Mémoire préparé en vue de l'obtention de l'**Habilitation à Diriger des Recherches**, par

Pavla ŠTÍPSKÁ

Caractérisation et interprétation de l'enregistrement métamorphique afin de définir les processus d'enfoncement et d'exhumation dans les orogènes (exemple du Massif de Bohême)

Deciphering and interpreting metamorphic record to infer processes of burial and exhumation in orogens (example of the Bohemian Massif)

Présenté le 23 Juin 2011, devant le jury composé de :

Gianreto Manatschal, Professeur, Université de Strasbourg, garant d'habilitation

Hubert Whitechurch, Professeur, Université de Strasbourg, rapporteur

Didier Marquer, Professeur, Université de Franche-Comté, Besançon, rapporteur

Michel Ballèvre, Professeur, Université Rennes 1, rapporteur

Roger Powell, Professeur, University of Melbourne, examinateur

Richard White, Professeur, University of Mainz, examinateur

Philippe Goncalves, Maître de conférences, Université de Franche-Comté, Besançon, examinateur

Here, I would like to express my sincere thanks to all people and colleagues who significantly influenced my professional career. Among them Karel Schulmann, my husband, deserves to be mentioned first, because he shown me that a rock can be understood, at least at some degree, and this was the beginning of my real interest in geology. When I started my diploma work, Karel invited to Prague Jean-Marc Lardeaux to give a series of courses in petrology. I heard for the first time, that rocks can travel in the crust and their path can be recognized by looking at their minerals and how they are arranged. This was actually the beginning of my interest in metamorphic petrology. My thanks are also directed to Pavel Pitra, my colleague, who taught me how to calculate P−T pseudosections and who shared his experience and knowledge with me. I was amazed discovering how these new diagrams help to understand what happens to the rocks during metamorphism and how the ideas we have about the rocks can be tested.

And then, I attended a course given by Roger Powell in Barcelona. There he said that everybody is welcome to work with him in Melbourne. For me this was the most important sentence. I dared to show him my work and to ask whether I can come − and he accepted! So, my special thanks are due to Roger for his precious time he spent with me, and all the discussions we have had not only of geology or petrology over coffee or wine or without these ingredients. I am grateful that I had the possibility to see his way how to think about the rocks and how to write about them. Most importantly, he gave me the self-confidence to write. I found this more difficult then calculating diagrams, and I believe that it is also the most horrible obstacle for many junior scientists. The receipt we found together is: When I am writing I should not imagine the great and famous geologists and the reviewers, but I should rather imagine the students to whom I am trying to explain a problem. Suddenly I become capable to write something at least partly reasonable! And the second part of the receipt is: "Write only once! Maybe it will take you the whole day to write a page, but if you do this every day you have a paper written in one month!" I am truly grateful that I had the possibility to work with a distinguished petrologist, who changed completely one geological domain, the metamorphic petrology − by his persistent work and continual collaboration with ordinary geologists and petrologists.

All this allowed me also to meet in person other great metamorphic geologists among which I would like to mention Mike Brown, who not only edited a number of my papers, but who gave unusual help in reshaping my ideas and who was extremely patient with my English. I would like to mention here also his extraordinary contribution to the whole scientific community of metamorphic geologists − in founding the Journal of Metamorphic Geology (not Petrology) and keeping it alive for so many fruitful years.

Another colleague who significantly influenced my work is Richard White whom I met for the first time while I was in Melbourne. I always admired his unusual and straightforward way of thinking and dealing with the migmatites including his remarkable way how to test and prove hypotheses by modeling. Many of my studies bear signs of his brilliant ideas.

I would like again to express my thanks to Karel Schulmann, my husband, and to Ondrej Lexa, my colleague. These are people with whom I spend most of my time in the field from whom I learned a lot about structures and tectonics. I am grateful for their over-simplified explanations of structures to me, and for being a witness of their scientific

conversations. The work with them brought me to the conclusion that nothing is ever certain and even the postulates and facts we find in books on structural geology (or metamorphic petrology) may and should be questioned. Even if I consider myself to be rather a metamorphic petrologist, thanks to them I keep always trying to link metamorphism with structural development in order to understand the lives of orogens.

There are, of course, many other colleagues I used to work with, discussed numerous issues or worked on electron microprobe, and who to various extent influenced my way of professional thinking. I have had nice time with them either in the field or lab, at home or abroad, and all of them I shall bear in my mind hoping they would forgive me for not quoting them in this acknowledgment.

Finally, I would like to express my deep and personal thanks of which the first goes to Petra, my daughter who must have suffered due to my often absence during my field works, teaching, participation in conferences, stays abroad and other activities that prevented me from spending as much time with her as was possible. I sincerely hope that she, being now older, can better understand that some professions require specific commitments. Another appreciation is directed to my mother who has always been ready to give me a hand whenever I needed in connection with my professional career and responsibilities involved. As for the future, I sincerely hope that my little twin daughters will be able to understand that I have to go to study some rocks for a month somewhere abroad, for example to Mongolia, and that I will be missing them a lot and loving them even more while away.

CURRICULUM VITAE

Née le 27 janvier 1967, à Prague, République Tchèque, nationalité : Tchèque, Situation de famille : mariée, 3 enfants, Adresse : 8, rue de la Carpe Haute 67000, Strasbourg, France

Situation professionnelle

Position depuis 2005 : Maître de Conférences à l'Université de Strasbourg.

Adresse professionnelle : Ecole et Observatoire des Sciences de la Terre, IPGS (CNRS UMR7516), Université de Strasbourg, 1 rue Blessig, 67084 Strasbourg, France, E-mail: stipska@unistra.fr

1994 : Chercheur et Maître de Conférences en Pétrologie Métamorphique au Département de Pétrologie et de Géologie Structurale de l'Université de Prague.

1992-99 : Thèse de doctorat de l'Université Charles de Prague (Ph.D.)

1991-92 : D.E.A. à l'Université Charles de Prague (titre Mgr.)

1986-91 : 4 années d'études intégrées à la Faculté de Sciences et à la Faculté de Lettres de l'Université Charles de Prague. Orientation : Géologie + Français + Russe

Publications *:* **29 publications A, Citations: 510, *h-facteur* = 13** (dans Scopus 5.4.2011)

Thématiques de recherche : La compréhension des *processus géodynamiques des chaînes de montagnes*, basée sur l'étude parallèle de la structure et des processus métamorphiques et magmatiques (le Massif de Bohême, l'Altaï en Mongolie). La reconstitution des trajets pression-température-déformation-temps à l'aide d'une analyse pétrologique et de la modélisation thermodynamique appliquée.

Collaborations professionnelles: 14 séjours de collaboration (1994-2010 : Melbourne, Australie ; Rennes, France ; ETH Zürich, Suisse ; Mayence, Allemagne ; ENS Lyon, France).

Programmes et projets de recherche : Participation au projet ANR Laterally forced overturns in orogens (2006-2010). Direction de 8 projets scientifiques (1996-2007, différentes agences en République Tchèque).

Encadrement : direction de deux thèses, participation en co-encadrement de cinq thèses, cinq stages D.E.A. (1997-2004), direction de cinq stages de master 1 et trois stages de master 2.

Enseignement : Des cours et des TP/TD dans tout le spectre de la pétrologie métamorphique (L2 Minéralogie, L2 optique cristalline, L3 Pétrologie métamorphique, M1 Modélisation en pétrologie, M2 Processus métamorphiques, M2 stages de terrain). En moyenne, 200h (équivalent TD) d'enseignement par an durant les dernières années.

EXPERIENCES PROFESSIONNELLES

Emplois, diplômes et études

2005 : Maître de Conférences à l'Université de Strasbourg.

1994 : Chercheur et Maître de Conférences en Pétrologie Métamorphique au Département de Pétrologie et de Géologie Structurale de l'Université de Prague.

1992-99 : Thèse de doctorat de l'Université Charles de Prague (Ph.D.), dirigée par Dr. Karel Schulmann : « Thermomechanical evolution of collisional boundary during the Variscan convergence - eastern margin of the Bohemian Massif (examples of the Staré Město Belt and the Thaya Dome) », soutenue le 19 novembre 1999 à Prague devant le jury composé de Prof. M. Rieder (Université Charles, Prague, République Tchèque), Prof. A.B. Thompson (ETH Zürich, Suisse), Prof. J-M. Lardeaux (Université Lyon, France), Prof. G. Zulauf (Université Erlangen, Allemagne), Prof. M. Novák (Université Brno, République Tchèque). (En anglais).

1991-92 : D.E.A. à l'Université Charles, Prague : « La zonation métamorphique dans la fenêtre de Dyje – le résultat de la mise en place des nappes Moldanubiennes » soutenu le 8 juillet 1992 avec la mention très bien (en tchèque).

1986-91 : 4 années d'études intégrées à la Faculté de Sciences et à la Faculté de Lettres de l'Université de Prague. Orientation : Géologie + Français + Russe

Distinction honorifique

2000 : Le prix du Groupe de Tectonique Tchécoslovaque « Radek Melka » pour la meilleure publication des jeunes chercheurs de l'année

Collaboration et séjours divers

2007 : Université de Melbourne, Australie, 1 mois, collaboration avec Prof. Roger Powell

2005 : Université Louis Pasteur, Strasbourg, France, chercheur invité, 6 mois

2004 : Université de Melbourne, Australie, 2 mois, collaboration avec Prof. Roger Powell (pendant une demi-année sabbatique)

2004 : Université de Strasbourg, projet Erasmus, 2 mois (pendant une demi-année sabbatique)

2004 : Université de Rennes 1, France, Maître de Conférences invité, 1 mois (pendant une demi-année sabbatique)

2003: ETH, Zürich, Suisse, cours de thermodynamique en pétrologie et application du programme THERMOCALC (par Prof. R. Powell, Melbourne, Australie), 3 jours

2003 : Université de Barcelone, Espagne : Cours de thermodynamique en pétrologie et application du programme THERMOCALC (par Prof. R. Powell, Melbourne, Australie), 3 jours

2003 : Université de Rennes 1, France, projet Erasmus, 3 semaines

2002 : Université de Rennes 1, France, Maître de Conférence invité, 1 mois

2001 : Université de Rennes 1, France, Maître de Conférence invité, 1 mois

2000 : Université de Mayence, Allemagne, collaboration avec Prof. A. Kröner, 1 mois

1999 : Université de Mayence, Allemagne, collaboration avec Prof. A. Kröner, 2 semaines

1995 : ETH Zürich, Suisse, collaboration avec Prof. A.B. Thompson, 1 mois

1994 : ENS Lyon, France, programme Tempus, 3 mois

Projets (direction, coordination ou participation) :

2006-2010 : Laterally forced overturns in orogens. Agence nationale de recherche, ANR, France. Participation.

2005-2007 : Lower and middle crustal behavior of the internal orogenic zone of the Bohemian massif: implication for exhumational models. GAČR, (Agence Nationale de la République Tchèque). Direction.

2002-2003 : L'exhumation des roches de haute pression dans le domaine de la racine orogénique (l'exemple du dôme de Śnieżnik). GUK 223/2002/B-GEO/PřF (Agence de l'Université Charles de Prague). Direction.

2002 : La corrélation des conditions P−T et des structures de l'exhumation dans le domaine de la racine orogénique FRVŠ 2315/2002 (Fondation de développement du système d' éducation). Direction.

2001-2003 : L'étude microstructurale des orthogneiss: le rôle de la vitesse de déformation, du stress et de la température. GAČR 205/00/D043 (Agence Nationale de la République Tchèque). Direction.

2000-2002 : La corrélation de l'évolution métamorphique et structurale dans la zone moldanubienne dans la Moravie du Sud: les implications pour la tectonique des nappes. GAUK 149/2000B/Geo (Agence de l'Université Charles de Prague). Direction.

1999-2001 : Les variations de la rhéologie de la croûte inférieure et moyenne pendant les processus orogéniques - l'exemple de la marge Nord-Est du Massif de Bohême. GAČR 205/99/1195 D043 (Agence Nationale de la République Tchèque). Direction.

1996-1998 : Du rifting vers l'extension tardive à la marge Nord-Est du Massif de Bohême - exemple de la ceinture de Staré Město. GAČR 205/96/0270 D043 (Agence Nationale de la République Tchèque). Direction.

1996-1998 : L' identification des environnements géotectoniques et des mécanismes de la mise en place des roches magmatiques à la limite des deux blocs crustaux – exemple de la ceinture de Staré Město. GAUK 245/1996 (Agence de l'Université Charles de Prague). Direction.

Enseignement

Grâce à mes expériences d'enseignement et de recherche, je dispense des cours et des TP/TD dans **tout le spectre de la pétrologie métamorphique** et en **optique cristalline**, j'ai aussi participé à l'encadrement d'étudiants lors **de stages de terrain.** J'ai assuré, en moyenne, 200h (équivalent TD) d'enseignement par an durant les dernières années. La répartition des heures était variable, en fonction du nombre des groupes. Ci-dessous un exemple concernant l'année universitaire 2009-2010 :

Sujet	année	heures	type
Optique cristalline	Licence 2	25	cours
		25	TD
Minéralogie	Licence 2	4	cours
Pétrologie métamorphique	Licence 3	25	cours
		25	TD
Modélisation en pétrologie	Master 1	25	cours
Processus métamorphiques	Master 2	25	cours

Encadrement

J'ai dirigé deux thèses à l'Université Charles de Prague, dont une en cotutelle avec M. Ballèvre (Université Rennes 1), j'ai **co-encadré trois thèses** à l'Université Louis Pasteur à Strasbourg et à l'Université Charles de Prague. Récemment je **participe en co-encadrement de deux thèses** à

l'Université de Strasbourg. Entre 1997 et 2004 j'ai aussi encadré **cinq stages DEA** (durée 2 ans) à l'Université de Prague. Pendant les cinq dernières années, j'ai dirigé **huit stages de master,** dont cinq stages de master 1 et trois stages de master 2 à l'Université Louis Pasteur et à l'Université de Strasbourg.

Encadrement de thèses

Košuličová, M. (2007) : Thermomechanical and temporal evolution of the Moravo-Silesian zone: examples of the Silesian domain and the Svratka window.

Racek, M. (2007) : Pressure, temperature and deformation evolution during viscous extrusion of orogenic lower crust driven by continental indentation, eastern margin of the Bohemian Massif. Thèse cotutelle avec M. Ballèvre, Université Rennes 1.

Participation en co-encadrement de thèses

Hasalová, P. (2007) : Microstructural, petrological and geochemical records of pervasive melt transport in the crust. Thèse en cotutelle de Université Louis Pasteur, Strasbourg et Charles University, Prague.

Franěk, J. (2007) : From microstructures to large-scale crustal deformations in collisional orogen: multidisciplinary approach. Thèse cotutelle de University Louis Pasteur, Strasbourg et Charles University, Prague.

Lehmann, J. (2009) : Mécanismes de déformation dans les systèmes d'accrétion paléozoïque. Université de Strasbourg.

Chopin, F. (2010) : Evolution du flux de matière, de l'architecture et de la rhéologie d'un prisme d'accrétion crustal (Dôme d'Orlica-Śnieżnik, Sudètes). Université de Strasbourg.

Skrzypek, E. (Soutenance prévue en septembre 2011) : Réorganisation géométrique et cinématique de la croûte dans les orogènes à gradient thermique élevé et super-élevé.

Encadrement de D.E.A. (durée 2 ans, 1997-2004)

Kolenovská, E. (1997) : L'évolution métamorphique et la déformation dans le Moldanubian dans la région de Jemnice. Université Charles de Prague, République Tchèque, (en tchèque).

Romanová, M. (2002) : L'évolution métamorphique et structurale de la convergence Varisque dans la série de Stronie dans le domaine de Lugicum. Université Charles de Prague, République Tchèque, (en tchèque).

Racek, M. (2003) : L'évolution structurale et métamorphique dans le prisme d'accrétion profond en relation avec le souscharriache de Brunovistulian (la Moravie du sud et l'Autriche). Université Charles de Prague, République Tchèque, (en tchèque).

Nahodilová, R. (2003) : La structure et le métamorphisme dans le prisme d'accrétion de la croûte inférieure dans le Moldanubian (l'Autriche). Université Charles de Prague, République Tchèque, (en tchèque).

Žáčková, E. (2004) : L'exhumation des roches dans la racine orogénique du dôme de Śnieżnik: l'évolution structurale et métamorphique dans la région de Miedzygorie et Králíky. Université Charles de Prague, République Tchèque, (en tchèque).

Encadrement de stages master (dernières 5 ans)

Skrzypek, E. (2006) : Le métamorphisme des éclogites de la zone de Śnieżnik, le Massif de Bohême. Master 1. Université Louis Pasteur, Strasbourg.

Askaribiyabani, M. (2006) : Le métamorphisme et la fusion le long du Main Central Thrust, Makalu. Master 1. Université Louis Pasteur, Strasbourg.

Skrzypek, E. (2007) : Etude d'enfouissement et d'exhumation : approche basée sur la modélisation thermodynamique, l'analyse microstructurale quantitative et la thermochronologie. Master 2. Université Louis Pasteur, Strasbourg.

Bollinger C. (2008) : Pétrologie et thermodynamique des éclogites issue de subduction de la marge passive. Master 1. Université Louis Pasteur, Strasbourg.

Vigouroux, E. (2008) : Les conditions UHP dans les granulites de la croûte continentale: étude pétrologique et modelisation thermodynamique. Master 1. Université Louis Pasteur, Strasbourg.

Bollinger, C. (2009) : Evolution pétrologique et analyse pression-température-déformation des éclogites de subduction du Massif de Bohême. Master 2. Université Louis Pasteur, Strasbourg.

Baur, A. (2010) : L'évolution prograde des granulites de haute pression dans le dôme de Śnieżnik (Massif de Bohême). Master 2. Université de Strasbourg.

Gicquel, A. (2011) : Les micaschistes du dôme d'Orlica : témoins d'un métamorphisme de haute pression ? Master 1. Université de Strasbourg.

RESUME DU TRAVAIL DE RECHERCHE

Thématiques de recherche

Mon domaine scientifique privilégié est la compréhension des **processus géodynamiques des chaînes de montagnes**, basée sur l'étude parallèle de la structure et des processus métamorphiques et magmatiques. Un travail sur **le terrain** représente donc pour moi la base nécessaire de cette approche. J'étudie les aspects géodynamiques des chaînes de collision essentiellement dans la chaîne Hercynienne sur l'exemple du Massif de Bohême, et ces dernières années, dans l'Altaï (Mongolie).

Le point fort de ma recherche est la reconstitution des trajets pression-température-déformation-temps à l'aide d'une **analyse pétrologique et une étude des microstrucures** et de la **modélisation thermodynamique**. Cette méthode comprend la construction de différents types de diagrammes de phases ainsi que l'étude de la stabilité des paragénèses minérales dans des roches de composition variée sous différentes conditions d'activité de fluides ou sous les conditions de fusion partielle. Je combine l'étude des processus métamorphiques par les méthodes classiques basées sur l'équilibre thermodynamique avec l'étude des microstructures et des textures.

Classiquement, les études des chemins pression-température des roches métamorphiques se concentrent majoritairement sur détermination **des conditions maximales et rétrogrades**, ce qui contribue, en liaison avec l'étude structurale, à la compréhension des mécanismes **d'exhumation** et d'évolution thermique pendant l'exhumation dans des différents contextes géodynamiques. Ces processus représentent un sujet majeur en géologie structurale, pétrologie métamorphique, géochronologie et dans le domaine de la modélisation numérique. Je les ai étudiés sur plusieurs exemples en collaboration avec des géochronologistes et des géologues structuraux.

Récemment, la modélisation des diagrammes de phases en liaison avec l'étude de la succession de cristallisation des phases et avec zonalité de croissance permet de quantifier **les chemins pression-température prograde**. La quantification des conditions prograde sert à évaluer les **conditions thermiques d'enfoncement** pendant **les stades précoces de l'orogenèse** ainsi qu'à caractériser les conditions thermiques **pré-orogéniques**, qui sont très rarement connues. Ces données issues de la pétrologie métamorphique sont utilisées dans la modélisation

de la formation des racines orogéniques et contribuent à notre compréhension des contextes géodynamiques qui précèdent l'orogenèse.

Les résultats majeurs

Parmi les thèmes géodynamiques majeurs de ma recherche, je citerai les mécanismes d'exhumation des roches, particulièrement de haute pression, déduits de leur évolution pression-température en relation avec le développement des structures. Ces études pétro-structurales que j'ai faites et que j'ai dirigées ont contribué de façon significative à la création d'un **nouveau modèle d'exhumation des roches profondes** pendant la collision, qui a été établi après plusieurs années d'études à la bordure Est du Massif de Bohême par le groupe de Karel Schulmann (Štípská *et al.*, 2004; Schulmann *et al.*, 2005; Štípská & Powell, 2005b; Štípská & Powell, 2005a; Racek *et al.*, 2006; Schulmann *et al.*, 2008a; Štípská *et al.*, 2008; Schulmann *et al.*, 2009a; Schulmann *et al.*, 2009b; Chopin *et al.*, en préparation-a; Chopin *et al.*, en préparation-b; Franěk *et al.*, 2011; Skrzypek *et al.*, 2011a; Štípská *et al.*, submitted). Il s'agit d' un modèle **d'extrusion verticale** de la croûte orogénique inférieure dans la racine orogénique, qui est initiée par le plissement des couches crustales. L'extrusion verticale est suivie par un **charriage subhorizontal** dans la croûte moyenne lié à l'indentation du domaine externe (Štípská *et al.*, 2004; Racek *et al.*, 2006; Schulmann *et al.*, 2008a; Štípská *et al.*, 2008). Nous avons proposé que de tels mécanismes sont probablement responsable de l'exhumation des roches profondes dans d'autres racines des chaînes de montagnes chaudes.

A cette thématique est liée l'étude tectono-métamorphique de **la zone orogénique extérieure** et le couplage de son évolution avec la zone interne, que j'ai aussi effectué sur la bordure Est du Massif de Bohême (Štípská & Schulmann, 1995; Parry *et al.*, 1997; Štípská *et al.*, 2000; Štípská *et al.*, 2001; Štípská *et al.*, 2004; Lexa *et al.*, 2005; Štípská *et al.*, 2006; Košuličová & Štípská, 2007; Schulmann *et al.*, 2008a). L'indentation de la zone externe dans la racine orogénique provoque son imbrication et la formation de nappes qui sont caractérisées par un métamorphisme inverse de type Barrovien. La profondeur de l'indentation et le degré de l'imbrication varient le long de la marge orogénique et dirigent la profondeur d'étalement et de charriage subhorizontal dans la zone interne.

Les interprétations géodynamiques de l'enfoncement et de l'exhumation dans le Massif de Bohême sont basées largement sur les résultats de mes travaux avec les **approches pétrologiques suivantes** :

La modélisation de la zonalité de croissance des phases dans des roches de différente composition, et selon des chemins variés pression-température, peut expliquer les zonalités des minéraux qui étaient jusqu'à maintenant interprétées seulement d'une façon qualitative et intuitive (Štípská & Powell, 2005a; Racek *et al.*, 2006; Štípská *et al.*, 2006; Košuličová & Štípská, 2007; Racek *et al.*, 2008; Štípská *et al.*, 2008; Skrzypek *et al.*, 2011a, Skrzypek *et al.*, 2011b; Štípská *et al.*, submitted). Par exemple, nous avons démontré grâce à l'étude des grenats prograde dans les éclogites de la zone interne que le gradient géothermique est déjà élevé au cours de l'enfoncement. Cela signifie que les éclogites dans la zone interne orogénique sont très différentes des éclogites formées dans les zones de subduction. Le gradient géothermique élevé pendant l'enfoncement de la racine est contemporain de la période du magmatisme qui traverse la marge active. Ce contexte est un des contextes géodynamiques proposé pour le Massif de Bohême. L'étude des chemins prograde des roches de haute pression et de la matrice métapélitique ou migmatitique a démontré que ces roches ont suivi des histoires différentes (Štípská *et al.*, 2006; Racek *et al.*, 2008; Štípská *et al.*, 2008). Les donnés pétrologiques ont servi de base pour proposer un modèle d'exhumation de la croûte profonde et de son fluage dans un canal migmatitique à la bordure de la racine orogénique (Racek *et al.*, 2006; Schulmann *et al.*, 2008a; Štípská *et al.*, 2008).

L'étude des porphyroblastes, des successions de cristallisation et des inclusions est une méthode classique pour étudier des déformations précoces. A partir de la modélisation des pseudo-sections (diagrammes d'équilibre des différents paragenèses), il est possible d'obtenir les données des conditions P−T de ces déformations. Ces données contribuent largement à la caractérisation des processus de l'enfoncement pendant la formation des orogènes (Racek *et al.*, 2006; Štípská *et al.*, 2006; Košuličová & Štípská, 2007; Štípská *et al.*, 2008; Skrzypek *et al.*, 2011a; Skrzypek *et al.*, 2011b; Štípská *et al.*, submitted). Les successions de cristallisation peuvent être les seuls témoins des réactions dans les roches de haute température où la composition chimique des minéraux est modifiée par diffusion. Les feldspaths ternaires associés

à des grenats avec une teneur importante en grossulaire sont classiquement utilisés dans les granulites de haute pression du Massif de Bohême pour estimer les conditions du métamorphisme à 18kbar et >1000°C. Des études microstructurales détaillées de ces granulites ont démontré l'existence de plusieurs générations de grenat, et que les grenats avec une teneur importante en grossulaire ne sont pas contemporains des feldspaths ternaires (Štípská & Powell, 2005b; Racek *et al.*, 2008).

La modélisation des migmatites est possible depuis l'invention du modèle granitique (Holland & Powell, 2001; White *et al.*, 2001). Cette modélisation n'est pas rectiligne, elle nécessite l'estimation de la teneur H_2O au début et pendant la fusion, l'estimation de la composition du liquide granitique, l'estimation de la quantité de liquide qui peut être perdue pendant l'anatexie, éventuellement la restitution du liquide perdu dans la composition de la roche totale. J'ai utilisé cette technique dans plusieurs travaux pour étudier les chemins P−T et pour estimer les quantités des liquides granitiques dans les migmatites et granulites (Štípská & Powell, 2005b; Racek *et al.*, 2006; Hasalová *et al.*, 2008c; Racek *et al.*, 2008; Schulmann *et al.*, 2008b; Štípská *et al.*, 2008; Chopin *et al.*, en préparation-a; Franěk *et al.*, 2011; Lexa *et al.*, 2011). Grâce à ces études nous avons proposé le modèle d'infiltration des liquides à l'échelle des grains, qui influence largement la rhéologie des roches quartzo-feldspathiques (Hasalová *et al.*, 2008a; Hasalová *et al.*, 2008b; Hasalová *et al.*, 2008c). La signification de la quantité du liquide impliqué dans la déformation des granulites et des orthogneiss pour la rhéologie de la croûte continentale est aussi discutée (Schulmann *et al.*, 2008b; Štípská *et al.*, 2008; Chopin *et al.*, in preparation-a; Franěk *et al.*, 2011).

Les microstructures en couronne sont largement discutées dans la littérature. Elles permettent souvent de déchiffrer les réactions au cours des chemins P−T. Leurs utilisation reste quand même controversée, la plupart des travaux essayant d'interpréter les relations temporaires de la croissance des couches individuelles et les domaines en équilibre, puis les utilisant pour la thermobarométrie ou pour la modélisation des pseudo-sections. Même si cette approche peut expliquer certaines réactions, elle ne peut pas expliquer l'arrangement spatial de minéraux dans la couronne réactionnelle. Pour cela il faut utiliser le calcul des potentiels chimiques. Un des premiers travaux qui utilise la modélisation du potentiel chimique avec les solutions solides est

donné dans Štípská *et al.* (2010a). Dans ce travail nous avons expliqué l'arrangement spatial des couronnes du plagioclase, du grenat et des symplectites du spinel-plagioclase qui se développent autour du disthène dans les granulites de haute pression.

La recherche future

Pour comprendre l'évolution des roches métamorphiques, il est nécessaire de continuer **les études détaillées de l'évolution microstructurale et de chimie des phases** en la combinant avec la **modélisation thermodynamique.** Ces études doivent être menées sur les zonalités de croissance, les successions de cristallisation, les textures coronitiques ou les domaines de fusion partielle. Le but est de continuer collaborer avec des géologues d'autres disciplines, en particulier avec des géologues structuraux, tectoniciens et géochronologistes, en amenant les outils de la pétrologie métamorphique pour comprendre les mécanismes d'évolution des parties profondes d'orogène et leurs exhumation.

J'ai l'expérience de ce type de recherche dans **le Massif de Bohême** où j'aimerai finaliser plusieurs études pétro-structurales, qui représentent une contribution importante à une synthèse majeure de l'évolution géodynamique d'un des massifs les plus importants de la chaîne varisque et qui sert d'exemple pour l'évolution géodynamique d'orogènes chauds.

Dans le futur, j'aimerais participer aux projets sur la formation **des Altaïdes**. J'y ai déjà travaillé lors de quatre expéditions dans le désert de Gobi dans le Sud-Ouest de la Mongolie (Kröner *et al.*, 2010; Lehmann *et al.*, 2010; Štípská *et al.*, 2010b). Mon intérêt dans ce domaine est aussi lié à mon expérience de travail dans le Massif de Bohême, car les Altaïdes représentent la continuation de la chaîne varisque en Asie. Contrairement aux massifs européens, qui sont dans leur majorité issus de la collision continentale, et donc formés par la croûte continentale réactivée, les grandes parties de l'orogène en Asie représentent en grande partie la formation de la croûte juvénile par accrétion de portions de la croûte continentale ancienne, de zones de subduction, d'arcs magmatiques et des bassins sédimentaires arrière-arc.

PUBLICATIONS

29 publications de rang A (parues)

Environ 90 présentations dans des colloques (liste non fournie).

510 citations, h-index=13 (en Scopus)

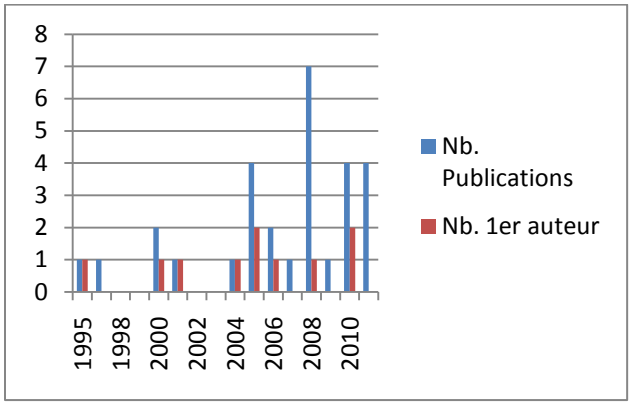

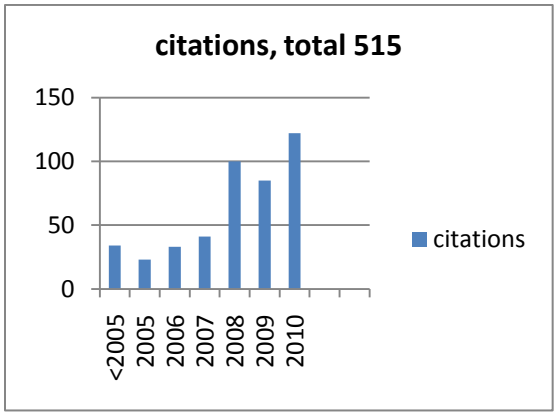

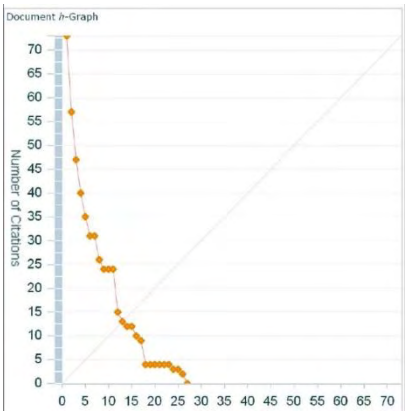

Par commodité, les publications sont présentées ci-dessous par ordre chronologique. (*IF*= IMPACT FACTOR (2009): 17 Journal of Metamorphic Geology (IF=4.16), 3 American Journal of Science (IF=2.28), 2 Tectonophysics (IF=1.94), 1 Geological Journal (IF=1.33), 1 Mineralogy and Petrology (IF=1.01), 1 Journal of Geophysical Research (IF=3.08), 1 Lithos (IF=3.54), 1 C. R. Geoscience (IF=0.93), 2 Geological Society London, special publications (sans IF)

Publications de rang A

1. **Štípská**, P. & Schulmann, K. (1995). Inverted metamorphic zonation in a basement-derived nappe sequence, Eastern margin of the Bohemian Massif. *Geological Journal*, 30, 385-413. DOI: 10.1002/gj.3350300315

2. Parry, M., **Štípská**, P., Schulmann, K., Hrouda, F., Ježek, J. & Kröner, A. (1997). Tonalite sill emplacement at an oblique plate boundary: NE margin of the Bohemian massif. *Tectonophysics*, 280, 61-81

3. **Štípská**, P., Schulmann, K. & Höck, V. (2000). Complex metamorphic zonation of the Thaya dome: result of buckling and gravitational collapse of imbricated nappe sequence. In: Cosgrove, J.W. and Ameen, M.S. (Eds), Forced folds and fractures, *Geological Society London, special publications*, 169, 197-211.

4. Kröner, A., **Štípská**, P., Schulmann, K. & Jaeckel, P. (2000). Chronological constraints on the pre-Variscan evolution of the northeastern margin of the Bohemian Massif, Czech Republic. In: Franke, W., Altherr, R., Haak, V., Oncken, O., Tanner, D. (Eds), Orogenic processes – quantification and modelling in the Variscan belt of central Europe. *Geological Society London, special publications*, 179, 175-197.

5. **Štípská** P., Schulmann K., Thompson, A.B., Ježek, J. & Kröner A. (2001). Thermo-mechanical role of a Cambro-Ordovician paleorift during the Variscan collision: the NE margin of the Bohemian Massif. In: Schulmann, K., Franke, W., Andersen, T.B. (Eds), Paleozoic Orogenesis and Crustal Evolution of the European Lithosphere. *Tectonophysics*, 332, 239-253.

6. **Štípská**, P., Schulmann, K. & Kröner, A. (2004). Vertical extrusion and middle crustal spreading of omphacite granulite: a model of syn-convergent exhumation (Bohemian Massif, Czech Republic). *Journal of Metamorphic Geology*, 22, 179-198.

7. Lexa O., **Štípská** P., Schulmann K., Baratoux L. & Kröner A. (2005). Contrasting textural record of two distinct metamorphic events of similar P−T conditions and different durations. *Journal of Metamorphic Geology*, 23, 649-666.

8. **Štípská**, P. & Powell, R. (2005a). Constraining the P−T path of a MORB-type eclogite using pseudosections, garnet zoning and garnet-clinopyroxene thermometry: an example from the Bohemian Massif. *Journal of Metamorphic Geology*, 23, 725-743. doi:10.1111/j.1525-1314.2005.00607.x

9. **Štípská**, P. & Powell, R. (2005b). Does ternary feldspar constrain the metamorphic conditions of high-grade meta-igneous rocks? Evidence from orthopyroxene granulites, Bohemian Massif. *Journal of Metamorphic Geology*, 23, 627-647. doi:10.1111/j.1525-1314.2005.00600.x.

10. Schulmann, K., Kröner, A., Hegner, E., Wendt, I., Konopásek, J., Lexa, O. & **Štípská**, P. (2005). Chronological constraints on the pre-orogenic history, burial and exhumation of deep-seated rocks along the eastern margin of the Variscan orogen, Bohemian Massif, Czech Republic. *American Journal of Science*, 305, 407-448.

11. **Štípská**, P., Pitra, P., Powell, R. (2006). Separate or shared metamorphic histories of eclogites and surrounding rocks? An example from the Bohemian Massif. *Journal of Metamorphic Geology*. 24, 219-240. doi:10.1111/j.1525-1314.2006.00634.x.

12. Racek, M., **Štípská**, P., Pitra, P., Schulmann, K. & Lexa, O. (2006). Metamorphic record of burial and exhumation of orogenic lower and middle crust: new tectonothermal model for the Drosendorf window (Bohemian Massif). *Mineralogy and Petrology*, 86, 221-251. doi 10.1007/s00710-005-0111-7.

13. Košuličová, M. & **Štípská, P**. (2007). Variations in the transient prograde geothermal gradient from chloritoid-staurolite equilibria: A case study from the Barrovian and Buchan type domains in the Bohemian Massif. *Journal of Metamorphic Geology*, 25, 19-35. doi:10.1111/j.1525-1314.2006.00674.x.

14. Schulmann K., Martelat, J.E., Ulrich, S., Lexa, O., **Štípská, P.** & Becker, J.K. (2008). Evolution of microstructure and melt topology in partially molten granitic mylonite: implications for rheology of felsic middle crust. *Journal of Geophysical Research*, **113**, B10406, doi:10.1029/2007JB005508

15. **Štípská**, P., Schulmann, K. and Powell, R. (2008). Contrasting metamorphic histories of lenses of high-pressure rocks and host migmatites with a flat orogenic fabric (Bohemian Massif, Czech Republic): a result of tectonic mixing within horizontal crustal flow? *Journal of Metamorphic Geology*, **26,** 623–646. doi:10.1111/j.1525-1314.2008. 00781.x.

16. Schulmann, K., Lexa, O., **Štípská**, P., Racek, M., Tajčmanová, L., Konopásek, J., Edel, J. B., Peschler, A. & Lehmann, J. (2008). Vertical extrusion and horizontal channel flow of orogenic lower crust: key exhumation mechanisms in large hot orogens? *Journal of Metamorphic Geology*, **26**, 273–297. doi:10.1111/j.1525-1314.2007.00755.x.

17. Racek, M., **Štípská, P.,** Powell, R. (2008). Garnet-clinopyroxene intermediate granulites in the St. Leonhard massif of the Bohemian Massif: ultrahigh-temperature metamorphism at high pressure or not? *Journal of Metamorphic Geology*, **26**, 253–271. doi:10.1111/j.1525-1314.2007.00754.x.

18. Hasalová, P., Janoušek, V., Schulmann, K., **Štípská**, P. & Erban, V. (2008a). From orthogneiss to migmatite: geochemical assessment of the melt infiltration model in the Gföhl Unit (Moldanubian Zone, Bohemian Massif). *Lithos*, **102**, 508–537. doi:10.1016 /j.lithos. 2007.07.021.

19. Hasalová, P., Schulmann, K., Lexa, O., **Štípská**, P., Hrouda, F., Ulrich, S., Haloda, J. & Týcová, P. (2008b). Origin of migmatites by deformation-enhanced melt infiltration of orthogneiss: a new model based on quantitative microstructural analysis. *Journal of Metamorphic Geology*, 26, 29-53. doi:10.1111/j.1525-1314.2007.00743.x.

20. Hasalová, P., **Štípská**, P., Powell, R., Schulmann, K., Janoušek, V. & Lexa, O. (2008c). Transforming mylonitic metagranite by open-system interactions during melt flow. *Journal of Metamorphic Geology*, 26, 55-80. doi:10.1111/j.1525-1314.2007.00744.x.

21. Schulmann, K., Konopásek, J, Janoušek, V., Lexa O., Lardeaux, J.M., Edel, J.B., **Štípská**, P. & Ulrich, S. (2009). An Andean type Palaeozoic convergence in the Bohemian Massif. *C. R. Geoscience*, **341**, 266–286. doi:10.1016/j.crte.2008.12.006.

22. **Štípská**, P., Powell, R., White, R.W. & Baldwin, J.A. (2010). Using calculated chemical potential relationships to account for coronas around kyanite: an example from the Bohemian Massif. *Journal of Metamorphic Geology*, **28**, 97–116. doi:10.1111/j.1525-1314.2009.00857.x

23. **Štípská**, P., Schulmann, K., Lehmann, J., Corsini, M., Lexa, O. & Tomurhuu, D. (2010): Cambrian eclogites in SW Mongolia: evidence that the Palaeo-Asian Ocean suture extends further east than expected. *Journal of Metamorphic Geology*, **28**, 915–933. doi:10.1111/j.1525-1314.2010.00899.x

24. Lehmann, J., Schulmann, K., Lexa, O., Corsini, M., Kröner, A., **Štípská, P.**, Tomurhuu, D. & Otgonbator, D. (2010). Structural constraints on the evolution of the Central Asian Orogenic Belt in Southern Mongolia. American Journal of Science, 310 (7), 575-628.

25. Kröner, A., Lehmann, J., Schulmann, K. Demoux, A., Lexa, O., Tomurhuu, D., **Štípská, P.**, Liu, D.Y. & Wingate, M.T.D. (2010). Lithostratigraphic and geochronological constraints on the evolution of the Central Asian Orogenic Belt in SW Mongolia: early Paleozoic rifting followed by late Paleozoic accretion. American Journal of Science, 310 (7), 523-574.

26. Lexa, O., Schulmann, K., Janoušek, V., **Štípská**, P., Guy, A. & Racek, M. (2011). Heat sources and trigger mechanisms of exhumation of HP granulites in Variscan orogenic root. *Journal of Metamorphic Geology*, **29**, 79–102. doi:10.1111/j.1525-1314.2010.00906.x

27. Franěk, J., Schulmann, K., Lexa, O., Ulrich, S., **Štípská**, P., Haloda, J. & Týcová, P. (2011). Origin of felsic granulite microstructure by heterogeneous decomposition of alkali feldspar and extreme weakening of orogenic lower crust during the Variscan orogeny. *Journal of Metamorphic Geology*, **29**, 103–130. doi: 10.1111/j.1525-1314.2010.00911.x

28. Skrzypek, E., **Štípská** P., Schulmann, K., Lexa, O. & Lexová, M. (2011a): Prograde and retrograde metamorphic fabrics – a key for understanding burial and exhumation in orogens (Bohemian Massif). *Journal of Metamorphic Geology*, **29**, 451–472. doi: 10.1111/j.1525-1314.2010.00924.x.

29. Skrzypek, E., Schulmann, K., **Štípská** P., Chopin, F., Lehmann, J., Lexa, O. & Haloda, J. (2011b): Tectono-metamorphic history recorded in garnet porphyroblasts: insights from thermodynamic modelling and electron backscatter diffraction analysis of inclusion trails. *Journal of Metamorphic Geology*, **29**, 473–496. doi: 10.1111/j.1525-1314.2010.00925.

Manuscrits soumis et en preparation pour submission en 2011 (rang A)

Štípská P., Chopin F., Skrzypek E., Schulmann K., Lexa O., Pitra, P., Martelat, J.E., Bollinger, C. Juxtaposition of eclogite-facies and mid-crustal rocks during exhumation: relative role of erosion and crustal-scale folding in a continentam wedge (Orlica-Śnieżnik dome, Bohemian Massif). Journal of Metamorphic Geology. soumis.

Chopin F., Schulmann K., **Štípská** P., Martelat, J.E., Pitra, P., Lexa, O., Petri, B. Prograde deformation gradient in subducted high-pressure orthogneiss (Orlica-Śnieżnik dome, Bohemian Massif): implications for reaction softening and strain localisation during continental subduction. Journal of Metamorphic Geology. soumis.

Chopin F., Schulmann K., Skrzypek E., Dujardin, J.R., Lehmann, Martelat, J.E., Lexa, O., Corsini, M., Edel, J.B., **Štípská P.**, Pitra, P. Multistage syn-convergent growth and collapse of mantled gneiss dome (Orlica-Śnieżnik dome, Bohemian Massif). préparé pour Tectonics.

Publications divers

Štípská P., Schulmann, K., Kröner, A, Ježek, J. & Konopásek, J. (2001). Structures related to the exhumation of HP rocks within the orogenic root domain: examples of the SE Moldanubian zone and the eastern Śnieżnik dome. *Mineralogical Society of Poland, Special Papers*, 19, 156-158.

Romanová, M. & Štípská, P. (2001). Structural and metamorphic evolution of the Stronie formation near Javorník. *Mineralogical Society of Poland, Special Papers*, 19, 147-149.

Krejzlíková, L., Schulmann, K., Lardeaux, J.M., Štípská, P., Lexa, O. & Gardien, V. (2001). Influence of microstructures on rheology of amphibolites during folding: example from the Jeseník amphibolite massif. *Mineralogical Society of Poland, Special Papers*, 19, 94-96.

Kolenovská, E., Schulmann, K., Klápová, H. & Štípská, P. (1999). Tectonometamorphic evolution of the Moldanubian Zone near Jemnice (South Moravia, Bohemian Massif). *Beih. Z. Eur. J. Mineral.*, 11, 91-94.

Traité

Konopásek, J., Štípská, P., Klápová, H. & Schulmann, K. (1998). Metamorphic petrology. (en tchèque). Karolinum. 241 pp.

SYNTHESE :

Deciphering and interpreting metamorphic record to infer processes of burial and exhumation in orogens (example of the Bohemian Massif)

Caractérisation et interprétation de l'enregistrement métamorphique afin de définir les processus d'enfoncement et d'exhumation dans les orogènes (exemple du Massif de Bohême)

Figures in the following text are meant to underline main points of the work rather than fully explain the details. Detailed explanations and complete figures can be found in the appendix.

ABSTRACT

A range of petrological and structural works carried in the Bohemian Massif largely contributed to establishment of the models of burial and exhumation mechanisms in the external and internal orogenic domains. The eastern margin of the Bohemian Massif is formed by the Brunia microcontinent that was underthrust below the westerly orogenic root of the Moldanubian-Lugian domain. The underthrusting produced in the Brunia basement approximately 50 kilometers wide zone of deformation and metamorphism, called the Moravo-Silesian zone. The Lugian-Moldanubian internal domain forms the core of the orogen and it is characterized by presence of high grade rocks, such as high-pressure felsic granulites, eclogites, garnetiferous and spinel peridotites and migmatites, low-grade rocks and magmatic bodies, preserving a complicated structural and metamorphic history of the deep orogenic root. The presence of high-pressure and low-temperature rocks in the Saxothuringian domain to the west is interpreted as a remnant of a subduction zone.

At the south-eastern margin of the Bohemian Massif, two large tectonic windows of the Moravian zone are emerging through a migmatitic nappe of the Moldanubian domain. We have shown that Barrovian prograde metamorphism in these tectonic windows, ranging from chlorite to kyanite zone, is related to continental underthrusting below the orogenic root, and retrograde P–T evolution to nappe stacking and inversion of metamorphic isograds. Complex pattern of isograds that obliquely crosscut tectonic boundaries in a present section is interpreted as a result of late folding of crustal sheets. In the northeastern margin of the Bohemian Massif occurs the Silesian domain, characterized by Barrovian and Buchan type metamorphism. In the kyanite zone, we described eclogite lenses in the metapelite matrix and demonstrated their separate metamorphic histories, indicating mixing of rocks at the tip of the underthrust crustal wedge. Further east, based on chloritoid-staurolite equilibria, we distinguished a high geothermal gradient during prograde metamorphism that is probably associated with inherited heat from a Devonian intracontinental rift, which can also explain the development of Buchan-type metamorphism.

In the north-eastern part of the contact between the Lugian domain and the Silesian zone occurs the Staré Město belt, composed of granodiorite, layered amphibolite, metagabbro and serpentinite. Combined structural and geochronological study revealed a structural unconformity

between subhorizontal fabrics in the granulites and amphibolites dated at 500 Ma and fabrics of the granodiorite sheet that are parallel to steep foliations reworking the gabbros, dated at 340 Ma on zircon. This allowed distinguishing relics of subhorizontal Ordovician fabrics for the first time in the whole Variscan European belt and interpreting these lithologies as a Cambro-Ordovician intracontinental rift. The Variscan tectono-metamorphic event is manifested by syn-convergent intrusion of the Carboniferous granodiorite sill and by HT-MP compressional deformation of the gabbros that produces foliations parallel with the structure of the granodiorite. Based on these criteria we interpreted the Staré Město belt as a preserved example of an intracontinental Cambro-Ordovician rift that has been reactivated and exhumed during the Variscan orogeny.

The studies in the Moldanubian-Lugian orogenic root domain shown that HP conditions are connected with early shallow-dipping fabric, and that HP rocks are exhumed during vertical crustal-scale folding that leads to extrusion of HP rocks along vertical channels. This produces a pattern of large-scale "synforms" cored commonly by HP granulites and large-scale "antiforms" dominated by metasediments. This model of crustal-scale folding and vertical extrusion is proposed as a possible major exhumation mechanism of HP rocks in hot orogens and a potential role of gravity in this process is discussed.

Studies of HP granulites from the Moldanubian orogenic root pointed to a problem of interpretation of equilibrium metamorphic assemblages in high-grade rocks and consequently to a problem of determining the peak metamorphic conditions. Classic combination of high-grossular garnet and high-temperature ternary feldspar led to estimation of metamorphic conditions to >1000 °C and 18−28 kbar. Microstructural analysis has shown that mafic granulites contain several generations of garnet, and that ternary feldspar and high-grossular garnet belong to two distinct episodes, and cannot be combined to infer metamorphic conditions. Detailed study of a Morb-type eclogite shows unusually hot prograde conditions that are interpreted as a result of Devonian thermal rejuvenation of continental back arc domain that was responsible for softening of a future orogenic root domain.

The steep foliations in the Lugian-Moldanubian domains are to a different degree reworked by shallow-dipping fabrics. At the eastern margin of the Bohemian Massif, kilometre-scale crustal boudins of HP granulites and eclogites enclosed in migmatites are present. The HP

lenses experienced first burial to 20 kbar and than exhumation to 10–7 kbar and the mid-crustal rocks revealed increase of pressure to 10 kbar. All the system was re-equilibrated at 7 kbar where the high pressure rocks cooled while mid-crustal rocks became heated. We interpreted this metamorphic pattern as a result of vertically extruded lower-crustal rocks into the middle crust, then travelling as fragments in a subhorizontal hot migmatitic channel above a continental margin. This is interpreted as a continental channel flow domain that developed in the orogenic root above the underthrust Brunia basement, and which is eroded along its total width of 120 km and length of 200 km.

A detailed petrological, microstructural and geochemical study of migmatites in the well developed shallow-dipping fabrics of the Moldanubian orogenic root allowed discussion about the evolution of the "channel flow" domain and about the melt migration in the crust. Four migmatite types collected in the steep and shallow-dipping structures show decreasing P−T conditions, indicating exhumation and cooling. Progressive changes in whole rock composition are interpreted in terms of open system behavior, caused by crustal-scale melt infiltration operating at grain boundaries. The mineral-equilibria modelling shown that such "metasomatism" by cirulating melt may cause the observed whole rock composition changes and was suggested as a new mechanism of melt transport in the crust.

In order to discuss the effects of melting on large-scale rheology during orogenic root deformations, pseudosection modeling of melt quantities was done to evaluate deformation mechanisms in various high-grade orthogneisses.

Simultaneous metamorphic and structural studies of lower- and middle crustal rocks permitted correlation of retrograde and very rarely preserved prograde metamorphic fabrics of the middle and lower orogenic crust, which started discussion of coupled and uncoupled mechanisms of burial and exhumation in the two crustal levels, but also with respect to the upper and lower plate.

INTRODUCTION

My scientific domain is the comprehension of tectonic and geodynamic processes in the mountain belts, based mainly on the parallel study of metamorphic processes and associated structural development.

I study the metamorphic processes by means of classic tools of metamorphic petrology, based for example on textural and microstructural analysis, microanalysis, interpretation of chemical equilibria and thermobarometry. I also use the method of mineral equilibria modeling that allows calculation of various phase diagrams for a large spectrum of metamorphic rocks. An extensive and detailed field study is for me a necessary base for interpretation of structural successions and their metamorphic conditions.

My studies, mainly in the eastern part of the Bohemian Massif of the Variscan belt contributed largely to interpretation of geodynamic evolution of the external and internal orogenic domains. The major results concern the various exhumation mechanisms and their thermal and barric characterization, as nappe stacking in the external domain, or vertical extrusion of lower orogenic crust followed by channel flow and ductile thinning in the middle orogenic crust of the internal domain. The results include also some aspects of the burial processes.

Metamorphic textures and microstructures; a key for understanding orogenic processes

Understanding of metamorphic microstructures is the key for revealing reaction history of rocks, pressure-temperature paths, relations to deformation and for understanding orogen-scale histories. Classic petrographic analysis combined with methods such as imaging on electron microscopy, electron microprobe or cathodoluminiscence provide compositional and physical information that can be used to interpret formation of metamorphic microstructures. Recent advances in thermodynamic modeling via pseudosections help to quantitatively evaluate hypothesis issued from petrographical observations, especially from the spatial arrangement of grains that may indicate succession of crystallization. Understanding of metamorphic microstructures combined with pseudosection modeling and structural studies is a key point of my research, which provided data that were extensively used in establishing large-scale orogenic models dealing with mechanisms of burial and exhumation.

The study of succession of crystallization based on *inclusions*, usually combined with interpretation of chemical zoning of porphyroblasts, is used to reveal prograde paths of the rocks (Štípská & Powell, 2005a; Racek *et al.*, 2006; Štípská *et al.*, 2006; Košuličová & Štípská, 2007; Štípská *et al.*, 2008; Skrzypek *et al.*, 2011a; Skrzypek *et al.*, 2011b). Careful study of textures related to succession of crystallization are especially important in high-grade rocks, where diffusion modified chemical composition of minerals and classic petrology methods, as for example thermobarometry, cannot be used. The *microstructural relationships*, even *in the matrix*, then can be an important and sometimes the only witness of a reaction history (Štípská & Powell, 2005b; Racek *et al.*, 2008) and may distinguish two or more metamorphic events and their relative timing.

Study of *porphyroblasts* is another classic tool that was used mainly to unravel early deformation. *Inclusion trails* and their orientation helps distinguishing deformation episodes (Košuličová & Štípská, 2007; Skrzypek *et al.*, 2011a; Skrzypek *et al.*, 2011b), or rotational vs. unrotational deformation regime (Skrzypek *et al.*, 2011a) during the porphyroblast growth. Based on sequential growth of porphyroblasts, inclusion trails and macroscopically preserved structures, Skrzypek *et al.* (2011b) have deciphered prograde and retrograde structures responsible for burial and exhumation of the middle orogenic crust. The same area was suitable for a contribution to a long-lasted discussion whether porphyroblasts rotate or not during various deformation regimes (Skrzypek *et al.*, 2011a). This work introduces a new technique, where the orientation of the inclusion trails of ilmenite in garnet is measured using the EBSD method, and their orientation is compared to macroscopically preserved structures. Small variations of ilmenite orientation in garnet suggest that a weak rotation of porphyroblasts occurred at the beginning of folding and during moderate buckling stage. During increasing intensity of deformation, the buckling stage was followed by passive flow with lack of porphyroblast rotation.

Another microstructure that always attracted petrologists are *coronas* (Fig. 1). These are reaction rims composed of monomineralic or polymineralic layers surrounding a mineral and separating it from the matrix or from another mineral. A major question is how and whether they can be used to reconstruct reaction history, metamorphic conditions and P−T paths. Usual approach is evaluating what chemical and textural subdomains represent an equilibrium assemblage suitable for thermodynamic analysis and what reactions are responsible for corona

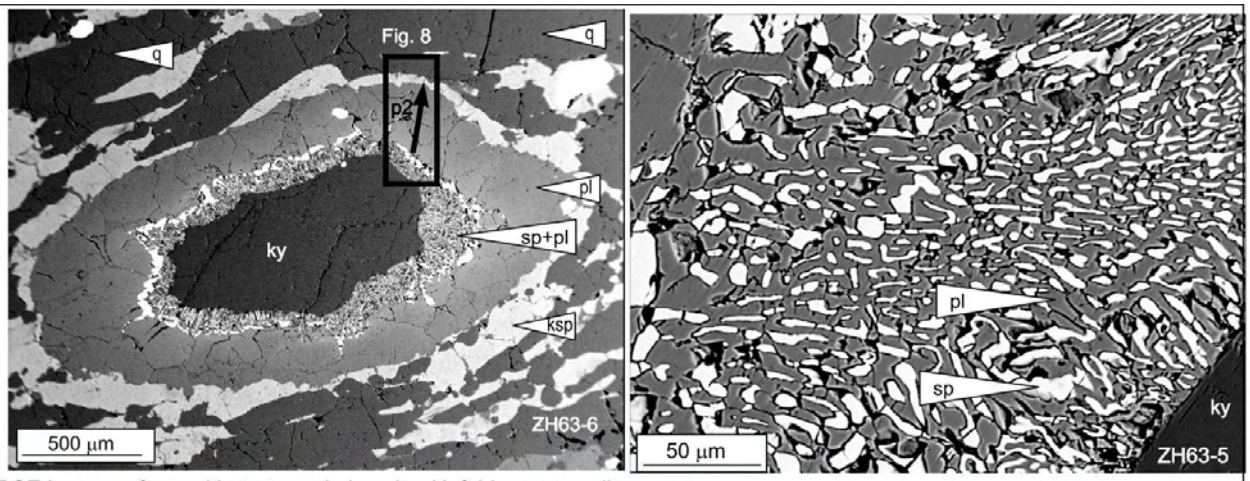

BSE images of coronitic textures in kyanite−K−feldspar granulite.

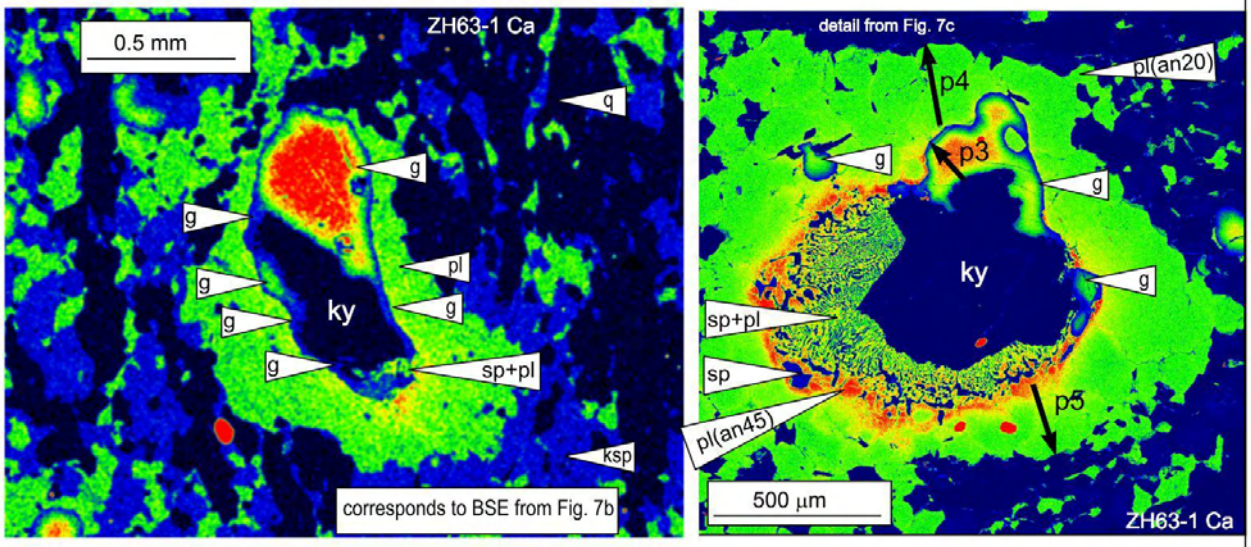

Compositional maps of Ca.

The spatial and compositional relations in the plagioclase-around-kyanite corona in a 3-D μ(SiO2)-μ(CaO)-μ(Na2O) diagram.

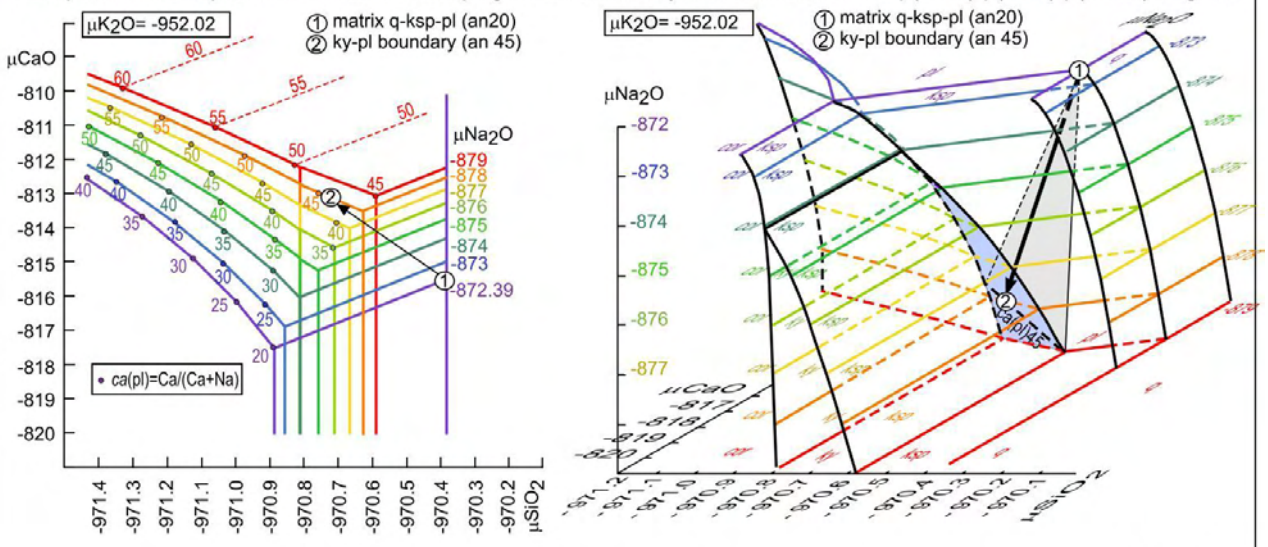

Fig. 1. Mineral equilibria modelling of coronitic structures in granulites. After Štípská et al. (2008).

formation. Such approach can eventually decipher metamorphic reactions, but cannot account for the spatial relationships. To understand the spatial relationships, mineral equilibria calculations explicitly involving chemical potentials are required. One of the first works that uses calculated chemical potential relationships for phase equilibria involving solid solutions is Štípská *et al.* (2010). The method is used to understand formation of corona textures involving plagioclase ± garnet around kyanite, and replacement of kyanite by plagioclase + spinel symplectite in kyanite-K-feldspar granulites in the Bohemian Massif.

Mineral equilibria modelling and its application in metamorphic petrology and tectonics

Thermodynamic calculations of phase diagrams for metamorphic and igneous rocks may be performed using several currently available programs such as THERMOCALC (Powell & Holland, 1988), Perplex (Connolly, 1990) or Theriak-Domino (De Capitani & Brown, 1987). Thermocalc uses a non linear equation solver to calculate user-specified equilibria, Perplex and Domino use Gibbs energy minimization. Although these programs use different calculation methods, they allow performing similar calculations. The possible calculations involve a wide range of phase diagrams, including P−T projections (petrogenetic grids), P−T pseudosections (a map of mineral assemblages for a specified whole rock composition and for variable pressure and temperature conditions), P−X , T−X or X−X pseudosections (a map of mineral assemblages for a specified rock composition, and for one or two compositional variables in the rock at fixed P and/or T), compatibility diagrams and μ−μ diagrams (chemical potential diagrams).

The P−T pseudosections are currently one of the best tools used in petrology in our attempt to understand P−T paths that the metamorphic rocks followed in the crust. Pseudosections are diagrams for a specified bulk rock composition and have only two degrees of freedom. The mineral proportions and mineral compositions are therefore uniquely defined at any point on the pseudosection, so that fields of individual mineral assemblages may be contoured for example for mineral molar (or volume) proportion or mineral composition. As the metamorphic rocks follow a P−T path during their burial and exhumation in the crust they are changing mineral assemblages in an attempt to minimize their Gibbs energy. The mineral assemblage of a metamorphic rock observed at the surface, including mineral proportions and mineral chemical composition, can be considered to reflect a state of preserved equilibrium along a P−T path at some scale (equilibration volume). A pseudosection calculated for such a rock or

for such an equilibration volume allows P–T information to be extracted. By comparison of the mineral assemblage and the chemistry of minerals with the calculated fields in the pseudosection and calculated mineral chemistry isopleths, peak P−T conditions are commonly successfully extracted. When mineral inclusions or growth zoning are preserved, pseudosections also allow extracting information about the prograde P−T path. Similarly, even partial development of retrograde minerals allows discussing the retrograde P−T path.

P−X and T−X pseudosections are useful diagrams for studying the influence of the bulk rock composition on the assemblages and chemistry of minerals. They are commonly used for example to study the effect of the quantity of H_2O on mineral equilibria at subsolidus conditions, to compare what is the difference between H_2O-saturated and H_2O-undersaturated equilibria. Such diagrams help for example understanding whether the equilibration along a particular P−T path will happen or not. It is supposed that the rock equilibrates when it releases H_2O, while when the reactions require H_2O, the equilibration stops, unless there is an external source of H_2O. Another commonly used variable is for example the Fe^{3+} or XFe to study the influence of the oxidation state of iron on mineral equilibria.

Another application of P−T, P−X and T−X pseudosection modelling is in supersolidus conditions, which started with the introduction of granitic melt model several years ago (Holland & Powell, 2001; White *et al.*, 2001). The modeling method is not straightforward, requires for example estimation of H_2O present at the onset or during melting, estimation of melt quantity that may have been lost during anatexis, its composition, and possibly reintegration of lost melt into the whole rock composition (White & Powell, 2002). These techniques were used in several studies (Štípská & Powell, 2005b; Racek *et al.*, 2006; Hasalová *et al.*, 2008c; Racek *et al.*, 2008; Schulmann *et al.*, 2008b; Štípská *et al.*, 2008; Franěk *et al.*, 2011b; Lexa *et al.*, 2011; Chopin *et al.*, submitted-a) that helped for example the quantification of melt production, quantification of melt extraction and revealed prograde and retrograde P−T paths of migmatites and granulites. Modeling of melt quantities was done to evaluate deformation mechanisms in high-grade granitic orthogneiss and in felsic granulites (Hasalová *et al.*, 2008c; Schulmann *et al.*, 2008b; Franěk *et al.*, 2011b; Lexa *et al.*, 2011; Chopin *et al.*, submitted-a), to help understanding of the processes of deformation mechanisms in order to discuss the effects of melting on large-scale rheology during orogenic root deformations.

While the P−T pseudosections and P−X or T−X pseudosection may help in understanding the P−T conditions of the assemblage formation, they cannot help in understanding of the spatial arrangement of the minerals in the rocks. For understanding of the arrangement in space, it is necessary to use the chemical potential diagrams (μ−μ diagrams). This was until now almost impossible, with exception of some very simple cases, but recent advances in the modelling approaches allow now these calculations to be done with models of solid solutions (Fig. 1) (White *et al.*, 2008; Štípská *et al.*, 2010).

For tectonic or geodynamic interpretations, the P−T paths of metamorphic rocks may be correlated with structures. This allows attributing to each structure a depth and temperature under which they developed. Structural successions combined with P−T paths of the rocks then represent basic information for interpretation of the behaviour of the crust during formation of the mountain belts. Combination with in situ dating adds quantitative information about the time-scales and may result in complete P−T−t−D paths (pressure-temperature-time-deformation) of rocks. If the P−T−t−D paths or at least parts of the P−T−t−D paths of the lower, middle and upper orogenic crust are known, they provide a database necessary for large-scale interpretations of orogenic processes (e.g. Schulmann *et al.*, 2008a).

Superposed orogenic fabrics and metamorphism – key to revealing tectonic evolution of an orogen

In the tectonic evolution of large orogenic root systems there are complexities that arise from the polyphase nature of vertical and horizontal material and heat transfer during long-lasting orogenic events. Therefore, detailed regional structural, petrological and geochronological studies of orogenic fabrics may provide a key to deciphering the succession, and length and time scales of processes responsible for mutual displacement of rocks and heat transfer within these large orogenic root systems. Tectonic models like continental underthrusting and corner flow, gravity redistribution or crustal scale folding should be associated with a typical succession of structures and typical P−T paths related to movement of rocks in individual crustal levels. Therefore, in order to correlate one of the models or their combination with the tectono-metamorphic evolution of an orogen, information about structural, petrological and geochronological evolutions of the orogenic lower, middle and upper crust is needed. Structural geology can compare successions of deformation fabrics from different crustal levels in order to

decide whether the lower and middle crust are mechanically coupled or decoupled during orogeny. Petrology provides information about vertical displacements and thermal evolution of rocks during orogeny. After establishing P−T paths of individual rocks it is possible to attribute these rocks to different crustal levels and to demonstrate their shared and/or unshared parts of metamorphic histories (Štípská *et al.*, 2006; Štípská *et al.*, 2008). Finally, combination of structural and petrological information into P−T−D (pressure-temperature-deformation) paths allows determining burial and/or exhumation character of individual fabrics. It allows also correlation of mutual horizontal and vertical displacements of rocks from different crustal levels during an orogenic cycle. Over last 15 years I applied these methods to reveal tectono-metamorphic history of the eastern margin of the Bohemian Massif.

THE BOHEMIAN MASSIF: A FIELD LABORATORY FOR STUDYING OROGENIC PROCESSES IN LARGE HOT OROGENS

The eastern margin of the Variscan Bohemian Massif is characterized by a boundary between the high-grade Moldanubian-Lugian and the Barrovian type Brunia-derived domains (Fig. 2). The boundary involves a major thrust of the internal Moldanubian domain over the external Brunian basement that produced in the latter a 300 km long and up to 50 km wide metamorphosed and deformed belt, the Moravo-Silesian domain (Suess, 1912; Suess, 1926). The boundary is marked by the so-called Micaschist zone, considered to be a retrogressed part of the structurally upper Moldanubian domain (Suess, 1926), or as the uppermost part of the structurally lower Brunian domain (Štípská & Schulmann, 1995; Štípská *et al.*, 2000; Konopásek *et al.*, 2002; Štípská *et al.*, 2006). The two major domains differ in protolith ages, character of Variscan metamorphism and style of deformation.

The Moldanubian-Lugian domain involves Cambro-Ordovician to Devonian magmatism that acted on Paleoproterozoic and Neoproterozoic protoliths (e.g. Kröner *et al.*, 2001; Friedl *et al.*, 2004; Lange *et al.*, 2005a; Lange *et al.*, 2005b). A major consequence of the Variscan orogenesis in the Moldanubian-Lugian domain is widespread anatexis and an alternation of medium- and high-pressure belts (e.g. Štípská *et al.*, 2004; Schulmann *et al.*, 2005). The high pressure belts are represented by felsic granulites and orthogneisses (O'Brien & Rötzler, 2003 and references therein), rare crustal eclogites (Medaris *et al.*, 1995b; Štípská & Schulmann,

1995; Medaris *et al.*, 1998) and intercalations of garnetiferous peridotites associated with mantle eclogites (e.g. Carswell, 1991; Medaris *et al.*, 1995a).

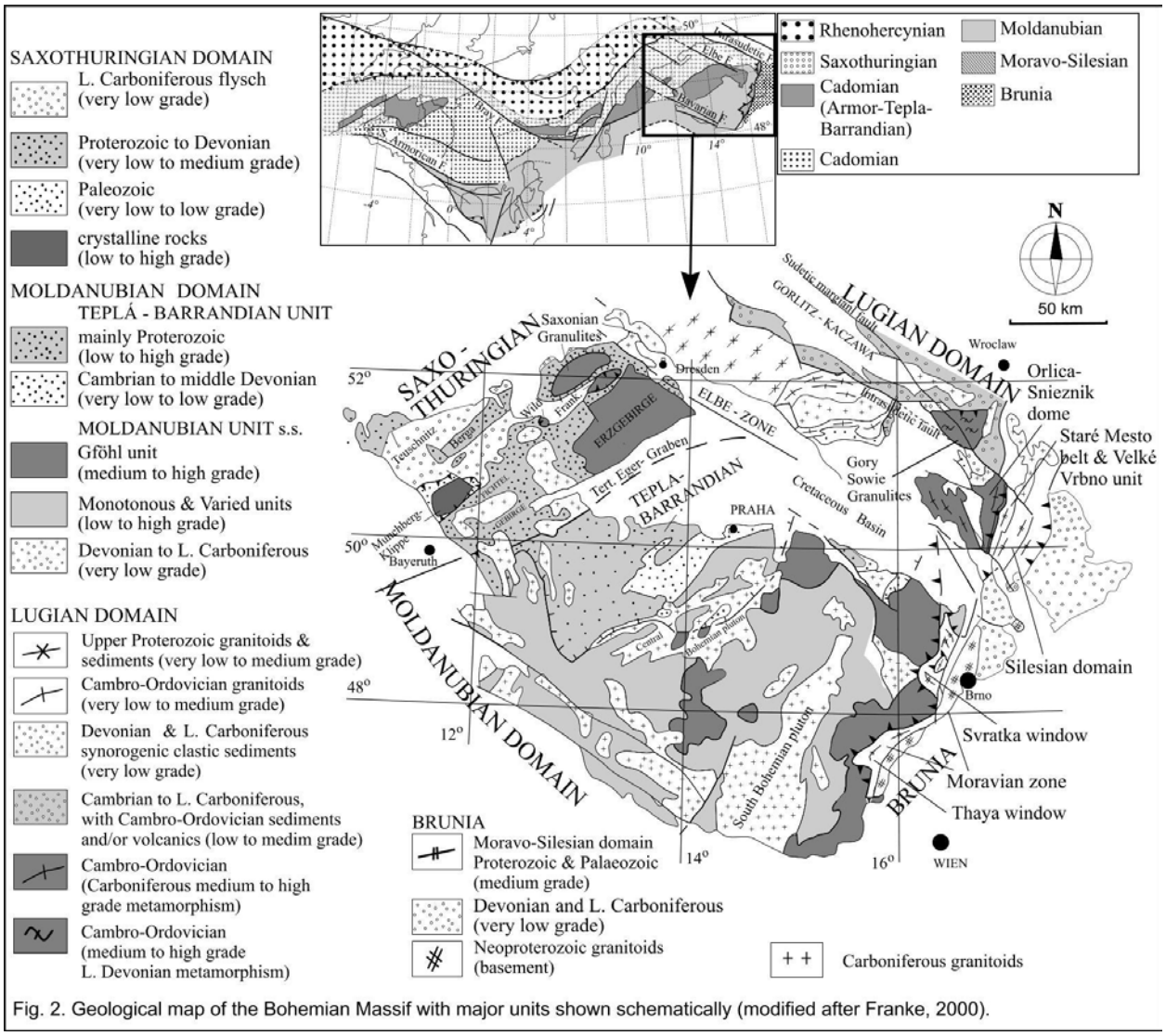

Fig. 2. Geological map of the Bohemian Massif with major units shown schematically (modified after Franke, 2000).

The Brunia basement is composed of Neoproterozoic granitoids (Kröner *et al.*, 2000, and references therein) and overlain by Cambro-Ordovician sedimentary rocks. During the Devonian, NE–SW-trending basins developed, characterized by shallow water and continental sedimentation in the south. In the north, the basins are deeper with marine sediments accompanied by volcanism, evolving in time into shallow-water sedimentation (Hladil, 1994; Hartley & Otava, 2001; Kalvoda *et al.*, 2003). The Cambro-Ordovician magmatism characteristic for the Moldanubian domain is here missing (Kröner *et al.*, 2000). Carboniferous compression produced an up to 50-km-wide deformation and metamorphic front in the

underthrust Brunia, the so-called Moravo-Silesian accretionary wedge that is characterised by Barrovian and Buchan type metamorphism (Schulmann & Gayer, 2000). This wedge emerges in the form of three tectonic windows, the southern Thaya window and the central Svratka window of the Moravian domain, and the northern Silesian domain. The compression was accompanied by Carboniferous, syn- to late tectonic magmatism in the Silesian domain.

The boundary of the Moldanubian-Lugian orogenic root with the continental Brunia margin offered a possibility to study geodynamic behavior of the underthrust plate, and of the hot orogenic root, including processes of their interaction during orogeny.

Barrovian metamorphism of the continental margin and the boundary with the Moldanubian domain

The Moravo-Silesian domain, a deformed and metamorphosed part of the Brunia basement that originated during the underthrusting below the orogenic root is the key region for understanding the inverted metamorphic sequences of the European Variscides. It is also a region that is important for understanding inverted metamorphism, channel flow tectonics and Himalayan metamorphic profile.

Various aspects, including the arguments for nappe stacking, metamorphic inversion and modification of the nappe pile by late crustal-scale folding are covered in Štípská & Schulmann (1995) and Štípská *et al.* (2000). A study of prograde metamorphic paths allowed discussion about the variations of the Brunia thermal state before the underthrusting, and contributed to understanding of the variations in metamorphic record along the Moravo-Silesian zone (Štípská *et al.*, 2006; Košuličová & Štípská, 2007). This metamorphism ranges from typical Barrovian assemblages in the southern and central part, to the Buchan type assemblages in the north, and shows the occurrence of eclogites in the uppermost trust sheets. The content of these works is summarized below.

The Moravo-Silesian zone as a deformed equivalent of the Brunia promontory (example of the Thaya window)

My early studies (Štípská & Schulmann, 1995; Štípská *et al.*, 2000) concerned inverted Barrovian metamorphism developed at the south-eastern margin of the Bohemian Massif, in two large tectonic windows emerging through a migmatitic nappe. The Brunian basement in the southern Thaya window responded to the underthrusting under the Moldanubian domain by

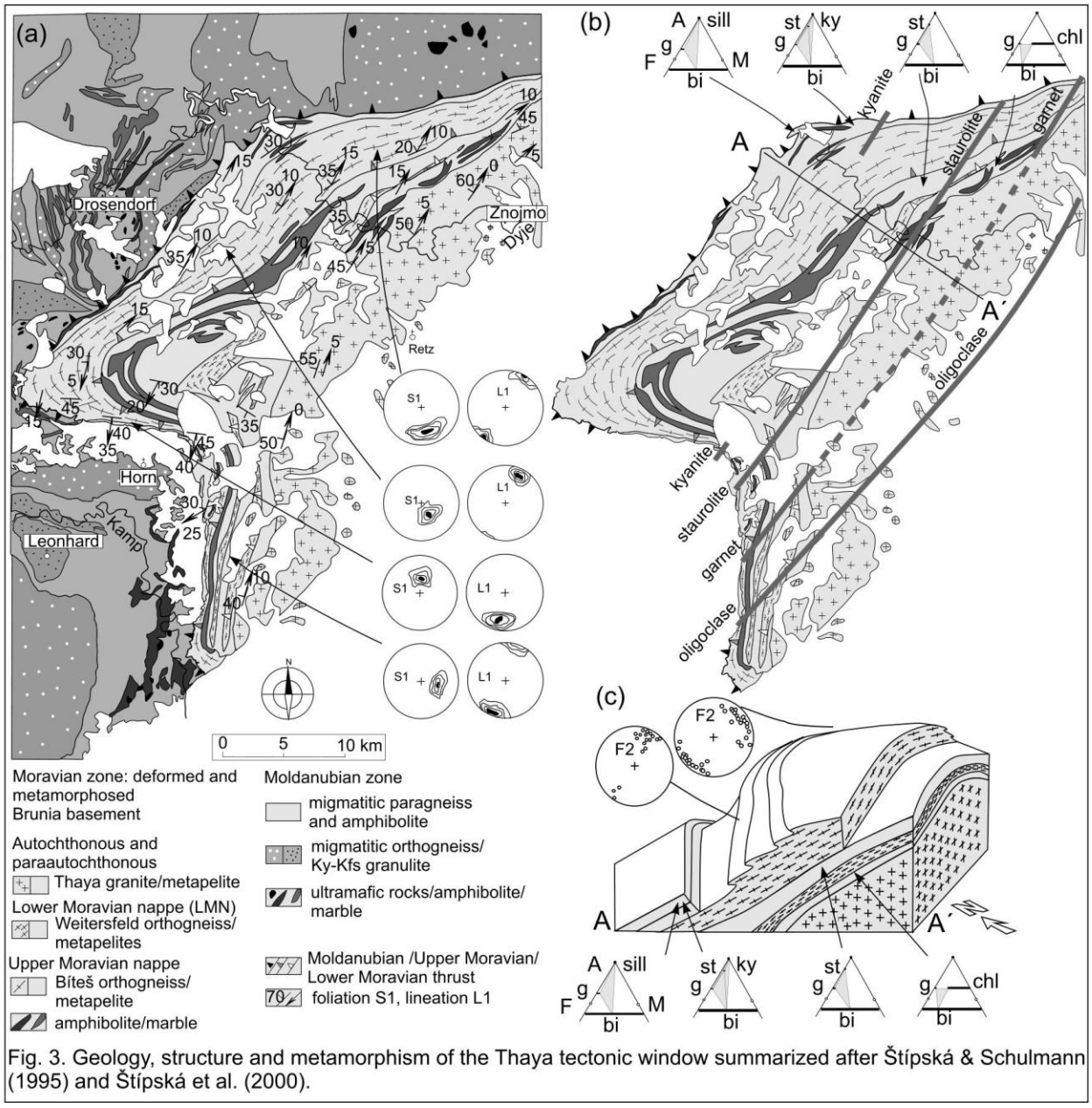

Fig. 3. Geology, structure and metamorphism of the Thaya tectonic window summarized after Štípská & Schulmann (1995) and Štípská et al. (2000).

formation of two crustal-scale nappes and deformation of the para-autochtonous basement (Figs 3 & 4). The nappes and the para-autochton are formed by an orthogneiss at the bottom and a metasedimentary sequence at the top. Within this basement-derived nappe sequence occurs inverted metamorphic zonation from chlorite to kyanite-sillimanite zone. Mineral reactions and geothermometry reveal an increase in temperature from 580–600 °C to 650 °C and an increase in pressure from 6 to 10 kbar from the bottom to the top of the nappe pile. Kinematic data and syntectonic crystallization of minerals indicate that the peak conditions were diachronously attained during a slow oblique underthrusting of the Brunia basement. Geochronological data

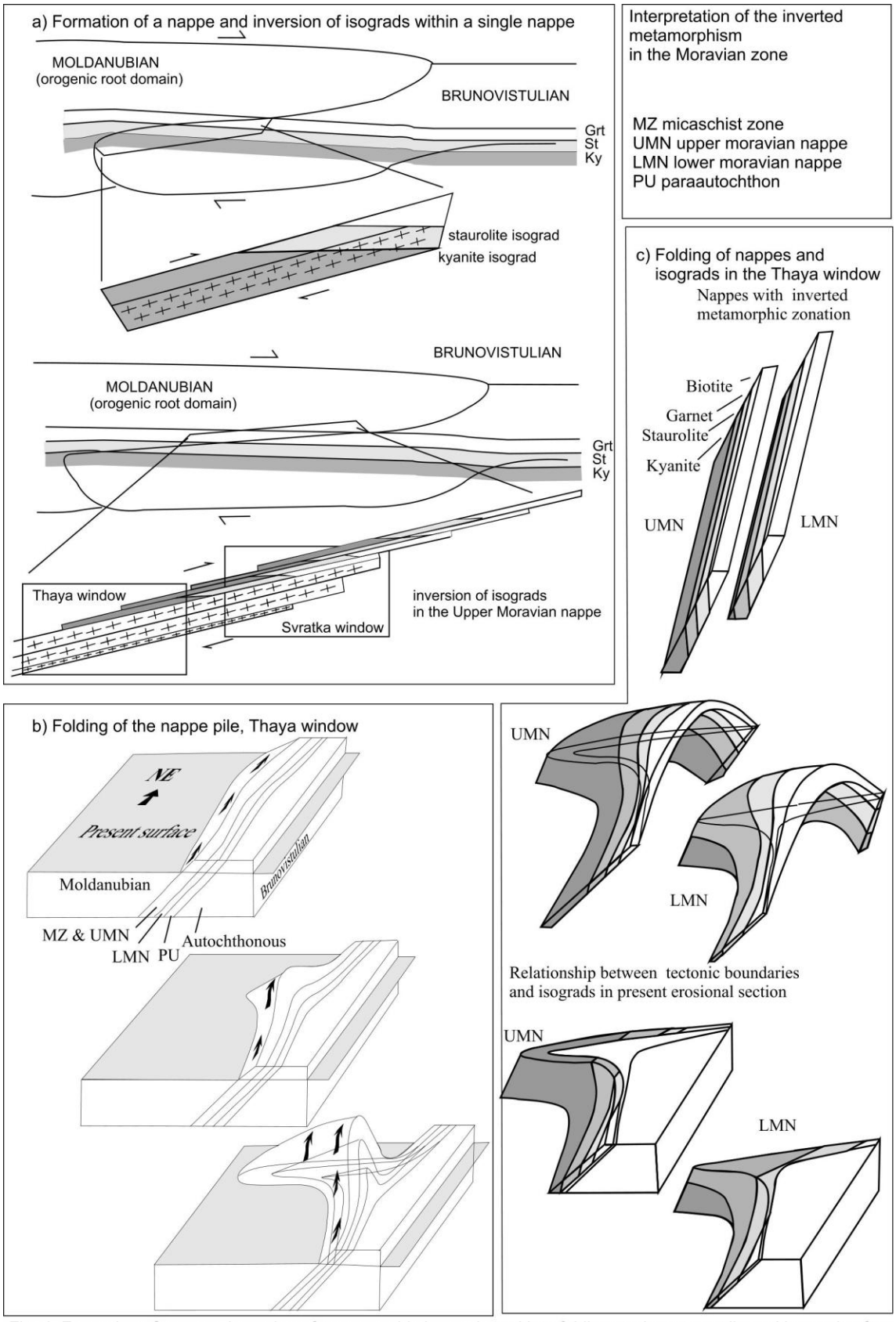

Fig. 4. Formation of nappes, inversion of metamorphic isograds and late folding on the nappe pile and isograds after Štípská & Schulmann (1995) and Štípská et al. (2000).

reveal about 20 Ma between granulite facies metamorphism of the upper plate and mineral cooling ages in the lower plate, precluding perturbation of the geotherm by underthrusting. We suggested a model showing a progressive break-up of the deepest parts of the underthrust Brunia and subsequent migration of the intraplate boundary to the base of the basement-derived thrust sheet. The uplift of this unit led to its decompression while the rest of the basement was subject to continuous underthrusting. The inverted metamorphic zonation within a single unit is explained using a model of heterogeneous deformation of upward transported units and passive inversion of initially subhorizontal isograds.

The pattern of isograds in a present section of the Thaya tectonic window is complex because the isograds obliquely crosscut the tectonic boundaries. We interpreted this pattern as a result of large-scale buckling of an imbricated nappe sequence (Štípská *et al.*, 2000). This large-scale mechanical instability was initiated by blocking of passively transported hot viscous rocks to shallow crustal levels. The wavelength and shape of the buckle fold is controlled by the greatest thickness of the uppermost nappe and by the low ratio of strong orthogneiss to weak micaschists in individual nappes. The steep inclinations of the thrust surfaces and the oblique movement of the crustal multilayer minimize the role of gravity on fold generation. Medium-scale gravitational folds originated at the end of the buckling of the nappes and are associated with the late sliding of the nappes away from the core of the anticline during late exhumation. Thermal, rheological and fold calculations are presented, which document and explain the mechanism of folding of large-scale crystalline nappes.

Prograde metamorphic evolution: evidence for the variable thermal state of the Brunia crust before underthrusting

Previous tectonometamorphic studies in the Silesian domain shown that this part of Brunia was largely modified by Devonian extension, including the formation of three crustal-scale boudins: the Desná dome, the Keprník nappe and the Velké Vrbno unit, and (volcano) sedimentary units between them (Schulmann & Gayer, 2000). The crustal boudins were underthrust individually during Carboniferous shortening with increasing burial depth to the west. The exhumation occurred under continuous compression accompanied by east-vergent folding with variable transposition into generally west-dipping foliation. Metamorphism is of Barrovian type (Souček, 1978; Schulmann & Gayer, 2000; Štípská *et al.*, 2006; Košuličová & Štípská, 2007), however,

complicated in detail by occurrence of eclogites within the staurolite-kyanite micaschists of the westernmost Velké Vrbno unit (Žáček, 1996; Štípská *et al.*, 2006), interpreted as mixing of the eclogites and the medium-grade metasediments at the tip of a crustal wedge. In the Silesian domain also occur Buchan-type paragenessies with andalusite and cordierite (Rozkošný & Souček, 1989; Cháb & Žáček, 1994). The Buchan type evolution was attributed partly to the heat from the neighbouring pluton, but the prograde transition from staurolite to sillimanite was ascribed to increased heat flow due to Devonian extension (Schulmann & Gayer, 2000; Baratoux *et al.*, 2005).

In Košuličová & Štípská (2007), we studied in detail the tectono-metamorphic evolution of the Silesian domain and we quantified the P−T paths using pseudosection modelling. In the staurolite zone, inclusions of chloritoid occur in garnet cores, while staurolite is included at garnet rims and is widespread in the matrix. Chloritoid X_{Fe} = 0.91 indicates transition to staurolite at 5 kbar and 550 °C and consequently, an early transient prograde geothermal gradient of 29 °C km^{-1}. The overall elevated thermal evolution is then reflected in prograde transition of staurolite to sillimanite and in achievement of peak temperature of 660 °C at relatively low pressure of 6.5 kbar. We compared the data with the results from the western Velké Vrbno unit (Štípská *et al.*, 2006) and from the southern Svratka window (Konopásek *et al.*, 2002). In these areas the high grade metamorphic zones record on prograde path evolution from staurolite to kyanite and development of sillimanite on decompression. Transition of chloritoid (X_{Fe} = 0.75–0.80) to staurolite occurs at 8–10 kbar and 560–580 °C indicating a transient prograde geothermal gradient of 16–18 °C km^{-1}. These data show variable barric evolutions along strike and across the Moravo-Silesian domain. Elevated prograde geothermal gradient coincides with areas of Devonian sedimentation and volcanism and Carboniferous intrusions. Therefore, we interpreted it as a result of heat inherited from Devonian rifting, further fuelled by syntectonic Carboniferous intrusions.

This contribution also showed that thermodynamic modelling of metamorphic rocks largely increased possibilities in deciphering prograde paths that provide important insights into early orogenic evolutions. We showed that chloritoid-staurolite transition is not only an indicator of temperature on prograde P−T paths, but also a useful indicator of pressure.

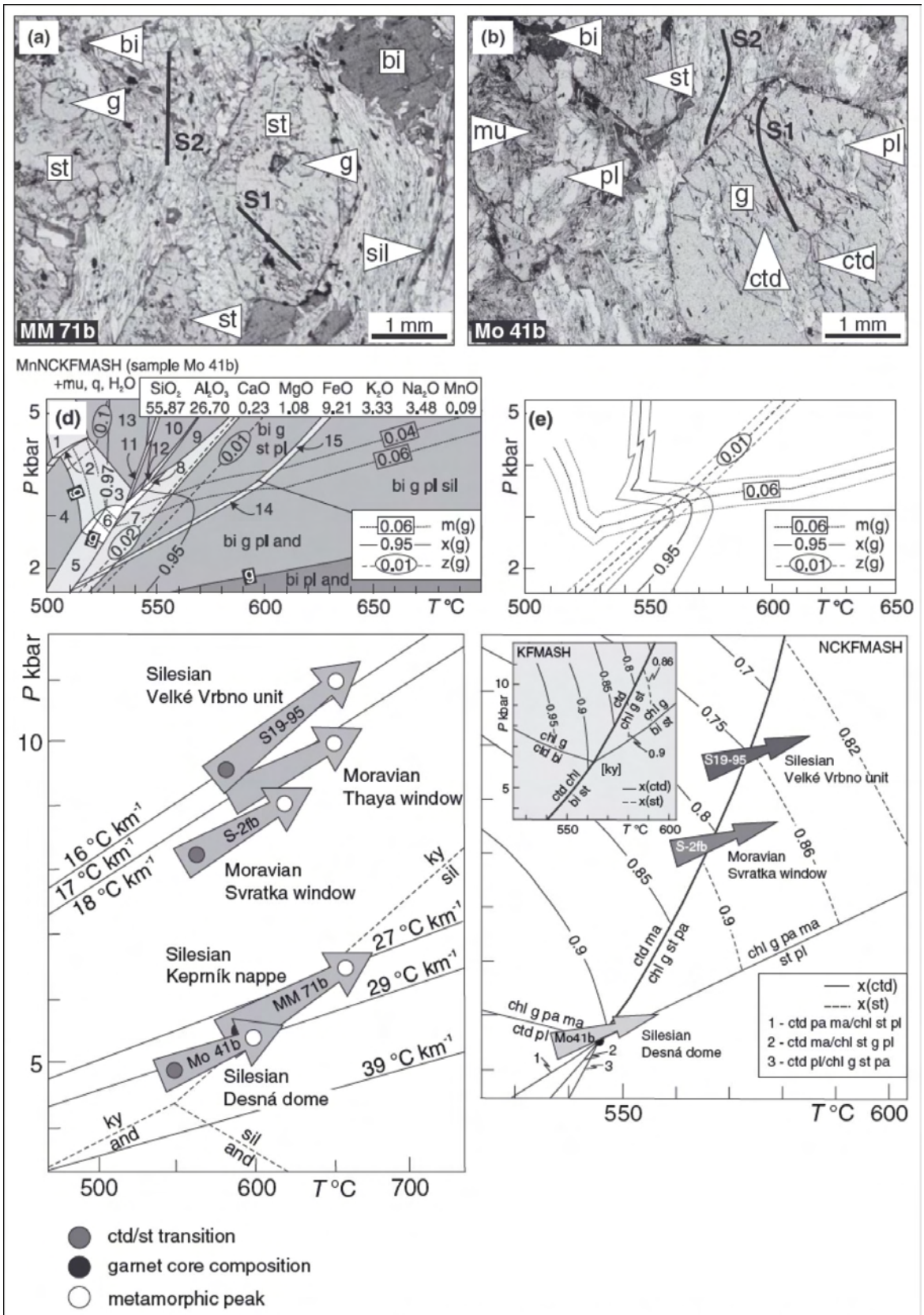

Fig. 5. Chloritoide-staurolite transition shows variable transient geothermal gradient on prograde path along the Moravo-Silesian zone. After Košuličová & Štípská (2007).

The processes of burial and exhumation at the tip of the underthrust Brunia (example of the Velké Vrbno unit)

In the Velké Vrbno unit, one published and several new zircon ages (Kröner *et al.*, 2000; Kröner, unpublished data) from the felsic orthogneisses are all Neoproterozoic, indicating a clear affinity to the Moravo-Silesian domain. Accordingly, we proposed that the major contact between the Moravo-Silesian and Moldanubian domains, originally placed at the base of the Velké Vrbno unit (the so-called Ramzová thrust), should be located at the top of this unit (the Nýznerov thrust).

Within the Velké Vrbno unit, eclogite boudins occur within an orthogneiss sheet enclosed in a Barrovian metapelite-dominated volcano-sedimentary sequence (Fig. 6a,b). A metamorphic and lithological break defines the base of the eclogite-bearing orthogneiss nappe, with a structurally lower sequence without eclogite exposed in a tectonic window. The structurally upper metapelites contain typically staurolite, kyanite and prograde-zoned garnet that includes from core to rim chloritoid–chlorite–paragonite–margarite, staurolite–chlorite–paragonite–margarite and kyanite–chlorite–rutile. In the pseudosection, the prograde path is traced from 9.5 kbar and 570 °C to the metamorphic peak at 11 kbar and 640 °C. Decompression through about 7 kbar is indicated by sillimanite and biotite growing at the expense of garnet. In the tectonic window, the structurally lower staurolite- and kyanite-bearing metapelites and garnetiferous amphibolites indicate a metamorphic peak of 10 kbar at 620 °C and 11 kbar and 610–660 °C, respectively, that is consistent with the other metapelites. The composition of pyroxene (jadeite 43%) and zoning of garnet in the eclogites are compatible in the pseudosection with burial under H_2O-undersaturated conditions to 18 kbar and 680 °C. Plagioclase, amphibole and epidote replaces garnet within foliated boudin margins, indicating that decompression occurred under decreasing temperature into garnet-free epidote−amphibolite facies conditions.

The prograde path of eclogites and metapelites up to the metamorphic peak cannot be shared, being along different geothermal gradients, of about 11°C and 17 °C/km, respectively, to metamorphic pressure peaks that are 6–7 kbar apart. The eclogite–orthogneiss sheet docked with metapelites at about 11 kbar and 650 °C, and from this depth the exhumation of the pile is shared. We interpret the separate metamorphic histories of the eclogite lenses and of the kyanite-metapelites as back thrusting of the eclogitized tip of the underthrust Brunia basement that is followed by mixing of eclogite-orthogneiss sheets with predominantly volcano-sedimentary

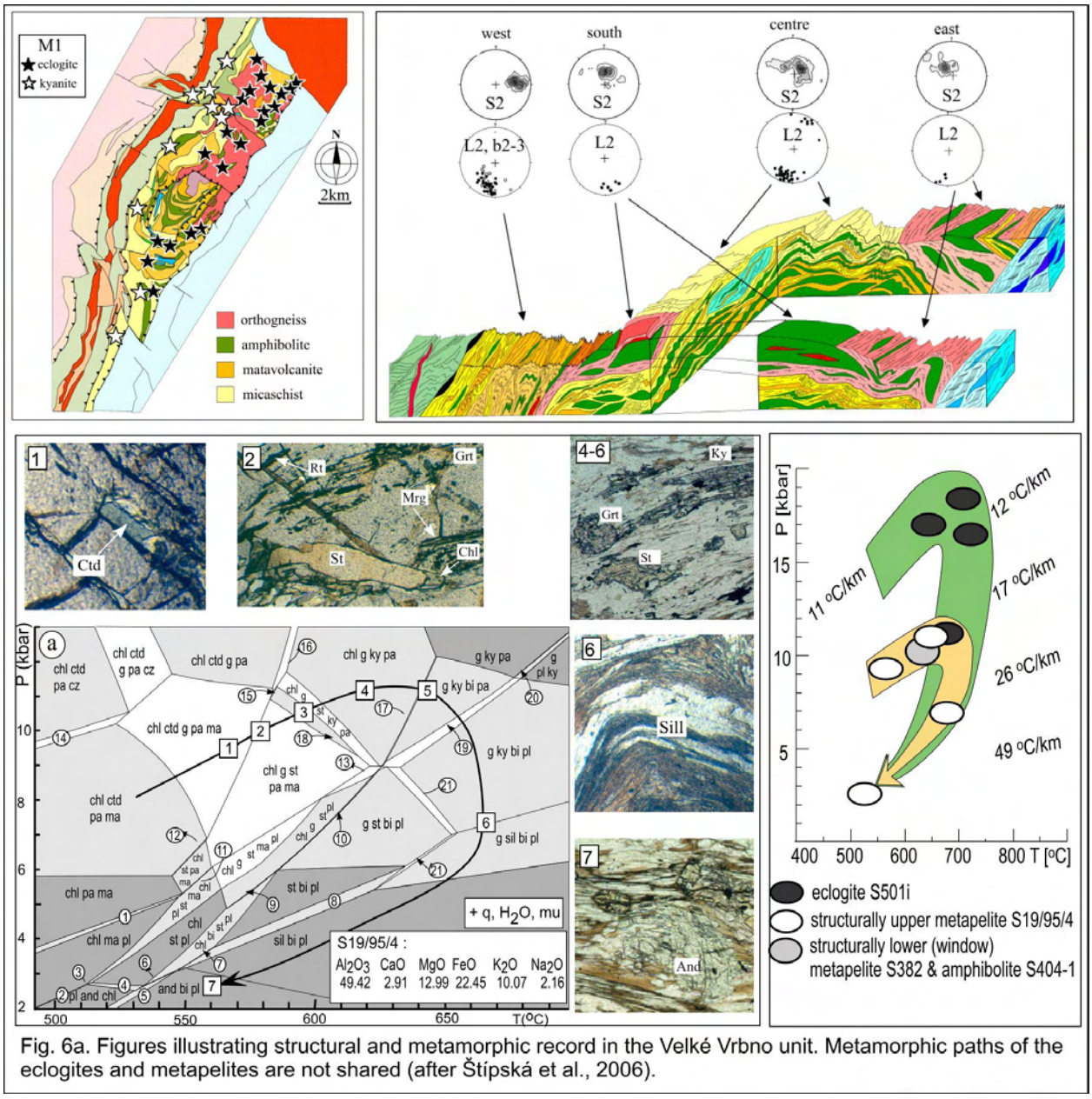

Fig. 6a. Figures illustrating structural and metamorphic record in the Velké Vrbno unit. Metamorphic paths of the eclogites and metapelites are not shared (after Štípská et al., 2006).

rocks under middle-pressure conditions in the crustal wedge (Fig. 6). Similar relationships were described by Konopásek *et al*. (2002) in the southern Moravian zone.

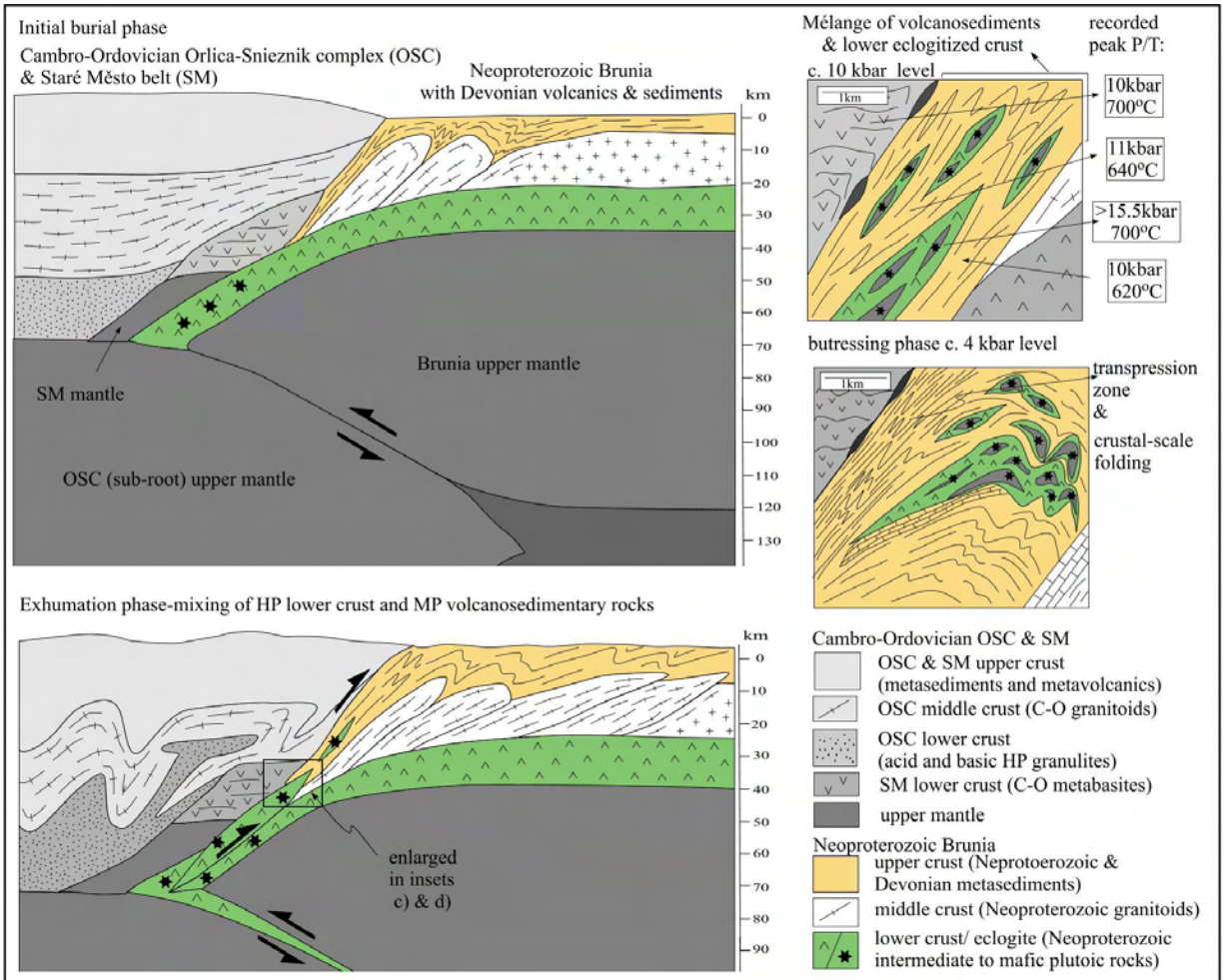

Fig. 6b. Tectonic interpretation showing burial of the Brunia microcontinent under the orogenic root, formation of the eclogite at the tip of the underthrust Brunia and mixing of eclogites with medium grade metasediments in the eccretionary wedge during exhumation. Unpublished results based on Štípská et al. (2006).

The transitional zone between the internal orogenic root domain and the continental margin

In the north-eastern part of the contact between the Moldanubian-Lugian and the Moravo-Silesian zones occurs the so-called Staré Město belt, composed of granodiorite, layered amphibolite, metagabbro and serpentinites (Figs 7 & 8). This unit was classically considered as the retrogressed base of the Moldanubian domain (Suess, 1926) but modern studies show that it represents a transitional zone between the easterly Brunia continental margin represented by Moravo-Silesian zone and westerly orogenic root domain represented by Lugian domain. In order to understand the role of this peculiar unit in the building of orogenic structure we have undertaken combined structural and geochronological study of individual lithologies forming the

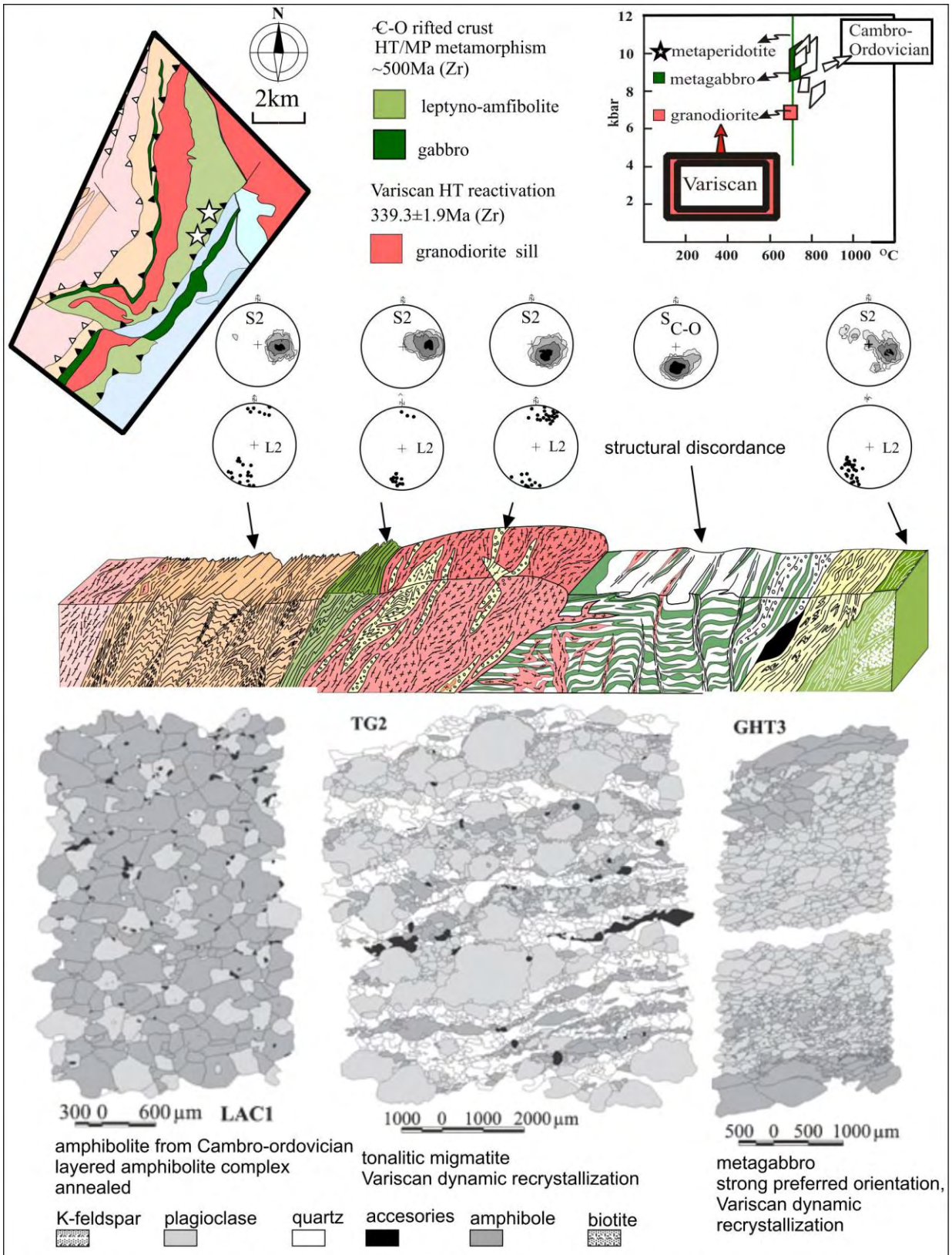

Fig. 7. Figures illustrate Cambro-Ordovician and Variscan structure, metamorphism and contrasting mircostructural record of Cambro-Ordovician and Variscan metamorphism in the Staré Město belt. After Parry et al. (1997), Kröner et al. (2000) and Lexa et al. (2005).

Staré Město belt. The first order marker is a structural disconformity between subhorizontal fabrics in the granulites and amphibolites dated at 500 Ma (Early Ordovician) and fabrics of the granodiorite sheet. The fabrics of the granodiorite sheet are parallel to steep foliations reworking the hangingwall gabbros, dated at 340 Ma using U-Pb zircon SHRIMP and Pb-Pb evaporation method. This allowed Parry *et al.* (1997) and later Kröner *et al.* (2000) to distinguish relics of subhorizontal Ordovician fabrics for the first time in the whole Variscan European belt. These studies shown that the gabbroic intrusions and layered amphibolite complex of the Staré Město belt can be interpreted as a Cambro-Ordovician intracontinental rift corresponding to an attenuated lower crustal segment of the Moldanubian-Lugian domain for which Cambro-Ordovician protolith ages are characteristic (Turniak *et al.*, 2000; Kröner *et al.*, 2001). The Variscan tectono-metamorphic event is manifested by syn-convergent intrusion of the Carboniferous granodiorite sill, HT-MP compressional deformation of the gabbros that produces foliations parallel with the structure of the granodiorite. Based on these criteria we interpreted the Staré Město belt as a preserved example of an intracontinental Cambro-Ordovician rift that has been reactivated during the Variscan orogeny.

Thermal structure and rheology of the continental rift during collision

In order to understand Carboniferous metamorphism related to dextral transpressive shearing associated with intrusion of the granodiorite sill, I have conducted a thermal modeling work (Fig. 8). This study shown that the Carboniferous metamorphism is limited to first kilometer distance from the sill on both sides and its duration was very short, around 100 000 years, because the sill intruded thermally equilibrated Ordovician lithosperic structure, which revealed 140 My of cooling (Štípská *et al.*, 2001). Numerical thermal and rheological modelling has demonstrated that the Staré Město paleorift after 140 Ma long cooling period represented a stiff heterogeneity in between the easterly situated Cadomian continent and the westerly lying crust of the future Variscan orogenic root zone. Carboniferous underplating of the paleorift by a granodioritic magma was probably responsible for partial thermal weakening of the upper mantle and the mafic lower crust and for subsequent exhumation of the remaining rigid part of the Cambro-Ordovician crust. All units were finally deformed in transpressional heterogeneous greenschist facies regime at a supracrustal level.

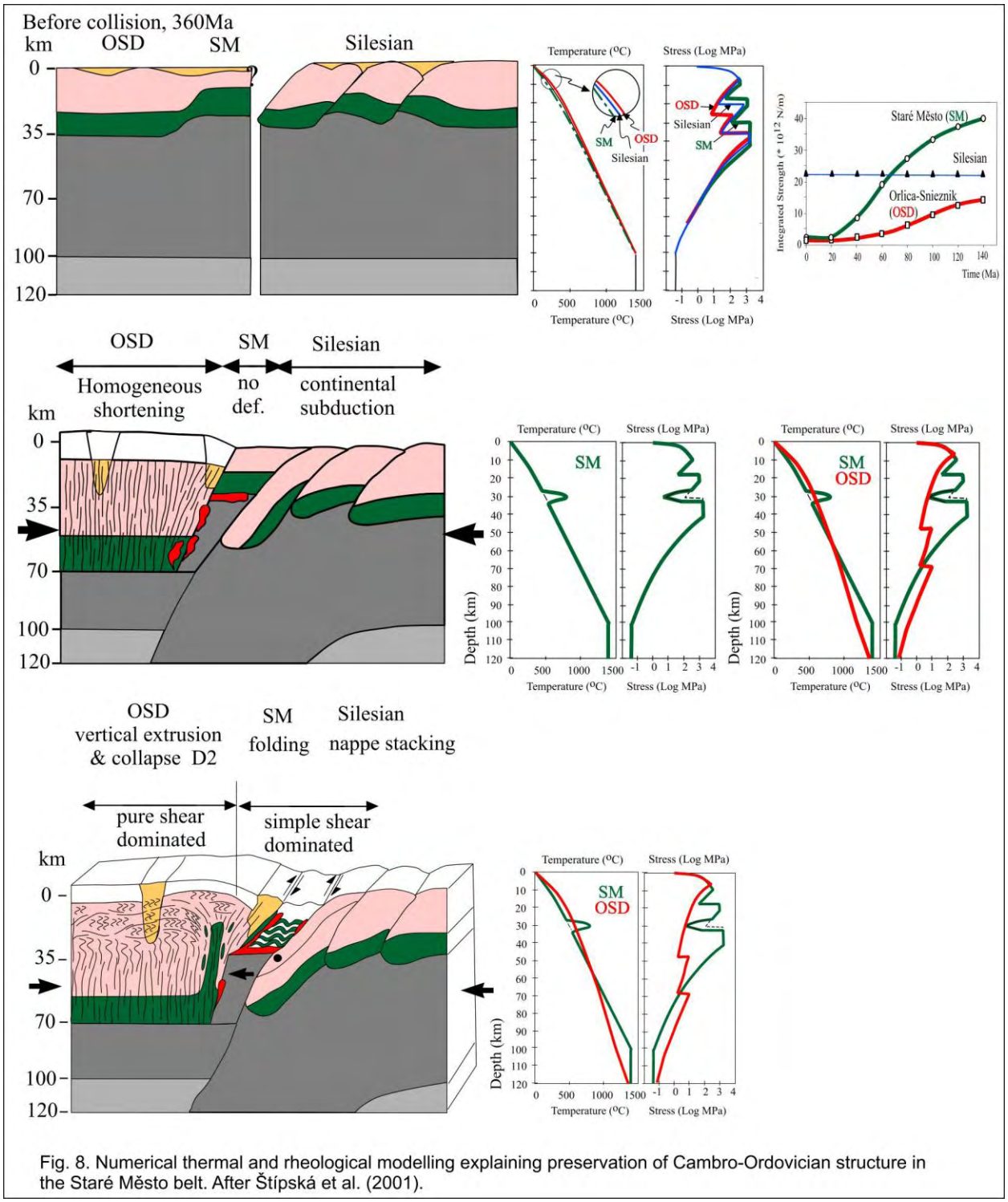

Fig. 8. Numerical thermal and rheological modelling explaining preservation of Cambro-Ordovician structure in the Staré Město belt. After Štípská et al. (2001).

Distinguishing metamorphism of similar degree but contrasting tectonic origin

The modeling study (Štípská *et al.*, 2001) demonstrated that the Ordovician metamorphic event is related to a large thermal anomaly associated with moderate continental thinning, while the

Carboniferous metamorphism is associated only with emplacement of the granodiorite sill into the same depth where the rift died more than 100 million year ago. The petrology study of Lexa *et al.* (2005) pointed to a problem of two metamorphic records of similar intensity but of very different age and tectonic setting (Fig. 7). The problem of polymetamorphism can be easily resolved if we study eclogitized granulites like in the Scandinavian Western gneiss Region or in the Alps. Here the issue is relatively straightforward, the anhydrous Proterozoic and Permian granulite assemblages are hydrated and eclogitized during Silurian and Eocene continental subduction, respectively. The Staré Město belt in the Bohemian Massif offers a challenging problem of distinguishing the Ordovician amphibolite and granulite facies metamorphism from Carboniferous metamorphism of similar metamorphic degree that is reworking in shear-zones the Ordovician gabbros.

The motivation of subsequent work was to understand how two metamorphic events of the same intensity but of different duration can be recognized. This question implies kinetic considerations and we have undertaken detailed microstructural analysis associated with petrological work. I have performed GIS measurements of a range of thin sections, which have been subsequently evaluated using the Poly Lx method (Lexa *et al.*, 2005) and we have demonstrated that the Ordovician microstructure reveals features of perfect textural maturity (like crystal size distribution typical for dominance of growth over nucleation, regular grain contact frequency distribution and absence of shape and boundary preferred orientations). All microstructural features are typical for solid state annealing leading to perfectly equilibrated granulite – amphibolites facies texture. In contrast, the Carboniferous texture was highly immature showing several high energy unstable features like nucleation dominated crystal size distribution, aggregate distribution and strong boundary and shape preferred orientation. These microstructural features are typical for solid state differentiation and development of high energy microstructure. We interpreted the marked difference in metamorphic textures as a result of different time scales of metamorphic equilibration under the same temperature. Consequently, we have introduced a term of textural attractor, which is linked with time scale of thermal event and associated textural maturation.

P−T evolution in Moldanubian-Lugian orogenic root, correlation with structures and models of burial and exhumation

Current concepts of burial and exhumation in deep orogenic roots

Current concepts of burial of continental crust involve 1) underthrusting of buoyant and radioactive crust underneath upper plate lithosphere and its attachment to bottom of hangingwall plate (Chemenda *et al.*, 2000; Gerya *et al.*, 2001; Gerya *et al.*, 2004; Franěk *et al.*, 2011a; Guy *et al.*, 2011; Lexa *et al.*, 2011), 2) influx of crust into deep apex of a continental wedge (Oncken, 1997; Chopin *et al.*, submitted-a; Chopin *et al.*, submitted-b) or 3) pure shear thickening of thermally weakened and moderately thinned crust (Thompson *et al.*, 2001; Collins, 2002; Schulmann *et al.*, 2002). The burial mechanisms differ in thermal regimes related to crustal thickening. The former case is characterized by LT and HP subduction type regime followed by more or less static heating of buried crust (Franěk *et al.*, 2011a; Franěk *et al.*, 2011b) leading to drastic rheological weakening of the lower crust and mantle lithosphere (Gerya *et al.*, 2001; Gerya *et al.*, 2004; Lexa *et al.*, 2011). The model of crustal influx into continental wedge is generally characterized by HP-LT metamorphic gradient which remains preserved even during subsequent exhumation associated with circulation effects along pro-side of the continental wedge (e.g. Allemand & Lardeaux, 1997). Hot and moderately thinned lithosphere represents a prerequisite of pure shear thickening, which may be associated with isothermal burial path (e.g. Schulmann *et al.*, 2002). In case of extremely hot thinned crust the pure shear thickening leads to burial associated with cooling (e.g. Thompson *et al.*, 2001). The metamorphic evolutions associated with burial of continental crust are so far poorly understood due to lack of systematic petrological studies. Rare studies carried out in the Bohemian Massif and the West Carpathians show that the understanding of syn-burial metamorphic path preserved in deep orogens can help to distinguish mechanisms of crustal thickening and thermal regimes of orogenic systems in general (Štípská & Powell, 2005a; Štípská *et al.*, 2006; Košuličová & Štípská, 2007; Jeřábek *et al.*, 2008; Skrzypek *et al.*, 2011b; Chopin *et al.*, submitted-a).

Current concepts of exhumation of deep-seated rocks in convergent orogens are generally based on the style of pressure–temperature–time (P–T–t) paths retrieved from high-pressure (HP) to ultra-high pressure (UHP) rocks (Duchène *et al.*, 1997). The way how the (U)HP rocks and mid-crustal rocks become exhumed depends on the mode of vertical elevation of rocks during

regional convergence or extension. The most commonly reported kinematic model in a convergent setting is displacement of deeply subducted rocks above lower pressure rocks along a crustal scale thrust (e.g. Chemenda *et al.*, 2000; Jolivet *et al.*, 2005). Crustal scale folding is another convergent kinematic model, which may explain exhumation (Burg *et al.*, 1998; Burg *et al.*, 2004). In the extensional setting, the emplacement of (U)HP rocks into middle to upper crustal levels may occur along a deep-seated extensional fault zone following a subduction event (e.g. Andersen & Fossen, 1993).

Advent of analogue and numerical orogenic scale models offered mechanical and dynamic explanation of burial and exhumation of rocks along convergent boundaries (Platt, 1987). A first group of models involves corner flow circulation of rocks above a downgoing plate in front of a rigid buttress (Platt, 1993; Allemand & Lardeaux, 1997; Gerya & Stöckhert, 2006), or above a gently inclined upper plate boundary (Beaumont *et al.*, 2001; Beaumont *et al.*, 2006). A second group of models is based on gravity driven exhumation and redistribution of deeply buried material. The most typical example are crustal scale "diapiric" domes (e.g. Gerya *et al.*, 2002; Gerya *et al.*, 2004), which may be enhanced by lateral forces leading to mixed diapiric and folding mechanisms (Burg *et al.*, 2004; Lexa *et al.*, 2011). Another example is horizontal spreading of a rebounded lower crust beneath a rigid orogenic lid (Koyi *et al.*, 1999) or a convective removal of a tectospheric root (England & Houseman, 1988; Andersen *et al.*, 1991). An alternative model has been developed for the large-scale horizontal movement of melt-bearing middle crust based on channel flow (Beaumont *et al.*, 2001; Beaumont *et al.*, 2006; Godin *et al.*, 2006b), and has been applied to explain the ductile extrusion of medium-pressure metamorphic rocks along the Himalayan front (Grujic *et al.*, 1996; Jamieson *et al.*, 2002; Godin *et al.*, 2006a; Jamieson *et al.*, 2006). Whereas the first group of models focuses on explaining vertical displacements of UHP and HP rocks, the second group of models emphasizes the importance of large-scale horizontal displacements in orogens.

Burial and peak metamorphic conditions of the lower orogenic crust

Metamorphic conditions estimated for the HP rocks in the Moldanubian and Lugian domain range from 750 °C to 1100 °C and from 18 kbar to 28 kbar (O'Brien & Rötzler, 2003and references therein). Some HP rocks studied in the Bohemian Massif reveal peak conditions around 700−850 °C and 18−22 kbar (Štípská & Powell, 2005a; Franěk *et al.*, 2011b; Chopin *et*

al., submitted-a; Štípská *et al.*, submitted), and some of them show features that point to preservation of structure, microstructure and/or mineral chemistry from the prograde path (Štípská & Powell, 2005a; Chopin *et al.*, submitted-a; Štípská *et al.*, submitted). The rocks with remnants of prograde features are especially eclogitic metagranites and eclogites from the Orlica-Śnieżnik dome in the Lugian domain (Chopin *et al.*, submitted-a; Štípská *et al.*, submitted). The eclogitic metagranites show increasing degree of deformation from augen to mylonitic orthogneiss types and preserve high grossular garnet and phengitic muscovite that point to a relatively cold prograde path from 600−650 °C and 12 kbar to 750 °C and 19 kbar (Chopin *et al.*, submitted-a). The eclogites enclosed in the metagranites contain garnet with prograde zoning, omphacite and phengitic muscovite that indicate similar metamorphic peak as the orthogneisses, around 700−750 °C and 22 kbar (Štípská *et al.*, submitted). All these petrological studies were performed in the Orlica-Śnieżnik dome, which was recently interpreted as a deep crustal wedge resulting from influx of Ordovician crust underneath Proterozoic autochthonous crust (Chopin *et al.*, submitted-a). The metamorphic evolutions studied by Chopin *et al*. (submitted-a) and Štípská *et al*. (submitted) show that high pressure-low temperature field gradient are typical features related to crustal influx thickening mode.

Detailed study of a Morb-type eclogite from the Moldanubian zone (Štípská & Powell, 2005a) shows unusually hot prograde conditions from 750 °C and 10 kbar to 750 °C and 18 kbar, based on preserved garnet chemical zoning and plagioclase and hornblende inclusions in garnet (Fig. 9). The hot prograde path is interpreted as a consequence of Devonian thermal rejuvenation of continental back arc domain that was responsible for softening of a future orogenic root domain.

Similar results have been obtained by Košuličová & Štípská (2007) for metapelites coming from thickened Devonian rift during Carboniferous collision. These two studies show importance of thermal weakening of continental crust for a thickening mode. In both cases it was an autochthonous Ordovician and Devonian crust of the upper plate which were thickened and buried to lower and middle crustal depths, respectively.

Last studies from the Bohemian Massif point out to the progressive and static heating of previously subducted continental crust in depths of 60–70 km (Franěk *et al.*, 2011a). The relics of high-pressure events is represented by kyanite and Ca-rich garnet enclosed in large feldspar blasts, which become discontinuously decomposed during onset of exhumation and partial

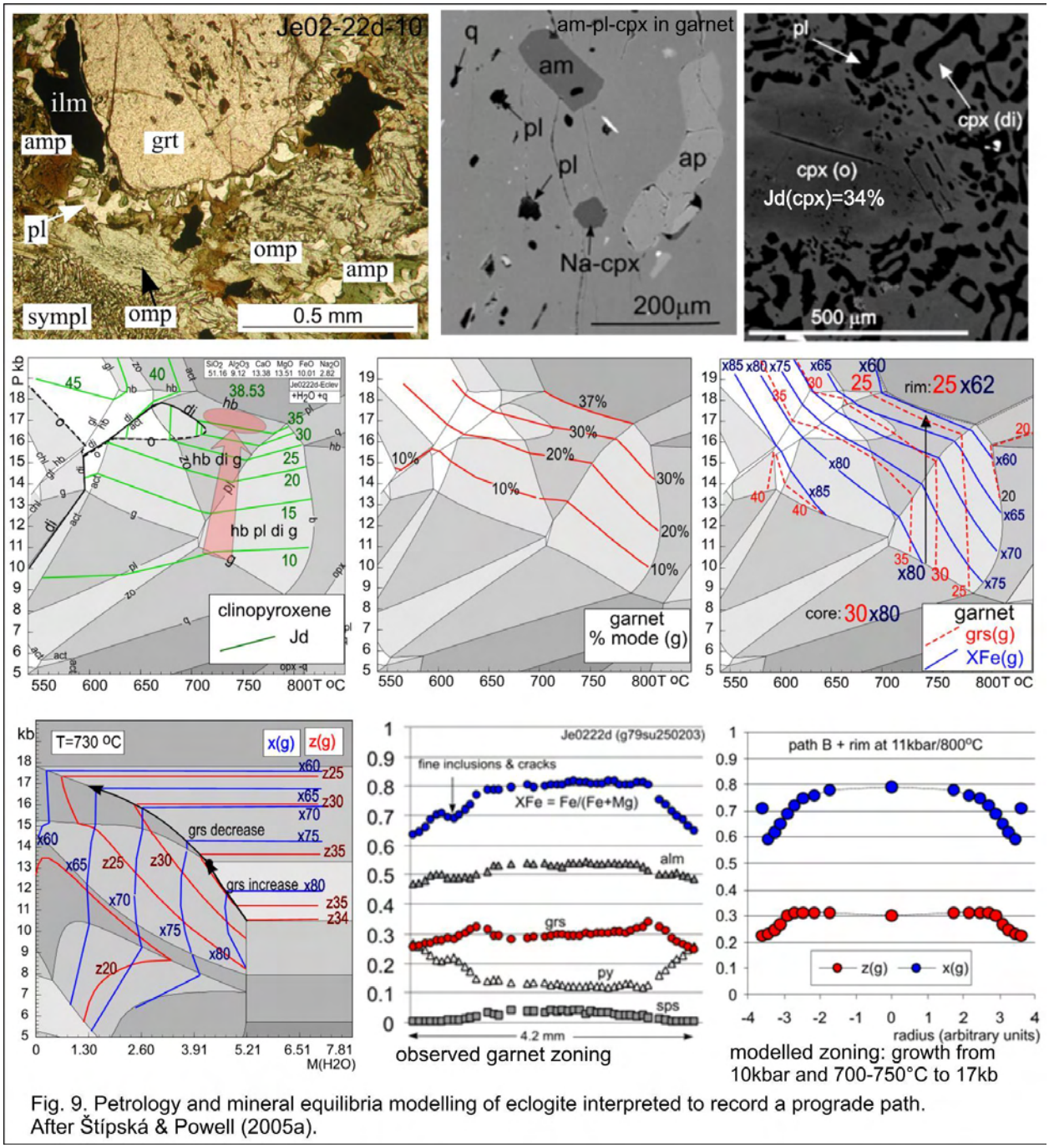

Fig. 9. Petrology and mineral equilibria modelling of eclogite interpreted to record a prograde path. After Štípská & Powell (2005a).

melting. The heating is attributed to decay of radiogenic elements leading to partial melting of felsic crust and underlying mantle (Lexa *et al.*, 2011). This petrological study indicate particular thermal and rheological evolution of orogenic roots resulting from thermal incubation of radiogenic crust tectonically underplated underneath thickened continents.

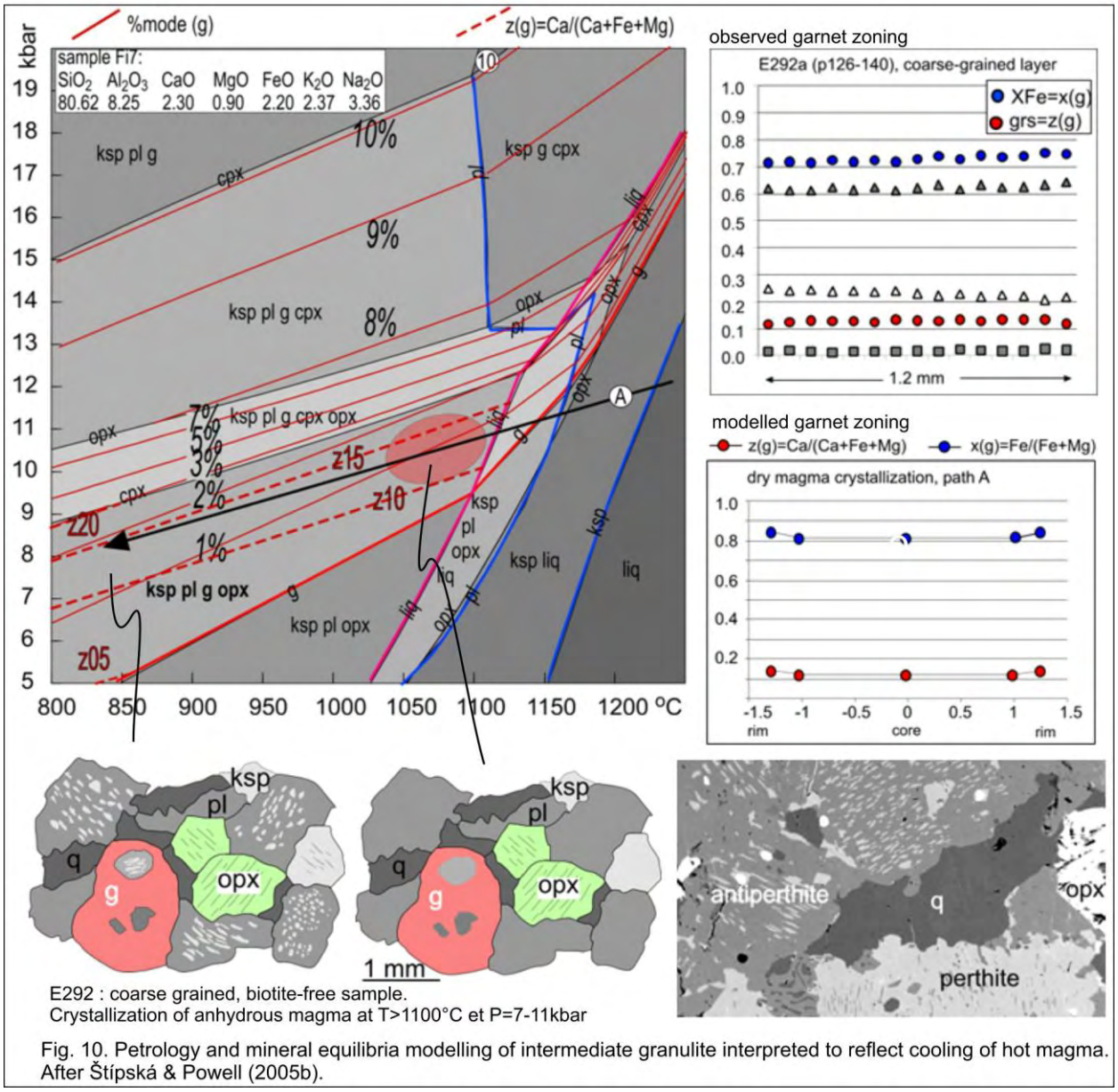

Fig. 10. Petrology and mineral equilibria modelling of intermediate granulite interpreted to reflect cooling of hot magma. After Štípská & Powell (2005b).

Studies of high-pressure granulites (Štípská & Powell, 2005b; Racek *et al.*, 2008) pointed to a problem of interpretation of equilibrium of metamorphic assemblages in high-grade rocks (Figs 10 & 11). It is usually the classic combination of high-grossular garnet and high-temperature ternary feldspar that led to estimation of metamorphic conditions to >1000 °C and 18−28 kbar. Our microstructural analysis has shown that mafic granulites contain several generations of garnet, that ternary feldspar is linked probably to a magmatic event and that ternary feldspar and high-grossular garnet belong to two distinct episodes, and cannot be combined to infer metamorphic conditions.

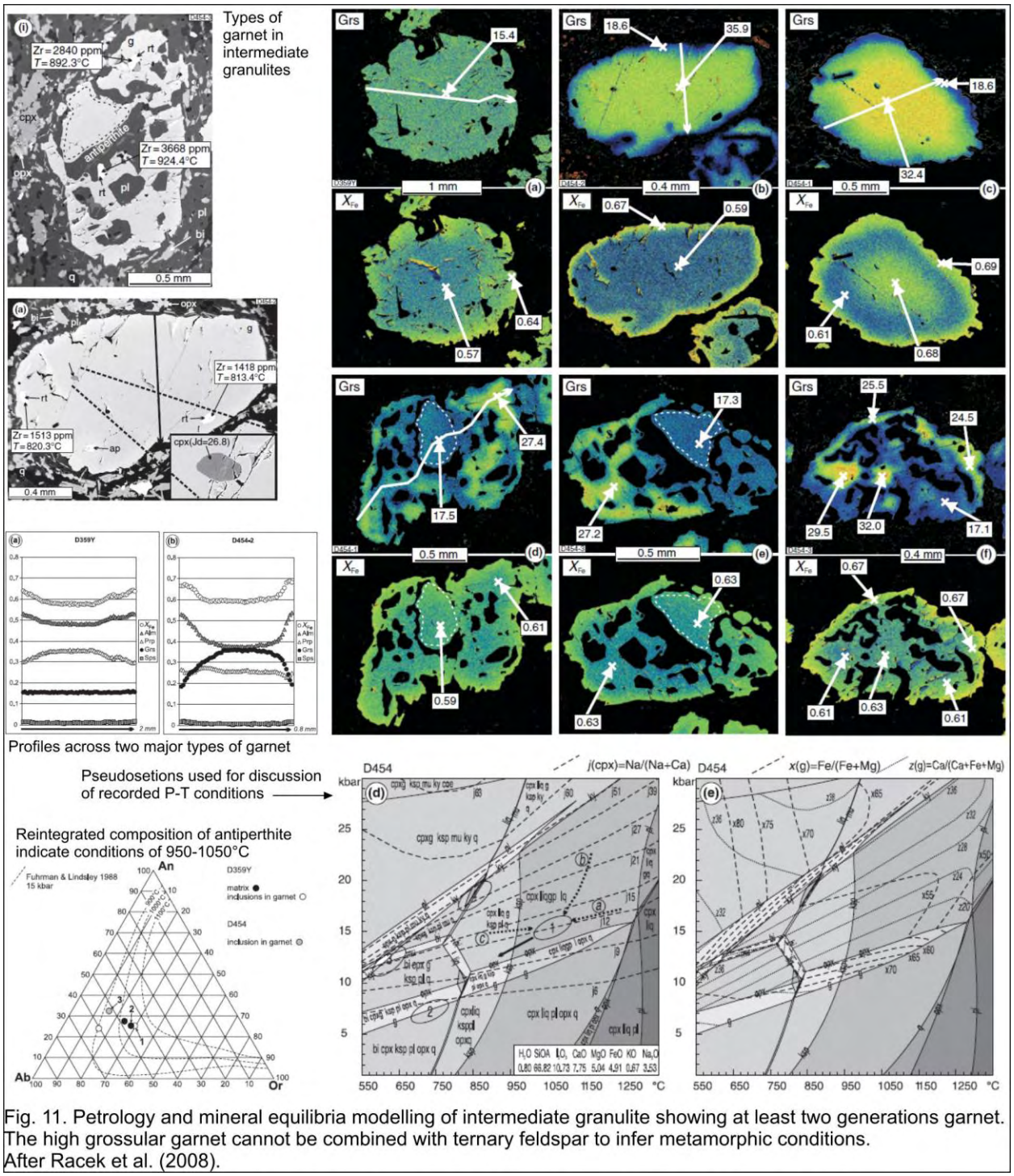

Fig. 11. Petrology and mineral equilibria modelling of intermediate granulite showing at least two generations garnet. The high grossular garnet cannot be combined with ternary feldspar to infer metamorphic conditions. After Racek et al. (2008).

Metamorphic record of burial and subsequent exhumation by subvertical crustal-scale folding

It was shown that high-pressure conditions are connected with early shallow-dipping fabric in the deep root (Chopin *et al.*, submitted-a; Štípská *et al.*, submitted), and that high-pressure rocks

are exhumed during vertical crustal-scale folding that leads to extrusion of high-pressure rocks along vertical channels (Štípská *et al.*, 2004; Racek *et al.*, 2006; Franěk *et al.*, 2011b; Skrzypek *et al.*, 2011b; Štípská *et al.*, submitted). This model of crustal-scale folding and vertical extrusion is proposed as a possible major exhumation mechanism of exhumation of high-pressure rocks in hot orogens (Schulmann *et al.*, 2005; Schulmann *et al.*, 2008a; Schulmann *et al.*, 2009; Chopin *et al.*, submitted-b).

The first area where this process was identified is the belt of eclogite facies granulites composed of omphacite-plagioclase-garnet-quartz-rutile, and located in the Rychleby Mts in the Lugian domain, eastern Czech Republic (Fig. 12) (Štípská *et al.*, 2004). The exhumation there was a localised process initiated by buckling of crustal layers in a thickened orogenic root. Folding and post-buckle flattening was followed by the main stage of exhumation that is characterized by vertical ductile extrusion. This process is documented by structural data, and the vertical ascent of rocks from a depth of ca. 70 to ca. 35 km is documented by metamorphic petrology. SHRIMP $^{206}Pb/^{238}U$ and $^{207}Pb/^{206}Pb$ evaporation zircon ages of 342±5 and 341.4±0.7 Ma date peak metamorphic conditions. The next stage of exhumation was associated with sideways flat thrusting associated with lateral viscous spreading of granulites and surrounding rocks over indenting adjacent continental crust at a depth of ca. 35−30 km. This stage was associated with syntectonic intrusion of a granodiorite sill at 345−339 Ma, emplaced at a crustal depth of ca. 25 km. The time required for cooling of the sill as well as for heating of the country rocks brackets this event to a maximum of 250 000 years. Therefore, similar ages of crystallization for the granodiorite magma and the peak of eclogite facies metamorphism of the granulite suggest a very short period of exhumation, limited by the analytical errors of the dating methods. Our calculations suggest that the initial exhumation rate during vertical extrusion was 3−15 mm/yr, followed by an exhumation rate of 24–40 mm/yr during further uplift along a magma-lubricated shear zone. The extrusion stage of exhumation was associated with a high cooling rate, which decreased during the stage of lateral spreading.

In the light of these new interpretations, we reinvestigated also the classic area in Lower Austria, where originated the idea of the high-grade Gföhl nappe, rooted some 150–300 km to the west, and thrust south-east-wards over hundreds of kilometres over middle-crustal units (e.g. Tollmann, 1982; Franke, 1989a; Franke, 1989b; Matte, 1991). This model is largely based on observations from the eastern margin of the Moldanubian, in Lower Austria (including the

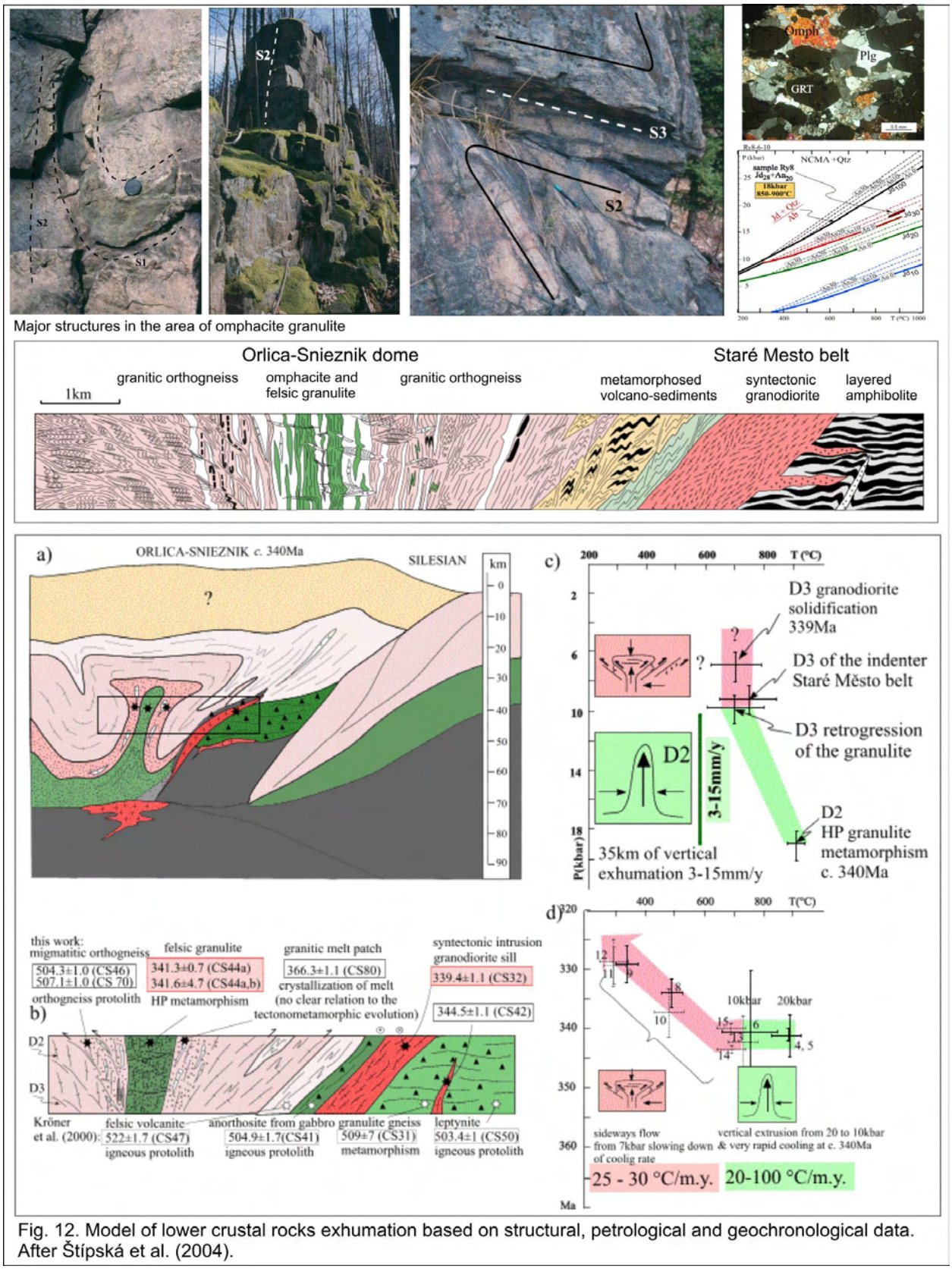

Fig. 12. Model of lower crustal rocks exhumation based on structural, petrological and geochronological data. After Štípská et al. (2004).

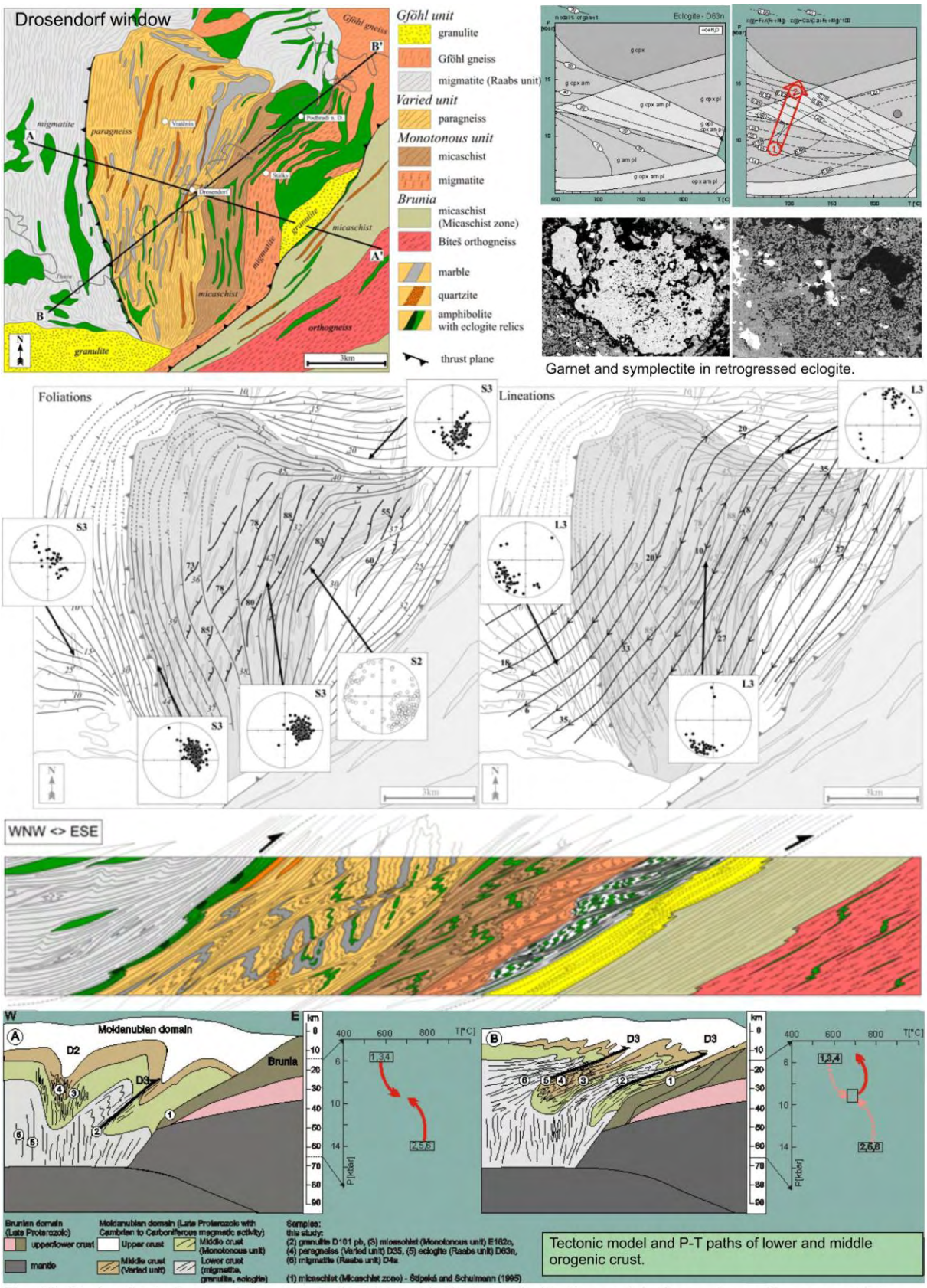

Fig. 13. Study of petrology and structure in the Drosendorf window led to the model of extrusions of lower crust into mid-crustal depth, followed by shallow-dipping thrusting over indenting Brunia microcontinent. After Racek et al. 2006.

“Drosendorf window”), where the “intra-Moldanubian” character of high-grade rocks thrust over the medium-grade metamorphic units was originally recognized (Suess, 1918). However, despite disagreements concerning the vergency and the age of the thrusting, such a distant origin of the nappes was not suggested, or was even explicitly rejected (Fuchs & Matura, 1976; Thiele, 1984). With respect to recent investigations, the opinion of Fuchs that the nappes are derived from the eastern Moldanubian zone and therefore have roots “on place”, without large thrust distances, is particularly important.

In the area of the Drosendorf window, a continuous, but attenuated section through orogenic lower and middle crust overthrust by a second lower-crustal complex was distinguished (Fig. 13) (Racek *et al.*, 2006). This indicates the existence of two lower-crustal "autochthonous" extrusions into middle crust that is not compatible with the model of "allochthonous" lower crustal klippen remaining after flat thrusting of the Gföhl nappe over large distances. The base of the lower crust is represented by a granulite body exhumed from ca. 15 kbar and 800 °C. A hangingwall complex of layered amphibolites gradually passes into amphibolite bearing paragneisses (the Monotonous unit) and micaschists intercalated with marbles at the top (the Varied unit). The metamorphic grade and anatexis decreases upwards and the micaschists preserve a prograde path to ca. 8 kbar and 700 °C. This sequence is overthrust by a second lower crustal strongly migmatitized Raabs complex marked by an eclogite-bearing belt at the base. The garnet zoning of eclogite indicates burial from 10 kbar to minimum 15 kbar. In all units, relics of a steep metamorphic fabric were identified, reworked by folding and a moderately west-dipping foliation. The conditions of 7–10 kbar and ca. 750 °C for the flat foliation were obtained in all units indicating that exhumation of the lower crust into a middle crustal level occurred earlier, probably during the development of steep fabrics. The intense shallow-dipping fabric is interpreted as a result of thrusting of the whole assembly over the middle crustal Brunian indentor. The P−T data and P−T paths of rocks from the bottom to the top of the structure are consistent with the "extrusion" exhumational model proposed by Štípská *et al*. (2004).

In the paper by Schulmann *et al*. (2005), key lithological units of the high-grade eastern margin of the Bohemian Massif were dated using the U-Pb and Pb-Pb methods on zircons in order to establish a chronological framework for the geodynamic evolution of the Variscan orogenic root. The protolith ages for metagranitoids, orthogneisses and granulites of thickened lower and middle crust reveal the existence of magmatic activity that occurred over a 100 million year time

interval from Cambro-Ordovician to early Devonian times, probably related to discontinuous intracontinental rifting of Neoproterozoic crust. Our geochronological data suggest that the eastern part of the orogenic root represents thermally softened and rifted Neoproterozoic crust, preserved farther to the east as the Brunia microcontinent. Zircon ages for felsic granulites, high-grade gneisses of the lower crust and of a syn-convergence granodioritic intrusion in the upper crust indicate that thickening and exhumation of the crust occurred during a narrow time interval between 370 and 340 Ma. Exhumation of the lower crust to mid-crustal levels was a localized process that occurred at ca. 340 Ma and was associated with crustal-scale folding in the internal part of the root as well as orogenic channel flow along the eastern collisional margin. Both types of exhumation mechanisms were driven by deep-level wedging (indentation) of the easterly Brunia continent, followed by deposition of heavy minerals and pebbles derived from high-pressure rocks in the adjacent foreland basin. Final orogenic development was characterized by NE-SW dextral transpressive shearing parallel to the Brunia margin as well as dextral transtension associated with activity along the Elbe lithospheric fault. These processes affected the marginal parts of the orogenic root and were accompanied by 330 to 325 Ma old syntectonic granitoid intrusions along reactivated lithotectonic boundaries. Rotation of the assembled orogenic belt, accompanied by lithospheric faulting driven by westerly subduction roll-back, may be the most plausible model to explain late deformation of the orogenic root.

Another area where the succession of exhumation structures and metamorphic conditions is in agreement with the model of Štípská *et al*. (2004) is the Blanský les granulite massif in the central part of the Bohemian Massif (Franěk *et al.*, 2006). In the paper by Franěk *et al.* (2011b), we studied in detail the question of origin and evolution of a granulitic microstructure typically developed in felsic granulites of the European Variscan belt. It shows that the precursor of the Variscan felsic granulites was a high-pressure alkali feldspar-rich coarse-grained layered orthogneiss. Its S1 subhorizontal layering is defined by the alignment of alkali feldspar porphyroclasts alternating with monomineralic bands of quartz and bands rich in plagioclase and garnet. The alkali feldspar porphyroclasts contain inclusions of quartz, garnet, kyanite, biotite and rutile, reflecting peak P–T conditions of 16–18 kbar and 850 °C during S1 formation. Superimposed steep folds and steep cleavage, S2, are associated with recrystallization of alkali feldspar, plagioclase and quartz, and garnet chemistry modifications that correspond to 9–10 kbar and 800 °C. During exhumation, involving 8 kbar decompression and cooling, the perthitic alkali

feldspar underwent an unusual process of heterogeneous decomposition along irregular reaction fronts forming a fine-grained matrix composed of plagioclase and K-feldspar grains. Regular grain distributions in the matrix, nucleation dominated crystal size distribution and preservation of lattice orientation of the parental perthite crystals are all explained by a discontinuous precipitation process. This heterogeneous decomposition of alkali feldspar solid solution is controlled by chemically and strain induced grain-boundary migration. During exhumation and decompression, the fine-grained matrix underwent viscous deformation, forming the typical microstructure of the Variscan granulites. Random phase distributions, minor coarsening and feldspar textures are interpreted as a result of strain softening due to diffusion creep accommodated grain-boundary sliding. Subordinate large quartz ribbons were rheologically stronger than the feldspar-dominated matrix due to the activity of different deformational mechanisms. Finally, in mid-crustal levels, the subvertical structure was overprinted by a perpendicular fabric associated with the growth of sillimanite, heterogeneous hydration and local partial melting, development of aggregate phase distributions and significant coarsening. This evolution is accompanied with the development of a strong lattice preferred orientation of quartz, K-feldspar and plagioclase, reflecting a switch to dislocation creep mechanism and a general hardening of the granulites under amphibolite facies conditions.

The major cause for the exhumation of the lower orogenic crust in the vertical channels are considered lateral compressive forces (Štípská *et al.*, 2004; Schulmann *et al.*, 2005; Racek *et al.*, 2006; Schulmann *et al.*, 2008a; Franěk *et al.*, 2011b), but because the lower orogenic crust in the Bohemian Massif is formed essentially by felsic rocks, we examined also a contribution of the gravitational forces in the paper by Lexa *et al.* (2011) (Fig. 14). The structural pattern of the Moldanubian domain may be described as the domes cored by felsic granulites of Ordovician protolith age that are separated from synclines of mid-crustal Neoproterozoic and Palaeozoic metasedimentary rocks by a late Ordovician to Silurian metabasic unit. Reflection and refraction seismic sections combined with gravity inversion modelling suggest the presence of a low density layer at the bottom of the crust (interpreted as felsic granulite) overlain by a denser layer (interpreted as amphibolite) with layers of intermediate density at the top (interpreted as metasedimentary rocks). It is proposed that the granulite domes surrounded by middle crustal rocks reflect transposed horizontal layering originally similar to that preserved in the deep crust and imaged by the geophysical surveys. This geological and geophysical structure is considered

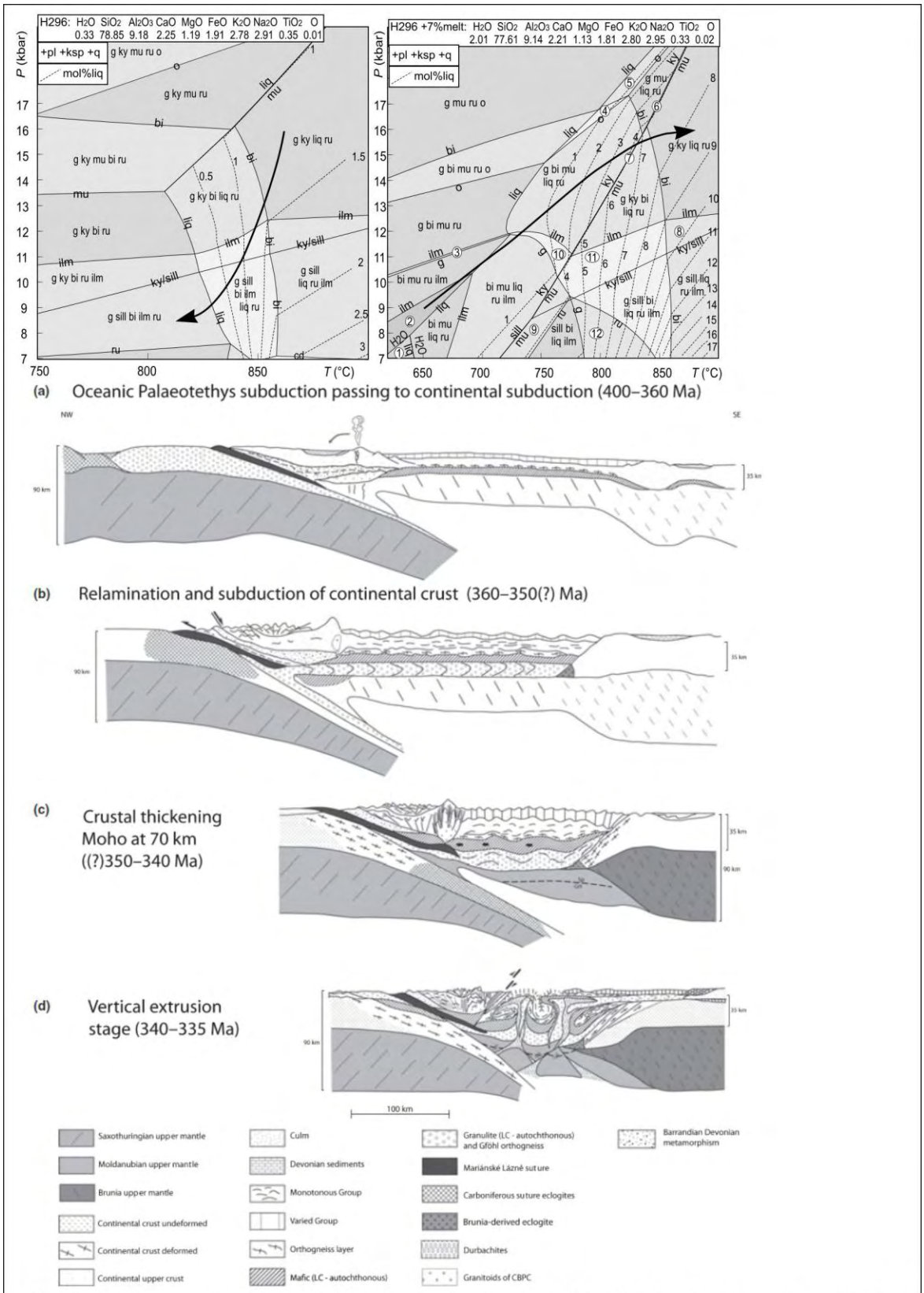

Fig. 14. Pseudosection modelling predicts that granulites lost around 8 mol% of melt during metamorphism. The role of their original radioactive heat production, followed by melt loss and therefore removal of radioactive heat production on the role of gravity in the exhulmation of granulties is discussed. After Lexa et al. (2011).

to be a result of Visean gravity redistribution initiated by radioactive heating of felsic crust tectonically emplaced at the bottom of the Palaeozoic orogenic root. The radioactive layer with heat production of 4 $\mu W/m^3$ corresponds geochemically and isotopically to Ordovician felsic metaigneous rocks of the Saxothuringian domain that have been emplaced at Moho depth under the thickened crust during the late Devonian–early Carboniferous continental subduction. Part of the continental crust continued to be subducted and produced fluids ⁄ low-volume melts, which directly contaminated and enriched the local lithospheric mantle by lithophile elements, most notably Cs, Rb, Li, Pb, U, Th and K. Thermal incubation of 10–15 Ma was sufficient to heat and convert the underplated felsic layer into granulites via dehydration melting and melt segregation. The process of melt loss was responsible for the removal of radioactive elements and for switching off the heat at the beginning of the exhumation process. At the same time, the metasomatized underlying mantle was heated producing characteristic ultrapotassic magmas. Gravitational instability was then induced by the density contrast between the light granulites and the overlaying denser mafic lower crustal layer and a viscosity drop related to thermal weakening and partial melting of the latter.

Early shallow-dipping burial fabrics in the lower orogenic crust

In several above-mentioned studies, there were indications that the structure of the lower orogenic crust was originally shallow dipping. These indications include the isoclinal upright rootless folds (Štípská *et al.*, 2004), shallow-dipping foliations in the area studied by Racek *et al.* (2006) or relicts of subhorizontal fabrics and upright folds in the Blanský Les massif (Franěk *et al.*, 2011b). These early shallow-dipping fabrics are largely obliterated in the Moldanubian domain, but are well preserved in some parts of the northern orogenic root domain, in the Orlica-Śnieżnik dome (Chopin *et al.*, submitted-a; Chopin *et al.*, submitted-b; Štípská *et al.*, submitted) that allows examining the mechanisms of burial and formation of the orogenic root (Figs 15−18).

The structural pattern around the eclogite belt and in the surrounding granitic orthogneiss in the Miedzygorie area (the Orlica-Śnieżnik dome), is characterized by well preserved shallow-dipping S1 foliation that is folded by upright folds (Štípská *et al.*, submitted) (Fig. 15). The rare S1 fabric in the eclogite is defined by alternation of garnet-rich (grs = 22−29 mol.%) and omphacite-rich (jd = 33−36 mol.%) layers with oriented muscovite (Si = 3.26−3.31 p.f.u.) and accessory kyanite, epidote, rutile and quartz. The assemblage and garnet zoning (grs_{core} = 29,

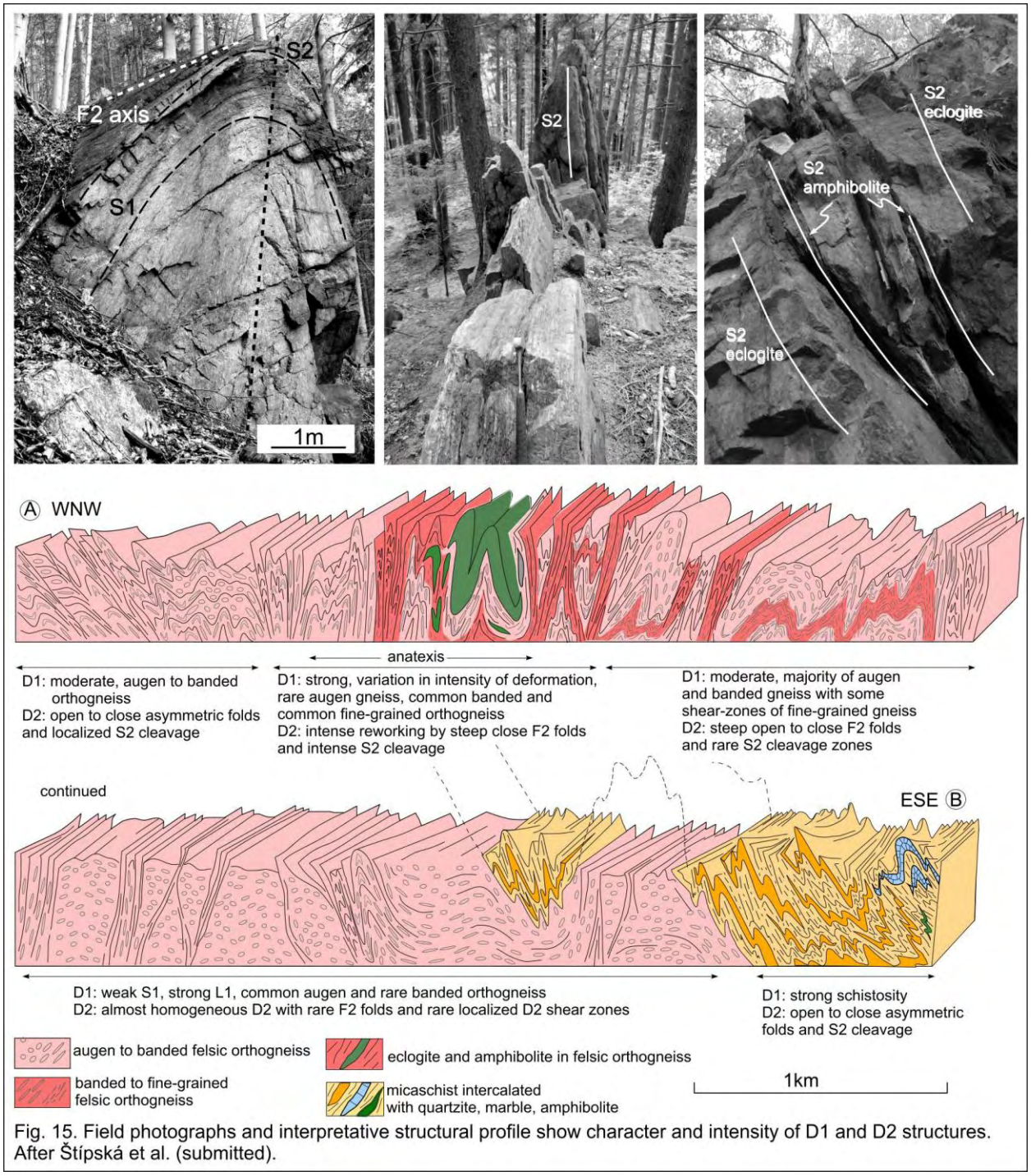

Fig. 15. Field photographs and interpretative structural profile show character and intensity of D1 and D2 structures. After Štípská et al. (submitted).

grs_{rim} = 22 mol.%) are compatible with a prograde P–T path from ~20 kbar and ~640 °C to ~22 kbar and ~720 °C achieved during the S1 fabric (Štípská *et al.*, submitted). The study of Chopin *et al.* (submitted-a) shows, that finite strain gradient in the S1 fabric in the granitic orthogneisses allows dividing into three distinct microstructural groups: type I - augen, type II - banded and type III- mylonitic orthogneiss, each representing an evolutionary stage of progressively

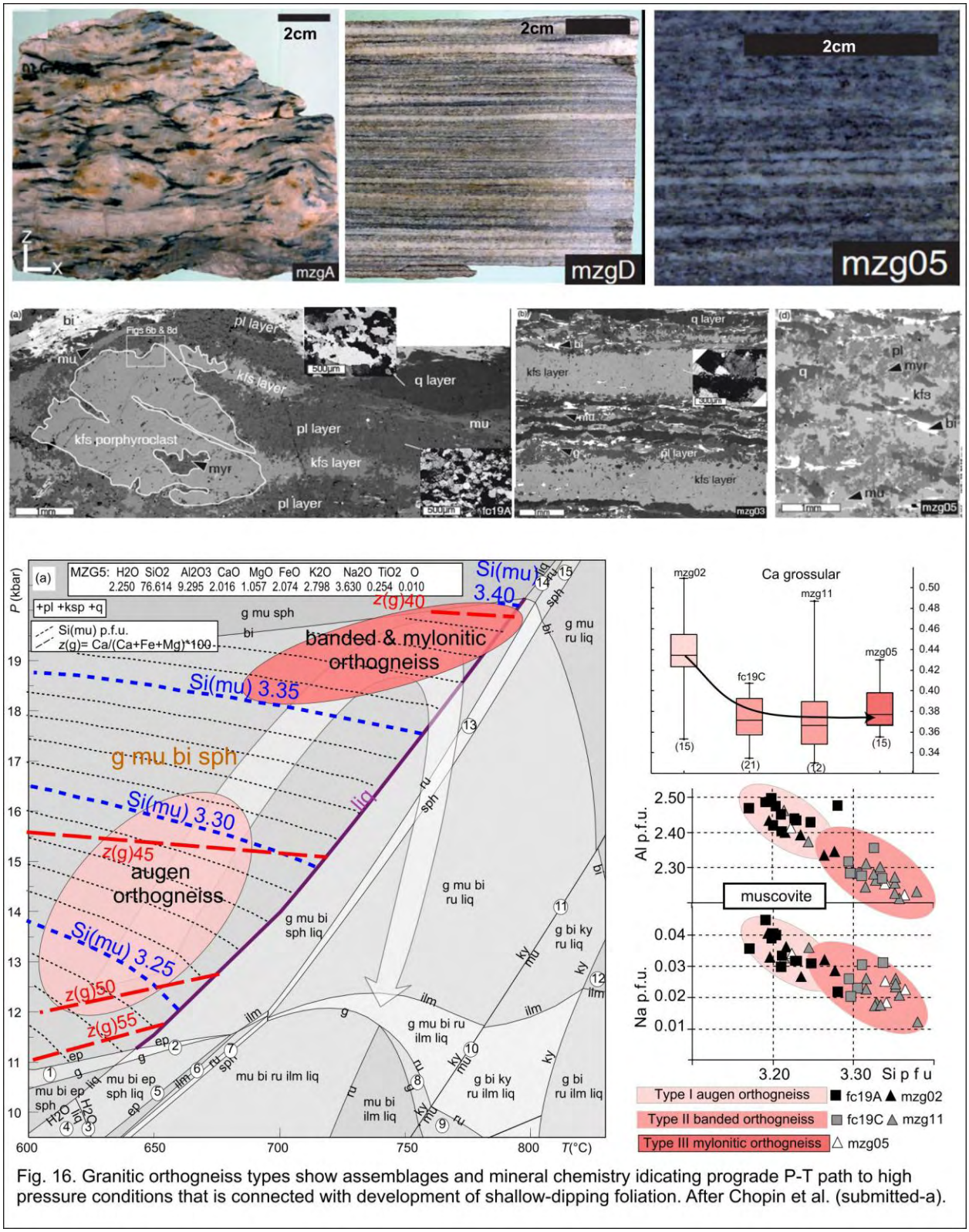

Fig. 16. Granitic orthogneiss types show assemblages and mineral chemistry idicating prograde P-T path to high pressure conditions that is connected with development of shallow-dipping foliation. After Chopin et al. (submitted-a).

deformed metagranite (Fig. 16). Type I orthogneiss is made of partially recrystallised K-feldspar phenocrysts, fully recrystallised quartz aggregates and interconnected monomineral layers of

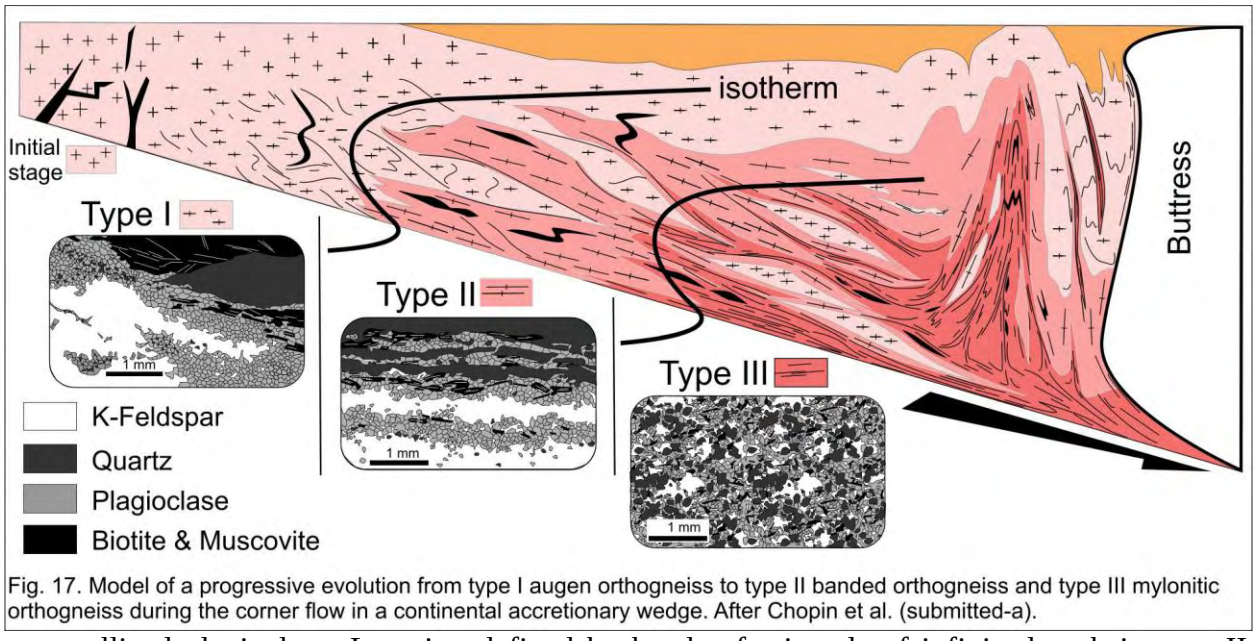

Fig. 17. Model of a progressive evolution from type I augen orthogneiss to type II banded orthogneiss and type III mylonitic orthogneiss during the corner flow in a continental accretionary wedge. After Chopin et al. (submitted-a).

recrystallized plagioclase. Layering defined by bands of minerals of infinite length in type II orthogneiss is marked by increasing proportion of interstitial phases and deformation of wide recrystallized myrmekite fronts affecting both plagioclase- and K-feldspar-rich layers. Type III orthogneiss reveals relics of quartz and K-feldspar ribbons preserved in fine grained polymineralic matrix. All the types reveal the same assemblage (q+pl+kfs+mu+bi+g+sph±ilm), but show variation in composition of muscovite (from Si p.f.u.=3.16−3.28 to Si p.f.u.=3.22−3.38) and garnet (from grs=0.42−0.46 to grs=0.35−0.40) from type I to type III. The assemblage and mineral composition variations are consistent in a pseudosection with a P−T path ranging from 12 kbar and 650 °C (type I orthogneiss) to 19 kbar and 750 °C (types II and III orthogneisses). The deformation types thus do not represent evolutionary stages of highly partitioned deformation at constant P−T conditions, but reflect progressive burial of continental crust (Figs 16 & 17). The microstructure of type I and type II orthogneisses result from a dislocation creep of quartz and K-feldspar while grain boundary sliding dominated diffusion creep regime is characteristic for the type III orthogneiss. The strain weakening related to transition from type I to type II microstructure is enhanced by recrystallization of wide myrmekite fronts, and further weakening and strain localisation in type III orthogneiss occur via incipient partial melting.

Regarding the microstructural and petrological evolution of the studied sequence, we propose that the orthogneiss records continuous progressive and prograde deformation along a cold metamorphic gradient (~10°C/km). The MP augen orthogneiss thus represents structural

and metamorphic relicts that were passively buried along shear-zones formed by banded and mylonitic orthogneiss to 22 kbar and 750 °C. This event is related to burial of continental felsic crust during continental subduction and influx of rocks into apex of a orogenic accretionary wedge, before fast extrusion close to the rigid buttress indentor (Chopin *et al.*, submitted-a; Chopin *et al.*, submitted-b; Štípská *et al.*, submitted) (Figs 17 & 18).

Correlation of the metamorphic record of the lower and middle orogenic crust

Complementary metamorphic and structural studies of lower- and middle crustal rocks (Racek *et al.*, 2006; Skrzypek *et al.*, 2011b; Štípská *et al.*, submitted) permitted discussion of coupled and uncoupled mechanisms of burial and exhumation in the two crustal levels.

In the early work by Racek *et al.* (2006) it has been shown that the prograde paths and peak P−T of the lower and the middle crustal rocks are not shared. In lower- and middle crustal rocks are preserved relics of a steep metamorphic fabric, reworked by folding and a moderately west-dipping foliation. The conditions of 7–10 kbar and ca. 750 °C for the shallow-dipping foliation were obtained in all units indicating that exhumation of the lower crust into a middle crustal level occurred earlier, probably during the development of steep fabrics. The intense shallow-dipping fabric is interpreted as a result of thrusting of the whole assembly over the middle crustal Brunian indentor. The P−T data and P−T paths of rocks from the bottom to the top of the structure show, that both crustal levels underwent horizontal shortening, but at various depth. During the vertical shortening the portions of the lower crust were exhumed in the middle crust and there both middle and lower crustal portions were reworked by shallow dipping fabric in the same middle crustal depth.

In the eastern part of the Orlica-Śnieżnik dome (NE Bohemian Massif), alternating belts of orthogneiss with high-pressure rocks and mid-crustal metasedimentary–metavolcanic rocks commonly display a dominant subvertical fabric deformed into a subhorizontal foliation (Skrzypek *et al.*, 2011a; Skrzypek *et al.*, 2011b). The first macroscopic foliation is subvertical, strikes NE– SW and is heterogeneously folded by open to isoclinal folds with subhorizontal axial planes parallel to the heterogeneously developed flat-lying foliation. The metamorphic evolution of the mid-crustal metasedimentary rocks involved successive crystallization of chlorite–muscovite–ilmenite–plagioclase–garnet, followed by staurolite-bearing and then kyanite-bearing assemblages in the subvertical fabric. This was followed by garnet retrogression, with

syntectonic crystallization of sillimanite and andalusite parallel to the shallow-dipping foliation. Elsewhere, andalusite and cordierite statically overgrew the flat-lying fabric. With reference to a P–T pseudosection for a representative sample, the prograde succession of mineral assemblages and the garnet zoning pattern with decreasing grossular, spessartine and XFe are compatible with a P–T path from 3.5–5 kbar and 490–520 °C to peak conditions of 6–7 kbar and 630 °C, suggesting burial from 12 to 25 km with increasing temperature. Using the same pseudosection, the retrograde succession of minerals shows decompression to sillimanite stability at 4 kbar and 630 °C and to andalusite–cordierite stability at 2–3 kbar indicating exhumation from 25 km to around 9–12 km. Subsequent exhumation to 6 km occurred without apparent formation of a deformation fabric. The structure and petrology together with the spatial distribution of the metasedimentary–metavolcanic rocks, and gneissic and high-pressure belts are compatible with a model of burial of limited parts of the upper and middle crust in narrow cusp-like synclines. This burial is synchronous with the exhumation of orogenic lower crust represented by the gneissic and high-pressure rocks in lobe-shaped and volumetrically more important anticlines. Converging P–T–D paths for the metasedimentary rocks and the adjacent high-pressure rocks are due to vertical exchanges between cold and hot vertically moving masses. Finally, the retrograde shallow-dipping fabric affects both the metasedimentary–metavolcanic rocks and the gneissic and high-pressure rocks, and indicates that the 15 km exhumation was mostly accommodated by heterogeneous ductile thinning associated with unroofing of a buoyant crustal root.

In the central part of the Orlica-Śnieżnik dome (Bohemian Massif), eclogite, felsic orthogneiss and garnet-staurolite metapelite with intercalations of amphibolite, quartzite and marble occur in a 5 km long profile (Štípská *et al.*, submitted). A structural study combined with petrographic observations and mineral equilibria modelling is used to understand the mechanism of such close juxtaposition of high pressure and medium pressure rocks in the crust (Figs 15 & 18). The structural succession in all lithologies shows an early shallow-dipping fabric S1 that is folded by upright folds and overprinted by a heterogeneously developed subvertical foliation S2. Late recumbent folds associated with a weak shallow-dipping axial plane cleavage S3 occur locally. The S1 fabric in the eclogite is defined by alternation of garnet-rich (grs = 22−29 mol.%) and omphacite-rich (jd = 33−36 mol.%) layers with oriented muscovite (Si = 3.26−3.31 p.f.u.) and accessory kyanite, epidote, rutile and quartz. The assemblage and garnet zoning (grs_{core} = 29, grs_{rim} = 22 mol.%) are compatible with a prograde P–T path from ~20 kbar and ~640 °C to ~22

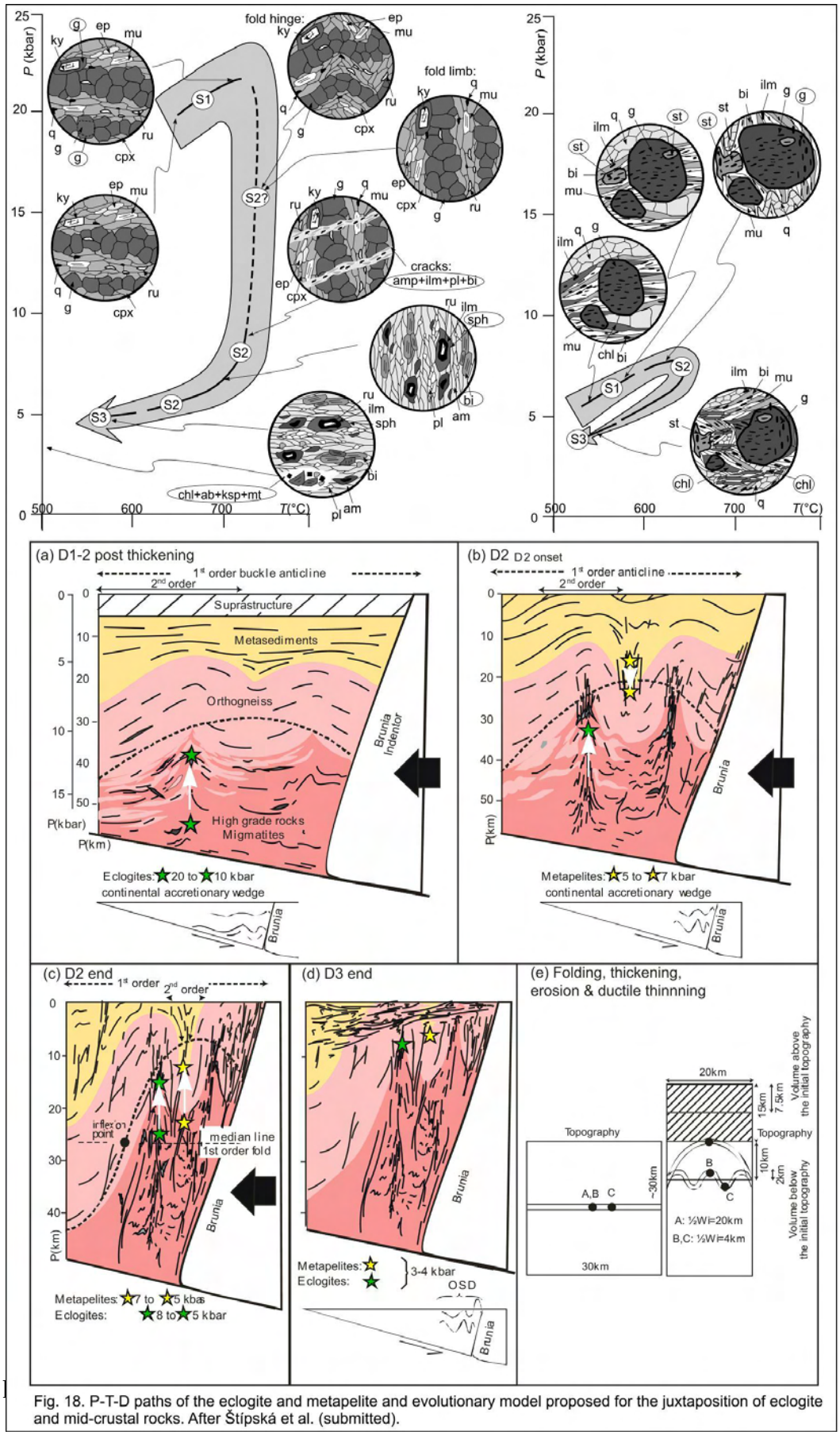

Fig. 18. P-T-D paths of the eclogite and metapelite and evolutionary model proposed for the juxtaposition of eclogite and mid-crustal rocks. After Štípská et al. (submitted).

is formed by amphibole, plagioclase, biotite and relict rutile surrounded by ilmenite and sphene that is compatible with decompression and cooling from ~9 kbar and ~730 °C to 5−6 kbar and 600−650 °C. The S3 fabric contains amphibole, plagioclase, biotite, ilmenite surrounded by sphene, and domains with albite, chlorite, K-feldspar and magnetite indicating cooling to greenschist facies conditions. The metapelites are composed of garnet, staurolite, muscovite, biotite, quartz, ilmenite and chlorite. Chemical zoning of garnet core that contains straight ilmenite and staurolite inclusion trails oriented perpendicular to the external S2 fabric indicates prograde growth from ~5 kbar and ~520 °C to ~7 kbar and ~610 °C during or after the formation of the S1 fabric. Inclusion trails parallel with the S2 fabric at garnet and staurolite rims are interpreted as continuation of the prograde path to ~7.5 and ~630 °C in the S2 fabric. Matrix chlorite parallel to the S2 foliation indicates that the subvertical fabric was still active below 550 °C. The prograde evolution of the eclogite and metapelite during/after the development of the early shallow-dipping fabric is interpreted as simultaneous burial of the lower and upper-middle orogenic crust along shallow-dipping surfaces within a continental accretionary wedge. Axial planar fabrics developed during upright folding and are associated with retrogression under amphibolite-facies conditions in the eclogite, and firstly with prograde and later with retrograde evolution in the metapelites. The shared part of the eclogite and metapelite P−T paths was achieved in the subvertical fabric and points to their common exhumation during fold amplification, which is only possible when erosion, ductile thinning or tectonic unroofing efficiently reduce the upper part of the thickened crust.

Significance of late shallow-dipping fabrics in the orogenic root zone

All the studied areas of the internal orogenic zone are affected to a different degree by late shallow-dipping fabrics (Figs 19−25). Their intensity varies from rare open folds with subhorizontal axial planes (Štípská *et al.*, 2004; Štípská *et al.*, submitted) through shallow-dipping cleavage heterogeneously reworking the earlier steep fabrics (Štípská *et al.*, 2004; Racek *et al.*, 2006; Skrzypek *et al.*, 2011b), to almost complete reworking of all lithologies by shallow dipping, commonly migmatitic fabric (Hasalová *et al.*, 2008a; Hasalová *et al.*, 2008b; Hasalová *et al.*, 2008c; Štípská *et al.*, 2008). There are two possible reasons for the development of these fabrics, which is the channel flow mechanism or ductile thinning mechanism. In the channel flow mechanism, the rocks of the internal domain flow out in a ductile channel over a rigid indentor.

To keep the channel operational it requires presence of a rigid superstructure above the channel that keeps the temperature high. Typical P−T paths of the rocks in the channel would be characterized by heating for mid-crustal rocks and decompression and cooling for lower crustal lumps surrounded by hot migmatitic matrix. In the ductile thinning mechanism, the whole thickened crust is later thinned, the superstructure is detached by extensional shear-zones and the P−T paths are characterized by concomitant cooling and decompression.

Channel flow

The significance of shallow-dipping fabrics reworking the early steep foliations was unraveled at the eastern margin of the Bohemian Massif where are present kilometre-scale crustal boudins of HP granulites and eclogites enclosed in migmatites (Racek *et al.*, 2006; Hasalová *et al.*, 2008a; Hasalová *et al.*, 2008b; Hasalová *et al.*, 2008c; Schulmann *et al.*, 2008a; Štípská *et al.*, 2008). These studies represent in fact unique dataset documenting a continental channel flow domain, which is eroded along its total width of 120 km and length of 200 km.

In Štípská *et al*. (2008) is presented a detailed analysis of P−T paths in the area where migmatites with sub-horizontal fabrics host lenses of eclogite, kyanite-K-feldspar granulite and marble within a migmatitic matrix of paragneiss and amphibolite (Fig. 19). Petrological study and pseudosection modelling have been used to establish whether the whole area experienced terrain-wide exhumation of lower orogenic crust, or whether smaller portions of higher-pressure lower crust were combined with a lower-pressure matrix. Kyanite-K-feldspar granulite shows peak conditions of 16.5 kbar and 850 °C with no clear indications of prograde path, while in the eclogite the prograde path indicates burial from 10 kbar and 700 °C to a peak of 18 kbar and 800 °C. Two contrasting prograde paths are identified within the host migmatitic paragneiss. The first path is inferred from the presence of staurolite and kyanite inclusions in garnet that contains preserved prograde zoning that indicates burial with simultaneous heating to 11 kbar and 800 °C. The second path is inferred from garnet overgrowths of a flat foliation defined by sillimanite and biotite. Garnet growth in such an assemblage is possible only if the sample is heated at 7–8 kbar to around 700–840 °C. Decompression is associated with strong structural reworking in the flat fabric that involves growth of sillimanite in paragneiss and kyanite-K-feldspar granulite at 7–10 kbar and 750–850 °C. The contrasting prograde metamorphic histories indicate that kilometre-scale portions of high-pressure lower orogenic crust were exhumed to middle crust levels,

Shallow-dipping foliation in the migmatites

Eclogite in the shallow-dipping foliation

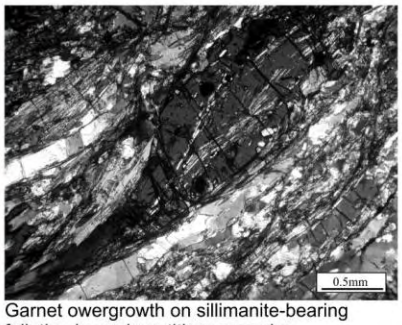

Garnet owergrowth on sillimanite-bearing foliation in a migmatitic paragneiss

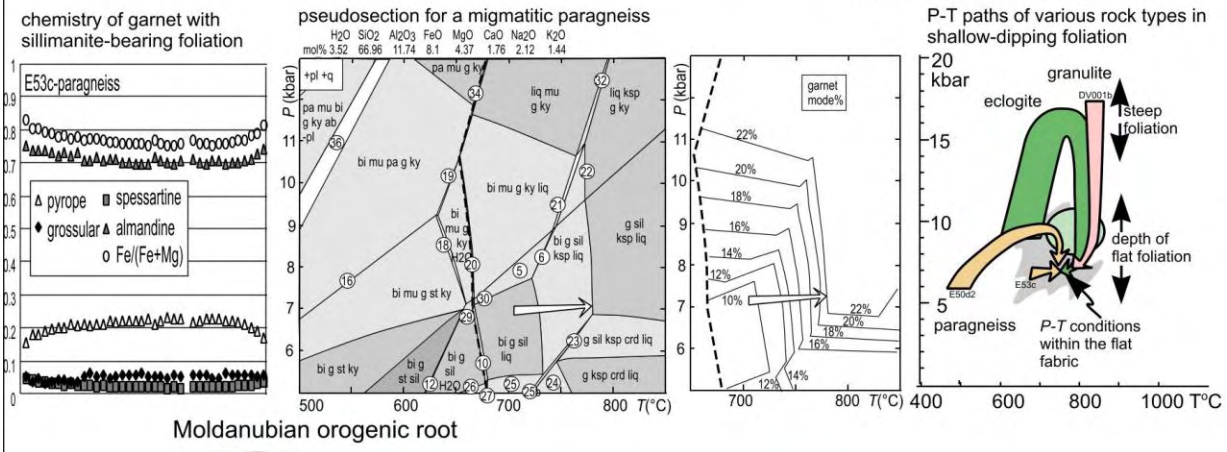

Moldanubian orogenic root

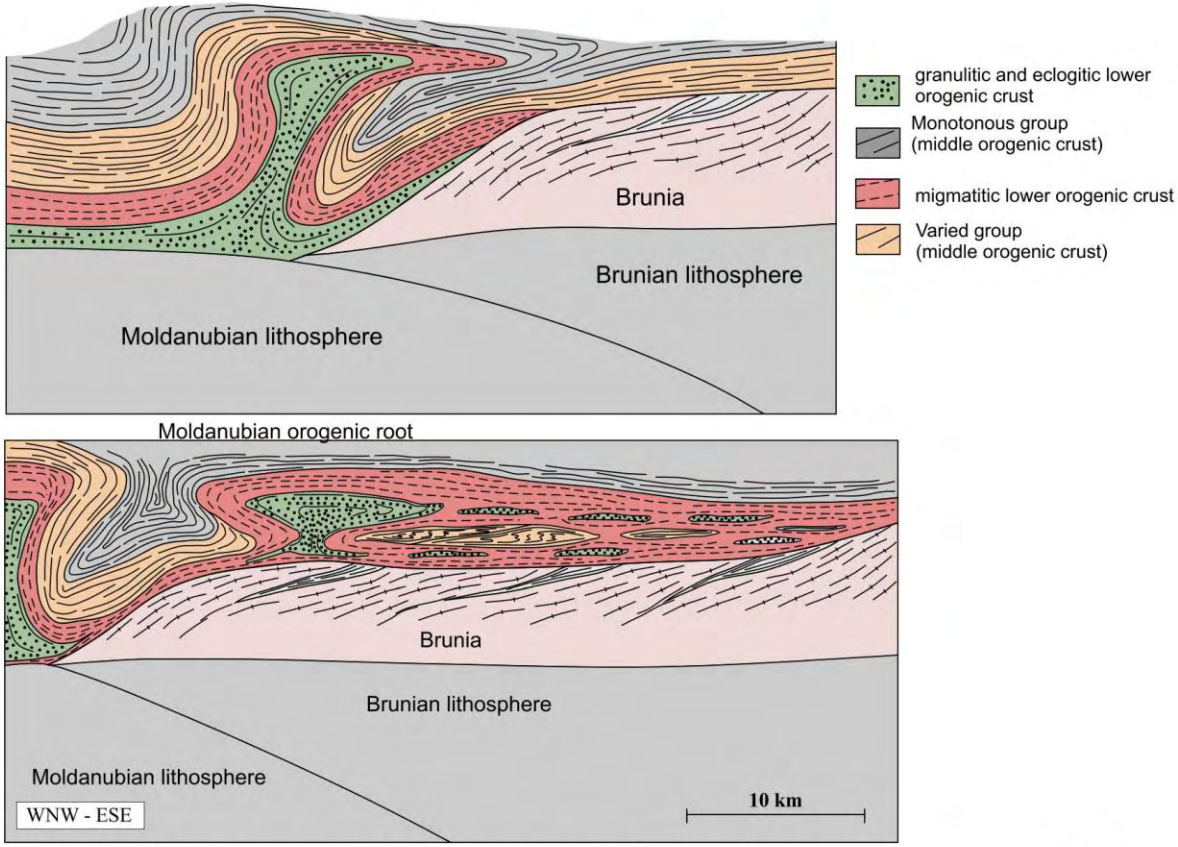

Fig. 19. Model of vertical extrusion followed by subhorizontal flow over the indenting Brunia microcontinent, based on structure, petrology and pseudosection modelling. After Štípská et al. (2008).

dismembered and mixed with a middle crustal migmatite matrix, simultaneously with the development of a flat foliation. The contrasting P−T paths with different pressure peaks show that tectonic models explaining high-pressure boudins in such a fabric cannot be the result of heterogeneous retrogression during ductile rebound of the whole orogenic root. The P−T paths are compatible with a model of heterogeneous vertical extrusion of lower crust into middle crust, followed by subhorizontal flow.

The most detailed microstructural, petrological and geochemical study of migmatites in the channel flow zone is done by Hasalová *et al.* (Hasalová *et al.*, 2008a; Hasalová *et al.*, 2008b; Hasalová *et al.*, 2008c) (Figs 20 & 21). Granitic gneisses and migmatites of the eastern part of Gföhl unit range from banded mylonitic orthogneiss with recrystallized monomineralic bands, through stromatic and schlieren migmatite, to isotropic nebulite. This sequence was classically attributed to increasing degree of anatexis. Under the microscope, the evolution is characterized by progressive destruction of the monomineralic banding that characterizes the original mylonitic orthogneiss. Throughout, the mineral assemblage is biotite–K-feldspar–plagioclase–quartz ± garnet ± sillimanite, but the mineral compositions exhibit systematic changes with progressive disintegration of the layering. From banded orthogneiss to nebulite, the garnet composition changes systematically, $Alm_{75->94}Prp_{17->0.8}Grs_{2.5->1.2}Sps_{2->11}$ and XFe = 0.45−>0.99 and for biotite, XFe =0.80−>1. This is consistent with a decrease in equilibration temperature and pressure from 790 °C and 8.5–6 kbar, to 690 °C and 5–4 kbar. There is also a systematic change of whole-rock composition, marked by an increase in SiO_2 (71 −> 77 wt%) and XFe (0.62 −> 0.85) and by a decrease in Al_2O_3 (16 −> 13 wt%) and CaO (1.50 −> 0.43 wt%). Assuming that the protoliths of the migmatites started with the same composition, these systematic changes indicate open-system behaviour. The predicted consequences of various open-system processes are assessed using thermodynamic modelling. The observed variations are interpreted as being a consequence of melt flow through, and interaction with the rocks, and, to change the rock composition sufficiently, a large volume of melt must have been involved. The textural and whole-rock chemical changes from banded orthogneiss to nebulitic migmatite are attributed to an increasing volume of melt that infiltrated through and interacted with the parental banded orthogneiss. The P–T path suggests that the melt infiltration operating at grain boundaries proceeded at progressively lower P–T conditions for types I–IV, which implies that melt flow changed from pervasive to channelized during exhumation corresponding to the

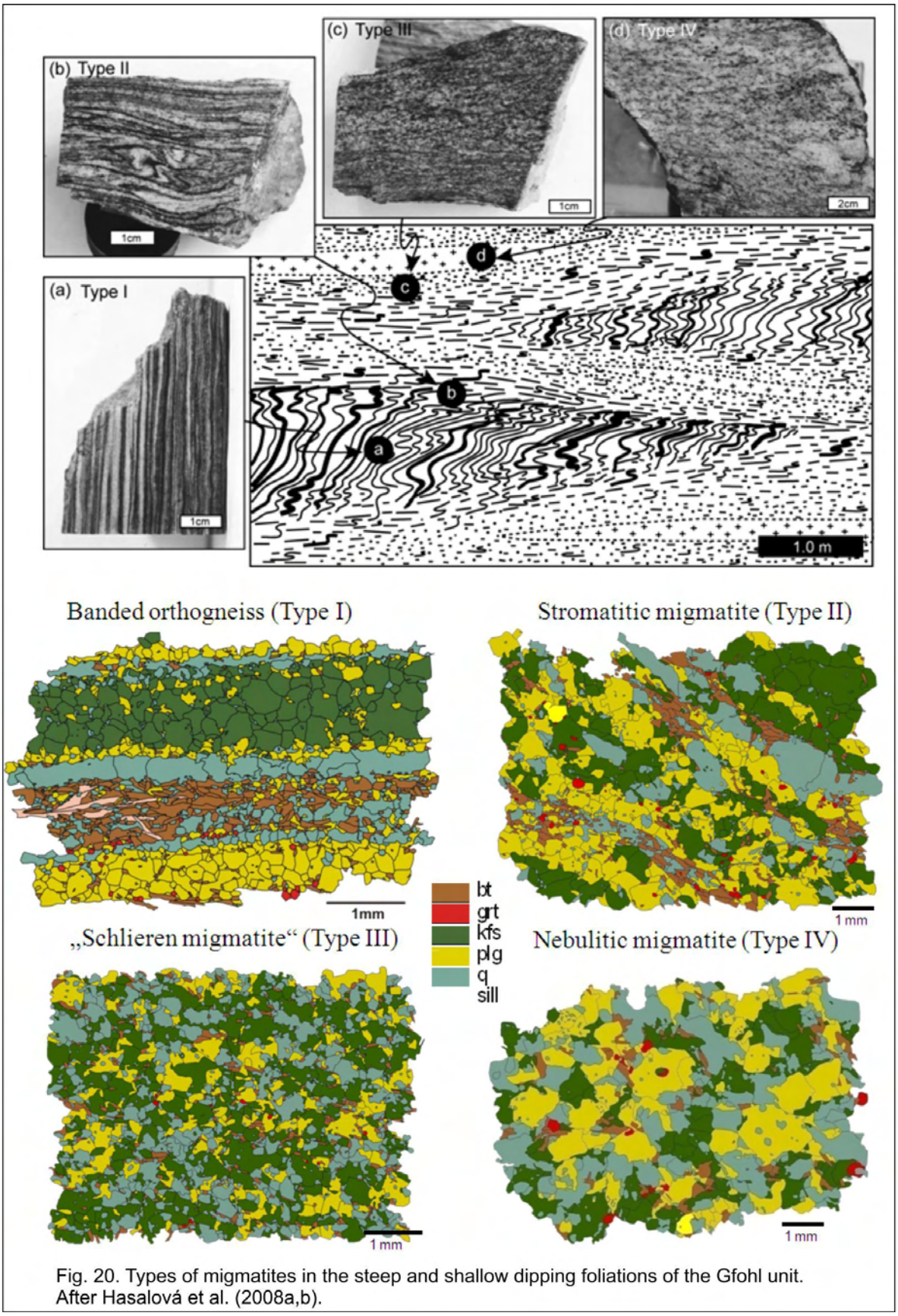

Fig. 20. Types of migmatites in the steep and shallow dipping foliations of the Gfohl unit. After Hasalová et al. (2008a,b).

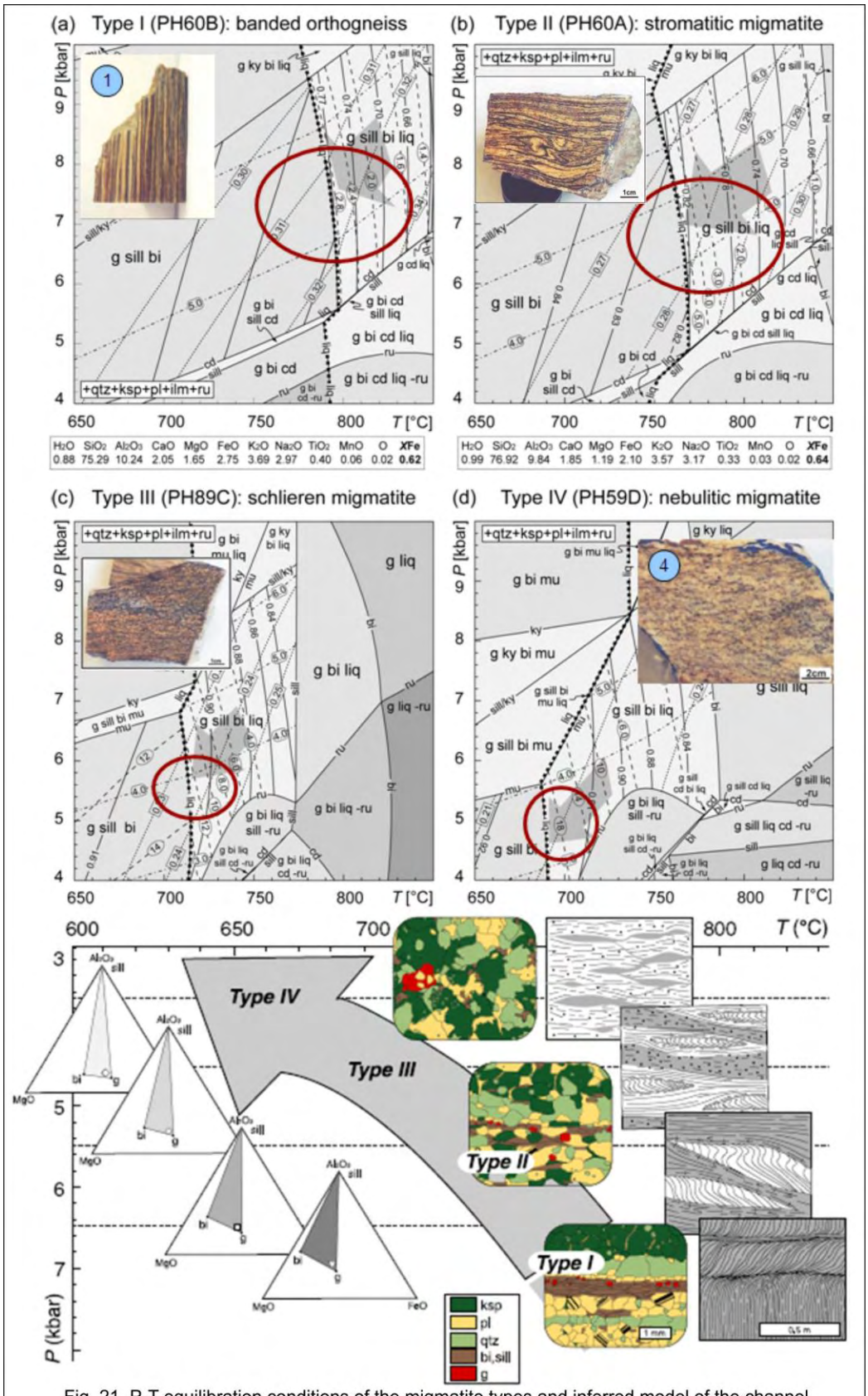

Fig. 21. P-T equilibration conditions of the migmatite types and inferred model of the channel flow domain evolution during exhumation. Based on Hasalová et al. (2008a,b, c).

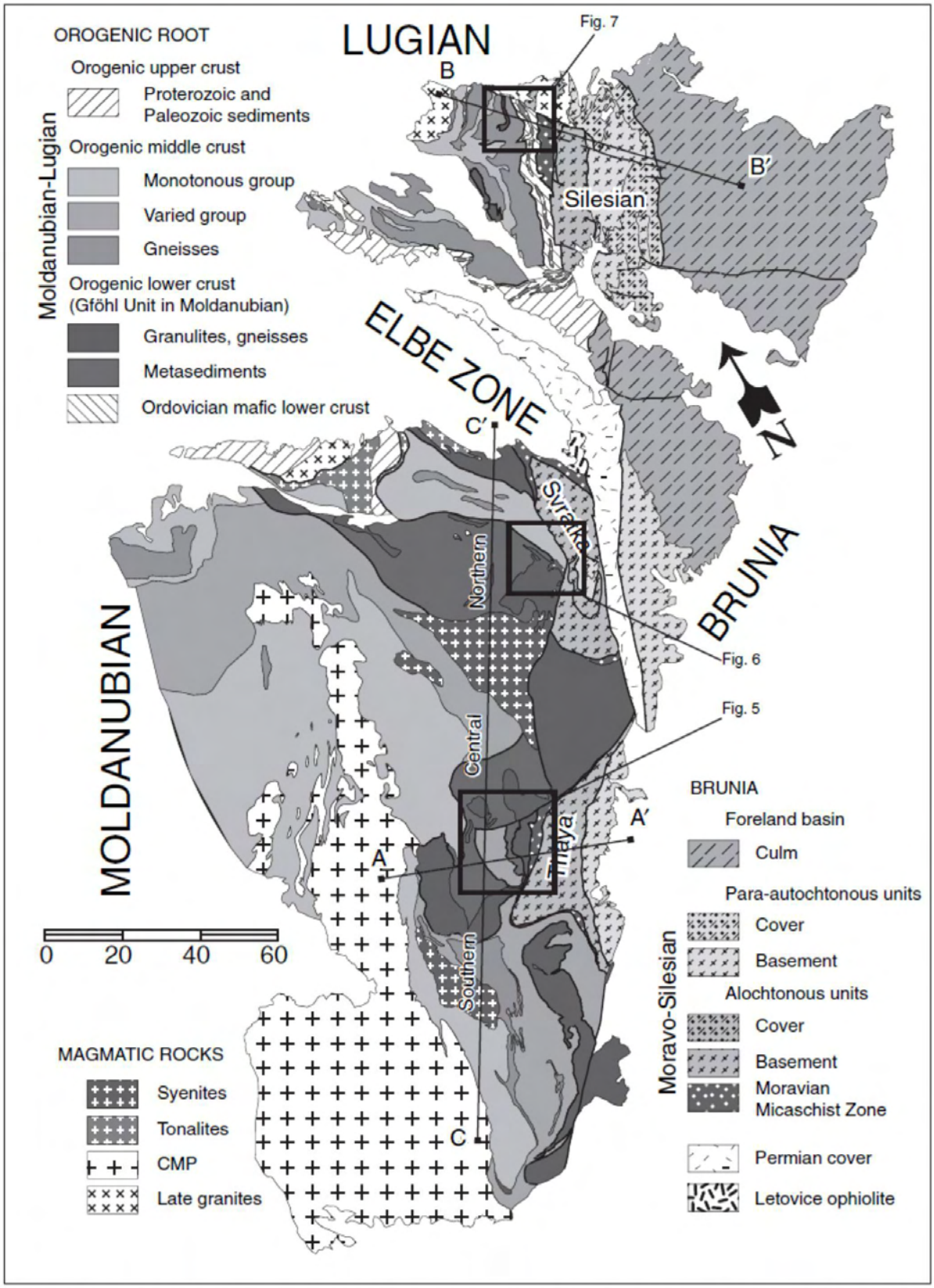

Fig. 22. Map of the eastern margin of the Bohemian massif. Location of the profiles shown in Fig. 23 is indicated. After Schulmann et al. (2008).

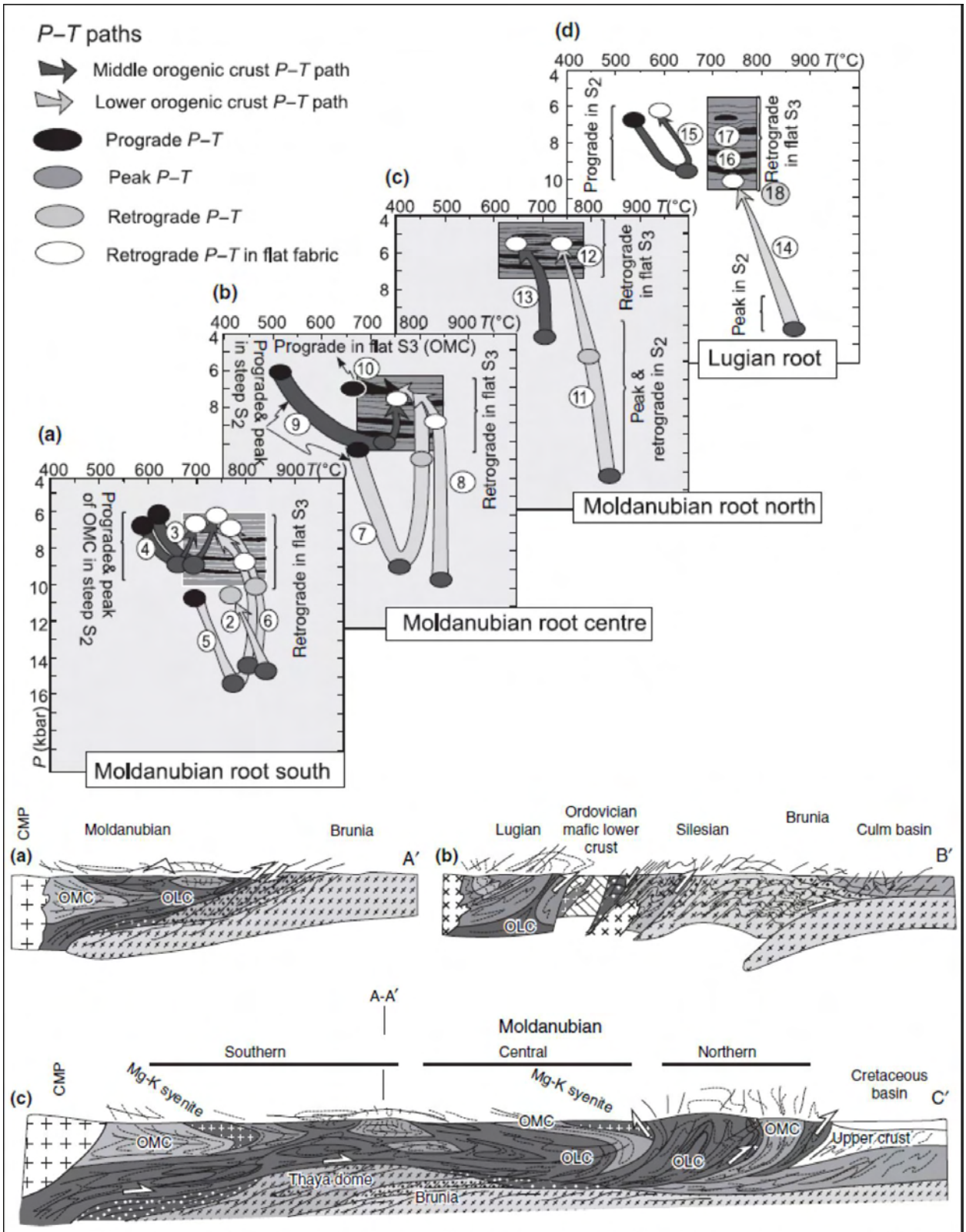

Fig. 23. P-T paths from the orogenic lower and middle crust and depth of development of the late shallow-dipping fabric. Interpretative profiles show channel flow development. After Schulmann et al. (2008).

observed relationships between the four rock types in the field. The model of crustal infiltration by melt is supported also by detailed geochemical, microstructural and EBSD studies (Hasalová *et al.*, 2008a; Hasalová *et al.*, 2008b).

The synthesis of works that describe the channel flow related structures, metamorphism and ages along the eastern margin of the Bohemian Massif is done in Schulmann *et al.* (2008a) (Figs 22 & 23). Fabrics that record the early vertical extrusion originated between 350 and 340 Ma, during building of a crustal orogenic root in response to SE-directed Saxothuringian continental subduction. Fabrics that record the later subhorizontal exhumation event relate to an eastern promontory of the Brunia continent indentating into the rheologically weaker rocks of the orogenic root. Indentation initiated thrusting or flow of the orogenic crust over the Brunia continent in a N-directed sub-horizontal channel. This sub-horizontal flow operated between 330 and 325 Ma, and was responsible for a heterogeneous mixing of blocks and boudins of lower and middle crustal rocks and for their progressive thermal re-equilibration. The erosion depth as well as the degree of reworking decrease from south to north, pointing to an outflow of lower crustal material to the surface and its subsequent erosion and sedimentation in a foreland basin.

Ductile thinning fabrics

The metamorphic evolution of late subhorizontal fabrics associated with ductile thinning were systematically studied on the example of the Stronie metasedimentary unit and adjacent granulites from the Orlica-Śnieżnik dome (Skrzypek *et al.*, 2011a; Skrzypek *et al.*, 2011b) (Fig. 24). Provided that the metamorphic evolution of the Stronie metasedimentary rocks and granulites during the formation of late subhorizontal foliation was coeval, the significance of metamorphic evolution of both units during exhumation can be discussed. The petrological data from the metapelites and granulites of the NE part of the Orlica-Śnieżnik dome (Skrzypek *et al.*, 2011a; Skrzypek *et al.*, 2011b) indicate a decrease in both pressure and temperature as long as the shallow-dipping fabric evolved. Although producing compatible retrograde P–T paths, the model of exhumation in the core of a large antiform associated with erosion (Burg *et al.*, 1998) can probably be ruled out because no shallow-dipping fabrics are created during this process. By contrast, the early retrograde P–T path of granulites suggested that strong erosion already occurred during the subvertical fabric development. This mechanism is likely to persist during later exhumation and may therefore enhance cooling of the crust, as demonstrated by erosional

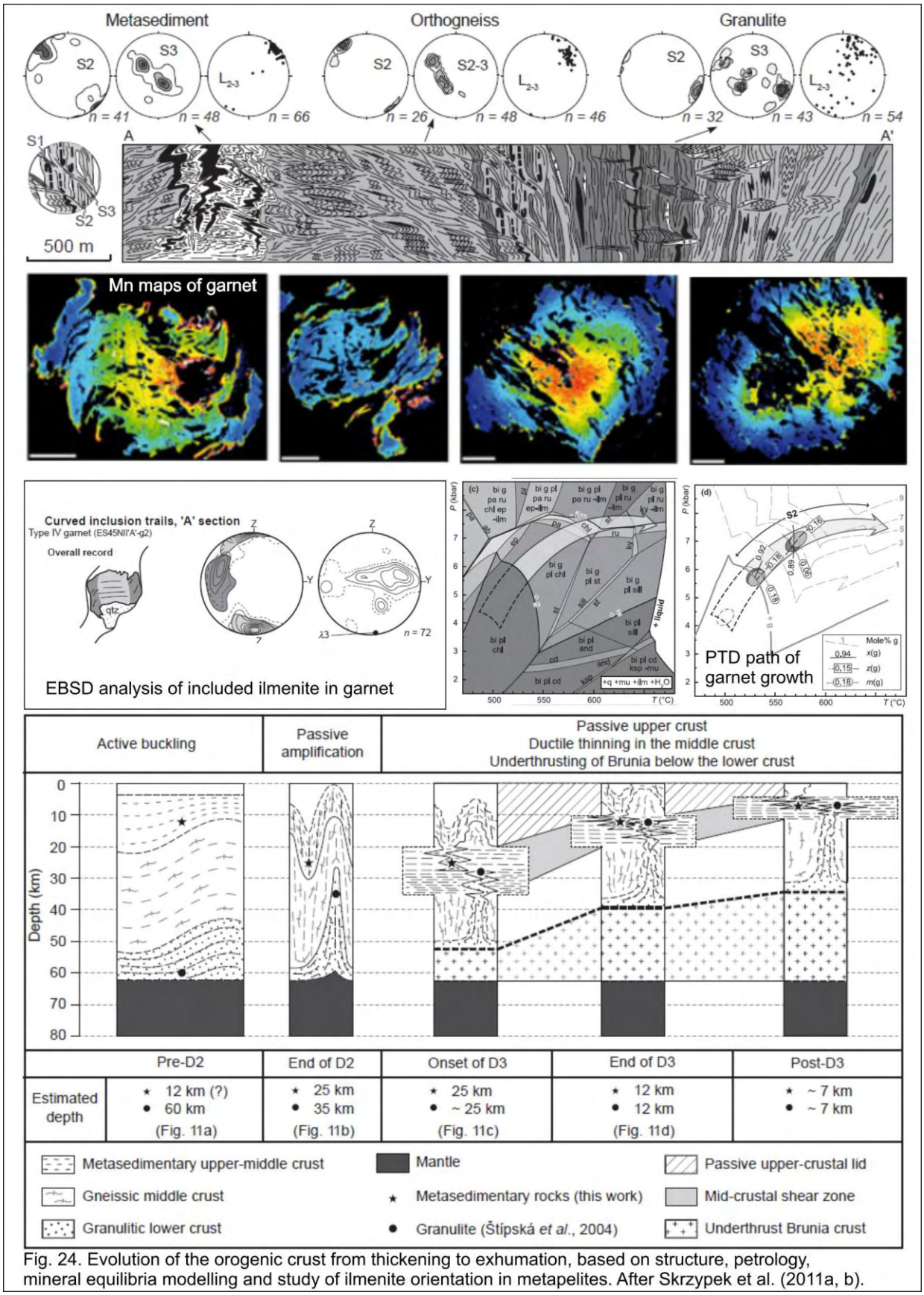

Fig. 24. Evolution of the orogenic crust from thickening to exhumation, based on structure, petrology, mineral equilibria modelling and study of ilmenite orientation in metapelites. After Skrzypek et al. (2011a, b).

models of Ruppel & Hodges (1994). Lack of additional heat could also be due to the relatively small amount of hot granulitic material that has been brought in contact with the middle crust. However, there is further need for an exhumation mechanism that would be responsible for the widespread flat-lying deformation observed in the whole area. The mechanism of ductile thinning (Ring & Brandon, 1999; Ring *et al.*, 1999) may be responsible for the unroofing of high-grade core of continental orogens either by homogeneous vertical shortening process (Vanderhaeghe & Teyssier, 2001), or by activity of localized extensional detachments (Platt, 1993).

In summary, the ductile thinning brings rocks closer to the surface by vertical shortening of the overlying crustal column at a given crustal level, in conjunction with continuous cooling, which accelerates as the rocks approach the surface (Feehan & Brandon, 1999). From structural, microstructural (Skrzypek *et al.*, 2011a; Skrzypek *et al.*, 2011b) and petrological observations, ductile thinning together with erosion can account for the retrograde P–T–D path of both granulites and metapelites. The driving force for the formation of the horizontal foliation and the ductile thinning process is suggested to be the underthrusting of the Orlica- Śnieżnik root by the eastern Brunovistulian continent during the Carboniferous. In the study area, the restoration of a standard crustal thickness of 35 km was probably achieved during late Carboniferous extensional stretching and thinning of the whole thickened crust (Schulmann & Gayer, 2000).

FUTURE STUDIES

Perspectives in the studies of the Moravo-Silesian zone

The perspective in this region is the study of the interactions of the Brunia microcontinent with the overriding Moldanubian orogenic root. The southern part of the Brunia microcontinent shows thick nappes and thick metamorphic zones in the basement, and well developed subhorizontal fabrics in the Moldanubain root, while the middle part, in the region of the Svratka window, shows thin nappes and thin metamorphic zones in the basement and poorly developed shallow-dipping fabrics in the overlying Moldanubian rocks. The structural and metamorphic pattern of the whole Moravian zone shows that the Brunia microcontinent played a major role in the development of the channel flow in the migmatitic and high-grade rocks of the above Moldanubian zone. We are preparing a publication that will use the structural and petrological

observations, and modelled P−T paths in the whole length of the Moravian zone, in order to quantify the time-scales necessary for development of the channel flow in the overriding root.

Perspectives in the studies of P−T evolution of the lower orogenic crust

The published extreme pressure and temperature conditions of the lower crustal rocks in the Moldanubian zone and the presence of garnetiferous and spinel peridotites attracted a lot of attention in past decades. However, the ultra-high pressure conditions inferred for the lower crustal rocks are mostly based on thermobarometry or pseudosection modeling, using assemblages that are not necessarily in chemical equilibrium (Štípská & Powell, 2005b; Racek *et al.*, 2008). Coesite and diamond have been recently found in felsic granulites (O'Brien & Kotková, unpublished results), close to the Saxothuringian domain where the remnants of crust subducted to diamond stability field were already described (Massonne & Nasdala, 2003). It this sense, there are perspectives in looking for the coesite and microdiamond in the crustal rocks of the Moldanubian-Lugian domain in order to map the extent of lumps of crust that were possibly subducted so deep. Other perspective is in understanding the relationship between garnetiferous and spinel peridotites and the felsic granulites in terms of their structure and metamorphism. Which parts of their structural and metamorphic evolution are common? The major questions that remain to be solved concern also the extreme temperature conditions (> 900 °C) that are based for example on the presence of ternary feldspar, exsolution of orthopyroxene in clinopyroxene or high zirconium content in rutile. Are these high temperatures local? What is the volume of the lower crustal rocks that has been exposed to these temperatures? What is the spatial distribution of these rocks with respect to rocks that did not experience such high temperatures and preserve even prograde metamorphic features? Are they linked with magmatic events, or do they occur only close to the peridotites? Are the ultra-high temperature conditions contemporaneous with metamorphism of other high-pressure rocks? At what depths did the ultra-high temperature conditions occur? These questions are important in order to understand the evolution of the large hot orogens, and there are several areas in the Moldanubian zone where I continue the research in order to provide at least partial answers to these questions.

Perspectives in understanding the significance of the shallow-dipping late orogenic structures

After complex tectonic evolution (Fig. 25), all the areas in the Moldanubian domain are affected to a various degree by late shallow-dipping structures. They range from weak open folds with subhorizontal plane to almost complete reworking by shallow dipping axial cleavage and pervasive, usually migmatitic foliation. Two studied areas, the eastern Moldanubian zone and the Orlica-Śnieżnik dome in the north show that these shallow-dipping fabrics are likely to result from different processes, the channel flow and ductile thinning mechanisms, respectively. These results initiated an idea, that the formation of the shallow-dipping fabrics marks the establishment of the infra- and superstructure transitional zone (ISTRA zone) and that it may have very different evolution in various types of orogens. This research initiated the ANR proposal that was submitted in collaboration with the Strasbourg group led by Karel Schulmann, Nice group led by Jean-Marc Lardeaux and the Rennes group led by Denis Gapais. The major questions may be summarized as follows:

1) In which depth does the ISTRA zone originate and what is its position with respect to the upper and lower plate? What is the thickness of infrastructure, superstructure and the ISTRA zone? Can this zone migrate vertically and change its thickness?
2) What are the criteria to recognize the ISTRA zone in the field?
3) What is the evolution of the crust before, during and after the establishment of the ISTRA zone?
4) When does the ISTRA zone originate and what is its evolution in time?
5) What are the mechanisms of localization and rheological evolution of the ISTRA zone?
6) What are the factors and processes responsible for the ISTRA development?

Main anticipated result of this project is to propose a modified view on orogenic systems by evaluating mechanisms of coupled deformation between the upper and lower plate during early stages of orogenesis followed by mechanical decoupling and development of the ISTRA zone, separating the orogenic infra and superstructure in various crustal depths. We will determine and characterize: (1) environmental and intrinsic parameters of the crust in time, like temperature, pressure, "lithological-density-rheological" stratification before and after the decoupling, (2) factors controlling vertical migration of the ISTRA zone in time, (3) strain localization mechanisms associated with the ISTRA zone formation.

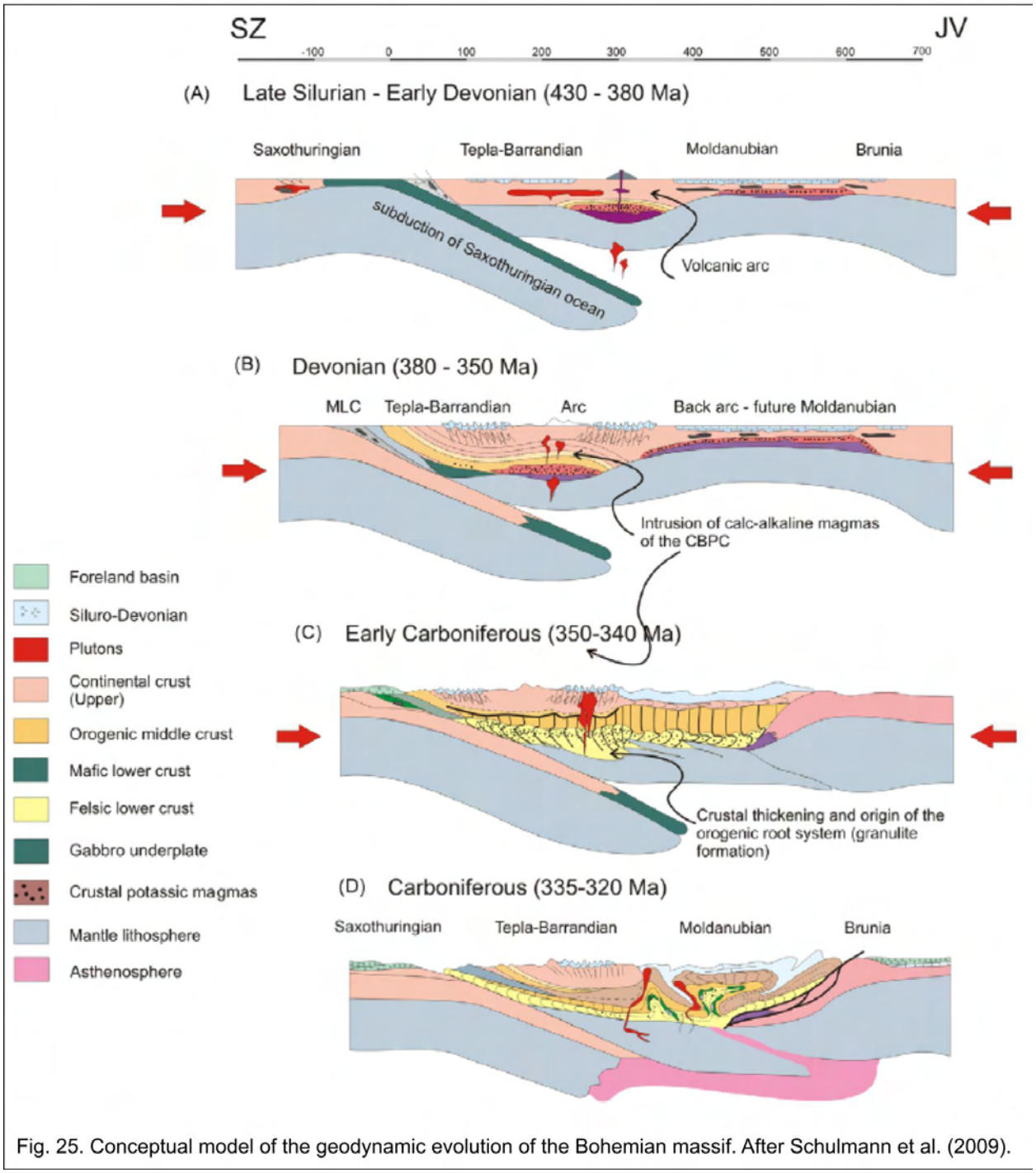

Fig. 25. Conceptual model of the geodynamic evolution of the Bohemian massif. After Schulmann et al. (2009).

These data will help to propose the mechanisms of formation of orogenic infra- and superstructure and the ISTRA zone in orogenic systems. The anticipated mechanisms are the channel flow, horizontal spreading, ductile thinning and detachment zones. The data will allow defining position of the ISTRA zone with respect to the lower/upper plate boundary.

REFERENCES

Allemand, P. & Lardeaux, J. M., 1997. Strain partitioning and metamorphism in a deformable orogenic wedge: Application to the Alpine belt. *Tectonophysics*, **280**, 157-169.

Andersen, T. B. & Fossen, H., 1993. The role of extensional tectonics in the Caledonides of south Norway-discussion and reply. *Journal of Structural Geology*, **15**, 1379-1383.

Andersen, T. B., Jamtveit, B., Dewey, J. F. & Swensson, E., 1991. Subduction and eduction of continental crust: major mechanisms during continent-continent collision and orogenic extensional collapse, a model based on the south Norwegian Caledonides. *Terra Nova*, **3**, 303-310.

Baratoux, L., Lexa, O., Cosgrove, J. W. & Schulmann, K., 2005. The quantitative link between fold geometry, mineral fabric and mechanical anisotropy: as exemplified by the deformation of amphibolites across a regional metamorphic gradient. *Journal Of Structural Geology*, **27**, 707-730.

Beaumont, C., Jamieson, R. A., Nguyen, M. H. & Lee, B., 2001. Himalayan tectonics explained by extrusion of a low-viscosity crustal channel coupled to focused surface denudation. *Nature*, **414**, 738-742.

Beaumont, C., Nguyen, M. H., Jamieson, R. A. & Ellis, S., 2006. Crustal flow modes in large hot orogens. Channel flow, ductile extrusion and exhumation in continental collision zones. *Geological Society Special Publications*, **268**, 91-145.

Burg, J. P., Kaus, B. J. P. & Podladchikov, Y. Y., 2004. Dome structures in collision orogens: Mechanical investigation of the gravity/compression interplay. *Geological Society of America Special Papers*, **380**, 47-66.

Burg, J. P., Nievergelt, P., Oberli, F., Seward, D., Davy, P., Maurin, J. C., Diao, Z. & Meier, M., 1998. The Namche Barwa syntaxis: evidence for exhumation related to compressional crustal folding. *Journal of Asian Earth Sciences*, **16**, 239-252.

Carswell, D. A., 1991. Variscan high P-T metamorphism and uplift history in the Moldanubian Zone of the Bohemian Massif in Lower Austria. *European Journal of Mineralogy*, **3**, 323-342.

Cháb, J. & Žáček, V., 1994. Geology of the Žulová pluton mantle (Bohemian Massif, Central Europe). *Bulletin of the Czech Geological Survey*, **69**, 1-12.

Chemenda, A. I., Burg, J. P. & Mattauer, M., 2000. Evolutionary model of the Himalaya-Tibet system: geopoem based on new modelling, geological and geophysical data. *Earth and Planetary Science Letters*, **174**, 397-409.

Chopin, F., Schulmann, K., Martelat, J. E., Štípská, P., Lexa, O. & Petri, B., submitted-a. Prograde deformation gradient in subducted HP orthogneiss (Orlica-Śnieżnik dome, Bohemian Massif): Implications for reaction softening and strain localization during continental subduction. *Journal of Metamorphic Geology*.

Chopin, F., Schulmann, K., Skrzypek, E., Dujardin, J. R., Lehmann, J., Martelat, J. E., Lexa, O., Corsini, M., Edel, J. B., Štípská, P. & Pitra, P., submitted-b. Multistage syn-convergent growth and collapse of mantled gneiss dome (Orlica-Śnieżnik Dome, Bohemian Massif). *Tectonics*.

Collins, W. J., 2002. Hot orogens, tectonic switching, and creation of continental crust. *Geology*, **30**, 535-538.

Connolly, J. A. D., 1990. Multivariable phase diagrams: An algorythm based on generalized thermodynamics. *American Journal of Science*, **290**, 666-718.

De Capitani, C. & Brown, T. H., 1987. The computation of chemical equilibrium in complex systems containing non-ideal solutions. *Geochimica and Cosmochimica Acta* **51**, 2639-2652.

Duchène, S., Lardeaux, J. M. & Albarède, F., 1997. Exhumation of eclogites: insights from depth-time path analysis. *Tectonophysics*, **280**, 125-140.

England, P. C. & Houseman, G. A., 1988. The mechanics of the Tibetan Plateau. *Philosophical Transactions of the Royal Society of London Series a-Mathematical Physical and Engineering Sciences*, **326**, 301-320.

Feehan, J. G. & Brandon, M. T., 1999. Contribution of ductile flow to exhumation of low-temperature, high-pressure metamorphic rocks: San Juan-Cascade nappes, NW Washington State *Journal of Geophysical Research*, **104**, 10883-10902.

Franěk, J., Schulmann, K. & Lexa, O., 2006. Kinematic and rheological model of exhumation of high pressure granulites in the Variscan orogenic root: example of the Blanský les granulite, Bohemian Massif, Czech Republic. *Mineralogy and Petrology*, **86**, 253-276.

Franěk, J., Schulmann, K., Lexa, O., Tomek, Č. & Edel, J. B., 2011a. Model of syn-convergent extrusion of orogenic lower crust in the core of the Variscan belt: implications for exhumation of high-pressure rocks in large hot orogens. *Journal of Metamorphic Geology*, 53–78.

Franěk, J., Schulmann, K., Lexa, O., Ulrich, S., Štípská, P., Haloda, J. & Týcová, P., 2011b. Origin of felsic granulite microstructure by heterogeneous decomposition of alkali feldspar and extreme weakening of orogenic lower crust during the Variscan orogeny. *Journal of Metamorphic Geology*, **29**, 103–130.

Franke, W., 1989a. Tectonostratigraphic units in the Variscan belt of central Europe. *Geological Society of America, Special Paper*, **230**, 67-90.

Franke, W., 1989b. Variscan plate tectonics in Central Europe - current ideas and open questions. *Tectonophysics*, **169**, 221-228.

Friedl, G., Finger, F., Paquette, J., Quadt, A., McNaughton, N. & Fletcher, I., 2004. Pre-Variscan geological events in the Austrian part of the Bohemian Massif deduced from U-Pb zircon ages. *International Journal of Earth Sciences*, **93**, 802-823.

Fuchs, G. & Matura, A., 1976. Zur Geologie des Kristallins der südlichen Böhmischen Masse. *Jahrbuch der Geologischen Bundesanstalt Wien*, **119**, 1-43.

Gerya, T. & Stöckhert, B., 2006. Two-dimensional numerical modeling of tectonic and metamorphic histories at active continental margins. *International Journal of Earth Sciences*, **95**, 250-274.

Gerya, T. V., Maresch, W. V., Willner, A. P., Van Reenen, D. D. & Smit, C. A., 2001. Inherent gravitational instability of thickened continental crust with regionally developed low- to medium-pressure granulite facies metamorphism. *Earth and Planetary Science Letters*, **190**, 221-235.

Gerya, T. V., Perchuk, L. L., Maresch, W. V. & Willner, A. P., 2004. Inherent gravitational instability of hot continental crust: Implications for doming and diapirism in granulite facies terrains. *Geological Society of America Special Papers* **380**, 97-115.

Gerya, T. V., Perchuk, L. L., Maresch, W. V., Willner, A. P., Van Reenen, D. D. & Smit, C. A., 2002. Thermal regime and gravitational instability of multi-layered continental crust: implications for the buoyant exhumation of high-grade metamorphic rocks. *European Journal of Mineralogy*, **14**, 687-699.

Godin, L., Gleeson, T. P., Searle Mike, P., Ullrich, T. D. & Parrish, R. R., 2006a. Locking of southward extrusion in favour of rapid crustal-scale buckling of the Greater Himalayan Sequence, Nar Valley, central Nepal.; Channel flow, ductile extrusion and exhumation in continental collision zones. *Geological Society Special Publications*, **268**, 269-292.

Godin, L., Grujic, D., Law, R. D. & Searle Mike, P., 2006b. Channel flow, ductile extrusion and exhumation in continental collision zones; an introduction.; Channel flow, ductile extrusion and exhumation in continental collision zones. *Geological Society Special Publications*, **268**, 1-23.

Grujic, D., Casey, M., Davidson, C., Hollister, L. S., Kundig, R., Pavlis, T. & Schmid, S., 1996. Ductile extrusion of the Higher Himalayan Crystalline in Bhutan: Evidence from quartz microfabrics. *Tectonophysics*, **260**, 21-43.

Guy, A., Edel, J. B., Schulmann, K., Tomek, Č. & Lexa, O., 2011. A geophysical model of the Variscan orogenic root (Bohemian Massif): Implications for modern collisional orogens *Lithos*, **124**, 144-157.

Hartley, A. J. & Otava, J., 2001. Sediment provenance and dispersal in a deep marine foreland basin: the Lower Carboniferous Culm Basin, Czech Republic. *Journal of the Geological Society*, **158**, 137-150.

Hasalová, P., Janoušek, V., Schulmann, K., Štípská, P. & Erban, V., 2008a. From orthogneiss to migmatite: geochemical assessment of the melt infiltration model in the Gföhl Unit (Moldanubian Zone, Bohemian Massif). *Lithos*, **102**, 508–537.

Hasalová, P., Schulmann, K., Lexa, O., Štípská, P., Hrouda, F., Ulrich, S., Haloda, J. & Týcová, P., 2008b. Origin of migmatites by deformation-enhanced melt infiltration of orthogneiss: a new model based on quantitative microstructural analysis. *Journal of Metamorphic Geology*, **26**, 29-53.

Hasalová, P., Štípská, P., Powell, R., Schulmann, K., Janoušek, V. & Lexa, O., 2008c. Transforming mylonitic metagranite by open-system interactions during melt flow. *Journal of Metamorphic Geology*, **26**, 55-80.

Hladil, J., 1994. Microfacies of Devonian Limestones in Moravia (part II.-Review of discerned microfacies). *Zemní plyn a nafta*, **39**, 19-70.

Holland, T. J. B. & Powell, R., 2001. Calculation of phase relations involving haplogranitic melts using an internally consistent thermodynamic dataset. *Journal of Petrology*, **42**, 673-683.

Jamieson, R. A., Beaumont, C., Nguyen, M. H. & Grujic, D., 2006. Provenance of the Greater Himalayan Sequence and associated rocks; predictions of channel flow models.; Channel flow, ductile extrusion and exhumation in continental collision zones. *Geological Society Special Publications*, **268**, 165-182.

Jamieson, R. A., Beaumont, C., Nguyen, M. H. & Lee, B., 2002. Interaction of metamorphism, deformation and exhumation in large convergent orogens. *Journal of Metamorphic Geology*, **20**, 9-24.

Jeřábek, P., Faryad, W. S., Schulmann, K., Lexa, O. & Tajčmanová, L., 2008. Alpine burial and heterogeneous exhumation of Variscan crust in the West Carpathians: insight from thermodynamic and argon diffusion modelling. *Journal of the Geological Society*, **165**, 479-498.

Jolivet, L., Raimbourg, H., Labrousse, L., Avigad, D., Leroy, Y., Austrheim, H. & Andersen, T. B., 2005. Softening trigerred by eclogitization, the first step toward exhumation during continental subduction. *Earth and Planetary Science Letters*, **237**, 532-547.

Kalvoda, J., Leichmann, J., Babek, O. & Melichar, R., 2003. Brunovistulian Terrane (Central Europe) and Istanbul Zone (NW Turkey): Late Proterozoic and Paleozoic tectonostratigrap development and paleogeography. *Geologica Carpathica*, **54**, 139-152.

Konopásek, J., Schulmann, K. & Johan, V., 2002. Eclogite-facies metamorphism at the eastern margin of the Bohemian Massif - subduction prior to continental underthrusting? *European Journal of Mineralogy*, **14**, 701-713.

Košuličová, M. & Štípská, P., 2007. Variations in the transient prograde geothermal gradient from chloritoid-staurolite equilibria: a case study from the Barrovian and Buchan-type domains in the Bohemian Massif. *Journal of Metamorphic Geology*, **25**, 19-35.

Koyi, H. A., Milnes, A. G., Schmeling, H., Talbot, C. J., Juhlin, C. & Zeyen, H., 1999. Numerical models of ductile rebound of crustal roots beneath mountain belts. *Geophysical Journal International*, **139**, 556-562.

Kröner, A., Jaeckel, P., Hegner, E. & Opletal, M., 2001. Single zircon ages and whole rock Nd isotopic systematics of early Palaeozoic granitoid gneisses from the Czech and Polish Sudetes (Jizerské hory, Krkonoše Mountains and Orlice-Sněžník Complex). *International Journal of Earth Sciences*, **90**, 304-324.

Kröner, A., Štípská, P., Schulmann, K. & Jaeckel, P., 2000. Chronological constraints on the pre-Variscan evolution of the northeastern margin of the Bohemian Massif, Czech Republic. In: *Orogenic processes; quantification and modelling in the Variscan Belt.* (eds Franke, W., Haak, V., Oncken, O. & Tanner, D.) *Geological Society of London Special Publications*, pp. 175-197, Geological Society of London. London, United Kingdom, 179, 175-197.

Lange, U., Bröcker, M., Armstrong, R., Trapp, E. & Mezger, K., 2005a. Sm-Nd and U-Pb dating of high-pressure granulites from the Zlote and Rychleby Mts (Bohemian Massif, Poland and Czech Republic). *Journal of Metamorphic Geology*, **23**, 133-145.

Lange, U., Bröcker, M., Armstrong, R., Żelaźniewicz, A., Trapp, E. & Mezger, K., 2005b. The orthogneisses of the Orlica-Śnieżnik complex (West Sudetes, Poland): geochemical characteristics, the importance of pre-Variscan migmatization and constraints on the cooling history. *Journal of the Geological Society*, **162**, 973-984.

Lexa, O., Schulmann, K., Janoušek, V., Štípská, P., Guy, A. & Racek, M., 2011. Heat sources and trigger mechanisms of exhumation of HP granulites in Variscan orogenic root. *Journal of Metamorphic Geology*, **29**, 79–102.

Lexa, O., Štípská, P., Schulmann, K., Baratoux, L. & Kröner, A., 2005. Contrasting textural record of two distinct metamorphic events of similar P-T conditions and different durations. *Journal of Metamorphic Geology*, **23**, 649-666.

Massonne, H. J. & Nasdala, L., 2003. Characterization of an early metamorphic stage through inclusions in zircon of a diamon-diferous quartzofeldspathic rock from the Erzgebirge, Germany. *American Mineralogist*, **88**, 883-889.

Matte, P., 1991. Accretionary history and crustal evolution of the Variscan belt in Western Europe. *Tectonophysics*, **196**, 309-337.

Medaris, L. G., Beard, B. L., Johnson, C. M., Valley, J. W., Spicuzza, M. J., Jelínek, E. & Mísař, Z., 1995a. Garnet pyroxenite and eclogite in the Bohemian Massif: geochemical evidence for Variscan recycling of subducted lithosphere. *Geologische Rundschau*, **84**, 489-505.

Medaris, L. G., Fournelle, J. H., Ghent, E. D., Jelínek, E. & Mísař, Z., 1998. Prograde eclogite in the Gföhl Nappe, Czech Republic: new evidence on Variscan high-pressure metamorphism. *Journal of Metamorphic Geology*, **16**, 563-576.

Medaris, L. G., Jelínek, E. & Mísař, Z., 1995b. Czech eclogites: Terrane settings and implications for Variscan tectonic evolution of the Bohemian Massif. *European Journal of Mineralogy*, **7**, 7-28.

O'Brien, P. J. & Rötzler, J., 2003. High-pressure granulites: formation, recovery of peak conditions and implications for tectonics. *Journal of Metamorphic Geology*, **21**, 3-20.

Oncken, O., 1997. Transformation of a magmatic arc and an orogenic root during oblique collision and it's consequences for the evolution of the European Variscides (Mid-German Crystalline Rise). *Geologische Rundschau*, **86**, 2-20.

Parry, M., Štípská, P., Schulmann, K., Hrouda, F., Ježek, J. & Kröner, A., 1997. Tonalite sill emplacement at an oblique plate boundary: northeastern margin of the Bohemian Massif. *Tectonophysics*, **280**, 61-81.

Platt, J. P., 1987. The uplift of high-pressure low-temperature metamorphic rocks. *Philosophical Transactions of the Royal Society of London*, **A321**, 87-103.

Platt, J. P., 1993. Exhumation of high-pressure rocks; a review of concepts and processes. *Terra Nova*, **5**, 119-133.

Powell, R. & Holland, T. J. B., 1988. An internally consistent dataset with uncertainties and correlations: 3. Applications to geobarometry, worked examples and a computer program. *Journal of Metamorphic Geology*, **6**, 173-204.

Racek, M., Štípská, P., Pitra, P., Schulmann, K. & Lexa, O., 2006. Metamorphic record of burial and exhumation of orogenic lower and middle crust: a new tectonothermal model for the Drosendorf window (Bohemian Massif, Austria). *Mineralogy and Petrology*, **86**, 221-251.

Racek, M., Štípská, P. & Powell, R., 2008. Garnet-clinopyroxene intermediate granulites in the St. Leonhard massif of the Bohemian Massif: ultrahigh-temperature metamorphism at high pressure or not? *Journal of Metamorphic Geology*, **26**, 253–271.

Ring, U. & Brandon, M. T., 1999. Ductile deformation and mass loss in the Franciscan Subduction Complex: implications for exhumation processes in accretionary wedges. *Geological Society Special Publication*, **154**, 55-86.

Ring, U., Brandon, M. T., Lister, G. S. & Willett, S. D., 1999. Exhumation processes: normal faulting, ductile flow and erosion. *Geological Society Special Publication*, **154**, 1-27.

Rozkošný, I. & Souček, J., 1989. Contribution to the petrology of the Žulová massif mantle. *Acta Universitatis Carolinae, Geologica*, **2**, 165-197.

Ruppel, C. & Hodges, K. V., 1994. Pressure-temperature-time paths from two-dimensional thermal models: prograde, retrograde and inverted metamorphism. *Tectonics*, **13**, 17-44.

Schulmann, K. & Gayer, R., 2000. A model for a continental accretionary wedge developed by oblique collision: the NE Bohemian Massif. *Journal of the Geological Society, London*, **157**, 401-416.

Schulmann, K., Konopásek, J., Janoušek, V., Lexa, O., Lardeaux, J. M., Edel, J. B., Štípská, P. & Ulrich, S., 2009. An Andean type Palaeozoic convergence in the Bohemian Massif. *Comptes Rendus Geoscience*, **341**, 266-286.

Schulmann, K., Kröner, A., Hegner, E., Wendt, I., Konopásek, J., Lexa, O. & Štípská, P., 2005. Chronological constraints on the pre-orogenic history, burial and exhumation of deep-seated rocks along the eastern margin of the Variscan orogen, Bohemian Massif, Czech Republic. *American Journal of Science*, **305**, 407-448.

Schulmann, K., Lexa, O., Štípská, P., Racek, M., Tajčmanová, L., Konopásek, J., Edel, J. B., Peschler, A. & Lehmann, J., 2008a. Vertical extrusion and horizontal channel flow of

orogenic lower crust: key exhumation mechanisms in large hot orogens? *Journal of Metamorphic Geology*, **26**, 273–297.

Schulmann, K., Martelat, J. E., Ulrich, S., Lexa, O., Štípská, P. & Becker, J. K., 2008b. Evolution of microstructure and melt topology in partially molten granitic mylonite: Implications for rheology of felsic middle crust. *Journal of Geophysical Research-Solid Earth*, **113**.

Schulmann, K., Schaltegger, U., Ježek, J., Thompson, A. B. & Edel, J. B., 2002. Rapid burial and exhumation during orogeny: Thickening and synconvergent exhumation of thermally weakened and thinned crust (Variscan orogen in Western Europe). *American Journal of Science*, **302**, 856-879.

Skrzypek, E., Schulmann, K., Štípská, P., Chopin, F., Lehmann, J., Lexa, O. & Haloda, J., 2011a. Tectono-metamorphic history recorded in garnet porphyroblasts: insights from thermodynamic modelling and electron backscatter diffraction analysis of inclusion trails. *Journal of Metamorphic Geology*, **29**, 473–496.

Skrzypek, E., Štípská, P., Schulmann, K., Lexa, O. & Lexová, M., 2011b. Prograde and retrograde metamorphic fabrics - a key for understanding burial and exhumation in orogens (Bohemian Massif). *Journal of Metamorphic Geology*, **29**, 451–472.

Souček, J., 1978. Metamorphic zones of the Vrbno and Rejvíz series, the Hrubý Jeseník Mountains, Czechoslovakia. *Tschermaks mineralogische und petrographische Mitteilungen*, **25**, 195-217.

Štípská, P., Chopin, F., Skrzypek, E., Schulmann, K., Lexa, O., Pitra, P., Martelat, J. E. & Bollinger, C., submitted. The role of large-scale folding and erosion on juxtaposition of eclogite and mid-crustal rocks (Orlica-Śnieżnik Dome, Bohemian Massif). *Journal of Metamorphic Geology*, **submitted**.

Štípská, P., Pitra, P. & Powell, R., 2006. Separate or shared metamorphic histories of eclogites and surrounding rocks? An example from the Bohemian Massif. *Journal of Metamorphic Geology*, **24**, 219-240.

Štípská, P. & Powell, R., 2005a. Constraining the P-T path of a MORB-type eclogite using pseudosections, garnet zoning and garnet-clinopyroxene thermometry: an example from the Bohemian Massif. *Journal of Metamorphic Geology*, **23**, 725-743.

Štípská, P. & Powell, R., 2005b. Does ternary feldspar constrain the metamorphic conditions of high-grade meta-igneous rocks? Evidence from orthopyroxene granulites, Bohemian Massif. *Journal of Metamorphic Geology*, **23**, 627-647.

Štípská, P., Powell, R., White, R. W. & Baldwin, J. A., 2010. Using calculated chemical potential relationships to account for coronas around kyanite: an example from the Bohemian Massif. *Journal of Metamorphic Geology*, **28**, 97-116.

Štípská, P. & Schulmann, K., 1995. Inverted metamorphic zonation in a basement-derived nappe sequence, eastern margin of the Bohemian Massif. *Geological Journal*, **30**, 385-413.

Štípská, P., Schulmann, K. & Höck, V., 2000. Complex metamorphic zonation of the Thaya dome: result of buckling and gravitational collapse of an imbricated nappe sequence. In: *Forced folds and fractures, Geological Society Special Publications, 169* (eds Cosgrowe, J. W. & Ameen, M. S.), pp. 197-211, Geological Society, London, Special publications.

Štípská, P., Schulmann, K. & Kröner, A., 2004. Vertical extrusion and middle crustal spreading of omphacite granulite: a model of syn-convergent exhumation (Bohemian Massif, Czech Republic). *Journal of Metamorphic Geology*, **22**, 179-198.

Štípská, P., Schulmann, K. & Powell, R., 2008. Contrasting metamorphic histories of lenses of high-pressure rocks and host migmatites with a flat orogenic fabric (Bohemian Massif, Czech Republic): a result of tectonic mixing within horizontal crustal flow? *Journal of Metamorphic Geology*, **26**, 623-646.

Štípská, P., Schulmann, K., Thompson, A. B., Ježek, J. & Kröner, A., 2001. Thermo-mechanical role of a Cambro-Ordovician paleorift during the Variscan collision: the NE margin of the Bohemian Massif. *Tectonophysics*, **332**, 239-253.

Suess, F. E., 1912. Die Moravischen Fenster und ihre Beziehung zum Grundgebirge des Hohen Gesenkes. *Akademie der Wissenschaften, Denkschrift Matematisch-Naturwissenschaftliche Klasse*, **88**, 541-631.

Suess, F. E., 1918. Bemerkungen zur neueren Literatur über die Moravischen Fenster. *Mitt Geol Ges* **11**, 71-128.

Suess, F. E., 1926. *Intrusionstektonik und Wandertektonik im variszichen Grundgebirge*. Verlag Bornttrager, Berlin.

Thiele, O., 1984. Zum Deckenbau und Achsenplan des Moldanubikums der südlichen Böhmischen Masse (Österreich). *Jahrbuch der Geologischen Bundesanstalt Wien*, **126**, 513-523.

Thompson, A. B., Schulmann, K., Ježek, J. & Tolar, V., 2001. Thermally softened continental extensional zones (arcs and rifts) as precursors to thickened orogenic belts. *Tectonophysics*, **332**, 115-141.

Tollmann, A., 1982. Großräumiger variszischer Deckenbau im Moldanubikum und neue Gedanken zum Variszikum Europas. *Geotektonische Forschungen*, **64**, 1-91.

Turniak, K., Mazur, S. & Wysoczanski, R., 2000. SHRIMP zircon geochronology and geochemistry of the Orlica-Śnieżnik gneisses (Variscan belt of Central Europe) and their tectonic implications. *Geodinamica Acta*, **13**, 1-20.

Vanderhaeghe, O. & Teyssier, C., 2001. Partial melting and flow of orogens. *Tectonophysics*, **342**, 451-472.

White, R. W. & Powell, R., 2002. Melt loss and the preservation of granulite facies mineral assemblages. *Journal of Metamorphic Geology*, **20**, 621-632.

White, R. W., Powell, R. & Baldwin, J. A., 2008. Calculated phase equilibria involving chemical potentials to investigate the textural evolution of metamorphic rocks. *Journal of Metamorphic Geology*, **26**, 181-198.

White, R. W., Powell, R. & Holland, T. J. B., 2001. Calculation of partial melting equilibria in the system Na2O-CaO-K2O-FeO-MgO-Al2O3-SiO2-H2O (NCKFMASH). *Journal of Metamorphic Geology*, **19**, 139-153.

Žáček, V., 1996. Retrograded eclogite from the Staré Město Belt, NE margin of the Bohemian Massif. *Journal of the Czech Geological Society*, **41**, 167-175.

APPENDIX

The appendix contains following publications that are grouped thematically. Within each group the publications appear in chronological order. Some publications cover several research subjects, which is discussed in the synthetic part of the text.

METAMORPHISM OF THE BRUNIA CONTINENTAL MARGIN

1. **Štípská**, P. & Schulmann, K. (1995). Inverted metamorphic zonation in a basement-derived nappe sequence, Eastern margin of the Bohemian Massif. *Geological Journal*, 30, 385-413. DOI: 10.1002/gj.3350300315
2. **Štípská**, P., Schulmann, K. & Höck, V. (2000). Complex metamorphic zonation of the Thaya dome: result of buckling and gravitational collapse of imbricated nappe sequence. In: Cosgrove, J.W. and Ameen, M.S. (Eds), Forced folds and fractures, *Geological Society London, special publications*, 169, 197-211.
3. **Štípská**, P., Pitra, P., Powell, R. (2006). Separate or shared metamorphic histories of eclogites and surrounding rocks? An example from the Bohemian Massif. *Journal of Metamorphic Geology*. 24, 219-240. doi:10.1111/j.1525-1314.2006.00634.x.
4. Košuličová, M. & **Štípská, P**. (2007). Variations in the transient prograde geothermal gradient from chloritoid-staurolite equilibria: A case study from the Barrovian and Buchan type domains in the Bohemian Massif. *Journal of Metamorphic Geology*, 25, 19-35. doi:10.1111/j.1525-1314.2006.00674.x.

THE TRANSITIONAL ZONE BETWEEN THE INTERNAL OROGENIC ROOT DOMAIN AND THE CONTINENTAL MARGIN

5. Parry, M., **Štípská**, P., Schulmann, K., Hrouda, F., Ježek, J. & Kröner, A. (1997). Tonalite sill emplacement at an oblique plate boundary: NE margin of the Bohemian massif. *Tectonophysics*, 280, 61-81.
6. Kröner, A., **Štípská**, P., Schulmann, K. & Jaeckel, P. (2000). Chronological constraints on the pre-Variscan evolution of the northeastern margin of the Bohemian Massif, Czech Republic. In: Franke, W., Altherr, R., Haak, V., Oncken, O., Tanner, D. (Eds), Orogenic processes – quantification and modelling in the Variscan belt of central Europe. *Geological Society London, special publications*, 179, 175-197.
7. **Štípská** P., Schulmann K., Thompson, A.B., Ježek, J. & Kröner A. (2001). Thermo-mechanical role of a Cambro-Ordovician paleorift during the Variscan collision: the

NE margin of the Bohemian Massif. In: Schulmann, K., Franke, W., Andersen, T.B. (Eds), Paleozoic Orogenesis and Crustal Evolution of the European Lithosphere. *Tectonophysics*, 332, 239-253.

8. Lexa O., **Štípská** P., Schulmann K., Baratoux L. & Kröner A. (2005). Contrasting textural record of two distinct metamorphic events of similar P−T conditions and different durations. *Journal of Metamorphic Geology*, 23, 649-666.

BURIAL AND PEAK METAMORPHIC CONDITIONS OF THE LOWER OROGENIC CRUST

9. **Štípská**, P. & Powell, R. (2005a). Constraining the P−T path of a MORB-type eclogite using pseudosections, garnet zoning and garnet-clinopyroxene thermometry: an example from the Bohemian Massif. *Journal of Metamorphic Geology*, 23, 725-743. doi:10.1111/j.1525-1314.2005.00607.x
10. **Štípská**, P. & Powell, R. (2005b). Does ternary feldspar constrain the metamorphic conditions of high-grade meta-igneous rocks? Evidence from orthopyroxene granulites, Bohemian Massif. *Journal of Metamorphic Geology*, 23, 627-647. doi:10.1111/j.1525-1314.2005.00600.x.
11. Racek, M., **Štípská, P.,** Powell, R. (2008). Garnet-clinopyroxene intermediate granulites in the St. Leonhard massif of the Bohemian Massif: ultrahigh-temperature metamorphism at high pressure or not? *Journal of Metamorphic Geology*, **26**, 253–271. doi:10.1111/j.1525-1314.2007.00754.x.

METAMORPHIC RECORD OF BURIAL AND SUBSEQUENT EXHUMATION BY SUBVERTICAL CRUSTAL-SCALE FOLDING

12. **Štípská**, P., Schulmann, K. & Kröner, A. (2004). Vertical extrusion and middle crustal spreading of omphacite granulite: a model of syn-convergent exhumation (Bohemian Massif, Czech Republic). *Journal of Metamorphic Geology*, 22, 179-198.
13. Schulmann, K., Kröner, A., Hegner, E., Wendt, I., Konopásek, J., Lexa, O. & **Štípská**, P. (2005). Chronological constraints on the pre-orogenic history, burial and exhumation of deep-seated rocks along the eastern margin of the Variscan orogen, Bohemian Massif, Czech Republic. *American Journal of Science*, 305, 407-448.
14. Racek, M., **Štípská**, P., Pitra, P., Schulmann, K. & Lexa, O. (2006). Metamorphic record of burial and exhumation of orogenic lower and middle crust: new

tectonothermal model for the Drosendorf window (Bohemian Massif). *Mineralogy and Petrology*, 86, 221-251. doi 10.1007/s00710-005-0111-7.

15. Schulmann K., Martelat, J.E., Ulrich, S., Lexa, O., **Štípská, P.** & Becker, J.K. (2008). Evolution of microstructure and melt topology in partially molten granitic mylonite: implications for rheology of felsic middle crust. *Journal of Geophysical Research*, **113**, B10406, doi:10.1029/2007JB005508

16. Schulmann, K., Lexa, O., **Štípská**, P., Racek, M., Tajčmanová, L., Konopásek, J., Edel, J. B., Peschler, A. & Lehmann, J. (2008). Vertical extrusion and horizontal channel flow of orogenic lower crust: key exhumation mechanisms in large hot orogens? *Journal of Metamorphic Geology*, **26**, 273–297. doi:10.1111/j.1525-1314.2007.00755.x.

17. Schulmann, K., Konopásek, J, Janoušek, V., Lexa O., Lardeaux, J.M., Edel, J.B., **Štípská**, P. & Ulrich, S. (2009). An Andean type Palaeozoic convergence in the Bohemian Massif. *C. R. Geoscience*, **341**, 266–286. doi:10.1016/j.crte.2008.12.006.

18. **Štípská**, P., Powell, R., White, R.W. & Baldwin, J.A. (2010). Using calculated chemical potential relationships to account for coronas around kyanite: an example from the Bohemian Massif. *Journal of Metamorphic Geology*, **28**, 97–116. doi:10.1111/j.1525-1314.2009.00857.x

19. Lexa, O., Schulmann, K., Janoušek, V., **Štípská**, P., Guy, A. & Racek, M. (2011). Heat sources and trigger mechanisms of exhumation of HP granulites in Variscan orogenic root. *Journal of Metamorphic Geology*, 79–102. doi:10.1111/j.1525-1314.2010.00906.x

20. Franěk, J., Schulmann, K., Lexa, O., Ulrich, S., **Štípská**, P., Haloda, J. & Týcová, P. (2011). Origin of felsic granulite microstructure by heterogeneous decomposition of alkali feldspar and extreme weakening of orogenic lower crust during the Variscan orogeny. *Journal of Metamorphic Geology*, **29**, 103–130. doi: 10.1111/j.1525-1314.2010.00911.x

21. Skrzypek, E., Schulmann, K., **Štípská** P., Chopin, F., Lehmann, J., Lexa, O. & Haloda, J. (2011a): Tectono-metamorphic history recorded in garnet porphyroblasts: insights from thermodynamic modelling and electron backscatter diffraction analysis of inclusion trails. *Journal of Metamorphic Geology*, **29**, 473–496. doi: 10.1111/j.1525-1314.2010.00925.

22. Skrzypek, E., **Štípská** P., Schulmann, K., Lexa, O. & Lexová, M. (2011b): Prograde and retrograde metamorphic fabrics – a key for understanding burial and exhumation

in orogens (Bohemian Massif). *Journal of Metamorphic Geology*, **29**, 451–472. doi: 10.1111/j.1525-1314.2010.00924.x.

EARLY SHALLOW-DIPPING BURIAL FABRICS IN THE LOWER OROGENIC CRUST

23. Štípská P., Chopin F., Skrzypek E., Schulmann K., Lexa O., Pitra, P., Martelat, J.E., Bollinger, C. submitted. Juxtaposition of eclogite-facies and mid-crustal rocks during exhumation: relative role of erosion and crustal-scale folding in a continentam wedge (Orlica-Śnieżnik dome, Bohemian Massif). *Journal of Metamorphic Geology*.

24. Chopin F., Schulmann K., **Štípská** P., Martelat, J.E., Pitra, P., Lexa, O., Petri, B. submitted. Prograde deformation gradient in subducted high-pressure orthogneiss (Orlica-Śnieżnik dome, Bohemian Massif): implications for reaction softening and strain localisation during continental subduction. *Journal of Metamorphic Geology*.

SIGNIFICANCE OF LATE SHALLOW-DIPPING FABRICS IN THE OROGENIC ROOT ZONE

25. Štípská, P., Schulmann, K. and Powell, R. (2008). Contrasting metamorphic histories of lenses of high-pressure rocks and host migmatites with a flat orogenic fabric (Bohemian Massif, Czech Republic): a result of tectonic mixing within horizontal crustal flow? *Journal of Metamorphic Geology*, **26,** 623–646. doi:10.1111/j.1525-1314.2008. 00781.x.

26. Hasalová, P., Janoušek, V., Schulmann, K., **Štípská**, P. & Erban, V. (2008a). From orthogneiss to migmatite: geochemical assessment of the melt infiltration model in the Gföhl Unit (Moldanubian Zone, Bohemian Massif). *Lithos*, **102**, 508–537. doi:10.1016 /j.lithos. 2007.07.021.

27. Hasalová, P., Schulmann, K., Lexa, O., **Štípská**, P., Hrouda, F., Ulrich, S., Haloda, J. & Týcová, P. (2008b). Origin of migmatites by deformation-enhanced melt infiltration of orthogneiss: a new model based on quantitative microstructural analysis. *Journal of Metamorphic Geology*, 26, 29-53. doi:10.1111/j.1525-1314.2007.00743.x.

28. Hasalová, P., **Štípská**, P., Powell, R., Schulmann, K., Janoušek, V. & Lexa, O. (2008c). Transforming mylonitic metagranite by open-system interactions during melt flow. *Journal of Metamorphic Geology*, 26, 55-80. doi:10.1111/j.1525-1314.2007.00744.x.

METAMORPHISM OF THE BRUNIA CONTINENTAL MARGIN

1. **Štípská**, P. & Schulmann, K. (1995). Inverted metamorphic zonation in a basement-derived nappe sequence, Eastern margin of the Bohemian Massif. *Geological Journal*, 30, 385-413. DOI: 10.1002/gj.3350300315
2. **Štípská**, P., Schulmann, K. & Höck, V. (2000). Complex metamorphic zonation of the Thaya dome: result of buckling and gravitational collapse of imbricated nappe sequence. In: Cosgrove, J.W. and Ameen, M.S. (Eds), Forced folds and fractures, *Geological Society London, special publications*, 169, 197-211.
3. **Štípská**, P., Pitra, P., Powell, R. (2006). Separate or shared metamorphic histories of eclogites and surrounding rocks? An example from the Bohemian Massif. *Journal of Metamorphic Geology*. 24, 219-240. doi:10.1111/j.1525-1314.2006.00634.x.
4. Košuličová, M. & **Štípská, P**. (2007). Variations in the transient prograde geothermal gradient from chloritoid-staurolite equilibria: A case study from the Barrovian and Buchan type domains in the Bohemian Massif. *Journal of Metamorphic Geology*, 25, 19-35. doi:10.1111/j.1525-1314.2006.00674.x.

GEOLOGICAL JOURNAL, VOL. 30, 385–413 (1995)

Inverted metamorphic zonation in a basement-derived nappe sequence, eastern margin of the Bohemian Massif

PAVLA ŠTÍPSKÁ and KAREL SCHULMANN

Institute of Petrology and Structural Geology, Faculty of Science, Charles University, Prague, Albertov 6, Czech Republic

Inverted metamorphic zonation is developed in the basement-derived nappe sequence at the eastern margin of the Bohemian Massif. Mineral reactions and geothermometry reveal an increase in temperature from 580–600°C to 650°C and an increase in pressure from 6 to 10 kbar from the bottom to the top of the nappe pile. Kinematic data and syntectonic crystallization of minerals indicate that the peak conditions were diachronously attained during a slow oblique underthrusting of the Brunovistulian basement. Geochronological data reveal about 20 Ma between granulite facies metamorphism of the upper plate and mineral cooling ages in lower plate, precluding perturbation of the geotherm by underthrusting. A model is suggested showing a progressive break-up of the deepest part of the underthrust Brunovistulicum and subsequent migration of the intraplate to the base of the basement-derived thrust sheet. The uplift of this unit led to its decompression while the rest of the basement was subject to continuous underthrusting. The inverted metamorphic zonation within a single unit is explained using a model of heterogeneous deformation of upward transported units and passive inversion of initially subhorizontal isograds.

KEY WORDS Barrovian metamorphic zonation; prograde metamorphism; continental underthrusting; post-metamorphic imbrication

1. INTRODUCTION

Continental collision zones provide examples for the development of inverted metamorphic zonation related to rapid convergence and crustal overthrusting, e.g. Tertiary collision in the Himalayan chain (Le Fort 1975; Pecher 1989) and Devonian collision in the European Palaeozoic belt (Burg *et al.* 1984; 1989).

The early one-dimensional thermal modelling of Oxburgh and Turcotte (1974), England and Richardson (1977) and England and Thompson (1984) have shown that the inverted thermal structure of orogens is controlled by processes of crustal thickening. The P–T–t paths, distribution of isograds and relative timing of mineral growth are apparently related to the thermal and tectonic evolution of orogenic belts (Thompson and England 1984; Thompson and Ridley 1987).

Inverted temperature gradients are attributed to: (1) instantaneous emplacement of hot on cold material called the 'hot iron effect' (Staubli 1989; Mohan *et al.* 1989; Hubbard 1989); (2) localized heating due to the dissipation of energy on the fault surface (England and Molnar 1993); (3) post-metamorphic imbrication disrupting the metamorphic sequence (Treloar *et al.* 1989; Burg *et al.* 1989; Brunel and Kienast 1986); and (4) the emplacement of granitoids along the thrust surface (Davidson *et al.* 1992).

Detailed tectono-metamorphic studies of inverted metamorphic sequences may help to distinguish between these four mechanisms. Do metamorphic inversions reflect a transient inverted geotherm or a polyphase stacking history? The basement-derived nappes at the eastern border of the Bohemian Massif offer a good opportunity for such a study. Large-scale overthrusting of high-grade Moldanubian rocks over cold Brunovistulian platform (Figure 1) during the Variscan orogeny has been discussed (Höck 1975; Höck *et al.* 1990; Schulmann *et al.* 1994). Imbricated Brunovistulian basement rocks forming the so-called Moravian zone (Suess 1912; 1926) appear in two large-scale tectonic windows (southern Dyje and northern

CCC 0072–1050/95/040385–29

Received 22 November 1994
Revised 26 July 1995

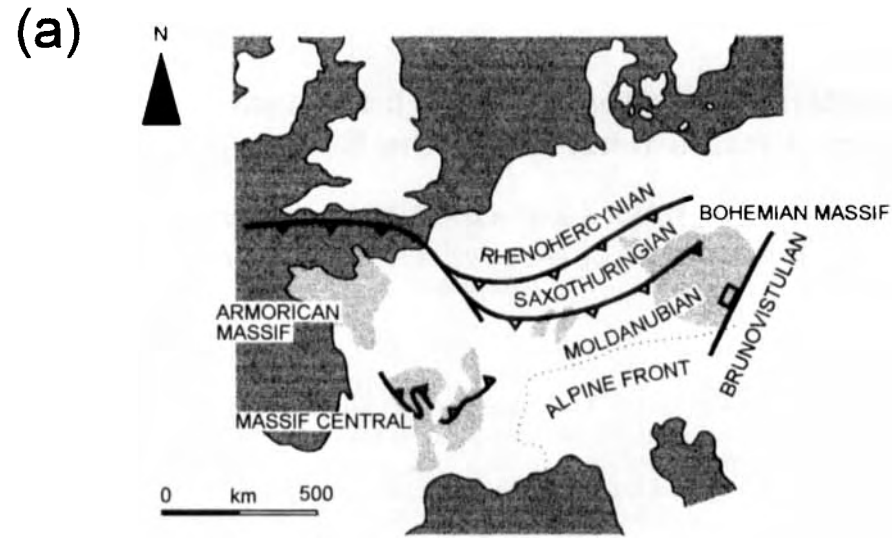
(a)
N
RHENOHERCYNIAN
SAXOTHURINGIAN
BOHEMIAN MASSIF
MOLDANUBIAN
BRUNOVISTULIAN
ALPINE FRONT
ARMORICAN MASSIF
MASSIF CENTRAL
0 km 500

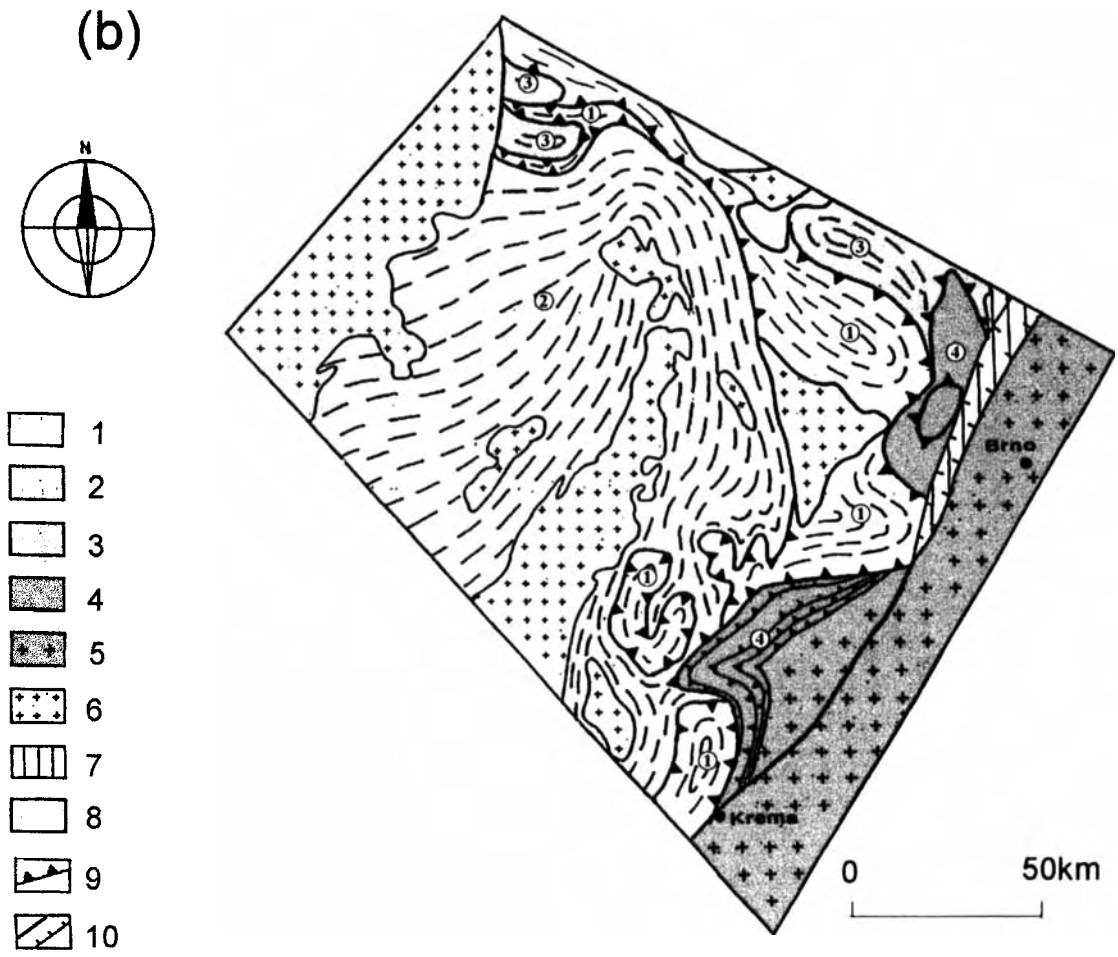
(b)
N
1
2
3
4
5
6
7
8
9
10
Brno
Krems
0
50km

Svratka) below the Moldanubian thrust. The Moravian nappe pile, together with the autochthonous basement rocks, exhibit a classic inversion of metamorphic isograds from chlorite to sillimanite zone (Suess 1912; 1926). The metamorphic inversion continues up to the hanging wall Moldanubian domain, where the uppermost Gföhl unit containing high-temperature eclogites and granulites overlies the high upper amphibolite facies Drosendorf unit (Matte 1991).

In this paper we present and discuss the P–T–t evolution of basement-derived units progressively metamorphosed and stacked in the Dyje window of the Moravian collision zone. Thermobarometry, inferred metamorphic reactions in metapelites and structural and kinematic data in individual stacked units are used to model the development of inverted metamorphic zonation in Moravian zone.

2. LITHOTECTONIC ZONATION

The area studied is situated in the northern part of the Dyje window (Figure 2). The sequence may be divided into six lithotectonic units, from the bottom up.

1. Brunovistulian basement (Dudek 1980), represented by the autochthonous Dyje granitic to granodioritic complex of Cadomian age (551 ± 6 Ma, Rb–Sr whole rock sample, Scharbert and Batik 1985).
2. Para-autochthonous metasedimentary roof (the PU) of the Dyje granite consisting of metagraywacke, quartzite, metapelite and hornfels (Preclik 1924; 1926). The Dyje granite discordantly penetrates the overlying metasediments producing late Proterozoic contact metamorphism (Preclik 1924; 1926; Frasl 1983; Höck *et al.* 1990).
3. Lower Moravian unit (the LMU) formed by strongly deformed Weitersfeld orthogneiss with sills concordant with the hanging wall, varied metasedimentary sequence consisting of mica schist, marble and calc-silicate rocks.
4. Upper Moravian unit (the UMU) formed by a thick slice of the Bítes orthogneiss, presumably of upper Proterozoic age (796 ± 11, Rb–Sr whole rock, Scharbert 1977; 480 ± 50, Rb–Sr whole rock, Van Breemen *et al.* 1982) and by an upper metasedimentary sequence formed by mica schist, quartzite, marble, amphibolite and graphitic schist. The overlying sediments are interlayered with sills of the Bítes orthogneiss.
5. Mica schist zone (the MZ) presented by mica schist, amphibolite, quartzite and concordant orthogneiss bodies.
6. The Moldanubian granulite slice and intrusion of peraluminous anatectic granite represents the highest member of the nappe pile.

It is widely accepted that the LMU and the UMU, called locally the Pleissing nappe and the Bítes nappe, are sheets derived from the Brunovistulian basement during the Variscan orogeny (Frasl 1983; Fritz and Neubauer 1993). This hypothesis is supported by the similarity of geochemical signature and pre-Variscan ages of deformed granitic material in the autochthonous domain as well as in sheared orthogneiss bodies at the base of the LMU and the UMU (Scharbert 1977; Scharbert and Batík 1985; Morauf and Jager 1982; Finger *et al.* 1989). Cooling ages of Variscan metamorphism have been determined using the Ar/Ar method: 325.5 ± 0.7 Ma on muscovite for the LMU, 328.7 ± 0.7 Ma on muscovite for the UMU and 341 ± 1.4 Ma on amphibole for the MZ (Dallmeyer *et al.* 1990).

3. STRUCTURAL GEOLOGY

The first Variscan deformational event comprised NNE compression due to crustal thickening and affects all the tectonic units of the Moravian zone. This event is characterized by the development of a metamorphic

Figure 1. (a) Location of the Bohemian Massif in the European Variscides. The study area is marked by a box. (b) Simplified geological map of the eastern margin of the Bohemian Massif with main tectonic units and major thrusts indicated. 1, Gföhl unit; 2, Drosendorf unit; 3, Svratka crystalline unit; 4, basement-derived nappes of the Moravian zone; 5, Brunovistulian basement; 6, Variscan granitoids; 7, Permian graben; 8, Lower Palaeozoic; 9, thrust boundaries; and 10, strike-slip and normal faults

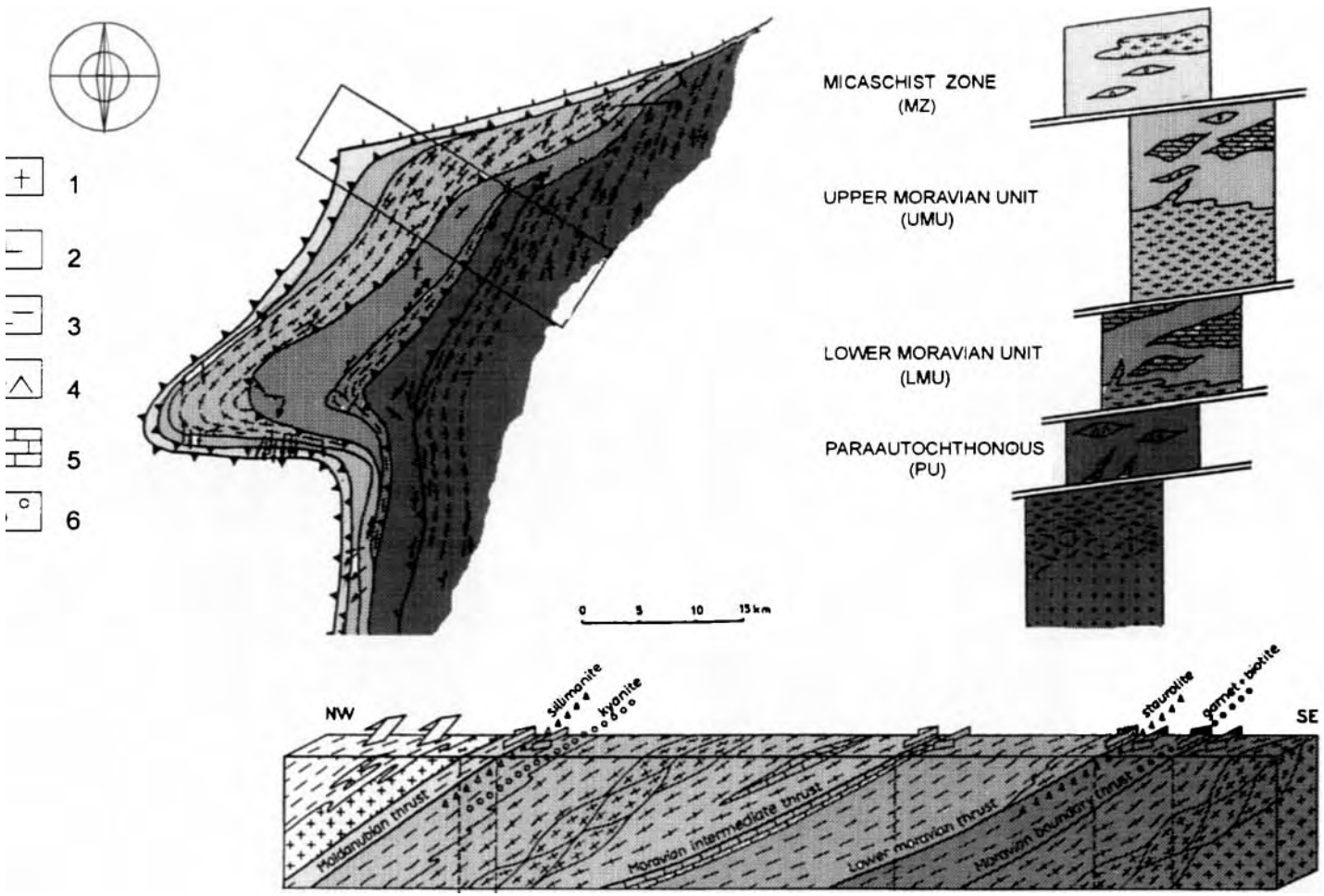

Figure 2. (a) Simplified geological map of the Dyje window. (b) Lithotectonic column: 1, Cadomian Dyje granite; 2, orthogneiss; 3, metapelite; 4, amphibolite; 5, marble and calcsilicate; and 6, quartzite. (c) Tectonic profile across the studied area with indicated metamorphic zones and main tectonic boundaries and sense of displacement along major thrusts

schistosity S_1 subparallel or locally oblique to the lithological bedding. It coincides with axial planes of close to isoclinal sheath F_1 folds. The S_1 planes are subparallel to major lithotectonic boundaries in the entire Dyje window (Figure 2). In the studied profile S_1 dips to the north-west at gentle to intermediate angles. This metamorphic foliation bears a subhorizontal north-east trending stretching lineation L_1. Associated kinematic indicators, e.g. asymmetrical porphyroclasts, shear bands and locally C-S fabrics, suggest top to the north-east oriented shearing (Schulmann *et al.* 1994).

The second major deformation is related to the detachment and strong heterogeneous deformation of two large-scale crustal nappes. The D_2 deformation is characterized by heterogeneous reactivation of the earlier homogeneous fabric and produces sillimanite-bearing shear zones in metapelites of the UMU and of the MZ, and mylonites in orthogneisses of the UMU and the LMU (Schulmann 1990; Schulmann *et al.* 1994; Lobkowicz *et al.* in press). Kinematic criteria again show top to the north-east movements. In the PU the S_2 foliation forms a flat crenulation cleavage deforming the S_1 foliation. Large- to medium-scale subhorizontal F_2 folding affects the highly anisotropic roofs of orthogneiss bodies of the LMU and the UMU.

Late D_3 deformation is retrogressive in all the tectonic units. It is associated with the formation of greenschist facies discontinuous shear zones, shear bands and extensional foliation boudinage with neck zones filled with quartz. D_3 mylonitization is strongest at the footwall of the LMU, where a 1 km thick zone of phyllonites developed (Preclik 1926; Schulmann *et al.* 1994). Kinematic criteria are consistent with north-eastward sliding of the hanging wall segments at the northern part of the Dyje window and with conjugate south-eastward oriented sliding of overlying segments in the south (Fritz 1990; Fritz and Neubauer 1993).

4. METAMORPHISM AND DEFORMATION

During D_1 the rocks of all tectonic units underwent a prograde metamorphic event M_1 with typical Barrovian mineral assemblages in S_1 foliation represented by: (1) st+ky+grt+bt in the MZ and in the UMU; (2) st+grt+bt in the LMU; (3) st+grt+bt in the uppermost part of the PU; and (4) grt+bt or grt+chl+bt in the lower part of the PU unit. The inverted metamorphic zonation is recorded by this spatial mineralogical distribution. Sigmoidal inclusion trails in syntectonic garnets are consistent with top to the north-east kinematics throughout the whole nappe pile (Figure 3b).

In the MZ and the UMU a late tectonic M_2 assemblage bt+sil has overgrown the main foliation in low strain domains or the late sillimanite and biotite grow in asymmetrical pressure shadows around garnets or in microshear zones indicating top to the north-east D_2 movements (Figure 4f).

Late D_3 shearing is associated with the growth of chlorite, muscovite and partly biotite (M_3) in asymmetrical pressure shadows or along late shear bands, indicating consistent top to the north-east movements in all the tectonic units. In low strain domains the chlorite, muscovite and biotite have overgrown the S_1–S_2 fabric. This indicates that in each unit the kinematics are consistently north-eastward during prograde (D_1, M_1) as well as retrograde (D_2, M_2 and D_3, M_3) parts of P–T–t path. The relationships between deformation phases and mineral growth are illustrated in Figure 3a and 3b and the metamorphic zonation in the studied profile is summarized in Figure 2c. The garnet and staurolite isograds lie within the PU in inverted sequence. The whole of the overlying the LMU lies in the staurolite zone. The kyanite and sillimanite isograds are nearly coincident towards the top of the UMU. This zonal scheme is essentially valid for the western margin of the Dyje window (Höck *et al.* 1990). In the northern Svratka window kyanite, staurolite and garnet isograds are found inverted within the UMU (Jaros and Mísar 1974) and the biotite and chlorite isograds are developed in the LMU. This suggests that the isograds transect the thrusts in the whole Moravian zone.

5. TEXTURES AND MINERAL PHASES

5a. Chlorite

In the PU chlorite is present as thin flakes intergrown with muscovite and biotite in the main S_1 foliation plane. Late chlorite also appears within pressure shadows around garnet and staurolite or replaces biotite. In

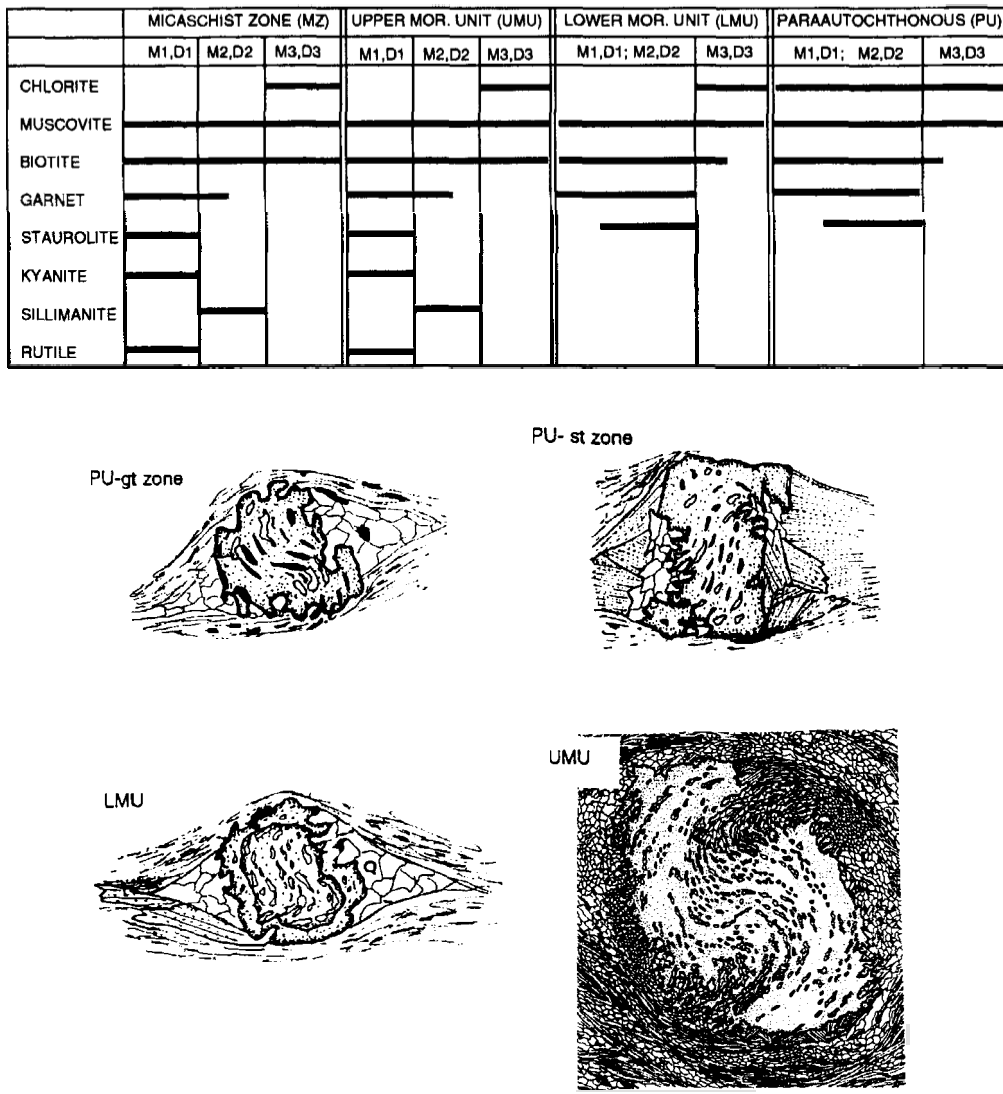

Figure 3. (a) Stability of minerals in relation to the main deformation phases and metamorphic events are indicated by black bars. (b) Inclusion trail patterns in rotated garnets in the UMU, the LMU and the PU. These garnets show consistent top to the north-east kinematics related to the D_1, M_1 event

all other units this late chlorite appears as large porphyroblasts that grew across the foliation plane or replaced garnet, staurolite and biotite in the pressure shadows, or that grew along retrograde D_3 shear bands. Chlorite has a ripidolite composition with X_{Fe} 0.40–0.55. Chlorite grown in fractures of large garnets in the UMU and the MZ exhibits an even higher X_{Fe} (0.55–0.80), reflecting the high X_{Fe} of the host garnet (Figure 5).

5b. White mica

In all the tectonic units white micas define the main foliation. In the PU and the LMU the preferred orientation of the white mica is distinct, whereas in the UMU and the MZ it is ill-defined. The grain size increases from the PU towards the hanging wall units. White micas are muscovites with a minor component of celadonite and paragonite. The paragonite content in white mica is higher in the staurolite zone of both the PU and the LMU and decreases towards the kyanite and sillimanite zone in the structurally high UMU

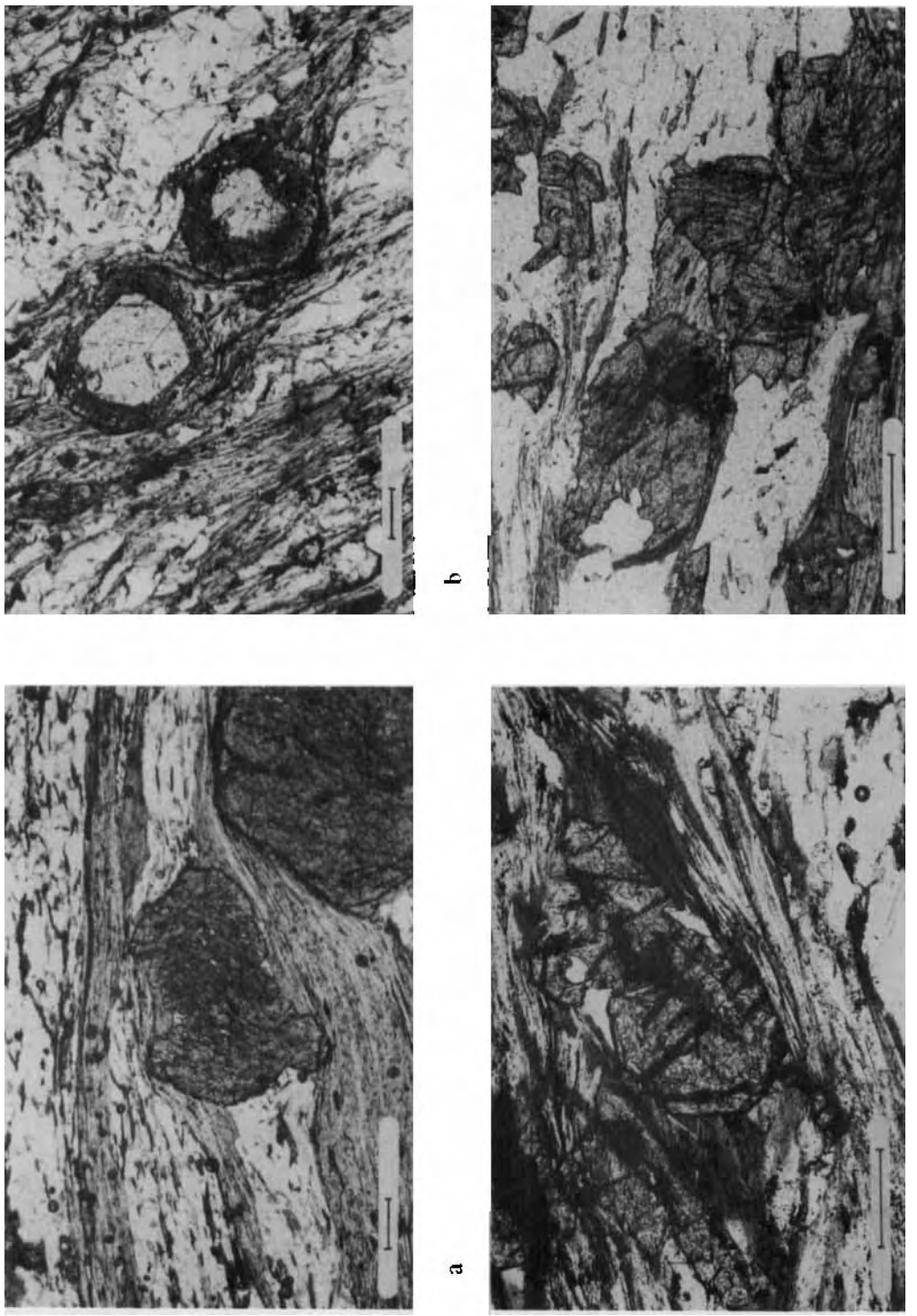

Figure 4. Micrographs of porphyroblast–foliation relationship and of principal textures. Black bar represents 0.3 mm. (a) Rotated garnet porphyroblasts in the PU showing curved inclusion trails. (b) Optically zoned garnets in the LMU showing clear garnet I cores and clouded garnet II rims. (c) Staurolite porphyroblast grown at the expense of garnet I in the LMU. (d) Staurolite porphyroblasts grown over the main foliation S_1 folded by syn-schistosity north-east vergent F_1 folds.

Figure 4 caption continued on next page

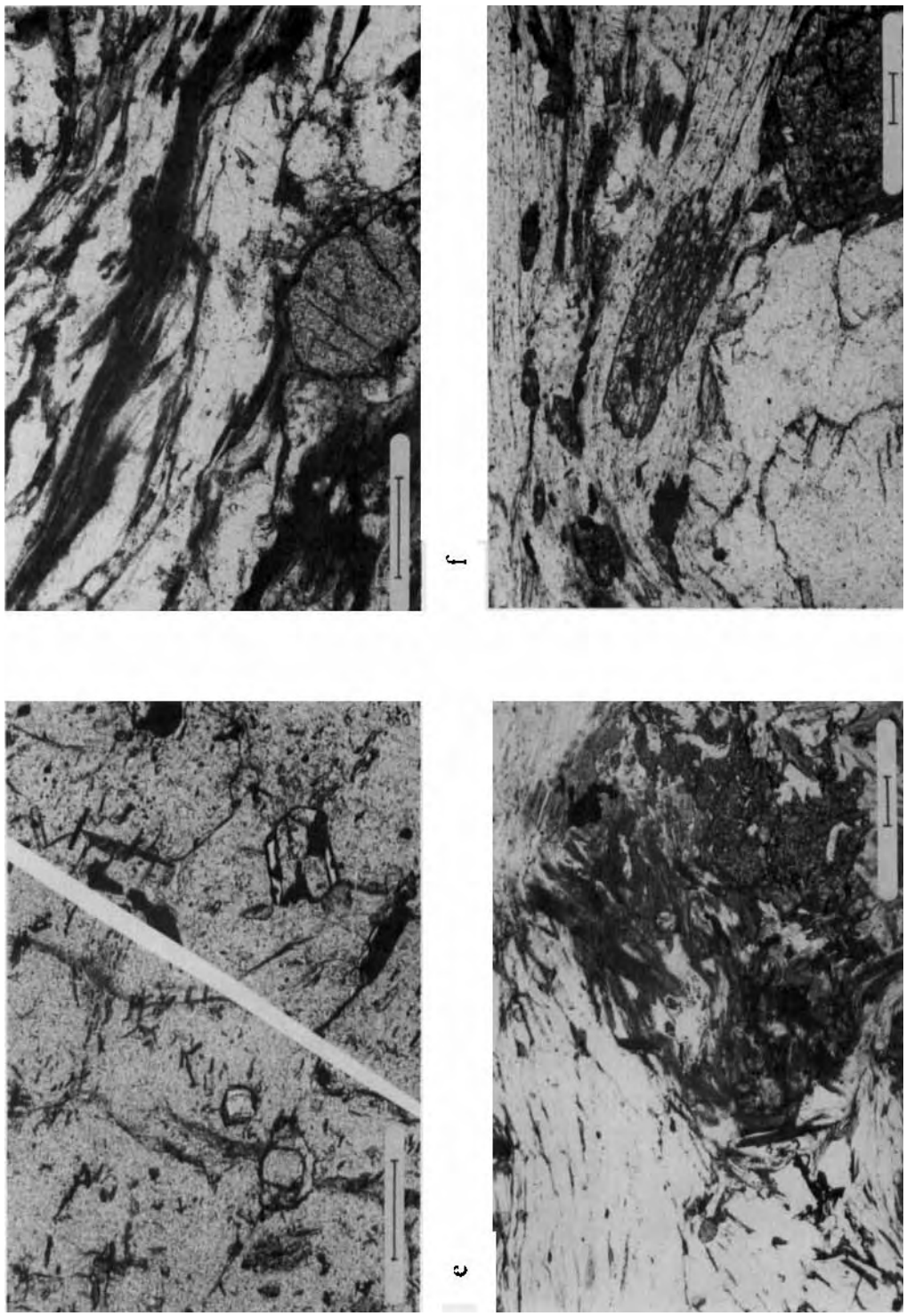

(e) Inclusions of staurolite, kyanite and rutile in large garnet of the UMU. (f) Sillimanite grown along north-east vergent microshear zones in the UMU. (g) Resorption of large garnet by biotite and sillimanite in the MZ. (h) Relict kyanite in a late S_3 shear zone formed by muscovite in the MZ

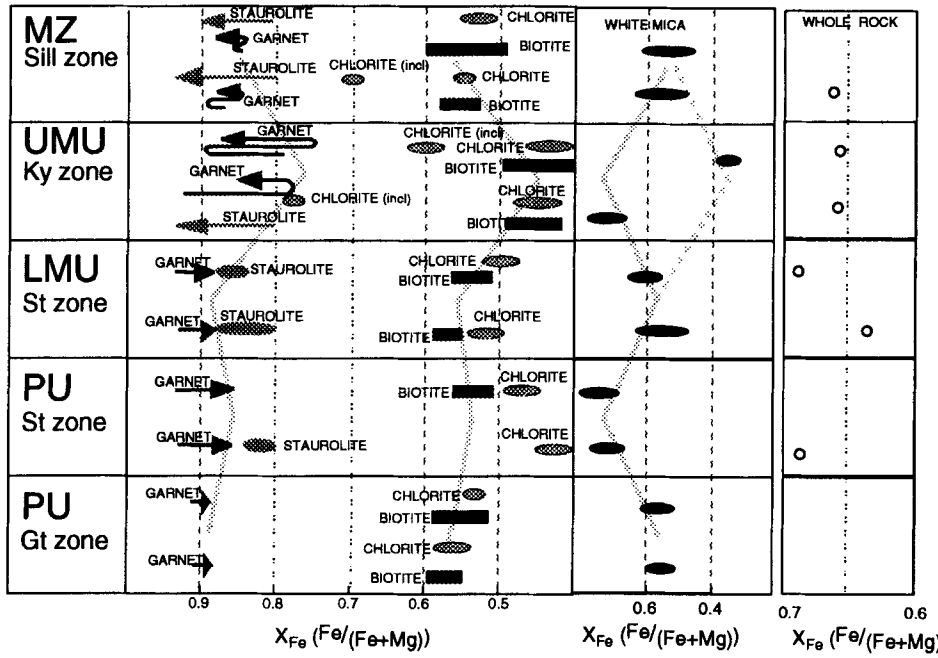

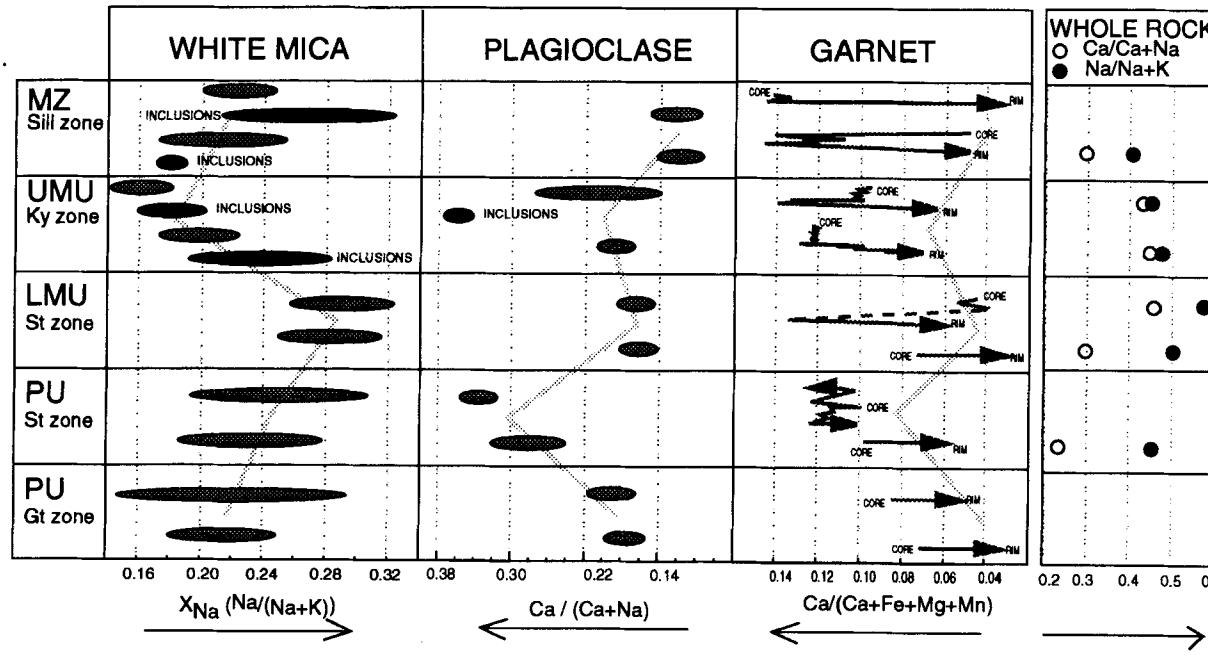

Figure 5. (a) Schematic T–X_{Fe} diagram showing the change in the composition of garnet, staurolite, biotite, chlorite and white micas with increasing metamorphic grade. (b) Variations of paragonite content in muscovite, anorthite content in plagioclase and grossular content in garnet with metamorphic grade. The X_{Fe}, X_{Ca}, X_{Na} values of the whole rock analyses are presented at the right-hand side of the diagrams

Table 1. Biotite — representative microprobe analyses

	Mica schist zone (MZ)		Upper unit (UMU)		Lower unit (LMU)		Para-autochthonous Unit (PU)	
MnO	0.06	0.02	0.23	0.26	0.00	0.00	0.13	0.06
NaO	0.41	0.13	0.20	0.26	0.29	0.26	0.15	0.33
K_2O	8.34	7.44	7.38	7.40	7.37	8.46	8.40	8.73
FeO_{tot}	19.04	19.61	17.54	18.73	20.71	19.62	20.51	17.37
MgO	8.34	8.68	10.00	10.26	9.09	9.21	9.41	8.64
CaO	0.00	0.05	0.02	0.00	0.00	0.03	0.00	0.00
ZnO	0.00	0.08	0.07	0.12	0.00	0.01	0.03	0.01
Al_2O_3	21.18	22.06	19.13	18.89	19.83	19.62	17.56	21.39
TiO_2	1.82	1.70	1.95	2.05	1.62	1.44	1.83	1.35
SiO_2	33.62	33.49	34.97	35.00	35.23	34.99	34.16	36.26
CrO	0.00	0.01	0.01	0.01	0.02	0.00	0.00	0.07
OH	3.85	3.89	3.85	3.89	3.92	3.88	3.78	3.97
Total	96.67	97.15	95.35	96.88	98.08	97.53	95.96	98.18
Mn	0.008	0.002	0.031	0.034	0.001	0.000	1.74	0.007
Na	0.125	0.038	0.060	0.077	0.087	0.078	4.69	0.096
K	1.654	1.461	1.464	1.455	1.438	1.664	1.697	1.681
Fe_{tot}	2.474	2.526	2.282	2.414	2.649	2.530	2.716	2.191
Mg	1.933	1.993	2.317	2.356	2.072	2.118	2.221	1.943
Ca	0.000	0.008	0.003	0.000	0.000	0.004	0.000	0.001
Zn	0.000	0.009	0.008	0.014	0.000	0.001	0.003	0.001
Al	3.879	4.002	3.507	3.432	3.574	3.566	3.277	3.803
Ti	0.212	0.196	0.228	0.238	0.186	0.167	0.218	0.153
Si	5.225	5.156	5.438	5.395	5.389	5.396	5.409	5.472
Cr	0.000	0.002	0.002	0.002	0.003	0.000	0.000	0.008
OH	2.000	2.000	2.000	2.000	2.000	2.000	2.000	2.000
	17.51	17.393	17.340	17.416	17.398	17.524	17.606	17.356
X_{Fe}	0.5622	0.5591	0.4992	0.5095	0.5611	0.5444	0.5517	0.5308

and the MZ (Figure 5b). Margarites were found as inclusions in garnets, sometimes together with chlorites with exceptionally high X_{Fe} up to 0.8 in the UMU and the MZ.

5c. Biotite

Primary biotite is a widespread phase in all the tectonic units, exhibiting a strong preferred orientation. In all the tectonic units rare biotite porphyroblasts overgrew S_1–S_2 foliation and replaced early garnets. Biotite shows extensive Fe–Mg solid solution with X_{Fe} varying from 0.4 to 0.5 in the kyanite zone of the UMU and from 0.5 to 0.6 in all other zones (Figure 5a, Table 1). The TiO_2 content in biotite tends to increase in conjunction with metamorphic grade.

5d. Garnet

In the PU, garnets contain numerous opaque and quartz inclusions. The shape of inclusion trails is irregular being perpendicular, curved to parallel with respect to the external foliation (Figures 3b and 4a).

Inclusion-free garnet I in the LMU is often rimmed by clouded garnet II, which is rich in quartz and opaque inclusions (Figure 4b). The younger garnet II also grew separately in the matrix. The inclusion trails are often curved, indicating syn-D_1 growth.

Large clear garnets in the UMU and the MZ contain inclusions of ky+rt+st+bt+ilm+pl+ms that are sometimes oriented. Snowball inclusion trails were observed, indicating syntectonic garnet growth in the main D_1 shear fabric.

Table 2. Garnet — representative microprobe analyses

	Mica schist zone (MZ)		Upper unit (UMU)		Lower unit (LMU)				Para-autochthonous unit (PU)	
	Core	Rim	Core	Rim	Core I	Rim I	Core II	Rim II	Core	Rim
MnO	2.35	3.59	8.07	4.74	7.11	1.8	1.36	0.64	7.94	3.92
NaO	0.000	0.000	0.000	0.000	0.01	0.000	0.01	0.07	0.06	0.000
K_2O	0.02	0.18	0.000	0.000	0.000	0.02	0.000	0.000	0.000	0.03
FeO_{tot}	32.84	31.96	28.65	30.22	32.00	35.62	32.57	35.71	28.14	31.83
MgO	2.89	2.04	1.54	2.91	1.48	2.55	2.12	2.57	1.84	2.88
CaO	2.59	2.47	4.24	3.81	1.31	1.12	4.22	1.86	3.07	2.34
ZnO	0.12	0.36	0.000	0.000	0.000	0.000	0.000	0.02	0.04	0.26
Al_2O_3	21.82	22.18	21.33	21.68	21.33	21.64	22.18	21.83	21.51	21.81
TiO_2	0.01	0.04	0.12	0.07	0.04	0.000	0.03	0.01	0.07	0.03
SiO_2	37.50	37.32	37.51	37.75	36.9	36.44	37.73	37.48	36.87	36.61
CrO	0.000	0.000	0.000	0.001	0.01	0.000	0.000	0.000	0.01	0.000
Total	100.14	100.16	101.45	101.20	100.18	99.19	100.21	100.19	99.55	99.91
Mn	0.317	0.487	0.864	0.510	0.977	0.248	0.184	0.087	1.089	0.534
Na	0.000	0.000	0.000	0.000	0.002	0.000	0.004	0.023	0.018	0.000
K	0.004	0.037	0.000	0.000	0.000	0.004	0.000	0.000	0.000	0.005
Fe_{tot}	4.386	4.281	3.713	3.933	4.340	4.848	4.334	4.781	3.809	4.282
Mg	0.688	0.487	0.356	0.676	0.357	0.620	0.504	0.612	0.444	0.692
Ca	0.443	0.424	0.703	0.635	0.227	0.196	0.720	0.319	0.533	0.4029
Zn	0.016	0.045	0.000	0.000	0.000	0.000	0.000	0.002	0.005	0.030
Al	4.107	4.184	3.895	3.977	4.077	4.150	4.157	4.119	4.103	4.136
Ti	0.001	0.005	0.014	0.008	0.005	0.000	0.003	0.001	0.009	0.004
Si	5.988	5.974	5.814	5.875	5.984	5.929	6.005	6.001	5.967	5.921
Cr	0.000	0.000	0.000	0.001	0.001	0.000	0.000	0.000	0.008	0.000
	51.950	15.922	15.359	15.615	15.971	15.995	15.912	15.947	15.978	16.008
X_{Fe}	0.8724	0.9075	0.9278	0.8680	0.9370	0.8916	0.8997	0.8883	0.9170	0.8744
Al	0.7518	0.7544	0.6598	0.6841	0.7358	0.8201	0.7551	0.8245	0.6490	0.7247
Py	0.1179	0.0856	0.0633	0.1175	0.0606	0.1048	0.0878	0.1056	0.0756	0.1170
Sp	0.0544	0.0857	0.1535	0.0887	0.1656	0.0420	0.0320	0.0150	0.1855	0.0904
Gr	0.0757	0.0735	0.1213	0.1081	0.0370	0.0330	0.1245	0.0548	0.0882	0.0673
Ad	0.0001	0.0007	0.0022	0.0013	0.0008	0.0000	0.0005	0.0002	0.0014	0.0006

5e. Garnet chemistry

Normal garnet growth zoning patterns are preserved in all the tectonic units, with some deviations depending on metamorphic grade. The pattern is characterized by Mn, Ca, X_{Fe} decreasing in a typical bell-shaped zoning curve and Mg, Fe increasing from core to rim. This zoning pattern (Figure 6a, Table 2) is attributed to prograde metamorphic conditions prevailing during the main metamorphic event. Ternary Mn–Fe–Mg plots exhibit decreasing fractionation of Mn and an increase in Fe and Mg (Figure 6b).

Garnet I in the LMU exhibits normal growth zoning curves of Mn, Mg and Fe, but differs in Ca content, which is flat and exceptionally low. The garnet II rimming the early garnet is characterized by the normal zoning pattern characteristic of all other units. The depletion of Mn may be explained by its fractionation during the growth of garnet I. The abrupt change in textural and compositional zoning might be attributed to the involvement of garnet in discontinuous reactions during its growth (Thompson 1976a; Burton *et al.* 1989). In the UMU and the MZ the normal zoning pattern is perturbed near the rim by an increase in Mn and X_{Fe} in conjunction with a decrease in Mg and Fe. This type of zoning is well demonstrated in the ternary Mn–Fe–Mg plot (Figure 6b) and reflects the resorption of garnet by a reaction producing biotite (Tracy *et al.* 1976). In the MZ, flat chemical profiles of garnet porphyroblasts are present. This type of chemical profile

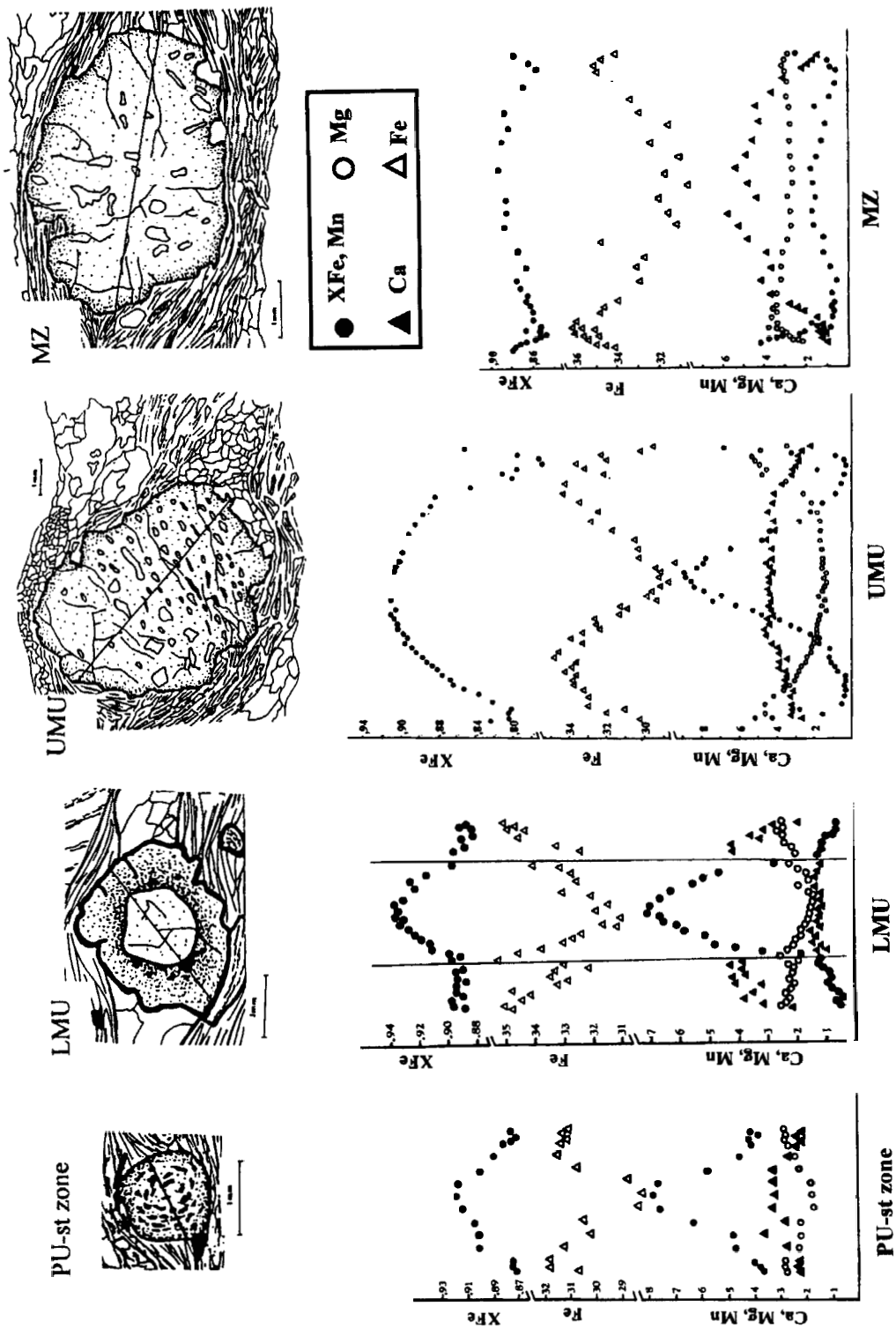
PU-st zone
LMU
UMU
MZ
● XFe, Mn ○ Mg
▲ Ca △ Fe
Ca, Mg, Mn
Fe
XFe

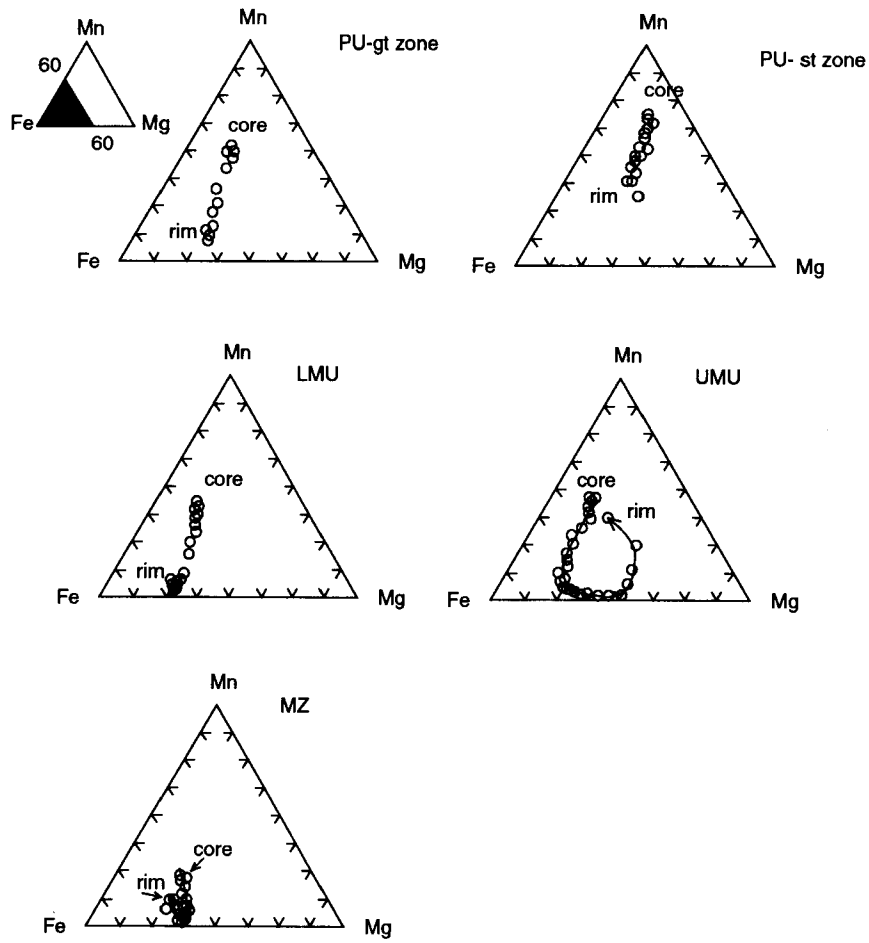

Figure 6. (a) Representative textural types of garnet and chemical profiles. (b) Ternary diagrams showing characteristic garnet zoning patterns in individual units

is characteristic of high-grade rock and the homogenization of garnet chemistry commonly attributed to intracrystalline diffusion.

5f. Staurolite

Small staurolite grains appear in the main foliation in the uppermost part of the PU. In the LMU staurolite replaces the inclusion-free garnets I (Figure 4c) and overgrows straight S_1 foliation or S_1 folded by recumbent F_1 folds (Figure 4d). These observations suggest continuous growth of staurolite during D_1, but slightly later than garnet I. Staurolite is a common inclusion in large garnets in the UMU and the MZ, together with kyanite (Figure 4e). In both units staurolite also grew within the main foliation. The amount of staurolite in the matrix of the MZ is lower compared with inclusions in garnet. Sometimes staurolite in the matrix is absent altogether. Matrix staurolite rarely contains inclusions of rt+qtz+bt+ms+opaque.

Staurolites from the UMU and the MZ are chemically zoned, exhibiting an increase in X_{Fe} from the core (0.8) towards the rim (0.93). Ti, Mg, Fe and Si contents decrease towards the rim, whereas Al increases, indicating the (Fe, Mg)Si→AlAl Tschermak's substitution (Figures 5a and 7, Table 3). The Zn content ranges between 0.0 and 1.6 wt.% and varies irregularly within a single grain irrespective of the metamorphic grade.

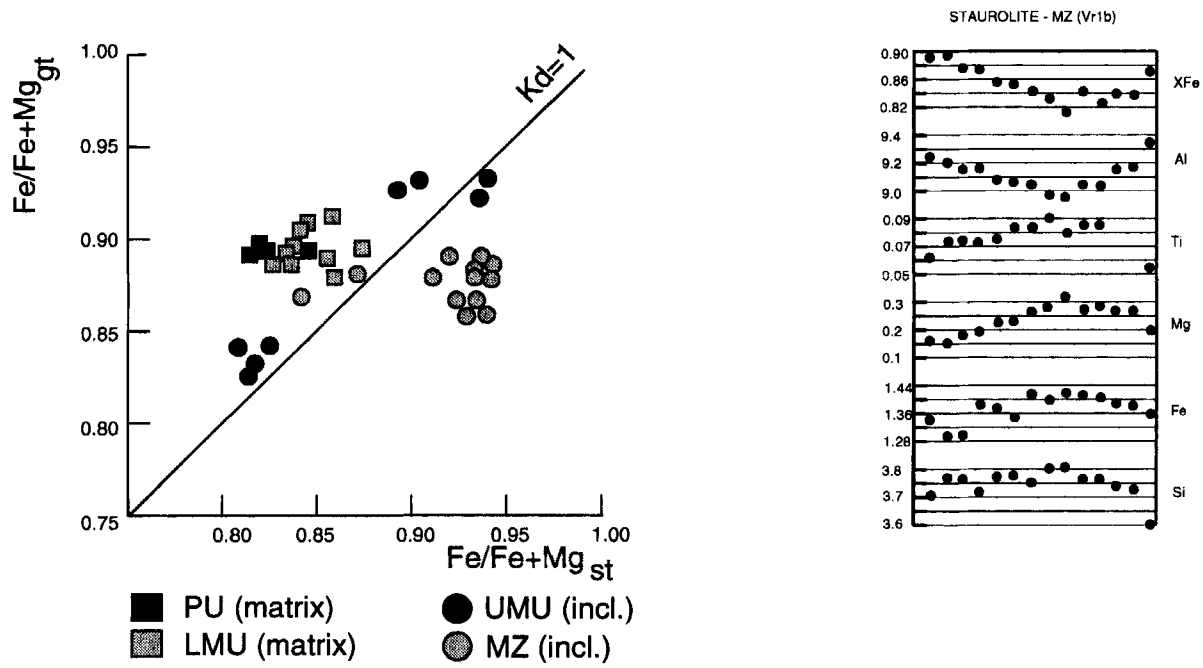

Figure 7. (a) Mineral chemistry of staurolite illustrating partitioning of Fe–Mg between garnet and staurolite in individual units. It shows Fe–Mg reversal in the MZ and partly in the UMU. (b) Chemical zoning profile in staurolite of the MZ revealing reverse zoning marked by X_{Fe} increase towards the rim

The partitioning of Fe–Mg between staurolite and garnet in the PU and the LMU shows $X_{Fe\ st} < X_{Fe\ Gt}$, whereas in the UMU and the MZ the reverse relationship in Fe–Mg partitioning is observed (Figure 7a). The reverse trend was also reported by Ballèvre *et al.* (1989) from HP metapelites.

5g. Plagioclase

Plagioclase in the PU occurs in some places as porphyroblasts that overgrew the S_1 fabric. Plagioclase composition in the PU is An_{24-36} and in the LMU is An_{14-18}. In the UMU some plagioclase inclusions in large garnets are An_{34-38} and the matrix plagioclase corresponds to An_{18-28}, whereas in the MZ both inclusions in garnets and matrix plagioclase are An_{10-14} (Figure 5b, Table 4).

5h. Kyanite

Kyanite appears in the UMU and the MZ as large tabular crystals in the foliation plane or as inclusions within garnets (Figure 4e). Kyanite and staurolite sometimes form intergrowths in the UMU. Large kyanite porphyroblasts rarely contain inclusions of bt+rt+qtz+ms+opaque+ma. Kyanite is often boudinaged, replaced and overgrown by muscovite (Figure 4h).

5i. Sillimanite

Sillimanite was recognized only within the UMU and the MZ. Fibrolitic sillimanite grows along the foliation planes and microshear zones in the UMU and towards the MZ the amount of sillimanite increases (Figure 4f). In the MZ a secondary complex intergrowth of biotite and fibrolite replaced early garnet (Figure 4g).

Table 3. Staurolite — representative microprobe analyses

	Mica schist zone (MZ)			Upper unit (UMU)			Lower unit (LMU)		Para-autochthonous unit (PU)
	Core	Rim	Inclusions	Core	Rim	Inclusions	Core	Rim	
MnO	00.23	0.21	0.11	0.44	0.38	0.85	0.14	0.05	0.38
NaO	0.00	0.08	0.02	0.00	0.09	0.00	0.16	0.02	0.19
K_2O	0.02	0.00	0.01	0.00	0.00	0.00	0.00	0.01	0.00
FeO_{tot}	12.03	11.96	13.28	12.51	12.32	12.06	13.29	13.34	12.42
MgO	1.36	1.32	0.56	1.96	1.75	0.82	1.50	1.37	1.55
CaO	0.00	0.02	0.00	0.00	0.01	0.05	0.00	0.01	0.00
ZnO	0.38	0.28	0.49	1.27	1.41	0.35	0.79	1.05	2.21
Al_2O_3	54.85	56.38	56.15	53.15	52.83	55.37	53.94	53.45	52.93
TiO_2	0.87	0.16	0.60	0.69	0.58	0.44	0.72	0.61	0.54
SiO_2	27.41	26.96	26.25	28.37	27.53	27.06	28.18	27.44	28.19
CrO	0.08	0.07	0.03	0.00	0.03	0.01	0.08	0.03	0.02
OH	2.16	2.17	2.15	2.17	2.13	2.16	2.18	2.14	2.16
Total	99.39	99.65	99.66	100.58	99.07	99.19	100.99	99.53	100.58
Mn	0.027	0.024	0.014	0.051	0.046	0.082	0.016	0.006	0.044
Na	0.000	0.022	0.005	0.000	0.024	0.000	0.044	0.006	0.050
K	0.004	0.000	0.002	0.000	0.000	0.000	0.000	0.001	0.000
Fe_{tot}	1.395	1.385	1.546	1.446	1.447	1.401	1.529	1.561	1.443
Mg	0.281	0.272	0.117	0.408	0.367	0.171	0.308	0.285	0.320
Ca	0.000	0.004	0.000	0.000	0.001	0.007	0.000	0.002	0.000
Zn	0.039	0.029	0.050	0.130	0.147	0.036	0.080	0.109	0.227
Al	8.969	9.182	9.217	8.654	8.745	9.067	8.749	8.813	8.663
Ti	0.091	0.016	0.082	0.072	0.061	0.046	0.074	0.065	0.056
Si	3.803	3.729	3.656	3.919	3.867	3.763	3.879	3.839	3.915
Cr	0.009	0.008	0.004	0.000	0.003	0.002	0.009	0.003	0.003
OH	1.000	1.000	1.000	1.000	1.000	1.000	1.000	1.000	1.000
	15.618	15.697	15.673	15.680	15.708	15.574	15.689	15.690	15.720
X_{Fe}	0.8351	0.8382	0.9303	0.7858	0.8027	0.8970	0.8340	0.8462	0.8230

6. METAMORPHIC REACTIONS

Most of the metamorphic reactions involving AFM minerals take place in the KFMASH system, K_2O–FeO–MgO–Al_2O_3–SiO_2–H_2O, in which sequences of continuous and discontinuous reactions have been described by Thompson (1976a; 1976b) using isobaric T–X_{Mg} diagrams. However, the application of this reaction scheme to natural rocks is complicated by the problematic persistence of AFM phases beyond fields predicted in the KFMASH system due to additional components, e.g. Na_2O, CaO and MnO (Yardley *et al.* 1980).

Mineral assemblages, mineral compositions and whole rock analyses of metapelites of individual units are portrayed using the AFM topologies of Thompson (1976a) in Figure 8. The relevant metamorphic reactions are deduced from textural relations, the chemical compositions of the AFM phases, plagioclase and muscovite.

6a. Staurolite zone of the PU

The staurolite zone of the PU is characterized by a small amount of biotite and by a large modal amount of chlorite and muscovite. The whole rock analysis shows a higher concentration of alumina than average pelite and plots on the garnet–chlorite tie line in the AFM space (Figure 8). However, the host rock iron content does not allow the production of chloritoid (Hoschek 1969) and consequently the garnet–chlorite–staurolite assemblage could not result from discontinuous reaction of chloritoid and quartz (Thompson *et al.* 1977).

Table 4. Plagioclase — representative microprobe analyses

	Mica schist zone (MZ)	Upper unit (UMU)	Lower unit (LMU)	Para-autochthonous (PU)
MnO	0.01	0.00	0.00	0.00
NaO	10.64	9.44	10.59	8.83
K_2O	0.05	0.08	0.05	0.06
FeO_{tot}	0.04	0.28	0.11	0.20
MgO	0.05	0.00	0.02	0.03
CaO	2.41	4.44	3.24	5.79
ZnO	0.04	0.09	0.00	0.00
Al_2O_3	22.10	23.97	22.29	24.67
TiO_2	0.00	0.00	0.00	0.00
SiO_2	62.91	60.32	62.76	59.89
CrO	0.00	0.00	0.00	0.00
Total	98.26	98.62	99.07	99.48
Mn	0.000	0.000	0.000	0.000
Na	0.928	0.826	0.919	0.768
K	0.003	0.005	0.003	0.003
Fe_{tot}	0.002	0.010	0.004	0.008
Mg	0.003	0.000	0.001	0.002
Ca	0.116	0.215	0.155	0.278
Zn	0.001	0.003	0.000	0.000
Al	1.171	1.275	1.175	1.304
Ti	0.000	0.000	0.000	0.000
Si	2.828	2.722	2.808	2.685
Cr	0.000	0.000	0.000	0.000
	5.052	5.558	5.065	5.048
Ab	88.61	79.02	85.28	73.16
Or	0.28	0.44	0.29	0.32
An	11.11	20.55	14.43	26.52

As was pointed out earlier, the metapelites just below the base of the LMU were strongly retrogressed during D_3 shearing in a zone 1 km thick (Preclik 1926). Therefore, we suggest a retrograde reaction destabilizing an early prograde assemblage of garnet–biotite–staurolite (Figure 8).

6b. Staurolite zone of the LMU

The increasing modal content of biotite and the growth of staurolite associated with the disappearance of primary chlorite are interpreted to result from the discontinuous reaction

$$\text{Muscovite} + \text{garnet} + \text{chlorite} = \text{staurolite} + \text{biotite} + \text{quartz} + H_2O \qquad \text{(R1)}$$

Biotite gains K^+ from muscovite and consequently the remaining muscovite is enriched in the Na component (Figure 5b) relative to muscovite in the garnet zone of the PU. This reaction was calibrated to 585°C at a pressure of 5 kbar (Thompson 1976b).

Growth of staurolite at the expense of garnet I (Figure 4c) suggests the continuous reaction (Delor *et al.* 1984)

$$\text{Fe garnet} + \text{Na muscovite} + \text{Ca plagioclase} = \text{Ca garnet} + \text{Na-poor muscovite} + \text{staurolite} + \text{albite} \qquad \text{(R2)}$$

The existence of this reaction is supported by the increase of CaO and decrease of FeO in garnet II (Figure 6) and decrease in X_{An} in matrix plagioclase (Figure 5b), which may result from an increase of P_{tot} (Crawford 1977). Reaction (R2) is temperature sensitive and was empirically calibrated to 590–600°C (Delor *et al.* 1984).

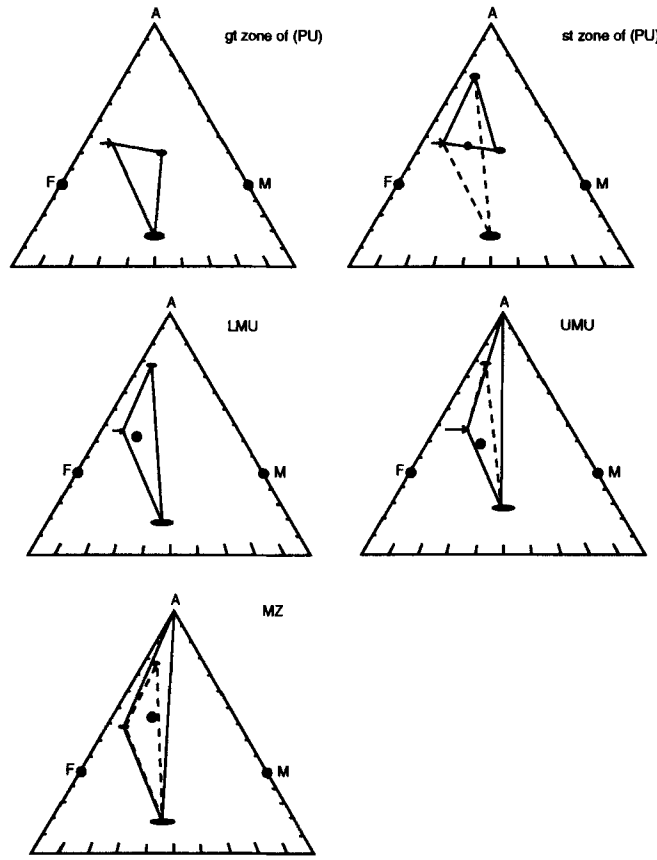

Figure 8. Mineral compositions plotted in AFM topologies of individual units. Black circle represents whole rock analyses. Thick tie lines and hatched lines indicate equilibrium and persisting assemblages, respectively

6c. Kyanite zone of the UMU

Staurolite crystals in the matrix exhibit a marked zoning with increasing X_{Fe} from the core towards the rim (Figure 7), which could result from the continuous reaction

$$\text{Staurolite} + \text{muscovite} + \text{quartz} = \text{biotite} + Al_2SiO_5 + H_2O \qquad \text{(R3)}$$

The X_{Fe} of all the product phases is lower than that of reactants. Hence reaction (R3) drives the three-phase field st–ky–bt towards the higher X_{Fe} side and could be explained as a continuous Fe–Mg reaction with $T_{Fe} > T_{Mg}$ (Thompson 1976a; 415).

The presence of Fe-staurolite and kyanite inclusions in garnet may indicate the discontinuous reaction

$$\text{Staurolite} + \text{quartz} = \text{kyanite} + \text{garnet} + H_2O \qquad \text{(R4)}$$

This sequence of reactions is consistent with an increase in temperature during prograde metamorphism (Thompson 1976a; 1976b). Reaction (R4) was calibrated by Spear and Cheney (1989) at 650°C, 11 kbar and 670°C, 9 kbar. The increase in the albite component in matrix plagioclase compared with plagioclase inclusions in large garnets and the decrease in the Na/(Na+K) ratio in muscovite (Figure 5b) compared with paragonite-rich muscovites in lower grade pelites may indicate the continuous reaction (Thompson *et al.* 1977; Hoke 1990)

$$\text{Na-rich muscovite} + \text{quartz} = \text{kyanite} + \text{albite} + \text{K-rich muscovite} + H_2O \qquad \text{(R5)}$$

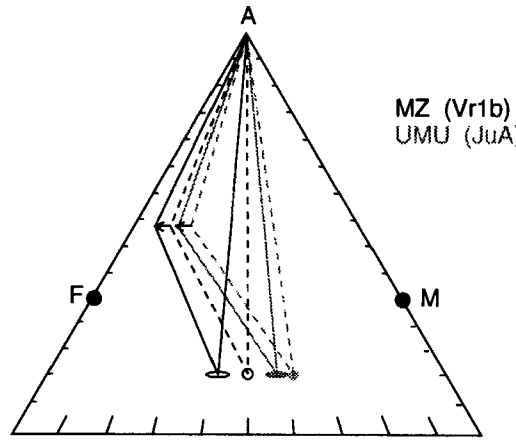

Figure 9. Continuous net transfer reaction (R6) portraying shift of mineral triangle sillimanite–biotite–garnet towards higher Fe

6d. Sillimanite zone of the UMU and the MZ

Garnet grains are often replaced by aggregates of sillimanite and biotite (Figure 4g). Such garnets exhibit reverse zoning at their rims (Figure 6). The garnet resorption together with this type of zoning indicates a continuous reaction

$$\text{Garnet} + \text{muscovite} = \text{sillimanite} + \text{biotite} + \text{quartz} \qquad \text{(R6)}$$

Biotite and garnet become more Fe-rich due to reaction (R6) resulting in a shift in the three-phase triangle garnet–biotite–sillimanite towards the higher X_{Fe} side of AFM diagram (Figure 9). The continuous reaction (R6) is characteristic of a decompression metamorphic path (Spear 1993).

7. CONDITIONS OF METAMORPHISM

The metamorphic conditions were estimated using rim compositions at mutual contacts of garnet–biotite, garnet–chlorite, garnet–staurolite and garnet–plagioclase. Calibrations of the garnet–biotite (gtbt) and garnet–chlorite (gtchl) Fe–Mg exchange (Hodges and Spear 1982) and garnet–staurolite (gtst) Fe–Mg exchange (Perchuk 1969) were used to determine the temperatures during metamorphism within individual units. The pressure conditions of metamorphism were evaluated using pressure-sensitive equilibria of garnet–plagioclase–Al_2SiO_5–quartz (GPAQ) and garnet–plagioclase–biotite–muscovite (GBMP) after Hodges and Crowley (1985).

7a. Results of thermometry

The results of thermometry are shown in Table 5 and in Figure 10. Garnet–biotite thermometry in the garnet zone of the PU yields temperature estimates of 520–600°C. In the retrograde shear zone at the top of the PU (staurolite zone) the garnet–biotite and garnet–chlorite calibrations give temperature estimates varying between 460 and 550°C. Temperature estimates for garnet–staurolite schists of the LMU vary in the range 530–560°C; results of sample L151 are interpreted as a late stage re-equilibration during M_3D_3. Temperatures of 560–650°C were calculated in staurolite–kyanite schists of the UMU and 550–640°C in sillimanite-bearing schists of the MZ. All the above temperature estimates were taken at 7 kbar.

Table 5. Pressure and temperature estimates in individual units (H&S = Hodges and Spear 1982, P = Perchuk 1969, H&C = Hodges and Crouley, 1985)

	T-GRT-BI (H&S)		T-GRT-ST (P)	T-GTBI (H&S) data of Hoeck	T_{max}	GBMP (H&C)		GBMP at T_{max}	GPAQ (H&C)		GPAQ at T_{max}
	5 kbar	7 kbar				500°C	600°C		500°C	600°C	
PU gt zone					600						
L75/2	513–587	520–594				4.0–5.5	6.0–7.5	6.0–7.5			
L78/5	570–620	577–600				4.4–5.2	6.3–7.2	6.3–7.2			
PU st zone				580–590	600						
L82	475–523	481–530				4.3–4.8	6.3–6.8	6.3–6.8			
L84 (gt–chl)	453–542	459–548	540–570			3.8–3.9	6.1–6.3	6.1–6.3			
LMU				598–610	600						
L151	409–443	415–449				3.8–4.6	5.6–6.6	5.6–6.6			
L159	518–550	525–558	550–580			5.8–7.7	7.8–10.3	7.8–10.3			
UMU					650						
Vr7b	554–633	561–640	580–610 incl.			6.4–7.0	8.6–9.4	9.8–10.7	6.4–7.4	8.5–9.2	9.6–10.2
JuA incl.									7.2–9.3	9.4–10.4	
JuA rim	616–643	624–651				5.0–6.0	7.1–8.1	6.6–8.7	4.9–6.0	6.8–8.1	8.0–9.3
MZ					650						
Vr1a	542–628	550–636	620–660 incl.			4.8–5.6	6.8–7.7	7.8–8.7	5.0–5.7	6.9–7.7	7.9–8.9
Vr1b	580–607	588–613	650–680 incl.			4.4–6.1	6.3–8.2	7.3–9.4	4.4–6.4	6.8–8.4	8.2–9.5

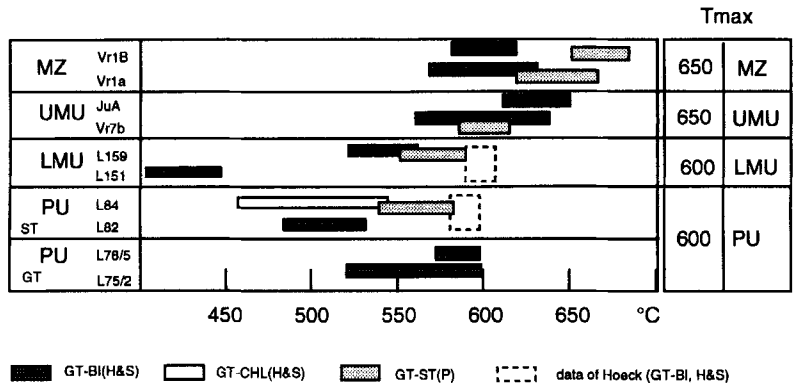

Figure 10. Variations in temperature estimates with increasing grade. The temperature has been calculated at 7 kbar using garnet–biotite (Hodges and Spear 1982), garnet–chlorite (Hodges and Spear 1982) and garnet–staurolite (Perchuk 1969) thermometry. Data of Höck *et al.* (1990) included

7b. Interpretation of thermometry

Maximum temperatures attained in the PU probably reached approximately 580–600°C, in agreement with the data of Höck (1993) from the Austrian part of the same unit. Significantly, lower temperature estimates coming from the staurolite zone of the PU are interpreted as a result of strong M_3 retrogression.

The maximum calculated temperatures (560°C) in the LMU are not consistent with petrography and are lower than for the garnet zone in the PU. This may be explained either by rapid diffusion modifying the garnet rim composition in the staurolite zone, resulting in low calculated temperature (Spear 1993), or by later re-equilibration during M_3 retrogression. The latter possibility is more probable in this instance because of the strong reduction in thickness and widespread retrogression of the LMU in our profile (Batík and Fediuková 1992). In the Austrian part of the LMU, higher temperatures of about 600°C were obtained by Höck *et al.* (1990) using the calibration of Hodges and Crowley (1985) and temperatures of 565–585°C were calculated by Bernroider (1989) using the method of Ghent and Stout (1981). The transition from garnet to staurolite zone at temperatures approaching 600°C is consistent with the discontinuous reaction (R1), which was calibrated to 585°C at a pressure of 5 kbar (Thompson 1976b). This is the reason why the values of Höck *et al.* (1990) have been taken into account in our tectonic interpretation.

Maximum temperature estimates in kyanite schists of the UMU and sillimanite schists of the MZ yield 650 and 640°C, respectively, which is apparently higher than in previous units and consistent with petrographical observations and the inferred metamorphic reaction (R3), which is calibrated to 650°C at pressures 9 to 10 kbar (Spear 1993).

The peak temperatures in the MZ were probably slightly higher than those in the UMU. This is indicated by strongly modified profiles of garnets by intracrystalline diffusion (Figure 6) in the MZ. However, slightly lower temperature estimates (640°C) are due to a late decompression reaction (garnet = sillimanite+biotite, Figure 4g). We therefore consider that the maximum temperatures reached in the MZ were at least the same as in the UMU.

Garnet–staurolite thermometry (Perchuk 1969) results are consistent with petrography and calibrations of reactions (R1, R2, R4) (Thompson 1976b; Delor *et al.* 1984; Spear and Cheney 1989) and show a steady increase in temperature according to the metamorphic grade (Figure 10).

The P–T conditions of cooling are difficult to estimate, but small, late Mn-rich rims around garnets in the LMU show 400–450°C (Höck *et al.* in press). This estimate is consistent with our sample L151 from the retrogressed part of the LMU, which yields 400–450°C at pressures of 4–4.5 kbar. Fluid inclusions in late quartz veins yield 300°C at 3.3–4 kbar (Fritz and Loitzenbauer 1994), indicating a later part of the cooling history.

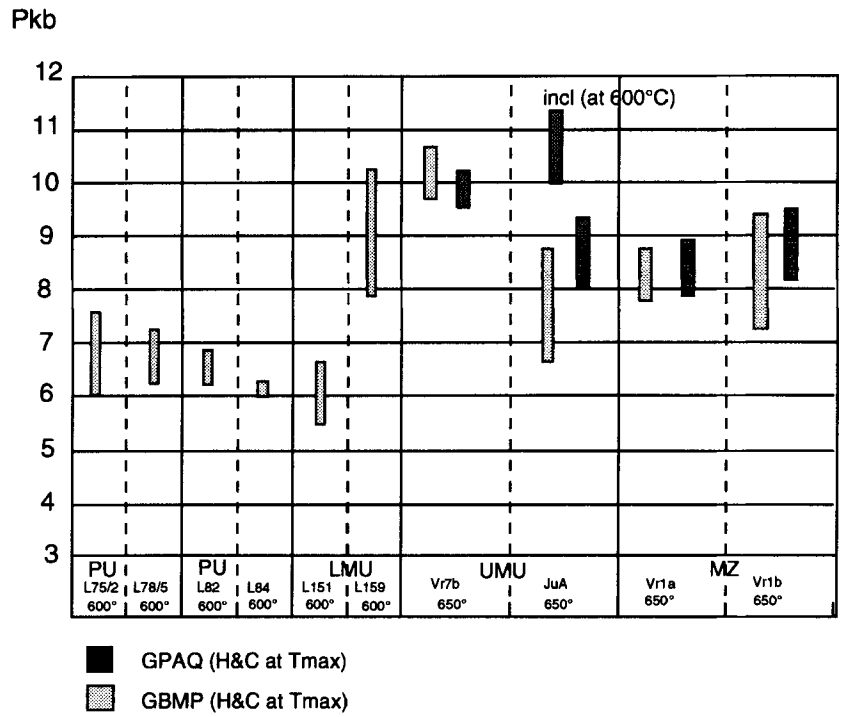

Figure 11. Variations in pressure with increasing metamorphic grade. The pressure range was calculated at maximum calculated temperatures using GPAQ and GBMP (Hodges and Crowley 1985)

7c. Results of barometry

Results of barometry are presented in Table 5 and Figure 11. The pressures were calculated for maximum attained temperatures in individual units, i.e. 600°C for both the PU and the LMU and 650°C for the UMU and the MZ.

GBMP calibration yields similar values of pressure estimates ranging from 6 to 7.5 kbar for the whole of the PU. GBMP estimations from staurolite schists of the LMU correspond to 6.6–10.3 kbar. Results from sample L151 represent a late stage re-equilibration. Estimates obtained from kyanite schists of the UMU using GBMP and GPAQ give 8–10.7 kbar. Sample JuA exhibits a low estimate of 6.6 to 8.7 kbar using the GBMP calibration, whereas the GPAQ calibration yields more reasonable results of 8–9.3 kbar. Plagioclase inclusions in garnet of the UMU give higher estimates (9.4–10.4 at 600°C) than those from matrix. Pressure estimates in sillimanite schists of the MZ using both GBMP and GPAQ give 7.3–9.5 kbar.

7d. Interpretation of geobarometry

The data for the PU are calculated from three samples yielding similar results. The lower pressure limit from the LMU fits well with results of Bernroider (1989) or of Höck *et al.* (1990), who obtained pressure estimates ranging between 5 and 7 kbar using the GBMP calibration of Ghent and Stout (1981) and the phengitic content of muscovites (Massone and Schreyer 1987). However, the upper value of 10.3 kbar seems to be an overestimate and an upper pressure limit of 7.8 kbar is used for tectonic interpretation. The comparison of pressure estimates based on plagioclase inclusions (9.4–10 kbar at 600°C) with that for matrix (8–10.7 at 650°C) indicates either isobaric heating during garnet growth or a metamorphic peak temperature below the peak pressure in a clockwise P–T–t loop. The increase in temperature is supported by the occurrence of the sequence of reactions (R3) and (R4).

Lower pressure estimates from pelites of the MZ compared with the UMU are explained by the modification of garnet rim composition related to reaction (R6) during the decompression phase D_2M_2. Moreover, significantly higher pressures, 12–14 kbar, were reported from the northern Svratka window from the same tectonic unit by Johan *et al.* (1990) and Lardeaux *et al.* (1991). Their estimates are based on a chloritoid, Mg-rich staurolite, paragonite and rutile assemblage included within garnet porphyroblasts and the presence of talc and phengite inclusions in muscovite.

8. DISCUSSION

In the Moravian metapelites we have used several published geothermometers and geobarometers consistent with observed mineralogy. It must be emphasized that the quantitative P–T estimates obtained this way are sometimes erratic and often contradict phase compatibilities. This can be interpreted, for instance, as a result of chemical disequilibrium probably related to heterogeneous diffusion, which can produce contrasted cooling effects giving rise either to zoning diffusion or short-range rim re-equilibration. Therefore the exchange thermobarometry is not always the most powerful technique in a metapelitic system and paragenetic analysis, i.e. phase compatibilities and possible reaction history, allow the temperature evolution to be better constrained.

In previous sections it was shown by combining textural relationships, inferred metamorphic reactions and thermobarometry that the metamorphic grade systematically increases from the basement towards the top of the Moravian nappe sequence (Figure 12). This inverted metamorphic gradient is indicated by temperature increase from ca. 580–600 to 650°C and the pressure increase from ca. 6–7 to 10 kbar towards the top of the pile.

Each tectonic unit exhibits its own distinct metamorphic and tectonic evolution, which is dated by Ar/Ar cooling ages and shows 341 ± 1.4 Ma on hornblende in the MZ, 328.7 ± 3.3 Ma on muscovite in the UMU and 325.5 ± 0.7 Ma on muscovite in the LMU (Dallmeyer *et al.* 1990).

The inversion of metamorphic gradient is also well developed in the overlying Moldanubicum (Figure 12). The Drosendorf unit of the Moldanubian zone in Austria shows peak conditions of 720–760°C and 7–9 kbar (Petrakakis 1986), whereas temperatures of 1000°C and pressures 16 kbar (Carswell and O'Brien 1993) from Austrian granulites and 1060°C, 15–22 kbar from associated eclogites (Beard *et al.* 1989; Dudek and Fediuková 1974) are typical for the uppermost Gföhl unit. P–T data from granulites neighbouring the Moravian zone in the Czech Republic show temperatures around 800°C and pressures of 12 kbar (Urban 1992). The subsequent amphibolite facies retrogression associated with north-eastward ductile deformation occurred in the range 600–800°C, 5–9 kbar (Petrakakis and Richter 1991) or at 700°C, 6–9 kbar (Urban 1992). The regionally relevant zircon and monazite ages of a granulite event range from 351 to 369 Ma, whereas the monazite age of an amphibolite facies overprint in Gföhl migmatites gives 337 ± 3 Ma (Van Breemen *et al.* 1982).

An essential piece of evidence is that the syn-metamorphic north-east directed kinematics of the Moravian zone is consistent in all lithotectonic units and is virtually independent of the metamorphic grade. This event could be correlated and decompressional amphibolite facies north-eastward deformation in the Gföhl granulites (Urban 1992), followed by melt-enhanced north-east shearing of the Gföhl orthogneiss (Cháb *et al.* 1994) and with widespread anatexis of the Gföhl unit (Matejovská 1975). Prograde metamorphism in the lower plate is characterized by dehydration reactions and the released fluids have probably catalysed the retrograde decompressional reactions in the upper plate (O'Brien and Carswell 1993).

The age constraints, P–T and kinematic data show that shortly after granulite formation, the Moldanubian lower crust was dextrally uplifted along a lateral Brunovistulian ramp at 340–337 Ma. The peak pressure conditions in all levels of progressively obliquely underthrusted Brunovistulicum were attained during one kinematically consistent event, D_1M_1. The tip of the underthrust slab represented by the MZ in the northern Svratka window was transported into depths corresponding to 12–14 kbar (Johan *et al.* 1990), the middle part of the slab (at present the UMU) into a depth corresponding to 9.4–10.7 kbar

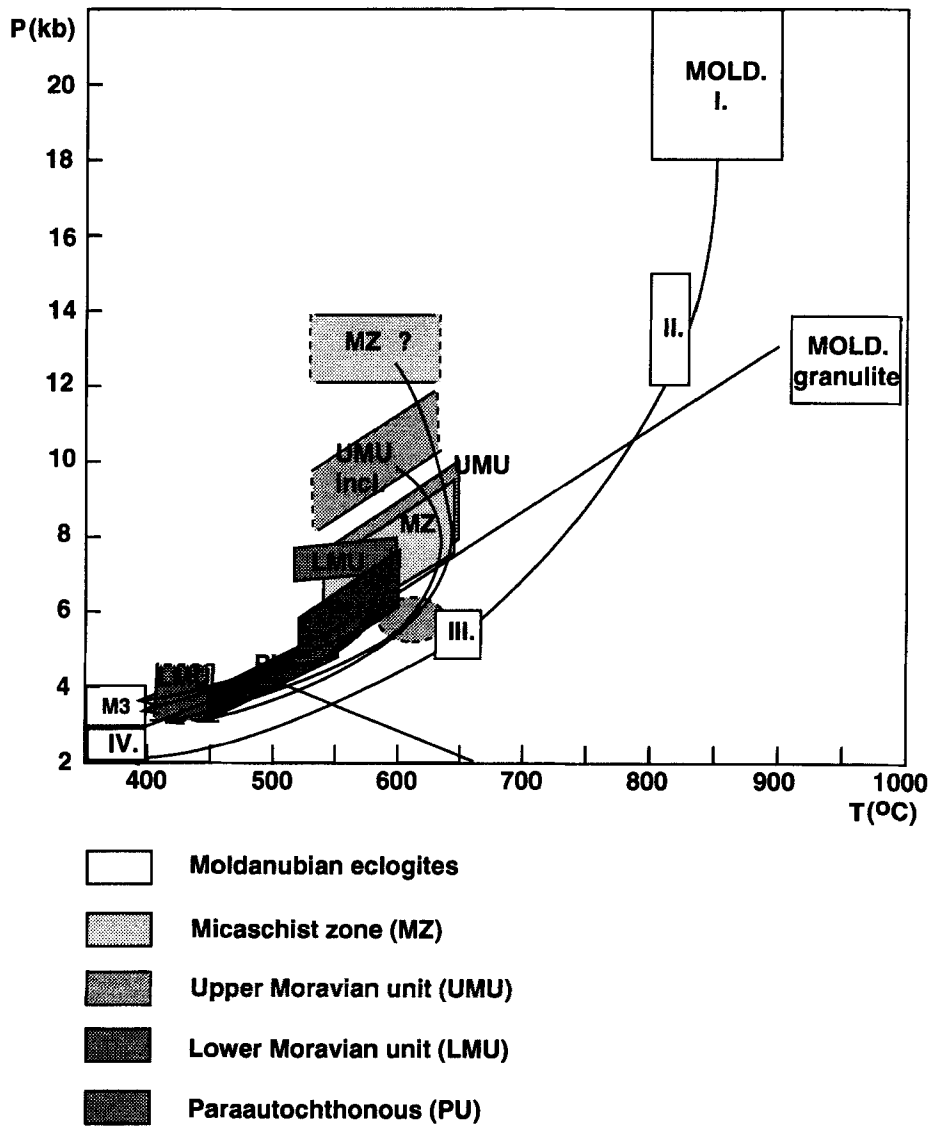

Figure 12. Conditions of metamorphism in individual units of the Moravian zone of the Dyje window. The P–T boxes calculated using garnet–biotite thermometry and GPAQ, GBMP barometry. The P–T conditions for Moldanubian granulites and for the Drosendorf pelites are taken from O'Brien and Carswell (1993) and from Petrakakis (1986), and for M3 retrogression in Moravian zone are from Fritz and Loitzenbauer (1994)

and the most distant part of the slab, the PU, into the shallowest depth of 6–7.5 kbar. Such a palaeo-burial depth gradient is shown in Figure 12.

It is also shown that the decompressional phase D_2M_2 marked by reaction (R6) in the MZ and the UMU is related to continuous top to the north-east oriented shearing.

The D_3M_3 greenschist facies retrogression of the whole stack is associated with north-eastward shearing, which indicates uplift of all Moravian units into supracrustal levels. This stage is terminated by widespread extensional tectonics in the Gföhl migmatites and in the Moravian zone under lower greenschist facies conditions (Schulmann *et al.* 1994). The conditions of cooling are constrained using the fluid inclusion study of Fritz and Loitzenbauer (1994) and yield 300–400°C and pressure 3–4 kbar.

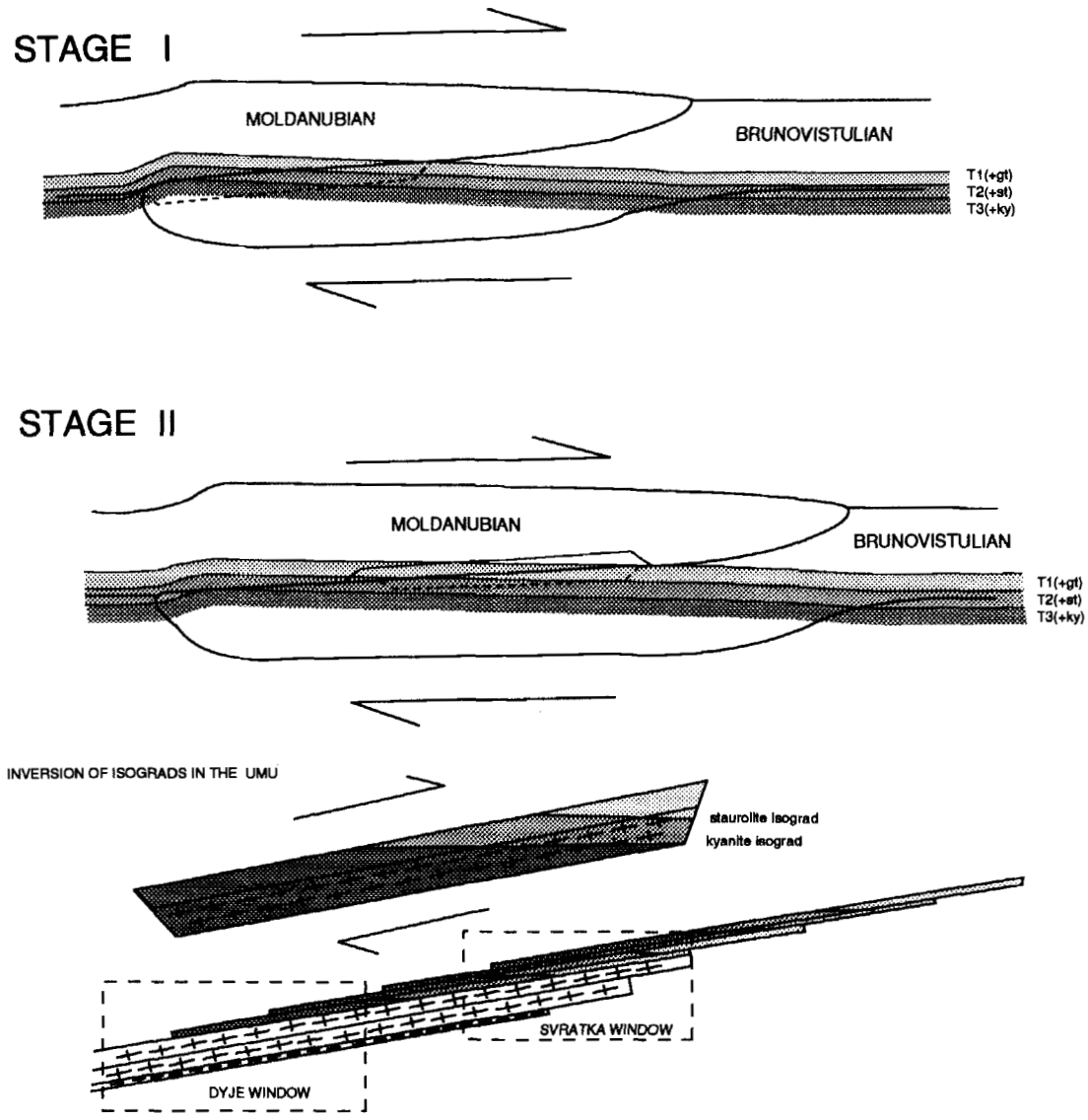

9. TECTONIC INTERPRETATION OF MORAVIAN INVERTED METAMORPHIC ZONATION

Several studies of inverted metamorphic zonation have sought to explain the physical factors controlling pressure and temperature evolution in collisional belts. The classic thermal model illustrates that instantaneous overthrusting of hot rock over cold rock causes major perturbations of steady-state geotherms due to a faster rate of heat emplacement than that of heat conduction (Oxburgh and Turcotte 1974; England and Thompson 1984). However, the perturbed geotherm relaxes towards the steady-state geotherm in several tens of millions years, leading to restoration of the original thermal profile. Models of P–T evolution combining thickening with erosion predict a peak temperature after peak pressure along a clockwise loop (England and Richardson 1977; England and Thompson 1984). A model of syn-metamorphic thrusting producing folding of isotherms has been suggested in several regions of the world, implying inversion of temperature near the thrust plane while the pressure trend resembles the lithostatic gradient (Hubbard 1989; Pecher 1989—Himalaya; Burg *et al.* 1989—Le Vibal klippe, French Massif Central).

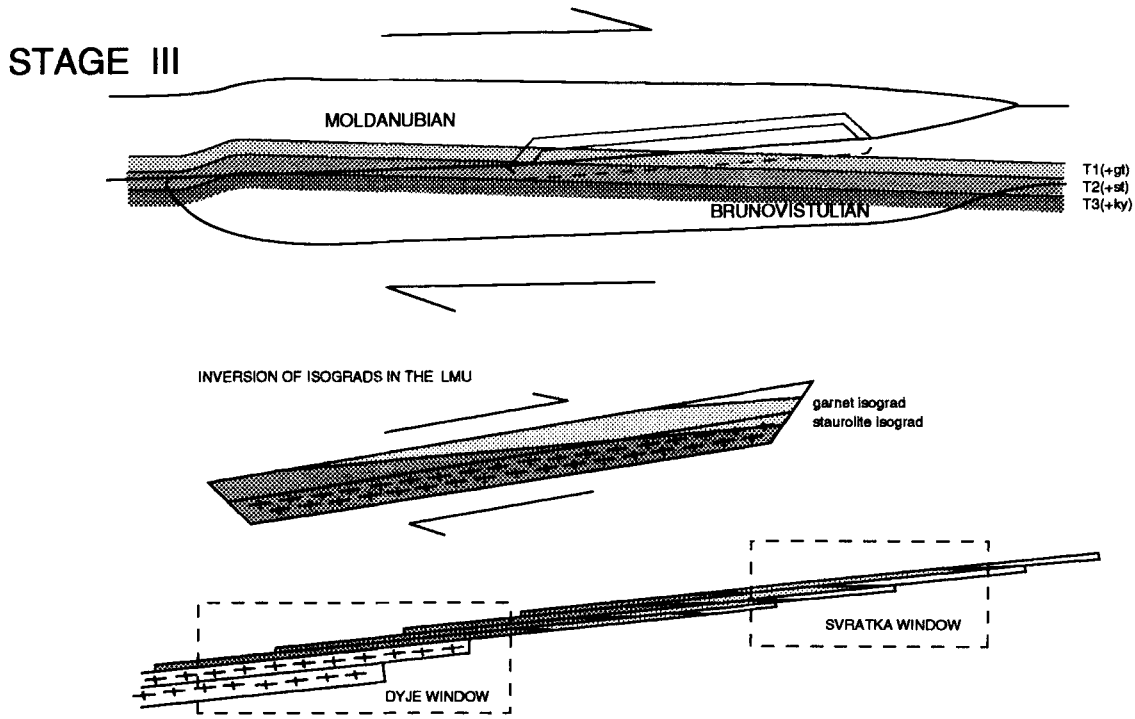

Figure 13. Schematic diagram illustrating, in three stages, the mechanical inversion of metamorphic isograds by transportation of metamorphic zones within nappes and their simple shear deformation

The two-dimensional thermal modelling of Shi and Wang (1987) has shown that the sawtooth-shaped geotherm could be produced provided that the convergence rates exceed 10^{-8} s^{-1}. Under normal convergent rates in collisional zones (Carter and Tsenn 1987), equal roughly to 10^{-13}–10^{-14} s^{-1}, the inversion of isotherms does not develop. The time interval between the age of granulite metamorphism of the Gföhl unit (369–351 Ma) and the cooling age of biotite in retrogressed granulites (Matte *et al.* 1985; 325 Ma), the latter corresponding to cooling ages in Moravian units, indicate realistically low convergence rates (tens of millimetres per year). Thus, perturbation of the geotherm probably did not occur in the Moldanubian/Brunovistulian convergence and the isotherms remained almost subhorizontal during D_1 underthrusting (Figure 13).

Once the underthrust continental crust has been subducted into depths of several tens of kilometres, its strength is significantly weakened (Van den Beukel 1992). This strength decrease of underthrusted crust is due to weakening processes associated with dynamic recrystallization (White *et al.* 1980) related to rock deformation and to metamorphic reactions. Resistive forces acting on underthrust crust due to friction at the plate contact and due to buoyancy of crustal material can lead to break-up of the lithosphere and formation of a new plate contact in the underthrust middle crust (Van den Beukel 1992).

We suggest that this mechanism can lead to the break-up of the deepest underthrust part of the Brunovistulian platform to produce the MZ and the UMU allochthons by migration of the intraplate boundary to the base of the UMU at a depth around 35 km (Figure 13). At this stage uplift and exhumation of the UMU, the MZ and Moldanubian granulites lead to decompressional reactions in all these units, e.g. reaction (R6) in the UMU and the MZ and decrease in pressure from 10 to 7 kbar and slight decrease in temperature registered using geothermobarometry.

The P–T one-dimensional thermal models of Spear and Peacock (1990) show that the temperature of 650°C at 8–10 kbar may be achieved after a time lag 30–40 Ma before the onset of erosion. To cross the kyanite–sillimanite phase boundary during isobaric heating implies an unrealistically long time interval of

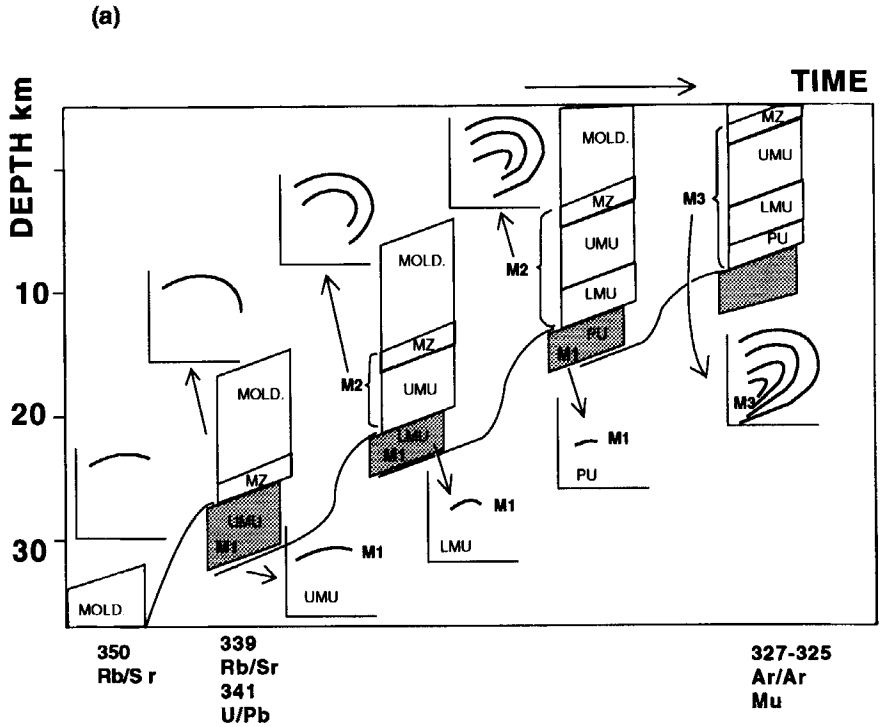

Figure 14. Simplified interpretative diagram showing progressive detachment of the UMU, the LMU and the PU and migration of the intraplate boundary with time and depth. Schematic P–T–t paths show decompression in uplifted units and simultaneous prograde metamorphism in underthrust units

burial before the start of erosion. So reaction (R6) must be associated with decompression and a reasonable erosion rate. During uplift and decompression of the UMU and the MZ the rest of the Brunovistulian platform is continuously underthrust and progressively metamorphosed under increasing temperature and pressure (Figures 13 and 14); see reaction (R2) in the LMU.

Further underthrusting of the rest of the Brunovistulian platform led to the detachment of the LMU and to the migration of the intraplate boundary downwards to depths corresponding to 5–8 kbar (Figures 13 and 14). At this stage of the Moldanubicum, the UMU and the LMU were uplifted, leading to continuous decompression in initially deep units and to the first decompression in the LMU. The rest of the Brunovistulian basement is still underthrust, resulting in growth of staurolite below the new plate boundary under pressures of 6–7.5 kbar (Figures 13 and 14). The decompression stage in the LMU might be recorded by low calculated rim temperatures.

In contrast with the homogeneous deformation and distribution of metamorphism related to slow underthrusting, the uplift-related structures are heterogeneous. This is supported by the heterogenous development of sillimanite-bearing shear zones in the MZ and the UMU. The heterogeneity of greenschist facies shear zone is even more pronounced, so that large pods of non-retrogressed rocks are preserved in the LMU and the PU, especially in the thick Austrian part of these units.

The passive transport of metamorphism from deep zones can explain the inversion of metamorphic zones on the scale of a nappe pile, but not in a single thrust sheet. The inversion of metamorphic zones is developed in the PU, but is also a typical feature of the LMU and the UMU on the scale of the whole Moravian zone. Several hypotheses have been put forward to explain the inversion of metamorphism in a single unit: (1) deformation in a simple shear zone (Mason 1984; Boyle 1987); and (2) shear heating (England and Molnar 1993).

A model similar to that proposed by Mason (1984) or by Burton *et al.* (1989) in the central Scandinavian Caledonides is the most suitable for this example. We suggest a heterogeneous network of

syn-decompressional to late metamorphic shear zones (Figure 4f and 4h) operating in individual units and transporting less deformed lithons to upper levels during the uplift stage (Figures 13 and 14). These zones have been mapped, e.g. by Schulmann (1990) in the orthogneiss body of the UMU and by Lobkowicz *et al.* (in press) in the Dyje granite. This type of deformation can actually produce an inversion of metamorphic zones and conserve the early 'subduction' related assemblages in low strain domains. The kinematic record of both homogeneous 'subduction' and heterogeneous 'uplift' remains the same.

The steep P–T–t loops in the overlying Moldanubicum indicate the important role of extensional faults in rapid unroofing (Thompson and Ridley 1987) of the Dyje window. This is consistent with observations of Schulmann *et al.* (1994), who have shown that migration of the thrusts downwards operated simultaneously with extension in the upper units.

ACKNOWLEDGEMENTS

We are grateful to Professor J. M. Lardeaux for substantial help in the early stages of this research and during the stays of P. Stípská in ENS Lyon. His critical comments are also highly appreciated. P. Jakes and F. Holub helped with early versions of the manuscript. We thank A. P. Boyle, P. Treloar and R. Mason for reviewing the manuscript and for improvement of the English style.

REFERENCES

Ballèvre, M., Pinardon, J. L., Kienast, J. L. and Vuichard, J. P. 1989. Reversal of Fe–Mg partitioning between garnet and staurolite in eclogite facies metapelites from the Champtoceaux nappe (Brittany, France). *Journal of Petrology* **30**, 1321–1349.

Bátik, P. and Fediuková, E. 1992. Garnet chemistry as an indicator of metamorphic development and deformations of the Moldanubicum in the Dyje dome. *Vestnik Ceskeho geologickeho ustavu* **67**, 1–24.

Beard, B. L., Medaris, L. G., Valley, J. W., Brueckner, H. K. and Misar, Z. 1989. Mantle-derived Variscan eclogites from the Bohemian Massif, Czechoslovakia. *Abstracts, Third International Eclogite Conference, Wurzburg*, 2–3.

Bernroider, M. 1989. Zur Petrogenese prekambrischer Metasedimente und cadomischer Magmatite im Moravikum. *Jahrbuch des Geologischen Bundesanstalt* **132**, 349–373.

Boyle, A. P. 1987. A model for stratigraphic and metamorphic inversions at Sulitjelma, central Scandes. *Geological Magazine* **124**, 451–466.

Brunel, M. and Kienast, J. R. 1986. Etude petro-structurale des chevauchements ductiles himalayens sur la transversale de l'Everest-Makalu (Nepal oriental). *Canadian Journal of Earth Sciences* **23**, 1117–1137.

Burg, J. P., Leyreloup, A., Marchand, J. and Matte, P. 1984. Inverted metamorphic zonation and large-scale thrusting in the Variscan Belt: an example in the French Massif Central. *In*: Hutton, D. H. W. and Sanderson, D. J. (eds) *Variscan Tectonics of the North Atlantic Region*. Blackwell Scientific, London, 47–61.

— — —, Delor, C. P., Leyreloup, A. F. and Romney, F. 1989. Inverted metamorphic zonation and Variscan thrust tectonics in the Rouergue area (Massif Central, France): P–T–t record from mineral to regional scale. *In*: Daly, J. S., Cliff, R. A. and Yardley, B. W. D. (eds), *Evolution of Metamorphic Belts*. Geological Society, London, Special Publication, **43**, 423–439.

Burton, K. W., Boyle, A. P., Kirk, W. L. and Mason, R. 1989. Pressure, temperature and structural evolution of the Sulitjelma fold-nappe, central Scandinavian Caledonides. *In*: Daly, J. S., Cliff, R. A. and Yardley, B. W. D. (eds), *Evolution of Metamorphic Belts*. Geological Society, London, Special Publication, **43**, 391–411.

Carswell, D. A. and O'Brien, P. J. 1993. Thermobarometry and geotectonic significance of high-pressure granulites: examples from the Moldanubian zone of the Bohemian Massif in Lower Austria. *Journal of Petrology* **34**, 427–459.

Carter, N. L. and Tsenn, M. C. 1987. Flow properties of continental lithosphere. *Tectonophysics* **136**, 27–63.

Cháb, M., Schulmann, K. and Holub, F. 1994. Evolution of stromatitic structures in the eastern part of the Czech part of Moldanubicum. *Abstracts, 11th Annual Meeting of the Swiss Tectonic Studies Group, Neuchatel.*

Chamberlain, C. P. 1986. Evidence for repeated folding of isotherms during regional metamorphism. *Journal of Petrology* **27**, 63–89.

Crawford, M. L. 1977. Calcium zoning in almandine garnet, Wissahickon Formation, Philadelphia. *Canadian Mineralogist* **15**, 243–249.

Dallmeyer, R. D., Neubauer, F. and Höck, V. 1992. Chronology of late Paleozoic tectonothermal activity in the southeastern Bohemian Massif, Austria (Moldanubian and Moravo- Silesian zones): $^{40}Ar/^{39}Ar$ mineral age controls. *Tectonophysics* **210**, 135–153.

Davidson, C., Hollister, L. S. and Schmid, S. M. 1992. Role of melt in the formation of deep-crustal compressive shear zone: the Maclaren glacier metamorphic belt, South Central Alaska. *Tectonics* **11**, 348–359.

Delor, C. P., Burg, J. P. and Leyreloup, A. F. 1984. Staurolite forming reactions and geothermobarometry of a high pressure thermal aureole in the French Massif Central. *Journal of Metamorphic Geology* **2**, 55–77.

Dudek, A. 1980. The crystalline basement block of the Outer Carpathians in Moravia. *Rozpravy Ceskoslovenske akademie ved* **90**, 1–85.

— — — and Fediuková, E. 1974. Eclogites of the Bohemian Moldanubicum. *Neues Jahrbuch für Mineralogische Anhaundlungen* **121**, 127–159.

England, P. C. and Molnar, P. 1993. The interpretation of inverted metamorphic isograds using simple physical calculations. *Tectonics* **12**, 145–157.

— — — **and Richardson, S. W. 1977.** The influence of erosion upon the mineral facies of rocks from different metamorphic environments. *Journal of the Geological Society of London* **134**, 201–213.

— — — **and Thompson, A. B. 1984.** Pressure–temperature–time paths of regional metamorphism I. Heat transfer during evolution of regions of thickened continental crust. *Journal of Petrology* **25**, 894–928.

Finger, F., Frasl, G., Höck, V. and Steyrer, H. P. 1989. The granitoids of the Moravian Zone of northeast Austria—products of a Cadomian active continental margin. *Precambrian Research* **45**, 235–245.

Frasl, G. 1983. Zur Geologie des Kristallins und Tertiars der weiteren Umgebung von Eggenburg. *Osterreichische Geologische Bundes Austalt, Excursion Guide.*

— — —, **Fuchs, G., Matura, A. and Thiele, P. 1977.** Einführing in die Geologie des Waldviertel Grundgebirges. *In: Arbeitstagung der Geologischen Bundesanstalt. Special Publication, Austrian Geological Survey, Vienna.*

Fritz, H. 1990. Structures and kinematics along the Moravian — Moldanubian boundary preliminary results. *Österreichische Beit räge zu Meteorologie und Geophysik* **3**, 77–96.

— — — **and Loitzenbauer, J. 1994.** Fluid activity during late stage of Variscan deformation in the Moravian nappe complex. *Mitteilungen der Osterreichischen Mineralogischen Gesselschaft* **139**, 47–49.

— — — **and Neubauer, F. 1993.** Kinematics of crustal stacking and dispersion in the south-eastern Bohemian Massif. *Geologische Rundschau* **82**, 556–565.

Ghent, E. D. and Stout, M. Z. 1981. Geobarometry and geothermometry of plagioclase–biotite–garnet–muscovite assemblages. *Contributions to Mineralogy and Petrology* **76**, 92–97.

Höck, V. 1975. Mineralzone in Metapeliten und Metapsammiten der Moravischen Zone in Niederosterreich. *Mitteilungen der Geologischen Gesselschaft* **66–67**, 49–60.

Höck, V., Marschallinger, R. and Topa, D. 1990. Granat-biotit-geothermometrie in metapeliten der Moravischen zone in Österreich. *Österreichische Beiträge zu Meteorologie und Geophysik* **3**, 149–167.

— — —, **Stipska, P. and Schulmann, K.** Complex metamorphic zonation of the Thaya Dome—a result of oblique collapse on inverted metamorphic isograd pattern. *Journal of Czech Geological Society* in press.

Hodges, K. V. and Crowley, P. D. 1985. Error estimation and empirical geothermombarometry for pelitic systems. *American Mineralogist* **70**, 702–709.

— — — **and Spear, F. S. 1982.** Geothermometry, geobarometry and the A12SIO5 triple point at Mt. Moosilauke, New Hampshire. *American Mineralogist*, **67**, 1118–1134.

Hoke, L. 1990. The Altkristallin of the Kreuzeck Mountains, SE Tauern Window, Eastern Alps—basement crust in a convergent plate boundary zone. *Jahrbuch des Geologischen Bundesanstalt* **133**, 5–87.

Hoschek, G. 1969. The stability of staurolite and chloritoid and their significance in metamorphism of pelitic rocks. *Contributions to Mineralogy and Petrology* **22**, 208–232.

Hubbard, M. S. 1989. Thermobarometric constraints on thermal history of the Main Central Thrust Zone and Tibetan Slab, eastern Nepal Himalaya. *Journal of Metamorphic Geology* **7**, 19–30.

Jaros, J. and Misar, Z. 1974. Der Deckenbau der Svratka-Kuppel und seine Bedeutung fur das geodynamische Modell der Bohmischen Masse. *Sbornik geologickych ved.* **26**, 69–82.

Johan, V., Autran, A., Ledru, P., Lardeaux, J.-M. and Melka, R. 1990. Discovery of relics of a high pressure metamorphism at the base of the Moldanubian Nappe Complex [abstract]. *Abstracts: International Conference on Paleozoic Orogens in Central Europe.*

Lardeaux, J.-M., Johan, V., Autran, A. and Ledru, P. 1991. Talc–phengite–kyanite bearing metapelites: high pressure metamorphism in the Moravian zone and its tectonic significant. *Abstracts: Geological Workshop; Moravian Windows.*

Le Fort, P. 1975. Himalaya: the collided range. Present knowledge of the continental arc. *American Journal of Science* **275A**, 1–44.

Lobkowicz, M., Melka, R. and Schulmann, K. Variscan polyphase deformation of the Moravian Cadomian basement: result of lateral ramp tectonics. *Geodinamica Acta*, in press.

Mason, R. 1984. Inverted isograds at Sulitjelma, Norway: the result of shear zone deformation. *Journal of Metamorphic Geology* **2**, 77–82.

Massone, H. J. and Schreyer, W. 1987. Phengite geobarometry based on limiting assemblage with K-feldspar, phlogopite and quartz. *Contributions to Mineralogy and Petrology* **96**, 212–224.

Matejovská, O. 1975. The Moldanubicum gneiss series of southwestern Moravia and its relation to granulites. *Vestnik Ustredniho ustavu geologickeho* **50**, 345–351.

Matte, P. 1991. Accretionary history and crustal evolution of the Variscan belt in Western Europe. *Tectonophysics* **196**, 309–337.

— — —, **Maluski, H. and Echtler, H. 1985.** Cisaillement ductiles varisques vers l'est-Sud Est dans les nappes du Waldviertel (Sud Est du Massif de Bohème, Autriche). Données microtectoniques et radiometriques 39AR-40 AR. *Comptes Rendu de Academie des Sciences* **301**, 721–724.

Mohan, A., Windley, B. F. and Searle, M. P. 1989. Geothermobarometry and development of inverted metamorphism in the Darjeeling–Sikkim region of the eastern Himalaya. *Journal of Metamorphic Geology* **7**, 95–110.

Morauf, W. and Jager, F. 1982. Rb–Sr whole rock ages for Bitesh Gneiss, Moravicum, Austria. *Terra Cognita* **2**, 60–61.

O'Brien, P. J. and Carswell, D. A. 1993. Tectonometamorphic evolution of the Bohemian Massif: evidence from high pressure metamorphic rocks. *Geologische Rundschau* **82**, 531–555.

Oxburgh, E. R. and Turcotte, D. L. 1974. Thermal gradients and regional metamorphism in underthrust terrains with special reference to the Eastern Alps. *Schweizerische Mineralogische und Petrographische Mitteilungen* **54**, 641–662.

Pecher, A. 1989. The metamorphism in the Central Himalaya. *Journal of Metamorphic Geology* **7**, 31–41.

Perchuk, L. L. 1969. The staurolite-garnet thermometer. *Akadamie Nauk USSR, Doklady* **186**, 1405–1407 [in Russian].

Petrakakis, K. 1986. Metamorphism of high-grade gneisses from the Moldanubian Zone, Austria, with particular reference to garnets. *Journal of Metamorphic Geology* **4**, 323–344.

— — — **and Richter, W. 1991.** MetamorphoseBedingungen in der Gfohler Einheit. *Zentralblat für Geologie und Palaontologie* **1**, 167–180.

Preclik, K. 1924. Zur Analyse des Moravischen Faltenwurfes im Thayatale. *Verhandlungen des Geologischen Bundesanstalt* No. 1924.180–191.

— — — **1926.** Die moravische Phyllitzone im Thayatale. *Sbornik statniho geologickeho ustavu* **6**, 221–274.

Scharbert, S. 1977. Neue Ergebnisse radiometrischer Altersbestimmungen an Gesteinen des Waldviertels. *Osterreichische Geologische Bundes Austalt* 10–13.

— — — **and Batik, P. 1985.** The age of the Thaya (Dyje) pluton. *Verhandlungen des Geologischen Bundesanstalt* **3**, 325–331.

Schulmann, K. 1990. fabric and kinematic study of the Bites orthogneiss (southwestern Moravia): result of large-scale shearing parallel to the Moldanubian/Moravian boundary. *Tectonophysics* **177**, 229–244.

— — —, **Melka, R., Lobkowicz, M., Ledru, P., Lardeaux, J.-M. and Autran, A. 1994.** Contrasting styles of deformation during progressive nappe stacking at the southeastern margin of the Bohemian Massif (Thaya Dome). *Journal of Structural Geology* **16**, 355–370.

Shi, Y. and Wang, Ch. 1987. Two-dimensional modelling of the P–T–t paths of regional metamorphism in simple underthrust terrains. *Geology* **15**, 1048–1051.

Spear, F. S. 1993. *Metamorphic Phase Equilibria and Pressure–Temperature–Time Paths.* Mineralogical Society of America, Washington.

— — — **and Cheney, J. T. 1989.** A petrogenetic grid for pelitic schists in the system SiO_2–Al_2O_3–FeO–MgO–K_2O–H_2O. *Contributions to Mineralogy and Petrology* **101**, 149–164.

— — — **and Peacock, S. M. 1990.** Metamorphic P–T–t paths: program manual and computer exercises for the calculation of metamorphic phase equilibria, pressure–temperature–time paths and thermal evolution of orogenic belts. *Geological Society of America, Short Course, Dallas, Texas,* 188 pp.

Staubli, A. 1989. Polyphase metamorphism and the development of the Main Central Thrust. *Journal of Metamorphic Geology* **7**, 73–93.

Suess, F. E. 1912. Die Moravischen fenster und ihre Beziehung zum Grundgebirge des Hohen Gesenkes. Denkschr. *Osterreichische Akademie der Wissenschft mathematik naturwissenschaft* **88**, 541–631.

— — — **1926.** *Intrusionstektonik und Wandertektonik im variszichen Grundgebirge.* Borntträger, Berlin.

Thompson, A. B. 1976a. Mineral reactions in pelitic rocks: I. prediction of P–T–X(Fe–Mg) phase relations. *American Journal of Science* **276**, 401–424.

— — —, **1976b.** Mineral reactions in pelitic rocks: II. Calculation of some P–T–X(Fe–Mg) phase relations. *American Journal of Science* **276**, 425–454.

— — — **and England, P. C. 1984.** Pressure–temperature–time paths of regional metamorphism II. Their inference and interpretation using mineral assemblages in metamorphic rocks. *Journal of Petrology* **25**, 929–955.

— — — **and Ridley, J. R. 1987.** Pressure–temperature–time (P–T–t) histories of orogenic belts. *Philosophical Transactions of the Royal Society* **A 321**, 27–45.

— — —, **Lyttle, P. T. and Thompson, J. B. 1977.** Mineral reactions and A–Na–K and A–F–M facies types in the Gassets schists. Vermont. *American Journal of Science* **277**, 1124–1151.

Tracy, R. J., Robinson, P. and Thompson, A. B. 1976. Garnet composition and zoning in the determination of temperature and pressure of metamorphism, central Massachusetts. *American Mineralogist* **61**, 762–775.

Treloar, P. J., Broughton, R. D., Williams, M. P., Coward, M. P. and Windley, B. F. 1989. Deformation, metamorphism and imbrication of the Indian plate, south of the Main Mantle Thrust, north Pakistan. *Journal of Metamorphic Geology* **7**, 111–125.

Urban, M. 1992. Kinematics of the Variscan thrusting in the Eastern Moldanubicum (Bohemian Massif, Czechoslovakia): evidence from the Namest granulite massif. *Tectonophysics* **201**, 371–391.

Van Breemen, O., Aftalion, M., Bowes, D. R., Dudek, A., Misar, Z., Povondra, P. and Vrana, S. 1982. Geochronological studies of the Bohemian Massif, Czechoslovakia, and their significance in the evolution of Central Europe. *Transaction of Royal Society of Edinburgh: Earth Sciences* **73**, 89–108.

Van den Beukel, J. 1992. Some thermomechanical aspects of the subduction of continental lithosphere. *Tectonics* **11**, 316–329.

White, S. H., Burrows, S. E., Carreras, J., Shaw, N. D. and Humphreys, F. J. 1980. On mylonites in ductile shear zones. *Journal of Structural Geology* **2**, 175–187.

Yardley, B. W. D., Leake, B. E. and Farrow, C. M. 1980. The Metamorphism of Fe-rich Pelites from Connemara, Ireland. *Journal of Petrology* **21**, 365–399.

Complex metamorphic zonation of the Thaya dome: result of buckling and gravitational collapse of an imbricated nappe sequence

P. ŠTÍPSKÁ[1,2], K. SCHULMANN[1] & V. HÖCK[3]

[1]*Institute of Petrology and Structural Geology, Charles University, Albertov 6, 12843 Prague, Czech Republic*

[2]*Geophysical Institute, Czech Academy of Science, Boční II/1401, 141 31, Prague, Czech Republic*

[3]*Institute of Geology and Palaeontology, University of Salzburg*

Abstract: The metamorphic isograd geometry and dome structure of the Thaya tectonic window, which emerges through the Moldanubian nappe pile at the eastern margin of the Bohemian Massif, is interpreted as a result of large-scale buckling of an imbricated nappe sequence. This large-scale mechanical instability was initiated by the blocking of passively transported hot viscous rocks to shallow crustal levels. The wavelength and shape of the buckle fold is controlled by the greatest thickness of the uppermost nappe and by the low ratio of strong orthogneiss to weak micaschists in individual nappes. The steep inclinations of the thrust surfaces and the oblique movement of the crustal multilayer minimizes the role of gravity on fold generation. Medium-scale gravitational folds originated at the end of the buckling of the nappes and are associated with the late sliding of the nappes away from the core of the anticline during late exhumation. Thermal, rheological and fold calculations are presented which document and explain the mechanism of folding of large-scale crystalline nappes.

Over the past two decades an increasing number of examples of thrust-related inverted metamorphic zonations have been reported, for example, from the Caledonides (Mason 1984), from the Variscides (Burg *et al.* 1989) and from the Tertiary Himalayan chain (Mohan *et al.* 1989; Treloar *et al.* 1989).

Several models have been proposed to explain the inversion of metamorphic zones. These are: (1) large-scale syn-metamorphic folding of isotherms; (2) conductive heating from the hot upper plate to a colder lower plate – the 'hot iron effect' (Hubbard 1989); (3) shear heating; (4) imbrication and tectonic stacking of metamorphic rocks with higher-grade rocks in the hangingwall and lower-grade rocks in the footwall (Treloar *et al.* 1989; Brunel & Kiénast 1986); and (5) inversion of metamorphic isograds by a superimposed zone of ductile shear (Mason 1984).

Whatever the mechanism of inversion, the metamorphic isograds should be subparallel to lithotectonic boundaries in trend and often also in dip. The close geometric relationship of isograds with tectonic boundaries is reported from many case studies (Mohan *et al.* 1989; Treloar *et al.* 1989).

The main feature of the eastern margin of the Bohemian Massif is the eastward thrusting of a hot Moldanubian unit over the easterly Brunovistulian continent. The deformation and metamorphism of the lower Brunovistulian plate led to the formation of a shear zone called the Moravian zone. This zone consists of a complicated nappe system derived from the Brunovistulian plate which emerges through the Moldanubian nappes in the form of north-northeast elongated tectonic windows (Fig. 1). The Brunovistulian nappe pile in the southern part of the Thaya window shows an inverted metamorphic zonation ranging from biotite to sillimanite zones (Höck 1975, 1995; Štípská & Schulmann 1995). An explanation of the inverted metamorphic zonation in this region, which involves the imbrication of metamorphic zones and their passive deformation (i.e. a combination of models 4 and 5) has been suggested by Štípská & Schulmann (1995). However, the NE-trending mineral zones are only parallel to the boundary of the window in its central part. In the south and in the north they cut the regional structure (Höck 1975, 1995). None of the above-mentioned models of inversion of metamorphic zones is able to explain this geometry.

This paper is not intended to explain the mechanism of inversion of metamorphic zones, but focuses on the elucidation of the oblique geometric relationship between the lithotectonic boundaries and metamorphic zonation in the dome-like structure of the Thaya tectonic window. This geometry is explained in terms of 'buckling' of a multilayer nappe pile during the

From: COSGROVE, J. W. & AMEEN, M. S. (eds). *Forced Folds and Fractures*. Geological Society, London, Special Publications, **169**, 197–211. 1-86239-060-6/00/$15.00

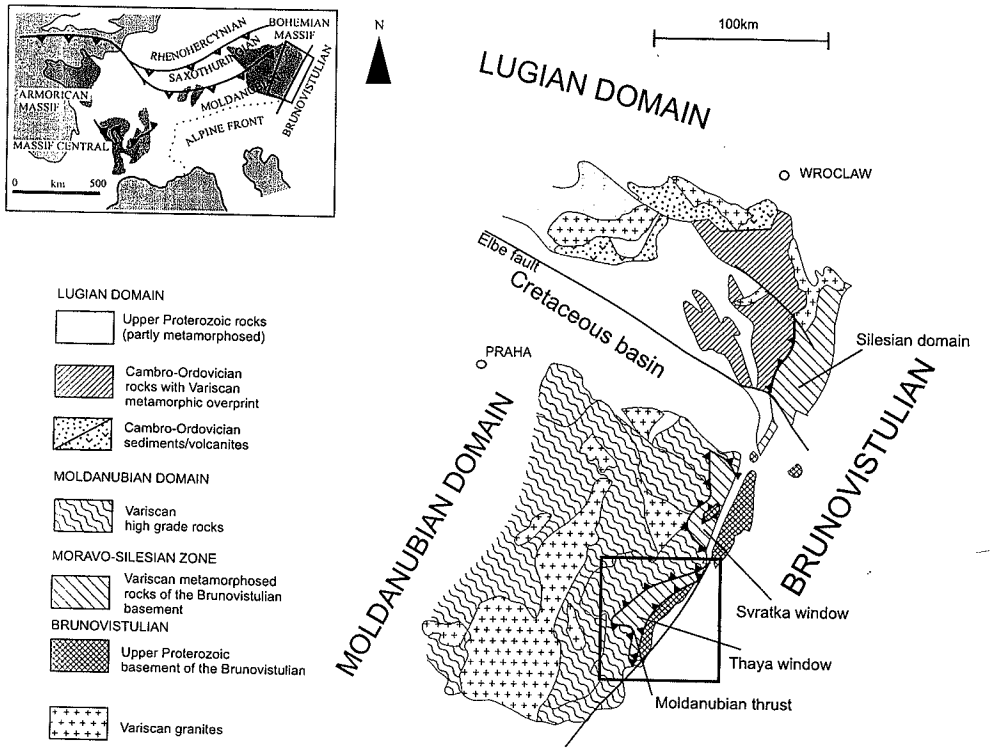

Fig. 1. Tectonic sketch map of the eastern margin of the Bohemian Massif. The Thaya window is situated to the south and the Svratka window to the north.

late stages of oblique convergence. The proposed mechanism of crustal-scale nappe buckling is supported by simple one-dimensional thermal and rheological modelling.

Geological setting

The lithology, structure and metamorphism of the Thaya window has been studied in detail since the end of the last century and the nappe structure, as well as the inversion of metamorphic zonation, had already been recognized by Suess (1912, 1926). Detailed descriptions of the geology of the Thaya window from the Austrian and Bohemian parts were presented by a number of workers (Preclik 1927; Waldmann 1930; Frasl 1970).

In addition the description of the structural evolution of the Thaya window (the polyphase structural history, the orientation of structures, the finite strain and the kinematics), has been the objective of detailed studies carried out over the past 10 years (Schulmann 1990; Fritz 1991; Fritz & Neubauer 1993; Schulmann *et al.* 1994; Kolaříková *et al.* 1997; Lobkowicz *et al.* 1998).

The metamorphic evolution of the Thaya dome (the mapping of the metamorphic isograds, the polyphase metamorphic evolution and the P–T estimates) has also been described in numerous papers (Frasl 1970; Höck 1975, 1995; Štípská & Schulmann 1995). The interested reader is referred to these works and only a short summary of the metamorphic and structural evolution is presented here.

Lithology

The Thaya tectonic window (Fig. 2), which is situated at the southeastern margin of the Bohemian Massif, consists of a para-autochthonous Brunovistulian basement (Dudek 1980) in the core rimmed by two basement-derived nappes. They show the following lithology and structure.

The structurally deepest Thaya granite of Cadomian age (550 Ma, Rb–Sr, Scharbert & Batík 1980) is overlain by a paraautochthonous Upper Proterozoic metapelitic to metapsammitic sequence forming the original roof of the intrusion.

The next, higher unit is a basement-derived Lower Moravian nappe (LMN) which has

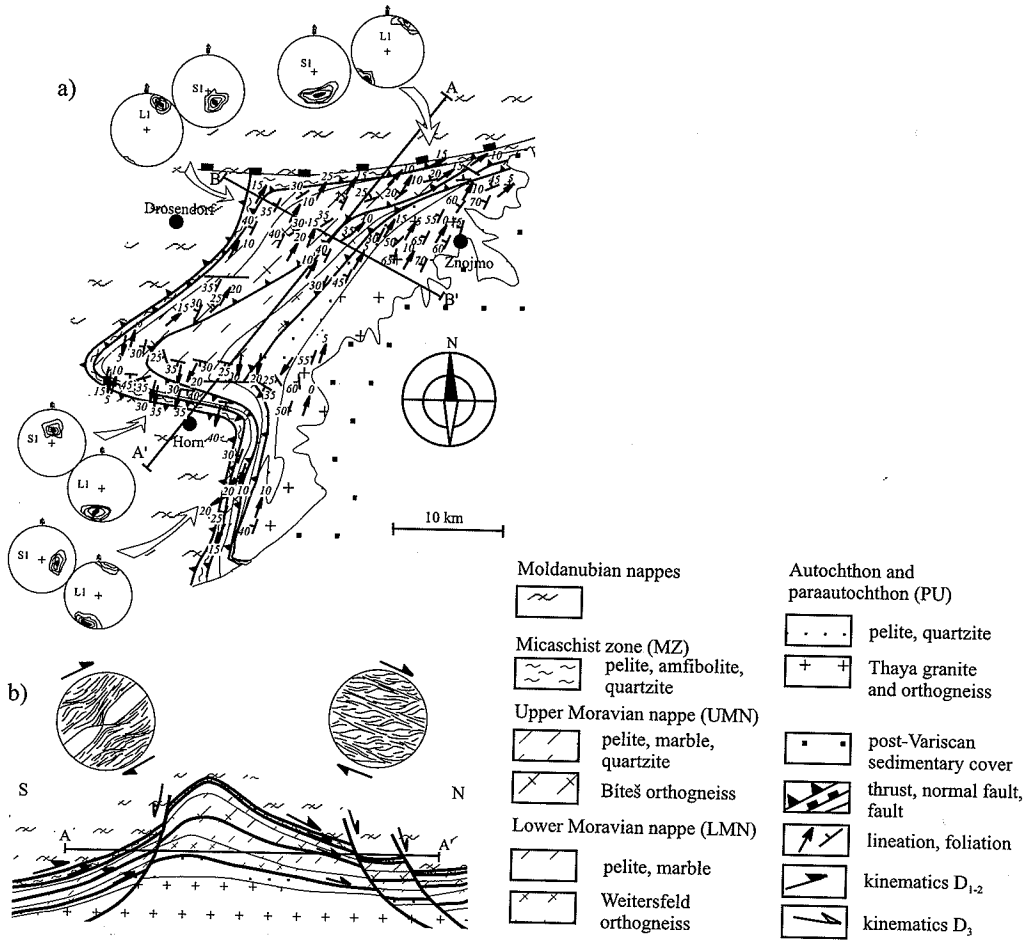

Fig. 2. Structural map and a northeast–southwest cross-section of the Thaya window. (**a**) Tectonic and structural map showing the major nappe structure of the window. The orientation diagrams of lineations and foliations show the structural pattern in the central strike-slip and northern and southern dip-slip domains (data from Fritz 1991; Schulmann 1990; Schulmann *et al.* 1994). (**b**) Schematic northeast–southwest cross-section of the Thaya window showing syn-metamorphic kinematic indicators after Fritz (1991), Fritz & Neubauer (1993) and Schulmann *et al.* (1994).

strongly sheared orthogneiss (the Weitersfeld orthogneiss) at the base overlain by meta-sedimentary cover sequences composed of metapelites, marbles and calcsilicate rocks. The Weitersfeld orthogneiss is restricted to the central part of the Thaya dome (Fig. 2).

The uppermost basement-derived Upper Moravian nappe (UMN) also has an orthogneiss body at its base (the Bíteš orthogneiss) and has a meta-volcano-sedimentary cover. The boundary between the Moldanubian nappes and the Brunovistulian basement-derived nappes is formed by the so-called Micaschist zone (MZ), a monotonous sequence of micaschists and subordinate amphibolites.

Structures

The main structural feature of the Thaya dome is the syn-metamorphic foliation S1 which parallels the lithotectonic boundaries and forms an S-shaped structure (Fig. 2). The S1 foliation bears a stretching and mineral lineation L1, and is

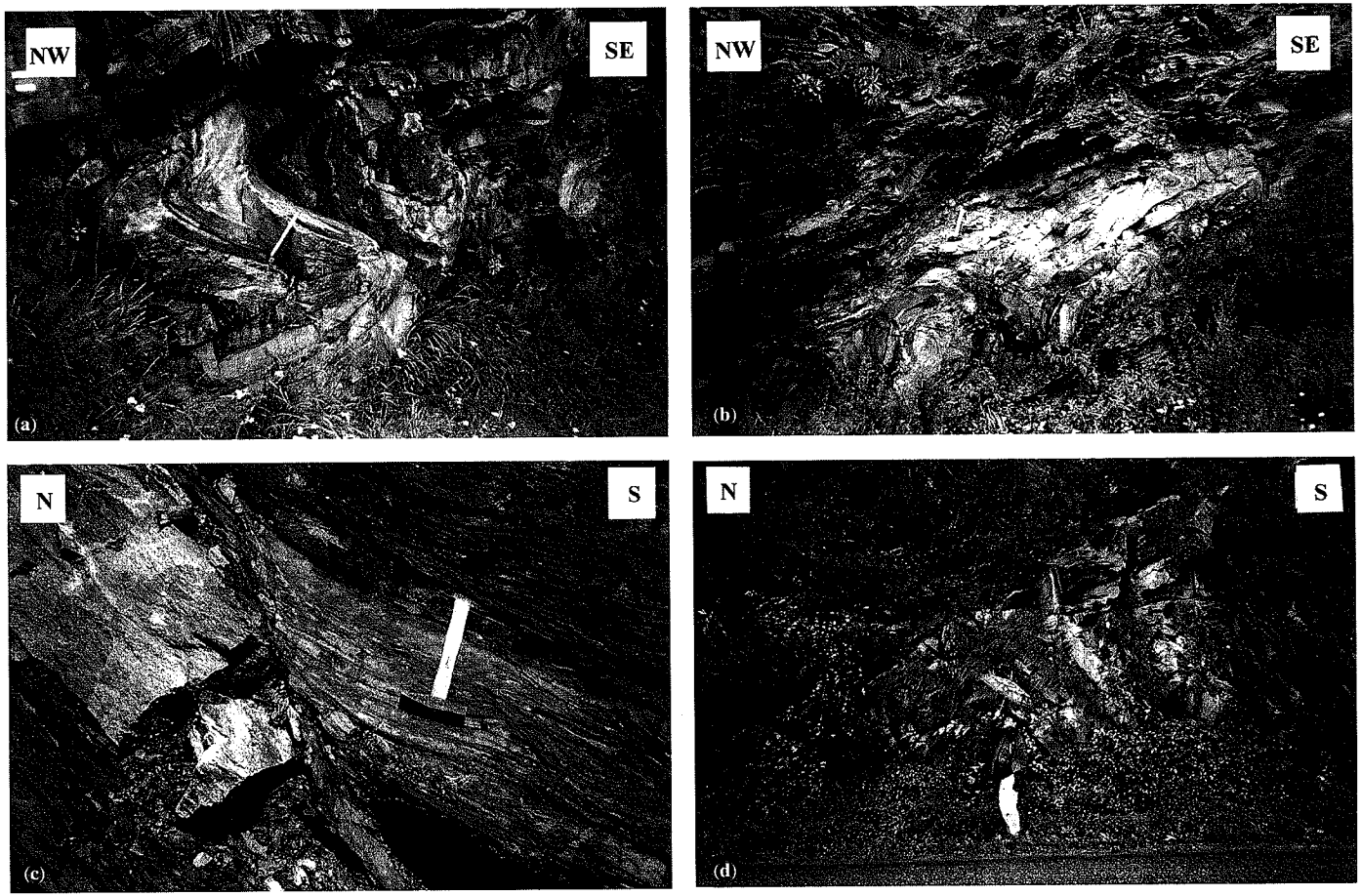

Fig. 3. Photographs of late gravitational structures. (**a**) West-facing late folds indicate the westward sliding of nappes in the upper part of the Bíteš orthogneiss (central domain, Vranov nad Dyjí). (**b**) Greenschist facies normal shear zone in the Bíteš orthogneiss indicating westward sliding (central domain, Vranov nad Dyjí). (**c**) Normal shear zone in the upper part of the Bíteš orthogneiss (southern dip-slip domain close to Horn). (**d**) Normal greenschist facies shear zone in Moldanubian migmatites associated with large-scale normal fault separating the Thaya window from the Moldanubian rocks (Bítov, north of Drosendorf).

associated with syn-schistose isoclinal sheath folds F1. The syn-metamorphic stretching lineation L1 trends north-northeast–south-southwest (Fig. 2) cutting the lithotectonic boundaries at various angles (Schulmann 1990; Fritz 1991).

Recent structural investigations (Fritz 1991; Fritz & Neubauer 1993; Schulmann *et al.* 1994) showed that the main deformation phase involved a top-to-the-north (north-northeast) inclined transpressional movement. This is indicated by the mineral stretching lineations and numerous shear-sense indicators which can be traced over large parts of the Moravian zone. The deformations have taken place in the central section in amphibolite facies conditions, which is in accordance with the mineral assemblages in the metapelites and metacarbonate rocks. Fritz (1991) has shown that in the southern dip-slip domain the kinematics exhibit the northeast thrust movements, whereas in the western part of the Thaya window dextral strike-slip movements occur (Schulmann 1990). Schulmann *et al.* (1994) reported that in the northern termination of the Thaya window the kinematic indicators reveal top-to-the-northeast dip-slip movements (Fig. 2). Detailed finite strain studies (Schulmann 1990; Fritz 1991) have shown oblate fabrics in both the southern and northern dip-slip domains, and plane strain fabric in the western strike-slip domain.

The syn-metamorphic structures are refolded by late-metamorphic W-facing recumbent F2 folds (Fig. 3a) developed as a result of the later exhumation of the nappe sequence (Schulmann *et al.* 1994). These folds vary in size from several metres to 100 m, and their hinges change orientation when traced around the dome

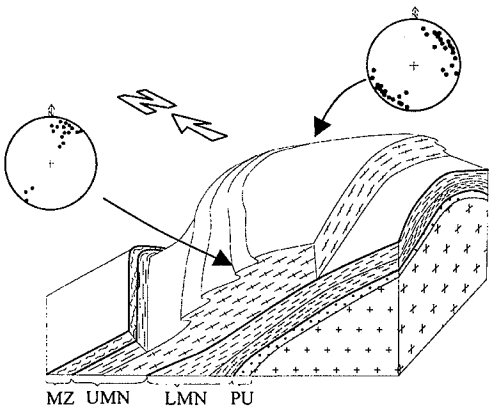

Fig. 4. Block diagram of the northern termination of the Thaya dome showing hinge orientations of late gravitational folds swinging around the Thaya dome.

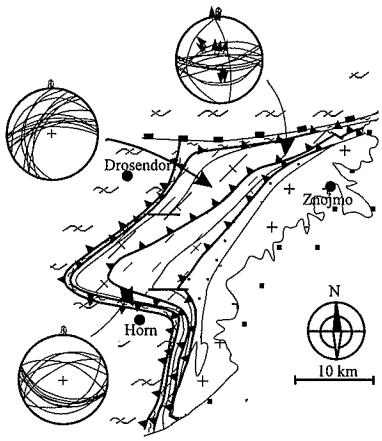

Fig. 5. Tectonic sketch map of the Thaya window and orientation diagrams showing the orientation of normal greenschist facies shear zones. Lower-hemisphere, equal area projection.

(Fig. 4) from northeast–southwest to almost east–west at the northern termination of the Thaya window (Schulmann 1990). Gravitational folding is associated with the development of medium-scale normal shear zones at the central W-dipping part of both the Upper and Lower Moravian nappes (Figs 3b and 5) which also indicate late westward gravitational sliding (Schulmann *et al.* 1994; Kolaříková *et al.* 1997). Numerous normal greenschist facies shear zones are symmetrically developed at the northern and southern terminations of the dome and in the overlying Moldanubian migmatites (Figs 3 and 5).

Normal greenschist facies shear zones developed in all levels of the nappe pile as well as the F2 folds, indicate gravitational sliding of a thick Moldanubian migmatitic sequence and Moravian nappes away from the core of the Thaya window (Lobkowicz *et al.* 1998). This gravitational sliding occurred at a relatively shallow crustal level as indicated by the associated retrogression which occurred under greenschist facies conditions (Kolaříková *et al.* 1997).

Metamorphic evolution

Metamorphic zonation

Two distinct metamorphic events have been recognized (Frasl 1970; Höck 1995). The first is related to the intrusion of the Thaya batholith and is of Upper Proterozoic age. The main regional metamorphism is of Variscan age. It is of

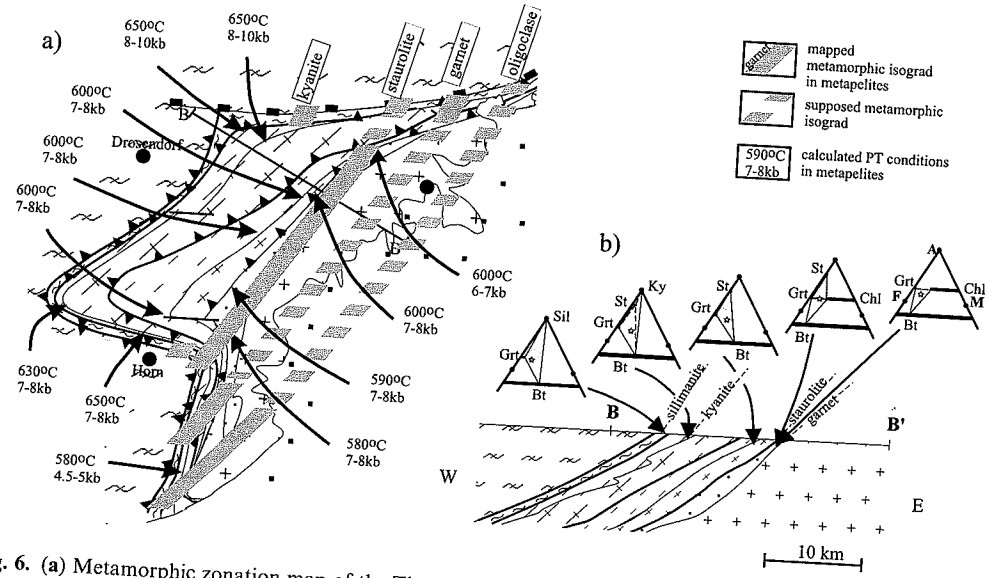

Fig. 6. (**a**) Metamorphic zonation map of the Thaya window after Höck (1975, 1995). The *P–T* estimates after Bernroider (1989), Höck (1995) and Štípská & Schulmann (1995). (**b**) Schematic northwest–southeast cross-section of the Thaya window (location in Fig. 2) showing the main mineral assemblages using AFM topologies in individual nappes and metamorphic zones. The stars in the AFM diagrams indicate whole rock compositions. Mineral compositions after Štípská & Schulmann (1995). Minerals: bt biotite; chl chlorite; grt garnet; ky kyanite; sil silmanite; st staurolite.

Barrovian type and was followed by greenschist facies retrogression. $^{40}Ar/^{39}Ar$ cooling ages of amphiboles from amphibolites in the Bíteš orthogneiss give 328.7 ± 3.3 Ma, muscovites from the Bíteš orthogneiss 328.7 ± 0.8 Ma and the muscovite of Weitersfeld orthogneiss yields 325.5 ± 0.7 Ma (Dallmeyer *et al.* 1992). These data reflect the intersection of approximately 500°C (amphibole) and 350°C (muscovite) isotherms, respectively during a rapid uplift and exhumation.

As Suess (1912), Preclik (1927) and Frasl (1970) pointed out, the metamorphic grade is highest in the western part and decreases towards the south, east and north. Therefore, the metamorphism is inverse, i.e. the structurally highest units exhibit the highest grade of metamorphism. In 1975, Höck identified four mineral zones with different assemblages in the metapelitic rocks striking parallel to the mineral stretching lineation (southwest–northeast), and cutting the regional structure (south–north to southwest–northeast), especially in the southern part of the window (Fig. 6a). Recent investigations by the present authors in the northern part of the Thaya window show that the mineral zonation also cuts the regional structure in this area.

The metamorphic zonation is defined by: (1) the albite–oligoclase boundary lying mainly in the autochthonous Thaya granite; (2) a garnet–biotite zone; and (3) a garnet–biotite–staurolite zone (Höck 1995). Kyanite and sillimanite zones (4) occur in the upper part of metapelites of the Upper Moravian nappe (Fig. 6). The peak metamorphic conditions attained in each unit are recorded in the central sector of the Thaya window where the sequence of mineral assemblages can be defined as follows: (1) grt + bt or grt + chl + bt in the lower part of the para-autochthonous unit and st + grt + bt in its upper part; (2) grt + st + bt in the Lower Moravian nappe; (3) grt + ky + st + bt in the Upper Moravian nappe and sil + bt + grt in its uppermost part (see Fig. 6) (Štípská & Schulmann 1995). These mineral assemblages are syn-tectonic with mainly top-to-the-northeast shearing (Schulmann *et al.* 1994). The garnet zoning in all tectonic units reflects the prograde temperature evolution (Höck 1995; Štípská & Schulmann 1995). As noted above, the mineral zones strike north-northeast, obliquely cutting the lithotectonic boundaries in the south, running parallel in the central sector and cutting these boundaries obliquely in the north (Fig. 6).

Pressure–temperature (P–T) estimates

We have used the published pressure and temperature estimates of Bernroider (1989) and Štípská & Schulmann (1995) for the northern part of the Thaya window and those of Höck (1995) and Höck *et al.* (1990) for its southern part. Detailed thermobarometry was performed in all tectonic units and includes estimates of maximum *P–T* conditions and, in some cases, also conditions of retrogression. Temperature estimates in the metapelites were obtained using both garnet–biotite and garnet–staurolite thermometers. Pressures were estimated using garnet–plagioclase geobarometers in the metapelites and phengite barometry in the orthogneisses. Pressure–temperature estimates of retrogression were obtained using late Mn-rich garnet rims compositions (Höck 1995) and fluid inclusions in late quartz veins (Fritz & Loitzenbauer 1994).

Peak metamorphic conditions

The peak metamorphic conditions are summarized in Figs 6 and 7. These conditions in the kyanite zone of the Upper Moravian nappe and the Micaschist zone were estimated at 630–650°C and 8–10 kbar in the northern section and 600–630°C and 9–10 kbar at the south. In the southernmost part of the Upper Moravian nappe Höck (1995) estimated pressures of 4.5–5 kbar at temperatures of 450–500°C. Calculated peak metamorphic conditions of the staurolite zone of the Lower Moravian nappe and the para-autochthonous unit are approximately 600°C and 7–8 kbars. Pressure–temperature estimates for the garnet zone of the para-autochthonous unit correspond to approximately 580°C and 7–8 kbars in the south, and about 600°C and 7–9 kbars in the northern part. Peak pressure conditions in the autochthonous deformed Thaya granite were estimated at approximately 6 kbar (Kolaříková *et al.* 1997).

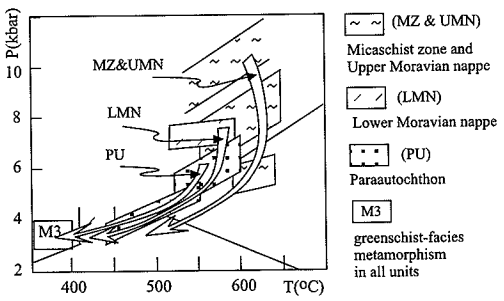

Fig. 7. The *P–T* estimates from metapelites of the Thaya window with indicated *P–T* paths. Calculations taken from Bernroider (1989), Höck (1995) and Štípská & Schulmann (1995).

Retrograde part of the pressure–temperature evolution

The retrograde stage in the Micaschist zone and the Upper Moravian nappe is marked by the growth of sillimanite at the expense of garnet under conditions of 600–630°C at 5.5–7 kbars and subsequent greenschist facies retrogression (Kolaříková *et al.* 1997). In the Lower Moravian nappe, small Mn-rich rims around the garnets reflect a stage in which 400–450°C was attained in both the southern and northern parts of the Thaya window (Höck 1995; Štípská & Schulmann 1995). In this unit, Fritz & Loitzenbauer (1994) calculated a pressure of 3.3 kbars and a temperature of 300°C from fluid inclusions in late quartz veins. In the para-autochthonous unit the minimum pressure and temperature of 4 kbar and 450°C were obtained for the retrograde part of the *P–T* path.

Inversion of metamorphic isograds

Extensive field observations and *P–T* calculations on the pelitic assemblages suggest a three-stage model for the Variscan evolution of the complex metamorphic zonation pattern. The prograde part of the *P–T* evolution is documented by the prograde zonation of garnets in all metamorphic zones (Štípská & Schulmann 1995). Based on garnet core compositions for both the Upper and Lower Moravian nappes, Höck (1995) suggests conditions of 400–500°C and 4–5.5 kbar for this stage. This stage is connected with continuous underthrusting of the Brunovistulian block beneath the hot Moldanubian block (Štípská & Schulmann 1995).

Continental underthrusting leads to complete equilibration of the continental geotherm after underthrusting, and to the restoration of the subhorizontal and parallel position of the isotherms (isograds) after a certain period of thermal relaxation. We suggest that this stage is connected with the maximum attained *P–T* conditions in the deepest part of the underthrust plate. At this time, the isograds formed an acute angle with the major thrust boundary (Fig. 8a).

The second stage is associated with the blocking of underthrusting as a result of buoyancy forces and shear stress at the thrust surface leading to a break up of the deepest part of the Brunovistulian plate. In this way, the first

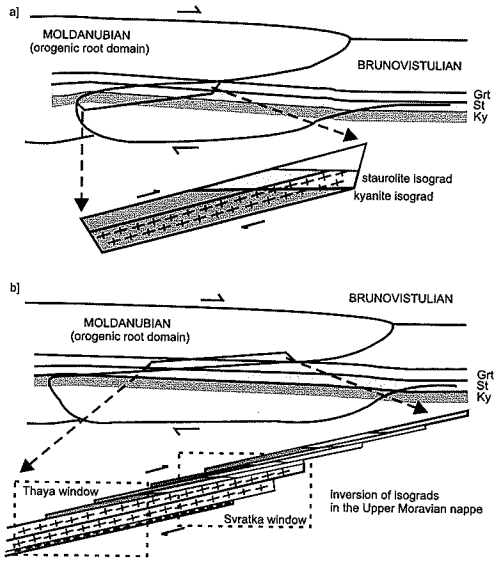

Fig. 8. Schematic diagram illustrating two stages of the mechanical inversion of metamorphic isograds by transportation of metamorphic zones within nappes and their heterogeneous simple shear deformation (modified from Štípská & Schulmann 1995).

high-grade nappes (the Micaschist zone and the Upper Moravian nappe) formed and were transported upwards together with the metamorphic zones. The rest of the Brunovistulian basement was being continuously underthrust. The Lower Moravian nappe originated in an identical manner and was thrust together with attached Upper Moravian nappe over the para-autochthon and autochthonous Thaya granite.

This process caused an apparent parallelism of the metamorphic zonation with the thrust boundaries. This parallelism was further enhanced by the heterogeneous simple shear deformation of fossil isograds (Fig. 8b) transported within the nappe.

Refolding of nappes and isograds

The evolution of inverted metamorphic zonation discussed above implies that the oblique angular relationship between metamorphic zones and lithotectonic boundaries that appears in the present erosional section must have been produced by a later post-peak metamorphic effect. We suggest a model involving the folding of the Moravian nappes that is supported by the following structural and metamorphic evidence.

The stretching lineations exhibit a constant southwest–northeast direction, whereas the foliation planes follow the shape of the western part of the Thaya window (Fig. 2a). The syn-metamorphic kinematic indicators show top-to-the-northeast thrust movements in the S-dipping dip-slip domain (near Horn), dextral movements in the western strike-slip domain (Fritz 1991) and down-slip movements in the northern termination of the Thaya window (Schulmann *et al.* 1994) (Fig. 2b). This suggests that the early kinematics have been refolded by a large-scale antiformal fold with an axis gently plunging to the west. The model of progressive folding of the Variscan nappes and associated kinematics is shown in Fig. 9.

Earlier in the paper we described how inverted metamorphic zonation occurs within individual tectonic units, i.e. the Upper Moravian and Lower Moravian nappes. The kinematic analysis

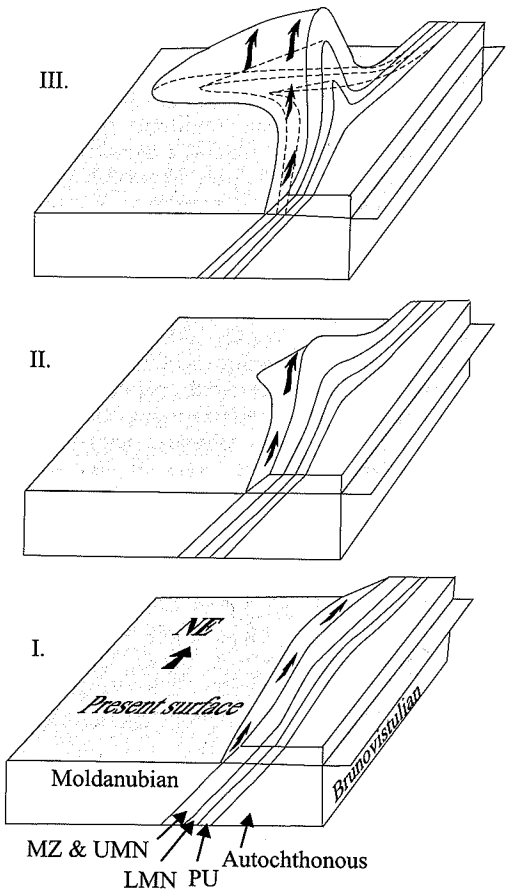

Fig. 9. Diagrammatic schematic evolution of the refolding of the Variscan nappes and their kinematic indicators around a gentle, W-plunging axis. Arrows mark syn-metamorphic kinematic indicators.

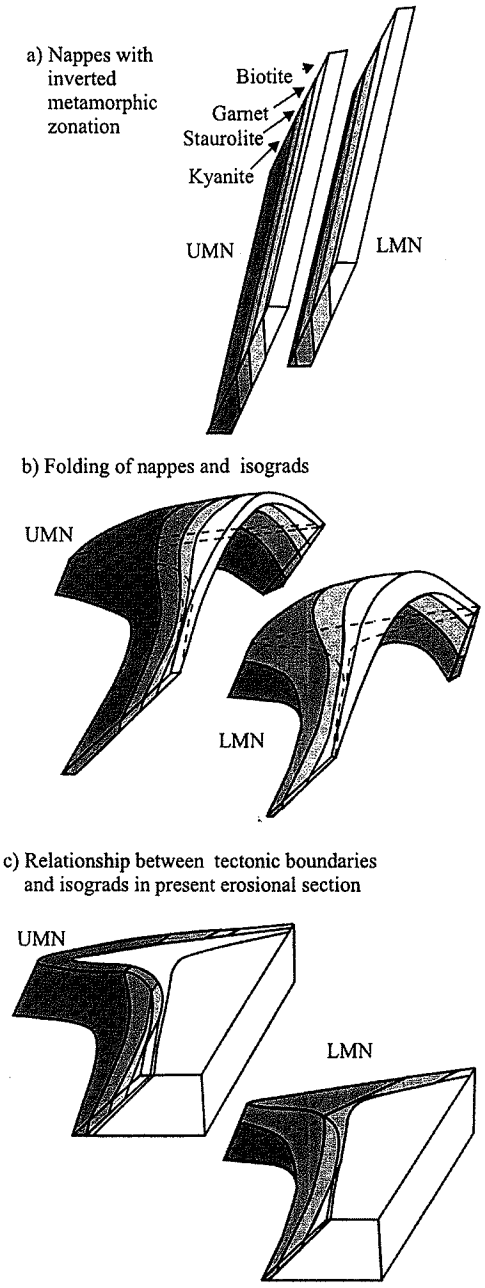

Fig. 10. Schematic diagram showing the refolding of the metamorphic isograds. (**a**) Inverted metamorphism in the individual nappes before folding.(b) Folding of the individual nappes with previously developed isograds. (**c**) The effect of isograds 'cross-cutting' tectonic boundaries in a horizontal section through this fold. Note lower metamorphism of the Lower Moravian nappe in the erosional section.

shows that the nappes were subsequently folded into a large-scale antiform with an axis plunging gently to the west. Figure 10a shows individual nappes with their inverted metamorphic zonation. If this nappe sequence is folded and subsequently cut by a horizontal section, it can be seen that the high-grade rocks would occur in the hinge zone and lower-grade rocks in the limb regions (Fig. 10b and c). This is because the metamorphic zones cut the individual lithotectonic boundaries obliquely. The same geometry is developed in both the Upper Moravian and the Lower Moravian nappes. The more or less continuous trends of the isograds crossing the entire window (Fig. 6a) can be explained by small differences in metamorphic grade between individual nappes and by the small thickness of the nappes. When both folded nappes are placed together, then the resulting trend of metamorphic isograds is achieved (Figs 6a and 10c).

From the observations presented above, we can conclude that the structure of the Thaya window can be viewed as a large-scale antiform plunging gently to the west with a wavelength of 40–45 km.

Thermal and rheological considerations

The basic assumption for the model presented above is that the high-grade nappes were transported upwards at a velocity sufficient to retain the temperature necessary for their viscous behaviour. England & Thompson (1984) have shown that the thermal budget of exhumed rocks depends on the rate of their vertical elevation. To estimate the rate of elevation of rocks within individual nappes, a numerical one-dimensional thermal model was used. This enabled the simulation of the P–T evolution of the Moravian nappes during their exhumation. The main parameters of the thermal numerical model are given in Table 1.

The P–T conditions likely to occur in the subducted crust, after the underthrusting of the Brunovistulian slab below the Moldanubian domain, can be approximated using a model of thickening of the crust by thrusting proposed by England & Thompson (1984). The thermal evolution in the Upper and Lower Moravian nappes were modelled separately and their vertical elevation corresponds to an erosion rate of $1.5\,\mathrm{mm\,year^{-1}}$. The model representing the thermal evolution of the Upper Moravian nappe was assumed to be instantaneously buried from a depth of 1 km to a depth of 36 km, and the model representing the metamorphic evolution

Table 1. *Parameters for the thermal numerical model presented in Fig. 11a*

Thermal diffusivity	$0.9 \times 10^{-6}\ m^2\ s^{-1}$
Thermal conductivity	$2.25\ W\ mK^{-1}$
Heat flow at MOHO	$40\ mW\ m^{-2}$
Radioactive heat	$2\ \mu W\ m^{-3}$
Depth of heat production	15 km
Time lag	25 Ma

of the Lower Moravian nappe was assumed to be instantaneously buried to a depth of 29 km. The effect of continuous underthrusting was simulated by assuming a time lag of 25 Ma for thermal relaxation.

According to this simple thermal model a temperature of 630°C is achieved at a depth of 36 km and the temperature of 580°C at a depth of 29 km, which corresponds approximately to the peak metamorphic conditions determined using geothermobarometry in the Upper and Lower Moravian nappes, respectively (Fig. 11a). The model predicts that after 6–7 Ma, the Upper Moravian nappe would have been exhumed to a depth of 28–25 km and that the temperature would have increased to 650°C (conditions of re-equilibration of the Upper Moravian nappe). At this depth (29 km, 580°C) the Lower Moravian nappe becomes detached and starts to be exhumed with the Upper Moravian nappe. After the next 8 Ma of joint exhumation the nappes rise to a depth of 13–15 km and the temperature decreases in both nappes to approximately the same temperature of 530–550°C (Fig. 11a).

In order to assess the mechanical behaviour of crustal nappes during the exhumation, it is important to know their rheological properties. Taking into account the lithological composition of Moravian nappes, the rheological properties of the Bíteš and Weitersfeld orthogneisses have been assumed to be similar to those of albitic rocks, and those of the surrounding metapelites assumed to be similar to the rheology of wet quartzitic rocks. The quartzite rheology was selected for the metapelites because the rheological data for the rheology for micaceous rocks are lacking and because quartz is significantly weaker than albite at all temperatures. The variations in creep strength, σ, with temperature and depth we have calculated for both albite and quartz (Ranalli & Murphy 1987) using equation (1) for a strain rate of $\dot{e} = 10^{-14}\ s^{-1}$:

$$\sigma = A\dot{e}^{n} \exp(Q/RT) \qquad (1)$$

where A is the pre-exponential function, n the creep exponent, Q the activation enthalpy of creep and R the universal gas constant.

The calculated shear stress values and viscosities for albite and quartzite for temperature range from 500 to 650°C are presented in Table 2. Calculated viscosity contrasts between albite and quartzite in individual nappes for temperatures taken from a thermal model (Fig. 11a) are shown in Table 3. An important feature is the decrease in viscosity contrast with decreasing temperature and increasing absolute values of shear stress for both the albitic rock and quartzite (Fig. 11b). The calculated shear stress values for albitic rock and quartzite from Table 2 were used to constrain the rheological evolution of the Upper and Lower Moravian nappes

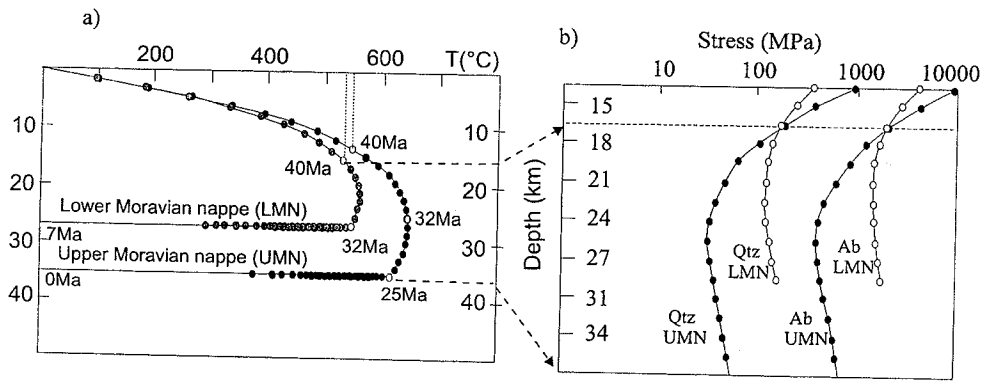

Fig. 11. Results of thermal modelling using a one-dimensional computer program showing P–T and rheological evolution of the Upper and Lower Moravian nappes during their exhumation after 25 Ma of thermal relaxation. (**a**) Model of P–T–t paths of the Lower Moravian nappe which starts after 7 Ma of exhumation of the Upper Moravian nappe. Both nappes reach the same thermal conditions after 8 Ma of joint exhumation. (**b**) Shear stress calculated for albite-rich rock (orthogneiss) and for quartzite (metapelites) using T values from the thermal model.

Table 2. *Calculated shear stress values and viscosities for albitic (orthogneiss) and quartzitic (metapelite) rock over the temperature range of 500–650°C*

T (C)	σ_{ab} (MPa)	σ_{qtz} (MPa)	μ_{ab} (Pa s)	μ_{qtz} (Pa s)
500	12777	1316	6.39×10^{23}	6.58×10^{22}
510	9630	969	4.81×10^{23}	4.84×10^{22}
520	7337	721	3.67×10^{23}	3.61×10^{22}
530	5648	543	2.82×10^{23}	2.72×10^{22}
540	4390	414	2.19×10^{23}	2.07×10^{22}
550	3443	318	1.72×10^{23}	1.59×10^{22}
560	2725	247	1.36×10^{23}	1.23×10^{22}
570	2174	193	1.09×10^{23}	9.66×10^{21}
580	1748	152	8.74×10^{22}	7.62×10^{21}
590	1416	121	7.08×10^{22}	6.07×10^{21}
600	1155	97	5.77×10^{22}	4.87×10^{21}
610	948	79	4.74×10^{22}	3.93×10^{21}
620	784	64	3.92×10^{22}	3.20×10^{21}
630	651	52	3.26×10^{22}	2.62×10^{21}
640	545	43	2.72×10^{22}	2.16×10^{21}
650	458	36	2.29×10^{22}	1.79×10^{21}

Ab, albite; qtz, quartzite.
Rheological parameters are taken from the experiments of Jaoul *et al.* (1984) for hydrous quartzite: $n = 2.4$, $Q = 163\,\mathrm{kJ\,m^{-1}}$, $A = 10^{-5}\,\mathrm{MPa^{-n}\,s^{-1}}$ and of Shelton & Tullis (1981) for albitic plagioclase: $n = 3.9$, $Q = 234\,\mathrm{kJ\,m^{-1}}$; $A = 2.51 \times 10^{-6}\,\mathrm{MPa^{-n}\,s^{-1}}$.

during their exhumation (Fig. 11b). The temperature values used for calculation of shear stress at different depths for each nappe were taken from the P–T model (Fig. 11a).

Our thermal modelling shows that the nappes during vertical elevation are transporting heat, and that the temperature during the early stages of exhumation increases. The temperature evolution is coupled with rheological behaviour of the crustal nappes during their exhumation. Consequently, the shear stress values decrease with increasing temperature in both nappes (Fig. 11b), which is followed by hardening with decreasing temperature at supracrustal levels. The Upper Moravian nappe, which was hotter than the Lower Moravian nappe, was significantly weaker for both albite and quartzitic lithologies. When the temperature converges (at 520–540°C) in both nappes at depths approximately corresponding to 15–16.5 km, the shear stress attains the same values for quartzite (414 MPa) and albitic rock (4390 MPa) in both units (Table 2, Fig. 11b).

Our thermal models show that rocks in the individual nappes were transported upwards to

Table 3. *Calculated viscosity ratios for albitic (orthogneiss) and quartzitic (metapelite) rock in the Upper and Lower Moravian nappes (UMU, LMU) during their exhumation*

Depth (km)	T (°C) UMN	T (°C) LMN	μ_{ab}/μ_{qtz} UMN	μ_{ab}/μ_{qtz} LMN	W_i (km) for μ_{ab}(UMN)/μ_{qtz}UMN	W_i (km) for μ_{ab}(UMN)/μ_{qtz}LMN
29.5	655	580	12.9	2.8	40.5	24.2
27	660	585	13.0	2.8	40.6	24.5
25.5	660	590	13.0	3.2	40.6	25.4
24.0	655	630	12.9	3.5	40.5	26.2
22.5	650	590	12.8	3.8	40.4	26.9
21	630	590	12.4	5.4	40.0	29.0
19.5	620	585	12.3	5.8	39.8	31.0
18	600	580	11.9	7.6	39.4	33.9
16.5	570	560	11.3	8.8	38.7	35.7
15	540	540	10.6	10.6	38.0	38.0

Ab, albite; qtz, quartzite.
Temperatures and depths are taken from the numerical model presented in Fig. 11a. The theoretical wavelength for the Biteš orthogneiss embedded in UMN metapelites (μ_{ab}UMN/μ_{qtz}UMN) and LMN metapelites (μ_{ab}UMN/μ_{qtz}LMN) has also been calculated (see Fig. 12b).

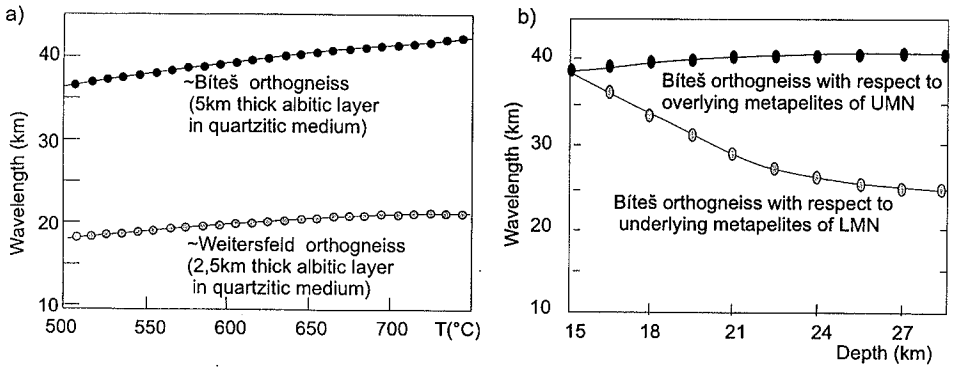

Fig. 12. Results of calculations of fold wavelength (using the Biot formula) for viscosities of albitic rock and quartzite and for different thickness of competent layers. **(a)** The wavelength is calculated for the Bíteš and Weitersfeld orthogneiss at temperatures ranging from 500 to 750°C. **(b)** Wavelength of the Bíteš orthogneiss layer calculated for viscosity contrast between the Bíteš orthogneiss and the overlying and underlying pelites. The viscosities of albite rock and quartzite were calculated using T and stress values from Fig. 11.

supracrustal levels rapidly enough to avoid significant temperature loss (Fig. 11a). Therefore, they could deform or fold in a ductile manner when they reached a relatively rigid and cold obstacle such as the autochthonous Thaya granite. It is important to point out that at a certain depth, which is controlled by the rate of exhumation, the rocks making up the nappes attain the same rheological properties (Fig. 11b).

Crustal multilayer

The development of folds in a multilayer made up of alternating competent and incompetent layers is controlled by the ratio of the thickness of the incompetent and competent layers ($n = d_2/d_1$) and their viscosity contrast μ_1/μ_2 (Ramberg 1962, 1964). The Upper Moravian nappe is marked by the presence of an orthogneiss body 4–5 km thick and a 2–3 km thick micaschist sequence in the hangingwall. The Lower Moravian nappe contains significantly less orthogneiss than micaschist, the former is about 2 km thick and the latter 3 km thick. The metasediments of the para-autochthonous unit have a thickness of 2 km and contain relatively small amounts of orthogneiss. Thus, the proportion of incompetent to competent layer thickness for the Moravian nappes approaches a value slightly higher than $n = 1$. This means that the multilayer system will fold harmonically, i.e. will behave mechanically as a multilayer where all layers develop the same wavelength rather than a series of single layers in which each competent layer develops its own wavelength according to the single-layer buckling equation (see equation 2) (see Price & Cosgrove 1990).

The folding of simplest multilayer system requires similar rheological properties of competent layers embedded in soft matrix with unique viscosity. The wavelength W_i of this multilayer system is controlled by the thickest competent layer (Ramberg 1970), and is calculated using the Biot (1961) and Ramberg (1964) formula:

$$W_i = d2\pi(\mu_1/6\mu_2)^{1/3} \qquad (2)$$

where W_i is the initial fold wavelength, d is the thickness of competent layer and μ_1/μ_2 is the viscosity contrast. However, the requirement of similar viscosity of competent layers is not fulfilled for the large part of exhumation history of the Moravian nappes. Figure 11b shows that the thicker Bíteš orthogneiss is rheologically weaker than the underlying Weitersfeld orthogneiss for depths deeper than 16.5 km.

If the folding is driven by stronger Weitersfeld orthogneiss, then the wavelength of the fold would reach 18–20 km only (Fig. 12a) which is not consistent with the observed wavelength of 40–45 km of the Thaya antiform (Fig. 2). However, when the fold wavelength is calculated for the Bíteš orthogneiss for the temperature range 500–650°C and viscosity contrast μ_{ab}/μ_{qtz} in the range 10–13 (Table 3), then the W_i values vary between 37 and 40 km (Fig. 12a, Table 3), i.e. the approximate wavelength exhibited by the Thaya antiform. We therefore suggest that the folding was driven by this thick competent layer. This is possible only when the Bíteš orthogneiss is of equal viscosity or is rheologically stronger than the underlying Weitersfeld orthogneiss, i.e. at depths of less than 16.5 km.

Another requirement of this buckling model is the unique viscosity of the weak medium embedding orthogneiss bodies. This requirement is not fulfilled at depths exceeding 16 km where the temperatures of both nappes become equilibrated. During joint exhumation of the Upper and Lower Moravian nappes, the viscosity ratio between the Bíteš orthogneiss and the overlying metasediments (μ_{ab}UMN/μ_{qtz}UMN) is different from the viscosity ratio between the Bíteš orthogneiss and the underlying metasediments of the Lower Moravian nappe (μ_{ab}UMN/μ_{qtz}LMN) (Table 3). We have calculated the fold wavelength for the Bíteš orthogneiss with respect to overlying (UMN) and underlying (LMN) metasediment viscosities, respectively (Table 3, Fig. 12b). The fold wavelength of the Bíteš orthogneiss if embedded in a medium of the underlying metasediments is 25 km at a depth of 29.5 km and steadily increases to $W_i = 38$ km at a depth of 15 km. At this depth, the temperature, as well as the viscosity of both the underlying and overlying metapelites, converge.

Discussion

The complex geometry of the inverted metamorphic isograds and their oblique relationship with respect to the main lithotectonic boundaries have been discussed, and detailed petrological data and structural observations used to argue that the complex pattern of metamorphic isograds is in part the result of large-scale buckling of the metamorphic nappe sequence. Pressure–temperature data in combination with thermal modelling have been used to estimate the rheological evolution of the nappe sequence during exhumation.

It is suggest that the buckling of the Moravian nappe pile started at a depth of 15 km during exhumation and that its wavelength was controlled by the Bíteš orthogneiss the thickest competent layer. At this depth the viscosities of the Bíteš and the Weitersfeld orthogneiss become equal and the viscosity of medium embedding the Bíteš orthogneiss (the underlying and overlying metasediments) becomes homogeneous. The calculated fold wavelength of 38 km is in good agreement with the observed wavelength of the Thaya antiform, 40–45 km. The estimated depth of 15 km, at which folding was initiated, roughly coincides with the depth estimate of 18 km (5-6 kbar, Kolaříková *et al.* 1997) for the burial of the autochthonous Thaya granite. It is argued that, at this depth, the autochthonous Thaya granite acted as a rigid buttress which inhibited further nappe thrusting and enhanced the buckling of the multilayer system.

The style of folding of the Moravian nappes multilayer sequence is controlled by relatively low ductility contrast ($\mu_{albite}/\mu_{quartz}$) and moderate ratio of incompetent to competent layer thickness. This relatively close spacing of the Bíteš and Weitersfeld orthogneiss ensures that a harmonic fold assemblage develops and that the zone of contact strain (Ramberg 1962) of the Bíteš orthogneiss is sufficiently large to control the folding of underlying sequences.

The relatively low viscosity contrast may have been responsible for important modification of fold geometry by homogeneous flattening which would lead to a thickening of both the competent and incompetent layers in the hinge zone and thinning in the fold limbs. The flattening of this megafold is well documented by its similar fold geometry and by the finite strain studies of Schulmann (1990) and Fritz (1991), which show oblate strain ellipsoids in the limb regions and plane strain fabrics in the fold hinge.

The folding of crustal nappes along an inclined surface is responsible for the rapid elevation of fold hinge into supracrustal levels in response to horizontal shortening (Fig. 2b). The overlying thick nappe of Moldanubian migmatites cannot be folded, and is therefore affected by extensional faulting where it lies above the fold limbs (Figs 2b and 3d). These huge extensional to transtensional faults place high-grade Moldanubian rocks in direct contact with low-grade Moravian rocks (Schulmann *et al.* 1994). Extensional faulting also affects the Moravian units and results in a reduction of their thickness in the northern and southern parts of the window (Figs 2b, 3b and c and 5). The extensional faulting is accompanied by the development of medium-scale gravitational folds in the highly anisotropic parts of Moravian nappes (Schulmann *et al.* 1994) which do not affect the whole crustal multilayer (Figs 3a and 4).

Ramberg (1968, 1970) demonstrated that gravity folding results in significantly greater fold wavelengths than buckling for horizontal layers thicker than 1 km. However, in the case of the Moravian nappes, the folding starts along a relatively steeply inclined surface (Figs 6b and 9). Therefore, it is argued that gravity did not play a major role in the formation of large-scale buckle folds. Instead, we suggest that in this example gravity influenced the sliding of nappes along extensional faults which developed on the limbs of the Thaya antiform. We interpret the extensional structures as secondary products of large-scale buckling of a nappe sequence.

Financial support of Czech National Grant Agency (No. 205/96/0277) and Ministry of Education (No. 2431 3005) are gratefully acknowledged.

References

BERNROIDER, M. 1989. Zur Petrogenese prekambrischer Metasedimente und cadomischer Magmatite im Moravikum. *Jahrbuch des Geologischen Bundesanstalt*, **132**, 349–373.

BIOT, M. A. 1961. Theory of folding of stratified, viscoelastic media and its applications in tectonics and orogenesis. *Geological Society of America Bulletin*, **72**, 1595–1632.

BRUNEL, M. & KIÉNAST, J. R. 1986. Etude petro-structurale des chevauchements ductiles himalayens sur la transversale de l'Everest-Makalu (Nepal oriental). *Canadian Journal of Earth Sciences*, **23**, 1117–1137.

BURG, J. P., DELOR, C. P., LEYRELOUP, A. F. & ROMNEY, F. 1989. Inverted metamorphic zonation and Variscan thrust tectonics in the Rouergue area (Massif Central, France): P–T–t record from mineral to regional scale. *In*: CLIFF, R. A., DALY, J. S. & YARDLEY, B. W. D. (eds) *Evolution of Metamorphic Belts*. Geological Society, London, Special Publications, **43**, 423–439.

DALLMEYER, R. D., NEUBAUER, F. & HÖCK, V. 1992. Chronology of late Paleozoic tectonothermal activity in the southeastern Bohemian massif, Austria (Moldanubian and Moravo-Silesian zones) – 40Ar/39Ar mineral age controls. *Tectonophysics*, **210**, 135–153.

DUDEK, A. 1980. The crystalline basement block of the Outer Carpathians in Moravia. *Rozpravy Československé akademie věd*, **90**, 1–85.

ENGLAND, P. C. & THOMPSON, A. B. 1984. Pressure–temperature–time paths of regional metamorphism, part I: heat transfer during the evolution of regions of thickened continental crust. *Journal of Petrology*, **25**, 894–928.

FRASL, G. 1970. Zur Metamorphose und Abgrenzung der Moravischen Zone im niederoesterreichischen Waldviertel. *Nachrichtungen Deutche Geologische Gesselschaft*, **2**, 55–60

FRITZ, H. 1991. Structures and kinematics along the Moravian–Moldanubian boundary: preliminary results. *Osterreichische Beitrage zu Meteorologie und Geophysik*, **3**, 77–96.

—— & LOITZENBAUER, J. 1994. Fluid activity during late stage of Variscan deformation in the Moravian nappe complex. *Mitteilungen der Osterreichischen Mineralogischen Gesselschaft*, **139**, 47–49.

—— & NEUBAUER, F. 1993. Kinematics of crustal stacking and dispersion in the south-eastern Bohemian Massif. *Geologische Rundschau*, **82**, 556–565.

HUBBARD, M.S. 1989. Thermobarometric constraints on thermal history of the Main Central Thrust Zone and Tibetan Slab, eastern Nepal Himalaya. *Journal of Metamorphic Geology*, **7**, 19–30.

HÖCK, V. 1975. Mineralzonen in Metapeliten und Metapsammiten der Moravischen Zone in Niederoesterreich. *Mitteilungen der Geologischen Gesselschaft*, **66–67**, 49–60.

—— 1995. Moravian zone: Metamorphic evolution. *In:* DALLMEYER, R. D., FRANKE, W. & WEBER, K. (eds) *Pre-Permian Geology of Central and Eastern Europe*, Springer-Verlag, Berlin, 541–553.

——, MARSCHALLINGER, R. & TOPA, D. 1990. Granat-Biotit-Geothermometrie in Metapeliten der Moravischen Zone in Osterreich. *Osterreichische Beitrage zu Meteorologie und Geophysik*, **3**, 149–167.

JAOUL, O., TULLIS, J. & KRONENBERG A. 1984. The effect of varying water content on the behaviour of Heavitree quartzite. *Journal of Geophysical Research*, **89**, 4298–4312.

KOLAŘÍKOVÁ, A., MARQUER, D. & SCHULMANN, K. 1997. Evolution of mass-transfer during progressive oblique under-thrusting of the Variscan foreland: eastern Bohemian Massif. *Geodinamica Acta*, **10**, 81–93.

LOBKOWICZ, M., SCHULMANN, K. & MELKA, R. 1998. Variscan deformation, microstructural zonation and extensional exhumation of the Moravian Cadomian basement. *Geodinamica Acta*, **11**(2/3), 119–137.

MASON, R. 1984. Inverted isograde at Sulitljema, Norway: the result of shear zone deformation. *Journal of Metamorphic Geology*, **2**, 77–82.

MOHAN, A., WINDLEY, B. F. & SEARLE, M. P. 1989. Geothermobarometry and development of inverted metamorphism in the Darjeeling–Sikkim region of the eastern Himalaya. *Journal of Metamorphic Geology*, **7**, 95–110.

PRECLIK, K. 1927. Zur Tektonik und Metamorphose der moravischen Aufwolbung am Ostrand der Bohmischen Masse. *Geologische Rundschau*, **18**, 81–103.

PRICE, N. J. & COSGROVE, J. W. 1990. *Analysis of Geological Structures*. Cambridge University Press, Cambridge.

RAMBERG, H. 1962. Contact strain and folding instability of a multilayered body under compression. *Geologische Rundschau*, **51**, 405–439.

—— 1964. Selective buckling of composite layers with contrasted rheological properties, a theory for simultaneous formation of several orders of folds. *Tectonophysics*, **4**, 307–341.

—— 1968. Instability of layered systems in the field of gravity. I, II. *Physics of the Earth and Planetary Interiors*, **1**, 427–447.

—— 1970. Folding of compressed multilayers in the field of gravity. I, II. *Physics of the Earth and Planetary Interiors*, **2**, 203–232.

RANALLI, G. & MURPHY, D. C. 1987. Rheological stratification of the lithosphere. *Tectonophysics*, **132**, 281–295.

SCHARBERT, S. & BATÍK, P. 1980. The Age of the Thaya (Dyje) Pluton. *Verhandlungen des Geologischen Bundesanstalt*, **3**, 325–331.

SCHULMANN, K. 1990. Fabric and kinematic study of the Bites orthogneiss (southwestern Moravia): Result of large-scale northeastward shearing parallel to the Moldanubian/Moravian boundary. *Tectonophysics*, **177**, 229–244.

——, MELKA, R., LOBKOWICZ, M., LEDRU, P., LARDEAUX, J. M. & AUTRAN, A. 1994. Contrasting styles of deformation during progressive nappe stacking at the southeastern margin of the Bohemian Massif (Thaya Dome). *Journal of Structural Geology*, **16**, 355–370.

SHELTON, G. & TULLIS, J. 1981. Experimental flow laws for crustal rocks. *Eos, Transactions of Americal Geophysical Union*, **62**, 396.

ŠTÍPSKÁ, P. & SCHULMANN, K. 1995. Inverted metamorphic zonation in a basement-derived nappe sequence, eastern margin of the Bohemian Massif. *Geological Journal*, **30**, 385–413.

SUESS, F. E. 1912. Die moravischen Fenster und ihre Beziehung zum Grundgebirge des Hohen Gesenke. *Akademie der Wissenschaften, Denkschrift Matematisch-Naturwissenschaftliche Klasse*, **83**, 541–631.

—— 1926. *Intrusionstektonik und Wandertektonik im variszichen Grundgebirge*. Bornttrager, Berlin.

TRELOAR, P. J., BROUGHTON, R. D., WILLIAMS, M. P., COWARD, M. P. & WINDLEY, B. F. 1989. Deformation, metamorphism and imbrication of the Indian plate, south of the Main Mantle Thrust, north Pakistan. *Journal of Metamorphic Geology*, **7**, 111–125.

WALDMANN, L. 1930. Zum geologischen Bau der Thayakuppel und ihre Metamorphose. *Mitteilungen der Geologischen Gesselschaft*, **21**, 133–152.

J. metamorphic Geol., 2006, **24,** 219–240 doi:10.1111/j.1525-1314.2006.00634.x

Separate or shared metamorphic histories of eclogites and surrounding rocks? An example from the Bohemian Massif

P. ŠTÍPSKÁ,[1,2] P. PITRA[3] AND R. POWELL[4]
[1]*Université Louis Pasteur, CGS/EOST, UMR 7517, 1 Rue Blessig, Strasbourg, France (stipska@gmail.com)*
[2]*Institute of Petrology and Structural Geology, Charles University, Albertov 6, Prague, Czech Republic*
[3]*Géosciences Rennes, UMR CNRS 6118, Université Rennes 1, Campus de Beaulieu, 35042 Rennes Cedex, France*
[4]*School of Earth Sciences, University of Melbourne, Melbourne, Victoria 3010, Australia*

ABSTRACT Eclogite boudins occur within an orthogneiss sheet enclosed in a Barrovian metapelite-dominated volcano-sedimentary sequence within the Velké Vrbno unit, NE Bohemian Massif. A metamorphic and lithological break defines the base of the eclogite-bearing orthogneiss nappe, with a structurally lower sequence without eclogite exposed in a tectonic window. The typical assemblage of the structurally upper metapelites is garnet–staurolite–kyanite–biotite–plagioclase–muscovite–quartz–ilmenite ± rutile ± silli-manite and prograde-zoned garnet includes chloritoid–chlorite–paragonite–margarite, staurolite–chlorite–paragonite–margarite and kyanite–chlorite–rutile. In pseudosection modelling in the system Na_2O–CaO–K_2O–FeO–MgO–Al_2O_3–SiO_2–H_2O (NCKFMASH) using THERMOCALC, the prograde path crosses the discontinuous reaction chloritoid + margarite = chlorite + garnet + staurolite + paragonite (with muscovite + quartz + H_2O) at 9.5 kbar and 570 °C and the metamorphic peak is reached at 11 kbar and 640 °C. Decompression through about 7 kbar is indicated by sillimanite and biotite growing at the expense of garnet. In the tectonic window, the structurally lower metapelites (garnet–staurolite–biotite–muscovite–quartz ± plagioclase ± sillimanite ± kyanite) and amphibolites (garnet–amphibole–plagioclase ± epidote) indicate a metamorphic peak of 10 kbar at 620 °C and 11 kbar and 610–660 °C, respectively, that is consistent with the other metapelites. The eclogites are composed of garnet, omphacite relicts (jadeite = 33%) within plagioclase–clinopyroxene symplectites, epidote and late amphibole–plagioclase domains. Garnet commonly includes rutile–quartz–epidote ± clinopyroxene (jadeite = 43%) ± magnetite ± amphibole and its growth zoning is compatible in the pseudosection with burial under H_2O-undersaturated conditions to 18 kbar and 680 °C. Plagioclase + amphibole replaces garnet within foliated boudin margins and results in the assemblage epidote–amphibole–plagioclase indicating that decompression occurred under decreasing temperature into garnet-free epidote–amphibolite facies conditions. The prograde path of eclogites and metapelites up to the metamorphic peak cannot be shared, being along different geothermal gradients, of about 11 and 17 °C km^{-1}, respectively, to metamorphic pressure peaks that are 6–7 kbar apart. The eclogite–orthogneiss sheet docked with metapelites at about 11 kbar and 650 °C, and from this depth the exhumation of the pile is shared.

Key words: Bohemian Massif; eclogite; incoherent *P–T* paths; metapelite; prograde garnet zoning; pseudosection.

INTRODUCTION

Eclogites and blueschists commonly occur as boudins within other rock types, such as felsic gneisses and metapelites, in subduction-related convergent orogens. Classic examples, as reviewed in Chopin (2003), occur in the Western Gneiss Region in Norway, the Dora-Maira Massif in Western Alps, the Kokchetav Massif in Kazakhstan, the Bohemian Massif in Europe, and the Dabie-Su-Lu in China, as well as the Sanbagawa Belt in Japan (Wallis & Aoya, 2000; Ko *et al.*, 2005) and the Alanya nappes in Turkey (Okay, 1989). The common question in these terranes is whether the high-pressure rocks and the rocks enclosing them shared their entire *P–T* history, just a part of it, or if their *P–T* histories are completely separate. It was originally proposed in many places that eclogites and blueschists are tectonically interleaved at mid-crustal depth and do not share a metamorphic history (e.g. Smith, 1988). Structural observations usually cannot help in answering this question. Whereas structures related to high-pressure metamorphism are commonly preserved in the mafic boudins, they are not observed in the country rocks, but this may be because they are obliterated there by later deformation as a consequence of being rheologically softer than the high-pressure mafic rocks.

Metamorphic studies are useful in revealing the prograde stage of the metamorphic history, demonstrating whether the peak conditions of the host rocks

are consistent with the peak conditions in eclogites, and in some cases may even indicate comparable prograde *P–T* paths. The discovery of coesite and microdiamond in both eclogites and surrounding rocks proved the coherence of their *P–T* paths in UHP terranes that were previously thought to have had separate histories (Chopin, 2003). In terranes, where the maximum pressure of mafic boudins is in the quartz–eclogite or blueschist facies, it is still necessary to rely on common mineral assemblages. Even if the felsic rocks react less, for example due to the lack of H_2O, and/or are more easily retrogressed (e.g. Heinrich, 1982; Proyer, 2003), with high-pressure assemblages being replaced in the matrix, careful petrographic study has demonstrated that even the felsic rocks are useful in determining prograde and peak conditions at high pressure (for references see Wei & Powell, 2004). Relics of prograde and peak assemblages armoured in garnet may occur, and garnet itself may preserve its growth zoning. Consequently, a shared history for mafic rocks and interlayered and/or surrounding felsic rocks has been demonstrated in high-pressure terranes (Meyre *et al*., 1999; Okay, 2002; Wei & Powell, 2004; Ko *et al*., 2005). However, the 'blocks' of high-pressure mafic rocks (possibly interlayered with portions of high-pressure felsic layers) are still being considered in other terranes to be a result of tectonic mixing with host rocks at lower pressure, for example in the Sanbagawa Belt (Takasu, 1984, 1989), in the mixed zone of the Nordfjord area in the Western Gneiss Region (Wain, 1997) and in the Alanya nappes in Turkey (Okay, 1989).

The exploitation of petrographic information has been improved enormously by thermodynamic modelling of both felsic and mafic lithologies allowing determination of *P–T* conditions of mineral assemblages via pseudosections (Meyre *et al*., 1999; Proyer, 2003; Wei *et al*., 2003; Wei & Powell, 2004). The power of pseudosections in solving such problems is in the ability of the approach to quantify the prograde part of *P–T* paths using mineral inclusions, their chemistry and garnet growth zoning. In this study, we apply the approach to eclogite boudins that occur in felsic orthogneisses surrounded by metapelites and metavolcanics at the eastern margin of the Bohemian Massif in the Velké Vrbno unit. We demonstrate that the prograde and peak metamorphic histories of eclogites and metapelites are separate, establish the depth of their docking, and show that their exhumation *P–T* path is shared.

GEOLOGICAL SETTING

Geology of the eastern margin of the Bohemian Massif

The Velké Vrbno unit, the object of this study, is situated at the boundary between the high-grade Moldanubian and the Barrovian type Brunia-derived domains at the eastern margin of the Variscan Bohemian Massif (Fig. 1). The boundary involves a major thrust of the internal Moldanubian domain over the external Brunian basement that produced in the latter a 300-km long metamorphosed and deformed belt, the Moravo-Silesian domain (Suess, 1912, 1926). The boundary is marked by the so-called Micaschist zone, involving the Velké Vrbno unit, considered to be a retrogressed part of the structurally upper Moldanubian domain (Suess, 1926), or as the uppermost part of the structurally lower Brunian domain (Štípská & Schulmann, 1995; Konopásek *et al*., 2002). The two major domains differ in protolith ages, character of Variscan metamorphism and style of deformation.

The Moldanubian domain

The Moldanubian domain involves Cambro-Ordovician to Devonian magmatism that acted on Paleoproterozoic and Neoproterozoic protoliths (e.g. Kröner *et al*., 2001; Friedl *et al*., 2004; Lange *et al*., 2005a,b). A major consequence of the Variscan orogenesis in this domain is widespread anatexis and an alternation of medium- and high-pressure belts (e.g. Štípská *et al*., 2004; Schulmann *et al*., 2005). The high-pressure belts are represented by felsic granulites and orthogneisses (O'Brien & Rötzler, 2003), rare crustal eclogites (Medaris *et al*., 1998; Klemd & Bröcker, 1999; Štípská & Powell, 2005) and intercalations of garnetiferous peridotites associated with 'mantle' eclogites (e.g. Carswell, 1991; Medaris *et al*., 1995).

The Brunian basement and the Moravo-Silesian zone

The Brunian basement contains Neoproterozoic granitoids that lack the Cambro-Ordovician magmatic rejuvenation typical of the Moldanubian domain (Kröner *et al*., 2000 and references therein). Variscan metamorphism in the Moravo-Silesian domain is of Barrovian type and is tectonically inverted (Souček, 1978; Schulmann & Gayer, 2000; Štípská *et al*., 2000). Remnants of eclogites were reported from the central part of the Moravo-Silesian domain (Konopásek *et al*., 2002), whereas Abukuma-type mineral assemblages (Rozkošný & Souček, 1989) are characteristic for some areas in the northern part.

NE margin of the Bohemian Massif and the Velké Vrbno unit

In the north-eastern part of the contact between the Moldanubian and the Moravo-Silesian domain, the transitional zone, defined by Kröner *et al*. (2000), consists of (1) the Staré Město belt and (2) the Velké Vrbno unit. These two units were considered by Suess (1926) as the retrogressed base of the Moldanubian domain, corresponding to the continuation of the Micaschist zone further to the south. Zircon dating in the Staré Město unit revealed its Cambro-Ordovician origin and this part is therefore interpreted as an attenuated lower crustal segment of the Moldanubian

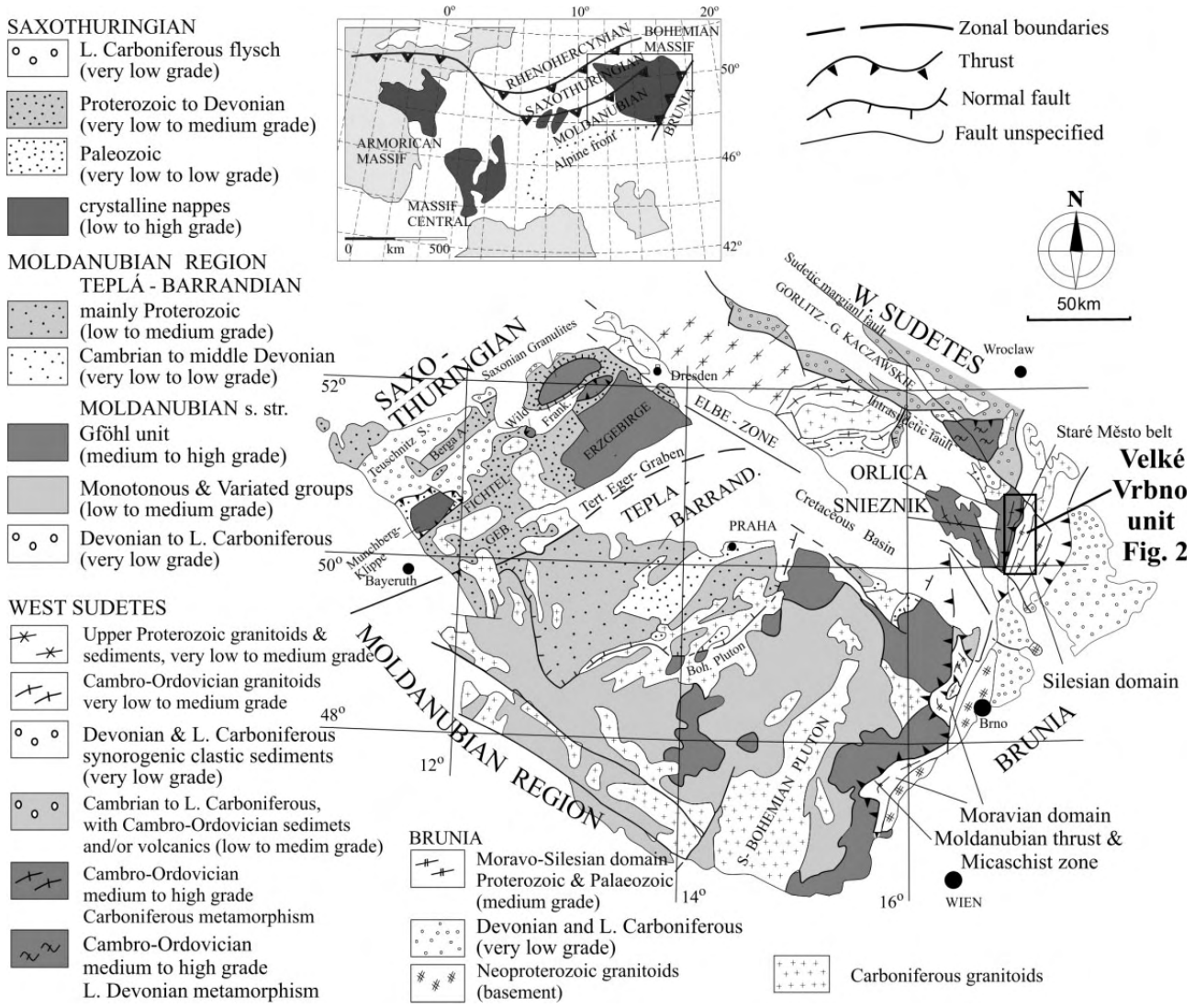

Fig. 1. Outline geological map of the Bohemian Massif with major units shown schematically (modified after Franke, 2000). Location of the study area (Fig. 2) is indicated. Upper left inset is position of study area in the framework of the European Variscides.

domain (Kröner *et al*., 2000; Štípská *et al*., 2001) for which Cambro-Ordovician protolith ages are characteristic (Turniak *et al*., 2000; Kröner *et al*., 2001). In the Velké Vrbno unit, one published and several new zircon ages (Kröner *et al*., 2000; A. Kröner, unpublished data) from the felsic orthogneisses are all Neoproterozoic, indicating a clear affinity with the Moravo-Silesian domain. Accordingly, the major contact between the Moravo-Silesian and Moldanubian domains (Fig. 2), originally placed at the base of the Velké Vrbno unit (the so-called Ramzová thrust; Suess, 1926), is thought to be located at the top of this unit (the Nýznerov thrust; Skácel, 1989).

The Velké Vrbno unit

The Velké Vrbno unit has an antiformal structure elongated in the NE–SW direction (Fig. 2), and according to the orthogneiss protolith ages represents the uppermost part of the Moravo-Silesian domain. The dominant feature of the unit is an eclogite-bearing orthogneiss-metavolcanic sheet (Žáček, 1996) thrust over a volcano-sedimentary sequence. The latter consists of marbles with graphitic schists, paragneisses and metapelites with structurally downwards increasing proportion of mafic and felsic meta-volcanics. Above the orthogneiss sheet there is a gradual upward change from dominant felsic orthogneiss into a bimodal metavolcanic sequence with increasing proportion of sedimentary component, up to a sequence of metapelites and paragneisses with minor metavolcanic intercalations at the top.

Deformation related to the eclogite facies conditions was not recognized, as the eclogites are fine-grained and massive. The main deformation phase (D2) is developed under amphibolite facies conditions in all

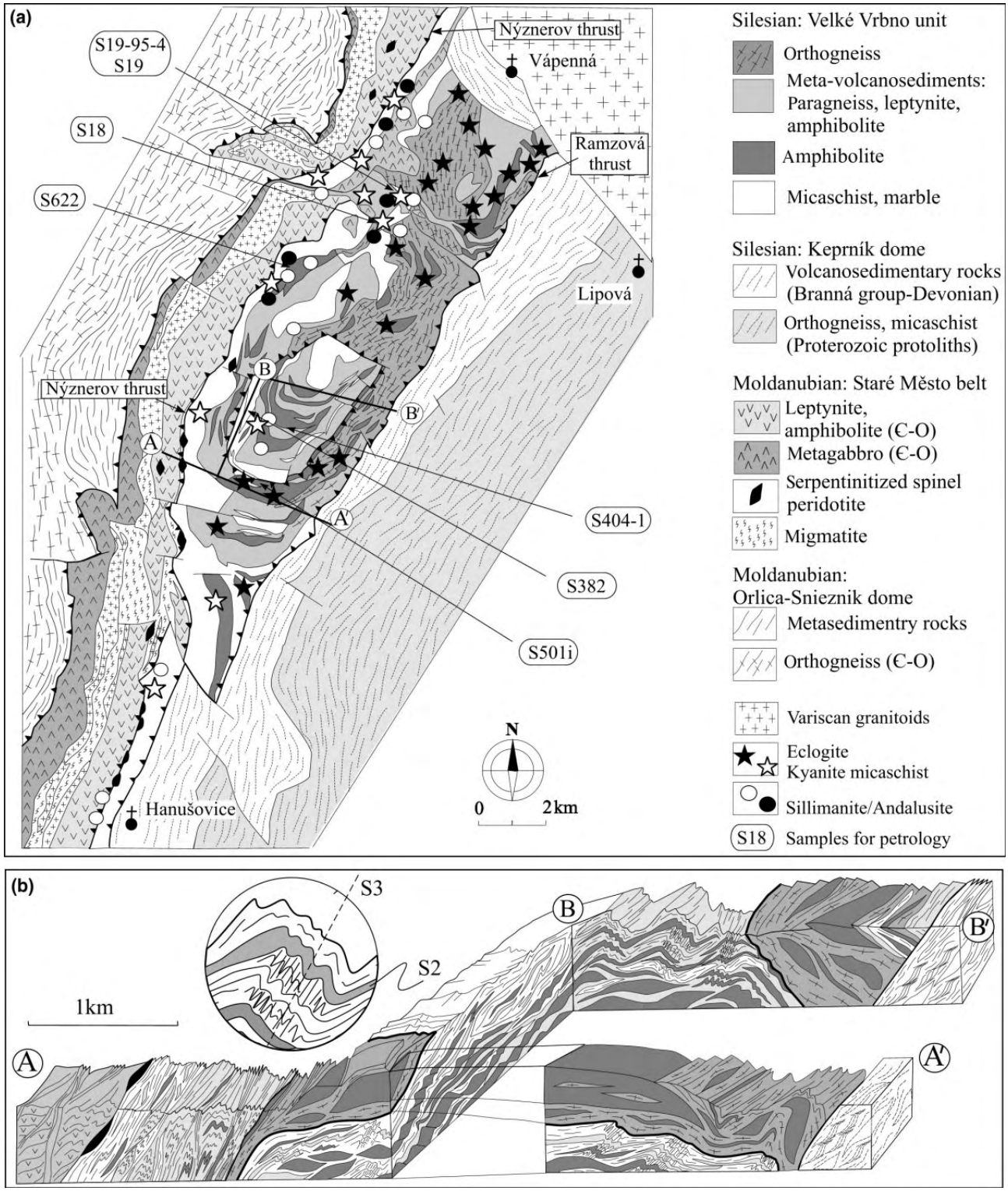

Fig. 2. (a) Simplified geological map of the Velké Vrbno unit and surroundings showing occurrence of eclogites and kyanite-bearing micaschists. Occurrences of sillimanite and andalusite overprints are also shown. Sample locations used for petrology and the position of the structural profile are indicated. (b) Interpretative geological cross section showing early D2 fabric and style of superimposed D3 deformation. Vertical axis not to scale.

the rock types. The S2 foliation dips to the east in the eastern part, to the west in the western part and to the south in the southern part, so defining the regional antiformal structure. The latter is attributed to the large-scale D3 folding that is recognizable on outcrop-scale in the form of east-vergent F3 folds with sub-horizontal hinges and west-dipping axial planes, characteristic of the whole Moravo-Silesian domain (Schulmann & Gayer, 2000). At the contact with the Staré Město belt, F3 folding is associated with the development of an intense S3 schistosity that may result in an almost penetrative transposition forming an S3 amphibolite to epidote–amphibolite facies mylonitic foliation.

METAMORPHIC EVOLUTION

Analytical procedures and abbreviations

Minerals have been analysed using the Cameca SX50 at ETH Zürich, the JEOL microprobe at Mainz University and the Cameca SX100 at the Geological Institute of the Czech Academy of Sciences, in point beam mode at 15 kV and 10 nA. Representative analyses recalculated with Holland's AX software (http://www.esc.cam.ac.uk/astaff/holland) are listed in Table 1.

The sign '$\rightarrow$' is used for a trend in mineral composition or for zoning and the sign '–' for a range of mineral compositions (p.f.u. = per formula unit). The mineral abbreviations used are: mu = muscovite, q = quartz, chl = chlorite, ctd = chloritoid, g = garnet, st = staurolite, bi = biotite, ky = kyanite, sil = sillimanite, and = andalusite, pa = paragonite, ma = margarite, cz = clinozoisite, pl = plagioclase, di = diopsidic clinopyroxene, o = omphacitic clinopyroxene, opx = orthopyroxene, am = amphibole, hb = hornblende, act = actinolite, gl = glaucophane, ep = epidote, law = lawsonite, ilm = ilmenite, tit = titanite, and ru = rutile. The isopleth notation used is: x(g, st, ctd, bi) = Fe/(Fe + Mg), z(g) = Ca/(Ca + Fe + Mg), an(pl) = Ca/(Ca + Na), j(di), j(o) = Al(Oct)/(Al(Oct) + Mg + Fe) = Na/(Na + Ca).

Previous metamorphic studies

The overall metamorphic evolution of the Velké Vrbno unit has not been studied systematically, although it was considered to be a part of the structurally-overlying upper Moldanubian domain to the west (Suess, 1926). The evidence for such a correlation comes mainly from the presence of eclogites (Žáček, 1996). Others correlated it with the westward and structurally lower Barrovian-type Moravo-Silesian domain (Skácel, 1989; Schulmann & Gayer, 2000), but these correlations were made on the basis of lithology, structure and protolith ages and not on the basis of metamorphic studies. In order to establish the overall metamorphic picture, the mineral assemblages in metapelites, mafic rocks and orthogneisses were mapped, correlating them with major deformational structures in the field and in thin section (Figs 2–4).

Felsic orthogneisses

The orthogneiss sheet is dominated by meta-granodiorites at the base with plagioclase and K-feldspar forming either augens or recrystallized monomineralic ribbons defining the S2 foliation together with quartz ribbons and aligned biotite. Garnet or amphibole is rarely present. In the upper part of the orthogneiss body, felsic metavolcanics consist of plagioclase, quartz, some K-feldspar and rare garnet and biotite. No minerals suspected of being formed at high pressure were found in the felsic orthogneisses.

Mafic rocks

Mafic rocks were investigated mainly for the presence of high-pressure relicts represented by omphacite and symplectite after omphacite, the mapped regional extent of eclogites is shown in Fig. 2. Eclogites occur as metre to several tens of metres long boudins in the orthogneiss sheet including in its upper metavolcanic sequence and one eclogite was found where upper metapelites start to occur.

The eclogite boudin cores consist of isotropic, fine-grained, greenish eclogite with millimetre-sized garnet, whereas the marginal parts are retrogressed to foliated garnet-free amphibolite. Under the microscope, the eclogite is composed of fine-grained clinopyroxene-plagioclase symplectite with omphacite relicts (up to 1 mm) and clusters of garnet and rutile (Fig. 4a). Coarse-grained amphibole–plagioclase domains, in some samples also involving epidote, are commonly developed within the symplectite. Abundant garnet (0.2–5 mm) exhibits cloudy cores with innumerable unidentified minute inclusions. Garnet commonly includes rutile, quartz, epidote and in some samples also one or more of clinopyroxene, kyanite, magnetite, muscovite, amphibole and albite. Matrix rutile is usually associated with ilmenite or rimmed by titanite. In amphibolitized samples, garnet is replaced by coronas or pseudomorphs of plagioclase with minor amphibole, resulting in the garnet-free assemblage pl–am–ilm ± ep ± tit ± q that defines the S2 foliation.

Structurally upwards, within the part dominated by micaschists, no eclogite relics were found, indicating that eclogite was never present here or was completely retrogressed. Within these micaschists the mafic rocks are amphibolites rarely containing garnet. Within the westernmost S3 mylonitic zone they are epidote-amphibolites (Fig. 4f) that exhibit a reduced grain size below 0.2 mm and the assemblage of pargasitic amphibole (Si p.f.u. = 6.29–6.53, X_{Fe} = 0.35–0.43), oligoclase (an24–30) and epidote with 35–36% of pistacite.

No eclogite relicts were found in the micaschists and volcano-sedimentary rocks below the orthogneiss

Table 1. (a) Representative mineral analyses, sample S19-95-4 (in – inclusion in garnet, mx – matrix). (b) Representative mineral analyses from eclogite (S501i). (c) Representative mineral analyses, sample S382. (d) Representative mineral analyses from amphibolites (S404-1, S622).

Mineral analysis	g-core 105	g-rim 59	chl-in 195	ctd-in 376	mu-in 41	ma-in 211	pa-in 213	st-in 18	mu-mx p27	pl-mx p23	st-mx p93	bi-mx p76
(a)												
SiO_2	37.93	38.02	25.14	25.08	46.46	35.17	43.49	27.24	46.17	59.63	27.73	35.78
TiO_2	0.09	0.08	0.13	0.00	0.30	0.11	0.17	0.22	0.49	0.02	0.67	1.84
Al_2O_3	21.28	21.68	22.27	41.23	39.06	47.55	42.34	54.68	37.60	26.04	54.42	20.88
FeO	32.67	34.92	27.32	21.95	0.96	1.16	0.97	14.95	0.89	0.15	14.01	17.85
MnO	0.52	0.06	0.10	0.02	0.03	0.00	0.00	0.04	0.00	0.00	0.16	0.03
MgO	2.24	5.44	13.61	4.10	0.25	0.28	0.18	1.25	0.66	0.00	1.78	9.50
CaO	6.28	1.27	0.00	0.00	0.03	8.42	2.51	0.00	0.00	7.93	0.00	0.00
Na_2O	0.00	0.00	0.00	0.00	1.13	2.72	5.43	0.01	0.86	7.26	0.00	0.30
K_2O	0.00	0.00	0.00	0.00	8.30	0.44	1.16	0.00	9.07	0.09	0.00	8.88
Total	101.02	101.47	88.57	92.38	96.52	95.85	96.25	98.39	95.74	101.12	98.77	95.06
Oxygen	12	12	14	6	11	11	11	46	11	8	46	11
Si	3.01	2.97	2.64	1.02	3.00	2.30	2.78	7.55	3.02	2.63	7.63	2.69
Ti	0.01	0.01	0.01	0.00	0.02	0.01	0.01	0.05	0.02	0.00	0.14	0.10
Al	1.99	2.00	2.76	1.98	2.97	3.67	3.19	17.87	2.90	1.36	17.65	1.85
Fe^{3+}	0.00	0.05	0.00	0.00	0.04	0.04	0.02	0.00	0.03	0.01	0.00	0.00
Fe^{2+}	2.17	2.23	2.40	0.75	0.02	0.02	0.03	3.47	0.02	0.00	3.22	1.12
Mn	0.04	0.00	0.01	0.00	0.00	0.00	0.00	0.01	0.00	0.00	0.04	0.00
Mg	0.26	0.63	2.14	0.25	0.02	0.03	0.02	0.52	0.06	0.00	0.73	1.06
Ca	0.53	0.11	0.00	0.00	0.00	0.59	0.17	0.00	0.00	0.38	0.00	0.00
Na	0.00	0.00	0.00	0.00	0.14	0.35	0.67	0.01	0.11	0.62	0.00	0.04
K	0.00	0.00	0.00	0.00	0.68	0.04	0.10	0.00	0.76	0.01	0.00	0.85
cat	8.00	8.00	9.96	3.99	6.89	7.03	6.99	29.47	6.92	5.00	29.41	7.73
X_{Fe}/an	0.89	0.78	0.53	0.75	0.40	0.41	0.67	0.87	0.19	0.38	0.82	0.51

	Eclogite S501i											
Mineral analysis	g-core 114su	g spike 104su	g-rim 430	cpx in 122	cpx mx 58	pl 110	am-core 117	am-rim 143su	ep in 78su	ep in 81su	ep mx 87	ep mx 89su
(b)												
SiO_2	38.07	38.86	38.58	54.30	54.31	63.89	41.90	54.21	38.87	39.58	38.52	39.42
TiO_2	0.15	0.03	0.07	0.14	0.15	0.02	0.82	0.19	0.00	0.03	0.05	0.06
Cr_2O_3	0.01	0.00	0.00	0.07	0.11	0.05	0.01	0.00	0.00	0.00	0.00	0.02
Al_2O_3	20.96	21.49	21.87	11.94	8.54	22.00	14.77	2.13	28.06	31.48	28.36	31.80
FeO	29.67	22.90	23.87	5.63	5.38	0.10	13.06	10.32	7.91	2.09	6.56	1.77
MnO	0.77	0.68	0.56	0.04	0.04	0.00	0.05	0.10	0.10	0.00	0.07	0.07
MgO	3.09	4.99	6.08	7.92	10.31	0.00	11.40	17.27	0.03	0.02	0.19	0.04
CaO	7.82	10.63	9.06	13.33	17.23	3.90	11.15	12.21	23.48	24.28	23.53	24.23
Na_2O	0.05	0.00	0.00	6.20	4.88	10.21	3.01	0.47	0.01	0.03	0.01	0.02
K_2O	0.01	0.00	0.00	0.01	0.00	0.09	0.88	0.05	0.00	0.01	0.00	0.00
Total	100.60	99.57	100.09	99.58	100.95	100.26	97.05	96.94	98.47	97.52	97.29	97.40
Oxygen	12	12	12	6	6	8	23	23	12.5	12.5	12.5	12.50
Si	2.99	3.00	2.97	1.94	1.94	2.81	6.20	7.72	3.03	3.02	3.02	3.01
Ti	0.01	0.00	0.00	0.00	0.00	0.00	0.09	0.02	0.00	0.00	0.00	0.00
Cr	0.00	0.00	0.00	0.00	0.00	0.00	0.00	0.00	0.00	0.00	0.00	0.00
Al	1.94	1.96	1.98	0.50	0.36	1.14	2.58	0.36	2.58	2.83	2.62	2.86
Fe^{3+}	0.05	0.05	0.05	0.02	0.02	0.03	0.10	0.09	0.05	0.05	0.05	0.05
Fe^{2+}	1.95	1.48	1.53	0.17	0.16	0.00	1.62	1.23	0.52	0.13	0.43	0.11
Mn	0.05	0.05	0.04	0.00	0.00	0.00	0.01	0.01	0.01	0.00	0.01	0.01
Mg	0.36	0.58	0.70	0.42	0.55	0.00	2.51	3.67	0.00	0.00	0.02	0.01
Ca	0.66	0.88	0.75	0.51	0.66	0.18	1.77	1.86	1.96	1.99	1.98	1.98
Na	0.01	0.00	0.00	0.43	0.34	0.87	0.86	0.13	0.00	0.00	0.00	0.00
K	0.00	0.00	0.00	0.00	0.00	0.01	0.17	0.01	0.00	0.00	0.00	0.00
cat	8.00	8.00	8.01	4.00	4.03	5.04	15.89	15.00	8.00	8.00	8.14	8.00
X_{Fe}/an	0.84	0.72	0.68	0.26	0.23	0.18	0.35	0.20				
grs/ep	0.22	0.30	0.25						0.05	0.05	0.42	0.05

Mineral analysis	g-rim p33-3	g-core p11-26	bi-mx p14-5	st-rim p28-3	mu 39	pl p31
(c)						
SiO_2	37.32	37.00	35.94	28.45	47.36	61.54
TiO_2	0.06	0.19	1.51	0.42	0.30	0.00
Al_2O_3	21.33	20.88	19.71	54.17	33.98	24.43
FeO	32.82	27.96	18.28	12.53	1.65	0.06
MnO	0.15	4.89	0.00	0.14	0.04	0.00
MgO	2.69	0.65	10.36	1.78	1.17	0.00
CaO	5.54	8.68	0.03	0.00	0.01	5.59
Na_2O	0.00	0.04	0.22	0.02	0.78	8.81
K_2O	0.00	0.01	9.47	0.01	9.55	0.09
Total	99.91	100.30	95.52	97.52	94.84	100.52

Table 1. *Cont'd*

Mineral analysis	g-rim p33-3	g-core p11-26	bi-mx p14-5	st-rim p28-3	mu 39	pl p31
Oxygen	6	6	11	46	11	8
Si	2.99	2.97	2.71	7.86	3.15	2.72
Ti	0.00	0.01	0.09	0.09	0.02	0.00
Al	2.01	1.98	1.75	17.63	2.67	1.27
Fe^{3+}	0.01	0.07	0.00	0.00	0.00	0.00
Fe^{2+}	2.18	1.81	1.15	2.89	0.09	0.00
Mn	0.01	0.33	0.00	0.03	0.00	0.00
Mg	0.32	0.08	1.16	0.73	0.12	0.00
Ca	0.48	0.75	0.00	0.00	0.00	0.27
Na	0.00	0.01	0.03	0.01	0.10	0.76
K	0.00	0.00	0.91	0.00	0.81	0.01
cat	8.00	8.00	7.80	29.25	6.96	5.02
X_{Fe}/an	0.87	0.96	0.50	0.80	0.44	0.26

	g-ep amphibolite S404-1				ep-amphibolite S622		
Mineral analysis	g p207-251	am 121a1	pl 132a1	ep 130a1	pl 58a3	am 61a3	ep 64
(d)							
SiO_2	38.35	44.53	60.84	39.49	60.83	43.49	37.75
TiO_2	0.17	0.68	0.00	0.12	0.00	0.77	0.18
Cr_2O_3	0.00	0.10	0.02	0.29	0.04	0.04	0.01
Al_2O_3	21.68	13.37	24.23	31.88	23.40	11.30	25.34
FeO	23.63	12.89	0.20	2.18	0.31	16.52	9.27
MnO	2.22	0.16	0.03	0.02	0.01	0.33	0.07
MgO	3.55	11.76	0.00	0.02	0.02	10.66	0.03
CaO	11.33	11.40	6.29	24.73	6.06	12.20	24.35
Na_2O	0.04	2.24	8.44	0.05	8.68	1.93	0.00
K_2O	0.00	0.51	0.15	0.00	0.15	0.72	0.00
Total	100.97	97.64	100.20	98.78	99.50	97.96	97.00
Oxygen	12	23	8	12.5	8	23	12.5
Si	2.97	6.50	2.69	2.99	2.71	6.47	2.98
Ti	0.01	0.08	0.00	0.01	0.00	0.09	0.01
Cr	0.00	0.01	0.00	0.02	0.00	0.00	0.00
Al	1.98	2.30	1.26	2.84	1.23	1.98	2.36
Fe^{3+}	0.06	0.15	0.01	0.14	0.01	0.32	0.61
Fe^{2+}	1.47	1.42	0.00	0.00	0.00	1.73	0.00
Mn	0.15	0.02	0.00	0.00	0.00	0.04	0.00
Mg	0.41	2.56	0.00	0.00	0.00	2.36	0.00
Ca	0.94	1.78	0.30	2.01	0.29	1.94	2.06
Na	0.01	0.63	0.72	0.01	0.75	0.56	0.00
K	0.00	0.10	0.01	0.00	0.01	0.14	0.00
cat	8.00	15.56	5.00	8.01	5.00	15.64	8.02
X_{Fe}/an	0.28	0.36	0.30		0.29	0.42	
grs/ep	0.31			0.14			0.61

sheet, where the amphibolites involve g–am–pl–q ± ep ± tit ± ru ± ilm. Garnet is commonly surrounded by variably developed plagioclase–amphibole coronas that are stretched within the S2 foliation. In some layers, garnet is completely pseudomorphed during the continued development of the S2 foliation on decompression that results in garnet-free amphibolite and epidote-amphibolite.

Metapelites

Metapelites above the orthogneiss sheet commonly contain kyanite as an index mineral, but many samples contain just staurolite (Fig. 2). The dominant matrix assemblage is g–st–ky–bi–pl–mu–q–ilm ± ru, locally with sillimanite, and late andalusite is limited to the NW part of the unit (Figs 2 & 3). All the minerals are aligned in the S2 foliation; sillimanite locally grows at the expense of garnet and staurolite. This foliation is wrapped around andalusite porphyroblasts, indicating at least local activity of the S2 foliation during late stages of exhumation (Fig. 3e). Inclusions of ctd–chl–pa–ma, st–chl–pa–ma and ky–chl–ru in garnet are present in some samples, and these are shown below to be valuable in establishing the prograde path of the metapelites.

Metapelites below the orthogneiss-eclogite sheet contain as an index mineral staurolite and in one case also kyanite (Fig. 2). The common assemblage is g–st–bi–mu–q ± pl ± sil. The foliation is defined by oriented micas, staurolite and quartz ribbons and the inclusion trails within garnet are continuous into the external S2 foliation, suggesting that it formed contemporaneously with peak metamorphic conditions. In some thin sections, biotite and sillimanite grow at the expense of garnet at its edges and in its pressure

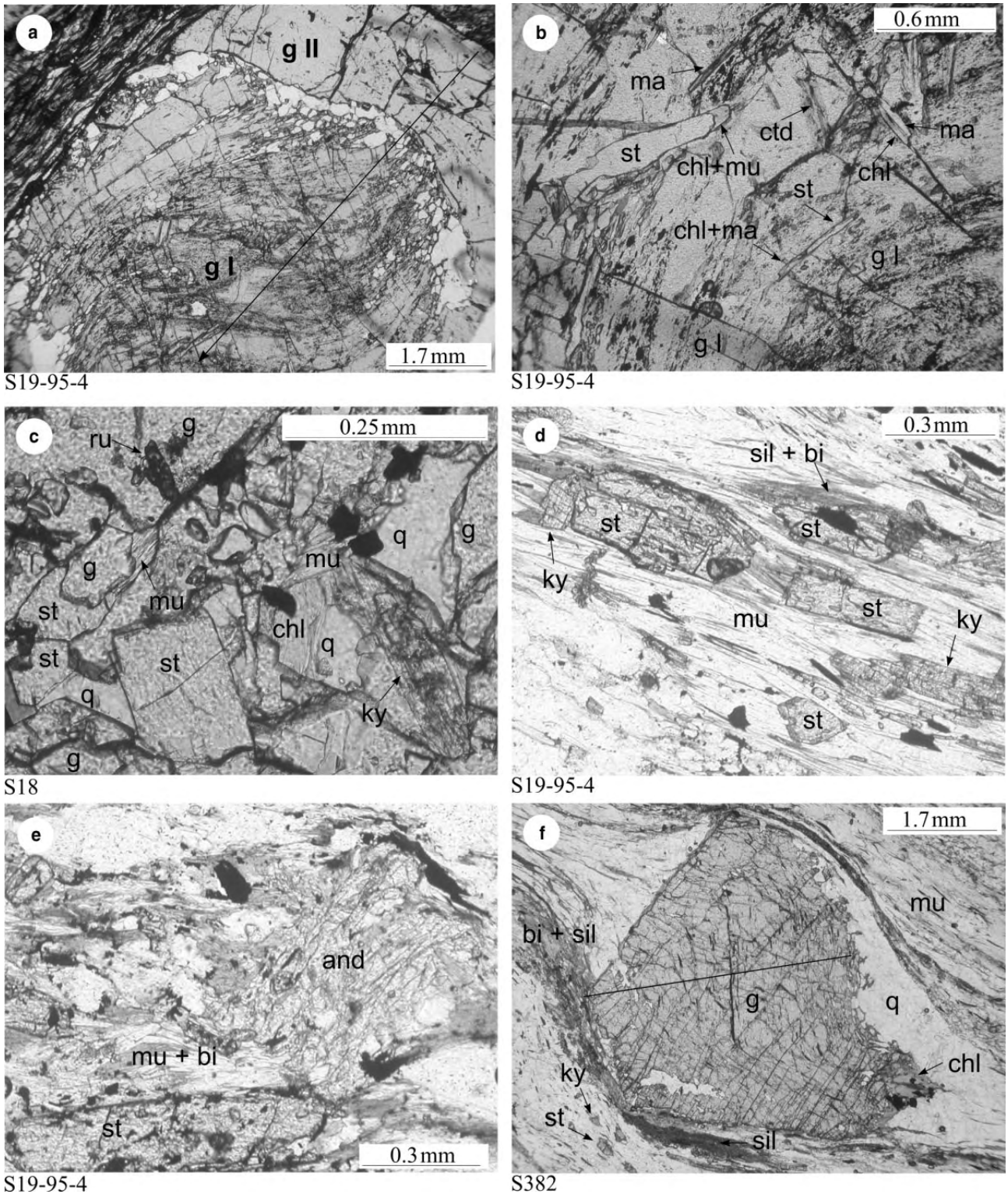

Fig. 3. Photomicrographs of metapelites in plane-polarized light. (a) Cloudy garnet I (g I) overgrown by clear garnet II (g II) (S19-95-4). Arrow indicates the profile in Fig. 5. (b) Prograde inclusions ctd–st–chl–ma–mu–ilm in garnet I (S19-95-4). (c) Inclusions of st–ky–chl–mu–ru at the boundary of garnet I and II (S18). (d) Kyanite and staurolite as part of the peak assemblage, partly replaced by sillimanite and biotite (S19-95-4). (e) Development of pressure shadows around late andalusite porphyroblasts wrapped by the foliation (S19-95-4). (f) Peak assemblage ky–st–g–bi–mu–pl with late sillimanite under the eclogite-bearing orthogneiss sheet (S382). Position of profile in Fig. 5 is indicated.

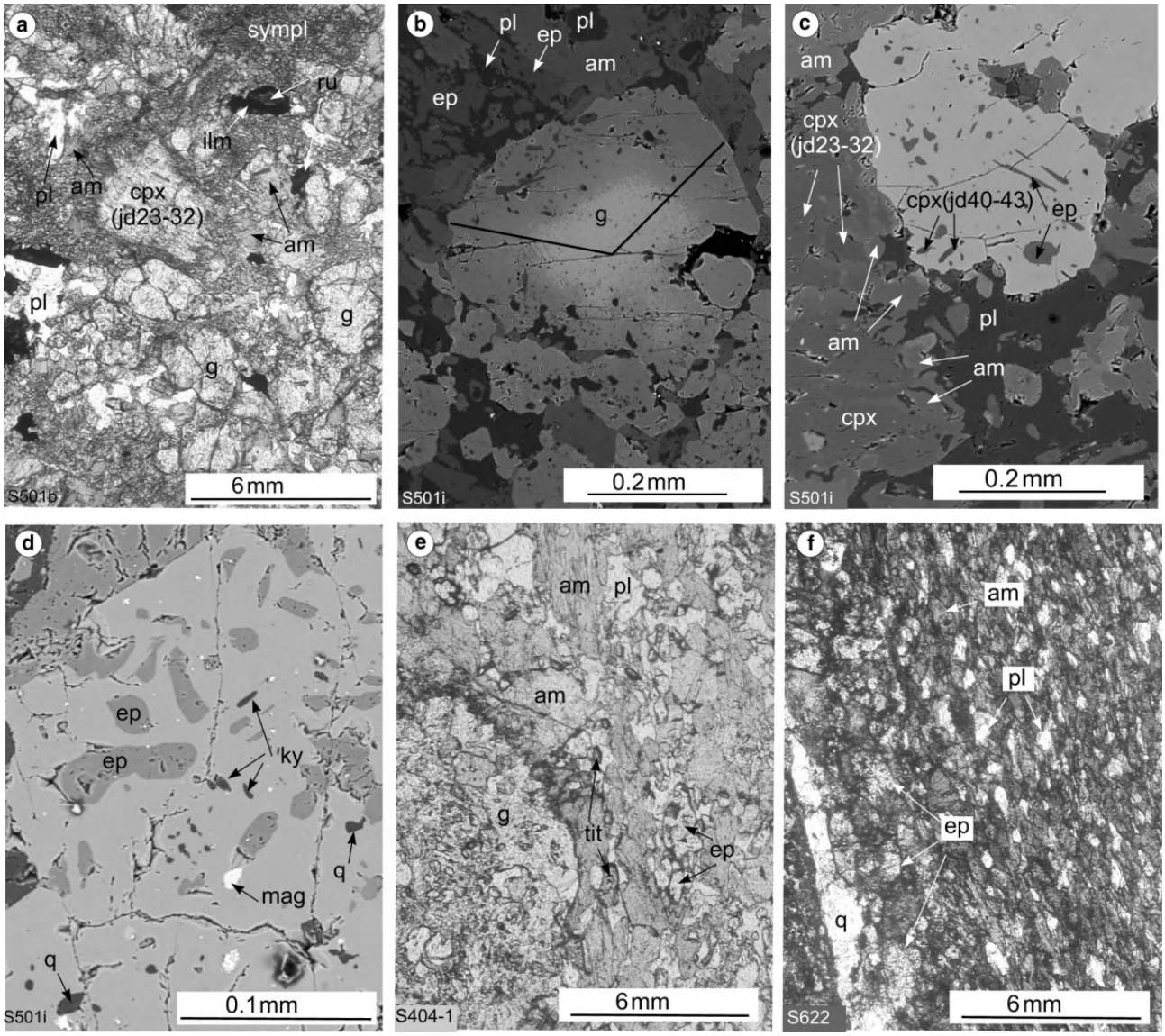

Fig. 4. Photomicrographs, plane-polarized light and BSE images of metabasic rocks. (a) Garnet, rutile and relict omphacite surrounded by fine-grained symplectite and coarse amphibole–plagioclase domains, typical of the HP assemblage in the eclogites (eclogite S501b). (b) Zoned garnet, the location of the profile from Fig. 5 is indicated (eclogite S501i), BSE. (c) Clinopyroxene and epidote included in garnet (eclogite S501i), BSE. (d) Kyanite, epidote, magnetite and quartz included in garnet (eclogite S501i), BSE. (e) Garnet, amphibole, plagioclase and epidote, the most common assemblage of metabasites under the eclogite-bearing orthogneiss sheet (amphibolite S404-1). (f) Fine-grained am–ep–pl–q without garnet, characteristic of the mylonite zone at the western boundary of the Velké Vrbno unit (amphibolite S622).

shadows (Fig. 3f), indicating that the S2 foliation was also active during decompression. Locally, metapelites exhibit restricted growth of chlorite. However, in the northern part, below the orthogneiss body, the metapelites are converted into phyllites within a reactivated S2 foliation.

Definition of an internal nappe structure

The metamorphic assemblages in the structurally lower metapelites and metabasites from the tectonic window do not reveal signs of high-pressure metamorphism, with mineral assemblages reflecting upper amphibolite facies peak conditions. The occurrence of meta-sedimentary rocks without eclogite below the orthogneiss-eclogite sheet indicates a metamorphic and lithological break that we interpret in terms of an internal nappe structure, with the thrust plane located at the bottom of the orthogneiss body, the underlying rocks appearing in a tectonic window. Towards the top of the nappe the lithological change is continuous, with the last eclogite found where metasedimentary intercalations start to occur: there is no clear tectonic and metamorphic boundary. The structurally upper metapelites,

even though they appear to be in lithological continuity within the high-pressure nappe, also do not reveal signs of high-pressure metamorphism in their upper-amphibolite facies mineral assemblages.

PETROLOGY, MINERAL CHEMISTRY AND *P–T* CONDITIONS

The major question is whether some of the rocks shared the high-pressure metamorphism with the eclogites, or whether some of the rock types were amalgamated later and, if so, to determine the depth that this occurred. The focus in further study is therefore on selected samples of metapelites and metabasites from the nappe and from the tectonic window as these lithologies have mineral assemblages and textures that are conducive for determination and comparison of their individual *P–T* paths and peak conditions (Fig. 2).

The eclogites were studied in detail and special attention was paid to structurally upper kyanite-bearing metapelites containing garnet with inclusions of chloritoid, paragonite, margarite and chlorite that could have potentially reflected garnet growth at high-pressure conditions (samples S19-95-4, S19, S18 in Fig. 2). Based on thin-section study, the rocks from the tectonic window were not suspected of attaining high pressure, so only quantifying the peak of metamorphism was attempted. The felsic orthogneisses did not reveal signs of high-pressure assemblages, nor were the assemblages suitable for determination of *P–T* conditions, and therefore they are not considered further here.

Structurally upper metapelites: petrology and mineral chemistry

Samples S19-95-4, S19 and S18b

The mineral assemblage is g–st–ky–bi–pl–mu–q–ilm ± ru ± sil ± an. Garnet has an inclusion-rich cloudy core with curved inclusion trails (garnet I) separated by a quartz-rich zone from a clear mantle (garnet II) (Fig. 3a). The core of garnet I includes ctd–ma–pa–mu–chl, st–rt appear towards the garnet I rim, where chloritoid disappears (Fig. 3b), and garnet II includes ru–st–ky–chl (S18, Fig. 3c). Garnet (S19-95-4) is almandine with negligible spessartine content and exhibits chemical zoning as portrayed in Fig. 5(a). The core is homogeneous with a high grossular content and high X_{Fe} [alm73 prp8 grs18 sps1; $X_{Fe} = Fe/(Fe + Mg) = 0.90–0.91$], followed by a sharp decrease in grossular and X_{Fe} towards the garnet I rim (alm73 → 77 prp8 → 14 grs18 → 8 sps1; $X_{Fe} = 0.90 \rightarrow 0.84$). Garnet II has low grossular, and X_{Fe} further decreases (alm77 → 71 prp16 → 29 grs8 → 0 sps0; $X_{Fe}0.84 \rightarrow 0.70$).

Chloritoid is included only within garnet I and its X_{Fe} decreases from the core towards the rim of garnet I ($0.91 \rightarrow 0.77$ in S19-95-4, $0.91 \rightarrow 0.70$ in S18b); its spessartine content is negligible. Chlorite inclusions ($X_{Fe} = 0.54–0.66$) are commonly in contact with white mica or staurolite in garnet I and are interpreted as primary. Secondary chlorite locally grows in the matrix. White mica inclusions within garnet I are muscovite (mu80–88 pa12–20 ma0), margarite (ma50–74 pa20–44 mu1–10) and paragonite (pa50–70 ma20–47 mu2–12) and the white mica in the matrix is muscovite (mu81–84 pa11–16, $X_{Al,M2A} = Al + Si-4 = 0.91–0.94$). Biotite inclusions were not found, but it is a widespread matrix mineral oriented parallel to the foliation ($X_{Fe} = 0.47–0.50$, $X_{Al,M1} = Al + Si-4 = 0.50–0.67$). Staurolite is included in the rims of garnet I and in garnet II and is a common matrix mineral. X_{Fe} of the inclusions decreases towards garnet rims ($0.90 \rightarrow 0.81$ in S19-95-4, $0.84 \rightarrow 0.80$ in S18b), whereas matrix porphyroblasts are unzoned ($X_{Fe} = 0.84–0.80$). The Ti-content in the inclusions (0.01–0.04 p.f.u.) is lower than in the matrix (0.05–0.09 p.f.u.) and the decrease in Al is correlated with an increase in Si in the formulae (inclusions: Al = 9.4–9.0, Si = 3.65–3.95; matrix: Al = 9.2–8.85, Si = 3.75–4.0). Kyanite is included at the limit of garnet I and in garnet II (S18), together with rutile and chlorite, and is abundant in the matrix. Small quantities of sillimanite associated with biotite locally replace garnet. Andalusite includes matrix staurolite, overgrows the foliation, but locally developed pressure shadows indicate a continuation of deformation after its growth (Fig. 3e). Plagioclase (an = 33–40) only occurs within the matrix. Ilmenite is coarse-grained in the rims of garnet I, in garnet II and within the matrix. Globular rutile first appears in the rim of garnet I and is common within garnet II; it is rarely included in staurolite and very rare within the matrix.

Structurally upper metapelites: *P–T* estimates

NCKFMASH grid

As a first step in constraining the *P–T* conditions, a petrogenetic grid in the system Na_2O–CaO–K_2O–FeO–MgO–Al_2O_3–SiO_2–H_2O (NCKFMASH) was calculated in order to establish the stability of the numerous univariant curves and invariant points that are seen by high-Al rock compositions. The grid is calculated for chl–ctd–bi–g–st–ky–sil–and–ma–pa–mu–pl–q–cz and H_2O. Muscovite, quartz and H_2O are taken to be in excess. The calculations were performed using THERMOCALC (Powell & Holland, 1988) and the internally consistent thermodynamic dataset 5.3 (Holland & Powell, 1998: May 2001 upgrade). Mixing models for most solid solutions were taken from Holland & Powell (1998), and the THERMOCALC documentation (Powell & Holland, 2002). The free energy of paragonite in margarite ($I_{pa,ma}$) was increased by 5 kJ mol^{-1} using the DQF approach, to fit constraints on compositions of natural coexisting mu–ma–pa (Höck, 1974; Feenstra, 1996). Plagioclase

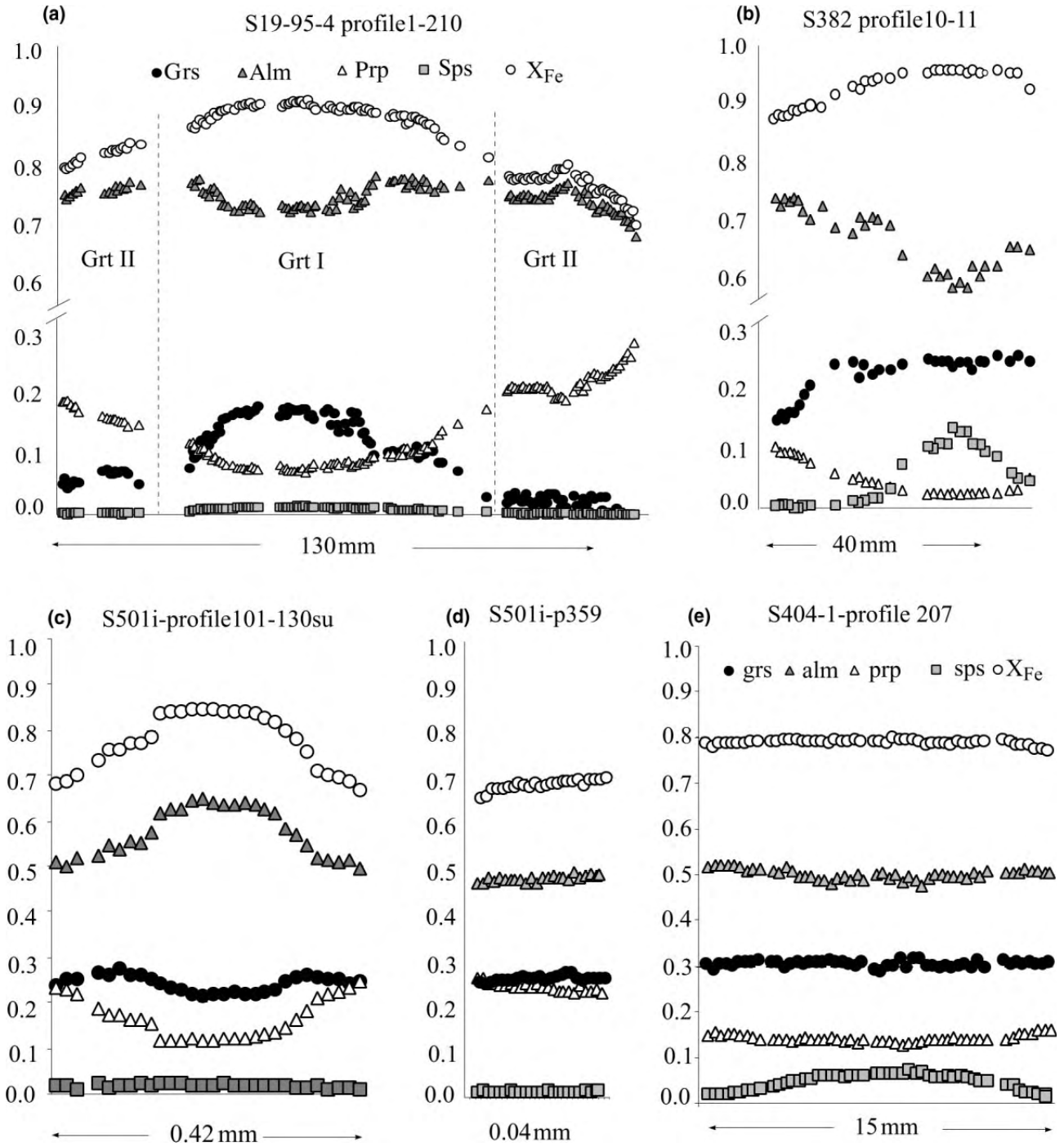

Fig. 5. Chemical profiles of garnet. See text for details.

was formulated using the model of Holland & Powell (1992). Our NCKFMASH grid (Fig. 6) differs from that of Worley & Powell (1998) because reactions involving chloritoid, sillimanite and andalusite were taken into account and biotite was not considered to be in excess. It differs from the grid of Wei & Powell (2006) by including margarite and clinozoisite (not zoisite), and not glaucophane, talc, lawsonite or omphacite. At lower temperature and at the highest pressures in Fig. 6, the phase relationships may be metastable with respect to glaucophane-, lawsonite- and omphacite-bearing assemblages. In addition, the grid will not apply to very magnesian assemblages in which talc would be stable. The calculated NCKF-

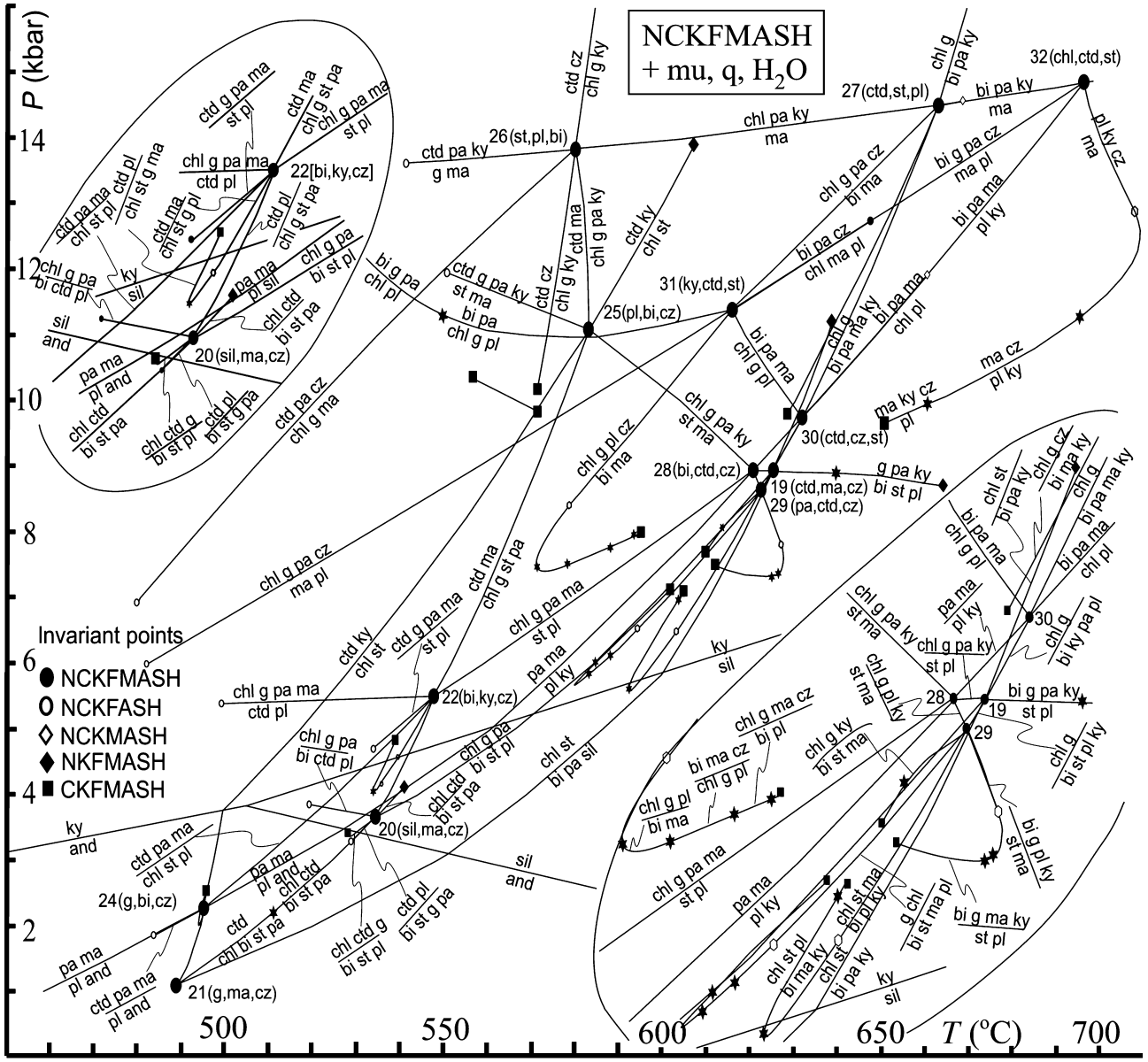

Fig. 6. NCKFMASH grid used for the construction of the pseudosection in Fig. 7. Mineral abbreviations: mu = muscovite, q = quartz, chl = chlorite, ctd = chloritoid, g = garnet, st = staurolite, bi = biotite, ky = kyanite, sil = sillimanite, and = andalusite, pa = paragonite, ma = margarite, cz = clinozoisite, pl = plagioclase.

MASH grid (Fig. 6) has 13 stable invariant points that are listed in Table 2 together with invariant points of all subsystems involved in the construction of the grid.

Pseudosection and P–T estimates

To constrain the *P–T* evolution of the metapelites, a *P–T* pseudosection for the bulk rock composition of sample S19-95-4 (Table 3) was constructed, and contoured with compositional isopleths for garnet, staurolite, chloritoid, plagioclase and biotite (Fig. 7). The pseudosection is able to predict a paragenetic sequence that matches the inclusions observed in garnet (Figs 3c & 7). The corresponding *P–T* path is discussed in terms of *P–T* areas labelled 1–7 in Fig. 7. Complementary information from samples S18b and S19 was also considered as these samples have similar mineral associations for similar high-Al rock compositions (Table 3).

Areas 1 and 2. Inclusions of chl–ctd–pa–ma in garnet cores (X_{Fe} = 0.90–0.86, grs = 0.18–0.15) suggest that this assemblage formed at 8.5–11 kbar and 550–580 °C (area 1). The rimward decrease of X_{Fe} in the chloritoid (0.90 → 0.70) further suggests an increase in temperature and/or pressure. The presence of staurolite

Table 2. Invariant points used for construction of the grid in Fig. 6.

	Phases	*P* (kbar)	*T* (°C)
Invariant point	ky, and, sil	3.82	505.1
KFMASH invariant points (g, st, bi, chl, ctd, ky, sil, and)			
[ctd]	g, chl, st, bi, ky	11.58	635.7
[bi]	chl, ctd, g, st, ky	13.93	607.7
[ky]	chl, ctd, st, g, bi	4.92	548.8
[g]	chl, ctd, st, bi, and	1.36	491.1
CASH invariant point (an, ky, ma, cz)			
	an, ky, ma, cz	9.68	651.1
CKFMASH invariant points (chl, ctd, g, st, bi, ky, sil, and, cz, ma, an)			
1 [an, cz, ctd]	chl, g, st, bi, ky, ma	7.70	610.0
2 [cz, ctd, ky]	chl, g, st, bi, ma, an	7.13	602.1
3 [ctd, g, cz]	chl, st, bi, ky, ma, an	7.12	605.1
4 [ctd, cz, chl]	g, st, bi, ky, ma, an	7.51	612.3
5 [ctd, ky, st]	chl, g, bi, cz, ma, an	8.00	595.4
6 [cz, an, bi]	chl, g, st, ky, ctd, ma	9.85	571.9
7 [cz, ky, bi]	chl, ctd, g, st, ma, an	4.83	539.3
8 [g, cz, ma]	chl, ctd, st, bi, and, an	1.36	491.0
9 [cz, sil, ma]	chl, ctd, g, st, bi, an	3.45	528.2
10 [g, bi, cz]	chl, ctd, st, and, ma, an	2.49	496.1
11 [st, an, bi]	chl, ctd, g, cz, ma, ky	10.20	571.6
12 [bi, chl, an]	ctd, g, st, ky, cz, ma	10.31	556.9
13 [an, st, ctd]	chl, g, bi ky, cz, ma	9.81	629.0
NKFMASH invariant points (chl, ctd, g, st, bi, ky, sil, and, pa, ab)			
14 [ab, ctd]	chl, g, st, bi, ky, pa	11.23	639.3
15 [bi, ab]	chl, ctd, g, st, ky pa	13.93	607.8
16 [chl, ctd]	g, st, bi, ky, pa, ab	8.71	664.6
17 [sil, ab]	chl, ctd, g, st, bi, pa	4.11	541.3
18 [g, ab]	st, ctd, chl, bi, pa, and	1.10	489.1
NCKFMASH inv. points (chl, ctd, g, st, bi, ky, and, pa, ma, pl, cz)			
19 [ma, ctd, cz]	chl, bi, g, st, ky, pa, pl	8.94	625.6
20 [sil, ma, cz]	chl, ctd, bi, g, st, pa, pl	3.66	534.7
21 [g, ma, cz]	chl, ctd, bi, st, and, pa, pl	1.10	489.0
22 [bi, ky, cz]	chl, ctd, g, st, ma, pa, pl	5.50	548.0
24 [g, bi, cz]	chl, ctd, st, and, ma, pa, pl	2.28	495.4
25 [pl, bi, cz]	chl, ctd, g, st, ky, ma, pa	11.09	583.5
26 [st, pl, bi]	chl, ctd, g, ky, ma, pa, cz	13.84	580.4
27 [ctd, st, pl]	chl, bi, g, ky, ma, pa, cz	14.51	663.3
28 [bi, ctd, cz]	chl, g, st, ky, ma, pa, pl	8.94	621.0
29 [pa, ctd, cz]	chl, bi, g, st, ky, ma, pl	8.65	622.8
30 [ctd, cz, st]	chl, bi, g, ky, ma, pa, pl	9.75	632.2
31 [ky, ctd, st]	chl, bi, g, ma, pa, pl, cz	11.40	616.1
32 [chl, ctd, st]	bi, g, ky, ma, pa, pl, cz	14.86	696.6

Table 3. Rock compositions (oxide in wt%, FeO[a]).

Sample	SiO_2	TiO_2	Al_2O_3	Fe_2O_3	FeO	MnO	MgO	CaO	Na_2O	K_2O	P_2O_5	H_2O-	CO_2	H_2O+	Tot	*A*	X_{Fe}
s19	60.08	1.15	19.41		6.75*	0.02	1.97	0.62	0.57	3.99	0.08	0.28	0.47	3.07	91.71	0.31	0.66
s19-95-4	62.36	1.03	18.87		6.04*	0.02	1.96	0.73	0.50	3.55	0.09	0.24	0.36	2.81	92.52	0.35	0.63
S501i	48.84	1.68	14.12	2.79	8.92	0.2	7.73	11.14	2.55	0.25	0.16	0.2	< 0.05	1.27	98.58		

[a]All Fe recalculated as FeO, standard wet chemical methods.
$A(\text{mol\%}) = (Al_2O_3{-}3K_2O)/(Al_2O_3{-}3K_2O + FeO + MgO)$, $X_{Fe}(\text{mol\%}) = FeO/(FeO + MgO)$.

($X_{Fe} = 0.85$–0.89) and the disappearance of chloritoid ($X_{Fe} = 0.70$) in the rim of garnet I indicates crossing of the discontinuous reaction ctd + ma = chl + g + st + pa at about 9.5 kbar and 570 °C (area 2).

Area 3. Kyanite appears through a continuous reaction in the divariant field chl–g–st–pa–ky at 10–11 kbar and 590–610 °C. X_{Fe} of staurolite in the inclusions as well as in the matrix decreases to a minimum value (0.80–0.82). X_{Fe} of garnet still increases ($0.86 \rightarrow 0.82$) but the grossular isopleths abruptly change their slope, so accounting for the sharp decrease of grossular in the rim of garnet I (down to grs = 0.10).

Areas 4 and 5. Crossing of the chl–g–pa-ky field is inferred from ky–chl inclusions in garnet II and from the garnet chemistry. Biotite appears through a continuous reaction in the chl–g–pa–ky–bi field, abundant matrix kyanite and biotite and absence of synfolial chlorite further suggest a transition to the

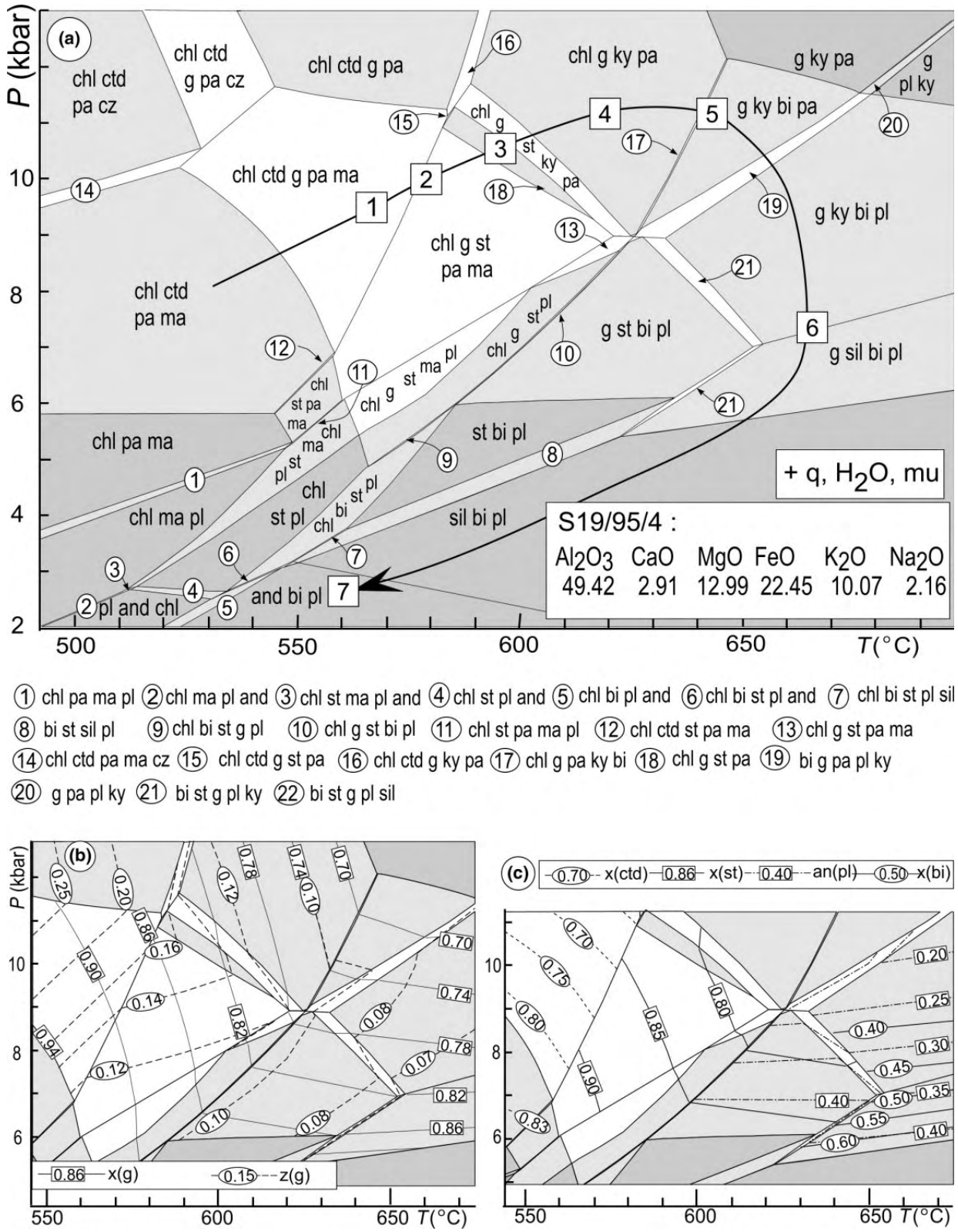

Fig. 7. (a) Pseudosection calculated for the rock composition of sample S19-95-4. *P–T* path is derived by comparing the modelled assemblages and isopleths with assemblages, chemistry and zoning of minerals observed in the sample. See text for details. (b,c) Enlarged parts of the pseudosection with calculated isopleths of mineral composition [x(g, st, ctd, bi) = Fe/(Fe + Mg), z(g) = Ca/(Ca + Fe + Mg), an(pl) = Ca/(Ca + Na)].

g–pa–ky–bi field. X_{Fe} and grossular in garnet II decrease ($0.83 \rightarrow 0.70$, $0.08 \rightarrow 0.04$) in agreement with the trend of model isopleths, and although the measured values for grossular are too low when compared with the model, the X_{Fe} in garnet indicates a minimum pressure of 11 kbar. During the transition to the g–pa–ky–bi field garnet is predicted to cease growing, and staurolite to become metastable.

Area 6. Intergrowths of bi–sil in the matrix, and sometimes also replacing garnet, suggest a transition to the g–sil–bi–pl field. Observed an(pl) = 35–40, and X_{Fe} of biotite ranging from 0.47 to 0.50, implies equilibration around 7 kbar and 650 °C.

Area 7. Andalusite growth indicates a pressure decrease to below 4 kbar. The equilibration volume during this phase is evidently small, and the *P–T* path in the andalusite stability field is difficult to estimate. Late chlorite may be associated with the growth of andalusite but may also be later.

In conclusion, the metapelites from above the eclogite-bearing orthogneiss sheet record a clockwise *P–T* loop with well-preserved prograde evolution from about 9.5 kbar and 570 °C to a peak pressure at 11 kbar and 640 °C (Fig. 7). Subsequent exhumation was essentially isothermal to about 7 kbar and 650 °C, and was followed by cooling and exhumation to <3 kbar and 500–570 °C. The sequence of implied mineral assemblages and the chemistry of the minerals show that these samples did not attain high-pressure conditions.

Eclogites: petrology and mineral chemistry

Sample S501i

The least retrogressed eclogite (S501i), with the assemblage of g–cpx–am–ep–pl–ky–ru–tit–mag–ilm–q, was considered in detail. Clusters of small garnet (0.1–0.5 mm) with cloudy cores are amalgamated into larger grains and include epidote, amphibole, omphacite, quartz, magnetite, globular rutile, and locally kyanite (Fig. 4b–d). Larger garnet is zoned with, from core to rim, alm65 $\rightarrow$ 49 py11 $\rightarrow$ 24 grs21 $\rightarrow$ 29 $\rightarrow$ 25 sps1–2; $X_{Fe} = 0.85 \rightarrow 0.67$ (Fig. 5c); smaller grains have asymmetrical or flat distribution of elements (alm46–51 py22–0.27 grs24–27 sps1–2; $X_{Fe} = 0.68$–0.71; Fig. 5d). Clinopyroxene included in garnet has a jadeite content of 40–43%, while clinopyroxene relics (up to 1 mm) in the matrix are irregularly zoned with lower jadeite between 10% and 33%. Pargasitic amphibole (0.2–0.4 mm, Si p.f.u. = 6.1–6.3, $X_{Fe} = 0.20$–0.35), locally rimmed by actinolite (Si p.f.u = 7.7, $X_{Fe} = 0.20$), grows around the symplectite and is associated with plagioclase (0.2–0.5 mm, an12.5–14.5). Epidote included in garnet and in the matrix both have two compositional ranges (pistacite 7–19 and 42–46), possibly reflecting a miscibility gap (Deer *et al.*, 1992, p. 93). Whereas rutile is abundant within garnet, ilmenite is associated with omphacite and amphibole in the matrix. Quartz occurs both in the matrix and within garnet.

Eclogites: pseudosections

The modelling was undertaken with THERMOCALC 3.23 (Powell *et al.*, 1998: recent upgrade) and the internally consistent thermodynamic dataset 5.5 (Holland & Powell, 1998: November 2003 upgrade) in the system Na_2O–CaO–FeO–MgO–Al_2O_3–SiO_2–H_2O–Fe_2O_3 (NCFMASHO). The datafile coding of the activity–composition relationships of the minerals used in the calculations involves the clinopyroxene model based on Holland & Powell (1996), the plagioclase model of Holland & Powell (2003), the epidote model of T.J.B. Holland (pers. comm.) and the amphibole model of Dale *et al.* (2005). In the absence of appropriate models for Fe^{3+} incorporation in clinopyroxene and amphibole, the only Fe^{3+}-bearing phase is epidote. This results in epidote being present everywhere in the pseudosections, whereas it is likely that it would react out in amphibole- and/or clinopyroxene-bearing assemblages to higher pressure and temperature. The highest temperature part of some of the pseudosections may be metastable with respect to melt-bearing assemblages that cannot yet be calculated in the absence of an appropriate melt model. In the pseudosections, where the composition of supra-solvus clinopyroxene varies through the composition of the solvus top in a field, the boundary is shown by a dashed line labelled di/o (for explanation see Štípská & Powell, 2005). Similarly, the solvus top of coexisting hornblende and glaucophane is extended into the suprasolvus region by a line labelled hb/gl. The rock composition of the sample, S501i (Fig. 2, Table 3) was used for the modelling. Even though the garnet is zoned, preliminary calculations have shown that simultaneous fractionation of garnet and clinopyroxene on the prograde path has little effect on effective bulk composition, so fractionation calculations are not presented (cf. Marmo *et al.*, 2002).

NCFMASHO H_2O-saturated pseudosection

The pseudosection in Fig. 8 is constructed for H_2O-saturated conditions. The major features involve a coexistence of two or three amphiboles at lower temperatures, garnet is stable only above 14 kbar and two pyroxenes coexist at 15–17 kbar and 610–720 °C. In the part of the pseudosection above the clinopyroxene solvus, the composition of clinopyroxene changes continuously but rapidly from 20% jadeite to >40% jadeite and clinopyroxene with >41% jadeite is stable only below 700 °C. The compositional isopleths of grossular range from 35% down to 20%.

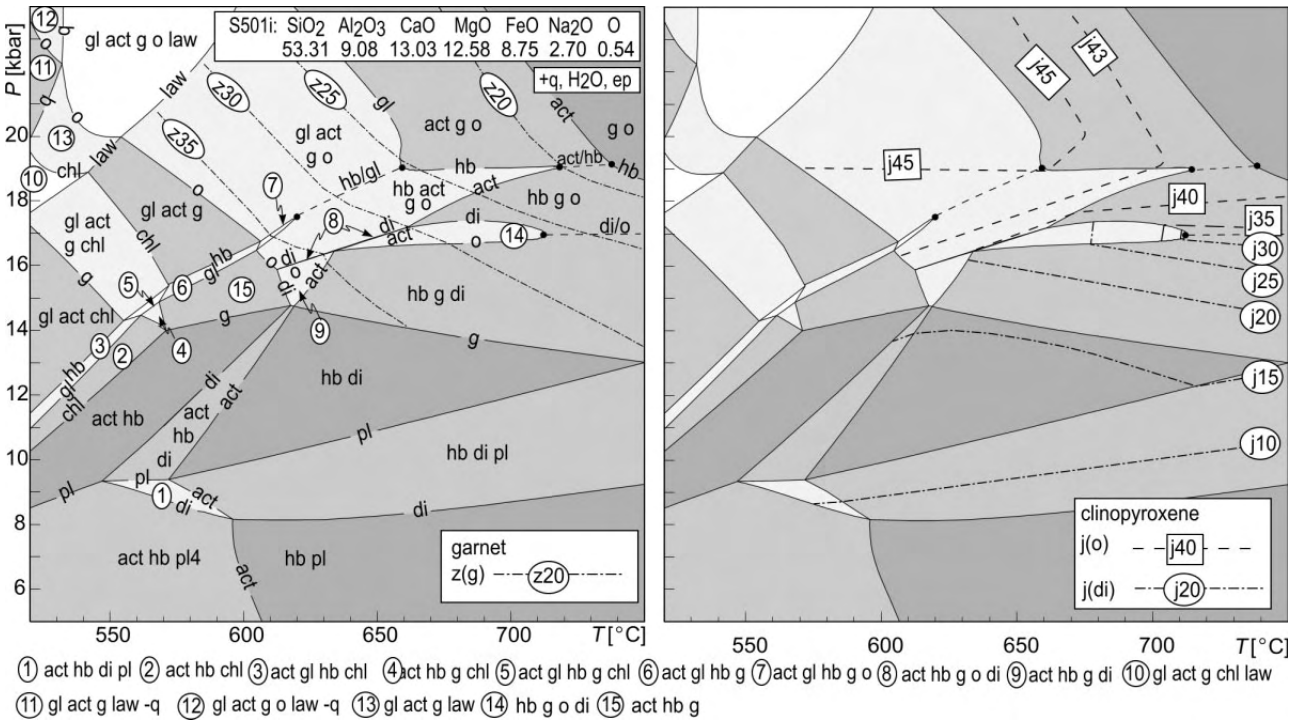

Fig. 8. Pseudosection for the composition of the eclogite, S501i, with epidote–quartz–H_2O in excess, contoured for compositional isopleths. Mineral abbreviations: pl = plagioclase, q = quartz, g = garnet, di = diopsidic clinopyroxene, o = omphacitic clinopyroxene, opx = orthopyroxene, hb = hornblende, act = actinolite, gl = glaucophane, ep = epidote, chl = chlorite, law = lawsonite. Isopleth notation: x(g) = Fe/(Fe + Mg), z(g) = Ca/(Ca + Fe + Mg), j(di), j(o) = Al(Oct)/(Al(Oct) + Mg + Fe) = Na/(Na + Ca).

The inclusions of omphacite with 41–43% of jadeite in garnet in sample S501i indicate garnet growth in the hb–act–g–o field, at 600–700 °C and 16–19 kbar. The prograde *P–T* path indicates equilibration at 700 °C and 17 kbar as indicated by matrix clinopyroxene with a maximum of 30–33% jadeite. Garnet grown along such a path should exhibit a decrease of grossular from 35 to 20% according to the pseudosection. However, this does not correspond to the observed zoning in sample S501i. To explain the grossular zoning, the dependence of the phase relationships on the H_2O content of the rock composition is investigated.

P–M(H_2O) pseudosection

The effect of H_2O undersaturation on assemblages and the composition of phases was studied in a *P–M*(H_2O) pseudosection at 620 °C (Fig. 9). The dashed line marks H_2O saturation, dividing the diagram into a part with assemblages coexisting with free H_2O, and a part with assemblages with H_2O only structurally bound in the minerals on the left-hand side of the pseudosection. The major effect of H_2O undersaturation is on the stability of garnet and on its composition.

On burial, the rock with H_2O in the range of 5.27–6 mol.% reaches the H_2O saturation line and evolves in the H_2O-undersaturated region up to 15–17 kbar where H_2O saturation occurs again. In the rock following the path indicated by the arrow, the garnet growth zoning involves an increase in grossular followed by a decrease, accompanied by a continuous decrease in X_{Fe} (z(g)20 → 32 → 30 and x(g) 80 → 75). This type of garnet zoning is similar to the observed profile in Fig. 5. However, the path on the diagram does not involve heating during burial as suggested by the two compositional ranges of clinopyroxene observed in the rock.

NCFMASH-O pseudosection with 5.16 mol.% of H_2O and P–T path

A pseudosection for the rock with a specified H_2O content corresponding to the path indicated by the arrow in Fig. 9 is shown in Fig. 10. The mineral assemblages are H_2O-undersaturated to lower pressure and temperature. The composition of garnet and clinopyroxene on the prograde path is also shown. With respect to H_2O-saturated conditions (Fig. 8), the garnet stability field is enlarged as well as its compositional range. The jadeite isopleths are almost unaffected by H_2O undersaturation.

The *P–T* path compatible with the assemblages and composition of the phases in sample S501i is discussed in terms of areas labelled 1–5. Area 1 represents the garnet core composition and the path directed towards

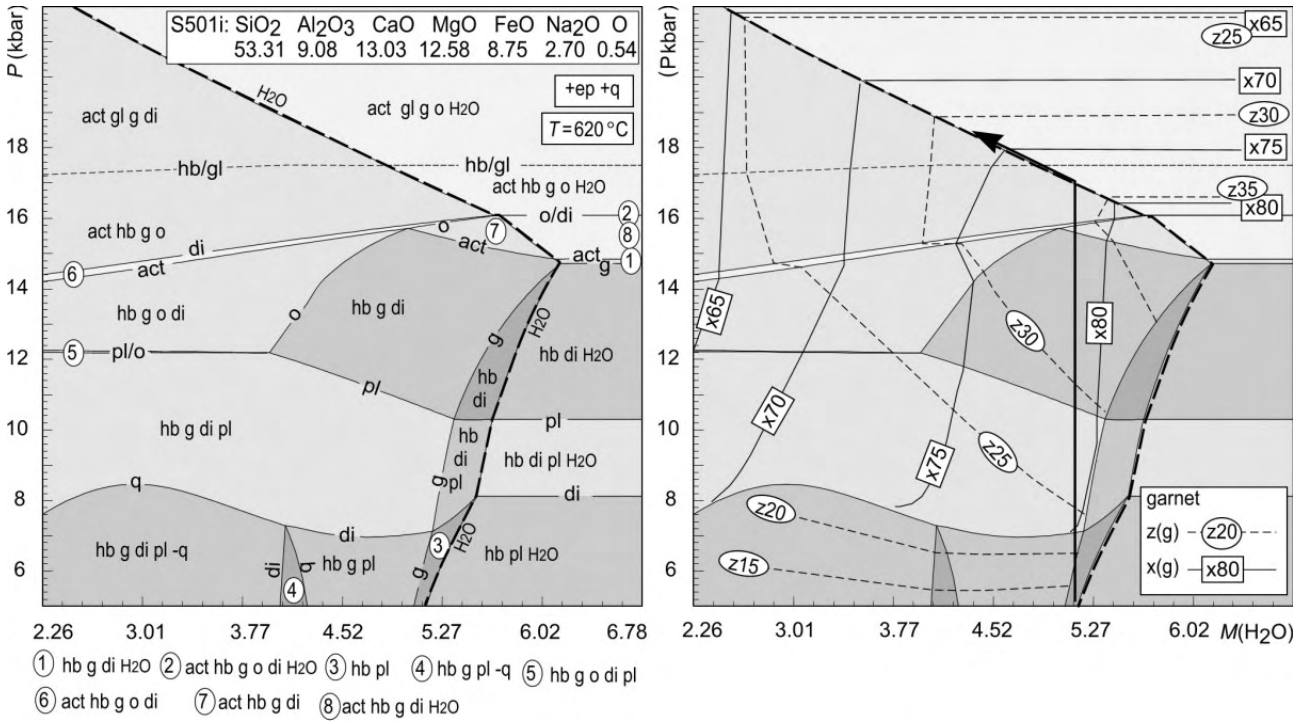

Fig. 9. *P–M*(H_2O) pseudosection for the eclogite, S501i, calculated at 620 °C with *M*(H_2O) ranging from 0 to 6.78 mol.%. Full arrow indicates a prograde path along which an H_2O-saturated rock is likely to equilibrate. The dashed line indicates the H_2O-undersaturated part of the path, along which the rock is likely to evolve until the H_2O saturation line is again reached at about 17 kbar. On this path, *z*(g) in the growing garnet first increases and than decreases, while *x*(g) decreases continuously.

area 2 is compatible with increase in grossular simultaneously with X_{Fe} decrease in garnet. Area 2 represents conditions where omphacite with 40–43% of jadeite is included by garnet and the path towards area 3 is compatible with simultaneous grossular and X_{Fe} decreases to $z(g) = 25$ and $x(g) = 65$, corresponding to the observed garnet rim composition. From this point, garnet is consumed. Area 4 represents conditions of matrix reequilibration at 700 °C and 17 kbar as indicated by matrix clinopyroxene with 30–33% of jadeite and garnet rims ($z(g) = 25$, $x(g) = 65$). This reequilibration requires addition of H_2O as implied by including area 4 on this fixed H_2O content pseudosection. Decompression is indicated by the observation of plagioclase–clinopyroxene–amphibole symplectites (area 5).

Metapelites and amphibolites of the tectonic window

Metapelites, sample S328

Sample S328 with the assemblage g–st–ky–bi–mu–ilm–q–sil–chl was studied in detail (Fig. 3f). Garnet has an inclusion-rich core with trails of ilm–q truncated at the boundary with a garnet overgrowth. Garnet exhibits a zoning profile with, from core to rim, alm53 → 79 py3 → 10 grs25 → 15 sps13 → 0, $X_{Fe} = 0.96 \rightarrow 0.87$ (Figs 3f & 5b). Muscovite (mu77–81 pa10–18; $X_{Al,M2A} = 0.88$–0.90) and biotite ($X_{Fe} = 0.48$–0.51; $X_{Al,M1} = 0.51$–0.60) are aligned in the foliation. Staurolite occurs only in the matrix ($X_{Fe} = 0.88$–0.80, Ti = 0.05–0.14 p.f.u., ZnO = 0.40–0.54 wt%, Mn is negligible) together with rare kyanite. Sillimanite is associated with biotite and replaces garnet. The plagioclase composition varies between 21 and 33% anorthite. Ilmenite is included in garnet and occurs within the matrix. Peak metamorphic conditions were calculated using the average *P–T* method in THERMOCALC. For the rim compositions of the assemblage g–st–ky–bi–mu–q–pl, the calculations yielded 616 ± 25 °C and 9.9 ± 0.9 kbar (1σ).

Amphibolites, sample S404-1

A garnetiferous amphibolite with the assemblage g–am–pl–q–ep (S404-1, Fig. 4) contains garnet (2 mm) that is in textural equilibrium with the am–pl ± q matrix (0.2–1.5 mm) or locally surrounded by a plagioclase-rich corona. Amphibole is magnesiohornblende (Si = 6.26–6.77 p.f.u., $X_{Fe} = 0.26$–0.40.) and plagioclase has 20–30% anorthite. Garnet shows a rimward decrease in spessartine, compensated by an increase in pyrope and almandine, whereas grossular is more or less constant (alm48 → 52 py13 → 16 grs28–32 sps8 → 2; X_{Fe} 0.80 → 0.78). Epidote has 11–16% pistacite. Relict rutile is included in amphibole, and is largely replaced by titanite in the matrix. Ilmenite is rare.

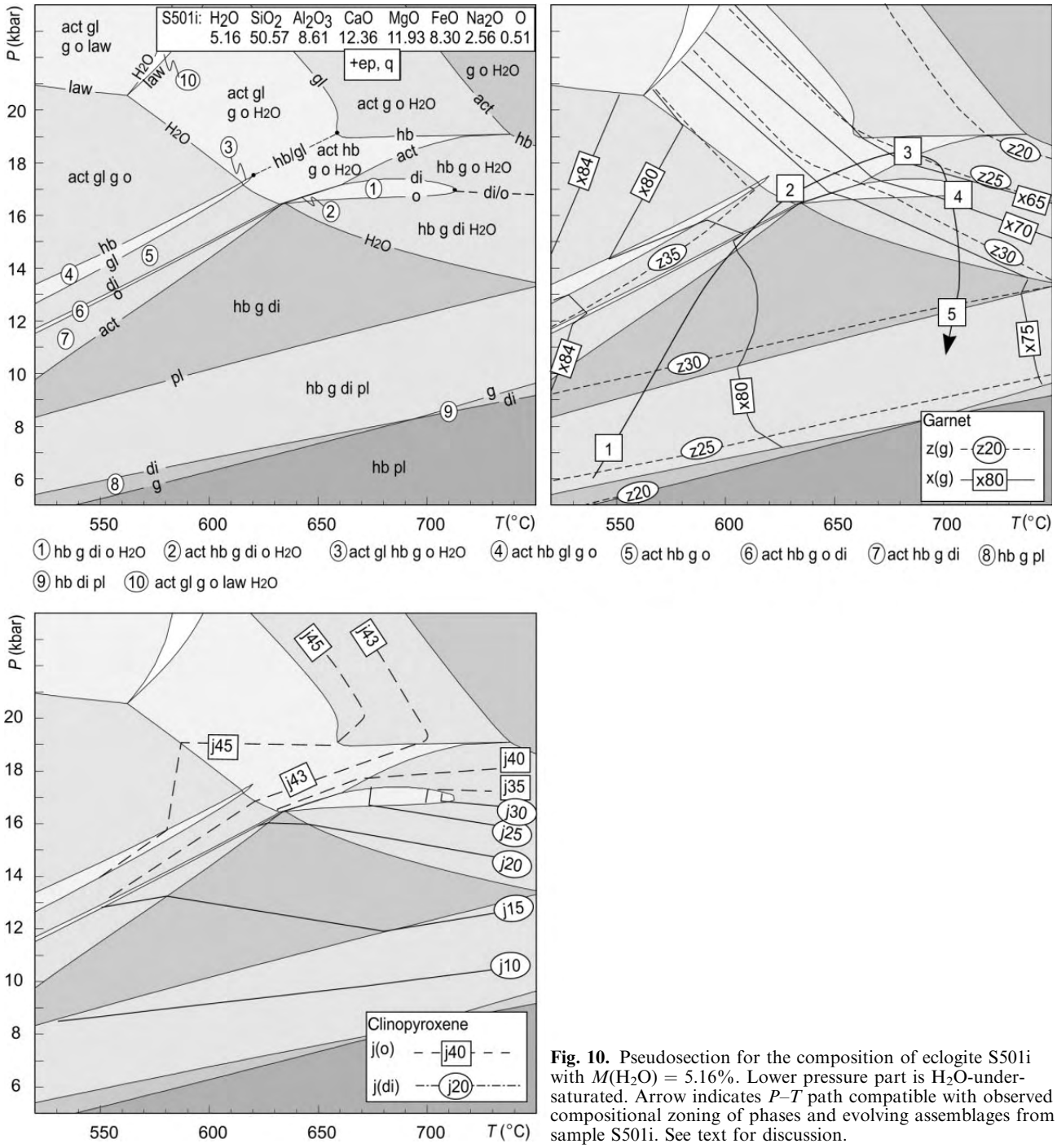

Fig. 10. Pseudosection for the composition of eclogite S501i with $M(H_2O) = 5.16\%$. Lower pressure part is H_2O-undersaturated. Arrow indicates *P–T* path compatible with observed compositional zoning of phases and evolving assemblages from sample S501i. See text for discussion.

Pressures obtained for S404-1 using the g–pl–hb barometers (Kohn & Spear, 1990) are 10.8 and 11.5 kbar for Mg and Fe end-member reactions, respectively. The am–pl thermometer (Holland & Blundy, 1994) yields 660 and 640 °C for the ed–tr and the ed–ri calibrations, respectively (at 10 kbar). Similar results (630 ± 75 °C, 10.5 ± 1.1 kbar) were obtained using the method of Dale *et al.* (2000). THERMOCALC average *P–T* calculations give 615 ± 60 °C and 11 ± 1.9 (1σ). These *P–T* estimates are consistent with the metamorphic peak deduced for the metapelites.

DISCUSSION AND CONCLUSIONS

P–T evolution

This metamorphic study has shown that the *P–T* paths for the eclogites and metapelites are different, regard-

ing their prograde histories and metamorphic peak, and that these rocks docked at about 11 kbar (Fig. 11). From this depth, their exhumation is shared. The evidence for the *P–T* paths of the different rock types is now summarized.

The pelitic rocks above the eclogite-bearing orthogneiss sheet (S19-95-4, S19, S18b) show a prograde evolution at increasing pressure that is well anchored at two points. One is the crossing of the discontinuous reaction ctd + ma = chl + g + st + pa that causes the disappearance of chloritoid with X_{Fe} of 0.70 at about 9.5 kbar and 570 °C. Second, the rocks reached their peak pressure at about 11 kbar and 640 °C in the field of g–pa–ky–bi as deduced from the mineral assemblage and the garnet zoning. The presence of staurolite in garnet, and the nature of the garnet zoning, appears to exclude the continuation of the *P–T* path to high pressure after the disappearance of chloritoid, supporting the overall middle-pressure evolution. The prograde part of the *P–T* path indicates a pressure and temperature increase at a thermal gradient of about 17 °C km^{-1} during burial to 11 kbar. The exhumation path is marked by essentially isothermal decompression to 7 kbar at 650 °C, followed by further decompression and cooling to 500–570 °C.

The prograde evolution of the eclogites under epidote–amphibolite facies conditions to eclogite facies is reflected in inclusions of epidote, amphibole and omphacite in garnet (sample S501i). The garnet zoning and the jadeite content of 40–43% in omphacite inclusions suggests that the prograde path occurred in the act–hb–g–o–ep field under H_2O-undersaturated conditions (Fig. 10). The maximum temperature of 700 °C and minimum pressure of 18 kbar is indicated by garnet rim compositions (grs25, $X_{Fe} = 65$) and the composition of omphacite inclusions. The maximum jadeite content in the matrix clinopyroxene of 33% with the garnet rim composition attest to equilibration at 700 °C at around 17 kbar. The thermal gradient for eclogite on the prograde path to peak pressure is about 11 °C km^{-1}. Breakdown of garnet to plagioclase in amphibolitized eclogite and the lack of garnet in the foliated external parts of boudins is interpreted in terms of further decompression and cooling into epidote–amphibolite facies conditions.

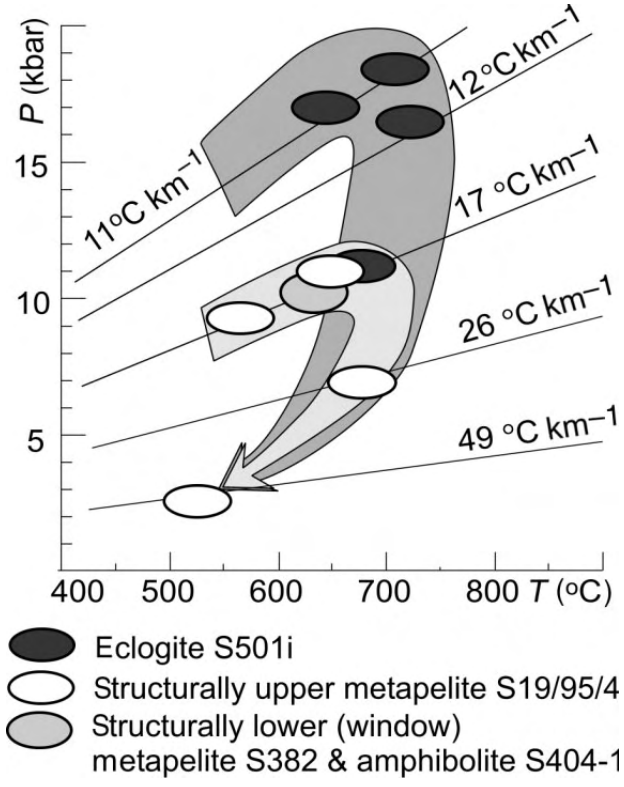

Fig. 11. Summary of *P–T* paths derived from metapelites and basic rocks from the Velké Vrbno unit. Geothermal gradients calculated for density 2.9 g cm^{-3}. See text for discussion.

Garnetiferous amphibolite (S404-1) and the metapelite (S328) from the tectonic window, below the eclogite-bearing orthogneiss sheet, show peak conditions of about 11 kbar and 610–660 °C and 10 kbar at 620 °C, respectively. These conditions are identical to those of the metapelites higher in the structural column, suggesting similar burial depth.

The eclogite boudins are scattered in the orthogneisses and therefore it seems reasonable to suppose that the whole eclogite-bearing orthogneiss sheet attained eclogite facies conditions, but the metagranitoids did not develop and/or preserve high-pressure mineral assemblages (cf. Proyer, 2003). The zoning in garnet of the eclogites, compatible with H_2O-undersaturated conditions during their prograde history, may thus reflect the H_2O-undersaturated environment of the surrounding orthogneisses. Eclogite boudins of variable size also occur within fine-grained metavolcanic rocks and metapelites to the west. Within the western, metapelite-dominated part, eclogite bodies disappear. This may indicate that either the eclogites were never present there, or that they have been completely retrogressed within the more hydrous metapelites.

Only part of the *P–T* path is shared

A comparison of the *P–T* paths from the eclogites and metapelites reveals that these rocks shared only part of their *P–T* history. The minimum difference in pressure on the prograde path and peak between eclogites and metapelites is 6–7 kbar. The type of inclusions within the metapelite and eclogite suggests that the prograde assemblages developed under hydrous and H_2O-undersaturated conditions, respectively, and both lithologies were reactive during burial. Therefore, the possibility that the metapelite could have been buried to greater depths together with the eclogites and did not react can be excluded as their medium-pressure prograde evolution can be documented. Moreover, the *P–T* conditions of the prograde evolution of the eclogite lie on a lower geothermal gradient than the

prograde conditions determined for the metapelites overlying the eclogite-bearing orthogneiss.

The eclogites and metapelites appear to share the same decompressional *P–T* path from about 11 kbar, which is the maximum pressure determined both in the metapelite overlying the orthogneiss sheet and from the tectonic window. The subsequent common exhumation *P–T* path is indicated by plagioclase–amphibole coronas stretched around garnet or pseudomorphs after garnet in the retrogressed eclogites and in the amphibolites, and by local development of sillimanite–biotite intergrowths in the pressure shadows of garnet in metapelites. The pressure interval of 11 to about 7 kbar is the amount of exhumation under amphibolite facies conditions that is common for all the rock types. This is corroborated also by the pervasive development of an amphibolite facies S2 foliation.

Geodynamic implications and comparison with other areas

The areas for which different *P–T* paths of eclogites and surrounding rocks have been suggested include, for example, the Sanbagawa belt (e.g. Takasu, 1989) and southern Turkey (Okay, 1989). The conditions reported from eclogites and schists of the Sanbagawa belt lie on a low geothermal gradient and this belt has been interpreted as a subduction-related accretionary prism (Takasu, 1989; Takasu *et al*., 1994; Inui & Toriumi, 2002; Ko *et al*., 2005). The relationship of the high-pressure rocks and surroundings is interpreted in terms of tectonic mixing in a mélange zone or in nappes (Takasu, 1989; Takasu *et al*., 1994; Wallis & Aoya, 2000).

The example studied here exhibits higher geothermal gradients during prograde and peak evolution than those typical for subduction zones. The eclogites and surrounding Neoproterozoic orthogneisses of the Velké Vrbno unit are interpreted to have reached eclogite facies conditions at 18 kbar and 700 °C during the underthrusting of the Brunian Neoproterozoic crust below the Moldanubian orogenic root, while the metapelites reached only the staurolite and kyanite grade during burial to about 11 kbar at 650 °C. The staurolite and kyanite micaschists of the Velké Vrbno unit represent therefore a logical continuation of the inverted Barrovian metamorphic sequence developed in the Brunian basement to the east (Schulmann & Gayer, 2000), with the eclogites representing slices of the Neoproterozoic Brunian basement buried to and exhumed from eclogite facies conditions.

We suggest that the Velké Vrbno unit and the Micaschist zone further south are the uppermost part of the *continental* accretionary prism of the Brunian basement (cf. Schulmann & Gayer, 2000; Konopásek *et al*., 2002). The development of an accretionary prism on the underthrust continental crust accounts for a higher geothermal gradient than is characteristic of the accretionary prisms formed above subduction zones. This context is similar to the Main Central thrust in the Himalayas where relatively high-temperature eclogites are found within an orthogneiss that occurs above the staurolite–kyanite metapelites at the boundary of the Lesser and Higher Himalayas (Lombardo *et al*., 1998; Lombardo & Rolfo, 2000).

ACKNOWLEDGEMENTS

Financial support to P.Š. by the Czech National Grant Agency (grant no. 205/99/1195) and by Charles University Grant Agency (grant No.223/2002/B-GEO/PrF) is gratefully acknowledged. Two visits of P.Š. to Mainz University for microprobe work were funded by the German Science Foundation (DFG), grant Kr 590/68-1 to A. Kröner and several visits of P.Š. to ETH Zürich were funded by the Swiss National Foundation ('Continuous Orogenesis' grant to A.B. Thompson). We gratefully acknowledge valuable discussions with K. Schulmann. E. Reusser, D. Siedler-Vavrecka (ETH, Zürich) and V. Böhmová (Geological Institute of the Czech Academy of Sciences) are thanked for operating the microprobes. P.Š. also received financial support from the Czech Ministry of Education (grant no. 24313005). R.P. acknowledges ARC Discovery Grant DP 0451770. N. Daczko and R. Kryza are thanked for their reviews, and D. Robinson for his editorial work.

REFERENCES

Carswell, D.A., 1991. Variscan high *P–T* metamorphism and uplift history in the Moldanubian Zone of the Bohemian Massif in Lower Austria. *European Journal of Mineralogy*, **3,** 323–342.

Chopin, C., 2003. Ultrahigh-pressure metamorphism: tracing continental crust into the mantle. *Earth and Planetary Science Letters*, **212,** 1–14.

Dale, J., Holland, T. & Powell, R., 2000. Hornblende-garnet-plagioclase thermobarometry: a natural assemblage calibration of the thermodynamics of hornblende. *Contributions to Mineralogy and Petrology*, **140,** 353–362.

Dale, J., Powell, R., White, R. W., Elmer, F. L. & Holland, T. J. B., 2005. A thermodynamic model for Ca-Na clinoamphiboles in Na_2O-CaO-FeO-MgO-Al_2O_3-SiO_2-H_2O-O for petrological calculations. *Journal of Metamorphic Geology*, **23,** 771–791.

Deer, W. A., Howie, R. A. & Zussman, J., 1992. *An Introduction to Rock-forming Minerals*. Longman Scientific & Technical, Harlow, Essex.

Feenstra, A., 1996. An EMP and TEM-AEM study of margarite, muscovite and paragonite in polymetamorphic metabauxites of Naxos (Cyclades, Greece) and the implications of fine-scale mica generations. *Journal of Petrology*, **37,** 201–233.

Franke, W., 2000. The mid-European segment of the Variscides: tectonostratigraphic units, terrane boundaries and kinematic evolution. In: *Orogenic Processes: Quantification and Modelling in the Variscan Belt, Special Publications, 179* (eds Franke, W., Haak, V., Oncken, O. & Tanner, D.), pp. 35–63. The Geological Society of London, London.

Friedl, G., Finger, F., Paquette, J., Quadt, A., McNaughton, N. & Fletcher, I., 2004. Pre-Variscan geological events in the Austrian part of the Bohemian Massif deduced from U-Pb zircon ages. *International Journal of Earth Sciences*, **93,** 802–823.

Heinrich, C. A., 1982. Kyanite-eclogite to amphibolite facies evolution of hydrous mafic and pelitic rocks, Adula Nappe, Central Alps. *Contributions to Mineralogy and Petrology*, **81,** 30–38.

Höck, V., 1974. Coexisting phengite, paragonite and margarite in metasediments of the Mittlere Hohe Tauern, Austria. *Contributions to Mineralogy and Petrology*, **43,** 261–273.

Holland, T. J. B. & Blundy, J. D., 1994. Non-ideal interactions in calcic amphiboles and their bearing on amphibole-plagioclase thermometry. *Contributions to Mineralogy and Petrology*, **116,** 433–447.

Holland, T. J. B. & Powell, R., 1992. Plagioclase feldspars: activity–composition relations based on Darkens Quadratic Formalism and Landau theory. *American Mineralogist*, **77,** 53–61.

Holland, T. J. B. & Powell, R., 1996. Thermodynamics of order-disorder in minerals. 2. symmetric formalism applied to solid solutions. *American Mineralogist*, **81,** 1425–1437.

Holland, T. J. B. & Powell, R., 1998. An internally consistent thermodynamic data set for phases of petrological interest. *Journal of Metamorphic Geology*, **16,** 309–343.

Holland, T. & Powell, R., 2003. Activity–composition relations for phases in petrological calculations: an asymmetric multicomponent formulation. *Contributions to Mineralogy and Petrology*, **145,** 492–501.

Inui, M. & Toriumi, M., 2002. Prograde pressure–temperature paths in the pelitic schists of the Sambagawa metamorphic belt, SW Japan. *Journal of Metamorphic Geology*, **20,** 563–580.

Klemd, R. & Bröcker, M., 1999. Fluid influence on mineral reactions in ultrahigh-pressure granulites: a case study in the Sneznik Mts. (West Sudetes, Poland). *Contributions to Mineralogy and Petrology*, **136,** 358–373.

Ko, Z. W., Enami, M. & Aoya, M., 2005. Chloritoid and barroisite-bearing pelitic schists from the eclogite unit in the Besshi district, Sanbagawa metamorphic belt. *Lithos*, **81,** 79–100.

Kohn, M. J. & Spear, F. S., 1990. Two new barometers for garnet amphibolites with applications to southeastern Vermont. *American Mineralogist*, **75,** 89–96.

Konopásek, J., Schulmann, K. & Johan, V., 2002. Eclogite-facies metamorphism at the eastern margin of the Bohemian Massif-subduction prior to continental underthrusting? *European Journal of Mineralogy*, **14,** 701–713.

Kröner, A., Štípská, P., Schulmann, K. & Jaeckel, P., 2000. Chronological constraints on the pre-Variscan evolution of the northeastern margin of the Bohemian Massif, Czech Republic. In: *Orogenic Processes; Quantification and Modelling in the Variscan Belt* (eds Franke, W., Haak, V., Oncken, O. & Tanner, D.), Geological Society of London, London, UK. *Geological Society of London Special Publications*, **179,** 175–197.

Kröner, A., Jaeckel, P., Hegner, E. & Opletal, M., 2001. Single zircon ages and whole rock Nd isotopic systematics of early Palaeozoic granitoid gneisses from the Czech and Polish Sudetes (Jizerské hory, Krkonoše Mountains and Orlice-Sneznik Complex). *International Journal of Earth Sciences*, **90,** 304–324.

Lange, U., Bröcker, M., Armstrong, R., Trapp, E. & Mezger, K., 2005a. Sm-Nd and U-Pb dating of high-pressure granulites from the Zlote and Rychleby Mts (Bohemian Massif, Poland and Czech Republic). *Journal of Metamorphic Geology*, **23,** 133–145.

Lange, U., Bröcker, M., Armstrong, R., Zelazniewicz, A., Trapp, E. & Mezger, K., 2005b. The orthogneisses of the Orlica-Snieznik complex (West Sudetes, Poland): geochemical characteristics, the importance of pre-Variscan migmatization and constraints on the cooling history. *Journal of the Geological Society, London*, **162,** 973–984.

Lombardo, B. & Rolfo, F., 2000. Two contrasting eclogite types in the Himalayas: implications for the Himalayan orogeny. *Journal of Geodynamics*, **30,** 37–60.

Lombardo, B., Pertusati, P., Rolfo, F. & Visona, D., 1998. First report of eclogites from the Eastern Himalaya: Implications for the Himalayan orogeny. *Memorie di scienze geologiche dell Universita di Padova*, **50,** 67–68.

Marmo, B. A., Clarke, G. L. & Powell, R., 2002. Fractionation of bulk rock composition due to porphyroblast growth: effects on eclogite facies mineral equilibria, Pam Peninsula, New Caledonia. *Journal of Metamorphic Geology*, **20,** 151–165.

Medaris, L. G., Jelínek, E. & Mísař, Z., 1995. Czech eclogites: terrane settings and implications for Variscan tectonic evolution of the Bohemian Massif. *European Journal of Mineralogy*, **7,** 7–28.

Medaris, L. G., Fournelle, J. H., Ghent, E. D., Jelínek, E. & Mísař, Z., 1998. Prograde eclogite in the Gföhl Nappe, Czech Republic: new evidence on Variscan high-pressure metamorphism. *Journal of Metamorphic Geology*, **16,** 563–576.

Meyre, C., De Capitani, C., Zack, T. & Frey, M., 1999. Petrology of high-pressure metapelites from the Adula nappe (Central Alps, Switzerland). *Journal of Petrology*, **40,** 199–213.

O'Brien, P. J. & Rötzler, J., 2003. High-pressure granulites: formation, recovery of peak conditions and implications for tectonics. *Journal of Metamorphic Geology*, **21,** 3–20.

Okay, A. I., 1989. An exotic eclogite blueschist slice in a Barrovian-style metamorphic terrain, Alanya nappes, Southern Turkey. *Journal of Petrology*, **30,** 107–132.

Okay, A. I., 2002. Jadeite-chloritoid-glaucophane-lawsonite blueschists in northwest Turkey: unusually high P/T ratios in continental crust. *Journal of Metamorphic Geology*, **20,** 757–768.

Powell, R. & Holland, T. J. B., 1988. An internally consistent dataset with uncertainties and correlations: 3. Applications to geobarometry, worked examples and a computer program. *Journal of Metamorphic Geology*, **6,** 173–204.

Powell, R., Holland, T. & Worley, B., 1998. Calculating phase diagrams involving solid solutions via non-linear equations, with examples using THERMOCALC. *Journal of Metamorphic Geology*, **16,** 577–588.

Powell, R. & Holland, T. J. B., 2002. Course notes for *THERMOCALC Workshop 2002: Calculating Metamorphic Phase Equilibria*, Barcelona. CD-ROM.

Proyer, A., 2003. The preservation of high-pressure rocks during exhumation: metagranites and metapelites. *Lithos*, **70,** 183–194.

Rozkošný, I. & Souček, J., 1989. Contribution to the petrology of the Žulová massif mantle. *Acta Universitatis Carolinae, Geologica*, **2,** 165–197.

Schulmann, K. & Gayer, R., 2000. A model for a continental accretionary wedge developed by oblique collision: the NE Bohemian Massif. *Journal of the Geological Society, London*, **157,** 401–416.

Schulmann, K., Kröner, A., Hegner, E., *et al*., 2005. Chronological constraints on the pre-orogenic history, burial and exhumation of deep-seated rocks along the eastern margin of the Variscan orogen, Bohemian Massif, Czech Republic. *American Journal of Science*, **305,** 407–448.

Skácel, J., 1989. Crossing of Lugian boundary fault with Nýznerov dislocation belt between Vápenná and Javorník in Silesia (in Czech). *Acta Universitatis Palackianae Olomucensis*, **95,** 31–45.

Smith, D. C., 1988. A review of the peculiar mineralogy of the "Norwegian eclogite province", with crystal chemical, petrological, geochemical, and geodynamical notes and an extensive bibliography. In: *Eclogites and Eclogite-Facies Rocks* (ed. Smith, D.C.), pp. 1–206. Elsevier, Amsterdam.

Souček, J., 1978. Metamorphic zones of the Vrbno and Rejvíz series, the Hrubý Jeseník Mountains, Czechoslovakia. *Tschermaks mineralogische und petrographische Mitteilungen*, **25,** 195–217.

Štípská, P. & Powell, R., 2005. Constraining the P–T path of a MORB-type eclogite using pseudosections, garnet zoning and garnet-clinopyroxene thermometry: an example from the Bohemian Massif. *Journal of Metamorphic Geology*, **23,** 725–743.

Štípská, P. & Schulmann, K., 1995. Inverted metamorphic zonation in a basement-derived nappe sequence, eastern margin of the Bohemian Massif. *Geological Journal*, **30,** 385–413.

Štípská, P., Schulmann, K. & Höck, V., 2000. Complex metamorphic zonation of the Thaya dome: result of buckling and gravitational collapse of an imbricated nappe sequence. In: *Forced Folds and Fractures* (eds Cosgrowe, J. W. & Ameen, M. S.), pp. 197–211. Geological Society of Special publications, London.

Štípská, P., Schulmann, K., Thompson, A. B., Ježek, J. & Kröner, A., 2001. Thermo-mechanical role of a Cambro-Ordovician paleorift during the Variscan collision: the NE margin of the Bohemian Massif. *Tectonophysics*, **332,** 239–253.

Štípská, P., Schulmann, K. & Kröner, A., 2004. Vertical extrusion and middle crustal spreading of omphacite granulite: a model of syn-convergent exhumation (Bohemian Massif, Czech Republic). *Journal of Metamorphic Geology*, **22,** 179–198.

Suess, F. E., 1912. Die Moravischen Fenster und ihre Beziehung zum Grundgebirge des Hohen Gesenkes. *Akademie der Wissenschaften, Denkschrift Matematisch-Naturwissenschaftliche Klasse*, **88,** 541–631.

Suess, F. E., 1926. *Intrusionstektonik und Wandertektonik im variszichen Grundgebirge*. Verlag Bornttrager, Berlin.

Takasu, A., 1984. Prograde and retrograde eclogites in the Sambagawa Metamorphic Belt, Besshi District, Japan. *Journal of Petrology*, **25,** 619–643.

Takasu, A., 1989. *P–T* histories of peridotite and amphibolite tectonic blocks in the Sanbagawa metamorphic belt, Japan. In: *The Evolution of Metamorphic Belts* (eds Daly, J. S., Cliff, R. A. & Yardley, B. W. D.). *Geological Society of London Special Publication*, **43,** 533–538.

Takasu, A., Wallis, S. R., Banno, S. & Dallmeyer, R. D., 1994. Evolution of the Sambagawa Metamorphic Belt, Japan. *Lithos*, **33,** 119–133.

Turniak, K., Mazur, S. & Wysoczanski, R., 2000. SHRIMP zircon geochronology and geochemistry of the Orlica-Snieznik gneisses (Variscan belt of Central Europe) and their tectonic implications. *Geodinamica Acta*, **13,** 1–20.

Wain, A., 1997. New evidence for coesite in eclogite and gneisses: Defining an ultrahigh-pressure province in the Western Gneiss Region of Norway. *Geology*, **25,** 927–930.

Wallis, S. & Aoya, M., 2000. A re-evaluation of eclogite facies metamorphism in SW Japan: proposal for an eclogite nappe. *Journal of Metamorphic Geology*, **18,** 653–664.

Wei, C. J. & Powell, R., 2004. Calculated phase relations in high-pressure metapelites in the system NKFMASH (Na_2O-K_2O-FeO-MgO-Al_2O_3-SiO_2-H_2O). *Journal of Petrology*, **45,** 183–202.

Wei, C. J. & Powell, R., 2006. Calculated phase relations in the system NCKFMASH (Na_2O-CaO-K_2O-FeO-MgO-Al_2O_3-SiO_2-H_2O) for high-pressure metapelties. *Journal of Petrology*, **47,** 385–408.

Wei, C. J., Powell, R. & Zhang, L. F., 2003. Eclogites from the south Tianshan, NW China: petrological characteristic and calculated mineral equilibria in the Na_2O- CaO-FeO-MgO-Al_2O_3-SiO_2-H_2O system. *Journal of Metamorphic Geology*, **21,** 163–179.

Worley, B. & Powell, R., 1998. Singularities in NCKFMASH (Na_2O-CaO-K_2O-FeO-MgO-Al_2O_3-SiO_2-H_2O). *Journal of Metamorphic Geology*, **16,** 169–188.

Žáček, V., 1996. Retrograded eclogite from the Staré Město Belt, NE margin of the Bohemian Massif. *Journal of the Czech Geological Society*, **41,** 167–175.

Received 22 August 2005; revision accepted 10 January 2005.

J. metamorphic Geol., 2007, **25,** 19–35 doi:10.1111/j.1525-1314.2006.00674.x

Variations in the transient prograde geothermal gradient from chloritoid-staurolite equilibria: a case study from the Barrovian and Buchan-type domains in the Bohemian Massif

M. KOŠULIČOVÁ[1,2] AND P. ŠTÍPSKÁ[3]
[1]*Institute of Petrology and Structural Geology, Charles University, Albertov 6, 12843, Prague, Czech Republic (monika.kosulicova@seznam.cz)*
[2]*Czech Geological Survey, Klárov 3, 11821, Prague, Czech Republic*
[3]*Université Louis Pasteur, CGS/EOST, UMR 7517, 1 Rue Blessig, Strasbourg, France*

ABSTRACT Thermodynamic modelling of metamorphic rocks increases the possibilities of deciphering prograde paths that provide important insights into early orogenic evolution. It is shown that the chloritoid–staurolite transition is not only an indicator of temperature on prograde P–T paths, but also a useful indicator of pressure. The approach is applied to the Moravo-Silesian eastern external belt of the Bohemian Massif, where metamorphic zones range from biotite to staurolite-sillimanite. In the staurolite zone, inclusions of chloritoid occur in garnet cores, while staurolite is included at garnet rims and is widespread in the matrix. Chloritoid $X_{Fe} = 0.91$ indicates transition to staurolite at 5 kbar and 550 °C and consequently, an early transient prograde geothermal gradient of 29 °C km^{-1}. The overall elevated thermal evolution is then reflected in the prograde transition of staurolite to sillimanite and in the achievement of peak temperature of 660 °C at a relatively low pressure of 6.5 kbar. To the south and to the west of the studied area, high-grade metamorphic zones record a prograde path evolution from staurolite to kyanite and development of sillimanite on decompression. Transition of chloritoid to staurolite was reported in two places, with chloritoid $X_{Fe} = 0.75$–0.80, occurring at 8–10 kbar and 560–580 °C, and indicating a transient prograde geothermal gradient of 16–18 °C km^{-1}. These data show variable barric evolutions along strike and across the Moravo-Silesian domain. Elevated prograde geothermal gradient coincides with areas of Devonian sedimentation and volcanism, and syn- to late Carboniferous intrusions. Therefore, we interpret it as a result of heat inherited from Devonian rifting, further fuelled by syntectonic Carboniferous intrusions.

Key words: Barrovian and Buchan metamorphism; Bohemian Massif; chloritoid–staurolite; prograde geotherm; pseudosection.

INTRODUCTION

The form of P–T paths of metamorphic rocks reflects their geodynamic histories and can be used to interpret thermal aspects of tectonic processes in mountain belts. The thermal state of an orogenic belt is manifested in the isograd distribution in the field, classically known as facies series, barric types or geothermal field gradients (Miyashiro, 1961). Isograds commonly reflect peak temperature conditions achieved after peak pressure at relatively late stages of evolution, while understanding of thermal processes at an early stage in mountain belts depends on the determination of prograde conditions.

Contrasting prograde geothermal gradients have been identified in adjacent domains of New England and the NW Iberian Massif (Florence *et al.*, 1993; Reche *et al.*, 1998; Spear *et al.*, 2002; Arenas & Catalan, 2003), and the contemporaneity of Barrovian and Buchan metamorphism has been demonstrated in the Scottish Caledonides (Baxter *et al.*, 2002). Different dP/dT conditions at an early stage of metamorphism have also been reported in the metamorphic zones of the Sanbagawa belt (Enami, 1998). All these contrasting prograde histories indicate variations in the thermal state of crust at early stages of burial and give rise to questions about possible causes, involving rate of burial, age of subducted slab, contribution of heat from syntectonic intrusions or the effects of pre-collisional extension and associated temporal aspects.

Prograde transient geothermal gradients are best deciphered from P–T paths of individual samples. On a prograde path, the assemblage tends to equilibrate if grain size is small and fluid is available. However, as a result of low element diffusion rates, a garnet preserves its composition until upper amphibolite facies (Ayres & Vance, 1997) and may be used for interpretation of prograde paths, for example using the Gibbs method (Spear & Selverstone, 1983; Spear, 1988). Garnet commonly includes other minerals that are isolated

and preserved, while in the matrix the same minerals will equilibrate and eventually disappear. Thus to decipher prograde conditions, it is usual to include reaction history and thermobarometry on inclusions within garnet (Thompson *et al*., 1977; Selverstone & Spear, 1985; St Onge, 1987).

Progress in mineral equilibria modelling by means of pseudosections allows a combination of various approaches in determining the prograde *P–T* conditions of rocks. In a pseudosection, prograde conditions may be deduced from mineral assemblages (Zeh, 2001), compositional isopleths of garnet (Vance & Mahar, 1998; Zeh & Millar, 2001; Zeh, 2001), modal proportions (Stüwe & Powell, 1995) or modelled garnet growth zoning along a specified *P–T* path (Zeh & Millar, 2001; Štípská & Powell, 2005a,b). Other possibilities involve the succession of mineral assemblages from inclusions and combinations with thermobarometry (Vance & Mahar, 1998). In using pseudosections, it is useful to find reliable points on prograde *P–T* paths, as for example the intersection of the lower stability limit of garnet with its core compositional isopleths or chlorite upper stability combined with barometry on inclusions (Vance & Mahar, 1998).

Another potential indicator of prograde conditions is the transition from chloritoid to staurolite that is common in high-alumina metapelites, and which has been recognized and demonstrated in a series of experiments and topological relations (Albee, 1972 and references therein). This transition is commonly used for demonstration of prograde temperature evolution on inclusions (Thompson *et al*., 1977; Spalla *et al*., 1999) but it is rarely used as a *P–T* indicator (Konopásek *et al*., 2002; Štípská *et al*., 2006). As the chloritoid–staurolite transition is temperature-sensitive and the X_{Fe} of minerals changes along univariant reactions, the X_{Fe} of chloritoid and staurolite at this transition should also provide information on pressure, and therefore on the transient prograde geothermal gradient.

In this contribution we present an example of metamorphic zones that shows the transition from staurolite to sillimanite, indicating a relatively high geothermal gradient at the metamorphic peak, similar to Abukuma or Buchan classical terranes. Isograd succession and peak evolution are compared with neighbouring Barrovian-type areas, which show the characteristic transition from staurolite to kyanite, and later to sillimanite. The major interest is, whether the difference in thermal evolution is a late phenomenon, or whether it applies also for prograde paths. It is suggested that the chloritoid–staurolite transition is a useful indicator of prograde *P–T* conditions and it is used to determine transient prograde geothermal gradient. Using this approach, different prograde geothermal gradients are identified in the study area and a possible cause is suggested for this phenomenon. Similar examples of contrasting barric evolutions reported in the literature are discussed.

GEOLOGY OF THE EASTERN MARGIN OF THE BOHEMIAN MASSIF

A 300-km-long contact between the internal high-grade Moldanubian domain thrust over the external Brunia basement is exposed at the eastern margin of the Variscan Bohemian Massif (Fig. 1) (Suess, 1912, 1926; Schulmann *et al*., 2005). Carboniferous compression produced an up to 50-km-wide deformation and metamorphic front in the underthrust Brunia, the so-called Moravo-Silesian accretionary wedge (Schulmann & Gayer, 2000). This wedge emerges in the form of three tectonic windows, the southern Thaya window, the central Svratka window (of the Moravian domain) and the northern Silesian domain (Fig. 1). The compression was accompanied by Carboniferous, syn- to late tectonic magmatism in the Silesian domain.

The Brunia basement is composed of Neoproterozoic granitoids (Kröner *et al*., 2000, and references therein) and overlain by Cambro-Ordovician sedimentary rocks. During the Devonian, NE–SW-trending basins developed, characterized by shallow water and continental sedimentation in the south. In the north, the basins are deeper with marine sediments accompanied by volcanism, evolving in time into shallow-water sedimentation (Hladil, 1994; Hartley & Otava, 2001; Kalvoda *et al*., 2003).

The Moravian domain: a review of metamorphic evolution

In the Thaya and Svratka windows, underthrusting caused basement imbrication into two crustal nappes, with orthogneiss bodies at the base and metasediments at the top. Peak temperature and pressure increases up the pile from the chlorite to kyanite–sillimanite zone. Transition from staurolite to kyanite occurred on prograde path, while sillimanite developed on decompression (Höck, 1975; Štípská & Schulmann, 1995). In the uppermost part, eclogites mixed with micaschists are found, in which the chloritoid–staurolite inclusions in garnet were used to demonstrate their different *P–T* paths (Konopásek *et al*., 2002).

Metamorphic inversion is explained by transport of deeper rocks over shallower rocks during a process of simultaneous nappe stacking and Brunia underthrusting (Štípská & Schulmann, 1995). The metamorphic pattern of isograds cutting lithotectonic boundaries in the present-day erosional section is interpreted as a late phenomenon developed during folding of the nappe pile and isograds at shallow crustal levels (Štípská *et al*., 2000).

The Silesian domain: a review of metamorphic evolution

The basement in the Silesian domain was largely modified by Devonian extension, including the formation of three crustal-scale boudins (Fig. 2): the Desná dome, the Keprník nappe and the Velké Vrbno unit, and (volcano) sedimentary units between them (Schulmann & Gayer,

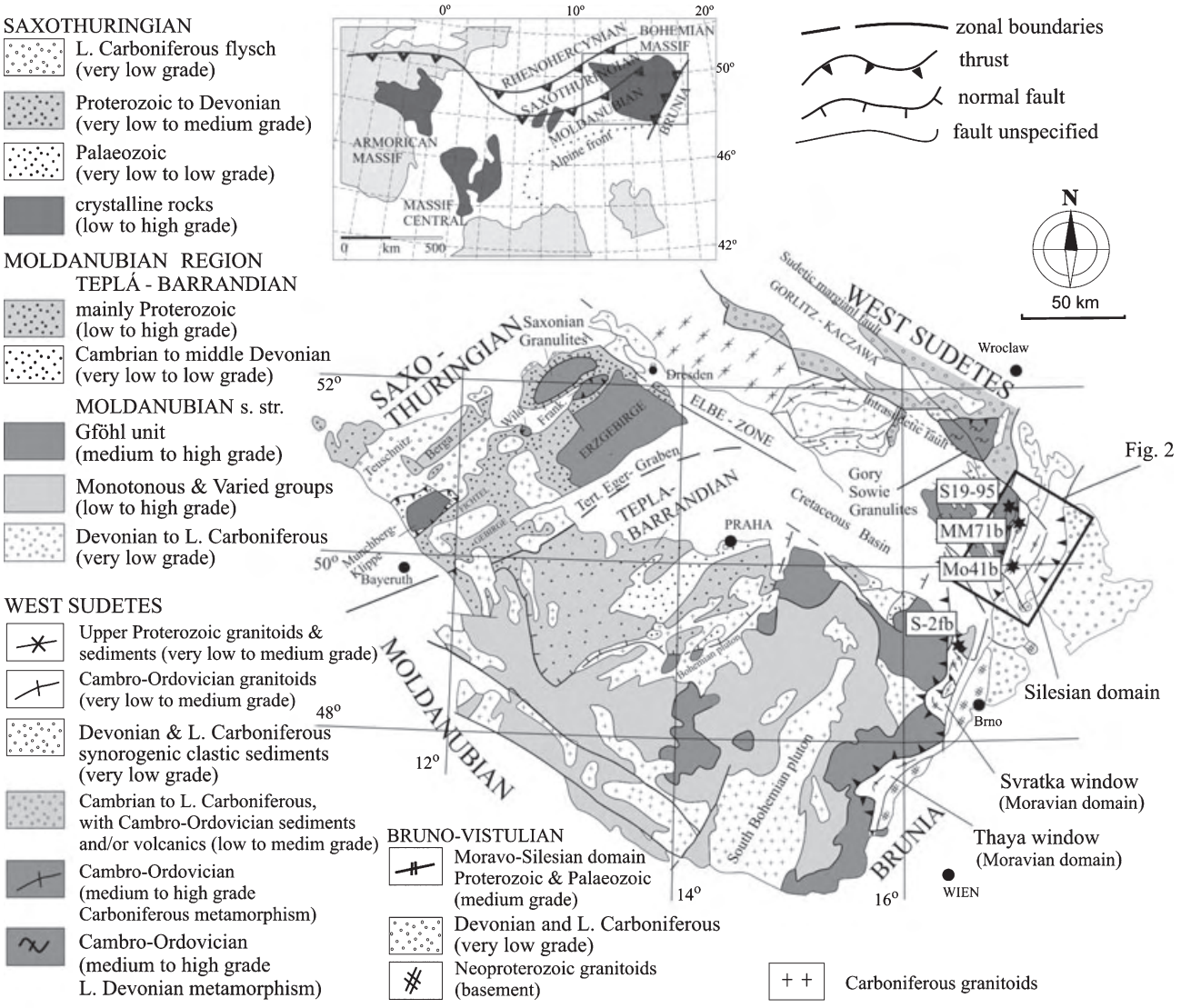

Fig. 1. Outline geological map of the Bohemian Massif with major units shown schematically (modified after Franke, 2000). Location of the study area (Fig. 2) is indicated together with position of the studied and discussed samples. Upper left inset is position of study area in the framework of the European Variscides.

2000). The crustal boudins were underthrust individually during Carboniferous shortening with increasing burial towards the west (Fig. 3). Exhumation occurred under continuous compression accompanied by east-vergent folding with variable transposition into generally west-dipping foliation. A zone of superimposed extension is localized between the Keprník and the Velké Vrbno domains (Schulmann & Gayer, 2000).

Metamorphism is of the Barrovian type (Souček, 1978; Schulmann & Gayer, 2000; Štípská *et al*., 2006), although complicated in detail by the presence of Buchan-type paragneisses (Rozkošný & Souček, 1989; Cháb *et al*., 1994). The Buchan-type evolution was attributed partly to the heat from the neighbouring pluton, but the prograde transition from staurolite to sillimanite was ascribed to increased heat flow caused by Devonian extension (Schulmann & Gayer, 2000; Baratoux *et al*., 2005).

Another complexity is the occurrence of eclogites within the staurolite–kyanite micaschists of the westernmost Velké Vrbno unit (Žáček, 1996; Štípská *et al*., 2006; Fig. 2). In the micaschists, the chloritoid and staurolite inclusions in garnet allowed determination of prograde conditions, the peak was inferred from the kyanite-bearing matrix, and restricted crystallization of sillimanite and andalusite occurred on decompression. The eclogites did not share the prograde path with the micaschists but were emplaced next to them at 10 kbar, from where their retrograde paths are shared (Štípská *et al*., 2006).

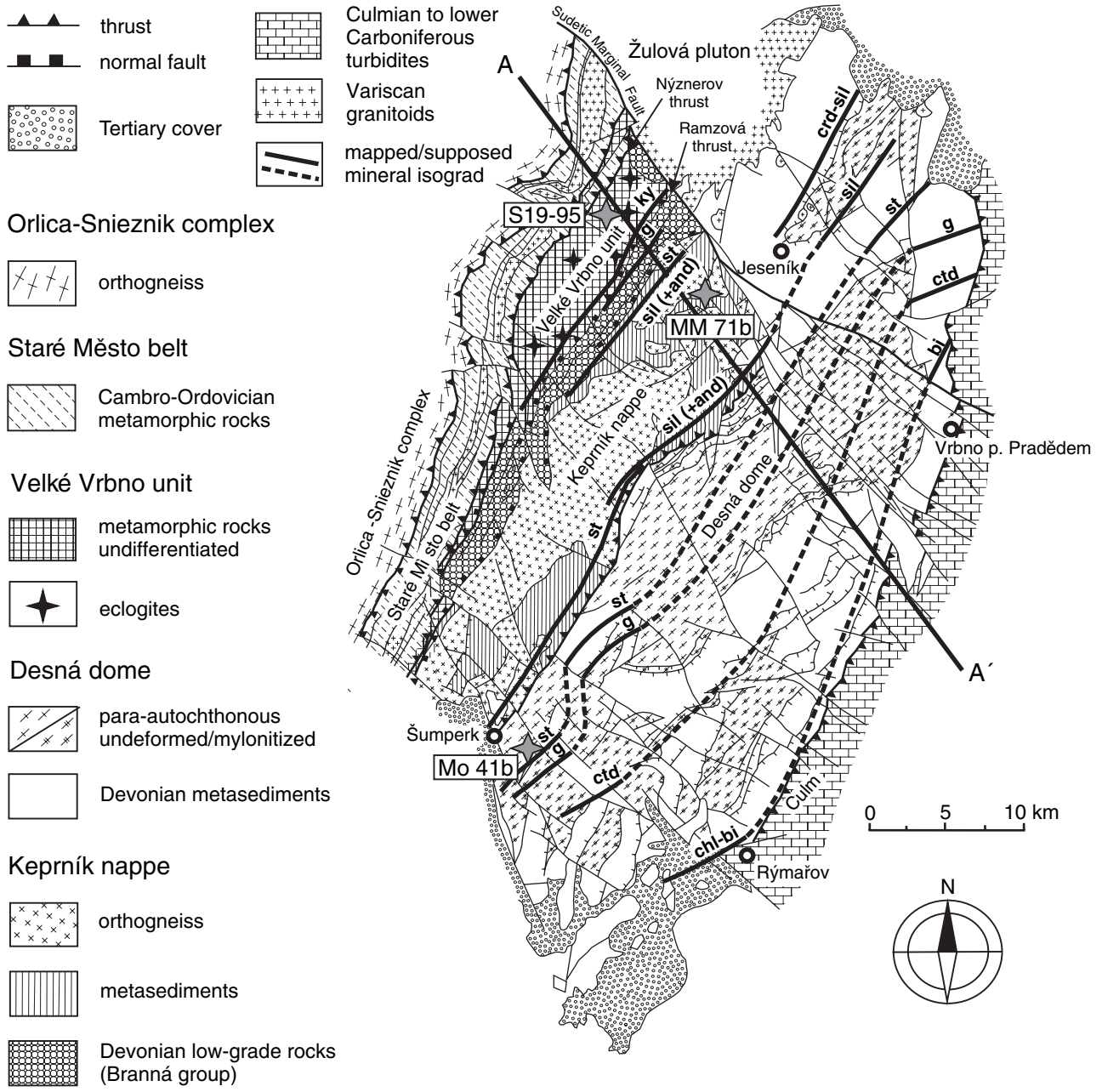

Fig. 2. Geological map of the Silesian domain based on unpublished geological maps of the Czech Geological Survey, modified after J. Cháb. The metamorphic zonality in the northern part is after Souček (1978). Location of the studied and discussed samples is indicated. A–A′ is the line of section in Fig. 3.

METAMORPHIC AND STRUCTURAL EVOLUTION OF THE SOUTHERN SILESIAN DOMAIN

The metamorphic foliation S1 is commonly crenulated and folded by east-vergent F2 folds that lead to variable transposition into a new west-dipping foliation S2. The western part of the Keprník nappe is affected by superimposed west-dipping extensional zone parallel to the D2 fabric (see also Cháb *et al.*, 1994; Schulmann & Gayer, 2000) (Fig. 3).

Within the metapelites of the southern Silesian domain, the following succession of index minerals was mapped from the east to the west in the Desná dome: biotite-chlorite, chloritoid, garnet and staurolite. In the Keprník nappe, the degree of metamorphism from the east to the west first increases from staurolite to staurolite–sillimanite grade, with a strong overprint and growth of widespread andalusite, especially in the western extensional zone. Towards the top of the Keprník nappe at its western side, the metamorphic

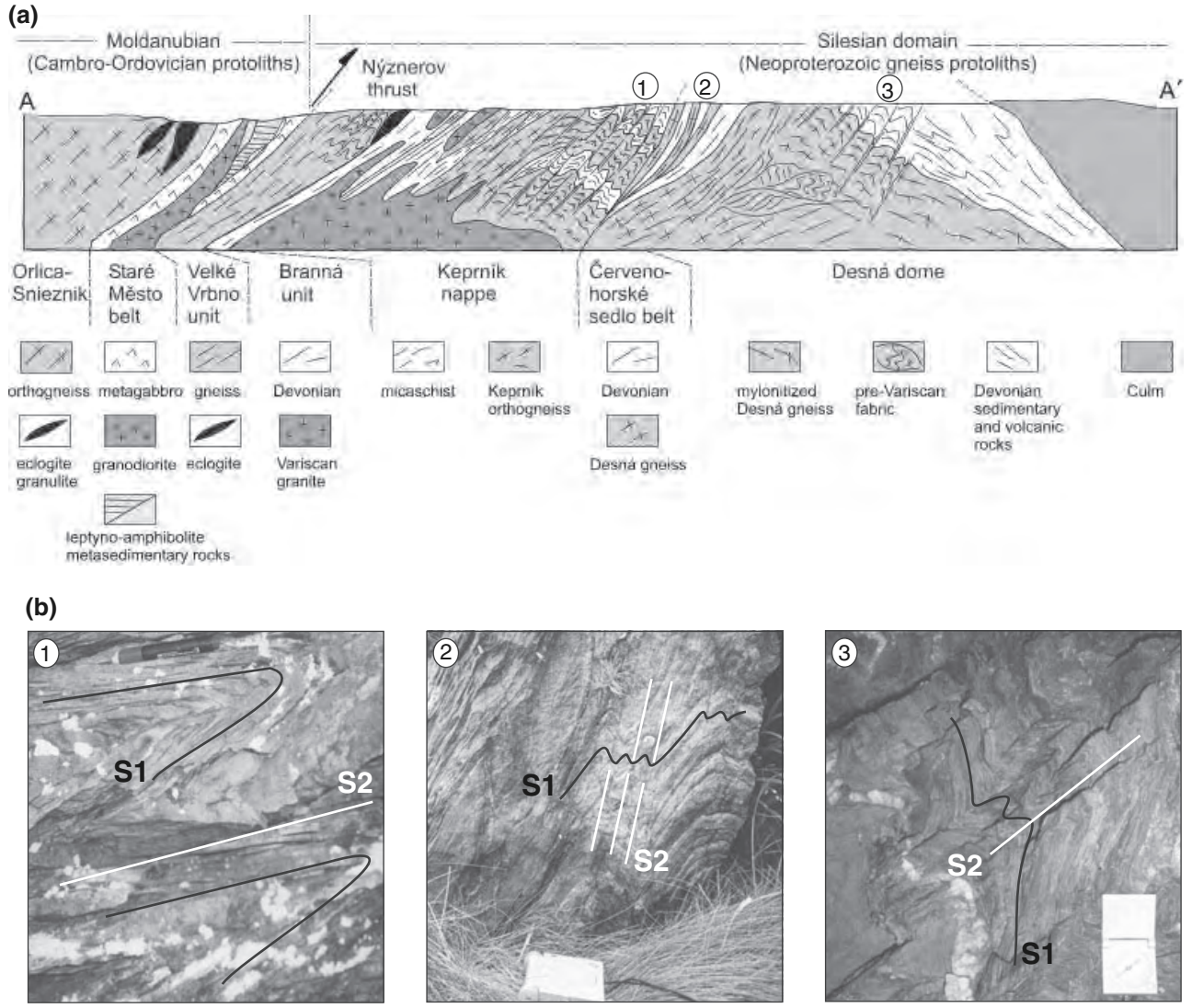

Fig. 3. (a) Geological cross-section (A–A′, shown in Fig. 2) of the Silesian domain showing major structures, lithological content of individual units and major tectonic boundaries (modified after Schulmann & Gayer, 2000). (b) Field photographs illustrating typical relationships of S1 and S2 foliations in the areas indicated 1, 2 and 3 in the cross-section.

degree within the extensional zone decreases to staurolite and garnet zones (Figs 2 & 4).

In the following description, we adapt the logic of relationship between multiple foliation development and simultaneous porphyroblast growth presented for example by Bell & Welch (2002), which establishes the relative timing between structures and metamorphism. The thin sections were cut perpendicular to the fold axis and intersection lineations of superimposed S1 and S2 foliations.

Petrography: the Desná dome

Chlorite-biotite and chloritoid zones

The micaschists are fine-grained (0.1–0.3 mm), with alternation of recrystallized plagioclase-quartz lenses and mica-rich layers, where muscovite, chlorite and biotite are parallel to the matrix foliation. The chloritoid porphyroblasts (0.8 mm) have overgrown the main foliation randomly or have radially nucleated on muscovite. The S1 foliation is crenulated, muscovite is locally aligned in the S2 planes. In some samples, chlorite replaces biotite or forms randomly oriented clusters, and plagioclase is converted to sericite.

Garnet zone

A typical assemblage is garnet, muscovite, quartz, plagioclase and ilmenite. In garnet (5 mm), straight inclusion trails of the S1 foliation are formed by muscovite, quartz and ilmenite, but curved inclusions of ilmenite at garnet rims indicate a continuation of garnet growth at the beginning of the D2 crenulation.

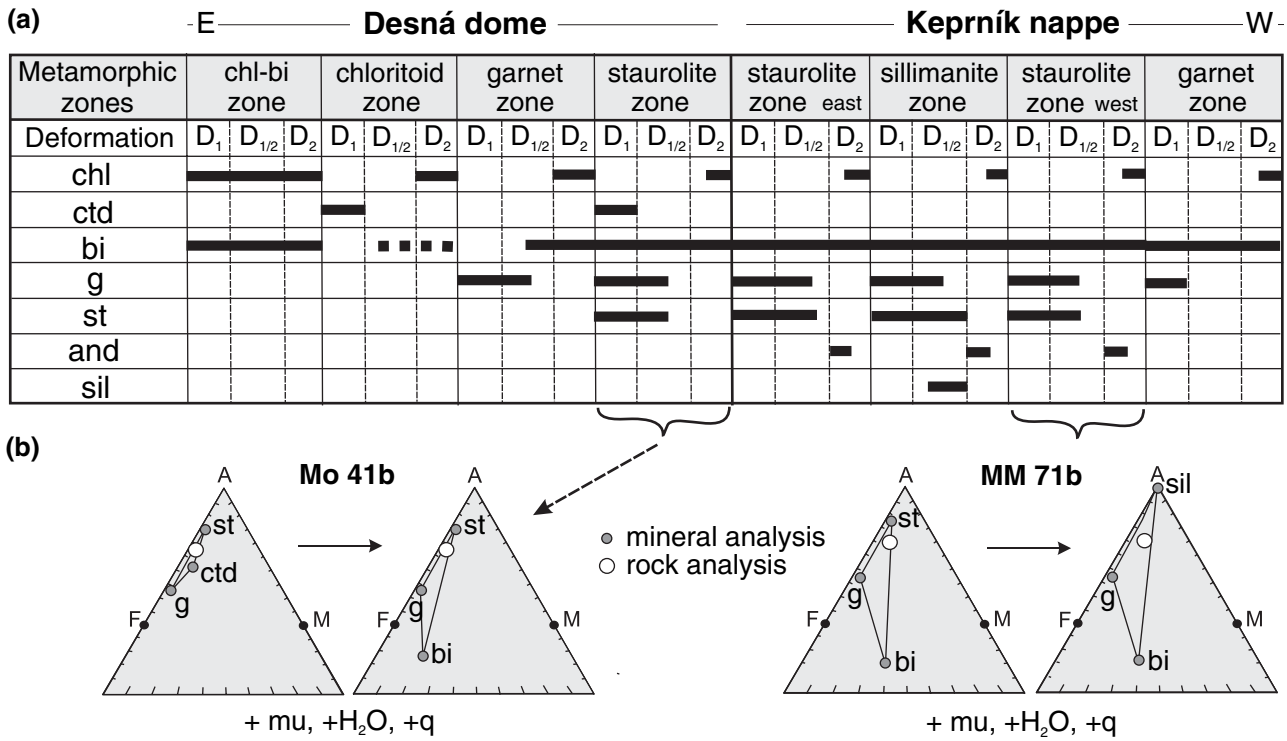

Fig. 4. (a) Crystallization–deformation relationships in individual zones, portrayed from the east to the west. Plagioclase, muscovite and quartz are always present. (b) Metamorphic evolution for the studied samples portrayed in AFM diagrams.

The external foliation defined by recrystallized lenses of quartz and plagioclase (0.3 mm), rare biotite and preferred orientation of muscovite is commonly crenulated and transposed into new S2 foliation oriented at high angle to the inclusion trails. Chlorite is a retrograde phase and grows locally parallel to the S2 planes or is randomly oriented.

Staurolite zone

The samples usually contain garnet, staurolite, biotite, ±chloritoid, muscovite, quartz, plagioclase, ilmenite and late chlorite. Garnet porphyroblasts (4 mm) include the S1 foliation marked by oriented inclusion trails of chloritoid, muscovite, quartz, plagioclase and ilmenite. Chloritoid (0.4 mm) is present only as inclusion in garnet, whereas staurolite is locally included at garnet rims and is widespread in the matrix (Fig. 5a). The inclusion trails are curved towards the garnet rims, indicating continuation of the garnet growth at the beginning of the S2 crenulation (Fig. 5b). Staurolite porphyroblasts have straight inclusion trails that are, in places, also curved towards the rim, and in some samples staurolite overgrows the crenulated foliation. Biotite and muscovite mark the S1 foliation, but they are stable also in the S2 cleavage that is commonly almost perpendicular to the inclusion trails. Chlorite replaces biotite or grows in the S2 cleavage.

Petrography: the Keprník nappe

The metamorphic zones are described from the east to the west.

Staurolite–(andalusite) zone – east

Micaschists from this zone contain staurolite, garnet, andalusite, muscovite, biotite, quartz, plagioclase, ilmenite and late chlorite. Porphyroblasts of staurolite (up to 2 cm) include garnet, biotite, ilmenite and quartz. Although the straight inclusion trails are commonly at high angles to the external foliation, in some cases, they are curved towards the rim indicating continuous growth at the start of the D2 deformation. Small garnet (up to 0.3 mm) is included in staurolite (Fig. 5c) or occurs in the matrix. Plagioclase porphyroblasts (0.3 mm) are randomly distributed in the matrix or are included in staurolite. Biotite (1.5 mm) commonly includes garnet, andalusite (1 mm) overgrows the S2 foliation and chlorite grows at the expense of biotite and staurolite. Chlorite is a retrograde phase.

Staurolite–sillimanite–(andalusite) zone

Micaschists from this zone are composed of staurolite, ±garnet, quartz, plagioclase, muscovite, biotite, sillimanite, andalusite, ilmenite and late chlorite. Garnet

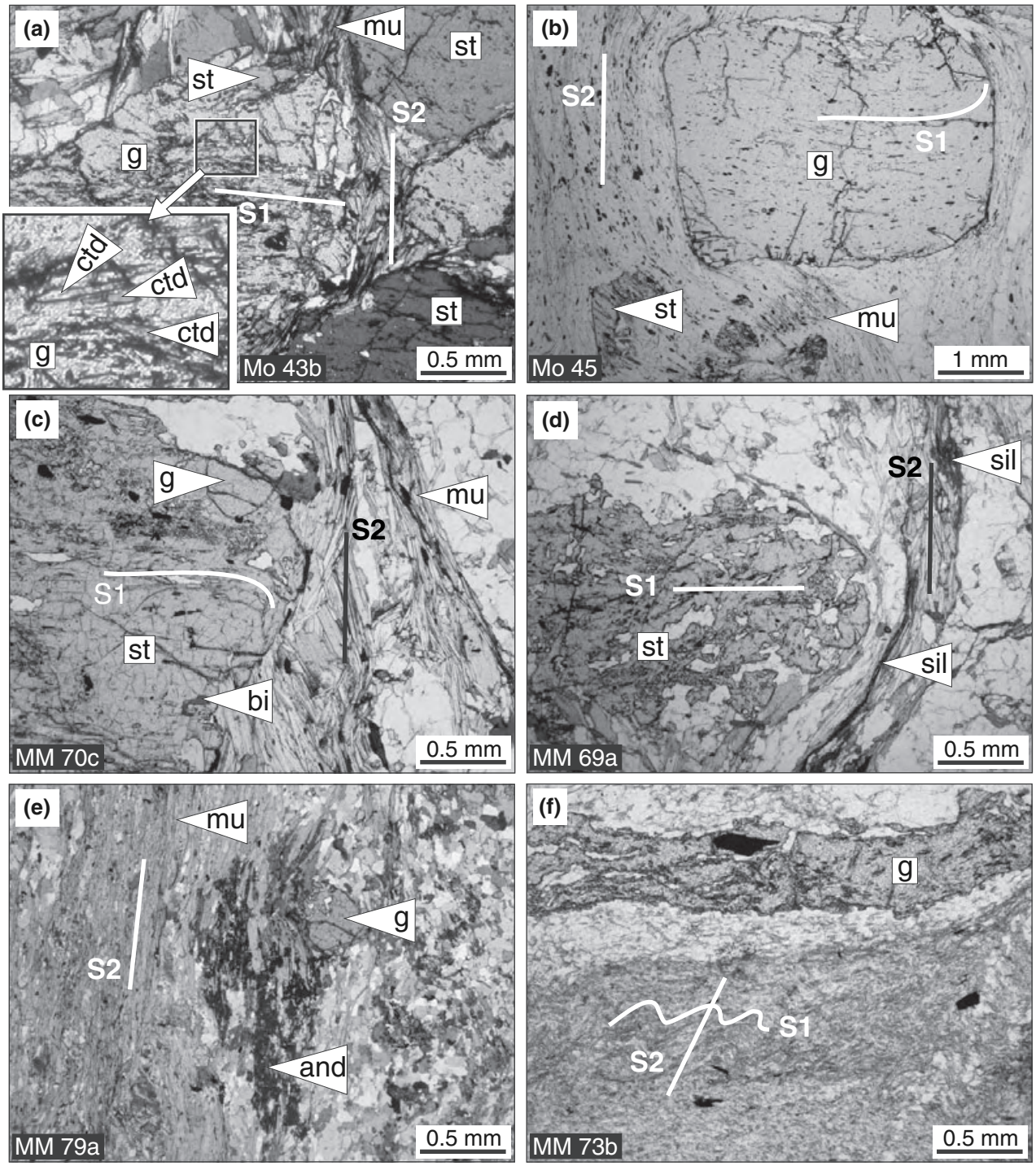

Fig. 5. Photomicrographs of metapelites showing crystallization-deformation relationships, plane polarized light. (a) Staurolite zone, Desná dome: inclusions of chloritoid and opaque minerals in garnet are perpendicular to external fabric. Staurolite is included at garnet rim. Inset shows detail of chloritoid inclusion. (b) Staurolite zone, Desná dome: straight inclusion trails curved towards the rim of garnet indicate its growth during D1 and D2 deformations. (c) Staurolite zone, Keprník nappe: Curved inclusion trails in staurolite rim show continuation of its growth during D2 deformation. Garnet is included at staurolite rim. (d) Staurolite–sillimanite–(andalusite) zone, Keprník nappe: staurolite with inclusions perpendicular to the external foliation marked by sillimanite. (e) Staurolite–sillimanite–(andalusite) zone, Keprník nappe: porphyroblast of andalusite overgrows the S2 foliation. (f) Garnet zone, Branná group, Keprník nappe: inclusions in an elongated garnet porphyroblast in the S2 foliation. The matrix is crenulated during D2 deformation.

porphyroblasts (0.1–1 mm) contain locally oriented quartz and ilmenite inclusion trails, indicating their growth in the S1 foliation. Staurolite (up to 3 cm) includes garnet, muscovite, biotite, quartz, plagioclase and ilmenite. Quartz and ilmenite trails in staurolite are straight and/or curved, indicative of its growth during S1 foliation and D2 crenulation (Fig. 5d). The straight inclusion trails are commonly at high angles to the external foliation, where muscovite and biotite-rich bands alternate with quartz–plagioclase bands in the S2 foliation. Fibrolitic sillimanite grows around staurolite, plagioclase or biotite in the S2 cleavage (Fig. 5d). Andalusite (up to 5 mm) contains quartz and ilmenite, and overgrows the S2 crenulation (Fig. 5e). Locally, biotite (1.5 mm) encloses garnet, and chlorite grows at contacts with biotite, garnet, staurolite and andalusite.

Staurolite–(andalusite) zone – west

Micaschists from this zone exhibit similar relations of porphyroblast growth as in the staurolite–sillimanite zone, but from the Al_2SiO_5 polymorphs contain only andalusite that is commonly overgrowing the S2 foliation.

Garnet zone

This zone is situated in the uppermost (westernmost) part of the Keprník nappe. The dominant foliation S2 is formed by fine-grained (0.1–0.5 mm) matrix of muscovite, biotite, quartz, plagioclase commonly retrogressed to white mica and rare chlorite. Crenulated S1 foliation is locally preserved in the hinge zones of F2 folds. There, oriented inclusion trails of quartz and micas in garnet (3 mm) and its shape give evidence of its growth during the S1 foliation (Fig. 5f).

PETROLOGY, MINERAL CHEMISTRY AND *P–T* EVOLUTION

Analytical procedures and abbreviations

Minerals have been analysed using the Cameca SX100 electron microprobe at the Institute of Geology, Czech Academy of Sciences and on CAM-SCAN S4 scanning electron microscope at the Institute of Geology, Charles University, Prague in point beam mode at 15 kV and 10 nA. Representative analyses are listed in Table 1. The mineral abbreviations used are: mu, muscovite; q, quartz; chl, chlorite; ctd, chloritoid; g, garnet; st, staurolite; bi, biotite; ky, kyanite; sil, sillimanite; and, andalusite; pa, paragonite; ma, margarite; pl, plagioclase; ilm, ilmenite; alm = Fe/(Ca + Fe + Mg + Mn); py = Mg/(Ca + Fe + Mg + Mn); grs = Ca/(Ca + Fe + Mg + Mn); sps = Mn/(Ca + Fe + Mg + Mn); the isopleth notation used is: x(g, st, ctd) = Fe/(Fe + Mg), z(g) = Ca/(Ca + Fe + Mg), m(g) = Mn/(Mn + Ca + Fe + Mg).

The overall pattern of the succession of metamorphic zones in the Desná dome and in the Keprník nappe indicates a higher metamorphic field gradient than in the southern Moravian windows and in the Velké Vrbno unit to the west. Several samples were studied in detail in order to determine their *P–T* evolution and to determine whether the higher geothermal gradient in the studied area is a late or an early phenomenon. Special attention was therefore paid to the determination of prograde conditions. Sample MM 71b from the staurolite–sillimanite zone of the Keprník nappe and sample Mo 41b from the staurolite zone of the Desná dome are presented in this section (Figs 2 & 6).

Sample MM 71b, staurolite–sillimanite transition: petrology and mineral chemistry

The sample contains bi + g + st + sil + mu + pl + ilm + q + chl. Muscovite and biotite form bands parallel to the foliation, alternating with quartz aggregates. Garnet (0.7 mm) contains few inclusions of quartz and ilmenite, is included in staurolite and is rarely present in the matrix. Porphyroblasts of staurolite (3.5 mm) contain numerous quartz and garnet inclusions (Fig. 6a). Biotite (1.5 mm) commonly includes garnet and in places is included in staurolite. Fibrolitic sillimanite forms clusters associated with staurolite or biotite, and is oriented preferentially parallel to the S2 crenulation (Fig. 6a). Chlorite is retrograde and is present in very small amount in the matrix, at contacts with biotite or staurolite.

Garnet is not zoned and there is no difference between garnet included in staurolite and matrix garnet ($alm_{77}prp_{10}grs_5sps_7$, $X_{Fe} = 0.88$–0.89; Fig. 7). Staurolite X_{Fe} value ranges between 0.84 and 0.85, the biotite X_{Fe} is 0.56–0.58 and Ti 0.10–0.11 p.f.u. Plagioclase has the anorthite content of 0.21–0.22.

Sample Mo 41b, chloritoid–staurolite transition: petrology and mineral chemistry

The sample contains ctd + bi + g + st + mu + pl + ilm + q + chl. The garnet porphyroblasts (4 mm) include chloritoid, plagioclase, muscovite, quartz and ilmenite. Relicts of chloritoid (0.5 mm) are included in garnet and are lacking in the matrix, while staurolite is widespread in the matrix where it includes biotite, muscovite, quartz and ilmenite (Fig. 6b). Inclusion trails within garnet are straight in the core and are curved towards the porphyroblast rims, with the internal part being perpendicular to the external foliation S2. In staurolite, the inclusion trails are generally straight. The matrix is dominated by crenulated muscovite and quartz-rich bands, contains plagioclase and rare biotite, and late chlorite locally grows in the S2 cleavage. From the succession of crystallization it is clear that prograde evolution starts with chloritoid and garnet followed by staurolite growth during the D1

Table 1. Representative analyses of the studied samples. (a) MM 71b, (b) Mo 41b.

Sample:	MM 71b g-core	MM 71b g-rim	MM 71b st-core	MM 71b st-rim	MM 71b bi	MM 71b mu	MM 71b chl	MM 71b pl
(a)								
SiO_2	36.93	37.16	26.52	26.77	36.02	46.36	24.83	62.09
TiO_2	0.00	0.00	0.53	0.56	1.85	0.60	0.16	0.00
Al_2O_3	21.07	21.33	54.76	55.16	20.61	37.51	23.74	23.83
FeO	34.14	34.16	14.22	13.96	20.39	0.77	27.32	0.23
MnO	3.13	3.39	0.19	0.23	0.00	0.00	0.00	0.00
MgO	2.46	2.61	1.56	1.39	8.87	0.41	13.35	0.00
CaO	1.83	1.83	0.00	0.00	0.00	0.00	0.00	4.68
Na_2O	0.00	0.00	0.00	0.00	0.00	1.35	0.00	9.11
K_2O	0.00	0.00	0.00	0.00	8.64	9.42	0.00	0.00
Total	99.56	100.49	97.78	98.07	96.38	96.42	89.40	99.94
Oxygen	12	12	48	48	11	11	18	12
Si	3.00	3.00	7.43	7.47	2.74	3.01	3.63	2.75
Ti	0.00	0.00	0.11	0.12	0.11	0.03	0.02	0.00
Al	2.02	2.02	18.09	18.13	1.85	2.87	4.10	1.24
Fe^{2+}	2.29	2.28	3.33	3.26	1.30	0.04	3.34	0.01
Mn	0.22	0.23	0.05	0.05	0.00	0.00	0.00	0.00
Mg	0.30	0.31	0.65	0.58	1.01	0.04	2.91	0.00
Ca	0.16	0.16	0.00	0.00	0.00	0.00	0.00	0.22
Na	0.00	0.00	0.00	0.00	0.00	0.17	0.00	0.78
K	0.00	0.00	0.00	0.00	0.84	0.78	0.00	0.00
$X_{Fe^{2+}}$	0.89	0.88	0.84	0.85	0.56	0.50	0.53	
x_{Alm}	0.77	0.77						
x_{Prp}	0.10	0.10					x_{An}	0.22
x_{Grs}	0.05	0.05					x_{Ab}	0.78
x_{Sps}	0.07	0.08					x_{Or}	0.00

Sample:	Mo 41b g-core	Mo 41b g-rim	Mo 41b ctd	Mo 41b st-core	Mo 41b st-rim	Mo 41b bi	Mo 41b mu	Mo 41b pl-in g	Mo 41b pl-core	Mo 41b pl-rim
(b)										
SiO_2	36.89	36.57	24.38	27.12	26.70	33.62	46.22	66.44	67.54	67.28
TiO_2	0.13	0.19	0.00	0.43	0.42	1.63	0.22	0.01	0.00	0.00
Al_2O_3	20.53	20.44	39.42	53.77	54.28	19.39	36.30	20.71	19.42	20.13
FeO	37.26	39.25	26.95	15.87	15.14	26.72	1.09	0.10	0.01	0.13
MnO	2.71	2.28	0.27	0.10	0.06	0.09	0.00	0.01	0.09	0.00
MgO	1.30	1.11	1.43	0.97	0.86	4.73	0.15	0.00	0.01	0.00
CaO	0.63	0.43	0.01	0.00	0.01	0.02	0.00	1.78	0.71	0.97
Na_2O	0.05	0.07	0.00	0.04	0.00	0.41	2.03	10.89	11.39	11.13
K_2O	0.00	0.01	0.00	0.00	0.01	8.86	8.46	0.06	0.05	0.06
Total	99.48	100.33	92.45	98.29	97.47	95.47	94.47	99.99	99.21	99.70
Oxygen	12	12	14	48	48	11	11	12	12	12
Si	3.03	2.99	2.55	3.85	3.81	2.71	3.08	2.91	2.98	2.95
Ti	0.01	0.00	0.00	0.05	0.05	0.10	0.01	0.00	0.00	0.00
Al	1.99	1.97	4.85	9.00	9.14	1.84	2.85	1.07	1.01	1.04
Fe^{2+}	2.56	2.69	2.35	1.88	1.81	1.80	0.06	0.00	0.00	0.01
Mn	0.19	0.16	0.02	0.01	0.01	0.01	0.00	0.00	0.00	0.00
Mg	0.16	0.14	0.22	0.20	0.18	0.57	0.01	0.00	0.00	0.00
Ca	0.06	0.04	0.00	0.00	0.00	0.00	0.00	0.08	0.03	0.05
Na	0.01	0.01	0.00	0.01	0.00	0.06	0.26	0.93	0.97	0.95
K	0.00	0.00	0.00	0.00	0.00	0.91	0.72	0.00	0.00	0.00
$X_{Fe^{2+}}$	0.94	0.95	0.91	0.90	0.91	0.76	0.81		0.03	0.05
x_{Alm}	0.81	0.86								
x_{Prp}	0.05	0.04					x_{An}	0.08	0.03	0.05
x_{Grs}	0.02	0.01					x_{Ab}	0.91	0.96	0.95
x_{Sps}	0.06	0.05					x_{Or}	0.00	0.00	0.00

phase. Garnet and staurolite grew until the beginning of the development of S2 crenulation.

Garnet is slightly zoned from core to rim (Fig. 7), with increasing almandine and decreasing pyrope, grossular and spessartine ($alm_{0.81\Rightarrow0.88}$ $prp_{0.05\Rightarrow0.04}$ $grs_{0.02\Rightarrow0.01}$ $sps_{0.07\Rightarrow0.04}$; $X_{Fe} = 0.94$–0.96). Chloritoid has X_{Fe} of 0.91–0.92. In other samples of the same locality, chloritoid has a similarly high X_{Fe} (0.88–0.89 and 0.94–0.95 in samples Mo 46 and Mo 43c, respectively). Staurolite is unzoned and its X_{Fe} value ranges between 0.90 and 0.91. The matrix biotite and biotite inclusions have similar composition with $X_{Fe} = 0.76$ and Ti = 0.10–0.11 p.f.u. Plagioclase is slightly zoned from An_3 in the core to An_5 at the rim, plagioclase in garnet has An_8.

Pseudosections

The pseudosections were calculated in the system Na_2O-CaO-K_2O-FeO-MgO-Al_2O_3-SiO_2-H_2O (NCKFMASH) for chl-ctd-bi-g-st-ky-sil-and-ma-pa-mu-pl-q and H_2O. Then, Mn was added to biotite, chlorite,

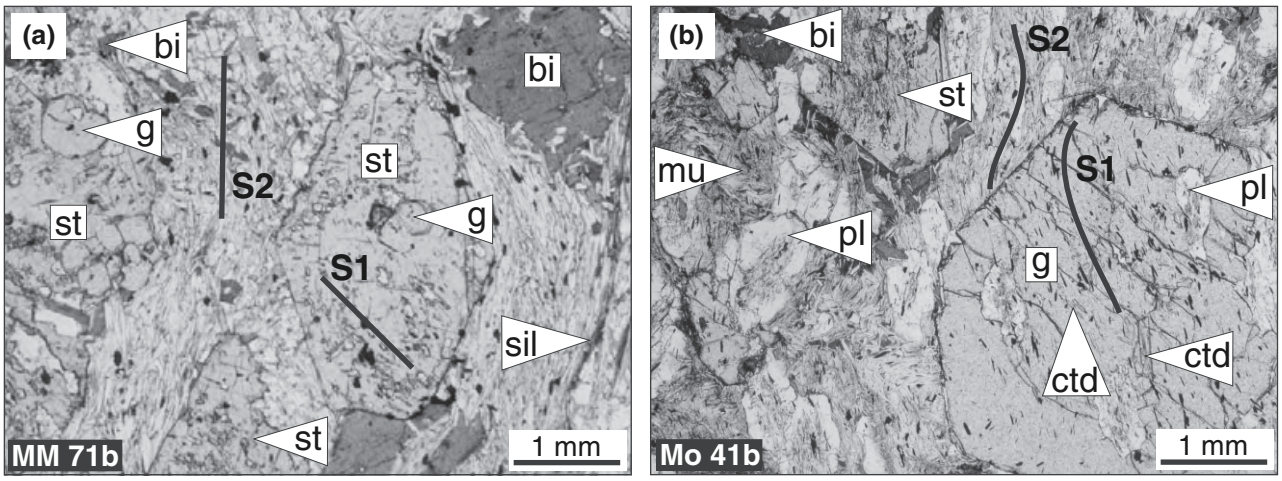

Fig. 6. Photomicrographs of the studied samples MM 71b and Mo 41b. (a) Staurolite–sillimanite–(andalusite) zone, Keprník nappe: staurolite with garnet inclusions, matrix is composed of muscovite, biotite, quartz and sillimanite. (b) Staurolite zone, Desná dome: garnet includes chloritoid and plagioclase, matrix is composed of staurolite, muscovite, biotite, plagioclase and quartz.

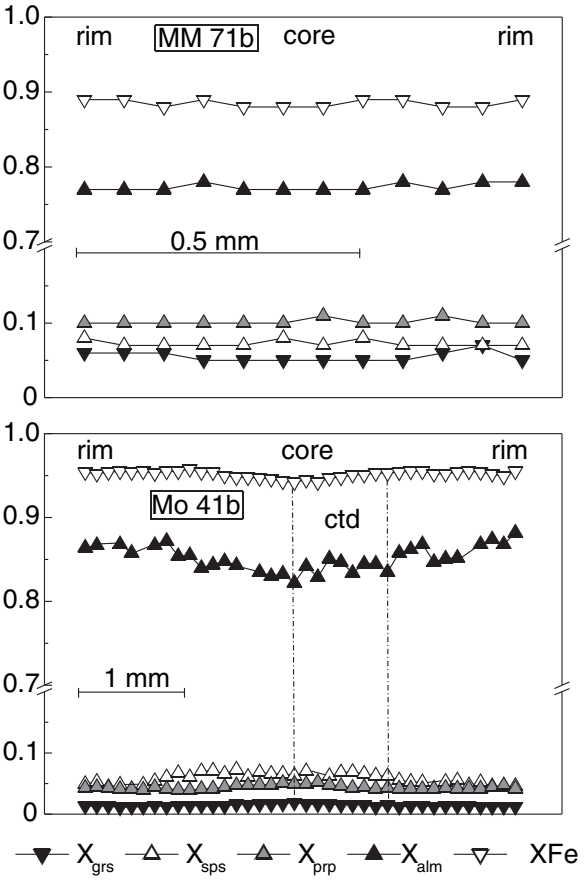

Fig. 7. Garnet profiles for samples MM 71b and Mo 41b.

chloritoid, staurolite and garnet to study its influence on garnet stability (Wang & Spear, 1991; Droop & Harte, 1995; Mahar *et al*., 1997). Muscovite, quartz and H_2O are taken to be in excess and the high-temperature parts of the pseudosections are metastable with respect to melt. For pseudosection calculations the rock compositions were used with all Fe treated as FeO, and with the molar amounts of the considered oxides recalculated to 100%. The fractionation of rock composition by porphyroblast growth is not considered. The calculations were performed using THERMOCALC 3.25 (Powell *et al*., 1998; 2005 upgrade) and the internally consistent thermodynamic data set 5.5 (Holland & Powell, 1998; November 2003 upgrade). Mixing models for most solid solutions were taken from White *et al*. (2001) and the THERMOCALC documentation (Powell & Holland, 2004). Plagioclase was formulated using the model of Holland & Powell (2003), the paragonite–muscovite solution formulated after Coggon & Holland (2002) and the paragonite-margarite solution as in Štípská *et al*. (2006). Mineral compositional and mole proportion isopleths were plotted for the phases of interest in order to study garnet growth and chemistry of chloritoid and staurolite.

P–T pseudosection for sample MM 71b, staurolite–sillimanite transition

The rock composition of the sample, MM 71b, was used for the modelling (in wt%: SiO_2 = 59.0, TiO_2 =1.10, Al_2O_3 = 19.95, FeO_{tot} = 9.26, MnO = 0.09, MgO = 2.17, CaO = 0.44, Na_2O = 1.11, K_2O = 3.30, P_2O_5 = 0.13; standard wet chemical methods). The major features in the NCKFMASH system involve stability of garnet above ~4 kbar (at < 630 °C), stability of staurolite between 520 °C (at ~2.3 kbar) and 665 °C (at ~7 kbar), and sillimanite stability above 590 °C (~4 kbar) and below ~7 kbar (at 665 °C) (Fig. 8a–c). With addition of Mn into the system, the stability limit of garnet is shifted to 510 °C and below 2 kbar (Fig. 8d, e). Muscovite is absent in the high-temperature and low-pressure part of the pseudosections.

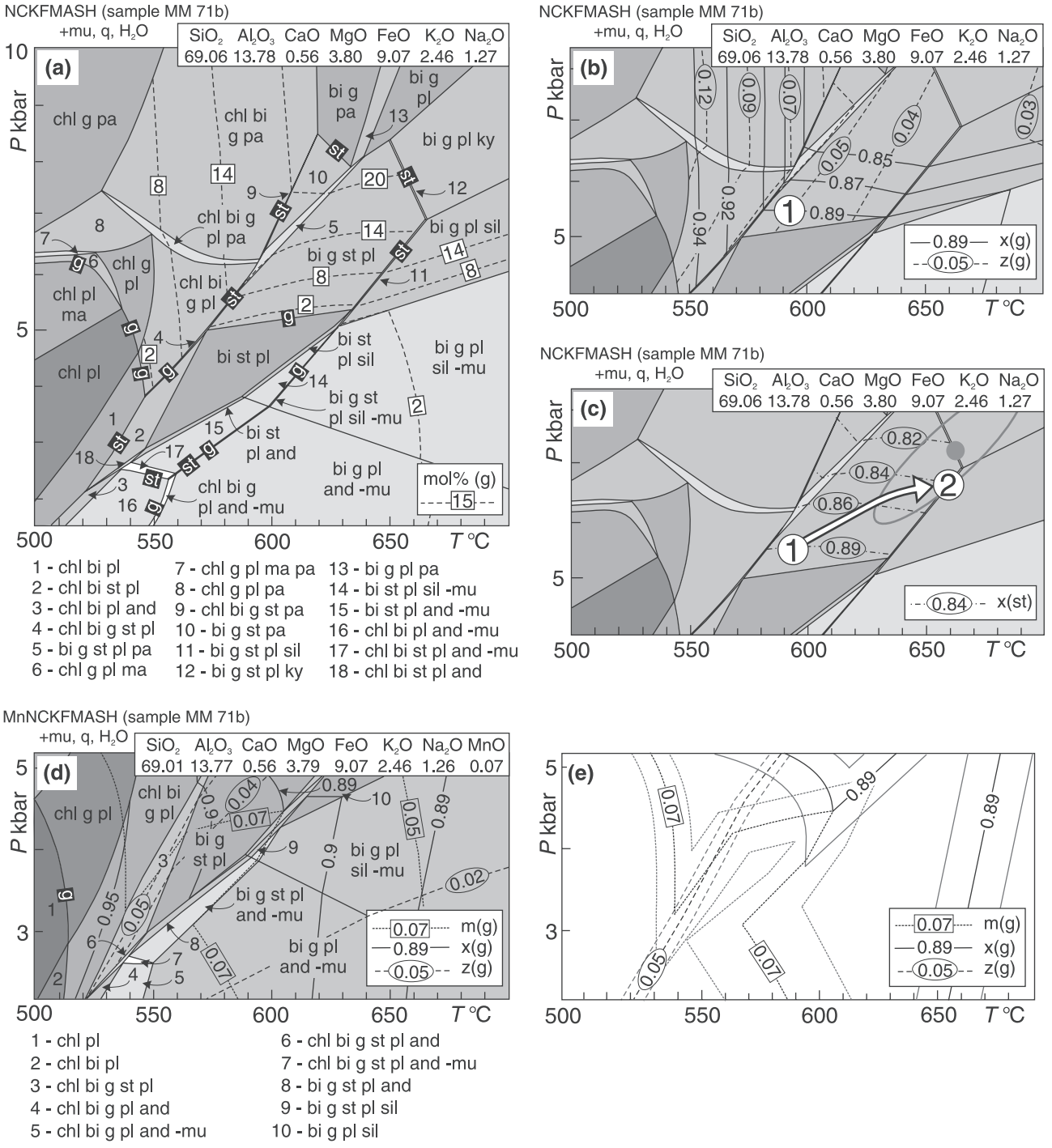

Fig. 8. Pseudosection for the micaschist sample MM 71b, the Keprník nappe. (a) NCKFMASH pseudosection with garnet mole proportions. (b) Compositional variables of garnet, point 1 indicates beginning of garnet growth. (c) Compositional variables of staurolite. Prograde *P–T* path is deduced from the assemblage and mineral compositions. Point 2 indicates peak metamorphic conditions deduced from staurolite–sillimanite transition. Result of average *P–T* calculation (grey ellipse) for metamorphic peak is shown with 1σ. (d) MnNCKFMASH pseudosection shows enlarged stability for garnet. (e) The compositional variables of garnet core with calculated uncertainties almost meet at ~4.5 kbar and 580 °C.

The sequence of growth in the sample involves garnet included in staurolite and matrix assemblage bi-g-st-sil-mu-pl-q. In the NCKFMASH system, the observed garnet composition (grs = 5%, X_{Fe} = 0.89) indicates growth in the trivariant assemblage bi-g-st-pl at 5.5 kbar and 590 °C that is inferred from the calculated molar and compositional isopleths of garnet (Fig. 8b–point 1). In the Mn-NCKFMASH system

(Fig. 8d, e), the isopleths meet in the area of 550–610 °C and 4–5 kbar, giving similar results for the beginning of garnet growth (grs = 5%, sps = 7%, $X_{Fe} = 0.89$). The observed continuation of staurolite growth that includes garnet and transition from staurolite to sillimanite in the matrix indicate temperature increase to 660 °C (Fig. 8c–point 2). The pressure of metamorphic peak is limited by the growth of sillimanite and by the absence of kyanite to the maximum of ~6.5 kbar. The average *P–T* calculations for the peak metamorphic assemblage in the matrix bi-g-st-sil-mu-pl (calculated with representative analyses, Table 1) yield 663 ± 29 °C and 7.3 ± 1.2 kbar, compatible with the results of the pseudosection modelling (Fig. 8c). Therefore, the prograde evolution deduced from the pseudosection starts at 550–610 °C and 4–5 kbar and continues to the peak at ~660 °C and 6.5 kbar.

Pseudosection for sample Mo 41b, chloritoid–staurolite transition

The rock composition of the sample, Mo 41b, was used for the modelling (in wt%: $SiO_2 = 43.4$, $TiO_2 = 2.36$, $Al_2O_3 = 35.2$, $FeO_{tot} = 9.52$, $MnO = 0.09$, $MgO = 0.55$, $CaO = 0.19$, $Na_2O = 2.78$, $K_2O = 4.00$, $P_2O_5 = 0.07$; standard wet chemical methods). The major features of the pseudosection in the NCKFMASH system involve garnet stability above ~3.5 kbar (at 540 °C) and staurolite stability between 510 °C (at ~2 kbar) and 670 °C (at ~7 kbar). With pressures increasing from ~2 to ~5.5 kbar, the lower stability limit of biotite increases from ~510 °C to ~590 °C; in a temperature range between 580 and 700 °C, the upper pressure stability limit of biotite shows only a slight variation between 5 and 6 kbar (Fig. 9a–c).

Sequentional growth observed in the thin section involves chloritoid and plagioclase included in garnet cores, staurolite included in garnet rims and matrix assemblage bi-g-st-mu-pl-q. This sequence is compatible with *P–T* path in the NCKFMASH pseudosection from the divariant field chl-ctd-g-pl-pa at 520–540 °C and ~4 kbar through the chloritoid-staurolite transition in the divariant field chl-ctd-g-st-pa and further through the staurolite-bearing fields to the trivariant bi-g-st-pl assemblage at 560–640 °C and 4–5 kbar (Fig. 9a). The observed X_{Fe} value (0.94–0.95) of garnet cores fits the calculated isopleths and indicates temperature of 550–560 °C, while the grossular content is slightly lower than that predicted by the pseudosection (Fig. 9c). The X_{Fe} of chloritoid of 0.91 is in a good agreement with temperature conditions deduced from the X_{Fe} of garnet, and additionally it indicates crossing of the chloritoid–staurolite transition slightly below 5 kbar (Fig. 9b–point 1). The composition of matrix staurolite and presence of biotite restrict peak conditions in the field of bi-g-st-pl to 5 kbar and 590–630 °C (Fig. 9b–point 2). The addition of Mn into the system enlarges garnet stability field below 2 kbar (at ~600 °C). Observed garnet composition ($sps_{0.06–0.05}grs_{0.01}$; $X_{Fe} = 0.95$) is close to the values in the field chl-ctd-g-st-pl-pa but the corresponding isopleths do not cross exactly there (Fig. 9d, e). The *P–T* path recorded by the assemblage and deduced from the pseudosection starts at 520–540 °C and ~3 kbar, crosses a well-anchored point at the chloritoid–staurolite transition at ~5 kbar and 550 °C and continues to the peak at 590–630 °C, slightly above 5 kbar. Insufficient number of independent reactions for the peak assemblage precluded average *P–T* calculations.

SOUTHERN SILESIAN DOMAIN, SUMMARY OF RESULTS

In the southern part of the Silesian domain studied, the metamorphic zones are from the east to the west biotite, garnet, chloritoid and staurolite in the autochthonous Desná domain, while almost the entire Keprník nappe is in the staurolite–sillimanite zone with late andalusite overprint. In the western part of the Keprník nappe, affected by late extensional shear zone, the grade decreases upwards to the staurolite and garnet zones.

The straight inclusion trails in garnet and staurolite show their crystallization mainly during the prograde deformational phase D1 and the high-angle curvatures in staurolite and garnet rims witness the change of deformational regime into D2 still during their growth (Fig. 5). The external foliation is commonly perpendicular or at high angles to the inclusion trails within the porphyroblasts, and in all the zones matrix foliation contains crenulated relicts of S1 in the hinge zones of microfolds. Matrix foliation is marked by muscovite, biotite, and in the Keprník nappe also by sillimanite. Crystallization of andalusite occurs later, as it grows in the S2 foliation or overgrows it. These deformational phases preserved as inclusion trails in porphyroblasts and in the matrix may be correlated with the burial and exhumational stages of Schulmann & Gayer (2000), but modified in that beginning of the second deformational stage is contemporaneous with prograde metamorphism.

A remarkable feature is the transition of staurolite to sillimanite, clearly achieved on a prograde path and indicating a higher geothermal gradient during prograde evolution, compared with a classical Barrovian terrane. Peak conditions for the sillimanite zone are 660 °C and 6.5 kbar which is equivalent to a transient geothermal gradient of 27 °C km^{-1} (Fig. 10). The transition of chloritoid to staurolite, preserved as inclusions in garnet of the staurolite zone is crossed at a relatively low pressure of 4.9 kbar at 550 °C, as deduced from the X_{Fe} of chloritoid and staurolite. Thus, the transient geothermal gradient during early prograde evolution is also elevated, and corresponds to 29 °C km^{-1} (Fig. 10). The late formation of andalusite indicates that during uplift, the metamorphic units have cooled along even higher geothermal gradient.

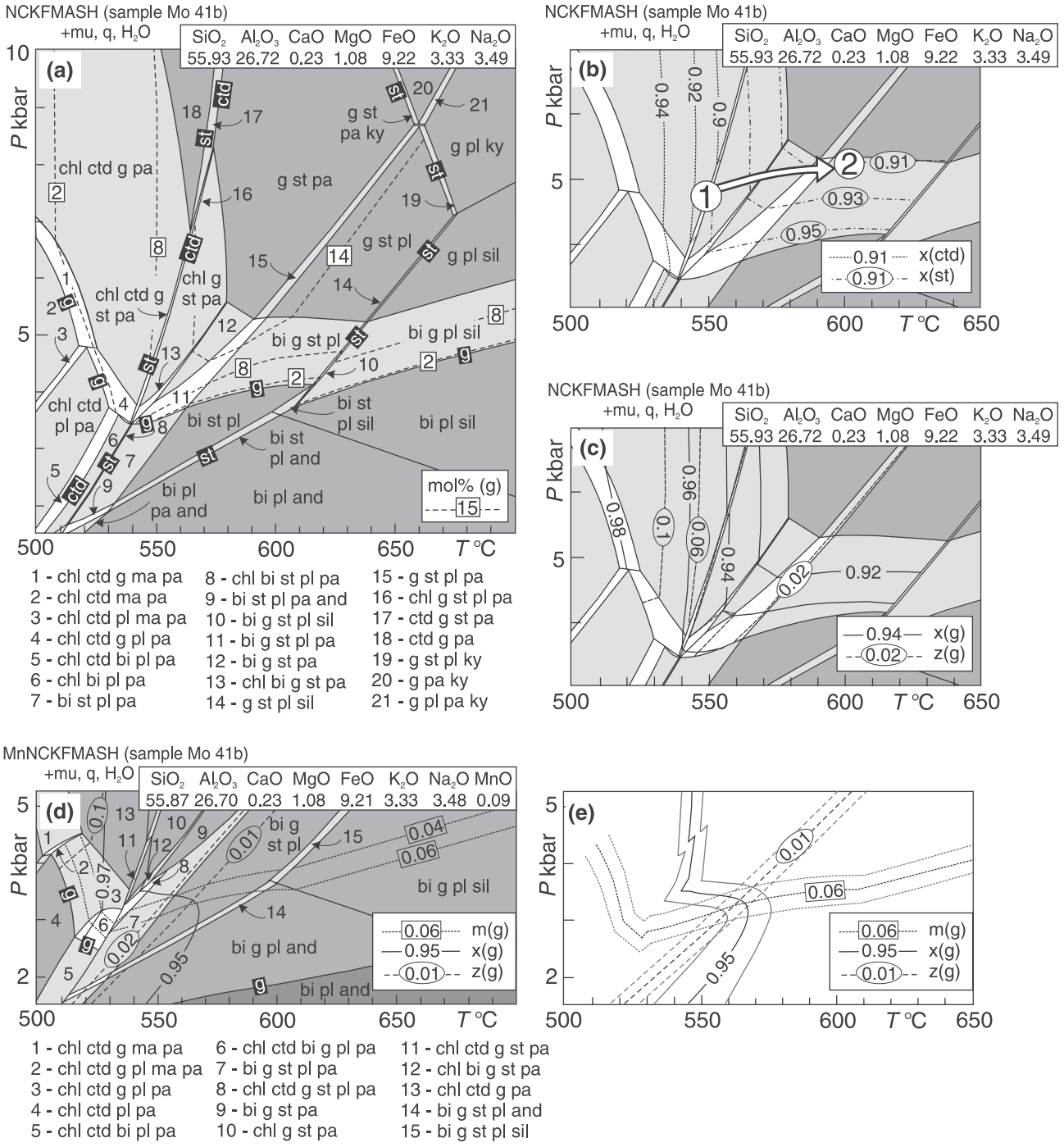

Fig. 9. Pseudosection for the micaschist sample Mo 41b, the Desná dome. (a) NCKFMASH pseudosection with garnet mole proportions. (b) Detail with chloritoid and staurolite compositional variables. Point 1 indicates crossing of chloritoid–staurolite transition at $x(\mathrm{ctd}) = 0.91$, point 2 indicates peak conditions, prograde P–T path is deduced from succession of mineral assemblages and mineral compositions. (c) Detail with garnet compositional variables. (d) In the MnNCKFMASH pseudosection garnet stability is enlarged. (e) Compositional variables in the MnNCKFMASH system with calculated uncertainties for garnet core.

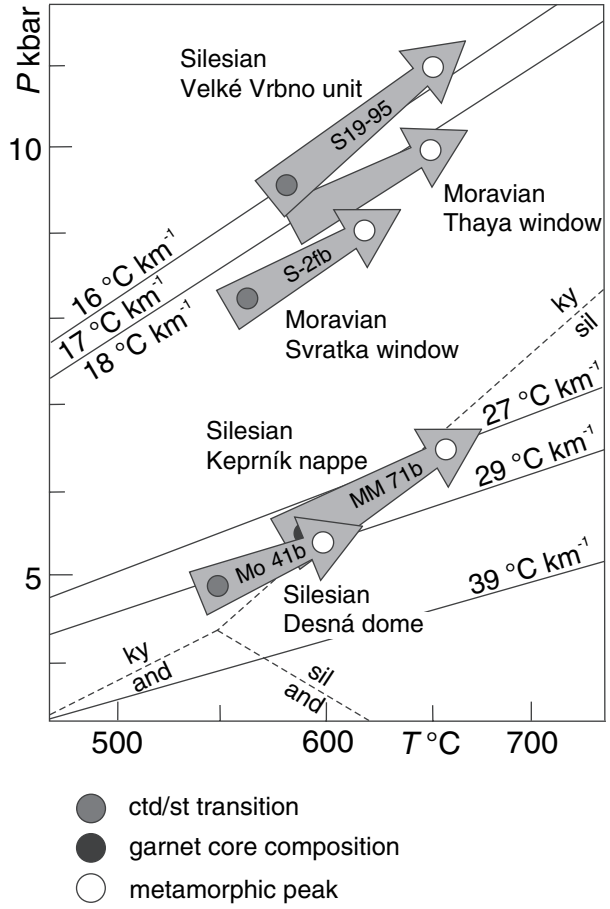

Fig. 10. Summary of prograde P–T paths from individual areas of the Moravo-Silesian zone shows a strong variation in transient prograde geothermal gradients. Gradients are calculated for density 2.7 g cm^{-3}.

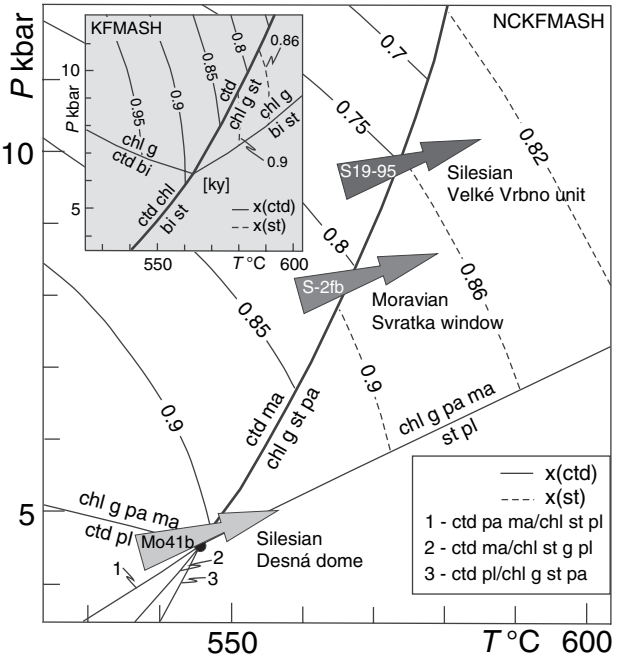

Fig. 11. Chloritoid–staurolite transition in the P–T grid for the NCKFMASH and KFMASH systems, with compositional isopleths of chloritoid and staurolite. The chloritoid–staurolite transition of the studied sample from the Desná dome (Mo 41b) is compared with other samples from the Moravo-Silesian domain (sample S2fb from Konopásek *et al.*, 2002; sample S19-95 from Štípská *et al.*, 2006).

DISCUSSION AND CONCLUSIONS

Chloritoid–staurolite transition as an indicator of dP/dT

In the KFMASH grid, the univariant reaction ctd = st + g + chl is a good indicator of temperature, and the X_{Fe} of minerals involved increases up pressure along the reaction (Fig. 11). Therefore, the X_{Fe} value of chloritoid and staurolite at this transition is also an indicator of pressure and consequently of dP/dT conditions along a prograde path. Such indications were already studied and reported for example by Schreyer (1988); Ballèvre *et al.* (1989) and Konopásek *et al.* (2002).

With the addition of Na_2O and CaO into the model system, the reaction in the NCKFMASH grid changes into ctd + ma = chl + g + st + pa, but remains at similar P–T conditions (Štípská *et al.*, 2006). This reaction is common for some Al-rich pelites (Štípská *et al.*, 2006), in others, the chloritoid–staurolite transition remains as a narrow field inherited from the KFMASH ctd = st + g + chl univariant reaction (Fig. 9). The addition of these components into the KFMASH grid modifies to some extent the slope and the position of x(ctd) and x(st) isopleths (Fig. 11), which affects the absolute determinations of dP/dT slightly, but has minor effect for relative comparisons.

We suggest that the determination of prograde conditions from chloritoid–staurolite transition is therefore a very useful method that has a significant potential in determining prograde geothermal gradients, with similar importance as for example the beginning of garnet growth and its compositional isopleths (Vance & Mahar, 1998). An advantage in determining prograde conditions from chloritoid–staurolite equilibria is that a point on a prograde path is defined by crossing of three lines inferred from just two minerals: the chloritoid to staurolite univariant transition and the X_{Fe} isopleths for chloritoid and staurolite.

Contrasting transient prograde geothermal gradients at the eastern margin of the Bohemian massif

The chloritoid–staurolite transition has been used to determine prograde conditions already on three places in the Moravo-Silesian domain: in this study, in the Svratka window (Konopásek *et al.*, 2002) and in the Velké Vrbno unit (Štípská *et al.*, 2006). These studies show that significant differences in the transient

prograde geothermal gradient exist in the adjacent areas of the Moravo-Silesian continental accretionary wedge and along its strike: the transition from chloritoid to staurolite during early prograde evolution is crossed in the range of 5–9.5 kbar, resulting in the differences of transient geothermal gradient to the order of 29–16 °C km^{-1} (Figs 1 & 10). The continuation of prograde path in the high-grade zones is characterized by transition of staurolite into sillimanite or into kyanite (Štípská & Schulmann, 1995; Schulmann & Gayer, 2000; Štípská *et al*., 2000, 2006), and coincides with the areas of higher and lower early geothermal gradients, respectively, determined from chloritoid–staurolite equilibria (Fig. 10).

The study of prograde metamorphic conditions shows that the thermal variations in the accreted Moravo-Silesian region existed already during early burial and were maintained until the late burial stage. Therefore, the whole area probably started thickening with initially variable geotherms and this implication should be considered in future tectonic considerations.

Possible causes of contrasting or high-prograde gradients

Similar features of contrasting prograde *P–T* paths in adjacent areas observed along the Moravo-Silesian domain have been reported elsewhere, for example from the NW Iberian Massif (Reche *et al*., 1998; Arenas & Catalan, 2003), the New England crystalline complex (Spear *et al*., 1990, 1995, 2002; Armstrong *et al*., 1992; Kohn *et al*., 1992; Florence *et al*., 1993), or from the classical terranes of the Scottish Caledonides (Baxter *et al*., 2002). Most of the models, including the above-mentioned examples, attempt to explain elevated geothermal gradients at metamorphic peak or rarely even for the period of prograde path by additional heat supply from magmas. Pre-compressional extension causing thinning of isotherms and increasing geothermal gradients is suggested as an alternative source of heat (Wickham & Oxburgh, 1986; Thompson, 1989a,b; Thompson *et al*., 2001). A region that is compressed and buried shortly after an extensional period should record an elevated geothermal gradient in its metamorphic evolution. Such process was suggested for example to explain metamorphism in the Slave province of the NW Canadian Shield (Thompson, 1989a,b), in the Palaeozoic belt of New England (Armstrong *et al*., 1992), in the Variscan Vosges (Schulmann *et al*., 2002) and in the Moldanubian domain of the Bohemian Massif (Schulmann *et al*., 2005; Štípská & Powell, 2005a,b).

The geological record of high-prograde metamorphic gradient exemplified by the southern Silesian domain reveals deep Devonian basins accompanied by bimodal back-arc volcanism (Patočka & Valenta, 1990; Kalvoda *et al*., 2003) and also numerous syn- to late tectonic Carboniferous intrusions (Schulmann & Gayer, 2000). In contrast, a shallow marine Devonian sedimentation and lack of Carboniferous intrusions are characteristic for the areas of low-prograde geothermal gradient and underthrusting of thick continental plate (Konopásek *et al*., 2002; Štípská *et al*., 2006). The logical explanation of the higher geothermal gradient during burial is therefore the inherited heat from Devonian rifting, already suggested by Schulmann & Gayer (2000). The high heat flow is possibly maintained by syn- to late tectonic Carboniferous intrusions that certainly provide additional heat for widespread sillimanite–andalusite areas and the cordierite–sillimanite zone. However, the relative and temporal role of Devonian extension and Carboniferous magmatism on metamorphic evolution may be resolved only if both metamorphic and magmatic events are dated in detail.

ACKNOWLEDGEMENTS

This work was financially supported by the Charles University Grant Agency (270/2005/B-GEO/PrF), the Czech Geological Survey (CGS 90-903 104) and the Czech National Grant Agency (205-05-2187). P. Štípská also acknowledges financial support from the French National Grant Agency (no. 06-1 148784). M. Košuličová benefited from financial support of the French embassy during her stays at the University Louis Pasteur in Strasbourg, France. We gratefully acknowledge valuable discussions with K. Schulmann and we thank P. Pitra for reading the early version of the manuscript. V. Böhmová from the Geological Institute of the Czech Academy of Sciences and J. Haloda from the Czech Geological Survey are thanked for operating the microprobe. We are grateful to M. Okrusch and an anonymous reviewer for constructive reviews and to D. Robinson for careful editorial work.

REFERENCES

Albee, A. L., 1972. Metamorphism of pelitic schists: reaction relations of chloritoid and staurolite. *Geological Society of America Bulletin*, **83,** 3249–3268.

Arenas, R. & Catalan, J. R. M., 2003. Low-P metamorphism following a Barrovian-type evolution. Complex tectonic controls for a common transition, as deduced in the Mondonedo thrust sheet (NW Iberian Massif). *Tectonophysics*, **365,** 143–164.

Armstrong, T. R., Tracy, R. J. & Hames, W. E., 1992. Contrasting styles of Taconian, Eastern Acadian and Western Acadian metamorphism, central and western New England. *Journal of Metamorphic Geology*, **10,** 415–426.

Ayres, M. V. & Vance, D., 1997. A comparative study of diffusion profiles in Himalayan and Dalradian garnets: constraints on diffusion data and the relative duration of the metamorphic events. *Contributions to Mineralogy and Petrology*, **128,** 66–80.

Ballèvre, M., Pinardon, J. L., Kienast, J. R. & Vuichard, J. P., 1989. Reversal of Fe-Mg partitioning between garnet and staurolite in eclogite-facies metapelites from the Champtoceaux nappe (Brittany, France). *Journal of Petrology*, **30,** 1321–1349.

Baratoux, L., Lexa, O., Cosgrove, J. W. & Schulmann, K., 2005. The quantitative link between fold geometry, mineral fabric

and mechanical anisotropy: as exemplified by the deformation of amphibolites across a regional metamorphic gradient. *Journal of Structural Geology*, **27,** 707–730.

Baxter, E. F., Ague, J. J. & Depaolo, D. J., 2002. Prograde temperature-time evolution in the Barrovian type-locality constrained by Sm/Nd garnet ages from Glen Clova, Scotland. *Journal of the Geological Society of London*, **159,** 71–82.

Bell, T. H. & Welch, P. W., 2002. Prolonged Acadian orogenesis: revelations from foliation intersection axis (FIA) controlled by monazite dating of foliations in porphyroblasts and matrix. *American Journal of Science*, **302,** 549–581.

Cháb, J., Mixa, P., Vaněček, M. J. & Žáček, V., 1994. Evidence of an extentional tectonics in the NW of the Hrubý Jeseník Mts (the Bohemian Massif, Central Europe). *Bulletin of Czech Geological Survey*, **69,** 7–15.

Coggon, R. & Holland, T. J. B., 2002. Mixing properties of phengitic micas and revised garnet-phengite thermobarometers. *Journal of Metamorphic Geology*, **20,** 683–696.

Droop, G. T. R. & Harte, B., 1995. The effect of Mn on the phase relations of medium-grade pelites: constraints from natural assemblages on petrogenetic grid topology. *Journal of Petrology*, **36,** 1549–1578.

Enami, M., 1998. Pressure-temperature path of the Sanbagawa prograde metamorphism deduced from grossular zoning of garnet. *Journal of Metamorphic Geology*, **16,** 97–106.

Florence, F. P., Spear, F. S. & Kohn, M. J., 1993. P–T paths from northwestern New Hampshire – metamorphic evidence for stacking in a thrust/nappe complex. *American Journal of Science*, **293,** 939–979.

Franke, W., 2000. The mid-European segment of the Variscides: tectonostratigraphic units, terrane boundaries and kinematic evolution. In: *Orogenic Processes: Quantification and Modelling in the Variscan Belt, Special Publication 179* (eds Franke, W., Haak, V., Oncken, O. & Tanner, D.), pp. 35–63. Geological Society, London.

Hartley, A. J. & Otava, J., 2001. Sediment provenance and dispersal in a deep marine foreland basin: the Lower Carboniferous Culm Basin, Czech Republic. *Journal of the Geological Society of London*, **158,** 137–150.

Hladil, J., 1994. Microfacies of Devonian limestones in Moravia (part II.-Review of discerned microfacies). *Zemní plyn a nafta*, **39,** 19–70.

Höck, V., 1975. Mineralzonen in Metapeliten und Metapsammiten der Moravischen Zone in Niederoesterreich. *Mitteilungen der Geologischen Gesselschaft*, **66–67,** 49–60.

Holland, T. J. B. & Powell, R., 1998. An internally consistent thermodynamic data set for phases of petrological interest. *Journal of Metamorphic Geology*, **16,** 309–343.

Holland, T. & Powell, R., 2003. Activity-composition relations for phases in petrological calculations: an asymmetric multicomponent formulation. *Contributions to Mineralogy and Petrology*, **145,** 492–501.

Kalvoda, J., Leichmann, J., Bábek, O. & Melichar, R., 2003. Brunovistulian terrane (Central Europe) and Istanbul zone (NW Turkey): Late Proterozoic and Paleozoic tectonostratigraphic development and paleogeography. *Geologica Carpathica*, **54,** 139–152.

Kohn, M. J., Orange, D. L., Spear, F. S., Rumble, D. & Harrison, T. M., 1992. Pressure, temperature, and structural evolution of West Central New Hampshire – hot thrusts over cold basement. *Journal of Petrology*, **33,** 521–556.

Konopásek, J., Schulmann, K. & Johan, V., 2002. Eclogite-facies metamorphism at the eastern margin of the Bohemian Massif – subduction prior to continental underthrusting? *European Journal of Mineralogy*, **14,** 701–713.

Kröner, A., Štípská, P., Schulmann, K. & Jaeckel, P., 2000. Chronological constraints on the pre-Variscan evolution of the northeastern margin of the Bohemian Massif, Czech Republic. In: *Orogenic Processes: Quantification and Modelling in the Variscan Belt; Special Publication 179* (eds Franke, W., Haak, V., Oncken, O. & Tanner, D.), pp. 175–197. Geological Society, London.

Mahar, E. M., Baker, J. M., Powell, R., Holland, T. J. B. & Howell, N., 1997. The effect of Mn on mineral stability in metapelites. *Journal of Metamorphic Geology*, **15,** 223–238.

Miyashiro, A., 1961. Evolution of metamorphic belt. *Journal of Petrology*, **2,** 277–311.

Patočka, F. & Valenta, J., 1990. Geochemistry of metatrachytes and metarhyolites of the southern part of the Devonian Vrbno Group in the Horní Město area and teconic setting of origin of the metavolcanic protoliths. *Časopis pro mineralogii a geologii*, **35,** 41–64.

Powell, R. & Holland, T., 2004. Course notes for "THERMOCALC workshop 2004: calculating metamorphic phase equilibria" (ETH Zurich). (CD-ROM).

Powell, R., Holland, T. & Worley, B., 1998. Calculating phase diagrams involving solid solutions via non-linear equations, with examples using THERMOCALC. *Journal of Metamorphic Geology*, **16,** 577–588.

Reche, J., Martínez, F. J. & Arboleya, M. L., 1998. Low- to medium-pressure Variscan metamorphism in Galicia (NW Spain): evolution of a kyanite-bearing synform and associated bounding antiformal domains. In: *What Drives Metamorphism and Metamorphic Reactions? Special Publications 138* (eds Trefoar, P. J. & O'Brien, P. J.), pp. 61–69. Geological Society, London.

Rozkošný, I. & Souček, J., 1989. Contribution to the petrology of the Žulová Massif mantle. *Acta Universitatis Carolinae, Geologica*, **2,** 165–197.

Schreyer, W., 1988. Experimental studies on metamorphism of crustal rocks under mantle pressures. *Mineralogical Magazine*, **52,** 1–26.

Schulmann, K. & Gayer, R., 2000. A model for a continental accretionary wedge developed by oblique collision: the NE Bohemian Massif. *Journal of the Geological Society of London*, **157,** 401–416.

Schulmann, K., Schaltegger, U., Ježek, J., Thompson, A. B. & Edel, J. B., 2002. Rapid burial and exhumation during orogeny: thickening and synconvergent exhumation of thermally weakened and thinned crust (Variscan orogen in Western Europe). *American Journal of Science*, **302,** 856–879.

Schulmann, K., Kröner, A., Hegner, E. *et al*., 2005. Chronological constraints on the pre-orogenic history, burial and exhumation of deep-seated rocks along the eastern margin of the Variscan orogen, Bohemian Massif, Czech Republic. *American Journal of Science*, **305,** 407–448.

Selverstone, J. & Spear, F. S., 1985. Metamorphic P–T paths from pelitic schists and greenstones from the Southwest Tauern Window, Eastern Alps. *Journal of Metamorphic Geology*, **3,** 439–465.

Souček, J., 1978. Metamorphic zones of the Vrbno and Rejvíz series, the Hrubý Jeseník Mountains, Czechoslovakia. *Tschermaks mineralogische und petrographische Mitteilungen*, **25,** 195–217.

Spalla, M. I., Carminati, E., Ceriani, S., Oliva, A. & Battaglia, D., 1999. Influence of deformation partitioning and metamorphic re-equilibration on P–T path reconstruction in the pre-Alpine basement of the central Southern Alps (Northern Italy). *Journal of Metamorphic Geology*, **17,** 319–336.

Spear, F. S., 1988. The Gibbs method and Duhem's theorem: The quantitative relationships among P, T, chemical potential, phase composition and reaction progress in igneous and metamorphic system. *Contributions to Mineralogy and Petrology*, **99,** 249–256.

Spear, F. S. & Selverstone, J., 1983. Quantitative P–T paths from zoned minerals: theory and tectonic applications. *Contributions to Mineralogy and Petrology*, **83,** 348–357.

Spear, F. S., Hickmott, D. D. & Selverstone, J., 1990. Metamorphic consequences of thrust emplacement, Fall Mountain, New-Hampshire. *Geological Society of America Bulletin*, **102,** 1344–1360.

Spear, F. S., Kohn, M. J. & Paetzold, S., 1995. Petrology of the regional sillimanite zone, west-central New Hampshire, Usa,

with implications for the development of inverted isograds. *American Mineralogist*, **80,** 361–376.
Spear, F. S., Kohn, M. J., Cheney, J. T. & Florence, F., 2002. Metamorphic, thermal, and tectonic evolution of central New England. *Journal of Petrology*, **43,** 2097–2120.
St Onge, M. 1987. Zoned poikiloblastic garnets: P–T paths and syn-metamorphic uplift through 30 km of structural depth, Wopmay orogen, Canada. *Journal of Petrology*, **28,** 1–21.
Štípská, P. & Powell, R., 2005a. Constraining the P–T path of a MORB-type eclogite using pseudosections, garnet zoning and garnet-clinopyroxene thermometry: an example from the Bohemian Massif. *Journal of Metamorphic Geology*, **23,** 725–743.
Štípská, P. & Powell, R., 2005b. Does ternary feldspar constrain the metamorphic conditions of high-grade meta-igneous rocks? Evidence from orthopyroxene granulites, Bohemian Massif. *Journal of Metamorphic Geology*, **23,** 627–647.
Štípská, P. & Schulmann, K., 1995. Inverted metamorphic zonation in a basement-derived nappe sequence, eastern margin of the Bohemian Massif. *Geological Journal*, **30,** 385–413.
Štípská, P., Schulmann, K. & Höck, V., 2000. Complex metamorphic zonation of the Thaya dome: result of buckling and gravitational collapse of an imbricated nappe sequence. In: *Forced Folds and Fractures, Special Publication 169* (eds Cosgrowe, J. W. & Ameen, M. S.), pp. 197–211. Geological Society, London.
Štípská, P., Pitra, P. & Powell, R., 2006. Separate or shared metamorphic histories of eclogites and surrounding rocks? An example from the Bohemian Massif. *Journal of Metamorphic Geology*, **24,** 219–240.
Stüwe, K. & Powell, R., 1995. PT paths from modal proportions: application to to the Koralm Complex, eastern Alps. *Contributions to Mineralogy and Petrology*, **119,** 83–93.
Suess, F. E., 1912. Die Moravischen Fenster und ihre Beziehung zum Grundgebirge des Hohen Gesenkes. *Akademie der Wissenschaften, Denkschrift Matematisch-Naturwissenschaftliche Klasse*, **88,** 541–631.
Suess, F. E., 1926. *Intrusionstektonik und Wandertektonik im variszichen Grundgebirge*. Verlag Borntträger, Berlin.
Thompson, P. H., 1989a. An empirical model for metamorphic evolution of the Archean Slave Province and adjacent Thelon Tectonic Zone, north-western Canadian Shield. In: *Evolution of Metamorphic Belts, Special Publications 43* (eds Daly, J. S., Cliff, R. A. & Yardley, B. W. D.), pp. 245–263. Geological Society, London.
Thompson, P. H., 1989b. Moderate overthickening of thinned sialic crust and the origin of granitic magmatism and regional metamorphism in low-P-high-T terranes. *Geology*, **17,** 520–523.
Thompson, A. B., Tracy, R. J., Lyttle, P. T. & Thompson, J. B., 1977. Prograde reaction histories deduced from compositional zonation and mineral inclusions in garnet from the Gassetts schists, Vermont. *American Journal of Science*, **277,** 1152–1167.
Thompson, A. B., Schulmann, K., Ježek, J. & Tolar, V., 2001. Thermally softened continental extensional zones (arcs and rifts) as precursors to thickened orogenic belts. *Tectonophysics*, **332,** 115–141.
Vance, D. & Mahar, E., 1998. Pressure-temperature paths from P–T pseudosections and zoned garnets: potential, limitations and examples from the Zanskar Himalaya, NW India. *Contributions to Mineralogy and Petrology*, **132,** 225–245.
Wang, P. & Spear, F. S., 1991. A field and theoretical-analysis of garnet + chlorite + chloritoid + biotite assemblages from the tri-state (Ma, Ct, Ny) area, USA. *Contributions to Mineralogy and Petrology*, **106,** 217–235.
White, R. W., Powell, R. & Holland, T. J. B., 2001. Calculation of partial melting equilibria in the system Na_2O-CaO-K_2O-FeO-MgO-Al_2O_3-SiO_2-H_2O (NCKFMASH). *Journal of Metamorphic Geology*, **19,** 139–153.
Wickham, S. M. & Oxburgh, E. R., 1986. A rifted tectonic setting for Hercynian high-thermal gradient metamorphism in the Pyrenees. *Tectonophysics*, **129,** 53–69.
Žáček, V., 1996. Retrograded eclogite from the Staré Město Belt, NE margin of the Bohemian Massif. *Journal of the Czech Geological Society*, **41,** 167–175.
Zeh, A., 2001. Inference of a detailed P–T path from P–T pseudsections using metapelitic rocks of variable composition from a single outcrop, Shackleton Range, Antarctica. *Journal of Metamorphic Geology*, **19,** 329–350.
Zeh, A. & Millar, I. L., 2001. Metamorphic evolution of garnet-epidote-biotite gneiss from the Moine Supergroup, Scotland, and geotectonic implications. *Journal of Petrology*, **2,** 529–554.

Received 3 May 2006; revision accepted 26 September 2006.

5. Parry, M., **Štípská**, P., Schulmann, K., Hrouda, F., Ježek, J. & Kröner, A. (1997). Tonalite sill emplacement at an oblique plate boundary: NE margin of the Bohemian massif. *Tectonophysics*, 280, 61-81.

6. Kröner, A., **Štípská**, P., Schulmann, K. & Jaeckel, P. (2000). Chronological constraints on the pre-Variscan evolution of the northeastern margin of the Bohemian Massif, Czech Republic. In: Franke, W., Altherr, R., Haak, V., Oncken, O., Tanner, D. (Eds), Orogenic processes – quantification and modelling in the Variscan belt of central Europe. *Geological Society London, special publications*, 179, 175-197.

7. **Štípská** P., Schulmann K., Thompson, A.B., Ježek, J. & Kröner A. (2001). Thermo-mechanical role of a Cambro-Ordovician paleorift during the Variscan collision: the NE margin of the Bohemian Massif. In: Schulmann, K., Franke, W., Andersen, T.B. (Eds), Paleozoic Orogenesis and Crustal Evolution of the European Lithosphere. *Tectonophysics*, 332, 239-253.

8. Lexa O., **Štípská** P., Schulmann K., Baratoux L. & Kröner A. (2005). Contrasting textural record of two distinct metamorphic events of similar P−T conditions and different durations. *Journal of Metamorphic Geology*, 23, 649-666.

ELSEVIER

Tectonophysics 280 (1997) 61–81

TECTONOPHYSICS

Tonalite sill emplacement at an oblique plate boundary: northeastern margin of the Bohemian Massif

Matthew Parry [a,*], Pavla Štípská [b], Karel Schulmann [b], František Hrouda [b], Josef Ježek [c], Alfred Kröner [d]

[a] *Department of Geology, Imperial College, Prince Consort Road, London, SW7 2BP, UK*
[b] *Institute of Petrology and Structural Geology, Faculty of Science, Charles University, Albertov 6, Prague, Czech Republic*
[c] *Institute of Applied Mathematics and Computer Science, Faculty of Science, Charles University, Albertov 6, Prague, Czech Republic*
[d] *Institut für Geowissenschaften, Johannes Gutenberg Universität, Saarstraße 21, Postfach 3980, D-6500 Mainz 1, Germany*

Received 20 March 1996; accepted 6 December 1996

Abstract

A tonalitic sill has been examined at the Variscan transpressive boundary of the Lugian and Silesian plates at the NE margin of the Bohemian Massif. A structural, petrological and geochronological study reveals that it was emplaced syn-tectonically with major ductile shearing in lower crustal rocks. Magmatic and pre-rheological critical melt percentage (RCMP) fabrics are concordant with the hanging wall structures but discordant with those of the footwall. The AMS study shows the predominance of flattening strain at the margins and plane strain fabrics in the core. Numerical modelling of AMS fabrics is in good agreement with the hypothesis of magma flow and deformation in oblique transpression. A tectonic model was developed explaining emplacement and syn-tectonic deformation of progressively cooled tonalitic intrusion.

Keywords: magma emplacement; plate boundary; anisotropy of magnetic sucsceptibility; Variscan belt

1. Introduction

This work deals with a tonalitic sill emplaced along an oblique collisional boundary at the eastern margin of the Bohemian Massif. Similar cases were found along other collisional boundaries, for example, the tonalitic intrusions along the Insubric Line (Schmid et al., 1989) or the Great Tonalite Sill of Alaska (Ingram and Hutton, 1994). These sills are very long bodies separating different terranes and are associated with transpressional regimes. All show fault-controlled magmatism in which the melts intrude an active contractional fault, which in general terms cannot create space as in extensional or strike-slip regimes (Hutton, 1988). Therefore, it is generally accepted that these sills are large dykes whose propagation is driven by magma overpressure at the tip (Lister and Kerr, 1991). Hutton (1992) states that the tonalite sheets exploit active shear planes because these represent important structural anisotropies, and the deformation of the sill reduces the cohesion parallel to the shear planes. The emplacement mechanism involves sheet wedging which is able to overcome the orogenic contractional stresses.

To date quantitative fabric studies of magmatic bodies, such as finite strain and anisotropy of mag-

* Corresponding author.

PII S0040-1951(97)00146-7

netic susceptibility (AMS) analysis, have been limited to large-scale plutons (Guineberteau et al., 1987; John and Blundy, 1993) and no analyses exist dealing with the mechanism of dyke intrusion in compressional fields. An understanding of the fabric development of syn-tectonically intruding dykes in conjunction with structural relationships in the surrounding country rock is essential to more fully understand the dynamics of tonalite sill emplacement at obliquely convergent plate boundaries.

We present here the result of a study on the emplacement of a tonalitic body 1 km thick and over 60 km long, situated between two continental plates at the northeastern margin of the Bohemian Massif (Fig. 1). We provide information on the relationship of internal structures of the sill with respect to the country rocks and describe the finite strain pattern using micro-structural and AMS analysis. The tonalite is considered as syn-tectonic on the basis of the following three criteria: (1) its shape is extremely elongate parallel to the regional fabric; (2) it shows structural concordance of foliation and lineation with one phase of the regional deformation; (3) it displays a continuum of fabric development from magmatic, through pre-rheological critical melt percentage (RCMP) to solid-state deformation with decreasing temperatures; this is the main criterion for recognising syn-tectonic intrusions (Paterson et al., 1989). We propose a mechanical model that accounts for magma propagation and cooling along the plate boundary during Variscan continental collision.

2. Geological setting

The eastern margin of the Bohemian Massif is characterized by oblique collision of the Moldanubian terrane with the easterly Pan-African Brunovistulian micro-continent as defined by Dudek (1980). The major collisional structure was recognized at the beginning of this century by Suess (1912, 1926) who developed the concept of large-scale Moldanubian overthrusting over an easterly-lying Moravian foreland along the whole 300 km length of the NE–SW-trending orogenic front.

At the northeastern margin of the Bohemian Massif there are two major units, the Lugian upper plate and the Silesian domain, representing the strongly deformed and imbricated Brunovistulian lower plate (Fig. 1). The Lugian domain is represented by high-grade rocks with protolith ages of 500–510 Ma (Oliver et al., 1993). The Silesian consists of imbricated Pan-African basement and Devonian cover sequences with inverted Barrovian metamorphic zonation. These plates are separated by the Staré Město belt whose rocks are derived partly from the mantle and partly from lower crustal rocks of the Lugian domain.

The general structure of the Staré Město belt (Štípská et al., 1995,) is characterized by NE–SW-trending lithologies. The base is marked by boudins of spinel peridotites along strongly retrograde schists derived from the lower plate. Above are located banded amphibolites intercalated with anatectic schists derived from the Lugian plate. These are intruded by the tonalite sill. In the hanging wall of the tonalite, a band of strongly sheared gabbros occurs and the top of the Staré Město tectonic sequence is formed by a strongly retrogressed metasedimentary unit (Fig. 2). In the northern part of the Staré Město sequence, the gabbroic belt is tectonically repeated below the banded amphibolites and spinel peridotite boudins.

3. Structural geology and petrology of the area

3.1. D1 high-temperature structures of wall rocks

The banded amphibolite unit in the footwall of the tonalite sill consists essentially of layers of fine-grained, sometimes garnet-bearing amphibolites, amphibole-bearing schists and acidic rocks. This layering is clearly metamorphic and represents at least D1. Transitions between layers are commonly gradual and sometimes sharp. This compositional banding dips north-northwest at shallow angles and is often deformed by isoclinal intrafolial folds and pinch and swell structures (D1). These show that during this deformation a low viscosity contrast existed between the layers, and hence indicates high-temperature conditions of deformation. The amphibolites dissipate into diffuse pockets of coarse-grained plagioclase and amphibole-bearing melts sometimes associated with normal shear bands and boudin neck zones.

The amphibole–clinopyroxene–plagioclase assemblage indicates a transition from upper amphi-

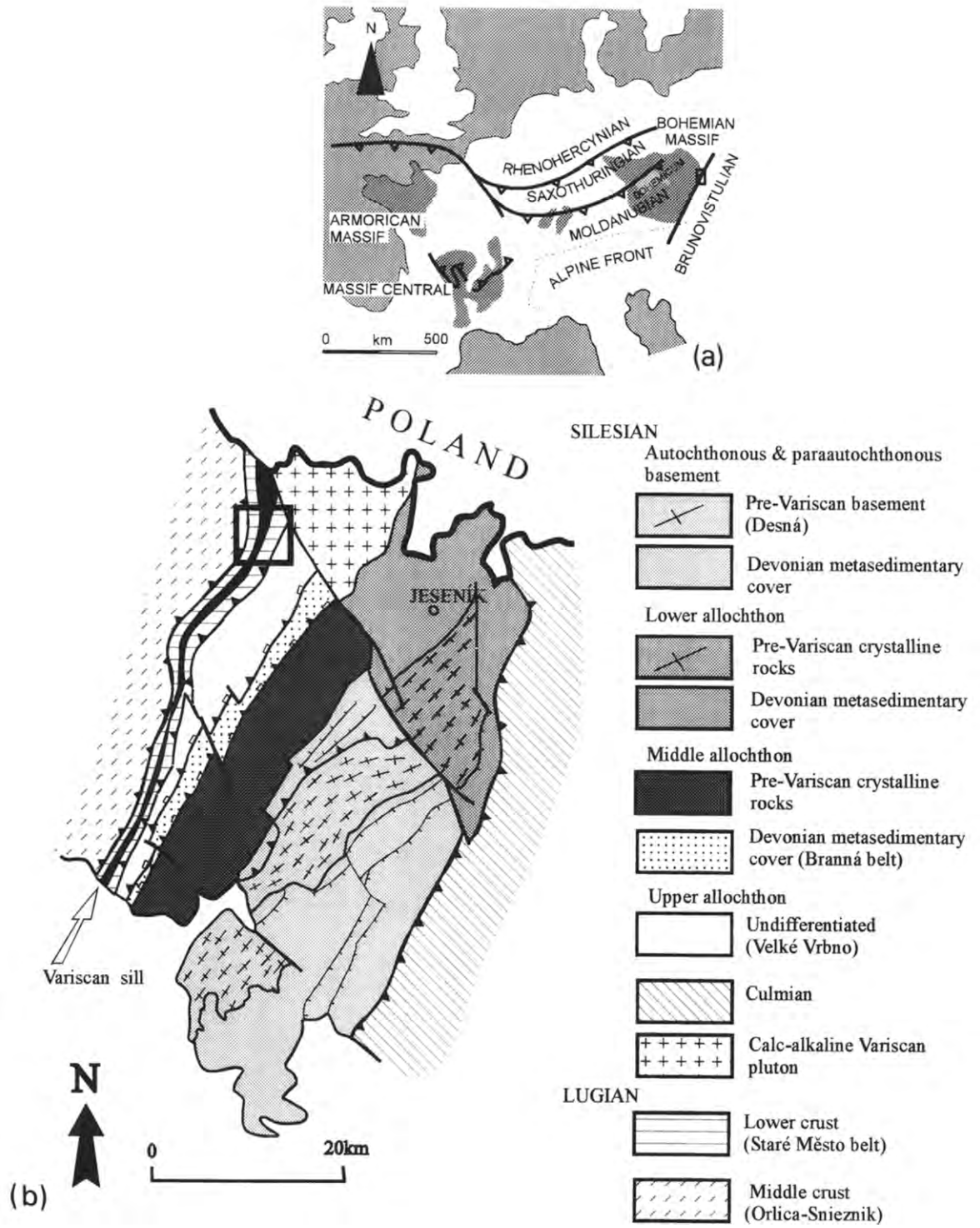

Fig. 1. Location map of the European Variscides, Bohemian Massif and the field area on the northeastern margin.

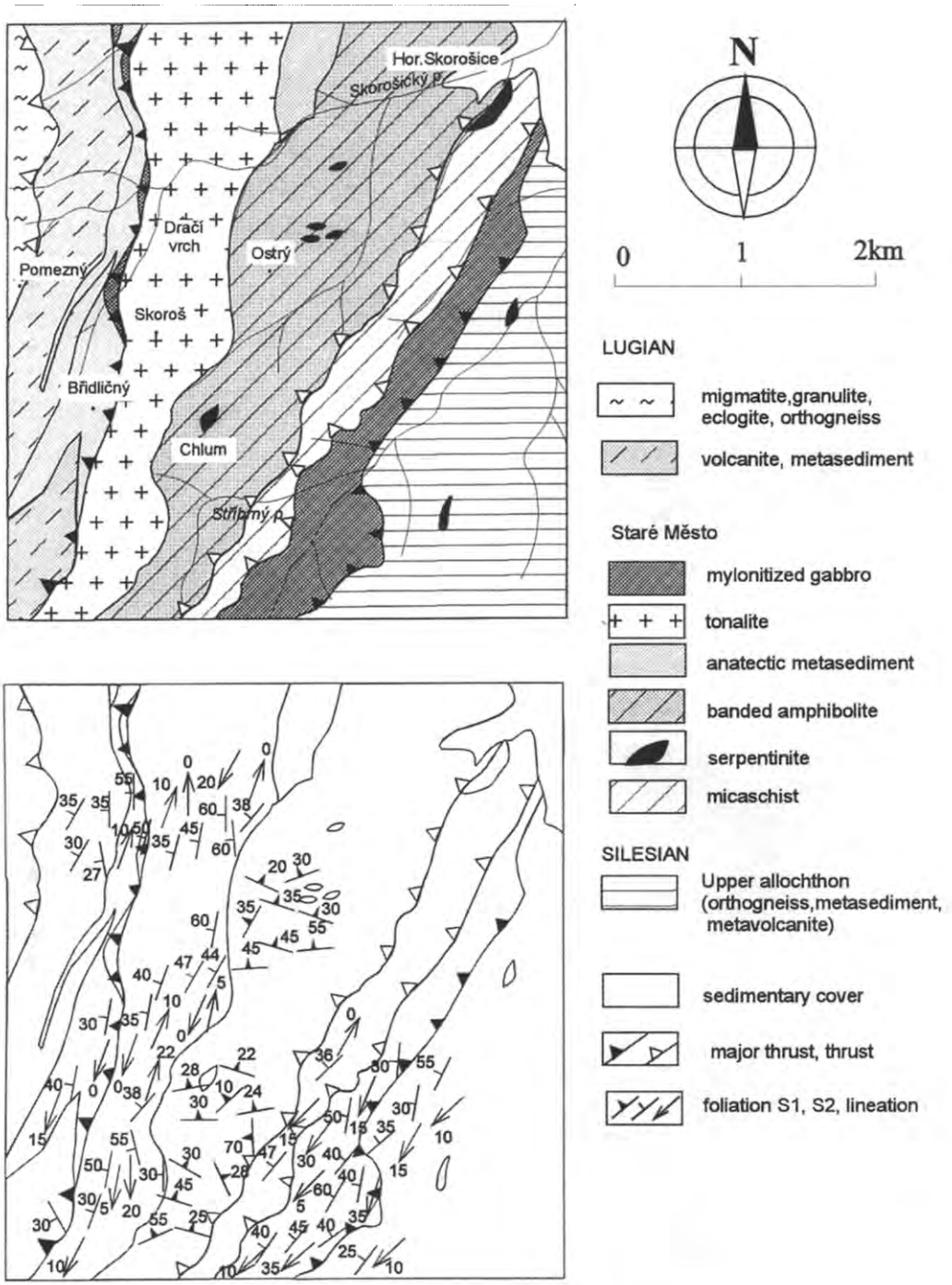

Fig. 2. (a) Lithological map of the northern part of the Staré Město belt. (b) Structural data for the same area.

bolite to granulite facies conditions with temperatures around 800°C (Fig. 4). These petrographic observations are in good agreement with temperature estimates of 750–850°C calculated using the amphibole–plagioclase thermometry of Holland and Blundy (1994). The pressure of this metamorphic event has been calculated at 8–10 kbar using the Grt–Hbl–Pl–Qtz barometry of Kohn and Spear (1989). Partly anatectic associated metasediments are marked by the mineral assemblage Grt–Pl–Qtz–Sil–Bt yielding temperatures of 800–900°C using Grt–Bt thermometry of Indares and Martignole (1985). Pressures estimated using Grt–Bt–Pl–Qtz barometry (Hodges and Crowley, 1985) are 7 to 9 kbar (Fig. 4). These *P–T* conditions show an exceptionally high thermal gradient for M1 metamorphism connected with high-temperature deformation D1 marked by a very low viscosity contrast between mafic and acid material. The compositional banding dips north-northwest at shallow angles. Single zircon evaporization gives Cambro–Ordovician ages of 500.5 ± 0.6 Ma to 505 ± 6 Ma for this metamorphic event.

3.2. D2 deformation

In the hanging wall of the tonalite is a thin layer of boudinaged and strongly sheared gabbros deformed during D2. The rock consists of banded mylonites dipping uniformly to the northwest at moderate angles sometimes refolded by intrafolial isoclinal folds. Intense stretching lineations plunge shallowly to the southwest. The gabbroic belt below the banded amphibolites is generally strongly deformed. However, in low-strain areas the original magmatic structures are represented by magmatic layering S0, strongly variable grain sizes of plagioclase and amphibole and original intrusive contacts of trondhjemite and basaltic dykes. The gabbros are heterogeneously deformed by ductile shear zones and are converted to banded mylonites in high-strain areas. The mylonitic foliation S2 dips moderately to the northwest and bears an intense stretching lineation plunging to the southwest. Sigmoidal amphibole porphyroclasts are occasionally preserved indicating top-to-the-NE movement. The mylonitic foliation is refolded by tight folds with NE-trending hinges and occasionally by sheath folds. The deformation of amphibole and plagioclase occurred via dynamic recrystallization by sub-grain rotation, leading to the development of monomineralic sharply separated layers. In contrast to the D1 fabric, which is produced by high-temperature static annealing, this mylonitic pattern is produced by a D2 deformational strain rate sensitive process.

The temperature of mylonitic deformation has been calculated at 700–750°C using plagioclase–amphibole thermometry (Holland and Blundy, 1994) on dynamically recrystallized grains. The pressure estimates based on Grt–Hbl–Qtz–Pl barometry (Kohn and Spear, 1989) yield 8–10 kbar for the recrystallized matrix. The mineral Pl–Cum–Hb assemblage in recrystallized gabbros is locally replaced by Opx–Hbl–Pl indicating a temperature increase during D2 (Spear, 1991). This is in agreement with an increasing An component towards the rim of recrystallized plagioclase.

D2 deformation of banded amphibolites in the footwall of tonalitic sill is represented by steep brittle–ductile NE-trending shear zones filled by granitic to pegmatitic melts (Fig. 3).

3.3. D3 greenschist facies deformation

The primary structures and the D2 banded mylonites in gabbros are affected by a heterogeneous network of steep D3 shear zones that were active during greenschist facies conditions. These are characterized by intense crenulation of anisotropic banded mylonites. The S3 cleavage strikes NE–SW and bears a sub-horizontal stretching lineation. The regions between late shear zones are affected by large-scale upright gentle folding with sub-horizontal NE-trending axes. This late folding affected probably also high-temperature fabric D1 in banded amphibolites.

The metasedimentary unit with migmatitic relics at the top of the sequence is strongly reworked under greenschist facies conditions which, because of thermal conditions, could be attributed to D3. This deformation is marked by development of an intense mylonitic NW-dipping foliation, upright NE-trending folds, SW-plunging lineation and numerous top-to-the-NE sense of shear criteria.

3.4. Tonalite structures

The sill composition varies over many kilometres between tonalite and granite. The tonalite includes

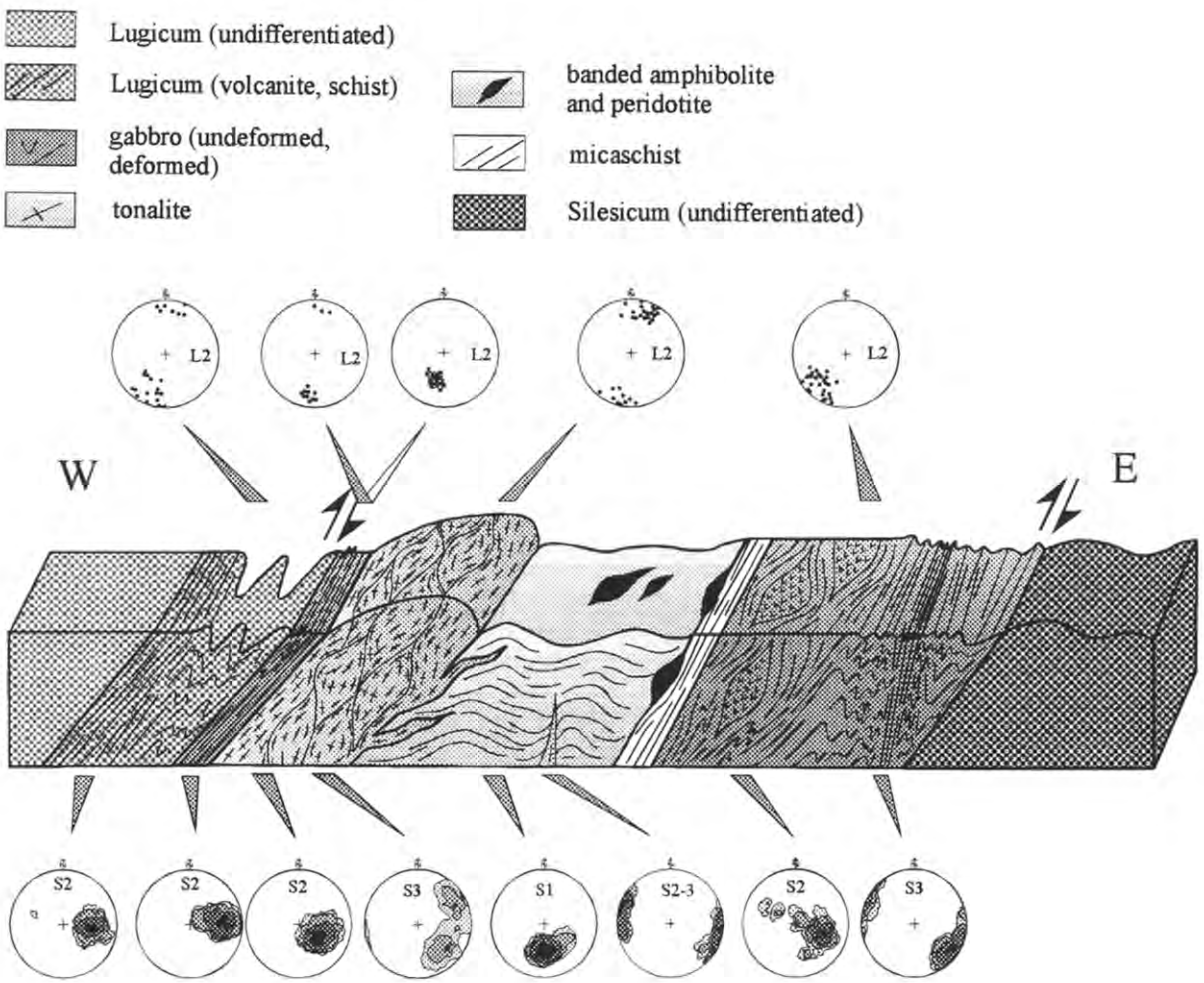

Fig. 3. Block diagram illustrating structural data. Orientation diagrams display orientation of foliations S1, S2, S3 and lineations L2. Contoured at multiples of uniform distribution per about 50 measurements per diagram. Lineation diagrams from gabbros are also taken from southern area out of the map (crosses).

sheet-like xenoliths of metamorphic rocks with pre-intrusion polyphase structures, which increase in number towards the top. Rare mafic xenoliths also occur, and it is unclear whether these are wall rock xenoliths or mantle enclaves. Intrusion of the sill is constrained at 339 ± 7 Ma by the $^{207}Pb/^{206}Pb$ single zircon evaporation technique.

At mesoscopic scale the sill shows a planar fabric of variable intensity. The fabric at the base of the sill is defined by preferred orientation of amphibole and biotite and by alignment of plagioclase. Near the base plagioclase phenocrysts are occasionally tiled indicating magmatic deformation and a high content of crystals in the melt (Den Tex, 1969). Towards the top of the sill the fabric intensity increases so that biotite and feldspars form elongate aggregates and the quartz is arranged in ribbons. The foliation dips uniformly to the northwest and bears a sub-horizontal mineral lineation characterized by alignment of feldspars and linear arrangement of mica aggregates. Rare pre-full crystallization lock-up shear bands (Ingram and Hutton, 1994) indicate a predominantly dextral sense of shear. Leucocratic dykes crosscutting the foliated tonalite are either folded parallel to or cut and translated along foliation planes, indicating the syn-tectonic nature of intrusion. The

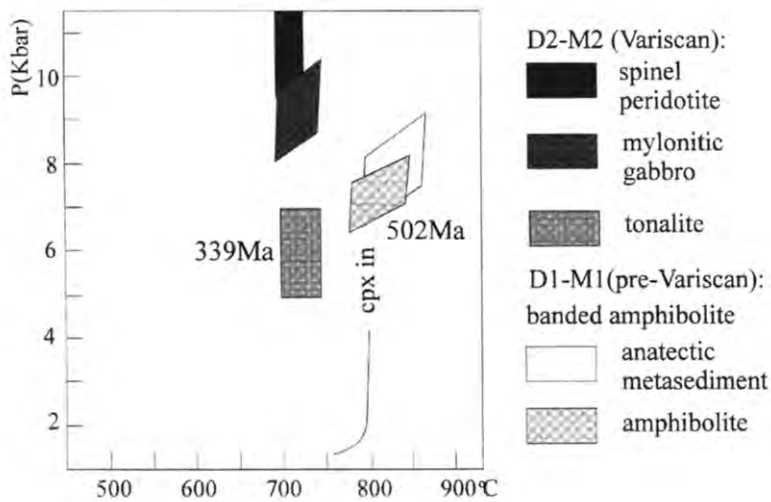

Fig. 4. *P–T* plot of the studied area. Two metamorphic events are distinguished: Variscan with temperatures around 700–750°C at variable pressures, and pre-Variscan MP granulite facies metamorphism.

structural pattern of the tonalite is geometrically and kinematically compatible with D2 structures in the mylonitized gabbros, but is discordant with respect to the D1 fabric in the banded amphibolites.

Late greenschist conjugate D3 shears cut the tonalite indicating a kinematic continuum of NE–SW extension (Fig. 3). These late structures may be correlated with D3 greenschist facies shear zones in the wall rock. (Fig. 4.)

The depth of crystallization of the tonalite according to the total aluminium content of the amphiboles (Schmidt, 1992) is 6–7 kbar. Typical values quoted in the literature for the solidus temperature of tonalite of around 700°C (De Yoreo et al., 1989) are in agreement with calculated temperatures at 710–730°C using the Hb–Plg thermometry of Holland and Blundy (1994).

4. Tonalite micro-structural evolution

The tonalite displays a micro-structural continuum of magmatic deformation, through pre-RCMP to solid-state deformation at decreasing temperatures. Four stages can be distinguished on the basis of discrete deformation mechanisms operating in different minerals.

Stage 1. Undeformed tonalite is composed of 45% plagioclase, 20% quartz, 20% amphibole, 10% biotite and less than 5% K-feldspar and accessory minerals. Rare magmatic texture is characterized by an almost idiomorphic shape of plagioclase, large randomly or weakly oriented flakes of biotite and irregular amphibole enclosing other mineral species. Quartz forms large blebs with irregular shape and boundaries (Fig. 5a).

Stage 2. Pre-RCMP fabric (Bouchez et al., 1992) is characterized by the shape preferred orientation of plagioclase phenocrysts and the onset of dynamic recrystallization at grain boundaries. Quartz blebs are weakly elongated and show strongly sutured boundaries indicating recrystallization by grain boundary migration. Biotite and amphibole are aligned and do not exhibit signs of internal strain or dynamic recrystallization (Gapais and Barbarin, 1986; Fig. 5b).

Stage 3. Solid-state deformation is characterized by rounded elongate feldspar augen (40% of the rock) and localization of ductile deformation in a matrix of recrystallized biotite and quartz (20%). This weak matrix is affected by a heterogeneous network of shear bands. Quartz grains make up 15% of the rock, they are very small and flattened close to the centre of shear bands and between rigid feldspar clasts but increase in size towards more protected regions (Fig. 5c).

Stage 4. Rocks in ductile shear zones are typically mylonites with more than 50% of ultrafine-grained dark matrix composed of recrystallized biotite, quartz and plagioclase. The remainder of the

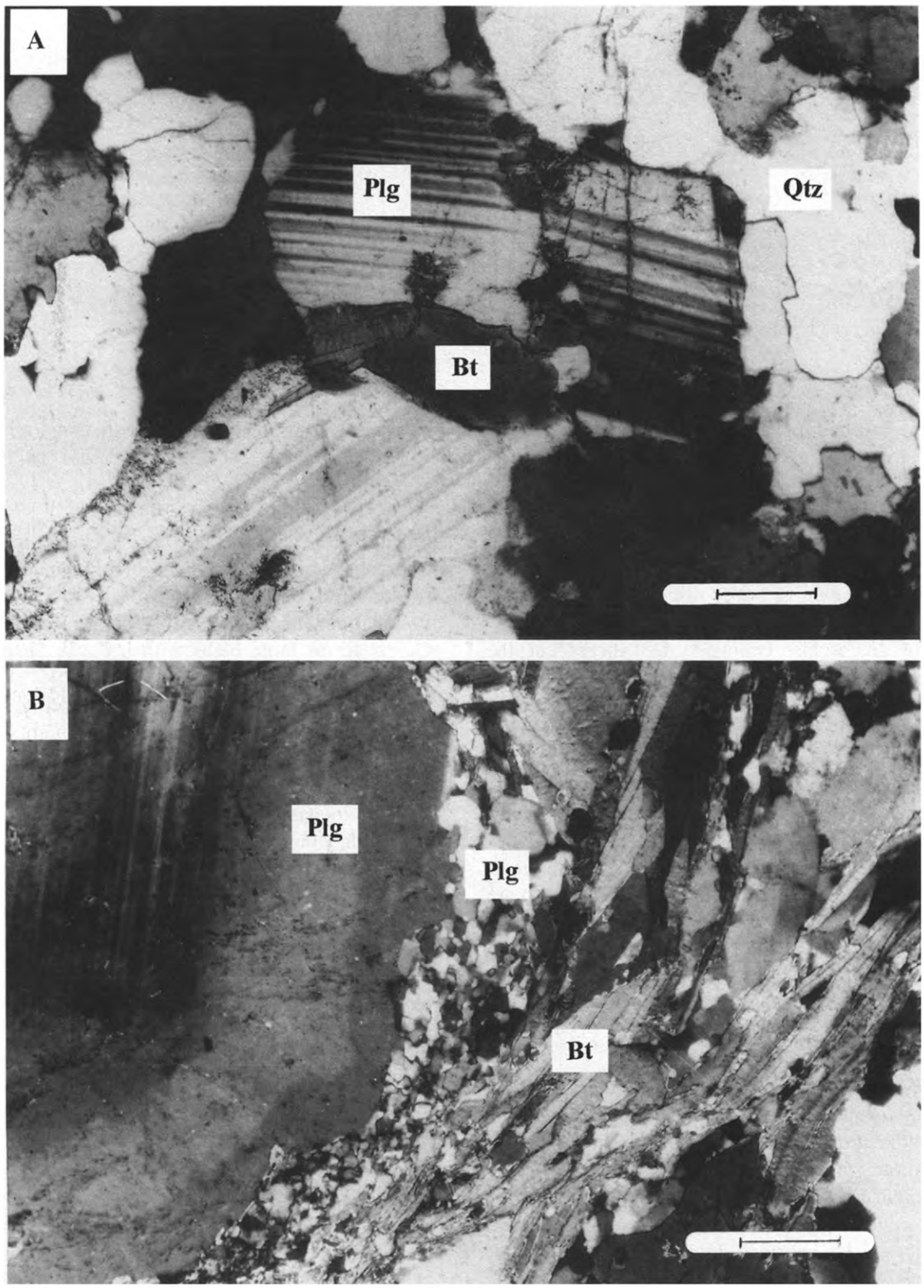

Fig. 5. Photographs of tonalite micro-structure: (a) stage 1 magmatic texture; (b) stage 2 sub-magmatic texture; (c) stage 3 solid state deformation; (d) stage 4 mylonite. Scale bar represents 0.2 mm.

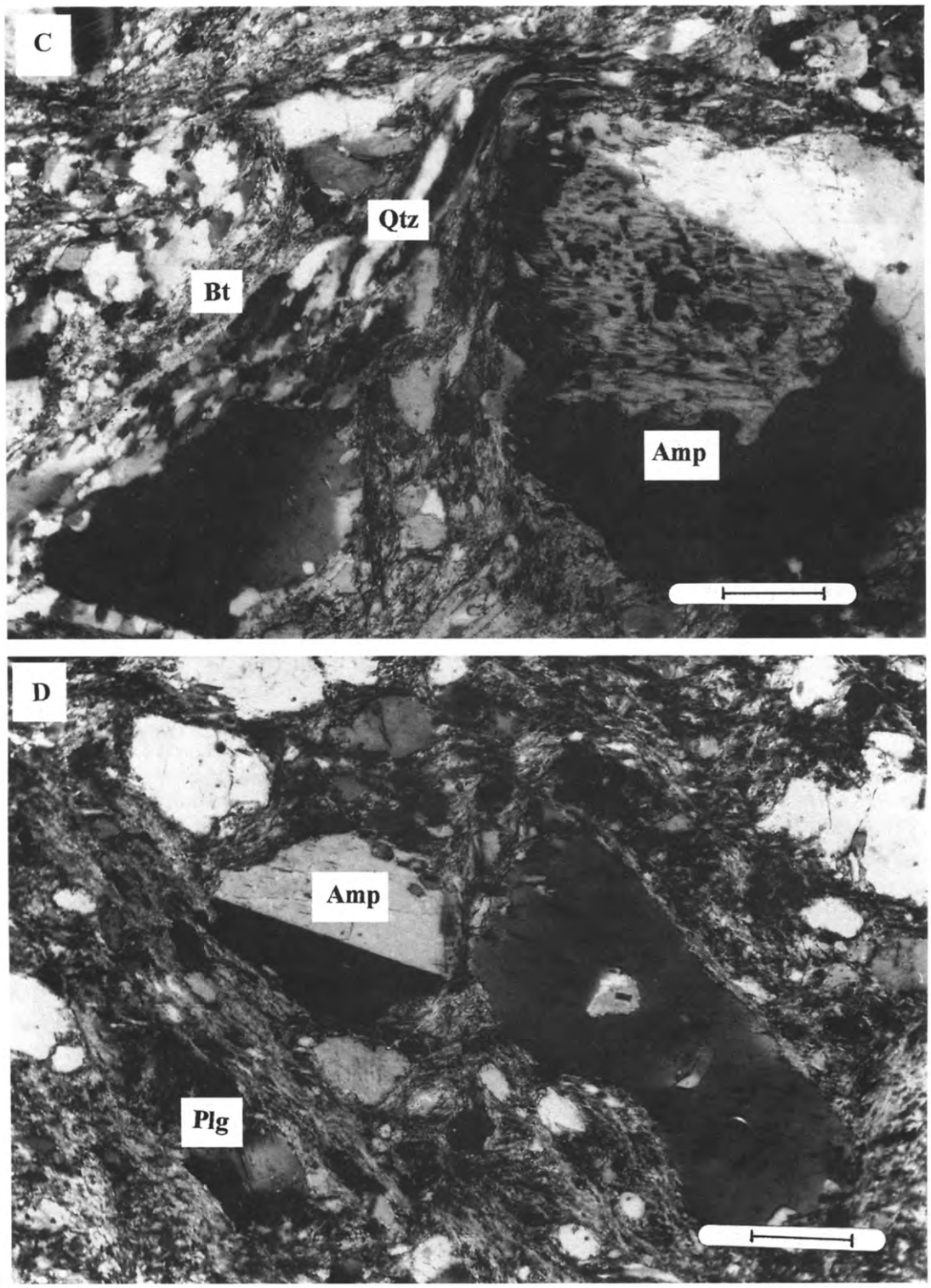

Fig. 5 (continued).

rock consists of isolated rounded clasts of plagioclase (30%) and amphibole (20%) floating in the matrix. Quartz and biotite are rare (Fig. 5d).

The magmatic stage 1 is developed only at the base of the sill while the pre-RCMP stage 2 is dominant throughout. Deformation in the solid state is developed only locally in heterogeneously developed discrete shear zones.

5. Quartz *c*-axis preferred orientation

Quartz *c*-axes have been measured using a universal stage and thin sections cut parallel to the lineation and perpendicular to the foliation. The quartz *c*-axis pattern from samples showing sub-solidus micro-structures display either small circle distribution around the pole of foliation (Fig. 6a) or an incomplete Lister type II cross girdle pattern (Fig. 6b) (Lister and Hobbs, 1980). The large opening angle of small-circle and maxima close to foliation plane may indicate simultaneous activity of basal $< a >$ and prism $< c >$ slip systems (Nicolas and Poirier, 1976). This type of fabric is indicative of high-temperature deformation. In tonalite deformed in the solid state large and small grains from stress-protected and stress-exposed areas were measured separately. *C*-axes of large grains exhibit either maxima close to the *Z*-axis (Fig. 6c,d) or an almost random distribution with some maxima located close to *X*-axis of finite strain. *C*-axes of small grains (Fig. 6e,f) form pair maxima symmetrically distributed between the *Z* and *Y* strain axes or strong sub-maximum at *Y*. The quartz *c*-axis pattern in stress-protected regions is interpreted as a result of dominant basal $< a >$ slip activity, while the grains in high-stress regions display dominant prism $< a >$ slip in combination with rhomb $< a + c >$ slip (Bouchez and Pécher, 1981). These results are in agreement with observations of Schmid and Casey (1986) and Handy (1990) suggesting that the prism $< a >$ slip is active at high strain rate and stress. A sample showing sub-solidus deformation from the top of the sill shows distribution of *c*-axes which could be interpreted as small circles around the *X*-axis of the finite strain (Fig. 6g). This type of fabric could be interpreted as resulting from constrictional flow (Lister and Hobbs, 1980).

The whole micro-fabric sequence documents the transition from HT deformation close to granite solidus, through solid-state micro-fabrics developed in HT to LT conditions. This is typically reported from syn-tectonically cooled granites.

5.1. Interpretation of micro-structures and micro-fabrics

Micro-structural studies show that the tonalite sill displays mostly pre-RCMP deformation with limited solid-state flow. Limited plastic deformation is concentrated in the rigid feldspars while the weak minerals (quartz and biotite) are shielded from stress. This type of micro-structure is typical of a load-bearing framework (LBF) structure (Handy, 1990). The quartz *c*-axes analyses show that high-temperature slip systems have been active and reflect also changing symmetry of deformation ranging from flattening to constriction. Only locally has the rigid feldspar skeleton been broken so that deformation is concentrated in weak phases. Intense stress partitioning reflected by variation of quartz grain size is characteristic of interconnected weak layer (IWL) structure with a high viscosity contrast and low amount of weak fraction (Handy, 1994).

The mineralogical composition of the tonalite is such that there is a relatively large volume of weak minerals such as quartz and biotite. This means that the LBF structure rapidly becomes unstable with increasing strain (Handy, 1990). Consequently, the dominance of LBF structures throughout the sill indicates that deformation in the solid state was very weak. Experiments with rock analogues show that the break down of LBF structures to IWL structures occurs with a maximum 20% of shortening (Jordan, 1987, 1988). Therefore, we suggest that most of the deformation occurred in the magmatic and pre-RCMP stages and the observed plastic deformation is related only to the locking up of the

Fig. 6. Quartz *c*-axis data measured with a universal stage on *XZ* sections: (a, b) from stage 2 LBF structures; (c, d) from large grains of stage 3 IWL structures; (e, f) from small grains of stage 3 IWL structures; (g) from a stage 2 LBF structure showing a possible constrictional pattern. Contoured at multiples of uniform distribution.

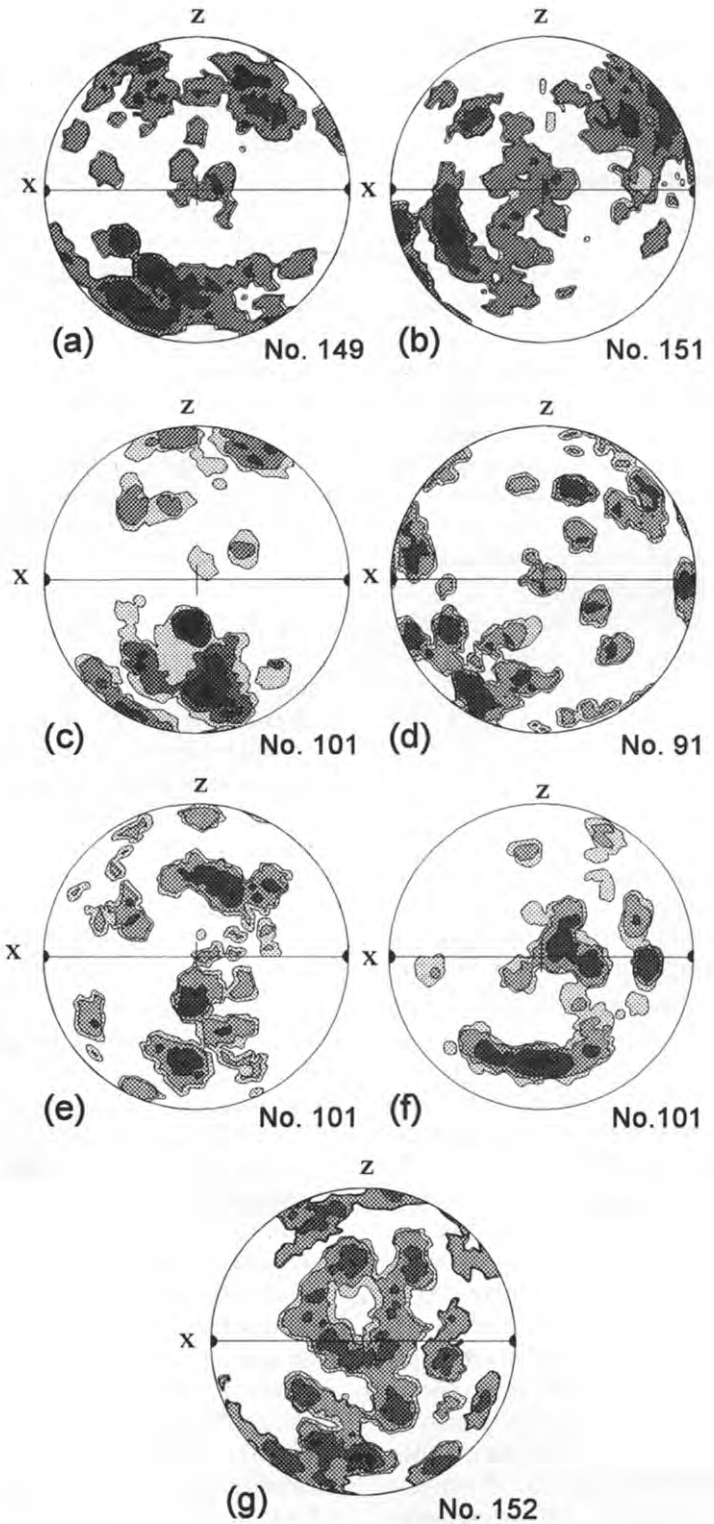
Z
X
X
(a)
No. 149
Z
X
X
(b)
No. 151
Z
X
X
(c)
No. 101
Z
X
X
(d)
No. 91
Z
X
X
(e)
No. 101
Z
X
X
(f)
No.101
Z
X
(g)
No. 152

movement with the full crystallization. The absence of pervasive S-C structures is a good indicator of weak solid-state strain in syn-tectonically intruding granitoids (Gapais, 1989).

6. Anisotropy of magnetic susceptibility of the tonalite

Three roughly equally spaced profiles across the tonalite were chosen on the basis of the amount of exposure available. Forty-six oriented samples were collected using a portable drilling machine. Their low field anisotropy of magnetic susceptibility (AMS) was measured with the KLY-3S Kappabridge (Jelínek and Pokorný, 1996) and the data were evaluated statistically using the ANISOFT program package (Hrouda et al., 1990).

The results of the AMS measurements are presented in terms of the mean susceptibility (k_m), the corrected degree of AMS (P') and the shape parameter (T) defined as follows (Jelínek, 1981):

$$k_m = (k_1 + k_2 + k_3)/3 \quad (1)$$

$$P' = \exp 2[(y_1 - y)^2 + (y_2 - y)^2 + (y_3 - y)^2] \quad (2)$$

$$T = 2\ln(k_2/k_3)/\ln(k_1/k_3) - 1 \quad (3)$$

where $k_1 \geq k_2 \geq k_3$ are the values of principal susceptibilities and $y_1 = \ln k_1$, $y_2 = \ln k_2$, $y_3 = \ln k_3$, $y = (y_1 + y_2 + y_3)/3$. If $1 \geq T > 0$, the magnetic fabric is predominantly planar, if $-1 \leq T < 0$, the magnetic fabric is predominantly linear.

6.1. Results

The mean bulk susceptibility is relatively low, in most specimens ranging from 200×10^6 to 800×10^6 (SI) (Fig. 7a). The most frequent value is around 400×10^{-6}. These relatively low values indicate that the carriers of magnetism are not only ferromagnetic minerals (sensu lato), but also paramagnetic minerals (probably amphibole and biotite). The magnetic minerals were identified through the investigation of temperature variation of bulk susceptibility of powdered specimens using the CS-2 apparatus and KLY-2 Kappabridge (Parma and Zapletal, 1991; Parma et al., 1993) and the resolution of the susceptibility into the paramagnetic and ferromagnetic components was made using the method of Hrouda (1994). The thermomagnetic curves show a paramagnetic hyperbola in the initial part and a rapid decrease in the vicinity of 580–590°C which corresponds to the curie temperature of magnetite. The susceptibility resolution into components shows that the paramagnetic minerals dominate the rock susceptibility of weakly magnetic specimens, while it is magnetite that controls the rock susceptibility in strongly magnetic specimens (Fig. 7b). Consequently, the AMS indicates the preferred orientation of paramagnetic minerals in weakly magnetic specimens, while it indicates the preferred orientation of magnetite in strongly magnetic specimens.

The degree of AMS (P') is relatively low (Fig. 7a), clearly lower than usual in metamorphic rocks of similar composition. In all three profiles it is lowest in the specimens from the eastern margin of the body and increases towards the top in the west (Fig. 8a).

The susceptibility ellipsoids are mostly oblate and only rarely prolate. The most strongly oblate ellipsoids are at the margins of the tonalite while the ellipsoids on the transition between oblate and prolate occur in the central areas (Fig. 8b).

The magnetic foliations and lineations are orientated parallel to the mesoscopic foliations and lineations in the tonalite. The magnetic foliations strike mostly NE–SW, dipping moderately to the northwest, the magnetic lineations are subhorizontal trending NE–SW (Fig. 9). There is no consistent spatial variation in the orientation of the magnetic lineation or foliation across any of the profiles.

6.2. Interpretation of AMS fabric

There is a question whether this magnetic fabric originated from magmatic flow or through tectonic deformation. In a flow magnetic fabric one would expect a low degree of AMS more or less homogeneous throughout the whole body, clearly triaxial susceptibility ellipsoids, magnetic foliation conformable to the body shape and the magnetic lineation vertical if the magma flowed vertically, or horizontal if the magma flowed horizontally (for numerous examples see Ellwood, 1975; Hrouda, 1982; Ernst, 1990; Ernst and Baragar, 1992). In a deformational magnetic fabric one would expect a relatively high degree of

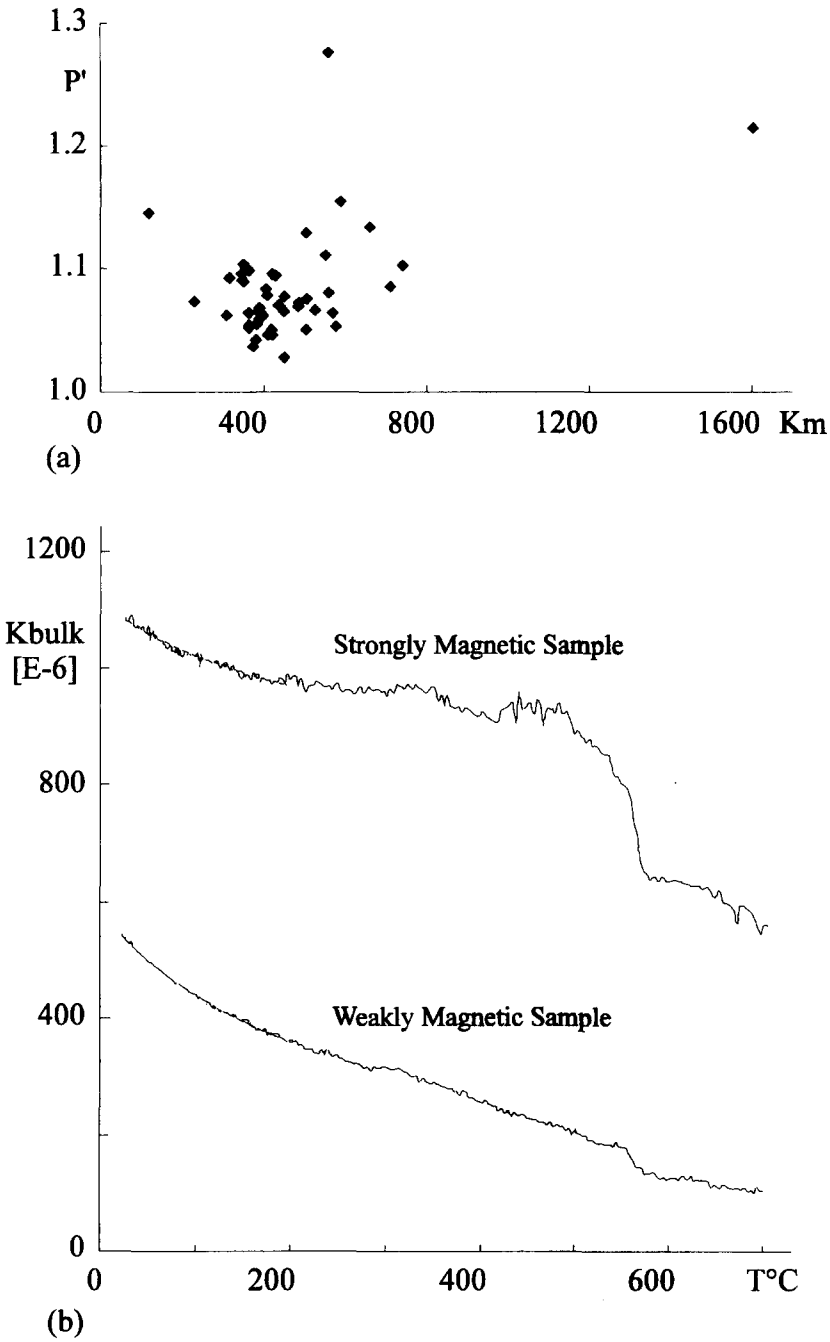

Fig. 7. (a) Plot of mean susceptibility k_m against the degree of intensity P'; note that the majority of samples plot between 200 and $800 \times 10^{-6} k_m$. (b) Plot of temperature against bulk susceptibility for strongly and weakly magnetic samples showing decreases in bulk susceptibility in the 580–590°C region.

AMS, the shape of the susceptibility ellipsoid to vary with the shape of the strain ellipsoid, the magnetic foliation pole and magnetic lineation parallel to the minimum and maximum strains, respectively. Indications of our AMS study suggest that magnetic fabric originated through magmatic flow acting during tec-

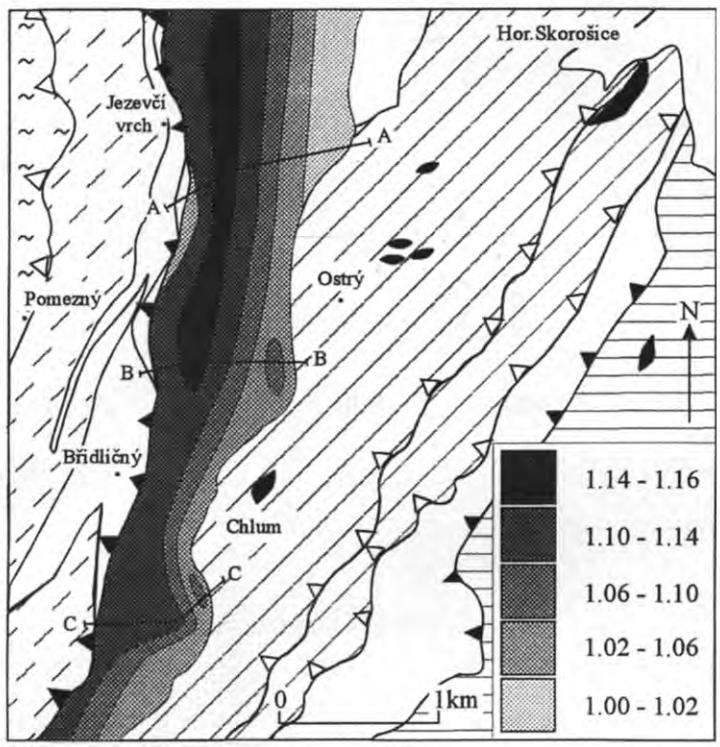
Hor.Skorošice
Jezevčí vrch
A
A
Ostrý
Pomezný
N
B
B
Břidličný
Chlum
C
C
1.14 - 1.16
1.10 - 1.14
1.06 - 1.10
1.02 - 1.06
1.00 - 1.02
0
1km

(a)

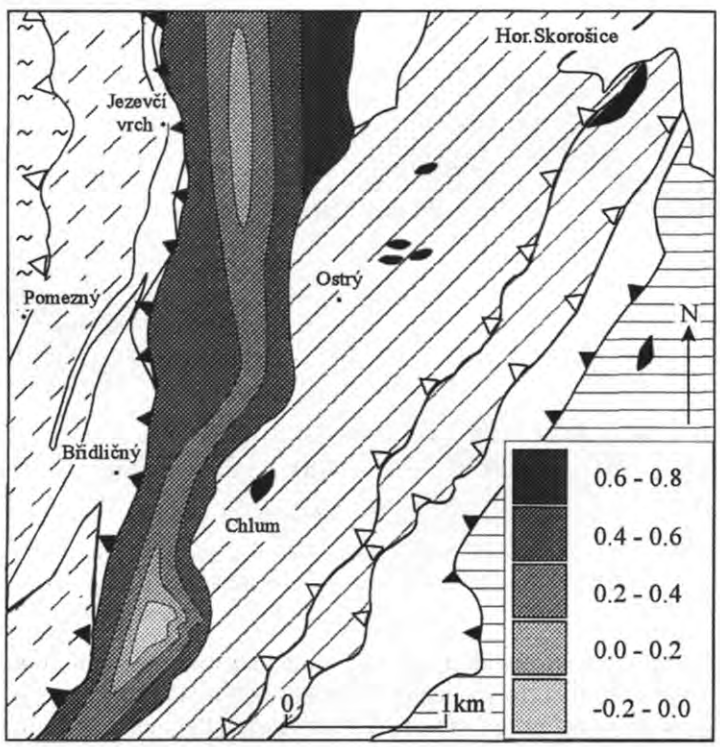
Hor.Skorošice
Jezevčí vrch
Ostrý
Pomezný
N
Břidličný
Chlum
0.6 - 0.8
0.4 - 0.6
0.2 - 0.4
0.0 - 0.2
-0.2 - 0.0
0
1km

(b)

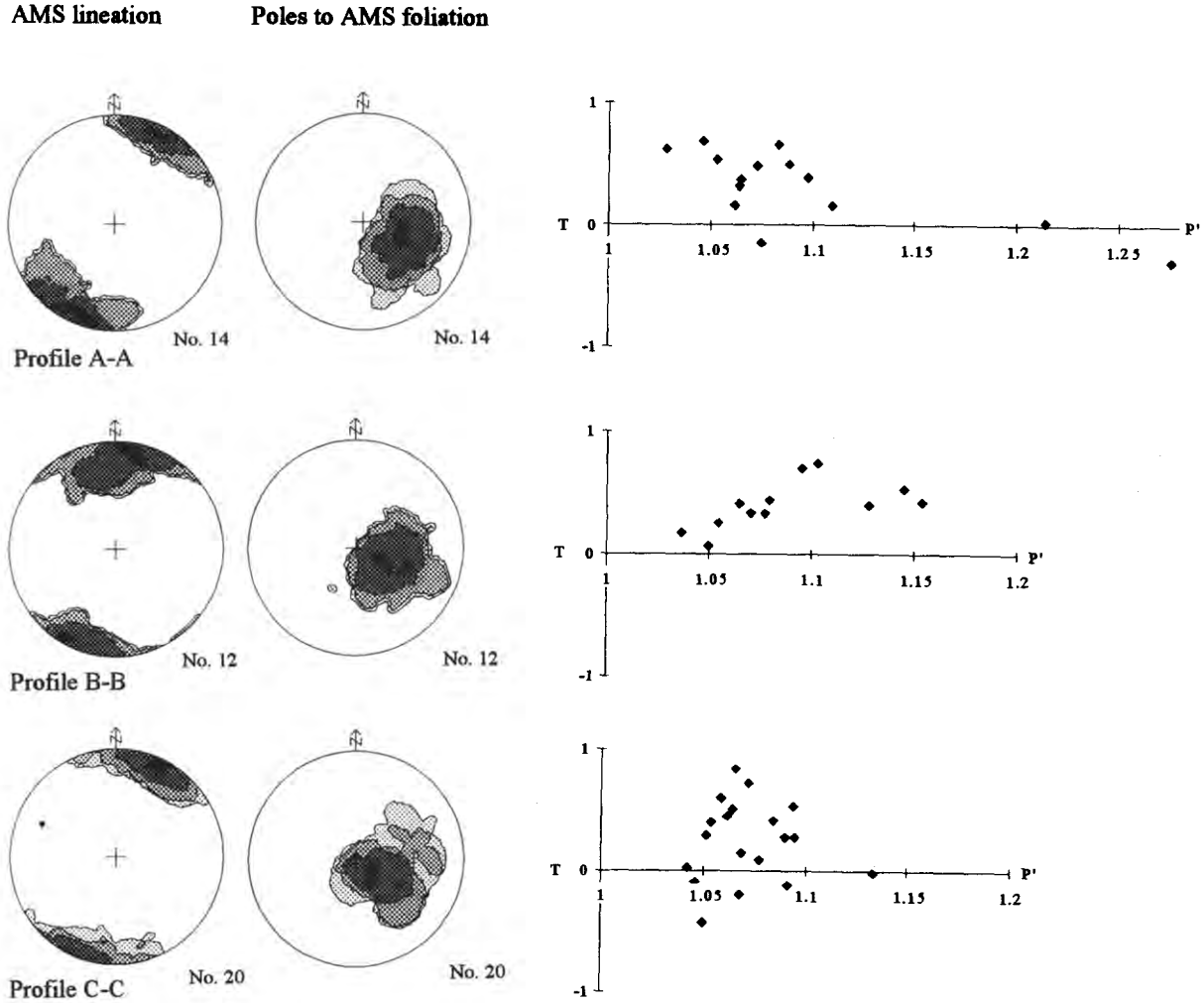

Fig. 9. AMS data for the three sampled profiles *A–A*, *B–B* and *C–C* (see Fig. 8). (a) Foliation and lineation data presented on lower hemisphere projections. (b) Plots of P' against T; $T > 0$ represents flattening, $T = 0$ plane strain, and $T < 0$ constriction.

tonic processes; this is in agreement with the results of micro-structural research. In order to constrain possible types of magmatic flow we used numerical modelling.

6.3. Modelling of AMS fabric

Provided the tonalite is dominated by pre-full crystallization micro-structures and displays a low degree of solid-state deformation, the model of Jeffery (1922) of non-interacting rigid particles in viscous fluid may be suitable for modelling of AMS fabric. For this modelling, we have used software of Ježek et al. (1994) complemented by AMS evaluating routines. The particles modelled are those found to bear the AMS, namely biotite and amphibole. Biotite is modelled as a platy mineral having an aspect ratio of 6 : 6 : 1 with a susceptibility ellipsoid

Fig. 8. Maps of tonalite showing contours of AMS parameters: (a) contours of the intensity of AMS represented by P' and the three profiles sampled *A–A*, *B–B*, and *C–C*; (b) contours of T – the shape of the AMS ellipsoid.

oriented such that k_3 is perpendicular to the plane of the particle and $k_1 = k_2$ in the plane of the particle (Zapletal, 1990). This assumes that the shape of the particle reflects the crystal lattice, as it will do in a crystal growing from the melt. Amphibole as an elongate mineral which can be compared to elongated rigid markers of general form is modelled with an aspect ratio of 3 : 2 : 1 and a susceptibility ellipsoid as suggested by Friedrich (1995). The model assumes initially isotropic distribution of orientations of these two equally populated minerals. During deformation biotites and amphiboles form separate sub-fabrics. Combination of these two sub-fabrics creates a global fabric which should correspond to AMS fabric measured from field specimens. The results of modelling are presented on horizontal lower hemisphere projections with poles to biotite, the lineation of amphibole, k_{1-3} of the resulting susceptibility ellipsoid, parameters P' and T of AMS, amount of simple shear γ and natural strain $\ln S$ (Fig. 10). It should be noted that the sense of shear is dextral but the X direction of the model does not correspond to the north direction of reality.

The geometry and structural pattern of wall rocks of the tonalitic sill indicate that the deformation of these rocks occurred in a dextral transpressive regime (Fig. 10). Measured AMS fabrics exhibit steeply inclined foliation and sub-horizontal lineation. Such a type of AMS fabric can be obtained by modelling in case of: (1) simple shear, or (2) strongly oblique transpression. Simple shear defined by horizontal movements of rigid blocks with vertical walls surrounding tonalitic magma may produce AMS fabric as shown in Fig. 10. Progressive simple shear results in the development of a maximum of poles of biotite close to the Y-direction and a horizontal lineation defined by long axes of amphiboles near to the X-direction. Calculated principal susceptibility directions and parameters T and P' are consistent with obtained field measurements (Figs. 8 and 9). T values remain close to plane strain geometry.

Teissyeire and Tikoff (1994) have shown that wrench-dominated transpressions representing oblique convergence with angle $\alpha < 20°$ for small strains produce horizontal lineations which progressively switch to a vertical direction. Similarly, our modelling of AMS in oblique transpression has shown that the multiparticle system of biotites and amphiboles for small strains created AMS fabric with a horizontal k_1 principal susceptibility direction (Fig. 10). The T and P' parameters are again in the frame of measured values but the T parameter exhibits a higher degree of oblateness than in case of simple shear. Increase of strain is responsible for a higher degree of oblateness and slightly stronger fabric intensity than those observed in the field. More importantly, the k_1 susceptibility evolves progressively towards a vertical direction similarly to the well known switch of the longest finite strain axis direction.

Comparison of numerical modelling with observed natural fabrics confirms the general idea of oblique transpression. In detail, in a natural fabric pattern, we can distinguish different zones of slightly differing symmetry and intensity. AMS fabrics along boundaries of sill exhibit oblate and weak fabrics with horizontal lineation and can be compared with the initial stages of oblique transpressional flow. In the central part of the sill the AMS pattern is characterized by plane strain and stronger fabrics which could be compared rather with simple shear.

7. Discussion

Rocks in the footwall of tonalitic sill show granulite low-pressure facies metamorphism which occurred during Cambro–Ordovician rifting of continental crust (Štípská et al., 1996). The granulite facies metamorphism is partly due to underplating by gabbroic intrusion. During the Variscan collision and intrusion of tonalitic sill granulite rocks and underlying gabbros suffered 170 Ma of cooling and therefore were in rigid state.

High-temperature mylonitic deformation of gabbros during the Variscan oblique collision is shown to have occurred at 700–750°C at pressures of 8–10 kbar and is characterized by macroscopically observed flattening of amphibole and plagioclase aggregates, SW-plunging lineation and dextral sense of shear criteria. The increase of temperature during deformation of the gabbros is documented by prograde continuous and discontinuous reactions in the recrystallized matrix. The most likely reason for such high temperatures is that heat flux from a tonalitic magma

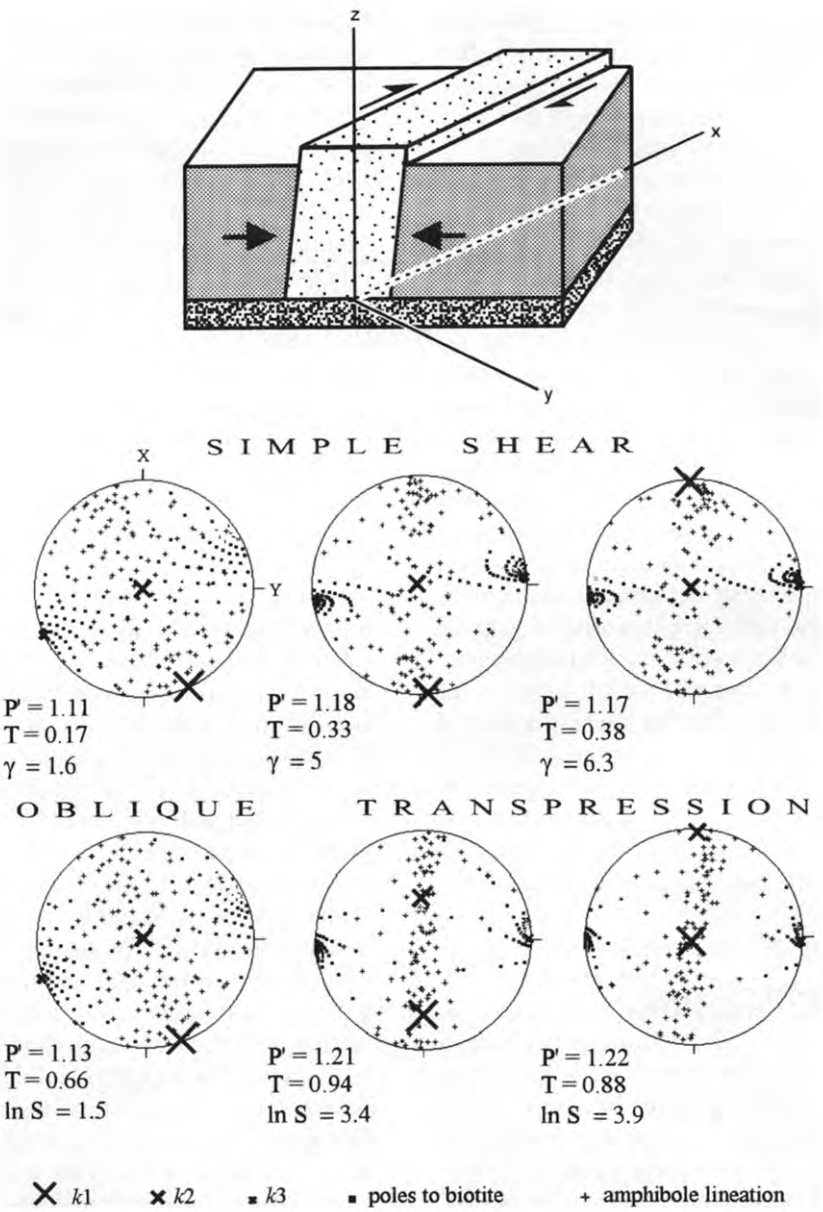

Fig. 10. Numerical modelling of particles in simple shear and oblique transpression; the upper part of the figure shows the geometry of the model. Simple shear and transpression models show different stages of progressive deformation. The resulting biotite and amphibole orientations and corresponding global AMS fabric are presented in lower-hemisphere, equal-area projection orientation diagrams.

reservoir formed below thinned Cambro–Ordovician crust.

In the tonalite sill the pressure estimates of amphibole crystallization are calculated at 5–7 kbar and calculated temperatures of tonalite solidus yield 710–730°C. Pressure data show that the magnetic minerals in tonalite crystallized at depths ca. 10 km shallower than where deformation of metagabbros occurred. Therefore, the AMS results describe fabric development of tonalite at this depth after an important proportion of amphibole and biotite has been fully crystallized. We assume that the AMS

data reflect the last stages of magma emplacement and probably slightly later solid-state deformation following magma solidification.

Similarly to the gabbroic mylonites in the hanging wall, the tonalite shows steeply dipping AMS foliation and sub-horizontal lineation throughout the whole body. The lower intensity of AMS in the eastern marginal part of the sill indicates a low amount of magma deformation due to the more rapid cooling of magma in contact with underlying cold rocks. Micro-structural analysis also shows that the magma is rapidly frozen preserving textural features typical for magmatic flow. On the other hand, the western marginal part was in contact with relatively warmer metagabbros and, therefore, was deformed for a longer time. This is responsible for a higher degree of AMS. Supporting evidence for this interpretation are micro-structural observations showing a higher degree of solid-state deformation at the western boundary of the sill where thrusting of gabbros continued during solidification of tonalitic magma. The rocks in the central part of the sill were hot for the longest period and exhibit the highest degree of AMS. Plane strain-like values of parameter T in the central part of the tonalitic body may be explained as resulting from dominating simple shear in elongated magmatic pockets surrounded by solid tonalite in the last period of overall solidification of the whole tonalitic sill.

Fig. 11 summarizes our tectonic model of intrusion of the tonalitic sill:

(1) *Stage I.* Solid Cambro–Ordovician gabbros at a depth of at least 30–36 km corresponding to a measured 8-10 kbar were heated from a tonalitic magmatic chamber. Such extreme heat input is responsible for weakening of amphibole gabbro, of which the rheology roughly corresponds to pyroxene-rich rocks that, according to experiments (Kirby, 1985; Ranalli and Murphy, 1987), require temperatures for viscous behaviour in the range 700–750°C.

(2) *Stage II.* Transpressive deformation developed a ductile shear zone in gabbroic rocks several hundred metres in width allowing oblique and dextral uplift of the western block and strong, observed, deformation of gabbros parallel to the shear zone boundary.

(3) *Stage III.* Continuous oblique transpression produced squeezing of the magma into the highly anisotropic lower-crustal mylonitic zone. The deformation in gabbroic mylonites weakens the zone in the lower crust and results in loss of cohesion (Hutton, 1992). It is envisaged that magma overpressure and viscous pressure drop (Lister and Kerr, 1991; Clemens and Mawer, 1992) allow the contractional stresses to be overcome and sheet wedging of magma to occur along this zone of weakness. Pressure estimates of magma solidification show depths of intrusion of 18–24 km corresponding to 5–7 kbar. High temperatures reported in tonalite at this depth indicate isothermal magma ascent and subsequent rapid cooling at shallow depths. The high velocity of tonalitic magma ascent is due to the low viscosity and density of magma (Petford et al., 1993; Petford, 1996) and eventually increased by the compressional component of transpression (Thompson et al., 1997). This period of magma ascent is not recorded by structural and AMS data because tonalite was not fully crystallized. During this magmatic stage the gabbroic mylonites have been passively transported to above the sill the underlying rocks being protected from ductile deformation due to inability of the magma to transmit shear stresses.

(4) *Stage IV.* New P–T conditions imposed by underlying cold wall rocks were responsible for rapid magma cooling starting from the eastern lower part of the tonalitic sill. This was accompanied by an increase of viscosity and by crystallization of large amounts of crystals. The preservation of LBF structures in most of the rock and the lack of pervasive S–C fabrics (Gapais, 1989) indicates that the crystallization of the magma blocked further movement in this area. Progressively solidifying magma was deformed in a transpressional regime. The magmatic flow stage was followed by solid-state deformation in the western boundary of the sill due to continuous overthrusting of gabbroic mylonites.

Acknowledgements

This work was funded by grant No. 30689 of the Czech National Foundation to Karel Schulmann. The analytical work was supported by a Continuous Orogenesis grant of the Swiss National Foundation to Prof. A.B. Thompson. We are grateful to Nick Petford for constructive criticism which substantially improved the manuscript.

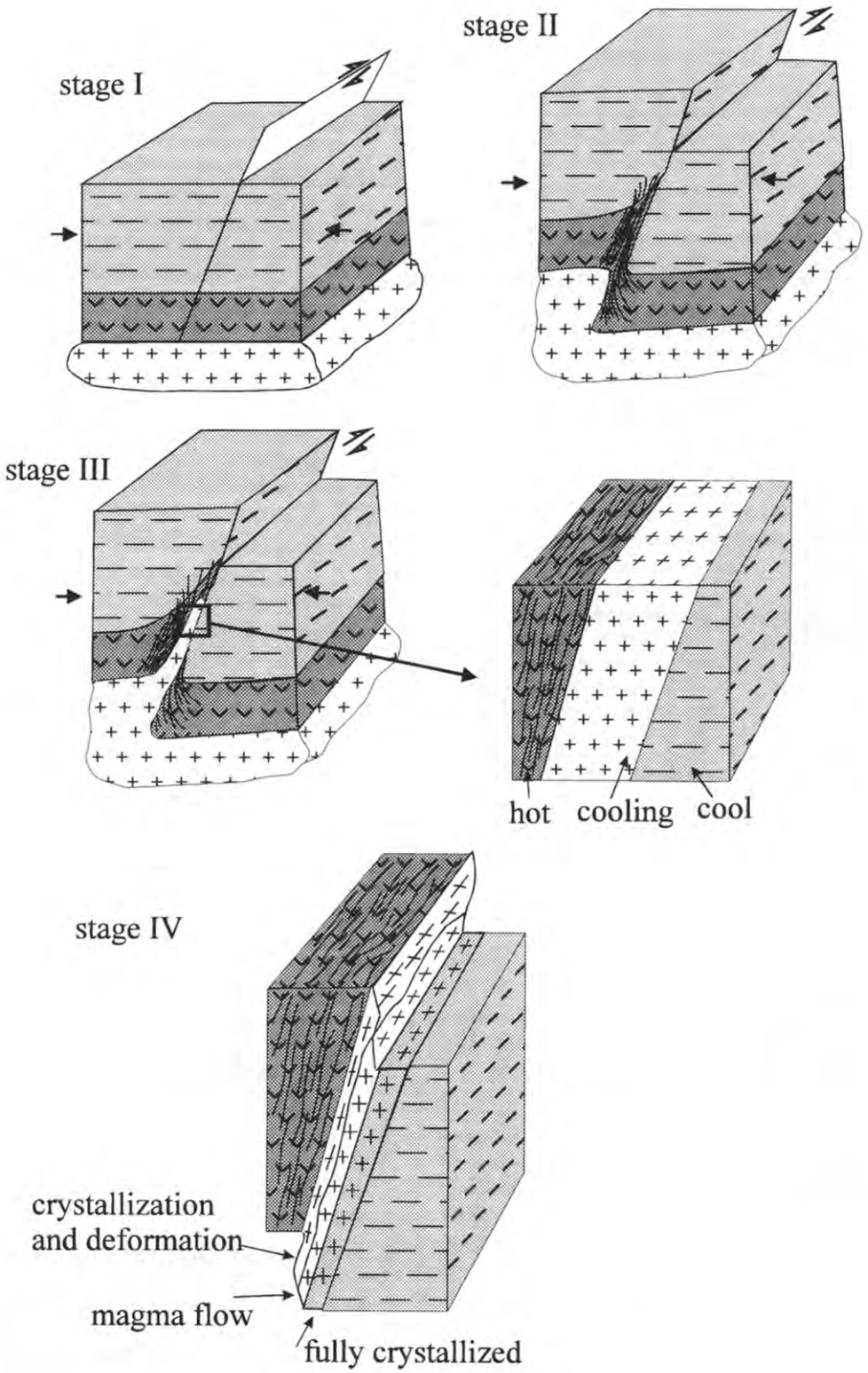

Fig. 11. Four stages of shear zone development, tonalite sill intrusion and magma deformation during cooling. See text for explanation.

References

Bouchez, J.L., Pécher, A., 1981. The Himalayan main central thrust pile and its quartz-rich tectonites in central Nepal. Tectonophysics 78, 23–50.

Bouchez, J.L., Deal, C., Gleizes, G., Nédélec, A., Cuney, M., 1992. Sub-magmatic microfractures in granites. Geology 20, 35–38.

Clemens, J.D., Mawer, C.K., 1992. Granitic magma transport by magma fracture propagation. Tectonophysics 204, 339–360.

De Yoreo, J.J., Lux, D.R., Guidotti, C.V., 1989. The role of crustal anatexis and magma migration in regions of thickened crust. In: Daly, J.G., Cliff, R.A., Yardley, B.W.D. (Eds.), Evolution of Metamorphic Belts. Geol. Soc. London, Spec. Publ. 43, 187–202.

Den Tex, E., 1969. Origin of ultramafic rocks, their tectonic setting and history: a contribution to the discussion of the paper 'The origin of ultramafic and ultrabasic rocks' by P.J. Wyllie. Tectonophysics 7, 457–488.

Dudek, A., 1980. The crystalline basement block of the Outer Carpathians in Moravia-Brunovistulicaum. Rozpr. Česk. Akad. Věd 90, 1–85.

Ellwood, B.B., 1975. Analysis of emplacement mode in basalt from DSDP holes 319A and 312 using anisotropy of magnetic susceptibility. J. Geophys. Res. 80, 4805–4808.

Ernst, R.E., 1990. Magma flow directions in two mafic Proterozoic dyke swarms of the Canadian Shield: As estimated using anisotropy of magnetic susceptibility data. In: Parker, A.J., Rickwood, P.C., Tucker, D.H., (Eds.) Mafic Dykes and Emplacement Mechanisms. Balkema, Rotterdam, pp. 231–235.

Ernst, R.E., Baragar, W.R.A., 1992. Evidence from magnetic fabric for the flow pattern of magma in the Mackenzie giant radiating dyke swarm. Nature 356, 511–513.

Friedrich, D., 1995. Gefügeuntersuchungen der Amphiboliten der böhmische Masse unter besonderer Berücksichtigung der Anisotropie der magnetischen Suszeptibilität. Geotekton. Forsch. 82, 1–448.

Gapais, D., 1989. Shear structures within deformed granites: mechanical and thermal indicators. Geology 17, 1144–1147.

Gapais, D., Barbarin, B., 1986. Quartz fabric transition in a cooling syntectonic granite (Hermitage Massif, France). Tectonophysics 125, 357–370.

Guineberteau, B., Bouchez, J.L., Vigneresse, J.L., 1987. The Mortagne granite pluton (France) emplaced by pull-apart along a shear zone: structural and gravimetric arguments and regional implication. Geol. Soc. Am. Bull. 99, 763–770.

Handy, M., 1990. The solid-state flow of polymineralic rocks. J. Geophys. Res. 95, 8647–8661.

Handy, M., 1994. Flow laws for rocks containing two non-linear viscous phases: a phenomenological approach. J. Struct. Geol. 16, 287–301.

Hodges, K.V., Crowley, P.D., 1985. Error estimation and empirical geothermobarometry for pelitic systems. Am. Mineral. 70, 702–729.

Holland, T.J.B., Blundy, J.D., 1994. Non-ideal interactions in calcic amphiboles and their bearing on amphibole–plagioclase thermometry. Contrib. Mineral. Petrol. 116, 433–447.

Hrouda, F., 1982. Magnetic anisotropy of rocks and its application in geology and geophysics. Geophys. Surv. 5, 37–82.

Hrouda, F., 1994. A technique for the measurement of thermal changes of magnetic susceptibility of weakly magnetic minerals and rocks by the CS-2 apparatus and KLY-2 Kappabridge. Geophys. J. Int. 118, 604–612.

Hrouda, F., Jelínek, V., Hrušková, L., 1990. A package of programs for statistical evaluation of magnetic anisotropy data using IBM-PC computers (abstr.). EOS Trans. AGU, p. 1289.

Hutton, D.H.W., 1988. Igneous emplacement in a shear-zone termination: the biotite granite at Strontian, Scotland. Geol. Soc. Am. Bull. 100, 1392–1399.

Hutton, D.H.W., 1992. Granite sheeted complexes: evidence for the dyking ascent mechanism. Trans. R. Soc. Edinburgh 83, 377–382.

Indares, A., Martignole, J., 1985. Biotite–garnet geothermometry in granulite facies; the influence of Ti and Al in biotite. Am. Mineral. 70, 272–278.

Ingram, G.M., Hutton, D.W.H., 1994. The Great Tonalite Sill: emplacement into a contractional shear zone and implications for Late Cretaceous to Early Eocene tectonics in southeastern Alaska and British Columbia. Geol. Soc. Am. Bull. 106, 715–728.

Jeffery, G.B., 1922. The motion of ellipsoidal particles immersed in a viscous fluid. Proc. R. Soc. London 102, 161–179.

Jelínek, V., 1981. Characterization of the magnetic fabric of rocks. Tectonophysics 79, T63–T67.

Jelínek, V., Pokorný, J., 1996. Some new concepts in technology of transformer bridges for measuring susceptibility and anisotropy of rocks. EGS abstracts.

Ježek, J., Melka, R., Schulmann, K., Venera, Z., 1994. The behaviour of rigid triaxial ellipsoid particles in viscous flows — modelling of fabric evolution in a multiparticle system. Tectonophysics 229 (3-4), 165–180.

John, B.E., Blundy, J.D., 1993. Emplacement-related deformation of granitoid magmas, southern Adamello Massif. Geol. Soc. Am. Bull. 105, 1517–1541.

Jordan, P., 1987. The deformational behaviour of bimineralic limestone–halite aggregates. Tectonophysics 135, 185–197.

Jordan, P., 1988. The rheology of polymineralic rocks — an approach. Geol. Rundsch. 77 (1), 285–294.

Kirby, S.H., 1985. Rheology of the lithosphere. Rev. Geophys. Space Phys. 21, 1458–1487.

Kohn, M.J., Spear, F.S., 1989. Empirical calibration of geobarometers for the assemblage garnet + hornblende + plagioclase + quartz. Am. Mineral. 74, 77–84.

Lister, J.R., Hobbs, B.E., 1980. The simulation of fabric development during plastic deformation and its application to quartzite: the influence of the deformation history. J. Struct. Geol. 2, 335–370.

Lister, J.R., Kerr, R.C., 1991. Fluid-mechanical models of crack propagation and their application to magma transport in dykes. J. Geophys. Res. 96, 10049–10077.

Nicolas, A., Poirier, P., 1976. Crystalline Plasticity and Solid State Flow in Metamorphic Rocks. Wiley, London, 444 pp.

Oliver, G.J.H., Corfu, F., Krogh, T.E., 1993. U–Pb ages from

SW Poland: evidence for a Caledonian suture zone between Baltica and Gondwana. J. Geol. Soc. London 150, 355–369.

Parma, J., Zapletal, K., 1991. CS-1 apparatus for measuring the temperature dependence of low-field susceptibility of minerals and rocks (in cooperation with the KLY-2 Kappabridge). Leaflet, Geofyzika Brno.

Parma, J., Hrouda, F., Pokorný, J., Wohlgemuth, L., Suza, P., Šilinger, P., Zapletal, K., 1993. A technique for measuring temperature dependent susceptibility of weakly magnetic rocks. EOS Trans. AGU 1993, 113, Spring meeting.

Paterson, S.R., Vernon, R.H., Tobisch, O.T., 1989. A review of criteria for the identification of magmatic and tectonic foliations in granitoids. J. Struct. Geol. 11, 349–363.

Petford, N., 1996. Dykes or diapirs?. Trans. R. Soc. Edinburgh: Earth Sci. 87, 105–114.

Petford, N., Kerr, R.C., Lister, J.R., 1993. Dike transport of granitoid magmas. Geology 21, 845–848.

Ranalli, G., Murphy, D.C., 1987. Rheological stratification of the lithosphere. Tectonophysics 132, 281–295.

Schmid, S.M., Casey, M., 1986. Complete fabric analysis of some commonly observed quartz *c*-axis patterns. In: Hobbs, B.E., Heard, H.C. (Eds.), Mineral and Rock Deformation: Laboratory Studies. AGU, Geophys. Monogr. 36, 236–286.

Schmid, S.M., Aebli, H.R., Heller, F., Zingg, A., 1989. The role of the Periadriatic Line in the tectonic evolution of the Alps. In: Coward, M.P., Dietrich, D., Park, R.G. (Eds.), Alpine Tectonics. Geol. Soc. London, Spec. Publ. 45, 153–171.

Schmidt, M.W., 1992. Amphibole composition in tonalite as a function of pressure: an experimental calibration of the Al-in-hornblende barometer. Contrib. Mineral. Petrol. 110, 304–310.

Spear, F., 1991. Metamorphic Phase Equilibria and Pressure–Temperature–Time Paths. Mineralogical Society of America, Washington, DC, 799 pp.

Štípská, P., Kröner, A., Jaeckel, P., Schulmann, K., 1995. Structural and regional boundary between two colliding crustal blocks at the NE margin of the Bohemian Massif. TMIDSR Conference, Prague, J. Czech Geol. Soc., abstr. vol. 40, 49–50.

Štípská, P., Schulmann, K., Kroener, A., Parry, M., 1996. Le comportement rhéologique à la limite des plaques pendant la collision varisque: l'exemple de la bordure NE du massif de la Bohème. 16me Réunion des Sciences de la Terre, Orléans, 10–12 avril 1996, Abstr. Vol. 60.

Suess, F.E., 1912. Die moravischen Fenster und ihre Beziehung zum Grundgebirge. Oesterr. Akad. Wiss. Math. Naturwiss. 88, 541–631.

Suess, F.E., 1926. Intrusions-Tektonik und Wander-Tektonik in Varistischen Gebirge. Bornträger, Berlin, 268 pp.

Teissyeire, C., Tikoff, B., 1994. Strain modelling of displacement field partitioning in transpressional orogens. J. Struct. Geol. 11, 1575–1588.

Thompson, A.B., Schulmann, K., Ježek, J., 1997. Thermal evolution and exhumation in obliquely convergent (transpressive) orogens. Tectonophysics 280, 171–184 (this issue).

Zapletal, K., 1990. Low-field susceptibility anisotropy of some biotite crystals. Phys. Earth Planet. Inter. 63, 85–97.

Chronological constraints on the pre-Variscan evolution of the northeastern margin of the Bohemian Massif, Czech Republic

A. KRÖNER[1], P. ŠTÍPSKÁ[2], K. SCHULMANN[2] & P. JAECKEL[1,3]

[1]*Institut für Geowissenschaften, Universität Mainz, D-55099 Mainz, Germany (e-mail: kroener@mail.uni-mainz.de)*

[2]*Department of Petrology, Charles University, Albertov 6, CS 12843, Praha 2, Czech Republic*

[3]*Max-Planck-Institut für Chemie, Postfach 3060, D-55020 Mainz, Germany*

Abstract: New single zircon ages enable us to provide an evolutionary scenario for the Neoproterozoic to Cambro-Ordovician tectonic history of part of the easternmost Sudetes along the northeastern margin of the Bohemian Massif. The easternmost crustal segment (Brunia) yields Neoproterozoic ages from both autochthonous and allochthonous Variscan units; these ages document a Cadomian (Pan-African) history that may be linked with the northern margin of Gondwana. A Cambro-Ordovician magmatic–thermal event in Brunia is represented by granitic to pegmatitic dykes intruding Neoproterozoic crust and by localized partial anatexis. Farther west a narrow zone of Cambro-Ordovician rifting is identified (Staré Městro belt), marked by gabbroic magmatism, bimodal volcanism and medium-pressure granulite facies metamorphism. The westernmost crustal domain (Orlica–Snieznik dome) is represented by Neoproterozoic crust intruded by Cambro-Ordovician plutons consisting of calk-alkaline granitoid rocks and affected by widespread Cambro–Ordovician anatexis. The geodynamic setting of the Neoproterozoic and Cambro-Ordovician domains is similar to that of the Western Sudetes, where both Cambro-Ordovician rifting and calc-alkaline magmatism were identified. We discuss the rifting mechanics in terms of sequential crustal thinning along the northern margin of Gondwana. The calc-alkaline magmatism, in conjunction with crustal rifting, is related to a back-arc geometry in front of a retreating south-dipping subduction zone during progressive closure of the Tornquist Ocean southeast of Avalonia.

The late Palaeozoic collisional history of the Variscan belt in central Europe is now reasonably well understood (Franke 1989, this volume; Matte *et al.* 1990), but there is still much discussion about the earlier, Neoproterozoic to early Palaeozoic, evolution of the various crustal segments constituting this belt. The Bohemian Massif is part of the axial zone of the Variscan belt and is composed of Mesoproterozoic to late Palaeozoic rock assemblages.

Three major zones have been recognized along the eastern margin of the Bohemian Massif (Schulmann & Gayer 2000) (see Fig. 1). They are, from bottom to top and east to west: (1) the undeformed lower plate Brunia, the Brunian domain; (2) a zone of intense Variscan deformation and metamorphism of the lower plate, the Moravo-Silesian domain; (3) the upper plate, consisting of middle- to upper-crustal rocks of the Moldanubian–Lugian domain. The Variscan structure of the eastern margin of the Bohemian Massif resulted from oblique collision between the combined Moldanubian–Lugian domain and the Neoproterozoic (Cadomian or Pan-African) Brunia domain (originally defined by Dudek (1980) as Brunovistulicum) to the east (see also Finger *et al.* this volume).

The Brunian domain, interpreted as a microcontinent (Matte *et al.* 1990), consists of Neoproterozoic high-grade metamorphic rocks intruded by numerous late Proterozoic granitoids (dated at *c.* 550 and 580 Ma) and overlain by a Devonian basin (see Chlupáč (1994) for review). The NE–SW-trending Moravo-Silesian domain is a belt of sheared and metamorphosed Brunia-derived rocks, piled up into a nappe sequence and consisting of three NE–SW-trending tectonic windows (Suess 1912). Variscan deformation and metamorphism have produced a tectonically inverted Barrovian metamorphic zonation ranging from a chlorite zone in the east to a kyanite–sillimanite zone in the west

From: FRANKE, W., HAAK, V., ONCKEN, O. & TANNER, D. (eds).
Orogenic Processes: Quantification and Modelling in the Variscan Belt.
Geological Society, London, Special Publications, **179**, 175–197. 0305-8719/00/$15.00

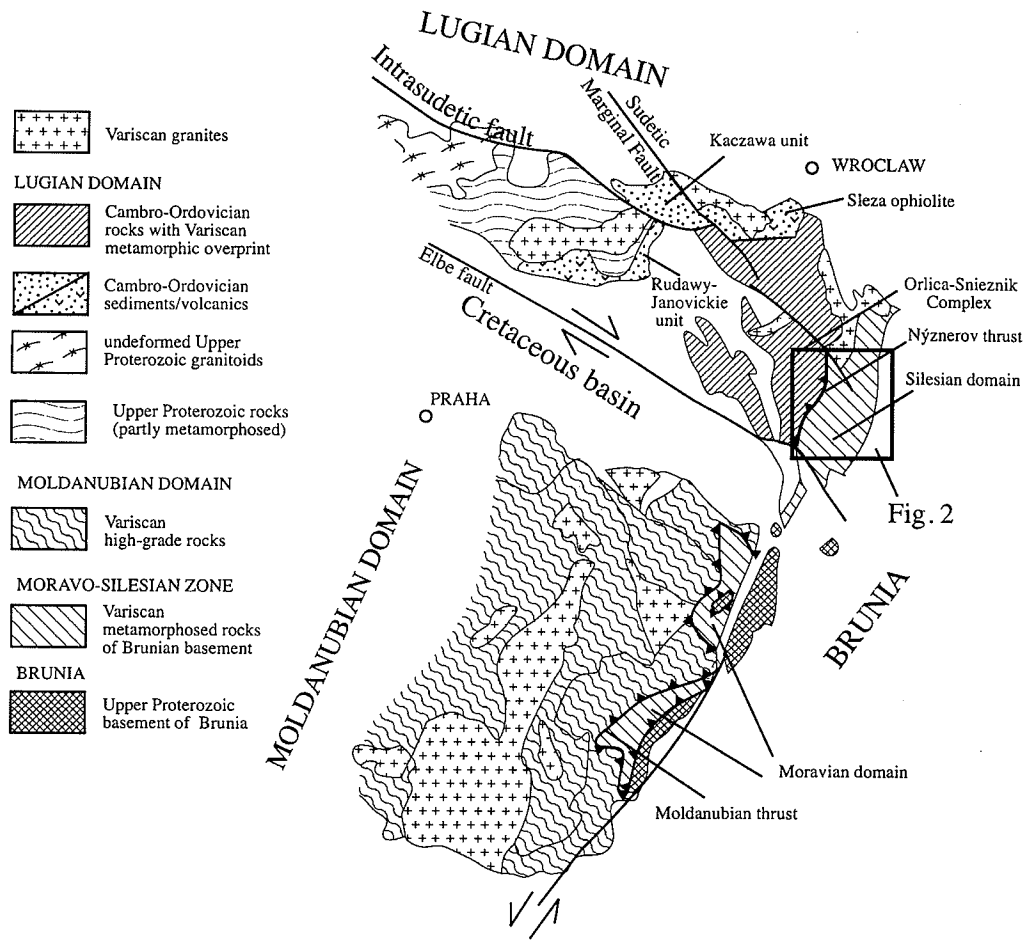

Fig. 1. Simplified geological map of the eastern and northeastern margin of the Bohemian Massif, showing major crustal units (after Matte *et al.* (1990) and Aleksandrowski *et al.* (1997)).

(Štípská & Schulmann 1995). The western Moldanubian domain is characterized by widespread Variscan anatexis, relics of high-pressure metamorphism and intrusion of large granitoid bodies. In the north, the Lugian domain consists mostly of medium-grade schists and high-grade rocks (migmatites and high-grade gneisses) as well as relics of high-pressure granulites and eclogites.

To be able to understand the geodynamic evolution of the contact zone between the Lugian and Brunia domains it is important to determine the composition, deformation, metamorphism and protolith age of the highly deformed rocks in this region. In this paper we present zircon age data from this critical tectonic boundary, in combination with whole-rock Nd mean crustal residence ages (Hegner & Kröner this volume), which document the pre-Variscan geological history of the Brunian and Lugian crustal segments.

Geology of the area studied

The geology of area studied is shown in the simplified map of Fig. 2, and a NW–SE cross-section is shown in Fig. 3. The Silesian domain has traditionally been subdivided into the low-grade eastern Desná dome and the allochthonous medium-grade western Keprník nappe. The precise western boundary of the Silesian domain is uncertain, and the rock assemblages west of the Keprník nappe are provisionally assigned to a transition zone between the Lugian and Silesian domains. From east to west this zone

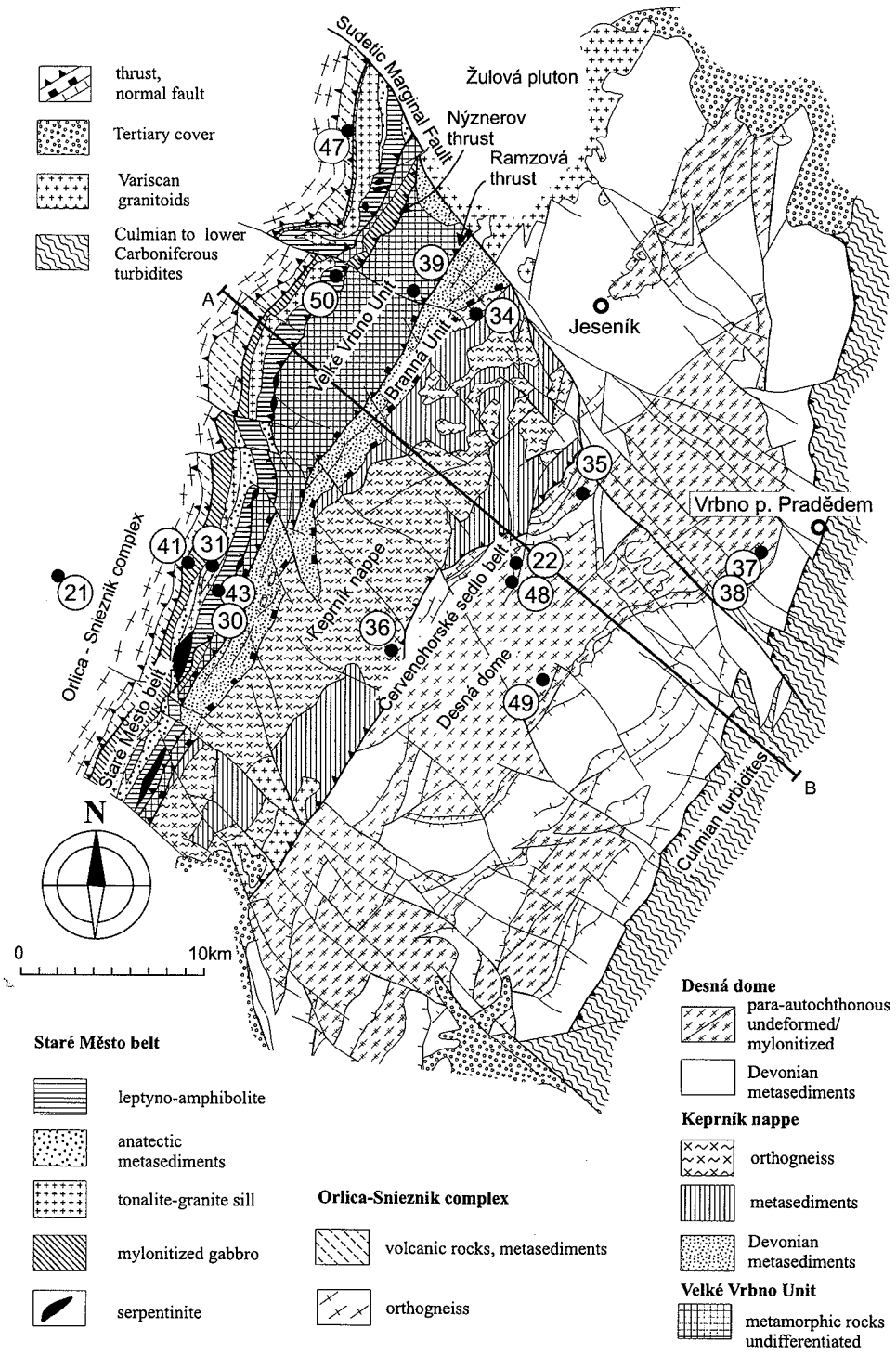

Fig. 2. Sketch map showing tectonic units of the Silesian and Lugian domains in the Jeseníky Mts, northeastern margin of the Bohemian Massif, eastern Czech Republic, and location of samples for which zircon ages were determined in this study (after Cháb, unpubl. map).

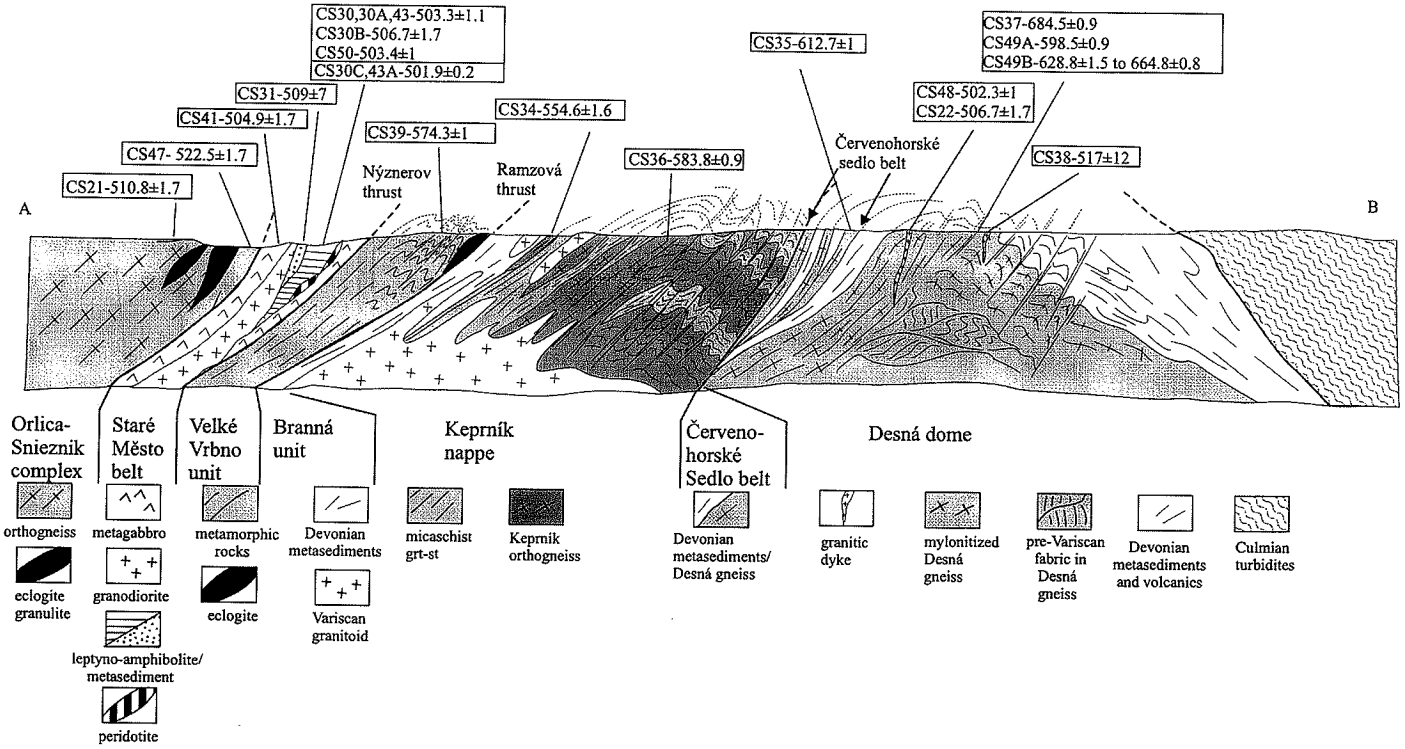

Fig. 3. Synoptic cross-section along line as indicated in Fig. 2 and showing various tectonic units, major tectonic boundaries and zircon ages reported in this paper. (For geological details, see Schulmann & Gayer (2000).)

consists of high-grade rocks of the Velké Vrbno unit and the Staré Město belt (Figs 2 and 3).

The Silesian domain has been affected by at least one pre-Variscan and two major Variscan tectono-metamorphic events. Pre-Variscan deformation (D1) and amphibolite facies metamorphism (M1) are locally preserved in crystalline complexes of the Desná dome and the Staré Město belt. The early Variscan deformation (D2) and metamorphism (M2) are related to major underthrusting of the entire Silesian domain below the Lugian domain (Schulman & Gayer 2000).

The parautochthonous core of the Desná dome is composed of medium-grade, biotite-rich layered gneisses and ophthalmitic to stromatitic migmatites. The cover sequence consists of quartzites of early Devonian (Pragian) age (Chlupáč 1994) as well as mica schists and metavolcanic rocks of mid-Devonian (Givetian) age (Fig. 3). The northwestern part of the cover is intruded by a Variscan calc-alkaline granite (the Žulová pluton, Fig. 2). The gneisses forming the core of the Desná dome display relics of pre-Variscan amphibolite facies metamorphism M1 (Fediuková *et al.* 1985), and these rocks were overprinted by Variscan greenschist to amphibolite facies deformation (Fig. 3).

The Keprník nappe is composed of a strongly deformed orthogneiss body tectonically intercalated with staurolite-bearing metapelites, calc-silicate rocks and quartzites. The Devonian sedimentary cover consists of low-grade polymictic conglomerates, quartzites, porphyroids, calc-silicate rocks and Devonian marbles. Variscan amphibolite facies deformation was later affected by strong D3 westward extension (Schulmann & Gayer 2000) (Fig. 3).

The Velké Vrbno unit (transitional zone) constitutes an anticlinal structure and is made up of sheets of felsic orthogneisses, metapelites, felsic and mafic metavolcanics, marbles and local occurrences of eclogites. All lithologies exhibit a strong amphibolite-facies metamorphic fabric.

Lower-crustal rocks of the Staré Město belt (transitional zone) define a narrow SW–NE trending linear domain (Fig. 2). The base is marked by a highly deformed sequence of leptyno-amphibolites associated with tonalitic gneisses and granulite facies metasediments that are intruded by a Variscan sill-like granodiorite body (Parry *et al.* 1997). In the hanging wall of the tonalite a layer of strongly sheared gabbro occurs. The earliest structures D1, and metamorphism M1, in rocks of the Staré Město belt are preserved in the leptyno-amphibolite sequence and associated metasediments. M1 reflects a transition from upper amphibolite to granulite facies conditions and exhibits temperatures of 800–900°C and pressures of 7–9 kbar (Parry *et al.* 1997; Štípská *et al.* 2000).

The eastern part of the Lugian domain consists of the Orlica–Snieznik dome, which is mainly built up of (1) granitic orthogneisses (Snieznik gneiss) and migmatites (Gieraltow gneiss) and (2) medium-grade staurolite schists with accompanying amphibolites, marbles and quartzites as well as low-grade felsic metavolcanic rocks, referred to in entirety as the Stronie Group. Locally there occur lensoid bodies of eclogite and intermediate to felsic high-pressure granulites (850°C, 19–22 kbar; Steltenpohl *et al.* 1993). The first fabric D1 is generally associated with high-temperature (HT) conditions and was affected by widespread D2 mylonitization under amphibolite facies conditions.

Previous geochronology

There are few precise ages for rocks in the area under discussion. Van Breeman *et al.* (1982) reported multigrain U–Pb zircon data for the Keprník gneiss and the Brno pluton, both part of the Brunia domain, and a Rb–Sr isochron age for the Snierznik gneiss of the Lugian domain. The Keprník gneiss sample revealed a complex zircon population of which six fractions are well aligned and yielded concordia intercept ages of $1422 + 191/-177$ and $546 + 6/-8$ Ma, respectively. The lower intercept age was interpreted to approximate the time of emplacement of the gneiss protolith, although considered by Van Breemen *et al.* as possibly being too low. The upper intercept age was ascribed to zircon inheritance from the source area of this crustally derived granite. Three discordant zircon fractions from a sample of Brno diorite (outside our study area) provided an upper concordia intercept age of 584 ± 5 Ma. Van Breemen *et al.* (1982) considered this to reflect the time of emplacement of the diorite. There are also K/Ar ages of uncertain significance ranging from 555 to 630 Ma on hornblende and biotite from the Brno pluton (Scharbert & Batík 1980).

Whole-rock samples of the Snieznik gneiss, sampled near the village of Žulová, yielded an Rb–Sr errorchron age of 487 ± 11 Ma (Van Breemen *et al.* 1982). Van Breemen *et al.* cautiously considered this to be the primary age of the gneiss protolith in view of the strong Variscan metamorphic overprint recorded in this area. Borkowska *et al.* (1990) reported an Rb–Sr whole-rock isochron age of 464 ± 18 Ma for Gieraltow migmatic gneisses and considered this to reflect the time of magmatic emplacement. Oliver *et al.* (1993) analysed three multigrain

zircon fractions from a mylonitized Sniezník gneiss collected near the Polish–Czech border, and the ambiguous results indicate crystallization of the gneiss precursor at either $488 + 4/-7$ or 504 ± 3 Ma ago. A SHRIMP single zircon study of Turniak *et al.* (2000) yielded identical ages of *c.* 500 Ma for both the Sniezník and Gieraltow gneisses and demonstrated the presence of numerous inherited cores as old as 2.6 Ga in the zircons analysed. Brueckner *et al.* (1991) presented Variscan Sm–Nd mineral isochron ages between 327 and 352 Ma for eclogites occurring as tectonic lenses in the Sniezník and Gieraltow gneisses in Poland.

Scharbert & Batík (1980) reported a 14-point Rb–Sr isochron age of 551 ± 6 Ma for widely scattered samples from the Thaya (Dyje) granite in the Brunian domain in the Czech–Austrian border region (outside our study area) and interpreted this as reflecting the time of emplacement. Recent SHRIMP zircon data for the Bittesch gneiss within the Thaya Batholith yielded a concordant mean $^{206}Pb/^{238}U$ age of 586 ± 7 Ma, whereas inherited cores yielded ages as old as 1377 Ma (Friedl *et al.* 1998)

Twenty-eight muscovite, biotite and amphibole $^{40}Ar/^{39}Ar$ ages were reported by Maluski *et al.* (1995) for the Desná, Keprník and Sniezník domes in the present study area, and these document a strong Variscan overprint with cooling ages ranging between 340 and 300 Ma. Laser analyses on single muscovite grains from mylonitic gneisses along the eastern rim of the Desná dome also produced older ages between 380 and 520 Ma, with the cores of these grains showing the older ages whereas the rims were apparently reset during the Variscan event (Maluski *et al.* 1995). No information concerning the primary emplacement age of these rocks can be extracted from these data.

Finally, Fritz *et al.* (1996) reported Neoproterozoic $^{40}Ar/^{39}Ar$ hornblende and muscovite ages from rocks of the Brunian domain north of Brno (outside our study area). These range between 610 and 565 Ma were interpreted to reflect a strong Cadomian event.

Description of samples, geochemistry and ages

The samples studied here were analysed for major and trace elements by X-ray fluorescence (XRF). Single zircons or groups of two grains each were analysed isotopically by evaporation, vapour digestion or ion microprobe (SHRIMP II), and the analytical procedures are summarized in the Appendix. The major and trace element compositions of the dated samples, a brief characterization of the zircon morphology as well as the evaporation analyses and the vapour digestion and SHRIMP analytical data, respectively, can be obtained from the Society Library or the British Library Document Supply Centre, Boston Spa, Wetherby, West Yorkshire LS32 7BQ, UK, as Supplementary Publication No. SUP 18148 (7 pages) The Nd mean crustal residence ages quoted below are based on a two-stage model, and details have been given by Hegner & Kröner (this volume). We present and discuss our samples and isotopic data in three groups, namely those from the Silesian domain, the Transition zone and the Lugian domain.

Silesian domain (core of the Desná dome)

The first two samples come from a quarry near Zámčisko at the hill Medvědí důl (Figs 2 and 3), where we found interlayered light grey (sample CS 49A) and dark grey (sample CS 49B) biotite schists interpreted as metagreywacke and folded together with, and intruded by, granitoid orthogneisses (Kölbl 1929). Sample 49A is a typical Desná plagioclase–biotite schist marked by a strong mylonitic fabric. It is composed of plagioclase, quartz, biotite and epidote $\pm$ muscovite. The foliation is enhanced by elongation of quartz aggregates and by alignment of biotite. Chemically the dated sample resembles a trondhjemite or dacite and this, together with the zircon morphology, suggests that this rock is of igneous derivation, either a dacitic lava or a tuff. Sample 49B is chemically, mineralogically and texturally similar to sample 49A. It is composed of plagioclase, quartz, biotite, epidote and some muscovite. The microstructure is mylonitic, and the foliation is enhanced by alignment of dispersed biotite and by flattening of quartz aggregates.

The zircons of sample CS 49A are perfectly idiomorphic, unlike detrital grains in a sedimentary rock. Five grains were evaporated individually and produced a combined mean age of 598.4 ± 0.9 Ma (Fig. 4a) that we interpret to reflect either the time of igneous emplacement of the host rock if it is a tuff or the age of the source rock if it is a volcanic greywacke. By implication, this is also the approximate age of deposition of the supracrustal sequence to which samples CS 49A and -B belong. The host rock is most probably derived from melting of crust that, if it was of volcanic origin, probably reflects magmatic material, perhaps generated in an arc environment. An $\varepsilon_{Nd(t)}$ value of -1.6 and a mean crustal residence age of 1.2 Ga (Hegner & Kröner this volume) suggest that the sample is

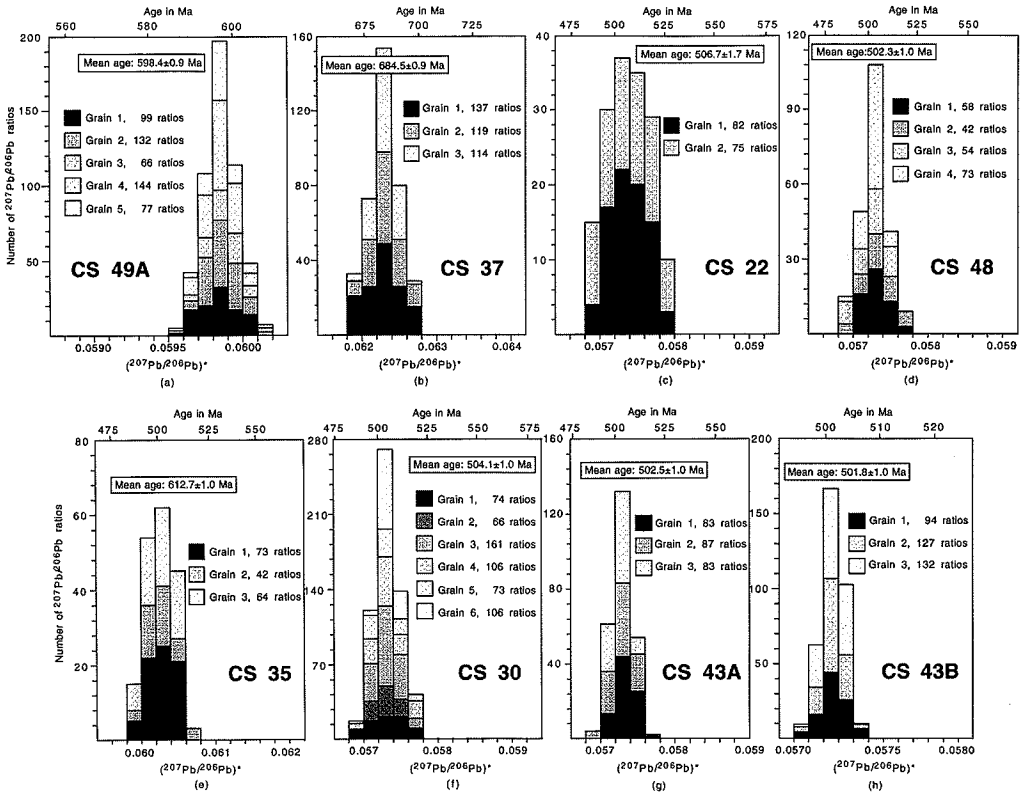

Fig. 4. Histograms showing distribution of radiogenic lead isotope ratios derived from evaporation of single zircons from Jeseníky Mts, northeastern Czech Republic. (**a**) Spectrum for five igneous zircons from metadacite or dacitic tuff sample CS 49A, quarry near Zámčisko. (**b**) Spectrum for three grains from leucocratic gneiss sample CS 37, Ludvíkov Cemetery, interpreted to reflect age of magmatic emplacement. (**c**) Spectrum for two grains from strongly foliated granite–gneiss sample CS 22, western Desná dome, east of Kouty nad Desnou, interpreted to reflect age of magmatic emplacement. (**d**) Spectrum for four grains from pegmatitic granite sample CS 48, forest SE of Kouty nad Desnou, Jeseníky Mts. (**e**) Spectrum for three grains from ultramylonitic orthogneiss sample CS 35, Filipovice. (**f**) Spectrum for six grains from tonalitic gneiss sample CS 30, Hanušovice quarry. (**g**) Spectrum for three grains from tonalitic gneiss sample CS 43A, Hanušovice quarry. (**h**) Spectrum for three grains from anatectic melt patch sample CS 43B, Hanušovice quarry. Analytical data are available as a Supplementary Publication (see p. 180).

derived from a source containing Grenvillian-age crustal material.

Metagreywacke sample CS 49B contains detrital zircons with morphologies that are typical of mechanical rounding during surface transport. Three grains were evaporated, and all have different ages ranging from 628.8 ± 1.5 to 664.8 ± 0.8 Ma, reflecting a Neoproterzoic source terrain. The $\varepsilon_{Nd(t)}$ value of -1.1 corresponds to a Nd mean crustal residence age of 1.2 Ga, identical to that of sample CS 49A (Hegner & Kröner this volume). This implies that the metagreywacke is derived from a source that contains a significant proportion of Grenvillian-age material, similar to the source of CS 49A.

Two other samples were collected from the northern termination of the Desná dome, which is composed of strongly mylonitic grandiorites and migratites (Novotný & Štelcl 1961; Fišera *et al.* 1986). The oldest rock dated in this region is a leucogranitic gneiss (sample CS 37, Figs 2 and 3) collected from a cliff NW of the Ludvíkov Cemetery some 20 km SSE of Jeseník, where it represents the main component of the Desná dome. The gneiss displays a strong foliation that is isoclinally folded with the development of a younger axial plane foliation. This younger foliation is folded together with a younger, 2 m wide dyke of porphyritic granite representing the youngest igneous phase of the pluton.

The dated sample is a mylonitized granite with relict clasts of plagioclase. It is composed of fine-grained albitic plagioclase, quartz, muscovite, relicts of biotite, chlorite and epidote. The microstructures as well as the mineralogy are consistent with very low grade conditions (chlorite zone) of deformation. Chemically the sample is a quartz monzonite.

The zircons have slightly rounded terminations, a feature common in metamorphic rocks and generally ascribed to metamorphic corrosion (for detailed discussion of this feature, see Kröner *et al.* (1994) and Kröner & Hegner (1998). Three grains were evaporated individually and yielded virtually identical $^{207}Pb/^{206}Pb$ isotopic ratios that combine to a mean age of 684.5 ± 0.9 Ma (Fig. 4b), which we interpret as reflecting the crystallization age of the gneiss protolith. One further grain with slightly more pronounced rounding at the ends yielded a significantly higher age of 864.0 ± 1.6 Ma; we interpret this grain as a xenocryst. As in the previous sample, the presence of xenocrysts suggests involvement of older crustal material in the generation of the host granitoid, but an $\varepsilon_{Nd(t)}$ value of +0.6 and a mean crustal residence age of 1.3 Ga (Hegner & Kröner this volume) make it likely that this crust has mixed with a considerable amount of juvenile material. We therefore suggest a continental-margin type magmatic arc for the generation of the Desná dome. The above granite emplacement age of *c.* 684 Ma is the oldest yet encountered anywhere along the eastern margin of the Bohemian Massif and clearly reflects the Cadomian (Pan-African)-age Brunia terrane outlined earlier.

The porphyritic dyke cross-cutting the gneiss has also been dated (sample CS 38) by both the vapour digestion and evaporation techniques. This rock is a porphyritic granite composed of K-feldspar, plagioclase, quartz, biotite and new phases of chlorite, muscovite and epidote. A weak foliation is underlined by microshear zones developed in the fine-grained matrix. Vapour digestion analysis of three very clear and idiomorphic zircon grains provided discordant results that can be fitted to a chord through the origin (mean square weighted deviates (MSWD) = 0.1) intersecting concordia at 517 ± 12 Ma (Fig. 5a). In view of the euhedral shape of the zircons we interpret this age as representing the time of crystallization of the porphyritic granite. Four further grains with slightly rounded terminations were evaporated and produced significantly older results between 594 and 911 Ma (Fig. 5a, inset); we interpret these grains as xenocrysts derived from the source region of the granite. The $\varepsilon_{Nd(t)}$ value of −4.3 and the Nd mean crustal residence age of 1.5 Ma (Hegner & Kröner this volume) support the conclusion that an appreciable amount of older crust was involved in the generation of the porphyritic granite. The emplacement age of 517 Ma is similar to early Palaeozoic ages elsewhere in the West Sudetes Mts (Oliver *et al.* 1993; Kröner *et al.* 1994, 1997; Kröner & Hegner 1998), and the significance of this will be discussed below.

Silisian domain (eastern margin of Desná dome)

The eastern part of the Desná dome is exposed in a broad belt east of the town of Šumperk (Figs 2 and 3), and two samples were dated from this area. The first is a massive, fine-grained ophthalmitic migmatite (sample CS 22) containing porphyroblasts of plagioclase and collected from the bank of the Desná River east of the village of Kouty nad Desnou (Figs 2 and 3). Chemically the rock is a granite. It has been described as a retrograded pearl gneiss (Fediuková *et al.* 1985) and consists of plagioclase, quartz, biotite and garnet ($\pm$ chlorite and muscovite). Plagioclase, quartz and biotite constitute the matrix minerals and define the foliation. The rock is locally affected by microshears parallel to an early foliation.

There are two zircon generations in this rock, one idiomorphic and one with slightly rounded terminations. Two grains of the first variety produced a mean $^{207}Pb/^{206}Pb$ age of 506.7 ± 1.7 Ma (Fig. 4c), which we interpret as the time of emplacement of the gneiss protolith. Seven grains of the second variety yielded variable $^{207}Pb/^{206}Pb$ ages ranging between 604 and 1106 Ma, and we interpret these gains as xenocrysts from an older basement. However, it is unlikely that the Desná gneiss was derived from anatexis of this basement, as its $\varepsilon_{Nd(t)}$ value of −0.3 and the mean crustal residence age of 1.2 Ga (Hegner & Kröner this volume) suggest that a fair amount of relatively young material was involved in its generation. The most plausible explanation for the Nd isotopic systematics is mixing of an igneous source, possibly from an underplated juvenile reservoir, with older crust. Like sample CS 38, the emplacement age of 507 Ma is similar to Cambro-Ordovician ages for granitoids along the entire eastern margin of the Bohemian Massif in the West Sudetes Mts of Poland and the Czech Republic (Oliver *et al.* 1993; Kröner *et al.* 1994; Kröner & Hegner 1998).

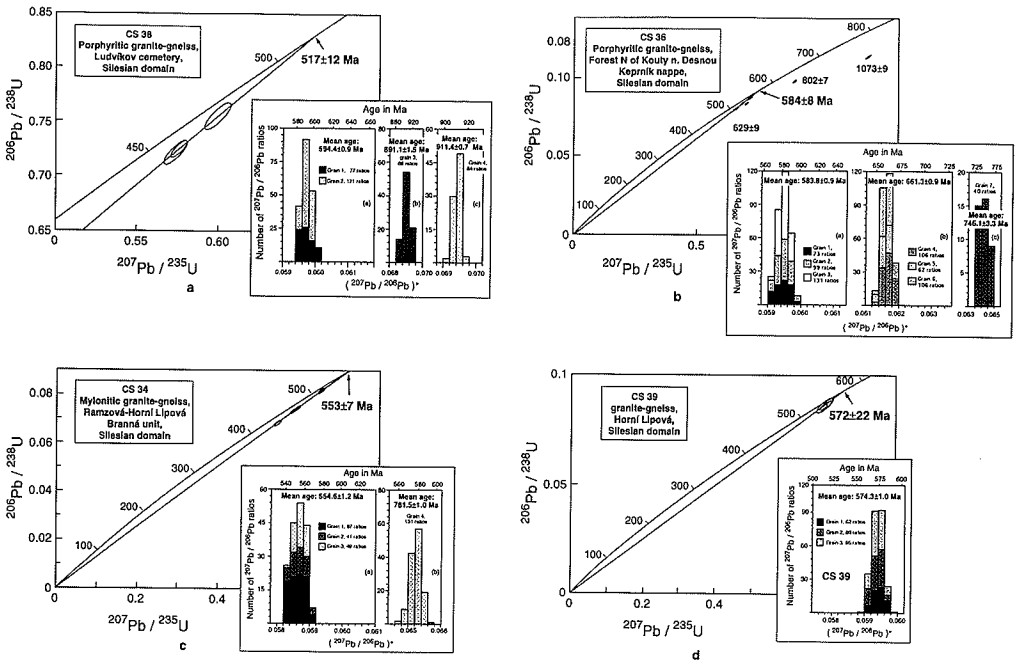

Fig. 5. Concordia diagrams showing analytical data for single zircons from rocks of the Jeseníky Mts, northeastern Czech Republic. (**a**) Porphyritic granite–gneiss sample CS 38. Inset shows histograms with distribution of radiogenic lead isotope ratios derived from evaporation of single zircons from same sample. (**b**) Keprník granite–gneiss sample CS 36, forest north of Kouty nad Desnou, Jeseníky Mts. Inset shows histograms with distribution of radiogenic lead isotope ratios derived from evaporation of single zircons from same sample. (**c**) Mylonitic orthogneiss sample CS 34, hill between Ramzová and Horní Lipová. Inset shows histograms with distribution of radiogenic lead isotopic ratios derived from evaporation of single zircons from same sample. (**d**) Granite–gneiss sample CS 39, Horní Lipová. Inset shows histogram with distribution of radiogenic lead isotope ratios derived from evaporation of single zircons from same sample. Analytical data are available as a Supplementary Publication (see p. 180).

The second sample (CS 48) is a whitish, coarse- to medium-grained, almost pegmatitic granite that cross-cuts the fabric in the Desná migmatitic gneiss and is itself slightly deformed. The sample was collected in the forest between the hills Medvědí and Tupý about 1.5 km SSE of sample CS 22 (Figs 2 and 3). Chemically this is a granite, and the sample is composed of K-feldspar, plagioclase, quartz and muscovite. It is affected by greenschist facies heterogeneous deformation and exhibits relict igneous textures. Four idiomorphic zircon grains were evaporated individually and yielded a combined mean $^{207}Pb/^{206}Pb$ age of 502.3 ± 1.0 Ma (Fig. 4d) that we interpret to reflect the time of magmatic emplacement. The $\varepsilon_{Nd(t)}$ value of -1.0 (Hegner & Kröner this volume) suggests that this rock is not entirely the result of remelting of old crust, but that some young material must have been involved in its generation. This sample is only marginally younger than our Desná gneiss sample CS 22, and this implies that the foliation seen in the Desná gneiss must have formed between 507 and 502 Ma ago, i.e. during an early Palaeozoic event and not during Variscan deformation as was previously thought (Fediuková *et al.* 1985).

Silesian domain (Červenohorské sedlo belt)

We dated only one sample from this domain, and this is a tightly folded, grey, fine-grained ultramylonitic granite (sample CS 35) that belongs to one of the sheets forming the strongly mylonitized Červenohorské sedlo belt, which occurs between the Keprník nappe and the Desná dome (Fig. 3). The sample was collected in a forest near the main Jeseník–Šumperk road about 1 km south of Filipovice (Figs 2 and 3). It is a mylonitic orthogneiss with rare relics of small porphyroclasts of K-feldspar (0.3 mm in size). The fine-grained matrix is composed of plagioclase, K-feldspar, quartz and biotite. The microstructure is consistent with medium-grade conditions (staurolite zone) of mylonitization.

The zircons are idiomorphic and appear completely unaffected by the intense mylonitization. Three grains were evaporated and provided a combined mean $^{207}Pb/^{206}Pb$ age of 612.7 ± 1.0 Ma (Fig. 4e) that we interpret as reflecting the time of the original granite emplacement. The $\varepsilon_{Nd(t)}$ value of 0.4 and the Nd mean crustal residence age of 1.2 Ga (Hegner & Kröner this volume) suggest that this rock is not derived from remelting of very old basement but that late Proterozoic material was involved in its generation.

Silesian domain (Keprník nappe)

We dated two samples from the pre-Variscan crystalline rocks of the Keprník nappe. The first is the porphyritic and well-foliated leucocratic Keprník gneiss (CS 36), which was collected in the forest north of Kouty nad Desnou (Figs 2 and 3). Chemically the gneiss is of granitic composition. Under the microscope the dated sample is a typical orthogneiss, composed of K-feldspar + plagioclase + quartz + muscovite. The foliation is defined by an alignment of biotite and elongation of quartz ribbons. The microstructures are characteristic of amphibolite facies conditions of deformation.

The zircons are slightly rounded at their terminations as a result of a metamorphic overprint. Six grains were analysed by vapour digestion, of which three are near-concordant and well aligned (MSWD = 0.06), providing a concordia intercept age of 584 ± 8 Ma (Fig. 5b). Two further grains have distinctly older $^{207}Pb/^{206}Pb$ minimum ages of 802 ± 7 and 1073 ± 9 Ma, and are interpreted as xenocrysts. The result for a further grain is slightly offset to the right of the discordia line, and the $^{207}Pb/^{206}Pb$ age is 629 ± 9 Ma (Fig. 5b). This grain is probably a mixture of old material and *c.* 584 Ma overgrowth and is not further considered here. Evaporation of three grains yielded a mean $^{207}Pb/^{206}Pb$ age of 583.8 ± 0.9 Ma, indistinguishable from the U–Pb age, whereas three further grains provided identical isotopic ratios that combine to a mean age of 661.3 ± 0.9 Ma. One further grain has an age of 746.1 ± 3.3 Ma (Fig. 5b, inset). We interpret all pre-584 Ma grains as xenocrysts, inherited from older crustal material, and suggest that there was a significant amount of 661 Ma crust in the source region of the gneiss, as suggested by the relative abundance of zircons of that age.

The two dating methods essentially provide the same picture, namely that crystallization of the gneiss precursor occurred at about 584 Ma, whereas the xenocrysts provide evidence of older crust dating back to 1073 Ma. The $\varepsilon_{Nd(t)}$ value is -5.8 and equivalent to a mean crustal residence age of 1.8 Ga (Hegner & Kröner this volume). These values clearly document a significant involvement of older crust in the generation of this rock. In fact, it is possible that the Keprník gneiss is entirely due to remelting of older curst. This is also supported by previous U–Pb zircon dating by Van Breemen *et al.* (1982), whose data for six strongly discordant multigrain fractions scatter about a discordia line with concordia intercept ages of $1422 + 191/-177$ Ma and $547 + 6/-8$ Ma, respectively. The disagreement between our crystallization age of 584 Ma and the lower intercept age of 547 Ma determined by Van Breemen *et al.* (1982) is not surprising, as the latter date is most probably the result of interpolation and Pb loss, and is therefore too low, as already noted by those workers. We conclude that the Keprník gneiss precursor was emplaced some 583 Ma ago and therefore belongs to the Cadomian-age Brunia terrane discussed above.

The second sample (CS 34) comes from the cover of the Keprník nappe, also known as the lower part of the Branná unit (Cháb 1986), and was collected on a steep hill below the railway line from Ramzová to Horní Lipová (Figs 2 and 3). This is a very fine-grained highly sheared pre-Devonian orthogneiss of granitic composition. Under the microscope it shows characteristic features of an ultramylonite composed of K-feldspar, plagioclase, quartz and biotite. The microstructural features are consistent with mylonitization of a granitic protolith under upper greenschist to lower amphibolite facies conditions.

The zircons are similar to those in sample CS 35 and were apparently not affected by mylonitization of the host rock. Four grains were analysed after vapour digestion and provided results that are between 5 and 25% discordant but can be fitted to a discordia line (MSWD = 0.44) with an upper concordia intercept at 553 ± 7 Ma (Fig. 5c). The same result was obtained by evaporation of three grains that yielded a mean $^{207}Pb/^{206}Pb$ age of 554.6 ± 1.2 Ma (Fig. 5c, inset). One grain had a significantly older $^{207}Pb/^{206}Pb$ age of 781.5 ± 1.0 Ma and is probably inherited from the source region of the original granite. Intracrustal melting is the most likely process by which the protolith of sample CS 34 was generated, and this is also supported by an $\varepsilon_{Nd(t)}$ value of -4.7, which corresponds to a mean crustal residence age of 1.6 Ga (Hegner & Kröner this volume). We consider that the age of *c.* 555 Ma approximates the time of

emplacement of the original granite and note that the mylonitic deformation has not affected the isotopic systematics of the zircons. Therefore, the time of mylonite formation remains undated. The mylonitized granite, like the previous samples, belongs to the Cadomian-age Brunia terrane that we have now identified within all three tectonic units of the Silesian domain.

Transitional zone (Velké Vrbno unit)

We have dated only one sample from this unit, a strongly foliated orthogneiss (sample CS 39) collected in a forest WNW of Horní Lipová (Figs 2 and 3). Chemically the rock is classified as a tonalite, and consists of plagioclase, quartz, amphibole and chloritized biotite. The dated sample displays a banded structure marked by alternation of polycrystalline aggregates of subsequent grains of plagioclase with layers rich in amphibole and biotite. The microstructures are consistent with high-grade conditions of fabric acquisition.

The zircons have well-rounded terminations, and analysis of three grains after vapour digestion provided almost concordant results with a mean $^{207}Pb/^{206}Pb$ age of 570 ± 6 Ma. If the tightly grouped data points are fitted to a chord through the origin (MSWD = 0.07) the intercept age is identical, but less precise, at 572 ± 22 Ma (Fig. 5d). Three further grains were evaporated and yielded a combined mean $^{207}Pb/^{206}Pb$ age of 574.3 ± 1.0 Ma (Fig. 5d, inset). We consider the age of *c.* 574 Ma as most closely reflecting the time of intrusion of the granitic gneiss precursor. The $\varepsilon_{Nd(t)}$ value of 1.9 and the Nd model age of 1.1 Ga (Hegner & Kröner this volume) indicate a significant involvement of young or juvenile material in the generation of this rock. The age of 574 Ma is in the same range as most ages for the Silesian domain discussed above and suggests at least part of the Velké Vrbno unit to be derived from a Cadomian-age crustal unit.

Transitional zone (Staré Město belt)

The first six samples came from the leptyno-amphibolite sequence in a quarry just west of the village of Hanušovice (Figs 2 and 3) where the amphibolites are intercalated with tonalitic gneisses. The dominant rock type in this quarry is a strongly foliated tonalitic gneiss that locally contains thin layers of granodioritic gneiss. The tonalite is transected by numerous high-temperature ductile extensional shear zones in which *in situ* melt patches occur, indicating local anatectic mobilization of the tonalitic material during a high-grade metamorphic event. The tonalite is concordant with the planar fabric of the enclosing leptyno-amphibolite complex. It is essentially composed of quartz, plagioclase, biotite, amphibole and garnet. Elongate aggregates of amphibole and biotite separate the leucocratic layers consisting of coarse elongate plagioclase and well-annealed quartz that occurs in large aggregates or in the form of drops between the plagioclase grains. The microstructure corresponds to very high temperature conditions of fabric acquisition.

We have dated zircons from the tonalitic gneiss where it is unaffected by later anatexis (samples CS 30, 30A and 43A, taken from different locations in the quarry), from a granodioritic gneiss intercalation (CS 30B) and from the *in situ* melt patches (CS 30C, 43B). Three grains from sample CS 30 and six grains from sample CS 30A were analysed by vapour digestion, and the results are between 10 and 20% discordant, but can be fitted to a chord through the origin (MSWD = 0.38) that intersects concordia at 504 ± 4 Ma (Fig. 6a). Six further grains from sample CS 30 were evaporated individually and produced almost identical $^{207}Pb/^{206}Pb$ ratios that combine to a mean age of 504.1 ± 1.0 Ma (Fig. 4f). Evaporation of four grains from sample CS 30A yielded an identical age of 503.2 ± 1.0 Ma (Fig. 6a, inset), and a mean $^{207}Pb/^{206}Pb$ age of 502.5 ± 1.0 could be calculated from evaporation of three grains from sample CS 43A (Fig. 4g). In summary, both dating methods yielded identical results, and we adopt a weighted mean age of 503.3 ± 1.0 Ma for the intrusion of the tonalitic gneiss precursor.

Zircons from the more leucocratic gneiss variety represented by sample CS 30B are identical to those in the previous samples. Analysis of three grains by vapour digestion produced very consistent results that are about 15% discordant and, if fitted on a chord through the origin, intersect the concordia at 507 ± 19 Ma (diagram not shown). The mean $^{207}Pb/^{206}Pb$ age is 506.7 ± 1.7 Ma. We conclude from this that the leucocratic phase of the Hanušovice gneiss is identical in age to the tonalitic phase. One further grain yielded a much higher $^{207}Pb/^{206}Pb$ minimum age of 818 ± 16 Ma; this again is a xenocryst, probably derived from the source region of the gneiss or taken up during its ascent.

The combined weighted mean age for all zircons evaporated from the tonalitic and granodioritic gneiss samples is 503.3 ± 0.8 Ma. This is in the same range of Cambro-Ordovician granitoid emplacement ages as found in the Orlické Hory Mts to the west and in other parts of the Sudetes Mts (Oliver *et al.* 1993; Kröner *et al.*

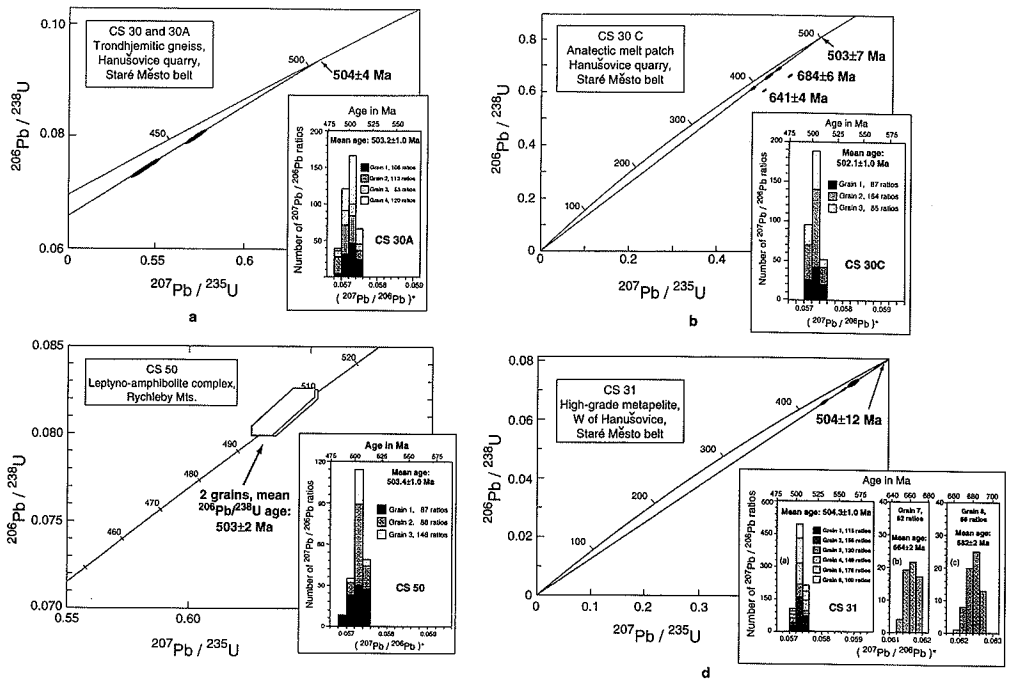

Fig. 6. Concordia diagrams showing analytical data from single zircons from rocks of the Jeseníky Mts, northeastern Czech Republic. (**a**) Eight grains from tonalitic gneiss samples CS 30 and 30A, Hanušovice quarry. Inset shows histogram with distribution of radiogenic lead isotope ratios derived from evaporation of four single zircons from sample CS 30A. (**b**) Six grains from anatectic melt patch sample CS 30C, Hanušovice quarry. Inset shows histogram with distribution of radiogenic lead isotope ratios derived from evaporation of three single zircons from same sample. (**c**) SHRIMP II analyses of two zircons from metarhyodacite sample CS 50, Skorošice, Rychleby Mts. Data boxes for each analysis are defined by standard errors in $^{207}Pb/^{235}U$, $^{206}Pb/^{238}U$ and $^{207}Pb/^{206}Pb$. Inset shows histogram with distribution of radiogenic lead isotope ratios derived from evaporation of three single zircons from same sample. (**d**) Three metamorphic zircons from metapelite sample CS 31, NE of Vlaské, Jeseníky Mts. Inset shows histograms with distribution of radiogenic lead isotope ratios derived from evaporation of single zircons from same sample. Analytical data are available as a Supplementary Publication (see p. 180).

1994). The Nd isotopic systematics of the two gneiss varieties are similar and preclude derivation of these rocks from anatectic melting of much older crust. Tonalite sample CS 30A has an $\varepsilon_{Nd(t)}$ value of +3.4 and a mean crustal residence age of 0.91 Ga, whereas granodioritic gneiss sample CS 30B has an $\varepsilon_{Nd(t)}$ value of 6.4 and an Nd model age of 0.67 Ga (Hegner & Kröner this volume). We suggest that the granitoid pluton from which the Hanušovice gneisses are derived formed from a mixture of juvenile material and minor late Proterozoic crust. Underplating of gabbroic magma at the base of the crust and interaction with the lower crust is a likely scenario for this process.

Anatectic melt patches of trondhjemitic composition within the tonalitic gneiss are coarse grained and, under the microscope, are composed of plagioclase (50–60 vol. %), weakly recrystallized quartz and rare (5 vol. %) biotite. Quartz is strongly annealed and forms isolated pockets in a framework of feldspar. Newly formed zircons in the anatectic melt samples CS 30C and 43B are exclusively short-prismatic and have sharp terminations. Six grains from sample CS 30C were analysed by vapour digestion and display a similar discordance pattern to the analyses discussed above. Four points are well aligned and define a chord intersecting concordia at 503 ± 7 Ma (Fig. 6b), whereas two grains are distinctly older with $^{207}Pb/^{206}Pb$ minimum ages of 641 ± 4 and 684 ± 6 Ma, respectively. Although no older cores could be seen under the optical microscope in these completely transparent grains, we suspect that the above ages reflect core-overgrowth relationships and signify the presence of older crustal material in the source region of the original tonalite from which the old grains must ultimately be derived. Three other idiomorphic

grains from sample CS 30C were evaporated and yielded a combined mean age of 502.1 ± 1.0 Ma (Fig. 6b, inset), identical to, but more precise than, the U–Pb age. Zircons from sample CS 43B were only evaporated, and three grains produced a combined mean age of 501.8 ± 1.0 Ma(Fig. 4h). Again, this age is indistinguishable from the two previous determinations. The weighted mean evaporation age of the two melt samples CS 30C and 43B is 501.9 ± 0.6 Ma, slightly younger than the mean age of 503.3 ± 0.8 Ma for the gneissic samples. The $\varepsilon_{Nd(t)}$ value for sample CS 30C is 2.3 and the mean crustal residence age is 0.99 Ga, very similar to that of sample CS 30A (Hegner & Kröner this volume). This is not surprising, as the Nd isotopic systematics are normally not affected by intracrustal melting and differentiation.

The above data for the Hanušovice quarry can be interpreted in two ways. Either the fabric-forming event and subsequent anatectic melting occurred almost immediately after emplacement of the original tonalite, and in this case high-grade metamorphism and extensional deformation was associated with this event or, alternatively, *all* zircons dated from the melt patches are inherited, and the melting and deformational event remains undated. We give preference to the first interpretation, as we have already demonstrated a fabric-forming event at just above 500 Ma in the Desná dome of the Silesian autochthonous domain, and there is also evidence for a *c.* 500 Ma granulite-facies metamorphic event in the Hanušovice area as discussed below.

Another sample from the northern part of the leptyno-amphibolite sequence in the Rychleby Mts is from a felsic layer of this sequence, exposed on a cliff in the forest near Stříbrný hill and near the Polish border (sample CS 50, see Figs 2 and 3). The sequence is tightly isoclinally folded and is also affected by high-grade metamorphism as shown by local melt patches. Chemically the sample CS 50 is a rhyodacite, and the mineral composition is plagioclase, quartz and minor amphibole. The foliation is defined by flattened grains or aggregates of quartz and plagioclase, and by compositional banding marked by alternations of layers rich in amphibole with layers composed only of felsic minerals.

Two zircon grains of sample CS 50 were analysed on SHRIMP II and produced concordant results (Fig. 6c) with a mean $^{206}Pb/^{238}U$ age of 503 ± 2 Ma. Evaporation of three further grains yielded identical results, and the combined mean $^{207}Pb/^{206}Pb$ age is 503.4 ± 1.0 Ma (Fig. 6c, inset). We interpret this to reflect the time of emplacement of the original rhyodacite, and this is time-equivalent with the intrusion of the Hanušovice tonalitic gneiss precursor. This age underlines the regional significance of the *c.* 500 Ma event in the Staré Město belt in particular and in the Lugian domain in general.

The next sample (CS 41) is an anorthositic gneiss collected from a unit of layered gabbroic gneiss exposed in the forest west of the village of Vlaské and some 2 km NW of the Hanušovice quarry (Figs 2 and 3). The exposure from which this sample was taken clearly reveals relict magmatic layering in a ductilely deformed metagabbro, strongly reminiscent of layered gabbros in ophiolite suites. The rock is medium grained and dominantly composed of plagioclase enclosing irregular small grains of quartz.

Zircons in this sample were rare, small (60–80 μm in length) and displayed slight rounding at their ends. To obtain a strong enough signal for Pb isotopes in the mass spectrometer, three grains were evaporated together in two batches and yielded almost identical results that combine to a mean age of 504.9 ± 1.0 Ma (Fig. 7a). This is interpreted to reflect the crystallization age of the anorthosite and, by implication, of the layered gabbro unit. If the interpretation of this unit as part of a dismembered ophiolite suite is correct (Mísař *et al.* 1984), then this is also the formation age of the oceanic crust from which this ophiolitic fragment is derived. The $\varepsilon_{Nd(t)}$ value for the meta-anorthosite is 0.5, and the Nd model age is 1.1 Ga (Hegner & Kröner this volume). These values make it unlikely that the layered gabbro unit is derived from Nd-depleted oceanic crust of mid-ocean ridge basalt (MORB) composition. We rather suspect that the ophiolite suite formed in a marginal basin where the input of Nd-enriched detritus led to contamination of the upper-mantle source region, similar to processes envisaged for the generation of supra-subduction zone ophiolites (Pearce 1987; Zimmer *et al.* 1995).

The last sample (CS 31) is a pelitic, granulite facies, garnetiferous paragneiss occurring tectonically above the tonalitic gneiss and collected some 1.5 km NW of the Hanušovice quarry at a roadcut on a narrow road leading to the village of Žleb (Figs 2 and 3). Under the microscope the rock consists essentially of plagioclase, biotite, quartz, garnet and rutile in the matrix, and plagioclase forms porphyroblasts up to 0.5 cm in size.

There are two types of zircon in this sample, detrital and metamorphic. The latter type has been described from many granulite terrains and is believed to form at temperatures above 800°C near or at the peak of high-grade metamorphism

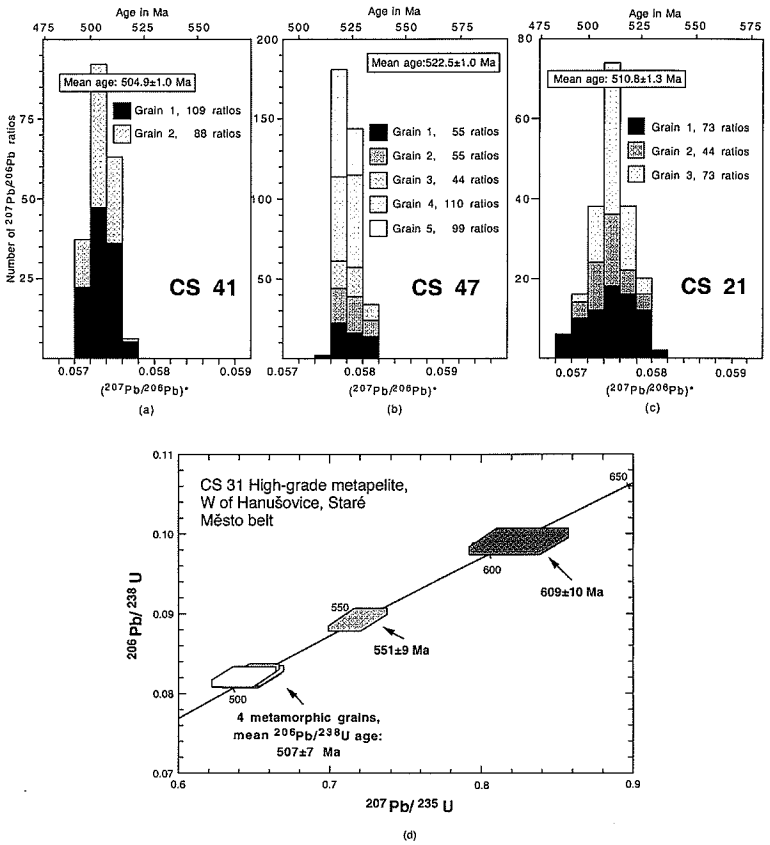

Fig. 7. Histograms (**a–c**) and concordia diagram (**d**) showing distribution of radiogenic lead isotope ratios for zircon analyses of samples from Jeseníky Mts, northeastern Czech Republic. (**a**) Spectrum for two fractions of three zircons each from anorthositic gneiss sample CS 41, west of Hanušovice. (**b**) Spectrum for five grains from felsic metadacite sample CS 47, Stronie Formation, Hraničná, Vojtovice, interpreted to reflect age of magmatic emplacement. (**c**) Spectrum for three grains from granitic augen-gneiss sample CS 21, Morava River, east of Králíky, Orlické Hory Mts. (**d**) SHRIMP II analyses of six metamorphic zircons from metapelite sample CS 31, NE of Vlaské, Jeseníky Mts. Data boxes as in Fig. 6c. Analytical data are available as a Supplementary Publication (see p. 180).

(see summary and references given by Kröner & Willner (1998). Cathodoluminescence photographs of these zircons reveal well-developed sector zoning, as is typical of metamorphic grains (Vavra 1990; Kröner & Willner 1998), and no older cores. Three metamorphic grains were analysed by vapour digestion and produced slightly discordant results that can be fitted on a chord through the origin (MSWD = 0.03) intersecting concordia at 504 ± 12 Ma (Fig. 6d). Six further grains were analysed by SHRIMP II and produced concordant results, of which four have a combined mean $^{206}Pb/^{238}U$ age of 509 ± 7 Ma (mean $^{207}Pb/^{206}Pb$ age is 502 ± 19 Ma), whereas the remaining grains have minimum ages of 551 ± 9 and 609 ± 10 Ma, respectively (Fig. 7d). The first four grains are clearly metamorphic, and their age is identical to that of the zircons analysed by vapour digestion, whereas the two additional grains are probably detrital (the difference between round, multifaceted grains and mechanically rounded detrital grains is almost impossible to see on mounted photographs for SHRIMP analysis). Six further multifaceted grains were evaporated and yielded virtually identical $^{207}Pb/^{206}Pb$ ratios that combine to a mean age of 504.3 ± 1.0 Ma (Fig. 6d, inset). Finally, we evaporated two of the detrital grains and obtained minimum ages of 663.5 ± 1.7 and 681.5 ± 1.5 Ma (Fig. 6d, inset). The detrital population analysed would suggest that the metapelite protolith was deposited after 551 Ma.

The $\varepsilon_{Nd(t)}$ value for sample CS 31 is 0.2, assuming depositional age of about 550 Ma, and the corresponding Nd mean crustal residence age is 1.2 Ga (Hegner & Kröner this volume). As in the case of metagreywacke sample CS 49B, the metapelite was not derived from erosion of ancient crust but from predominantly young (Neoproterozoic) crustal material, probably a Cadomian-age magmatic arc terrane. We conclude from the zircon and Nd data that the pelitic sediment from which sample CS 31 originated was deposited at some time after 551 Ma, probably as the erosion product of a Neoproterozoic magmatic arc terrane, and was metamorphosed to granulite-facies conditions at about 504 Ma.

Lugian domain

The first sample (CS 47) was collected just west of the Staré Město belt, in the Rychleby Mts about 500 m west of the village of Vojtovice (Figs 2 and 3). It is a well-layered felsic metavolcanic rocks, chemically a dacite, that is part of the sequence of metasediments. Under the microscope the rock consists essentially of plagioclase, quartz, K-feldspar and minor muscovite and biotite. The foliation is accentuated by elongation of quartz ribbons, plagioclase aggregates and by alignment of fine-grained muscovite and biotite. Five zircon grains were evaporated and produced a combined mean age of 522.5 ± 1.0 Ma (Fig. 7b) that we interpret to reflect the time of extrusion of the metadacite precursor. This age is identical to a single zircon evaporation age for a metadacite from the type locality of the Stronie formation near Romanov in the Orlica–Snieznik dome, Poland (Kröner & Don, unpubl. data), and confirms the correlation of the two units. One further zircon grain from sample CS 47 yielded a much higher $^{207}Pb/^{206}Pb$ age of 1752.5 ± 2.1 Ma and is most probably a xenocryst. The $\varepsilon_{Nd(t)}$ value of -5.0 and the mean crustal residence age of 1.6 Ga (Hegner & Kröner this volume) attest to the crustal origin of this metadacite whose source region is distinctly different from, and older than, the samples in the southern part of the Staré Město belt discussed above.

The Orlica–Snieznik dome is largely made up of granitoid gneisses (Fig. 2), and we report the results for only one sample from this rock type, as additional zircon ages and Nd isotopic characteristics will be published elsewhere (Kröner *et al.* 2000). Sample CS 21 is a well-foliated augen-gneiss of granitic composition, collected on the bank of the Morava River, east of Králíky (Figs 2 and 3). It is similar to many of the granitic gneisses exposed in the Orlické Hory Mts farther west and consists of plagioclase, quartz, biotite, muscovite and subordinate K-feldspar. The foliation is enhanced by the preferred orientation of biotite.

Three zircon grains were evaporated and yielded a combined mean $^{207}Pb/^{206}Pb$ age of 510.8 ± 1.3 Ma (Fig. 6c). The $\varepsilon_{Nd(t)}$ value is -3.9 and corresponds to a mean crustal residence age of 1.5 Ga (Hegner & Kröner this volume). These data suggest generation of the gneiss protolith by intracrustal melting, and the age and Nd isotopic characteristics of this granite gneiss are similar to those of several other granitoid gneisses from the Orlické Hory Mts farther west (Kröner *et al.* 2000), suggesting that this part of the Lugian domain is the result of a major Cambro-Ordovician magmatic event that is evident almost everywhere in the Czech and Polish Sudetes Mts along the eastern margin of the Bohemian Massif (Oliver *et al.* 1993; Kröner & Hegner 1998).

Discussion and conclusions

Our new zircon ages enable us to reconstruct the Neoproterozoic to Cambro-Ordovician evolution of part of the northeastern Bohemian Massif, in particular the contact zone between the Brunia and Lugian domains.

Silesian domain, westernmost part of Neoproterozoic Brunia

The myolitized gneisses of the major constituents of the Silesian domain (the Desná dome and the Keprník nappe) exhibit Neoproterozoic ages of emplacement. Moreover, the ultramylonitic rocks of thrust sheets located between the Desná dome and Keprník nappe (Červenohorské sedlo mylonitic belt) and in the footwall of the Devonian cover of the Keprník nappe (Branná Group) are also of Neoproterozoic age. We therefore interpret the Silesian domain as the northernmost part of the Brunia plate, which was underthrust below the Lugian plate, subsequently imbricated in the form of large crystalline nappes and then exhumed (Fig. 3). One of the major problems is the definition of the western limit of the Brunia plate, which is traditionally placed between the Devonian cover of the Keprník nappe and the Velké Vrbno unit. Our study has shown that at least part of the Velké Vrbno high-grade rocks are also derived from the Brunia plate. This, together with the presence of undoubtedly Variscan Barrovian metamorphism (kyanite schists) and

medium-temperature (MT) eclogites, indicates that the Velké Vrbno unit represents the most deeply buried part of the Brunia microplate. Therefore, the Ramzová overthrust of Suess (1926) can no longer be considered as the easternmost limit of the Brunia plate; the boundary must be placed farther west, below the Staré Město belt.

Silesian domain; Cambro-Ordovician event

Our zircon ages document Cambro-Ordovician magmatic and metamorphic activity affecting the Brunia microplate. The thermal effect of this event was weak and is documented only by granitic (CS 38) and pegmatitic dykes (CS 48). Metamorphism locally reached the stage of partial melting, e.g. sample CS 22, but the precise PT conditions, as a result of the strong Variscan overprinting (Fediuková *et al.* 1985), cannot be determined. The Nd isotopic systematics for two of the above samples (CS 22 and CS 48) suggest participation of primitive material in the generation of these rocks. The Cambro-Ordovician dykes and metamorphism in the Brunia plate represent the easternmost extremity of this thermal even in central Europe.

Cambro-Ordovician event in the Staré Město belt

Felsic volcanic rocks of the leptyno-amphibolite sequence and associated tonalite–trondhjemite intrusive rocks at the base of the Staré Město belt yielded Cambro-Ordovician ages of emplacement (502–504 Ma). During high-temperature solidification and associated extensional deformation, these rocks have been metamorphosed under granulite facies conditions (8–10 kbar, 800–850°C, Štipská *et al.* 2000 that locally led to remelting. Zircons from melt patches in extensional lock-up shear bands as well as from an anorthositic layer in highly differentiated gabbro also yielded Cambro-Ordovician ages of emplacement. Finally, migmatitic, pelitic sediments, which are associated with these magmatic rocks and reached medium-pressure granulite facies metamorphism (7–9 kbar, 800–850°C, Štipská *et al.* 2000), contain metamorphic zircons, also of Cambro-Ordovician age.

We interpret the association of large volumes of gabbroic rocks (Fig. 2), highly differentiated dykes and bimodal volcanism (leptyno-amphibolite unit) as signifying an important rifting and underplating event at about 500 Ma ago. The geochemistry of these early Palaeozoic amphibolites in the Staré Město belt indicates MORB affinities, although the nature of crustal contamination suggests that the basaltic precursor was emplaced in a rifted ensialic environment (Floyd *et al.* 1996). Moreover, MP–HT metamorphism, also of Cambro-Ordovician age, and associated extensional tectonics suggest exceptionally high heat flow during thinning of the continental crust. Melting of crustal material was associated with this event, as documented by melt patches and the intrusion of granodioritic to tonalitic rocks that are probably products of melting of juvenile mafic (gabbroic?) material. The exceptionally hot geotherm, extensional tectonics and bimodal volcanism are all interpreted in terms of crustal thinning. The effect of gabbro underplating probably resulted in dehydration melting of lower mafic crust and the production of tonalitic magmas and associated granulite facies metamorphism. The geological environment and the chemistry of the Staré Město amphibolites (Floyd *et al.* 1996) as well as their MP–HT metamorphism indicate that crustal attenuation was insufficient to develop proper oceanic crust.

Cambro-Ordovician rifting is also documented in the Kaczawa Mountains (GK in Fig. 8) of the Polish West Sudetes Mts (Furnes *et al.* 1989), where diabase sills, pillow lavas, felsic volcanogenic calc-alkaline rocks and subsequent metabasalt flows of tholeiitic composition are attributed to this rifting event. Similar mafic volcanism (505 ± 5 Ma, Oliver *et al.* 1993) and gabbroic magmatism (494 ± 2 Ma, Oliver *et al.* 1993) was dated from the Rudawy–Janowicke region (Fig. 1) and is interpreted as ocean-floor magmatism and island-arc formation (Oliver *et al.* 1993). In addition, geochemical affinities of a mafic blueschist protolith to ocean-floor and ocean-island basalts in the Rýchory Mts (Maluski & Patočka 1997) suggest formation of oceanic crust in Ordovician time. However, no relics of Cambro-Ordovician granulite facies metamorphism were found in this region. In contrast to the Kaczawa Mts, the Rudawy–Janowicke region and southerly Rýchory Mts, where an oceanic stage had been reached, continental separation has not take place in the Staré Město belt.

Cambro-Ordovician event in the Orlica–Snieznik dome

Granitoid rocks in the Orlica–Sniezník dome have previously been dated between 487 and 505 Ma (Van Breemen *et al.* 1982; Liew & Hofmann 1988; Oliver *et al.* 1993). This age range is now extended to *c.* 522 Ma and suggests

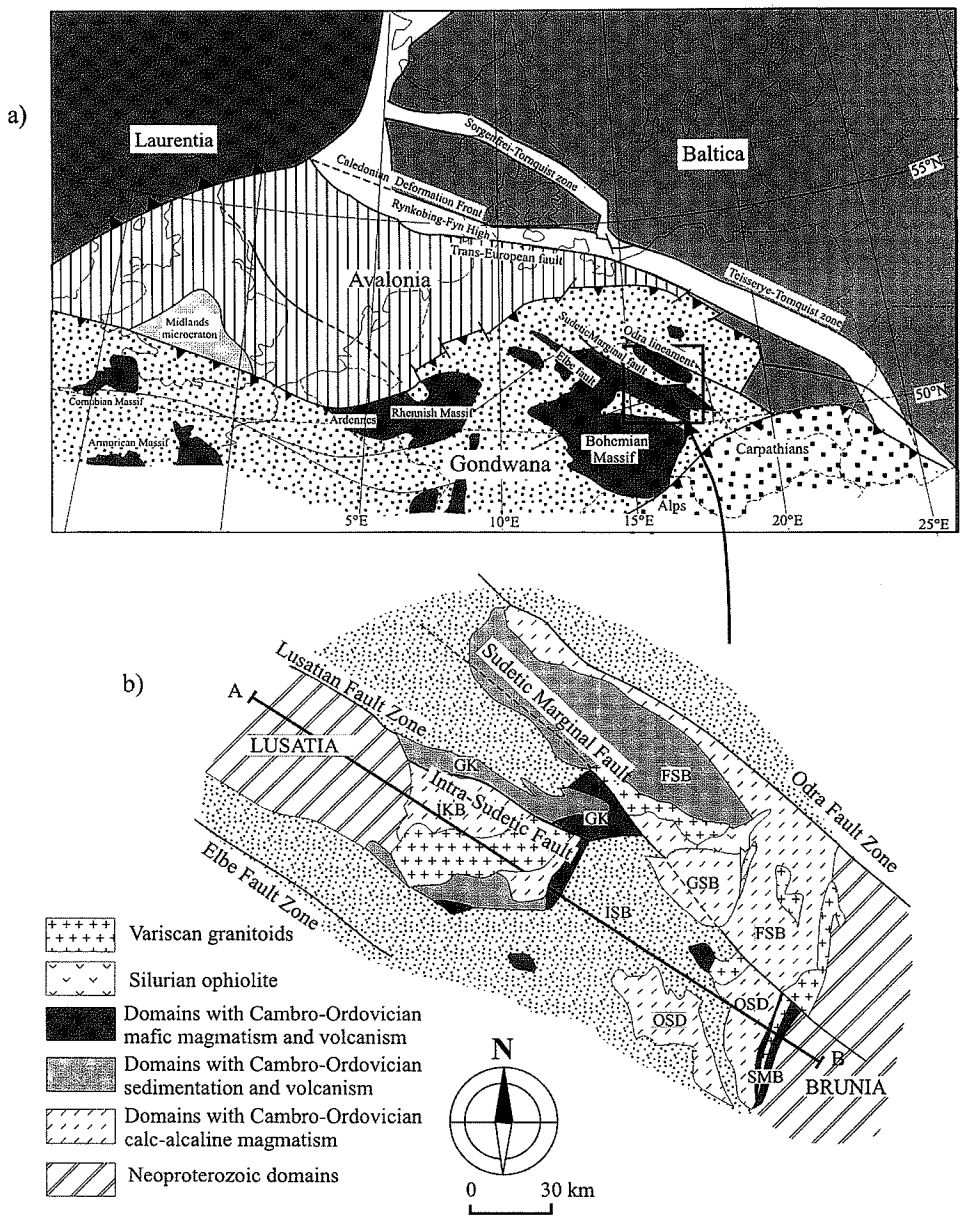

Fig. 8. (**a**) Position of western Sudetes with respect to recent geometry and boundaries of Avalonia and the Teisseyre–Tornquist zone (after Pharaoh *et al.* 1997). (**b**) Simplified geological map of the western Sudetes showing regional distribution of Neoproterozoic and Cambro-Ordovician domains (simplified after Żelaźniewicz 1997). FSB, Fore-Sudetic Block; GK, Gory Kaczawskie; GSB, Góry Sowie Block; IKB, Izera–Karkonosze Block; ISB, Intra-Sudetic Basin; OSD, Orlica–Śnieżník dome; SMB, Staré Město belt.

that the dome constitutes a composite granitoid pluton. Nd isotopic characteristics of the dated samples (CS 21 and CS 47) suggest derivation from pre-existing continental crust (Hegner & Kröner this volume). The Orlica–Śnieżník dome is a predominantly continental domain consisting of pre-Cadomian crust (Nd-model ages 1460–1660 Ma) and large volumes of Cambro-Ordovician granitoids of calc-alkaline composition similar to orogenic granite suites, which

support a subduction-related origin (Kröner *et al.* 2000). This Cambro-Ordovician granitoid and gneissic complex is situated between two NE–SW-trending rifted domains (Kaczawa–Rudawy–Janowicke and Staré Město) that have been amalgamated during the Variscan Orogeny (Schulmann & Gayer 2000).

Cambro-Ordovician tectonics in the Sudetic region

The geometry and sedimentary sequences overlying Neoproterozoic and Cambro-Ordovician domains of the Sudetes Mts were discussed by Żelaźniewicz (1997). According to Cymerman *et al.* (1997), the lithostratigraphic terranes in the Sudetes exhibit a symmetrical distribution with a central region of Cambro-Ordovician basinal–oceanic rocks bordered by sialic domains with Cambro-Ordovician magmatic activity from the west (Izera and South Karkonosze region) and east (Orlica–Sniezník dome) (Fig. 8). This large domain of Cambro-Ordovician tectonothermal activity is bordered by Neoproterozoic Gondwana-derived terranes to the west (Lusatian domain) and east (Brunia domain). Our data demonstrate that, in addition to this simple scheme, Cambro-Ordovician crustal attenuation also occurred between the Orlica–Sniezník domain and the Brunia domain, but without the development of proper oceanic crust. Therefore, the major tectonic pattern of the Sudetes is probably represented by an alternation of rifted domains with sialic regions during Gondwana fragmentation at the Cambro-Ordovician boundary (Figs 8 and 9).

In modern coordinates, the fragmentation of northern Gondwana occurred in a NW–SE direction so that NE–SW-trending belts of rifted and sialic domains developed. These units were displaced along the NW–SE Intrasudetic fault system and are separated from the more southerly units by the Elbe zone and from more northerly units by the Odra lineament (Fig. 8). The age of these major NW–SE transcurrent fault systems is disputed (Aleksandrowski *et al.* 1997; Bula *et al.* 1997), but it is likely that they acted as transfer faults during the rifting period and were later reactivated.

Ordovician fragmentation and crustal thinning of the northern margin of Gondwana may have originated through several mechanisms. The Cambro-Ordovician rifted regions of the western Sudetes (e.g. the Rudawy–Janowicke and Staré Město domains) differ significantly from each other in terms of the degree of crustal thinning. The Staré Město belt experienced gabbroic underplating, granulite facies metamorphism and structures related to crustal extension. In contrast, the Rudawy–Janowicke domain exhibits extensive rifting leading to the development of oceanic crust (see Fig. 9).

The geometry of the Staré Město belt may therefore be interpreted in terms of rifting along the northern Gondwana passive margin with the formation of a narrow zone of crustal attenuation (several tens of kilometres), located several tens to a maximum of 100 km away from the major site of break-up (Rudawy–Janowicke terrane). Magmatic activity along the passive margin was relatively weak in the western part of Brunia, where only some granitic dykes were emplaced in extensional gashes (the Desná dome). Farther west, thinning of the crust in the Staré Město region was likely to be more pronounced, and the minimum crustal thickness was 24–28 km (equivalent to a pressure of 7–8 kbar).

Limited crustal thinning may have been responsible for a substantial increase in lithospheric strength (Bertotti *et al.* 1997), causing final break-up of the crust to have occurred in a different region. With analogy to the southern Alpine rifted margin, for example, we suggest that the Staré Město belt represents only a zone of local lithospheric thinning along a stable Neoproterozoic continental margin of Gondwana, whereas break-up occurred farther west in what is now the Rudawy–Janowicke domain.

However, early Palaeozoic rifting in the Rudawy–Janowicke and Staré Město zones seems difficult to reconcile with Cambro-Ordovician calc-alkaline magmatism in the Orlica–Sniezník dome, the Góry Sowie Mts and the Izera Mts, where a subduction environment has been postulated (Oliver *et al.* 1993; Kröner *et al.* 1994, 2000; Kröner & Hegner 1998). A geotectonic position similar to that of the present Indonesian Archipelago could be suggested, implying subduction of oceanic crust below continental domains associated with pulling and fragmentation of hanging-wall continental crust. This type of tectonic setting could explain both successive fragmentation of continental crust and the development of transfer fault systems, as well as crustal thinning associated with back-arc-related bimodal volcanism and subduction-related magmatism as postulated for the Lugian domain.

Analogous models of back-arc extension (Faccenna *et al.* 1996) use the concept of retreating subduction as a driving mechanism of successive break-up of the upper plate. In such models the zone of early thinning is progressively migrating away from the retreating subduction zone. Consequently, the zone of maximum

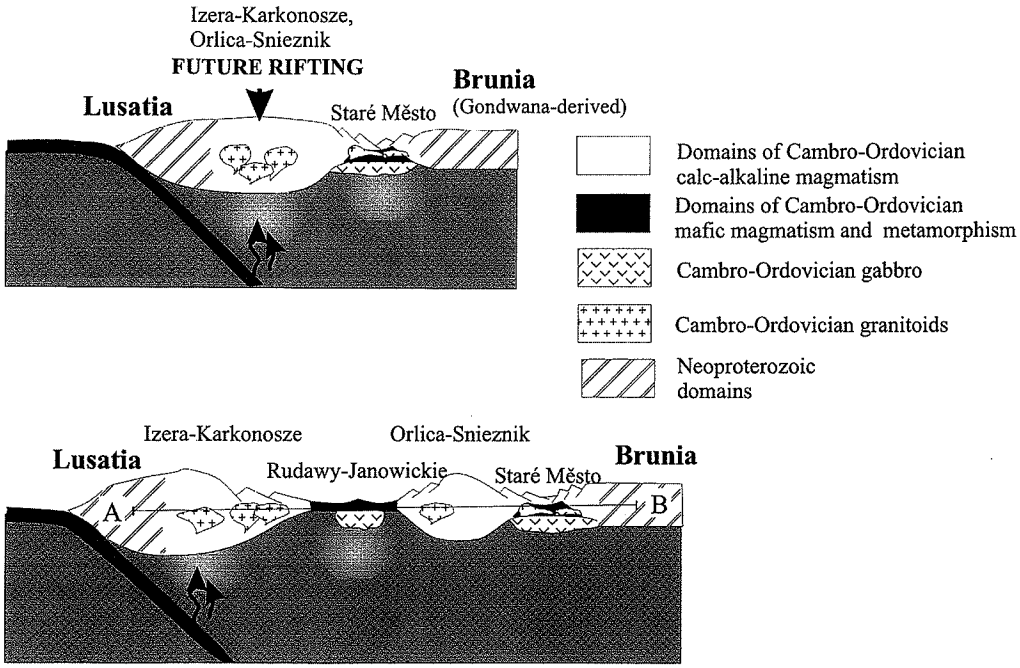

Fig. 9. Tectonic model of early Palaeozoic sequential rifting and related magmatism in the western Sudetes. The upper sketch shows early back-arc rifting in the Staré Město zone and supposed subduction-related calc-alkaline magmatism in sialic domains. Further trench retreat produced further rifting of softened sialic domains and development of oceanic crust west of the Staré Město rift.

crustal thinning is also migrating towards the trench. Therefore, the upper, extended, plate is made up of several rift zones separating large-scale boudins of continental crust.

A possible model for the development of a narrow intracontinetal rift zone in the eastern Bohemian Massif could be seen in the progressive closure of the Tornquist Ocean south of Avalonia (Tait *et al.* 1994, 1995; Torsvik *et al.* 1996), with a subduction zone dipping below the northern margin of Gondwana. This caused calc-alkaline magmatism, supra-subduction zone rifting and fragmentation on the overriding Gondwana plate (Fig. 9).

Relics of an early Palaeozoic rift, the Raabs sea, is preserved in a similar structural position as the Staré Město belt in the southern, Austrian, part of the eastern margin of the Bohemian Massif, as noted by Finger & Steyrer (1995). Those workers suggested that the Raabs sea was an immature intra-continental rift that opened through a process of continental back-arc rifting. In their model, the Staré Město belt, the Raabs unit and the Rudawy–Janowicke ophiolite represent relics of narrow oceans, which became curved after closure as a result of forceful indentation of the 'Moldanubian terrane' and clockwise rotational oroclinal bending around the eastern flank of the Bohemian Massif in early Carboniferous time (Tait *et al.* 1996). However, this model is not supported by sufficient data to rule out alternative opinions.

Financial support to A.K. by the Deutsche Forschungsgemeinschaft (DFG) within the Priority Programme 'Orogenic Processes' (Grant Kr 590/35) is gratefully acknowledged. A.K. also appreciates mass spectrometer analytical facilities in the Max-Planck-Institut für Chemie in Mainz. Some zircon analyses were carried out on the Sensitive High Resolution Ion Microprobe mass spectrometer (SHRIMP II) operated by a consortium consisting of Curtin University of Technology, the Geological Survey of Western Australia and the University of Western Australia with the support of the Australian Research Council. We appreciate the advice of A. A. Nemchin, A. Kennedy and D. Nelson during SHRIMP analysis and data reduction. This research was also funded by Grant 205/96/0270 of the Czech National Science Foundation to Pavla Štípská. We are grateful to Jan Cháb for making available his unpublished geological map of the Jeseníky Mts (Fig. 2) and for assistance during sample collection. F. Finger, V. Janoušek and G. Rogers considerably improved the manuscript through their comments. This is a contribution to EUROPROBE and the German Priority Programme 'Orogenic Processes'.

References

ALEKSANDROWSKI, P., KRYZA, R., MAZUR, S. & ZABA, J. 1997. Kinematic data on major Variscan strike-slip faults and shear zones in the Polish Sudetes, northeast Bohemian Massif. *Geological Magazine*, **134**, 727–739.

BERTOTTI, G., TER VOORDE, M., CLOETINGH, S. & PICOTTI, V. 1997. Thermomechanical evolution of the South Alpine rifted margin (North Italy): constraints on the strength of passive continental margins. *Earth and Planetary Science Letters*, **146**, 181–193.

BORKOWSKA, M., CHOUKROUNE, P., HAMEURT, J. & MARTINEAU, F. 1990. A geochemical investigation of the age, significance and structural evolution of the Caledonian–Variscan granite–gneisses of the Snieżnik metamorphic area, central Sudetes. *Geologica Sudetica*, **25**, 1–27.

BRUECKNER, H. K., MEDARIS, L. G., JR. & BAKUN-CZUBAROW, N. 1991. Nd and Sr age and isotope patterns from Variscan eclogites of the eastern Bohemian Massif. *Neues Jahrbuch für Mineralogie, Abhandlungen*, **163**, 169–196.

BULA, Z., JACHOWICZ, M. & ZABA, J. 1997. Principal characteristics of the Upper Silesian Block and Malopolska Block border zone (southern Poland). *Geological Magazine*, **134**, 669–677.

CHÁB, J. 1986. [Structure of the Moravo-Silesian branch of the European Upper Palaeozoic orogen (a working hypothesis)]. *Věstník Ústředního Ústavu Geologického*, **61**, 113–120 [in Czech].

CHLUPÁČ, I. 1994. Facies and biogeographic relationships in Devonian of the Bohemian Massif. *Courier Forschungsinstitut Senckenberg*, **169**, 299–317.

CYMERMANN, Z., PIASECKI, M. & SESTON, M. 1997. Terranes and terrane boundaries in the Sudetes, NE Bohemian Massif. *Geological Magazine*, **134**, 717–725.

DUDEK, A. 1980. The crystalline basement block of the Outer Carpathians in Moravia. *Rozpravy Československé Akademie Ved*, **90**, 1–85.

FACCENNA, C., DAVY, P., BRUN, J. P., FUNICIELLO, R., GIARDINI, D., MATTEI, M. & NALPAS, N. 1996. The dynamics of back-arc extension: an experimental approach to the opening of the Tyrrhenian Sea. *Geophysical Journal International*, **126**, 781–795.

FEDIUKOVÁ, E., FIŠERA, M., Cháb, J., Kopečný, V. & RYBKA, R. 1985. Garnets of the pre-Devonian rocks in the eastern part of the Hruby Jesenik Mts. (North Moravia, Czechoslovakia). *Acta Universitatis Carolinae Geologica*, **3**, 197–234.

FINGER, F. & STEYRER, H. P. 1995. A tectonic model for the eastern Variscides: indication from a chemical study of amphibolites in the south-eastern Bohemian Massif. *Geologica Carpathic*, **46**, 137–150.

——, HANŽL, P., PIN, C., VAN QUADT, A. & STEYRER, H. P. 2000. The Brunovistulian: Avalonian Precambrian sequence at the eastern end of the central European Variscides? *This volume*.

FIŠERA, M., SOUČEK, J. & NOVOTNÝ, P. 1986. [Blastomylonites of the Orlík nappes group, Hrubý Jesení Mts]. *Věstník Ústředního Ústavu Geologického*, **61**, 321–331 [in Czech].

FLOYD, P. A., WINCHESTER, J. A., CIESIELCZUK, J., LEWANDOWSKA, A., SZCZEPANSKI, J. & TURNIAK, K. 1996. Geochemistry of early Palaeozoic amphibolites from the Orlica–Snieznik dome, Bohemian Massif: petrogenesis and palaeotectonic aspects. *Geologische Rundschau*, **85**, 225–238.

FRANKE, W. 1989. Variscan plate tectonics in Central Europe—current ideas and open questions. *Tectonophysics*, **169**, 221–228.

—— 2000. The mid-European segment of the Variscides: tectono-stratigraphic units, terrane boundaries and plate evolution. *This volume*.

FRIEDL, G., MCNAUGHTON, N., FLETCHER, I. R. & FINGER, F. 1998. New SHRIMP-zircon ages for orthogneisses from the south-eastern part of the Bohemian Massif (Lower Austria). *Act Universitatis Carolinae—Geologica*, **42**, 251–252.

FRITZ, H., DALLYMEYER, R. D., NEUBAUER, F. & URBAN, M. 1996. Thick-skinned versus thin skinned thrusting: rheologically controlled thrust propagation in the Variscan collisional belt in the southeastern Bohemian Massif (Czech Republic–Austria). *Tectonics*, **15**, 1389–1413.

FURNES, H., KRYZA, R. & MUSZYNSKI, A. 1989. Geology and Geochemistry of Early Palaeozoic Volcanics of the Swierzawa Unit, Kaczawa Mts. W. Sudetes, Poland. *Nues Jahrbuch Für Geologie und Paläontologie, Montatshefte*, **3**, 136–154.

HEGNER, E. & KRÖNER, A. 2000. Review of ND isotopic data and xenocrystic and detrital zircon ages from the pre-Variscan basement in the eastern Bohemian Massif: speculations on palinspastic reconstructions. *This Volume*.

JAECKEL, P., KRÖNER, A., KAMO, S. L., BRANDL, G. & WENDT, J. I. 1997. Late Archaean to early Proterozoic granitoid magmatism and high-grade metamorphism in the central Limpopo belt, South Africa. *Journal of the Geological Society, London*, **154**, 25–44.

KOBER, B. 1986. Whole-grain evaporation for $^{207}Pb/^{206}Pb$-age-investigations on single zircons using a double-filament thermal ion source. *Contributions to Mineralogy and Petrology*, **93**, 482–490.

—— 1987. Single-zircon evaporation combined with Pb^+ emitter-bedding for $^{207}Pb/^{206}Pb$-age investigations using thermal ion mass spectrometry, and implications to zirconology. *Contributions to Mineralogy and Petrology*, **96**, 63–71.

KÖLBL, L. 1929. Die alpine Tektonik des Altvatergebirges. *Mitteilungen der Geologischen Gesellschaft*, **22**, 65–124.

KRÖNER, A. & HEGNER, E. 1998. Geochemistry, single zircon ages and Sm–Nd systematics of granitoid rocks from the Góry Sowie (Owl) Mts, Polish West Sudetes: evidence for early Palaeozoic arc-related plutonism. *Journal of the Geological Society, London*, **155**, 711–724.

—— & TODT, W. 1988. Single zircon dating constraining the maximum age of the Barberton greenstone belt, souther Africa. *Journal of Geophysical Research*, **93**, 15329–15337.

—— & WILLNER, A. P. 1998. Time of formation and peak of Variscan HP–HT metamorphism of quartz–feldspar rocks in the central Erzgebirge, Saxony, Germany. *Contributions Mineralogy and Petrology*, **132**, 1–20.

——, HEGNER, E. & JAECKEL, P. 1997. Cambrian to Ordovician granitoid orthogneisses in the Polish and Czech West Studies Mts and their geodynamic significance. *Terra Nostra*, **97**(11), 67–68.

——, JAECKEL, P., HEGNER, E. & OPLETAL, M. 2000. Single zircon ages and whole-rock Nd isotopic systematics of granitoid gneisses from the Czech Sudetes (Jizerské hory, Krkonoše and Orlice–Sniežník Dome). *Geologische Rundschau*, in press.

——, —— & OPLETAL, M. 1994. Pb–Pb and U–Pb zircon ages for orthogneisses from eastern Bohemia: further evidence for a major Cambro-Ordovician magmatic event. *Journal of the Czech Geological Society*, **39**, 61.

——, ——, REISCHMANN, T. & KRÖNER, U. 1998. Further evidence for an early Carboniferous (~340 Ma) age of high grade metamorphism in the Saxonian Granulite Complex. *Geologische Rundschau*, **86**, 751–766.

——, WINDLEY, B. F., JAECKEL, P., BREWER, T. S. & RAZAKAMANANA, T. 1999. New zircon ages and regional significance for the evolution of the Pan-African orogen in Madagascar. *Journal of the Geological Society, London*, **156**, 1125–1135.

LASKOWSKI, N. & KRÖNER, A. 1985. Geochemical characteristics of Archaean and late Proterozoic to Palaeozoic fine-grained sediments from southern Africa and significance for the evolution of the continental crust. *Geologische Rundschau*, **74**, 1–9.

LIEW, T. G. & HOFMANN, A. W. 1988. Precambrian crustal components, plutonic associations, plate environment of the Hercynian Fold Belt of Central Europe: indications from a Nd and Sr isotopic study. *Contributions to Mineralogy and Petrology*, **98**, 129–138.

LUDWIG, K. R. 1994. *ISOPLOT, a plotting and regression program for radiogenic-isotope data, version 2.75*. US Geological Survey, Open-File Report **91–45**.

MALUSKI, H. & PATOČKA, F. 1997. Geochemistry and ^{40}Ar–^{39}Ar geochronology of the mafic metavolcanic rocks from the Rychory Mountains complex (west Sudetes, Bohemian Massif): palaeotectonic significance. *Geological Magazine*, **134**, 703–716.

——, RAILICH, P. & SOUCEK, J. 1995. Pre-Variscan, Variscan and early Alpine thermo-tectonic history of the northeastern Bohemian Massif: a $^{40}Ar/^{39}Ar$ study. *Geologische Rundschau*, **84**, 345–358.

MATTE, Ph., MALUSKI, H., RAJLICH, P. & FRANKE, W. 1990. Terrane boundaries in the Bohemian Massif: results of large-scale Variscan shearing. *Tectonophysics*, **177**, 151–170.

NELSON, D. R. 1997. *Compilation of SHRIMP U–Pb zircon geochronology data, 1996*. Geological Survey of Western Australia, Record. **1997/2**.

NOVOTNÝ, M. & ŠTELCL, J. 1961. *Petrograpy of the northeastern part of the Hrubý Jeseník*. Státni Pedagogické Nakladatelství, Praha, Czech Republic.

O'CONNOR, J. T. 1965. *A classification for quartz-rich igneous rocks based on feldspar ratio*. US Geological Survey, Professional Papers, **525B**, 79–84.

OLIVER, G. J. H., CORFU, F. & KROUGH, T. E. 1993. U–Pb ages from SW Poland: evidence for a Caledonian suture zone between Baltica and Gondwana. *Journal of the Geological Society, London* **150**, 355–369.

PARRY, M., ŠTÍPSKÁ, P., SCHULMANN, K., HROUDA, F., JEŽEK, J. & KRÖNER, A. 1997. Tonalite sill emplacement at an oblique plate boundary: northeastern margin of the Bohemian Massif. *Tectonophysics*, **280**, 61–81.

PEARCE, J. A. 1987. An expert system for the tectonic characterization of ancient volcanic rocks. *Journal of Volcanology and Geothermal Research*, **32**, 51–65.

PHARAOH, T. C., ENGLAND, R. W., VERNIERS, J. & ŻELAŹNIEWICZ, A. 197. Introduction: geological and geophysical studies in the Trans-European suture zone. *Geological Magazine*, **5**, 585–590.

SCHARBERT, S. & BATÍK, S. 1980. The age of the Thaya (Dyje) pluton. *Verhandlungen der Geologischen Bundesanstalt*, **1980**, 325–331.

SCHULMANN, K. & GAYER, R. 2000. A model for an obliquely developed continental accretionary wedge: NE Bohemian massif. *Journal of the Geological Society, London*, **157**, 401–406.

STACEY, J. S. & KRAMERS, J. D. 1975. Approximation of terrestrial lead isotope evolution by a two-stage model. *Earth and Planetary Science Letters*, **26**, 207–221.

STELTENPOHL, M. G., CYMERMAN, Z., KROGH, T. E. & KUNK, M. J. 1993. Exhumation of eclogitized continental basement during Variscan lithospheric delamination and gravitational collapse, Sudety Mountains, Poland. *Geology*, **21**, 1111–1114.

ŠTÍPSKÁ, P. & SCHULMANN, K. 1995. Inverted metamorphic zonation in a basement-derived nappe sequence, eastern margin of the Bohemian Massif. *Geological Journal*, **30**, 385–413.

——, ——, THOMPSON, A. B. & JEŽEK, J. 2000. Thermomechanical role of a Cambro-Ordovician palaeorift during the Variscan collision: the NE margin of the Bohemian Massif. *Tectonophysics*, in press.

SUESS, F. E. 1912. Die moravischen Fenster und ihre Beziehung zum Grundgebirge des Hohen Gesenkes. *Denkschriften der kaiserlichen Akademie der Wissenschaften*, **88**, 541–631.

—— 1926. *Intrusionstektonik und Wandertektonik im variszischen Grundgebirge*. Borntraeger, Berlin.

TAIT, J., BACHTADSE, V. & SOFFEL, H. C. 1994. Silurian palaeogeography of Armorica: new palaeomagnetic data from central Bohemia. *Journal of Geophysical Research*, **99**, 2897–2907.

——, —— & —— 1995. Upper Ordovician palaeogeography of the Bohemian Massif: implications

for Armorica. *Geophysical Journal International*, **122**, 211–218.

——, —— & —— 1996. Eastern Variscan fold belt: Paleomagnetic evidence for oroclinical bending. *Geology*, **24**, 871–874.

TORSVIK, T. H., SMETHURST, M. A., MEERT, J. G. *et al.* 1996. Continental break-up and collision in the Neoproterozoic and Palaeozoic—a tale of Baltica and Laurentia. *Earth-Science Reviews*, **40**, 229–258.

TURNIAK, K., MAZUR, S. & WYSOCZAŃSKI, R. 2000. SHRIMP zircon geochronology and geochemistry of the Orlica–Snieznik gneisses (Sudetes, SW Poland) and implications for the evolution of the Variscides in East–Central Europe. *Geodynamica Acta*, in press.

VAN BREEMEN, O., AFTALION, M., BOWES, D. R., DUDEK, A., MISAŘ, Z., POVONDRA, P. & VRÁNA, S. 1982. Geochronological studies of the Bohemian Massif, Czechoslovakia, and their significance in the evolution of Central Europe. *Transactions of the Royal Society*, **73**, 89–108.

VAVRA, G. 1990. On the kinematics of zircon growth and its petrogenetic significance: a cathodoluminescence study. *Contributions to Mineralogy and Petrology*, **106**, 90–99.

YORK, D. 1969. Least squares fitting of a straight line with correlated errors. *Earth and Planetary Science Letters*, **5**, 320–324.

Żelaźniewicz, A. 1997. The Sudetes as a Palaeozoic orogen in central Europe. *Geological Magazine*, **134**, 691–702.

ZIMER, M., KRÖNER, A., JOCHUM, K. P., REISCHMANN, T. & TODT, W. 1995. The Gabal Gerf complex: a Precambrian N-MORB ophiolite in the Nubian Shield, NE Africa. *Chemical Geology*, **123**, 29–51.

Appendix

Analytical methods

Major oxides and trace elements were determined by XRF spectrometry on whole-rock fused glass discs and powder pellets, respectively, at the University of Mainz using a Philips PW 1404 XRF spectrometer and procedures as outlined by Laskowski & Kröner (1985). The results are presented as a Supplementary Publication (see p. 180). Heavy minerals were separated from whole-rock samples weighing about 5 kg each by standard procedures. Zircons were then handpicked for single grain analysis using the HF vapour digestion and evaporation techniques in Mainz and SHRIMP II in Perth.

Single zircon evaporation. Our laboratory procedures follow Kober (1986, 1987) with slight modifications (Kröner & Hegner 1988; Kröner & Todt 1988). Isotopic measurements were carried out on a Finnigan-MAT 261 mass spectrometer at the Max-Planck-Institute für Chemie in Mainz. Common lead was corrected, where necessary, using the model of Stacey & Kramers (1975).

Repeated analysis of single grains of an internal zircon standard during this study yielded a value of 0.126635 ± 0.000062 (2σ error of the population), and this error is considered the best estimate for the reproducibility of our evaporation data (Kröner *et al.* 1999). The calculated $^{207}Pb/^{206}Pb$ ratios and their 2σ (mean) errors are presented as a Supplementary Publication (see p. 180), together with a summary of the zircon morphology. The $^{207}Pb/^{206}Pb$ spectra are shown as histograms to permit visual assessment of the data distribution from which the ages are derived. As the evaporation technique provides only Pb isotopic ratios, all $^{207}Pb/^{206}Pb$ ages determined by this method are necessarily minimum ages. Kröner & Hegner (1998) discussed this problem and provided reliability criteria for evaporation analyses.

Vapour-digestion U–Pb analysis. Our laboratory procedures and instrumental conditions have been described by Jaeckel *et al.* (1997) and Kröner *et al.* (1999). Blank values were 3 pg for Pb and 10 pg for U. The Pb composition of the blank was $^{206}Pb/^{204}Pb = 17.78$, $^{207}Pb/^{204}Pb = 14.97$, $^{208}Pb/^{204}Pb = 36.57$. Isotopic measurements were performed on a Finnigan-MAT 261 mass spectrometer at the Max Planck-Institut für Chemie in Mainz. Common-Pb correction followed the two-stage model of Stacey & Kramers (1975). All errors are given at the $2\sigma_{ext.}$ level. The ages of 2σ errors of intercepts of the best-fit with concordia were determined using the regression calculation of York (1969). The analytical data are listed as a Supplementary Publication (see p. 180).

SHRIMP II procedure. Zircons were handpicked and mounted in epoxy resin together with chips of the Perth Consortium standard CZ3. The mount was then polished, cleaned, etched in 48% HF, photographed and then repolished as detailed by Kröner *et al.* (1998). Isotopic analyses were performed on the Perth Consortium SHRIMP II, and instrumental conditions have been summarized by Kröner *et al.* (1998). The 1σ error in the ratio $^{206}Pb/^{238}U$ during analysis of all standard zircons during this study was between 1.3 and 1.65%, and the primary beam intensity was between 2.2 and 2.8 nA. Sensitivity varied between 20 and 30 c.p.s. $ppm^{-1}Pb$. Raw data reduction followed the method described by Nelson (1997). Common-Pb corrections have been applied, assuming that common Pb is surface related and using the isotopic

composition of Broken Hill. The analytical data are presented as a Supplementary Publication (see p. 180). Errors given on individual analyses are based on counting statistics and are at the 1σ level. Errors for pooled analyses are at 2σ or 95% confidence. The ages and 2σ errors of intercepts of the best-fit line with concordia were calculated using the method of Ludwig (1994).

ELSEVIER

Tectonophysics 332 (2001) 239–253

TECTONOPHYSICS

www.elsevier.com/locate/tecto

Thermo-mechanical role of a Cambro-Ordovician paleorift during the Variscan collision: the NE margin of the Bohemian Massif

P. Štípská[a,b,*], K. Schulmann[a], A.B. Thompson[c], J. Ježek[d], A. Kröner[e]

[a]*Institute of Petrology and Structural Geology, Charles University, Albertov 6, 12843 Prague, Czech Republic*
[b]*Geophysical Institute, Czech Academy of Science, Boční II/1401, 141 31, Prague, Czech Republic*
[c]*Department Erdwissenschaften, Institute für Mineralogie und Petrologie, ETH E64, Sonneggstr. 5, Zurich, CH-8092, Switzerland*
[d]*Institute of Applied Mathematics and Computer Science, Faculty of Science, Charles University, Albertov 6, Prague, Czech Republic*
[e]*Institut für Geowissenschaften, Universität Mainz, 55099 Mainz, Germany*

Abstract

The Staré Město (SM) belt (NE margin of the Bohemian Massif) represents a preserved example of an intracontinental Cambro-Ordovician rift that has been shortened during the Variscan orogeny. The rifted sequence consists of gabbroic intrusions and a leptyno-amphibolite complex of Cambro-Ordovician protolith age. The latter suffered medium pressure, granulite facies, Cambro-Ordovician metamorphism associated with extension in a continental protorift. The Variscan tectonometamorphic event is manifested by convergent orogenesis with syn-convergent intrusion of a Carboniferous tonalitic sill, high temperature–medium pressure compressional deformation of gabbros and high temperature metamorphism of peridotites.

Numerical thermal and rheological modelling suggests that the SM paleorift after 140 Ma of cooling represented a stiff heterogeneity between an easterly situated Cadomian continent and a westerly lying Variscan orogenic root zone. Carboniferous underplating of the paleorift by tonalitic magma was probably responsible for the thermal weakening of both the upper mantle and the mafic lower crust, and the subsequent uplift of the remaining rigid part of the Cambro-Ordovician crust. All the units were later deformed in transpressional heterogeneous greenschist facies regime at a supracrustal level.

Keywords: Cambro-Ordovician rifting; Variscan collision; rheology; intracontinental paleorift exhumation; Bohemian Massif

1. Introduction

Inherited lithology influences the rheology and dynamics of the continental deformation in former intracontinental extended domains (e.g. Oxburgh, 1982; Cloetingh et al., 1995). The initial depth to Moho and thermal state of an originally extended domain determines the strength distribution during subsequent convergence (e.g. Allemand and Brun, 1991). Thompson et al., 2000 argue that, immediately after continental rifting, the sub-rift lithosphere is weaker than the adjacent continental lithosphere. In agreement with a suggestion by Oxburgh (1982), the thickness of the sub-rift lithosphere progressively increases with time during cooling, so that the sub-rift mantle becomes stronger than the adjacent continental lower crust. The mafic lower crust generated during a rifting event may contribute greatly to the strength of the sub-rift lithosphere following cooling (e.g. Bertotti et al., 1997). This strength distribution will play a significant role in determining the tectonic style during

* Corresponding author.
E-mail address: stipacka@natur.cuni.cz (P. Štípská).

0040-1951/01/$ - see front matter
PII: S0040-1951(00)00259-6

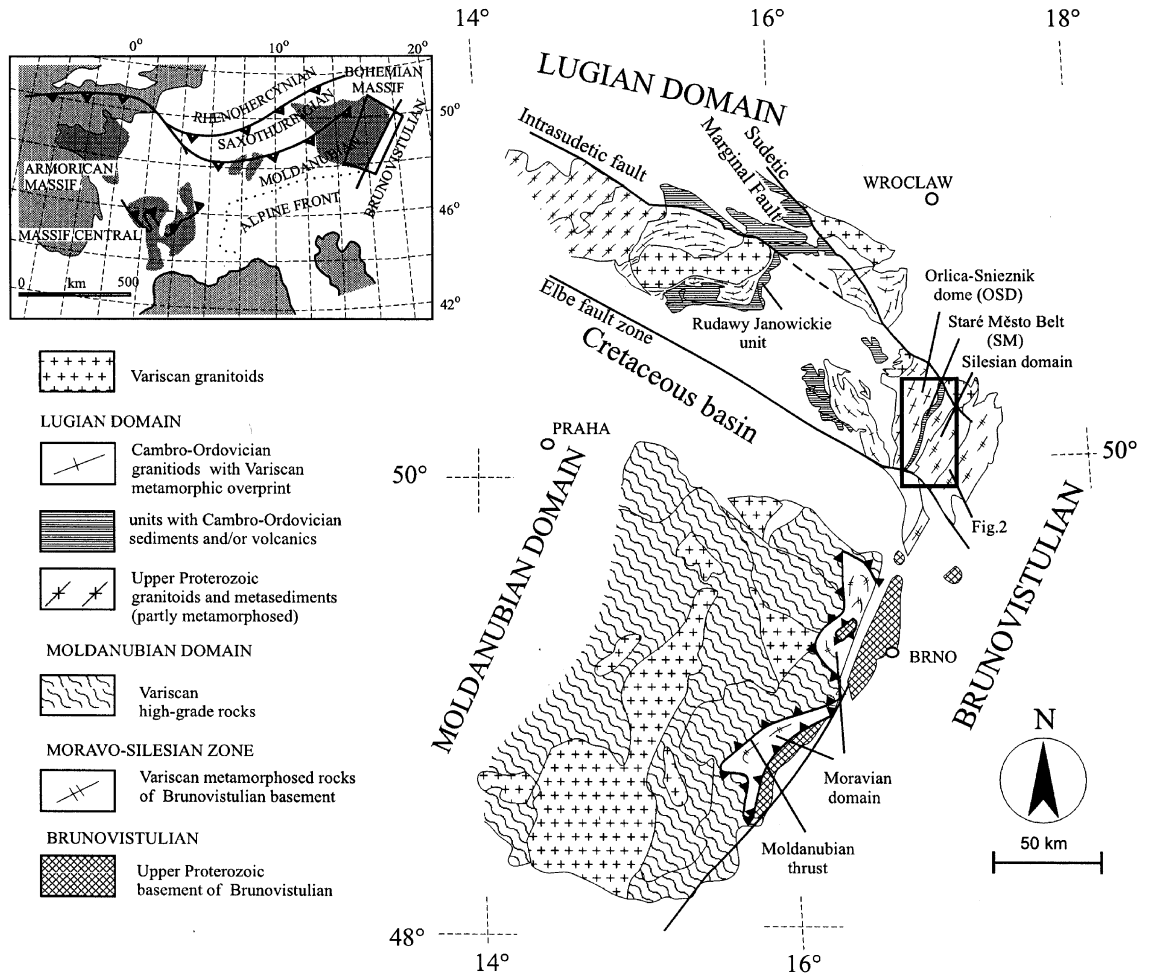

Fig. 1. Outline geological map of the eastern part of the Bohemian Massif with the major units shown schematically. The location of the studied area (Fig. 2) is indicated. Upper left inset is the position of the studied area in the framework of European Variscides.

compression of the continental domains which contain rifted regions. Cooled rifted domains represent stiff heterogeneities against the adjacent continental lithosphere, and their exhumation during later convergence is not well understood. To distinguish a paleorift thermomechanical history from the history of subsequent convergence and exhumation, detailed structural, petrological and geochronological information is needed.

On the basis of structural, geochronological and petrological data (Parry et al., 1997; Kröner et al., 2000; Štípská, 1999; Štípská et al., 2000), this study suggests that a Cambro-Ordovician rift, with preserved anomalous high temperature–medium pressure (HT–MP) metamorphic conditions and Cambro-Ordovician structures, was incorporated during Variscan collision along the NE margin of the Bohemian Massif. We attempt to explain the mechanical behaviour of this rifted lithospheric segment, using combined thermal and rheological modelling. The thermal and mechanical interplay and the history of compression of the extended lithosphere over 140 Ma of cooling, are the subject of our modelling.

2. Geological setting of the NE margin of the Bohemian Massif

The major Variscan collisional structure of the eastern margin of the Bohemian Massif was recognized by Suess (1926) who developed a concept of large-scale Moldanubian–Lugian thrusting over the Moravo-Silesian metamorphic belt, in the east (Fig. 1).

Two major units are usually distinguished along the NE margin of the Bohemian Massif: the tectonically upper Orlica–Snieznik dome (OSD) to the west, forming the easternmost part of the Lugian domain, and the tectonically lower Silesian domain to the east (Fig. 1). The OSD is composed of medium- to high-grade gneisses, schists and granitoids with Cambro-Ordovician protolith ages (480–522 Ma; Don et al., 1990; Oliver et al., 1993; Kröner et al., 2000). The high-grade gneisses contain boudins of eclogites and granulites, indicating metamorphic pressure and temperature conditions ranging from 18 to 25 kbar and 800 to 900°C, respectively (Kryza et al., 1996). A Sm–Nd garnet–clinopyroxene whole-rock age of ~340 Ma for the Snieznik eclogite is interpreted to approximate closely the time of the eclogite-facies temperature maximum (Steltenpohl et al., 1993). The $^{40}Ar/^{39}Ar$ cooling age of hornblende from eclogite (332 ± 2 Ma) is interpreted to reflect carboniferous cooling (Steltenpohl et al., 1993).

The Silesian domain consists of Pan-African (Cadomian) basement (~554–684 Ma; U–Pb and Pb–Pb zircon ages, Van Breemen et al., 1982; Kröner et al., 2000) overlain by a thick Devonian sedimentary sequence which was strongly involved in Variscan nappe tectonics. The Silesian domain is affected firstly by prograde Barrovian-type metamorphism ranging from the chlorite zone in the east to the kyanite zone in the west, and then overprinted in some areas by an HT–LP metamorphic event (e.g. staurolite and kyanite are replaced by sillimanite and andalusite). This later event was associated with intrusions of granitic magmas (Souček, 1978; Schulmann and Gayer, 2000). Relics of retrograde eclogites in the western part (of supposed Variscan age, although they have not been dated) indicate pressures of ca. 16 kbar at temperatures of ca. 650°C (Žáček, 1996). Variscan cooling ages for amphibole, muscovite and biotite from the rocks of the Silesian domain vary between 300 and 315 Ma (Ar–Ar method, Maluski et al., 1995).

The OSD and the Silesian domain are separated by the Staré Město (SM) belt (Fig. 2), the subject of this study, which consists of an upper mantle and lower crustal complex thinned during Cambro-Ordovician rifting (Kröner et al., 2000), and which was later involved in the Variscan collision. The general structure of the SM belt is characterized by NE–SW trending lithologies (Fig. 2). The top of the tectonic sequence is represented by a strongly retrogressed volcano-sedimentary unit, which tectonically underlies high-grade gneisses and granulites of the OSD. Structurally below, there occurs a layer of strongly sheared gabbro constituting a ductile shear zone along which a tonalitic sill was emplaced (Parry et al., 1997). In the footwall of the tonalite sill, the so-called leptyno-amphibolite complex comprises a layered sequence of alternating amphibolites and fine-grained quartzo-feldspathic rocks (leptynites), as well as tonalitic gneisses associated with high-grade metasediments showing evidence of anatexis. This complex is marked at its base by boudins of serpentinized spinel peridotite. Only in the northern part of the SM sequence is the gabbroic belt tectonically repeated below the LAC sequence and the spinel peridotite boudins.

3. Tectonothermal evolution of the boundary between the Silesian and Lugian domains

Two major tectonometamorphic events were recognized in the studied area. The first event was recognized in the SM belt only and is interpreted as a result of Cambro-Ordovician intracontinental rifting. The second polyphase event is Variscan in age and affects all the units of the eastern margin of the Bohemian Massif. The abbreviated description of tectonometamorphic evolution is based on the detailed structural and petrological work of Parry et al. (1997) and Štípská (1999), and the detailed geochronological investigations ($^{207}Pb/^{206}Pb$ single zircon evaporation technique, U–Pb vapour digestion and $^{206}Pb/^{238}U$ on SHRIMP II) of Kröner et al. (2000). Details of structural succession, critical mineral assemblages, *PT* estimates and geochronological data used in the thermal and rheological modelling are presented in Table 1.

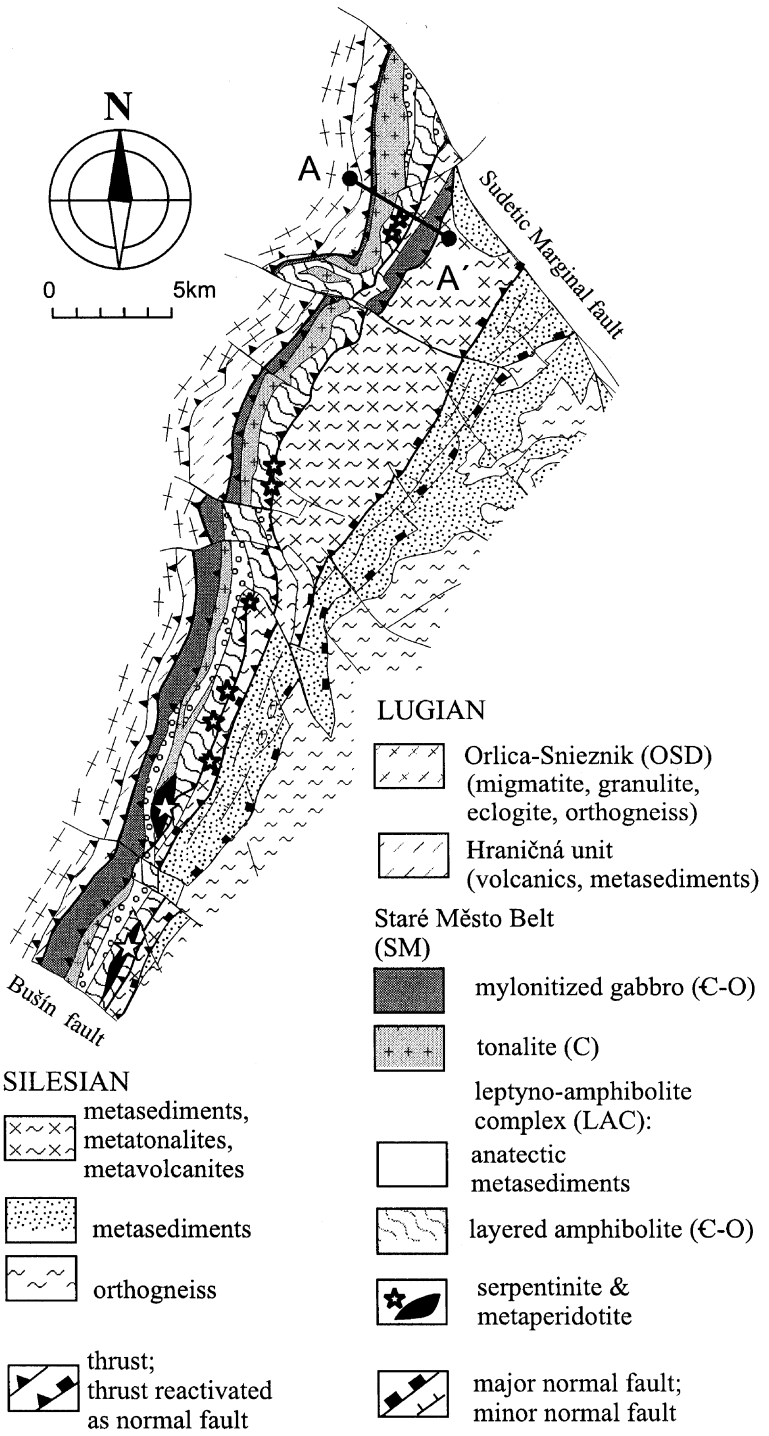

Fig. 2. Geological map of the SM belt based on unpublished geological maps 1: 25,000 provided by courtesy of the Czech Geological Survey (Dr M. Opletal). Geological cross-section A–A′ is shown in Fig. 3.

Table 1
Summary of *PT* estimates and ages from different lithologies of the SM belt according to Štípská (1999) and Kröner et al. (2000)

Rock type	Texture	*T* (°C) (Štípská, 1999)	*P* (kbar) (Štípská, 1999)	Zircon age (Ma)
Lithologies associated to D_1 Cambro-Ordovician structure				
Layered amphibolites	Weak shape preferred orientation, annealed	730–860	8.5–10	503.4 ± 1.0 (Pb–Pb single zircon evaporation), 503 ± 2 (U–Pb, SHRIMP II), protolith age (Kröner et al., 2000)
Tonalitic gneiss	Weak shape preferred orientation, annealed	700–770	9.2–10.1	Weighted mean age 503.3 ± 0.8 (Pb–Pb single zircon evaporation, U–Pb vapour digestion), protolith age (Kröner et al., 2000)
Melt patch within tonalitic gneiss	Random orientation	750–770	7.9–8.7	Weighted mean age 501.9 ± 0.6 (Pb–Pb single zircon evaporation, U–Pb vapour digestion), remelting or protolith age (Kröner et al., 2000)
Migmatitic paragneiss	Weak shape preferred orientation, annealed	790–900	7.3–8.2	Mean age 504.3 ± 1.0 (Pb–Pb single zircon evaporation), 509 ± 7 (U ± Pb SHRIMP II), metamorphic age (Kröner et al., 2000)
Lithologies associated to D_2 Variscan structure				
Metagabbro	Strong preferred orientation, dynamic recrystallization of Pl, Amp	710–740	7.8–10.1	504.9 ± 1 (Pb–Pb evaporation of three grains), protolith age (Kröner et al., 2000)
Metaperidotite	Relics of peak assemblage	666–703	–	–
Tonalite	Dynamic recrystallization of Pl, Qtz	670–725	6.5–7	339 ± 1.1 (Pb–Pb single zircon evaporation), protolith age (Parry et al., 1997)

3.1. Cambro-Ordovician evolution of the Staré Město belt

The earliest structures (D_1) and metamorphism (M_1) are Cambro-Ordovician in age and were recognized only in the leptyno-amphibolite complex while the igneous features of the Cambro-Ordovician event have been distinguished in the weakly deformed part of the metagabbro belt. The leptyno-amphibolite complex consists predominantly of amphibolite alternating with leptynite dated at 502 ± 1.7–503 ± 2 Ma. The layered amphibolites are associated with tonalitic migmatitic gneiss dated at 503 ± 0.8 Ma, and migmatitic metasediments containing intercalations of quartzites and calc-silicate rocks (Table 1).

The leptyno-amphibolite complex is affected by a D_1 event. The variably dipping foliation S_1 is characterized by compositional banding and migmatitic layering affected by a range of melt collection structures such as extensional shear bands filled with melts, neck zones of intrafolial boudinage and irregular melt patches (Fig. 3). This extensional melting episode has been dated at 501.9 ± 0.6 Ma.

Important to understanding the history is the discovery of magmatic structures preserved in low strain domains of a belt of highly mylonitized metagabbros. These structures are represented by magmatic layering marked by the alternation of gabbro layers with different grain size and dikes of fine-grained trondhjemites. The trondhjemitic dike yields an age of 504.9 ± 1 Ma.

The physical conditions of metamorphism in different lithologies of the leptyno-amphibolite complex were estimated using standard geothermobarometry (Štípská, 1999; Štípská et al., 2000). The mineral assemblage of the layered amphibolites is composed of hornblende, plagioclase, clinopyroxene, rare garnet and quartz. The metamorphic *PT* conditions, calculated with the calibrations of Holland and Blundy (1994) and Kohn and Spear (1990), range between 730 and 860°C and 8.5 and 10 kbar (Table 1). The tonalitic gneiss and melt patches of the same rock consist of hornblende, garnet, plagioclase, quartz,

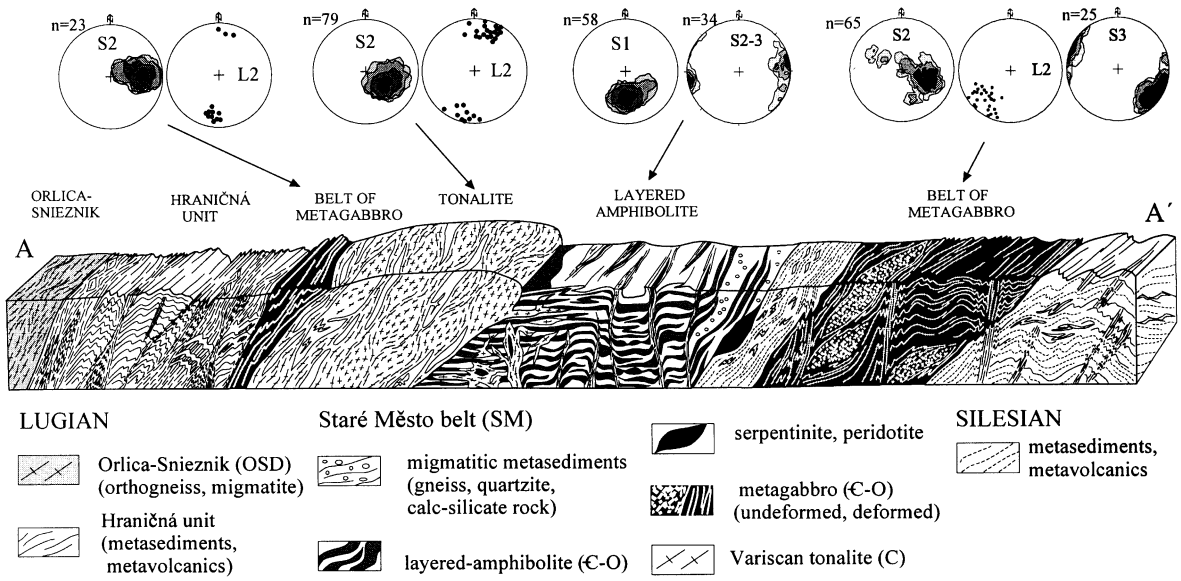

Fig. 3. Geological cross-section A–A′ (shown in Fig. 2) of the SM belt showing major structures, lithology of individual units and major tectonic boundaries. Equal-area, lower-hemisphere stereoplots show D_1, D_2 and D_3 planar and linear structures. Vertical axis is not to scale.

biotite, titanite and magnetite. The metamorphic *PT* conditions for the tonalitic migmatites were determined as ~700–770°C and 9.2–10.1 kbar, and in melt patches within the tonalitic gneiss as ~750–770°C and 7.9–8.7 kbar, using the calibrations of Holland and Blundy (1994), Kohn and Spear (1990) and Schmidt (1992). In the migmatitic paragneiss composed of plagioclase, biotite, garnet, K-feldspar, prismatic sillimanite, rutile and ilmenite, the *PT* conditions of metamorphism were calculated as ~790–900°C and 7.3–8.2 kbar, using the calibrations of Ferry and Spear (1978), Thompson (1976), Koziol (1989) and Bohlen et al. (1983). The age of this metamorphism is dated at ca. 504–509 Ma — from football-shaped, multifaceted grains of zircon of metamorphic origin in migmatitic paragneiss (Pb–Pb single zircon evaporation and SHRIMP II, Kröner et al., 2000).

These observations document that the HT metamorphism that occurred close to the amphibolite to granulite facies transition at a depth of 30–35 km was associated with extension. This was coeval with the magmatic emplacement of the layered amphibolites, tonalitic migmatites and gabbros during the Cambro-Ordovician event.

3.2. Variscan tectonometamorphic evolution of the Staré Město belt

Variscan deformation (D_2) affects all units of the SM belt. It is mostly characterized by the syntectonic emplacement of a tonalite sill (single zircon ^{207}Pb–^{206}Pb evaporation age of 339 ± 1.1 Ma) between a band of mylonitic metagabbro to the west and the leptyno-amphibolite complex to the east (Parry et al., 1997). The foliation S_2 of the sill is mostly syn-magmatic, dipping to the NW and bearing sub-horizontal mineral and stretching lineations L_2 (Fig. 3). Shear bands indicate a dextral sense of shear. The fabric of the sill is broadly concordant with the mylonitic fabric of the hanging-wall gabbro but strongly discordant to the D_1 fabric of the underlying leptyno-amphibolite complex.

The gabbro in the hanging wall of the sill is affected by intense deformation marked by the development of a mylonitic foliation S_2 (formed by monomineralic layers of recrystallized amphibole and plagioclase) within a several to hundred metres thick ductile shear zone (Figs. 2 and 3). This foliation dips to the WNW and bears an intense stretching lineation plunging to the SW. Kinematic criteria such as sigmoidal

amphibole clasts indicate a dextral sense of shear. Variscan deformation in the leptyno-amphibolite complex is marked by open to closed F_2 folds of an originally flat-lying Cambro-Ordovician foliation S_1. Fold hinges are sub-parallel to the regional Variscan stretching direction and are locally cut by NE–SW and NW–SE conjugate shear zones filled with melts.

The Variscan metamorphism may be studied in the mylonitic shear zone of metagabbros and elongate boudins of serpentinized metaperidotites at the base of the leptyno-amphibolite complex. The determination of *PT* conditions of the Variscan metamorphism is summarized in Table 1. The depth of magmatic crystallization of the tonalite was estimated at 6.5–7.0 kbar at a temperature of 671–724°C, using the calibrations of Schmidt (1992) and Holland and Blundy (1994). The mineral assemblage in metagabbro (composed of recrystallized plagioclase, and amphibole, garnet, rutile and rare quartz) is related to dynamic recrystallization. The *PT* conditions of the mylonitization in the metagabbro were estimated on recrystallized grains at 711–740°C, and 7.8 and 10.1 kbar according to the calibrations of Holland and Blundy (1994) and Kohn and Spear (1990). Serpentinized spinel metaperidotites show relic peak mineral assemblage composed of olivine, orthopyroxene, amphibole, chlorite and spinel. The mineral compositions, as well as the zoning of amphiboles, provide evidence for a prograde character of the M_2 metamorphism, at least from the lower to the upper amphibolite facies. In spinel metaperidotites, the temperature range is between 660 and 700°C, deduced from the alumina content of orthopyroxene rims (Gasparik and Newton, 1984).

Late D_3 Variscan deformation affected the D_1 and D_2 structures or developed gradually from the D_2 structures under retrograde (greenschist facies) metamorphic conditions. The foliation S_2 was reactivated under greenschist facies conditions and locally cross-cut by steep D_3 shear zones. The regions between these late D_3 shear zones were folded by open metre-scale F_3 folds with sub-horizontal NE–SW trending hinges. Kinematic indicators associated with the NE trending stretching lineation show a dextral sense of movement.

4. Modelling of the tectonometamorphic evolution of the Staré Město belt

4.1. Interpretation of Cambro-Ordovician magmatism and metamorphism

Dating of gabbros, tonalitic migmatitic gneiss, layered amphibolites of the leptyno-amphibolite complex and melts in shear zones within tonalitic gneiss indicate that the emplacement of gabbro (~504 Ma), the tonalitic gneiss precursor (~503 Ma) and the bimodal sequence of layered amphibolites (~502 Ma) are almost coeval with the main metamorphic–anatectic event (~503 Ma). In migmatitic paragneiss, the metamorphic-type zircon population (~504 Ma) directly indicates the age of Cambro-Ordovician metamorphism. The structures and fabrics of the leptyno-amphibolite complex indicate an extensional regime associated with high-grade metamorphic conditions.

Mineral assemblages and estimated *PT* conditions in layered amphibolite (~730–860°C/8.5–10 kbar), in tonalitic gneiss (~700–770°C/9.2–10.1 kbar), in melt patches within tonalitic gneiss (~750–770°C/7.9–8.7 kbar) and in migmatitic paragneiss (~790–900°C/7.3–8.2 kbar) suggest that during the Cambro-Ordovician period, the leptyno-amphibolite complex was metamorphosed close to the amphibolite–granulite facies transition at a depth of 30–35 km. This range in pressure is interpreted as reflecting an isothermal decompression, from ~8.2–10 to ~7.3–8.7 kbar, that is inferred from pressure differences between tonalitic migmatite and melt within shear zones of the same rock. The *PT* conditions of Variscan metamorphism recorded in peridotite and mylonitic gabbro suggest a similar range of pressure (ca. 9 kbar) — yet slightly lower temperatures than in the case of Cambro-Ordovician metamorphism (Table 1). This indicates that the lithotectonic column before the Variscan metamorphic episode consisted of gabbros above the upper mantle rocks but below the leptyno-amphibolite complex. The coincidence of Cambro-Ordovician and Variscan pressure conditions of metamorphism may indicate the crustal thickness resulting from the Cambro-Ordovician extension. Therefore, the pressure range quoted above indicates that the Cambro-Ordovician crust had an approximate thickness of

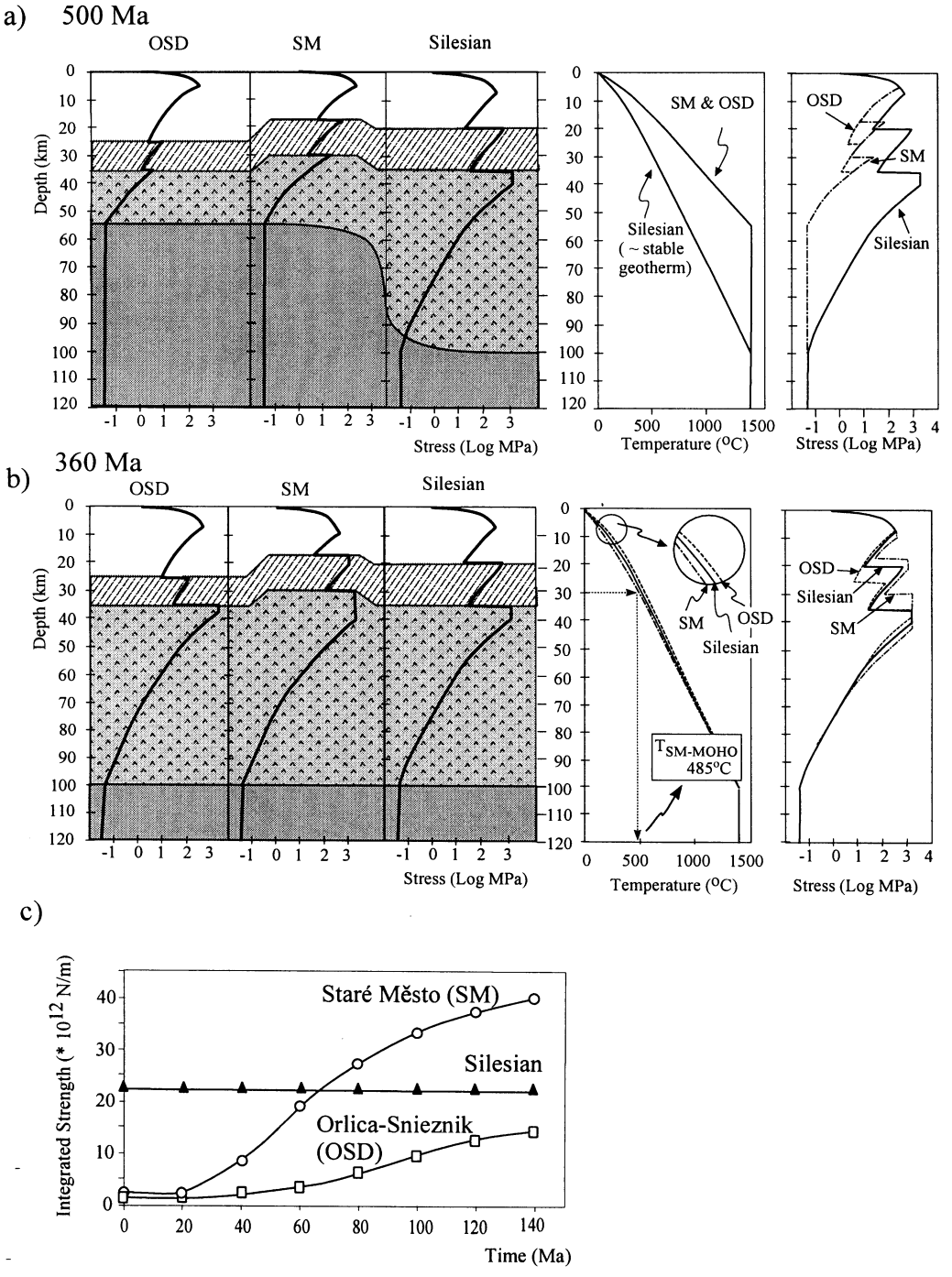
a) 500 Ma
OSD
SM
Silesian
Depth (km)
Stress (Log MPa)
SM & OSD
Silesian
(~ stable
geotherm)
Temperature (°C)
OSD
SM
Silesian
Stress (Log MPa)
b) 360 Ma
OSD
SM
Silesian
Depth (km)
Stress (Log MPa)
SM
OSD
Silesian
T SM-MOHO
485°C
Temperature (°C)
OSD
Silesian
SM
Stress (Log MPa)
c)
Integrated Strength (* 10^12 N/m)
Staré Město (SM)
Silesian
Orlica-Snieznik
(OSD)
Time (Ma)

35 km which decreased to about 30 km during the extension. The estimated average temperature close to 800–850°C suggests a very hot Cambro-Ordovician geotherm (Fig. 4(a)). This type of thermal gradient may develop during lithospheric thinning marked by significant stretching of the mantle (δ) coupled with weak stretching of the crust (β, McKenzie, 1978). Such a type of lithospheric thinning ($\delta \gg \beta$) is connected with mantle upwelling, adiabatic decompression and partial melting of peridotite resulting in intrusions of large volumes of magmas advecting heat towards crustal levels (e.g. Morgan and Ramberg, 1987). The argument for a thermal contribution of gabbroic underplating in the SM domain is presently seen in the close spatial relationship of the leptyno-amphibolite complex and the exceptionally large volumes of gabbroic material. Massive underplating by gabbro and the mostly mafic sequence of layered amphibolite generated several kilometres of new, predominantly mafic lower crust. This led to significant modification of the lithological composition in the lithospheric section of the SM rift (Fig. 4(a)).

4.2. Post-rifting thermal evolution of the Staré Město belt and surrounding lithospheric segments

The post-rifting thermal evolution of the SM and the surrounding lithosphere is crucial for their mechanical behaviour during subsequent Variscan deformation. We assume that the cooling of the SM paleorift occurred in the interval between the rifting at 500 Ma and the onset of Variscan convergence that occurred in Sudetes probably during the Late Devonian (ca. 360 Ma; Ar–Ar ages, Maluski and Patočka, 1997), and culminated during the Early Carboniferous (as dated by the intrusion of the tonalite sill at 339 Ma). The minimum interval of SM paleorift cooling is therefore about 140 Ma.

The emplacement of large volumes of granitoids in the OSD also occurred during Cambro-Ordovician times (~480–522 Ma; Oliver et al., 1993; Kröner et al., 2000). Therefore, we speculate that the massive Cambro-Ordovician granitoid magmatism in the OSD is responsible for the development of a hot geotherm and possibly also an increase in thickness of the granitic layer with high radioactive heat production. The Silesian domain was not affected by the Cambro-Ordovician rifting and is, therefore, considered as a reference standard geotherm (e.g. England and Thompson, 1984) for this region (Fig. 4).

4.3. Estimates of lithospheric strength during Cambro-Ordovician rifting and after 140 Ma of cooling

The yield strength envelopes (strength profiles) were constructed using the computer program 'IBAROOT' (Ježek, 1998), where the strength for the brittle domain σ_β of the crust and mantle is calculated using Byerlee's constants (Byerlee, 1968). To calculate the strength of a ductile domain σ_ϖ, the power-law creep equation using the constants quoted in Ranalli and Murphy (1987) has been applied.The values of the creep parameters and the composition of individual crustal segments used in the model are given in Table 2 and Fig. 4. The integrated strength values for the entire lithosphere were calculated after England (1987).

The strength profile for the SM domain is constructed for a hot geotherm, assuming that the crust is thinned from 35 to 30 km, with ~840°C at

Fig. 4. Results of numerical thermal and rheological modelling. Upper crust (dry granite); OSD = 25 km, SM = 17 km, and Silesian = 20 km. Lower crust (diabase); OSD from 25 to 35 km, SM from 17 to 30 km, and Silesian from 20 to 35 km. Geotherms were defined as follows: depth of radioactive heat production (D) = 15 km for OSD, D = 10 km for SM, and D = 12 km for Silesian domain; heat production (A) = 2.8 μW m^{-3}; thermal conductivity (K) = 2.25 W m^{-1} K^{-1}; density (ρ) = 3.0 g cm^{-3}; specific heat (c) = 1000 J kg^{-1} K^{-1}; and thermal diffusivity (κ) = 9×10^{-7} m^2 s^{-1}. Temperature at the base of 100 km thick lithosphere = 1400°C. Thinning of stable geotherm by factor 0.55 corresponds to the temperatures estimated in SM paleorift for the Cambro-Ordovician rifting. Similar value of thinning of the geotherm is suggested for OSD, and corresponds to surface heat flow measured in volcanic arcs. (a) Geotherms in the SM belt, OSD and Silesian domains at 500 Ma and corresponding yield strength envelopes. (b) Calculated geotherms for SM paleorift and OSD at the onset of Variscan collision and corresponding yield strength envelopes at 360 Ma, after 140 Ma of thermal relaxation. (c) Progressive evolution of integrated strength values during this 140 Ma of cooling due to relaxation of perturbed geotherm for the SM paleorift and the OSD compared with stable Silesian domain.

Table 2
Experimental flow law data used for construction of yield strength envelopes, after Ranalli and Murphy (1987)

	Upper crust granite (dry)	Lower crust diabase	Mantle olivine
A ($MPa^{-n}\ s^{-1}$)	1.25×10^{-9}	2.2×10^{-4}	4×10^{6}
Q ($kJ\ mol^{-1}$)	123	260	540
β	0.75	0.75	0.75
n	3.2	3.4	3.0

the base, according to calculated *PT* conditions. Consequently, assuming that the thinning was homogeneous, the upper crust of thickness 20 km and the mafic lower crust of 15 km were thinned to 17 and 13 km, respectively (Fig. 4(a)). The strength profile for the OSD was constructed for a 'hot' post-magmatic geotherm, for upper and lower crust thicknesses of 25 and 10 km, respectively. The strength profile of the Silesian domain consisting of 20 km upper crust and 15 km lower crust is constructed for a stable continental geotherm ('standard' geotherm, England and Thompson, 1984; Fig. 4). These values represent very rough estimates of crustal lithological and thermal structures based on rheological profiles of the European lithosphere (e.g. Cloetingh and Burov, 1996). The presented estimates try to underline the first-order effects of the variations of thickness of crustal layers, inherited from the Cambro-Ordovician rifting, on the subsequent contrasting mechanical behaviour of individual lithospheric segments during the Variscan collision.

Subsequent cooling of SM and OSD geotherms is simulated using numerical solutions of the heat conduction equation for relaxation of perturbed geotherms (e.g. Morgan and Ramberg, 1987; Thompson et al., 2000). These calculations are based on the time necessary for conductive cooling (related to the depth of the Cambro-Ordovician perturbation) with respect to a stable continental geotherm for an equilibrium European lithosphere thickness of ca. 100 km (Babuška and Plomerová, 1993). We have simultaneously examined the strength evolution of both the OSD and the SM domains during cooling compared to the stable Silesian lithosphere (Fig. 4(b) and (c)). The strength of the OSD expressed by integrated strength values increased with cooling but after 140 Ma, the OSD was still weaker than the stable Silesian lithosphere. This is due to the thick granitic upper crust of the OSD and to the higher radioactive heat production being responsible for the slow cooling of the upper part of the lithosphere (Fig. 4(b) and (c)). The strength profile and integrated strength values for the SM show that immediately after rifting, this domain was weaker than the Silesian domain but during subsequent cooling, the SM lithosphere became significantly stronger than both the OSD and the Silesian lithospheres.

4.4. Variscan convergence: interpretation of Variscan metamorphism and deformation

The major argument for Variscan deformation in the SM belt is based on the structure, fabric and emplacement age of the tonalitic sill (~339 Ma). It was shown that the preserved Cambro-Ordovician structures of the leptyno-amphibolite complex are discordant to the Variscan syntectonic fabric of the tonalitic sill. However, the mylonitic fabric of metagabbro is fully concordant with the foliation, lineation and dextral transpression kinematics of the tonalitic sill (Parry et al., 1997). The petrological analysis has shown that prograde zoning occurred in dynamically recrystallized minerals in mylonitic gabbro and metaperidotite.

The remaining but important problem involves the *PT* estimates of Variscan metamorphism resembling closely those of the Cambro-Ordovician event. An important question is the estimate of temperature at the Moho below the SM domain before Variscan convergence. The modelling of the thermal relaxation of the hot, Cambro-Ordovician geotherm has shown that after 140 Ma the temperature close to Moho cooled down to ca. 485°C (Fig. 4(b)). However, the Variscan M_2 metamorphism of metagabbro and metaperidotite shows temperatures of 700–750°C, suggesting that the cooled mantle and the lower crustal rocks were to a large extent heated up at a pressure

Table 3
Parameters adopted in the thermal model of magmatic underplating (parameters chosen for the thermal and rheological modelling presented in Figs. 5 and 6 are in bold)

		Reference
Half width of intrusion (m)	250, 500, 600, 750, **1000**, 1100	
Temperature of country rocks (T at MOHO below SM after 140 Ma of cooling) (°C)	485	Thermal model, Fig. 4(b)
Temperature of intrusion (interval of crystallization for basaltic magma) (°C)	1100 (450), 1150 (500), 1200 (550), 1250 (600)	Čermák et al. (1982)
Temperature of intrusion (interval of crystallization for tonalite magma) (°C)	1000 (350), **1050 (400)**	Johannes and Holtz (1996)
Heat of crystallization (kJ kg^{-1})	200	Peacock (1989)
Thermal conductivity of hornblende gabbro at 500°C (W m^{-1} K^{-1})	2.58	Čermák et al. (1982)
Heat capacity of gabbro (J kg^{-1} K^{-1})	1000	Čermák et al. (1982)
Density of gabbro (kg m^{-3})	3060	Čermák et al. (1982)

not exceeding 10 kbar. The comparison of the pressure attributed to the Variscan metamorphic event with the pressure developed during the Cambro-Ordovician metamorphism of the leptyno-amphibolite complex indicates that the SM domain was not considerably thickened during the Variscan convergence.

4.5. Exhumation of the Staré Město belt — weakening of the upper mantle and lower crust due to magmatic underplating

The high ductility and degree of metamorphism of metagabbro, as well as thermal conditions related to the metaperidotite, indicate external heat input responsible for perturbation of the continental geotherm during the Variscan collision. A possible external thermal source can be attributed to plutonic processes such as the Variscan tonalitic sill intruded beneath the metagabbro (Figs. 2 and 3). Local weakening of gabbro and peridotite may have been a consequence of this tonalitic magma underplating below the SM paleorift.

In the model, it is assumed that the magma ascended to the Moho (a major rheological boundary, e.g. Vigneresse, 1995) where a horizontally elongate magma chamber developed. A series of contact metamorphic calculations were made employing the 'CONTACT' software of Peacock (1989). The input parameters are given in Table 3. A temperature of 485°C is considered appropriate for the temperature at the Moho below the SM after 140 Ma of cooling (Fig. 4(b)). Modelling was carried out to estimate the magma temperature and thickness of a magma chamber which would determine minimum metamorphic conditions of 700°C for an average thickness of 500 m of gabbroic shear zone (Fig. 5(a)). The results have shown that these temperature conditions are achieved only for magma with its temperature above 1000°C. According to the results of Johannes and Holtz (1996), temperatures exceeding 1000°C are achieved by completely molten tonalitic magma with less than ca. 5 wt% of water. Our modelling has shown that the minimum half thickness of the chamber for tonalitic magma with a temperature of 1050°C is about 1000 m (Fig. 5(a)). Such a thickness of the magma chamber roughly approximates the actual thickness of the tonalite sheet.

The country rocks were modelled with the physical parameters quoted for a hornblende gabbro (Table 3; Čermák et al., 1982) with the initial temperature of 485°C (Fig. 4(b)). The simulation shows that the temperature produced by tonalite intrusion exceeds 700°C at a distance of up to 500 m from the magma chamber. The maximum increase in temperature for samples located 500 m from the contact occurred after 40,000 years, and then the temperature gradually decreased (Fig. 5(b)). This thermal perturbation after 40,000 years was incorporated into the previously calculated geotherm, and its influence on the strength profile can be seen in Fig. 6(a). The bottom of the mafic lower crust and the originally 'brittle' uppermost layer

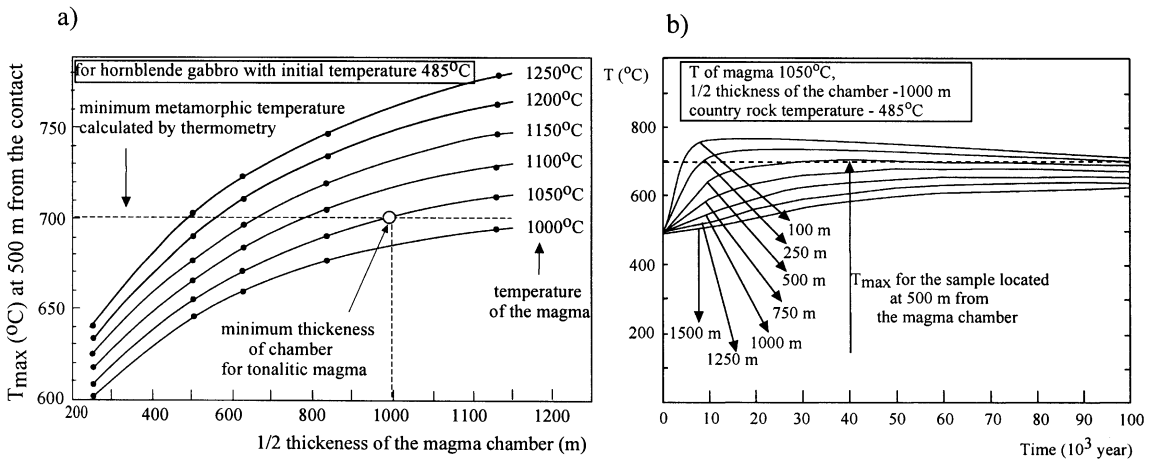

Fig. 5. (a) Maximum temperature achieved in country rocks at a distance of 500 m from the contact of the magma chamber calculated for different magma temperatures and different half thicknesses of the magma chamber. The diagram is calculated for thermal conductivity of hornblende gabbro with initial temperature of 485°C (Čermák et al., 1982). (b) Thermal influence of 2 km thick slab of tonalitic magma on the surrounding rocks (calculated for hornblende gabbro).

of the mantle are greatly weakened while the top of the lower crust remains strong and the central part rigid. The strength in the mantle increases downwards away from the magmatic chamber, and at ~34 km the strength decreases with depth.

We suggest that tonalitic magma underplating the SM paleorift may explain the metamorphic conditions found in metagabbro and metaperidotite, and allow the strain to be localized in both lithologies (Fig. 6(b)). The thrust development was accompanied by syntectonic intrusion of tonalite (Parry et al., 1997). As the heat from the magma chamber is insufficient to weaken the entire lower crust, its upper part represented by the leptyno-amphibolite complex remains rigid, almost undeformable, and unaffected by Variscan metamorphism (Fig. 6(a)).

5. Discussion and conclusions

The primary result of the investigations presented by Kröner et al. (2000), Parry et al. (1997), Štípská (1999) and Štípská et al. (2000) is that the leptyno-amphibolite complex, together with the gabbroic belt, represents Cambro-Ordovician lower crust deformed during the Variscan orogeny. The rifting period significantly changed the lithological stratification of the SM lithosphere. Tommasi and Vauchez (1997) and Vauchez et al. (1998) have shown that cold paleorifts may represent stiff heterogeneities responsible for strain localization and shear zone development along their margins during later intracontinental deformation. In agreement with their suggestion, we observe contrasting mechanical behaviour of the SM domain with respect to the surrounding lithospheric segments.

The present study shows that at the onset of Variscan collision, the SM domain represented a strong block surrounded by a very weak OSD to the west and relatively weaker Silesian lithosphere to the east. The Variscan metamorphic evolution of the OSD indicates important thickening at ~340 Ma (Steltenpohl et al., 1993). The Silesian domain was underthrust to the west below the SM belt during the Variscan period resulting in Barrovian-type metamorphism in the Silesian domain (Schulmann and Gayer, 2000). The above-described metamorphic trends suggest that both the units surrounding the SM belt suffered significant burial resulting in the development of HP metamorphism whereas the petrological data of Variscan metamorphism from the SM belt indicate that less thickening occurred there (Fig. 6(c)). This difference can be interpreted as a maximum thickening of the OSD (orogenic root domain) in front of the undeformable SM paleorift, which represents a strong obstacle to the easterly

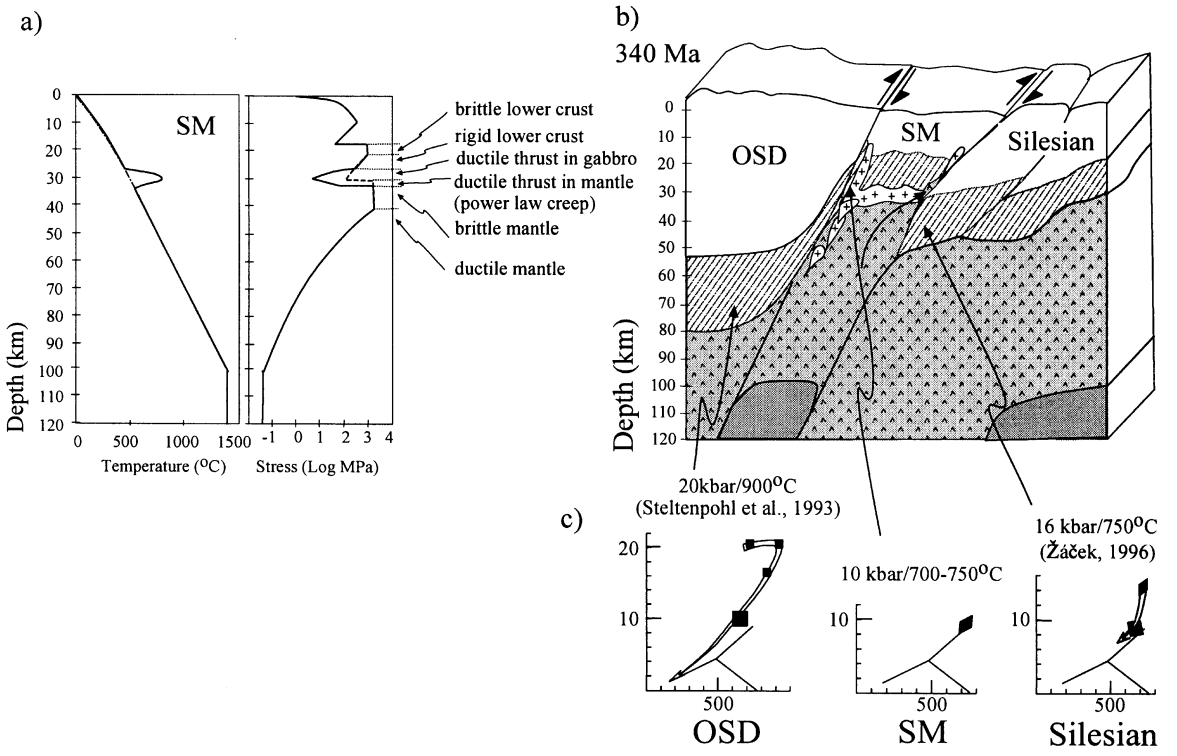

Fig. 6. (a) Calculated thermal perturbance 40,000 years after the emplacement of magma incorporated into the previously calculated geotherm and its influence on the strength profile of the SM domain. (b) Variscan exhumation of rigid lower crust of the SM paleorift sandwiched between thickened lithosphere of the OSD and underthrust Silesian domain. (c) *PT* space to the left shows *PT* evolution of HP rocks of the OSD (Steltenpohl et al., 1993) and *PT* space to the right shows metamorphic evolution for Silesian eclogites (Žáček, 1996). Central *PT* diagram shows peak metamorphic conditions of Variscan metamorphism in the SM. Thickness of sub-crustal mantle is estimated on the base of yield strength envelopes for all three domains from Fig. 4(b).

propagating Variscan deformation (Fig. 6(b) and (c)). The SM belt at the time of collision represented the strongest domain of the whole region with a rigid mantle and rigid lower mafic crust elevated higher than the adjacent mantle of the Silesian domain. This geometry determines the migration of the collisional front to the east and the subsequent continental underthrusting of the Silesian domain below both the SM paleorift and the OSD. The thickening of the OSD in front of the westward underthrusting of the Silesian domain below the SM paleorift can be explained by the mechanical properties and relative vertical position of the subcrustal mantle of all three domains at the onset of convergence.

The exhumation of the SM rocks is explained by significant weakening of the uppermost part of the mantle, and of the lower crust, due to magmatic underplating represented by the tonalite sill. We envisage tonalite magma generation to result from continued eastward subduction of the Saxothuringian domain below the easterly Variscan root lithosphere (OSD). Local weakening of gabbro and peridotite allow enhanced strain to be localized in both lithologies. The entire almost undeformed overlying lower crust — leptyno-amphibolite complex — was subsequently exhumed along ductile gabbroic and peridotite thrusts into supracrustal levels (Fig. 6). The vertical movements of the leptyno-amphibolite complex were accompanied by syntectonic intrusion of tonalite as described by Parry et al. (1997).

Acknowledgements

Financial support to P. Štípská by the Czech National Grant Agency with the grant No. 205/99/1195 is gratefully acknowledged. Software for thermal and rheological modelling was developed as part of grant No. 296/1997/B GEO to J. Ježek. This work benefited from several visits of P.Š. to ETH Zürich, financed by the Swiss National Foundation ('Continuous Orogenesis' grant to A.B. Thompson). P. Štípská, K. Schulmann and J. Ježek were supported financially by the grant No. 24313005 of the Ministry of Education of the Czech Republic. We are grateful to G. Zulauf for constructive and helpful review, and to J.P. Burg for acting as editor.

References

Allemand, P., Brun, J.-P., 1991. Width of continental rifts and rheological layering of the lithosphere. Tectonophysics 188, 63–69.

Babuška, V., Plomerová, J., 1993. Lithospheric thickness and velocity anisotropy — seismological and geothermal aspects. Tectonophysics 225, 79–89.

Bertotti, G., ter Voorde, M., Cloetingh, S., Picotti, V., 1997. Thermomechanical evolution of the South Alpine rifted margin (North Italy): constraints on the strength of passive continental margins. Earth Planet. Sci. Lett. 146, 181–193.

Byerlee, J.D., 1968. Brittle ductile transition in rocks. J. Geophys. Res. 73 (14), 4741–4750.

Bohlen, S.R., Wall, V.J., Boettcher, A.L., 1983. Experimental investigations and geological applications of equilibria in the system $FeO–TiO_2–Al_2O_3–SiO_2–H_2O$. Am. Mineral. 68, 1049–1058.

Čermák, V., Huckenholz, H.G., Rybach, L., Schmid, R. Schopper, J.R., Schuch, M., Stöffler, D., Wohlenberg, J., 1982. Physical properties of rocks. In: Angenheister, H. (Ed.), Landolt-Börnstein, Numerical Data and Functional Relationships in Science and Technology, Group V: Geophysics and Space Research, pp. 305–370.

Cloetingh, S., van Wees, J.D., van der Beek, P.A., Spadini, G., 1995. Role of pre-rift rheology in kinematics of extensional basin formation: constraints from thermomechanical models of Mediterranean and intracratonic basins. Marine and Petroleum Geology 12, 793–807.

Cloetingh, S., Burov, E., 1996. Thermomechanical structure of European continental lithosphere: constraints from rheological profiles and EET estimates. Geophys. J. Int. 124, 695–723.

Don, J., Dumicz, M., Wojciechowska, I., Zelazniewicz, A., 1990. Lithology and tectonics of the Orlica–Snieznik Dome, Sudetes. Recent state of knowledge. N. Jb. Geol. Paläont. Abh. 179, 159–188.

England, P.C., 1987. Diffuse continental deformation — length scales, rates and metamorphic evolution. Philos. Trans. R. Soc. London, Ser. A — Mathl. Phys. Engng. Sci. 321, 3–22.

England, P.C., Thompson, A.B., 1984. Pressure–temperature–time paths of regional metamorphism I: heat transfer during the evolution of regions of thickened continental crust. J. Petrol. 25, 894–928.

Ferry, J.M., Spear, F.S., 1978. Experimental calibration of the partitioning of Fe and Mg between biotite and garnet. Contrib. Mineral. Petrol. 66, 113–117.

Gasparik, T., Newton, R.C., 1984. The reversed alumina contents of orthopyroxene in equilibrium with spinel and forsterite in the system $MgO–Al_2O_3–SiO_2$. Contrib. Mineral. Petrol. 85, 186–196.

Holland, T.J.B., Blundy, J.D., 1994. Non-ideal interactions in calcic amphiboles and their bearing on amphibole–plagioclase thermometry. Contrib. Mineral. Petrol. 116, 433–447.

Ježek, J., 1998. Thermal and rheological modelling of lithosphere. TMR Summer School handout. Imperial College, London (unpublished results).

Johannes, W., Holtz, F., 1996. Petrogenesis and experimental petrology of granitic rocks. In: Goresy, A. El., von Engelhardt, Hahn, T. (Eds.). Minerals and Rocks 22. Springer, Berlin (335 pp.).

Kohn, M.J., Spear, F.S., 1990. Two new barometers for garnet amphibolites with applications to southeastern Vermont. Am. Mineral. 75, 89–96.

Koziol, A.M., 1989. Recalibration of the garnet–plagioclase–Al_2SiO_5–quartz (GASP) geobarometer and application to natural parageneses. Trans. Am. Geophys. Un. 70, 493.

Kröner, A., Štípská, P., Schulmann, K., Jaeckel, P., 2000. Chronological constraints on the pre-Variscan evolution of the northeastern margin of the Bohemian Massif, Czech Republic. Orogenic Processes — Quantification and Modelling in the Variscan Belt of Central Europe (Special Volume), Franke, W., Altherr, R., Haak, V., Oncken, O., Tanner, D. (Eds.). Geol. Soc. Spec. Publ. 179, 175–197.

Kryza, R., Pin, C., Vielzeuf, D., 1996. High-pressure granulites from the Sudetes (south-west Poland): evidence of crustal subduction and collisional thickening in the Variscan Belt. J. Metamorph. Geol. 14, 531–546.

Maluski, H., Patožka, F., 1997. Geochemistry and 40Ar/39Ar geochronology of the mafic metavolcanic rocks from the Rúchory Mountains complex (west Sudetes, Bohemian Massif): paleotectonic significance. Geol. Mag. 134, 703–716.

Maluski, H., Rajlich, P., Souček, J., 1995. Pre-Variscan, Variscan and early Alpine thermo — tectonic history of the northeastern Bohemian Massif: an 40Ar/39Ar study. Geol. Rdsch. 84, 345–358.

McKenzie, D., 1978. Some remarks on the development of sedimentary basins. Earth Planet. Sci. Lett. 40, 25–32.

Morgan, P., Ramberg, I.B., 1987. Physical changes in the lithosphere associated with thermal relaxation after rifting. Tectonophysics 143, 1–11.

Oliver, G.J.H., Corfu, F., Krogh, T.E., 1993. U–Pb ages from SW Poland: evidence for a Caledonian suture zone between Baltica and Gondwana. J. Geol. Soc. (Lond.) 150, 355–369.

Oxburgh, E.R., 1982. Heterogeneous lithospheric stretching in early

history of orogfenic belts. In: Hsu, K.J. (Ed.), Mountain building processes. Academic Press, London, 85–95.

Parry, M., Štípská, P., Schulmann, K., Hrouda, F., Ježek, J., Kröner, A., 1997. Tonalite sill emplacement at an oblique plate boundary: northeastern margin of the Bohemian Massif. Tectonophysics 280, 61–81.

Peacock, S.M., 1989. Thermal modelling of metamorphic pressure–temperature paths: a forward approach. In: Spear, F.S., Peacock, S.M. (Eds.), Metamorphic Pressure–Temperature–Time Paths. American Geophysical Union, Short Course in Geology, 102 pp.

Ranalli, G., Murphy, D.C., 1987. Rheological stratification of the lithosphere. Tectonophysics 132, 281–295.

Schmidt, M.W., 1992. Amphibole composition in tonalite as a function of pressure: an experimental calibration of the Al-in-hornblende barometer. Contrib. Mineral. Petrol. 110, 304–310.

Schulmann, K., Gayer, R., 2000. A model for an obliquely developed continental accretionary wedge: NE Bohemian Massif. J. Geol. Soc. London. 157, 401–416.

Souček, J., 1978. Metamorphic zones of the Vrbno and Rejvíz series, the Hrub_ Jeseník Mountains, Czechoslovakia. Tschermaks Mineral. Petrogr. Mitt. 25, 195–217.

Steltenpohl, M.G., Cymerman, Z., Krogh, E.J., Kunk, M.J., 1993. Exhumation of eclogitized continental basement during Variscan lithospheric delamination and gravitational collapse, Sudety Mountains, Poland. Geology 21, 1111–1114.

Štípská, P., 1999. Thermomechanical evolution of collisional boundary during Variscan convergence — eastern margin of the Bohemian Massif (examples of the Staré Město belt and the Thaya dome). PhD thesis, Charles University, Prague, 175 pp.

Štípská, P., Schulmann, K., Kröner, A., Thompson, A.B., 2000. Discovery of the Cambro-Ordovician metamorphism related to intracontinental rifting within the Variscan belt: NE margin of the Bohemian Massif (submitted for publication).

Suess, F.E., 1926. Intrusionstektonik und Wandertektonik im variszichen Grundgebirge. Borntträger, Berlin.

Thompson, A.B., 1976. Mineral reactions in pelitic rocks: II. Calculation of some P–T–X (Fe–Mg) phase relations. Am. J. Sci. 276, 425–454.

Thompson, A.B., Schulmann, K., Ježek, J., Tolar, V., 2001. Thermally softened continental extensional zones (arcs and rifts) as precursors to thickened orogenic belts. Tectonophysics 332 (1/2) 115–141.

Tommasi, A., Vauchez, A., 1997. Continental-scale rheological heterogeneities and complex intraplate tectono-metamorphic patterns: insights from a case-study and numerical models. Tectonophysics 279, 327–350.

Van Breemen, O., Aftalion, M., Bowes, D.R., Dudek, A., Mísař, Z., Povondra, P., Vrána, S., 1982. Geochronological studies of the Bohemian Massif, Czechoslovakia, and their significance in the evolution of Central Europe. Trans. Edinb. Geol. Soc. Earth Sci. 72, 89–108.

Vauchez, A., Tommasi, A., Barruol, G., 1998. Rheological heterogeneity, mechanical anisotropy and deformation of the continental lithosphere. Tectonophysics 296, 61–86.

Vigneresse, J.L., 1995. Crustal regime deformation and ascent of granitic magma. Tectonophysics 249, 187–202.

Žáček, V., 1996. Retrograded eclogite from the Staré Město Belt, NE margin of the Bohemian Massif. J. Czech Geol. Soc. 41, 167–175.

J. metamorphic Geol., 2005, **23,** 649–666 doi:10.1111/j.1525-1314.2005.00601.x

Contrasting textural record of two distinct metamorphic events of similar *P–T* conditions and different durations

O. LEXA,[1,2] P. ŠTÍPSKÁ,[1,2] K. SCHULMANN,[1,2] L. BARATOUX[1] AND A. KRÖNER[3]
[1]*Institute of Petrology and Structural Geology, Charles University, Albertov 6, 128 43 Prague, Czech Republic (lexa@natur.cuni.cz)*
[2]*Université Louis Pasteur, CGS/EOST, UMR 7517, 1 rue Blessig, Strasbourg 67084, France*
[3]*Institut für Geowissenschaften, Universität Mainz, 55099 Mainz, Germany*

ABSTRACT A structural, metamorphic and geochronological study of the Staré Město belt implies the existence of two distinct metamorphic events of similar peak *P–T* conditions (700–800 °C, 8–10 kbar) during the Cambro-Ordovician and the Carboniferous tectonometamorphic events. The hypothesis of two distinct periods of metamorphism was suggested on the basis of structural discordance between an undoubtedly Carboniferous granodiorite sill intrusion and earlier Cambro-Ordovician fabrics of a banded amphibolite complex. The analysis of crystal size distribution (CSD) shows high nucleation density (N_0) and low average growth rate (Gt) for Carboniferous mylonitic metagabbros and mylonitic granodiorites. The parameter N_0 decreases whereas the quantity Gt increases towards higher temperatures progressively approaching the values obtained from the Cambro-Ordovician banded amphibolite complex. The spatial distribution of amphibole and plagioclase shows intense mechanical mixing for lower-temperature mylonitic metagabbros. In high-temperature mylonites a strong aggregate distribution is developed. Cambro-Ordovician amphibolites unaffected by Carboniferous deformation show a regular to anticlustered spatial distribution resulting from heterogeneous nucleation of individual phases. This pattern, together with CSD, was subsequently modified by the grain growth and textural equilibration controlled by diffusive mass transfer during Carboniferous metamorphism. The differences between the observed textures of the amphibolites are interpreted to be a consequence of the different durations of the Carboniferous and Cambro-Ordovician thermal events.

Key words: Cambro-Ordovician and Carboniferous metamorphism; quantitative textural analysis; crystal size distributions; grain contact frequencies.

INTRODUCTION

Identifying distinct metamorphic episodes in domains with a polymetamorphic history is possible providing the *P–T* conditions of a younger metamorphic event are markedly different from those of a preceding one. The problem becomes more complex when the more recent metamorphic event affects units which previously suffered a metamorphic event of a similar grade. In this particular case it is only the geological context and geochronological data that can indicate the existence of distinct tectonometamorphic episodes.

Polymetamorphic domains are commonly studied using analysis of polyphase deformations and individual tectonic events are attributed to distinct deformational phases (Turner & Weiss, 1963). In favourable situations tectonic regimes responsible for the formation of two distinct deformational phases can be distinguished. However, polyphase structures commonly result from the continuous activation of local mechanical instabilities during a single deformation event (Burg, 1999).

The tools of metamorphic petrology are able to provide *P–T* estimates of peak metamorphic conditions, and important fragments of *P–T* paths can be reconstructed when thermodynamic modelling is applied (Powell & Holland, 1988). However, metamorphic and phase petrology do not reveal information about the duration of metamorphic events. The time span between individual metamorphic-deformation events and the duration of metamorphic reworking can be determined in principle by geochronology.

When metamorphic rocks are reworked by a following tectonometamorphic event after a significant period of time but under similar *P–T* conditions, it is unlikely that the duration of events, strain rates and kinematics of deformation are also the same. However, the texture of metamorphic tectonites results from nucleation, grain growth and various recrystallization mechanisms that are strongly controlled by temperature, time and strain rate/stress ratio (Hickey & Bell, 1996). Therefore, the analysis of metamorphic textures is a method that is capable of distinguishing between two metamorphic events under similar *P–T* conditions of different durations.

Here, we consider an example of Cambro-Ordovician metamorphism associated with crustal thinning

followed by moderate crustal thickening and magma underplating during the Carboniferous (Variscan) orogeny (Štípská *et al.*, 2001). The results of a structural, petrological and geochronological study allow a preliminary distinction of two metamorphic events, which exhibit similar *P–T* conditions. The structural and geochronological arguments presented here are not sufficiently unambiguous to distinguish between metamorphic fabrics developed during the Cambro-Ordovician thinning and the Carboniferous moderate thickening. Therefore, quantitative textural analysis of pairs of rock samples with similar mineralogical compositions has been used to show the influence of the Cambro-Ordovician and Carboniferous events on final textures.

GEOLOGICAL SETTING

The Staré Město belt was a Cambro-Ordovician rift, separating high-grade gneisses of a thickened continental crust (Orlica-Snieznik dome) in the west from the Neo-Proterozoic continental margin (Silesian domain) in the east (Fig. 1), at the eastern margin of the Bohemian Massif (Kröner *et al.*, 2000a,b). The Staré Město belt consists of a lower crustal complex which was later affected by the Variscan collisional tectonics (Kröner *et al.*, 2000a,b; Štípská *et al.*, 2001). The overall structure of this unit is marked by NE–SW trending lithologies generally dipping to the west (Figs 2 & 3). The top of the tectonic sequence and the boundary with the rocks of the Orlica-Snieznik dome is represented by a layer of strongly sheared metagabbro (504.9 ± 1.0 Ma; Kröner *et al.*, 2000a,b). This boundary represents a ductile shear zone along which a Variscan granodiorite sill was emplaced (Parry *et al.*, 1997). Zircon from the northern and southern parts of the granodiorite sill were dated at 339.4 ± 1.1 and 344.5 ± 0.4 Ma, respectively, reflecting the time of magma crystallization. The banded amphibolite complex located structurally below comprises a layered sequence of alternating banded amphibolites and fine-grained quartzofeldspathic rocks (503 ± 2 and 502.1 ± 1.7 Ma; Kröner *et al.*, 2000a,b), subordinate tonalitic gneisses (503.3 ± 0.8 and 501.9 ± 0.6 Ma; Kröner *et al.*, 2000a,b) and high-grade metasediments showing evidence of anatexis (age of metamorphism – *c.* 504 Ma; Kröner *et al.*, 2000a,b). In the northern part of the Staré Město belt the mylonitic metagabbros are tectonically repeated underneath the banded amphibolite complex (Fig. 1).

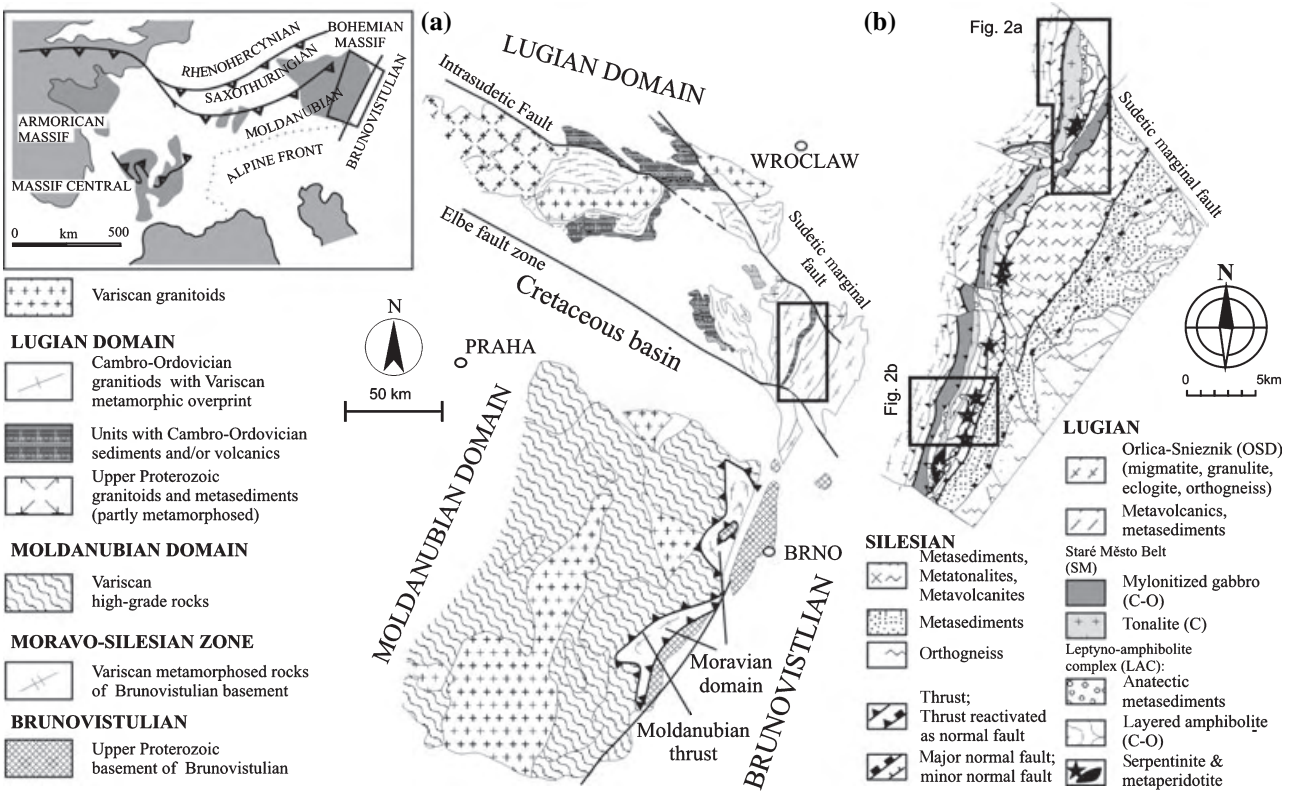

Fig. 1. (a) The schematic outlines of the major units of the Bohemian Massif. The location of the studied area is indicated. Upper left inset shows the position of the studied area in the frame of European Variscides. (b) Geological map of the Staré Město belt based on geological maps 1:25 000 provided by courtesy of the Czech Geological Survey. Important thrust faults and normal faults are indicated. Frames mark location of maps shown in Fig. 2.

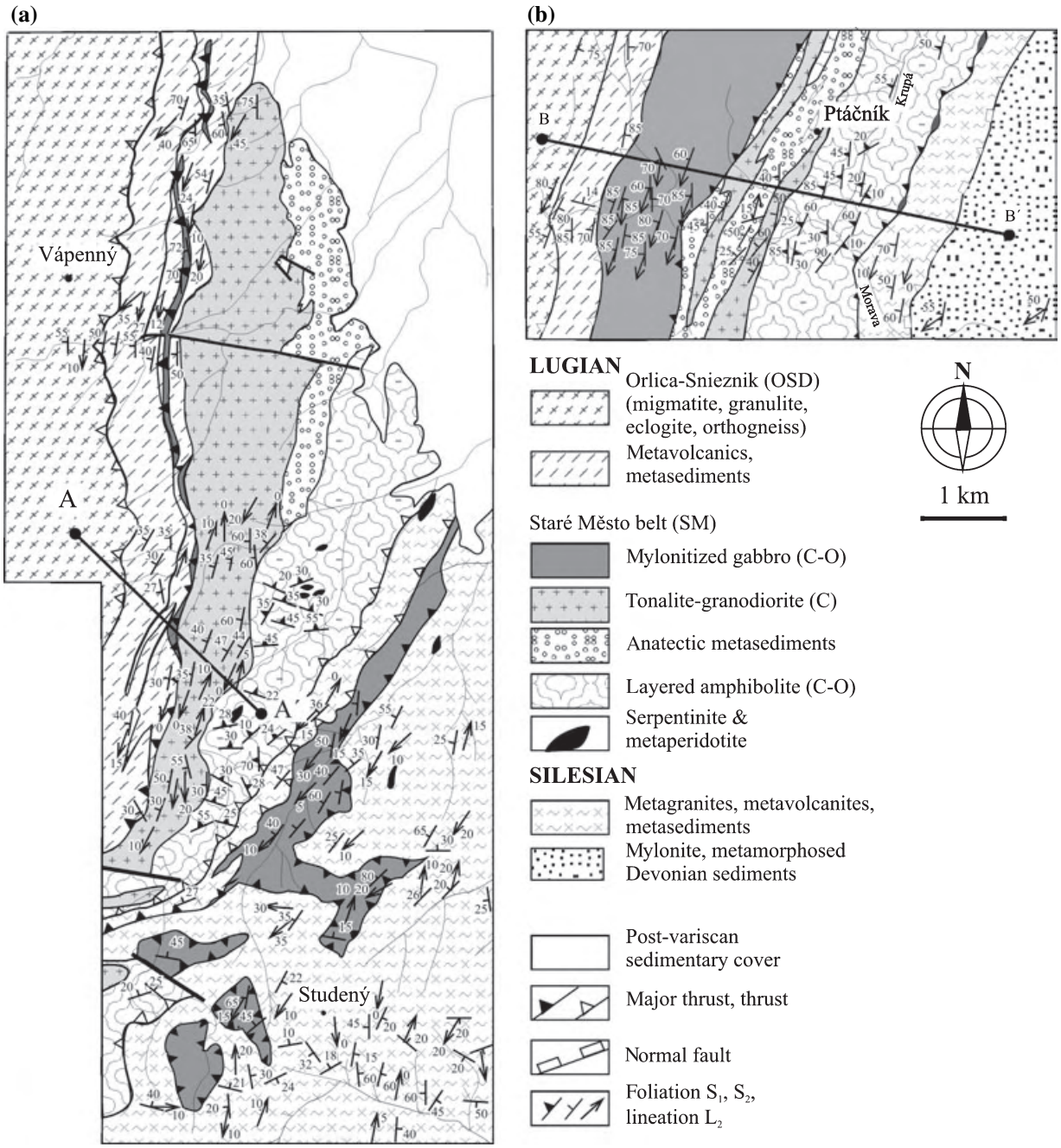

Fig. 2. Geological and structural maps of the Staré Město belt. Foliations, mineral lineations and major thrust and normal faults are indicated. (a) Northern area, see Fig. 1 for location. A–A′ is the cross-section shown in Fig. 4. (b) Southern area, see Fig. 1 for location. B–B′ is the cross-section shown in Fig. 3.

STRUCTURAL CHARACTERIZATION OF VARISCAN AND CAMBRO-ORDOVICIAN FABRICS

Structural relationships between the granodiorite sill, mylonitic metagabbros and banded amphibolite complex combined with geochronological data by Kröner *et al.* (2000a,b) allowed Štípská *et al.* (2001) to distinguish Cambro-Ordovician and Variscan tectonometamorphic events in the study area. This hypothesis was based on structural relationships between the banded amphibolite complex and the superposed granodiorite intrusion in the northern part of the Staré Město belt (Štípská *et al.*, 2001). In the south, however, the presumed Variscan and Cambro-Ordovician fabrics are concordant, and are almost indistinguishable from each other in the field (Fig. 3b).

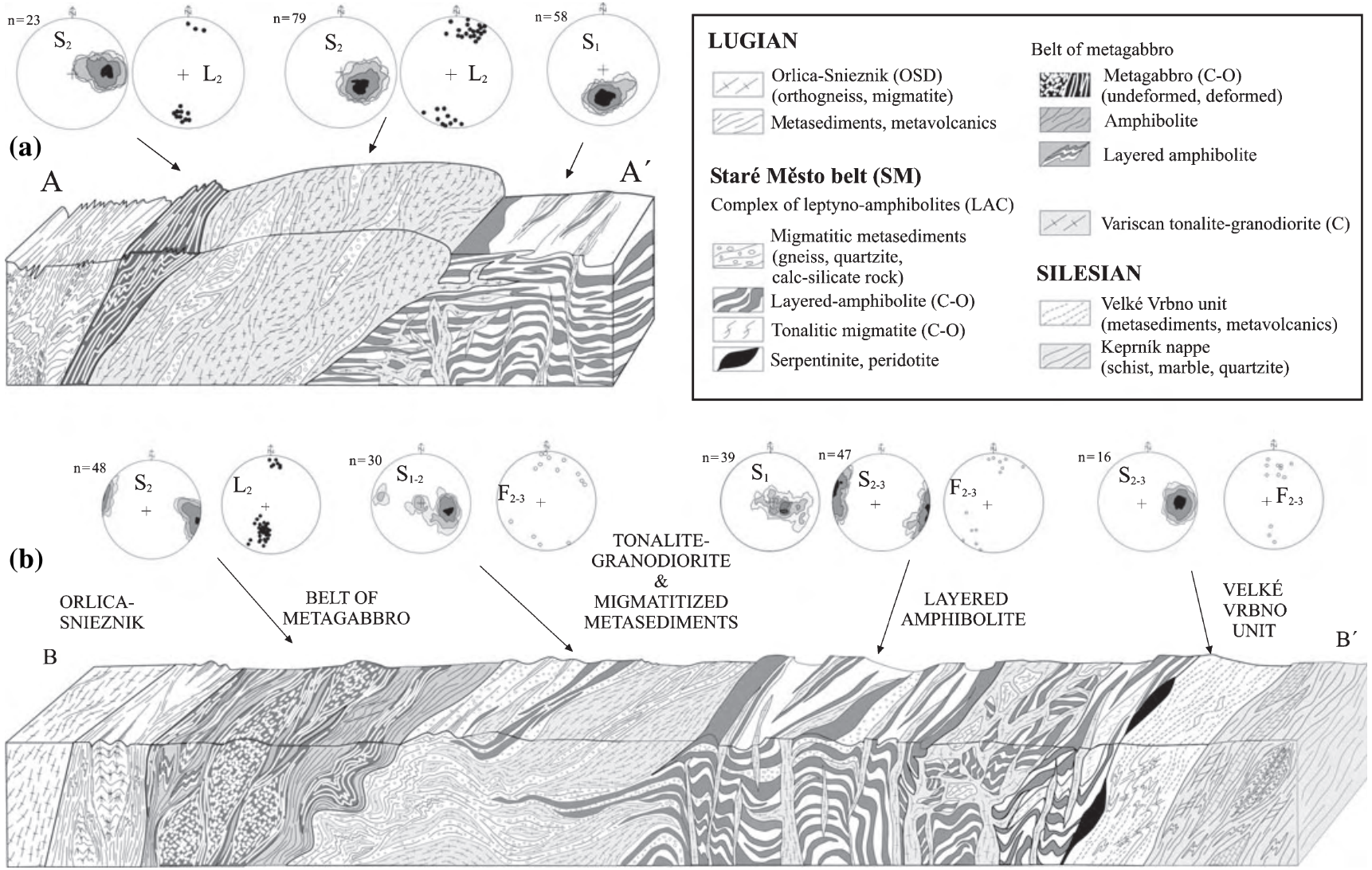

Fig. 3. Geological cross-sections A–A′ and B–B′ (shown in Fig. 2) of the Staré Město belt disclosing major structures, lithology of individual units and major tectonic boundaries. Equal-area, lower-hemisphere stereoplots show D_1, D_2 and D_3 planar and linear structures. Each stereoplot is contoured at regular multiples of distribution. Drawings are made according to field photographs and field notes and show principal structural features.

Structures in Variscan granodiorite

The Variscan granodiorite sill is syntectonically emplaced between the mylonitic metagabbro to the west, and the banded amphibolite complex to the east (Parry *et al.*, 1997). The structural pattern of the granodiorite sill varies from SW to NE along the length of the intrusion (Figs 2 & 3). The magmatic to subsolidus foliation (S_2) dips to the NW and bears an intense subhorizontal mineral lineation (L_2) defined by an alignment of amphibole (Fig. 3a,b). Rare lock-up shear-bands filled with residual melt indicate a dextral sense of shear. In the south, the granodiorite does not form a continuous body but occurs as numerous sills in surrounding amphibolites and anatectic metasediments (Fig. 3b). The granodiorite locally forms dykes emplaced along conjugate steep brittle–ductile NW–SE or NE–SW trending shear zones at high angle to the initially flat-lying S_1 foliation (Fig. 3a,b).

Structures of mylonitic metagabbros

Although the western metagabbro belt was strongly reworked during the Variscan orogeny, magmatic structures are preserved in the low-strain domains (Fig. 4c). Here, the metagabbro exhibits either a medium-grained isotropic texture and homogeneous composition, or layering marked by alternating layers of variable grain size ranging from a few mm up to 2 cm (Fig. 4c). The mylonitic metagabbros exhibit the development of S_2 mylonitic foliation, defined by alternating monomineralic ribbons of recrystallized plagioclase and amphibole (Figs 4c & 5c). This foliation dips at medium to high angles to the WNW. Towards the south, the foliation tends to become subvertical (Fig. 2b). A strong mineral L_2 lineation is defined by recrystallized aggregates of amphibole and is associated with numerous kinematic indicators suggesting dextral shearing. The S_2 foliation is locally affected by late F_3 folds with hinges sub-parallel to L_2 lineation or by development of S_3 crenulation cleavage. The complete structural and kinematic coherency between the metagabbros and underlying granodiorite sill suggests their common Variscan deformation history.

The eastern metagabbro was affected by heterogeneous shear zones (Fig. 4d) during the Variscan deformation. The metagabbros are strongly mylonitized at the upper and lower contacts with the hangingwall and

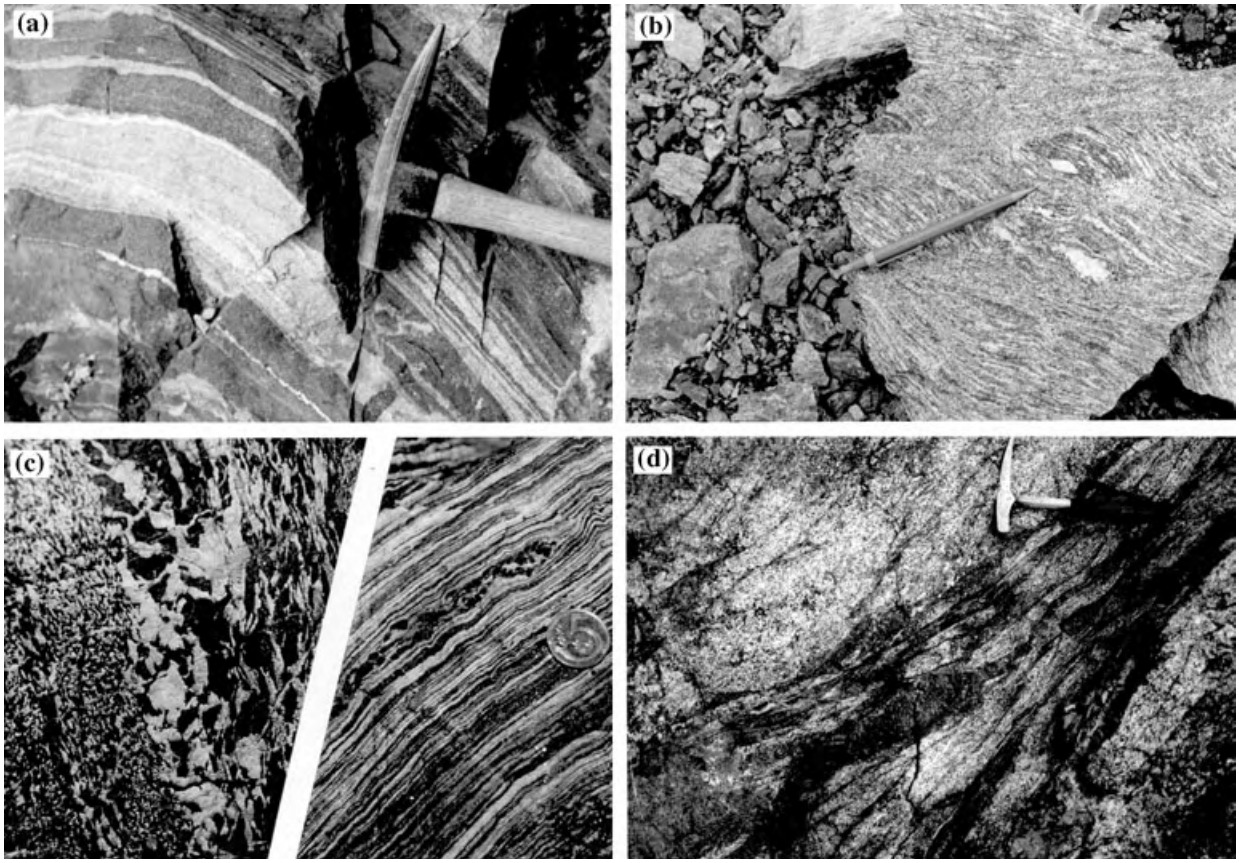

Fig. 4. Field photographs showing main structural features of important lithologies of the Staré Město belt. (a) Metamorphic layering M_1 of banded amphibolite complex. (b) Extensional melt-filled shear-bands D_1 in tonalitic migmatitic gneiss of the banded amphibolite complex. (c) Coarse-grained C-O metagabbro (left photograph) mylonitized during D_2 (right photograph) from western belt. (d) Coarse-grained C-O metagabbro mylonitized by localized shear zones during D_2 from eastern belt.

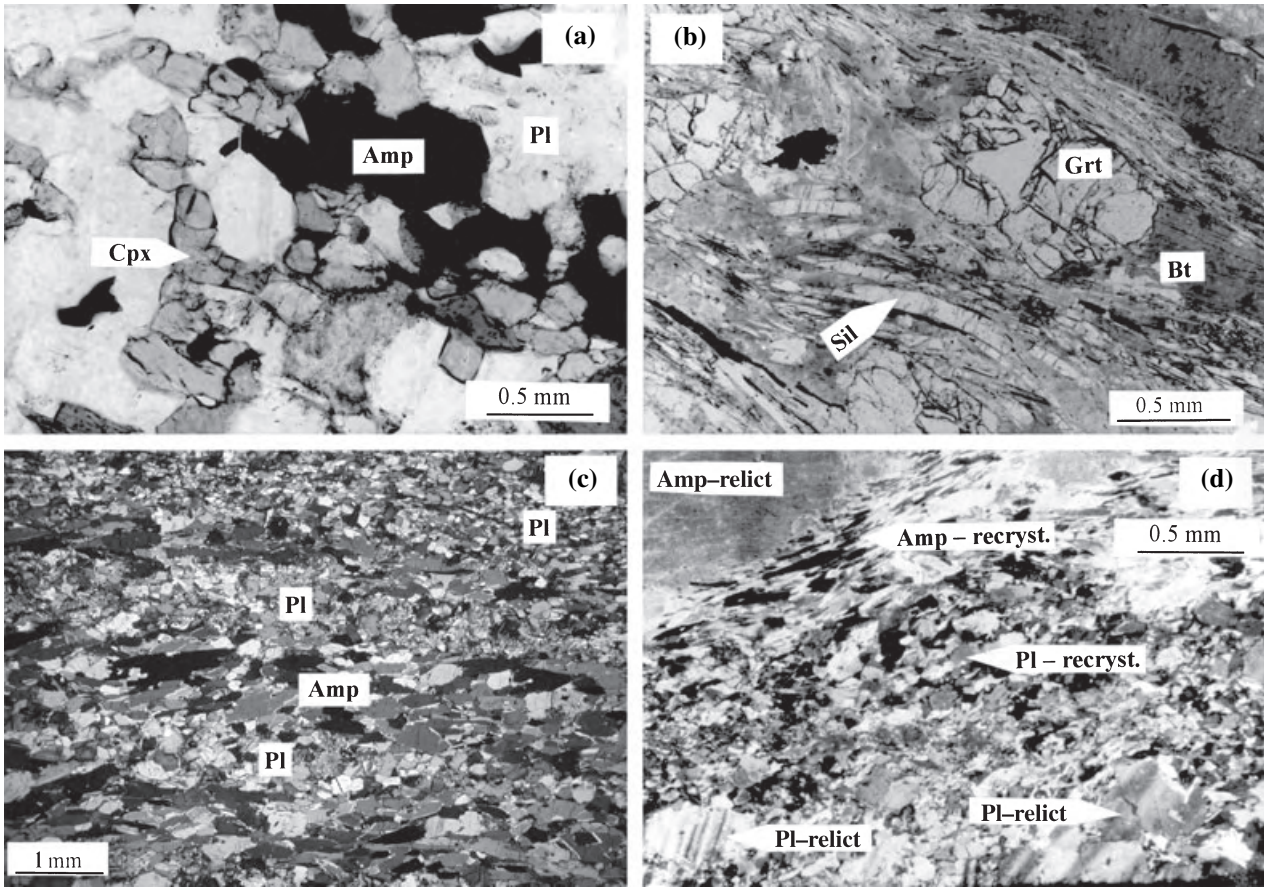

Fig. 5. Photomicrographs of characteristic mineral assemblages and textures from the Staré Město belt: (a) M_1 assemblage Cpx–Amp–Pl–Qtz of layered amphibolite showing equilibrated annealed texture. (b) M_1 assemblage Grt–Bt–Sil in anatectic paragneiss. (c) Variscan dynamic M_2 recrystallization of C-O metagabbro from the western belt leading to strong mineral banding of amphibole and plagioclase. (d) Variscan dynamic M_2 recrystallization of amphibole and plagioclase in C-O metagabbro from the eastern belt marked by strong cataclastic grain-size reduction.

footwall metapelites, respectively, while magmatic structures are preserved in the inner part. The geometry of S_2 fabric and kinematics of deformation are identical with those of the western metagabbro sheet (Fig. 3).

Structures of the banded amphibolite complex

The banded amphibolite complex is affected by a high-temperature metamorphic event characterized by a range of melt-collecting structures. The S_1 foliation is marked by a metamorphic compositional layering best seen in the banded amphibolites and in the tonalitic migmatites (Figs 3a & 4a). In the northern part of the study area, S_1 dips to the NNE at shallow angles (Figs 2a & 3a). To the south, the S_1 moderately dips to the west in the migmatitic metasediments and is generally flat-lying in the banded amphibolites (Figs 2b & 3b). The S_1 compositional and metamorphic layering is locally folded into rootless isoclinal F_1 folds or is affected by asymmetrical pinch and swell boudinage with melt collecting in some neck-zones. In the tonalitic gneisses and more rarely in the layered amphibolites the planar fabric is affected by extensional shear zones filled with an amphibole-bearing tonalitic melt, or the planar fabric dissipates in coarse-grained melt patches (Fig. 4b).

The Variscan D_2 deformation in the banded amphibolite complex is marked by folding of the originally flat-lying Cambro-Ordovician S_1 foliation. These open to close F_2 folds strike NE–SW with sub-horizontal hinges and wavelengths ranging from a few metres to several tens of metres (Fig. 3). Fold hinges are locally cut by subvertical, NE–SW or NW–SE trending, conjugated shear and fracture zones filled with granitic melts. The internal foliation within these shear zones bears a NE–SW trending stretching L_2 lineation (Fig. 3). Similar to mylonitic metagabbros, older foliations are locally affected by late F_3 folds with hinges sub-parallel to the L_2 lineation or by development of a late S_3 crenulation cleavage sub-parallel to the S_2 foliation, indicating deformation continuity towards lower metamorphic conditions.

Table 1. Mineral assemblages and textures of samples used for thermobarometry.

Sample	Unit	Locality	Rock type	Texture	Grt	Pl	Hbl	Cum	Cpx	Qtz	Bt	Kfs	Sil	Rt	Ilm	Ttn	Mag	Opx
Samples associated with D1 Cambro-Ordovician structure																		
LAC4a	LAC	66 g	Grt-amphibolite	Preferred shape orientation, annealed	×	×	×	–	–	×	–	–	–	–	×	–	×	–
LAC4b	LAC	S149e	Cpx-amphibolite	Weak shape preferred orientation, annealed	–	×	×	–	×	×	–	–	–	–	×	–	×	–
LAC4c	LAC	S149f	Melt patches within amphibolite	Random orientation	–	×	×	–	–	×	–	–	–	–	–	–	–	–
TG1a	LAC	S24-1b	Tonalitic migmatite	Weak shape preferred orientation, annealed	×	×	×	–	–	×	×	–	–	–	–	–	–	–
TG1b	LAC	S24-5a	Tonalitic migmatite	Weak shape preferred orientation, annealed	×	×	×	–	–	×	×	–	–	–	–	–	–	–
TG1c	LAC	S24-6e	Melt patches within migmatite	Random orientation	–	×	×	–	–	×	×	×	–	–	–	×	×	–
MP1	LAC	Heg3	Metapelite	Weak shape preferred orientation, annealed	×	×	–	–	–	×	×	×	×	×	×	–	–	–
Samples associated with D2 Variscan structure																		
GAHT	Western gabbroic belt	S33b	Grt-amphibolite	Strong preferred orientation, dynamic recrystalliation of Pl, Qtz	×	×	×	×	–	×	–	–	–	–	×	–	×	–
GHT3	Western gabbroic belt	S151	Metagabbro	Strong preferred orientation of Amp, dynamic recrystalliation of Pl, Amp	–	×	×	×	×	–	–	–	–	–	×	×	–	×
GLT2	Eastern gabbroic belt	S130	Metagabbro	Strong preferred orientation of Amp, dynamic recrystalliation of Pl, Amp	–	×	×	–	–	–	–	–	–	–	×	×	–	–
T3	Sill		Granodiorite	Dynamic recrystallization of Pl, Qtz	–	×	×	–	–	×	×	×	–	–	×	×	×	–

PETROLOGY, METAMORPHIC TEXTURES AND *P–T* ESTIMATES

Sample selection for petrological study and analytical procedures

The study samples were selected according to their structural position with respect to assumed Cambro-Ordovician and Variscan fabrics. Mineral analyses were carried out on a CAMECA SX 50 at ETH Zürich and a JEOL microprobe at the University of Mainz. Operating conditions were 15 kV acceleration voltage and beam current of 20 nA. Representative samples with mineral assemblages are given in Table 1 and corresponding mineral compositions are summarized in Table 2. Mineral abbreviations used in text and tables follow Kretz (1983). Representative mineral analyses are listed in Tables 3–6. Amphibole formulae were calculated after Holland & Blundy (1994) and classified according to Leake *et al.* (1997). The geothermometers and geobarometers used for calculations are given in Table 7. For each sample, five to 10 sets of analyses were used for *P–T* calculations and the results are shown in Table 7 and Fig. 6.

Metamorphic textures and mineral compositions of the granodiorite sill and mylonitic metagabbros

The granodiorite sill is composed of Pl + Qtz + Amp + Bt + Kfs + Ttn + Mag + Ilm + Ap. It shows magmatic, sub-magmatic and solid-state microstructures marked by dynamic recrystallization of plagioclase, amphibole and quartz (Parry *et al.*, 1997). Amphibole correspond to magnesiohornblende and tschermakite (i.e. Si p.f.u. = 6.3–6.7, X_{Mg} = 0.54–0.64) and plagioclase is $An_{34–37}$ andesine.

The proportions of plagioclase and amphibole in the western mylonitic metagabbro vary significantly and the rock locally consists of up to 90% plagioclase or 90% amphibole. Minor clinopyroxene occurs in the core of large amphibole. Titanite is an abundant accessory mineral. Non-recrystallized amphibole is interpreted as magmatic in origin and the composition corresponds to a magnesiohornblende (i.e. Si p.f.u. = 7.00–7.25, X_{Mg} = 0.84–0.89). The magmatic plagioclase is a $An_{55–62}$ labradorite.

The mineral assemblage of highly reworked metagabbro with banded mylonitic structure (Figs 4c & 5c) includes Pl + Amp ± Cum ± Cpx ± Opx ± Grt ± Ttn ± Rt ± Ilm. A granulite facies mineral assemblage, comprising saphirine and corundum, is re-equilibrated during subsequent amphibolite facies reworking (Baratoux *et al.*, 2005). Both amphibole and plagioclase show strong compositional variations between those of old magmatic and metamorphic grains (Table 1). Rare garnet-bearing amphibolite developed through the deformation and metamorphism of a tonalitic migmatitic gneiss associated with metagabbro in the lower part of the gabbroic sheet. It exhibits mineral assemblage Hbl ± Cum ± Grt + Pl + Qtz ± Mag ± Ilm (Table 1) which allows the pressure during the Variscan metamorphism to be estimated.

Recrystallized plagioclase exhibits an increase in the anorthite content from the core towards the rim in the metagabbro ($An_{37 \rightarrow 60}$) and garnet-amphibolite ($An_{15 \rightarrow 27}$). Recrystallized amphibole in the metagabbro corresponds to tschermakite, and tschermakite or ferrotschermakite in the garnet-amphibolite. Garnet shows an increase in almandine, grossular, pyrope and X_{Mg} (Fig. 7d), accompanied by depletion of spessar-

Table 2. Summarized compositions of minerals used for thermobarometry.

Sample	Rock type	Locality	Grt					Pl	Amp			Cpx	Bt	Ilm
			X_{Mg}	Alm	Py	Grs	Sps	An	Compositional name[a]	X_{Mg}	Si (pfu)	X_{Mg}	X_{Mg}	X_{Ilm}
Samples associated with D1 Cambro-Ordovician structure														
LAC4a	Grt-amphibolite	66 g	0.16–0.18	62–65	12–14	11–21	4–5	31–33	Ts, Fe-Ts	0.47–0.54	6.27–6.37	–	–	–
LAC4b	Cpx-amphibolite	S149c	–	–	–	–	–	44–50	Mg-Hbl, Ts, Ed, Prg	0.59–0.68	6.36–6.71	0.67[b]	–	–
LAC4c	Melt patche within amphibolite	S149f	–	–	–	–	–	38–43	Ts	0.63–0.74	6.25–6.50	–	–	–
TG1a	Tonalitic migmatite	S24-1b	0.10–0.11	55 (51)	7 (8)	28 (29)	6 (13)	33–35	Fe-Prg, Hs	0.34–0.37	5.8–6.2	–	0.34–0.36	–
TG1b	Tonalitic migmatite	S24-5a	0.11–0.12	58 (50)	8 (6)	25 (31)	9 (14)	31–34	Fe-Prg, Hs	0.25–0.40	5.8–6.2	–	0.33–0.35	–
TG1c	Melt patche within migmatite	S24-6e	–	–	–	–	–	32–35	Fe-Prg, Hs	0.34–0.38	5.95–6.25	–	0.32–0.33	–
MP1	Metapelite	Heg3	0.15 (0.26–0.28)[b]	75 (69)	15 (26)	4 (4)	5 (1)	24–26	–	–	–	–	0.50–0.53	0.95–0.98
Samples associated with D2 Variscan structure														
GAHT	Grt-amphibolite	S33b	0.15 (0.05)	70 (57)	12 (3)	15 (27)	3 (12)	15–27 (15)	Fe-Ts, Ts	0.46–0.67	6.1–6.3	–	–	–
									Cum	0.48–0.50	7.7–7.9			
GHT3	Metagabbro	S151	–	–	–	–	–	37–60	Ts,	0.82–0.88	6.0–6.3	–	–	–
									Cum	0.64	5.3			
GLT2	Metagabbro	S130	–	–	–	–	–	48–62 (25)	Mg-Hbl, Ts	0.74–0.88	6.24–6.64	–	–	–
T3	Granodiorite		–	–	–	–	–	34–37	Mg-Hbl, Ts	0.54–0.64	6.3–6.7	–	–	–

Values in brackets represent core compositions of zoned minerals. Notes: $Alm = 100 \times Fe^{2+}/(Mg + Ca + Mn + Fe^{2+})$, $An = 100 \times Ca/(Ca + Na + K)$, $X_{Mg} = Mg/(Mg + Fe^{2+})$.
[a]Amphibole compositional name from classification of Leake *et al.* (1997): Prg, pargasite; Ts, tschermakite; Ed, edenite; Hs, hastingsite; Tr, tremolite; Mg-Hbl, magnesio-hornblende.
[b]$X_{Mg} = Mg/(Mg + Fe_{tot})$.

tine from the core to the rim (i.e. $Alm_{57 \rightarrow 70}$ $Grs_{2 \rightarrow 15}Py_{3 \rightarrow 12}Sps_{12 \rightarrow 3}$; $X_{Mg} = 0.05 \rightarrow 0.15$).

A relic magmatic assemblage in the eastern mylonitic metagabbro is represented by Pl + Hbl ± Cpx ± Ttn ± Ilm. Magmatic plagioclase (0.5–5 mm) shows zoning marked by a rimward increase of anorthite from 50 to 60%, whereas recrystallization of the plagioclase (0.05–0.1 mm) is accompanied by a decrease in anorthite content (i.e. An_{45}). Magmatic amphibole (0.5–5 mm) with pyroxene relics in the cores is magnesiohornblende (6.8–7.0 Si p.f.u., $X_{Mg} =$ 0.72–0.77). Recrystallized grains (0.02–0.1 mm) correspond to magnesiohornblende with a slightly lower content of Si and X_{Mg} (6.6–6.7 Si p.f.u., $X_{Mg} = 0.69$–0.74) in comparison with original grains.

P–T conditions of Variscan metamorphism

The pressure of crystallization of the granodiorite (T3) was calculated as 6.5–7.0 kbar using the Al-content of amphibole (Schmidt, 1992) at a temperature of 670–725 °C inferred from the Pl–Hbl thermometer of Holland & Blundy (1994). In the western mylonite metagabbro the temperature was estimated as 770 ± 50 °C using the thermometer by Holland & Blundy (1994) in metagabbro (GHT3), while in garnet-amphibolite the temperature was estimated as 710–740 °C (GAHT). A similar temperature of 750 ± 50 °C is reported by Baratoux *et al.* (2005) for 40 amphibole–plagioclase couples. Pressure conditions between 8 and 10 kbar were calculated only in Qtz-bearing garnet-amphibolite by means of the Kohn & Spear (1990) barometer. Based on 30 amphibole–plagioclase couples from the eastern mylonite metagabbro, Baratoux *et al.* (2005) estimated temperature as 650 ± 50 °C using the Pl–Hbl thermometer of Holland & Blundy (1994). The pressure could not be calculated because of the lack of garnet.

Mineral textures and mineral compositions of rocks of the banded amphibolite complex

Mineral assemblages and selected mineral compositions of all study rocks are given in Table 1 and summarized in Table 2, respectively.

Banded amphibolites are characterized by the mineral assemblage Amp + Pl + Qtz ± Cpx ± Grt ± Mag ± Ilm. Three types of microstructures marked by straightened grain boundaries without indications of dynamic recrystallization are distinguished: (1) Equigranular aggregates (grain size 0.05–1.0 mm) of amphibole, plagioclase and quartz (Fig. 5a); (2) amphibole-rich layers alternating with elongate aggregates (grain size 0.05–1.0 mm) of quartz and plagioclase; and (3) coarse-grained aggregates (grain size 1–5 mm) of randomly distributed plagioclase and quartz sometimes with amphibole occur in melt patches. In types (1) and (2) the mineral grains are aligned and elongated parallel to the compositional

Table 3. Representative electron probe analyses of garnet.

Garnet analyses recalculated to 12 oxygen								
Event	C-O						Varis.	
Sample/analyses	TG1a/grt23-rim	TG1a/grt44-core	TG1b/grt27-rim	LAC4a/grt43-rim	MP1/grt379-core[a]	MP1/grt313-rim[a]	GAHT/grt5-15-core	GAHT/grt114-rim
SiO_2	37.96	37.65	37.44	37.95	37.69	36.79	37.14	37.47
TiO_2	0.06	0.13	0.14	0.07	0.08	0.08	0.07	0.04
Al_2O_3	20.64	20.53	20.77	20.46	21.21	20.82	21.17	20.98
FeO	26.47	24.70	27.05	30.02	32.60	35.12	25.97	32.46
MnO	4.28	5.78	5.19	1.84	0.56	2.25	6.15	1.25
MgO	1.80	1.54	1.75	3.06	6.54	3.62	0.85	3.12
CaO	10.05	10.28	8.31	7.34	1.33	1.33	9.92	5.28
Total	101.26	100.61	100.65	100.74	100.01	100.01	101.27	100.60
Si	2.99	2.98	2.98	3.00	2.97	2.97	2.94	2.97
Ti	0.00	0.08	0.01	0.00	0.00	0.00	0.00	0.00
Al	1.92	1.92	1.95	1.90	1.97	1.98	1.98	1.96
Fe^{3+}	0.10	0.11	0.09	0.09	0.00	0.00	0.13	0.09
Fe^{2+}	1.65	1.53	1.71	1.89	2.15	2.37	1.59	2.07
Mn	0.29	0.39	0.35	0.12	0.04	0.15	0.41	0.08
Mg	0.21	0.18	0.21	0.36	0.77	0.44	0.10	0.37
Ca	0.85	0.87	0.71	0.62	0.11	0.12	0.84	0.45

[a]Fe^{3+} not calculated.

Table 4. Representative electron probe analyses of amphibole.

Amphibole analyses recalculated after Holland & Blundy (1994)											
Event	C-O						Varis.				
Sample/analyses	LAC4a/amp37	LAC4b/amp16	LAC4c/amp482	TG1a/amp45	TG1b/amp12-6	TG1c/amp64	GAHT/amp115	GAHT/cum6-7[a]	GHT3/amp48	GLT2/amp-102	T3/amp18
SiO_2	42.06	45.27	42.58	39.82	39.12	39.38	41.64	51.85	43.34	45.11	43.59
TiO_2	1.59	1.47	1.75	0.91	1.05	0.94	0.53	0.05	0.20	0.61	1.26
Al_2O_3	11.58	9.68	11.73	12.96	13.51	13.40	12.42	1.35	17.66	13.94	11.85
FeO	20.83	15.88	17.00	23.31	23.52	23.46	22.17	27.34	11.03	9.82	16.03
MnO	0.12	0.32	0.24	0.57	0.54	0.46	0.46	0.59	0.13	0.18	0.24
MgO	7.87	11.69	10.54	5.66	5.45	5.55	7.28	13.95	12.09	13.98	10.89
CaO	10.62	11.34	10.68	11.13	11.41	11.31	10.57	2.51	11.29	12.42	11.05
Na_2O	2.11	1.50	1.86	1.45	1.33	1.39	1.77	0.18	1.95	1.71	1.25
K_2O	0.07	0.55	0.78	1.47	1.65	1.63	0.23	0.01	0.27	0.32	1.48
Total	96.85	97.70	97.16	97.28	97.58	97.52	97.07	97.83	97.95	98.09	97.64
Si	6.38	6.65	6.34	6.16	6.05	6.09	6.30	7.75	6.15	6.43	6.44
Ti	0.18	0.16	0.20	0.11	0.12	0.11	0.06	0.01	0.02	0.07	0.14
Al	2.07	1.68	2.06	2.36	2.46	2.44	2.22	0.24	2.95	2.34	2.07
Fe^{3+}	0.58	0.50	0.61	0.66	0.70	0.67	0.91	0.19	0.70	0.34	0.51
Fe^{2+}	2.06	1.45	1.50	2.36	2.34	2.36	1.90	3.23	0.61	0.83	1.47
Mn	0.02	0.04	0.03	0.08	0.07	0.06	0.06	0.08	0.02	0.02	0.03
Mg	1.78	2.56	2.34	1.30	1.26	1.28	1.64	3.11	2.56	2.97	2.40
Ca	1.73	1.79	1.70	1.84	1.89	1.87	1.71	0.40	1.72	1.90	1.75
Na	0.62	0.43	0.54	0.44	0.40	0.42	0.52	0.05	0.54	0.47	0.36
K	0.01	0.10	0.15	0.29	0.33	0.32	0.04	0.00	0.05	0.06	0.28

[a]Cummingtonite recalculated on the basis of 23 oxygen and 15 cations + Na + K.

layering. Regardless of textural type, the minerals are not zoned. Almandine-rich garnet reveals flat chemical profiles ($Alm_{62-65}Grs_{11-21}Py_{12-14}Sps_{4-5}$; $X_{Mg} = 0.16$–0.18; Fig. 7a). Amphibole is magnesiohornblende or tschermakite, rarely edenite or pargasite. Plagioclase is andesine (An_{30-50}) and X_{Mg} of rare clinopyroxene equals 0.65–0.67.

Tonalitic migmatitic gneiss is made up of Qtz + Pl + Bt + Amp ± Grt. Its structure is characterized by alternations of leucosome, mesosome and melanosome layers several mm to 1 cm in thickness. Weak layering is defined by amphibole–plagioclase aggregates alternating with quartz-rich domains (Fig. 4b). Plagioclase and amphibole are elongated (length 0.2–3 mm) in the leucosome and restitic layers, whereas plagioclase is isometric (up to 3 mm). Biotite (0.2–1 mm) is oriented parallel to the foliation together with amphibole in melanosome. Garnet porphyroblasts (0.3 mm) occur in mesosome and melanosome. Large coarse-grained quartz aggregates occurs in leucosome. Chemical profiles across garnet show slight zoning with cores being more spessartine-rich; the X_{Mg} ratio is constant (0.10–0.12) (Fig. 7c). Amphibole is homogeneous ferropargasite or hastingsite, regardless of the textural position and type of aggregate. X_{Mg} in biotite ranges between 0.32 and 0.36, and the Ti content between 0.14 and 0.22 p.f.u. The composition of plagioclase in both the leucosome and melt patches is An_{31-35} andesine.

Table 5. Representative electron probe analyses of plagioclase.

Event	C-O							Varis						
Sample/ analyses	LAC4b/ pl13	LAC4c/ pl82-1	LAC4a/ pl50	TG1a/ pl46-5	TG1b/ pl26	TG1c/ pl2-8	MP1/ pl137	GAHT/ pl113 -rim	GHT3/ pl122-core	GHT3/ pl101-rim	GLT2/ pl122-core	GLT2/ pl101-rim	GLT2/ pl79-core	T3/ pl19
SiO_2	56.92	58.57	60.07	59.94	60.11	59.82	61.64	62.51	59.02	52.36	64.73	56.05	62.00	59.35
TiO_2	0.00	0.03	0.00	0.01	0.01	0.00	0.01	0.03	0.00	0.00	0.00	0.00	0.01	0.01
Al_2O_3	27.18	26.20	25.01	25.54	25.26	25.09	24.01	23.64	25.92	30.48	22.01	27.73	23.42	26.19
FeO	0.22	0.13	0.35	0.05	0.17	0.17	0.00	0.35	0.00	0.00	0.07	0.18	0.00	0.05
CaO	9.74	8.53	6.60	7.09	6.99	7.31	5.28	4.95	7.17	12.18	3.27	10.09	5.26	7.02
Na_2O	6.30	6.73	8.16	7.65	7.73	7.44	8.76	8.77	7.63	4.50	9.70	5.93	8.66	7.59
K_2O	0.12	0.30	0.05	0.18	0.12	0.35	0.20	0.07	0.00	0.00	0.15	0.03	0.12	0.15
Total	100.48	100.49	100.19	100.46	100.39	100.18	99.90	100.32	99.74	99.52	99.93	100.01	99.47	100.36
Si	2.54	2.61	2.66	2.66	2.67	2.66	2.73	2.76	2.64	2.37	2.86	2.52	2.76	2.63
Ti	0.00	0.00	0.00	0.00	0.00	0.00	0.00	0.00	0.00	0.00	0.00	0.00	0.00	0.00
Al	1.43	1.38	0.00	1.34	1.32	1.32	1.25	1.23	1.36	1.63	1.15	1.47	1.23	1.37
Fe^{3+}	0.01	0.00	0.01	0.00	0.01	0.01	0.00	0.00	0.00	0.00	0.00	0.01	0.00	0.00
Ca	0.47	0.41	0.31	0.34	0.33	0.35	0.25	0.23	0.34	0.59	0.15	0.49	0.25	0.33
Na	0.55	0.58	0.70	0.66	0.66	0.64	0.75	0.75	0.66	0.40	0.83	0.52	0.75	0.65
K	0.01	0.02	0.00	0.01	0.01	0.02	0.01	0.00	0.00	0.00	0.01	0.00	0.01	0.01

Table 6. Representative electron probe analyses of biotite and clinopyroxene.

Bt analyses recalculated to 11 oxygen, cpx to 6 oxygen

Event	C-O			
Mineral	cpx	bt		
Sample/analyses	LAC4b/cpx20	TG1a/bt25	TG1b/bt45	MP1/bt343
SiO_2	50.88	33.95	35.10	36.06
TiO_2	0.24	2.92	3.15	1.57
Al_2O_3	2.35	15.71	15.76	19.78
FeO	11.11	25.22	24.39	18.03
MnO	0.35	0.30	0.35	0.05
MgO	12.04	7.23	7.37	10.83
CaO	22.14	0.02	0.07	0.00
Na_2O	0.58	0.04	0.05	0.22
K_2O	0.01	9.51	9.40	9.03
Total	99.70	94.90	95.64	95.57
Si	1.93	2.74	2.80	2.75
Ti	0.01	0.18	0.19	0.09
Al	0.11	1.49	1.48	1.78
Fe^{3+}	0.03	0.00	0.00	0.00
Fe^{2+}	0.32	1.70	1.63	1.15
Mn	0.01	0.02	0.02	0.00
Mg	0.68	0.87	0.88	1.23
Ca	0.90	0.00	0.01	0.00
Na	0.04	0.01	0.01	0.03
K	0.00	0.98	0.96	0.88

The mineral assemblage of the migmatitic paragneisses is Pl + Bt + Qtz ± Grt ± Kfs ± Sil ± Rt ± Ilm. Plagioclase and quartz form large isometric grains up to 10 mm in size. With an increasing degree of anatexis, quartz and plagioclase (0.3–5 mm) coalesce to form lenses bordered by biotite-rich rims occasionally containing sillimanite. Both the leucosome and melanosome aggregates contain garnet. In the nebulitic stage diffuse pockets of leucosome of different size developed. Garnet forms poikilitic crystals (0.1–1 cm) with inclusions of quartz and biotite. Scarce K-feldspar occurs in leucosome lenses. The distribution of elements in garnet cores is homogeneous ($Alm_{69}Grs_4Py_{26}Sps_1$; $X_{Mg} = 0.26$–0.28) but within the outer 100 μm rim or around biotite inclusions garnet is enriched with almandine and spessartine and depleted in pyrope ($Alm_{75}Grs_4Py_{26}Sps_5$; $X_{Mg} = 0.15$; Fig. 7b). This zoning is attributed to continuous Fe–Mg re-equilibration between garnet and biotite during cooling. The X_{Mg} of matrix biotite ranges from 0.50 to 0.53 and its Ti-content varies between 0.07 and 0.21 p.f.u. Plagioclase is a homogeneous An_{28-31} oligoclase-andesine.

P–T conditions of Cambro-Ordovician metamorphism

The temperature of metamorphism in amphibolites (LAC4a, LAC4b and LAC4c) was estimated with the Pl–Hbl thermometer by Holland & Blundy (1994). The temperature ranges of 725–825 and 730–860 °C were inferred for amphibolites and melt patches, respectively. A comparable temperature span of 715–770 and 750–770 °C was established for the tonalitic gneiss and associated melt patches, respectively (TG1a, TG1b & TG1c). The pressure in amphibolites was estimated as 8.5–10 kbar, and in tonalitic gneisses as 9–10 kbar using the Grt–Hbl–Pl–Qtz barometer (Kohn & Spear, 1990). A similar range of 8–10 kbar was obtained from the aluminium content of amphibole (Schmidt, 1992) within the tonalitic gneisses. Similarly, a pressure 8–9 kbar was estimated from melt patches crystallized in the small-scale shear zones. A pressure of 7.5 kbar was obtained from garnet core and matrix plagioclase using the GASP barometer (Koziol, 1989), calculated by means of the 'Thermobarometry' software (Spear *et al.*, 1991). Pressure calculated using the GRAIL barometer (Bohlen *et al.*, 1983) gives a range of 7.5–8 kbar for garnet cores containing rutile and ilmenite inclusions.

QUANTITATIVE TEXTURAL ANALYSIS

A quantitative microstructural analysis was carried out on three samples of the banded amphibolite complex, assumed to be exclusively the result of the Cambro-

Table 7. Results of *P–T* calculations using the following geothermometers and geobarometers: HB, Holland & Blundy (1994); T, Thompson (1976); FS, Ferry & Spear (1978); NW, O'Neill & Wall (1987); GN, Gasparik & Newton (1984); KS (Mg), Kohn & Spear (1990); KS (Fe), Kohn & Spear (1990); K, Koziol (1989); Bh, Bohlen *et al.* (1983); S, Schmidt (1992). Errors are given in table headings.

Sample	Rock type	Combination	*T* calculated at a *P* (kbar) of	Pl–Hbl (HB)		Grt-Bt (T)	Grt-Bt (FS)	*P* calculated at a *T* (°C) of	Grt–Hbl–Pl–Qtz (KS)		Al in Hbl (S)	GASP (K)	GRAIL (Bh)
				T (Ed-Tr)	T (Ed-Ri)				*P* (Mg)	*P* (Fe)			
				± 40 °C	± 40 °C	± 50 °C	± 50 °C		± 0.5	± 0.5	± 0.6	Not given	± 0.5
Samples associated with D1 Cambro-Ordovician structure													
LAC4a	Grt-amphibolite	Rims	10	731–770	772–823	–	–	700	8.6–9.0	9.5–9.8	–	–	–
LAC4b	Cpx-amphibolite	Rims	10	727–787	775–825	–	–	700	–	–	–	–	–
LAC4c	Melt patches within amphibolite	Rims	10	732–765	796–857	–	–	–	–	–	–	–	–
TG1a	Tonalitic migmatite	Rims	10	715–755	732–772	700–738	685–737	700	9.7–10.0	9.8–10.1	8.2–10.0	–	–
TG1b	Tonalitic migmatite	Rims	10	717–762	712–768	712–727	702–722	700	9.2–9.9	9.5–9.8	8.4–10.0	–	–
TG1c	Melt patches within migmatite	Rims	10	750–756	759–770	–	–	–	–	–	7.9–8.7	–	–
MP1	Metapelite	Cores	7	–	–	788–840	838–905	800	–	–	–	7.3–7.4	7.6–8.2
		Rims	7	–	–	581–616	549–593	–	–	–	–	–	–
Samples associated with D2 Variscan structure													
GAHT	Grt-amphibolite	Rims	10	711–730	724–737	–	–	700	7.8–8.4	9.6–10.1	–	–	–
GHT3	Metagabbro	Rims	10	716–836	711–837	–	–	–	–	–	–	–	–
T3	Tonalite	Rims	6	671–691	714–724	–	–	–	–	–	6.5–7.0	–	–

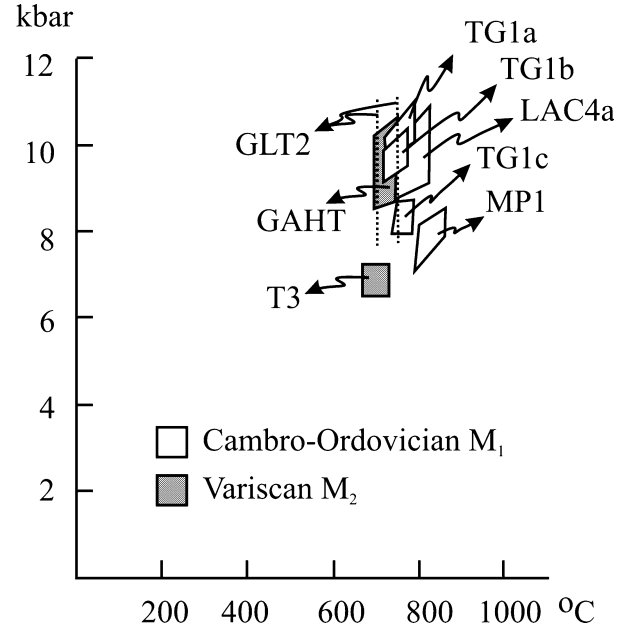

Fig. 6. *P–T* diagram with blank boxes for C-O metamorphism. *P–T* estimates for Variscan assemblages are presented in grey boxes. Dashed lines show temperature estimates from metagabbros and from metaperidotites. Numbers correspond to samples presented in Tables 1, 2 and 7.

Ordodvician metamorphism. We investigated also six samples representing the Variscan granodiorite, tonalitic tectonites and mylonitic metagabbros, in which, only the Variscan metamorphic history is assumed to be preserved. Polished thin sections of the samples parallel to lineation and perpendicular to foliation (XZ section) were prepared for optical microscopy and back-scattered electron image (BSEI) analysis. The BSEI analysis was carried out using the Camscan S4 instrument fitted with a high-resolution backscatter detector. Line drawings of optical microscopy photographs and BSE images were digitized (Fig. 8) and processed in ESRI ArcView desktop GIS in order to obtain a map of boundaries between individual grains (Lexa, 2003). The analysis of crystal size distributions (CSD), shape preferred orientation of grains (SPO) and grain boundaries preferred orientation (GBPO), as well as grain contact frequencies were carried out in PolyLX MATLAB^{TM} Toolbox (Lexa, 2003).

Crystal size distributions

The theory of CSD is a well-established method in chemical engineering, metallurgy and ceramics to reveal information about nucleation, growth rates and growth times of crystals (Randolph & Larson, 1971). CSD in many metamorphic and igneous rocks show a loglinear relationship between grain size L and population density N according to the following equation

$$N = N_0 \, e^{-L/Gt}, \qquad (1)$$

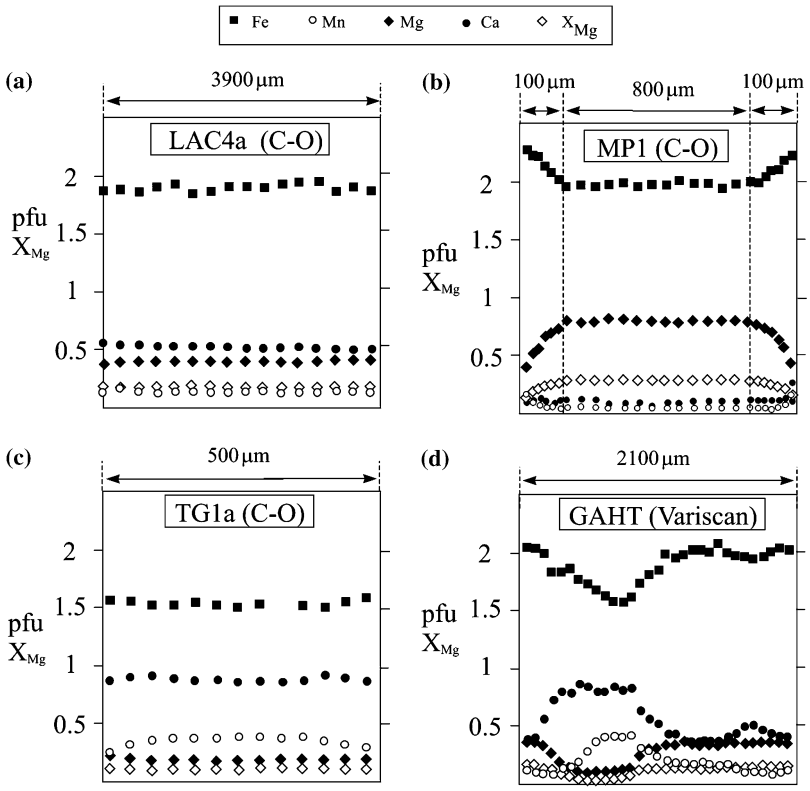

Fig. 7. Chemical profiles of garnet: (a) in layered amphibolite showing flat patterns, (b) in sillimanite-bearing paragneiss with well-developed flat profiles in core and margin affected by late diffusion, (c) in tonalitic migmatitic gneiss and (d) in Grt-amphibolite within metagabbro. Numbering of samples corresponds to numbers in Tables 1, 2 and 7. See text for discussion.

where N_0 and Gt are constants and may be related to nucleation density and growth rate of crystal (Cashman & Ferry, 1988; Marsh, 1988).

CSD plots of all samples constructed according to the method by Peterson (1996) exhibit linear correlations between logarithm of population density (i.e. number of crystals per size per volume) and crystal size (Fig. 9b). Therefore, applying the theory of CSD, such distributions could be parameterized by zero size intercept N_0 (nucleation density) and slope Gt (growth rate multiplied by time). These two parameters plotted in a N_0–Gt space (Fig. 9) exhibit an inverse correlation, and the samples with a comparable metamorphic grade and deformation history form distinct clusters. The metagabbros (samples GLT1 & GLT2, Fig. 8b) sheared during the Variscan episode from the eastern mylonitic belt (*c.* 650 ± 50 °C) form a group with the highest N_0 and lowest Gt values, while metagabbros (samples GHT1 & GHT2) adjacent to the granodiorite sill (*c.* 750 ° ± 50 °C) exhibit a decrease in N_0 in conjunction with increasing Gt. The samples LAC1, LAC3 and TG2 (Fig. 8a,d) of banded amphibolites and amphibole-bearing tonalitic gneisses that originated during the Cambro-Ordovician metamorphism (*c.* 750–850 °C) plot in the centre of the diagram (lower N_0, higher Gt). The undeformed Variscan granodiorite (sample T1, Fig. 8c) exhibits lowest values of N_0 and highest values of Gt.

Grain shapes, shape preferred orientation and grain boundary preferred orientation

Plagioclase is a low-symmetry mineral characterized by weakly elongated to round shapes under most metamorphic conditions. Degree of elongation of plagioclase grains is therefore an indication of intracrystalline deformation. In contrast, amphibole is highly elongate in low-metamorphic grade rocks, while at high-grade ones it becomes spherical (Brodie & Rutter, 1987). Therefore, shape analysis combined with SPO provides information about the degree of deformation of both plagioclase and amphibole aggregates.

Both grain shapes and SPO were evaluated using the PolyLX toolbox (Lexa, 2003). The grain shapes are characterized by preferred orientation of the long axes and by mean axial ratio R of the best-fit ellipse on the individual grains using the area-moments ellipse fitting method. To evaluate an overall single phase SPO, individual linear segments of grain boundaries of individual phases were treated as independent vectors contributing to the bulk Scheidegger–Watson orientation-tensor. The eigenvalue analysis determines two eigenvalues and assigns them to mutually perpendicular directions. The ratio of eigenvalues R_e is considered as a rough estimate of the degree of SPO for the given phase. Grain boundary preferred orientation was assessed by a similar technique, with the bulk

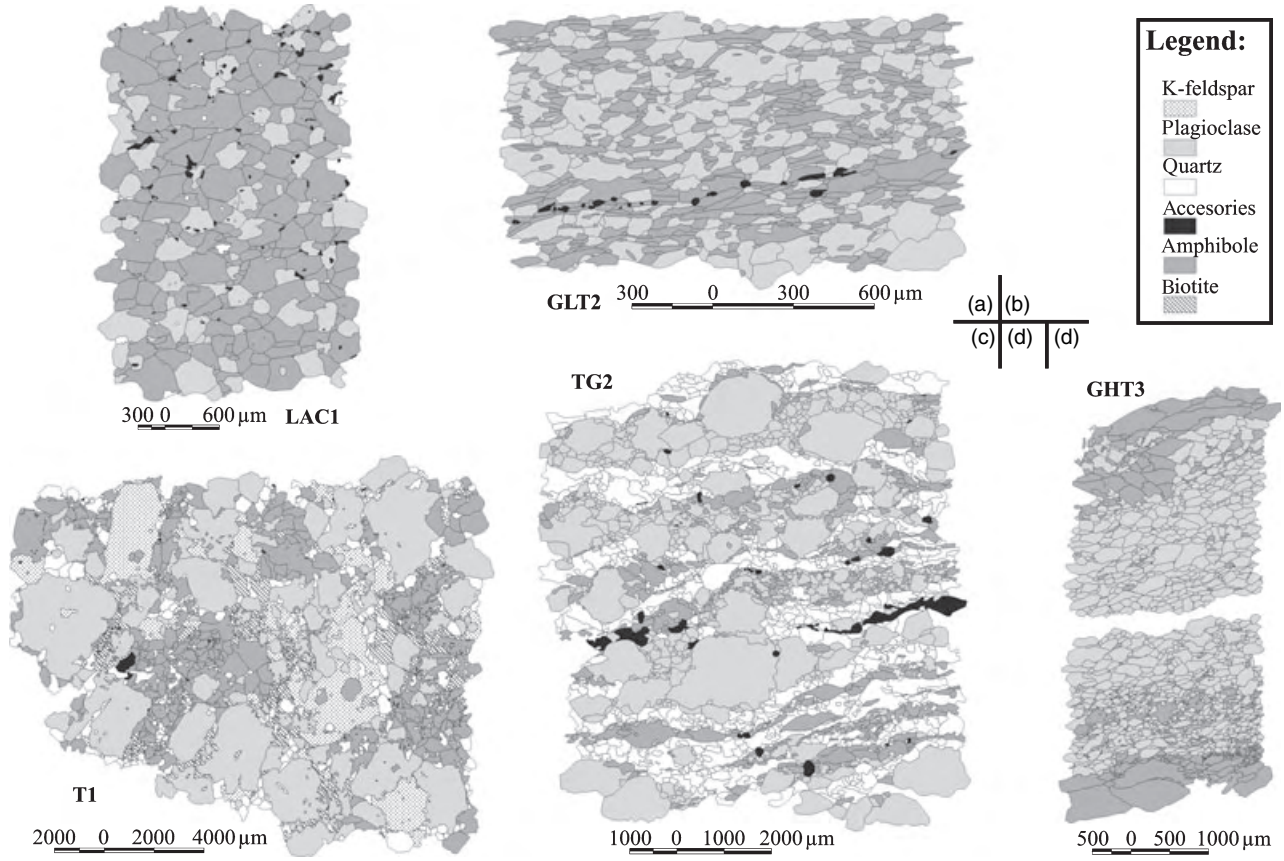

Fig. 8. Representative digitized microstructures used in textural analyses. See text for detailed sample description.

Scheidegger–Watson orientation-tensor formed from the individual linear segments of boundary traces between the chosen phases. Resulting eigenvalues ratio R_b is considered as a rough estimate of the degree of GBPO.

Results of the grain shape analysis and SPO analysis are shown in Fig. 10. Both amphibole (Fig. 10b) and plagioclase (Fig. 10a) show systematic changes. While samples with preserved magmatic textures (T1) and LAC samples (LAC1, TG2) exhibit very weak SPO and lowest values of axial ratios (*c*. 1.5), samples of mylonitic metagabbros show a significant increase in the average axial ratio (2–3) and increase of the SPO degree with decreasing temperature.

Grain contact frequencies

Grain contact frequencies allow the statistical deviation from random spatial distribution of grain boundaries to be examined (Kretz, 1994). So far, the degree of deviation of grain boundaries distribution from random distribution have been evaluated by plotting observed/expected ratio of like–like contacts of the two major minerals against each other. Here we propose a diagram where χ value

$$\chi = \frac{\text{Observed} - \text{Expected}}{\sqrt{\text{Expected}}} \qquad (2)$$

is plotted against the ratio of orientation-tensor eigenvalues, i.e. the degree of GBPO. The major advantage of this diagram is in simple visual evaluation of the degree of deviation from an expected random distribution of grain contacts ($\chi = 0$).

Results of this analysis are presented in Fig. 10. The amphibolite facies mylonitic metagabbros exhibit almost a random distribution at higher strains (GLT2) and tend to develop more of an aggregate-type of microstructure (χ values are positive for like–like and negative for unlike contacts in Fig. 10c,d) at lower strains (GLT1) accompanied by a significant decrease of preferred orientation of amphibole–amphibole and amphibole–plagioclase contacts. The high-grade mylonitic metagabbros (GHT1 & GHT2) exhibit a strong aggregate distribution and a moderate preferred orientation of grain boundaries. Samples from the banded amphibolite complex (TG2 & LAC1) show a tendency towards a regular distribution (negative like–like χ values and positive unlike χ values) and a low degree of GBPO. The tonalitic gneiss weakly overprinted by the Variscan deformation (LAC3) shows

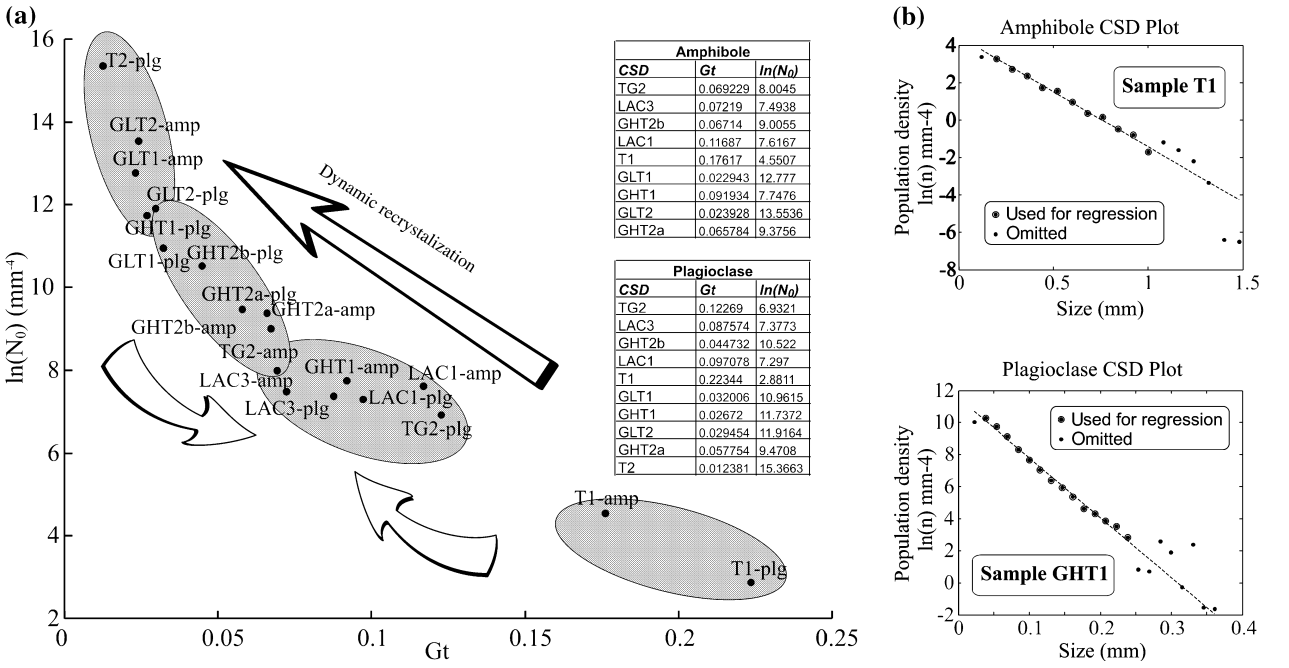

Fig. 9. (a) Plot of crystal size distribution (CSD) parameters N_0 and Gt. Parameters are obtained from CSD plots, where straight line is fitted on plotted data. Gt represents the slope and N_0 the intercept of fitted line. Shaded ellipses from upper left to lower right corner mark domains of LT metagabbros, HT metagabbros, banded amphibolites and magmatic rocks. See discussion. (b) Examples of CSD plots used for N_0 and Gt parameter estimates.

transitional values of χ and R_b between those of the banded amphibolite complex and the mylonitic metagabbro samples. The Variscan undeformed granodiorite sill shows nearly a random distribution of grain contacts and an absence of GBPO.

DISCUSSION

The study samples of mafic lithologies from the Cambro-Ordovician and Variscan structures exhibit remarkably similar mineral assemblages. In addition, the presence of garnet in metamorphosed mafic rocks indicates the medium pressure conditions for both Cambro-Ordovician and Variscan structures. Local occurrence of orthopyroxene bearing mineral assemblages in the banded amphibolites as well as in the western metagabbro mylonite belt (Table 1) indicates that both Cambro-Ordovician and Variscan metamorphic events reached a boundary between granulite and amphibolite facies conditions.

The metamorphic assemblages and P–T estimates of the Cambro-Ordovician metamorphic conditions of banded amphibolite complex calculated overlap within the likely uncertainties with those of the Variscan mylonitic metagabbros and granodiorite. Moreover, in the southern part of the region studied, the Variscan and Cambro-Ordovician fabrics are concordant and therefore slight differences in metamorphic conditions are indistinguishable. We suggest that in this case the standard methods of metamorphic petrology cannot discriminate the two distinct metamorphic events from each other.

Interpretation of crystal size distributions

The grain-size distribution in metamorphic rocks (Cashman & Ferry, 1988; Eberl *et al.*, 1998) is primarily controlled by the interaction between nucleation rate which is sensitive to temperature overstepping (Cahn, 1957), and the growth rate which is an approximately linear function of overstepping (Ridley & Thompson, 1986). A further process that influences CSD is textural coarsening driven by a tendency to decrease the excess of interfacial energy to reach a lower energy state (Voorhees, 1992). The transfer of material from smaller grains to larger ones occurs by diffusion and is commonly expressed by the Lifshitz–Slyozov–Wagner (LSW) equation (Lifshitz & Slyozov, 1961) for Ostwald ripening, or by the communicating neighbours theory (CN) by DeHoff (1991) where a diffusion length scale is spatially dependent. This difference between the theories is expressed in the way that the CSD is modified during coarsening (Higgins, 1998). In the case of LSW the descriptive parameters N_0 and Gt remain constant, while the CN theory implies a decrease in N_0 and Gt during coarsening.

Experimental studies have shown that the size of dynamically recrystallized grains is strongly dependent on recrystallization mechanisms that are controlled by stress and temperature (Twiss, 1977). Low-temperature

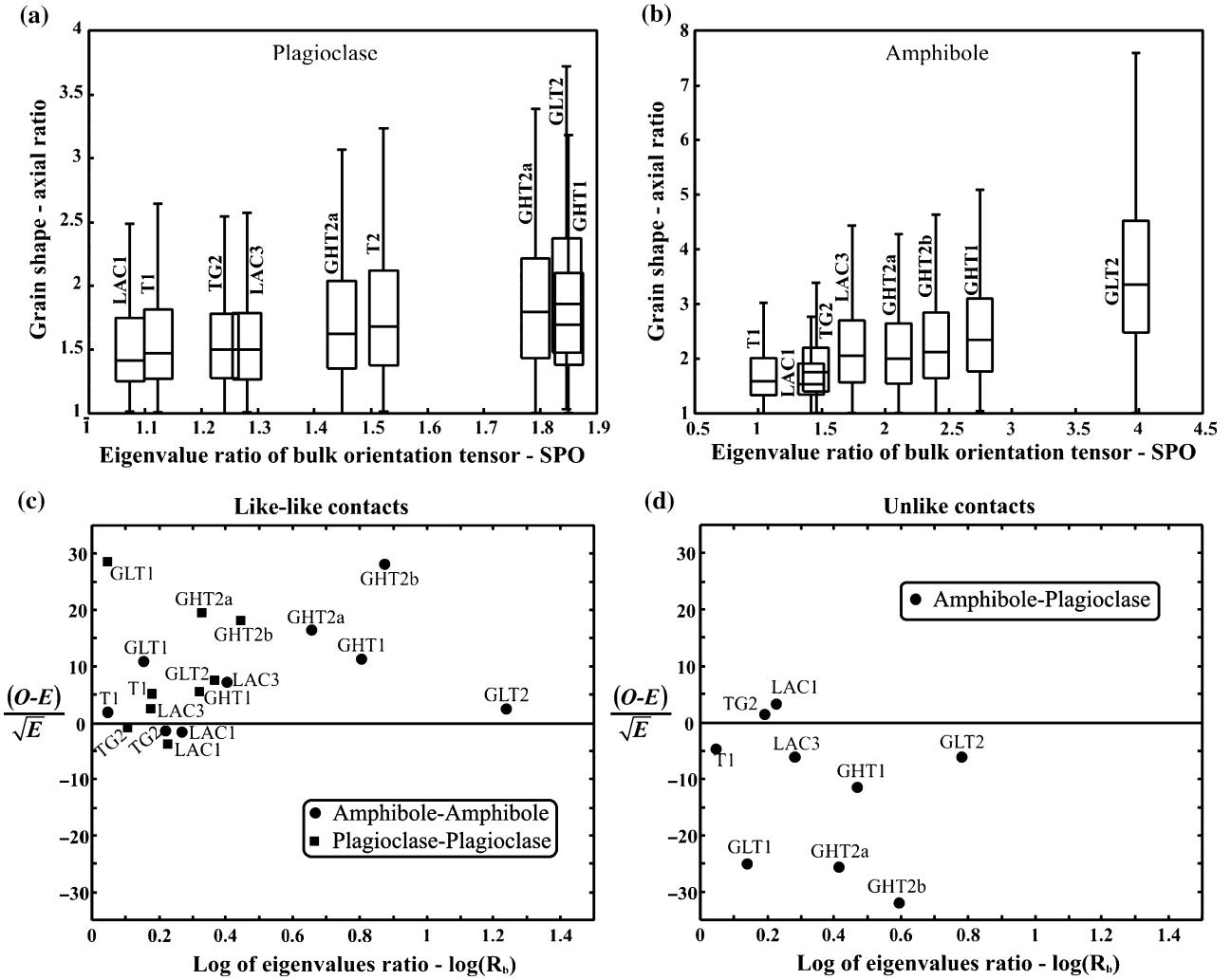

Fig. 10. (a, b) Plot of grains shape preferred orientation (SPO) of amphibole and plagioclase in studied samples. The results are summarized by a boxplot-type plot of axial ratios *v.* eigenvalue ratios for individual phases. Individual boxes showing median, first and third quartile values. The whiskers represent statistical estimate of range of data while outliers are not shown. Vertical axis characterizes a shape of grains, while horizontal axis represents area-weighted degree of preferred orientations. (c, d) Grain boundary frequencies. Plots of deviations from random spatial distribution *v.* degree of preferred orientation. The value of deviation from random spatial distribution is obtained by contact-frequency method (Kretz, 1969) and length-weighted degree of preferred orientation is estimated as ratio of eigenvalues of bulk matrix of inertia. Plot of like–like and unlike boundaries is separated into two panels.

recrystallization mechanisms such as bulging and subgrain rotation recrystallization (Poirier & Guillope, 1979) are processes dominated by heterogeneous nucleation and grain-size reduction. On the contrary, grain-boundary migration recrystallization is often connected with grain coarsening (Urai *et al.*, 1986). Hickey & Bell (1996) suggested that the syntectonic growth of minerals is primarily controlled by gradients in lattice strain energy, which results from inhomogeneous deformation involving dislocation creep. Decreasing the strain rate to temperature ratio ($\dot{e}/T$) leads to a decrease in the ratio of nucleation to growth rate (N/G), and coarser grain size can develops. On the contrary, increase of $\dot{e}/T$ ratio leads to increasing N/G, and therefore the grain size decreases. This hypothesis has been supported by Azpiroz & Fernández (2003) who used CSD plots to analyse dynamically recrystallized metabasites across a metamorphic gradient.

The CSD in the mylonitic metagabbros studied are characterized by a decrease in N_0 and an increase in Gt values with increasing metamorphic temperature estimates, and are projected in areas of high N_0 values and low Gt in the N_0–Gt plot. If all these results are interpreted in terms of CSD theory, the above-described evolutionary trend indicates a decreasing dominance of nucleation processes over grain growth with increasing temperature. The correlation of metamorphic temperature and grain-size distribution could be explained as a result of textural coarsening using the CN theory (Higgins, 1998). However, the microstructural observations of the

onset of dynamic recrystallization in weakly deformed metagabbros show that the lower-temperature mylonites exhibit a smaller initial recrystallization grain size than the new recrystallized grains of the high-temperature mylonites (Baratoux *et al.*, 2005). In addition, inspection of the N_0–Gt plot shows that highly deformed samples (GLT2, GHT2a,b, T2) exhibit higher N_0 and lower Gt values relative to weakly deformed samples (GLT1, GHT1). Based on these two observations, we suggest that the differences in CSD parameters are not the result of textural coarsening but are merely controlled by temperature- and strain rate-dependent mechanisms of dynamic recrystallization. Azpiroz & Fernández (2003) reported an increase in N_0 but a constant Gt (slope) with decreasing temperature and increasing Gt values for constant N_0 with increasing finite strain in the Iberian Massif metabasites. However, it is proposed that in our study the N_0 and Gt change simultaneously due to temperature and strain intensity variations and that the temperature change plays a key role in the resulting CSD shape.

Samples from the banded amphibolite complex are marked by lower N_0 and higher Gt values in comparison with the mylonitic metagabbros. The CSD is developed in both amphibolites and tonalitic gneiss, which indicates that it is independent on a relative proportion of amphibole and plagioclase in both rock types. These data in the N_0–Gt diagram show a continuous trend together with the above-described samples from the mylonitic metagabbros. In addition, results of Hb–Pl thermometry reveal an increase in estimated temperatures from the eastern mylonite metagabbros, through the western mylonite metagabbros to the banded amphibolite complex. Such an evolutionary trend is likely to be interpreted as the result of a textural coarsening comparable with the results of Cashman & Ferry (1988) reinterpreted by Higgins (1998).

Interpretation of spatial distribution minerals and grain boundaries

Seng (1936) and later DeVore (1959) proposed that the spatial distribution of crystals in high-grade gneisses is dominantly determined by interfacial energy. This concept was adopted by Flinn (1969) who explained a prevailing number of unlike boundaries in granulites through the insertion of grains of one phase between grains of other phases. Flinn (1969) suggested that this feature is a consequence of a smaller interfacial energy of unlike boundaries in comparison with like–like boundaries. However, Ramberg (1952) suggested that differences in interfacial energies are too small to drive diffusional mass transfer in high-grade rocks.

Modern material science experimental studies show that during the wetting process the low-energy (low-misorientation angle) boundaries in one phase are preserved while another phase preferentially precipitates on high-energy (high-misorientation angle) boundaries (e.g. Kim & Rohrer, 2004). In other words, the highest energy boundaries are progressively eliminated from an inherited population by 'infiltration' of the other phase. This is in agreement with the known fact that in granular-polygonal aggregates the minor phase precipitates on triple points to achieve lower total interfacial energy (Spry, 1969; Vernon, 1974). Such a tendency was documented by Dallain *et al.* (1999) who showed that the predominance of unlike contacts in polycrystalline aggregates originated through wetting of grain boundaries by fluids or melts, and subsequent precipitation of other phases on like–like contacts.

In contrast, the solid-state differentiation resulting from dynamic recrystallization leads to the development of monomineralic aggregates or bands due to coalescence of like phases at high strains (Schulmann *et al.*, 1996; Kruse & Stünitz, 1999). Therefore, the like–like contacts prevail and the so-called aggregate-type distribution develops, which is a typical feature of high-temperature deformation of polyphase rocks such as gabbros and granites (Dallain *et al.*, 1999; Baratoux *et al.*, 2005).

The high-temperature mylonitic metagabbros from the study area exhibit high-grain SPO and GPBO associated with the development of a strong aggregate distribution. The lower-temperature mylonitic metagabbros are characterized by extreme values of SPO in conjunction with an almost random grain distribution. We suggest that in the case of high-temperature mylonitic metagabbros the process controlling the development of a strong aggregate distribution is solid-state differentiation due to a different efficiency of dislocation creep in hornblende and plagioclase. This process is likely to be accompanied by some diffusional mass transfer responsible for preferential heterogeneous nucleation (Kruse & Stünitz, 1999) of interstitial plagioclase in coarse-grained amphibole aggregates (Baratoux *et al.*, 2005). On the contrary, in the lower-temperature metagabbro mylonites, the random mineral distribution and the lack of crystallographic preferred orientation of plagioclase were interpreted to be the result of mechanical mixing due to grain-boundary sliding during granular flow.

Samples from the banded amphibolite and tonalitic gneiss show a low SPO, a very weak elongation of both plagioclase and amphibole, a weak GBPO connected with a weak dominance of unlike contacts indicating a regular to anticlustered grain distribution. Such a grain distribution and the large grain size of both phases exclude mechanical mixing as a process explaining this texture. We are of the opinion that the spatial distribution of plagioclase and amphibole (e.g. sample LAC1) can result from heterogeneous nucleation of plagioclase in an amphibole aggregates. However, an original grain-size distribution characteristic of nucleation and growth processes is completely obliterated by elimination of the small grains. Very low-grain

elongation, SPO and GBPO, similar CSD of both phases and regular grain distribution indicate that the aggregates tend to achieve a state with a minimum interfacial energy. As mentioned above, the processes of heterogeneous nucleation of minor phase lead to occupation of the high-energy grain boundaries at early stages of the texture development. However, in the rocks studied it is impossible to distinguish a minor phase from the host aggregate, which indicates that the process of interfacial energy reduction is more advanced due to significant diffusional mass transfer. As the driving differences in bulk interfacial energies are too small (Ramberg, 1952), the only plausible explanation is the long time-scale of the process.

Different time-scales of Cambro-Ordovician and Variscan metamorphic events

Štípská *et al.* (2001) proposed a tectonic model in which the Cambro-Ordovician metamorphism is related to large-scale rifting while the Variscan metamorphic event was connected with a thermal effect induced by the syntectonic granodiorite sill intrusion, and was spatially restricted to the host rocks of the intrusion. The thermal time constant τ is given by the relationship:

$$\tau \propto \frac{l^2}{\kappa}, \qquad (3)$$

where l is the characteristic length of thermal event and κ is the thermal diffusivity (Carlslaw & Jaeger, 1959). This equation indicates that duration of thermal equilibration increases with the square of the size of the thermal anomaly. Based on the proposed tectonic model, we assume that a relaxation of the perturbed temperature field generated by the continental rift differs in time-scale by at least one order of magnitude from that generated by an intrusion of several km in size. In other words, the metamorphic P–T conditions attained at a similar depth level may yield similar temperatures but the time required for metamorphic equilibration and development of specific metamorphic textures may differ substantially.

ACKNOWLEDGEMENTS

This research is a part of an ongoing collaboration between Charles University, Prague, Mainz University, Germany, and ETH Zürich, Switzerland. Financial support to P. Štípská by the Charles University Grant Agency (grant no. 223/2002/B-GEO/PrF) and the Czech National Grant Agency (GA205/00/D043 and GA205/99/1195) is gratefully acknowledged. The microprobe work at ETH Zürich was financed by the Swiss National Foundation ('Continuous Orogenesis' grant to A.B. Thompson). Two visits of P. Štípská to Mainz University and a part of the microprobe work were funded by the German Science Foundation (DFG, grant Kr 68-1, Kr 590/35). The grant no. 24313005 of the Ministry of Education of the Czech Republic provided funds for O. Lexa, P. Štípská and K. Schulmann.

REFERENCES

Azpiroz, M. D. & Fernández, C., 2003. Characterization of tectono-metamorphic events using crystal size distribution (CSD) diagrams. A case study from the Acebuches metabasites (SW Spain). *Journal of Structural Geology*, **25,** 935–947.

Baratoux, L., Schulmann, K., Ulrich, S. & Lexa, O., 2005. Contrasting microstructures and deformation mechanisms in metagabbro mylonites contemporaneously deformed under different temperatures (c. 650 and c. 750 °C). In: *Deformation Mechanisms, Rheology and Tectonics: from Minerals to the Lithosphere* (eds Gapais, D., Brun, J. P. & Cobbold, P. R.), *Geological Society Special Publications*, pp. 97–125. Geological Society of London, London, UK.

Bohlen, S. R., Wall, V. J. & Boettcher, A. L., 1983. Experimental investigations and geological applications of equilibria in the system FeO–TiO_2–Al_2O_3–SiO_2–H_2O. *American Mineralogist*, **68,** 1049–1058.

Brodie, K. H. & Rutter, E. H., 1987. The role of transiently fine-grained reaction-products in syntectonic metamorphism – natural and experimental examples. *Canadian Journal of Earth Sciences*, **24,** 556–564.

Burg, J.-P., 1999. Ductile structures and instabilities: their implication for Variscan tectonics in the Ardennes. *Tectonophysics*, **309,** 1–25.

Cahn, J. V., 1957. Nucleation on dislocations. *Acta Metallurgica*, **5,** 169–172.

Carlslaw, H. S. & Jaeger, J. C., 1959. *Conduction of Heat in Solids*. Oxford University Press, Oxford.

Cashman, K. V. & Ferry, J. M., 1988. Crystal size distribution (CSD) in rocks and the kinetics and dynamics of crystallization; 3, Metamorphic crystallization. *Contributions to Mineralogy and Petrology*, **99,** 401–415.

Dallain, C., Schulmann, K. & Ledru, P., 1999. Textural evolution in the transition from subsolidus annealing to melting process, Velay Dome, French Massif Central. *Journal of Metamorphic Geology*, **17,** 61–74.

DeHoff, R. T., 1991. A geometrically general-theory of diffusion controlled coarsening. *Acta Metallurgica Et Materialia*, **39,** 2349–2360.

DeVore, G. W., 1959. Role of minimum interfacial free energy in determining the macroscopic features of minerals assemblages. *Journal of Geology*, **67,** 211–227.

Eberl, D. D., Drits, V. A. & Srodon J., 1998. Deducing growth mechanisms for minerals from the shapes of crystal size distributions. *American Journal of Science*, **298,** 499–533.

Ferry, J. M. & Spear, F. S., 1978. Experimental calibration of the partitioning of Fe and Mg between biotite and garnet. *Contributions to Mineralogy and Petrology*, **66,** 113–117.

Flinn, D., 1969. Grain contacts in crystalline rocks. *Lithos*, **2,** 361–370.

Gasparik, T. & Newton, R. C., 1984. The reversed alumina contents of orthopyroxene in equilibrium with spinel and forsterite in the system MgO–Al_2O_3–SiO_2. *Contributions to Mineralogy and Petrology*, **85,** 186–196.

Hickey, K. A. & Bell, T. H., 1996. Syn-deformational grain growth: matrix coarsening during foliation development and regional metamorphism rather than by static annealing. *European Journal of Mineralogy*, **8,** 1351–1373.

Higgins, M. D., 1998. Origin of anorthosite by textural coarsening: quantitative measurements of a natural sequence of textural development. *Journal of Petrology*, **39,** 1307–1323.

Holland, T. J. B. & Blundy, J. D., 1994. Non-ideal interactions in calcic amphiboles and their bearing on amphibole–plagio-

clase thermometry. *Contributions to Mineralogy and Petrology*, **116,** 433–447.
Kim, C.-S. & Rohrer, G. S., 2004. Geometric and crystallographic characterization of WC surfaces and grain boundaries in WC-Co composites. *Interface Science*, **12,** 19–27.
Kohn, M. J. & Spear, F. S., 1990. Two new barometers for garnet amphibolites with applications to southeastern Vermont. *American Mineralogist*, **75,** 89–96.
Koziol, A. M., 1989. Recalibration of the garnet–plagioclase–Al_2SiO_5–quartz (GASP) geobarometer and application to natural parageneses. *Transactions of the American Geophysical Union*, **70,** 493.
Kretz, R., 1969. On the spatial distribution of crystals in rocks. *Lithos*, **2,** 39–66.
Kretz, R., 1983. Symbols for rock forming minerals. *American Mineralogist*, **68,** 277–279.
Kretz, R., 1994. *Metamorphic Crystallization*. John Wiley & Sons, Chichester.
Kröner, A., O'Brien, P. J., Nemchin, A. A. & Pidgeon, R. T., 2000a. Zircon ages for high pressure granulites from South Bohemia, Czech Republic, and their connection to Carboniferous high temperature processes. *Contributions to Mineralogy and Petrology*, **138,** 127–142.
Kröner, A., Štípská, P., Schulmann, K. & Jaeckel, P., 2000b. Chronological constraints on the pre-Variscan evolution of the northeastern margin of the Bohemian Massif, Czech Republic. In: *Orogenic Processes: Quantification and Modelling in the Variscan Belt* (eds Franke, W., Haak, W., Oncken, O. & Tanner, D.), *Geological Society, London, Special Publications*, **179,** 175–197.
Kruse, R. & Stünitz, H., 1999. Deformation mechanisms and phase distribution in mafic high- temperature mylonites from the Jotun Nappe, southern Norway. *Tectonophysics*, **303,** 223–249.
Leake, B. E., Woolley, A. R., Arps, C. E. *et al*., 1997. Nomenclature of amphiboles: Report of the Subcommittee on Amphiboles of the International Mineralogical Association Commission on new minerals and mineral names. *Mineralogical Magazine*, **61,** 295–321.
Lexa, O., 2003. *Numerical Approaches in Structural and Microstructural Analyses*. Unpublished PhD Thesis, Charles University, Prague.
Lifshitz, I. M. & Slyozov, V. V., 1961. The kinetics of precipitation from supersaturated solid solutions. *Journal of Physics and Chemistry of Solids*, **19,** 35–50.
Marsh, B. D., 1988. Crystal size distribution (CSD) in rocks and the kinetics and dynamics of crystallization; 1, Theory. *Contributions to Mineralogy and Petrology*, **99,** 277–291.
O'Neill, H. S. C. & Wall, V. J., 1987. The olivine–orthopyroxene–spinel oxygen geobarometer, the Nickel precipitation curve, and the oxygen fugacity of the Earth's upper mantle. *Journal of Petrology*, **28,** 1169–1191.
Parry, M., Štípská, P., Schulmann, K., Hrouda, F., Ježek, J. & Kröner, A., 1997. Tonalite sill emplacement at an oblique plate boundary: northeastern margin of the Bohemian Massif. *Tectonophysics*, **280,** 61–81.
Peterson, T. D., 1996. A refined technique for measuring crystal size distributions in thin section. *Contributions to Mineralogy and Petrology*, **124,** 395–405.
Poirier, J. P. & Guillope, M., 1979. Deformation induced recrystallisation of minerals. *Bulletin de Mineralogie*, **102,** 67–74.
Powell, R. & Holland, T. J. B., 1988. An internally consistent dataset with uncertainties and correlations: 3. Applications to geobarometry, worked examples and a computer program. *Journal of Metamorphic Geology*, **6,** 173–204.
Ramberg, H., 1952. *The Origin of Metamorphic and Metasomatic Rocks*. University of Chicago Press, Chicago, IL.
Randolph, A. D. & Larson, M. A., 1971. *Theory of Particle Processes*. Academic Press, New York.
Ridley, J. & Thompson, A. B., 1986. The role of mineral kinetics in the development of metamorphic microtextures. In: *Fluid–Rock Interactions during Metamorphism* (eds Walther, J. V. & Wood, B. J.), pp. 154–193. Springer-Verlag, New York.
Schmidt, M. W., 1992. Amphibole composition in tonalite as a function of pressure: an experimental calibration of the Al-in-hornblende barometer. *Contributions to Mineralogy and Petrology*, **110,** 304–310.
Schulmann, K., Mlcoch, B. & Melka, R., 1996. High-temperature microstructures and rheology of deformed granite, Erzgebirge, Bohemian Massif. *Journal of Structural Geology*, **18,** 719–733.
Seng, H., 1936. Die Migmatitfrage und der Mechanismus parakristalliner Prägung. *Geologische Rundschau*, **27,** 471–492.
Spear, F. S., Peacock, S. M., Kohn, M. J., Florence, F. P. & Menard, T., 1991. Computer programs for petrologic P–T–t path calculations. *American Mineralogist*, **76,** 2009–2012.
Spry, A. H., 1969. *Metamorphic Textures*. Pergamon Press, Oxford.
Štípská, P., Schulmann, K., Thompson, A. B., Ježek, J. & Kröner, A., 2001. Thermo-mechanical role of a Cambro-Ordovician paleorift during the Variscan collision: the NE margin of the Bohemian Massif. *Tectonophysics*, **332,** 239–253.
Thompson, A. B., 1976. Mineral reactions in pelitic rocks: II. Calculation of some P–T–X (Fe–Mg) phase relations. *American Journal of Science*, **276,** 425–454.
Turner, J. T. & Weiss, L. E., 1963. *Structural Analysis of Metamorphic Tectonictes*. McGraw-Hill, San Francisco, CA.
Twiss, R. J., 1977. Theory and applicability of a recrystallized grain size paleopiezometer. *Pure and Applied Geophysics*, **115,** 227–244.
Urai, J. L., Means, W. D. & Lister, G. S., 1986. Dynamic recrystallization of minerals. *AGU Geophysical Monograph*, **36,** 161–199.
Vernon, R. H., 1974. Controls of mylonitic compositional layering during non-cataclastic ductile deformation. *Geological Magazine*, **111,** 121–123.
Voorhees, P. V., 1992. Ostwald ripening of two-phase mixtures. *Annual Review of Materials Science*, **22,** 197–215.

Received 3 June 2005; revision accepted 17 July 2005.

9. **Štípská**, P. & Powell, R. (2005a). Constraining the P−T path of a MORB-type eclogite using pseudosections, garnet zoning and garnet-clinopyroxene thermometry: an example from the Bohemian Massif. *Journal of Metamorphic Geology*, 23, 725-743. doi:10.1111/j.1525-1314.2005.00607.x

10. **Štípská**, P. & Powell, R. (2005b). Does ternary feldspar constrain the metamorphic conditions of high-grade meta-igneous rocks? Evidence from orthopyroxene granulites, Bohemian Massif. *Journal of Metamorphic Geology*, 23, 627-647. doi:10.1111/j.1525-1314.2005.00600.x.

11. Racek, M., **Štípská, P.,** Powell, R. (2008). Garnet-clinopyroxene intermediate granulites in the St. Leonhard massif of the Bohemian Massif: ultrahigh-temperature metamorphism at high pressure or not? *Journal of Metamorphic Geology*, **26**, 253–271. doi:10.1111/j.1525-1314.2007.00754.x.

J. metamorphic Geol., 2005, **23,** 725–743 doi:10.1111/j.1525-1314.2005.00607.x

Constraining the *P–T* path of a MORB-type eclogite using pseudosections, garnet zoning and garnet-clinopyroxene thermometry: an example from the Bohemian Massif

P. ŠTÍPSKÁ[1,2,3] AND R. POWELL[4]
[1]*Institute of Petrology and Structural Geology, Charles University, Albertov 6, 12843, Prague, Czech Republic (stipska@illite.u-strasbg.fr)*
[2]*Czech Geological Survey, Klárov 3, 118 21, Prague, Czech Republic*
[3]*Centre de Géochimie de Surface, UMR CNRS 7517, 1 Rue Blessig, Strasbourg, France*
[4]*School of Earth Sciences, University of Melbourne, Melbourne, Victoria 3010, Australia*

ABSTRACT A mid-ocean ridge basalt (MORB)-type eclogite from the Moldanubian domain in the Bohemian Massif retains evidence of its prograde path in the form of inclusions of hornblende, plagioclase, clinopyroxene, titanite, ilmenite and rutile preserved in zoned garnet. Prograde zoning involves a flat grossular core followed by a grossular spike and decrease at the rim, whereas Fe/(Fe + Mg) is also flat in the core and then decreases at the rim. In a pseudosection for H_2O-saturated conditions, garnet with such a zoning grows along an isothermal burial path at *c.* 750 °C from 10 kbar in the assemblage plagioclase-hornblende-diopsidic clinopyroxene-quartz, then in hornblende-diopsidic clinopyroxene-quartz, and ends its growth at 17–18 kbar. From this point, there is no pseudosection-based information on further increase in pressure or temperature. Then, with garnet-clinopyroxene thermometry, the focus is on the dependence on, and the uncertainties stemming from the unknown Fe^{3+} content in clinopyroxene. Assuming no Fe^{3+} in the clinopyroxene gives a serious and unwarranted upward bias to calculated temperatures. A Fe^{3+}-contributed uncertainty of ±40 °C combined with a calibration and other uncertainties gives a peak temperature of 760 ± 90 °C at 18 kbar, consistent with no further heating following burial to eclogite facies conditions. Further pseudosection modelling suggests that decompression to *c.* 12 kbar occurred essentially isothermally from the metamorphic peak under H_2O-undersaturated conditions (*c.* 1.3 mol.% H_2O) that allowed the preservation of the majority of garnet with symplectitic as well as relict clinopyroxene. The modelling also shows that a MORB-type eclogite decompressed to *c.* 8 kbar ends as an amphibolite if it is H_2O saturated, but if it is H_2O-undersaturated it contains assemblages with orthopyroxene. Increasing H_2O undersaturation causes an earlier transition to SiO_2 undersaturation on decompression, leading to the appearance of spinel-bearing assemblages. Granulite facies-looking overprints of eclogites may develop at amphibolite facies conditions.

Key words: Bohemian Massif; garnet-clinopyroxene thermometry; MORB eclogite; prograde garnet zoning; pseudosection.

INTRODUCTION

Eclogite, *sensu lato*, a rock dominated by garnet and clinopyroxene (with significant jadeite component; commonly omphacitic), can have a considerable range of minerals occurring in minor proportion as inclusions or within the matrix. These minor minerals may give important clues to the pressure–temperature (*P–T*) conditions of formation of the eclogite (e.g. Hacker *et al.*, 2003). Inclusions within garnet involve hydrous minerals like chlorite, white mica, zoisite or epidote, amphibole and lawsonite and are usually interpreted as relicts trapped on the prograde path through the greenschist, amphibolite or blueschist facies (e.g. Krogh, 1982; Carson *et al.*, 1999; Page *et al.*, 2003).

However, outside the stability limits of these hydrous minerals, there is an open-ended region to high pressure and high temperature in which such eclogites can be formed. In this region, establishing peak metamorphic conditions is difficult because the minerals change composition only slowly with *P–T*, although progress is being made when phengite is additionally present (Krogh Ravna & Terry, 2004). For phengite-free eclogites, the determination of peak conditions hinges on the garnet-clinopyroxene (g-cpx) Fe-Mg exchange thermometer. One difficulty arises from the continuous Fe-Mg exchange during retrogression that makes interpretation of the 'peak' values questionable, at least for higher-temperature eclogites. The g-cpx thermometer is also much less precise than commonly claimed because the uncertainties associated with, for example, the unknown content of ferric iron in garnet and clinopyroxene are rarely reported (e.g. Proyer *et al.*, 2004). Moreover, the commonly

adopted tactic of assuming all Fe as Fe^{2+} in clinopyroxene biases temperature strongly upwards. However, as discussed below, g-cpx thermometry can give useful results, albeit with much larger uncertainties than commonly reported.

Establishing the prograde part of the *P–T* path in the making of an eclogite has relied on the inclusions in garnet. Eclogites that were formed on a cooler path through the blueschist facies involve inclusions of glaucophane, epidote and even lawsonite (e.g. Will *et al*., 1998; Carson *et al*., 1999; Dachs & Proyer, 2001; Marmo *et al*., 2002; Wei *et al*., 2003). Garnet in higher-temperature eclogites have inclusions of hornblende, epidote and/or anhydrous minerals like plagioclase and clinopyroxene. These eclogites have been interpreted to form on a warmer path through the amphibolite facies (e.g. Krogh, 1982; Krogh *et al*., 1994; Medaris *et al*., 1995; Franceschelli *et al*., 1998; Möller, 1998; Elvevold & Gilotti, 2000; Will & Schmädicke, 2001; Page *et al*., 2003; Wei *et al*., 2003).

Garnet growth zoning constrains the equilibria in which the garnet grew, and provides information on the prograde path, even if prograde (hydrous) minerals are not preserved at the metamorphic peak. Garnet zoning has been interpreted as prograde in eclogites, based on the shape of zoning with respect to Fe/(Fe + Mg) and also on the nature of the inclusions (e.g. O'Brien & Vrána, 1995; O'Brien, 1997a; Möller, 1998; Medaris *et al*., 1998; Elvevold & Gilotti, 2000; Will & Schmädicke, 2001; Marmo *et al*., 2002; Shervais *et al*., 2003). However, explanation of the garnet-zoning patterns in relation to the evolving assemblage and estimation of the prograde *P–T* path from such zoning has not been undertaken in metabasic rocks. In contrast, attempts to characterize the prograde path have been undertaken, based on the increase in the modal proportion of garnet in a particular assemblage (e.g. Carson *et al*., 1999; Marmo *et al*., 2002; Wei *et al*., 2003), on evolving chemistry of amphibole (e.g. Willner *et al*., 2004) and on thermobarometry on inclusions (e.g. Elvevold & Gilotti, 2000; Page *et al*., 2003).

Decompression primarily causes the formation of plagioclase-diopsidic clinopyroxene symplectites after more Na-rich clinopyroxene, and amphibole-plagioclase kelyphites around garnet (e.g. Will & Schmädicke, 2001; Yang, 2004). Other types of symplectites and kelyphites in the middle- to higher-temperature eclogites also involve, for example, combinations of orthopyroxene, spinel, sapphirine and olivine (e.g. O'Brien & Vrána, 1995; O'Brien, 1997a,b; Dirks & Sithole, 1999; Möller, 1999; Elvevold & Gilotti, 2000; O'Brien & Rötzler, 2003). Such replacement textures should constrain a segment of the *P–T* path, but thermobarometric studies have revealed a large range of mineral chemistry and, as a consequence, a large scatter in calculated *P–T* conditions making thermobarometric results in these textures unreliable (O'Brien & Vrána, 1995; Yang, 2004). Some of these textures have been interpreted as granulite facies overprints reflecting either isothermal decompression or even a temperature increase during exhumation (O'Brien & Vrána, 1995; O'Brien, 1997a; Dirks & Sithole, 1999; Möller, 1999). A major uninvestigated reason for the variety of assemblages is the degree of H_2O and SiO_2 undersaturation rather than the variation in *P–T* conditions of retrogression.

Placing rocks in the context of a *P–T* path is best done with calculated pseudosections, but this has been difficult to apply to eclogites in a wide *P–T–M*(H_2O) range because of the absence of an appropriate thermodynamic model for amphibole, a key mineral in the prograde and retrograde history of eclogite, even if it is commonly absent at the metamorphic peak. Now, with a recently developed amphibole model (Dale *et al*., 2005), we show here the power of the pseudosection approach combined with garnet-clinopyroxene thermometry for constraining the *P–T* evolution of eclogite as applied to a mid-ocean ridge basalt (MORB)-type crustal eclogite from the Bohemian Massif.

GEOLOGICAL SETTING AND PETROLOGY

Geological and tectonic framework

The eclogite considered here is from the Moldanubian zone that forms the internal part of the European Variscan orogen in the Bohemian Massif (Fig. 1; for references, see Franke, 2000; Schulmann *et al*., 2005). The Moldanubian zone consists of the Gföhl, Varied and Monotonous metamorphic units and numerous Variscan plutons. The Gföhl unit is dominated by felsic kyanite-K-feldspar granulites and felsic orthogneisses with subordinate intermediate and basic rock types, and with associated garnet peridotite. The Varied and Monotonous units are named according to the character of the dominant sedimentation and are metamorphosed mostly at medium grade.

The eclogites occur in all three units and their classification has been influenced by and created within a previously accepted tectonic framework in which the Gföhl unit was interpreted as the uppermost long-distance-sourced nappe thrust over lower-grade Varied and Monotonous units (Tollmann, 1982; Franke, 1989, 2000; Matte *et al*., 1990). This classical view is now disputed in a series of structural and metamorphic studies that interpret the granulite complexes and associated high-pressure rocks (including the eclogites) within the Moldanubian domain as 'autochtonous' vertical extrusions of the lower crust of the thickened orogenic root spread into the middle crust (Štípská *et al*., 2004; Schulmann *et al*., 2005; Racek *et al*., 2006). In this view, not only did the Gföhl unit form the lower part of the orogenic crust, but, in some places, parts of the originally superficial Varied and Monotonous units were also buried to eclogite facies conditions, prior to their exhumation (Racek *et al*., 2006). The peak of high-pressure metamorphism and onset of exhumation within the Moldanubian zone is

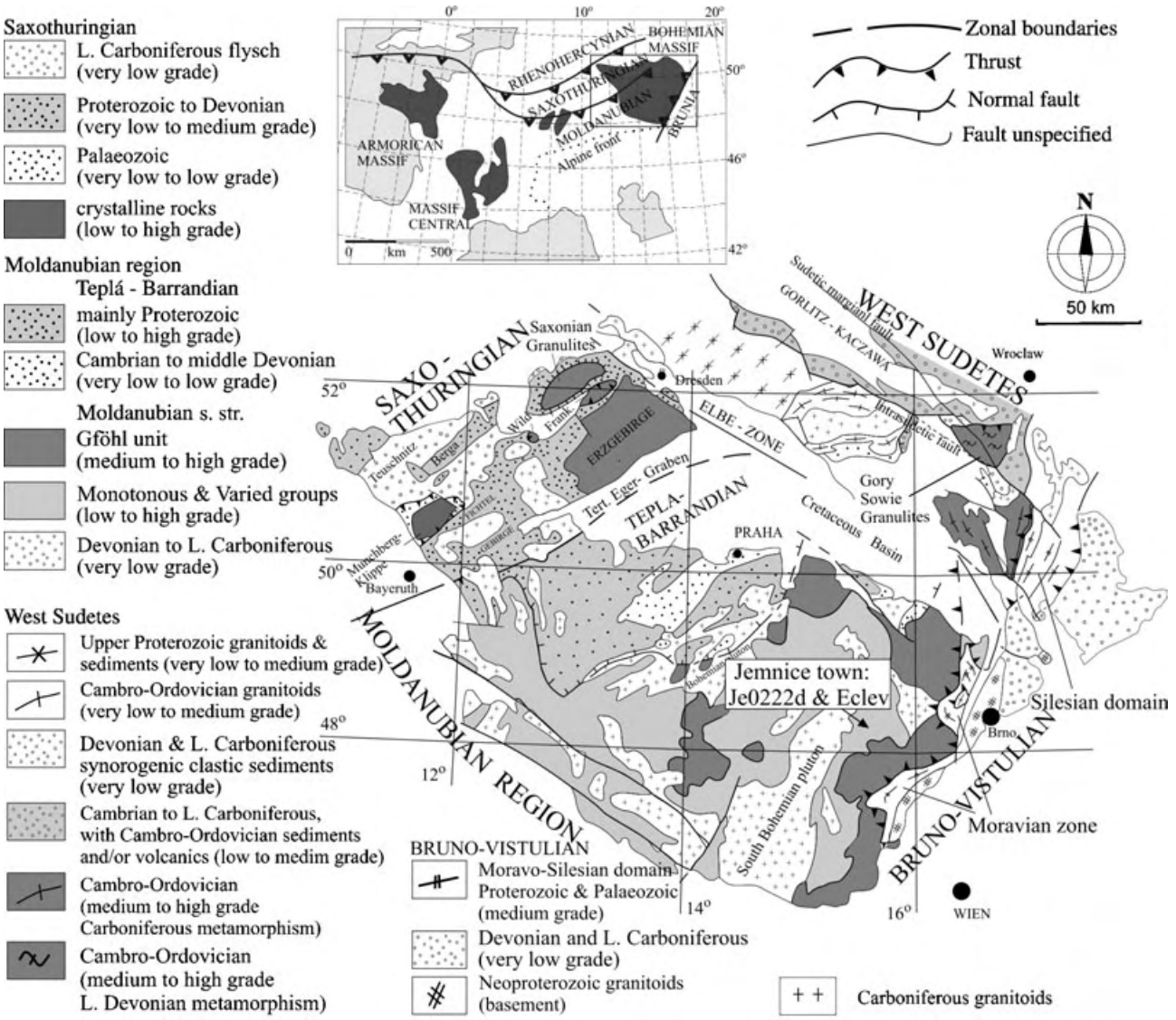

Fig. 1. Outline geological map of the Bohemian Massif with major units shown schematically (modified after Franke (2000). Location of sample studied is indicated. The upper left inset is the position of the study area in the framework of the European Variscides.

interpreted as Carboniferous (e.g. Kröner *et al*., 2000; Schulmann *et al*., 2005).

Occurrence and classification of eclogites within the Moldanubian zone

All the Moldanubian eclogites belong to the middle–high temperature groups of Carswell (1990) and the major distinction that has been made is in the geological occurrence and metamorphic history (Dudek & Fediuková, 1974; Medaris *et al*., 1995). Within the Gföhl unit, the eclogites inside garnet peridotites have been interpreted as high-pressure crystal accumulation of garnet and clinopyroxene, whereas eclogites derived from basalt protoliths occur with felsic granulites, spinel peridotites, serpentinites and other mafic rocks (Medaris *et al*., 1995, 1998). A special group that is interpreted to be metamorphosed at high pressure, but with granulite facies mineral assemblages are garnet-clinopyroxene gneisses (e.g. Cooke, 2000; Cooke & O'Brien, 2001; O'Brien & Rötzler, 2003).

Eclogites were classified as 'prograde' if they exhibit prograde garnet zoning and contain prograde inclusions in garnet (Medaris *et al*., 1995). These 'prograde' eclogites occur, for example, within the Varied and Monotonous units (e.g. Medaris *et al*., 1995; O'Brien & Vrána, 1995; O'Brien, 1997a); the first 'prograde' eclogite from a Gföhl granulite body was described by Medaris *et al*. (1998). Their prograde character has been suggested on the basis of inclusions within garnet that involve amphibole, epidote-group minerals, plagioclase, clinopyroxene and titanite and on a variety

of prograde garnet profiles (Medaris *et al.*, 1995, 1998; O'Brien & Vrána, 1995; O'Brien, 1997a). The peak assemblage in common types of eclogite is formed by garnet-omphacite-rutile. Rarer varieties have kyanite and/or quartz in addition. Epidote-group minerals within the matrix are scarce.

The retrograde evolution of eclogites commonly includes formation of diopsidic clinopyroxene-plagioclase symplectites after omphacite, accompanied by plagioclase-amphibole kelyphites around garnet. In some cases, complex coronitic symplectites and kelyphites develop, including the growth of orthopyroxene in domains of garnet and clinopyroxene, and sapphirine, spinel, corundum, and anorthite in domains replacing kyanite (O'Brien & Vrána, 1995; O'Brien, 1997a,b). These symplectites have been considered to be the result of decompression under granulite facies conditions, while the amphibole-bearing symplectites have been interpreted to reflect lower temperatures (Messiga & Bettini, 1990; Medaris *et al.*, 1995).

Previously estimated metamorphic conditions

Peak conditions for prograde eclogites have been inferred almost exclusively from garnet-clinopyroxene thermometry, and barometry using the jadeite content of clinopyroxene. For the prograde eclogites of the Varied and Monotonous units, the *P–T* conditions vary (according to author) within a range of *c.* 650–800 °C and 14–19 kbar (Medaris *et al.*, 1995; O'Brien & Vrána, 1995; O'Brien, 1997a) and for the unique Gföhl prograde eclogite, 890 °C and 18 kbar (Medaris *et al.*, 1998). Reported *P–T* conditions for prograde garnet-clinopyroxenites are 830 °C and 13 kbar (Medaris *et al.*, 1998). However, more recently, for other garnet-clinopyroxene gneisses of the Gföhl unit metamorphic conditions of 950–1050 °C and 14–19 kbar have been proposed (Cooke, 2000; Cooke & O'Brien, 2001; O'Brien & Rötzler, 2003). Ultrahigh-temperature (UHT) metamorphic conditions attained at high pressure were also suggested for felsic granulites, based on the occurrence of ternary feldspar (for references, see O'Brien & Rötzler, 2003). These UHT metamorphic conditions are however disputed by Štípská & Powell (2005) who interpreted such ternary feldspar to be of magmatic origin. Thermobarometric attempts to quantify the *P–T* conditions of decompression resulted in a large scatter that did not establish whether the retrograde path was isothermal or had an increase or decrease in temperature (O'Brien & Vrána, 1995).

Eclogite example

Eclogite samples (thin section Je0222d and sample for rock analysis Eclev) were collected in an eclogite body, several tens of metres thick, occurring at the contact with a kyanite-K-feldspar granulite in Jemnice town (Fig. 1). The migmatitic upper-amphibolite facies foliation in the area is effectively horizontal over large distances obliterating previous vertical structures that pre-date this fabric elsewhere (e.g. Štípská *et al.*, 2004; Schulmann *et al.*, 2005; Racek *et al.*, 2006). It is therefore not clear as to whether the eclogite body shared its whole evolution with the kyanite-K-feldspar granulite and therefore belongs to the Gföhl unit or not.

The matrix is formed of diopsidic clinopyroxene-plagioclase symplectite with abundant relicts of more sodic clinopyroxene and omphacite that together constitute 50–60 modal% of the rock (Fig. 2). The modal content of garnet is 30–40%, it has an inclusion-rich core with plagioclase, amphibole, clinopyroxene, quartz, rutile, ilmenite and titanite inclusions and a clear rim with rare inclusions of rutile (Fig. 2b). Amphibole forms a maximum of 10% of the sample. Amphibole-plagioclase kelyphites surround garnet (Fig. 2a) and in places amphibole invades plagioclase-clinopyroxene symplectite. Minor quartz was observed within the matrix. Rutile also occurs as inclusions in clinopyroxene and amphibole, and with secondary ilmenite in the matrix.

Minerals have been analysed using the Cameca SX100 at the Czech Academy of Sciences in point beam mode at 15 kV and 10 nA. Representative analyses are listed in Table 1. Relict matrix clinopyroxene (up to 1 mm across), recalculated on the basis of four cations per six oxygen basis, has a maximum Na = 0.30–0.33 pfu, Fe/(Fe + Mg) = 0.27–0.35 (all Fe as Fe^{2+}), and $Fe^{2+}/(Fe^{2+} + Mg)$ = 0.2–0.3 (with Fe^{2+} converted to Fe^{3+} on charge balance). Clinopyroxene inclusions in garnet have Na = 0.28 pfu, Fe/(Fe + Mg) = 0.40, and $Fe^{2+}/(Fe^{2+} + Mg)$ = 0.32, and clinopyroxene within the symplectites is diopsidic with Na = 0.01–0.10 pfu and $Fe^{2+}/(Fe^{2+} + Mg)$ = 0.24–0.30.

The garnet (up to 5 mm across) has a compositionally flat core [$Alm_{56}Grs_{30}Py_{11}Sps_4$, Fe/(Fe + Mg) = 80], a sharp increase of grossular content up to 33% near the garnet rim, followed by a grossular decrease at the actual rim [$Alm_{46}Grs_{25}Py_{28}Sps_0$, Fe/(Fe + Mg) = 63]. In the NCFMASH system, this corresponds to $x(g)$ = Fe/(Fe + Mg) of 80⇒63, and $z(g)$ = Ca/(Ca + Mg + Fe) of 31⇒33⇒25 (Fig. 3, Table 1).

Plagioclase has a composition that varies according to its textural position. Inclusions in garnet are an = Ca/(Ca + Na) of 0.1–0.3, within the fine-grained symplectite 0.1–0.2, in the matrix domains of coarse-grained amphibole plagioclase 0.25–0.35 and within the plagioclase-amphibole kelyphites around garnet it increases from 0.3 to 0.5 at the garnet contact.

Amphibole in all textural positions is pargasitic. It is recalculated on 23 oxygen with 13 cations + Na + Ca + K. Si (pfu) and Al,M2 varies according to textural position: in the inclusions Si = 6.03 pfu and octahedral (M2-site) Al = 0.55; near garnet it is

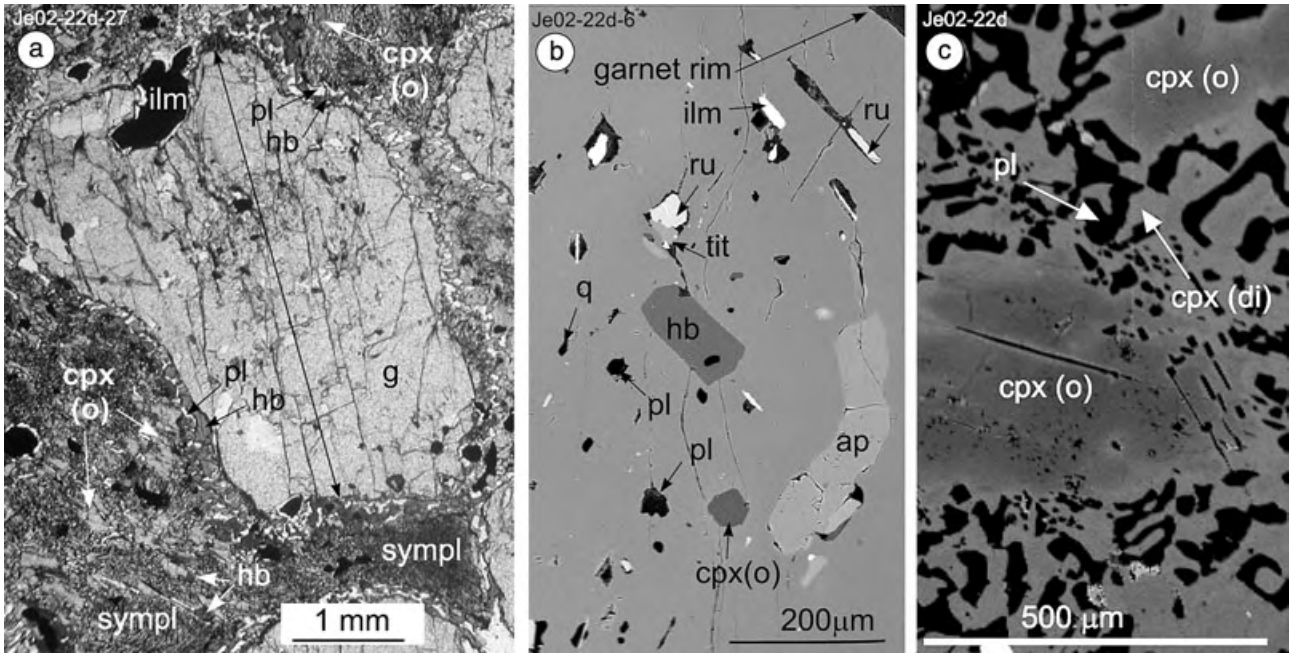

Fig. 2. (a) Photomicrograph of garnet, with profile indicated, and kelyphite of plagioclase, amphibole and ilmenite. Relicts of omphacite set in a symplectitic matrix. Amphibole also invades the clinopyroxene-plagioclase symplectites. (b) BSE image of inclusions of plagioclase, quartz, amphibole, omphacitic clinopyroxene, rutile, titanite, ilmenite and apatite in garnet. (c) BSE image of relict of omphacitic clinopyroxene (dark grey) set in a symplectite of diopsidic clinopyroxene (light grey) and plagioclase (black).

6.0–6.1 and 0.51–0.58, and near or within clinopyroxene-plagioclase symplectites it is 6.2–6.4 and 0.26–0.40. Amphibole in all textural positions has Fe/(Fe + Mg) = 0.36–0.44 (for all Fe as Fe^{2+}), Fe^{2+}/(Fe^{2+} + Mg) = 0.23–0.36, A-site Na = 0.49–0.64, and M4-site Na = 0.22–0.35.

Table 1. Representative mineral analyses.

Sample:	Je0222d	Je0222d	Je0222d	Je0222d	Je0222d	Je0222d	Je0222d	Je0222d	je0222d	je0222d
Mineral:	cpx	cpx	cpx	cpx	g	g	g	am	am	am
Position:	in	mx relic	mx relic	sympl	core	spike	rim	in	near g	sympl
Analysis:	27	58-6	58-8	72	65h240303	45h240303	37h240303	24	37	56
SiO_2	51.07	54.66	53.70	51.70	38.63	38.27	38.94	40.28	40.80	43.50
TiO_2	0.75	0.21	0.25	0.24	0.00	0.00	0.00	3.19	0.95	0.78
Cr_2O_3	0.09	0.05	0.06	0.02	0.00	0.00	0.00	0.06	0.17	0.00
Al_2O_3	7.82	8.97	8.80	5.26	21.77	21.80	22.09	14.32	14.85	11.78
FeO	10.02	6.66	6.73	8.71	25.28	22.47	23.26	14.30	15.28	13.75
MnO	0.18	0.06	0.06	0.14	1.28	0.63	0.23	0.19	0.04	0.19
MgO	8.47	9.23	9.67	12.02	3.32	5.23	6.87	10.18	11.09	13.02
CaO	16.82	15.90	16.70	20.18	10.68	11.50	8.98	10.31	11.00	10.93
Na_2O	3.81	4.67	4.18	1.72	0.00	0.00	0.00	2.89	3.21	2.75
K_2O	0.01	0.02	0.00	0.00	0.00	0.00	0.00	0.91	0.35	0.31
Total	99.02	100.43	100.15	99.99	100.96	99.90	100.37	96.63	97.75	97.00
Si	1.90	1.97	1.95	1.91	3.00	2.96	2.98	6.03	5.99	6.35
Ti	0.02	0.01	0.01	0.01	0.00	0.00	0.00	0.36	0.11	0.09
Cr	0.00	0.00	0.00	0.00	0.00	0.00	0.00	0.01	0.02	0.00
Al	0.34	0.38	0.38	0.23	1.99	1.99	1.99	2.53	2.57	2.03
Fe^{3+}	0.09	0.00	0.01	0.06	0.00	0.09	0.04	0.38	0.77	0.84
Fe^{2+}	0.23	0.20	0.19	0.21	1.64	1.36	1.45	1.41	1.11	0.83
Mn	0.01	0.00	0.00	0.00	0.08	0.04	0.01	0.02	0.00	0.02
Mg	0.47	0.50	0.52	0.66	0.38	0.60	0.78	2.27	2.43	2.83
Ca	0.67	0.61	0.65	0.80	0.89	0.95	0.74	1.65	1.73	1.71
Na	0.27	0.33	0.29	0.12	0.00	0.00	0.00	0.84	0.91	0.78
K	0.00	0.00	0.00	0.00	0.00	0.00	0.00	0.17	0.07	0.06
Total	4.00	4.00	4.00	4.00	8.00	8.00	8.00	15.66	15.71	15.55
$X_{Fe(Fe^{2+})}$	0.32	0.29	0.27	$0.24X_{Fe(Fe^{2+})}$	0.81	0.69	$0.65X_{Fe(Fe^{2+})}$	0.38	0.31	0.23
				Grs	0.30	0.32	0.25Al6	0.55	0.57	0.38
							NaA	0.49	0.64	0.49
							NaM4	0.35	0.27	0.29

in, inclusion; mx, matrix; sympl, symplectite.

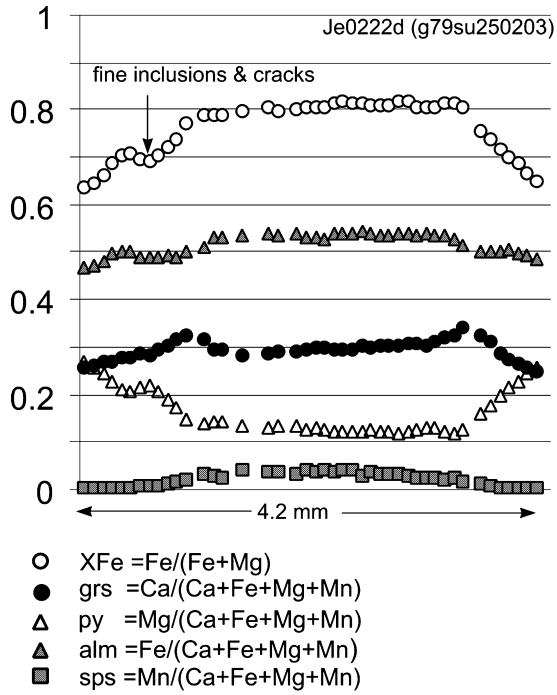

Fig. 3. Large garnet (4.2 mm) exhibits flat core with slight decrease in spessartine, spikes of grossular near the garnet rim followed by decrease in grossular and x(g) to the rim.

CALCULATED PSEUDOSECTIONS

In order to constrain the P–T path, the observed mineral assemblages, mineral compositions and textural relationships are compared with the stability and compositions of the phases in P–T–X pseudosections. The fields on P–T pseudosections calculated for dry and H_2O-saturated conditions are contoured for garnet modes in order to ascertain where garnet grows and where it is consumed. The fields are also contoured for mineral composition to identify in which fields and along which paths the observed prograde garnet zoning can be produced. The retrograde path is considered via the compositions of clinopyroxene, plagioclase and amphibole. The effect of H_2O content in the prograde and retrograde evolution is then studied in P–$M(H_2O)$ pseudosections, $M(H_2O)$ being the mol.% of H_2O in the bulk composition (Guiraud *et al.*, 2001). We study the likely evolution of incompletely hydrated protolith, to investigate whether there is sufficient H_2O in the protolith during the prograde history for the rock to be fluid-present and to involve continuous dehydration. We also investigate the effect of incomplete rehydration of the peak assemblage when it occurs during the retrograde history.

The pseudosection modelling was undertaken with THERMOCALC 3.23 (Powell *et al.*, 1998: recent upgrade) and the internally consistent thermodynamic dataset 5.5 (Holland & Powell, 1998: November 2003 upgrade) in the system Na_2O-CaO-FeO-MgO-Al_2O_3-SiO_2-H_2O (NCFMASH). The datafile coding of the activity–composition relationships of the minerals used in the calculations involves the orthopyroxene model used by White *et al.* (2001), a clinopyroxene model based on the study of Holland & Powell (1996), the plagioclase model of Holland & Powell (2003), and the amphibole model of Dale *et al.* (2005). The high-T part of some of the pseudosections is metastable with respect to melt-bearing assemblages, as discussed in the sections below, in the absence of an appropriate melt model for basic systems.

The calculated clinopyroxenes extend from below the top of the omphacite-diopsidic clinopyroxene solvus to the supra-solvus region. The composition of the solvus top is at *c.* 32% jadeite in the pseudosections. Clinopyroxene with less than this jadeite content is referred to as diopsidic clinopyroxene, whereas clinopyroxene with greater (up to *c.* 70% jadeite) is referred to as omphacite, whether its structure is ordered or disordered. In the pseudosections, where the composition of supra-solvus clinopyroxene varies through the composition of the solvus top in a field, the boundary is shown by a dashed line labelled di/o.

The rock composition of the sample, Eclev, from the eclogite body was used for the modelling (in wt%: $SiO_2 = 48.18$, $TiO_2 = 1.58$, $Al_2O_3 = 14.57$, $FeO_{tot} = 11.27$, $MnO = 0.19$, $MgO = 8.54$, $CaO = 11.76$, $Na_2O = 2.74$, $K_2O = 1.03$, $P_2O_5 = 0.14$; standard wet chemical methods). It differs only slightly in NCFMASH from the composition of unaltered MORB, Table 2 (Pearce, 1976; Hacker *et al.*, 2003). Even though the garnet in the eclogite is zoned, bulk composition fractionation calculations are not presented (c.f. Marmo *et al.*, 2002). Preliminary calculations showed that with garnet and clinopyroxene fractionating, the bulk composition barely changes. Although zoning in the clinopyroxene is not very well established because of the conversion of clinopyroxene to kelyphite as well as retrograde re-equilibration, the range of composition in the inclusion and matrix clinopyroxene suggests prograde (as well as retrograde) zoning. Thus the one Eclev bulk composition, Table 2, is used for all the calculated phase diagrams.

Table 2. The rock composition (sample Eclev) from the eclogite body studied compared to mid-ocean ridge basalt (MORB: Pearce, 1976; Hacker *et al.*, 2003) in NCFMASH.

Sample	Eclev (wt%)	MORB (wt%)	% difference
SiO_2	49.6	51.5	−3.7
Al_2O_3	15.0	16.0	−6.1
FeO	11.6	10.8	7.6
MgO	8.8	7.7	13.6
CaO	12.1	11.3	7.2
Na_2O	2.8	2.6	6.7
Tot	100	100	
Fe/(Fe + Mg)	0.57	0.58	−2.3

Dry *P–T* pseudosections

The dry pseudosection is characterized at high temperature by a pressure-dependent pattern of fields with the characteristic garnet-omphacite-quartz assemblage at high pressure and the appearance of plagioclase on lowering pressure (Fig. 4). Disappearance of quartz on further decrease of pressure affects the lower-pressure fields in comparison with those for SiO_2-saturated conditions. To illustrate the importance of SiO_2 undersaturation on the calculated phase relations we present also the corresponding pseudosection for Eclev but with SiO_2 added so that the rock composition is SiO_2 saturated to lower pressure (Fig. 5). The SiO_2 undersaturation below the quartz-out line causes the appearance of spinel before the appearance of orthopyroxene and the disappearance of garnet (Fig. 4). This topology is slightly modified in the low temperature side of the pseudosection (Fig. 4), where instead of a one-clinopyroxene field occur two-clinopyroxene fields with a solvus top at *c*. 670–680 °C.

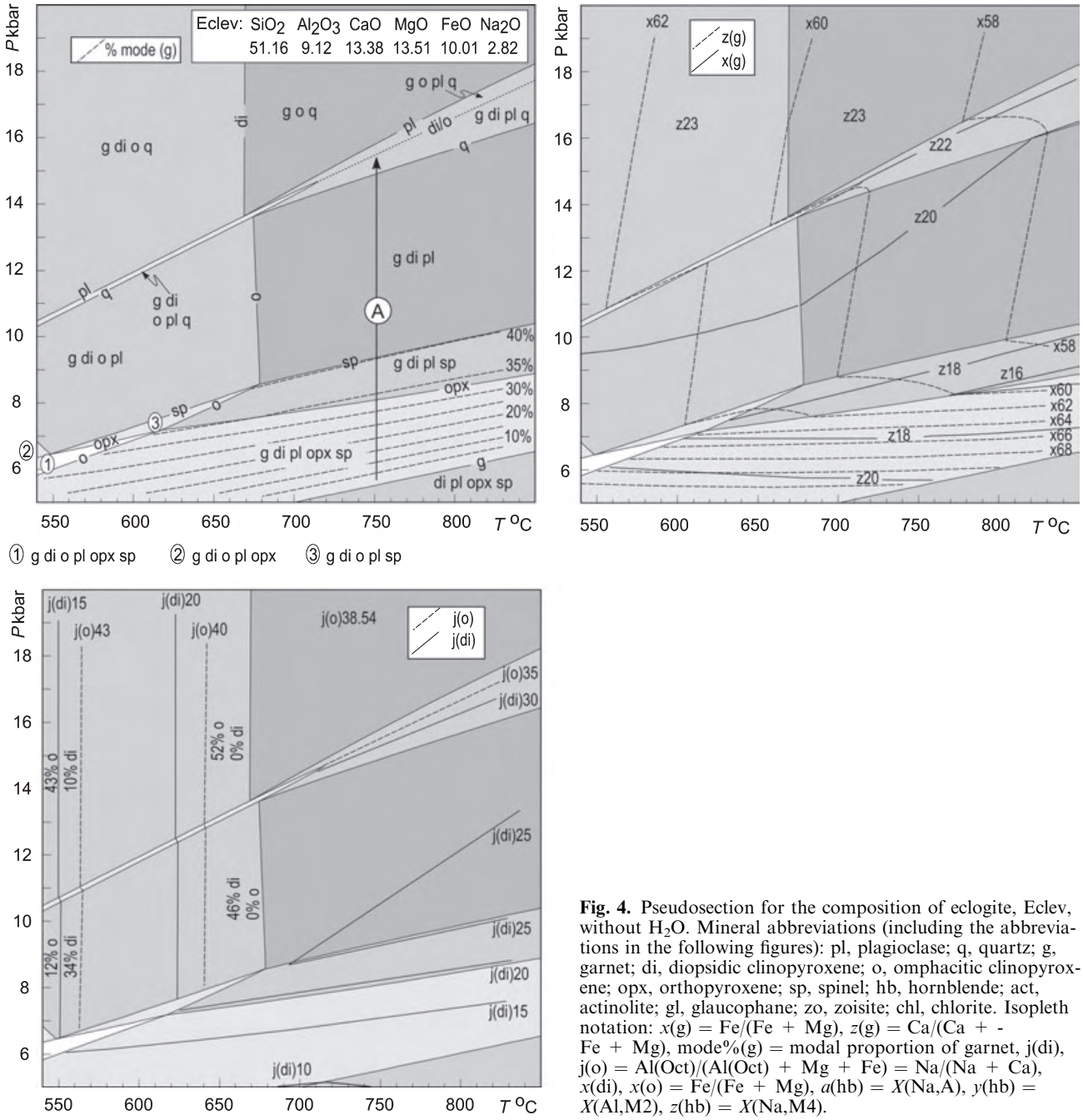

Fig. 4. Pseudosection for the composition of eclogite, Eclev, without H_2O. Mineral abbreviations (including the abbreviations in the following figures): pl, plagioclase; q, quartz; g, garnet; di, diopsidic clinopyroxene; o, omphacitic clinopyroxene; opx, orthopyroxene; sp, spinel; hb, hornblende; act, actinolite; gl, glaucophane; zo, zoisite; chl, chlorite. Isopleth notation: $x(g) = Fe/(Fe + Mg)$, $z(g) = Ca/(Ca + -Fe + Mg)$, mode%(g) = modal proportion of garnet, j(di), $j(o) = Al(Oct)/(Al(Oct) + Mg + Fe) = Na/(Na + Ca)$, $x(di)$, $x(o) = Fe/(Fe + Mg)$, $a(hb) = X(Na,A)$, $y(hb) = X(Al,M2)$, $z(hb) = X(Na,M4)$.

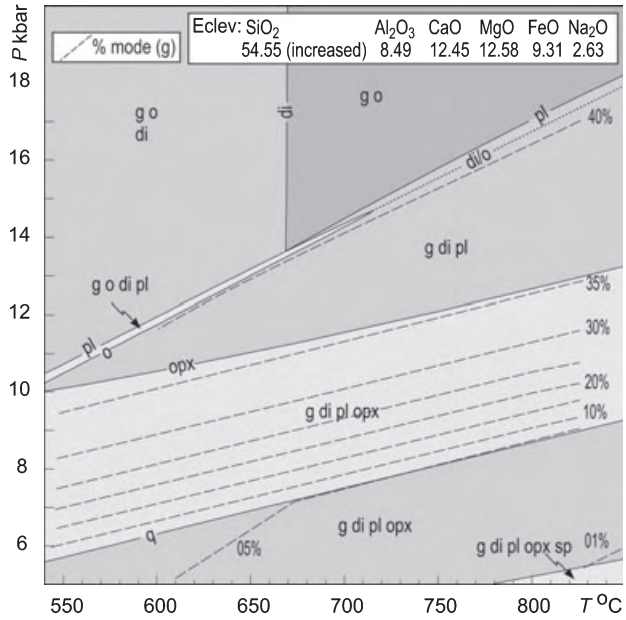

Fig. 5. Pseudosection for the composition of eclogite, Eclev, without H_2O and with increased SiO_2 content to show the importance of SiO_2 undersaturation (in Fig. 4) on the calculated equilibria.

The dry pseudosection in Fig. 4 shows that garnet can grow on the prograde path (for example path A) only in the presence of spinel. However, the z(g) (see caption of Fig. 4 for notation and abbreviations) of such garnet is too low [z(g) = 0.17–0.20] and cannot explain the observed garnet zoning in the sample studied. The peak conditions are not well constrained, but lie in the vicinity of j30 and j35 in Fig. 4, where the composition of garnet does correspond approximately to the observed z(g) rim value. The dry pseudosection (Fig. 4) may explain the formation of the diopsidic clinopyroxene-plagioclase symplectites that indicate decompression, but cannot produce amphibole relationships and does not provide information on the temperature during the retrograde path.

H_2O-saturated *P–T* pseudosection

An H_2O-saturated pseudosection is applicable to the prograde path only if the eclogite protolith was H_2O saturated. Then it would also be H_2O saturated at the peak, becoming H_2O undersaturated at the start of decompression (e.g. Guiraud *et al.*, 1996, 2001; Carson *et al.*, 1999). An H_2O-saturated pseudosection is only applicable to the retrograde path if H_2O infiltration occurs to keep the rock completely hydrated.

The stability of hydrous minerals modifies the pattern of anhydrous assemblages in the dry pseudosection, except at high temperature and pressure (Figs 6 & 7). Zoisite is stable in the low-temperature part up to *c.* 710 °C. The low-temperature/high-pressure side is characterized by the presence of two and three amphibole fields, involving glaucophane, actinolite and hornblende, with these names being used *sensu lato*. Accordingly, actinolite can range in composition towards winchite and edenite, glaucophane towards nyboite, and hornblende can range towards pargasite, tschermakite, barroisite and even sadanagaite; when the three amphiboles coexist, hornblende has higher A-site Na than the other amphiboles, and intermediate M4-site Na and M2-site Al (see Dale *et al.*, 2005, for a detailed discussion). The one-amphibole field, with only hornblende present, starts with the disappearance of actinolite at *c.* 550–650 °C at low and medium pressure and at *c.* 700 °C at high pressure. Plagioclase is stable on the high-temperature side of the plagioclase-in line that heads diagonally from the low-pressure/low-temperature to the high-pressure/high-temperature side of the pseudosection. Garnet is stable on the high-pressure side of the garnet-in line and clinopyroxene is present in most fields of the *P–T* range presented, with two-clinopyroxene fields at *c.* 16–17 kbar and below *c.* 715 °C. The assemblages at the high-temperature side below *c.* 16 kbar and on the low-pressure/high-temperature side are quartz-undersaturated, which has a major effect on the mineral stabilities in comparison with quartz-saturated conditions. The assemblages on the high-temperature side of the pseudosection may be metastable with respect to assemblages involving melt, or at least will have melt in them. Although not well constrained by experiment, an estimate for the (K_2O-free) NCFMASH wet solidus at intermediate pressures is of the order of 750–800 °C (e.g. Wolf & Wyllie, 1994; Pattison, 2003). That leucosome-bearing partially melted granulite facies metabasic rocks have the same assemblages as shown on Fig. 6, suggests that the topology of the phase relationships is similar, that the field boundaries may not move much, and also that the proportion of melt in this *P–T* range is not large (e.g. Wolf & Wyllie, 1994).

The prograde history of eclogite involves the progressive breakdown of hydrous minerals and eventually the growth of clinopyroxene and garnet. The garnet growth zoning depends on the fields in which garnet growth occurred via the equilibrium between garnet and the other minerals involved, and therefore on the precise *P–T* path. In the *P–T* range presented, these fields involve, with increasing temperature, as hydrous minerals two and three amphibole fields with zoisite (without plagioclase), hornblende-zoisite (without plagioclase) and hornblende (with plagioclase). Garnet grown along path A may include zoisite, hornblende, and clinopyroxene while garnet grown along path B may include plagioclase, hornblende and clinopyroxene. Garnet growth zoning resulting from paths A and B, for garnet modal increase increments of 5% converted to radius, is presented in Fig. 8. The profile resulting from path A under hydrous conditions shows continuous decrease in z(g) and x(g) from core to rim, while the profile

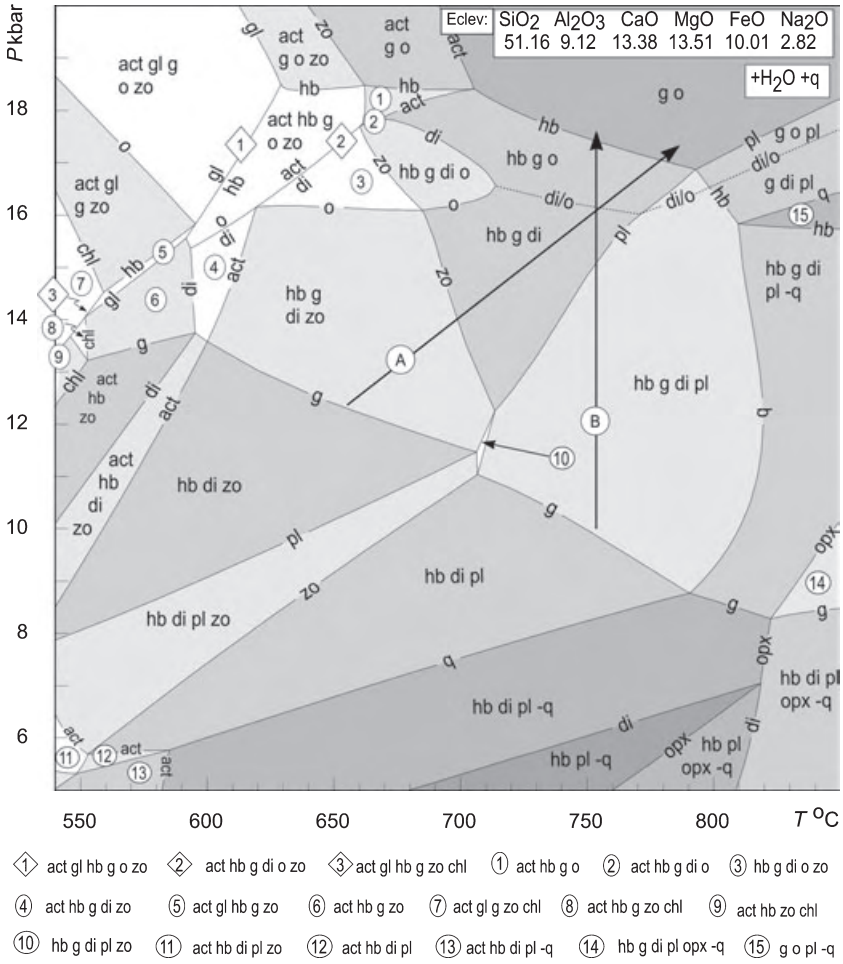

Fig. 6. Pseudosection for the composition of the eclogite, Eclev, calculated for H_2O- and quartz-saturated conditions, -q denotes quartz-absent assemblages. Garnet profiles resulting from the growth along paths A and B are shown in Fig. 8.

resulting from path B exhibits a continuous decrease in x(g) and a plateau in z(g) in the core with slight z(g) increase that is followed by z(g) decrease towards the rim (Fig. 8).

The observed inclusions in garnet are hornblende, plagioclase and omphacitic clinopyroxene, and the observed garnet zoning best correlates with path B. This suggests that the prograde path involved essentially isothermal burial within the plagioclase-hornblende stability field at the relatively high temperature of *c*. 750 °C. The effect of H_2O content – being less than that for H_2O saturation – on the relative stability of zoisite, plagioclase and garnet, and on the garnet zoning along a path at lower temperature is examined below. Prograde along path B, the mineral assemblage evolved until all amphibole was consumed and the rock entered the garnet-clinopyroxene field at *c*. 750 °C and 17–18 kbar with the garnet rim composition corresponding to the predicted value. From this point, if the rock continued to higher *P–T*, it traverses a field with little thermobarometric pseudosection-based information, as the modes of garnet and omphacite do not change. The main concern therefore is whether it is possible to recognize if the sample was heated further and, if it was, what was the maximum temperature. A possible answer is provided by garnet-clinopyroxene Fe-Mg exchange thermometry, but as the x(di) and x(g) isopleths in the g-cpx and g-cpx-pl fields have large spacing, the thermometric information will not be strong.

At the peak, the assemblage is anhydrous and at the beginning of decompression will become H_2O-undersaturated at the *P–T* where hydrous minerals would become stable if H_2O were available. The formation of diopsidic clinopyroxene-plagioclase symplectites was shown above to be consistent with decompression on a path in the dry pseudosection. However, retrograde amphibole-plagioclase intergrowths suggest that the rock was rehydrated in the amphibole stability field during decompression. Amphibole and plagioclase compositions tend to correspond to the calculated isopleths on the high-temperature side of the hb-g-cpx-pl-q field and to a pressure of 11–13 kbar. The upper stability limit of amphibole cannot be calculated in the absence of an appropriate melt model, but experimental data would

suggest that it is in excess of 900 °C (e.g. Wolf & Wyllie, 1994; Rapp, 1995).

P–M(H_2O) pseudosections

The *P–M*(H_2O) pseudosections were constructed to qualify the above conclusions drawn from the *P–T* diagram for H_2O-saturated conditions. For decreasing H_2O content, the assemblages contain lower modal proportions of hydrous minerals and are replaced progressively by anhydrous minerals.

Prograde evolution: P–M(H_2O) pseudosection at 650 °C

The effect of H_2O-undersaturation on the relative stability of zoisite, plagioclase and garnet was considered in order to verify whether the observed garnet zoning and inclusions of plagioclase could also be explained by a prograde path at lower temperature (Fig. 9).

With increasing pressure at 650 °C, for H_2O-saturated conditions, quartz appears, then zoisite, followed by plagioclase disappearing and then garnet

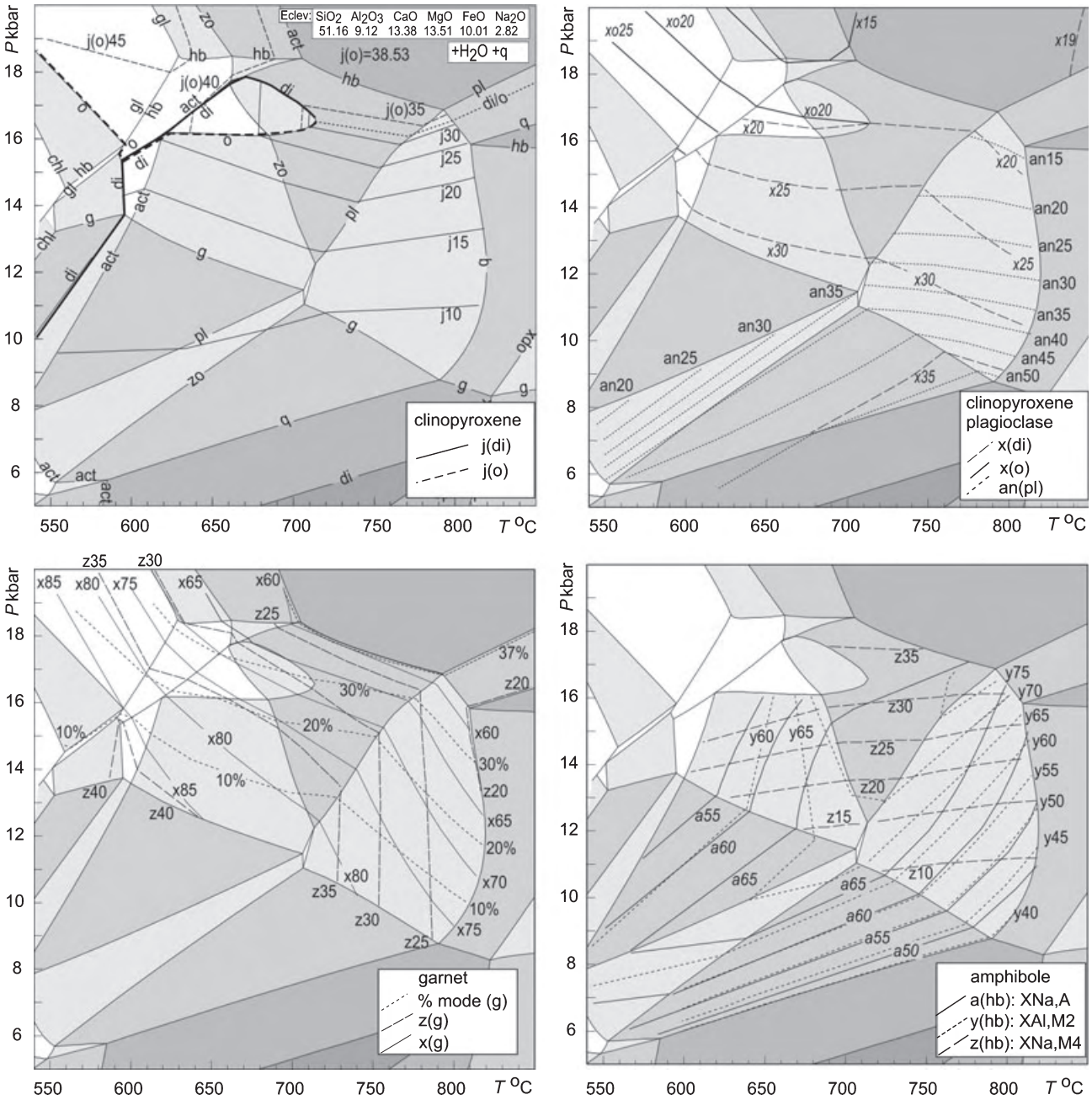

Fig. 7. H_2O-saturated pseudosection from Fig. 6 contoured for modal and compositional isopleths. See caption of Fig. 4 for notation and abbreviations. Thick dashed line is omphacite-out, thick full line is diopside-out.

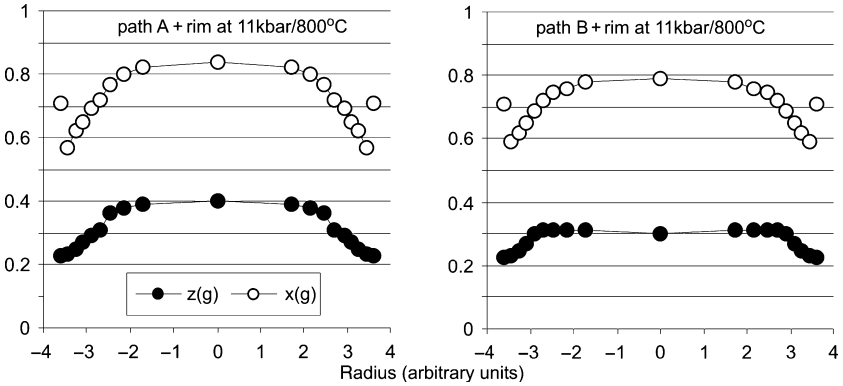

Fig. 8. Calculated garnet profiles resulting from growth along paths A and B from Fig. 6. Garnet growth increments of 5 modal% are converted into radius (in arbitrary units). Rims in profiles represent the compositions towards which garnet may equilibrate after decompression. Profile from path B corresponds to the measured garnet profile (Fig. 3).

appears. For H_2O-undersaturated conditions, garnet is present in all fields, and, with increasing pressure, quartz appears, plagioclase disappears, zoisite appears and eventually the rock becomes H_2O saturated at high pressure. In the H_2O-undersaturated fields, garnet grows a little in the plagioclase-present fields (5–7 modal%) and can therefore include plagioclase (and also clinopyroxene and hornblende). At high pressure, garnet can include in addition zoisite and actinolite, but not plagioclase. The garnet profile exhibits first an increase in z(g) with the starting value dependent on the pressure and degree of H_2O undersaturation [in the range of $z(g) = 0.16$ and 0.38]. After reaching the zoisite-in line and H_2O-saturation line, z(g) decreases to $z(g) = 0.30$. This equilibrium evolution of the rock in the absence of a fluid phase may not happen, unless deformation occurs causing recrystallization (Guiraud *et al.*, 2001). For an H_2O-undersaturated protolith and in the absence of deformation it is likely that the original protolith assemblage is preserved until the H_2O saturation line is reached, and then the metastably preserved minerals would be overgrown by garnet. Such garnet would appear as a rim on already-present garnet cores (e.g. from a magmatic or from another metamorphic event) or as new grains in the matrix. Depending from where the H_2O saturation line is reached, the first newly formed garnet has the z(g) composition in the range from *c.* 0.38 to 0.30.

The H_2O-saturated protolith follows the H_2O saturation line at *c.* 5.2 mol.% of H_2O up to *c.* 9 kbar. There, with the appearance of zoisite, the rock becomes H_2O-undersaturated following a vertical path on Fig. 9, unless fluid infiltration occurs. It is likely that the assemblage from this point (hb-di-pl) is preserved metastably until the H_2O saturation line is again reached at 13–14 kbar. There, garnet appears, increases its modal proportion to 15% and overgrows metastably-preserved plagioclase (and clinopyroxene and hornblende) and also newly grown zoisite. However, z(g) of such a garnet is 0.38 which is too high compared with the observed grossular content in the garnet cores of the sample studied, but such an explanation of compound pl-zo-di-hb inclusions may be applicable to other eclogite examples.

For an H_2O-undersaturated protolith, it is therefore possible, for example, for a garnetiferous amphibolite with hb-g-cpx-q-pl to persist metastably up to the H_2O saturation line and from this point dehydrate and evolve in equilibrium. The observed increase in grossular content near the garnet rim to 33% followed by grossular decrease is therefore possible with a path at *c.* 650 °C under H_2O-undersaturated conditions (between 2 and 4 modal% H_2O). In this interpretation, the garnet cores with amphibole and plagioclase inclusions would have to be preserved from a previous metamorphic (or magmatic) event and the boundary with the new grossular-richer overgrowth smoothed diffusively. The garnet rim could include metastably preserved plagioclase too. We consider this possibility to be unlikely for the sample studied, because for example the x(g) zoning would then be expected to be more smoothed than z(g).

Prograde evolution: P–M(H_2O) pseudosection at 730 °C

A prograde path outside the zoisite stability field was studied in a *P–M*(H_2O) pseudosection at 730 °C (Fig. 10). The important effect of H_2O undersaturation is to shift the quartz-out line to higher pressure. This induced quartz undersaturation stabilizes orthopyroxene to higher pressure compared with hydrous conditions, stabilizes spinel for very H_2O-undersaturated conditions below 9 kbar and extends the stability of garnet to lower pressure.

A rock that is H_2O saturated at the beginning of burial at 730 °C, for example, through its own dehydration reactions, or through dehydration reactions in surrounding metasediments, follows the H_2O saturation line and progressively dehydrates along the arrow in Fig. 10. Garnet would start to grow at *c.* 10.5 kbar with the composition of $z(g) = 0.34$ and $x(g) = 0.84$. With increasing pressure, the grossular

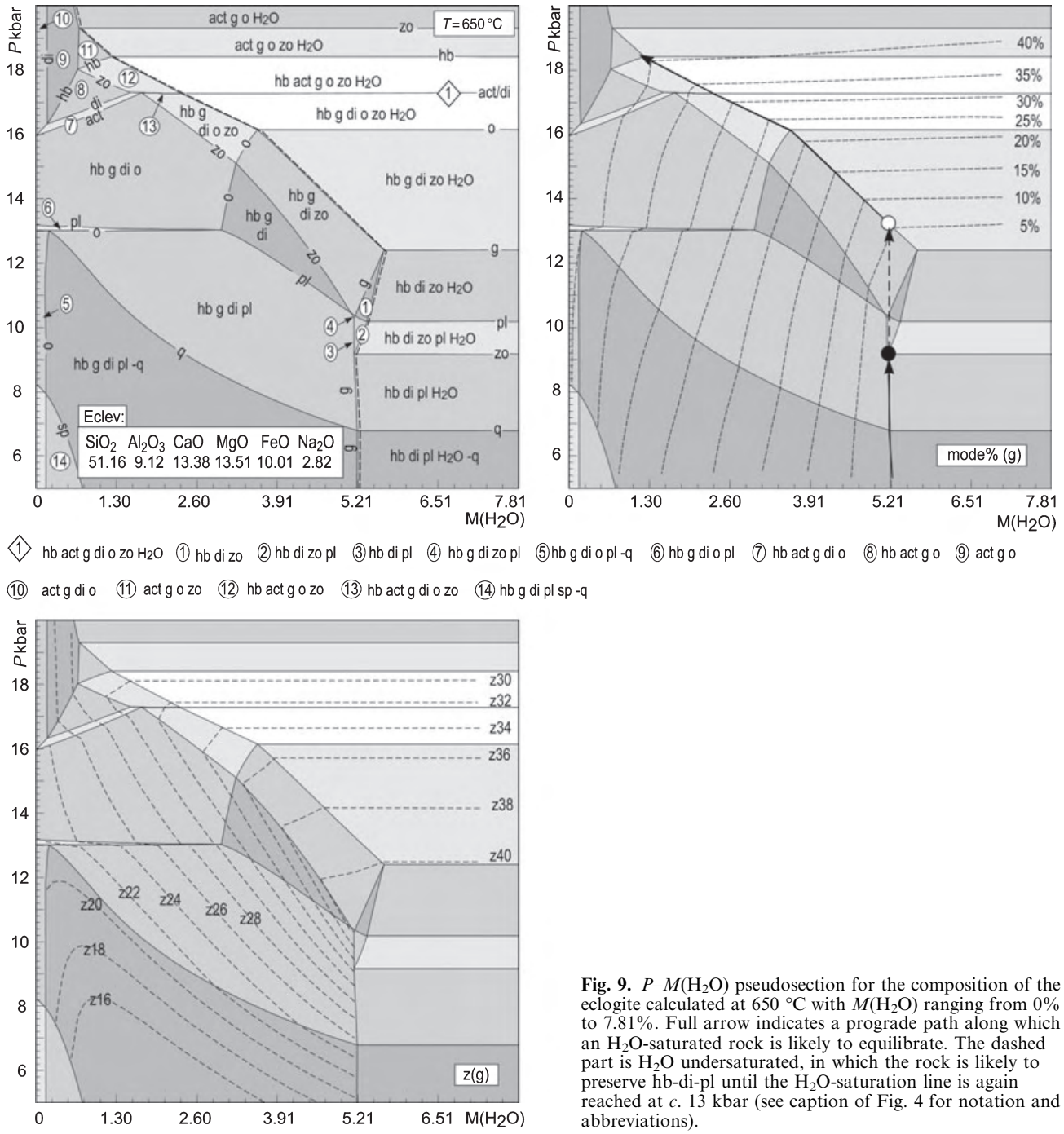

Fig. 9. *P–M*(H_2O) pseudosection for the composition of the eclogite calculated at 650 °C with *M*(H_2O) ranging from 0% to 7.81%. Full arrow indicates a prograde path along which an H_2O-saturated rock is likely to equilibrate. The dashed part is H_2O undersaturated, in which the rock is likely to preserve hb-di-pl until the H_2O-saturation line is again reached at *c*. 13 kbar (see caption of Fig. 4 for notation and abbreviations).

content first increases up to $z(g) = 0.35$, then from the plagioclase-out line decreases down to $z(g) = 0.25$; $x(g)$ decreases continuously to 0.60. A garnet profile that results from growth in this sequence of assemblages, but at slightly higher temperature is presented in Fig. 8. The effect of conversion of garnet modal content into radius (in arbitrary units) reproduces almost exactly the garnet profile from the sample studied, even with the slight increase in $z(g)$ near the rim.

Retrograde evolution: P–M(H_2O): pseudosection at 785 °C

The effect of H_2O undersaturation on the mineral assemblages during decompression was studied in a *P–M*(H_2O) pseudosection at 785 °C (Fig. 11). The consequence of a lower H_2O content is the earlier consumption of quartz from the assemblage on decompression. Orthopyroxene forms below 11 kbar and on further decompression garnet disappears, but at a lower pressure than under H_2O-saturated condi-

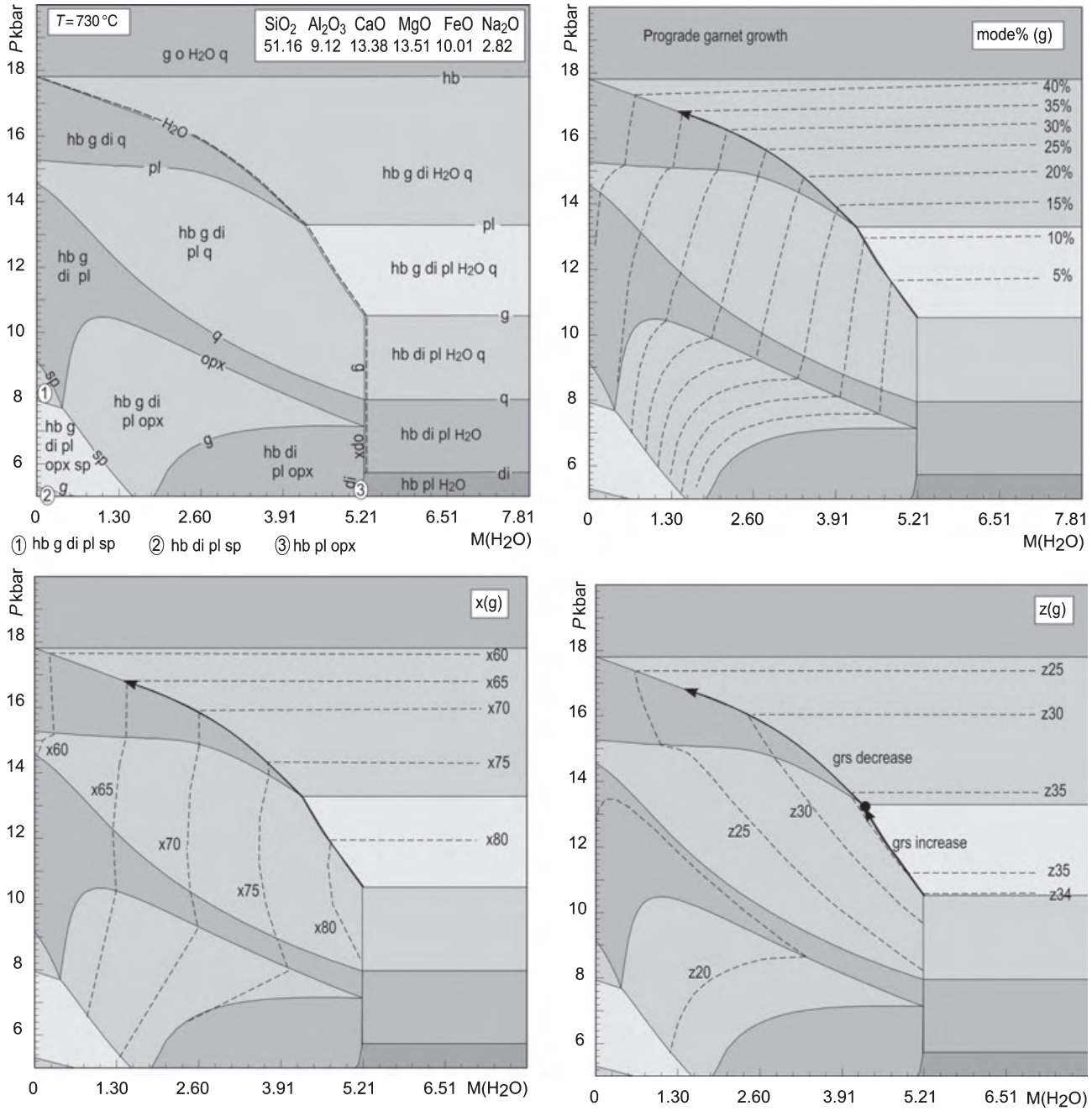

Fig. 10. *P–M*(H_2O) pseudosection for the composition of the eclogite calculated at 730 °C with *M*(H_2O) ranging from 0% to 7.81%. The arrow indicates a prograde path for a H_2O-saturated rock; *z*(g) in the growing garnet first increases up to the full circle and than decreases, while *x*(g) decreases continuously (see caption of Fig. 4 for notation and abbreviations).

tions. At very H_2O-undersaturated conditions, minor spinel forms below 10 kbar. The major effect that H_2O undersaturation has is on the composition of amphibole in the quartz-free fields. In both the hb-g-cpx-pl-q-H_2O and hb-g-cpx-pl-q fields *y*(hb) decreases during decompression. However, the slope of the *y*(hb) isopleths change dramatically across the quartz-out line. On loss of quartz for a particular H_2O content, the *y*(hb) remains constant during decompression. Below the opx-in line the *y*(hb) even increases with further decompression. A similar effect is observed in the trend of the *a*(hb) isopleths. The effect on the *z*(hb) isopleths is less: on decompression, the *z*(hb) decreases less in H_2O-undersaturated fields than under H_2O-saturated conditions. Increasing quartz undersaturation with decreasing H_2O content also affects the

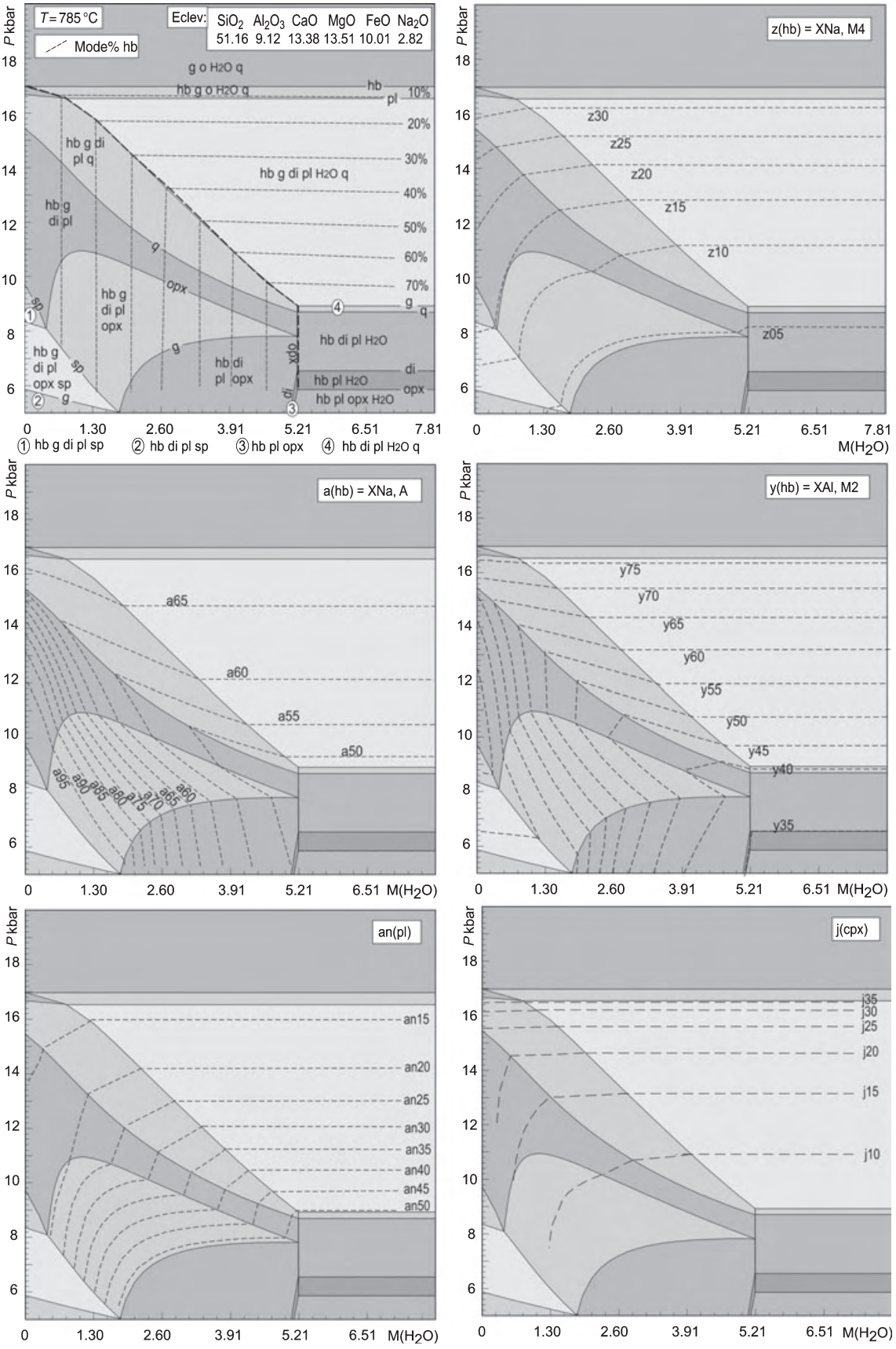

composition of plagioclase: it becomes less-anorthite rich and clinopyroxene becomes more jadeite rich.

From the amphibole modal isopleths it may be concluded that the rock studied, having approximately observed 10 modal% of amphibole, corresponds to a water content of a maximum of 1 mol.% of H_2O. The observed composition of the amphibole, in terms of a(hb) = A-site Na = 0.49–0.64, z(hb) = (M4-site Na)/2 = 0.11–0.18, reflects this level of H_2O undersaturation, in the pressure range of 10–13 kbar. Whereas the observed M2-site Al is too low compared with the calculated y(hb) isopleths, if the observed M2-site Al and Fe^{3+} are combined they give 0.61–0.66, comparing favourably with the calculated y(hb) in the suggested pressure range.

On decompression, the rock became domainal, with the subsequent textural development around the omphacitic clinopyroxene and the garnet being different. These domains will have formed and evolved as the garnet and clinopyroxene reacted, and reacted with the infiltrating fluid, during decompression. Modelling such a situation, controlled by chemical potential gradients as well as the H_2O influx, is beyond the scope of this study. As a consequence, the modelling in this section can be applied only in a general way. Nevertheless, the conclusion that the rock did not become H_2O saturated during fluid influx, and that this fluid influx took place at *c*. 10–13 kbar appears to be defensible.

GARNET-CLINOPYROXENE THERMOMETRY

The established approach for estimating temperatures of formation of eclogites is garnet-clinopyroxene (g-cpx) Fe-Mg exchange thermometry. Whereas such thermometry in principle should be performable via isopleths on the pseudosections, the g-cpx thermometer is sufficiently sensitive to the chemistry of the minerals (e.g. ferric iron in clinopyroxene, if only via its effect on the content of ferrous iron) that a thermometer that does not take account of such things will not work. The calibration of the g-cpx thermometer of Krogh Ravna (2000) is used here, but with a new assessment of minimum uncertainties associated with g-cpx temperatures. This calibration is the best available, but it should be amenable to improvements using dataset estimates of the entropy and volume changes for the exchange reaction using Holland & Powell (1998), and also van Laar activity coefficients of the end-members (Holland & Powell, 2003).

It is not new to point out that uncertainties on g-cpx temperatures are generally under-reported (Krogh Ravna & Terry, 2004), at least partly because of ignored contributions from estimating ferric iron (Sobolev *et al*., 1999; Schmid *et al*., 2003), and it is this aspect that is focused on here. It is assumed that the standard deviation on a calculated temperature stemming from the calibration in Krogh Ravna (2000) is, at a minimum, 30 °C (from propagating the uncertainty on the leading term, A, in Table 3 of Krogh Ravna, 2000).

A key point is that the common practice of assuming that there is no ferric iron in the clinopyroxene does regularize the calculation of temperature by removing the element of variability introduced by this estimation, but it strongly *biases* the calculated temperature on the high side (i.e. temperature is seriously overestimated). This point can be easily shown, as in Fig. 12, and is obvious given that converting FeO to Fe_2O_3 in a clinopyroxene analysis directly affects the ln $K(D)$ of the exchange reaction.

An average garnet rim analysis is combined with each of 26 clinopyroxene analyses from larger clinopyroxene grains. Analyses from diopsidic clinopyroxene-plagioclase symplectites were not used. The contribution to the uncertainty in temperature arising from the choice of garnet analysis and the estimation of ferric iron in garnet are not included below as they are of second order (although, their inclusion will increase overall temperature uncertainties slightly).

Although error propagation from the weight % (wt%) in a mineral analysis (standard deviation on a wt% is taken to be 1% relative) is the approach commonly used to consider analysis-derived uncertainties, we start by using the approach of Carson & Powell (1997). Given that estimation of ferric iron by charge balance is inherently uncertain, an alternative approach is to *specify* a certain conversion of FeO to Fe_2O_3, x, and then to modify the original analysis (via least squares) to determine the 'best' analysis that is charge balanced for this value of x (Carson & Powell, 1997). Clearly the 'best' analysis is identical to the original analysis when the x for charge balance, x(cb), is specified.

Using the 'best' analysis approach, Fig. 12 shows the dependence of the calculated temperature using the method of Krogh Ravna (2000) on the conversion of FeO to Fe_2O_3, x, for the 26 clinopyroxene analyses, at 18 kbar. The dot along each line corresponds to x(cb). The upward bias on temperature of assuming no ferric iron is clear. The lines form two groups, in fact corresponding directly to Mg# in the clinopyroxene (as the one garnet composition was used to calculate all the lines).

Fig. 11. *P–M*(H_2O) pseudosection for the composition of the eclogite calculated at 785 °C with $M(H_2O)$ ranging from 0% to 7.81%. H_2O-undersaturation on decompression causes SiO_2 undersaturation that is responsible for the stabilization of orthopyroxene at much higher pressure than for H_2O-saturated conditions, and also stabilizes spinel. The modal and compositional variables for amphibole, plagioclase and clinopyroxene are strongly modified with respect to H_2O-saturated conditions (see caption of Fig. 4 for notation and abbreviations).

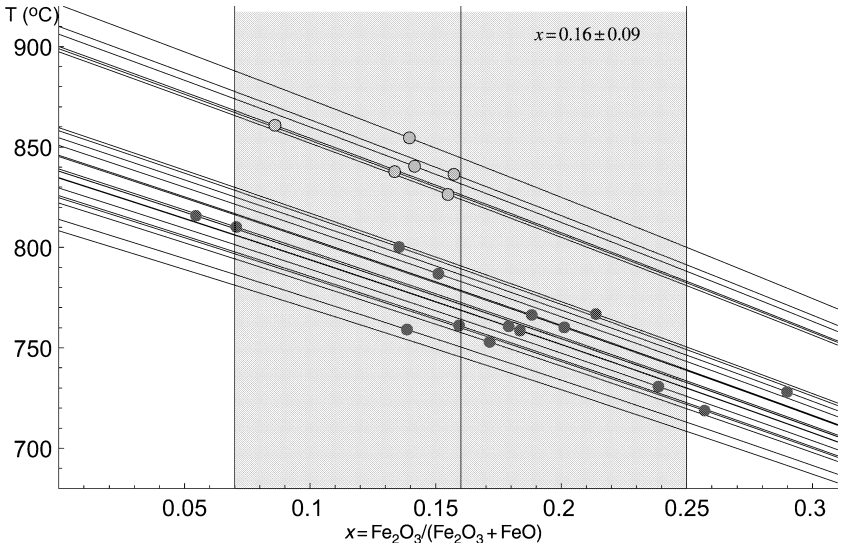

Fig. 12. A 'best analysis' approach to g-cpx thermometry for 26 omphacite analyses combined with one rim garnet composition: the shaded symbol along each line corresponds to the charge-balance value of the conversion of FeO to Fe_2O_3 (see text).

The upper group in Fig. 12 involves clinopyroxene with the lower Mg# and also the more diopsidic composition, being transitional in composition to the diopsidic clinopyroxene in the symplectites. This group gives *higher* temperatures, even though the clinopyroxenes in this group most likely reflect re-equilibration during decompression and presumably cooling. As this group was calculated with 18 kbar, it is interesting to note that the lines come down in temperature as this pressure is decreased, overlapping the top of the main group of lines if 12 kbar is used. Equally, this feature may reflect the fact that these clinopyroxenes were not in equilibrium with garnet (at least not one of the composition used) so that these calculated temperatures are meaningless.

Ignoring the three analyses that gave negative x(cb), the average x(cb) of the remaining 23 clinopyroxene analyses is 0.16 ± 0.09 (2 σ), giving the shaded band on Fig. 12. Using the main group, a temperature range of 710–830 °C is indicated. To get an estimate of the likely uncertainty stemming from ferric estimation using the above estimate of x(cb) = 0.16, an error propagation was undertaken using one of the clinopyroxene analyses, the individual x(cb) of which is close to the average. First, just the 1% relative on the wt% oxides was used, as though there was no information on the uncertainty on x(cb), giving Fig. 13(a), with ±90 °C (2 σ) on the temperature estimate. However using 1% relative on the wt% *and* a standard deviation of 0.045 on x(cb) gives the histogram in Fig. 13(b), with ±40 °C (2 σ) on the temperature estimate. This shows that an effort to combine calculations on several clinopyroxene analyses is worthwhile in terms of the reduction in the temperature uncertainty stemming from ferric estimation.

When the reduced uncertainty, ±40 °C, is combined with the calibration uncertainty, ±70 °C results, still a minimum value for the uncertainty on the calculated temperature given that the contribution from garnet is not included, and that the calibration uncertainty is most likely larger. Adopting a conservative estimate of uncertainty, with a cumulative uncertainty from other

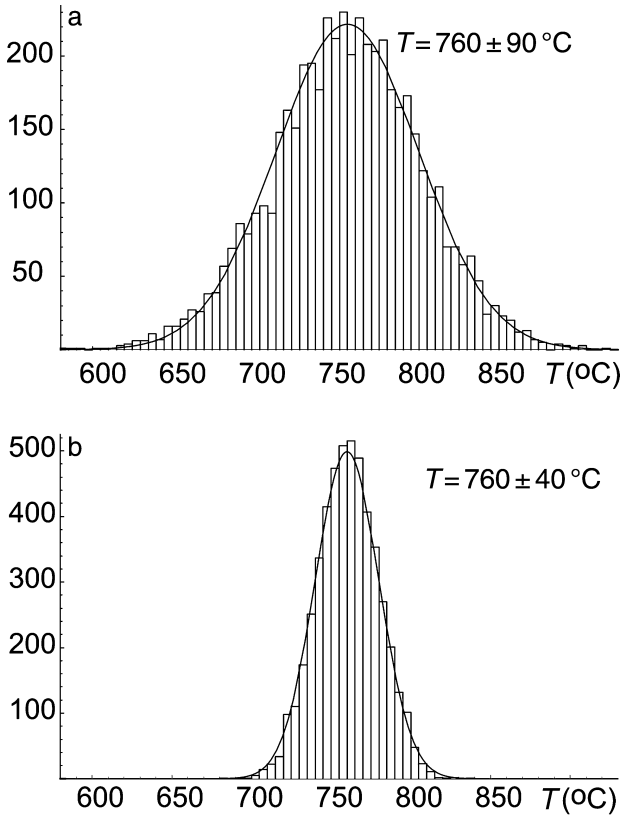

Fig. 13. Monte Carlo simulation of error propagation of the garnet-clinopyroxene Fe-Mg exchange thermometer applied to a particular omphacite-garnet pair in Je0222d; (a) with 1% relative uncertainty on the wt% of the omphacite analysis; (b) with 1% relative uncertainty on the wt% of the omphacite analysis *and* with the estimated value and its uncertainty on the conversion of FeO to Fe_2O_3 (see text).

sources contributing just 25 °C, this rock has a peak metamorphic temperature of, say, 760 ± 90 °C at 18 kbar.

DISCUSSION AND CONCLUSIONS

The findings presented here document an example of *P–T* path determination for a MORB-type eclogite using a pseudosection approach with a recently developed amphibole model, combined with g-cpx thermometry.

While the observed garnet zoning is impossible to obtain under dry conditions, it is compatible with a prograde path in the H_2O-saturated pseudosection (path B, on Figs 6 & 7). The observed garnet zoning is consistent with isothermal burial at 730–750 °C up to *c*. 17–18 kbar under continuous dehydration (Figs 8 & 10). Garnet has apparently grown in the presence of hornblende and its zoning reflects a H_2O-present metamorphic environment during its prograde history. Additionally, from the identity of the trapped inclusions it has grown in the presence of plagioclase rather than zoisite.

There is no pseudosection-based thermobarometric information on a possible increase in pressure or temperature after the prograde disappearance of amphibole above 17–18 kbar. However, garnet-clinopyroxene Fe-Mg exchange thermometry (Krogh Ravna, 2000) gives 760 ± 90 °C, a result consistent with the eclogite not heating up further once it had become amphibole-free.

The decompression occurred in the stability of hornblende and outside the stability of zoisite. The total modal content of amphibole (*c*. 10%) indicates strongly H_2O-undersaturated conditions that allowed the preservation of the majority of the peak assemblage represented by garnet and omphacitic clinopyroxene. The clinopyroxene was decomposed into plagioclase-diopsidic clinopyroxene symplectites and plagioclase-amphibole kelyphites developed around garnet. The composition of amphibole and plagioclase, and the absence of orthopyroxene indicates mineral reaction on decompression down to 11–12 kbar at a similar temperature to that prior to burial.

General implications

Garnet from intermediate-temperature eclogites commonly shows flat grossular cores even if it is zoned in Fe/(Fe + Mg) and/or spessartine, and it has been interpreted as growing prograde (Medaris *et al*., 1995, 1998; O'Brien & Vrána, 1995; Möller, 1998). It is noteworthy, that if the *x*(g) of a garnet profile with prograde flat grossular is diffusively flattened, then such garnet may look like completely diffusively flattened granulite facies garnet and may lead to an overestimation of metamorphic temperature. Similar compositional profiles with flat grossular cores followed by spikes in grossular have been interpreted as possible overgrowths on an older garnet core from another metamorphic event or as the change in the reaction assemblage (Medaris *et al*., 1995; O'Brien, 1997a; Möller, 1998; Will & Schmädicke, 2001). It has been suggested that such prograde garnet has grown under greenschist, amphibolite, eclogite and even under granulite facies conditions (Shervais *et al*., 2003). Here, it has been shown that such a type of garnet zoning with grossular spikes is able to grow under H_2O-saturated conditions along an isothermal burial path at *c*. 730–750 °C, starting to grow in the amphibolite facies at 9–10 kbar and ending its growth at eclogite facies conditions. In this case, the relatively hot start of the *P–T* path is consistent with some current models of the Moldanubian zone involving a Devonian arc and back-arc region before Carboniferous collision (Thompson *et al*., 2001; Schulmann *et al*., 2002, 2005). The mineral assemblage in the eclogite studied is interpreted to have formed during crustal thickening, not in a subduction zone.

The formation of plagioclase-diopsidic clinopyroxene symplectites and amphibole-plagioclase kelyphites around garnet is a well-known effect in eclogites of decompression. Other coronas that are usually interpreted as a granulite facies overprint of eclogite involve formation of orthopyroxene, spinel or olivine, and in the kyanite-bearing eclogites also sapphirine, spinel, corundum and Ca-plagioclase after kyanite (for references, see O'Brien & Rötzler, 2003). In some cases, these assemblages have been accounted for with an increase in temperature after the eclogite facies metamorphism (O'Brien & Vrána, 1995; O'Brien, 1997a,b). Moreover, orthopyroxene + spinel-bearing coronas have been interpreted as a higher-temperature overprint compared with amphibole-plagioclase kelyphite (e.g. Messiga & Bettini, 1990). Here, however, we show that both types of retrograde reaction texture can form along the same general path under different H_2O-undersaturated conditions. In general, textures that have been interpreted to be of granulite facies origin can be formed under amphibolite facies conditions under H_2O-undersaturated conditions, particularly in SiO_2-undersaturated rock compositions.

The approach advocated here for g-cpx thermometry needs to be further investigated and tested elsewhere. On recognition of the strong upward bias of g-cpx temperatures when clinopyroxenes are assumed to be ferric-free, literature examples where this assumption has been made should be re-evaluated, including applications in the Bohemian massif. UHT metamorphic conditions at high pressure have also been inferred for felsic granulites, based on the occurrence of ternary feldspar (for references, see O'Brien & Rötzler, 2003), but this result is disputed based on the interpretation of a magmatic origin for this feldspar (Štípská & Powell, 2005).

In the absence of measurement of ferric iron in the clinopyroxene, the statistical approach used above can

be used to improve uncertainties on calculated temperatures while using a charge-balance calculation for ferric iron. However, this approach does assume that the clinopyroxene involves four cations per six oxygen (as normally applied). As discussed by Proyer *et al*. (2004), this is not an appropriate assumption for UHP eclogites where the omphacitic clinopyroxene may be slightly eskolaitic. In this case standard charge balance calculations will fail, commonly by giving near-zero (or negative) ferrous to ferric conversion, providing a (further) justification for the commonly-indefensible assumption of the clinopyroxene being ferric-free. In general, there is no substitute for a direct measurement of ferric iron for calculations as sensitive as g-cpx thermometry.

ACKNOWLEDGEMENTS

This work was financially supported by the Charles University Grant Agency (No.149/2000/B-GEO/PrF) and the Czech National Grant Agency (No. 205-05-2187). The visit of P.Š. to University of Melbourne was partly funded by the Czech Ministry of Education (No. 24313005). R.P. acknowledges ARC Discovery Grant DP0209461. We gratefully acknowledge V. Böhmová from the Czech Academy of Sciences for operating the microprobe. P.Š. thanks P. Pitra for introducing her to pseudosection calculations, and also for numerous discussions. We acknowledge valuable discussions with R. White.

REFERENCES

Carson, C. J. & Powell, R., 1997. Garnet-orthopyroxene geothermometry and geobarometry: error propagation and equilibration effects. *Journal of Metamorphic Geology*, **15,** 679–686.

Carson, C. J., Powell, R. & Clarke, G. L., 1999. Calculated mineral equilibria for eclogites in CaO-Na_2O-FeO-MgO-Al_2O_3-SiO_2-H_2O: application to the Pouebo Terrane, Pam Peninsula, New Caledonia. *Journal of Metamorphic Geology*, **17,** 9–24.

Carswell, D. A., 1990. Eclogite and the eclogite facies: definitions and classification. In: *Eclogite Facies Rocks* (ed. Carswell, D. A.), pp. 1–13. Blackie, Glasgow.

Cooke, R. A., 2000. High-pressure/temperature metamorphism in the St. Leonhard Granulite Massif, Austria: evidence from intermediate pyroxene-bearing granulites. *International Journal of Earth Sciences*, **89,** 631–651.

Cooke, R. A. & O'Brien, P. J., 2001. Resolving the relationship between high P-T rocks and gneisses in collisional terranes: an example from the Gföhl gneiss-granulite association in the Moldanubian Zone, Austria. *Lithos*, **58,** 33–54.

Dachs, E. & Proyer, A., 2001. Relics of high-pressure metamorphism from the Grossglockner region, Hohe Tauern, Austria: Paragenetic evolution and PT-paths of retrogressed eclogites. *European Journal of Mineralogy*, **13,** 67–86.

Dale, J., Powell, R., White, R. W. & Elmer, F., 2005. A thermodynamic model for clinoamphiboles in Na_2O–CaO–FeO–MgO–Al_2O_3–SiO_2–H_2O–O for petrological calculations. *Journal of Metamorphic Geology*, **23,** 771–791. Doi: 10.1111/j.1525-1314.2005.00609.x

Dirks, P. & Sithole, T. A., 1999. Eclogites in the Makuti gneisses of Zimbabwe: implications for the tectonic evolution of the Zambezi Belt in southern Africa. *Journal of Metamorphic Geology*, **17,** 593–612.

Dudek, A. & Fediuková, E., 1974. Eclogites of the Bohemian Moldanubicum. *Neues Jahrbuch Für Mineralogie-Abhandlungen*, **121,** 127–159.

Elvevold, S. & Gilotti, J. A., 2000. Pressure-temperature evolution of retrogressed kyanite eclogites, Weinschenk Island, North-East Greenland Caledonides. *Lithos*, **53,** 127–147.

Franceschelli, M., Eltrudis, A., Memmi, I., Palmeri, R. & Carcangiu, G., 1998. Multi-stage metamorphic re-equilibration in eclogitic rocks from the Hercynian basement of NE Sardinia (Italy). *Mineralogy and Petrology*, **62,** 167–193.

Franke, W., 1989. Tectonostratigraphic units in the Variscan belt of central Europe. *Geological Society of America, Special Paper*, **230,** 67–90.

Franke, W., 2000. The mid-European segment of the Variscides: tectonostratigraphic units, terrane boundaries and kinematic evolution. In: *Orogenic Processes: Quantification and Modelling in the Variscan Belt, Special Publications, 179* (eds Franke, W., Haak, V., Oncken, O. & Tanner, D.), pp. 35–63. The Geological Society of London, London.

Guiraud, M., Powell, R. & Cottin, J. Y., 1996. Hydration of orthopyroxene-cordierite-bearing assemblages at Laouni, central Hoggar, Algeria. *Journal of Metamorphic Geology*, **14,** 467–476.

Guiraud, M., Powell, R. & Rebay, G., 2001. H_2O in metamorphism and unexpected behaviour in the preservation of metamorphic mineral assemblages. *Journal of Metamorphic Geology*, **19,** 445–454.

Hacker, B. R., Abers, G. A. & Peacock, S. M., 2003. Subduction factory – 1. Theoretical mineralogy, densities, seismic wave speeds, and H_2O contents. *Journal of Geophysical Research–Solid Earth*, **108,** 1–26.

Holland, T. J. B. & Powell, R., 1996. Thermodynamics of order–disorder in minerals. 2. Symmetric formalism applied to solid solutions. *American Mineralogist*, **81,** 1425–1437.

Holland, T. J. B. & Powell, R., 1998. An internally consistent thermodynamic data set for phases of petrological interest. *Journal of Metamorphic Geology*, **16,** 309–343.

Holland, T. & Powell, R., 2003. Activity–composition relations for phases in petrological calculations: an asymmetric multicomponent formulation. *Contributions to Mineralogy and Petrology*, **145,** 492–501.

Krogh, E. J., 1982. Metamorphic evolution of Norwegian country-rock eclogites, as deduced from mineral inclusions and compositional zoning of garnet. *Lithos*, **15,** 305–321.

Krogh, E. J., Oh, C. W. & Liou, J. G., 1994. Polyphase and anticlockwise P-T evolution for Franciscan eclogites and blueschists from Jenner, California, USA. *Journal of Metamorphic Geology*, **12,** 121–134.

Krogh Ravna, E. J., 2000. The garnet-clinopyroxene Fe^{2+}-Mg geothermometer: an updated calibration. *Journal of Metamorphic Geology*, **18,** 211–219.

Krogh Ravna, E. J. & Terry, M. P., 2004. Geothermobarometry of UHP and HP eclogites and schists – an evaluation of equilibria among garnet-clinopyroxene-kyanite-phengite-coesite/quartz. *Journal of Metamorphic Geology*, **22,** 579–592.

Kröner, A., O'Brien, P. J., Nemchin, A. A. & Pidgeon, R. T., 2000. Zircon ages for high pressure granulites from South Bohemia, Czech Republic, and their connection to Carboniferous high temperature processes. *Contributions to Mineralogy and Petrology*, **138,** 127–142.

Marmo, B. A., Clarke, G. L. & Powell, R., 2002. Fractionation of bulk rock composition due to porphyroblast growth: effects on eclogite facies mineral equilibria, Pam Peninsula, New Caledonia. *Journal of Metamorphic Geology*, **20,** 151–165.

Matte, P., Maluski, H., Rajlich, P. & Franke, W., 1990. Terrane boundaries in the Bohemian Massif: Result of large-scale Variscan shearing. *Tectonophysics*, **177,** 151–170.

Medaris, L. G., Jelínek, E. & Mísař, Z., 1995. Czech eclogites: terrane settings and implications for Variscan tectonic evolution of the Bohemian Massif. *European Journal of Mineralogy*, **7,** 7–28.

Medaris, L. G., Fournelle, J. H., Ghent, E. D., Jelínek, E. & Mísař, Z., 1998. Prograde eclogite in the Gföhl Nappe, Czech Republic: new evidence on Variscan high-pressure metamorphism. *Journal of Metamorphic Geology*, **16,** 563–576.

Messiga, B. & Bettini, E., 1990. Reactions behaviour during kelyphite and symplectite formation – a case-study of mafic granulites and eclogites from the Bohemian Massif. *European Journal of Mineralogy*, **2,** 125–144.

Möller, C., 1998. Decompressed eclogites in the Sveconorwegian (-Grenvillian) orogen of SW Sweden: petrology and tectonic implications. *Journal of Metamorphic Geology*, **16,** 641–656.

Möller, C., 1999. Sapphirine in SW Sweden: a record of Sveconorwegian (-Grenvillian) late-orogenic tectonic exhumation. *Journal of Metamorphic Geology*, **17,** 127–141.

O'Brien, P. J., 1997a. Garnet zoning and reaction textures in overprinted eclogites, Bohemian Massif, European Variscides: a record of their thermal history during exhumation. *Lithos*, **41,** 119–133.

O'Brien, P. J., 1997b. Granulite facies overprints of eclogites: short-lived events deduced from diffusion modelling. In: *Precambrian Geology and Metamorphic Petrology, Proceedings 30th International Geological Congress, 17, part II* (eds Qian, X., You, Z., Jahn, B. M. & Halls, H. C.), pp. 157–171.

O'Brien, P. J. & Rötzler, J., 2003. High-pressure granulites: formation, recovery of peak conditions and implications for tectonics. *Journal of Metamorphic Geology*, **21,** 3–20.

O'Brien, P. J. & Vrána, S., 1995. Eclogites with a short-lived granulite facies overprint in the Moldanubian Zone, Czech Republic: petrology, geochemistry and diffusion modelling of garnet zoning. *Geologische Rundschau*, **84,** 473–488.

Page, F. Z., Essene, E. J. & Mukasa, S. B., 2003. Prograde and retrograde history of eclogites from the Eastern Blue Ridge, North Carolina, USA. *Journal of Metamorphic Geology*, **21,** 685–698.

Pattison, D. R. M., 2003. Petrogenetic significance of orthopyroxene-free garnet plus clinopyroxene plus plagioclase +/– quartz-bearing metabasites with respect to the amphibolite and granulite facies. *Journal of Metamorphic Geology*, **21,** 21–34.

Pearce, J. A., 1976. Statistical analysis of major element patterns in basalts. *Journal of Petrology*, **17,** 15–43.

Powell, R., Holland, T. & Worley, B., 1998. Calculating phase diagrams involving solid solutions via non- linear equations, with examples using THERMOCALC. *Journal of Metamorphic Geology*, **16,** 577–588.

Proyer, A., Dachs, E. & McCammon, C., 2004. Pitfalls in geothermobarometry of eclogites: Fe^{3+} and changes in the mineral chemistry of omphacite at ultrahigh pressures. *Contributions to Mineralogy and Petrology*, **147,** 305–318.

Racek, M., Štípská, P., Pitra, P., Schulmann, K. & Lexa, O., 2006. Metamorphic record of burial and exhumation of orogenic lower and middle crust: new tectonothermal model for the Drosendorf window, Bohemian Massif. *Mineralogy and Petrology*, in press.

Rapp, R. P., 1995. Amphibole-out phase boundary in partially melted metabasalt, its control over liquid fraction and composition, and source permeability. *Journal of Geophysical Research*, **100,** 15601–15610.

Schmid, R., Wilke, M., Oberhansli, R. *et al*., 2003. Micro-XANES determination of ferric iron and its application in thermobarometry. *Lithos*, **70,** 381–392.

Schulmann, K., Schaltegger, U., Ježek, J., Thompson, A. B. & Edel, J. B., 2002. Rapid burial and exhumation during orogeny: Thickening and synconvergent exhumation of thermally weakened and thinned crust (Variscan orogen in Western Europe). *American Journal of Science*, **302,** 856–879.

Schulmann, K., Kröner, A., Hegner, E. *et al*., 2005. Geodynamics of eastern margin of the Variscan thickened orogenic root, model based on structural, petrological and new geochronological data. *American Journal of Science*, in press.

Shervais, J. W., Dennis, A. J., McGee, J. J. & Secor, D., 2003. Deep in the heart of Dixie: Pre-Alleghanian eclogite and HP granulite metamorphism in the Carolina terrane, South Carolina, USA. *Journal of Metamorphic Geology*, **21,** 65–80.

Sobolev, V. N., McCammon, C. A., Taylor, L. A., Snyder, G. A. & Sobolev, N. V., 1999. Precise Mossbauer milliprobe determination of ferric iron in rock-forming minerals and limitations of electron microprobe analysis. *American Mineralogist*, **84,** 78–85.

Štípská, P. & Powell, R., 2005. Does ternary feldspar constrain the metamorphic conditions of high-grade meta-igneous rocks? Evidence from orthopyroxene gneisses, Bohemian Massif. *Journal of Metamorphic Geology*, **23,** 627–647. Doi: 10.1111/j.1525-1314.2005.00600.x.

Štípská, P., Schulmann, K. & Kröner, A., 2004. Vertical extrusion and middle crustal spreading of omphacite granulite: a model of syn-convergent exhumation (Bohemian Massif, Czech Republic). *Journal of Metamorphic Geology*, **22,** 179–198.

Thompson, A. B., Schulmann, K., Ježek, J. & Tolar, V., 2001. Thermally softened continental extensional zones (arcs and rifts) as precursors to thickened orogenic belts. *Tectonophysics*, **332,** 115–141.

Tollmann, A., 1982. Großräumiger variszischer Deckenbau im Moldanubikum und neue Gedanken zum Variszikum Europas. *Geotektonische Forschungen*, **64,** 1–91.

Wei, C. J., Powell, R. & Zhang, L. F., 2003. Eclogites from the south Tianshan, NW China: petrological characteristic and calculated mineral equilibria in the Na_2O- CaO-FeO-MgO-Al_2O_3-SiO_2-H_2O system. *Journal of Metamorphic Geology*, **21,** 163–179.

White, R. W., Powell, R. & Holland, T. J. B., 2001. Calculation of partial melting equilibria in the system Na_2O-CaO-K_2O-FeO-MgO-Al_2O_3-SiO_2-H_2O (NCKFMASH). *Journal of Metamorphic Geology*, **19,** 139–153.

Will, T. M. & Schmädicke, E., 2001. A first find of retrogressed eclogites in the Odenwald Crystalline Complex, Mid-German Crystalline Rise, Germany: evidence for a so far unrecognised high-pressure metamorphism in the Central Variscides. *Lithos*, **59,** 109–125.

Will, T., Okrusch, M., Schmädicke, E. & Chen, G. L., 1998. Phase relations in the greenschist-blueschist-amphibolite-eclogite facies in the system Na_2O-CaO-FeO-MgO-Al_2O_3-SiO_2-H_2O (NCFMASH), with application to metamorphic rocks from Samos, Greece. *Contributions to Mineralogy and Petrology*, **132,** 85–102.

Willner, A.P., Glodny, J., Garya, T.V., Godoy, E. & Massonne, H.J., 2004. A counterclokwise PTt path of high-pressure/low temperature rocks from the Coastal Cordillera accretionary complex of south-central Chile: constraints for the earliest stage of subduction mass flow. *Lithos*, **75,** 283–310.

Wolf, M. B. & Wyllie, P. J., 1994. Dehydration-melting of amphibolite at 10 kbar: the effects of temperature and time. *Contributions to Mineralogy and Petrology*, **115,** 369–383.

Yang, T. N., 2004. Retrograded textures and associated mass transfer: evidence for aqueous fluid action during exhumation of the Qinglongshan eclogite, Southern Sulu ultrahigh pressure metamorphic terrane, eastern China. *Journal of Metamorphic Geology*, **22,** 653–669.

Received 23 March 2005; revision accepted 9 August 2005.

J. metamorphic Geol., 2005, **23,** 627–647 doi:10.1111/j.1525-1314.2005.00600.x

Does ternary feldspar constrain the metamorphic conditions of high-grade meta-igneous rocks? Evidence from orthopyroxene granulites, Bohemian Massif

P. ŠTÍPSKÁ[1,2,3] AND R. POWELL[4]
[1]*Institute of Petrology and Structural Geology, Charles University, Albertov 6, 12843, Prague, Czech Republic (stipska@illite.u-strasbg.fr)*
[2]*Czech Geological Survey, Klárov 3, 118 21, Prague, Czech Republic*
[3]*Centre de Géochimie de Surface, UMR CNRS 7516, 1 Rue Blessig, Strasbourg, France*
[4]*School of Earth Sciences, University of Melbourne, Victoria 3010, Australia*

ABSTRACT The presence of ternary feldspar in high-grade meta-igneous rocks, and the recognition of the thermometric significance of this mineral, has led recent researchers to postulate peak metamorphic temperatures in excess of 1000 °C. However, it needs to be established that such ternary feldspar is not in fact a survivor of the original high-temperature crystallization of the igneous protolith. After exsolution, the host and lamellae in the ternary feldspar grains may be stable throughout subsequent history as long as recrystallization does not occur. Such a history may involve rehydration and metamorphism, including H_2O-saturated conditions, with the compositions and proportions of the host and lamellae being modified to reflect the *P–T* conditions experienced. In the case of the high-grade meta-igneous rocks from the Moldanubian of the Bohemian Massif, some samples that contain ternary feldspar preserve a substantial measure of their igneous heritage. Orthopyroxene-bearing granulites not only include types that are barely affected by the metamorphism, but also others that have undergone hydration of the igneous protolith prior to the development of a metamorphic overprint. A key to establishing the igneous origin of the ternary feldspar grains is their preservation in garnet that is either itself igneous, or of a relatively low-temperature metamorphic origin. Applying the logic to the other ternary feldspar-bearing meta-igneous rocks deprives the Moldanubian of its ultrahigh temperature (UHT) metamorphic status.

Key words: Bohemian Massif; garnet zoning; orthopyroxene granulite; ternary feldspar; UHT metamorphism.

INTRODUCTION

Establishing the metamorphic conditions of high-grade metamorphic rocks formed much above 750 °C is difficult because conventional thermobarometric methods, primarily relying on Fe-Mg exchange between minerals, do not return reliable results because of re-equilibration of the minerals on cooling (Fitzsimmons & Harley, 1994; Pattison & Begin, 1994). Ultrahigh temperature (UHT) conditions have been established via the stability of mineral assemblages involving, e.g. sapphirine-quartz (e.g. Kelsey *et al.*, 2004) and pigeonite (e.g. Sandiford & Powell, 1986), but these require the presence of unusual rock compositions (Mg-Al-rich metasediments and metaironstones respectively). However, in these cases, there is no doubt that the UHT mineral assemblages developed are of metamorphic origin, as they are developed in metasedimentary rocks.

The presence of ternary feldspar in meta-igneous rocks has been used to suggest UHT metamorphism in terranes that otherwise have no unambiguous record of UHT conditions, on the assumption that the ternary feldspar is metamorphic (e.g. Bohemian Massif, Carswell & O'Brien, 1993; Snowbird tectonic zone, Snoeyenbos *et al.*, 1995). In contrast, in the UHT Napier Complex in Antarctica (Ellis *et al.*, 1980), there is abundant diverse evidence of extreme metamorphic conditions, including the presence of ternary feldspar in a variety of rock types (e.g. Harley, 1998; Hokada, 2001). Hayob *et al.* (1989) also presented an example of UHT metamorphism established via the presence of ternary feldspar in sillimanite gneiss xenoliths from the deep crust. Whereas ternary feldspar may have a metamorphic origin in some rocks under UHT metamorphic conditions, it is possible that in other cases it formed from high-temperature igneous crystallization and that it has survived subsequent metamorphism.

To address the question of the origin of ternary feldspar in meta-igneous rocks, we use petrography, mineral chemistry and mineral equilibrium methods on meta-igneous rocks from the Bohemian Massif, in the light of the likely igneous and metamorphic processes involved in the origin and evolution of such rocks. The

rocks chosen for study are orthopyroxene-garnet-two feldspar-quartz granulites from the Gföhl unit of the Moldanubian in the Bohemian Massif, henceforth referred to as opx granulites. The current view is that the metamorphism is UHT primarily on the basis of the occurrence of ternary feldspar (O'Brien & Rötzler, 2003 and references therein). We consider the development of mineral assemblages containing ternary feldspar in the context of an igneous–metamorphic history, also contributing to the ongoing discussion of the metamorphic conditions in the Bohemian Massif.

Mineral assemblages in igneous rocks depend on magma chemistry and the P–T of crystallization. Mineral assemblages in metamorphic rocks depend on rock chemistry and the P–T path. Rock chemistry may evolve along the P–T path, particularly as a consequence of addition or loss of H_2O via a fluid or melt. A major control on the origin and evolution of a meta-igneous rock is the H_2O content and the way it changes during the history of the rock. Magmatic rocks involved in a metamorphic process may not equilibrate continuously along a prograde path and may preserve relicts of igneous assemblages, especially if rocks are coarse-grained, deformation is not penetrative, H_2O availability is limited and if the temperature of metamorphism is lower compared with that of magma crystallization. These relicts may be recognized texturally, or from the presence of minerals incompatible with the superimposed metamorphism (e.g. Rubie, 1990). In other cases, magmatic rocks on metamorphism may equilibrate continuously along a prograde path and preserve a peak metamorphic mineral assemblage with no igneous features preserved. Meta-igneous rocks may record only a part of their metamorphic history and metamorphic transformations may not be complete on the scale of a hand specimen or thin section.

For granulite facies metamorphism, the metamorphic mineral assemblage may be similar to an original magmatic mineral assemblage, and so may not be useful for distinguishing these processes. Prior to trying to constraining the metamorphic conditions, the possibility of relicts of the igneous protolith being preserved needs to be addressed. Then the metamorphic overprint may be considered, involving distinguishing prograde and retrograde metamorphic features. Here, to do this, petrographic observations, especially textures, and compositions and zoning of the minerals are combined with predictions arising from mineral equilibria calculations, mainly using pseudosections.

OVERVIEW OF PROCESSES

It is necessary to have a conceptual framework in order to consider the origin and evolution of the mineral assemblages, textures and mineral chemistry of meta-igneous rocks. The metamorphic part of such a framework is outlined in Powell *et al.* (2005), based on a more or less consensual view of an equilibrium model of metamorphism that has been built over recent decades. This view can be extended to igneous crystallization: in essence, it involves the idea that the formation, destruction, new formation and preservation of minerals in different stages of a composite igneous–metamorphic history will largely be dependent on the presence, absence or availability of H_2O and/or melt (e.g. Guiraud *et al.*, 2001; Brown, 2002; White & Powell, 2002), and also on the presence or absence of deformation, in its ability to recrystallize and destroy pre-existing mineral grains and also to promote re-equilibration of mineral assemblages.

In an igneous context, a working hypothesis is that mineral assemblages tend to re-equilibrate in the presence of melt over the crystallization interval, the focus here being on plutonic rocks. Mineral assemblages will then be preserved from the vicinity of the solidus temperature where the last melt crystallized, or from an 'effective' solidus temperature where most melt has crystallized (or residual melt has been lost). Considering more felsic melts, the solidus temperature depends primarily on the amount of H_2O in the magma. The dry solidus is at a very high temperature and the crystallization interval tends to be small. The crystallization interval for hydrous melts is much larger, with the solidus occurring at lower temperature. The probability of preservation of early-crystallized minerals in hydrous melt depends on the amount of H_2O and the resulting evolution of the melt proportion during crystallization. Survival of early-formed crystals is possible if the effective solidus is at a high temperature. However, it is unlikely for H_2O-rich melt, where a continuous re-equilibration of the mineral assemblage down to a relatively low temperature is expected to occur.

Adopting this rationale, the solidus temperature of crystallized magma may be deduced from the magmatic mineral assemblage present in the rock, at least if sufficient mineral assemblage has survived. If a magmatic rock contains only anhydrous minerals, then the melt was dry and had a very high-temperature solidus (or melt loss occurred from the magma at such a temperature). Hydrous mineral assemblages imply a lower effective solidus temperature. During cooling and until the time when the metamorphic history starts, little is likely to happen to this solidus assemblage unless local hydration associated with deformation occurs, e.g. through the development of shear zones. Little is likely to happen to the mineral assemblage of a rock along the P–T path if it contains no hydrous minerals, fluid or melt are not added, and in the absence of deformation.

THERMOBAROMETRIC METHODS

Ternary feldspar

Regardless of whether ternary feldspar in a meta-igneous rock is igneous or metamorphic, it may give

thermometric information with an appropriate calibration and with a successful reintegration of the original feldspar grain from the compositions and proportions of host and lamellae. Aspects of calibration and reintegration are discussed below in the context of understanding the observations made on the ternary feldspar in the opx granulites, which are also relevant to other ternary feldspar applications.

The formulation and calibration of the thermodynamics of feldspar in the system $NaAlSi_3O_8$-$KAlSi_3O_8$-$CaAl_2Si_2O_8$ is a significant step in ternary feldspar thermometry, because the experimental data used in the calibration are at relatively low pressure and temperature with respect to the conditions of formation of the ternary feldspar of interest (Seck, 1971a,b; Elkins & Grove, 1990). Moreover, the pressure and temperature range of the experimental data is small. A substantial extrapolation of the data via thermodynamic equations is involved, with the P–T experimental range being insufficient to support the extrapolation.

Of the main published thermodynamic models, all but one (Holland & Powell, 2003) use a sub-regular model (Fuhrman & Lindsley, 1988; Elkins & Grove, 1990; Benisek *et al*., 2003). Fuhrman & Lindsley (1988) calibrated primarily from Seck's experiments, Elkins & Grove (1990) from their own experiments, and Benisek *et al*. (2003) from both sets. Each of them incorporated available calorimetric and volumetric data to various degrees. However, they all ignored the structural transition in plagioclase, rendering the use of their equations for extrapolation problematic. Holland & Powell (2003) do explicitly model the structural transition, but do not include recent data on the An-Or join, nor fully incorporate available volume data on ternary feldspar. Thus, this model is unlikely to extrapolate well either. In presenting the model, the authors aimed only to show that it interpolated the Elkins & Grove (1990) experiments with a model containing few adjustable parameters. That these differences are significant in terms of extrapolation can be seen in Fig. 1.

A satisfactory model for extrapolation, and thus for thermometry on rocks, is yet to be constructed: ideally, it would involve additional experiments at higher pressures as well as temperatures. An indication of the most acceptable extrapolation, at least at 8 kbar, may be given by the ternary feldspar reintegration data for the Napier Complex of Hokada (2001). Considering the metamorphic temperature to be between 1000 and 1100 °C at 8 kbar (e.g. Kelsey *et al*., 2004), the Fuhrman & Lindsley boundary of the ternary one-phase feldspar field looks to be most appropriate, as also suggested by Hokada (2001). Given that pressure and temperature extrapolations are involved, it is possible that the Fuhrman & Lindsley equation is less appropriate at other pressure and temperature values.

The reintegration of the host and lamellae in ternary feldspar presents its own problems because of the possibility of open-system behaviour amongst various other processes accompanying and following exsolution. Reintegrated feldspar may become more ternary by the action of these processes, thus giving temperatures that are too high. As a background to considering the vectors that represent the way that the composition of a ternary feldspar may move, it is relevant to consider the compositional modification of ternary feldspar grains in general. Prior to the onset of exsolution, compositional change may occur, possibly concomitant with grain growth: such change is non-recoverable in the determination of original feldspar composition. Once exsolution has started, a ternary feldspar grain should be considered as being made up of the two minerals that constitute the host and the lamellae. Attendant on volume and diffusion constraints, the subsequent history of a ternary feldspar grain may show modification of both the compositions and the proportions of the host and lamellae, thus modifying the composition of the ternary grain as a whole. Such effects may well be of a different magnitude in different textural settings, for example between inclusions in garnet and the matrix. An early-formed ternary feldspar grain, in its exsolved form, may survive in a rock that suffers hydration and a prograde-retrograde metamorphic cycle, as long as it is not broken up and/or forced to recrystallize, for example as a consequence of deformation. A ternary feldspar grain in this context may be thought of as a mixture of the phases that constitute the host and lamellae.

Some possible vectors for the compositional modification of ternary feldspar grains are shown in Fig. 2. Of these, most are chemical processes, but for matrix grains in deformed rocks the physical process of the

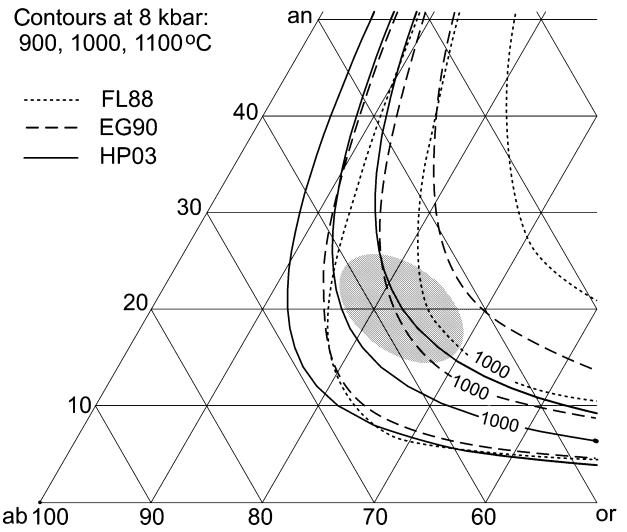

Fig. 1. Comparison of the position of the boundary of the one-phase field in $NaAlSi_3O_8$-$KAlSi_3O_8$-$CaAl_2Si_2O_8$ as a function of temperature calculated with the SOLVCALC program (Wen & Nekvasil, 1994) for the equations of Fuhrman & Lindsley (1988), Elkins & Grove (1990), and using THERMOCALC for the thermodynamic model of Holland & Powell (2003), for FL88, EG90 and HP03 respectively. The shaded field represents a cluster of reintegrated compositions from the samples studied (see also Fig. 7).

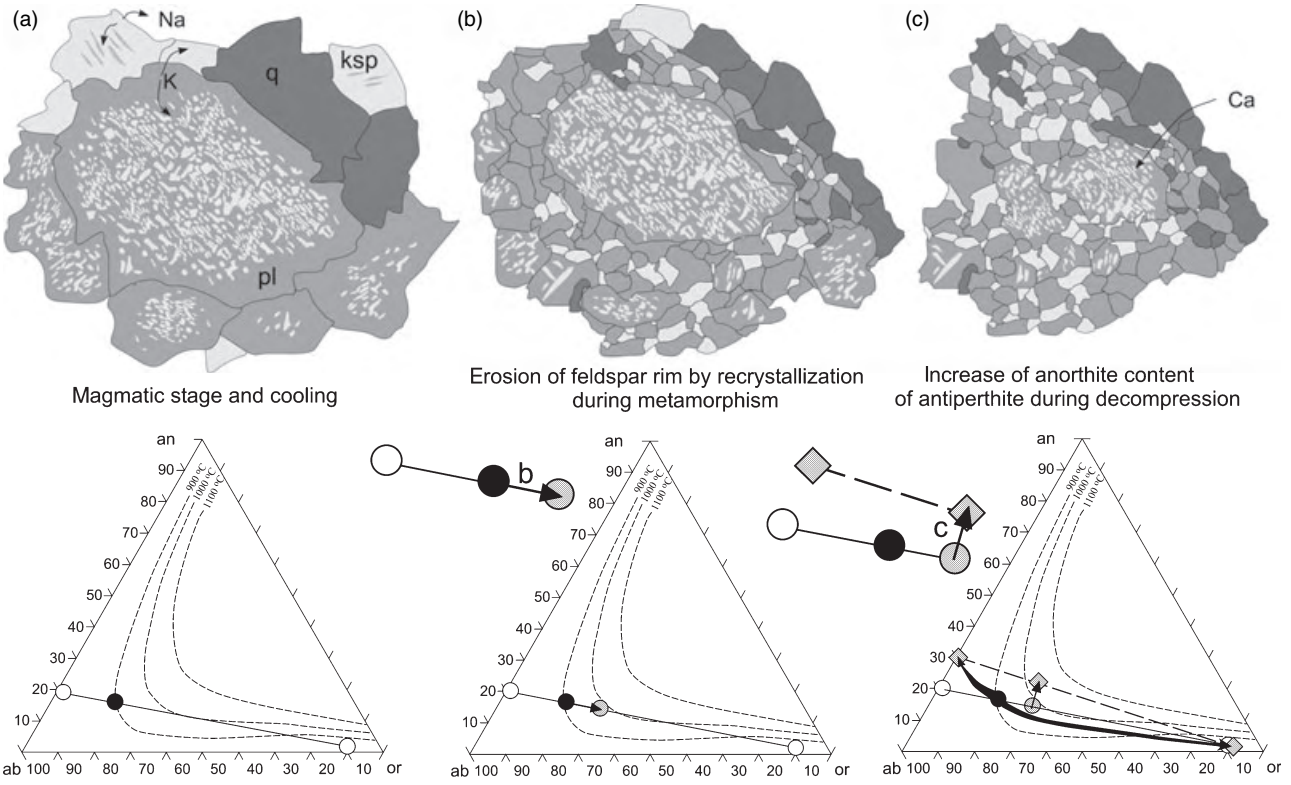

Fig. 2. Vectors indicating the direction of modification of the composition of reintegrated ternary feldspar for the schematically-shown processes. (a) During exsolution an exsolution-free rim originates from which K diffused into the matrix or towards the core of the grain. (b) Recrystallization removes the exsolution-free rim, thus resulting in a lower proportion of plagioclase in the grain. (c) Re-equilibration during decompression causes the plagioclase to become more calcic (best seen at the margin of antiperthite inclusions in garnet).

erosion of the margin of the host (which is commonly lamella-free) would change the composition of grains making them more ternary. Benisek *et al.* (2003) focussed on Na=K exchange processes for composition modification. Whereas there are good diffusion-related reasons that they provide for this being an important type of modification, the supposedly difficult NaSi=CaAl exchange does occur commonly, as reflected in garnet and plagioclase zoning where these minerals contact (e.g. Whitney, 1991). For thermometry, it is necessary to look at many ternary feldspar grains in each rock, and use those grains deduced to have involved the least compositional modification in order to determine the likely original ternary feldspar composition (see Bohlen & Essene, 1977).

Pseudosections

Pseudosections are, for example, *P–T* phase diagrams that represent phase equilibria as a function of *P–T* for a specified rock composition. Such diagrams are excellent for placing an observed mineral assemblage in a *P–T* context, and when diagrams are contoured for mineral proportions and compositions (isopleths), they provide essential information regarding mineral composition zoning. Pseudosections reveal aspects of the *P–T* path that a rock followed, not just the conditions that might be estimated by conventional thermobarometry. In high-grade rocks, pseudosections have the advantage over conventional thermobarometry of not being dependent on deducing the original compositions of the minerals, given that these may have been irretrievably modified by re-equilibration during cooling.

Pseudosection modelling was undertaken with THERMOCALC 3.23 (Powell *et al.*, 1998) and the internally consistent thermodynamic dataset 5.5 (Holland & Powell, 1998: Nov. 2003 upgrade). The datafile coding of the activity–composition relationships of the minerals and melt used in the calculations is that of White *et al.* (2001), with the feldspar model of Holland & Powell (2003). The model used for H_2O-free melt is adapted from that used by White *et al.* (2001). This datafile is available as supplementary material.

EXAMPLE: OPX GRANULITES FROM THE BOHEMIAN MASSIF

Geological setting

The Bohemian Massif is a part of the Variscan orogen in Europe (for a recent review, see Franke, 2000).

From the NW to the SE, it consists of three main domains – Saxothuringian, Moldanubian and Brunovistulian (Fig. 3). The Moldanubian domain is dominated by medium- to high-grade metamorphic rocks intruded by numerous plutons. Large granulite massifs up to 24 km in length, that mostly correspond geochemically to slightly peraluminous, fractionated granitic rocks (e.g. Fiala *et al*., 1987; Janoušek *et al*., 2004), form a substantial part of the high-grade Gföhl unit. Traditionally, these massifs were interpreted as klippe of a distantly sourced nappe, but they are now thought to be exhumed lower crust reaching vertically into the middle crust and being laterally spread at mid-crustal levels (Štípská *et al*., 2004; Schulmann *et al*., 2005). The major rock type of these massifs is a kyanite-K-feldspar-garnet felsic granulite that hosts bodies of garnet peridotites and spinel peridotites associated with mantle eclogites, prograde crustal eclogites, clinopyroxene-garnet granulites and orthopyroxene-garnet granulites (Carswell, 1991; Medaris *et al*., 1995, 1998; Petrakakis & Jawecki, 1995; O'Brien & Rötzler, 2003; Janoušek *et al*., 2004). There is a similar granulite massif within the Saxothuringian domain that contains the granulite 'type locality' (O'Brien & Rötzler, 2003 and references therein), and in the Góry Sowie Massif in Poland with an uncertain geological position (O'Brien *et al*., 1997).

Orthopyroxene commonly occurs in clinopyroxene-garnet granulites as orthopyroxene-plagioclase symplectites, and O'Brien & Rötzler (2003) interpreted all orthopyroxene in high-*P* granulites of Variscan Europe as retrograde, forming during decompression

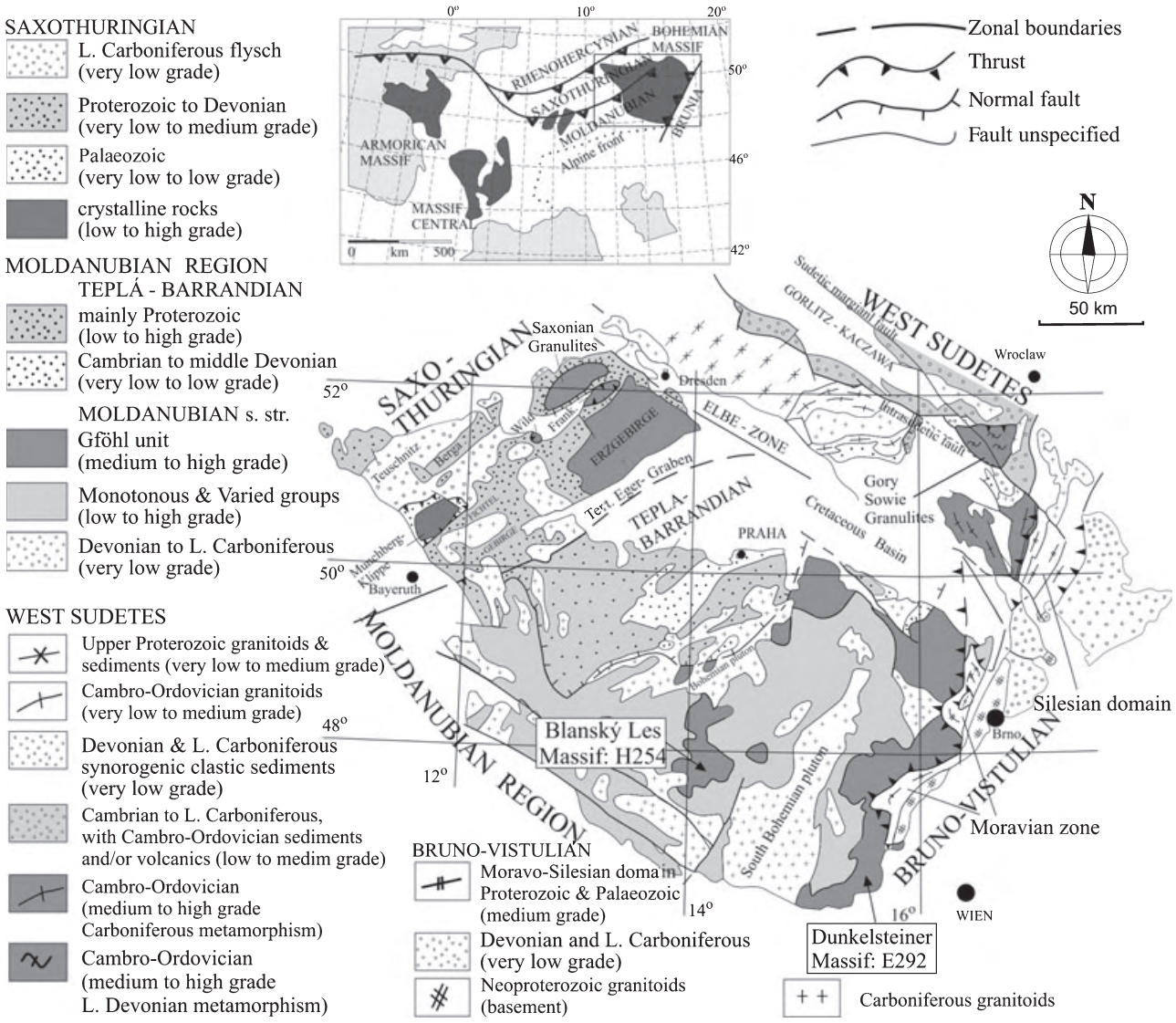

Fig. 3. Outline geological map of the Bohemian Massif with major units shown schematically (modified after Franke, 2000). Location of samples studied is indicated. The upper left inset is the position of the study area in the framework of the European Variscides.

from the metamorphic peak. However, other granulites with sub-idioblastic orthopyroxene were described by Petrakakis & Jawecki (1995) and Petrakakis (1997) from the Dunkelsteiner granulite massif. Garnet-orthopyroxene and orthopyroxene-clinopyroxene granulites in the Líšov Massif were interpreted as syn-metamorphic igneous rocks (Vrána & Jakeš, 1982). Other garnet-orthopyroxene granulites from Lower Austria were interpreted as containing orthopyroxene at the metamorphic peak (Carswell & O'Brien, 1993). All of the pyroxene in orthopyroxene granulites did not form during decompression.

Two types of garnet have been described from orthopyroxene granulites. One porphyroblastic type is characterized by a decrease in grossular from *c*. 30–40% to *c*. 12–15% and increasing x(g) (for abbreviations see caption for Fig. 8) at garnet rims, interpreted to be the result of decompression (Petrakakis & Jawecki, 1995; Owen & Dostal, 1996; Petrakakis, 1997). This porphyroblastic garnet is, in places, resorbed and a plagioclase corona is developed around it, rimmed by an orthopyroxene-rich corona (Owen & Dostal, 1996). Petrakakis (1997) reported a similar garnet, but with decrease in x(g) followed by an increase towards the rim, and he proposed that the initial x(g) decrease may represent prograde zoning. Another type of garnet reported from Opx-granulites is of a coronitic variety that grows around pseudomorphs composed mostly of spinel, anorthite and corundum (Petrakakis & Jawecki, 1995; Owen & Dostal, 1996). This coronitic garnet commonly has idiomorphic boundaries towards matrix and shows zoning similar to the rims of the first type of garnet (Petrakakis & Jawecki, 1995). Unfortunately, neither representative analyses nor the x(g) were reported, but from the compositional profiles x(g) seems to increase slightly (in the order of 0.76 to >0.72). In the study of Owen & Dostal (1996), there is just one representative analysis and a statement that coronitic garnet has a low grossular content (*c*. 13–14%). As the primary interest of our study is in establishing the early stages of the evolution of the garnet-orthopyroxene granulites, samples with coronitic garnet were not considered.

Using ternary feldspar (interpreted as metamorphic) coexisting with kyanite and garnet in kyanite-K-feldspar granulites and garnet-clinopyroxene thermometry in mafic granulites yields peak *P–T* conditions of *c*. 1000 °C at 14–22 kbar (e.g. Carswell & O'Brien, 1993; O'Brien *et al*., 1997; Cooke *et al*., 2000; Cooke, 2000; Kröner *et al*., 2000; Cooke & O'Brien, 2001; Rötzler & Romer, 2001; O'Brien & Rötzler, 2003) and >1000 °C and >25 kbar (e.g. Kryza *et al*., 1996; Klemd & Bröcker, 1999). Given the uncertainty in conventional thermometry, the postulation of UHT conditions hinges primarily on the metamorphic origin of ternary feldspar.

We focus on two samples, E292 and H254. Sample E292 is from one of the dark orthopyroxene-garnet granulite bodies that appear as boudins that are several tens of metres long in the Dunkelsteiner kyanite-K-feldspar granulite massif in Lower Austria (boulders near the quarry Rosenthal, north of Karlstetten; Fig. 3). The sample is divided along a foliation-parallel boundary into two layers that are considered separately – E292a is a coarse-grained variety and E292b is finer grained (Fig. 4a,b). Sample H254 is from a 100 m long boudin of dark granulite that occurs in the kyanite-K-feldspar granulite body of the Blanský Les Massif in the Czech Republic (5.2 km NNW from Český Krumlov and 550 m SSE from the hill Klet'; Fig. 3). For analyses see Table 1.

E292a: coarse-grained layer (Dunkelsteiner Massif)

The coarse-grained layer E292a consists of a 1 mm grain-size felsic matrix formed of antiperthite, perthite, plagioclase, K-feldspar and quartz (95%), with garnet (3%), orthopyroxene (2%), and accessory biotite and ilmenite (Fig. 4a–c). The matrix has no noticeable preferred orientation; some felsic grains exhibit lobate grain boundaries. The coarse antiperthite and perthite grains exhibit variable exsolution of K-feldspar and plagioclase, respectively, and they commonly have exsolution-free rims (Fig. 5a). Smaller grains or elongated intergranular films of plagioclase and K-feldspar tend to be without exsolution features. Myrmekite is locally developed around perthite grains. Garnet up to 1.5 mm in size contains composite inclusions of K-feldspar-plagioclase-quartz (Fig. 5b). A few biotite grains occur within the matrix and at contacts with orthopyroxene.

Antiperthite grains that show most exsolution optically, combined with thin exsolution-free rims, are composed of 26% of K-feldspar and 74% of plagioclase (an = 0.30–34), which yields a reintegrated composition of ab54 an22 or24 (point 1 in Table 2; Fig. 7). Two other grains with abundant exsolution were reintegrated to yield similar compositions (points 2 & 3 in Table 2; Fig. 7). Perthite occurs locally within the cores of K-feldspar grains and is composed of up to 14% of plagioclase exsolution within the K-feldspar host. Such grains yield a reintegrated composition of ab19 an4 or76 (point 4 in Table 2; Fig. 7). The temperature deduced from the antiperthite grains is *c*. 1000 °C at 8 kbar, according to the Fuhrman & Lindsley (1988) calibration.

Garnet (alm60–63 py26–21 grs12–14 sps2–3) has a flat profile with respect to $z(g) = Ca/(Fe + Mg + Ca) = 0.12–0.14$ and $x(g) = Fe/(Fe + Mg) = 0.71–0.75$ (Figs 4f & 6). Orthopyroxene has $x(opx) = Fe/(Fe + Mg) = 0.48–0.50$ and $Al = 0.057–0.074$ pfu. Biotite has $x(bi) = Fe/(Fe + Mg) = 0.45–0.50$ with $TiO_2 = 5.8–6.4$ wt% (0.34–0.37 pfu).

Key observations include the random coarse-grained texture with abundant antiperthite and perthite, presence of orthopyroxene, and the very dry nature of

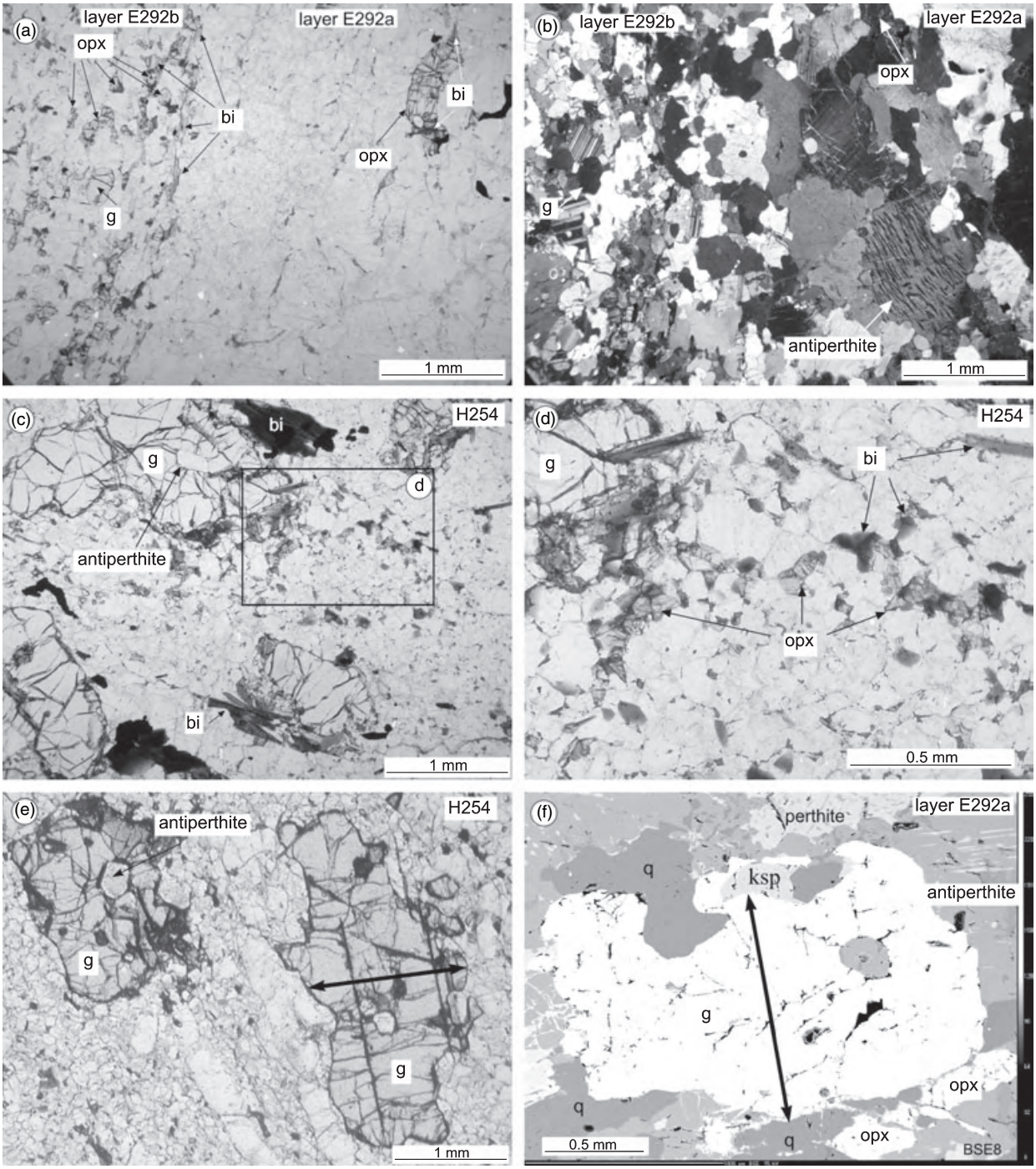

Fig. 4. (a) & (b) Coarse-grained (E292a) and finer-grained (E292b) layers with similar assemblage of orthopyroxene-garnet-feldspar-quartz-biotite. Coarse-grained layer (E292a) contains large antiperthites and perthites and only a few biotite grains. Garnet has different compositions (see text). (c) & (d) Sample H254 is composed of orthopyroxene-garnet-biotite-feldspar-quartz. Felsic matrix is fine-grained and foliation is marked by biotite. Antiperthite inclusions occur in garnet. (e) Garnet profile from sample H254. (f) Garnet with indicated profile from sample E292a has contacts to antiperthite, quartz, K-feldspar and orthopyroxene.

the mineralogy. Garnet has contacts to matrix mesoperthite, K-feldspar, quartz and orthopyroxene (Fig. 4f) and does not exhibit coronas of plagioclase rimmed by orthopyroxene.

E292b: finer-grained layer (Dunkelsteiner Massif)

The finer-grained layer (0.2 mm grain size) consists of a felsic matrix composed of quartz, plagioclase and

Table 1. Representative analyses of garnet and orthopyroxene. Minerals were analysed using the Cameca SX100 at the Czech Academy of Sciences in point beam mode at 15 kV and 10 nA.

Sample:	E292A	E292B	E292B	H254	H254	H254	E292A	E292B	H254
Mineral:	g	g	g	g	g	g	opx	opx	opx
Position:	Core	Core	Rim	Core	At fsp incl.	Rim	Matrix	Matrix	Matrix
Analysis:	p128	p85	p92	p69	p38	p53	103	p101	6
SiO_2	38.32	38.24	38.15	38.16	38.70	38.60	50.47	51.15	52.23
TiO_2	0.11	0.14	0.02	0.22	0.03	0.06	0.11	0.09	0.09
Al_2O_3	21.16	21.08	21.09	21.02	21.41	21.21	1.37	1.20	0.70
Cr_2O_3	0.12	0.00	0.04	0.08	0.03	0.03	0.00	0.00	0.00
FeO	28.43	25.02	29.48	21.18	26.39	25.60	30.92	30.01	27.18
MnO	0.70	0.63	1.18	0.59	0.48	0.71	0.33	0.52	0.37
MgO	6.34	4.49	5.66	3.07	7.03	7.48	16.52	17.07	19.05
CaO	4.68	10.21	4.21	15.16	5.66	5.72	0.33	0.37	0.43
Na_2O	0.01	0.00	0.01	0.05	0.03	0.03	0.00	0.01	0.03
Total	99.87	99.80	99.84	99.54	99.75	99.42	100.05	100.42	100.08
cat/charges	8/24	8/24	8/24	8/24	8/24	8/24	4/8	4/8	4/8
Si	3.00	2.99	3.00	2.99	3.01	3.00	1.95	1.97	1.99
Ti	0.01	0.01	0.00	0.01	0.00	0.00	0.00	0.00	0.00
Cr	0.01	0.00	0.00	0.01	0.00	0.00	0.00	0.00	0.00
Al	1.95	1.94	1.95	1.94	1.96	1.94	0.06	0.05	0.03
Fe^{3+}	0.03	0.05	0.03	0.07	0.03	0.05	0.02	0.01	0.00
Fe^{2+}	1.83	1.59	1.91	1.32	1.69	1.61	0.98	0.96	0.87
Mn	0.05	0.04	0.08	0.04	0.03	0.05	0.01	0.02	0.01
Mg	0.74	0.52	0.66	0.36	0.81	0.87	0.95	0.98	1.08
Ca	0.39	0.86	0.36	1.27	0.47	0.48	0.01	0.02	0.02
Na	0.00	0.00	0.00	0.01	0.01	0.00	0.00	0.00	0.00
XFe^{2+}	0.71	0.75	0.74	0.79	0.67	0.65	0.51	0.50	0.45
xCa	0.13	0.28	0.12	0.42	0.16	0.16	0.01	0.01	0.01

K-feldspar (90%), with abundant biotite (8%), minor garnet and orthopyroxene (2%) and accessory ilmenite (Figs 4a,b & 5d). The feldspar grains do not exhibit exsolution features. Biotite defines a strong foliation that is parallel to the boundary with the coarse-grained layer, whereas felsic minerals are not preferentially oriented and have straight grain boundaries (Fig. 4a,b).

Feldspar does not have ternary compositions, plagioclase contains 30–34% of anorthite (ab63–65 an30–33 or1–4) and K-feldspar has low albite content between 2% and 3% (ab2–3 an0.2 or96–97). Garnet of size 0.6 mm exhibits a zoning profile with, from core to rim, alm52⇒66 py18⇒21 grs30⇒11 sps1, with a constant x(g) = 0.75–0.78 (Figs 5d & 6). Orthopyroxene x(opx) = 0.50–0.51 and Al = 0.04–0.07 pfu. Biotite has x(bi) = 0.44–0.48 and TiO_2 = 5–6 wt%.

Key observations, contrasting with the coarse-grained layer, include the more hydrous nature of the mineralogy, the biotite foliation, smaller grain size and absence of exsolution features within the feldspar. Remarkable is the strong grossular zoning, with high grossular content in garnet cores (30%) in garnet that is smaller than the ones in the coarse-grained layer that exhibit flat low-grossular zoning profiles.

H254 (Blanský Les Massif)

The sample H254 is composed of a felsic matrix containing quartz, K-feldspar, and plagioclase (88%), with garnet (7%), orthopyroxene (1%), biotite (4%), relicts of antiperthite, and accessory rutile and ilmenite (Figs 4b,c & 5e,f). The foliation in the matrix (0.1 mm) is defined by elongated quartz ribbons that alternate with equigranular feldspar-rich layers composed of randomly distributed quartz, plagioclase and K-feldspar with straight grain boundaries (Fig. 4c,d). Biotite is oriented parallel to this foliation. The feldspar within the recrystallized matrix does not show exsolution features apart from a few larger (0.7 mm) antiperthite relicts (Fig. 5e). Antiperthites are also preserved as inclusions within garnet (Figs 4c & 5f). They exhibit plagioclase exsolution-free rims that separate the part of the grain with exsolution lamellae from the contact with garnet, with the rim in optical continuity with the plagioclase in the core (Fig. 5f,g).

Plagioclase within the recrystallized matrix contains 24–34% of anorthite and K-feldspar has about 10% of albite. Two relicts of antiperthite within the matrix give the reintegrated composition of ab45–49 an15–16 or35–41, using the plagioclase analyses within the K-feldspar exsolutions that contain 24–26% of anorthite (points 5 & 6 in Table 2). Inclusions of antiperthite within garnet exhibit strong variation of the composition of the plagioclase host from 32% to 20% of anorthite from the contact with garnet to the contact with exsolved K-feldspar (Fig. 7). For the reintegration the value of 25–26% of anorthite was used, however the range of possible reintegrations with different anorthite contents can be deduced from Fig. 7. The reintegrated compositions that include the exsolution-free rim are much closer to the reintegrated values obtained from the matrix relicts than when the plagioclase rim was not included, and therefore the latter reintegration is considered as incorrect (point 9b

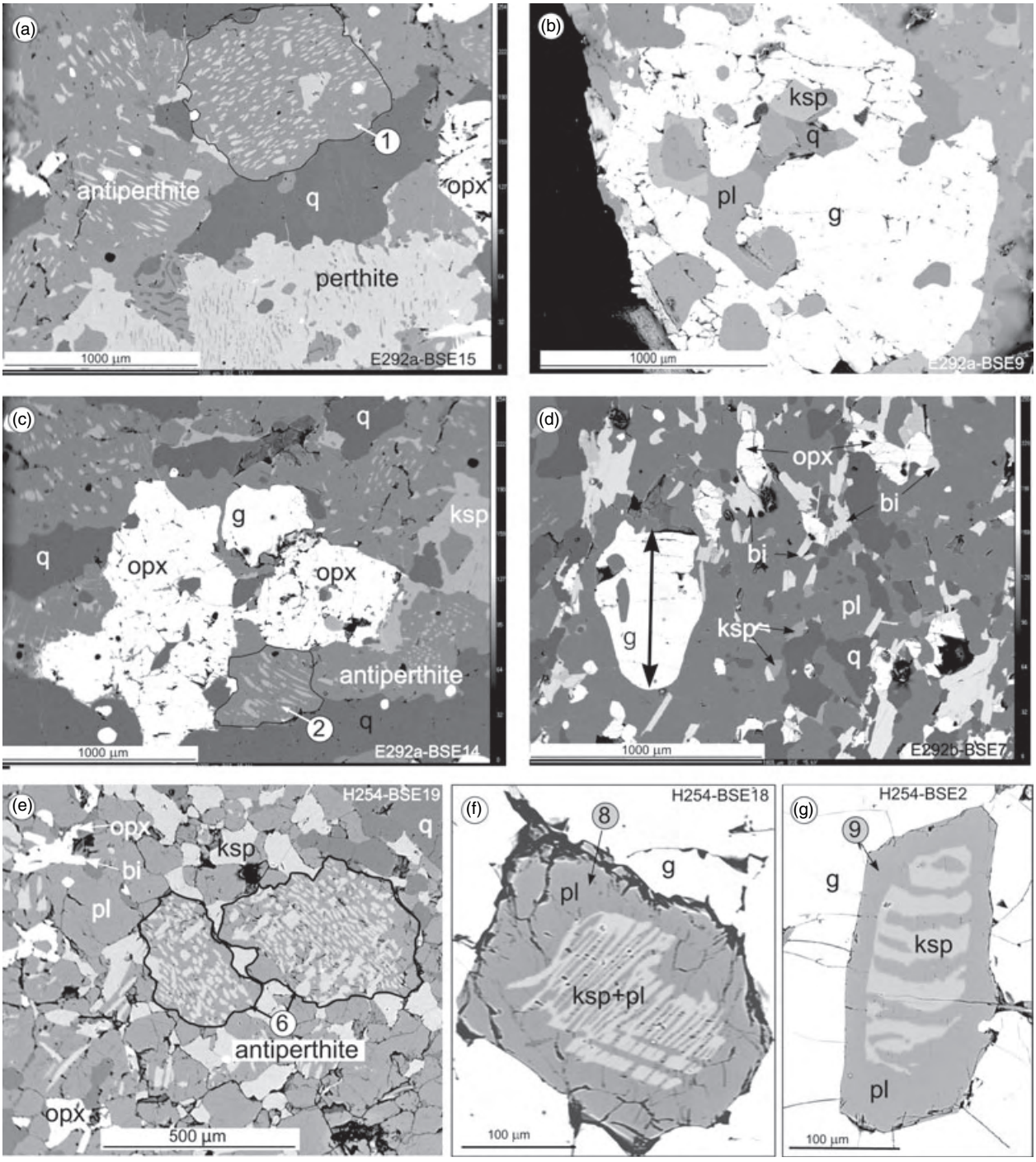

Fig. 5. (a) Randomly oriented antiperthite, perthite and quartz with lobate grain boundaries in the coarse grained layer (E292a). (b) Large garnet with composite inclusion of K-feldspar-plagioclase and quartz that may represent trapped melt. (c) Large orthopyroxene set within a matrix of ternary feldspar and quartz (E292a). (d) Finer-grained layer (E292b) rich in biotite and feldspar (not ternary). Foliation marked by biotite orientation is parallel to the boundary with E292a. (e) Relicts of larger antiperthite grains within the fine-grained matrix of plagioclase-K-feldspar-quartz (H254). (f) & (g) Antiperthite inclusions within garnet with an exsolution-free rim of plagioclase that separates the exsolution-rich core from the contact with garnet (H254). Circled numbers correspond to reintegrated feldspar in Fig. 7.

in Fig. 7). Reintegrations of antiperthite inclusions within garnet are less potassic than reintegrations of matrix antiperthite relicts, consistent with the antiperthite within the matrix having had an exsolution-free rim that was eroded via recrystallization and incorporation in the finer-grained matrix. Antiperthite

Table 2. Reintegrated feldspar with the proportion of the host and exsolutions and their compositions.

			Integrated			Plagioclase				K-feldspar			
No.	Sample	Texture	ab	an	or	pl%	ab	an	or	ksp%	ab	an	or
1	E292a (BSE15)	Coarse matrix	0.54	0.22	0.24	74	0.69	0.30	0.01	26	0.10	0.00	0.90
2	E292a (BSE14)	Coarse matrix	0.54	0.25	0.21	78	0.67	0.32	0.01	22	0.06	0.00	0.94
3	E292a (BSE13)	Coarse matrix	0.59	0.24	0.17	84	0.69	0.29	0.02	16	0.08	0.00	0.92
4	E292a (BSE16)	Coarse matrix (whole grain)	0.19	0.04	0.76	14	0.66	0.33	0.01	86	0.14	0.01	0.85
4b	E292a (BSE16)	Coarse matrix (only core)	0.21	0.06	0.73	14	0.66	0.33	0.01	86	0.14	0.01	0.85
5	H254 (BSE3)	Relict in recrystallized matrix	0.49	0.16	0.35	61	0.74	0.26	0.01	39	0.10	0.00	0.90
6	H254 (BSE19)	Relict in recrystallized matrix	0.45	0.15	0.41	56	0.73	0.26	0.01	44	0.08	0.00	0.92
7	H254 (BSE17)	Incl. in garnet	0.54	0.18	0.28	69	0.73	0.26	0.01	31	0.10	0.00	0.90
8	H254 (BSE18)	Incl. in garnet	0.60	0.19	0.21	78	0.74	0.25	0.01	23	0.10	0.00	0.90
9	H254 (BSE2)	Incl. in garnet	0.53	0.18	0.30	69	0.73	0.26	0.01	31	0.08	0.00	0.92
9b	H254 (BSE2)	Incl. in garnet (only core)	0.35	0.11	0.53	43	0.73	0.26	0.01	57	0.08	0.00	0.92

Reintegration was done via BSE images, with grain boundaries checked under the optical microscope. The proportion of lamellae and host was calculated using the point-counting planimetric method. Within the matrix exsolved grains, the composition of plagioclase and K-feldspar vary little, and the average compositions were used for reintegration. Within the ternary feldspar included in garnet, the composition of the plagioclase host varies significantly (see Fig. 7); for reintegration the average of analyses among K-feldspar exsolutions was used.

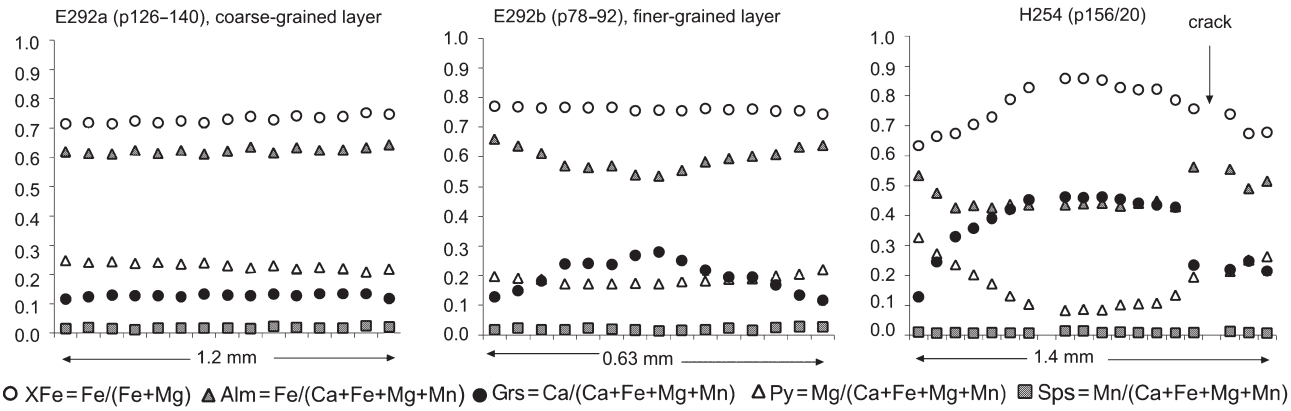

Fig. 6. (a) Flat chemical profile across 1.2 mm size garnet from the coarse-grained layer (E292a). (b) Profile across smaller garnet (0.6 mm) from finer-grained layer (E292b) shows strong zoning in grossular. (c) Large garnet (1.4 mm) from sample H254 exhibits strong zoning in grossular and X(Fe). This garnet contains inclusions of antiperthite grains.

included in garnet was protected from such erosion. The reintegrated values for inclusions are therefore considered to be closer to the original composition, even if the anorthite content of the plagioclase host was modified towards garnet and K-feldspar contacts. The temperature deduced from the composition of antiperthite inclusions in garnet is 1000 °C according to the Fuhrman & Lindsley (1988) calibration.

Garnet is zoned with z(g) and x(g) decreasing from core to rim or towards feldspar inclusions (alm42 $\Rightarrow$ 55 py16 $\Rightarrow$ 30 grs45 $\Rightarrow$ 10 sps = 0, x(g) = 73 $\Rightarrow$ 65) (Figs 4e & 6). Biotite from the matrix has x(bi) = 0.35–0.41 and Ti *c*. 5 wt%. Orthopyroxene has x(opx) = 0.44–0.47 and Al = 0.03–0.05 pfu.

Key observations include the presence of antiperthite relicts in the matrix and especially the antiperthite inclusions within garnet that itself is strongly zoned with respect to z(g) and x(g). The garnet forms large grains, the zoning is symmetrical and does not show several chemically distinct cores. The presence of abundant biotite indicates the important H_2O content of the sample.

PSEUDOSECTIONS FOR OPX GRANULITES

Calculated pseudosections are a powerful tool for unravelling the history of complex metamorphic rocks as several stages in the evolution of a rock may be considered on one diagram, at least if the rock varies little in composition during its evolution. In principle the igneous and metamorphic stages in a specified *P–T* evolution may be considered simultaneously. Conversely, with an interpretation of the observed mineral assemblages and textures, the *P–T* path may be constrained.

On pseudosections, mol.% changes along a specified *P–T* path may be tracked allowing the growth and consumption of phases to be considered. The main questions that arose from petrographic observations concerning the textural and chemical relationship of ternary feldspar and garnet may be discussed using pseudosections. Primary interest is focussed on deciphering *P–T* paths that allow ternary feldspar to be included in garnet and that may explain at the same time the observed garnet-zoning patterns.

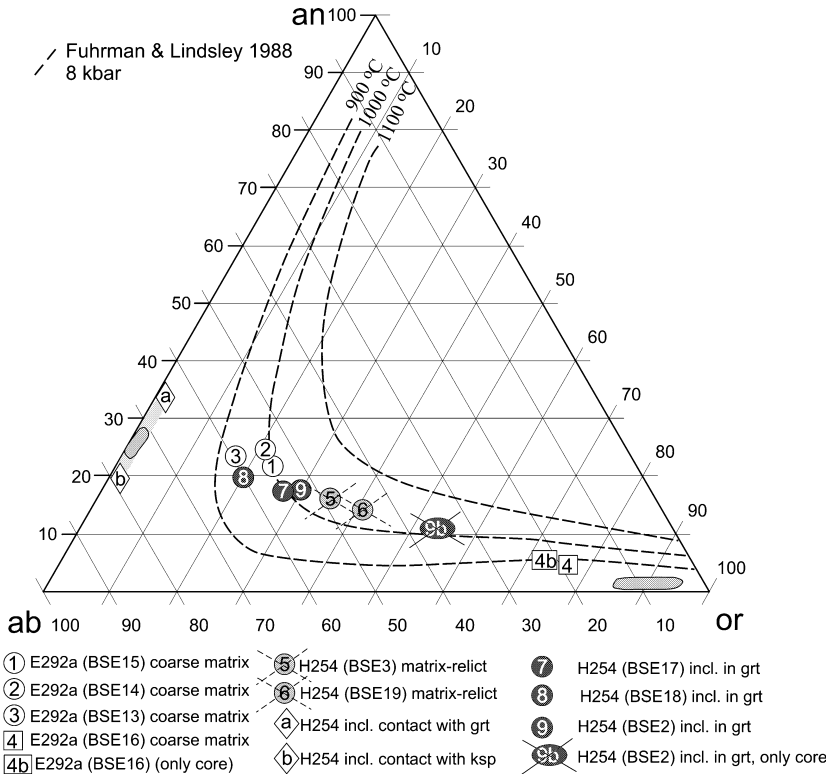

Fig. 7. Plotted compositions of reintegrated ternary feldspar. Most ternary antiperthites from sample E292a and inclusions within garnet from sample H254 plot around the isopleth of 1000 °C (from Fuhrman & Lindsley, 1988) and are considered to approximate the temperature of their formation. Point 9a is an antiperthite inclusion where the core was reintegrated without its plagioclase rim (H254), the approach being considered to be inappropriate. Points 5 & 6 are matrix antiperthites and their composition is interpreted to be modified by removal of an exsolution-free rim by recrystallization (H254) (see Fig. 2). Points a and b represent the anorthite content of plagioclase next to garnet and K-feldspar exsolution in the included antiperthites respectively. Examples 1, 2, 6, 8 and 9 are presented in Fig. 5.

Orthopyroxene granulites reported from the Gföhl unit are composed of quartz, plagioclase, K-feldspar, orthopyroxene and garnet ± clinopyroxene (e.g. Fiala *et al*., 1987; Petrakakis & Jawecki, 1995; Owen & Dostal, 1996). Fiala *et al*. (1987) provided an average chemical analysis of garnet-orthopyroxene granulites (group B1-7, here named Fi7) that is used here for the pseudosection calculations. Their granulites are granoblastic, fine-grained, composed of mesoperthite and perthitic orthoclase, (total 29% of plagioclase, 27% of alkali feldspar), quartz (37%), orthopyroxene (4%), garnet (1%), biotite (1%), ±ilmenite, zircon and apatite. Carswell & O'Brien (1993) described similar granulites (group B, average of three analyses, here named CwB) of similar composition to Fi7 (see inset of Fig. 8b). The rock composition is considered to approach the effective rock composition along a metamorphic path, with the ternary feldspar considered in terms of their constituent minerals. Fractionation by prograde growth of garnet is not significant because of the low garnet proportion. Our modelling additionally investigates the consequence of varying the water content of the bulk composition, in mol.%, $M(H_2O)$.

P–T pseudosections were constructed for the range 5–20 kbar and 600–1050 °C where the primary interest was in the metamorphic evolution and in the range 5–20 kbar and 800–1250 °C to study magmatic processes. A pseudosection was constructed for $M(H_2O) = 0$, and then the effect of H_2O addition was studied in a T–$M(H_2O)$ section at an appropriate pressure (7.8 kbar). Pseudosections involving H_2O were constructed for a representative H_2O-undersaturated case, and for H_2O saturation at the solidus. Mineral compositional and mole proportion isopleths were plotted for the phases of interest and especially in order to study garnet growth and its zoning along specified *P–T* trajectories. Magma crystallization involving cooling with a little decompression is represented by path A in Figs 8(b) and 10(a). The trajectories B and C in Fig. 10(a) were chosen to represent garnet zoning during prograde metamorphism for (B) burial accompanied by heating within the range of geothermal gradients of 16–12 °C km^{-1} and for (C) isothermal burial at 750 °C.

P–T pseudosection for $M(H_2O) = 0$

The solidus in the 'dry' [$M(H_2O) = 0$] pseudosection occurs in the range 1020–1250 °C and for orthopyroxene-bearing fields it is located at *c*. 1100 °C (Fig. 8). The dominant feature of the pseudosection is the pressure-sensitive pattern of mineral assemblage fields below the solidus. From high to low pressure these assemblages are characterized by the Fe–Mg phases: g, g-cpx, g-cpx-opx, g-opx, and opx, corresponding to the known sequence for granulite facies rocks. The upper stability of orthopyroxene occurs at 14–15 kbar at 1200–1100 °C, but on isobaric cooling orthopyroxene disappears in favour of an orthopyroxene-free assemblage containing garnet and clinopyroxene. A reasonable upper pressure limit from which orthopyroxene is likely to be preserved on cooling (assuming cooling is

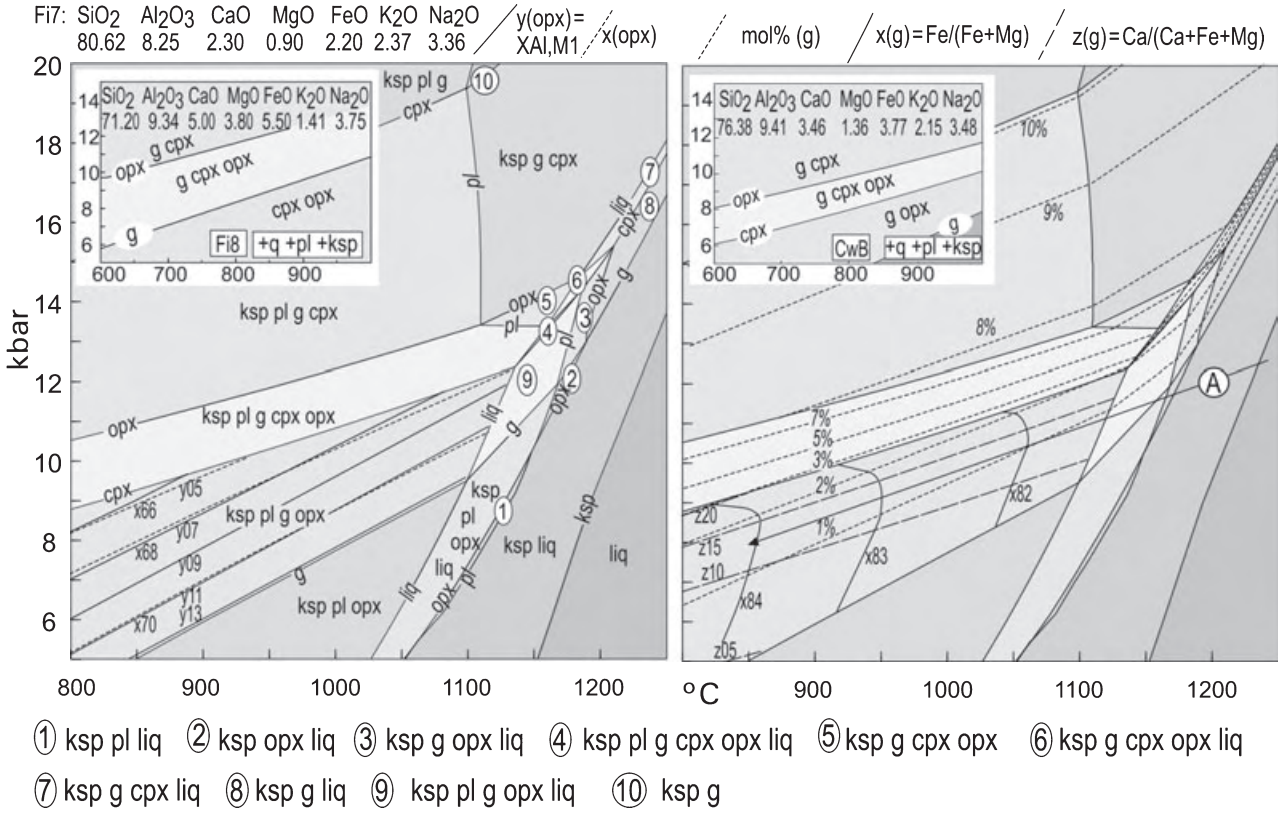

Fig. 8. Pseudosection for the composition of opx granulite without H_2O (group 7 from Fiala *et al.*, 1987). Left inset: pseudosection for the granulite group 8 of Fiala *et al.*, 1987. Right inset: pseudosection for the composition of g-opx granulite from Carswell & O'Brien, 1993. Mineral abbreviations: ksp = K-feldspar, pl = plagioclase, q = quartz, g = garnet, cpx = clinopyroxene, opx = orthopyroxene, liq = liquid, bi = biotite, mu = muscovite. Isopleths: y(opx) = X(Al,M1), x(opx) = Fe/(Fe + Mg), x(g) = Fe/(Fe + Mg), z(g) = Ca/(Ca + Fe + Mg), mol.%(g) = mol.% of garnet.

approximately isobaric) is 12 kbar and then it coexists with clinopyroxene and garnet, whereas below 10 kbar it occurs without clinopyroxene. The order of crystallization of phases from a melt of this rock composition at 9–11 kbar is quartz, K-feldspar, and then, in various order depending on the exact pressure, orthopyroxene, plagioclase and garnet in a narrow interval of *c.* 100 °C. At a slightly lower temperature, the last liquid disappears. An important observation is that garnet therefore may contain inclusions of ternary K-feldspar and ternary plagioclase (and also of quartz and orthopyroxene). The compositional range of grossular in the opx-g field is large, from 5 to 20 mol.%, isopleths are flat and garnet may therefore preserve pressure information on melt crystallization, if profiles are not diffusively flattened at these high temperatures. Isopleths of x(g) in the g-opx field have a steep slope, but the variation over the large interval of 850–1100 °C is only from 0.81 to 0.84 and therefore x(g) contains little thermometric information in this field. The orthopyroxene composition variables y(opx) and x(opx) are both pressure sensitive; y(opx) may have barometric information because of the relatively large compositional range between 0.05 and 0.13, but x(opx) varies little. However, as this is a relatively high-variance field, it is likely that x(g) and x(opx) are as dependent on bulk-rock composition as on pressure and temperature.

The phase relationships for composition Fi8, an orthopyroxene-clinopyroxene granulite (Fiala *et al.*, 1987), are shown as an inset on Fig. 8. The main difference in the calculated assemblages of these two rock types is the different proportion of the minerals in the g-opx-cpx trivariant field at medium pressure and consequently the disappearance of either clinopyroxene or garnet towards lower pressure.

T–M(H_2O) pseudosection at 7.8 kbar

The effect of H_2O in the bulk-rock composition on the stability and preservation of mineral assemblages during cooling is presented in a *T–M*(H_2O) section at 7.8 kbar (Fig. 9). An infinitesimal amount of H_2O lowers the solidus from *c.* 1120 °C for dry conditions to *c.* 800 °C, stabilizing an infinitesimal amount of biotite, infinitesimal melt being present in the lower 300 °C of this temperature range (Figs 8 & 9). Larger amounts of H_2O lower the solidus to *c.* 650 °C stabilizing additionally the hydrous minerals, muscovite and hornblende. H_2O plays a major role on the

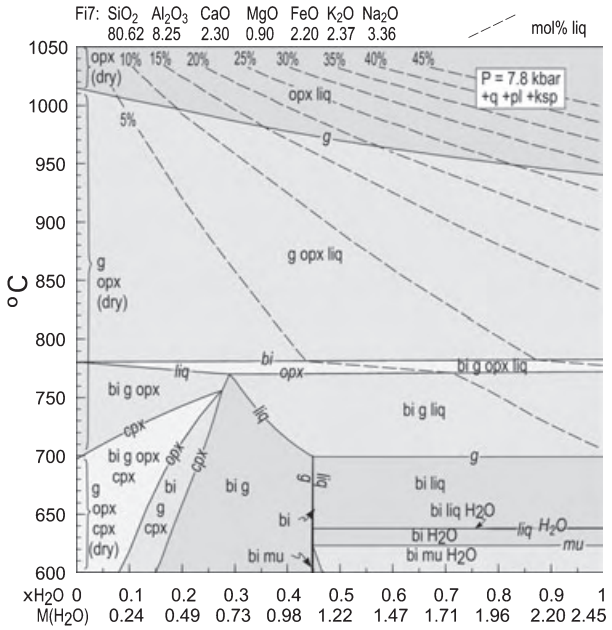

Fig. 9. *T*–*M*(H_2O) pseudosection for the composition of the opx granulite calculated at 7.8 kbar with M(H_2O) ranging from 0 to 2.45 mol.%. For abbreviations see caption for Fig. 8.

stability of Fe-Mg phases at the solidus. With increasing H_2O content, the Fe-Mg phases at the solidus are opx-g, opx-g-bi, g-bi, bi-H_2O, and bi ± mu(± hb)-H_2O just below the solidus. The preservation of orthopyroxene is therefore likely only for a low H_2O content (max 0.72 mol.%). Based on these calculations, *P*–*T* pseudosections were calculated for 0.5 and 1.19 mol.% of H_2O. These pseudosections are used to consider metamorphic processes as well as melt crystallization.

P–*T* pseudosection for *M*(H_2O) = 0.5 (H_2O-undersaturated at solidus)

An H_2O-undersaturated pseudosection (Fig. 10) was constructed to study crystallization of hydrous magma and metamorphism affecting the products of igneous crystallization from originally dry melt that has been partially hydrated subsequently. The solidus is lowered to 700–800 °C, the stability of clinopyroxene and orthopyroxene is reduced and garnet proportions are reduced via the appearance of biotite and muscovite. At higher *T* the same pressure-dependent pattern of fields as in the dry pseudosection occurs, with g, g-cpx, g-cpx-opx, g-opx and opx, but here in the presence of melt. However, the amount of melt is small, between 1000 and 950 °C it decreases from 10 to 5 mol.% and then it decreases further to the solidus at *c*. 780 °C (Fig. 9).

The order of crystallization from melt at 7–8 kbar is K-feldspar, plagioclase, orthopyroxene then garnet. On cooling, the question arises as to whether high-*T* ternary feldspar are likely to reequilibrate to non-ternary compositions, because melt is present down to 750–800 °C, but in very small proportion (< 10 to 5 mol.%). Biotite comes in just above the solidus in garnet-orthopyroxene fields; however, the amount of H_2O is sufficient to convert only part of the orthopyroxene to biotite. On further cooling, clinopyroxene may come in at the expense of orthopyroxene, but this may not happen for kinetic reasons, unless cooling is accompanied by deformation. The likely preserved assemblage is the solidus assemblage bi-g-opx-pl-ksp-q with possible relicts of ternary feldspar. Garnet may preserve pressure information on melt crystallization because the z(g) isopleths are relatively flat, but x(g) from 1000 °C has little variation and is unlikely to reflect the temperature evolution, additionally because of diffusive re-equilibration at these high temperatures. Orthopyroxene y(opx) isopleths are relatively flat but steeper than z(g), therefore the y(opx) may decrease over a large interval on cooling and x(opx) varies little below 1000 °C.

For the study of metamorphism, an important feature of this pseudosection is the high grossular content in the medium-*P*/low-*T* fields where garnet mol.% contours also change significantly. In these fields, garnet grows on prograde paths such as B and C (Fig. 10), mostly at the expense of biotite in the presence of muscovite or melt. Such paths do not involve orthopyroxene and path B ends with the assemblage g-cpx-liq. However the amount of clinopyroxene produced is very small (max. 1.2 mol.%). On a retrograde path, or during isobaric heating in the orthopyroxene-bearing fields, garnet is consumed. Garnet profiles represented for 1 mol.% increments, converted to radius for path A and path B, reveal strong zoning in x(g), but flat z(g) (Fig. 11).

The pseudosections also help to establish along what part of the *P*–*T* path garnet may include ternary feldspar. Along the prograde *P*–*T* path garnet grew up to 14 kbar and 750 °C and may therefore have included feldspar, but the feldspar is ternary only if magmatic relicts with already exsolved plagioclase and K-feldspar are present. During further increase in *P*–*T*, garnet did not grow and cannot therefore include metamorphic ternary feldspar even if temperatures reached 1000 °C. Moreover, during decompression from 1000 °C and 18 kbar, garnet proportion decreases. Along path A, for melt crystallization, garnet starts to grow after feldspar and increases in proportion, so that it includes ternary feldspar (and also plagioclase or K-feldspar at lower *T*).

P–*T* pseudosection for *M*(H_2O) = 1.19 (H_2O-saturated at solidus)

The pseudosection for the rock composition with sufficient H_2O for it to be H_2O-saturated at the solidus (at 9.8 kbar and 623 °C) was constructed in order to study the prograde metamorphism following complete rehydration of the products of igneous crystallization (Fig. 12). The high-*T* mineral assemblages are the same

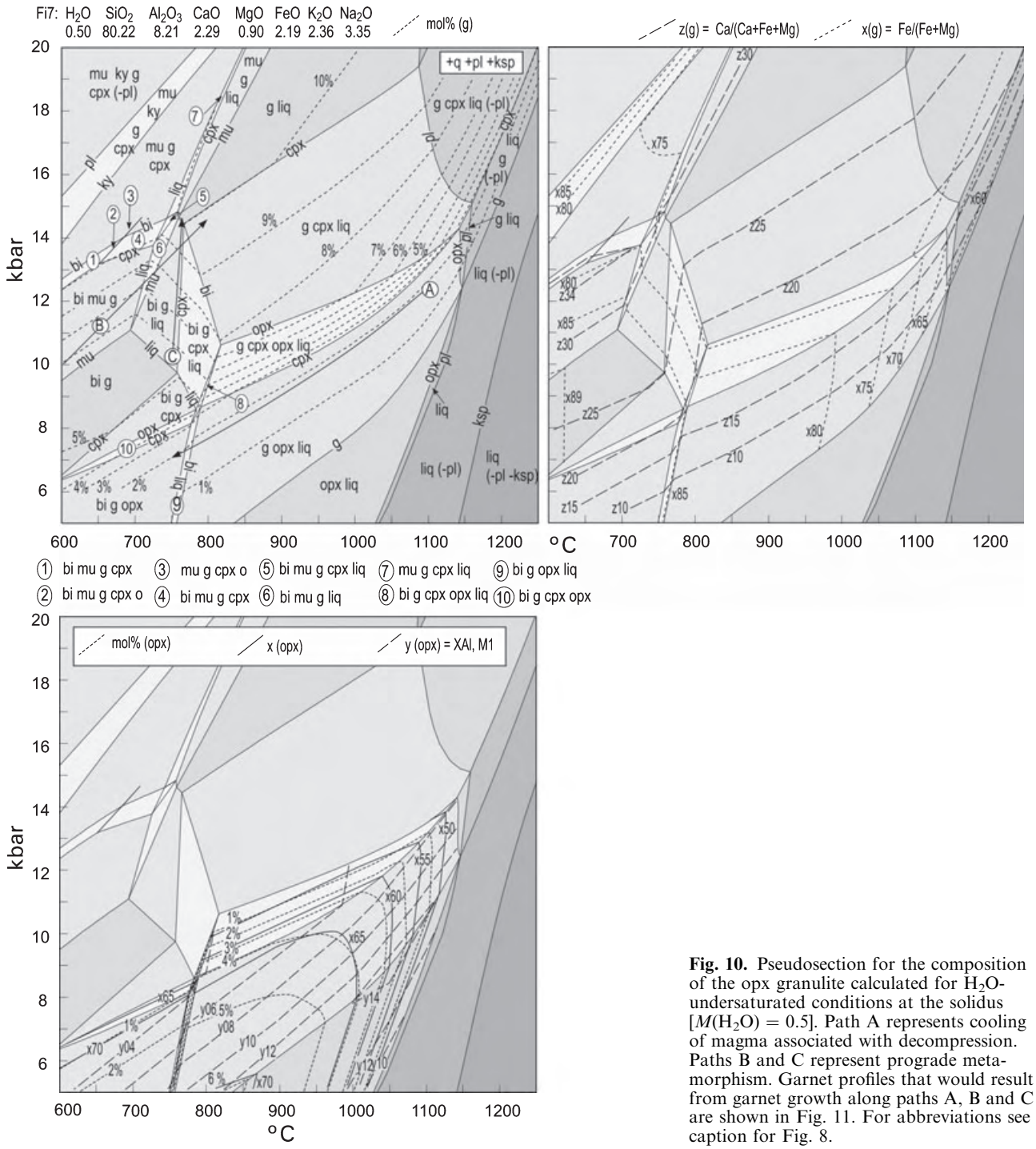

Fig. 10. Pseudosection for the composition of the opx granulite calculated for H_2O-undersaturated conditions at the solidus [$M(H_2O) = 0.5$]. Path A represents cooling of magma associated with decompression. Paths B and C represent prograde metamorphism. Garnet profiles that would result from garnet growth along paths A, B and C are shown in Fig. 11. For abbreviations see caption for Fig. 8.

as for undersaturated conditions. However, with cooling, the H_2O content is sufficient for all of the orthopyroxene to be replaced by biotite by *c*. 750–800 °C, and to markedly restrict not only the stability of clinopyroxene and orthopyroxene but also that of garnet. Muscovite is stable at lower *T*, and hornblende is stabilized below *c*. 600 °C (but does not appear in the *P*–*T* range presented). Up to 9.8 kbar the solidus is H_2O-saturated and occurs below 650 °C, then from this point it is (slightly) H_2O-undersaturated to 800 °C at higher pressure.

Low-temperature fields are characterized by a very high grossular content in garnet that is even higher than for H_2O-undersaturated conditions, and by a strong variation in garnet proportion. The compositional patterns resulting from garnet growth along

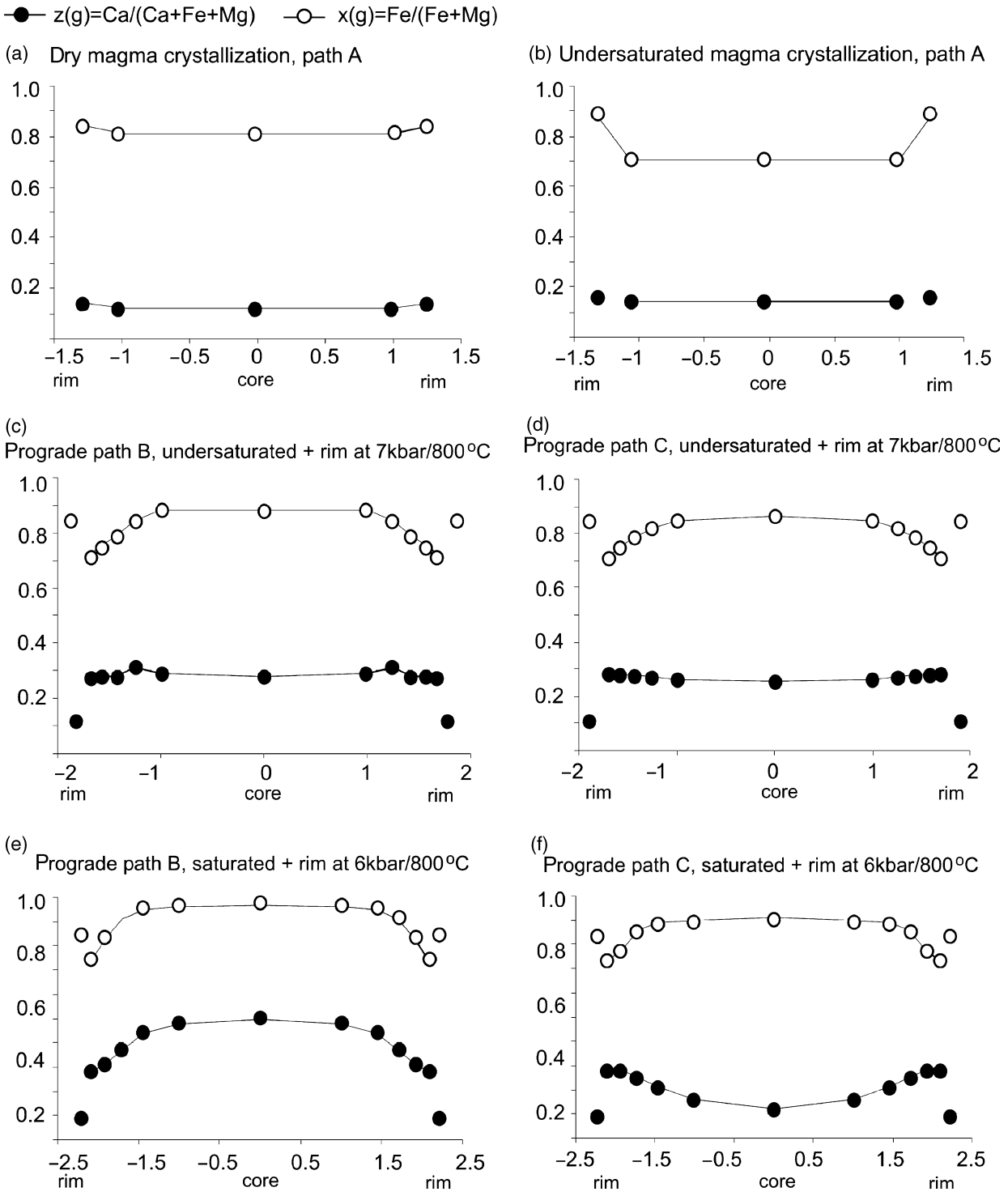

Fig. 11. Garnet profiles resulting from growth along paths A, B and C from Figs 10 and 12. Garnet growth increments of 1 mol.% are converted into radius (in arbitrary units). Rims in profiles for paths B and C represent the compositions towards which garnet may equilibrate after decompression.

path B and C are presented for growth increments of 1 mol.% in Fig. 11. They are characterized by very high x(g) in the cores decreasing towards the rims. For path B, z(g) is very high in the core and decreases towards the rim while for path C, z(g) increases. The outside points represent the garnet composition at 6–7 kbar and 800 °C, towards which rims may tend to equilibrate after subsequent decompression. Segments

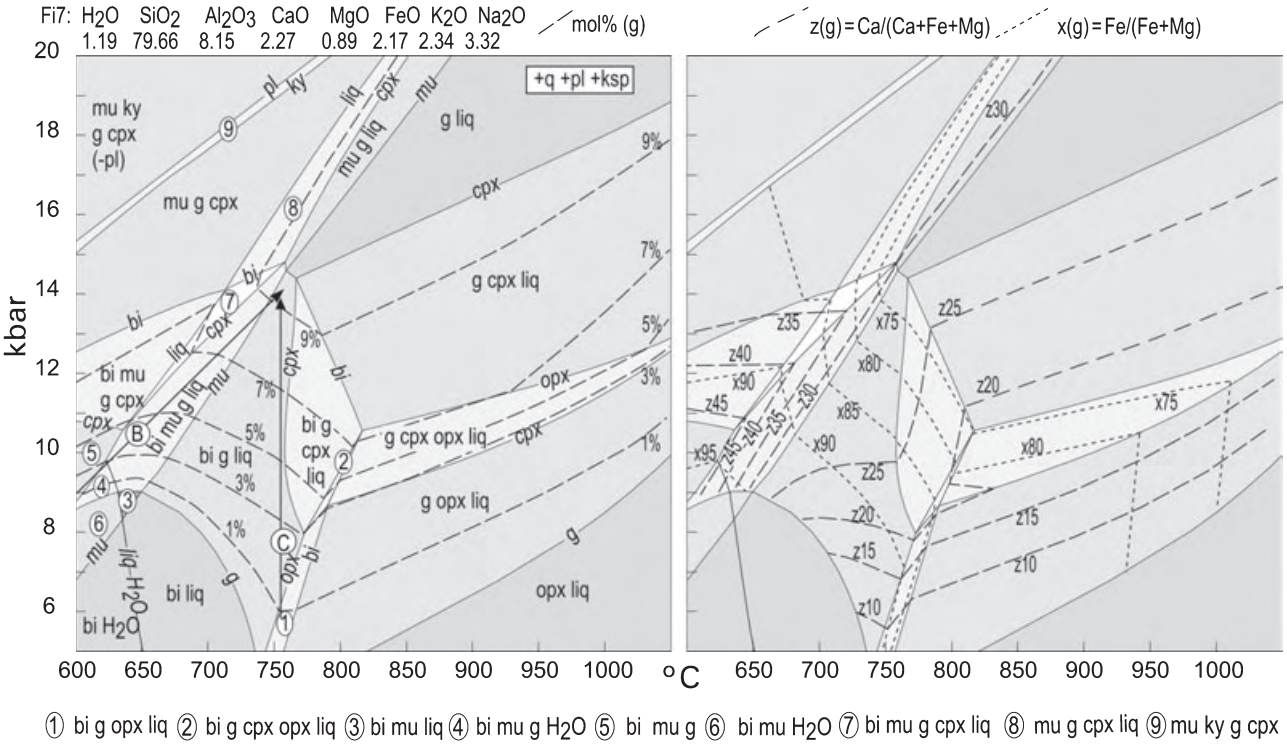

Fig. 12. Pseudosection for the composition of the opx granulite calculated for H_2O-saturated conditions at the solidus at 9.8 kbar [$M(H_2O) = 1.19$]. Garnet profiles resulting from the growth along paths B and C are shown in Fig. 11. For abbreviations see caption for Fig. 8.

of *P–T* paths along which garnet grew and may therefore include ternary or other feldspar are almost identical to the segments described for undersaturated conditions. For rocks where orthopyroxene is preserved, this pseudosection is likely to be useful only for the prograde path and then melt must be lost in order to decrease the H_2O content to a value necessary for preservation of orthopyroxene during decompression and cooling.

INTERPRETATION

Opx granulite E292a: coarse-grained layer

Comparison of the characteristics of the coarse-grained layer with pseudosections points strongly to the high temperature side of the ksp-pl-opx-g field in the dry pseudosection or to the ksp-pl-opx-g-liq field in the H_2O-undersaturated pseudosection. Reintegrated compositions of ternary plagioclase coexisting with ternary K-feldspar correspond to a temperature of *c.* 1000 °C using the calibration of Fuhrman & Lindsley (1988) (Fig. 7). Grossular content of garnet (12–13%) indicates a pressure between 8 and 13 kbar. Similar pressure conditions were interpreted for g-opx and g-cpx granulites forming the Líšov Massif (Vrána & Jakeš, 1982). These authors also adopted a magmatic interpretation of these rocks. The observed composition of garnet [x(g) = 0.71–0.76] and orthopyroxene [x(opx) = 0.48–0.50] is consistent with the isopleths in the high-temperature part of the H_2O-undersaturated pseudosection. Biotite occurring at orthopyroxene grain boundaries (Fig. 4a) may reflect crystallization at the solidus, and may be an indication of the small amount of H_2O in the melt, but may also indicate later H_2O addition. The compositional variables are compatible with UHT conditions at intermediate pressure, and we interpret these conditions to reflect crystallization of dry or H_2O-undersaturated *magma*, and *not* as a result of metamorphism. The coarse-grained equigranular texture of the sample that resembles a granulite facies texture may be achieved during the growth of the minerals over a small crystallization interval from a dry melt, or a similarly narrow interval for a H_2O-undersaturated melt having only 5 mol.% melt remaining as cooling occurs through 1050 °C. The texture of the rock is likely to have continued to be modified to a lower temperature, but at still high-temperature conditions. There is no evidence in this rock of a response to the metamorphism that affected other Moldanubian rocks, including E292b, presumably through an absence of deformation and rehydration (see below).

Opx granulite E292b: finer-grained biotite-rich layer

The observed assemblage and chemistry of the minerals, especially the garnet zoning, may be modelled in

the H_2O-undersaturated or -saturated pseudosections. The high grossular cores of the garnet can grow only in the fields at lower temperature, where garnet proportion also changes significantly. Therefore, garnet growth may occur during a prograde metamorphic path in the presence of hydrous phases, biotite and/or muscovite and/or melt. The constant x(g) does not fit the patterns obtained for the theoretical garnet zoning (Fig. 11) but may be accounted for by diffusional flattening at higher *T*. The peak pressure is difficult to infer, but the sample could have attained peak pressure in the bi-g-liq field or in cpx-bearing fields outside the stability of biotite (where clinopyroxene has low proportion). On decompression the orthopyroxene may have come in at the expense of clinopyroxene outside the biotite-stability field or within the biotite stability but only for H_2O-undersaturated conditions. Further cooling can be studied only in the H_2O-undersaturated pseudosection. If the prograde metamorphism occurred under H_2O-saturated conditions then melt loss must have occurred in order to preserve orthopyroxene at the solidus. If the sample was outside the stability of biotite, then biotite would have appeared on the solidus mainly at the expense of orthopyroxene.

The biotite-rich layer can be interpreted as a shear zone within a dry magmatic body (represented by sample E292a) that was hydrated and affected by prograde metamorphism including growth of prograde garnet. Peak pressure and peak temperature are difficult to constrain. It is even questionable whether the sample reached the clinopyroxene stability field or whether the sample passed outside the biotite stability field. An indication of medium rather than very high temperature is the composition and texture of feldspar, that is not ternary and does not show exsolution. We consider that the maximum reasonable temperature for prograde metamorphism to be below *c*. 800–850 °C. A similar orthopyroxene-bearing sample with strongly zoned garnet was described by Petrakakis & Jawecki (1995) and by Petrakakis (1997) from the same granulite massif. Interestingly, they found a small amount of clinopyroxene that may be considered as an indication of a prograde path into the g-cpx field at peak pressure, as was predicted from the garnet zoning in the pseudosections discussed above. Orthopyroxene would then need to develop retrogressively during decompression.

Opx granulite H254

Reintegrated ternary feldspar compositions give a temperature of *c*. 1000 °C when the calibration of Fuhrman & Lindsley (1988) is used (Fig. 7). This feldspar is included in garnet, and consequently garnet must have grown when ternary feldspar was already present in the rock. The garnet-zoning profile, with high grossular content, and x(g) pattern showing a decrease from core to rim is not possible to achieve in the dry and H_2O-undersaturated pseudosections. The only fields where the z(g) and x(g) isopleths are comparable with the observed values in the garnet core occur in the low-temperature/medium-pressure part of the H_2O-saturated pseudosection. The observed garnet zoning is compatible with the zoning pattern produced during garnet growth along the prograde *P–T* path B, characterized by simultaneous increase in pressure and temperature, heading into the g-cpx field (Fig. 11c). However, similar garnet zoning would result also from burial with *P–T* paths within the bi-mu-g-cpx field. The pressure peak is difficult to assess because clinopyroxene would appear in small proportion at higher pressure, and then would be replaced by orthopyroxene during decompression. The decompression path that must follow the prograde evolution cannot be deduced from the H_2O-saturated pseudosection because melt loss must occur in order to preserve orthopyroxene during cooling. However, the drop of grossular content to 8 mol.% at the garnet rim and at the contact with feldspar inclusions most probably reflects rim reequilibration at lower pressure.

DISCUSSION AND CONCLUSIONS

The main conclusion from this study of opx granulites is that the ternary feldspar in these rocks is of igneous origin, based on textural and mineral chemical observations combined with the pseudosection modelling. We have shown that it is impossible to include a metamorphic ternary feldspar at *c*. 1000 °C and 18 kbar in a prograde garnet along a *P–T* path as proposed for example by Carswell & O'Brien (1993). This requires a re-evaluation of the maximum metamorphic temperature in the Moldanubian, which had become constrained completely by the presumption that the ternary feldspar grew during the metamorphism. There is currently no strong evidence that the Moldanubian is a UHT metamorphic terrane.

The survival of igneous ternary feldspar grains requires an absence of recrystallization, so that plagioclase and K-feldspar occurring as lamellae and host in ternary feldspar grains are able to survive as long as plagioclase and alkali feldspar continue to be stable. For recrystallization to occur, deformation is likely to have been necessary. Even with deformation, unrecrystallized ternary feldspar may be preserved in garnet, or as augen in the matrix. Rehydration, as long as it is not accompanied or followed by recrystallization, does not preclude the survival of already-exsolved ternary feldspar grains. The garnet in which ternary feldspar is preserved may be original igneous or prograde metamorphic, and the study of garnet zoning may lead to the possibility of distinguishing between these cases. It is conceivable that the polyphase inclusions occur in garnet that is interpreted to have been igneous, are more or less modified original melt inclusions.

It has been suggested that the metamorphism in the Moldanubian, involving burial of at least some

mid- to lower-crustal rocks to eclogite facies conditions, is relatively short-lived (e.g. O'Brien & Vrána, 1995; O'Brien, 1997a,b). Although tectonic settings are not discussed here, the time-scale of metamorphism is relevant when considering the preservation of growth zoning in garnet. The diffusive flattening of growth zoning is a function of temperature and time. Typically, in regional metamorphic terranes, Fe-Mg growth zoning in garnet is flattened at a temperature of the order of 650 °C, whereas Ca zoning is flattened at a (much) higher temperature (Tracy, 1982; Chakraborty & Ganguly, 1991; Schwandt *et al.*, 1996). It is noted that Fe-Mg growth zoning is preserved in some of the orthopyroxene granulite garnet, which we infer to have experienced a maximum temperature of 850 °C. This provides circumstantial evidence that UHT conditions were not involved, unless the time-scale of metamorphism is many orders of magnitude shorter than in typical regional metamorphism. Given the horizontal scale of the effects of the heating to produce the metamorphism in the granulite massifs (of the order of up to 450 km^2), if temperatures exceeded 850 °C regionally, both the time scale of conductive heating and cooling, and the rates of diffusion at UHT conditions, should have homogenized these garnet compositions.

The Opx granulites constrain two segments of the overall igneous and metamorphic history in the Moldanubian. First, the magmatic relicts represented by ternary feldspar reflect a very high temperature of crystallization, implying that the magma was dry or at least quite H_2O-undersaturated. The second part of the history is represented by prograde garnet that has core compositions requiring hydration of the host rock early during the prograde *P–T* path or prior to it. The rest of the prograde *P–T* path including the pressure peak and decompression cannot be interpreted unambiguously from these rocks, although the retrograde re-equilibration at garnet-plagioclase grain contacts (at garnet rims and in garnet inclusions) reflects decompression to lower pressure, of the order of 6–7 kbar. The *P–T* of the metamorphic peak is suggested by crustal eclogites that occur in a similar way to the Opx granulites within the kyanite-K-feldspar granulite, at least where they do occur (Medaris *et al.*, 1998). Garnet-clinopyroxene thermometry (on garnet-clinopyroxene-bearing rocks) has suggested higher temperatures (e.g. Carswell & O'Brien, 1993; Cooke, 2000; Cooke *et al.*, 2000; Cooke & O'Brien, 2001), but these may point to original magmatic rather than to metamorphic conditions. A new mineral equilibrium study of eclogites with clear prograde features suggests metamorphic peak conditions of *c.* 18 kbar and, at

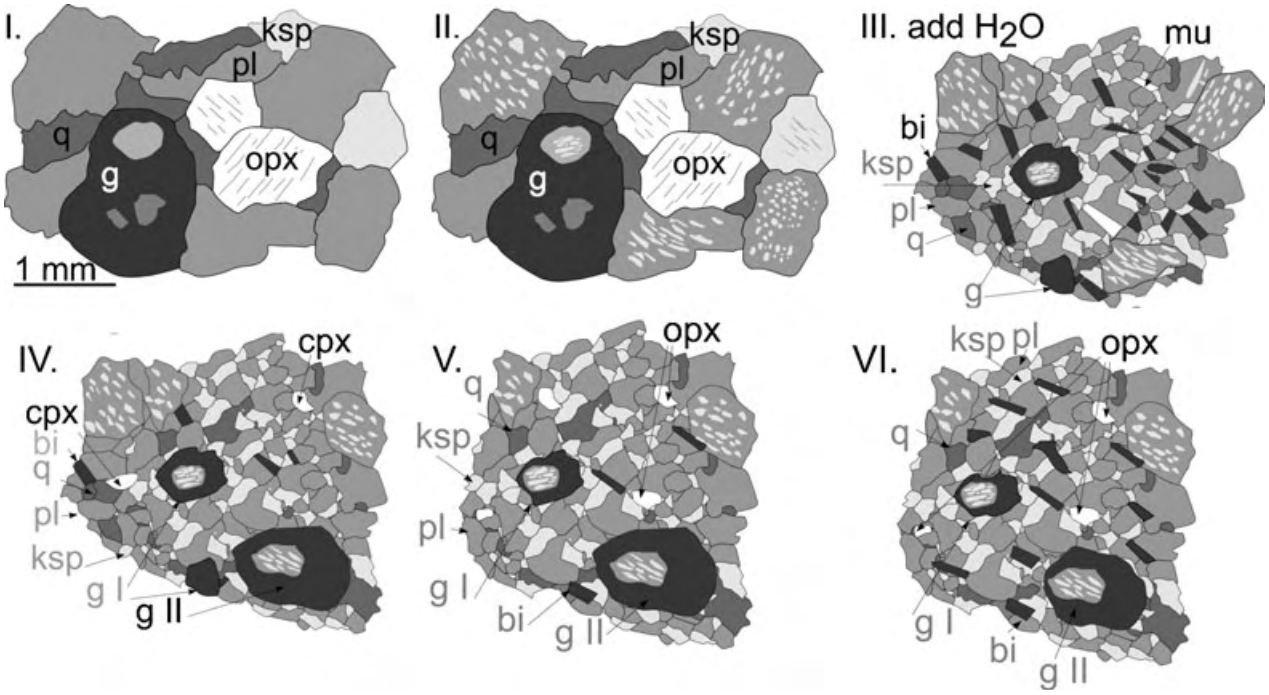

Fig. 13. Idealised reconstruction of the textural and mineral evolution of an opx granulite based on observation and the pseudosections, relating to the magmatic and metamorphic path on Fig. 14. (I) Texture and assemblage resulting from high-temperature melt crystallization involves orthopyroxene, garnet, quartz, ternary plagioclase and K-feldspar. Ternary feldspar is included in garnet. (II) On cooling, ternary feldspar develops exsolution lamellae. (III) Hydration producing biotite at the expense of orthopyroxene and garnet, and minor muscovite. (IV) Growth of high grossular garnet with high X(Fe) overgrowing relict grains of originally igneous ternary feldspar. Clinopyroxene forms. (V) On decompression clinopyroxene is consumed and orthopyroxene grows. Melt loss occurs to preserve orthopyroxene at the solidus. (VI) Melt crystallizes and releases H_2O that causes the growth of biotite.

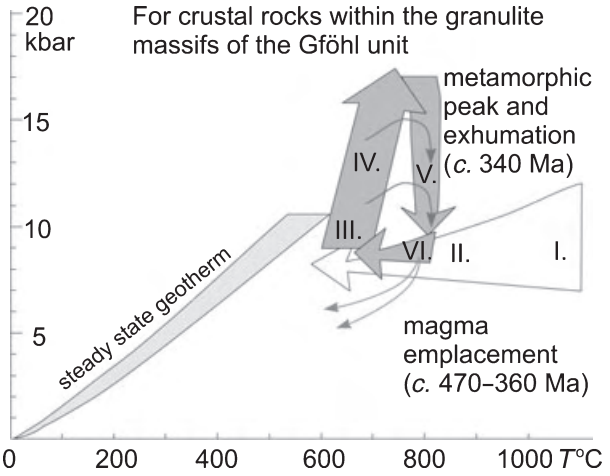

Fig. 14. *P–T* evolution suggested for the crustal rocks within the granulite massifs of the Gföhl unit, based on the study of opx granulites. In the first stage magma intrudes, crystallizes (I) and cools towards a steady state geotherm (II). Prograde metamorphism starts to be detectable at 8–10 kbar and 600–700 °C (III). Peak pressure for some rocks is at c. 18 kbar (e.g. Medaris *et al.*, 1998), for others it may be at lower pressure (IV). Decompression occurs at max 850 °C (V) and is followed by cooling (VI).

most 850 °C (Štípská & Powell, 2005). In the light of this study, the higher temperatures for the garnet-clinopyroxene-bearing rocks) may also be due to temperature overestimation. It is not clear whether a pressure of the order of 18 kbar was achieved generally, as this is not constrained by the Opx granulites. E292a appears to have been completely unresponsive during the metamorphism, whereas the orthopyroxene in the other samples is interpreted to be mainly retrogressive, after clinopyroxene. A pressure peak of 18 kbar is therefore not precluded. A cartoon representation of the likely *P–T* evolution is shown in Figs 13 & 14.

The *P–T* path also contributes to the recent discussion of the origin and time of formation of the granulite massifs. Some authors have suggested the formation of magmatic protoliths and a subsequent prograde metamorphic overprint, while others prefer a history in which high-*P* magmatic rocks attain a metamorphic character primarily during cooling and decompression with accompanying deformation (e.g. Vrána & Jakeš, 1982; Vrána, 1989; Carswell, 1991; Roberts & Finger, 1997; Kotková & Harley, 1999; Kröner *et al.*, 2000; Janoušek *et al.*, 2004). The common age of *c.* 340 Myr on rounded zircon in felsic granulites is generally accepted to date the metamorphic peak (e.g. van Breemen *et al.*, 1982; Kröner *et al.*, 1988, 2000; Aftalion *et al.*, 1989; Wendt *et al.*, 1994). Some inherited zircon cores and long prismatic magmatic zircon from felsic granulites are in the range of 470 to 357 Ma (e.g. Wendt *et al.*, 1994; Kröner *et al.*, 2000; Friedl *et al.*, 2004; Štípská *et al.*, 2004; Schulmann *et al.*, 2005) and these older ages are interpreted to date the magmatic emplacement (e.g. Friedl *et al.*, 2004; Schulmann *et al.*, 2005). Ordovician to Devonian zircon ages may be correlated with the magmatic part of the *P–T* path, whereas the Carboniferous age is interpreted to correspond to the peak of prograde metamorphism and exhumation (Fig. 14).

Although the magmatic-metamorphic evolution proposed here is deduced from just the study of Opx granulites, we suggest, by analogy, that this type of evolution was experienced also by other rock types (for example, garnet-clinopyroxene granulites), including the volumetrically more important felsic granulite host to the Opx granulites. Whereas the argument for igneous mineral grain survivors has focussed on the ternary feldspar, it is worth observing that other minerals, e.g. pyroxene and garnet, may well also survive from the igneous protolith. If the Moldanubian is not a UHT metamorphic terrane, it would be appropriate to re-examine the evidence for other terranes that have been proposed to be UHT primarily on the basis of ternary feldspar (see O'Brien & Rötzler, 2003, for a recent compilation).

ACKNOWLEDGEMENTS

This work was supported financially by the Charles University Grant Agency (No.149/2000/B-GEO/PrF to P.Š.) and the Czech National Grant Agency (No. 205-04-2065 to O. Lexa). The visit of P.Š. to the University of Melbourne was partly funded by the Czech Ministry of Education (No. 24313005). R.P. acknowledges ARC Discovery Grant DP0209461, and the hospitality of ETH, Zurich, where some of the work was undertaken. Mineral analyses were carried out on a CAMECA SX100 at the Czech Academy of Sciences, and we gratefully acknowledged V. Böhmová for operating the microprobe. P.Š. thanks P. Pitra for introducing her to the world of pseudosections, and also for numerous discussions. Jan Franěk provided the sample H254. E. Essene and P. O'Brien are thanked for their detailed and constructive reviews, and M. Brown is thanked for his careful editorial work.

REFERENCES

Aftalion, M., Bowes, D. R. & Vrána, S., 1989. Early carboniferous U-Pb zircon age for garnetiferous, perpotassic granulites, Blanský Les Massif, Czechoslovakia. *Neues Jahrbuch Für Mineralogie-Monatshefte*, 145–152.

Benisek, A., Kroll, H., Cemic, L., Kohl, V., Breit, U. & Heying, B., 2003. Enthalpies in (Na,Ca)- and (K,Ca)-feldspar binaries: a high-temperature solution calorimetric study. *Contributions to Mineralogy and Petrology*, **145,** 119–129.

Bohlen, S.R. & Essene, E.J., 1977. Feldspar and oxide thermometry of granulites in the Adirondack Highlands. *Contributions to Mineralogy and Petrology*, **62,** 153–169.

van Breemen, O., Aftalion, M., Bowes, D. R. *et al.*, 1982. Geochronological studies of the Bohemian Massif, Czechoslovakia, and their significance in the evolution of Central Europe. *Transactions of the Royal Society of Edinburgh, Earth Sciences*, **73,** 89–108.

Brown, M., 2002. Retrograde processes in migmatites and granulites revisited. *Journal of Metamorphic Geology*, **20,** 25–40.

Carswell, D. A., 1991. Variscan high P-T metamorphism and uplift history in the Moldanubian Zone of the Bohemian Massif in Lower Austria. *European Journal of Mineralogy*, **3,** 323–342.

Carswell, D. A. & O'Brien, P. J., 1993. Thermobarometry and geotectonic significance of high-pressure granulites: examples from the Moldanubian Zone of the Bohemian Massif in Lower Austria. *Journal of Petrology*, **34,** 427–459.

Chakraborty, S. & Ganguly, J., 1991. Compositional zoning and cation diffusion in garnets. In: *Diffusion, Atomic Ordering and Mass Transport* (ed. Ganguly, J.), pp. 120–175. Springer-Verlag, New York.

Cooke, R. A., 2000. High-pressure/temperature metamorphism in the St. Leonhard Granulite Massif, Austria: evidence from intermediate pyroxene-bearing granulites. *International Journal of Earth Sciences*, **89,** 631–651.

Cooke, R. A. & O'Brien, P. J., 2001. Resolving the relationship between high P-T rocks and gneisses in collisional terranes: an example from the Gföhl gneiss-granulite association in the Moldanubian Zone, Austria. *Lithos*, **58,** 33–54.

Cooke, R. A., O'Brien, P. J. & Carswell, D. A., 2000. Garnet zoning and the identification of equilibrium mineral compositions in high-pressure-temperature granulites from the Moldanubian Zone, Austria. *Journal of Metamorphic Geology*, **18,** 551–569.

Elkins, L. T. & Grove, T. L., 1990. Ternary feldspar experiments and thermodynamic models. *American Mineralogist*, **75,** 544–559.

Ellis, D. J., Sheraton, J. W., England, R. N. & Dallwitz, W. B., 1980. Osumilite-sapphirine-quartz granulites from Enderby Land, Antarctica: mineral assemblages and reactions. *Contributions to Mineralogy and Petrology*, **72,** 123–143.

Fiala, J., Matějovská, O. & Vaňková, V., 1987. Moldanubian granulites: source material and petrogenetic considerations. *Neues Jahrbuch für Mineralogie Abhandlungen*, **157,** 133–165.

Fitzsimmons, I. C. & Harley, S. L., 1994. The influence of cation retrograde exchange on granulite PT estimates and a convergent technique for the recovery of peak metamorphic conditions. *Journal of Petrology*, **35,** 543–576.

Franke, W., 2000. The mid-European segment of the Variscides: tectonostratigraphic units, terrane boundaries and kinematic evolution. In: *Orogenic Processes: Quantification and Modelling in the Variscan Belt, Special Publications, 179*, (eds Franke, W., Haak, V., Oncken, O. & Tanner, D.), pp. 35–63, The Geological Society of London, London.

Friedl, G., Finger, F., Paquette, J., Quadt, A., McNaughton, N. & Fletcher, I., 2004. Pre-Variscan geological events in the Austrian part of the Bohemian Massif deduced from U-Pb zircon ages. *International Journal of Earth Sciences*, **93,** 802–823.

Fuhrman, M. L. & Lindsley, D. H., 1988. Ternary-feldspar modeling and thermometry. *American Mineralogist*, **73,** 201–215.

Guiraud, M., Powell, R. & Rebay, G., 2001. H_2O in metamorphism and unexpected behaviour in the preservation of metamorphic mineral assemblages. *Journal of Metamorphic Geology*, **19,** 445–454.

Harley, S. L., 1998. Ultrahigh temperature granulite metamorphism (1050°C, 12 kbar) and decompression in garnet (Mg_{70})-orthopyroxene-sillimanite gneisses from the Rauer Group, East Antarctica. *Journal of Metamorphic Geology*, **16,** 541–562.

Hayob, J. L., Essene, E. J., Ruiz, J., Ortega-Gutiérrez, F. & Aranda-Gómez, J. J., 1989. Young high-temperature granulites from the base of the crust in central Mexico. *Nature*, **342,** 265–268.

Hokada, T., 2001. Feldspar thermometry in ultrahigh-temperature metamorphic rocks: Evidence of crustal metamorphism attaining similar to 1100°C in the Archean Napier Complex, East Antarctica. *American Mineralogist*, **86,** 932–938.

Holland, T. J. B. & Powell, R., 1998. An internally consistent thermodynamic data set for phases of petrological interest. *Journal of Metamorphic Geology*, **16,** 309–343.

Holland, T. & Powell, R., 2003. Activity-composition relations for phases in petrological calculations: an asymmetric multicomponent formulation. *Contributions to Mineralogy and Petrology*, **145,** 492–501.

Janoušek, V., Finger, F., Roberts, M. P., Frýda, J., Pin, C. & Dolejš, D., 2004. Deciphering petrogenesis of deeply buried granites: whole-rock geochemical constraints on the origin of largely undepleted felsic granulites from the Moldanubian Zone of the Bohemian Massif. *Transactions of the Royal Society of Edinburgh, Earth Sciences*, **95,** 141–154.

Kelsey, D. E., White, R. W., Holland, T. J. B. & Powell, R., 2004. Calculated phase equilibria in K_2O-FeO-MgO-Al_2O_3-SiO_2-H_2O for sapphirine-quartz-bearing mineral assemblages. *Journal of Metamorphic Geology*, **22,** 559–578.

Klemd, R. & Bröcker, M., 1999. Fluid influence on mineral reactions in ultrahigh-pressure granulites: a case study in the Sneznik Mts. (West Sudetes, Poland). *Contributions to Mineralogy and Petrology*, **136,** 358–373.

Kotková, J. & Harley, S. L., 1999. Formation and evolution of high-pressure leucogranulites: experimental constraints and unresolved issues. *Physics and Chemistry of the Earth Part A – Solid Earth and Geodesy*, **24,** 299–304.

Kröner, A., Wendt, I., Liew, T. C. *et al.*, 1988. U-Pb zircon and Sm-Nd model ages of high grade Moldanubian metasediments, Bohemian Massif, Czechoslovakia. *Contributions to Mineralogy and Petrology*, **99,** 257–266.

Kröner, A., O'Brien, P. J., Nemchin, A. A. & Pidgeon, R. T., 2000. Zircon ages for high pressure granulites from South Bohemia, Czech Republic, and their connection to Carboniferous high temperature processes. *Contributions to Mineralogy and Petrology*, **138,** 127–142.

Kryza, R., Pin, C. & Vielzeuf, D., 1996. High-pressure granulites from the Sudetes (south-west Poland): evidence of crustal subduction and collisional thickening in the Variscan Belt. *Journal of Metamorphic Geology*, **14,** 531–546.

Medaris, L. G., Jelínek, E. & Mísař, Z., 1995. Czech eclogites: Terrane settings and implications for Variscan tectonic evolution of the Bohemian Massif. *European Journal of Mineralogy*, **7,** 7–28.

Medaris, L. G., Fournelle, J. H., Ghent, E. D., Jelínek, E. & Mísař, Z., 1998. Prograde eclogite in the Gföhl Nappe, Czech Republic: new evidence on Variscan high-pressure metamorphism. *Journal of Metamorphic Geology*, **16,** 563–576.

O'Brien, P. J., 1997a. Garnet zoning and reaction textures in overprinted eclogites, Bohemian Massif, European Variscides: a record of their thermal history during exhumation. *Lithos*, **41,** 119–133.

O'Brien, P. J., 1997b. Granulite facies overprints of eclogites: short-lived events deduced from diffusion modelling. In: *Precambrian Geology and Metamorphic Petrology, Proceedings 30th International Geological Congress, 17, part II* (eds Qian, X., You, Z., Jahn, B. M. & Halls, H. C.), pp. 157–171. Dordrecht, Netherlands.

O'Brien, P. J. & Rötzler, J., 2003. High-pressure granulites: formation, recovery of peak conditions and implications for tectonics. *Journal of Metamorphic Geology*, **21,** 3–20.

O'Brien, P. J. & Vrána, S., 1995. Eclogites with a short-lived granulite facies overprint in the Moldanubian Zone, Czech Republic: petrology, geochemistry and diffusion modelling of garnet zoning. *Geologische Rundschau*, **84,** 473–488.

O'Brien, P. J., Kröner, A., Jaeckel, P., Hegner, E., Zelazniewicz, A. & Kryza, R., 1997. Petrological and isotopic studies on palaeozoic high-pressure granulites, Gory Sowie Mts, Polish Sudetes. *Journal of Petrology*, **38,** 433–456.

Owen, J. V. & Dostal, J., 1996. Contrasting corona structures in mafic granulite from the Blanský Les Complex, Bohemian Massif, Czech Republic. *Canadian Mineralogist*, **34,** 959–966.

Pattison, D. R. M. & Begin, N. J., 1994. Zoning patterns in orthopyroxene and garnet in granulites – Implications for

geothermometry. *Journal of Metamorphic Geology*, **12,** 387–410.
Petrakakis, K., 1997. Evolution of Moldanubian rocks in Austria: review and synthesis. *Journal of Metamorphic Geology*, **15,** 203–222.
Petrakakis, K. & Jawecki, C., 1995. High-grade metamorphism and retrogression of Moldanubian granulites, Austria. *European Journal of Mineralogy*, **7,** 1183–1203.
Powell, R., Holland, T. & Worley, B., 1998. Calculating phase diagrams involving solid solutions via non- linear equations, with examples using THERMOCALC. *Journal of Metamorphic Geology*, **16,** 577–588.
Powell, R., Guiraud, M. & White, R. W., 2005. Truth and beauty in metamorphic phase equilibria: conjugate variables and phase diagrams. *Canadian Mineralogist*, **43,** 21–33.
Roberts, M. P. & Finger, F., 1997. Do U-Pb zircon ages from granulites reflect peak metamorphic conditions? *Geology*, **25,** 319–322.
Rötzler, J. & Romer, R. L., 2001. P-T-t evolution of ultrahigh-temperature granulites from the Saxon Granulite Massif, Germany. Part I: Petrology. *Journal of Petrology*, **42,** 1995–2013.
Rubie, D. C., 1990. Role of kinetics in the formation and preservation of eclogites. In: *Eclogite Facies Rocks* (ed. Carswell, D.A.), pp. 111–140. Blackie, Glasgow; Chapman and Hall, New York.
Sandiford, M. J. & Powell, R., 1986. Pyroxene exsolution in granulites from Fyfe Hills, Enderby Land, Antarctica: evidence for 1000°C metamorphic temperatures in Archean continental crust. *American Mineralogist*, **71,** 946–954.
Schulmann, K., Kröner, A., Hegner, E. *et al*., 2005. Geodynamics of eastern margin of the Variscan thickened orogenic root, model based on structural, petrological and new geochronological data. *American Journal of Science*, in press.
Schwandt, C. S., Cygan, R. T. & Westrich, H. R., 1996. Ca self-diffusion in grossular garnet. *American Mineralogist*, **81,** 448–451.
Seck, H. A., 1971a. Der Einfluss des Drucks auf die Zusammensetzung koexistierender Alkalifeldspäte und Plagioklase. *Contributions to Mineralogy and Petrology*, **31,** 67–86.
Seck, H. A., 1971b. Koexistierende Alkalifeldspäte und Plagioklase von 650°C bis 900°C. *Neues Jahrbuch Für Mineralogie Abhandlungen*, **115,** 315–345.
Snoeyenbos, D. R., Williams, M. L. & Hanmer, S., 1995. Archean high-pressure metamorphism in the western Canadian shield. *European Journal of Mineralogy*, **7,** 1251–1272.
Štípská, P. & Powell, R., 2005. Constraining the *P–T* path of a MORB-type eclogite using pseudosections, garnet zoning and garnet-clinopyroxene thermometry: an example from the Bohemian Massif. *Journal of Metamorphic Geology*, **23,** 725–743. doi: 10.1111/j.1525-1314.2005.00607.x.
Štípská, P., Schulmann, K. & Kröner, A., 2004. Vertical extrusion and middle crustal spreading of omphacite granulite: a model of syn-convergent exhumation (Bohemian Massif, Czech Republic). *Journal of Metamorphic Geology*, **22,** 179–198.
Tracy, R. J., 1982. Compositional zoning and inclusions in metamorphic minerals. In: *Characterization of Metamorphism through Mineral Equilibria, Reviews in Mineralogy, 10*, (ed. Ferry, J.M.), pp. 355–397, Mineralogical Society of America.
Vrána, S., 1989. Perpotassic granulites from Southern Bohemia – a new rock-type derived from partial melting of crustal rocks under upper mantle conditions. *Contributions to Mineralogy and Petrology*, **103,** 510–522.
Vrána, S. & Jakeš, P., 1982. Orthopyroxene and two-pyroxene granulites from a segment of charnockitic crust in southern Bohemia. *Bulletin of the Czech Geological Survey*, **57,** 129–143.
Wen, S. & Nekvasil, H., 1994. SOLVCALC: An interactive graphics program package for calculating ternary feldspar solvus and for two-feldspar thermometry. *Computers & Geosciences*, **20,** 1025–1040.
Wendt, J. I., Kröner, A., Fiala, J. & Todt, W., 1994. U-Pb zircon and Sm-Nd dating of Moldanubian HP/HT granulites from South Bohemia, Czech Republic. *Journal of the Geological Society, London*, **151,** 83–90.
White, R. W. & Powell, R., 2002. Melt loss and the preservation of granulite facies mineral assemblages. *Journal of Metamorphic Geology*, **20,** 621–632.
White, R. W., Powell, R. & Holland, T. J. B., 2001. Calculation of partial melting equilibria in the system Na_2O-CaO-K_2O-FeO-MgO-Al_2O_3-SiO_2-H_2O (NCKFMASH). *Journal of Metamorphic Geology*, **19,** 139–153.
Whitney, D. L., 1991. Calcium depletion halos and Fe-Mn-Mg zoning around faceted plagioclase inclusions in garnet from a high-grade pelitic gneiss. *American Mineralogist*, **76,** 493–500.

Received 22 November 2005; revision accepted 30 June 2005.

J. metamorphic Geol., 2008, **26,** 253–271 doi:10.1111/j.1525-1314.2007.00754.x

Garnet–clinopyroxene intermediate granulites in the St. Leonhard massif of the Bohemian Massif: ultrahigh-temperature metamorphism at high pressure or not?

M. RACEK,[1,2,3] P. ŠTÍPSKÁ[4] AND R. POWELL[5]
[1]*Institute of Petrology and Structural Geology, Charles University, Albertov 6, 12843, Prague, Czech Republic (martin.racek@geology.cz)*
[2]*Czech Geological Survey, Geologická 6, 15 200 Prague, Czech Republic*
[3]*Géosciences Rennes, UMR CNRS 6118, Université Rennes 1, France*
[4]*CGS/EOST, Université Louis Pasteur, UMR CNRS 7517, 1 Rue Blessig, Strasbourg, France*
[5]*School of Earth Sciences, University of Melbourne, Victoria 3010, Australia*

ABSTRACT Garnet–clinopyroxene intermediate granulites occur as thin layers within garnet–kyanite–K–feldspar felsic granulites of the St. Leonhard granulite body in the Bohemian Massif. They consist of several domains. One domain consists of coarser-grained coexisting ternary feldspar, clinopyroxene, garnet, quartz and accessory rutile and zircon. The garnet has 16–20% grossular, and the clinopyroxene has 9% jadeite and contains orthopyroxene exsolution lamellae. Reintegrated ternary feldspar and the Zr-in-rutile thermometer give temperatures higher than 950 °C. Mineral equilibria modelling suggests crystallization at 14 kbar. The occurrence and preservation of this mineral assemblage is consistent with crystallization from hot dry melt. Between these domains is a finer-grained deformed matrix made up of diopsidic clinopyroxene, orthopyroxene, plagioclase and K-feldspar, apparently produced by reworking of the coarser-grained domains. Embedded in this matrix, and pre-dating the reworking deformation, are garnet porphyroblasts that contain clinopyroxene, feldspar, quartz, rutile and zircon inclusions. In contrast with the garnet in the coarser-grained domains, the garnet generally has $>30\%$ grossular, the included clinopyroxene has 7–27% jadeite and the Zr content of rutile indicates much lower temperatures. Some of these high-grossular garnet show zoning in Fe/(Fe + Mg), decreasing from 0.7 in the core to 0.6 and then increasing to 0.7 at the rim. These garnet are enigmatic, but with reference to appropriate pseudosections are consistent with localized new mineral growth from 650 to 850 °C and 10 to 17 kbar, or with equilibration at 20 kbar and 770 °C, modified by two-stage diffusional re-equilibration of rims, at 10–15 and 8 kbar. The strong pervasive deformation has obscured relationships that might have aided the interpretation of the origin of these porphyroblasts. The evolution of these rocks is consistent with formation by igneous crystallization and subsequent metamorphism to high-*T* and high-*P*, rather than an origin by ultrahigh-*T* metamorphism. Regarding the petrographic complexity, combination of the high grossular garnet with the ternary feldspar to infer ultrahigh-*T* metamorphism at high pressure is not justified.

Key words: Bohemian Massif; clinopyroxene granulite; rutile thermometer; ternary feldspar; UHT metamorphism.

INTRODUCTION

Ultrahigh temperature in excess of 1000 °C at 15–22 kbar has been suggested as the peak metamorphic conditions for the granulite massifs of the Gföhl Unit in the Moldanubian Zone, Bohemian Massif (for summary, see O'Brien & Rötzler, 2003). These conditions have been obtained by thermobarometric methods combining antiperthite with kyanite and high-grossular garnet in felsic granulites and either antiperthite with orthopyroxene and garnet in intermediate orthopyroxene granulites or antiperthite with clinopyroxene and high-grossular garnet in intermediate clinopyroxene granulites (e.g. Carswell & O'Brien, 1993; O'Brien *et al.*, 1997; Cooke, 2000; Cooke *et al.*, 2000; Kröner *et al.*, 2000; Cooke & O'Brien, 2001; Rötzler & Romer, 2001; O'Brien & Rötzler, 2003).

In these studies, it has been assumed that all the minerals in each rock type result from metamorphic mineral growth and that they constitute equilibrium mineral assemblages. However, these granulites had igneous protoliths and it is reasonable to suppose that they may preserve magmatic relicts. Clearly such relicts, unless re-equilibrated under metamorphic conditions, cannot be used to infer peak metamorphic conditions. In general, it is crucial to decide which phases are considered to have once been in equilibrium, for example if minerals grew in several 'events'

in texturally complex rocks. In the rocks of interest the central question is whether ternary feldspar is part of the metamorphic assemblage and can be combined with high grossular garnet to determine peak *P–T* by conventional thermobarometry.

Magmatic relicts in the granulites have been suggested to occur in the Líšov massif (Vrána & Jakeš, 1982; Janoušek *et al.*, 2006) and in the Dunkelsteiner Wald and Blanský les massifs (Štípská & Powell, 2005a). In the Líšov massif, clinopyroxene with orthopyroxene exsolution lamellae, orthopyroxene and feldspar porphyroclasts are interpreted as magmatic relicts. There are no minerals indicative of higher pressure such as kyanite or high-grossular garnet and therefore ultrahigh temperature metamorphism at high-pressure has not been suggested for this massif.

Štípská & Powell (2005a) studied orthopyroxene–garnet granulites that contain antiperthite and modelled these rocks using pseudosections. A coarse-grained texture formed by antiperthite, perthite, quartz, orthopyroxene and low-grossular garnet (12–14%) was interpreted to be the result of crystallization of dry melt at around 1000 °C and 8 kbar. In another sample, large antiperthite porphyroclasts are present in a highly recrystallized fine-grained matrix formed by plagioclase, K-feldspar, quartz, orthopyroxene and biotite. The reintegrated compositions of the perthite and antiperthite are consistent with crystallization at >1000 °C. This sample contains a diagnostic texture, in which antiperthite is included in strongly zoned garnet. The garnet core has high grossular (45%) and $X_{Fe} = Fe/(Fe + Mg)$ of 0.73, which indicate conditions of 650 °C and 10 kbar in pseudosections, with chemical zoning that is consistent with prograde growth during an increase in *P–T* conditions. Therefore the high-grossular garnet core cannot have been in equilibrium with the ternary feldspar inclusions, but it can have been in equilibrium with the host plagioclase and K-feldspar lamellae that represent two separate mineral phases after exsolution. The exsolution texture survives at low temperature unless it is destroyed by deformation and/or is recrystallized. This study showed that ternary feldspar included in garnet is either magmatic feldspar in a magmatic garnet, or a magmatic feldspar relict in a metamorphic garnet. Therefore the ternary feldspar in these orthopyroxene granulites cannot be combined with high-grossular metamorphic garnet for thermobarometric purposes.

In this contribution, a study of garnet–clinopyroxene granulites that contain high-temperature antiperthite as well as high grossular garnet is presented. They occur as thin discontinuous layers in garnet–kyanite–K-feldspar granulites in the St. Leonhard massif in the Bohemian Massif in Austria. We examine the textural relationships of the minerals, mineral compositions, especially of garnet, clinopyroxene and antiperthite, and model the rock evolution using pseudosections and combine them with temperatures obtained from the Zr content of rutile. It is shown that the rocks are complex petrographically, and that the high grossular garnet and antiperthite were unlikely to have been part of an equilibrium assemblage, and so should not be used in combination to determine *P–T*. The parts of the rocks that have ultrahigh-temperature features are consistent with crystallization from a dry melt.

GEOLOGICAL SETTING AND PREVIOUS PETROLOGY

The Bohemian Massif is composed of three main tectonic domains (from west to east): Saxothuringia, Moldanubian Region and Brunia (Fig. 1). They preserve characteristic metamorphic patterns interpreted to be remnants of a Variscan subduction zone, an internal, Andean-type orogenic root and a continental indentor, respectively (Schulmann *et al.*, 2005). The Moldanubian domain is dominated by medium- to high-grade metamorphic rocks that are intruded by Devonian to Carboniferous plutonic rocks, ranging from calcalkaline arc-type intrusions to late-tectonic granites (e.g. Holub *et al.*, 1997; Janoušek *et al.*, 2000, 2004). The lithological subdivision of the Moldanubian domain includes the high-grade Gföhl unit, interpreted as lower orogenic crust, and the Monotonous and Varied paragneiss-dominated units, generally showing metamorphic conditions of an anatectic orogenic middle crust (Schulmann *et al.*, 2005). The Gföhl unit is exposed in two large NE–SW-trending belts, and within these belts the lower orogenic crust was exhumed and juxtaposed to middle orogenic levels along vertical structures, and then laterally spread out within/and over the middle crust (Štípská *et al.*, 2004; Schulmann *et al.*, 2005; Tajčmanová *et al.*, 2006; Franěk *et al.*, 2006; Racek *et al.*, 2006). Massifs lithologically similar to the Gföhl unit occur also within the Saxothuringian domain (O'Brien & Rötzler, 2003 and references therein), and in the Góry Sowie massif in Poland (O'Brien *et al.*, 1997) with an uncertain geological position.

The Gföhl unit is dominated by felsic anatectic orthogneiss and several kilometre-large bodies of kyanite–K-feldspar granulites (O'Brien & Rötzler, 2003; and references therein). The felsic granulites are interpreted as having magmatic protoliths and correspond geochemically to slightly peraluminous fractionated granites (e.g. Fiala *et al.*, 1987; Janoušek *et al.*, 2004; Janoušek & Holub, 2007). They contain minor, chemically intermediate varieties of granulite, commonly of two types with either garnet–clinopyroxene or garnet–orthopyroxene (Vrána & Jakeš, 1982; Carswell & O'Brien, 1993; Petrakakis & Jawecki, 1995; Petrakakis, 1997; Cooke, 2000; Cooke *et al.*, 2000; Cooke & O'Brien, 2001; O'Brien & Rötzler, 2003; Janoušek *et al.*, 2006; Štípská *et al.*, 2004). The orthogneisses and granulites also host garnet and spinel peridotites, and mantle and crustal eclogites (Medaris *et al.*, 1995, 1998; Carswell, 1991; Štípská & Powell, 2005b).

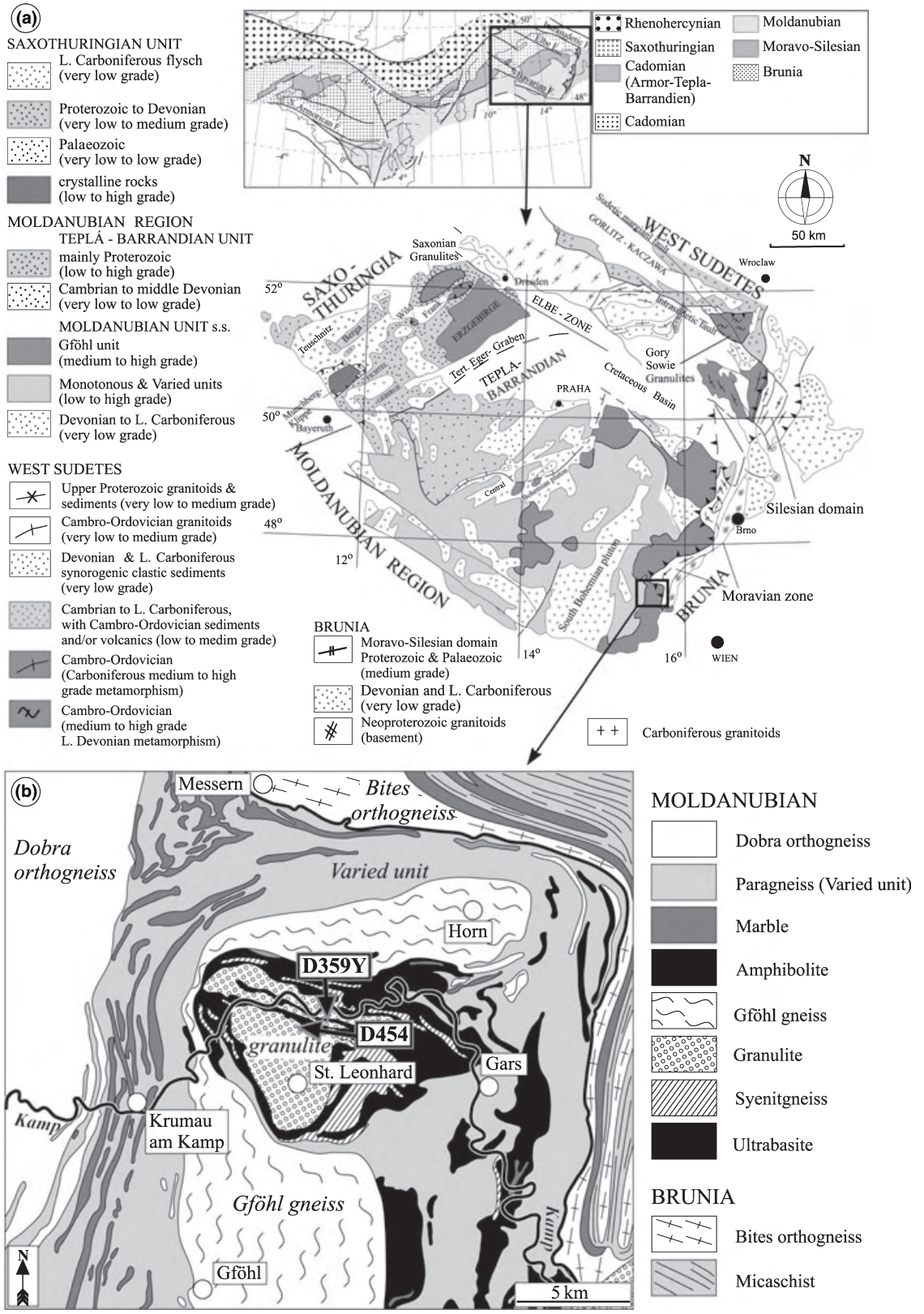

Fig. 1. (a) Geological map of the Bohemian Massif. The upper inset shows the position of the Bohemian Massif in the European Variscides. (b) Geological map of the studied area with major units shown. Indicated are the locations of the studied samples D359Y and D454.

The most common age of zircon from the granulites is *c*. 340 Ma and it is commonly interpreted as dating the peak metamorphic conditions (e.g. Aftalion *et al*., 1989; Kröner *et al*., 1988, 2000; van Breemen *et al*., 1982; Wendt *et al*., 1994; Štípská *et al*., 2004; Lange *et al*., 2005). Older ages between 470 and 350 Ma are reported from zircon cores and from prismatic varieties (e.g. Friedl *et al*., 2004; Kröner *et al*., 2000; Schulmann *et al*., 2005; Wendt *et al*., 1994; Klemd & Bröcker, 1999; Lange *et al*., 2005; Janoušek *et al*., 2006), interpreted partly in terms of inheritance and partly in terms of magmatic crystallization of the granulite protoliths.

The St. Leonhard granulite massif in Lower Austria is a 8 by 5 km body tectonically overlying the middle orogenic crust of the Varied unit composed of anatectic paragneisses, amphibolites, marbles, and less abundant quartzites and metamorphosed acid volcanic rocks (Fig. 1b). The massif is dominated by kyanite–K-feldspar granulites that contain rare garnet–antiperthite–clinopyroxene granulites as centimetre-scale layers and boudins within the felsic granulites (Cooke, 2000). The massif is surrounded by garnet–clinopyroxene rocks that do not contain antiperthite and that form also a several kilometres long, east- to west-trending belt that divides the body (Cooke *et al*., 2000). In its northern part there is a belt of garnet peridotites (e.g. Scharbert & Carswell, 1983; Carswell, 1991; Becker, 1997).

The garnet–clinopyroxene–antiperthite rocks, the subject of this study, have already been investigated by Cooke (2000). He combined the reintegrated compositions of ternary feldspar, aluminous centres of clinopyroxene and high grossular centres of garnet and using conventional thermobarometric methods obtained 15–19 kbar and 950–1050 °C that he interpreted as the peak metamorphic conditions. He also distinguished later metamorphic recrystallization at 8–12 kbar and cooling to 500 °C. Similar garnet–clinopyroxene–antiperthite granulites from the Saxothuringian domain have also been studied, where the peak metamorphic conditions were estimated to be more than 1000 °C and 20 kbar (Rötzler & Romer, 2001; O'Brien & Rötzler, 2003).

PETROGRAPHY

The clinopyroxene-bearing granulites of this study are dark fine-grained massive rocks that occur as centimetre- to tens of centimetre-thick discontinuous bands and lenses in the main body of felsic kyanite–K-feldspar granulite of the St. Leonhard massif. The rocks are commonly fine-grained and appear isotropic, rarely showing a weak macroscopic foliation. Under the microscope all granulite types show a strong foliation that is defined mainly by bands of recrystallized quartz and feldspar and by the preferred orientation of biotite.

Several samples of the clinopyroxene-bearing granulites were studied. They are composed of antiperthitic plagioclase, plagioclase, quartz, garnet, clinopyroxene, orthopyroxene, minor biotite and K-feldspar, with accessory rutile, zircon, ilmenite and apatite. These minerals occur in three petrographic contexts (Figs 2–4). The first involves a coarse-grained texture (Fig. 2). The second is a fine-grained matrix texture that appears to have resulted from strong overprinting involving recrystallization accompanying the strain responsible for the dominant rock foliation (Fig. 3). The samples show various degrees of preservation of the coarse-grained texture as a result of the heterogeneous nature of this reworking. There are also texturally distinct high grossular garnet that occur in the recrystallized matrix, that are numerous in some samples. These, constituting the third petrographic context, are termed enigmatic garnet (Fig. 4) as the relationship between these garnet, the coarser-grained texture, and the fine-grained texture derived from it, is unclear. The features of these three petrographic contexts will be described separately for the two rock specimens studied in detail.

Coarse-grained texture

Relicts of the coarse-grained texture are preserved to some extent in all of the samples studied, but the texture is best preserved in D359Y.

Sample D359Y

The sample D359Y is characterized by the presence of well-preserved relicts of the coarse-grained texture. Large garnet, up to 2 mm in diameter, are commonly interstitial to antiperthite. They commonly contain large inclusions of antiperthite (Fig. 2a) and less abundant and smaller inclusions of clinopyroxene (up to 0.3 mm) (Fig. 2b), but some large garnet have almost no inclusions (Fig. 5a). Many garnet have oriented rutile rods and the included clinopyroxene commonly has thin orthopyroxene exsolution lamellae. The coarse-grained texture is also preserved in the form of abundant relicts of large antiperthite (Fig. 2c) and clinopyroxene porphyroclasts (up to 1.2 mm) in the matrix (Fig. 2d,e).

Fig. 2. Relicts of coarse-grained texture in BSE images. (a) Antiperthite in garnet (D359Y). (b) Matrix clinopyroxene and its inclusions in garnet show orthopyroxene exsolution (D359Y). (c) Relict antiperthite in recrystallized matrix (D359Y). (d & e) Clinopyroxene porphyroclasts with antiperthite and garnet inclusions enveloped by coronas of orthopyroxene (D359Y) (f) Skeletal garnet includes antiperthite and clinopyroxene (D454). (g) Matrix clinopyroxene with orthopyroxene exsolution (D454). (h) Inclusion-poor garnet with rutile rods (D454). The arrow corresponds to the compositional profile in Fig. 6e. (i) Garnet with rutile rods (marked by dashed line) is surrounded by enigmatic garnet free of rutile rods (D454). The areas marked by dashed line in (a & c & f) correspond to reintegrated feldspar compositions 1, 2 & 3 in Fig. 7.

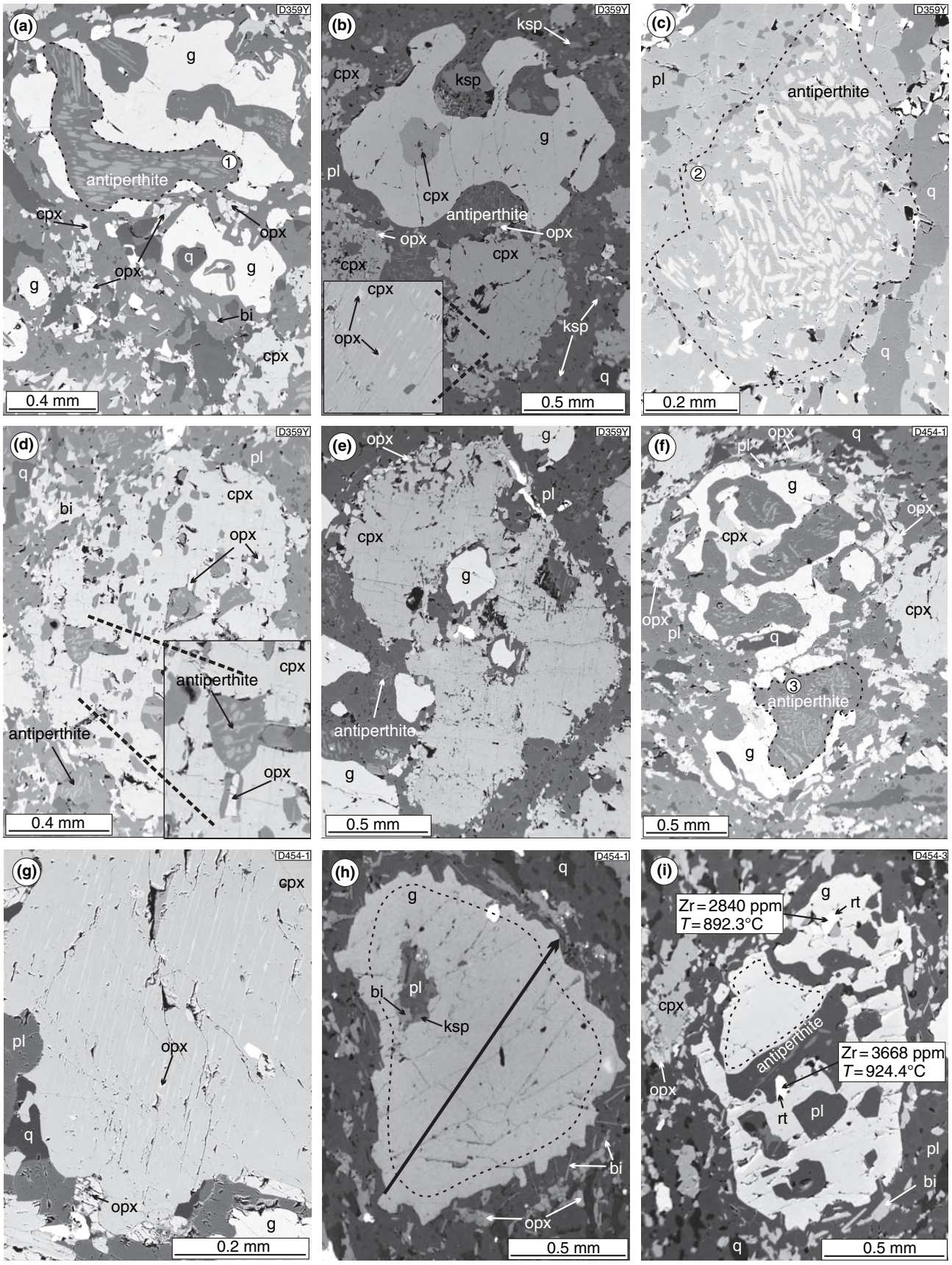

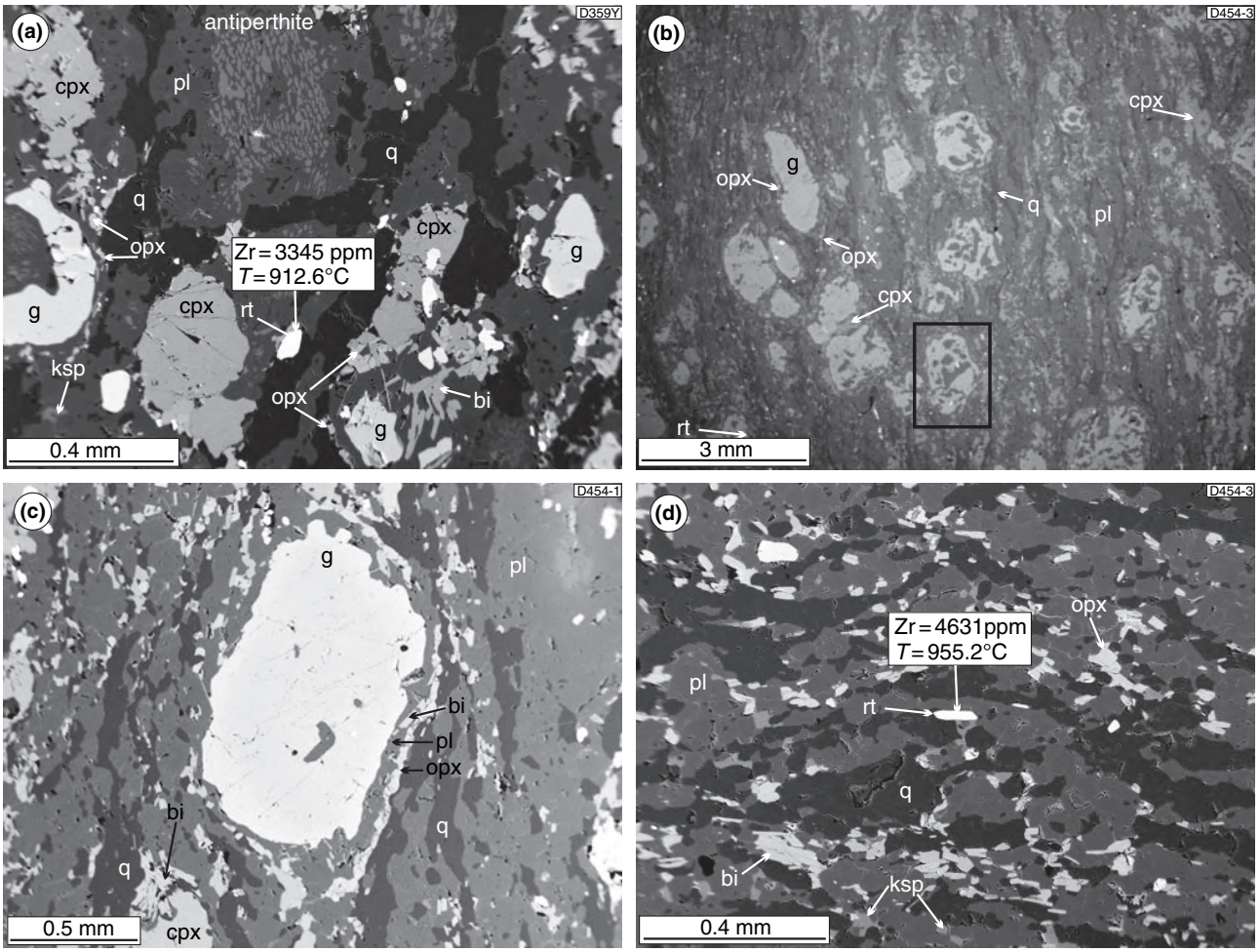

Fig. 3. Fine-grained matrix texture in BSE images: (a) Bands of fine-grained feldspar formed at the expense of antiperthite and recrystallized quartz ribbons. Garnet enveloped by plagioclase–orthopyroxene corona (D359Y). (b) Strongly recrystallized matrix of quartz ribbons, bands of fine-grained feldspar, orthopyroxene, clinopyroxene and biotite anastomosing around mostly enigmatic garnet. Rectangle indicates position of the compositional map in Fig. 5e (D454). (c) Plagioclase–orthopyroxene corona around garnet in recrystallized matrix (D454). (d) Detail of recrystallized matrix with quartz ribbons alternating with fine-grained feldspar bands and with fine-grained orthopyroxene, clinopyroxene and biotite. Zr content of rutile and calculated temperature using Tomkins *et al.* (2007) are indicated (a & d).

These clinopyroxene exhibit orthopyroxene exsolution lamellae (Fig. 2b inset) and rarely contain inclusions of antiperthite (Fig. 2d inset) and small garnet (Fig. 2e). The antiperthite inclusions at the contact with garnet have a plagioclase rim without K-feldspar exsolution lamellae that is in optical continuity with the host in the antiperthite. The matrix antiperthite is surrounded by recrystallized plagioclase. Accessory rutile and zircon are included in garnet, antiperthite and clinopyroxene and occur in the matrix (Fig. 3a).

Sample D454

The features of the relict coarse-grained texture are similar to those of D359Y, however, their preservation is not as good. Sample D454 contains only a few garnet with large inclusions of antiperthite and clinopyroxene (Fig. 2f). In places, there is a difficulty in distinguishing texturally the garnet associated with coarse-grained texture from the enigmatic garnet. However, some garnet has rutile rods, which are considered to be a high-temperature feature. In a few cases garnet exhibiting rutile rods and associated antiperthite is largely surrounded by enigmatic garnet (Figs 2i & 4c), and some inclusion-poor garnet also shows rutile rods (Fig. 2h). A few large clinopyroxene porphyroclasts with orthopyroxene exsolution occur in the matrix (Fig. 2g) and apart from a few small relicts, antiperthite is present only as inclusions in garnet (Fig. 2f). Accessory rutile and zircon are present in garnet and clinopyroxene and occur in the matrix (Fig. 2i).

Fine-grained matrix texture

The reworking of the coarse-grained texture occurred in all the samples, producing recrystallized bands

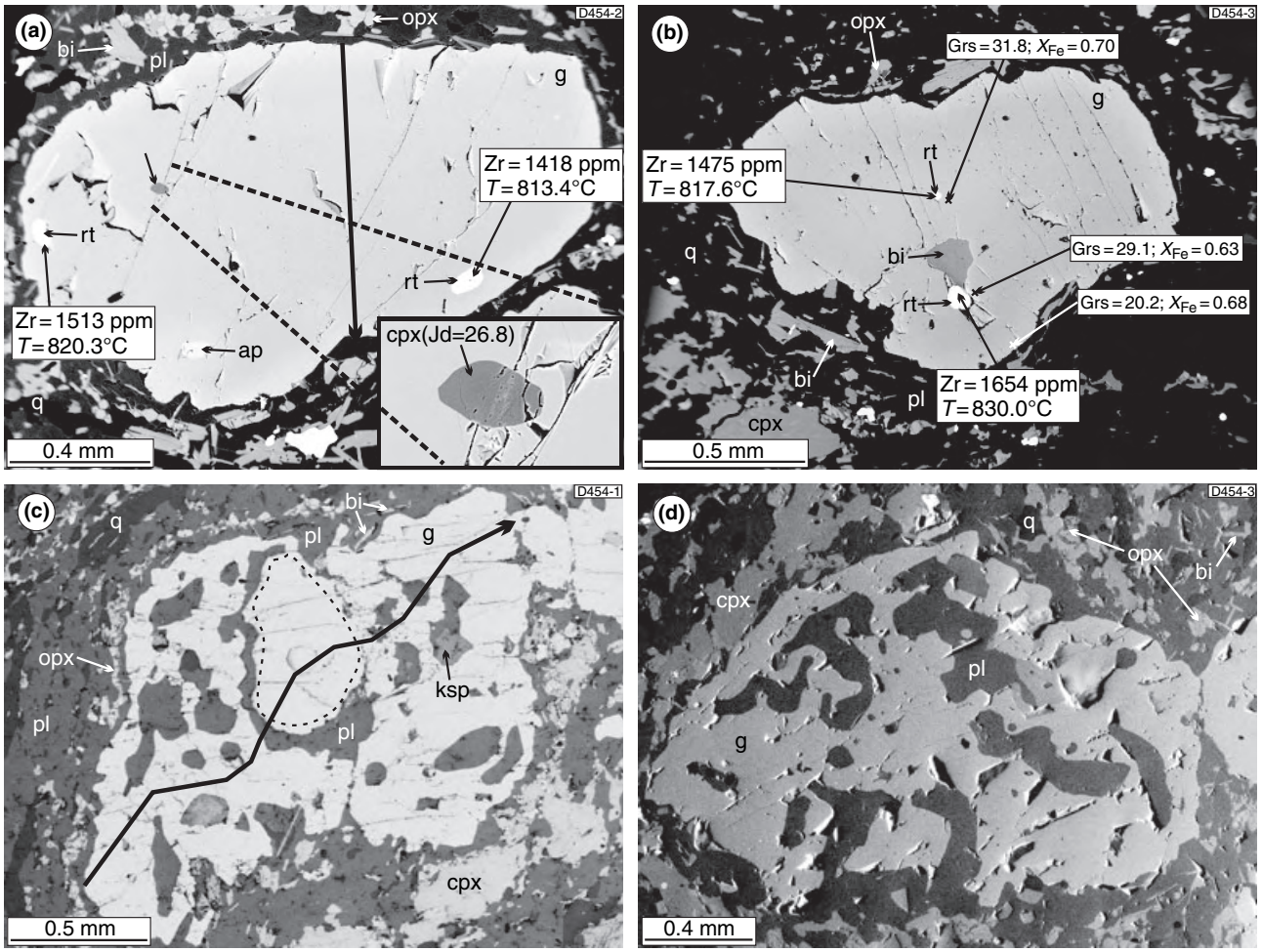

Fig. 4. Enigmatic garnet (D454) in BSE images: (a & b) Inclusion-poor garnet includes rutile, clinopyroxene (a) and biotite (b). (c) Garnet with rutile rods (marked by dashed line) is surrounded by enigmatic garnet free of rutile rods with plentiful inclusions of feldspar (D454) (d) Numerous amoeboid inclusions of plagioclase in enigmatic garnet. Zr content of rutile and calculated temperature after Tomkins *et al.* (2007) are indicated (a & b). Arrows across garnet in (a & c) correspond to the compositional profiles in Fig. 6b & d.

that define the main rock fabric (Fig. 3). Feldspar in these bands is a fine-grained (10–50 μm) mixture of plagioclase and less abundant K-feldspar that contains also minor small grains of clinopyroxene, orthopyroxene and biotite (10–50 μm). Quartz forms monomineralic ribbons of recrystallized grains with larger grain size (50–200 μm). The matrix contains accessory rutile, zircon, apatite and ilmenite.

Sample D359Y

Sample D359Y shows the lowest degree of reworking. The coarse-grained quartzo-feldspathic texture is heterogeneously affected by a network of fine-grained recrystallized monomineralic quartz ribbons (grain size 50–200 μm, Fig. 3a) and by development of a fine-grained matrix composed of plagioclase with minor K-feldspar and quartz that forms at the expense of former antiperthite (Fig. 3a). The relict antiperthite is surrounded by recrystallized plagioclase. The recrystallization is connected also with growth of small grains of clinopyroxene and orthopyroxene (10–50 μm) in the matrix (Fig. 2a). Orthopyroxene preferentially grows at the contact with relict clinopyroxene porphyroclasts and forms discontinuous coronas around them (Fig. 2e). Orthopyroxene grains also participate in the development of more complex coronas around garnet, being separated from garnet by a plagioclase corona (Fig. 3a). Biotite is oriented parallel to the foliation or forms around partly resorbed garnet (Fig. 3a).

Sample D454

The degree of fine-grained recrystallization in sample D454 is much higher than in sample D359Y. The matrix is almost completely recrystallized into monomineralic bands of fine-grained quartz alternating with recrystallized feldspar, with some biotite, quartz and

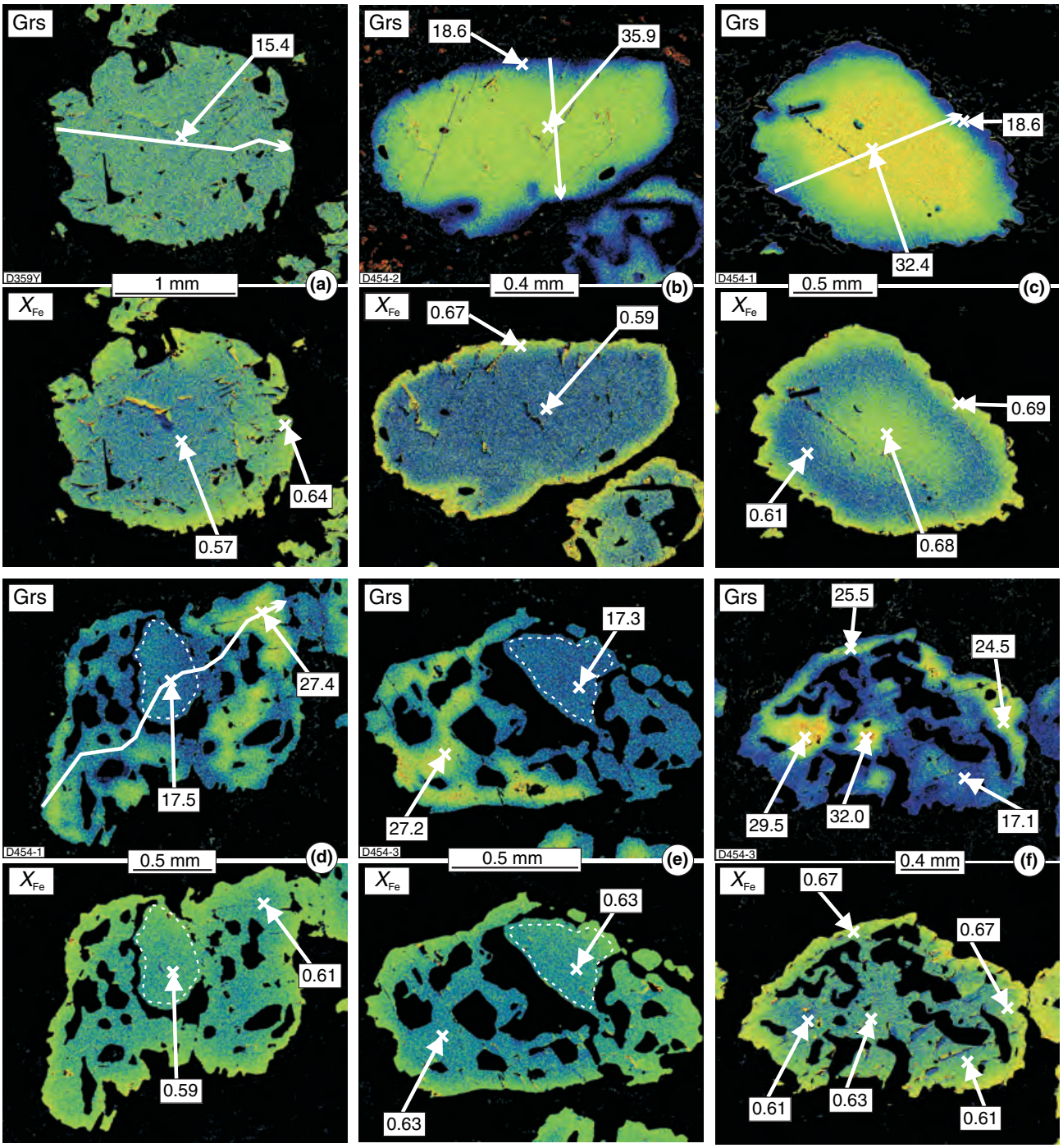

Fig. 5. Garnet compositional maps of grossular and X_{Fe} ratio. (a) Inclusion-poor garnet with low and constant grossular content and X_{Fe} ratio increasing at the rim (magmatic garnet, D359Y). (b-f) Enigmatic garnet from sample D454: (b) Garnet with X_{Fe} and high grossular plateau in the core. At the rim grossular decreases and X_{Fe} increases. (c) Garnet with high grossular plateau in the core and strong zoning in X_{Fe} that is high in the core, decreases, and again increases at the rim. (d & e) Garnet with inclusion-free part containing rutile rods (marked by dashed line) have flat distribution of elements with low grossular and are enclosed by inclusion-rich garnet with considerably higher grossular content. Arrows in (a–d) mark positions of compositional profiles in Fig. 6a–d. (f) Garnet with numerous amoeboid plagioclase inclusions show variable grossular content with peaks away from the matrix and plagioclase inclusions.

small grains of orthopyroxene and clinopyroxene (Fig. 3b,c & d). The relict large clinopyroxene porphyroclasts are enveloped by fine-grained orthopyroxene (Fig. 2g) and most garnet has a corona of plagioclase and orthopyroxene, in places also with biotite (Figs 2f & 3c).

Enigmatic garnet

Besides the coarse-grained texture and superimposed fine-grained recrystallization that are observed in all the samples, many of the rocks studied also contain garnet with different internal textural characteristics that only rarely have a clear relationship to the textures described above. Sample 359Y does not contain enigmatic garnet, so the following relates to sample D454. This sample contains a range of large (up to 1 mm) enigmatic garnet. The most distinctive are those that contain only a few small inclusions from amongst plagioclase, clinopyroxene, rutile or zircon (Fig. 4a,b). The clinopyroxene inclusions have not exsolved orthopyroxene (inset in Fig. 4a) and plagioclase is not antiperthitic. There is an apparent continuum from such 'clean' garnet to those with numerous large, angular to amoeboid plagioclase inclusions (Fig. 4c,d) as well as clinopyroxene, rutile, zircon and rarely biotite ('inclusion-rich' garnet). Adjacent plagioclase inclusions may be optically continuous (Fig. 4d). Parts of the plagioclase inclusions may be coarsely antiperthitic (Fig. 2i). Some garnet and some parts of a single garnet contain numerous oriented rods of rutile (Figs 2i,h & 4c). In few clear cases, referred to above, enigmatic garnet with numerous plagioclase inclusions largely surrounds coarse-grained texture garnet with rutile rods, with adjacent antiperthite (Figs 2i & 4c).

MINERAL CHEMISTRY

The composition of minerals in the two samples is described in terms of the three textural contexts. Mineral analyses were performed on an electron microprobe CAMECA SX-100 at the Geological Institute of Academy of Science of the Czech Republic and on an electron microprobe CAMECA SX-50 at the French Research Institute for Exploitation of the Sea in Brest. The compositional maps of garnet were obtained on a scanning electron microscope CamScan CS 3200 at the Czech Geological Survey in Prague and on a scanning electron microscope VEGA\\XMU (Vega) at the University Louis Pasteur in Strasbourg. Zr content of rutile was measured on an electron microprobe CAMECA SX-100 at the Institute of Mineralogy at the University of Stuttgart.

Silicate minerals were analysed in point beam mode at 15 kV and 15 nA. The average composition of the clinopyroxene porphyroclasts with orthopyroxene lamellae was obtained by analysing an area of 20×20 μm in the scanning mode at 15 kV and 3 nA on the electron microscope CamScan CS. Rutile was analysed in point-beam mode at 15 kV and 50 nA. Representative analyses are listed in Tables 1–3.

Mineral abbreviations, end-members and variables

q, quartz; pl, plagioclase; ksp, K-feldspar; g, garnet; cpx, clinopyroxene; opx, orthopyroxene; o, omphacite; ky, kyanite; mu, muscovite; bi, biotite; coe, coesite; liq, silicate melt; ap, apatite; rt, rutile.

X_{Fe} = $Fe_{tot}/(Fe_{tot} + Mg)$; Alm – almandine = $Fe_{tot}/(Fe_{tot} + Mg + Ca + Mn)$; Prp – pyrope = $Mg/(Fe_{tot} + Mg + Ca + Mn)$; Grs – grossular = $Ca/(Fe_{tot} + Mg + Ca + Mn)$; Sps – spessartine = $Mn/(Fe_{tot} + Mg + Ca + Mn)$; An – anorthite = Ca/

Table 1. Representative analyses of garnet.

Sample	D359Y	D359Y	D359Y	D454	D454	D454	D454	D454	D454	D454	D454	D454	D454
Mineral	g	g	g	g	g	g	g	g	g	g	g	g	g
Position	Core-1	Core-2	Rim	Core	Rim	Core	Between	Rim	Core	H-Ca	Rim	Core	Rim
Texture	Coarse	Coarse	Coarse	Enigm	Enigm	Enigm	Enigm	Enigm	Coarse/enigm	Coarse/enigm	Coarse/enigm	Coarse	Coarse
SiO_2	39.67	39.10	38.81	39.28	38.06	39.16	39.45	38.39	39.74	39.57	39.11	39.54	38.93
TiO_2	0.18	0.22	0.01	0.17	0.01	0.17	0.20	0.06	0.00	0.00	0.05	0.00	0.08
Cr_2O_3	0.01	0.08	0.09	0.08	0.00	0.02	0.00	0.05	0.00	0.00	0.00	0.00	0.00
Al_2O_3	21.88	21.87	21.84	22.47	21.73	21.82	21.92	21.90	22.51	22.50	22.35	22.61	22.55
FeO	22.72	21.79	24.16	17.61	25.08	21.38	20.71	25.88	22.49	20.26	24.83	21.08	24.81
MnO	0.42	0.58	0.38	0.39	1.08	0.35	0.28	0.87	0.38	0.55	0.81	0.42	0.50
MgO	9.39	8.30	8.38	7.22	7.30	5.68	7.33	6.60	8.67	7.39	6.99	9.20	7.99
CaO	6.04	7.75	5.68	13.68	6.34	11.90	10.81	6.31	6.34	9.99	6.42	7.10	4.86
Na_2O	0.01	0.01	0.00	0.05	0.01	0.04	0.04	0.03	0.00	0.00	0.00	0.00	0.00
Total	100.33	99.71	99.35	100.94	99.60	100.53	100.73	100.09	100.13	100.25	100.55	99.94	99.72
cat/charge	8/24	8/24	8/24	8/24	8/24	8/24	8/24	8/24	8/24	8/24	8/24	8/24	8/24
Si	3.01	2.99	2.99	2.95	3.02	3.00	2.99	2.97	3.02	3.01	3.00	3.00	3.00
Ti	0.01	0.01	0.00	0.01	0.00	0.01	0.01	0.00	0.00	0.00	0.00	0.00	0.00
Cr	0.00	0.00	0.01	0.00	0.00	0.00	0.00	0.00	0.00	0.00	0.00	0.00	0.00
Al	1.96	1.97	1.99	1.99	2.02	1.97	1.96	2.00	2.02	2.02	2.02	2.02	2.05
Fe^{3+}	0.00	0.01	0.02	0.09	0.00	0.02	0.05	0.05	0.00	0.00	0.00	0.00	0.00
Fe^{2+}	1.44	1.38	1.54	1.01	1.61	1.35	1.27	1.63	1.43	1.29	1.59	1.34	1.60
Mn	0.03	0.04	0.02	0.02	0.07	0.02	0.02	0.06	0.02	0.04	0.05	0.03	0.03
Mg	1.06	0.95	0.96	0.81	0.66	0.65	0.83	0.76	0.98	0.84	0.80	1.04	0.92
Ca	0.49	0.64	0.47	1.10	0.61	0.98	0.88	0.52	0.52	0.81	0.53	0.58	0.40
Na	0.00	0.00	0.00	0.01	0.00	0.01	0.01	0.00	0.00	0.00	0.00	0.00	0.00
X_{Fe}	0.58	0.60	0.62	0.58	0.71	0.68	0.61	0.69	0.59	0.61	0.67	0.56	0.64
Alm (%)	47.71	46.25	51.66	36.39	0.55	45.38	43.22	55.54	48.42	43.30	53.59	44.86	54.18
Prp (%)	35.16	31.42	31.95	26.58	0.22	21.50	27.29	25.23	33.27	28.14	26.89	34.89	31.10
Grs (%)	16.24	21.08	15.56	36.21	0.21	32.37	28.91	17.35	17.49	27.36	17.74	19.35	13.60
Sps (%)	0.90	1.25	0.83	0.82	0.02	0.75	0.58	1.88	0.83	1.20	1.78	0.90	1.11

Table 2. Representative analyses of clinopyroxene.

Sample	D359Y	D359Y	D454	D454	D359Y	D359Y	D359Y	D359Y	D454	D454	D454	D454
Mineral	cpx	cpx	cpx	cpx	cpx	cpx	cpx + opx	cpx	cpx	cpx	cpx	cpx
Position	mx-core	mx-rim	mx-core	mx-rim	incl-core	incl-rim	Matrix	Matrix	Matrix	Incl	Incl	Incl
Texture	Coarse	Coarse	Coarse	Coarse	Coarse	Coarse	Coarse	Fine	Fine	Enigm	Enigm	Enigm
SiO_2	51.75	52.95	51.38	51.25	51.97	52.62	51.69	52.66	52.22	49.54	50.33	49.08
TiO_2	0.54	0.21	0.64	0.37	0.57	0.39	0.64	0.21	0.36	0.55	0.32	0.64
Cr_2O_3	0.01	0.08	0.12	0.05	0.05	0.02	0.00	0.12	0.06	0.11	0.03	0.00
Al_2O_3	4.56	1.86	4.51	3.15	5.11	3.41	4.60	1.64	3.26	11.40	13.27	10.31
FeO	7.90	7.22	8.12	9.24	6.89	7.15	9.59	8.11	8.69	4.85	4.01	6.25
MnO	0.15	0.00	0.22	0.26	0.20	0.12	0.00	0.06	0.19	0.08	0.06	0.00
MgO	12.78	14.11	12.67	13.34	12.89	14.21	13.86	14.05	13.43	11.15	9.49	10.57
CaO	20.83	22.03	21.55	21.90	20.63	21.16	18.19	21.93	21.40	19.69	18.28	22.01
Na_2O	0.89	0.35	0.85	0.54	1.12	0.67	0.77	0.34	0.44	2.24	3.83	1.25
Total	99.41	98.80	100.07	100.10	99.44	99.74	99.35	99.11	100.04	99.61	99.61	100.12
cat/charge	4/12	4/12	4/12	4/12	4/12	4/12	4/12	4/12	4/12	4/12	4/12	4/12
Si	1.93	1.98	1.91	1.90	1.93	1.95	1.93	1.97	1.94	1.81	1.82	1.81
Ti	0.02	0.01	0.02	0.01	0.02	0.01	0.02	0.01	0.01	0.01	0.01	0.02
Cr	0.00	0.00	0.00	0.00	0.00	0.00	0.00	0.00	0.00	0.00	0.00	0.00
Al	0.07	0.02	0.09	0.10	0.07	0.05	0.07	0.03	0.14	0.49	0.56	0.45
Fe^{3+}	0.13	0.07	0.10	0.04	0.15	0.09	0.13	0.05	0.00	0.00	0.00	0.00
Fe^{2+}	0.00	0.00	0.01	0.07	0.00	0.00	0.00	0.00	0.00	0.02	0.05	0.00
Mn	0.25	0.23	0.24	0.22	0.21	0.22	0.30	0.25	0.27	0.13	0.07	0.19
Mg	0.00	0.00	0.01	0.01	0.01	0.00	0.00	0.00	0.01	0.00	0.00	0.00
Ca	0.00	0.00	0.00	0.00	0.00	0.00	0.00	0.00	0.00	0.00	0.00	0.00
Na	0.71	0.79	0.70	0.74	0.71	0.78	0.77	0.78	0.74	0.61	0.51	0.58
Ca	0.83	0.88	0.86	0.87	0.82	0.84	0.73	0.88	0.85	0.77	0.71	0.87
Na	0.06	0.03	0.06	0.04	0.08	0.05	0.06	0.02	0.03	0.16	0.27	0.09
Jd (%)	6.40	2.57	6.12	3.88	8.05	4.77	5.60	2.49	3.16	15.84	26.79	8.93
X_{Fe}	0.26	0.22	0.26	0.28	0.23	0.22	0.28	0.24	0.27	0.20	0.19	0.25
Opx (%)	9.62	7.97	7.93	8.51	8.95	10.84	20.80	9.19	10.91	7.09	2.39	4.18
CaTs (%)	4.14	0.11	4.09	0.40	3.99	3.16	3.65	1.19	3.71	13.90	11.40	15.86

Table 3. Representative analyses of feldspar, orthopyroxene and biotite.

Sample	D359Y	D454	D359Y	D454	D359Y	D454	Sample	D359Y	D359Y	D454	Sample	D359Y	D454
Mineral	pl	pl	ksp	ksp	pl	ksp	Mineral	opx	opx	opx	Mineral	bi	bi
Position	Antipert	Antipert	Antipert	Antipert	Matrix	Matrix	Position	Exsol	Matrix	Matrix	Position	Matrix	Incl
Texture	Coarse	Coarse	Coarse	Coarse	Fine	Fine	Texture	Coarse	Fine	Fine	Texture	Fine	Enigm
SiO_2	59.59	59.12	64.21	64.12	58.97	65.24	SiO_2	51.63	52.92	52.50	SiO_2	37.62	37.51
TiO_2	0.00	0.00	0.00	0.00	0.01	0.00	TiO_2	0.08	0.05	0.02	TiO_2	6.91	7.19
Cr_2O_3	0.00	0.00	0.00	0.00	0.02	0.02	Cr_2O_3	0.00	0.03	0.06	Cr_2O_3	0.20	0.04
Al_2O_3	25.28	25.96	18.52	18.52	25.74	19.08	Al_2O_3	3.15	1.16	1.04	Al_2O_3	13.85	13.28
FeO	0.14	0.13	0.05	0.02	0.33	0.01	FeO	24.15	23.23	23.91	FeO	13.50	11.61
MnO	0.00	0.00	0.00	0.00	0.06	0.03	MnO	0.38	0.41	0.29	MnO	0.05	0.02
MgO	0.01	0.01	0.00	0.01	0.00	0.00	MgO	20.35	21.99	20.92	MgO	14.06	16.23
CaO	7.38	7.81	0.05	0.06	7.98	0.12	CaO	0.61	0.51	0.51	CaO	0.01	0.02
Na_2O	7.28	6.85	0.81	0.62	6.79	1.15	Na_2O	0.01	0.01	0.04	Na_2O	0.00	0.08
K_2O	0.31	0.51	16.26	16.43	0.48	14.67	K_2O	0.01	0.02	0.00	K_2O	10.09	9.62
Total	99.99	100.39	99.90	99.78	100.37	100.32	Total	100.38	100.33	99.30	Total	96.27	95.60
cat/charge	5/16	5/16	5/16	5/16	5/16	5/16	cat/charge	4/12	4/12	4/12	cat/charge	8/22	8/22
Si	2.66	2.64	2.96	2.96	2.63	3.00	Si	1.93	1.97	1.98	Si	2.87	2.87
Ti	0.00	0.00	0.00	0.00	0.00	0.00	Ti	0.00	0.00	0.00	Ti	0.47	0.37
Cr	0.00	0.00	0.00	0.00	0.00	0.00	Cr	0.00	0.00	0.00	Cr	0.00	0.02
Al	1.33	1.36	1.01	1.01	1.35	1.03	Al	0.14	0.05	0.05	Al	1.23	1.27
Fe	0.01	0.00	0.00	0.00	0.01	0.00	Fe^{3+}	0.00	0.01	0.00	Fe	0.87	0.86
Mn	0.00	0.00	0.00	0.00	0.00	0.00	Fe^{2+}	0.76	0.71	0.76	Mn	0.00	0.00
Mg	0.00	0.00	0.00	0.00	0.00	0.00	Mn	0.01	0.01	0.01	Mg	1.60	1.63
Ca	0.35	0.37	0.00	0.00	0.38	0.01	Mg	1.13	1.22	1.18	Ca	0.00	0.00
Na	0.63	0.59	0.07	0.06	0.59	0.10	Ca	0.02	0.02	0.02	Na	0.02	0.00
K	0.02	0.03	0.96	0.97	0.03	0.86	Na	0.00	0.00	0.00	K	0.93	0.98
							K	0.00	0.00	0.00			
An	0.35	0.38	0.00	0.00	0.38	0.01					X_{Fe}	0.35	0.35
Or	0.02	0.03	0.93	0.94	0.03	0.89	X_{Fe}	0.40	0.37	0.39			
Ab	0.63	0.60	0.07	0.05	0.59	0.11							

(Ca + Na + K); Ab – albite = Na/(Ca + Na + K), Or – orthoclase = K/(Ca + Na + K), Jd – jadeite = Na, Opx – orthopyroxene = $[Fe^{2+} + Mg - (Ca - Al/2 - Cr/2 - Fe^{3+}/2 + Na/2)]/2$; CaTs – Ca-Tschermack = $Al^{IV} - (Ti*2 + Cr + Fe^{3+})$. Isopleth notations for pseudosections: $x(g) = Fe/(Fe + Mg)$; $z(g) = Ca/(Ca + Fe + Mg)$; $j(cpx) = Na/(Na + Ca)$.

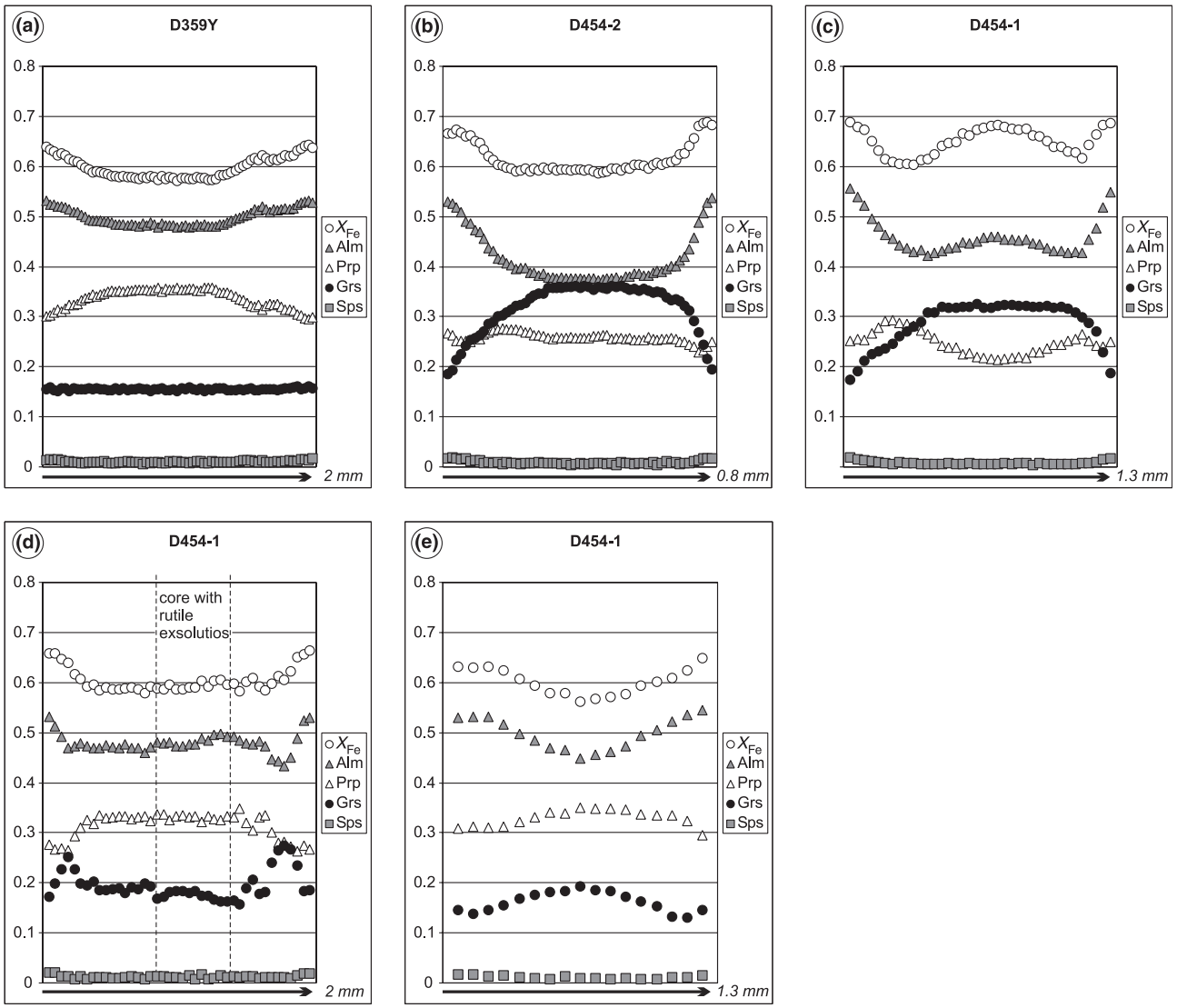

Fig. 6. Garnet chemical profiles: (a) Low-grossular garnet (magmatic garnet, D359Y, Fig. 5a). (b) Enigmatic garnet with grossular and X_{Fe} plateau in the core (D454, Figs 4a & 5b). (c) Garnet with grossular plateau and strong X_{Fe} zoning marked by high X_{Fe} ratio in the core (D454, Fig. 5c). (d) Enigmatic garnet with high grossular content enclosing the low-grossular magmatic garnet with rutile rods (D454, Figs 4c & 5d). (e) Inclusion-poor garnet with low grossular content and rutile rods (magmatic garnet, D454, Fig. 2h). For detailed discussion see text.

Coarse-grained texture

Sample D359Y

Garnet shows weak zoning with almandine and X_{Fe} increasing and pyrope decreasing from core to the rim (X_{Fe} = 0.57 → 0.62, Alm = 0.48 → 0.52, Prp = 0.36 → 0.32, Grs = 0.16) (Figs 5a & 6a). In a few cases a slightly higher grossular content is present in the core, connected with slightly higher X_{Fe}, giving core to rim zoning X_{Fe} = 0.61 → 0.58, Alm = 0.47, Prp = 0.31 → 0.35, Grs = 0.21 → 0.17, then continuing to X_{Fe} = 0.67, Alm = 0.55, Prp = 0.27, Grs = 0.17.

Plagioclase in the antiperthite has An = 33–41% and the K-feldspar exsolution lamellae have 3–8% of albite. The reintegrated composition of antiperthite from garnet and matrix, that also includes the exsolution free rim that is in optical continuity with the antiperthite in the case of inclusions, is in the range of An = 24–27%, Or = 15–30% and Ab = 48–61% (points 1 & 2 in Figs 2a,c & 7).

Clinopyroxene outside of garnet shows weak zoning with decreasing jadeite and X_{Fe} from core to rim (Jd = 6.4% → 2.5%, X_{Fe} = 0.26 → 0.23, Opx = 9.6 → 8.0%, CaTs = 4.1% → 0%), the clinopyroxene inclusions in garnet commonly have slightly higher

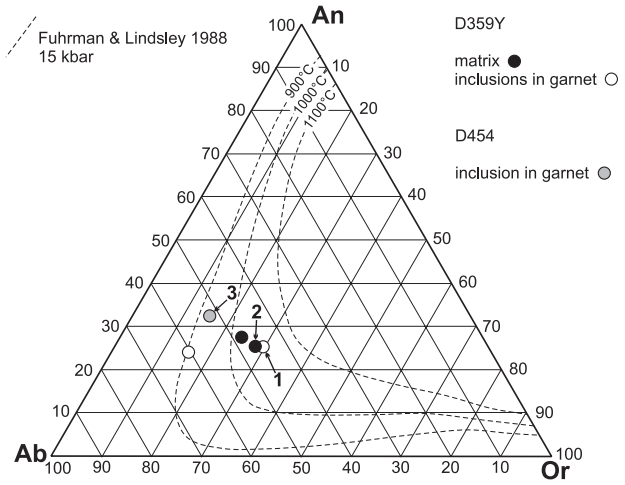

Fig. 7. Reintegrated antiperthites from garnet and matrix. The temperature isopleths are calculated after Fuhrman & Lindsley (1988) for 15 kbar. Numbered points correspond to the antiperthites in Fig. 2a,c,f.

jadeite content that decreases towards their rims (Jd = 8.1 → 4.8%, X_{Fe} = 0.23 → 0.22, Opx = 8.8 → 10.8%, CaTs = 4.0% → 3.2%). The orthopyroxene exsolution lamellae have X_{Fe} = 0.37 and Al content = 0.10–0.14 p.f.u. (calculated for 4 cations in formula). The average composition of the clinopyroxene porphyroclasts with orthopyroxene lamellae obtained by analysing of grains in the scanning mode is Jd = 5.6–6.2%, X_{Fe} = 0.28–0.30, Opx = 16.3–20.8%, CaTs = 3.3–4.9%.

Sample D454

Garnet with numerous large antiperthite and clinopyroxene inclusions, texturally similar to the garnet from sample D359Y, have generally low grossular content (X_{Fe} = 0.59–0.62, Alm = 0.46–0.5, Prp = 0.29–0.32, Grs = 0.16–0.20, Fig. 2f). The garnet that exhibits rutile rods has always grossular content lower than 20% (Figs 2h,i, 4c, 5d,e, 6d,e).

The antiperthite is composed of plagioclase with An = 35–40% and K-feldspar exsolution lamellae with Ab = 3–7%. The reintegrated composition of antiperthite from garnet, including the exsolution free rim that is in optical continuity with the antiperthite is An = 33%, Or = 15% and Ab = 52% (point 3 in Figs 2f & 7).

Clinopyroxene porphyroclasts have a similar composition to the clinopyroxene in sample D359Y, with the jadeite content of the matrix porphyroclasts decreasing slightly from core to rim (Jd = 6.1% → 3.9%, X_{Fe} = 0.25–0.28, Opx = 7.9 → 8.7%, CaTs = 4.1 → 0.4%) and the inclusions in garnet having slightly higher jadeite in their cores (Jd = 8.7% → 4.6%, X_{Fe} = 0.23, Opx = 8.2 → 9.5%, CaTs = 4.2 → 2.8%).

Fine-grained matrix texture

Composition of the minerals present in the recrystallized matrix including the fine-grained feldspar, biotite, orthopyroxene and clinopyroxene, is in the same range for all of the samples studied, and thus will be presented together. The recrystallized plagioclase in the matrix and in the plagioclase coronas around garnet shows considerable range of compositions ranging from An = 30–44%. Less abundant fine-grained K-feldspar contains 3–12% of albite. The small grains of matrix clinopyroxene have low jadeite (Jd = 2.5–4.1%, X_{Fe} = 0.24–0.26, Opx = 6.8–10.9%, CaTs = 0.8–3.7%), orthopyroxene has X_{Fe} = 0.35–0.40 and contains 0.05 p.f.u. of Al (calculated for 4 cations in formula) and biotite has X_{Fe} = 0.27–0.35 and Ti = 0.25–0.4 p.f.u. (calculated for 8 cations in formula).

Enigmatic garnet

The following relates to sample D454. The 'clean' inclusion-poor garnet has a pronounced central high grossular compositional plateau with Grs > 0.3, in marked contrast to the Grs < 0.2 of the coarse texture. In some garnet there is also an almandine, pyrope and X_{Fe} plateau in the core, with a decrease of grossular and increase of X_{Fe} at the rim (X_{Fe} = 0.57 → 0.7, Alm = 0.37 → 0.54, Prp = 0.27 → 0.26, Grs = 0.36 → 0.20, Sps = 0.00 → 0.02) (Figs 5b & 6b). In other 'clean' garnet, in the area of the high grossular plateau there is a decrease in X_{Fe}, followed by decrease of grossular and increase of X_{Fe} at the rim (X_{Fe} = 0.68 → 0.60 → 0.69, Alm = 0.46 → 0.42 → 0.56, Prp = 0.22 → 0.29 → 0.25, Grs = 0.32 → 0.29 → 0.17, Sps = 0.00 → 0.00 → 0.02) (Figs 5c & 6c). It is not clear whether this distinction is related to position-of-section of the garnet, with the latter cut more centrally.

A few garnet with inclusion-free part containing rutile rods, with 'inclusion-rich' garnet partially enclosing it, alluded to above, have in their coarse-texture part a typically flat distribution of elements with low grossular content (Grs = 0.17, X_{Fe} = 0.59, Figs 5d,e & 6d). However in the surrounding plagioclase inclusion-rich part it has considerably higher grossular (up to Grs = 0.27, X_{Fe} = 0.59–0.63, Figs 5d,e & 6d). In addition there are a few inclusion-free garnet, also with numerous rutile rods, that have much lower grossular content in the core compared to the above 'clean' garnet and their zoning is characterized by an increase of X_{Fe} at the rim and only slight decrease of grossular (X_{Fe} = 0.56 → 0.65, Alm = 0.46 → 0.55, Prp = 0.35 → 0.29, Grs = 0.19 → 0.14, Sps = 0.00 → 0.02) (Figs 2h & 6e). They are most likely also to be coarse-grained texture garnet.

The grossular content in all the garnet grains decreases to values of 0.17–0.20 in the vicinity of

plagioclase inclusions, whereas the X_{Fe} may decrease slightly, contrary to the increasing X_{Fe} at the garnet rim. This is correlated with increasing anorthite content at the rims of the plagioclase inclusions.

Three small inclusions of clinopyroxene in high grossular garnet (Grs = 0.26–0.35) have a considerably different composition compared to other inclusions and matrix clinopyroxene. Two of them have higher content of Na and Al (Jd = 15.9% and 26.8%; X_{Fe} = 0.20 and 0.19; Opx = 7.0% and 2.4%, CaTs = 13.8% and 11.4%, respectively) (Fig. 4a). The third inclusion has exceptionally high Al (Jd = 8.9%; X_{Fe} = 0.25; Opx = 4.2%, CaTa = 15.9%). There are also other small clinopyroxene inclusions with lower jadeite content (Jd = 2–4.8%; X_{Fe} = 0.24–0.25; Opx = 6.7–8.2%, CaTs = 0–2%) that are mostly enclosed together with plagioclase. Biotite inclusions in the enigmatic garnet have generally higher Ti content than biotite in the matrix (X_{Fe} = 0.29–0.35, Ti = 0.35–0.47 p.f.u., calculated for eight cations in formula).

THERMOMETRY

Ternary feldspar

The reintegrated composition of antiperthite present in garnet and in the matrix was used to estimate the temperature of the formation of the coarse-grained texture. The reintegrated composition was calculated from analysis of plagioclase host and K-feldspar exsolution lamellae and the modal proportion that was obtained by image analysis of the BSE images. This composition is in the range of An = 24–33%, Or = 15–30% and Ab = 48–61%. Accepting that the more ternary of these are likely to represent the original feldspar composition, a temperature in excess of 1000 °C is indicated (after Fuhrman & Lindsley, 1988), noting that the pressure dependence of the feldspar solvus is essentially unknown (Štípská & Powell, 2005b) (Fig. 7).

Zr in rutile

Rutile is a common accessory phase, occurring with zircon and quartz. It is present in various textural positions: in the matrix, enclosed in various types of garnet and in clinopyroxene (Figs 2i, 3a,d & 4a,b). The Zr content of rutile was used to calculate the temperature using the new calibration of Tomkins *et al.* (2007) that includes a pressure dependence for the thermometer. The results are presented in Fig. 8 in the form of box-plots for each textural setting, calculated for a pressure of 15 kbar. The features of each box-plot increase in temperature by 30 °C for each additional 5 kbar. In a box-plot, the box is given by the interquartile range of the data (the middle half of the data), the line across the box is at the median of the data, and the whiskers extend out to the furthest datapoint that

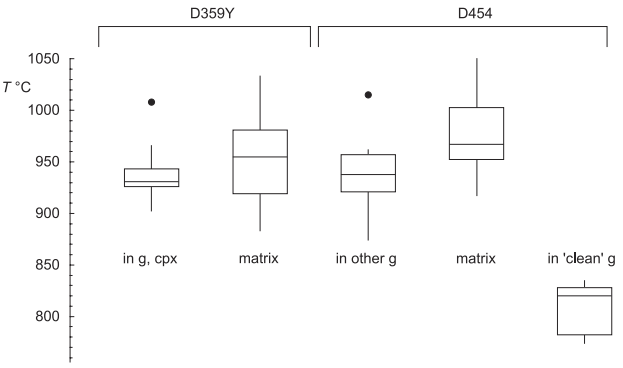

Fig. 8. Temperature from the Zr-in-rutile thermometer of Tomkins *et al.* (2007). The results are presented in the form of box-plots (see text) for each textural setting (in the matrix, enclosed in various types of garnet and in clinopyroxene), calculated at 15 kbar. The number of analyses involved in the box-plots are, respectively, 19, 19, 17, 12 and 11 across the figure.

is within 1.5 times the interquartile range from the box. Dots are points beyond the whiskers (outliers). Given that temperatures may be too high if the rutile was not in communication with quartz when it grew, and may be too low if the rutile was not in communication with zircon, it is not appropriate to just take the highest temperature as being representative of the temperature of formation. The proposal of Tomkins *et al.* (2007) is to use the upper temperature end of the box as a conservative estimate of temperature of formation. In such hot rocks, there is the additional problem that the closure temperature is likely to be at or below the formation conditions (Watson *et al.*, 2006), so temperatures may be progressively reset during cooling, depending on rutile grain size and cooling rate (see below). Regardless, the temperatures from the matrix rutile are the hottest so far recorded by crustal rocks to our knowledge (compare Tomkins *et al.*, 2007).

Sample D359Y

Rutile included in garnet shows a narrow range of Zr-content of 2900–3900 ppm. A few rutile occur in large clinopyroxene porphyroclasts with a Zr content of 3800–4900 ppm. Combining the inclusion data gives an interquartile range on temperature of 925–945 °C (Fig. 8). The range of the Zr-content of matrix rutile is much larger (2500–7600 ppm). The interquartile range on temperature is 920–980 °C (Figs 3a & 8).

Sample D454

The matrix rutile has a large range of Zr-content = 3300–8700 ppm (Fig. 3d), resulting in an interquartile range on temperature of 950–1005 °C, consistent with that for D359Y. Rutile inclusions in garnet have a much larger range of Zr = 930–9300 ppm, but a range of textural contexts is represented, from 'clean' garnet to what is most likely

coarse-grained texture garnet, through those that are difficult or impossible to classify. Rutile in 'clean' (high grossular) garnet give an interquartile range on temperature of 780–830 °C, much lower than for any other category of garnet (Fig. 4a,b). Such rutile has not been observed anywhere else in the rock.

Rutile in coarse-grained texture garnet and those impossible to classify give an interquartile range on temperature of 920–940 and 930–960 °C, respectively (Fig. 2i). Given that they are similar, and involve few analyses (six each), they are combined in Fig. 8. The results are consistent with matrix results but are quite different from the results for the 'clean' garnet.

Closure in Zr-in-rutile thermometry

The availability of new experimental data for the diffusion of Zr (and Hf) in rutile (Cherniak *et al.*, in press) allows the Zr-in-rutile thermometric results above to be considered in terms of closure of rutile to diffusive Zr loss with cooling in the assemblage rutile-zircon-quartz. The approach of Cherniak *et al.* (in press, Fig. 10), based on Dodson (1973), allows closure temperature relationships as a function of cooling rate and grain size (radius of rutile grains considered as cylinders) to be calculated (Fig. 9). In this it is assumed that closure occurs from a temperature that is sufficiently high that rutile is open to Zr at the beginning (Ganguly & Tirone, 1999). The data used are for Hf diffusion at right angles to the c axis in rutile, given that the results for Hf and Zr are effectively the same parallel to c, and data are not reported for Zr at right angles to c.

The rutile grains in the rocks are of the order of 20 to 30 μm. Superimposing this on Fig. 9, with the range of temperatures given by the thermometer, 940 to 1000 °C, gives a very high cooling rate, conservatively well in excess of 1000 °C Myr^{-1}. This provides an additional constraint on likely rock-forming processes, as discussed below.

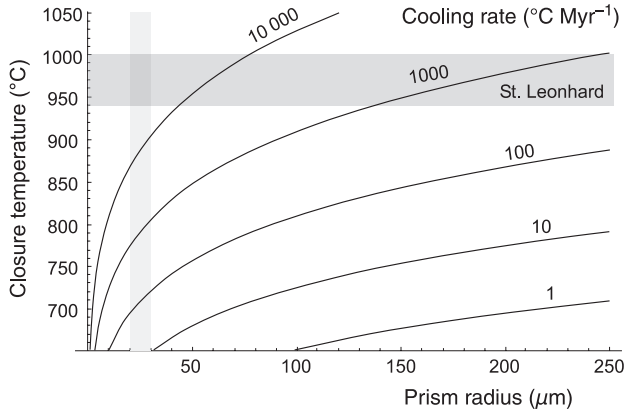

Fig. 9. Calculated closure temperature relationships as a function of cooling rate and grain size (radius of rutile grains considered as cylinders) based on Cherniak *et al.* (in press). The rutile grain-size and range of temperatures given by the thermometer for the studied samples are marked as grey areas.

MODELS

In this section, we summarize the critical textural and mineral chemical information for the three petrographic contexts and discuss how they may have formed.

Coarse-grained texture

The coarse-grained texture is characterized by minerals that all show high-temperature features. Antiperthite reintegrated compositions give temperature of formation above 1000 °C, low grossular (Grs = 0.18–0.20) garnet (Figs 5a & 6a) rarely containing oriented rutile rods (Figs 2h, i & 5c), clinopyroxene with 6–9% jadeite showing orthopyroxene lamellae and rutile containing significant Zr corresponding to temperatures well in excess of 900 °C.

The coarse-grained texture is best preserved in sample D359Y, so this sample is used to investigate via pseudosections the conditions of coarse-grained texture formation. This modelling was undertaken in the system NCKFMASH using THERMOCALC 3.25 (Powell *et al.*, 1998; recent upgrade) and the internally consistent thermodynamic dataset 5.5 (Holland & Powell, 1998; November 2003 upgrade). The coding of activity–composition relationships of the minerals was taken from White *et al.* (2001), with the model of feldspar from Holland & Powell (2003) and the clinopyroxene model from Holland & Powell (1996). The bulk composition used for the pseudosection was gained from an XRF analysis of the whole rock of sample D359Y (SiO_2 = 55.20, TiO_2 = 1.32, Al_2O_3 = 16.10, CaO = 7.81, MgO = 5.49, FeO = 10.40, K_2O = 0.82, Na_2O = 2.69, MnO = 0.15, P_2O_5 = 0.25, in wt%, with TiO_2, MnO and P_2O_5 ignored to reduce the composition for NCKFMASH). The water content H_2O = 0.8 used was chosen to involve a small proportion of melt (5.6–9.9 mol.% at 1000 °C and 10–15 kbar), which then makes a correspondingly small proportion of biotite at the solidus.

Thez *P–T* pseudosection for sample D359Y is characterized by clinopyroxene stability over the whole *P–T* range of the diagram (Fig. 9a–c). The high-temperature part is characterized by a typical granulite facies succession of ferromagnesian assemblages with decreasing pressure: garnet–clinopyroxene, garnet–clinopyroxene–orthopyroxene and clinopyroxene–orthopyroxene (see also Štípská & Powell, 2005a,b, inset in Fig. 8). Down temperature, a two-feldspar assemblage is established by approximately 800–950 °C. At and below the solidus, biotite is stable in the low- and middle-pressure part, to be replaced by muscovite at higher pressure. At high-pressure/low-temperature kyanite appears, related to the breakdown

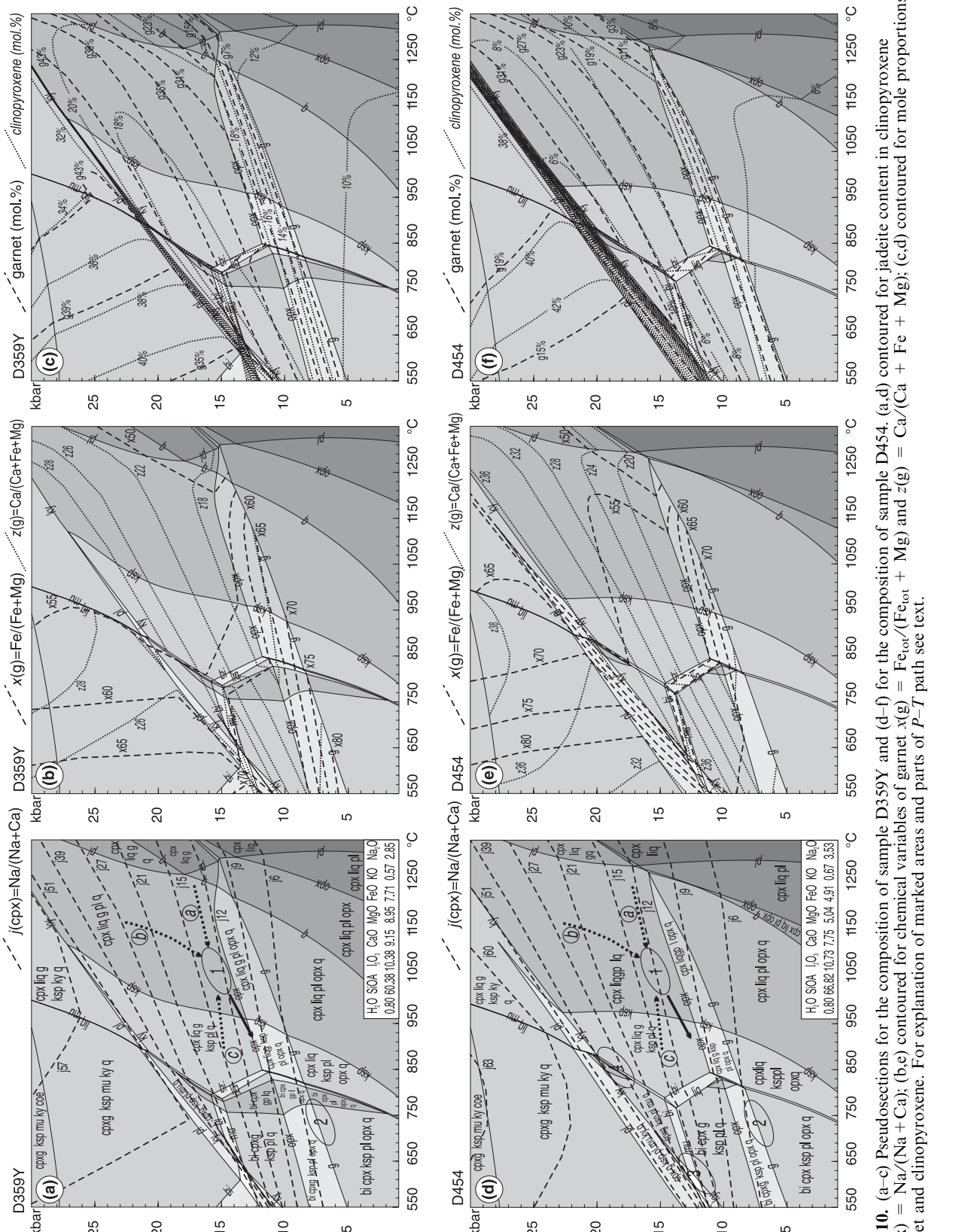

Fig. 10. (a–c) Pseudosections for the composition of sample D359Y and (d–f) for the composition of sample D454. (a,d) contoured for jadeite content in clinopyroxene $j(\mathrm{cpx}) = \mathrm{Na}/(\mathrm{Na}+\mathrm{Ca})$; (b,e) contoured for chemical variables of garnet $x(\mathrm{g}) = \mathrm{Fe}_{\mathrm{tot}}/(\mathrm{Fe}_{\mathrm{tot}} + \mathrm{Mg})$ and $z(\mathrm{g}) = \mathrm{Ca}/(\mathrm{Ca} + \mathrm{Fe} + \mathrm{Mg})$; (c,d) contoured for mole proportions of garnet and clinopyroxene. For explanation of marked areas and parts of P–T path see text.

of plagioclase with increasing pressure. The diagram is contoured with mole proportion and composition isopleths for garnet and clinopyroxene, (Fig. 10a–c), to relate to the observed mineral assemblage and mineral compositions.

In the pseudosection, clinopyroxene with 6–9% of jadeite, garnet with 18–20% of grossular and antiperthite at a temperature in excess of 1000 °C corresponds to a pressure of about 15 kbar. Growth of garnet of this grossular content, enclosing antiperthite, with clinopyroxene, occurs with cooling and some decompression above the orthopyroxene-in line, (Fig. 10, solid arrow). From the closure systematics of the Zr-in-rutile thermometer, this cooling must have been very fast, at least initially. Given the absence of evidence for the *P–T* path prior to reaching 1000 °C and 15 kbar, establishing the overall path is contentious. Our strong preference is for the formation of the coarse-grained texture to be the result of magma crystallization at a depth corresponding to 15 kbar (Fig. 10, dashed arrow, a), followed by rapid cooling to the ambient crustal temperature.

However alternatives have been proposed. Carswell & O'Brien (1993) and Cooke (2000) suggested decompression from higher pressure (Fig. 10, dashed arrow, b), based on thermobarometry combining high grossular garnet with ternary feldspar. On Fig. 10f, decompression from about 25 kbar is implied, at a temperature of > 1000 °C. However, as argued here, these two minerals did not form part of the same assemblage, and therefore such an early high pressure history is not indicated. Another alternative is a short-lived thermal event involving fast isobaric heating (and fast cooling) (O'Brien & Vrána, 1995) (Fig. 10, dashed arrow, c). However, from the garnet mineral proportion contours on Fig. 10c,f, most garnet growth has occurred at lower temperature on such a path, so that garnet cannot be expected to enclose ternary feldspar (see also Štípská & Powell, 2005a,b).

Fine-grained matrix texture

The development of the fine-grained matrix is associated with an anastomosing foliation around coarse-grained porphyroclasts and relicts of coarse-grained texture. The recrystallized matrix involves plagioclase, quartz, K-feldspar, orthopyroxene, clinopyroxene (Jd = 3–4%), and biotite that formed during recrystallization. The rutile in this matrix preserves high-temperature compositions so is not likely to have recrystallized. The embedded porphyroclasts involve garnet, clinopyroxene with orthopyroxene lamellae and antiperthite. These appear to have once been part of the coarse-grained texture material. Also involved are enigmatic garnet, commonly of a high grossular composition. Garnet porphyroclasts are surrounded by orthopyroxene and orthopyroxene–plagioclase coronas.

For the *P–T* interpretation of the fine-grained recrystallization the pseudosection for sample D359Y is used. As the recrystallization took place in the stability field of orthopyroxene, biotite and clinopyroxene with 3–4% of jadeite, this suggests conditions of 5–7 kbar and < 800 °C in the pseudosection (area 2 in Fig. 10a). As only a small amount of biotite (1–2%) is produced at the solidus, the conditions of recrystallization took place under H_2O-undersaturated conditions. This is likely to have contributed to the preservation of porphyroclast relicts and their chemistry.

From the textural observations, the last significant textural and mineral chemical modification that these rocks experienced was connected with development of this fine-grained matrix texture. This took place largely at the expense of coarse-grained texture material that we interpret as magmatic. It is likely that this deformation and recrystallization destroyed textural information that might have allowed the formation of the enigmatic garnet to be more thoroughly understood. In particular the equilibration of garnet near plagioclase at this stage, in inclusions and the matrix, produced garnet compositions that are similar to coarse-grained texture garnet compositions. Areas of such low grossular garnet may therefore be early or late, and this critical distinction may be difficult or impossible to make.

Enigmatic garnet

Under the term enigmatic garnet we group two types that show high grossular content, or are interpreted to have had high grossular contents, and do not contain rutile rods: 'clean' garnet and 'inclusion-rich' garnet. Although such garnet does not occur in sample D359Y, they are common in D454. The 'clean' garnet form large porphyroclasts with core compositions of Grs = 35–38% that contain rare inclusions of plagioclase, clinopyroxene without orthopyroxene lamellae and with jadeite content up to 27%, and containing rutile with low Zr content giving low temperatures (Fig. 4a,b). The 'inclusion-rich' garnet also have elevated grossular (Grs > 30%) away from the common plagioclase inclusions, but reduced values (Grs < 20%) towards the plagioclase inclusions.

The origin of the enigmatic garnet is discussed in the context of a pseudosection constructed for a whole-rock composition of sample D454 (Fig. 10d–f) that contains high grossular garnet. The bulk composition used for this pseudosection gained from an XRF analysis of D454 is (SiO_2 = 62.01, TiO_2 = 0.69, Al_2O_3 = 16.75, CaO = 6.59, MgO = 3.14, FeO = 5.48, K_2O = 0.99, Na_2O = 3.35, MnO = 0.06, P_2O_5 = 0.11, in wt%). However, this pseudosection can only be used as a rough guide as this composition does not necessarily represent the composition in which these enigmatic garnet grew, depending on how they formed. The topology of this pseudosection is

similar to that for the sample D359Y. The main difference is in the position of the mole proportion contours of clinopyroxene and garnet and in the position of the grossular and jadeite isopleths. The molar content of garnet and clinopyroxene is lower at similar *P–T* compared with the pseudosection for D359Y. The clinopyroxene content is nearly constant in the area below the stability of kyanite (5–7 mol.%), but it increases rapidly with the appearance of kyanite and consumption of plagioclase to 34–37 mol.% over an interval of 2 kbar. In comparison to the pseudosection for D359Y, the grossular isopleths show higher values at comparable pressure, with the maximum reaching $z(g) = 36–38$ in two different *P–T* regions: at high temperature and at low-temperature/mid-pressure. The jadeite isopleths are at nearly the same position as in the pseudosection D359Y in the area below kyanite stability, but they increase more abruptly and reach higher values in the kyanite stability field at high pressure.

The origin of the enigmatic garnet hinges on whether there is a continuum between the garnet with few inclusions and a high grossular plateau in their cores (the 'clean' garnet), and the 'inclusion-rich' garnet that contains numerous large plagioclase inclusions. If there is not a continuum then it is possible that the two sorts of garnet have different origins; if not, then a single origin seems much more likely.

We start by considering the simplest model, that there is a continuum and a single origin for enigmatic garnet. The critical observation is that high grossular garnet overgrows low grossular garnet with rutile rods (Fig. 5d,e), antiperthite (Fig. 2i) and can enclose relatively high-temperature rutile (Fig. 2i). This necessarily places the growth of enigmatic garnet to be after the igneous crystallization of the coarse-grained texture (and before the development of the fine-grained matrix). It must involve a prograde metamorphic reworking of magmatic rock (the coarse-grained texture material). Accepting that equilibration at a late stage has modified the garnet composition adjacent to plagioclase, much of what is observed can be reconciled. In particular, the plagioclase inclusions are relicts of igneous antiperthite, and indeed they do contain rare lamellae away from obvious coarse-grained texture material. However difficulties do remain: how to account for the high grossular plateau in the 'clean' garnet, the lower temperature nature of their rutile, and why the low temperature rutile does not appear to occur in the matrix.

The high grossular plateau (Figs 5b & 6b) may be accounted for by prograde growth following a grossular isopleth [in the pseudosection $z(g) = 32–36$ from 10 kbar and 600 °C to 18 kbar and 800 °C] that would also produce zoning in X_{Fe}, then diffusionally modified on decompression (areas 3 & 4 in Fig. 10d). The absence of simultaneous growth of high-jadeite pyroxene may be explained by almost no increase in the molar clinopyroxene proportion from 10 to 18 kbar (Fig. 10f). Pre-existing but diffusionally-modified clinopyroxene would then account for the rare higher jadeite inclusions found in 'clean' garnet. The predominance of fine grain-size low-jadeite clinopyroxene in the matrix is testament to the ease of reequilibration of clinopyroxene, at least for small grains.

The remaining problem to be resolved in a prograde reworking model is why the rutile in the 'clean' garnet gives much lower temperatures than, for example, the matrix rutile, and why such lower temperature rutile is not found in the matrix, if it is assumed that the garnet overgrew the matrix (Fig. 8). Given that the solubility of Zr in garnet increases dramatically with grossular content (H. Tomkins, pers. comm.), it is possible that the rutile that was overgrown crystallized at high temperature, and that they were diffusionally modified by interaction with the garnet after inclusion. Such a view might also account for why matrix rutile gives somewhat higher temperatures than rutile included in the other sorts of garnet. Otherwise the origin and evolution of the rutile in 'clean' garnet remains unresolved.

Given that it is hard to deny that the 'inclusion-rich' garnet formed by reworking of the coarse-grained texture material, it remains to be considered whether the enigmatic garnet and the 'clean' garnet formed separately. One possibility is that the enigmatic garnet represent xenocrysts from a rock several hundreds of degrees cooler than the magma that was picked up and dismembered during emplacement. We see only the garnet. Such a rock could have been at 18 kbar and 800 °C, as already derived from the pseudosection, although in this model, the pressure cannot be properly estimated from the garnet zoning itself, because the pseudosection may not correspond to the rock in which the garnet grew. The only clues that can be used to better constrain the *P–T* conditions of this garnet are inclusions of clinopyroxene with high jadeite content (up to 27%, Fig. 4a) giving high pressures of about 18 kbar and rutile with low Zr content giving low temperatures of about 800 °C. Moreover the plateau of high grossular could be interpreted as diffusionally equilibrated at high pressure following incorporation in the magma, and the drop to 18% of grossular at the rims as diffusional reequilibration on decompression in the magma. The X_{Fe} zoning (Figs 5c & 6c) would then need to be interpreted as twice diffusionally modified, with an original plateau formed at high pressure (in the pseudosection at 20 kbar, $X_{Fe} = 0.7$, area 4 in Fig. 10d), modified due to decompression (in the pseudosection to $X_{Fe} = 0.6$ at 10 kbar), and finally modified during fine-grained reworking (in the pseudosection at 8 kbar, to $X_{Fe} = 0.7$, area 2 in Fig. 10d).

Reworking

The final stage of the history of these rocks saw recrystallization into a foliation marked by the assemblage

of orthopyroxene, diopsidic clinopyroxene, biotite, plagioclase, quartz. It is also associated with formation of clinopyroxene–orthopyroxene coronas around magmatic clinopyroxene porphyroclasts, and plagioclase–orthopyroxene coronas around garnet. This reworking occurred at 650–750 °C and 6–8 kbar (see also Cooke, 2000) and obliterated the textural relationships of the inclusion-poor high-grossular garnet with respect to the igneous, coarse-grained texture.

CONCLUSIONS

In previous work on granulites in the Bohemian Massif, antiperthite was assumed to be in equilibrium with high grossular garnet, leading to estimated metamorphic conditions of >1000 °C at around 18 kbar (starting for example with Carswell & O'Brien, 1993). Features pointing to a magmatic origin for part of a mineral assemblage were first identified in orthopyroxene–garnet–antiperthite granulites by Štípská & Powell (2005a,b). These authors proposed a history involving first magma crystallization at 1000 °C and 8 kbar, followed later by metamorphic reworking at higher pressure and lower temperature.

The garnet–clinopyroxene–antiperthite granulites from the St. Leonhard massif also show more complex petrographic relations than previously reported for similar rock types in the Bohemian Massif. The rocks preserve, to a different degree, a coarse-grained texture formed by quartz, antiperthite, high-Zr rutile, low grossular garnet commonly containing rutile rods and clinopyroxene (Jd = 7–9%) with orthopyroxene exsolution. We interpret this texture to be the result of crystallization of dry magma at about 14–15 kbar and 1000 °C. Some samples contain signs of metamorphic crystallization at about 18 kbar and 800 °C, inferred from high grossular garnet (Grs = 36–38%) that includes clinopyroxene with 27% jadeite and rutile with low-Zr contents. The key point is that there appears to be two distinct parts to a discontinuous high-pressure history represented, with evidence of the *P–T* discontinuity not being recorded in the mineral assemblages. We suggest that the combination of ternary feldspar with high grossular garnet for thermobarometry in these and similar rocks is unlikely to be appropriate as these minerals grew in the different parts of the history, magmatic and metamorphic respectively.

ACKNOWLEDGEMENTS

This work was financially supported by the Charles University Grant Agency (no. 253/2005/B-GEO/Prf to M.R.), Czech National Grant Agency (no. 205-05-2187 to P.Š.) and French National agency (no. 06-1 14 8784 to Karel Schulmann). We gratefully acknowledge T. Theye from the Institute of Mineralogy at the University of Stuttgart, M. Bohn from the French Research Institute for Exploitation of the Sea in Brest, Z. Korbelová, A. Langrová and V. Böhmová from the Geological institute of Academy of Science of the Czech Republic for operating the microprobes. R.P. acknowledges support of ARC DP0451770. We also gratefully acknowledge S. Chakraborty and D. Pattison for constructive reviews and M. Brown for editorial handling and corrections.

REFERENCES

Aftalion, M., Bowes, D. R. & Vrána, S., 1989. Early carboniferous U-Pb zircon age for garnetiferous, perpotassic granulites, Blanský Les Massif, Czechoslovakia. *Neues Jahrbuch Für Mineralogie-Monatshefte*, **4,** 145–152.

Becker, H., 1997. Sm–Nd garnet ages and cooling history of high-temperature garnet peridotite massifs and high-pressure granulites from lower Austria. *Contributions to Mineralogy and Petrology*, **127,** 224–236.

van Breemen, O., Aftalion, M., Bowes, D. R. *et al.*, 1982. Geochronological studies of the Bohemian Massif, Czechoslovakia, and their significance in the evolution of Central Europe. *Transactions of the Royal Society of Edinburgh, Earth Sciences*, **73,** 89–108.

Carswell, D. A., 1991. Variscan high P-T metamorphism and uplift history in the Moldanubian Zone of the Bohemian Massif in Lower Austria. *European Journal of Mineralogy*, **3,** 323–342.

Carswell, D. A. & O'Brien, P. J., 1993. Thermobarometry and geotectonic significance of high-pressure granulites: examples from the Moldanubian Zone of the Bohemian Massif in Lower Austria. *Journal of Petrology*, **34,** 427–459.

Cherniak, D.J., Manchester, J. & Watson, E.B., (2007) **261,** 267–279. Zr and Hf diffusion in rutile. *Earth and Planetary Science Letters*.

Cooke, R. A., 2000. High-pressure/temperature metamorphism in the St. Leonhard Granulite Massif, Austria: evidence from intermediate pyroxene-bearing granulites. *International Journal of Earth Sciences*, **89,** 631–651.

Cooke, R. A. & O'Brien, P. J., 2001. Resolving the relationship between high P-T rocks and gneisses in collisional terranes: an example from the Gföhl gneiss-granulite association in the Moldanubian Zone, Austria. *Lithos*, **58,** 33–54.

Cooke, R. A., O'Brien, P. J. & Carswell, D. A., 2000. Garnet zoning and the identification of equilibrium mineral compositions in high-pressure-temperature granulites from the Moldanubian Zone, Austria. *Journal of Metamorphic Geology*, **18,** 551–569.

Dodson, M.H., 1973. Closure temperature in cooling geochronological and petrological systems. *Contributions to Mineralogy and Petrology*, **40,** 259–274.

Fiala, J., Matějovská, O. & Vaňková, V., 1987. Moldanubian granulites: source material and petrogenetic considerations. *Neues Jahrbuch für Mineralogie Abhandlungen*, **157,** 133–165.

Franěk, J., Schulmann, K. & Lexa, O., 2006. Kinematic and rheological model of exhumation of high-pressure granulites in the Variscan orogenic root: example of the Blanský les granulite, Bohemian Massif, Czech Republic. *Mineralogy and Petrology*, **86,** 253–276.

Friedl, G., Finger, F., Paquette, J., Quadt, A., McNaughton, N. & Fletcher, I., 2004. Pre-Variscan geological events in the Austrian part of the Bohemian Massif deduced from U–Pb zircon ages. *International Journal of Earth Sciences*, **93,** 802–823.

Fuhrman, M. L. & Lindsley, D. H., 1988. Ternary-feldspar modelling and thermometry. *American Mineralogist*, **73,** 201–215.

Ganguly, J. & Tirone, M, 1999. Diffusion closure temperature and age of a mineral with arbitrary extent of diffusion: theoretical formulation and applications. *Earth and Planetary Science Letters*, **170,** 131–140.

Holland, T. J. B. & Powell, R., 1996. Thermodynamics of order–disorder in minerals. 2. Symmetric formalism applied to solid solutions. *American Mineralogist*, **81,** 1425–1437.

Holland, T. J. B. & Powell, R., 1998. An internally consistent thermodynamic data set for phases of petrological interest. *Journal of Metamorphic Geology*, **16,** 309–343.

Holland, T. & Powell, R., 2003. Activity–composition relations for phases in petrological calculations: an asymmetric multicomponent formulation. *Contributions to Mineralogy and Petrology*, **145,** 492–501.

Holub, F. V., Machart, J. & Manová, M., 1997. The Central Bohemian Plutonic Complex: geology, chemical composition and genetic interpretation. *Journal of Geological Sciences – Economic Geology, Mineralogy*, **31,** 27–50.

Janoušek, V. & Holub, F. V., 2007. The causal link between HP-HT metamorphism and ultrapotasic magmatism in collisional orogens: case study from the Moldanubian Zone of the Bohemian Massif. *Proceedings of the Geologists' Association*, **118,** 75–86.

Janoušek, V., Bowes, D. R., Rogers, G., Farrow, C. M. & Jelínek, E., 2000. Modelling diverse processes in the petrogenesis of a composite batholith: the Central Bohemian Pluton, Central European Hercynides. *Journal of Petrology*, **41,** 511–543.

Janoušek, V., Finger, F., Roberts, M. P., Frýda, J., Pin, C. & Dolejš, D., 2004. Deciphering petrogenesis of deeply buried granites: whole-rock geochemical constraints on the origin of largely undepleted felsic granulites from the Moldanubian Zone of the Bohemian Massif. *Transactions of the Royal Society of Edinburgh, Earth Sciences*, **95,** 141–154.

Janoušek, V., Gerdes, A., Vrána, S. *et al*., 2006. Low-pressure Granulites of the Lišov Massif, Southern Bohemia: Viséan Metamorphism of Late Devonian Plutonic Arc Rocks. *Journal of Petrology*, **47,** 705–744.

Klemd, R. & Bröcker, M., 1999. Fluid influence on mineral reactions in ultrahigh-pressure granulites: a case study in the Sneznik Mts. *(West Sudetes, Poland)*. *Contributions to Mineralogy and Petrology*, **136,** 358–373.

Kröner, A., Wendt, I., Liew, T. C. *et al*., 1988. U-Pb zircon and Sm-Nd model ages of high grade Moldanubian metasediments, Bohemian Massif, Czechoslovakia. *Contributions to Mineralogy and Petrology*, **99,** 257–266.

Kröner, A., O'Brien, P. J., Nemchin, A. A. & Pidgeon, R. T., 2000. Zircon ages for high pressure granulites from South Bohemia, Czech Republic, and their connection to Carboniferous high temperature processes. *Contributions to Mineralogy and Petrology*, **138,** 127–142.

Lange, U., Bröcker, M., Armstrong, R., Trapp, E. & Mezger, K., 2005. Sm-Nd and U-Pb dating of high-pressure granulites from the Zote and Rychleby Mts (Bohemian Massif, Poland and Czech Republic). *Journal of Metamorphic Geology*, **23,** 133–145.

Medaris, L. G., Jelínek, E. & Mísař, Z., 1995. Czech eclogites: Terrane settings and implications for Variscan tectonic evolution of the Bohemian Massif. *European Journal of Mineralogy*, **7,** 7–28.

Medaris, L. G., Fournelle, J. H., Ghent, E. D., Jelínek, E. & Mísař, Z., 1998. Prograde eclogite in the Gföhl Nappe, Czech Republic: new evidence on Variscan high-pressure metamorphism. *Journal of Metamorphic Geology*, **16,** 563–576.

O'Brien, P. J. & Rötzler, J., 2003. High-pressure granulites: formation, recovery of peak conditions and implications for tectonics. *Journal of Metamorphic Geology*, **21,** 3–20.

O'Brien, P. J. & Vrána, S., 1995. Eclogites with a short-lived granulite facies overprint in the Moldanubian Zone, Czech Republic: petrology, geochemistry and diffusion modelling of garnet zoning. *International Journal of Earth Sciences*, **84,** 473–488.

O'Brien, P. J., Kröner, A., Jaeckel, P., Hegner, E., Zelazniewicz, A. & Kryza, R., 1997. Petrological and isotopic studies on palaeozoic high-pressure granulites, Gory Sowie Mts, Polish Sudetes. *Journal of Petrology*, **38,** 433–456.

Petrakakis, K., 1997. Evolution of Moldanubian rocks in Austria: review and synthesis. *Journal of Metamorphic Geology*, **15,** 203–222.

Petrakakis, K. & Jawecki, C., 1995. High-grade metamorphism and retrogression of Moldanubian granulites, Austria. *European Journal of Mineralogy*, **7,** 1183–1203.

Powell, R., Holland, T. & Worley, B., 1998. Calculating phase diagrams involving solid solutions via non- linear equations, with examples using THERMOCALC. *Journal of Metamorphic Geology*, **16,** 577–588.

Racek, M., Štípská, P., Pitra, P., Schulmann, K. & Lexa, O., 2006. Metamorphic record of burial and exhumation of orogenic lower and middle crust: new tectonothermal model for the Drosendorf window (Bohemian Massif, Austria). *Mineralogy and Petrology*, **86,** 221–251.

Rötzler, J. & Romer, R. L., 2001. P-T-t evolution of ultrahigh temperature granulites from the Saxon Granulite Massif, Germany. *Part I: Petrology*. *Journal of Petrology*, **42,** 1995–2013.

Scharbert, H. G. & Carswell, D. A., 1983. Petrology of garnet-clinopyroxene rocks in a granulite facies environment, Bohemian Massif of Lower Austria. *Bullettin Mineralogie*, **106,** 761–774.

Schulmann, K., Kröner, A., Hegner, E. *et al*., 2005. Chronological constraints on the pre-orogenic history, burial and exhumation of deep- seated rocks along the eastern margin of the Variscan orogen, Bohemian Massif, Czech Republic. *American Journal of Science*, **305,** 407–448.

Štípská, P. & Powell, R., 2005a. Does ternary feldspar constrain the metamorphic conditions of high-grade meta-igneous rocks? Evidence from orthopyroxene granulites, Bohemian Massif *Journal of Metamorphic Geology*, **23,** 627–647.

Štípská, P. & Powell, R., 2005b. Constraining the P–T path of a MORB-type eclogite using pseudosections, garnet zoning and garnet-clinopyroxene thermometry: an example from the Bohemian Massif. *Journal of Metamorphic Geology*, **23,** 725–743.

Štípská, P., Schulmann, K. & Kröner, A., 2004. Vertical extrusion and middle crustal spreading of omphacite granulite: a model of syn-convergent exhumation (Bohemian Massif, Czech Republic). *Journal of Metamorphic Geology*, **22,** 179–198.

Tajčmanová, L., Konopásek, J. & Schulmann, K., 2006. Thermal evolution of the orogenic lower crust during exhumation within a thickened Moldanubian root of the Variscan belt of Central Europe. *Journal of Metamorphic Geology*, **24,** 119–134.

Tomkins, H. S., Powell, R. & Ellis, D. J, 2007. The pressure dependence of the zirconium-in-rutile thermometer. *Journal of Metamorphic Geology*, **25,** 703–713.

Vrána, S. & Jakeš, P., 1982. Orthopyroxene and two-pyroxene granulites from a segment of charnockitic crust in southern Bohemia. *Bulletin of the Czech Geological Survey*, **57,** 129–143.

Watson, E. B., Wark, D. A. & Thomas, J. B., 2006. Crystallization thermometers for zircon and rutile. *Contribution to Mineralogy and Petrology*, **151,** 413–433.

Wendt, J. I., Kröner, A., Fiala, J. & Todt, W., 1994. U-Pb zircon and Sm-Nd dating of Moldanubian HP/HT granulites from South Bohemia, Czech Republic. *Journal of the Geological Society, London*, **151,** 83–90.

White, R. W., Powell, R. & Holland, T. J. B., 2001. Calculation of partial melting equilibria in the system Na_2O-CaO-K_2O-FeO-MgO-Al_2O_3-SiO_2-H_2O (NCKFMASH). *Journal of Metamorphic Geology*, **19,** 139–153.

Received 18 March 2007; revision accepted 26 November 2007.

12. **Štípská**, P., Schulmann, K. & Kröner, A. (2004). Vertical extrusion and middle crustal spreading of omphacite granulite: a model of syn-convergent exhumation (Bohemian Massif, Czech Republic). *Journal of Metamorphic Geology*, 22, 179-198.

13. Schulmann, K., Kröner, A., Hegner, E., Wendt, I., Konopásek, J., Lexa, O. & **Štípská**, P. (2005). Chronological constraints on the pre-orogenic history, burial and exhumation of deep-seated rocks along the eastern margin of the Variscan orogen, Bohemian Massif, Czech Republic. *American Journal of Science*, 305, 407-448.

14. Racek, M., **Štípská**, P., Pitra, P., Schulmann, K. & Lexa, O. (2006). Metamorphic record of burial and exhumation of orogenic lower and middle crust: new tectonothermal model for the Drosendorf window (Bohemian Massif). *Mineralogy and Petrology*, 86, 221-251. doi 10.1007/s00710-005-0111-7.

15. Schulmann K., Martelat, J.E., Ulrich, S., Lexa, O., **Štípská, P.** & Becker, J.K. (2008). Evolution of microstructure and melt topology in partially molten granitic mylonite: implications for rheology of felsic middle crust. *Journal of Geophysical Research*, **113**, B10406, doi:10.1029/2007JB005508

16. Schulmann, K., Lexa, O., **Štípská**, P., Racek, M., Tajčmanová, L., Konopásek, J., Edel, J. B., Peschler, A. & Lehmann, J. (2008). Vertical extrusion and horizontal channel flow of orogenic lower crust: key exhumation mechanisms in large hot orogens? *Journal of Metamorphic Geology*, **26**, 273–297. doi:10.1111/j.1525-1314.2007.00755.x.

17. Schulmann, K., Konopásek, J, Janoušek, V., Lexa O., Lardeaux, J.M., Edel, J.B., **Štípská**, P. & Ulrich, S. (2009). An Andean type Palaeozoic convergence in the Bohemian Massif. *C. R. Geoscience*, **341**, 266–286. doi:10.1016/j.crte.2008.12.006.

18. **Štípská**, P., Powell, R., White, R.W. & Baldwin, J.A. (2010). Using calculated chemical potential relationships to account for coronas around kyanite: an example from the Bohemian Massif. *Journal of Metamorphic Geology*, **28**, 97–116. doi:10.1111/j.1525-1314.2009.00857.x

19. Lexa, O., Schulmann, K., Janoušek, V., **Štípská**, P., Guy, A. & Racek, M. (2011). Heat sources and trigger mechanisms of exhumation of HP granulites in Variscan orogenic root. *Journal of Metamorphic Geology*, 79–102. doi:10.1111/j.1525-1314.2010.00906.x

20. Franěk, J., Schulmann, K., Lexa, O., Ulrich, S., **Štípská**, P., Haloda, J. & Týcová, P. (2011). Origin of felsic granulite microstructure by heterogeneous decomposition of alkali feldspar and extreme weakening of orogenic lower crust during the Variscan orogeny. *Journal of Metamorphic Geology*, **29**, 103–130. doi: 10.1111/j.1525-1314.2010.00911.x

21. Skrzypek, E., **Štípská** P., Schulmann, K., Lexa, O. & Lexová, M. (2011a): Prograde and retrograde metamorphic fabrics – a key for understanding burial and exhumation in orogens (Bohemian Massif). *Journal of Metamorphic Geology*, **29**, 451–472. doi: 10.1111/j.1525-1314.2010.00924.x.

22. Skrzypek, E., Schulmann, K., **Štípská** P., Chopin, F., Lehmann, J., Lexa, O. & Haloda, J. (2011b): Tectono-metamorphic history recorded in garnet porphyroblasts: insights from thermodynamic modelling and electron backscatter diffraction analysis of inclusion trails. *Journal of Metamorphic Geology*, **29**, 473–496. doi: 10.1111/j.1525-1314.2010.00925.

J. metamorphic Geol., 2004, **22,** 179–198 doi:10.1111/j.1525-1314.2004.00508.x

Vertical extrusion and middle crustal spreading of omphacite granulite: a model of syn-convergent exhumation (Bohemian Massif, Czech Republic)

P. ŠTÍPSKÁ,[1] K. SCHULMANN[1] AND A. KRÖNER[2]
[1]*Institute of Petrology and Structural Geology, Charles University, Albertov 6, 12843, Prague, Czech Republic (stipacka@natur.cuni.cz)*
[2]*Institut für Geowissenschaften, Universität Mainz, 55099 Mainz, Germany*

ABSTRACT The exhumation of eclogite facies granulites (Omp–Plg–Grt–Qtz–Rt) in the Rychleby Mts, eastern Czech Republic, was a localised process initiated by buckling of crustal layers in a thickened orogenic root. Folding and post-buckle flattening was followed by the main stage of exhumation that is characterized by vertical ductile extrusion. This process is documented by structural data, and the vertical ascent of rocks from a depth of *c*. 70 to *c*. 35 km is documented by metamorphic petrology. SHRIMP $^{206}Pb/^{238}U$ and $^{207}Pb/^{206}Pb$ evaporation zircon ages of 342 ± 5 and 341.4 ± 0.7 Ma date peak metamorphic conditions. The next stage of exhumation was associated with sideways flat thrusting associated with lateral viscous spreading of granulites and surrounding rocks over indenting adjacent continental crust at a depth of *c*. 35–30 km. This stage was associated with syntectonic intrusion of a granodiorite sill at 345–339 Ma, emplaced at a crustal depth of *c*. 25 km. The time required for cooling of the sill as well as for heating of the country rocks brackets this event to a maximum of 250 000 years. Therefore, similar ages of crystallization for the granodiorite magma and the peak of eclogite facies metamorphism of the granulite suggest a very short period of exhumation, limited by the analytical errors of the dating methods. Our calculations suggest that the initial exhumation rate during vertical extrusion was 3–15 mm yr^{-1}, followed by an exhumation rate of 24–40 mm yr^{-1} during further uplift along a magma-lubricated shear zone. The extrusion stage of exhumation was associated with a high cooling rate, which decreased during the stage of lateral spreading.

Key words: Bohemian Massif; crustal folding; eclogite facies granulite; lateral spreading; vertical exhumation; zircon dating.

INTRODUCTION

Exhumation is a process, which refers to the upward motion of a rock relative to the surface (England & Molnar, 1990). The rate of exhumation is commonly estimated from the pressure, and therefore from the depth, of equilibration of mineral associations and from their age (Duchène *et al*., 1997). This type of analysis is critically dependent on the cooling history of rocks evaluated by temperature–time paths, which is possible by dating mineral assemblages and interpretation of closure temperatures of different isotopic systems (Parrish, 2001). To understand the depth–time and time–temperature paths of exhumed rocks a number of mechanistic exhumation models have been established, which emphasise the roles of different processes such as erosion, normal faulting and ductile thinning, etc. (see Ring *et al*., 1999 for summary). These authors listed diagnostic structural and petrological features of exhumation processes as well as problems related to quantification of the exhumation rates. At deep crustal levels the formation of subhorizontal ductile foliations is generally interpreted to be diagnostic of ductile thinning which is attributed to exhumation of deep-seated rocks (e.g. Krabbendam & Dewey, 1998). The other popular model to explain syn-convergent exhumation of HP rocks along subduction zones is based on the high buoyancy of subducted continental crust (Chemenda *et al*., 1997). Another group of syn-convergent tectonic exhumation models assumes corner flow circulation in accretionary wedges (Cloos, 1982) which was later generalised to large wedges and rocks of high metamorphic grade (Allemand & Lardeaux, 1997; Platt, 1993). Burg *et al*. (1997, 1998) have shown that the exhumation of lower crustal rocks may also be related to compressional crustal-scale folding. The last important group of exhumation models emphasises the role of lateral forces responsible for the development of vertical fabrics during exhumation due to ductile extrusion of lower crustal rocks between two rigid walls (Merle & Guillier, 1989; Thompson *et al*., 1997a,b). The ductile extrusion process can be approximated quantitatively by channel flow models (Grujic *et al*., 1996) as was shown for the Himalayan orogenic front (Hodges *et al*., 2001).

Structural, petrological and geochronological data and anisotropy of magnetic susceptibility (AMS) are used to examine a *P–T–t–d* path associated with exhumation of a high-pressure (HP) granulite belt. We discuss several of the above-mentioned exhumation models and their relative contribution to the bulk exhumation path of the studied rocks. The rate of exhumation is assessed through petrological and geochronological data in order to estimate the magnitude and time of vertical elevation of HP rocks and the *P–T* conditions and timing of lateral spreading at mid-crustal depth. These data are further used to discuss a well-dated temperature–time path and cooling patterns of the entire orogenic domain.

GEOLOGICAL SETTING

The Orlica–Snieznik complex (OSC) represents the easternmost unit of the West Sudetes, being bordered by the NW-trending Elbe and Intrasudetic faults (Fig. 1). The OSC is composed of medium- to high-grade orthogneisses and supracrustal metasedimentary rocks. High-grade orthogneisses known as the Snieznik gneiss (coarse-grained, porphyritic) and Gieraltow gneiss (fine-grained mylonitized and/or migmatitic) are tectonically interlayered with eclogite facies rocks and medium-grade metasediments and metavolcanics of the Stronie and Mlynowiec Groups. The complex structural and metamorphic history of the OSC was summarized by Don *et al.* (1990). Zelazniewicz (1988)

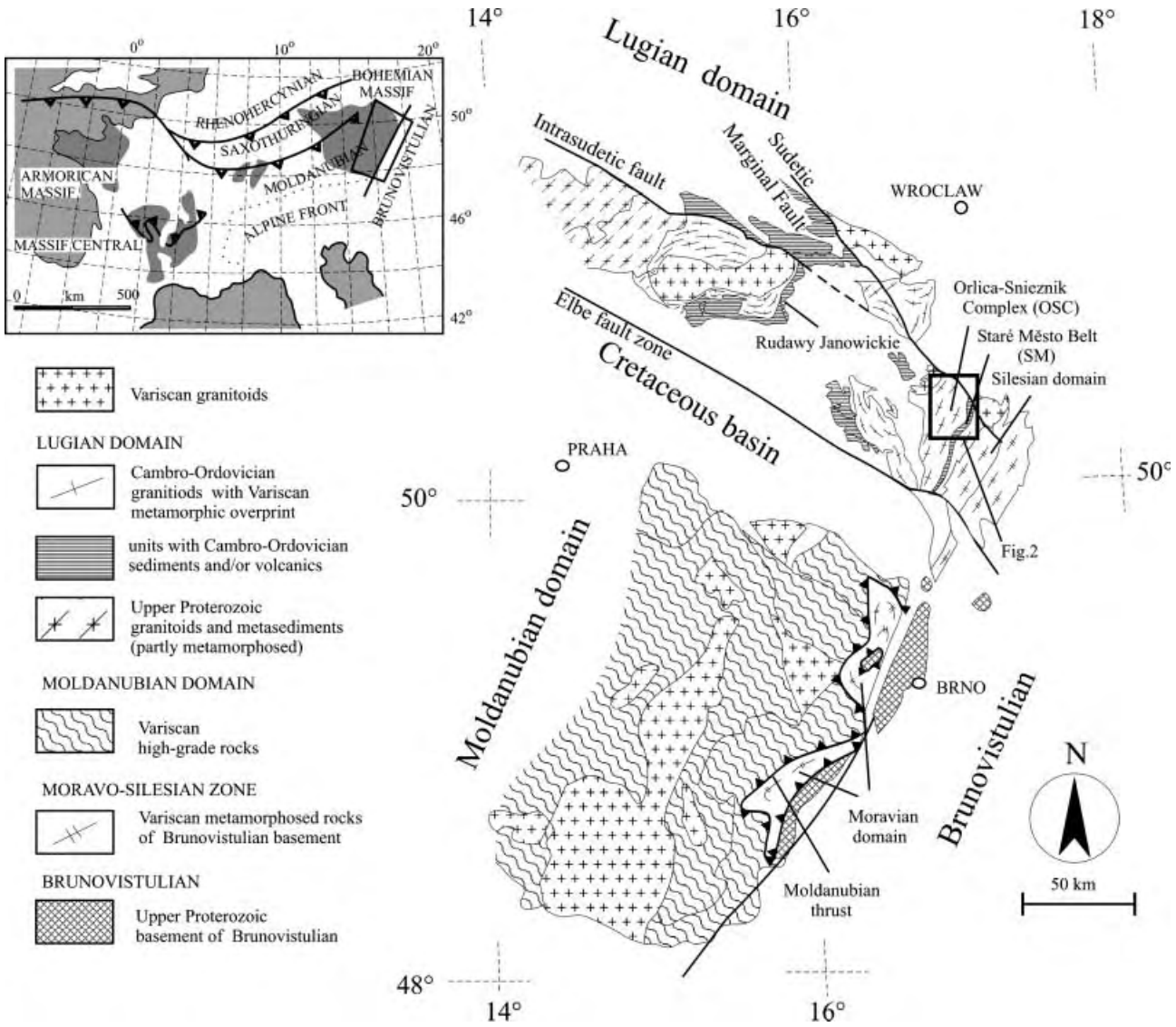

Fig. 1. Outline geological map of the eastern part of the Bohemian Massif with the major units shown schematically. Location of study area (Fig. 2) is outlined. Upper left inset depicts location of the study area within the Variscan belt of Europe.

argued that the main fabric of the Snieznik orthogneiss resulted from irrotational strain associated with E–W regional shortening whereas Cymerman (1992) suggested NE directed non-coaxial thrusting. Some workers considered the main foliation to result from a late Caledonian process, whereas others emphasise the importance of Carboniferous events (Aleksandrowski *et al*., 2000; Don *et al*., 1990; Kröner *et al*., 2001a; Turniak *et al*., 2000).

The example studied here is represented by a NE–SW trending, 15 km long and approximately 1 km wide belt of eclogite facies omphacite and Ky–Kfs granulites (Pouba *et al*., 1985) with stable plagioclase during the peak of eclogite facies metamorphism (see review of O'Brien & Rötzler, 2003). The belt is located in the eastern part of the OSC in the Rychleby and Zlote Mts (Fig. 2). The Rychleby granulites consist of dark, fine-grained garnet–omphacite granulite locally retrogressed to amphibolite and interlayered with felsic fine-grained, Ky–Kfs granulite. The surrounding orthogneisses are strongly mylonitized and exhibit an increasing degree of anatexis and an increasing number of amphibolite bodies, between several tens of cm and several metres wide, towards the granulite belt. Both types of orthogneiss, the porphyritic, layered and coarse-grained (Snieznik) and fine-grained (Gieraltow) are present.

The metamorphic evolution is best studied in eclogite facies rocks (Smulikowski, 1967) which exhibit different thermal evolutions. The peak pressures for the eclogites, the Rychleby granulites and surrounding gneisses are believed to lie in the coesite stability field (Bakun–Czubarow, 1992; Bröcker & Klemd, 1996; Klemd & Bröcker, 1999; Kryza *et al*., 1996). Amphibolite facies retrogression in different domains of the OSC span a wide range, between 2 and 11 kbar

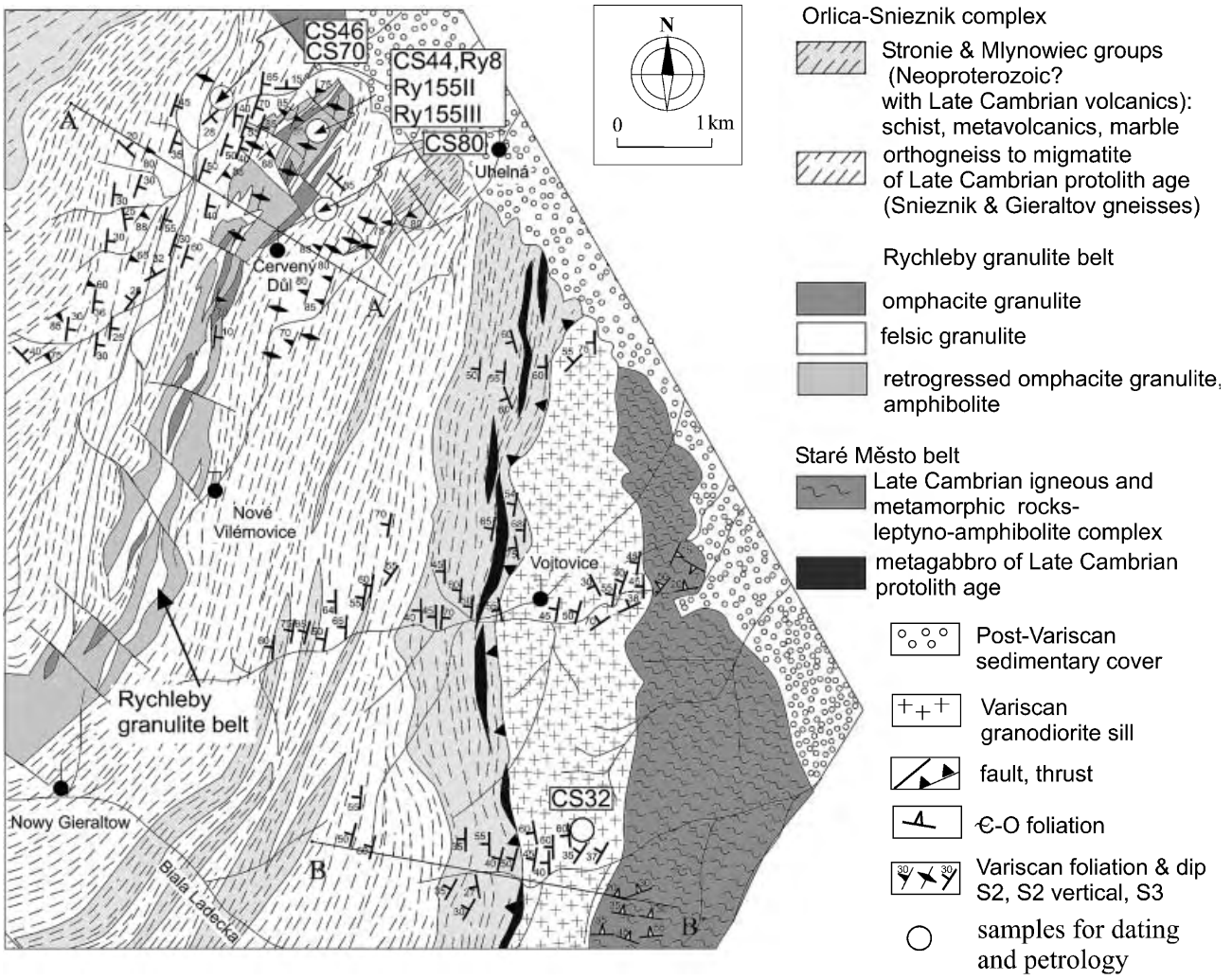

Fig. 2. Geological and structural map of the Rychleby granulite belt, surrounding orthogneisses and adjacent Staré Město belt. Location of samples for zircon geochronology and metamorphic petrology are shown. Lines A–A′ and B–B′ indicate the position of interpretative structural profile (Fig. 3).

and 600–650 °C (e.g. Bröcker & Klemd, 1996; Klemd *et al.*, 1995; Steltenpohl *et al.*, 1993). Metamorphic conditions in the adjacent Stronie rocks reached the staurolite or staurolite–kyanite grade (Smulikowski, 1979), and orthogneisses locally underwent partial melting (Turniak *et al.*, 2000).

The intrusion ages of the orthogneiss precursors and metavolcanic rocks of the Stronie Group all correspond to a widespread and voluminous Cambro–Ordovician magmatic event (e.g. Kröner *et al.*, 2001a; Oliver *et al.*, 1993). The Variscan history is documented by Sm–Nd garnet–clinopyroxene-whole rock ages of 341 ± 7, 329 ± 6 and 337 ± 4 Ma for eclogite lenses (Brueckner *et al.*, 1991). Klemd & Bröcker (1999) provided conventional U–Pb multigrain zircon ages of 369–360 Ma for magmatic zircon from granulites of the Rychleby belt, and Turniak *et al.* (2000) dated high-U rims around igneous zircon of an anatectic Gieraltow gneiss variety, which yielded a SHRIMP age of 342 ± 6 Ma. Muscovite and biotite $^{40}Ar/^{39}Ar$ ages of the Snieznik orthogneiss are 328 ± 1.7 and 328 ± 2 Ma (Steltenpohl *et al.*, 1993). Lange *et al.* (2002) presented a Rb–Sr phengite-whole rock and Rb–Sr biotite-whole rock ages of 337 ± 2.3 and 328.6 ± 4.4 Ma, respectively, for sheared Sniezznik orthogneiss.

The OSC is bounded to the east by the Staré Město belt which consists of a lower crustal complex that was thinned during Cambro–Ordovician rifting and was subsequently involved in Variscan collision (Štípská *et al.*, 2001). The boundary between the OSC and Staré Město belt strikes NE–SW, parallel to the general lithotectonic sequence. The volcano–sedimentary unit at the top of the Staré Město tectonic sequence is interpreted to belong to the Stronie Group (Kröner *et al.*, 2000b). Structurally below is a layer of sheared gabbro and a leptyno–amphibolite suite, both having Cambro–Ordovician ages of emplacement, but Variscan and Cambro–Ordovician ages of metamorphism, respectively (Kröner *et al.*, 2000b). A Variscan granodiorite sill was syntectonically emplaced along the boundary between the sheared gabbro and the leptyno–amphibolite. Farther to the east occurs the Neoproterozoic basement – the Silesian domain that was underthrust below the Staré Město belt and OSC during Carboniferous convergence (Kröner *et al.*, 2000b; Schulmann & Gayer, 2000).

STRUCTURAL EVOLUTION OF THE RYCHLEBY GRANULITE BELT

Deformational sequence resulting in a steep structural fan

The dominant structure within the Rychleby granulite belt is a NE–SW trending vertical foliation defined by an alternation of mafic and felsic layers varying in thickness from several centimetres to several metres (Figs 3 & 4). The earliest and relict structure is marked by mafic layers refolded by F2 isoclinal folds with steep axial planes, indicating the existence of a metamorphic foliation S1, the orientation and character of which is impossible to assess (Fig. 4a). These folded mafic layers are boudinaged and tectonically dismembered, thus indicating complete transposition of an early S1 fabric into a new vertical S2 foliation (Fig. 4b).

Mafic and felsic granulite types are macroscopically isotropic, and a mineral alignment parallel to compositional layering is ill defined. Therefore, the anisotropy of magnetic susceptibility (AMS) method was used to determine the internal fabric of the granulite belt. Sixty oriented samples were taken using a portable drill at nine sampling sites along an E–W section across the widest part of the belt. The AMS data were statistically evaluated using the ANISOFT package of programs (Hrouda

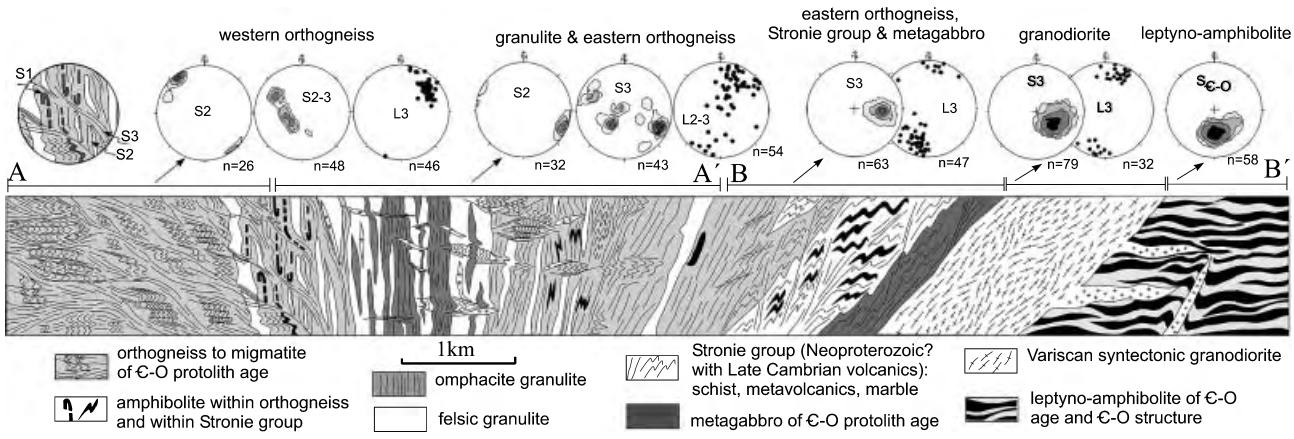

Fig. 3. Interpretative geological cross-section showing relics of S1 fabric in the granulite belt, major vertical structure S2 and the style of superimposed D3 deformation in the granulite belt and surrounding orthogneisses. The contact of the OSC with the Staré Město belt is concordant with the sheared gabbro and syntectonic granodiorite intrusion, but discordant with the Cambro–Ordovician structure of the leptyno–amphibolite complex. Equal-area, lower-hemisphere stereoplots show D2 and D3 planar and linear structures. Vertical axis is not to scale.

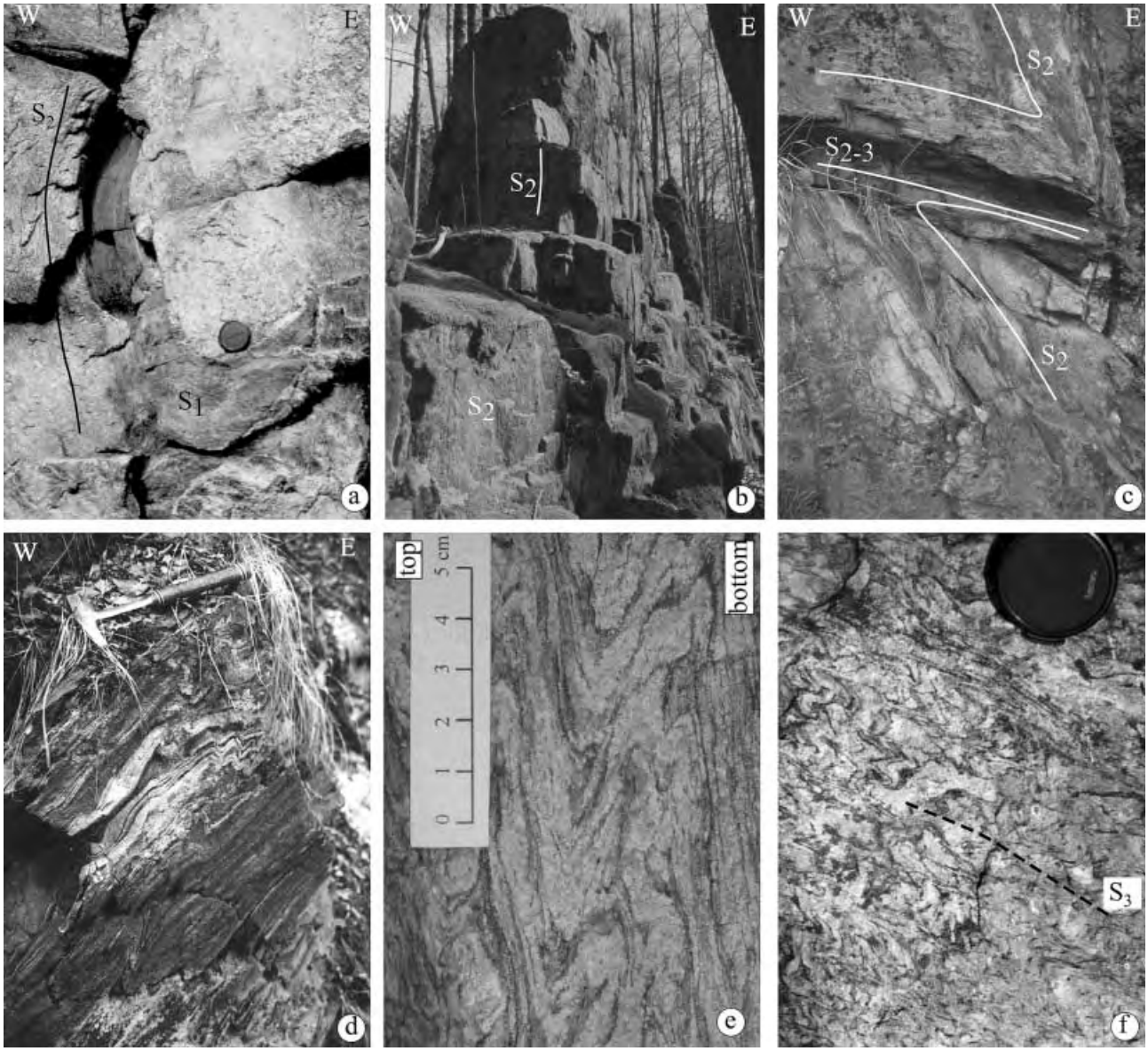

Fig. 4. Field photographs showing structural features of the granulite belt and surrounding orthogneiss. (a) The S1 metamorphic fabric of a mafic layer is preserved in an isoclinal dismembered F2-fold within the vertical S2 foliation. (b) Vertical S2 foliation in the granulite belt. (c) F3-folds with axial planes and axial cleavage S3 in the western orthogneiss and dipping to the east towards the granulite belt. (d) East-vergent F3-folds in the eastern orthogneiss and in the Stronie Group close to the Staré Město belt indicate eastward thrusting. (e) Detail of HT S2 foliation in the orthogneiss, folded by F3-fold. (f) Detail of the development of S3 axial cleavage in banded orthogneiss.

et al., 1990; Jelínek, 1978). The AMS study revealed two major groups of fabrics (Fig. 5). The first group exhibits steep NE–SW striking magnetic foliations (poles to K3) and almost sub-horizontal NE–SW trending magnetic lineations. These fabrics are both oblate and prolate and have a very low degree of anisotropy. Only locally is a stronger magnetic fabric developed for moderately oblate strains. The other group of samples is marked by flat magnetic foliations dipping west, south-east or north-east. The magnetic lineation plunges shallowly to the SE. The shape of the AMS ellipsoid is mostly of plane strain type, and the degree of anisotropy is very low, in agreement with the almost isotropic macroscopic appearance of the rocks.

In order to obtain a more complete picture of the structural development we studied the surrounding orthogneisses in a *c*. 2.5 km wide belt to the west (referred to here as western orthogneiss) and to the east towards the contact with the Staré Město belt (eastern orthogneiss) (Figs 2 & 3). In the western orthogneiss the NE–SW striking vertical foliation S2 is defined by strongly elongated ribbons of recrystallized

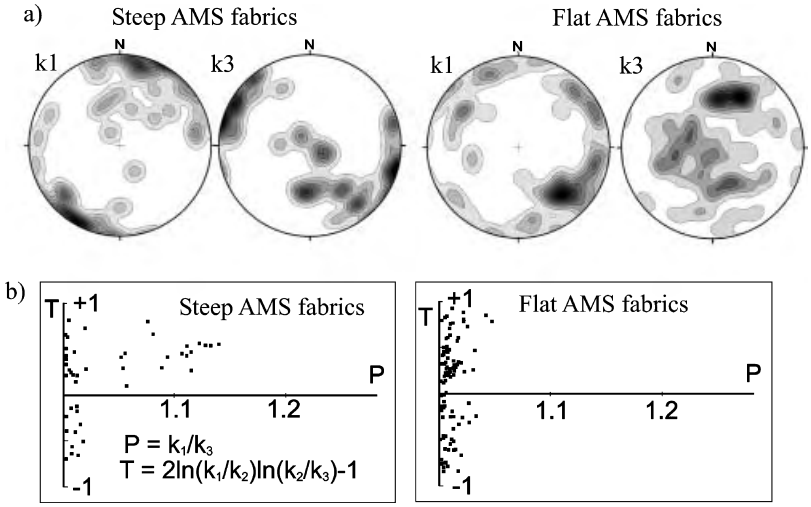

Fig. 5. Results of AMS study of the Rychleby granulites. (a) Orientation of K1 (magnetic lineation) and K3 (magnetic foliation) for vertical fabric (S2) and thrust zones (S3), respectively. (b) *P–T* diagrams showing degree of magnetic susceptibility and variations in shape of AMS ellipsoid.

K-feldspar, plagioclase and quartz and by the preferred orientation of biotite. Microstructural features, such as dynamic recrystallization of both feldspars and a low viscosity contrast between quartz and feldspar, indicate the HT nature of the mylonitic fabric (Přikryl *et al.*, 1996). In the fine-grained gneiss variety, the foliation is generally defined by relicts of recrystallized feldspar ribbons but locally only by a planar arrangement of biotite in a granoblastic quartz–feldspar matrix. Towards the granulite belt, the boundaries of the recrystallized ribbons of individual minerals become diffuse and progressively disappear in conjunction with the development of leucosome layers, reflecting an increasing degree of migmatization. Here, both types of gneiss were transformed into layered, leucocratic migmatites.

Within the eastern orthogneiss the dip of the NE–SW striking sub-vertical foliation becomes progressively shallower going to the east (Figs 3 & 4d). In addition, the textural character of the foliation changes from migmatitic to mylonitic towards the contact with the underlying Stronie Group and Staré Město belt. The fabric in the Stronie Group rocks is concordant with that of the hanging wall gneiss. The gneissosity is folded into tight to isoclinal, locally asymmetric and east-vergent folds with sub-horizontal hinges and rounded shapes (Fig. 4d).

Sub-horizontal reworking of the steep fabric

The dominant vertical fabric S2 was reworked in all lithologies to varying degree by D3 shear zones and recumbent F3-folds with a mylonitic axial cleavage S3 that developed during amphibolite facies conditions locally leading to anatexis (Figs 2, 3 & 4). Within the main granulite belt, rare HT D3 shear zones associated with melting are developed. The dip of these NE–SW striking shear zones ranges from vertical to sub-horizontal, and the shear planes frequently bear a vertical to sub-horizontal NE-trending stretching lineation.

Different late structures were identified in the western and eastern orthogneiss belts (Figs 3 & 4). In the western belt, the early HT D2-fabric was refolded by metre- to several metre-scale asymmetrical F3-folds with axial planes dipping east. The foliation in the east-dipping long limbs is frequently reworked and transformed into mylonite, whereas the short, steep, NW-dipping limbs contain a strong, east-dipping crenulation cleavage (Fig. 4e,f). The attitude of the fold axial planes and of the cleavage progressively changes from steeply east-dipping to sub-horizontal going to the west, where the folds become symmetrical. The metamorphic grade associated with this F3-folding and shearing corresponds to the amphibolite facies as indicated by the ductile character of mylonitization parallel to the long limbs. Rocks adjacent to the granulite belt were retrograded during a localized amphibolite facies overprint, as seen in steeply east-dipping melt-collecting shear zones. Folding is developed between these shear zones, but much less intense than farther east.

Flat isoclinal F3-folds rarely overprint the early and dominant steep fabric in the eastern orthogneiss belt. Along the contact with the Stronie Group, the early HT foliation was reactivated by medium- to low-temperature shearing, leading to disintegration of the anatectic or HT layered texture and to the development of fine-grained quartzo–feldspatic mylonites. The mylonite foliation S2-3 dips W at moderate angles and often contains a vertical to sub-horizontal stretching lineation. Decimetre-scale shear bands and asymmetrical folds (Fig. 4d) related to the mylonites near the contact with the Stronie rocks indicate thrusting to the east or a dextral sense of shear.

Structures in the Staré Město belt

The structural evolution of the Staré Město belt was described in detail by Parry *et al.* (1997) and Štípská

et al. (2001). The Variscan deformation in this area is defined by emplacement of a large syntectonic granodiorite sill, which is concordant with the fabric of the hangingwall mylonitic gabbro (Fig. 3). The Variscan fabric dips to the NW at steep to intermediate angles and bears a sub-horizontal mineral lineation. Importantly, the leptyno–amphibolite complex in the footwall of the granodiorite intrusion exhibits a discordant flat planar fabric, which is Cambro–Ordovician in age (Kröner *et al.*, 2000b). The Cambro–Ordovician metamorphic rocks of the leptyno–amphibolite complex experienced fairly weak Variscan deformation, manifested by brittle–ductile dextral shear zones and open folding. This structural discordance with respect to the Variscan pervasive fabric of the granodiorite sill, mylonitic gabbros and adjacent OSC rocks implies that these rocks behaved as a rigid block during Variscan convergence (Fig. 3).

METAMORPHIC EVOLUTION OF THE RYCHLEBY GRANULITES

To characterize metamorphic conditions of the subvertical (D2–M2) and flat fabric (D3–M3), one sample of omphacite granulite (Ry8) and two samples of granulite retrogressed in amphibolite facies shear zones were studied (Ry155II & Ry155III). Mineral analyses were carried out on a CAMECA SX 50 at ETH Zürich and a JEOL microprobe at the University of Mainz. Representative mineral analyses are listed in Table 1. Errors given in thermobarometric calculations are 1σ.

Eclogite facies stage M2

Petrography and mineral chemistry

Sample Ry8 is a fine-grained (0.1–1 mm) garnet–clinopyroxene granulite with a macroscopically ill-defined foliation. The matrix assemblage is composed of Grt–Omp–Ky–Plg–Qtz–Rt, where feldspar and quartz show a weak shape-preferred orientation and the oval-shaped garnet as well as the cleavage of the omphacite are preferably aligned parallel to the foliation (Fig. 6a). Based on these textural criteria, the matrix assemblage is interpreted to correspond to *P–T* conditions during development of the vertical S2 foliation. Kyanite is overgrown by a corona of garnet or plagioclase (Fig. 6b). Garnet is zoned with rather homogeneous cores and narrow rims marked by a decrease in grossular and an increase in pyrope ($Alm_{39 \rightarrow 42}Grs_{35 \rightarrow 26}Py_{21 \rightarrow 28}Sps_1Andr_{4 \rightarrow 3}$; $X_{Mg35 \rightarrow 40}$). In the omphacite a trend of highest jadeite contents in the cores decreasing at the rims from Jd_{28} to Jd_{20} was observed; X_{Mg} varies between 0.79 and 0.74. Plagioclase is unzoned andesine ($Ab_{78-82}An_{17-20}Or_{2-3}$).

Table 1. Representative mineral analyses of omphacite granulite sample Ry8 and retrogressed granulite samples Ry155II and Ry155III.

Sample	Ry8	Ry8	Ry8	Ry8	Ry8	Ry155II	Ry155II	Ry155II	Ry155II	Ry155III	Ry155III	Ry155III
Analysis	199	371b	287	287	329	407	435	391	378	75	39	116
Mineral	grt core	grt rim	cpx core	cpx rim	plg	grt core	grt rim	amp	plg	amp	cpx	plg
Wt%												
SiO_2	39.43	39.59	52.28	51.33	64.49	39.94	39.47	44.47	58.05	45.23	53.48	57.17
TiO_2	0.10	0.13	0.59	0.59	0.00	0.11	0.06	0.42	0.08	0.87	0.06	0.04
Cr_2O_3	–	–	0.05	0.05	–	–	–	–	–	–	–	–
Al_2O_3	22.53	22.60	10.80	10.49	23.33	22.44	21.98	12.09	26.38	10.66	0.67	26.69
FeO	19.51	21.32	6.83	6.67	0.16	20.77	24.16	15.96	0.17	14.82	8.20	0.14
MnO	0.36	0.48	0.04	0.04	0.00	0.49	1.46	0.34	0.00	0.23	0.28	0.01
MgO	5.45	7.54	9.57	9.92	0.00	7.66	6.26	10.85	0.00	11.47	13.17	0.00
CaO	14.27	10.26	17.50	17.97	4.05	9.99	7.96	11.46	8.30	11.87	23.74	9.10
Na_2O	0.00	0.00	4.00	3.41	9.06	0.01	0.02	1.47	6.94	1.13	0.29	6.63
K_2O	0.00	0.00	0.04	0.01	0.50	0.01	0.02	0.75	0.23	1.08	0.00	0.21
Total	101.65	101.92	101.70	100.48	101.59	101.42	101.35	97.81	100.15	97.36	99.89	99.99
Cations/Charges	8/24	8/24	4/12	4/12	5/16	8/24	8/24	13 + K + Na + Ca/23	5/16	13 + K + Na + Ca/23	4/12	5/16
Si	2.97	2.97	1.87	1.86	2.81	3.00	3.01	6.50	2.59	6.67	2.00	2.56
Ti	0.01	0.01	0.02	0.02	0.00	0.01	0.00	0.05	0.00	0.10	0.00	0.00
Cr	–	–	0.00	0.00	–	–	–	–	–	–	–	–
Al	2.00	2.00	0.45	0.45	1.20	1.99	1.98	2.08	1.39	1.85	0.03	1.41
Fe^{3+}	0.04	0.06	0.06	0.04	0.00	0.00	0.00	0.67	0.01	0.34	0.00	0.01
Fe^{2+}	1.19	1.28	0.15	0.16	0.01	1.31	1.54	1.29	0.00	1.49	0.26	0.00
Mn	0.02	0.03	0.00	0.00	0.00	0.03	0.09	0.04	0.00	0.03	0.01	0.00
Mg	0.61	0.84	0.51	0.54	0.00	0.86	0.71	2.36	0.00	2.52	0.73	0.00
Ca	1.15	0.82	0.67	0.70	0.19	0.80	0.65	1.80	0.40	1.87	0.95	0.44
Na	0.00	0.01	0.28	0.24	0.77	0.00	0.00	0.42	0.60	0.32	0.02	0.58
K	0.00	0.00	0.00	0.00	0.03	0.00	0.00	0.14	0.01	0.20	0.00	0.01
Total	8.00	8.00	4.00	4.00	5.00	8.00	8.00	15.34	5.00	15.39	4.00	5.00
X_{Mg}	0.34	0.40	0.78	0.77		0.40	0.32	0.65		0.63	0.74	
X_{py}	0.21	0.28				0.29	0.24					
X_{alm}	0.40	0.43				0.44	0.51					
X_{grs}	0.39	0.28				0.27	0.22					
X_{sps}	0.01	0.01				0.01	0.03					

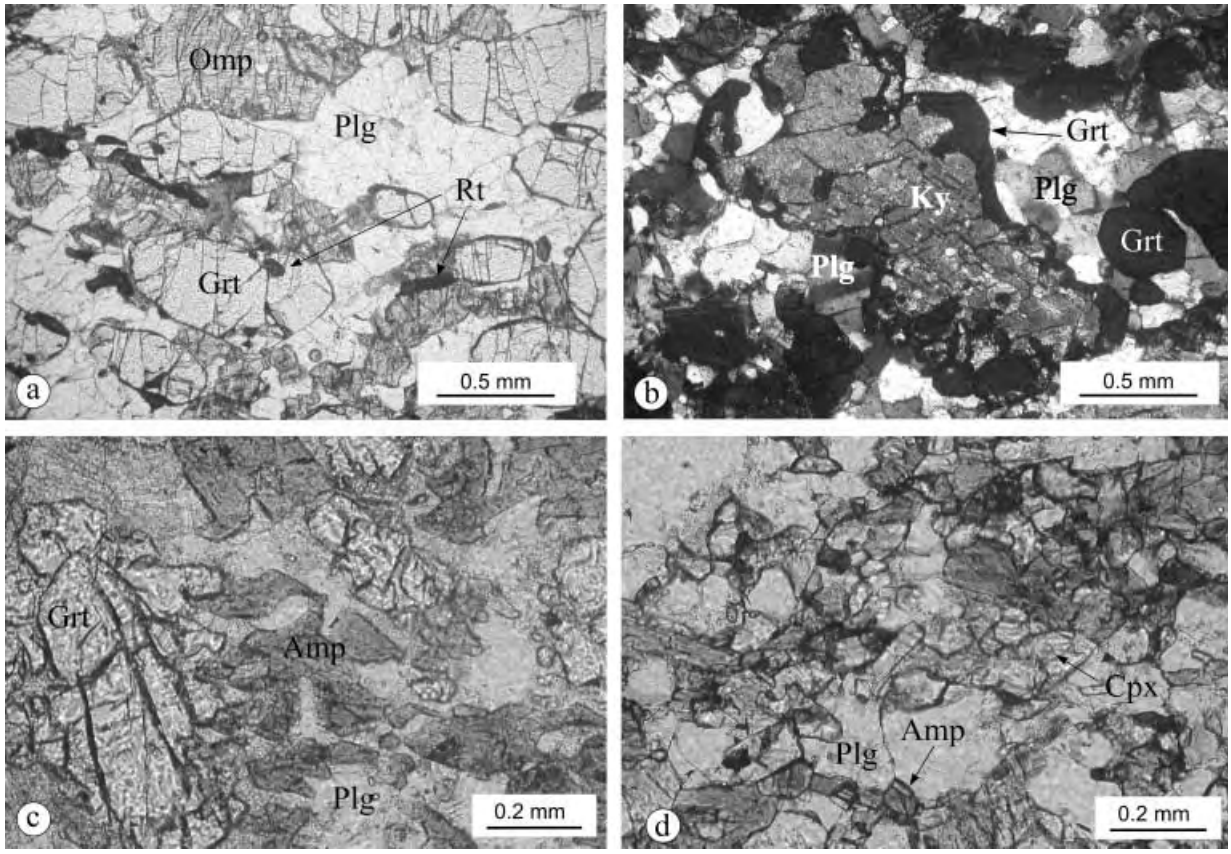

Fig. 6. Photomicrographs showing metamorphic evolution of the omphacite granulite. (a) HP assemblage consists of garnet, omphacite, quartz and plagioclase arranged parallel to the vertical foliation (sample Ry8). (b) Corona of garnet around kyanite. (c) Retrograde amphibolite facies stage with the assemblage garnet, plagioclase and amphibole (sample Ry155II) or (d) amphibole, plagioclase and clinopyroxene (sample Ry155III).

Thermobarometry and modelling of the eclogite facies stage

It was assumed in the calculations that garnet cores were equilibrated with high jadeite omphacite cores and that garnet rims were re-equilibrated with the omphacite rims. Garnet and pyroxene cores (Grs_{33-35}, Jd_{25-27}, $n = 13$, at 18 kbar) yielded a temperature of 913 ± 23 and 897 ± 25 °C and garnet and pyroxene rims (Grs_{23-27}, Jd_{18-24}, $n = 14$, 18 kbar) gave a temperature of 869 ± 10 and 860 ± 6 °C, according to Ellis & Green (1979) and Powell (1985), respectively.

To understand the relative contribution of the CaO component in pyroxene and plagioclase on the pressure estimates, modelling was undertaken using the VERTEX program (Connolly, 1990) with the thermodynamic dataset of Holland & Powell (1990). Mixing properties of feldspar are after Fuhrman & Lindsley (1988) and the disordered model of Gasparik (1985) was used for pyroxene. The discontinuous reaction

$$Ab = Jd + Qtz \quad (1)$$

becomes continuous with addition of CaO. If CaO only enters clinopyroxene, its stability field is extended to lower pressure with respect to the reaction (1) (thick lines in Fig. 7). Plagioclase occurs on the low pressure side of the reaction therefore the addition of CaO into albite extends its stability field to higher pressures (dashed isopleths). The relative contribution of diopside and anorthite end-members for Jd_{28}–An_{20} (Ry8) provides a pressure of *c.* 18.5 kbar (at 900 °C) and plots above the 'higher' isopleth of Jd_{30}–Ab. The uncertainties for reaction (1) were calculated after Powell & Holland (1988) to 0.93 kbar and 34 °C. The pressure estimate was confirmed by Holland's barometer (1983), yielding 18.3 kbar at 900 °C for Jd_{28}–An_{20} and assuming molecular mixing for both phases.

Amphibolite facies overprint M3

Sample Ry155II is a retrogressed granulite with a coarse-grained matrix of Amp–Plg–Qtz (Fig. 6c). Garnet is surrounded by a corona of plagioclase with minor amphibole. The garnet cores and contacts with amphibole are rather homogeneous ($Alm_{43}Grs_{26}Py_{29}Sps_1$, $X_{Mg0.40}$), whereas the composition at contacts with plagioclase changes ($Alm_{54}Grs_{22}Py_{19}Sps_4$, $X_{Mg0.26}$). Amphibole corresponds to tschermakite and

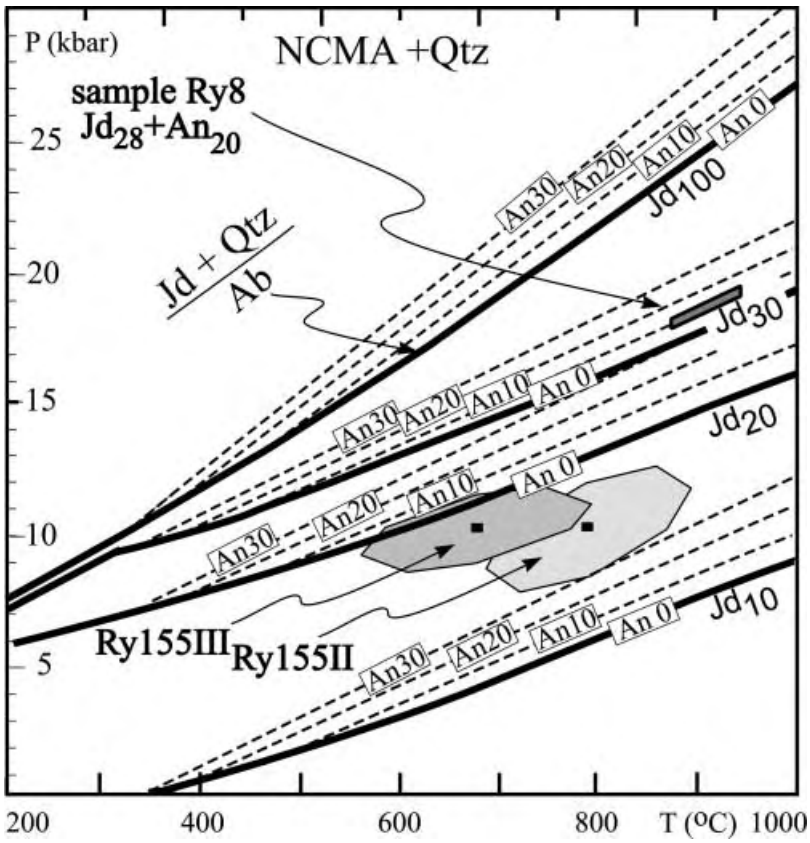

Fig. 7. Results of thermodynamic calculations using the Vertex program (Connolly, 1990), thermometry and average *P–T* calculations. The solid lines represent contours for increasing jadeite content in omphacite C2/c in equilibrium with pure albite. The dashed isopleths labelled An_{10-30} emanating from solid lines are equilibria for increasing content of anorthite in plagioclase with a given omphacite. Equilibria for sample Ry8 (Jd_{28} and An_{20}) are indicated; the temperature for sample Ry8 was calculated using the Grt–Cpx thermometer (Powell, 1985). *P–T* conditions of re-equilibration for samples Ry155II, Ry155III were calculated using average *P–T* method in THERMOCALC.

magnesiohornblende. Plagioclase varies from An_{20} to An_{40}. Sample Ry155III is composed of Amp–Plg–Qtz–Cpx with no garnet relicts. Amphibole is magnesiohornblende, tschermakite, edenite or pargasite. Plagioclase varies between An_{35} and An_{42}, jadeite content in clinopyroxene is *c*. 0.02 and X_{Mg} ranges between 73 and 77. In both samples rutile is preserved within amphibole, and matrix ilmenite is overgrown by titanite.

The pressure calculated in sample Ry155II for the Grt–Plg contacts and matrix amphibole, using the calibration of Kohn & Spear (1990) gave 10.9 ± 0.9 and 10.3 ± 0.7 kbar for the Mg and Fe end-member reactions, respectively (at 700 °C, $n = 13$). Plg–Amp pairs were used to calculate the temperature according to Holland & Blundy (1994). The ed–tr and ed–ri calibrations provided a temperature of 683 ± 30 and 685 ± 34 °C, respectively (at 10 kbar, $n = 11$). Average *P–T* calculations using THERMOCALC (Powell & Holland, 1988) for Grt–Plg contacts and matrix amphibole yielded 788 ± 83 °C and 10.2 ± 1.9 kbar. In sample Ry155III, the temperatures calculated using the calibration of Holland & Blundy (1994) are 679 ± 16 and 699 ± 15 °C for the ed–tr and ed–ri end–members, respectively (at 10 kbar, $n = 12$). Average *P–T* calculations on rim compositions provided 692 ± 94 °C and 10.4 ± 1.3 kbar.

Significance of the *P–T* evolution

Our maximum *P–T* estimates for the Rychleby granulites are 18 kbar and 900 °C and correspond to the development of the vertical structure S2. Kryza *et al.* (1996) and Klemd & Bröcker (1999) obtained using the two-feldspar thermometry and Grt–Als–Qtz–Plg barometry peak conditions for associated Ky–Kfs granulites of up to 35 kbar/1100 °C and 28 kbar/1000 °C, respectively. We caution that these UHP may be overestimated due to the possibility that non-equilibrium compositions may have been used for the calculations. The radial cracks around quartz inclusions interpreted by Bakun–Czubarow (1992) as pseudomorphs after coesite are also an indication for UHP. However, Wendt *et al.* (1993) emphasized that radial cracks around quartz may result from dilation of α-quartz and do not necessarily indicate the existence of former coesite. Thus a maximum pressure of 20 kbar is preferred, but in the following discussion the consequences of possible UHP metamorphism are also taken into consideration.

Despite the large range and errors for the retrogression stage, the data indicate that decompression occurred during decreasing temperature and passed the amphibolite facies field at approximately 10 kbar and 700 °C. Therefore, the exhumation along the vertical zone reflects transport of *c*. 35 km between peak

pressure and retrograde metamorphic conditions during D3.

ZIRCON GEOCHRONOLOGY

SHRIMP analyses: Isotopic analyses were performed on the Perth Consortium SHRIMP II ion microprobe (De Laeter & Kennedy, 1998), and the analytical procedures are described in Compston *et al.* (1992) and Nelson (1997). The error in the ratio Pb*/U during analysis of all standard zircons during this study was 1.28%. Analyses of samples and standards were alternated to allow assessment of Pb^+/U^+ discrimination. Raw data reduction followed the method of Nelson (1997). Common Pb corrections were applied using the ^{204}Pb-correction method, assuming that common lead is surface-related (Kinny, 1986) and therefore using the isotopic composition of Broken Hill lead. Errors on individual analyses are at the 1-σ level, are based on counting statistics and include the uncertainty in the standard U/Pb age (Nelson, 1997). Errors for pooled analyses are at 2σ.

Single zircon evaporation: The laboratory procedures as well as comparisons with conventional and ion-microprobe zircon dating are detailed in Kröner *et al.* (1991) and Kröner & Hegner (1998). Isotopic measurements were carried out on a Finnigan-MAT 261 mass spectrometer at the Max-Planck-Institut für Chemie in Mainz.

New U–Pb and Pb–Pb zircon ages

In order to constrain the tectonic history associated with exhumation of the Rychleby granulites, single zircon or small grain fractions were dated from critical rocks (Fig. 2) using SHRIMP II and/or the evaporation technique. The analytical data are shown in Tables 2 and 3 and in Figs 8 & 9.

Fine-grained felsic granulite samples CS44a and CS44b are composed of Plg–Ksp–Qtz–Grt–Bt–Rt–Ky. The zircon population consists predominantly of near-spherical, translucent, multifaceted grains, some 40–80 μm in diameter and clearly of metamorphic origin.

Concordant SHRIMP ^{206}Pb/^{238}U isotopic ratios for eight metamorphic grains from both samples (Table 2) yielded a combined mean age of 342 ± 5 Ma (Fig. 8), whereas three small zircon fractions of three to four grains each from sample CS44a produced a combined mean ^{207}Pb/^{206}Pb evaporation age of 341.4 ± 0.7 Ma (Table 3, Fig. 8, inset). These ages are interpreted to reflect new growth of metamorphic zircon near the peak of metamorphism. The core of metamorphic grain 7 in sample CS44b provided a ^{206}Pb/^{238}U age of 473 ± 8 Ma (Table 2), and the significance of this age is uncertain, although it is likely that this dates an event in the history of the granulite protolith.

Sample CS46, resampled as CS70, is a porphyritic, foliated granitic gneiss of anatectic origin consisting of Plg–Kfs–Qtz–Bt–Grt. Sample CS46 showed advanced migmatization and yielded a preliminary Pb–Pb mean zircon age of *c.* 456 Ma which is difficult to interpret and is suspected to be a mixture of *c.* 500 Ma igneous crystallization and *c.* 340 Ma overgrowths. Therefore, the least migmatitic part of this rock was resampled at the same locality as CS70. The zircon in both samples are clear or light- to yellow-brown, stubby to long-prismatic crystals with idiomorphic or with variously rounded terminations. Cathodoluminescence images of zircon from CS70 show oscillatory zoning, typical of magmatic growth. A total of eight grains was evaporated individually and produced variable results (Table 3, Fig. 9a–c). The three youngest grains have a combined mean ^{207}Pb/^{206}Pb age of 507.1 ± 1.0 Ma. This is similar to zircon ages obtained for other granitoids in the OSC and is interpreted to represent the protolith age. Three further grains yielded identical but significantly higher ^{207}Pb/^{206}Pb ratios corresponding to a mean age of 565.5 ± 0.9 Ma, and we interpret these as xenocrysts reflecting the predominantly late Neoproterozoic source region from which the original porphyritic granite was derived through melting. One further grain with rounded terminations is still older with a minimum age of 665.6 ± 0.9 Ma and most probably is also a xenocryst from a Precambrian basement.

Careful selection of five near-idiomorphic grains from the more migmatitic sample CS46 yielded a mean ^{207}Pb/^{206}Pb age of 504 ± 1.0 Ma (Table 3), which is slightly younger than the age for sample CS70 and may reflect a small component of younger overgrowth that was not removed during evaporation. Nevertheless, the ages for CS46 and CS70 are almost identical, within error, and approximate the time of protolith emplacement. One additional grain with slightly

Table 2. SHRIMP II analytical data for spot analyses of single zircons from granulite samples CS44a and CS44b.*

Sample (p.p.m.)	U (p.p.m.)	Th	^{206}Pb/^{204}Pb	^{208}Pb/^{206}Pb	^{207}Pb/^{206}Pb	^{206}Pb/^{238}U	^{207}Pb/^{235}U	$^{206}/_{238}$ age ± 1 σ	$^{207}/_{235}$ age ± 1 σ	$^{207}/_{206}$ age ± 1 σ
Granulite sample CS 44a										
CS 44a-1	95	33	1191	0.1090 ± 117	0.0534 ± 51	0.0539 ± 9	0.397 ± 39	338 ± 6	339 ± 28	347 ± 216
CS 44a-2	364	35	786	0.0296 ± 66	0.0530 ± 30	0.0543 ± 9	0.396 ± 24	341 ± 6	339 ± 17	327 ± 127
Granulite sample CS 44b										
CS 44b-1	272	56	5120	0.0724 ± 192	0.0577 ± 83	0.0543 ± 10	0.431 ± 64	341 ± 6	364 ± 45	517 ± 289
CS 44b-2	745	36	2801	0.0108 ± 27	0.0518 ± 13	0.0545 ± 9	0.389 ± 12	342 ± 6	333 ± 9	275 ± 57
CS44b-3	1051	323	11684	0.0939 ± 17	0.0533 ± 8	0.0550 ± 9	0.405 ± 96	345 ± 6	345 ± 7	342 ± 34
CS44b-4	844	50	8007	0.0191 ± 18	0.0530 ± 9	0.0552 ± 9	0.403 ± 10	346 ± 6	344 ± 7	330 ± 39
CS44b-5	446	137	6819	0.0957 ± 28	0.0539 ± 13	0.0538 ± 9	0.400 ± 12	338 ± 5	342 ± 9	367 ± 54
CS44b-6	540	51	5208	0.0308 ± 27	0.0549 ± 13	0.0545 ± 9	0.412 ± 13	342 ± 6	350 ± 9	408 ± 53
CS44b-7	311	137	13553	0.1385 ± 27	0.0563 ± 12	0.0762 ± 13	0.591 ± 17	473 ± 8	472 ± 11	464 ± 47

* 1 is spot on grain 1, 2 is spot on grain 2, etc.

Table 3. Isotopic data from single grain zircon evaporation.

Sample Locality	Zircon colour and morphology	Grain #	Mass scans[1]	Evaporation T°C	Mean $^{207}Pb/^{206}Pb$ ratio[2] and 2-σm error	$^{207}Pb/^{206}Pb$ age and 2-σm error
CS 32 granodiorite (Skorošický brook, about 1 km NW of Ostrý Hill)						
	clear to light brown,	1	130	1600	0.053241 ± 30	339.1 ± 1.3
	long-prismatic,	2	130	1599	0.053244 ± 25	339.2 ± 1.1
	idiomorphic	3	96	1598	0.053252 ± 42	339.6 ± 1.8
		4	62	1599	0.057326 ± 45	340.0 ± 1.9
mean of 4 analyses		1–4	418		0.053248 ± 17	**339.4 ± 1.1**
CS 42 granodiorite (Morava river close to Hanušovice town -not shown on the map in Fig. 2)						
	clear to light yellow,	1	110	1600	0.053359 ± 24	344.1 ± 1.4
	long-prismatic,	2	130	1597	0.053368 ± 21	344.4 ± 0.9
	idiomorphic	3	153	1598	0.053374 ± 10	344.7 ± 0.4
mean of 3 analyses		1–3	393		0.053368 ± 10	**344.5 ± 1.1**
CS 44a felsic granulite (Račí valley, 400 m east of Pustý zámek)						
	clear, near-spherical,	1	95	1619	0.053284 ± 33	340.9 ± 1.4
	multifaceted	2	90	1612	0.053308 ± 28	341.9 ± 1.2
		3	49	1638	0.053290 ± 23	341.2 ± 1.0
mean of 3 analyses		1–3	323		0.053294 ± 16	**341.3 ± 0.7**
CS 46 migmatitic orthogneiss (Račí valley, 600 m north of Pustý zámek)						
	clear to yellow-	1	148	1597	0.057313 ± 13	503.6 ± 0.5
	brown, short- and	2	86	1599	0.057318 ± 19	503.8 ± 0.7
	long-prismatic,	3	86	1596	0.057323 ± 16	504.0 + 0.6
	ends little rounded	4	96	1599	0.057360 + 22	504.4 ± 0.8
		5	64	1598	0.057362 ± 22	504.5 ± 0.8
mean of 5 analyses		1–5	480		0.057332 ± 8	**504.3 ± 1.0**
	ends rounded	8	129	1595	0.067660 ± 17	858.2 ± 0.8
CS 70 migmatitic orthogneiss (Račí valley, 600 m north of Pustý zámek)						
	light to yellow-	1	126	1596	0.057392 ± 33	506.6 ± 1.3
	brown, short & long	2	86	1598	0.057403 ± 31	507.1 ± 1.2
	prismatic, ends rd.	3	108	1599	0.057416 ± 29	507.5 ± 1.1
mean of 3 analyses		1–3	320		0.057403 ± 18	**507.1 ± 1.0**
	as above	4	173	1598	0.058884 ± 34	562.8 ± 1.3
		5	129	1600	0.058869 ± 34	562.3 ± 1.3
		6	108	1599	0.058869 ± 29	562.3 ± 1.1
mean of 3 analyses		4–6	410		0.058875 ± 19	**562.5 ± 1.0**
	ends rounded	7	151	1598	0.061754 ± 25	665.6 ± 0.9
CS 80 granitic melt patch (Červený brook, 600 m NE from the village Červený Důl)						
	clear, stubby to	1	74	1596	0.053895 ± 48	366.7 ± 2.0
	long-prismatic,	2	88	1598	0.053883 ± 44	366.2 ± 1.8
	idiomorphic	3	85	1597	0.053876 ± 29	365.9 ± 1.2
		4	81	1598	0.053888 ± 23	366.4 ± 1.0
mean of 4 analyses		1–4	451		0.053885 ± 18	**366.3 ± 1.1**

[1] Number of $^{207}Pb/^{206}Pb$ ratios evaluated for age assessment. [2] Observed mean ratio corrected for nonradiogenic Pb where necessary. Errors based on uncertainties in counting statistics.

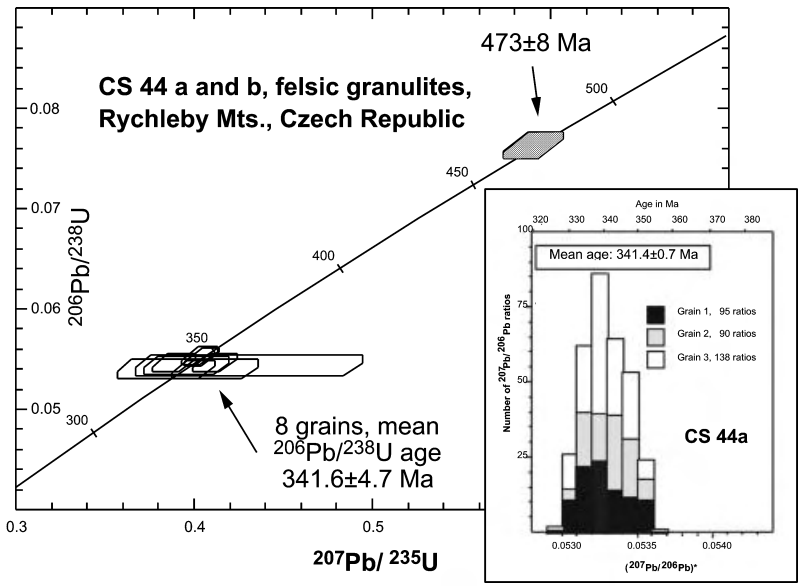

Fig. 8. Concordia diagram showing SHRIMP II analyses of metamorphic zircon from felsic granulite samples CS44a and 44b. Data boxes for each analysis are defined by standard errors in $^{207}Pb/^{235}U$, $^{206}Pb/^{238}U$ and $^{207}Pb/^{206}Pb$. Inset shows histogram with distribution of radiogenic lead isotope ratios derived from evaporation of three small zircon fractions from sample CS44a, integrated from 323 ratios.

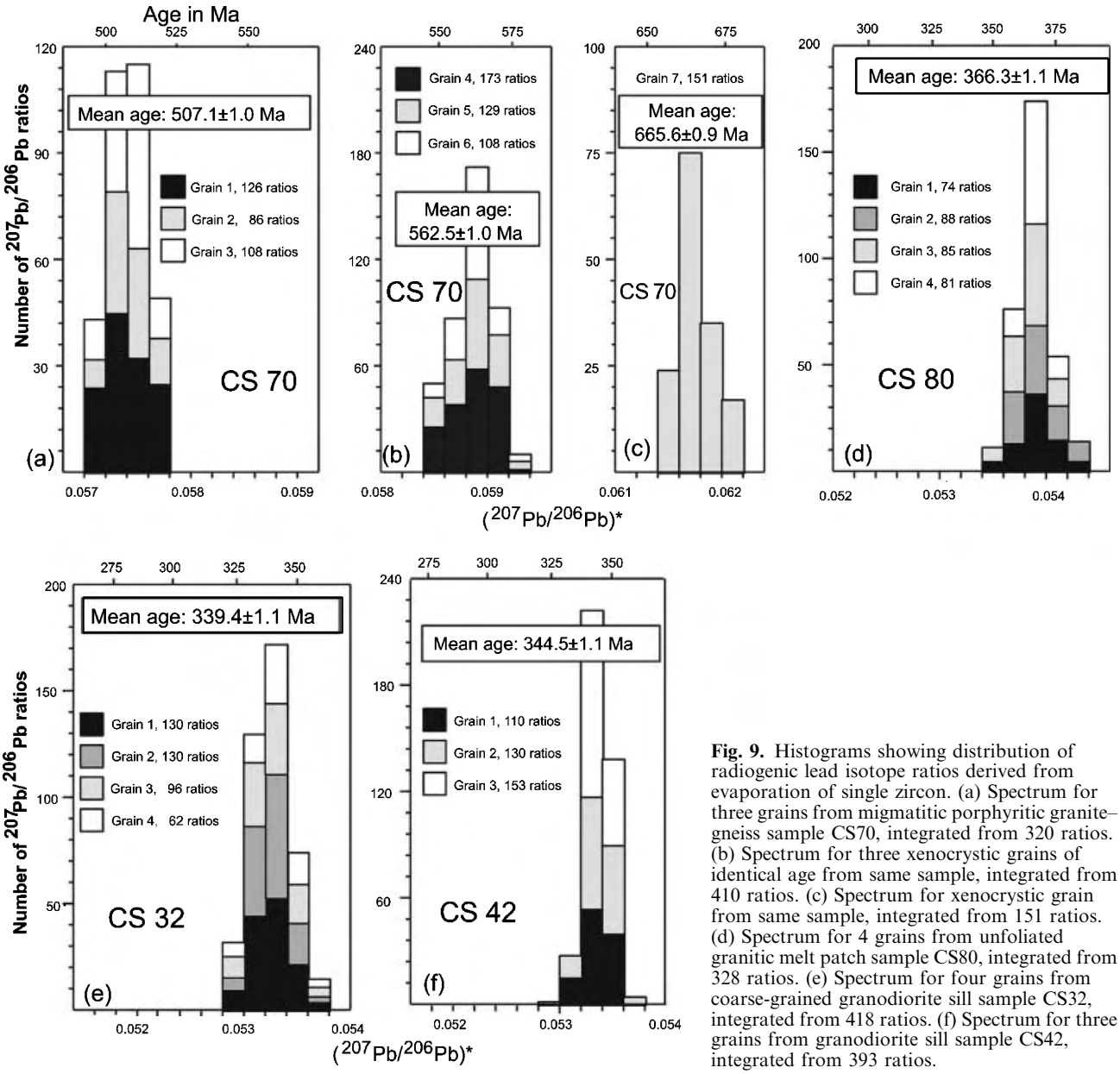

Fig. 9. Histograms showing distribution of radiogenic lead isotope ratios derived from evaporation of single zircon. (a) Spectrum for three grains from migmatitic porphyritic granite–gneiss sample CS70, integrated from 320 ratios. (b) Spectrum for three xenocrystic grains of identical age from same sample, integrated from 410 ratios. (c) Spectrum for xenocrystic grain from same sample, integrated from 151 ratios. (d) Spectrum for 4 grains from unfoliated granitic melt patch sample CS80, integrated from 328 ratios. (e) Spectrum for four grains from coarse-grained granodiorite sill sample CS32, integrated from 418 ratios. (f) Spectrum for three grains from granodiorite sill sample CS42, integrated from 393 ratios.

rounded terminations produced a much older age of 858.2 ± 0.8 Ma and is interpreted as a xenocryst.

Sample CS80 is an unfoliated granite collected from a large melt patch within the anatectic orthogneiss. The sample consists of Kfs–Plg–Qtz–Bt–Ms and has a typical magmatic texture with random orientation of the minerals. The zircon are clear, stubby or long-prismatic crystals with idiomorphic sharp terminations, typical of magmatic growth. No metamorphic overgrowth was visible on cathodoluminiscence images. Three long-prismatic grains were evaporated and provided a mean $^{207}Pb/^{206}Pb$ age of 366.3 ± 1.1 Ma (Table 3, Fig. 9d) that is interpreted to reflect magmatic crystallization of the protolith. Klemd & Bröcker (1999) reported similar $^{207}Pb/^{206}Pb$ ages of 369–360 Ma from the same granulite belt in southern Poland and ascribed these to protolith formation or melting during the early stages of high-grade metamorphism.

Sample CS32 is a coarse-grained granodiorite composed of Plg–Kfs–Qtz–Amp–Bt. The strong magmatic foliation is marked by the preferred orientation of amphibole and biotite. Four long-prismatic, euhedral grains of typical magmatic habit were evaporated individually and yielded a mean age of 339.4 ± 1.1 Ma (Table 3, Fig. 9e) that we interpret to reflect the time of granodiorite emplacement during major S3 shearing.

The sample CS42 was collected from the southern part of the granodiorite sill, where numerous dykes cut

the leptyno-amphibolite complex of the Staré Město belt. The zircon is clear to light yellow, long-prismatic and idiomorphic. Three zircon grains from this sample CS42 yielded identical isotopic ratios that provide a mean age of 344.5 ± 1.1 Ma (Table 3, Fig. 9f). Here again we consider this to reflect emplacement of the granodiorite.

Significance of new zircon ages

One of the main difficulties of this study is the correct interpretation of the above zircon ages in terms of the HP event. U–Pb multigrain ages of 369–360 Ma for a felsic granulite from the OSC (Klemd & Bröcker, 1999) were interpreted to reflect protolith emplacement, similar to the South Bohemian data of Wendt *et al.* (1994). In a similar way the 366.3 ± 1.1 Ma age of sample CS80 is interpreted to reflect magmatic crystallization. We speculate that this event is probably related to processes above the subduction zone located farther west, in the Rudawy Janowickie and Rýchory Mts, where blueschist facies metamorphism was dated at *c.* 360 Ma (Fig. 1; Maluski & Patočka, 1997). However, it still remains unclear whether this melting process occurred before or during the early stages of HP metamorphism in the OSC.

The combined mean metamorphic zircon age of 341.6 ± 4.7 for samples CS44a and 44b is interpreted to reflect growth near the peak of metamorphism and is in excellent agreement with granulite zircon ages in other parts of the Bohemian massif (Kröner *et al.*, 1998; O'Brien *et al.*, 1997; Kröner & Willner, 1998; Kröner *et al.*, 2000a). Roberts & Finger (1997) suggested that zircon crystallization in hot isothermally uplifted granulites postdates the pressure peak of the *P–T* path and, consequently, metamorphic zircon would grow after exhumation to mid-crustal levels. However, Kröner *et al.* (2000a) dated single zircon on SHRIMP, which were included in HP minerals and confirmed the 340 Ma crystallization age for the South Bohemian HP event. In addition, Sm–Nd garnet–WR–cpx isochrons of Brueckner *et al.* (1991) from nearby OSC eclogites yielded ages of 341 ± 7 and 337 ± 4 Ma which are identical to our zircon ages. Because of the high closure temperatures for diffusion of Pb and REE (Lee *et al.*, 1997; Van Orman *et al.*, 2002) we interpret all these data as reflecting the age of eclogite facies metamorphism, rather than retrogression of these rocks.

In addition, orthogneisses in which the Rychleby granulites are found yielded only Cambro–Ordovician emplacement ages, indicating that eclogite facies metamorphism was restricted to the narrow belt in which Carboniferous metamorphic zircon growth occurred. The above interpretation is also supported by a U–Pb SHRIMP age of 342 ± 6 Ma for high-U magmatic rims surrounding *c.* 500 Ma igneous grains and interpreted to reflect anatexis in the Gieraltow gneiss in Miedzygorze in Poland (Turniak *et al.*, 2000). All available evidence therefore supports the interpretation that metamorphic zircon growth within the Rychleby granulites occurred close to peak *P–T* conditions. However, taking all Sm–Nd and U–Pb zircon data into account, it cannot be excluded that the duration of HP–HT metamorphism may have ranged from *c.* 366 to *c.* 340 Ma.

The question of precise timing of the S3 fabric is raised by different ages for samples CS32 (339.4 ± 1.1 Ma) with strong magmatic fabric and CS42 (344.5 ± 1.1 Ma) collected from one of numerous dykes cross-cutting the Cambro-Ordovician structure of the leptyno–amphibolite complex in the Staré Město belt. The magmatic activity may have been long-lasted and the older age may be related to an early magma pulse predating development of the S3 shear zone. The younger age dates the syntectonic granodiorite pulse associated with S3 shearing and extrusion of hot lower crustal rocks over rigid buttress of the Staré Město belt.

DISCUSSION

Kinematic significance of ductile structures

It has been shown that within the steep fabric of the granulite belt and surrounding gneisses a relict fabric is preserved, which was refolded by steep isoclinal folds. Therefore, the new steep fabric originated through transposition of the S1-foliation which was probably sub-horizontal originally. It has also been shown that the S2-fabric in the granulite belt developed at *c.* 18 kbar and *c.* 900 °C. Although the *P–T* conditions of steep fabric development within the surrounding orthogneiss were not determined, the degree of anatexis indicates a gradual decrease in metamorphic conditions away from the granulite belt. This implies that juxtaposition of the granulites with the surrounding lower-grade rocks occurred due to differential vertical movements. In addition, the AMS study revealed a vertical magnetic foliation with a horizontal lineation and a variable shape for the ellipsoid of magnetic susceptibility. In agreement with Hrouda *et al.*, 2000), we interpret the horizontal AMS lineations to reflect the orientation of preserved hinges of isoclinal folds and, consequently, they do not represent the transport direction.

A steep anastomosing network of amphibolite facies D3 shear zones developed during late increments of viscous extrusion and indicates a vertical direction of flow in this tabular zone. In contrast, rare flat shear zones are interpreted as a result of collapse of vertical fabrics. The S3-fabric in the surrounding gneisses dipping towards the core of the granulite zone is interpreted to reflect a transition from vertical flow to sideways thrusting at a crustal depth corresponding to *c.* 10 kbar. The AMS study in the granulite belt confirmed flat magnetic foliations bearing SE–NW-oriented lineations, which are perpendicular to the

trend of the granulite belt. It is suggested that these fabrics most likely reflect the direction of sideways thrusting, whereas the NE–SW trending linear structures measured in the field may correspond to the intersections between the S2- and S3-foliations and to the trend of F3-fold hinges.

The D2-pattern reveals a predominantly coaxial structural history related to NE–SW shortening and vertical extrusion along a NE-trending zone. The transition to amphibolite facies sub-horizontal D3-flow was probably still coaxial as shown by an almost symmetrical structural pattern around the granulite core and by the AMS fabrics. However, the degree of non-coaxiality of deformation increases towards the east, where it is manifested by dextral reactivation near and within the Staré Město belt, as described from metagabbros and the granodiorite sill (Parry *et al.*, 1997).

Mechanisms of granulite exhumation

In analogy to mesoscopic folding, the development of a vertical tabular zone of granulites surrounded by medium-grade rocks may have originated through folding of crustal layers of significantly larger scale. These large-scale anticlines with high-grade gneisses in their cores and medium-grade metasedimentary rocks in synclines were already recognised by Don (1964, 1982). From the consideration of theoretical and physical models, it can be concluded that there are several stages in the formation of a fold (Fig. 10).

The thickened crust should originally have exhibited horizontal rheological stratification controlled by the thermal gradient and lithological differences between lower and upper crust (Burg & Podladchikov, 1999, 2000). In our model the lower layer is represented by felsic and intermediate HP granulites, whereas the orthogneisses and metasedimentary rocks represent the upper layer. Layer-parallel shortening of such a stratified system will generate passive amplification of initial surface irregularities to give a characteristic cuspate–lobate geometry of the folded interface with cusps of the hotter and therefore weaker granulitic rocks pointing upwards and lobes of the upper crust pointing downwards (Biot, 1964). Such types of folds were described in high-grade terranes but only at a scale of hundreds of metres (Kisters *et al.*, 1996), while the initial size of cusp proposed in this study has to be in the range of several kilometres. As shown by Fletcher (1982), the formation of high-amplitude cusps requires a large amount of shortening. High strain may in our case be related to the proximity of a rigid indenter which, according to Štípská *et al.* (2001), is represented by Cambro–Ordovician rocks of the Staré Město belt. The process of folding thus led to the formation of a narrow, vertical, tabular zone composed of granulites and surrounded by a wider domain composed of granitoid gneiss and metasedimentary rocks. It is likely that the above-described mechanism is not sufficient to explain the amount of exhumation of rocks from the base of the thickened crust as determined by petrology. We suggest that post-buckle flattening may have generated strong viscous partitioning (Schulmann *et al.*, 2003) which was probably responsible for differential velocities of exhumation of lower crustal rocks along a weak channel as modelled by Thompson *et al.* (1997a), provided that a rigid bottom layer exists. This rigid compensation level may represent the sub-crustal mantle as suggested by Thompson *et al.* (2001). The final stage of extrusion occurred along the marginal zone of retrogressed granulites and partially molten gneisses, whereas the granulite core was almost passively transported upwards in form of a rigid plug. However, the granulite core itself experienced some deformation during this late stage as shown by the presence of a heterogeneous network of D3 shear zones.

The transition from steep to flat fabric in the OSC has already been described by Dumicz (1979), who interpreted steep fabrics to be a result of lateral shortening and the transition to flat fabric as a consequence of gravitational load and sideways mass flow. The origin of ductile sub-horizontal fabrics in the deep crust has been explained as a result of gravity-driven ductile rebound of the orogenic root (Koyi *et al.*, 1999; Milnes & Koyi, 2000). The concept of sideways flow, termed 'lateral extrusion' (Bird, 1991), 'sub-surface collapse' (Avouac & Burov, 1996) or 'lower crustal spreading' (England & Holland, 1979) is based on buoyant return of low-bulk-density and high-pressure rocks (Dewey *et al.*, 1993), that rebound against a rigid lid marked by the brittle-ductile transition. We suggest that the transition from steep 'channel flow' to sub-horizontal 'lateral spreading' fabrics in our study area is not related to gravity-driven ductile rebound, but was probably initiated by an eastward movement of the Staré Město indenter. Gently inclined amphibolite facies fabrics of the Rychleby granulites that developed at *c.* 10 kbar and 700 °C may be correlated with Variscan mylonitization of Cambro–Ordovician gabbros at the western margin of the Staré Město belt, which occurred at similar conditions of 710–740 °C at 8–10 kbar (Štípská *et al.*, 2001). The preservation of Cambro–Ordovician metamorphic conditions of 730–850 °C at 8–10 kbar in the internal part of the Staré Město belt suggests that only its western margin was reworked during Variscan burial. This implies that the Staré Město belt acted as a rigid ramp which was pushed into the weak and thickened orogenic root (Fig. 10a,b). The observed strain pattern is remarkably similar to that of extruding-spreading analogous models explaining superficial spreading nappes (Merle, 1989). However, in our case study the spreading operated at deep crustal levels.

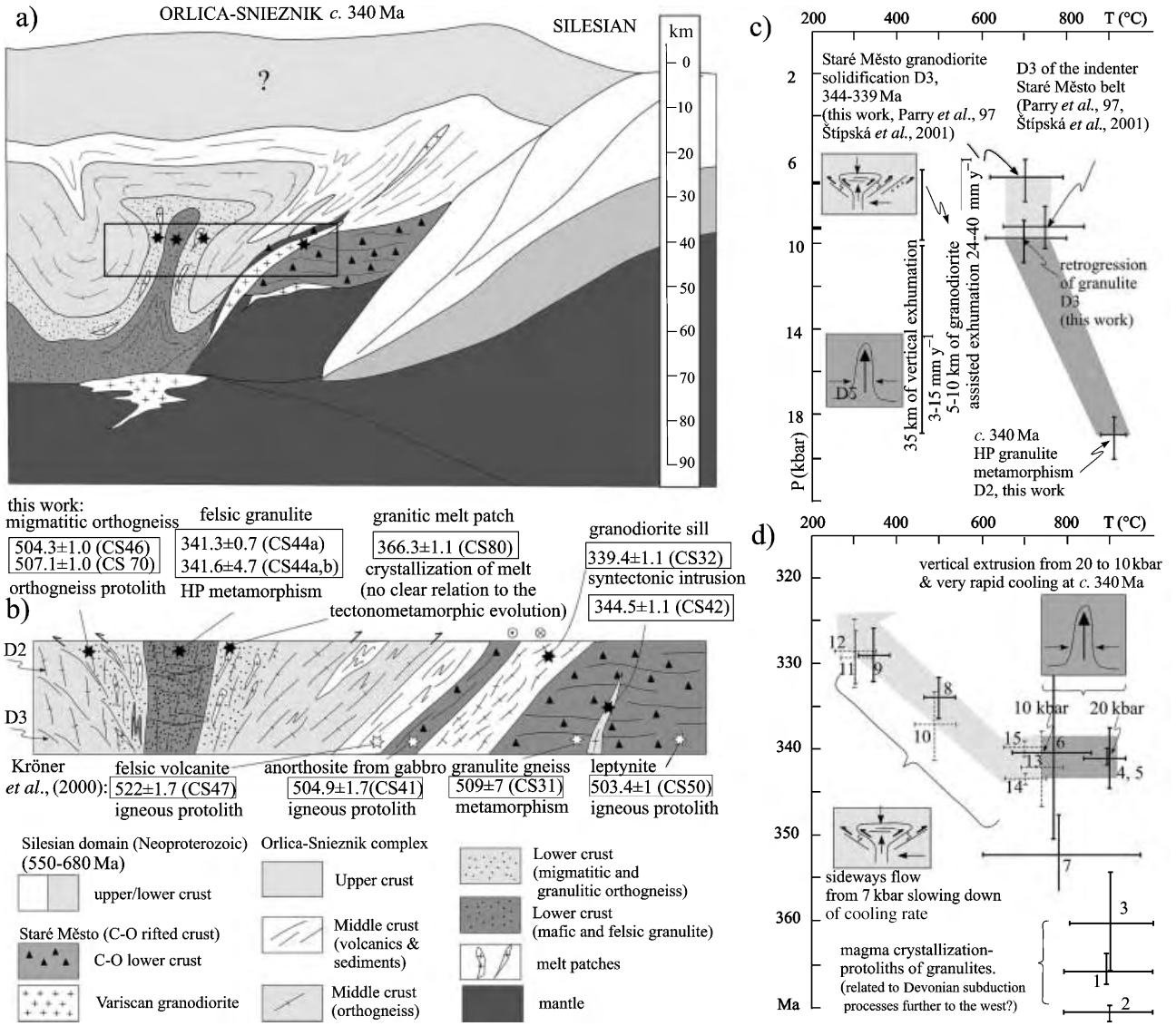

Fig. 10. Model for the tectonic evolution of the study area and summary *P–T–t–D* plots. (a) Schematic sketch showing the situation at the end of ductile extrusion and the beginning of lateral spreading. The indenting rigid block of the Staré Město belt was responsible for both D2 extrusion of granulites from *c.* 70 km and their lateral D3 spreading at a depth of 35 km. A granodiorite sill was emplaced parallel to D3 fabrics. (b) Enlarged section shows position of new geochronological data with respect to structural fabrics as well as earlier data sampled east of the granulite belt. (c) Summary *P–T–D* plot for the studied granulites and the Staré Město belt. The *P–T* conditions for amphibolite facies retrogression of granulite and of metamorphism of the Staré Město rocks are dated by the age of the syntectonic intrusion of the granodiorite sill during D3. The exhumation rates for stages D2 and D3 are shown. (d) Temperature–time path for Rychleby granulite belt (thick lines) and for the entire OSC (dashed lines). Numbers of individual age determinations refer to Tables 2 and 3. Cooling rate paths are shown for vertical extrusion of the granulite belt and for the lateral spreading stage.

Exhumation and cooling rates

Evaluation of the velocity of vertical ascent requires knowledge of the maximum pressures which the rocks experienced and the pressures reflecting their retrogression (Duchène *et al.*, 1997). These data permit the determination of the magnitude of the minimum vertical path along which the exhumed rocks travelled. The other necessary information is the dating of peak pressure conditions and the age of *P–T* conditions associated with retrogression. This may be done by dating of a petrologically established crystallization depth of rapidly cooled granitic intrusions syn-tectonically emplaced along retrograde shear zones.

Depth–time path

The exhumation rate of the granulites is now estimated, taking into account the zircon ages for peak

HP metamorphism and granodiorite emplacement at a depth at least 35 km shallower than granulite formation. Since these ages are identical, within error, the time span indicated by the error in the least precise age must be considered, which is at most 10 Myr. However, the time span is only 2 Myr. if the difference between the age of 341.3 ± 0.7 Ma for the granulite (CS44a) and the age of 339.4 ± 1.1 Ma (CS39) for the granodiorite is taken into account.

First exhumation occurred along a vertical channel from a depth of 70 km (18 kbar) to 35 km (10 kbar) (Fig. 10c). For the time interval of 10 Myr for this stage, the minimum exhumation rate is 3 mm year^{-1} or 6.5 mm year^{-1} if the peak pressure values suggested by Kryza *et al.* (1996) are considered. The highest exhumation rate is 15 mm year^{-1} and 30 mm year^{-1} for the time span of 2 Myr as calculated for our pressure estimates and those of Kryza *et al.* (1996), respectively.

As shown above, sideways thrusting of granulites and gneisses at 10 kbar was correlated with the development of thrust-related metamorphism at 8–10 kbar along the western margin of the Staré Město gabbros. This thrusting was associated with syntectonic emplacement of a granodiorite sill whose depth of intrusion was estimated at 6.5–7 kbar. Therefore, the vertical transport, corresponding to the 3 kbar difference between shearing in the gabbros and granodiorite solidification, was accommodated within the Staré Město belt. According to Paterson & Tobisch (1992), solidification of granodioritic magma takes about 250 000 years on average, at mid to shallow crustal levels. This implies that the late exhumation increment corresponds to *c.* 3 kbar over a period of 250 000 years, which is equivalent to an exhumation rate in the range of 24–40 mm year^{-1}. These rates are in agreement with the predictions of Hollister (1993) and Davidson *et al.*, 1994) and confirm that lubrication of a shear zone by syn-tectonically emplaced magma is a very efficient mechanism of rock exhumation, even for very short time scales. Lateral spreading or other mechanisms such as, for example, ductile thinning and/or erosion may be responsible for continuation of the exhumational process to shallow crustal levels as proposed by Bröcker & Klemd (1996).

Temperature–time path

The *P–T* estimates suggested here are consistent with a high rate of temperature decrease from 900 to 700 °C for peak and retrogressive conditions, respectively (Fig. 10). The temperature decrease would even be greater if the peak temperature of 1100 °C estimated by Kryza *et al.* (1996) is taken into account. The 342 Ma zircon ages determined for peak conditions of granulite and syn-D3 granodiorite emplacement indicate cooling rates of 20 or 100 °C Myr^{-1} assuming 2 or 10 Myr^{-1} for the duration of the exhumation process. Various metamorphic and cooling ages determined for the OSC by Brueckner *et al.* (1991), Steltenpohl *et al.* (1993), Klemd & Bröcker (1999), Turniak *et al.* (2000), Lange *et al.* (2002) and Borkowska *et al.* (1990) indicate cooling from 700–650 °C to 300 °C during the time interval from 342 to 328 Ma, thus implying an average cooling rate of 25–30 °C Myr^{-1} (Table 4 & Fig. 10d). Even if the structural position of these samples is unknown, we suppose that most of the cooling ages are related to D3-deformation. This means that the rocks cooled rapidly during the vertical extrusion, whereas the cooling rate slowed down during the lateral spreading stage.

In agreement with Burg *et al.* (1998) a high cooling rate during the early exhumation stage is assumed to

Table 4. Summary of ages related to the metamorphism in the OSC.

N	Localization/rock	Age (Ma)	Method	Interpretation	Reference
	Rychleby (Zlote) granulite belt				
1	granitic melt patch within orthogneiss	366.3 ± 1.1	Pb/Pb, single Zrn evaporation	melt crystallization	this work
2	mafic granulite	369 ± 1	Pb/Pb Zrn multigrain	protolith crystallization from melt	Klemd & Bröcker (1999)
3	mafic granulite	360 ± 6	Pb/Pb Zrn multigrain	protolith crystallization from melt	Klemd & Bröcker (1999)
4	felsic granulite	341.6 ± 4.7	Zrn SHRIMP	HP metamorphism	this work
5	felsic granulite	341.4 ± 0.7	Pb/Pb, single Zrn evaporation	HP metamorphism	this work
6	mafic granulite	341 ± 10, 343 ± 11	Sm/Nd, Grt-WR	HP metamorphism	Klemd & Bröcker (1999)
7	mafic granulite	352 ± 4	Sm/Nd, Grt-Cpx-WR	HP metamorphism?	Brueckner *et al.* (1991)
	near Rychleby (Zlote) granulite belt				
8	eclogite	332.6 ± 2.3	Ar/Ar, Hbl	cooling through 500°C	Steltenpohl *et al.* (1993)
9	orthogneiss	328 ± 2	Ar/Ar, Ms	cooling through 350°C	Steltenpohl *et al.* (1993)
10	orthogneiss	328.8 ± 1.7	Ar/Ar, Bt	cooling through 300°C	Steltenpohl *et al.* (1993)
	Miedzygorze belt				
11	orthogneiss	337.4 ± 2.3	Rb/Sr, Ms-WR	cooling through 500°C	Lange *et al.* (2002)
12	orthogneiss	328.6 ± 4.4	Rb/Sr, Ms-WR	cooling through 300°C	Lange *et al.* (2002)
13	orthogneiss	342 ± 6	Zrn SHRIMP	metamorphism & anatexis	Turniak *et al.* (2000)
	Staré Město granodiorite				
14	granodiorite	344.5 ± 0.4	Pb/Pb, single Zrn evaporation	pre-D3 melt crystallization	this work
15	granodiorite	339.4 ± 1.1	Pb/Pb, single Zrn evaporation	syn-D3 melt crystallization	this work
	Other ages (not plotted in Fig. 10)				
16	eclogite	341 ± 7, 337 ± 4, 329 ± 6	Sm/Nd, Grt-Cpx-WR	HP metamorphism or uplift?	Brueckner *et al.* (1991)
17	orthogneiss	335 ± 5	Rb/Sr, Bt-Ms-WR	cooling	Borkowska *et al.* (1990)

be due to fast exhumation coupled with significant lateral heat transfer responsible for efficient cooling of vertically extruded small volumes of granulites through colder mid-crustal rocks. However, the Ar–Ar and Rb–Sr cooling ages reported for the entire OSC probably reflect the cooling rate for the entire complex and, moreover, for the stage when lateral movements were important (Fig. 10c,d). In fact, during D3 the granulite body became part of a large system with its own thermal budget and cooling history. Our data show a different pattern of cooling rates than that reported by other authors (e.g. Duchène *et al*., 1997), and also contradict results of numerical modelling (Grasemann *et al*., 1998; Thompson *et al*., 1997a). This is because these models were constructed for simple boundary conditions and to explain exhumation of entire orogens, whereas natural exhumation processes are diachronous, polyphase and operate through various mechanisms on smaller length scales.

CONCLUSIONS

(1) Exhumation of the HP granulite belt in the Orlica–Snieznik complex was initiated by buckling of crustal layers of thickened continental crust due to lateral shortening.
(2) Folding was followed by vertical ductile extrusion from a depth of 70 km (18 kbar) to mid-crustal level of 35 km (10 kbar) due to viscous partitioning between stronger cores of synforms and weaker cores of antiforms dominated by granulites. The vertical ascent is attributed to E–W compression and not to gravity-driven doming or diapirism.
(3) The final stage of exhumation was associated with lateral viscous spreading of the HP granulites and surrounding rocks at a depth corresponding to 10 kbar. This process was controlled by indentation of a rigid continental ramp and is dated by a syntectonic granodiorite intrusion.
(4) The exhumation succession described here, especially the extrusion stage, was a localized process heterogeneously affecting the orogenic root. It is suggested that it may be of general validity for the exhumation of HP rocks in hot orogenic roots.
(5) The exhumation rate of granulites during vertical extrusion ranges between 3 and 15 mm $year^{-1}$. Tabular intrusion of a granodiorite sill served as an efficient lubricant along which the final exhumation increment of 24–40 mm $year^{-1}$ occurred.
(6) The granulites cooled rapidly during vertical extrusion (20–100 °C Myr^{-1}) and the cooling rate decreased to 25–30 °C Myr^{-1} during the lateral spreading stage.

ACKNOWLEDGEMENTS

We are grateful to F. Hrouda for providing the AMS measurements and for helpful discussions. Some of the zircon analyses were carried out on the Sensitive High Resolution Ion Microprobe mass spectrometer (SHRIMP II) operated by a consortium consisting of Curtin University of Technology, the Geological Survey of Western Australia and the University of Western Australia with the support of the Australian Research Council. We appreciate the advice of A. A. Nemchin and A. Kennedy during SHRIMP analysis. This research is part of an ongoing collaboration between Charles University, Prague, Mainz University, Germany, and ETH Zürich, Switzerland. Financial support to P.Š. by the Czech National Grant Agency (grant no. 205/99/1195) and Charles University Grant Agency (grant No.223/2002/B-GEO/PřF) is gratefully acknowledged**.** Zircon geochronology was funded by the German Science Foundation (DFG, grant Kr 68–1) to A.K. as were two visits of P.Š. to Mainz University. Several visits of P.Š. to ETH Zürich were funded by the Swiss National Foundation ('Continuous Orogenesis' grant to A. B. Thompson). P.Š. & K.S. also received financial support from the Czech Ministry of Education, grant no. 24313005. We thank P. O'Brien and an anonymous reviewer for constructing comments and a careful review of the manuscript.

REFERENCES

Aleksandrowski, P., Kryza, R., Mazur, S., Pin, C. & Zalasiewicz, J. A., 2000. The Polish Sudetes: Caledonian or Variscan? *Transactions of the Royal Society of Edinburgh-Earth Sciences*, **90,** 127–146.

Allemand, P. & Lardeaux, J. M., 1997. Strain partitioning and metamorphism in a deformable orogenic wedge: Application to the Alpine belt. *Tectonophysics*, **280,** 157–169.

Avouac, J. P. & Burov, E. B., 1996. Erosion as a driving mechanism of intracontinental mountain growth. *Journal of Geophysical Research*, **101,** 17 747–17 769.

Bakun-Czubarow, N., 1992. Quartz pseudomorphs after coesite and quartz exsolutions in eclogitic omphacites of the Zlote Mountains in the Sudetes (SW Poland). *Archiwum Mineralogiczne*, **48,** 3–25.

Biot, M. A., 1964. Theory of viscous buckling and gravity instability of multilayers with large deformation. *Geological Society of America Bulletin*, **76,** 371–378.

Bird, P., 1991. Lateral extrusion of lower crust from under high topography, in the isostatic limit. *Journal of Geophysical Research*, **96,** 10 275–10 286.

Borkowska, M., Choukroune, P., Hameurt, J. & Martineau, F., 1990. A geochemical investigation of the age, significance and structural evolution of the Caledonian-Variscan granite-gneisses of the Snieznik metamorphic area (Central Sudetes, Poland). *Geologia Sudetica*, **15,** 1–27.

Bröcker, M. & Klemd, R., 1996. Ultrahigh-pressure metamorphism in the Snieznik Mountains (Sudetes, Poland): P-T constraints and geological implications. *Journal of Geology*, **104,** 417–433.

Brueckner, H. K., Medaris, L. G. & Bakun-Czubarow, N., 1991. Nd and Sr age and isotope patterns from Variscan eclogites of the eastern Bohemian Massif. *Neues Jahrbuch für Mineralogie, Abhandlungen*, **163,** 169–196.

Burg, J. P., Davy, P., Nievergelt, P., Oberli, F., Seward, D., Diao, Z. Z. & Meier, M., 1997. Exhumation during crustal folding in the Namche-Barwa syntaxis. *Terra Nova*, **9,** 53–56.

Burg, J. P., Nievergelt, P., Oberli, F. *et al.* 1998. The Namche Barwa syntaxis: evidence for exhumation related to compressional crustal folding. *Journal of Asian Earth Sciences*, **16,** 239–252.

Burg, J. P. & Podladchikov, Y., 1999. Lithospheric scale folding: numerical modelling and application to the Himalayan syntaxes. *International Journal of Earth Sciences*, **88,** 190–200.

Burg, J. P. & Podladchikov, Y., 2000. From buckling to asymmetric folding of the continental lithosphere; numerical modelling and application to the Himalayan syntaxes. In: *Tectonics of the Nanga Parbat Syntaxis and the Western Himalaya, Special Publication, 170* (eds Khan, M. A., Treloar, P. J., Searle, M. P. & Jan, M. Q.), pp. 219–236. Geological Society, London

Chemenda, A., Matte, P. & Sokolov, V., 1997. A model of Palaeozoic obduction and exhumation of high-pressure/low-temperature rocks in the southern Urals. *Tectonophysics*, **276,** 217–227.

Cloos, M., 1982. Flow melanges – numerical modeling and geologic constraints on their origin in the Franciscan Subduction Complex, California. *Geological Society of America Bulletin*, **93,** 330–345.

Compston, W., Williams, I. S., Kirschvink, J. L., Zhang, Z. & Ma, G., 1992. Zircon U-Pb ages for the Early Cambrian time-scale. *Journal of the Geological Society of London*, **149,** 171–184.

Connolly, J. A. D., 1990. Multivariable phase diagrams: An algorithm based on generalized thermodynamics. *American Journal of Science*, **290,** 666–718.

Cymerman, Z., 1992. Rotational ductile deformations in the Snieznik metamorphic complex. *Geological Quarterly*, **36,** 393–420.

Davidson, C., Schmid, S. M. & Hollister, L. S., 1994. Role of melt during deformation in the deep crust. *Terra Nova*, **6,** 133–142.

De Laeter, J. R. & Kennedy, A. K., 1998. A double focusing mass spectrometer for geochronology. *International Journal of Mass Spectrometry*, **178,** 43–50.

Dewey, J. F., Ryan, P. D. & Andersen, T. B., 1993. Orogenic uplift and collapse, crustal thickness, fabrics and metamorphic phase changes; the role of eclogites. In: *Magmatic Processes and Plate Tectonics, Special Publications, 76*, (eds Prichard, H. M., Alabaster, T., Harris, N. B. W. & Neary, C. R.). pp. 325–343. Geological Society, London.

Don, J., 1964. The Zlote and Krowiarki Mountains as structural elements of the Snieznik metamorphic massif. *Geologia Sudetica*, **1,** 79–117.

Don, J., 1982. The Sienna synform and the relationship of gneisses to the deformational stages distinguished in the Snieznik metamorphic massif (Sudetes). *Geologia Sudetica*, **17,** 130–124.

Don, J., Dumicz, M., Wojciechowska, I. & Zelazniewicz, A., 1990. Lihology and tectonics of the Orlica-Snieznik Dome, Sudetes: recent state of knowledge. *Neues Jahrbuch für Geologie und Paläontologie, Abhandlungen*, **179,** 159–188.

Duchène, S., Lardeaux, J. M. & Albarède, F., 1997. Exhumation of eclogites: insights from depth-time path analysis. *Tectonophysics*, **280,** 125–140.

Dumicz, M., 1979. Tectogenesis of the metamorphosed series of the Klodzko district: a tentative explanation. *Geologia Sudetica*, **14,** 29–44.

Ellis, D. J. & Green, D. H., 1979. An experimental study of the effect of Ca upon garnet-clinopyroxene Fe-Mg exchange equilibria. *Contributions to Mineralogy and Petrology*, **71,** 13–22.

England, P. C. & Holland, T. J. B., 1979. Archimedes and the Tauern eclogites – role of buoyancy in the preservation of exotic eclogite blocks. *Earth and Planetary Science Letters*, **44,** 287–294.

England, P. & Molnar, P., 1990. Surface uplift, uplift of rocks, and exhumation of rocks. *Geology*, **18,** 1173–1177.

Fletcher, R. C., 1982. Analysis of the flow in layered fluids at small, but finite, amplitude with application to mullion structures. *Tectonophysics*, **81,** 51–66.

Fuhrman, M. L. & Lindsley, D. H., 1988. Ternary-feldspar modeling and thermometry. *American Mineralogist*, **73,** 201–215.

Gasparik, T., 1985. Experimental study of subsolidus phase relations and mixing properties of pyroxeneand plagioclase in the system Na_2O-CaO-Al_2O_3-SiO_2. *Contributions to Mineralogy and Petrology*, **89,** 346–357.

Grasemann, B., Ratschbacher, L. & Bradley, H., 1998. Exhumation of ultrahigh-pressure rocks: Thermal boundary conditions and cooling history. In: *When Continents Collide: Geodynamics and Geochemistry of Ultrahigh-Pressure Rocks* (eds Hacker, B. R. & Liou, J. G.), pp. 117–139. Kluwer Academic.

Grujic, D., Casey, M., Davidson, C., Hollister, L. S., Kundig, R., Pavlis, T. & Schmid, S., 1996. Ductile extrusion of the Higher Himalayan Crystalline in Bhutan: Evidence from quartz microfabrics. *Tectonophysics*, **260,** 21–43.

Hodges, K. V., Hurtado, J. M. & Whipple, K. X., 2001. Southward extrusion of Tibetan crust and its effect on Himalayan tectonics. *Tectonics*, **20,** 799–809.

Holland, T. J. B., 1983. The experimental determination of activities in disordered and short-range ordered jadeitic pyroxenes. *Contributions to Mineralogy and Petrology*, **82,** 214–220.

Holland, T. J. B. & Blundy, J. D., 1994. Non–ideal interactions in calcic amphiboles and their bearing on amphibole-plagioclase thermometry. *Contributions to Mineralogy and Petrology*, **116,** 433–447.

Holland, T. J. B. & Powell, R., 1990. An enlarged and updated internally consistent thermodynamic dataset with uncertainties and correlations: the system K_2O-Na_2O-CaO-MgO-MnO-FeO-Fe_2O_3-Al_2O_3-TiO_2-SiO_2-C-H_2-O_2. *Journal of Metamorphic Geology*, **8,** 89–124.

Hollister, L. S., 1993. The role of melt in the uplift and exhumation of orogenic belts. *Chemical Geology*, **108,** 31–48.

Hrouda, F., Jelínek, V. & Hrušková, L., 1990. A package of programs for statistical evaluation of magnetic data using IBM-PC computers. *Eos, Transactions of the American Geophysical Union*, **71,** 43.

Hrouda, F., Krejči, O. & Otava, J., 2000. Magnetic fabric in folds of the easternmost Rheno-Hercynian Zone. *Physics and Chemistry of the Earth Part a – Solid Earth and Geodesy*, **25,** 505–510.

Jelínek, V., 1978. Statistical processing of anisotropy of magnetic susceptibility measured on groups of specimens. *Studia Geophysica et Geodetica*, **22,** 50–62.

Kinny, P. D., 1986. 3820 Ma zircons from a tonalitic Amitsoq Gneiss in the Godthaab District of southern West Greenland. *Earth and Planetary Science Letters*, **79,** 337–347.

Kisters, A. F. M., Charlesworth, E. G., Gibson, R. L. & Anhaeusser, C. R., 1996. Steep structure formation in the Okiep copper district, South Africa: Bulk inhomogeneous shortening of a high-grade metamorphic granite-gneiss sequence. *Journal of Structural Geology*, **18,** 735–751.

Klemd, R. & Bröcker, M., 1999. Fluid influence on mineral reactions in ultrahigh-pressure granulites: a case study in the Sneznik Mts. (West Sudetes, Poland). *Contributions to Mineralogy and Petrology*, **136,** 358–373.

Klemd, R., Bröcker, M. & Schramm, J., 1995. Characterization of amphibolite facies fluids of Variscan eclogites from the Orlica-Snieznik Dome (Sudetes, SW Poland). *Chemical Geology*, **119,** 101–113.

Kohn, M. J. & Spear, F. S., 1990. Two new barometers for garnet amphibolites with applications to southeastern Vermont. *American Mineralogist*, **75,** 89–96.

Koyi, H. A., Milnes, A. G., Schmeling, H., Talbot, C. J., Juhlin, C. & Zeyen, H., 1999. Numerical models of ductile rebound of crustal roots beneath mountain belts. *Geophysical Journal International*, **139,** 556–562.

Krabbendam, M. & Dewey, J. F., 1998. Exhumation of UHP rocks by transtension in the Western Gneiss region, Scandinavian Caledonides. In: *Continental Transpressional and*

Transtensional Tectonics, Special Publications, 135, (eds Holdsworth, R. E., Strachan, R. A. & Dewey, J. F.), pp. 159–181. Geological Society of London, London.

Kröner, A., Byerly, C. R. & Lowe, D. R., 1991. Chronology of early Archean granite-greenstone evolution in the Barberton Mountain Land, South Africa, based on precise dating by single zircon evaporation. *Earth and Planetary Science Letters*, **103,** 41–54.

Kröner, A. & Hegner, E., 1998. Geochemistry, single zircon ages and Sm-Nd systematics of granitoid rocks from the Gory Sowie (Owl Mts, polish West Sudetes: evidence for early Palaeozoic arc-related plutonism. *Journal of the Geological Society of London*, **155,** 711–724.

Kröner, A., Jaeckel, P., Hegner, E. & Opletal, M., 2001a. Single zircon ages and whole rock Nd isotopic systematics of early Palaeozoic granitoid gneisses from the Czech and Polish Sudetes (Jizerské hory, Krkonoše Mountains and Orlice-Sneznik Complex). *International Journal of Earth Sciences*, **90,** 304–324.

Kröner, A., Jaeckel, P., Reischmann, T. & Kroner, U., 1998. Further evidence for an early Carboniferous (similar to 340 Ma) age of high-grade metamorphism in the Saxonian granulite complex. *Geologische Rundschau*, **86,** 751–766.

Kröner, A., O'Brien, P. J., Nemchin, A. A. & Pidgeon, R. T., 2000a. Zircon ages for high pressure granulites from South Bohemia, Czech Republic, and their connection to Carboniferous high temperature processes. *Contributions to Mineralogy and Petrology*, **138,** 127–142.

Kröner, A., Štípská, P., Schulmann, K. & Jaeckel, P., 2000b. Chronological constraints on the pre-Variscan evolution of the northeastern margin of the Bohemian Massif, Czech Republic. In: *Orogenic Processes; Quantification and Modelling in the Variscan Belt, Special Publications, 179*, (eds Franke, W., Haak, V., Oncken, O. & Tanner, D.), pp. 175–197. Geological Society of London. London.

Kröner, A. & Willner, A. P., 1998. Time of formation and peak of Variscan HP-HT metamorphism of quartz-feldspar rocks in the central Erzgebirge, Saxony, Germany. *Contributions to Mineralogy and Petrology*, **132,** 1–20.

Kryza, R., Pin, C. & Vielzeuf, D., 1996. High-pressure granulites from the Sudetes (south-west Poland): evidence of crustal subduction and collisional thickening in the Variscan Belt. *Journal of Metamorphic Geology*, **14,** 531–546.

Lange, U., Bröcker, M., Mezger, K. & Don, J., 2002. Geochemistry and Rb-Sr geochronology of a ductile shear zone in the Orlica-Snieznik dome (West Sudetes, Poland). *International Journal of Earth Sciences*, **91,** 1005–1016.

Lee, J. K. W., Williams, I. S. & Ellis, D. J., 1997. Pb, U and Th diffusion in natural zircon. *Nature*, **390,** 159–161.

Maluski, H. & Patočka, F., 1997. Geochemistry and ^{40}Ar-^{39}Ar geochronology of the mafic metavolcanic rocks from the Rýchory Mountains complex (west Sudetes, Bohemian Massif): palaeotectonic significance. *Geological Magazine*, **134,** 703–716.

Merle, O., 1989. Strain models within spreading nappes. *Tectonophysics*, **165,** 57–71.

Merle, O. & Guillier, B., 1989. The building of the Central Swiss Alps – an experimental approach. *Tectonophysics*, **165,** 41–56.

Milnes, A. G. & Koyi, H. A., 2000. Ductile rebound of an orogenic root; case study and numerical model of gravity tectonics in the Western gneiss complex, Caledonides, southern Norway. *Terra Nova*, **12,** 1–7.

Nelson, D. R., 1997. Compilation of SHRIMP U-Pb zircon geochronology data, 1996, 189 p., Geological Survey of Western Australia, Record 1997/1.

O'Brien, P. J., Kröner, A., Jaeckel, P., Hegner, E., Zelazniewicz, A. & Kryza, R., 1997. Petrological and isotopic studies on Palaeozoic high pressure granulites with a medium pressure overprint, Góry Sowie (Owl) Mts., Polish Sudetes. *Journal of Petrology*, **38,** 433–456.

O'Brien, P. J. & Rötzler, J., 2003. High-pressure granulites: formation, recovery of peak conditions and implications for tectonics. *Journal of Metamorphic Geology*, **21,** 3–20.

Oliver, G. J. H., Corfu, F. & Krogh, T. E., 1993. U-Pb ages from SW Poland: evidence for a Caledonian suture zone between Baltica and Gondwana. *Journal of the Geological Society of London*, **150,** 355–369.

Parrish, R. R., 2001. The response of mineral chronometers to metamorphism and deformation in orogenic belts. In: *Continental Reactivation and Reworking, Special Publications, 184*, (eds Miller, J. A., Holdsworth, R. E., Buick, I. S. & Hand, M.), pp. 289–301. Geological Society of London. London.

Parry, M., Štípská, P., Schulmann, K., Hrouda, F., Ježek, J. & Kröner, A., 1997. Granodiorite sill emplacement at an oblique plate boundary: northeastern margin of the Bohemian Massif. *Tectonophysics*, **280,** 61–81.

Paterson, S. R. & Tobisch, O. T., 1992. Rates of processes in magmatic arcs – implications for the timing and nature of pluton emplacement and wall rock deformation. *Journal of Structural Geology*, **14,** 291–300.

Platt, J. P., 1993. Exhumation of high-pressure rocks; a review of concepts and processes. *Terra Nova*, **5,** 119–133.

Přikryl, R., Schulmann, K. & Melka, R., 1996. Perpendicular fabrics in the Orlické Hory orthogneisses (western part of the Orlice-Snìžník Dome, Bohemian Massif) due to high temperature E-W deformational event and late lower temperature N-S overprint. *Èasopis Pro Mineralogii a Geologii*, **41,** 156–166.

Pouba, Z., Padìra, K. & Fiala, J., 1985. Omphacite granulite from the NE margin of the Bohemian Massif (Rychleby Mts). *Neues Jahrbuch für Mineralogie, Abhandlungen*, **151,** 29–52.

Powell, R., 1985. Regression diagnostics and robust regression in geothermometer geobarometer calibration – the garnet clinopyroxene geothermometer revisited. *Journal of Metamorphic Geology*, **3,** 231–243.

Powell, R. & Holland, T. J. B., 1988. An internally consistent dataset with uncertainties and correlations: 3. Applications to geobarometry, worked examples and a computer program. *Journal of Metamorphic Geology*, **6,** 173–204.

Ring, U., Brandon, M. T., Willett, S. D. & Lister, G. S., 1999. Exhumation processes. In: *Exhumation Processes; Normal Faulting, Ductile Flow and Erosion, Special Publications, 154*, (eds Ring, U., Brandon, M. T., Lister, G. S. & Willett, S. D.), pp. 1–27. Geological Society of London, London.

Roberts, M. P. & Finger, F., 1997. Do U-Pb zircon ages from granulites reflect peak metamorphic conditions? *Geology*, **25,** 319–322.

Schulmann, K. & Gayer, R., 2000. A model for a continental accretionary wedge developed by oblique collision: the NE Bohemian Massif. *Journal of the Geological Society of London*, **157,** 401–416.

Schulmann, K., Thompson, A. B., Lexa, O. & Ježek, J., 2003. Strain distribution and fabric development modeled in active and ancient transpressive zones. *Journal of Geophysical Research-Solid Earth*, **108,** 1–14.

Smulikowski, K., 1967. Eclogites of the Snieznik Mts in the Sudetes. *Geologia Sudetica*, **3,** 157–174.

Smulikowski, K., 1979. Polymetamorphic evolution of the crystalline complex of Snieznik and Gory Zlote Mts in the Sudetes. *Geologia Sudetica*, **14,** 7–76.

Steltenpohl, M. G., Cymerman, Z., Krogh, E. J. & Kunk, M. J., 1993. Exhumation of eclogitized continental basement during Variscan lithospheric delamination and gravitational collapse, Sudety Mountains, Poland. *Geology*, **21,** 1111–1114.

Štípská, P., Schulmann, K., Thompson, A. B., Ježek, J. & Kröner, A., 2001. Thermo-mechanical role of a Cambro-Ordovician paleorift during the Variscan collision: the NE margin of the Bohemian Massif. *Tectonophysics*, **332,** 239–253.

Thompson, A. B., Schulmann, K. & Ježek, J., 1997a. Extrusion tectonics and elevation of lower crustal metamorphic rocks in convergent orogens. *Geology*, **25,** 491–494.

Thompson, A. B., Schulmann, K. & Ježek, J., 1997b. Thermal evolution and exhumation in obliquely convergent (transpressive) orogens. *Tectonophysics*, **280,** 171–184.

Thompson, A. B., Schulmann, K., Ježek, J. & Tolar, V., 2001. Thermally softened continental extensional zones (arcs and rifts) as precursors to thickened orogenic belts. *Tectonophysics*, **332,** 115–141.

Turniak, K., Mazur, S. & Wysoczanski, R., 2000. SHRIMP zircon geochronology and geochemistry of the Orlica-Snieznik gneisses (Variscan belt of Central Europe) and their tectonic implications. *Geodinamica Acta*, **13,** 1–20.

Van Orman, J. A., Grove, T. L., Shimizu, N. & Layne, G. D., 2002. Rare earth element diffusion in a natural pyrope single crystal at 2.8 GPa. *Contributions to Mineralogy and Petrology*, **142,** 416–424.

Wendt, A. S., D'Arco, P., Goff, B. & Oberhansli, R., 1993. Radial cracks around alpha-quartz inclusions in almandine: constraints on the metamorphic history of the Oman mountains. *Earth and Planetary Science Letters*, **114,** 449–461.

Wendt, J. I., Kröner, A., Fiala, J. & Todt, W., 1994. U-Pb zircon and Sm-Nd dating of Moldanubian HP/HT granulites from South Bohemia, Czech Republic. *Journal of the Geological Society of London*, **151,** 83–90.

Zelazniewicz, A., 1988. Orthogneisses due to irrotational extension, a case from the Sudetes, Bohemian Massif. *Geologische Rundschau*, **77,** 671–682.

Received 8 October 2003; revision accepted 2 January 2004.

[American Journal of Science, Vol. 305, May, 2005, P. 407–448]

CHRONOLOGICAL CONSTRAINTS ON THE PRE-OROGENIC HISTORY, BURIAL AND EXHUMATION OF DEEP-SEATED ROCKS ALONG THE EASTERN MARGIN OF THE VARISCAN OROGEN, BOHEMIAN MASSIF, CZECH REPUBLIC

KAREL SCHULMANN*, ALFRED KRÖNER**, ERNST HEGNER***, IMMO WENDT***, JIŘÍ KONOPÁSEK****·******, ONDREJ LEXA*·****, and PAVLA ŠTÍPSKÁ*·****

ABSTRACT. Key lithological units of the high-grade eastern margin of the Bohemian Massif were dated using the U-Pb and Pb-Pb methods on zircons in order to establish a chronological framework for the geodynamic evolution of the Variscan orogenic root. The protolith ages for metagranitoids, orthogneisses and granulites of thickened lower and middle crust reveal the existence of magmatic activity that occurred over a 100 million year time interval from Cambro-Ordovician to early Devonian times, probably related to discontinuous intracontinental rifting of Neoproterozoic crust. Our geochronological data suggest that the eastern part of the orogenic root represents thermally softened and rifted Neoproterozoic crust, preserved farther to the east as the Brunia microcontinent. Zircon ages for felsic granulites, high-grade gneisses of the lower crust and of a syn-convergence granodioritic intrusion in the upper crust indicate that thickening and exhumation of the crust occurred during a narrow time interval between 370 and 340 Ma. Exhumation of the lower crust to mid-crustal levels was a localized process that occurred at ~340 Ma and was associated with crustal-scale folding in the internal part of the root as well as orogenic channel flow along the eastern collisional margin. Both types of exhumation mechanisms were driven by deep-level wedging (indentation) of the easterly Brunia continent, followed by deposition of heavy minerals and pebbles derived from high-pressure rocks in the adjacent foreland basin. Final orogenic development was characterized by NE-SW dextral transpressive shearing parallel to the Brunia margin as well as dextral transtension associated with activity along the Elbe lithospheric fault. These processes affected the marginal parts of the orogenic root and were accompanied by 330 to 325 Ma old syntectonic granitoid intrusions along reactivated lithotectonic boundaries. Rotation of the assembled orogenic belt, accompanied by lithospheric faulting driven by westerly subduction roll-back, may be the most plausible model to explain late deformation of the orogenic root.

INTRODUCTION

Thickened orogenic root systems form during prolonged convergence of lithospheric plates (Dewey and Bird, 1970). Crustal thickening during collision is generally associated with intense ductile deformation and high-grade metamorphism with peak pressure conditions corresponding to double average crustal thickness, and temperatures permitting for extensive melting to occur in mica- and amphibole-rich rocks (Thompson, 1999). An important consequence of melting of rocks buried to the bottom of an orogenic root is the obliteration of the pre-collisional history of most rock assemblages and resetting of many isotopic systems. The exhumation of such deeply buried rocks late in the collisional history may also involve further decompression

*Université Louis Pasteur, Centre de Geochimie de la Surface, UMR-CNRS 7517, 1 rue Blessig, 67084 Strasbourg cedex, France; schulman@illite.u-strasbg.fr
**Institut für Geowissenschaften, Universität Mainz, 55099 Mainz, Germany
***Department für Geo- und Umweltwissenschaften, Universität München, Theresienstrasse 41, 80333 München, Germany
****Institute of Petrology and Structural Geology, IPSG, Charles University, Albertov 6, CS 12843 Prague, Czech Republic
*****Czech Geological Survey, Klarov 3, Prague, 11821, Czech Republic

melting. Another consequence of exhumation processes within orogenic root systems is juxtaposition of crustal units showing distinctly different peak pressure metamorphic records (Štípská and others, 2004). The intrusion of syntectonic granitoids frequently follows important structural boundaries of exhumed units and, because of rapid cooling, these intrusive rocks best record the timing of melting processes in the remaining root.

Lithotectonic units with specific P-T histories may be assigned to lower, middle, and upper crustal segments. However, this interpretation neglects the depositional and early orogenic evolution of supracrustal and pre-orogenic intrusive assemblages. Therefore, rocks forming the orogenic root of a collisional system are often not placed and interpreted in terms of their pre-collisional paleogeographic geodynamic setting and position in the crust.

The U-Pb and Pb-Pb isotopic systems in zircon are very resistant to even high-grade metamorphism and so may be used to extract information on older events such as primary magmatism and initial metamorphism, despite multiple phases of high-grade metamorphism (Mezger and Krogstad, 1997; Möller and others, 2002). This behavior offers the opportunity to obtain information on the timing of early magmatic events prior to formation of the orogenic root and on late melting events associated with maximum burial and exhumation of the host rocks. Therefore, deciphering the P-T evolution of an orogenic root, combined with precise dating of individual high-T events, provides a basis for understanding the mechanisms of formation and exhumation of orogenic root systems through time.

The Variscan orogen in Europe represents such a hot orogenic root system (Dewey and Burke, 1973) which allows observation of the finite metamorphic and structural patterns at considerable detail that cannot be studied in active modern orogens. The Variscan orogeny occurred during Devonian to Carboniferous convergence of peri-Gondwanan crustal segments and the northern European plate, also known as Baltica (Ziegler, 1986; Tait and others, 1996). Prior to this convergence all Neoproterozoic units forming the Bohemian Massif (the Saxothuringian, the Teplá Barrandian and Moldanubian domains; Franke, 1989) were affected by large-scale Cambro-Ordovician rifting processes which are commonly interpreted as a result of fragmentation of the northern Gondwana margin and drift of lithospheric terranes to the north (Kröner and others, 2000b; Štípská and others, 2001; Friedl and others, 2004; this work). During the early Devonian a major switch in plate movement occurred, resulting in the development of the SE-dipping Saxothuringian subduction zone (in present-day coordinates) (Franke, 2000). This paleo-subduction zone is characterized by the development of high-pressure, low-temperature metamorphism during the Devonian and obduction of eclogites on top of the Saxuthuringian plate (Franke, 2000). The Saxothuringian oceanic and continental crust were subducted underneath an upper continental plate that is today represented by the Teplá-Barrandian and Moldanubian domains (fig. 1), and this subduction created a large-scale magmatic arc in the area of Central Bohemian Pluton (Žák and others, 2005). Carboniferous collision of the Saxothuringian plate with the hanging-wall Teplá-Barrandian and Moldanubian domains involved major crustal thickening and development of an internal orogenic zone represented by a thickened orogenic root that is exposed today between the Saxothuringian domain in the northwest and the late Neoproterozoic Brunia terrane in the southeast (Dudek, 1980).

The lack of precise protolith ages for rocks constituting the principal units of the Moldanubian domain has so far prevented an in-depth understanding of its development. Therefore, we present new U-Pb and Pb-Pb zircon ages for key lithologies in the eastern part of the Variscan orogenic root, whose structural and metamorphic evolution is now well understood. The protolith and metamorphic ages of felsic rocks

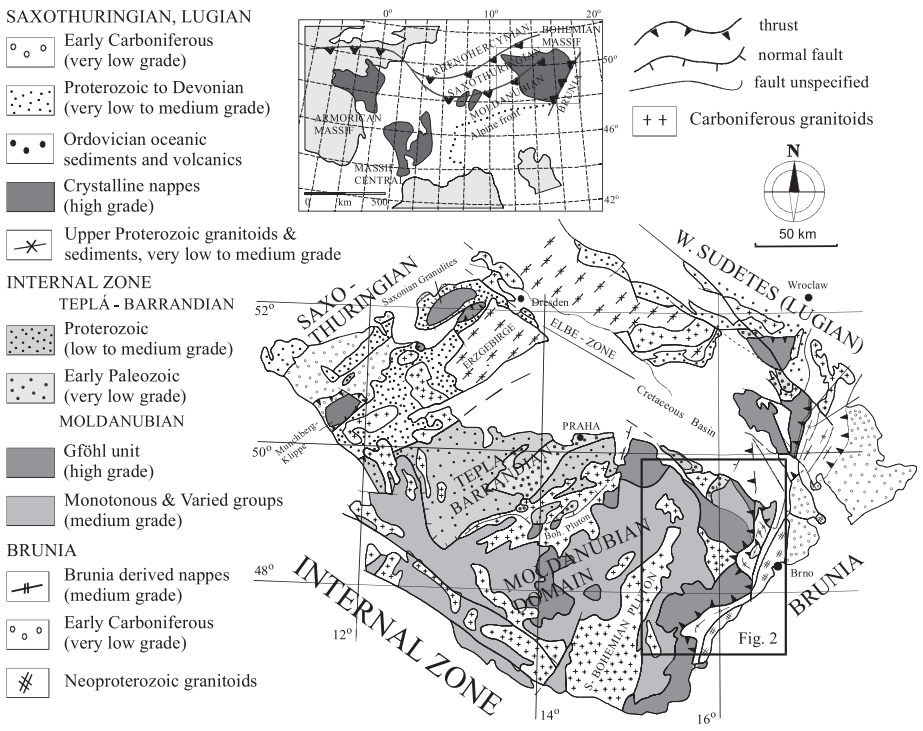

Fig. 1. Outline geological map of the eastern part of the Bohemian Massif with major units shown schematically. The location of the study area (fig. 2) is indicated. Upper left inset is the position of the study area within the framework of the European Variscides. (Modified after Franke, 2000.)

(essentially metavolcanic layers, granitoid orthogneisses, granulites and granitoids) were determined in order to establish a geodynamic framework including the pre- and syncollisional evolution of the eastern part of the Variscan orogen. Finally, from the present position of individual crustal units, we infer their different burial histories and the temporal evolution of crustal-scale buckling and syn-convergent exhumation of the deepest parts of the orogenic root, connected with lithospheric indentation of the Brunia foreland. The final increment of exhumation was dated by syntectonic intrusions associated with dextral wrenching along the NE-SW trending Brunia continental margin and the NW-SE oriented Elbe shear zone (fig. 1), thereby disrupting the orogenic fabric. Based on the new age data and existing paleomagnetic models we discuss the possible role of far-field forces on late exhumation processes within a hot orogenic root system.

GEOLOGY OF THE EASTERN MARGIN OF THE BOHEMIAN MASSIF

The eastern margin of the Bohemian Massif provides a detailed picture of its geological inventory as has already been recognized by Suess (1912, 1926). The eastern segment of the Brunia foreland is made up of unmetamorphosed and virtually undeformed Neoproterozoic granitoids (for example, Finger and others, 2000; Kröner and others, 2000b), which intruded into Neoproterozoic high-grade schists and migmatites (Fritz and others, 1996). This basement is unconformably overlain by Cambro-Ordovician clastic and pelitic metasediments, bimodal metavolcanic rocks, shallow marine Devonian sediments and Carboniferous foreland basin sediments (Hartley and Otava, 2001; Kalvoda and others, 2003). A NE-SW trending belt of

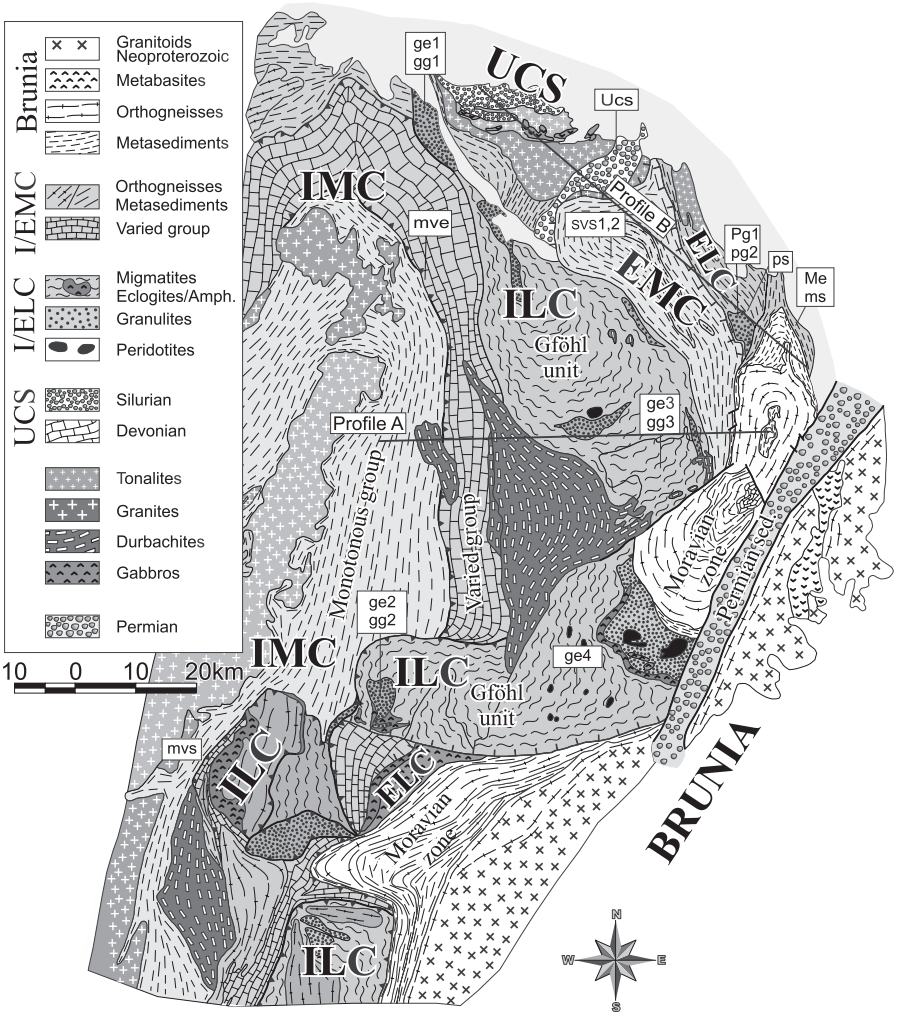

Fig. 2. Geological map of the eastern margin of the Bohemian Massif showing the distribution of crustal levels. Sample localities for geochronology are shown. Abbreviations: IMC – internal middle crustal belt; EMC – extrenal middle crustal belt; ILC – internal lower crustal belt; ELC – external lower crustal belt; UC – upper crustal segment; ge – Gföhl eclogite; gg – Gföhl granulite; ucs – upper crustal schists; svs – Svratka Unit schists; pg – Policka Unit granulites; ps – Policka Unit schists; me – Moravian Zone eclogites; ms – Moravian Zone schists; mve – Monotonous and Varied Units eclogites; mvs - schists of Monotonous and Varied Units. Positions of cross-sections A and B from figure 5 are marked by thick lines.

sheared and metamorphosed Brunia-derived rocks represents a zone of deformation along the western margin of the Brunia continent. This 300 km long and 50 km wide belt was named the Moravian zone in its southern part and consists of two NE-SW elongated tectonic windows emerging through high-grade rocks of the overlying Moldanubian domain: the southern Thaya window and northern Svratka window (fig. 2, Suess, 1926). The interface between the Moravian zone and the overthrust Moldanubian domain is marked by a narrow belt of kyanite-bearing micaschists interpreted as a major shear zone along which the high-grade Moldanubian gneisses and migmatites were retrogressed and thrust to the east (Moravian Micaschist Zone of Suess, 1912, 1926).

The Moldanubian domain (MD) east of Central Moldanubian pluton (fig. 1) has been subdivided into three major lithotectonic units that were previously identified and defined in Lower Austria (Thiele, 1976; Matura, 1984; Fuchs, 1986), namely the Monotonous Unit to the west and the Varied and Gföhl Units to the east, adjacent to the Moravian Zone (fig. 2). Tollmann (1982) grouped the Monotonous and Varied Units into the so-called Drosendorf terrane, based on their relatively low degree of metamorphism compared to the high-grade Gföhl Unit. This lithotectonic subdivision is valid for the entire Moldanubian domain in which the Monotonous Unit represents the structurally lowermost unit. It consists of K-feldspar-sillimanite±cordierite migmatitic paragneisses (metagraywacke) interlayered with leucocratic, K-feldspar-rich granitoid orthogneisses and rare eclogitic tectonic lenses (Dudek and Fediuková, 1974; O'Brien, 1997; O'Brien and Vrána, 1997). The Varied Unit occurs structurally above the Monotonous Unit, and their mutual contact is defined by uniformly deformed bodies of granitic gneiss (Fuchs and Matura, 1976). The Varied Unit consists of a strongly deformed, thick sequence of biotite-plagioclase gneisses with garnet, sillimanite and/or interlayered calc-silicate rocks, quartzite, intercalations of marble, graphite schists and numerous bodies of amphibolite. The Gföhl Unit is made up of a large body of granitoid gneiss associated with migmatites and K-feldspar-sillimanite paragneisses, locally accompanied by partially molten amphibolite bodies at its base. Today it represents the uppermost structural level of the Moldanubian zone and contains numerous bodies of Ky-Kfs granulite as well as tectonic lenses of eclogite and garnet and/or spinel peridotite. According to many authors the Gföhl Unit constitutes the highest part of the Moldanubian nappe pile, tectonically overlying the Drosendorf terrane (Fuchs, 1986; Franke, 1989; Matte and others, 1990).

P-T Evolution and Previous Geochronology of the Study Area

The NE-SW oriented Variscan structure of the eastern Bohemian Massif is intersected by the crustal-scale NW-SE trending Elbe Fault Zone (EFZ) that separates the northerly Sudetic realm from the main part of the Bohemian Massif (fig. 1). Our study area (fig. 2) covers the eastern part of the orogenic root between the EFZ to the north and the Moravian Zone on the east.

The basement granitoids of the Brunia continent in the study area yielded Neoproterozoic ages as documented by zircon as well as $^{40}Ar/^{39}Ar$ cooling ages (van Breemen and others, 1982; Fritz and others, 1996; Finger and others, 2000; table 1). These rocks and unconformably-overlying shallow marine Devonian metasediments show weak Variscan deformation and lower greenschist-facies metamorphism (Špaček and others, 2001; Franců and others, 2002). The metamorphic pattern of the Brunia-derived Svratka tectonic window shows a well-developed tectonically inverted Barrovian zonation ranging from the chlorite to sillimanite zone (Schulmann and others, 1991). The age of this metamorphism is Carboniferous on the basis of $^{40}Ar/^{39}Ar$ geochronology (Macintyre and others, 1992; Fritz and others, 1996; table 1).

In the north, high-grade rocks of the Gföhl Unit contain eclogite lenses with estimated minimum pressures of 18 to 19 kbar and temperatures of ~890 °C, surrounded by felsic granulite (Medaris and others, 1998; ge1 in figs. 2 and 3). Similar eclogites of the Gföhl Unit were overprinted at medium pressures of 9 to 12 kbar and temperatures of 750 to 850 °C (Kolenovská and others, 1999; ge2 in figs. 3 and 4). The common feature of these eclogite bodies is their basaltic composition and spatial association with felsic granulites, suggesting a crustal origin for these rocks (Medaris and others, 1998). Associated felsic granulites in the inner part of the Gföhl Unit reveal PT conditions of 825 to 840 °C at 11 to 17.5 kbar (Medaris and others, 1998; gg1 in figs. 3 and 4) and 800 to 850 °C at 9.5 to 11 kbar (Kolenovská and others, 1999; gg2 in figs. 3 and 4), the latter of which are considered to reflect conditions of re-equilibration. Granulites of the study area reveal temperatures of 840 °C at 18 to 19 kbar, re-

TABLE 1

List of published geochronological data from the studies area.

Unit	Rock type	Age	Method	Reference
Brunia domain				
Brno Massif	Metarhyolite	725 ± 15	Pb-Pb (zircon evapor.)	Finger and others (2000)
	Diorite	584 ± 5	U/Pb (zircon)	van Breemen and others (1982)
	Diorite	598.9 ± 1.0	Ar/Ar plateau (amphibole)	Fritz and others (1996)
	Diorite	586.9 ± 0.5	Ar/Ar plateau (amphibole)	
	Pegmatite	565.3 ± 0.8	Ar/Ar plateau (muscovite)	
Letovice Complex	Amphibolite	346 ± 3	Ar/Ar plateau (amphibole)	Macintyre and others (1992)
	Amphibolite	336 ± 5	Ar/Ar plateau (amphibole)	
	Amphibolite	343 ± 5	Ar/Ar plateau (amphibole)	
Thaya dome	Amphibolite	341 ± 2.2	Ar/Ar isotope corr. (amphibole)	Fritz and others (1996)
	Metagranite	582 ± 10	U/Pb (zircon)	Friedl and others (2004)
	Metagranite	566 ± 10	U/Pb (zircon)	
	Metagranite	568 ± 10	U/Pb (zircon)	
	Orthogneiss	1643 ± 10	Pb/Pb (zircon)-inherited core	
	Orthogneiss	595 ± 7	U/Pb (zircon)	
	Orthogneiss	581 ± 9	U/Pb (zircon)	
	Orthogneiss	589 ± 7	U/Pb (zircon)	
	Granite	551 ± 6	Rb/Sr whole rock isochron	Scharbert and Batík (1985)
	Orthogneiss	326.5 ± 0.4	Ar/Ar plateau (muscovite)	
	Amphibolite	341.1 ± 1.4	Ar/Ar isotope corr. (amphibole)	Dallmeyer and others (1992)
	Amphibolite	328.7 ± 3.3	Ar/Ar isotope corr. (amphibole)	
	Orthogneiss	325.5 ± 0.7	Ar/Ar isotope corr. (muscovite)	
	Orthogneiss	328.7 ± 0.8	Ar/Ar isotope corr. (muscovite)	
Svratka dome	Amphibolite	575.6 ± 2.2	Ar/Ar isotope corr. (amphibole)	Fritz and others (1996)
	Orthogneiss	326.5 ± 0.6	Ar/Ar plateau (muscovite)	
	Micaschist	330.0 ± 0.5	Ar/Ar plateau (muscovite)	

TABLE 1
(continued)

Unit	Rock type	Age	Method	Reference
ILC				
Raabs Complex	Orthogneiss	428 ± 6	U/Pb (zircon)	Finger and von Quadt (1995)
Strážek Complex	Granulite	347 ± 9	U/Pb (zircon)	Kröner and others (1998)
	Grt pyroxenite	373 ± 7	Sm/Nd (WR-mineral)	Brueckner and others (1991)
Gföhl Unit	Orthogneiss	493 ± 7	U/Pb (zircon)	Friedl and others (2004)
	Orthogneiss	484 ± 7	U/Pb (zircon)	
	Orthogneiss	478 ± 7	U/Pb (zircon)	
	Orthogneiss	474 ± 6	U/Pb (zircon)	
	Orthogneiss	433 ± 6	U/Pb (zircon)	
	Orthogneiss	335 ± 5	U/Pb (zircon)	
	Orthogneiss	334 ± 5	U/Pb (zircon)	
	Granulite	2336 ± 23	Pb/Pb (zircon)-inherited core	
	Granulite	446 ± 59	Pb/Pb (zircon)	
	Granulite	437 ± 9	U/Pb (zircon)	
	Granulite	433 ± 8	U/Pb (zircon)	
	Eclogite	324 ± 5	Sm/Nd (WR-mineral)	
	Eclogite	341 ± 7	Sm/Nd (WR-mineral)	
	Eclogite	323 ± 7	Sm/Nd (WR-mineral)	Beard and others (1992)
	Eclogite	336 ± 16	Sm/Nd (WR-mineral)	
	Eclogite	342 ± 9	Sm/Nd (WR-mineral)	
	Grt pyroxenite	343 ± 17	Sm/Nd (WR-mineral)	Medaris and others (1995)
	Eclogite	344 ± 6	Sm/Nd (WR-mineral)	

TABLE 1
(continued)

Unit	Rock type	Age	Method	Reference
IMC				
Variegated Unit	Metabasalt	358 ± 6	U/Pb (zircon)	Friedl and others (1993)
	Orthogneiss	2336 ± 23	Pb/Pb (zircon)-inherited core	Friedl and others (2004)
	Orthogneiss	621 ± 8	U/Pb (zircon)	
	Orthogneiss	622 ± 9	U/Pb (zircon)	
	Orthogneiss	618 ± 8	U/Pb (zircon)	
Southern Bohemian Batholith	Bt-granite	323 ± 4	U/Pb (monazite)	refs in Finger and others (1997)
		327 ± 5	U/Pb (monazite)	
		328 ± 5	U/Pb (monazite)	
	Granodiorite	328 ± 4	U/Pb (zircon)	
	Bt-granite	319 ± 6	U/Pb (monazite)	
	Ms-Bt-granite	327 ± 4	U/Pb (monazite)	
ELC				
Polička Complex	Orthogneiss	338 ± 3	U/Pb (monazite)	van Breemen and others (1982)

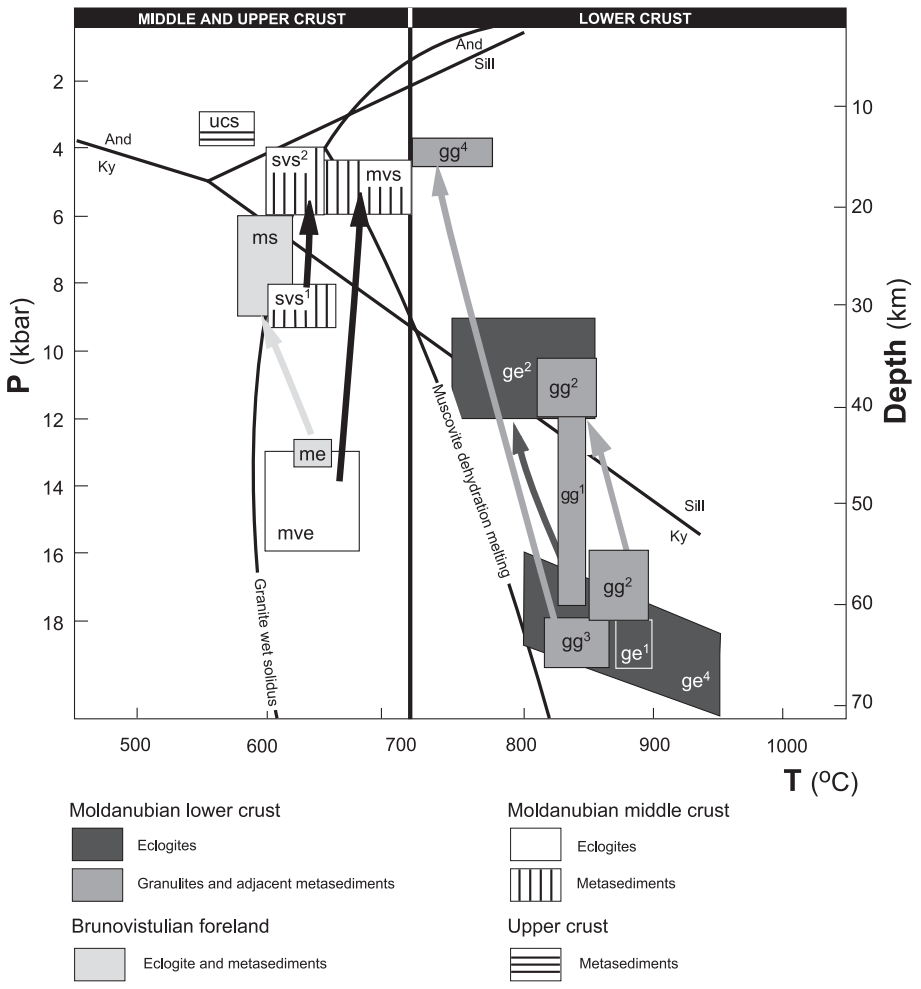

Fig. 3. Temperature-depth diagram showing P-T estimates for Variscan assemblages along the eastern margin of the Bohemian Massif and assuming lithostatic pressure (P = 1 ρgh). Dark gray boxes show peak (gg1, gg3, pg1) and re-equilibration (gg2, gg3, gg4, pg2) conditions for felsic ILC and ELC granulites (Medaris and others, 1998; Kolenovská and others, 1999; Schulmann and others, 1999; Tajčmanová and others, 2005). Black boxes show estimates of peak (ge1, ge3) and re-equilibration (ge2) stages for ILC eclogites by Medaris and others (1995a, 1998) and Kolenovská and others (1999). White box shows peak conditions for IMC eclogites (mve; Medaris and others, 1995a). Vertically hatched boxes show peak and re-equilibration conditions for IMC and EMC micaschists (mvs, svs1, svs2; Vrána, 1995; Pitra and Guiraud, 1996; Petrakakis, 1997). Light gray boxes show peak conditions for Brunia-derived eclogites and micaschists (me, ms; Konopásek and others, 2002). Horizontally hatched box shows peak conditions of UC (ucs; Pitra and others, 1994; Pitra and Guiraud, 1996). Reaction 1 – alumosilicate triple point, 2 – biotite dehydration melting, 3 – muscovite dehydration melting, 4 – pelite wet solidus, 5 – Alb = Jd+Qtz, 6 - Bio+Alb+Sil+Qtz → Grt +Crd+Kfsp+L (compiled by Thompson, 1999, 2000).

equilibrated at 760 to 800 °C and 10 to 13 kbar and later at 720 to 777 °C and 4 to 4.5 kbar (Tajčmanová and others, 2005; gg3 in figs. 3 and 4). The Gföhl Unit in the study area contains numerous tectonically emplaced bodies of garnet and spinel peridotite (T 900 – 1300 °C, P 28 – 44 kbar), associated with lenses of eclogite (T 800 – 950 °C, P 16 – 20 kbar) and clinopyroxenite, representing high-pressure partial melts of the upper mantle (Medaris and others, 1995a; Medaris, 1999; ge4 in figs. 3 and 4).

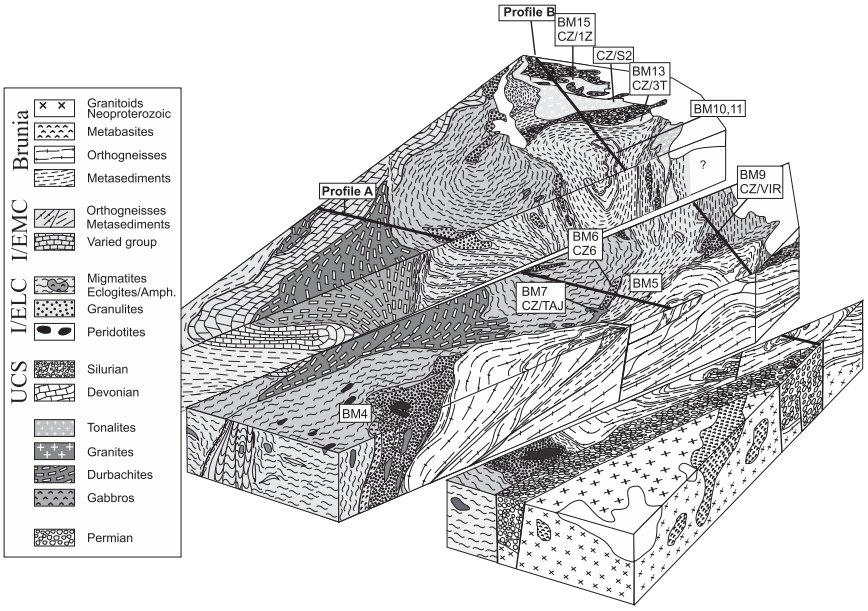

Fig. 4. Schematic block diagrams of three critical areas showing main structural features and orogenic fabric in the study area along NE-SW oriented sections. Intermediate block diagram shows tectonic style of imbrication of the Brunia foreland and overthrusting of the Moldanubian lower crust according to Schulmann and others (1991). Eastern block-diagram shows relationships between IMC (the Monotonous and Varied Units), ILC (the Gföhl Unit), EMC (The Svratka Crystalline Complex) and ELC (The Polička Unit) along a section perpendicular to the Elbe Shear Zone. Positions of cross-sections A and B from figure 5 are marked by thick lines. The scale is arbitrary.

Multigrain zircon and monazite fractions from granulites of the Gföhl Unit yielded U-Pb ages between 370 and 337 Ma (van Breemen and others, 1982; Kröner and others, 1988; table. 1). Eclogites of the same unit yielded Sm-Nd whole-rock-garnet ages ranging between 341 and 323 Ma, whereas associated peridotites show both Devonian and Carboniferous ages (Brueckner and others, 1991; Beard and others, 1992; Medaris and others, 1995b; table 1).

To the west, the Gföhl Unit is bordered by the Varied and Monotonous Units containing rare lenses of eclogite revealing minimum PT conditions of 600 to 680 °C at 13 to 16 kbar (Dudek and Fediuková, 1974; Medaris and others, 1995a, 1998; O'Brien, 1997; O'Brien and Vrána, 1997; mve in figs. 3 and 4). Metamorphic conditions in the surrounding gneisses yielded 600 to 720 °C at 4.5 to 6 kbar (Vrána, 1995; Petrakakis, 1997; mvs in fig. 4).

To the north and northeast, the Gföhl Unit is in contact with a medium-grade unit (Svratka Crystalline Complex), which lithologically resembles the Monotonous Unit and consists of garnet-sillimanite paragneisses interlayered with numerous bodies of porphyritic and fine-grained granitoid gneiss and migmatite. Kyanite-bearing paragneisses reveal peak P-T conditions of 8 to 9 kbar and 610 to 660 °C and re-equilibration conditions at 4 to 6 kbar and 600 to 650 °C in the sillimanite stability field (Pitra and Guiraud, 1996; svs1 and svs2 in figs. 3 and 4). $^{40}Ar/^{39}Ar$ dating indicates Carboniferous cooling ages of 325 to 332 Ma for samples of the Svratka Crystalline Complex (Fritz and others, 1996). The boundary between the high-grade Gföhl Unit and this medium-grade unit is marked by small-scale finger-like intrusions of K- and Mg-rich syenite (locally known as durbachite; Holub and others, 1997) that constitutes a large batholith within the Gföhl Unit farther to the south.

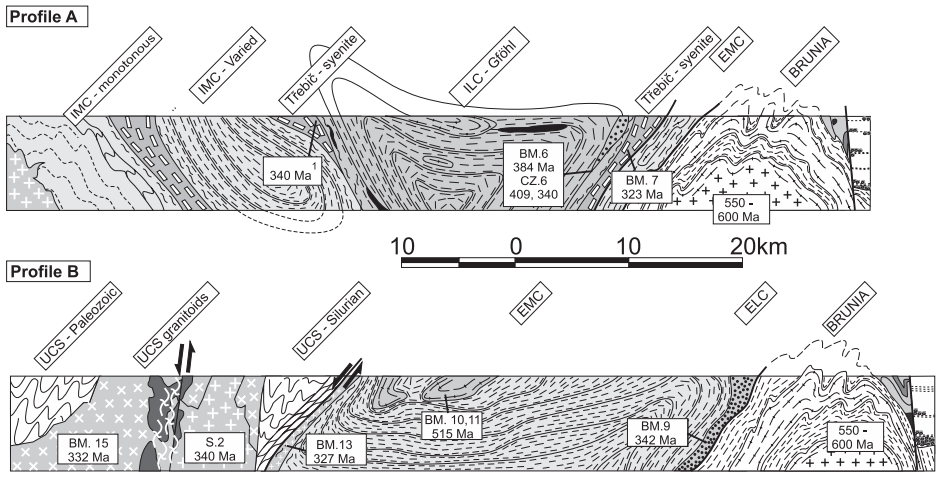

Fig. 5. Schematic sections across the eastern margin of the Bohemian Massif showing major structures, lithologies of individual domains and main tectonic boundaries. (A) NE-SW section from the ILC (the Gföhl Unit) in the west to the Brunia foreland to the east, (B) NW-SE section from the UC (Chrudim and Hlinsko Paleozoic) in the W, EMC (the Svratka Crystalline Complex) to the Brunia foreland to the east. Age data from Kröner and others (1988), van Breemen and others (1982) and Fritz and others (1996). Horizontal scale is shown, vertical scale is arbitrary.

To the north and east, the sillimanite schists and orthogneisses are bordered by the Polička Unit, composed of garnet-kyanite micaschists with intercalations of felsic granulite and partly anatectic amphibolite (Schulmann and others, 1999; pg1 and pg2, fig. 3). Monazites from one of these granulite bodies produced a multigrain U-Pb age of 338 ± 3 Ma (van Breemen and others, 1982). Farther south, this unit is strongly tectonically reduced and overlies a narrow strip of kyanite-bearing micaschists of the Moravian Micaschist Zone, rimming the entire eastern margin of Brunia-derived tectonic windows. Staurolite-bearing micaschists (580 – 620 °C, 6 – 9 kbar) of this belt also occur along the eastern flank of the Svratka window and contain eclogite boudins which exhibit minimum pressure conditions of 13 kbar at temperatures of 625 to 655 °C (Konopásek and others, 2002; ms, me in figs. 3 and 4).

A sequence of weakly metamorphosed Silurian to Devonian metasediments (the Paleozoic Hlinsko and Chrudim rocks) is separated by a major normal shear zone from the underlying NW- termination of the above-mentioned medium-grade unit of sillimanite para- and orthogneisses (Pitra and others, 1994; ucs in figs. 4 and 5). The NE-SW trending contact between these two units is marked by the sheet-like intrusion of a granodiorite sill. Intrusion of this sill was probably accompanied by metamorphism of Silurian metapelites at a pressure of ~4 kbar and temperatures of 550 to 590 °C (Pitra and others, 1994; Pitra and Guiraud, 1996).

Lithotectonic Zonation of the Moldanubian Orogenic Crust

The lithological content and inferred metamorphic conditions of the main units of the Moldanubian domain can be used to define a lithotectonic zonation that corresponds to crustal levels existing during maximum thickening of the orogenic root. The main reason for such a classification is to understand the spatial pattern of units that experienced different vertical displacement during exhumation. Interpretation of these units as syn-thickening crustal levels, their geometry and structural record may help to unravel mechanisms of exhumation and burial of these units. According to the lithological content and peak PT conditions described above, the Gföhl Unit can

be defined as a granulite-eclogite unit representing thickened crust that reached a depth of ~60 km and will be further described as *orogenic lower crust*. The granulite-bearing sillimanite paragneiss unit adjacent to the deformed margin of the Neoproterozoic Brunia foreland is considered to represent an *external orogenic lower crust* (ELC), whereas the main body of the Gföhl Unit represents an *internal orogenic lower crust* (ILC). The middle crustal sillimanite-paragneiss unit that is sandwiched between the ILC and ELC is defined here as an *external orogenic middle crust* (EMC), whereas the Monotonous and Varied Units in the west are defined as an *internal orogenic middle crust* (IMC). The Silurian and Devonian sediments in the NE part of the study area represent the uppermost, least metamorphosed sequence of the orogenic root and are defined here as an *upper orogenic crust* (UC), insignificantly buried during the Variscan orogeny. The Moravian nappe sequence exposed in the Svratka window represents a metamorphosed and imbricated part of the Neoproterozoic Brunia foreland.

Tectonic Evolution of the Eastern Part of the Bohemian Massif

The main features of the tectonic evolution along the eastern margin of the Variscan orogenic front in the Bohemian Massif are shown in figures 4 and 5. The study area exhibits the transition from a NE-SW-trending orogenic fabric adjacent to the Brunia foreland to a NW-SE trend parallel to the Elbe fault zone. This continuous curvature in orogenic trend was already recognized by Suess (1926), but its kinematic significance was not discussed and understood.

Several studies have documented that the Moldanubian root system was thrust over the Brunia foreland along a major dextral transpressional zone associated with northeastward imbrication of the basement and formation of the Moravian Zone (for example, Fritz and others, 1996). In the study area, the underthrust Brunia foreland formed a pile of internally imbricated basement- and cover-derived thrust sheets forming the so-called Svratka tectonic window (Suess, 1912; Schulmann and others, 1991; fig 4). Granulites, ultramafic rocks and eclogites of the ELC, associated with micaschists of the Moravian Zone, were thrust over the Brunia foreland, thereby forming klippen east of the Svratka tectonic window (eastern parts of cross-sections A and B, fig. 5; Konopásek and others, 2002). The entire internally imbricated system of lower crustal rocks and basement-derived sheets was refolded along large-scale upright folds during final E-W shortening (Schulmann and others, 1991). This folding also affected the Culmian foreland basin of Visean to early Namurian age, suggesting the age of latest shortening to be around 320 Ma (Hartley and Otava, 2001).

The EMC displays early west-verging compressive structures, strongly reworked by non-coaxial extensional deformation with a NW-SE oriented stretching axis parallel to the Elbe zone (Melka and others, 1992). The ILC was thrust over this unit in the south, whereas farther to the north the EMC occurs in the hanging wall of ILC high-pressure granulites and migmatites (Němec, 1968; see fig. 4). This is associated with a change in trend of both belts from NNE-SSW in the south to NW-SE and parallel to the Elbe zone farther north. The ILC shows multiple structures as follows: (1) An early, steep, N-S-striking foliation and isoclinal folds associated with high-pressure mineral assemblages in granulites are interpreted as a result of E-W compression at lower crustal levels (Schulmann and others, 1999; Tajčmanová and others, 2005). (2) A second, gently inclined thrust-related amphibolite-facies fabric is associated with partial melting at medium to low pressures (Tajčmanová and others, 2005). This secondary fabric is more penetrative in schists and migmatites and is generally associated with a NE-SW stretching lineation and kinematic criteria, suggesting top-to-the-NE thrusting (Schulmann and others, 1994). Finger-like durbachite bodies were emplaced syntectonically during this late thrusting event at several localities along the boundary between the ILC and EMC belts (fig. 4). The main body of durbachite masks the contact between metasediments of the Varied Unit of the IMC and the ILC to the west and the fabric of

high-grade rocks of the ILC (fig. 2). However, in general the medium-grade schists and marbles of the IMC occur in the footwall of west-dipping high-grade rocks and granulites of the ILC (fig. 4 and western part of cross-section A in fig. 5). The ILC rocks also exhibit a polyphase character of deformation marked by refolding of an early, steeply dipping metamorphic fabric into a flat-lying migmatitic fabric. The large-scale structure of the high-grade gneisses of the ILC exhibit a bivergent structural pattern (a positive flower structure), which is perturbed in the vicinity of the Elbe fault zone (cross-section A in fig. 5).

Paleozoic metasediments of the UC in the northeastern part of the study area (fig. 1) were refolded along kilometer-scale steep folds (NW part of cross-section B in fig. 5; Pitra and others, 1994). These rocks were intruded by granodiorites and tonalites of calc-alkaline affinity (Holub and others, 1997), showing steep magmatic to solid-state fabrics (Hrouda and others, 1999). These authors suggested syntectonic emplacement of the granitoids during regional folding and, therefore, their crystallization age may determine the age of main shortening of the upper crustal Silurian sediments. Melka and others (1992) and Pitra and others (1994) documented intense normal shearing which affected the entire central and western part of the EMC and also postdates shortening-related fabrics in the hanging wall Silurian metasediments of the studied upper crustal segment (cross-section B in fig. 5). This ductile shearing is parallel in strike to the Elbe Fault Zone and is compatible with top-to-the-NW normal movement (Synek and Oliveriová, 1993). A late granodiorite sill was syntectonically emplaced along the boundary between the EMC and UC and delineates the so-called Hlinsko detachment (Pitra and others, 1994). Steep normal shear zones are developed farther west in the UC and also affected rocks of the granodiorite-tonalite suite (NW part of the cross-section B in fig. 5). Late granites intruded during normal shearing and were emplaced at supracrustal levels between a tonalite intrusion to the east and unmetamorphosed Silurian sediments to the west (Hrouda and others, 1999). A normal solid-state shear zone was developed in the older tonalite, whereas in the late granite the fabric is magmatic to subsolidus-state.

RESULTS OF ZIRCON DATING

Gföhl Orthogneiss and Migmatite at the Boundary Between ILC and EMC

Anatectic and strongly deformed orthogneiss sample BM 4 was collected in the Rokytka valley close to the village of Biskupice (fig. 4). The rock is composed of recrystallized K-feldspar and plagioclase layers; quartz ribbons are strongly annealed, and garnet occurs in biotite-rich bands with abundant sillimanite. In the outcrop sampled, the orthogneiss locally passes into migmatite and contains pockets of granitic melt. Migmatitic gneiss sample BM 5 comes from the Loučka valley close to the village of Skryje (fig. 4). It contains a considerable amount of anatectic melt, layers of recrystallized K-feldspar, plagioclase, quartz, biotite and sillimanite. We interpret these two samples as representing originally porphyritic coarse-grained granite that was strongly deformed under high-grade conditions and partially melted.

Abraded ball-shaped cores of originally euhedral, brown, transparent zircon grains of Gföhl orthogneiss sample BM 4 and three small fractions of migmatite sample BM 5 containing clear to milky euhedral grains and needles with little rounding at their terminations were analyzed after vapor dissolution (table 2) and plot on a regression line (MSWD = 1.3) with intercept ages at 394 ± 6 and 1374 ± 36 Ma (fig. 6). The long-prismatic grain morphologies in both samples indicate a magmatic origin. We therefore consider the lower intercept age of 394 ± 6 Ma to most closely reflect the time of crystallization of the magmatic protolith, whereas the upper intercept reflects the mean age of the Mesoproterozoic source from which the original granite was derived.

TABLE 2

U-Pb isotopic analyses of Bohemian zircons after dissolution using HF vapor transfer

Sample	Zircon description	$^{206}Pb/^{204}Pb^{m}$	$^{206}Pb/^{238}U^{c}$	% error	$^{207}Pb/^{235}U^{c}$	% error	$^{207}Pb/^{206}Pb^{c}$	$^{206}Pb/^{238}U$ age [Ma]	$^{207}Pb/^{235}U^{c}$ age [Ma]	$^{207}Pb/^{206}Pb$ age [Ma]	Corr. coeff.
BM 1-1	Abraded, 15 euhedral, clear grains	297 ± 5	0.1181	0.57	1.0787	1.42	0.0662 ± 8	719.6 ±4.1	743.0± 10.6	815±25	0.542
BM 1-2	Abraded, 15 well rounded grains, milky to clear	198 ± 3	0.0753	0.32	0.6349	1.51	0.0611 ± 8	468.0±1.5	499.1± 7.5	644±30	0.495
BM 1-3	10 clear, euhedral, grains, 100-125 μm	168 ± 3	0.0584	0.98	0.4375	2.19	0.0543 ± 10	365.9±3.6	368.5± 8.1	383±42	0.549
BM 1-4	6 purple, euhedral, clear, grains, > 125 μm	135 ± 1	0.0641	0.52	0.4931	2.46	0.0558 ± 13	400.5±2.1	407.0± 10.0	445±50	0.465
BM 1-5	Abraded, 6 brown euhedral grains, 100-125 μm, well rounded after abrasion	717 ± 16	0.0577	0.84	0.4453	1.19	0.0559 ± 4	361.6±3.0	374.0±4.5	450±18	0.747
BM 1-6	Abraded, 8 euhedral, brown grains 100-125 μm. Well rounded after abrasion	801 ± 16	0.06	0.59	0.4548	0.96	0.0600 ± 4	375.6±2.2	380.6± 3.7	604±13	0.673
BM 1-7	14 clear, euhedral, grains, rounded at tips	516 ± 4	0.0595	0.66	0.4581	0.83	0.0558 ± 3	372.6±2.5	382.9± 3.2	445±11	0.811
BM 1-8	14 tiny, clear, euhedral grains	357 ± 4	0.0517	0.24	0.4304	0.55	0.0546 ± 3	325.0±0.8	363.5± 2.0	397±11	0.518
BM 1-9	1 brown, clear, stubby grain	576 ± 6	0.0773	0.94	0.6293	1.01	0.0590 ± 2	480.0±4.5	495.7± 5.0	568±8	0.939
BM 1-10	1 brown, euhedral, patchy grain	1052 ± 30	0.0543	2.19	0.4085	3.28	0.0545 ± 9	340.9±7.5	347.8± 11.4	394±39	0.773
BM 1-11	3 clear, stubby grains	335 ± 1	0.0513	0.51	0.5183	0.88	0.0733 ± 4	322.5±1.6	424.0± 3.7	1023±12	0.635
BM 1-12	2 long prismatic grains	247 ± 7	0.0439	0.65	0.3524	5.35	0.0583 ± 30	277.0±1.8	306.5± 16.4	540±112	0.081
BM 1-13	1 euhedral, grayish, zircon tip	807 ± 97	0.0478	1.23	0.3541	6.04	0.0537 ± 267	301.0±3.7	307.8± 18.6	362±112	0.216
BM 3-1	Abraded, 3 grains, clear, brown, stubby	1251 ± 33	0.1137	0.48	1.1446	0.71	0.0730 ± 4	694.2±3.3	774.7± 5.5	1014±10	0.731
BM 3-2	Abraded, 3 grains, clear, brown, prismatic	2892 ± 58	0.121	0.54	1.2903	0.59	0.0773 ± 2	736.3±4.0	841.4± 5.0	1129±4	0.926
BM 3-3	3 brown, stubby grains	2330 ± 47	0.0745	0.78	0.6325	0.82	0.0616 ± 2	463.2±3.6	497.7± 4.1	660±5	0.951
BM 3-4	8 prismatic clear, brown grains	1250 ± 13	0.0908	0.75	0.7601	0.96	0.0607 ± 4	560.3±4.2	574.1±5.5	630±13	0.781
BM 3-5	4 clear euhedral grains	2985 ± 60	0.0837	0.72	0.8854	0.9	0.0767 ± 4	518.2±3.7	643.9±5.8	1115±11	0.802
BM 3-6	Abraded, 4 rounded, pink, formerly prismatic grains	773 ± 31	0.0976	0.4	0.9706	0.57	0.0721 ± 3	600.3±2.4	688.8±3.9	990±8	0.74
BM 3-7	Abraded, 3 prismatic brown milky grains	1030 ± 13	0.0773	0.24	0.6174	1.13	0.0579 ± 6	480.0±1.2	488.2±5.5	526±23	0.474
BM 3-8	Abraded, 2 prismatic clear grains, slightly polished	684 ± 27	0.092	0.35	0.802	0.86	0.0633 ± 5	567.4±2.0	598.0±5.1	717±16	0.528
BM 4-1	Abraded, 5 clear, slender, pink still oval shaped grains	475 ± 8	0.1239	0.38	1.8354	0.61	0.1074 ± 5	753.0±2.9	1058.2±6.5	1756±8	0.67

TABLE 2
(continued)

Sample	Zircon description	$^{206}Pb/^{204}Pb^*$	$^{206}Pb/^{238}U^c$	% error	$^{207}Pb/^{235}U^c$	% error	$^{207}Pb/^{206}Pb^c$	$^{206}Pb/^{238}U$ age [Ma]	$^{207}Pb/^{235}U^c$ age [Ma]	$^{207}Pb/^{206}Pb$ age [Ma]	Corr. coeff.
BM 4-2	Abraded, 4 ball shaped brown transparent grains	287 ± 7	0.0986	0.27	0.9571	1.24	0.0704 ± 8	606.2±1.6	681.8±8.5	940±24	0.373
BM 4-3	Abraded, 4 ball shaped brown transparent grains	197 ± 2	0.1043	0.36	1.0459	1.33	0.0727 ± 9	639.6±2.3	726.8±9.7	1006±24	0.508
BM 5-1	8 clear grains, < 75 μm	729 ± 10	0.0604	0.58	0.4795	0.75	0.0576 ± 3	378.1±2.2	397.7±3.0	513±10	0.799
BM 5-2	7 clear, stubby grains	839 ± 6	0.0879	0.57	0.6955	0.64	0.0574 ± 2	543.1±3.1	536.1±3.4	505±6	0.904
BM 5-3	6 euhdral needles	630 ± 17	0.0649	0.6	0.4839	0.85	0.0540 ± 3	405.4±2.4	400.7±3.4	372±13	0.732
BM 5-4	9 tiny euhedral, clear needles	375 ± 8	0.0567	0.76	0.4199	1.84	0.0537 ± 8	355.5±2.7	356.0±6.6	359±36	0.526
BM 5-5	15 subrounded clear grains, <63 μm	412 ± 6	0.0641	0.44	0.5412	1.05	0.0612 ± 6	400.5±1.8	439.2±4.6	647±19	0.518
BM 5-6	8 euhedral clear grains, <63 μm	533 ± 14	0.068	0.86	0.5921	1.59	0.0632 ± 8	424.1±3.6	472.2±7.5	715±27	0.622
BM 5-7	8 prismatic grains, milky with rounded tips	274 ± 4	0.0656	0.37	0.5121	1.69	0.0566 ± 9	409.6±1.5	419.9±7.1	477±34	0.478
BM 5-8	Clear needles with rounded tips	245 ± 4	0.0659	0.37	0.5111	1.34	0.0563 ± 7	411.4±1.5	419.2±5.6	463±27	0.466
BM 6-1	4 irregulary shaped grains, clear with spots	476 ± 7	0.0587	0.73	0.4312	1.27	0.0533 ± 5	367.7±2.7	364.0±4.6	340±22	0.67
BM 6-2	3 short, prismatic, clear, stubby grains	219 ± 1	0.0605	0.59	0.4471	1.53	0.0536 ± 7	378.7±2.2	375.2±5.7	354±30	0.49
BM 6-3	4 well rounded, clear grains	747 ±12	0.0612	0.57	0.4569	0.89	0.0542 ± 4	382.9±2.2	382.1±3.4	378±15	0.68
BM 7-1	2 stubby slightly brown and clear grains	3140 ± 7	0.0645	0.74	0.4705	0.95	0.0529 ± 1	402.9±3.0	391.5±3.7	325±6	0.943
BM 7-2	1 brown, short prismatic, clear grain	3742 ± 144	0.0422	1.01	0.307	1.52	0.0527 ± 2	266.5±2.7	271.9±4.1	317±10	0.905
BM 7-3	1 tip of a clear pinkish grain	1586 ± 12	0.0439	0.52	0.32	0.87	0.0528 ± 2	277.0±1.4	281.9±2.5	321±9	0.776
BM 9-1	3 clear, stubby grains, <63 μm	800 ± 40	0.0493	0.9	0.3603	3.14	0.0532 ± 9	310.2±2.8	312.4±9.8	339±39	0.322
BM 9-2	2 clear, stubby grains	805 ± 16	0.0502	0.52	0.3609	1.28	0.0534 ± 4	315.7±1.6	312.9±4.0	344±18	0.357
BM 10-1	Abraded, 3 brown clear elongated grains	1576 ± 16	0.2141	0.41	3.1423	0.45	0.106 ± 2	1250.6±5.1	1443.1±6.5	1739±3	0.93
BM 10-2	Abraded, 6 tiny, small and clear grains	235 ± 6	0.0836	0.44	0.6755	3.19	0.0586 ± 17	517.6±2.3	524.1±16.7	554±65	0.581
BM 10-3	Abraded, 4 prismatic, clear grains	467 ± 11	0.0893	0.73	0.8041	1.48	0.0653 ± 8	551.4±4.0	599.1±8.9	784±25	0.59
BM 10-4	Abraded, 5 well rounded clear grains	212 ± 3	0.1069	0.61	1.1031	1.84	0.0748 ± 12	654.7±4.0	754.8±13.9	1064±32	0.516
BM 11-1	Abraded, 1 prismatic clear grain	215 ± 2	0.0669	0.39	0.5209	1.48	0.0565 ± 8	417.5±1.6	425.8±6.3	471±29	0.463

TABLE 2
(continued)

Sample	Zircon description	$^{206}Pb/^{204}Pb^{m}$	$^{206}Pb/^{238}U^{c}$	% error	$^{207}Pb/^{235}U^{c}$	% error	$^{207}Pb/^{206}Pb^{c}$	$^{206}Pb/^{238}U$ age [Ma]	$^{207}Pb/^{235}U^{c}$ age [Ma]	$^{207}Pb/^{206}Pb$ age [Ma]	Corr. coeff.
BM 12-1	6 clear, irregular shaped grains, >100 μm	376 ± 5	0.0647	0.33	0.5074	1.01	0.0568 ± 5	404.1±1.3	416.7±4.2	486±20	0.485
BM 12-2	8 clear, euhedral grains, >100 μm	716 ± 9	0.0679	0.33	0.5182	0.66	0.0554 ± 3	423.5±1.4	423.9±2.8	428±12	0.572
BM 12-3	6 clear, pinkish euhedral grains, > 100 μm	850 ± 42	0.0586	0.65	0.5554	0.87	0.0688 ± 4	367.1±2.4	448.5±3.9	892±11	0.781
BM 12-4	7 clear, stubby grains, > 63-100 μm	464 ± 6	0.0642	0.67	0.4707	1.13	0.0532 ± 5	401.1±2.7	391.7±4.4	338±20	0.641
BM 13-1	6 brownish, euhedral grains with cracks	845 ± 5	0.05	0.26	0.365	0.39	0.0529 ± 1	314.5±0.8	315.9±1.2	326±6	0.688
BM 13-2	5 clear, euhedral grains, rounded tips	208 ± 1	0.0519	0.26	0.3791	1.49	0.0533 ± 5	326.2±0.8	326.4±4.9	344±22	0.446
BM 13-3	5 pink, euhedral clear grains	147 ± 1	0.0592	0.27	0.4354	1.05	0.0529 ± 7	370.8±1.0	367.0±3.9	326±32	0.466
BM 14-1	Abraded, 10 prismatic grains, rounded tips	216 ± 3	0.0549	0.44	0.3896	1.84	0.0514 ± 9	344.5±1.5	334.1±6.1	284±54	0.441
BM 14-2	3 stubby to euhedral, clear, grains	564 ± 23	0.0516	0.42	0.3698	2.51	0.0520 ± 12	324.3±1.4	319.5±8.0	305±17	0.428
BM 15-1	Abraded, 2 brown, elongated grains	818 ± 18	0.0556	0.34	0.4018	0.85	0.0524 ± 4	348.8±1.2	343.0±2.9	330±17	0.513
BM 15-2	Abraded, 7 prismatic, pink grains	294 ± 2	0.0555	0.32	0.4063	1.01	0.0530 ± 5	348.2±1.1	346.2±3.5	330±21	0.451
BM 15-3	Abraded, 10 clear well rounded grains. Formerly euhedral grains	280 ± 5	0.0614	0.47	0.4576	1.99	0.0540 ± 10	384.1±1.8	382.6±7.6	373±41	0.463

m = measured ratio; c = ratio corrected for common lead (Stacey and Kramers, 1975), spike, mass fractionation, and blank. All errors are 2 sigma.

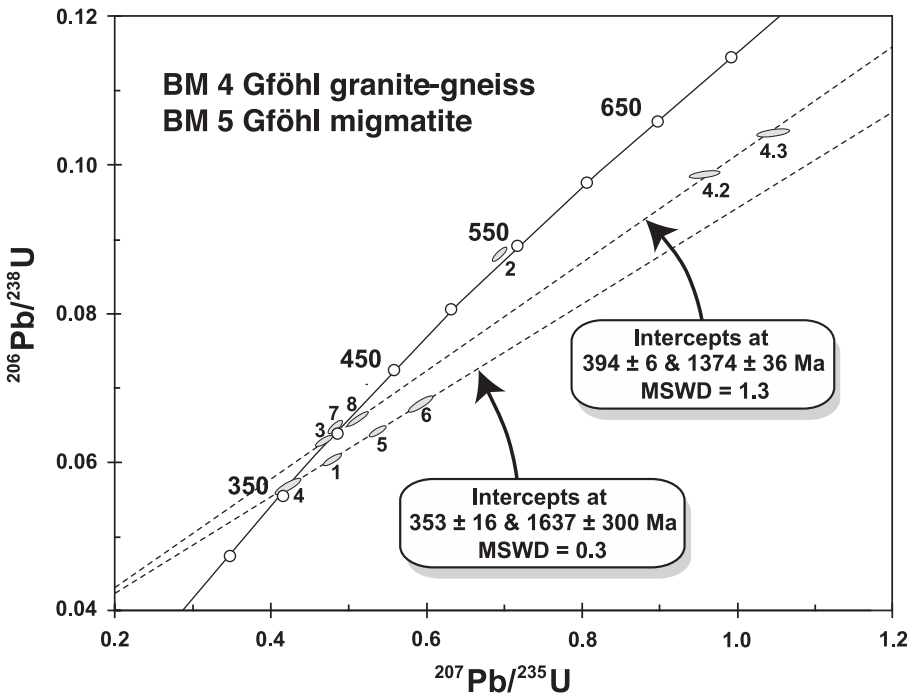

Fig. 6. Concordia diagram showing analytical data for zircons from Gföhl granitic gneiss sample BM 4 and migmatitic gneiss sample BM 5. Error ellipses are 2-sigma.

A distinctly different population of clear, stubby zircons in the same samples with variable degrees of partial dissolution at the originally pyramidal terminations as well as thin, euhedral and needle-like grains probably represent new zircon growth during advanced migmatization and partial anatexis. Several fractions of the stubby grains are discordant, whereas the clear needles are nearly concordant. All fractions are aligned along a chord (MSWD = 2.3), yielding a significantly younger lower intercept age of 353f ± 16 Ma and a poorly constrained upper intercept at 1637 ± 300 Ma (fig. 6). We interpret the younger age to reflect zircon crystallization during partial melting, whereas the upper intercept age of ~1637 Ma appears to reflect a similar crustal source as in the older zircon population.

A sample of least deformed, non-migmatitic Gföhl gneiss (CZ 14/4) was collected at locality Biskupice, 2 km east of sample BM 4, and is petrographically similar to BM 4. The homogeneous zircon population consists of long-prismatic grains, little rounded at their terminations, and clearly of igneous origin. Five grains were evaporated individually and yielded similar $^{207}Pb/^{206}Pb$ ratios that combine to a mean age of 550.6 ± 1.0 Ma (table 3, fig. 7A). This is likely to reflect the time of igneous emplacement of the gneiss precursor. Two similar looking zircons yielded significantly higher ages of 791.5 ± 2.8 Ma and 848.2 ± 2.9 Ma respectively (table 3, figs. 7B, C) and are interpreted as xenocrysts. The difference in age as compared to samples BM 4 and 5 and the lack of much older xenocrysts suggest that sample CZ 14/4 represents a distinct gneiss unit within the Gföhl assemblage and supports the assumption that the term "Gföhl gneiss" may include a variety of orthogneisses of different ages and origins.

TABLE 3

Pb isotopic data from single grain zircon evaporation.

Sample Number	Zircon color and morphology	Grain #	Mass scans[1]	Evaporation temp. in °C	Mean $^{207}Pb/^{206}Pb$ ratio[2] and 2-σm error	$^{207}Pb/^{206}Pb$ age and error
CZ 14/4	yellow-brown, long-prismatic, slightly rounded terminations	1	114	1596	0.058547±29	550.3±1.1
		2	62	1595	0.058564±61	550.9±2-3
		3	87	1589	0.058541±37	550.1±1.4
		4	127	1594	0.058566±22	550.1±0.8
		5	122	1596	0.058556±22	550.6±0.8
mean of 5 grains		1-5	512		0.058555±14	***550.6±1.0**
	yellow-brown, ends well rounded	6	83	1599	0.065534±88	791.5±2.8
		7	110	1598	0.067335±92	848.2±2.9
CZ-1Z	clear to light brown, stubby to long-prismatic, euhedral	1	110	1599	0.053072±46	331.9±2.0
		2	88	1600	0.053082±49	332.3±2.1
		3	66	1598	0.053091±58	332.7±2.5
mean of 3 grains		1-3	264		0.053080±29	332.2**±1.2**
2S	yellow-brown, long-prismatic, euhedral	1	87	1599	0.053267±33	340.2±1.4
		2	84	1600	0.053252±33	339.5±1.4
		3	122	1598	0.053271±29	340.4±1.2
mean of 3 grains		1-3	293		0.053264±18	***340.1±1.1**
CZ-3T	clear to yellowish-brown, long-prismatic, euhedral	1	81	1598	0.053017±37	329.5±1.6
		2	95	1597	0.053012±32	329.3±1.4
		3	94	1599	0.053046±24	330.8±1.0
mean of 3 grains		1-3	187		0.053025±18	***329.9±1.1**
CZ/TAJ	brown, long-prismatic, idiomorphic	1	106	1595	0.052869±38	323.2±1.6
		2	84	1594	0.052884±39	323.8±1.7
		3	103	1592	0.052874±30	323.4±1.3
		4	103	1594	0.052888±40	324.0±1.7
		5	63	1596	0.052881±29	323.7±1.2
		6	88	1595	0.052877±33	323.5±1.4
mean of 6 grains		1-5	547		0.052877±15	***323.5±1.1**
CZ 6	clear, near-spherical, multifaceted	1	133	1605	0.053264±23	340.1±1.0
		2	100	1604	0.053268±23	340.2±1.0
		3	99	1607	0.053254±27	339.6±1.2
		4	121	1602	0.053273±24	340.4±1.0
		5	107	1610	0.053259±19	339.8±0.8
		6	129	1609	0.053260±13	339.9±0.5
mean of 6 grains		1-6	689		0.053263± 9	***340.0±1.1**
		7	44	1596	0.054926±61	409.2±2.5
		8	98	1598	0.054323±25	384.5±1.0
		9	83	1597	0.054331±27	384.8±1.1
mean of 2 grains		8&9	181		0.0543	***384.6±1.1**
CZ/Vir	clear to yellowish-brown, long-prismatic, euhedral	1	89	1598	0.053227±35	338.5±1.5
		2	97	1597	0.053256±33	339.7±1.4
		3	68	1599	0.053238±46	339.0±2.0
mean of 3 grains		1-3	254		0.053241±21	***339.1±1.1**

[1]Number of $^{207}Pb/^{206}Pb$ ratios evaluated for age assessment. [2]Observed mean ratio corrected for nonradiogenic Pb where necessary. Errors based on uncertainties in counting statistics. *Error based on reproducibility of internal standard.

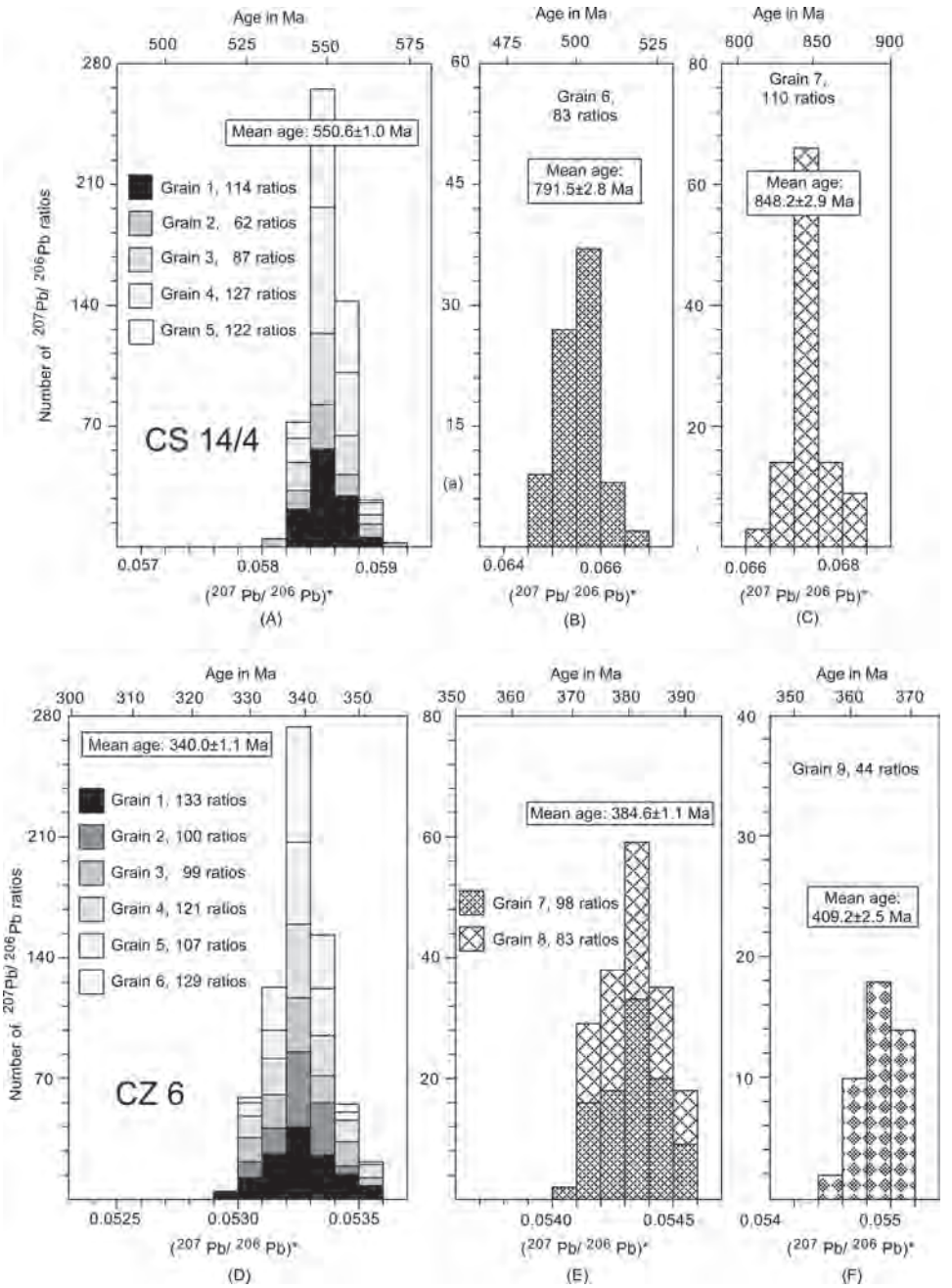

Fig. 7. Histograms showing distribution of radiogenic lead isotope ratios derived from evaporation of single zircons from rocks of the Variscan root zone, southern Bohemia, Czech Republic. (A) Spectrum for 5 grains from porphyritic granite-gneiss sample CZ 14/4, integrated from 512 ratios and interpreted to reflect age of protolith emplacement. (B, C) Spectra for xenocrystic grains. (D) Spectrum for 6 grain fractions of 3-4 metamorphic zircons each from granulite sample CZ 6, integrated from 689 ratios and interpreted to reflect age of high-grade metamorphism. (E) Spectrum for 2 igneous grains, integrated from 181 ratios and interpreted to reflect emplacement of granulite protolith. (F) Xenocrystic grain.

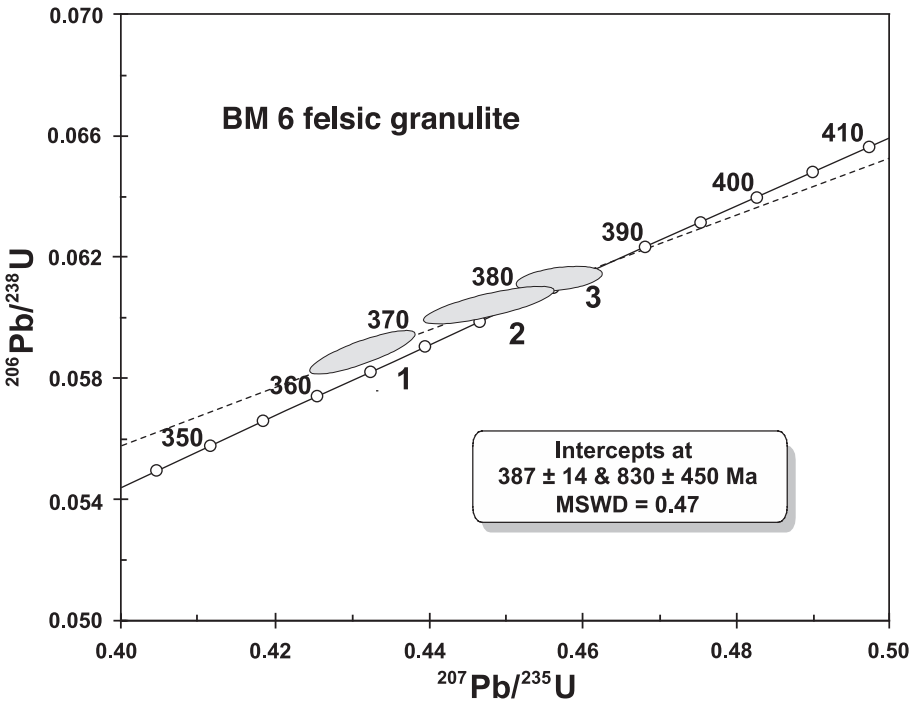

Fig. 8. Concordia diagram showing analytical data for zircons from felsic granulite sample BM 6. Errors as in figure 6.

Felsic Granulite Close to the Contact Between ILC and EMC

Felsic granulite sample BM 6 comes from the least retrograded portion of a granulite body in the Loučka Valley of the Drahonín area, close to the border between the Gföhl and Svratka crystalline units (fig. 4). The granulites in this area contain two contrasting metamorphic assemblages. The early assemblage is characterized by kyanite + garnet + biotite + plagioclase + quartz + mesoperthite, whereas the later assemblage contains sillimanite + garnet + spinel + biotite.

Sample BM 6 contains clear, oval-shaped and stubby zircons as well as irregularly-shaped grains with no internal zoning as is common in high-grade rocks. Six small fractions containing two to four grains each are slightly reversely discordant, presumably due to U-loss in the internal domains of the grain (Williams and others, 1984) or due to laboratory procedures, but plot near the concordia curve (fig. 8). Two oval-shaped grains of fraction 3 are 45 percent discordant and yielded an intercept age of 383 ± 3 Ma. The U-Pb data obtained from cores of clear, stubby and oval-shaped grains of fractions 5 and 6 are also reversely discordant but are well aligned (MSWD = 0.22) and, together with the remaining four fractions of oval-shaped grains, project to a concordia intercept age of 387 ± 14 Ma (table 2, fig. 8). Early Neoproterozoic inheritance is revealed by an ill-defined upper intercept age of 803 ± 450 Ma. The high degree of concordance of the abraded zircons makes it unlikely that these grains contain considerable amounts of older material, and we therefore interpret the age of 387 ± 14 Ma to reflect the time of crystallization of the granulite precursor. Wendt and others (1994) reported similar U-Pb zircon protolith emplacement ages of 365 to 373 Ma for South Bohemian granulites from the Blanský les massif.

An additional sample of felsic granulite was collected from the same locality (CZ 6) and contained abundant ball-shaped, clear, multifaceted zircons of metamorphic origin as well as clear to yellowish long-prismatic grains with well rounded terminations which appear to be of igneous derivation. Six small fractions of 3 to 4 grains each (~60 – 90 μm in diameter) of the metamorphic population were evaporated individually at high temperatures and yielded consistent $^{207}Pb/^{206}Pb$ ratios corresponding to a mean age of 340.0 ± 1.1 Ma (table 3, fig. 7D). This age is identical to metamorphic ages obtained from numerous granulite samples throughout the Bohemian Massif and reflects the peak of HP/HT metamorphism (Kröner and others, 2000a).

In contrast, the rounded, long-prismatic grains provided variable results. Two grains yielded similar isotopic ratios with a mean age of 384.6 ± 1.1 Ma, whereas one grain has a $^{207}Pb/^{206}Pb$ minimum age of 409.2 ± 2.5 Ma (table 3, figs. 7E, F). The former result is identical to the lower intercept age obtained by the vapor transfer method and, in our view, reflects the time of crystallization of the granulite precursor. The most plausible interpretation for the older age of ~409 Ma is mixing of the ~385 Ma magmatic components with an older source (core?) as reflected by the upper concordia intercept of the vapor transfer data (fig. 8). The "age" is therefore considered to be geologically meaningless.

Mg-K Syenite (Durbachite) Emplaced at the ILC and EMC Boundary

Sample BM 7 of dark porphyritic durbachite was collected close to the village of Drahonín (fig. 4) and is composed of K-feldspar phenocrysts, biotite, actinolitic hornblende, quartz and rare plagioclase.

The zircon population comprises short-prismatic and euhedral, clear to pink grains with no rounding at the ends. Two single grains and a micro-fraction of two stubby grains were analyzed by the vapor transfer method. The U-Pb data can be fitted to a regression line (MSWD = 0.43) through the origin and with an upper concordia intercept corresponding to an age of 323 ± 7 Ma (fig. 9). In view of the igneous nature of the zircons this is interpreted to date the time of emplacement of the durbachite.

Long-prismatic, euhedral single zircons from a second durbachite sample (CZ/TAJ) and collected from the same locality were evaporated and yielded a mean $^{207}Pb/^{206}Pb$ age of 323.5 ± 1.1 Ma (table 3, fig. 9, inset). This result is identical, but more precise, than the vapor transfer result and places a younger age limit on the steep fabric in the Gföhl granulites.

Granitic Gneisses from the EMC

Strongly deformed and recrystallized Svratka granitic augen-gneiss sample BM 10 was collected close to the village of Sněžná north of the town of Nové Město (fig. 4). The rock is composed of K-feldspar augens, recrystallized plagioclase, quartz ribbons as well as muscovite and biotite aggregates. The augen-gneiss is surrounded by sillimanite micaschists with a sillimanite + biotite + garnet + muscovite + plagioclase + quartz assemblage. Microgranite gneiss sample BM 11 was also collected close to the village of Sněžná and represents a typical example of the SCC, similar to augen-gneiss BM 10. It shows a strong planar fabric reflecting intense solid-state deformation and is composed of recrystallized K-feldspar, plagioclase and quartz. Muscovite is abundant, whereas biotite is rare.

Zircons from sample BM 10 are mostly subhedral and clear, transparent to light brown and translucent. Four small fractions of 3 to 6 morphologically identical grains each were treated in an air abrasion cell to remove potential metamorphic overgrowths. The grains of fraction 3 were only slightly abraded and thus at least partly kept their original, euhedral shape. The remaining fractions 1, 2 and 4 consisted of well-rounded, oval grains after abrasion, and the analytical data (table 2) show considerable dispersion in the Concordia diagram (fig. 10). Regression through all

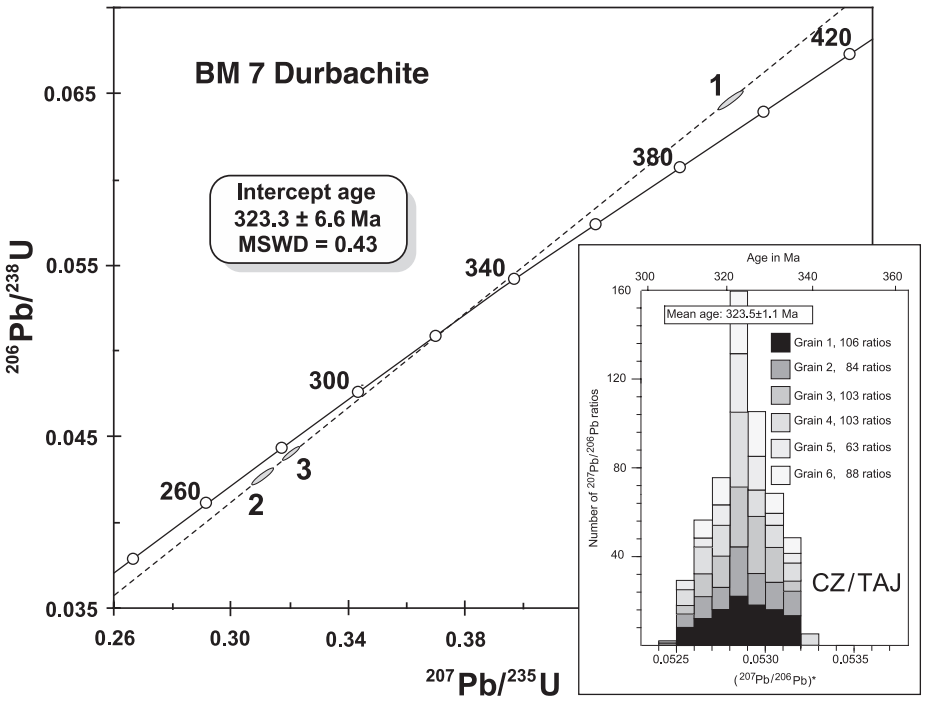

Fig. 9. Concordia diagram showing analytical data for zircons from porphyritic durbachite sample BM 7. Inset is histogram showing distribution of radiogenic lead isotope ratios derived from evaporation of 6 zircon grains from durbachite sample CZ/TAJ, integrated from 547 ratios.

four poorly aligned data points (MSWD = 5.6) yielded intercept ages of 508 ± 30 and 1927 ± 60 Ma. If the result for slightly abraded fraction 3 is excluded from the regression calculation, the MSWD significantly improves to 1.4, and the resulting discordia line yields statistically equivalent but better constrained intercept ages of 515 ± 9 and 1932 ± 7 Ma (fig. 10). The fact that the slightly polished grains plot below the 515 Ma discordia either suggests Pb-loss during high-grade metamorphism at ~340 Ma or metamorphic overgrowth at 340 Ma, or both. The age of 515 ± 9 Ma is thus interpreted to approximate the time of protolith emplacement, whereas the upper intercept age of 1932 ± 7 Ma suggests that the gneiss protolith resulted from melting of late Paleoproterozoic basement.

A single, elongate and abraded zircon grain was analyzed from microgranite-gneiss sample BM 11 (table 2), and the results plot well below the 515 Ma discordia for sample BM 10 (fig. 10). The corresponding $^{207}Pb/^{206}Pb$ minimum age of 471 ± 29 Ma is considered to reflect Pb-loss at an unspecified time in the past, and the result is therefore difficult to interpret. We shall therefore not consider this sample in the following discussion.

Melt Patch from Migmatitic Metabasite of the ELC

Sample BM 9 represents melt patches within amphibolites associated with the Vír granulite body and sampled in a quarry north of the village of Vír (fig. 4). Adjacent granulites exhibit a homogeneously developed high-grade metamorphic fabric related to severe retrogression and partial melting. The melt patches occur in neck zones of intrafolial boudin necks in lock-up shear bands. The rock is composed of a hbl-plg-

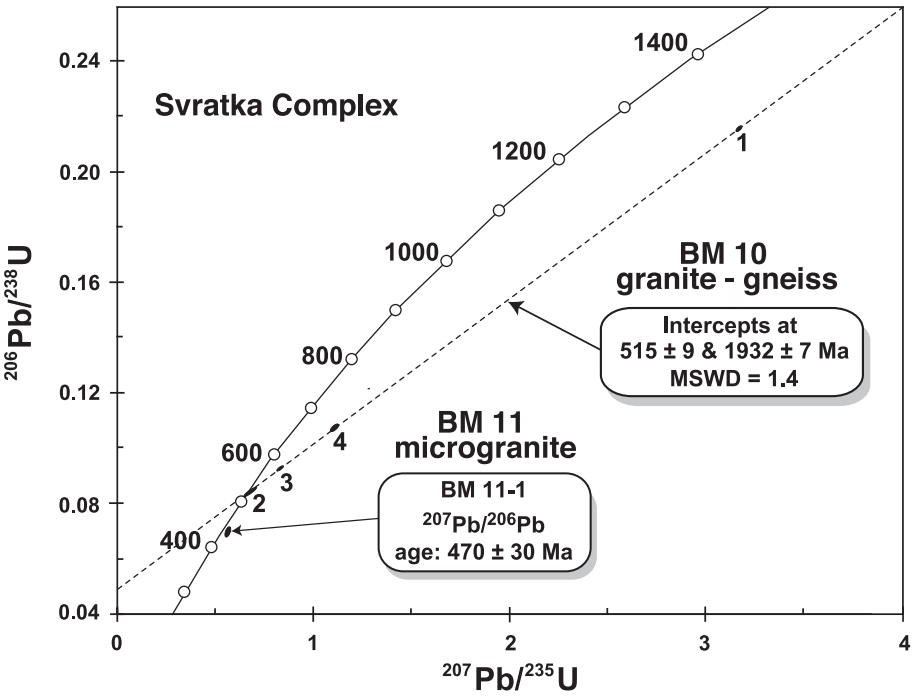

Fig. 10. Concordia diagram showing U-Pb zircon data for Svratka orthogneiss samples BM 10 and BM 11. Errors as in figure 6.

titanite assemblage, and the surrounding amphibolite is characterized by the assemblage hbl-plg-qtz±grt±cpx. The melt patches are interpreted as the result of *in-situ* melting of high-grade amphibolite.

The zircon population consists of clear, short prismatic to stubby grains, whereas milky-gray (metamict) grains are rare. Two fractions of two grains each and three transparent, stubby grains were analyzed after vapor transfer and provided slightly discordant isotopic ratios (table 2, fig. 11) and $^{207}Pb/^{206}Pb$ ages of 339 ± 39 and 344 ± 18 Ma with a mean of 341.6 ± 6 Ma (fig. 11) that we interpret to reflect the formation of melt patches in the Vír granulite body. Due to the slight discordance, the $^{206}Pb/^{238}U$ apparent age of this sample is distinctly younger at 310 Ma.

Zircons from a further sample of coarse-grained melt patch from the same locality (CZ/Vír) were clear to yellowish-brown, long-prismatic and euhedral. Evaporation of three large grains produced identical isotopic ratios that combine to a mean $^{207}Pb/^{206}Pb$ age of 339.1 ± 1.1 Ma (table 3, fig. 11, inset). This is identical to, but more precise than, the conventional $^{207}Pb/^{206}Pb$ age and is considered to be the best estimates for the time of melt patch formation.

Granodiorite Sill Emplaced at the Boundary Between EMC and UC

Strongly sheared granodioritic gneiss sample BM 13 was collected from a sill near the village of Krouna in the Krouna River valley (fig. 4). The sill was affected by solid state normal shearing marked by a strong NW-SE trending stretching lineation, but granodiorite veins cross-cut the main fabric and indicate a syntectonic origin for the intrusion (Pitra and others, 1994). The rock contains relict plagioclase porphyroclasts, locally strongly recrystallized, recrystallized biotite, amphibole and quartz.

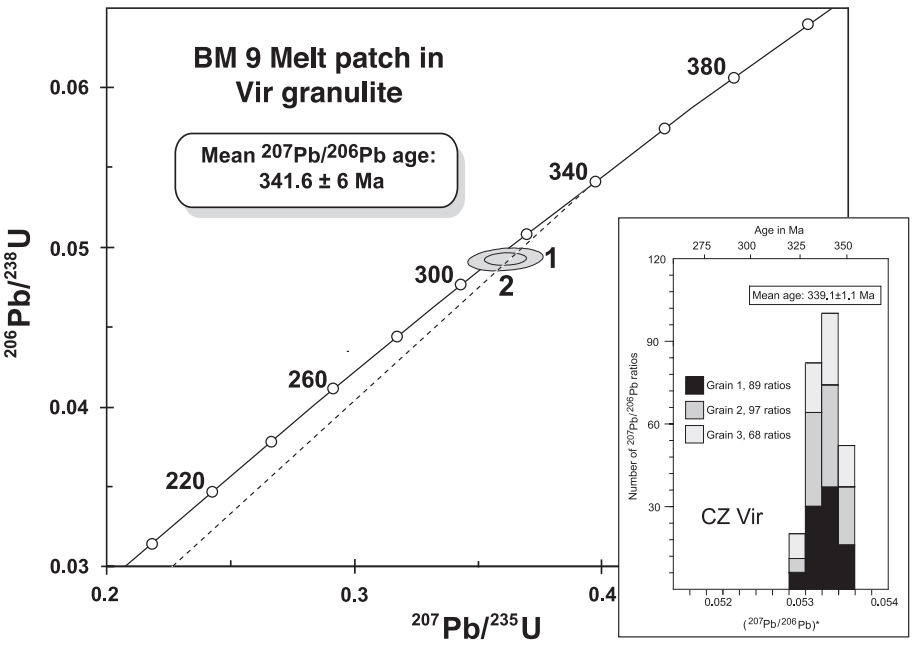

Fig. 11. Concordia diagram showing U-Pb zircon data for meltpatch sample BM 9 within amphibolites of the Vír granulite. Inset is histogram showing distribution of radiogenic lead isotope ratios derived from evaporation of 3 zircon grains from granulite sample CZ/Vir, integrated from 254 ratios.

The zircons are brownish to clear and predominantly euhedral, but there are also grains with slightly rounded terminations. The analytical results after vapor transfer dissolution of three fractions containing 5 to 6 grains each are presented in table 2 and figure 12. Euhedral grains with cracks (fraction 1) document recent Pb-loss and, together with two additional fractions of euhedral grains, one concordant and one grossly reversely discordant, can be fitted to a regression line (MSWD = 1.3) from the origin to an upper intercept age of 327 ± 6 Ma (fig. 12). This is considered to reflect the time of emplacement of the gneiss protolith.

The additional sample CZ/3T was collected from the same locality as BM 13, and individual evaporation of three euhedral zircon grains yielded consistent $^{207}Pb/^{206}Pb$ ratios with a mean age of 323.5 ± 1.1 (table 3, fig. 12, inset). This is identical to, but more precise than, the vapor transfer data and provides a well-constrained older age limit for the shearing event.

Granitoids Emplaced into the Upper Crust

This plutonic complex consists of two major intrusive phases, namely an older amphibole-bearing granodiorite (sample CZ/2S) and younger pink granite (sample BM 15) representing a shallow intrusion of subvolcanic character. The granodiorite was sampled at the locality Švihov and is composed of plagioclase, K-feldspar, quartz, biotite and amphibole.

The zircon population is uniformly yellow-brown, long-prismatic and euhedral, and three grains were evaporated individually, yielding identical $^{207}Pb/^{206}Pb$ ratios that combine to a mean age of 340.1 ± 1.1 Ma (table 3, fig. 13). This is consistent with ages from similar calc-alkaline granodiorites from the Central Bohemian Pluton (Holub and others, 1997) and also with ages for granodiorite sills dated in the

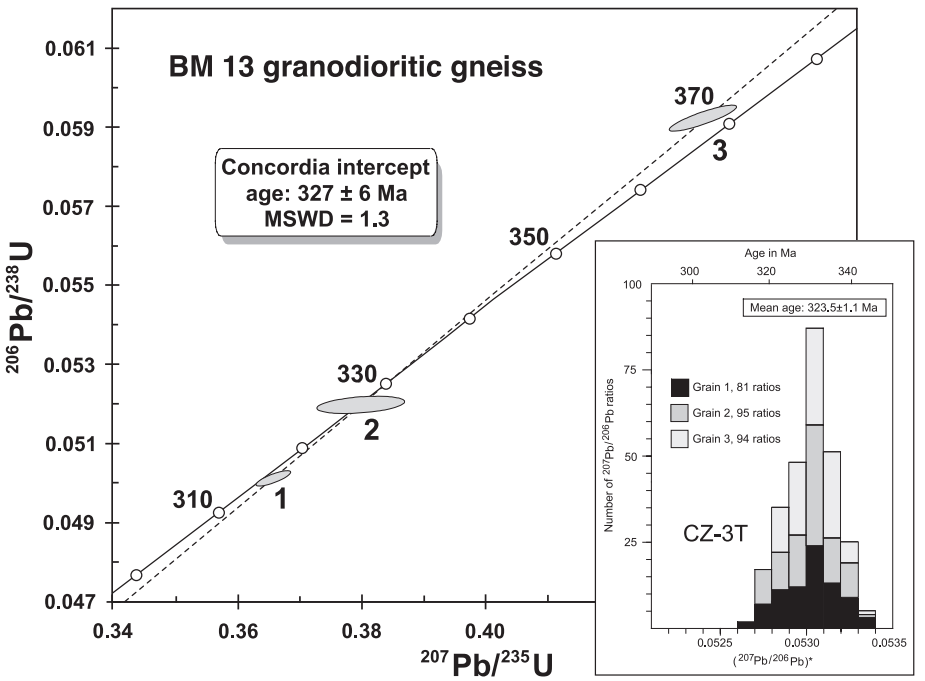

Fig. 12. Concordia diagram showing U-Pb zircon data for granodioritic gneiss sample BM 13. Inset is histogram showing distribution of radiogenic lead isotope ratios derived from evaporation of 3 zircon grains from granodiorite sample CZ/TAJ, integrated from 270 ratios.

northern part of the Bohemian Massif (Štípská and others, 2004). A common feature of all these granodioritic to tonalitic intrusions is their syntectonic, transpressional emplacement into upper crustal levels.

Pink granite sample BM 15 was collected at a dam on the Chrudimka River close to the village of Nasavrky (fig. 4). It is composed of K-feldspar, plagioclase, quartz and some biotite. Granophyric textures were observed locally. The granite caused contact metamorphism in the adjacent metasediments as indicated by the development of an orthitic chloritoid + muscovite + chlorite assemblage, indicating very low pressures and a shallow level of contact metamorphism. The Silurian country rocks exhibit evidence of intense compressional imbrication predating granite emplacement.

U-Pb dating results for abraded, originally subhedral, zircon fractions analyzed after vapor dissolution are presented in table 2 and in the Concordia diagram of figure 14. A fraction of pink, oval-shaped zircons and a fraction of two brown, sub-transparent grains are reversely discordant but plot close to concordia. They combine to an intercept age of 332 ± 20 Ma, whereas a third fraction containing 10 small, well rounded, abraded grains of originally clear euhedral shape produced a concordant $^{207}Pb/^{206}Pb$ age of 373 ± 25 Ma that may be interpreted to reflect an inherited component assimilated from wall rocks during ascent. However, since the fraction consisted of ten grains, the above "age" is most likely a geologically meaningless mixture between the 332 Ma populations and some older crustal component whose true age remains unspecified.

Resampling of the Nasavrky pink granite at the same locality as above (sample CZ/1Z) yielded clear, euhedral zircons, and evaporation of three grains produced a mean $^{207}Pb/^{206}Pb$ age of 332.2 ± 1.2 Ma (table 3, fig. 14, inset), identical to the

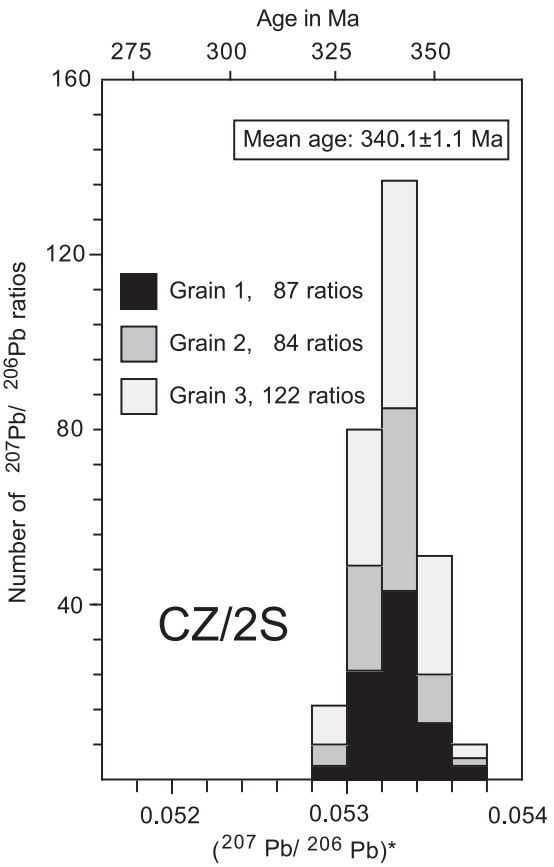

Fig. 13. Histogram showing distribution of radiogenic lead isotope ratios derived from evaporation of 3 zircon grains from granitoid gneiss sample CZ/2S, integrated from 320 ratios.

younger of the two vapor transfer results. No xenocrysts were identified in this sample. We are therefore confident, that the age of 332 reflects the time of emplacement of the pink granite.

Sm-Nd Whole-Rock Isotopic Systematics

Sm and Nd whole-rock isotopic data for most dated samples are listed in table 4 and are plotted in the isotopic evolution diagram of figure 15. Several samples show $^{147}Sm/^{144}Nd$ ratios considerably higher than 0.12 as is typically found in mature continental crust, and it is obvious that the light rare earth elements (LREE) in these samples have been modified by crystal fractionation involving LREE-enriched accessory phases such as apatite, or possibly metamorphism. Therefore, using these modified Sm/Nd ratios in the calculation of model ages yields meaningless data. However, it is helpful to use a 2-stage Nd isotopic evolution model (Liew and Hofmann, 1988) to calculate Nd mean crustal residence ages where the measured Sm/Nd ratio is used to define the isotopic evolution of the sample until its time of crystallization or its last modification of the Sm/Nd ratio (second stage), for example, metamorphism, migmatization or anatexis. The first (earlier) stage, namely the isotopic evolution path of Nd in the sample from its time of separation from the mantle, is then determined with an

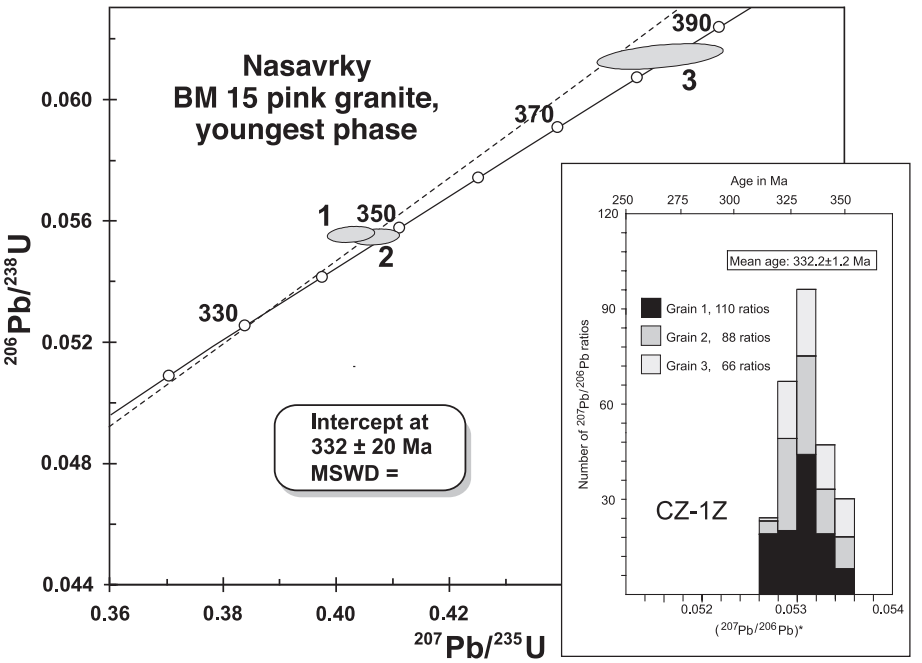

Fig. 14. Concordia diagram showing U-Pb zircon data for Zumberk pink granite-gneiss sample BM 15. Inset is histogram with distribution of radiogenic lead isotope ratios derived from evaporation of 3 zircons from pink granite-gneiss sample CZ/1Z, integrated from 264 ratios.

average crustal $^{147}Sm/^{144}Nd$ ratio of 0.12. The mean crustal residence ages thus calculated for the Bohemian granitoid rocks range from 1.43 to 1.96 Ga (fig. 15) and are considerably older than the magmatic protolith crystallization ages, indicating that substantial melting of older crustal sources must have occurred. The $\epsilon_{Nd(t)}$ values were calculated for the inferred times of high-grade metamorphism (340 Ma) or emplacement ages of the protoliths as determined by zircon dating.

As can be seen from figure 15, the majority of samples show $\epsilon_{Nd(t)}$ values of -3 to −8, consistent with melting of lower crustal material having an average mean crustal residence age of ~1.5 Ga. There is no evidence for involvement of significantly rejuvenated crust such as underplated, juvenile, mantle-derived material. Samples of ca. 400 to 500 Ma show similar $\epsilon_{Nd(t)}$ values, suggesting ongoing melting of isotopically similar crustal protoliths. Only during the latest Variscan development a "fanning-out" of the $\epsilon_{Nd(t)}$ values suggests involvement of limited amounts of juvenile material. When comparing the Bohemian root data with those from neighboring units, the data plot on the isotopic evolution paths of the gneisses from the Desná Dome and the Lugian Domain (Hegner and Kröner, 2000). This relationship suggests a uniform isotopic composition of different crustal levels in this part of the Bohemian Massif.

INTERPRETATION OF THE ISOTOPIC AGES

Isotopic Ages Testifying to Cambro-Ordovician Rifting along the Northern Gondwana Margin

The oldest rock of this study is represented by Gföhl Gneiss sample CZ 14/4 of the Internal Lower Crustal Belt with a protolith age of 550.6 ± 1.0 Ma (fig. 16). Similar or older Neoproterozoic ages are reported from the tectonic boundaries between the Varied and Monotonous Units of the Internal Middle Crustal Belt (for example,

TABLE 4

Sm-Nd isotopic data for samples from the Variscan root zone, southern Bohemia.

Sample	Sample	Age*	Nd [ppm]	Sm [ppm]	$^{147}Sm/^{144}Nd$	$^{143}Nd/^{144}Nd_{meas.}$	$^{143}Nd/^{144}Nd(t)$	e(t)	Model age [Ga]**
BM 1	Metarhyolite - Varied Group	350	11.21	2.33	0.1255	0.512104 ± 9	0.511817	-7.2	1.63
BM 2	Granitoid orthogneiss - Varied Group	350	4.22	1.47	0.1099	0.512204 ± 19	0.511952	-4.6	1.42
BM 3	Rhyolite - Drosendorf Group	530	5.78	1.70	0.1780	0.512072 ± 12	0.511454	-9.8	1.96
BM 4	Granitoid orthogneiss - Gföhl unit	400	8.98	2.41	0.1625	0.512195 ± 9	0.511769	-6.9	1.64
BM 5	Migmatite - Gföhl unit	350	15.37	3.74	0.1470	0.512199 ± 8	0.511862	-6.4	1.56
BM 6	Felsic granulite	390	9.03	2.33	0.1561	0.512193 ± 9	0.511794	-6.7	1.61
BM 7	Durbachite	320	58.6	12.66	0.1306	0.512119 ± 9	0.511846	-7.4	1.62
BM 8	Felsic granulite - Vir unit	350	4.09	1.02	0.1502	0.512252 ± 12	0.511907	-5.5	1.49
BM 9	Melt patch - Vir unit	310	9.75	1.95	0.1210	0.512521 ± 9	0.512275	0.7	0.97
BM10	Granite gneiss - Svratka complex	510	19.63	4.53	0.1394	0.512158 ± 9	0.511692	-5.7	1.63
BM11	Granite gneiss - Svratka complex	470	2.28	0.82	0.2161	0.512381 ± 11	0.511716	-6.2	1.64
BM12	Migmatite - Svratka complex	430	6.23	1.67	0.1616	0.512238 ± 8	0.511783	-5.9	1.58
BM13	Granodioritic gneiss	330	25.57	5.03	0.1190	0.512216 ± 9	0.511959	-5.0	1.43
BM14	Granodiorite - Nasavrky complex	350	3.88	0.49	0.1468	0.512284 ± 12	0.511948	-4.7	1.43
BM15	Pink biotite granite	330	28.98	5.40	0.1127	0.512279 ± 8	0.512036	-3.5	1.32

meas. = measured
*Crystallization age based on U-Pb or Pb-Pb zircon ages of this study.
**Nd model age, 2-stage Sm-Nd evolution after Liew and Hofmann (1988)

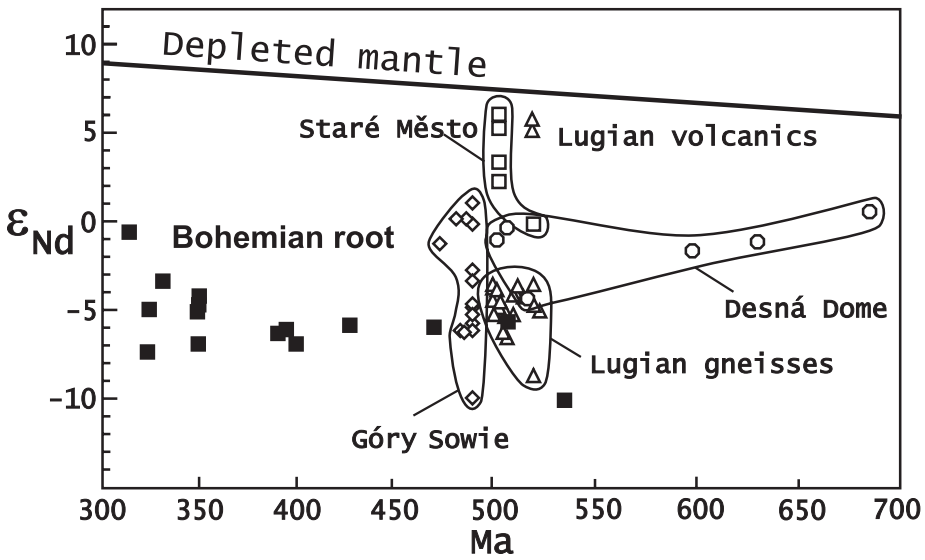

Fig. 15. Nd evolution diagram showing Sm-Nd systematics of dated samples of the Variscan root in southern Bohemia (full squares) compared with data for the Czech and Polish West Sudetes as compiled by Hegner and Kröner (2000).

Wendt and others, 1993; Gebauer and Friedl, 1994; Košler and others, 1996). These protolith ages show a striking similarity with those of adjacent Brunia granitoids (van Breemen and others, 1982; Scharbert and Batík, 1985; Fritz and others, 1996; Finger and others, 2000; Friedl and others, 2004) and granitoids of the Silesian Domain in the northerly West Sudetes (Kröner and others, 2000b).

Cambro-Ordovician magmatism is documented by zircon ages of samples BM 10 (515 ± 9 Ma) and BM 11, representing granitoid and volcanic rocks in the External Middle Crustal Belt (fig. 16). Both the zircon ages and Nd isotopic systematics of the studied Cambro-Ordovician gneisses from the EMC reveal remarkable similarities with calc-alkaline granitoid rocks in the West Sudetes which are interpreted to be of subduction-related origin (Kröner and others, 2000a, 2000b; Hegner and Kröner, 2000). Similar early Paleozoic emplacement ages of ~480 Ma for granitoid rocks have also been reported from the Gföhl gneiss in Lower Austria (Friedl and others, 1998, 2004) and from the Lower Crustal unit in South Bohemia (Vrána and Kröner, 1995). In addition, the onset of Ordovician-Silurian intracontinental rifting is documented by 428 ± 6 Ma old bimodal volcanism (Finger and von Quadt, 1995), now preserved in high-grade rocks of the Internal Lower Crustal Belt (Gföhl Unit in Lower Austria). Cambro-Ordovician volcanic activity was also reported from the upper crustal levels of the Teplá-Barrandian Unit (Chlupáč, 1994). However, the Brunia continent in general does not show such magmatism except in felsic dikes dated by Kröner and others (2000b) in the northern part of this segment (fig. 16). All these data are consistent with a concept of rifting along the northern Gondwana margin which, in the area of the Moldanubian domain, did not reach oceanic separation (Štípská and others, 2001). The intensity of Cambro-Ordovician deep crustal magmatic activity and volcanic and sedimentary additions at supracrustal levels are gradually increasing towards the northwest, leading to opening of the Saxothuringian ocean in between the Saxothuringian and Teplá-Barrandian domains (Franke, 2000). This Cambro-Ordovcian thinning of the Gondwana northern margin was recently interpreted either as a result of

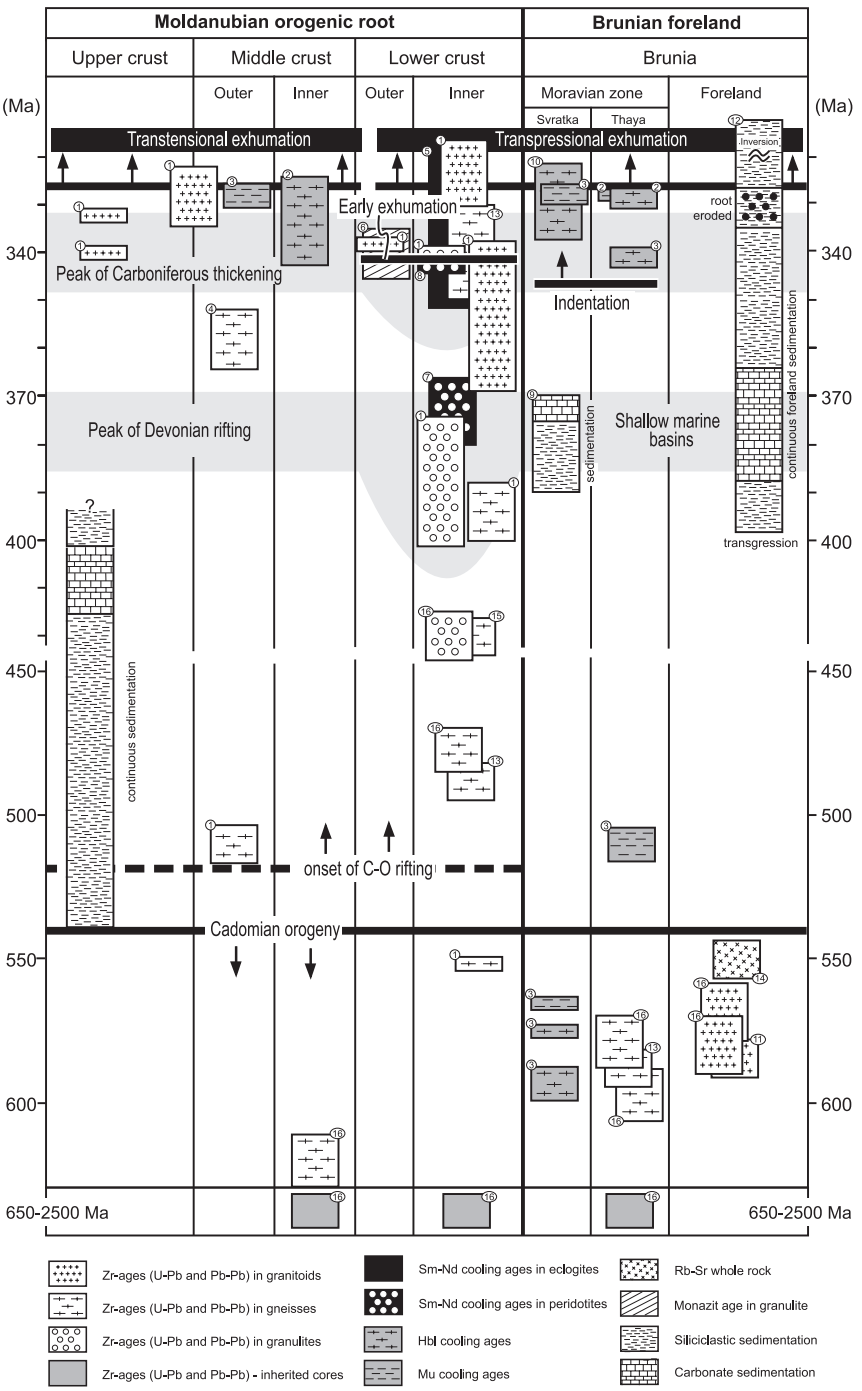

Fig. 16. Summary of published and new U-Pb and Pb-Pb zircon ages, published Nd-Sm cooling ages and published ^{40}Ar-^{39}Ar cooling ages from all crustal levels of the Moldanubian orogenic root and the Brunia continent from the entire eastern margin of the Bohemian massif (fig. 2). Stratigraphic columns of the Upper Crustal segment in the Barrandian area and the Brunia foreland according to Chlupáč (1994). Dark gray area in the diagram indicates duration of Paleozoic rifting as documented by geochronology and the sedimentary record. The light gray area shows the time span of compression including burial and

development of an intracontinental back arc basin above a giant subduction zone which must be located behind the Saxothuringian plate (Kröner and others, 2000b), or in terms of thinning of northern Gondwana (Winchester and others, 2002).

Isotopic Ages Testifying to Devonian Intracontinetal Back Arc Extension

A major change in plate configuration occurred in the early Devonian and was associated with subduction of the Saxothuringian Ocean to the southeast (in present-day coordinates; Franke, 1989; Krohe, 1998). This subduction led to the development of a magmatic arc in the region of Central Bohemian plutonic complex (Žák and others, 2005). During this period the Moldanubian domain occupied the position of a back-arc in the Saxothuringian subduction system (Carswell, 1991).

A Devonian age of 394 ± 6 Ma for zircons from Gföhl Gneiss samples BM 4 and 5 is interpreted to approximate the time of emplacement of the magmatic protoliths. Furthermore, we obtained an imprecise magmatic protolith age of 387 ± 14 Ma for felsic granulite sample BM 6 and 384.6 ± 1.1 for zircons in sample CZ-6 (fig. 16). U-Pb and Pb-Pb zircon protolith emplacement ages of 373 ± 12 Ma, 366.3 ± 1.1 Ma and 369 to 360 Ma were also reported from other Bohemian granulite massifs by Wendt and others (1994), Klemd and Bröcker (1999) and Štípská and others (2004), respectively. These ages agree well with a Devonian Sm-Nd cooling age of 373 Ma for nearby garnet peridotites from the ILC (Carswell and Jamtveit, 1990; Brueckner and others, 1991; table 1). Importantly, a late Devonian age of 358 Ma was also determined for felsic volcanic rocks of the IMC (Friedl and others, 1993), and massive magmatism represented by dolerite dykes occurred at the Silurian and Devonian boundary in the Paleozoic cover (Chlupáč, 1994).

A magmatic event leading to the emplacement of igneous rocks – precursors of felsic granulites, at 387 and 394 Ma, suggests a major period of magmatism in the Devonian. Our U-Pb and Pb-Pb data, combined with cooling ages for peridotites, may indicate an important Devonian thermal reworking of the Moldanubian lower crust. The products of volcanic activity preserved in the middle crustal Varied group support the existence of a Devonian basin that developed during crustal thinning (Finger and Steyrer, 1995). The timing of all these events correlates with first records of subduction activity at the eastern margin of the Saxothuringian domain (Franke, 2000) and with subsequent development of a magmatic arc in the area of the Central Bohemian Pluton (Košler and others, 1993; Holub and others, 1997; Venera and others, 2000). This concept is supported by geochemistry studies of garnet pyroxenite layers contained in garnet peridotites that indicate melting of sub-lithospheric mantle triggered by melts of fluids derived from subducting slab at greater depth (Becker, 1996a, 1996b). The geodynamic position of the Moldanubian domain with respect to the location of the subduction zone and related magmatic arc leads us to the conclusion, that the Devonian emplacement ages of magmatic rocks in the orogenic lower crust confirm the existence of a period of back arc extension in this region suggested by Carswell (1991).

A Devonian episode of shallow-water clastic sedimentation and volcanic activity was also reported from the western margin of Brunia (fig. 16). Here, deepening of the

---

exhumation of the lower crust related to the Brunia indentation process. The light gray area shows the duration of compression including burial and exhumation of the lower crust related to the Brunia indentation process. (1) – data of this study, (2) – Dallmeyer and others (1992), (3) – Fritz and others (1996), (4) – Friedl and others (1993), (5) – Brueckner and others (1991); Beard and others (1992), (6) – van Breemen and others (1982), (7) – Brueckner and others (1991), (8) - Beard and others (1992), (9) – Simplified after Galle and others (1995), (10) – Macintyre and others (1992), (11) – van Breemen and others (1982), (12) – Simplified after Kalvoda and others (2003) and Hartley and Otava (2001), (13) Friedl and others (1998), 14) – Scharbert and Batik (1985), (15) – Finger and von Quadt (1995), (16) – Friedl and others (2004).

Devonian sedimentary basin increased towards the north, where it was associated with voluminous bimodal volcanism and a deep marine sedimentary infill (Patočka and Valenta, 1990; Galle and others, 1995). This may indicate that the Brunia Neoproterozoic granitoids and metasediments represent a margin of the Devonian back arc domain, whereas the Monotonous Group corresponds to its highly stretched central part. We suggest that elevated temperatures during Devonian rifting may be responsible for significant melting of the lower part of the Neoproterozoic crust and crystallization of zircons from melts forming precursors of at least some varieties of the Gföhl gneiss and felsic granulites. In addition, numerical thermo-rheological models proposed by Thompson and others (2001) indicate that such a thermally weakened domain represents a suitable precursor for a thickened orogenic belt.

Isotopic Ages Related to Crustal Thickening

The youngest geochronological record pointing to a Devonian rifting process is represented by an U-Pb age of 358 Ma for felsic metavolcanic rocks reported by Friedl and others (1993) from the IMC (fig. 16). This age coincides remarkably well with termination of sedimentation within the early Paleozoic basin in the Prague area (fig. 1; Chlupáč, 1994). In addition, an angular unconformity between folded Givetian strata and overlying early Carboniferous sediments was reported from a drill hole reaching the base of the Cretaceous basin (in Chlupáč, 1994). The onset of convergence on the Brunia continent is marked by the transition from Famenian carbonate platform sedimentation to early Carboniferous flysh-type sediments at the Famenian-Frasnian boundary (Hartley and Otava, 2001). All these data indicate an important change in the tectonic regime at about 360 to 350 Ma (fig. 16).

The next younger reported ages correspond to the peak of high-pressure metamorphism in eclogites and granulites of the ILC and ELC. Metamorphic zircons from a HP granulite (sample CZ 6) yielded a $^{207}Pb/^{206}Pb$ evaporation age of 340.0 ± 1.1 Ma. A slightly older age of 353 ± 16 was obtained for magmatic emplacement of the Gföhl gneiss (samples BM4 and BM 5). This corresponds to ages from a nearby Ky-Kfs granulite (Kröner and others, 1988) and the Gföhl gneiss of the IMC, as well as an U-Pb monazite age for a granulite of the ILC (van Breemen and others, 1982). This age is also known from other granulite bodies elsewhere in the Bohemian Massif (Kotková and others, 1996; Kröner and Willner, 1998; Klemd and Bröcker, 1999; Kröner and others, 2000a; Svojtka and others, 2002; Štípská and others, 2004). Kröner and others (2000a) argued that the 340 Ma old zircons occur as inclusions in minerals defining the HP-phase as well as in the matrix and concluded that these zircons must have grown near or during peak pressure conditions.

The important discovery of this study is the age of syn-convergent calc-alkaline plutonism (340.1 ± 1.1 Ma; sample CZ/2S) for a granite intruding Paleozoic sediments in the upper crust (Hrouda and others, 1999). Corresponding ages of 350 to 340 Ma were reported for syn-convergent calc-alkaline plutons intruding upper crustal Paleozoic sediments (Holub and others, 1997; Janoušek and Gerdes, 2003) or thickened middle crustal units (Štípská and others, 2004). All these data suggest that the entire crust underwent progressive thickening during the early Carboniferous (fig. 16) after 10 to 20 Ma of convergence.

Relationship Between Isotopic Ages and the Exhumation Process

There are four important isotopic ages which permit to constrain the timing of exhumation processes related to the final structural pattern of the orogenic root. Mean ages of 341 ± 6 (sample BM 9) and 339.1 ± 1.1 Ma (sample CZ/Vir) were obtained from melt patches in high-temperature amphibolites associated with Ky-Kfs granulites of the ELC. The melting event is connected with retrogression of granulite and, therefore, reflects the earliest stage of the exhumation process. Similarily,

thrusting of the ILC over the IMC is dated by the emplacement of large portions of mantle-derived magmas of the Třebíč Massif dated at 340 Ma (Holub and others, 1997). This study yielded a group of ages from granitoids syntectonically emplaced along major intra-root tectonic boundaries and late granites intruding the upper crust. The age of durbachite emplacement (323 ± 7 and 323.5 ± 1.1 Ma; samples BM7 and CZ/TAJ) along the boundary between the ILC and EMC reflects the timing of oblique northeast-verging thrusting of the lower crust over the middle crust at a pressure of ~4 kbar (fig. 16). Similarly, the age of a syntectonic granodiorite (327 ± 6 and 323.5 ± 1.1 Ma; samples BM13 and CZ/3T) at the boundary between the EMC and UC suggests extensional unroofing along the middle/upper crustal boundary (Pitra and others, 1994). A similar age has been obtained for the youngest granite generation (332 ± 20 and 332.2 ± 1.1 Ma; samples BM15 and CZ/1Z) that intruded the previously folded upper crustal rocks along a major normal shear zone.

Our data are in agreement with emplacement ages for a large S-type granite pluton in the axial part of the IMC (see Finger and others, 1997 for review). The existing PT estimates for the contact aureole indicate a depth of emplacement corresponding to ~4 kbar (Petrakakis, 1997). The above-listed ages correspond to numerous muscovite and biotite Ar-Ar data from the EMC, ELC and metamorphosed Brunia-derived nappes from the eastern margin of the Bohemian Massif ranging between 330 and 325 Ma (Dallmeyer and others, 1992; Fritz and others, 1996). The $^{40}Ar/^{39}Ar$ ages from the internal part of the root reflect a similar time span (Dallmeyer and others, 1992). A-type eclogites from our study area yielded Sm-Nd cooling ages of 336 ± 16 and 323 ± 7 Ma respectively, which have been interpreted as exhumation ages (Beard and others, 1992). However, other Sm-Nd data reported from root eclogites suggest older cooling ages up to 377 Ma (Brueckner and others, 1991; Beard and others, 1992; Klemd and Bröcker, 1999). The tectonic setting of the eclogites is often poorly constrained and, therefore, these cooling ages are difficult to interpret.

A study of heavy minerals from sediments in the foreland basin documented the first appearance of a garnet-rich heavy mineral assemblage at the beginning of the late Visean (~335 Ma), indicating the first exhumation of high-grade metamorphic rocks (Hartley and Otava, 2001). The most important evidence for exhumation of the orogenic lower crustal rocks is the presence of granulite-facies rocks, durbachites and migmatites in pebbles within middle Visean conglomerates, indicating the onset of deposition of lower crustal material in the foreland basin at around 330 to 327 Ma (Hartley and Otava, 2001). These granulitic pebbles experienced their high-pressure metamorphism at ~340 Ma (Vrána and Novák, 2000; Kotková and others, 2001). All the above data indicate that exhumation of rocks from the bottom of the root to the surface occurred within a time span of 10 to 15 Ma (fig. 16). Such a high exhumation rate has already been estimated by Svojtka and others (2002) and Štípská and others (2004) for other parts of the Bohemian Massif.

GEODYNAMIC INTERPRETATION

The rapid transition from Devonian rifting to shortening at about 350 Ma ago (fig. 17B) indicates that the entire lithosphere in the domain of the future orogenic root was exceptionally weak, because there was a very short period of temperature decay before the onset of collision (Loosveld and Etheridge, 1990). As shown by Thompson and others (2001) and Schulmann and others (2002) such a weakened lithosphere can be homogeneously thickened. Their calculations show that a thickening timescale of 10 to 15 Ma is required to transport the Moho to a depth of 60 km without significant heat transfer. Therefore, temperatures of 800 to 900 °C recorded at peak pressures of 18 to 20 kbar in eclogites and HP granulites (Steltenpohl and others, 1993; Medaris and others, 1998), may correspond to temperatures existing in the lower crust of the rifted domain prior to thickening (Štípská and Powell, 2005a, 2005b). We assume that

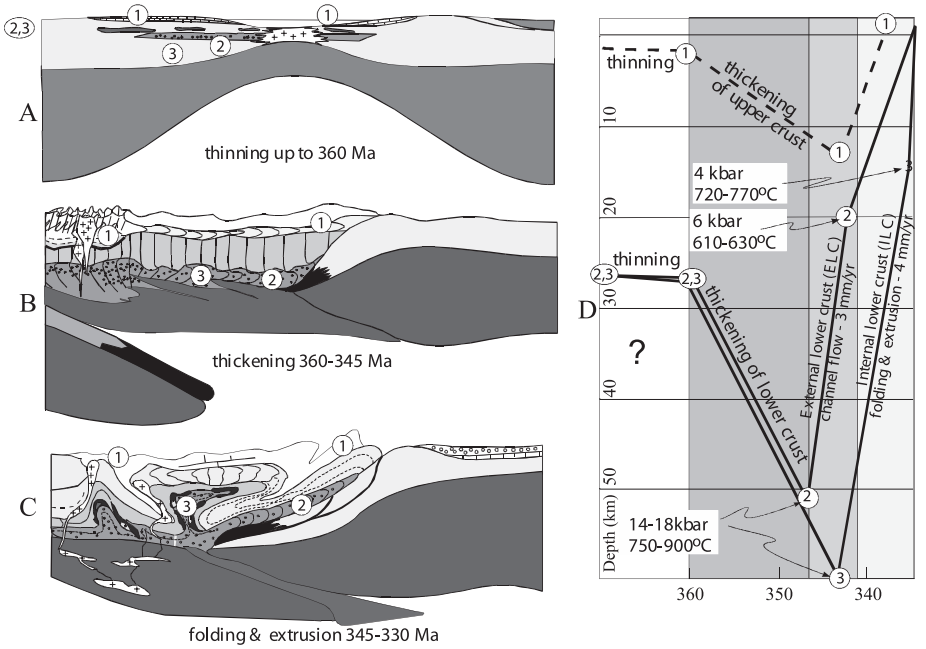

Fig. 17. Series of evolutionary cross sections through the eastern margin of the Variscan orogen showing: (A) Development of large-scale intracontinental rifting during the Devonian between 390 and 360 Ma. (B) Geometry of root units at ~350 Ma prior to exhumation along eastern margin of Bohemian Massif. (C) Geometry of root and continental margin during exhumation at ~340 Ma associated with channel flow of lower crust along the external part of the root and folding of the entire crustal sequence in the more internal part of the root. (D) Depth-time diagram showing integrated rates of thickening following lithospheric thinning and subsequent exhumation, relative to several P-T constraints from geothermobarometry (Medaris and others, 1995a; Schulmann and others, 1999; Tajcmanova and others, 2005). Two lines are constructed for exhumation along a lower crustal antiform and orogenic channel, respectively, on the assumption of a lower pressure for granulite-facies metamorphism in the EMC and higher pressure in the ILC, respectively.

the thickening process led to the formation of a root composed of three horizontal crustal layers defined by maximum pressure conditions estimated for individual lithologies of thickened lower crust (18 – 20 kbar), middle crust (8 – 10 kbar) and upper crust (4 kbar), respectively (fig. 17B). The tectonic model presented here can be compared with modern thermomechanical models in which the mechanical and metamorphic evolution of large convergent orogens is driven by subduction of suborogenic mantle lithosphere (Willet and others, 1993; Beaumont and others, 2004). Evolution of continental plateaus above subducting mantle lithosphere was modeled by Vanderhaeghe and others (2003) as a result of prolonged thickening of the crust during orogenesis. However, this model of crustal thickening is connected with long lasting growth of a plateau 750 km wide during ~75 Ma and is not associated with a pre-existing thermal anomaly.

Indentation-Induced Lower Crustal Flow and Exhumation

Our model of exhumation of lower crust in the study area is based on the assumption that after thickening the buried sub-rift (sub-root) upper mantle becomes stronger than the adjacent continental mantle below a depth of 60 to 70 km. We assume that any further descent of the root is blocked, but the lower crust in the thickened domain is significantly weaker than the adjacent continental mantle.

Consequently, the Moldanubian sub-root mantle was underthrust below the Brunia continental mantle at about 350 to 340 Ma (figs. 17 B, C). This led to continuous convergent motion of the Brunia indenter in form of a lithospheric flake, and the Brunia upper mantle slid along the sub-root rigid floor of the mantle wedge and squeezed the weak parts of the inner root upwards. It is this indentation process that generated major shortening of the root domain, leading to perturbation of its original horizontal rheological stratification. In our view, the exhumation of deeply buried crust is the result of a continuous indentation process of the Brunia continent in front of which granulitized lower crust was rapidly extruded to higher crustal levels. We suggest that the alternation of crustal levels presented in this study resulted from folding of these horizontal rheological boundaries in form of a large lower crustal antiform in front of the indenting plate. The laterally different extent of vertical amplification of the lower crustal antiform representing the future ILC belt was controlled by the thickness of the indenting Brunia ramp.

The mechanism of initiation of the original cusp at the lower-middle crustal boundary, the amplification of folds, and final transition to flat fabrics into mid-crustal levels by a lateral spreading mechanism is explained and discussed elsewhere (Štípská and others, 2004). Here we only discuss the finite geometry of the root crustal level by combined mechanisms of folding of the lower and middle crustal interface and ductile extrusion of the lower crust close to the indenting continental lithosphere. The lower crustal rocks were also extruded along a narrow zone or channel following the boundary of the Brunia indenter forming the ELC belt. The extrusion of weak lower crustal material led to a high ascent velocity of HP rocks to a shallow crustal level as shown by the steep decompression PT path for eclogites (Konopásek and others, 2002). A high exhumation velocity is documented by the 338 ± 3 Ma monazite U-Pb age from fresh granulite (van Breemen and others, 1982), 340 Ma U-Pb zircon age for a melt patch in opx-bearing amphibolite surrounding a granulite body (Sample BM 9, this work), and a ^{40}Ar-^{39}Ar amphibole cooling age of 340 Ma in nearby retrograde eclogites at the Brunia margin (Macintyre and others, 1992). Since the ages of the low pressure overprint and peak conditions of granulite metamorphism (Schulmann and others, 1999) are identical, within analytical error, we must consider the time span indicated by the error in the least precise age, which is a maximum of 6 Ma. Therefore, the extrusion rate within the ELC belt corresponds to ~7 mm/y (fig. 17C). This indicates that the lower crustal rocks reached shallow crustal levels earlier in the area of the ELC belt than in the lower crustal antiform farther to the west. Moreover, the rate of vertical extrusion in this belt is significantly higher compared to calculated exhumation rates of granulites in the large-scale antiform of the ILC belt estimated at about 3 mm/y (Tajčmanová and others, 2005).

Comparison of orogenic structure of eastern margin of the Bohemian Massif with existing numerical models shows the development of a lower crustal antiform and asymmetrical upper crustal thickening similar to results shown by Jamieson and others (2002). However, their latest models show the effects of doming triggered by underthrusting of rigid lower crust, extrusion of the dome in a channel above the frontal ramp or near-symmetric thrust extrusion located on the side of the orogen adjacent to subducting plate (Beaumont and others, 2004, fig. 12), which is in contradiction with distribution of lower crustal rocks along the eastern margin of the Bohemian Massif.

Late Transpressional and Transtensional Deformation

The most prominent late tectonic feature in the Carboniferous evolution of the eastern margin of the Bohemian Massif is dextral transpressive deformation along the Brunia margin (Schulmann, 1990; Fritz and Neubauer, 1993; Schulmann and others, 1994). This deformation was connected with large-scale oblique folding of Brunia-derived crystalline nappes (Štípská and others, 2000). The age of these processes is well

constrained at 325 to 300 Ma by ^{40}Ar-^{39}Ar ages (Fritz and others, 1996). The durbachite bodies dated at 323 Ma in this study and emplaced along the ILC and EMC boundary, display a magmatic to solid-state fabric consistent with dextral shearing. Reactivation of these major tectonic boundaries indicates that the horizontal shear stress was also transmitted into the root.

The other important feature of the northern part of the study area is the continuous change of fabric orientation towards parallelism with the Elbe shear zone. Here, transpressive NE-SW trending deformation parallel to the Brunia margin progressively passes into transtensional dextral shearing and extensional deformation in a region parallel to the Elbe zone (Melka and others, 1992; Pitra and others, 1994). The age of this shearing is well constrained by syn-extensional emplacement of a granodiorite sill along the EMC-UC boundary and by dating of emplacement of an S-type granite in the upper crust that is also coeval with NW-directed normal shearing. These deformations were responsible for exhumation of middle crust up to 4 kbar in conjunction with downthrow of the upper crust to similar depth (Pitra and Guiraud, 1996). Hence, our study has shown that dextral transpressive shearing parallel to the root-continent boundary, and dextral transtension parallel to the Elbe zone operated at the same time and at similar crustal levels. This deformation was restricted to a maximum distance of 20 km from the continental margin and the Elbe zone, but had a profound effect on the final geometrical pattern of the study area. Transpressive shearing along Brunia and transtensional deformation parallel to the Elbe zone were responsible for displacement of the ELC and EMC to the northeast and their dramatic attenuation in the south. The upper crustal segment, which was originally sitting upon the EMC, was extended, thinned and transported to the NW along a major normal shear zone. If the combined effect of NE-directed transpression and NW-transtension is removed, a simple tectonic pattern emerges, resulting from the early stages of large-scale buckling and an orogenic channel parallel to the Brunia margin. This pattern is manifested by alternating belts of lower and middle crust parallel to the main collisional boundary.

In order to explain simultaneous compression and transtension along the root margins, a tectonic model implying far-field forces is proposed. Edel and others (2003) suggested that the Carboniferous evolution of the Variscan belt can be regarded as the result of major clockwise rotation of a previously assembled orogenic system, compensated by large, dextral NW-SE striking lithospheric faults (fig. 5 in Edel and others, 2003). The blocks defined by these faults are antithetically rotating in a book-shelf manner and thus produced anticlockwise rotations. We suggest that the dextral shearing parallel to the Elbe zone is fully compatible with the model proposed by Edel and others (2003), but its activity must have been accompanied by clockwise rotation of the Brunia block, producing coeval transpressive deformation of the eastern margin of the root. These authors suggested that rotation of the Variscan belt was most likely initiated by closure of the westerly located Rhenohercynian ocean during the early Carboniferous (Oncken and others, 1999; Franke, 2000) which correlates well with the above-described transpressive and transtensional movements during the time span of 330 to 320 Ma.

ACKNOWLEDGMENTS

This research resulted from a collaborative project between Charles University, Prague, and Mainz and Munich Universities, Germany. Financial support to Karel Schulmann by the Czech Science Foundation (grant no. 2005/98/K004) is gratefully acknowledged. The isotopic work was funded by the German Science Foundation (DFG, grant Kr 68-1) to Alfred Kröner and Ernest Hegner. Karel Schulmann, Ondrej Lexa, Pavla Štípská, and Jiří Konopásek also received financial support from the Czech Ministry of Education, grant no. 24313005, Alfred Kröner acknowledges the use of

mass spectrometer analytical facilities in the Max-Planck-Institut für Chemie in Mainz. Thorough reviews of Onno Oncken, Patrick O'Brien, Jean Pierre Burg and John Dewey significantly helped to improve the manuscript and are gratefully acknowledged.

Appendix: analytical procedures

Zircons were separated using a Wilfley table, magnetic separator, heavy liquids, and final handpicking under a binocular microscope. In order to obtain information on the internal structures and zircon morphologies, cathodoluminiscence (CL) and back scatter electron (BSE) images were studied before selecting zircons for isotopic analysis.

U-Pb Zircon Analysis after Vapor Transfer

Single zircon grains or small grain fractions consisting of morphologically identical grains were dissolved by the vapor transfer technique (Krogh, 1978; Parrish, 1987; Wendt and Todt, 1991). The method requires no chemical separation of U and Pb and produces low degrees of sample contamination (typically ~3 pg Pb blank contribution per zircon sample). For blank corrections the following Pb ratios were used: $^{206}Pb/^{204}Pb = 18.15$; $^{207}Pb/^{204}Pb = 15.63$; $^{208}Pb/^{204}Pb = 38.14$. As samples were not weighed prior to decomposition, U and Pb concentrations could not be determined. However, use of a mixed $^{205}Pb/^{233}U$ spike solution enabled us to calculate the the U/Pb ratios and corresponding U-Pb ages.

Isotopic ratios were measured on a Finnigan-MAT 261 mass spectrometer equipped with a secondary electron multiplier at the University of Munich. The analytical data and calculated ages are listed in table 2 and were corrected for instrumental mass fractionation (ca. 2. 2 ‰ per atomic mass unit) and total procedural blank (<10 pg Pb per analysis). Regression analysis of the U-Pb isotopic data was performed with the ISOPLOT program of Ludwig (1999), using the algorithm of York (1969) and the decay constants recommended by Steiger and Jäger (1977). Errors are at the 2-sigma (95% confidence) level.

Zircon Evaporation

Single zircons or small grain fractions of 3 to 4 crystals each were handpicked after careful optical inspection and analyzed by the evaporation method (Kober, 1987). $^{207}Pb/^{206}Pb$ isotopic ratios were measured on a Finnigan-MAT 261 mass spectrometer at the Max-Planck-Institut für Chemie in Mainz. The procedures as well as comparisons with conventional and ion-microprobe zircon dating are detailed in Kröner and others (1991) and Kröner and Hegner (1998).

The calculated ages and their uncertainties are based on the means of all ratios and their 2-σ (mean) errors. Mean ages and errors for several zircons from the same sample are presented as weighted means of the entire data set. Repeated analysis of an internal zircon standard suggests an error of about 0.2 percent as best estimate for the reproducibility of the $^{207}Pb/^{206}Pb$ ages. In the case of combined data sets the 2-σ_m error may become very low, and whenever this error was less than the reproducibility of the internal standard, we have used the latter value (that is, 0.2 %).

The zircon evaporation data are presented in table 3, and the $^{207}Pb/^{206}Pb$ spectra are shown in histograms that permit visual assessment of the data distribution. Due to the lack of U concentrations there is no *a priori* way to determine whether the zircons behaved as closed systems and the measured $^{207}Pb/^{206}Pb$ ratio reflects a concordant age. However, comparative studies using evaporation, conventional U–Pb dating, and ion-microprobe analysis have shown excellent agreement, even for zircons from complex metamorphic terrains (Kröner and others, 1991, 2001; Cocherie and others, 1992; Jaeckel and others, 1997; Karabinos, 1997).

Sm-Nd Whole-Rock Isotopic Analysis

Sm and Nd isotopes of whole-rock samples were analyzed at the University of Munich, employing procedures outlined in Hegner and others (1995). The Nd isotopic ratios were measured in a dynamic quadruple mass collection mode using a Finnigan MAT 261, whereas a static collection mode was used for Sm isotopes. $^{143}N/^{144}Nd$ isotope ratios were normalized to $^{146}Nd/^{144}Nd \cong 0.7219$ and Sm isotopic ratios to $^{147}Sm/^{152}Sm = 0.56081$. Total procedural blanks were ca. 70 pg Nd and ca. 20 pg Sm. Within-run precision ($2\sigma_{mean}$) for $^{143}Nd/^{144}Nd$ was $\pm$ 1.3 x 10^{-5}. Repeated measurements of the $^{143}N/^{144}Nd$ isotopic ratio in our Ames Nd standard yielded a value of 0.512138 $\pm$ 12 (2σ, N= 26), corresponding to 0.511850 in the La Jolla Nd standard. The Nd model ages were calculated with a 2-stage isotopic evolution model as defined in Liew and Hofmann (1988) due to the fact that about half of the samples have high Sm/Nd ratios, unlike typical continental crust, thus preventing the calculation of meaningful single-stage Nd model ages as outlined in

DePaolo (1981). The Sm-Nd isotopic data and Nd model ages are listed in table 4. We interpret the Nd model ages in terms of mean crustal residence ages (Arndt and Goldstein, 1987).

References

Arndt, N. T., and Goldstein, S. L., 1987, Use and abuse of crust-formation ages: Geology, v. 15, p. 893–895.

Beard, B. L., Medaris, L. G., Johnson, C. M., Brueckner, H. K., and Mísař, Z., 1992, Petrogenesis of Variscan high-temperature group-A eclogites from the Moldanubian zone of the Bohemian Massif, Czechoslovakia: Contributions to Mineralogy and Petrology, v. 111, p. 468–483.

Beaumont, C., Jamieson, R. A., Nguyen, M. H., and Medvedev, S., 2004, Crustal channel flows: 1. Numerical models with applications to the tectonics of the Himalayan-Tibetan orogen: Journal of Geophysical Research, v. 109, B06406.

Becker, H., 1996a, Crustal trace element and isotopic signatures in garnet pyroxenites from garnet peridotites massifs from lower Austria: Journal of Petrology, v. 37, p. 785–810.

——— 1996b, Geochemistry of garnet peridotite massifs from lower Austria and the composition of deep lithosphere beneath a Paleozoic convergent plate margin: Chemical Geology, v. 134, p. 49–65.

Brueckner, H. K., Medaris, L. G., and Bakun-Czubarow, N., 1991, Nd-Sm age and isotope patterns from Variscan eclogites of the eastern Bohemian Massif: Neues Jahrbuch für Mineralogie-Abhandlungen, v. 163, p. 169–196.

Carswell, D. A., 1991, Variscan high P-T metamorphism and uplift history in the Moldanubian Zone of the Bohemian Massif in Lower Austria: European Journal of Mineralogy, v. 3, p. 323 – 342.

Carswell, D. A., and Jamtveit, B., 1990, Variscan Sm-Nd ages for the high-pressure metamorphism in the Moldanubian Zone of the Bohemian Massif, Lower Austria: Neues Jahrbuch für Mineralogie-Abhandlungen, v. 162, p. 69–78.

Chlupáč, I., 1994, Facies and biogeographic relationships in Devonian of the Bohemia Massif: Courier Forschungsintitut Senckenberg, v. 169, p. 299–317.

Cocherie, A., Guerrot, C., and Rossi, P., 1992, Single-zircon dating by step-wise Pb evaporation – comparison with other geochronological techniques applied to the Hercynian granites of Corsica, France: Chemical Geology, v. 101, p. 131–141.

Dallmeyer, R. D., Neubauer, F., and Höck, V., 1992, Chronology of Late Paleozoic tectonothermal activity in the southeastern Bohemian Massif, Austria (Moldanubian and Moravo-Silesian zones) - Ar^{40}/Ar^{39} mineral age controls: Tectonophysics, v. 210, p. 135–153.

DePaolo, D. J., 1981, A Nd and Sr isotopic study of Mesozoic calc-alkaline granitic batholiths of the Sierra Nevada and Peninsular Ranges, California: Journal of Geophysical Research, v. 86, p. 10370–10488.

Dewey, J. F., and Bird, J. M., 1970, Mountain belts and the new global tectonics: Journal of Geophysical Research, v. 75, p. 2625–2647.

Dewey, J. F., and Burke, K., 1973, Tibetan, Variscan and Precambrian basement reactivation: Products of continental collision: Journal of Geology, v. 81, p. 683–692.

Dudek, A., 1980, The crystalline basement block of the Outer Carpathians in Moravia: Rozpravy Československé Akademie Věd, v. 90, p. 1–85.

Dudek, A., and Fediuková, E., 1974, Eclogites of the Bohemian Moldanubicum: Neues Jahrbbuch für Mineralogie Abhandlungen, v. 121, p. 127–159.

Edel, J. B., Schulmann, K., and Holub, F. V., 2003, Anticlockwise and clockwise rotations of the Eastern Variscides accommodated by dextral lithospheric wrenching: palaeomagnetic and structural evidence: London, Journal of the Geological Society, v. 160, p. 209–218.

Finger, F., and Steyrer, H. P., 1995, A tectonic model for the eastern Variscides: Indications from a chemical study of amphibolites in the south-eastern Bohemian Massif: Geologica Carpatica, v. 46, p. 137–150.

Finger, F., and von Quadt, A., 1995, U/Pb ages of zircons from a plagiogranite-gneiss in the SE Bohemian Massif, Austria – further evidence for an important early Palaeozoic rifting episode in the eastern Variscides: Schweizerische Mineralogische und Petrographische Mitteilungen, v. 75, p. 265–270.

Finger, F., Roberts, M. P., Haunschmid, B., Schermaier, A., and Steyrer, H. P., 1997, Variscan granitoids of central Europe: their typology, potential sources and tectonothermal relations: Mineralogy and Petrology, v. 61, p. 67–96.

Finger, F., Tichomirowa, M., Pin, C., and Hanžl, P., 2000, Relics of an early-Panafrican metabasite-metarhyolite formation in the Brno Massif, Moravia, Czech Republic: International Journal of Earth Sciences, v. 89, p. 328–335.

Franců, E., Franců, J., Kalvoda, J., Poelchau, H. S., and Otava, J., 2002, Burial and uplift history of the Palaeozoic Flysch in the Variscan foreland basin (SE Bohemian Massif, Czech Republic), *in* Bertotti, G., Schulmann, K., and Cloetingh, S., editors, Continental collision and the tectonosedimentary evolution of forelands: European Geophysical Society, Stephen Mueller Special Publication Series, v. 1, p. 167–179.

Franke, W., 1989, Variscan plate tectonics in Central Europe – current ideas and open questions: Tectonophysics, v. 169, p. 221–228.

——— 2000, The mid-European segment of the Variscides: tectonostigratigraphic units, terrane boundaries and plate tectonic evolution, *in* Franke, W., Haak, W., Oncken, O., and Tanner, D., editors, Orogenic processes: Quatification and modelling in the Variscan belt: Geological Society of London Special Publication, v. 179, p. 35–63.

Friedl, G., von Quadt, A., Ochsner, A., and Finger, F., 1993, Timing of the Variscan orogeny in the Southern Bohemian Massif (NE Austria) deduced from new U-Pb zircon and monazite dating: Terra Abstracts, v. 5, p. 235–236.

Friedl, G., McNaughton, N., Fletcher, I. R., and Finger, F., 1998, New SHRIMP-zircon ages for orthogneisses from the south-eastern part of the Bohemian Massif (Lower Austria), *in* Schulmann, K., editor, Proceedings of the International conference - Palaeozoic orogenesis and crustal evolution of European lithosphere: Acta Universitatis Carolinae, v. 42, p. 251–252.

Friedl, G., Finger, F., Paquette, J. L., von Quadt, A., McNaughton, N. J., and Fletcher, I. R., 2004, Pre-Variscan geological events in the Austrian part of the Bohemian Massif deduced from U-Pb zircon ages: International Journal of Earth Sciences, v. 93, p. 802–823.

Fritz, H., and Neubauer, F., 1993, Kinematics of crustal stacking and dispersion in the south-eastern Bohemian massif: Geologische Rundschau, v. 82, p. 556–556.

Fritz, H., Dallmeyer, R. D., and Neubauer, F., 1996, Thick-skinned versus thin-skinned thrusting: rheology-controlled thrust propagation in the Variscan collisional belt (the southeastern Bohemian Massif, Czech Republik - Austria): Tectonics, v. 15, p. 1389–1413.

Fuchs, G., 1986, Zur Diskussion um den Deckenbau der Böhmischen Masse: Jahrbuch der Geologischen Bundesanstalt, v. 129, p. 41–49.

Fuchs, G., and Matura, A., 1976, Die Geologie des Kristallins der südlichen Böhmischen Masse: Jahrbuch der Geologischen Bundesanstalt, v. 119, p. 1–43.

Galle, A., Hladil, J., and Isaacson, P. E., 1995, Middle Devonian biogeography of closing south Laurussia – North Gondwana Variscides: Examples from the Bohemian Massif (Czech Republic), with emphasis on Horní Benešov: Palaios, v. 10, p. 221–239.

Gebauer, D., and Friedl, G., 1994, A 1.38 Ga protolith age for the Dobra orthogneiss (Moldanubian Zone) of the southern Bohemian Massif, NE-Austria); evidence from ion-microprobe (SHRIMP) dating of zircon: Journal of the Czech Geological Society, v. 39, p. 34–35.

Hartley, A. J., and Otava, J., 2001, Sediment provenance and dispersal in a deep marine foreland basin: the Lower Carboniferous Culm Basin, Czech Republic: Journal of the Geological Society London, v. 158, p. 137–150.

Hegner, E., and Kröner, A., 2000, Review of Nd isotopic data and xenocryst and detrital zircon ages from the pre-Variscan basement in the eastern Bohemian Massif: speculations on palinspasic reconstructions, *in* Franke, W., Haak, V., Oncken, O., and Tanner, D., editors, Orogenic processes: quantification and modelling in the Variscan belt: Geological Society of London Special Publication, no. 179, p. 113–129.

Hegner, E., Walter, H. J., and Satir, M., 1995, Pb-Sr-Nd isotopic compositions and trace element geochemistry of megacrysts and melilitites from the Tertiary Urach volcanic field: source composition of small volume melts under SW Germany: Contributions to Mineralogy and Petrology, v. 122, p. 322–335.

Holub, F. V., Cocherie, A., and Rossi, P., 1997, Radiometric dating of granitic rocks from the Central Bohemian Plutonic Complex (Czech Republic); constraints on geochronology of thermal and tectonic events along the Moldanubian-Barrandian boundary: Comptes Rendus de 'l Academie des Sciences, Serie II, v. 325, p. 19–26.

Hrouda, F., Táborská, Š., Schulmann, K., Ježek, J., and Dolejš, D., 1999, Magnetic fabric and rheology of co-mingled magmas in the Nasavrky Plutonic Complex (E. Bohemia): implications for intrusive strain regime and emplacement mechanism: Tectonophysics, v. 307, p. 93–111.

Jaeckel, P., Kröner, A., Kamo, S. L., Brandl, G., and Wendt, J. I., 1997, Late Archaean to early Proterozoic granitoid magmatism and high-grade metamorphism in the central Limpopo belt, South Africa: London, Journal of the Geological Society, v. 154, p. 25–44.

Jamieson, R. A., Beaumont, C., Nguyen, M. H., and Lee, B., 2002, Interactions of metamorphism, deformation and exhumation in large convergent orogens: Journal of Metamorphic Geology, v. 20, p. 9–24.

Janoušek, V., and Gerdes, A., 2003, Timing the magmatic activity within the Central Bohemian Pluton, Czech Republic: Conventional U-Pb ages for the Sázava and Tábor intrusions and their geotectonic significance: Journal of the Czech Geological Society, v. 48, p. 70–71.

Kalvoda, J., Leichmann, J., Bábek, O., and Melichar, R., 2003, Brunovistulian Terrane (Central Europe) and Istanbul Zone (NW Turkey): Late Proterozoic and Paleozoic tectonostratigraphic development and paleogeography: Geologica Carpathica, v. 54, p. 139–152.

Karabinos, P., 1997, An evaluation of the single-grain zircon evaporation method in highly discordant samples: Geochimica et Cosmochimica Acta, v. 61, p. 2467–2474.

Klemd, R., and Bröcker, M., 1999, Fluid influence on mineral reactions in ultrahigh-pressure granulites: a case study in the Snieznik Mts. (West Sudetes, Poland): Contributions to Mineralogy and Petrology, v. 136, p. 358–373.

Kober, B., 1987, Single-zircon evaporation combined with Pb+emitter-bedding for $^{207}Pb/^{206}Pb$-age investigations using thermal ion mass spectrometry, and implications to zirconology: Contributions to Mineralogy and Petrology, v. 96, p. 63–71.

Kolenovská, E., Schulmann, K., Klápová, H., and Štípská, P., 1999, Tectonometamorphic evolution of the Moldanubian zone near Jemnice (south Moravia, Bohemian Massif): Beihefte zur European Journal of Mineralogy, v. 11, p. 91–110.

Konopásek, J., Schulmann, K., and Johan, V., 2002, Eclogite-facies metamorphism at the eastern margin of the Bohemian Massif - subduction prior to continental underthrusting?: European Journal of Mineralogy, v. 14, p. 701–713.

Košler, J., Aftalion, M., and Bowes, D. R., 1993, Mid-Late Devonian plutonic activity in the Bohemian Massif - U-Pb zircon isotopic evidence from the Staré Sedlo and Mirotice gneiss complexes, Czech Republic: Neues Jahrbuch für Mineralogie – Monatshefte, v. 9, p. 417–431.

Košler, J., Aftalion, M., Vokurka, K., Klečka, M., and Svojtka, M., 1996, Early Cambrian granitoid magmatism in the Moldanubian Zone: U-Pb zircon isotopic evidence from the Stráž orthogneiss (in Czech): Zprávy o geologických výzkumech - ČGU Praha, p. 109–110.

Kotková, J., Kröner, A., Todt, W., and Fiala, J., 1996, Zircon dating of north Bohemian granulites, Czech Republic: Further evidence for the lower carboniferous high-pressure event in the Bohemian Massif: Geologische Rundschau, v. 85, p. 154–161.

Kotková, J., Novák, M., Leichmann, J., and Houzar, S., 2001, Nature and Provenance of Exotic Rock Types from Lower Carboniferous Conglomerates (Eastern Bohemian Massif): Geolines, v. 13, p. 81.

Krogh, T. E., 1978, Vapour transfer for the dissolution of zircons in a multi-sample capsule, at high pressure, *in* Zartman, R. E., editor, 4th International conference of Geochronology, Cosmochronology, Isotope Geology, 1978: United States Geological Survey, Open-File Report, v. 78–701, p. 233–234.

Krohe, A., 1998, Extending a thickened crustal bulge: toward a new geodynamic evolution model of the paleozoic NW Bohemian Massif, German Continental Deep Drilling site (SE Germany): Earth-Science Reviews, v. 44, p. 95–145.

Kröner, A., and Hegner, E., 1998, Geochemistry, single zircon ages and Sm-Nd systematics of granitoid rocks from the Góry Sowie (Owl Mts.), Polish West Sudetes: evidence for early Palaeozoic arc-related plutonism: London, United Kingdom, Journal of the Geological Society, v. 155, p. 711–724.

Kröner, A., and Willner, A., 1998, Time of formation and peak of Variscan HP-HT metamorphism of quartz-feldspar rocks in the central Erzgebirge, Saxony, Germany: Contributions to Mineralogy and Petrology, v. 132, p. 1–20.

Kröner, A., Wendt, J. I., Liew, T. C., Compston, W., Todt, W., Fiala, J., Vaňková, V., and Vaněk, J., 1988, U-Pb zircon and Sm-Nd model ages of high-grade Moldanubian metasediments, Bohemian Massif, Czechoslovakia: Contributions to Mineralogy and Petrology, v. 99, p. 257–266.

Kröner, A., Byerly, C. R., and Lowe, D. R., 1991, Chronology of early Archean granitegreenstone evolution in the Barberton Mountain Land, South Africa, based on precise dating by single zircon evaporation: Earth and Planetary Science Letters, v. 103, p. 41–54.

Kröner, A., O'Brien, P. J., Nemchin, A. A., and Pidgeon, R. T., 2000a, Zircon ages for high-pressure granulites from South Bohemia, Czech Republic, and their connection to Carboniferous high temperature processes: Contributions to Mineralogy and Petrology, v. 138, p. 127–142.

Kröner, A., Štípská, P., Schulmann, K., and Jaeckel, P., 2000b. Chronological constraints on the pre-Variscan evolution of the northeastern margin of the Bohemian Massif, Czech Republic, *in* Franke, W., Haak, W., Oncken, O., and Tanner, D., editors, Orogenic processes: Quantification and modelling in the Variscan belt: Geological Society of London Special Publication, no. 179, p. 175–198.

Kröner, A., Jaeckel, P., Hegner, E., and Opletal, M., 2001, Single zircon ages and whole rock Nd isotopic systematics of early Palaeozoic granitoid gneisses from the Czech and Polish Sudetes (Jizerske hory, Krkonose Mountains and Orlice-Sneznik Complex): International Journal of Earth Sciences, v. 90, p. 304–324.

Liew, T. C., and Hofmann, A. W., 1988, Precambrian crustal components, plutonic associations, plate environment of the Hercynian fold belt of central Europe: indications from a Nd and Sr isotopic study: Contributions to Mineralogy and Petrology, v. 98, p. 129–138.

Loosveld, R. J. H., and Etheridge, M. A., 1990, A model for low-pressure facies metamorphism during crustal thickening: Journal of Metamorphic Geology, v. 8, p. 257–267.

Ludwig, K. R., 1999, ISOPLOT/Ex version 2.01. a Geochronological toolkit for Microsoft Excel: Berkeley Special Publications Center, Special Publications, 1a.

Macintyre, R. M., Bowes, D. R., Hamidullah, S., and Onscott, T. C., 1992, K-Ar and Ar-Ar study of amphibolites from meta-ophiolite complexes, eastern Bohemian Massif, *in* Kukal, Z., editor, Proceedings of the 1st International Conference on the Bohemian Massif: Prague, Czech Geological Survey, p. 195–199.

Matte, Ph., Maluski, H., Raijlich, P., and Franke, W., 1990, Terrane boundaries in the Bohemian Massif: Result of large-scale Variscan shearing: Tectonophysics, v. 177, p. 151–170.

Matura, A., 1984, Das Kristallin am Südostrand der Böhmischen Masse zwischen Ybbs/Donau und St. Pölten: Jahrbuch der Geologischen Bundesanstalt, v. 127, p. 13–27.

Medaris, L. G., 1999, Garnet peridotites in Eurasian high-pressure and ultrahigh-pressure terranes: A diversity of origins and thermal histories: International Geology Review, v. 41, 799 – 815.

Medaris, L. G., Jelínek, E., and Mísař, Z., 1995a, Czech eclogites: Terrane settings and implications for Variscan tectonic evolution of the Bohemian massif: European Journal of Mineralogy, v. 7, p. 7–28.

Medaris, L. G., Beard, B. L., Johnson, C. M., Valley, J. W., Spicuzza, M. J., Jelínek, E., and Mísař, Z., 1995b, Garnet pyroxenite and eclogite in the Bohemian Massif: geochemical evidence for Variscan recycling of subducted lithosphere: Geologische Rundschau, v. 84, p. 489–505.

Medaris, L. G., Fournelle, J. H., Ghent, E.D., Jelínek, E., and Mísař, Z., 1998, Prograde eclogite in the Gfşhl nappe, Czech Republic: new evidence on Variscan high-pressure metamorphism: Journal of Metamorphic Geology, v. 16, p. 563–576.

Melka, R., Schulmann, K., Schulmannová, B., Hrouda, F., Lobkowicz, M., and Figar, S., 1992, Perpendicular linear fabrics in synkinematically emplaced tourmaline granite: Journal of Structural Geology, v. 14, p. 605–620.

Mezger, K., and Krogstad, E. J., 1997, Interpretation of discordant U-Pb zircon ages: an evaluation: Journal of Metamorphic Geology, v. 15, p. 127–140.

Möller, A., O'Brien, P. J., Kennedy, A., and Kröner, A., 2002, Polyphase zircon in ultrahigh-temperature granulites (Rogaland, SW Norway): constraints for Pb diffusion: Journal of Metamorphic Geology, v. 20, p. 727–740.

Němec, D., 1968, Die Metamorphose des NE-Randes des Kernes der Bşhmischen Masse: Verhandlungen der geologischen Bundesanstalt, v. 1–2, p. 189–203.

O'Brien, P. J., 1997, Garnet zoning and reaction textures in overprinted eclogites, Bohemian Massif, European Variscides: A record of their thermal history during exhumation: Lithos, v. 41, p. 119–133.

O'Brien, P. J., and Vrána, S., 1997, Eclogites with a short-lived granulite facies overprint in the Moldanubian zone, Czech Republic: petrology, geochemistry and diffusion modelling of garnet zoning: Geologische Rundschau, v. 84, p. 473–488.
Oncken, O., von Winterfeld, C., and Dittmar, U., 1999, Accretion of a passive rifted margin: the Late Paleozoic Rhenohercynian fold and thrust belt (Middle European Variscides): Tectonics, v. 18, p. 75–91.
Parrish, R. R., 1987, An improved microcapsule for zircon dissolution in U-Pb geochronology: Isotope Geosciences, v. 66, p. 99–102.
Patočka, F., and Valenta, J., 1990, Geochemistry of metatrachytes and metarhyolites of the southern part of the Devonian Vrbno Group in the Horní Město area and tectonic setting of origin of the metavolcanic protoliths: Časopis pro mineralogii a geologii, v. 35, p. 41–46.
Petrakakis, K., 1997, Evolution of Moldanubian rocks in Austria: Review and synthesis: Journal of Metamorphic Geology, v. 15 (2), p. 203–222.
Pitra, P., and Guiraud, M., 1996, Probable anticlockwise P-T evolution in extending crust: Hlinsko region, Bohemian Massif: Journal of Metamorphic Geology, v. 14, p. 49–60.
Pitra, P., Burg, J. P., Schulmann, K., and Ledru, P., 1994, Late-orogenic extension in the Bohemian Massif: Petrostructural evidence in the Hlinsko region: Geodinamica Acta, v. 6, p. 15–31.
Scharbert, S., and Batík, P., 1985, The age of the Thaya (Dyje) pluton: Verhandlungen der Geologischen Bundesanstallt, v. 3, p. 325–331.
Schulmann, K., 1990, Fabric and kinematic study of the Bíteš orthogneiss (southwestern Moravia) – result of large-scale northeastward shearing parallel to the Moldanubian boundary: Tectonophysics, v. 177, p. 229–244.
Schulmann, K., Ledru, P., Autran, A., Melka, R., Lardeaux, J. M., Urban, M., and Lobkowicz, M., 1991, Evolution of nappes in the eastern margin of the Bohemian massif: a kinematic interpretation: Geologische Rundschau, v. 80, p. 73–92.
Schulmann, K., Melka, R., Lobkowicz, M., Ledru, P., Lardeaux, J. M., and Autran, A., 1994, Contrasting styles of deformation during progressive nappe stacking at the southeastern margin of the Bohemian Massif (Thaya dome): Journal of Structural Geology, v. 16, p. 355–370.
Schulmann, K., Štoudová, S., Konopásek. J., and Martelat, J. E., 1999, Excursion to the Czech part of Moldanubia – The northern margin of the core of the Bohemian massif (processes at boundary of the orogenic root): Beiheft zur European Journal of Mineralogy, v. 11, p. 95–104.
Schulmann, K., Schaltegger, U., Ježek, J., Thompson, A. B., and Edel, J. B., 2002, Rapid burial and exhumation during orogeny: Thickening and synconvergent exhumation of thermally weakened and thinned crust (Variscan orogen in Western Europe): American Journal of Science, v. 302, p. 856–879.
Špaček, P., Kalvoda, J., Franců, E., and Melichar, R., 2001, Variation of deformation mechanisms within the progressive-retrogressive mylonitization cycle of limestones: Brunovistulian sedimentary cover (the Variscan orogeny of the Southeastern Bohemian Massif): Geologica Carpathica, v. 52, p. 263–275.
Steiger, E. H., and Jäger, E., 1977, Subcommission on geochronology, convention of the use of decay constants in geo- and cosmochronology: Earth and Planetary Science Letters, v. 19, p. 321–329.
Steltenpohl, M. G., Cymerman, Z., Krogh, E. J., and Kunk, M. J., 1993, Exhumation of eclogitized continental basement during Variscan lithospheric delamination and gravitational collapse, Sudetes Mountains, Poland: Geology, v. 21, p. 1111–1114.
Štípská, P., and Powell, R., 2005a, Do ternary feldspars constrain the metamorphic conditions of high-grade meta-igneous rocks? Evidence from orthopyroxene gneisses, Bohemian Massif: Journal of Metamorphic Geology.
——— 2005b, Constraining the P-T path of crustal eclogites (an example from the Bohemian Massif): Journal of Metamorphic Geology.
Štípská P., Schulmann , K., and Höck, V., 2000, Complex metamorphic zonation of the Thaya dome: result of buckling and gravitational collapse of imbricated nappe sequence, *in* Cosgrowe, J. W., and Ameen, M. S., editors, Forced folds and fractures: Geological Society of London Special Publication, v. 169, p. 197–211.
Štípská, P., Schulmann, K., Kröner, A., Ježek, J., and Thompson, A. B., 2001, Thermo-mechanical role of Cambro-Ordovician paleorift during Variscan collision. NE margin of the Bohemian Massif: Tectonophysics, v. 332, p. 211–239.
Štípská, P., Schulmann, K., and Kröner, A., 2004, Vertical extrusion and middle crustal spreading of omphacite granulite: a model of syn-convergent exhumation (Bohemian Massif, Czech Republic): Journal of Metamorphic Geology, v. 22, p. 179–198.
Suess, F. E., 1912, Die moravischen Fenster und ihre Beziehung zum Grundgebirge des Hohen Gesenke: Denkschrichte des Koeniglischen Akademie der Wissenscahft, Mathematik, Naturwissenschaft, v. 83, p. 541–631.
——— 1926, Intrusionstektonik und Wandertektonik im variszichen Grundgebirge: Berlin, Borntträger, 269 p.
Svojtka, M., Košler, J., and Venera, Z., 2002, Dating granulite-facies structures and the exhumation of lower crust in the Moldanubian Zone of the Bohemian Massif: International Journal of Earth Sciences, v. 91, p. 373–385.
Synek, J., and Oliveriová, D., 1993, Terrane character of the northeast margin of the Moldanubian zone – the Kutná hora crystalline complex, Bohemian Massif: Geologische Rundschau, v. 82, p. 566–582.
Tait, J., Bachtadse, V., and Soffel, H., 1996, Eastern Variscan fold belt: paleomagnetic evidence for oroclinal bending: Geology, v. 24, p. 871–874.
Tajčmanová L., Konopásek J., and Schulmann, K., 2005, Thermal evolution of the lower crust during exhumation within thickened orogenic root (Variscan belt of Central Europe): Journal of Metamorphic Geology.

Thiele, O., 1976, Ein westvergenter kaledonischer Deckenbau im niederösterechischen Waldviertel: Jahrbuch der Geologischen Bundesanstalt, v. 119, p. 75–81.
Thompson, A. B., 1999, Some time-space relationships for crustal melting and granitic intrusion at various depths, *in* Castro, A., Fernadez, C., and Vigneresse, J. L., editors, Understanding granites: Integrating new and classical techniques: Geological Society of London Special Publication, v. 168, p. 7–25.
——— 2000, Clockwise P/T paths for crustal melting and H_2O recycling in granite source regions and migmatite terrains: Lithos, v. 56, p. 33–45.
Thompson, A. B., Schulmann, K., Ježek, J., and Tolar, V., 2001, Thermally softened continental extensional zones (arcs and rifts) as precursors to thickened orogenic belts: Tectonophysics, v. 332, p. 115–141.
Tollman, A., 1982, Grossräumiger variszischer Deckenbau im Moldanubikum und neue Gedanken zum Variszikum Europas: Geotektonische Forschungen, v. 64, p. 1–91.
van Breemen, O., Aftalion, M., Bowes, D. R., Dudek, A., Mísař, Z., Povondra, P., and Vrána, S., 1982, Geochronological studies of the Bohemian Massif, Czechoslovakia, and their significance in the evolution of central Europe: Transactions of the Royal Society of Edinburgh, Earth Science Series, v. 73, p. 89–108.
Vanderhaeghe, O., Medvedev, S., Fullsack, P., Beaumont, C., and Jamieson, R. A., 2003, Evolution of orogenic wedges and continental plateaux: insights from crustal thermal-mechanical models overlying subducting mantle lithosphere: Geophysical Journal International, v. 153, p. 27–51.
Venera, Z., Schulmann, K., and Kröner, A., 2000, Intrusion within a transtensional tectonic domain: the istá granodiorite (Bohemian Massif)—structure and rheological modelling: Journal of Structural Geology, v. 22, p. 1437–1454.
Vrána, S., 1995, The Moldanubian Zone in the Czech Republic, *in* Dallmeyer, R. D., Franke, W., and Weber, K., editors, Pre-Permian Geology of Central and Eastern Europe: Berlin, Springer, p. 456–460.
Vrána, S., and Kröner, A., 1995, Pb-Pb zircon ages for tourmaline alkali-feldspar orthogneiss from Hluboká nad Vltavou in southern Bohemia: Journal of the Czech Geological Society, v. 40, p. 127–131.
Vrána, S., and Novák, M., 2000, Petrology and geochemistry of granulite clasts in the Visean Luleč conglomerate, Kulm in central Moravia, Czech Republic: Věstník Českého geologického ústavu, v. 75, p. 405–413.
Wendt, J. I., and Todt, W., 1991, A vapour digestion method for dating single zircons by direct measurement of U and Pb without chemical separation: Terra Abstracts, v. 3/1, p. 507–508.
Wendt, J., Kröner, A., Fiala, J., and Todt, W., 1993, Evidence from zircon dating for existence of approximately 2.1 Ga old crystalline basement in Southern Bohemia, Czech Republic: Geologische Rundschau, v. 82, p. 42–50.
Wendt, J. I., Kröner, A., Fiala, J., and Todt, W., 1994, U-Pb zircon and Sm-Nd dating of Moldanubian high-P/high-T granulites from south Bohemia, Czechoslovakia: London, Journal of the Geological Society, v. 151, p. 83–90.
Willet, S. D., Beamont, C., and Fullsack, P., 1993, Mechanical model for the tectonics of doubly vergent compressional orogens: Geology, v. 21, p. 371 – 374.
Williams, I. S., Compston, W., Black, L. P., Ireland, T. R., and Foster, J. J., 1984, Unsupported radiogenic Pb in zircon: a cause of anomalously high Pb-Pb, U-Pb and Th-Pb ages: Contributions to Mineralogy and Petrology, v. 88, p. 322–327.
Winchester, J. A., and The PACE TMR Network Team (contract ERBFMRXCT 97-0136), 2002, Palaeozoic amalgamation of Central Europe: new results from recent geological and geophysical investigations: Tectonophysics, v. 360, p. 5 – 21.
York, D., 1969, Least squared fitting of a straight line with correlated errors: Earth and Planetary Science Letters, v. 5, p. 320–324.
Žák, J., Holub, V. F., and Verner, K., 2005, Tectonic evolution of a continental magmatic arc from transpression in the upper crust to exhumation of mid-crustal orogenic root recorded by episodically emplaced plutons: the Central Bohemian Plutonic Complex (Bohemian Massif): International Journal of Earth Sciences, v. 94, p. 385–400.
Ziegler, P. A., 1986, Geodynamic model for the Palaeozoic crustal consolidation of Western and Central Europe: Tectonophysics, v. 126, p. 303–328.

Mineralogy and Petrology (2006) 86: 221–251
DOI 10.1007/s00710-005-0111-7

Mineralogy and Petrology

Metamorphic record of burial and exhumation of orogenic lower and middle crust: a new tectonothermal model for the Drosendorf window (Bohemian Massif, Austria)

M. Racek[1,3], **P. Štípská**[2,4], **P. Pitra**[3], **K. Schulmann**[2], and **O. Lexa**[1,2]

[1] Institute of Petrology and Structural Geology, Charles University, Praha, Czech Republic
[2] Centre de Géochimie de Surface, UMR CNRS 7517, Strasbourg, France
[3] Géosciences Rennes, UMR CNRS 6118, Université Rennes 1, France
[4] Czech Geological Survey, Prague, Czech Republic

Editorial handling: V. Janoušek

Summary

A continuous, but attenuated section through orogenic lower and middle crust overthrust by a second lower-crustal complex was distinguished at the eastern margin of the Bohemian Massif. This indicates the existence of two lower-crustal ''autochthonous'' extrusions into middle crust that is not compatible with the model of ''allochthonous'' lower crustal klippen remaining after flat thrusting of the Gföhl nappe over large distances. The base of the lower crust is represented by a granulite body exhumed from c. 15 kbar and 800 °C. A hangingwall complex of layered amphibolites gradually passes into amphibolite bearing paragneisses (the Monotonous unit) and micaschists intercalated with marbles at the top (the Varied unit). The metamorphic grade and anatexis decreases upwards and the micaschists preserve a prograde path to c. 8 kbar and 700 °C. This sequence is overthrust by a second lower crustal strongly migmatitized complex, referred to as the Raabs complex, which is marked by an eclogite-bearing belt at the base. The garnet zoning of eclogite indicates burial from 10 kbar to min. 15 kbar. In all units, relics of a steep metamorphic fabric were identified, reworked by folding and a moderately west-dipping foliation. The conditions of 7–10 kbar and approximately 750 °C for the flat foliation were obtained in all units indicating that exhumation of the lower crust into a middle crustal level occurred earlier, probably during the development of steep fabrics. The intense flat fabric is interpreted as a result of thrusting of the whole assembly over the middle crustal Brunian indentor.

Introduction

The internal domain of the Variscan Bohemian Massif – the Moldanubian zone – is characterised by the presence of high-pressure units overlying mostly intermediate- to low-pressure migmatites. The generally accepted models of the Moldanubian zone interpret the high-grade domains as relics of one single or composite Gföhl nappe complex, rooted some 150–300 km to the west, beneath the Barrandian domain, and thrust south-east-wards over hundreds of kilometres over middle-crustal units (e.g. *Tollmann*, 1982; *Franke*, 1989; *Matte*, 1991). This model is largely based on observations from the eastern margin of the Moldanubian, in Lower Austria (including the ''Drosendorf window''), where the ''intra-Moldanubian'' character of high-grade rocks thrust over the medium-grade metamorphic units was originally recognized (e.g. *Suess*, 1918; *Kober*, 1938; *Fuchs*, 1971, 1976; *Thiele*, 1976). However, regardless of disagreements concerning the vergency and the age of the thrusting, such a distant origin of the nappes was not suggested, or was even explicitly rejected by these earlier authors (e.g. *Fuchs*, 1976; *Thiele*, 1984). With respect to the ideas that follow, the opinion of Fuchs that the nappes are derived from the eastern Moldanubian zone and therefore have roots ''on place'', without large thrust distances, is particularly important.

Štípská et al. (2004) and *Schulmann* et al. (2005) proposed a new interpretation of the orogenic structure and exhumational history of the lower crust within a hot orogenic root along the eastern collisional front of the Bohemian Massif, marked by alternations of steep lower and middle crustal belts. This model is based on the presence of steep structures preserved in high-pressure rocks that were interpreted as reflecting the vertical extrusion of the orogenic lower crust into middle crustal levels. It was suggested that the ductile extrusion was initiated by steep folding of crustal layers. Subsequent flat reworking of extruded high-pressure and middle-pressure rocks was attributed to the indentation of the external Brunian domain into the weak orogenic root.

In the light of these new interpretations, we reinvestigate the classical area in Lower Austria, where the original idea of the high-grade Gföhl nappe originated. In order to discuss the vertical movements in individual lithologies, we present a series of petrological data, set into a well-defined structural frame, from rocks selected in a continuous E–W oriented profile that runs across the Drosendorf window. Field observations and petrological data indicate the existence of two lower-crustal extrusions, where the first exhumes a continuous lower-middle crustal section that is overthrust by a second lower-crustal complex. The mid-crustal reworking of the whole sequence is discussed in terms of the indentation of Brunia. The PT data and PT paths of rocks from the bottom to the top of the structure are consistent with the ''extrusion'' exhumational model proposed by *Štípská* et al. (2004) and *Schulmann* et al. (2005) in other parts of the collisional front.

Geological setting

The eastern margin of the Bohemian Massif (Fig. 1) is characterized by a contact between the Moldanubian and Brunian domains that represents one of the major boundaries of internal and external zones in the European Variscan orogen (*Suess*, 1912, 1926). The Brunia external domain is composed of undeformed Late

Proterozoic granitoids and high-grade schists (e.g. *Scharbert* and *Batík*, 1980; *van Breemen* et al., 1982; *Finger* et al., 2000a, b; *Kröner* et al., 2000b) overlain by Cambro-Ordovician sediments, metavolcanics and shallow marine Devonian sediments (e.g. *Dudek*, 1960; *Hartley* and *Otava*, 2001; *Kalvoda* et al., 2003). Variscan deformation caused the east-ward thrusting of the Moldanubian over the western margin of the Brunia domain and produced a 300 km long and up to 50 km wide belt of metamorphosed rocks emerging through hot lower crustal nappes in form of tectonic windows. The metamorphism is tectonically inverted within imbricated orthogneiss-metasedimentary nappes from kyanite zone in the west to chlorite zone in the east (*Höck*, 1975; *Fritz* and *Neubauer*, 1993; *Schulmann* et al., 1994, 1995; *Štípská* and *Schulmann*, 1995; *Fritz* et al., 1996; *Schulmann* and *Gayer*, 2000; *Štípská* et al., 2000).

The Moldanubian internal domain consists at its eastern margin, from the top to the bottom, of the high-grade Gföhl unit overlying the generally lower-grade Varied and Monotonous units, all intruded by mostly Carboniferous plutons (*Fuchs*, 1976; *Fuchs* and *Matura*, 1976; *Thiele*, 1976, 1984). The Gföhl unit is dominated by felsic kyanite – K-feldspar granulite massifs with minor intermediate and mafic granulite types with mostly magmatic protoliths (*Fiala* et al., 1987; *Janoušek* et al., 2004) that are associated with garnetiferous peridotites. It comprises also felsic anatectic orthogneisses (the Gföhl gneiss). Amphibolite-dominated, usually highly anatectic complexes interlayered with felsic metavolcanics and paragneisses are collectively called the Raabs unit and are generally considered as a lower part of the Gföhl unit (*Thiele*, 1984; *Fritz* and *Neubauer*, 1993; *Finger* and *Steyrer*, 1995). An increasing number of U–Pb zircon ages from the Gföhl gneiss, granulite massifs and bimodal magmatic rocks revealed the significant period of magmatic activity in the eastern Moldanubian domain between c. 500–350 Ma that gave probably rise to the majority of magmatic protoliths of the Gföhl unit (*Finger* and *von Quadt*, 1995; *Friedl* et al., 2004; *Schulmann* et al., 2005).

The Varied unit is formed by paragneisses with quartzites, marbles, graphite schists, amphibolites and bodies of granitic gneisses. The granitic gneisses are Late Proterozoic in age and/or display a Late Proterozoic anatectic overprint. Dating of a felsic layer within the amphibolites yielded a U–Pb age of 358 Ma (*Friedl* et al., 1993). This can lead to interpretations, that carbonate-rich sedimentation of the Varied unit is Early Paleozoic (presumably Devonian) in age (*Friedl* et al., 1993, 2004; *Gebauer* and *Friedl*, 1994). The Monotonous unit is dominated by paragneisses and contains minor quartzite, calc-silicate and mafic rocks with presumed Late Proterozoic age of sedimentation (*Kröner* et al., 1988).

There is a great number of petrological studies in the southern Moldanubian domain, but they are often scattered and rarely linked with structural evolution. The remarkable feature is the common and widespread overprint of all the units that occurred in the range of 700–800 °C and 8–11 kbar. This overprint was followed by an isobaric cooling to c. 6 kbar, 650–500 °C and was interpreted to be related to the thrusting of the Moldanubian assembly over Brunia (*Petrakakis*, 1997 and references therein).

The metamorphic evolution of the granulite massifs was interpreted as prograde, with peak metamorphic assemblage of garnet-kyanite-mesoperthite-quartz

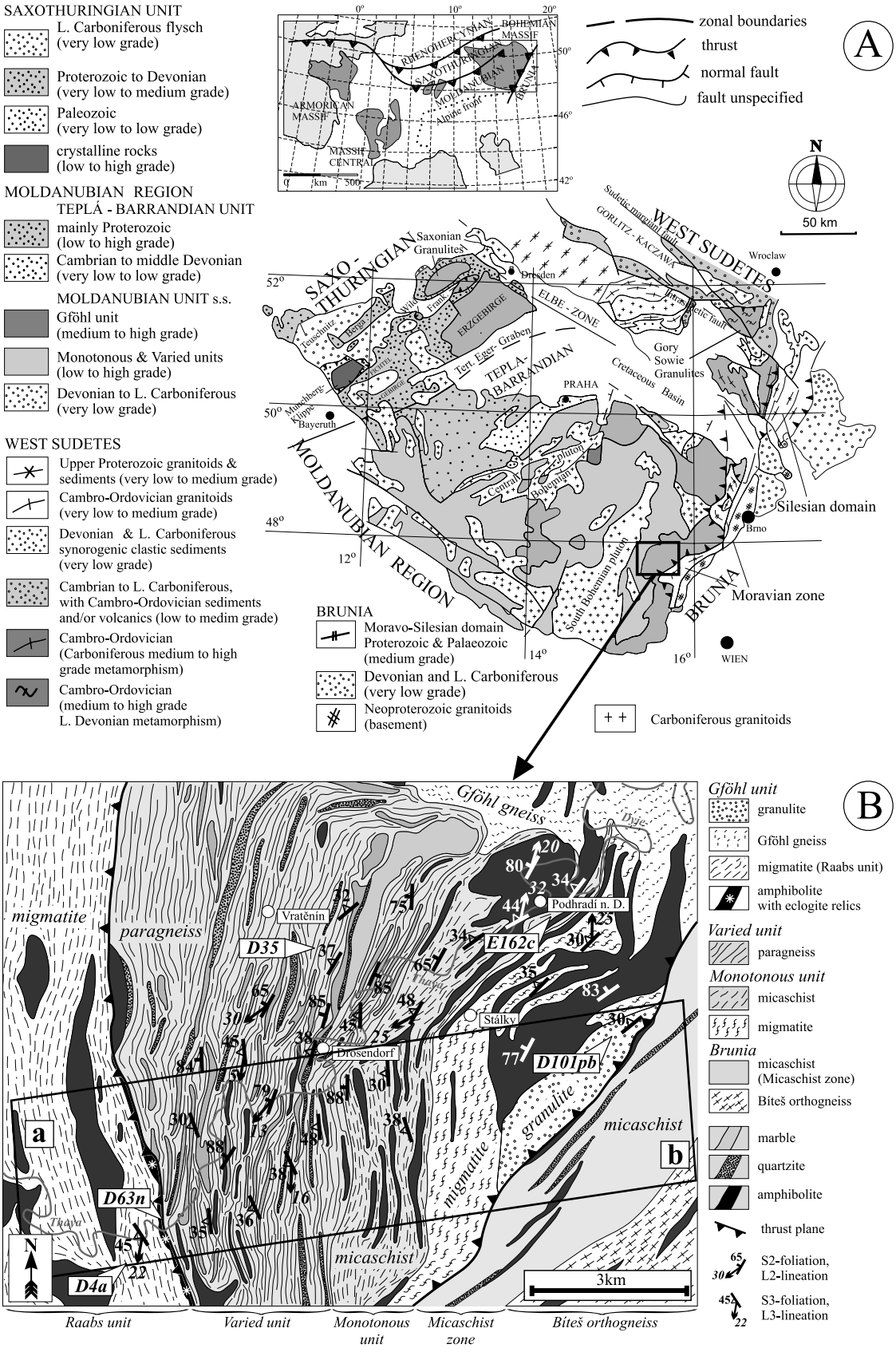
SAXOTHURINGIAN UNIT
L. Carboniferous flysch (very low grade)
Proterozoic to Devonian (very low to medium grade)
Paleozoic (very low to low grade)
crystalline rocks (low to high grade)
MOLDANUBIAN REGION
TEPLÁ - BARRANDIAN UNIT
mainly Proterozoic (low to high grade)
Cambrian to middle Devonian (very low to low grade)
MOLDANUBIAN UNIT s.s.
Gföhl unit (medium to high grade)
Monotonous & Varied units (low to high grade)
Devonian to L. Carboniferous (very low grade)
WEST SUDETES
Upper Proterozoic granitoids & sediments (very low to medium grade)
Cambro-Ordovician granitoids (very low to medium grade)
Devonian & L. Carboniferous synorogenic clastic sediments (very low grade)
Cambrian to L. Carboniferous, with Cambro-Ordovician sediments and/or volcanics (low to medim grade)
Cambro-Ordovician (Carboniferous medium to high grade metamorphism)
Cambro-Ordovician (medium to high grade L. Devonian metamorphism)
BRUNIA
Moravo-Silesian domain Proterozoic & Palaeozoic (medium grade)
Devonian and L. Carboniferous (very low grade)
Neoproterozoic granitoids (basement)
Carboniferous granitoids
zonal boundaries
thrust
normal fault
fault unspecified
A
N
50 km
SAXO-THURINGIAN
MOLDANUBIAN REGION
WEST SUDETES
BRUNIA
Saxonian Granulites
Dresden
Wroclaw
ELBE - ZONE
ERZGEBIRGE
Tert. Eger- Graben
TEPLA-BARRANDIAN
PRAHA
Gory Sowie Granulites
Cretaceous Basin
Munchberg-Klippe
Bayeruth
Central Bohemian pluton
South Bohemian pluton
Silesian domain
Brno
Moravian zone
WIEN
52°
50°
48°
12°
14°
16°
B
Gföhl gneiss
migmatite
paragneiss
Vratěnin
Podhradí n. D.
Stálky
Drosendorf
D35
E162c
D101pb
D63n
D4a
granulite
micaschist
migmatite
a
b
3km
Gföhl unit
granulite
Gföhl gneiss
migmatite (Raabs unit)
amphibolite with eclogite relics
Varied unit
paragneiss
Monotonous unit
micaschist
migmatite
Brunia
micaschist (Micaschist zone)
Biteš orthogneiss
marble
quartzite
amphibolite
thrust plane
S2-foliation, L2-lineation
S3-foliation, L3-lineation
Raabs unit
Varied unit
Monotonous unit
Micaschist zone
Biteš orthogneiss

and clinopyroxene-garnet-mesoperthite indicating conditions of c. 1000–1050 °C and 16–18 kbar (*Carswell* and *O'Brien*, 1993; *Cooke*, 2000; *Cooke* et al., 2000; *Cooke* and *O'Brien*, 2001). *Cooke* and *O'Brien* (2001) estimated that the peak conditions within the Gföhl gneiss were similar to those of the granulites – between 14–16 kbar at >950 °C, while in other areas of the Gföhl gneiss the metamorphic peak was calculated to approximately 8 kbar and 750 °C (*Owen* and *Dostal*, 1996). An alternative PT path for granulite massifs was suggested by *Štípská* and *Powell* (2005a). They attribute the ultra-high temperature conditions to the magmatic emplacement of granulite protoliths at moderate depth of c. 7–13 kbar, followed by cooling. The prograde metamorphic overprint from moderate into high pressure and decompression presumably occurred at moderate temperature, lower than 850 °C (*Štípská* and *Powell*, 2005a, b).

In the Varied unit in Lower Austria, the prograde evolution to 700–800 °C and 7–9 kbar is documented within the paragneisses on muscovite and kyanite inclusions in garnet and the common matrix assemblage is garnet-sillimanite-K-feldspar-biotite. Amphibolites are composed of hornblende-plagioclase ± garnet with local formation of orthopyroxene with peak conditions of 730–780 °C and 7–8.5 kbar (*Petrakakis*, 1986; *Büttner* and *Kruhl*, 1997; *Petrakakis*, 1997). Migmatitic paragneisses of the Monotonous unit in Lower Austria preserve the prograde evolution in the form of a staurolite-kyanite-garnet-biotite assemblage included in plagioclase and indicating pressures in excess of 8 kbar (*Büttner* and *Kruhl*, 1997). Around granitoid bodies, the biotite-plagioclase-quartz ± garnet ± sillimanite bearing matrix is often overgrown by cordierite formed at c. 4.5 kbar and 750–800 °C (*Linner*, 1996; *Büttner* and *Kruhl*, 1997). Rare presence of eclogites was reported by *Linner* (1996) and *O'Brien* (1997) within the paragneisses of the Monotonous unit and from the limit of Gföhl and Varied unit (*Štípská* and *Powell*, 2005b). The post-peak re-equilibration associated with widespread recrystallization in the Varied and Gföhl units was determined to 7–11 kbar and 700–850 °C (*Petrakakis*, 1997; *Kolenovská* et al., 1999; *Štípská* and *Powell*, 2005b).

From the tectonic point of view, the Gföhl unit, namely the granulite massifs and the Gföhl gneiss, form klippen thrust over the Monotonous and Varied units (e.g. *Suess*, 1918; *Kober*, 1938; *Fuchs*, 1971, 1976; *Thiele*, 1976). There is general agreement, that the overall structure of this nappe is east-vergent, coherent with the thrusting of the Moldanubian unit over Brunia, but opinions on its origin and formation are contrasting. *Fuchs* (1971, 1976) proposed that the nappe has its root in the easternmost Moldanubian and was thrust to the west during Caledonian or early Variscan times. This was followed by thrusting of the Moldanubian over the Brunia during Variscan times, resulting in the east-vergent fabric of the thrust that affects the whole nappe sequence including the thrust boundaries. *Thiele* (1976,

Fig. 1. **A** Outline geological map of the Bohemian Massif with major units shown schematically (modified after *Franke*, 2000). The upper left inset is position of the Bohemian Massif in the framework of the European Variscides. **B** A map of the studied area simplified after *Suess* et al. (1925). Dominant metamorphic fabrics D2 and D3 and position of the studied petrological samples are shown. Rectangle corresponds to location of the cross-section in Fig. 2

1984) and *Tollmann* (1982) disagreed with this model and proposed that the nappe was thrust from the west to the east and is Variscan in age. *Tollmann* (1982) put the root of the nappe underneath the Teplá-Barrandian domain, implying displacements of 150–300 km. This idea was adopted by later authors (e.g. *Franke*, 1989; *Matte*, 1991) and generalized for the entire Bohemian Massif. *Thiele* (1984) located the root zone of the Gföhl nappe in the area west of Dunkelstein and Wieselburg, which demands the thrusting of only tens of kilometres. The general structure in the eastern Moldanubian domain resulting from E–W compression is modified towards the Brunia domain by an increasing transpressional component with NNE-directed transport (*Schulmann*, 1990; *Schulmann* et al., 1991; *Fritz* and *Neubauer*, 1993; *Štípská* and *Schulmann*, 1995; *Fritz*, 1996; *Štípská* et al., 2000).

According to numerous studies, the age of high-grade metamorphism within the Moldanubian zone is Carboniferous (*Kröner* et al., 2000a; *Friedl* et al., 2003, and references therein). However, aside from the Carboniferous metamorphic peak, important Ordovician, Silurian and Devonian magmatic activity was reported from the eastern Moldanubian zone (*Finger* and *von Quadt*, 1995; *Friedl* et al., 2004; and *Schulmann* et al., 2005), that may be associated also with tectonic activity and metamorphism (*Schulmann* et al., 2005).

Lithology and structure across the Drosendorf window

The study area is located along a cross-section that includes the Drosendorf window and the adjacent lower crustal rocks of the Gföhl unit (*Fuchs* and *Matura*, 1976) (Fig. 1B). Here, the NE–SW trending western boundary of the Brunia domain is marked by a felsic granulite body elongated parallel to the Brunia margin. A complex of banded amphibolites and an augen-orthogneiss body, interpreted as the base of the Monotonous unit (*Tollmann*, 1982), occurs in the hangingwall of the granulite sheet. Towards the west, the amount of amphibolite and leptynite decreases and the dominant lithology is represented by a sequence of metapelites and paragneisses. All the rock types are migmatitic, but the degree of anatexis decreases westwards. The westerly-situated Varied unit is composed of metasedimentary rocks, represented by paragneisses with numerous sheets of marbles up to several metres thick, calc-silicate rocks and subordinate quartzite. The metasediments are accompanied by garnetiferous amphibolites and rare felsic metavolcanics. The degree of anatexis, locally developed in the paragneisses, is very low. At the western border of the Varied unit, the Gföhl unit (called here traditionally the Raabs unit) occurs, that comprises a 100 m thick amphibolite sheet at its base, containing relicts of retrogressed eclogites. To the west and structurally above this eclogite-bearing sheet, a large body of a migmatitic felsic gneiss (the Kolmitz gneiss) passes into a metamorphosed bimodal magmatic complex interlayered with paragneisses. The degree of anatexis is high in all the lithologies.

Three main deformational events were identified in the studied profile (Fig. 1B; Fig. 2). The earliest metamorphic foliation S1 is folded by F2 folds with steep axial planes and subhorizontal N–S trending fold-axes that are well preserved in the Varied unit and locally in the amphibolites of the Monotonous unit. The resulting steep foliation S2 includes lineation L2 that plunges mostly under shallow to intermediate angles towards the SW.

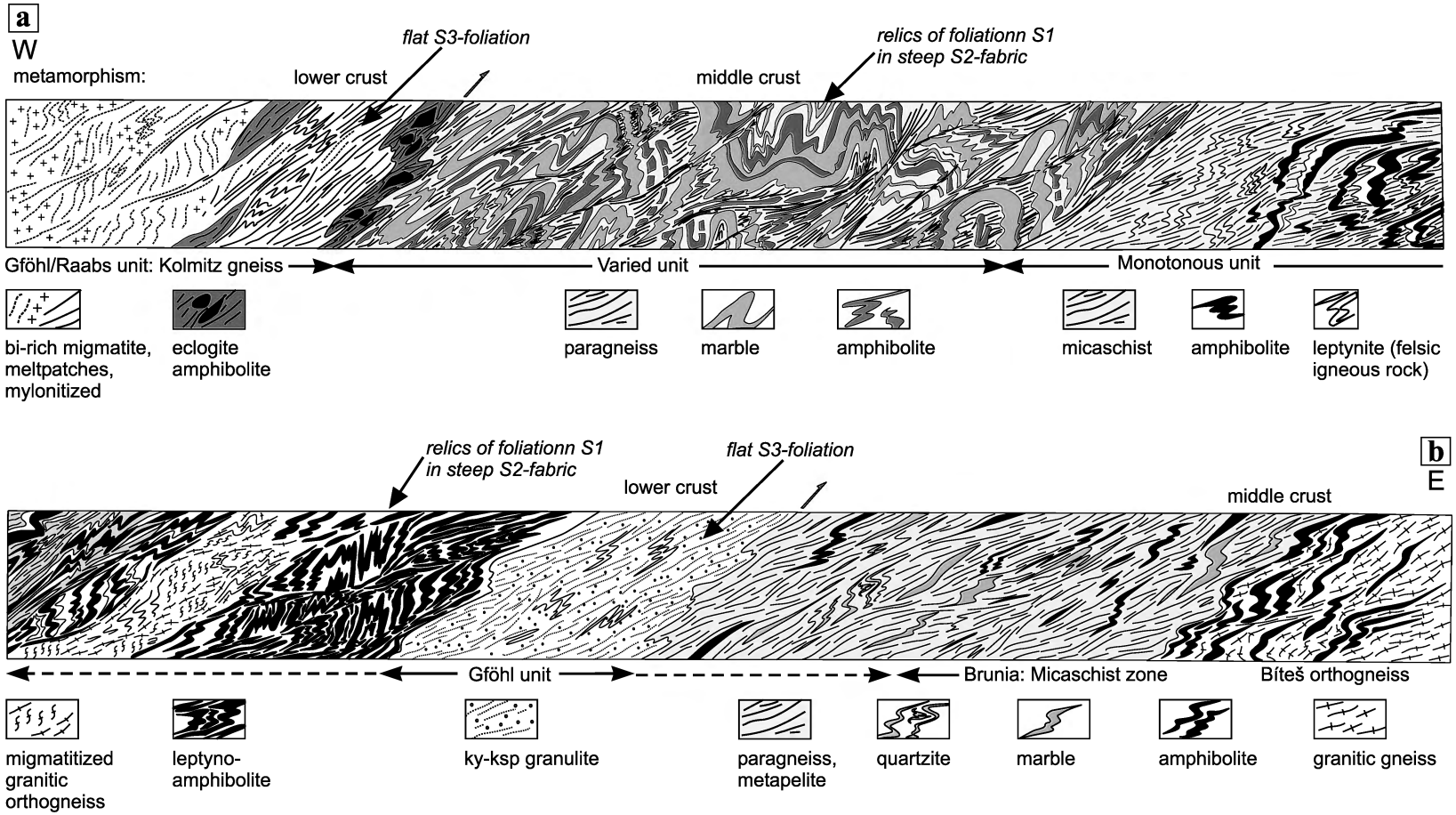

Fig. 2. Interpretative geological and structural cross-section showing three main metamorphic fabrics and style of dominant D3 deformation. Vertical axis not to scale

The third deformation event is characterized by reworking of these subvertical fabrics by F3 folds with west-dipping axial planes and N–S trending axes. This leads to the widespread transposition into a moderately west-dipping foliation S3. The D3 deformation is heterogeneously developed, and locally the earlier structures are completely transposed by several tens of metres wide zones of moderately to shallowly W to SW dipping foliation S3. These zones are mostly developed parallel to the long limbs of large scale F3 folds. The D3 shear deformation affects homogeneously the eastern granulite belt that shows complete mylonitic transposition. The intensity of the D3 deformation affecting the steep fabrics of the Varied unit systematically increases towards the western contact with high-grade metamorphic gneisses and migmatites in the hangingwall. Here, the migmatites of the Raabs unit are converted to mylonitic gneisses and underlying schists of the Varied unit show complete transposition associated with development of sheath folds and strong N-trending stretching lineation.

Petrology and mineral chemistry

To characterize the PT evolution in the units of the studied profile, we have chosen two samples of felsic granulite (D101pb, D101c), a micaschist from the Monotonous unit (E162c), a paragneiss from the Varied unit (D35), a retrogressed eclogite from the bottom of the Raabs unit (D63n) and one migmatitic gneiss from the Raabs unit (D4a) (Fig. 1B).

Mineral analyses were performed on an electron microprobe CAMECA SX-100 at the Geological institute of Academy of Science of the Czech Republic and on a scanning electron microscope CAM-SCAN S4 at the Faculty of Science, Charles University in Prague. The size of defocused beam used for measuring of average composition of perthitic K-feldspar in samples of granulite was 50 µm. Representative analyses of minerals are listed in Tables 1 and 2 and mineral chemistry of the studied samples is summarized in Table 3.

Ky-ksp granulite (samples D101pb, D101c)

The granulites are composed of K-feldspar, plagioclase and quartz (90%), garnet (Fig. 3A), kyanite (Fig. 3B), minor biotite, sillimanite and accessory rutile and ilmenite. They are strongly recrystallized and the foliation (S3) is defined by bands of recrystallized quartz and feldspar and the preferred orientation of kyanite, sillimanite and biotite. Within the fine-grained matrix (0.1–0.5 mm) up to 2 mm large porphyroclasts of garnet, perthitic K-feldspar, quartz and in few samples also antiperthitic plagioclase are preserved indicating a former coarser-grained texture. Garnet (1–4 mm) contains inclusions of K-feldspar (frequently perthitic), plagioclase, quartz and rutile. Biotite underlies the matrix foliation or grows at the expense of garnet. It is absent from sample D101pb. Locally, short needles of sillimanite form at garnet rims or on kyanite. Muscovite is generally absent, but in some samples it grows at the expense of kyanite.

Garnet in the sample D101pb (Fig. 3A) is a relatively pyrope-rich almandine and is zoned with a grossular-rich core and a decreasing content of Ca towards

Table 1. *Representative analyses of minerals in samples of granulite (D101pb, D101c) and micaschist from the Monotonous unit (E162c)*

Lithology:	Granulite								Micaschist (Monoton. unit)						
Sample	D101pb	D101pb	D101pb	D101pb	D101c	D101c	D101c	D101c	E162c	E162c	E162c	E162c	E162c	E162c	E162c
Mineral	g	g	ksp	pl	g	bi	ksp	pl	g	g	bi	mu	st	ksp	pl
Position	core	rim	matrix	matrix		matrix	matrix	matrix	core	rim	matrix	matrix	inclusion	matrix	matrix
Wt% oxide															
SiO_2	38.75	38.97	65.21	65.61	38.21	35.77	65.24	64.21	37.06	36.75	33.94	45.69	26.21	64.49	59.99
TiO_2	0.01	0.05	0.00	0.04	0.00	2.80	0.01	0.00	0.08	0.04	4.27	1.24	0.77	0.00	0.01
Cr_2O_3	0.00	0.07	0.00	0.00	0.00	0.00	0.00	0.00	0.00	0.00	0.06	0.00	0.01	0.01	0.03
Al_2O_3	21.51	21.24	18.02	21.92	21.38	19.14	18.29	22.35	20.58	20.43	19.17	36.29	55.10	18.52	25.20
FeO	28.29	29.94	0.00	0.00	34.76	18.79	0.08	0.00	34.80	38.34	23.93	1.18	13.93	0.11	0.05
MnO	0.99	0.94	0.06	0.00	0.86	0.00	0.00	0.00	0.55	0.37	0.18	0.00	0.22	0.06	0.00
MgO	6.62	7.35	0.00	0.00	3.31	9.45	0.00	0.00	0.87	1.78	5.50	0.34	0.75	0.01	0.00
CaO	3.43	2.04	0.03	2.84	1.91	0.00	0.05	3.06	6.06	2.62	0.00	0.00	0.00	0.05	6.91
Na_2O	0.04	0.03	1.27	10.25	0.00	0.00	0.93	10.23	0.03	0.00	0.11	0.42	0.03	1.33	7.54
K_2O	0.00	0.02	15.29	0.15	0.00	9.66	14.61	0.08	0.00	0.00	9.58	9.61	0.00	14.86	0.17
ZnO	–	–	–	–	–	–	–	–	–	–	–	–	1.08	–	–
Total	99.62	100.67	99.90	100.81	100.43	95.61	99.21	99.93	100.03	100.34	96.74	94.77	98.10	99.44	99.90
Cations/Charges	8/24	8/24	5/16	5/16	8/24	8/24	5/16	5/16	8/24	8/24	8/24	7/24	15/47	5/16	5/16
Si	3.03	3.02	3.00	2.86	3.05	2.79	3.04	2.82	3.00	2.98	2.70	3.08	3.73	2.98	2.68
Ti	0.00	0.00	0.00	0.00	0.00	0.16	0.00	0.00	0.00	0.00	0.26	0.06	0.08	0.00	0.00
Cr	0.00	0.00	0.00	0.00	0.00	0.00	0.00	0.00	0.00	0.00	0.00	0.00	0.00	0.00	0.00
Al	1.98	1.94	0.98	1.13	2.01	1.76	1.00	1.16	1.96	1.95	1.80	2.88	9.24	1.01	1.33
Fe^{3+}	0.00	0.01	0.00	0.00	0.00	0.00	0.00	0.00	0.03	0.09	0.00	0.00	0.00	0.00	0.00
Fe^{2+}	1.85	1.93	0.00	0.00	2.32	1.23	0.00	0.00	2.33	2.51	1.59	0.07	1.66	0.00	0.00
Mn	0.07	0.06	0.00	0.00	0.06	0.00	0.00	0.00	0.04	0.03	0.01	0.00	0.03	0.00	0.00
Mg	0.77	0.85	0.00	0.00	0.39	1.10	0.00	0.00	0.11	0.22	0.65	0.03	0.16	0.00	0.00
Ca	0.29	0.17	0.00	0.13	0.16	0.00	0.00	0.14	0.53	0.23	0.00	0.00	0.00	0.00	0.33
Na	0.01	0.01	0.11	0.87	0.00	0.00	0.08	0.87	0.01	0.00	0.02	0.05	0.01	0.12	0.65
K	0.00	0.00	0.90	0.01	0.00	0.96	0.87	0.00	0.00	0.00	0.97	0.83	0.00	0.88	0.01
Zn	–	–	–	–	–	–	–	–	–	–	–	–	0.09	–	–
Total	8.00	8.00	5.00	5.00	8.00	8.00	5.00	5.00	8.00	8.00	8.00	7.00	15.00	5.00	5.00
XFe	0.71	0.70	*An* 0.00	0.13	*XFe*	0.85	0.53	*An* 0.00	0.14	*XFe*	0.96	0.92	0.71	0.66	0.91	*An* 0.00	0.33
Alm	0.62	0.64	*Ab* 0.11	0.86	*Alm*	0.79		*Ab* 0.09	0.85	*Alm*	0.78	0.85				*Ab* 0.12	0.66
Prp	0.26	0.28	*Or* 0.89	0.01	*Prp*	0.13		*Or* 0.91	0.00	*Prp*	0.03	0.07				*Or* 0.88	0.01
Grs	0.10	0.06			*Grs*	0.06				*Grs*	0.17	0.07					
Sps	0.02	0.02			*Sps*	0.02				*Sps*	0.01	0.01					

q quartz, *pl* plagioclase, *ksp* K-feldspar, *g* garnet, *ilm* ilmenite, *am* amphibole, *cpx* clinopyroxene, *opx* orthopyroxene, *o* omphacite, *cd* cordierite, *ky* kyanite, *sill* sillimanite, *and* andalusite, *mu* muscovite, *bi* biotite, *pa* paragonite, *crn* corundum, *liq* silicate melt. *Xfe* Fe(tot)/(Fe(tot) + Mg), *Alm* almandine = Fe(tot)/(Fe(tot) + Mg + Ca + Mn), *Prp* pyrope = Mg/(Fe(tot) + Mg + Ca + Mn), *Grs* grossular = Ca/(Fe(tot) + Mg + Ca + Mn), *Sps* spessartine = Mn/(Fe(tot) + Mg + Ca + Mn), *An* anorthite = Ca/(Ca + Na + K), *Ab* albite = Na/(Ca + Na + K), *Or* orthoclase = K/(Ca + Na + K)

Table 2. *Representative analyses of minerals in samples of paragneiss from the Varied unit (D35), eclogite from the Raabs unit (D63n) and migmatite from the Raabs unit (D4a)*

Lithology:	Paragneiss (Varied unit)					Ecogite						Migmatite (Raabs unit)			
Sample	D35	D35	D35	D35	D35	D63n	D63n	D63n	D63n	D63n	D63n	D4a	D4a	D4a	D4a
Mineral	g	g	bi	st	pl	g	g	g	cpx	am	pl	g	bi	pl	ksp
Position	core	rim	matrix	inclusion	matrix	core	core/rim	rim	symplect	matrix	symplect		matrix	matrix	matrix
Wt% oxide															
SiO_2	37.07	37.57	36.81	26.79	63.99	38.04	37.86	38.63	52.45	44.97	60.08	37.47	35.71	64.44	64.75
TiO_2	0.08	0.05	3.80	1.22	0.00	0.05	0.08	0.10	0.15	1.61	0.02	0.00	3.13	0.00	0.00
Cr_2O_3	0.00	0.03	0.00	0.00	0.00	0.00	0.01	0.10	0.02	0.03	0.00	0.00	0.00	0.00	0.00
Al_2O_3	21.27	21.66	17.43	54.59	22.45	20.94	20.95	20.83	1.04	9.72	24.92	20.69	18.75	22.54	18.93
FeO	29.25	30.52	14.66	13.30	0.00	27.09	27.62	26.53	12.99	17.30	0.21	36.23	21.43	0.00	0.00
MnO	2.46	0.26	0.00	0.02	0.00	2.29	0.96	0.62	0.05	0.00	0.01	2.21	0.00	0.00	0.00
MgO	2.47	4.02	12.91	2.51	0.00	2.95	2.24	3.73	11.66	10.28	0.00	2.60	7.51	0.00	0.00
CaO	7.40	5.88	0.01	0.02	3.63	8.66	10.69	8.79	21.42	11.08	6.69	0.81	0.00	3.16	0.00
Na_2O	0.05	0.01	0.19	0.00	9.50	0.01	0.00	0.05	0.27	1.34	7.58	0.00	0.00	9.87	1.52
K_2O	0.01	0.01	9.67	0.01	0.22	0.00	0.00	0.00	0.01	0.90	0.43	0.00	9.66	0.34	14.49
ZnO	–	–	–	0.25	–	–	–	–	–	–	–	–	–	–	–
Total	100.06	100.01	95.48	98.71	99.80	100.02	100.40	99.37	100.05	97.24	99.93	100.01	96.19	100.35	99.69
Cations/Charges	8/24	8/24	8/24	15/47	5/16	8/24	8/24	8/24	4/12	15 + K + Na/23	5/16	8/24	8/24	5/16	5/16
Si	2.95	2.97	2.82	3.75	2.83	3.01	2.99	3.06	1.99	6.79	2.68	3.03	2.81	2.83	2.98
Ti	0.00	0.00	0.22	0.13	0.00	0.00	0.00	0.01	0.00	0.18	0.00	0.00	0.19	0.00	0.00
Cr	0.00	0.00	0.00	0.00	0.00	0.00	0.00	0.01	0.00	0.00	0.00	0.00	0.00	0.00	0.00
Al	2.00	2.02	1.57	9.01	1.17	1.95	1.95	1.94	0.05	1.73	1.31	1.98	1.74	1.17	1.03
Fe^{3+}	0.10	0.04	0.00	0.00	0.00	0.02	0.06	0.00	0.00	0.00	0.01	0.00	0.00	0.00	0.00
Fe^{2+}	1.85	1.98	0.94	1.56	0.00	1.78	1.76	1.76	0.41	2.18	0.00	2.45	1.41	0.00	0.00
Mn	0.17	0.02	0.00	0.00	0.00	0.15	0.06	0.04	0.00	0.00	0.00	0.15	0.00	0.00	0.00
Mg	0.29	0.47	1.47	0.52	0.00	0.35	0.26	0.44	0.66	2.31	0.00	0.31	0.88	0.00	0.00
Ca	0.63	0.50	0.00	0.00	0.17	0.73	0.90	0.75	0.87	1.79	0.32	0.07	0.00	0.15	0.00
Na	0.01	0.00	0.03	0.00	0.81	0.00	0.00	0.01	0.02	0.39	0.66	0.00	0.00	0.84	0.14
K	0.00	0.00	0.94	0.00	0.01	0.00	0.00	0.00	0.00	0.17	0.02	0.00	0.97	0.02	0.85
Zn	–	–	–	0.02	–	–	–	–	–	–	–	–	–	–	–
Total	8.00	8.00	8.00	15.00	5.00	8.00	8.00	8.00	4.00	15.57	5.00		8.00	5.00	5.00
XFe	0.87	0.81	0.39	0.75	*An* 0.17	*XFe* 0.84	0.87	0.80	0.38	0.49	*An* 0.32	*XFe* 0.89	0.62	*An* 0.15	0.00
Alm	0.64	0.67			*Ab* 0.82	*Alm* 0.59	0.60	0.59			*Ab* 0.66	*Alm* 0.82		*Ab* 0.83	0.14
Prp	0.10	0.16			*Or* 0.01	*Prp* 0.11	0.09	0.15			*Or* 0.02	*Prp* 0.10		*Or* 0.02	0.86
Grs	0.21	0.17				*Grs* 0.24	0.30	0.25				*Grs* 0.02			
Sps	0.05	0.01				*Sps* 0.05	0.02	0.01				*Sps* 0.05			

q quartz, *pl* plagioclase, *ksp* K-feldspar, *g* garnet, *ilm* ilmenite, *am* amphibole, *cpx* clinopyroxene, *opx* orthopyroxene, *o* omphacite, *cd* cordierite, *ky* kyanite, *sill* sillimanite, *and* andalusite, *mu* muscovite, *bi* biotite, *pa* paragonite, *crn* corundum, *liq* silicate melt. *Xfe* Fe(tot)/(Fe(tot) + Mg), *Alm* almandine = Fe(tot)/(Fe(tot) + Mg + Ca + Mn), *Prp* pyrope = Mg/(Fe(tot) + Mg + Ca + Mn), *Grs* grossular = Ca/(Fe(tot) + Mg + Ca + Mn), *Sps* spessartine = Mn/(Fe(tot) + Mg + Ca + Mn), *An* anorthite = Ca/(Ca + Na + K), *Ab* albite = Na/(Ca + Na + K), *Or* orthoclase = K/(Ca + Na + K)

Table 3. *Summary of mineral chemistry of all the studied samples*

Unit	Rock type	Sample	Garnet					K-feldspar	
			position	*XFe*	*Alm*	*Prp*	*Grs*	*Sps*	position	*Ab*
granulite	granulite	D101pb	core	0.71	0.62	0.26	0.10	0.02	inclusion	0.21–0.26
			rim	0.70	0.64	0.28	0.06	0.02	perthite	0.36–0.39
									matrix	0.11–0.13
		D101c	–	0.81–0.85	0.75–0.79	0.13–0.19	0.04–0.06	0.02	perthite	0.34
									matrix	0.09–0.13
Monotonous	micaschist	E162c	core	0.96	0.78	0.03	0.17	0.01		
			rim	0.92	0.85	0.07	0.07	0.01	matrix	0.12–0.16
Varied	paragneiss	D35	core	0.87	0.64	0.10	0.21	0.05		
			rim	0.81	0.67	0.16	0.17	0.01		
Raabs	eclogie	D63n	core	0.84	0.59	0.11	0.24	0.05		
			core/rim	0.87	0.60	0.09	0.30	0.02		
			rim	0.80	0.59	0.15	0.25	0.01		
Raabs	migmatite	D4a	–	0.86–0.91	0.81–0.85	0.09–0.12	0.02–0.03	0.04–0.06	inclusion	0.4
									porphyrocl.	0.15–0.31
									matrix	0.09–0.17

Unit	Rock type	Sample	Plagioclase		Biotite (matrix)		Staurolite (inclusions)		Clinopyroxene (symplect.)	
			position	*An*	*XFe*	*Ti* (*pfu.*)	*XFe*	*Zn* (*pfu.*)	*XFe*	*Ca*/(*Ca* + *Fe* + *Mg*)
granulite	granulite	D101pb	inclusion	0.13–0.17						
			matrix	0.08–0.13						
		D101c			0.53	0.16				
			matrix	0.14						
Monotonous	micaschist	E162c	inclusion	0.34–0.38	0.69–0.76	0.18–0.26	0.91	0.09–0.12		
			matrix	0.31–0.33						
Varied	paragneiss	D35	matrix	0.15–0.22	0.37–0.43	0.14–0.22	0.75	0.02–0.03		
Raabs	eclogie	D63n	symplect.	0.32–0.35					0.37–0.38	0.47–0.48
Raabs	migmatite	D4a			0.62–0.65	0.18–0.26				
			matrix	0.15–0.18						

q quartz, *pl* plagioclase, *ksp* K-feldspar, *g* garnet, *ilm* ilmenite, *am* amphibole, *cpx* clinopyroxene, *opx* orthopyroxene, *o* omphacite, *cd* cordierite, *ky* kyanite, *sill* sillimanite, *and* andalusite, *mu* muscovite, *bi* biotite, *pa* paragonite, *crn* corundum, *liq* silicate melt. *Xfe* Fe(tot)/(Fe(tot) + Mg), *Alm* almandine = Fe(tot)/(Fe(tot) + Mg + Ca + Mn), *Prp* pyrope = Mg/(Fe(tot) + Mg + Ca + Mn), *Grs* grossular = Ca/(Fe(tot) + Mg + Ca + Mn), *Sps* spessartine = Mn/(Fe(tot) + Mg + Ca + Mn), *An* anorthite = Ca/(Ca + Na + K), *Ab* albite = Na/(Ca + Na + K), *Or* orthoclase = K/(Ca + Na + K)

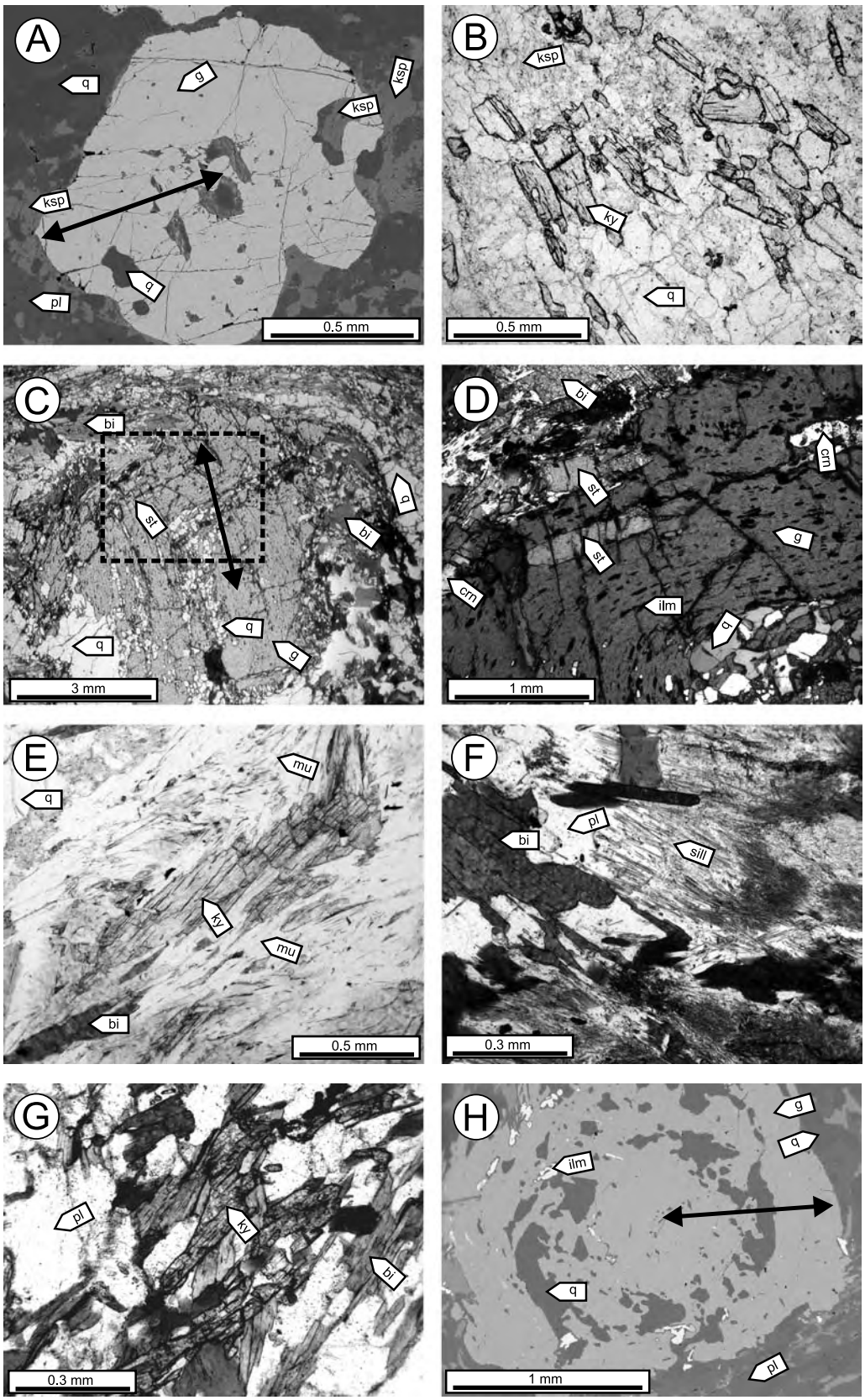
A
q
g
ksp
ksp
ksp
q
pl
0.5 mm
B
ksp
ky
q
0.5 mm
C
bi
str
q
bi
q
q
g
3 mm
D
bi
crn
str
g
str
crn
ilm
q
1 mm
E
mu
q
ky
mu
bi
0.5 mm
F
pl
bi
sill
0.3 mm
G
pl
ky
bi
0.3 mm
H
g
q
ilm
q
pl
1 mm

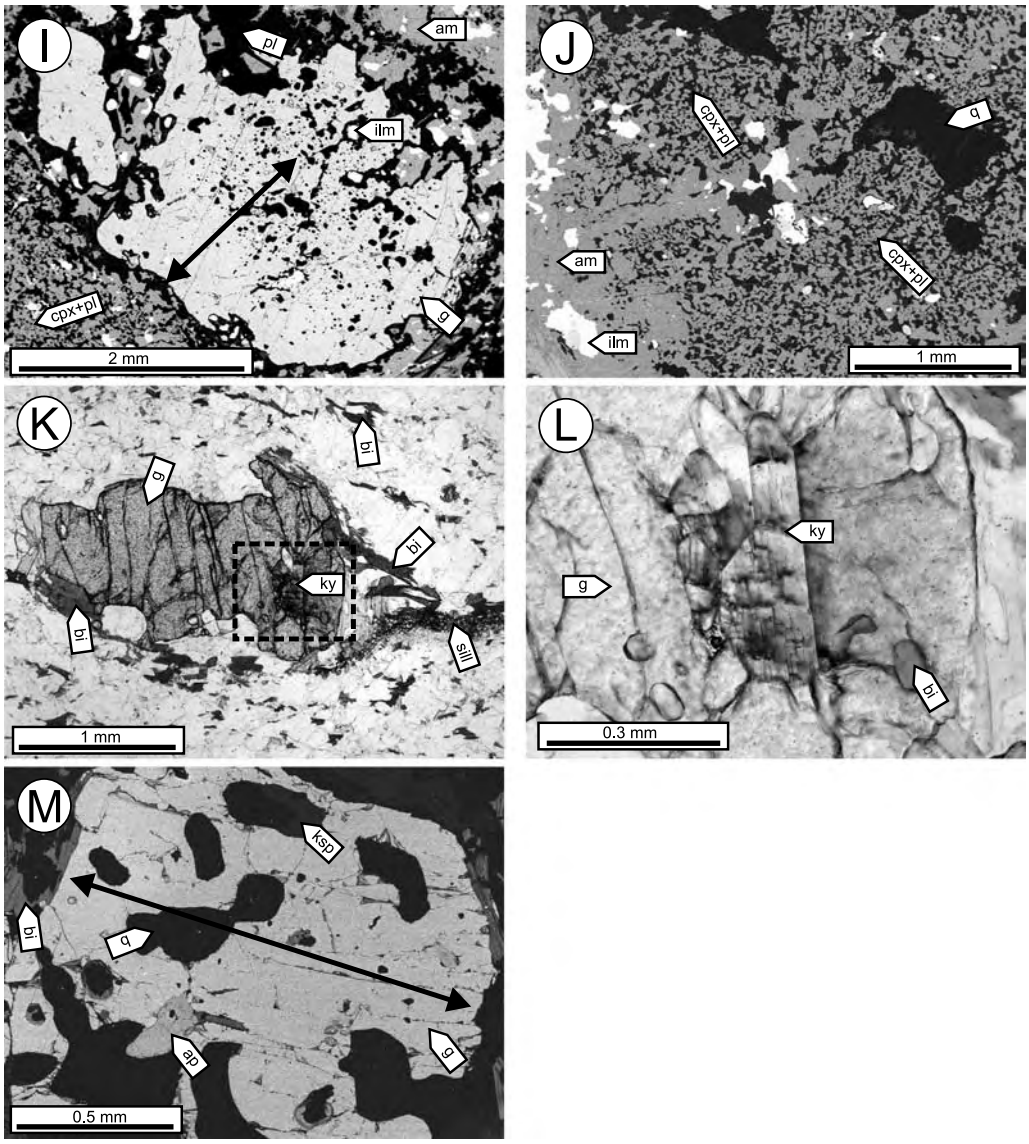

Fig. 3. Microphotographs of granulite sample D101pb: **A** Garnet with inclusions of quartz and K-feldspar, surrounded by matrix of K-feldspar, plagioclase and quartz. Arrow corresponds to the garnet profile in Fig. 4A (BSE-image). **B** Kyanite aligned in the recrystallized granulite matrix. Micaschist sample E162c of the Monotonous unit: **C** Garnet includes staurolite, plagioclase, ilmenite, quartz and locally corundum. Two foliations systems were overgrown by garnet during prograde path. Arrow corresponds to the profile in Fig. 4B. **D** Detail of staurolite inclusions in the garnet-rim (from Fig. 3C, crossed polars with gypsum plate). **E** Relic kyanite in the matrix, partially resorbed by muscovite. **F** Fibrolitic sillimanite with biotite and plagioclase in the S3 foliation. Paragneiss sample D35 of the Varied unit: **G** Kyanite in the matrix of biotite and plagioclase. **H** Arrow in the garnet corresponds to the profile in Fig. 4C (BSE-image). Eclogite sample D63n of the Raabs unit: **I** Garnet porphyroblast with inclusion-rich core and inclusion-poor rim, surrounded by corona of plagioclase in the matrix of clinopyroxene-plagioclase symplectites and amphibole. Arrow corresponds to the garnet profile in Fig. 4D (BSE-image). **J** Matrix of eclogite with clinopyroxene-plagioclase symplectites, amphibole, ilmenite and a cluster of quartz (BSE-image). Migmatite sample D4a of the Raabs unit: **K** Garnet with kyanite inclusion. Biotite and sillimanite define the S3 foliation. **L** Detail of kyanite inclusion in garnet (from Fig. 3K). **M** Garnet porphyroblast with inclusions of plagioclase and quartz. Arrow corresponds to the garnet profile in Fig. 4E (BSE-image)

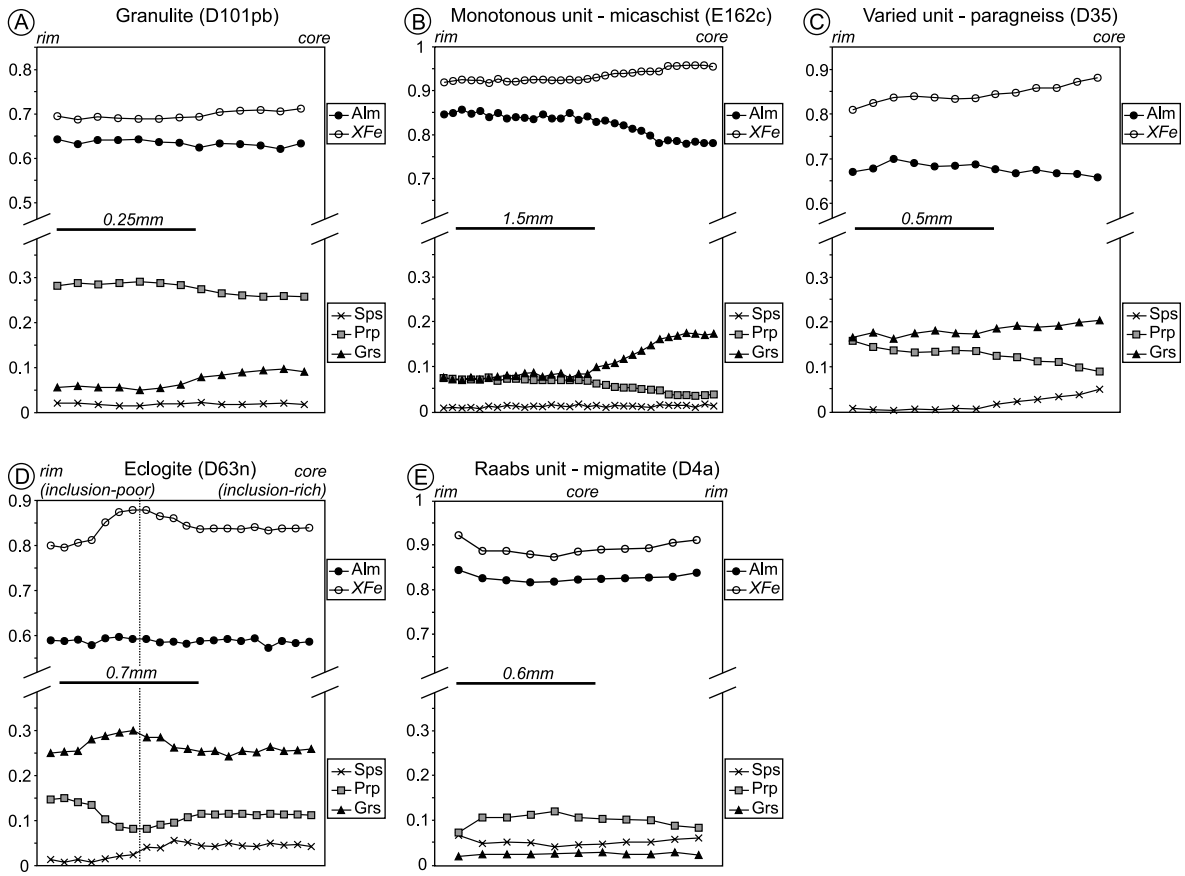

Fig. 4. Compositional profiles of garnets from **A** granulite, **B** micaschist of the Monotonous unit, **C** paragneiss of the Varied unit, **D** eclogite of the Raabs unit, **E** migmatite of the Raabs unit. Their positions are marked by arrows in Fig. 3A, C, H, I, M

the rim (Alm62 → 64, Prp26 → 28, Grs10 → 6, Sps2; XFe = 0.7–0.71) (Fig. 4A). The average composition of perthitic K-feldspar porphyroclasts measured by defocused beam is Or57–62Ab36–39An3. K-feldspar inclusions in garnet contain 21–26% of albite whereas the recrystallized K-feldspar has a lower albite amount (11–13%). Plagioclase in garnet contains 13–17% of anorthite whereas matrix plagioclase has lower anorthite content (An8–13).

Garnet in the sample D101c is unzoned and the composition is Alm75–79, Prp13–19, Grs4–6, Sps2; XFe = 0.81–0.85. The average composition of perthitic K-feldspar porphyroclasts is Or63, Ab34, An3, K-feldspar inclusions in garnet contain 26% of albite, recrystallized fine-grained K-feldspar has lower albite content (9–13%). Plagioclase has 14% of anorthite component. Biotite has XFe = 0.53 and its Ti content is negligible (0.16 pfu).

Micaschist (Monotonous unit, sample E162c)

The micaschists of the Monotonous unit are banded rocks composed of 1–2 millimetre thick monomineralic bands of quartz alternating with bands composed of

biotite, plagioclase and K-feldspar. This banding together with the preferred orientation of biotite defines the S3 foliation that wraps around large garnets (2–8 millimetres). Locally, sillimanite and muscovite are present on S3 foliation planes. In the eastern part of the Monotonous unit, the metapelitic rocks become strongly anatectic, and the S3 foliation is marked by layers of coarse-grained quartzo-feldspathic leucosome parallel to the original micaschist banding.

In sample E162c, garnet (2–8 millimetres) includes staurolite, plagioclase, quartz, ilmenite, apatite and locally corundum (Fig. 3C, D). The inclusion trails are generally S-shaped with the internal foliation (S2) in the garnet core oriented almost perpendicularly to the external foliation S3 and becoming parallel to the S3 at the garnet rims (Fig. 3C). Locally, rare kyanite is present in the matrix, partially pseudomorphed by muscovite (Fig. 3E). Fibrolitic sillimanite forms clusters commonly associated with biotite and muscovite in garnet pressure shadows (Fig. 3F).

Garnet is almandine-rich and strongly zoned (Fig. 4B) with decreasing grossular and XFe from core to rim (Alm78 $\rightarrow$ 85, Prp3 $\rightarrow$ 7, Grs17 $\rightarrow$ 7, Sps1; XFe = 0.96 $\rightarrow$ 0.92). Staurolite XFe is 0.91 and it contains 0.09–0.12 pfu of Zn. Biotite has XFe ranging from 0.69 to 0.76, and Ti = 0.18–0.26 pfu. Matrix plagioclase contains a lower amount of anorthite (An31–33) than plagioclase enclosed in garnet-cores (An38–44). K-feldspar contains 12–16% of albite.

Paragneiss (Varied unit, sample D35)

Paragneisses from the Varied unit contain biotite, sillimanite, muscovite, plagioclase, quartz and rare kyanite. Garnet is rarely preserved, being in general partly or totally replaced by common sillimanite-biotite nodules. These paragneisses are penetratively affected by the S3 foliation, marked by the preferred orientation of mica and sillimanite.

Sample D35 contains a well-preserved garnet in a matrix composed of biotite, plagioclase, quartz and kyanite (Fig. 3G). Garnet core and mantle are distinctly separated by a zone rich in inclusions of quartz and plagioclase (Fig. 3H). It also includes rutile and staurolite.

Garnet is zoned from core to rim: Alm64 $\rightarrow$ 67, Prp10 $\rightarrow$ 16, Grs21 $\rightarrow$ 17, Sps5 $\rightarrow$ 1; XFe = 0.87 $\rightarrow$ 0.81 (Fig. 4C). Biotite has XFe ranging between 0.37–0.43, its Ti content is 0.14–0.22 pfu. Staurolite has XFe around 0.75 and it contains 0.02–0.03 pfu of Zn. The composition of plagioclase in the matrix and in garnet is similar and ranges Ab78–84, An15–22, Or1.

Eclogite (D63n)

The retrogressed eclogite from the bottom of the Raabs unit is a massive coarse-grained rock with ill-defined foliation. It forms boudins in the garnet-free amphibolite sheet, almost penetratively affected by S3 foliation.

In the core of the boudins, the eclogite contains large garnets (up to 6 millimetres) in a matrix composed of coarse-grained clinopyroxene-plagioclase symplectite, amphibole, abundant quartz that forms monomineral clusters (up to 2 millimetres), accessory ilmenite and rutile. Garnet includes titanite and quartz and

is surrounded by coronas of plagioclase. Towards the margins of the boudins, garnet is replaced by plagioclase, the clinopyroxene-plagioclase symplectite is progressively replaced by amphibole-plagioclase and the S3 fabric becomes more intense. The surrounding amphibolite consists of amphibole, plagioclase, quartz and titanite.

The studied sample D63n is a massive coarse-grained eclogite from the boudin core, characterized by well-preserved clinopyroxene-plagioclase symplectites and large (4–6 millimetres) garnets that form up to 30% of this rock.

Garnet contains numerous inclusions of quartz titanite and ilmenite in the core, whereas the margins are inclusion-poor (Fig. 3I). Plagioclase coronas with amphibole develop around the garnet porphyroblasts and indicate its resorption. The matrix is formed by domains of coarse-grained clinopyroxene-plagioclase symplectite (Fig. 3J) with clinopyroxene being partly replaced by amphibole and domains of coarse-grained amphibole-plagioclase symplectites. Approximately 20% of the matrix is formed by large (2–4 millimetres) clusters of quartz. A considerable amount of ilmenite is present in the matrix.

The inclusion-rich garnet core is zoned with increasing grossular-content and XFe (Alm59 $\rightarrow$ 60, Prp11 $\rightarrow$ 9, Grs24 $\rightarrow$ 30, Sps5 $\rightarrow$ 2; XFe = 0.84–0.87), while in the inclusion-poor margin grossular and XFe decreases to Alm59, Prp15, Grs25, Sps1; XFe = 0.80 (Fig. 4D). Clinopyroxene has XFe = 0.37–0.38 and $Ca/(Ca + Fe + Mg) = 0.47$–0.48. Amphibole is Mg-hornblende with XFe = 0.46–0.49 and Si = 6.61–6.82 pfu. Plagioclase contains 32–35% of anorthite.

Felsic migmatitic gneiss (the Raabs unit, sample D4a)

The migmatitic gneisses (the Kolmitz gneiss) occur at the base of the Raabs unit, above the eclogite-bearing belt. They are heterogeneous leucocratic migmatites, composed predominantly of K-feldspar, plagioclase and quartz, forming about 80% of the rock, biotite-rich melanosomes, garnet and occasional sillimanite. Kyanite is rarely present in some samples as small inclusions in garnet and plagioclase. Patches of granitic appearance occur within the migmatite, have variable size up to several metres and probably represent crystallized melt. Although the migmatitic foliation is ill-defined, the biotite-rich restites, in general un-oriented, in places mark a steep foliation S2. Superimposed solid-state deformation D3 develops flat-lying shear zones. The intensity increases towards the east where at the border with the Varied unit the gneisses display a penetrative foliation S3. It is accompanied by dynamic recrystallization of feldspars and quartz and by the growth of biotite and sillimanite on the S3 foliation planes.

The sample D4a (Fig. 3K, L, M) represents a migmatite with superimposed solid-state deformation. It contains small garnet porphyroblasts (1–4 millimetres 5 modal %), minor biotite (5%) and prismatic sillimanite aligned in the S3 foliation. Garnet includes feldspars, quartz and kyanite. Kyanite is also present as small inclusions in matrix plagioclase.

Garnet is slightly zoned (Alm81–85, Prp9–12, Grs2–3, Sps4–6; XFe = 0.86–0.91) (Fig. 4E). Large K-feldspar porphyroclasts (Ab15–31) and inclusions in garnet (Ab40) have higher content of albite than recrystallized matrix K-feldspar (Ab9–17). Plagioclase contains 15–18% of anorthite and 1–3% of orthoclase. Biotite has XFe = 0.62–0.65 and Ti = 0.18–0.26 pfu.

Pseudosections and PT evolution

The observed mineral assemblages, mineral compositions and textural relationships are compared with the stability and compositions of the phases in P–T–X pseudosections in order to determine the PT evolution of the studied samples. The pseudosection modelling was undertaken with THERMOCALC 3.23 (*Powell* et al., 1998: recent upgrade) and the internally-consistent thermodynamic dataset 5.5 (*Holland* and *Powell*, 1998: Nov. 2003 upgrade). The datafile coding of the activity-composition relationships of the minerals and melt used in the calculations is that of *White* et al. (2001), with the feldspar model of *Holland* and *Powell* (2003) and amphibole model from *Wei* et al. (2003). The rock compositions were calculated from the modal proportions of the minerals and their chemical compositions according to the method outlined in *Stüwe* and *Powell* (1995). PT conditions of matrix reequilibration were calculated using the THERMOCALC average PT method. The results are presented with 1σ uncertainty.

Ky-ksp granulite (samples D101pb, D101c)

One of the major problems when calculating pseudosections at the amphibolite-/granulite-facies transition, is the estimation of the amount of available H_2O that has an important influence on the mineral stability, especially during the retrograde PT evolution (*Powell* and *Downes*, 1990; *White* and *Powell*, 2002). In order to determine the H_2O content of the studied granulite, a TX pseudosection with varying H_2O content was constructed (Fig. 5A) and compared with the observed mineralogy of the sample. The H_2O amount of the rock (0.99% mol.) was chosen so that it allows the observed stability of alumosilicate below the solidus. The pressure used for the calculation of TX-pseudosection (7.5 kbar) was chosen approximately according to the conditions of retrogression (see below).

The main features of the PT pseudosection for the granulite (Fig. 5B, C) involve the positive slope of the solidus between 650 and 870 °C and the character of biotite stability that is pressure-dependent below the solidus and temperature-dependent in the presence of melt. The upper temperature limit of 2-feldspar stability field is 880 °C.

The peak mineral assemblage in the granulite is garnet, kyanite, plagioclase, K-feldspar and quartz, and it situates the PT conditions in the large g-ky-pl-liq field. The garnet cores with high Ca-content (Grs = 10%, XFe = 0.71) then constrain the peak PT conditions to approximately 800 °C and 15 kbar (Fig. 5C; pt. 1). In the following stage, garnet is overgrown by biotite, kyanite is locally replaced by sillimanite and the recrystallised matrix is composed of K-feldspar, plagioclase and quartz. These features indicate that PT conditions were in the g-sill-bi-pl-liq field (Fig. 5C; pt. 2), in the PT range between 700–760 °C and 5–10 kbar. This is also supported by the composition of garnet rims (Grs = 5%, XFe = 0.7), where the grossular content constrains pressure to approximately 9 kbar. The average PT calculation for the assemblage g-ky-bi-pl-ksp-q for the sample D101c yields 759 ± 50 °C and 10.7 ± 1.5 kbar (1σ), which is coherent with the pseudosection topology.

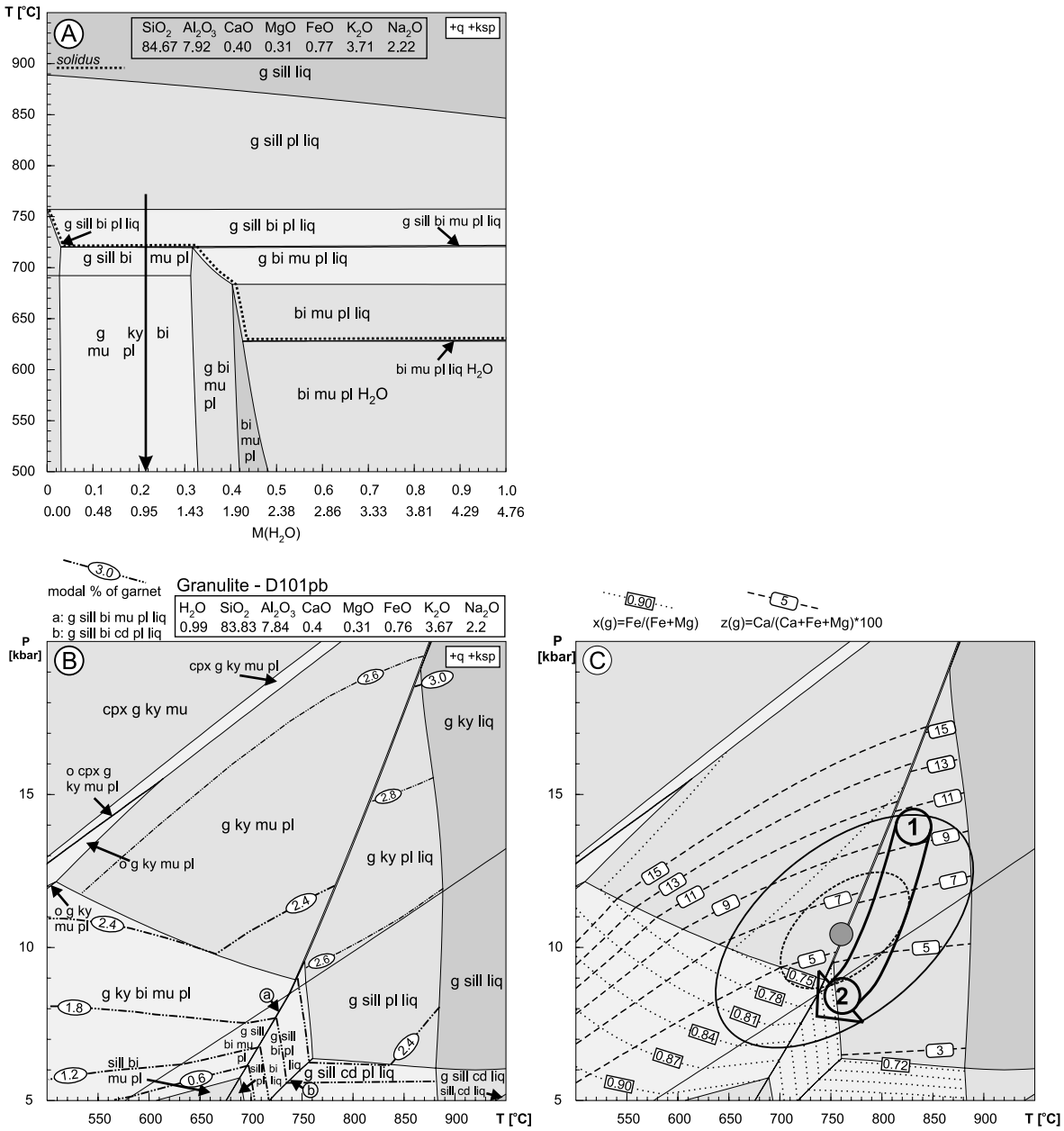

Fig. 5. **A** T-XH_2O pseudosection at 7.5 kbar for the granulite (D101pb). The modal proportion of H_2O (M(H_2O)) in the rock composition ranges between 0 and 4.76% and the position of the solidus and the solidus assemblages vary with increasing H_2O content. The observed matrix assemblage g-sill-bi-pl ± mu restricts the H_2O proportion at solidus for the studied sample to 0.15–1.5 modal %. An intermediate value of 0.99% H_2O is used for the construction of PT pseudosection. **B** PT pseudosection for the granulite sample D101pb contoured for the modal proportion of garnet and **C** contoured for the XFe and grossular-content in garnet PT-path (also discussed in the text): (1) grossular-rich garnet core, (2) grossular-poor garnet rims. The results of average PT calculations for the retrogression are plotted with 1σ and 2σ uncertainties

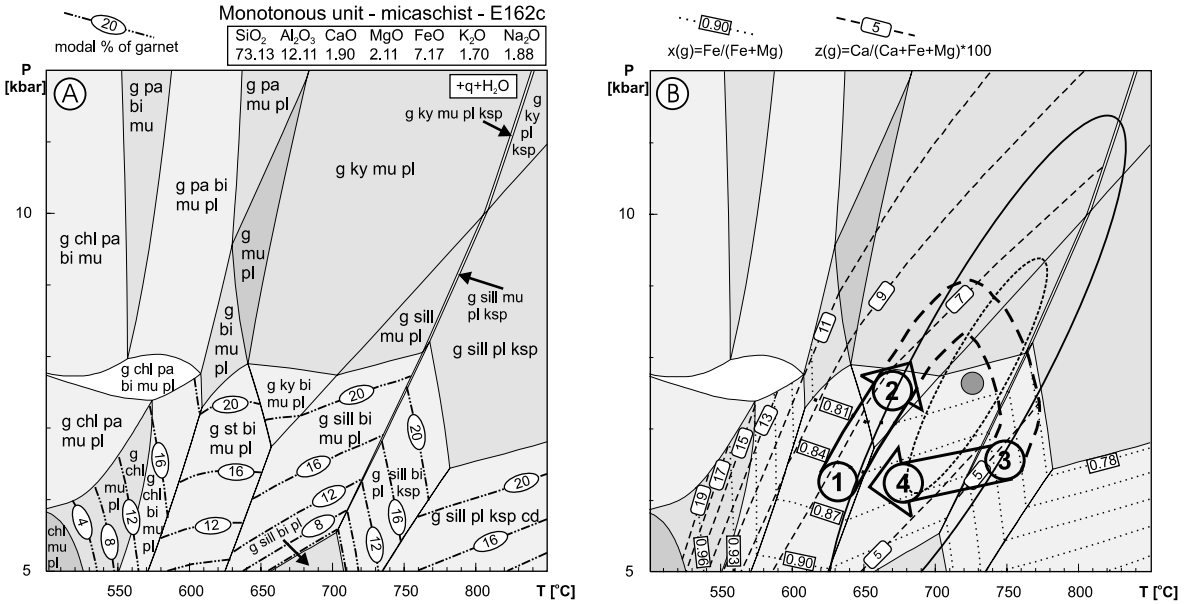

Fig. 6. PT pseudosection for the micaschist from the Monotonous unit (sample E162c). PT-path: (1) staurolite inclusions in garnet, (2) kyanite relics in matrix, (3) occurrence of sillimanite and K-feldspar, (4) appearance of muscovite. The dashed part of PT-path corresponds to the uncertain constraint of pressure in the kyanite stability field

Micaschist (Monotonous unit, sample E162c)

The bulk composition used to calculate the PT pseudosection for the micaschist E162c from the Monotonous unit was one supposed effective for the crystallisation of the garnet rims and matrix minerals. Consequently, the strongly zoned garnet cores were not taken into account in the calculation of the bulk composition. The main features of the pseudosection (Fig. 6) involve the stability of staurolite that occurs below 650 °C and 8 kbar and the stability of alumosilicate (kyanite or sillimanite) above 5 kbar and 620 °C. The upper stability of biotite is at about 8 kbar and 780 °C. The pseudosection was calculated with H_2O in excess and its high-temperature side is metastable with respect to melt.

The succession of three mineral assemblages was deduced from textural relationships. Staurolite inclusions in the garnet rim belong to the first assemblage that correlates with the trivariant field g-st-bi-mu-pl, restricting the PT conditions to 550–650 °C and 4–8 kbar (Fig. 6B; pt. 1). The second mineral assemblage involves the kyanite relics in the matrix that reflect the shift to the g-ky-bi-mu-pl trivariant field and to the conditions of 630–700 °C and 6–8 kbar (Fig. 6B; pt. 2). However, kyanite could grow also above the biotite-out curve and the micaschist could reach higher pressure. The stable grossular content (approximately 7%) of the garnet rims is consistent with this prograde path, although the isopleths of XFe in the pseudosection have lower values than those measured in the garnet. This is ascribed to the diffusional re-equilibration of XFe. Sillimanite and K-feldspar that are present in the biotite-bearing matrix reflect an equilibration in the g-sill-bi-pl-ksp field (700–790 °C, 4–8 kbar) (Fig. 6B; pt. 3). This assemblage is here interpreted to be reached on decompression, but an isobaric increase in temperature

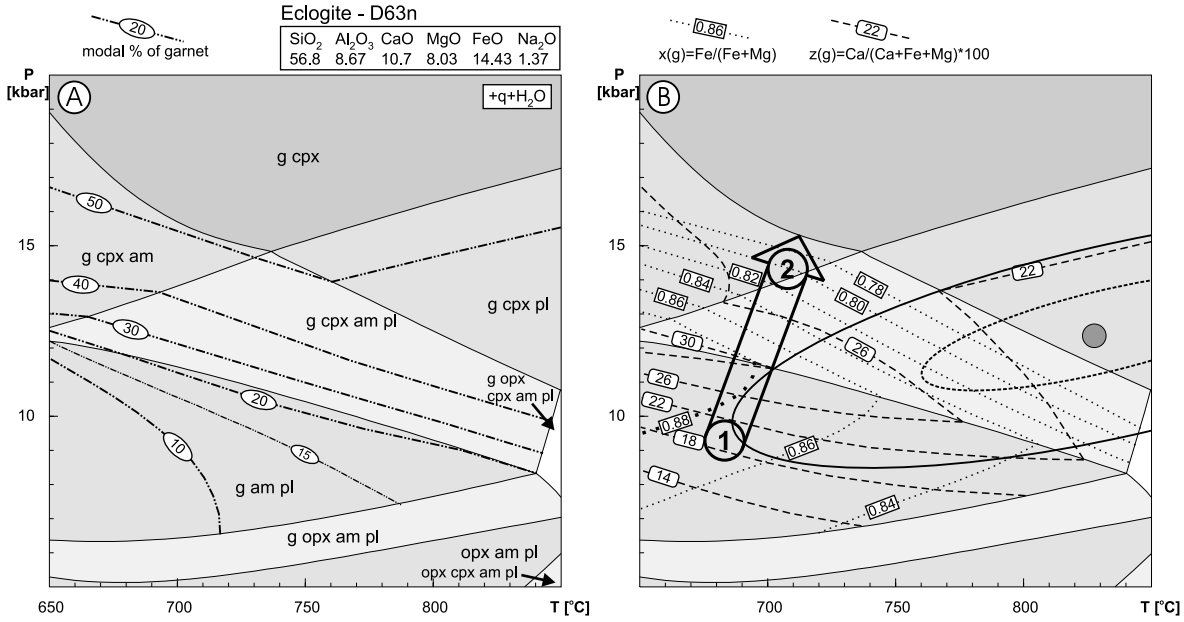

Fig. 7. PT pseudosection for the eclogite from the bottom of the Raabs unit (sample D63n) Prograde PT-path is deduced from the garnet zoning. (1) Inclusion-rich core, (2) inclusion-poor rim

cannot be excluded. The late crystallization of matrix muscovite in apparent equilibrium with sillimanite reflects cooling to the g-sill-bi-mu-pl stability field; T = 610–750 °C, P = 4–8 kbar (Fig. 6B; pt. 4). The average PT calculations for this mineral assemblage (g-sill-bi-mu-pl-q) yield PT conditions 730 ± 41 °C and 7.7 ± 1.5 kbar.

Eclogite (D63n)

The pseudosection for the eclogite (Fig. 7) was calculated with H_2O in excess and is metastable with respect to melt at high temperature. Garnet is stable above 5–7 kbar and clinopyroxene occurs above 8–12 kbar. The plagioclase stability limit has a positive slope and ranges between 13–17 kbar, whereas the line restricting the stability of amphibole runs from 19 to 11 kbar with a negative slope.

The eclogite does not contain any relics of jadeite-rich clinopyroxene. The main target therefore was to understand the significance of the garnet zoning in order to use it for the determination of peak pressure conditions (Fig. 4D). This approach is flawed, however, by the insufficiency of available solid-solution models for amphibole. The results have therefore a qualitative rather than quantitative significance. According to the trend of the grossular and XFe isopleths (Fig. 7B), garnet records the growth under increasing pressure. The observed increase of grossular and XFe at the border of the core region corresponds to the increase of pressure in the quadrivariant field g-amp-pl (Fig. 7B; pt. 1). The following decrease of both values (Grs = 30 → 25%, XFe = 0.88 → 0.80) is consistent with further increase in pressure to the g-cpx-amp ± pl fields (Fig. 7B; pt. 2) reaching

the maximum at c. 14–15 kbar at a temperature of around 700 °C. This is a minimum pressure because the garnet rims are resorbed as indicated by plagioclase-amphibole coronas.

The result of the average PT calculations for the matrix assemblage g-cpx-amp-pl-q is 837 ± 82 °C and 12.4 ± 1.5 kbar. However, the widespread presence of symplectites suggests that this result corresponds to a partial equilibration during decompression and does not reflect the PT conditions during the development of the S3 foliation. We interpret the peak temperature of metamorphism to be in the lower temperature side of the uncertainty ellipse, say <850 °C, because of the preservation of garnet growth zoning.

Felsic migmatitic gneiss (the Raabs unit, sample D4a)

The H_2O-content for the calculation of the PT pseudosection for the migmatite from the Raabs unit was estimated in the same way as for the granulite (see Fig. 5A). The solidus with positive slope ranges between 700 and 860 °C, biotite is stable up to 10–13 kbar and 750 °C (Fig. 8).

The observed relics of kyanite included in garnet and plagioclase suggest early conditions in the kyanite stability field. Because kyanite can be included in garnet only during garnet growth, the texture indicates a record of a prograde path (Fig. 8B; pt. 1). However, the lack of additional information, as for example preserved garnet zoning, does not allow specifying these conditions. The following stage is recorded by the matrix equilibrium between K-feldspar, plagioclase, quartz,

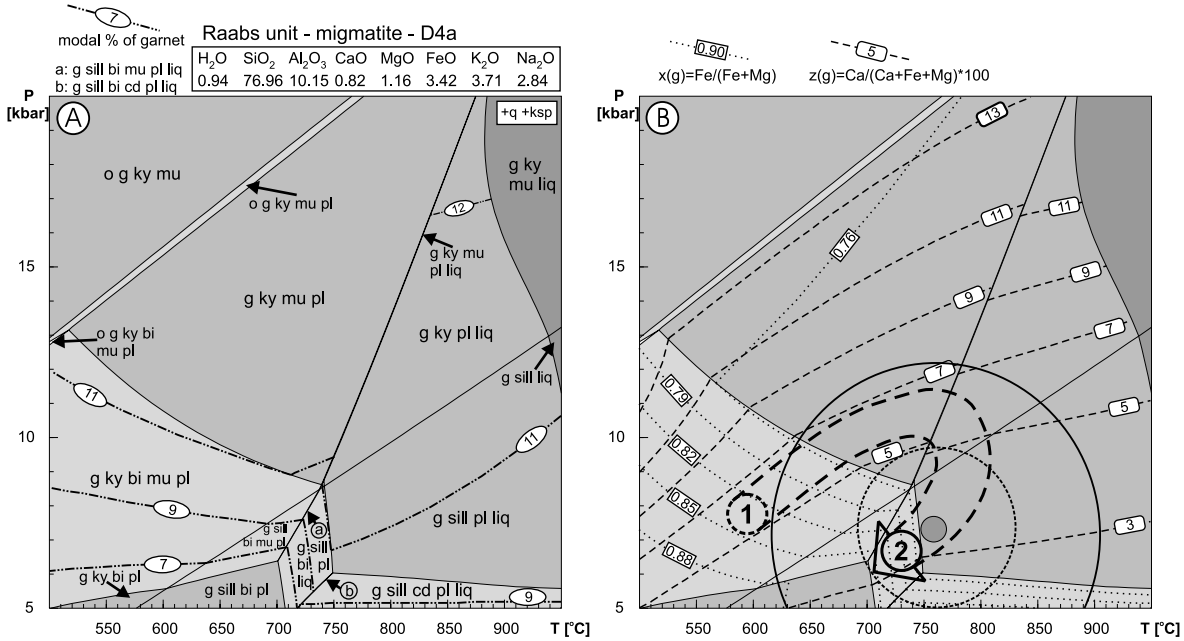

Fig. 8. PT pseudosection for the migmatite from the Raabs unit (sample D4a). The prograde path is deduced from kyanite overgrown by garnet that corresponds in the pseudosection to the increase in garnet modal content in the kyanite stability field. The dashed pattern is used due to impossibility of any PT constrain. Pt. 2 corresponds to retrogression

garnet, sillimanite and minor biotite and corresponds to the field g-sill-bi-pl-liq between 700–750 °C and 4–9 kbar or to the field g-sill-bi-pl (550–710 °C, 3–6 kbar) (Fig. 8B; pt. 2). The composition of garnet (Grs = 3%, XFe = 0.87) constrains the conditions to approximately 700 °C and 5–6 kbar. The average PT calculations for the assemblage g-sill-bi-pl-ksp-q give 761 ± 58 °C and 7.5 ± 1.9 kbar.

Discussion

The contrasting prograde and peak PT conditions within orogenic lower and middle crust

The petrological investigation across the Drosendorf window reveals contrasting PT evolution in individual units, where medium-pressure rocks are sandwiched between two high-pressure belts. The eastern high-pressure belt is represented by a granulite sheet, where no prograde features were found, and the pressure of approximately 15 kbar indicates burial depth down to about 55 kilometers (Fig. 9). The second high pressure belt is represented by the eclogite-bearing amphibolite at the base of the Raabs unit, where prograde burial from about 10 kbar (~36 kilometers) to a minimum depth of 15 kbar (~55 kilometers) is recorded by the preserved prograde garnet zoning. Although the temperature in the granulite and in the eclogite at the pressure peak is difficult to constrain precisely, a minimum of c. 800 °C is indicated by the absence of primary muscovite in the granulite. A calculated temperature of 837 ± 87 °C in the retrogressed eclogite, even if imprecise and attained on decompression path, also indicates high temperature conditions. No direct relation of the high pressure assemblages to the structure is preserved, but they clearly pre-date the flat D3 mylonitization.

The degree of anatexis above the granulite belt decreases to the top of the middle crustal sequence from where two micaschist samples, one from the Monotonous unit and one from the Varied unit, preserve the prograde evolution. The garnet growth zoning, staurolite inclusions and matrix kyanite in both samples indicate the burial from c. 600 °C and 6 kbar to min. 8 kbar and 650–700 °C (Fig. 9). The preserved XFe zoning in the sample from the Varied unit may be a sign of slightly lower temperature conditions with respect to the Monotonous unit, where the XFe is interpreted to be diffusionally flattened and where muscovite breakdown and K-feldspar growth indicate temperatures of at least 750 °C.

PT conditions of D3 deformation

The D3 deformation in the granulite is marked by strong matrix recrystallization, reorientation of kyanite, growth of sillimanite and decrease of grossular content at garnet rims. These retrograde features are consistent with calculated PT conditions of 10.7 ± 1.5 kbar and 759 ± 50 °C (Fig. 9). In the micaschist sample from the Monotonous unit the decompression into the sillimanite field occurred in the stability field of K-feldspar, which constraints the minimum temperature to 750 °C at pressure of 7–8 kbar. The widespread muscovite growth on the S3 foliation planes indicates further near isobaric cooling as confirmed also by corresponding average PT calculation of 730 ± 41 °C and 7.7 ± 1.5 kbar. Similar PT conditions

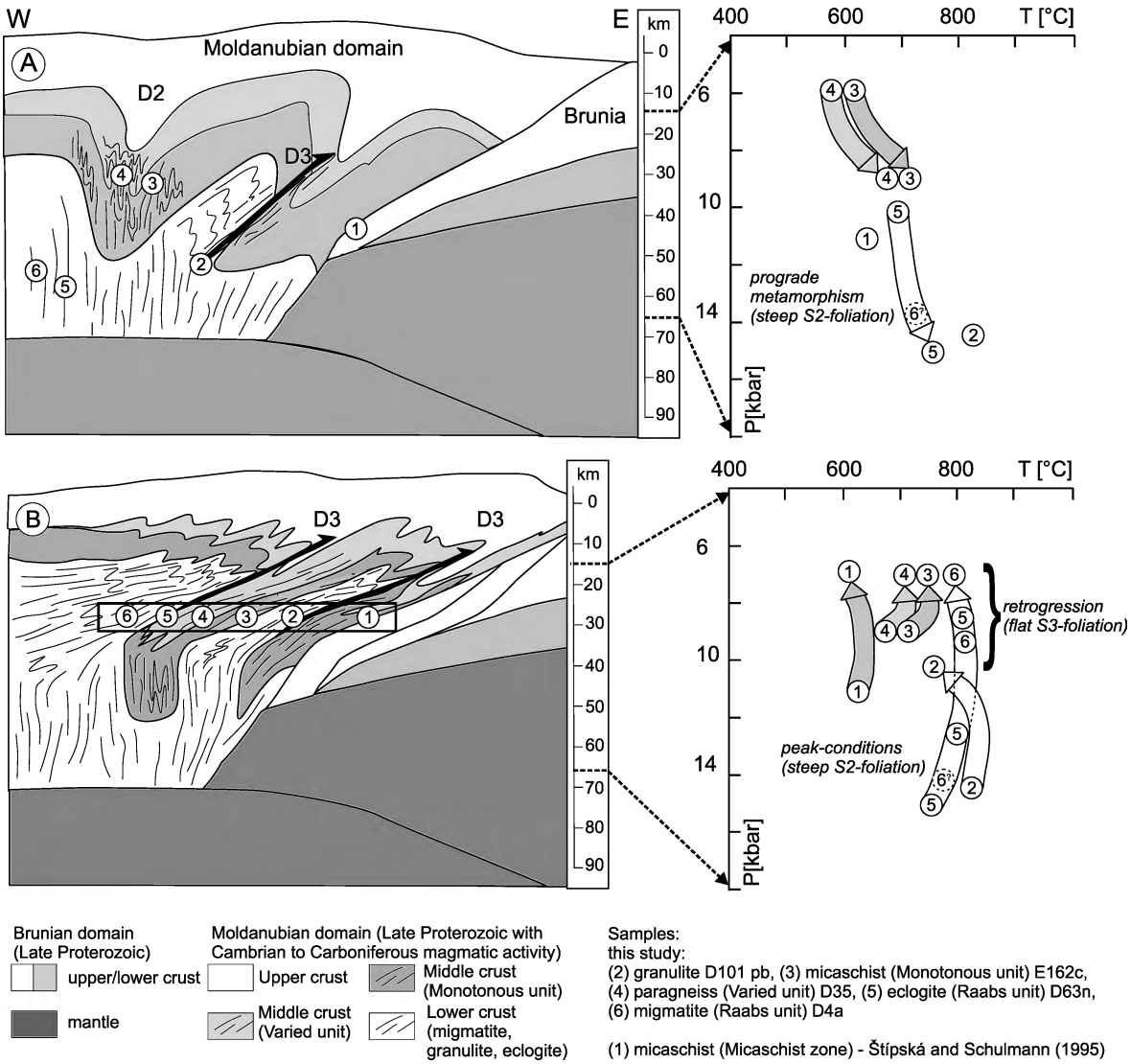

Fig. 9. A tectonic model proposed for the evolution of the Drosendorf window as deduced from structure and PT paths of the studied samples. **A** The generation of steep foliation S2 due to the E–W compression. Thickening and prograde metamorphism in all levels is followed by vertical extrusion of lower crust into middle crustal depth. **B** Localized exhumation along steep fabrics brings portions of high-pressure lower crust against the middle-crustal samples. The originally vertical alternation of middle and lower crustal belts is affected at 7–10 kbar by flat foliation S3 that is attributed to the indentation depth of the Brunia basement

of retrogression are deduced from the micaschist within the Varied unit. The S3 retrogression in the Raabs unit is achieved after decompression, as deduced from the migmatite sample that contains kyanite inclusions in garnet. The mylonitic foliation S3 is marked by sillimanite and biotite, and very low grossular content in garnet, which indicates diffusional reequilibration at low pressure, consistent with calculated average PT conditions of 761 ± 58 °C and 7.5 ± 1.9 kbar.

The significance of prograde and peak metamorphic evolution and comparison with other parts of the Moldanubian domain

The well preserved prograde metamorphic evolution in the Monotonous and Varied units of the Drosendorf window indicates burial to about 28 kilometers (~8 kbar) that corresponds to the PT conditions reported from other parts of Lower Austria (*Petrakakis*, 1997) and from the middle crustal structures further to the north by *Pitra* and *Guiraud* (1996). However, the occurrence of eclogites was reported from other parts of the Moldanubian domain within the Monotonous and Varied units (e.g. *Medaris* et al., 1995; *O'Brien* and *Vrána*, 1995; *Linner*, 1996; *O'Brien*, 1997). These units were therefore buried into various depth levels in different parts of the Moldanubian domain and in some parts middle crust became a part of the lower orogenic crust. In these cases, it is difficult to define exactly which lithology forms a part of the Monotonous and Varied units (lithological criterion) and which rock assemblage shows metamorphic conditions corresponding to the so-called Gföhl high-grade unit (metamorphic criterion). This nomenclature problem arises also in the present study, indeed, no tectonic contact is observed between the base of the Monotonous unit and the high-grade lower crustal layered amphibolite and the ''Gföhl'' granulite. It is therefore possible that these rocks represent a continuous lithological and metamorphic lower-middle crustal section, which is in agreement with the evolution of the PT conditions. The layered amphibolite and granulite that are in other Moldanubian areas called the Gföhl unit, may therefore be viewed here as the base of the Monotonous unit.

The prograde evolution deduced from the garnet zoning in the eclogite at the base of the western Gföhl-Raabs unit indicates its burial from 10 to a minimum of 15 kbar and consequently the thickening to 55 kilometers, if the minimum pressure estimate is taken into account (Fig. 9). Similar garnet zoning profiles from eclogites with peak pressure of about 18 kbar associated with the Gföhl granulites were also interpreted as prograde by *Medaris* et al. (1998) and *Štípská* and *Powell* (2005b). Another well documented prograde PT evolution was suggested for burial of the Gföhl lower crust by *Štípská* and *Powell* (2005a) on the example of prograde garnet from orthopyroxene granulites. These prograde paths of eclogites and granulites of the Gföhl and Raabs-type lithologies indicate important process of thickening from approximately 35 up to 65 kilometers in units that we call the ''orogenic lower crust'' (Fig. 9).

From the ternary feldspar and garnet-clinopyroxene thermometry it was suggested that the temperature at the base of the thickened lower crust at about 18 kbar attained more than 1000 °C (e.g. *Carswell* and *O'Brien*, 1993; *Cooke*, 2000; *Cooke* and *O'Brien*, 2001). However, based on textural relationships of ternary feldspars included in prograde garnets, *Štípská* and *Powell* (2005a) suggest that this very high temperature was attained at much lower pressure and resulted from hot magma emplacement and crystallization that was followed by a period of major thickening. The preservation of prograde garnet zoning in the eclogite from this study (even for the XFe), and from other eclogites found within the Varied, Monotonous and Gföhl units (*Medaris* et al., 1995, 1998; *O'Brien* and *Vrána*, 1995; *Štípská* and *Powell*, 2005b) also supports the lower temperature estimates for the base of the thickened crust, say of maximum 850 °C, at least in some parts of the orogenic root.

Correlation of the Drosendorf metamorphic sequence with other parts of the collisional front

There exist two recent studies along the eastern Variscan collisional front that describe structure and exhumation of orogenic lower crust in the thickened Moldanubian root adjacent to the Brunian continental margin (*Štípská* et al., 2004; *Schulmann* et al., 2005) and similar structures are also described from the southern part of the Moldanubian domain by *Franěk* et al. (this volume).

Štípská et al. (2004) studied a 2 km wide HP granulite belt that occurs in the northernmost termination of the eastern Variscan collisional front and proposed a new exhumation model of lower crust by its ductile vertical extrusion in front of a rigid indenting block. These authors described the transition from vertical extrusion from about 18 kbar to lateral spreading in a depth level of about 10 kbar at approximately 700 °C. The lateral spreading of the exhumed lower crust is manifested by the development of amphibolite facies shear zones in the HP granulites as well as in the adjacent middle crust that is compatible with thrusting over the easterly rigid indentor.

Schulmann et al. (2005) examined the central sector of the eastern collisional margin and defined alternations of orogenic lower and middle crustal belts that show fairly similar structural pattern to that described in this work. These authors interpreted the internal lower crustal belt as a large scale, 20 kilometers wide extrusion that was thrust in a bivergent manner over the middle crustal synclines. They further interpreted the structural and metamorphic pattern of the external lower crustal belt as a result of a hot lower crustal channel flow driven by lateral movements of a rigid continental indentor.

We suggest that the superpositions of high-grade lower crustal rocks (the granulite and the Raabs migmatite) over middle crustal units observed in the studied area represent two lower crustal extrusions over middle crustal units and are equivalent to the orogenic middle and lower crustal alternations described by *Schulmann* et al. (2005). In our interpretation, the eastern granulite belt was extruded along a lower crustal channel parallel to the Brunian crustal indentor from a depth of at least 55 kilometers (∼15 kbar) to about 35 kilometers (∼10 kbar) (Fig. 9). The section from the eastern lower crustal granulite up to the Monotonous and Varied units that form the core of the Drosendorf window represents, according to our knowledge, the best preserved continuous section of the thickened orogenic crust. The retrogression and thrusting started at about 10 kbar that indicates the depth level of indentation of the upper part of the lithospheric Brunian continental indentor into the adjacent hot root (Fig. 9). The depth of thrusting of orogenic lower crust over the rigid indentor is supported by peak pressure of 10–12 kbar reported from the western Brunia derived thrust sheet (the ''Micaschist zone'') by *Štípská* and *Schulmann* (1995).

This indentation scenario is fundamentally similar to the tectonic models proposed by *Štípská* et al. (2004, Fig. 10) and *Schulmann* et al. (2005, Fig. 18). We suggest that the structural relationships between orogenic lower and middle crusts as well as the peak pressure conditions are similar in all these studied sectors. The lower crustal extrusions into middle crust occur along steep channels initiated by steep folding of thickened crustal layers. The flat thrusting of lower crust over

middle crust (here of the Raabs unit over the Varied unit and the eastern granulite over the Brunia) is interpreted in terms of lateral spreading of the Moldanubian root over the indenting Brunia continent. The main difference is in the level of lateral spreading or D3 flat thrusting that vary from 10 kbar in the north (*Štípská* et al., 2004) to 7–10 kbar in the Drosendorf cross section. We suggest that it is the tectonic evolution of the indenting plate, namely the degree of its imbrication that controls the depth level of the lower crustal spreading in different parts of the orogenic front.

Correlation of the new interpretation of the Drosendorf sequence with classical studies from Lower Austria

The intra-Moldanubian structure of the high-grade Gföhl unit thrust over the lower grade Monotonous and Varied units that was firstly described in a series of papers by *Fuchs* (1971, 1976), *Fuchs* and *Matura* (1976) and *Thiele* (1976) is perfectly valid for the lower-crustal Raabs unit thrust over the middle-crustal Varied unit in the western part of the Drosendorf window. However, in the eastern part of the window, there is a lithological and metamorphic continuity from the lower-crustal complexes with the Gföhl type granulite and the Raabs-type layered amphibolite at the base, continuously passing upwards into the Monotonous sequence of paragneisses with progressively decreasing amount of layered amphibolites. This lithological continuity is also accompanied by a decrease in metamorphic grade. Instead of one continuous thrust of the Gföhl high-grade nappe that was supposed to be overturned by folding in the eastern part of the Drosendorf window by *Fuchs* (1971, 1976) and then adopted in the large-scale interpretations by *Tollmann* (1982), *Franke* (1989) and *Matte* (1991), we interpret the eastern sequence as a complete attenuated lower-middle crustal section with a thrust located at the base of the eastern granulite. Our interpretation of two subvertical extrusions derived from lower crust and then laterally spread over middle crust is however in agreement with the proposal of the ''autochtonous'' nature of the lower-crustal nappes by *Fuchs* (1976).

Conclusions

1. The petrological and structural study across the Drosendorf window revealed preservation of a continuous, but attenuated profile of lower-middle crustal orogenic section overthrust by a second lower-crustal complex. The asymmetrical lithological and metamorphic structure precludes the existence of a Gföhl thrust overturned by folding as suggested by *Fuchs* (1971, 1976) in the eastern part of the window. Consequently, the presented data do not support the concept of a far-travelled large-scale lower-crustal Gföhl nappe thrust over the mid-crustal Monotonous and Varied units (*Tollmann*, 1982; *Franke*, 1989; *Matte*, 1991), but indicate the presence of two lower-crustal ''autochtonous'' extrusions into middle crust similarly as described from sections further to the north (*Štípská* et al., 2004; *Schulmann* et al., 2005).
2. The first thrust is located at the base of the granulite and formed at a minimum pressure of 15 kbar and 800 °C, and it exhumed a lower crustal (Raabs-type) layered amphibolite complex and the middle-crustal Monotonous and Varied

units at the top. The continuity within the section is indicated by gradual lithological changes and by continuous decrease in metamorphic grade up to the micaschists of the Monotonous and Varied units that preserve prograde evolution from approximately 6 kbar and 600 °C to about 8 kbar and 650–700 °C.

3. The second lower-crustal complex of migmatites (the Raabs unit) was thrust over the Varied unit from minimum pressures of 15 kbar as indicated by an eclogite-bearing belt at its base. Importantly, the eclogite also preserves a prograde garnet zoning developed under burial from about 10 kbar to a minimum of 15 kbar thus reflecting important thickening within the orogenic lower crust prior to the exhumation.
4. An intense moderately-dipping foliation has developed at 7–10 kbar and approximately 750 °C and affects the entire lower-middle crustal sequence. It indicates that the exhumation of the orogenic lower crust into middle crustal level occurred earlier, probably along a steep fabric that is locally preserved in all the units. The intense reworking is associated with flat thrusting within the Moldanubian root and with thrusting of the Moldanubian domain over the Brunia. The level in which the reworking occurred is attributed to the indentation depth of the Brunian continental crust.

Acknowledgements

This work was financially supported by the Charles University Grant Agency (No. 149/2000/B-GEO/PrF to P. Štípská) and the Czech National Grant Agency (No. 205-05-2187 to P. Štípská). *P. Štípská, K. Schulmann* and *O. Lexa* also received financial support from the Czech Ministry of Education (No. 24313005). We would like to thank reviewers *F. Neubauer* and *E. Dachs* for constructive corrections and remarks to this paper and *V. Janoušek* for editorial handling. We gratefully acknowledge *Z. Korbelová* and *A. Langrová* from the Geological Institute of the Czech Academy of Sciences and *J. Haloda* from the Czech Geological Survey for operating the microprobe.

References

Büttner S, Kruhl JH (1997) The evolution of a late-Variscan high-T/low-P region: the southeastern margin of the Bohemian Massif. Geol Rundsch 86: 21–38

Carswell DA, O'Brien PJ (1993) Thermobarometry and geotectonic significance of high-pressure granulites: examples from the Moldanubian Zone of the Bohemian Massif in Lower Austria. J Petrol 34: 427–459

Cooke RA (2000) High-pressure/temperature metamorphism in the St. Leonhard Granulite Massif, Austria: evidence from intermediate pyroxene-bearing granulites. Int J Earth Sci 89: 631–651

Cooke RA, O'Brien PJ (2001) Resolving the relationship between high P–T rocks and gneisses in collisional terranes: an example from the Gföhl gneiss-granulite association in the Moldanubian Zone, Austria. Lithos 58: 33–54

Cooke RA, O'Brien PJ, Carswell DA (2000) Garnet zoning and the identification of equilibrium mineral compositions in high-pressure-temperature granulites from the Moldanubian Zone, Austria. J Metamorph Geol 18: 551–569

Dudek A (1960) Krystalické břidlice a devon východně od Znojma. Sbor Ústř úst geol 26: 101–141

Fiala J, Matějovská O, Vaňková V (1987) Moldanubian granulites: source material and petrogenetic considerations. Neues Jb Mineral Abh 157: 133–165

Finger F, Steyrer HP (1995) A tectonic model for the eastern Variscides: indications from a chemical study of amphibolites in the south-eastern Bohemian Massif, Austria. Geol Carpath 46: 1–14

Finger F, von Quadt A (1995) U/Pb ages of zircons from a plagiogranite-gneiss in the south-eastern Bohemian Massif, Austria – further evidence for an important Early Paleozoic rifting episode in the Eastern Variscides. Schweiz Mineral Petrogr Mitt 75: 265–270

Finger F, Hanžl P, Pin C, von Quadt A, Steyrer HP (2000a) The Brunovistulian: Avalonian Precambrian sequence at the eastern end of the Central European Variscides? In: *Franke W, Haak V, Oncken O, Tanner D* (eds) Orogenic processes: quantification and modelling in the Variscan Belt. Geol Socond Spec Pub 179: 103–112

Finger F, Tichomirowa M, Pin C, Hanžl P (2000b) Relics of an early-Panafrican metabasite-metarhyolite formation in the Brno Massif, Moravia, Czech Republic. Int J Earth Sci 89: 328–335

Franěk J, Schulmann K, Lexa O (2006) Kinematic and rheological model of exhumation of high-pressure granulites in the Variscan orogenic root: example of the Blanský les granulite, Bohemian Massif, Czech Republic. Mineral Petrol 86: 253–276

Franke W (1989) Tectonostratigraphic units in the Variscan belt of central Europe. Geol Soc Am Spec Paper 230: 67–90

Franke W (2000) The mid-European segment of the Variscides: tectonostratigraphic units, terrane boundaries and kinematic evolution. In: *Franke W, Haak V, Oncken O, Tanner D* (eds) Orogenic processes: quantification and modelling in the Variscan Belt. Geol Soc Lond Spec Publ 179: 35–63

Friedl G, von Quadt A, Ochsner A, Finger F (1993) Timing of the Variscan orogeny in the Southern Bohemian Massif (NE Austria) deduced from new U–Pb zircon and monazite dating. Terra Nova 1(5): 235–236

Friedl G, Cooke R, Finger F, McNaughton NJ, Fletcher I (2003) U–Pb SHRIMP dating and trace element investigations on multiple zircons from a South-Bohemian granulite. J Czech Geol Soc 48: 51

Friedl G, Finger F, Paquette J, Quadt A, McNaughton N, Fletcher I (2004) Pre-Variscan geological events in the Austrian part of the Bohemian Massif deduced from U–Pb zircon ages. Int J Earth Sci 93: 802–823

Fritz H (1996) Geodynamic and tectonic evolution of the southeastern Bohemian Massif: the Thaya section (Austria). Mineral Petrol 58: 253–258

Fritz H, Neubauer F (1993) Kinematics of crustal stacking and dispersion in the south-eastern Bohemian Massif. Geol Rundsch 82: 556–565

Fritz H, Dallmeyer RD, Neubauer F (1996) Thick-skinned versus thin-skinned thrusting: rheology controlled thrust propagation in the Variscan collisional belt (the southeastern Bohemian Massif, Czech Republic – Austria). Tectonics 15: 1389–1413

Fuchs G (1971) Zur Tektonik des östlichen Waldviertels (N.Ö.). Verh Geol B-A 3: 424–440

Fuchs G (1976) Zur Entwicklung der Böhmischen Masse. Jb Geol B-A 119: 45–61

Fuchs G, Matura A (1976) Zur Geologie des Kristallins der südlichen Böhmischen Masse. Jb Geol B-A 119: 1–43

Gebauer D, Friedl G (1994) A 1.38 Ga protolith age for the Dobra orthogneiss (Moldanubian zone of the southern Bohemian Massif, NE-Austria): evidence from ion-microprobe (SHRIMP) dating of zircon. J Czech Geol Soc 39: 34–35

Hartley AJ, Otava J (2001) Sediment provenance and dispersal in a deep marine foreland basin: the Lower Carboniferous Culm Basin, Czech Republic. J Geol Soc 158: 137–150

Höck V (1975) Mineralzonen in Metapeliten und Metapsammiten der Moravischen Zone in Niederösterreich. Mitt Geol Ges 66–67: 49–60

Holland TJB, Powell R (1998) An internally consistent thermodynamic data set for phases of petrological interest. J Metamorph Geol 16: 309–343

Holland TJB, Powell R (2003) Activity-composition relations for phases in petrological calculations: an asymmetric multicomponent formulation. Contrib Mineral Petrol 145: 492–501

Janoušek V, Finger F, Roberts MP, Frýda J, Pin C, Dolejš D (2004) Deciphering petrogenesis of deeply buried granites: whole-rock geochemical constraints on the origin of largely undepleted felsic granulites from the Moldanubian Zone of the Bohemian Massif. Trans Roy Soc Edinb Earth Sci 95: 141–159

Kalvoda J, Leichmann J, Bábek O, Melichar R (2003) Brunovistulian Terrane (Central Europe) and Istanbul Zone (NW Turkey): late Proterozoic and Paleozoic tectonostratigrapic development and paleogeography. Geol Carpath 54: 139–152

Kober L (1938) Der Geologische Aufbau Österreichs. Springer, Wien, 204 pp

Kolenovská E, Schulmann K, Klápová H, Štípská P (1999) Tectonometamorphic evolution of the Moldanubian zone near Jemnice (South Moravia, Bohemian Massif). Beih Eur J Mineral 11: 91–94

Kröner A, Wendt I, Liew TC, Compston W, Todt W, Fiala J, Vaňková V, Vaněk J (1988) U–Pb zircon and Sm–Nd model ages of high grade Moldanubian metasediments, Bohemian Massif, Czechoslovakia. Contrib Mineral Petrol 99: 257–266

Kröner A, O'Brien PJ, Nemchin AA, Pidgeon RT (2000a) Zircon ages for high pressure granulites from South Bohemia, Czech Republic, and their connection to Carboniferous high temperature processes. Contrib Mineral Petrol 138: 127–142

Kröner A, Štípská P, Schulmann K, Jaeckel P (2000b) Chronological constraints on the pre-Variscan evolution of the northeastern margin of the Bohemian Massif, Czech Republic. In: *Franke W, Haak V, Oncken O, Tanner D* (eds) Orogenic processes; quantification and modelling in the Variscan Belt. Geol Soc Lond Spec Publ 179: 175–197

Linner M (1996) Metamorphism and partial melting of paragneisses of the Monotonous Group, SE Moldanubicum (Austria). Mineral Petrol 58: 215–234

Matte P (1991) Accretionary history and crustal evolution of the Variscan belt in Western Europe. Tectonophysics 196: 309–337

Medaris LG, Jelínek E, Mísař Z (1995) Czech eclogites: Terrane settings and implications for Variscan tectonic evolution of the Bohemian Massif. Eur J Mineral 7: 7–28

Medaris LG, Fournelle JH, Ghent ED, Jelínek E, Mísař Z (1998) Prograde eclogite in the Gföhl Nappe, Czech Republic: new evidence on Variscan high-pressure metamorphism. J Metamorph Geol 16: 563–576

O'Brien PJ (1997) Garnet zoning and reaction textures in overprinted eclogites, Bohemian Massif, European Variscides: a record of their thermal history during exhumation. Lithos 41: 119–133

O'Brien PJ, Vrána S (1995) Eclogites with a short-lived granulite facies overprint in the Moldanubian Zone, Czech Republic: petrology, geochemistry and diffusion modelling of garnet zoning. Geol Rundsch 84: 473–488

Owen JV, Dostal J (1996) Prograde metamorphism and decompression of the Gföhl gneiss, Czech Republic. Lithos 38: 259–270

Petrakakis K (1986) Metamorphism of high-grade gneisses from the Moldanubian Zone, Austria, with particular reference to garnets. J Metamorph Geol 4: 323–344

Petrakakis K (1997) Evolution of Moldanubian rocks in Austria: review and synthesis. J Metamorph Geol 15: 203–222

Pitra P, Guiraud M (1996) Probable anticlockwise P–T evolution in extending crust: Hlinsko region, Bohemian Massif. J Metamorph Geol 14: 49–60

Powell R, Downes J (1990) Garnet porphyroblast-bearing leucosomes in metapelites: mechanisms, phase diagrams, and an example from Borken Hill, Australia. In: *Ashworth JR, Brown M* (eds) High temperature metamorphism and crustal anatexis. The Mineralogical Society series. Unwin Hyman, London, pp 105–123

Powell R, Holland T, Worley B (1998) Calculating phase diagrams involving solid solutions via non-linear equations, with examples using THERMOCALC. J Metamorph Geol 16: 577–588

Scharbert S, Batík P (1980) The age of the Thaya (Dyje) pluton. Verh Geol B-A 3: 325–331

Schulmann K (1990) Fabric and kinematics study of the Bíteš orthogneiss (southwest Moravia): result of large-scale northeastward shearing parallel to the Moldanubian/Moravian boundary. Tectonopysics 177: 229–244

Schulmann K, Gayer R (2000) A model for a continental accretionary wedge developed by oblique collision: the NE Bohemian Massif. J Geol Soc 157: 401–416

Schulmann K, Ledru P, Autran A, Melka R, Lardeaux JM, Urban M, Lobkowicz M (1991) Evolution of nappes in the eastern margin of the Bohemian Massif: a kinematic interpretation. Geol Rundsch 80: 73–92

Schulmann K, Melka R, Lobkowicz M, Ledru P, Lardeaux JM, Autran A (1994) Contrasting styles of deformation during progressive nappe stacking at the southeastern margin of the Bohemian Massif (Thaya Dome). J Struct Geol 16: 355–370

Schulmann K, Lobkowicz M, Melka R, Fritz H (1995) Structure of the allochthonous Moravo-Silesian units. In: *Dallmeyer RD, Franke W, Weber K* (eds) Pre-permian geology of Central and Eastern Europe. Springer, Berlin Heidelberg New York Tokyo, pp 530–540

Schulmann K, Kröner A, Hegner E, Wendt I, Konopásek J, Lexa O, Štípská P (2005) Chronological constraints on the pre-orogenic history, burial and exhumation of deep-seated rocks along the eastern margin of the Variscan orogen, Bohemian Massif, Czech Republic. Am J Sci 305: 407–448

Štípská P, Powell R (2005a) Does ternary feldspar constrain the metamorphic conditions of high-grade meta-igneous rocks? Evidence from orthopyroxene granulites, Bohemian Massif. J Metamorph Geol 23: 627–647

Štípská P, Powell R (2005b) Constraining the P–T path of a MORB-type eclogite using pseudosections, garnet zoning and garnet-clinopyroxene thermometry: an example from the Bohemian Massif. J Metamorph Geol 23: 725–743

Štípská P, Schulmann K (1995) Inverted metamorphic zonation in a basement-derived nappe sequence, eastern margin of the Bohemian Massif. Geol J 30: 385–413

Štípská P, Schulmann K, Höck V (2000) Complex metamorphic zonation of the Thaya dome: result of buckling and gravitational collapse of an imbricated nappe sequence. In: *Cosgrowe JW, Ameen MS* (eds) Forced folds and fractures. Geol Soc Lond Spec Publ 169: 197–211

Štípská P, Schulmann K, Kröner A (2004) Vertical extrusion and middle crustal spreading of omphacite granulite: a model of syn-convergent exhumation (Bohemian Massif, Czech Republic). J Metamorph Geol 22: 179–198

Stüwe K, Powell R (1995) PT Paths from modal proportions: application to the Koralm Complex, Eastern Alps. Contrib Mineral Petrol 119: 83–93

Suess FE (1912) Die Moravischen Fenster und ihre Beziehung zum Grundgebirge des Hohen Gesenkes. Österr Akad Wiss math-naturw Kl, Denkschr 88: 541–631

Suess FE (1918) Bemerkungen zur neueren Literatur über die Moravischen Fenster. Mitt Geol Ges 11: 71–128

Suess FE (1926) Intrusionstektonik und Wandertektonik im variszischen Grundgebirge. Bornträger, Berlin, 268 pp

Suess FE, Gerhart H, Beck H (1925) Geologische Spezialkarte, Blatt Drosendorf, 1: 75 000. Geol B-A, Wien

Thiele O (1976) Zur Tektonik des Waldviertels in Niederösterreich (südliche Böhmische Masse). Nova Acta Leopoldina 45: 67–82

Thiele O (1984) Zum Deckenbau und Achsenplan des Moldanubikums der südlichen Böhmischen Masse (Österreich). Jb Geol B-A 126: 513–523

Tollmann A (1982) Großräumiger variszischer Deckenbau im Moldanubikum und neue Gedanken zum Variszikum Europas. Geotekt Forsch 64: 1–91

van Breemen O, Aftalion M, Bowes DR, Dudek A, Mísař Z, Povondra P, Vrána S (1982) Geochronological studies of the Bohemian Massif, Czechoslovakia, and their significance in the evolution of Central Europe. Trans Roy Soc Edinb Earth Sci 73: 89–108

Wei CJ, Powell R, Zhang LF (2003) Eclogites from the south Tianshan, NW China: petrological characteristic and calculated mineral equilibria in the Na_2O–CaO–FeO–MgO–Al_2O_3–SiO_2–H_2O system. J Metamorph Geol 21: 163–179

White RW, Powell R (2002) Melt loss and the preservation of granulite facies mineral assemblages. J Metamorph Geol 20: 621–632

White RW, Powell R, Holland TJB (2001) Calculation of partial melting equilibria in the system Na_2O–CaO–K_2O–FeO–MgO–Al_2O_3–SiO_2–H_2O (NCKFMASH). J Metamorph Geol 19: 139–153

Authors' addresses: *M. Racek*, Institute of Petrology and Structural Geology, Charles University, Albertov 6, Praha 2, 12843, Czech Republic, e-mail: martin.racek@centrum.cz; *P. Štípská* (e-mail: stipska@illite.u-strasbg.fr), *K. Schulmann* (e-mail: schulman@illite.u-strasbg.fr), and *O. Lexa* (e-mail: lexa@illite.u-strasbg.fr), Centre de Géochimie de Surface, UMR CNRS 7517, 1 Rue Blessig, 67084 Strasbourg Cedex, France; *P. Pitra*, Géosciences Rennes, UMR CNRS 6118, Université Rennes 1, Campus de Beaulieu, 263 Av. du gen. Leclerc, 35042 Rennes Cedex, France, e-mail: pavel.pitra@univ-rennes1.fr

J. metamorphic Geol., 2008, **26,** 273–297 doi:10.1111/j.1525-1314.2007.00755.x

Vertical extrusion and horizontal channel flow of orogenic lower crust: key exhumation mechanisms in large hot orogens?

K. SCHULMANN,[1] O. LEXA,[1,3] P. ŠTÍPSKÁ,[1] M. RACEK,[2] L. TAJČMANOVÁ,[2,4] J. KONOPÁSEK,[2,3] J.-B. EDEL,[1] A. PESCHLER[1] AND J. LEHMANN[1]
[1]*Université Louis Pasteur, EOST, UMR 7516 - 7517, 1 Rue Blessig, Strasbourg 67 084, France*
[2]*Czech Geological Survey, Klárov 3, 118 21 Praha 1, Czech Republic*
[3]*Institute of Petrology and Structural geology, Charles University, Albertov 6, 128 43, Prague, Czech Republic*
[4]*Dipartimento di Mineralogia e Petrologia, Università di Padova, Corso Garibaldi 37, I-35 137 Padova, Italy*

ABSTRACT A large database of structural, geochronological and petrological data combined with a Bouguer anomaly map is used to develop a two-stage exhumation model of deep-seated rocks in the eastern sector of the Variscan belt. An early sub-vertical fabric developed in the orogenic lower and middle crust during intracrustal folding followed by the vertical extrusion of the lower crustal rocks. These events were responsible for exhumation of the orogenic lower crust from depths equivalent to 18–20 kbar to depths equivalent to 8–10 kbar, and for coeval burial of upper crustal rocks to depths equivalent to 8–9 kbar. Following the folding and vertical extrusion event, sub-horizontal fabrics developed at medium to low pressure in the orogenic lower and middle crust during vertical shortening. Fabrics that record the early vertical extrusion originated between 350 and 340 Ma, during building of an orogenic root in response to SE-directed Saxothuringian continental subduction. Fabrics that record the later sub-horizontal exhumation event relate to an eastern promontory of the Brunia continent indenting into the rheologically weaker rocks of the orogenic root. Indentation initiated thrusting or flow of the orogenic crust over the Brunia continent in a north-directed sub-horizontal channel. This sub-horizontal flow operated between 330 and 325 Ma, and was responsible for a heterogeneous mixing of blocks and boudins of lower and middle crustal rocks and for their progressive thermal re-equilibration. The erosion depth as well as the degree of reworking decreases from south to north, pointing to an outflow of lower crustal material to the surface, which was subsequently eroded and deposited in a foreland basin. Indentation by the Brunia continental promontory was highly noncoaxial with respect to the SE-oriented Saxothuringian continental subduction in the Early Visean, suggesting a major switch of plate configuration during the Middle to Late Visean.

Key words: Bohemian Massif; channel flow; exhumation; orogenic lower crust; Variscan belt.

INTRODUCTION

Current concepts of exhumation of deep-seated rocks in convergent orogens are generally based on the style of the pressure–temperature–time (*P–T–t*) path retrieved from high-pressure (HP) to ultra-high-pressure (UHP) rocks (e.g. Duchene *et al.*, 1997). One group of exhumation mechanisms for these rocks has been inferred from conceptual or numerical models driven by subduction–accretion processes that result in either corner flow circulation within an accretionary wedge (Platt, 1986, 1993; Allemand & Lardeaux, 1997; Gerya & Stockhert, 2006) or buoyancy-driven exhumation of subducted continental crust (Chemenda *et al.*, 1995). Another group of conceptual models has been developed for gravity-driven exhumation of HP rocks in thickened orogenic root systems. In these models, processes such as convective removal of a tectospheric root (England & Houseman, 1988; Andersen *et al.*, 1991) or lateral variations in gravitational potential energy of thickened continental lithosphere (Milnes & Koyi, 2000; Rey *et al.*, 2001; Vanderhaeghe & Teyssier, 2001) drive the exhumation. Recently, an alternative model has been developed for the large-scale horizontal movement of melt-bearing middle crust based on channel flow (Beaumont *et al.*, 2001, 2006; Godin *et al.*, 2006), and has been applied to explain the ductile extrusion of medium-pressure metamorphic rocks along the Himalayan front (Grujic *et al.*, 1996; Jamieson *et al.*, 2002, 2004). Whereas the first group of models focuses on explaining vertical displacements of UHP and HP rocks, the second group of models emphasizes the importance of large-scale horizontal displacements in orogens.

Monocyclic continuous models of orogenic lower crust exhumation may be supported by structural and kinematic field studies that emphasize the 2D character of the exhumation process (e.g. Milnes & Koyi, 2000). However, more commonly there are complexities in the 3D character of the tectonic evolution of large

orogenic root systems that arise from the polyphase nature of vertical and horizontal material and heat transfer during long-lasting orogenic events that make these systems more difficult to unravel. The polyphase and discontinuous character of orogeny may be due to major changes in plate configurations (e.g. Dewey *et al.*, 1989) or to the existence of inherited rheological heterogeneities and variations in mechanical anisotropy (e.g. Burg, 1999). Therefore, detailed regional structural, petrological and geochronological studies of orogenic fabrics may provide a key to deciphering the succession, and length and time scales of processes responsible for material and heat transfer within these large orogenic root systems.

Classically, the Palaeozoic Variscan orogen in Western and Central Europe (Fig. 1) is a large, hot, bivergent orogen that is interpreted to have developed during prolonged convergence between Laurussia and Gondwana (e.g. Ziegler, 1986; Matte *et al.*, 1990). Traditionally, burial and exhumation of UHP and HP rocks are thought to be the result of a kinematic continuum of coaxial subduction and subsequent collision processes (e.g. O'Brien & Carswell, 1993; Konopásek & Schulmann, 2005), and as a consequence petrological and geochronological data may fit in one of the 2D conceptual models discussed above.

In this study, we present structural, petrological and geochronological data acquired during the last two decades from the eastern termination of the European Variscan front within an area of about 20 000 km^2 (Figs 1 & 2). It is shown that exhumation of the orogenic lower crust occurred during two distinct periods related to a major change in the configuration of lithospheric plates during the Visean. The first exhu-

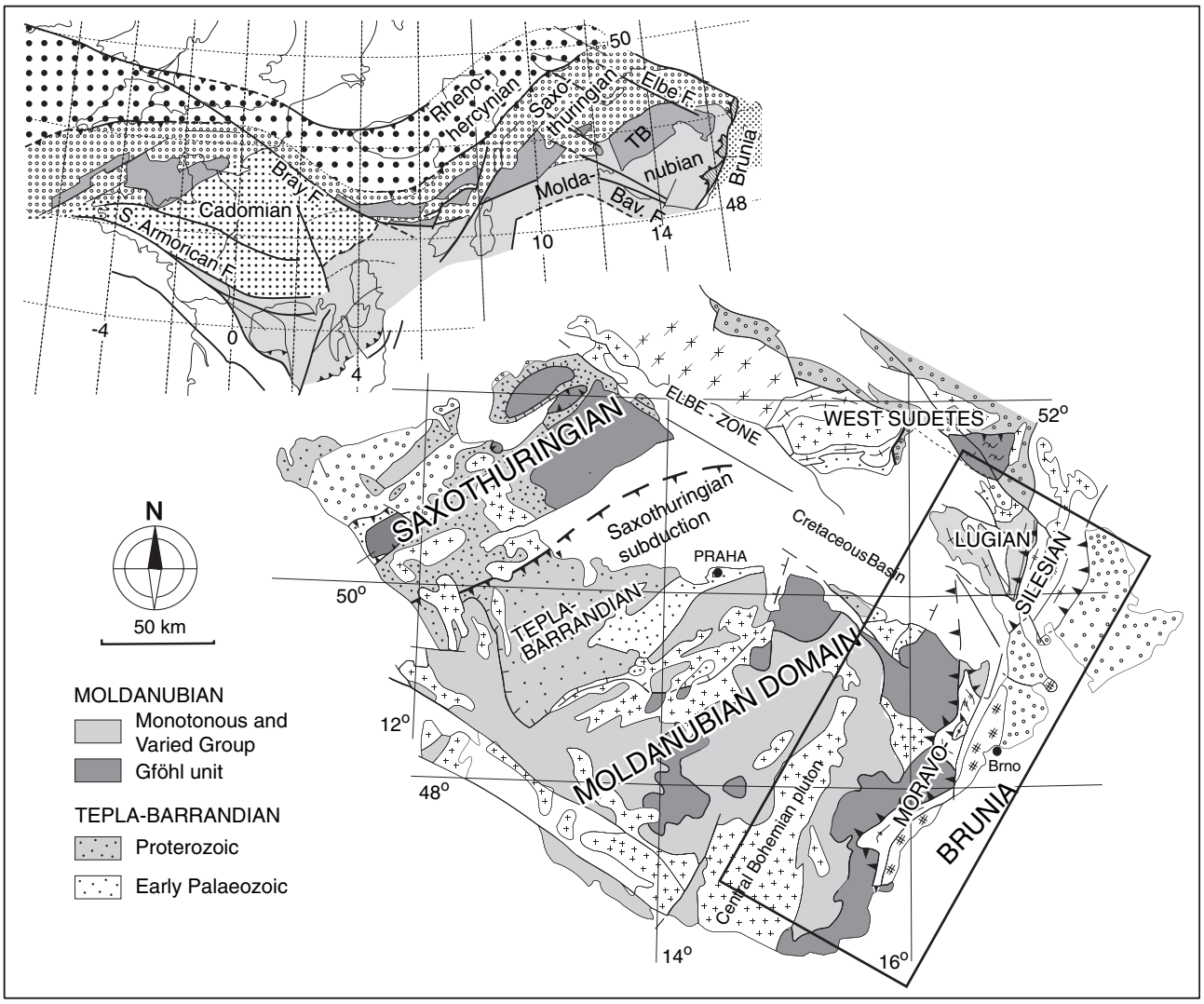

Fig. 1. Outline geological map of the Bohemian Massif with major units shown schematically (modified after Franke, 2000). Upper inset is the position of the Bohemian Massif in the framework of the European Variscides (after Edel *et al.*, 2003). The area discussed in this review is marked by a rectangular box.

mation event was related to almost vertical material transfer, which was driven by S-E directed oceanic and continental (Armorican–Saxothuringian) subduction dynamics during the Devonian and Tournasian to Early Visean (Fig. 1). Following this early evolution, during the Middle to Late Visean indentation from the east by a promontory of the Brunia continent at a high angle to the Saxothuringian subduction direction resulted in horizontal flow and transport of the extruded orogenic lower crust over the rigid continent as a hot fold nappe.

GEOTECTONIC SETTING

Suess (1912, 1926) described the geology of the eastern Variscan front and divided the crystalline complexes of the Bohemian Massif into two parts, an internal Moldanubian–Lugian domain and an external Moravo–Silesian Zone (Figs 1 & 2). Dudek (1980) completed this subdivision and defined a Brunia continent with the Moravo–Silesian Zone as its western deformed margin. The eastern segment of the Brunia continent is built up of unmetamorphosed to weakly metamorphosed Neoproterozoic granites, high-grade schists and migmatites. This basement is unconformable, covered by Lower Carboniferous foreland basin sedimentary rocks, by Devonian shallow marine sedimentary rocks, and locally by Cambro-Ordovician clastic, pelitic metasediment rocks and bimodal metavolcanic rocks (Franke, 2000; Hartley & Otava, 2001).

The Moravo–Silesian Zone represents a NE–SW-trending belt of sheared and metamorphosed rocks derived from the Brunia continent. This 300 km long, 30–50 km wide belt consists of three NE–SW-elongated tectonic windows emerging through structurally overlying high-grade rocks of the Moldanubian–Lugian domain: a southern Thaya window; a central Svratka window; and a northern Silesian domain (Fig. 2). Schulmann *et al.* (2005) identified the Moldanubian–Lugian domain in the Bohemian Massif as the deep orogenic root system of the Variscan orogen (Fig. 2). The Elbe zone (Fig. 2) divides rocks of the Moldanubian–Lugian domain into two: a larger high-grade Moldanubian domain to the south and a smaller high-grade Lugian domain to the north (Suess, 1926).

The Moldanubian domain (Figs 1 & 2) has been subdivided into three major lithotectonic units (e.g. Fuchs, 1986), namely the amphibolite facies Monotonous and Varied Groups, which together with gneisses make up the orogenic middle crust, and the predominantly granulite facies Gföhl Unit, which is inferred to be the orogenic lower crust (Fig. 2). The Varied Group outcrops structurally above the Monotonous Group, with a contact that is commonly marked by bodies of granite gneiss. The Monotonous Group consists of migmatitic paragneisses (metagraywacke) interlayered with granite orthogneisses, quartzites and rare eclogites (Dudek & Fediuková, 1974; Petrakakis, 1997). The Varied Group consists of a thick sequence of paragneisses interlayered with calcsilicate rocks, marbles, quartzites, graphite schists, amphibolites and felsic metavolcanic rocks. The Gföhl Unit is composed of large areas of migmatitic granite gneiss, called the Gföhl gneiss, and of areas of various highly anatectic migmatites and paragneisses that are in places accompanied by migmatitic amphibolites at the base. The Gföhl Unit includes numerous bodies of Ky–Kfs felsic granulite as well as tectonic lenses of eclogite and garnet and/or spinel peridotite.

The main part of the Lugian domain is composed of medium- to high-grade granite gneisses and metamorphosed volcano-sedimentary rocks with Cambro–Ordovician protolith ages (Kröner *et al.*, 2001, and references therein). The granite gneisses contain boudins of eclogite and a belt of garnet–omphacite granulite, and are considered an equivalent of the Gföhl Unit, whereas the belts of medium-grade schists of volcano-sedimentary origin are regarded as an equivalent of either the Monotonous or the Varied Groups (Fig. 2). An Ordovician leptyno-amphibolite lower crustal complex (the Staré Město belt) occurs in the eastern part of the Lugian domain (Štípská *et al.*, 2001).

DEFINITION OF BASEMENT AND OROGENIC CRUSTAL LEVELS

In this section, multiple criteria, such as the peak pressure conditions attained by individual units, the character and the age of the protolith and chronology of metamorphic zircon, are used to decipher the relative vertical position of crustal units during the Lower Palaeozoic and the Devonian. This information is then used to propose a model for the stratification of the orogenic crust along the eastern Variscan front.

The Brunia continent

Based on zircon protolith ages (Fig. 3a) and $^{40}Ar/^{39}Ar$ cooling ages ranging from 600 to 540 Ma, granites and migmatites forming the basement of the Brunia continent are inferred to have originated during the Pan-African orogenic events (Van Breemen *et al.*, 1982; Fritz *et al.*, 1996; Finger *et al.*, 2000; Friedl *et al.*, 2004). Tectonic imbrication of Devonian metasedimentary rocks and basement, and metamorphism to lower greenschist facies occurred at the western margin of the Brunia continent during the Carboniferous (Franců *et al.*, 2002). In the northern Silesian domain (Fig. 2), the metamorphic pattern of nappes derived from the Brunia continent shows an inverted Barrovian zonation ranging from chlorite grade in the east to kyanite/sillimanite grade in the west (Štípská & Schulmann, 1995; Schulmann & Gayer, 2000). The western termination of the Moravo–Silesian Zone in the north reached eclogite facies conditions (Fig. 4; Štípská *et al.*, 2006), and it is likely that the western tip of the Moravo–Silesian Zone in the south has been

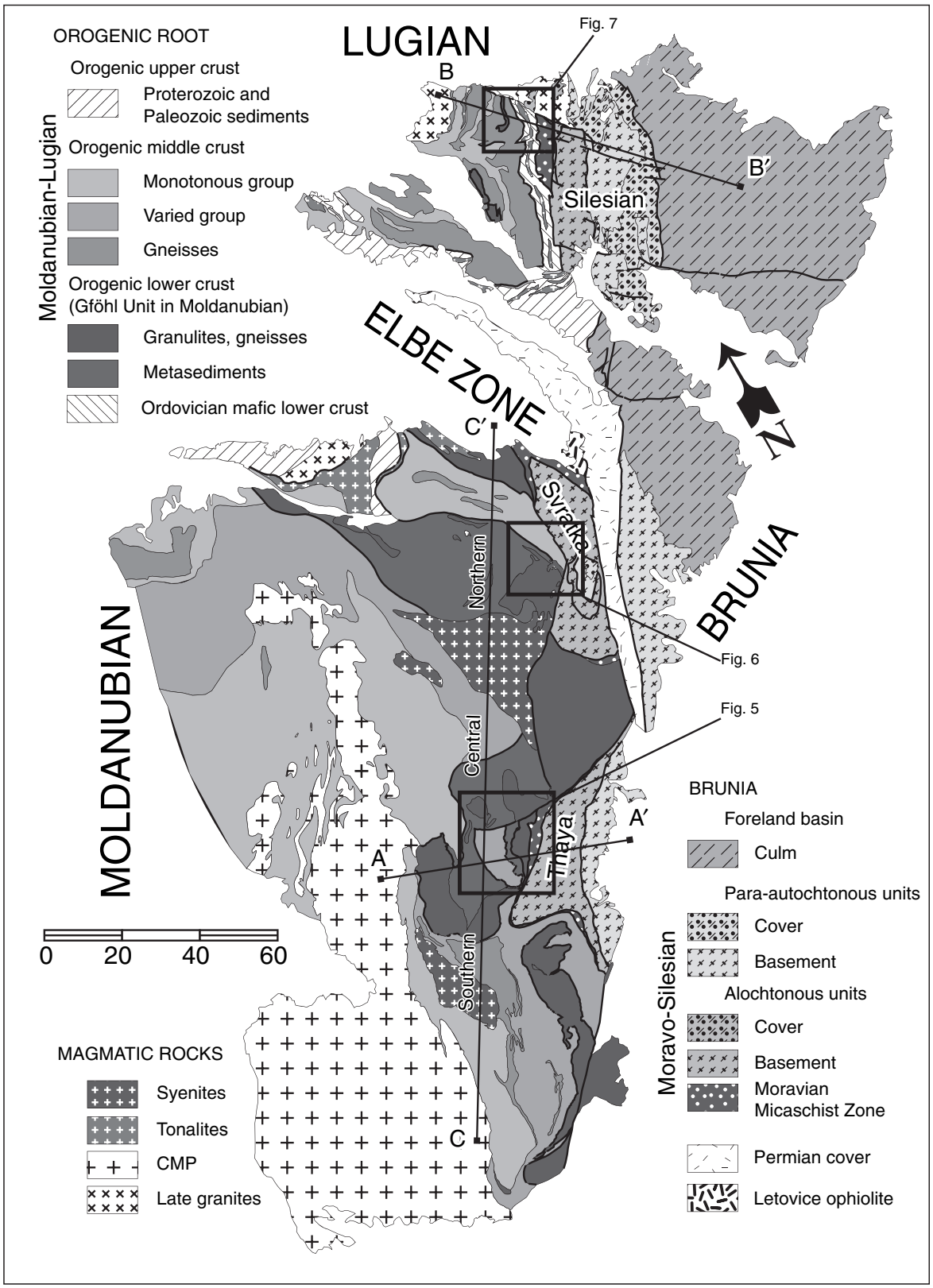

Fig. 2. Map of the eastern margin of the Bohemian Massif to show inferred orogenic crustal levels and the locations of Figs 5, 6 & 7, which are indicated by rectangular boxes. Also shown are the positions of interpretative cross sections A–A′, B–B′ and C–C′ presented in Fig. 10.

underthrust to eclogite conditions as well (Konopásek *et al.*, 2002).

The orogenic root

The Gföhl Unit and Lugian high-grade rocks

The Gföhl Unit (Fig. 2) is composed predominantly of felsic granulites (11–20 kbar, 800–1000 °C) and high-grade gneisses (e.g. O'Brien & Rötzler, 2003; Štípská & Powell, 2005b) that contain eclogite lenses of basaltic composition, suggesting a crustal origin (18–19 kbar, 800–900 °C, Fig. 4; e.g. Medaris *et al.*, 1998; Štípská & Powell, 2005a and references therein). The eclogites and granulites, as well as other lithologies of the Gföhl Unit, were overprinted at amphibolite facies conditions (4–12 kbar, 750–850 °C, Fig. 4; e.g. Petrakakis, 1997; Hasalová *et al.*, 2008b). The Gföhl Unit contains numerous tectonically emplaced bodies of garnet and spinel peridotite (28–44 kbar, 900–1300 °C, Fig. 4), associated with lenses of eclogite (16–20 kbar, 800–950 °C) and clinopyroxenite, representing partial melt crystallized in the upper mantle (Medaris *et al.*, 1995). The Lugian eclogites and granulites (18–20 kbar, 800–900 °C, Fig. 4; e.g. Steltenpohl *et al.*, 1993; Štípská *et al.*, 2004) are considered to reflect UHP conditions (Kryza *et al.*, 1996), but this has not been confirmed; they were re-equilibrated at variable *P–T* conditions (4–11 kbar, 700–800 °C, Fig. 4).

Multigrain zircon and monazite fractions from granulites and high-grade gneisses of the Gföhl Unit yielded conventional upper intercept U–Pb ages between 550 and 510 Ma, interpreted to date the formation of the protoliths (Fig. 3b; e.g. Van Breemen *et al.*, 1982; Schulmann *et al.*, 2005). In addition, xenocrystic cores and prismatic zircon from felsic granulites and Gföhl gneiss yield Silurian to Devonian U–Pb ages also interpreted to date the formation of the protoliths (Fig. 3b; Friedl *et al.*, 2004). However, a majority of U–Pb zircon ages fall in the range 360–340 Ma with a prominent peak at *c.* 340 Ma, which is interpreted to record the age of Variscan metamorphism (Fig. 3d). Ultra-potassic syenites (durbachites) spatially related to Ky–Kfs granulites yield ages around 338 Ma and 325 Ma (Fig. 3e; Holub *et al.*, 1997; Janoušek & Holub, 2007).

The Monotonous and Varied Groups

In the Moldanubian domain, paragneisses of the Monotonous and Varied Groups generally record medium-pressure metamorphism (8–9 kbar, 610–660 °C) associated at higher temperatures with widespread anatexis (~ 9 kbar, 700–800 °C), followed by re-equilibration in the sillimanite stability field at conditions around 4–6 kbar and 600–800 °C (Fig. 4; e.g. Petrakakis, 1997). The metamorphic conditions of the Monotonous Group paragneisses are

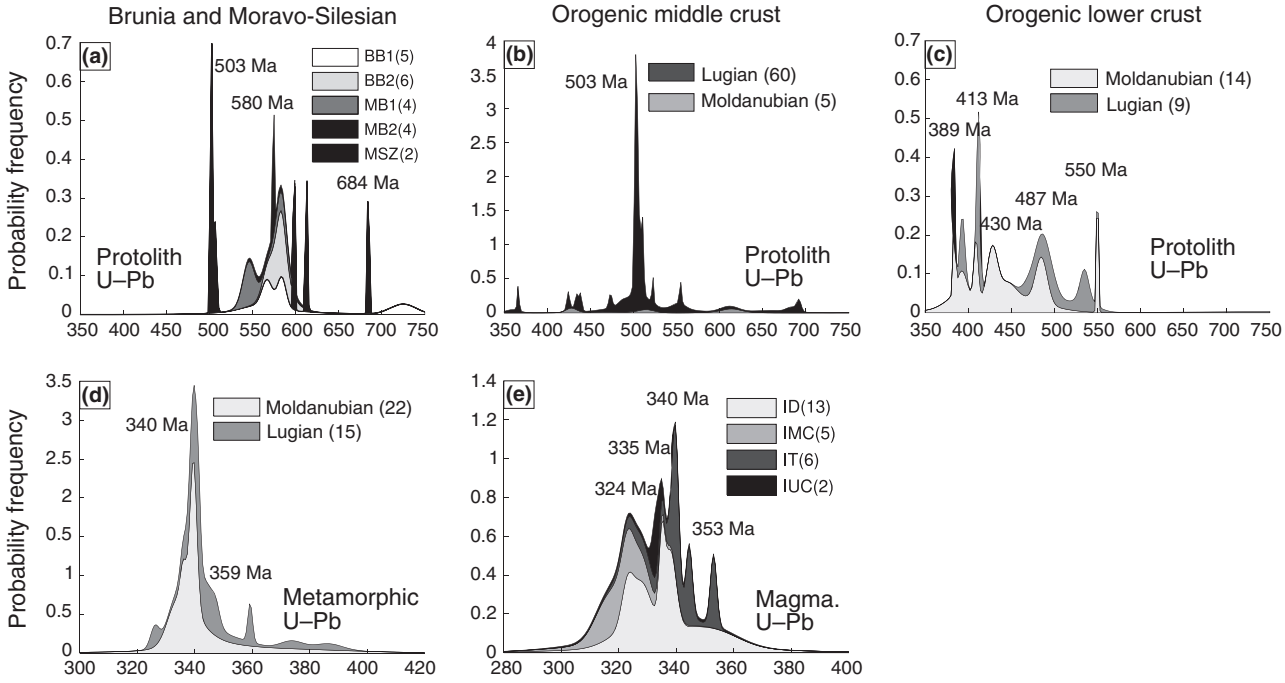

Fig. 3. Probability curves of age histograms to show existing zircon U–Pb ages. For the Brunia continent and the Moravo–Silesian Zone (a), Moldanubian and Lugian domain (b, c & d) and intrusive rocks (e). BB1, Brunia basement south of the Elbe zone; BB2, Brunia basement north of the Elbe zone; MB1, Moravian domain basement rocks; MB2, Silesian domain basement rocks; MSZ, Moravian Micaschist Zone; ID, Mg-rich syenites (durbachites) of the orogenic lower crust; IMC, intrusive rocks of the middle crust; IT, tonalite–granodiorite intrusions; IUC, granites in upper crustal units. Numbers in parentheses stand for number of available ages.

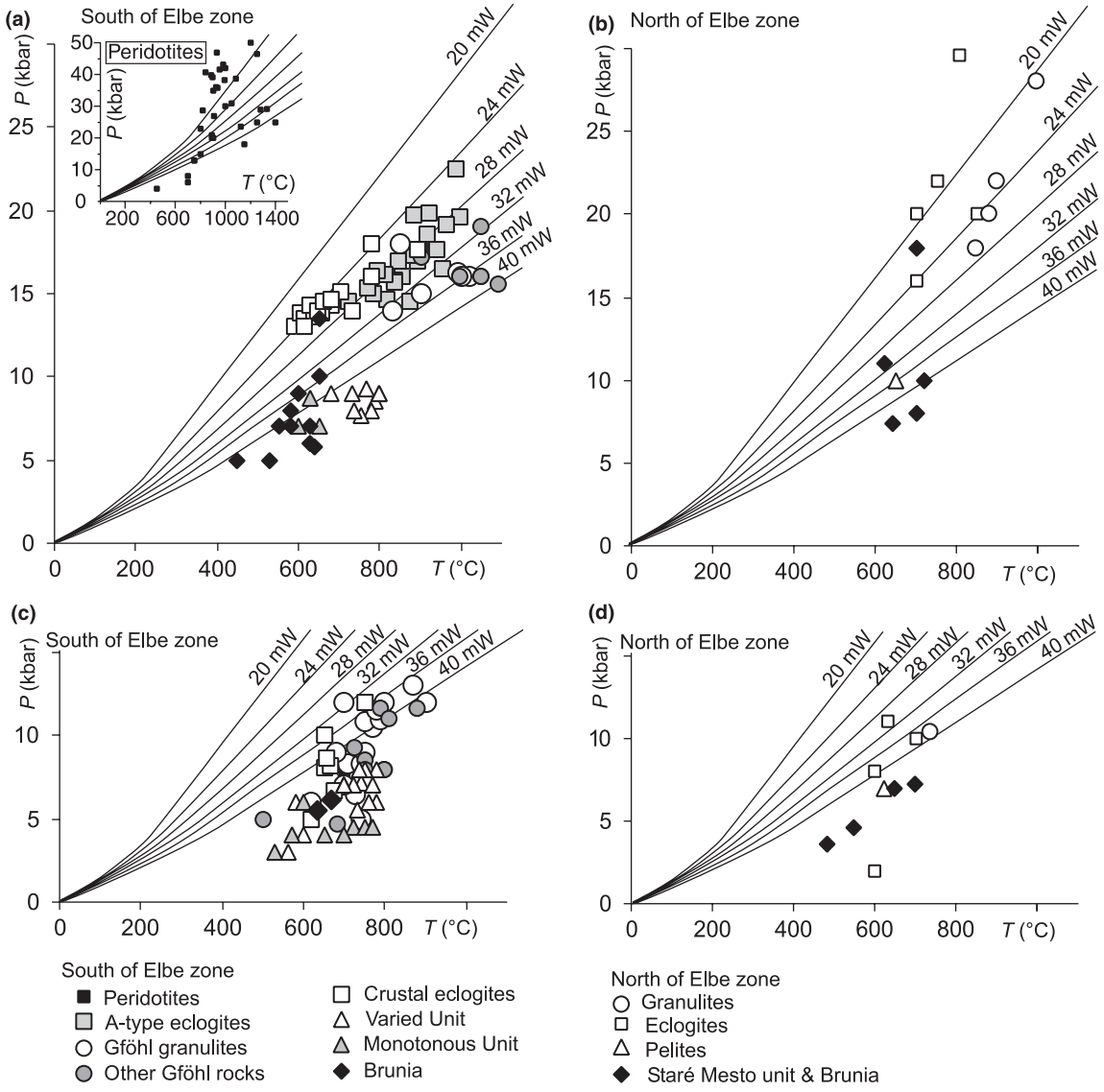

Fig. 4. *P–T* conditions for (a) peak metamorphism in the orogenic root and Brunia continent south of the Elbe Zone; (b) peak metamorphism in the orogenic root and Brunia continent north of the Elbe Zone; (c) retrograde conditions in the orogenic root and Brunia continent south of the Elbe Zone; and (d) retrograde conditions in the orogenic root and Brunia continent north of the Elbe Zone. Source of data: Carswell & O'Brien (1993), Steltenpohl *et al.* (1993), Medaris *et al.* (1995), Štípská & Schulmann (1995), Bröcker & Klemd (1996), Kryza *et al.* (1996), Pitra & Guiraud (1996), Parry *et al.* (1997), Petrakakis (1997), Medaris *et al.* (1998), Klemd & Bröcker (1999); Romanová & Štípská (2001); Konopásek *et al.* (2002); O'Brien & Rötzler (2003); Štípská *et al.* (2004); Lexa *et al.* (2005); Štípská & Powell (2005a,b); Racek *et al.* (2006); Štípská *et al.* (2006); Tajčmanová *et al.* (2006); also shown are steady-state geotherms calculated for various mantle heat flows (as indicated in the figure) and exponential radioactive heat production.

commonly re-equilibrated in the stability field of cordierite at conditions around 4.5–6 kbar and 600–720 °C (Petrakakis, 1997), inferred to be due to the thermal effect of Carboniferous intrusions emplaced at 330–310 Ma (Fig. 3e). Despite the overall medium-pressure character, in the Moldanubian domain the Varied and Monotonous Group rocks include rare lenses of eclogite that register conditions of 13–16 kbar at 600–680 °C (Fig. 4; Medaris *et al.*, 1995). The peak metamorphism of the volcano-sedimentary rock series in the Lugian domain varies from garnet to kyanite grade, yielding 7–9 kbar at 550–650 °C (Romanová & Štípská, 2001; Jastrzębski, 2005; Murtezi, 2006) with re-equilibration in the sillimanite stability field at sub-solidus conditions of 5–6 kbar at around 600 °C.

In the Monotonous and Varied Groups of the Moldanubian domain, scarce U–Pb zircon data from orthogneisses and metavolcanic rocks yield Neoproterozoic and Cambrian protolith ages (Fig. 3c; Schulmann *et al.*, 2005). U–Pb zircon data from metavolcanic rocks and granites of the Lugian domain

yield predominantly Cambrian protolith ages (Fig. 3c; e.g. Kröner *et al.*, 2000 and references therein).

Neoproterozoic and Lower Palaeozoic low-grade sequences

A sequence of weakly metamorphosed Neoproterozoic and Silurian to Devonian sedimentary rocks is separated by a crustal-scale detachment from the underlying medium- and high-grade rocks of the Moldanubian and Lugian domains (Pitra *et al.*, 1994; Mazur *et al.*, 2005). The NE–SW-trending contact of the upper crustal sedimentary rocks and middle crustal metamorphic rocks is marked by granodiorite sills, which yield U–Pb zircon ages of 350–340 Ma (Fig. 3e). Intrusion of the sills was accompanied by metamorphism of the hangingwall rocks at conditions around 4 kbar and 550–590 °C (Fig. 4). Locally, granite plutons, which yield U–Pb zircon ages around 330 Ma, intrude these low-grade rocks (e.g. Schulmann *et al.*, 2005).

Definition of crustal levels within the Moldanubian–Lugian orogenic root

The lithologies and metamorphic conditions of the main units of the Moldanubian and Lugian domains are used to define a lithotectonic zonation that corresponds to different crustal levels that existed during maximum thickening of the orogenic root. In turn, the present map distribution of the different crustal levels defines the spatial pattern of crustal units that experienced different vertical displacements. Interpretation of these different crustal levels associated with thickening and the differences in vertical displacement, together with the geometry and structural record within each unit may allow us to unravel the mechanism(s) of exhumation of these units.

According to the lithologies and peak P–T conditions described above, the Gföhl Unit is a granulite–eclogite unit representing the lower part of a thickened crust that reached lithostatic pressures of 18–20 kbar, corresponding to a depth of 60–70 km, which we define as the orogenic lower crust. In addition, the geochronological and petrological data show a systematic correlation of protolith age, metamorphic age and peak pressures (Figs 3 & 4). Only the high-grade rocks of the Gföhl Unit and the Lugian granulites record Devonian protolith ages, Early Carboniferous metamorphic ages and peak pressures of 18–20 kbar. For these reasons, Schulmann *et al.* (2005) suggested that the orogenic lower crust in the Bohemian Massif represents Neoproterozoic–Cambro-Ordovician continental crust that experienced a major thermal reworking during Devonian intra-continental (back-arc) rifting.

The Monotonous and Varied Groups yield peak pressure conditions not exceeding 12 kbar and are interpreted to have reached maximum crustal depths around 40 km under an elevated thermal gradient. We define these units as representing the orogenic middle crust. The Monotonous and Varied Groups and low-grade units yield only Neoproterozoic and Ordovician protolith ages, they lack a Devonian thermal reworking and they are interpreted as forming shallower crustal levels during the Devonian and Carboniferous. Using the same reasoning, the weakly metamorphosed Neoproterozoic and Lower Palaeozoic rocks that show peak pressures around 4 kbar, and no evidence of Devonian thermal reworking are defined as the orogenic upper crust.

During the Carboniferous history of building the orogenic root, the rocks occupying structurally deeper positions were transported upwards, whereas shallower units were moved downwards. The result is that the orogenic lower and middle crusts now form subparallel belts at the surface. Exceptionally, the Varied and Monotonous Groups reached lower orogenic crustal conditions during their burial, and in this case, they become part of the orogenic lower crust.

TECTONICS OF THE EASTERN PART OF THE BOHEMIAN MASSIF

Structural evolution of the Brunia continental margin: the Moravo–Silesian Zone

The Brunia continent forms a pile of internally imbricated basement- and cover-derived thrust sheets, termed the Moravo–Silesian Zone, which developed during Carboniferous dextral–oblique thrusting of the Moldanubian–Lugian domain (Schulmann *et al.*, 1991). As a result, the whole Moravo–Silesian Zone experienced intense non-coaxial NE-directed deformation (Schulmann *et al.*, 1994; Fritz *et al.*, 1996). Crustal-scale folds with west-plunging hinges refold the nappe pile during the final stages of NE-directed deformation (Schulmann, 1990; Štípská *et al.*, 2000). Finally, the Svratka dome and the Silesian domain were folded by west-facing folds that also affected the Culm foreland basin, suggesting the age of latest shortening to be around 310 Ma (Hartley & Otava, 2001).

Orogenic structure of the crustal root

The eastern branch of the Moldanubian domain located between Central Moldanubian pluton and Moravo–Silesian Zone (Fig. 1) is examined here. In order to characterize structural and petrological variations along-strike of the orogenic margin we introduce the southern, central and northern Moldanubian domains.

The large-scale structure of the Moldanubian domain is characterized from west to east as follows: (i) first, there is a sequence of east-dipping schists and marbles of the Monotonous and Varied groups, which is intruded by the Central Moldanubian pluton; (ii) to the east, this sequence is overlain by high-grade

gneisses, migmatites and granulites containing numerous inclusions of peridotites and eclogites; (iii) further east, this orogenic lower crust is thrust over west-dipping middle crustal rocks that are composed of sillimanite micaschists, orthogneiss or leptynitic amphibolite of Cambro-Ordovician age in the south (Figs 5c & 6c); and (iv) finally, the easternmost extremity of the Moldanubian sequence is characterized by a lower crustal segment of mafic and felsic granulites associated with migmatitic biotite paragneiss and a few mantle slivers (Fig. 5c). All these units trend parallel to the continental margin represented by Moravian nappes of the Thaya and Svratka domes, respectively (Fig. 2). This sequence of rocks is generally valid for the northern and southern parts of the Moldanubian domain, but in contrast the central part is dominated by orogenic lower crust rocks intruded by Mg–K-rich syenite intrusions (figs 4 & 5 in Schulmann *et al.*, 2005).

The geological structure of the Lugian domain (Fig. 7) is characterized by alternations of orthogneisses with metasedimentary and metavolcanic rocks that comprise the orogenic middle crust. In the central part of the orthogneiss belt there is a narrow NE-trending belt of garnet–omphacite granulite and migmatite that represents the orogenic lower crust. A Carboniferous granodiorite sill marks the eastern boundary of the Lugian domain, with an Ordovician leptyno-amphibolite unit extending further to the east (Fig. 7c). Directly in the footwall of the Lugian domain there is an eclogite unit derived from the lower crust of the Brunia continent (Štípská *et al.*, 2006). Imbricated Brunia basement and cover thrust sheets of the Moravo–Silesian domain represent the structurally deepest unit of the section. Superposed orogenic fabrics observed in the field and their petrological characteristics in four representative areas are described below, three from the Moldanubian domain and one from the Lugian domain, where the spatial relationships between the orogenic lower crust and the adjacent orogenic middle crust may be critically evaluated.

Structural development of the Moldanubian domain

The most characteristic structural feature of the Moldanubian domain is the widespread flat-lying foliation. In the southern Moldanubian domain (Figs 2 & 5), the flat fabric gently dips to the east in the western part and to the west in the eastern part. This geometry led Austrian geologists to define a large-scale Gföhl nappe resting on middle crustal rocks in synformal structures (Tollmann, 1982; Fuchs, 1986). However, recent studies have shown that the sub-horizontal fabrics (S_3) were superimposed on vertical fabrics (S_2), and although the superposition is of variable intensity, it occurs in almost all the rock types of the lower and middle crust.

For the Moldanubian domain, we review three areas where the relationship of the steep to the flat fabrics has been studied in detail (Kolenovská *et al.*, 1999; Racek *et al.*, 2006; Tajčmanová *et al.*, 2006; P. Štípská & K. Schulmann, unpublished data). First, the structural succession is described on the macroscopic scale, where the S_2 fabric, defined mainly by steep lithological alternation and/or steep internal rock layering, was reworked by multiple mechanisms into a flat-lying S_3 fabric of variable intensity (Fig. 8). Later a detailed discussion is given of the metamorphic characterization of the steep S_2 fabric and metamorphic conditions of the flat D_3 reworking in individual lithologies.

The first area is located in the northernmost termination of the southern Moldanubian domain (Figs 2 & 5; Racek *et al.*, 2006). Here, exceptionally well-preserved S_2 fabrics occur as steep alternations of paragneisses, marbles, felsic volcanic rocks, amphibolites and quartzites of the middle crust that are surrounded by migmatites and granulites of the orogenic lower crust (Fig. 5, stereoplot E). The S_2 fabric was the result of isoclinal steep folding and from transposition of compositional banding S_1 in amphibolites (Fig. 8d). The S_2 foliation was refolded by open to close recumbent F_3 folds in the central part of the middle crustal domain (Fig. 8f), and approaching the contacts with surrounding orogenic lower crust the degree of flat D_3 reworking increases in conjunction with development of S_3 axial planar schistosity (Fig. 8e). The mineral stretching lineation trends NE–SW over the whole area, in accordance with the orientation of the hinges of the F_3 folds (Fig. 5, stereoplot F). The S_3 foliation clearly changes its orientation and dip, following the form of the orogenic middle crust, and similarly, the L_3 lineation plunges either to the SSW or

Fig. 5. (a) Structural map of a critical area of the southern Moldanubian domain with S_2 and S_3 fabrics (after Racek *et al.*, 2006). See Fig. 2 for regional location. The map shows a large area of orogenic middle crust, called the Drosendorf window, that is entirely surrounded by orogenic lower crustal rocks. Structural trends (thin lines – S3 fabrics, thick lines – S_2 fabrics) indicate extrapolations of the major orientation of structural fabrics in the field. The density of trend lines indicates the homogeneity of fabric elements in the field. (b) Stereograms: A – stereogram showing poles to S_3 fabrics in the area of orogenic lower crust north of the orogenic middle crustal domain; B – poles to S_3 fabrics from the orogenic lower crust and orogenic middle crust close to the northern termination of the orogenic middle crust domain; C – poles to S_3 fabrics from the orogenic lower crust and orogenic middle crust along the western border of the orogenic middle crust domain; D – poles to S_3 fabrics from the orogenic lower crust underlying the orogenic middle crust domain; E – stereogram showing poles to relicts of S_2 preserved within central part of the orogenic middle crust domain; F – stereogram showing L_3 mineral and stretching lineations from the whole area. Equal area projection, lower hemisphere, contoured at multiples of uniform distribution. (c) Interpretative cross-section shows main structural features described in the text. The numbers on the cross-section and map show locations of samples used for *P–T* calculations shown in Fig. 9.

NNE according to the lenticular shape of the orogenic middle crustal (Fig. 5, stereoplots B, C & D).

The second area is the southernmost part of the 3000 km^2 region of orogenic lower crust of the central Moldanubian domain (central part of Fig. 2, and northern part of Fig. 5; Kolenovská *et al.*, 1999). Here, the orogenic lower crust is a vast domain typically composed of felsic migmatitic orthogneisses and migmatites containing large bodies of Ky–Kfs granulite, eclogite and peridotite. The whole area is

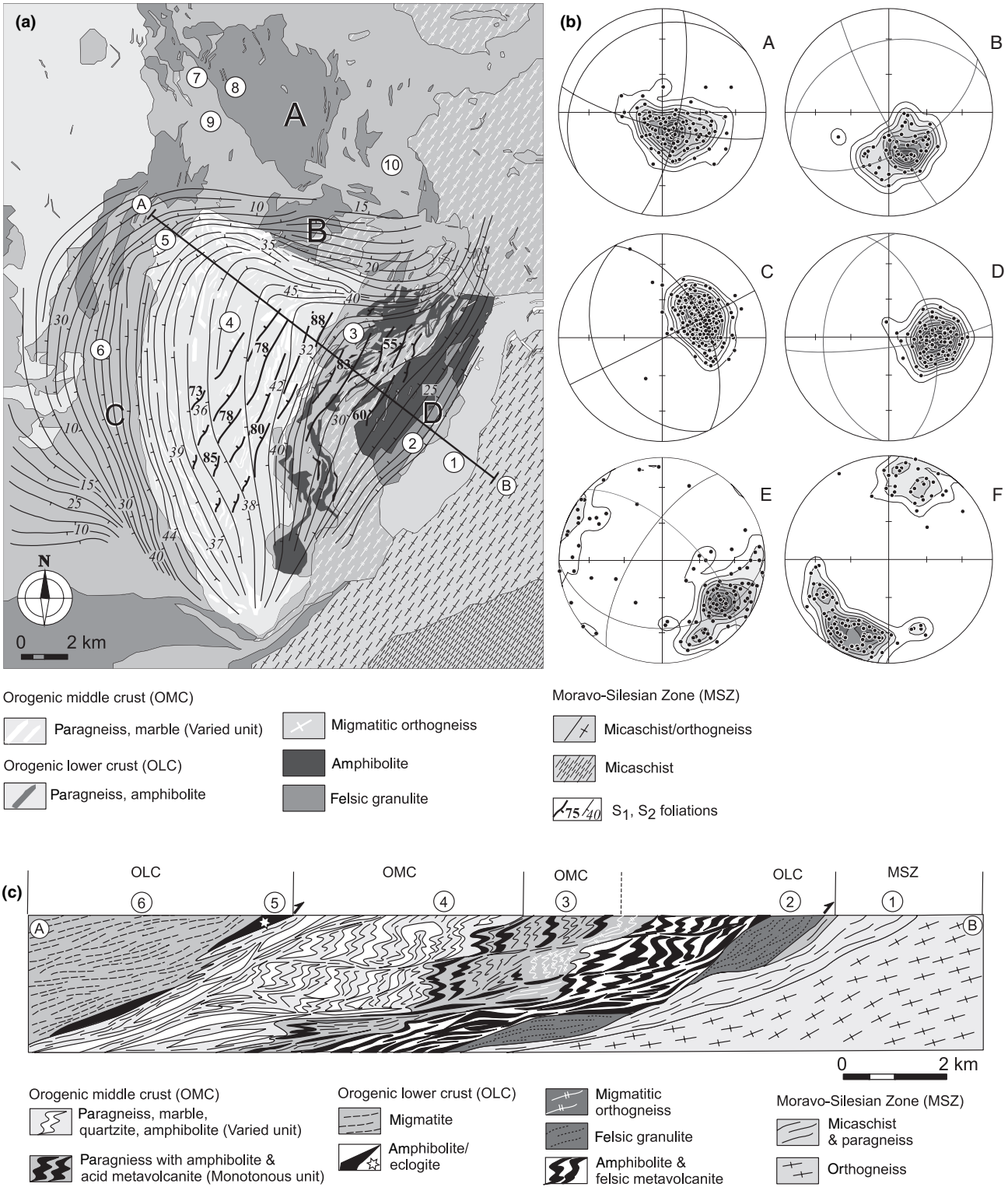

characterized by a flat migmatitic S_3 foliation (Fig. 5, stereoplot A) that is axial planar to rare isoclinal folds with hinges generally trending NNE–SSW, parallel to stretching and mineral lineations. Numerous shear bands filled with leucosome indicate a dominant top-to-the-NE shearing (Urban, 1992; Schulmann *et al.*, 1994). The eclogites and granulites form lozenge-shaped boudins surrounded by migmatitic fabric. These rocks locally contain relics of early NE-trending steep S_2 fabric, but because of their scarce occurrence,

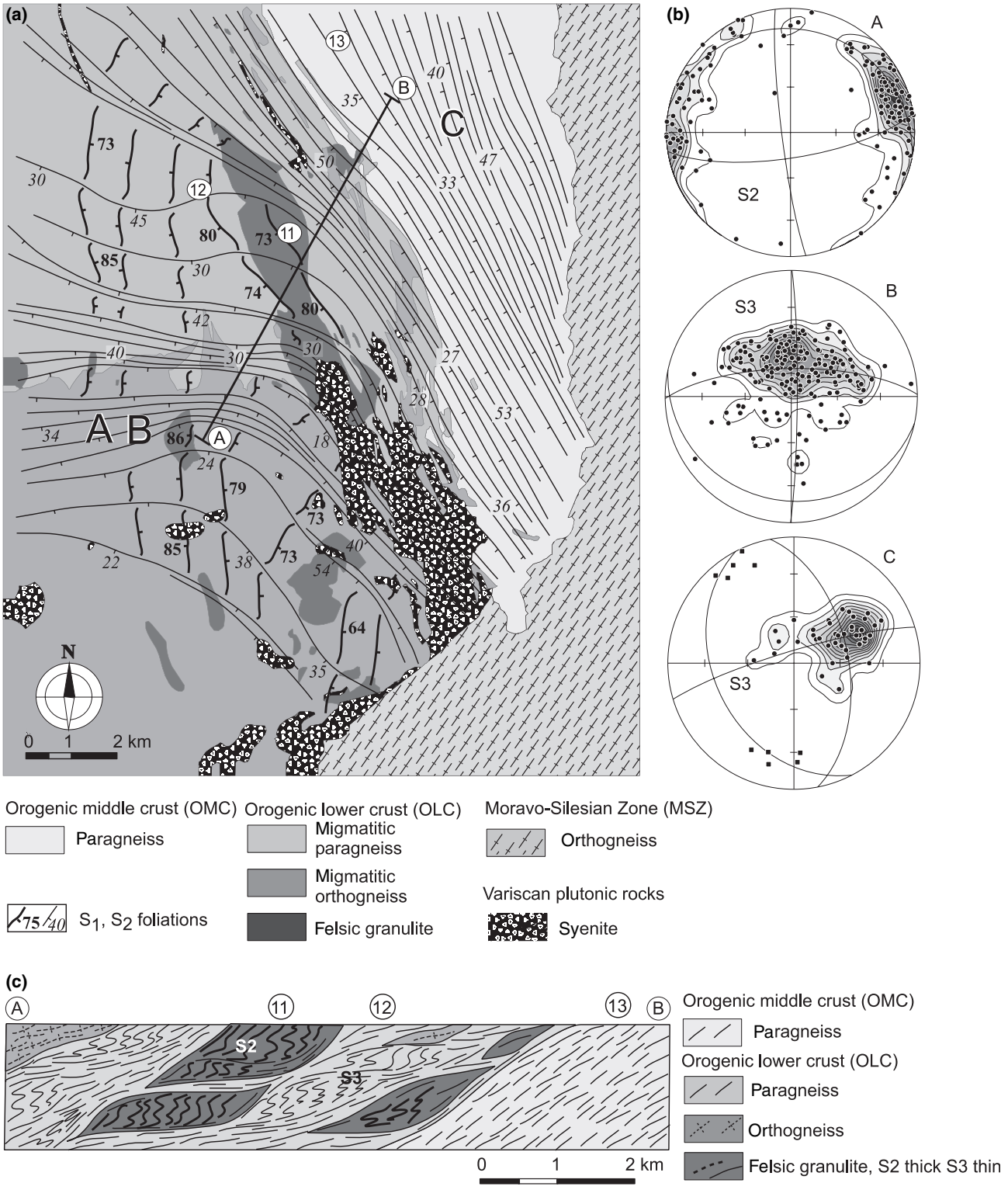

we cannot demonstrate the regional extent of the S_2 fabric in this area (Fig. 8h).

The third area is located in the northern Moldanubian domain (Figs 2 & 6) and is characterized by thrusting of a NNW–SSE-elongated granulite body over the middle crust (Fig. 6a, c). The granulite shows an exceptionally well-preserved steep NNW–SSE-trending granulite-to-amphibolite facies S_2 foliation (Fig. 6, stereoplot A). D_3 shallow to moderately steep, south-dipping shear zones, which show top to the NNE shear sense, cut the S_2 fabric heterogeneously. The surrounding migmatites and migmatitic orthogneisses exhibit predominantly S_3 fabric, which dips gently to moderately to the south (Fig. 6, stereoplot B). This foliation, formed essentially by migmatitic banding, contains numerous close to isoclinal F_3 folds with hinges trending NNE–SSW parallel to mineral lineation. Within the adjacent middle crust, the deformation is also polyphase, comprising an early foliation that dips steeply to the SW, which was reworked by a schistosity that dips gently in the same direction (Fig. 6, stereoplot C).

Structural development of the Lugian domain

The northern part of the Lugian domain is characterized by a central granulite belt surrounded on the western and eastern sides by strongly migmatized orthogneisses (Figs 7c & 8b). The granulite and the adjacent orthogneisses reveal the NNE–SSW-trending vertical S_2 foliation parallel to the trend of the orogenic lower crust (Fig. 7, stereoplot A). This S_2 foliation contains rootless folds formed by layers of metabasite that preserve evidence of an early S_1 foliation (Štípská *et al.*, 2004).

East of the granulite belt, the orthogneisses and migmatite show reworking of the vertical S_2 fabric by moderately west-dipping S_3 foliation (Fig. 8g). The dip of the S_3 fabric progressively decreases eastwards towards the underlying Ordovician lower crustal leptyno-amphibolite unit (Fig. 7, stereoplot B); a granodiorite sill emplaced syntectonic with the D_3 deformation marks the boundary between this unit and the Lugian orthogneiss, dating the D_3 structures at *c*. 340 Ma (Parry *et al.*, 1997; Štípská *et al.*, 2001). Importantly, the structure of the leptyno-amphibolite unit is discordant with respect to D_3 fabrics of the western Lugian orthogneisses; the leptyno-amphibolite unit is inferred to be of Early Ordovician age, based on U–Pb zircon dates that yield an age of *c*. 510 Ma (Fig. 7, cross-section; Štípská *et al.*, 2001; Lexa *et al.*, 2005).

To the NW from the granulite belt, the S_2 fabric is affected by sub-horizontal, variably dipping amphibolite facies S_3 fabric (Fig. 8a,b). This S_3 fabric has intensely reworked the steep S_2 foliation of the adjacent orogenic middle crust to the point that it progressively passes into a several hundred metre wide normal-sense shear zone dipping gently to the NE (Fig. 8c).

P–T–t history of the Moldanubian–Lugian root

The relationship between the prograde and retrograde *P–T* paths and orogenic fabrics is a key piece of information necessary to understand the thermo-mechanical processes that operated within the orogenic root. Microstructural, petrological and thermodynamic modelling studies during the last five years have revealed a systematic pattern of *P–T* evolution related to the early steep fabrics in both the orogenic lower and middle crust. In addition, combination of the *P–T* evolution with Sm–Nd and $^{40}Ar/^{39}Ar$ cooling ages reveals important differences in the thermo-chronological evolution of the orogen.

Microstructural and petrographic characterization of S_2 and S_3 fabrics

In the orogenic lower crust, the steep fabric is characterized by compositional banding formed by mafic and felsic granulite (Štípská *et al.*, 2004). More commonly S_2 is defined by a mineral fabric, marked by oriented kyanite, biotite and recrystallized ribbons of quartz and feldspar in the case of the felsic granulite (Tajčmanová *et al.*, 2006), and by the elongated shape of garnet and aligned omphacite grains in the case of the mafic granulite (Štípská *et al.*, 2004). In the orogenic lower crust composed of migmatitic orthogneisses, the S_2 fabric is defined by alternation of infinite monomineralic recrystallized bands of quartz, plagioclase and K-feldspar, in an assemblage with kyanite, biotite and garnet that results from a high-temperature

Fig. 6. (a) Structural map of an area showing thrusting of the orogenic lower crust over the orogenic middle crustal in the NE part of the Moldanubian domain, with regional S_2 and S_3 fabrics as shown in Fig. 5 (after Tajčmanová *et al.*, 2006). See Fig. 2 for regional location. The map shows a large body of orogenic lower crustal granulites that preserve relicts of the S_2 fabrics. The structural trends (thin layers – S_3 fabrics, thick layers – S_2 fabrics) indicate extrapolations of major orientations of structural fabrics in the field. The density of trend-lines indicates the homogeneity of fabric elements in the field. (b) Stereograms: A – stereogram shows poles to S_2 fabrics in the orogenic lower crustal granulites; B – stereogram of poles to S_3 fabrics from the orogenic middle crust. Squares in stereogram show integrated directions of L_3 lineations from the area. C – Stereogram of poles to S_3 fabrics from the orogenic lower crustal granulites and associated migmatites. Equal area projection, lower hemisphere, contoured at multiples of uniform distribution. (c) Simplified cross-section shows well-preserved S_2 fabrics in competent granulites surrounded by cordierite migmatites completely reworked by S_3 fabric. The migmatites and granulites of the orogenic lower crust are thrust over orogenic middle crust to the east. The numbers on the cross-section and map show locations of samples used for *P–T* calculations in Fig. 9.

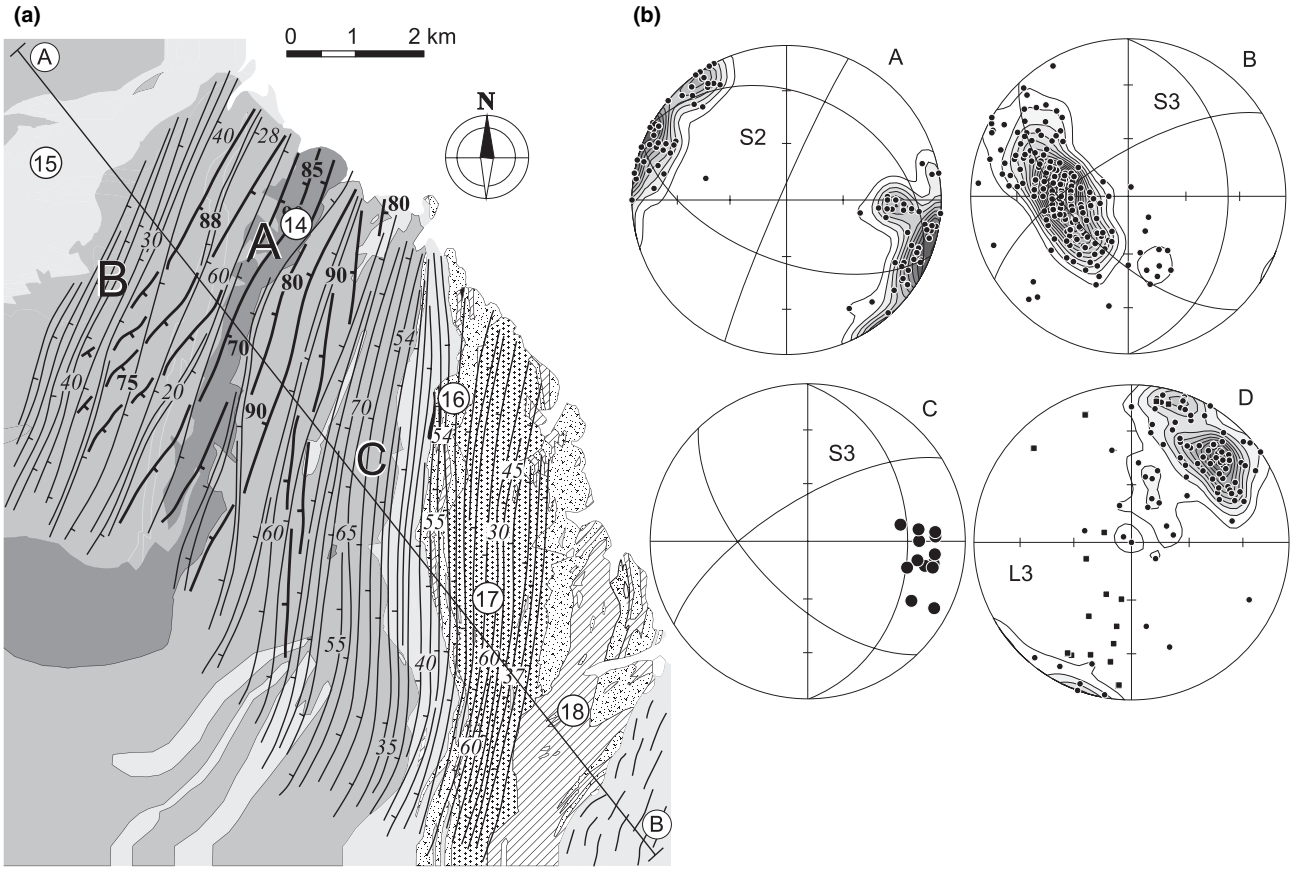

Orogenic middle crust (OMC)
Orthogneiss & orthogneiss migmatite
Metasediments & metavolcanics

Orogenic lower crust (OLC)
Omphacite granulite
Cambro-Ordovician metamorphic complex
Layered mafic & felsic metavolcanites
Felsic migmatite

Variscan plutonic rocks
Granodiorite
Moravo-Silesian Zone (MSZ)
Metasediments & metavolcanics
S_1, S_2 foliations

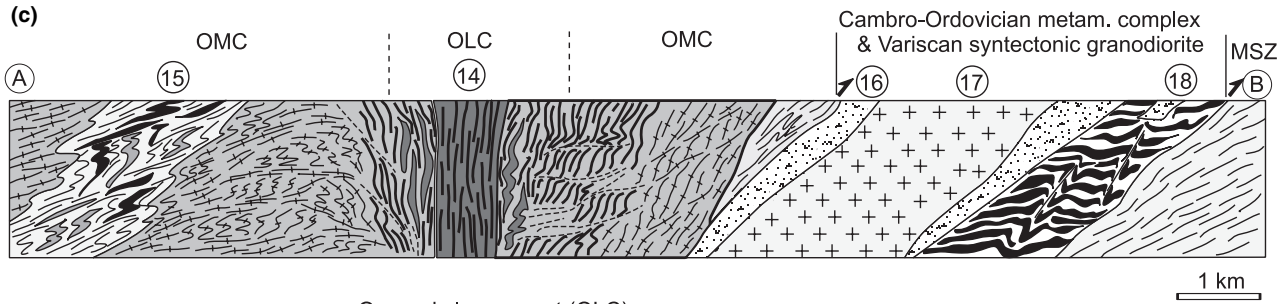

Orogenic middle crust (OMC)
Orthogneiss migmatite
Orthogneiss
Metasediments & metavolcanics

Orogenic lower crust (OLC)
Omphacite granulite
Cambro-Ordovician metamorphic complex
Layered mafic & felsic metavolcanites
Felsic migmatite

Variscan plutonic rocks
Granodiorite
Moravo-Silesian Zone (MSZ)
Metasediments & metavolcanics
S_1, S_2 foliations

and medium- to high-pressure recrystallization of coarse-grained granite (Hasalová *et al*., 2008a). In areas inferred to be a part of the orogenic lower crust, based on the presence of HP relicts and the high degree of anatexis, the S_2 fabric is defined by steep compositional layering in amphibolites, felsic metavolcanic rocks, orthogneisses and paragneisses.

In the orogenic middle crust the S_2 fabric is characterized by a steep lithological alternation of paragneisses with amphibolites, felsic metavolcanic rocks, quartzites, marbles and calcsilicate rocks (Romanová & Štípská, 2001; Racek *et al*., 2006). In the amphibolites, the steep fabric is characterized by aligned hornblende and recrystallized plagioclase ribbons in association with garnet that indicates medium-pressure conditions for formation of this fabric. Evidence of the prograde fabrics in the paragneisses of the Moldanubian domain occurs only as rare oriented inclusions of staurolite and kyanite in garnet and remnants of these minerals in the matrix (Racek *et al*., 2006). Even in some areas of the Moldanubian domain where the macroscopic fabric of the paragneisses remained steep, the higher-grade assemblages were commonly overprinted passively by lower-grade assemblages with sillimanite or cordierite, which we ascribe to the high reactivity of the paragneisses in the presence of melt. As the other lithologies do not show variation of the assemblage with changing *P–T* conditions, the main guide in characterizing the steep fabric in the orogenic middle crust of the Moldanubian domain is the steep lithological alternation combined with peak *P–T* conditions.

In the Lugian domain, in the orogenic middle crust the characterization of the steep fabric is much better constrained because of the absence of anatexis in the metasedimentary rocks and the absence or limited extent of anatexis in the orthogneisses. In the orthogneisses, the S_2 fabric is marked by steep alternation of recrystallized augen and ribbons of quartz and feldspar and by the orientation of biotite and muscovite. Steep localized ultramylonitic zones are developed locally. The prograde and peak *P–T* conditions of the steep fabrics in Lugian metapelites are constrained by the successive growth of garnet, staurolite and kyanite in the micaschists (Romanová & Štípská, 2001; Jastrzębski, 2005; Murtezi, 2006).

As described above, the flat fabric in the orogenic lower and middle crust commonly originates through horizontal folds affecting the steep fabric and is only rarely associated with sub-horizontal or gently dipping, thrust-related shear zones. Highly anisotropic rocks, such as banded orthogneisses, show strong axial planar crenulation cleavage, which, in places, passes gradually into a sub-horizontal foliation with evidence of the early vertical anisotropy occurring only as a few rootless folds (Fig. 8h). The intensity and characteristic mineralogy of the flat reworking is variable depending on the specific area, lithology and degree of metamorphism. However, some mineralogical features are common for the Ky–Kfs granulites, the orthogneisses and the paragneisses. These include the widespread development of the assemblages garnet–sillimanite–K-feldspar, in the Moldanubian domain, and garnet–muscovite ± sillimanite, in the Lugian domain, showing the overall moderate pressure character of the S_3 reworking and the higher temperature in the Moldanubian domain compared with the Lugian domain. Because of the variability of the S_3 structures along the orogen, the detailed mineralogical characteristics and *P–T* conditions for both the S_2 and S_3 fabrics for the four areas identified above are described below.

P–T *evolution of the Moldanubian domain*

Racek *et al*. (2006) examined petrological relationships between the steep and flat fabrics in the orogenic lower and middle crust of the southern Moldanubian domain (Figs 5 & 9a). Modelling of garnet zoning in eclogite from the western part of the orogenic lower crust (no. 5 in Figs 5 & 9a) indicates burial process to have taken place from around 10 kbar and 700 °C to around 15–16 kbar and 800 °C. Similar peak conditions are determined for kyanite–sillimanite migmatite structurally above the eclogite (around 14 kbar at 750 °C; no. 6 in Figs 5 & 9a). However, these prograde and peak conditions are associated with the steep S_2 fabric only as the early structural relations of relict minerals

Fig. 7. (a) Structural map of a critical area showing thin vertical belt of the orogenic lower crust surrounded by orogenic middle crust in the eastern part of the Lugian domain with regional S_2 and S_3 fabrics as in Fig. 5 (after Štípská *et al*., 2004). See geological map in Fig. 2 for regional location. The map shows a narrow body of the orogenic lower crustal granulites, preserving relicts of the S_2 fabrics, and the surrounding fabric of the orogenic middle crust. The fabric in the mafic lower crust and the syntectonic tonalite is also shown. The structural trends (thin layers – S_3 fabrics, thick layers – S_2 fabrics) indicate extrapolations of major orientations of structural fabrics in the field. Density of trend lines indicates the homogeneity of fabric elements in the field. Stereograms: A – stereogram of poles to S_2 fabrics in the garnet–omphacite-bearing granulites; B – stereogram of poles to S_3 fabrics from the orogenic lower crust and surrounding orogenic middle crust rocks represented by thin dots and contoured. Thick dots in the stereograms show S_3 foliations typical for the Ordovician metagabbros and Carboniferous tonalite sill of the Lugian mafic complex. C – Stereogram of L_3 directions from the granulite belt and surrounding orogenic middle crust (thin dots and contoured data). Black squares show mineral and stretching lineations from mylonitized gabbros and granodiorite sill. Note strong discrepancy in orientations of S_3 foliations and L_3 lineations between granulite belt and adjacent Ordovician mafic complex. Equal area projection, lower hemisphere, contoured at multiples of uniform distribution. (c) Simplified cross-section shows the vertical central granulite belt showing thrusting of the orogenic lower crust over the Ordovician leptyno-amphibolite complex. Note the syntectonic D_3 intrusion of the 340 Ma granodiorite sill and discordant fabrics in the 510 Ma leptyno-amphibolite complex.

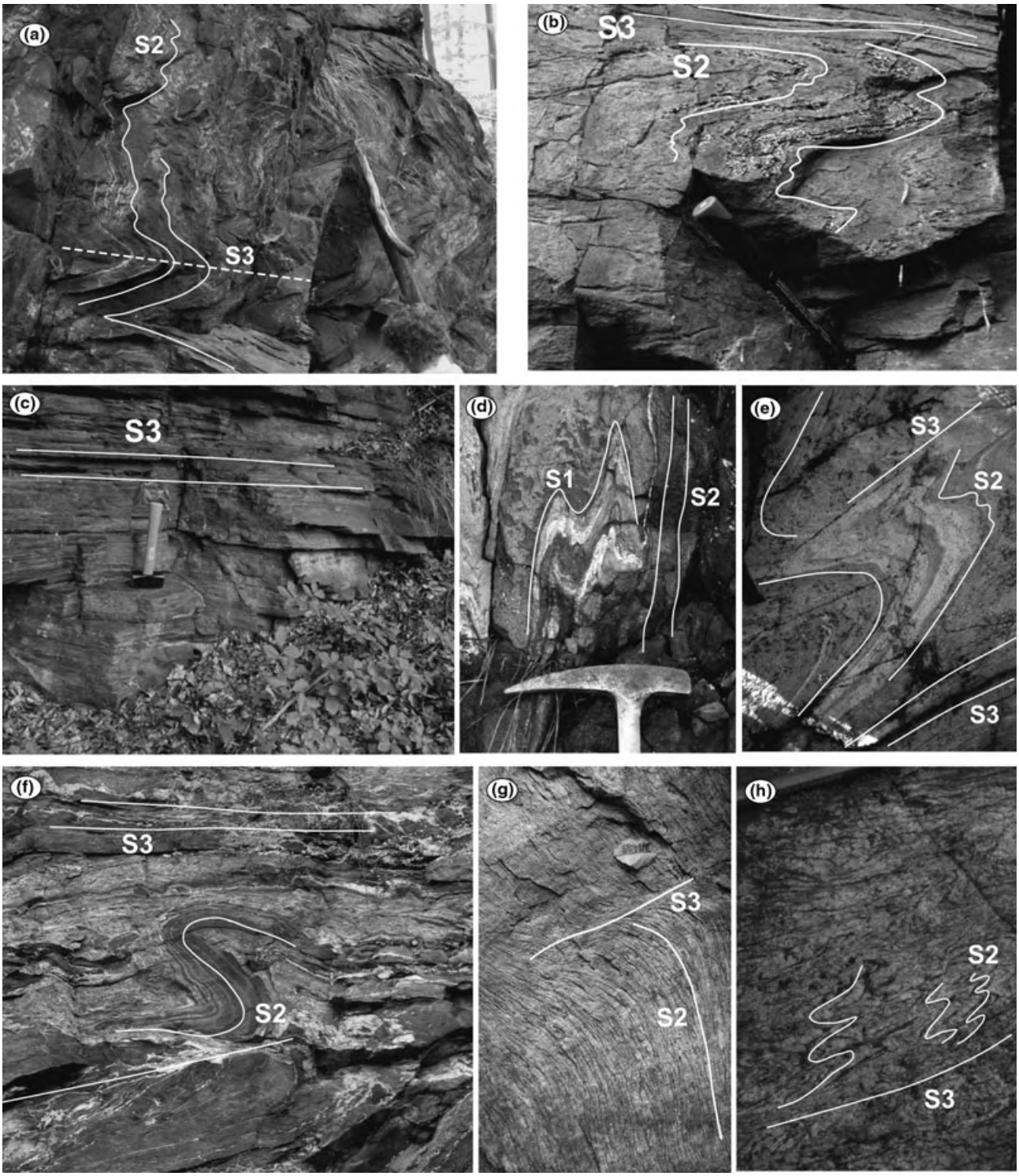

Fig. 8. Field photographs of the S_2–S_3 relationships. (a) Well preserved S_2 fabric in the garnetiferous amphibolite in the orogenic middle crust of the Lugian domain. (b) Strongly reworked S_2 fabric in the amphibolite in the orogenic middle crust of the Lugian domain. (c) Complete transposition of early fabric in new S_3 in epidote amphibolite in the orogenic middle crust of the Lugian domain. (d) Excellent preservation of the steep S_2 fabric in garnetiferous amphibolite in the orogenic middle crust of the southern Moldanubian domain. (e) S_2 folded by F_3 folds in the felsic granulite of the orogenic lower crust in the southern Moldanubian domain. (f) Asymmetrical folding of the S_2 fabric in the S_3 channel-flow fabric of the orogenic lower crust in southern Modanubian domain. (g) Character of S_2 foliation in high-grade banded orthogneiss of the Lugian domain. (h) Microfolding and partial transposition of high-grade S_2 fabric in the Gföhl gneiss of the southern Moldanubian domain.

were obliterated by strong S_3 reworking. High-pressure conditions are also reported from the Ky–Kfs granulite body to the east (~15 kbar, 800 °C, no. 2 in Figs 5 & 9a), also part of the orogenic lower crust, where the retrieved *P–T* is clearly related to the S_2 fabric.

The retrograde path of rocks from the orogenic lower crust situated far from the Brunia margin is characterized by an almost isothermal decompression to about 7 kbar, as recorded by the S_3 assemblage garnet-hornblende-plagioclase in eclogite and garnet–sillimanite–biotite in migmatite (no. 5, 6 in Fig. 9a). Unlike the central part of the Moldanubian, the Ky–Kfs granulite forming the orogenic lower crust at the boundary with the Brunia margin shows cooling with decompression (no. 2 in Fig. 9a). Modelling of zoning in garnet that is syntectonic with the S_2 fabrics in paragneisses of the orogenic middle crust is consistent with increase of *P–T* conditions to about 9 kbar and 700 °C (nos 3 & 4 in Figs 5 & 9a). The retrograde *P–T* path of the sillimanite-bearing S_3 fabric in rocks of the orogenic middle crust is associated with decrease of pressure coupled with increase of temperature, to about 7 kbar and 700–750 °C (nos 3 & 4 in Fig. 9a).

Kolenovská *et al*. (1999), Štípská & Powell (2005a) and P. Štípská & K. Schulmann (unpublished data) examined the *P–T* evolution of rocks and relics of both the orogenic lower and middle crust over a large area dominated by flat S_3 fabric in the central Moldanubian domain (Fig. 2). Here, Ky–Kfs granulites register peak conditions around 18 kbar and 850 °C with no clear indication of the prograde path (no. 8 in Figs 5 & 9b). In contrast, a MORB-type eclogite provides evidence of the prograde path from about 10 kbar and 750 °C to 17–18 kbar in the form of inclusions of hornblende and plagioclase in a prograde garnet (no. 7 in Fig. 9b). Both samples from the orogenic lower crust show almost isothermal decompression and strong D_3 reworking at 7–10 kbar and 750–850 °C (nos 7 & 8 in Fig. 9b). Associated paragneisses from the orogenic lower crust contain early staurolite and kyanite inclusions in garnet that preserves prograde zoning, indicating burial to about 10 kbar and 700 °C (no. 9 in Figs 5 & 9b; P. Štípská & K. Schulmann, unpublished data). The matrix was completely transposed by the D_3 deformation, as marked by sillimanite and biotite developed during decompression (no. 9 in Figs 5 & 9b). In another paragneiss the flat sillimanite–biotite-bearing fabric was overgrown by garnet, indicating heating at around 7–8 kbar and 700–850 °C (no. 10 in Fig. 9b; P. Štípská & K. Schulmann, unpublished data). The prograde conditions and peak pressures from samples of this area could not be directly linked to the steep fabric because of almost complete transposition of rocks by the S_3 fabric. However, the prograde inclusions in garnet from the eclogite and from the paragneiss form straight, sub-vertical internal fabrics oriented at a high angle to the external S_3 foliation, indicating that these garnet have probably grown in the steep fabric.

The steep S_2 fabric in the granulite body rimming the NE margin of the Moldanubian domain is marked by garnet, kyanite and K-feldspar indicating conditions of about 18 kbar at 850 °C, whereas the crystallization of biotite in the same fabric occurred during decompression accompanied by slight cooling (no. 11 in Figs 6 & 9c; Tajčmanová *et al*., 2006). Within the S_2 fabric, sillimanite–biotite intergrowths replacing garnet indicate significant decompression and cooling (no. 11 in Fig. 9c). The S_3 fabric is associated with hercynite-rimming metastable kyanite in the granulite and with the development of cordierite, sillimanite and biotite in adjacent gneisses and migmatites, indicating conditions of around 4 kbar and 700 °C (nos 12, 25 in Figs 6 & 9c). Muscovite–biotite schists of the adjacent orogenic middle crust contain sillimanite that overgrows relicts of kyanite in the matrix. The peak *P–T* conditions estimated by Pitra & Guiraud (1996) are 8–9 kbar at 610–660 °C, which was followed by near-isothermal decompression, as recorded in the whole middle crustal complex, to 4–6 kbar (no. 13 in Figs 5 & 9c).

P–T *evolution of the Lugian domain*

Early petrological studies of granulite from the orogenic lower crust suggested peak conditions of about 28 kbar at 1000 °C (Bröcker & Klemd, 1996; Kryza *et al*., 1996; Klemd & Bröcker, 1999), based on two-feldspar thermometry and Grt–Ky–Qtz–Pl barometry. However, Štípská *et al*. (2004) questioned these results because of the possibility of non-equilibrium compositions, which may have been involved in the calculations. Instead, these authors proposed that peak pressures were around 18–20 kbar at 800–900 °C (no. 14 in Figs 7 & 9d). Štípská *et al*. (2004) further proposed that these conditions are characteristic for the steep S_2 foliation. These authors also constrained conditions to around 10 kbar and 700 °C for the amphibolite facies retrogression within the S_3 fabric (no. 14 in Fig. 9d). Petrological studies and modelling of prograde garnet zoning from rocks of the Ky–St–Grt micaschists revealed a prograde path up to about 10 kbar and 650 °C (no. 15 in Figs 7 & 9d; Romanová & Štípská, 2001; Jastrzębski, 2005). A microstructural study confirmed that the growth of prograde garnet was syntectonic with the steep S_2 fabric. The main reworking in the horizontal S_3 fabrics occurred in the field of sillimanite stability at about 7 kbar and 650 °C (no. 15 in Fig. 9d).

The Ordovician metamorphic fabric in the leptyno-amphibolite unit developed at about 10 kbar and 800 °C (no. 18 in Figs 7 & 9d; Štípská *et al*., 2001; Lexa *et al*., 2005). Carboniferous metamorphism related to the S_3 reworking of rocks at the western margin of this unit, close to the Carboniferous sill intruded at around 7 kbar (no. 17 in Figs 7 & 9d; Lexa *et al*., 2005), occurred under similar conditions of around 8 kbar and 750 °C (no. 16 in Figs 7 & 9d; Baratoux *et al*., 2005).

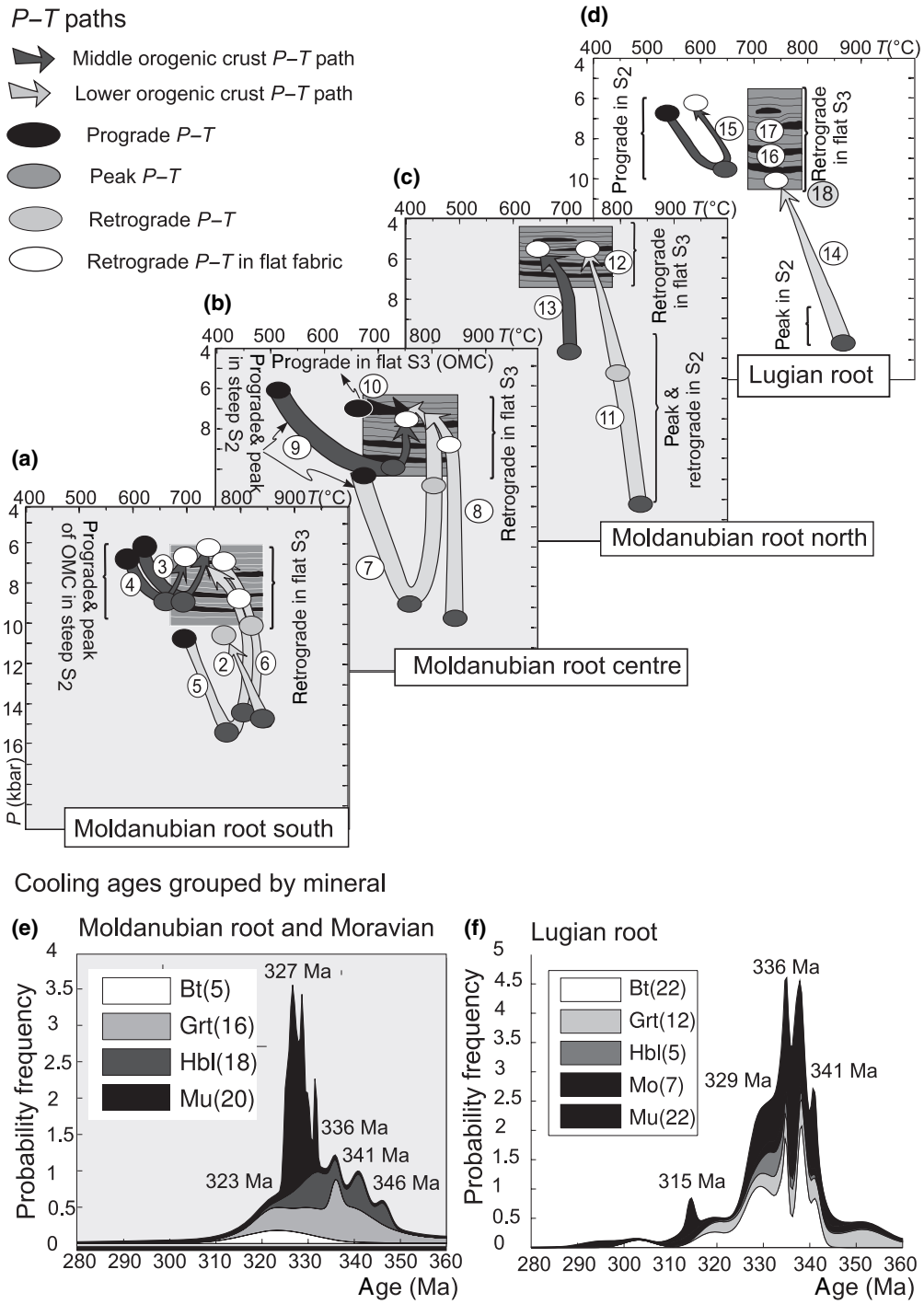

Fig. 9. *P–T* diagrams showing prograde and retrograde *P–T* paths of samples studied in the structural context discussed in the text. (a) Southern Moldanubian area in Fig. 5: Source of data: 1 – kyanite micaschist (Štípská & Schulmann, 1995); 2 – Ky–Kfs granulite (Racek *et al*., 2006); 3 – kyanite micaschist (Racek *et al*., 2006); 4 – staurolite-kyanite paragneiss (Racek *et al*., 2006); 5 – retrogressed eclogite (Racek *et al*., 2006); 6 – sillimanite migmatite (Racek *et al*., 2006). (b) Central Moldanubian area in Fig. 5: 7 – eclogite (Štípská & Powell, 2005a); 8 – Ky–Kfs granulite (P. Štípská & K. Schulmann, unpublished data), 9 – migmatitic paragneiss (P. Štípská & K. Schulmann, unpublished data); 10 – migmatitic paragneiss (P. Štípská & K. Schulmann, unpublished data). (c) Central Moldanubian area in Fig. 6: 11 – Ky–Kfs granulite (Tajčmanová *et al*., 2006); 12 – cordierite gneiss (Tajčmanová *et al*., 2006); 13 – metapelite (Pitra & Guiraud, 1996). (d) Lugian domain in Fig. 7: 14 – garnet–omphacite-bearing granulite (Štípská *et al*., 2004); 15 – staurolite–kyanite micaschist (Romanová & Štípská, 2001); 16 – amphibolite (Lexa *et al*., 2005); 17 – granodiorite (Parry *et al*., 1997); 18 – Ordovician metapelitic granulite (Lexa *et al*., 2005). (e, f): Probability curves of age histograms dealing with existing Moldanubian and Lugian Sm–Nd and $^{40}Ar/^{39}Ar$ cooling ages. Bt – biotite $^{40}Ar/^{39}Ar$ cooling ages; Grt–Cpx and Grt–whole rock, Sm–Nd ages; Hbl – hornblende and Mu – muscovite, Ar^{40}/Ar^{39} cooling ages.

Thermochronology of Moldanubian and Lugian domains

The distribution of isotopic ages reflects a two-stage cooling, related to exhumation processes. An older stage is marked by cooling ages from minerals with high blocking temperatures (Sm–Nd system in garnet, 700–750 °C, Hensen & Zhou, 1995; $^{40}Ar/^{39}Ar$ in hornblende, around 480 °C, Harrison *et al*., 1985). Systematically, younger cooling ages are retrieved from minerals with low blocking temperatures ($^{40}Ar/^{39}Ar$ in muscovite, around 350 °C, and in biotite, around 280 °C, Harrison *et al*., 1985). Peridotites and associated eclogites yield Sm–Nd whole-rock–garnet ages between 350 and 325 Ma (Brueckner *et al*., 1991; Beard *et al*., 1992; Medaris *et al*., 1995). The peak for Sm–Nd ages for both types of rocks is around 336 Ma (Fig. 9e). The $^{40}Ar/^{39}Ar$ hornblende data are compatible with the distribution of Sm–Nd ages, whereas the $^{40}Ar/^{39}Ar$ muscovite data record systematically younger ages ranging from 331 to 325 Ma (Fig. 9e; Matte *et al*., 1990; Dallmeyer *et al*., 1992; Fritz *et al*., 1996).

The Variscan cooling history of the Lugian eclogites is documented by Sm–Nd garnet–clinopyroxene–whole-rock ages of 340–330 Ma (Brueckner *et al*., 1991). Recently, Lange *et al*. (2005) provided Sm–Nd isochrons for the Lugian granulites that define ages between 357 and 337 Ma, which fit the existing $^{40}Ar/^{39}Ar$ hornblende and biotite cooling ages from this region (Schneider *et al*., 2006). The $^{40}Ar/^{39}Ar$ muscovite ages from all lithologies of the Lugian domain are similar to Sm–Nd garnet, $^{40}Ar/^{39}Ar$ hornblende and $^{40}Ar/^{39}Ar$ biotite data from granulites and eclogites, indicating a rapid and monocyclic cooling history (Fig. 9f).

Polyphase fabric and metamorphic evolution of the orogenic belt

The structural pattern in the Lugian domain reveals a well-preserved D_2 vertical fabric in the orogenic lower and middle crust as well as coherency of these units, defined by sub-parallel alternations of continuous belts of orogenic lower and middle crust on the geological map. Here, the geometry of the geological units and map patterns are fully controlled by the D_2 deformation. The D_3 deformation was generally weak and heterogeneous, being mostly concentrated close to the thrust of the Lugian domain over the Ordovician leptyno-amphibolite unit to the east and close to the area of flat fabric and the normal-sense shear zone bounding the Lugian domain in the west (Figs 7 & 8). Normal-sense non-coaxial shearing developed continuously from the earlier pure shear deformation and probably this was responsible for displacement of schists of the orogenic middle crust to the NW and unroofing of the orogenic lower crust.

In the orogenic lower and middle crust of the Lugian domain, petrology indicates that retrograde conditions of omphacite-bearing granulites and peak pressure conditions of adjacent micaschists are similar. In the orogenic middle crust, the prograde mineral growth is clearly related to the steep S_2 fabric (Romanová & Štípská, 2001), whereas in the granulites from the orogenic lower crust, development of the S_2 fabric is related to their retrogression (Štípská *et al*., 2004). The remarkable differences in prograde and retrograde *P–T* paths of rocks from the orogenic middle and lower crust, respectively, related to steep S_2 foliations makes this region the best example of vertical material and heat transfer during D_2.

Štípská *et al*. (2001) further discussed the significance of similar Carboniferous and Ordovician metamorphic conditions for the easterly lower crustal leptyno-amphibolite complex. They concluded that this complex cooled after Ordovician rifting and remained stable in the crust before the onset of Variscan deformation. Heterogeneous Variscan amphibolite facies deformation was localized in the western margin of the Ordovician block and shares the same *P–T* conditions and kinematics with amphibolite facies retrograde fabric of the easternmost orogenic lower crust. Consequently, Štípská *et al*. (2004) suggested that the transition from the steep-to-the-west moderately dipping fabrics in the orogenic lower crust was linked to thrusting of these rocks over a rigid lower crustal block made up of leptyno-amphibolite unit rocks at a depth equivalent to about 10 kbar (Fig. 5c).

In contrast, the horizontal S_3 fabrics affecting rocks of the orogenic lower crust and the normal-sense shear zone developed in the west were linked to the development of retrograde and syntectonic mineral assemblages indicating an important decrease of temperature and pressure typical for detachment zones (e.g. Vanderhaeghe & Teyssier, 2001). The Lugian root records a single-stage cooling history characterized by telescoping of ages for minerals with different blocking temperatures.

The structural development of the NE termination of the Moldanubian domain shares a number of features with the Lugian domain. In this area, the S_2 foliation was well preserved in felsic granulites in conjunction with a weak D_3 reworking, which emphasizes a coherency of the lower and middle orogenic crust and indicates that the map pattern developed during D_2 vertical movements, similar to that in the Lugian domain. The steep fabric in the orogenic lower crust records retrogression to the sillimanite stability field, suggesting that the orogenic lower crust was exhumed to middle crustal conditions along the S_2 fabric. The HP characteristics of this fabric are not necessarily always preserved, preservation being dependent mainly on whether the crust avoids re-hydration during exhumation. However, in contrast with the Lugian domain, the heterogeneous D_3 deformation does not show any normal-sense component of shear and is exclusively associated with

top-to-the-NE-oriented thrusting in the stability field of cordierite at low pressures of 3–4 kbar.

Structural and petrological studies of the southern and central Moldanubian domains show that similar *P–T* conditions around 7 kbar at 750 °C are characteristic for all crustal levels during development of the flat S_3 fabric. Rocks from different depths were mixed and reworked together during the D_3 deformation, as evidenced by contrasting prograde *P–T* paths with different pressure peaks. The increase of temperature in the orogenic middle crust and the slight decrease of temperature in the orogenic lower crust during retrogression suggest a mutual thermal equilibration during development of the S_3 flat fabric.

Structural observations show that all rocks were strongly deformed during D_3 horizontal flow, although more competent lithologies, mostly middle crust and some granulites, retained their original steep S_2 fabric, whereas in the less competent, weak lower crust, the horizontal top-to-the-NE D_3 ductile shearing dominates. During this process, the originally coherent orogenic middle and lower crust was disaggregated to form boudins and rootless folds in a pervasively flowing migmatitic matrix. We suggest that providing the volume of orogenic middle crustal is high enough, the mineral assemblages from the D_2 vertical fabrics are preserved (Figs 6 & 9a). In contrast, the smaller boudins were completely re-equilibrated and even heated in the flowing mass of hot orogenic lower crust (Figs 6 & 9b). The metamorphic conditions associated with the D_3 flow show clearly that pressure, temperature and intensity of D_3 reworking decreases from south to north across the whole continental margin.

Based on dating of metamorphic zircon from granulites, the timing of HP metamorphism and S_2 fabric formation in the Moldanubian domain was estimated by Schulmann *et al.* (2005) and Tajčmanová *et al.* (2006) to occur between 350 and 340 Ma. This age span corresponds with cooling ages of minerals with high blocking temperatures in the northern Moldanubian domain (Matte *et al.*, 1990; Macintyre *et al.*, 1992), and indicates that already during the D_2 stage an important cooling and exhumation of this area was taking place, similar to the Lugian domain. The younger 330–325 Ma $^{40}Ar/^{39}Ar$ cooling ages obtained for muscovite and biotite imply a second distinct period of thermal reworking and isotopic resetting in the region, correlated with the strong D_3 reworking in the south.

Geophysical imagery of the subsurface shape of the Brunia continental promontory

It is apparent that the thrust-related horizontal flow, which dominates the deformation of the Moldanubian domain at around 325 Ma, does not exist in the Lugian domain. This indicates a significant difference in the bulk exhumation processes between the two crustal segments and the important involvement of the Brunia continent in the Moldanubian exhumation history. In order to discuss the relative contribution of the Brunia basement in the tectonic evolution of the orogenic root it is necessary to know the sub-surface extent of the basement promontory underneath the orogenic root rocks. Therefore, after the compilation of gravity data, a Bouguer anomaly map of the area (Fig. 10) was produced.

At a large scale, the Bouguer anomaly map (Fig. 10) shows two main domains: (i) to the west, a domain characterized by low- and intermediate-gravity anomalies, inferred to be associated with rocks that have low to intermediate densities; and (ii) to the east, a domain with a succession of gravity highs inferred to be associated with significantly denser rocks. In the NE, the low- to intermediate-gravity anomalies coincide with the Lugian domain, whereas the gravity highs are associated with the Brunia continent. The steep horizontal gradient in gravity reflects a steep boundary between the Lugian domain and the Brunia continent. In the SW, the Moldanubian domain west of the NNE–SSW-striking Central Moldanubian pluton is characterized by low- and intermediate-gravity anomalies similar to the Lugian domain. Similar to the north, we infer that the gravity highs over the Brunia continent in the SE represent mostly dense rocks. However, these gravity highs continue to the west, into the eastern part of Moldanubian domain as far as the Central Moldanubian pluton. Therefore, the observation made in the north, where the gravity boundary coincides with the geological boundary between the Lugian domain and Brunia, is not valid in the south, where the geophysical boundary is located about 50–70 km west of the mapped geological boundary.

Within the eastern Moldanubian domain, the rocks at outcrop are similar west and east of the South Bohemian pluton, and rocks with high densities that could explain the gravity high in the eastern part of the Moldanubian domain are not represented at outcrop. Consequently, the dense rocks must be located at a greater depth. The gentle gradient of the gravity highs in the west indicates that the dense Brunia continental promontory dips towards the west, beneath the eastern Moldanubian rocks. This interpretation is confirmed by preliminary 3D modelling, which shows that the boundary between the dense Brunia basement and the low- to intermediate-density rocks of the Moldanubian domain has a gentle dip down to a depth of some 2–3 km near the Central Moldanubian pluton, where it dips more steeply beneath the pluton (60–70°).

Implication of Bouguer anomaly pattern

This analysis of the Bouguer anomaly map in Fig. 10 reveals striking differences between the Moldanubian and Lugian domains, which may be interpreted in terms of the presence of Brunia basement under a thin layer of Moldanubian rocks. This interpretation is consistent with the suggestion that the S_3 fabric in the

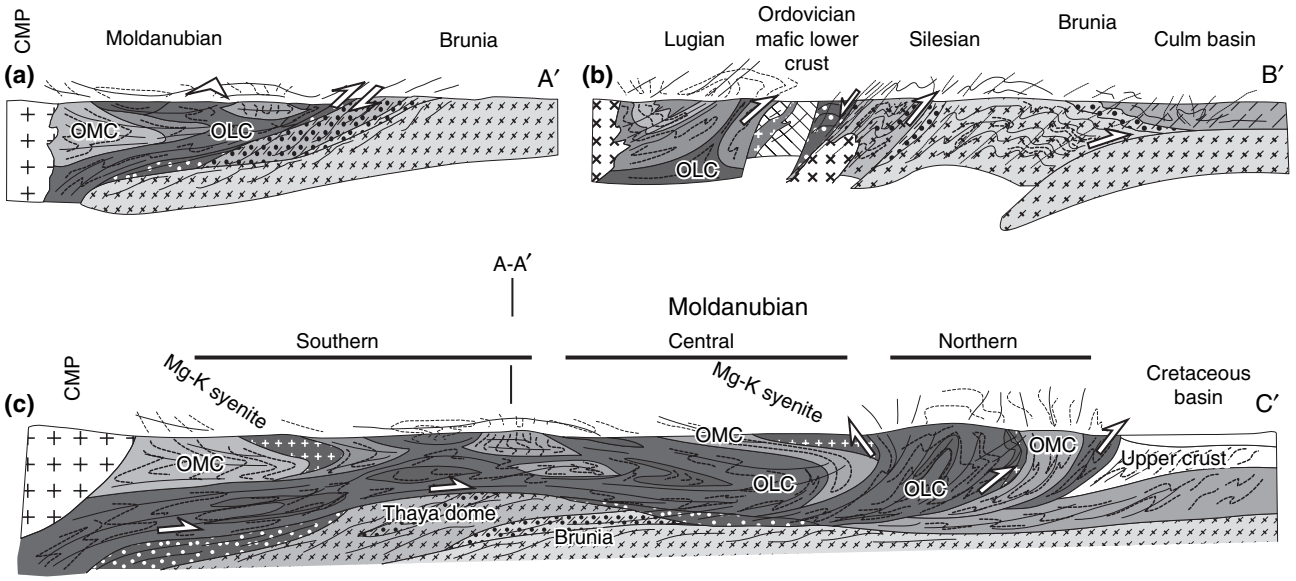

Fig. 10. Interpretative cross-sections located in Fig. 2, showing distribution of the orogenic lower, middle and upper crust of the orogenic root and the Brunia continent. (a) East to west cross-section of southern Moldanubian showing synformal structure. The S_3 fabric associated with channel flow is dominant in the orogenic lower crust, whereas in the orogenic middle crust the steep S_2 fabric is dominant. Dismembered orogenic middle crust forms large-scale boudins surrounded by migmatitic S_3 fabric. (b) Cross-section of Lugian–Silesian domain, to show relationships between the D_2 extrusion of the orogenic lower crust that was thrust over the Ordovician leptyno-amphibolite complex and the S_3 fabric associated with ductile thinning in the Lugian section. (c) North to south cross-section of the Moldanubian domain. Figure shows strong D_3 deformation of the rear part of the system with important mixing of orogenic lower crust and orogenic middle crust in the channel flow fabric and weak D_3 deformation in the northern part of the section.

Moldanubian domain may result from underthrusting of the Brunia continental promontory. In contrast, the absence of a gravity high over the Lugian domain, coupled with the structural and geochronological criteria discussed above, indicate that the Brunia continent was not underthrust beneath the orogenic root of the Lugian domain. In other words, the horizontal fabrics in the Lugian domain cannot be explained by the mechanical interaction between the Brunia continent and the Lugian root system.

DISCUSSION

Tectonic significance of steep orogenic fabrics

The zone of vertically foliated Lugian domain granulites that are surrounded by migmatized and highly sheared orthogneisses that also preserve a steep metamorphic S_2 fabric represents a key area for understanding the early stage of exhumation of the lower orogenic crust. Thrusting or normal faulting exhumation mechanisms cannot explain the steep S_2 fabric in the granulite and orthogneisses, which we have interpreted instead as recording a vertical channel along which upward extrusion of the orogenic lower crust occurred.

Another important observation is that the S_2 foliation results from macroscopic refolding of an early sub-horizontal fabric at the scale of both the mesoscopic sub-horizontal compositional anisotropy and the orogenic crust (Štípská *et al.*, 2004; Racek *et al.*, 2006). In addition, petrological studies show that the S_2 fabric in rocks of the orogenic middle crust adjacent to the granulites is associated with the prograde metamorphic evolution to a metamorphic peak at around 9 kbar, whereas in the orogenic lower crust the S_2 fabric is related with retrogression from high pressures around 18–20 kbar to pressures around 7–10 kbar.

The structural pattern and opposite metamorphic evolution developed in the kinematically similar S_2 fabrics indicates vertical material transfer compatible with large-scale folding. We suggest that folding of the crustal layers was responsible for the exhumation of the orogenic lower crust in cores of large antiforms and burial of the orogenic middle and upper crust in synformal regions. Furthermore, we suggest that the alternations of vertical belts of orogenic lower and middle crust that parallel the continental margin originated during this D_2 event. At the end of this process most of the orogenic middle and lower crust had already cooled below the blocking temperatures for the $^{40}Ar/^{39}Ar$ system in hornblende and partly also the $^{40}Ar/^{39}Ar$ system in muscovite.

In the Polish part of the Lugian domain large-scale folding of crustal layers was recognized by Don (1964) and Dumicz (1979). Moreover, a theoretical background for exhumation of lower crust by folding has been provided by (Burg & Podladchikov, 1999) and applied to the exhumation of lower crustal rocks for

example in the area of the Namche Barwa syntaxis (Burg *et al.*, 1997).

Based on shape analysis of macroscopic folds, Franěk *et al.* (2006) proposed that the folding of lower crustal layers occurred at granulite facies conditions by passive amplification mechanisms. Consequently, these authors suggested that the folding started by the development of cuspate structures at the boundary between the lower and middle crust because of a low-viscosity contrast at this interface (cf. Kisters *et al.*, 1996). Growth of the upward-pointing cusps was replaced by vertical extrusion as the whole domain became sufficiently shortened and the horizontal anisotropy was replaced by a vertical anisotropy. At that stage, the difference in the integrated vertical bulk viscosity between a weak lower crustal cusp and an adjacent stronger middle crustal lobe increased. These viscosity differences lead to strain partitioning and vertical extrusion of the weak orogenic lower crust but slower exhumation of adjacent middle crust (Ježek *et al.*, 1998).

To make the mechanism of vertical extrusion possible a rigid floor is required (Schulmann *et al.*, 2003), which is represented by a strong sub-root mantle in the model proposed here. The strength of the sub-crustal mantle was modelled for a given thermal gradient by Thompson *et al.* (2001) and Schulmann *et al.* (2002), who showed that at least 40 km of rigid mantle lithosphere was likely to have existed at the onset of exhumation of the thermally weakened lower crust. The occurrence of slivers of mantle peridotite, which have sharp boundaries and discordant internal fabrics with respect to the flow fabric of the surrounding granulites, within the orogenic lower crust provides further evidence for the existence of a strong mantle and implies an important strength contrast between the mantle and the orogenic lower crust (Medaris *et al.*, 2006). Although the granulite extrusion structures described in this study resemble extrusions of lower-crust driven by density inversion (Martinez *et al.*, 2001), they were controlled mostly by lateral shortening forces in this case, as shown in Fig. 11a.

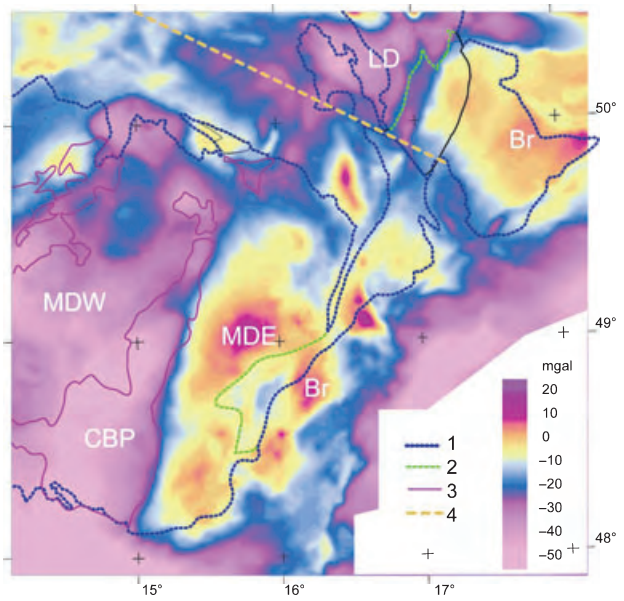

Fig. 11. Bouguer anomaly map of the eastern margin of the Bohemian Massif (provided by the Czech Geological Survey). Thick lines superimposed on the Bouguer anomaly map are limits of geological unit boundaries and orogenic crustal levels from Fig. 2. Br, Brunia continent; MDE, eastern branch of the Moldanubian domain; CMP, the Central Moldanubian pluton; MDW, western branch of the Moldanubian domain; LD, the Lugian domain.

Horizontal flow of orogenic lower crust

A transition from vertical S_2 fabrics to horizontal S_3 fabrics occurs in almost all examples of lower crustal vertical structures in the Moldanubian and Lugian domains. Therefore, the main questions that arise are: is there a causal relationship between vertical extrusion and the development of horizontal flow? and what are the driving forces for the deformation?

Ductile thinning and collapse of vertical fabric in the Lugian domain

A satisfactory tectonic model to explain the structural, petrological and geochronological data from the Lugian domain is one involving folding of a layered orogenic crust followed by the asymmetrical north-eastward extrusion of the orogenic lower crust caused by the indentation of an Ordovician mafic lower crustal block at *c.* 340 Ma. Extrusion of the orogenic lower crust was associated with the development of the horizontal D_3 fabric accompanied with detachment of the western units and complete reworking of the orogenic middle crust in adjacent synforms. Consequently, the horizontal fabric in the Lugian domain cannot have been created in response to intracrustal flow because of lateral variations in lithostatic pressure/gravitational potential energy of thickened crust/lithosphere (Milnes & Koyi, 2000; Vanderhaeghe & Teyssier, 2001).

A more likely explanation is a model in which the vertically moving material experiences a reversal in the principal strain-rate directions (Feehan & Brandon, 1999), which was expressed as a switch from the vertical fabric at depth to the sub-horizontal fabric at shallow crustal levels (Ring & Brandon, 1999). However, such a model requires the presence of a thick continental accretionary wedge, as proposed by Platt (1986), which has a mixed flow field involving vertical thickening at depth and vertical thinning near the surface.

Previously Schulmann & Gayer (2000) interpreted the Lugian domain as an obliquely convergent wedge developed above the Saxothuringian subduction zone. In this model, the Ordovician mafic lower crustal block

represents a relict of the rigid backstop and the normal-sense shear zone in the west reflects the collapse of vertically extruded material (Fig. 11b). Importantly, the U–Pb zircon data show Ordovician protolith ages for both the felsic orogenic root (orogenic lower and middle crust) and the Ordovician mafic lower crustal block to the east. These data, together with the coincidence of the gravity and geological boundaries between the Lugian domain and the Brunia continent (Fig. 10), indicate that the transition from vertical to horizontal fabric results from an intra-Lugian mechanical interaction and that the Brunia continent was not involved in this process (Fig. 12).

Heterogeneous channel flow and hot fold nappe fabrics in the Moldanubian domain

There are a number of differences associated with the development of the flat fabric in the Moldanubian domain compared with the development of the flat fabric in the Lugian domain. In the southern part of the Moldanubian domain, the horizontal S_3 fabric developed at decreasing pressure from south to north (Figs 4 & 5d) in conjunction with decreasing intensity of the D_3 reworking. This is associated with an increase in temperature and decrease in pressure in the orogenic middle crust concomitant with a decrease in temperature and pressure of the orogenic lower crust. In addition, migmatized gneisses of the orogenic lower crust commonly surround blocks and boudins of the orogenic middle crust that preserve evidence of the early HP metamorphism. The D_3 deformation shows constant NNE–SSW-oriented stretching and top-to-the-NNE thrust-related shear movement, which is consistent with oblique transpressive deformation in the adjacent Moravo–Silesian Zone. The common geometry and oblique thrust kinematics of the D_3 deformation are the chief features of the mechanical interaction between the Moldanubian domain, Moravo–Silesian Zone and the Brunia continent. The geophysical observations confirm the hypothesis of large-scale displacement of the Brunia basement underneath the Moldanubian domain, which interpretation locates the sub-surface margin of the Brunia continental promontory far to the west from the present Moldanubian domain and Moravo–Silesian Zone boundary.

This highly non-coaxial deformation correlates with young cooling ages (330–325 Ma) for muscovite and biotite $^{40}Ar/^{39}Ar$ systems compared with older (350–340 Ma) hornblende $^{40}Ar/^{39}Ar$ data, Sm–Nd cooling ages from HP metamorphic rocks and metamorphic ages from zircon, preserved mainly in the north. Muscovite and biotite from the adjacent Moravo–Silesian Zone nappes and the deformed Brunia continent show similar young $^{40}Ar/^{39}Ar$ cooling ages, which correspond to those of detrital muscovite fractions from the Culm foreland basin. The detrital muscovite shows convergence of the stratigraphic age of sedimentation and the $^{40}Ar/^{39}Ar$ cooling ages at 330–325 Ma (F. Neubauer, pers. comm.). Pebbles of granulite and Mg-rich syenite (durbachite) in the foreland conglomerates have yielded similar information from U–Pb dating of zircon, where two groups of ages occur at *c.* 340 and *c.* 325 Ma, the latter being consistent with the stratigraphic age of 330–320 Ma (Kotková *et al.*, 2007).

We suggest that the D_3 deformation, which involved subhorizontal top-to-the-NE thrusting of the Moldanubian domain over the Brunia continent, occurred

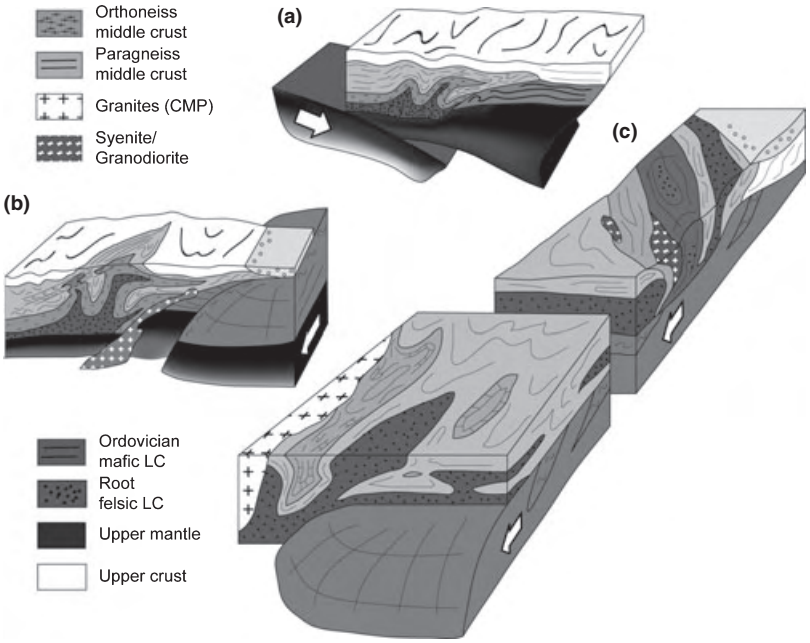

Fig. 12. Sequence of block diagrams to show the principal exhumation mechanisms and progressive tectonic evolution of the eastern margin of the Bohemia Massif. (a) Early stage of crustal folding and extrusion associated with vertical material and heat transfer. (b) Second stage (*c.* 340 Ma) of development of a flat fabric due to collapse of the vertical anisotropy – probably due to ductile thinning mechanisms that accompany detachments of the upper crust. (c) Weak orogenic root deformed by the Brunia continental promontory and the development of large hot nappes during D_3 at 330–325 Ma. The section shows a northward attenuation of the crust together with a northward-facing topographic slope with coeval surface erosion in the North. The latter is consistent with the geometry of the Brunia continent.

at 330–325 Ma and was associated with exhumation of HP metamorphic rocks to the surface, as demonstrated by sedimentation of granulite pebbles and metamorphic muscovite in the foreland basin. The earlier ages clustering around 340 Ma correspond to D_2 event, i.e. to the vertical material transfer associated with crustal-scale folding, evidence of which is partially preserved in flat-lying migmatites.

The structure of the Moldanubian domain is consistent with the 'stage 3' of the channel-flow model – the hot fold nappe (Beaumont *et al.*, 2006; Culshaw *et al.*, 2006). In these channel-flow models, stage 3 coincides with the arrival of a lower crustal block that forces weak middle and lower crust into large-scale gently inclined fold nappes rooted in the thickened Moho.

The hot fold nappe model can be applied to the Moldanubian root system, keeping in mind that the model represents the result of a continuous 2D history whereas the Moldanubian root system comprises an exhumation history in two stages that are kinematically independent. Nevertheless, the hot fold nappe model simulates well the relatively weakly deformed NE part of the Moldanubian system with well-preserved D_2 fabric, which reaches shallow crustal levels and ultimately the surface (Figs 8 & 11). To the south, the extruded nappes were derived from more internal and hotter parts of the orogen. Increasingly large volumes of weak lower crust were gradually transported southwards over the Brunia continent leading to an increase in the amount of lower crustal material at the surface.

The channel flow is heterogeneous, as predicted by Beaumont *et al.* (2001, 2006), because of the previous history, which generates important crustal strength variations. The implication of this model is that the heterogeneous crust makes the geometry and composition of the channel flow similarly heterogeneous. In the Moldanubian case, the channel transports detached blocks and boudins of distinctly different compositions such as HP granulites and mid-crustal segments that still preserve relicts of the D_2 fabric. In this southern part of the channel all isotopic systems are re-equilibrated and the cooling ages are younger in comparison with the non-uniformly reset isotopic systems in the north.

CONCLUSIONS

This study has shown that exhumation of the orogenic lower crust in the eastern sector of the Variscan orogenic belt is characterized by two independent stages. (1) The first stage is best preserved in the Lugian domain, where it is characterized by an intra-crustal folding that is responsible for vertical material transfer associated with exhumation of the deep orogenic lower crust to shallower crustal levels corresponding to pressures around 10 kbar at about 350 to 340 Ma. The folding and vertical extrusion events are followed by a vertical shortening leading to development of sub-horizontal fabrics at medium to low pressures. The early horizontal shortening was probably triggered by the existence of a rigid Ordovician block, part of which is preserved at the eastern boundary of the Lugian domain. We suggest that this early exhumation event was related kinematically to Saxothuringian continental subduction to the east, creating a convergent continental accretionary wedge – the Lugian domain. Mechanical interactions with the large Brunia continent during the exhumation process remain unconstrained.

(2) The Moldanubian domain has steep fabrics in similar orientations to those preserved in the Lugian domain. Vertical material transfer during the Lower Carboniferous led to the development of alternations of steeply inclined domains of lower and middle orogenic crust, similar to Lugian domain. However, this tectonic event was followed by a NNE-directed sub-horizontal shearing at about 330–325 Ma resulting from subsurface indentation by the Brunia continental promontory into the Moldanubian domain. The arrival of the Brunia continent is responsible for the progressive emplacement of hot fold nappes and heterogeneous channel flow in the rear (western) part of the system generating mixtures of middle and lower crustal units with preserved early exhumation fabrics.

ACKNOWLEDGEMENTS

This study was made possible thanks to the ANR project 'LFO in orogens' funding as well as to financial support of CNRS (UMRs 7516 and 7517) and the Czech Science Foundation (GACR 205/05/2187 and GACR 205/04/2065). Ondrej Lexa is indebted to the Université Louis Pasteur for covering his salary. We are grateful to J. Platt, D. Grujic and an anonymous reviewer for constructive reviews. The editorial work of M. Brown is highly appreciated.

REFERENCES

Allemand, P. & Lardeaux, J. M., 1997. Strain partitioning and metamorphism in a deformable orogenic wedge: Application to the Alpine belt. *Tectonophysics*, **280,** 157–169.

Andersen, T. B., Jamtveit, B., Dewey, J. F. & Swensson, E., 1991. Subduction and eduction of continental crust: major mechanisms during continent–continent collision and orogenic extensional collapse, a model based on the south Norwegian Caledonides. *Terra Nova*, **3,** 303–310.

Baratoux, L., Schulmann, K., Ulrich, S. & Lexa, O., 2005. Contrasting microstructures and deformation mechanisms in metagabbro mylonites contemporaneously deformed under different temperatures (c. 650 °C and c. 750 °C). In: *Deformation Mechanisms, Rheology and Tectonics: From Minerals to the Lithosphere, Special Publication 243* (eds Gapais, D., Brun, J.-P. & Cobbold, P. R.), pp. 97–125. Geological Society, London.

Beard, B. L., Medaris, L. G., Johnson, C. M., Brueckner, H. K. & Mísař, Z., 1992. Petrogenesis of Variscan high-temperature group–A eclogites from the Moldanubian zone of the Bohemian Massif, Czechoslovakia. *Contributions to Mineralogy and Petrology*, **111,** 468–483.

Beaumont, C., Jamieson, R. A., Nguyen, M. H. & Lee, B., 2001. Himalayan tectonics explained by extrusion of a low-viscosity crustal channel coupled to focused surface denudation. *Nature*, **414,** 738–742.

Beaumont, C., Nguyen, M. H., Jamieson, R. A. & Ellis, S., 2006. Crustal flow modes in large hot orogens. In: *Channel Flow, Ductile Extrusion and Exhumation in Continental Collision Zones, Special Publication 268* (eds Law, R. D., Searle, M. P. & Godin, L.), pp. 91–145. Geological Society, London.

Bröcker, M. & Klemd, R., 1996. Ultrahigh-pressure metamorphism in the Snieznik Mountains (Sudetes, Poland): P–T constraints and geological implications. *Journal of Geology*, **104,** 417–433.

Brueckner, H. K., Medaris, L.G. & Bakun-Czubarow, N., 1991. Nd–Sm age and isotope patterns from Variscan eclogites of the eastern Bohemian Massif. *Neues Jahrbuch für Mineralogie Abhandlungen*, **163,** 169–196.

Burg, J.-P., 1999. Ductile structures and instabilities: their implication for Variscan tectonics in the Ardennes. *Tectonophysics*, **309,** 1–25.

Burg, J.-P. & Podladchikov, Y., 1999. Lithospheric scale folding: numerical modelling and application to the Himalayan syntaxes. *International Journal of Earth Sciences*, **88,** 190–200.

Burg, J. P., Davy, P., Nievergelt, P. *et al.*, 1997. Exhumation during crustal folding in the Namche-Barwa syntaxis. *Terra Nova*, **9,** 53–56.

Carswell, D. A. & O'Brien, P. J., 1993. Thermobarometry and geotectonic significance of high-pressure granulites: examples from the Moldanubian Zone of the Bohemian Massif in Lower Austria. *Journal of Petrology*, **34,** 427–459.

Chemenda, A. I., Mattauer, M., Malavieille, J. & Bokun, A. N., 1995. A mechanism for syn-collisional rock exhumation and associated normal faulting: results from physical modelling. *Earth & Planetary Science Letters*, **132,** 225–232.

Culshaw, N.G., Beaumont, C. & Jamieson, R.A., 2006. The orogenic superstructure–infrastructure concept: revisited, quantified, and revived. *Geology*, **34,** 733–736. doi:10.1130/G22793.1.

Dallmeyer, R. D., Neubauer, F. & Hock, V., 1992. Chronology of late Paleozoic tectonothermal activity in the southeastern Bohemian Massif, Austria (Moldanubian and Moravo–Silesian zones): $^{40}Ar/^{39}Ar$ mineral age controls. *Tectonophysics*, **210,** 135–153.

Dewey, J. F., Cande, S. & Pitman, W. C., 1989. Tectonic evolution of the India/Eurasia Collision Zone. *Eclogae Geologicae Helvetiae*, **82,** 717–734.

Don, J., 1964. The Zlote and Krowiarki Mountains as structural elements of the Snieznik metamorphic massif. *Geologia Sudetica*, **1,** 79–117.

Duchene, S., Lardeaux, J. M. & Albarede, F., 1997. Exhumation of eclogites: insights from depth–time path analysis. *Tectonophysics*, **280,** 125–140.

Dudek, A., 1980. The crystalline basement block of the Outer Carpathians in Moravia. *Rozpravy Československé Akademie Věd*, **90,** 1–85.

Dudek, A. & Fediuková, E., 1974. Eclogites of the Bohemian Moldanubicum. *Neues Jahrbbuch für Mineralogie Abhandlungen*, **121,** 127–159.

Dumicz, M., 1979. Tectogenesis of the metamorphosed series of the Klodzko district: a tentative explanation. *Geologica Sudetica*, **14,** 29–44.

Edel, J. B., Schulmann, K. & Holub, F. V., 2003. Anticlockwise and clockwise rotations of the Eastern Variscides accommodated by dextral lithospheric wrenching: palaeomagnetic and structural evidence. *Journal of the Geological Society*, **160,** 209–218.

England, P. C. & Houseman, G. A., 1988. The mechanics of the Tibetan Plateau. *Philosophical Transactions – Royal Society of London, Series A*, **326,** 301–320.

Feehan, J. G. & Brandon, M. T., 1999. Contribution of ductile flow to exhumation of low-temperature, high-pressure metamorphic rocks: San Juan–Cascade nappes, NW Washington State. *Journal of Geophysical Research B: Solid Earth*, **104,** 10 883–10 902.

Finger, F., Tichomirowa, M., Pin, C. & Hanžl, P., 2000. Relics of an early Panafrican metabasite–metarhyolite formation in the Brno Massif, Moravia, Czech Republic. *International Journal of Earth Sciences*, **89,** 328–335.

Franců, E., Franců, J., Kalvoda, J., Poelchau, H.S. & Otava, J., 2002. Burial and uplift history of the Palaeozoic Flysch in the Variscan foreland basin (SE Bohemian Massif, Czech Republic). In: *Continental Collision and the Tectonosedimentary Evolution of Forelands, Stephen Mueller Special Publication Series* (eds Bertotti, G., Schulmann, K. & Cloetingh, S.), pp. 167–179. European Geophysical Society, Berlin.

Franěk, J., Schulman, K. & Lexa, O., 2006. Kinematic and rheological model of exhumation of high pressure granulites in the Variscan orogenic root: example of the Blanský les granulite, Bohemian Massif, Czech Republic. *Mineralogy and Petrology*, **86,** 253–276.

Franke, W., 2000. The mid-European segment of the Variscides: tectonostratigraphic units, terrane boundaries and plate tectonic evolution. In: *Orogenic Processes: Quatification and Modelling in the Variscan Belt, Special Publication 179* (eds Franke, W., Haak, W., Oncken, O. & Tanner, D.), pp. 35–63. Geological Society, London.

Friedl, G., Finger, F., Paquette, J.L., von Quadt, A., McNaughton, N. J. & Fletcher, I. R., 2004. Pre-Variscan geological events in the Austrian part of the Bohemian Massif deduced from U–Pb zircon ages. *International Journal of Earth Sciences*, **93,** 802–823.

Fritz, H., Dallmeyer, R. D. & Neubauer, F., 1996. Thick-skinned versus thin-skinned thrusting: rheology controlled thrust propagation in the Variscan collisional belt (the southeastern Bohemian Massif, Czech Republic–Austria). *Tectonics*, **15,** 1389–1413.

Fuchs, G., 1986. Zur Diskussion um den Deckenbau der Böhmischen Masse. *Jahrbuch der Geologischen Bundesanstalt*, **129,** 41–49.

Gerya, T. & Stockhert, B., 2006. Two-dimensional numerical modeling of tectonic and metamorphic histories at active continental margins. *International Journal of Earth Sciences*, **95,** 250–274.

Godin, L., Grujic, D., Law, R.D. & Searle, M.P., 2006. Channel flow, ductile extrusion and exhumation in continental collision zones: an introductionIn: *Channel Flow, Ductile Extrusion and Exhumation in Continental Collision Zones, Special Publication 268* (eds Law, R. D., Searle, M. P. & Godin, L.), pp. 1–23. Geological Society, London.

Grujic, D., Casey, M., Davidson, C. *et al.*, 1996. Ductile extrusion of the Higher Himalayan Crystalline in Bhutan: evidence from quartz microfabrics. *Tectonophysics*, **260,** 21–43.

Harrison, T. M., Duncan, I. & McDougall, I., 1985. Diffusion of ^{40}Ar in biotite; temperature, pressure and compositional effects. *Geochimica et Cosmochimica Acta*, **49,** 2461–2468.

Hartley, A. J. & Otava, J., 2001. Sediment provenance and dispersal in a deep marine foreland basin: The Lower Carboniferous Culm Basin, Czech Republic. *Journal of the Geological Society*, **158,** 137–150.

Hasalová, P., Schulmann, K., Lexa, O. *et al.*, 2008a. Origin of migmatites by deformation enhanced melt infiltration of orthogneiss: a new model based on quantitative microstructural analysis. *Journal of Metamorphic Geology*, **26,** 29–53.

Hasalová, P., Štípská, P., Powell, R., Schulmann, K., Janoušek, V. & Lexa, O., 2008b. Transforming mylonitic metagranite by open-system interactions during melt flow. *Journal of Metamorphic Geology*, **26,** 55–80.

Hensen, B.J. & Zhou, B., 1995. Retention of isotopic memory in garnets partially broken down during an overprinting granulite-facies metamorphism: implications for the Sm–Nd closure temperature. *Geology*, **23,** 225–228.

Holub, F. V., Cocherie, A. & Rossi, P., 1997. Radiometric dating of granitic rocks from the Central Bohemian Plutonic Complex (Czech Republic): constraints on the chronology of

thermal and tectonic events along the Moldanubian-Barrandian boundary. *Comptes Rendus de l'Academie de Sciences – Serie IIa: Sciences de la Terre et des Planetes*, **325,** 19–26.

Jamieson, R. A., Beaumont, C., Nguyen, M. H. & Lee, B., 2002. Interaction of metamorphism, deformation and exhumation in large convergent orogens. *Journal of Metamorphic Geology*, **20,** 9–24.

Jamieson, R. A., Beaumont, C., Medvedev, S. & Nguyen, M. H., 2004. Crustal channel flows: 2. Numerical models with implications for metamorphism in the Himalayan–Tibetan orogen. *Journal of Geophysical Research B: Solid Earth*, **109,** B06407, 1–24.

Janoušek, V. & Holub, F. V., 2007. The causal link between HP–HT metamorphism and ultrapotassic magmatism in collisional orogens: case study from the Moldanubian Zone of the Bohemian Massif. *Proceedings of the Geologists Association*, **118,** 75–86.

Jastrzębski, M., 2005. The tectonometamorphic evolution of the marbles in the Lądek–Śnieżnik Metamorphic Unit, West Sudetes. *Geologica Sudetica*, **37,** 1–26.

Ježek, J., Schulmann, K. & Thompson, A. B., 1998. Modelling of strain partitioning in transpression zones. In: *Proceedings of the Fourth Annual Conference of the International Association for Mathematical Geology* (eds Buccianti, A., Nardi, G. & Potenza, R.), pp. 827–832. De Frede, Naples.

Kisters, A. F. M., Charlesworth, E. G., Gibson, R. L. & Anhaeusser, C. R., 1996. Steep structure formation in the Okiep copper district, South Africa: bulk inhomogeneous shortening of a high-grade metamorphic granite–gneiss sequence. *Journal of Structural Geology*, **18,** 735–751.

Klemd, R. & Bröcker, M., 1999. Fluid influence on mineral reactions in ultrahigh-pressure granulites: a case study in the Snieznik Mts (West Sudetes, Poland). *Contributions to Mineralogy and Petrology*, **136,** 358–373.

Kolenovská, E., Schulmann, K., Klápová, H. & Štípská, P., 1999. Tectonometamorphic evolution of the Moldanubian zone near Jemnice (south Moravia, Bohemian Massif). *Beihefte zum European Journal of Mineralogy*, **11,** 91–110.

Konopásek, J. & Schulmann, K., 2005. Contrasting Early Carboniferous field geotherms: evidence for accretion of a thickened orogenic root and subducted Saxothuringian crust (Central European Variscides). *Journal of the Geological Society*, **162,** 463–470.

Konopásek, J., Schulmann, K. & Johan, V., 2002. Eclogite-facies metamorphism at the eastern margin of the Bohemian Massif – subduction prior to continental underthrusting? *European Journal of Mineralogy*, **14,** 701–713.

Kotková, J., Gerdes, A., Parrish, R.R. & Novák, M., 2007. Clasts of Variscan high-grade rocks within Upper Viséan conglomerates – constraints on exhumation history from petrology and U–Pb chronology. *Journal of Metamorphic Geology*, **25,** 781–801.

Kröner, A., Štípská, P., Schulmann, K. & Jaeckel, P., 2000. Geochronological constraints on the pre-Variscan evolution of the northeastern margin of the Bohemian Massif, Czech Republic. In: *Quantification and Modelling in the Variscan Belt, Special Publication 179* (eds Franke, W.H.V., Oncken, O. & Tanner, D.), pp. 175–197. Geological Society, London.

Kröner, A., Jaeckel, P. & Hegner, E., 2001. Single zircon ages and whole-rock Nd isotopic systematics of Early Palaeozoic granitoid gneissess from the Czech and Polish Sudetes. (Jizerské Hory, Krkonoše mountains and Orlice-Sněžník complex). *International Journal of Earth Sciences*, **90,** 304–324.

Kryza, R., Pin, C. & Vielzeuf, D., 1996. High-pressure granulites from the Sudetes (south-west Poland): evidence of crustal subduction and collisional thickening in the Variscan Belt. *Journal of Metamorphic Geology*, **14,** 531–546.

Lange, U., Bröcker, M., Armstrong, R., Trapp, E. & Mezger, K., 2005. Sm–Nd and U–Pb dating of high-pressure granulites from the Zlote and Rychleby Mts (Bohemian Massif, Poland and Czech Republic). *Journal of Metamorphic Geology*, **23,** 133–145.

Lexa, O., Štípská, P., Schulmann, K., Baratoux, L. & Kröner, A., 2005. Contrasting textural record of two distinct metamorphic events of similar P–T conditions and different durations. *Journal of Metamorphic Geology*, **23,** 649–666.

Macintyre, R. M., Bowes, D.R., Hamidullah, S. & Onscott, T.C., 1992. K–Ar and Ar–Ar study of amphibolites from meta-ophiolite complexes, eastern Bohemian Massif. In: *Proceedings of 1st International Conference on the Bohemian Massif*, Czech Geological Survey, Prague, pp. 195–199.

Martinez, F., Goodliffe, A. M. & Taylor, B., 2001. Metamorphic core complex formation by density inversion and lower crust extrusion. *Nature*, **411,** 930–934.

Matte, P., Maluski, H., Rajlich, P. & Franke, W., 1990. Terrane boundaries in the Bohemian Massif: result of large-scale Variscan shearing. *Tectonophysics*, **177,** 151–170.

Mazur, S., Aleksandrowski, P. & Szczepanski, J., 2005. The presumed Teplá–Barrandian/Moldanubian terrane boundary in the Orlica Mountains (Sudetes, Bohemian Massif): structural and petrological characteristics. *Lithos*, **82,** 85–112.

Medaris, G., Jelínek, E. & Mísař, Z., 1995. Czech eclogites: terrane settings and implications for Variscan tectonic evolution of the Bohemian Massif. *European Journal of Mineralogy*, **7,** 7–28.

Medaris, L. G., Fournelle, J. H., Ghent, E. D., Jelínek, E. & Mísař, Z., 1998. Prograde eclogite in the Gföhl Nappe, Czech Republic: new evidence on Variscan high-pressure metamorphism. *Journal of Metamorphic Geology*, **16,** 563–576.

Medaris, L. G., Beard, B. L. & Jelínek, E., 2006. Mantle-derived, UHP garnet pyroxenite and eclogite in the Moldanubian Gföhl nappe, Bohemian Massif: a geochemical review, new P–T determinations, and tectonic interpretation. *International Geology Review*, **48,** 765–777.

Milnes, A. G. & Koyi, H. A., 2000. Ductile rebound of an orogenic root: case study and numerical model of gravity tectonics in the Western Gneiss Complex, Caledonides, southern Norway. *Terra Nova*, **12,** 1–7.

Murtezi, M., 2006. The acid metavolcanic rocks of the Orlica–Śnieżnik Dome (Sudetes): their origin and tectono-metamorphic evolution. *Geologica Sudetica*, **38,** 1–38.

O'Brien, P. J. & Carswell, D. A., 1993. Tectonometamorphic evolution of the Bohemian Massif: evidence from high pressure metamorphic rocks. *Geologische Rundschau*, **82,** 531–555.

O'Brien, P. J. & Rötzler, J., 2003. High-pressure granulites: formation, recovery of peak conditions and implications for tectonics. *Journal of Metamorphic Geology*, **21,** 3–20.

Parry, M., Štípská, P., Schulmann, K., Hrouda, F., Ježek, J. & Kröner, A., 1997. Tonalite sill emplacement at an oblique plate boundary: northeastern margin of the Bohemian Massif. *Tectonophysics*, **280,** 61–81.

Petrakakis, K., 1997. Evolution of Moldanubian rocks in Austria: review and synthesis. *Journal of Metamorphic Geology*, **15,** 203–222.

Pitra, P. & Guiraud, M., 1996. Probable anticlockwise P–T evolution in extending crust: Hlinsko region, Bohemian Massif. *Journal of Metamorphic Geology*, **14,** 49–60.

Pitra, P., Burg, J.-P., Schulmann, K. & Ledru, P., 1994. Late orogenic extension in the Bohemian Massif: petrostructural evidence in the Hlinsko region. *Geodinamica Acta*, **7,** 15–30.

Platt, J. P., 1986. Dynamics of orogenic wedges and the uplift of high-pressure metamorphic rocks. *Geological Society of America Bulletin*, **97,** 1037–1053.

Platt, J. P., 1993. Exhumation of high-pressure rocks: a review of concepts and processes. *Terra Nova*, **5,** 119–133.

Racek, M., Štípská, P., Pitra, P., Schulmann, K. & Lexa, O., 2006. Metamorphic record of burial and exhumation of orogenic lower and middle crust: a new tectonothermal model for the Drosendorf window (Bohemian Massif, Austria). *Mineralogy and Petrology*, **86,** 221–251.

Rey, P., Vanderhaeghe, O. & Teyssier, C., 2001. Gravitational collapse of the continental crust: definition, regimes and modes. *Tectonophysics*, **342,** 435–449.

Ring, U. & Brandon, M. T., 1999. Ductile deformation and mass loss in the Franciscan Subduction Complex: implications for exhumation processes in accretionary wedges. In: *Exhumation Processes: Normal Faulting, Ductile Flow and Erosion, Special Publication 154* (ed. Ring, U., Brandon, M.T., Lister, G.S. & Willet, S.D.), pp. 55–86. Geological Society, London.

Romanová, M. & Stípská, P., 2001. Structural and metamorphic evolution of the Stronie formation near Javorník. *Mineralogical Society of Poland, Special Papers*, **19,** 147–149.

Schneider, D. A., Zahniser, S. J., Clascock, J. M., Gordon, S. M. & Manecki, M., 2006. Thermochronology of the West Sudetes (Bohemian Massif): rapid and repeated eduction in the eastern Variscides, Poland and Czech Republic. *American Journal of Science*, **306,** 846–873.

Schulmann, K., 1990. Fabric and kinematic study of the Bites orthogneiss (southwestern Moravia): result of large-scale northeastward shearing parallel to the Moldanubian/Moravian boundary. *Tectonophysics*, **177,** 229–244.

Schulmann, K. & Gayer, R., 2000. A model for a continental accretionary wedge developed by oblique collision: The NE Bohemian Massif. *Journal of the Geological Society*, **157,** 401–416.

Schulmann, K., Ledru, P., Autran, A. *et al*., 1991. Evolution of nappes in the eastern margin of the Bohemian Massif: a kinematic interpretation. *Geologische Rundschau*, **80,** 73–92.

Schulmann, K., Melka, R., Lobkowicz, M. Z., Ledru, P., Lardeaux, J.-M. & Autran, A., 1994. Contrasting styles of deformation during progressive nappe stacking at the southeastern margin of the Bohemian Massif (Thaya Dome). *Journal of Structural Geology*, **16,** 355–370.

Schulmann, K., Schaltegger, U., Ježek, J., Thompson, A.B. & Edel, J.-B., 2002. Rapid burial and exhumation during orogeny: thickening and synconvergent exhumation of thermally weakened and thinned crust (Variscan orogen in Western Europe). *American Journal of Science*, **302,** p 856–879.

Schulmann, K., Thompson, A. B., Lexa, O. & Ježek, J., 2003. Strain distribution and fabric development modeled in active and ancient transpressive zones. *Journal of Geophysical Research–Solid Earth*, **108**(B1), 2023, doi: 10.1029/200/JB000632./.

Schulmann, K., Kroner, A., Hegner, E. *et al*., 2005. Chronological constraints on the pre-orogenic history, burial and exhumation of deep-seated rocks along the eastern margin of the Variscan orogen, Bohemian Massif, Czech Republic. *American Journal of Science*, **305,** 407–448.

Steltenpohl, M. G., Cymerman, Z., Krogh, E. J. & Kunk, M. J., 1993. Exhumation of eclogitized continental basement during Variscan lithospheric delamination and gravitational collapse, Sudety Mountains, Poland. *Geology*, **21,** 1111–1114.

Štípská, P. & Powell, R., 2005a. Constraining the P–T path of a MORB-type eclogite using pseudosections, garnet zoning and garnet–clinopyroxene thermometry: an example from the Bohemian Massif. *Journal of Metamorphic Geology*, **23,** 725–743.

Štípská, P. & Powell, R., 2005b. Does ternary feldspar constrain the metamorphic conditions of high-grade meta-igneous rocks? Evidence from orthopyroxene granulites, Bohemian Massif *Journal of Metamorphic Geology*, **23,** 627–647.

Štípská, P. & Schulmann, K., 1995. Inverted metamorphic zonation in a basement-derived nappe sequence, eastern margin of the Bohemian Massif. *Geological Journal*, **30,** 385–413.

Štípská, P., Schulmann, K. & Höck, V., 2000. Complex metamorphic zonation of the Thaya dome: result of buckling and gravitational collapse of an imbricated nappe sequence. In: *Forced Folds and Fractures, Special Publication*, 169 (eds Cosgrove, J. W. & Ameen, M. S.), pp. 197–211. Geological Society, London.

Štípská, P., Schulmann, K., Thompson, A. B., Ježek, J. & Kröner, A., 2001. Thermomechanical role of a Cambro–Ordovician paleorift during the Variscan collision: the NE margin of the Bohemian Massif. *Tectonophysics*, **332,** 239–253.

Štípská, P., Schulmann, K. & Kröner, A., 2004. Vertical extrusion and middle crustal spreading of omphacite granulite: a model of syn-convergent exhumation (Bohemian Massif, Czech Republic). *Journal of Metamorphic Geology*, **22,** 179–198.

Štípská, P., Pitra, P. & Powell, R., 2006. Separate or shared metamorphic histories of eclogites and surrounding rocks? An example from the Bohemian Massif *Journal of Metamorphic Geology*, **24,** 219–240.

Suess, F. E., 1912. Die moravischen Fenster und ihre Beziehung zum Grundgebirge des Hohen Gesenke. *Denkschrichte des Koeniglischen Akademie der Wissenscahft, Mathematik. Naturwissenschaft*, **12,** 541–631.

Suess, F. E., 1926. *Intrusionstektonik und Wandertektonik im variszichen Grundgebirge*. Borntträger, Berlin.

Tajčmanová, L., Konopásek, J. & Schulmann, K., 2006. Thermal evolution of the orogenic lower crust during exhumation within a thickened Moldanubian root of the Variscan belt of Central Europe. *Journal of Metamorphic Geology*, **24,** 119–134.

Thompson, A. B., Schulmann, K., Ježek, J. & Tolar, V., 2001. Thermally softened continental extensional zones (arcs and rifts) as precursors to thickened orogenic belts. *Tectonophysics*, **332,** 115–141.

Tollmann, A., 1982. Großraumiger variszischer Deckenbau im Moldanubikum und neue Gedanken zum Variszikum Europas. *Geotektektonische Forschungen*, **64,** 1–91.

Urban, M., 1992. Kinematics of the Variscan thrusting in the Eastern Moldanubicum (Bohemian Massif, Czechoslovakia): evidence from the Namest granulite massif. *Tectonophysics*, **201,** 371–391.

Van Breemen, O., Aftalion, M., Bowes, D. R. *et al*., 1982. Geochronological studies of the Bohemian massif, Czechoslovakia, and their significance in the evolution of Central Europe. *Transactions of the Royal Society of Edinburgh: Earth Sciences*, **73,** 89–108.

Vanderhaeghe, O. & Teyssier, C., 2001. Partial melting and flow of orogens. *Tectonophysics*, **342,** 451–472.

Ziegler, P. A., 1986. Geodynamic model for the Palaeozoic crustal consolidation of western and central Europe. *Tectonophysics*, **126,** 303–328.

Received 3 April 2007; revision accepted 27 November 2007.

JOURNAL OF GEOPHYSICAL RESEARCH, VOL. 113, B10406, doi:10.1029/2007JB005508, 2008

Evolution of microstructure and melt topology in partially molten granitic mylonite: Implications for rheology of felsic middle crust

Karel Schulmann,[1] Jean-Emmanuel Martelat,[2] Stanislav Ulrich,[3,4] Ondrej Lexa,[4] Pavla Štípská,[1] and Jens K. Becker[5]

Received 19 November 2007; revised 27 April 2008; accepted 30 July 2008; published 24 October 2008.

[1] The deformation study of midcrustal porphyritic granite reveals exceptionally high strain intensities of feldspar aggregates compared to stronger quartz. Three types of microstructures corresponding to evolutionary stages of deformed granite were recognized: (1) the metagranite marked by viscous flow of plagioclase around strong alkali feldspar and quartz, (2) quartz augen orthogneiss characterized by development of banded mylonitic structure of recrystallized plagioclase and K-feldspar surrounding augens of quartz, and (3) banded mylonite characterized by alternation of quartz ribbons and mixed aggregates of feldspars and quartz. The original weakening of alkali feldspar is achieved by decomposition into albite chains and K-feldspar resulting from a heterogeneous nucleation process. The subsequent collapse of alkaline feldspar and development of monomineralic layering is attributed to the onset of syn-deformational dehydration melting of Mu-Bi layers associated with production of ~2% melt. The final deformation stage is marked by mixing of feldspars which is explained by higher melt production due to introduction of external water. An already small amount of melt is responsible for extreme weakening of the feldspar because of Melt Connectivity Threshold effect triggering grain boundary sliding deformation mechanisms. The grain boundary sliding controls diffusion creep at small melt fraction and evolves to particulate flow at high melt fractions. Strong quartz shows a dislocation creep deformation mechanism throughout the whole deformation history marked by variations in the activity of the slip systems, which are attributed to variations in stress and strain rate partitioning with regard to changing rheological properties of the deforming feldspars.

Citation: Schulmann, K., J.-E. Martelat, S. Ulrich, O. Lexa, P. Štípská, and J. K. Becker (2008), Evolution of microstructure and melt topology in partially molten granitic mylonite: Implications for rheology of felsic middle crust, *J. Geophys. Res.*, *113*, B10406, doi:10.1029/2007JB005508.

1. Introduction

[2] Rheology of the continental crust is dominated by quartzo-feldspathic rocks, which are represented mainly by metagranitoids, orthogneisses and felsic volcanics [*Carter and Tsenn*, 1987]. To date, the models of crustal rheology use laboratory derived laws described by constitutive equations that are established for minerals or monomineralic rocks such as quartzites and anorthosites [*Ranalli*, 1995]. Most of laboratory experiments show that the quartz is weaker than plagioclase for the same homologous temperatures [*Ranalli and Murphy*, 1987; *Schmid*, 1982]. However, the natural quartzo-feldspathic rocks are mixtures with different proportions of strong feldspars and weak quartz with variable grain shapes and grain size distributions. The deformation of such natural rocks leads to strain partitioning between the different components and nonuniform deformation [*Handy*, 1990]. *Handy* [1994a] defined the load-bearing framework structure and interconnected weak layer structure and proposed comprehensive empirical equations that determine the strength of polyphase composites. *Handy* [1994a] applied this concept to quartzo-feldspathic rocks and concluded that the proportion of weaker quartz controls the bulk rheology. The basis of these models is the coexistence of two nonlinear viscous phases; the bulk rheology is a consequence of the rock structure and the relative proportions of the two mineral phases [*Ji and Zhao*, 1994].

[3] Microstructural studies show that the progressive orthogneiss deformation is associated with strain partitioning and variations in the deformation mechanisms of feldspars and quartz [*Handy et al.*, 1999; *Schulmann et al.*, 1996; *Simpson*, 1985]. For instance *Gapais* [1989] and

[1]Centre de Géochimie de la Surface, UMR7516, Université Louis Pasteur, CNRS, Strasbourg, France.
[2]Laboratoire de Géodynamique des Chaînes Alpines, UMR5025, Université Joseph Fourier, Observatoire des Sciences de l'Univers de Grenoble, CNRS, Grenoble, France.
[3]Geophysical Institute, Czech Academy of Sciences, Prague, Czech Republic.
[4]Institute of Petrology and Structural Geology, Charles University, Prague, Czech Republic.
[5]Institut für Geowissenschaften, Universität Tübingen, Tübingen, Germany.

0148-0227/08/2007JB005508$09.00

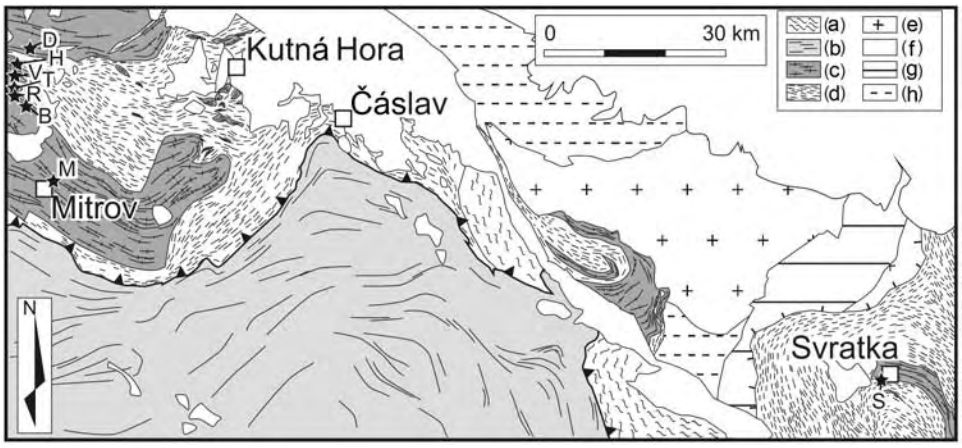

Figure 1. Geological map of the central part of Bohemian Massif modified after *Beneš* [1964] and *Synek and Oliverová* [1993]. Black stars and capitalized letters refer to studied samples (B, D, H, M, R, S, T, and V). (a) Lower crustal rocks (granulites and eclogites), (b) the midcrustal monotonous metasedimentary unit, (c) the midcrustal orthogneiss unit, (d) the kyanite micaschist unit, (e) the intrusives, (f) Cretaceous and Quaternary rocks, (g) the undifferenciated Lower Palaeozoic rocks, and (h) the Neo-Proterozoic metasediments.

Schulmann et al. [1996] have shown that at amphibolite facies the feldspars show evolution from dislocation creep to grain boundary sliding with increasing strain intensity in conjunction with variations in the activity of the quartz slip systems. Therefore, the viscosity contrast between feldspars and quartz was not constant but varied with increasing degree of strain as the rheological role of individual minerals evolved as shown by a range of experimental and natural studies [*Handy*, 1994b; *Ji et al.*, 2000; *Rybacki and Dresen*, 2004; *Stünitz and Fitz Gerald*, 1993]. However, the aforementioned studies all neglect a possible role of the melt on the deformation of the polyphase rocks.

[4] The aim of this paper is to show, through detailed microstructural study and thermodynamical modeling, the contribution of interstitial melt to the rheology of progressively deformed granites under midcrustal conditions. We use natural examples of a sequence of granite mylonites to document the melt enhanced rheological inversion of disproportionately stronger quartz compared to the weak feldspars in midcrustal rocks. This work also shows that with increasing melt fraction the deformation mechanisms of feldspars varies from the grain boundary sliding accommodated dislocation creep to granular flow while the quartz is only deformed in the dislocation creep field.

2. Geological Setting

[5] The study area located in the central part of the Bohemian Massif in the Czech Republic is known for the extreme deformation of porphyritic granites in a crustal-scale shear zone [*Synek and Oliverová*, 1993]. The porphyritic granite mylonites studied are of Cambro-Ordovician protolith age and come from an orthogneiss-bearing, midcrustal unit that overlies kyanite micaschists in the west (Figure 1). In the east a similar rock assemblage occurs in an equivalent structural unit, although these orthogneiss bodies exist within kyanite-sillimanite bearing micaschists. According to *Schulmann et al.* [2005] both units record a Carboniferous tectono-metamorphic history between 340 and 325 Ma. The midcrustal unit is overlain by kyanite bearing migmatites and granulites of the orogenic lower crustal unit that contain eclogite lenses with estimated minimum pressures of 18–19 kbar and temperatures of 800–900°C [*Medaris et al.*, 1998]. The P-T conditions of the kyanite bearing micaschists in the footwall of the mylonitic orthogneiss sheet have experienced temperatures of 620–710°C at pressures of 6.5–9.5 kbar [*Kachlík*, 1999] similarly to 8–9 kbar and 610–660°C estimated in the micaschists in the eastern part of the studied area [*Pitra and Guiraud*, 1996].

[6] The geological structure of the studied rocks was described by *Synek and Oliverová* [1993] who interpreted the middle crustal orthogneiss-bearing unit and the overlying orogenic lower crustal unit as a crustal nappe stack resulting from a Carboniferous deformation. On the basis of the structural position of the midcrustal orthogneiss and the regional metamorphic field gradient, the PT conditions of metamorphism and deformation of the studied rocks are estimated to be between 9 and 18 kbar and 650–850°C. More precise P-T estimations were not established because of the lack of pressure and temperature sensitive mineral assemblages that are necessary for standard thermobarometric methods.

3. Shape Analysis of Quartz and Feldspars

[7] Undeformed porphyritic granitoids may serve as an excellent example of multiphase mixtures of originally spherical (ellipsoidal) clasts with constant phase fractions. When these rocks are subjected to deformation, mineral grains reach different strain intensities, which can be easily quantified using standard finite strain techniques [*Ramsay and Huber*, 1983]. Measurement of the shapes of naturally deformed minerals in originally coarse-grained and porphyritic granitoids may thus help to track the viscous behavior of individual phases for different bulk strain intensities

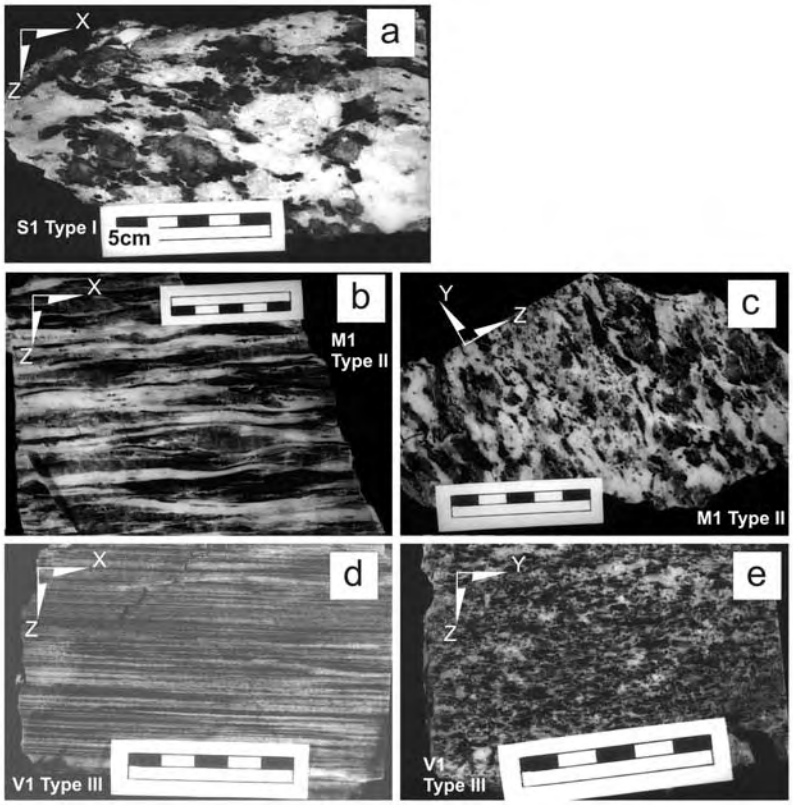

Figure 2. Macroscopic samples of deformed metagranite divided in three types according to the deformation intensity and the macroscopic appearance. X, Y, and Z refer to the axes of the finite strain ellipsoid. (a) Sample S1 is a weakly deformed metagranite with large centimeter-sized grains of quartz and feldspar representing Type I rock. (b, c) Sample M1 is an augen orthogneiss corresponding to Type II rocks and intermediate strain intensity (equivalent to samples T1, T2, M2, and R4), (d, e) Sample V1 is a banded mylonite corresponding to Type III rock and the highest intensity of deformation (equivalent to other highly strained samples R5, R3, V2, and H1).

[*Treagus*, 2002]. This allows constraining the degree of strain partitioning in rocks and the viscosity ratios between the individual mineral phases.

[8] The shape analysis of the feldspars and the quartz polycrystalline aggregates was carried out on 17 sections cut both perpendicular to the foliation and parallel to the stretching lineation and perpendicular to both the foliation and the lineation, i.e., parallel to the XZ and YZ sections of the finite strain ellipsoid (Figure 2). The K-feldspar cannot be distinguished from plagioclase in highly deformed macroscopic samples and therefore both minerals were grouped together for finite strain measurements. All studied samples are composed on average of 60–70% feldspars, 35–25% quartz and up to 10% of biotite and muscovite. The almost constant mineral composition for highly variable strain intensities and constant bulk rock chemistry shows the lack of chemical variations with strain (Table 1).

[9] In our study we classified three major types of deformed orthogneiss according to the deformation intensities at the macroscopic scale: Type I is represented by weakly deformed metagranite (Figure 2a); Type II corresponds to augen orthogneiss with quartz porphyroclast (Figures 2b and 2c); Type III is a banded mylonite orthogneiss (Figures 2d and 2e).

[10] Mineral shape data are plotted into a Flinn diagram [*Flinn*, 1965] (Figure 3). The analyses of feldspar polycrystalline aggregates and quartz of the individual samples are connected by tie lines with the vertical ellipse representing the bulk strain value of the whole rock. An important feature of all the studied samples is that feldspars show higher strain intensities than quartz for any bulk strain (Figures 3a and 3b). In several samples of the so-called Doubravčany pencil gneiss, the strain intensities cannot be identified because the stretching of feldspar and quartz layers exceeds the length of the samples (Figure 2d). The strain symmetry, represented by the K values of *Flinn* [1965], varies from prolate to oblate shapes (K = 2.7 to 0.3). For quartz with prolate shapes, the corresponding feldspar strain symmetry is close to plane strain, while for oblate quartz, the feldspars show the same shape or slightly more oblate shapes (Figure 3b). Strain intensities are expressed using Ramsay's D value, which is an alternative expression of viscosity ratio values of *Gay* [1968a, 1968b] also used by *Schulmann et al.* [1996]. The inspection of the diagram in Figure 3b shows that the highest strain ratios are achieved between D_{fel}/D_{qtz} for Type III orthogneiss and some Type II orthogneiss samples marked by high bulk strain intensities. The relatively small ratio between D_{fel}/D_{qtz} suggests similar yield-

Table 1. Bulk Rock Chemistry of Midcrustal Orthogneisses

Sample	S1	M1	V1	D1
SiO_2	72, 9	70, 9	73, 0	70, 2
TiO_2	0, 3	0, 3	0, 2	0, 4
Al_2O_3	13, 3	14, 7	13, 7	14, 7
Fe_2O_3	1, 9	1, 4	1, 8	2, 6
FeO	0, 9	1, 0	0, 7	0, 7
MnO	0, 0	0, 1	0, 0	0, 0
MgO	0, 5	0, 6	0, 4	0, 8
CaO	1, 1	1, 4	0, 8	1, 0
Na_2O	2, 3	2, 6	2, 5	1, 8
K_2O	4, 5	4, 7	4, 7	4, 6
P_2O_5	0, 2	0, 2	0, 2	0, 2
H_2O-	0, 2	0, 3	0, 3	0, 2
H_2O^+	1, 0	1, 2	1, 0	2, 1
CO_2	0, 2	0, 2	0, 4	0, 2
Total	99, 5	99, 5	99, 7	99, 6

ing of both mineral phases for low bulk strains for several samples of weakly deformed Type II orthogneiss.

4. Microstructure Development of Deformed Metagranitoids

[11] The microstructural investigations covered the qualitative description of the rock and mineral structure using optical microscope and scanning electron microscope imaging. The microprobe work complements the scanning electron microscope (SEM) study to identify compositional variations of the recrystallized feldspars (Tables 2a, 2b, and 2c).

4.1. Type I: Metagranite and Weakly Deformed Orthogneiss

[12] The metagranite samples show K-feldspar phenocrysts up to 10 cm in size surrounded by quartz blebs. Elongated plagioclase polycrystalline aggregates range from 1 to 3 cm in size (Figure 2a). Light and SEM microscopies show that the plagioclase forming recrystallized aggregates (labeled Pl1 in Figure 4) corresponds to oligoclase An_{15}. The Pl1 plagioclase has an average grain size of 50 -70 μm, straight boundaries and subequant shapes (Figure 4 and Table 2c). The quartz blebs consist of large grains ($\sim$400 μm in size) with irregular and highly serrated boundaries. Biotite and muscovite are present as elongated recrystallized aggregates. The plagioclase grains within alkaline feldspar phenocrysts are labeled Pl1b here. These plagioclases are 10 to 50 μm in size, correspond to albite An_{1-8} and are usually arranged into chains mostly parallel to (100) or locally along (010) planes of the host K-feldspar (Figures 4a and 4b and Table 2c). The K-feldspars themselves show subgrains of $\sim$80 μm in size. Subgrain boundaries are straight and meet in triple point junctions. At a smaller scale, the feldspars show kinked domains along which the Pl1b chains are rotated (Figure 4a). These kinked domains show internal strain marked by irregular undulatory extinction. Microprobe analyses show that K-feldspar cores exhibit rather constant composition revealing approximately 10 mol % of albite (Table 2a). Only around enclosed Pl1b chains the alkali feldspar shows a rapid decrease of the albite component (Figure 5).

4.2. Type II: Orthogneiss With Quartz Augens

[13] This rock is characterized by the presence of isolated and elongated quartz augens surrounded by highly elongated K-feldspar and plagioclase polycrystalline aggregates forming almost monomineralic layers (Figure 6). Biotite and muscovite are forming elongated monomineralic aggregates located at boundaries between feldspars and quartz or within plagioclase layers. Quartz augens are composed of grains 150–1000 μm in size with serrated boundaries. Plagioclase (Pl1) polycrystalline aggregates are composed of oligoclase An_{10-20} subequant grains (50–150 μm in

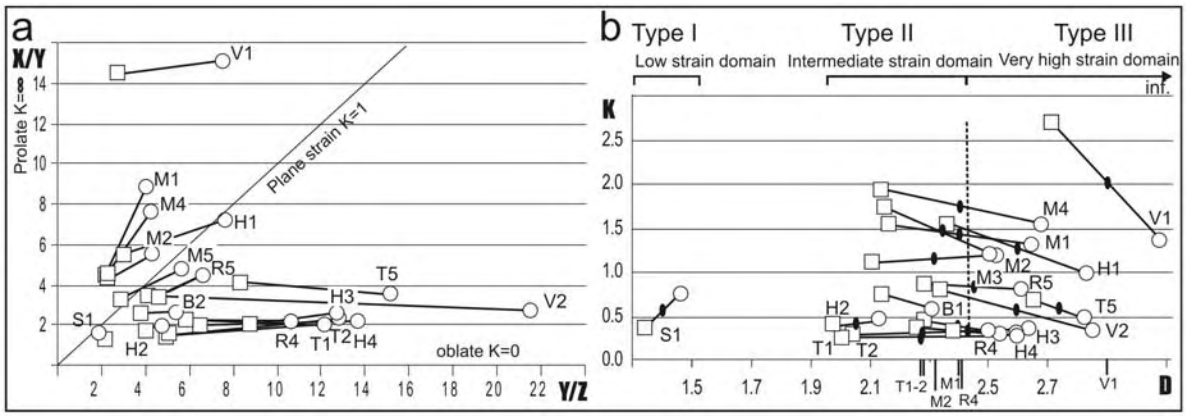

Figure 3. (a) Flinn diagram after *Ramsay and Huber* [1983] shows the shapes of deformation ellipsoids represented as projections of X/Y axial ratios on the ordinate and Y/Z ratios on the abscissa in the graph. This diagram allows to visualize the shapes of the strain ellipsoid and the intensity of deformation in the 2-D diagram. (b) Diagram showing strain intensity expressed as the D parameter on the abscissa against shape K parameter on the ordinate; K = (X/Y-1)/(Y/Z-1) varies from 0 for oblate shapes, to 1 for plane strain shapes, and to infinity for prolate shapes, $D = (((X/Y-1)^2 + ((Y/Z-1)^2)^{1/2}$. The values are obtained by measuring 30 ellipses (harmonic sum) from XZ and YZ sections (principal planes of finite strain ellipsoid). Squares show quartz, and circles show undifferentiated feldspar. Rock types are determined according to the bulk strain intensity and macroscopic appearance (Figure 2) from weakly deformed metagranite S1; intermediate strained augen orthogneiss samples T1, T2, M2, M1, and R4; and highly strained banded orthogneiss samples H1, T5, V1, and V2.

Table 2a. K-Feldspar Compositions[a]

Sample	S1	S1	M1	M1	V1	V1
Analysis	50	48	71	79	92	104
SiO_2	65, 27	64, 07	64, 09	65, 05	64, 63	64, 96
Al_2O_3	18, 69	18, 42	18, 22	18, 56	18, 73	18, 71
CaO	0, 00	0, 03	0, 04	0, 00	0, 03	0, 04
Na_2O	1, 20	0, 49	0, 29	1, 37	1, 10	0, 59
K_2O	15, 87	16, 46	16, 86	15, 52	15, 90	16, 48
Total	101, 04	99, 49	99, 50	100, 54	100, 40	100, 82
Si	2, 986	2, 985	2, 990	2, 988	2, 978	2, 984
Al	1, 008	1, 011	1, 002	1, 005	1, 017	1, 013
Ca	0, 000	0, 002	0, 002	0, 000	0, 002	0, 002
Na	0, 106	0, 044	0, 026	0, 122	0, 098	0, 053
K	0, 926	0, 978	1, 004	0, 910	0, 935	0, 966
Total	5, 026	5, 020	5, 024	5, 024	5, 030	5, 017
X_{Or}	89, 69	95, 53	97, 27	88, 17	90, 36	94, 66
X_{Ab}	10, 31	4, 32	2, 54	11, 83	9, 50	5, 15
X_{An}	0, 00	0, 15	0, 19	0, 00	0, 14	0, 19

[a]Structural formulae calculated on the basis of 8(O).

Table 2c. Large or Interconnected Plagioclase: Pl1 Compositions[a]

Sample	S1	T1	M1	M1	V1
Analysis	43	114	67	91	109
SiO_2	64, 60	64, 70	65, 62	63, 75	65, 55
Al_2O_3	22, 72	22, 84	21, 43	23, 06	22, 22
CaO	3, 48	3, 76	2, 36	4, 38	3, 07
Na_2O	9, 88	10, 03	11, 03	9, 48	10, 23
K_2O	0, 23	0, 13	0, 10	0, 27	0, 22
Total	100, 91	101, 46	100, 56	100, 97	101, 30
Si	2, 827	2, 819	2, 878	2, 797	2, 854
Al	1, 172	1, 173	1, 108	1, 192	1, 140
Ca	0, 163	0, 176	0, 111	0, 206	0, 143
Na	0, 838	0, 847	0, 938	0, 806	0, 864
K	0, 013	0, 007	0, 006	0, 015	0, 012
Total	5, 013	5, 022	5, 040	5, 017	5, 013
X_{Or}	1, 26	0, 70	0, 53	1, 47	1, 20
X_{Ab}	82, 65	82, 26	88, 95	78, 49	84, 75
X_{An}	16, 09	17, 04	10, 52	20, 04	14, 05

[a]Structural formulae calculated on the basis of 8(O).

size) with straight boundaries meeting at triple point junctions (Figures 5 and 6c and Table 2c). Plagioclase polycrystalline aggregates often contain biotite flakes parallel to the foliation or interstitial quartz and new plagioclase An_{1-10} (Pl2). K-feldspar polycrystalline aggregates are composed of slightly elongate to subequant grains with straight boundaries forming a well developed triple point network lined by narrow films of pure albite An_{1-10} (Pl2). Disintegration of the K-feldspar layers into elongate aggregates surrounded by fine-grained Pl1 matrix was observed in some samples. This process is connected to the development of bands filled with recrystallized Pl1 grains up to 150 μm wide oblique with respect to the long axis of the feldspar polycrystalline aggregates (Figure 6b). Finally, elongated thin aggregates of Pl1 are smeared out in the K-feldspar rich matrix. Quartz also forms weakly elongated polymineralic aggregates characterized by highly irregular boundaries with the surrounding feldspar matrix. Common feature are the lobes of quartz and cusps of the K-feldspar pointing in the direction perpendicular to the long face of the aggregate and to the macroscopic foliation.

4.3. Type III: Banded Mylonitic Orthogneiss and Ultramylonite

[14] Banded mylonitic orthogneiss is marked by thin quartz ribbons less than 1000 μm wide. They are surrounded by polymineralic layers of plagioclase, quartz and K-feldspar (Figure 7b). Micas are generally dispersed in the matrix or form narrow layers parallel to the foliation (Figures 7c and 7d). Disintegrated relics of plagioclase aggregates are composed of Pl1 grains An_{14-20} (Figure 5 and Table 2c) and of K-feldspar grains 50–100 μm in size (rarely 200 μm) and of irregular shapes. The interfacial boundaries with K-feldspar are generally straight and commonly lined by rims of Pl2 (An_{4-12}) or thin layers of quartz. Locally, relics of the K-feldspar layers that are a few grains wide ($\sim$250 μm) occur with straight mutual boundaries lined by Pl2 films. The quartz commonly occurs in the form of isolated grains with serrated boundaries and cusps pointing perpendicular and parallel to the macroscopic foliation. However, the most common are few hundred microns wide quartz ribbons composed by elongate, 200–300 μm wide and up to 1000 μm long grains with highly serrated boundaries.

[15] A rather exceptional kind of Type III microstructure is represented by the exceptionally coarse-grained, mylonitic orthogneiss sample B2. This rock type is characterized by polymineralic layers with poorly defined boundaries and a large average grain size of plagioclase and K-feldspar ranging from 160 to 200 μm. The Pl1 grains in relict plagioclase aggregates show sutured boundaries and wide Pl2 rims while the interstitial Pl2 grains in the K-feldspar rich aggregates form wide films and cuspate pools. The interstitial quartz (100 μm in size) occurs in the form of serrated grains in triple point junctions of K-feldspar and Pl1 relict aggregates.

Table 2b. Isolated Plagioclase Pl1b and Pl2 Compositions[a]

Sample	S1	T1	T1	M1	V1
Analysis	52	119	115	77	105
SiO_2	68, 72	69, 06	67, 94	68, 67	67, 69
Al_2O_3	19, 70	19, 74	20, 19	19, 78	20, 69
CaO	0, 31	0, 10	0, 78	0, 22	1, 28
Na_2O	11, 84	12, 14	11, 27	11, 77	11, 19
K_2O	0, 05	0, 12	0, 12	0, 54	0, 23
Total	100, 62	101, 19	100, 30	101, 01	101, 09
Si	2, 986	2, 986	2, 963	2, 980	2, 938
Al	1, 009	1, 006	1, 038	1, 012	1, 058
Ca	0, 014	0, 005	0, 037	0, 010	0, 060
Na	0, 998	1, 018	0, 953	0, 991	0, 942
K	0, 003	0, 007	0, 007	0, 030	0, 013
Total	5, 010	5, 022	4, 998	5, 023	5, 010
X_{Or}	0, 28	0, 64	0, 67	2, 90	1, 26
X_{Ab}	98, 30	98, 91	95, 67	96, 11	92, 87
X_{An}	1, 42	0, 45	3, 66	0, 99	5, 87

[a]Structural formulae calculated on the basis of 8(O).

4.4. Topology of Interstitial Phases in Plagioclase and K-Feldspar Aggregates

[16] The most common interstitial phase at the grain scale are thin films of Pl2 and quartz up to 50 μm long and 10 μm wide located along the mutual plagioclase boundaries, often at high angle to the foliation or in the form of cuspate pools at triple point junctions. The mutual boundaries of Pl1 aggregate grains are often lined by narrow rims of new plagioclase An_{1-10} (Pl2). In Type II orthogneiss samples showing strongly elongated recrystallized K-feldspar and Pl1 grains (samples T1, T2), the Pl2 films exhibit preferred orientation parallel to the direction of maximum stretching, i.e., along the crystal faces parallel to the foliation (Figure 8). In the M1, M2 samples of the orthogneiss Type II, the shape preferred orientation of the recrystallized feldspar is low,

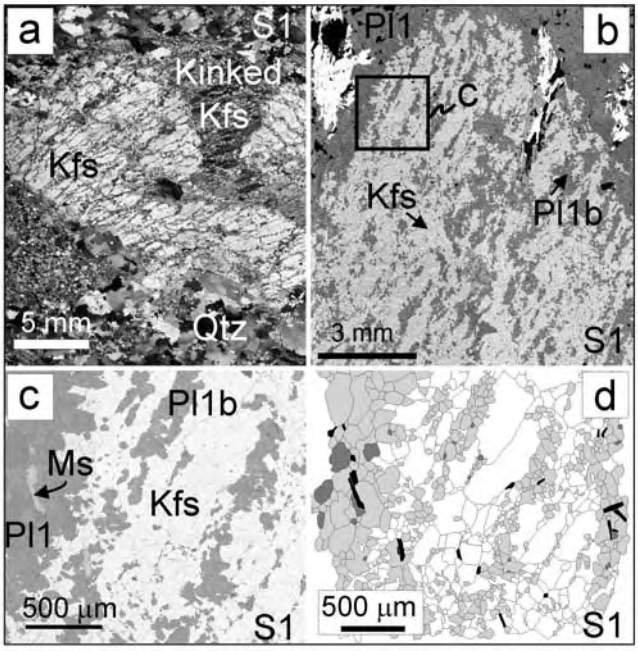

Figure 4. Type I microstructure (S1 sample). (a) Type I metagranite marked by large alkaline feldspar clasts decomposed into albite chains and K-feldspar and (b) scanning electron microscope (SEM) image of alkaline feldspar decomposition. Rectangle indicates the position of the detailed SEM image. (c) The detail of the SEM image showing the shapes of new bulbous albite grains. (d) Corresponding ArcView Geographical Information Systems (GIS) image used for the quantitative mirostructural analysis. Scanning electron microscope images obtained in backscattered electron mode (Camscan microscope, Institute of Petrology and Structural Geology Prague). K-feldspar is represented in light gray, biotite is represented as white laths, quartz and plagioclase are shown in dark gray, and rectangular white mica laths are shown in light gray. In ArcView GIS images the K-feldspar is represented in white, white mica and biotite are represented in black, plagioclase is represented in light gray, and quartz is represented in dark gray. The ArcView Geographical Information System was used as an ideal environment for digitizing mineral shapes [*Lexa et al.*, 2005]. Mineral abbreviations correspond to those of *Kretz* [1983].

which corroborates the development of thin albite-quartz films along the feldspar faces oriented along two maxima with respect to the macroscopic layering (Figure 8). The mean orientation of the Pl2 and quartz seams form an angle of 10–15° with respect to the foliation trace. Interstitial convex quartz grains often occur at triple point junctions but locally line the feldspar boundaries as narrow films (Figures 6c and 6d).

[17] The presence of interstitial phases is the most pronounced in Type III orthogneiss (samples R3, V1 and B2 in particular) where the recrystallized feldspar grains exhibit no shape preferred orientation. Here, wider cuspate-lobate pools and narrow films of Pl2 and quartz occur at a high angle to the macroscopic foliation. The B2 sample shows an extreme orientation of Pl2 seams which form an angle of up to 70° with the foliation trace.

[18] Another important feature is the development of intragranular, wedge shaped fractures that are predominantly developed in elongated feldspar grains with stronger SPO in samples T1 and T2 (Figure 8). These gently curved fractures often originate at the foliation-parallel grain boundaries or triple point junctions, terminate in the interior of the grains and are oriented at low angles (15–30°) to the maximum stretching. In Type III orthogneiss samples (e.g., sample B2) the intragranular fractures occur as well being oriented at high angle to the principal stretching direction.

5. Quantitative Textural Analysis

[19] The quantitative analysis of grain shapes and boundaries was carried out in an ArcView GIS environment. Examples of analyzed samples are shown in Figures 4d, 6d, and 7d. The statistical parameters involving grains size distributions, shape preferred orientation, degree of grain elongation and grain contact frequencies were performed using the MATLAB PolyLX toolbox [*Lexa et al.*, 2005] in order to quantify the above described microstructural sequence of rock types. The grain size distribution was evaluated as an important parameter in deformed rocks because of its sensitivity to stress and temperature [*Schmid et al.*, 1999]. The correct determination of grain size is essential in polyphase systems, where stress and strain rate partitioning are expected [*Handy*, 1990]. Another important parameter is the shape of recrystallized grains, which is strongly dependent on the type of deformation mechanisms and grain growth history [*Boullier and Guéguen*, 1975; *Schmid et al.*, 1987]. Grain contact distribution in the rock yields information about the evolution of spatial distribution of the different minerals in rocks with deformation or melting [*Lexa et al.*, 2005; *Hasalová et al.*, 2008]. This is expressed by the grain contact frequency (GCF) that statistically quantifies the deviation of the grain contact distribution from random [*Kretz*, 1969]. The aggregate distribution, marked by the dominant presence of like-like contacts, represents one end-member of the spatial distribution of grain boundaries that is resulting from the solid state differentiation process [*McLellan*, 1983]. The regular distribution is characterized by the predominance of unlike contacts in rock and is considered as a second end-member

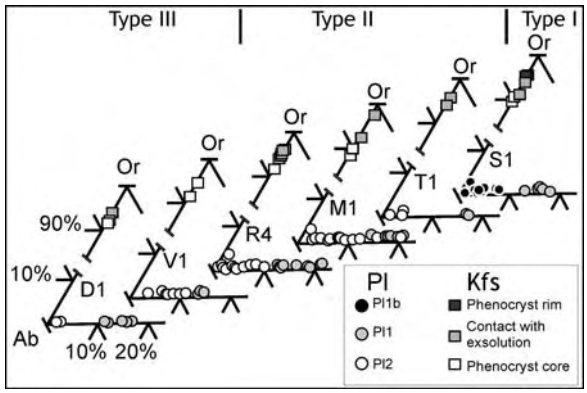

Figure 5. Ternary diagrams showing the composition of feldspars in different samples. Pl1 corresponds to isolated plagioclase aggregate (see text for explanation).

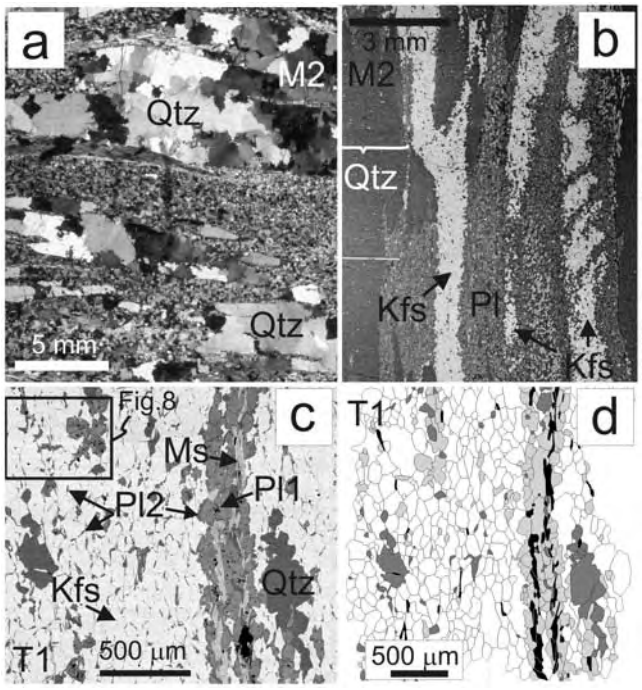

Figure 6. Type II microstructure. (a) Micrograph of sample M2 Type II microstructure characterized by large quartz ribbons and fine-grained feldspar matrix, (b) SEM image of the M2 sample showing typical monominerallic layering and plagioclase aggregate bridges, and (c) detailed SEM image of the T1 sample showing K-feldspar and plagioclase polycrystalline aggregate microstructure. The characteristic feature is the high elongation of feldspar grains lined with Pl2 films, (d) corresponding ArcView GIS drawing of Type II microstructure of the T1 sample. The SEM and ArcView GIS colors are the same as in Figure 4.

of the spatial distribution of the grain boundaries that develops mostly because of solid state annealing [*Flinn*, 1969], mechanical mixing [*Kruse and Stünitz*, 1999] or crystallization of the interstitial melt [*Dallain et al.*, 1999; *Hasalová et al.*, 2008].

5.1. Crystal Size Distribution

[20] The grain size distributions of recrystallized quartz, K-feldspar and of plagioclase have been determined on the basis of more than 500 measured grains per thin section for each sample (except of about 200 measurements in coarse-grained sample B2). Because of the ubiquitous lognormal distribution of the grain populations, the median value was considered to be the most reliable statistical value and the spread of the grain size distribution was evaluated as a difference between the third and first quartile instead of the standard deviation.

[21] The K-feldspar shows a similar grain size distribution for all rock types and is characterized by the median grain size ranging from 60 to 180 μm (Figure 9a). Except sample B2 with exceptionally large grain size, the grain size spread does not follow any systematic pattern. However, the interstitial quartz shows an increasing median grain size value from 20 to 50 μm in the Type II orthogneiss to 80–100 μm in Type III orthogneiss. The plagioclase was examined for the interstitial and aggregate positions separately. The most striking feature is a progressive increase of the aggregate plagioclase grain size from 60 μm (median value) in metagranite to 90 μm in augen orthogneiss to 110 μm in banded orthogneiss, and to 170 μm for sample B2 (Figure 9a). We also observe a systematically higher grain size of aggregate grains compared to the interstitial plagioclase grains for all rock types. In addition, the median value of the aggregate plagioclase grains is shifted toward the third quartile value, while in the interstitial grains it is closer to the first quartile value.

[22] In order to obtain information about the crystal nucleation and growth, the crystal size distribution (CSD) method was applied in the studied samples. The theory of CSD is a well-established technique in metallurgy, ceramics and chemical engineering to reveal information about nucleation, growth rates and growth times of crystals [*Randolph and Larson*, 1971]. CSD in many metamorphic and igneous rocks show a log linear relationship between the grain size L and the population density N according to the equation

$$N = N_0 e^{-L/Gt}$$

where N_0 and Gt are constants and may be related to the nucleation density and growth rate of the crystals [*Higgins*, 1998]. This technique was previously successfully applied to the metamorphic rocks by *Cashman and Ferry* [1988], *Hasalová et al.* [2008], and *Lexa et al.* [2005]. CSD plots of

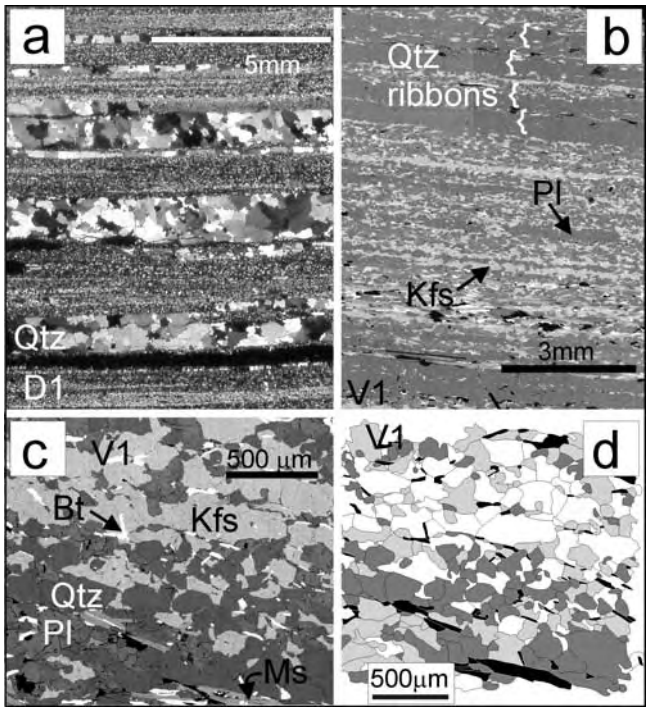

Figure 7. Type III microstructure of banded orthogneiss. (a) Micrograph of sample D1 showing layers of quartz alternating with mixed layers of feldspars and quartz, (b) SEM image of the sample V1 showing quartz and feldspar mixing and poor definition of layer boundaries, (c) detailed SEM image of K-feldspar and plagioclase mixing in the matrix, and (d) corresponding ArcView GIS drawing. The SEM and ArcView GIS colors are the same as in Figure 4.

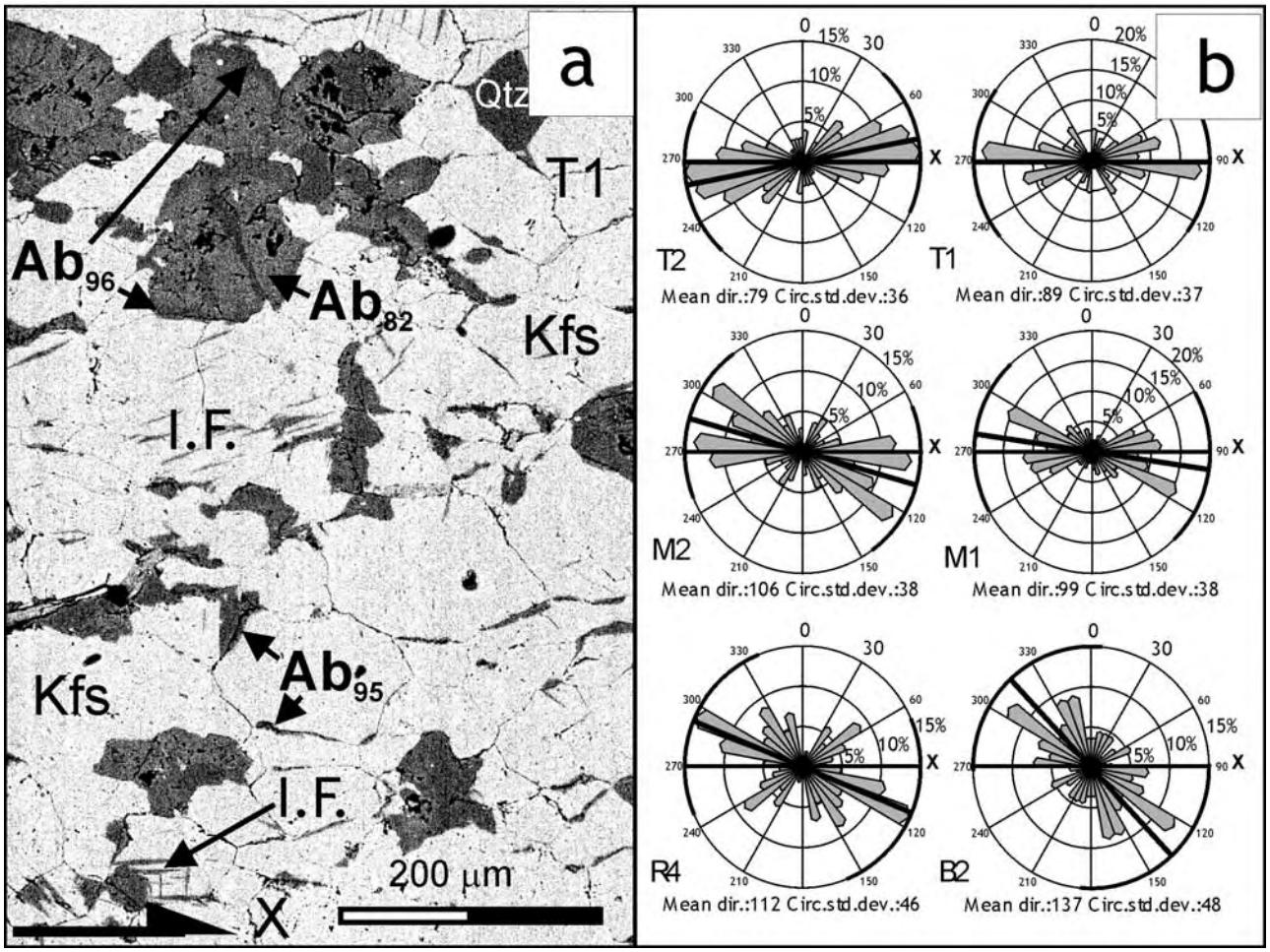

Figure 8. (a) Detail from the backscattered scanning electron image of sample T1 (location of Figure 8a is shown in SEM image in Figure 6c). The image shows the distribution of albite seams along boundaries of K-feldspar grains, character of compositional zoning of the plagioclase in the top left, and intragranular fractures filled with albite (I.F.). (b) Rose diagrams show preferred orientation of ~100 interstitial quartz and Pl2 seams in K-feldspar aggregate. The mean direction and standard circular deviation are shown in the bottom of each diagram. The thick horizontal line represents the orientation of lineation (X), and the thin line shows the orientation of the mean direction.

all the samples constructed according to the method by *Peterson* [1996] exhibit linear correlations between the logarithm of the population density (i.e., the number of crystals per size per volume) and the crystal size (Figure 9b). Applying the theory of CSD, such distributions could be parameterized by the zero size intercept N_0 (nucleation density) and slope Gt (growth rate multiplied by time). These two parameters are plotted in a N_0-Gt diagram [*Lexa et al.*, 2005] where the samples form a distinct trend. Trends in the grain size distributions using CSD method are visualized in Figure 9b. The crystal size distribution plot of the plagioclase aggregates is the most pronounced and shows a systematic decrease of N_0 and an increase of the G_t values with increasing degree of deformation i.e., from Type I to Type III rocks.

5.2. Grain Shapes and Shape Preferred Orientation (SPO)

[23] The aspect ratio median value of plagioclase and K-feldspar varies between 1.5 to 3.1 and no systematic pattern related to the type of rocks and the degree of deformation is obvious (Figure 10). However, the SPO of plagioclase and K-feldspar in most of Type II and III orthogneiss samples is higher compared to the Type I sample with exceptionally high SPO for samples T1 and T2. There is a difference between the aggregate plagioclase (Pl1) and the interstitial albite (Pl2) marked by a systematically higher SPO for the former compared to the latter.

5.3. Grain Contact Frequencies (GCF) and Grain Boundary Preferred Orientation (GBPO)

[24] The combination of the GCF analysis with the studies of the preferred orientation of the like-like (like–like contacts = boundaries of minerals of the same species) and unlike grain boundaries (GBPO) yields important information about the organization of the grain boundaries with respect to the deformation processes [*Lexa et al.*, 2005]. So far the degree of deviation of the grain boundary distributions from the random distribution has been evaluated by plotting the observed/expected ratio of the like–like

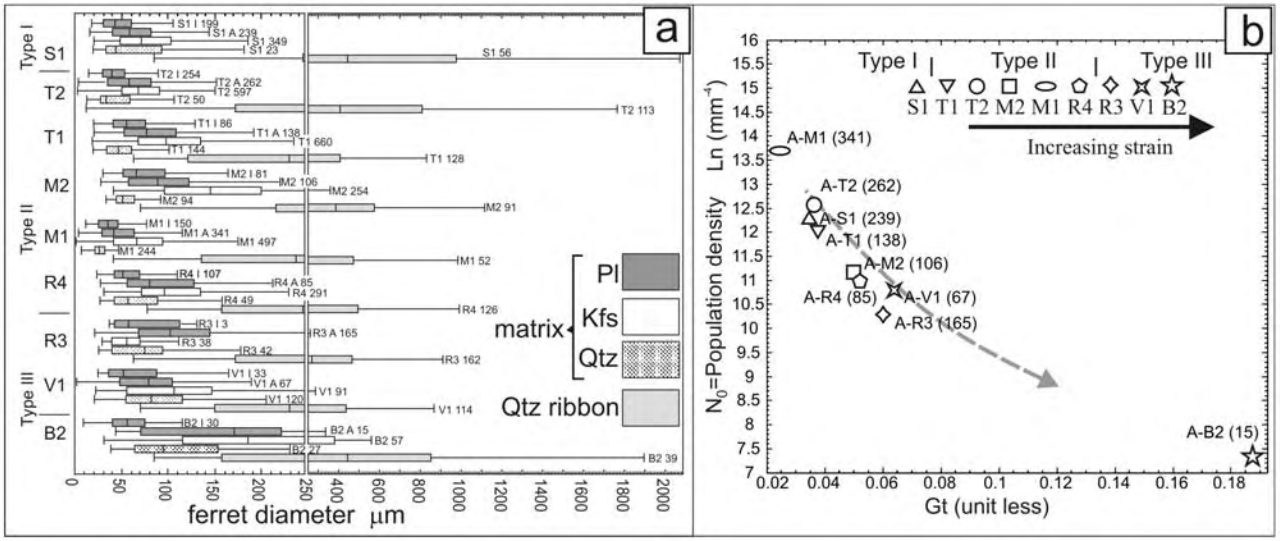

Figure 9. (a) Grain size statistics for the studied samples presented in box-and-whiskers diagrams. Horizontal axis corresponds to the ferret diameter of grain size in micrometers, and the thick bar represents the median of grain size distribution. Vertical axis shows samples arranged according to the degree of deformation from least deformed S1 to most intensely deformed sample V1. B2 represents an exceptionally coarse-grained mylonitic banded orthogneiss. For each sample the plagioclase grain size statistics for interstitial phases (I = Pl2 grains), and for recrystallized grains forming aggregates (A = Pl1 grains) are shown. The number of grains is indicated. Grain size distributions of isolated quartz in the matrix and quartz grains forming centimetric ribbons or augen are also differentiated. This diagram shows progressive coarsening of both Pl1 (aggregate) and Pl2 (interstitial) grains. (b) Plot of crystal size distribution (CSD) for plagioclases (I = Pl2 interstitial grain, A = Pl1 recrystallized grains in aggregates). N_0 ln(mm^{-4}) values on vertical axis represent density of grains per volume, and dimensionless Gt values reflect the grain size frequency distribution. This diagrams show decrease of N_0 values and increase of Gt values which in classical CSD plots represent decreasing values of the intercept of the CSD curve with vertical axis associated with decreasing slope [*Higgins*, 1998]. In the CSD theory this evolution means decreasing nucleation rate and increasing growth rate contribution to the shape of the grain size frequency histogram [*Lexa et al.*, 2005].

contacts of the two major minerals against each other [e.g., *McLellan*, 1983]. *Lexa et al.* [2005] proposed a new diagram where the χ value

$$\chi = \frac{Observed - Expected}{\sqrt{Expected}}$$

is plotted against the ratio of orientation tensor eigenvalues that represent the degree of GBPO. If the solidified melt is identified in a rock the GBPO may yield information about the types of channel networks as defined by *Sawyer* [2001] and quantified by *Hasalová et al.* [2008] and *Závada et al.* [2007].

[25] In this work we use a method proposed by *Lexa et al.* [2005] where the grain contact frequencies are used to assess the character of the spatial distributions of grain boundaries. Figure 11a shows that the plagioclase like-like contacts for the Type I metagranite plots in an intermediate part of the diagram and is characterized by a rather small aggregate distribution. This is due to the presence of the two plagioclase populations resulting from the recrystallization of the large plagioclase crystals (high aggregate distribution) and from the disintegration of the large alkaline feldspar crystals into a mixture of albite and K-feldspar (Figure 4). With increasing deformation a clear evolution of the grain contact frequency toward strongly aggregated distribution for weakly deformed samples of the Type II microstructure can be observed. This is probably due to the coalescence of feldspar and plagioclase layers. At very high strain intensities the plagioclase grain contact frequencies evolve toward the random or regular types of distribution in Type III microstructure. This type of evolution indicates an almost perfect mixing of the plagioclase with other mineral phases. The degree of GBPO of the like-like boundaries for plagioclase does not evolve with the above described trend but remains rather constant for any degree of the finite strain. The K-feldspar grain contact frequency shows a similar behavior to the plagioclase but for some samples a rather strong GBPO coupled with a decreasing grain contact frequency was observed. The evolution of the unlike plagioclase-K-feldspar grain boundaries exactly mirrors the evolution of the plagioclase like-like contact frequency behavior (Figure 11b). For the observed constant grain size it is a geometrical necessity that an increase of the like-like contacts causes a corresponding decrease of the unlike contacts of feldspars.

6. Crystallographic Preferred Orientation

[26] The lattice-preferred orientation (LPO) of quartz, plagioclase and K-feldspar was determined using the electron backscatter diffraction (EBSD) technique [*Bascou et*

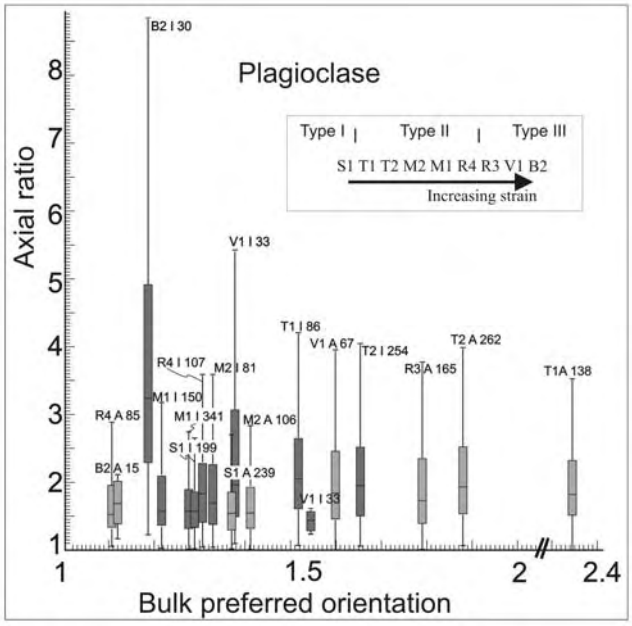

Figure 10. Plot of the grain shape preferred orientations (SPO) of plagioclase and K-feldspar in studied samples. The results are summarized by a box-type plot of axial ratios versus eigenvalue ratios of bulk shape preferred orientation for individual phases. Individual boxes show median and first and third quartile values. The whiskers represent a statistical estimate of the range of data, while outliers are not shown. Vertical axis characterizes the shape of grains, while horizontal axis represents the area-weighted degree of preferred orientation. Plagioclase (I = interstitial Pl2 grains, A = recrystallized Pl1 grains forming aggregates). This diagram shows generally low aspect ratios of plagioclase grains for all samples and exceptionally strong SPO of some samples of Type II and III microstructures.

al., 2001]. The lattice preferred orientation of quartz is presented in the pole figures of the crystallographic directions < c > and < a > (Figure 12). In the case of plagioclase and K-feldspar, the list of operative slip systems [*Kruse et al.*, 2001; *Tullis*, 1983] has been used and measured data has been plotted in the pole figures of these crystallographic planes and directions. Pole figures of principal slip directions and slip planes showing the best coincidence with the main axes of the finite strain ellipsoid of every sample are presented (Figure 13). In the assessment of the maxima position in the pole figures, it has been taken into account that samples M1, V1 reveal prolate shapes of the strain ellipsoid. Hence the maxima of poles in the slip planes might occur along a girdle perpendicular to the slip direction.

6.1. Quartz Augens and Ribbons Crystallographic Preferred Orientation (CPO)

[27] The quartz c axis fabric for Type I microstructure (sample S1) shows a strong central maximum and weaker submaxima close to the periphery of the diagram suggesting an ill-defined oblique cross girdle pattern with opening angles of around 45° (Figure 12). The fabric is a result of the dominant prism < a > and subordinate basal < a > slip systems and a plane strain noncoaxial deformation. Type II microstructures (samples T2 and M1) show strong, central c axis maxima. There is also a tendency to form a single girdle of c axes distribution oriented oblique to the foliation (T2). This c axis pattern is commonly interpreted as a result of a prism < a > slip activity and a noncoaxial deformation [*Schmid and Casey*, 1986]. The Type III microstructure (samples R3 and V1) is characterized by maxima located either at the periphery of the diagram or in an intermediate position. The maxima are organized either along single girdles oblique to the foliation (sample R3) or symmetrically in case of sample V1. These c axis patterns developed from combined activity of the basal < a > and rhomb < a + c > slip systems with a minor contribution of the prism < a > slip during the noncoaxial deformation.

6.2. Plagioclase and K-Feldspar CPO

[28] Plagioclase CPO shows a weakening and an increased activity of secondary and tentative slip systems with microstructural evolution from Type I to Type III microstructures (Figure 13). A frequently described slip system (010)[100] [*Kruhl*, 1996; *Martelat et al.*, 1999; *Schulmann et al.*, 1996] has been observed only in the Type I microstructures (S1) and shows an asymmetry of the position of the maxima with respect to the foliation. The plagioclase from the Type II and III microstructures showed less common slip systems that are supposed to be secondary or tentative [*Kruse et al.*, 2001]. In the Type II microstructure (T2 and M1), the CPO shows active slip systems with dissociated Burgers vectors [*Montardi and Mainprice*, 1987; *Olsen and Kohlstedt*, 1985] namely $1/2[112](11\bar{1})$ and $1/2[111](10\bar{1})$ in the sample T2, and $1/2[1\bar{1}2](110)$ and $1/2[1\bar{1}2](20\bar{1})$ in the sample M1. Brief inspection of both pairs of slip systems shows that each pair occupies a close position in the plagioclase crystal [*Kruse et al.*, 2001, Figure 2] and it is very likely that they operated simultaneously. The Type III microstructures show very weak crystallographic preferred orientation of the plagioclase and sample R3 again reveals an activity on the $1/2[1\bar{1}2](110)$ slip systems with dissociated Burgers vector (Figure 13).

[29] The K-feldspar phenocryst and albite neoblasts of Type I orthogneiss show the same crystallographic orientations (sample S1, Figure 13) that do not coincide with any known slip systems. Albite neoblasts originate along the strings that are parallel to (100) planes. In the Types II and III microstructures, the CPO of K-feldspar recrystallized grains reveal similar pattern indicative of the slip direction parallel to the 1/2[110] in all samples that operate on the (001), $(1\bar{1}1)$ slip planes (Figure 13). A less pronounced slip system $[101](10\bar{1})$ has been recognized in the augen gneiss sample T2 from the Type II microstructure.

7. Petrological Modeling

[30] The structural position and shapes of interstitial phases, the character of mineral zoning and the compositional variations of the plagioclase (Pl2) in both Type II and III microstructures indicate the presence of some kind of fluid during the deformation [*Fitz Gerald and Stünitz*, 1993; *Sawyer*, 2001; *Hasalová et al.*, 2008; *Závada et al.*, 2007]. Therefore, the pseudosection modeling was performed in order to examine whether the deformation process in the studied orthogneisses occurred in the presence of a melt or an aqueous fluid.

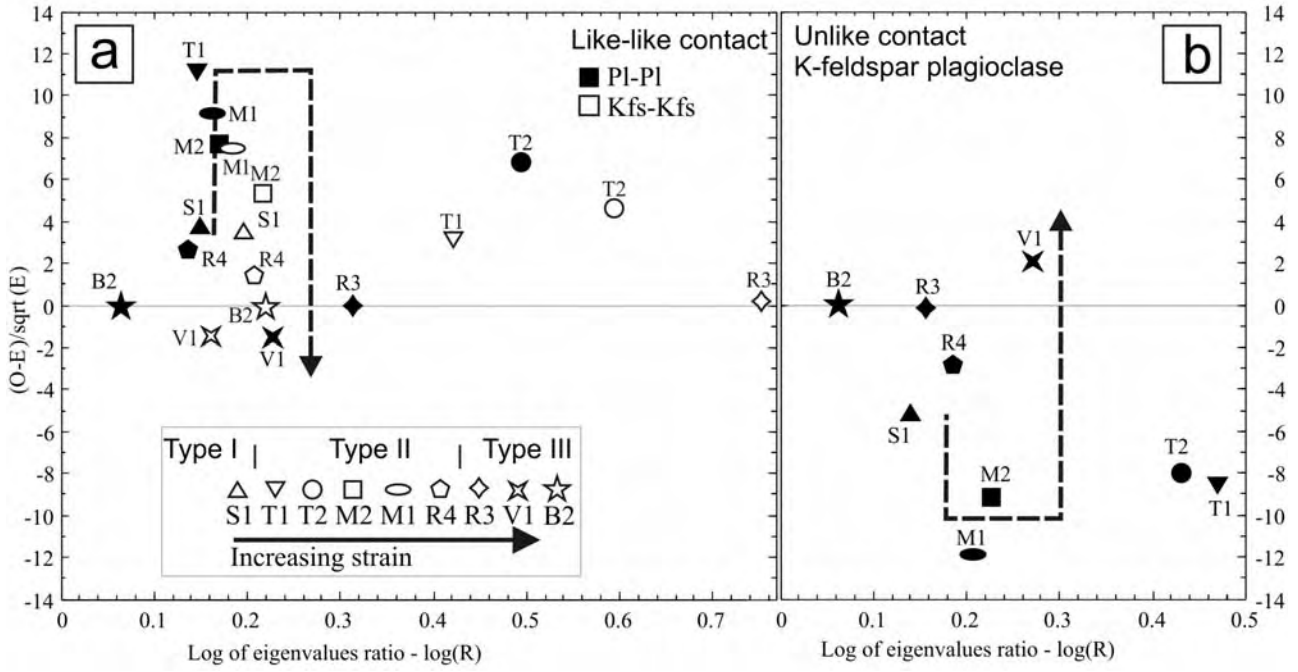

Figure 11. Plot of the grain boundary frequencies. Plots of the deviations from random spatial distribution versus the degree of grain boundary preferred orientation. The value of the deviation from random spatial distribution is obtained by the contact frequency method [*Kretz*, 1969], and the length-weighted degree of preferred orientation is estimated as the ratio of eigenvalues of the bulk matrix of inertia. The plot of the like-like and unlike boundaries is separated. (a) The diagram of feldspars like-like boundaries shows a trend from the weak aggregate distribution of Type 1 microstructure, to the highly aggregate distribution in Type II microstructures, and almost random distribution in highly mixed Type III microstructures. (b) The diagram of feldspar unlike boundaries mirrors the like-like evolutionary trend.

7.1. Modeling Method

[31] The pseudosections were calculated in the system Na_2O-CaO-K_2O-FeO-MgO-Al_2O_3-SiO_2-H_2O (NCKFMASH). All the Fe was treated as FeO and molar amounts of the considered oxides were recalculated to 100 mol %. The calculations were performed using THERMOCALC 3.25 [*Powell et al.*, 1998] and the data set 5.5 [*Holland and Powell*, 1998]. The mixing models for the most solid solutions were taken from *White et al.* [2001] and the THERMOCALC documentation [*Powell and Holland*, 2004]. The feldspars are formulated using the model of *Holland and Powell* [2003], the paragonite-muscovite solution is after *Coggon and Holland* [2002]. The quartz, K-feldspar and plagioclase are in excess and the pseudosections are contoured for liquid mole isopleths.

7.2. Results

[32] The first pseudosection is calculated with the amount of H_2O, $M(H_2O)$ = 2.68 mol % in the whole rock composition, which is the amount of H_2O tied in micas in the assemblage biotite-muscovite-plagioclase-K-feldspar-quartz (Bt-Ms-Pl-Kfs-Qtz) at 8 kbar and 600°C (Figure 14a). The limiting maximum pressure for the studied rock with the assemblage Bt-Ms-Pl-Kfs-Qtz is the appearance of garnet at 8–9 kbar, the maximum temperature limit is the beginning of biotite dehydration melting marked by the appearance of garnet at temperatures of 680–700°C and the breakdown of muscovite at 680–700°C below 6 kbar that is not observed. The minimum pressure and temperature conditions cannot be determined from the assemblage of the studied sample, therefore, we used the P-T path of *Pitra and Guiraud* [1996] that was determined in the neighboring metapelites. It is characterized by decompression from 8–9 kbar and 610–660°C to 4–5 kbar and 600–650°C. Path 1 (Figure 14a) is characterized first by heating followed by decompression. Melting in the assemblage Bt-Ms-Pl-Kfs-Qtz without external H_2O starts at c. 660°C and 8 kbars and the maximum amount of melt produced in the field of Bt-Ms-Pl-Kfs-Qtz-Liq is less then 1 mol %.

[33] The evolution of assemblages that the rock composition produces with a varying amount of H_2O ($M(H_2O)$ = 0–4.78 mol %) on heating at 8 kbar is examined in Figure 14b. The evolution for the amount of H_2O tied in micas (=2.68 mol %) in a rock with the starting assemblage Bt-Ms-Pl-Kfs-Qtz is indicated by path 1, and is equivalent to the isobaric heating path in Figure 14a. The assemblage Bt-Ms-Pl-Kfs-Qtz starts to melt at c. 660°C, and produces less then 0.5% of melt at c. 685°C (path 1 in Figure 14b). The upper temperature limit is the appearance of garnet at c. 690°C that is not observed in the studied rocks. The lower amount of H_2O in the rock stabilizes the anhydrous phases such as the garnet or kyanite and higher amounts of H_2O indicates the presence of free aqueous fluid below 630°C.

[34] If above the temperature of c. 630°C appears free H_2O in the rock that follows the path 1, the rock composition is immediately drawn to the right side, and starts to

melt (for example path 2 in Figure 14a). This leucocratic melt is generated by the water released by the dehydration process in which water migrates upward into the melt-fertile rocks that are above the wet-solidus temperature [*Scaillet et al.*, 1990; *Thompson and Connolly*, 1995]. The quantity of produced melt depends on the amount of available external H_2O. For example the total amount of H_2O for path 2 is $M(H_2O)$ = 4.28 mol %, which is 1.60 mol % of H_2O added to 2.68 mol % H_2O already present in the micas. Such H_2O addition results in the production of 5 mol % of melt at 660°C and 8 kbar.

[35] The evolution during decompression was also studied in P-$M(H_2O)$ sections at 660°C. Following a decompression from 8 to 4.5 kbar, the rock with the original H_2O tied in micas increases the amount of melt to 1 mol %. In a rock that contains added H_2O, the melt fraction increases by 1–2.5%, for example for path 2 the total amount of melt at 4.5 kbar is 7.5 mol % because of 1.6 mol % added H_2O on the prograde path.

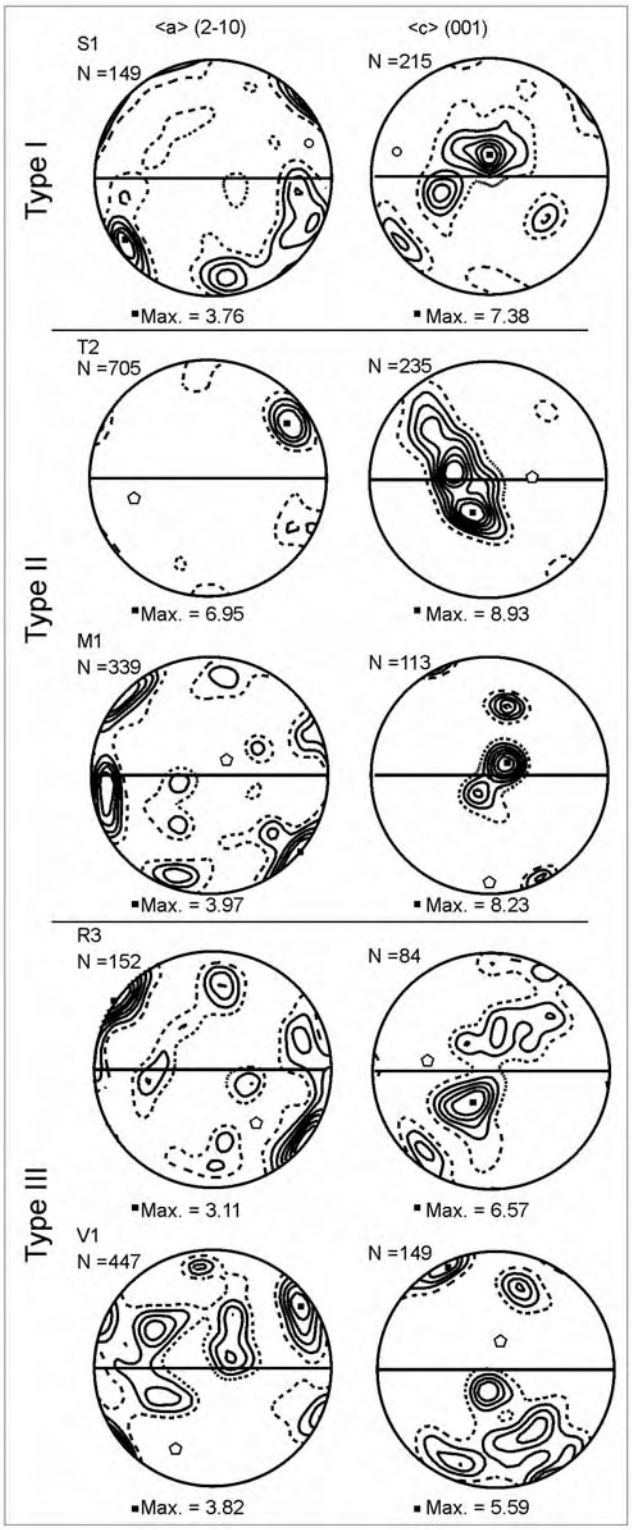

8. Discussion

[36] Here we discuss the anomalously weak K-feldspar and plagioclase compared to quartz in light of the strain data and quantitative microstructural and textural analysis. The quartz-feldspar rheology inversion is discussed as a result of the alkaline feldspar breakdown and the formation of a fine-grained feldspar matrix. Finally, we propose a model of mixing of the recrystallized plagioclase and K-feldspar grains with the silicate melt associated with grain boundary sliding controlled diffusion creep followed by a granular flow at higher melt proportions.

8.1. Comparative Quartz and K-Feldspar Rheology

[37] On the basis of the number of experimental data, the quartz can be considered to be significantly weaker compared to the K-feldspar and plagioclase for a wide range of temperatures [*Jaoul et al.*, 1984; *Kronenberg and Tullis*, 1984; *Tullis*, 1990]. This is supported by a number of studies of quartzo-feldspathic rocks deformed at medium- to high-temperature conditions [*Gapais*, 1989; *Handy*, 1994a; *Schulmann et al.*, 1996]. It is only at greenschist facies conditions and in the presence of hydrous fluids, when feldspars become weaker than quartz via destabilization and breakdown to mixture of retrograde fine-grained reaction products as white mica, quartz (K-feldspar breakdown) and epidote, albite ± garnet (plagioclase breakdown) [*Fitz Gerald and Stünitz*, 1993; *Handy*, 1990; *Stünitz and Fitz Gerald*, 1993]. Nevertheless, it is assumed that the strength of feldspars is generally several orders of magnitude higher than that of quartz [*Handy*, 1994a; *Handy et al.*, 1999; *Ranalli and Murphy*, 1987].

[38] The shapes of quartz and feldspar polycrystalline aggregates measured in this work clearly show that for

Figure 12. Electron backscatter diffraction in situ measurements on quartz ribbons. Pole diagrams showing contoured crystallographic orientation (projected in lower hemisphere equal area). Contoured at multiples of uniform distribution (maximum 10 uniform). The foliation normal is N-S, and the stretching lineation is E-W. Black squares correspond to the pole of the mean orientation. The pole figures show evolution of active slip systems with increasing deformation from activity of combined prism < a > and basal < a > slip systems for weakly deformed Type I microstructures, via the activity of prism < a > slip system in intermediate Type II microstructures to combined activity of basal < a > and rhomb < a + c > slip systems in highly strained Type III microstructures.

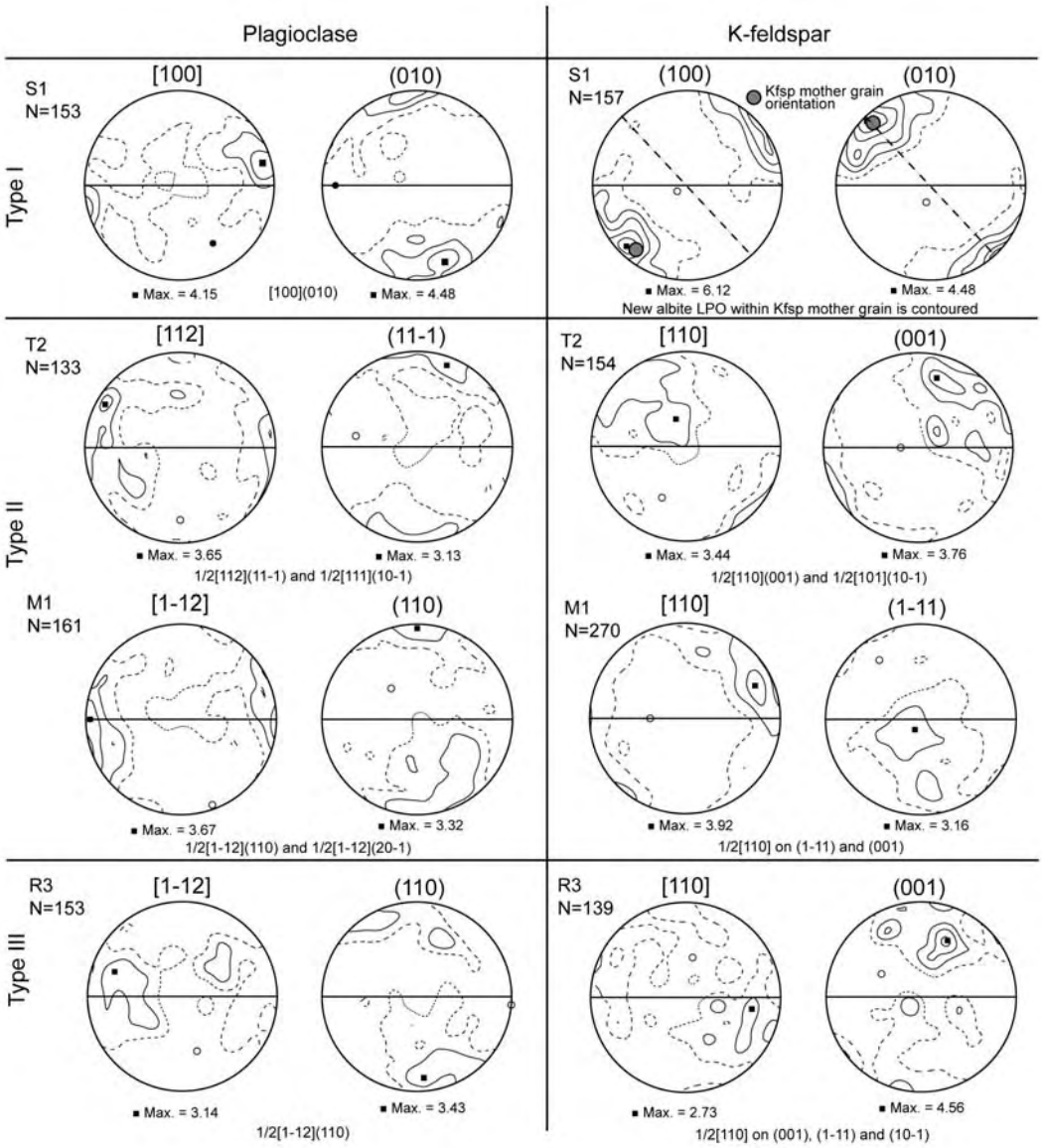

Figure 13. Contoured pole figures of the most characteristic slip direction and slip plane of K-feldspar and plagioclase from the Type I to the Type III microstructures. Equal area projection, lower hemisphere. Contoured at interval 1.0 times of the uniform distribution. Foliation (full line) is horizontal, and lineation is in this plane in the E-W direction. N is the number of measured grains. Maximum densities (black square in the pole figures) are marked below the pole figure. Plagioclase shows commonly reported slip system only for Type I microstructure and activity of secondary and tentative slip systems with dissociated Burgers vectors for Type II and III microstructures. The top right pole figures show dependency of CPO of the new exsolved albite grains Pl1b on the orientation of alkali feldspar host. K-feldspar reveals also slip systems with dissociated Burgers vectors for Types II and III microstructures. See text for discussion.

various deformation intensities the quartz aggregates are less deformed than the feldspar aggregates and the difference of D values between feldspar and quartz aggregates increases with increasing bulk deformation. We suggest that the studied samples reveal a higher competency of quartz compared to the feldspar polycrystalline aggregates for all examined strain intensities at high-temperature conditions. The strength reversal between the quartz and feldspar in experimentally deformed aplite was documented by *Dell'Angelo and Tullis* [1996]. These authors showed that at 700°C, the dispersed quartz grains in the aplite remain less deformed than the feldspar grains while at higher temperatures the interconnected quartz becomes weaker than feldspars.

8.2. Structural Evolutionary Trends of Polyphase Mylonites

[39] We discuss here a hypothesis of microstructural evolutionary trend in which the Types I, II and III microstructures represent different deformation stages along a

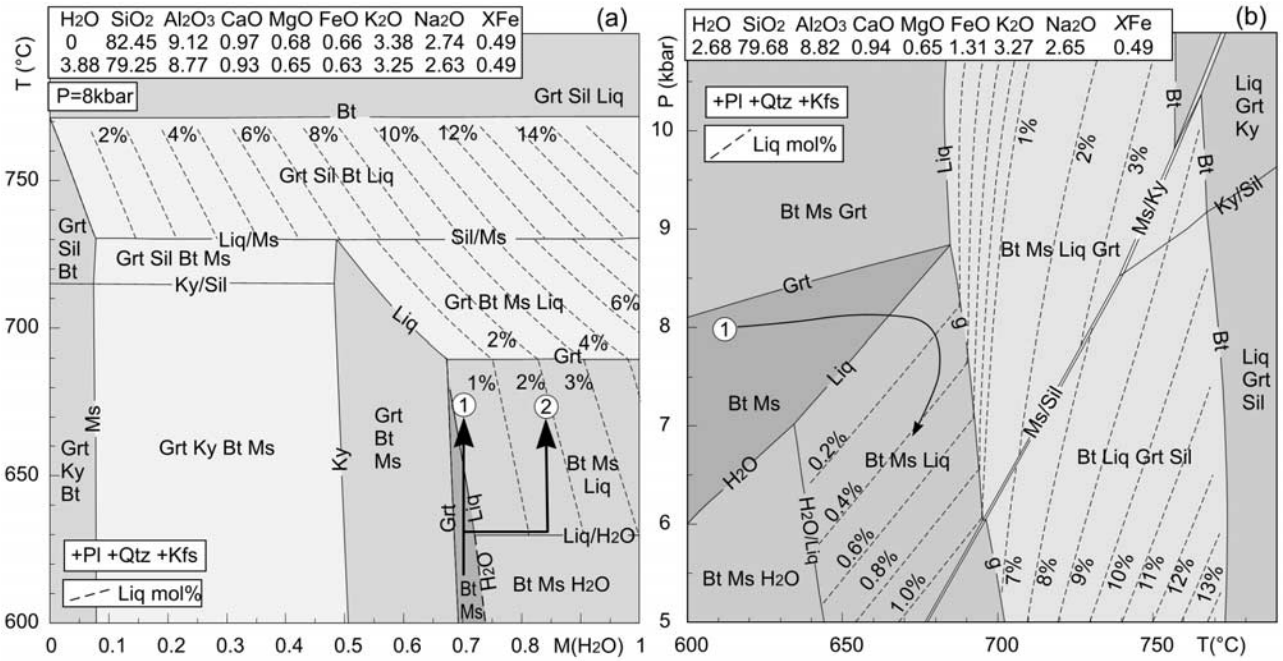

Figure 14. (a) Pseudosection showing the evolution of assemblages that the rock composition produces with varying amounts of H_2O (M(H_2O) = 0–3.88 mol %) on heating at 8 kbar. (b) The pseudosection calculated with the amount of H_2O tied in micas, deduced from pseudosection (Figure 14a). The pseudosection shows a prograde path between 7 and 8 kbar along which the melt appears above 640°C in the stability of Bt-Ms-Liq-Pl-Ksp-Qtz. For comparison, the contours of melt production in other fields are also shown. Mineral abbreviations correspond to those of *Kretz* [1983].

progressive deformation path. Theoretically, the load-bearing framework (LBF) minerals (LBF = interconnected strong phase) should shield a weak phase from viscous deformation for weak phase fractions lower than 20% [*Handy*, 1990]. With increasing strain the weak phase starts to interconnect along localized shear bands, leading finally to the development of a banded structure of alternating monomineralic layers [*Jordan*, 1988]. This corresponds to an evolution from high-viscosity contrast toward low-viscosity contrast interconnected weak layer (IWL) structures [*Handy*, 1994a].

[40] The microstructure of the Type I orthogneisses show interconnected recrystallized aggregates of plagioclase (representing the weakest phase) surrounding strong clasts of quartz and alkali feldspar. This kind of microstructure corresponds to IWL microstructure with the deformation highly localized into rheologically weak plagioclase and a relatively high volume (up to 60 vol. %) of strong fraction (Figure 15a). This observation is valid for the macroscopic scale, but different rheological behavior can be observed at the scale of the individual feldspar clasts. The internal structure of the alkali feldspar phenocrysts shows typical characteristics for a LBF structure formed by K-feldspar and aggregates of recrystallized plagioclase representing an isolated weak phase [*Eudier*, 1962; *Jordan*, 1987; *Tharp*, 1983]. A rather high volume of weak pockets (20–30%) indicates a low stability of the LBF structure for small strain intensities [*Handy*, 1994a]. This is consistent with the observed onset of coalescence of plagioclase chains along microshear bands in Figure 6b [*Jordan*, 1988].

[41] The Type II microstructures are characterized by the collapse of the internal LBF structure of alkali feldspar through the interconnection of recrystallized plagioclase and K-feldspar. This evolution is documented by the presence of oblique ''bridges'' of recrystallized plagioclases crossing recrystallized K-feldspar aggregates and connecting surrounding plagioclase matrix (Figure 6b). From a rheological point of view, the volume of the weak matrix increased from $\sim$ 30 to 60 vol. % through the addition of entirely recrystallized plagioclase and K-feldspar from original phenocrysts of Type I rock to already recrystallized plagioclase of Type II orthogneiss (Figure 15b). This evolution leads to the development of IWL structures at all scales marked by a low volume of strong phases (quartz) and a moderate viscosity contrast indicated by the elongated shapes of quartz aggregates. An important feature of this stage is the coalescence of K-feldspar and plagioclase leading to the development of almost monomineralic layers (Figure 6).

[42] The Type III microstructure is characterized by the destruction of feldspar monomineralic layering through progressive mixing of the feldspars and the subordinate small quartz grains forming a fine-grained matrix. The final microstructure is represented by highly elongated quartz ribbons surrounded by the homogeneously deformed feldspar-quartz matrix. This type of rock microstructure corresponds to the IWL structures and is marked by a very low-viscosity contrast between the quartz and the weak phases. The stronger quartz can be seen as a deformable inclusions in weak matrix (Figure 15c). In order to develop such a microstructure the deformation mechanisms of feldspars have to evolve toward similar efficiency.

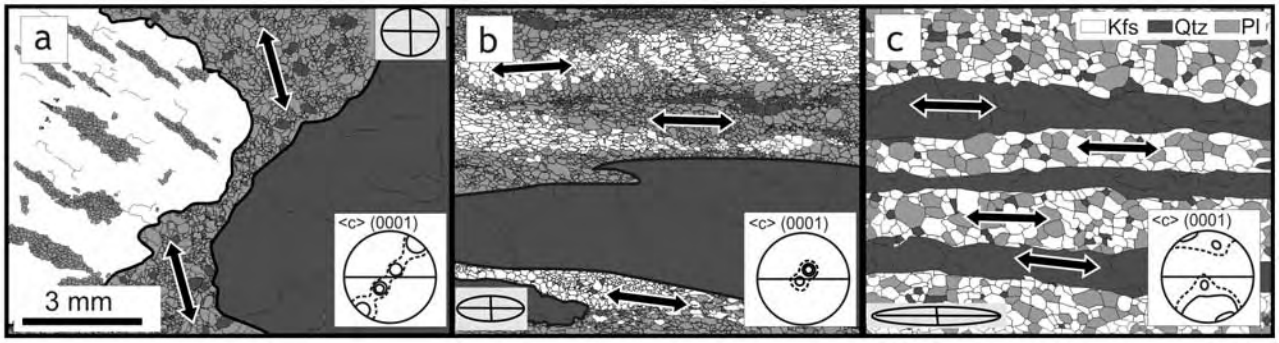

Figure 15. The evolutionary trend of the metagranite deformation. (a) Orthogneiss Type I showing interconnected weak layer (IWL) structure with strain concentration in plagioclase. The K-feldspar shows internal load-bearing framework structure with weak plagioclase strings, while quartz exhibits weak CPO, both indicating shielding of quartz and feldspar from viscous flow. (b) Orthogneiss Type II is marked by almost uniform flow in plagioclase and K-feldspar monomineralic layers around the strong quartz-IWL structure with low viscosity contrast. The rock shows development of monomineralic layering and intense yielding of quartz marked by strong CPO and activity of prism < a > slip. (c) Orthogneiss Type III shows a uniform flow of all mineral phases and mixing of feldspars associated with important crystal growth. The quartz texture exhibits weakening comparing to the previous stage and activity of the basal < a > slip.

8.3. Mechanism of Alkali Feldspar Breakdown: Transition From Type I to II Rock

[43] The key element controlling the rheological development of the bulk rock is the mechanism of decomposition of originally large alkali feldspar phenocrysts into chains of plagioclase grains and adjacent K-feldspar hosts (Figure 4). EBSD measurements have shown that the texture of the new plagioclase crystals in any structural position is almost identical to that of the K-feldspar hosts (Figure 13), indicating an orientation relationship between the host and the inclusion.

[44] The above described features do not have an unambiguous explanation. The coherent texture of the plagioclase and host K-feldspar grain may reflect a heterogeneous nucleation process [*Putnis et al.*, 2003; *Ribbe*, 1983]. The Time-Temperature-Transformation diagrams for the feldspar exsolution during cooling suggest that a process of heterogeneous nucleation is the most likely mechanism because of the slow cooling rates (which are likely to occur in deep seated intrusions) [*Putnis et al.*, 2003]. Our microstructural analyses show that the shape and size of the exsolution patterns is determined by the structure of the host namely by (100) and (010) planes of alkali feldspars. The experiments of *Putnis et al.* [2003] show that the albite rich regions originate as a monoclinic feldspar exsolution in the K-rich host. With falling temperatures the albite changes to a high-albite triclinic structure. The strain generated at the lamella interface leads to the segmentation of the lamella by the albite twinning reducing the strain energy across the interface region. It is possible that such twinned lamellae coarsen during the subsequent annealing which may lead to the development of new albite grains. The process of coarsening may have been enhanced by the thermally induced deformation so that first subgrains and subsequently developed new grains originated from the progressively deforming twinned lamellae. All these processes may result in the development of chains of albite grains subparallel to the former exsolution domains. The process of the heterogeneous nucleation is supported by the compositional profiles which show a decrease of albite components in the host K-feldspar toward the albite boundary of rather constant composition similarly to the profiles published by *Putnis et al.* [2003]. In theory the exsolution process should be related either to the cooling history of crystallization of the granite or to the deformation-metamorphism process as suggested by *White and Mawer* [1986, 1988]. However, the spatial distribution of plagioclase chains in the feldspar host and the crystallographic coherency suggest that the transformation of the original alkali feldspar was achieved by heterogeneous nucleation.

8.4. Consequences of Feldspar Breakdown: Monomineralic Layering in Type II Rocks

[45] The progressive textural evolution toward aggregate distribution in the Type II microstructure is a typical feature of the high-grade deformation of granitoids [*Gapais*, 1989; *Handy*, 1994a; *Schulmann et al.*, 1996]. The onset of granite deformation is marked by the high stress concentrations in the plagioclase grains due to the relative rheological inactivity of the quartz and K-feldspar at the onset of the metagranite deformation (Type I microstructure). The grain size increase of the recrystallized plagioclase and K-feldspar associated with the development of monomineralic layering can be interpreted in terms of stress relaxation [*Hobbs*, 1981] coupled with a flow stress increase in the quartz aggregates indicated by the activity of the prism < a > slip system compared to the basal < a > in the Type I microstructure [*Schmid and Casey*, 1986]. Alternatively, the evolution of the quartz slip system can be attributed to the increasing strain intensity in the Type II microstructure [*Heilbronner and Tullis*, 2006]. Rather unusual feldspar slip systems like once in Type II rocks (Figure 13) have been reported by *Baratoux et al.* [2005] from high-grade mylonitic metagabbros and by *Franěk et al.* [2006] from partially molten granulites. These authors interpreted the observed slip systems as a result of a grain boundary sliding accompanied with a crystal plastic deformation. All this

implies a progressive homogenization of the stress field during this stage. Differences in the efficiency of the deformation mechanisms lead to the development of monomineralic layering precluding effective mechanical mixing. We emphasize that the involvement of feldspars in the homogeneous flow increases the proportion of the weak material up to 60%, which provided a significant drop of the bulk strain rate or stress assuming constant far field stresses or a bulk strain rate, respectively (Figure 15b). The effective weakening mechanism could be regarded in the presence of fluid or melt phase at grain boundaries in Type II rocks which is represented by the interstitial albitic Pl2 and quartz forming thin films parallel to the K-feldspar and Pl1 boundaries or as small cuspate grains in triple point junctions.

8.5. Reasons for Transition From Type II to Type III Rock: Melt-Assisted Mineral Mixing

[46] Type III microstructures correspond to a mixing of fine-grained plagioclase and K-feldspar by two competitive processes: a mechanical mixing accompanied by syn-deformational mass transfer either by diffusion [*Baratoux et al.*, 2005; *Kruse and Stünitz*, 1999] or by melt/fluid redistribution along grain boundaries during the in situ melting [*Závada et al.*, 2007; *Hasalová et al.*, 2008] or infiltration of hydrous fluids, respectively [*Stünitz and Fitz Gerald*, 1993]. The mechanical mixing process is supported by the progressive thinning of the plagioclase aggregates in a K-feldspar matrix associated with the extreme stretching of the rock at very high strains. This process is inevitably associated with a grain boundary sliding mechanism and diffusion dominated creep. The growth of albite and quartz rims around the K-feldspar grains and the overall grain size increase of both feldspars can result from the above mentioned mass transfer mechanisms.

[47] The intensity of quartz CPO in Type III microstructures decreases compared to Type II microstructures. This is due to a switch of the active slip system from prism < a > toward basal < a > and rhomb < a + c > slip systems in Type III microstructure (Figure 15c). These slip systems are not common in partially molten high-grade mylonites where the activity of prism < c > glide is reported [e.g., *Gapais and Barbarin*, 1986; *Martelat et al.*, 1999]. Our observations do not indicate a late reworking during a low-temperature event and we therefore suggest that the activity of the "low-temperature" slip systems in high-grade mylonites results from strain rate or stress conditions which are currently unconstrained [*Závada et al.*, 2007; *Hasalová et al.*, 2008]. Consequently, the deformation mechanism in quartz is the dislocation creep and the evolution of slip systems suggest a decrease of the flow stress or strain rate compared to previous stages [*Handy*, 1990; *Herwegh et al.*, 1997; *Schmid and Casey*, 1986]. However, the diffusional creep in the feldspar matrix supported by grain shapes and crystallographic preferred orientations (Figure 13) shows that the Type III microstructures represent a deformation stage marked by the overall flow stress drop associated with the increase of homogeneity of the strain distribution. This overall weakening is consistent with interstitial phases forming a substantial proportion of the rock volume and shapes of pools or thick films of Pl2 and quartz grains that are similar to the melt topology described by *Sawyer* [2001] or *Marchildon and Brown* [2003].

8.6. Quantitative Microstructural and Petrological Arguments for Syn-deformational Melting

[48] The CSD curves (Figure 9b) show decreasing N_0 and increasing G_t values in relict plagioclase aggregates toward Type III rocks. The trend from Type II to Type III rocks (Figure 9b) consistent with the rapid nucleation of interstitial Pl2 is marked by the presence of thin isolated films in SEM images of Type II microstructures (Figure 6, samples T1 and M2, and Figure 8). The decrease of N_0 and increase of G_t values in Type III microstructures correspond to a growth of Pl2 pools and large new Pl2 rims in a K-feldspar dominated matrix (Figure 7, samples V1 and D1). This evolution corrobarates the weakening of the aggregate distribution in Type II microstructures toward an almost random distribution in Type III microstructures and an associated development of important proportion of the interstitial phases (Figure 11).

[49] The pseudosection modeling indicates that the only fluid that could be present during the deformation of the orthogneiss at the estimated temperatures of 650–680°C is a silicate melt (Figure 14). Either the temperature increase or the pressure drop along the path estimated by *Pitra and Guiraud* [1996] or *Tajcmanová et al.* [2006] for associated metapelites can be responsible for the dehydration melting of the muscovite-biotite bearing orthogneiss assemblage. The amount of melting may even be increased by external fluids introduced from the surrounding metapelites [*Thompson and Connolly*, 1995].

[50] The nucleation dominated part of the deformation-melting history in Type II microstructures is probably associated with the onset of the melting reaction and heterogeneous nucleation of the melt droplets at high-energy triple points or noncoherent grain boundaries. The growth dominated process associated with the Type III microstructures reflects a more advanced melting leading to the development of large pools and the coalescence of small nuclei along all boundaries in deformed aggregates. This process is best exemplified by the sample B2 which resembles a migmatitic structure at the macroscopic scale.

8.7. Grain Boundary Sliding Diffusional Creep and Variations in Melt Topology With Increasing Melt Fraction

[51] The studied microstructural sequence is characterized by the increasing deformation intensity (Figure 3), the increasing melt fraction (Figures 4, 6, and 7), grain size (Figure 9) and random grain contact distribution as well as the low aspect ratio of grains (Figures 10 and 11). This evolutionary trend is accompanied by a change in orientation of the melt seams (Figures 8 and 16) from an orientation subparallel to the foliation to seams oriented at high angle to the foliation.

[52] Melt seams preferentially located along grain boundaries parallel to the foliation in Type II microstructures are commonly reported in natural samples [*Sawyer*, 2001; *Rosenberg and Berger*, 2001] and in some experimental or analog studies [*Daines and Kohlstedt*, 1997; *Groebner and Kohlstedt*, 2006; *Walte et al.*, 2005]. This geometry can be observed in microstructures of the T1 and T2 samples and is compatible with the combined activity of grain boundary sliding and crystal-plastic deformation mechanisms at very low melt fractions (<2%). Therefore, the

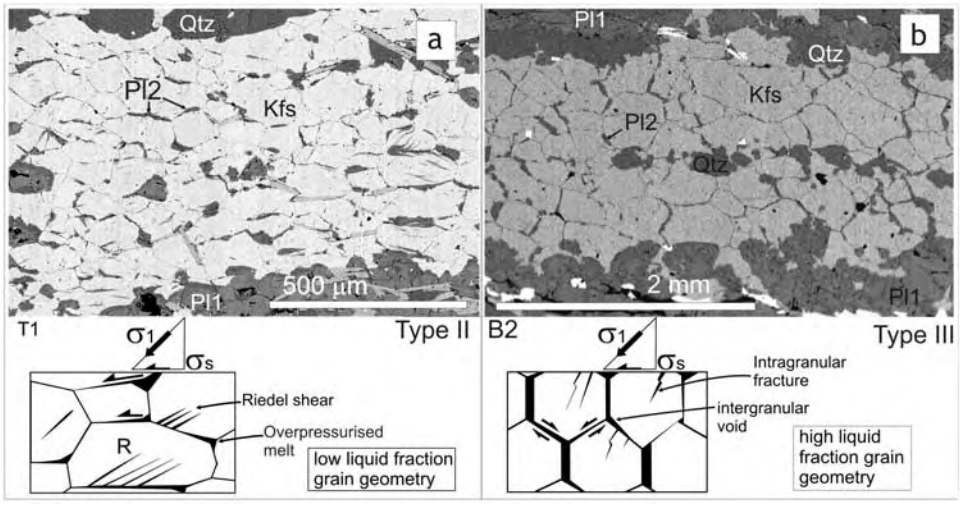

Figure 16. The evolution of (a) shear plane-parallel melt preferred orientation at low melt fractions and (b) shear plane-perpendicular melt preferred orientation at high melt fractions. At low melt fractions, shear is accommodated by the grain boundary sliding parallel to the shear direction. Since grain boundary sliding means a loss of the cohesion along these boundaries, they represent an easy path for melt which accumulates at these boundaries (bottom left, Figure 16a). At higher melt fractions, a switch from shear plane parallel to shear plane-perpendicular melt preferred orientation can be observed. This is probably because of stress concentrations at grain boundaries oriented perpendicular to simple shear and accompanying dilation/cavitation of these boundaries (bottom right, Figure 16b). See text for further explanations.

orientation of melt seams can be explained by a loss of cohesion at boundaries oriented parallel to the foliation. Because of shearing, the melt concentrated at triple points suffers an increasing overpressure. We suggest that the combination of loss of cohesion and build up of melt overpressure leads to the injection of melt between actively moving grain boundaries oriented at a high angle to the principal compressive stress, i.e., parallel to the macroscopic foliation (Figure 16a). Oblique intragranular fractures can be interpreted as Riedel shears channeling melt from overpressured, dilatant grain boundaries accompanying movements along foliation-parallel grain boundaries [*Rosenberg and Handy*, 2000]. The M1 and M2 samples are characterized by a general constrictional deformation, lower aspect ratio of grains and low melt fraction (<2%). Similarly to the T1 and T2 samples these grain aggregates exhibit microscopic features compatible with grain boundary sliding and plastic deformation. The preferred orientation of melt is weaker compared to the T1 and T2 samples, which can be explained by a smaller dimension of active grain boundaries and also by a prolate shape of the strain ellipsoid.

[53] The overpressured melt is therefore injected in between grain boundaries of variable orientation with a mean direction parallel to the foliation. This orientation is therefore a function of (1) melt fraction, where little melt behaves as isolated weak pockets localizing strain (Figure 16a); and (2) deformation mechanisms probably corresponding to the grain boundary sliding–grain boundary locking transitional regime defined by *Walte et al.* [2005]. This regime is marked by the transition from grain boundary sliding to crystal-plastic framework deformation promoting foliation parallel to the elongation associated with the development of a strong melt preferred orientation parallel to the principal stretching direction [*Groebner and Kohlstedt*, 2006].

[54] In Type III microstructures (samples R3, V1, B2) the melt pools and intragranular melt filled fractures are oriented at a high angle to the stretching direction but show rather weak preferred orientations (Figure 16b). Experimental studies by *Dell'Angelo et al.* [1987] and *Dell'Angelo and Tullis* [1988] show that melt pockets are perpendicular to the maximum stress direction for high differential stress and relatively low melt fractions of 3–5%. Analogue studies of *Walte et al.* [2005] and *Park and Means* [1996] show comparable development of melt pockets oriented parallel to the principal stress at melt fractions ranging from 4 to 10%. Consequently, we suggest that the Type III microstructures result from the distributed granular flow, which operated at higher melt fractions between 5–10%, and where the higher melt fraction and connectivity promote grain boundary sliding and dynamic dilation (Figure 16b).

[55] *Závada et al.* [2007] explain the development of melt films perpendicular to the stretching direction by the mechanisms of intergranular and/or intragranular fracturing during grain boundary sliding at melt fractions between 2–5%. They propose that the dilation represents a final creep failure state which resulted from a cavitation process accompanying the grain boundary sliding controlled diffusion creep. They also suggested that, in analogy to the experimental works of *Sklenička et al.* [1977] and *Kassner and Hayes* [2003]; the distributed intergranular cavitation in K-feldspar is consistent with relatively slow strain rates typical for diffusion type creep. Another possible model proposes that the melt is overpressured and therefore can overcome the least principal stress as well as the cohesion of

suitably oriented planes in the aggregate [*Hubbert and Rubey*, 1959]. As a result of melt overpressure, the feldspar aggregate dilates and the melt is accumulated in intergranular and intragranular pockets and fractures.

[56] It is likely that the evolution in the orientation of melt pockets is caused by the increasing melt fraction and/or by the change in differential stress magnitude and orientation [*Cosgrove*, 1997]. The implication of the increasing melt fraction and connectivity certainly influences the distribution of local compressive and shear stress magnitudes and orientations and the active deformation mechanism (Figure 16). In this context, it is not likely that the melt preferred orientation is controlled by the variations in differential stress [*Gleason et al.*, 1999], hydrostatic annealing [*Daines and Kohlstedt*, 1997] or variations in the wetting angle [*Walte et al.*, 2005]. In order to further explain this relationship between melt seam orientations and melt fractions more analogs and possibly numerical modeling is needed.

[57] In Type II microstructures the diffusion creep rates of both feldspars were effectively enhanced by the interstitial melt phase wetting their boundaries and leading to a rapid strength drop within the MCT field as proposed by [*Rosenberg and Handy*, 2005]. This is consistent with a low amount of melt <2% produced by the continuous metamorphic reaction in the absence of externally introduced fluid as inferred from petrological modeling. However, Type III microstructures are characterized by higher proportions of melt which can be produced by the introduction of external fluids into the system. The increase of the melt fraction is responsible for a substantial modification of the bulk deformation mechanism from crystalline plasticity assisted grain boundary sliding to granular flow.

9. Conclusions

[58] 1. Extreme weakness of feldspars is reported in midcrustal granite mylonite which is marked by disproportionately higher strain intensities of the feldspar polycrystalline aggregates compared to quartz.

[59] 2. Three types of microstructures corresponding to the evolutionary stages of deformed granite were recognized: Type I (metagranite marked by a viscous flow of plagioclase around the strong alkali feldspar and quartz), Type II (quartz augen orthogneiss characterized by the development of a banded mylonitic structure of recrystallized plagioclase and K-feldspar surrounding augens of quartz), and Type III (banded orthogneiss characterized by the alternation of quartz ribbons and mixed aggregates of feldspars and quartz).

[60] 3. The weakening of the alkali feldspar is achieved by the decomposition into albite chains and K-feldspar resulting from a heterogeneous nucleation process.

[61] 4. The extreme deformation of feldspars and their progressive mixing are attributed to syn-deformational melting of muscovite-biotite rich layers associated with the grain boundary sliding controlled diffusion creep of feldspars.

[62] 5. The strong quartz shows a dislocation creep deformation mechanism throughout the deformation history marked by the variations in activity of the slip systems, which are attributed to variations in the stress and strain rate partitioning with regard to changing rheological properties of the deforming feldspars.

[63] 6. The orientation of melt seams varies with increasing strain; this can be explained as a consequence of a concomitant increase in the melt fraction associated with a change in the far field and local stress field conditions.

[64] **Acknowledgments.** The grant to Stanislav Ulrich of the Research Council of the Czech Academy of Science is gratefully acknowledged. This study was made possible thanks to the ANR project "LFO in Orogens" funding as well as to financial support of CNRS (UMRs 7516 and 7517). We are grateful to Ed Sawyer and Denis Gapais for fruitful and constructive reviews.

References

Baratoux, L., K. Schulmann, S. Ulrich, and O. Lexa (2005), Contrasting microstructures and deformation mechanisms in metagabbro mylonites contemporaneously deformed under different temperatures (c. 650°C and c. 750°C), in *Deformation Mechanisms, Rheology and Tectonics: From the Minerals to the Lithosphere*, edited by D. Gapais, J. P. Brun, and P. R. Cobbold, *Geol. Soc. Spec. Publ.*, *243*, 97–125.

Bascou, J., G. Barruol, A. Vauchez, D. Mainprice, and M. Egydio-Silva (2001), EBSD-measured lattice-preferred orientations and seismic properties of eclogites, *Tectonophysics*, *342*, 61–80, doi:10.1016/S0040-1951(01)00156-1.

Beneš, K. (1964), Geologická mappá ČSSR, map, scale 1:200,000, Ústřední Ústav Geol., Prague.

Boullier, A. M., and Y. Guéguen (1975), SP-Mylonites: Origin of some mylonites by superplastic flow, *Contrib. Mineral. Petrol.*, *50*, 93–104, doi:10.1007/BF00373329.

Carter, N. L., and M. Tsenn (1987), Flow properties of continental lithosphere, *Tectonophysics*, *136*, 27–63, doi:10.1016/0040-1951(87)90333-7.

Cashman, K. V., and J. M. Ferry (1988), Crystal size distribution (CSD) in rocks and the kinetics and dynamics of crystallization III. Metamorphic crystallization, *Contrib. Mineral. Petrol.*, *99*, 401–415, doi:10.1007/BF00371933.

Coggon, R., and T. J. B. Holland (2002), Mixing properties of phengitic micas and revised garnet-phengite thermobarometers, *J. Metamorph. Geol.*, *20*, 683–696, doi:10.1046/j.1525-1314.2002.00395.x.

Cosgrove, J. W. (1997), The influence of mechanical anisotropy on the behaviour of the lower crust, *Tectonophysics*, *280*, 1–14.

Daines, M. J., and D. L. Kohlstedt (1997), Influence of deformation on melt topology in peridotites, *J. Geophys. Res.*, *102*, 10,257–10,272, doi:10.1029/97JB00393.

Dallain, C., K. Schulmann, and P. Ledru (1999), Textural evolution in the transition from subsolidus annealing to melting process, Velay Dome, French Massif Central, *J. Metamorph. Geol.*, *17*, 61–74, doi:10.1046/j.1525-1314.1999.00176.x.

Dell'Angelo, L. N., and J. Tullis (1988), Experimental deformation of partially melted granitic aggregates, *J. Metamorph. Geol.*, *6*, 495–515, doi:10.1111/j.1525-1314.1988.tb00436.x.

Dell'Angelo, L. N., and J. Tullis (1996), Textural and mechanical evolution with progressive strain in experimentally deformed aplite, *Tectonophysics*, *256*, 57–82, doi:10.1016/0040-1951(95)00166-2.

Dell'Angelo, L. N., J. Tullis, and R. A. Yund (1987), Transition from dislocation creep to melt-enhanced diffusion creep in fine-grained granitic aggregates, *Tectonophysics*, *139*, 325–332, doi:10.1016/0040-1951(87)90107-7.

Eudier, M. (1962), Mechanical properties of sintered low-alloy steels, *Powder Metall.*, *9*, 278–290.

Fitz Gerald, J. D., and H. Stünitz (1993), Deformation of granitoids at low metamorphic grades. I. Reactions and grainsize reduction, *Tectonophysics*, *221*, 269–297, doi:10.1016/0040-1951(93)90163-E.

Flinn, D. (1965), On the symmetry principle and the deformation ellipsoid, *Geol. Mag.*, *102*, 36–45.

Flinn, D. (1969), Grain contacts in crystalline rocks, *Lithos*, *3*, 361–370.

Franěk, J., K. Schulmann, and O. Lexa (2006), Kinematic and rheological model of exhumation of high pressure granulites in the Variscan orogenic root: Example of the Blanský les granulite, Bohemian Massif, Czech Republic, *Mineral. Petrol.*, *86*, 253–276, doi:10.1007/s00710-005-0114-4.

Gapais, D. (1989), Shear structures within deformed granites; mechanical and thermal indicators, *Geology*, *17*, 1144–1147, doi:10.1130/0091-7613(1989)017<1144:SSWDGM>2.3.CO;2.

Gapais, D., and B. Barbarin (1986), Quartz fabric transition in a cooling syntectonic granite (Hermitage massif, France), *Tectonophysics*, *125*, 357–370, doi:10.1016/0040-1951(86)90171-X.

Gay, N. C. (1968a), Pure shear and simple shear deformation of inhomogeneous viscous fluids. 1. Theory, *Tectonophysics*, *5*, 211–234, doi:10.1016/0040-1951(68)90065-6.

Gay, N. C. (1968b), Pure shear and simple shear deformation of inhomogeneous viscous fluids. 2. The deformation of the total finite strain in a rock from objects such as deformed pebbles, *Tectonophysics*, *5*, 295–302, doi:10.1016/0040-1951(68)90033-4.

Gleason, G. C., V. Bruce, and H. W. Green (1999), Experimental investigation of melt topology in partially molten quartzo-feldspathic aggregates under hydrostatic and non-hydrostatic stress, *J. Metamorph. Geol.*, *17*, 705–722, doi:10.1046/j.1525-1314.1999.00228.x.

Groebner, N., and D. L. Kohlstedt (2006), Deformation induced metal melt networks in silicates: Implications for core-mantle interactions in planetary bodies, *Earth Planet. Sci. Lett.*, *245*, 571–580, doi:10.1016/j.epsl.2006.03.029.

Handy, M. R. (1990), The solid-state flow of polymineralic rocks, *J. Geophys. Res.*, *95*, 8647–8661, doi:10.1029/JB095iB06p08647.

Handy, M. R. (1994a), The energetics of steady-state heterogeneous shear in mylonitic rock, *Mater. Sci. Eng. A*, *175*, 261–272, doi:10.1016/0921-5093(94)91065-0.

Handy, M. R. (1994b), Flow laws for rocks containing two non-linear viscous phases: A phenomenological approach, *J. Struct. Geol.*, *16*, 287–301, doi:10.1016/0191-8141(94)90035-3.

Handy, M. R., S. Wissing, and J. E. Streit (1999), Strength and structure of mylonite with combined frictional-viscous rheology and varied bimineralic composition, *Tectonophysics*, *303*, 175–191, doi:10.1016/S0040-1951(98)00251-0.

Hasalová, P., K. Schulmann, O. Lexa, P. Štípská, and F. Hrouda (2008), Origin of felsic migmatites by progressive destruction of metamorphic layering during ductile shearing and melt infiltration, *J. Metamorph. Geol.*, *26*, 29–53.

Heilbronner, R., and J. Tullis (2006), Evolution of c axis pole figures and grain size during dynamic recrystallization: Results from experimentally sheared quartzite, *J. Geophys. Res.*, *111*, B10202, doi:10.1029/2005JB004194.

Herwegh, M., M. R. Handy, and R. Heilbronner (1997), Temperature- and strain-rate-dependent microfabric evolution in monomineralic mylonite: Evidence from in situ deformation of norcamphor, *Tectonophysics*, *280*, 83–106, doi:10.1016/S0040-1951(97)00139-X.

Higgins, M. D. (1998), Origin of anorthosite by textural coarsening: Quantitative measurements of a natural sequence of textural development, *J. Petrol.*, *39*, 1307–1325, doi:10.1093/petrology/39.7.1307.

Hobbs, B. E. (1981), The influence of metamorphic environment upon the deformation of minerals, *Tectonophysics*, *78*, 335–383, doi:10.1016/0040-1951(81)90020-2.

Holland, T. J. B., and R. Powell (1998), An internally consistent thermodynamic data set for phases of petrological interest, *J. Metamorph. Geol.*, *16*, 309–343, doi:10.1111/j.1525-1314.1998.00140.x.

Holland, T. J. B., and R. Powell (2003), Activity-composition relations for phases in petrological calculations: An asymmetric multicomponent formulation, *Contrib. Mineral. Petrol.*, *145*, 492–501, doi:10.1007/s00410-003-0464-z.

Hubbert, M. K., and W. W. Rubey (1959), Role of fluid pressure in mechanics of overthrust faulting, *Geol. Soc. Am. Bull.*, *70*, 116–166.

Jaoul, O., J. Tullis, and A. Kronenberg (1984), The effect of varying water contents on the creep behavior of Heavitree Quartzite, *J. Geophys. Res.*, *89*, 4298–4312, doi:10.1029/JB089iB06p04298.

Ji, S., and P. Zhao (1994), Strength of two-phase rocks: A model based on fiber-loading theory, *J. Struct. Geol.*, *16*, 253–262, doi:10.1016/0191-8141(94)90108-2.

Ji, S., R. Wirth, E. Rybacki, and J. Zhenting (2000), High-temperature plastic deformation of quartz-plagioclase multilayers by layer-normal compression, *J. Geophys. Res.*, *105*, 16,651–16,664, doi:10.1029/2000JB900130.

Jordan, P. G. (1987), The deformational behaviour of bimineralic limestone-halite aggregates, *Tectonophysics*, *135*, 185–197, doi:10.1016/0040-1951(87)90160-0.

Jordan, P. G. (1988), The rheology of polymineralic rocks — An approach, *Geol. Rundsch.*, *77*, 285–294, doi:10.1007/BF01848690.

Kachlík, V. (1999), Relationship between Maldanubicum (Central Bohemia, Czech Republic): A result of the polyphase Variscan nappe tectonics, *J. Czech Geol. Soc.*, *44*, 201–291.

Kassner, M. E., and T. A. Hayes (2003), Creep cavitation in metals, *Int. J. Plast.*, *19*, 1715–1748, doi:10.1016/S0749-6419(02)00111-0.

Kretz, R. (1969), On the spatial distribution of crystals in rocks, *Lithos*, *2*, 39–66, doi:10.1016/S0024-4937(69)80005-8.

Kretz, R. (1983), Symbols for rock-forming minerals, *Am. Mineral.*, *68*, 277–279.

Kronenberg, A., and J. Tullis (1984), Flow strengths of quartz aggregates; grain size and pressure effects due to hydrolytic weakening, *J. Geophys. Res.*, *89*, 4281–4297, doi:10.1029/JB089iB06p04281.

Kruhl, J. H. (1996), Prism- and basal-plane parallel subgrain boundaries in quartz: A microstructural geothermobarometer, *J. Metamorph. Geol.*, *14*, 581–589, doi:10.1046/j.1525-1314.1996.00413.x.

Kruse, R., and H. Stünitz (1999), Deformation mechanisms and phase distribution in mafic high-temperature mylonites from the Jotun Nappe, southern Norway, *Tectonophysics*, *303*, 223–249, doi:10.1016/S0040-1951(98)00255-8.

Kruse, R., H. Stünitz, and K. Kunze (2001), Dynamic recrystallization processes in plagioclase porphyroclast, *J. Struct. Geol.*, *23*, 1781–1802, doi:10.1016/S0191-8141(01)00030-X.

Lexa, O., P. Štípská, K. Schulmann, L. Baratoux, and A. Kröner (2005), Contrasting textural record of two distinct metamorphic events of similar P-T conditions and different durations, *J. Metamorph. Geol.*, *23*, 649–666, doi:10.1111/j.1525-1314.2005.00601.x.

Marchildon, N., and M. Brown (2003), Spatial distribution of melt-bearing structures in anatectic rocks from Southern Brittany: Implications for melt-transfer at grain- to orogen-scale, *Tectonophysics*, *364*, 215–235, doi:10.1016/S0040-1951(03)00061-1.

Martelat, J.-E., K. Schulmann, J.-M. Lardeaux, and C. Nicollet (1999), Granulite microfabric and deformation mechanisms in southern Madagascar, *J. Struct. Geol.*, *21*, 671–687, doi:10.1016/S0191-8141(99)00052-8.

McLellan, E. L. (1983), Contrasting textures in metamorphic and anatectic migmatites: An example from the Scottish Caledonides, *J. Metamorph. Geol.*, *1*, 241–262, doi:10.1111/j.1525-1314.1983.tb00274.x.

Medaris, L. G., J. H. Fournelle, E. D. Ghent, E. Jelínek, and Z. Mísař (1998), Prograde eclogite in the Gföhl Nappe, Czech Republic: New evidence on Variscan high-pressure metamorphism, *J. Metamorph. Geol.*, *16*, 563–576, doi:10.1111/j.1525-1314.1998.00158.x.

Montardi, Y., and D. Mainprice (1987), A transmission electron microscopic study of the plastic deformation of calcic plagioclase (An 68–70), *Bull. Mineral.*, *110*, 1–14.

Olsen, T. S., and D. L. Kohlstedt (1985), Natural deformation and recrystalization of some intermediate plagioclase feldspars, *Tectonophysics*, *111*, 107–131, doi:10.1016/0040-1951(85)90067-8.

Park, Y., and W. D. Means (1996), Direct observation of deformation processes in crystal mushes, *J. Struct. Geol.*, *18*, 847–858, doi:10.1016/S0191-8141(96)80017-4.

Peterson, T. D. (1996), A refined technique for measuring crystal size distributions in thin section, *Contrib. Mineral. Petrol.*, *124*, 395–405, doi:10.1007/s004100050199.

Pitra, P., and M. Guiraud (1996), Probable anticlockwise P-T evolution in extending crust: Hlinsko region, Bohemian Massif, *J. Metamorph. Geol.*, *14*, 49–60, doi:10.1111/j.1525-1314.1996.t01-1-00049.x.

Powell, R., and T. J. B. Holland (2004), Course notes for "THERMOCALC Workshop 2004: Calculating metamorphic phase equilibria [CD-ROM], report, Eidg. Tech. Hochsch., Zurich, Zurich, Switz.

Powell, R., T. Holland, and B. Worley (1998), Calculating phase diagrams involving solid solutions via non-linear equations, with examples using THERMOCALC, *J. Metamorph. Geol.*, *16*, 577–588, doi:10.1111/j.1525-1314.1998.00157.x.

Putnis, A., C. M. Pina, J. M. Astilleros, L. Fernández-Díaz, and M. Prieto (2003), Nucleation of solid solutions crystallizing from aqueous solutions, *Philos. Trans. R. Soc. London, Ser. A*, *361*, 615–632, doi:10.1098/rsta.2002.1142.

Ramsay, J. G., and M. I. Huber (1983), *The Techniques of Modern Structural Geology*, vol. 1, *Strain Analysis*, 307 pp., Elsevier, London.

Ranalli, G. (1995), *Rheology of the Earth*, 2nd ed., 366 pp., CRC Press, London.

Ranalli, G., and D. C. Murphy (1987), Rheological stratification of the lithosphere, *Tectonophysics*, *132*, 281–295, doi:10.1016/0040-1951(87)90348-9.

Randolph, A. D., and M. A. Larson (1971), *Theory of Particle Processes*, 251 pp., Elsevier, San Diego, Calif.

Ribbe, P. H. (1983), Chemistry structure and nomenclature of feldspars, in *Feldspar Mineralogy*, *Rev. Mineral.*, vol. 2, 2nd ed., edited by P. H. Ribbe, pp. 21–55, Mineral. Soc. of Am., Washington, D. C.

Rosenberg, C. L., and A. Berger (2001), Syntectonic melt pathways in granite, and melt-induced transition in deformation mechanisms, *Phys. Chem. Earth, Part A*, *26*, 287–293.

Rosenberg, C. L., and M. R. Handy (2000), Syntectonic melt pathways during simple shearing of a partially molten rock analogue (Norcamphor-Benzamide), *J. Geophys. Res.*, *105*, 3135–3149, doi:10.1029/1999JB900371.

Rosenberg, C. L., and M. R. Handy (2005), Experimental deformation of partially melted granite revisited: Implications for the continental crust,

J. Metamorph. Geol., *23*, 19–28, doi:10.1111/j.1525-1314.2005.00555.x.

Rybacki, E., and G. Dresen (2004), Deformation mechanism maps for feldspar rocks, *Tectonophysics*, *382*, 173–187, doi:10.1016/j.tecto.2004.01.006.

Sawyer, E. W. (2001), Melt segregation in the continental crust: Distribution and movement of melt in anatectic rocks, *J. Metamorph. Geol.*, *19*, 291–309, doi:10.1046/j.0263-4929.2000.00312.x.

Scaillet, B., C. France-Lanord, and P. Le Fort (1990), Badrinath-Gangotri plutons (Garhwal, India): Petrological and geochemical evidence for fractionation processes in a high Himalayan leucogranite, *J. Volcanol. Geotherm. Res.*, *44*, 163–188, doi:10.1016/0377-0273(90)90017-A.

Schmid, S. M. (1982), Microfabric studies as indicators of deformation mechanisms and flow laws operative in mountain building, in *Mountain Building Processes*, edited by K. J. Hsü, pp. 95–110, Elsevier, London.

Schmid, S. M., and M. Casey (1986), Complete fabric analysis of some commonly observed quartz c-axis patterns, in *Mineral and Rock Deformation: Laboratory Studies*, *Geophys. Monogr. Ser.*, vol. 36, edited by B. E. Hobbs and H. C. Heard, pp. 263–286, AGU, Washington, D. C.

Schmid, S. M., R. Panozzo, and S. Bauer (1987), Simple shear experiments on calcite rocks: Rheology and microfabric, *J. Struct. Geol.*, *9*, 747–778, doi:10.1016/0191-8141(87)90157-X.

Schmid, S. M., R. Heilbronner, and H. Stünitz (1999), Deformation mechanisms in nature and experiment (editorial remarks), *Tectonophysics*, *303*, vii–ix, doi:10.1016/S0040-1951(98)00302-3.

Schulmann, K., B. Mlcoch, and R. Melka (1996), High-temperature microstructures and rheology of deformed granite, Erzgebirge, Bohemian Massif, *J. Struct. Geol.*, *18*, 719–733, doi:10.1016/S0191-8141(96)80007-1.

Schulmann, K., A. Kröner, E. Hegner, I. Wendt, J. Konopásek, O. Lexa, and P. Štípská (2005), Chronological constraints on the pre-orogenic history, burial and exhumation of deep-seated rocks along the eastern margin of the Variscan Orogen, Bohemian Massif, Czech Republic, *Am. J. Sci.*, *305*, 407–448, doi:10.2475/ajs.305.5.407.

Simpson, C. (1985), Deformation of granitic rocks across the brittle-ductile transition, *J. Struct. Geol.*, *7*, 503–511, doi:10.1016/0191-8141(85)90023-9.

Sklenička, V., J. Saxl, and J. Čadek (1977), Intercrystalline fracturing at high temperature creep of metals and alloys (in Czech), report, 108 pp., Czech. Acad. of Sci., Prague.

Stünitz, H., and J. D. Fitz Gerald (1993), Deformation of granitoids at low metamorphic grades. II. Granular flow in albite-rich mylonites, *Tectonophysics*, *221*, 299–324, doi:10.1016/0040-1951(93)90164-F.

Synek, J., and D. Oliverová (1993), Terrane character of the north-east margin of the Moldanubian Zone: The Kutná Hora Crystalline Complex, Bohemian Massif, *Geol. Rundsch.*, *82*, 566–582, doi:10.1007/BF00212417.

Tajcmanová, L., J. Konopásek, and K. Schulmann (2006), Thermal evolution of the orogenic lower crust during exhumation within a thickened Moldanubian root of the Variscan belt of Central Europe, *J. Metamorph. Geol.*, *24*, 119–134, doi:10.1111/j.1525-1314.2006.00629.x.

Tharp, T. M. (1983), Analogies between the high-temperature deformation of polyphase rocks and the mechanical behavior of porous powder metal, *Tectonophysics*, *96*, 1–11, doi:10.1016/0040-1951(83)90216-0.

Thompson, A. B., and J. A. D. Connolly (1995), Melting of the continental crust: Some thermal and petrological constraints on anatexis in continental collision zones and other tectonic settings, *J. Geophys. Res.*, *100*, 15,565–15,580, doi:10.1029/95JB00191.

Treagus, S. H. (2002), Modelling the bulk vicosity of two-phase mixtures in term of clast shape, *J. Struct. Geol.*, *24*, 57–76, doi:10.1016/S0191-8141(01)00049-9.

Tullis, J. (1983), Deformation of feldspars, in *Feldspar Mineralogy*, *Rev. Mineral.*, vol. 2, 2nd ed., edited by P. H. Ribbe, pp. 297–323, Mineral. Soc. of Am., Washington, D. C..

Tullis, J. (1990), Experimental studies of deformation mechanisms and microstructures in quartzo-feldspathic rocks, in *Deformation Processes in Minerals, Ceramics and Rocks*, edited by D. Barbour and P. Meredith, pp.190–227, CRC Press, Cambridge, U. K.

Walte, N. P., P. D. Bons, and C. W. Passchier (2005), Deformation of melt-bearing systems — Insight from in situ grain-scale analogue experiments, *J. Struct. Geol.*, *27*, 1666–1679, doi:10.1016/j.jsg.2005.05.006.

White, J. C., and C. K. Mawer (1986), Extreme ductility of feldspars from a mylonite, Parry Sound, Canada, *J. Struct. Geol.*, *8*, 133–143, doi:10.1016/0191-8141(86)90104-5.

White, J. C., and C. K. Mawer (1988), Dynamic recrystallization and associated in perthites: Evidence of deep crustal thrusting, *J. Geophys. Res.*, *93*, 325–337, doi:10.1029/JB093iB01p00325.

White, R. W., R. Powell, and T. J. B. Holland (2001), Calculation of partial melting equilibria in the system $Na_2O-CaO-K_2O-FeO-MgO-Al_2O_3-SiO_2-H_2O$ (NCKFMASH), *J. Metamorph. Geol.*, *19*, 139–153, doi:10.1046/j.0263-4929.2000.00303.x.

Závada, P., K. Schulmann, J. Konopásek, O. Lexa, and S. Ulrich (2007), Melt topology in deformed quartzo-feldspathic rocks: Implication for rheology and grain-scale migration of melt in partially molten crust, *J. Geophys. Res.*, *112*, B10210, doi:10.1029/2006JB004820.

J. K. Becker, Institut für Geowissenschaften, Universität Tübingen, Sigwartstrasse 10, D-72076 Tübingen, Germany.

O. Lexa, Institute of Petrology and Structural Geology, Charles University, Albertov 6, 12843 Praha 2, Czech Republic.

J.-E. Martelat, Laboratoire de Géodynamique des Chaînes Alpines, UMR5025, Université Joseph Fourier, Observatoire des Sciences de l'Univers de Grenoble, CNRS, F-38041 Grenoble Cedex 9, France.

K. Schulmann and P. Štípská, Centre de Géochimie de la Surface, UMR7516, Université Louis Pasteur, CNRS, F-67084 Strasbourg Cedex, France.

S. Ulrich, Geophysical Institute, Czech Academy of Sciences, Bočni II/1401, 14131 Praha 4, Czech Republic.

Available online at www.sciencedirect.com
ScienceDirect
C. R. Geoscience 341 (2009) 266–286
COMPTES RENDUS GEOSCIENCE

Tectonics

An Andean type Palaeozoic convergence in the Bohemian Massif

Karel Schulmann [a,*], Jiří Konopásek [b,c], Vojtěch Janoušek [b], Ondrej Lexa [c], Jean-Marc Lardeaux [d], Jean-Bernard Edel [a], Pavla Štípská [a], Stanislav Ulrich [e]

[a] *EOST, UMR 7517, université Louis-Pasteur, 1, rue Blessig, 67084 Strasbourg, France*
[b] *Czech Geological Survey, Klárov 3, 118 21 Praha 1, Czech Republic*
[c] *Institute of Petrology and Structural geology, Charles University, Albertov 6, 128 43 Prague, Czech Republic*
[d] *Géosciences Azur, UMR CNRS 6526, université de Nice Sophia-Antipolis, parc Valrose, 06108 Nice cedex 02, France*
[e] *Geophysical Institute, Czech Academy of Sciences, Boční II/1401, 141 31 Praha 4, Czech Republic*

Received 24 December 2008; accepted after revision 24 December 2008
Available online 25 February 2009

Written on invitation of the Editorial Board

Abstract

The geological inventory of the Variscan Bohemian Massif can be summarized as a result of Early Devonian subduction of the Saxothuringian ocean of unknown size underneath the eastern continental plate represented by the present-day Teplá-Barrandian and Moldanubian domains. During mid-Devonian, the Saxothuringian passive margin sequences and relics of Ordovician oceanic crust have been obducted over the Saxothuringian basement in conjunction with extrusion of the Teplá-Barrandian middle crust along the so-called Teplá suture zone. This event was connected with the development of the magmatic arc further east, together with a fore-arc basin on the Teplá-Barrandian crust. The back-arc region – the future Moldanubian zone – was affected by lithospheric thinning which marginally affected also the eastern Brunia continental crust. The subduction stage was followed by a collisional event caused by the arrival of the Saxothuringian continental crust that was associated with crustal thickening and the development of the orogenic root system in the magmatic arc and back-arc region of the orogen. The thickening was associated with depression of the Moho and the flux of the Saxothuringian felsic crust into the root area. Originally subhorizontal anisotropy in the root zone was subsequently folded by crustal-scale cusp folds in front of the Brunia backstop. During the Visean, the Brunia continent indented the thickened crustal root, resulting in the root's massive shortening causing vertical extrusion of the orogenic lower crust, which changed to a horizontal viscous channel flow of extruded lower crustal material in the mid- to supra-crustal levels. Hot orogenic lower crustal rocks were extruded: (1) in a narrow channel parallel to the former Teplá suture surface; (2) in the central part of the root zone in the form of large scale antiformal structure; and (3) in form of hot fold nappe over the Brunia promontory, where it produced Barrovian metamorphism and subsequent imbrications of its upper part. The extruded deeper parts of the orogenic root reached the surface, which soon thereafter resulted in the sedimentation of lower-crustal rocks pebbles in the thick foreland Culm basin on the stable part of the Brunia continent. Finally, during the Westfalian, the foreland Culm wedge was involved into imbricated nappe stack together with basement and orogenic channel flow nappes. ***To cite this article: K. Schulmann et al., C. R. Geoscience 341 (2009).***

Résumé

Convergence paléozoïque de type Andin dans le Massif de Bohême. Le Massif varisque de Bohême est le résultat de la subduction, au Dévonien supérieur, de l'océan Saxothuringien sous la plaque continentale représentée à l'est par les zones actuelles

* Corresponding author.
E-mail address: schulmann.karel@gmail.com (K. Schulmann).

1631-0713/$ – see front matter © 2009 Published by Elsevier Masson SAS on behalf of Académie des sciences.
doi:10.1016/j.crte.2008.12.006

de Teplá-Barrandien et de Moldanubien. L'ampleur de cet océan demeure inconnue. Pendant le Dévonien moyen, les séries sédimentaires de la marge passive saxothuringienne et les reliques de la croûte océanique ordovicienne ont été obductées sur le socle saxothuringien alors que, dans le même temps, la croûte moyenne Teplá-barrandienne était extrudée le long de la suture de Teplá. Plus à l'est, cet événement était associé au développement d'un arc magmatique et à la formation d'un bassin avant-arc sur le socle Teplá-Barrandien. Le domaine arrière-arc – la future zone moldanubienne – subissait un amincissement lithosphérique qui affectait aussi en partie la croûte continentale de Brunia. La subduction s'est achevée avec la collision de la croûte continentale saxothuringienne et s'est traduite par un épaississement crustal et la formation d'une racine orogénique dans les zones de l'arc magmatique et de l'arrière-arc. L'épaississement était associé à une dépression du Moho et au flux de croûte felsique saxothuringienne dans la racine orogénique. L'anisotropie sub-horizontale de la racine a donné suite à un plissement serré, d'échelle crustale, au front du butoir continental de Brunia. Pendant le Viséen, le continent Brunia a indenté la racine crustale épaissie en provoquant un important raccourcissement de la racine, l'extrusion verticale de la croûte inférieure de l'orogène passant à un flux visqueux en chenal horizontal, de matériaux de la croûte inférieure à des niveaux médio- et supra-crustaux. Les roches de la croûte inférieure orogénique ont été extrudées (1) dans d'étroits chenaux parallèles à la surface de l'ancienne suture de Teplá, (2) au centre de la zone de racine sous la forme d'un large antiforme et (3) en nappe plissée chaude au-dessus du promontoire de Brunia, tout en produisant un métamorphisme barrovien, ainsi que l'imbrication des niveaux supérieurs. Les roches extrudées les plus profondes de la racine ont atteint la surface, puis ont été reprises, peu de temps après, sous la forme de galets dans la sédimentation de type Culm dans l'épais bassin d'avant-pays qui recouvre la partie stable du continent Brunia. Enfin, pendant le Westphalien, le prisme d'accrétion du Culm, ainsi que le socle et les nappes de chenaux crustaux ont été repris dans une suite de nappes imbriquées. ***Pour citer cet article : K. Schulmann et al., C. R. Geoscience 341 (2009).***

Keywords: Bohemian Massif; Saxothuringian oceanic subduction; Building of Variscan orogenic root system; Channel flow

Mots clés : Massif de Bohême ; Subduction océanique saxothuringienne ; Formation de la racine orogénique varisque ; Flux en chenal

1. Introduction

Starting with [16] and followed by [33] and [93,94], the eastern Variscan belt is interpreted as the result of Devonian to Carboniferous continent–continent collision, resembling the (sub-)recent Himalayan-Tibetan type collisional system. However, there is a wealth of data (see for example [93,94]) suggesting that this orogenic belt could have resulted from an Andean type convergence, i.e. as a typical upper plate orogen located above a long-lasting Devonian–Carboniferous subduction system.

The aim of this article is to show that all the current criteria defining an Andean type of convergent margin are present and surprisingly well preserved in the Variscan Bohemian Massif. These criteria are in particular [66,71,122,157]:

- the development of Franciscan type blueschist-facies metamorphism in the lower plate;
- arc type magmatism marked by calc-alkaline to potassium-rich (shoshonitic) series in the distance of 150–200 km from the trench;
- back-arc basin developed on continental upper plate crust and replaced by thick continental root;
- deep granulite-facies metamorphism associated with supposed underplating of the crust by mafic magmas at the bottom of the root;
- continental lithosphere thrust underneath the thickened root system.

Based on these criteria, the architecture of the eastern Variscan belt is interpreted as the result of a large-scale and long-lasting subduction process associated with crustal tectonics, metamorphism, magmatic and sedimentary additions that developed over the width of at least 500 km, in present-day coordinates, and time scale of ∼80 Ma.

2. Present-day architecture of the Bohemian Massif and location of Palaeozoic sutures

The Bohemian Massif occurs at the eastern extremity of the European Variscan belt, representing one of its largest exposures (Fig. 1). From west to east, the Eastern Variscan belt forming the Bohemian Massif can be subdivided into four major units:

- the Saxothuringian Neoproterozoic basement with its Palaeozoic cover corresponding to the continental crust of the Armorican plate [87,105,147];
- the Teplá-Barrandian Unit consisting of Neoproterozoic basement and its Early Palaeozoic cover interpreted as an independent crustal block (the Bohemia Terrane of South Armorica *sensu* [34]);
- the Moldanubian high- to medium-grade metamorphic domain intruded by numerous Carboniferous

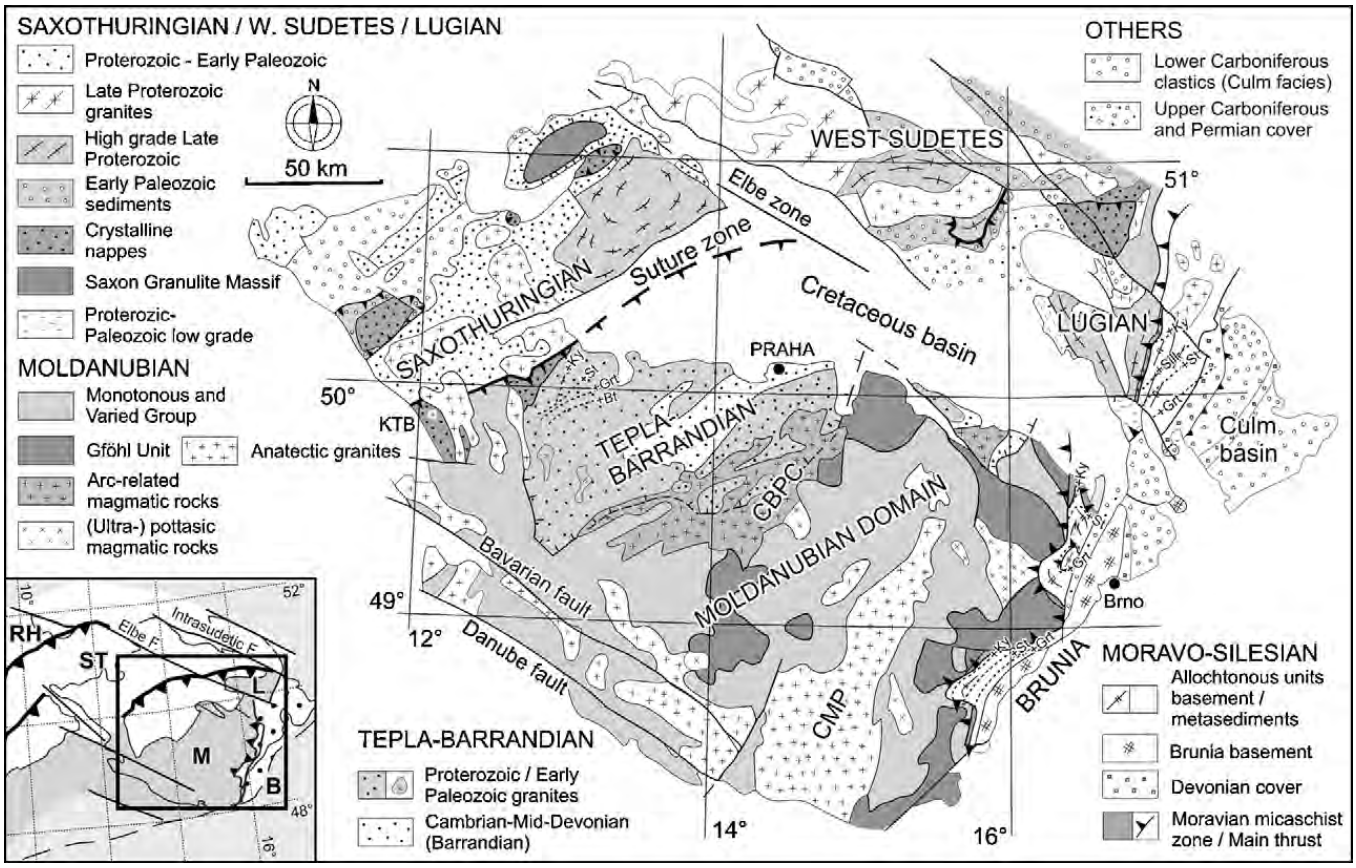

Fig. 1. Simplified geological map of the Bohemian Massif (modified after [34]). CBPC: Central Bohemian Plutonic Complex; CMP: Central Moldanubian Pluton. The lower left insert shows position of the Bohemian Massif in the frame of the European Variscides (modified [22]). RH: Rhenohercynian zone; ST: Saxothuringian Zone; M: Moldanubian Zone; B: Brunia Continent; L: Lugian domain.

Fig. 1. Carte géologique simplifiée du Massif de Bohême (modifiée d'après [34]). CBPC : Complexe plutonique de Bohême centrale ; CMP : Pluton central moldanubien. L'encart du bas à gauche montre la position du Massif de Bohême dans le cadre des Variscides européennes (modifié d'après [22]). RH : Zone rhénohercynienne ; ST : Zone saxothuringienne ; M : Zone moldanubienne ; B : Brunia ; L : Zone lugienne.

granitic plutons, altogether forming the high-grade core of the orogeny;

- the eastern Brunia Neo-Proterozoic basement with Early to Late Palaeozoic cover [35,140].

The palaeontological record of Lower Palaeozoic (Cambrian and Ordovician) sediments of the Saxothuringian and Teplá-Barrandian domains shows affinities to the Gondwana faunas implying that these blocks were derived from the northern Gondwana margin [20,27,28,68]. In addition, there is a range of isotopic and U–Pb zircon data suggesting a Gondwanan provenance of all units composing the Bohemian Massif [96,106].

2.1. Saxothuringian domain

This domain is represented by Neoproterozoic par-autochthonous rocks (580–550 Ma) formed by migmatites and paragneisses intruded by Cambro-Ordovician calc-alkaline porphyritic granitoids converted to augen orthogneiss during the Variscan orogeny [38,39,76,89]. These rocks are unconformably covered by Cambrian and Ordovician rift sequences (Fig. 1) overlain by Late Ordovician to Famennian pelagic sediments and Famennian to Visean flysh of the Thuringian facies [85,125,144]. The par-autochthon is overthrust by allochthonous units containing deep-water equivalents of the Ordovician to Devonian rocks of the para-autochthon, and by proximal flysh sediments (the Bavarian facies).

The allochthonous units occur in Münchberg, Wildenfels and Frankenberg klippens and exhibit pile of thrust sheets marked by decreasing pressure and metamorphic age from the top to the bottom [34]. In the hangingwall occur thrust sheets with Mid-Ocean Ridge Basalt (MORB)-type metabasites of Ordovician protolith age eclogitized (Fig. 2; $P = \sim 25$ kbar, $T = 650$ °C)

[34] during the Devonian ~395 Ma [102]. Structurally deeper occur sheets marked by medium pressure (MP) assemblages and Late Devonian (~365 Ma) zircon and hornblende cooling ages. This rock pile represents both distal and proximal Late Ordovician to Devonian passive margin rocks tectonically inverted during the Devonian convergence [44,134]. In the Sudetic part (Figs. 1 and 2) of the Bohemian Massif, the Ordovician rift sequences are well developed and marked by the presence of deep marine sediments and MORB-type volcanics followed by Silurian and Devonian sedimentary sequences [95]. The Ordovician oceanic rocks are enhanced by a blueschist-facies metamorphic overprint of Late Devonian age [33,34].

However, a later Carboniferous underthrusting of the Saxothuringian/Armorican continental rocks underneath the easterly Teplá-Barrandian block was identified suggesting a continuous convergence in this area, which was responsible for eclogitization of both the oceanic and continental crust resulting from continental underthrusting [90] at ~340 Ma [71]. The continental underthrusting reached even the pressure conditions of the diamond stability [150]. This event is responsible for the global reworking of the Saxothuringian terrane at HP conditions, imbrication of subducted continental crust and exhumation of deep rocks in form of crustal scale nappes [92]. Thus, the structure of the Saxothurinigian domain is defined by par-autochthonous domain (Fig. 2; $P = 13–15$ kbar, $T = 580–630$ °C) [69,70,72] and eclogite-bearing ''lower'' crustal nappe ($P = 20–26$ kbar, $T = 630–700$ °C) [70]. The highest tectonic unit, ''the upper nappe'' reached the high pressure (HP) granulite facies peak conditions ($P = 15–20$ kbar, $T = 800$ °C [69,116]) at 340 Ma [79,154]. The exhumation of granulite facies unit occurred at 340 Ma as shown by $^{40}Ar/^{39}Ar$ cooling ages [80,83].

2.2. The Saxothuringian–Teplá-Barrandian boundary

The boundary between the two crustal domains is characterized by the presence of units with high proportion of ultramafic and mafic rocks (Fig. 1; Mariánské Lázně Complex and Erbendorf–Vohenstrauss Zone). The former complex is marked by a presence of serpentinites at the bottom overlain by a thick sequence of amphibolites, eclogites and metagabbros. The U–Pb zircon protolith ages discriminate the mafic rocks into two main groups with Cambrian (~540 Ma [145]) and Ordovician (~496 Ma [5]) ages. On the other hand, the metamorphic and cooling ages (Sm–Nd garnet–pyroxene and Ar–Ar hornblende) are Devonian, ranging between 410 and 370 Ma [4,15]). Similarly, the newly determined U–Pb ages for metamorphic zircon in mafic rocks, as well as monazite from orthogneiss, and titanite in leucosome all cluster around 380 Ma and possibly date the exhumation of the whole Mariánské Lázně Complex [163]. The Devonian metamorphic evolution started with eclogite-facies metamorphism (Fig. 2; $P = 16–18$ kbar, $T = 640–715$ °C) [145] and continued at *c.* 380 Ma by granulite-facies re-equilibration [99]. The Erbendorf–Vohenstrauss Zone further west shows similar lithological and petrological zonation as the Mariánské Lázně Complex and it is thus commonly interpreted as a part of the same tectonic unit [101,145].

2.3. Teplá-Barrandian domain

Stratigraphically, the Teplá-Barrandian Unit (Fig. 1) consists of Neoproterozoic basement with the lower arc-related volcano-sedimentary sequence (the Kralupy–Zbraslav Group), followed by siliceous black shales and a flyshoid sequence (shales, greywackes and conglomerates, [35]). The Neoproterozoic basement is unconformably overlain by a thick sequence (1500–2000 m) of Lower Cambrian conglomerates, greywackes, and sandstones [19,82] followed by shales and a rift-related volcanic sequence in the Upper Cambrian. The development of the Lower Palaeozoic Prague Basin [17] is marked by Early Ordovician (Tremadocian) transgression followed by mid-Ordovician rifting associated with volcanic activity, and with sedimentation of Silurian graptolite shales. The sedimentation continued mainly with carbonates, namely the Upper Silurian to Devonian calcareous flyshoid sequence. The Early Silurian was associated with important volcanic activity, accompanied by basaltic and ultramafic intrusions [51]. The sedimentation terminated in mid-Devonian with distal turbidites of the Srbsko Formation (Givetian) containing, among others, detrital zircons of Devonian (~390 Ma) age [108].

The whole sequence is folded by steep folds presumably of Late Devonian age as shown by Culm facies sediments unconformably deposited on folded Ordovician strata [135]. The deformation affected also the underlying Neoproterozoic basement, having intensity and age increasing progressively to the west. In the same direction rises also the metamorphic grade reaching amphibolite-facies conditions close to the Teplá-Barrandian/Saxothuringian boundary [10]. In this area is developed a typical Barrovian metamorphic zonation ranging from biotite–garnet zone (Fig. 2a; $P = 3–4$ kbar, $T = 450–520$ °C) [146,156,160,161] in

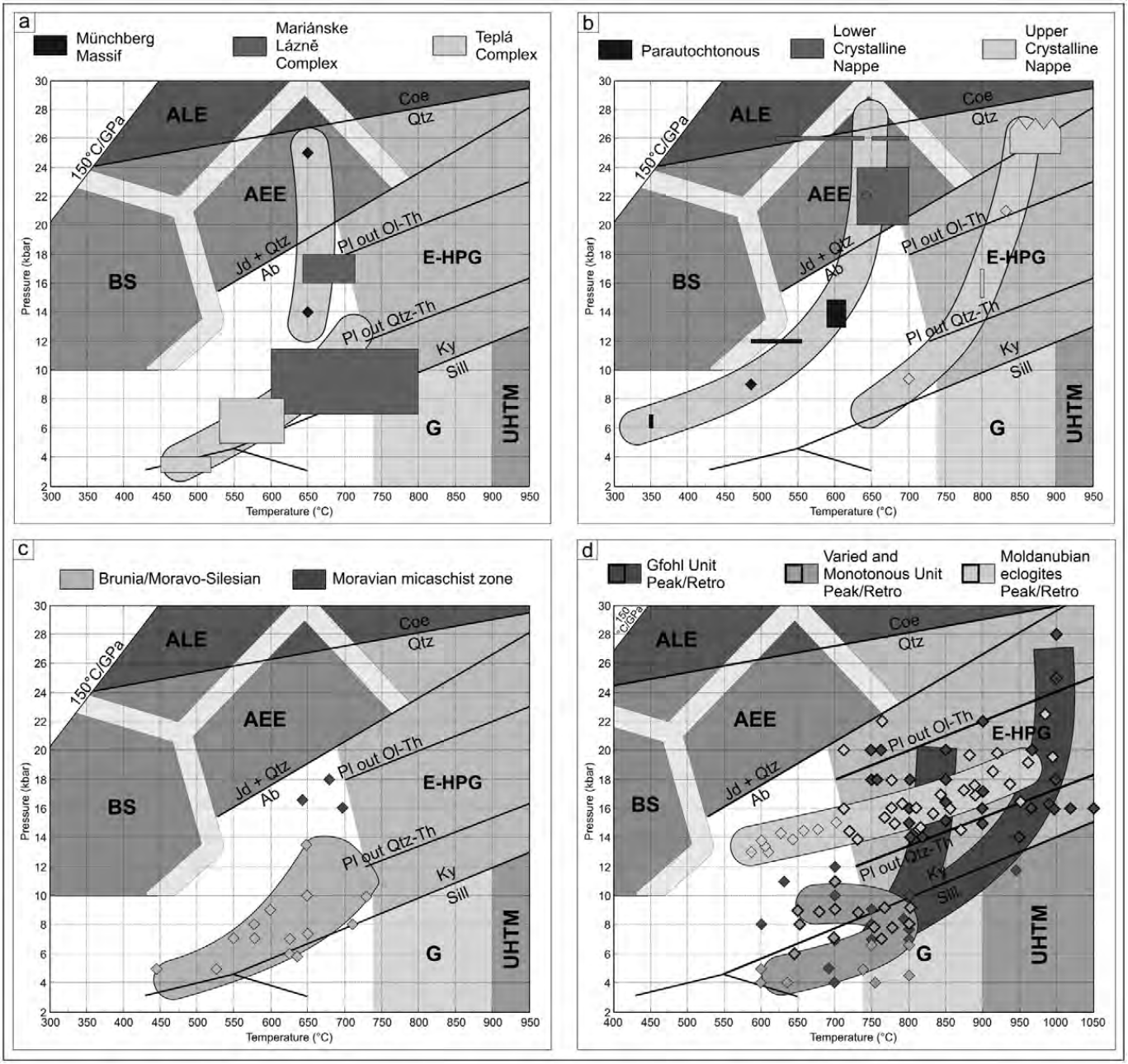

Fig. 2. Pressure–temperature (*P–T*) diagram showing the location of the principal metamorphic facies in the *P–T* space (after Brown, [6]). BS: blueschist facies; AEE: amphibole-epidote eclogite facies; ALE: amphibole-lawsonite eclogite facies; LE: lawsonite eclogite facies; AE: amphibole eclogite facies; GS: greenschist facies; A: amphibolite facies; E-HPG: medium-temperature eclogite facies – high-pressure granulite metamorphism; G: granulite facies; UHTM: the ultra-high-temperature metamorphic part of the granulite facies. **a**: Devonian HP–LT metamorphism (390–380 Ma) from the Münchberg and Mariánské Lázně units contrasted to Devonian (380 Ma) MP metamorphism of the western part of the Teplá-Barrandian; **b**: Carboniferous (340 Ma) HP–LT metamorphism from the Saxothuringian par-autochthon and lower nappe contrasted to the HP–HT metamorphism of the granulite bearing upper nappe (modified after [71]); **c**: Carboniferous (340 Ma) HP–HT metamorphism of the orogenic lower crustal belt from the Moldanubian domain, HT–MP and LP metamorphism related to the exhumation of the orogenic lower crust contrasted to the MP–MT peak metamorphism of the orogenic middle crust followed by heating during exhumation (modified after [123]; **d**: Carboniferous HP–MT metamorphism of the Moravian eclogites contrasted to the MP–MT Barrovian metamorphism of the Moravian Zone (modified after [77]).

Fig. 2. Diagramme pression–temperature (*P–T*) montrant la localisation des principaux faciès métamorphiques dans l'espace *P–T* (d'après [6]). BS : faciès schiste bleu ; AEE : faciès éclogitique à amphibole-épitote ; ALE : faciès éclogitique à amphibole-lawsonite ; LE : faciès éclogitique à lawsonite ; E-HPG : métamorphisme à éclogite de moyenne température et à granulite de haute pression ; G : faciès granulite ; UHTM : partie métamorphique d'ultrahaute température du faciès granulite. **a** : métamorphisme dévonien HP–LT (390–380 Ma) des unités de Münchberg et Mariánské Lázně contrastant avec le métamorphisme MP (380 Ma) de la partie occidentale de l'unité de Teplá-Barrandien ; **b** : métamorphisme carbonifère HP–LT (340 Ma) du parautochtone Saxothuringien et de la nappe inférieure, contrastant avec le métamorphisme HP–HT de la granulite

the east up to kyanite zone (Figs. 1 and 2a; $P = 5–8$ kbar, $T = 530–620$ °C) [156] in the west marked by a ''normal'' gradient (increase of pressure and temperature to the structural footwall). The $^{40}Ar/^{39}Ar$ muscovite and hornblende dating yielded exclusively Middle Devonian cooling ages [155].

2.4. The Teplá-Barrandian–Moldanubian domains boundary – the Central Bohemian Plutonic Complex

The igneous activity in the area of the Central Bohemian Plutonic Complex (Fig. 1) started with intrusions of calc-alkaline Devonian (protolith ~370 Ma) tonalites to granodiorites, latter transformed into highly sheared orthogneisses [74]. The first unmetamorphosed plutonic rocks were Late Devonian (~354 Ma) calc-alkaline tonalites, granodiorites, trondhjemites, quartz diorites and gabbros of the Sázava suite [62,64,158]. Their Sr–Nd isotopic ratios and trace-element signature indicate that the source of the basic magmas was a slightly depleted mantle above a subduction zone. In addition, a significant role for mixing with acidic magmas is to be assumed [60,64]. Further south/southeast occur voluminous Early Carboniferous (~349–346 Ma [18,55,56]) high-K calc-alkaline plutonic bodies of the Blatná suite (mainly granodiorites with minor quartz monzonite and monzogabbro bodies). The intermediate rock types resulted from mixing of slightly enriched mantle-derived and crustal magmas [61]. Finally, further east occur syn-deformational bodies or post-tectonic elliptical intrusions of (ultra-)potassic rocks of mid-Carboniferous (~343–337 Ma) ages [53,55,63,157]. Both the Sázava and Blatná suites contain numerous xenoliths, screens and roof pendants of the Barrandian-like Palaeozoic and Neo-Proterozoic sequences, indicating a major role for stopping as an emplacement mechanism [159].

All these features indicate that the Central Bohemian Plutonic Complex corresponds to a relatively shallow section (<10 km) through the Devonian–Carboniferous magmatic arc, which widened and expanded to the east with time. There is also a remarkable temporal trend of increase in the potassic character of magmas, presumably as the basic magmas tapped increasingly more enriched mantle sources [56,60,62].

2.5. The Moldanubian domain

According to Fuchs [41,42], three major units define this domain (Fig. 1):

- the ''Monotonous Group'' of Proterozoic metasediments, with numerous Late Proterozoic to Early Palaeozoic orthogneisses [25,39,153], quartzites and amphibolites. The Monotonous group is traditionally considered to represent the structurally deepest tectonic unit;
- structurally above the ''Varied Group'' composed of plagioclase-bearing paragneisses, quartzites and marbles intercalated with amphibolites and leptynites. The protoliths of metasediments are supposed to be at least partly Early Palaeozoic in age, based on the depleted-mantle Nd model ages of 430–500 Ma for the amphibolite layers [67] or on the Devonian age of the intimately associated felsic metavolcanics [37];
- structurally highest the ''Gföhl Unit'' (Fig. 1) composed of orthogneiss with Ordovician protolith ages [39], amphibolitized eclogites, granulites, garnet- and spinel-bearing peridotites surrounded by felsic migmatites.

The upper amphibolite-facies metamorphism developed on the regional scale in the Monotonous and Varied groups reflecting maximal pressures of 10 kbar at temperatures of 650–700 °C (Fig. 2) [109,112]. However, higher grade (eclogitic) boudins have been identified, generally at the boundary between both groups (Fig. 2) [23,97].

Metamorphism of the Gföhl Unit is characterized by early eclogite facies (Fig. 2; ~20 kbar, 650 °C) [97,129] followed by granulite-facies re-equilibration [103,129] and retrogression under amphibolite-facies conditions [131,142]. The granulites of the Gföhl Unit are considered as a product of prograde metamorphism with peak metamorphic assemblage of garnet-kyanite-mesoperthite-quartz in felsic protoliths and clinopyroxene-garnet-mesoperthite in the intermediate varieties indicating P–T conditions of c. 1000–1050 °C and 16–18 kbar (Fig. 2c) [8]. Associated Gföhl orthogneiss shows peak metamorphic conditions similar to granulites between 14–16 kbar above 950 °C (Fig. 2) [12]. However, Štípská and Powell [128] attributed the ultra-high temperature

incluant la nappe supérieure (modifié d'après [71]) ; **c** : métamorphisme carbonifère HP–HT (340 Ma) de la ceinture orogénique crustale inférieure du domaine moldanubien, le métamorphisme HT–MP et LP, en liaison avec l'exhumation de la croûte orogénique inférieure contrastant avec le pic MP–MT du métamorphisme de la croûte orogénique moyenne, suivi d'une élévation de température pendant l'exhumation (modifié d'après [123]) ; **d** : métamorphisme carbonifère HP–MT des éclogites moraviennes, contrastant avec le métamorphisme MT barrovien de la zone moravienne (modifié d'après [77]).

conditions to the magmatic emplacement of granulite protoliths at moderate depth of c. 7–13 kbar, followed by cooling and prograde metamorphic overprint and decompression occuring at temperatures lower than 850 °C [128,129]. The granulite-facies overprint is probably Visean in age as shown by a number of zircon ages [1,84,122,131,153] but recent studies indicate possible Devonian age of ~370 Ma [2].

Based on existing pressure-temperature (*P–T*) estimates two NW–SE trending belts of HP rocks (granulites, eclogites and peridotites) are distinguished, one located close to the Barrandian–Moldanubian boundary (the western belt of Finger et al. [29]) and the other rimming the eastern margin of the Bohemian Massif. These belts alternate with MP units, represented by the Varied and Monotonous groups, which also form NW–SE trending wide belts.

The deformation history in the Moldanubian Zone reveals early vertical NNE–SSW trending fabrics, associated with crystallization of HP mineral assemblages [31,113,131,142,151]. These are reworked by flat deformation fabrics that are associated with MP to low-pressure (LP) and high-temperature (HT) mineral assemblages [50,133,142,143,151]. The flat fabrics show intense NE–SW trending mineral lineation that is commonly associated with generalized ductile flow towards northeast and this kind of deformation is typical of the whole eastern margin of the Bohemian Massif. The early steep fabrics are dated at 350 to 340 Ma [122], while the ages of the flat ones cluster generally around 335 Ma [123]. In the southwestern part of the Moldanubian domain, younger set of steep NW–SE metamorphic fabrics reworks the flat foliation, having been associated with LP metamorphic conditions at around 325–315 Ma [29,138].

The HP granulites are spatially, structurally and temporally associated with (ultra-)potassic melasyenites to melagranites, which can be divided into two groups differing in modal mineralogy and textures:

- coarsely porphyritic K-feldspar melasyenites to melagranites of the so-called durbachite group/series with a ''wet'' mineral assemblage Mg-biotite plus actinolitic hornblende (e.g., Čertovo břemeno and Třebíč intrusions);
- even-grained melasyenites–melagranites (Tábor and Jihlava intrusions), containing a variously retrogressed, originally almost ''dry'', assemblage of two pyroxenes plus Mg-biotite [29,53,59,149].

For the most basic ultra-potassic rocks, the high contents of Cr and Ni with high melting point to derivation from an olivine-rich source (i.e., Earth's mantle). On the other hand, elevated concentrations of U, Th, LREE and LILE, pronounced depletion in HFSE as well as high K/Na and Rb/Sr ratios seem to contradict the mantle origin. This dual geochemical character and crustal-like Sr–Nd isotopic compositions require melting of anomalous lithospheric mantle sources, metasomatised and contaminated by mature crustal material ([59] and references therein), and interaction of these mafic melts with crustally-derived leucogranitic magmas.

The Moldanubian metamorphic units were penetrated by numerous and voluminous anatectic plutons loosely grouped into the Moldanubian (or South Bohemian) Plutonic Complex [26,45,46,54]. These are mostly felsic–intermediate, two-mica granitic to granodioritic intrusions with either S- or transitional I/S type character [26,88,148]. High-resolution conventional U–Pb zircon and monazite dating showed that the bulk of the Moldanubian Plutonic Complex (*c.* 80%) was emplaced at 331–323 Ma. The fine-grained granodiorites associated with minor diorites followed in a second, less important event at 319–315 Ma [47]. The post-tectonic intrusions of the Moldanubian Plutonic Complex postdated shortly the thermal peak of the regional metamorphism, but were significantly younger than the emplacement of both the Central Bohemian Plutonic Complex and (ultra-)potassic plutonic rocks scattered throughout the Moldanubian domain.

Granitic rocks in the southwestern sector of the Bohemian Massif (Bavarian Forest) have largely independent position. Here, large-scale crustal anatexis was connected with a significant reheating (LP–HT regional metamorphism) and a tectonic remobilisation of the crust (Bavarian Phase *sensu* [29]). The intrusions northeast of the Bavarian Pfahl Zone are dated between 328 and 321 Ma, whereas ages between 324 and 321 Ma are obtained southwest of this zone. It apparently represents an important terrane boundary and the granitic intrusions sampled distinct basement units [124].

2.6. The Moldanubian–Brunia continental transition zone

This boundary was defined by Suess [136,137] as a zone of severe deformation and metamorphism of continental rocks (the so-called Moravo-Silesian Zone, Fig. 1). In his seminal work, Suess [136] defined the deep thrusting of the Moldanubian Zone over more external and shallower Moravo-Silesian Zone, the latter emerging through Moldanubian nappe in a form of several tectonic windows. The contact between these units is marked by a particular unit, the Moravian ''micaschist zone'', which

is composed of kyanite-bearing micaschists that were interpreted by Suess [136] as a result of deep crustal retrogression (''diaftorism'') of the Moldanubian gneisses. Modern studies by Konopásek et al. [73] and Štípská et al. [132] have shown that this zone contains boudins of eclogites (Fig. 2; $P = \sim 16$ kbar, $T = \sim 650$ °C), HP granulites and peridotites embedded in the metapelites. This zone, which contains elements of both Moravian and Moldanubian parentage, is thus regarded as a first order tectonic boundary.

The underlying Moravo-Silesian Zone (Fig. 1) is characterized by two nappes composed of orthogneisses at the bottom and a metapelite sequence at the top. These nappes are thrust over the Neoproterozoic basement which is often imbricated with its Pragian to Famennian cover [9,43]. A number of isotopic studies (e.g. [28]) show that the orthogneisses of the Moravian Zone are derived from the underlying Brunia continent [20]. This 50 km wide and 300 km long zone of intense deformation is marked by an inverted metamorphic sequence ranging from chlorite to kyanite-sillimanite zones and *P–T* conditions ranging from 5–10 kbar and 550–650 °C (Fig. 2) [77,127]. The prograde metamorphism is interpreted as a result of continental underthrusting associated with intense top-to-the-NNE oriented shearing, development of sheath folds and gneissification of Brunia-derived granite protoliths [118,121]. The subsequent deformation is connected with recumbent folding and imbrication of Neoproterozoic gneisses with Devonian cover [119,120]. This later phase is interpreted as late imbrications of metamorphosed Brunia crust in a kinematic continuum with early underthrusting event. The cooling after the Barrovian metamorphism is constrained at 340–325 Ma by hornblende Ar–Ar data [14,40] and monazite inclusions in garnets yielding 340–330 Ma CHIME ages [78].

2.7. The Brunia continent

The Brunia continental foreland (Fig. 1) originally called the Bruno-Vistulicum by Dudek [20] consists of Neoproterozoic granitoids, migmatites and schists. They reveal the existence of a 680-Ma-old crust, intruded by 550-Ma-old granites [28,40]. This basement is unconformably overlain by Cambrian strata [7], Ordovician and shallow marine Lower Devonian quartzites and conglomerates followed by Givetian carbonate platform sedimentation [3,68]. Since the Early Carboniferous (~350 Ma), foreland sedimentary environment developed being accompanied by extensional faulting indicating the flexural subsidence of the Brunia margin [49,96]. From 345 until 300 Ma, a 7.5 km thick Variscan flysch (Culm facies) was deposited onto the Brunia foreland. This sedimentation was coeval with the onset of massive exhumation in the neighbouring Moldanubian domain and the continuous loading of the Brunia continent [49]. Low-grade source rocks associated with clastic muscovites dated at 345–330 Ma [117] gradually pass to a high-grade metamorphic source material marked by pyrope-rich mineral fraction and granulite pebbles dated at 340–330 Ma [13,49,81,152]. Since 330 Ma, began also lateral shortening of the flysch basin marked by a deformation front progressively migrating from eastward in conjunction with decreasing intensity of deformation [30,57]. Deformation of this flysch terminated at c. 300 Ma as indicated by Ar–Ar cooling ages of the metamorphosed Culm facies in the west [91] and deformation of the Variscan molasse further east [11].

3. Geodynamic evolution of the Bohemian Massif

The spatial and temporal distribution of geological units, magmatic fronts and metamorphic zones can be interpreted in an evolutionary scheme very similar to that currently reported from the Andean type orogeny. The following account provides a succession of tectonic events that can be interpreted in terms of south-eastward (in the present-day coordinates) oceanic subduction underneath an active continental margin, obduction of the Saxothuringian oceanic domain, formation of a fore-arc region, growth of magmatic arc and development of a large-scale back-arc system on the continental lithosphere. The early oceanic subduction event could have been followed by a continental underthrusting of the Armorican plate leading to increased friction between the upper and lower plates, gradual flattening of the subduction zone marked by eastward migration of arc and subsequent crustal thickening. The latter event could have been responsible for the development of a thick continental root due to thickening of the upper plate represented by the Teplá-Barrandian and Moldanubian crustal material. The final evolution is marked by the continental indentation of eastern Brunia continent into a weak orogenic root, exhumation of the Moldanubian orogenic lower crust, collapse of the Teplá-Barrandian lid and Moldanubian thrusting over the Brunia platform.

3.1. Early Devonian oceanic subduction underneath the active continental margin

The contact between the Saxothuringian-Armorican plate and the overriding Teplá-Barrandian continent is

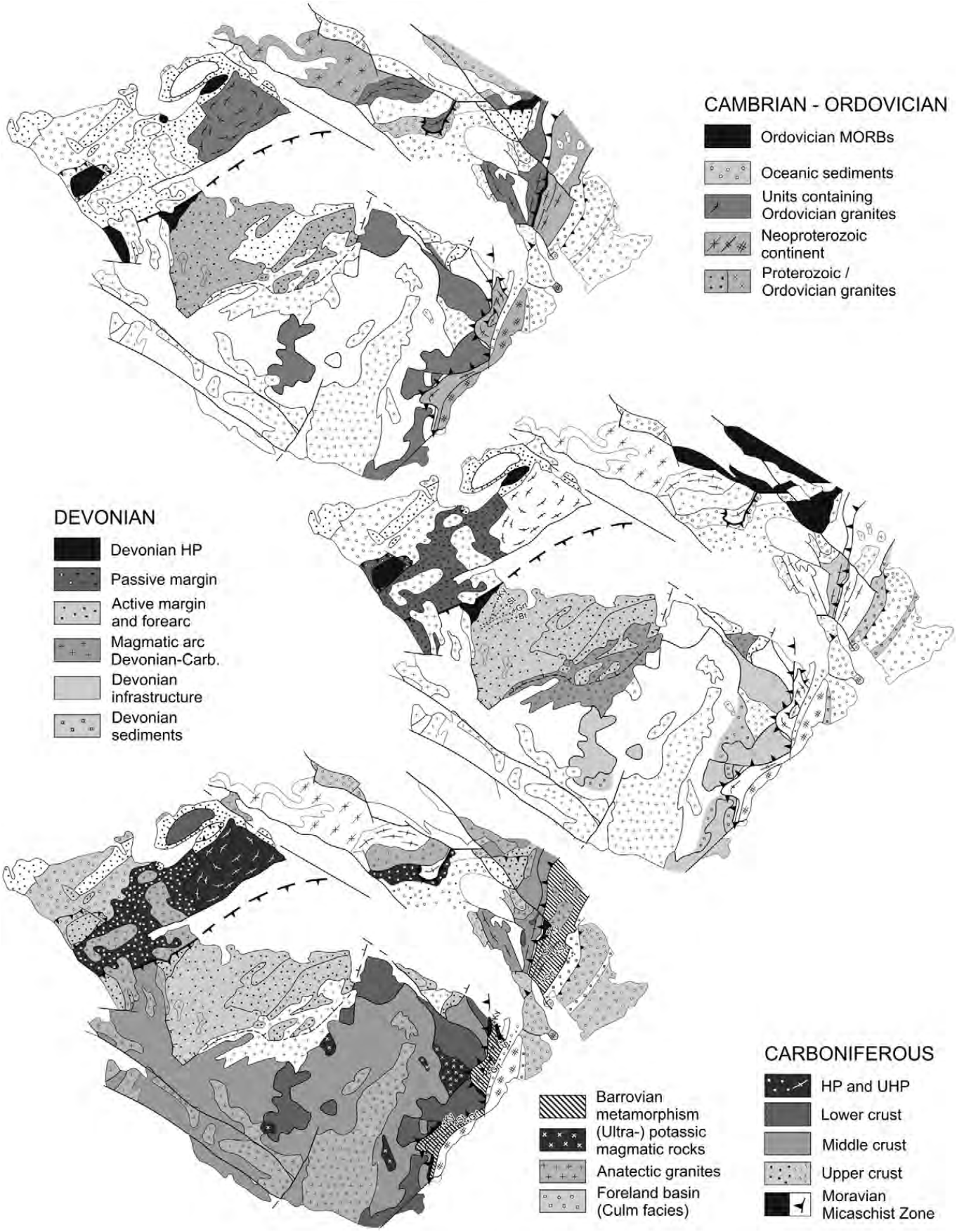

marked by relics of Ordovician MORB eclogites and metabasites locally associated with Ordovician sediments metamorphosed under blueschist–eclogite facies conditions indicating a Mid-Devonian oceanic subduction [34] and an existence of Lower Palaeozoic Saxothuringian oceanic domain (Fig. 3a). The exact age and size of the Saxothuringian ocean is not known, because the differences of Ordovician and Lower Devonian faunas between Saxothuringian and Barrandian continental domains are not confirmed, precluding an existence of large oceanic barrier of biogeographical significance [10,52,106]. Therefore, the oceanic domain must have been narrow and potentially short lived in order not to be recorded by palaeobiogeographic faunal evidence. The only existing argument for larger oceanic separation are from palaeomagnetic data of Tait et al., [141] suggesting that the Saxothuringian and Tepla-Barrandian blocks rotated independently during Silurian and Devonian times.

The hornblende and mica cooling ages of the Vohenstraus–Erbendorf Zone, Mariánské Lázně complex and the Sovie Gory granulites cluster around 380 Ma, which indicates early collision between the Teplá-Barrandian and Saxothuringian domains (Figs. 3middle and 4B). This is also confirmed by Famennian flysh sediments of the Saxothuringian basin that contain detrital zircons dated at 380 Ma [114] which is a direct evidence of mutual contact between the Teplá-Barrandian and Saxothuringian domains during Famennian but most likely already during mid-Devonian. The Barrovian metamorphic zonation developed at the western flank of the Teplá-Barrandian domain (Figs. 3middle and 4B) is potentially related to deformation of the overriding Teplá-Barrandian continental margin and is consistent with a model of extrusion of lower part of the Teplá-Barrandian crust during Devonian shortening event [160,161]. The folding of the eastern very low grade shales and volcanics of the Neoproterozoic sequences is interpreted as a supracrustal response to the same deformation event affecting high grade rocks in the west [161]. Thus, the exhumation of HP rocks in the Mariánské Lázně Complex and the deformation of the Teplá-Barrandian basement are coupled and related to convergent processes at the Saxothuringian plate boundary (Figs. 3middle and 4B).

The strong argument for eastward subduction of the Saxothuringian ocean underneath the eastern Teplá-Barrandian continent is a Devonian–Lower Carboniferous magmatic arc that is firmly founded on the continental crust. This arc, the Central Bohemian Plutonic Complex, separated the Teplá-Barrandian domain from the future Moldanubian domain and in this model the former unit represented a fore-arc region during Devonian (Figs. 3middle and 4B). Thus, the position of Devonian HP rocks thrust over the Saxothuringian basement, existence of the Mariánské Lázně Complex – the oceanic fragment at suture position, and location of calc-alkaline magmatic rocks further east confirm a polarity of the oceanic subduction underneath the eastern fore-arc and magmatic arc system during Late Devonian (Figs. 3middle and 4B). The distance between the arc and the trench area represented by the suture indicates that the dip of subduction zone was probably moderate (30–40°, Fig. 4B). The temporal evolution of magma geochemistry from calc-alkaline to more potassic/shoshonitic affinities (from 370 to 336 Ma) is compatible with flattening of the subduction zone and increased melting of continental material during Early Carboniferous. The Barrandian (Prague) Basin is interpreted as a part of the fore-arc basin marked by 380-Ma-old detrital zircons found in Mid-Devonian flyshoid sequences [135] suggesting early erosion of the eastern magmatic arc.

The most problematic question in the Devonian subduction model for the Bohemian massif is the role of the future Moldanubian domain as well as the position of the Brunia continent. The amphibolites derived from Siluro-Devonian tholeiitic basalts associated with carbonates, widespread in Lower Austria and South Bohemia, are interpreted as volcanic products of a relic

Fig. 3. Time slices maps showing the chronological and tectonic significance of the various units of the Bohemian Massif. Top: Ordovician time slice showing the location of Ordovician MORB and deep marine sediments, and that of the Proterozoic units containing the Ordovician magmatism; middle: Devonian time slice showing the location of Devonian high pressure (HP) rocks, the passive margin sequences, the active margin metamorphism, the fore-arc region, the magmatic arc, the location of Devonian infrastructure and sediments; bottom: Carboniferous time slice shows the location of orogenic lower and middle crust belts in the Moldanubian domain, the metamorphism of the Moravian Zone, the Moravian Micaschist Zone, the HP units in Saxothuringian domain and the various types of magmatic rocks.

Fig. 3. Cartes selon des tranches de temps montrant la signification chronologique et tectonique des diverses unités du Massif de Bohême. En haut : tranche de temps ordovicienne montrant la localisation du MORB ordovicien et des sédiments marins profonds et celle des unités protérozoïques incluant le magmatisme ordovicien ; au milieu : tranche de temps dévonienne montrant la localisation des roches de haute pression (HP) dévoniennes, les séquences de marge active, le domaine avant-arc, l'arc magmatique et la localisation de l'infrastructure et des sédiments dévoniens ; en bas : tranche de temps carbonifère montrant la localisation des chaînes orogéniques crustales inférieure et moyenne du Domaine moldanubien, le métamorphisme de la zone moravienne, de la zone des micaschistes moraviens, des unités HP du domaine saxothuriningien et des différents types de roches magmatiques.

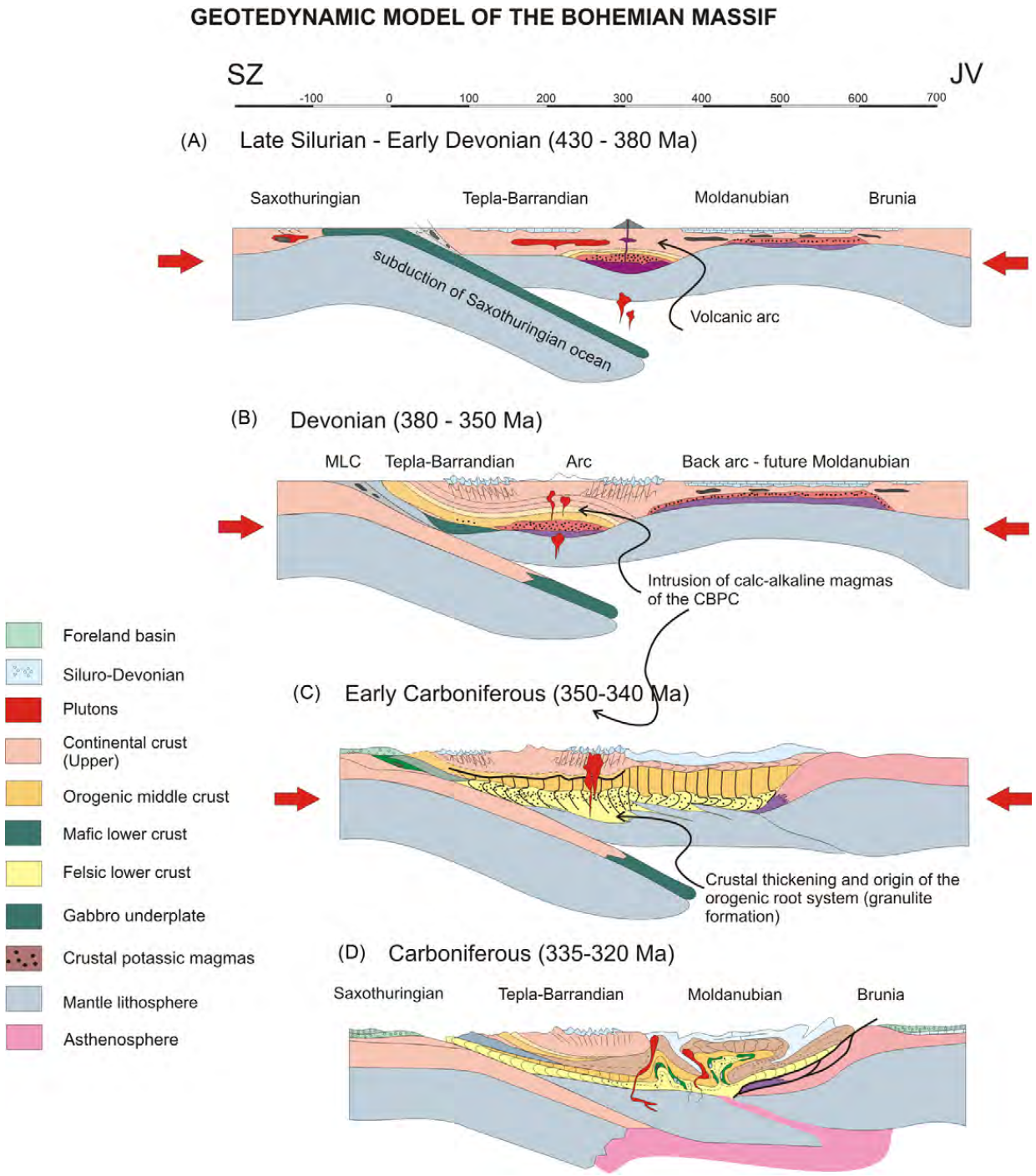

Fig. 4. Conceptual model of the geodynamic evolution of the Bohemian Massif shown as schematic cross sections through the orogen. **A**. Silurian–Early Devonian subduction setting with the beginning of arc and back-arc formation on upper plate. **B**. Onset of the Mid-Devonian continental underthrusting of Saxothuringian lithosphere, deformation of active margin, formation of magmatic arc and persistence of back-arc region on the upper plate. **C**. Crustal thickening processes marked by the influx of Saxothuringian crust and progressive individualization of the Brunia active margin. **D**. Brunia continent indentation associated with the channel flow process, imbrications of underthrust Brunia and the formation of the Moravian Zone.

Fig. 4. Modèle conceptuel de l'évolution géodynamique du Massif de Bohême représenté par des coupes schématiques au travers de l'orogène. **A**. Subduction Silurien–Dévonien inférieur se mettant en place avec le début de la formation de l'arc et de l'arrière-arc sur la plaque supérieure. **B**. Au Dévonien moyen, mise en place du sous-charriage continental et de la lithosphère saxothuringienne, déformation de la marge active, formation de l'arc magmatique et persistance de la zone d'arrière-arc sur la plaque supérieure. **C**. Processus d'épaississement crustal marqué par la venue de croûte saxothuringienne et individualisation progressive de la marge active de Brunia. **D**. Indentation de Brunia, associée à un processus de flux de chenal, imbrications du sous-charriage de Brunia et formation de la zone moravienne.

of large-scale back-arc system [24,67]. In addition, the felsic metavolcanics and amphibolite layers in the Varied Group are regarded as the continuity of back-arc bimodal volcanism till Givetian [37]. However, the supposed depositional Devonian age of the Varied group is questioned thanks to low Sr isotopic ratios which indicate shallow marine environment during Late Proterozoic rather than Palaeozoic [32]. Schulmann et al. [122] interpreted the common occurrence of Late Silurian–Early Devonian zircons in the high grade amphibolites of the Moldanubian domain as a result of important magmatic reworking of the lower part of the continental crust associated with mafic magmatic additions during lithospheric thinning of this domain (Fig. 3middle). In their model, the Monotonous Group represents relic of Proterozoic middle crust that is less affected by thermal and magmatic reworking while the upper crust recorded sedimentary and volcanic evolution related to the Silurian–Devonian extensional event. A back-arc environment is further supported by bimodal volcanic activity in narrow Devonian basins developed on the north-eastern margin of the Brunia continent [107] suggesting only minor thinning of continental crust at the easternmost termination of the back-arc system (Figs. 3middle and 4B). In this concept the rest of the Brunia platform represents a stable continental domain not affected by the back-arc spreading.

The Devonian Saxothuringian oceanic subduction and onset of continental underthrusting of the Saxothuringian–Armorican lower plate underneath the upper plate is thus recorded in all units forming the present-day Bohemian Massif (Fig. 5). The following contemporaneous processes were identified:

- eclogitization of the Saxothuringian crust and its exhumation along the Teplá suture;
- sedimentation of Mid-Devonian distal turbidites of the Srbsko Formation followed by inversion of the fore-arc basin in the Teplá-Barrandian domain, origin of the magmatic arc in the area of the Central Bohemian Plutonic Complex and exhumation of the western metamorphosed margin of the Teplá unit suggesting convergent processes in the upper plate;
- formation of the back-arc system on the continental lithosphere as shown by isotopic data in the Moldanubian domain and marginally in the Devonian basins affecting western margin of the Brunia continent (here, the formation of small oceanic basin is not excluded). All existing data point out to the subduction process that operated at least 45 million years from 400 to 355 Ma (Fig. 5).

3.2. The Early Carboniferous crustal thickening of the upper plate

This event is recognized in all units except the Teplá-Barrandian supracrustal unit. The western margin of the Bohemian Massif is characterized by the arrival of the Saxothuringian continental crust and its subduction underneath the eastern Teplá-Barrandian–Moldanubian domain (Fig. 4B). The main thrust boundary migrated further west, so that the continental crust was thrust underneath the fossil Devonian suture and former fore-arc region [71]. At the same time the deformation regime changed in the far field back-arc region (future Moldanubian domain), which recorded the progressive thickening of the whole previously thinned and thermally softened domain as indicated by several recent petrological studies (e.g. [77,128]). Recent structural studies have shown that the earliest preserved fabrics have been sub-horizontal [31,112,123,131], which may indicate that the lower crustal material was originally flowing horizontally from the area of the continental subduction channel towards the region of eastern backstop in a manner proposed by [104] for the closure of the Rhenohercynian Basin and formation of the Mid-German Crystalline Rise.

Indeed, the influx of lower crustal material transported by south-east dipping Saxothuringian continental subduction zone underneath the fore arc (the Teplá-Barrandian domain) and further below the former back-arc domain is regarded to be at the origin of the future ‘‘Gföhl Unit’’. This hypothesis is in line with the whole-rock geochemical and Sr–Nd isotopic composition as well as the zircon inheritance patterns in the Moldanubian HP–HT granulites [59,65]. Importantly, the crustal material involved in the subduction and extruded over the sub-arc and sub-back-arc mantle lithosphere may have been turned into voluminous HP granulites known from many regions of the Bohemian Massif [59,100]. Such a processing of the lower plate continental lithosphere in a subduction zone and its extrusion above mantle wedge was successfully modelled by Gerya and Stockert [48]. Alternatively, the back-arc domain with high thermal budget inherited from Devonian stretching may have been thickened and the partially molten lower crust may have been transported downwards and transformed into the HP granulites as suggested by Štípská and Powell [129] or Schulmann et al.[122]. However, this model fails to explain the occurrence of the Gföhl gneiss and felsic granulites in the lower crustal position.

The onset of thickening of the root is not recorded in the Teplá domain (Fig. 4C), which behaved as a

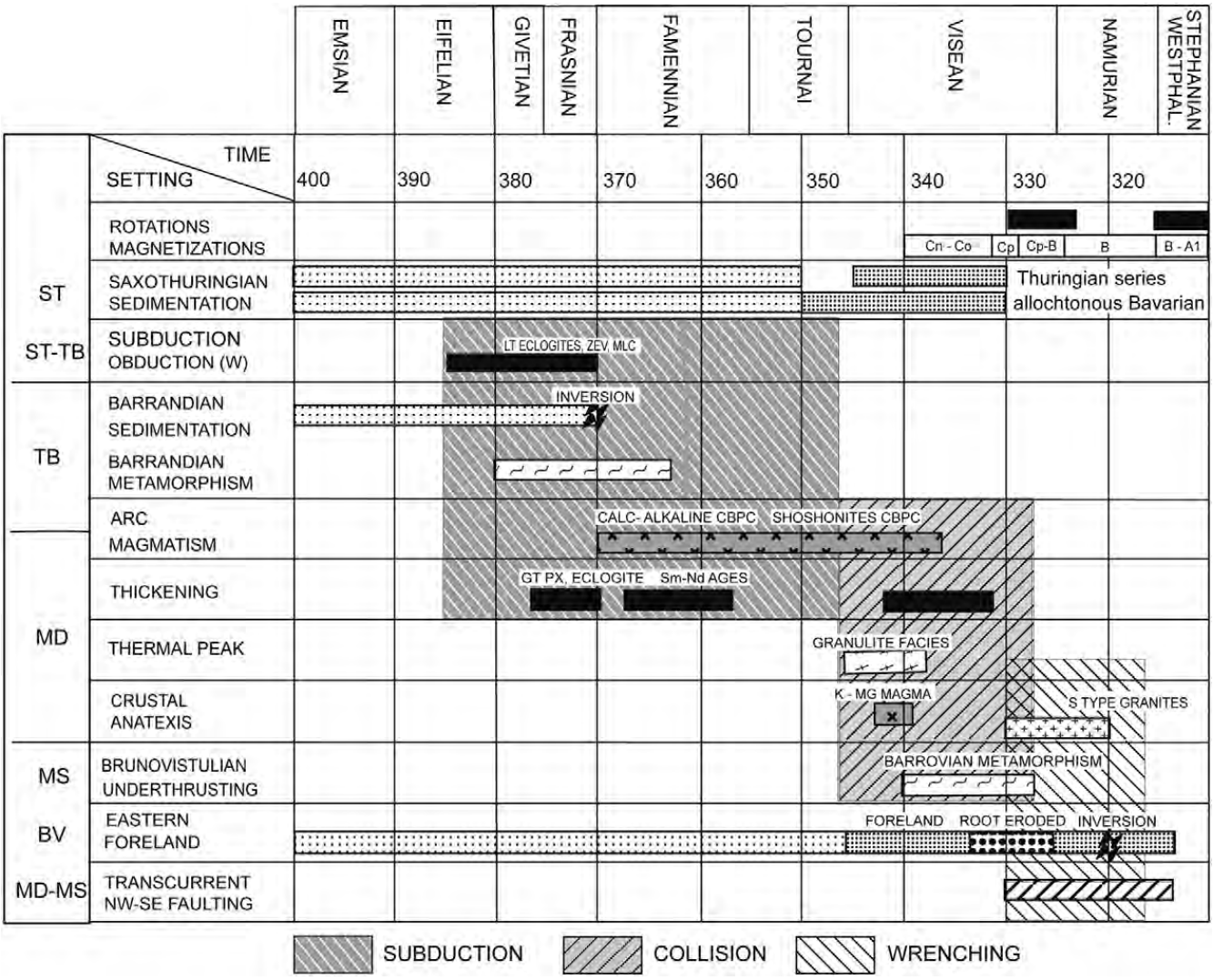

Fig. 5. Summary of geochronology data showing the time scales of the three major events forming the Bohemain Massif: oceanic subduction and continental underthrusting of Saxothuringian domain, building of thick orogenic root system and collapse of orogen due to indentation of Brunia.

Fig. 5. Résumé des données chronologiques montrant les échelles de temps des trois évènements majeurs de la formation du Massif de Bohême : subduction océanique et sous-charriage du domaine saxothuringien, édification de l'épais système d'enracinement orogénique et « collapse » de l'orogène, en raison de l'indentation de Brunia.

supra-structural unit at this time, but it is shown by deformation of the Lower Palaeozoic rocks of the Prague basin and adjacent Late Proterozoic rocks. Here, the steep fabric is well dated by syntectonic calc-alkaline plutons at about 355–345 Ma [64,122,158]. In contrast, the eastern sector of the orogen records onset of loading of the Brunia platform (Fig. 4C) during Tournaisian manifested by destruction of the Givetian carbonate platform and sedimentation of coarse basal clastics [49].

The timing of crustal thickening is relatively poorly constrained compared to the subduction and later exhumation processes (Fig. 5). However, the Tournaisian and Early Visean massive clastic sedimentation on both Saxothuringian and Brunia plates suggests load of both continental lithospheric plates and high topography in between them. This corroborates the peak metamorphic ages in the granulites and the Moldanubian eclogites as well as the Visean age of compression of the magmatic arc. All geochronological and other geological information point to a crustal thickening period that was very short and did not last more than 20 million years, from 355 to 335 Ma, with a peak around 340 Ma (Fig. 5).

3.3. Late Visean exhumation of orogenic lower crust of the upper plate

The exhumation of the Variscan lower crust during Early Carboniferous is exemplified by the three NE–SW

trending belts of granulites, eclogites and peridotites (Fig. 3c) intimately associated with the (ultra-)potassic magmatites [29,59]. The first granulite belt is represented by narrow strip of felsic granulites that occur at the Saxothuringian–Teplá-Barrandian boundary and it is interpreted as an extrusion of the orogenic lower crust along a large scale crustal shear zone at ∼340 Ma [71,163]. The coeval ∼340 Ma age of the Saxothuringian eclogites and of the felsic granulites [80,150] led Konopásek and Schulmann [71] to propose a model of simultaneous exhumation of nappes derived from the Saxothuringian crust and viscous extrusion of orogenic lower crust from underneath the Teplá-Barrandian supracrustal unit (Fig. 4D) [36]. The second belt, recognized east of the Central Bohemian Plutonic Complex, i.e., "the magmatic arc", was exhumed along huge west dipping detachment zone [111,157,158], which was also responsible for collapse of the upper part of the magmatic arc system and the downthrow of the whole Barrandian section [115,157]. Such a huge vertical material transfer (Fig. 4D) could have been responsible for vertical exchange of the lower crustal and upper crustal material in a range of 50 km with final throw of 15 km [110,162]. The cooling ages from the lower crustal domain show that the granulites have crossed the 300 °C isotherm during Carboniferous (∼330–310 Ma) [75,138] suggesting the time at which the lower crustal bulge reached shallow position in the upper plate.

The third lower crustal belt rims the eastern margin of the Bohemian Massif, i.e. the boundary with the Brunia continent (Fig. 4D). Here the granulite fabric is also vertical and interpreted in terms of massive vertical exchanges with orogenic middle crust [123]. The zone of the lower crustal bulge is interpreted as an enormous zone of vertical extrusion surrounded by a middle crust coevally transported downwards in form of a crustal scale synform. The vertical material transfer along the Moldanubian lower crustal belts was a matter of research for several Czech authors during the last five years [31,112,123,131,142]. The model of vertical extrusion is based on the concept of buckling of the lower and mid-crustal interface followed by growth of crustal scale antiforms. This process is thought to be triggered by rheological and thermal instabilities in the arc region, while to the east it is forced by rigid backstop, preserved only locally [130].

However, the most important feature of the eastern Variscan front is the development of horizontal fabrics in the Moldanubian root zone parallel to the Brunia continental margin. The intense deformation of the Brunia continent leading to the formation of the Moravo-Silesian imbricated nappe system was associated with the development of tectonically inverted Barrovian metamorphism (Fig. 4D) and formation of crustal mélange in its upper part (the Moravian Micaschist Zone). These phenomena, as well as mixing of HP rocks and migmatites in the overlying Moldanubian nappe have been recently interpreted in terms of indentation of the Brunia continent into the hot and thick continental root [123]. This lower crustal indentation and flow of hot lower crustal rocks in supracrustal levels are consistent with a model of continental channel flow driven by the arrival of a crustal plunger, a model which is advocated for two decades for the deformation of the Eastern Cordillera in the Andes (e.g. [87]). Finally, the continuous load of the Brunia platform related to deep indentation process led to the development and eastward propagation of the foreland basin. In our model, as the hot Moldanubian rocks advance over the Brunia platform, an imbricated footwall nappe system is generated and thrust over the progressively buried foreland basin rocks.

The time scale of exhumation of the orogenic lower crust is well constrained due to a set of well dated diachronous processes that start with the exhumation of the West-Bohemian granulites, growth of western and eastern orogenic lower crustal antiforms and a shallow channel flow of partially molten lower crust associated with the inversion of the eastern foreland basin. All that is linked with a major thermal event in the mantle as shown by the ages of a syn-extrusion high potassic magmatism, the exhumation of large number of mantle fragments and the overall melting of the Moldanubian crust. The time scale of all these processes was surprisingly short, i.e., about of 20 Ma, and ranges from 335 to 315 Ma (Fig. 5).

4. Palaeographic constraints for Andean type orogeny in the Bohemian Massif

Finger and Steyrer [24] attempted to explain the tectonic processes at the Moldanubian–Moravian boundary with a plate tectonic model involving the subduction of a Silurian–Devonian oceanic domain westward beneath the Moldanubian zone. This concept supposes large rotation of the Brunia platform forming a part of an Old Red continent (Avalonia) around the core of the Bohemian Massif during Visean times [140]. The model of westward subduction is also based on the presence of Silurian MORB-type amphibolites [25] within the Gföhl Unit, which are interpreted as relics of oceanic crust of the Rheic Ocean. In addition, the occurrences of eclogites located along the eastern

Variscan front [73,132] can serve as an additional argument for this subduction model.

However, the palaeomagnetic investigations carried out on granitoids of the Central Bohemian Pluton and its extension to the east (the Nasavrky Plutonic Complex [58]) demonstrate that the Teplá-Barrandian, the Moldanubian as well as Brunia domains had a common geodynamic behaviour since the Late Visean (335–330 Ma according to Edel et al. [22]). Therefore, the interpretation of palaeomagnetic directions from Devonian sediments of the Brunovistulian platform [86,98,139] in terms of an oroclinal bending of the Rhenohercynian domain along the Moldanubian core cannot be valid for several reasons:

- the consistency of these ''Devonian'' palaeomagnetic directions with Middle-Late Carboniferous directions (Cp directions at 330–325 Ma and B directions at 320–315 Ma, Fig. 6) in the Moldanubian zone suggests that the Devonian sediments overlying the Brunia continent were re-magnetized in Late Variscan time. Consequently, no relative rotation between the Brunia continent and the Moldanubian core can be considered prior to 330 Ma;
- magnetic overprinting of the Devonian sequences on the Brunia continent is supported by important deformation and burial of Culm and Devonian sediments during Late Carboniferous deformation of the Brunia margin [30,120,126]. Hence, it is unlikely that primary magnetizations could have survived such a severe structural and thermal reworking of the Devonian sediments. We suggest that magnetic overprinting was the result of the Carboniferous tectonothermal processes associated with the underthrusting of the Brunia platform together with Culm accretionary wedge [11] underneath the hot Moldanubian root zone and with later uplift and erosion of the Moldanubian–Moravian nappe sequence.

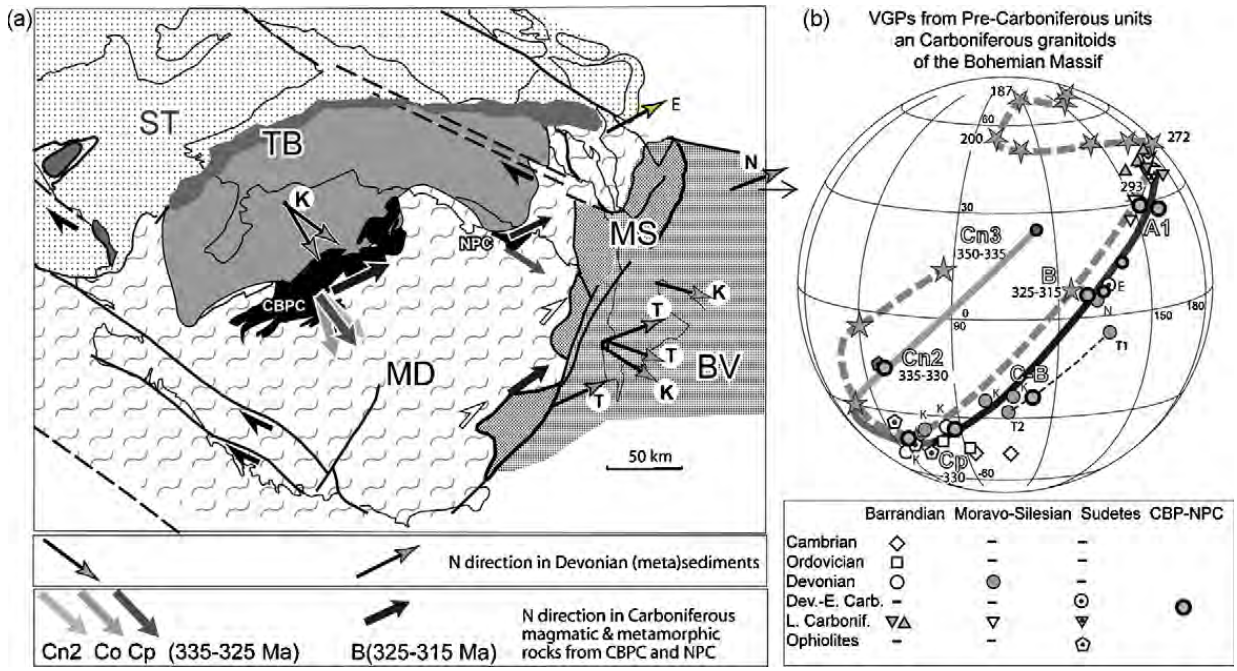

Fig. 6. **a**: paleomagnetic north directions obtained in Devonian (meta)sediments from the Teplá-Barrandian and Brunia zones (K: [86]; N: [98]; T: [139]; E: [21]) and from Early Carboniferous granitoids from Central Bohemian Pluton and Nasavrky Pluton [22]. Cn and Co directions represent magnetizations acquired at the end of the NW–SE shortening and the uplift of the Moldanubian root; Cp and B directions correspond to overprints acquired during NNE–SSW compression and clockwise rotation of the Variscides. Note the similarity of ''Devonian'' directions with Carboniferous directions; **b**: published mean virtual geomagnetic poles (VGPs) and associated apparent polar wander curve (grey dashed line) from Early Paleozoic rocks of the Bohemian Massif and mean poles from western Europe Variscides (stars with ages of magnetization) and associated apparent polar wandering curve (dark grey line) [22].

Fig. 6. **a** : directions du nord paléomagmatique obtenues dans les (méta)sédiments dévoniens des zones Teplá-barrandienne et Brunia (K :[86] ; N :[98] ; T :[139] ; E :[21]) et dans les granitoïdes du Carbonifère inférieur et du Pluton Nasavrky [22]. Les directions Cn et Co représentent les magnétisations acquises à la fin du raccourcissement NW–SE et du soulèvement de la racine moldanubienne ; les directions Cp et B correspondent à des réaimantations acquises durant la compression NNE–SSW et la rotation dans le sens des aiguilles d'une montre des Variscides. À noter, la similarité des directions « dévoniennes » et carbonifères ; **b** : pôles géomagnétiques virtuels (VGP) publiés, associés à la courbe de dérive apparente des pôles (ligne en tiretés) pour les roches du Paléozoïque inférieur du Massif de Bohême et pôles moyens pour les Variscides d'Europe occidentale (étoiles avec âges de la magnétisation), associés à la courbe de dérive des pôles (ligne continue gris foncé) [22].

The Siluro-Devonian basin in the area of the Moldanubian zone existed as a back-arc basin above the Saxothuringian subduction zone [122] but the question of development of oceanic crust in this area remains a matter of discussions. Therefore, in contrast to the generally accepted rotation of a Brunia continent independent of a stationary Moldanubian domain associated with a closure of a large (Rheic) oceanic domain we propose a model of common geodynamic history of the Bohemian Massif during Devonian and Early Carboniferous (Fig. 5). In our model the palaeomagnetic, crustal scale geophysical and structural data are in favour of an early counterclockwise rotation of composite blocks (Saxothuringian, Barrandian, Moldanubian and Brunia altogether) accommodated by a large scale NW–SE trending dextral wrench zones (such as the Elbe, Pfahl, Franconian and Pays de Bray faults) during Early Visean [22]. These movements could have resulted from northwest drift of Gondwana continental masses and continued after 330 Ma by clockwise rotation of the whole Variscan belt around the Euler pole that was continuously translated westward parallel to the Teysseire–Tornquist zone (southern margin of the Baltica).

Acknowledgements

The French National Science Foundation project ‘‘ANR LFO in orogens’’, internal research funds of CNRS UMR 7615 and grant MSM0021620855 of the Ministry of Education of the Czech Republic are acknowledged for financial support and salary of Ondrej Lexa. Jiří Konopásek appreciates the financial support of the Grant Agency of the Charles University (project No. B-GEO-270/2006), as well as the support by the Ministry of Education, Youth and Sports of the Czech Republic through the Scientific Centre ‘‘Advanced Remedial Technologies and Processes’’ (identification code 1M0554).

References

[1] M. Aftalion, D. Bowes, S. Vrána, Early Carboniferous U-Pb zircon age for garnetiferous, perpotassic granulites, Blanský les massif, Czechoslovakia, Neues Jarhb. Miner. Monat. 4 (1989) 145–152.

[2] R. Anczkiewicz, J. Szczepański, S. Mazur, C. Storey, Q. Crowley, I. Villa, M. Thirlwall, T. Jeffries, Lu–Hf geochronology and trace element distribution in garnet: Implications for uplift and exhumation of ultra-high pressure granulites in the Sudetes, SW Poland, Lithos 95 (2007) 363–380.

[3] O. Bábek, Č. Tomek, R. Melichar, J. Kalvoda, J. Otava, Structure of unmetamorphosed Variscan tectonic units of the southern Moravo-Silesian zone, Bohemian Massif: a review, Neues Jahrb. Geol. Palaontol. Abh. 239 (2006) 37–75.

[4] B.L. Beard, L.G. Medaris, C.M. Johnson, E. Jelínek, J. Tonika, L.R. Riciputi, Geochronology and geochemistry of eclogites from the Mariánské Lázně Complex, Czech Republic: implications for Variscan orogenesis, Geol. Rundsch. 84 (1995) 552–567.

[5] D.R. Bowes, M. Aftalion, U-Pb zircon isotopic evidence for Early Ordovician and Late Proterozoic units in the Mariánské Lázné complex, Central European Hercynides, Neues Jahrb. Miner. Monat. (1991) 315–326.

[6] M. Brown, Metamorphic conditions in Orogenic Belts: a record of secular change, Int. Geol. Rev. 49 (2007) 193–234.

[7] Z. Bula, M. Jachowicz, J. Zaba, Principal characteristics of the Upper Silesian Block and Malopolska Block border zone (southern Poland), Geol. Mag. 134 (1997) 669–677.

[8] D. Carswel, P. O’Brien, Thermobarometry and geotectonic significance in the Moldanubian Zone of the Bohemian Massif in Lower Austria, J. Petrol. 34 (1993) 427–459.

[9] I. Chlupáč, Fossil communities in the metamorphic Lower Devonian of the Hrubý Jeseník Mts., Czechoslovakia, Neues Jahrb. Geol. Palaontol. Abh. 177 (1989) 367–392.

[10] I. Chlupáč, Facies and biogeographic relationships in Devonian of the Bohemian Massif, Courier Forschungsinstitut Senckenberg 169 (1994) 299–317.

[11] P. Čížek, Č. Tomek, Large-scale thin-skinned tectonics in the eastern boundary of the Bohemian Massif, Tectonics 10 (1991) 273–286.

[12] R. Cooke, P. O’Brien, Resolving the relationship between high P–T rocks and gneisses in collisional terranes: an example from the Gföhl gneiss–granulite association in the Moldanubian Zone, Austria, Lithos 58 (2001) 33–54.

[13] R. Čopjaková, P. Sulovský, B. Paterson, Major and trace elements in pyrope–almandine garnets as sediment provenance indicators of the Lower Carboniferous Culm sediments, Drahany Uplands, Bohemian Massif, Lithos 82 (2005) 51–70.

[14] R. Dallmeyer, F. Neubauer, V. Höck, Chronology of Late Paleozoic tectonothermal activity in the southeastern Bohemian Massif, Austria (Moldanubian and Moravo-Silesian zones): $^{40}Ar/^{39}Ar$ mineral age controls, Tectonophysics 210 (1992) 135–153.

[15] R. Dallmeyer, M. Urban, Variscan vs Cadomian tectonothermal activity in northwestern sectors of the Teplá-Barrandian zone, Czech Republic: constraints from $^{40}Ar/^{39}Ar$ ages, Geol. Rundsch. 87 (1998) 94–106.

[16] J.F. Dewey, K.C.A. Burke, Tibetan, Variscan and Precambrian basement reactivation: products of continental collision, J. Geol. 81 (1973) 683–692.

[17] W. Dörr, G. Zulauf, J. Fiala, W. Franke, Z. Vejnar, Neoproterozoic to Early Cambrian history of an active plate margin in the Teplá–Barrandian unit—a correlation of U–Pb isotopic-dilution-TIMS ages (Bohemia, Czech Republic), Tectonophysics 352 (2002) 65–85.

[18] W. Dörr, J. Fiala, W. Franke, U. Haack, S. Philippe, J. Schastok, D. Scheuvens, Z. Vejnar, G. Zulauf, Cambrian vs. Variscan tectonothermal evolution within the Teplá-Barrandian: evidence from U-Pb zircon ages of syn-tectonic plutons (Bohemian Massif, Czech Republic), Acta Univ. Carol. Geol. 42 (1998) 229–230.

[19] K. Drost, U. Linnemann, N. McNaughton, O. Fatka, P. Kraft, M. Gehmlich, C. Tonk, J. Marek, New data on the Neoproterozoic–Cambrian geotectonic setting of the Teplá-Barrandian

volcano-sedimentary successions: geochemistry, U-Pb zircon ages, and provenance (Bohemian Massif, Czech Republic), Int. J. Earth Sci. 93 (2004) 742–757.

[20] A. Dudek, The crystalline basement block of the outer Carpathians in Moravia – Brunovistulicum, Rozpravy Československé Akademie věd, Rada matematika prirodni ved 90 (1980) 85.

[21] J. Edel, T. Aïfa, M. Jelenska, M. Kodzialko-Hofmokl, A. Zelazniewicz, Réaimantations des formations paléozoïques des Sudètes polonaises et courbe de dérive des pôles géomagnétiques d'Europe du Carbonifère moyen au Jurassique moyen, C. R. Acad. Sci. Ser. IIa 325 (1997) 479–486.

[22] J.B. Edel, K. Schulmann, F.V. Holub, Anticlockwise and clockwise rotations of the eastern Variscides accommodated by dextral lithospheric wrenching: palaeomagnetic and structural evidence, J. Geol. Soc. 160 (2003) 209–218.

[23] S. Faryad, M. Perraki, S. Vrána, P–T evolution and reaction textures in retrogressed eclogites from Světlík, the Moldanubian Zone (Czech Republic), Mineral. Petrol. 88 (2006) 297–319.

[24] F. Finger, H.P. Steyrer, A tectonic model for the eastern. Variscides: indications from a chemical study of amphibolites in. the southeastern Bohemian Massif, Geol. Carpath. 46 (1995) 137–150.

[25] F. Finger, A. von Quadt, U/Pb ages of zircons from a plagiogranite-gneiss in the south-eastern Bohemian Massif, Austria-further evidence for an important Early Paleozoic rifting episode in the eastern Variscides, Schweiz, Mineral. Petrogr. Mitt. 75 (1995) 265–270.

[26] F. Finger, M. Roberts, B. Haunschmid, A. Schermaier, H. Steyrer, Variscan granitoids of central Europe: their typology, potential sources and tectonothermal relations, Mineral. Petrol. 61 (1997) 67–96.

[27] F. Finger, M. Tichomirowa, C. Pin, P. Hanžl, Relics of an Early-Panafrican metabasite-metarhyolite formation in the Brno Massif, Moravia, Czech Republic, Int. J. Earth Sci. 89 (2000) 328–335.

[28] F. Finger, P. Hanžl, C. Pin, A. von Quadt, H.P. Steyrer, The Brunovistulian: Avalonian Precambrian sequence at the eastern end of the central European Variscides? Geol. Soc. London Spec. Publ. 179 (2000) 103–112.

[29] F. Finger, A. Gerde, V. Janoušek, M. Ren, G. Riegier, Resolving the Variscan evolution of the Moldanubian sector of the Bohemian Massif: the significance of the Bavarian and the Moravo–Moldanubian tectonometamorphic phases, J. Geosci. 52 (2007) 9–28.

[30] E. Franců, J. Franců, J. Kalvoda, H. Poelchau, J. Otava, Burial and uplift history of the Palaeozoic Flysch in the Variscan foreland basin (SE Bohemian Massif, Czech Republic), in: Continental collision and the tectonosedimentary evolution of forelands, 2002, pp. 167–179.

[31] J. Franěk, K. Schulmann, O. Lexa, Kinematic and rheological model of exhumation of high pressure granulites in the Variscan orogenic root: example of the Blanský les granulite, Bohemian Massif, Czech Republic, Mineral. Petrol. 86 (2006) 253–276.

[32] W. Frank, S. Hammer, F. Popp, S. Scharbert, M. Thöni, Isotopengeologische Neuergebnisse zur Entwicklungsgeschichte der Böhmischen Masse. Proterozoische Gesteinsserien und variscische Hauptorogenese, Osterr. Beitr. Meteorol. Geophys. 3 (1990) 185–228.

[33] W. Franke, Variscan plate tectonics in central Europe—current ideas and open questions, Tectonophysics 169 (1989) 221–228.

[34] W. Franke, The mid-European segment of the Variscides: tectonostratigraphic units, terrane boundaries and plate tectonic evolution, Geol. Soc. London Spec. Publ. 179 (2000) 35–61.

[35] W. Franke, The Variscan orogen in central Europe: construction and collapse, Geol. Soc. London Mem. 32 (2006) 333–343.

[36] W. Franke, E. Stein, Exhumation of high-grade rocks in the Saxo-Thuringian Belt: geological constraints and geodynamic concepts, Geol. Soc. London Spec. Publ. 179 (2000) 337–354.

[37] G. Friedl, A. von Quadt, A. Oshner, F. Finger, Timing of the Variscan orogeny in the southern Bohemian Massif (NE Austria) deduced fro new U-Pb zircon and monazite dating, Terra Nova 5 (1993) 235–236.

[38] G. Friedl, F. Finger, N.J. McNaughton, I.R. Fletcher, Deducing the ancestry of terranes: SHRIMP evidence for South America-derived Gondwana fragments in central Europe, Geology 28 (2000) 1035–1038.

[39] G. Friedl, F. Finger, J.-L. Paquette, A. von Quadt, N.J. McNaughton, I.R. Fletcher, Pre-Variscan geological events in the Austrian part of the Bohemian Massif deduced from U–Pb zircon ages, Int. J. Earth Sci. 93 (2004) 802–823.

[40] H. Fritz, R.D. Dallmeyer, F. Neubauer, Thick-skinned versus thin-skinned thrusting: Rheology controlled thrust propagation in the Variscan collisional belt (The southeastern Bohemian Massif, Czech Republic - Austria), Tectonics 15 (1996) 1389–1413.

[41] G. Fuchs, Zur Entwicklung der Böhmischen Masse, Jahrb. Geol. Bundelsansalt 129 (1976) 41–49.

[42] G. Fuchs, Zur Diskussion um den Deckenbau der Böhmischen Masse, Jahrb. Geol. Bundelsansalt 129 (1986) 41–49.

[43] A. Galle, J. Hladil, P. Isaacson, Middle Devonian biogeography of closing South Laurussia; North Gondwana Variscides; examples from the Bohemian Massif (Czech Republic), with emphasis on Horní Benešov, Palaios 10 (1995) 221–239.

[44] D. Gebauer, M. Grünenfelder, U–Pb zircon and Rb–Sr mineral dating of eclogites and their country rocks. Example: Münchberg Gneiss Massif, Northeast Bavaria, Earth Planet. Sci. Lett. 42 (1979) 35–44.

[45] A. Gerdes, Geochemische und thermische Modelle zur Frage der spätorogenen Granitgenese am Beispiel des Südböhmischen Batholiths: Basaltisches Underplating oder Krustenstapelung, Unpublished Ph.D. thesis, University of Göttingen (1997) 113.

[46] A. Gerdes, G. Wörner, A. Henk, Post-collisional granite generation and HT-LP metamorphism by radiogenic heating: the Variscan South Bohemian Batholith, J. Geol. Soc. 157 (2000) 577–587.

[47] A. Gerdes, G. Friedl, R. Parrish, F. Finger, High-resolution geochronology of Variscan granite emplacement–the South Bohemian Batholith, J. Czech. Geol. Soc. 48 (2003) 53.

[48] T. Gerya, B. Stockhert, Two-dimensional numerical modeling of tectonic and metamorphic histories at active continental margins, Int. J. Earth Sci. 95 (2006) 250–274.

[49] A.J. Hartley, J. Otava, Sediment provenance and dispersal in a deep marine foreland basin: the Lower Carboniferous Culm Basin, Czech Republic, J. Geol. Soc. 158 (2001) 137–150.

[50] P. Hasalová, P. Štípská, R. Powell, K. Schulmann, V. Janoušek, O. Lexa, Transforming mylonitic metagranite by open-system interactions during melt flow, J. Metamorph. Geol. 26 (2008) 55–80.

[51] V. Havlíček, Development of a linear sedimentary depression exemplified by the Prague Basin (Ordovician–Middle Devonian; Barrandian area–central Bohemia), Sb. Geologick. Ved Geol. 35 (1981) 7–48.

[52] V. Havlíček, J. Vaněk, O. Fatka, Perunica microcontinent in the Ordovician (its position within the Mediterranean Province, series division, benthic and pelagic associations), Sb. Geologick. Ved Paleontol. 46 (1994) 23–56.

[53] F. Holub, Ultrapotassic plutonic rocks of the durbachite series in the Bohemian Massif: petrology, geochemistry and petrogenetic interpretation, J. Geol. Sci. Econ. Geol. Min. 31 (1997) 5–26.

[54] F. Holub, M. Klečka, D. Matějka, Moldanubian Zone VII. C. 3. Igneous activity, in : R. Dallmeyer, W. Franke, K. Weber (Eds.), Pre-Permian Geology of central and eastern Europe, Springer, Berlin, 1995, pp. 444–452.

[55] F. Holub, A. Cocherie, P. Rossi, Radiometric dating of granitic rocks from the Central Bohemian Plutonic Complex (Czech Republic): constraints on the chronology of thermal and tectonic events along the Moldanubian-Barrandian boundary, C. R. Acad. Sci. Ser. IIa 325 (1997) 19–26.

[56] F. Holub, J. Machart, M. Manová, The Central Bohemian Plutonic Complex: geology, chemical composition and genetic interpretation, J. Geol. Sci. Econ. Geol. Min. 31 (1997) 27–50.

[57] F. Hrouda, O. Krejčí, J. Otava, Magnetic fabric in folds of the easternmost Rheno-Hercynian Zone, Phys. Chem. Earth Part A. 25 (2000) 505–510.

[58] F. Hrouda, Š. Taborská, K. Schulmann, J. Ježek, D. Dolejš, Magnetic fabric and rheology of co-mingled magmas in the Nasavrky Plutonic Complex (E Bohemia); implications for intrusive strain regime and emplacement mechanism, Tectonophysics 30 (1999) 93–111.

[59] V. Janoušek, F. Holub, The causal link between HP/HT metamorphism and ultrapotassic magmatism in collisional orogens: case study from the Moldanubian Zone of the Bohemian Massif, Proc. Geol. Assoc. 118 (2007) 75–86.

[60] V. Janoušek, G. Rogers, D. Bowes, Sr-Nd isotopic constraints on the petrogenesis of the Central Bohemian Pluton, Czech Republic, Int. J. Earth Sci. 84 (1995) 520–534.

[61] V. Janoušek, D.R. Bowes, C.J.R. Braithwaite, G. Rogers, Microstructural and mineralogical evidence for limited involvement of magma mixing in the petrogenesis of a Hercynian high-K calc-alkaline intrusion: the Kozárovice granodiorite, Central Bohemian Pluton, Czech Republic, Trans. R. Soc. Edinburgh Earth Sci. 91 (2000) 15–26.

[62] V. Janoušek, D.R. Bowes, G. Rogers, C.M. Farrow, E. Jelínek, Modelling diverse processes in the petrogenesis of a composite batholith: the Central Bohemian Pluton, Central European Hercynides, J. Petrol. 41 (2000) 511–543.

[63] V. Janoušek, F. Holub, A. Gerdes, K-rich magmatism in the Moldanubian Unit, Bohemian Massif – a complex story featuring variably enriched lithospheric mantle melts and their interaction with the crust, Geolines 16 (2003) 48–49.

[64] V. Janoušek, C. Braithwaite, D. Bowes, A. Gerdes, Magma-mixing in the genesis of Hercynian calc-alkaline granitoids: an integrated petrographic and geochemical study of the Sázava intrusion, Central Bohemian Pluton, Czech Republic, Lithos 78 (2004) 67–99.

[65] V. Janoušek, S. Vrána, V. Erban, K. Vokurka, M. Drábek, Metabasic rocks in the Varied Group of the Moldanubian Zone, southern Bohemia – their petrology, geochemical character and possible petrogenesis, J. Geosci. 53 (2008) 31–64.

[66] V. Janoušek, F. Finger, M. Roberts, J. Frýda, C. Pin, D. Dolejš, Deciphering the petrogenesis of deeply buried granites: whole-rock geochemical constraints on the origin of largely undepleted felsic granulites from the Moldanubian Zone of the Bohemian Massif, Trans. R. Soc. Edinburgh: Earth Sci. 95 (2004) 141–159.

[67] V. Janoušek, A. Gerdes, S. Vrána, F. Finger, V. Erban, G. Friedl, C.J.R. Braithwaite, Low-pressure granulites of the Lišov Massif, southern Bohemia: Visean metamorphism of Late Devonian plutonic arc rocks, J. Petrol. 47 (2006) 705–744.

[68] J. Kalvoda, O. Bábek, O. Fatka, J. Leichmann, R. Melichar, S. Nehyba, P. Špaček, Brunovistulian terrane (Bohemian Massif, central Europe) from Late Proterozoic to late Paleozoic: a review, Int. J. Earth Sci. 97 (2008) 497–518.

[69] H. Klápová, J. Konopásek, K. Schulmann, Eclogites from the Czech part of the Erzgebirge multi-stage metamorphic and structural evolution, J. Geol. Soc. 155 (1998) 567–583.

[70] J. Konopásek, K. Schulmann, Variscan transpressional deformation and crustal folding in the Krkonose Mountains (northern margin of the Bohemian Massif), in : K. Schulmann (Ed.), Palaeozoic orogenesis and crustal evolution of European lithosphere, Univerzita Karlova, Prague, Czech Republic, 1998, pp. 279–280.

[71] J. Konopásek, K. Schulmann, Contrasting Early Carboniferous field geotherms: evidence for accretion of a thickened orogenic root and subducted Saxothuringian crust (central European Variscides), J. Geol. Soc. 162 (2005) 463–470.

[72] J. Konopásek, K. Schulmann, O. Lexa, Structural evolution of the central part of the Krusne hory (Erzgebirge) Mountains in the Czech Republic - evidence for changing stress regime during Variscan compression, J. Struct. Geol. 23 (2001) 1373–1392.

[73] J. Konopásek, K. Schulmann, V. Johan, Eclogite-facies metamorphism at the eastern margin of the Bohemian Massif – subduction prior to continental underthrusting? Eur. J. Mineral. 14 (2002) 701–713.

[74] J. Košler, M. Aftalion, D. Bowes, Mid–Late Devonian plutonic activity in the Bohemian Massif: U–Pb zircon isotopic evidence from the Staré Sedlo and Mirotice gneiss complexes, Czech Republic, Neues Jahrb. Miner. Monat. (1993) 417–431.

[75] J. Košler, S. Kelley, D. Vance, M. Svojtka, Independent dating of cooling and decompression of high grade rocks in the Southern Bohemian Massif with Ar-Ar, Sm-Nd and U-Pb Techniques, J. Conf. Abs. 4 (1999) 39.

[76] J. Košler, D.R. Bowes, J. Konopásek, J. Míková, Laser ablation ICPMS dating of zircons in Erzgebirge orthogneisses: evidence for Early Cambrian and Early Ordovician granitic plutonism in the western Bohemian Massif, Eur. J. Mineral. 16 (2004) 15–22.

[77] M. Košuličová, P. Špaček, Variations in the transient prograde geothermal gradient from chloritoid-staurolite equilibria: a case study from the Barrovian and Buchan-type domains in the Bohemian Massif, J. Metamorph. Geol. 25 (2007) 19–36.

[78] M. Košuličová, R. Montigny, K. Schulmann, P. Špaček, Late Paleozoic thermal overprints exemplified by Th-U-Pb monazite and K-Ar mica dating at the eastern margin of the Bohemian Massif (West Sudets, Czech Republic), Bull. Soc. geol. France (2008), submitted for publication.

[79] J. Kotková, Tectonometamorphic history of lower crust in the Bohemian Massif: example of north Bohemian granulites, Czech Geol. Surv. Spec. Paper 2 (1993) 1–42.

[80] J. Kotková, A. Kröner, W. Todt, J. Fiala, Zircon dating of North Bohemian granulites, Czech Republic: further evidence for the Lower Carboniferous high-pressure event in the Bohemian Massif, Geol. Rundsch. 85 (1996) 154–161.

[81] J. Kotková, A. Gerdes, R. Parrish, M. Novák, Clasts of Variscan high-grade rocks within Upper Visean conglomerates-cons-

traints on exhumation history from petrology and U-Pb chronology, J. Metamorph. Geol. 25 (2007) 781–801.

[82] B. Kříbek, Z. Pouba, V. Skoček, J. Waldhausrová, Neoproterozoic of the Teplá-Barrandian Unit as a part of the Cadomian orogenic belt: a review and correlation aspects, Bull. Czech Geol. Soc. 75 (2000) 175–196.

[83] A. Kröner, A. Willner, Time of formation and peak of Variscan HP-HT metamorphism of quartz-feldspar rocks in the central Erzgebirge, Saxony, Germany, Contrib. Mineral. Petrol. 132 (1998) 1–20.

[84] A. Kröner, P. O'Brien, A. Nemchin, R. Pidgeon, Zircon ages for high pressure granulites from South Bohemia, Czech Republic, and their connection to Carboniferous high temperature processes, Contrib. Mineral. Petrol. 138 (2000) 127–142.

[85] A. Kröner, A. Willner, E. Hegner, A. Frischbutter, J. Hofmann, R. Bergner, Latest Precambrian (Cadomian) zircon ages, Nd isotopic systematics and PT evolution of granitoid orthogneisses of the Erzgebirge, Saxony and Czech Republic, Int. J. Earth Sci. 84 (1995) 437–456.

[86] M. Krs, P. Pruner, Paleomagnetism, Palaeogeography of the Variscan Formations of the Bohemian Massif, J. Czech. Geol. Soc. 40 (1995) 3–45.

[87] S. Lamb, L. Hoke, L. Kennan, J. Dewey, Cenozoic evolution of the central Andes in Bolivia and northern Chile, Geol. Soc. London Spec. Publ. 121 (1997) 237–264.

[88] T. Liew, F. Finger, V. Höck, The Moldanubian granitoid plutons of Austria: chemical and isotopic studies bearing on their environmental setting, Chem. Geol. 76 (1989) 41–55.

[89] U. Linnemann, N.J. McNaughton, R.L. Romer, M. Gehmlich, K. Drost, C. Tonk, West African provenance for Saxo-Thuringia (Bohemian Massif): did Armorica ever leave pre-Pangean Gondwana? U/Pb-SHRIMP zircon evidence and the Nd-isotopic record, Int. J. Earth Sci. 93 (2004) 683–705.

[90] H. Maluski, F. Patočka, Geochemistry and $^{40}Ar/^{39}Ar$ geochronology of the mafic metavolcanic rocks from the Rýchory Mountains complex (West Sudetes, Bohemian Massif): palaeotectonic significance, Geol. Mag. 134 (1997) 703–716.

[91] H. Maluski, P. Rajlich, J. Souček, Pre-Variscan, Variscan and early Alpine thermo-tectonic history of the north-eastern Bohemian Massif; an (super 40) Ar/ (super 39) Ar study, Geol. Rundsch. 84 (1995) 345–358.

[92] H.J. Massonne, Early metamorphic evolution and exhumation of felsic high-pressure granulites from the north-western Bohemian Massif, Springer Wien, 2006, pp. 177–202.

[93] P. Matte, The Variscan collage and orogeny (480–290 Ma) and the tectonic definition of the Armorica microplate: a review, Terra Nova 13 (2001) 122–128.

[94] P. Matte, H. Maluski, P. Rajlich, W. Franke, Terrane boundaries in the Bohemian Massif – result of large-scale Variscan shearing, Tectonophysics 177 (1990) 151.

[95] S. Mazur, P. Aleksandrowski, R. Kryza, T. Oberc-Dziedzic, The Variscan Orogen in Poland, Geol. Q. 50 (2006) 89–118.

[96] W.S. McKerrow, C. Mac Niocaill, P.E. Ahlberg, G. Clayton, C.J. Cleal, R.M.C. Eagar, The Late Palaeozoic relations between Gondwana and Laurussia, Geol. Soc. London Spec. Publ. 179 (2000) 9–20.

[97] G. Medaris, E. Jelínek, Z. Mísař, Czech eclogites. Terrane settings, interpretation for Variscan tectonic evolution of the Bohemian Massif, Eur. J. Mineral. 7 (1995) 7–28.

[98] J. Nawrocki, The Devonian–Carboniferous platform paleomagnetic directions from the Silesian–Krakow area and their importance for Variscan paleotectonic reconstructions, Geol. Q. 37 (1993) 397–430.

[99] P. O'Brien, Garnet zoning and reaction textures in overprinted eclogites, Bohemian Massif, European Variscides: a record of their thermal history during exhumation, Lithos 41 (1997) 119–133.

[100] P. O'Brien, The fundamental Variscan problem: high-temperature metamorphism at different depths and high-pressure metamorphism at different temperatures, in: W. Franke, V. Haak, O. Oncken, D. Tanner (Eds.), Orogenic Processes: Quantification and Modelling in the Variscan Belt, Geological Society, London, 2000, pp. 369.

[101] P. O'Brien, C. Rohr, M. Okrush, M. Patzak, Eclogite facies relics and a multistage breakdown in metabasites of the KTB pilot hole, NE Bavaria: implications for the Variscan tectonometamorphic evolution of the NW Bohemian Massif, Contrib. Mineral. Petrol. 112 (1992) 261–278.

[102] P.J. O'Brien, D.A. Carswell, Tectonometamorphic evolution of the Bohemian Massif - evidence from high-pressure metamorphic rocks, Geol. Rundsch. 82 (1993) 531–555.

[103] P.J. O'Brien, S. Vrána, Eclogites with a short-lived granulite-facies overprint in the Moldanubian Zone, Czech Republic – petrology, geochemistry and diffusion modeling of garnet zoning, Geol. Rundsch. 84 (1995) 473–488.

[104] O. Oncken, C. von Winterfeld, U. Dittmar, Accretion of a rifted passive margin: the Late Paleozoic Rhenohercynian fold and thrust belt (Middle European Variscides), Tectonics 18 (1999) 75–91.

[105] O. Oncken, D. Hindle, J. Kley, K. Elger, P. Victor, K. Schemmann, Deformation of the central Andean Upper Plate System—facts, fiction, and constraints for plateau models, in : O. Oncken, et al. (Eds.), The Andes, Springer Verlag, 2006, pp. 3–27.

[106] F. Paris, Early Palaezoic palaeography of northern Gondwana regions, Acta Univ. Carol. Geol. 42 (1998) 473–483.

[107] F. Patočka, J. Valenta, Geochemistry of the Late Devonian intermediate to acid metavolcanic rocks from the southern part of the Vrbno Group, the Jeseniky Mts. (Moravo-Silesian Belt, Bohemian Massif, Czech Republic): paleotectonic implications, Geolines 4 (1996) 42–54.

[108] F. Patočka, P. Vlašímský, K. Blechová, Geochemistry of Early Paleozoic volcanics of the Barrandian Basin (Bohemian Massif, Czech Republic): implications for Paleotectonic reconstructions, Jahrb. Geol. Bundelsansalt 136 (1993) 871–894.

[109] K. Petrakakis, Evolution of Moldanubian rocks in Austria: review and synthesis, J. Metamorph. Geol. 15 (1997) 203–222.

[110] P. Pitra, J.P. Burg, M. Giraud, Late-Variscan strike-slip tectonics between the Teplá-Barrandian and Moldanubian terranes (Czech Bohemian Massif): petrostructural evidence, J. Geol. Soc. 156 (1999) 1003–1020.

[111] P. Pitra, J.P. Burg, K. Schulmann, P. Ledru, Late Orogenic extension in the Bohemian Massif – petrostructural evidence in the Hlinsko Region, Geodin. Acta 7 (1994) 15–30.

[112] M. Racek, P. Štípská, P. Pitra, K. Schulmann, O. Lexa, Metamorphic record of burial and exhumation of orogenic lower and middle crust: a new tectonothermal model for the Drosendorf window (Bohemian Massif, Austria), Mineral. Petrol. 86 (2006) 221–251.

[113] P. Rajlich, J. Synek, M. Sarbach, K. Schulmann, Hercynian-thrust related shear zones and deformation of the Varied Group on the contact of granulites/southern Moldanubian, Bohemian Massif, Int. J. Earth Sci. 75 (1986) 665–683.

[114] J. Schäfer, W. Dörr, Ergebnisse zur Liefergebietsanbindung des saxothuringischen Flyschs durch Stoffbestandsuntersuchungen und U–Pb-Datierungen detrischer Zirkone, Terra Nostra 984 (1994) 95–96.

[115] D. Scheuvens, G. Zulauf, Exhumation, strain localization, and emplacement of granitoids along the western part of the central Bohemian shear zone (Bohemian Massif), Int. J. Earth Sci. 89 (2000) 617–630.

[116] E. Schmädicke, M. Okrusch, W. Schmidt, Eclogite-facies rocks in the Saxonian Erzgebirge Germany: high pressure metamorphism under contrasting P-T conditions, Contrib. Mineral. Petrol. 1992 (1992) 226–241.

[117] D. Schneider, S. Zahniser, J. Glascock, S. Gordon, M. Manecki, Thermochronology of the West Sudetes (Bohemian Massif): Rapid and repeated eduction in the eastern Variscides, Poland and Czech Republic, Am. J. Sci. 306 (2006) 846.

[118] K. Schulmann, Fabric and kinematic study of the Bites Orthogneiss (Southwestern Moravia) – result of large-scale northeastward shearing parallel to the Moldanubian Moravian Boundary, Tectonophysics 177 (1990) 229–244.

[119] K. Schulmann, R. Gayer, A model for a continental accretionary wedge developed by oblique collision; the NE Bohemian Massif, J. Geol. Soc. 157 Part 2 (2000) 401–416.

[120] K. Schulmann, P. Ledru, A. Autran, R. Melka, J. Lardeaux, M. Urban, M. Lobkowicz, Evolution of nappes in the eastern margin of the Bohemian Massif: a kinematic interpretation, Int. J. Earth Sci. 80 (1991) 73–92.

[121] K. Schulmann, R. Melka, M. Lobkowicz, P. Ledru, J. Lardeaux, A. Autran, Contrasting styles of deformation during progressive nappe stacking at the southeastern margin of the Bohemian Massif (Thaya Dome), J. Struct. Geol. 16 (1994) 355–370.

[122] K. Schulmann, A. Kroner, E. Hegner, I. Wendt, J. Konopásek, O. Lexa, P. Štípská, Chronological constraints on the pre-orogenic history, burial and exhumation of deep-seated rocks along the eastern margin of the Variscan Orogen, Bohemian Massif, Czech Republic, Am. J. Sci. 305 (2005) 407–448.

[123] K. Schulmann, O. Lexa, P. Štípská, M. Racek, L. Tajčmanová, J. Konopásek, J.B. Edel, A. Peschler, J. Lehmann, Vertical extrusion and horizontal channel flow of orogenic lower crust: key exhumation mechanisms in large hot orogens? J. Metamorph. Geol. 26 (2008) 273–297.

[124] W. Siebel, C. Shang, E. Reitter, J. Rohrmuller, K. Breiter, Two distinctive granite suites in the SW Bohemian Massif and their record of emplacement: Constraints from geochemistry and zircon $^{207}Pb/^{206}Pb$ chronology, J. Petrol. 49 (2008) 1853–1872.

[125] W. Siebel, H. Raschka, W. Irber, H. Kreuzer, K. Lenz, I. Wendt, Early Palaeozoic acid magmatism in the Saxothuringian Belt: new insights from a geochemical and isotopic study of orthogneisses and metavolcanic rocks from the Fichtelgebirge, SE Germany, J. Petrol. 38 (1997) 203–229.

[126] P. Špaček, J. Kalvoda, E. Franců, R. Melichar, Variation of deformation mechanisms within the progressive-retrogressive mylonitization cycle of limestones: Brunovistulian sedimentary cover (the Variscan orogeny of the southeastern Bohemian Massif), Geol. Carpath. 52 (2001) 263–275.

[127] P. Štípská, K. Schulmann, Inverted metamorphic zonation in a basement-derived nappe sequence; eastern margin of the Bohemian Massif, Geol. J. 30 (1995) 385–413.

[128] P. Štípská, R. Powell, Constraining the PT path of a MORB-type eclogite using pseudosections, garnet zoning and garnet-clinopyroxene thermometry: an example from the Bohemian Massif, J. Metamorph. Geol. 23 (2005) 725–743.

[129] P. Štípská, R. Powell, Does ternary feldspar constrain the metamorphic conditions of high-grade meta-igneous rocks? Evidence from orthopyroxene granulites, Bohemian Massif, J. Metamorph. Geol. 23 (2005) 627–647.

[130] P. Štípská, K. Schulmann, A.B. Thompson, J. Ježek, A. Kröner, Thermo-mechanical role of a Cambro-Ordovician paleorift during the Variscan collision: the NE margin of the Bohemian Massif, Tectonophysics 332 (2001) 239–253.

[131] P. Štípská, K. Schulmann, A. Kröner, Vertical extrusion and middle crustal spreading of omphacite granulite: a model of syn-convergent exhumation (Bohemian Massif, Czech Republic), J. Metamorph. Geol. 22 (2004) 179–198.

[132] P. Štípská, P. Pitra, R. Powell, Separate or shared metamorphic histories of eclogites and surrounding rocks? An example from the Bohemian Massif, J. Metamorph. Geol. 24 (2006) 219–240.

[133] P. Štípská, K. Schulmann, R. Powell, Contrasting metamorphic histories of lenses of high-pressure rocks and host migmatites with a flat orogenic fabric (Bohemian Massif, Czech Republic): a result of tectonic mixing within horizontal crustal flow? J. Metamorph. Geol. 26 (2008) 623–646.

[134] H. Stosch, G. Lugmair, Geochemistry and evolution of MORB-type eclogites from the Münchberg Massif, southern Germany, Earth Planet. Sci. Lett. 99 (1990) 230–249.

[135] L. Strnad, M. Mihaljevič, Sedimentary provenance of Mid-Devonian clastic sediments in the Teplá-Barrandian Unit (Bohemian Massif): U–Pb and Pb–Pb geochronology of detrital zircons by laser ablation ICP-MS, Mineral. Petrol. 84 (2005) 47–68.

[136] F.E. Suess, Die moravischen Fenster und ihre Beziehung zum Grundgebirge des Hohen Gesenkes, Denkschr. K. K. Akad. Wiss. 83 (1912) 541–631.

[137] F.E. Suess, Intrusionstektonik und Wandertektonik im variszischen Grundgebirge, Verlag von Gebrüder Borntraeger, Berlin, 1926p. 268.

[138] M. Svojtka, J. Košler, Z. Venera, Dating granulite-facies structures and the exhumation of lower crust in the Moldanubian Zone of the Bohemian Massif, Int. J. Earth Sci. 91 (2002) 373–385.

[139] J. Tait, V. Bachtadse, H. Soffel, Eastern Variscan fold belt; paleomagnetic evidence for oroclinal bending, Geology 24 (1996) 871–874.

[140] J.A. Tait, V. Bachtadse, W. Franke, H.C. Soffel, Geodynamic evolution of the European Variscan fold belt: palaeomagnetic and geological constraints, Geol. Rundsch. 86 (1997) 585–598.

[141] J. Tait, V. Bachtadse, J. Dinares-Turell, Paleomagnetism of Siluro-Devonian sequences, NE Spain, J. Geophys. Res. 105 (2000) 23,595–23,603.

[142] L. Tajčmanová, J. Konopásek, K. Schulman, Thermal evolution of the orogenic lower crust during exhumation within a thickened Moldanubian root of the Variscan belt of central Europe, J. Metamorph. Geol. 24 (2006) 119–134.

[143] L. Tajčmanová, J. Konopásek, J. Connolly, Diffusion-controlled development of silica-undersaturated domains in felsic granulites of the Bohemian Massif (Variscan belt of central Europe), Contrib. Mineral. Petrol. 153 (2007) 237–250.

[144] M. Tichomirowa, Die Gneise des Erzgebirges-hochmetamorphe Äquivalente von Neoproterozoisch-frühpaläozoischen Grauwacken und Granitoiden der Cadomiden, Technische Universität Bergakademie Freiberg, 2003.

[145] H. Timmermann, V. Štědrá, A. Gerdes, S.R. Noble, R.R. Parrish, W. Dörr, The problem of dating high-pressure metamorphism: a U-Pb isotope and geochemical study on eclogites

and related rocks of the Marianské Lázně Complex, Czech Republic, J. Petrol. 45 (2004) 1311–1338.

[146] H. Timmermann, W. Dörr, E. Krenn, F. Finger, G. Zulauf, Conventional and in situ geochronology of the Teplá crystalline unit, Bohemian Massif: implications for the processes involving monazite formation, Int. J. Earth Sci. 95 (2006) 629–647.

[147] R.B. Trumbull, U. Riller, O. Oncken, E. Scheuber, K. Munier, F. Hongn, The time-space distribution of Cenozoic volcanism in the South-Central Andes: a new data compilation and some tectonic implications, in : O. Oncken, et al. (Eds.), The Andes, Springer Verlag, 2006, pp. 29–43.

[148] C. Vellmer, K. Wedepohl, Geochemical characterization and origin of granitoids from the South Bohemian Batholith in Lower Austria, Contrib. Mineral. Petrol. 118 (1994) 13–32.

[149] K. Verner, J. Žák, R. Nahodilová, F. Holub, Magmatic fabrics and emplacement of the cone-sheet-bearing Knížecí Stolec durbachitic pluton (Moldanubian Unit, Bohemian Massif): implications for mid-crustal reworking of granulitic lower crust in the central European Variscides, Int. J. Earth Sci. 97 (2008) 19–33.

[150] A. von Quadt, D. Gebauer, Evolution of eclogitic rocks in the Erzgebirge: a conventional and SHRIMP U-Pb zircon and Sm-Nd study, Acta Univ. Carol. Geol. 42 (1998) 324–1324.

[151] S. Vrána, Polyphase shear folding and thrusting in the Moldanubicum of southern Bohemia, Vestn. Ustr. Ust. Geol. 51 (1979) 75–86.

[152] S. Vrána, M. Novák, Petrology and geochemistry of granulite clasts in the Visean Luleč conglomerate, Kulm in central Moravia, Czech Republic, Bull. Czech Geol. Soc. 75 (2000) 405–413.

[153] J.I. Wendt, A. Kröner, J. Fiala, W. Todt, U-Pb zircon and Sm-Nd dating of Moldanubian HP/HT granulites from South Bohemia, Czech Republic, J. Geol. Soc. 151 (1994) 83–90.

[154] A. Willner, K. Roetzler, W. Maresch, Pressure-temperature and fluid evolution of quartzo-feldspathic metamorphic rocks with a relic high-pressure, granulite-facies history from the central Erzgebirge (Saxony, Germany), J. Petrol. 38 (1997) 307–336.

[155] V. Žáček, Garnets and metamorphic evolution of the Teplá crystalline complex, western Bohemia, Zentralbl. Geologie. Palaontol. 1 (1994) 847–856.

[156] V. Žáček, J. Cháb, Metamorphism in the Tepla upland, Bohemian massif, Czech Republic (preliminary report), Bull. Czech Geol. Soc. 68 (1993) 33.

[157] J. Žák, F. Holub, K. Verner, Tectonic evolution of a continental magmatic arc from transpression in the upper crust to exhumation of mid-crustal orogenic root recorded by episodically emplaced plutons: the Central Bohemian Plutonic Complex (Bohemian Massif), Int. J. Earth Sci. 94 (2005) 385–400.

[158] J. Žák, K. Schulmann, F. Hrouda, Multiple magmatic fabrics in the Sázava pluton (Bohemian Massif, Czech Republic): a result of superposition of wrench-dominated regional transpression on final emplacement, J. Struct. Geol. 27 (2005) 805–822.

[159] J. Žák, F. Holub, V. Kachlík, Magmatic stoping as an important emplacement mechanism of Variscan plutons: evidence from roof pendants in the Central Bohemian Plutonic Complex (Bohemian Massif), Int. J. Earth Sci. 95 (2006) 771–789.

[160] G. Zulauf, Von der Anchizone bis zur Eklogitfazies: Angekippte Krustenprofile als Folge der cadomischen und variscischen Orogenese im Teplá-Barrandium (Böhmische Masse), Geotekton. Forsch. 89 (1997) 1–302.

[161] G. Zulauf, Structural style, deformation mechanisms and paleodifferential stress along an exposed crustal section: constraints on the rheology of quartzofeldspathic rocks at supra- and infrastructural levels (Bohemian Massif), Tectonophysics 332 (2001) 211–237.

[162] G. Zulauf, C. Bues, W. Dörr, Z. Vejnar, 10 km Minimum throw along the West Bohemian shear zone: evidence for dramatic crustal thickening and high topography in the Bohemian Massif (European Variscides), Int. J. Earth Sci. 91 (2002) 850–864.

[163] G. Zulauf, W. Dörr, J. Fiala, J. Kotková, H. Maluski, P. Valverde-Vaquero, Evidence for high-temperature diffusional creep preserved by rapid cooling of lower crust (North Bohemian shear zone, Czech Republic), Terra Nova 14 (2002) 343–354.

J. metamorphic Geol., 2010, **28,** 97–116 doi:10.1111/j.1525-1314.2009.00857.x

Using calculated chemical potential relationships to account for coronas around kyanite: an example from the Bohemian Massif

P. ŠTÍPSKÁ,[1] R. POWELL,[2] R. W. WHITE[3] AND J. A. BALDWIN[4]
[1]*Ecole et Observatoire des Sciences de la Terre, IPGS (CNRS UMR7516), Université de Strasbourg, 1 rue Blessig, 67084 Strasbourg, France (stipska@gmail.com)*
[2]*School of Earth Sciences, The University of Melbourne, Melbourne, Vic. 3010, Australia*
[3]*Institute for Geosciences, University of Mainz, D-55099 Mainz, Germany*
[4]*Department of Geosciences, University of Montana, Missoula, MT 59812, USA*

ABSTRACT Corona textures around kyanite, involving for example zoned plagioclase separating kyanite from the matrix, reflect the instability of kyanite with the matrix on changing *P–T* conditions, commonly related to decompression. The chemical potential gradients set up between the kyanite and the matrix as a consequence of slow Al diffusion drive corona development, with the zoning of the plagioclase reflecting the gradients. Calculated mineral equilibria are used to account for corona textures involving plagioclase ± garnet around kyanite, and replacement of kyanite by plagioclase + spinel symplectite, in quartz + plagioclase + K-feldspar + garnet + kyanite granulite facies gneiss from the Blanský les massif in the Bohemian massif, Czech Republic. In the garnet-bearing coronas, a commonly discontinuous garnet layer lies between the kyanite and the continuous plagioclase layer in the corona, with both the garnet and the plagioclase appearing mainly to replace matrix rather than kyanite. The garnet layer commonly extends around kyanite from original matrix garnet adjacent to the kyanite. Where garnet is missing in the corona, the kyanite itself may be replaced by a spinel–plagioclase corona. In a local equilibrium model, the mineral and mineral compositional spatial relationships are shown to correspond to paths in $\mu(Na_2O)$–$\mu(CaO)$–$\mu(K_2O)$–$\mu(FeO)$–$\mu(MgO)$–$\mu(SiO_2)$ in the model chemical system, Na_2O–CaO–K_2O–FeO–MgO–Al_2O_3–SiO_2 (NCKFMAS). The discontinuous nature of the garnet layer in coronas is accounted for by the effect of the adjacent original garnet on the chemical potential relationships. The replacement of kyanite by spinel + plagioclase appears to be metastable with respect to replacement by corundum + plagioclase, possibly reflecting the difficulty of nucleating corundum.

Key words: Bohemian massif; chemical potential; ky–K-feldspar granulite; plagioclase ± garnet around kyanite; plagioclase–spinel symplectite.

INTRODUCTION

In an equilibrium model of metamorphism, a mineral assemblage and the mineral compositions are at equilibrium on some length scale at the prevailing pressure–temperature (*P–T*) conditions (e.g. Powell *et al*., 2005), building on the idea of local or mosaic equilibrium (Korzhinskii, 1959; Thompson, 1959). If a new mineral does not nucleate with changing conditions, the equilibrium will be a metastable one, rather than the stable one. If the scale of equilibration is vanishingly small, no visible change occurs. Equilibration itself is dependent on rates of intergranular (i.e. grain boundary, or intercrystalline) and intracrystalline diffusion, which in turn depend on temperature, rate of change of temperature with time, fluid/melt presence/absence, grain size, strain in the minerals, etc.

Assuming equalized *P–T* between the different parts of a mineral assemblage, equilibration involves equalizing of chemical potentials. If, with changing *P–T*, minerals in an assemblage are no longer in equilibrium with each other, chemical potential gradients are established between them. Reaction will then occur in an attempt to flatten out the gradients. As discussed in White *et al*. (2008), such reaction may proceed to completion, with chemical potential gradients removed, while still leaving spatial and compositional consequences of the reaction path, particularly for reaction in the prograde history. Reaction in the retrograde history commonly does not proceed to completion, with effective reaction ceasing during cooling because the rate of equilibration becomes too slow even though chemical potential gradients are still present. This, combined with the coarser-grained nature of higher temperature mineral assemblages, results in the characteristic feature of retrograde reaction in higher grade rocks: the development of coronas.

A situation in which corona development may occur is in response to chemical potential gradients established between a mineral and other parts of a mineral

assemblage when they are no longer in equilibrium with each other with changed *P–T*. This appears to be commonly the case for kyanite. With the assumption of local equilibrium in the corona around the mineral, the minerals and their compositions will be the (stable or metastable) equilibrium ones at the chemical potentials that exist at that position along the spatially developed chemical potential gradients.

There are two lineages for considering the consequences of chemical potential gradients to account for reaction textures in a local equilibrium context that start with Korzhinskii, as outlined by White *et al.* (2008). One lineage runs through Thompson (1959, 1970), Brady (1977) and Rumble (1982) to the present day. In this lineage, the chemical potential relationships are the primary focus, but, for example, the paths across chemical potential diagrams are essentially qualitative. The other, with a focus on physical modelling of coronas, starts with Fisher (1973), and proceeds through Joesten (1977), and for example Ashworth & Birdi (1990) to the present day. In this lineage, in principle, the paths across chemical potential diagrams should be able to be calculated, but the information is not available to do that currently, except in simple situations. So, for example, systems involving solid solutions cannot be handled in a general way, yet most coronas of interest do involve solid solutions, as do the ones under consideration here. In accord with White *et al.* (2008), this study follows the first lineage by calculating chemical potential relationships for phase equilibria involving solid solutions, accepting that the paths in chemical potential will be essentially qualitative. Here we use calculated chemical potential relationships to account for corona textures around kyanite in felsic granulite from the Blanský les massif in the Bohemian massif, Czech Republic (Fig. 1).

GEOLOGICAL BACKGROUND

The classical lithological division of the Variscan Moldanubian internal orogenic zone in the Bohemian Massif includes the Gföhl unit and Monotonous and Varied groups (e.g. Fuchs, 1986; Fig. 1). The Gföhl unit is characterized by high-grade rocks, interpreted as orogenic lower crust (Schulmann *et al.*, 2005, 2008), that typically includes kyanite–K-feldspar granulite and migmatite orthogneiss, hosting mafic and intermediate granulite, peridotite and eclogite (e.g. Carswell, 1991; Medaris *et al.*, 1995, 2005; O'Brien & Rötzler, 2003; Hasalová *et al.*, 2008; Štípská *et al.*, 2008). The Monotonous and Varied groups are dominated by paragneisses that generally underwent upper amphibolite facies metamorphism and anatexis (Petrakakis, 1997; Schulmann *et al.*, 2008) and are interpreted as an orogenic middle crust (Schulmann *et al.*, 2008; Štípská *et al.*, 2008). The kyanite–K-feldspar granulites form bodies up to several kilometres long that appear in two N–S-trending belts, one in the middle of the Bohemian massif that includes the locality studied, and the other along its eastern margin (Fig. 1).

Kyanite–K-feldspar granulites commonly contain kyanite, garnet, K-feldspar, plagioclase, quartz ±perthite and/or antiperthite ±biotite ±sillimanite and rutile. The prograde path and peak conditions of the granulite massifs are disputed, with some authors preferring a high-pressure and high-temperature peak ~16–18 kbar and 800–850 °C, whereas others prefer ultrahigh pressure and/or ultrahigh temperature conditions (for recent discussions, see O'Brien & Rötzler, 2003; Štípská & Powell, 2005; O'Brien, 2008; Racek *et al.*, 2008). The retrograde path involves decompression to at least 10 kbar and in some areas may have continued to as low as 4 kbar almost isothermally or associated with some cooling, followed by strong cooling with moderate or minor decompression (Petrakakis, 1997; O'Brien & Rötzler, 2003; Racek *et al.*, 2006; Tajčmanová *et al.*, 2006; Schulmann *et al.*, 2008; Štípská *et al.*, 2008). The metamorphic peak is dated to *c.* 340 Ma (van Breemen *et al.*, 1982; Kröner *et al.*, 1988; Schulmann *et al.*, 2005; Janoušek *et al.*, 2006) and amphibolite facies retrogression to 335–325 Ma (Matte *et al.*, 1985; Brueckner *et al.*, 1991; Beard *et al.*, 1992; Dallmayer *et al.*, 1992; Friedl *et al.*, 2003; Schulmann *et al.*, 2008).

One of the major petrological features associated with the retrograde path is the transition of kyanite to sillimanite, with kyanite being commonly associated with the steep fabric and growth of abundant sillimanite in the areas of late intense flat fabric reworking (Tajčmanová *et al.*, 2006; Štípská *et al.*, 2008). Kyanite is commonly surrounded by plagioclase coronas in samples that may or may not contain sillimanite (O'Brien & Rötzler, 2003), and their progressive development has been described by Tajčmanová *et al.* (2007). In some areas there are also abundant coronitic structures around kyanite that involve other minerals such as spinel, garnet, sapphirine or corundum in addition to plagioclase (O'Brien & Rötzler, 2003). Some textural features, such as spinel-rich cores in some garnet, are also interpreted as pseudomorphs after kyanite (O'Brien & Rötzler, 2003). Analogous occurrences of plagioclase–around–kyanite coronas are described in the literature, that may also involve various other minerals such as corundum, spinel, sapphirine, garnet and cordierite (e.g. Dasgupta *et al.*, 1995; Okay, 1995; Owen & Dostal, 1996; Möller, 1998; O'Brien, 1999; Nakamura & Hirajima, 2000; Nakamura, 2002; O'Brien & Rötzler, 2003; Baldwin *et al.*, 2007).

PETROGRAPHY

Analytical procedures

The minerals were analysed using the Cameca SX100 at the Institute of Mineralogy, Petrology and

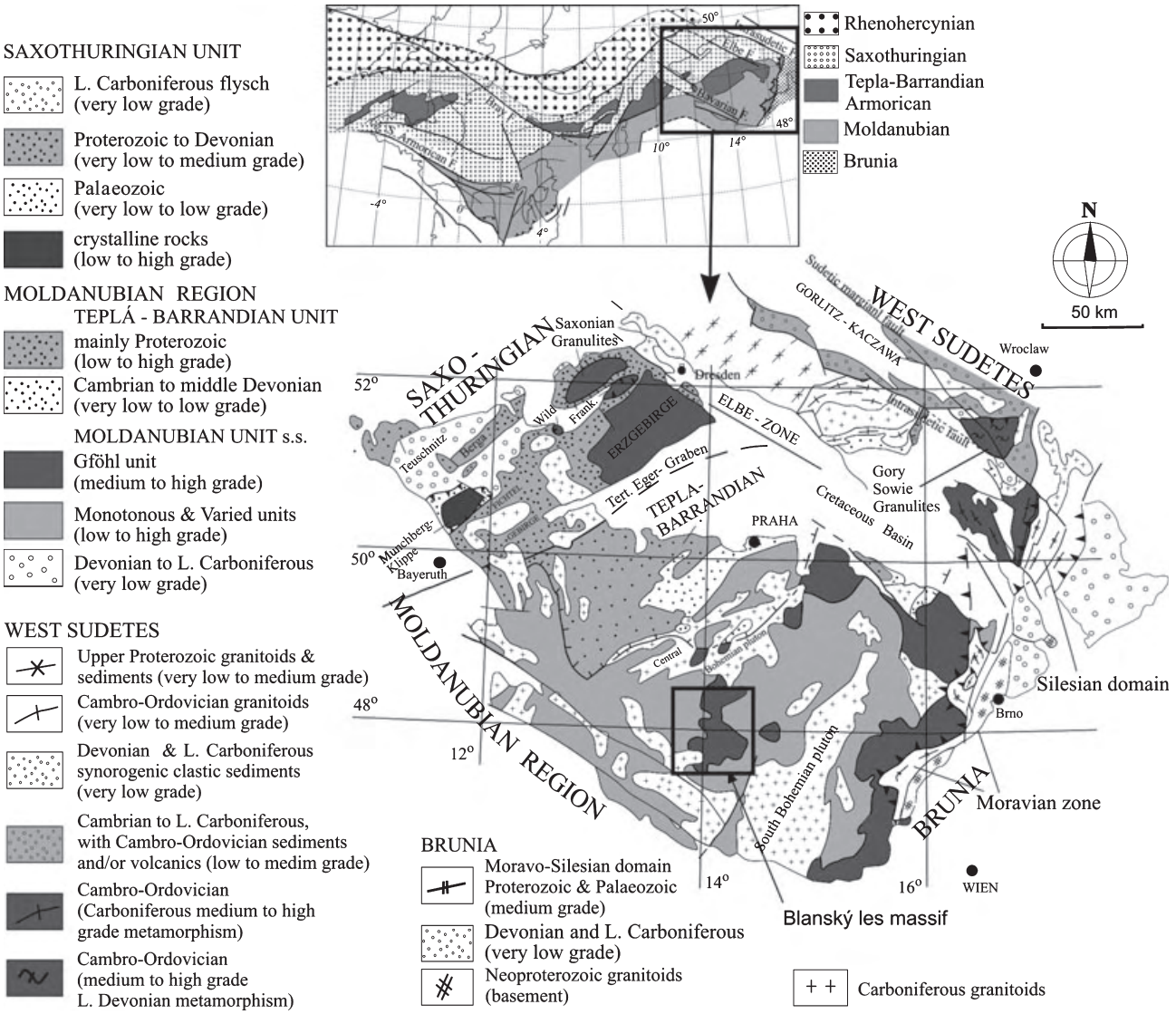

Fig. 1. Geological map of the Bohemian Massif with major units shown schematically (modified after Franke, 2000). Location of the study area is indicated. Upper left inset is position of study area in the framework of the European Variscides (modified after Edel *et al.*, 2003).

Geochemistry at the University of Freiburg, by WDS in point beam mode at 15 kV and 10 nA and the compositional maps were obtained on a scanning electron microscope VEGA\\XMU (Vega) at the University Louis Pasteur in Strasbourg. The sign '⇒' is used for a trend in mineral composition or for zoning and the sign '–' for a range of mineral compositions; p.f.u. is the per formula unit. Representative mineral analyses are summarized in Table 1, the mineral abbreviations and isopleth notation used are listed in the footnote of Table 1. Petrography and mineral chemistry are illustrated in Figs 2–6.

Kyanite–K-feldspar granulites

The samples studied are kyanite–K-feldspar granulites from the Zrcadlová huť quarry in the Blanský les massif (48°53′12.073″N, 14°13′53.852″E; for recent publications, see O'Brien & Rötzler, 2003; Franěk *et al.*, 2006). The samples studied (ZH20, ZH63 & ZH51) are white-grey fine-grained gneisses with small abundant pale rose-coloured garnet (max 1 mm), disseminated accessory amount of biotite and rutile and small green patches of spinel (max 1 mm). Foliation is marked by recrystallized feldspar and quartz bands (up to 4 mm thick) and oriented biotite and

Table 1. Representative mineral analyses, including list of mineral abbreviations and isopleth notations used in the text.

Sample ZH63-1									
Mineral	g-c	g-r	g-r	sp	pl	pl	pl	pl	bi
Position	Corona	Corona	Next to sp-pl sympl	In sympl	pl corona contact sp	pl corona contact mx	In sympl	pl mx	bi mx
Analysis	36	50	18	2	1	20	4	34	33
SiO_2	38.82	38.79	38.43	0.06	56.27	61.83	57.53	61.22	36.16
TiO_2	0.08	0.02	0.01	0.00	0.02	0.01	0.02	0.05	6.13
Cr_2O_3	0.00	0.00	0.00	0.02	0.00	0.00	0.00	0.01	0.07
Al_2O_3	21.97	21.97	22.13	61.53	27.81	23.78	27.44	23.96	15.69
FeO	24.71	28.67	31.62	27.21	0.22	0.01	0.47	0.09	12.79
MnO	0.39	0.52	0.76	0.08	0.01	0.01	0.00	0.02	0.02
MgO	6.39	8.31	7.40	9.88	0.00	0.01	0.12	0.00	14.01
CaO	8.71	2.57	0.74	0.04	9.35	4.96	8.26	4.90	0.00
Na_2O	0.00	0.00	0.00	0.00	6.32	8.93	6.88	8.97	0.12
K_2O	0.00	0.00	0.00	0.00	0.15	0.15	0.20	0.17	9.48
ZnO	0.00	0.00	0.00	0.52	0.00	0.00	0.00	0.00	0.00
Total	101.08	100.84	101.09	98.81	100.16	99.69	100.92	99.39	94.47
Cations (Fe^{2+}/Fe^{3+} charge balance)									
Si	2.97	2.97	2.97	0.00	2.52	2.74	2.55	2.72	2.80
Ti	0.00	0.00	0.00	0.00	0.00	0.00	0.00	0.00	0.36
Cr	0.00	0.00	0.00	0.00	0.00	0.00	0.00	0.00	0.00
Al	1.98	1.99	2.02	1.97	1.47	1.24	1.43	1.26	1.43
Fe^{3+}	0.08	0.07	0.05	0.02	0.01	0.00	0.02	0.00	0.00
Fe^{2+}	1.50	1.77	1.99	0.60	0.00	0.00	0.00	0.00	0.83
Mn	0.03	0.03	0.05	0.00	0.00	0.00	0.00	0.00	0.00
Mg	0.73	0.95	0.85	0.40	0.00	0.00	0.01	0.00	1.62
Ca	0.71	0.21	0.06	0.00	0.45	0.24	0.39	0.23	0.00
Na	0.00	0.00	0.00	0.00	0.55	0.77	0.59	0.77	0.02
K	0.00	0.00	0.00	0.00	0.01	0.01	0.01	0.01	0.94
Zn	0.00	0.00	0.00	0.02	0.00	0.00	0.00	0.00	0.00
Total	8.00	8.00	8.00	3.00	5.00	5.00	5.00	5.00	8.00
$X_{Fe(tot)}$/an	0.68	0.66	0.71	0.61	0.45	0.23	0.39	0.23	0.34
alm(Fe_{tot})/ab	0.52	0.61	0.68		0.55	0.76	0.59	0.76	
py(Fe_{tot})/or	0.24	0.31	0.28		0.01	0.01	0.01	0.01	
grs(Fe_{tot})	0.23	0.07	0.02						
sps(Fe_{tot})	0.01	0.01	0.02						

mu, muscovite; q, quartz; g, garnet; bi, biotite; cd, cordierite; cor, corundum; pl, plagioclase; ksp, K-feldspar; liq, granitic liquid; ilm, ilmenite; ru, rutile; sp, spinel; mx, matrix; sympl, symplectite; c, core; r, rim; alm, Fe/(Ca + Fe + Mg + Mn); prp, Mg/(Ca + Fe + Mg + Mn); grs, Ca/(Ca + Fe + Mg + Mn); sps, Mn/(Ca + Fe + Mg + Mn); X_{Fe}, Fe/(Fe + Mg); an, Ca/(Ca + Na + K); ab, Na/(Ca + Na + K); or, K/(Ca + Na + K). The isopleth notation used is: x(g, sp) = Fe/(Fe + Mg) × 100, z(g) = Ca/(Ca + Fe + Mg) × 100, ca(pl) = Ca/(Ca + Na) × 100.

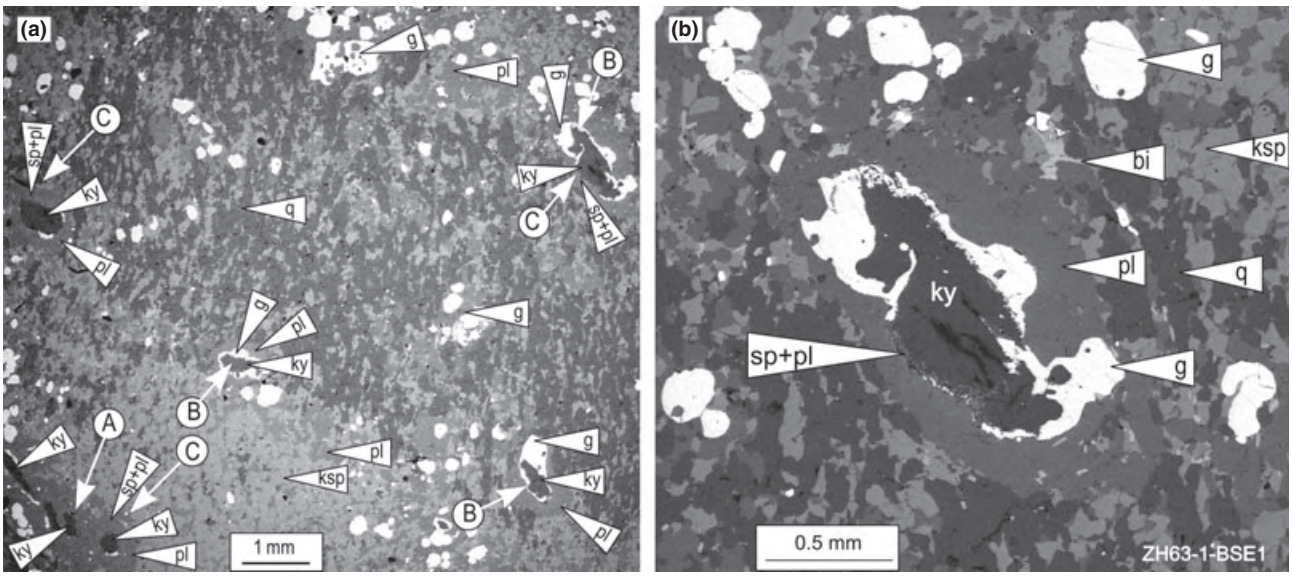

Fig. 2. (a) Banded kyanite–K-feldspar granulite (BSE). Indicated are kyanite grains with (A) just a plagioclase corona, (B) a plagioclase–garnet corona and (C) a plagioclase corona and spinel–plagioclase symplectite. (b) Enlarged view of a corona around kyanite involving plagioclase, discontinuous garnet and spinel–plagioclase symplectite.

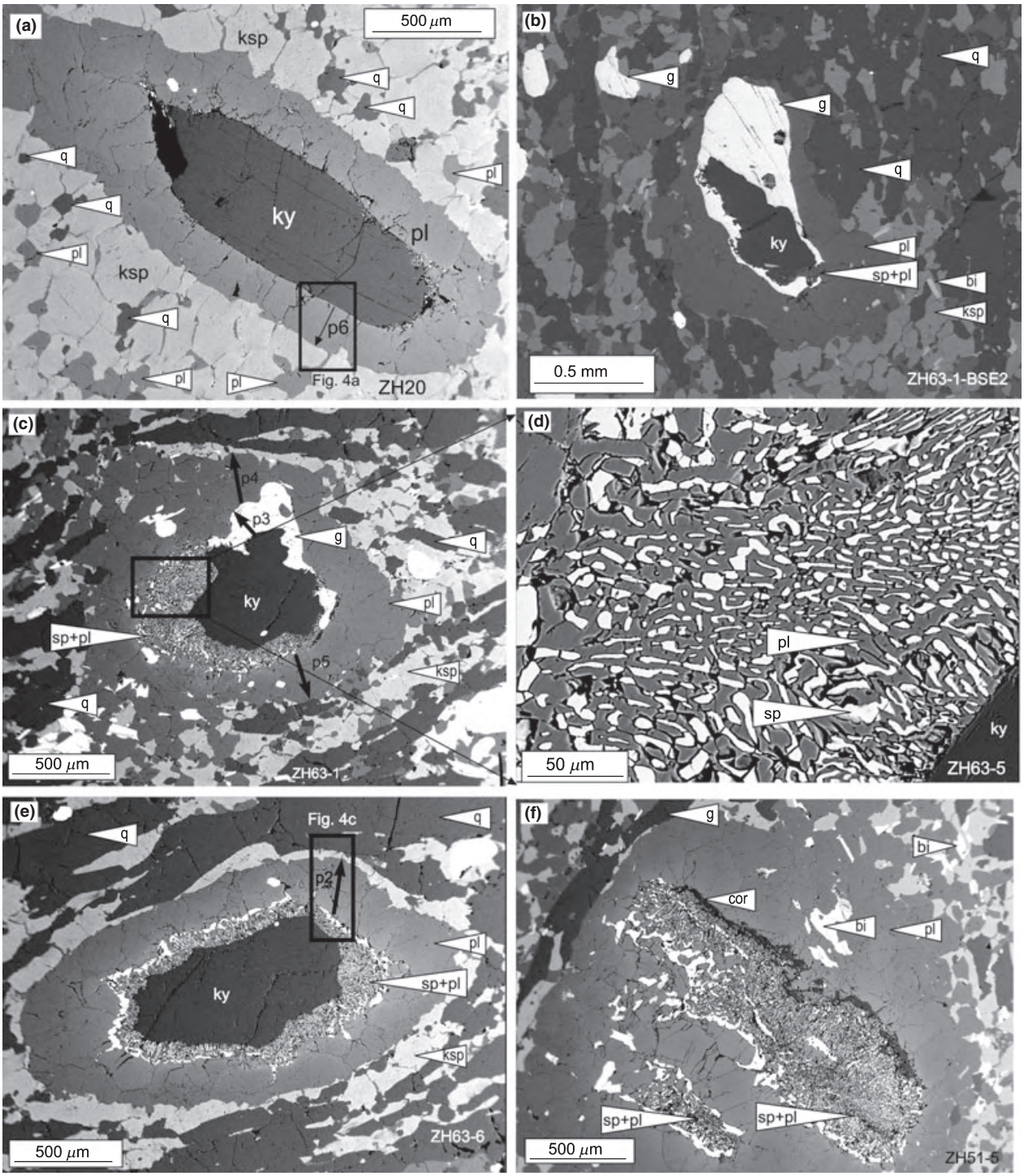

Fig. 3. BSE images of coronitic textures in kyanite–K-feldspar granulite. (a) Plagioclase corona separates kyanite from a matrix composed essentially of K-feldspar, quartz and plagioclase. (b, c) Discontinuous garnet around kyanite in between the kyanite and the plagioclase layer. A thin garnet corona extends from one or more larger garnet grains. The plagioclase corona layer is very thin or does not exist where a large garnet grain is present and is much thicker where the garnet extension is present or where the garnet layer is missing. Where the garnet corona is absent a spinel–plagioclase symplectite commonly develops. (d) Detail of spinel–plagioclase symplectite from (c). (e) Spinel–plagioclase symplectite with simple plagioclase–around–kyanite corona. Some boundaries of the spinel–plagioclase symplectite towards plagioclase are straight, interpreted as a former kyanite grain boundary. The symplectite is coarser-grained towards plagioclase and finer-grained at its contact with kyanite. (f) In a plagioclase corona a corundum–plagioclase symplectite is developed at one side of the spinel–plagioclase symplectite. Arrows in (a,) (c) and (e) indicate position of chemical profiles shown in Figs 5 & 6, rectangles in (a) and (e) are localizations of compositional maps from Fig. 4.

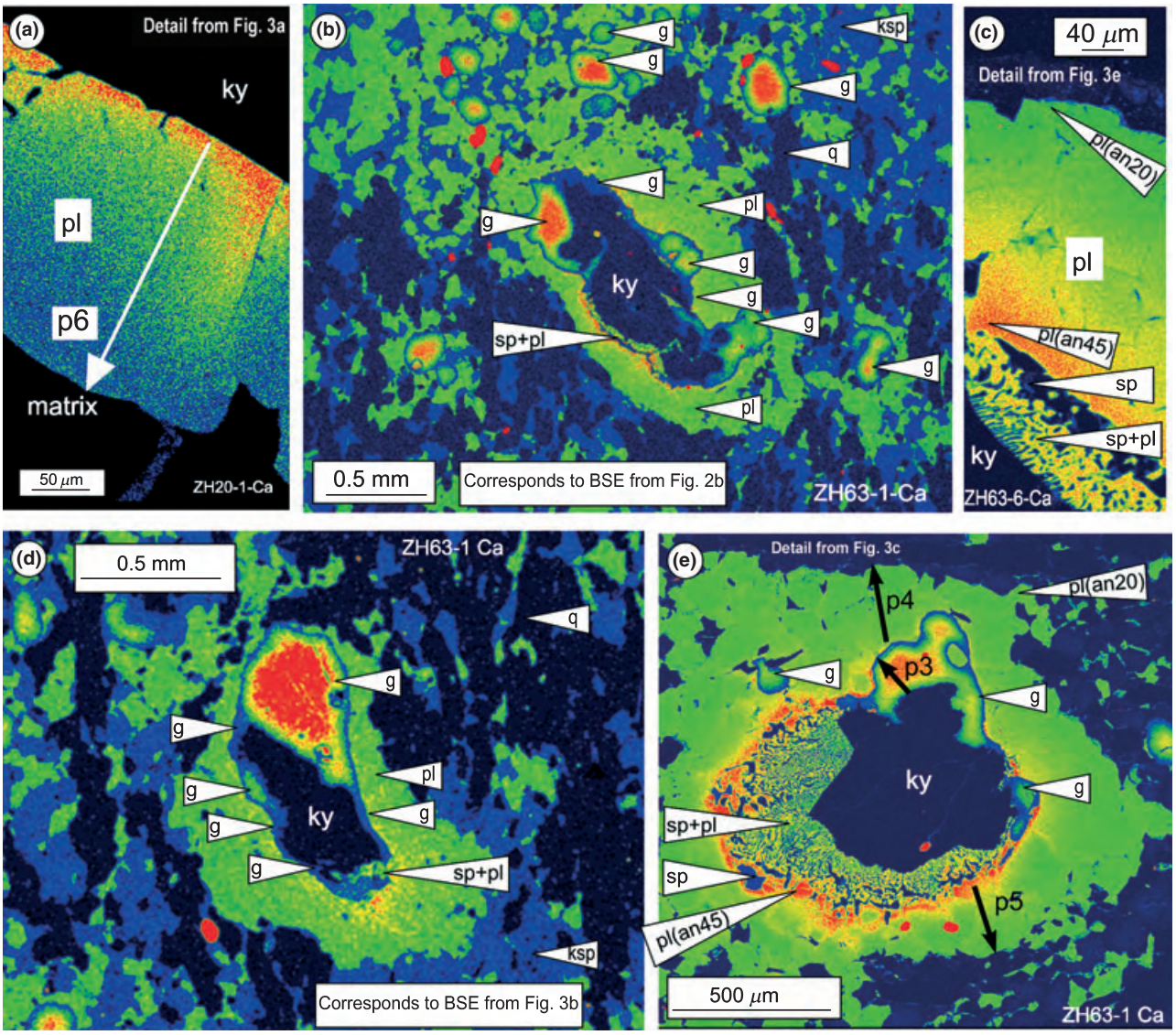

Fig. 4. Compositional maps of Ca. (a) Decrease in Ca content of plagioclase from kyanite to matrix in a simple plagioclase–around–kyanite corona. (b) Cores of garnet in the matrix and large garnet next to kyanite exhibit high Ca content (red), garnet rims and thin garnet corona around kyanite (dark blue) have low Ca content (light blue). Zoning of plagioclase corona is stronger where a garnet extension is missing and where spinel–plagioclase symplectite is developed (orange) than where a garnet layer is present (yellow-green). (c) Plagioclase corona shows strong zoning in Ca in between spinel–plagioclase symplectite and matrix. Plagioclase composition within the spinel–plagioclase symplectite is nearly constant. (d) Large high-Ca garnet (red) and almost continuous low-Ca (blue) garnet extensions along kyanite–plagioclase boundary. (e) Weak Ca zoning next to garnet across a plagioclase corona contrasts with strong Ca zoning next to spinel–plagioclase symplectite. Plagioclase composition within the spinel–plagioclase symplectite shows no zoning. Arrows indicate positions of chemical profiles presented in Figs 5 & 6.

spinel patches. Kyanite is only rarely visible macroscopically.

A back-scattered electron image of half a thin section is shown in Fig. 2a. This shows that the rock is layered with respect to the proportions of quartz and feldspar, and that there is a well-developed second fabric defined by quartz grain shape. The samples contain characteristic coronas around kyanite that involve plagioclase and, variously, garnet and spinel–plagioclase and corundum–plagioclase symplectites (Figs 2 & 3). The matrix is fine-grained (0.1 mm), composed of recrystallized K-feldspar, plagioclase and quartz, with numerous small garnet (1 mm) and kyanite, and accessory biotite, rutile and zircon. Matrix garnet and large garnet adjacent to kyanite have the same type of zoning, with core to rim being alm_{50}–py_{21}–grs_{24}–sps_0 and X_{Fe} = 68–70 to $alm_{60–65}$–py_{30}–$grs_{4–6}$–sps_0 and X_{Fe} = 65 (Figs 4 & 5). Plagioclase in the matrix has anorthite content ~20–23 mol.%. Biotite has X_{Fe} ~0.34 and Ti = 6.13 wt%.

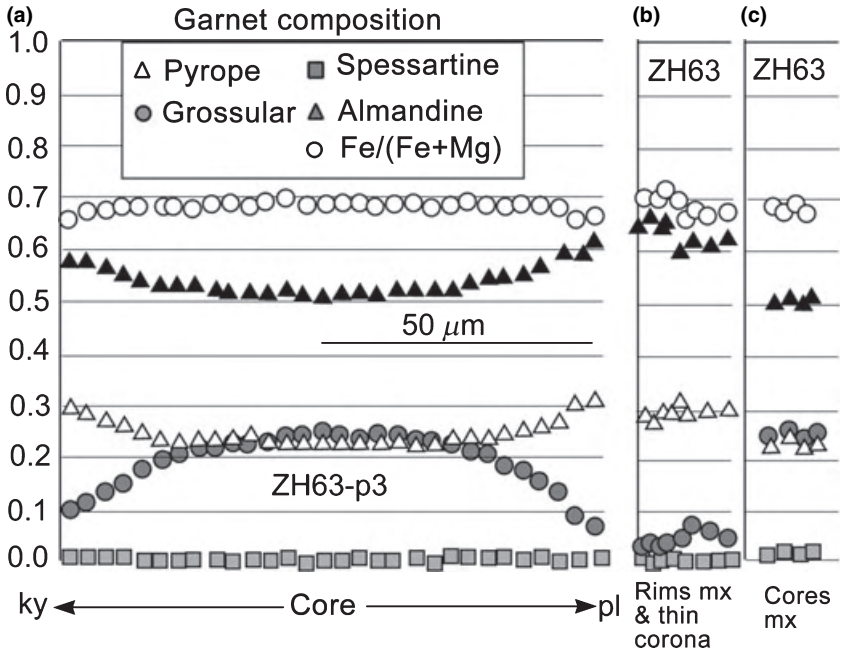

Fig. 5. Composition and zoning of garnet in textural positions as indicated.

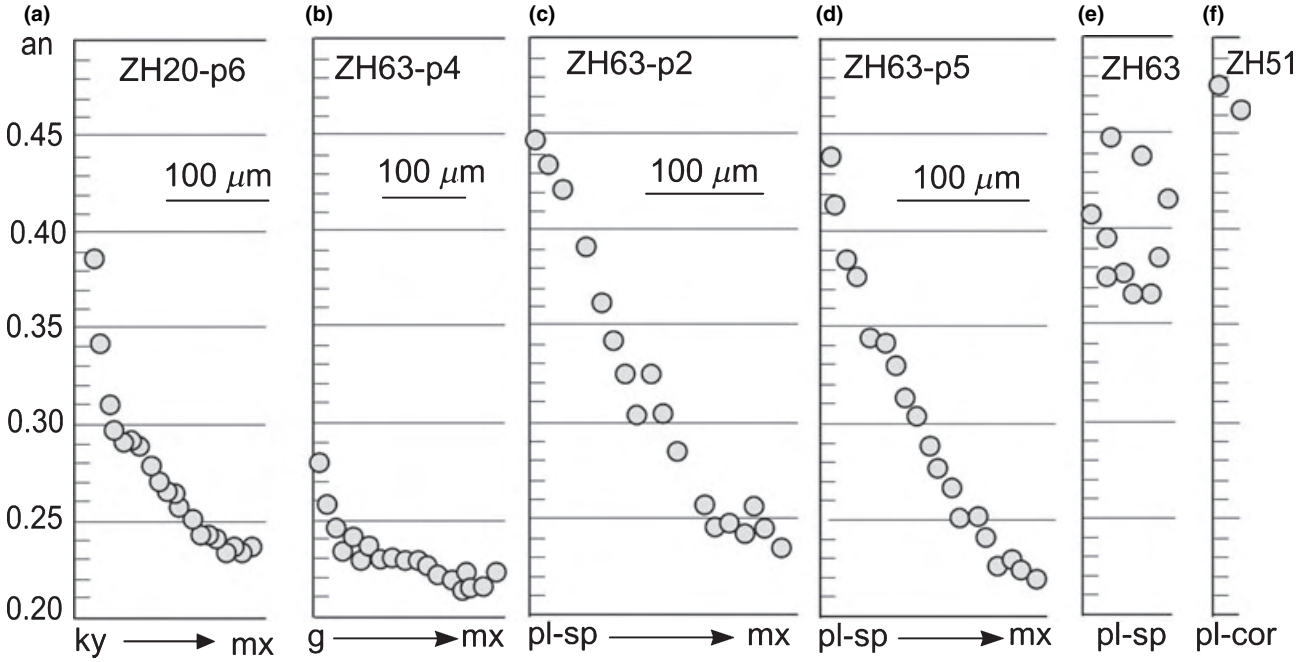

Fig. 6. Composition and zoning of plagioclase in textural positions as indicated.

Plagioclase–around–kyanite coronas

Kyanite in the kyanite–K-feldspar granulites of the Blanský les massif is commonly surrounded by a polycrystalline but monomineralic plagioclase corona that separates kyanite from a matrix that is composed essentially of K-feldspar, quartz and plagioclase (Fig. 3a). Texturally the kyanite appears not to be substantially replaced (e.g. not greatly embayed), so the plagioclase corona is considered to have grown mainly at the expense of the matrix. The plagioclase is strongly zoned, with anorthite content increasing from 20–23 mol.% at the contact with the matrix to 38–45 mol.% at the kyanite–plagioclase boundary

(Figs 4a & 6a). Orthoclase content in plagioclase is constant and ranges between 1–1.7 mol.%. The zoning is parallel to the kyanite edge, passing continuously across plagioclase grain boundaries in the corona (Fig. 4a)

Garnet–plagioclase coronas

Garnet may be present discontinuously around kyanite, occurring between the kyanite and the plagioclase layer in the overall corona. There is commonly one or more larger garnet grains adjacent to kyanite from which a thin garnet corona extends along the kyanite–plagioclase boundary (Figs 2b & 3b,c). The plagioclase corona layer is very thin or does not exist where a larger garnet grain is present and is much thicker where the garnet extension is present or where the garnet layer is missing (Figs 2b & 3b,c).

Large garnet grains in the corona are concentrically zoned, similar to the matrix garnet grains, with core to rim being alm_{50}–py_{21}–grs_{24}–sps_0 and X_{Fe} = 68–70 to $alm_{60–65}$–py_{30}–$grs_{4–6}$–sps_0 and X_{Fe} = 65 (Figs 4 & 5). The composition of the thin garnet extensions corresponds to the garnet rim compositions (Figs 4 & 5). Rare solitary garnet grains that occur next to spinel–plagioclase symplectites have very low grossular contents, with the composition of alm_{71}–py_{28}–grs_{02}–sps_{02} and X_{Fe} = 71. Plagioclase zoning where the garnet layer is present ranges from an = 20–22 mol.% at the contact with matrix to an = 38 mol.% at the contact with garnet (Figs 4b–d & 6b) and is thus commonly less strongly zoned than that in the simple plagioclase around kyanite coronas (from an = 20–22 mol.% in the matrix to an = 40–45 mol.% at kyanite–plagioclase boundary) (Figs 4a & 6a). Orthoclase content in plagioclase is constant and ranges between 1 and 1.8 mol.%.

The textural and compositional relations in the garnet-bearing coronas are consistent with the larger garnet grains in the coronas having been present prior to the development of the reaction textures, belonging to the stage when kyanite was in equilibrium with the matrix, while the garnet extension developed with the existing plagioclase corona at conditions when kyanite had become metastable.

Spinel–plagioclase symplectites in coronas

Spinel–plagioclase symplectite occurs both in samples with simple plagioclase–around–kyanite coronas and in samples where garnet coronas are developed, but in the latter, the spinel–plagioclase symplectite occurs only where the garnet corona is absent. The spinel–plagioclase symplectite typically forms a layer that separates kyanite from a monomineralic plagioclase layer. Some boundaries of the spinel–plagioclase symplectite towards plagioclase are straight and are interpreted as former kyanite grain boundaries (Figs 3e,f & 4c), indicating that the spinel–plagioclase symplectite develops primarily at the expense of kyanite. The spinel–plagioclase symplectite is commonly coarser-grained towards plagioclase and finer-grained at its contact with kyanite (Figs 3c,e,f & 4c,e). The mineral proportions in the symplectites vary between 35–40 vol.% spinel and 65–60 vol.% plagioclase.

The composition of spinel within the symplectites is constant with X_{Fe} = 60–63 and negligible Zn content of ~0.01 cations p.f.u. The monomineralic plagioclase corona is strongly zoned, from an = 21–24 at the contact with the matrix up to an = 45 at the contact with the spinel–plagioclase symplectite (Fig. 6c,d). Within the symplectite the plagioclase composition varies between an = 35 mol.% and an = 45 mol.% with or = 1–1.7 mol.% and does not show any regular zoning (Figs 4b–e & 6e).

The theoretical proportion of spinel and plagioclase obtained by decomposition of kyanite at fixed Al:Si of 2:1 and for plagioclase with an = 35 mol.% and an = 50 mol.% is 36:64 and 39:61, respectively. The ratio of the two phases in the symplectites (35–40 vol.% of spinel and 65–60 vol.% of plagioclase with an = 35–45 mol.%) is therefore consistent with the relative immobility of Al_2O_3 and SiO_2 as the spinel–plagioclase symplectite replacing kyanite developed.

Corundum–plagioclase and garnet–spinel symplectite in coronas

Corundum–plagioclase symplectite after kyanite is present rarely and is associated with spinel–plagioclase symplectite (Fig. 3f). The plagioclase composition in such symplectites has a high anorthite content of ~45–48% (Fig. 6f). Garnet-spinel symplectite occurs in some samples (data not shown). A kyanite relic is present very rarely inside the texture, indicating that they are also a result of kyanite replacement.

MODELLING

Introduction to modelling

In order to provide a *P–T* context for the textures, a *P–T* pseudosection in the system, Na_2O-CaO–K_2O–FeO–MgO–Al_2O_3–SiO_2–H_2O–TiO_2–O (NCKFMASHTO), is presented in Fig. 7 for sample ZH63 (SiO_2 = 69.46, TiO_2 = 0.42, Al_2O_3 = 14.95, FeO_{tot} = 3.68, MnO = 0.04, MgO = 0.90, CaO = 1.98, Na_2O = 3.07, K_2O = 4.73, P_2O_5 = 0.17 in wt%). The calculations were performed with THERMOCALC 3.26 (Powell & Holland, 1988) and DATASET 5.5 (Holland & Powell, 1998; November 2003 upgrade), with the activity-composition models for biotite, orthopyroxene and melt from White *et al.* (2007), garnet from White *et al.* (2007) modified by Diener *et al.* (2008), feldspar from Holland & Powell (2003), white mica from Coggon & Holland (2002) and ilmenite from White *et al.* (2000).

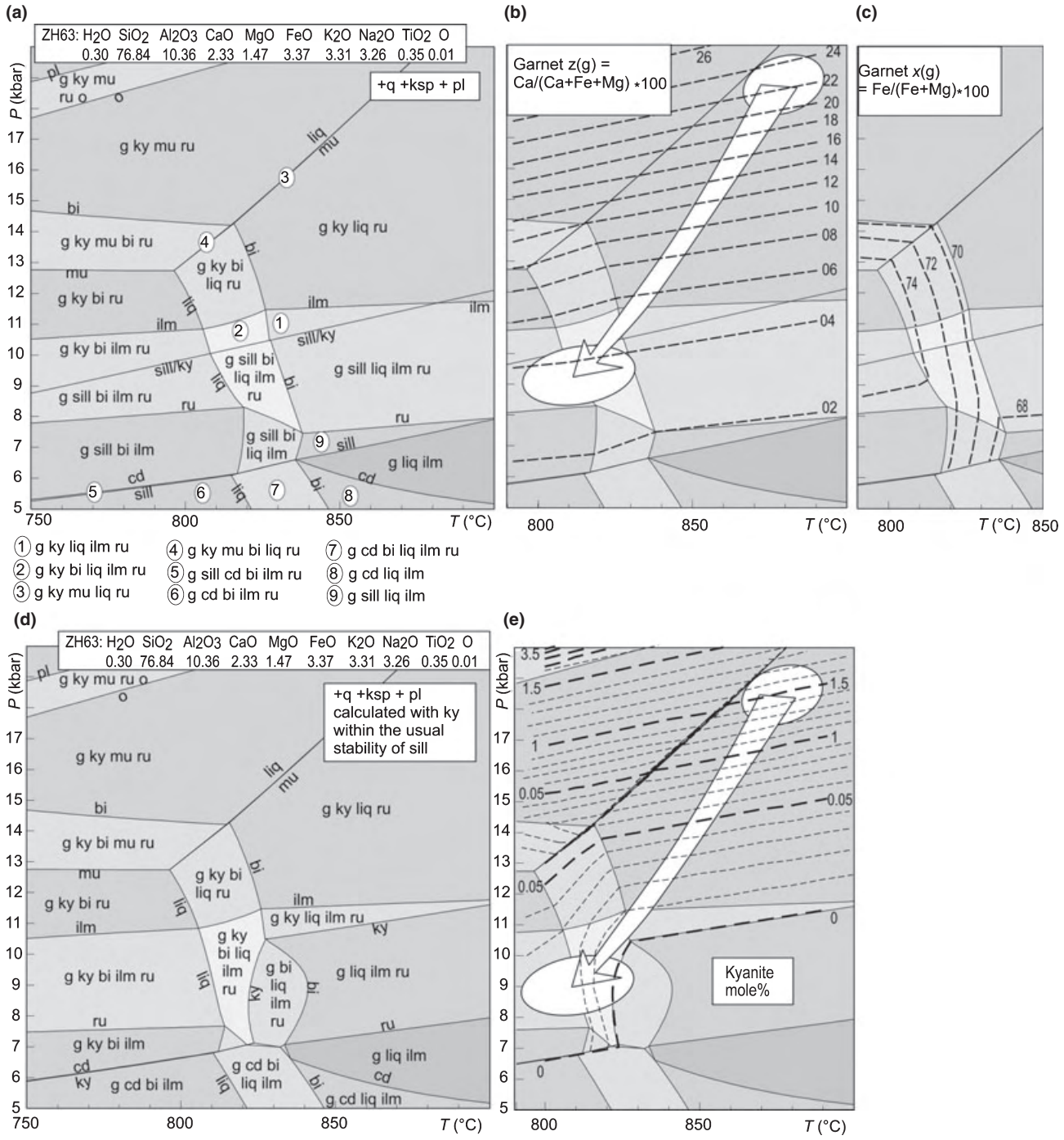

Fig. 7. Pseudosections calculated for the rock composition of the granulite sample ZH63 show equilibrium relations with sillimanite (a–c), and with metastable kyanite within the stability of sillimanite (d–e). *P–T* path is derived by comparing the modelled assemblages and isopleths with assemblages, chemistry and zoning of minerals observed in the sample. (b, c, e) Enlarged parts of the pseudosections with calculated isopleths of mineral composition and molar proportions.

For the pseudosection the analysed whole rock composition of ZH63 was modified slightly by adding a small amount of alumina to enable an aluminosilicate to be stable at the estimated peak metamorphic conditions. H_2O = 0.30 mol.% in the rock composition allows the inferred lower pressure assemblage g–bi–ky–ru–pl–ksp–q–liq with garnet X_{Fe} = 0.7 to be stable on the pseudosection. Higher H_2O shifts the liquid-out line to lower temperature where *x*(g) is higher than observed in the sample, and lower H_2O

moves the liquid-out line to higher temperature where $x(g)$ is lower than observed. The mineral composition and molar proportion isopleths (abbreviations listed in Table 1) were plotted for the phases of interest.

Equilibrium relations with sillimanite are shown in Fig. 7a–c, and relations with metastable kyanite within the stability of sillimanite in Fig. 7d–e. The position of the garnet compositional isopleths for assemblages with sillimanite (Fig. 7b,c) is similar to those of metastable kyanite-bearing assemblages (data not shown). With the original minerals inferred to have been quartz, K-feldspar, plagioclase, garnet, kyanite, rutile and melt and using the garnet core composition with 22–24 mol.% of grossular, the peak metamorphic *P–T* conditions are estimated to have been ~19 kbar and 880 °C. On the basis of the garnet rim composition with 3–4 mol.% of grossular, $X_{Fe} = 0.7$, and the presence of biotite, the *P–T* conditions of the corona development, at least that involving garnet, is consistent with formation at ~8.5 kbar and 800 °C, and this *P–T* is used in the modelling below. The pseudosection predicts that sillimanite would be stable at pressures less than ~10 kbar. Given that it is not present in the sample studied, the kyanite observed is considered to be metastable with respect to sillimanite and the calculations in the following sections are performed with kyanite rather than sillimanite.

Following equilibration of the mineral assemblage at 19 kbar, decompression to 8.5 kbar occurred, with the matrix mineral assemblage, including the rim composition of garnet, reflecting these conditions (Fig. 7e). Whereas in the calculations in the next section, in NCKAS rather than in NCKFMASHTO, kyanite is indeed not stable with the matrix at 8.5 kbar, in the pseudosection kyanite is still present at 8.5 kbar and 800 °C, admittedly at very small molar content (< 0.03 mol.%, Fig. 7e). This apparent inconsistency can be ascribed to the bulk composition used for the pseudosection being slightly too aluminous, or the thermodynamic models of the minerals allowing alumina to be left over resulting in a small amount of kyanite being made. Similarly, a small variation in H_2O can move the solidus down through 800 °C.

Modelling the observed corona textures involves superimposing on such a *P–T* history an idea of when and how the corona developed. Although it is possible that the corona developed continuously during decompression, it is plausible that little happened during decompression, and that corona development initiated at lower pressure. This then could be considered, in the first instance, to have occurred at one *P–T*; this simplification is adopted here as it considerably simplifies the analysis. The original mineral assemblage in which kyanite was an equilibrium participant is considered to have decompressed to 8.5 kbar and 800 °C with little or no reaction, and only then did the mineral assemblage attempt to re-equilibrate. If at these new conditions, with kyanite not stable with the matrix, all elements are sufficiently mobile then the kyanite will simply be consumed, the key elements being the slowest diffusers, which plausibly are Al, followed by Si (Carlson, 2002). The presence of a corona around kyanite indicates that Al diffusion has been sufficiently slow to not allow simple consumption.

Coronas consist of a layer or layers between the reacting mineral and the matrix, each involving one or more phases that reflect the chemical potential gradients that existed then. In order to understand the development of such coronas it is necessary to consider how and why the gradients were initiated. Consumption of kyanite involves Al diffusing away, and at the same time other elements diffusing in. Clearly, the existence of the plagioclase corona reflects that the diffusion of Al could not occur fast enough. The start of the attempted flattening of the chemical potential of Al occurred by growth of more anorthitic plagioclase on the kyanite, presumably initially grown on the less anorthitic plagioclase in the matrix (garnet could also be involved, as discussed below). In this way a monomineralic plagioclase corona developed, in which the plagioclase is zoned from an anorthite content typical of the matrix, to a much higher value in contact with the kyanite. Continued corona growth, trying to flatten the chemical potential gradient of Al, involved replacement of matrix and, to a much lesser extent, kyanite by plagioclase. The stoichiometry and zoning of the plagioclase will have at least partially constrained the chemical potential gradients of other oxides between the kyanite and the matrix.

The number of phases in each layer of a corona contains information about the effective mobility of the elements involved. In this limiting case of a monomineralic layer (plagioclase) all components need to be mobile on the time and length scale of interest. But if a layer is bimineralic (as occurs with kyanite being replaced by spinel + plagioclase), then two components are effectively immobile on the time and length scale of interest. In fact, there is a hierarchy of mobilities, or more strictly diffusivities, from the slowest (Al) to the fastest (K in NCKMAS?) in this case. For the purpose of phase equilibria modelling, it is convenient to subdivide the elements on the basis of their mobilities (on the time and length scale), to be effectively immobile, mobile (but having chemical potentials that vary on the scale of the corona) and completely mobile (whose chemical potentials are constant and superimposed on the corona), as discussed in White *et al.* (2008). This is an arbitrary device given that the diffusivities of the various components are in a continuum (i.e. nothing is likely to be completely mobile or completely immobile), but it allows the modelling to be undertaken. In the context of intensive *v.* extensive variables (e.g. Powell *et al.*, 2005), mobile elements are considered in terms of their chemical potentials (intensive variables), whereas the immobile ones are considered in terms of composition

(extensive variables) (see Powell *et al*., 2005; White *et al*., 2008, based on Munster, 1970; Callen, 1985).

Although the initial calculations to place the rocks in an overall *P–T* context have been performed in NCKFMASHTO (see above), the modelling of the corona texture can be performed in Na_2O–CaO–K_2O–FeO–MgO–Al_2O_3–SiO_2 (NCKFMAS). But even in this smaller system there are considerable issues regarding representation of the mineral equilibria. A monomineralic zone of plagioclase occurring around kyanite implies that six oxides in this system need to be handled as chemical potential variables that change across the corona, rather than composition variables, the seventh being dependent on the other chemical potentials via the Gibbs-Duhem equation. Fortunately, prior to considering ferromagnesian minerals, the system can be reduced further to NCKAS, and, with an assumption about the mobility of K_2O (taken to be completely mobile), the mineral equilibria can be represented completely in μ(CaO)–μ(Na_2O)–μ(SiO_2) at fixed *P–T*. With a line representing the chemical potential gradients in the corresponding 3D diagram, variations in μ(MgO) and μ(FeO) can then be addressed in order to consider the stability of ferromagnesian minerals. This is the approach followed below.

In the modelling, the equilibria in the matrix are used to set the values of the chemical potentials that are superimposed on the edge of the corona. It is assumed that the reacting mineral (kyanite) makes up a minority of the rock, so reaction is focused on that mineral (in the form of the corona), the matrix acting effectively as an infinite reservoir, changing little as a consequence of the reaction except immediately adjacent to the mineral. Thus, the superimposed chemical potentials are not considered to vary as the corona develops.

The calculations in NCKFMAS were performed with THERMOCALC 3.31 (Powell & Holland, 1988) and DATASET 5.5 (Holland & Powell, 1998; November 2003 upgrade), with the activity-composition relationships of garnet, biotite and orthopyroxene used in White *et al*. (2001), feldspar from Holland & Powell (2003), white mica from Coggon & Holland (2002) and melt from White *et al*. (2007).

Plagioclase–around–kyanite coronas in the system NCKAS

The spatial relations from matrix K-feldspar + quartz, through the plagioclase corona, to kyanite can be illustrated on a calculated μ(SiO_2)–μ(CaO) diagram in the NCKAS system. The matrix is considered to provide the chemical potential environment for the development of the plagioclase corona. In calculating the values of the matrix chemical potentials, it is assumed that the corona developed at the *P–T* conditions reflected in the mineral rim compositions, 8.5 kbar and 800 °C (see above). The matrix assemblage g–bi–pl–ksp–q–liq is effectively divariant in NCKFMASH if two mineral composition variables are set, allowing chemical potentials to be calculated at specified *P–T*. At 8.5 kbar and 800 °C, with z(g) = 0.04 and ca(pl) = 20, corresponding to the observed rim values of garnet and plagioclase, the chemical potentials in NCKAS are μ(Al_2O_3) = −1772.0 kJ, μ(SiO_2) = −970.4 kJ, μ(CaO) = −815.5 kJ, μ(Na_2O) = −872.4 kJ and μ(K_2O) = −952.0 kJ. In the μ(SiO_2)–μ(CaO) diagrams in Fig. 8 each is calculated at a specified μ(Na_2O). K_2O is taken to be

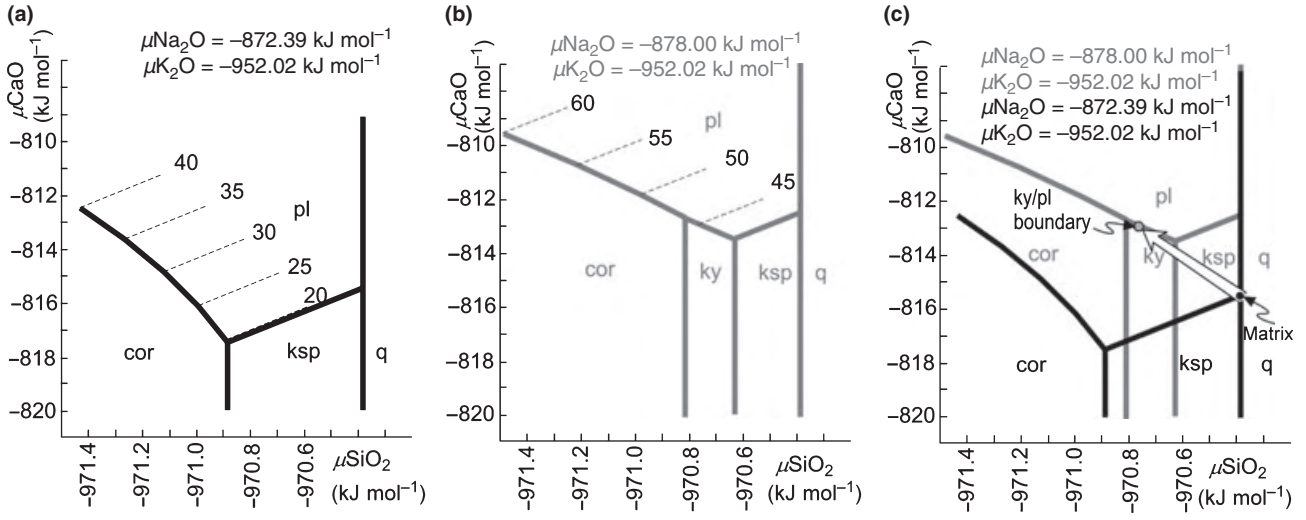

Fig. 8. Calculated μ(SiO_2)–μ(CaO) diagrams in the NCKAS system: (a) with specified μ(K_2O) and μ(Na_2O) taken from the assumed-equilibrated matrix assemblage g–bi–pl–ksp–q–liq with z(g) = 0.04 and ca(pl) = 20 at 8.5 kbar and 800 °C. On the corresponding diagram kyanite is not stable. (b) μ(Na_2O) is varied until the kyanite–plagioclase boundary with ca(pl) = 45 appears on the diagram, thus representing observed relations in the corona. (c) Gradients in the chemical potentials from the matrix to the kyanite–plagioclase boundary are represented by a vector in μ(SiO_2)–μ(CaO)–μ(Na_2O) space when the two diagrams (a, b) are superimposed.

completely mobile, with $\mu(K_2O)$ held constant on all the $\mu(SiO_2)$–μ(CaO) diagrams, and so considered to be specified and superimposed on the corona as it develops (see Appendix for the calculation approach).

On the $\mu(SiO_2)$–μ(CaO) diagram for the matrix value of $\mu(Na_2O)$ (Fig. 8a) kyanite is not stable. As kyanite is present in the rock the values of the chemical potentials both within kyanite and at the kyanite–plagioclase interface must differ from those in the matrix. Therefore, the $\mu(Na_2O)$ was varied until the kyanite–plagioclase boundary with *ca*(pl) = 45 appears on the diagram, thus representing observed relations in the corona (Fig. 8b). On such a diagram, kyanite may also be in contact with corundum, plagioclase or K-feldspar, but not in contact with quartz. The values of $\mu(SiO_2)$, μ(CaO) and $\mu(Na_2O)$ at the plagioclase–kyanite boundary being different from those in the matrix result in chemical potential gradients between the matrix and the kyanite–plagioclase boundary. These variations are represented by a vector in $\mu(SiO_2)$–μ(CaO)-$\mu(Na_2O)$ space when the two diagrams are superimposed (Fig. 8c). To visualize better these relationships, first a series of two-dimensional $\mu(SiO_2)$–μ(CaO) diagrams at varying $\mu(Na_2O)$ and superimposed $\mu(K_2O)$ are calculated (Fig. 9a). These are then arranged to make a three-dimensional figure (Fig. 9b). The grey area shows a projection plane from the matrix (contact of quartz, K-feldspar and plagioclase) onto the kyanite–plagioclase plane with an intersection at *ca*(pl) = 45. The black arrow represents a vector in this plane that is chosen for construction of further diagrams below.

The 3D $\mu(SiO_2)$–μ(CaO)–$\mu(Na_2O)$ diagram illustrates the spatial and compositional relations that are observed in the plagioclase–around–kyanite coronas. It shows that the kyanite, unstable with the matrix yet not reacted out, causes chemical potential gradients to be developed between the kyanite and the matrix. Reaction attempting to flatten the chemical potential gradients has produced the strongly zoned plagioclase corona, whose inner side is in contact with kyanite and whose outer side coexists with a matrix composed of quartz, K-feldspar and plagioclase.

Plagioclase–around–kyanite coronas with garnet in the system NCKFMAS

To involve MgO and FeO in the modelling, μ(MgO) and μ(FeO) variations are superimposed on the $\mu(SiO_2)$–μ(CaO)–$\mu(Na_2O)$ vector obtained for the simple plagioclase–around–kyanite corona. These calculations are an extension of the ones above, so they result in one-phase fields on the μ–μ diagrams. The calculations with the superposition of μ(MgO) and μ(FeO) are performed for $\mu(SiO_2)$–μ(CaO)–$\mu(Na_2O)$–$\mu(K_2O)$ in three points on the vector: for the matrix, for the plagioclase–kyanite boundary and inside kyanite (Fig. 10). The resulting topology shows a garnet stability field at high μ(FeO) and low μ(MgO) and an orthopyroxene field at low μ(FeO) and high μ(MgO), with the progressive shift in the plagioclase (kyanite)-garnet-orthopyroxene point to lower μ(FeO) and higher μ(MgO) along the $\mu(SiO_2)$–μ(CaO)–$\mu(Na_2O)$ vector (Fig. 10). On these diagrams spinel is metastable. Garnet compositional isopleths x(g) are plotted within the garnet stability field. The arrow in the μ(MgO)–μ(FeO) diagram represents a vector coincident with the x(g) = 70 isopleth (corresponding to the measured garnet composition in the coronas).

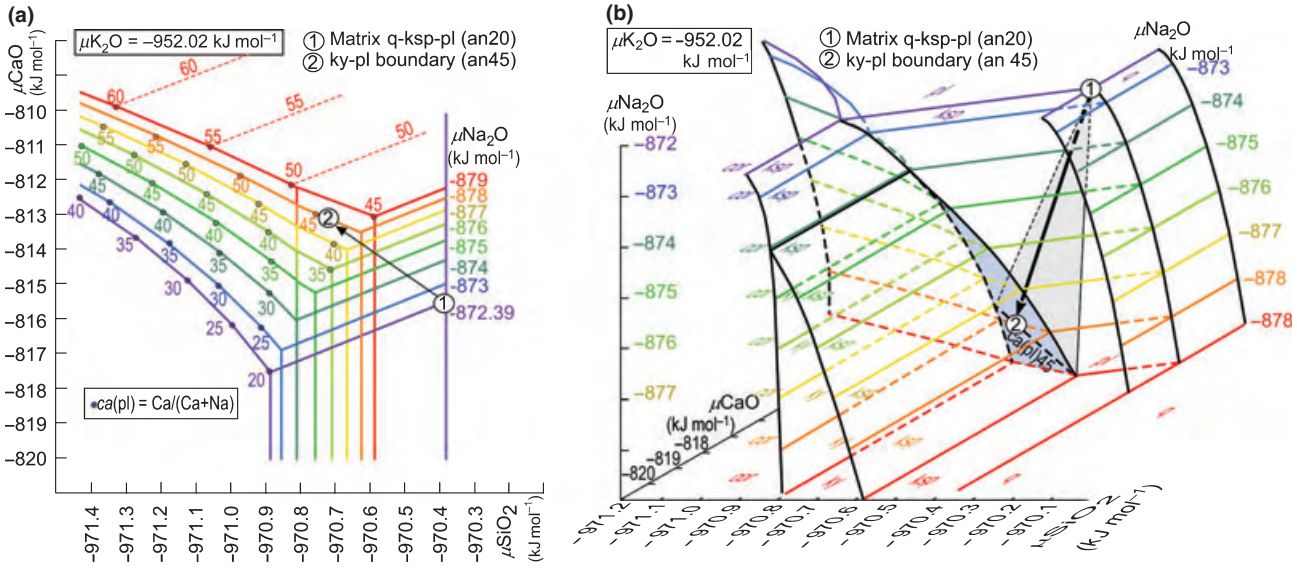

Fig. 9. (a) A series of two-dimensional $\mu(SiO_2)$–μ(CaO) diagrams at varying $\mu(Na_2O)$ and superimposed $\mu(K_2O)$ used for construction of the 3D $\mu(SiO_2)$–μ(CaO)–$\mu(Na_2O)$ diagram in (b). (b) The spatial and compositional relations in the plagioclase–around–kyanite corona in a 3D $\mu(SiO_2)$–μ(CaO)–$\mu(Na_2O)$ diagram. For details, see text.

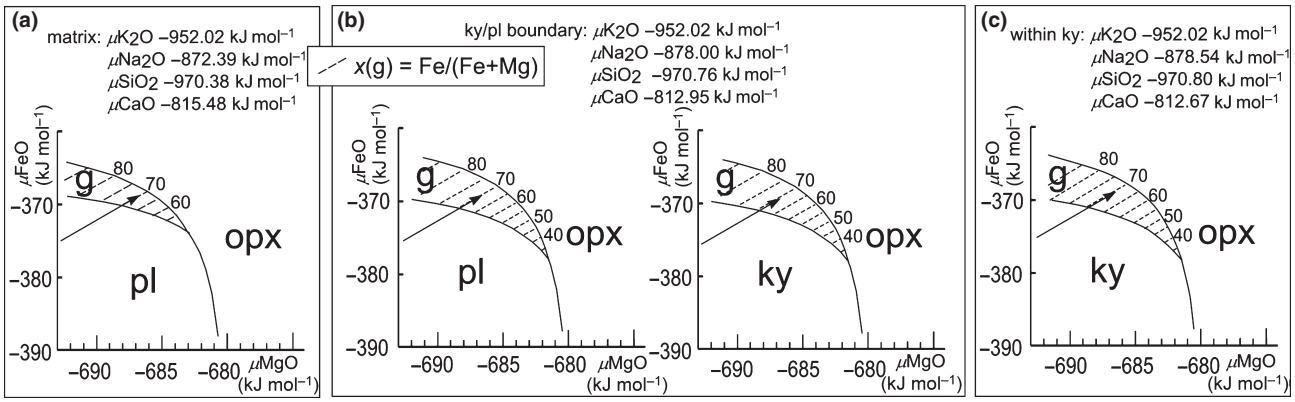

Fig. 10. Superimposed μ(MgO) and μ(FeO) variations on the $\mu(SiO_2)$–μ(CaO)–$\mu(Na_2O)$ vector from Fig. 9: (a) for the matrix, (b) for the plagioclase–kyanite boundary and (c) inside kyanite. The topology shows garnet and orthopyroxene fields while spinel is metastable. Garnet compositional isopleths x(g) are plotted within the garnet stability field. The arrow is a vector coincident with the $x(g) = 70$ isopleth.

Relations along a slice at approximately fixed μ(MgO)/μ(FeO), corresponding to the vector along $x(g) = 70$ (Fig. 10) are combined with the phase relations along the vector $\mu(SiO_2)$–μ(CaO)–$\mu(Na_2O)$ (Fig. 9), which results in the phase topology shown in Fig. 11. In Fig. 11, one phase fields of plagioclase, garnet and kyanite intersect at a point, and a field of orthopyroxene occurs at higher μ(MgO)/μ(FeO). In Fig. 11, dashed arrow (a) shows a path from kyanite across plagioclase towards the matrix without garnet present; dashed arrow (b) shows a path from kyanite across garnet and plagioclase towards the matrix. The values of the compositional isopleths *ca*(pl) decrease from the kyanite field towards the matrix. A path that intersects the garnet field has a lower *ca*(pl) next to garnet than plagioclase at the kyanite–plagioclase boundary without garnet, in agreement with the observed plagioclase compositions in the two textures. The simplest explanation of the presence/absence of garnet in the corona is that the μ(MgO)–μ(FeO) in the vicinity of kyanite is affected by the presence of pre-existing garnet. Thus, with garnet present, the μ(MgO)–μ(FeO) as provided by the matrix is augmented such that garnet occurs as a layer in the corona.

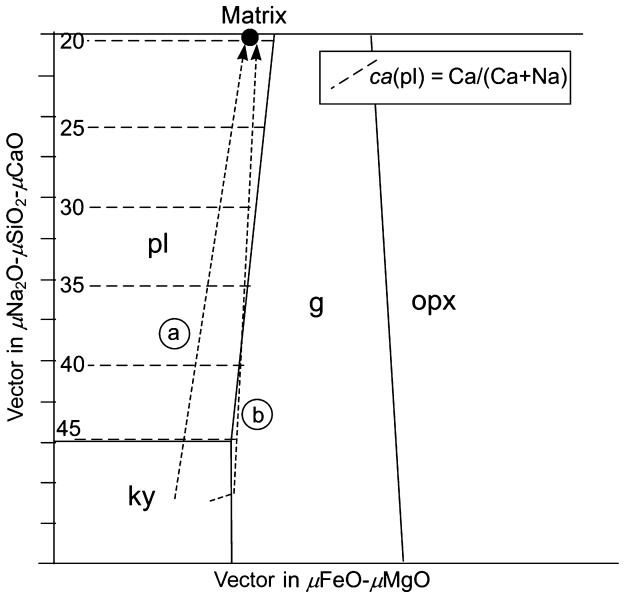

Fig. 11. Phase topology obtained by manual combination of the calculated phase relations along a slice at approximately fixed μ(MgO)/μ(FeO) (along $x(g) = 70$) from Fig. 10 with the calculated phase relations along the vector $\mu(SiO_2)$–μ(CaO)–$\mu(Na_2O)$ from Fig. 9, contoured with compositional isopleths *ca*(pl). The dashed arrow (a) shows a path from kyanite across plagioclase towards the matrix and decreasing values of *ca*(pl). The dashed arrow (b) shows a path from kyanite across garnet and plagioclase towards the matrix and decreasing values of *ca*(pl), starting at lower values then in (b).

Spinel–plagioclase and other symplectites in the system NCKAS and NCKFMAS

In the above, for example in Fig. 9, SiO_2 was considered to be mobile [SiO_2 considered via $\mu(SiO_2)$], and μ–μ diagrams involved one-phase fields. Now both Al_2O_3 and SiO_2 will be treated as immobile, resulting in the fields in μ–μ diagrams being labelled with Al_2O_3–SiO_2 bar compatibility diagrams, with SiO_2 considered as the composition variable [conjugate to $\mu(SiO_2)$].

Initially the assumption is made that symplectite growth occurred at the same P–T as plagioclase ± garnet corona formation. Considering the phase relationships involving kyanite, corundum, plagioclase and quartz in the NCKAS system, with SiO_2 and Al_2O_3 immobile, reactions such as ky = cor + pl are involved, as can be seen on the $\mu(Na_2O)$–μ(CaO) diagram at 8.5 kbar, 800 °C at the matrix $\mu(K_2O)$ (Fig. 12). This figure is equivalent to Fig. 9b, with a reaction like ky = cor + pl being equivalent to

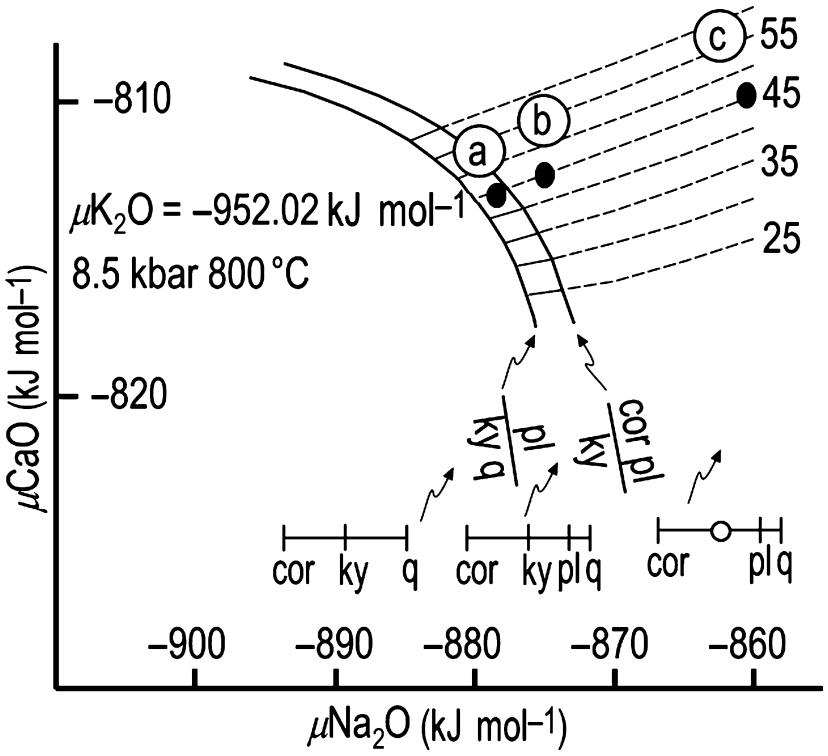

Fig. 12. Phase relationships involving kyanite, corundum, plagioclase and quartz in the NCKAS system at fixed $\mu(K_2O)$ from the matrix, at 800 °C and 8.5 kbar, with SiO_2 and Al_2O_3 immobile. Contours of *ca*(pl) for the assemblage kyanite–plagioclase are shown as full lines in the stable region, and as dashed lines where they extend into the region where this assemblage is metastable with respect to corundum. The line *ca*(pl) = 45 and black points (a), (b) and (c) represent conditions for which relations involving the Fe-Mg minerals in Fig. 13 are calculated. Open circle is where the composition of kyanite plots.

an edge between one-phase fields in the μ–μ–μ diagram. The diagram, Fig. 12, is contoured for *ca*(pl) for the assemblage kyanite–plagioclase, and the contours are extended from the stable region for this assemblage (full lines) into the region where this assemblage is metastable with respect to corundum (dashed lines), if for example corundum did not nucleate.

In Fig. 9 it is clear that the arrow between the matrix and the kyanite, represented by the conditions at the kyanite–plagioclase boundary, implies that any attempt at equalizing the chemical potentials will involve the growth of a plagioclase corona between the matrix and the kyanite, as outlined above. The equivalent equalization in Fig. 12, going from where kyanite is stable, for example point 'a', to the right, involves the crossing of the ky = pl + cor reaction, implying the growth of a plagioclase + corundum symplectite replacing kyanite in the NCKAS system. Although this replacement is observed, it is uncommon. Instead the dominant replacement involves spinel + plagioclase. To consider this, FeO and MgO must be considered in addition, via μ(FeO)–μ(MgO) diagrams.

The line *ca*(pl) = 45 (Fig. 12) is the focus of attention because it corresponds to the common plagioclase composition at the contact of the plagioclase corona with kyanite in the samples studied. The μ(FeO)–μ(MgO) diagrams are drawn to consider the phase relations of Fe–Mg-bearing phases at the kyanite edge under the μ(CaO)–μ(Na_2O) values for three points along the *ca*(pl) = 45 line (Fig. 13). For kyanite to coexist with plagioclase, as at the kyanite edge, the bar diagram needs to have a field with ky + pl, as at point 'a' in Fig. 12. For 'a', μ(FeO)–μ(MgO) relationships are shown in Fig. 13a, the solid lines being the stable relationships. The lines ky = cor + g and pl + ky = g, and the lines ky = cor + opx and pl = opx + ky are effectively coincident, because kyanite and plagioclase for these μ(CaO)–μ(Na_2O)–μ(K_2O) have a similar stability. Stable relations predict that with increasing μ(FeO) kyanite should decompose to corundum-garnet and then to spinel-garnet and with increasing μ(MgO) to corundum-orthopyroxene and spinel-orthopyroxene. Such symplectites are not observed in the samples studied, and, moreover the main symplectite type involving spinel + plagioclase is not predicted. The problem is that the reaction stabilizing spinel, cor = sp, occurs at too high μ(FeO) and μ(MgO), well beyond where both plagioclase and kyanite have reacted out.

A resolution of this problem is to propose that corundum has difficulty nucleating. The solid lines in Fig. 13a are the stable equilibria, the dashed lines are the metastable equilibria. The equilibria metastable with respect to corundum are therefore given by the dashed lines and the solid lines that do not involve corundum, with corundum being replaced by spinel in the bar diagrams. Even with this assumption the diagram predicts with increasing μ(FeO) formation of spinel-garnet symplectite and for high μ(MgO) formation of spinel-orthopyroxene symplectite, not spinel–plagioclase. Using point 'b' from Fig. 12, the

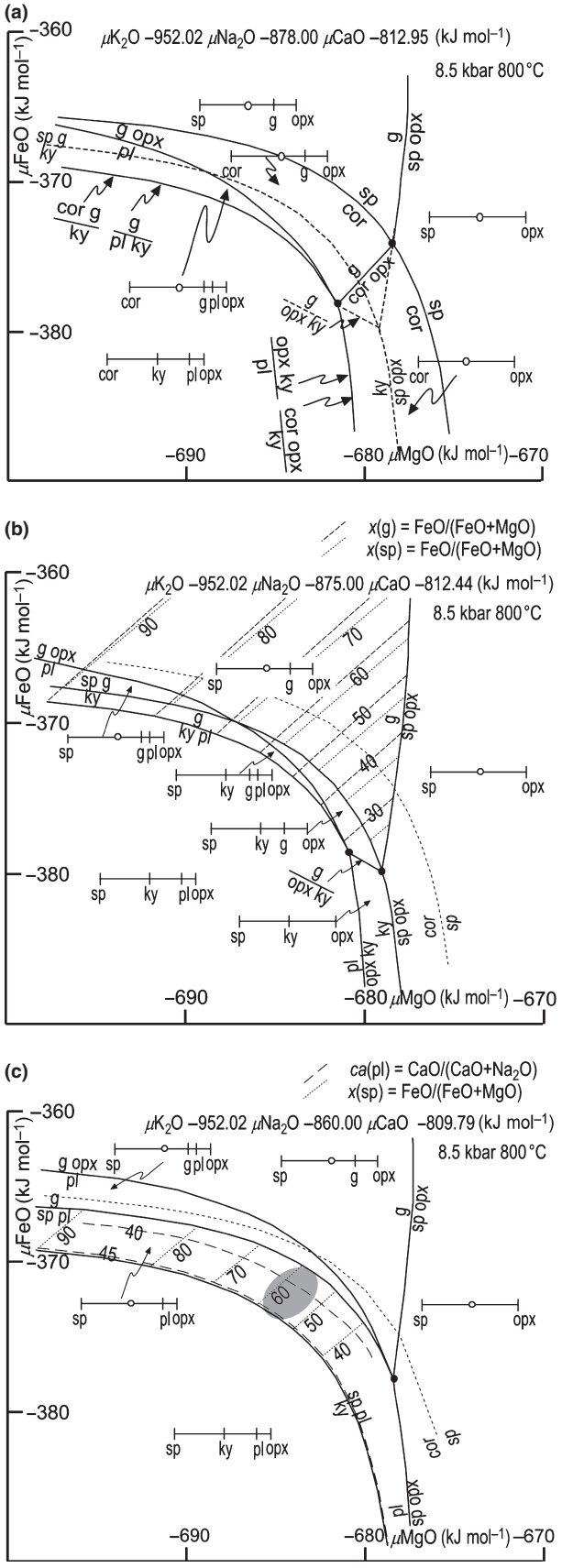

same applies (Fig. 13b). But for point 'c' from Fig. 12, there is a stable field for spinel + plagioclase (Fig. 13c). In Fig. 13b,c, the position of the stable transition cor = sp (dashed line) is indicated but the other stable relations with corundum are not shown, and instead the metastable spinel-bearing relations are plotted (solid lines).

Only with corundum considered to be metastable are the symplectite assemblages of interest predicted. The diagrams are contoured for x(g) and x(sp) for garnet-spinel assemblage in Fig. 13b and for ca(pl) and x(sp) in Fig. 13c. In the samples studied the plagioclase within the plagioclase-spinel symplectite has anorthite content of 35–45 mol.% and X(sp) ~60–63, which corresponds to the calculated values in the spinel–plagioclase field in Fig. 13c (shaded area). The calculations predict that spinel–plagioclase symplectites can be developed at 8.5 kbar and 800 °C, under the conditions that SiO_2 and Al_2O_3 are immobile, corundum did not nucleate and that the value for $\mu(Na_2O)$ is relatively high.

Conceivably symplectite growth occurred with further decompression from the P–T of corona formation. To address this, chemical potential relations with decreasing pressure, at 7 kbar and 5.5 kbar, at 800 °C have also been calculated (Fig. 14a,b respectively). First, the chemical potentials for the matrix assemblage g–bi–pl–ksp–q–liq are calculated, with fixed z(g) = 0.03 and 0.02, respectively, and with ca(pl) = 25 (corresponding to the trends of decreasing grossular and increasing anorthite content with decreasing pressure in the pseudosection, and close to the range of observed compositions).

The same $\mu(Na_2O)$ as in Fig. 13c is taken to calculate the μ(FeO)–μ(MgO) diagrams at 7 kbar and 5.5 kbar (Fig. 14). Fields of spinel–garnet and spinel–orthopyroxene occur at high μ(FeO) and μ(MgO). The field for the spinel–plagioclase symplectite progressively extends to lower μ(FeO) and μ(MgO) compared with relations at 8.5 kbar (Fig. 13c), and is larger for lower pressure. A decrease in pressure therefore favours formation of spinel–plagioclase symplectites.

The antipathetic occurrence of garnet layers in coronas and the replacement of kyanite by spinel + plagioclase appears to relate to the lower $\mu(Na_2O)$ and also higher μ(FeO) and μ(MgO) of the garnet + kyanite boundary, resulting in spinel + plagioclase not being stable there.

Fig. 13. μ(FeO)–μ(MgO) diagrams for the μ(CaO)–$\mu(Na_2O)$ along the ca(pl) = 45 line, shown as black dots (a), (b) and (c) in Fig. 12, with SiO_2 and Al_2O_3 immobile. The results in the fields are labelled with Al_2O_3–SiO_2 bar diagrams and the fields are contoured for x(g), x(sp) and ca(pl). See text. Grey ellipse shows region of plagioclase-spinel symplectite where mineral compositions correspond to observed values (an(pl) = 35–45 mol.% and X_{Fe}(sp) = 60–63). Open circle is where the composition of kyanite plots.

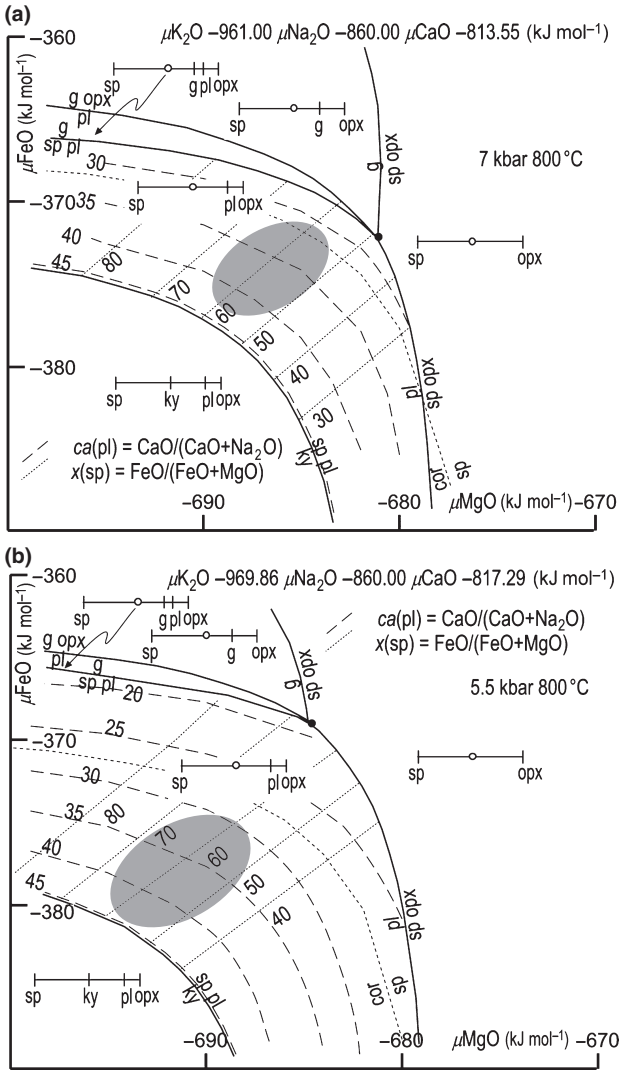

Fig. 14. μ(FeO)–μ(MgO) diagrams along the *ca*(pl) = 45 line at values of $\mu(Na_2O)$ from a point (c) in Fig. 12, calculated at 800 °C and at decreasing pressure of 7 kbar (a) and 5.5 kbar (b). SiO_2 and Al_2O_3 are immobile, the results in the fields are labelled with Al_2O_3–SiO_2 bar diagrams and the fields are contoured for *x*(g), *x*(sp) and *ca*(pl). See text. Grey ellipses show regions of plagioclase–spinel symplectite where mineral compositions correspond to observed values (an(pl) = 35–45 mol.% and X_{Fe}(sp) = 60–63).

DISCUSSION AND CONCLUSIONS

The observed corona development around kyanite can be accounted for with calculated mineral equilibria in $\mu(Na_2O)$–μ(CaO)–$\mu(K_2O)$–μ(FeO)–μ(MgO)–$\mu(Al_2O_3)$–$\mu(SiO_2)$ (i.e. in NCKFMAS). For the example considered here, with Al_2O_3 being the least mobile component that caused the corona to form, the plagioclase layer in the corona is consistent with gradients established in $\mu(Na_2O)$–μ(CaO)–$\mu(SiO_2)$ at 8.5 kbar and 800 °C, with $\mu(K_2O)$ being taken to be constant across the corona. These *P*–*T* conditions were estimated using constraints from *P*–*T* pseudosections. Considering additionally μ(FeO) and μ(MgO), garnet may form a layer in the corona between the plagioclase and the kyanite at these conditions. Generally garnet occurs only as an extension from larger pre-existing garnet grains adjacent to kyanite, implying that the chemical potential relationships are influenced by this pre-existing garnet. The textures are consistent with the plagioclase and garnet layers in the corona having mainly replaced the matrix rather than the kyanite grains. Whereas these layers are monomineralic, implying that less than two components are immobile, the replacement of kyanite is bimineralic, implying that two components are effectively immobile during the replacement. The proportions of spinel and plagioclase in the spinel–plagioclase symplectites after kyanite are consistent with the immobile components being Al_2O_3 and SiO_2. The calculated stability relations relating to the spinel–plagioclase symplectites imply that there was a decrease in pressure subsequent to the growth of the monomineralic corona layers, and that corundum had difficulty nucleating.

It would be useful to be able to predict when garnet should be expected as a layer in plagioclase–around–kyanite coronas, and to predict when kyanite should be expected to be replaced by spinel + plagioclase or sapphirine + plagioclase or corundum + plagioclase symplectites, or symplectites involving cordierite. But because this depends on the underlying μ(CaO)–$\mu(Na_2O)$–$\mu(SiO_2)$ relationships this is difficult to do. Built into the above calculations is the observed anorthite content of the plagioclase at the plagioclase–kyanite contact, and this is known to vary between rocks in different rock types and in different terranes.

If the growth of the plagioclase ± garnet corona around kyanite made way for symplectite growth during decompression, why did the replacement of kyanite by plagioclase + spinel cease during subsequent cooling? This reaction has a positive volume change and it is possible that the environment of the texture is not able to deform to accommodate this volume change as cooling progresses, thus effectively terminating reaction. Other kinetic reasons may contribute, including simply the slowing of diffusion with cooling due to the strong temperature dependence of such processes.

If corona reaction proceeded to completion the chemical potential gradients between the matrix and the kyanite would be completely flattened out, with the complete consumption of kyanite. Nevertheless a spatial distribution of reaction products is likely to remain, particularly the plagioclase layer (e.g. White *et al.*, 2008). An essential feature of equilibration would be the removal of the zoning of plagioclase across the plagioclase layer. Several outcomes are possible. If the reaction had proceeded to completion prior to symplectite growth, the result is likely to be a clump of garnet grains sitting within an unzoned plagioclase moat, or, in the absence of garnet, a pool of unzoned plagioclase where the kyanite and its

plagioclase moat had been. However, if chemical potential gradients for those components considered to be mobile were flattened during the stage of the symplectite growth, by implication this would not involve flattening the chemical potential gradients of Al_2O_3 and SiO_2 both of which by this stage are effectively immobile. Thus the plagioclase zoning is preserved, reflecting the fact that a fractionation from the matrix through into the kyanite with respect to Al_2O_3 and SiO_2 had already taken place prior to the start of symplectite growth, and diffusion at that stage was too slow to change them. As a consequence the matrix is quartz-saturated whereas the environment of the kyanite is SiO_2-undersaturated. In the absence of corundum nucleation the result would be a spinel + plagioclase aggregate located within a moat of zoned plagioclase, the zoning reflecting equalized chemical potentials for all components except Al_2O_3 and SiO_2. If corundum did nucleate the result would be a corundum + plagioclase aggregate located within a moat of zoned plagioclase. Interestingly, if this was preceded by replacement of kyanite by spinel + plagioclase, it would involve FeO and MgO diffusing through the plagioclase to make the spinel, then diffusing out again when the texture was replaced by corundum + plagioclase.

An alternative logic for the development of the observed coronas is that kyanite is consumed by a corona as a consequence of sillimanite growing in an adjacent part of the rock, so that kyanite is primarily unstable with the matrix due to the presence of sillimanite there. In this case the overall reaction may simply be kyanite = sillimanite, as in Carmichael (1969) who considered the appearance of sillimanite in kyanite-bearing metapelites in Barrovian-type metamorphism. Indeed slightly more aluminous gneiss does develop sillimanite. In this case the chemical potential relationships will be different to those in Fig. 9, with the chemical potential differences established between a sillimanite-bearing matrix assemblage and the kyanite. Developing this is beyond the scope of this paper, but the logic should be analogous to that in White *et al*. (2008).

Complex reaction textures on aluminosilicate porphyroblasts are a reasonably common feature (e.g. Pitra & de Waal, 2001; White *et al*., 2002; Marschall *et al*., 2003; Johnson *et al*., 2004; Tajčmanová *et al*., 2007) and have been interpreted using a range of qualitative and quantitative methods. Plagioclase–around–kyanite textures similar to those considered here have been investigated using calculated mineral equilibria in a recent study by Tajčmanová *et al*. (2007), but without explicit consideration of chemical potential relationships. The idea followed in Tajčmanová *et al*. (2007) is to choose a volume of rock including the texture that can be considered to be effectively a closed system during texture development. That development then involves a redistribution of material within the volume. A pseudosection is drawn for this overall rock volume which is then used to interpret the texture. In the case of some simple textures, for example the orthopyroxene and sillimanite layers in the corona texture developed between sapphirine and quartz discussed in White *et al*. (2008), the reaction corresponds to passage across a univariant line in *P–T* in the system FMAS: sapphirine + quartz = orthopyroxene + sillimanite.

Whereas the reaction accounts for the minerals in the corona, it cannot account for the spatial relationships. In this case, fortuitously, the chemical potential gradients that do account for the spatial relationships involve only the minerals in this reaction. In contrast, the occurrence of corundum in a part of this texture cannot be predicted by the pseudosection for the whole volume (which is quartz-saturated). Tajčmanová *et al*. (2007) tried to surmount this type of problem by making a *T–x* pseudosection, with the *x*-axis attempting to represent the composition change across the texture. It is simply not possible to do this and reproduce the mineral assemblages other than in a very generalized way, not least because variance considerations force too many minerals to be involved in each pseudosection field, some of which will commonly not occur in the corona. The point is that the components that are mobile involve chemical potential gradients across the corona within the overall volume, and these components in being treated as chemical potentials must then not be present in the bulk composition used to draw the pseudosections (see also White *et al*., 2008). Moreover, the way in which the chemical potentials change within the corona control which minerals are stable, and these may well be ones not stable in the pseudosections (although an arbitrary choice of the bulk compositions to use in the *T–x* pseudosection may allow them to appear). In general, such a pseudosection approach will be unsuccessful in accounting for corona textures, and mineral equilibria calculations explicitly involving chemical potentials are required.

ACKNOWLEDGEMENTS

This work was financially supported by the French National agency (No. 06-1 148784 to K. Schulmann). R.P. and R.W.W. thank the Australian Research Council for support from ARC DP0451770 and DP0557013. We gratefully acknowledge H. Müller-Sigmund from the Institute of Mineralogy, Petrology and Geochemistry at the University of Freiburg for operating the microprobe. We thank B. Carlson, F. Spear and P. Pitra for their interesting and helpful reviews. M. Brown is thanked for his editorial work.

REFERENCES

Ashworth, J.R. & Birdi, J.J., 1990. Diffusion modelling of coronas around olivine in an open system. *Geochimica et Cosmochimica Acta*, **54,** 2389–2401.

Baldwin, J.A., Powell, R., Williams, M.L. & Goncalves, P., 2007. Formation of eclogite, and reaction during exhumation to mid-crustal levels, Snowbird tectonic zone, western Canadian Shield. *Journal of Metamorphic Geology*, **25,** 953–974.

Beard, B.L., Medaris, L.G., Johnson, C.M., Brueckner, H.K. & Mísař, Z., 1992. Petrogenesis of Variscan high-temperature group A eclogites from the Moldanubian Zone of the Bohemian Massif, Czechoslovakia. *Contributions to Mineralogy and Petrology*, **111,** 468–483.

Brady, J.B., 1977. Metasomatic zones in metamorphic rocks. *Geochimica et Cosmochimica Acta*, **41,** 113–125.

van Breemen, O., Aftalion, M., Bowes, D.R. *et al*., 1982. Geochronological studies of the Bohemian Massif, Czechoslovakia, and their significance in the evolution of Central Europe. *Transactions of the Royal Society of Edinburgh, Earth Sciences*, **73,** 89–108.

Brueckner, H.K., Medaris, L.G. & Bakun-Czubarow, N., 1991. Nd and Sr age and isotope patterns from Variscan eclogites of the eastern Bohemian Massif. *Neues Jahrbuch für Mineralogie, Abhandlungen*, **163,** 169–196.

Callen, H.B., 1985. *Thermodynamics and an introduction to thermostatistics*. John Wiley & Sons, New York, 493 pp.

Carlson, W.D., 2002. Scales of disequilibrium and rates of equilibration during metamorphism. *American Mineralogist*, **87,** 185–204.

Carmichael, D.M., 1969. On the mechanism of prograde metamorphic reactions in quartz-bearing pelitic rocks. *Contributions to Mineralogy and Petrology*, **20,** 244–267.

Carswell, D.A., 1991. Variscan high *P–T* metamorphism and uplift history in the Moldanubian Zone of the Bohemian Massif in Lower Austria. *European Journal of Mineralogy*, **3,** 323–342.

Coggon, R. & Holland, T.J.B., 2002. Mixing properties of phengitic micas and revised garnet-phengite thermobarometers. *Journal of Metamorphic Geology*, **20,** 683–696.

Dallmayer, R.D., Neubauer, F. & Höck, V., 1992. Chronology of late Paleozoic tectonothermal activity in the southeastern Bohemian Massif, Austria (Moldanubian and Moravo-Silesian zones): $^{40}Ar/^{39}Ar$ mineral age controls. *Tectonophysics*, **210,** 135–153.

Dasgupta, S., Sengupta, P., Ehl, J., Raith, M. & Bardhan, S., 1995. Reaction textures in a suite of spinel granulites from the Eastern-Ghats Belt, India – evidence for polymetamorphism, a partial petrogenetic grid in the system KFMASH and the roles of ZnO and Fe_2O_3. *Journal of Petrology*, **36,** 435–461.

Diener, J.F.A., White, R.W. & Powell, R., 2008. Granulite facies metamorphism and subsolidus fluid-absent reworking, Strangways Range, Arunta Block, central Australia. *Journal of Metamorphic Geology*, **26,** 603–622.

Edel, J.B., Schulmann, K. & Holub, F.V., 2003. Anticlockwise and clockwise rotations of the Eastern Variscides accommodated by dextral lithospheric wrenching: palaeomagnetic and structural evidence. *Journal of the Geological Society*, **160,** 209–218.

Fisher, G.W., 1973. Nonequilibrium thermodynamics as a model for diffusion-controlled metamorphic processes. *American Journal of Science*, **273,** 897–924.

Franěk, J., Schulmann, K. & Lexa, O., 2006. Kinematic and rheological model of exhumation of high pressure granulites in the Variscan orogenic root: example of the Blanský les granulite, Bohemian Massif, Czech Republic. *Mineralogy and Petrology*, **86,** 253–276.

Franke, W., 2000. The mid-European segment of the Variscides: tectonostratigraphic units, terrane boundaries and kinematic evolution. In: *Orogenic Processes: Quantification and Modelling in the Variscan Belt, Special Publications, 179* (eds Franke, W., Haak, V., Oncken, O. & Tanner, D.), pp. 35–63, The Geological Society of London, London.

Friedl, G., Cooke, R., Finger, F., McNaughton, N.J. & Fletcher, I., 2003. U-Pb shrimp dating and trace element investigations on multiple zircons from a South-Bohemian granulite. *Journal of the Czech Geological Society*, **48,** 51.

Fuchs, G., 1986. Zur Diskussion um den Deckenbau der Böhmischen Masse. *Jahrbuch der Geologischen Bundesanstalt*, **129,** 41–49.

Hasalová, P., Štípská, P., Powell, R., Schulmann, K., Janoušek, V. & Lexa, O., 2008. Transforming mylonitic metagranite by open-system interactions during melt flow. *Journal of Metamorphic Geology*, **26,** 55–80.

Holland, T.J.B. & Powell, R., 1998. An internally consistent thermodynamic data set for phases of petrological interest. *Journal of Metamorphic Geology*, **16,** 309–343.

Holland, T. & Powell, R., 2003. Activity–composition relations for phases in petrological calculations: an asymmetric multicomponent formulation. *Contributions to Mineralogy and Petrology*, **145,** 492–501.

Janoušek, V., Gerdes, A., Vrána, S. *et al*., 2006. Low-pressure granulites of the Líšov Massif, Southern Bohemia: Visean metamorphism of Late Devonian plutonic arc rocks. *Journal of Petrology*, **47,** 705–744.

Joesten, R., 1977. Evolution of mineral assemblage zoning in diffusion metasomatism. *Geochimica et Cosmochimica Acta*, **41,** 649–670.

Johnson, T., Brown, M., Gibson, R. & Wing, B., 2004. Spinel-cordierite symplectites replacing andalusite: evidence for melt-assisted diapirism in the Bushveld Complex, South Africa. *Journal of Metamorphic Geology*, **22,** 529–545.

Korzhinskii, D.S., 1959. *Physicochemical Basis of the Analysis of the Paragenesis of Minerals*. Consultants Bureau, New York, 142 pp.

Kröner, A., Wendt, I., Liew, T.C. *et al*., 1988. U-Pb zircon and Sm-Nd model ages of high grade Moldanubian metasediments, Bohemian Massif, Czechoslovakia. *Contributions to Mineralogy and Petrology*, **99,** 257–266.

Marschall, H.R., Kalt, A. & Hanel, M., 2003. *P–T* evolution of a Variscan lower-crustal segment: a study of granulites from the Schwarzwald, Germany. *Journal of Petrology*, **44,** 227–253.

Matte, P., Maluski, H. & Echtler, H., 1985. Cissaillements ductiles varisques vers l'Est - Sud-Est dans les nappes du Waldviertel (Sud-Est du Massif de Bohême, Autriche). Données microtectoniques et radiométriques 39Ar/40Ar. *Comptes rendus de l'Académie des Sciences Paris, série II*, **301,** 721–726.

Medaris, L.G., Jelínek, E. & Mísař, Z., 1995. Czech eclogites: terrane settings and implications for Variscan tectonic evolution of the Bohemian Massif. *European Journal of Mineralogy*, **7,** 7–28.

Medaris, G., Wang, H., Jelínek, E., Mihaljevič, M. & Jakeš, P., 2005. Characteristics and origins of diverse Variscan peridotites in the Gföhl Nappe, Bohemian Massif, Czech Republic. *Lithos*, **82,** 1–23.

Möller, C., 1998. Decompressed eclogites in the Sveconorwegian (-Grenvillian) orogen of SW Sweden: petrology and tectonic implications. *Journal of Metamorphic Geology*, **16,** 641–656.

Munster, A., 1970. *Classical Thermodynamics*. Wiley Inter-Science, London.

Nakamura, D., 2002. Kinetics of decompressional reactions in eclogitic rocks - formation of plagioclase coronas around kyanite. *Journal of Metamorphic Geology*, **20,** 325–333.

Nakamura, D. & Hirajima, T., 2000. Granulite-facies overprinting of ultrahigh-pressure metamorphic rocks, northeastern Su-Lu region, eastern China. *Journal of Petrology*, **41,** 563–582.

O'Brien, P.J., 1999. Asymmetric zoning profiles in garnet from HP-HT granulite and implications for volume and grain-boundary diffusion. *Mineralogical Magazine*, **63,** 227–238.

O'Brien, P.J., 2008. Challenges in high-pressure granulite metamorphism in the era of pseudosections: reaction textures, compositional zoning and tectonic interpretation with examples from the Bohemian Massif. *Journal of Metamorphic Geology*, **26,** 235–251.

O'Brien, P.J. & Rötzler, J., 2003. High-pressure granulites: formation, recovery of peak conditions and implications for tectonics. *Journal of Metamorphic Geology*, **21,** 3–20.

Okay, A.I., 1995. Paragonite eclogites from Dabie-Shan, China – re-equilibration during exhumation. *Journal of Metamorphic Geology*, **13,** 449–460.
Owen, J.V. & Dostal, J., 1996. Contrasting corona structures in mafic granulite from the Blanský Les Complex, Bohemian Massif, Czech Republic. *Canadian Mineralogist*, **34,** 959–966.
Petrakakis, K., 1997. Evolution of Moldanubian rocks in Austria: review and synthesis. *Journal of Metamorphic Geology*, **15,** 203–222.
Pitra, P. & de Waal, S.A., 2001. High-temperature, low-pressure metamorphism and development of prograde symplectites, Marble Hall Fragment, Bushveld Complex (South Africa). *Journal of Metamorphic Geology*, **19,** 311–325.
Powell, R. & Holland, T.J.B., 1988. An internally consistent dataset with uncertainties and correlations: 3. Applications to geobarometry, worked examples and a computer program. *Journal of Metamorphic Geology*, **6,** 173–204.
Powell, R., Guiraud, M. & White, R.W., 2005. Truth and beauty in metamorphic phase equilibria: conjugate variables and phase diagrams. *Canadian Mineralogist*, **43,** 21–33.
Racek, M., Štípská, P., Pitra, P., Schulmann, K. & Lexa, O., 2006. Metamorphic record of burial and exhumation of orogenic lower and middle crust: a new tectonothermal model for the Drosendorf window (Bohemian Massif, Austria). *Mineralogy and Petrology*, **86,** 221–251.
Racek, M., Štípská, P. & Powell, R., 2008. Garnet-clinopyroxene intermediate granulites in the St. Leonhard massif of the Bohemian Massif: ultrahigh-temperature metamorphism at high pressure or not? *Journal of Metamorphic Geology*, **26,** 253–271.
Rumble, D., 1982. The role of perfectly mobile components in metamorphism. *Annual Review of Earth and Planetary Sciences*, **109,** 221–233.
Schulmann, K., Kröner, A., Hegner, E. *et al*., 2005. Chronological constraints on the pre-orogenic history, burial and exhumation of deep-seated rocks along the eastern margin of the Variscan orogen, Bohemian Massif, Czech Republic. *American Journal of Science*, **305,** 407–448.
Schulmann, K., Lexa, O., Štípská, P. *et al*., 2008. Vertical extrusion and horizontal channel flow of orogenic lower crust: key exhumation mechanisms in large hot orogens? *Journal of Metamorphic Geology*, **26,** 273–297.
Štípská, P. & Powell, R., 2005. Does ternary feldspar constrain the metamorphic conditions of high-grade meta-igneous rocks? Evidence from orthopyroxene granulites, Bohemian Massif. *Journal of Metamorphic Geology*, **23,** 627–647.
Štípská, P., Schulmann, K. & Powell, R., 2008. Contrasting metamorphic histories of lenses of high-pressure rocks and host migmatites with a flat orogenic fabric (Bohemian Massif, Czech Republic): a result of tectonic mixing within horizontal crustal flow? *Journal of Metamorphic Geology*, **26,** 623–646.
Tajčmanová, L., Konopásek, J. & Schulmann, K., 2006. Thermal evolution of the orogenic lower crust during exhumation within a thickened Moldanubian root of the Variscan belt of Central Europe. *Journal of Metamorphic Geology*, **24,** 119–134.
Tajčmanová, L., Konopásek, J. & Connolly, J.A.D., 2007. Diffusion-controlled development of silica-undersaturated domains in felsic granulites of the Bohemian Massif (Variscan belt of Central Europe). *Contributions to Mineralogy and Petrology*, **153,** 237–250.
Thompson, J.B., 1959. Local equilibrium in metasomatic processes. In: *Researches in Geochemistry* (ed. Abelson, P.H.), pp. 427–457. Wiley, New York.
Thompson, J.B., 1970. Geochemical reaction and open systems. *Geochimica et Cosmochimica Acta*, **34,** 529–551.
White, R.W., Powell, R., Holland, T.J.B. & Worley, B.A., 2000. The effect of TiO_2 and Fe_2O_3 on metapelitic assemblages at greenschist and amphibolite facies conditions: mineral equilibria calculations in the system K_2O-FeO-MgO-Al_2O_3-SiO_2-H_2O-TiO_2-Fe_2O_3. *Journal of Metamorphic Geology*, **18,** 497–511.
White, R.W., Powell, R. & Holland, T.J.B., 2001. Calculation of partial melting equilibria in the system Na_2O-CaO- K_2O-FeO-MgO-Al_2O_3-SiO_2-H_2O (NCKFMASH). *Journal of Metamorphic Geology*, **19,** 139–153.
White, R.W., Powell, R. & Clarke, G.L., 2002. The interpretation of reaction textures in Fe-rich metapelitic granulites of the Musgrave Block, central Australia: constraints from mineral equilibria calculations in the system K_2O-FeO-MgO-Al_2O_3-SiO_2-H_2O-TiO_2-Fe_2O_3. *Journal of Metamorphic Geology*, **20,** 41–55.
White, R.W., Powell, R. & Holland, T.J.B., 2007. Progress relating to calculation of partial melting equilibria for metapelites. *Journal of Metamorphic Geology*, **25,** 511–527.
White, R.W., Powell, R. & Baldwin, J.A., 2008. Calculated phase equilibria involving chemical potentials to investigate the textural evolution of metamorphic rocks. *Journal of Metamorphic Geology*, **26,** 181–198.

APPENDIX: CALCULATING μ–μ DIAGRAMS WITH THERMOCALC

The mineral spatial relations in the corona are illustrated here in a simple system and qualitative way (e.g. White *et al*., 2008). The oxides necessary to describe

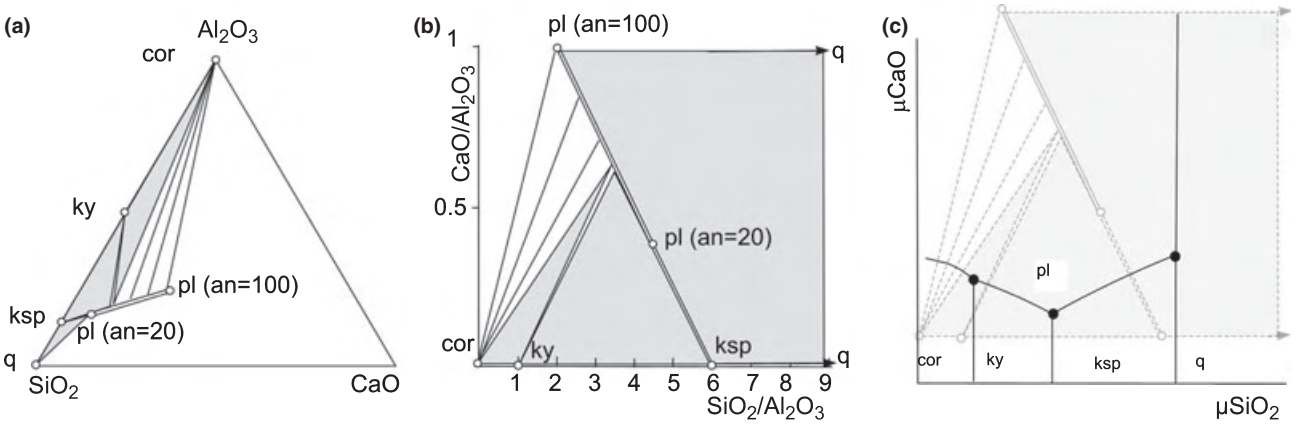

Fig. A1. Derivation of mineral spatial relations of the plagioclase around kyanite corona in a qualitative μ–μ diagram from a compatibility diagram. (a) The mineral relations on a triangular diagram and (b) on an orthogonal diagram. (c) Qualitative $\mu(SiO_2)$–μ(CaO) diagram.

the observed sequence kyanite to plagioclase to K-feldspar + quartz involve Na_2O, CaO, K_2O, Al_2O_3 and SiO_2. In this the chemical potentials of K_2O and Na_2O are considered as constant, in order to draw a qualitative $\mu(CaO)$–$\mu(SiO_2)$ diagram. Al_2O_3 is considered to be the least mobile component. The mineral relations can be then plotted on a triangular diagram with CaO–SiO_2–Al_2O_3 apices or on an orthogonal phase diagram with SiO_2/Al_2O_3 and CaO/Al_2O_3 as the axes (Fig. A1a,b). Because the tie-lines in a compatibility diagram are orthogonal to the lines in the corresponding μ–μ diagram, the relations in the compatibility diagram in Fig. A1b can be used to construct the qualitative $\mu(SiO_2)$–$\mu(CaO)$ diagram (Fig. A1). Phase points in the compatibility diagram occur as fields in the μ–μ diagram, tie lines as reaction lines and tie triangles as intersections.

This relationship between a compatibility diagram and a corresponding μ–μ diagram, provides a connection with how THERMOCALC is used to calculate μ–μ diagrams. Whereas it can work at specified μ values (via the setmu script, see http://www.metamorph.geo.uni-mainz.de/thermocalc/), the information for μ–μ diagrams is calculated indirectly. With the calcmu script, THERMOCALC will calculate the chemical potentials of the components for any equilibrium. So, in this case, with the chemical potentials of K_2O and Na_2O set via setmu, THERMOCALC would be used to calculate the divariant equilibrium, pl–ksp–ky, for example, giving the composition of the phases at the specified P–T. In addition, it gives the chemical potentials that define the coordinates of the invariant point in the μ–μ diagram. In the same way trivariants are calculated to provide the information for the univariant lines in the μ–μ diagram.

Received 26 May 2009; revision accepted 6 October 2009.

Journal of
METAMORPHIC GEOLOGY

J. metamorphic Geol., 2011, **29,** 103–130 doi:10.1111/j.1525-1314.2010.00911.x

Origin of felsic granulite microstructure by heterogeneous decomposition of alkali feldspar and extreme weakening of orogenic lower crust during the Variscan orogeny

J. FRANĚK,[1,2] K. SCHULMANN,[2] O. LEXA,[1,3] S. ULRICH,[4] P. ŠTÍPSKÁ,[2] J. HALODA[1] AND P. TÝCOVÁ[1]
[1]*Czech Geological Survey, Klárov 3, 118 21 Prague, Czech Republic (honzaf2@seznam.cz)*
[2]*Institut de Physique du Globe de Strasbourg, IPGS – UMR 7516, CNRS et Université de Strasbourg (EOST), 1 Rue Blessig, 67084 Strasbourg, France*
[3]*Institute of Petrology and Structural Geology, Charles University, Albertov 6, 128 43 Prague, Czech Republic*
[4]*Institute of Geophysics, Czech Academy of Sciences, Boční II/1401, 141 31 Prague, Czech Republic*

ABSTRACT This study answers the question of origin and evolution of a granulitic microstructure typically developed in felsic granulites of the European Variscan belt. It shows that the precursor of the Variscan felsic granulites was a high-pressure alkali feldspar-rich coarse-grained layered orthogneiss. Its S1 subhorizontal layering is defined by the alignment of alkali feldspar porphyroclasts alternating with monomineralic bands of quartz and bands rich in plagioclase and garnet. The alkali feldspar porphyroclasts contain inclusions of quartz, garnet, kyanite, biotite and rutile, reflecting peak *P–T* conditions of 1.6–1.8 GPa and 850 °C during S1 formation. Superimposed steep folds and steep cleavage, S2, are associated with recrystallization of alkali feldspar, plagioclase and quartz, and garnet chemistry modifications that correspond to 0.9–1.0 GPa and 800 °C. During exhumation, involving 0.8 GPa decompression and cooling, the probably perthitic alkali feldspar underwent an unusual process of heterogeneous decomposition along irregular reaction fronts forming a fine-grained matrix composed of plagioclase and K-feldspar grains. Regular grain distributions in the matrix, nucleation-dominated crystal size distribution and preservation of lattice orientation of the parental perthite crystals are all explained by a discontinuous precipitation process. This heterogeneous decomposition of alkali feldspar solid solution is controlled by chemically and strain induced grain-boundary migration. During exhumation and decompression, the fine-grained matrix underwent viscous deformation, forming the typical microstructure of the Variscan granulites. Random phase distributions, minor coarsening and feldspar textures are interpreted as a result of strain softening due to diffusion creep-accommodated grain-boundary sliding. Subordinate large quartz ribbons were rheologically stronger than the feldspar-dominated matrix due to the activity of different deformational mechanisms. Finally, in mid-crustal levels, the subvertical structure was overprinted by a perpendicular steep fabric associated with the growth of sillimanite, heterogeneous hydration and local partial melting, development of aggregate phase distributions and significant coarsening. This evolution is accompanied with the development of a strong lattice preferred orientation of quartz, K-feldspar and plagioclase, reflecting a switch to dislocation creep mechanism and a general hardening of the granulites under amphibolite facies conditions.

Key words: felsic granulites; Moldanubian domain; quantitative microstructural analysis; quartz and feldspar rheology; Variscan belt.

INTRODUCTION

Felsic high-pressure (HP) granulites represent the most abundant deep crustal rocks exposed in the Palaeozoic Variscan belt in Europe and form large accumulations of the orogenic lower crust, e.g. in the Vosges Massif (Gayk & Kleinschrodt, 2000) and the Bohemian Massif (O'Brien & Carswell, 1993), where the classic example is the Saxony Granulite Massif (Behr, 1961). These rocks are characterized by a fine-grained recrystallized matrix of K-feldspar and plagioclase containing kyanite, garnet and quartz ribbons. These highly deformed rocks have attracted the interest of structural geologists for decades (e.g. Behr, 1961; Lister & Dornsiepen, 1982), who have studied the quartz textures and considered the granulite microstructure a testimony to deep crustal flow. However, despite the generally accepted opinion that granulites represent deep-seated tectonites reflecting deformation in the deep crust, the parental rocks as well as physical conditions and mechanism of deformation remain matters of discussion. Therefore, the key issue of this work is understanding the formation of the granulite microstructures and related deformation mechanisms

in terms of thermal conditions and deformational processes. Unravelling the complex deformational behaviour of the felsic granulites should assist broader considerations of rheology and mechanical behaviour of orogenic lower crust during various stages of deformation and exhumation.

The deformation mechanisms governing rheology of lower crustal rocks are often hard to determine due to changes of the microstructures during exhumation, recrystallization in later deformations or retrogression (e.g. Rutter & Brodie, 1992). At granulite facies conditions, the ductile strain is usually accommodated by dislocation creep, or diffusion creep that may be complemented by grain-boundary sliding (GBS) (Martelat *et al*., 1999; Garlick & Gromet, 2004), each mechanism having variable importance. Grain-boundary diffusion or the presence of silicate melts may favour the diffusion creep or GBS according to new results of Schulmann *et al*. (2008) and Závada *et al*. (2007). The GBS may then operate at the expense of other mechanisms and promote granular flow, particularly in fine-grained rocks (Závada *et al*., 2007; Schulmann *et al*., 2008).

Feldspar, the main constituent of the felsic granulites, is an essential component of the Earth's crust. Nevertheless, its deformational behaviour is not yet fully understood, mainly due to complex solid solution mixing and variation in crystallographic structure with cooling (e.g. Ribbe, 1983; Putnis *et al*., 2003; Abart *et al*., 2009). A common process is exsolution with cooling, which modifies the rheological behaviour of alkali feldspar and may lead to drastic weakening of the orogenic lower crust (Schulmann *et al*., 2008).

Feldspar recrystallization, driven mainly by chemical disequilibrium of the Or–Ab–An solid solution, has been studied in natural examples (Stünitz, 1998; Putnis, 2002) or experimentally (Stünitz & Tullis, 2001), but these studies have focused mainly on medium-temperature water-assisted processes below ~500 °C. At these conditions the original chemically unstable feldspar undergoes dissolution and precipitates as two separate feldspars of different composition. Such results cannot be easily extrapolated to the granulite water under-saturated HT conditions of at least 850 °C (O'Brien & Rötzler, 2003; Štípská & Powell, 2005), where the available fluid is represented by silicate melt, rather than water.

In order to address the above-mentioned aspects, we present a microstructural analysis of exceptionally preserved samples of lower-crustal felsic granulites from an 8.5 × 2.5 km domain (Franěk *et al*., 2006, 2011) with well-preserved granulite facies fabrics. These rocks form part of the Blanský les Granulite Massif (BLG) in the southern Bohemian Moldanubian domain, which belongs to the Variscan collisional chain in central Europe. The combined microstructural and petrological analysis shows evidence of a complex evolution of alkali feldspar rheology during granulite formation and exhumation. Changes in ductility are ascribed to chemically and deformationally driven recrystallization, variations in grain size as well as changing temperature and the amount of interstitial melt.

Geological setting

The Bohemian Massif (Fig. 1a,b) represents the eastern exposure of the Variscan orogen in Europe. During the Variscan orogenesis (380–300 Ma), involving Saxothuringian oceanic subduction and subsequent continental underthrusting, a ~300-km wide orogenic chain evolved. From the NW to the SE, the following tectonic sequence is developed (Schulmann *et al*., 2009): the Saxothuringian domain represented by Neoproterozoic basement covered by Palaeozoic sedimentary rocks, the Teplá suture zone and the supra-crustal Teplá–Barrandian Unit. Further to the SE, the arc-related granitoid plutons separate the Teplá–Barrandian folded sedimentary rocks from the high-grade Moldanubian Zone, which shows widespread anatexis and contains slices of lower-crustal and mantle rocks. This pervasively deformed root domain is further to the east bounded by the Brunia microplate (e.g. Schulmann *et al*., 2005), which is only marginally affected by Variscan tectonometamorphic processes.

The Moldanubian Zone consists of middle- and lower-crustal segments, offering an excellent opportunity to examine evidence of the exhumation processes operating in a collisional setting. The exhumed lower crust, designated as the Gföhl Unit (Fuchs, 1976), is represented by felsic granulites and anatectic gneisses that enclose small bodies of mafic granulites, mantle rocks and eclogites. The mid-crustal paragneiss-dominated level has been divided according to the prevailing lithology into the Monotonous Group, with only limited content of intercalations, such as amphibolites or quartzites, and the Varied Group, bearing a large proportion of intercalated amphibolites, quartzites and marbles (Fuchs, 1976; Matte *et al*., 1990). The studied BLG is the largest granulite body in Southern Bohemia, and belongs to the Gföhl Unit, which is located in a complex stack between the Monotonous and Varied groups, being accompanied by several neighbouring granulite bodies (Fig. 2).

Previous studies of South Bohemian granulites

P–T estimates (Fig. 3) of peak metamorphic conditions have been calculated by various authors using either conventional thermobarometry yielding ~1000 °C/1.6 GPa (e.g. Vrána, 1989; O'Brien & Seifert, 1992; Carswell & O'Brien, 1993; Cooke, 2000), thermodynamic modelling in THERMOCALC software that yields a maximum of 850 °C/1.6–1.8 GPa (Štípská & Powell, 2005) or TWEEQU yielding 970–1000 °C/1.6–1.7 GPa (Kröner *et al*., 2000). The conditions for the amphibolite facies overprint are estimated to 700–800 °C and 0.5–0.8 GPa (Kröner *et al*., 2000; Štípská & Powell, 2005; Verner *et al*., 2007).

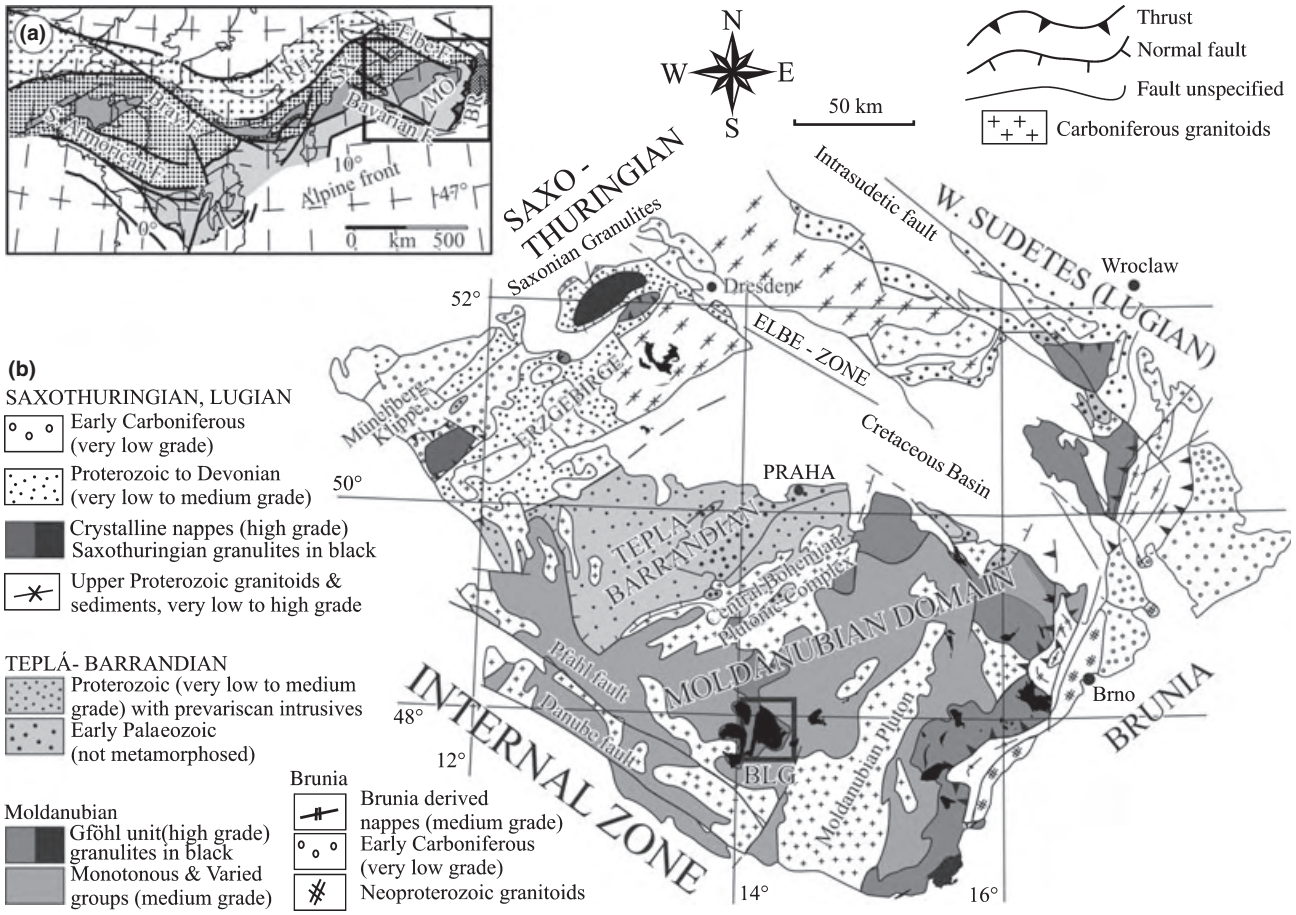

Fig. 1. (a) Position of the Bohemian Massif in the Variscan chain in Europe. (b) Simplified geological architecture of the Bohemian Massif. Rectangle marks the study area depicted in Fig. 2. Modified after Franke (2000).

Radiometric ages ascribed to protolith crystallization of the South Bohemian felsic granulites give between 469 ± 4 and 357 ± 2 Ma using the U–Pb method on zircon (Wendt *et al*., 1994; Kröner *et al*., 2000). Subsequent peak HP metamorphism took place between 351 ± 6 Ma (Wendt *et al*., 1994) and 341 ± 3Ma (Kröner *et al*., 2000). Retrogression under amphibolite facies conditions proceeded immediately after exhumation to mid-crustal levels, between 340 ± 3 and 338 ± 3 Ma (both U–Pb on zircon, Kröner *et al*., 2000). Cooling below ~500 °C is constrained by the 331 ± 1 Ma ^{40}Ar–^{39}Ar age of hornblende from an amphibolite adjacent to the BLG (Košler *et al*., 1999).

Protolith to the felsic granulites is still debated, but the majority of studies consider the protolith to have been a granitic igneous rock (e.g. Fiala *et al*., 1987; Jakeš, 1997; Kotková & Harley, 1999; Finger *et al*., 2003; Janoušek *et al*., 2004, 2006; Tropper *et al*., 2005; Janoušek & Holub, 2007). Janoušek *et al*. (2004) suggested an Ordovician granitic protolith with a model age of *c*. 450 Ma, which is supported by the radiometric U–Pb zircon ages of Kröner *et al*. (2000) and Friedl *et al*. (2003).

Franěk *et al*. (2006) reported a succession of three ductile fabrics in the BLG (Fig. 2). The oldest subhorizontal fabric S1 is preserved in an 8.5 km × 2.5 km elliptical area of the BLG and macroscopically is defined by an alternation of up to 1-cm thick white bands formed by recrystallized alkali feldspar, up to 1-cm thick quartz-rich bands and 1- to 3-mm thick darker plagioclase–garnet-dominated bands (Fig. 4a,b). Large perthite porphyroclasts, up to a centimetre in diameter, are preserved in the feldspar-rich bands. The S1 foliation is folded by metre-scale passive F2 folds with steeply inclined axial planes and pervasively developed penetrative cleavage S2, which is macroscopically characterized by strong subhorizontal elongation of quartz ribbons and biotite aggregates. Within the limbs, the S1 compositional layering is stretched and progressively rotated towards the N–S striking steep S2 cleavage, which contains the subhorizontal L2 stretching and mineral lineation. In strongly reworked areas, the only relicts of the S1 fabric are highly attenuated remnants of the S1 compositional layering parallel to S2. Macroscopically, the D2 structures are best seen in the form

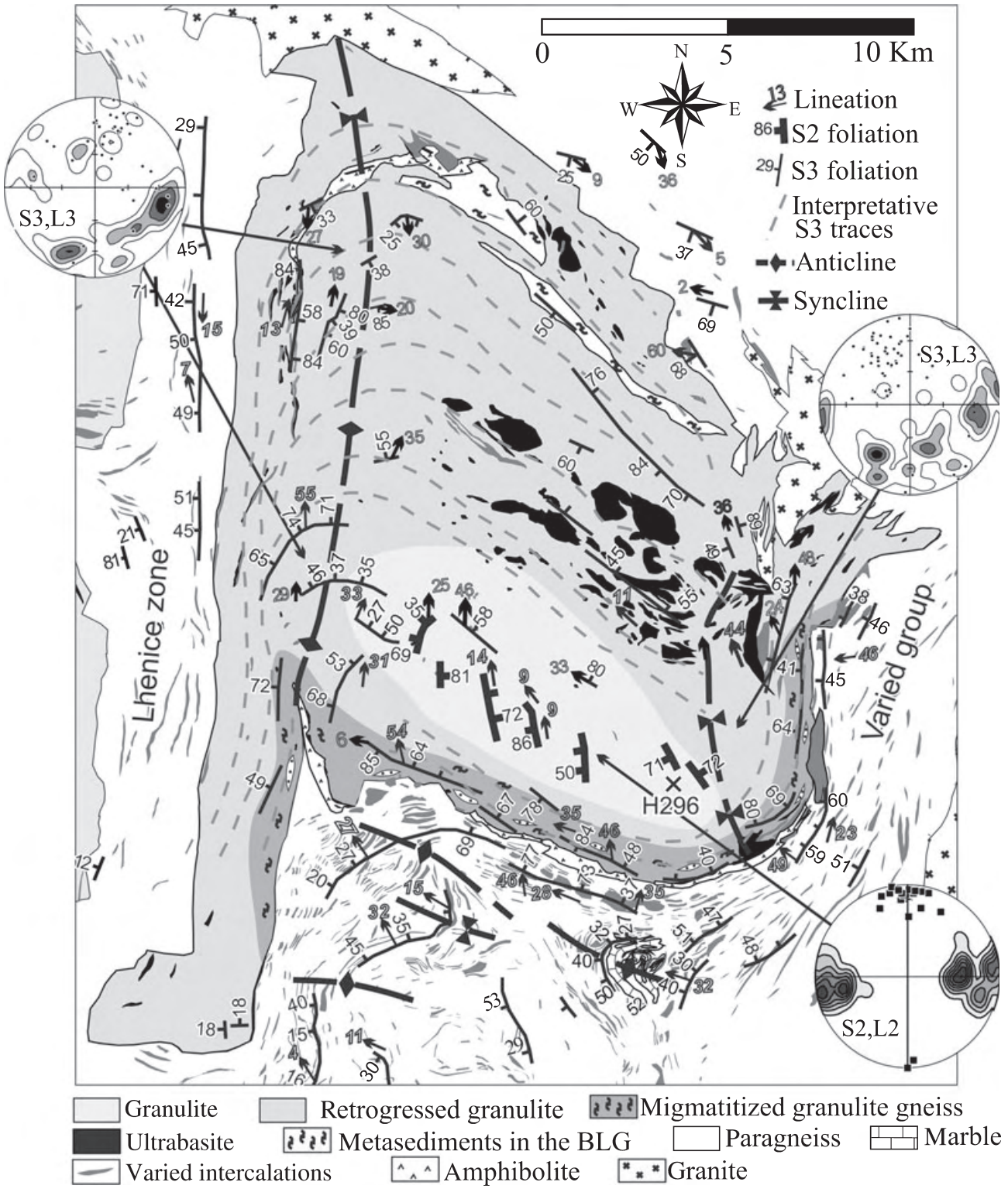

Fig. 2. Structural map of the Blanský les Granulite (modified after Franěk *et al*., 2006). Stereographic projections depict contoured densities of foliation poles and dots mark corresponding lineations: S2 – 55 foliations and 24 lineations; S3 – west 51 foliations and 35 lineations; S3 – east 51 foliations and 54 lineations. Note that in all cases the foliation poles are distributed along great circle(s) whereas the lineations plunge subparallel to π-axes corresponding to these great circles.

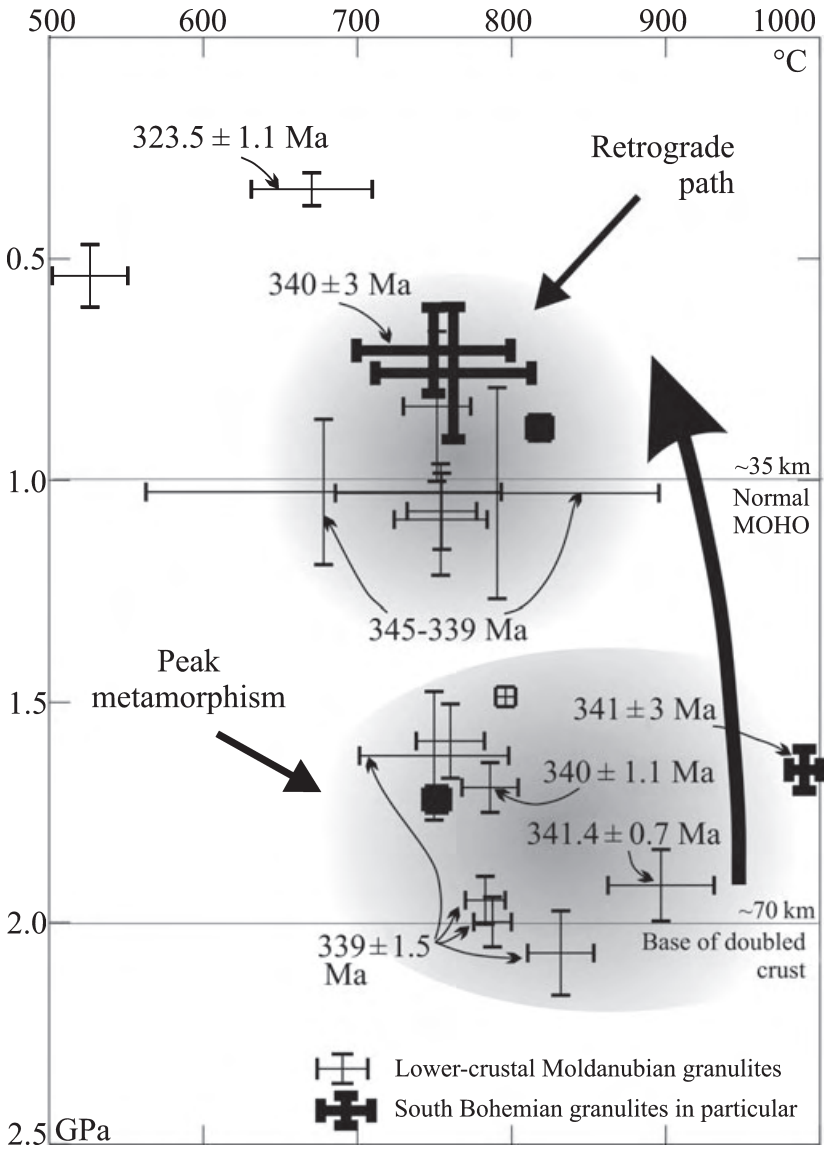

Fig. 3. *P–T* estimates from Moldanubian granulites accompanied by relevant radiometric ages suggest almost isothermal rapid exhumation from peak metamorphic conditions to mid-crustal levels. Results from south Bohemian bodies emphasized by thick lines. For references, see fig. 3 in Franěk *et al*. (2011).

of the elongated quartz ribbons and biotite aggregates that show a strong shape-preferred orientation. Both the S1 and S2 foliations show a mineral assemblage of Grt–Ky–Bt–Kfs–Pl–Qtz, indicating HP granulite facies conditions. Mafic boudins enclosed in S2 are crosscut by Grt–Ky–Kfs–Pl–Qtz felsic dykes. At the marginal part of the elliptical structural relict domain, the S2 foliation is folded by outcrop-scale F3 folds with the formation of axial gneissosity S3 (Fig. 4c). This gneissosity penetratively transposes all previous fabrics in the majority of the BLG and shows synkinematic retrogressive breakdown of garnet to biotite and kyanite to sillimanite (Fig. 5f), constraining the deformation to mid-crustal conditions. The detailed tectonic history and exhumation in a form similar to a forced diapir are described in Franěk *et al*. (2011) and Lexa *et al*. (2011).

PETROLOGY

Analytical procedures

The minerals were analysed using the scanning electron microscopes Tescan VEGA\\ XMU at 15 kV and 0.4 nA at the Strasbourg University and CamScan CS 3200 at 15 kV and 3 nA at the LAREM laboratory of the Czech Geological Survey in Prague. Compositional maps of the feldspar were complemented by spot or area analyses of representative places. Mineral formulae and end-member proportions were calculated using the NORM software (Ulmer, 1986). Microstructural types are qualitatively described according to the deformational fabrics (S1–S3) and subsequently they were quantitatively evaluated using the program PolyLX (Lexa *et al*., 2005) and by electron

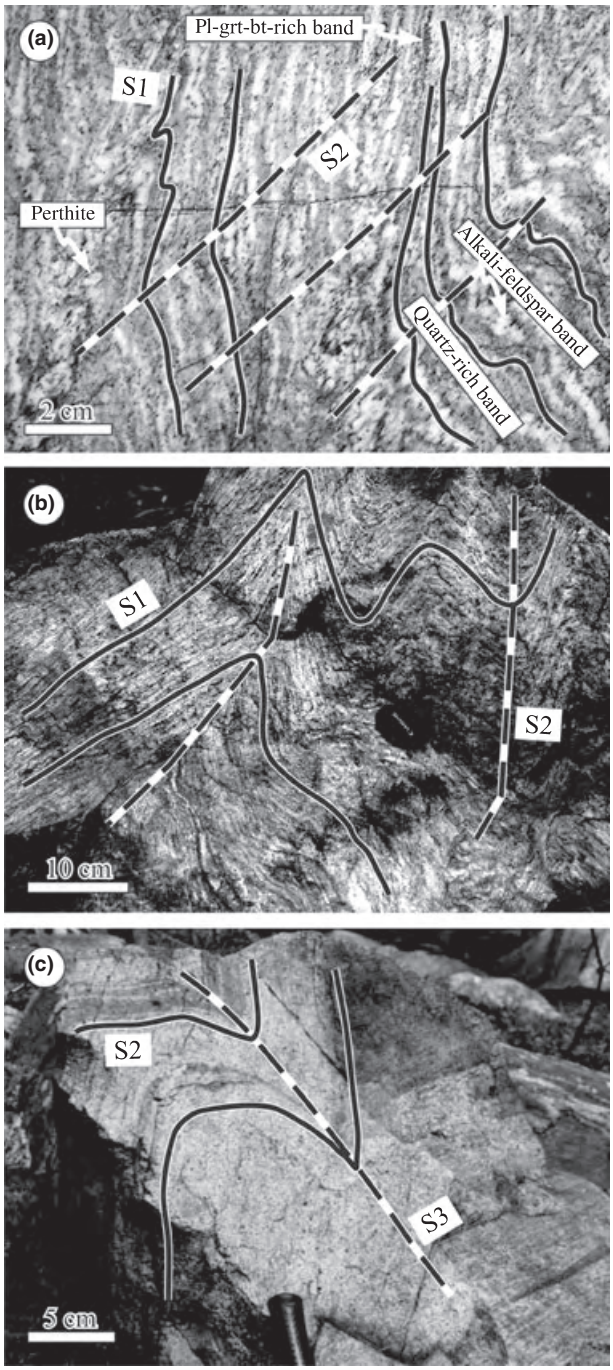

Fig. 4. Field photographs of (a and b) passive F2 folds depicting penetrative development of S2 axial cleavage across the folded S1 compositional layering. (c) F3 folds reworking at amphibolite facies conditions the granulite facies S2 mylonite.

back-scattered diffraction (EBSD). To study the transition from the S1 fabric into the S2 cleavage and the associated *P–T* path, the rocks were collected from one locality within the elliptical relict structural domain (outcrop H296; Fig. 2; 48°51′52.343″N, 14°19′14.135″E). Sixty thin sections containing ~350 large perthite porphyroclasts were oriented with respect to the penetrative S2 foliation and L2 lineation, representing XY, XZ and YZ sections.

Petrography of the granulites with the S1 fabric

Rocks at outcrop H296 are white-grey, fine-grained granulites composed of alkali feldspar, quartz, plagioclase and garnet (~0.2 mm), with minor biotite, kyanite (~0.3 mm) and porphyroclasts (up to 17 mm) of perthitic alkali feldspar. The rocks record evidence of the complete granulite facies structural evolution described above. Microscopically, S1 contains discontinuous bands or lenses dominated by plagioclase that contain numerous garnet, kyanite, some quartz and biotite (Fig. 5b,d). The almost monomineralic S1 quartz bands are recrystallized into elongated S2 ribbons and only quartz accumulation into stripes indicates the original S1 layering (Fig. 5c). Less elongated quartz grains are rarely preserved in pressure shadows of perthite porphyroclasts. Large perthite porphyroclasts with numerous lensoidal to lamellar oligoclase exsolutions are recrystallized at their grain boundaries to a mixture of small K-feldspar grains (~0.063 mm) with rare perthitic exsolution lamellae and oligoclase grains (~0.047 mm). The feldspar-dominated bands with rare garnet are predominantly composed of this K-feldspar–plagioclase mixture with minor quartz (~0.055 mm), ascribed to the D2 recrystallization process (Figs 5a & 6a,b). In the recrystallized matrix composed of K-feldspar, plagioclase and quartz, minor garnet, kyanite, biotite, rutile, ilmenite, zircon, monazite and apatite also occur (Fig. 6g,h).

The perthitic porphyroclasts (up to 17 mm across) contain inclusions of quartz, garnet and kyanite, and more rarely biotite, rutile, ilmenite, zircon, monazite, apatite and Fe-sulphide (Fig. 6a–f). Quartz inclusions (up to 1 mm across) commonly consist of a single crystal with oval or euhedral shape. Garnet (up to 1.2 mm across) enclosed in perthite is euhedral and is commonly surrounded by a thin corona of plagioclase. Subhedral kyanite inclusions are also separated from perthite by a thick plagioclase corona. Biotite inclusions in perthite have short prismatic habits, and are in places partially retrogressed to chlorite.

Mineral chemistry

To specify the *P–T* path for the S1 and S2 fabrics, one sample (H296-S1A) with the S1 layering affected by the S2 cleavage, as described above, was analysed in detail. It contains garnet, kyanite, perthitic K-feldspar, plagioclase, quartz, biotite, rutile, ilmenite, apatite and zircon. The composition of the minerals in the individual bands is similar. Large perthite grains include quartz, garnet, kyanite, rutile, ilmenite, apatite and zircon. Garnet included in large perthite and garnet from the matrix are zoned from core to rim with

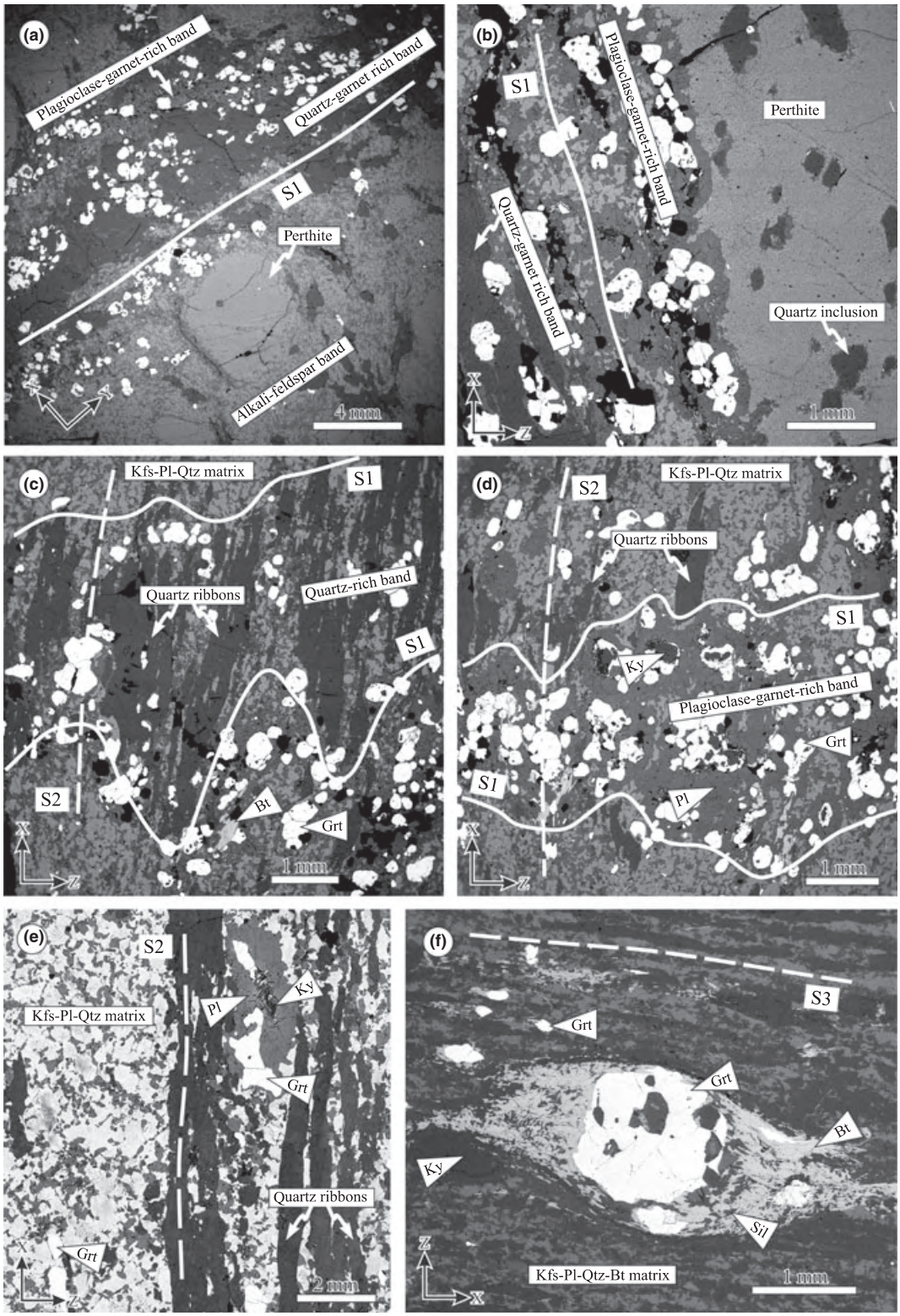

Fig. 5. BSE images characterizing the three examined fabrics. (a) S1 compositional layering. (b) S1 rotated subparallel to S2 in a fold limb; note quartz shapes in perthite and in the matrix. (c) Quartz-rich S1 band recrystallized to S2 ribbons. (d) Grt–Ky–Pl-rich S1 band affected by the D2 deformation. (e) Penetratively developed S2 granulitic mylonite; note plagioclase corona around kyanite. (f) Amphibolite facies S3 fabric; note biotite with sillimanite growing around garnet and a relict kyanite.

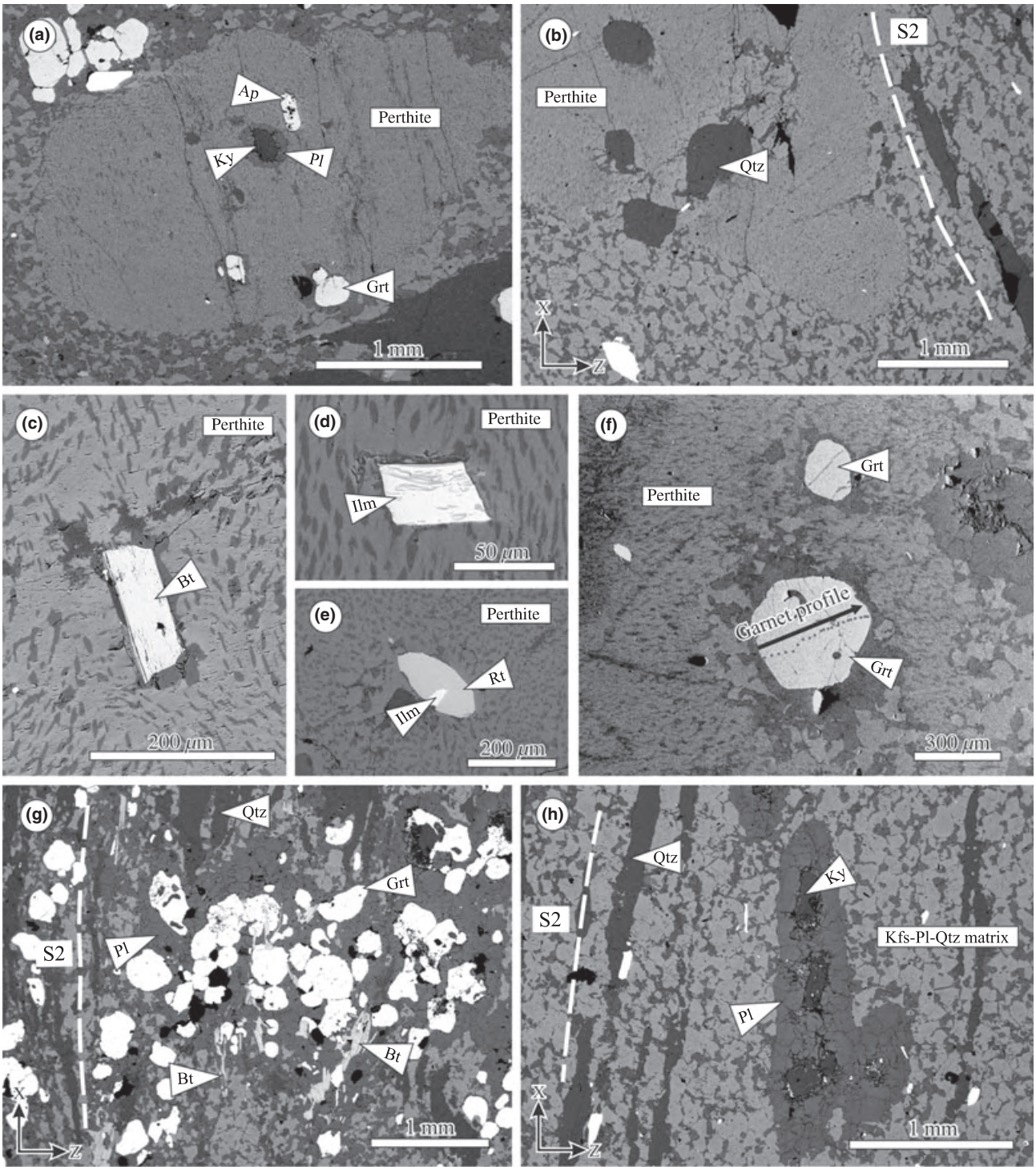

Fig. 6. BSE images of S1 layering. (a–f) Inclusions in the large perthite grains reflect peak metamorphic assemblage. A microchemical profile across garnet in (f) is presented in Fig. 7. (g) Grt–Ky–Pl-rich S1 band containing biotite, which grows parallel to S2. (h) K-feldspar-rich band enclosing kyanite with typical well-developed plagioclase corona.

decreasing grossular, increasing pyrope and almandine, and flat X_{Fe} ($Alm_{0.52 \Rightarrow 0.61}Grs_{0.23 \Rightarrow 0.04}Prp_{0.22 \Rightarrow 0.28}Sps_{0.00–0.01}$; X_{Fe} = Fe/(Fe + Mg) = 0.70, Fig. 7b). The X_{Fe} of biotite in the matrix ranges from 0.33 to 0.35 with Ti = 0.21–0.26 (pfu based on 22 oxygen). Recrystallized K-feldspar and plagioclase are zoned from core to rim, with $Or_{77 \rightarrow 97}Ab_{23 \rightarrow 03}An_{0.0}$ and $Or_{02 \rightarrow 01}Ab_{81 \rightarrow 77}An_{18 \rightarrow 21}$, respectively. Kyanite,

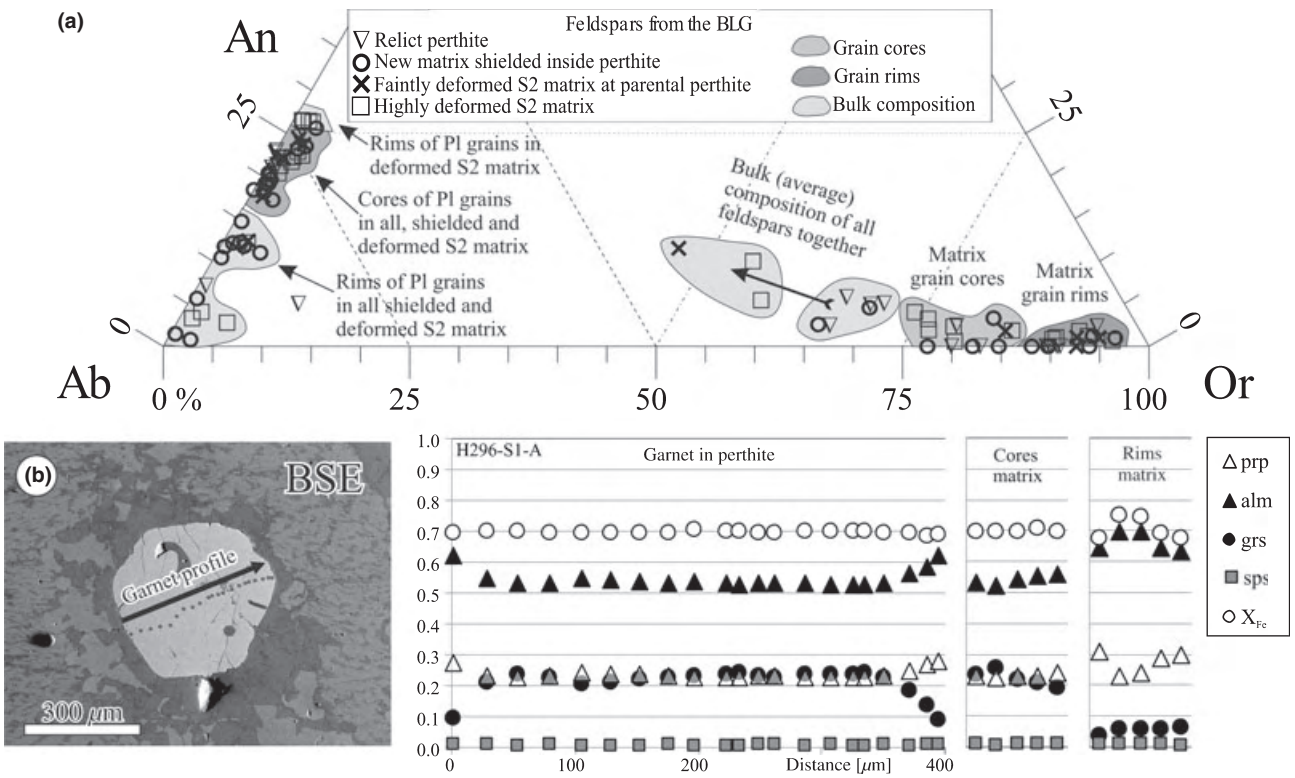

Fig. 7. (a) Ternary plot of feldspar compositions acquired from microchemical analyses of perthite recrystallization and S2 fabric. Similar bulk compositions of parental perthites and shielded matrix are contrasted against areal analyses of deformed matrix. Zoning of plagioclase and to a lesser extent also of K-feldspar are highlighted in the description of data clusters. (b) Microchemical profile across garnet enclosed in large perthite showing a wide flat grossular-rich core, gradual compositional zoning at both rims and almost constant X_{Fe} across the whole crystal.

both included in perthite and in the matrix, is surrounded by a plagioclase corona.

The studied sample H296-S1A lacks biotite inclusions in the perthite porphyroclasts, and because biotite and garnet inclusions in perthite are generally rare, the other five samples from the same macroscopically homogeneous outcrop were analysed to test whether there is a difference in composition between biotite and garnet inclusions in perthite and those in the matrix. The biotite X_{Fe} ranges from 0.23 to 0.40 and Ti = 0.15–0.34 pfu, and there is no clear difference between biotite inclusions and biotite in the matrix (Table 1). Garnet in other thin sections shows the same zoning as that from the sample H296-S1A, but additionally a decrease in X_{Fe} to 0.68 at some garnet rims was detected.

The composition of the large unzoned perthite grains was acquired in several samples from the same outcrop by areal analyses performed by scanning of regions containing ~100 plagioclase exsolution lamellae. It corresponds on average to 68.2% Or, 27.3% Ab and 4.5% An (Fig. 7a). The K-feldspar domains of perthite porphyroclasts contain on average 87.1% Or, 12.3% Ab and 0.6% An. The relict perthite porphyroclasts reveal two generations of plagioclase exsolution lamellae (e.g. Fig. 6c). The coarser exsolution lamellae, presumably older, exhibit elongated braided shapes and are 0.8% Or, 76.7% Ab and 22.5% An in composition. The second micro- to crypto-perthitic generation of exsolution lamellae was not analysed because of its small thickness. Detailed feldspar compositions studied in relation to the recrystallization mechanisms for individual deformation episodes are given below.

P–T path for S1 and S2 fabrics

A pseudosection was calculated using THERMOCALC 3.30 (Powell & Holland, 1988) and DATASET 5.5 (Holland & Powell, 1998; November 2003 upgrade), in the system NCKFMASHTO (Na_2O–CaO–K_2O–FeO–MgO–Al_2O_3–SiO_2–H_2O–TiO_2–O) with biotite and melt models from White *et al.* (2007), garnet from Diener *et al.* (2008), ilmenite from White *et al.* (2000), feldspar from Holland & Powell (2003), white mica from Coggon & Holland (2002) and cordierite from the THERMOCALC documentation (Powell & Holland, 2004). Mineral composition isopleths x(g, bi) = Fe/(Fe + Mg), z(g) = Ca/(Ca + Fe + Mg) and t(bi) = XTi(M1) were plotted for garnet and biotite. The analysed composition of the sample H296-S1A (in wt% SiO_2 = 71.98, TiO_2 = 0.42, Al_2O_3 = 13.53, FeO = 2.1, MnO = 0.03, MgO = 0.73, CaO = 1.93,

Table 1. Representative microchemical analyses of principal minerals constituting the sample H296-S1 used for calculation of the *P–T* pseudosection in Fig. 8.

Mineral	Grt	Grt	Bt	Kfs	Kfs	Pl	Pl	Pl
Sample	H296-S1A	H296-S1A	H296-S1A	H296-S1A	H296-S1A	H296-S1A	H296-S1A	H296-S1A
Analysis	1 g-c	1 g-r	43	44	45	46	5	47
Position	core matrix	rim matrix	matrix	core	rim	core	rim	very rim
SiO_2	38.67	38.79	39.40	65.54	64.95	63.46	63.02	67.40
TiO_2	na	na	4.37	0.00	0.00	0.00	0.00	0.00
Al_2O_3	21.51	21.48	16.88	18.66	18.34	22.66	23.06	20.41
FeO	24.93	29.93	12.37	0.00	0.00	0.35	0.00	0.00
MnO	0.40	0.44	−0.13	0.00	0.00	0.00	0.00	0.00
MgO	5.96	7.99	12.95	0.00	0.00	0.00	0.00	0.00
CaO	8.49	1.41	0.00	0.00	0.00	3.76	4.47	2.09
Na_2O	na	na	0.34	2.48	0.32	9.41	9.17	10.31
K_2O	na	na	9.73	12.87	15.80	0.16	0.32	0.22
Total	99.95	100.05	95.91	99.55	99.42	99.79	100.04	100.43
Si	3.00	3.01	3.00	3.01	3.03	2.81	2.79	2.96
Ti	0.00	0.00	0.25	0.00	0.00	0.00	0.00	0.00
Al	1.97	1.97	1.51	1.01	1.01	1.18	1.20	1.06
Fe^{3+}	0.04	0.00	0.00	0.00	0.00	0.01	0.00	0.00
Fe^{2+}	1.58	1.94	0.79	0.00	0.00	0.00	0.00	0.00
Mn	0.03	0.03	−0.01	0.00	0.00	0.00	0.00	0.00
Mg	0.69	0.93	1.47	0.00	0.00	0.00	0.00	0.00
Ca	0.70	0.12	0.00	0.00	0.00	0.18	0.21	0.10
Na	0.00	0.00	0.05	0.22	0.03	0.81	0.79	0.88
K	0.00	0.00	0.94	0.75	0.94	0.01	0.02	0.01
Total	8.00	8.00	8.00	5.00	5.00	5.00	5.01	5.00
Prp/An	0.23	0.31		0.00	0.00	0.18	0.21	0.10
Alm/Ab	0.53	0.64		0.23	0.03	0.81	0.77	0.89
Grs/Or	0.23	0.04		0.77	0.97	0.01	0.02	0.01
Sps	0.01	0.01						
X_{Fe} (Fe^{2+})	0.70	0.68	0.35					

Na_2O = 2.76, K_2O = 4.01, P_2O_5 = 0.15, H_2O_- = 0.22, H_2O_+ = 0.56, CO_2 = 0.03) was modified for modelling by adding 1 mol.% of kyanite to enable a small amount of aluminosilicate to be stable at the estimated peak metamorphic conditions, as it is observed in the thin section. The amount of H_2O = 0.33 mol.% was chosen after the construction of T–M_{H2O} sections, as it allows the garnet X_{Fe} = 0.70 to be stable in the pseudosection (not shown; see Hasalová *et al.*, 2008a for approach). The major features of the pseudosection involve melt being stable above 810 °C, biotite stable up to 1.6 GPa and 860 °C, ilmenite stable below 1.26 GPa, cordierite stable below 0.7 GPa, and a muscovite-out line heading from 750 °C to 810 °C at 1.35 GPa and then continuing to 880 °C and 2.0 GPa (Fig. 8).

The textural features indicate that perthite and minerals included in perthite (kyanite, garnet, biotite, rutile and quartz) belong to the early assemblage, whereas recrystallized plagioclase and K-feldspar, matrix biotite, rutile, ilmenite and quartz belong to a later assemblage. Because of intense D2 recrystallization, the original plagioclase composition is not known, but the recrystallized monomineralic plagioclase bands and lenses indicate the stability of plagioclase with alkali feldspar within the S1 structure. Chloritized biotite and probably ilmenite in perthite porphyroclasts are considered as resulting from re-equilibration. The flat profile of garnet X_{Fe} is interpreted as having equilibrated during the later stage of metamorphism, even for the garnet included in perthite porphyroclasts, whereas strong grossular zoning is consistent with the core composition having been preserved from the early metamorphic stage, and the rim having equilibrated during the later stage. In the pseudosection, the grossular compositional isopleth of garnet z(g) = 23 occurs outside the biotite stability field (Fig. 8), whereas biotite also belongs to the observed peak assemblage. However, the biotite-present field is only 0.15 GPa and 30 °C apart from the compositional isopleth z(g) = 23, and the peak is therefore estimated as the area between these lines, to ~1.6–1.8 GPa and 850–880 °C (area 1 in Fig. 8). The X_{Fe} of the garnet (=70) and the grossular content at the garnet rim (grs = 4) indicate conditions of ~0.9–1.0 GPa and 825 °C for the second stage (area 2 in Fig. 8). An attempt was made to correlate the biotite composition with the two metamorphic stages, but even if the compositions fit approximately the calculated values in the pseudosection, it is likely that the measured range (X_{Fe} = 0.29–0.36, and Ti = 0.19–0.26 pfu) reflects partial re-equilibration on decompression, as does the X_{Fe} of garnet, and therefore cannot be used for more precise estimation of *P*–T conditions. The feldspar from the pseudosection calculations is not used for thermobarometric

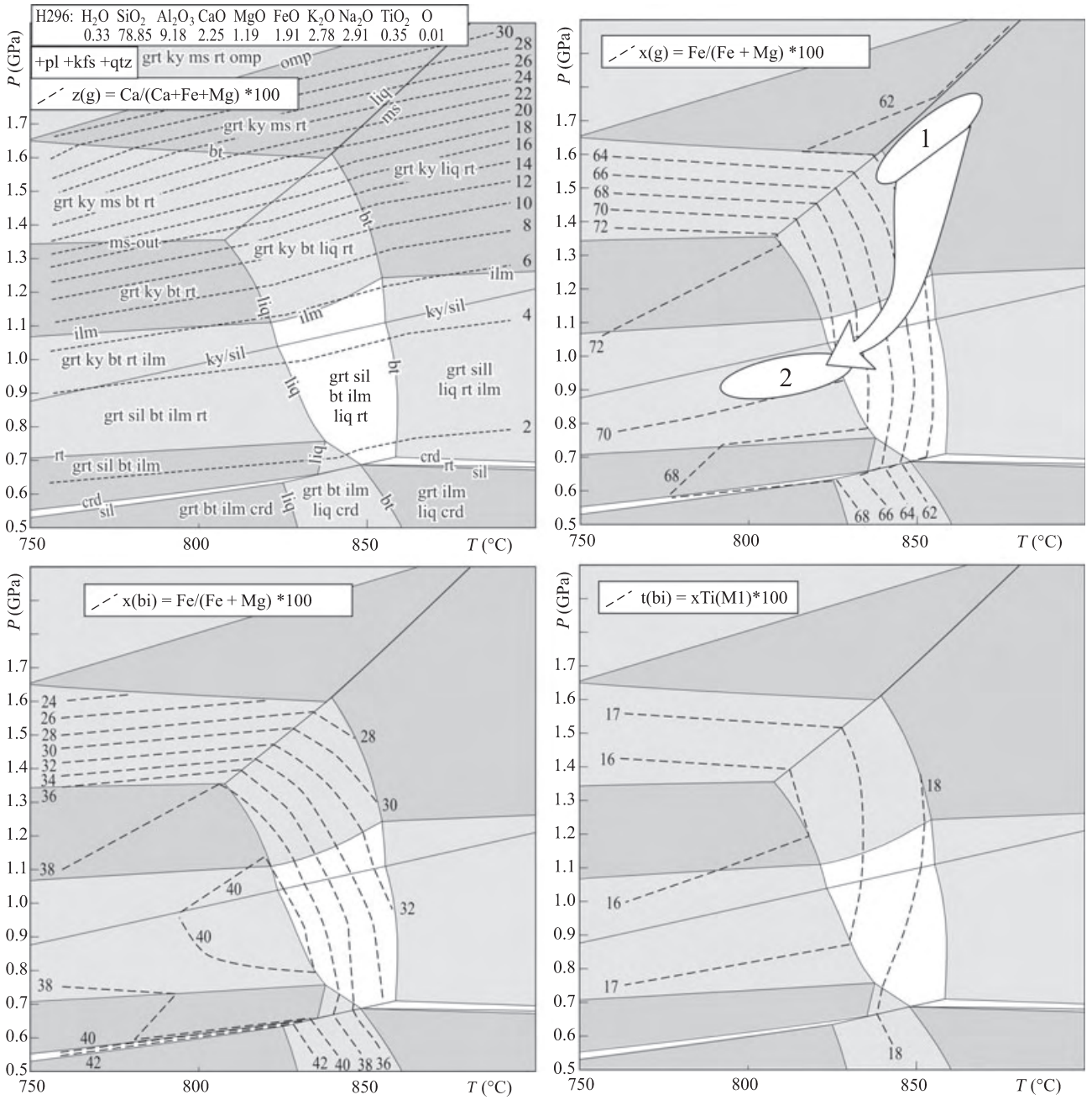

Fig. 8. *P–T* pseudosection calculated in THERMOCALC software for a felsic granulite sample H296-S1. The indicated *P–T* path reflects coarse-grained alkali feldspar growth at peak conditions followed by decompression during S2 fabric development.

estimations, because recent models use significant extrapolations from relatively low pressure and temperature with respect to the conditions of formation of the ternary feldspar of interest (see discussion in Štípská & Powell, 2005). The lack of a clear difference between the chemistry of biotite inclusions and matrix biotite in the other studied thin sections is interpreted as being due to partial chemical re-equilibration on decompression, even within perthite porphyroclasts. A decrease in X_{Fe} to 0.68 at some garnet rims in the other studied thin sections (Fig. 7b) may be explained by further decompression in liquid-absent conditions where x(g) decreases, or by heating. Plagioclase coronas around kyanite reflect decompression (Tajčmanová *et al.*, 2007; Štípská *et al.*, 2010).

In summary, the peak *P–T* conditions ~1.6–1.8 GPa and 850–880 °C are inferred for the stage when alkali feldspar porphyroclasts were stable with garnet, kyanite, biotite, rutile, plagioclase and quartz, presumably within the S1 layering. The S2 fabric started to develop

at these *P–T* conditions and re-equilibrated to the assemblage corresponding to the garnet rim composition, recrystallized K-feldspar, plagioclase, biotite, rutile, ilmenite and quartz, whereas kyanite separated by plagioclase from the equilibrated matrix was metastable (see also Štípská *et al.*, 2010). The *P–T* estimate for the second stage is 0.9–1.0 GPa and 825 °C, showing ~0.8 GPa of decompression associated with cooling within the S2 fabric.

Granular microstructures

Progressive recrystallization of the original coarse-grained microstructure into the fine-grained granular matrix is recorded in finger-like granular matrix domains preserved in large perthite crystals shielded from D2 deformation (Fig. 9a,b,e). In this context, the S2 matrix originated by growth and coalescence of the granular domains preserved in the perthites (Fig. 9a,b) and the perthite grains, as well as the plagioclase aggregates, represent precursors of the fine-grained granular matrix (Fig. 9c,d). A penetratively developed S2 mylonitic foliation is characterized by a granular matrix composed of fine-grained K-feldspar, plagioclase and quartz, and elongated coarse-grained 'platy' quartz ribbons (Figs 5e & 9e). The S2–S3 transition is marked by a substantial change of the granulite mylonitic microstructure towards orthogneiss-like rocks mainly by phase redistribution and grain coarsening (Franěk *et al.*, 2006).

Type I: microstructure of granular domains within perthites

Development of the granular microstructure started with the formation and growth of finger-like, fine-grained domains inside the perthite porphyroclasts (Type I microstructure, Fig. 9a,b). These domains commonly show a lack of preferred orientation in all the studied orthogonal sections; only in XZ sections are they locally elongated subparallel to the X direction of the D2 strain. The Type I microstructure developed dominantly inside perthite porphyroclasts or along two adjacent perthite crystals and garnet–perthite grain boundaries (Fig. 6f), whereas along quartz–perthite or kyanite–perthite boundaries it develops rarely.

The K-feldspar grains in the Type I microstructure show mainly oval shapes of small axial ratio compared with plagioclase. The plagioclase grains range from circular at K-feldspar triple junctions to highly elongated where it coats boundaries between either new K-feldspar crystals or between relict perthite and new K-feldspar (Figs 9b,f & 10a). At the recrystallization front, the phase boundaries of K-feldspar and plagioclase are curved and irregular, whereas in the recrystallized granular matrix the feldspar boundaries are straighter (Fig. 10a,b).

Areal microchemical analyses of the Type I microstructure (regions containing ~100 grains) yield an average composition of 67.3% Or, 29.1% Ab and 3.6% An, similar to that of neighbouring parental perthite grains. On average, the K-feldspar composition is 87.6% Or, 11.8% Ab and 0.6% An, and plagioclase cores consist of 1.5% Or, 78.1% Ab and 20.4% An. Compositional maps reveal a sharp reaction front separating parental perthite from the newly formed Type I microstructure (Fig. 10a). The boundary is easily distinguishable by crypto-perthitic exsolutions, which are abundant in the parental perthite but absent from K-feldspar of the Type I microstructure. New K-feldspar grains reveal weak gradual zoning from Or_{82} in cores to Or_{93} at grain boundaries. The matrix plagioclase grains show strong zoning marked by $An_{18–23}$ cores surrounded by $An_{11–12}$ rims. Locally, irregular patches of pure albite occur at the edges of plagioclase grains.

At the edges of the perthite grains, the new matrix is weakly deformed, showing still the Type I microstructure. Nevertheless, increasing elongation of quartz inclusions with weakly recrystallized Type I microstructure (Fig. 9a) documents the influence of D2 deformation. This Transitional type II microstructure differs by the occurrence of quartz grains in the matrix, which suggests exchange of chemical components with the perthite surroundings. The feldspar composition of this transitional type also shows significant differences (Fig. 7a). Area analyses yield an average feldspar composition of 46.5% Or, 42.0% Ab and 11.5% An, which is significantly different from both the parental perthites and the shielded recrystallized domains. The K-feldspar grains are 90.9% Or, 8.1% Ab and 1.0% An, and the plagioclase is on average 1.6% Or, 76.5% Ab and 21.9% An.

The compositional map acquired at the outer edge of a decomposing perthite also reflects the chemical changes. Plagioclase zoning exhibits a distinct pattern, in which An_{24} homogeneous grains contain only isolated remnants of $An_{11–13}$ outer domains. Weak gradual zoning of K-feldspar, in which the rims are depleted in albite, resembles K-feldspar in the matrix shielded inside perthite.

Plagioclase aggregates at this stage are completely recrystallized to an equi-dimensional mosaic marked by equigranular grains with straight boundaries, commonly meeting in triple point junctions (Fig. 9d). Minor quartz and K-feldspar locally occur at triple junctions. Quartz forms weakly elongated aggregates surrounded by the feldspar matrix.

Type II: microstructure of penetrative fabric S2

The Type II microstructure is linked to D2 deformation and it is the dominant microstructural type throughout the 8.5-km wide relict granulite facies domain. The Type II microstructure is defined by a feldspar-dominated granular matrix enclosing large quartz ribbons. The feldspar aggregate is a mixture of plagioclase and K-feldspar, forming an

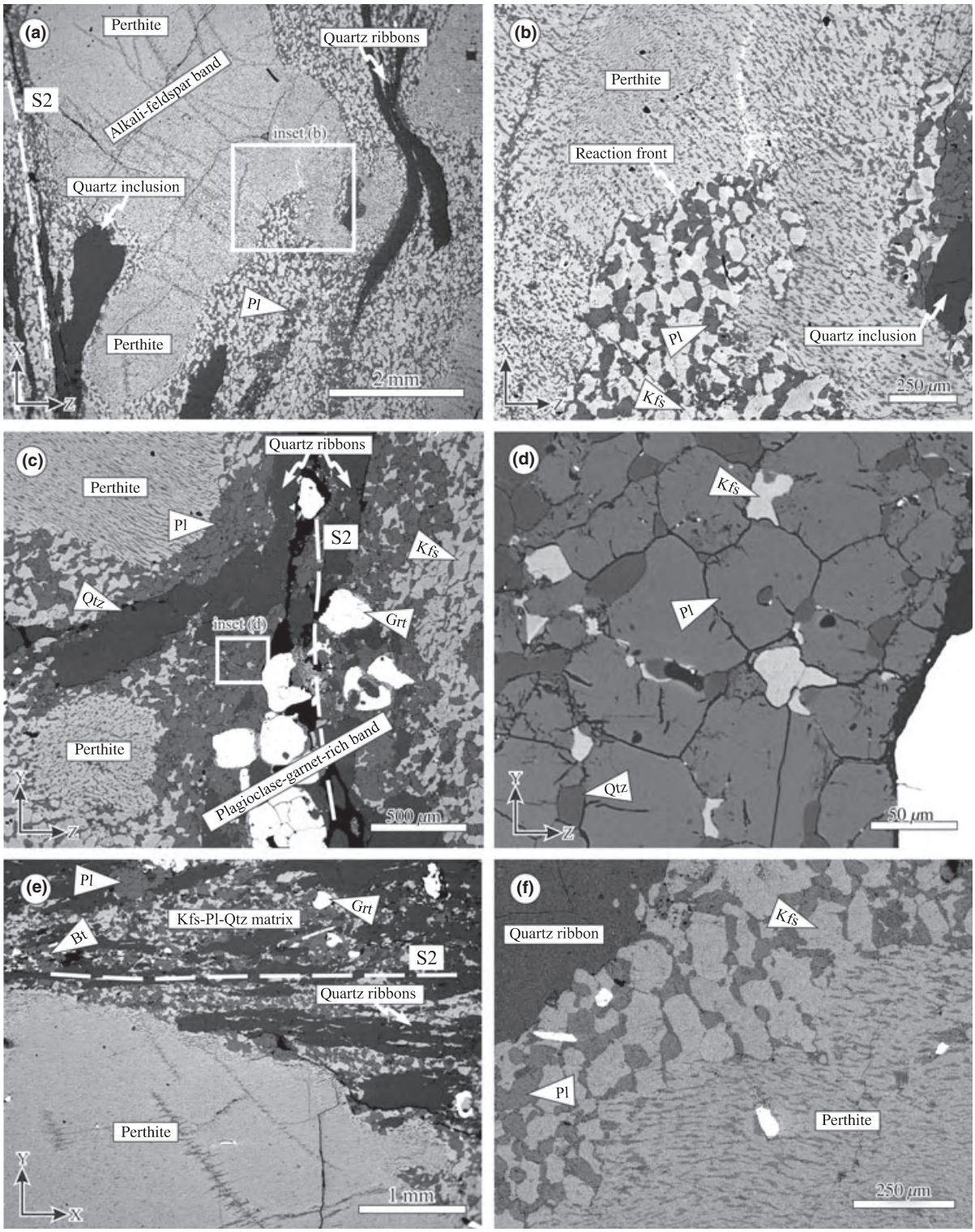

Fig. 9. BSE images documenting recrystallization of large perthite and formation of the fine-grained granular matrix. (a and b) Heterogeneous recrystallization of the parental perthite at a sharp reaction front in domains partly parallel to trace of the S2 fabric. Note the elongation of a quartz inclusion released from the perthite documenting D2 strain. (c and d) Recrystallized Pl–Grt-rich band with interstitial quartz and cuspate geometry of several K-feldspar grains. (e) Recrystallization of a perthite grain partly exposed to the D2 strain (top of the porphyroclast) and partly in a pressure shadow (right side). (f) Detail of a shape-preferred orientation of plagioclase in a newly formed granular matrix adjacent to a parental perthite.

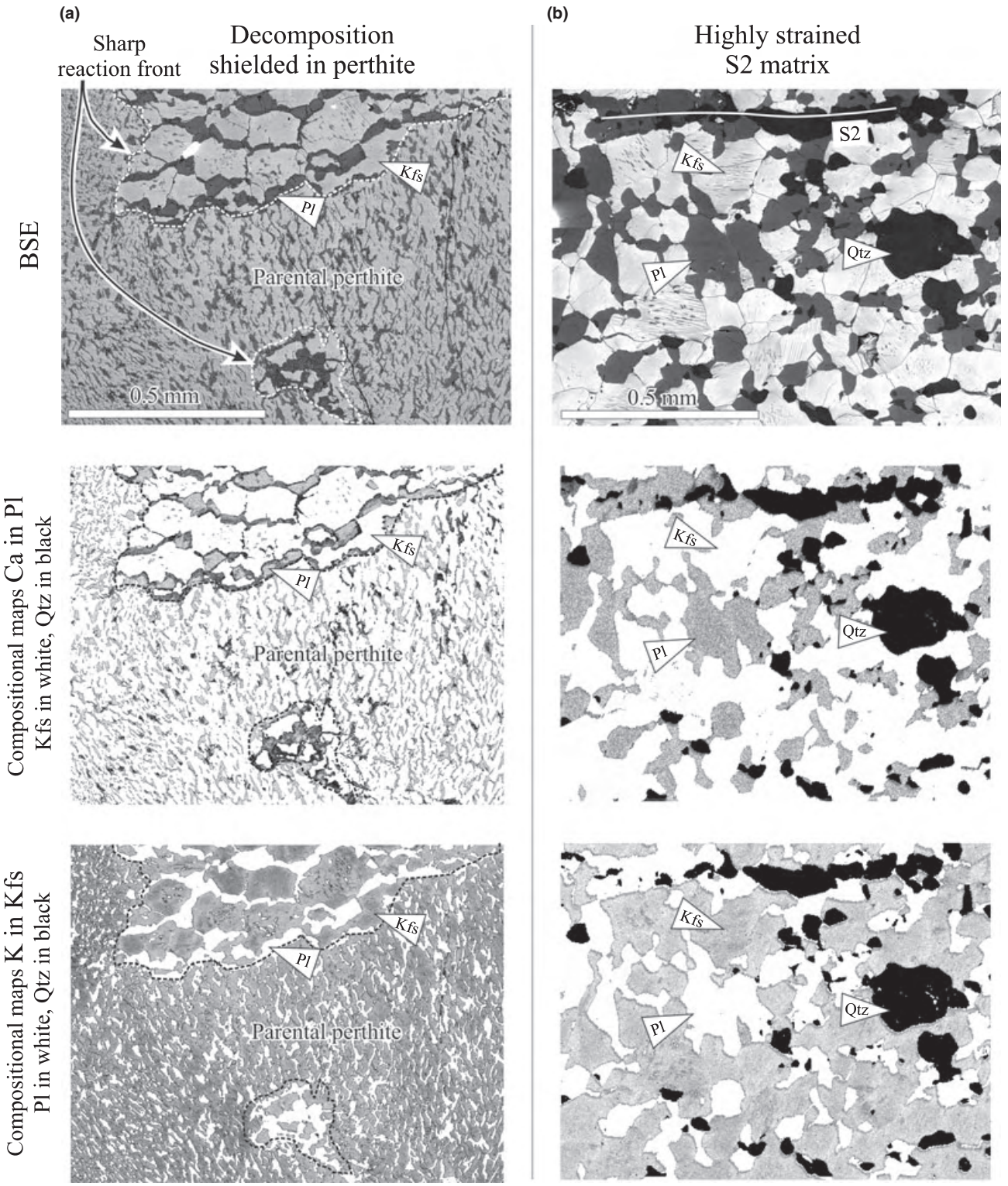

Fig. 10. Compositional maps of Ca and K from (a) matrix shielded inside parental perthite and (b) progressively deformed matrix in the S2 fabric. For Ca, the K-feldspar and quartz grains are masked by white and black colour to emphasize the Ca zoning in plagioclase. Similarly, the plagioclase and quartz grains are masked in the K distribution maps to demonstrate the K zoning in K-feldspar. The BSE images are offered for better orientation in phase distribution.

equi-dimensional mosaic (Fig. 5e). Transposition of S1 compositional layering into the S2 fabric via rotation and attenuation suggests intense deformation during D2 (Fig. 9a). The quartz bands inherited from S1 disintegrated to form the ribbons parallel to S2 and were further dynamically recrystallized along ribbon boundaries, leading to significant reduction of quartz grain size (Fig. 11a). Numerous new small quartz grains nucleated in triple junctions of feldspar grains in the matrix. The garnet grains became dispersed in the matrix and kyanite crystals deformed by kinking. Isolated biotite flakes lie parallel to S2 and, together with quartz ribbons, define a strong L > S fabric.

Areal analysis of a Type II matrix region covering ~100 feldspar grains yields an average feldspar composition of 56.4% Or, 35.9% Ab and 7.7% An (Fig. 7a). The average composition of the K-feldspar is 84.7% Or, 13.5% Ab and 1.8% An, and the plagioclase is composed of 1.8% Or, 74.6% Ab and 23.6% An.

Two compositional maps acquired from the feldspar-dominated matrix (one depicted in Fig. 10b) reveal typical mild zoning of K-feldspar, reflecting the loss of Na around grain boundaries. Plagioclase exhibits uniform An_{23} composition with a weak increase of 2–3% anorthite content towards rims. Locally, thin films of albite occur along plagioclase–K-feldspar and K-feldspar–K-feldspar boundaries; they are significantly thinner than rims in the Type I microstructure.

Type III: microstructure of S3 amphibolite facies fabric

The S3 fabrics prevailing in the felsic granulites of the BLG reveal highly variable degrees of retrogression of the previous mineral assemblage. Contemporaneous hydration of granulites heterogeneously increases towards the boundaries of the granulite massif, where it is accompanied by widespread partial melting and segregation of the melt into mm–dm thick bands parallel to S3 (Kodym, 1972; Franěk *et al*., 2006). The quartz, K-feldspar and plagioclase show irregular grain boundaries and develop into monomineralic aggregates (Fig. 12), whereas the quartz ribbons typical for the S2 entirely disappear. The aspect ratios of quartz grains significantly decrease, compared with the S2 fabric, in conjunction with coarsening of feldspar mosaic (Figs 5f & 11b). The abundant biotite flakes lie parallel to the foliation planes and sillimanite in some instances defines the lineation. The resulting S3 microstructure resembles a common Bt + Sil ± Grt orthogneiss more than a retrograde granulite.

In order to eliminate the effect of strain localization into melt bands or biotite stripes that developed during D3, only macroscopically homogeneous S3 samples with dispersed biotite were studied. The petrology and microchemistry of a steep fabric from a neighbouring Křišťanov Granulite Massif, analogous to the S3 in the BLG, are given in Verner *et al*. (2007).

Quantitative microstructural analysis

The previous section defined three types of microstructures developed from the coarse-grained precursor of the felsic granulites: Type I corresponds to granular microstructure inside coarse perthite and a transitional type in the vicinity of coarse perthite grains; Type II microstructure corresponds to the pervasively developed granulitic S2 fabric; and Type III microstructure corresponds to the S3 fabric developed under amphibolite facies conditions. According to the principle of fabric superposition (Wilson, 1961), the succession of microstructural types is seen as an evolutionary microstructural trend reflecting deformation stages along the exhumation path of the granulites. The coarse-grained orthogneiss precursor microstructure cannot be sufficiently described using quantitative methods. In order to compare the three microstructural stages, we have quantified several parameters characterizing the microstructures using the PolyLX toolbox (Lexa *et al*., 2005) for the MATLAB™ software package and CSD-correction program (e.g. Higgins, 1998). Four thin sections oriented parallel to the lineation and perpendicular to the foliation (XZ sections) from representative samples of the S2 (956 & 1252 grains) and S3 fabrics (848 & 886 grains) were digitalized in an ArcView GIS environment (Fig. 11a,b) and analysed by the PolyLX and CSD-correction software. In order to obtain statistically significant results, we have merged four areas of the Type I microstructure yielding 801 grains. Before merging, the individual areas were rotated with respect to the trace of S2. In addition, the transitional matrix area at the boundary between the perthite and D2 matrix was digitalized, covering 868 grains.

Different microstructural types have been quantified in plots of bulk grain-boundary preferred orientation (GBPO) against contact frequencies (Fig. 12) and slope of linear regression from crystal size distribution (CSD) analysis *v*. regression intercept (Fig. 13). The grain size as well as other quantitative characteristics are statistically evaluated in Table 2, more detailed description of the quantitative data is given in Appendix S1.

The contact frequency method (Kretz, 1969) compares the observed (O) count of contacts between two minerals with the value expected (E) for a perfectly random distribution. The calculation involves modal proportions of phases, only a scatter in grain size may cause a limited uncertainty of the results. The boundaries are designated as 'like–like' for contacts between grains of one phase or 'unlike' for the case of boundary between two different phases. The resulting χ^2-value $(O - E)/\mathrm{sqrt}(E)$ is a measure of the deviation of mineral spatial distribution from random. It is positive for like–like contacts and negative for unlike contacts if the corresponding microstructure tends to form monomineralic aggregates (Lexa *et al*., 2005). On the other hand, the unlike contacts exhibit positive values,

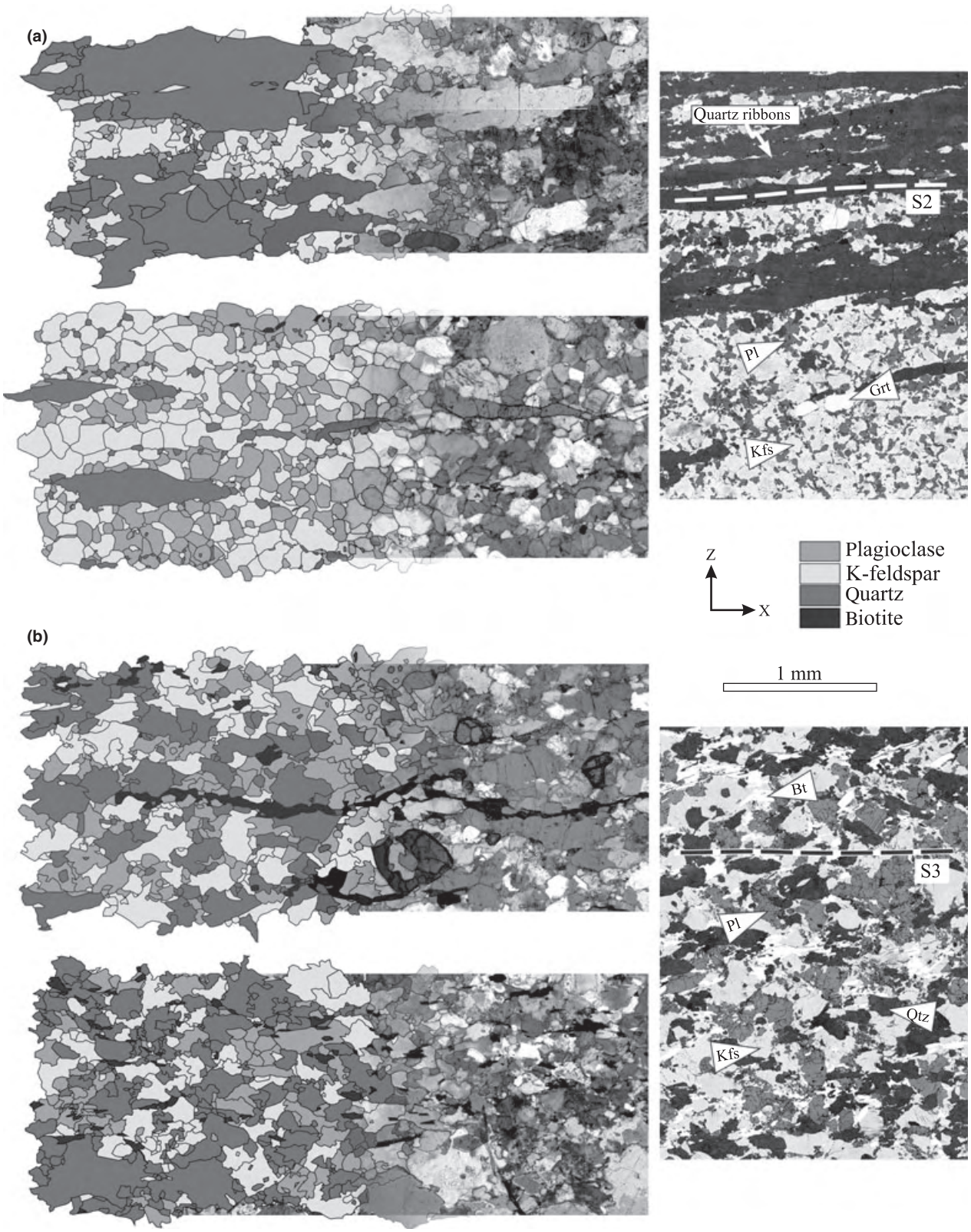

Fig. 11. Microstructural character of XZ sections (X is parallel to lineation, Z normal to foliation) of the two fabrics quantified in the felsic granulites: (a) the granulite facies S2 and (b) the amphibolite facies S3. The left column combines optical image under crossed polarizers with its vectorized form used for statistical analysis in Fig. 12. The right column presents BSE images pointing out phase distribution.

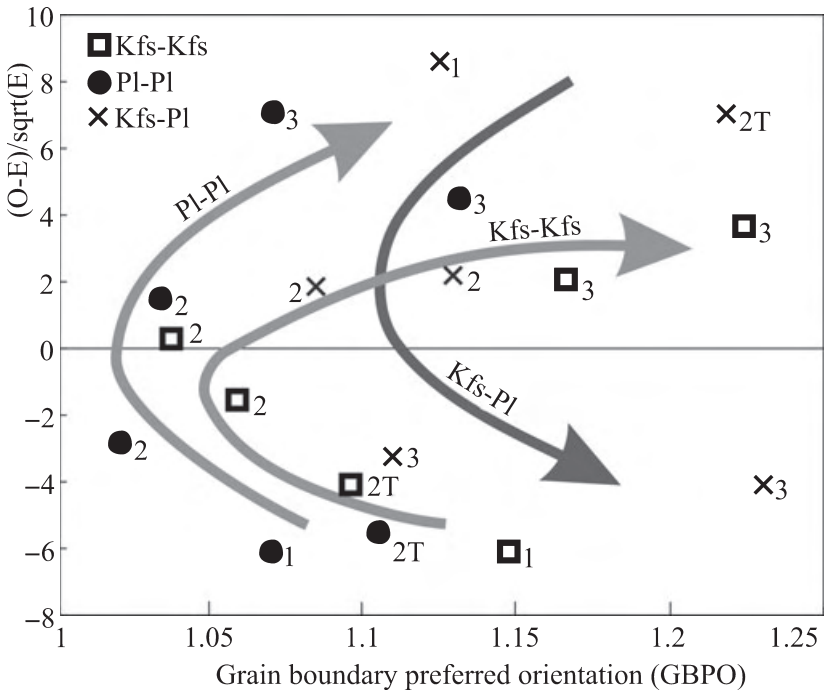

Fig. 12. Quantitative microstructural analysis of the degree of grain boundary-preferred orientation *v.* contact frequencies for like and unlike boundaries of feldspars. Numbers at individual data points refer to the evolution stages defined in the section Granular microstructures.

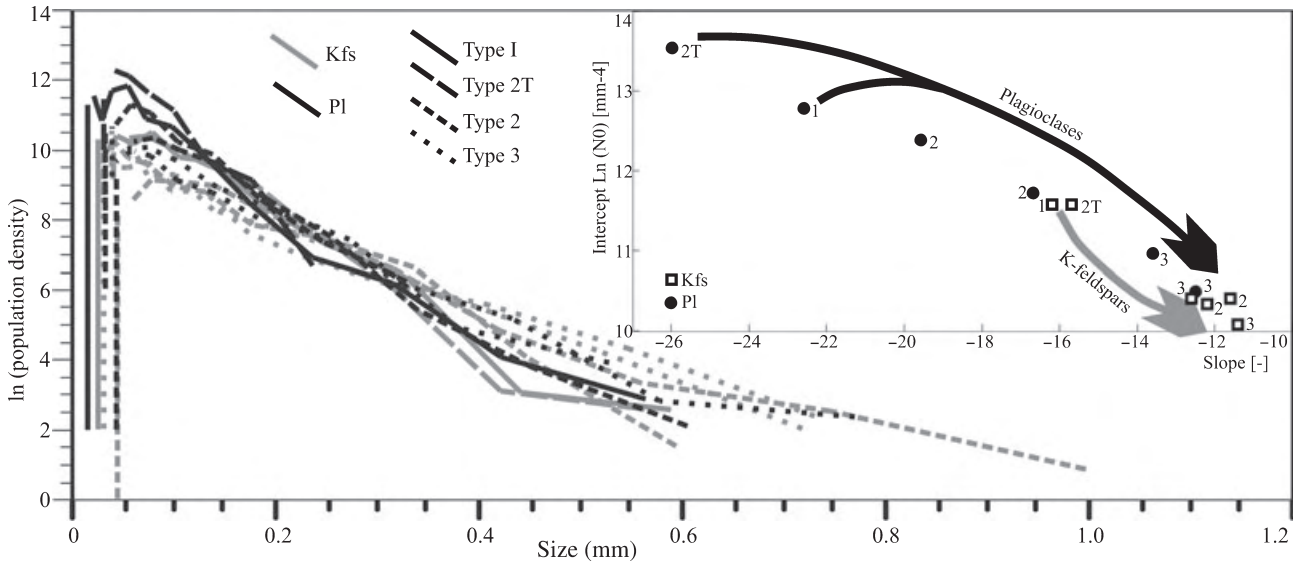

Fig. 13. Crystal size distribution curves for both feldspars. Values of slope and upper intercept of linear regression are plotted together in the inset showing an evolutionary trend for both the feldspars. Numbers at individual data points refer to the evolution stages defined in the section Granular microstructures.

whereas the like–like contacts are negative where the phases tend to be regularly distributed.

Crystal size distributions measured in metamorphic rocks yield quantitative information about crystal nucleation and growth rates, growth times and the degree of overstepping of reactions during metamorphism (Cashman & Ferry, 1988). The CSDs are described as the population density function of the cumulative number of crystals per unit volume per linear crystal size. The data are plotted in log-normal space and a linear regression of points is the characteristic. The intercept values ($N0$) are proportional to the nucleation density of the examined phase at the onset of nucleation (size 0), and the slope (Gt) is proportional to the modification of original grain-size distribution by a variety of coarsening processes such

Table 2. Quantitative characteristics of the microstructural evolution.

		EAD (μm)			Bulk SPO	Axial ratio	CSD intercept	CSD slope
		Q1	Median	Q3				
1-shielded granular	Kfs	33.7	56.3	84.4	1.21	1.53	11.57	−16.2
matrix	Pl	26.8	42.3	59.4	1.22	1.51	12.78	−22.6
2T-weakly deformed	Qtz	18.0	26.6	40.9	2.90	1.67		
matrix	Kfs	44.8	67.1	90.8	1.40	1.49	11.57	−15.7
	Pl	29.2	40.3	59.0	1.20	1.53	13.54	−26.0
2-S2 granulitic matrix	Qtz	14.7	22.5	45.2	2.12	1.49		
	Kfs	56.5	83.9	126.7	1.30	1.43	10.40	−11.6
	Pl	46.3	64.7	90.6	1.14	1.48	11.73	−16.7
3-S3 retrograde fabric	Qtz	39.5	59.8	104.2	1.50	1.46		
	Kfs	42.7	67.4	109.2	1.40	1.54	10.07	−11.4
	Pl	40.9	67.2	111.5	1.27	1.43	10.50	−12.5

Equal area diameter (EAD) statistical characteristics depicting K-feldspar, plagioclase and quartz grain-size evolution from the perthite recrystallization process to amphibolite facies syntectonic retrogression. Q1 and Q3 refer to 1st and 3rd quartiles. The bulk SPO is calculated as the ratio of eigenvalues of bulk orientation tensor according to Lexa *et al.* (2005), the axial ratio values represent modus of their lognormal distribution.

as Ostwald ripening or 'communicating neighbours' theory (Marsh, 1988). Although the individual absolute values are meaningless without knowledge of kinetic parameters, they can be used to compare individual stages of the textural maturation history in a single rock type (Lexa *et al.*, 2005; Hasalová *et al.*, 2008b; Schulmann *et al.*, 2008). The SPO and GBPO are calculated as ratios of eigenvalues of the orientation tensors of long axes of minerals and grain boundaries, respectively (Lexa *et al.*, 2005), and their values usually depend on types of active recrystallization and/or deformation mechanisms. The aspect ratio, SPO and GBPO are relatively high for dynamically recrystallized grains deformed by dislocation creep (Kruse *et al.*, 2001; Ulrich *et al.*, 2002; Baratoux *et al.*, 2005), whereas low values commonly characterize GBS-controlled diffusion creep associated with mutual rotation of individual grains (Boullier & Gueguen, 1975; Behrmann & Mainprice, 1987).

Grain contact frequency evolution

The grain contact frequency method yields a well-defined evolutionary trend of like–like contacts for both Kfs and Pl. The two minerals reveal fairly similar and highly negative values of $(O - E)/\mathrm{sqrt}(E)$ ratio (−6) for Type I microstructure (Fig. 12), suggesting highly regular spatial distribution of both feldspars. Both feldspars also reveal distinct GBPO (1.07–1.15). The Type II microstructure shows an important increase of like–like grain contact frequency in Fig. 12, reaching zero, which suggests an almost perfectly random distribution of both feldspars, coupled with almost complete loss of GBPO. Finally, the Type III microstructure reveals a further increase of $(O - E)/\mathrm{sqrt}(E)$ values, suggesting a progressively developing aggregate distribution (higher for plagioclase compared to K-feldspar) associated with an increase of GBPO values. The evolution of K-feldspar–plagioclase grain boundary frequencies mirrors the trend of like–like contacts, but the GBPO remains more developed for all stages, compared with like–like boundaries, with peaks in Types I and III microstructures. The progressive evolution of rock structure from a regular distribution of grains through random to an aggregate distribution indicates a process of solid-state differentiation and development of mineral layering. The fluctuation of GBPO suggests destruction of the original preferred orientation of grain boundaries by D2, whereas D3 was responsible for the development of a new GBPO.

Grain-size evolution

The grain-size statistics (Table 2, Appendix S1) has a rather constant and low value (55–70 μm) for recrystallized K-feldspar of the Type I microstructure and transitional microstructures adjacent to perthite crystals, and a slightly larger grain size for the Types II and III microstructures (84 & 67 μm, respectively). Similarly, fine-grained plagioclase has a small and constant grain size for the Type I microstructure (42 μm) and a larger grain size for Types II and III ($\sim$66 μm). The quartz grain size first decreases from the transitional microstructure (26 μm) to the Type II microstructure (23 μm), and increases in the Type III microstructure (60 μm). In general, the K-feldspar recrystallized grain size is the largest of all the studied minerals ($\sim$70 μm).

The CSD analyses reveal a two stage grain-size evolution for both plagioclase and K-feldspar (Fig. 13). Both minerals show decrease of N0 values and increase of Gt values from the Type I to Types II and III microstructures. For plagioclase the evolution is marked by gradual decrease in the N0 value, coupled with an increase in the Gt value from the Types II to III microstructures. Importantly, although the evolution of the plagioclase and K-feldspar grain size starts from very different positions in the Gt–N0 plot (higher N0 and smaller Gt in plagioclase, compared with K-feldspar), they end up with nearly the same values of both parameters for the Type III microstructure. Both minerals reach the greatest difference in grain-size parameters for the Type II microstructure, for which plagioclase shows significantly higher N0 values and smaller Gt values compared with K-feldspar.

Shape-preferred orientation and grain elongation

The aspect ratio remains constant for both K-feldspar and plagioclase during the whole deformation sequence and the bulk shape-preferred orientation (SPO) of plagioclase remains similarly low, whereas K-feldspar SPO is slightly higher for Types II and III microstructures (Table 2). Quartz reaches the highest degree of SPO (mean value $\sim$ 2–3) for Type II, together with a relatively high aspect ratio. The Type III microstructure is characterized by a decrease of the quartz SPO in conjunction with a significant decrease in the aspect ratio (Table 2).

Lattice-preferred orientation

Lattice-preferred orientation (LPO) measurements of quartz, K-feldspar and plagioclase grains from all the described microstructural types were additionally carried out in order to evaluate operative deformation mechanisms. A strong LPO usually originates during plastic deformation via dislocation creep, whereas the diffusion-accommodated GBS generally weakens the LPO of deforming grains (e.g. Jiang *et al*., 2000). The slip systems accommodating dislocation creep are well known for quartz (e.g. Schmid & Casey, 1986) and plagioclase (e.g. Tullis, 1983; Montardi & Mainprice, 1987; Kruse *et al*., 2001; Stünitz *et al*., 2003), but less known for K-feldspar (Tullis, 1983). To ensure high quality of measurements, the crystal lattice orientations were collected manually via EBSD in the LAREM laboratory of the Czech Geological Survey and at the Institute of Petrology and Structural Geology at Charles University in Prague. LPO data for each sample (XZ thin section) were plotted separately as non-polar projections on a lower hemisphere and important slip planes and directions for quartz, K-feldspar and plagioclase were projected.

Type I microstructure

At first, the EBSD study was carried out in domains consisting of perthite and the newly formed Type I matrix enclosed within the perthite, therefore protected from D2 and D3 deformation. The Type I K-feldspar and plagioclase grains reveal roughly the same lattice orientation as the K-feldspar host and plagioclase exsolutions in parental perthite. When passing outside the protected matrix into the Transitional type II microstructure, a continuous increase of LPO scattering with respect to the parental perthite orientation occurs in the matrix without any tendency to develop a new LPO (Fig. 14).

Type II microstructure

The pole figures of matrix quartz show incomplete high-angle Type II cross-girdle (Lister & Price, 1978) of c-axes (Fig. 15a). High opening angle and central maximum are consistent with dominance of prism <a> and <c> slip systems, being variably accompanied by rhomb <a> + <c> slip (e.g. Lister & Dornsiepen, 1982). The large quartz ribbons have an irregular size and distribution of subgrains, with inclined subgrain boundaries and a strong central maximum sometimes accompanied with minor submaxima oriented close to the lineation. This typical granulite pattern (Behr, 1961) results from predominance of the prism <a> slip, only rarely accompanied by subordinate prism <c> slip (Schmid & Casey, 1986).

In plagioclase, the LPO shows an incomplete girdle of (010) poles normal to the lineation direction and maxima of [201], [101] and [001] subparallel to the lineation. It indicates the activity of primary [001] (010)

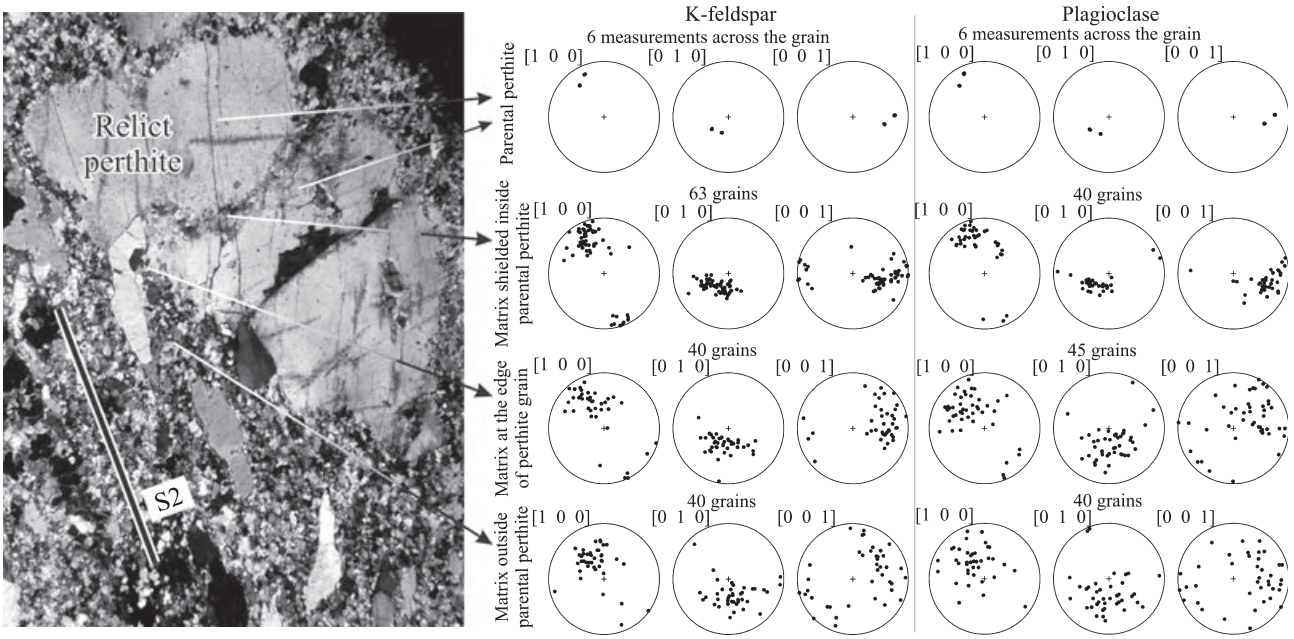

Fig. 14. Electron back-scattered diffraction measurements of a perthite domain undergoing recrystallization to granular matrix and initial D2 deformation. The crystal lattice orientation of both K-feldspar background and plagioclase exsolutions in parental perthite are compared to both feldspars in the granulitic matrix located inside the perthite, at the edge of the perthite and in the deformed matrix adjacent to the perthite grain. The elongation of quartz grains reflects D2 strain intensity and depicts orientation of S2 fabric. Lower hemisphere non-polar equal-area projections.

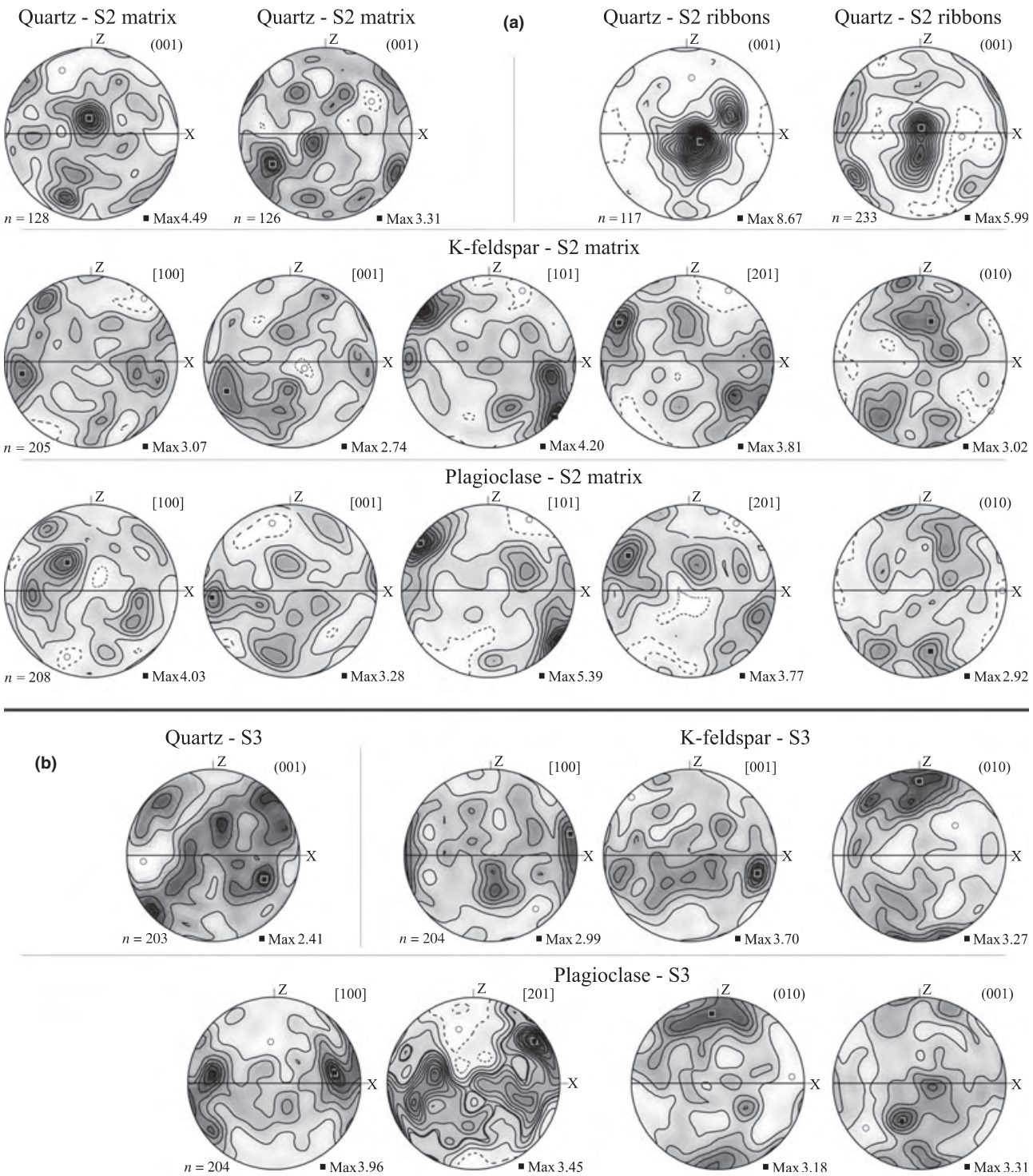

Fig. 15. Polar diagrams of lattice preferred orientation of quartz, K-feldspar and plagioclase from XZ sections of felsic granulites exhibiting penetrative (a) S2 and (b) S3 fabrics. Only the slip planes significant for each mineral are presented; lower hemisphere non-polar equal-area projections.

as well as secondary [101] (010) and [201] (010) slip systems according to Kruse *et al.* (2001). The LPO of K-feldspar is similar to that of plagioclase suggesting activity of the same slip systems. Additional slip system [100] (010) in K-feldspar makes the only difference between both of the feldspars. It is noteworthy that pole figures of both feldspars show double maxima of single crystal orientations close to each other.

Type III microstructure

The quartz LPO shows a high angle Type II cross-girdle of c-axes distribution with a maximum either in the centre or near edges of the girdle. The LPO is similar to those measured from the S2 matrix microstructure and implies a combination of prism <a> and rhomb <a> + <c> slip (Fig. 15b). Plagioclase shows the (010) and (001) planes subparallel to foliation and a girdle distribution of [100] and [201] along the foliation with single maxima parallel to the lineation. This pattern points to activity of three slip systems, namely [100] (010), [201] (010) and [100] (001). In the case of K-feldspar, all samples show a pronounced maximum of (010) planes parallel to foliation, whereas other common slip planes do not show such relationship. A girdle distribution is observed for the [001] and [100] directions, with a maximum of the [001] direction oriented parallel to the stretching lineation. These attributes indicate that the activity of [100](010) slip system is the characteristic for both feldspars.

DISCUSSION

We discuss the origin and petrological significance of the S1 fabric as a precursor for development of characteristic granular microstructure of Variscan felsic granulites. Subsequently, an attempt is made to discuss the origin of granular fabric, its specific quantitative microstructural characteristics and its importance for understanding deep crustal flow processes. Finally, the petrology, microstructure and LPO of various types of granulites are discussed in terms of the rheological evolution of orogenic lower crust and its extrusion (Franěk *et al*., 2011) during the Variscan orogeny in Europe. Figure 16 puts the microstructural evolution in context with the tectonic history.

Interpretation of S1 fabric: HP orthogneiss

The observed structural succession, field distribution of the S1 relicts and microstructural relations imply that the perthitic alkali feldspar, plagioclase and quartz aggregates preserved locally within the S1 compositional layering represent a remnant of the precursor of the Blanský les felsic granulites. The best preserved relicts of the S1 layering contain a substantial amount of large alkali feldspar (presently perthite) and large quartz grains in the microstructure. The inclusions of kyanite, high-grossular garnet and rutile suggest that the large alkali feldspar crystallized at HP conditions (Figs 8 & 16). Despite diffusional re-equilibration of most minerals, the peak *P–T* conditions related to the growth of large alkali feldspar are estimated at 1.6–1.8 GPa and 850–880 °C. The abundant idiomorphic or oval-shaped quartz inclusions in the large perthite porphyroclasts point to a lack of plastic deformation during alkali feldspar growth. Such inclusions may develop either in granites, or during melt-assisted recrystallization in migmatites (Mehnert, 1968, pp. 111, 192). The lenticular plagioclase-rich aggregates are interpreted as completely recrystallized remnants of large plagioclase grains complementary to the alkali feldspar porphyroclasts (Figs 9c,d & 16, 3D block diagram 1). Consequently, the original rock was a coarse-grained granite/orthogneiss crystallized under HP conditions in the kyanite stability field. Existence of two complementary feldspars at peak conditions contrasts with laboratory experiments of Tropper *et al*. (2005) focused on the South-Bohemian felsic granulites, where only a single alkali feldspar existed above 850 °C.

The S1 layering of initially coarse-grained quartz, K-feldspar and plagioclase-rich layers may be interpreted as a result of solid-state deformational segregation of minerals with different plasticity at high temperatures, a process common in formation of, e.g. layered orthogneisses. The length of the bands then indicates significant strain during the D1 phase. Assuming growth of large alkali feldspar during the D1 episode, the overgrowth of quartz, garnet and biotite by the large feldspar indicates a dominance of growth processes resulting in overall coarsening of the gneiss (Higgins, 1998; Lexa *et al*., 2005). Such crystal growth indicates that the temperature/strain rate ratio was rather high and thermodynamic modelling (Fig. 8) suggests contemporaneous partial melting. High-*P* peak conditions (~1.6–1.8 GPa) indicate that the flow occurred at the bottom of thickened crust as also suggested by other studies (e.g. Štípská & Powell, 2005; Racek *et al*., 2006; Tajčmanová *et al*., 2006). Therefore, the S1 fabric probably originated during lower crustal flow at the bottom of a thickened crustal root and at progressively increasing temperatures (Fig. 16).

The inclusions within the perthite porphyroclasts, the S1 compositional layering and the S2 mylonitic foliation in the BLG are similar to the oldest structures described from the Saxonian Granulitgebirge (Behr, 1961). In addition, all of the Variscan felsic granulites reveal similar geochemistry and geochronology (340 Ma peak). Consequently, both the mentioned massifs and other Variscan felsic granulite massifs as well may have evolved from such HP coarse-grained orthogneisses.

Origin of granular matrix in granulites

The microchemical and textural relations indicate that the initial large alkali feldspar underwent heterogeneous step-by-step recrystallization during the D2 event, which resulted in formation of a fine-grained matrix. This recrystallization probably postdated exsolution of the coarse perthitic plagioclase because (i) the newly formed Type I K-feldspar in the granulitic matrix is devoid of such large braided exsolutions, and (ii) the perthite exsolutions reveal ~1–2% higher anorthite content than the cores of Type I matrix plagioclase indicating a bit higher temperature of formation (Fig. 16, 3D block diagram 2). Nevertheless, it

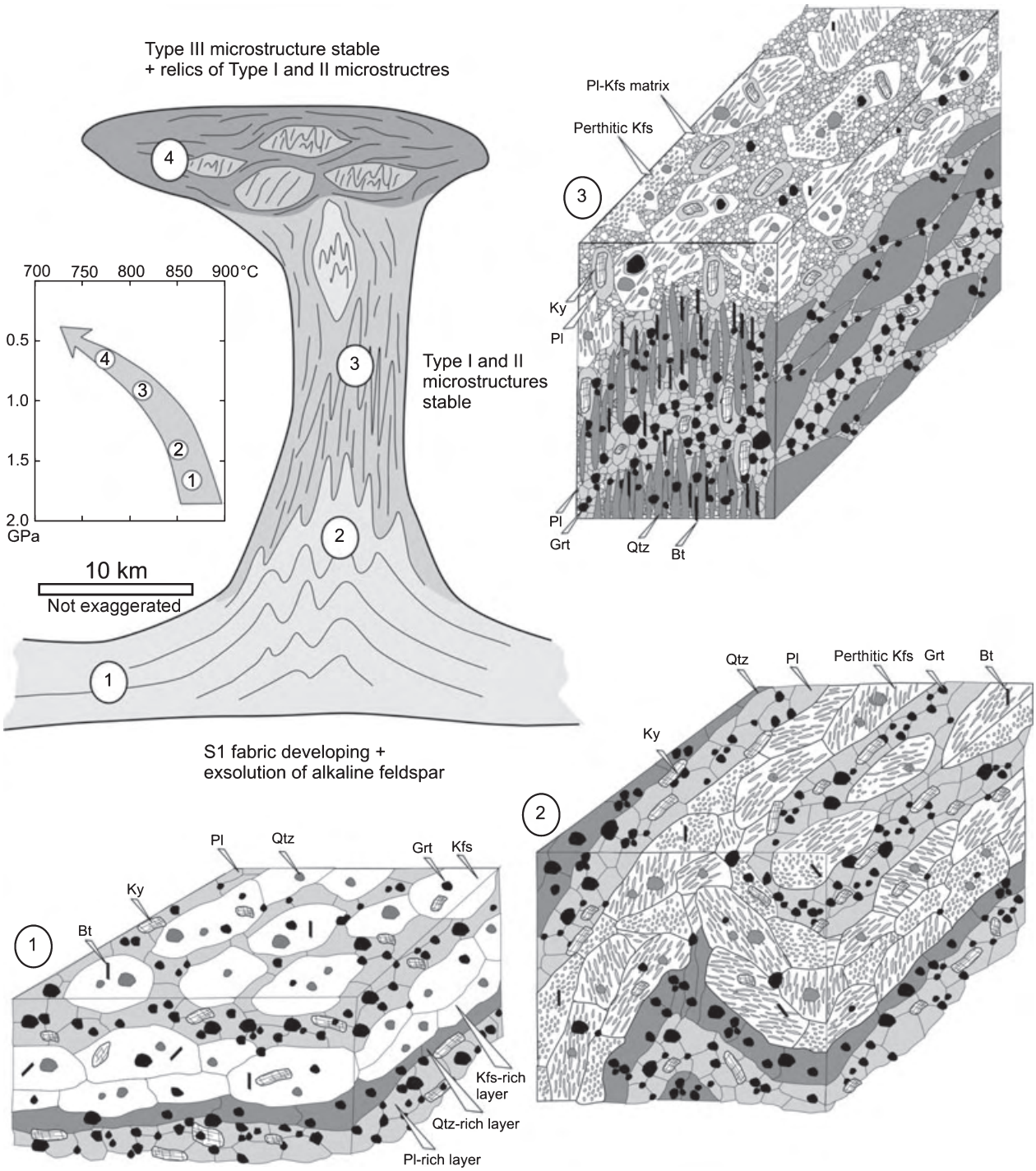

Fig. 16. Interpretative 3D scheme of the microstructural evolution of felsic granulites from the coarse-grained layered HP granulite precursor to granulite facies mylonite developed during exhumation in a crustal scale 'diapiric' dome according to Franěk *et al.* (2011). The block diagram 1 shows the tentative model of original layered orthogneiss microstructure with numerous kyanite, quartz and garnet crystals in large feldspar porphyroblasts. The model of 'diapiric' exhumation (Franěk *et al.*, 2011; Lexa *et al.*, 2011) shows the position of this microstructure at the bottom of the crust and its *P–T* conditions (1). The extent of preservation of the S1 fabric is marked by light shading at the bottom of diapiric extrusion. The block diagram (2) shows the development of perthites at the beginning of exhumation with decompression and limited cooling. The block diagram (3) exhibits the development of typical granulite fabric, such as platy quartz and granular microstructures of Types I and II. Relicts of kyanite preserved in perthite porphyroclasts and matrix with decompression kelyphitic haloes are shown. This microstructure is developed in the main vertical channel of the 'diapir' and is marked by intermediate shading in the structural model. The 'diapir' head shows the stability of Type III granular microstructure (dark shading) and rotated relict domains preserving Type II microstructure.

cannot be fully excluded that the large perthitic exsolutions in alkali feldspar porphyroclasts originated during later stages of cooling and decompression along the exhumation path.

The recrystallization must have initiated by deformation-induced conversion of the (perthitic) parental alkali feldspar directly into small K-feldspar grains by an uncommon process, which is discussed in the next paragraphs. Plagioclase was then gradually redistributed along the new K-feldspar grain boundaries (e.g. Fig. 9b,f), presumably via grain-boundary diffusion. The sharp compositional boundaries between An_{23} cores and An_{12} rims of the Type I plagioclase (Fig. 10a) indicate that they did not develop by continuous growth and that they were not significantly affected by later diffusion. We suggest that at first, the An_{23} plagioclase grains coalesced in triple junctions of the new K-feldspar grains by grain-boundary diffusion mechanism. They originated by reduction of surface and coalescence of preexisting coarse and compositionally similar An_{24} plagioclase perthitic exsolutions, assuming perthitic nature of the parental alkali feldspar. The new grain boundaries were subsequently overgrown by An_{12} plagioclase, the components for which were probably released from surrounding K-feldspar by volume diffusion. This process is indicated by gradual zoning at rims of adjacent K-feldspar grains (Fig. 10a). The CSD patterns (Fig. 13) show that the formation of the Type I K-feldspar–plagioclase mosaic originated by a nucleation-dominated process accompanied by limited crystal growth, compared with the later Types II and III microstructure (Lexa *et al*., 2005; Hasalová *et al*., 2008b). The nucleation density of plagioclase was significantly higher than that of K-feldspar.

The most important manifestation of the perthite recrystallization is redistribution of Or, Ab and An components on a micro-scale in a chemically closed system, resulting in development of the fine-grained granular matrix (Fig. 16, 3D block diagram 3). The high amount of unlike grain boundaries in the granular matrix preserved inside parental perthite indicates a tendency to regular distribution and thus active intermixing of the K-feldspar and plagioclase. The regular distribution represents the energetically lowest state of such a polyphase material (Seng, 1936; DeVore, 1959) and progressive straightening of grain boundary geometries of K-feldspar and plagioclase further minimizes the surface energy by grain shape simplification typical for grain boundary reduction (Passchier *et al*., 1992). According to this model the recrystallization then appears to be substantially driven by a decrease of chemical and surface energy in the metastable (perthitic) alkali feldspar. The concept of surface energy minimization was suggested by Flin (1969), who proposed that the regular distribution is a consequence of a smaller interfacial energy of unlike boundaries in comparison with like–like boundaries. However, Ramberg (1952) considered the interfacial energies to be too small to drive diffusional mass transfer in granulites.

The weak but systematic scatter of lattice orientations of new plagioclase and K-feldspar grains with respect to the parental perthite (Fig. 14) points to contribution of stress to the bulk recrystallization process. Such a process of non-coherent decomposition of metastable alkali feldspar may be triggered either by water addition or by the application of external stress (Brown & Parsons, 1989 and references therein). As a lack of hydrous phases and presumably lack of water is typical for the granulite facies evolution of these rocks, the activity of external stress seems to be better candidate to trigger the recrystallization process.

The almost identical LPO of plagioclase and K-feldspar, regular grain distribution and high nucleation density CSD pattern of the polymineralic aggregate developed by recrystallization of solid solution crystal has not been previously described in nature. The sharp recrystallization front advancing into parental perthites represents a moving grain boundary driven by both chemical and deformational processes. According to Stünitz (1998), such recrystallization can be considered as a combination of strain- and chemically induced grain boundary migration processes. At the temperature and chemical conditions given during the D2, the activation energy of the grain boundary migration process was probably lower than that of dynamic recrystallization of the metastable (perthitic) alkali feldspar. Material science literature (e.g. Saheb *et al*., 1995; Sennour *et al*., 2004) has examples of sharp recrystallization fronts advancing gradually into intact grains of alloys (Fig. 9a,b,f) explained by the chemically induced grain boundary migration or a similar discontinuous precipitation process, which in many aspects resembles the alkali feldspar recrystallization. According to Yoon (1995), the discontinuous precipitation in metastable alloys represents largely autocatalytic recrystallization driven mainly by coherency strain energy. Activation of this process depends upon composition, temperature, stress and strain, elastic anisotropy, crystallographic relations and boundary curvature of involved grains (Yoon, 1995). Once triggered, e.g. by external strain, it causes very efficient heterogeneous decomposition of oversaturated solid solutions (like alkali feldspar) via (mainly chemically driven) grain boundary migration (Hay & Evans, 1987; Saheb *et al*., 1995; Sennour *et al*., 2004).

In conclusion, the formation of the granular matrix resembles the discontinuous precipitation triggered by straining of the probably perthitic alkali feldspar grains during D2 deformation (Fig. 16). The process starts preferably on pre-existing grain boundaries with other feldspar porphyroclasts or with garnet. The migration of the recrystallization front is driven mainly by the metastability of the (perthitic) alkali feldspar. In turn, the metastability of parental feldspar controls the

development of the irregular to amoeboid domains (e.g. Fig. 9a,b) of fine-grained regularly distributed K-feldspar and plagioclase matrix.

Lower crustal ascent and strength evolution of felsic granulites

The onset of the D2 deformation is marked by highly non-cylindrical folding of the S1 anisotropy prior to the S2 cleavage development (Figs 4a,b & 16, block diagram 3). The formation of a typical Variscan felsic granulite fine-grained microstructure with highly elongated quartz ribbons is the main result of the D2 deformation (Figs 5e & 9e) that is contemporaneous with the development of the granular Type I microstructure. Petrological modelling and mineral zoning, particularly the decrease of the grossular component in garnet, suggest that between the perthite growth and the end of the D2 there was significant decompression of ~0.8 GPa at slightly decreasing temperature over a time span of several million years (Figs 8 & 16). That means the S2 microstructure developed at slightly lower temperature compared with the S1 and under continuously decreasing pressure as indicated by a number of decompression microstructures such as plagioclase rims around kyanite and garnet (Figs 5e & 6h). This conclusion agrees with the observations of spinel–plagioclase and garnet coronas developed around kyanite, which form characteristic decompression microstructures in S2 (Štípská *et al.*, 2010). The common denominator of these coronas is that they are elongated parallel to S2 foliation (Fig. 6h) and therefore developed at the end of the D2 deformation.

The small interstitial quartz grains, discontinuous albite films at plagioclase or K-feldspar boundaries and cuspate feldspar grain shapes (Fig. 9d) are consistent with the presence of syn-deformational intergranular partial melt in the granulitic S2 matrix, a conclusion previously suggested by Franěk *et al.* (2006) and supported also by dykes of felsic granulite crosscutting mafic boudins embedded in S2. Tajčmanová *et al.* (2006, 2007) inferred a low content of partial melt (< 5%) and very fast diffusion for Moldanubian felsic granulites, either at the peak conditions (~850 °C/1.8 GPa) or during decompressional event equivalent to our D2 phase. Syn-deformational partial melting during the rapid D2 decompression is in agreement also with the laboratory experiments of Tropper *et al.* (2005) who produced significant amount of partial melt during simulated isothermal decompression of a felsic rock from HP granulite facies conditions.

The phase contact frequency analysis of highly strained S2 microstructures (Fig. 12) reveals intermixing of all the three major phases (quartz, K-feldspar and plagioclase) to almost ideally random distribution. The SPO and GBPO of both feldspars in S2 reach the lowest values from all the samples analysed and the axial ratio of S2 matrix grains shows low values as well (Fig. 12). CSD calculations show a decrease in N_0 values compared to Gt values of both K-feldspar and plagioclase, when compared with the Type I microstructure. This is in accord with increased grain size of both the feldspars. In order to increase the grain size at constant temperature, it is necessary to either decrease strain rate, which is not very likely during D2 deformation, or to decrease the flow stress by, e.g. strain softening via activation of GBS (e.g. Rutter & Brodie, 1988; Knipe, 1989). On the other hand, the elongation of isolated quartz ribbons, their curved like–like boundaries and adjacent small quartz grains (Fig. 11a) suggest the importance of dislocation creep and a combination of grain boundary migration with grain-size reduction by a subgrain rotation mechanism. Dominance of less-efficient dislocation creep, grain-size reduction and non-connectivity of the quartz ribbons imply that the quartz ribbons were rheologically stronger than the surrounding feldspar matrix.

In conclusion, the quantitative microstructural characteristics of the fine-grained matrix point to the importance of diffusion-controlled GBS, which best explains the studied microstructure (Schulmann *et al.*, 2008). Slow volume diffusion cannot accommodate the high strains attained in the short time span of the exhumation of the granulite, but the more efficient grain boundary diffusion is likely to operate in such a fine-grained matrix under granulite facies temperatures. It usually enables GBS, which is also capable of accommodating high strain rates in such a fine-grained matrix. The grain boundary diffusion accommodated GBS is certainly enhanced by the presence of a small volume of silicate melt, which is suggested by microscopic and microchemical observations. Rosenberg & Handy (2005) and the experimental studies of Dell'Angelo *et al.* (1987) have shown that the presence of several percent of silicate melt may decrease the bulk strength of a rock by several orders of magnitude.

The GBS activity in feldspar is also supported by LPO scattering of newly formed matrix at the edges of parental perthite (Fig. 14), instead of reorientation to clusters, which is to be expected for dislocation creep. However, the LPO developed in both feldspars in the Type II microstructure indicates that some intracrystalline deformation, e.g. dislocation glide on easy slip systems, still operated. Preservation of the LPO even at high strains during GBS has been documented for albite (Jiang *et al.*, 2000) and calcite (Casey *et al.*, 1998) mylonites. The latter study proposed that the partitioning of deformation between intra- and intercrystalline mechanisms results in a pulsating strain state in the grains, contributing to the maintenance of subequant grains. They argued that lattices of constituent grains rotate continuously with no stable end orientation and that this can lead to a steady-state texture (Casey *et al.*, 1998).

D3 switch in rheology of feldspar *v.* quartz

The microstructural characteristics of the S3 microfabric (Type III microstructure) differ significantly compared with those of the S2. The high number of like–like boundaries in the feldspar-dominated matrix (Fig. 12) indicates significant coalescence of individual phases into monomineralic aggregates, and the SPO, GBPO and axial ratio of both feldspars also increase. In contrast, quartz grains exhibit a decrease in SPO as well as in axial ratio. The Type III microstructure is clearly characterized by a growth-dominated process, especially in the case of K-feldspar. The N0–Gt values of Types I, II and III microstructures project on a curve indicating simultaneous change of N0 and Gt due to temperature and strain variations and suggest that strain rate change probably plays a key role in the resulting CSD shape. Such an evolutionary trend is often interpreted as a result of grain coarsening, which unusually occured at lower temperature related to upper amphibolite facies metamorphism during D3 (700–800 °C) compared with the D2 granulite facies conditions (800–850 °C) (Figs 3 & 8). Therefore, the starting D2 recrystallized grain size was not in equilibrium with the temperature-corrected strain rate (Zener & Holomon, 1944, parameter Z), such that the microstructure was located in the grain-coarsening field (fig. 1 of Ulrich *et al*., 2006 modified after Sakai & Jonas, 1984). In conclusion, only a significant strain rate decrease can explain the observed S3 grain coarsening at decreased temperature.

The S3 microstructure tendency for monomineralic aggregate distribution, high SPO and the general prevalence of grain growth over nucleation compared with S2 are in agreement with the strong LPO, suggesting that the quartz, K-feldspar and plagioclase deformed predominantly by dislocation creep. The irregular grain boundaries in the S3 microstructure are also typical of dislocation creep rather than GBS or diffusional mechanisms. The dominance of dislocation creep indicates hardening of the felsic granulites, where the less plastic feldspar forms a low viscosity contrast load-bearing framework (LBF, Handy, 1990) that resulted in high bulk strength of the retrograde felsic rock in mid-crustal levels.

CONCLUSIONS

The precursor of the Blanský les felsic granulites was an HP alkali feldspar–plagioclase–quartz–garnet–biotite–kyanite bearing coarse-grained layered orthogneiss that developed via deformational solid-state segregation of quartz and feldspars. It records peak P–T conditions of ~1.6–1.8 GPa and 850–880 °C (Fig. 16).

Granular matrix (Type I microstructure) formed by recrystallization of ~10 mm large and probably perthitic strong alkali feldspar porphyroclasts into a weak fine-grained (~0.055 mm) plagioclase–K-feldspar matrix. This transition occurred via a process resembling discontinuous precipitation mechanism in metal alloys. It was driven mainly by chemically and strain induced grain boundary migration, but triggered by stress build up during early stages of D2. Newly formed matrix grains maintained roughly the lattice orientation of the parental alkali feldspar crystal. They have a sufficiently small grain size to allow flow by GBS.

The fine-grained S2 granulitic matrix (Type II microstructure) with a very low content of silicate melt deformed predominantly via diffusion creep-controlled GBS. The large quartz ribbons were rheologically stronger than the feldspar-dominated matrix due to the activity of different deformational mechanisms. During this stage, in only several million years, the linearly viscous granulite matrix containing low amount of interstitial melt was extruded upwards through a vertical channel (Franěk *et al*., 2011) from pressures of ~1.7 GPa at 850 °C to ~1.0 GPa at 800 °C (Fig. 16).

After cooling and crystallization of the syn-D2 partial melt along grain boundaries, the granulites deformed at lower P–T conditions in the middle crust during D3 episode by less-efficient dislocation creep. Local hydration produced partial melt that segregated from solid matrix into isolated bands instead of coating grain boundaries.

ACKNOWLEDGEMENTS

The work was supported by Grants of the Czech Science Foundation (GACR 205/05/2187 and 205/09/0539) and the internal project of the Czech Geological Survey (No. 326700). Stays of J. Franěk at Strasbourg University were funded by the French Government Foundation (BGF). The French National Grant Agency (No.06-1148784) and Grant MSM0021620855 of the Ministry of Education of the Czech Republic are acknowledged for financial support of K. Schulmann and O. Lexa. We are grateful to J.-E. Martelat for constructive suggestions. We also thank R. Vernon, H. Stünitz and J. Tullis for their constructive revisions. We also thank M. Brown and R. White for careful editorial work.

REFERENCES

Abart, R., Petrishcheva, E., Rhede, D. & Wirth, R., 2009. Exsolution by spinodal decomposition: II: perthite formation during slow cooling of anatexites from Ngornghoro, Tanzania. *American Journal of Science*, **309,** 450–475; doi: 10.2475/06.2009.02.

Baratoux, L., Lexa, O., Cosgrove, J.W. & Schulmann, K., 2005. The quantitative link between fold geometry, mineral fabric and mechanical anisotropy: as exemplified by the deformation of amphibolites across a regional metamorphic gradient. *Journal of Structural Geology*, **27,** 707–730.

Behr, H.J., 1961. Beitrage zur petrographischen und tektonischen Analyse des sachsischen Granulitgebirges. *Frebierger Forschungshefte C*, **119,** 5–118.

Behrmann, J.H. & Mainprice, D., 1987. Deformation mechanisms in a high-temperature quartz-feldspar mylonite: evidence for super-plastic flow in the lower crust. *Tectonophysics*, **140,** 297–305.

Boullier, A.M. & Gueguen, Y., 1975. SP-mylonites; origin of some mylonites by superplastic flow. *Contributions to Mineralogy and Petrology*, **50,** 93–104.

Brown, W.L. & Parsons, I., 1989. Alkali feldspars: ordering rates, phase transformations and behaviour diagrams for igneous rocks. *Mineralogical Magazine*, **53,** 25–42.

Carswell, D.A. & O'Brien, P.J., 1993. Thermobarometry and geotectonic significance of high-pressure granulites – examples from the Moldanubian Zone of the Bohemian Massif in Lower Austria. *Journal of Petrology*, **34,** 427–459.

Casey, M., Kunze, K. & Olgaard, D.L., 1998. Texture of Solnhofen limestone deformed to high strains in torsion. *Journal of Structural Geology*, **20,** 255–267.

Cashman, K.V. & Ferry, J.M., 1988. Crystal size distribution (CSD) in rocks and the kinetics and dynamics of crystallization – III. Metamorphic crystallization. *Contributions to Mineralogy and Petrology*, **99,** 401–415.

Coggon, R. & Holland, T., 2002. Mixing properties of phengitic micas and revised garnet-phengite thermobarometers. *Journal of Metamorphic Geology*, **20,** 683–696.

Cooke, R.A., 2000. High-pressure/temperature metamorphism in the St. Leonhard Granulite Massif, Austria: evidence from intermediate pyroxene-bearing granulites. *International Journal of Earth Sciences*, **89,** 647–651.

Dell'Angelo, L.N., Tullis, J. & Yund, R.A., 1987. Transition from dislocation creep to melt-enhanced diffusion creep in fine-grained granitic aggregates. *Tectonophysics*, **139,** 325–332.

DeVore, G.W., 1959. Role of minimum interfacial free energy in determining the macroscopic features of mineral assemblages. I. The model. *Journal of Geology*, **67,** 211–227.

Diener, J.F.A., White, R.W. & Powell, R., 2008. Granulite facies metamorphism and subsolidus fluid-absent reworking, Strangways Range, Arunta Block, central Australia. *Journal of Metamorphic Geology*, **26,** 603–622.

Fiala, J., Matějovská, O. & Vaňková, V., 1987. Moldanubian granulites: source material and petrogenetic considerations. *Neues Jahrbuch fur Mineralogie, Abhandlungen*, **157,** 133–165.

Finger, F., Cooke, R., Janoušek, V. *et al.*, 2003. Petrogenesis of the south Bohemian granulites: the importance of crystal-melt relationships. *Journal of the Czech Geological Society*, **48,** 44–45.

Flin, D., 1969. Grain contacts in crystalline rocks. *Lithos*, **2,** 361–370.

Franěk, J., Schulman, K. & Lexa, O., 2006. Kinematic and rheological model of exhumation of high pressure granulites in the Variscan orogenic root: example of the Blanský les granulite, Bohemian Massif, Czech Republic. *Mineralogy and Petrology*, **86,** 253–276.

Franěk, J., Schulman, K., Lexa, O., Tomek, C. & Edel, J.B., 2011. Model of syn-convergent extrusion of orogenic lower crust in the core of the Variscan belt: implications for exhumation of high-pressure rocks in large hot orogens. *Journal of Metamorphic Geology*, **29,** 53–78.

Franke, W., 2000. The mid-European segment of the Variscides: tectonostratigraphic units, terrane boundaries and plate tectonic evolution. *Geological Society Special Publication*, **179,** 35–56.

Friedl, G., Cooke, R., Finger, F., McNaughton, N.J. & Fletcher, I., 2003. U-Pb SHRIMP dating and trace element investigations on multiple zoned zircons from a South-Bohemian granulite. *Journal of the Czech Geological Society*, **48,** 51.

Fuchs, G., 1976. Zur Entwicklung der Böhmischen Masse. *Jahrbuch des Geologischen Bundesanstalts*, **119,** 45–61.

Garlick, S.R. & Gromet, L.P., 2004. Diffusion creep and partial melting in high temperature mylonitic gneisses, Hope Valley shear zone, New England Appalachians, USA. *Journal of Metamorphic Geology*, **22,** 45–62.

Gayk, T. & Kleinschrodt, R., 2000. Hot contacts of garnet peridotites in middle/upper crustal levels: new constraints on the nature of the late Variscan high-T/low-P event in the Moldanubian (Central Vosges/NE France). *Journal of Metamorphic Geology*, **18,** 293–305.

Handy, M., 1990. The solid state flow of polymineralic rocks. *Journal of Geophysical Research*, **95,** 8647–8661.

Hasalová, P., Štípská, P., Powell, R., Schulmann, K., Janoušek, V. & Lexa, O., 2008a. Transforming mylonitic metagranite by open-system interactions during melt flow. *Journal of Metamorphic Geology*, **26,** 55–80.

Hasalová, P., Schulmann, K., Lexa, O. *et al.*, 2008b. Origin of migmatites by deformation-enhanced melt infiltration of orthogneiss: a new model based on quantitative microstructural analysis. *Journal of Metamorphic Geology*, **26,** 29–53.

Hay, R.S. & Evans, B., 1987. Chemically induced grain boundary migration in calcite: temperature dependence, phenomenology, and possible applications to geologic systems. *Contributions to Mineralogy and Petrology*, **97,** 127–141.

Higgins, M.D., 1998. Origin of anorthosite by textural coarsening: quantitative measurements of a natural sequence of textural development. *Journal of Petrology*, **39,** 1307–1323.

Holland, T. & Powell, R., 1998. An internally consistent thermodynamic data set for phases of petrological interest. *Journal of Metamorphic Geology*, **16,** 309–343.

Holland, T. & Powell, R., 2003. Activity–composition relations for phases in petrological calculations: an asymmetric multicomponent formulation. *Contributions to Mineralogy and Petrology*, **145,** 492–501.

Jakeš, P., 1997. Melting in high-P region – case of Bohemian granulites. *Acta Universitatis Carolinae, Geologica*, **41,** 113–125.

Janoušek, V. & Holub, F.V., 2007. The causal link between HP-HT metamorphism and ultrapotassic magmatism in collisional orogens: case study from the Moldanubian Zone of the Bohemian Massif. *Proceedings of the Geologists Association*, **118,** 75–86.

Janoušek, V., Finger, F., Roberts, M., Frýda, J., Pin, C. & Dolejš, D., 2004. Deciphering the petrogenesis of deeply buried granites: whole-rock geochemical constraints on the origin of largely undepleted felsic granulites from the Moldanubian Zone of the Bohemian Massif. *Transactions of the Royal Society of Edinburgh – Earth Sciences*, **95,** 141–159.

Janoušek, V., Gerdes, A., Vrána, S. *et al.*, 2006. Low-pressure granulites of the Lišov Massif, Southern Bohemia: visean metamorphism of Late Devonian plutonic arc rocks. *Journal of Petrology*, **47,** 705–744.

Jiang, Z., Prior, D.J. & Wheeler, J., 2000. Albite crystallographic preferred orientation and grain misorientation distribution in a low-grade mylonite: implications for granular flow. *Journal of Structural Geology*, **22,** 1663–1674.

Knipe, R.J., 1989. Deformation mechanisms – recognition from natural tectonites. *Journal of Structural Geology*, **11,** 127–146.

Kodym, O., 1972. Multiphase deformation in the Blanský les granulite massif (South Bohemia). *Krystalinikum*, **9,** 91–105.

Košler, J., Kelley, S.P., Vance, D. & Svojtka, M., 1999. Independent dating of cooling and decompression of high grade rocks in the southern Bohemian Massif with Ar-Ar, Sm-Nd and U-Pb techniques. *Journal of Conference Abstracts*, **4,** 39.

Kotková, J. & Harley, S.L., 1999. Formation and evolution of high-pressure leucogranulites: experimental constraints and unresolved issues. *Physics and Chemistry of the Earth Part A – Solid Earth and Geodesy*, **24,** 299–304.

Kretz, R., 1969. On the spatial distribution of crystals in rocks. *Lithos*, **2,** 39–65.

Kröner, A., O'Brien, P.J., Nemchin, A.A. & Pidgeon, R.T., 2000. Zircon ages for high pressure granulites from South Bohemia, Czech Republic, and their connection to Carboniferous high temperature processes. *Contributions to Mineralogy and Petrology*, **138,** 127–142.

Kruse, R., Stunitz, H. & Kunze, K., 2001. Dynamic recrystallization processes in plagioclase porphyroclasts. *Journal of Structural Geology*, **23,** 1781–1802.
Lexa, O., Štípská, P., Schulmann, K., Baratoux, L. & Kröner, A., 2005. Contrasting textural record of two distinct metamorphic events of similar P–T conditions and different durations. *Journal of Metamorphic Geology*, **23,** 649–666.
Lexa, O., Schulmann, K., Janoušek, V., Štípská, P., Guy, A. & Racek, M., 2011. Heat sources and trigger mechanisms of exhumation of HP granulites in Variscan orogenic root. *Journal of Metamorphic Geology*, **29,** 79–102.
Lister, G.S. & Dornsiepen, U.F., 1982. Fabric transition in the Saxony granulite terrain. *Journal of Structural Geology*, **4,** 81–92.
Lister, G.S. & Price, G.P., 1978. Fabric development in a quartz–feldspar mylonite. *Tectonophysics*, **49,** 37–78.
Marsh, B.D., 1988. Crystal size distributions (CSD) in rocks and the kinetics and dynamics of crystallization – I. Theory. *Contributions to Mineralogy and Petrology*, **99,** 277–291.
Martelat, J.E., Schulmann, K., Lardeaux, J.M., Nicollet, C. & Cardon, H., 1999. Granulite microfabrics and deformation mechanisms in southern Madagascar. *Journal of Structural Geology*, **21,** 671–687.
Matte, P., Maluski, H., Rajlich, P. & Franke, W., 1990. Terrane boundaries in the Bohemian Massif: result of the large–scale Variscan shearing. *Tectonophysics*, **177,** 151–170.
Mehnert, K.R., 1968. *Migmatites and the Origin of Granitic Rocks*. Elsevier, Amsterdam, 393 pp.
Montardi, Y. & Mainprice, D., 1987. A transmission electron microscopy study of the natural plastic deformation of calcic plagioclases (An 68–70). *Bulletin de Mineralogie*, **110,** 1–14.
O'Brien, P.J. & Carswell, D.A., 1993. Tectonometamorphic evolution of the Bohemian Massif – evidence from high-pressure metamorphic rocks. *Geologische Rundschau*, **82,** 531–555.
O'Brien, P.J. & Rötzler, J., 2003. High-pressure granulites: formation, recovery of peak conditions and implications for tectonics. *Journal of Metamorphic Geology*, **21,** 3–20.
O'Brien, P.J. & Seifert, K., 1992. P–T–t paths as records of orogenic processes: examples and problems from the crystalline of the Bohemian Massif. *Terra Nostra*, **1992,** 58–59.
Passchier, C.W., Trouw, R.A.J., Zwart, H.J. & Vissers, R.L.M., 1992. Porphyroblast rotation – Eppur-Si-Muove. *Journal of Metamorphic Geology*, **10,** 283–294.
Powell, R. & Holland, T., 1988. An internally consistent dataset with uncertainties and correlations. 3. Applications to geobarometry, worked examples and a computer-program. *Journal of Metamorphic Geology*, **6,** 173–204.
Powell, R. & Holland, T., 2004. Course notes for 'THERMOCALC workshop 2004: calculating metamorphic phase equilibria' (ETH Zurich, Switzerland). CD-ROM.
Putnis, A., 2002. Mineral replacement reactions: from macroscopic observations to microscopic mechanisms. *Mineralogical Magazine*, **66,** 689–708.
Putnis, A., Pina, C.M., Astilleros, J.M., Fernández-Díaz, L. & Prieto, M., 2003. Nucleation of solid solutions crystallising from aqueous solutions. *Philosophical Transactions of the Royal Society A: Mathematical, Physical and Engineering Sciences*, **361,** 615–632.
Racek, M., Štípská, P., Pitra, P., Schulmann, K. & Lexa, O., 2006. Metamorphic record of burial and exhumation of orogenic lower and middle crust: a new tectonothermal model for the Drosendorf window (Bohemian Massif, Austria). *Mineralogy and Petrology*, **86,** 221–251.
Ramberg, H., 1952. *The Origin of Metamorphic and Metasomatic Rocks*. University of Chicago Press, Chicago, 317 pp.
Ribbe, P.H. (ed.), 1983. *Feldspar Mineralogy*, 2nd edn. Mineralogical society of America, Washington, 362 pp.
Rosenberg, C.L. & Handy, M.R., 2005. Experimental deformation of partially melted granite revisited: implications for the continental crust. *Journal of Metamorphic Geology*, **23,** 19–28.
Rutter, E.H. & Brodie, K.H., 1988. The role of tectonic grain size reduction in the rheological stratification of the lithosphere. *Geologische Rundschau*, **77,** 295–307.
Rutter, E.H. & Brodie, K.H., 1992. Rheology of the lower crust. In: *Continental Lower Crust* (eds Fountain, D.M., Arculus, R. & Kay, R.W.), pp. 201–267. Elsevier, Amsterdam.
Saheb, N., Boumerzoug, Z., Hamana, D., Laoui, T. & Van Der Biest, O., 1995. Different types of discontinuous precipitation in Cu-15 Wt% in alloy. *Scripta Metallurgica et Materiala*, **32,** 1453–1458.
Sakai, T. & Jonas, J.J., 1984. Dynamic recrystallization: mechanical and microstructural consideration. *Acta Metallurgica*, **32,** 198–209.
Schmid, S.M. & Casey, M., 1986. Complete fabric analysis of some commonly observed quartz c-axis patterns. In: *Mineral and Rock Deformation: Laboratory Studies* (eds Hobbs, B.E. & Heard, H.C.), pp. 263–286. American Geophysical Union Monograph, Vol. 36, Washington, DC.
Schulmann, K., Kröner, A., Hegner, E. *et al*., 2005. Chronological constraints on the pre-orogenic history, burial and exhumation of deep-seated rocks along the eastern margin of the Variscan Orogen, Bohemian Massif, Czech Republic. *American Journal of Science*, **305,** 407–448.
Schulmann, K., Martelat, J.-E., Ulrich, S., Lexa, O., Štípská, P. & Becker, J.K., 2008. Evolution of microstructure and melt topology in partially molten granitic mylonite: implications for rheology of felsic middle crust. *Journal of Geophysical Research*, **113,** B10406.
Schulmann, K., Konopásek, J., Janoušek, V. *et al*., 2009. An Andean type Palaeozoic convergence in the Bohemian Massif. *Comptes Rendus – Geoscience*, **341,** 266–286.
Seng, H., 1936. Die Migmatitfrage und der Mechanismus parakristalliner Pragung. *Geologische Rundschau*, **27,** 471–492.
Sennour, M., Jouneau, P.H. & Esnouf, C., 2004. TEM and EBSD investigation of continuous and discontinuous precipitation of CrN in nitrided pure Fe-Cr alloys. *Journal of Materials Science*, **39,** 4521–4531.
Štípská, P. & Powell, R., 2005. Does ternary feldspar constrain the metamorphic conditions of high-grade metaigneous rocks? Evidence from orthopyroxene granulites, Bohemian Massif. *Journal of Metamorphic Geology*, **23,** 627–647.
Štípská, P., Powell, R., White, R.W. & Baldwin, J.A., 2010. Using calculated chemical potential relationships to account for coronas around kyanite: an example from the Bohemian Massif. *Journal of Metamorphic Geology*, **28,** 97–116.
Stünitz, H., 1998. Syndeformational recrystallization – dynamic or compositionally induced? *Contributions to Mineralogy and Petrology*, **131,** 219–236.
Stünitz, H. & Tullis, J., 2001. Weakening and strain localization produced by syn-deformational reaction of plagioclase. *International Journal of Earth Sciences*, **90,** 136–148.
Stünitz, H., Fitz Gerald, J.D. & Tullis, J., 2003. Dislocation generation, slip systems, and dynamic recrystallization in experimentally deformed plagioclase single crystals. *Tectonophysics*, **372,** 215–233.
Tajčmanová, L., Konopásek, J. & Schulmann, K., 2006. Thermal evolution of the orogenic lower crust during exhumation within a thickened Moldanubian root of the Variscan belt of Central Europe. *Journal of Metamorphic Geology*, **24,** 119–134.
Tajčmanová, L., Konopásek, J. & Connolly, J.A.D., 2007. Diffusion-controlled development of silica-undersaturated domains in felsic granulites of the Bohemian Massif (Variscan belt of Central Europe). *Contributions to Mineralogy and Petrology*, **153,** 237–250.
Tropper, P., Konzett, J. & Finger, F., 2005. Experimental constraints on the formation of high-P/high-T granulites in the

Southern Bohemian Massif. *European Journal of Mineralogy*, **17,** 343–356.
Tullis, J., 1983. Deformation of feldspars. In: *Feldspar Mineralogy* (ed. Ribbe, P.H.), pp. 297–323. Mineralogical Society of America, Washington.
Ulmer, P., 1986. *Norm-Program for Cation and Oxygen Mineral Norms*. Computer Library IKP-ETH, Zürich.
Ulrich, S., Schulmann, K. & Casey, M., 2002. Microstructural evolution and rheological behaviour of marbles deformed at different crustal levels. *Journal of Structural Geology*, **24,** 979–995.
Ulrich, S., Thompson, A.B., Schulmann, K. & Casey, M., 2006. Microstructure mechanism map of dynamically recrystallized marble. *Tectonophysics*, **412,** 173–182.
Verner, K., Žák, J., Nahodilová, R. & Holub, F.V., 2007. Magmatic fabrics and emplacement of the cone-sheet-bearing Knížecí Stolec durbachitic pluton (Moldanubian Unit, Bohemian Massif): implications for mid-crustal reworking of granulitic lower crust in the Central European Variscides. *International Journal of Earth Sciences*, **97,** 19–33.
Vrána, S., 1989. Perpotassic granulites from Southern Bohemia – a new rock-type derived from partial melting of crustal rocks under upper mantle conditions. *Contributions to Mineralogy and Petrology*, **103,** 510–522.
Wendt, J.I., Kröner, A., Fiala, J. & Todt, W., 1994. U-Pb zircon and Sm-Nd dating of Moldanubian HP/HT granulites from south Bohemia, Czech Republic. *Journal of the Geological Society London*, **151,** 83–90.
White, R.W., Powell, R., Holland, T. & Worley, B.A., 2000. The effect of TiO_2 and Fe_2O_3 on metapelitic assemblages at greenschist and amphibolite facies conditions: mineral equilibria calculations in the system K_2O–FeO–MgO–Al_2O_3–SiO_2–H_2O–TiO_2–Fe_2O_3. *Journal of Metamorphic Geology*, **18,** 497–511.
White, R.W., Powell, R. & Holland, T., 2007. Progress relating to calculation of partial melting equilibria for metapelites. *Journal of Metamorphic Geology*, **25,** 511–527.
Wilson, G., 1961. The tectonic significance of small–scale structures, and their importance to the geologist in the field. *Annales de la Société Géologique de Belgique*, **84,** 423–595.
Yoon, D.Y., 1995. Theories and observations of chemically induced interface migration. *International Materials Reviews*, **40,** 149–179.
Závada, P., Schulmann, K., Konopásek, J., Ulrich, S. & Lexa, O., 2007. Extreme ductility of feldspar aggregates – melt-enhanced grain boundary sliding and creep failure: rheological implications for felsic lower crust. *Journal of Geophysical Research B: Solid Earth*, **112,** B10210.
Zener, C. & Holomon, J.H., 1944. Effect of strain rate upon plastic flow of steel. *Journal of Applied Physics*, **15,** 22–32.

SUPPORTING INFORMATION

Additional Supporting Information may be found in the online version of this article:

Appendix S1. Quantitative characteristics of the individual microstructural evolutionary stages.

Please note: Wiley-Blackwell are not responsible for the content or functionality of any supporting materials supplied by the authors. Any queries (other than missing material) should be directed to the corresponding author for the article.

Received 26 March 2010; revision accepted 6 September 2010.

Journal of
METAMORPHIC GEOLOGY

J. metamorphic Geol., 2011, **29,** 79–102 doi:10.1111/j.1525-1314.2010.00906.x

Heat sources and trigger mechanisms of exhumation of HP granulites in Variscan orogenic root

O. LEXA,[1] K. SCHULMANN,[2] V. JANOUŠEK,[1,3] P. ŠTÍPSKÁ,[2] A. GUY[2,4] AND M. RACEK[1,3]
[1]*Institute of Petrology and Structural Geology, Faculty of Science, Charles University in Prague, Albertov 6, 128 43 Prague 2, Czech Republic (lexa@natur.cuni.cz)*
[2]*Institute de Physique de Globe, UMR 7516, École et Observatoire de Science de la Terre, Université de Strasbourg, 1 Rue Blessig, Strasbourg 67084, France*
[3]*Czech Geological Survey, Klárov 3, 118 21 Prague 1, Czech Republic*
[4]*Department of Geophysics, Faculty of Mathematics and Physics, Charles University in Prague, V Holešovičkách 3, 180 00 Prague 8, Czech Republic*

ABSTRACT The structure of the Moldanubian domain is marked by felsic granulites of Ordovician protolith age forming the cores of domes that are separated from mid-crustal Neoproterozoic and Palaeozoic metasedimentary rocks that occur in synclines by a late Ordovician to Silurian metabasic unit. Reflection and refraction seismic sections combined with gravity inversion modelling suggest the presence of a low density layer at the bottom of the crust (interpreted as felsic granulite) overlain by a denser layer (interpreted as amphibolite) with layers of intermediate density at the top (interpreted as metasedimentary rocks). It is proposed that the granulite domes surrounded by middle crustal rocks reflect transposed horizontal layering originally similar to that preserved in the deep crust and imaged by the geophysical surveys. This geological and geophysical structure is considered to be a result of Viséan gravity redistribution initiated by radioactive heating of felsic crust tectonically emplaced at the bottom of a Palaeozoic orogenic root. The radioactive layer with heat production of 4 μW m^{-3} corresponds geochemically and isotopically to Ordovician felsic metaigneous rocks of the Saxothuringian domain that have been emplaced at Moho depth under thickened crust during late Devonian–early Carboniferous continental subduction. Part of the continental crust continued to be subducted and produced fluids/low-volume melts which directly contaminated and enriched the local lithospheric mantle by lithophile elements, most notably Cs, Rb, Li, Pb, U, Th and K. Thermal incubation of 10–15 Myr was sufficient to heat and convert the underplated felsic layer into granulites via dehydration melting and melt segregation. The process of melt loss was responsible for the removal of radioactive elements and for switching off the heat at the beginning of the exhumation process. At the same time, the metasomatized underlying mantle was heated producing characteristic ultrapotassic magmas. Gravitational instability was then induced by the density contrast between the light granulites and the overlaying denser mafic lower crustal layer and a viscosity drop related to thermal weakening and partial melting of the latter.

Key words: crustal structure; exhumation of lower crust; heat sources; radioactive heating.

Mineral abbreviations: bi, biotite; mu, muscovite; g, garnet; ky, kyanite; sill, sillimanite; cd, cordierite; pl, plagioclase; ksp, K-feldspar; liq, granitic liquid; o, omphacitic clinopyroxene; ilm, ilmenite; ru, rutile.

INTRODUCTION

The Variscan Bohemian Massif, Czech Republic, is characterized by the occurrence of large high-pressure (HP) granulite bodies within the central high-grade part of the orogen. These granulite bodies are mainly composed of alkali feldspar-garnet-kyanite granulites, eclogites and fragments of mantle peridotites surrounded by mid-crustal rocks. The exhumation and emplacement of the whole assemblage is commonly interpreted in terms of two contrasting models. In the first model, granulite massifs are inferred to be allochthonous, representing klippen of far travelled nappes rooted in the central part of the Bohemian Massif (e.g. Franke, 2000), whereas in the second model, granulites correspond to eroded windows of the orogenic infrastructure that have been vertically extruded to mid-crustal levels from lower crustal depths (e.g. Štípská *et al.*, 2004; Schulmann *et al.*, 2005). The latter model is analogous to that proposed for the Saxonian granulite Massif by Behr (1978) and Weber (1984).

The problem of exhumation of granulite lower crust has been discussed by a number of authors in relation to Archean and Mesoproterozoic orogenic belts (e.g. Perchuk, 1989). In these terranes, the emplacement of hot granulite lower crust has been interpreted in terms of gravity overturn driven by an inverted density profile (e.g. Roering *et al.*, 1992), whereby heavy mafic

rocks (greenstone belts) rest upon light intermediate to felsic TTG rocks [Tonalite-Trondhjemite-Granodiorite gneisses]. Perchuk (1989) proposed that such crustal gravity redistributions are triggered by heat flux resulting from large-scale plume tectonics.

Gerya *et al.* (2001) proposed a conceptually similar model of crustal-scale gravity redistribution to explain the emplacement of felsic orogenic crust into supracrustal levels of Palaeozoic orogens. In contrast to Archean and Mesoproterozoic orogenic belts, the heat source is inferred to be bulk radioactive heat production within a granodioritic lower crustal layer located at the bottom of the crustal pile (Gerya *et al.*, 2002, 2004). These authors suggested that the gravitational instability of doubly stacked lithologically heterogeneous crust is related to an initial density contrast of dissimilar intercalated layers enhanced by high-temperature phase transformations.

In this article, it is argued that the granulite bodies abundant in the central parts of the Bohemian Massif could have originated through a similar kind of gravity redistribution enhanced by lateral forcing. Using gravity inversion modelling, we demonstrate that relics of an original stratification with density inversion are still preserved in the Variscan crust of the Bohemian Massif, with a high density mafic middle crustal layer resting upon ~10 km of felsic crust (Guy *et al.*, 2010). It is also shown that the internal structure within each of the granulite massifs forms a pattern consistent with deceleration of vertically emplaced diapiric-like bodies and horizontal spreading of low-viscosity, partially molten rocks at supracrustal levels. Geochemical and geochronological data are used to argue that the felsic lower crust (FLC) is an allochthonous body emplaced underneath the pre-existing mafic lower crust during late Devonian–early Carboniferous continental subduction. The time-scales of thermal processes driving the gravity redistribution are estimated for two end-member scenarios: (i) a model of radioactive heat production solely in the FLC and/or mantle; and (ii) a large-scale thermal anomaly in the mantle caused by deep mantle processes such as tectospheric root delamination (Dewey *et al.*, 1993) or slab break off (Chemenda *et al.*, 2000) as proposed for the Bohemian Massif by Janoušek & Holub (2007). Finally, we offer a dynamic numerical model which is consistent with the available geological and geophysical data and allows assessment of exhumation metamorphic paths of the granulite rocks in the core of the Bohemian Massif.

GEOLOGICAL SETTING

Traditionally the Bohemian Massif has been subdivided into four main tectonic domains, which are, from the west to the east (Fig. 1): the Saxothuringian, the Teplá-Barrandian, the Moldanubian and the Brunia domains. The Saxothuringian domain is regarded as a Neoproterozoic continental block accreted in the Devonian to, and partly subducted under, the more easterly Teplá-Barrandian (suprastructure or orogenic lid) and Moldanubian (infrastructure or deep orogenic root) continental domains of the Variscan orogen (Schulmann *et al.*, 2009). The oceanic Teplá suture, left over after the closure of Saxothuringian ocean, is represented by Devonian to Carboniferous HP and ultra high-pressure rocks, gabbros and mantle fragments located between the Saxothuringian and the Teplá-Barrandian domains (Mlčoch & Konopásek, 2010 and references therein). The whole system is bounded from the east by a Neoproterozoic Brunia promontory, which indented the Moldanubian orogenic root during the early Carboniferous (Schulmann *et al.*, 2008).

Moldanubian domain

The Moldanubian domain is composed mostly of the orogenic middle crustal unit subdivided into two lithostratigraphic groups: the Monotonous Group of probable Neoproterozoic age (Friedl *et al.*, 2004), and the Varied Group, at least partly of early Palaeozoic affinity (e.g. Janoušek *et al.*, 2008). Their mutual contact is defined by uniformly deformed bodies of granitic gneiss of Neoproterozoic to Mesoproterozoic age (Wendt *et al.*, 1993; Friedl *et al.*, 2004). The Varied Group is composed of metasedimentary rocks intercalated with amphibolites, quartzites, marbles and calc silicates. The Monotonous Group consists of paragneisses intercalated with orthogneiss bodies. The lower part of the latter group is characterized by a thick sequence of amphibolites and metagabbros (Racek *et al.*, 2006) locally containing eclogites (O'Brien & Vrána, 1995).

The orogenic lower crust is represented by the Gföhl Unit (Fuchs, 1976), which comprises felsic and intermediate HP granulites accompanied by A type eclogites, garnet pyroxenites and peridotites (Medaris *et al.*, 1995), amphibolites accompanied by Mid-Ocean Ridge Basalt-type eclogites (Štípská & Powell, 2005a) and anatectic Gföhl orthogneisses.

Today the structure of the Moldanubian domain is characterized by alternation of three, NE–SW trending orogenic lower crustal and middle crustal belts (Fig. 1; Behr, 1978; Finger *et al.*, 2007). The first occurs mostly in south Bohemia, the second belt follows the eastern boundary between the Moldanubian domain and Brunia continent and the third is a less extensive belt of granulite rocks tracing the contact between the Teplá-Barrandian and the Saxothuringian domains The last large occurrence of granulites is represented by the NE–SW trending domal structure of the Saxonian granulite Massif (e.g. Franke, 2000).

Recent studies of the principal granulite bodies reveal a systematic lithotectonic pattern marked by granulite lenses rimmed by amphibolite–gabbro belts (AGB) of the local 'Begleit' (= accompanying) series and Gföhl orthogneiss (Fig. 2). The boundary between the AGB and the Monotonous Group is not clearly defined, and hence these basic rocks are sometimes

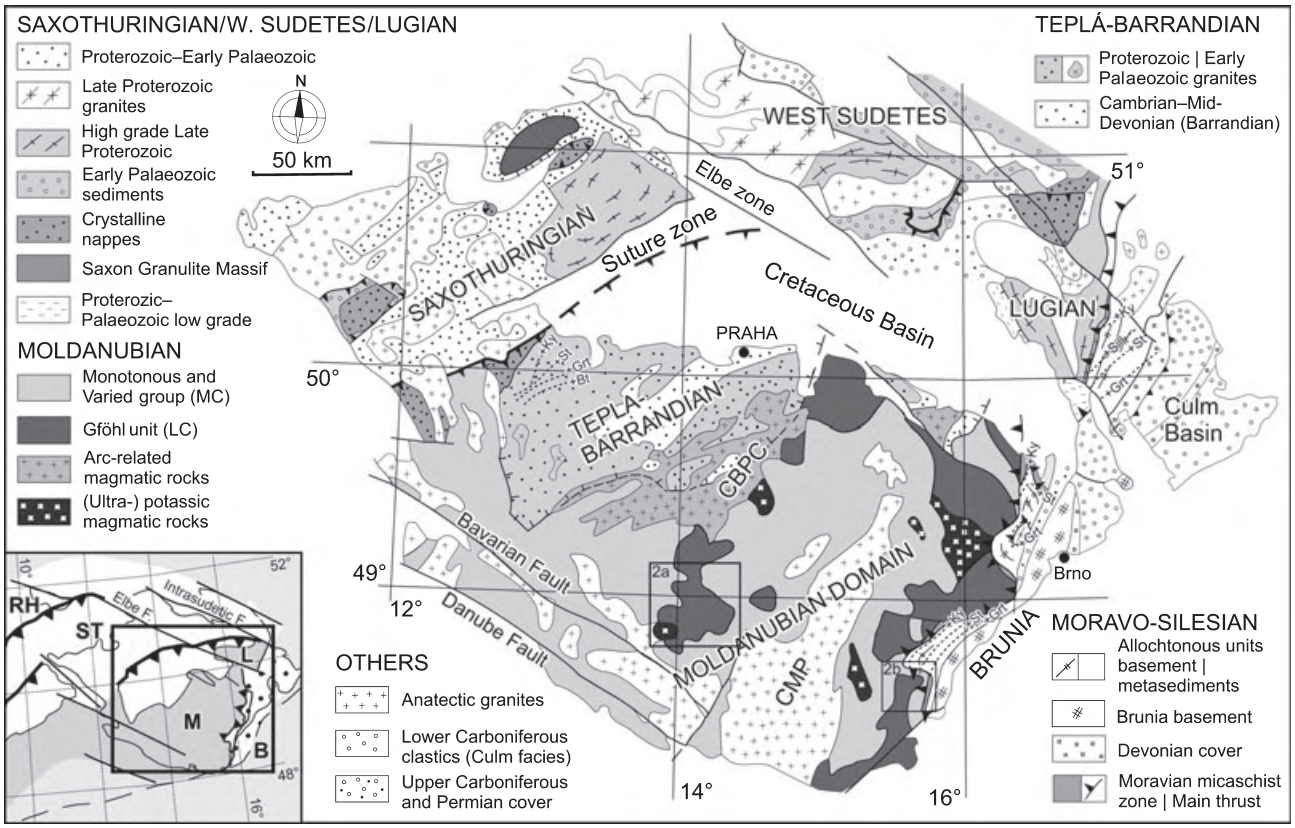

Fig. 1. Simplified geological map of the Bohemian Massif (modified after Franke, 2000). CBPC: Central Bohemian Plutonic Complex; CMP: Central Moldanubian Pluton. The lower left insert shows the position of the Bohemian Massif in the European Variscides (modified after Edel *et al*., 2003). RH: Rhenohercynian zone; ST: Saxothuringian Zone; M: Moldanubian Zone; B: Brunia Continent; L: Lugian domain.

attributed to the lowermost part of the Monotonous Group (Racek *et al*., 2006) and sometimes to the Gföhl Unit (Fuchs, 1976). In addition, the general pattern is complicated by the presence of large accumulations of amphibolites within the Varied and Monotonous groups without clear tectonostratigraphic affinity. The amphibolites and gabbros in Lower Austria reach several kilometres in thickness, but locally narrow to several hundred metres (e.g. Tajčmanová *et al*., 2010) and in some places they are cut out completely (Franěk *et al*., 2006). Because of the regional significance of these rocks, they are interpreted by some authors as a relict of the Silurian (*c*. 430 Ma) oceanic crust (Finger & von Quadt, 1995) or as the result of late Ordovician igneous activity related to thinning of continental crust (Schulmann *et al*., 2009). In contrast, the Gföhl orthogneiss yields dominantly Neoproterozoic protolith U–Pb zircon ages (e.g. 550 ± 1 Ma; Schulmann *et al*., 2005) accompanied by early Ordovician ages (e.g. 488 ± 6 Ma; Friedl *et al*., 2004). The Moldanubian felsic–intermediate granulites reveal a more complex spectrum of protolith U–Pb zircon ages clustering at *c*. 360, *c*. 400 and 470–450 Ma (Kröner *et al*., 2000; Friedl *et al*., 2004; Janoušek *et al*., 2004b).

CURRENT DEEP STRUCTURE OF THE FORMER VARISCAN ROOT

A new model of the structure and composition of Variscan crust in the Bohemian Massif was recently proposed by Guy *et al*. (2010) based on 3D gravity modelling, geological data and seismic refraction and reflection sections (Tomek *et al*., 1997; Hrubcová *et al*., 2005; Růžek *et al*., 2007). All results suggest that the deep structure of the Bohemian Massif crust, which was consolidated during the Variscan orogeny, reflects tectonic processes related to Palaeozoic subduction and collision at the subcrustal lithosphere level as well (Babuška *et al*., 2010).

According to this model, the crust is characterized by a succession of positive and negative anomalies of ~60–80 km wavelength for a nearly constant Moho depths. The central part of the Bohemian Massif displays a large negative Bouguer anomaly corresponding to the Palaeozoic crustal root represented by the Moldanubian domain (Fig. 3). The adjacent Neoproterozoic Brunia microcontinent displays an important gravity high caused by mafic and intermediate medium-grade metamorphic and magmatic rocks. However, the strong gradient marking the deep crustal

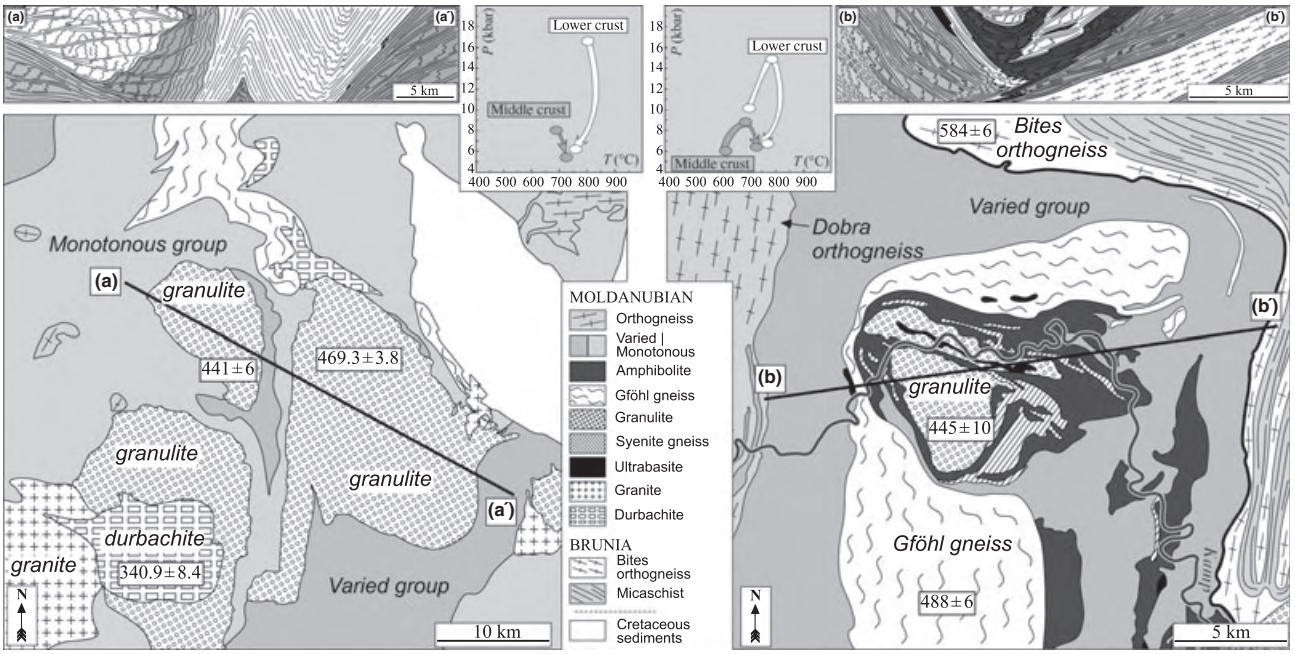

Fig. 2. Geological maps of Blanský les and St. Leonhard granulite areas with schematic structural profiles. Two *P–T* space insets show the metamorphic evolution of lower crustal and middle crustal rocks (Petrakakis, 1997; Pitra *et al*., 1999; Scheuvens, 2002; Štípská & Powell, 2005b; Racek *et al*., 2006, 2008). Protolith ages (Kröner *et al*., 2000; Friedl *et al*., 2004; Verner *et al*., 2008) of major rock types are shown on the map.

boundary between the root domain and the Brunia microcontinent is shifted 50–70 km westwards relative to their contact on the surface suggesting that the high density basement rocks are covered by a thin sheet of light granulites and migmatites in this area (Schulmann *et al*., 2008). North-west of the Moldanubian domain there is an important gravity high corresponding to the Neoproterozoic basement of the Teplá-Barrandian Unit. This is limited to the north by southeast dipping reflectors of the Teplá suture, which is characterized by high density eclogites and ultramafic rocks. The footwall of the suture corresponds to low density felsic crust of the Saxothuringian basement.

The seismic reflection and refraction sections and gravity modelling suggest a complex lithological structure of the Moldanubian domain marked by a low density, 5–10 km thick lower crustal layer located above the Moho, a 5–10 km thick dense mafic layer, a 10-km thick mid-crustal layer of intermediate density and a locally developed 2–5 km thick low density layer at the top (Fig. 3). The low density lower crust correlates well with low-*P* velocities in the range 6.0–6.4 km s^{-1} in the CEL09 section (Růžek *et al*., 2007). Guy *et al*. (2010) proposed that the low density layer located above the Moho corresponds to felsic rocks, which are interpreted as deep crustal equivalents of surface outcrops of the Gföhl Unit. These authors interpreted the high density thick layer located above light granulites as an equivalent of the AGB (Fig. 3). The intermediate density layer forming recent upper crust of the Moldanubian domain is interpreted as Monotonous and Varied group rocks, whereas the low density rocks on the surface are directly correlated with exposures of the Gföhl Unit. It is suggested that this layered structure of the Variscan crust reflects that of the original thick root, which was thinned by late Variscan and Permian extensional processes (Burg *et al*., 1994).

Exhumation model connecting deep crustal geophysics and surface geology

Guy *et al*. (2010) and Franěk *et al*. (2011a) proposed a model connecting the deep structure of the Variscan crust with surface distribution of lower and mid-crustal rocks. The layered structure of the orogenic root reported by geophysics thus represents a relict of Carboniferous distribution of horizontally layered crust prior to exhumation. In addition, it is supposed that the observed vertically layered distribution of orogenic lower crust surrounded by middle crustal units reflects steepening of the deep crustal horizontal layering. The model connecting deep crustal layering with surface geology is based on several recent studies suggesting that the granulites were exhumed along steep channels from lower crustal depth by a ductile extrusion mechanism (Štípská *et al*., 2004; Schulmann *et al*., 2005; Franěk *et al*., 2006, 2011a; Tajčmanová *et al*., 2006).

In this view, the granulites represented, before exhumation, the structurally deepest orogenic lower crust located at a depth of 60–70 km (18–20 kbar,

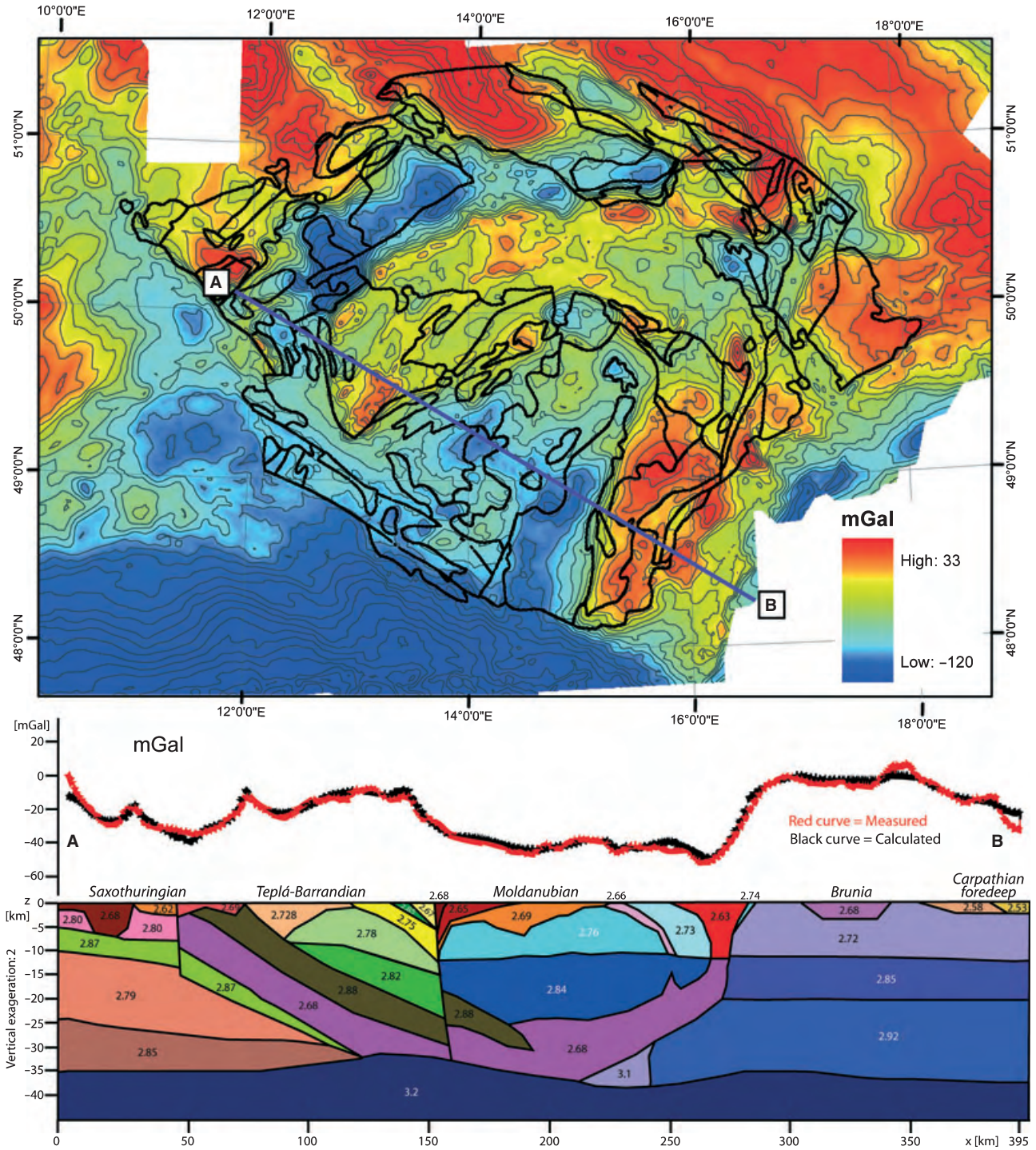

Fig. 3. Bouguer anomaly map of the Bohemian Massif (combined data provided by the Czech Geological Survey and Guy *et al.* (2010)) and gravimetric model for section A–B (profile no. 4 in Guy *et al.*, 2010). The main lithological unit boundaries are represented by superimposed thick black lines. The section A–B emphasizes the present density structure of the Moldanubian Domain with relicts of felsic rocks in the lower crust.

800–900 °C; Štípská & Powell, 2005b; Tajčmanová *et al.*, 2006). Structurally above were mafic rocks of the AGB, which formed during early Palaeozoic magmatic underplating of the Proterozoic crust of the Monotonous Group (Schulmann *et al.*, 2005, figs 16 & 17), and the structurally highest Varied Group corresponding to supracrustal early Palaeozoic sequences (Schulmann *et al.*, 2009). According to this hypothesis, the extrusion

mechanism lead to inversion of this crustal profile so that the granulites presently form cores of crustal anticlines, surrounded by AGB, variably thinned during extrusion, and by the Gföhl gneiss followed by metamorphic sequences of the Monotonous and Varied groups. In many places, the whole structure is even inverted because of the lateral spreading of vertically extruded lower crustal material (Fig. 2). This model is corroborated by detailed structural and petrological data, which show that the granulites and surrounding rocks exhibit common vertical fabrics which are associated with HP–high temperature (HT) mineral assemblages. The flat fabric, which locally may have a bowl shape, is superimposed on vertical extrusion fabrics and developed during subsurface spreading of the extruded partially molten lower crust (7–4 kbar, 700–650 °C; Racek *et al.*, 2006; Tajčmanová *et al.*, 2006; Hasalová *et al.*, 2008b).

CHRONOLOGY OF THE VARISCAN CALC-ALKALINE TO POTASSIC MAGMATISM – CONSTRAINTS ON TIME-SCALES OF THE OCEANIC AND CONTINENTAL SUBDUCTION

The contact of the Teplá-Barrandian and Moldanubian units is marked by voluminous granitic plutons of Variscan age with (normal or potassic) calc-alkaline chemistry and large ion lithophile element (LILE)/-high field strength element (HFSE) enrichment resembling magmatic associations of active continental margins. The oldest vestige of this igneous activity initiated by a late Devonian–early Carboniferous Andean-type subduction is preserved in the Čistá and Štěnovice plutons (Venera *et al.*, 2000; Žák *et al.*, 2010) as well as orthogneisses in the roof of the large Central Bohemian Plutonic Complex, CBPC (protolith *c.* 370–360 Ma; Košler *et al.*, 1993). A newly identified member of the subduction-related association is the mafic Lišov low-pressure granulite unit in southern Bohemia, the protolith of which was emplaced at *c.* 360 Ma into middle crustal levels (~15–20 km) of the same igneous arc (Janoušek *et al.*, 2006).

After a significant time gap, subduction-related members of the CBPC were emplaced, including the normal calc-alkaline gabbros, quartz diorites and tonalites of the Sázava suite (354.1 ± 3.5 Ma; Janoušek *et al.*, 2004a) and the high-K calc-alkaline, mainly granodioritic Blatná suite (347 + 4/−3 Ma; Dörr & Zulauf, 2010; 346.4 ± 1.1 Ma; Janoušek *et al.*, 2010) with associated monzonitic bodies. Finally, further east, commonly in association with HP granulite massifs and high-grade Gföhl orthogneisses, syn-deformational or post-tectonic intrusions of early Carboniferous (343–336 Ma) (ultra-) potassic rocks were emplaced (Holub, 1997; Holub *et al.*, 1997; Janoušek *et al.*, 2003; Verner *et al.*, 2008; Kotková *et al.*, 2010; Kusiak *et al.*, 2010). The time lag between the end of normal calc-alkaline magmatism (*c.* 354 Ma) and the onset of intrusion of K-rich magmas (*c.* 346 Ma) can be related to the transition from ocean plate subduction to continental underthrusting.

PETROLOGY AND GEOCHEMISTRY OF MOLDANUBIAN GRANULITES AND POTASSIC MAGMATIC ROCKS

A peculiar feature of the Moldanubian domain in the Bohemian Massif is an intimate spatial and temporal association between felsic HP, kyanite–garnet granulites and large ultrapotassic plutonic bodies (Janoušek & Holub, 2007). Whereas the granulites tend to be depleted in the radioactive elements U, Th and K, the (ultra-) potassic rocks are characterized by strong enrichment in these elements that shows clearly in the radiometric map (Fig. 4). Thus, understanding of the K, U and Th depletion/enrichment in individual rock types at various stages of the Viséan HP metamorphism and igneous activity seems to be a key to deciphering the thermal history of the Moldanubian orogenic crust.

Moldanubian HP granulites

High-pressure granulites represent a voluminous and ubiquitous component of the Gföhl Assemblage in both Austria and the Czech Republic. The most typical are felsic types consisting essentially of garnet, quartz and hypersolvus feldspar, and commonly containing kyanite. Rutile, zircon, apatite, ilmenite ± monazite are the common accessories (O'Brien & Rötzler, 2003). The felsic Moldanubian granulites were considered as former rhyolites/granites that acquired their high-grade metamorphic character during the Variscan collision and which suffered only limited HP melting (Fiala *et al.*, 1987a; Vellmer, 1992; Janoušek *et al.*, 2004b). Indeed, some granulites in rare domains that escaped later mylonitization/recrystallization are migmatitic in appearance (Franěk *et al.*, 2006). On the other hand, other authors (Vrána & Jakeš, 1982; Jakeš, 1997; Kotková & Harley, 1999) suggested that the felsic granulites represent HP granitic liquids that formed and separated from their source during the Variscan metamorphic cycle. There seem to be several arguments against such a model (Janoušek *et al.*, 2004b): (i) concentrations of Zr are far too low compared to calculated saturation levels at ≥900 °C, coupled with significant, mainly Ordovician zircon inheritance; (ii) consistently low (~750 °C) zircon and monazite saturation temperatures, whereas pre-Variscan inheritance is by no means rare, documenting that saturation was reached (Janoušek, 2006); (iii) preservation of Ordovician–Silurian whole rock and thin slab Rb–Sr ages corresponding to the principal inherited component in granulite zircon; and (iv) high heavy rare earth element + Y contents, ruling out the presence of large amounts of garnet in the residue and thus indicating a rather low-*P* melting.

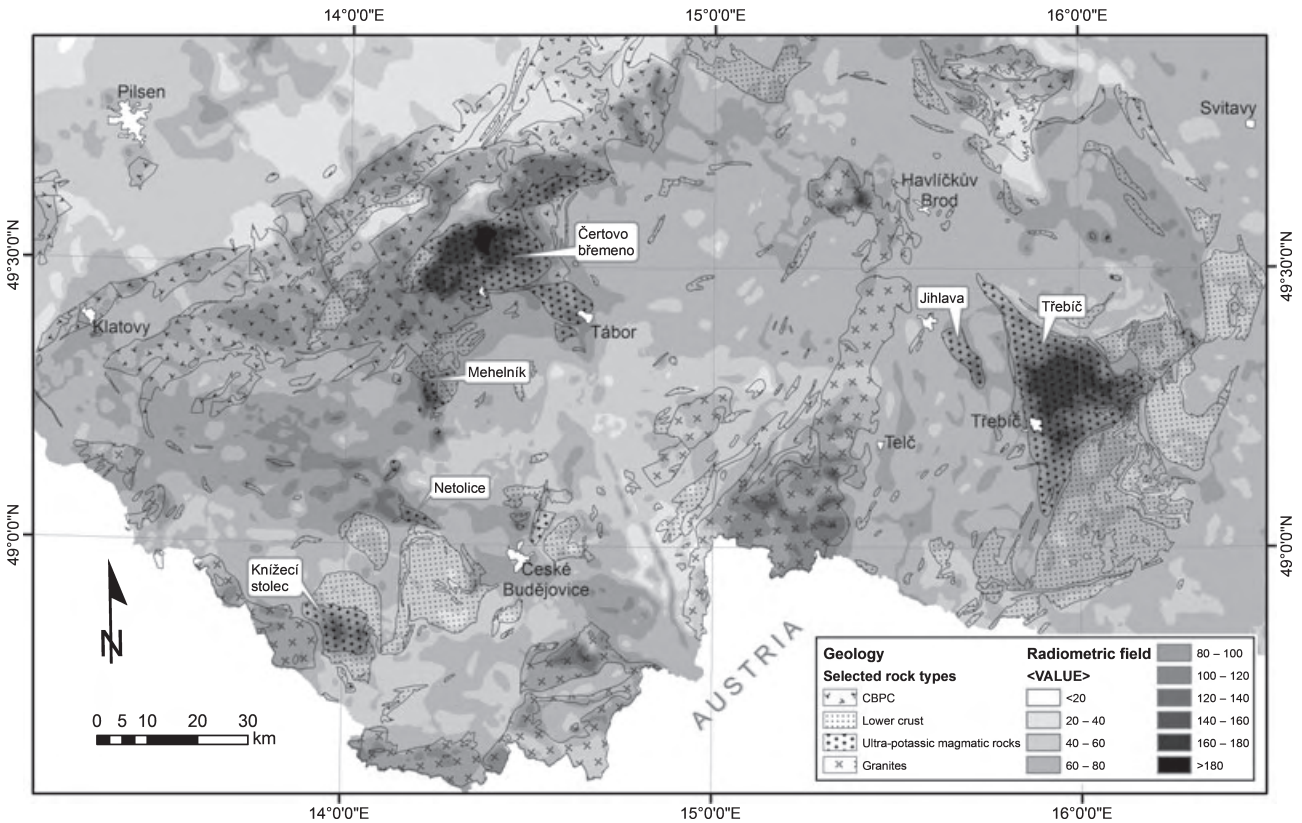

Fig. 4. Radiometric map of the south-eastern Bohemian Massif with isolines of natural air absorbed dose rate (nGy h^{-1}). The main bodies of ultrapotassic rocks (durbachite series and melasyenitoids *sensu* Holub, 1997) that show very high radioactivity are identified by name. The Variscan granites (crosses) and HP granulites (dots) are outlined. Source: Czech Geological Survey Map Server, http://www.geology.cz.

The most peculiar feature of the felsic Moldanubian granulites is the lack of LILE depletion, except for Cs, U and Th (Fiala *et al.*, 1987a,b; Janoušek *et al.*, 2004b). Thus, unlike in many other granulite terranes worldwide (Rudnick & Presper, 1990; Rudnick & Gao, 2003), prograde metamorphism appears to have been largely isochemical. As shown by Janoušek *et al.* (2004b), the composition of felsic Moldanubian granulites matches well with felsic Ordovician–Silurian metaigneous rocks from the Saxothuringian domain, for instance orthogneisses and meta-rhyolites from the Fichtelgebirge. The similarities include whole-rock geochemistry (excluding the most mobile elements Cs, Rb, Th, U, Pb and Li – Fig. 5a), Sr–Nd isotopic compositions and protolith ages of *c.* 480–455 Ma (Siebel *et al.*, 1997; Wiegand, 1997), forming an important maximum within the spectrum of inherited ages in the granulites.

A good candidate for complementary small-volume, HP–HT (> 900 °C) melt that managed to separate from the calc-alkaline granulites are the rare hyperpotassic granulites from Plešovice, Blanský les Massif (Vrána, 1989; Janoušek *et al.*, 2007). These rocks, which are composed essentially of K-feldspar, garnet, zircon and apatite, show rather extreme geochemical compositions (e.g. strong enrichments in Cs, Ba, Rb, U, Th, K, P and Zr; Fig. 5b). They yielded U–Pb zircon ages of 338 ± 1 Ma (Aftalion *et al.*, 1989) and 337.13 ± 0.37 Ma (Sláma *et al.*, 2008), which is close to the established best estimate of the HP metamorphic climax in the granulite massifs (*c.* 340 Ma – see above).

Moreover, rare coeval glimmerite veins in peridotite fragments enclosed by granulite bodies show high concentrations of LILE, U and Th, accompanied by low Rb/Cs and K/Rb ratios as well as low HFSE contents (Fig. 5c); the Sr and Nd isotopic compositions overlap with the granulites (Becker *et al.*, 1999). The glimmerites were interpreted as having crystallized from an ultrapotassic, F-rich aqueous-carbonic fluid, bearing a direct witness for the HP–HT devolatilization of granulite massifs.

Viséan (ultra-) potassic magmatism in the Moldanubian domain

In the Moldanubian domain of the Bohemian Massif, relatively large volumes of (ultra-) potassic plutonic rocks constitute several plutons and stocks spatially associated to granitoids of the Central Bohemian Plutonic Complex, the Moldanubian Plutonic Complex,

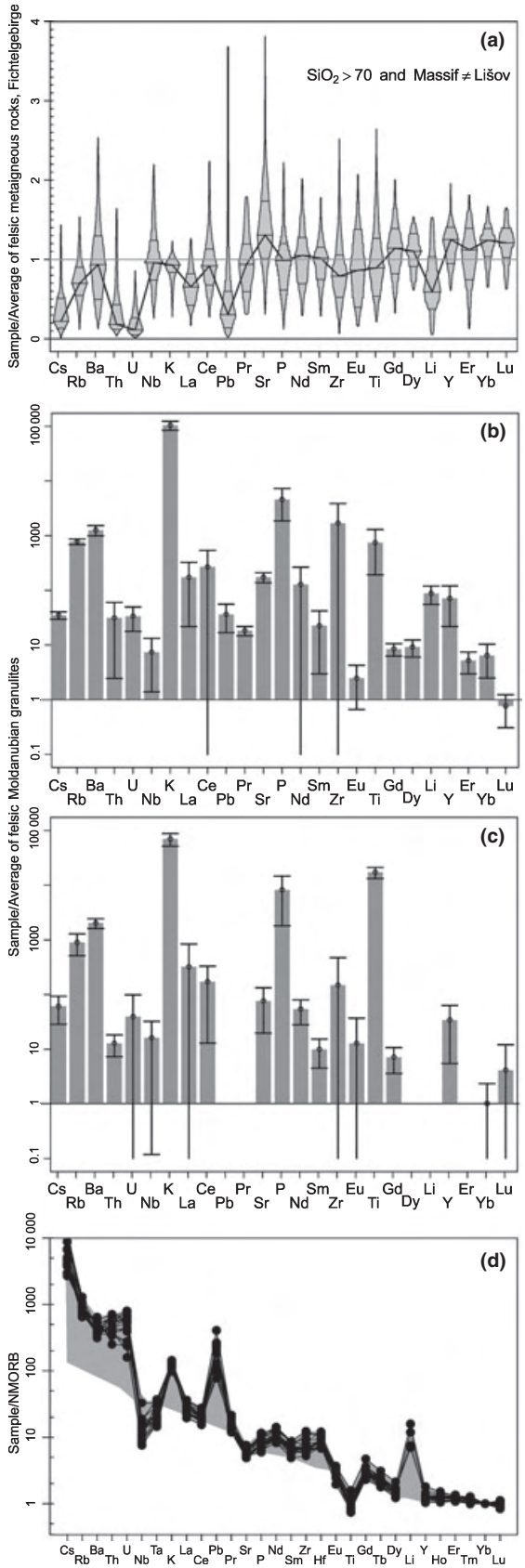

and high-grade metamorphic rocks of the Gföhl Assemblage, most notably felsic HP granulites. This prominent group represents the late-syntectonic durbachite series (e.g. Čertovo břemeno, Třebíč and Knížecí stolec intrusions – Žák *et al.*, 2005; Verner *et al.*, 2008) (Fig. 4) of quartz melasyenites to melagranites with hydrous ferromagnesian minerals, Mg-rich biotite and actinolitic amphibole. These are mainly coarsely porphyritic rocks that contain abundant K-feldspar phenocrysts and ultrapotassic mafic microgranular enclaves. The spatially associated, less deformed, or even post-tectonic, biotite–two-pyroxene melasyenites to melagranites (Tábor and Jihlava intrusions) are characterized by a 'drier' ferromagnesian mineral assemblage of orthopyroxene, clinopyroxene and Mg-biotite and lack the porphyritic texture (Žák *et al.*, 2005).

The petrogenesis of the Moldanubian (ultra-) potassic igneous rocks has been a matter of debate as even the basic, Mg and K-rich members or primitive lamprophyric dykes have a mixed geochemical character. While their high contents of Cr and Ni with high mg# point to derivation from an olivine-rich source (mantle peridotite), the elevated concentrations of U, Th, light rare earth element (LREE) and LILE, depletion in Ti, Nb and Ta (Fig. 5d) and high K_2O/Na_2O and Rb/Sr ratios apparently contradict a mantle origin (Holub, 1997; Janoušek & Holub, 2007). These features led several authors to invoke partial melting of anomalous (LILE- and LREE-enriched) lithospheric mantle domains (e.g. Janoušek *et al.*, 1995; Holub, 1997; Wenzel *et al.*, 1997, 2000; Janoušek & Holub, 2007), followed by mixing with lower crustal leucogranitic melts (Holub, 1997; Gerdes *et al.*, 2000). In any case, the crustal-like Sr–Nd isotopic signatures cannot be reconciled solely by crustal assimilation/contamination during the ascent of any primitive, mantle-derived magmas and require contamination by the subducted continental crust directly in the source

Fig. 5. Multi-element variation diagrams. (a) Box and percentile plots for felsic (SiO_2 > 70 wt%) Moldanubian granulites, normalized to an average of felsic metaigneous rocks from the Fichtelgebirge (Siebel *et al.*, 1997; Wiegand, 1997). See Janoušek *et al.* (2004b and references therein) for the data set. The distribution of each of the normalized trace-element contents is plotted as irregular polygons, the width of which at any given height is proportional to the empirical cumulative distribution. As in box plots, the median, 25th and 75th percentiles are marked with horizontal lines across the box. Compositions of the hyperpotassic Plešovice granulites (data from Janoušek *et al.*, 2007) (b) and Lower Austrian glimmerite veins (Becker *et al.*, 1999) (c) normalized by an average of felsic (SiO_2 > 70 wt%) HP Moldanubian granulites, except Lišov (taken from Janoušek *et al.*, 2004b). (d) Multi-element variation diagram for selected ultrapotassic rocks (durbachite series and syenitoids) from the Moldanubian Zone of the Bohemian Massif (Janoušek & Holub, 2007) normalized by N-MORB and then adjusted to $Yb_N = 1$ to minimize the effects of fractional crystallization (Pearce & Stern, 2006).

(Janoušek & Holub, 2007). As noted by the same authors, multi-element plots for the Moldanubian felsic granulites (Fig. 5a) and ultrapotassic rocks (Fig. 5d) are largely mutually complementary. The most striking are the cases of Cs, Rb, Th, U, Pb and Li, which are impoverished in the felsic granulites but strongly enriched in the ultrapotassic magmatic rocks.

NUMERICAL MODELLING CONSTRAINTS ON HEAT SOURCES AND EMPLACEMENT MECHANISMS OF THE OROGENIC LOWER CRUST

To constrain the heat source driving the tectonic processes of vertical extrusion three contrasting, but not mutually exclusive, hypotheses will be tested. Heat could be generated by: (i) *in situ* decay of radioactive elements contained in the FLC (U, Th and K); (ii) radioactive elements present in the metasomatized or crustally contaminated mantle; and (iii) a large-scale thermal anomaly generated in the mantle as a result of slab break off or mantle delamination.

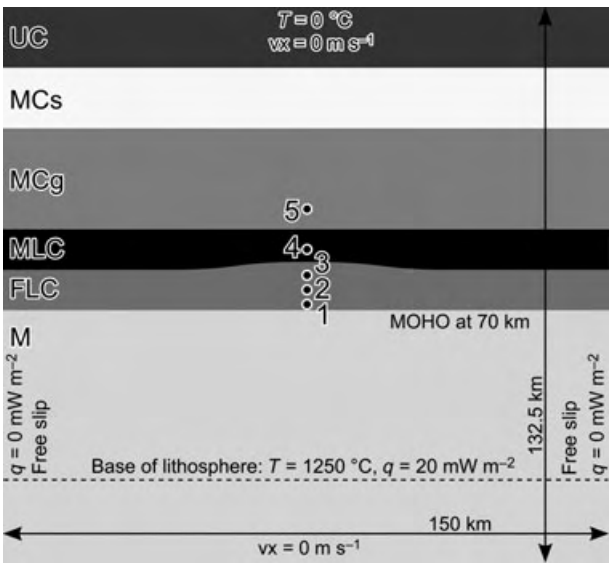

Fig. 6. Model geometry, initial lithology distribution, boundary conditions and location of tracked samples used for numerical simulations.

The annual thermal productions were calculated following the method of Kramers *et al.* (2001), using decay constants and specific heat production data summarized by van Schmus (1995; table 8). The past annual heat production (μW kg^{-1}) can be obtained from the elemental concentrations of K, U and Th using the equation:

$$\mathrm{H}(\mu\mathrm{W\ kg^{-1}}) = \mathrm{K}\frac{3.45\times10^{-6}}{\mathrm{e}^{-0.554t}} + \mathrm{Th}\frac{2.638\times10^{-2}}{\mathrm{e}^{-0.0495t}} + \mathrm{U}\left(\frac{4.03777\times10^{-3}}{\mathrm{e}^{-0.985t}} + \frac{9.396852\times10^{-2}}{\mathrm{e}^{-0.1551t}}\right), \quad (1)$$

where t represents age in Ga and K, U, Th are concentrations in ppm.

Model setup

The numerical model studies outlined below describe the transient thermal evolution of a thickened orogenic domain (Fig. 6) characterized by the presence of tectonically accreted felsic rocks, including granulites, within orogenic lower crust. This FLC directly underlies a mafic layer which was added to Neoproterozoic crust during early Palaeozoic crustal stretching and magmatic under-plating. The presence of low density FLC below a dense mafic layer introduces significant gravitational instability within the lower crust (Gerya *et al.*, 2001) which could trigger crustal diapirism (Ramberg, 1981; Perchuk, 1989) and perturbate the thermal field. We use thermal and dynamic numerical models to examine the role of high radioactive heat production located in the FLC as a main candidate triggering the gravitational instability as a result of pronounced progressive generation of heat and subsequent change in density because of thermal expansion.

The model is set up to allow the definition of different material domains with different thermal and mechanical properties (Table 2) on high-resolution Lagrangian markers initially arranged in a rectangular grid (Gerya & Yuen, 2003). Properties are mapped to a Eulerian staggered grid where governing equations are solved for temperature change (ΔT) and velocity. In each time, step markers are advected according to the updated velocity field and all temperature-dependent variables

Table 1. Calculated radioactive heat production values for Fichtelgebirge metaigneous rocks, felsic Moldanubian granulites and Moldanubian peridotite (present and at 340 Ma).

Rock type	Age (Ma)	Density (kg m^{-3})	Concentrations (ppm)							A (μW m^{-3})	
			K	Th	U	^{40}K	^{232}Th	^{235}U	^{238}U	Present	Past
Fichtelgebirge	340	2700	38642.550	13.00	9.00	7.3421	13.00	0.064	8.935	3.670	3.920
Moldanubian granulites	340	2750	38601.045	2.10	1.00	7.3342	2.10	0.007	0.993	0.788	0.885
Horní Bory peridotite	340	3200	940.537	0.11	0.57	0.1787	0.11	0.004	0.568	0.176	0.214

Data sources for averaged whole-rock compositions: Fichtebeirge metaigneous rocks: Siebel *et al.* (1997), Wiegand (1997).
Felsic Moldanubian granulites (SiO_2 > 70 wt%): Janoušek *et al.* (2004b and references therein).
Horní Bory peridotite: Ackerman *et al.* (2009).

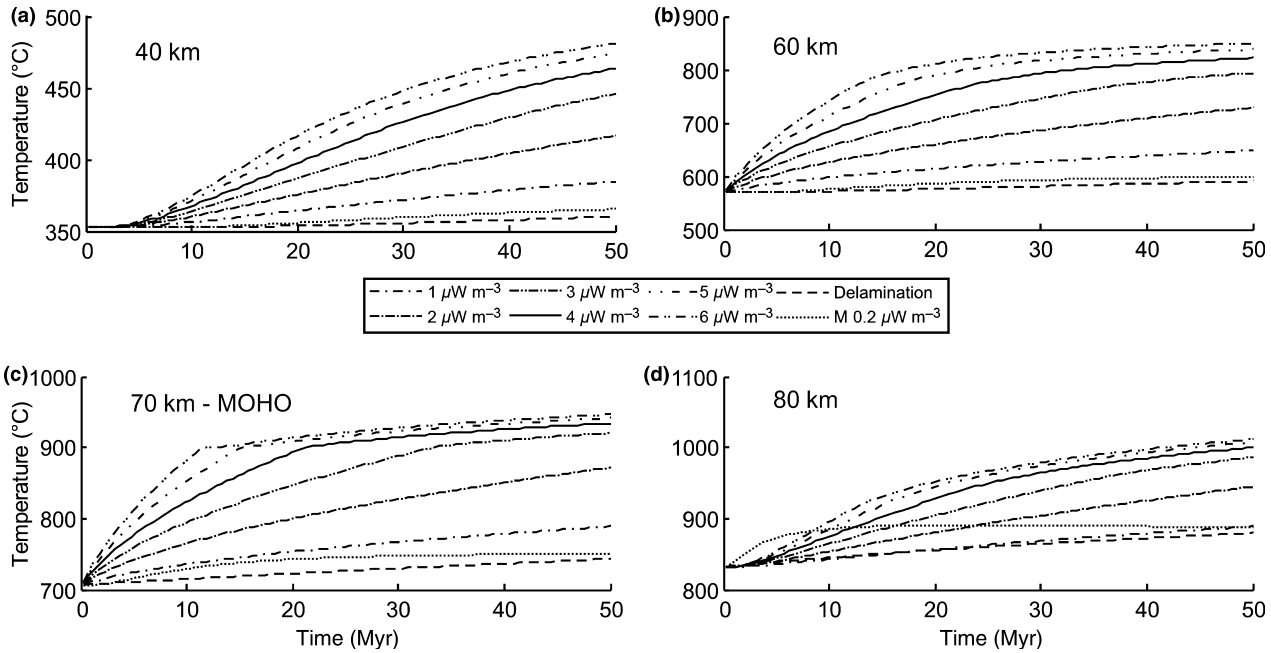

Fig. 7. Results of 1D static thermal models to compare temperature evolution controlled by different radioactive heat production of felsic lower crust (FLC; curves labelled 1–6 according to heat production) and radioactive heat production within the lithospheric mantle (dotted line) with thermal evolution caused by lithospheric delamination at 90 km depth (dashed line).

such as thermal diffusivity, specific heat, viscosity and density are recalculated according to temperature dependence for each marker (see Appendix).

The geometry of the model, the distribution of material layers and the boundary conditions of the numerical simulations are depicted in Fig. 6. The initial layered geometry introduces an artificial perturbation in the interface between felsic and mafic lower crust to allow immediate relaxation of gravitational instability in the central part of the computational domain. The initial temperature distribution is calculated as the steady-state solution of Eqn A.3, with heat sources located only in the upper crust. The lower crustal radioactive heat production is accounted only for transient development. One of the important features of the model is the ability to progressively eliminate sources of radioactive heat production according to the temperature achieved. As argued above using the available geochemical data, at a certain stage of the evolution of the lower crust, most of the radioactive elements, in particular U and Th, were stripped from the felsic granulites into partial melt or 'fluid' and transported, together with K-rich magmas, into the middle–upper crust. In the models, two values are used to cut-off heat production to simulate radioactive element evacuation via fluid or via melt.

Heat sources

The effect of such behaviour on thermal evolution was first examined in terms of a 1D static thermal model (Fig. 7). A sharp change in heating rate in Fig. 7c corresponds to the time when heat production is switched off in most of the lower crust. To compare the scale and magnitude of temperature change as a result of processes like delamination or heat production within lithospheric mantle, the plot is overlaid with results of two additional numerical simulations. The dotted line represents the results of a 1D model to simulate production of heat within a >60 km thick lithospheric mantle with a radioactive heat production of 0.2 μW m^{-3} calculated on the basis of the whole-rock geochemical data of Ackerman *et al.* (2009) for the Horní Bory garnet peridotite (Table 1). It is evident that even such an enriched mantle cannot provide sufficient heat to be responsible for the significant increase of temperature within the lower crust (Fig. 7c). Similarly, we argue that the process of lithosphere delamination (simulated by instantaneous replacement of lithospheric mantle below 90 km by asthenosphere in the model) cannot provide the necessary heat input. Results related to the mantle delamination process are shown by the dashed line in Fig. 7.

A series of numerical experiments was set up to study the influence of radioactive heat production located within the FLC (Fig. 7). Our calculations show that the temperature required for partial melting of mica-bearing felsic crust located at a depth of 70 km (~850–900 °C) are reached after 20 Myr for radioactive heat production of 2 μW m^{-3} and in 7 Myr for radioactive heat production of 4 μW m^{-3}. At 60 km depth, which is the assumed upper limit of the felsic layer, the melting temperature is reached in >50 Myr and in

Table 2. Mechanical properties (density, thermal expansivity and coefficients of temperature-dependent viscosity) of individual lithologies used for numerical simulations.

Material	Description	Reference density	Thermal expansion coefficient	Temperature-dependent viscosity range and coefficients			Radioactive heat production
		ρ_0 (kg m^{-3})	α	Effect. viscosity (Pa s^{-1})	C_1	C_2	H_r (μW m^{-3})
UC	Upper crust	2700	0	10^{22}	Viscosity const.		2×10^{-6}
MCs	Middle crust (schists)	2800	2×10^{-5}	1.5×10^{20} to 2.5×10^{19}	10^{16}	6000	0
MCg	Middle crust (gneisses)	2800	2×10^{-5}	2.5×10^{20} to 3.5×10^{19}	10^{17}	6000	0
MLC	Mafic lower crust	2950	0	2×10^{21} to 5×10^{20}	10^{18}	7000	0
FLC	Felsic lower crust	2750	3×10^{-5}	1.5×10^{19} to 6×10^{18}	10^{17}	5000	2×10^{-6} to 8×10^{-6}
M	Lithospheric mantle	3300	0	5×10^{21}	Viscosity const.		0 (2×10^{-7})

c. 20 Myr for the two radioactive heat production values, respectively. Keeping in mind the time-scales of magmatic and metamorphic events related to Palaeotethys subduction discussed above, the time of 5–15 Myr available between the arrival of continental crust into the subduction zone (354–346 Ma) and the metamorphic climax (*c*. 340 Ma) corresponds to the thermal incubation time estimated for radiogenic heat production of 4 μW m^{-3}.

Results of 2D modelling

The distribution of densities and viscosities for all models generally resulted in the development of a diapiric structure located at the introduced perturbation. The *P–T* of selected samples (samples 1–3 are within lower crust, sample 4 in mafic layer and sample 5 in middle crust; for locations, see Fig. 6), tracked during the model evolution are plotted on Figs 8–10. Similar to the static 1D models, the simulations show a clear relation between the initial temperature increase (20–150 °C) and radioactive heat production within lower crust.

Two types of evolution have been calculated: (i) a diapiric structure formed because of mantle heat source (heat production 0.2 μW m^{-3}); and (ii) a diapiric structure caused by radioactive heat production within the FLC for radioactive heat productivities ranging from 1 to 6 μW m^{-3}. The results of the numerical simulations for the case of mantle heat production are shown in Fig. 8. For the case of radioactive heat production within the FLC, it was terminated at 900 and 1000 °C. These results are presented together with a simulation in which the radioactive heat production was not switched off (Fig. 9) allowing a direct comparison of differences in *P–T* evolution (Fig. 10).

Several major conclusions can be drawn from these results. The diapir reflecting the mantle heat source (Fig. 8) exhibits a typical bell shape during the first 30 Myr and most importantly shows contrasting *P–T* evolution for samples located in different units and initial depths. Whereas the upper part of the mantle (Fig. 7d) is almost isobarically heated, the samples located in the felsic crust, mafic lower crustal layers and the middle crust reveal relatively slow exhumation and moderate heating associated with the diapir growth.

In contrast, experiments assuming high radiogenic heat production show typical bollard type diapirs. After 10–20 Myr imposed gravitational instability and variable radioactive heat production within lower crust, the viscosity of the overlying mafic layer is significantly reduced allowing relatively fast exchange of material and development of the central diapir. There are differences in rates of vertical exchange between individual simulations as increased heat production cause increase of buoyancy forces and decrease of viscosity of the diapir surroundings (samples 4 and 5).

The growth of bollard type diapirs is associated with either isothermal decompression or important cooling linked to diapir growth for samples located in deep felsic lower crustal layer. These are indeed the *P–T* evolutions retrieved from for Bohemian Massif granulites (Štípská *et al*., 2004; Racek *et al*., 2006; Tajčmanová *et al*., 2006). The samples located originally higher in the column and at the middle crustal levels reveal important heating associated with exhumation, which is also in accord with recent petrological studies (Racek *et al*., 2006; Štípská *et al*., 2008). The other important consequence is that rocks from any original position show convergence of *P–T* conditions after exhumation to mid-crustal depths. The time-scales of heating (10–20 Myr) and exhumation (5–10 Myr) calculated in this model are also in agreement with petrological and geochronological data reported by Štípská *et al*. (2004) and Tajčmanová *et al*. (2006, 2010). It should be noted that time-scales of our models are directly controlled by the rheology of the materials, which in our simulations is significantly simplified (Eqn A.3, Table 2).

Closer inspection of Fig. 10 confirms that the best fit of modern petrological and geochronological data with calculated *P–T* paths is with an initial radioactive heat production of 4 μW m^{-3}. Here, the maximum temperatures attained at the bottom of thickened crust are ~950 °C, while samples located in the central part of the felsic crustal column reach a maximum 800 °C at the thermal peak. These values may reconcile modern THERMOCALC modelling data of Štípská & Powell (2005b), Tajčmanová *et al*. (2006) and Racek *et al*. (2008) who reported peak temperatures ~800 °C with

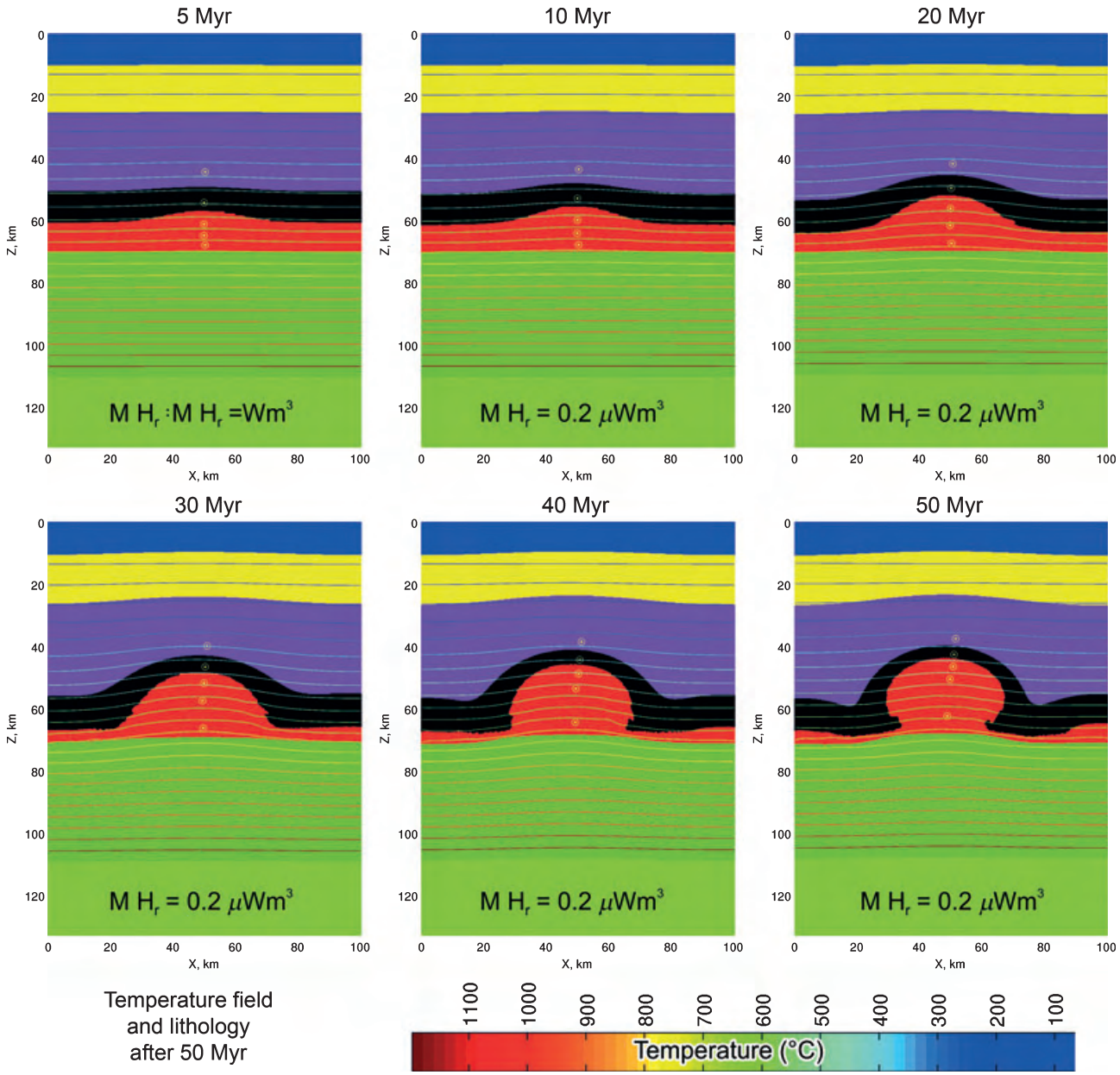

Fig. 8. Results of numerical simulation of radioactive heat production within the lithospheric mantle showing distribution of lithologies and temperature field developed during 50 Myr. Light shade of the mantle colour marks the asthenosphere (adiabatic geotherm and no heat production).

those of O'Brien (2000) and Cooke & O'Brien (2001) who reached significantly higher peak temperature estimates. Higher heat production would produce significantly higher peak temperatures of nearly 1000 °C maintained even at pressures as low as 12–13 kbar, which is in contradiction with modern petrological studies (see Schulmann *et al.*, 2008 for review).

Other important information comes from the temperature distribution in the core of the diapiric structure. The diagrams calculated for elevated radioactive heat production show areas where the temperature condition of radioactive heat production switch off (i.e. partial melting associated with release of radioactive elements) was attained during the evolution (the pinkish colour inside the diapirs in Fig. 9).

As shown above, the metaigneous rocks from Fichtelgebirge are thought to be the best candidates for precursors of the Moldanubian felsic granulites. Therefore, these rocks are interpreted as material that could have formed the felsic lower crustal layer, which was subsequently heated, partially melted and transformed to typical felsic Moldanubian granulites.

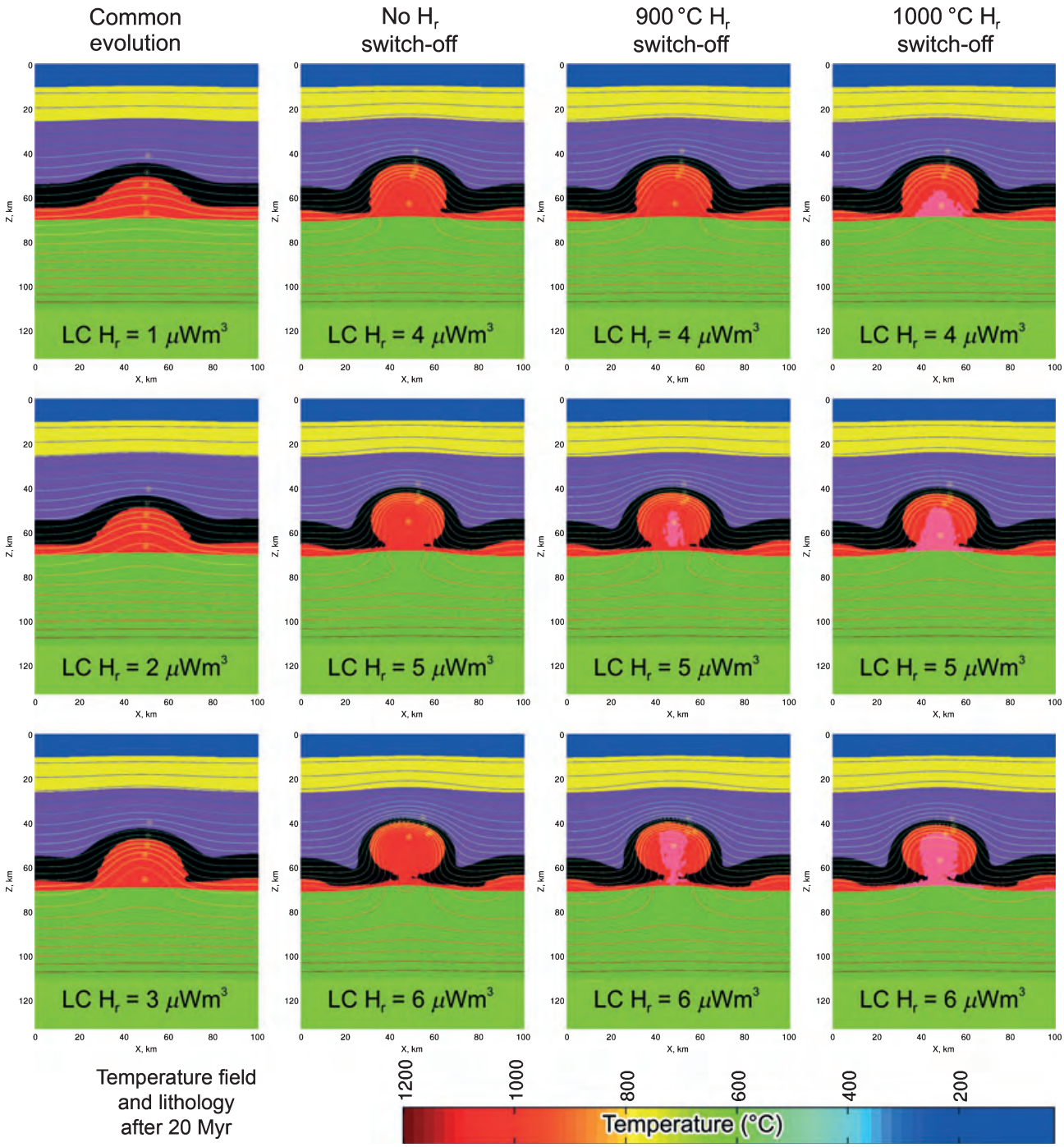

Fig. 9. Results of numerical simulations showing distribution of lithologies and temperature field developed after 20 Myr. Light shade of the lower crustal colour marks places where removal of radioactive heat production occurred while light shade of the mantle colour marks asthenosphere (adiabatic geotherm and no heat production). First column shows results for low radioactive heat production and lithology and temperature fields are identical for all switch-off conditions as they are not reached during 20 Myr. The second column gives results for no switch-off condition, whereas the third and fourth columns shows results of simulations with 900 and 1000 °C switch off for the lower crustal layer.

The metaigneous rocks from Fichtelgebirge yield an average radioactive heat production of 3.9 μW m^{-3} obtained from the average elemental concentrations of K, U and Th (Siebel *et al.*, 1997; Wiegand, 1997) using Eqn 1 (Table 1). However, the radioactive heat production for the average felsic granulites (SiO_2 > 70, Table 1) is extremely low (0.9 μW m^{-3}), suggesting that the radioactive elements were mostly lost during

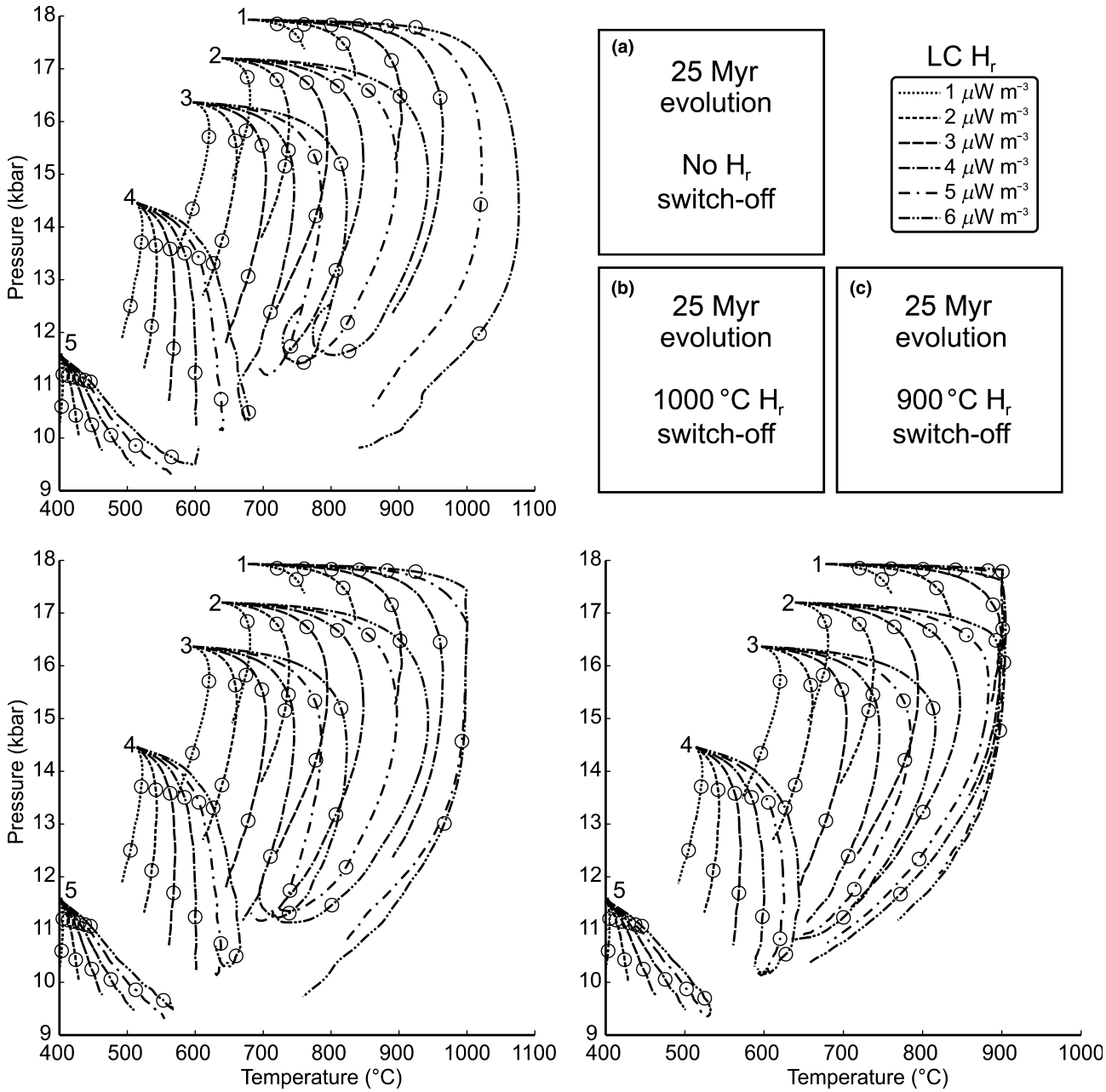

Fig. 10. *P–T* evolution of six tracked samples for models with different radioactive heat production values for the felsic lower crust (FLC). Samples 1, 2 and 3 were located in felsic lower crust, sample 4 within the mafic layer (MLC) and samples 5 and 6 are located in the middle crust. (a) No radioactive elements removed, (b) 900 °C and (c) 1000 °C threshold for radioactive element removal from the lower crust. Circles mark 10 Myr time step.

the partial melting connected with the granulite facies metamorphism.

In conclusion, the thermal structure which fits best the petrological and geochronological data obtained so far from the Moldanubian granulite massifs is that calculated with an initial radioactive heat production of 4 μW m^{-3} located in the felsic layer. The *P–T–t* evolutions of the AGB (mafic lower crust) and of the overlying mid-crustal rocks are also in good agreement with the model results, despite the fact that the simulated evolution represents only the initial part of a complex polyphase exhumation.

DISCUSSION

In this article, we discuss a particular structural pattern in the Variscan orogenic root in which orogenic lower crust composed of felsic granulites of Ordovician

protolith age forming cores of domes that are separated from mid-crustal Neoproterozoic and Palaeozoic metasedimentary rocks in synclines by a late Ordovician–Silurian metabasic layer. We argue that the origin of these structures was related to diapiric material exchange within the orogenic lower crust. The key element in deciphering the Viséan development is the occurrence of FLC underneath dense mafic crust as depicted by geology and geophysics. To understand the formation of this peculiar lithological sandwich the possible emplacement models for the FLC at the bottom of the root need to be discussed. Subsequently, we shall address the particular role of this felsic layer for the origin of the felsic granulite–(ultra-) potassic magma association. Finally, a model of gravity inversion is discussed together with thermal consequences for *P–T–t* paths of rocks in different positions with respect to the diapiric structure.

Model of relamination of felsic crust to early Palaeozoic mafic lower crust

The relamination of FLC has been proposed as an alternative to the model of Chemenda *et al.* (2000) to explain the structure of the Tibetan Plateau. The Tibetan Plateau is characterized by an exceptionally large gravity low indicating dominantly a felsic root underplated by Indian felsic crust, the density of which corresponds to felsic granulite at a pressure of 20 kbar (Hetényi *et al.*, 2007). Indeed, Le Pichon *et al.* (1997) argued that the high topography of the Tibetan Plateau is due to presence of low density granulites at depth. A similar gravity low is typical of the Altiplano Plateau in central Andes, having been interpreted as a result of underthrusting of the Brazilian crust underneath the Andean root (Oncken *et al.*, 2006). The gravity anomaly associated with the Moldanubian domain resembles remarkably the Tibetan and Altiplano plateaux density structure, which in this case is reduced by subsequent isostatic reequilibration (Burg *et al.*, 1994). The common denominator of all these geophysical observations is the occurrence of felsic crust at lower crustal depths. This is explained either as continental crust underthrusting thin lithospheric mantle (Chemenda *et al.*, 2000) or directly by influx of felsic crust into the orogenic root at Moho depth lifting the original lower crust and depressing the mantle lithosphere (Behr, 1978; Plesch & Oncken, 1999; Avouac, 2008).

In the western Bohemian Massif, the influx of ductile lower crust at granulite/eclogite facies conditions was proposed by O'Brien (2000). In Fig. 11a,b, the influx of Saxothuringian crust into the root domain is visualized in the form of a 10-km wide channel splitting the early Palaeozoic mafic lower crust from lithospheric mantle, whereas the other part of the continental crust is continuously subducted, contaminating the local mantle and sampling the mantle lithosphere. The term relamination (Hacker *et al.*, 2007) is accepted as being suitable for the addition of low density crust underneath the dense root, in contrast to the term delamination to describe loss of heavy root material and its replacement by the asthenosphere.

As discussed before, oceanic subduction had to have ceased by 354–346 Ma to be replaced by continental underthrusting. Incidentally, a Sm–Nd age of 354 ± 6 Ma was determined by dating of calcium-rich cores of garnet from the South Bohemian granulites indicating the onset of eclogitization of continental crust at this time (Prince *et al.*, 2000). If true, such a scenario allows a 5–15 Myr period to *c.* 340 Ma, the granulite facies metamorphic climax, for the subducted continental crust to thermally incubate and elevate the orogenic geotherm (England & Thompson, 1984). Based on *P–T* estimates, crustal thickening had to produce a ~70-km thick crust at this time (Fig. 11c). Melting of this continental crust started at *c.* 345 Ma, as indicated by high-K calc-alkaline magmatism of the Blatná suite. The maximum melt production at both the base of this crust and in the underlying mantle lithosphere occurred during, or soon after, the HP metamorphic climax at *c.* 340 Ma, as indicated by intrusions of ultrapotassic syenites at mid- to high-crustal levels.

The origin of the felsic granulite–ultrapotassic plutonic rock association and the heat source

Roberts & Finger (1997) proposed that heating of relatively refractory felsic metaigneous rocks, the likely source of the felsic granulites, to temperatures as high as 1000 °C would result in production of 5–15 vol.% of partial melt. This notion was confirmed by thermodynamic modelling of Janoušek *et al.* (2004b), who suggested that the initial melting, limited by mica availability, would not exceed 10 vol.% for any of the prospective granulite decompression paths and rapid increase of the melt fraction would occur only at ~1100 °C. However, it is important to correctly assess the melt production for the most typical felsic granulites. The most likely protolith for the felsic granulites is considered to be granite or orthogneiss of the 'Fichtelgebirge chemistry' that must have lost some melt during metamorphic evolution in order to preserve the high-pressure assemblage. Therefore, to estimate the degree of melt loss, pseudosections were calculated using THERMOCALC for a granulite with the oldest known preserved fabric from the Blanský les Massif (sample H296-S1 from Franěk *et al.*, 2011b; for details, see Appendix).

The sample modelled contains relict porphyroclasts of perthitic feldspar with inclusions of kyanite, garnet with 24 mol.% of grossular, rutile and biotite, which constrains the peak *P–T* conditions to ~16–18 kbar and 860 °C (Fig. 12a; Franěk *et al.*, 2011b). It is necessary to add 7 mol.% of melt into the rock composition to obtain assemblages containing biotite and muscovite without garnet or alumosilicate at

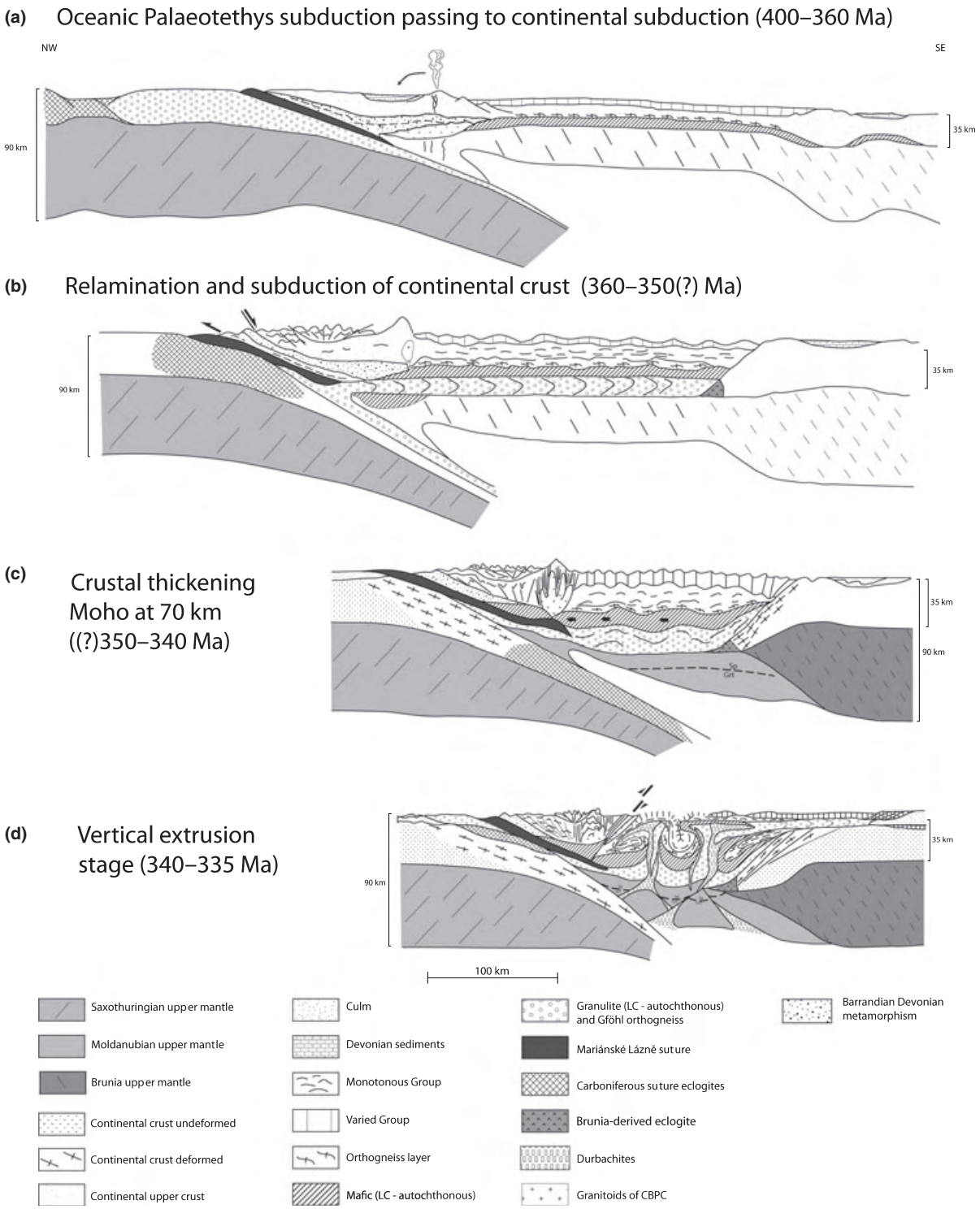

Fig. 11. Model proposed for the tectonic evolution of the orogenic root domain in the Bohemian Massif. (a) Model of continental underthrusting with development of the Barrandian forearc region, CBPC magmatic arc and backarc region represents the future Moldanubian domain. The position of the Palaeotethys suture is indicated as the future Mariánské Lázně Complex. (b) Relamination model with part of the allochthonous Saxothuringian crust injected between the Moho and the continental lithosphere. The other part is subducted thereby producing metasomatism of the overlying mantle. (c) Crustal thickening of the former backarc domain (Schulmann *et al.*, 2005, 2009). (d) Vertical extrusion and gravity redistribution of relaminated Saxothuringian crust at the end of Variscan orogeny.

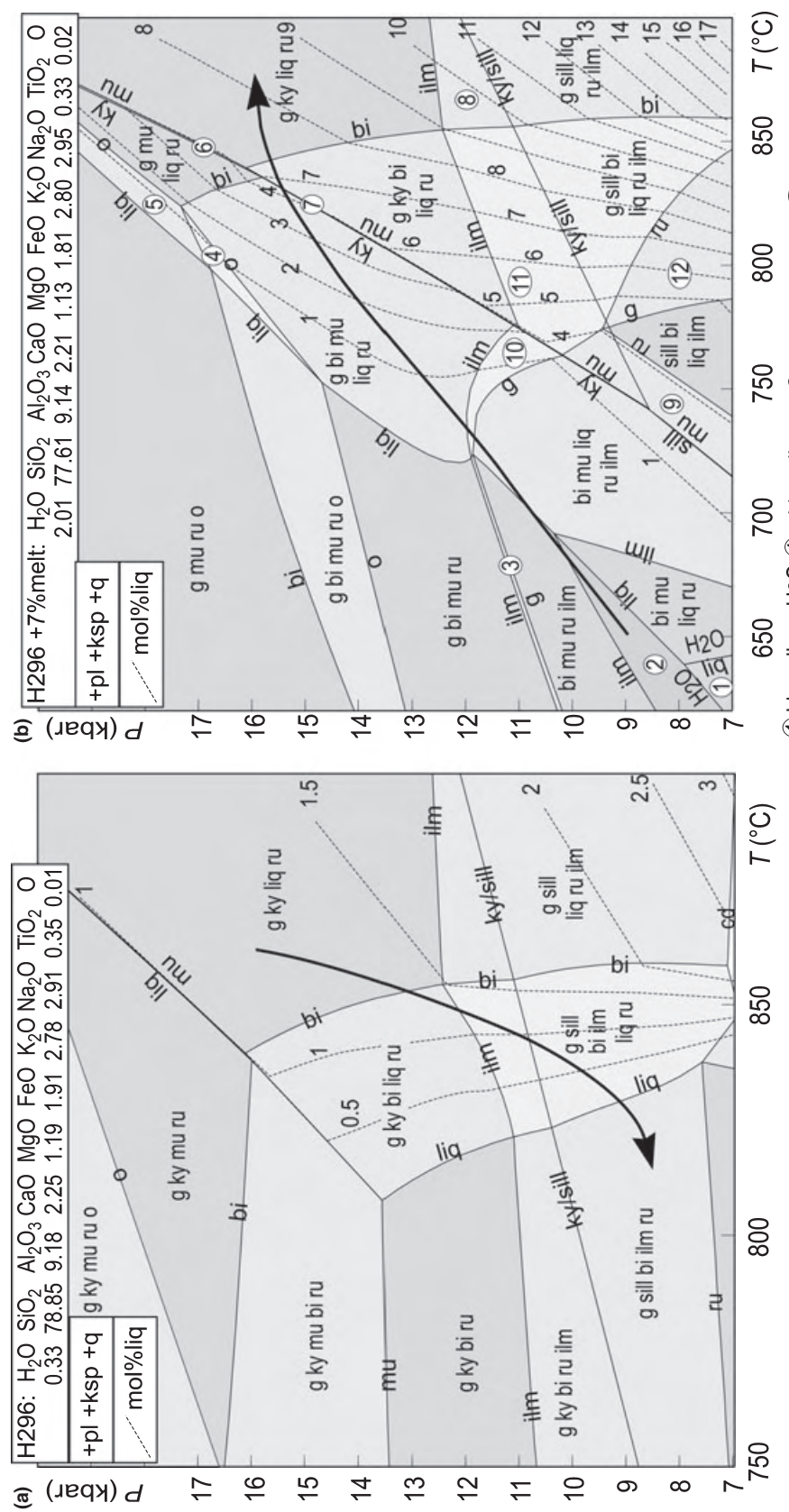

Fig. 12. (a) Pseudosection for granulite sample H296-S1 (Blanský les Massif) to show the *P–T* path from the peak assemblage of g–ky–pl–ksp–q–liq–ru at 16 kbar and 860 °C by decompression to 8 kbar and 820 °C (modified from Franěk *et al.*, 2011b). Molar percentage of melt is very low and allows the preservation of the peak assemblage on decompression and cooling. (b) Pseudosection for sample H296-S1 with 7 mol.% of melt added allows the stability of the mu–bi–pl–ksp–q assemblage at subsolidus conditions. Such a reconstructed granite whole-rock and mineral composition predicts 8 mol.% of melt at peak *P–T* conditions and 12 mol.% of melt at 8 kbar and 860 °C. Some melt must be lost to preserve the peak g–ky–pl–ksp–q–liq–ru assemblage.

subsolidus conditions. Such a reconstructed granite mineral composition calculated at 650 °C and 9 kbar is 8 mol.% muscovite, 6.5 mol.% biotite, 39 mol.% quartz, 30 mol.% plagioclase and 16 mol.% K-feldspar (Fig. 12b). On heating, the melt proportion for the reconstructed granite at 16 kbar and 860 °C is 8 mol.%, and on isothermal decompression to 8 kbar and 860 °C it increases to 13 mol.%. The calculations predict 14 mol.% of melt at 16 kbar and 1000 °C that increases to 37 mol.% at 8 kbar and 1000 °C, confirming the earlier estimates by Roberts & Finger (1997) and Janoušek *et al.*(2004b).

The modelling demonstrates that heating of granitic crust with a restricted amount of muscovite and biotite can generate a garnet-bearing residue and up to 7 mol.% of melt at temperatures ~900 °C. This temperature was used as a threshold for melt loss related removal of radioactive elements and the switching off of the heat production in lower crustal rocks in the numerical experiments.

The detailed microstructural studies of Franěk *et al.* (2006, 2011b) showed that the origin of the granulite microstructure is related to significant deformation, dynamic recrystallization and viscous flow during the vertical extrusion stage. Before the vertical extrusion stage, the granulite facies rocks acquired a metamorphic fabric in a rather static environment. The deformation occurred via diffusion-assisted grain boundary sliding, which is an efficient mechanism to extract melt from a continuously deforming source by a combination of dynamic dilation and compaction (Závada *et al.*, 2007). The mechanism of dynamically developed porosity and melt extraction was discussed by Hasalová *et al.* (2008a), who showed that a small amount of melt may be efficiently extracted from the source far below the rheologically critical melt percentage threshold (> 20–25 vol.% melt; Vigneresse *et al.*, 1996). Therefore, we consider 900 °C to be a reasonable temperature when melt can be extracted from the parent rock via the grain boundary sliding mechanism leaving behind a garnet-bearing mylonitic rock – the Moldanubian granulite. However, this process required significant deformation related to the vertical extrusion event to extract the melt. It is the pervasive early vertical fabric which is related to the efficient loss of melt (even at very small melt fraction), resulting in significant depletion of the parental rocks in U, Th, Cs, Li ± Rb, but leaving the rest of the geochemical signature unaffected.

A consequence of melting and melt extraction is the removal of a significant part of the radioactive element budget from the system. This is particularly true for U and Th hosted by accessories such as zircon or monazite, which would resist fluid loss in course of the progressive heating. On the other hand, they should dissolve readily even at low degrees of melting, as the partial melt was likely to be rather corrosive, being hot and rich in alkalis with fluorine (Finger & Cooke, 2004; Janoušek *et al.*, 2007). In granitic rocks, the relevant accessories are mostly enclosed in biotite (Bea, 1996) that was undergoing melting. Moreover, as argued by Watson *et al.* (1989) on theoretical grounds, the larger accessories are likely to be progressively concentrated at grain boundaries in the course of high-grade metamorphism. Finally, there is a direct evidence for the presence of low-degree, high-*T*, trace-element-rich melt in the felsic HP granulites, as the newly grown metamorphic zircon and rutile are rich in U, Th and LREE or Zr and Nb, respectively (Finger & Cooke, 2004). Thus, the accessories hosting U and Th in the protolith to the HP Moldanubian granulites seem to have been largely accessible to, and dissolved in, the low-degree HP melt.

The 1D thermal modelling has demonstrated that, for radioactive heat production of 4 μW m^{-3}, the temperature threshold of 900 °C would be reached in deeply buried crust after 7 Myr (at 70 km) to 15 Myr (at 60 km). A radioactive heat production of 4 μW m^{-3} is similar to the average radioactive heat production at *c.* 340 Ma calculated for the Fichtelgebirge metaigneous crust, which is considered to correspond to the most appropriate protolith of felsic granulites (Janoušek & Holub, 2007). Moreover, the modelling shows that heat necessary for crustal melting indeed could have been produced internally, within the time frame allowed by the available geochronological data (5–15 Myr).

The heat source located at lower crustal depths would also lead eventually to partial melting of the underlying metasomatized and hydrated subcrustal mantle lithosphere. Melting of such an anomalous and fertile mantle source could have produced, soon after the HP metamorphic peak, ultrapotassic rocks with mixed crustal–mantle signatures. The effective removal of U and Th from the partially molten felsic metaigneous rocks (future felsic granulites) by melt extraction would have grave consequences for the thermal evolution of the whole system. First, the depletion of radioactive elements from the granulite means that the melting process must have rapidly switched off. Second, the extracted melts could have partly mixed with enriched mantle-derived ultrapotassic magmas, which invaded the overlying partially molten crust, contributing to their further enrichment by U and Th.

However, this mixing was probably volumetrically rather insignificant and essentially different from another, large-scale hybridization event with S-type leucogranitic magmas assumed for the durbachite series in Bohemia (Holub, 1997) and the Rastenberg suite in Lower Austria (Gerdes *et al.*, 2000). The hybrid magmas finally intruded syn-tectonically or post-tectonically at mid- to high-crustal levels in close spatial and temporal association with the HP granulite and orthogneiss complexes so typical of the Variscan orogenic crust in the Moldanubian domain of the Bohemian Massif (Schulmann *et al.*, 2005; Žák *et al.*, 2005; Tajčmanová *et al.*, 2006; Janoušek & Holub, 2007).

Gravity overturns and 340 Ma crustal redistribution in the Bohemian Massif

Gerya *et al*. (2001, 2002) in their pioneering work proposed a model of gravity redistribution of granodioritic rocks and overlying mafic crust using radioactive heat production localized in granodioritic crust. This progressive heating of the FLC leads to its viscosity drop and density decrease triggering diapiric process. However, the time-scales required for gravity overturns proposed by these authors are not compatible with those reported for the Variscan orogeny (discussed before; see also Schulmann *et al*., 2009). Therefore, the temperature increase must have been significantly more radical and density contrasts higher than those predicted by Gerya *et al*. (2002, 2004). This is consistent with the gravity inversion modelling results of Guy *et al*. (2010) who have shown that the density contrast between residual FLC and an overlying thick gabbroic layer (Fig. 3) may be greater than that estimated by Gerya *et al*. (2001). Moreover, an additional source of gravity potential may be seen in the presence of eclogites in the thickened Ordovician–Silurian AGB layer (50–60 km), overlying the felsic crust at a depth of 60–70 km (Štípská & Powell, 2005a,b).

The scenario presented here (Fig. 11d) resembles the explanation of the formation of migmatitic domes in hot orogenic belts driven by gravitational collapse of thickened continental crust (Rey *et al*., 2001; Vanderhaeghe & Teyssier, 2001; Vanderhaeghe, 2009). All these conceptual models suggest partial melting of the lower crust to be a trigger mechanism for development of gravitational instability in both fossil and modern orogenic belts. The main difference of our model is in quantification of the gravitational instability, the rate of the heating and also the rate of the development of the diapiric structures. The initial position of less dense but highly radioactive felsic material below more dense mafic lower crust seems to be the necessary prerequisite for driving the tectonic evolution of the Variscan orogeny in the Bohemian Massif. Importantly, in our numerical models, the development of granulite domes is caused solely by gravitational instability. However, the structural data suggest that domes are initiated by folding of the lower and mid-crustal interfaces (e.g. Štípská *et al*., 2004; Schulmann *et al*., 2005) and the linear distribution of elongate granulite belts indicates that lateral shortening was an important component (Burg *et al*., 2004) related to the growth of granulite domes (Fig. 11d). Therefore, the combination of gravity and laterally forced extrusion of orogenic crust may lead to a development of gravity overturns more rapidly compared with the numerical models presented herein.

Our work shows that only a model of internal heating to drive the tectonic and gravity redistribution of orogenic lower crust can satisfactorily explain the temporarily restricted orogenic event at *c*. 340 Ma, which is responsible for most of the Variscan tectonothermal events reported so far in the Bohemian Massif. Thus, the timing of growth of these laterally forced diapirs seems to be connected with orogenic collapse and the major plate reorganization of the whole Variscan belt (Edel *et al*., 2003). The co-existence of *c*. 340 Ma ultrapotassic plutons and extruded felsic HP granulites thus defines a key thermomechanical event, which probably signified a rheological collapse of the whole Variscan belt in Europe (e.g. Rossi *et al*., 2009; Rubatto *et al*., 2010).

CONCLUSIONS

The exhumation of *c*. 340 Ma felsic granulites in the Bohemian Massif is interpreted in terms of tectonically triggered gravity redistribution of felsic orogenic lower crust and high density mafic crust. The model shows that radioactive heat production of 4 μW m^{-3} for lower crustal rocks, which is corroborated by calculated values from likely protolith rocks, and the calculated *P–T–t* evolution satisfy the thermal and geochronological evolution of the Bohemian Massif granulites. This radioactive heat production is typical of Ordovician felsic igneous rocks in the Fichtelgebirge (Saxothuringian domain), which are believed to have been relaminated at the bottom of thickened continental crust during the early Viséan continental underthrusting. The mutually complementary geochemical characteristics of granulites and ultrapotassic magmas highlight the shared thermomechanical history governed by radioactive heating of the lower crustal layer, culminating in partial melting of both the felsic lower crustal layer itself and its underlying fertile (metasomatized/contaminated) mantle lithosphere. Gravity-driven redistribution tectonics initiated by internal heating is interpreted to be the principal agent controlling the rheological collapse of the Variscan orogenic crust at *c*. 340 Ma.

ACKNOWLEDGEMENTS

We acknowledge grant MSM0021620855 from the Ministry of Education of the Czech Republic and internal research funds from CNRS UMR 7615 for salary and research support of Ondrej Lexa, and the French National Science Foundation ANR project 'LFO in orogens' for additional research support. We thank C. Clark and T. Gerya for their thorough reviews and highly appreciate the comments and suggestions, which significantly contributed to improving the quality of the publication. M. Brown is acknowledged for careful editorial work.

APPENDIX

Governing equations used for numerical modelling of gravity overturns

To simulate the thermal evolution, we use a numerical model based on the solution of the coupled equations

of momentum (Eqn A.1) and energy (Eqn A.3), subject to an incompressibility constraint (Eqn A.2) known as the Boussinesq approximation (Hansen & Yuen, 2000):

$$\frac{\partial \sigma_{ij}}{\partial x_i} = \frac{\partial P}{\partial x_i} - \rho g_i, \tag{A.1}$$

$$\frac{\partial v_i}{\partial x_i} = 0, \tag{A.2}$$

$$\frac{\partial T}{\partial t} + v_i \frac{\partial T}{\partial x_i} = \frac{1}{\rho C_\mathrm{p}} \frac{\partial}{\partial x_i} \kappa \rho C_\mathrm{p} \frac{\partial T}{\partial x_i} + \frac{A}{\rho C_\mathrm{p}}, \tag{A.3}$$

where x denotes the coordinates in m, v velocity in m s^{-1}, t time in s; σ_{ij} is stress tensor, P is pressure in Pa, g is gravitational acceleration (9.81 m s^{-2}), T is temperature in K, κ denotes thermal diffusivity and C_p denotes the specific heat capacity. The constitutive relationship between stress and strain is governed by the transport coefficient η representing viscosity:

$$\sigma_{ij} = 2\eta \dot{\varepsilon}_{ij}, \tag{A.4}$$

where $\dot{\varepsilon}_{ij}$ is the strain-rate tensor in s^{-1}. For the purpose of this work, we used a simplified flow law with only temperature-dependent viscosity according to the simple exponential equation:

$$\eta = C_1 \mathrm{e}^{\left(\frac{C_2}{T}\right)}, \tag{A.5}$$

where C_1 and C_2 are coefficients used to calculate effective viscosity from prescribed range (see Table 2). Density ρ is given by equation of state:

$$\rho = \rho_0[1 - \alpha(T - T_0)], \tag{A.6}$$

where α is the coefficient of thermal expansion and ρ_0 is the reference density at reference temperature T_0. Thermal diffusivity κ and specific heat capacity C_p are recalculated according to temperature using the following equations (Whittington *et al.*, 2009):

$$\kappa = 3.19 \times 10^{-7} + 1.214 \times 10^{-6} \mathrm{e}^{\left(\frac{273.15-T}{285.2}\right)}, \tag{A.7}$$

$$C_\mathrm{p} = 1538.39 - \frac{3.224 \times 10^5}{T} + \frac{2.714 \times 10^7}{T^2}, \tag{A.8}$$

derived from laser-flash analysis to provide realistic values for geologically relevant temperatures. These equations are solved for temperature and velocity and describe the fundamental physics required for modelling the thermal evolution during crustal diapirism.

Calculation methods used for thermodynamic modelling

The pseudosections were calculated using THERMOCALC 3.30 (Powell *et al.*, 1998) and the data set 5.5 (Holland & Powell, 1998; November 2003 upgrade), in the system Na_2O–CaO–K_2O–FeO–MgO–Al_2O_3–SiO_2–H_2O–TiO_2–O (NCKFMASHTO) with the biotite and melt models from White *et al.* (2007), garnet from Diener *et al.* (2008), ilmenite from White *et al.* (2000), feldspar from Holland & Powell (2003), white mica from Coggon & Holland (2002) and cordierite from THERMOCALC documentation (Powell & Holland, 2004). The analysed rock composition of sample H296 (in wt% $SiO_2 = 71.98$, $TiO_2 = 0.42$, $Al_2O_3 = 13.53$, FeO = 2.1, MnO = 0.03, MgO = 0.73, CaO = 1.93, $Na_2O = 2.76$, $K_2O = 4.01$, $P_2O_5 = 0.15$, $H_2O^- = 0.22$, $H_2O^+ = 0.56$, $CO_2 = 0.03$), was modified for modelling by adding 1 mol.% of kyanite to enable a small amount of aluminosilicate to be stable at the estimated peak metamorphic conditions, as is observed in thin section.

The reconstruction of a biotite–muscovite granite protolith requires several steps. It involves determination of the H_2O content in the final assemblage, consideration of open-system behaviour with respect to melt, and modification of the whole-rock composition by adding melt (White & Powell, 2002; White *et al.*, 2004; Štípská *et al.*, 2008). Tracking of the *P–T* path is therefore undertaken backwards in time, from the matrix assemblage to the early prograde evolution and to the protolith mineralogical composition. The amount of H_2O for the modelling shown in Fig. 12a is set such that it allows the stability of the observed matrix assemblage with garnet rim chemistry on cooling (not shown; see Franěk *et al.*, 2011b; see Hasalová *et al.*, 2008b for the approach followed). As the whole-rock composition is expected to change along the *P–T* path as a result of loss of melt, it has to be decided from which point on the *P–T* path the melt composition will be taken. Crossing the upper stability of muscovite causes an abrupt increase in melt proportion and is considered a likely condition for melt loss (White & Powell, 2002; White *et al.*, 2004); therefore, melt composition reintegrated was undertaken at 16 kbar and 860 °C.

REFERENCES

Ackerman, L., Jelínek, E., Medaris, G., Ježek, J., Siebel, W. & Strnad, L., 2009. Geochemistry of Fe-rich peridotites and associated pyroxenites from Horní Bory, Bohemian Massif: insights into subduction-related melt-rock reactions. *Chemical Geology*, **259,** 152–167.

Aftalion, M., Bowes, D. & Vrána, S., 1989. Early Carboniferous U-Pb zircon age for garnetiferous, perpotassic granulites, Blanský les massif, Czechoslovakia. *Neues Jahrbuch für Mineralogie-Monatshefte*, **4,** 145–152.

Avouac, J.P., 2008. Dynamic processes in extensional and compressional settings – mountain building: from earthquakes to geological deformation. In: *Treatise on Geophysics, Volumes 1-11* (ed. Schubert, G.), pp. 377–439. Elsevier, Amsterdam.

Babuška, V., Fiala, J. & Plomerová, J., 2010. Bottom to top lithosphere structure and evolution of western Eger Rift (Central Europe). *International Journal of Earth Sciences*, **99,** 891–907.

Bea, F., 1996. Residence of REE, Y, Th and U in granites and crustal protoliths; implications for the chemistry of crustal melts. *Journal of Petrology*, **37,** 521–552.

Becker, H., Wenzel, T. & Volker, F., 1999. Geochemistry of glimmerite veins in peridotites from Lower Austria – implications for the origin of K-rich magmas in collision zones. *Journal of Petrology*, **40,** 315–338.

Behr, H., 1978. Subfluenz-Prozesse im Grundgebirgs-Stockwerk Mitteleuropas. *Zeitschrift der Deutschen Gesellschaft für Geowissenschaften*, **129,** 283–318.

Burg, J.-P., Van Den Driessche, J. & Brun, J.-P., 1994. Syn-to post-thickening extension in the Variscan Belt of Western Europe: modes and structural consequences. *Géologie de la France*, **3,** 33–51.

Burg, J.-P., Kaus, B. & Podladchikov, Y., 2004. Dome structures in collision orogens. Mechanical investigation of the gravity/compression interplay. In: *Gneiss Domes in Orogeny*, Vol. 380 (eds Whitney, D.L., Teyssier, C. & Siddoway, C.S.), pp. 47–66, Geological Society of America Special Papers, Boulder, Colorado.

Chemenda, A., Burg, J.-P. & Mattauer, M., 2000. Evolutionary model of the Himalaya–Tibet system: geopoem based on new modelling, geological and geophysical data. *Earth and Planetary Science Letters*, **174,** 397–409.

Coggon, R. & Holland, T.J.B., 2002. Mixing properties of phengitic micas and revised garnet–phengite thermobarometers. *Journal of Metamorphic Geology*, **20,** 683–696.

Cooke, R. & O'Brien, P.J., 2001. Resolving the relationship between high P–T rocks and gneisses in collisional terranes: an example from the Gföhl gneiss–granulite association in the Moldanubian Zone, Austria. *Lithos*, **58,** 33–54.

Dewey, J.F., Ryan, P.D. & Andersen, T.B., 1993. Orogenic uplift and collapse, crustal thickness, fabrics and metamorphic phase changes: the role of eclogites. In: *Magmatic Processes and Plate Tectonics*, Vol. 76 (eds Prichard, H.M., Alabaster, T., Harris, N.B.W. & Neary, C.R.), pp. 325–343, Geological Society, Special Publications, London.

Diener, J.F.A., Powell, R. & White, R.W., 2008. Quantitative phase petrology of cordierite–orthoamphibole gneisses and related rocks. *Journal of Metamorphic Geology*, **26,** 795–814.

Dörr, W. & Zulauf, G., 2010. Elevator tectonics and orogenic collapse of a Tibetan-style plateau in the European Variscides: the role of the Bohemian shear zone. *International Journal of Earth Sciences*, **99,** 299–325.

Edel, J.B., Schulmann, K. & Holub, F.V., 2003. Anticlockwise and clockwise rotations of the Eastern Variscides accommodated by dextral lithospheric wrenching: palaeomagnetic and structural evidence. *Journal of the Geological Society*, **160,** 209–218.

England, P.C. & Thompson, A.B., 1984. Pressure temperature time paths of regional metamorphism. 1. Heat-transfer during the evolution of regions of thickened continental crust. *Journal of Petrology*, **25,** 894–928.

Fiala, J., Matějovská, O. & Vaňková, V., 1987a. Moldanubian granulites and related rocks: petrology, geochemistry and radioactivity. *Rozpravy Československé Akademie Věd, Řada Matematických a Přírodních Věd*, **97,** 1–102.

Fiala, J., Matějovská, O. & Vaňková, V., 1987b. Moldanubian granulites: source material and petrogenetic considerations. *Neues Jahrbuch für Mineralogie, Abhandlungen*, **157,** 133–165.

Finger, F. & Cooke, R., 2004. Evidence for the presence of a trace-element-loaded interstitial partial melt in a Moldanubian leucocratic granulite derived from LA-ICP-MS analyses on zircons and rutiles. In: *International Workshop on Petrogenesis of Granulites and Related Rocks, Náměšť nad Oslavou, October 1-3, 2004. Excursion Guide & Abstract Volume* (ed. Janoušek, V.), pp. 35–36. Moravian Museum, Brno.

Finger, F. & von Quadt, A., 1995. U/Pb ages of zircons from a plagiogranite-gneiss in the south-eastern Bohemian Massif, Austria-further evidence for an important early Paleozoic rifting episode in the eastern Variscides. *Schweizerische Mineralogische und Petrographische Mitteilungen*, **75,** 265–270.

Finger, F., Gerdes, A., Janoušek, V., René, M. & Riegler, G., 2007. Resolving the Variscan evolution of the Moldanubian sector of the Bohemian Massif: the significance of the Bavarian and the Moravo–Moldanubian tectonometamorphic phases. *Journal of Geosciences*, **52,** 9–28.

Franěk, J., Schulmann, K. & Lexa, O., 2006. Kinematic and rheological model of exhumation of high pressure granulites in the Variscan orogenic root: example of the Blanský les granulite, Bohemian Massif, Czech Republic. *Mineralogy and Petrology*, **86,** 253–276.

Franěk, J., Schulmann, K., Lexa, O., Tomek, Č. & Edel, J.-B., 2011a. Model of syn-convergent extrusion of orogenic lower crust in the core of the Variscan belt: implications for exhumation of high-pressure rocks in large hot orogens. *Journal of Metamorphic Geology*, **29,** 53–78.

Franěk, J., Schulmann, K., Lexa, O. *et al.*, 2011b. The precursor of Variscan felsic granulites, process of its granulitization, and inversed rheology of feldspars and quartz in the lower-crustal conditions. *Journal of Metamorphic Geology*, **29,** 103–130.

Franke, W., 2000. The mid-European segment of the Variscides: tectonostratigraphic units, terrane boundaries and plate tectonic evolution. *Geological Society, London, Special Publications*, **179,** 35–61.

Friedl, G., Finger, F., Paquette, J.-L., von Quadt, A., McNaughton, N.J. & Fletcher, I.R., 2004. Pre-Variscan geological events in the Austrian part of the Bohemian Massif deduced from U–Pb zircon ages. *International Journal of Earth Sciences*, **93,** 802–823.

Fuchs, G., 1976. Zur Entwicklung der Böhmischen Masse. *Jahrbuch der Geologischen Bundesanstalt*, **129,** 41–49.

Gerdes, A., Worner, G. & Finger, F., 2000. Hybrids, magma mixing and enriched mantle melts in post-collisional Variscan granitoids: the Rastenberg Pluton, Austria. In: *Orogenic Processes: Quantification and Modelling in the Variscan Fold Belt*, Vol. 179 (eds Franke, W., Haak, V., Oncken, O. & Tanner, D.), pp. 415–431, Geological Society, Special Publications, London.

Gerya, T. & Yuen, D.A., 2003. Characteristics-based marker-in-cell method with conservative finite-differences schemes for modeling geological flows with strongly variable transport properties. *Physics of the Earth and Planetary Interiors*, **140,** 293–318.

Gerya, T., Maresch, W., Willner, A., Van Reenen, D. & Smit, C., 2001. Inherent gravitational instability of thickened continental crust with regionally developed low-to medium-pressure granulite facies metamorphism. *Earth and Planetary Science Letters*, **190,** 221–235.

Gerya, T., Perchuk, L., Maresch, W., Willner, A., Van Reenen, D. & Smit, C., 2002. Thermal regime and gravitational instability of multi-layered continental crust: implications for the buoyant exhumation of high-grade metamorphic rocks. *European Journal of Mineralogy*, **14,** 687–699.

Gerya, T.V., Perchuk, L.L., Maresch, W.V. & Willner, A.P., 2004. Inherent gravitational instability of hot continental crust: implications for doming and diapirism in granulite facies terrains. In: *Gneiss Domes in Orogeny*, Vol. 380 (eds Whitney, D.L., Teyssier, C. & Siddoway, C.S.), pp. 97–115, Geological Society of America, Special Papers, Boulder, Colorado.

Guy, A., Edel, J.-B., Schulmann, K., Tomek, Č. & Lexa, O., 2010. A geophysical model of the Variscan orogenic root (Bohemian Massif): Implications for modern collisional orogens. *Lithos*, in press. doi:10.1016/j.lithos.2010.08.008.

Hacker, B.R., Kelemen, P.B. & Behn, M.D., 2007. Continental relamination drives compositional and physical-property changes in the lower crust, Eos Trans. AGU, 88, Fall Meeting Suppl., Abstract V32A-06.

Hansen, U. & Yuen, D.A., 2000. Extended-Boussinesq thermal-chemical convection with moving heat sources and variable viscosity. *Earth and Planetary Science Letters*, **176,** 401–411.

Hasalová, P., Schulmann, K., Lexa, O. *et al.*, 2008a. Origin of migmatites by deformation-enhanced melt infiltration of orthogneiss: a new model based on quantitative microstructural analysis. *Journal of Metamorphic Geology*, **26,** 29–53.

Hasalová, P., Štípská, P., Powell, R., Schulmann, K., Janoušek, V. & Lexa, O., 2008b. Transforming mylonitic metagranite by open-system interactions during melt flow. *Journal of Metamorphic Geology*, **26,** 55–80.

HeténYi, G., Cattin, R., Brunet, F. *et al*., 2007. Density distribution of the India plate beneath the Tibetan plateau: geophysical and petrological constraints on the kinetics of lower-crustal eclogitization. *Earth and Planetary Science Letters*, **264,** 226–244.

Holland, T.J.B. & Powell, R., 1998. An internally consistent thermodynamic data set for phases of petrological interest. *Journal of Metamorphic Geology*, **16,** 309–343.

Holland, T.J.B. & Powell, R., 2003. Activity–composition relations for phases in petrological calculations: an asymmetric multicomponent formulation. *Contributions to Mineralogy and Petrology*, **145,** 492–501.

Holub, F.V., 1997. Ultrapotassic plutonic rocks of the durbachite series in the Bohemian Massif: petrology, geochemistry and petrogenetic interpretation. *Journal of Geological Sciences-Economic Geology, Mineralogy*, **31,** 5–26.

Holub, F.V., Cocherie, A. & Rossi, P., 1997. Radiometric dating of granitic rocks from the Central Bohemian Plutonic Complex (Czech Republic): constraints on the chronology of thermal and tectonic events along the Moldanubian–Barrandian boundary. *Comptes Rendus de l'Academie des Sciences Series IIA Earth and Planetary Science*, **325,** 19–26.

Hrubcová, P., Środa, P., Špičák, A. *et al*., 2005. Crustal and uppermost mantle structure of the Bohemian Massif based on CELEBRATION 2000 data. *Journal of Geophysical Research-Solid Earth*, **110**(B11)**,** B11305.

Jakeš, P., 1997. Melting in high-P region – case of Bohemian granulites. *Acta Universitatis Carolinae Geologica*, **41,** 113–125.

Janoušek, V., 2006. *Saturnin*, R language script for application of accessory-mineral saturation models in igneous geochemistry. *Geologica Carpathica*, **57,** 131–142.

Janoušek, V. & Holub, F.V., 2007. The causal link between HP/HT metamorphism and ultrapotassic magmatism in collisional orogens: case study from the Moldanubian Zone of the Bohemian Massif. *Proceedings of the Geologists' Association*, **118,** 75–86.

Janoušek, V., Rogers, G. & Bowes, D.R., 1995. Sr-Nd isotopic constraints on the petrogenesis of the Central Bohemian Pluton, Czech Republic. *Geologische Rundschau*, **84,** 520–534.

Janoušek, V., Holub, F.V. & Gerdes, A., 2003. K-rich magmatism in the Moldanubian Unit, Bohemian Massif – a complex story featuring variably enriched lithospheric mantle melts and their Interaction with the crust. *Geolines*, **16,** 48–49.

Janoušek, V., Braithwaite, C.J.R., Bowes, D.R. & Gerdes, A., 2004a. Magma-mixing in the genesis of Hercynian calc-alkaline granitoids: an integrated petrographic and geochemical study of the Sázava intrusion, Central Bohemian Pluton, Czech Republic. *Lithos*, **78,** 67–99.

Janoušek, V., Finger, F., Roberts, M., Frýda, J., Pin, C. & Dolejš, D., 2004b. Deciphering the petrogenesis of deeply buried granites: whole-rock geochemical constraints on the origin of largely undepleted felsic granulites from the Moldanubian Zone of the Bohemian Massif. *Transactions of the Royal Society of Edinburgh, Earth Sciences*, **95,** 141–159.

Janoušek, V., Gerdes, A., Vrána, S. *et al*., 2006. Low-pressure granulites of the Lišov Massif, Southern Bohemia: Viséan metamorphism of late Devonian plutonic arc rocks. *Journal of Petrology*, **47,** 705–744.

Janoušek, V., Krenn, E., Finger, F., Míková, J. & Frýda, J., 2007. Hyperpotassic granulites from Blanský les (Moldanubian Zone, Bohemian Massif) revisited. *Journal of Geosciences*, **52,** 73–112.

Janoušek, V., Vrána, S., Erban, V., Vokurka, K. & Drábek, M., 2008. Metabasic rocks in the Varied Group of the Moldanubian Zone, southern Bohemia – their petrology, geochemical character and possible petrogenesis. *Journal of Geosciences*, **53,** 31–64.

Janoušek, V., Wiegand, B.A. & Žák, J., 2010. Dating the onset of Variscan crustal exhumation in the core of the Bohemian Massif: new U–Pb single zircon ages from the high-K calc-alkaline granodiorites of the Blatná suite, Central Bohemian Plutonic Complex. *Journal of the Geological Society*, **167,** 347–360.

Košler, J., Aftalion, M. & Bowes, D.R., 1993. Mid–late Devonian plutonic activity in the Bohemian Massif: U–Pb zircon isotopic evidence from the Staré Sedlo and Mirotice gneiss complexes, Czech Republic. *Neues Jahrbuch für Mineralogie-Monatshefte*, **1993,** 417–431.

Kotková, J. & Harley, S., 1999. Formation and evolution of high-pressure leucogranulites: experimental constraints and unresolved issues. *Physics and Chemistry of the Earth, Part A*, **24,** 299–304.

Kotková, J., Schaltegger, U. & Leichmann, J., 2010. Two types of ultrapotassic plutonic rocks in the Bohemian Massif – coeval intrusions at different crustal levels. *Lithos*, **115,** 163–176.

Kramers, J., Kreissig, K. & Jones, M., 2001. Crustal heat production and style of metamorphism: a comparison between two Archean high grade provinces in the Limpopo Belt, southern Africa. *Precambrian Research*, **112,** 149–163.

Kröner, A., O'Brien, P.J., Nemchin, A. & Pidgeon, R., 2000. Zircon ages for high pressure granulites from South Bohemia, Czech Republic, and their connection to Carboniferous high temperature processes. *Contributions to Mineralogy and Petrology*, **138,** 127–142.

Kusiak, M., Dunkley, D., Suzuki, K. *et al*., 2010. Chemical (non-isotopic) and isotopic dating of Phanerozoic zircon – a case study of durbachite from the Třebíč Pluton, Bohemian Massif. *Gondwana Research*, **17,** 153–161.

Le Pichon, X., Henry, P. & Goffé, B., 1997. Uplift of Tibet: from eclogites to granulites – implications for the Andean Plateau and the Variscan belt. *Tectonophysics*, **273,** 57–76.

Medaris, L.G., Jelínek, E. & Mísař, Z., 1995. Czech eclogites. Terrane settings, interpretation for Variscan tectonic evolution of the Bohemian Massif. *European Journal of Mineralogy*, **7,** 7–28.

Mlčoch, B. & Konopásek, J., 2010. Pre-late Carboniferous geology along the contact of the Saxothuringian and Teplá–Barrandian zones in the area covered by younger sediments and volcanics (western Bohemian Massif, Czech Republic). *Journal of Geosciences*, **55,** 81–94.

O'Brien, P.J., 2000. The fundamental Variscan problem: high-temperature metamorphism at different depths and high-pressure metamorphism at different temperatures. In: *Orogenic Processes: Quantification and Modelling in the Variscan Belt*, Vol. 179 (eds Franke, W., Haak, V., Oncken, O. & Tanner, D.), pp. 369–386, Geological Society, Special Publications, London.

O'Brien, P.J. & Rötzler, J., 2003. High-pressure granulites: formation, recovery of peak conditions and implications for tectonics. *Journal of Metamorphic Geology*, **21,** 3–20.

O'Brien, P.J. & Vrána, S., 1995. Eclogites with a short-lived granulite-facies overprint in the Moldanubian Zone, Czech Republic – petrology, geochemistry and diffusion modeling of garnet zoning. *Geologische Rundschau*, **84,** 473–488.

Oncken, O., Hindle, D., Kley, J., Elger, K., Victor, P. & Schemmann, K., 2006. Deformation of the Central Andean upper plate system – facts, fiction, and constraints for plateau models. In: *The Andes–Active Subduction Orogeny* (eds Oncken, O., Chong, G., Franz, G., Giese, P., Götze, H.-J., Ramos, V.A., Strecker, M.R. & Wigger, P.), pp. 3–27, Springer-Verlag, Heidelberg.

Pearce, J. & Stern, R., 2006. Origin of back-arc basin magmas: trace element and isotope perspectives. In: *Back-Arc Spreading Systems: Geological, Biological, Chemical, and Physical Interactions* (eds Christie, D.M., Fisher, C.R., Lee, S.-M. & Givens, S.), pp. 63–86, American Geophysical Union, Geophysical Monograph Series 166, Washington.

Perchuk, L., 1989. P–T–fluid regimes of metamorphism and related magmatism with specific reference to the granulite-

facies Sharyzhalgay complex of Lake Baikal. In: *Evolution of Metamorphic Belts* (eds Daly, J.S., Cliff, R.A. & Yardley, B.W.D.), pp. 275–292, 43, Blackwell Scientific Publications, Oxford.

Petrakakis, K., 1997. Evolution of Moldanubian rocks in Austria: review and synthesis. *Journal of Metamorphic Geology*, **15,** 203–222.

Pitra, P., Burg, J.-P. & Guiraud, M., 1999. Late Variscan strike-slip tectonics between the Tepla-Barrandian and Moldanubian terranes (Czech Bohemian Massif): petrostructural evidence. *Journal of the Geological Society, London*, **156,** 1003–1020.

Plesch, A. & Oncken, O., 1999. Orogenic wedge growth during collision – constraints on mechanics of a fossil wedge from its kinematic record (Rhenohercynian FTB, Central Europe). *Tectonophysics*, **309,** 117–139.

Powell, R. & Holland, T.J.B., 2004. *Course Notes for "THERMOCALC Workshop 2004: Calculating Metamorphic Phase Equilibria" (CD ROM)*. ETH, Zürich.

Powell, R., Holland, T.J.B. & Worley, B., 1998. Calculating phase diagrams involving solid solutions via non-linear equations, with examples using THERMOCALC. *Journal of Metamorphic Geology*, **16,** 577–588.

Prince, C.I., Košler, J., Vance, D. & Günther, D., 2000. Comparison of laser ablation ICP-MS and isotope dilution REE analyses – implications for Sm-Nd garnet geochronology. *Chemical Geology*, **168,** 255–274.

Racek, M., Štípská, P., Pitra, P., Schulmann, K. & Lexa, O., 2006. Metamorphic record of burial and exhumation of orogenic lower and middle crust: a new tectonothermal model for the Drosendorf window (Bohemian Massif, Austria). *Mineralogy and Petrology*, **86,** 221–251.

Racek, M., Štípská, P. & Powell, R., 2008. Garnet–clinopyroxene intermediate granulites in the St. Leonhard massif of the Bohemian Massif: ultrahigh-temperature metamorphism at high pressure or not? *Journal of Metamorphic Geology*, **26,** 253–271.

Ramberg, H., 1981. *Gravity Deformation and the Earth's Crust: In Theory, Experiments, and Geological Application*. Academic Press, London.

Rey, P., Vanderhaeghe, O. & Teyssier, C., 2001. Gravitational collapse of the continental crust: definition, regimes and modes. *Tectonophysics*, **342,** 435–449.

Roberts, M. & Finger, F., 1997. Do U–Pb zircon ages from granulites reflect peak metamorphic conditions? *Geology*, **25,** 319–322.

Roering, C., Van Reenen, D., Smit, C. *et al*., 1992. Tectonic model for the evolution of the Limpopo Belt. *Precambrian Research*, **55,** 539–552.

Rossi, P., Oggiano, G. & Cocherie, A., 2009. A restored section of the 'southern Variscan realm' across the Corsica-Sardinia microcontinent. *Comptes Rendus Geosciences*, **341,** 224–238.

Rubatto, D., Ferrando, S., Compagnoni, R. & Lombardo, B., 2010. Carboniferous high-pressure metamorphism of Ordovician protoliths in the Argentera Massif (Italy), Southern European Variscan belt. *Lithos*, **116,** 65–76.

Rudnick, R.L. & Gao, S., 2003. Composition of the Continental Crust. In: *Treatise on Geochemistry* (eds Holland, H.D. & Turekian, K.K.), pp. 1–64. Pergamon, Oxford.

Rudnick, R.L. & Presper, T., 1990. Geochemistry of intermediate- to high-pressure granulites. In: *Granulites and Crustal Evolution* (eds Vielzeuf, D. & Vidal, P.), pp. 523–550. Kluwer Academic Publishers, Dordrecht.

Růžek, B., Hrubcová, P., Novotný, M., Špičák, A. & Karousová, O., 2007. Inversion of travel times obtained during active seismic refraction experiments CELEBRATION 2000, ALP 2002 and SUDETES 2003. *Studia Geophysica et Geodaetica*, **51,** 141–164.

Scheuvens, D., 2002. Metamorphism and microstructures along a high-temperature metamorphic field gradient: the north–eastern boundary of the Královský Hvozd Unit (Bohemian Massif, Czech Republic). *Journal of Metamorphic Geology*, **20,** 413–428.

van Schmus, W., 1995. Natural radioactivity of the crust and mantle. In: *Global Earth Physics: A Handbook of Physical Constants* (ed. Ahrens, T.J.), pp. 283–291. American Geophysical Union, AGU Reference Shelf Series, Washington, DC.

Schulmann, K., Kröner, A., Hegner, E. *et al*., 2005. Chronological constraints on the pre-orogenic history, burial and exhumation of deep-seated rocks along the eastern margin of the Variscan orogen, Bohemian Massif, Czech Republic. *American Journal of Science*, **305,** 407–448.

Schulmann, K., Lexa, O., Štípská, P. *et al*., 2008. Vertical extrusion and horizontal channel flow of orogenic lower crust: key exhumation mechanisms in large hot orogens? *Journal of Metamorphic Geology*, **26,** 273–297.

Schulmann, K., Konopásek, J., Janoušek, V. *et al*., 2009. An Andean type Palaeozoic convergence in the Bohemian Massif. *Comptes Rendus-Géoscience*, **341,** 266–286.

Siebel, W., Raschka, H., Irber, W. *et al*., 1997. Early Palaeozoic acid magmatism in the Saxothuringian belt: new insights from a geochemical and isotopic study of orthogneisses and metavolcanic rocks from the Fichtelgebirge, SE Germany. *Journal of Petrology*, **38,** 203–230.

Sláma, J., Košler, J., Condon, D. *et al*., 2008. Plešovice zircon – a new natural reference material for U–Pb and Hf isotopic microanalysis. *Chemical Geology*, **249,** 1–35.

Štípská, P. & Powell, R., 2005a. Constraining the P-T path of a MORB-type eclogite using pseudosections, garnet zoning and garnet-clinopyroxene thermometry: an example from the Bohemian Massif. *Journal of Metamorphic Geology*, **23,** 725–743.

Štípská, P. & Powell, R., 2005b. Does ternary feldspar constrain the metamorphic conditions of high-grade meta-igneous rocks? Evidence from orthopyroxene granulites, Bohemian Massif *Journal of Metamorphic Geology*, **23,** 627–647.

Štípská, P., Schulmann, K. & Kröner, A., 2004. Vertical extrusion and middle crustal spreading of omphacite granulite: a model of syn-convergent exhumation (Bohemian Massif, Czech Republic). *Journal of Metamorphic Geology*, **22,** 179–198.

Štípská, P., Schulmann, K. & Powell, R., 2008. Contrasting metamorphic histories of lenses of high-pressure rocks and host migmatites with a flat orogenic fabric (Bohemian Massif, Czech Republic): a result of tectonic mixing within horizontal crustal flow? *Journal of Metamorphic Geology*, **26,** 623–646.

Tajčmanová, L., Konopásek, J. & Schulmann, K., 2006. Thermal evolution of the orogenic lower crust during exhumation within a thickened Moldanubian root of the Variscan belt of Central Europe. *Journal of Metamorphic Geology*, **24,** 119–134.

Tajčmanová, L., Soejono, I., Konopásek, J., Košler, J. & Klötzli, U., 2010. Structural position of high-pressure felsic to intermediate granulites from NE Moldanubian domain (Bohemian Massif). *Journal of the Geological Society*, **167,** 329–345.

Tomek, Č., Dvořáková, V. & Vrána, S., 1997. Geological interpretation of the 9HR and 503M seismic profiles in western Bohemia. In: *Geological Model of Western Bohemia Related to the KTB Borehole in Germany* (eds Vrána, S. & Štědrá, V.), pp. 43–50, *Journal of Geological Sciences, Geology*, **47,** Prague.

Vanderhaeghe, O., 2009. Migmatites, granites and orogeny: flow modes of partially-molten rocks and magmas associated with melt/solid segregation in orogenic belts. *Tectonophysics*, **477,** 119–134.

Vanderhaeghe, O. & Teyssier, C., 2001. Partial melting and flow of orogens. *Tectonophysics*, **342,** 451–472.

Vellmer, C., 1992. *Stoffbestand und Petrogenese von Granuliten und Granitischen Gesteinen der Südlichen Böhmischen Masse in Niederösterreich*. Unpublished PhD thesis, Georg-August-Universität, Göttingen.

Venera, Z., Schulmann, K. & Kröner, A., 2000. Intrusion within a transtensional tectonic domain: the Čistá granodiorite

(Bohemian Massif) – structure and rheological modelling. *Journal of Structural Geology*, **22,** 1437–1454.
Verner, K., Žák, J., Nahodilová, R. & Holub, F., 2008. Magmatic fabrics and emplacement of the cone-sheet-bearing Knížecí Stolec durbachitic pluton (Moldanubian Unit, Bohemian Massif): implications for mid-crustal reworking of granulitic lower crust in the Central European Variscides. *International Journal of Earth Sciences*, **97,** 19–33.
Vigneresse, J., Barbey, P. & Cuney, M., 1996. Rheological transitions during partial melting and crystallization with application to felsic magma segregation and transfer. *Journal of Petrology*, **37,** 1879–1600.
Vrána, S., 1989. Perpotassic granulites from southern Bohemia. *Contributions to Mineralogy and Petrology*, **103,** 510–522.
Vrána, S. & Jakeš, P., 1982. Orthopyroxene and two-pyroxene granulites from a segment of charnockitic crust in southern Bohemia. *Bulletin of the Czech Geological Survey*, **57,** 129–143.
Watson, E., Vicenzi, E. & Rapp, R., 1989. Inclusion/host relations involving accessory minerals in high-grade metamorphic and anatectic rocks. *Contributions to Mineralogy and Petrology*, **101,** 220–231.
Weber, K., 1984. Variation in tectonic style with time (Variscan and Proterozoic systems). In: *Patterns of Change in Earth Evolution* (eds Holland, H.D. & Trendall, A.F.), pp. 371–386. Springer Verlag, Berlin.
Wendt, J.I., Kröner, A., Fiala, J. & Todt, W., 1993. Evidence from zircon dating for existence of approximately 2.1 Ga old crystalline basement in southern Bohemia, Czech Republic. *Geologische Rundschau*, **82,** 42–50.
Wenzel, T., Mertz, D., Oberhänsli, R., Becker, T. & Renne, P., 1997. Age, geodynamic setting, and mantle enrichment processes of a K-rich intrusion from the Meissen Massif (northern Bohemian Massif) and implications for related occurrences from the mid-European Hercynian. *Geologische Rundschau*, **86,** 556–570.
Wenzel, T., Oberhänsli, R. & Mezger, K., 2000. K-rich plutonic rocks and lamprophyres from the Meissen Massif (northern Bohemian Massif): geochemical evidence for variably enriched lithospheric mantle sources. *Neues Jahrbuch für Mineralogie, Abhandlungen*, **175,** 249–293.
White, R.W. & Powell, R., 2002. Melt loss and the preservation of granulite facies mineral assemblages. *Journal of Metamorphic Geology*, **20,** 621–632.
White, R.W., Powell, R., Holland, T.J.B. & Worley, B.A., 2000. The effect of TiO_2 and Fe_2O_3 on metapelitic assemblages at greenschist and amphibolite facies conditions: mineral equilibria calculations in the system K_2O-FeO-MgO-Al_2O_3-SiO_2-H_2O-TiO_2-Fe_2O_3. *Journal of Metamorphic Geology*, **18,** 497–511.
White, R.W., Powell, R. & Halpin, J.A., 2004. Spatially-focussed melt formation in aluminous metapelites from Broken Hill, Australia. *Journal of Metamorphic Geology*, **22,** 825–845.
White, R.W., Powell, R. & Holland, T.J.B., 2007. Progress relating to calculation of partial melting equilibria for metapelites. *Journal of Metamorphic Geology*, **25,** 511–527.
Whittington, A.G., Hofmeister, A.M. & Nabelek, P.I., 2009. Temperature-dependent thermal diffusivity of the Earth's crust and implications for magmatism. *Nature*, **458**(7236)**,** 319–321.
Wiegand, B., 1997. Isotopengeologische und geochemische Untersuchungen zur prävariszischen magmatischen und sedimentären Entwicklung im saxothuringisch–moldanubischen Übergangsbereich (Grenzgebiet BRD/CR). *Geotektonische Forschungen*, **88,** 1–177.
Žák, J., Holub, F. & Verner, K., 2005. Tectonic evolution of a continental magmatic arc from transpression in the upper crust to exhumation of mid-crustal orogenic root recorded by episodically emplaced plutons: the Central Bohemian Plutonic Complex (Bohemian Massif). *International Journal of Earth Sciences*, **94,** 385–400.
Žák, J., Kratinová, Z., Trubač, J., *et al*., 2010. Structure, emplacement, and tectonic setting of Late Devonian granitoid plutons in the Teplá-Barrandian unit, Bohemian Massif. *International Journal of Earth Sciences, in press*. doi:10.1007/s00531-010-0565-7.
Závada, P., Schulmann, K., Konopásek, J., Ulrich, S. & Lexa, O., 2007. Extreme ductility of feldspar aggregates – melt-enhanced grain boundary sliding and creep failure: rheological implications for felsic lower crust. *Journal of Geophysical Research*, **112**(B10)**,** 1–15.

Received 16 March 2010; revision accepted 18 August 2010.

Journal of
METAMORPHIC GEOLOGY

J. metamorphic Geol., 2011, **29,** 451–472 doi:10.1111/j.1525-1314.2010.00924.x

Prograde and retrograde metamorphic fabrics – a key for understanding burial and exhumation in orogens (Bohemian Massif)

E. SKRZYPEK,[1] P. ŠTÍPSKÁ,[1] K. SCHULMANN,[1] O. LEXA[2,3] AND M. LEXOVÁ[4]
[1]*Ecole et Observatoire des Sciences de la Terre – UMR 7516, Université de Strasbourg, 1, rue Blessig, 67084 Strasbourg, France (etienne.skrzypek@eost.u-strasbg.fr)*
[2]*Institute of Petrology and Structural Geology, Charles University, Albertov 6, 12843 Prague, Czech Republic*
[3]*Czech Geological Survey, Klárov 3, 11000 Prague, Czech Republic*
[4]*Mykuna, Nad Hercovkou 15, 18000 Prague 8, Czech Republic*

ABSTRACT In the Orlica–Śnieżnik Dome (NE Bohemian massif), alternating belts of orthogneiss with high-pressure rocks and belts of mid-crustal metasedimentary–metavolcanic rocks commonly display a dominant subvertical fabric deformed into a subhorizontal foliation. The first macroscopic foliation is subvertical, strikes NE–SW and is heterogeneously folded by open to isoclinal folds with subhorizontal axial planes parallel to the heterogeneously developed flat-lying foliation. The metamorphic evolution of the mid-crustal metasedimentary rocks involved successive crystallization of chlorite–muscovite–ilmenite–plagioclase–garnet, followed by staurolite-bearing and then kyanite-bearing assemblages in the subvertical fabric. This was followed by garnet retrogression, with syntectonic crystallization of sillimanite and andalusite parallel to the shallow-dipping foliation. Elsewhere, andalusite and cordierite statically overgrew the flat-lying fabric. With reference to a *P–T* pseudosection for a representative sample, the prograde succession of mineral assemblages and the garnet zoning pattern with decreasing grossular, spessartine and X_{Fe} are compatible with a *P–T* path from 3.5–5 kbar/490–520 °C to peak conditions of 6–7 kbar/~630 °C suggesting burial from 12 to 25 km with increasing temperature. Using the same pseudosection, the retrograde succession of minerals shows decompression to sillimanite stability at ~4 kbar/~630 °C and to andalusite–cordierite stability at 2–3 kbar indicating exhumation from 25 km to around 9–12 km. Subsequent exhumation to ~6 km occurred without apparent formation of a deformation fabric. The structure and petrology together with the spatial distribution of the metasedimentary–metavolcanic rocks, and gneissic and high-pressure belts are compatible with a model of burial of limited parts of the upper and middle crust in narrow cusp-like synclines, synchronous with the exhumation of orogenic lower crust represented by the gneissic and high-pressure rocks in lobe-shaped and volumetrically more important anticlines. Converging *P–T–D* paths for the metasedimentary rocks and the adjacent high-pressure rocks are due to vertical exchanges between cold and hot vertically moving masses. Finally, the retrograde shallow-dipping fabric affects both the metasedimentary–metavolcanic rocks and the gneissic and high-pressure rocks, and indicates that the ~15-km exhumation was mostly accommodated by heterogeneous ductile thinning associated with unroofing of a buoyant crustal root.

Key words: Bohemian Massif; burial and exhumation; prograde and retrograde fabrics; *P–T–D* path; *P–T* pseudosection.

INTRODUCTION

Combined petrological and geochronological studies that constrain *P–T–t* paths have contributed significantly to the understanding of the thermal processes related to exhumation of deep-seated rocks in orogens (e.g. Duchêne *et al.*, 1997; Rubatto & Hermann, 2001; Carswell *et al.*, 2003). However, these studies are commonly not combined with petrological and microstructural investigations of metamorphic fabrics, precluding fuller understanding of tectonic mechanisms of exhumation. Several studies show that shallow-dipping fabrics are commonly associated with retrograde metamorphic assemblages and telescoped cooling ages which are interpreted as a result of exhumation processes driven by extension or gravitational spreading of thickened crust (e.g. Dewey *et al.*, 1993; Koyi *et al.*, 1999; Vanderhaeghe *et al.*, 1999). By contrast, other petrological and structural studies show that the retrograde *P–T* evolution in orogenic lower-crustal rocks may be connected with subvertical fabrics suggesting vertical extrusion flow to be a major exhumation mechanism (e.g. Štípská *et al.*, 2004).

Both concepts are deduced from studies of deep-seated rocks of the orogenic lower crust, but the link between structural and metamorphic records in nearby mid- to supracrustal rocks is rarely concurrently explored (e.g. Racek *et al.*, 2006). Once lower- and mid-crustal rocks with convergent *P–T* paths reach lower-grade conditions, they commonly show the same deformation pattern (e.g. Štípská *et al.*, 2006) indicating that they shared the same tectonic evolution during the last part of the exhumation process. Because exhumed lower-crustal rocks lack sensitive records of the late *P–T* evolution, it may be possible to use the retrograde fabrics and associated metamorphic records of mid-crustal rocks to infer the exhumation evolution of the whole crust. Moreover, in mid-crustal units the tectono-metamorphic record related to the thickening process is commonly better preserved because the exhumation structures are heterogeneous and less intense. Therefore, the petrological and structural evolution of mid-crustal rocks is also likely to provide information about the burial process that is not preserved by the orogenic lower crust.

An area where these burial and exhumation processes can be deciphered occurs in the internal part of the Bohemian Massif (Fig. 1). There, recent determinations of the *P–T–D* paths in lower- and mid-crustal rocks led to the development of an exhumation model involving vertical extrusion of deep-seated rocks and subsequent subhorizontal deformation at a mid-crustal level (Štípská *et al.*, 2004; Franěk *et al.*, 2006; Tajčmanová *et al.*, 2006). This concept differs from diapiric models (Warren & Ellis, 1996; Lexa *et al.*, 2010) in invoking the predominance of lateral forces (e.g. Bell & Johnson, 1989) instead of buoyancy forces (Whitney *et al.*, 2004) as the driving mechanism for exhumation. However, the tectono-metamorphic

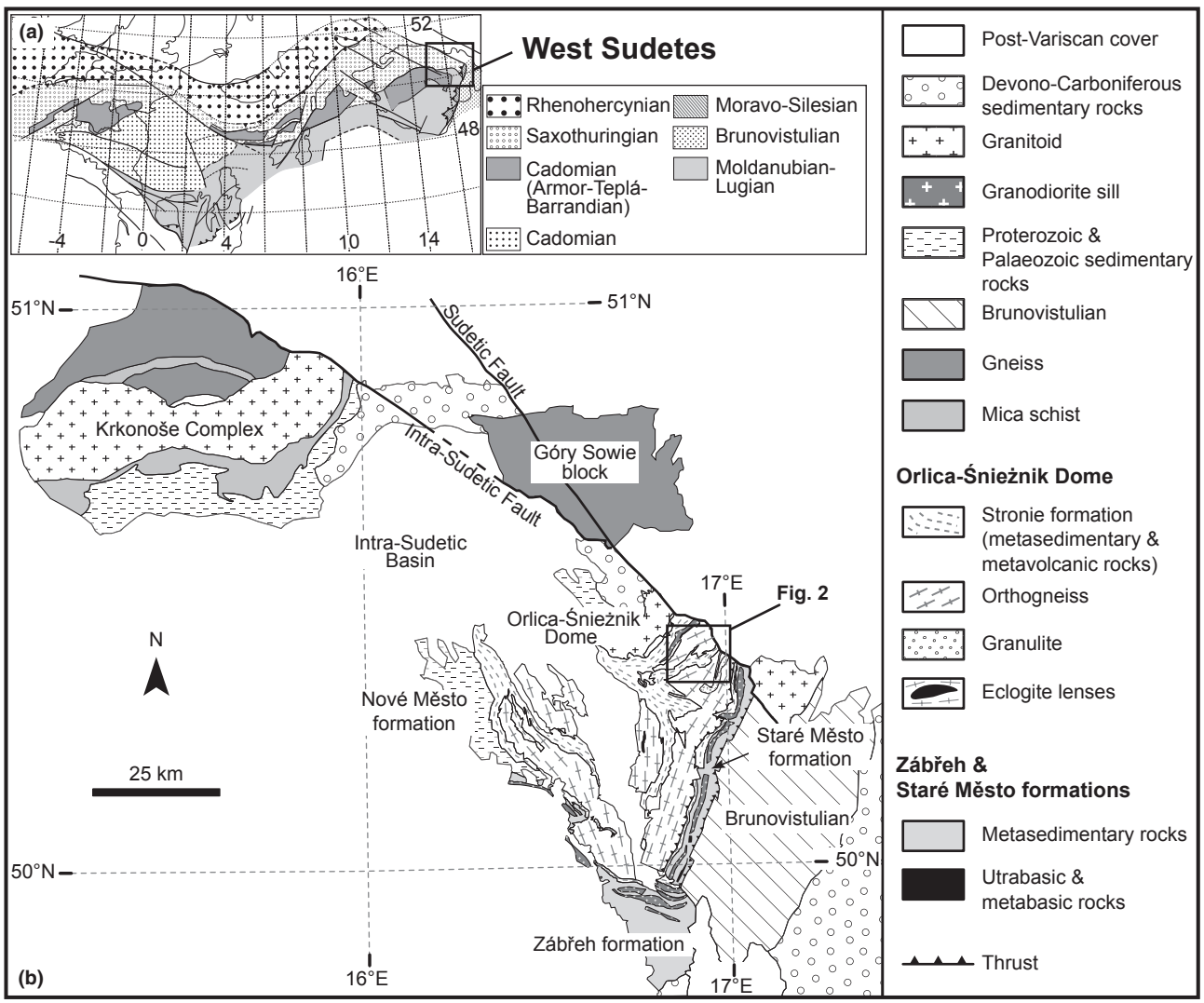

Fig. 1. Tectonic setting of the area of study. (a) Position of the area in the framework of the European Variscides (modified after Edel *et al.*, 2003). (b) Geological map of the West Sudetes (modified after Mazur *et al.*, 2005).

evolution of the middle crust probably results from crustal-scale folding (Racek *et al*., 2006), which is a process already proposed by e.g. Chamberlain (1986).

Here, we present an example of a structural succession in a metasedimentary sequence of the Orlica–Śnieżnik Dome (OSD) (NE Bohemian Massif), and decipher the prograde and retrograde fabrics, based on the relationships of fabric development and porphyroblast growth. The prograde and retrograde parts of the *P–T* path, determined via succession of porphyroblast growth and garnet zoning combined with pseudosection modelling are correlated with fabric development into a *P–T–D* path. The structural and metamorphic succession in the metasedimentary belt is correlated with the tectono-metamorphic evolution of an omphacite-bearing and felsic granulite belt that occurs only 5 km to the east. The implications for the burial and exhumation mechanisms of the continental crust are further discussed using existing conceptual models and associated *P–T–D* paths.

GEOLOGICAL SETTING

In the West Sudetes (Fig. 1), the OSD is interpreted as a remnant of the lower and middle crust of the Variscan orogenic root. The OSD is surrounded by narrow belts of low grade rocks (the Nové Město and Zábřeh formations) thought to represent the upper orogenic crust (Mazur *et al*., 2005; Schulmann *et al*., 2008). To the west, the presence of blueschists and oceanic sedimentary rocks in the western Krkonoše Complex (e.g. Maluski & Patočka, 1997) suggests a Late Devonian–Early Carboniferous east-dipping oceanic and continental subduction of the Saxothuringian zone (Collins *et al*., 2000). To the east, the boundary is marked by the Staré Město formation interpreted as a remnant of a Cambro–Ordovician intracontinental rift (Parry *et al*., 1997; Kröner *et al*., 2000; Štípská *et al*., 2001) and by the Neoproterozoic Brunovistulian continental blocks (Schulmann & Gayer, 2000; Košuličová & Štípská, 2007) that collided during Carboniferous compression.

Geology of the Orlica–Śnieżnik Dome (OSD)

The OSD is composed of orthogneisses, belts of metamorphosed volcano-sedimentary rocks of the Stronie (–Młynowiec) formation and bodies of high-pressure rocks (Don *et al*., 1990; Fig. 1b). The orthogneisses vary from an augen to a banded Śnieżnik type and a fine-grained mylonitic to migmatitic Gierałtów type. The Stronie formation is dominated by mica schist and paragneiss containing intercalations of acid to basic metavolcanic rocks (Floyd *et al*., 1996), calcitic and dolomitic marble and quartzitic schist (Wojciechowska, 1972). High-pressure rocks are represented by eclogite (Smulikowski, 1967) and omphacite-bearing granulite (Kozłowski, 1965) that form isolated bodies or N–S striking belts within the orthogneiss.

U–Pb zircon ages of 500–450 Ma are generally accepted to reflect the emplacement of granitic precursors of the Gierałtów and Śnieżnik gneisses (Turniak *et al*., 2000; Kröner *et al*., 2001; Lange *et al*., 2005b). Rare U–Pb zircon ages between 370 and 360 Ma from high-grade lithologies have been attributed to an Early Variscan HT event (Lange *et al*., 2005a), whereas Anczkiewicz *et al*. (2007) interpreted a *c*. 370 Ma Lu–Hf age of garnet from felsic granulites as a vestige of prograde UHP metamorphism. However, Štípská *et al*. (2004) and Bröcker *et al*. (2009) considered Early Carboniferous metamorphism between 345 and 330 Ma as a dominant event as also confirmed by Sm–Nd ages of 350–340 Ma on garnet and clinopyroxene in eclogites (Brueckner *et al*., 1991). In addition, recent Sm–Nd Garnet–WR dating from the Stronie formation provided an age of 346.5 ± 4.4 Ma interpreted as reflecting peak metamorphic conditions of mid-crustal rocks (Jastrzębski, 2008). Rb–Sr data from orthogneisses and ^{40}Ar–^{39}Ar dating on biotite, muscovite and hornblende from metapelites, orthogneisses and retrogressed eclogites yield 340–330 Ma ages documenting cooling of the massif (Steltenpohl *et al*., 1993; Lange *et al*., 2002; Schneider *et al*., 2006).

Major structural features recognized by Don *et al*. (1990) across the OSD involve folds, mylonitic zones in orthogneiss and east-directed thrust faults. Dumicz (1979) observed a subvertical schistosity deformed by folds with flat-lying axial planes and interpreted these structures as a result of Carboniferous tangential compression followed by vertical shortening due to gravitational loading. This fabric succession was confirmed by Štípská *et al*. (2004) around a granulite belt in the NE part of the OSD (Fig. 2). Apart from relics of a shallow-dipping fabric which have been locally preserved in the subvertical foliation, the vertical fabric linked with HP granulite facies metamorphism is deformed with variable intensity by a shallow-dipping fabric under amphibolite facies conditions. A similar fabric succession was reported by Jastrzębski (2005, 2008) in rocks from the Stronie formation where subvertical planes with remnants of a shallow-dipping structure are deformed into flat-lying structures displaying top-to-the-N sense of shear. According to this work, the horizontal compression at greenschist facies conditions is followed by prograde syn-burial subvertical shortening and subsequent decompression with later northward thrusting reactivating the flat-lying anisotropy.

Some authors report peak metamorphic conditions of eclogites and granulites of 18–22 kbar and 700–900 °C (Steltenpohl *et al*., 1993; Štípská *et al*., 2004), whereas other studies suggest UHP conditions of 27 kbar (Bakun-Czubarow, 1991; Bröcker & Klemd, 1996). Retrogression in the amphibolite facies is constrained between 4 and 11 kbar at 600–700 °C (Steltenpohl *et al*., 1993; Bröcker & Klemd, 1996; Štípská *et al*., 2004) for both eclogites and granulites.

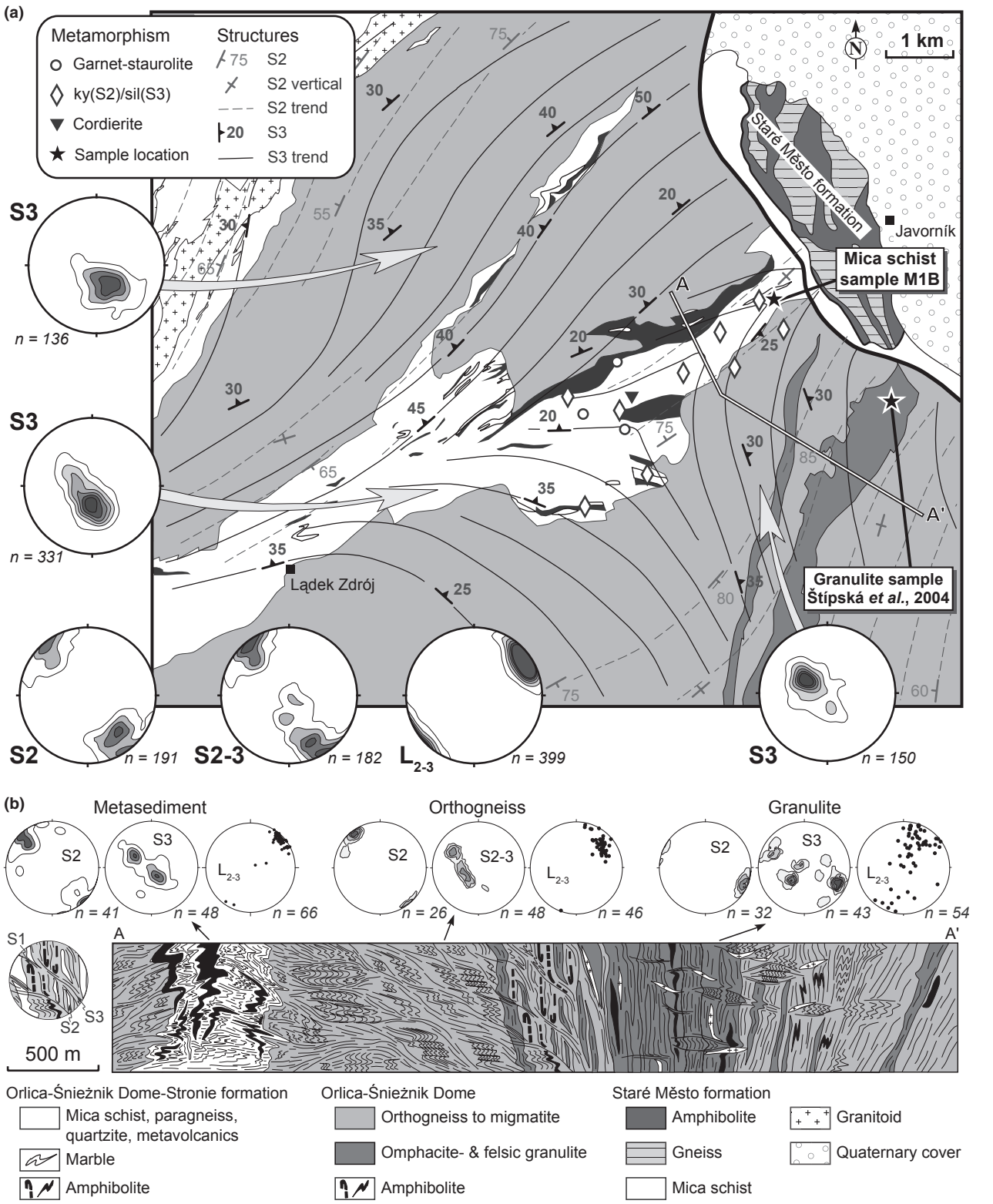

Fig. 2. (a) Simplified geological and structural map of the Lądek–Javorník area. Occurrences of metamorphic minerals, location of sample used for petrology and position of the structural profile are indicated. Plots show the orientation of S2, S3 and L_{2-3} structures (Schmidt net, lower-hemisphere projection). (b) Interpretative geological cross-section showing the early subvertical structure S2 and the style of superimposed D3 deformation in the rocks of the Stronie belt, the surrounding orthogneiss and the granulites. Equal-area, lower-hemisphere stereoplots show D2 and D3 planar and linear structures. Vertical axis is not to scale. Eastern part of the section is modified after Štípská *et al.* (2004).

The metamorphic studies on marbles, metapelites (Jastrzębski, 2005, 2008) and metavolcanics (Murtezi, 2006) from the Stronie formation show increasing metamorphic grade from the west to the east ranging from the garnet to the kyanite zone and peak pressures of 9–10 kbar achieved at 510–650 °C in the subvertical fabric. In addition, Jastrzębski (2008) suggested that in metapelites, a temperature increase from 510 to 620 °C at 7–8 kbar occurred in the shallow-dipping fabric.

STRUCTURAL EVOLUTION IN THE LĄDEK–JAVORNÍK AREA

The investigated part of the Stronie formation forms an ENE–WSW striking belt surrounded by augen to banded orthogneiss at the NE margin of the OSD (Fig. 2a). To the east, where the structural succession was documented by Štípská *et al.* (2004), a granulite belt is mantled by migmatitic orthogneiss.

Subvertical structure S2

The earliest mesoscopic structure in the metasedimentary rocks is a subvertical NE–SW striking metamorphic foliation S2 that is best preserved in the north-eastern termination of the belt. It is defined by compositional banding in marble, amphibolite and quartzitic schist (Figs 3a,b & 4a) and by alternation of mica-, quartz- and plagioclase-rich layers in the mica schist (Fig. 4c). In the surrounding orthogneiss, recrystallized quartz and feldspar augen and ribbons alternating with biotite- and muscovite-rich layers define the S2 foliation. In the granulite belt located to the SE, this dominant NE–SW striking S2 fabric dips steeply to the NW or SE (Štípská *et al.*, 2004; Fig. 2a).

Subhorizontal structure S3

The subvertical S2 fabric is heterogeneously deformed by metre- to millimetre-scale open to isoclinal folds F3 (Fig. 3b,c) with subhorizontal axial planes and subhorizontal, NE–SW trending hinges (Fig. 2a). In the eastern part, in places rich in marble and amphibolite, the F3 folds are commonly open to close, whereas in areas where mica schist dominates, the folds tend to be close to isoclinal (Fig. 4a,c). The hinge zones of the folds are commonly crenulated on the centimetre to millimetre-scale (Fig. 4c), and in the mica schist, the S3 cleavage defined by millimetre-spaced alternation of mica- and quartz-rich layers develops parallel to the axial planes. The open to close F3 folds show a varying asymmetry from symmetric to highly asymmetric folds with weakly deformed subvertical short limb and stretched, subhorizontal long limb nearly parallel to the axial plane (Fig. 4b). In the central and western part of the belt, the F3 folding commonly leads to almost complete transposition of the S2 foliation into the shallow-dipping S3 cleavage (Fig. 3c). There, the remnants of the S2 fabric are present only in low strain areas, as rare open and more abundant almost close to isoclinal folds in marble and amphibolite, and as frequent isoclinal and rootless isoclinal folds in the mica schist.

The shallow-dipping S3 foliation is the dominant structure in orthogneiss located on both sides of the metasedimentary belt. Close to isoclinal metre-scale folds with shallow-dipping axial planes are locally preserved, and hinge zones show isoclinally microfolded quartz-, feldspar- and biotite-rich bands. These hinge zones with axial-plane cleavage are in many places the only witness of the earlier steeply dipping S2 foliation. The D3 deformation is weaker in the granulites, resulting mostly in open F3 folds and localized shallow-dipping shear-zones (Štípská *et al.*, 2004).

The orientation of the S3 cleavage varies slightly. It is moderately dipping towards the NW in the northern part of the area, towards the N to NE in the centre and towards the SE near the granulite belt (Fig. 2a,b). Superposition of the S2 and S3 fabrics leads also to the development of a NE–SW subhorizontal intersection lineation L_{2-3} that is parallel to the F3 fold hinge (Fig. 2).

PETROGRAPHY

To determine the thermal and tectonic evolution of the structural succession, mica schist samples from the Stronie formation were used in this study. It is assumed that the orientation of pre-S3 minerals is preserved in the hinge zone during F3 fold development whereas minerals in the limbs may rotate and could acquire a different orientation. This assumption is supported by a quantitative microstructural study of garnet porphyroblasts from the same area (Skrzypek *et al.*, 2010). Observing relationships in the hinge zone facilitates interpretation of the relative growth of the minerals with respect to the structural development. Therefore, samples with well-preserved S2 fabric as well as from hinge zones of the F3 folds with variable intensity of the S3 cleavage development were investigated. The petrography is illustrated in Figs 5 and 6 and the interpretation of the relative mineral growth with respect to the deformational phases is summarized in Fig. 7.

Mineral abbreviations used are defined as follows: and, andalusite; bt, biotite; chl, chlorite; crd, cordierite; czo, clinozoisite; g, garnet (with end-members: Alm, almandine; Grs, grossular; Prp, pyrope; Sps, spessartine) ; ilm, ilmenite; kfs, K-feldspar; ky, kyanite; ms, muscovite; pg, paragonite; pl, plagioclase (Ab, albite; An, anorthite; Or, orthoclase); qtz, quartz; sil, sillimanite; st, staurolite.

Samples within the S2 foliation

Samples collected within the well-preserved S2 fabric in the eastern termination of the Stronie belt display

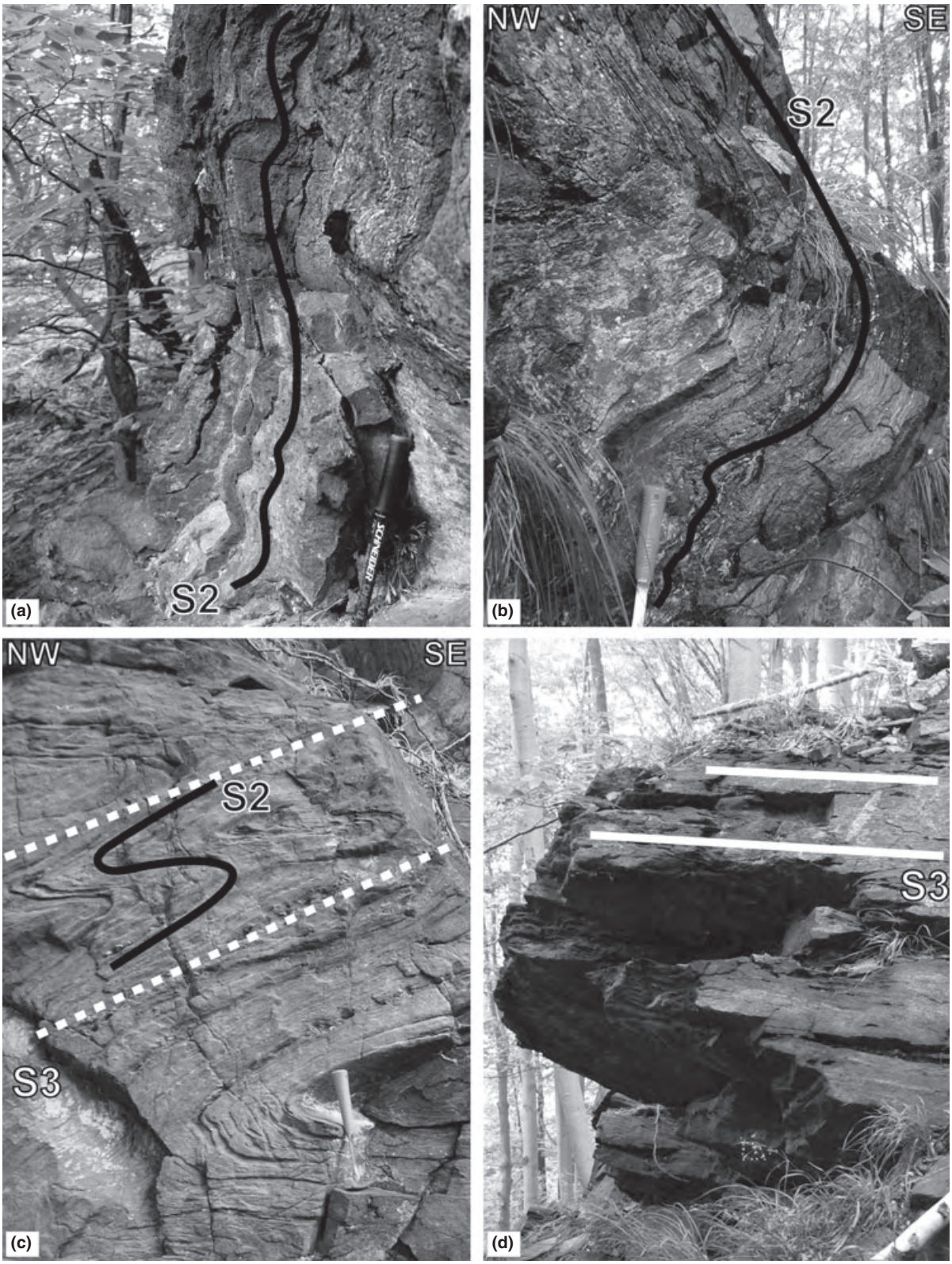

Fig. 3. Field photographs illustrating typical structural relationships. (a) Steeply dipping S2 foliation in interlayered marble and amphibolite. (b) Steeply dipping foliation folded by open F3 folds in amphibolite. (c) Isoclinal F3 folds in amphibolite. (d) Subhorizontal S3 foliation in mica schist.

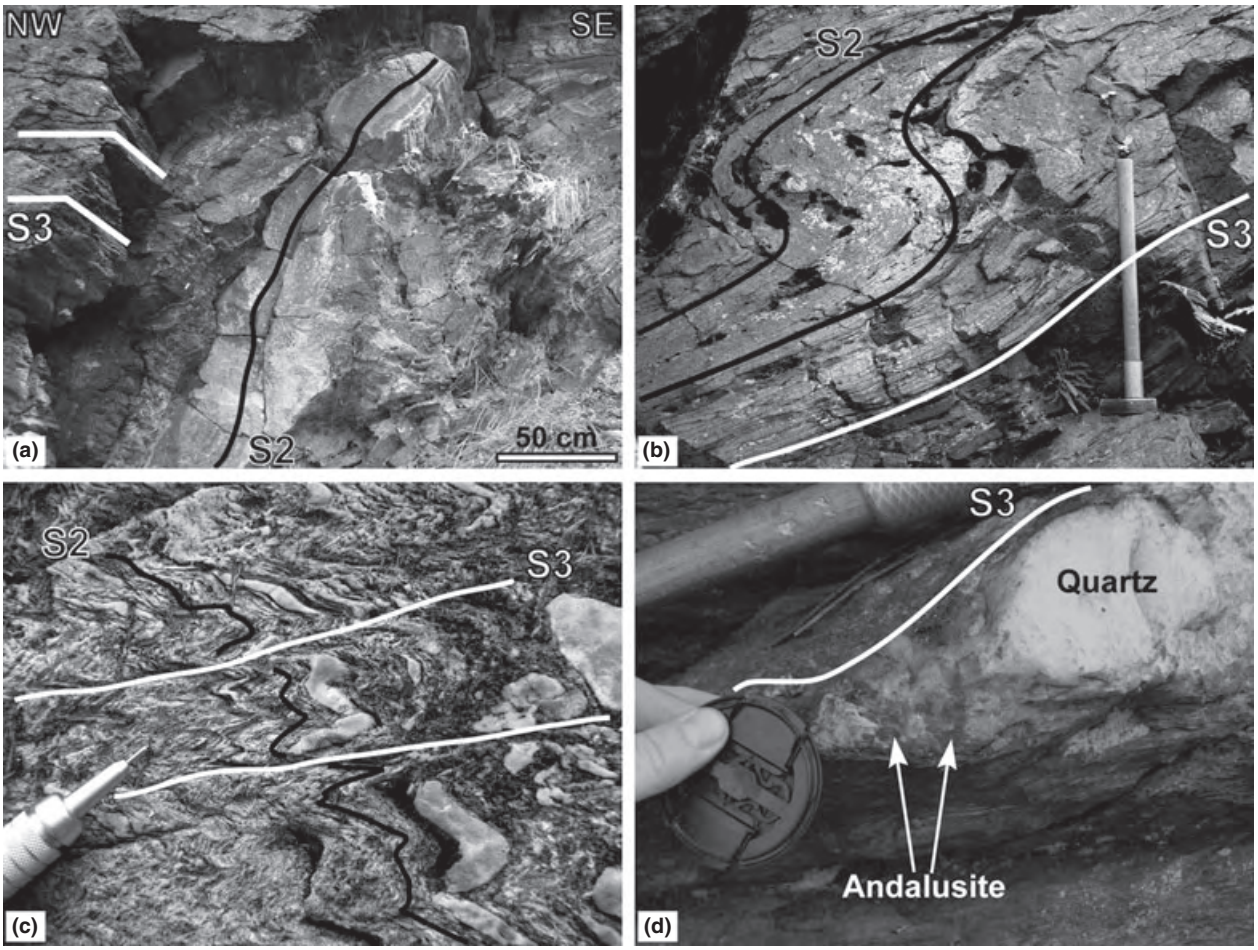

Fig. 4. Field photographs illustrating structural details. (a) Rheological contrast between marble with steeply dipping S2 foliation and surrounding mica schist transposed into the S3 fabric. (b) Asymmetric F3 fold in amphibolite with attenuated subhorizontal limbs. (c) Detail of subhorizontal crenulation cleavage S3 in the hinge of quartzitic mica schist. (d) Andalusite in quartz exudation parallel to the flat-lying S3 fabric in mica schist.

coarse-grained quartz-rich ribbons that alternate with muscovite-rich layers containing a variable amount of biotite oriented parallel to the S2 foliation (Fig. 5a–c). Garnet porphyroblasts (2–4 mm) are commonly elongated parallel to the S2 fabric and contain straight inclusion trails of quartz and ilmenite that are continuous with the external S2 foliation (Fig. 5a). Plagioclase forms large elongated porphyroblasts (1–4 mm) that commonly include oriented ilmenite, quartz, white mica and rare chlorite parallel to the external S2 fabric (Fig. 5b). Plagioclase also occurs as small grains in the matrix. Kyanite (up to 1 mm) is present only locally and is elongated parallel to the S2 foliation (Fig. 5c). Staurolite was not found in samples with the well-preserved subvertical S2 fabric but it is included in garnet that contains S2 inclusion trails perpendicular to the surrounding S3 foliation (Figs 5d & 8d). Other common accessory phases in the matrix are apatite and tourmaline and rare rutile is included in garnet.

Samples within the hinges of the F3 folds

Samples that were collected in the hinge zones of the F3 folds exhibit variable intensity of the S3 cleavage development and variable degree of preservation of the S2 structures. With increasing intensity of the F3 folding, three stages are distinguished based on the microstructural pattern of the matrix. First, the matrix composed of the quartz- and mica-rich S2 layers was microfolded (Fig. 5a–c). Then, a spaced S3 cleavage developed, marked by the orientation of biotite and muscovite with some preserved isoclinal and rootless folds composed of quartz-rich ribbons (Fig. 5e). In the last stage, the matrix was completely deformed (Fig. 6); quartz- and mica-rich layers are subhorizontal and rarely contain rootless folds of quartz-rich layers.

Porphyroblasts and inclusion trails in porphyroblasts of the hinge zone show variable orientation. In some cases, the inclusion trails of several neighbouring porphyroblasts are straight and oriented almost

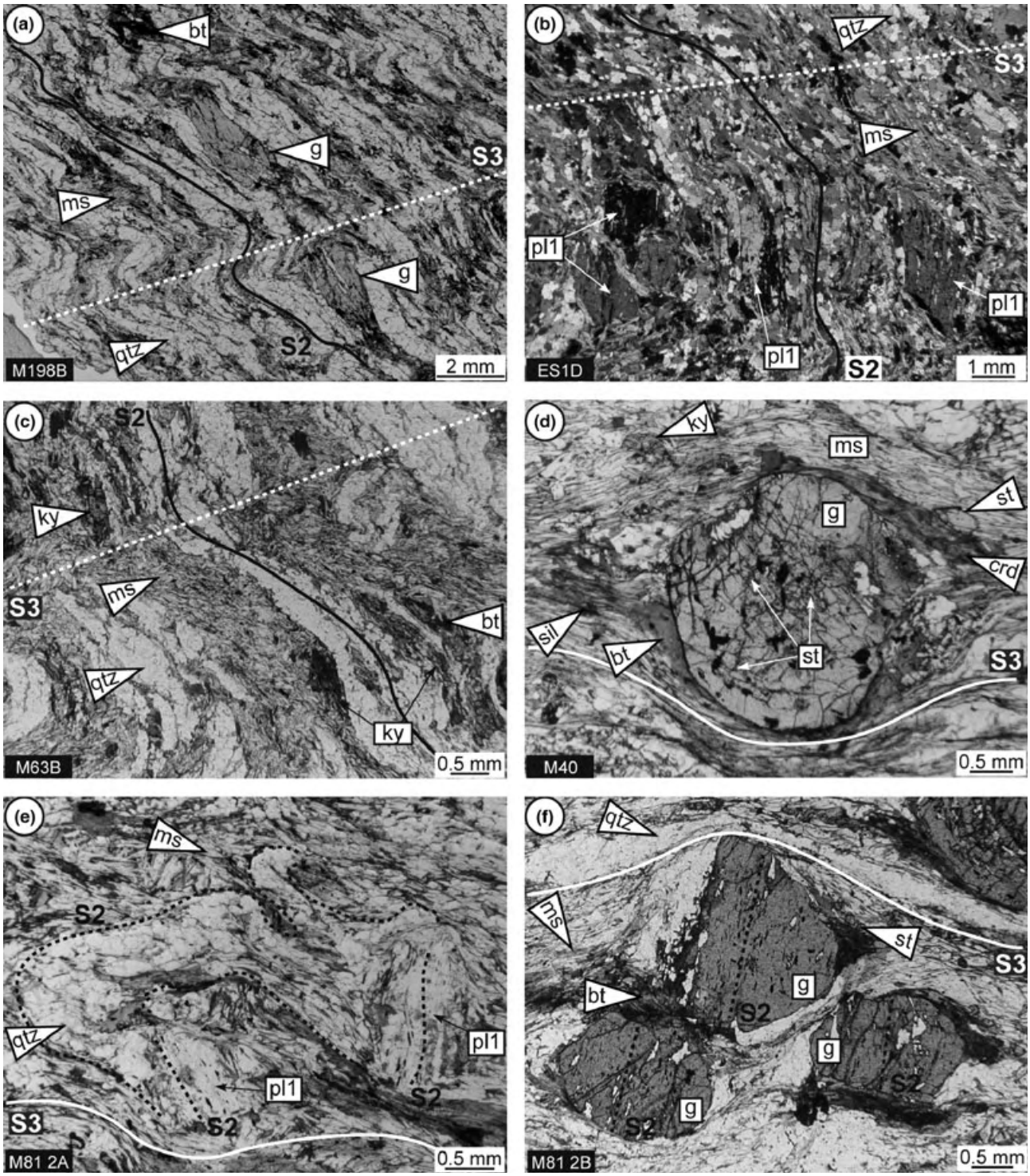

Fig. 5. Photomicrographs illustrating the relationships between the porphyroblasts and the S2 fabric (a–d), and the common porphyroblast orientation within the hinge zones of the F3 macrofolds (e–f). (a) Garnet and (b) plagioclase are elongated, and have inclusion trails parallel to the S2 metamorphic layering. (c) Kyanite crystals parallel to the S2 fabric. (d) Staurolite included in garnet with ilmenite inclusion trails perpendicular to the external S3 fabric. (e) Plagioclase elongation and orientation of the inclusion trails are perpendicular to the S3 fabric in the hinge of the F3 crenulation and oblique in the limb. (f) Garnet porphyroblasts with consistent inclusion trails perpendicular to the external S3 fabric. Full lines indicate the dominant foliation whereas dashed lines denote the inferred internal foliation in porphyroblasts or the orientation of the superimposed cleavage. Plane-polarized light except for (b).

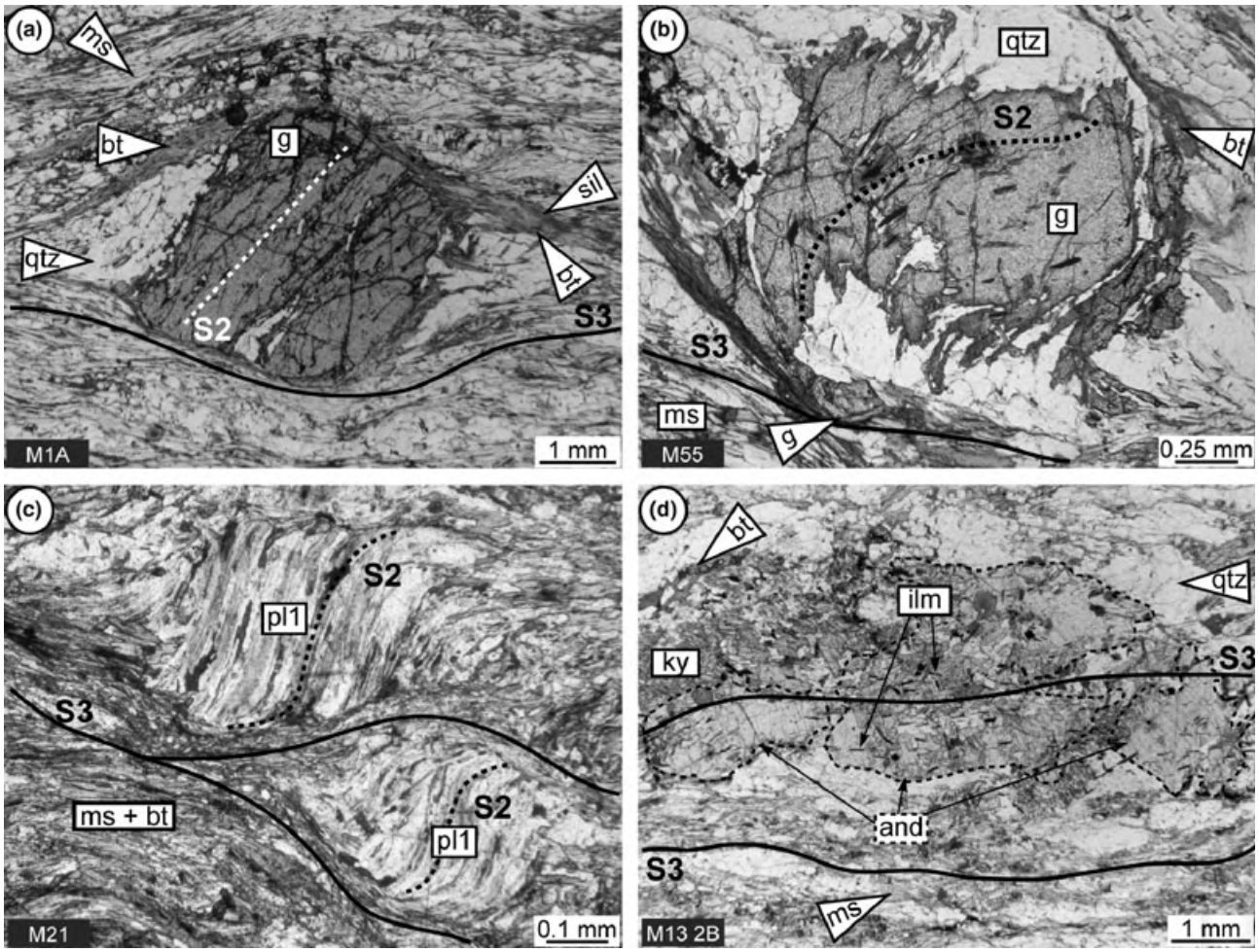

Fig. 6. Photomicrographs illustrating the relationships between the metamorphic minerals and the S3 fabric. (a) Garnet with inclusion trails oblique to the external S3 foliation and sillimanite–biotite intergrowths in the pressure shadows parallel to S3. (b) Garnet with inclusion trails at high angle to the external S3 foliation in the core and parallel to the S3 fabric at its outermost rim. (c) Plagioclase porphyroblasts with inclusion trails in the core at high angle to the external S3 fabric and inclusion trails in the rim passing continuously into the anastomosing S3 foliation. (d) Large and randomly oriented andalusite crystals with aligned ilmenite passing continuously into the external S3 fabric. Full lines indicate the dominant foliation whereas dashed lines denote the inferred foliation in porphyroblasts or relics of older fabrics. Plane-polarized light.

perpendicular with respect to the external foliation (Fig. 5f). They are therefore interpreted as porphyroblasts that grew during or after the formation of the S2 fabric and that did not rotate during the F3 folding while the matrix was deformed into the S3 fabric. In some samples, neighbouring porphyroblasts show straight inclusion trails that are oriented at a high angle with respect to each other and at variable angle to the S3 cleavage. In these samples, the different orientation of the inclusion trails is probably caused by rotation of the grains with the limbs of the microfolds (Fig. 5e). The exact orientation of the S2 fabric cannot be inferred from such porphyroblasts, but their growth can still be assigned to the S2 fabric.

Garnet (up to 6 mm) includes numerous ilmenite and quartz grains, and rare chlorite, staurolite and rutile grains. Ilmenite and quartz generally form straight inclusion trails that are oriented at high angle to the external S3 foliation (Fig. 6a). Some garnet porphyroblasts show straight inclusion trails in the core and curved inclusion trails in the outermost rim passing continuously into the S3 fabric (Fig. 6b). The microstructural relationships suggest that the major garnet growth occurred during development of the S2 fabric, but in some samples a small amount of garnet crystallized during development of the S3 fabric. Skrzypek *et al.* (2010) reported garnet porphyroblasts with inclusion trails in the inner core oriented at high angle with respect to the S2 fabric, and suggested the presence of an earlier foliation S1 that is not preserved macroscopically. In a few cases, this inferred S1 foliation seems crenulated and preserved in garnet (Fig. 8d).

Plagioclase forms porphyroblasts (2 mm) and small grains (0.3 mm) within the matrix. Porphyroblasts contain numerous ilmenite, white mica, some quartz

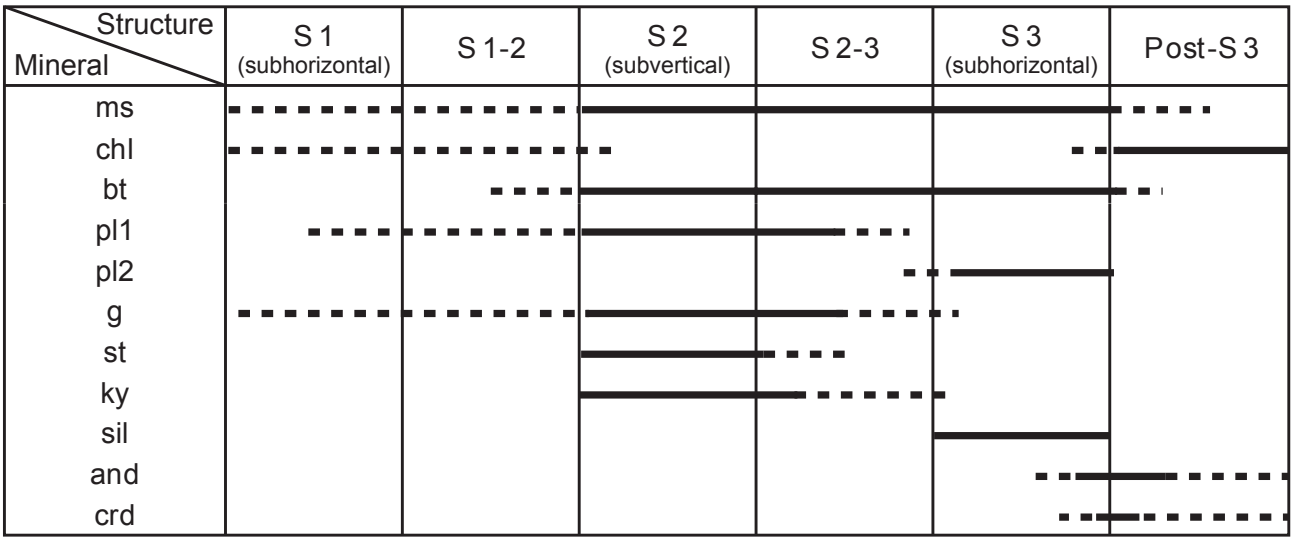

Fig. 7. Crystallization–deformation relationships. Quartz and ilmenite are always present. For details see text.

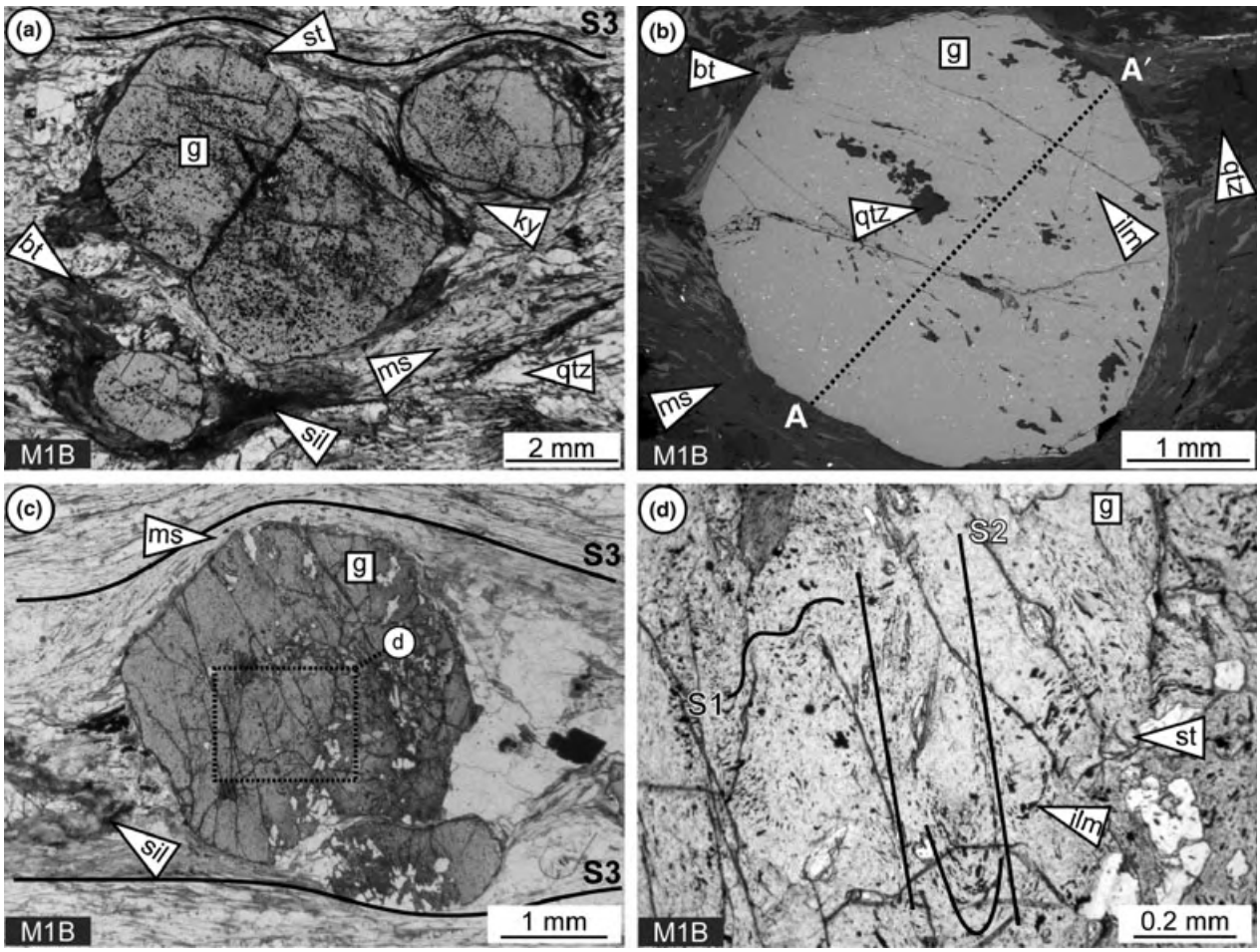

Fig. 8. Photomicrographs and BSE image of sample M1B selected for mineral chemistry and mineral equilibria modelling. (a) Garnet, staurolite, kyanite and sillimanite in muscovite–biotite schist. (b) Location of the garnet profile presented in Fig. 9 (BSE). (c) Sillimanite in the D3 pressure shadow of a garnet that contains staurolite and crenulated ilmenite inclusions. (d) Detail of the garnet core shows crenulated S1 inclusion trails and S2 cleavage that is perpendicular to the external S3 fabric. Plane-polarized light.

and rare chlorite. Ilmenite needles usually form straight inclusion trails oriented at high angle to the external foliation and rarely, the inclusion trails are curved at porphyroblast rims and continue into the S3 foliation (Fig. 6c). Small recrystallized plagioclase occurs within micaceous layers of the S3 cleavage and in samples that show almost complete transposition of the S3 foliation, the majority of plagioclase is present as small recrystallized grains in the matrix. The major porphyroblast growth is therefore assigned to the S2 fabric with a small amount assigned to the beginning of the S3 fabric development. The recrystallized small grains are associated with the S3 cleavage development.

Staurolite (1–2 mm) is sometimes included in garnet (Figs 5d & 8d) and commonly occurs in the matrix. In samples exhibiting relicts of the S2 quartz-rich layers, it is oriented parallel to the S2 fabric. Its orientation in the matrix of strongly deformed samples is random or parallel to the S3 fabric. Staurolite inclusions in garnet and oriented staurolite parallel to the S2 fabric indicate its growth during the D2 deformation. Its orientation parallel to the S3 fabric in strongly overprinted samples is assigned to reorientation during the D3 event.

Kyanite (0.5–1 mm) is common in the matrix and was not found in garnet. It is oriented parallel to the S2 quartz-rich layers in microfolded samples but the elongated grains are generally rotated with the limbs of the microfolds. In samples exhibiting strong D3 deformation without relicts of folded quartz-rich domains, kyanite orientation is random or mostly parallel to the S3 cleavage (Fig. 5d). Kyanite growth is assigned to the S2 fabric only; its orientation parallel to the S3 fabric in some samples is explained by reorientation during F3 microfolding.

Mica in weakly folded samples mostly occurs parallel to the S2 quartz-rich layers, and is slightly rotated with the limbs of the microfolds. A small amount of biotite and white mica occurs in the spaced S3 cleavage. In strongly overprinted samples, the mica is oriented parallel to the S3 fabric and biotite prevails over muscovite. In some samples with strong S3 fabric, biotite-rich pressure shadows commonly associated with sillimanite are developed around garnet (Fig. 6a) and occasional biotite ribbons with sillimanite are parallel to the S3 foliation. It is assumed that the majority of mica grew during the D2 event, but a significant amount also grew in the S3 spaced cleavage. In strongly overprinted samples, it is impossible to distinguish the S2 from the newly grown S3 mica, and it is likely that the mica chemically equilibrated during the D3 event. The biotite associated with sillimanite is assigned to the S3 fabric.

Sillimanite occurs only in samples that show strong D3 deformation. It is associated with biotite in the pressure shadows around garnet and in biotite-rich layers, always oriented parallel to the S3 foliation. It was never found microfolded. Its growth is therefore assigned to the D3 deformation.

Andalusite is commonly found only in samples with strong D3 deformation. It occurs in quartz–andalusite segregations parallel to the S3 fabric (Fig. 4d), in some pressure shadows of garnet and it forms large, randomly oriented porphyroblasts in the matrix. Andalusite commonly includes ilmenite oriented parallel to the S3 fabric and continuously passing into the matrix (Fig. 6d). Andalusite in the pressure shadows indicates that its growth started probably during the D3 deformation, but the majority of porphyroblasts is interpreted as late andalusite overgrowths on the already developed S3 foliation.

Cordierite was found in one sample as elongated stripes (1.5 mm), or small highly pinitized grains in the S3 matrix and around garnet porphyroblasts (Fig. 5d). Its growth is interpreted as post-tectonic with respect to the D3 deformation.

Chlorite occurs in the cores of some garnet and plagioclase porphyroblasts and rare chlorite is randomly oriented around garnet porphyroblasts. Chlorite included in garnet and plagioclase is assigned to the S2 event while the matrix chlorite replacing garnet is assigned to the late, post-D3 evolution.

CHEMISTRY AND *P–T* ESTIMATES

Analytical procedure

Chemical analyses have been carried out in Centre de Géochimie de la Surface in Strasbourg on a TESCAN VEGA XMU electron microscope with operating conditions of 15 kV and 15 nA. Mineral analyses are listed in Table 1.

Sample M1B

Sample M1B shows alternating quartz- and mica-rich bands corresponding to the S3 fabric (Fig. 8a,c). It is composed of garnet, staurolite, kyanite, sillimanite, biotite, muscovite, plagioclase and quartz with accessory ilmenite. Because samples from the area of study commonly preserve the same mineralogy (Fig. 2), sample M1B is considered as representative of this part of the Stronie formation.

Garnet (< 5%) and plagioclase (2–3%) form porphyroblasts (1–4 mm) that sometimes display inclusion trails oblique to the external S3 foliation. Plagioclase porphyroblasts (pl1) have outermost rims recrystallized into fine-grained aggregate (pl2) and tiny plagioclase grains (pl2) occur within the S3 matrix. Relics of staurolite and kyanite appear as small grains (0.5 mm) randomly distributed within the matrix lying next to garnet porphyroblasts but staurolite is also included in garnet with inclusions trails perpendicular to S3 (Fig. 8d). Intergrowths of biotite and sillimanite commonly appear in the garnet pressure shadows or as thin layers in the S3 matrix. Garnet shows strong zoning from core ($Alm_{0.60}$ $Prp_{0.04}$ $Grs_{0.16}$ $Sps_{0.21}$; X_{Fe} = 0.94) to rim ($Alm_{0.79}$

Table 1. Representative chemical analyses for minerals from sample M1B.

Sample	M1B								
Mineral position	g core	g rim	st core	st rim	bt matrix	ms matrix	pl 1 core	pl 1 rim	pl 2 matrix
Wt%									
SiO_2	37.24	37.21	27.16	26.63	36.12	46.15	67.20	64.87	64.89
TiO_2	0.16	0.29	0.85	0.93	2.35	0.76	0.00	0.05	0.00
Al_2O_3	21.09	21.43	54.38	53.98	20.49	37.21	20.80	21.73	22.32
FeO	28.23	35.23	11.57	12.07	19.61	0.94	0.25	0.19	0.16
MnO	7.85	1.98	0.56	0.56	0.00	0.05	0.00	0.05	0.00
MgO	1.06	2.66	1.35	1.36	8.70	0.65	0.16	0.11	0.10
CaO	5.17	2.34	0.14	0.06	0.00	0.00	0.63	1.64	2.22
Na_2O	0.11	0.00	0.00	0.00	0.36	1.14	11.24	10.51	10.48
K_2O	0.09	0.10	0.07	0.08	9.07	9.30	0.18	0.10	0.09
ZnO	n.a.	n.a.	2.23	2.01	n.a.	n.a.	n.a.	n.a.	n.a.
Total	101.00	101.24	98.31	97.68	96.70	96.20	100.46	99.25	100.26
Cations									
Si	2.98	2.96	7.69	7.59	2.79	3.03	2.93	2.87	2.84
Ti	0.01	0.02	0.18	0.20	0.14	0.04	0.00	0.00	0.00
Al	1.99	2.01	18.15	18.14	1.86	2.88	1.07	1.13	1.15
Fe^{3+}	0.05	0.03	0.00	0.00	0.00	0.00	0.01	0.01	0.01
Fe^{2+}	1.84	2.31	2.74	2.88	1.27	0.05	0.00	0.00	0.00
Mn	0.53	0.13	0.13	0.14	0.00	0.00	0.00	0.00	0.00
Mg	0.13	0.32	0.57	0.58	1.00	0.06	0.01	0.01	0.01
Ca	0.44	0.20	0.04	0.02	0.00	0.00	0.03	0.08	0.10
Na	0.02	0.00	0.00	0.00	0.05	0.15	0.95	0.90	0.89
K	0.01	0.01	0.03	0.03	0.89	0.78	0.01	0.01	0.01
Zn	n.a.	n.a.	0.47	0.42	n.a.	n.a.	n.a.	n.a.	n.a.
Total	8.00	8.00	30.00	30.00	8.00	7.00	5.00	5.00	5.00
X_{Fe}	0.94	0.88	0.83	0.83	0.56	An	0.03	0.08	0.10
Alm	0.62	0.78				Ab	0.96	0.91	0.89
Prp	0.04	0.11				Or	0.01	0.01	0.01
Grs	0.15	0.07							
Sps	0.18	0.05							

Structural formulae calculated on the basis of 12 oxygen for garnet, 46 for staurolite, 22 for biotite and muscovite and 8 for plagioclase.
n.a., not analysed.

$Prp_{0.13}$ $Grs_{0.06}$ $Sps_{0.04}$; X_{Fe} = 0.85) (Figs 8b & 9a). Staurolite is not zoned and its X_{Fe} varies from 0.81 to 0.85. All plagioclase is albite, but porphyroblasts show lower anorthite content (An_3) than the rims or small grains in the matrix ($An_{7–10}$). Typical X_{Fe} values for biotite are 0.55–0.57 and titanium clusters around 0.15 p.f.u.

Mineral equilibria modelling

Calculation method

A pseudosection in the MnO–Na_2O–CaO–K_2O–FeO–MgO–Al_2O_3–SiO_2–H_2O (MnNCKFMASH) system has been calculated for the whole-rock composition of sample M1B (in wt%: SiO_2 = 61.44; TiO_2 = 0.99; Al_2O_3 = 19.76; Fe_2O_3 = 0.99; FeO = 4.82; MnO = 0.37; MgO = 1.73; CaO = 0.89; Na_2O = 1.00; K_2O = 3.96; P_2O_5 = 0.08; standard wet chemical methods) with THERMOCALC 3.26 (Powell *et al.*, 1998) and the database 5.5 (November 2003 update; Holland & Powell, 1998). The activity–composition relationships of feldspar are from Holland & Powell (2003), white mica from Coggon & Holland (2002), silicate melt from White *et al.* (2007), Mn-bearing models from Mahar *et al.* (1997), chlorite from Holland *et al.* (1998) and biotite as in Powell & Holland (1999). Abbreviations for composition isopleths are x(g, st, bt) = Fe/(Fe + Mg); z(g) = Ca/(Fe + Mg + Ca + Mn); m(g) = Mn/(Fe + Mg + Ca + Mn). Quartz, muscovite and H_2O are set as excess phases.

Preliminary tests of pseudosection calculation for Stronie samples taking into account the fractionation of elements in garnet have shown such fractionation to be of small importance. This is in agreement with the study of Zuluaga *et al.* (2005) on pelitic schists with $<5\%$ modal garnet. The observed garnet zoning (Fig. 9a) suggests that cation diffusion was limited during the metamorphic evolution. Therefore, the calculations do not take into account element fractionation or intra-crystalline diffusion.

Pseudosection for sample M1B and P–T evolution

The pseudosection was calculated up to the *P–T* conditions where melt appears (640–680 °C). The major features of the pseudosection (Fig. 10a) include garnet stability over the range of calculated *P–T* conditions, staurolite stability from 550 °C (at 3.1 kbar) to 630 °C (at 6.2 kbar), chlorite stability up to 575–615 °C, and biotite stability above 500–550 °C. Kyanite is stable above ~610 °C (between 6 and 8.6 kbar), sillimanite from 580 °C (at 4 kbar) to 660 °C (at 6 kbar), andalusite between 520 and 630 °C at 2.4–4 kbar and

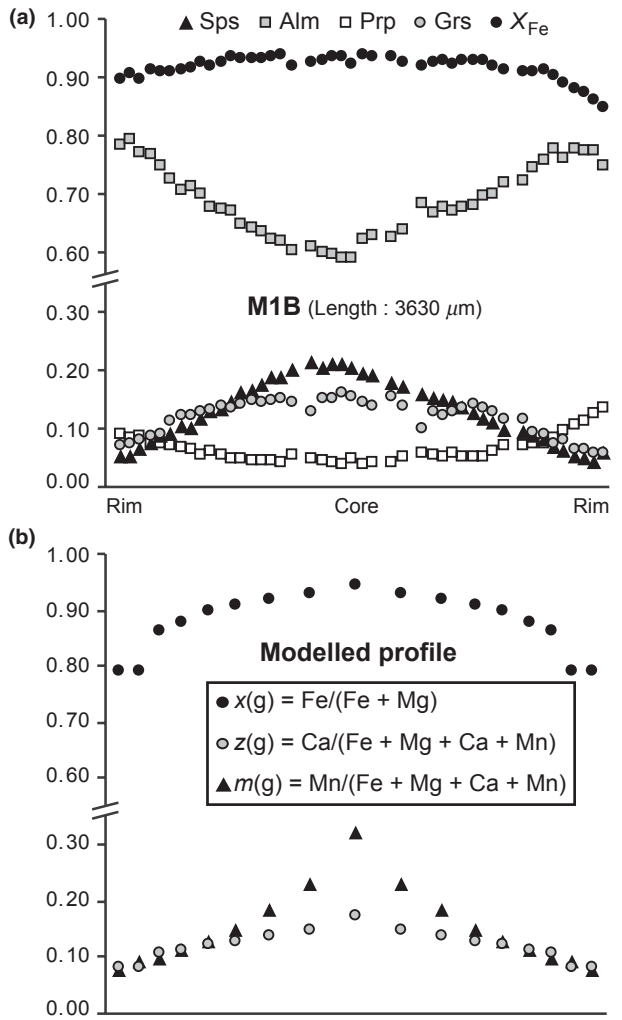

Fig. 9. (a) Garnet profile from sample M1B. The line of the profile is shown in Fig. 8b. (b) Modelled garnet profile for the *P–T* path represented by the white arrow (stages 1–2) in Fig. 10.

cordierite between 500 and 650 °C with an upper pressure limit at 3–3.5 kbar.

Sequential growth observed in the thin section involves oriented ilmenite, chlorite and white mica in plagioclase porphyroblasts, and garnet porphyroblasts with straight inclusion trails of ilmenite. This is complemented by the presence of randomly oriented staurolite and kyanite in the S3 matrix and sillimanite in garnet S3 pressure shadows as well as parallel to the S3 matrix foliation. This suggests a medium pressure prograde path starting in the quinivariant g–pl–chl field, continuing across the quadrivariant bt–g–pl–st field to the bt–g–pl–ky field followed by a pressure drop into the bt–g–pl–sil field.

The beginning of the *P–T* path is deduced from garnet core chemistry where grossular and X_{Fe} values (X_{Fe} = 0.94; Grs = 0.16) fit approximately the isopleths, but modelled *m*(g) = 0.32 is higher than the measured spessartine (Sps = 0.21) content (Fig. 9b). This discrepancy is probably due to excessive Mn incorporation in garnet. Indeed, in the present calculations garnet and chlorite are the only phases with Mn-bearing models present at low *P–T* conditions. However, a significant amount of MnO can also be trapped in other minerals (Spear & Cheney, 1989), especially in ilmenite (Caddick & Thompson, 2008) which is generally abundant in the matrix of pelitic samples and therefore, calculations taking into account TiO_2 would be likely to decrease *m*(g) values at low *P–T* conditions. This issue has been addressed by Skrzypek *et al.* (2010), where MnNCKFMASHTO pseudosections yielded similar *P–T* estimates for the onset of garnet growth but with a better match between *m*(g) and spessartine values. It is therefore proposed that the *P–T* evolution starts at 3.5–5 kbar and 490–520 °C (Fig. 10a–c, stage 1).

Inclusions in garnet porphyroblasts together with staurolite and kyanite occurrences in the matrix indicate further prograde *P–T* evolution. This is confirmed by staurolite chemistry (X_{Fe} = 0.81–0.85) compatible with the calculated isopleths (Fig. 10b) and by observed grossular and spessartine content at the garnet rim (Grs = 0.06; Sps = 0.04) that lie very close to the calculated isopleths of *z*(g) and *m*(g) in the kyanite field. This indicates *P–T* conditions of about 6–7 kbar and ~630 °C for the peak of metamorphism (Fig. 10a–c, stage 2), supported by the modelled garnet zoning closely reproducing the measured garnet profile (Fig. 9). In the absence of migmatization, the maximum temperature is bounded by the liquid-in line at 670 °C (Fig. 9a).

The interpretation of the sillimanite and biotite growing at the expense of garnet in the pressure shadows is compatible with pressure decrease and decrease in the modal proportions of garnet. This retrograde reaction is likely to modify the garnet rim chemistry. If Fe–Mg exchange is considered to be dominant during this process, this could result in the observed difference between garnet rim X_{Fe} and the calculated *x*(g) isopleths at the pressure peak (Figs 9b & 10b), while grossular and spessartine contents remain relatively unchanged. Therefore, the modelled values of *x*(bt) = 0.55–0.57 and *x*(g) = 0.85 similar to X_{Fe} of biotite and garnet rim suggest that garnet–biotite re-equilibration occurred in the sillimanite stability field. This points to retrogression towards ~4 kbar and ~630 °C (Fig. 10b, stage 3).

Additional petrographic information from other samples is also correlated with the pseudosection to roughly estimate the *P–T* evolution during further decompression. Because andalusite is widespread in samples with penetrative S3 foliation, and it is not stable in the pseudosection above 4 kbar, it is only possible to draw a cooling curve that lies below this upper pressure limit (Fig. 10a). Cordierite is present in one sample only; it is associated with andalusite, biotite, garnet, plagioclase, muscovite and quartz, which allows speculation that pressure decrease in the area of study, at least locally, continued to ~2–3 kbar at

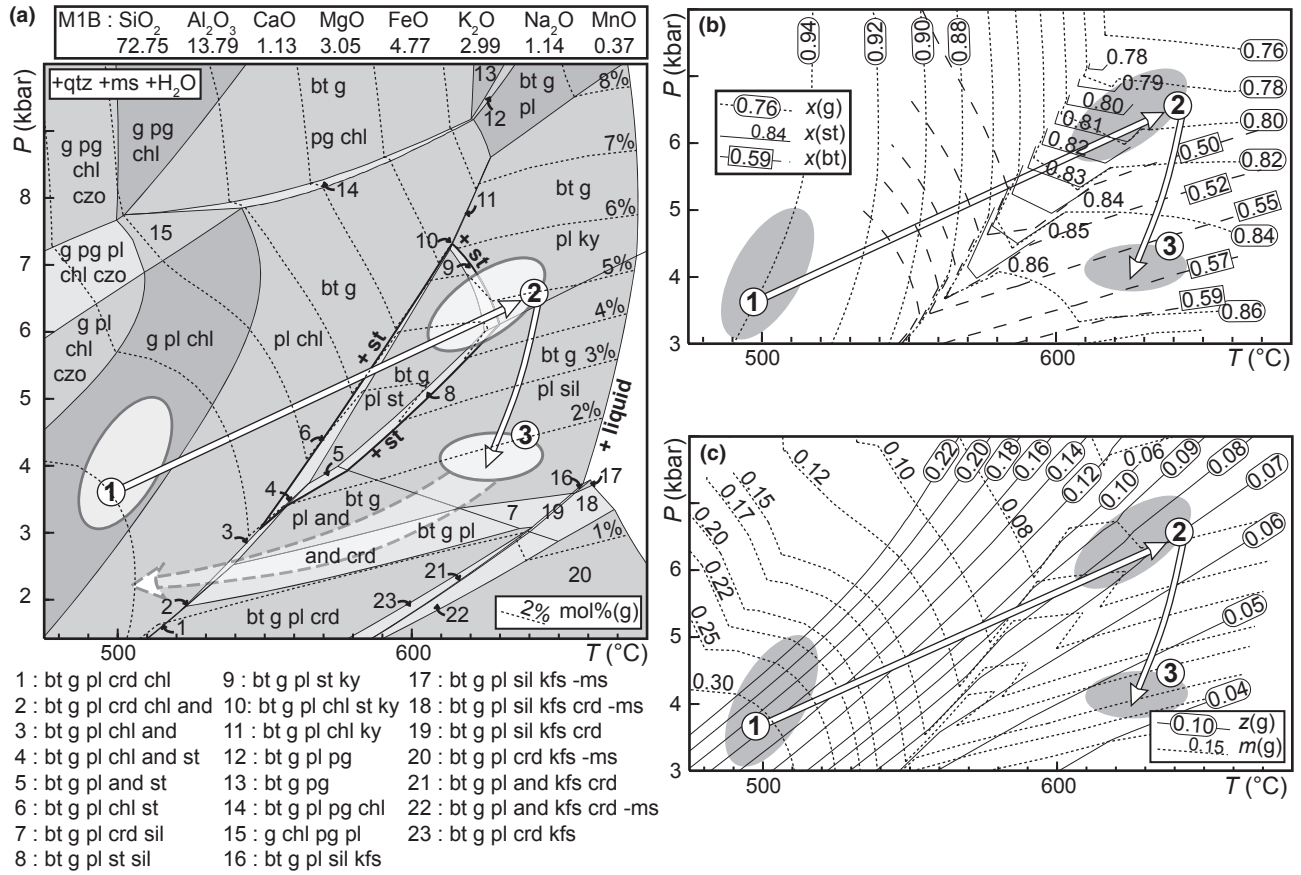

Fig. 10. (a) *P–T* pseudosection in the MnNCKFMASH system for sample M1B (in moles adjusted to 100%), contoured for garnet modal proportion. Full and dashed white lines indicate prograde and retrograde evolution derived by comparing the modelled assemblages and isopleths with observed assemblages, chemistry and zoning of minerals. Ellipses denote the probable *P–T* ranges for the different stages of the *P–T* path. See text for details. (b, c) Simplified part of the pseudosection with calculated isopleths of mineral composition.

temperatures above 530–630 °C, where this assemblage occurs in the pseudosection. The widespread presence of chlorite indicates further cooling below 530 °C.

DISCUSSION

In the following sections, structural and metamorphic observations are combined into a *P–T–D* path reflecting burial and subsequent exhumation of the metasedimentary rocks. This evolution is correlated with the *P–T–D* path from neighbouring lower-crustal granulites (Štípská *et al.*, 2004) and the tectonic significance of these *P–T–D* paths is discussed in the light of *P–T* paths established for conceptual tectonic settings. This approach is finally used to suggest that the observed *P–T–D* paths may be diagnostic of crustal-scale folding and ductile thinning.

Mineral growth and *P–T* conditions of the metamorphic fabrics in metasedimentary rocks

Although the major garnet growth has been ascribed to the S2 foliation based on microstructural observations, there is no evidence for garnet crystallization being restricted to this fabric. Some garnet porphyroblasts have core inclusion trails (S1) at high angle to the S2 fabric and indicate crystallization in an older, probably shallow-dipping S1 fabric that was completely obliterated on the macroscopic scale (Fig. 11a). These polyphase garnet porphyroblasts are therefore likely to document the very early stage of the prograde evolution (Skrzypek *et al.*, 2010).

The D2 deformation produced a NE–SW striking subvertical fabric visible in all the lithologies. In metapelites, oriented inclusion trails of white mica, chlorite and ilmenite in plagioclase and garnet porphyroblasts together with shape preferred orientation of kyanite and staurolite document growth of these minerals during the formation of the S2 foliation (Fig. 11b). The Barrovian succession of mineral growth together with the character of garnet zoning (Fig. 10) points to a prograde *P–T* path from 3.5–5 kbar and 490–520 °C to 6–7 kbar and ~630 °C.

The D3 deformation locally affects the S2 fabric by open to isoclinal folds but commonly entirely transposes the previous metamorphic banding into a new,

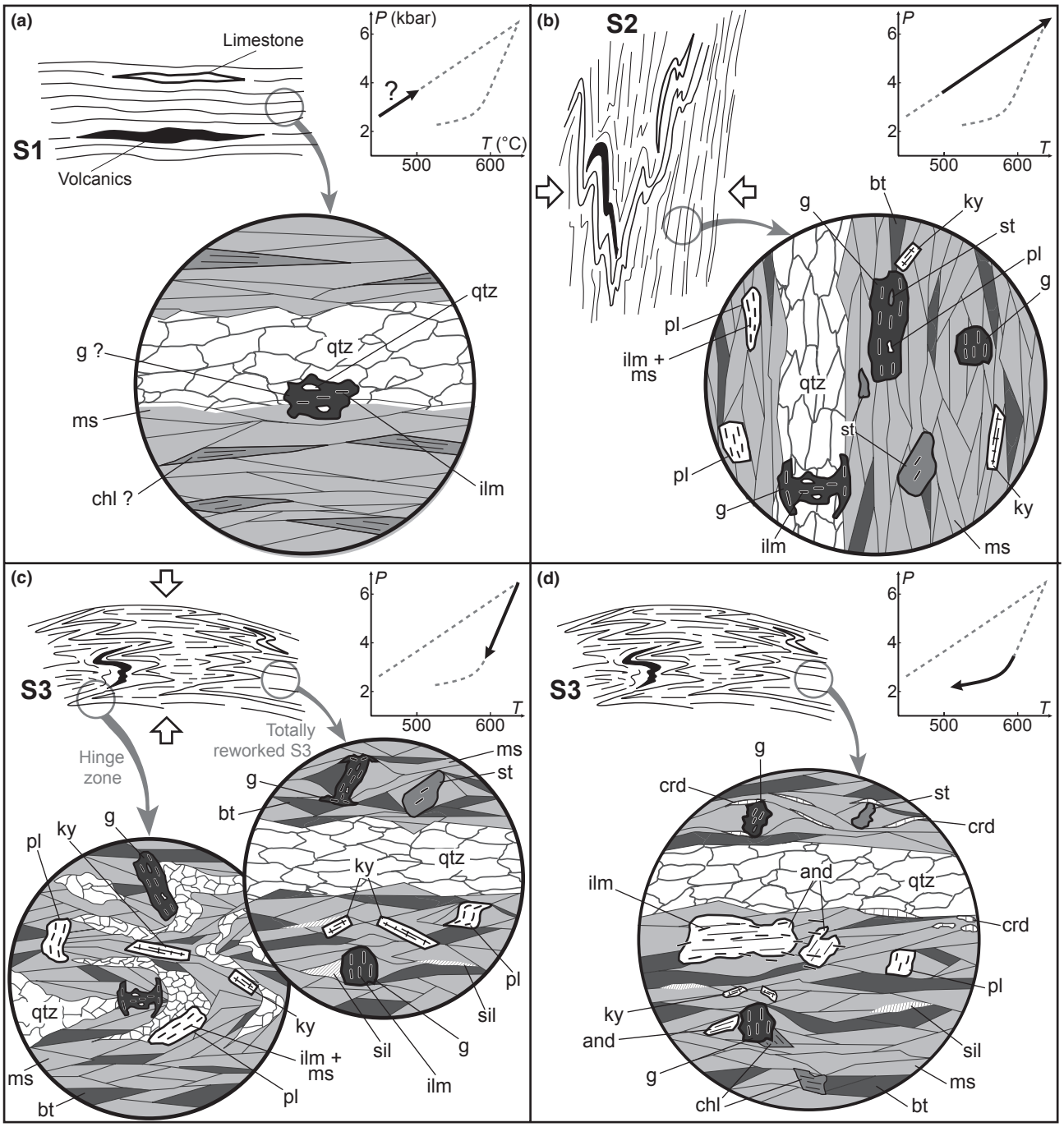

Fig. 11. (a–d) Sketches showing evolution of macrostructures, petrological succession and inferred *P*–*T* path. The orientation of inclusion trails within porphyroblasts and orientation of minerals with respect to the external structures shows the interpretation of the structural development of mineral assemblages during successive deformation phases. For discussion, see text.

flat-lying S3 structure. Some garnet and plagioclase rims parallel to the S3 fabric show that the shallow-dipping fabric started to develop at the metamorphic peak, where garnet stopped growing (Fig. 11c). Microstructural evidence of sillimanite–biotite growth in the garnet pressure shadows and in the shallow-dipping foliation suggests a crossing of the kyanite–sillimanite transition during the development of the S3 fabric and therefore indicates a drop in pressure towards ~4 kbar at temperatures still above 600 °C (Fig. 10). The andalusite in the pressure shadows of garnet and andalusite in quartz segregations oriented parallel to the S3 fabric (Fig. 11d) indicates that the D3 deformation and mineral growth continued down to ~3 kbar. Some andalusite and cordierite overgrow post-tectonically the S3 foliation indicating further

decrease in pressure to 2–3 kbar at temperatures between 530–630 °C after the D3 deformation (Fig. 10). Post-tectonic chlorite shows further cooling below 530 °C.

P–T–D–t relationships between metasedimentary rocks and neighbouring granulites

The *P–T–D* path (Figs 10 & 11) shows that rocks from the middle crust probably underwent early burial to 12 km under greenschist facies during formation of an early shallow-dipping fabric. Further burial from 12 km (~3.5 kbar) to 25 km (6–7 kbar) occurred during development of the regionally well-preserved subvertical fabric together with an increase in temperature from ~500 to 630–660 °C (Fig. 11). The age of the metamorphic peak may correspond to the *c*. 345 Ma Sm–Nd Garnet–WR isochron age from a kyanite-bearing metapelite located farther south where garnet growth was ascribed to the steeply dipping fabric by Jastrzębski (2008). A subsequent exhumation stage within the late shallow-dipping foliation is responsible for a minimum of 10 km of vertical displacement towards a depth of ~12 km (Fig. 12), evidenced by andalusite or cordierite growth, at still elevated temperatures of ~580 °C (Fig. 10).

An identical succession of fabrics in pelites, as well as in orthogneiss and granulite (Štípská *et al*., 2004), indicates a complete structural continuity between the investigated metasedimentary rocks and the high-pressure granulites located only 1–5 km to the SE (Fig. 2). Therefore, the tectono-metamorphic history of metasedimentary rocks can be compared to that of granulites. In granulites, an early, probably flat-lying, S1 fabric is folded into the subvertical S2 foliation that develops at a pressure peak of ~18 kbar and ~850 °C and is followed by heterogeneous shallow-dipping D3 deformation at 6–10 kbar and ~700 °C (Fig. 12). The prograde character of the remnants of the early shallow-dipping fabric is not demonstrated, but it is likely that the metamorphic peak of granulites is achieved before the onset of the D2 deformation (Štípská *et al*., 2004). The timing of the metamorphic peak is constrained by a SHRIMP U–Pb age of football-shaped zircon yielding *c*. 342 Ma, and the time span of granulite exhumation was estimated by the age of a syntectonic granodiorite sill emplaced in the Staré Město formation (Fig. 1) at *c*. 339 Ma (Pb–Pb zircon age) parallel to the S3 fabric in adjacent rocks (Parry *et al*., 1997; Štípská *et al*., 2001; Lexa *et al*., 2005). This shallow-dipping S3 fabric affected the hinge zone of the orthogneiss–granulite anticline, but because of the lack of pressure and temperature sensitive equilibria, the amount of vertical movement associated with the formation of the shallow-dipping fabric was not assessed in these rocks. Nevertheless, Štípská *et al*.

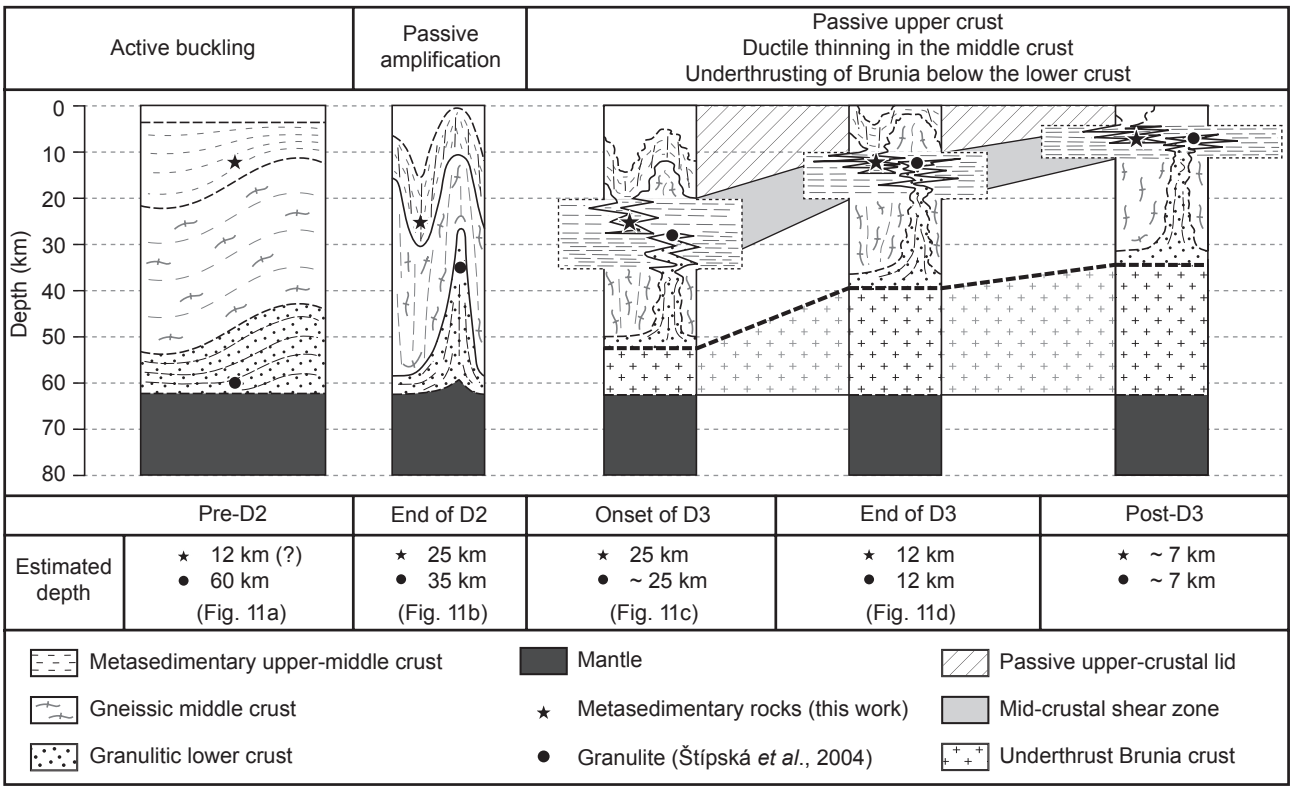

Fig. 12. Schematic evolution of the orogenic crust from thickening to exhumation. Inferred position of the Stronie formation metasedimentary rocks (black star) and neighbouring granulites (black circle) are indicated.

(2004) showed that the shallow-dipping fabric was probably associated with exhumation of the granulite belt from 10 to 6 kbar (Fig. 12).

In this way, the originally supracrustal metasedimentary rocks and the lower-crustal granulites were juxtaposed at a depth of 25–35 km during the formation of the steeply dipping S2 fabric (Fig. 12). The peak metamorphic conditions in the metasedimentary rocks and the retrograde amphibolite facies conditions in the granulites were roughly achieved at the same time of 345–340 Ma. This implies that the burial and exhumation events were fast, occurring in *c*. 5 Myr, and that the metasedimentary rocks and the granulites reached the same crustal level as a result of synchronous, but opposite, vertical movements. The subsequent evolution during the D3 deformation involved exhumation of both lithologies towards a depth of ~12 km (Fig. 12).

Burial–exhumation mechanisms and associated *P–T* paths

Although several mechanisms can account for burial and/or exhumation of mid- and lower-crustal rocks, they produce distinct *P–T* paths. An overview of observed and modelled *P–T* evolutions is likely to provide a basis for further discussing the different tectonic scenarii (Fig. 13).

Isothermal decompression is a typical metamorphic evolution in *orogenic lower-crustal lithologies* (e.g. Brown & Dallmeyer, 1996). Nevertheless, several processes can produce steep *retrograde P–T* paths (Fig. 13a). This could either be the result of diapiric rise (Teyssier & Whitney, 2002; Gerya *et al*., 2004), vertical extrusion (e.g. Thompson *et al*., 1997) or crustal-scale folding (Schulmann *et al*., 2005; Tajčmanová *et al*., 2006), where limited thermal exchange due to rapid exhumation is a key parameter and cooling is only reported for late parts of the *P–T* evolution. By contrast, a temperature increase followed by cooling during decompression is observed for erosional unroofing models (England & Thompson, 1984; Thompson *et al*., 1997).

These mechanisms related to lower-crustal exhumation have contrasted thermal consequences for *prograde P–T* paths of associated *mid-crustal rocks* (Fig. 13b). As an example, rocks from a syncline rimming a diapiric dome may follow a *P–T* path associated with exceptionally strong heating (Warren & Ellis, 1996), whereas models involving pure shear crustal thickening (Ruppel & Hodges, 1994) or crustal-scale folding reveal only moderate increase of temperature during burial (Chamberlain, 1986; Kim & Bell, 2005).

Subsequent exhumation of *juxtaposed orogenic lower- and mid-crustal rocks* from mid-crustal levels to shallower crustal levels can also occur along distinct *retrograde P–T* paths (Fig. 13c). During this phase, the time that elapses before rocks reach a colder level, i.e. the duration of thermal relaxation at depth, plays a major role on the shape of the *P–T* loop (England & Thompson, 1984; their fig. 2). The result is a more or less pronounced temperature increase after peak pressure or even a decrease in both pressure and temperature. This timing is critical for ductile extrusion models where mid-crustal rocks surrounding the hot channel are exhumed more slowly than the low-viscosity deep crustal rocks (e.g. Jamieson *et al*., 2002).

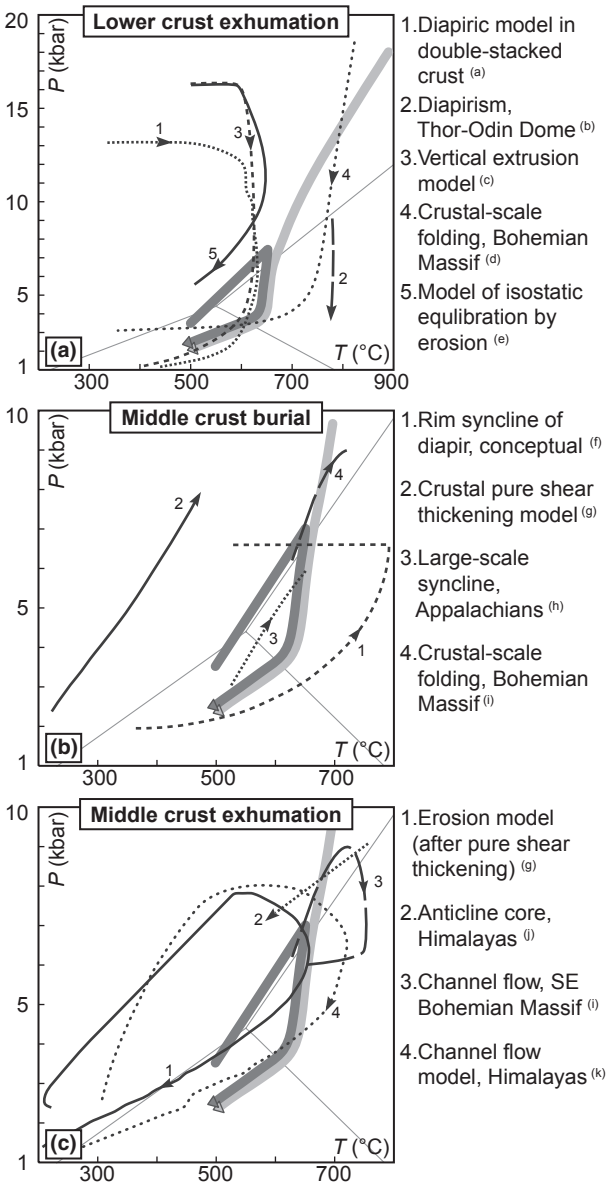

Fig. 13. Comparison between *P–T* paths for metasedimentary rocks (dark grey) and granulites (light grey) investigated by Štípská *et al*. (2004), and published *P–T* paths for different mechanisms of (a) exhumation of the orogenic lower crust, (b) burial of associated mid-crustal rocks and (c) exhumation of mid-crustal level. Modelled or observed *P–T* paths are after: (a) Gerya *et al*. (2004), (b) Norlander *et al*. (2002), (c, e) Thompson *et al*. (1997), (d) Tajčmanová *et al*. (2006), (f) Warren & Ellis (1996), (g) Ruppel & Hodges (1994), (h) Chamberlain (1986), (i) Racek *et al*. (2006), (j) Burg *et al*. (1997) and (k) Jamieson *et al*. (2004). Al_2SiO_5 phase diagram is shown for orientation.

Tectonic significance of metamorphic record in the vertical fabric

Štípská *et al.* (2004) interpreted the *P–T–D* path of granulites in terms of vertical flow of the orogenic lower crust towards mid-crustal levels. Different processes can account for such a retrograde path (Fig. 13a) and it is therefore essential to examine the *P–T* record of associated rocks from the middle crust.

If the granulites are considered as a diapirically rising dome for which isothermal decompression paths are classically documented (e.g. Norlander *et al.*, 2002; Duchêne *et al.*, 2006), neighbouring rocks from the rim syncline should record an anticlockwise *P–T* evolution (Fig. 13b) as proposed by Warren & Ellis (1996). However, cooling of the granulite during exhumation together with clockwise prograde path, high initial temperature and low density of the middle crust all seem to invalidate the diapiric hypothesis. By contrast, folding mechanisms involving burial in synforms are likely to produce prograde *P–T* paths similar to that one presented in Fig. 10 (e.g. Chamberlain, 1986; Fig. 13b). In the model of Sleep (1979), buckling of the lithological boundaries involves conservation of mass but does not allow shortening to occur parallel to the fold axial-plane surface. It follows that the rate of heating within synforms should be similar to the cooling rate within antiforms. However, given the discrepancy between heating of the Stronie metasedimentary rocks and cooling of granulites (Fig. 13), a different folding mechanism should be envisaged.

Field observations suggest that the fold pattern resembles an alternation of orthogneiss antiforms with rounded shape and large wavelength and pinched synforms of the Stronie rocks with shorter wavelength (Dumicz, 1979; Don, 1982). Such geometry has also been observed to the south of the OSD where eclogites and metasedimentary rocks are pinched on both sides of an orthogneiss body. Therefore, a mechanism of passive amplification of an initially cuspate–lobate interface producing large-scale folds to explain the vertical exchange between the middle and the lower crust in the subvertical S2 fabric is preferred. Microstructural observations suggest that this pervasive S2 fabric affecting the whole area probably results from pure shear dominated deformation, as also suggested by Skrzypek *et al.* (2010).

This concept of crustal-scale folding is similar to detachment folding modelled by Burg *et al.* (2004). In this view, the retrograde path in granulites could be compatible with extrusion models (e.g. Thompson *et al.*, 1997; Fig. 13a) also involving a significant erosional contribution to account for the observed cooling. Strong erosion during this period is potentially witnessed in the Intra-Sudetic Basin by abundant Lower Carboniferous sediment supply showing southeast provenance (Teisseyre, 1968, 1971, 1975). Cooling of the exhumed granulites could also be the result of thermal exchange with metasedimentary rocks because the rocks were stopped at mid-crustal level instead of being further rapidly extruded as in the case of diapiric models. In addition, the associated prograde *P–T* path in metasedimentary rocks can be explained by burial in the neighbouring syncline (Chamberlain, 1986; Fig. 13b).

Tectonic significance of metamorphic record in the shallow-dipping fabric

Provided that the metamorphic evolution of the Stronie metasedimentary rocks and granulites during the D3 deformation was coeval, the significance of metamorphic evolution of both units during the formation of the shallow-dipping fabric can be discussed.

In the SE part of the Bohemian Massif, mid- and lower-crustal rocks record juxtaposition at a similar crustal level by opposite vertical movements followed by a subhorizontal deformation (Racek *et al.*, 2006). In this region, the middle crust was further heated from 650 to ~750 °C after peak pressure (Fig. 13c), indicating that thermal relaxation or additional heat supply had to occur. These observations have been explained in terms of horizontal influx of hot granulitic and migmatitic rocks into colder mid-crustal lithologies that were subsequently mixed in a crustal channel (Racek *et al.*, 2006; Schulmann *et al.*, 2008; Štípská *et al.*, 2008). This process is described as a heterogeneous channel flow, where a mass of hot lower-crustal rocks transports remnants of mid-crustal synclines over continental basement. Evolution in a hot horizontal channel is also documented in the Himalayas by Jessup *et al.* (2006) and associated *P–T* paths involving post-peak heating (Fig. 13c) have been modelled by e.g. Jamieson *et al.* (2004).

However, petrological data presented in this work do not fit the channel flow model. Indeed, metapelites and granulites indicate a decrease in both pressure and temperature as long as the shallow-dipping fabric evolved (Figs 10 & 13c). Although producing compatible retrograde *P–T* paths, the model of exhumation in the core of a large antiform associated with erosion (Burg *et al.*, 1997) can probably be ruled out because no shallow-dipping fabrics are created during this process. By contrast, the early retrograde *P–T* path of granulites suggested that strong erosion already occurred during the subvertical fabric development. This mechanism is likely to persist during later exhumation and may therefore enhance cooling of the crust (Fig. 13c), as demonstrated by erosional models of Ruppel & Hodges (1994). Lack of additional heat could also be due to the relatively small amount of hot granulitic material that has been brought in contact with the middle crust, compared to the southern Moldanubian domain.

However, there is further need for an exhumation mechanism that would be responsible for the widespread flat-lying deformation observed in the whole area (Fig. 2). The mechanism of ductile thinning (Ring

& Brandon, 1999; Ring *et al*., 1999) may be responsible for the unroofing of high-grade core of continental orogens either by homogeneous vertical shortening process (Vanderhaeghe & Teyssier, 2001), or by activity of localized extensional detachments (Platt, 1993). In summary, the ductile thinning brings rocks closer to the surface by vertical shortening of the overlying crustal column at a given crustal level (Fig. 12), in conjunction with continuous cooling, which accelerates as the rocks approach the surface (Feehan & Brandon, 1999). From structural, microstructural (Skrzypek *et al*., 2010) and petrological observations, ductile thinning together with erosion can account for the retrograde *P–T–D* path of both granulites and metapelites.

The driving force for the formation of the horizontal foliation and the ductile thinning process is suggested to be the underthrusting of the Orlica–Śnieżnik root by the eastern Staré Město formation and the Brunovistulian continent during the Carboniferous (Fig. 12). This was proposed for example by Schulmann & Gayer (2000), Štípská *et al*. (2004, 2006). Isostatic re-equilibration of a thickened root leads to horizontal flow, generally localized underneath the rigid lid (Dewey *et al*., 1993; Koyi *et al*., 1999; Milnes & Koyi, 2000). In the study area, the restoration of a standard crustal thickness of 35 km (Fig. 12) was probably achieved during late Carboniferous extensional stretching and thinning of the whole thickened crust due to the activity of a major detachment zone (the Ramzová detachment) located close to the OSD and the imbricated Brunovistulian boundary (Schulmann & Gayer, 2000).

Diagnostic paired *P–T–D* paths?

A wide range of mechanisms can usually be related to any observed *P–T* path, but because the resolution of petrology is generally not sufficient, a strong link between deformation structures and metamorphism can help distinguish between different tectonic processes. In the present case, two major mechanisms, i.e. diapirism and large-scale folding, can account for vertical transfers between shallow and deep crustal rocks and subsequent flattening of exhumed lithologies (Burg *et al*., 2004). However, important features of the diapiric model such as the lack of flat-lying deformation in the buried rocks and the high thermal regime (Warren & Ellis, 1996) are incompatible with both the observed structural *and* metamorphic records in the investigated metasedimentary rocks and neighbouring granulites (Štípská *et al*., 2004). By contrast, the observed converging *P–T* paths of mid- and lower-crustal rocks associated to vertical flow are compatible with vertical exchanges of material through crustal-scale folding (Racek *et al*., 2006) whereas the subsequent joint decompression and cooling experienced by both lithologies in a shallow-dipping foliation suggest that exhumation was achieved by dominant ductile thinning (Ring & Brandon, 1999) and erosional unroofing. We finally suggest that the identification of paired *P–T–D* paths with similar features to those presented in this study could be further used to favour the proposed burial and exhumation processes, not only in the Variscan belt of Europe but also in other continental wedges worldwide.

ACKNOWLEDGEMENTS

E. Skrzypek kindly acknowledges funding by BRGM and Région Alsace. Financial support of the French National Grant Agency (06-1148784 to K. Schulmann) is gratefully acknowledged. The grant MSM0021620855 of the Ministry of Education of the Czech Republic is acknowledged for salary and financial support of O. Lexa. We are indebted to M. Caddick for thorough petrological comments and to J. Selverstone for useful suggestions on the discussion. M. Brown is thanked for careful editorial work.

REFERENCES

Anczkiewicz, R., Szczepański, J., Mazur, S. *et al*., 2007. Lu–Hf geochronology and trace element distribution in garnet: Implications for uplift and exhumation of ultra-high pressure granulites in the Sudetes, SW Poland. *Lithos*, **95,** 363–380.

Bakun-Czubarow, N., 1991. On the possibility of occurence of quartz pseudomorph after coesite in the eclogite-granulite rock series of the Złote Mountains in the Sudetes (SW Poland). *Archiwum Mineralogiczne*, **47,** 5–16.

Bell, T.H. & Johnson, S.E., 1989. Porphyroblast inclusion trails; the key to orogenesis. *Journal of Metamorphic Geology*, **7,** 279–310.

Bröcker, M. & Klemd, R., 1996. Ultrahigh-pressure metamorphism in the Śnieżnik Mountains (Sudetes, Poland): P-T constraints and geological implications. *Journal of Geology*, **104,** 417–433.

Bröcker, M., Klemd, R., Cosca, M., Brock, W., Larionov, A.N. & Rodionov, N., 2009. The timing of eclogite facies metamorphism and migmatization in the Orlica–Śnieżnik complex, Bohemian Massif: constraints from a multimethod geochronological study. *Journal of Metamorphic Geology*, **27,** 385–403.

Brown, M. & Dallmeyer, R.D., 1996. Rapid Variscan exhumation and the role of magma in core complex formation; southern Brittany metamorphic belt, France. *Journal of Metamorphic Geology*, **14,** 361–379.

Brueckner, H.K., Medaris, L.G. & Bakun-Czubarow, N., 1991. Nd and Sr age and isotope patterns from Variscan eclogites of the eastern Bohemian Massif. *Neues Jahrbuch für Mineralogie, Abhandlungen*, **163,** 169–196.

Burg, J.-P., Davy, P., Nievergelt, P. *et al*., 1997. Exhumation during crustal folding in the Namche-Barwa syntaxis. *Terra Nova*, **9,** 53–56.

Burg, J.-P., Kaus, B.J.P. & Podlachikov, Y.Y., 2004. Dome structures in collision orogens: mechanical investigation of the gravity/compression interplay. In: *Gneiss Domes in Orogeny* (eds Whitney, D.L., Teyssier, C. & Siddoway, C.S.), pp. 47–66. Geological Society of America Special Paper, Boulder, CO, USA.

Caddick, M. & Thompson, A.B., 2008. Quantifying the tectono-metamorphic evolution of pelitic rocks from a wide range of tectonic settings: mineral compositions in equilibrium. *Contributions to Mineralogy and Petrology*, **156,** 177–195.

Carswell, D.A., Brueckner, H.K., Cuthbert, S.J., Mehta, K. & O'Brien, P.J., 2003. The timing of stabilisation and the exhumation rate for ultra-high pressure rocks in the Western

Gneiss Region of Norway. *Journal of Metamorphic Geology*, **21,** 601–612.
Chamberlain, C.P., 1986. Evidence for the repeated folding of isotherms during regional metamorphism. *Journal of Petrology*, **27,** 63–89.
Coggon, R. & Holland, T.J.B., 2002. Mixing properties of phengitic micas and revised garnet-phengite thermobarometers. *Journal of Metamorphic Geology*, **20,** 683–696.
Collins, A.S., Kryza, R. & Zalasiewicz, J., 2000. Macrofabric fingerprints of Late Devonian-Early Carboniferous subduction in the Polish Variscides, the Kaczawa complex, Sudetes. *Journal of the Geological Society, London*, **157,** 283–288.
Dewey, J.F., Ryan, P.D. & Andersen, T.B., 1993. Orogenic uplift and collapse, crustal thickness, fabrics and metamorphic phase changes; the role of eclogites. In: *Magmatic Processes and Plate Tectonics* (eds Prichard, H.M., Alabaster, T., Harris, N.B.W. & Neary, C.R.), *Geological Society of London Special Publications*, **76,** 325–343.
Don, J., 1982. The Sienna synform and the relationship of gneisses to the deformational stages distinguished in the Śnieżnik metamorphic massif (Sudetes). *Geologia Sudetica*, **17,** 103–124.
Don, J., Dumicz, M., Wojciechowska, I. & Zelazniewicz, A., 1990. Lihology and tectonics of the Orlica-Śnieżnik Dome, Sudetes: recent state of knowledge. *Neues Jahrbuch für Geologie und Paläontologie, Abhandlungen*, **179,** 159–188.
Duchêne, S., Lardeaux, J.M. & Albarede, F., 1997. Exhumation of eclogites: insights from depth-time path analysis. *Tectonophysics*, **280,** 125–140.
Duchêne, S., Aïssa, R. & Vanderhaeghe, O., 2006. Pressure-temperature-time evolution of metamorphic rocks from Naxos (Cyclades, Greece): constraints from thermobarometry and Rb/Sr dating. *Geodinamica Acta*, **19,** 301–321.
Dumicz, M., 1979. Tectogenesis of the metamorphosed series of the Kłodzko district: a tentative explanation. *Geologia Sudetica*, **14,** 29–44.
Edel, J.-B., Schulmann, K. & Holub, F.V., 2003. Anticlockwise and clockwise rotations of the Eastern Variscides accommodated by dextral lithospheric wrenching: palaeomagnetic and structural evidence. *Journal of the Geological Society, London*, **160,** 209–218.
England, P.C. & Thompson, A.B., 1984. Pressure-temperature-time paths of regional metamorphism I. Heat-transfer during the evolution of regions of thickened continental-crust. *Journal of Petrology*, **25,** 894–928.
Feehan, J.G. & Brandon, M.T., 1999. Contribution of ductile flow to exhumation of low-temperature, high-pressure metamorphic rocks: San Juan Cascade nappes, NW Washington State. *Journal of Geophysical Research*, **104,** 10,883–10,902.
Floyd, P.A., Winchester, J.A., Ciesielczuk, J., Lewandowska, A., Szczepanski, J. & Turniak, K., 1996. Geochemistry of early Palaeozoic amphibolites from the Orlica-Śnieżnik dome, Bohemian Massif: petrogenesis and palaeotectonic aspects. *Geologische Rundschau*, **85,** 225–238.
Franěk, J., Schulmann, K. & Lexa, O., 2006. Kinematic and rheological model of exhumation of high pressure granulites in the Variscan orogenic root: example of the Blanský les granulite, Bohemian Massif, Czech Republic. *Mineralogy and Petrology*, **86,** 253–276.
Gerya, T.V., Perchuk, L.L., Maresch, W.V. & Willner, A.P., 2004. Inherent gravitational instability of hot continental crust: implications for doming and diapirism in granulite facies terrains. In: *Gneiss Domes in Orogeny* (eds Whitney, D.L., Teyssier, C. & Siddoway, C.S.), pp. 97–115. Geological Society of America Special Paper, Boulder, CO, USA.
Holland, T.J.B. & Powell, R., 1998. An internally consistent thermodynamic data set for phases of petrological interest. *Journal of Metamorphic Geology*, **16,** 309–343.
Holland, T. & Powell, R., 2003. Activity-composition relations for phases in petrological calculations: an asymmetric multicomponent formulation. *Contributions to Mineralogy and Petrology*, **145,** 492–501.
Holland, T.J.B., Baker, J. & Powell, R., 1998. Mixing properties and activity-composition relationships of chlorites in the system MgO-FeO-Al_2O_3-SiO_2-H_2O. *European Journal of Mineralogy*, **10,** 395–406.
Jamieson, R.A., Beaumont, C., Nguyen, M.H. & Lee, B., 2002. Interaction of metamorphism, deformation and exhumation in large convergent orogens. *Journal of Metamorphic Geology*, **20,** 9–24.
Jamieson, R.A., Beaumont, C., Medvedev, S. & Nguyen, M.H., 2004. Crustal channel flows: 2. Numerical models with implications for metamorphism in the Himalayan-Tibetan orogen. *Journal of Geophysical Research*, **109,** B06407.
Jastrzębski, M., 2005. The tectonometamorphic evolution of the marbles in the Lądek-Śnieżnik Metamorphic Unit, West Sudetes. *Geologia Sudetica*, **37,** 1–26.
Jastrzębski, M., 2008. A Variscan continental collision of the West Sudetes and the Brunovistulian terrane: a contribution from structural and metamorphic record of the Stronie Formation, the Orlica-Śnieżnik Dome, SW Poland. *International Journal of Earth Sciences*, **8,** 1901–1923.
Jessup, M.J., Law, R.D., Searle Mike, P. & Hubbard, M.S., 2006. Structural evolution and vorticity of flow during extrusion and exhumation of the Greater Himalayan Slab, Mount Everest Massif, Tibet/Nepal: implications for orogen-scale flow partitioning. In: *Channel flow, Extrusion, and Exhumation in Continental Collision Zones* (eds Law, R.D., Searle, M.P. & Godin, L.), *Geological Society of London Special Publications*, **268,** 355–378.
Kim, H.S. & Bell, T.H., 2005. Combining compositional zoning and foliation intersection axes (FIAs) in garnet to quantitatively determine early P-T-t paths in multiply deformed and metamorphosed schists: north central Massachusetts, USA. *Contributions to Mineralogy and Petrology*, **149,** 141–163.
Košuličová, M. & Štípská, P., 2007. Variations in the transient prograde geothermal gradient from chloritoid-staurolite equilibria: a case study from the Barrovian and Buchan-type domains in the Bohemian Massif. *Journal of Metamorphic Geology*, **25,** 19–35.
Koyi, H.A., Milnes, A.G., Schmeling, H., Talbot, C.J., Juhlin, C. & Zeyen, H., 1999. Numerical models of ductile rebound of crustal roots beneath mountain belts. *Geophysical Journal International*, **139,** 556–562.
Kozłowski, K., 1965. The granulitic complex of Stary Gierałtów – East Sudetes. *Archiwum Mineralogiczne*, **25,** 5–112.
Kröner, A., Štípská, P., Schulmann, K. & Jaeckel, P., 2000. Chronological constraints on the pre-Variscan evolution of the northeastern margin of the Bohemian Massif, Czech Republic. In: *Orogenic Processes; Quantification and Modelling in the Variscan Belt* (eds Franke, W., Haak, V., Oncken, O. & Tanner, D.). *Geological Society of London Special Publications*, **179,** 175–197.
Kröner, A., Jaeckel, P., Hegner, E. & Opletal, M., 2001. Single zircon ages and whole rock Nd isotopic systematics of early Palaeozoic granitoid gneisses from the Czech and Polish Sudetes (Jizerské hory, Krkonoše Mountains and Orlica-Sněžník Complex). *International Journal of Earth Sciences*, **90,** 304–324.
Lange, U., Bröcker, M., Mezger, K. & Don, J., 2002. Geochemistry and Rb-Sr geochronology of a ductile shear zone in the Orlica-Śnieżnik dome (West Sudetes, Poland). *International Journal of Earth Sciences*, **91,** 1005–1016.
Lange, U., Brocker, M., Armstrong, R., Trapp, E. & Mezger, K., 2005a. Sm-Nd and U-Pb dating of high-pressure granulites from the Złote and Rychleby Mts (Bohemian Massif, Poland and Czech Republic). *Journal of Metamorphic Geology*, **23,** 133–145.
Lange, U., Brocker, M., Armstrong, R., Zelazniewicz, A., Trapp, E. & Mezger, K., 2005b. The orthogneisses of the Orlica-Śnieżnik complex (West Sudetes, Poland): geochemical characteristics, the importance of pre-Variscan migmatization and constraints on the cooling history. *Journal of the Geological Society, London*, **162,** 973–984.

Lexa, O., Stipska, P., Schulmann, K., Baratoux, L. & Kroner, A., 2005. Contrasting textural record of two distinct metamorphic events of similar *P-T* conditions and different durations. *Journal of Metamorphic Geology*, **23,** 649–666.

Lexa, O., Schulmann, K., Janoušek, V., Štípská, P., Guy, A. & Racek, M., 2010. Heat sources and trigger mechanisms of exhumation of HP granulites in Variscan orogenic root. *Journal of Metamorphic Geology*, **29,** 79–102.

Mahar, E.M., Baker, J.M., Powell, R., Holland, T.J.B. & Howell, N., 1997. The effect of Mn on mineral stability in metapelites. *Journal of Metamorphic Geology*, **15,** 223–238.

Maluski, H. & Patočka, F., 1997. Geochemistry and $^{40}Ar/^{39}Ar$ geochronology of the mafic metavolcanic rocks from the Rýchory Mountains complex (west Sudetes, Bohemian Massif): paleotectonic significance. *Geological Magazine*, **134,** 703–716.

Mazur, S., Aleksandrowski, P. & Szczepański, J., 2005. The presumed Teplá-Barrandian/Moldanubian terrane boundary in the Orlica Mountains (Sudetes, Bohemian Massif): structural and petrological characteristics. *Lithos*, **82,** 85–112.

Milnes, A.G. & Koyi, H.A., 2000. Ductile rebound of an orogenic root; case study and numerical model of gravity tectonics in the Western Gneiss Complex, Caledonides, southern Norway. *Terra Nova*, **12,** 1–7.

Mųrtezi, M., 2006. The acid meta-volcanic rocks of the Orlica-Śnieżnik Dome (Sudetes): their origin and tectono-metamorphic evolution. *Geologia Sudetica*, **38,** 1–38.

Norlander, B.H., Whitney, D.L., Teyssier, C. & Vanderhaeghe, O., 2002. Partial melting and decompression of the Thor-Odin dome, Shuswap metamorphic core complex, Canadian Cordillera. *Lithos*, **61,** 103–125.

Parry, M., Stipska, P., Schulmann, K., Hrouda, F., Jezek, J. & Kroener, A., 1997. Tonalite sill emplacement at an oblique plate boundary; northeastern margin of the Bohemian Massif. In: *Thermal and Mechanical Interactions in Deep-seated Rocks* (ed. Schulmann, K.), pp. 61–81. Elsevier, Amsterdam, The Netherlands.

Platt, J.P., 1993. Exhumation of high-pressure rocks; a review of concepts and processes. *Terra Nova*, **5,** 119–133.

Powell, R. & Holland, T.J.B., 1999. Relating formulations of the thermodynamics of mineral solid solutions; activity modeling of pyroxenes, amphiboles, and micas. *American Mineralogist*, **84,** 1–14.

Powell, R., Holland, T. & Worley, B., 1998. Calculating phase diagrams involving solid solutions via non-linear equations, with examples using THERMOCALC. *Journal of Metamorphic Geology*, **16,** 577–588.

Racek, M., Štípská, P., Pitra, P., Schulmann, K. & Lexa, O., 2006. Metamorphic record of burial and exhumation of orogenic lower and middle crust: a new tectonothermal model for the Drosendorf window (Bohemian Massif, Austria). *Mineralogy and Petrology*, **86,** 221–251.

Ring, U. & Brandon, M.T., 1999. Ductile deformation and mass loss in the Franciscan Subduction Complex: implications for exhumation processes in accretionary wedges. In: *Exhumation Processes; Normal Faulting, Ductile Flow and Erosion* (eds Ring, U., Brandon, M.T., Willett, S.D. & Lister, G.S.), *Geological Society of London Special Publications*, **154,** 55–86.

Ring, U., Brandon, M.T., Willett, S.D. & Lister, G.S. 1999. Exhumation processes. In: *Exhumation Processes; Normal Faulting, Ductile Flow and Erosion* (eds Ring, U., Brandon, M.T., Willett, S.D. & Lister, G.S.), *Geological Society of London Special Publications*, **154,** 1–27.

Rubatto, D. & Hermann, J., 2001. Exhumation as fast as subduction? *Geology*, **29,** 3–6.

Ruppel, C. & Hodges, K.V., 1994. Pressure-temperature-time paths from two-dimensional thermal models: prograde, retrograde and inverted metamorphism. *Tectonics*, **13,** 17–44.

Schneider, D.A., Zahniser, S.J., Glascock, J.M., Gordon, S.M. & Manecki, M., 2006. Thermochronology of the West sudetes (Bohemian Massif): rapid and repeated eduction in the eastern Variscides, Poland and Czech Republic. *American Journal of Science*, **306,** 846–873.

Schulmann, K. & Gayer, R., 2000. A model for a continental accretionary wedge developed by oblique collision: the NE Bohemian Massif. *Journal of the Geological Society, London*, **157,** 401–416.

Schulmann, K., Kröner, A., Hegner, E. *et al*., 2005. Chronological constraints on the pre-orogenic history, burial and exhumation of deep-seated rocks along the eastern margin of the Variscan orogen, Bohemian Massif, Czech Republic. *American Journal of Science*, **305,** 407–448.

Schulmann, K., Lexa, O., Štípská, P. *et al*., 2008. Vertical extrusion and horizontal channel flow of orogenic lower crust: key exhumation mechanisms in large hot orogens? *Journal of Metamorphic Geology*, **26,** 273–297.

Skrzypek, E., Schulmann, K., Štípská, P. *et al*., 2011. Tectonometamorphic history recorded in garnet porphyroblasts: insights from thermodynamic modelling and electron backscatter diffraction analysis of inclusion trails. *Journal of Metamorphic Geology*, in press.

Sleep, N.H., 1979. A thermal constraint on the duration of folding with reference to Acadian Geology, New England (USA). *Journal of Geology*, **87,** 583–589.

Smulikowski, K., 1967. Eclogites of the Śnieżnik Mts in the Sudetes. *Geologia Sudetica*, **3,** 157–174.

Spear, F.S. & Cheney, J.T., 1989. A petrogenetic grid for pelitic schists in the system SiO_2-Al_2O_3-FeO-MgO-K_2O-H_2O. *Contributions to Mineralogy and Petrology*, **101,** 149–164.

Steltenpohl, M.G., Cymerman, Z., Krogh, E.J. & Kunk, M.J., 1993. Exhumation of eclogitised continental basement during Variscan lithospheric delamination and gravitational collapse, Sudety Mountains, Poland. *Geology*, **21,** 1111–1114.

Štípská, P., Schulmann, K., Thompson, A.B., Ježek, J. & Kröner, A., 2001. Thermo-mechanical role of a Cambro-Ordovician paleorift during the Variscan collision: the NE margin of the Bohemian Massif. *Tectonophysics*, **332,** 239–253.

Štípská, P., Schulmann, K. & Kröner, A., 2004. Vertical extrusion and middle crustal spreading of omphacite granulite: a model of syn-convergent exhumation (Bohemian Massif, Czech Republic). *Journal of Metamorphic Geology*, **22,** 179–198.

Štípská, P., Pitra, P. & Powell, R., 2006. Separate or shared metamorphic histories of eclogites and surrounding rocks? An example from the Bohemian Massif. *Journal of Metamorphic Geology*, **24,** 219–240.

Štípská, P., Schulmann, K. & Powell, R., 2008. Contrasting metamorphic histories of lenses of high-pressure rocks and host migmatites with a flat orogenic fabric (Bohemian Massif, Czech Republic): a result of tectonic mixing within horizontal crustal flow? *Journal of Metamorphic Geology*, **26,** 623–646.

Tajčmanová, L., Konopásek, J. & Schulmann, K., 2006. Thermal evolution of the orogenic lower crust during exhumation within a thickened Moldanubian root of the Variscan belt of Central Europe. *Journal of Metamorphic Geology*, **24,** 119–134.

Teisseyre, A.K., 1968. Sedimentology of the lowermost continental Culm deposits in the northern part of the Intra-Sudetic Basin. *Geologia Sudetica*, **4,** 221–298.

Teisseyre, A.K., 1971. Sedimentology of the Culm from Ciechanowice and palaeogeography of the lowermost Culm deposits of the Intra-Sudetic Basin. *Geologia Sudetica*, **5,** 237–280.

Teisseyre, A.K., 1975. Sedimentology and palaeogeography of the Culm alluvial fans in the Western the Intra-Sudetic Basin. *Geologia Sudetica*, **9,** 7–135.

Teyssier, C. & Whitney, D.L., 2002. Gneiss domes and orogeny. *Geology*, **30,** 1139–1142.

Thompson, A.B., Schulmann, K. & Ježek, J., 1997. Extrusion tectonics and elevation of lower crustal metamorphic rocks in convergent orogens. *Geology*, **25,** 491–494.

Turniak, K., Mazur, S. & Wysoczanski, R., 2000. SHRIMP zircon geochronology and geochemistry of the Orlica-Śnieżnik

gneisses (Variscan belt of Central Europe) and their tectonic implications. *Geodinamica Acta*, **13,** 1–20.
Vanderhaeghe, O. & Teyssier, C., 2001. Partial melting and flow of orogens. *Tectonophysics*, **342,** 451–472.
Vanderhaeghe, O., Burg, J.P. & Teyssier, C., 1999. Exhumation of migmatites in two collapsed orogens; Canadian Cordillera and French Variscides. In: *Exhumation Processes; Normal Faulting, Ductile Flow and Erosion* (eds Ring, U., Brandon, M.T., Lister, G.S. & Willett, S.D.), pp. 181–204. Geological Society Special Publications, Geological Society of London, London, UK.
Warren, R.G. & Ellis, D.J., 1996. Mantle underplating, granite tectonics, and metamorphic P-T-t paths. *Geology*, **24,** 663–666.
White, R.W., Powell, R. & Holland, T.J.B., 2007. Progress relating to calculation of partial melting equilibria for metapelites. *Journal of Metamorphic Geology*, **25,** 511–527.
Whitney, D.L., Teyssier, C. & Vanderhaeghe, O., 2004. Gneiss domes and crustal flow. In: *Gneiss Domes in Orogeny* (eds Whitney, D.L., Teyssier, C. & Siddoway, C.S.), pp. 15–33. Geological Society of America Special Paper, Boulder, CO, USA.
Wojciechowska, I., 1972. Preliminary results of investigations on so-called "Quartzites" in the neighbourhood of Romanowo (Stronie Complex), NW Part of Krowiarki (East Sudetes). *Bulletin de l'Académie Polonaise des Sciences, série Sciences de la Terre*, **20,** 273–277.
Zuluaga, C.A., Stowell, H.H. & Tinkham, D., 2005. The effect of zoned garnet on metapelite pseudosection topology and calculated metamorphic P-T paths. *American Mineralogist*, **90,** 1619–1628.

Received 17 September 2010; revision accepted 7 December 2010.

Journal of
METAMORPHIC GEOLOGY

J. metamorphic Geol., 2011, **29,** 473–496 doi:10.1111/j.1525-1314.2010.00925.x

Tectono-metamorphic history recorded in garnet porphyroblasts: insights from thermodynamic modelling and electron backscatter diffraction analysis of inclusion trails

E. SKRZYPEK,[1] K. SCHULMANN,[1] P. ŠTÍPSKÁ,[1] F. CHOPIN,[1] J. LEHMANN,[1] O. LEXA[2,3] AND J. HALODA[3]

[1]*Ecole et Observatoire des Sciences de la Terre – UMR 7516, Université de Strasbourg, 1, rue Blessig, 67084 Strasbourg, France (etienne.skrzypek@eost.u-strasbg.fr)*

[2]*Institute of Petrology and Structural Geology, Charles University, Albertov 6, 128 43 Prague, Czech Republic*

[3]*Czech Geological Survey, Klárov 3, 110 00 Prague, Czech Republic*

ABSTRACT In a Barrovian metamorphic sequence, garnetiferous mica schists document a heterogeneously developed superposition of sub-orthogonal fabrics and multiple garnet growth episodes. In the variably deformed domains, four types of garnet porphyroblasts have been defined based on inclusion trail patterns. Modelled garnet zoning in the MnNCKFMASHTO system indicates a prograde evolution from 4–4.5 kbar and 490–510 °C to 5–6 kbar and 520–550 °C in the earliest subhorizontal fabric progressing towards 6.5–7.5 kbar and 560–590 °C in the subsequent subvertical foliation. This fabric is heterogeneously deformed into a shallow-dipping retrograde foliation associated with garnet resorption. *In situ* electron backscatter diffraction measurements of ilmenite inclusions in individual garnet grains yield precise data on included planar and linear elements. Consistent orientations of internal foliations, lineations and foliation intersection axis sets indicate a superposition of three sub-orthogonal foliation systems. Weak variations of internal records with increasing intensity of deformation suggest that a moderate buckling stage occurred, but apparent lack of porphyroblast rotation is interpreted as a result of dominant passive flow. Coupling the orientation of internal fabric sets with *P–T* estimates is used to complement the tectono-metamorphic evolution of the thickened crust. We demonstrate that garnet porphyroblasts preserve features which reflect large-scale tectonic processes in orogens.

Key words: electron backscatter diffraction; foliation intersection axes; garnet porphyroblasts; inclusion trails; thermodynamic modelling.

INTRODUCTION

Porphyroblastic minerals are common in polydeformed and polymetamorphosed rocks. Because they preserve primary features relatively undisturbed by subsequent tectono-metamorphic events, they have been the focus of numerous studies. Indeed, porphyroblasts may document the stability of older minerals when these are present as inclusions, the succession of mineral fabrics if included minerals define clear trails, and *P–T* evolution if chemical zoning is preserved. Careful study of porphyroblasts can therefore help in solving key issues such as: (i) the deformation regime during and after their formation and (ii) *P–T* conditions under which they formed. Combining these pieces of information can unravel the deformational and metamorphic history of rocks during distinct episodes of the orogenic evolution.

Porphyroblasts are commonly used to access information about overprinting tectono-metamorphic events. This approach assumes that the porphyroblasts have not been perturbed, either chemically or tectonically, by any subsequent orogenic evolution. Whereas petrological studies emphasize the minor role of diffusional resetting in medium-grade rocks, the significance of inclusion trail microstructures remains strongly debated. Not only the quantification of porphyroblast internal records but also their tectonic implications are matters of discussion. It is therefore necessary to demonstrate how strongly inclusion trail data reflect past tectonic processes. This is the purpose of this contribution that compares orogenic fabrics with precise measurements of garnet internal records.

In the Orlica–Śnieżnik Dome (OSD) (West Sudetes), garnet-bearing metapelites that underwent polyphase deformation and associated metamorphism (Dumicz, 1979; Jastrzębski, 2008) display a succession of subhorizontal and subvertical fabrics. Because the different deformation events heterogeneously affected the whole unit, relics of earlier-formed structures and progressive stages of foliation superposition are well preserved. This area is therefore ideal for investigating

tectono-metamorphic processes and porphyroblast behaviour during polyphase deformation.

Garnet porphyroblasts preserving consistent inclusion trails have been investigated through zones showing variable intensity of crenulation cleavage development. The porphyroblast–matrix microstructural relationships are used to define four major garnet types preserving different internal fabrics. Pseudosection modelling of the main garnet types is then carried out to determine the *P–T* conditions corresponding to each fabric. This information is linked to precise measurements of the different inclusion trail microstructures using a new approach based on electron backscatter diffraction (EBSD) measurements of tabular ilmenite inclusions. The combined petrological and microstructural data are then used to discuss the use of porphyroblast records in orogenic belts.

BACKGROUND

Porphyroblasts commonly host rows of oriented inclusions that have been extensively used to infer crystallization-deformation relationships (e.g. Zwart, 1962) and decipher orogenic processes (e.g. Bell & Johnson, 1989). Microstructural studies of matrix foliation (S_e) and porphyroblast inclusion trails (S_i) have improved understanding of the deformational regimes during porphyroblast growth (e.g. Olesen, 1978; Vernon, 1978; Vernon *et al.*, 1993; Johnson & Vernon, 1995; Bell *et al.*, 1998). However, the accumulated data have continued the debate about rotation and non-rotation of porphyroblasts during growth (e.g. Bell *et al.*, 1992; Passchier *et al.*, 1992; Fay *et al.*, 2008; Bons *et al.*, 2009). Today, both rotational (Prior, 1987; Chan & Crespi, 1999; Ikeda *et al.*, 2002) and non-rotational (Fyson, 1980; Johnson, 1990; Aerden, 1995) behaviours have been documented in nature. The observed geometries of inclusion trails have been explained, for instance, by flexural flow folding (Visser & Mancktelow, 1992), coaxial deformation associated with passive folding (Ramsay, 1962; Stallard & Hickey, 2001; Timms, 2003), or deformation partitioning of bulk non-coaxial deformation into pure and simple shear components (Bell, 1981; Lister & Williams, 1983).

The different porphyroblast records have been investigated using a wide range of techniques. To retrieve orientation data from inclusion trails, serial thin sectioning (Bell *et al.*, 1995), serial polishing of samples (Jung *et al.*, 1999), statistical fitting of inclusion traces (Aerden, 2003) or more recently, computed X-ray tomography (Huddlestone-Holmes & Ketcham, 2005; Robyr *et al.*, 2007) have been used. The *P–T* conditions of porphyroblast growth have been assessed via thermobarometry (e.g. St Onge, 1987) or pseudosection modelling of chemical zoning (Kim & Bell, 2005), while absolute time constraints were generally based on electron microprobe U–Th–Pb dating of monazite inclusions (Bell & Welch, 2002).

GEOLOGICAL SETTING

Regional geology

The study area (Fig. 1) is located in the West Sudetes (Czech Republic, Poland), in the OSD. The OSD lies within the Moldanubian–Lugian internal domain (Fig. 1a), which is in contact with basement rocks of the Brunovistulian microcontinent to the east (Schulmann & Gayer, 2000; Štípská *et al.*, 2001; Lexa *et al.*, 2005; Kalvoda *et al.*, 2008). The OSD (Fig. 1b) is composed of orthogneisses and metasedimentary rocks, with scarce occurrences of granulite and eclogite (Don *et al.*, 1990). The investigated rocks belong to the Stronie (–Młynowiec) formation, which is mostly composed of mica schist and paragneiss with intercalations of amphibolite, marble and quartzite.

Geochronological and geochemical investigations suggest that the Stronie formation represents the infill of a Neoproterozoic to Middle Cambrian rifted intracontinental basin (Gunia, 1984a,b; Floyd *et al.*, 1996; Jastrzębski *et al.*, 2010). These were intruded at *c.* 500 Ma by granitic precursors of the orthogneisses (Turniak *et al.*, 2000; Kröner *et al.*, 2001). Peak metamorphism in the Stronie formation occurred during the Carboniferous, as suggested by a Sm–Nd Garnet–WR age of 346.5 ± 4.4 Ma (Jastrzębski, 2008), while later exhumation is documented by 340–330 Ma ^{40}Ar–^{39}Ar cooling ages on muscovite and biotite (Schneider *et al.*, 2006).

Several authors have already emphasized the polydeformed character of metapelite (Jastrzębski, 2008; Skrzypek *et al.*, 2010), gneiss (Dumicz, 1979; Żelażniewicz, 1988; Don *et al.*, 1990) and granulite (Štípská *et al.*, 2004) of the OSD. They recognized that a subvertical fabric was subsequently reworked and transposed into a flat-lying fabric. In addition, Štípská *et al.* (2004) pointed out that the earliest metamorphic fabric was probably flat-lying.

Petrological studies indicate that the Stronie formation underwent metamorphism reaching amphibolite facies conditions. In the central part of the OSD, Jastrzębski (2008) documented prograde metamorphism up to 10 kbar and 510 °C associated with the subvertical fabric, followed by a temperature increase to 620 °C at 7–8 kbar in the shallow-dipping fabric. In the eastern part of the OSD, Skrzypek *et al.* (2010) proposed a prograde evolution up to 7 kbar and 630 °C in the subvertical fabric, followed by a decrease of both temperature and pressure during development of the flat-lying fabric.

The poorly constrained earliest flat-lying structure is thought to record peak crustal thickening (Štípská *et al.*, 2004). According to Dumicz (1979), the subvertical fabric results from E–W shortening and is responsible for the alternation of antiforms cored by gneisses and synforms cored by metasedimentary rocks (Don, 1982), whereas the subsequent subhorizontal fabric results from subvertical shortening triggered by gravitational

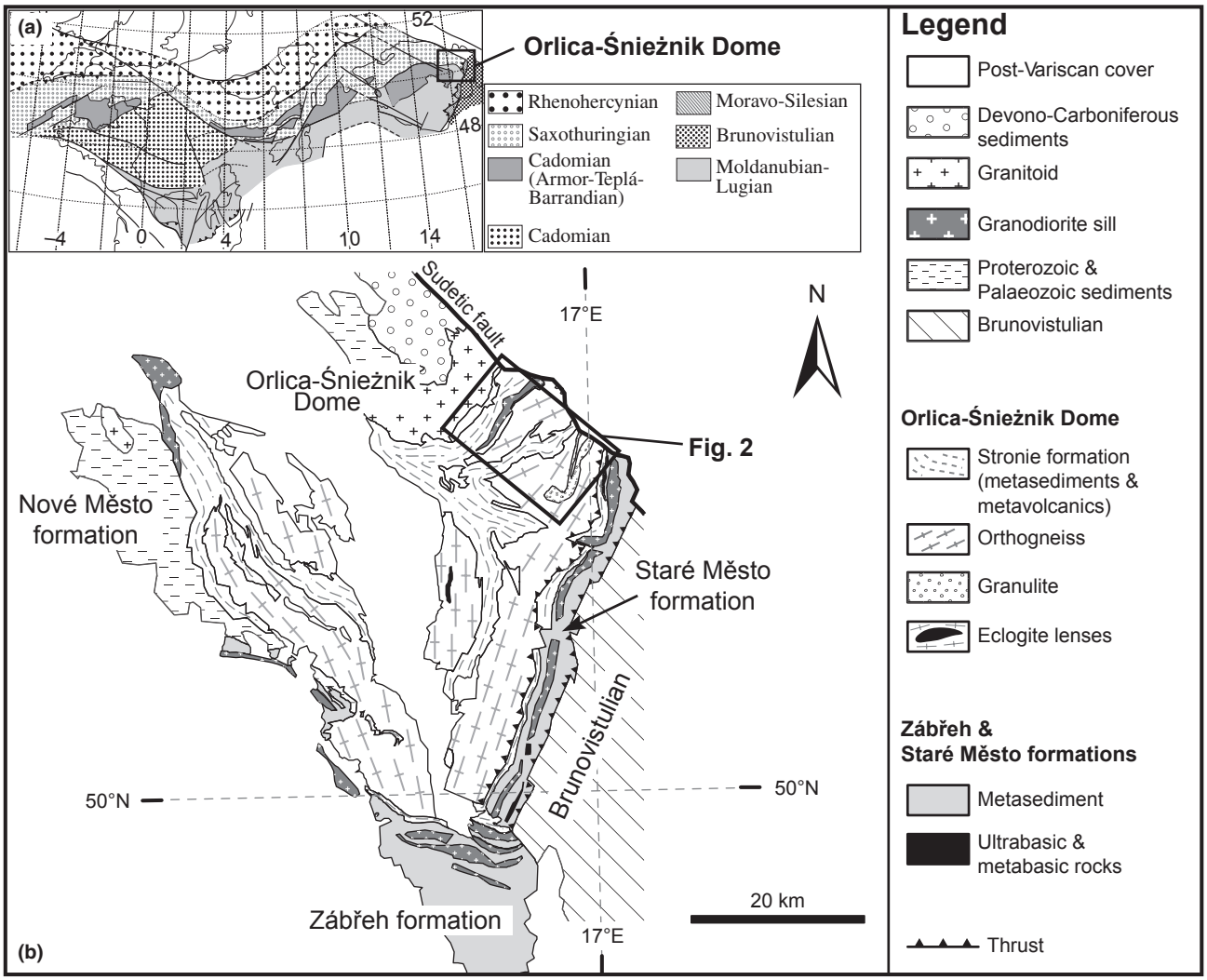

Fig. 1. Tectonic setting and geology of the study area. (a) Position of the West Sudetes in the European Variscides (after Edel *et al*., 2003). (b) Geological map of the Orlica-Śnieżnik Dome (modified after Don *et al*., 2003 and Żelaźniewicz *et al*., 2006).

loading. Štípská *et al*. (2004) and Skrzypek *et al*. (2010) related the subvertical structure to extrusion of granulites and contemporaneous burial of metasedimentary rocks by folding, while exhumation of both units is associated with development of the shallow-dipping fabric and is ascribed to ductile thinning.

Structural succession

S1 foliation

The first foliation only rarely occurs in the Bílá Voda valley located in the NW part of the study area (Fig. 2). It is preserved in quartz-rich lithologies as a weak, flat-lying schistosity without a distinct metamorphic differentiation (Fig. 3a). In orthogneiss, it is commonly refolded by rootless isoclinal folds (Fig. 3b). The regional orientation of S1 is difficult to determine, but rare outcrops (Fig. 3a) suggest that it was predominantly subhorizontal. The S1 foliation was also observed by Štípská *et al*. (2004), although only rarely, in granulite located to the SE (Fig. 2).

D2 structures

The subhorizontal S1 foliation was subsequently transposed into a NE–SW subvertical S2 foliation. This structure is dominant in the Bílá Voda valley, but can only be observed locally in few competent intercalations in the SE Javorník valley (Fig. 2). In the Bílá Voda valley, the S1 foliation is deformed by close to isoclinal upright F2 folds and a subvertical S2 discontinuous crenulation cleavage developed parallel to the F2 axial plane (Fig. 3b). In the SE Javorník valley, S1 is entirely transposed into a continuous S2 foliation. The F2 folds exhibit axial-plane and S2 cleavage steeply dipping to the NW or SE (Figs 2 & 3c), with fold hinges plunging shallowly to moderately to the NE or

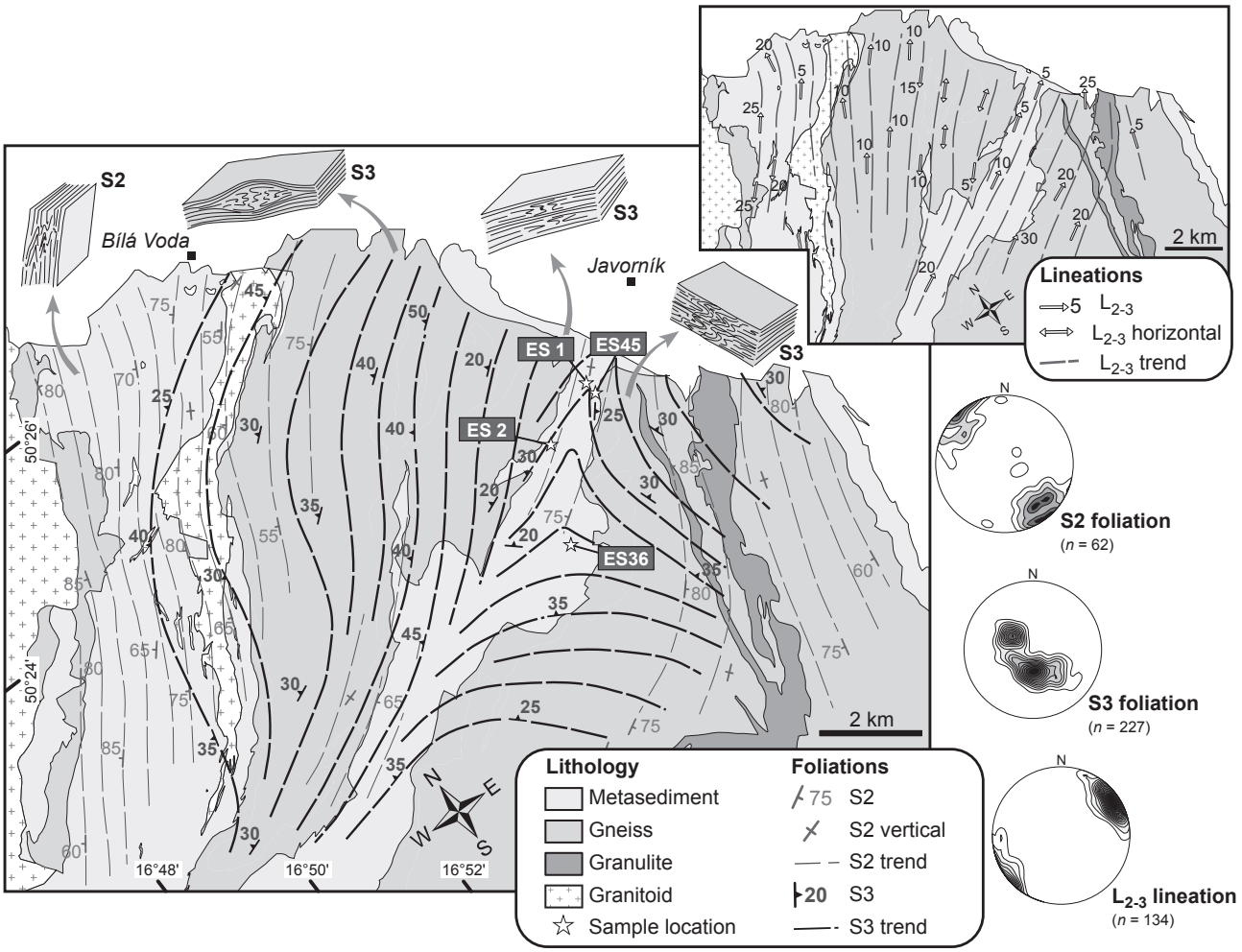

Fig. 2. Geological and structural map of the NE part of the Orlica-Śnieżnik Dome. Schematic blocks illustrate the dominant structural patterns across the area and stereonets show the orientation of the D2 and the D3 structures (Schmidt's net, lower hemisphere projection). The locations of samples used for petrology and EBSD analysis are indicated.

SW. In metapelitic rocks, the S2 foliation consists of a regularly spaced alternation of quartz- and mica-rich layers where small (0.5–1 cm) garnet crystals are occasionally present. The S2 foliation in the orthogneiss is composed of quartz–feldspar ribbons and thin (< 1 mm) continuous biotite-rich layers.

D3 structures

The D3 event heterogeneously deformed the subvertical S2 fabric and produced the subhorizontal S3 foliation. This fabric is dominantly developed in the Javorník valley (Fig. 2) but only weakly in the Bílá Voda valley. To the NW, the S2 is weakly folded into open recumbent folds with minor development of the subhorizontal S3 axial-plane cleavage. Towards the SE, the intensity of the D3 increases. Competent intercalations of marble and amphibolite show open to close, commonly asymmetric and recumbent F3 folds with a weak S3 axial-plane cleavage (Fig. 3d). Mica schist and paragneiss exhibit close to isoclinal F3 folds of similar geometry with a flat-lying S3 cleavage strongly affecting both hinge and limb zones (Fig. 3e). The surrounding orthogneiss is also heterogeneously deformed, and exhibits tightly folded to completely transposed alternations of quartz–feldspar- and mica-rich layers, preserving rare cm-scale low-strain domains (Fig. 2). The S3 foliation is subhorizontal (Fig. 3f), and dips shallowly to the NW in the northern part or to the NE in the southern part of the area (Fig. 2). The F3 folds always show flat-lying axial planes and subhorizontal NE–SW trending hinges parallel to the L_{2-3} intersection lineation (Fig. 3g). The term L_{2-3} will therefore be used for both the fold hinges and the intersection lineation (Fig. 2).

GARNET TYPES SAMPLED IN THE DIFFERENT STRUCTURAL DOMAINS

Ten mica schist samples containing abundant macroscopically visible garnet have been collected at four localities in the Javorník valley (Fig. 2). In all samples,

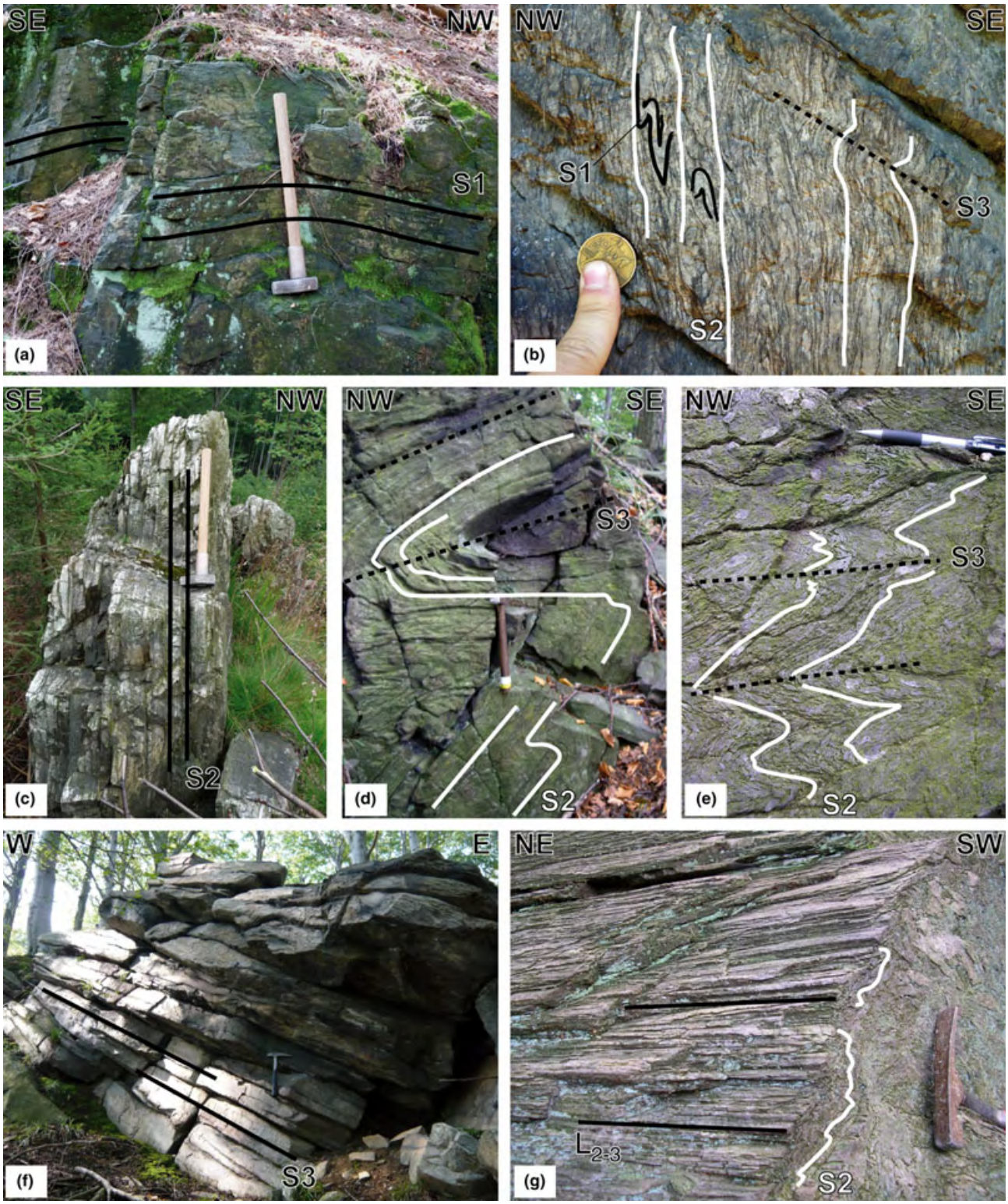

Fig. 3. Photographs illustrating the succession of structures in the investigated area. (a) Subhorizontal S1 foliation in quartzitic schist, (b) isoclinally folded relics of S1 in orthogneiss exhibiting the S2 cleavage, and (c) subvertical S2 foliation in orthogneiss from the Bílá Voda valley. (d) Open F3 fold in amphibolite, (e) close F3 folds and S3 axial-plane cleavage in mica schist, (f) subhorizontal S3 foliation in orthogneiss and (g) L_{2-3} intersection lineation in mica schist from the Javorník valley.

the S3 foliation and L_{2-3} intersection lineation were measured to allow precise reorientation in the laboratory. To quantify inclusion trail microstructures in sections parallel and perpendicular to F3 fold axis (L_{2-3}), two types of thin sections have been cut (Fig. 4): sections perpendicular to both the S3 and the L_{2-3} ('A' sections), and sections perpendicular to the S3 and parallel to the L_{2-3} ('B' sections). In the different structural domains where S2 is progressively overprinted by weak to intense S3 cleavage (Fig. 4), thin sections have been prepared parallel to the S3 foliation or the axial plane of F3 microfolds.

Structural domains of crenulation cleavage development

Four sampling domains were distinguished according to the intensity of the D3 overprinting and the position of samples with respect to the F3 folds (Figs 4 & 5). These domains are regarded as different stages of crenulation cleavage development as defined by Bell & Rubenach (1983).

Domain of preserved S2 foliation – Stages 1–2 of crenulation cleavage development

Metre-scale domains preserve the steeply dipping S2 foliation, which was only gently folded during D3 deformation. The axial-plane cleavage of F3 folds is discontinuous and produces an L_{2-3} intersection lineation, which is highly visible on the S2 surfaces. In thin section, the dominant metamorphic layering corresponds to the subvertical S2 fabric and appears as a millimetre-spaced alternation of quartz- and mica-rich domains (Fig. 5a). This layering is weakly crenulated, reorientation of mica is limited, and there is no evidence for a new metamorphic differentiation.

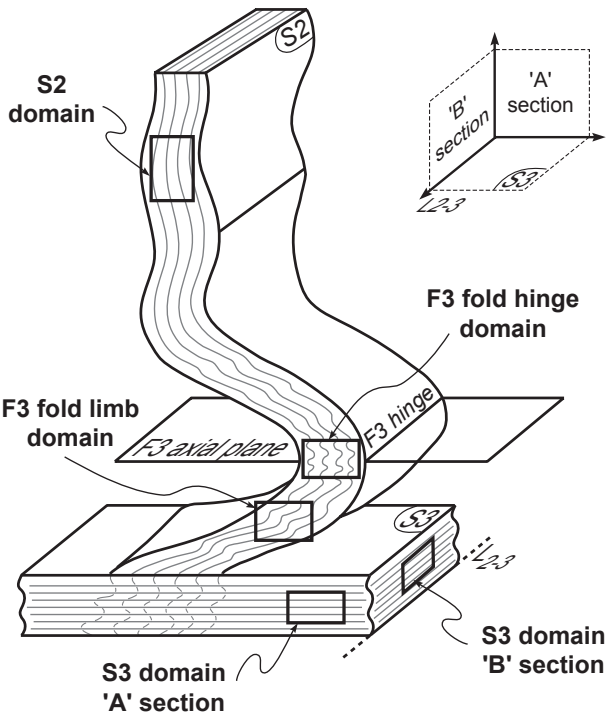

Fig. 4. Idealized schematic view of the different structural domains related to the progressive transposition of the S2 into the S3 foliation. Arbitrary reference frame used for thin sections (upper right hand corner) is based on the D3 structures.

Domain of F3 fold hinge – Stages 2–4 of crenulation cleavage development

Despite strong D3 deformation in mica schist, it is possible to observe metre-scale, close to isoclinal F3 folds (Fig. 3e). They exhibit narrow hinge zones with smaller-scale crenulation of quartz- and mica-rich layers of the S2 foliation. Thin sections display varying degrees of crenulation cleavage development (Fig. 5b,c). In weakly deformed hinges, open to tight symmetric F3 microfolds are defined by the continuous S2 layering, but the thickness of quartz-rich domains is highly variable (Fig. 5b). In places, where the D3 deformation is more intense, micro-crenulations become tight to isoclinal and the S2 quartz–mica layering is completely disrupted. The resulting microstructural pattern shows rootless folds of thick quartz lithons separated by thin mica-rich S3 cleavage planes (Fig. 5c).

Domain of F3 fold limb – Stage 4 of crenulation cleavage development

The limbs of F3 folds show asymmetric folding of the originally subvertical S2 fabric. This results in 'S'- or 'Z'-shaped microfolds, that are crosscut by mica-rich bands parallel to S3 (Fig. 5d). Mica is variably reoriented parallel to the S3 cleavage. It forms an irregular network that wraps around rare garnet or plagioclase porphyroblasts, and quartz grains aggregated in isolated lenses.

Domain of continuous S3 foliation – Stages 5–6 of crenulation cleavage development

The shallow-dipping S3 foliation corresponds to a new continuous metamorphic schistosity. It consists of thin quartz-rich layers alternating with thicker mica-rich layers (in both 'A' and 'B' sections). A variable amount of garnet and plagioclase is also present (Fig. 5e). The S3 alternation can be locally deflected around garnet and plagioclase porphyroblasts.

Garnet types

Across the sequence of structural domains defined above, four types of garnet porphyroblasts are distinguished according to their morphology and shape of the inclusion trails (Fig. 6). Although different cuts may reveal contrasted shapes, the representative

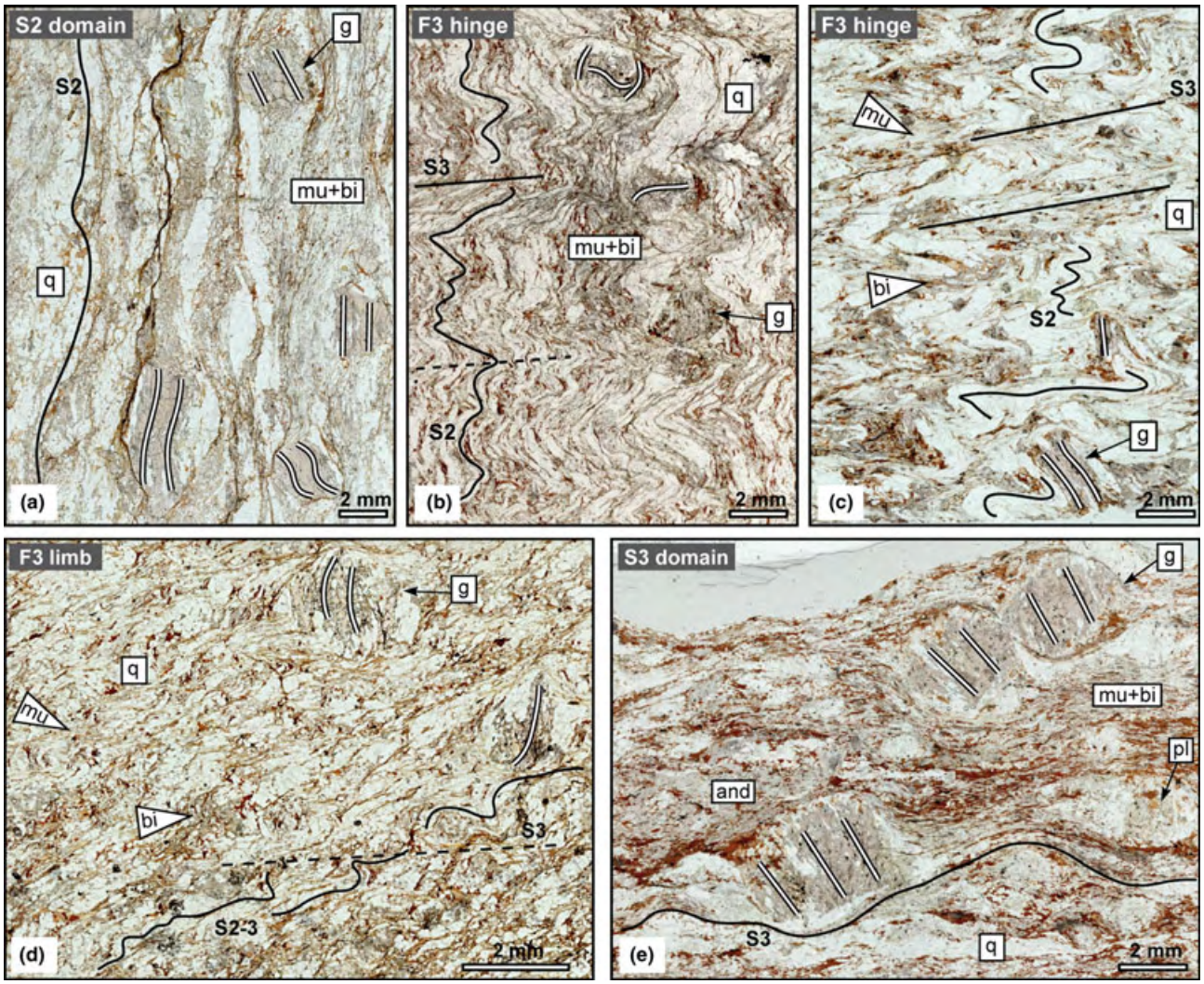

Fig. 5. Photomicrographs illustrating the microstructural pattern of the matrix in the different structural domains. (a) Continuous S2 layering in the domain of preserved S2 foliation (sample M76B). (b, c) Variable microfolding of the S2 foliation and incipient S3 cleavage in the F3 fold hinge domain (samples ES2CII and ES20C). (d) 'S'-shaped S2 layering in the F3 fold limb domain (sample ES2i). (e) Continuous S3 foliation wrapped around garnet and plagioclase porphyroblasts in the S3 domain (sample ES36L). Vertical 'A' sections, upper edge of photomicrographs is horizontal. Plane-polarized light. For mineral abbreviations, see Appendix.

features described for each garnet type rely on the observation of numerous orthogonal thin sections. In all garnet porphyroblasts, inclusion trails are dominated by rounded to elongated quartz grains and ilmenite needles. Preliminary assumptions about the significance of inclusion trails are based on garnet shapes and S_i–S_e relationships.

Type I garnet

Type I garnet occurs only in the F3 fold hinge domain. It usually shows an irregular shape with lobate boundaries and small skeletal apophyses (Fig. 6a) that can even be absent. Rare euhedral crystals also occur. Porphyroblasts (2–4 mm) mostly include quartz and are partly mantled by large quartz grains. This garnet type is characterized by a staircase shape of the inclusion trails (Fig. 6a,b). A relatively large core (1–2 mm) with subhorizontal inclusion trails is surrounded by a narrow rim (0.1–0.2 mm) where the inclusion trails become progressively subvertical and continuous with the external crenulated S2 foliation. In thin section, Type I garnet porphyroblasts commonly show nearly parallel inclusion trails. The succession of inclusion trail patterns suggests that the garnet rims record the S2 foliation, whereas the core pattern could represent the S1 foliation (Fig. 6b).

Type II garnet

Type II garnet is found in the domain of preserved S2 foliation, in F3 fold limb domain, and in samples

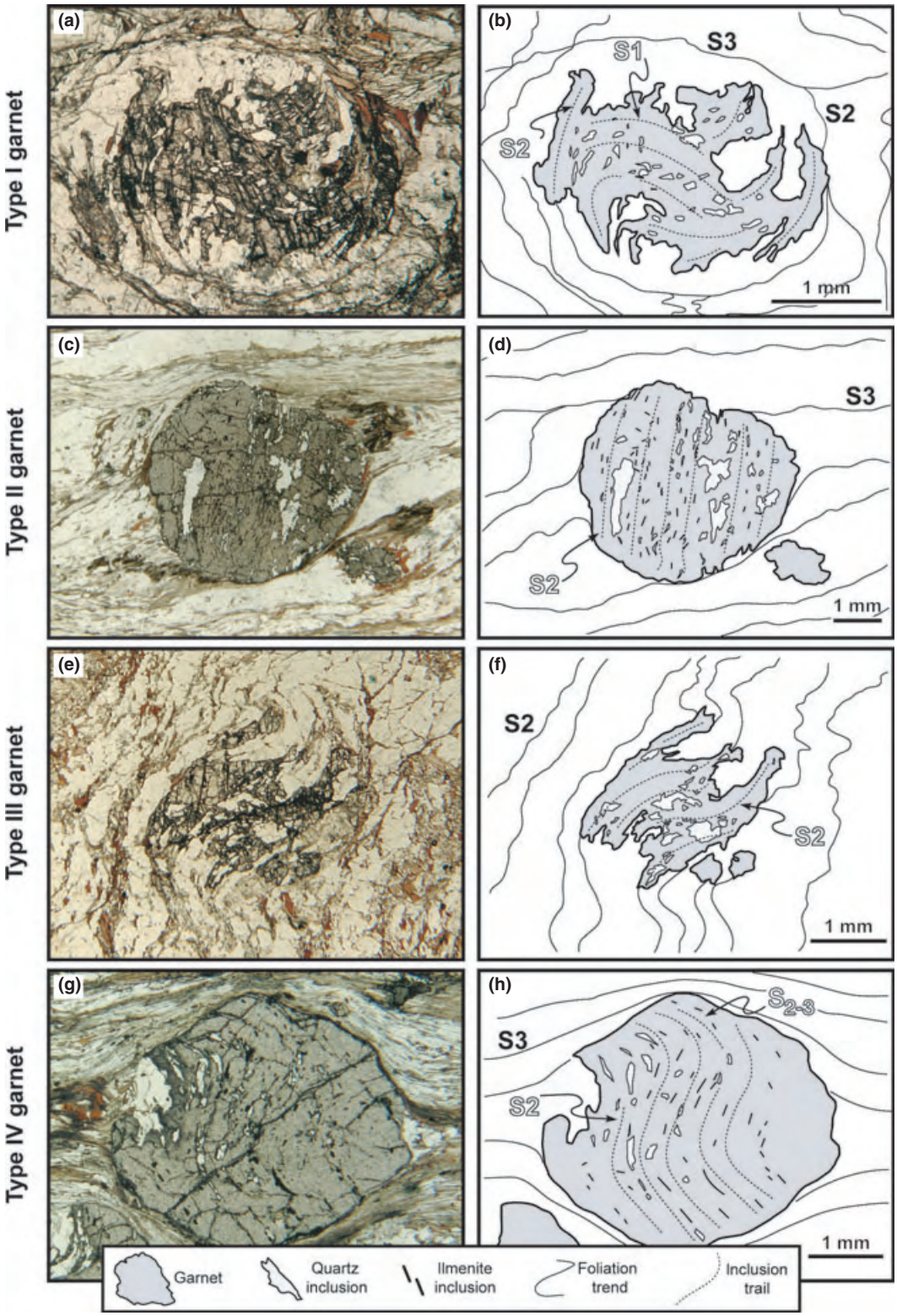

Fig. 6. Photomicrographs and associated line drawings exemplifying the different garnet types. (a, b) Type I garnet with staircase inclusion trails (sample ES2CII). (c, d) Type II garnet with straight inclusion trails (sample M1B). (e, f) Type III garnet with smoothly folded inclusion trails (sample ES2CII). (g, h) Type IV garnet with curved inclusion trails (sample M1A). Vertical sections, upper edge of photomicrographs is horizontal. Plane-polarized light.

showing the continuous S3 foliation. Porphyroblasts (up to 5 mm) are subhedral, commonly rounded, and contain abundant ilmenite inclusions (Fig. 6c). The inclusions mostly define straight patterns that are either nearly continuous with the subvertical foliation in the S2 domain, or truncated and almost perpendicular to the external subhorizontal S3 foliation in domains overprinted by D3 (Fig. 6c,d). A striking feature of this garnet type is the nearly consistent orientation of inclusion trails in porphyroblasts present in the same thin section, especially in the S3 domain (Fig. 5e). S_i–S_e relationships suggest that the growth of Type II garnet could have occurred during or after the development of the S2 foliation (Fig. 6d).

Type III garnet

Type III garnet is only observed in F3 fold hinge domains. Porphyroblasts are commonly elongated (2–4 mm), exhibit a curved shape, and occur as single anhedral crystals or small skeletal grains partly enclosing larger quartz (Fig. 6e). The skeletal growth results in the formation of larger garnet crystals in mica-rich layers, and only small apophyses along quartz grain boundaries in quartz-rich layers (Fig. 6e,f). Inclusion trails, although diffuse, display a smoothly curved pattern that coincides with the garnet shape and the gently folded outer S2 foliation (Fig. 6f). The continuity between S_i and S_e suggests that Type III garnet possibly records the S2 fabric weakly folded by the D3 deformation.

Type IV garnet

Type IV garnet is observed in all structural domains except in F3 fold limbs. Porphyroblasts are rounded to slightly elongated (1–3 mm) and commonly exhibit rims with asymmetric inclusion trails (Fig. 6g). Abundant ilmenite inclusions define sigmoidal trails that are subvertical in garnet core, but gradually curve into a subhorizontal position in the rims (Fig. 6g,h). In the S2 domain, the core inclusion trails are parallel to the external S2 fabric, whereas inclusions in the rim seem to be parallel to an ill-defined S3 cleavage. In the S3 domain, the rim trails are continuous with the matrix S3 foliation. These observations indicate that Type IV garnet could have entrapped both the S2 foliation and, to a lesser extent, the S3 foliation (Fig. 6h).

PETROLOGY

Samples and garnet chemistry

The analysed samples correspond to different stages of D3 deformation and were selected because they preserve a variable mineralogy and distinct garnet types.

Sample ES2C, F3 fold hinge domain, Type I and Type III garnet porphyroblasts

Sample ES2C was collected in the hinge of a F3 fold. This is a quartz-rich metapelite with thick quartz lithons separated by thin muscovite–biotite layers (Fig. 5b). The crenulated S2 layering contains garnet, plagioclase and a small amount of chlorite. Plagioclase porphyroblasts (2.5 mm) commonly host inclusions of white mica, biotite and ilmenite oriented parallel to the S2 layering, whereas chlorite is replacing garnet.

Type I and Type III porphyroblasts have inclusion trails defined by elongated quartz and ilmenite needles. Type I garnet exhibits a succession of subhorizontal and subvertical inclusion trails in the core and in the rim, respectively. It shows significant zoning in Mn and Mg whereas Fe and Ca remain relatively constant (Fig. 7a). Zoning of Type I garnet (Fig. 7b, Table 1) shows a core which varies from $Alm_{0.66}$ $Prp_{0.04}$ $Grs_{0.16}$ $Sps_{0.12}$ (X_{Fe} = 0.92) to $Alm_{0.71}$ $Prp_{0.08}$ $Grs_{0.14}$ $Sps_{0.08}$ (X_{Fe} = 0.90), followed by a decrease in X_{Fe} and Sps towards the rim ($Alm_{0.72}$ $Prp_{0.10}$ $Grs_{0.14}$ $Sps_{0.04}$; X_{Fe} = 0.88). Type III garnet shows smoothly curved inclusion trails continuously passing into the crenulated S2 foliation. Compositional mapping (Fig. 7a) reveals a weak zoning with respect to Mn and Mg, and core ($Alm_{0.72}$ $Prp_{0.07}$ $Grs_{0.13}$ $Sps_{0.07}$; X_{Fe} = 0.91) and rim ($Alm_{0.71}$ $Prp_{0.09}$ $Grs_{0.14}$ $Sps_{0.06}$; X_{Fe} = 0.88) analyses differ only slightly (Fig. 7b, Table 1). The composition of Type III garnet is comparable to the rim of Type I garnet but compositions similar to the core of the Type I garnet are never observed.

Sample ES36L, S3 domain, Type II garnet porphyroblasts

Sample ES36L was collected in a zone showing the continuous S3 foliation. This is a muscovite–biotite schist where thick micaceous bands wrap around quartz lenses, plagioclase and garnet porphyroblasts (Fig. 5e). Relics of staurolite are observed in the matrix and Al_2SiO_5 polymorphs are common. Kyanite is found in the matrix as small (0.5 mm), randomly oriented prisms and fibrous sillimanite occurs rarely. The most abundant polymorph is represented by andalusite porphyroblasts that host numerous ilmenite inclusions and lie parallel to S3 (2–4 mm).

Type II garnet porphyroblasts preserve numerous ilmenite needles that define straight trails oriented nearly perpendicular (60–90°) to the external S3 foliation. It is strongly zoned (Fig. 7a) showing decreasing spessartine and increasing pyrope (Fig. 7b, Table 1) from core ($Alm_{0.72}$ $Prp_{0.05}$ $Grs_{0.18}$ $Sps_{0.05}$; X_{Fe} = 0.93) to rim ($Alm_{0.74}$ $Prp_{0.08}$ $Grs_{0.16}$ $Sps_{0.01}$; X_{Fe} = 0.89).

Pseudosections and *P–T* estimates

Pseudosections have been calculated for samples ES2C and ES36L in the MnNCKFMASHTO system (for whole-rock compositions and activity–composition

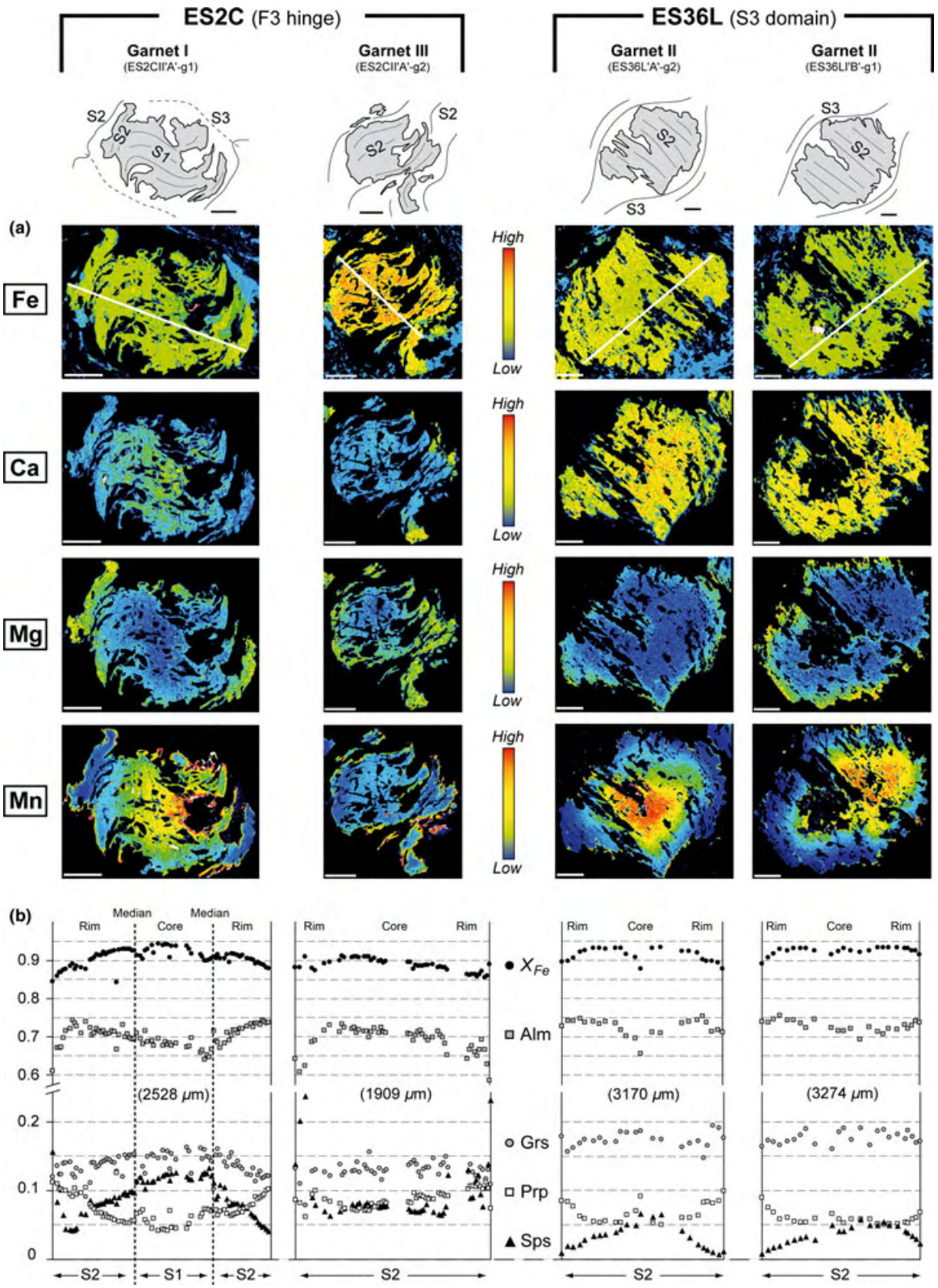

Fig. 7. Qualitative and quantitative garnet chemistry for samples ES2C (F3 fold hinge domain) and ES36L (S3 domain). (a) Compositional X-ray maps of Fe, Ca, Mg and Mn distribution in Types I, II and III garnet porphyroblasts. (b) Chemical profiles across Types I, II and III garnet porphyroblasts. Locations of the profiles are indicated on Fe X-ray maps. Scale bar is always 1 mm.

Table 1. Representative chemical analyses of garnet.

Structural domain	F3 hinge					S3 domain			
Garnet type	Garnet I			Garnet III		Garnet II		Garnet II	
Sample	ES2CII'A'-g1			ES2CII'A'-g2		ES36L'A'-g2		ES36LI'B'-g1	
Position	Core	Median	Rim	Core	Rim	Core	Rim	Core	Rim
Wt%									
SiO_2	36.68	36.71	37.28	36.22	36.18	36.22	36.87	35.66	36.73
TiO_2	0.17	0.13	0.12	0.13	0.15	0.16	0.19	0.15	0.11
Al_2O_3	20.64	21.08	21.33	20.84	20.96	21.00	21.28	20.57	21.15
FeO	30.72	32.69	33.42	33.60	33.14	34.42	34.64	33.21	34.50
MnO	5.11	3.40	1.95	3.17	2.75	1.86	0.60	2.08	0.33
MgO	1.51	1.88	2.51	1.76	2.28	1.30	2.08	1.23	2.21
CaO	5.56	4.82	4.88	4.38	4.64	6.27	5.69	6.21	5.64
Na_2O	0.00	0.00	0.00	0.00	0.00	0.00	0.00	0.00	0.00
K_2O	0.00	0.00	0.00	0.00	0.00	0.00	0.00	0.00	0.00
Total	100.39	100.70	101.47	100.08	100.10	101.21	101.36	99.11	100.66
Cations									
Si	2.95	2.94	2.95	2.93	2.91	2.89	2.93	2.91	2.93
Ti	0.01	0.01	0.01	0.01	0.01	0.01	0.01	0.01	0.01
Al	1.96	1.99	1.99	1.99	1.99	1.98	1.99	1.98	1.99
Fe^{3+}	0.11	0.11	0.09	0.14	0.17	0.21	0.13	0.18	0.13
Fe^{2+}	1.95	2.08	2.12	2.13	2.06	2.09	2.17	2.08	2.17
Mn	0.35	0.23	0.13	0.22	0.19	0.13	0.04	0.14	0.02
Mg	0.18	0.22	0.30	0.21	0.27	0.15	0.25	0.15	0.26
Ca	0.48	0.41	0.41	0.38	0.40	0.54	0.48	0.54	0.48
Na	0.00	0.00	0.00	0.00	0.00	0.00	0.00	0.00	0.00
K	0.00	0.00	0.00	0.00	0.00	0.00	0.00	0.00	0.00
Total	8.00	8.00	8.00	8.00	8.00	8.00	8.00	8.00	8.00
Prp	0.06	0.08	0.10	0.07	0.09	0.05	0.08	0.05	0.09
Alm	0.66	0.71	0.72	0.72	0.71	0.72	0.74	0.71	0.74
Grs	0.16	0.14	0.14	0.13	0.14	0.18	0.16	0.19	0.16
Sps	0.12	0.08	0.04	0.07	0.06	0.04	0.01	0.05	0.01
XF_e	0.92	0.90	0.88	0.91	0.88	0.93	0.90	0.93	0.89

Structural formulae calculated on the basis of 12 oxygen.

relationships, see Appendix). In the calculations, quartz, muscovite and H_2O are set in excess and the calcium contents of the whole-rock compositions are corrected for apatite.

Provided that chemical zoning reflects changes in pressure, temperature and composition of the matrix (Pattison & Bégin, 1994), garnet composition may be used to infer *P–T* conditions. Because analysed porphyroblasts show strong compositional zoning (Fig. 7), intra-crystalline diffusion was not taken into account, and the effect of element fractionation in garnet, regarded as negligible by e.g. Tinkham *et al.* (2001), was not considered.

Pseudosection for sample ES2C

The pseudosection for sample ES2C is bounded by the liquid-in line at 660–670 °C; the stability of garnet and ilmenite are highlighted by thick lines (Fig. 8a). Garnet is stable above 470–500 °C except for the low-pressure region between 520 and 650 °C and ilmenite is stable in almost all the investigated *P–T* range except for the region in the upper pressure range.

Inclusions of muscovite, biotite and ilmenite in plagioclase and garnet porphyroblasts suggest an evolution starting in the bi–g–pl–chl field (Fig. 8a). The onset of garnet growth is estimated at 4–4.5 kbar and 490–510 °C where the modelled isopleths [x(g) = 0.92; z(g) = 0.16] are compatible with observed X_{Fe} and Grs values in the core of Type I garnet (Fig. 8b). The core zoning of Type I garnet represents an evolution towards 5–5.5 kbar and 530–550 °C where the measured values of X_{Fe} = 0.90 and Grs = 0.14 lie close to x(g) and z(g) isopleths. The rim of Type I garnet (X_{Fe} = 0.88 and Grs = 0.14) is comparable to x(g) and z(g) values at 6–6.5 kbar and 570–590 °C and indicates the end of the *P–T* path in the bi–g–pl field (Fig. 8a,b), which is in agreement with the absence of chlorite in the matrix. The evolution from ~5 kbar and ~535 °C to ~6 kbar and ~575 °C is further supported by the composition of Type III garnet that is interpreted to grow contemporaneously with garnet I rims because X_{Fe} and Grs values are similar (Fig. 8b, Table 1).

Pseudosection for sample ES36L

The pseudosection for sample ES36L (Fig. 8c) is bounded by the liquid-in line at 660–670 °C; garnet and ilmenite stability (highlighted by thick lines) is reduced compared to the pseudosection for sample ES2C.

The presence of mica inclusions in garnet and plagioclase porphyroblasts together with matrix staurolite suggests a prograde evolution from the bi–g–pl–chl field to the bi–g–pl–st field (Fig. 8c). Crystallization relationships among the Al_2SiO_5 polymorphs indicate

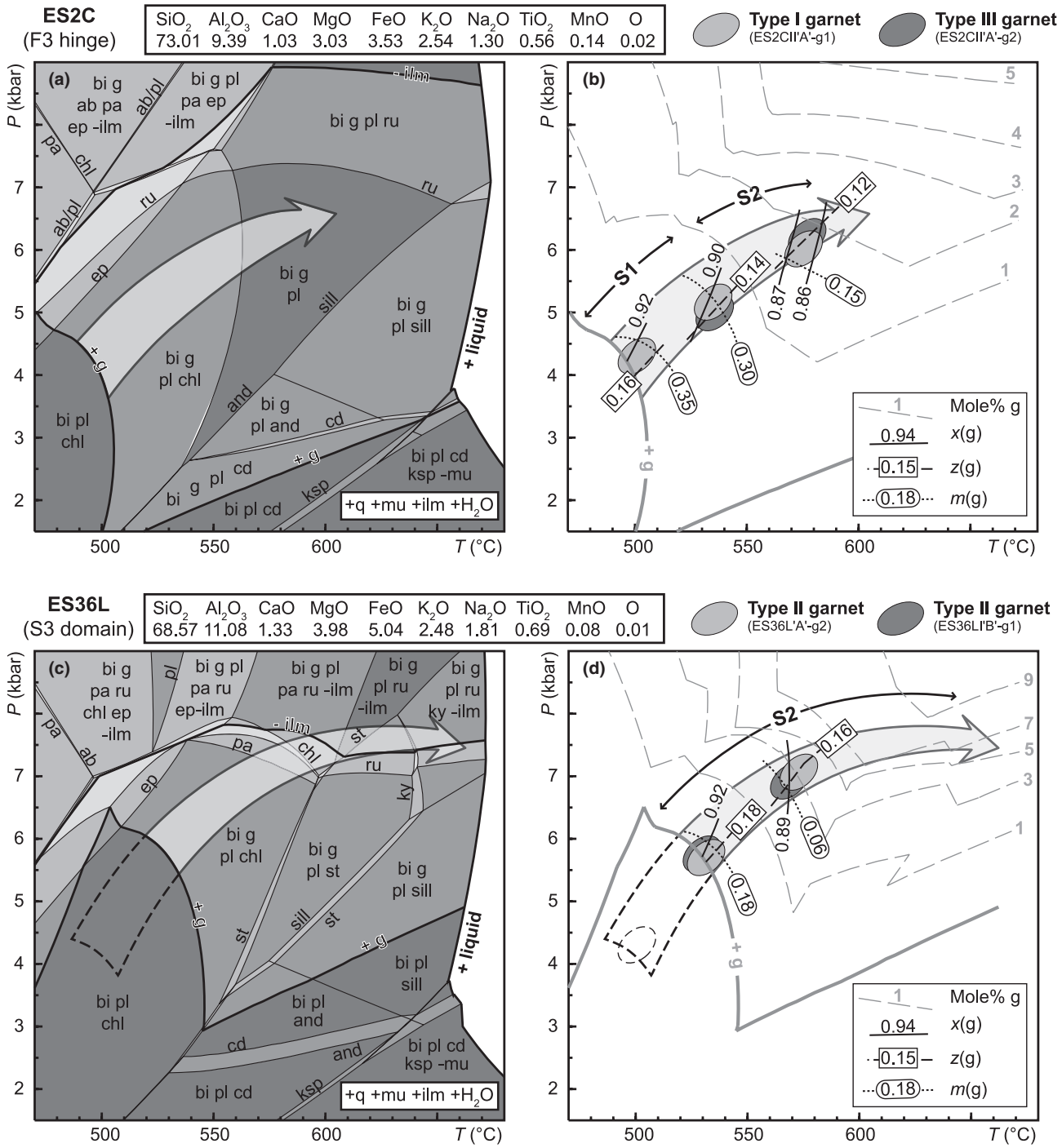

Fig. 8. *P–T* pseudosections and modelled compositional isopleths of garnet for representative samples. (a, b) Metamorphic evolution of sample ES2C (F3 fold hinge domain) derived from Type I and Type III garnet porphyroblasts. (c, d) Metamorphic evolution of sample ES36L (S3 domain) derived from Type II garnet porphyroblasts. Compositional isopleths are as follows: x(g) = Fe/(Fe + Mg); z(g) = Ca/(Fe + Mg + Ca + Mn); m(g) = Mn/(Fe + Mg + Ca + Mn).

earliest growth of kyanite, followed by sillimanite, and later growth of large andalusite. This points to the end of the prograde path in the bi–g–pl–ky–ilm–ru field (Fig. 8c). Core composition of Type II garnet (X_{Fe} = 0.93 and Grs = 0.18–0.19) matches the modelled x(g) and z(g) isopleths at 5.5–6 kbar and 520–540 °C, close to the garnet-in line (Fig. 8c,d). Values of X_{Fe} = 0.89 and Grs = 0.16 at the rim indicate increase in pressure and temperature to 6.5–7.5 kbar and 560–580 °C (Fig. 8d). Further progression

towards the kyanite stability field to 6.5–7.5 kbar and 640–670 °C is nearly isobaric and occurs parallel to garnet modal isopleths (Fig. 8d). This is compatible with very limited garnet growth at the end of the prograde *P–T* path and with the general absence of kyanite inclusions in garnet.

MICROSTRUCTURAL ANALYSIS

Measurement technique

When viewed in 'A' and 'B' sections, matrix and included ilmenite needles commonly define discontinuous trails (Figs 5 & 6). Nevertheless, SEM images of ilmenite trapped in porphyroblasts reveal that the apparent needles are sections of tabular crystals. We can therefore infer that the shape-preferred orientation of matrix or included ilmenite platelets corresponds to a foliation plane. Accessing ilmenite lattice-preferred orientation (LPO) via EBSD analysis is likely to test the following assumptions. Does the LPO of matrix ilmenite trails correspond to the macroscopic foliation and, if so, could the LPO of included ilmenite trails be related to earlier structures?

Data processing

The EBSD results were processed with PFch5 software (Mainprice, 2005) to provide a[100] and c[001] axis patterns of ilmenite (Fig. 9; for analytical details, see Appendix). However, because of hexagonal pseudo-symmetry in ilmenite, [a] axis patterns show data repetition. It is therefore more convenient to focus on ilmenite [c] axis patterns; the ilmenite [c] axis is usually the direction parallel to the short dimension in tabular ilmenite (Moseley, 1981), i.e. the pole to ilmenite platelets. Eigenvalues (E1, E2, E3) and eigenvectors ($\lambda 1$, $\lambda 2$, $\lambda 3$) of the [c] axis distribution were determined (Scheidegger, 1965), and two end-members are recognized. In the first end-member, [c] axis data show a cluster-type distribution, implying that tabular ilmenite crystals define a plane which is perpendicular to the direction of the smallest eigenvector $\lambda 3$ (Fig. 9b). In the second end-member, [c] axis data show a girdle-type distribution, implying that tabular ilmenite crystals define a zone axis, i.e. a linear structure which is parallel to the direction of the smallest eigenvector $\lambda 3$ (Fig. 9d). Provided that the [c] axis distribution is well-constrained, principal direction data can be transformed into geographic coordinates, and compared to the orientation of S3 and L_{2-3}.

Matrix ilmenite data

This procedure was applied to matrix ilmenite trails defining the S3 foliation (sample ES36L from S3 domain). Both [a] and [c] axis patterns are tightly constrained and define a plane that is subparallel to S3 measured in the field (Fig. 9a). The slight misfit is attributable to a minor deflection of matrix S3 around garnet porphyroblasts. This result demonstrates that the LPO of matrix ilmenite crystals corresponds to the macroscopic foliation.

Included ilmenite data

Because the LPO data from matrix ilmenite reveal a planar structure, the same approach was used for ilmenite inclusions in porphyroblasts. Representative end-members of [c] axis distribution are now presented.

Garnet porphyroblasts with straight to smoothly curved inclusion trails (Type II or III) show a cluster-type distribution of [c] axis patterns in 'A' sections. Moreover, the [a] axis patterns show a continuous girdle distribution instead of three isolated clusters (Fig. 9b). This confirms that the tabular objects define a plane which can be rotated back to geographic coordinates.

Porphyroblasts which contain curved inclusion trails (Type I or IV) follow the same example, but preserve distinct trails that can be separated according to BSE images. In this case, the [c] axis pattern defines an incomplete girdle formed by two broad maxima that reflect the presence of two planar fabrics (Fig. 9c). Separating core and rim data allows the incomplete girdle to be split into two [c] axis clusters associated with two different [a] axis girdles (Fig. 9c). These records are then used to reconstruct two different internal foliations.

In 'B' sections, garnet porphyroblasts generally display relatively straight inclusion trails (Type II). However, instead of a single cluster, ilmenite [c] axis patterns exhibit a girdle-type distribution (Fig. 9d). This suggests that ilmenite crystals define a linear internal structure (L_i).

These observations demonstrate that the LPO of included ilmenite trails not only corresponds to planar structures, but could also define linear elements, depending on the analysed section. In addition, the quantification of internal foliations allows definition of two types of foliation intersection axis (FIA): FIA resulting from the intersection between two internal foliations (*sensu* Bell *et al.*, 1995), and FIA corresponding to the intersection between an internal foliation and the matrix foliation (Fig. 9c).

Interpretation of quantitative internal records

Internal foliations

It has been demonstrated that the LPO of ilmenite inclusions defines planar structures (Fig. 9) that represent foliations. Thus, quantitative measurements can be correlated with the orientation of macroscopic field fabrics (Figs 10–12 & Table 2).

Type I garnet porphyroblasts document a polyphase history. Rare subhorizontal planes are preserved in the

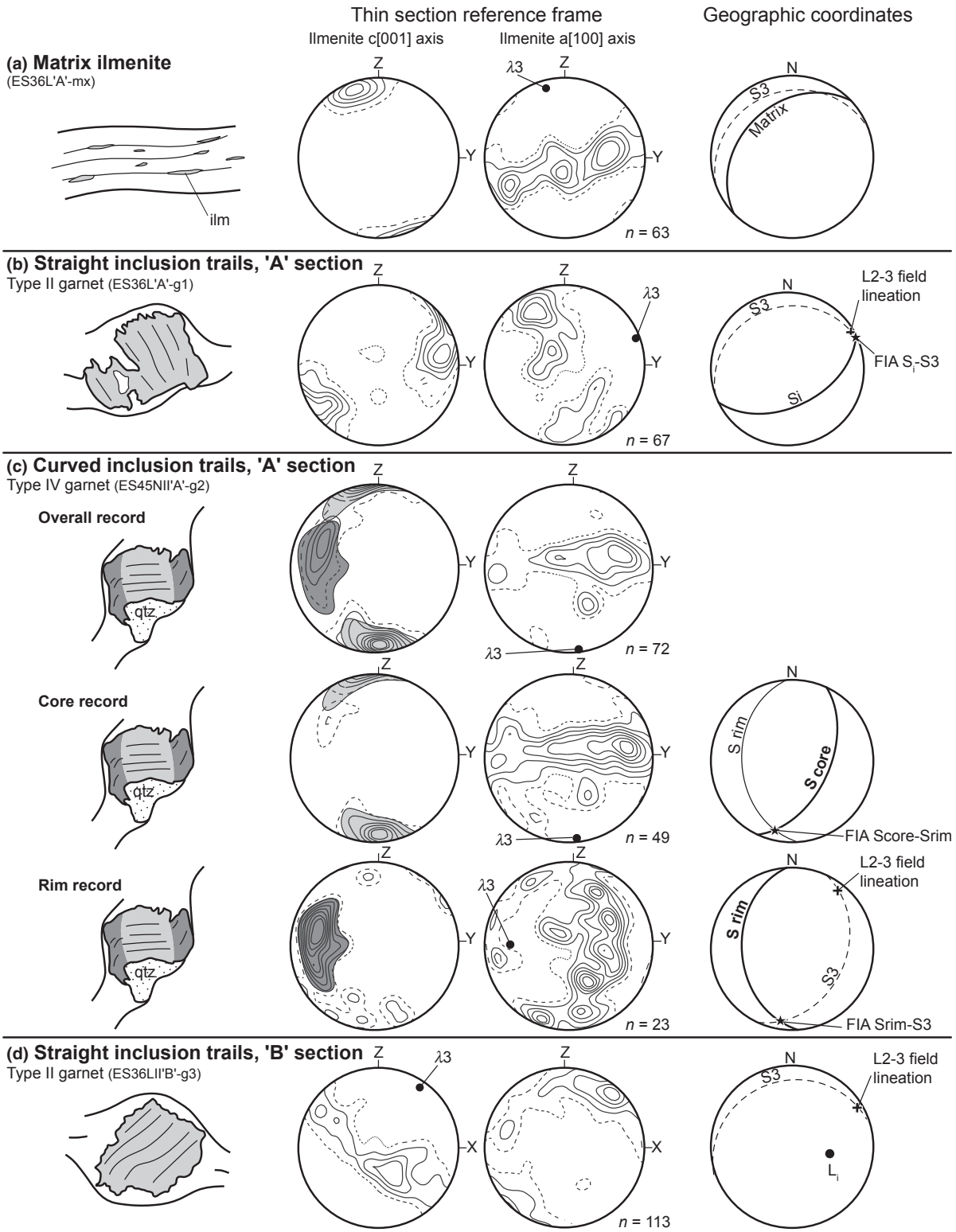

Fig. 9. Data processing and representative microstructural results obtained using EBSD analysis of (a) matrix ilmenite and (b–d) included ilmenite. (a) Matrix ilmenite data defining the S3 foliation. (b) Single foliation recorded in Type II garnet with straight inclusion trails, 'A' section. (c) Distinct foliations preserved in Type IV garnet with curved inclusion trails, 'A' section. (d) Lineation recorded in Type II garnet with straight inclusion trails, 'B' section. Stereonets are contoured at multiples of the uniform distribution. For details, see text.

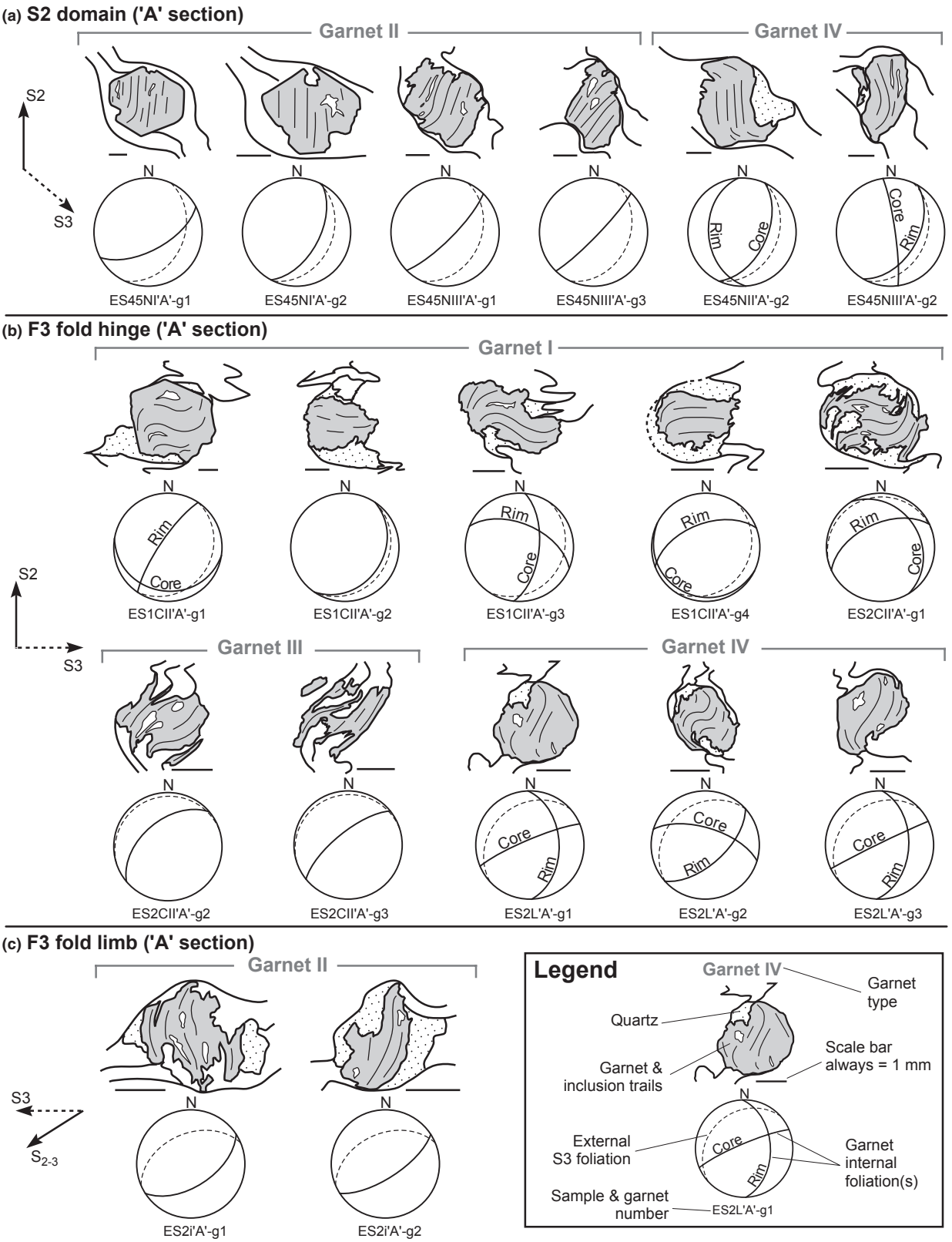

Fig. 10. Schematic sketches of S_i–S_e relationships in garnet porphyroblasts and associated microstructural results. Porphyroblasts ('A' section) are from (a) S2 domain, (b) F3 fold hinge domain and (c) F3 fold limb domain. Orientation of the external foliation is indicated.

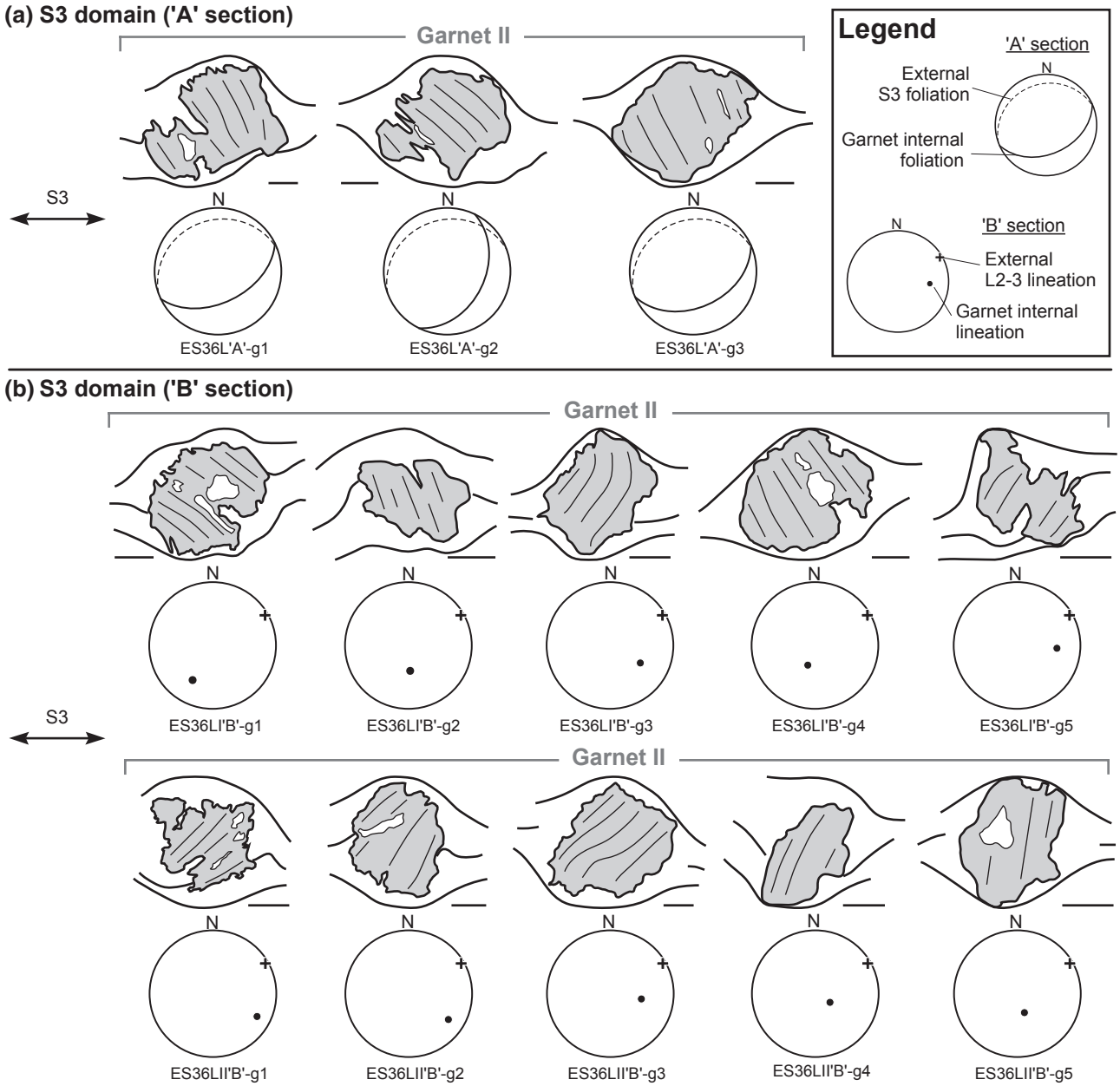

Fig. 11. Schematic sketches of S_i–S_e relationships in garnet porphyroblasts from S3 domain and associated microstructural results. Porphyroblasts are from (a) 'A' section, and (b) 'B' section. Orientation of the external foliation is indicated. For further details on the legend, see Fig. 10.

cores, and rims generally show NE–SW planes moderately to steeply (54–88°) dipping to the NW (Fig. 10a). The core record could correspond to the poorly preserved S1 foliation, whereas the rim record is mostly similar to the subvertical S2 fabric (Fig. 10a). This shows that garnet porphyroblasts from different hinge zones consistently preserved the succession of S1 and S2 fabrics (Fig. 12).

In all the structural domains where they are observed, Type II garnet porphyroblasts reveal NE–SW striking planes compatible with the S2 foliation (Figs 10a–c & 11a). Nevertheless, a progressive decrease of the dip angle with increasing intensity of the D3 deformation is observed. In the domain of preserved S2 foliation, NE–SW planes are subvertical, whereas they are moderately dipping (56–69°) to the SE in the F3 limb domain, and gently dipping (40–49°) to the SE in the S3 domain (Fig. 12).

Smoothly curved inclusion trails from Type III garnet porphyroblasts define steeply to moderately dipping, NE–SW striking foliations (Fig. 10b). This suggests that, although Type III porphyroblasts were

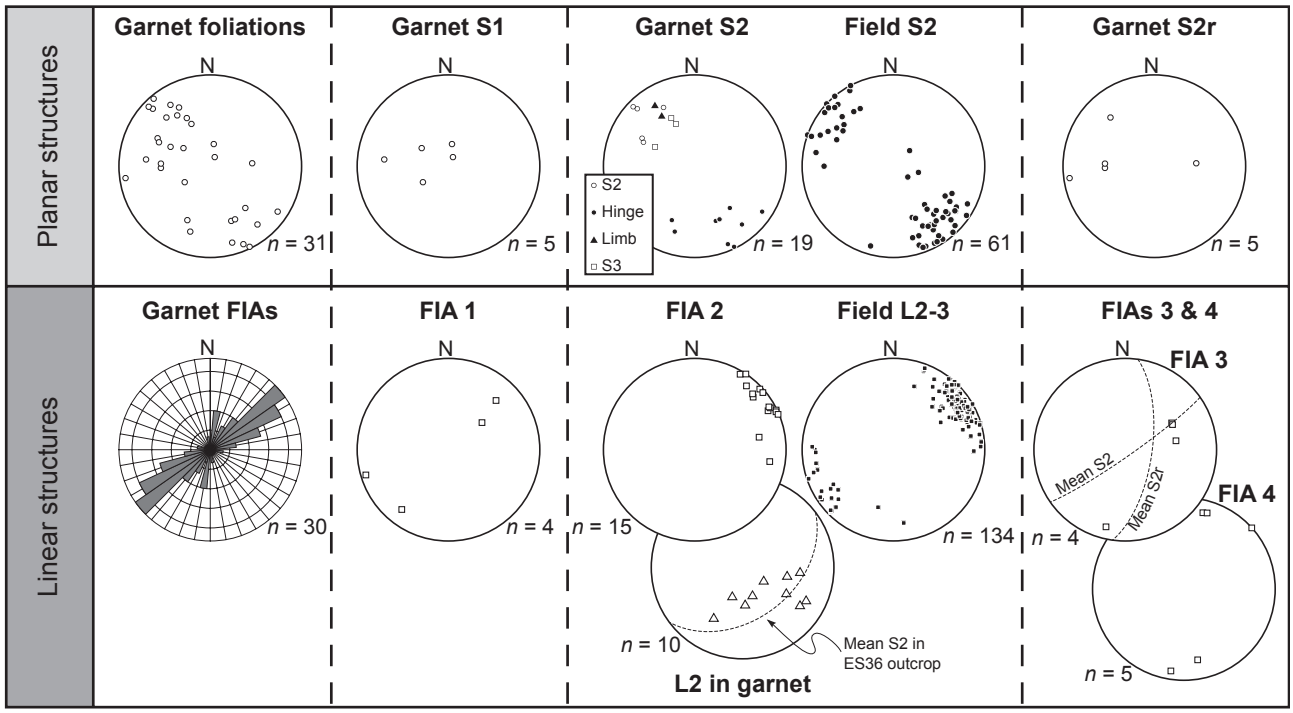

Fig. 12. Summary of planar and linear structures measured in garnet porphyroblasts and comparison with field data.

interpreted to have grown early during D3 deformation, they consistently preserve planar fabrics that are subparallel to the S2 foliation (Fig. 12).

In Type IV garnet porphyroblasts, core inclusions preserve nearly subvertical planes striking either N–S (S2 domain) or NE–SW (F3 hinge domain). These records are attributed to the S2 foliation. However, rim records show N–S planes moderately dipping to the E or W that are different from the matrix S3 foliation (Fig. 10a,b). These trails, previously considered as S3, could correspond to S2 that rotated halfway towards S3 at the onset of D3 deformation (Fig. 12). This rotated S2 foliation will be termed S2r.

Internal lineation

The study of Type II garnet porphyroblasts suggests that the LPO ilmenite pattern depends on the analysed section. Indeed, while LPO data reveal the planar S2 foliation in 'A' sections, they define lines moderately plunging to the SE in 'B' sections (Fig. 11b). This lineation is coplanar with the orientation of S2 obtained in 'A' sections (Fig. 12, L2 lineation).

If it is assumed that the S2 foliation is predominantly entrapped in Type II garnet, it follows that: 'A' sections should display thin traces of S2, whereas 'B' sections, which are by definition subparallel to S2, should exhibit a higher proportion of tabular ilmenite. This is evidenced by the dependence of ilmenite aspect ratios on the [c] axis plunge (Fig. 13). In addition, if the internal foliation is considered to be weakly folded, as shown by studies using computed X-ray tomography (e.g. Huddlestone-Holmes & Ketcham, 2005), the ilmenite LPO in 'B' sections could well define a line corresponding to the axis of the microfolded foliation (Fig. 14a).

In this view, the internal lineation recorded in Type II porphyroblasts is interpreted as the hinge of microfolds affecting the S2 fabric (Fig. 14a) and not as a proper FIA. The former interpretation is favoured because no evidence for an intersection between two distinct planes is observed. This lineation will be termed L2.

Foliation intersection axis

Foliation intersection axes commonly result from the intersection between superposed subvertical and subhorizontal foliations. Bell *et al.* (1995) underlined that the orientation of the FIA is controlled by the azimuth of the vertical foliation and does not depend on the direction of shearing in the flat-lying foliation. In addition, Bell & Johnson (1989) had previously proposed that the FIA lies perpendicular to the direction of bulk compression during orogenesis. We therefore tried to constrain the origin, relative timing and orientation of the FIA sets to further test their use as tectonic indicators. Using the quantification of included foliations and the orientation of matrix S3, four different FIA sets were defined (Fig. 14b).

Foliation intersection axis 1 is rare and is only revealed by Type I porphyroblasts. It is defined by the intersection between the internal S1 and S2 foliations (Fig. 14b), and corresponds to a shallowly

Table 2. Orientation data of internal structures measured using single grain inclusion trail analysis.

Sample	g	Part	Garnet type	Analysed inclusions	Internal structure				FIA		
					Type	Measurement		Interpretation	Measurement		Interpretation
						Azimut	Dip		Azimut	Dip	
S2 domain											
ES45NI'A'	g1	–	II	35	Planar	152	62	S2	79	29	FIA 2
ES45NI'A'	g2	–	II	12	Planar	118	55	S2	31	4	FIA 2
ES45NII'A'	g2	Rim	IV	23	Planar	266	38	S2r	189	10	FIA 4
ES45NII'A'	g2	Core	IV	49	Planar	115	52	S2	194	14	FIA 3
ES45NIII'A'	g1	–	II	40	Planar	135	78	S2	48	15	FIA 2
ES45NIII'A'	g2	Rim	IV	11	Planar	120	48	S3	–	–	–
ES45NIII'A'	g2	Core	IV	17	Planar	82	83	S2r	169	22	FIA 4
ES45NIII'A'	g3	–	II	18	Planar	134	83	S2	46	13	FIA 2
F3 hinge											
ES0lCII'A'	g1	Rim	I	7	Planar	304	78	S2	34	0	FIA 2
ES0lCII'A'	g1	Core	I	10	Planar	189	20	S1	218	18	FIA 1
ES0lCII'A'	g2	–	I	27	Planar	124	29	S1	–	–	–
ES0lCII'A'	g3	Rim	I	11	Planar	23	54	S2	99	18	FIA 2
ES0lCII'A'	g3	Core	I	9	Planar	96	60	S1	51	51	FIA 1
ES0lCII'A'	g4	Rim	I	6	Planar	339	54	S2	62	10	FIA 2
ES0lCII'A'	g4	Core	I	12	Planar	206	9	S1	253	6	FIA 1
ES2CII'A'	g1	Rim	I	8	Planar	335	54	S2	64	1	FIA 2
ES2CII'A'	g1	Core	I	15	Planar	58	27	S1	44	26	FIA 1
ES2CII'A'	g2	–	III	9	Planar	320	50	S2	47	3	FIA 2
ES2CII'A'	g3	–	III	12	Planar	321	71	S2	50	3	FIA 2
ES2L'A'	g1	Rim	IV	14	Planar	88	45	S2r	14	15	FIA 4
ES2L'A'	g1	Core	IV	30	Planar	337	82	S2	60	41	FIA 3
ES2L'A'	g2	Rim	IV	15	Planar	138	61	S2r	48	0	FIA 4
ES2L'A'	g2	Core	IV	34	Planar	17	64	S2	80	43	FIA 3
ES2L'A'	g3	Rim	IV	13	Planar	93	45	S2r	17	14	FIA 4
ES2L'A'	g3	Core	IV	9	Planar	334	88	S2	62	41	FIA 3
F3 limb											
ES2i	g1	–	II	24	Planar	147	56	S2	61	6	FIA 2
ES2i	g2	–	II	20	Planar	147	69	S2	60	7	FIA 2
S3 domain 'A' section											
ES36L'A'	g1	–	II	67	Planar	154	49	S2	65	2	FIA 2
ES36L'A'	g2	–	II	40	Planar	116	40	S2	39	11	FIA 2
ES36L'A'	g3	–	II	65	Planar	156	42	S2	67	1	FIA 2
S3 domain 'B' section											
ES36LI'B'	g1	–	II	44	Linear	210	37	L2	–	–	–
ES36LI'B'	g2	–	II	39	Linear	176	57	L2	–	–	–
ES36LI'B'	g3	–	II	65	Linear	120	44	L2	–	–	–
ES36LI'B'	g4	–	II	73	Linear	200	63	L2	–	–	–
ES36LI'B'	g5	–	II	26	Linear	94	37	L2	–	–	–
ES36LII'B'	g1	–	II	42	Linear	117	23	L2	–	–	–
ES36LII'B'	g2	–	II	77	Linear	123	26	L2	–	–	–
ES36LII'B'	g3	–	II	117	Linear	100	49	L2	–	–	–
ES36LII'B'	g4	–	II	31	Linear	121	68	L2	–	–	–
ES36LII'B'	g5	–	II	35	Linear	160	64	L2	–	–	–

plunging, NE–SW trending lineation (Fig. 12). Because FIA 1 results from the superposition of the subvertical S2 on the subhorizontal S1, it is interpreted as an indicator of a NW–SE directed D2 shortening event.

Foliation intersection axis 2 is reconstructed from garnet porphyroblasts that preserve S2 and that are truncated by the matrix S3 foliation. It is therefore defined by the intersection between S2 and S3 foliations (Fig. 14b). FIA 2 corresponds to a consistent set of subhorizontal, NE–SW trending lines (Fig. 12) that is similar to the macroscopic L2–3 intersection lineation. This illustrates that, although internal S2 records may show variable dip, their NE–SW strike is consistently preserved in garnet porphyroblasts.

Nevertheless, a stage of S2 reorientation (S2r) is evidenced by rims of Type IV garnet porphyroblasts. This allows the definition of FIA 3 and FIA 4. FIA 3 corresponds to the intersection between S2 and S2r internal records in Type IV porphyroblasts (Fig. 14b), and results in rare lines moderately plunging to the NE (Fig. 12). This FIA set can be considered as the axis of microfolds deforming S2 into S2r.

More importantly, FIA 4 is defined by the intersection between the internal S2r and the matrix S3 foliations in Type IV garnet porphyroblasts (Fig. 14b). This yields few subhorizontal NNE–SSW trending lines (Fig. 12). Because FIA 4 represents the overprinting of the N–S striking S2r foliation by the subhorizontal S3 fabric, it is interpreted as an indicator of E–W directed shortening at the onset of D3 deformation.

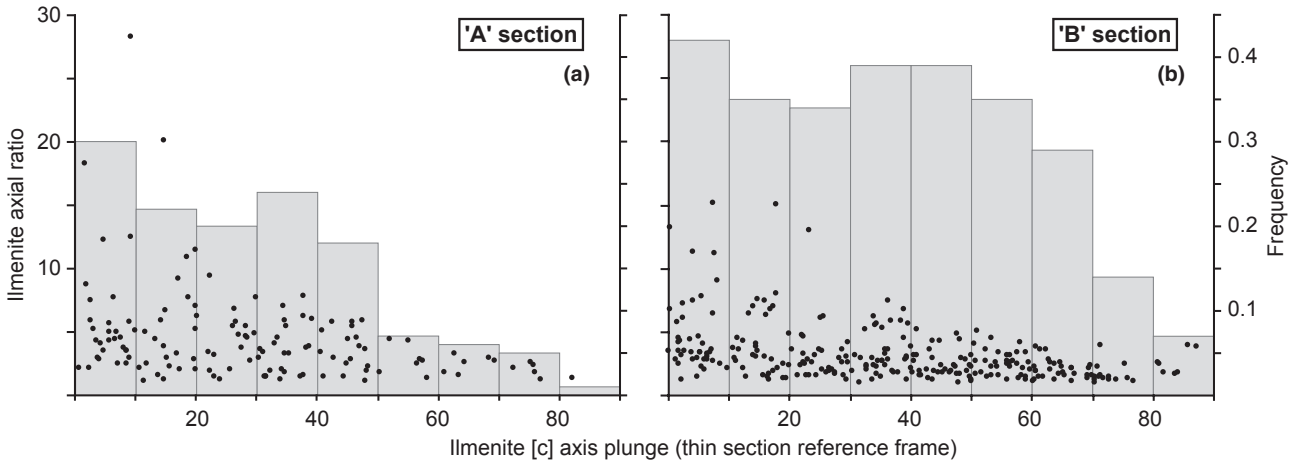

Fig. 13. Plot of ilmenite axial ratio as a function of [c] axis plunge and histogram of [c] axis plunge values for inclusions viewed in 'A' and 'B' sections. [c] axis plunge is given in thin section coordinates, i.e. vertical [c] axis is normal to the thin section. (a) Results for five porphyroblasts viewed in 'A' section. Note that [c] axis plunge rarely exceeds 50°. (b) Results for five porphyroblasts viewed in 'B' section. Note the dependence of axial ratio on [c] axis plunge.

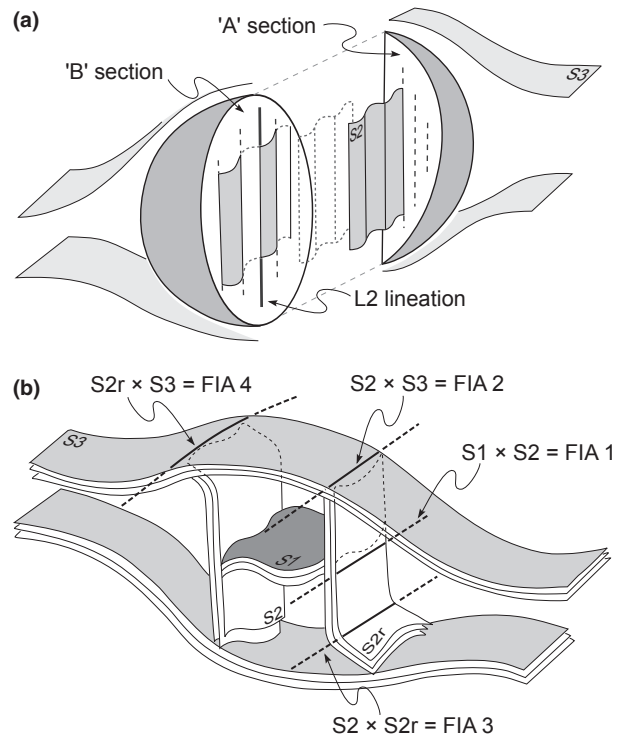

Fig. 14. Idealized sketches illustrating garnet internal records. (a) L2 lineation in garnet. (b) FIA sets defined by the intersections of internal and/or external foliations.

DISCUSSION AND CONCLUSIONS

Single grain inclusion trail analysis

Previous methods for studying the three-dimensional orientation of inclusion trails mostly relied on correlations between trails from different crystals measured in differently oriented thin sections (e.g. Bell *et al.*, 1998; Johnson *et al.*, 2006). Internal records were determined either by comparing the asymmetry of inclusion trails ('Asymmetry' technique, Hayward, 1990; Bell *et al.*, 1995) or using statistical fitting of inclusion trails ('FitPitch' technique, Aerden, 2003) from radial thin sections. However, these techniques only yield average values for all porphyroblasts in a hand specimen, assuming that all crystals remained nearly fixed relative to each other.

By contrast, this study presents a quantitative approach based on measurements of ilmenite inclusions in single garnet crystals (Fig. 9). The technique assumes that the ilmenite LPO, measured using EBSD, can correspond to macroscopic structures. This is validated by the compatibility between the LPO of matrix ilmenite and the orientation of the macroscopic foliation (Fig. 9a). Applying this technique to ilmenite inclusion trails gives access to both planar and linear internal structures and allows the reconstruction of FIA sets (Fig. 12). The comparison with field data shows that garnet inclusion trails preserve structures which have been partly or even entirely obliterated in the matrix.

Thus, this work introduces a new and precise technique for determining internal records preserved in porphyroblasts. The advantage of this method is that it allows *in situ* quantification of structures preserved in single porphyroblasts from a same thin section or sample. The present technique can serve for garnet with straight inclusion trails, i.e. when the 'Asymmetry' technique cannot be used (Sayab, 2005), but also reveals three-dimensional orientations of polyphase inclusion trails (Fig. 9c). The only limit of the technique probably resides in the number of ilmenite inclusions in porphyroblasts, but ~20 grains already

seem to provide reliable fabric patterns. Consequently, we propose that, in addition to platy ilmenite, other strongly anisotropic and oblate minerals like mica can be suitable to quantify inclusion trail patterns in staurolite, andalusite or other porphyroblastic minerals in metapelites.

Microstructural evolution: garnet rotation and non-rotation

Detailed inspection of quantitative microstructural results shows a variation of internal S2 records through the different structural domains (Fig. 12). The S2 foliation shows minor fluctuation in the hinges of F3 folds, whereas the dip of S2 notably decreases from F3 fold hinges to S3 domains (Figs 10 & 11). This could result from (i) garnet growth over an already folded S2 foliation, (ii) reorientation of porphyroblasts due to vorticity in the matrix, or (iii) non-coaxial deformation during D3.

The small variation observed in the hinge of F3 folds, where D3 is supposed to be mostly coaxial, could be explained by static overgrowth. It can equally be produced by matrix vorticity, because D3 produces a crenulation with a wavelength nearly similar to the grain size of garnet porphyroblasts. However, both hypotheses suppose non-systematic reorientation of garnet records. This contradicts the apparent decrease in S2 dip with increasing intensity of the D3 deformation (Fig. 12, garnet S2 records). Williams & Jiang (1999) demonstrated that porphyroblast rotation increasing with the fold limb dip can occur during pure shear folding associated with layer-parallel shearing. Because such shearing was not observed, we believe that the microstructural S2 records indicate an episode of non-coaxial deformation involving limited, but systemic garnet rotation with respect to the position of samples in F3 folds. This could be achieved during a D3 buckling stage.

Nevertheless, in the case of dominant non-coaxial deformation, porphyroblasts from different structural domains may show a spread of inclusion trail data (e.g. Johnson *et al.*, 2006). This was not observed in garnet porphyroblasts analysed in this study. By contrast, the EBSD data show that garnet consistently records the succession of subhorizontal and subvertical fabrics (Fig. 12). Some EBSD results even show that crystals with contrasted shapes preserve the same internal records (see for example ES2L'A'-g1 and -g2 in Fig. 10a). This appears to be in contradiction with the theoretical motion of rigid particles in a simple shear dominated viscous flow that depends, among other factors, on the shape of the particles (e.g. Jeffery, 1922; Ježek *et al.*, 1996; Ceriani *et al.*, 2003).

All these microstructural arguments suggest that no significant rotation occurred during the polyphase tectonic history. Natural (e.g. Aerden, 2004) and numerical (e.g. Jiang, 2001) examples have been used to argue that limited rotation due to deformation partitioning (Bell, 1981; Lister & Williams, 1983) can occur in non-coaxial deformation. However, macroscopic shear indicators were not observed and porphyroblasts do not show systematic development of asymmetric tails. We therefore favour a pure shear folding mechanism (Ramsay, 1962), also suggested by Ilg & Karlstrom (2000) to explain the presence together of rotated and non-rotated porphyroblasts. In this view, the foliation passively rotates around static porphyroblasts and is subsequently overgrown (Fig. 15). Consequently, the preservation of primary orientations in garnet porphyroblasts is interpreted as a result of dominant coaxial deformation.

Metamorphic evolution: polyphase garnet growth and resorption

The core of Type I garnet preserves the flat-lying S1 foliation (Fig. 12) and is associated with a prograde evolution from 4–4.5 kbar and 490–510 °C to 5–6 kbar and 520–550 °C (Fig. 8a,b). This first garnet growth episode therefore documents prograde metamorphism during or after development of the subhorizontal S1 foliation (Fig. 15).

Ilmenite inclusion trails in the rims of Type I garnet and in Types II and III porphyroblasts are interpreted as relicts of the S2 foliation (Fig. 12). The composition of Type I garnet rims and Type III garnet points to a second garnet growth episode from 5–6 kbar and 520–550 °C to 6.5–7.5 kbar and 560–590 °C (Fig. 8b). Despite a different pseudosection topology resulting from lower Mn content in the rock (Fig. 8), the sample containing Type II garnet indicates *P–T* conditions consistent with this second garnet growth episode (Fig. 8d). Staurolite and kyanite, which have been ascribed to the S2 fabric by Skrzypek *et al.* (2010), document the end of the *P–T* path at 6.5–7.5 kbar and 640–670 °C (Fig. 8c,d). All these observations point to a prograde evolution occurring during development of the subvertical S2 foliation (Fig. 15).

Limited garnet growth at the onset of D3 is documented by S2r records (Fig. 12). However, garnet is commonly replaced by sillimanite and biotite in the pressure shadows associated with the D3 deformation (Skrzypek *et al.*, 2010). In addition, the crystallization of andalusite parallel to the S3 foliation (Fig. 5e) indicates further pressure decrease during D3. This textural evidence indicates garnet resorption associated with retrograde *P–T* conditions during development of the subhorizontal S3 foliation (Fig. 15).

Tectonic significance of garnet records

Constraints on burial and exhumation processes

Field structural analysis reveals a succession of three superposed quasi-orthogonal foliations (Fig. 2). Because these fabrics have also been preserved in garnet porphyroblasts, *P–T* conditions associated with each fabric can be derived from garnet composition

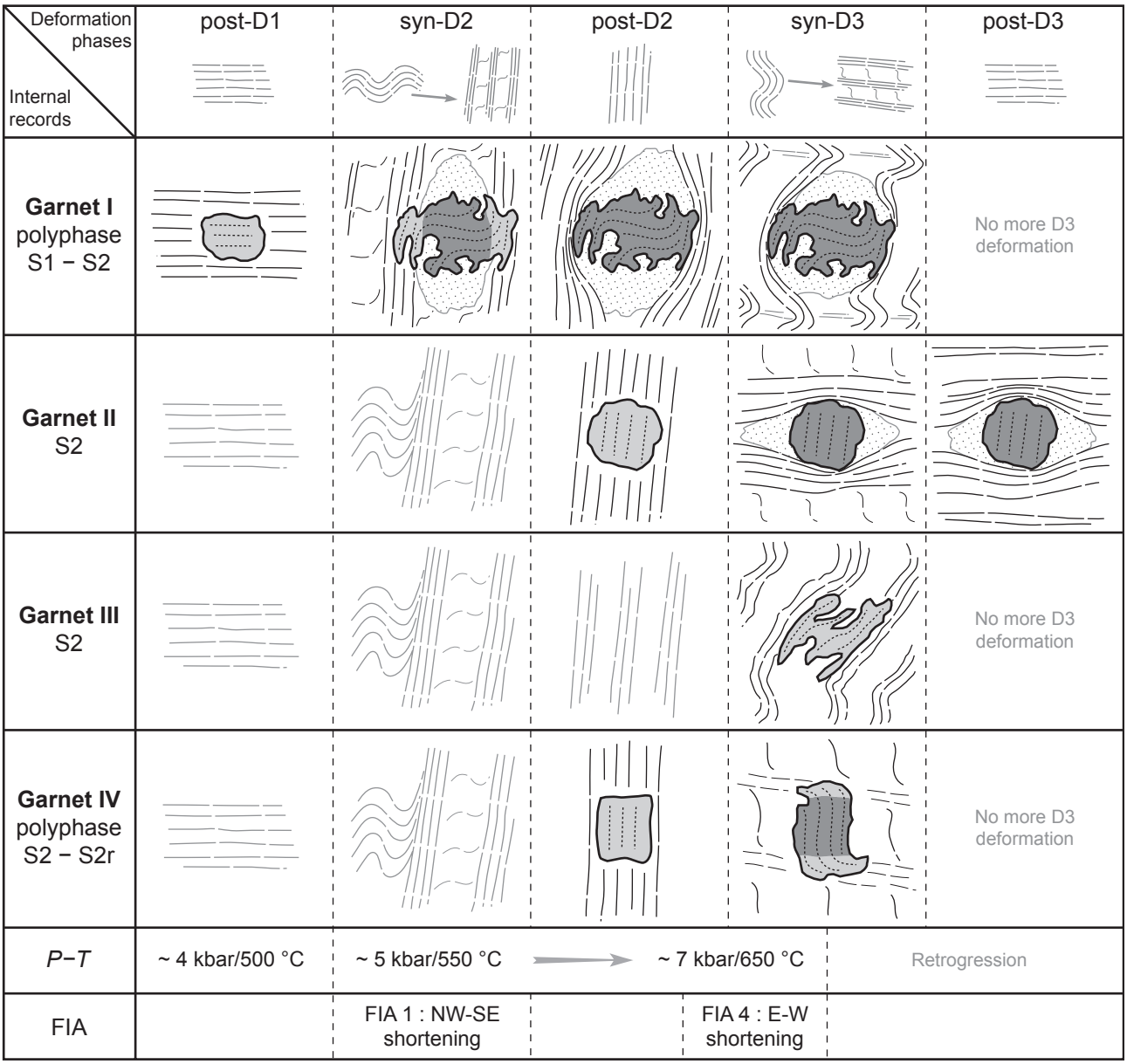

Fig. 15. Summary of crystallization–deformation relationships, metamorphic record and microstructural data associated with the different types of garnet porphyroblasts. Light grey = newer garnet, dark grey = older garnet.

(Fig. 8). The resulting *P–T–d* path is used to further constrain the tectono-metamorphic evolution.

Prograde metamorphism is documented during or after the development of the subhorizontal S1 foliation as well as during the formation of the subvertical S2 foliation (Fig. 8). This indicates continuous burial of metasedimentary rocks starting in a flat-lying fabric and culminating during horizontal shortening. Conversely, the pressure decrease associated with the development of the subhorizontal S3 foliation points to a subsequent exhumation.

This *P–T–d* path is not only in agreement with the model proposed by Skrzypek *et al.* (2010) but also places new constraints, especially on early stages of the evolution. Indeed, garnet records not only unravel the prograde character of the early S1 foliation but also suggest dominant pure shear deformation during the whole history. In the present case, combining compositional and microstructural records preserved in porphyroblasts with previous works (Štípská *et al.*, 2004; Skrzypek *et al.*, 2010) allows a more precise characterization of burial and exhumation processes in the root zone of the Variscan ororgen.

Constraints on large-scale tectonics: FIA implications

Different FIA sets were reconstructed (Fig. 14) to use them as indicators of compression during orogenesis

(Bell *et al.*, 1995). The trend of FIA 1 and FIA 4 correlates well with the general NE–SW or N–S strike of metasedimentary belts in the OSD (Fig. 1b). This geometry of synforms cored by metasedimentary rocks was already interpreted as a result of vertical shortening during the Carboniferous (Dumicz, 1979), but FIA records provide a more detailed history. They indicate NW–SE compression during D2 deformation, followed by E–W compression at the onset of D3.

Distinct FIAs have already been used to decipher a polyphase orogenic evolution (Aerden & Sayab, 2008). In the same way, we can propose that the first NW–SE compression reflects the Saxothuringian subduction recognized farther to the NW (Fig. 1a; Maluski & Patočka, 1997; Konopásek & Schulmann, 2005), whereas the subsequent E–W compression represents the influence of the N–S striking boundary of the Brunovistulian continent to the E (Fig. 1b; Štípská *et al.*, 2001). However, these FIAs may solely be linked to variations in the geometry of the Brunovistulian indentor (Fig. 1b). This suggests that the use of FIA as a tectonic indicator is subordinated to a careful understanding of the mechanical role of all major boundaries surrounding the investigated area.

ACKNOWLEDGEMENTS

E. Skrzypek acknowledges funding by BRGM and Région Alsace. Financial support of the French National Grant Agency (06–1148784 to K. Schulmann) is acknowledged. P. Týcová (Czech Geological Survey, Prague) is thanked for sample preparation and help during EBSD analyses. We also acknowledge the help from T. Theye (Universität Stuttgart) for chemical analyses and X-ray maps. Support from J-E. Martelat (UCB, Lyon) during field work was greatly appreciated. We are grateful to D. Aerden and M. Williams for detailed and constructive comments and to N. Timms for pushing us to clarify our work. M. Brown is thanked for careful editorial work.

REFERENCES

Aerden, D.G.A.M., 1995. Porphyroblast non-rotation during crustal extension in the Variscan Lys-Caillaouas Massif, Pyrenees. *Journal of Structural Geology*, **17,** 709–725.

Aerden, D.G.A.M., 2003. Preferred orientation of planar microstructures determined via statistical best-fit of measured intersection-lines: the 'FitPitch' computer program. *Journal of Structural Geology*, **25,** 923–934.

Aerden, D.G.A.M., 2004. Correlating deformation in Variscan NW-Iberia using porphyroblasts; implications for the Ibero-Armorican Arc. *Journal of Structural Geology*, **26,** 177–196.

Aerden, D.G.A.M. & Sayab, M., 2008. From Adria- to Africa-driven orogenesis: evidence from porphyroblasts in the Betic Cordillera, Spain. *Journal of Structural Geology*, **30,** 1272–1287.

Bell, T.H., 1981. Foliation development – the contribution, geometry and significance of progressive, bulk, inhomogeneous shortening. *Tectonophysics*, **75,** 273–296.

Bell, T.H. & Johnson, S.E., 1989. Porphyroblast inclusion trails; the key to orogenesis. *Journal of Metamorphic Geology*, **7,** 279–310.

Bell, T.H. & Rubenach, M.J., 1983. Sequential porphyroblast growth and crenulation cleavage development during progressive deformation. *Tectonophysics*, **92,** 171–194.

Bell, T.H. & Welch, P.W., 2002. Prolonged Acadian Orogenesis: revelations from foliation intersection axis (FIA) controlled monazite dating of foliations in porphyroblasts and matrix. *American Journal of Science*, **302,** 549–581.

Bell, T.H., Johnson, S.E., Davis, B., Forde, A., Hayward, N. & Witkins, C., 1992. Porphyroblast inclusion-trail orientation data: eppure non son girate! *Journal of Metamorphic Geology*, **10,** 295–307.

Bell, T.H., Forde, A. & Wang, J., 1995. A new indicator of movement direction during orogenesis – measurement technique and application to the Alps. *Terra Nova*, **7,** 500–508.

Bell, T.H., Hickey, K.A. & Upton, G.J.G., 1998. Distinguishing and correlating multiple phases of metamorphism across a multiply deformed region using the axes of spiral, staircase and sigmoidal inclusion trails in garnet. *Journal of Metamorphic Geology*, **16,** 767–794.

Bons, P.D., Jessell, M.W. & Griera, A., 2009. Porphyroblast rotation versus nonrotation: conflict resolution! COMMENT. *Geology*, **37,** e182–e188.

Ceriani, S., Mancktelow, N.S. & Pennacchioni, G., 2003. Analogue modelling of the influence of shape and particle/matrix interface lubrication on the rotational behaviour of rigid particles in simple shear. *Journal of Structural Geology*, **25,** 2005–2021.

Chan, Y.C. & Crespi, J.M., 1999. Albite porphyroblasts with sigmoidal inclusion trails and their kinematic implications: an example from the Taconic Allochthon, west-central Vermont. *Journal of Structural Geology*, **21,** 1407–1417.

Coggon, R. & Holland, T.J.B., 2002. Mixing properties of phengitic micas and revised garnet–phengite thermobarometers. *Journal of Metamorphic Geology*, **20,** 683–696.

Don, J., 1982. The Sienna synform and the relationship of gneisses to the deformational stages distinguished in the Śnieżnik metamorphic massif (Sudetes). *Geologia Sudetica*, **17,** 103–124.

Don, J., Dumicz, M., Wojciechowska, I. & Żelażniewicz, A., 1990. Lihology and tectonics of the Orlica-Śnieżnik Dome, Sudetes: recent state of knowledge. *Neues Jahrbuch für Geologie und Paläontologie, Abhandlungen*, **179,** 159–188.

Don, J., Skácel, J. & Gotowała, R., 2003. The boundary zone of the East and West Sudetes on the 1:50 scale geological map of the Velké Vrbno, Staré Město and Śnieżnik Metamorphic Units. *Geologia Sudetica*, **35,** 25–59.

Dumicz, M., 1979. Tectogenesis of the metamorphosed series of the Kłodzko district: a tentative explanation. *Geologia Sudetica*, **14,** 29–44.

Edel, J.-B., Schulmann, K. & Holub, F.V., 2003. Anticlockwise and clockwise rotations of the Eastern Variscides accommodated by dextral lithospheric wrenching: palaeomagnetic and structural evidence. *Journal of the Geological Society, London*, **160,** 209–218.

Fay, C., Bell, T.H. & Hobbs, B.E., 2008. Porphyroblast rotation versus non-rotation: conflict resolution! *Geology*, **36,** 307–310.

Floyd, P.A., Winchester, J.A., Ciesielczuk, J., Lewandowska, A., Szczepanski, J. & Turniak, K., 1996. Geochemistry of early Palaeozoic amphibolites from the Orlica-Śnieżnik dome, Bohemian Massif: petrogenesis and palaeotectonic aspects. *Geologische Rundschau*, **85,** 225–238.

Fyson, W.K., 1980. Fold fabrics and emplacement of an Archean granitoid pluton, Cleft Lake, Northwest Territories. *Canadian Journal of Earth Sciences*, **17,** 325–332.

Gunia, T., 1984a. Microflora of the crystalline limestones from the vicinity of Nowy Waliszów (Krowiarki Mts., Central Sudetes). *Geologia Sudetica*, **19,** 75–86.

Gunia, T., 1984b. Microfossils from the quartzitic schists in vicinity of Goszów, Śnieżnik Kłodzki Massif, Central Sudetes. *Geologia Sudetica*, **18,** 47–57.

Hayward, N., 1990. Determination of early fold axis orientations in multiply deformed rocks using porphyroblast inclusion trails. *Tectonophysics*, **179,** 353–369.

Holland, T.J.B. & Powell, R., 1998. An internally consistent thermodynamic data set for phases of petrological interest. *Journal of Metamorphic Geology*, **16,** 309–343.

Holland, T. & Powell, R., 2003. Activity-composition relations for phases in petrological calculations: an asymmetric multicomponent formulation. *Contributions to Mineralogy and Petrology*, **145,** 492–501.

Holland, T.J.B., Baker, J. & Powell, R., 1998. Mixing properties and activity-composition relationships of chlorites in the system MgO-FeO-Al_2O_3-SiO_2-H_2O. *European Journal of Mineralogy*, **10,** 395–406.

Huddlestone-Holmes, C.R. & Ketcham, R.A., 2005. Getting the inside story: using computed X-ray tomography to study inclusion trails in garnet porphyroblasts. *American Mineralogist*, **90,** ea1–ea17.

Ikeda, T., Shimobayashi, N., Wallis, S.R. & Tsuchiyama, A., 2002. Crystallographic orientation, chemical composition and three-dimensional geometry of sigmoidal garnet: evidence for rotation. *Journal of Structural Geology*, **24,** 1633–1646.

Ilg, B.R. & Karlstrom, K.E., 2000. Porphyroblast inclusion trail geometries in the Grand Canyon; evidence for non-rotation and rotation? *Journal of Structural Geology*, **22,** 231–243.

Jastrzębski, M., 2008. A Variscan continental collision of the West Sudetes and the Brunovistulian terrane: a contribution from structural and metamorphic record of the Stronie Formation, the Orlica-Śnieżnik Dome, SW Poland. *International Journal of Earth Sciences*, **8,** 1901–1923.

Jastrzębski, M., Żelaźniewicz, A., Nowak, I., Murtezi, M. & Larionov, A., 2010. Protolith age and provenance of metasedimentary rocks in Variscan allochthon units: U–Pb SHRIMP zircon data from the Orlica-Śnieżnik Dome, West Sudetes. *Geological Magazine*, **147,** 416–433.

Jeffery, G.B., 1922. The motion of ellipsoidal particles immersed in a viscous fluid. *Proceedings of the Royal Society, London*, **102,** 161–179.

Ježek, J., Schulmann, K. & Segeth, K., 1996. Fabric evolution of rigid inclusions during mixed coaxial and simple shear flows. *Tectonophysics*, **257,** 203–221.

Jiang, D., 2001. Reading history of folding from porphyroblasts. *Journal of Structural Geology*, **23,** 1327–1335.

Johnson, S.E., 1990. Lack of porphyroblast rotation in the Otago schists, New Zealand; implications for crenulation cleavage development, folding and deformation partitioning. *Journal of Metamorphic Geology*, **8,** 13–30.

Johnson, S.E. & Vernon, R.H., 1995. Stepping stones and pitfalls in the determination of an anticlockwise P-T-t-deformation path: the low-*P*, high-*T* Cooma Complex, Australia. *Journal of Metamorphic Geology*, **13,** 165–183.

Johnson, S.E., Dupee, M.E. & Guidotti, C.V., 2006. Porphyroblast rotation during crenulation cleavage development: an example from the aureole of the Mooselookmeguntic pluton, Maine, USA. *Journal of Metamorphic Geology*, **24,** 55–73.

Jung, W.S., Ree, J.H. & Park, Y., 1999. Non-rotation of garnet porphyroblasts and 3-D inclusion trail data; an example from the Imjingang Belt, South Korea. *Tectonophysics*, **307,** 381–395.

Kalvoda, J., Bábek, O., Fatka, O. *et al*., 2008. Brunovistulian terrane (Bohemian Massif, Central Europe) from late Proterozoic to late Paleozoic: a review. *International Journal of Earth Sciences*, **97,** 497–518.

Kim, H.S. & Bell, T.H., 2005. Combining compositional zoning and foliation intersection axes (FIAs) in garnet to quantitatively determine early P-T-t paths in multiply deformed and metamorphosed schists: north central Massachusetts, USA. *Contributions to Mineralogy and Petrology*, **149,** 141–163.

Konopásek, J. & Schulmann, K., 2005. Contrasting Early Carboniferous field geotherms: evidence for accretion of a thickened orogenic root and subducted Saxothuringian crust (Central European Variscides). *Journal of the Geological Society, London*, **162,** 463–470.

Kröner, A., Jaeckel, P., Hegner, E. & Opletal, M., 2001. Single zircon ages and whole rock Nd isotopic systematics of early Palaeozoic granitoid gneisses from the Czech and Polish Sudetes (Jizerské hory, Krkonoše Mountains and Orlica-Sněžník Complex). *International Journal of Earth Sciences*, **90,** 304–324.

Lexa, O., Stipska, P., Schulmann, K., Baratoux, L. & Kroner, A., 2005. Contrasting textural record of two distinct metamorphic events of similar *P-T* conditions and different durations. *Journal of Metamorphic Geology*, **23,** 649–666.

Lister, G.S. & Williams, P.F., 1983. The partitioning of deformation in flowing rock masses. *Tectonophysics*, **92,** 1–33.

Mahar, E.M., Baker, J.M., Powell, R., Holland, T.J.B. & Howell, N., 1997. The effect of Mn on mineral stability in metapelites. *Journal of Metamorphic Geology*, **15,** 223–238.

Mainprice, D., 2005. *PFch5* [Computer software]. Available at: ftp://www.gm.univ-montp2.fr/mainprice//CareWare_Unicef_Programs/ (last accessed on 27 July 2005).

Maluski, H. & Patočka, F., 1997. Geochemistry and $^{40}Ar/^{39}Ar$ geochronology of the mafic metavolcanic rocks from the Rýchory Mountains complex (west Sudetes, Bohemian Massif): paleotectonic significance. *Geological Magazine*, **134,** 703–716.

Moseley, D., 1981. Ilmenite exsolution in olivine. *American Mineralogist*, **66,** 976–979.

Olesen, N.Ø., 1978. Distinguishing between inter-kinematic and syn-kinematic porphyroblastesis. *Geologische Rundschau*, **67,** 278–287.

Passchier, C.W., Trouw, R.A.J., Zwart, H.J. & Vissers, R.L.M., 1992. Porphyroblast rotation; eppur si muove? *Journal of Metamorphic Geology*, **10,** 283–294.

Pattison, D.R.M. & Bégin, N.J., 1994. Zoning patterns in orthopyroxene and garnet in granulites – implications for geothermometry. *Journal of Metamorphic Geology*, **12,** 387–410.

Powell, R., Holland, T. & Worley, B., 1998. Calculating phase diagrams involving solid solutions via non-linear equations, with examples using THERMOCALC. *Journal of Metamorphic Geology*, **16,** 577–588.

Prior, D.J., 1987. Syntectonic porphyroblast growth in phyllites: textures and processes. *Journal of Metamorphic Geology*, **5,** 27–39.

Ramsay, J.G., 1962. The geometry and mechanics of formation of "similar" type folds. *Journal of Geology*, **70,** 309–327.

Robyr, M., Vonlanthen, P., Baumgartner, L.P. & Grobety, B., 2007. Growth mechanism of snowball garnets from the Lukmanier Pass area (Central Alps, Switzerland): a combined lCT/EPMA/EBSD study. *Terra Nova*, **19,** 240–244.

Sayab, M., 2005. Microstructural evidence for N–S shortening in the Mount Isa Inlier (NW Queensland, Australia): the preservation of early W–E-trending foliations in porphyroblasts revealed by independent 3D measurement techniques. *Journal of Structural Geology*, **27,** 1445–1468.

Scheidegger, A.E., 1965. On the statistics of the orientation of bedding planes, grain axes, and similar sedimentological data. *U.S. Geological Survey Professional Paper*, **525,** 164–167.

Schneider, D.A., Zahniser, S.J., Glascock, J.M., Gordon, S.M. & Manecki, M., 2006. Thermochronology of the West sudetes (Bohemian Massif): rapid and repeated eduction in the eastern Variscides, Poland and Czech Republic. *American Journal of Science*, **306,** 846–873.

Schulmann, K. & Gayer, R., 2000. A model for a continental accretionary wedge developed by oblique collision: the NE Bohemian Massif. *Journal of the Geological Society, London*, **157,** 401–416.

Skrzypek, E., Štípská, P., Schulmann, K., Lexa, O. & Lexová, M., 2011. Prograde and retrograde metamorphic fabrics – a

key for understanding burial and exhumation in orogens (Bohemian Massif). *Journal of Metamorphic Geology*, (in press).
St Onge, M.R., 1987. Zoned poikiloblastic garnets: P-T paths and syn-metamorphic uplift through 30 km of structural depth, Wopmay Orogen, Canada. *Journal of Petrology*, **987,** 1–21.
Stallard, A. & Hickey, K.A., 2001. Fold mechanisms in the Canton schist: constraints on the contribution of flexural flow. *Journal of Structural Geology*, **23,** 1865–1881.
Štípská, P., Schulmann, K., Thompson, A.B., Ježek, J. & Kröner, A., 2001. Thermo-mechanical role of a Cambro-Ordovician paleorift during the Variscan collision: the NE margin of the Bohemian Massif. *Tectonophysics*, **332,** 239–253.
Štípská, P., Schulmann, K. & Kröner, A., 2004. Vertical extrusion and middle crustal spreading of omphacite granulite: a model of syn-convergent exhumation (Bohemian Massif, Czech Republic). *Journal of Metamorphic Geology*, **22,** 179–198.
Timms, N.E., 2003. Garnet porphyroblast timing and behaviour during fold evolution: implications from a 3-D geometric analysis of a hand-sample scale fold in a schist. *Journal of Metamorphic Geology*, **21,** 853–873.
Tinkham, D.K., Zuluaga, C.A. & Stowell Harold, H., 2001. Metapelite phase equilibria modeling in MnNCKFMASH: the effect of variable Al_2O_3 and MgO/(MgO + FeO) on mineral stability. *Geological Materials Research*, **3,** 1–42.
Turniak, K., Mazur, S. & Wysoczanski, R., 2000. SHRIMP zircon geochronology and geochemistry of the Orlica-Śnieżnik gneisses (Variscan belt of Central Europe) and their tectonic implications. *Geodinamica Acta*, **13,** 1–20.
Vernon, R.H., 1978. Porphyroblast-matrix microstructural relationships in deformed metamorphic rocks. *Geologische Rundschau*, **67,** 288–305.
Vernon, R.H., Paterson, S.R. & Foster, D., 1993. Growth and deformation of porphyroblasts in the Foothills terrane, central Sierra Nevada, California: negotiating a microstructural minefield. *Journal of Metamorphic Geology*, **11,** 203–222.
Visser, P. & Mancktelow, N.S., 1992. The rotation of garnet porphyroblasts around a single fold, Lukmanier Pass, Central Alps. *Journal of Structural Geology*, **14,** 1193–1202.
White, R.W., Pomroy, N.E. & Powell, R., 2005. An in situ metatexite-diatexite transition in upper amphibolite facies rocks from Broken Hill, Australia. *Journal of Metamorphic Geology*, **23,** 579–602.
White, R.W., Powell, R. & Holland, T.J.B., 2007. Progress relating to calculation of partial melting equilibria for metapelites. *Journal of Metamorphic Geology*, **25,** 511–527.
Williams, P.F. & Jiang, D., 1999. Rotating garnets. *Journal of Metamorphic Geology*, **17,** 367–378.
Żelażniewicz, A., 1988. Orthogneisses due to irrotational extension, a case from the Sudetes, Bohemian Massif. *Geologische Rundschau*, **77,** 671–682.
Żelażniewicz, A., Nowak, I., Larionov, A. & Presnyakov, S., 2006. Syntectonic Lower Ordovician migmatite and post-tectonic Upper Viséan syenite in the western limb of the Orlica- Śnieżnik Dome, West Sudetes: U-Pb SHRIMP data from zircons. *Geologia Sudetica*, **38,** 63–80.
Zwart, H.J., 1962. On the determination of polymetamorphic mineral associations, and its application to the Bosost area (central Pyrenees). *Geologische Rundschau*, **52,** 38–69.

APPENDIX

Mineral abbreviations

Mineral abbreviations are as follows: ab, albite; and, andalusite; bi, biotite; chl, chlorite; cd, cordierite; ep, epidote; g, garnet (with end-members: Alm, almandine; Grs, grossular; Prp, pyrope; Sps, spessartine); ilm, ilmenite; ksp, K-feldspar; ky, kyanite; mu, muscovite; pa, paragonite; pl, plagioclase; q, quartz; ru, rutile; sill, sillimanite; st, staurolite.

Whole-rock data and activity–composition relationships used for pseudosection modelling

Pseudosections have been calculated in the MnO–Na_2O–CaO–K_2O–FeO–MgO–Al_2O_3–SiO_2–H_2O–TiO_2–O_2 system using whole-rock compositions of sample ES2C (ICP-ES whole-rock analysis in wt%: SiO_2 = 69.22; TiO_2 = 0.70; Al_2O_3 = 15.11; Fe_2O_3 = 0.49; FeO = 4.00; MnO = 0.16; MgO = 1.93; CaO = 1.08; Na_2O = 1.27; K_2O = 3.77; P_2O_5 = 0.14) and ES36L (ICP-ES whole-rock analysis in wt%: SiO_2 = 63.76; TiO_2 = 0.85; Al_2O_3 = 17.49; Fe_2O_3 = 0.69; FeO = 5.60; MnO = 0.09; MgO = 2.48; CaO = 1.33; Na_2O = 1.74; K_2O = 3.61; P_2O_5 = 0.15). In the calculations, O is set to small values (O = 0.01–0.02), mostly to evaluate ilmenite stability.

Calculations were performed using THERMOCALC 3.33 (Powell *et al*., 1998) and the thermodynamic database 5.5 from Holland & Powell (1998). The activity–composition relationships are as follows: for feldspar from Holland & Powell (2003), for white mica from Coggon & Holland (2002), for silicate melt from White *et al*. (2007), for epidote from Holland & Powell (1998), for Mn-bearing garnet, staurolite, cordierite and chlorite from Mahar *et al*. (1997) and Holland *et al*. (1998), and for Ti-bearing biotite and ilmenite from White *et al*. (2005).

Analytical procedure for EBSD analysis

Thin sections were polished and prepared for EBSD measurements using a CamScan CS 3200 electron microscope of the Czech Geological Survey, Prague. Operating conditions of 20-kV accelerating voltage, 5-nA beam current and 33-mm working distance were used for samples tilted at 70°.

Received 17 September 2010; revision accepted 4 December 2010.

EARLY SHALLOW-DIPPING BURIAL FABRICS IN THE LOWER OROGENIC CRUST

23. **Štípská** P., Chopin F., Skrzypek E., Schulmann K., Lexa O., Pitra, P., Martelat, J.E., Bollinger, C. Juxtaposition of eclogite-facies and mid-crustal rocks during exhumation: relative role of erosion and crustal-scale folding in a continentam wedge (Orlica-Śnieżnik dome, Bohemian Massif). Journal of Metamorphic Geology. soumis.

24. Chopin F., Schulmann K., **Štípská** P., Martelat, J.E., Pitra, P., Lexa, O., Petri, B. Prograde deformation gradient in subducted high-pressure orthogneiss (Orlica-Śnieżnik dome, Bohemian Massif): implications for reaction softening and strain localisation during continental subduction. Journal of Metamorphic Geology. soumis.

Microstructural and petrological evolution of a high pressure granitic orthogneiss during continental subduction (Orlica-Śnieżnik dome, NE Bohemian Massif)

F. CHOPIN [1], K. SCHULMANN [1], P. ŠTÍPSKÁ [1], J.E. MARTELAT[2], P. PITRA [3], O. LEXA [4,5], and B. PETRI [1]

[1]*Ecole et Observatoire des Sciences de la Terre, Institut de Physique du Globe – CNRS UMR7516, Université de Strasbourg, 1 rue Blessig, F-67084, Strasbourg Cedex, France*

[2]*Laboratoire de Géologie de Lyon – CNRS UMR5276, Université Claude Bernard et Ecole Normale Supérieure, F-69622, Villeurbanne, France*

[3]*Géosciences Rennes – CNRS UMR6118, Université Rennes 1, Campus de Beaulieu, F-35042 Rennes Cedex, France*

[4]*Institute of Petrology and Structural Geology, Charles University, Albertov 6, 128 43 Prague, Czech Republic*

[5]*Czech Geological Survey, Klárov 3, 110 00, Prague, Czech Republic*

Short title: Deformation of HP granitic orthogneiss

Key words: quantitative microstructural analysis, Thermocalc modeling, crust rheology, eclogite granitic orthogneiss, Bohemian Massif.

submitted to Journal of Metamorphic Geology

ABSTRACT

A microstructural and petrological study of a naturally deformed MP to HP granitic orthogneiss (Orlica-Śnieżnik dome, NE Bohemian Massif) allows examining the behaviour of the felsic crust during progressive burial along a subduction-type geothermal gradient (~10 °C/km). Along the studied finite strain gradient, the granitic orthogneisses develops three distinct microstructural groups: type I - augen, type II - banded and type III- mylonitic orthogneiss, each representing an evolutionary stage of a progressively deformed metagranite. Type I orthogneiss is made of partially recrystallized K-feldspar porphyroclasts surrounded by wide fronts of myrmekites, fully recrystallized quartz aggregates and interconnected monomineralic layers of recrystallized plagioclase. Layering defined by mineral bands in type II orthogneiss is marked by an increasing proportion of interstitial phases and the deformation of recrystallized myrmekite fronts affecting both plagioclase- and K-feldspar-rich layers. Type III orthogneiss reveals relics of quartz and K-feldspar ribbons preserved in a fine-grained polymineralic matrix. All the types have the same assemblage (q+pl+kfs+mu+bi+g+sph±ilm), but show systematic variations in the composition of muscovite and garnet from type I to type III. This is consistent with the equilibration of the three types at different positions along a prograde $P-T$ path ranging from P<15 kbar and T<700 °C (type I orthogneiss) to P = 19-20 kbar and T>700 °C (types II and III orthogneisses). The deformation types thus do not represent evolutionary stages of a highly partitioned deformation at constant $P-T$ conditions, but reflect progressive formation during the burial of the continental crust. The microstructure of type I and type II orthogneisses result from the dislocation creep of quartz and K-feldspar while grain boundary sliding-dominated diffusion creep regime is characteristic for the type III orthogneiss. Strain weakening related to transition from type I to type II microstructure is enhanced by the recrystallization of wide myrmekite fronts, and further weakening and strain localization in type III orthogneiss occur via partial melting (5 mol.%).

INTRODUCTION

Quartzo-feldspathic rocks form the most important part of the continental crust and the understanding of their rheological behaviour in a wide range of natural physical conditions is therefore the subject of many microstructural studies (e.g. Gapais, 1989; Handy, 1990). A detailed study of deformation gradients in metagranites is a common approach to evaluate the role of strain partitioning between mineral phases of contrasting rheology (Handy, 1994) and variations in mechanisms of dynamic recrystallization in progressively strained rocks (e.g. Schulmann *et al.*, 1996). Several studies have shown that quartz and feldspars in metagranites recrystallize dynamically by dislocation creep at greenschist facies (Shigematsu & Tanaka, 2000; Ishii *et al.*, 2007; Menegon *et al.*, 2008) or amphibolite facies conditions (Bose & Sengupta, 2003). At granulite facies conditions, dislocation creep is still an important deformation mechanism operating both in quartz and feldspars (Martelat *et al.*, 1999). At low metamorphic grades and high strain intensities, grain size reduction and crystallization of new phases from aqueous fluids leads to the development of granular flow of fine-grained polyphase aggregates (Stünitz & Fitzgerald, 1993; Lonka *et al.*, 1998; Jeřábek *et al.*, 2007). At amphibolite and granulite facies conditions and high strain intensities a small fraction of

interstitial melt is responsible for the transition from dislocation creep to grain boundary sliding-accommodated diffusion creep (Závada *et al.*, 2007; Schulmann *et al.*, 2008).

Studies of progressive deformation in (U)HP metagranites associated with burial of the continental crust into great depths are rare (Lenze & Stöckhert, 2007). Metagranites commonly form large scale boudins, which do not experience important deformation during either burial or exhumation (e.g. Lenze & Stöckhert, 2007; Hacker *et al.*, 2010). Only locally, plastic flow operating at high-pressure conditions was reported, for instance in the Qinling–Dabie–Sulu orogenic belt (Zhao *et al.*, 2005). The lack of distributed deformation in granitoids buried to great depths can be explained by the low level of differential stress or more likely, due to strain localisation in narrow shear zones or weaker lithologies such as HP metasediments (Stöckhert & Renner, 1998; Stöckhert, 2002). In addition, granitic orthogneisses spatially associated with eclogites do not typically reveal mineral assemblages characteristic for (U)HP conditions (Menold *et al.*, 2009; Peterman *et al.*, 2009) and it is therefore not clear whether they shared the same metamorphic evolution with the rocks bearing the eclogite facies assemblages (e.g. Cooke & O'Brien, 2001; Štípská *et al.*, 2006).

Consequently, there is a complete lack of observations allowing to understand how felsic material behaves during burial and subduction at (U)HP conditions and what can be the aspect of the rocks that experienced prograde deformation in terms of their microstructure and petrology. In order to fill this gap we examined a deformation gradient in a (U)HP eclogite-bearing granitic orthogneiss from the Orlica-Śnieżnik dome, where eclogites appear as large bodies in generally weakly deformed metagranites. The occurrence of eclogite slivers is associated with strong deformation gradients in the surrounding granitic orthogneiss. We performed a detailed microstructural, geochemical and petrological study combined with pseudosection modeling on granitic orthogneisses that show deformational gradients from augen, through banded to mylonitic types. We estimated the P−T conditions of deformation and identified various deformation mechanisms in the studied rock types. An attempt is made to discuss the possible reasons for major strain localization during continental subduction.

GEOLOGICAL SETTING

The Orlica-Śnieżnik dome (OSD) is situated in the north-eastern termination of the Bohemian Massif at the contact with the Brunia microcontinent (Mazur *et al.*, 2006, Fig. 1a). The OSD (Fig. 1b) is made of belts of high grade granitoid orthogneiss, sometimes cored by (U)HP rocks (Bröcker & Klemd, 1996; Štípská *et al.*, 2004), and surrounded by amphibolite facies metasediments altogether forming the Lugian root of the Variscan orogen (Skrzypek *et al.*, 2011b). The dome is mantled by supracrustal units of supposed Neo-Proterozoic age in the south (the Nové Město and Zábřeh units) (Mazur & Aleksandrowski, 2001) and by relics of Cambro-Ordovician rift sequences (the Staré Město unit) (Parry *et al.*, 1997; Kröner *et al.*, 2000; Štípská *et al.*, 2001) that collided with the Brunia microcontinent in the east (Schulmann & Gayer, 2000; Štípská *et al.*, 2006; Košuličová & Štípská, 2007). The protoliths of the orthogneisses (Kröner *et al.*, 2001) and the metapelites (Jastrzębski *et al.*, 2010) have a coeval Cambro-Ordovician origin, whereas the protolith of the (U)HP rocks remains discussed (Bröcker *et al.*, 2010). ^{40}Ar-^{39}Ar cooling ages of hornblende and micas (Schneider *et al.*, 2006) and metamorphic zircons (Bröcker *et al.*, 2009 and references therein) from both gneisses and metasediments cluster around 340 Ma. Recent studies have highlighted the

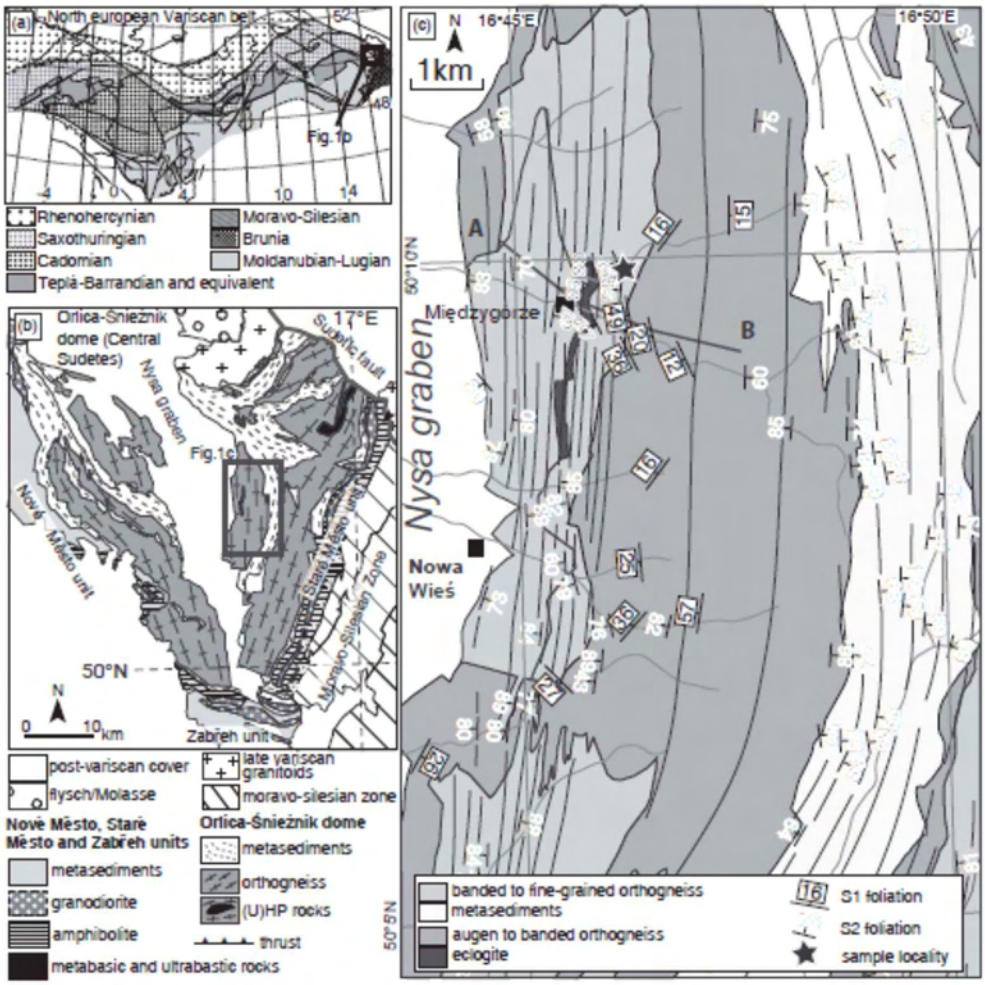

Fig. 1: Tectonic setting and geology of the studied area. (a) Position of the Orlica-Śnieżnik dome in the Variscan belt of Europe (modified after Edel *et al.*, 2003). (b) Geological map of the Orlica-Śnieżnik dome (modified after Aleksandrowski *et al.*, 1997; Don *et al.*, 2003; Żelaźniewicz *et al.*, 2006). (c) Structural map of the studied area (lithology after Don *et al.*, 2003).

succession of three main episodes of deformation: the remnants of early Variscan flat fabrics related to crustal thickening are followed by steep structures associated with E-W lateral shortening. Both are overprinted by ubiquitous flat supracrustal fabrics connected with ductile thinning and unroofing of the thickened crustal root (Skrzypek *et al.*, 2011a, Skrzypek *et al.*, 2011b).

The study area is located in the surroundings of the Międzygórze town, at the eastern periphery of the eclogite belt (Smulikowski, 1967; Dumicz, 1989) (Fig. 1c). In this area, the early flat fabric S1 is well preserved in the granitic orthogneiss that shows various macroscopic textural varieties ranging from augen orthogneiss (referred to as the Śnieżnik type in the literature; e.g. Fisher, 1936) to banded and fine grained mylonitic orthogneiss (the Gierałtów type). It has been shown that both orthogneiss types are derived from the same protolith of predominantly porphyric granite and represent different degrees of deformation (Lange *et al.*, 2005). The banded and mylonitic orthogneiss is most abundant in an approximately 1.5 kilometer wide zone around the eclogite belt, while further away the augen type is dominant (Figs 1c & 2). The S1 fabrics are affected by E-W directed D2 lateral

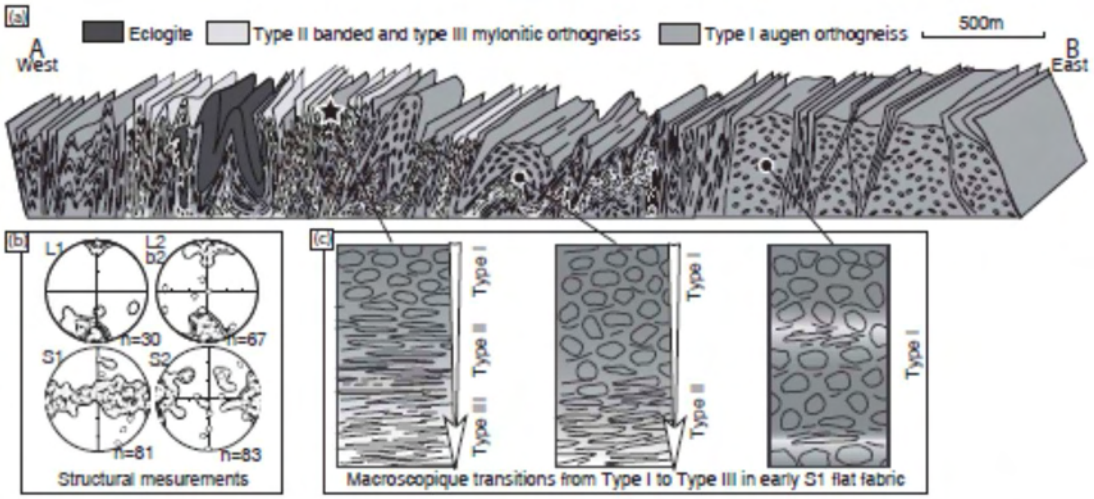

Fig. 2: (a) Geological cross-section in the Śnieżnik massif (A–B) showing principal structural features. Dark gray: type I augen to type II banded orthogneiss; Light grey: type III mylonitic orthogneiss. (b) Equal-area, lower-hemisphere projections of D1 and D2 planar and linear structures (contoured at regular multiples of distribution). (c) Spatial and macroscopic evolution of metagranite with increasing strain and corresponding types in S1 fabric (type I augen orthogneiss, type II banded orthogneiss and type III mylonitic orthogneiss).

shortening, which leads to the steepening of the N-S trending metamorphic fabric S1 and development of a new steep foliation S2 mainly in the vicinity of the eclogite (Figs. 1c & 2). The S2 fabric is associated with melt-filled shear bands indicating partial melting during exhumation.

Definition of structural types according to the finite strain gradient

All samples were taken in one outcrop close to the eclogite belt near the Międzygórze town (Figs 1c & 2). There, the metagranites exhibit a subhorizontal S1 foliation bearing a N-S trending lineation and are affected by a decimeter- to meter-scale finite D1 strain gradient (Fig. 2). The S1 foliation is affected by open to close N-S trending F2 folds, up to several tens of metres in amplitude. Macroscopically, three types of rocks are recognized, representing different degrees of the D1 deformation of a porphyric granite: type I augen orthogneiss, type II banded orthogneiss, and type III mylonitic orthogneiss (Fig. 3a−h).

Representative samples of the three rock types, have been cut parallel to the XZ and YZ sections of the finite strain ellipsoid in order to evaluate the evolution of the deformation intensity of K-feldspar clasts in the three types of rocks (Ramsay & Huber, 1983). The results of the finite strain analysis are presented in the Flinn's diagram (Flinn, 1965) (Fig. 3i,j). Type I and type II samples show a moderate increase of bulk strain intensity associated with weak variations of strain symmetry from plane strain to oblate shapes. The type III sample reveals a dramatic increase of finite strain intensity associated with an oblate shape.

Whole rock composition

The whole rock analyses were performed by ICP-AES in the Acme laboratories (Canada) and are presented in Table 1. Figure 4b shows that all samples display the same type of REE pattern. Type III mylonitic orthogneiss (samples mzg05 and mzg10) are slightly depleted in LREE compared to orthogneiss types I and II. The representation in an isocon diagram

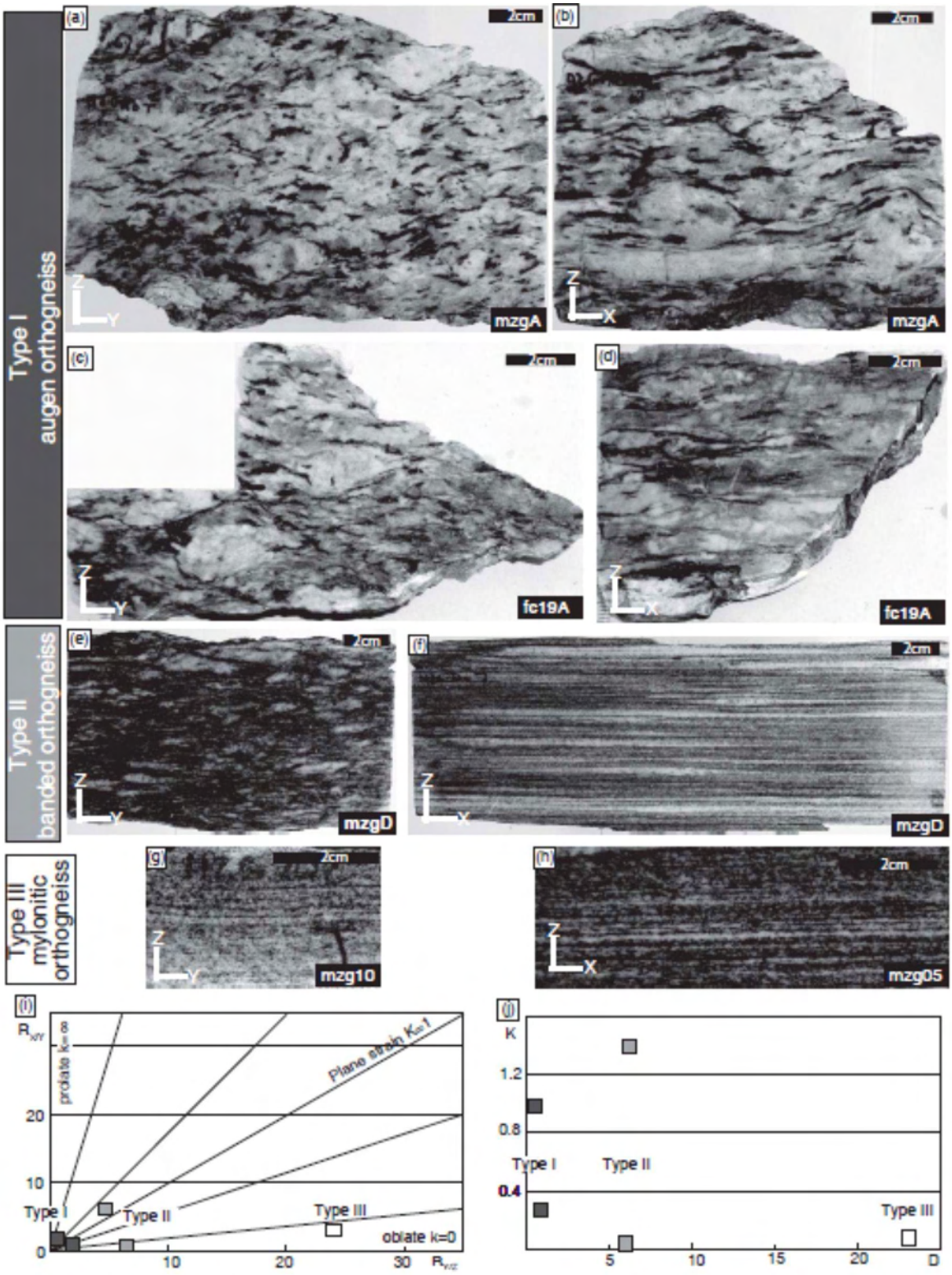

Fig. 3.: Illustration of the three metagranite types defined macroscopic pattern and deformation intensity. X, Y, and Z refer to the axes of the finite strain ellipsoid. (a-d) Type I augen orthogneiss. (e, f) Type II banded orthogneiss. (g, h) Type III mylonitic orthogneiss. (i) Diagram of Flinn (1965) showing the shapes of deformation ellipsoids. (j) Diagram showing strain intensity expressed by the shape parameter K as a function of bulk strain intensity parameter D. Strain analysis (i–j) was done for K-feldspar.

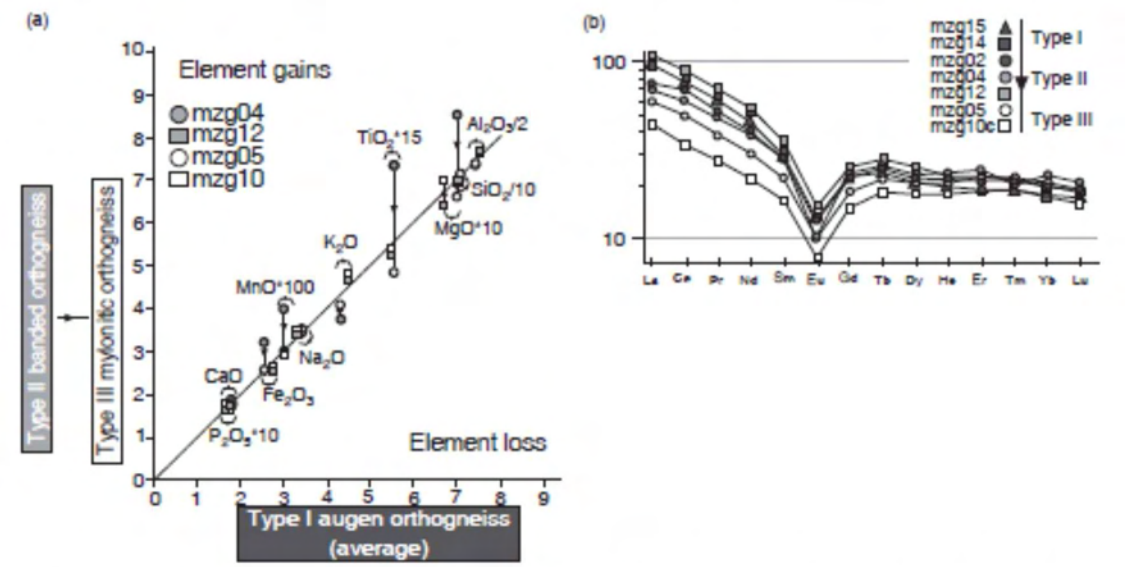

Fig. 4: (a) Isocon diagram after Grant (1986) comparing chemistry of type II and III samples (vertical axe) with average bulk rock composition of type I samples (horizontal axe). This diagram shows loss and/or gain of elements with respect to the type I average composition (reference line). Concentrations are scaled to fit in the plot. (b) REE patterns of the rocks sequences normalized to chondrites (Evensen *et al.*, 1978).

(Grant, 1986) (Fig. 4a) shows that the samples have a constant composition with negligible losses or gains of major elements in the rock sequence (i.e. no deviation from the reference line). The results are consistent with those carried out in the same rock sequences and in the same area by Lange *et al.* (2002). In agreement with these authors, we conclude that there are no indications for deformation- and/or fluid-enhanced element mobility and element redistribution in these progressively deformed rocks in this area.

MICROSTRUCTURAL AND PETROLOGICAL CHARACTERISTICS

The qualitative characterization of the rock types has been carried out using optical microscope, back scattered electron images (Figs 5−7) and microprobe analysis of feldspars, micas and garnet (Figs 8 & 9, Tables 2, 3 & 4). BSE images have been acquired with a Tescan VEGA\\XMU electron microscope at the EOST laboratory (University of Strasbourg). Mineral analyses were performed on a EPMA JEOL 8200 microprobe at the University of Lausanne (WDS mode, 15kV acceleration voltage, 10nA beam current, 5µm spot diameter, 20–30s counting time) and on a scanning electron microscope Tescan VEGA\\XMU at the University of Strasbourg in point beam mode at 15 kV and 10 nA. All studied samples show constant modal proportions of major phases (30−35% of quartz, 25−30% of K-feldspar, 30−35% of plagioclase and 10−15% of micas).

Type I: Augen orthogneiss

The type I augen orthogneiss is made of K-feldspar porphyroclasts (up to 3cm in size) and quartz ribbons (1−5mm thick) alternating with continuous layers of plagioclase and biotite-muscovite (1−3mm thick) (Fig. 5a). The limits between the feldspar aggregates and quartz are straight, whereas the limits between the plagioclase and K-feldspar layers are more irregular (Fig. 6a). K-feldspar porphyroclasts (Fig 5a) are the only remnants preserved from the original magmatic texture, while no relics of magmatic plagioclase or quartz are preserved.

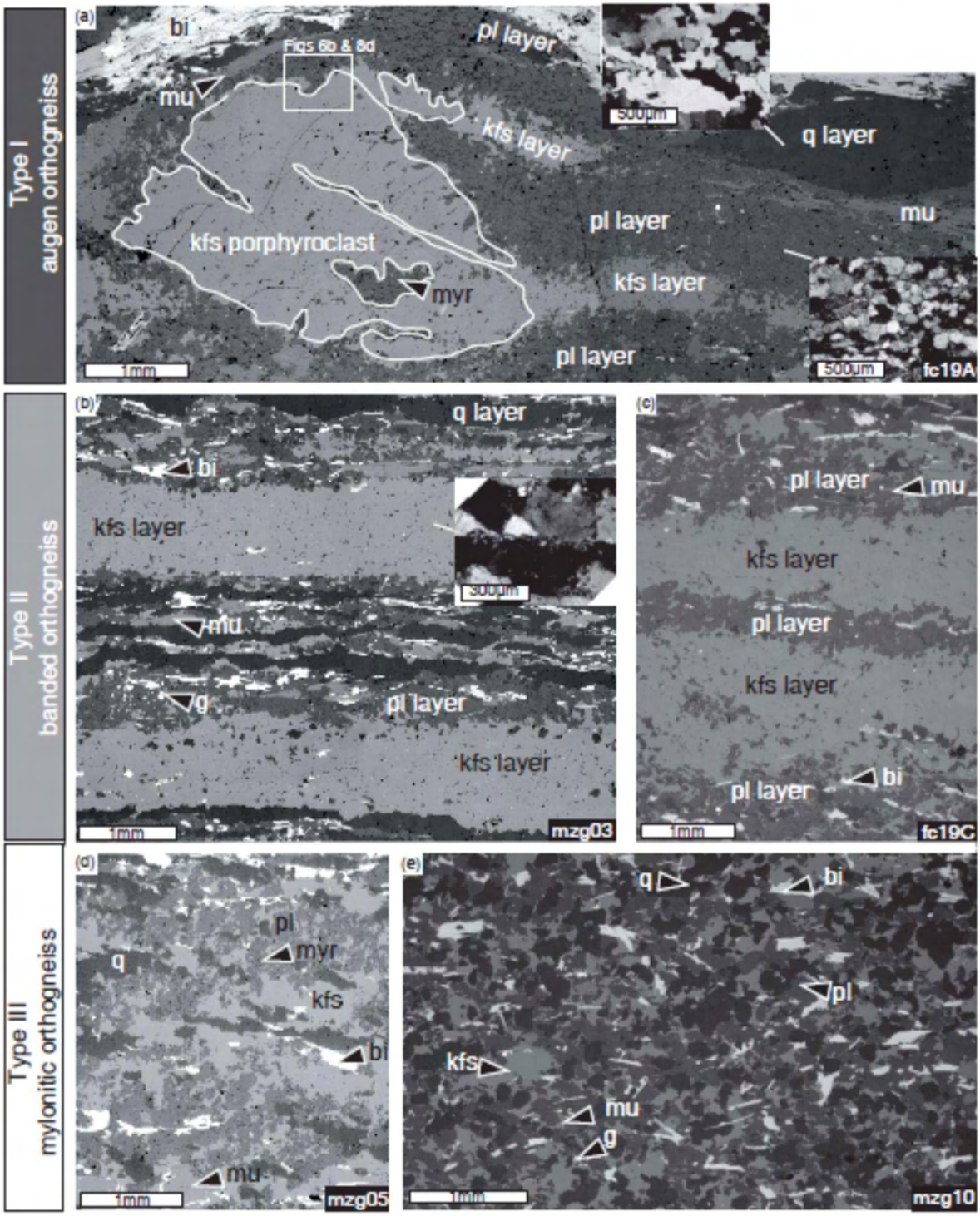

Fig. 5: Back scattered electron (BSE) images showing evolution of layering in the deformation gradient. (a) Type I augen orthogneiss with K-feldspar porphyroclasts showing recrystallized tail and with recrystallized augens of quartz and plagioclase layer. (b, c) Well-developed ribbons of feldspar and quartz in type II banded orthogneiss. Plagioclase-rich layers are enriched in micas and accessory minerals (e.g. garnet). (c, d) Weak layering and mixing of quartz and feldspar in a homogeneous matrix. In (a) and (b) small inserted cross polar microphotos precise the grain geometry. The mineral abbreviations used are mu = muscovite, q = quartz, g = garnet, bi = biotite, mu = muscovite, ksp = K-feldspar, pl = plagioclase, ilm = ilmenite; sph = sphene, myr = myrmekite.

Quartz forms completely recrystallized monomineralic aggregates in the form of lenses or highly elongated ribbons, made of large grains (150−300µm in size) with highly lobate boundaries (Fig. 5a, inset).

Relics of primary K-feldspar porphyroclasts (or_{91}) (Fig. 8a,c & Table 2) up to 3cm in size are recrystallized forming chains of fine grains flatenned in the foliation in the form of monomineralic ribbons (Fig. 5a). Newly formed and recrystallized K-feldspar (or_{90-92}) (Fig. 8c & Table 2) is present in the form of equidimensional grains (80−150µm) with straight boundaries (Fig. 5a). Plagioclase is present in the recrystallized K-feldspar layers in the form of less than 10µm thick and highly elongated interstitial grains (an_{03-22}) or myrmekitic aggregates (an_{24-26}) at triple junction sites or rimming the K-feldspar grains (Fig. 7b) (Fig. 8a,b & Table 3). Large quartz grains (20−100µm) also form an interstitial phase located between K-feldspar grains, preferentially along the margins of recrystallized layers (Figs 6a & 7b). Myrmekite is very common in the type I orthogneiss and occurs preferentially along the boundaries of K-feldspar porphyroclasts in the form of wide zones of vermicular quartz-plagioclase intergrowths (Fig. 6b) or inside K-feldspar porphyroclasts along perthitic exsolution lamellae (Fig. 5a). Myrmekites (an_{24-26}) (Fig. 8a,b & Table 3) have irregular and bulbous shapes and typical convex boundaries towards K-feldspar (Menegon *et al.*, 2006). Myrmekitic fronts form the inner rim of K-feldspar porphyroclasts, gradually passing into a wide outer rim composed of a fine-grained plagioclase (an_{22-25})-quartz mixture (Fig. 6b). No variation of composition of K-feldspar porphyroclasts has been detected close to the myrmekites (Fig. 8d). The outer rim is always adjacent to recrystallized plagioclase layers.

Plagioclase layers (Figs 5a, 6a) are made of an equilibrated mosaic of plagioclase grains (60−80µm in size) with a granoblastic texture (Figs 5a & 6b). They have a composition of an_{22-25} with a common enrichment in the albite content at the border (5-20µ) of the grains (Fig. 8a,b & Table 3). They contain interstitial crystals of rounded quartz (20−100µm, Figs 6a & 7a) and highly cuspate K-feldspar grains (or_{90-91}; 20−50µm in size) (Fig. 8a,c & Table 2) located at triple junctions (Figs 7a).

In the plagioclase layers, garnet forms clusters up to 500µm thick, made of small garnet grains (5−50µm, $alm_{0.48-0.53}py_{0.01-0.02}grs_{0.42-0.46}sps_{0.01-0.02}$, X_{Fe}=0.95−0.99) (Fig. 9a & Table 4). Muscovite laths occur either in biotite rich aggregates or as small grains inside the plagioclase layers with Si=3.18−3.28 p.f.u. and Na=0.02−0.04 p.f.u. (Fig. 9b & Table 4). Biotite forms large aggregates or single grains in plagioclase layers and exhibits X_{Fe}=0.63−0.67 and Ti= 0.10−0.25 p.f.u. (Fig. 9c & Table 4). Sphene, ilmenite and apatite are frequent in the plagioclase-rich layers.

Type II: Banded orthogneiss

The type II banded orthogneiss is characterized by an alternation of interconnected ribbons of quartz (0.3−2mm thick), plagioclase and K-feldspar (1−5mm thick) (Fig. 5b,c). Boundaries between the feldspar layers are poorly defined and interlobed with adjacent minerals (Fig. 5b,c), whereas the limits between quartz and the feldspar aggregates are straighter (Figs 5b, 6d).

Thin quartz monomineralic ribbons (Fig. 5b) are composed of recrystallized grains (50−100µm in size) with less serrated boundaries compared to the type I augen orthogneiss (Fig. 6d).

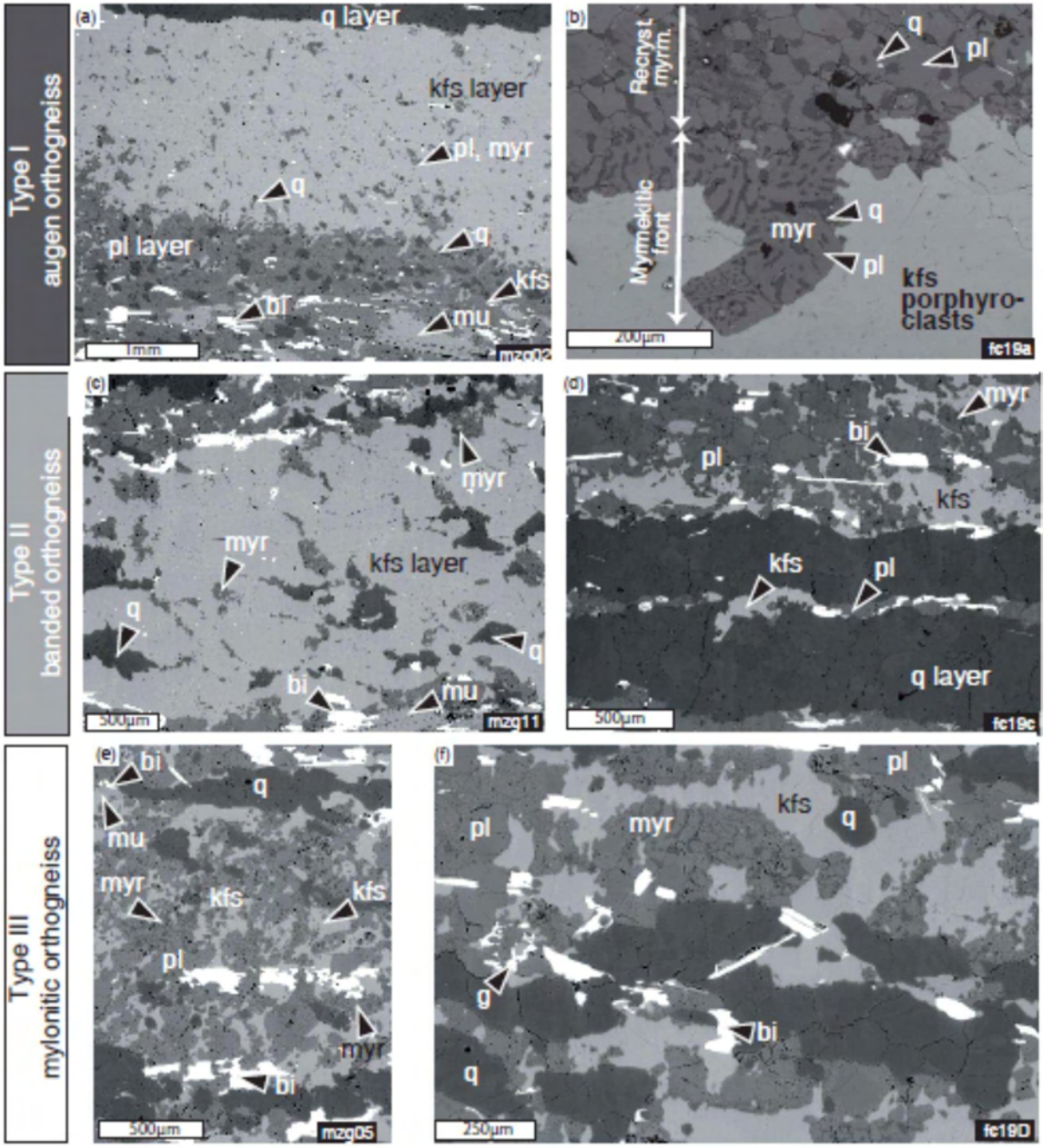

Fig. 6: Back scattered electron (BSE) images showing progressive mixing of phases. (a) Straight boundaries between K-feldspar- and quartz-rich layers, irregular boundaries between feldspar and plagioclase layers with rounded quartz at the interface. Micas and accessories mineral preferentially occur in plagioclase layers. (b) Development of myrmekitic front throughout a K-feldspar porphyroclasts. (c) Interstitial phases in K-feldspar-rich layer. (d) Two small quartz ribbons and irregular K-feldspar in plagioclase-rich layer. (e, f) Relics of quartz and feldspar ribbon with intersticial plagioclase and myrmekite.

K-feldspar rich layers are free of relic K-feldspar porphyroclasts (Fig. 5b,c). They are made of completely recrystallized subequant K-feldspar grains (50−80µm) with a constant composition (or_{89-91}) (Fig. 8a,c & Table 2), which show almost straight boundaries commonly covered by numerous interstitial phases (Fig. 6c). These are represented by (1) small aggregates of plagioclase that exhibit compositions ranging from an_{05} to an_{20} (Fig. 8a,b & Table 3), (2) isolated myrmekites pool 200 µm in size (Figs 6c,d & 7c,d) oriented at high

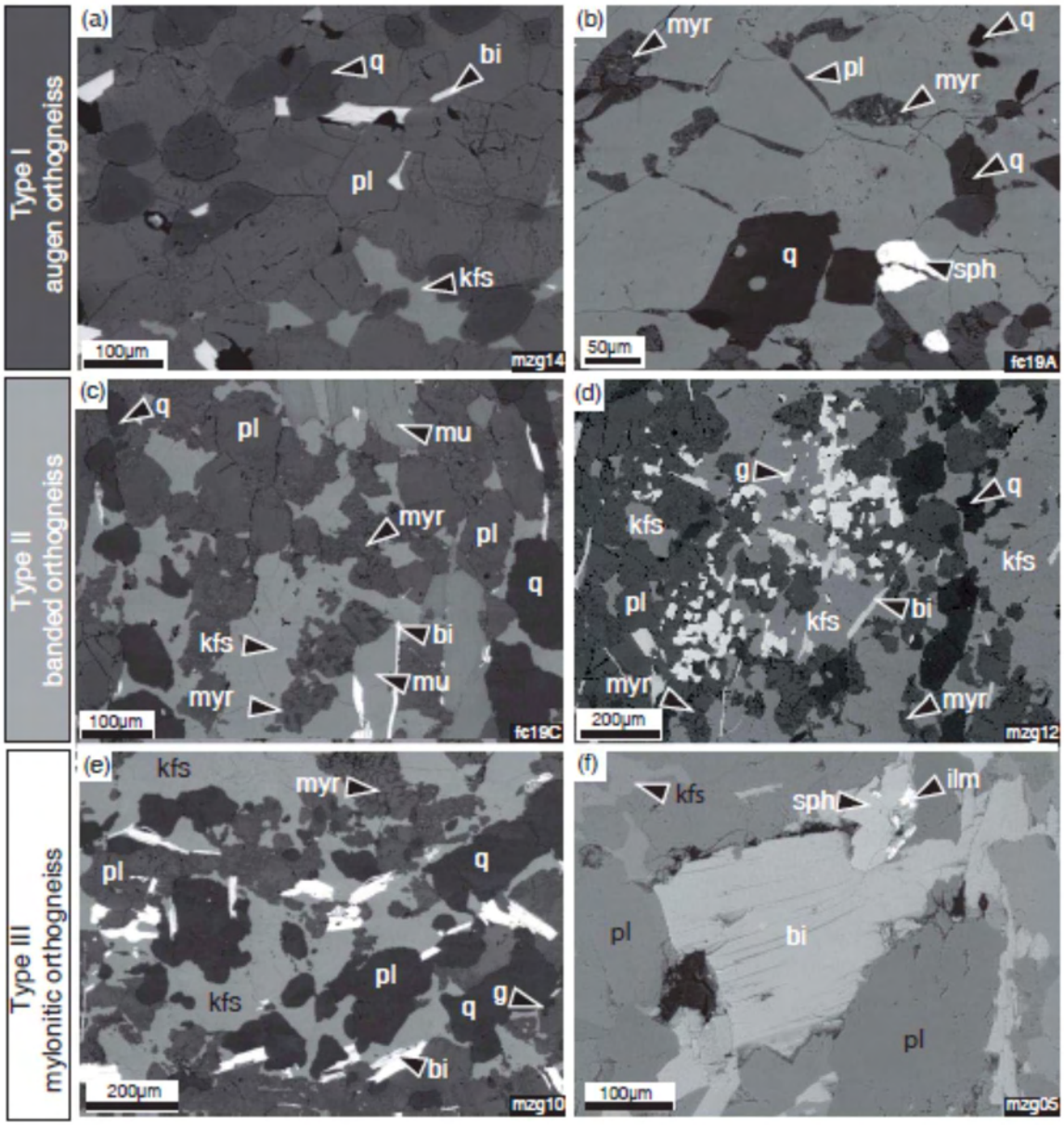

Fig. 7: Detailed back scattered images (BSE) showing distribution of interstitial phases in originally monomineralic layers. (a) Rounded quartz and cuspate K-feldspar at triple junction of plagioclase foam structure. (b) Interstitial plagioclase film, myrmekite and small rounded quartz in K-feldspar-rich layer (c). Small rounded quartz, myrmekite and K-feldspar embayment in a plagioclase-rich layer. (d) Garnet, embayment of K-feldspar, rounded quartz and myrmekite in a K-feldspar and plagioclase-rich layers. (e) Matrix of quartz, K-feldspar, plagioclase and myrmekite. (f) Sphene mantled by ilmenite.

angle to stretching direction and (3) isolated small rounded quartz grains (20−50µm) or quartz aggregates up to 100µm in diameter mostly located at triple junctions (Fig. 6c). Myrmekitic plagioclase shows a composition (an_{25}) (Fig. 8b & Table 3) similar to that present in type I orthogneiss.

Numerous grains of quartz, K-feldspar (or_{91}) (Fig. 8b,c & Table 2), micas and accessory minerals (Fig. 5b,c) occur within the layers dominated by plagioclase. Compared to the type I orthogneiss, the foam structure of the originally subequant plagioclase is disintegrated by numerous highly cuspate insterstitial K-feldspar grains (Fig. 6d) that line rounded and lobated plagioclase (Fig. 7c). Small myrmekites (an_{25}) (Fig. 8b & Table 3), and

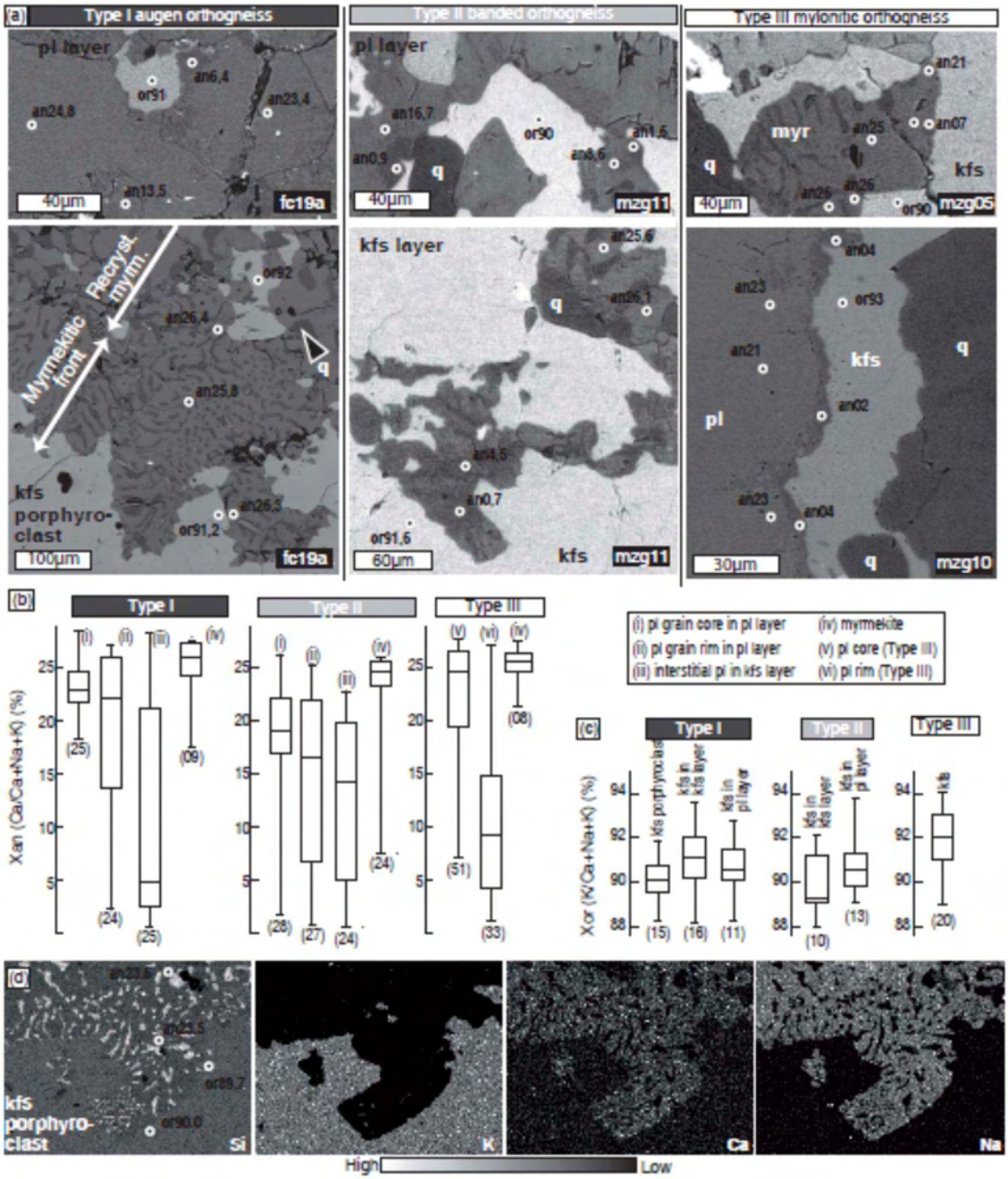

Fig. 8: Composition of texturally different feldspars throughout the rock sequence (a) BSE images showing typical positions of analysis. Plagioclase (b) and K-feldspar (c) composition summarized in box-plots of anorthite and orthoclase content (mol.%) *v.* rock type respectively with number of analyses in brackets. Individual box-and-whiskers plots show median and first and third quartile of the component content. The whiskers represent a statistical estimate of the data range. The number of analyses is marked. Representative analyses are listed in Table 2 & 3. (d) Compositional maps of the myrmekite shown in Fig. 6b.

interstitial rounded quartz grains (50µm) are also present within the recrystallized K-feldspar layers and along their boundaries (Fig. 7c,d). Plagioclase commonly shows an increase in the albite content from the core to the rim (Fig. 8a,b & Table 3). Compared to type I augen orthogneiss, small garnets (5−50µm in size, Fig. 7d) are richer in spessartine and pyrope ($alm_{0.49-0.52}py_{0.03}grs_{0.33-0.49}sps_{0.05-0.08}$, X_{Fe}=0.94−0.96) (Fig. 9a & Table 4). No core-rim chemical variations have been observed. Muscovite (Si=3.22–3.37 p.f.u. and Na=0.01–0.04 p.f.u.) shows a higher amount of the celadonite component compared to the type I orthogneiss (Fig 9b & Table 4). Biotite has X_{Fe}=0.63−0.73 and Ti= 0.07−0.25 p.f.u. (Fig. 9c & Table 4).

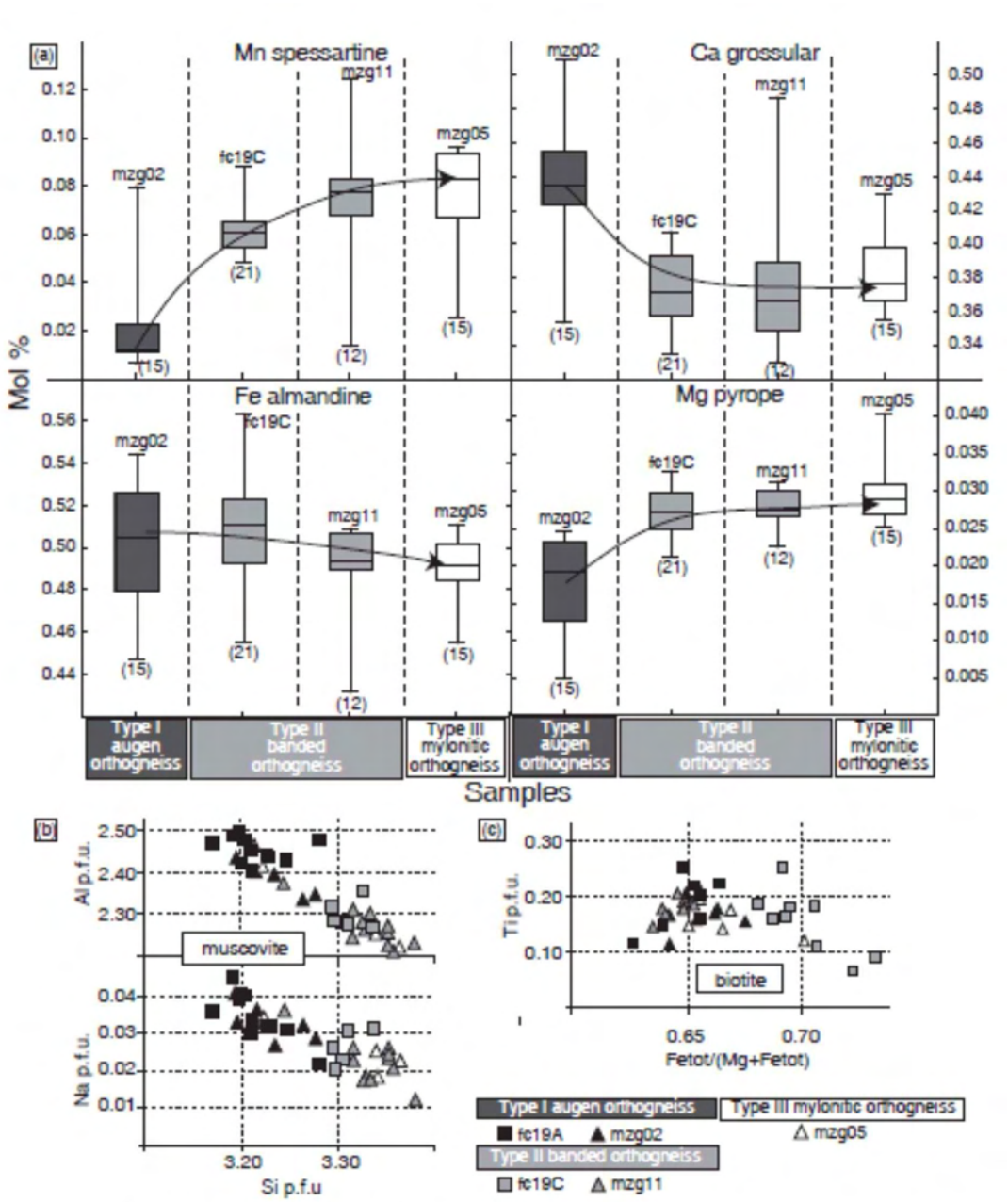

Fig. 9: (a) Garnet composition trends of spessartine, grossular, almandine and pyrope throughout the rock sequence. The data are summarized in box-and-whiskers plots of individual component content (mol.%) vs. rock type (for detail see caption of Fig. 8). Composition of muscovite (b) and biotite (c) for the three orthogneiss types. Note the increase in Si p.f.u. content in muscovite from type II to type III. Representative analyses are listed in Table 4.

Sphene, ilmenite and apatite are frequent in the plagioclase-rich layers and are mostly associated with biotite.

Type III: Mylonitic orthogneiss

In the type III mylonitic orthogneiss, discontinuous and narrow ribbons of feldspars and quartz less than 1mm and 200µm thick, respectively are only a few millimeters long (Fig. 5d) and in some samples these ribbons are almost absent (Fig. 5e). K-feldspar (or_{92})(Fig. 8a,c & Table 2), and quartz are mixed with zoned plagioclase (an_{20-26} for the core; an_{04-15} for the rim) (Fig. 8a,b & Table 3) and micas (Fig. 6e,f). Boundaries between K-feldspar (50µm),

plagioclase (50µm) and myrmekitic aggregates (an_{25}) (Fig. 8a,b & Table 3) are highly irregular with cuspate K-feldspar and lobate plagioclase (Fig. 6e,f), whereas boundaries between the plagioclase grains are almost straight (Fig. 7e). Small aggregates or isolated grains of quartz (50µm) show rounded boundaries. Micas are completely dispersed. Small garnet (5−50µm in size) is associated with micas and plagioclase, and compared to the orthogneiss type I and II it is richer in spessartine ($alm_{0.48-0.50}py_{0.03}grs_{0.37-0.40}sps_{0.07-0.09}$) (Fig. 9a & Table 4). Muscovite has a high Si content around 3.35 p.f.u. associated with a low Na content close to 0.02 p.f.u. (Fig. 9b & Table 4). Biotite exhibits a similar compositional variation (XFe=0.65−0.70 and Ti= 0.12−0.19 p.f.u.) as in the orthogneiss type I and II (Fig. 9c & Table 4). Sphene is locally mantled by ilmenite (Fig. 7f).

PETROLOGICAL MODELLING

Pseudosections were calculated using THERMOCALC (Powell *et al.*, 1998) and the dataset 5.5 (Holland & Powell, 1998; November 2003 upgrade), in the system Na_2O-CaO-K_2O-FeO-MgO-Al_2O_3-SiO_2-H_2O-TiO_2-O (NCKFMASHTO) with the garnet, biotite and melt models from White *et al.* (2007), ilmenite from White *et al.* (2000), feldspars from Holland & Powell (2003), white mica from Coggon & Holland (2002) and epidote from Holland & Powell (1998). The mineral abbreviations used are: bi = biotite, ep = epidote, g = garnet, ilm = ilmenite, ksp = K-feldspar, ky = kyanite, liq = liquid, mu = muscovite, pl = plagioclase, qtz = quartz, ru = rutile, sph = sphene.

P−T pseudosection

The pseudosection calculated for the analyzed composition of the type III orthogneiss mzg05 (Table 1; Fig. 10) is used for the discussion of the *P*−*T* conditions during deformation of the three orthogneiss types, because of their closely similar bulk compositions (Fig. 4). There is no evidence for the presence of granitic liquid during the development of the D1 fabrics. Consequently, the amount of H_2O (2.25 mol.%) is chosen to allow the stability of melt-absent assemblages on the prograde *P*−*T* path. The HP part of the pseudosection is metastable with respect to omphacite (above a line running approximately from 11 kbar and 650 °C to 17 kbar and 850 °C). This point is discussed later.

The major features of the pseudosection involve melt being stable above the line heading approximately from 11 kbar and 650 °C to 20 kbar and 810 °C, biotite stability up to 19−20 kbar in the melt-absent field and up to 800−850 °C in the melt-present fields, muscovite-out and kyanite-in line heading from 750 °C and 9 kbar to 830 °C and 16 kbar. Ilmenite is stable in the low pressure part of the pseudosection, sphene is stable in the low temperature and high pressure part of the pseudosection limited by the line heading from 640 °C and 9.5 kbar to 810 °C and 20 kbar. Rutile is stable in the high-temperature part limited by a line subparallel to the sphene stability with the exception of a small rutile-absent area at low pressure.

Metamorphic conditions

Textural features indicate that the observed assemblage composed of garnet, muscovite, biotite, plagioclase, K-feldspar, sphene, ilmenite and quartz is stable in the S1 foliation of all three orthogneiss types. This assemblage occurs in the pseudosection (Fig. 10a) as the g-mu-

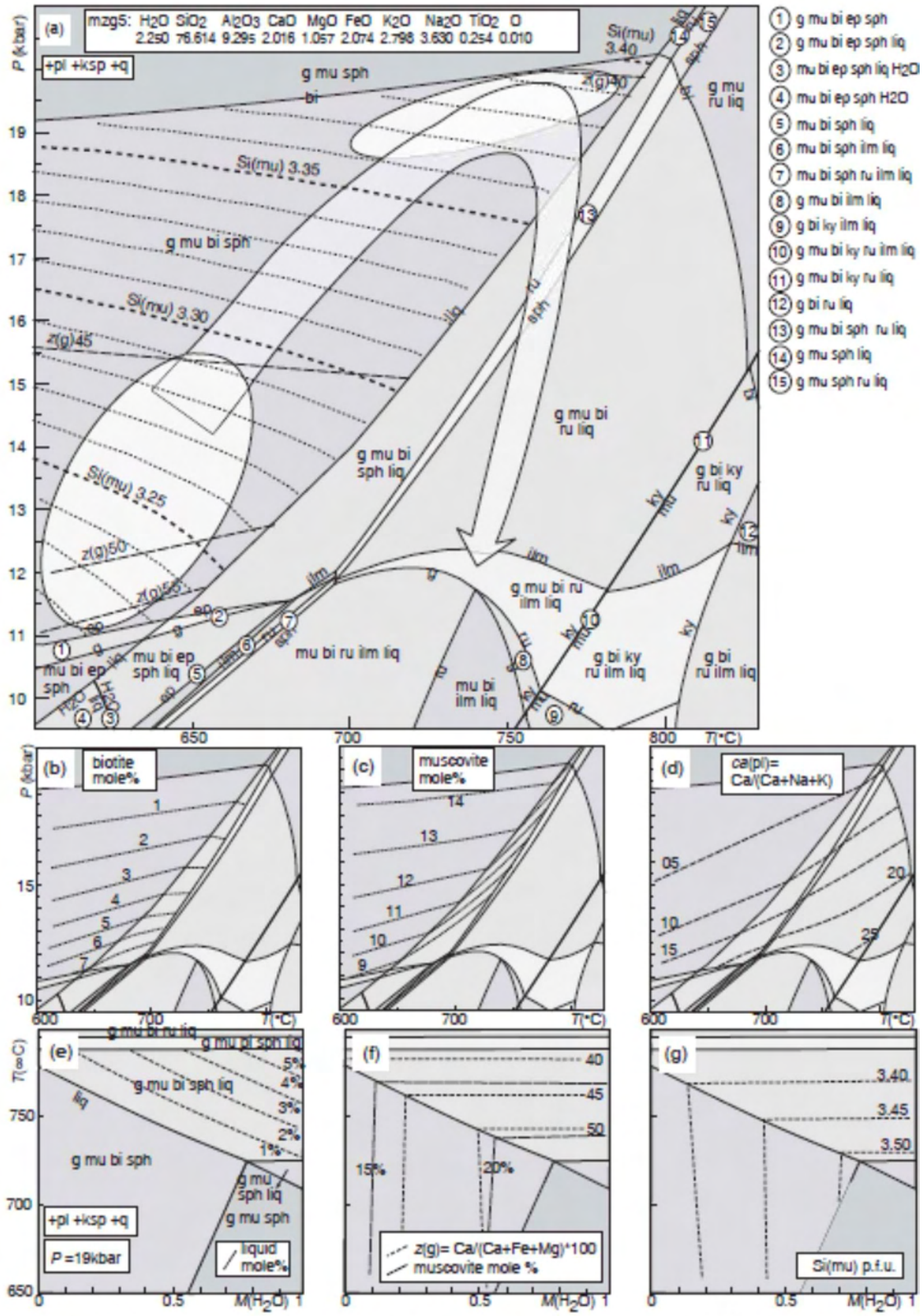

Fig. 10: (a) *P–T* pseudosection for the rock composition of the sample mzg05. Compositional isopleths of muscovite (Si p.f.u.) and garnet *z*(g) are shown. For discussion of the *P*−*T* path see text. (b, c) Simplified pseudosection with the calculated molar proportion of biotite (b) and muscovite (c). (d) Simplified pseudosection with the calculated isopleths of plagioclase. (e, f, g) T–*M*(H2O) pseudosection at 19 kbar with calculated isopleths and molar proportions of various minerals. *M*(H_2O) ranges from 2.25 to 3.85 mol.%.

bi-sph field, located in the low-temperature and high-pressure part of the pseudosection, from 11 kbar up to 20 kbar and 800 °C. However, the least deformed type I has garnet with a higher grossular (grs=0.42−0.50) and muscovite with a lower celadonite content (Si p.f.u.=3.16−3.28) than the more deformed orthogneiss types II and III (garnet: grs=0.37−0.40, muscovite: Si p.f.u.=3.22−3.38). The relatively wide range of the observed mineral compositions does not allow precise estimations of the P–T conditions. Nevetheless, the mineral compositions measured in the type I orthogneiss point to an equilibration in the lowermost part of the g-mu-bi-sph stability field, at pressures lower than 15 kbar and temperatures lower than 700 °C. On the other hand, mineral compositions of garnet and muscovite in the type II and III orthogneiss suggest that these rocks equilibrated in the uppermost part of the same field, at pressures between 19 and 20 kbar and temperatures higher than 700 °C.

T–M(H2O) pseudosection at 19 kbar

Although no clear evidence for the presence of melt during the D1 deformation was observed, it can not be excluded that a small amount of melt was present. Indeed, the presence of small quantities of melt (<10%) is generally very difficult or impossible to prove based on macroscopic and microscopic observations. Nevertheless, even such small quantities have major rheological consequences.

The major factor controlling the first appearance of a granitic liquid in a rock is the amount of H_2O. Therefore, in order to study the conditions of its appearance, its molar proportion and its influence on the mineral compositions around the estimated peak conditions, a T–$M(H_2O)$ pseudosection was calculated at 19 kbar (Fig. 10e−g). The temperature of the solidus decreases from 780 °C to 700 °C with increasing $M(H_2O)$ and the amount of magmatic liquid reaches up to 5 mol.% for the investigated T–$M(H_2O)$ range. The mineral compositional isopleths for the grossular content of garnet, z(g), Si content of muscovite and the molar proportion of muscovite are almost independent on the $M(H_2O)$ in the liquid-present field g-mu-bi-sph-liq. The observed grossular content in garnet, the Si content of muscovite and the molar content of muscovite that correspond to the estimated peak temperature between 730 and 770 °C would not be influenced strongly by a slightly higher amount of H_2O or by the presence of several percent of melt. It is therefore suggested that at the peak, the orthogneiss may have been fluid absent, or may have contained several percent of melt.

QUANTITATIVE MICROSTRUCTURAL ANALYSIS

Quantitative microstructural analysis is the statistical study of the spatial distribution of grains, their size, shape and boundaries. These microstructural parameters are sensitive to variations in physical conditions, strain intensity and mineral reactions, allowing to define rock microstructures using quantitative values. This approach permits to follow microstructural trends and better constrain processes like grain coarsening, annealing, nucleation and syn-deformational growth.

In order to evaluate quantitatively the microstructural sequence described above, we evaluated the grain size, the crystal size distribution (CSD), the grain shape preferred orientation (SPO), the grain boundary preferred orientation (GBPO) and the grain contact frequency (GCF). For this, we manually digitized 9 portions of XZ sections of representative

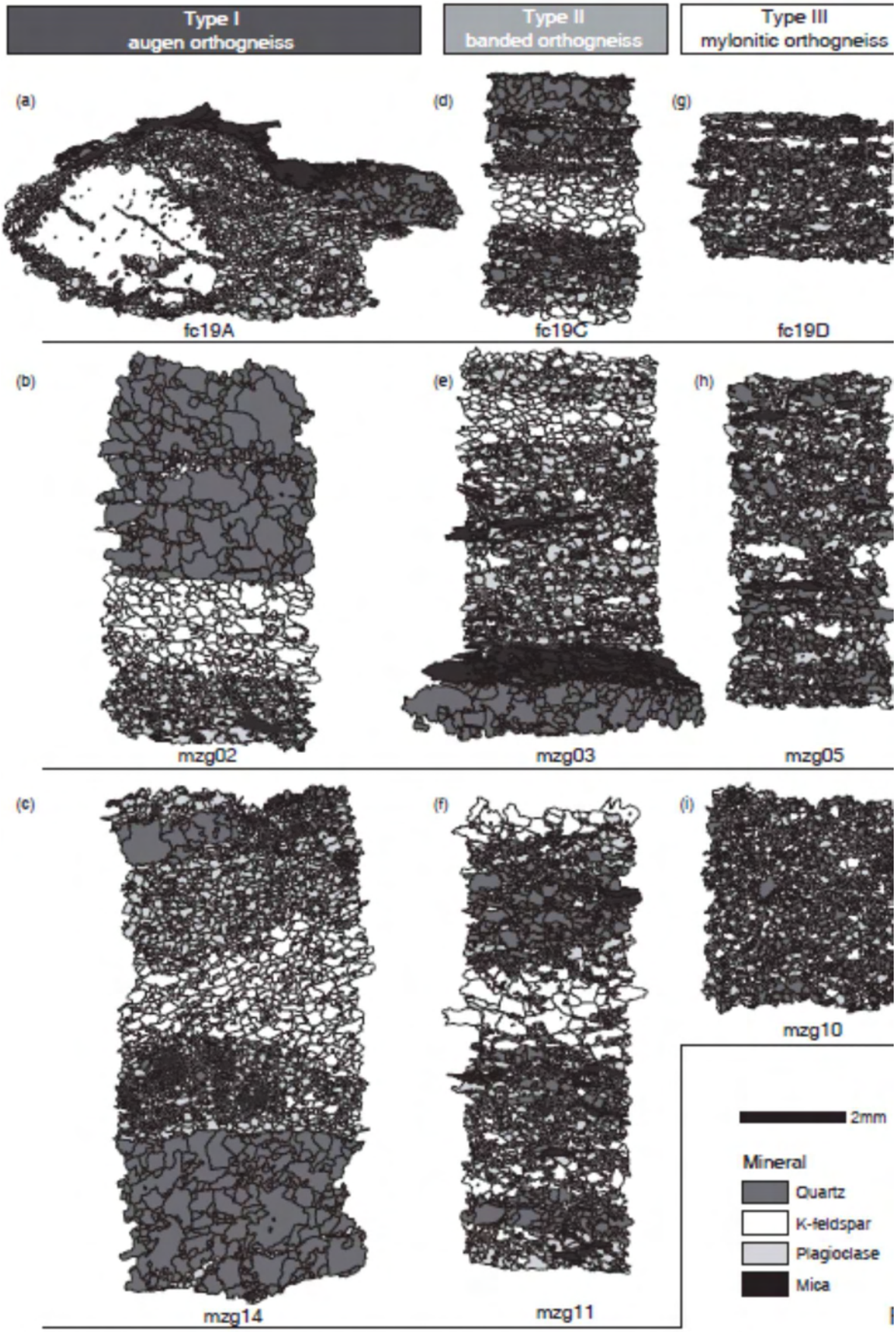

Fig. 11: Digitalized microstructures of the three orthogneiss types that have been used for quantitative microstructural analysis (see text for method). (a, b, c) Type I augen orthogneiss. (d, e, f) Type II banded orthogneiss. (g, h, i) Type III mylonitic orthogneiss.

thin sections (three per each type) (Fig. 11) with ESRI ArcMap desktop Gis using the superposition of BSE and classical optical images (as example compare Fig 5a with Fig. 11a). The maps of grains with full topology (between 2000−5000 grains per map), was carried out using the MATLAB^{TM} PolyLX toolbox V2.0. (Lexa, 2003; http://petrol.natur.cuni.cz/ ondro/). Except for the sample mzg10 (type III) that shows a complete mixing of phases, we also separated aggregates (monophase-rich layers) from interstitial phases.

Grain size statistics and crystal size distribution (CSD)

The evolution of the crystal size has been first evaluated using the grain size (Ferret diameter) in aggregates ("a") and interstitial phases ("i"). Results are presented for each sample in a box-whisker plot (Fig. 12a), which shows the median value (second quartile) and the grain size spread as the first and third quartile. From the type I to the type III orthogneiss, quartz aggregates show a decrease of mean grain size from 110 to 50µm in conjunction with a decrease of grain size spread. A similar trend is visible for both, the grain size mean (from 150 to 50µm) and the grain size spread of K-feldspar aggregates. Plagioclase grains in aggregates are more equant with a slight decrease of the mean grain size from 90 to 50µm in all the rocks types. Interstitial plagioclase in K-feldspar-rich layers shows a weak increase of grain size from 30 to 50µm with increasing finite strain, whereas the mean grain size of interstitial quartz in feldspar layers and interstitial K-feldspar in plagioclase-rich layers remains constant (~10−50µm).

The crystal nucleation and crystal growth can be revealed using the technique of crystal size distribution (CSD, Randolph & Larson, 1971). This technique has been used for metamorphic rocks by Cashman & Ferry (1988) or Díaz Aspiroz & Fernández (2003) and more recently by Franěk *et al.* (2011 and references therein). The latter authors apply the method not to determine the kinetics of crystal growth and nucleation but to obtain numerical values, which may compare individual grain size distributions. This method allows finding subtle trends in growth and nucleation histories compared to simple visual inspection of grain size histograms. We used the method of Peterson (1996), where the construction of a linear regression by plotting L as a function of ln (N) give access to a constant ln (N_0) (intercept) and G_t (slope). Each sample has been plotted separately using the method of Lexa *et al.* (2005) (Fig. 12b−d).

Quartz, K-feldspar and plagioclase show a systematic evolution of G_t and N_0 values from the type I to the type III microstructure. The weakly deformed type I microstructure developed at lowest metamorphic temperatures and form a group with the highest G_t (time-integrated growth rates) and lowest N_0 (nucleation density) values. The type II and III banded mylonite and ultramylonitic microstructures developed at significantly higher temperatures (c. 700 – 750 ° C) and exhibit an increase in N_0 in conjunction with decreasing G_t. This evolution is indicated by steepening of the slopes of the CSD curves associated with an increase in their upper intercept with the ordinate axis (insets in Fig. 12d). The sample fc19A (type I) that shows high value of N_0 for K-feldspar, and the sample mzg05 (type III) with a low N_0 value for plagioclase compared to samples of the same type, are exceptional.

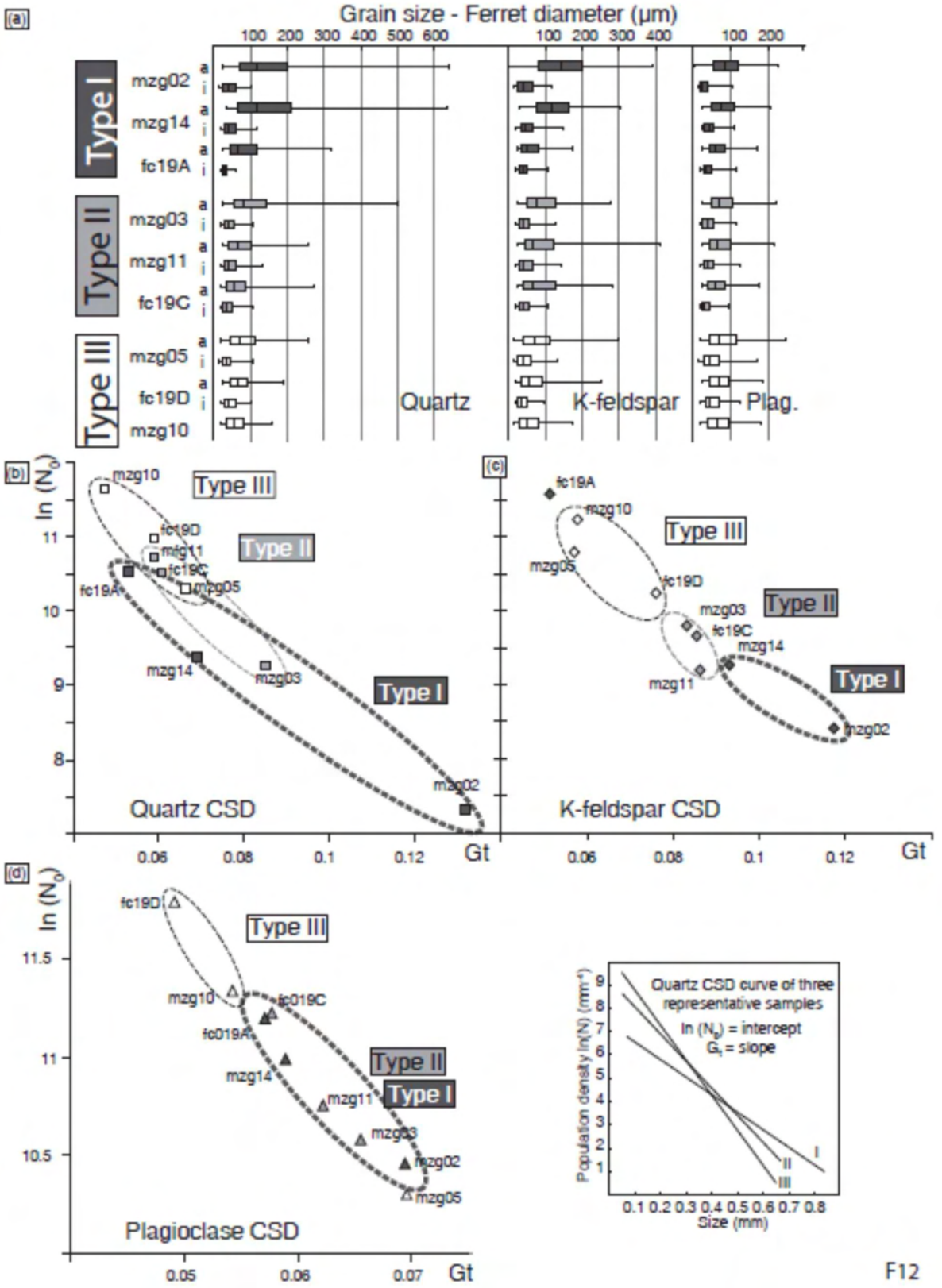

Fig. 12: Evolution of grain size diameter and crystal size distribution (CSD) in the deformation gradient. (a) Grain size diameter (i.e. Ferret diameter, or equivalent area diameter) presented in box-and-whiskers plot for aggregates ("a") and for interstitial phases ("i") from type I to type III. N_0 distinction between aggregates and interstitial phases for sample mzg10 (type III). Plot of crystal size distribution (CSD) parameters N_0 and G_t of (b) quartz, (c) K-feldspar and (d) plagioclase. Inset shows examples of linearized CSD curves used for G_t and N_0 estimates. See text for explanation.

Grain shapes and shape preferred orientation (SPO)

The aspect ratio, i.e. the ratio between the long and the short axis of the best fit ellipse, characterize the grain shape (Panozzo, 1984). The shape preferred orientation (SPO) is calculated using the eigenvalue ratio of the Scheidegger-Watson orientation tensor of individual linear segments of grain boundaries of each phase (Lexa *et al.*, 2005). In dynamically recrystallized rocks, a high SPO is interpreted to reflect a recrystallization by dislocation creep, whereas low SPO can be related to diffusion creep regime or annealing postdating deformation.

In "mono" mineralic aggregates, a constant and low aspect ratio of each phase is observed for all orthogneiss types (<1.6) (Fig. 13). Except for the quartz aggregates, where no clear variation is visible (not shown), shape preferred orientation increases from type I to type II and decrease from type II to type III (Fig. 13). Interstitial feldspar (plagioclase and K-feldspar in K-feldspar- and plagioclase-rich layers, respectively) show slightly higher aspect ratios associated with weaker shape preferred orientation compared to aggregate grains (Fig. 13).

Grain contact frequency (GCF) and grain boundary preferred orientation (GBPO)

The grain contact frequency method (Kretz, 1994) allows studying the statistical deviation from random spatial distribution of grains. A random distribution corresponds to rocks with the same proportion of like-like contact (contact between grains of the same phases) and unlike contact (contact between grains of different phases). In aggregate distribution, the quantity of like-like contacts is higher than the quantity of unlike contacts, whereas regular distribution shows preferentially unlike contacts (Fig. 14d, inset). The degree of deviation from random distribution is measured by using the following equation:

$$\chi = \frac{Observed - Expected}{\sqrt{Expected}}$$

For the like-like contacts, McLellan (1983) interprets the random distribution (i.e. χ=0) to be the result of rapid quenching of granitic melt. Regular distribution (i.e. $\chi < 0$) is expected in the process of extensive solid-state annealing (Flinn, 1969; Vernon, 1976; McLellan, 1983; Lexa *et al.*, 2005) in order to reduce the surface energy (Seng, 1936; DeVore, 1959), and also by mechanical mixing, and heterogeneous nucleation (Kruse & Stünitz, 1999; Baratoux *et al.*, 2005). Aggregate distribution (i.e. $\chi > 0$) is formed by solid-state differentiation mostly by dynamic recrystallization of rheologically different phases (Vernon, 1976; McLellan, 1983; Schulmann *et al.*, 1996).

The results are presented in plots of grain contact frequency (GCF) against grain boundary preferred orientation (ratio of the eigenvalues of the bulk matrix of inertia, length-weighted; Lexa *et al.*, 2005) showing the spatial evolution of grains from type I to type III (Fig. 14). For the like-like contacts, quartz shows an increase of aggregate distribution from type I to type II associated with a decrease of GBPO terminated with a decrease of aggregate distribution towards the type III (Fig. 14a). Both K-feldspar and plagioclase show a decrease of aggregate distribution from type I to type III towards a random to slightly regular distribution. GBPO of K-feldspar increases from type I to type II and decreases towards type III orthogneiss, whereas GBPO of plagioclase monotonously decreases (Fig. 14b, c). The

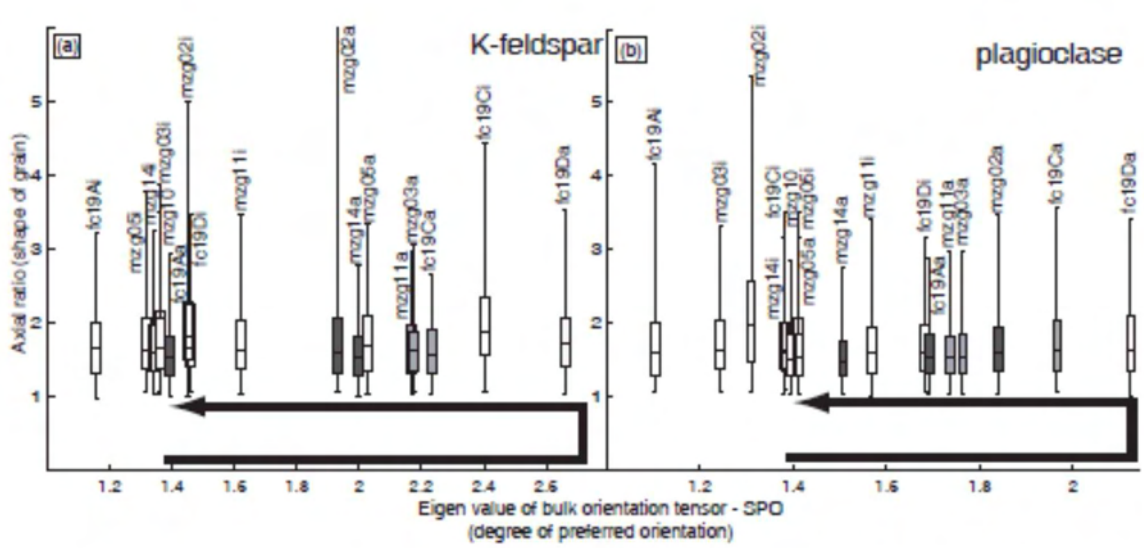

Fig. 13: Plot of the shape and shape preferred orientation of (a) K-feldspar and (b) plagioclase grains. Box-and-whiskers plots display axial ratio (representing the shape of grains) vs. eigenvalue of bulk preferred orientation (showing the degree of preferred orientation of grains). Full lines correspond to aggregates while dashed lines stand for interstitial phases. For the aggregates, note the constant axial ratio in all three types and the first increase and final decrease of SPO. Note also the weak SPO of interstitial phases.

distribution of quartz-plagioclase contacts remains constant, but their GBPO values increase with increasing degree of deformation (Fig. 14d). In contrast, the number of K-feldspar-plagioclase contacts is increasing continuously with slightly increasing GBPO (Fig. 14e).

LATTICE PREFERRED ORIENTATION (LPO)

The lattice preferred orientation (LPO) or crystallographic preferred orientation (CPO) has been measured in aggregates (except in sample mzg10 where no ribbon is visible) of representative thin sections of each type for quartz and K-feldspar. The acquisition of data has been done in manual mode using the electron back-scattered diffraction technique (Prior *et al.*, 1999; Bascou *et al.*, 2001; Prior *et al.*, 2009) on a scanning electron microscope Tescan VEGA\\XMU in the EOST laboratory, University of Strasbourg. Direct visualization of kikuchi bands patterns associated with the comparison of back scattered and optical images permit to plot only one measurement per grain.

LPO of quartz

LPO of quartz c-axes in type I aggregates (sample mzg02) shows strong maxima in an intermediate position close to the YZ plane and weaker sub-maxima at the periphery of the diagram forming an asymmetric incomplete single girdle. This suggests a mean activity of the rhomb <a + c> and sub-ordinate basal <a> slip system in a top-to-the north non-coaxial shearing. The quartz c-axis fabric in type II aggregates is similar for the sample mzg03 with the activity of the rhomb <a + c> and basal <a> slip systems resulting in a single asymmetric cross-girdle, whereas the fabric of the sample mzg04 shows the development of an incomplete asymmetric cross-girdle and suggests the addition of prism <a> activity (Lister & Paterson, 1979; Lister & Hobbs, 1980). For the type III microstructure, the activities of the above mentioned slip systems decrease, but maxima are still visible in the periphery (sample mzg05)

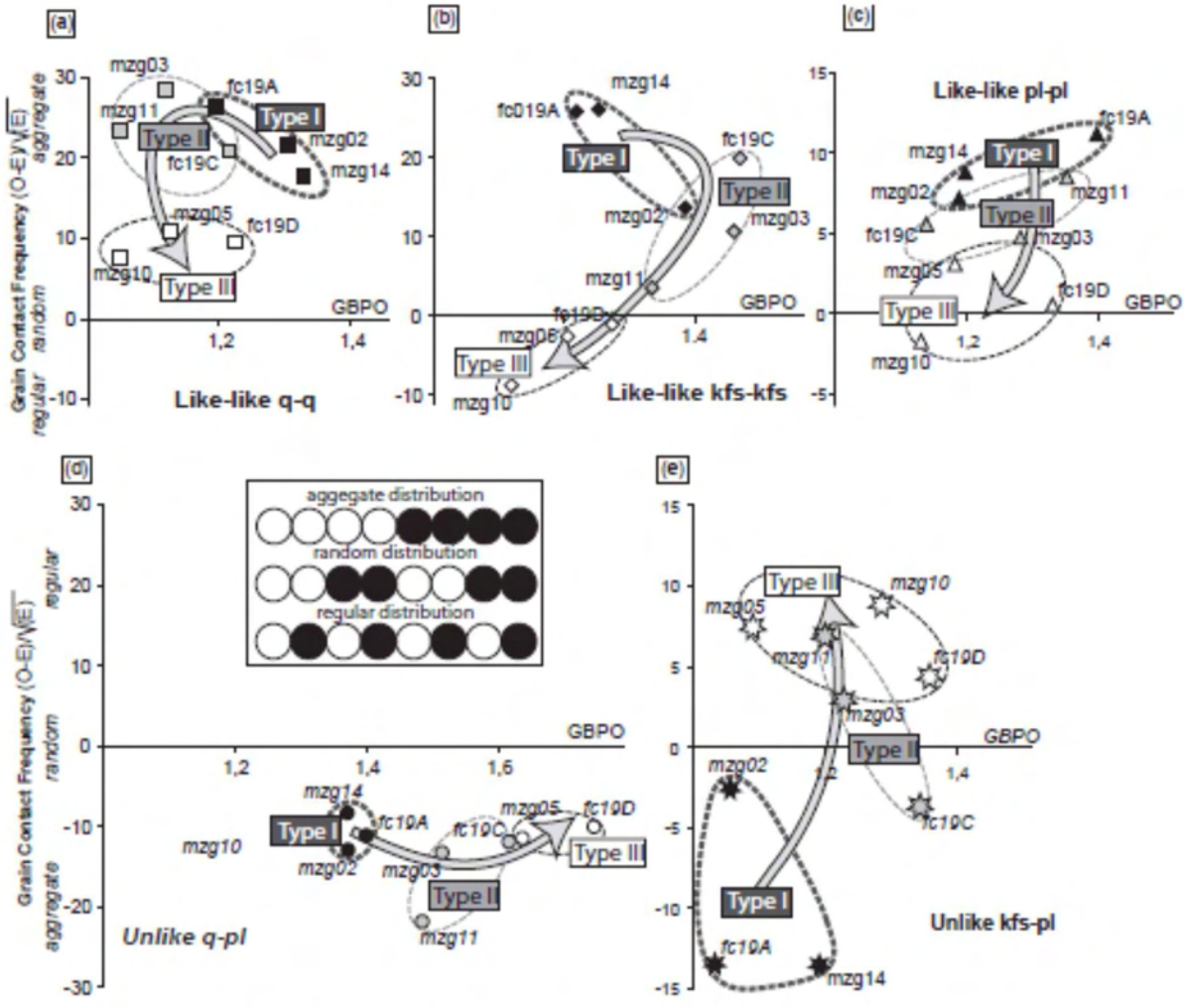

Fig. 14: Plot of the grain boundaries statistics for (a) quartz, (b) K-feldspar and (c) plagioclase. Deviation from random spatial distribution vs. degree of grain boundary preferred orientation (GBPO) is calculated using grain contact frequency method and ratio of eigenvalues of the bulk matrix of inertia (see text for details). Aggregates and intersticial phases have not been distinguished for this statistic. Like-like statistics for quartz shows a decrease of GBPO and a loose of aggregate distribution in rock sequences, whereas like-like contacts in feldspar show a small increase followed by a decrease of GBPO associated to the transition from aggregates to random distribution. Unlike K-feldspar – plagioclase contacts mirror this late evolution.

or in intermediate part of the diagram (sample mzg10), with the development of either a crossed or a single asymmetric girdle in samples mzg05 and mzg10, respectively, corresponding to a weak activity of basal <a>, rhomb <a+c> and prism <a> slip systems (Schmid & Casey, 1986). The characteristic feature of all the diagrams is the constant kinematics of non-coaxial shearing towards the north.

LPO of K-feldspar

LPO of K-feldspar in monomineralic aggregates in the type I microstructure (sample mzg02) shows a strong preferred orientation of the (010) plane parallel to the sample foliation plane. This planar preferred orientation is associated with a strong preferred orientation of the [001] axes parallel to the lineation. This suggests the activation of the classic [001](010) slip system (Willaime *et al.*, 1979; Sacerdoti *et al.*, 1980; Schulmann *et al.*, 1996; Franěk *et al.*, 2006). In the type II aggregates (sample mzg04), activity of [001](010) is still visible but with weaker

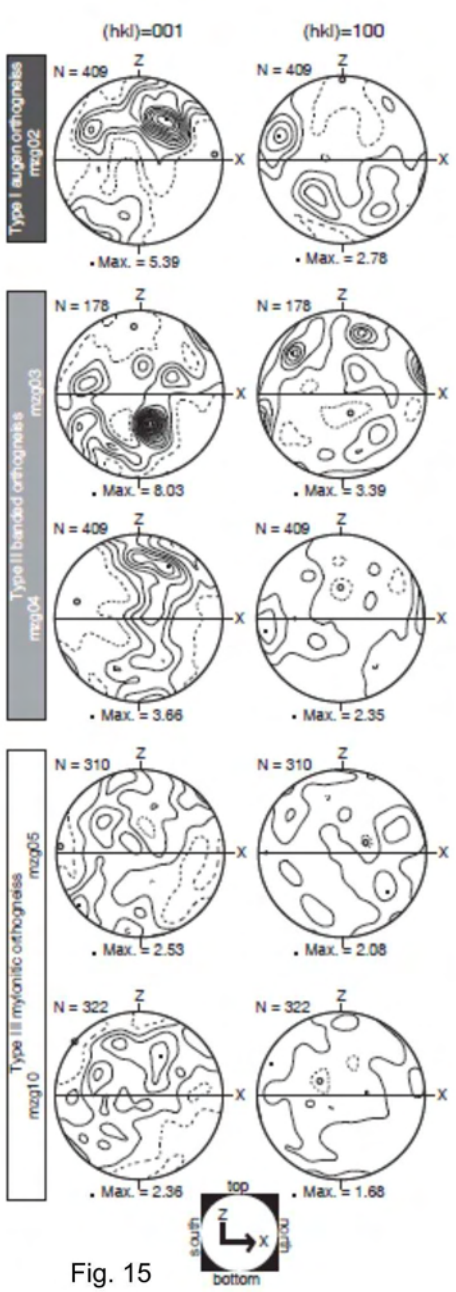

Fig. 15

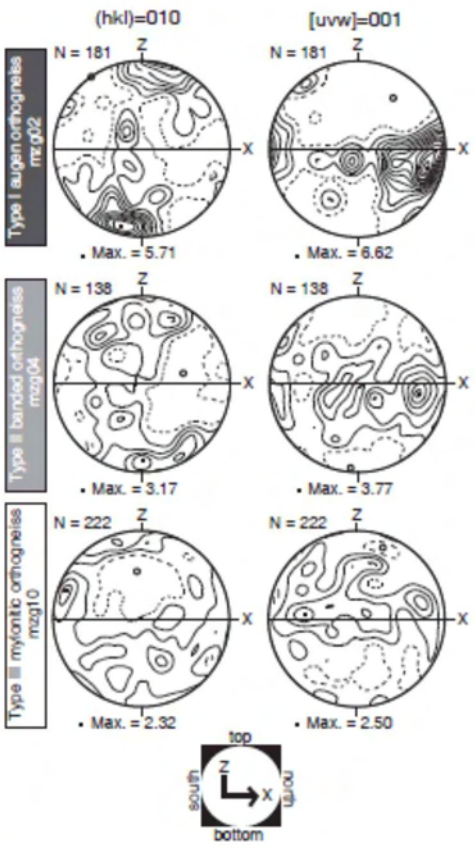

Fig. 16

Fig. 15: Crystallographic preferred orientation of quartz ribbons from electron backscattered diffraction in situ measurements. Pole diagrams are represented in equal area, lower hemisphere projection, contoured at intervals of 0.5 times uniform distribution. X and Z refer to the direction of lineation and pole to the foliation, respectively. Quartz shows activity of basal <a>, rhomb <a> and weak prism <a> slip systems in type I and II that are decreasing in type III orthogneiss.

Fig. 16: Crystallographic preferred orientation of K-feldspar ribbons using electron backscattered diffraction in situ measurements. Output .ang data files (TSL ASCII) have been transformed into .ctf file using HKL technology in order to be read and plot using PFch5 software (ftp://ftp.dstu.univ-montp2.fr/pub/TPHY/david/pc/). The results are presented in lower hemisphere equal area stereographic projection in homogeneous sample coordinates (Z direction (pole to foliation) up directed, and X (lineation) in horizontal right direction). LPO of quartz is presented in the pole figure of the crystallographic direction < c > (001) and < a > (100) (Fig. 15). For K-feldspar, we only plot crystallographic plane and directions that fit with the main axes of the finite strain ellipsoid (Fig. 16). K-Feldspar shows strong activity of (010)[001] glide system in types I and II, whereas this pattern decreases in the type III.

maxima compared to the type I microstructure. This trend further continues in K-feldspar from the poly-mineral matrix of the type III microstructure (sample mzg10), where the distribution of wide and weak maxima suggests a minor activity of the [001](010) slip system.

DISCUSSION

Significance of the estimated P−T conditions

It has been repeatedly reported that in many areas recording high-pressure metamorphism in basic lithologies, the surrounding quartzo-feldspatic rocks commonly lack evidence of high-pressure minerals. In some cases, the only witness of (ultra)high pressure metamorphism is the presence of coesite or diamond (Proyer, 2003; Peterman *et al.*, 2009). It has been suggested that quartzo-feldspatic rocks do not typically transform at (ultra)high pressure conditions (Peterman *et al.*, 2009) and the absence of omphacite in granitic orthogneisses was explained for instance by kinetic arguments (Oberhänsli *et al.*, 1983; Koons *et al.*, 1987) or by the fact that in natural high-pressure metagranites clinopyroxene is less stable than garnet (Proyer, 2003).

Similar features are observed in the studied granitic orthogneiss, where the high Si content of muscovite and presence of Ca-rich garnet indicate that these rocks were metamorphosed at high-pressure conditions. However, all samples are lacking omphacite even if they experienced strong deformation accompanied by dynamic recrystallization of feldspars and quartz. It was therefore assumed that omphacite did not nucleate and accordingly, mineral equilibria were modeled without considering omphacite and are therefore thermodynamically metastable with respect to omphacite. This allowed modeling the observed assemblage in the pseudosection, including the stability of sphene at high pressure (not observed in the presence of omphacite). The coherence between the observed and modeled assemblages justifies *a posteriori* this approach. The assemblage, the compositional isopleths and the mineral composition of garnet and muscovite in the orthogneiss types II and III suggest equilibration at around 19−20 kbar and T>700 °C, interpreted as the *P–T* conditions of the mylonitic deformation. The composition of garnet and muscovite in the type I orthogneiss suggests equilibration at about P<15 kbar and T<700 °C. Because the three rock types are sampled in a continuous strain gradient, less than 1 m thick, affecting the same metagranite, it is difficult to imagine that they had different *P−T* paths in the crust. The conditions for the least deformed orthogneiss type I are therefore interpreted as the conditions of the earliest increments of the D1 deformation encountered by the entire rock sequence on the prograde segment of their P–T evolution. Their preservation results from incomplete equilibration of the mineral assemblage at high-pressure. This is coherent with the weakly deformed character of this rock, since deformation is known to promote chemical equilibration. Such interpretation suggests that the different orthogneiss types preserve and reflect different stages of a single progressive prograde deformation at different crustal depths.

Interpretation of deformation microstructres across a finite strain gradient

The microstructure of the type I augen orthogneiss indicates that at this stage plagioclase is the weakest phase whereas K-feldspar +/- quartz form a rigid framework. Increasing deformation allows the formation of a layering indicating equal viscosity of deformed mineral aggregates in the type II banded orthogneiss. A quartz-feldspar mixture developed in the type

III mylonitic orthogneiss is associated with equalization of rheological properties of individual minerals.

Type I microstructre

K-feldspar porphyroclasts are surrounded by wide foliation-parallel myrmekite fronts indicating a competing role of stress and fluid access associated with the myrmekite origin (Vernon, 1991; Simpson & Wintsch, 1989). Similarly to the study of Menegon *et al.* (2006), the X ray compositional mapping does not reveal any zoning of K, Na and Ca in myrmekite or in the host K-feldspar (Fig. 8d) implying the exclusive role of diffusion of external Na^+ along grain boundaries. Temperature conditions of myrmekite origin can be semi-quantitatively estimated using lamellar spacing (~10 μm) yielding values in the range of ~580 – 660 °C (Harlov & Wirth, 2000; Wirth & Voll, 2004). The myrmekite rims around feldspar porphyroclasts are surrounded by a wider outer rim composed by a mixture of bulbous elongated quartz and partly recrystallized plagioclase which is in chemical and structural continuity with the myrmekitic one (Fig. 8a,b,d). This microstructure is interpreted as the result "dynamic" of dynamic coarsening of vermicular myrmekites entirely replacing original myrmekitic fronts in some samples (Fig. 11a,b). We suggest that the coarsening of quartz results from the coalescence of vermicular quartz grains by the grain boundary diffusion process along boundaries of plagioclase grains. Similarly, the plagioclase mosaic originated also by reduction of surface and coalescence of plagioclase forming larger grains of irregular shape and size. This recrystallization and grain coarsening implies the importance of grain boundary diffusion in the formation of a texturally more mature microstructure due to post-deformational annealing.

The recrystallized quartz and plagioclase layers originated by deformation and dynamic recrystallization of original porphyroclasts. This microstructure is characterized by the strongest LPO of both recrystallized quartz and K-feldspar from all rock types, which indicates intense plastic deformation. The triple junction network developed in the recrystallized plagioclase matrix (Fig. 7a,b) and the large surface of highly lobated quartz point to an important contribution of the surface area reduction (Passchier & Trouw, 1996).

The “corrosion” of strong feldspars by myrmekites and their recrystallization suggest an important contribution of hydrous fluids during the deformation. The strong LPO of quartz and K-feldspar together with a texturally mature microstructure are attributed to dominant dislocation creep controlling the deformation of rock. The static recrystallization of myrmekites and the development of the triple junction network in the plagioclase mosaic point to an important role of post-deformation solid state annealing (Passchier & Trouw, 1996).

Type II microstructure

The collapse of K-feldspar porphyroclasts in banded orthogneiss is mainly controlled by deformation of recrystallized myrmekitic (so its dynamic) zones inside the K-feldspar crystals and of the weak polymineralic matrix and myrmekites forming the rims of the porphyroclasts.

Compared to the type I microstructure this rock reveals a decreasing grain size and grain size spread (Fig. 12b−d). However, it also recorded a temperature increase of at least 100 °C (Fig. 10), which should theoretically lead to coarsening of the granoblastic microstructure. Therefore, the decrease of the mean grain size during increasing temperature has to result either from a dynamic recrystallization due to an increased applied stress and/or

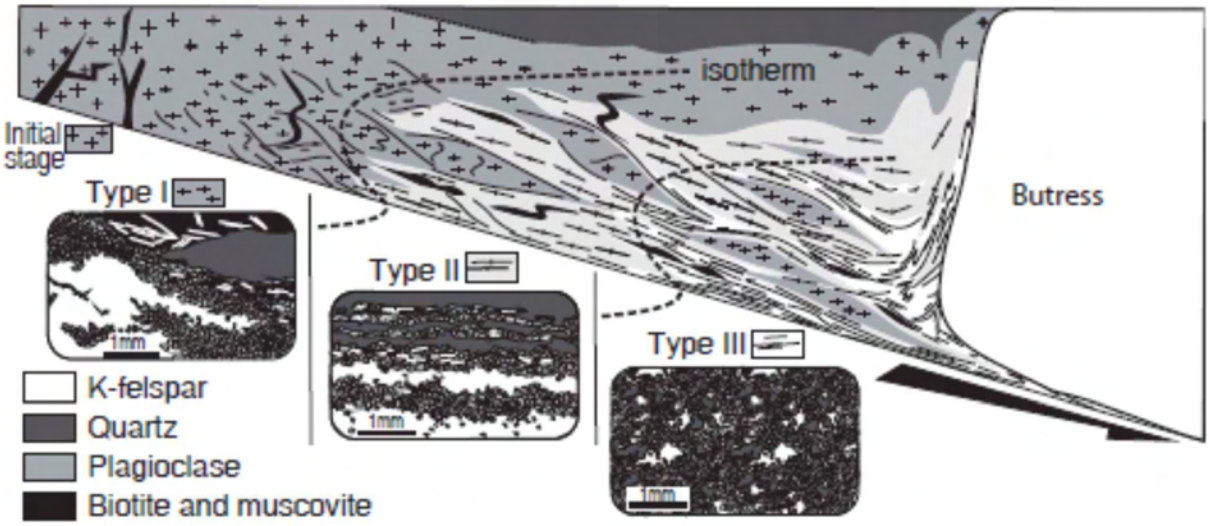

Fig. 17: Model of a progressive evolution from type I augen orthogneiss to type II banded orthogneiss and type III mylonitic orthogneiss during the corner flow in a continental accretionary wedge. During the burial, the porphyritic granite is progressively transformed into type I orthogneiss. Increasing strain triggers the formation of the type II orthogneiss at the expense of the type I orthogneiss. At this stage, the already deformed type I orthogneiss is passively transported. Ongoing burial and deformation leads to the development of the type III mylonitic orthogneiss at the expense of both type I and II orthogneisses, which are passively buried in the apex of the corner forming the root. Mafic dyke intrusions could represent the protolith of the eclogites found inside the orthogneiss.

strain rate (Shimizu, 1998, 2008; Ulrich *et al.*, 2002) or from a heterogeneous nucleation process (e.g. Hasalová *et al.*, 2008b). The trend in grain size evolution is also related to the increase of the volume of interstitial phases in feldspar-dominated layers, which favors the hypothesis of heterogeneous nucleation associated with the resorption of large crystals and suppressed crystal growth. This kind of nucleation dominated process is supported by the presence of highly cuspate boundaries of interstitial K-feldspar and plagioclase suggesting high mobility of grain boundaries (Gower & Simpson, 1992). In addition, small myrmekites occur in the form of blebs between adjacent but differently oriented recrystallized grains of alkali feldspar (Fig. 6c). This type of myrmekite is commonly called the intergranular myrmekite (Wirth & Voll, 1987) and may indicate reaction of K-feldspar with crystallizing melt. developed in dilatants structures (Fig. 6c)

Compared to the type I microstructure, the type II orthogneiss reveals distinct but weaker LPO of quartz and K-feldspar (Figs 15 & 16), incompatible with high strain intensities (Fig. 3i,j) (Heilbronner & Tullis, 2006). The prevailing deformation mechanism of quartz and K-feldspar is dislocation creep but diffusion creep component cannot be excluded in the plagioclase and polyminerallic aggregates.

Type III microstructure

The type III mylonitic orthogneiss is characterized by further decrease of grain size (Fig. 12) and the loss of lattice preferred orientation of all mineral phases (Fig. 15 & 16). The crystal size distribution diagram reveals a further increase of N_0 values associated with a vigorous decrease of G_t values compared to the type II microstructure (Fig. 14) which is normally interpreted as the result of an increased applied stress (e.g. Lexa *et al.*, 2005). These authors have shown that grain size reduction driven by an increased stress leads generally to solid state differentiation and the development of strong aggregate distribution. In contrast, the

grain size reduction of the type III microstructure is related to an important mixing of mineral phases resulting in a strong regular distribution. Kruse and Stünitz (1999) have shown that the regular (anticlustered) distribution in highly deformed rocks results from grain boundary sliding (Ashby & Verall, 1973) accompanied by heterogeneous nucleation of minor phases at matrix grain boundaries consistent with numerous highly cuspated interstitial minerals (Fig. 7). We suggest that the transition of type II to type III microstructure is characteristic for the transition from dislocation creep to diffusion-accommodated grain boundary sliding deformation mechanism enhanced by heterogeneous nucleation of interstitial phases in the presence of melt (e.g. Berger & Stünitz, 1996; Handy & Stünitz, 2002). Diffusion creep is responsible for a major weakening of the rock and results in exceptionally high strain intensities measured in this rock type.

Role and nature of the fluid phase

The feldspar microstructures (Figs 5d, 6e & 7e) and lining of large K-feldspar grains by albite (Fig. 7b) can be attributed to an incursion of external fluids or melts. However, the influx of external fluids or melt has to be associated with a major modification of bulk rock chemistry and REE patterns as shown by Marquer & Burkhard (1992) and Hasalová *et al.* (2008c), respectively. This was not observed in our study (Fig. 4) indicating that the system can be considered as chemically closed. Therefore, unlike the microstructural sequence studied by Hasalová *et al.* (2008a; 2008b; 2008c) the studied microstructural gradient originated in a chemically closed system.

The estimated P-T conditions for the type I orthogneiss are at the limit of the wet solidus for a granite system and therefore the fluid responsible for the growth of myrmekites can be either melt or a hydrous fluid. This is consistent with myrmekite chemistry typical for Na+ cation transport in hydrous fluid (Vernon, 2004, Menegon *et al.*, 2006).

The orthogneiss types II and III reveal P-T conditions clearly above the wet solidus of granite. Consequently, the rocks were fluid absent or contained melt (Fig. 10e−g). This is consistent with the microstructural observations showing intergranular myrmekites, mineral mixing, monomineral films and cuspate pools of plagioclase, K-feldspar and quartz mimicking former melt (Sawyer, 2001; Rosenberg, 2001, Holness *et al.*, 2005, Holness, 2008). The amount of indicators of former melt is volumetrically very low in all studied samples of type II and III around 5% (Závada *et al.*, 2007; Schulmann *et al.*, 2008) which is consistent with the absence of melt loss indicated by the lack of variation in bulk rock chemistry. The low amount melt is also indicated by pseudosection modelling (Fig. 10).

Strain localisation and softening during continental subduction

There arises a question whether the localization of deformation into narrow zones of ultramylonitic type III orthogneiss may be caused by reaction softening (Holyoke Lii & Tullis 2006a, b), for example by reactions leading to an increased amount of micas. It is demonstrated that the observed structures develop on a prograde path, during the increase of pressure and temperature, with the assemblage g-mu-bi-sph, and at least a part of this $P-T$ path is melt-absent. The molar amount of white mica increases and the molar amount of biotite decreases along a prograde path in the g-mu-bi-sph field, but the total volume of mica is approximately the same (Fig. 10b,c). In the samples, the approximate amount of mica is 10−15%, independently of the orthogneiss type. Therefore, our study does not reveal an increase of fine grained reaction products that could modify the deformation mechanisms and

induce a dramatic softening of the rock. The localization of the deformation cannot be caused by reactions leading to substantial changes of mineral proportions in sense of Holyoke Lii & Tullis (2006a).

While the type I augen orthogneiss was deformed at P<15 kbar and T<700 °C, the type II banded and type III mylonitic orthogneisses reveal pressures of of 18–20 kbar at T>700 °C. This indicates that the strain partitioning did not occur at constant $P-T$ conditions as it was shown in other natural examples (Schulmann *et al.*, 1996; Závada *et al.*, 2007; Schulmann *et al.*, 2008; Oliot et al., 2010). In our example the Śnieżnik orthogneiss was buried 20 km along a shear zone few km thick. For an inclination of the subduction zone of 30°, the Śnieżnik orthogneiss was passively transported 40 km into the depth of 60-75km where the mylonitic orthogneiss was finally reequilibrated (Fig. 17). The shear strain along the zone may vary between 20 to 40 γ depending on the width of the zone of active deformation (2 to 1 km, Fig 1c). This kind of strain localization requires extremely efficient weakening mechanisms. We argue that in the present case, this was achieved by the rheological collapse of strong feldspar porphyroclasts through the recrystallization of myrmekites in the type I microstructure and development of the banded structure of the type II rocks. Usually, in similar lithologies, rheological collapse of strong alkali feldspar at granulite facies conditions was achieved by recrystallization of exsolution lamellae (Shulmann et al., 2008; Franek et al., 2011). In contrast, in the studied example the weakening is due to formation and recrystallization of myrmekites developed along a prograde path with a strong pressure increase (<15 kbar <750 °C). Gorwth of myrmekites is associated with volume deacrease of 8.5% (Menegon et al., 2006) which may reflect increasing pressure. Further weakening and strain localization were induced by melting leading to the development of type III mylonites. It is proposed that such a microstructural evolution may represent a model for subduction of relatively undeformed crustal blocks in other HP terrains (Fig. 17).

Whole-rock compositions (ICP-AES)							
Rock type	Type I augen orthogneiss			Type II banded orthogneiss		Type III mylonitic orthogneiss	
Sample	mzg02	mzg15	mzg14	mzg04	mzg12	mzg05	mzg10
wt%							
SiO_2	70.80	69.59	71.10	70.43	70.05	71.29	69.69
TiO_2	0.37	0.37	0.36	0.49	0.35	0.32	0.36
Al_2O_3	14.86	15.45	14.71	14.67	15.37	14.68	15.27
Fe_2O_3	2.55	2.80	2.70	3.18	2.55	2.57	2.63
MnO	0.03	0.03	0.03	0.04	0.03	0.03	0.03
MgO	0.70	0.66	0.68	0.85	0.64	0.66	0.70
CaO	1.75	1.73	1.74	1.85	1.74	1.75	1.65
Na_2O	3.40	3.26	3.34	3.44	3.37	3.48	3.50
K_2O	4.30	4.98	3.97	3.72	4.62	4.08	4.81
P_2O_5	0.18	0.18	0.15	0.17	0.16	0.17	0.18
Sum	99.87	99.84	99.86	99.80	99.83	99.87	99.85
Xfe	0.65	0.68	0.67	0.65	0.67	0.66	0.65

Tab 1: Representative whole-rock analyses of samples from the deformation sequence.

Representative analyses of K-feldspars							
Rock type	Type I augen orthogneiss			Type II banded orthogneiss		Type III mylonitic orthogneiss	
Sample	fc19A			mzg11		mzg05	mzg10
Analysis n°	A118	B103	A141	ls486	ls466	mzg0509	mzg1027
Position	porphyroclast	in kfs layer	in pl layer	in kfs layer	in pl layer	matrix	matrix
Wt%							
SiO_2	64.69	64.58	64.49	65.29	64.74	65.25	63.38
TiO_2	0.00	0.00	0.00	0.00	0.00	0.07	0.20
Al_2O_3	18.45	18.47	18.60	18.36	18.35	18.47	18.15
FeO	0.10	0.34	0.10	0.01	0.00	0.05	0.19
MgO	0.11	0.05	0.03	0.00	0.01	0.04	0.05
CaO	0.34	0.31	0.28	0.02	0.01	0.25	0.35
Na_2O	0.83	0.77	0.77	1.17	0.66	1.03	0.66
K_2O	16.11	16.41	16.08	15.00	15.25	15.90	16.21
Sum	100.63	100.93	100.35	99.84	99.01	101.06	99.19
Structural formulae calculated on the basis of 5 cations							
Cations							
Si	2.96	2.95	2.96	3.01	3.02	2.97	2.95
Ti	0.00	0.00	0.00	0.00	0.00	0.00	0.01
Al	1.00	0.99	1.01	1.00	1.01	0.99	1.00
Fetot	0.00	0.01	0.00	0.00	0.00	0.00	0.01
Mg	0.01	0.00	0.00	0.00	0.00	0.00	0.00
Ca	0.02	0.02	0.01	0.00	0.00	0.01	0.02
Na	0.07	0.07	0.07	0.10	0.06	0.09	0.06
K	0.94	0.96	0.94	0.88	0.91	0.92	0.96
Sum	5.00	5.00	5.00	5.00	5.00	5.00	5.00
an	0.02	0.01	0.01	0.00	0.00	0.01	0.02
ab	0.07	0.07	0.07	0.11	0.06	0.09	0.06
or	0.91	0.92	0.92	0.89	0.94	0.90	0.93

an = Ca/(Ca + Na + K); ab = Na/(Ca + Na + K); or = K/(Ca + Na + K)

Tab. 2: Representative analyses of K-feldspar

Representative analyses of plagioclases

Rock type	Type I augen orthogneiss							Type II banded orthogneiss							Type III Mylonitic orthogneiss				
Sample	mzg02			fc19A				mzg11				fc19C			mzg05			mzg10	
Analysis n°	ls364	ls365	ls379	ls793	ls805	ls781	A126	ls485	ls478	ls491	C71	ls737	ls756	ls766	mzg521	mzgAT21	mzgAT65	mzg1016	mzg1010
Position	pl (i)	pl (ii)	pl (iii)	pl (i)	pl (ii)	pl (iii)	pl (iv)	pl (i)	pl (ii)	pl (iii)	pl (iv)	pl (i)	pl (ii)	pl (iii)	pl (v)	pl (vi)	pl (iii)	pl (v)	pl (vi)
Wt%																			
SiO_2	62.91	67.58	73.29	62.97	64.48	68.08	62.32	63.08	63.41	65.53	63.3	63.77	64.17	68.34	62.60	66.36	62.53	61.89	65.48
TiO_2	0.05	0.05	0.00	0.00	0.01	0.02	0.00	0.01	0.02	0.00	0.00	0.00	0.02	0.00	0.07	0.13	0.00	0.07	0.07
Al_2O_3	23.40	20.93	16.82	23.31	22.13	19.77	23.46	22.71	23.01	21.79	23.2	22.80	21.70	20.45	23.48	20.95	23.43	22.71	20.21
FeO	0.01	0.00	0.04	0.01	0.12	0.08	0.17	0.02	0.02	0.11	0.29	0.01	0.15	0.01	0.06	0.27	0.33	0.24	0.13
MgO	0.00	0.01	0.00	0.00	0.00	0.01	0.09	0.01	0.01	0.05	0.07	0.00	0.00	0.03	0.04	0.07	0.09	0.04	0.09
CaO	4.91	1.51	0.72	4.70	2.24	0.53	5.17	4.14	2.99	1.52	4.39	4.14	1.69	1.47	5.18	1.68	5.06	4.75	1.45
Na_2O	9.08	10.99	9.21	9.14	10.00	11.93	7.86	9.32	9.20	10.54	8.18	9.43	10.02	9.91	7.60	9.27	7.80	7.77	9.50
K_2O	0.27	0.04	0.28	0.23	0.43	0.11	0.19	0.25	0.91	0.61	0.25	0.20	0.92	0.55	0.31	0.25	0.27	0.29	0.11
Sum	100.63	101.10	100.35	100.37	99.41	100.52	99.26	99.55	99.57	100.16	99.60	100.36	98.66	100.76	99.34	98.98	99.51	97.76	97.04
Structural formulae calculated on the basis of 5 cations																			
Cations																			
Si	2.77	2.93	3.27	2.77	2.85	2.95	2.80	2.80	2.81	2.87	2.83	2.81	2.86	3.00	2.81	2.97	2.81	2.83	2.98
Al	1.21	1.07	0.88	1.21	1.15	1.01	1.24	1.19	1.20	1.12	1.22	1.18	1.14	1.06	1.24	1.11	1.24	1.22	1.09
Ca	0.23	0.07	0.03	0.22	0.11	0.02	0.25	0.20	0.14	0.07	0.21	0.20	0.08	0.07	0.25	0.08	0.24	0.23	0.07
Na	0.77	0.92	0.80	0.78	0.86	1.00	0.68	0.80	0.79	0.89	0.71	0.80	0.86	0.84	0.66	0.81	0.68	0.69	0.84
K	0.02	0.00	0.02	0.01	0.02	0.01	0.01	0.01	0.05	0.03	0.01	0.01	0.05	0.03	0.02	0.01	0.02	0.02	0.01
Sum	5.00	5.00	5.00	5.00	5.00	5.00	5.00	5.00	5.00	5.00	5.00	5.00	5.00	5.00	5.00	5.00	5.00	5.00	5.00
an	0.23	0.07	0.04	0.22	0.11	0.02	0.26	0.19	0.14	0.07	0.23	0.19	0.08	0.07	0.27	0.09	0.26	0.25	0.08
ab	0.76	0.93	0.94	0.77	0.87	0.97	0.72	0.79	0.80	0.89	0.76	0.80	0.87	0.89	0.71	0.89	0.72	0.73	0.92
or	0.01	0.00	0.02	0.01	0.02	0.01	0.01	0.01	0.05	0.03	0.01	0.01	0.05	0.03	0.02	0.02	0.02	0.02	0.01

an = Ca/(Ca + Na + K); ab = Na/(Ca + Na + K); or = K/(Ca + Na + K)

Tab. 3: Representative analyses of plagioclase with indicated position (see Fig. 8)

Representative analyses of muscovite, biotite and garnet

Rock type	Type I augen orthogneiss					Type II banded orthogneiss						Type III mylonitic orthogneiss		
Sample	mzg02			fc19A		mzg11			fc19C			mzg05		
Analysis n°	350	516	339	815	825	515	520	455	705	702	726	420	257	408
Mineral	mu	bi	g	mu	bi	mu	bi	g	mu	bi	g	mu	bi	g
Wt%														
SiO_2	47.19	36.05	37.36	47.25	35.96	48.94	35.93	38.08	49.07	34.67	37.40	49.29	35.66	37.45
TiO_2	0.54	2.97	0.02	0.59	4.18	0.53	2.97	0.04	0.66	1.81	0.03	0.51	2.00	0.017
Cr	0.00	0.04	0.00	0.04	0.01	0.00	0.05	0.01	0.01	0.00	0.00	0.04	0.07	0.00
Al_2O_3	29.90	17.27	21.35	30.29	17.58	28.48	17.08	21.42	29.48	17.36	21.02	27.64	17.26	21.32
FeO	3.28	22.91	24.55	3.15	21.62	3.18	22.78	23.02	2.58	25.66	25.05	3.41	25.13	22.94
MnO	0.01	0.31	0.53	0.03	0.28	0.00	0.30	3.72	0.03	0.37	2.73	0.03	0.36	4.07
MgO	1.99	6.53	0.43	1.86	6.57	2.12	6.93	0.79	1.54	5.98	0.75	2.11	6.02	0.74
CaO	0.00	0.01	15.46	0.00	0.01	0.00	0.00	12.78	0.22	0.02	13.10	0.00	0.00	12.82
Na_2O	0.27	0.11	0.00	0.31	0.10	0.13	0.00	0.00	0.72	0.04	0.00	0.17	0.04	0.00
K_2O	10.70	9.57	0.00	10.85	9.35	10.98	9.65	0.00	10.03	8.51	0.00	10.92	8.91	0.00
Sum	93.87	95.78	99.70	94.38	95.65	94.37	95.68	99.86	94.35	94.41	100.09	94.12	95.45	99.35
Structural formulae calculated on the basis of 12 oxygens for garnet. 22 for biotite and muscovite														
Cations														
Si	3.22	2.88	2.97	3.20	2.88	3.33	2.87	3.03	3.33	2.87	2.97	3.36	2.87	2.99
Ti	0.03	0.18	0.00	0.03	0.25	0.03	0.18	0.00	0.03	0.18	0.00	0.03	0.12	0.00
Cr	0.00	0.00	0.00	0.00	0.00	0.00	0.00	0.00	0.00	0.00	0.00	0.00	0.01	0.00
Al	2.40	1.62	2.00	2.42	1.66	2.28	1.61	2.01	2.36	1.61	1.97	2.22	1.64	2.01
Fetot	0.19	1.53	1.63	0.18	1.45	0.18	1.52	1.53	0.15	1.52	1.67	0.20	1.69	1.53
Mn	0.00	0.02	0.04	0.00	0.02	0.00	0.02	0.25	0.00	0.02	0.18	0.00	0.02	0.28
Mg	0.20	0.78	0.05	0.19	0.78	0.22	0.82	0.09	0.16	0.82	0.09	0.22	0.72	0.09
Ca	0.00	0.00	1.32	0.00	0.00	0.00	0.00	1.09	0.02	0.00	1.12	0.00	0.00	1.10
Na	0.04	0.02	0.00	0.04	0.02	0.02	0.00	0.00	0.10	0.00	0.00	0.02	0.01	0.00
K	0.93	0.97	0.00	0.94	0.95	0.95	0.98	0.00	0.87	0.98	0.00	0.95	0.92	0.00
Sum	7.00	8.00	8.00	7.00	8.00	7.00	8.00	8.00	7.00	8.00	8.00	7.00	8.00	8.00
X Fe	0.48	0.66	0.97	0.49	0.65	0.46	0.649	0.94	0.48	0.65	0.95	0.48	0.70	0.95
Prp			0.02					0.03			0.04			0.03
Alm			0.50					0.49			0.51			0.51
Grs			0.42					0.35			0.36			0.37
Sps			0.01					0.08			0.06			0.09

XFe = Fe/(Fe + Mg); Prp = Mg/(Fe +Mg+Ca+Mn); Alm = Fe/(Fe + Mg + Ca + Mn); Grs = Ca/Fe + Mg + Ca + Mn); Sps = Mn/(Fe + Mg + Ca + Mn).

Tab. 4: Representative analyses of muscovite, biotite and garnet

ACKNOWLEDGMENTS

Financial support of the French National Grant Agency (06-1148784 to K. Schulmann) is acknowledged. We thank James Alibon (Université de Lausanne) and Gilles Morvan (Université de Strasbourg) for technical support. Karim Malamoud (Université Joseph Fourier) provided the .ang (TSL ASCII) to .ctf (HKLtechnology) conversion, which was used in this work.

References

Aleksandrowski, P., Kryza, R., Mazur, S. & Żaba, J., 1997. Kinematic data on major Variscan strike-slip faults and shear zones in the Polish Sudetes, northeast Bohemian Massif. *Geological Magazine*, **134**(5), 727-739.

Ashby, M. F. & Verrall, R. A., 1973. Diffusion-Accomodated Flow and Superplasticity. *Acta Metallurgica*, **21**, 149-163.

Baratoux, L., Schulmann, K., Ulrich, S. & Lexa, O., 2005. Contrasting microstructures and deformation mechanisms in metagabbro mylonites contemporaneously deformed under different temperatures (c. 650°C and c. 750°C). In: *Deformation Mechanisms, Rheology and Tectonics: from Minerals to Lithosphere, Special Publications, 243* (eds Gapais, D., Brun, J. P. & Cobbold, P. R.), pp. 97–125, Geological Society of London, London.

Bascou, J., Barruol, G., Vauchez, A., Mainprice, D. & Egydio-Silva, M., 2001. EBSD-measured lattice-preferred orientations and seismic properties of eclogites. *Tectonophysics*, **342**(1-2), 61-80.

Berger, A. & Stünitz, H., 1996. Deformation mechanisms and reaction of hornblende: Examples from the Bergell tonalite (Central Alps). *Tectonophysics*, **257**(2-4), 149-174.

Bose, S. & Sengupta, S., 2003. High Temperature Mylonitization of Quartzofelspathic Gneisses: Example from the Schirmacher Hills, East Antartica. *Gondwana Research*, **6**(4), 805-816.

Bröcker, M., Klemd, R., Cosca, M., Brock, W., Larionov, A. N. & Rodionov, N., 2009. The timing of eclogite facies metamorphism and migmatization in the Orlica-Snieznik complex, Bohemian Massif: constraints from a multimethod geochronological study. *Journal of Metamorphic Geology*, **27**(5), 385-403.

Bröcker, M. & Klemd, R., 1996. Ultrahigh-pressure metamorphism in the Snieznik Mountains (Sudetes, Poland): P-T constraints and geological implications. *Journal of Geology*, **104**(4), 417-433.

Bröcker, M., Klemd, R., Kooijman, E., Berndt, J. & Larionov, A., 2010. Zircon geochronology and trace element characteristics of eclogites and granulites from the Orlica-Snieznik complex, Bohemian Massif. *Geological Magazine*, **147**(3), 339-362.

Cashman, K. V. & Ferry, J. M., 1988. Crystal size distribution (CSD) in rocks and the kinetics and dynamics of crystallization; 3 Metamorphic crystallization. *Contributions to Mineralogy and Petrology*, **99**(4), 401–415.

Coggon, R. & Holland, T. J. B., 2002. Mixing properties of phengitic micas and revised garnet- phengite thermobarometers. *Journal of Metamorphic Geology*, **20**(7), 683-696.

Cooke, R. A. & O'Brien, P. J., 2001. Resolving the relationship between high P-T rocks and gneisses in collisional terranes: an example from the Gföhl gneiss-granulite association in the Moldanubian Zone, Austria. *Lithos*, **58**(1-2), 33-54.

DeVore, G. W., 1959. Role of minimum interfacial free energy in determining the macroscopic features of minerals assemblages. *Journal of Geology*, **67**, 211–227.

Díaz Aspiroz, M & Fernández, C., 2003. Characterization of tectono-metamorphic events using crystal size distribution (CSD) diagrams. A case study from the Acebuches metabasites (SW Spain). *Journal of Structural Geology*, **25**, 935–947

Don, J., Skácel, J. & Gotowała, R., 2003. The boundary zone of the East and West Sudetes on the 1:50 000 scale geological map of the Velké Vrbno, Staré Město and Śnieznik Metamorphic Units. *Geologia Sudetica*, **35**(1), 25-59.

Dumicz, M. 1989. Następstwo serii gnejsowych Masywu Śnieżnika w świetle analizy mezostrukturalnej wybranych obszarów w jednostkach geologicznych Międzygórza i Gierałtowa (The Śnieżnik Mts gneisses sequence in the light of mesostructural analysis of some areas of the Międzygórze and Gierałtów units). *Geologia Sudetica*, **24**, 139-189.

Edel, J. B., Schulmann, K. & Holub, F. V., 2003. Anticlockwise and clockwise rotations of the Eastern Variscides accommodated by dextral lithospheric wrenching: palaeomagnetic and structural evidence. *Journal of the Geological Society*, **160**, 209-218.

Evensen, N. M., Hamilton, P. J. & O'Nions, R. K., 1978. Rare-earth abundances in chondritic meteorites. *Geochimica et Cosmochimica Acta*, **42**, 1199-1212.

Fisher, G., 1936. Der Bau des Glatzer Schneegebirges. *Jahrbuch der Preußischen Geologischen Landesanstalt*, **56**, 712-732.

Flinn, D., 1965. On the symmetry principle and the deformation ellipsoid. *Geological Magazine*, **102**(1), 36-45.

Flinn, D., 1969. Grain contacts in crystalline rocks. *Lithos*, **2**(4), 361–370.

Franěk, J., Schulmann, K. & Lexa, O., 2006. Kinematic and rheological model of exhumation of high pressure granulites in the Variscan orogenic root: example of the Blanský les granulite, Bohemian Massif, Czech Republic. *Mineralogy and Petrology*, **86**(3-4), 253-276.

Franěk, J., Schulmann, K., Lexa, O., Ulrich, S., Štípská, P., Haloda, J. & Týcová, P., 2011. Origin of felsic granulite microstructure by heterogeneous decomposition of alkali feldspar and extreme weakening of orogenic lower crust during the Variscan orogeny. *Journal of Metamorphic Geology*, **29**(1), 103-130.

Gapais, D., 1989. Shear structures within deformed granites: Mechanical and thermal indicators. *Geology*, **17**, 1144-1147.

Gower, R. J. W. & Simpson, C., 1992. Phase boundary mobility in naturally deformed, high-grade quartzofeldspathic rocks: evidence for diffusional creep. *Journal of Structural Geology*, **14**(3), 301–313.

Grant, J. A., 1986. The isocon diagram-a simple solution to Gresens' equation for metasomatic alteration. *Economic Geology*, **81**(8), 1976-1982.

Hacker, B. R., Andersen, T. B., Johnston, S., Kylander-Clark, A. R. C., Peterman, E. M., Walsh, E. O. & Young, D., 2010. High-temperature deformation during continental-margin subduction & exhumation: The ultrahigh-pressure Western Gneiss Region of Norway. *Tectonophysics*, **480**(1-4), 149-171.

Handy, M. R., 1990. The Solid-State Flow of Polymineralic Rocks. *Journal of Geophysical Research-Solid Earth and Planets*, **95**(B6), 8647-8661.

Handy, M. R., 1994. Flow laws for rocks containing two non-linear viscous phases: a phenomenological approach. *Journal of Structural Geology*, **16**, 287-301.

Handy, M. R. & Stünitz, H., 2002. Strain localization by fracturing and reaction weakening - A mechanism for initiating exhumation of subcontinental mantle beneath rifted margins. In: *Deformation Mechanisms, Rheology and Tectonics: Current Status and Futur Perspectives, Special Publication, 200* (eds De Meers, S., De Bresser, J. H. P. & Pennock, G.), pp. 387-407, Geological Society of London, London.

Harlov, D. E. & Wirth, R., 2000. K-feldspar–quartz and K-feldspar–plagioclase phase boundary interactions in garnet–orthopyroxene gneiss's from the Val Strona di Omegna, Ivrea–Verbano Zone, northern Italy. *Contributions to Mineralogy and Petrology*, **140**(2), 148-162.

Hasalová, P., Janoušek, V., Schulmann, K., Štípská, P. & Erban, V., 2008a. From orthogneiss to migmatite: geochemical assessment of the melt infiltration model in the Gföhl Unit (Moldanubian Zone, Bohemian Massif). *Lithos*, **102**, 508-537.

Hasalová, P., Schulmann, K., Lexa, O., Štípská, P., Hrouda, F., Ulrich, S., Haloda, J. & Týcová, P., 2008b. Origin of migmatites by deformation-enhanced melt infiltration of orthogneiss: a new model based on quantitative microstructural analysis. *Journal of Metamorphic Geology*, **26**, 29-53.

Hasalová, P., Štípská, P., Powell, R., Schulmann, K., Janoušek, V. & Lexa, O., 2008c. Transforming mylonitic metagranite by open-system interactions during melt flow. *Journal of Metamorphic Geology*, **26**(1), 55-80.

Heilbronner, R. & Tullis, J., 2006. Evolution of c axis pole figures and grain size during dynamic recrystallization: Results from experimentally sheared quartzite. *Journal of Geophysical Research B: Solid Earth*, **111**(10).

Holland, T. J. B. & Powell, R., 1998. An internally consistent thermodynamic data set for phases of petrological interest. *Journal of Metamorphic Geology*, **16**(3), 309-343.

Holland, T. J. B. & Powell, R., 2003. Activity-composition relations for phases in petrological calculations: an asymmetric multicomponent formulation. *Contributions to Mineralogy and Petrology*, **145**, 492-501.

Holness, M. B., 2008. Decoding migmatite microstructures. In: *Working with Migmatites, Short Course Series Volume 38* (ed Sawyer, E.W.), pp. 57-76, Mineralogical Association of Canada, Quebec City.

Holness, M. B., Cheadle, M. J. & McKenzie, D., 2005. On the uses of changes in dihedral angle to decode late-stage textural evolution in cumulates. *Journal of Petrology*, **46**, 1565-1583.

Holyoke Iii, C. W. & Tullis, J., 2006a. The interaction between reaction and deformation: An experimental study using a biotite + plagioclase + quartz gneiss. *Journal of Metamorphic Geology*, **24**(8), 743-762.

Holyoke Iii, C. W. & Tullis, J., 2006b. Mechanisms of weak phase interconnection and the effects of phase strength contrast on fabric development. *Journal of Structural Geology*, **28**(4), 621-640.

Ishii, K., Kanagawa, K., Shigematsu, N. & Okudaira, T., 2007. High ductility of K-feldspar and development of granitic banded ultramylonite in the Ryoke metamorphic belt, SW Japan. *Journal of Structural Geology*, **29**(6), 1083-1098.

Jastrzębski, M., Żelaźniewicz, A., Nowak, I., Murtezi, M. & Larionov, A. N., 2010. Protolith age and provenance of metasedimentary rocks in Variscan allochthon units: U-Pb SHRIMP zircon data from the Orlica-Snieznik Dome, West Sudetes. *Geological Magazine*, **147**(3), 416-433.

Jeřábek, P., Stünitz, H., Heilbronner, R., Lexa, O. & Schulmann, K., 2007. Microstructural-deformation record of an orogen-parallel extension in the vepor unit, West Carpathians. *Journal of Structural Geology*, **29**, 1722-1743.

Koons, P. O., Rubie, D. C. & Fruehgreen, G., 1987. The Effects of Disequilibrium and Deformation on the Mineralogical Evolution of Quartz Diorite During Metamorphism in the Eclogite Facies. *Journal of Petrology*, **28**(4), 679-700.

Košuličová, M. & Štípská, P., 2007. Variations in the transient prograde geothermal gradient from chloritoid-staurolite equilibria: a case study from the Barrovian and Buchan-type domains in the Bohemian Massif. *Journal of Metamorphic Geology*, **25**(1), 19-35.

Kretz, R., 1994. *Metamorphic Crystallization*. Wiley, New York.

Kröner, A., Jaeckel, P., Hegner, E. & Opletal, M., 2001. Single zircon ages and whole rock Nd isotopic systematics of early Palaeozoic granitoid gneisses from the Czech and Polish Sudetes (Jizerské hory, Krkonoše Mountains and Orlice-Sneznik Complex). *International Journal of Earth Sciences*, **90**(2), 304-324.

Kröner, A., Štípská, P., Schulmann, K. & Jaeckel, P., 2000. Chronological constraints on the pre-Variscan evolution of the northeastern margin of the Bohemian Massif, Czech Republic. In: *Orogenic processes; quantification and modelling in the Variscan Belt, Special Publication, 179* (eds Franke, W., Haak, V., Oncken, O. & Tanner, D.), pp. 175-197, Geological Society of London, London.

Kruse, R. & Stünitz, H., 1999. Deformation mechanisms and phase distribution in mafic high-temperature mylonites from the Jotun Nappe, southern Norway. *Tectonophysics*, **303**, 223–249.

Lange, U., Bröcker, M., Armstrong, R., Żelaźniewicz, A., Trapp, E. & Mezger, K., 2005. The orthogneisses of the Orlica-Snieznik complex (West Sudetes, Poland): geochemical characteristics, the importance of pre-Variscan migmatization and constraints on the cooling history. *Journal of the Geological Society*, **162**, 973-984.

Lange, U., Bröcker, M., Mezger, K. & Don, J., 2002. Geochemistry and Rb-Sr geochronology of a ductile shear zone in the Orlica-Snieznik dome (West Sudetes, Poland). *International Journal of Earth Sciences*, **91**(6), 1005-1016.

Lenze, A. & Stöckhert, B., 2007. Microfabrics of UHP metamorphic granites in the Dora Maira Massif, western Alps - No evidence of deformation at great depth. *Journal of Metamorphic Geology*, **25**(4), 461-475.

Lexa, O., 2003. *Numerical approaches in structural and microstructural analyses*. Unpub. PhD Thesis, Charles University, Prague.

Lexa, O., Štípská, P., Schulmann, K., Baratoux, L. & Kröner, A., 2005. Contrasting textural record of two distinct metamorphic events of similar P-T conditions and different durations. *Journal of Metamorphic Geology*, **23**(8), 649-666.

Lister, G. S. & Hobbs, B. E., 1980. The simulation of fabric development during plastic deformation and its application to quartzite: the influence of deformation history. *Journal of Structural Geology*, **2**(3), 355-370.

Lister, G. S. & Paterson, M. S., 1979. The simulation of fabric development during plastic deformation and its application to quartzite: fabric transitions. *Journal of Structural Geology*, **1**(2), 99-115.

Lonka, H., Schulmann, K. & Venera, Z., 1998. Ductile deformation of tonalite in the Suomusjarvi shear zone, south-western Finland. *Journal of Structural Geology*, **20**(6), 783-798.

Marquer, D. & Burkhard, M., 1992. Fluid circulation, progressive deformation and mass-transfer processes in the upper crust: the example of basement-cover relationships in the External Crystalline Massifs, Switzerland. *Journal of Structural Geology*, **14**(8-9), 1047-1057.

Martelat, J. E., Schulmann, K., Lardeaux, J. M., Nicollet, C. & Cardon, H., 1999. Granulite microfabrics and deformation mechanisms in southern Madagascar. *Journal of Structural Geology*, **21**(6), 671-687.

Mazur, S. & Aleksandrowski, P., 2001. The Tepla(?)/Saxothuringian suture in the Karkonosze-Izera massif, western Sudetes, central European Variscides. International Journal of Earth Sciences, **90**(2), 341-360.

Mazur, S., Aleksandrowski, P., Kryza, R. & Oberc-Dziedzic, T., 2006. The Variscan Orogen in Poland. *Geological Quarterly*, **50**(1), 89-118.

McLellan, E. L., 1983. Contrasting textures in metamorphic and anatectic migmatites - an example from the Scottish Caledonides. *Journal of Metamorphic Geology*, **1**(3), 241-262.

Menegon, L., Pennacchioni, G., Heilbronner, R. & Pittarello, L., 2008. Evolution of quartz microstructure and c-axis crystallographic preferred orientation within ductilely deformed granitoids (Arolla unit, Western Alps). *Journal of Structural Geology*, **30**(11), 1332-1347.

Menegon, L., Pennacchioni, G. & Stünitz, H., 2006. Nucleation and growth of myrmekite during ductile shear deformation in metagranites. *Journal of Metamorphic Geology*, **24**(7), 553-568.

Menold, C. A., Manning, C. E., Yin, A., Tropper, P., Chen, X. H. & Wang, X. F., 2009. Metamorphic evolution, mineral chemistry and thermobarometry of orthogneiss hosting ultrahigh-pressure eclogites in the North Qaidam metamorphic belt, Western China. *Journal of Asian Earth Sciences*, **35**(3-4), 273-284.

Oberhänsli, R., Hunziker, J. C., Martinotti, G. & Stern, W. B., 1983. Geochemistry, geochronology and petrology of Monte Mucrone: an example of eo-Alpine eclogitization of Permian granitoids in the Sesia –Lanzo zone, Western Alps, Italy. *Chemical Geology*, **52**, 165-184.

Oliot, E., Goncalves, P. & Marquer, D., 2010. Role of plagioclase and reaction softening in a metagranite shear zone at mid-crustal conditions (Gotthard Massif, Swiss Central Alps). *Journal of Metamorphic Geology*, **28**(8), 849-871.

Panozzo, R., 1984. Two-Dimensional Strain from the Orientation of Lines in a Plane. *Journal of Structural Geology*, **6**(1-2), 215-221.

Parry, M., Štípská, P., Schulmann, K., Hrouda, F., Ježek, J. & Kröner, A., 1997. Tonalite sill emplacement at an oblique plate boundary: northeastern margin of the Bohemian Massif. *Tectonophysics*, **280**(1-2), 61-81.

Passchier, C. W. & Trouw, R. A. J., 1996. *Microtectonics*. Springer-Verlag Berlin Heidelberg New York.

Peterman, E. M., Hacker, B. R. & Baxter, E. F., 2009. Phase transformations of continental crust during subduction and exhumation: Western Gneiss Region, Norway. *European Journal of Mineralogy*, **21**(6), 1097-1118.

Peterson, T. D., 1996. A refined technique for measuring crystal size distributions in thin section. *Contributions to Mineralogy and Petrology*, **124**, 395–405.

Powell, R., Holland, T. & Worley, B., 1998. Calculating phase diagrams involving solid solutions via non- linear equations, with examples using THERMOCALC. *Journal of Metamorphic Geology*, **16**(4), 577-588.

Prior, D. J., Boyle, A. P., Brenker, F., Cheadle, M. C., Austin, D., Lopez, G., Peruzzo, L., Potts, G. J., Reddy, S., Spiess, R., Timms, N. E., Trimby, P., Wheeler, J. & Zetterström, L., 1999. The application of electron backscatter diffraction and orientation contrast imaging in the SEM to textural problems in rocks. *American Mineralogist*, **84**(11-12), 1741-1759.

Prior, D. J., Mariani, E. & Wheeler, J., 2009. EBSD in the Earth Sciences: Applications, Common Practice, and Challenges. In: *Electron Backscatter Diffraction in Materials Science* (eds Schwartz, A. J., Kumar, M., Adams, B. L. & Field, D. P.), pp. 345-360, Springer-Verlag Berlin Heidelberg New York.

Proyer, A., 2003. The preservation of high-pressure rocks during exhumation: metagranites and metapelites. *Lithos*, **70**(3-4), 183-194.

Ramsay, J. G. & Huber, M. I., 1983. *The techniques of modern structural geology. Volume 1: Strain Analysis.* Academic Press, London.

Randolph, A. D. & Larson, M. A., 1971. *Theory of Particle Processes*. Academic Press, New York.

Rosenberg, C., 2001. Deformation of partially molten granite: a review and comparison of experimental and natural case studies. *International Journal of Earth Sciences*, **90**, 60–76.

Sacerdoti, M., Labernardière, H. & Gandais, M., 1980. Transmission electron microscope (TEM) study of geologically deformed potassic feldspars. *Bulletin de Minéralogie*, **103**, 148-155.

Sawyer, E. W., 2001. Melt segregation in the continental crust: distribution and movement of melt in anatectic rocks. *Journal of Metamorphic Geology*, **19**, 291–309.

Schmid, S. M. & Casey, M., 1986. Complete fabric analysis of some commonly observed quartz c-axis patterns. In: *Mineral and Rock Deformation: Laboratory Studies; the Paterson Volume, Geophysical Monograph, 36* (eds Hobbs, B. E. & Heard, H. C.), pp. 263-286, American Geophysical Union, Washington, DC.

Schneider, D. A., Zahniser, S. J., Glascock, J. M., Gordon, S. M. & Manecki, M., 2006. Thermochronology of the West Sudetes (Bohemian Massif): Rapid and repeated eduction in the Eastern Variscides, Poland and Czech Republic. *American Journal of Science*, **306**(10), 846-873.

Schulmann, K. & Gayer, R., 2000. A model for a continental accretionary wedge developed by oblique collision: the NE Bohemian Massif. *Journal of the Geological Society, London*, **157**, 401-416.

Schulmann, K., Mlčoch, B. & Melka, R., 1996. High-temperature microstructures and rheology of deformed granite, Erzgebirge, Bohemian Massif. *Journal of Structural Geology*, **18**(6), 719-733.

Schulmann, K., Martelat, J. E., Ulrich, S., Lexa, O., Štípská, P. & Becker, J. K., 2008. Evolution of microstructure and melt topology in partially molten granitic mylonite: Implications for rheology of felsic middle crust. *Journal of Geophysical Research-Solid Earth*, **113**, B10406.

Seng, H., 1936. Die Migmatitfrage und der Mechanismus parakristalliner Prägung. *Geologische Rundschau*, **27**, 471–492.

Shigematsu, N. & Tanaka, H., 2000. Dislocation creep of fine-grained recrystallized plagioclase under low-temperature conditions. *Journal of Structural Geology*, **22**(1), 65-79.

Shimizu, I., 1998. Stress and temperature dependence of recrystallized grain size: A subgrain misorientation model. *Geophysical Research Letters*, **25**(22), 4237-4240.

Shimizu, I., 2008. Theories and applicability of grain size piezometers: The role of dynamic recrystallization mechanisms. *Journal of Structural Geology*, **30**(7), 899-917.

Simpson, C. & Wintsch, R. P., 1989. Evidence for deformation-induced K-feldspar replacement by myrmekite. *Journal of Metamorphic Geology*, **7**, 261-275.

Skrzypek, E., Schulmann, K., Štípská, P., Chopin, F., Lehmann, J., Lexa, O. & Haloda, J., 2011a. Tectono-metamorphic history recorded in garnet porphyroblasts: insights from thermodynamic modelling and electron backscatter diffraction analysis of inclusion trails. *Journal of Metamorphic Geology*, **29**(4), 473-496.

Skrzypek, E., Štípská, P., Lexa, O., Schulmann, K. & Lexová, M., 2011b. Prograde and retrograde metamorphic fabrics – a key for understanding burial and exhumation in orogens (Bohemian Massif). *Journal of Metamorphic Geology*, **29**(4), 451-472.

Smulikowski, K., 1967. Eklogity Gór Śnieznickich w Sudetach (Eclogites of the Snieznik Mts in the Sudetes). *Geologia Sudetica*, 3, 157-174.

Štípská, P., Schulmann, K., Thompson, A. B., Ježek, J. & Kröner, A., 2001. Thermo-mechanical role of a Cambro-Ordovician paleorift during the Variscan collision: the NE margin of the Bohemian Massif. *Tectonophysics*, **332**(1-2), 239-253.

Štípská, P., Schulmann, K. & Kröner, A., 2004. Vertical extrusion and middle crustal spreading of omphacite granulite: a model of syn-convergent exhumation (Bohemian Massif, Czech Republic). *Journal of Metamorphic Geology*, **22**(3), 179-198.

Štípská, P., Pitra, P. & Powell, R., 2006. Separate or shared metamorphic histories of eclogites and surrounding rocks? An example from the Bohemian Massif. *Journal of Metamorphic Geology*, **24**(3), 219-240.

Stöckhert, B., 2002. Stress and deformation in subduction zones: Insight from the record of exhumed metamorphic rocks. In: *Deformation Mechanisms, Rheology and Tectonics, Special Publications, 200* (eds De Meers, S., Drury, M. R., De Bresser, J. H. P. & Pennock, G.), pp. 255-274, Geological Society of London, London.

Stöckhert, B. & Renner, J., 1998. Rheology of Crustal Rocks at Ultrahigh Pressure. In: *When Continents Collide: Geodynamics and Geochemistry of Ultrahigh-Pressure Rocks* (eds Hacker, B. R. & Liou, J. G.), pp. 57-95, Kluwer Academic Publishers, Dordrecht.

Stünitz, H. & Fitzgerald, J. D., 1993. Deformation of Granitoids at Low Metamorphic Grade. 2. Granular Flow in Albite-Rich Mylonites. *Tectonophysics*, **221**(3-4), 299-324.

Ulrich, S., Schulmann, K. & Casey, M., 2002. Microstructural evolution and rheological behaviour of marbles deformed at different crustal levels. *Journal of Structural Geology*, **24**(5), 979-995.

Vernon, R. H., 1976. *Metamorphic Processes: Reactions and Microstructure Development*. Wiley, New York.

Vernon, R. H., 1991. Questions about myrmekite in deformed rocks. *Journal of Structural Geology*, **13**(9), 979-985.

Vernon, R. H., 2004. *A Practical Guide to Rock Microstructures*. Cambridge University Press, Cambridge.

White, R. W., Powell, R. & Holland, T. J. B., 2007. Progress relating to calculation of partial melting equilibria for metapelites. *Journal of Metamorphic Geology*, **25**(5), 511-527.

White, R. W., Powell, R., Holland, T. J. B. & Worley, B. A., 2000. The effect of TiO_2 and Fe_2O_3 on metapelitic assemblages at greenschist and amphibolite facies conditions: mineral equilibria calculations in the system K_2O-FeO-MgO-Al_2O_3-SiO_2- H_2O-TiO_2-Fe_2O_3. *Journal of Metamorphic Geology*, **18**(5), 497-511.

Willaime, C., Christie, J. M. & Kovacs, M.-P., 1979. Experimental deformation of K-feldspar single crystals. *Bulletin de Minéralogie*, **102**, 168-177.

Wirth, R. & Voll, G., 1987. Cellular intergrowth between quartz and sodium-rich plagioclase (myrmekite) – an analogue of discontinuous precipitation in metal alloys. *Journal of Materials Science*, **22**, 1913-1918.

Závada, P., Schulmann, K., Konopásek, J., Ulrich, S. & Lexa, O., 2007. Extreme ductility of feldspar aggregates - Melt-enhanced grain boundary sliding and creep failure: Rheological implications for felsic lower crust. *Journal of Geophysical Research-Solid Earth*, **112**, B10210.

Żelaźniewicz, A., Nowak, I., Larionov, A. & Presnyakov, S., 2006. Syntectonic Lower Ordovician migmatite and post-tectonic Upper Viséan syenite in the western limb of the Orlica-Śnieżnik Dome, West Sudetes: U-Pb SHRIMP data from zircons. *Geologia Sudetica*, **38**, 63-80.

Zhao, Z. Y., Wei, C. J. & Fang, A. M., 2005. Plastic flow of coesite eclogite in a deep continent subduction regime: Microstructures, deformation mechanisms and rheologic implications. *Earth and Planetary Science Letters*, **237**(1-2), 209-222.

The role of large-scale folding and erosion on juxtaposition of eclogite and mid-crustal rocks (Orlica-Śnieżnik Dome, Bohemian Massif)

P. ŠTÍPSKÁ[1], F. CHOPIN[1], E. SKRZYPEK[1], K. SCHULMANN[1], O. LEXA[2,3], P. PITRA[4], J.E. MARTELAT[5], C. BOLLINGER[6]

[1]*Ecole et Observatoire des Sciences de la Terre, Institut de Physique du Globe – CNRS UMR 7516, Université de Strasbourg, 1 rue Blessig, F-67084 Strasbourg Cedex, France*
[2]*Institute of Petrology and Structural Geology, Charles University, Albertov 6, CZ-12843 Praha, Czech Republic*
[3]*Czech Geological Survey, Klárov 3, 110 00, Praha, Czech Republic*
[4]*Geosciences Rennes – CNRS UMR6118, Université Rennes 1, Campus de Beaulieu, F-35042 Rennes Cedex, France*
[5]*Laboratoire des Sciences de la Terre – CNRS UMR5570, Université de Lyon 1, F-69622, Villeurbanne, France*
[6]*Unité Matériaux et Transformations – CNRS UMR8207, Université Lille 1, Bât. C6, F-59655 Villeneuve d'Ascq, France*

Short title: Eclogite and mid-crustal rocks juxtaposition

submitted to Journal of Metamorphic Geology

ABSTRACT

Eclogite, felsic orthogneiss and garnet-staurolite metapelite with intercalations of amphibolite, quartzite and marble occur in a 5 km long profile in the area of Międzygórze in the Orlica-Śnieżnik dome (Bohemian Massif). A structural study combined with petrographic observations and mineral equilibria modelling is used to understand the mechanism of such close juxtaposition of high pressure and medium pressure rocks in the crust. The structural succession in all lithologies shows an early shallow-dipping fabric S1 that is folded by upright folds and overprinted by a heterogeneously developed subvertical foliation S2. Late recumbent folds associated with a weak shallow-dipping axial plane cleavage S3 occur locally. The S1 fabric in the eclogite is defined by alternation of garnet-rich (grs = 22−29 mol.%) and omphacite-rich (jd = 33−36 mol.%) layers with oriented muscovite (Si = 3.26−3.31 p.f.u.) and accessory kyanite, epidote, rutile and quartz. The assemblage and garnet zoning (grs_{core} = 29, grs_{rim} = 22 mol.%) are compatible with a prograde *P–T* path from ~20 kbar and ~640 °C to ~22 kbar and ~720 °C. The assemblage in the localized retrograde foliation S2 is formed by amphibole, plagioclase, biotite and relict rutile surrounded by ilmenite and sphene that is compatible with decompression and cooling from ~9 kbar and ~730 °C to 5−6 kbar and 600−650 °C. The S3 fabric contains amphibole, plagioclase, biotite, ilmenite surrounded by sphene, and domains with albite, chlorite, K-feldspar and magnetite indicating cooling to greenschist facies conditions. The metapelites are composed of garnet, staurolite, muscovite, biotite, quartz, ilmenite and chlorite. Chemical zoning of garnet core that contains straight ilmenite and staurolite inclusion trails oriented perpendicular to the external S2 fabric indicates prograde growth from ~5 kbar and ~520 °C to ~7 kbar and ~610 °C during or after the formation of the S1 fabric. Inclusion trails parallel with the S2 fabric at garnet and staurolite rims are interpreted as continuation of the prograde path to ~7.5 and ~630 °C in the S2 fabric. Matrix chlorite parallel to the S2 foliation indicates that the subvertical fabric was still active below 550 °C. The prograde evolution of the eclogite and metapelite during/after the development of the early shallow-dipping fabric is interpreted as simultaneous burial of the lower and upper-middle orogenic crust along shallow-dipping surfaces within a continental accretionary wedge. Axial planar fabrics developed during upright folding and are associated with retrogression under amphibolite-facies conditions in the eclogite, and firstly with prograde and later with retrograde evolution in the metapelites. The shared part of the eclogite and metapelite *P−T* paths was achieved in the subvertical fabric and points to their common exhumation during fold amplification, which is only possible when erosion, ductile thinning or tectonic unroofing efficiently reduce the upper part of the thickened crust.

Key words: Bohemian Massif, crustal-scale folding, eclogite, exhumation, pseudosection modelling.

INTRODUCTION

Orogenic belts are sites of common tectonic emplacement of (U)HP rocks at middle and upper crustal depth (Duchene *et al.*, 1997). The way how the (U)HP rocks and mid-crustal rocks become juxtaposed is critically dependent on the exhumation mechanism, i.e. on the mode of vertical elevation of rocks during regional convergence or extension. The most commonly reported kinematic model in a convergent setting is displacement of deeply subducted rocks above lower pressure rocks along a crustal scale thrust (e.g. Chemenda *et al.*, 2000; Jolivet *et al.*, 2005). Crustal-scale folding is another convergent kinematic model that may explain tectonic juxtaposition of high- and low-pressure rocks (Burg *et al.*, 1998; Burg *et al.*, 2004). In extensional setting, emplacement of (U)HP rocks into middle to upper crustal levels may occur along a deep-seated extensional fault zone following a subduction event (e.g. Andersen & Fossen, 1993).

Advent of analogue and numerical orogenic-scale models offered mechanical and dynamic explanation of burial and exhumation of rocks along convergent boundaries (Platt, 1987), which may lead to a close juxtaposition of high- and low-pressure rocks. A first group of models involves corner flow circulation of rocks above a downgoing plate in front of a rigid buttress (Platt, 1993; Allemand & Lardeaux, 1997; Gerya & Stöckhert, 2006), or above a gently inclined upper plate boundary (Beaumont *et al.*, 2001; Beaumont *et al.*, 2006). A second group of models is based on gravity-driven exhumation and redistribution of deeply buried material. The most typical example are crustal-scale "diapiric" domes (e.g. Gerya *et al.*, 2002; Gerya *et al.*, 2004), which may be enhanced by lateral forces leading to mixed diapiric and folding mechanisms (Burg *et al.*, 2004; Lexa *et al.*, 2011). Another example is horizontal spreading of a rebounded lower crust beneath a rigid orogenic lid (Koyi *et al.*, 1999).

Each model should be associated with a typical succession of structures and typical $P-T$ paths related to the movement of rocks in individual crustal levels. Therefore, in order to correlate one of the above models or their combination with the tectono-metamorphic evolution of an orogen, information about structural, petrological and geochronological evolutions of the orogenic lower, middle and upper crust is needed. Structural geology can compare successions of deformation fabrics from different crustal levels in order to explore mechanical coupling or decoupling between the lower and upper crust during orogeny. Structural investigations may also show whether the juxtaposition of high- and low-pressure rocks results from tectonic movements related to orogenesis or with late to post-orogenic faulting or shearing. Petrology provides additional information about vertical displacements and thermal evolution of rocks during orogeny. Establishing $P-T$ paths of individual rocks allows relating these rocks to different crustal levels and demonstrating their shared or unshared metamorphic histories (Racek *et al.*, 2006; Štípská *et al.*, 2006; Štípská *et al.*, 2008). Combination of structural and petrological information into $P-T-d$ paths allows determining burial and/or exhumation character of individual fabrics. It also allows correlation of relative horizontal and vertical displacements of rocks from different crustal levels during an orogenic cycle.

The polyphase structural and petrological evolution of lower crustal eclogite, felsic orthogneiss and adjacent mid-crustal metasediments is described in this work. The structural succession and associated metamorphic evolution of these rocks is evaluated in order to characterize burial and exhumation related fabrics in two contrasting crustal levels during the Variscan orogeny. Comparison of the $P-T-d$ paths of the eclogite and the metapelite allows discussing fabrics and deformation processes that are responsible for the close juxtaposition of the lower and the mid-crustal rocks. Finally, the structural and $P-T$ records of the individual fabrics are discussed in the frame of the kinematic and dynamic models introduced above.

GEOLOGICAL SETTING

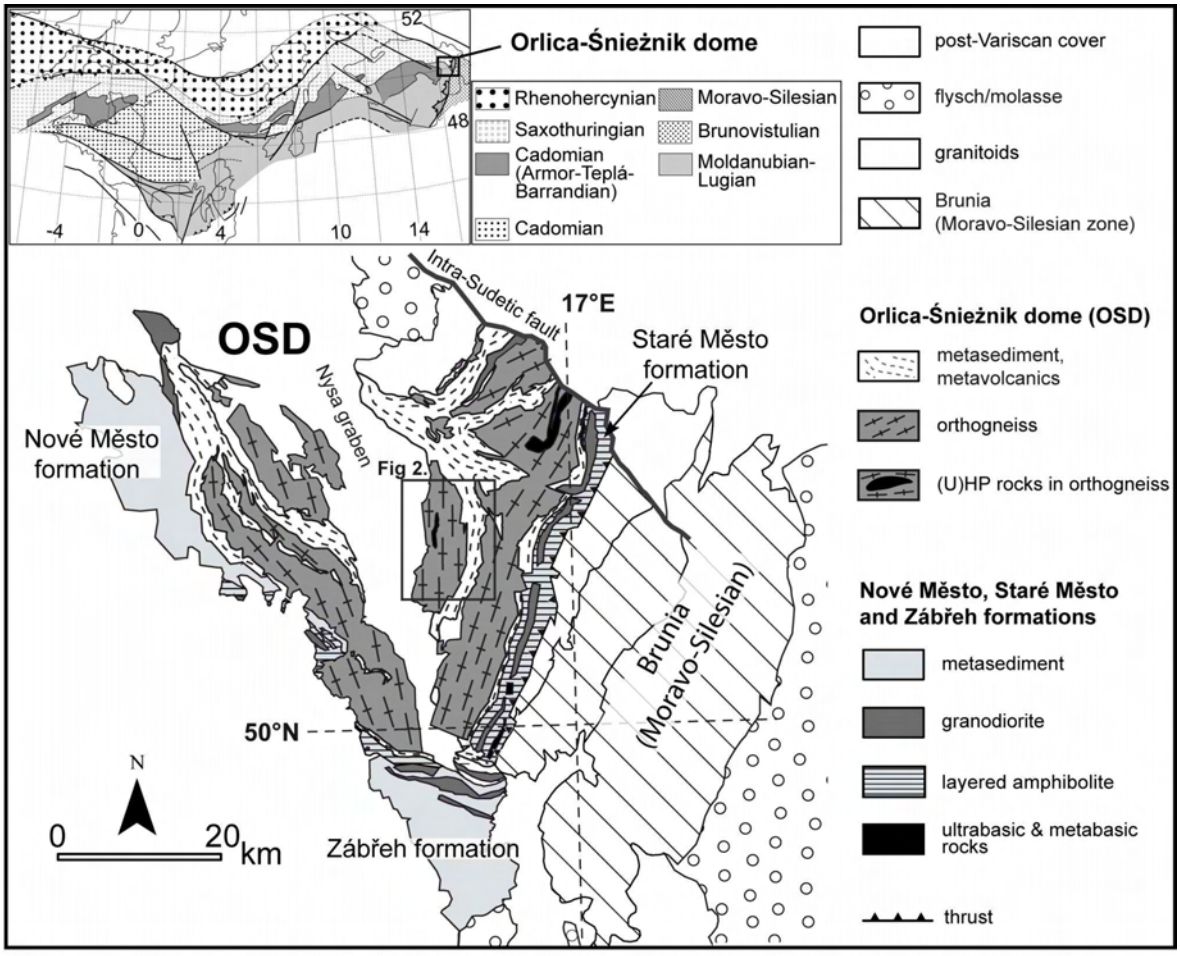

Fig. 1. Geological map of the Orlica-Śnieżnik dome (OSD) (modified after Aleksandrowski *et al.*, 1997; Don *et al.*, 2003; Żelaźniewicz *et al.*, 2006). Location of the study area (Fig. 2) is indicated. Upper left inset shows position of the study area in the framework of the European Variscides (modified after Edel, 2003).

The Orlica-Śnieżnik dome (OSD) is located in the easternmost part of the Bohemian Massif (Fig. 1). It is interpreted as part of the orogenic root of the Moldanubian-Lugian zone (e.g. Schulmann *et al.*, 2009) bordered to the east by the Staré Město formation, a remnant of a Late Cambrian intracontinental rift (Parry *et al.*, 1997; Kröner *et al.*, 2000; Štípská *et al.*, 2001; Lexa *et al.*,

2005), and the Moravo-Silesian zone, a deformed and metamorphosed part of the Neoproterozoic Brunovistulian (Brunia) microcontinent (Schulmann & Gayer, 2000; Štípská *et al.*, 2006; Košuličová & Štípská, 2007). The south-western and southern part of the OSD are surrounded by low grade rocks of the Nové Město and the Zábřeh formations interpreted as the upper orogenic crust (Mazur *et al.*, 2005; Schulmann *et al.*, 2008).

Lithology and protolith ages

The OSD (Fig. 1) is dominated by felsic orthogneiss, locally containing lenses of (U)HP rocks (eclogite and granulite), alternating with generally N−S trending belts of the volcanosedimentary Młynowiec-Stronie formation (Don *et al.*, 2003). The felsic orthogneisses are traditionally subdivided into two main types (Fig. 2): an augen and banded variety (the Śnieżnik type) and a fine-grained and/or migmatitic variety (the Gierałtów type) (Don *et al.*, 1990). Several authors suggest that both types result from variable reworking of the same porphyritic granite (Turniak *et al.*, 2000; Lange *et al.*, 2002; Lange *et al.*, 2005b) although this view is questioned by other authors (Żelaźniewicz *et al.*, 2006). The fine-grained and migmatitic Gierałtów types are volumetrically more abundant around the eclogite and granulite occurrences. Eclogitic bodies form a 3 km long N−S trending belt in the area of the Międzygórze town (Fig. 2), and occur as scattered lenses or loose blocks in the felsic orthogneiss mainly in the eastern and central parts of the OSD (Smulikowski, 1967). High-pressure basic and felsic granulites are restricted to a NNE−SSW trending 12 km long belt to the northeast (Pouba *et al.*, 1985; Štípská *et al.*, 2004). The metasedimentary unit is subdivided into the Młynowiec formation comprising plagioclase paragneiss and micaschist, and the Stronie formation composed of micaschist, paragneiss, quartzite, marble, amphibolite and acid volcanic rocks (Don *et al.*, 1990).

Zircon dating of both felsic orthogneiss varieties spans between 490 and 520 Ma, which is interpreted as the emplacement of the granitic precursor (Oliver *et al.*, 1993; Kröner *et al.*, 2000; Turniak *et al.*, 2000; Kröner *et al.*, 2001; Štípská *et al.*, 2004; Lange *et al.*, 2005b; Bröcker *et al.*, 2009). Sedimentation of the Młynowiec formation is older than 530 Ma (Jastrzębski *et al.*, 2010) and the Stronie sediments and volcanics are deposited between 520−470 Ma (Kröner *et al.*, 2000; Jastrzębski *et al.*, 2010). Despite the difficulties to determine the protolith ages of (U)HP rocks in the OSD (Bröcker *et al.*, 2010), they are probably older than 470 Ma (Štípská *et al.*, 2004; Lange *et al.*, 2005a; Bröcker *et al.*, 2010).

Previous structural studies

Structural studies focused mainly on the explanation of the generally N−S trending alternation of metasediments and felsic orthogneisses, cored in places by the (U)HP rocks. A succession of three major deformation events was recognized: an early shallow-dipping metamorphic foliation was followed by upright folding and development of a new metamorphic foliation, and subsequently reworked by folds with shallow-dipping to subhorizontal axial planes and

associated cleavage (Don, 1964; Dumicz, 1979; Don, 1982; Don *et al.*, 1990; Štípská *et al.*, 2004; Jastrzębski, 2009; Skrzypek *et al.*, 2011b).

Previous metamorphic and geochronological studies

Detailed petrography and occurrences of the eclogite types is given in Smulikowski (1967). Based on possible pseudomorphs after coesite and thermobarometry, several authors suggested pressures above 27 kbar for the eclogite (Bröcker & Klemd, 1996) and granulite (Bakun-Czubarow, 1992; Klemd & Bröcker, 1999), while other authors proposed maximum pressures of about 18−22 kbar for granulite (Steltenpohl *et al.*, 1993; Štípská *et al.*, 2004). Peak temperature is estimated at 700−800 °C for the eclogite (Bröcker & Klemd, 1996) and 800−1000 °C for the granulite (Pouba *et al.*, 1985; Bakun-Czubarow, 1992; Steltenpohl *et al.*, 1993; Kryza *et al.*, 1996; Klemd & Bröcker, 1999; Štípská *et al.*, 2004; Bröcker *et al.*, 2010). The retrograde evolution in the eclogite is estimated to lie at 4−9 kbar and 550−650 °C (Bröcker & Klemd, 1996), and is also constrained by fluid inclusion study that shows isothermal decompression from 8 kbar to 3 kbar at 600 °C, followed by almost isobaric cooling to 200 °C (Klemd *et al.*, 1995). Retrogression in the granulite is estimated between 9.5−12.5 kbar at 560−680 °C (Steltenpohl *et al.*, 1993) and 10 kbar at 700−800 °C (Štípská *et al.*, 2004).

Lu−Hf ages on garnet and U−Pb zircon ages clustering between 360 and 380 Ma are reported, but their geological meaning is questioned in terms of incomplete resetting (Anczkiewicz *et al.*, 2007; Bröcker *et al.*, 2010). In contrast, Sm−Nd data on whole-rock and garnet, and U−Pb geochronology on zircon bracket the age of (U)HP metamorphism between 350 and 330 Ma (Brueckner *et al.*, 1991; Klemd & Bröcker, 1999; Štípská *et al.*, 2004; Lange *et al.*, 2005a; Bröcker *et al.*, 2010). This is confirmed by the trace element characteristics of metamorphic zircon suggesting contemporaneous crystallization with garnet and indicating that zircon dates the (U)HP event and not a middle pressure overprint (Bröcker *et al.*, 2010). $^{40}Ar–^{39}Ar$ cooling ages range between 340 and 350 Ma around the Międzygórze eclogite belt (Schneider *et al.*, 2006; Bröcker *et al.*, 2009) and between 330 and 340 Ma around the granulite belt (Steltenpohl *et al.*, 1993; Schneider *et al.*, 2006; Bröcker *et al.*, 2009).

Metamorphic studies of metapelites in the OSD are commonly linked with deciphering the relationships between the structures and the degree of metamorphism (Jastrzębski, 2005; Mazur *et al.*, 2005; Murtezi, 2006; Jastrzębski, 2009; Skrzypek *et al.*, 2011b). The first record of prograde metamorphism is connected with the early shallow-dipping fabric (Skrzypek *et al.*, 2011b). Peak $P-T$ conditions subsequently attained in the superimposed subvertical fabric show a continuous increase from the chlorite to the kyanite zone from the W to the E of the dome. They are estimated at 5−9 kbar and 460−650 °C (Murtezi, 2006; Jastrzębski, 2009; Skrzypek *et al.*, 2011a; Skrzypek *et al.*, 2011b). Decompression to 2−3.5 kbar at 530−600 °C is connected with a late shallow-dipping and heterogeneously developed foliation (Skrzypek *et al.*, 2011b). The peak metamorphism is associated with a Sm−Nd garnet−whole-rock age of 346.5 ± 4.4 Ma for a Stronie micaschist (Jastrzębski, 2009).

In the orthogneisses around eclogite, the composition of phengitic muscovite reported by Bröcker *et al.* (2009) suggests high-pressure metamorphism. Based on garnet−zoisite−titanite−rutile−quartz thermobarometry, Bröcker & Klemd (1996) proposed ultra-high pressure metamorphism around 28 kbar. Close to the Międzygórze eclogite belt, the age of metamorphism is constrained as Carboniferous based on zircon overgrowths in the fine-grained felsic orthogneiss (342±6 Ma, Turniak *et al.*, 2000), or by leucosomes in migmatite around granulite (330−355 Ma, Štípská *et al.*, 2004; Lange *et al.*, 2005a; Lange *et al.*, 2005b; Anczkiewicz *et al.*, 2007; Bröcker *et al.*, 2009).

STRUCTURAL GEOLOGY

Structure was studied in the area of the Międzygórze eclogite belt, in the surrounding felsic orthogneiss, and to the east in the Stronie metasedimentary formation (Fig. 2). Major structural patterns are shown in the map (Fig. 2), in an interpretative profile (Fig. 3) and documented in Figs 4 & 5.

D1 deformation

The earliest structure is a shallow-dipping foliation S1 that is characterized in the felsic orthogneiss by a deformation gradient ranging from a weakly deformed coarse-grained granite, through an augen and a banded felsic orthogneiss to a fine-grained felsic orthogneiss (Fig. 4a, b). In the augen and banded varieties, the subhorizontal S1 foliation bears a N−S trending subhorizontal L1 lineation. The foliation and the lineation are well defined by almost monomineralic recrystallized augen and layers of quartz, plagioclase and K-feldspar, and by the preferred orientation of biotite and muscovite (Fig. 4b). In the fine-grained felsic orthogneiss, the S1 foliation is defined by biotite and/or muscovite and by rare thin monomineralic recrystallized layers of K-feldspar or quartz, although the majority of quartz and feldspar grains is randomly distributed and forms a fine-grained matrix.

The fine-grained felsic orthogneiss occurs in zones of variable thickness, ranging from several centimetres up to several tens of meters, and is volumetrically more abundant in a 2–3 km wide belt around the eclogite (Figs 2 & 3). Approximately 2 km to the east of the eclogite belt, the felsic augen orthogneiss with rare banded varieties occurs. In this area, the S1 foliation in the augen felsic orthogneiss is commonly very weak and ill-defined by oriented biotite and recrystallized quartz ribbons. However, the N−S trending L1 lineation is strong and marked by elongated rods of recrystallized quartz, K-feldspar and plagioclase. To the west of the eclogite belt, the majority of the felsic orthogneiss is banded, with subordinate augen and fine-grained orthogneiss types.

In a 2 km wide area to the west of the eclogite near Międzygórze, the S1 foliation is folded by metre-scale N-verging open folds with subvertical short limbs and long limbs gently dipping to the south (Fig. 5a–e, these folds are not represented in Fig. 3). Close to isoclinal folds also occur locally. The short limbs of the N-verging folds are in places affected by tensional

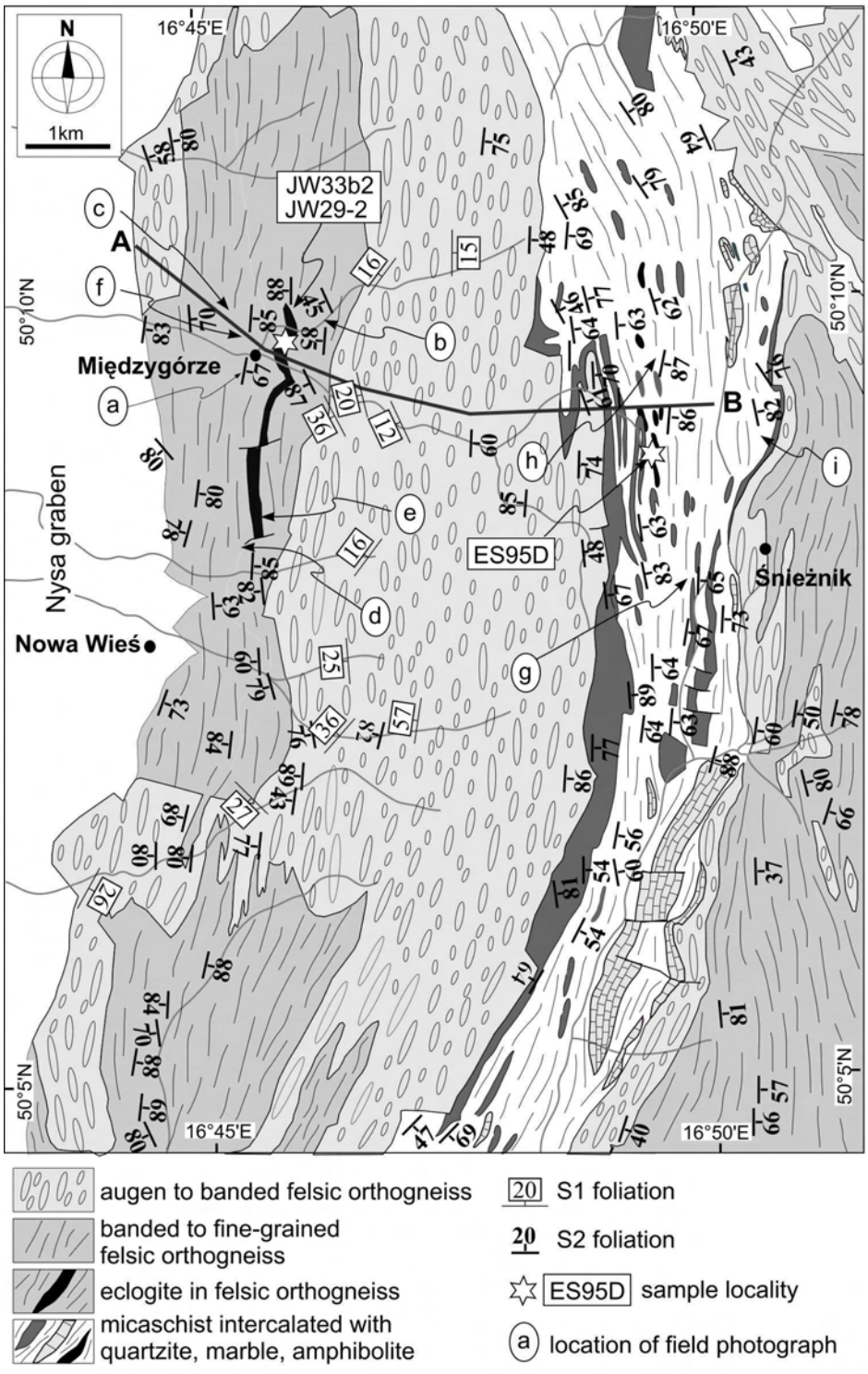

Fig. 2. Structural map of S1 and S2 foliations. Location of structural profile (Fig. 3), field photographs (Fig. 4) and samples used for petrology are indicated. Lithological map is after Don *et al.* (2003).

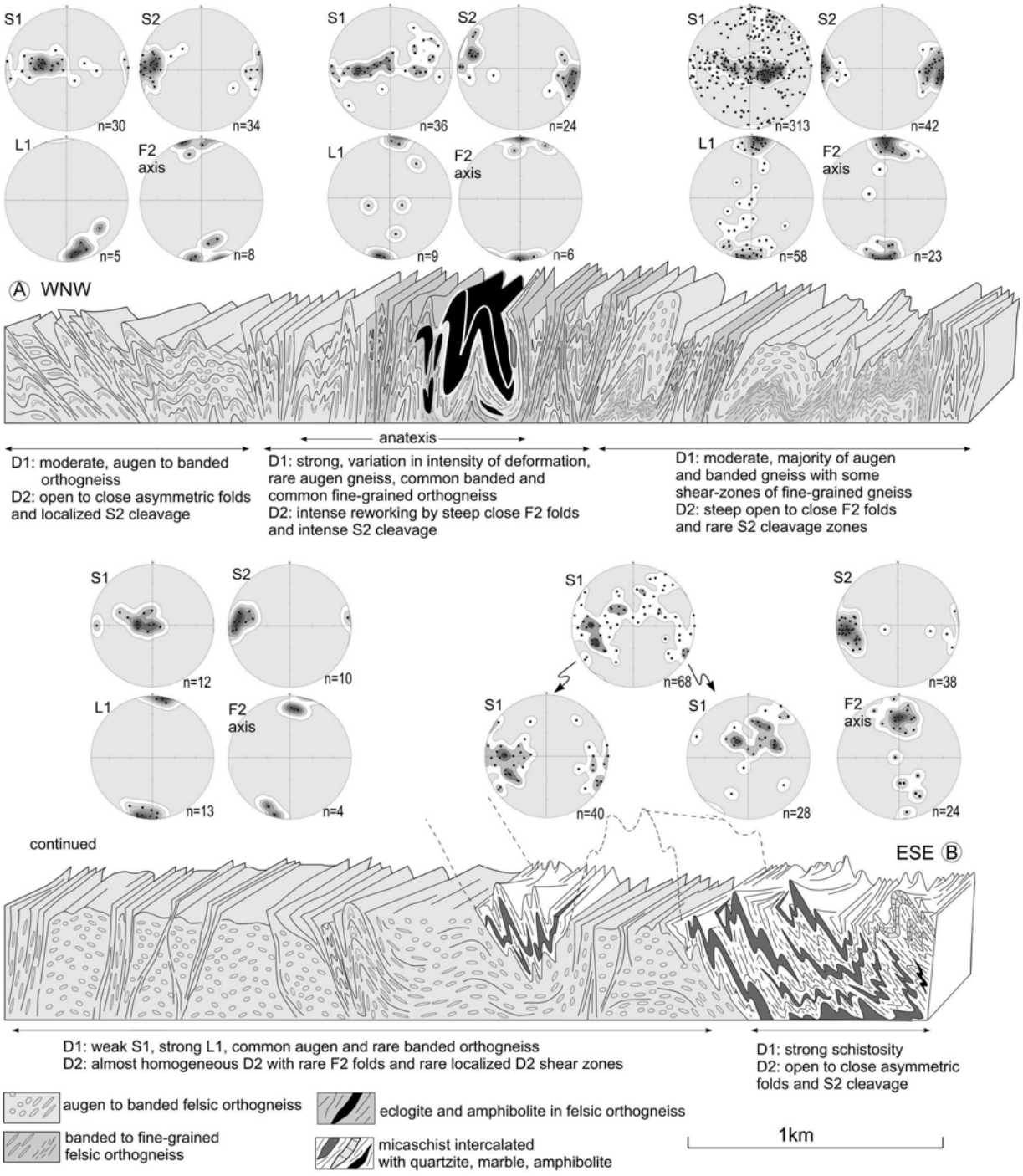

Fig. 3. Interpretative geological cross-section showing early shallow-dipping fabric S1 and style of superimposed subvertical deformation D2 in individual parts of the studied profile. Structures associated with the S1 foliation and late D3 structures are not shown (for these structures see Figs 4 & 5). Equal-area, lower-hemisphere stereoplots show D1 and D2 planar and linear structures. Vertical axis not to scale.

gashes filled with quartz (Fig. 5b) and by an axial planar cleavage. Fold hinges are oriented E−W or SE−NW in the open to close folds, and tend to be oriented SE−NW to N−S in the close to

isoclinal folds. The folds described above are attributed to the D1 deformation where the open asymmetric folds are interpreted in terms of moderate folding of a highly anisotropic multilayer system represented by the banded and the mylonitic felsic orthogneisses in a bulk simple shear (e.g. Grocott & Watterson, 1980; Skjernaa, 1980). In such a system, the fold hinges of the progressively attenuated folds rotate towards maximum stretching direction leading to the development of the close to isoclinal folds with fold hinges parallel to the stretching lineation, the so-called sheath folds (Cobbold & Quinquis, 1980).

In the eclogite, there are no common outcrop-scale remnants of the shallow-dipping S1 foliation. An area several tens of centimetres large of the shallow-dipping S1 foliation affected by the subvertical S2 crenulation cleavage (eclogite sample JW33b2) (Fig. 5g) was found at one place only.

In the Stronie metasedimentary belt, the S1 foliation is defined by an alternation of quartzite, garnet- and garnet−staurolite-bearing micaschist, marble and amphibolite, and by the orientation of micas and quartz ribbons in the micaschist and quartzite. Because of the strong intensity of the subsequent D2 reworking, the orientation of the S1 foliation cannot be constrained precisely. However, the F2 fold axes are variably plunging either to the north or to the south (Fig. 2b), which suggests that before the D2 deformation, the S1 foliation was probably affected by late-stage F1 folding characterised by E–W trending hinges and variably north- or south-dipping fold limbs. This is similar to the above-described behaviour in the felsic orthogneiss located to the west of the eclogite.

D2 deformation

In the felsic orthogneiss, where the D1 deformation led to development of the fine-grained and the banded orthogneiss varieties, the shallow-dipping S1 foliation is affected by upright metre- to several-metre-scale folding (Figs 4c & 5f–h). The folds are open to isoclinal, with subhorizontal N−S trending hinges and subvertical N−S striking axial planes. An axial plane cleavage is usually developed within the fold hinges, commonly showing almost complete transposition into the S2 foliation. The limbs of the tight to isoclinal folds show further attenuation, visible on the more flattened form of the augen and bands of recrystallized K-feldspar, compared to the hinge zone. In the areas with abundant N-vergent F1 folds, the steep N- or S-dipping limbs are also refolded by the F2 folds that have upright hinges and N−S striking vertical axial planes (Fig. 5d). Locally, the S1 foliation is crosscut by localized, several centimetres up to several metres wide subvertical N−S trending D2 shear zones. These shear zones show a sharp deformation gradient from the banded or augen felsic orthogneiss to the fine-grained felsic orthogneiss in the core of the shear zone. The S2 foliation in the felsic orthogneiss around the eclogite belt and especially to the west of the eclogite has commonly a migmatitic appearance, which is mostly visible from diffuse boundaries of the individual recrystallized bands and from the presence of quartz and plagioclase within the originally monomineralic K-feldspar layers. The migmatitic character is confirmed by the presence of centimetre-scale zones of fine-grained, macroscopically isotropic granite that occurs within the subvertical S2 cleavage (Fig. 4c).

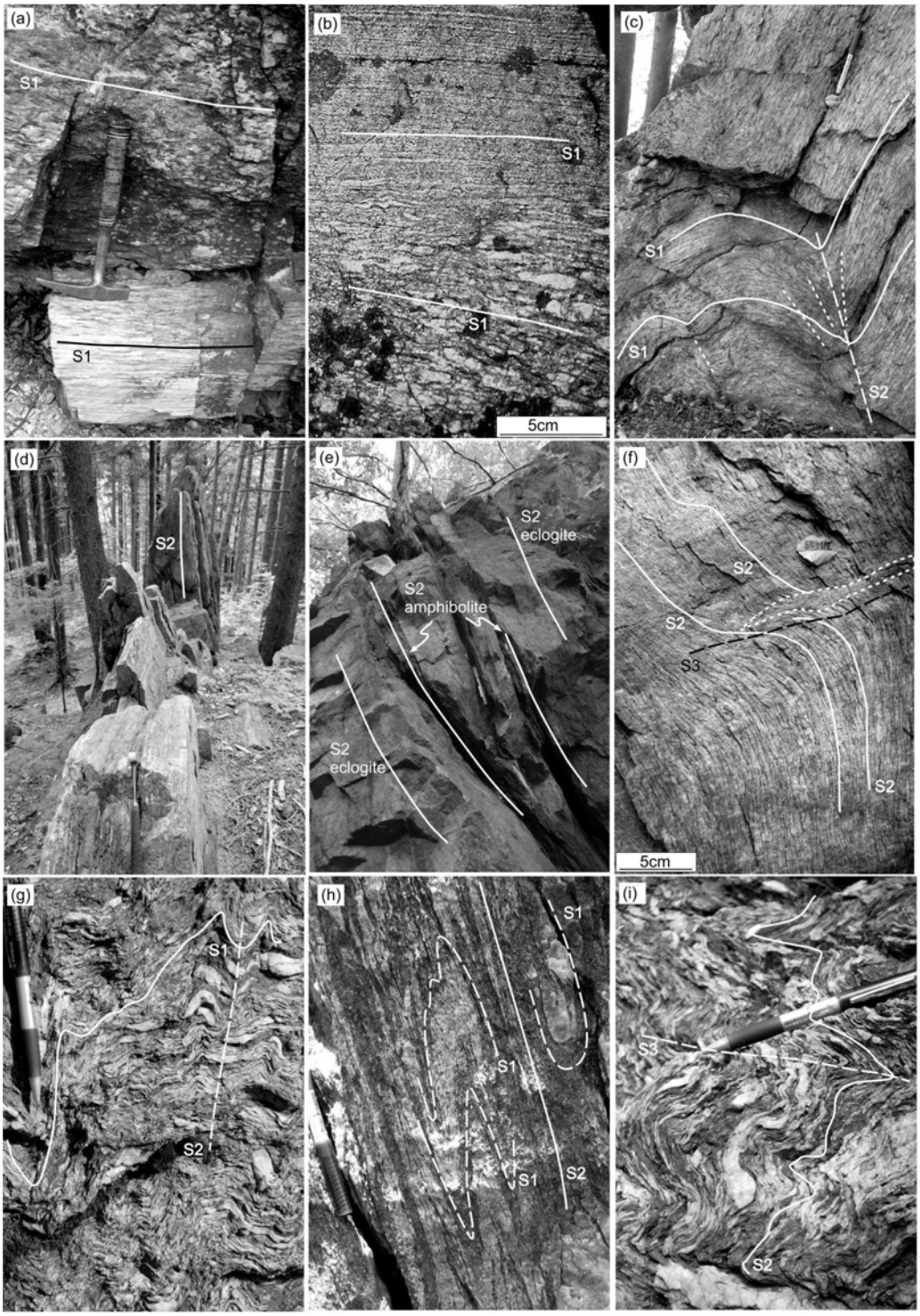

Fig. 4. Field photographs illustrating typical structural relationships. (a) Shallow-dipping foliation S1 in felsic orthogneiss showing deformational gradient from augen to banded variety. (b) Detail of shallow-dipping foliation S1 in the felsic orthogneiss with deformational gradient from augen to fine-grained variety. (c) S1 foliation of the banded felsic orthogneiss folded by upright open F2 folds. Melt-filled cleavage is subparallel to the axial plane (dashed lines). (d) Subvertical foliation S2 in the felsic orthogneiss. (e) Subvertical eclogite facies foliation S2 and amphibolite facies shear zones in the eclogite. (f) Subvertical foliation S2 in the banded felsic orthogneiss affected by S3 melt-filled shear zone (white dashed line). (g) Shallow-dipping S1 foliation in Stronie metasediments (highlighted by quartz bands) folded by open subvertical F2 folds. (h) S1 foliation in Stronie metasediments folded by close to isoclinal F2 folds leading to transposition into the subvertical S2 foliation. (i) Subvertical S2 foliation in Stronie metasediments affected by recumbent F3 folding.

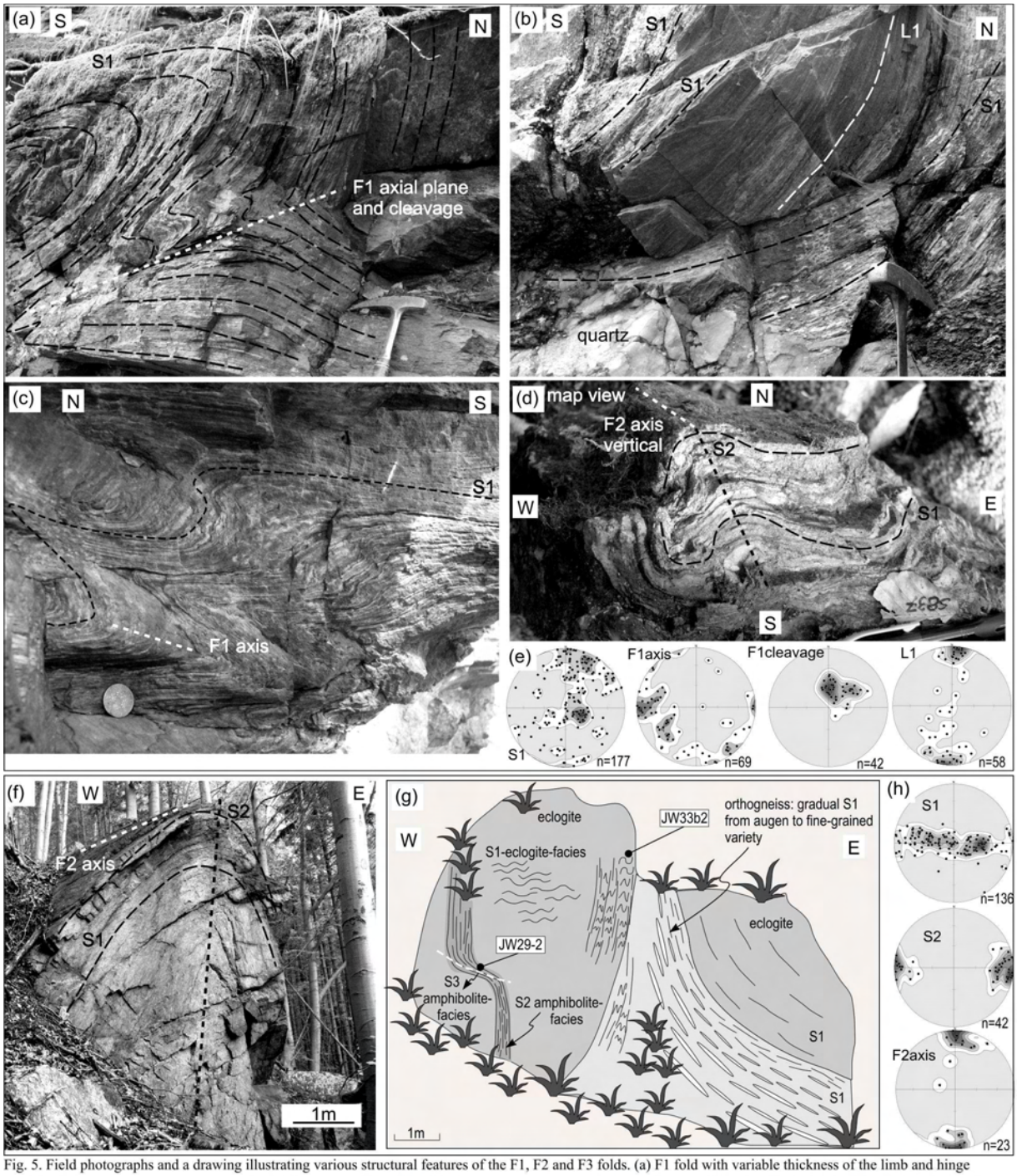

Fig. 5. Field photographs and a drawing illustrating various structural features of the F1, F2 and F3 folds. (a) F1 fold with variable thickness of the limb and hinge region, shallowly S-dipping axial plane and cleavage and E−W trending subhorizontal axis. Asymmetry marked by long S-dipping limb and short vertical or steeply S-dipping limb indicate N-directed movement. (b) Detail of the F1 fold showing short steeply-dipping limb that bears steepened L1 lineation. Short limb is gashed with the discontinuity filled by quartz. (c) Domain of the S1 foliation with close to isoclinal F1 folds showing E−W trending axis and variable thickness in the hinge and limb regions. (d) Short subvertical limb of the F1 fold is folded by open F2 folds with subvertical N−S trending axial plane. (e) Equal-area, lower-hemisphere stereoplots show D1 planar and linear structures in a domain affected by F1 folds (E of the eclogite). (f) Upright F2 fold with horizontal N−S trending axis affects the banded foliation S1 in the felsic felsic orthogneiss. (g) Field sketch showing relations of D1, D2 and D3 in the eclogite and surrounding felsic orthogneiss and sample position. (h) Equal-area, lower-hemisphere stereoplots show D1 and D2 planar and linear structures in an area strongly affected by F2 folds (around and E of the eclogite).

The F2 folding and foliation transposition into the S2 fabric is very intense in an about 2–3 km wide belt around the eclogite, leading to mostly vertical orientation of the foliations in the

field (Fig. 4d, e). To the west of the eclogite belt, the folds are open to close and overturned to the west, whereas to the east, the folds are open to close with subvertical axial planes. Further east, where augen felsic orthogneiss with very a weak S1 foliation and prolate deformation dominates, the D2 deformation can be recognized locally as millimetre-scale crenulations of S1 quartz ribbons or feldspar augen. It is suggested that the D2 deformation in this area is globally homogeneous, and leads to an intensification of the linear appearance of the augen orthogneiss. Heterogeneous N−S striking subvertical shear zones marked by the presence of the banded to fine-grained felsic orthogneiss are locally developed.

The eclogite outcrops show generally a steeply-dipping eclogite facies S1 foliation (Fig. 5e). The subvertical eclogite foliation is crosscut by amphibolite facies fractures and affected by centimetre-scale subvertical garnet-free amphibolite facies S2 zones. Meter- to several-metre-scale bodies of amphibolite with the subvertical S2 foliation occur also around the eclogite belt within the orthogneiss.

In the Stronie metasedimentary belt, F2 folds have steep east-dipping axial planes and N−S trending fold hinges that are variably (25−65°) plunging to the north or to the south. The folds are locally open, but more commonly close to isoclinal (Fig. 4g,h), ranging from metre-scale folds to millimetre-scale crenulations. In the micaschist, the D2 deformation leads to an almost complete transposition into the S2 foliation that contains rootless F2 folds defined by quartz ribbons or quartz-rich layers (Fig. 4h).

D3 deformation

Open metre- to several-metre-scale recumbent F3 folds with subhorizontal axial planes and N−S trending hinges are locally developed in the areas where the felsic orthogneiss displays an intense subvertical foliation. Shallow-dipping centimetre-scale S3 shear zones, marked by the banded or fine-grained orthogneiss variety are rarely localized in one of the limbs of the F3 folds or are crosscutting the subvertical S2 foliation. In the vicinity of the eclogite and in the area to the west of the eclogite, the D3 shear zones in the felsic orthogneiss are filled by isotropic fine-grained granite (Fig. 4f).

Rare open F3 folds also affect the subvertical foliation in the eclogite and the steep zones of S2 amphibolite facies foliation within the eclogite. The areas of S2 amphibolite facies foliation are rarely affected by localized centimetre-scale shallow-dipping S3 shear zones (eclogite-amphibolite sample JW29-2) (Fig. 5g).

In the Stronie metasedimentary belt, rare open to close F3 folds with subhorizontal axial planes and N−S trending subhorizontal hinges occur (Fig. 4i). This weak folding produces crenulations on the S2 planes defining a subhorizontal L3 lineation.

PETROLOGY

In order to assign $P-T$ conditions to the observed structures, oriented eclogite and metapelite samples with the S1, S2 and S3 foliations were studied.

Analytical procedures and abbreviations

Whole-rock analyses were preformed in the Acme laboratories, Canada. Mineral analyses were performed on a scanning electron microscope VEGA\\XMU at the Strasbourg University in point beam mode at 15 kV and 10 nA.

Petrography is documented in Figs 6 & 7, representative mineral analyses are summarized in Tables 1−3, and mineral chemistry is shown in Fig 8. The sign "=>" is used for a trend in mineral composition or for zoning and the sign "–" for a range of mineral compositions; p.f.u. = per formula unit. For amphibole, the variables and isopleths notations are used as in Dale *et al.* (2005) and Diener *et al.* (2007) in order to compare the chemical variability of amphibole with isopleths in pseudosections.

Mineral abbreviations: g=garnet, cpx=diopsidic clinopyroxene, o=omphacitic clinopyroxene, am=amphibole, hb=hornblende, act=actinolite, gl=glaucophane, ep=epidote, chl=chlorite, mu=muscovite, pl=plagioclase, q=quartz, ilm=ilmenite, ru=rutile, sph=sphene, mt=magnetite, bi=biotite, pa=paragonite, ky=kyanite, sill=sillimanite, and=andalusite, cd=cordierite, st=staurolite, ksp=K-feldspar; garnet: alm=Fe/(Ca + Fe + Mg + Mn), prp=Mg/(Ca + Fe + Mg + Mn), grs=Ca/(Ca + Fe + Mg + Mn), sps=Mn/(Ca + Fe + Mg + Mn), XFe=Fe/(Fe + Mg); plagioclase: an=Ca/(Ca + Na + K), ab=Na/(Ca + Na + K); clinopyroxene: jd=Na/(Na + Ca); amphibole: Z=xNa(M4)=Na(M4)/2, Y=xAl(M2)=Al^{VI}/2, A=xNa(A)=Na(A), C=xCa(M4)=Ca/2.

The isopleth notation used in the NCKFMASHTO system is: *x*(g, cpx)=Fe/(Fe+Mg), *z*(g)=Ca/(Ca+Fe+Mg)*100, *j*(cpx)=Na/(Na+Ca)*100, *z*(am)=xNa(M4)=Na(M4)/2*100, *y*(am)=xAl(M2)=Al^{VI}/2*100, *a*(am)=xNa(A)=Na(A)*100, Na(mu)=Na/(Na+K), y(mu)=4-Al^{IV}. The isopleth notation used in the MnNCKFMASHTO system is: *x*(g)=Fe/(Ca+Fe+Mg+Mn)*100, *z*(g)=Ca/(Ca+Fe+Mg+Mn)*100, *m*(g)=Mn/(Ca+Fe+Mg+Mn)*100, *x*(st)=Fe/(Fe+Mg)*100.

Eclogite and amphibolitized eclogite

The major eclogite type in the area of Międzygórze is composed of garnet (30−50 vol.%), omphacite (40−50 vol.%), epidote (0−8 vol.%), accessory muscovite, rutile, kyanite and quartz.

The shallow-dipping foliation S1 is defined by garnet-rich and omphacite-rich layers, elongated quartz ribbons, chains of rutile grains and by omphacite and muscovite preferred orientation (Fig. 6a, sample JW33b2). Some epidote commonly occurs in the matrix. The S1 foliation is folded by open millimetre-scale upright crenulation folds (Fig. 6a, sample JW33b2).

The dominant vertical foliation S2 in the eclogite is defined by the same features as the S1 foliation (Fig. 6b). The vertical amphibolite facies zones D2 are composed of preferentially oriented amphibole, biotite and elongated aggregates of sphene surrounding ilmenite, with rutile locally preserved in the central area (Fig. 6c). Plagioclase is scattered in the matrix or forms plagioclase-rich layers. Brittle cracks affecting the eclogite are filled with amphibole, plagioclase, biotite and ilmenite, indicating amphibolite facies conditions (Fig. 6b).

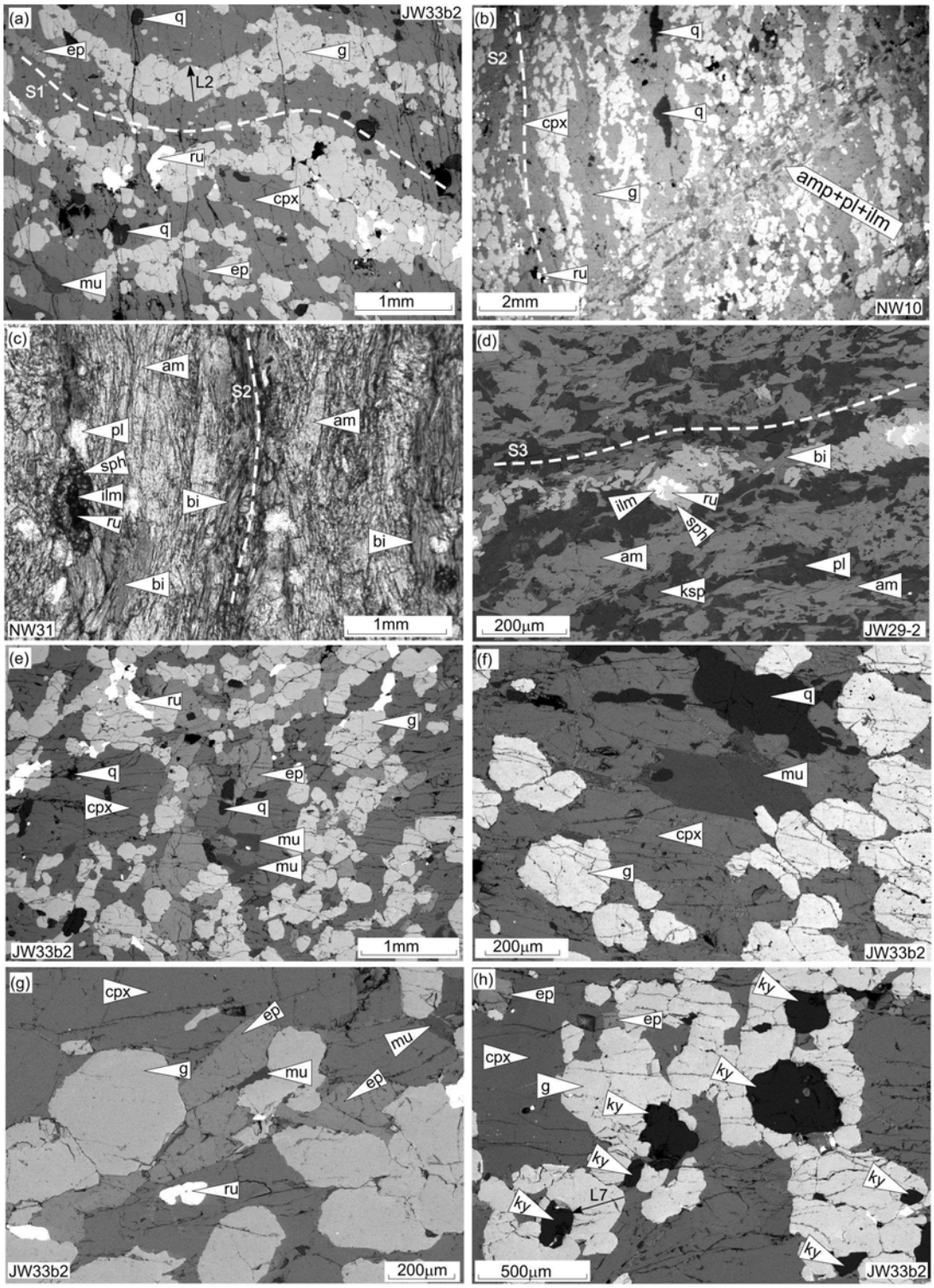

Fig. 6. Photomicrographs (plane-polarized light and BSE) of eclogite and amphibolitized eclogite showing relation of structure and mineral assemblage (a–d) and textural details of the eclogite sample JW33b2 (e–h). (a) S1 shallow-dipping foliation folded by F2 open folds. S1 defined by alternation of garnet- and clinopyroxene-rich bands. Black arrow indicates the profile in Fig. 8. (b) Subvertical S2 foliation marked by alternation of garnet- and clinopyroxene-rich bands affected by amphibolite facies fractures. (c) Subvertical S2 foliation defined by preferred orientation of amphibole, biotite, and elongated aggregates of ilmenite surrounded by sphene. (d) Attenuated limb of the F3 fold (see Fig. 5g) indicates activity of the D3 deformation, with S3 foliation marked mainly by oriented amphibole, biotite and chains of elongated aggregates of sphene. (e) Detail of matrix formed by g-cpx-ep-ru-q. (f) Clinopyroxene and muscovite oriented parallel to shallow-dipping S1 foliation. (g) Detail of epidote having net boundaries with respect to garnet, pyroxene and rutile. (h) Kyanite surrounded by coronas of garnet. Black arrow indicates profile in Fig. 8b.

The rare shallow-dipping shear-zones S3 affecting the vertical amphibolite facies foliation S2 are composed of oriented amphibole, biotite, chains of sphene aggregates located around ilmenite and rutile, and of feldspar-rich bands (Fig. 6d). Aggregates rich in chlorite and K-feldspar with some magnetite or chlorite replacing biotite occur locally within the S3 foliation.

Eclogite sample JW33b2

The mineral assemblage is formed by garnet (40%), omphacite (45%), epidote (3%), accessory muscovite, rutile, quartz and kyanite (Figs 6a, e−h). All minerals occur within the shallow-dipping foliation S1 (Figs 5g & 6a). Epidote is randomly distributed within the matrix, with areas that are richer, and areas that are almost free of epidote (Figs 6e−g). Kyanite is commonly surrounded by garnet but contacts with matrix minerals also occur (Fig. 6h).

The grossular content of zoned garnet in the matrix increases from around 26 mol.% in the core ($alm_{0.35}py_{0.37}grs_{0.26}sps_{0.01}$, XFe=0.47), to 29 mol.% ($alm_{0.34}py_{0.36}grs_{0.29}sps_{0.01}$, XFe=0.49) and decreases to 25−22 mol.% at the rim ($alm_{0.37}py_{0.39}grs_{0.23}sps_{0.01}$, XFe=0.48) (Fig. 8a). The zoning is asymmetric in garnet that occurs around kyanite, with core region next to kyanite and rim next to the matrix (Fig. 8b). The majority of garnet lacks the low grossular core, and has a flat profile with a composition that corresponds to the grossular peak ($alm_{0.34-36}py_{0.36-37}grs_{0.28-29}sps_{0.01}$, XFe=0.47−49) and lower grossular rims (Fig. 8c). Muscovite has Si=3.26−3.31 p.f.u. and Na=0.05−0.12 p.f.u. Clinopyroxene is omphacite with 33−36 mol.% of jadeite, up to 3 mol.% of Ca-tschermak component, and XFe=0.12−0.16. Epidote has Fe^{3+} content between 0.05−0.10 p.f.u.

Amphibolitized eclogite JW29-2

Amphibolitized eclogite sample JW29-2 was collected on the same outcrop as the eclogite sample JW33b2. It is located within the steeply-dipping amphibolite facies shear zone S2 that affects the eclogite, and that is further folded by open F3 folds. The sample is taken from an attenuated limb of the F3 fold (Fig. 5g). It contains amphibole, biotite, plagioclase, sphene, ilmenite, rutile, chlorite, K-feldspar and magnetite. Amphibole is elongated parallel to the S2 foliation and is associated with aggregates of preferentially oriented biotite. Plagioclase grains are disseminated in plagioclase-rich layers, and occasionally are associated with K-feldspar. Sphene is commonly arranged in chains parallel to the foliation, it occurs in form of elongated aggregates that surround ilmenite, which have in places rutile in the core. Aggregates with chlorite associated with K-feldspar and magnetite, and chlorite replacing biotite occur locally. Samples taken next to JW29-2 in the amphibolite facies S2 foliation that is not affected by the F3 folding are composed of amphibole, plagioclase, biotite and elongated sphene and ilmenite surrounding rutile, preferentially arranged in the S2 foliation.

Amphibole composition in the sample JW29-2 vary between tschermakitic hornblende and hornblende (Na(M4)=0.12−0.26, $Al^{IV=}$0.9−1.7, XFe=0.25−0.36, Y=Al^{VI}/2=0.45−0.79, Z=Na(M4)/2=0.06−0.13, C=Ca/2=0.85−0.92, A=Na(A)=0.04−0.15) (Fig. 8). Biotite chemistry

shows XFe=0.43−0.46 and Ti=1.64−2.23 p.f.u. The anorthite content of plagioclase varies generally between 30 mol.% and 50 mol.%. However, plagioclase with lower anorthite content (up to an=0) is locally associated with chlorite.

Metapelites

The S1 metamorphic layering is preserved rarely in the form of close to isoclinally folded alternation of quartz- and muscovite-rich bands (Fig. 7a). Discontinuous layers rich in garnet and staurolite following the S1 foliation are commonly observed (Fig. 7a). Garnet (1−2 mm) and staurolite (up to 1 mm) show inclusion trails parallel to the S1 foliation and containing quartz and ilmenite, with some minute crystals of staurolite in garnet. In places, larger staurolite grains are included at the outer rim of garnet porphyroblasts that show S1 inclusion trails oblique to the S2 cleavage (Fig. 7b). Biotite parallel to the S1 foliation is scarce.

The S2 fabric ranges from a weak spaced cleavage to a continuous metamorphic schistosity (Fig. 7b). Biotite (0.5 mm) shows preferential orientation parallel to the S2 axial plane cleavage and is more abundant than in the S1 fabric. Garnet with straight to weakly crenulated inclusion trails of the S1 fabric is overgrown by garnet with ilmenite inclusions continuous with the external S2 foliation (Fig. 7c, e). Staurolite porphyroblasts with S1 inclusion trails are in places overgrown by rims with ilmenite inclusions parallel to the matrix S2 foliation (Fig. 7d). Some samples exhibit widespread chlorite parallel to the S2 fabric (Fig. 7e). Some chlorite aggregates show sharp contact with garnet rims, but clearly replace staurolite (Fig. 7d, e). Chlorite occurs also in the axial plane of the F3 microfolds (areas highlighted in Fig. 7f).

Metapelite sample ES95DI

Sample ES95DI was collected in the hinge of a F2 fold to study the relationship between crystallization and deformation and to assign $P-T$ conditions to the individual deformational phases. The sample contains garnet, staurolite, biotite, muscovite, quartz, few plagioclase and accessory ilmenite, tourmaline, chlorite and apatite. The matrix displays microfolded quartz- and muscovite-rich S1 bands and S2 cleavage that is marked mostly by oriented biotite. Garnet porphyroblasts (2−4 mm) host inclusions of quartz, ilmenite, tourmaline, rare muscovite and plagioclase, which are commonly oriented at high angle to the axial plane of the F2 microfolds (similarly as in Fig. 7a). A small curvature continuous with the external S2 foliation locally occurs at the rim. It is interpreted as garnet growth during or after the formation of the shallow-dipping S1 foliation with some garnet rims formed within the subvertical S2 fabric.

Garnet shows zoning with decreasing spessartine, grossular and XFe, and increasing pyrope and almandine from core to rim ($alm_{0.60 => 0.75}$ $py_{0.04 => 0.15}$ $grs_{0.17 => 0.08}$ $sps_{0.19 => 0.02}$, XFe=0.94 => 0.83) (Fig. 8d & Table 3). Small staurolite crystals are also partly enclosed by garnet rims. Staurolite (up to 1mm) is abundant in the matrix and includes quartz, ilmenite and tourmaline that are oriented at high angle to the external S2 fabric in the core and parallel to the S2 fabric at the rim (Fig. 7d). This is interpreted as syn- or post-D1 staurolite growth followed by

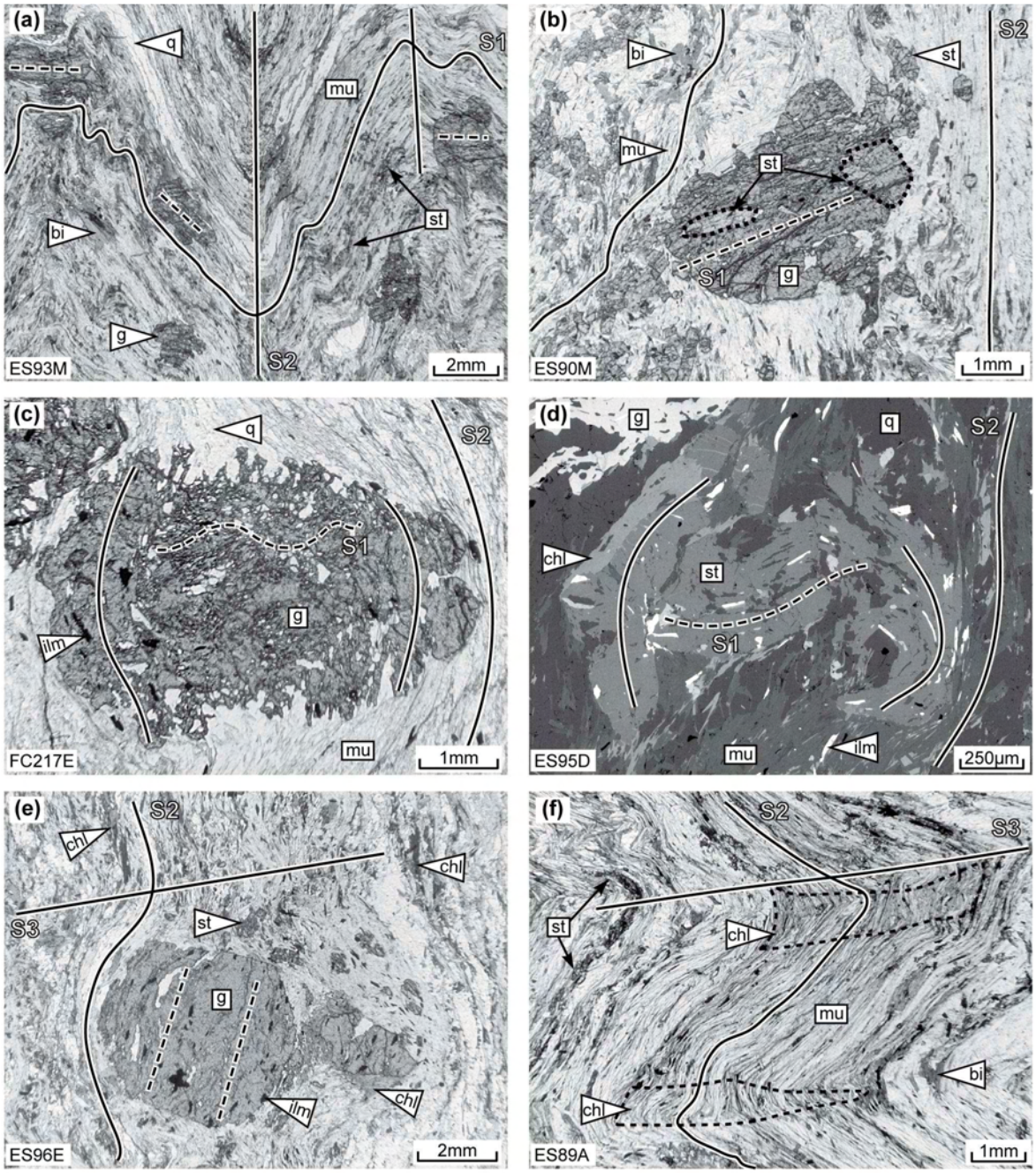

Fig. 7. Photomicrographs (plane-polarized light and BSE) of crystallization-deformation relationships in micaschists. (a) S1 foliation containing muscovite, quartz, biotite, garnet, and staurolite affected by F2 folds. (b) Garnet with staurolite inclusions (highlighted by dashed lines) and straight inclusion trails oriented oblique to the surrounding S2 foliation. (c) Garnet with quartz inclusion trails in the core marking crenulated S1 foliation and ilmenite inclusions at the rim, continuous with external S2 foliation. (d) Staurolite with quartz and ilmenite oriented at high angle to external S2 foliation in the core and subparallel at the rim. (e) Chlorite grows parallel to S2 foliation and rarely surrounds staurolite and garnet. (f) Domains rich in chlorite (highlighted by dashed lines) located in axial planes of F3 folds.

continuous growth during development of the subvertical S2 cleavage. Staurolite is not regularly zoned and its XFe varies between 0.82 and 0.86, Zn=0.07−0.14 p.f.u. and Ti=0.10−0.15 p.f.u. (Table 3). Rare plagioclase has an=0.15−0.19, biotite has XFe=0.53−0.55 and Ti=0.07−0.10 p.f.u. Chlorite (XFe=0.56−0.60) is found mostly around garnet and staurolite.

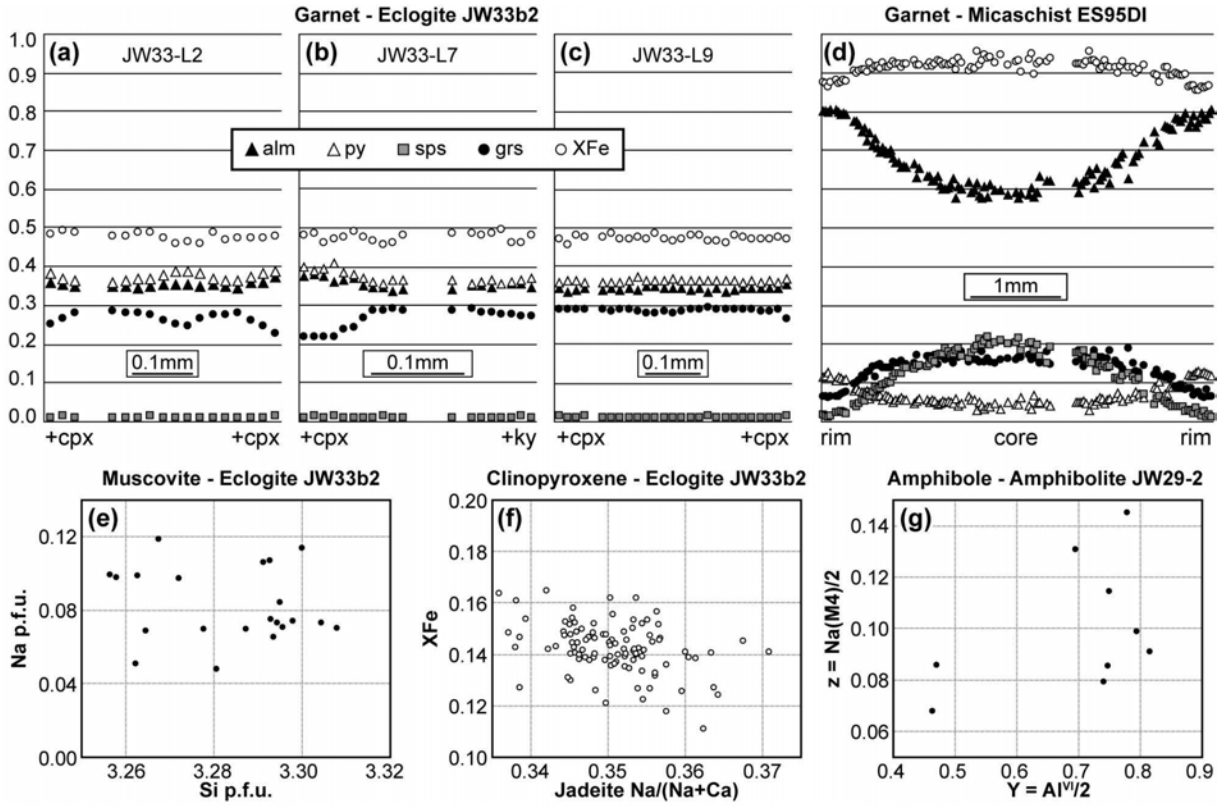

Fig. 8. Diagrams illustrating mineral chemistry in the eclogite, in the amphibolitized eclogite and in the micaschist. For details see text.

MINERAL EQUILIBRIA MODELLING

Calculation methods

Pseudosections were calculated using THERMOCALC 3.3 (Powell *et al.*, 1998, 2009 version) and the dataset 5.5 (Holland & Powell, 1998, November 2003 upgrade). The pseudosection for metabasic rocks (Fig. 9) is calculated in the model system Na_2O-CaO-K_2O-FeO-MgO-Al_2O_3-SiO_2-H_2O-TiO_2-O (NCKFMASHTO) with the amphibole model from Diener *et al.* (2007), clinopyroxene from Green *et al.* (2007), garnet from White *et al.* (2007) modified by Diener *et al.* (2008), feldspar from Holland & Powell (2003), paragonite-muscovite from Coggon & Holland (2002), chlorite from Holland *et al.* (1998), epidote from Holland & Powell (1998), ilmenite from White *et al.* (2000). The pseudosection for metapelite is calculated in the model system MnO-Na_2O-CaO-K_2O-FeO-MgO-Al_2O_3-SiO_2-H_2O-TiO_2-O (MnNCKFMASHTO) (Fig. 12). The activity-composition relationships for feldspars are from Holland & Powell (2003), white mica from Coggon & Holland (2002), silicate melt from White *et al.* (2007), epidote from Holland & Powell (1998), Mn-bearing models of staurolite, cordierite and chlorite from Mahar *et al.* (1997), Holland *et al.* (1998) and Holland & Powell (1998), and models of garnet, biotite and ilmenite as in White *et al.* (2005).

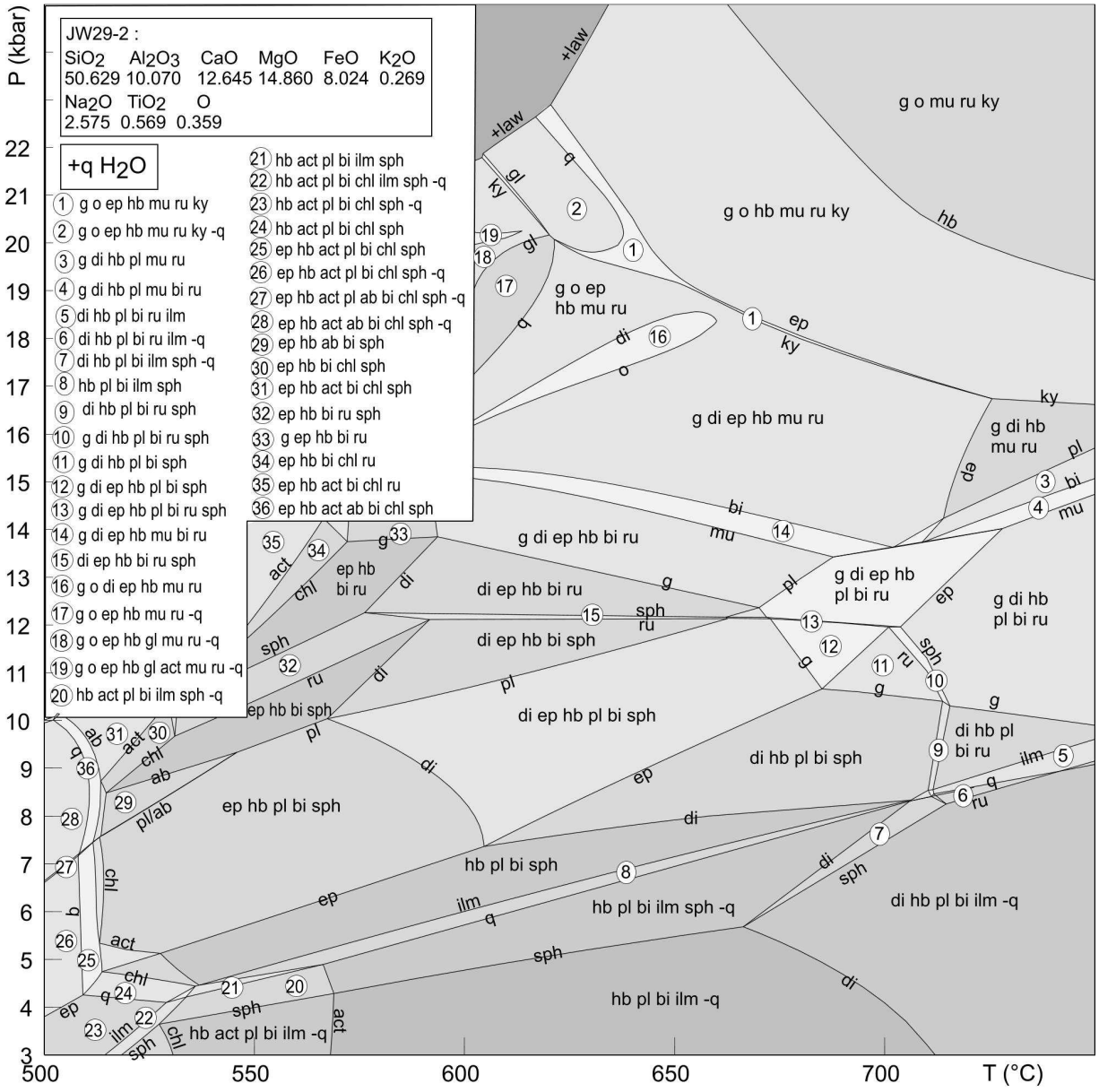

Fig. 9. Pseudosection calculated for the rock composition of the amphibolitized eclogite sample JW29-2 (NCKFMASHTO system, whole-rock composition in moles adjusted to 100%). $P-T$ range is chosen to discuss the high-pressure evolution and retrogression detailed in Figs 10 & 11. Abbreviations on field boundaries indicate the phase that is gained or lost on this transition.

Pseudosection for eclogite and amphibolitized eclogite

The H_2O-saturated pseudosection (Figs 9, 10 & 11) is calculated for the analyzed whole-rock composition of the sample JW29-2 that is an amphibolitized eclogite described above (in wt%: SiO_2=48.40, Al_2O_3=16.33, FeO=8.35, Fe_2O_3=0.90, MnO=0.16, MgO=9.53, CaO=11.28, Na_2O=2.54, K_2O=0.41, TiO_2=0.72, P_2O_5=0.01). This whole-rock composition is used also for discussion of the $P-T$ evolution of the studied eclogite sample JW33b2 with preserved S1 foliation, due to difficulty to sample this part of the outcrop, and for discussion of the $P-T$

evolution of the sample taken next to JW29-2 from the S2 foliation that is not affected by the F3 folding. Because the rock composition does not come from the same sample as the described thin sections of the eclogite and the amphibolite with the S2 foliation, the results should be taken only as a guide in determination of approximate *P–T* conditions, but should be able to allow discussion of the overall shape of the *P–T* path and of the relation of the *P−T* conditions to structural evolution. The pseudosection shows fields of mineral assemblages stable at eclogite and amphibolite facies conditions. The high-pressure and low-pressure parts of the pseudosection are contoured with the calculated compositional isopleths for muscovite, clinopyroxene, garnet, and amphibole (Figs 10 & 11) in order to discuss the high-pressure *P−T* evolution and the retrogression of the eclogite.

P−T evolution of the eclogite sample JW33b2

The minerals observed in the S1 foliation are garnet, omphacite, epidote, muscovite, quartz, rutile and kyanite. This assemblage is not stable in the pseudosection. The stability of epidote with kyanite is restricted to a very narrow field labeled 1, located between ~ 17 and 22 kbar. The calculated proportion of amphibole is between 20 and 40 mol.% in this field, which does not correlate with the absence of amphibole in the sample. The observed mineral compositions for garnet rim ($alm_{0.37}py_{0.39}grs_{0.22}sps_{0.01}$, XFe=0.47−0.49), muscovite (Si=3.26−3.31 p.f.u., Na=0.05−0.12 p.f.u.) and omphacite (jd=0.33−0.36, XFe=0.12−0.16) fit well to calculated compositional isopleths in the g−o−mu−ru−ky field that occurs in the high-pressure and high-temperature part of the diagram (Fig. 10a−f). Therefore, it is considered that some epidote persists metastably to higher pressure than predicted by the pseudosection, up to the amphibole-free field, and that peak conditions for the eclogite S1 foliation correspond to ~ 20−23 kbar and 700−750 °C (black circle labelled S1 in Fig. 10a−d).

Part of the prograde path may be discussed based on the garnet zoning and on the textural relation with respect to kyanite. Garnet that nucleated on kyanite has 26 mol.% of grossular at the boundary with kyanite, then grossular increases to 29 mol.% and again decreases to 22 mol.% at the rim. Such type of garnet zoning occurs in the pseudosection along a path that begins at the ky-in line and ends at the estimated peak *P−T* conditions, as indicated by the arrow in Figure 10d. Because this garnet is arranged in the garnet-rich bands parallel to the S1 foliation, this part of the prograde path from ~ 19.5 kbar and 640 °C to ~ 20−23 kbar and 700−750 °C is interpreted to occur during the development of the S1 fabric (black circles labelled S1 and the arrow in Fig. 10a−d).

P−T evolution of the amphibolitized eclogite sample JW29-2

The sample comprises amphibole, biotite, plagioclase, sphene, ilmenite, rutile, chlorite, K-feldspar and magnetite, quartz is absent. These minerals and the measured range of mineral compositions suggest a *P−T* path dominated by decompression under amphibolite and

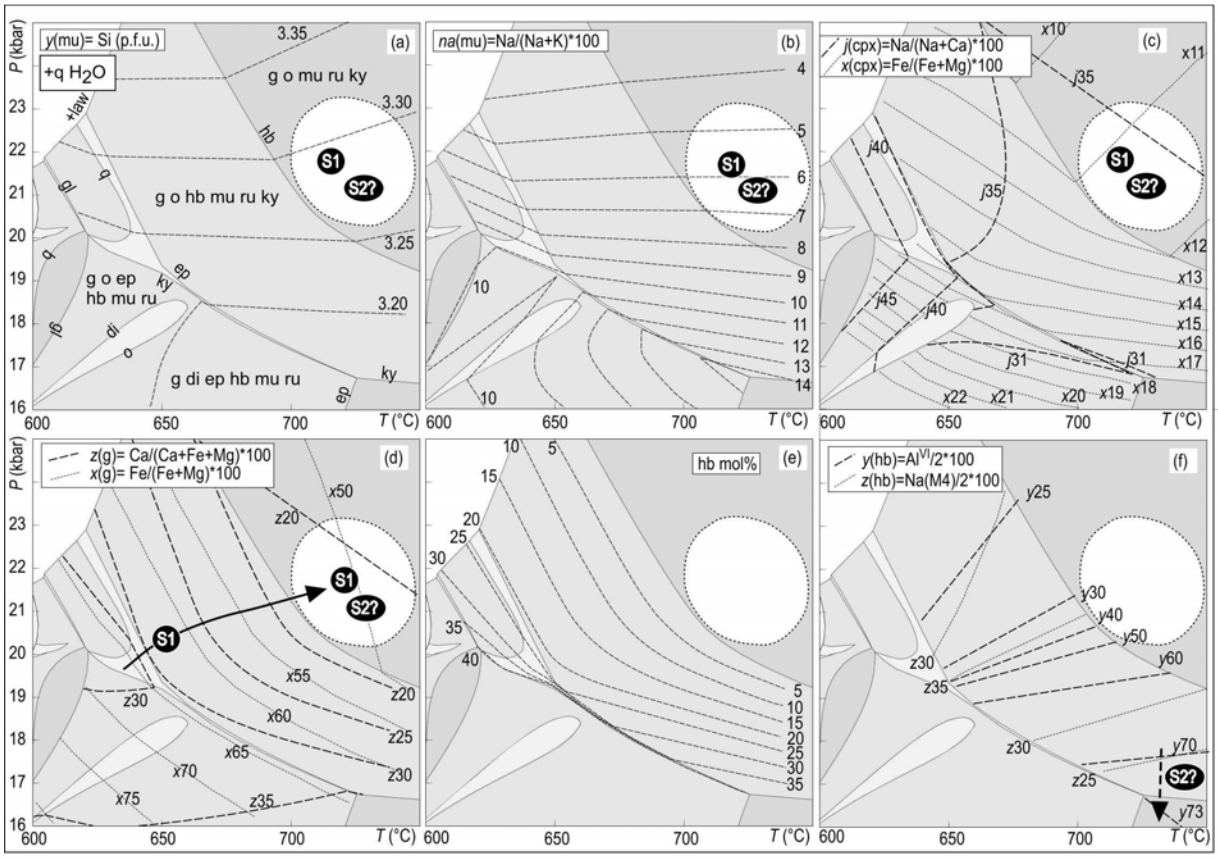

Fig. 10. (a−f) Enlarged and simplified high-pressure part of the pseudosection from Fig. 9. Pseudosections are contoured with calculated isopleths of mineral composition and molar proportions. Arrows and black circles indicate parts of *P–T* path and conditions of equilibration for individual structures, derived by comparing the modeled assemblages and isopleths with observed assemblages, chemistry and zoning of minerals. See text for details.

greenschist facies conditions. Absence of epidote indicates a path outside the stability of epidote, absence of muscovite and appearance of biotite indicate crossing the muscovite-out and biotite-in lines between ~ 700−750 °C and below 14−15 kbar. The overgrowth of sphene around ilmenite and rutile in the core indicates first nucleation of ilmenite on rutile and subsequent growth of sphene around ilmenite. Such succession occurs in the pseudosection along a path at temperature above ~ 720 °C, where the ilmenite-in line is crossed at about 9 kbar and sphene-in line is crossed during subsequent decrease of temperature at ~ 5−8 kbar and 660−710 °C (arrow in Fig. 11). The amphibole composition corresponding to tschermakitic hornblende and hornblende (XFe=25−36, Y=Al^{VI}/2=0.45−0.79, Z=Na(M4)/2=0.06−0.13) is in agreement with the calculated isopleths along the decompression path from about ~ 16 kbar and 700−750 °C (black circle labelled S2 and arrow in Fig. 10f) to the field hb−pl−bi−ilm−sph without quartz at ~ 4−7 kbar and 570−700 °C (Fig. 11b). The wide range of plagioclase compositions (from an=30 mol.% to an=50 mol.%) is in agreement with the modelled isopleths along the same decompression path (Fig. 11c). Plagioclase with lower anorthite content is locally associated with chlorite. XFe of biotite and amphibole closely fit the isopleths in the hb−pl−bi−ilm−sph field without quartz (Fig. 11c). Chlorite replacing biotite, aggregates of chlorite, K-feldspar and magnetite (not shown)

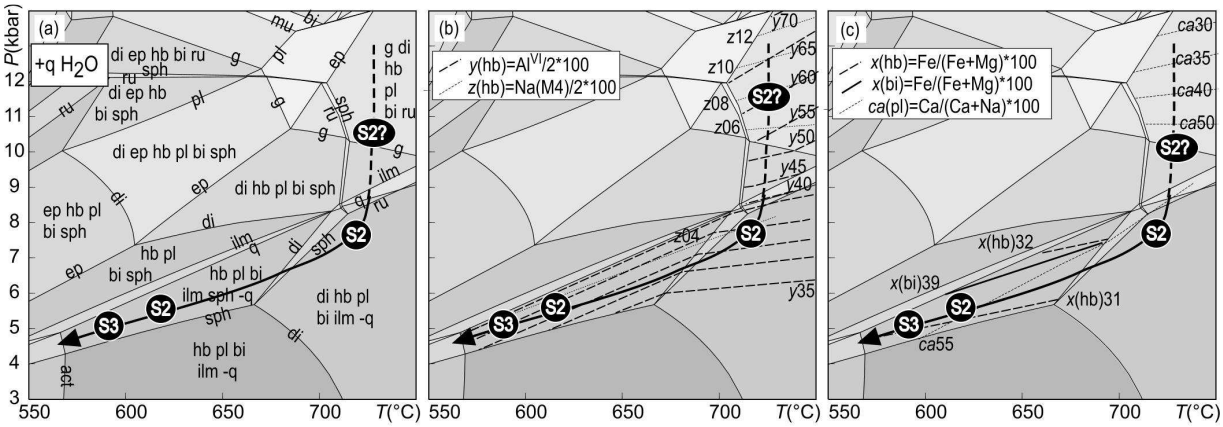

Fig. 11. Enlarged and simplified low-pressure part of the pseudosection from Fig. 9 contoured with calculated isopleths of mineral composition in the fields of interest. Arrows and black circles indicate parts of *P–T* path and conditions of equilibration for individual structures, derived by comparing the modeled assemblages and isopleths with observed assemblages and chemistry of minerals. See text for details.

together with the local presence of albite are interpreted as inhomogeneous greenschist facies retrogression at lower temperature then the *P*−*T* range of the pseudosection.

The inferred *P*−*T* path is also related to the structure development (black circles labelled S2 and S3 in Fig 11). Tschermakitic hornblende and plagioclase with an=30−50 mol.% are interpreted as phases that may be associated with the development of the subvertical amphibole-bearing fabric S2 associated with the decompression from 16 kbar to ~ 7 kbar at 700−750 °C. However, the first clear microstructural indication that the steeply-dipping foliation was mechanically active during D2 is the growth of elongated aggregates of ilmenite and sphene around rutile in the samples that are not affected by the D3 foliation (several centimetres next to the sample JW29-2). Sphene started to grow still during the formation of the S2 fabric, which is correlated with the hb−pl−bi−ilm−sph field without quartz that occurs at ~ 5−7 kbar and 560−700 °C. The S3 foliation represented by incomplete fabric transposition in the small scale shear zone (Fig. 5g) is correlated also with the hb−pl−bi−ilm−sph field without quartz, with amphibole compositions that correspond to hornblende s.s., plagioclase with an=50 mol.%, together with XFe of the biotite and hornblende (Fig. 11). The *P*−*T* conditions for the beginning of the S3 fabric are thus estimated to ~ 5 kbar and 600 °C. The presence of the domains with K-feldspar, chlorite, albite and magnetite suggests that the S3 fabric was mechanically active also under greenschist facies conditions.

Pseudosection for metapelite sample ES95D

The pseudosection (Fig. 12) is calculated for the analyzed whole-rock composition of the sample ES95D (in wt%: SiO_2=65.87, TiO_2=0.84, Al_2O_3=17.05, Fe_2O_3=7.03, MnO=0.08, MgO=2.09, CaO=0.64, Na_2O=1.01, K_2O=3.69, P_2O_5=0.34) with quartz, muscovite and H_2O in excess. The pseudosection is contoured with the calculated compositional isopleths for garnet and staurolite in order to discuss the *P*−*T* evolution of the metapelite.

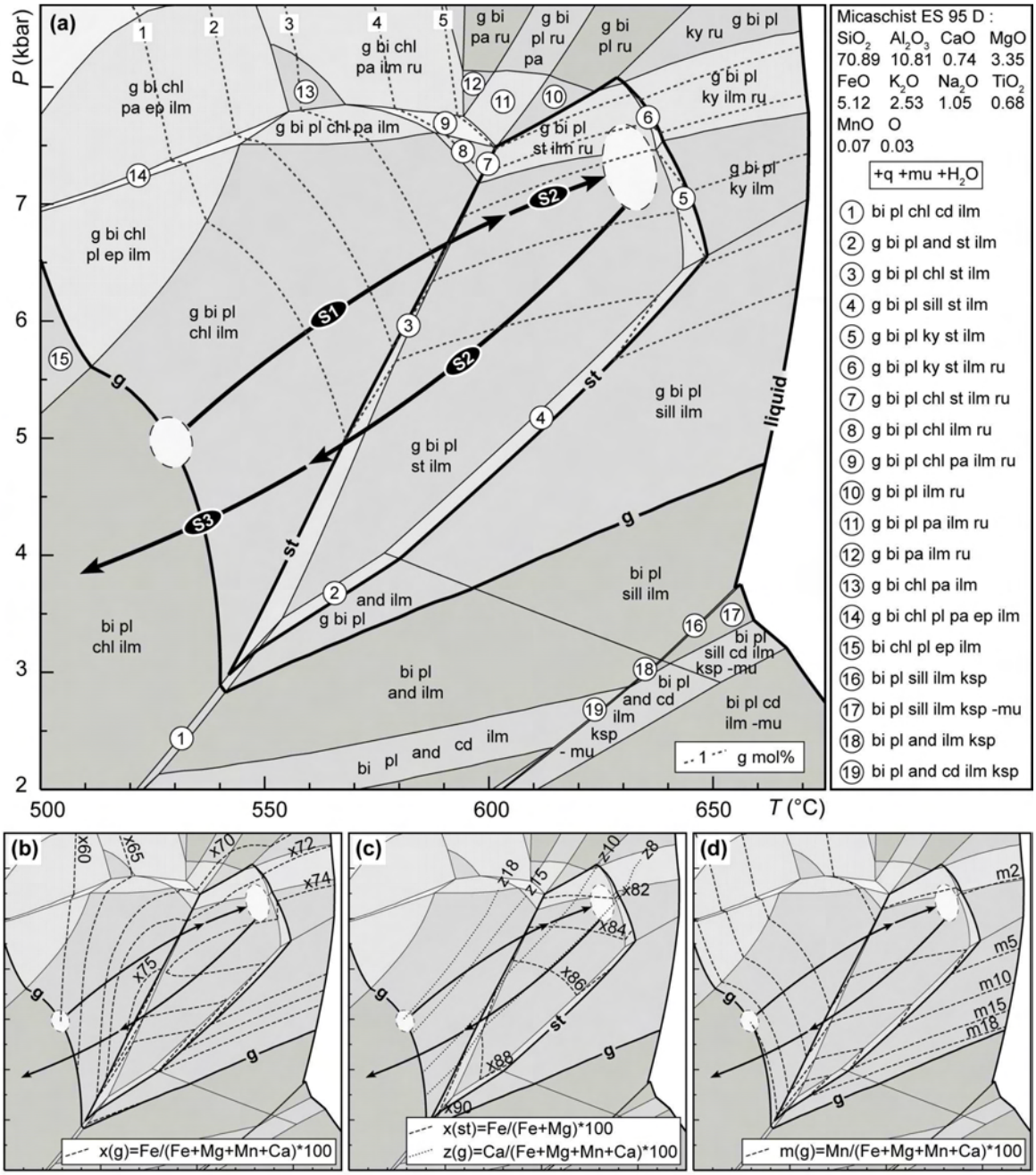

Fig. 12. (a) Pseudosection calculated for the rock composition of the metapelite sample ES95D (MnNCKFMASHTO system, whole-rock composition in moles adjusted to 100%), contoured with molar proportions of garnet. (b–d) Simplified parts of the pseudosection with calculated isopleths of mineral composition. Garnet, staurolite and granitic melt stability are highlighted. White ellipses show areas corresponding to garnet core and rim compositions. Arrows and black circles indicate parts of *P–T* path and conditions of equilibration for individual structures, derived by comparing the modeled assemblages and isopleths with observed assemblages and chemistry of minerals. See text for details.

P−T evolution of the micaschist sample ES95D

The stability of quartz, muscovite, garnet, staurolite, biotite and ilmenite has been documented in both the S1 and S2 foliations. The modelled compositional isopleths of garnet with values

similar to garnet core ($alm_{0.60}$ $grs_{0.17}$ $sps_{0.19}$) intersect at the garnet-in line and constrain the onset of garnet growth to ~ 5 kbar and 530 °C (Fig. 12b−d). The observed garnet zoning is compatible with prograde evolution crossing the staurolite-in line, which is in agreement with the occurrence of staurolite inclusions only close to the garnet rim. This $P-T$ path reaches the g−bi−pl−st−ilm field (Fig. 12a) at ~ 7 kbar and 630 °C where x(g), z(g), m(g) and x(st) values (Fig. 12b−d) are close to staurolite (XFe=0.82) and garnet rim compositions ($alm_{0.75}$ $grs_{0.08}$ $sps_{0.02}$). Garnet and staurolite rims (Fig. 7c,d) are associated with the S2 fabric indicating that the transition from the shallow-dipping S1 fabric into the subvertical S2 foliation started near the peak $P-T$ conditions (black ellipses labelled S1 and S2 in Fig. 12). Chlorite replacing staurolite in the S2 foliation can be correlated with a retrograde path crossing the chlorite-in line, possibly connected also with garnet rim ($alm_{0.75}$) re-equilibration below ~ 570 °C at the end of the D2 deformation (Fig. 12b). Further evolution during the D3 deformation is associated with chlorite occurrence in the F3 fold hinges indicating temperatures lower than ~ 540 °C for the end of the retrograde path in the bi−pl−chl−ilm field (Fig. 12a).

DISCUSSION AND CONCLUSIONS

Tectonic significance of orogenic fabrics

The heterogeneous character of the D1 deformation is best expressed by the highly deformed fine-grained and the banded felsic orthogneiss types around the eclogite, by the weakly deformed augen felsic orthogneiss further away from the eclogite and by the highly foliated metasedimentary belt. In addition, structural observations show that the felsic orthogneiss records a non-coaxial top to the north shearing expressed by the metre-scale N-verging asymmetric F1 folds. Parallelism of the eclogite fabric with that of the surrounding felsic orthogneiss suggests a shared deformation history. The metasedimentary rocks also display a strong S1 schistosity, which is concordant with the structure of the adjacent orthogneiss. In summary, both the deep- and the mid-crustal tectonites experienced similar N−S oriented subhorizontal flow, but the D1 deformation was highly localized in the fine-grained and banded felsic orthogneiss and in the metasediments, leaving the augen felsic orthogneiss only weakly deformed.

The subsequent D2 deformation causes upright folding associated with the development of N−S striking foliations. This is interpreted as the result of a subhorizontal E−W shortening. A characteristic feature is the intense folding and the fabric transposition of the felsic orthogneiss around the eclogite and of the metasediments in contrast to the several-kilometres large domain of the augen felsic orthogneiss that is only moderately affected by the D2 deformation (Fig. 3). This clearly indicates that the intensity of the F2 folding and its wavelengths are controlled by the degree of mechanical anisotropy of the individual lithologies achieved during the D1 deformation. The highly anisotropic banded felsic orthogneiss and the metasediments responded to horizontal shortening by intense folding with a common observed wavelength of several metres, while the competent augen felsic orthogneiss marked by a low degree of mechanical

anisotropy responded by homogeneous flattening rarely localized into shear zones (Fig. 3). Evaluation of the intensity of the D2 deformation in the eclogite is more difficult. The crenulation of the S1 eclogite facies fabric was observed at one place only and suggests that the eclogite is only locally affected by the F2 folding. It is proposed that the subvertical eclogite facies foliations are mostly steepened S1 fabrics, rotated in the limbs of the large F2 folds. The rare D2 amphibolite facies shear zones that affect the eclogite are thin and heterogeneous, and probably represent the axial plane cleavage of the large-scale F2 folds.

The recumbent F3 folds and the subhorizontal S3 cleavage heterogeneously affect the S2 foliation in all the lithological types. This weak deformation reflects vertical shortening and does not influence significantly the dominant D2 pattern.

P−*T*−*D* paths

The petrological study shows that the shallow-dipping S1 fabric in the eclogite is marked by prograde and peak mineral assemblage, for which the metamorphic *P*−*T* path is estimated from ~19.5 kbar and ~640 °C to 20−23 kbar and 700−750 °C. The S1 fabric in the felsic orthogneiss around the eclogite belt is probably co-facial with the eclogite, as indicated by the composition of white mica (Si = 3.30−3.43 p.f.u., Bröcker *et al.*, 2009). In the metapelites, minerals related to the S1 foliation show pressure and temperature increase from ~5 kbar and ~520 °C to ~7 kbar and ~630 °C (Fig. 13). The formation of the S1 fabric is therefore related to progressive burial of both the eclogite and the metasediments, but within different crustal depths. Consequently, eclogites and adjacent felsic orthogneiss are considered as a part of an orogenic lower crust, while the metapelites as a part of an orogenic middle crust within a continental wedge structure (Fig. 14a, inset). These crustal levels are separated by a thick layer of the augen orthogneiss for which the *P*−*T* conditions remain unknown (Fig. 14a).

The metamorphic conditions in the eclogite at the onset of the S2 fabric are difficult to estimate. In numerous sites the subvertical eclogite foliation is affected by fractures filled by amphibolite facies assemblages and by centimetre-scale subvertical amphibolite facies shear zones (Fig. 13a). In some places the subvertical foliation surrounding the eclogite developed entirely under amphibolite facies conditions and amphibolite bodies with a steeply-dipping foliation occur within the orthogneiss. The subsequent part of the retrograde *P*−*T* path from ~9 kbar to greenschist facies conditions is relatively well correlated with the structural development of the eclogite and the amphibolitized eclogite, but the part of the *P*−*T* path between the peak and ~ 9 kbar cannot be unambiguously correlated neither with S1 nor with S2 structures. Microstructural observations from the metapelites indicate that the *P*−*T* evolution related to the S2 fabric can be separated in two parts (Fig. 13b). The first part is associated with the growth of garnet and staurolite rims parallel to the S2 foliation reflecting continuation of burial to ~7.5 kbar and ~630 °C (Fig. 13b). The second part of the *P*−*T* path is related to syntectonic growth of chlorite in the S2 fabric, suggesting cooling bellow 550 °C, probably accompanied by decompression.

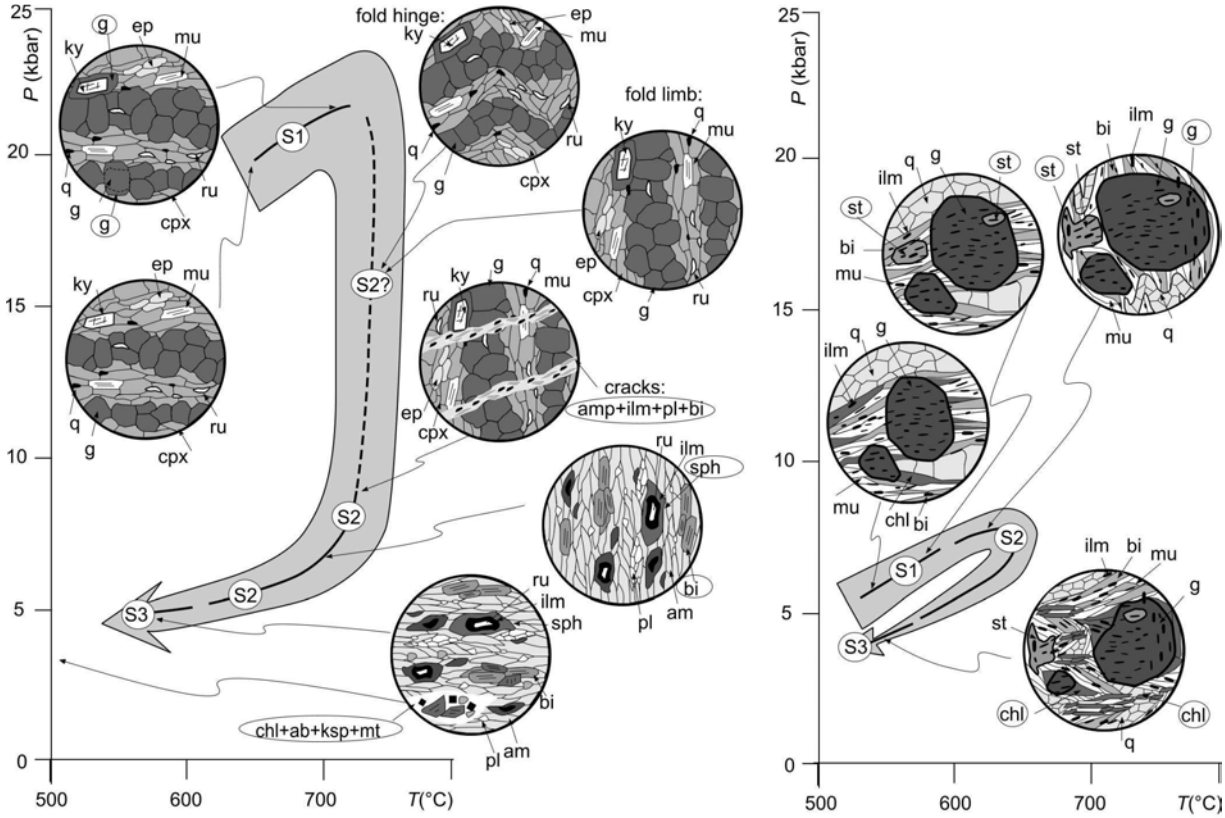

Fig. 13. Summary of $P-T$ data and associated microstructures. See text for discussion.

The petrological analysis shows that the eclogite and the metasediments were metamorphosed during the D2 deformation at different crustal levels corresponding to the orogenic lower and middle crust, respectively. The main difference is that during the F2 folding the eclogite experienced only exhumation, whereas the metapelite experienced first a burial increment (Fig. 14b) and then exhumation (Fig. 14c). Importantly, the coupled $P-T-d$ paths (Fig. 13) show that the F2 folding during the D2 deformation brings portions of the orogenic lower and middle crust into the same crustal level (Fig. 14b). The subsequent metamorphic evolution of the amphibolitized eclogite and the metasediments terminates at the same pressure of ~4−5 kbar (Fig. 13) and suggests that the final part of the exhumation was shared in the D2 fabric.

The mineral assemblages for both eclogite and metasediments in the S3 fabric are associated with temperature and pressure decrease below 550 °C and 4−5 kbar (Fig. 13). At this stage the metamorphic evolution of the eclogite and metasediments was shared and occurred at the same crustal level (Fig. 14d).

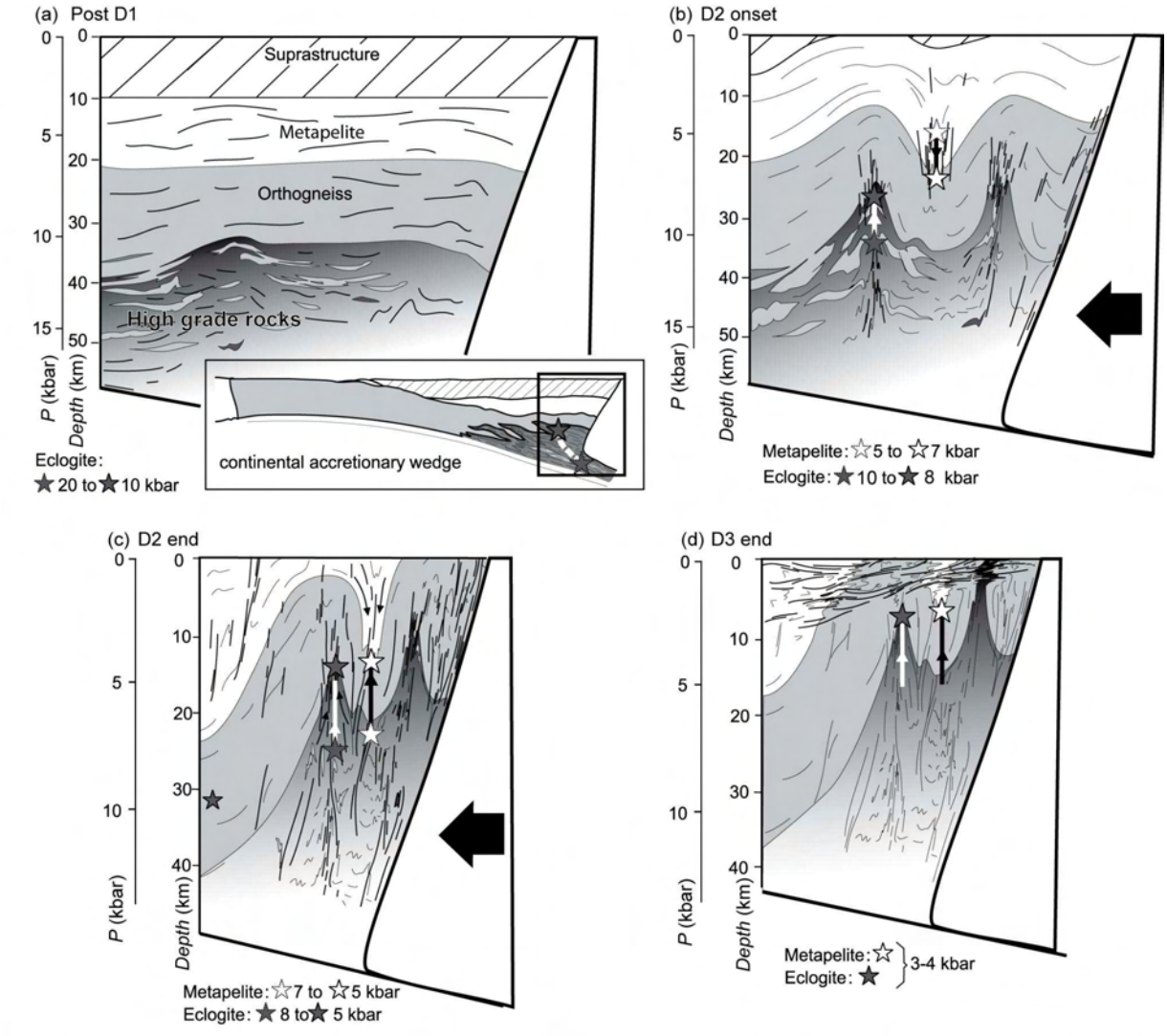

Fig. 14. Evolutionary model proposed for the juxtaposition of eclogite and mid-crustal rocks. (a) Crustal structure after burial of eclogite and metapelite in a continental accretionary wedge. Inset shows the general structure of the wedge. (b) Development of large-scale folds allowing exhumation of eclogite and burial of metapelite and (c) their subsequent joint exhumation. (d) Final exhumation by erosion and limited ductile thinning.

Constraining the juxtaposition of eclogite and metapelites

Folding and erosion model

While the thermal evolution of folded terrains is generally a non-trivial problem, changes in pressure could be successfully correlated with changes in distance between the surface and the studied sample. Therefore, the major processes affecting pressure evolution are those responsible for the reduction (i.e. ductile thinning, detachment-related thinning and/or erosion) or the thickening of the overburden. For clarity and the purpose of our 2D kinematic model, the overburden removal is approximated by “erosion”, while the vertical elongation of the modelled domain results from bulk homogeneous shortening. The pressure evolution of an originally sub-

horizontal layer is governed by these bulk vertical displacements but may be modified by fold-related displacements governed by the scaled amplification equation.

In order to explain the relative contribution of erosion and the D2 folding on the complex $P-T-d$ evolution of the metapelites in the synform and the eclogite in the antiform, we apply a kinematic model of buckling of a single layer during orogenic shortening. The single layer buckling originates from a mechanical instability developed during layer-parallel shortening and produces a lateral gradient in vertical displacement within the folded layer. The analytical results show that the growth rate of the single-layer fold amplitude is a function of the fold wavelength, where the maximum growth rate corresponds to the so-called dominant wavelength, which tends to be preferred during progressive shortening (Biot, 1961). Moreover, if the growth rate and the wavelength are non-dimensionalised by the layer-parallel shortening strain rate and the layer thickness respectively, the growth rate only depends on the wavelength and the viscosity contrast between the layer and the surrounding material (Fletcher, 1977). Schmalholz (2006) showed, that the horizontal and vertical hinge distances of many natural folds may be well correlated with the analytical parameters of wavelength and amplitude, respectively, using the scaled amplification equation describing fold amplification during viscous single-layer folding up to high amplitudes:

$$S_S = \left(\frac{\bar{A}}{\bar{A}_0} \right)^{\frac{1}{2+\alpha_0}} \left(\frac{\bar{L}}{\bar{L}_0} \right)^{\frac{\alpha_0}{2+\alpha_0}} \left(\pi \bar{A}_0 \sqrt{2\alpha_0} \right)^{\frac{1}{2+\alpha_0}} \quad (1)$$

where S_S is scaled stretch, $\bar{A}_0$, $\bar{A}$ are dimensionless initial and final fold amplitude, $\bar{L}_0$, $\bar{L}$ are initial and final dimensionless fold arc length and $\alpha_0 = (4R/3)^{2/3}$ is the dimensionless initial maximal growth rate dependent on the viscosity contrast between layer and matrix. In summary, the scaled amplification equation (Eq. 1) together with the growth rate equation (Biot, 1961; Fletcher, 1974; Schmalholz, 2006) represent a suitable mathematical framework to describe the main mechanical characteristics of finite amplitude buckling of a single viscous layers. The results of this model are summarized in Figure 15.

Burial and exhumation paths

We studied 3 different scenarii: (i) The “no erosion” model is characterized by progressive thickening of the overburden related to bulk shortening. (ii) The “full erosion” model, the overburden removal is more effective than shortening, so that the overall thickness does not change with time. (iii) The “increasing erosion” model has a progressive increase in efficiency of the overburden removal.

The “no erosion” model shows differential burial of all the folded layers with typical exponential relation between final depth and finite strain, while deeper initial positions of the folded layer corresponds to deeper final depths (Fig. 15a). It should be noted that final vertical displacement is partially reduced by isostatic re-equilibration due to overall thickening. The “full erosion” model shows overall exhumation of all folded layers with exception of the layers that

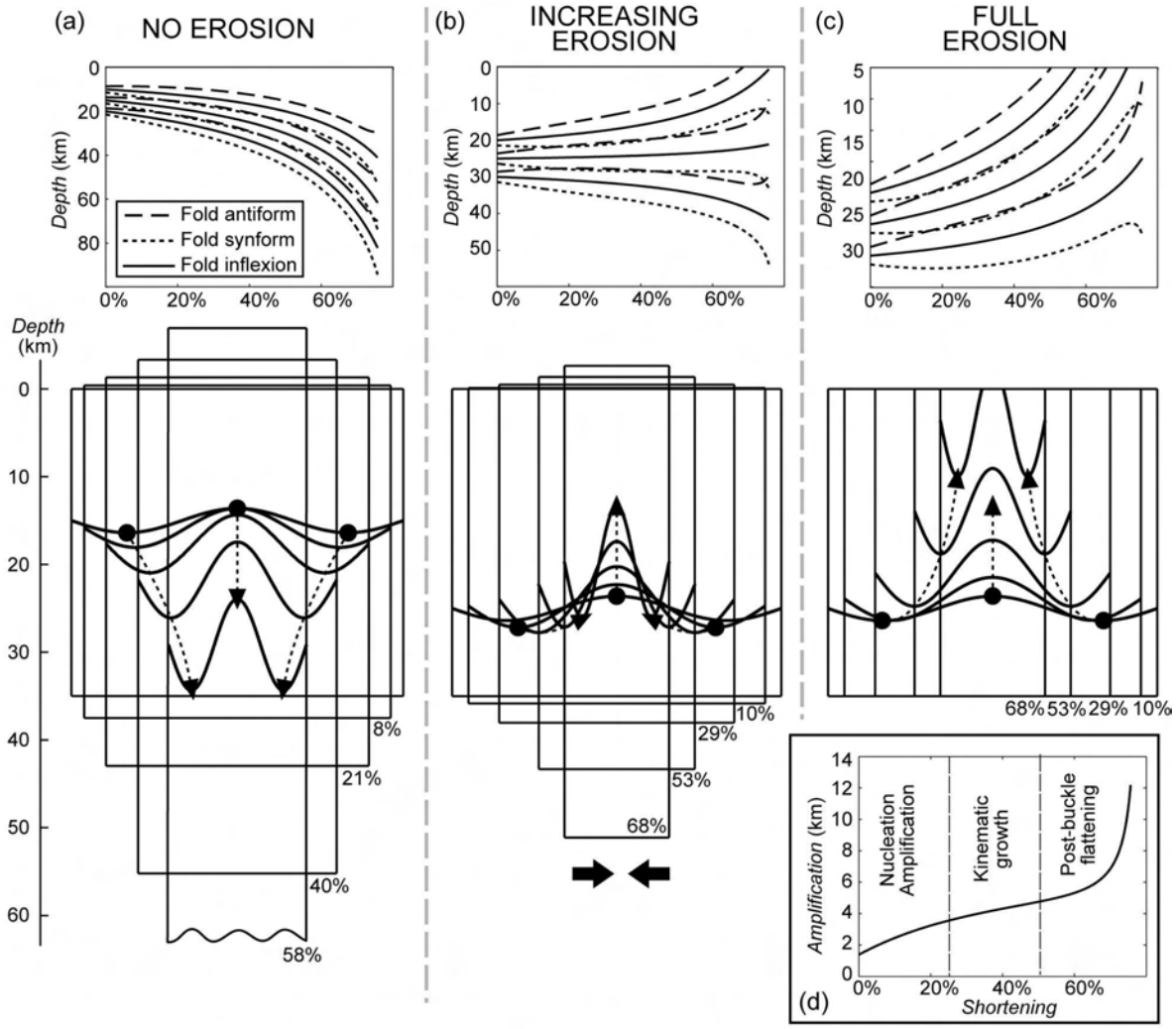

Fig. 15. Schematic evolution of vertical displacement of folded single-layer during bulk shortening for (a) "no erosion", (b) 'increasing erosion" and (c) "full erosion" models. The differential vertical movements of fold antiform, synform and inflexion line as a function of bulk shortening are plotted in diagrams along the bottom of the figure. (d) The non-linear evolution of buckle-fold amplification is plotted in amplification vs. shortening diagram in the central inset.

are located very close to the bottom of the system, where synformal parts of the folded layers resist to exhumation during early stages of shortening (Fig. 15c). The bulk rate of exhumation is slightly higher compared to burial rate in the "no erosion" model due to the absence of isostatic re-equilibration.

In the "increasing erosion" model, the early stages are characterized by a low amount of the overburden removal and an affinity to the "no erosion" model, with burial of the synformal parts of the initially shallower layer and the overall burial of the initially deeper layers (Fig. 15b). Once the overburden removal starts to dominate, the vertical displacements progressively change and fold antiforms together with fold synforms of the initially shallower layers are exhumed.

The modelling shows that neither the "no erosion", nor the "full erosion" model satisfies the complex $P-T-d$ evolution of the studied rocks. The 2D kinematic model indicates that in

order to develop progressive burial followed by exhumation during large-scale folding, the overburden removal processes like erosion or tectonic unroofing have to be significantly involved and have to be synchronous with bulk shortening. From the three tested situations it is the progressively "increasing erosion rate" model that satisfies the $P-T$ record of the studied rocks. The small burial recorded in the metapelites associated with an important exhumation in the eclogite fits well with this model (Fig. 15). For small erosion, the burial in synforms is possible but the point at the top of the antiform shows already important exhumation (Fig. 15b).

With increasing erosion, both antiforms and synforms exhibit an important exhumation for continuous shortening with the ongoing development of close to isoclinal folds. These modelled parameters fit well with the second stage of the $P-T$ history where both metapelite and eclogite show important exhumation related to the development of the S2 cleavage and the decrease of the fold interlimb angle. The vertical movements of rocks located in synforms and antiforms are also associated with typical evolutionary stages of folding starting with early nucleation (active) amplification, which is rapid and effectively competes with "erosion" thereby bringing rocks quickly down or up. This stage is followed by slower kinematic amplification where vertical movements are prevailing, followed by post-buckling stage at the late evolutionary history of fold life. The two latter fold evolutionary stages are connected with an active elevation of the whole system due to the progressively growing erosion rate.

Our model also shows that in order to simulate the simultaneous evolution of eclogite and metapelites, both rocks have to be located relatively high in the crustal column before the onset of folding. The eclogite layer located in a depth of 60 km and the metapelite at 25 km would never produce the $P-T$ evolutions reported in this work and the juxtaposition of both lithologies. The modelling therefore suggests that both eclogite and metapelites were located close to each other before the initiation of the folding event. They were probably separated by a ~10 km thick orthogneiss layer at a depth of 25–30 km.

$P-T-D$ evolution in the frame of existing orogenic models

The development of the S1 subhorizontal foliations related to an increase of pressure and temperature in the different crustal levels is typical for the model of burial of the crust in a continental wedge (Fig. 14a, inset) (Platt, 1993; Jeřábek *et al.*, 2008). The steep geometry of the D2 fabrics related to the exhumation is compatible with the corner flow circulation in the crustal wedge model (Platt, 1993; Allemand & Lardeaux, 1997). However, this model does not take into account the F2 folding reported in this work, which brings the orogenic lower and middle crustal rocks together (for similar examples see also Štípská *et al.*, 2004; Racek *et al.*, 2006; Schulmann *et al.*, 2008; Franěk *et al.*, 2011a; Franěk *et al.*, 2011b; Lexa *et al.*, 2011)(Fig. 14b). This part of the tectono-metamorphic history of the studied rocks can be best explained by the model proposed by Burg *et al.* (2004), which is the only model that takes into account crustal-scale folding due to horizontal shortening.

Numerical modelling (Fig. 15) shows that the juxtaposition between lower and mid-crustal rocks via crustal-scale folding can only occur if eclogite and metapelites are separated by

~10 km (Fig. 14a). This requires a first exhumation stage of eclogitic bodies prior to the D2 deformation. We can propose that the eclogite facies fabric S1 was passively exhumed to mid-crustal depths by back-thrusting along a predisposed subduction plane (S1). This mechanism may not leave a structural trace in the exhumed eclogite as shown in other parts of the Bohemian Massif (Klápová *et al.*, 1998; Konopásek & Schulmann, 2005). In such case the F2 folding would start to deform the eclogite at amphibolite facies conditions.

The shallow-dipping amphibolite to greenschist facies fabric D3 is geometrically compatible with the horizontal spreading of rocks proposed by Koyi *et al.* (1999). However, in their model the horizontal flow occurs due to the gravitational rebound of the root and affects the whole thickened crust. In the continental wedge model, the horizontal spreading is attributed to ductile thinning mechanism and occurs only at higher crustal levels (Ring *et al.*, 1999), which is compatible with the $P-T$ estimations of the D3 structures. In the absence of pervasive D3 deformation in the study area we favour erosion as the dominant mechanism responsible for the removal of the overburden.

sample	JW33b2						
mineral	g	g	g	cpx	mu	am	ep
position	core	peak	rim	mx	mx	in g	mx
analysis	A157-L2	A155-L2	A108-L1	16	A277-L4	32	12
SiO_2	39.95	40.15	39.79	55.05	50.03	43.29	39.41
TiO_2	0.12	0.26	0.14	0.20	1.10	0.26	0.08
Al_2O_3	22.93	23.01	22.58	10.82	29.14	18.05	33.29
FeO	17.03	16.32	17.87	3.18	1.34	7.31	1.63
MnO	0.48	0.40	0.44	0.16	0.10	0.07	0.12
MgO	10.15	9.69	10.42	10.10	3.61	13.51	0.23
CaO	9.92	10.41	8.59	15.42	0.05	10.23	23.38
Na_2O	0.00	0.00	0.04	5.02	0.57	3.00	0.07
K_2O	0.14	0.03	0.10	0.02	10.22	0.48	0.03
Total	100.72	100.27	99.97	99.97	96.16	96.20	98.24
Si	2.97	3.00	2.98	1.96	3.30	6.18	2.98
Ti	0.01	0.01	0.01	0.01	0.05	0.03	0.00
Al	2.01	2.03	1.99	0.46	2.27	3.04	2.97
Fe^{3+}	0.05	0.00	0.04	0.00	0.00	0.50	0.07
Fe^{2+}	1.00	1.02	1.08	0.09	0.07	0.37	0.03
Mn	0.03	0.03	0.03	0.00	0.01	0.01	0.01
Mg	1.12	1.08	1.16	0.54	0.36	2.87	0.03
Ca	0.79	0.83	0.69	0.59	0.00	1.56	1.90
Na	0.00	0.00	0.01	0.35	0.07	0.83	0.01
K	0.01	0.00	0.01	0.00	0.86	0.09	0.00
Total	8.00	8.00	8.00	4.00	7.00	15.48	8.00
XFe	0.47	0.49	0.48	0.15	0.17	0.11	
alm/an/jd/Y	0.35	0.34	0.37	0.35		0.91	
py/ab/Z	0.37	0.36	0.39			0.22	
grs/or/A	0.26	0.28	0.23			0.39	
sps/C	0.01	0.01	0.01			0.78	
Al^{IV}						1.82	

Table 1. Representative mineral analyses: eclogite JW33b2.

sample	JW29-2	JW29-2	JW29-2	JW29-2	JW29-2	JW29-2	JW29-2	JW29-2	JW29-2
mineral	am	am	bi	pl	ksp	ab	chl	ilm	sph
position	mx	mx	mx	mx	mx	mx	mx	mx	mx
analysis	51	67	46	52	34	35	65	59	58
SiO_2	43.64	49.39	36.63	61.71	64.46	67.23	42.87	0.16	30.51
TiO_2	0.62	0.43	2.20	0.06	0.00	0.06	0.00	55.30	39.40
Al_2O_3	14.51	7.79	16.75	24.73	19.09	20.10	10.42	0.15	1.23
FeO	13.63	12.33	18.29	0.41	0.25	0.33	9.96	41.51	0.54
MnO	0.31	0.33	0.15	0.09	0.00	0.00	0.00	3.40	0.24
MgO	10.48	14.28	12.18	0.18	0.24	0.00	21.78	0.28	0.05
CaO	11.45	12.15	0.00	4.95	0.00	0.39	0.44	0.27	27.83
Na_2O	1.20	0.67	0.12	8.15	0.18	10.59	0.77	0.04	0.08
K_2O	0.64	0.40	9.09	0.16	16.35	0.09	0.29	0.06	0.12
Total	96.48	97.77	95.41	100.44	100.57	98.79	86.53	101.17	100.00
Si	6.41	7.07	2.83	2.73	2.96	2.99	8.72	0.00	0.99
Ti	0.07	0.05	0.13	0.00	0.00	0.00	0.00	1.03	0.96
Al	2.51	1.32	1.53	1.29	1.03	1.05	2.50	0.00	0.05
Fe^{3+}	0.46	0.46	0.00	0.00	0.01	0.00	0.00	0.00	0.01
Fe^{2+}	1.21	1.02	1.18	0.02	0.00	0.01	1.69	0.86	0.00
Mn	0.04	0.04	0.01	0.00	0.00	0.00	0.00	0.07	0.01
Mg	2.29	3.05	1.40	0.01	0.02	0.00	6.61	0.01	0.00
Ca	1.80	1.86	0.00	0.23	0.00	0.02	0.10	0.01	0.97
Na	0.34	0.19	0.02	0.70	0.02	0.91	0.30	0.00	0.01
K	0.12	0.07	0.90	0.01	0.96	0.01	0.08	0.00	0.00
Total	15.26	15.12	8.00	5.00	5.00	5.00	20.00	2.00	3.00
XFe	0.35	0.25	0.46				0.20		
alm/an/jd/Y	0.79	0.46		0.25	0.00	0.02			
py/ab/Z	0.10	0.07		0.74	0.02	0.97			
grs/or/A	0.14	0.05		0.01	0.98	0.01			
sps/C	0.90	0.93							
Al^{IV}	1.59	0.93							

Table 2. Representative mineral analyses: amphibolitized eclogite JW29-2.

sample	ES95DI							
mineral	g	g	st	st	bi	chl	mu	pl
position	core	rim	core	rim	mx	mx	mx	mx
analysis	14	248	117	105	38	29	37	41
SiO_2	36.40	37.00	27.97	27.55	36.50	23.24	44.83	64.04
TiO_2	0.15	0.55	0.56	0.73	1.73	0.27	0.26	0.00
Al_2O_3	21.08	22.40	54.30	54.58	20.06	22.60	37.68	23.08
FeO	26.61	33.73	12.19	12.64	19.03	28.76	0.91	0.11
MnO	8.11	1.07	0.21	0.25	0.00	0.10	0.00	0.00
MgO	0.83	2.65	1.48	1.27	9.56	11.59	0.51	0.08
CaO	5.74	2.31	0.10	0.08	0.07	0.14	0.00	3.29
Na_2O	0.00	0.08	0.33	0.26	0.40	0.00	2.45	8.89
K_2O	0.00	0.16	0.00	0.00	8.61	0.03	7.33	0.00
ZnO	n.a.	n.a.	0.57	0.37	n.a.	n.a.	n.a.	n.a.
Total	98.92	99.93	97.71	97.72	95.97	86.73	93.97	99.49
Cations								
Si	2.98	2.97	7.91	7.74	2.82	5.07	2.99	2.85
Ti	0.01	0.03	0.12	0.15	0.10	0.04	0.01	0.00
Al	2.03	2.12	18.09	18.03	1.83	5.81	2.96	1.21
Fe^{3+}	0.00	0.00	0.00	0.00	0.00	0.00	0.00	0.00
Fe^{2+}	1.82	2.26	2.88	3.12	1.23	5.25	0.05	0.00
Mn	0.56	0.07	0.05	0.08	0.00	0.02	0.00	0.00
Mg	0.10	0.32	0.62	0.58	1.10	3.77	0.05	0.01
Ca	0.50	0.20	0.03	0.02	0.01	0.03	0.00	0.16
Na	0.00	0.01	0.18	0.15	0.06	0.00	0.32	0.77
K	0.00	0.02	0.00	0.00	0.85	0.01	0.62	0.00
Zn	-	-	0.12	0.14	-	-	-	-
Total	8.00	8.00	30.00	30.00	8.00	20.00	7.00	5.00
XFe	0.95	0.88	0.82	0.84	0.53	0.58		
alm/an	0.61	0.79						0.83
py/ab	0.03	0.11						0.17
grs/or	0.17	0.07						0.00
sps	0.19	0.03						

n.a. = not analyzed

Table 3. Representative mineral analyses: metapelite ES95DI.

ACKNOWLEDGEMENTS

The French National Grant Agency (06-1148784 to K. Schulmann) is gratefully acknowledged. The grant MSM0021620855 of the Ministry of Education of the Czech Republic and internal research funds of CNRS UMR 7615 are acknowledged for salary and financial support of O. Lexa. J. Lehmann is thanked for helpful discussions.

REFERENCES

Aleksandrowski, P., Kryza, R., Mazur, S. & Zaba, J., 1997. Kinematic data on major Variscan strike-slip faults and shear zones in the Polish Sudetes, northeast Bohemian Massif. *Geological Magazine*, **134**, 727-739.

Allemand, P. & Lardeaux, J. M., 1997. Strain partitioning and metamorphism in a deformable orogenic wedge: Application to the Alpine belt. *Tectonophysics*, **280**, 157-169.

Anczkiewicz, R., Szczepanski, J., Mazur, S., Storey, C., Crowley, Q., Villa, I. M., Thirlwall, M. E. & Jeffries, T. E., 2007. Lu-Hf geochronology and trace element distribution in garnet: Implications for uplift and exhumation of ultra-high pressure granulites in the Sudetes, SW Poland. *Lithos*, **95**, 363-380.

Andersen, T. B. & Fossen, H., 1993. The role of extensional tectonics in the Caledonides of south Norway-discussion and reply. *Journal of Structural Geology*, **15**, 1379-1383.

Bakun-Czubarow, N., 1992. Quartz pseudomorphs after coesite and quartz exsolutions in eclogitic omphacites of the Zlote Mountains in the Sudetes (SW Poland). *Archiwum Mineralogiczne*, **48**, 3-25.

Beaumont, C., Jamieson, R. A., Nguyen, M. H. & Lee, B., 2001. Himalayan tectonics explained by extrusion of a low-viscosity crustal channel coupled to focused surface denudation. *Nature*, **414**, 738-742.

Beaumont, C., Nguyen, M. H., Jamieson, R. A. & Ellis, S., 2006. Crustal flow modes in large hot orogens. Channel flow, ductile extrusion and exhumation in continental collision zones. *Geological Society Special Publications*, **268**, 91-145.

Biot, M. A., 1961. Theory of folding of stratified viscoelastic media and its implications in tectonics and orogenesis. *Geological Society of America Bulletin*, **72**, 1595-1620.

Bröcker, M. & Klemd, R., 1996. Ultrahigh-pressure metamorphism in the Śnieżnik Mountains (Sudetes, Poland): P-T constraints and geological implications. *Journal of Geology*, **104**, 417-433.

Bröcker, M., Klemd, R., Cosca, M., Brock, W., Larionov, A. N. & Rodionov, N., 2009. The timing of eclogite facies metamorphism and migmatization in the Orlica-Śnieżnik complex, Bohemian Massif: constraints from a multimethod geochronological study. *Journal of Metamorphic Geology*, **27**, 385-403.

Bröcker, M., Klemd, R., Kooijman, E., Berndt, J. & Larionov, A., 2010. Zircon geochronology and trace element characteristics of eclogites and granulites from the Orlica-Śnieżnik complex, Bohemian Massif. *Geological Magazine*, **147**, 339-362.

Brueckner, H. K., Medaris, L. G. & Bakun-Czubarow, N., 1991. Nd and Sr age and isotope patterns from Variscan eclogites of the eastern Bohemian Massif. *Neues Jahrbuch für Mineralogie, Abhandlungen*, **163**, 169-196.

Burg, J. P., Kaus, B. J. P. & Podladchikov, Y. Y., 2004. Dome structures in collision orogens: Mechanical investigation of the gravity/compression interplay. *Geological Society of America Special Papers*, **380**, 47-66.

Burg, J. P., Nievergelt, P., Oberli, F., Seward, D., Davy, P., Maurin, J. C., Diao, Z. & Meier, M., 1998. The Namche Barwa syntaxis: evidence for exhumation related to compressional crustal folding. *Journal of Asian Earth Sciences*, **16**, 239-252.

Chemenda, A. I., Burg, J. P. & Mattauer, M., 2000. Evolutionary model of the Himalaya-Tibet system: geopoem based on new modelling, geological and geophysical data. *Earth and Planetary Science Letters*, **174**, 397-409.

Cobbold, P. R. & Quinquis, H., 1980. Development of sheath folds in shear regimes. *Journal of Structural Geology*, **2**, 119-126.

Coggon, R. & Holland, T. J. B., 2002. Mixing properties of phengitic micas and revised garnet-phengite thermobarometers. *Journal of Metamorphic Geology*, **20**, 683-696.

Dale, J., Powell, R., White, R. W., Elmer, F. L. & Holland, T. J. B., 2005. A thermodynamic model for Ca-Na clinoamphiboles in Na_2O-CaO-FeO-MgO-Al_2O_3-SiO_2-H_2O-O for petrological calculations. *Journal of Metamorphic Geology*, **23**, 771-791.

Diener, J. F. A., Powell, R., White, R. W. & Holland, T. J. B., 2007. A new thermodynamic model for clino- and orthoamphiboles in the system Na_2O-CaO-FeO-MgO-Al_2O_3-SiO_2-H_2O-O. *Journal of Metamorphic Geology*, **25**, 631-656.

Diener, J. F. A., White, R. W. & Powell, R., 2008. Granulite facies metamorphism and subsolidus fluid-absent reworking, Strangways Range, Arunta Block, central Australia. *Journal of Metamorphic Geology*, **26**, 603-622.

Don, J., 1964. The Zlote and Krowiarki Mountains as structural elements of the Śnieżnik metamorphic massif. *Geologia Sudetica*, **1**, 79-117.

Don, J., 1982. The Sienna synform and the relationship of gneisses to the deformational stages distinguished in the Śnieżnik metamorphic massif (Sudetes). *Geologia Sudetica*, **17**, 130-124.

Don, J., Dumicz, M., Wojciechowska, I. & Żelaźniewicz, A., 1990. Lihology and tectonics of the Orlica-Śnieżnik Dome, Sudetes: recent state of knowledge. *Neues Jahrbuch für Geologie und Paläontologie, Abhandlungen*, **179**, 159-188.

Don, J., Skácel, J. & Gotowała, R., 2003. The boundary zone of the East and West Sudetes on the 1:50 000 scale geological map of the Velké Vrbno, Staré Město and Śnieznik Metamorphic Units. *Geologia Sudetica*, **35**, 25-59.

Duchene, S., Lardeaux, J. M. & Albarede, F., 1997. Exhumation of eclogites: insights from depth-time path analysis. *Tectonophysics*, **280**, 125-140.

Dumicz, M., 1979. Tectogenesis of the metamorphosed series of the Klodzko district: a tentative explanation. *Geologia Sudetica*, **14**, 29-44.

Edel, J. B., 2003. Magnetic overprints in granitoids and metamorphic rocks from Limousin (France): evidence for Late Variscan rotations, crustal folding and tilting. *Tectonophysics*, **363**, 225-241.

Fletcher, R. C., 1974. Wavelength selection in the folding of a single layer with power-law rheology. *American Journal of Science*, **274**, 1029-1043.

Fletcher, R. C., 1977. Folding of a single viscous layer: exact infinitesimal-amplitude solution. *Tectonophysics*, **39**, 593-606.

Franěk, J., Schulmann, K., Lexa, O., Tomek, C. & Edel, J. B., 2011a. Model of syn-convergent extrusion of orogenic lower crust in the core of the Variscan belt: implications for exhumation of high-pressure rocks in large hot orogens. *Journal of Metamorphic Geology*, **29**, 53–78.

Franěk, J., Schulmann, K., Lexa, O., Ulrich, S., Štípská, P., Haloda, J. & Týcová, P., 2011b. Origin of felsic granulite microstructure by heterogeneous decomposition of alkali feldspar and extreme weakening of orogenic lower crust during the Variscan orogeny. *Journal of Metamorphic Geology*, **29**, 103–130.

Gerya, T. & Stöckhert, B., 2006. Two-dimensional numerical modeling of tectonic and metamorphic histories at active continental margins. *International Journal of Earth Sciences*, **95**, 250-274.

Gerya, T. V., Perchuk, L. L., Maresch, W. V. & Willner, A. P., 2004. Inherent gravitational instability of hot continental crust: Implications for doming and diapirism in granulite facies terrains. *Geological Society of America Special Papers* **380**, 97-115.

Gerya, T. V., Perchuk, L. L., Maresch, W. V., Willner, A. P., Van Reenen, D. D. & Smit, C. A., 2002. Thermal regime and gravitational instability of multi-layered continental crust: implications for the buoyant exhumation of high-grade metamorphic rocks. *European Journal of Mineralogy*, **14**, 687-699.

Green, E., Holland, T. & Powell, R., 2007. An order-disorder model for omphacitic pyroxenes in the system jadeite-diopside-hedenbergite-acmite, with applications to eclogitic rocks. *American Mineralogist*, **92**, 1181-1189.

Grocott, J. & Watterson, J., 1980. Strain profile of a boundary within a large ductile shear zone. *Journal of Structural Geology*, **2**, 111-117.

Holland, T. J. B., Baker, J. & Powell, R., 1998. Mixing properties and activity-composition relationships of chlorites in the system MgO-FeO-Al_2O_3-SiO_2-H_2O. *European Journal of Mineralogy*, **10**, 395-406.

Holland, T. J. B. & Powell, R., 1998. An internally consistent thermodynamic data set for phases of petrological interest. *Journal of Metamorphic Geology*, **16**, 309-343.

Holland, T. J. B. & Powell, R., 2003. Activity-composition relations for phases in petrological calculations: an asymmetric multicomponent formulation. *Contributions to Mineralogy and Petrology*, **145**, 492-501.

Jastrzębski, M., 2005. The tectonometamorphic evolution of the marbles in the Lądek- Śnieżnik Metamorphic Unit, West Sudetes. *Geologia Sudetica*, **37**, 1-26.

Jastrzębski, M., 2009. A Variscan continental collision of the West Sudetes and the Brunovistulian terrane: a contribution from structural and metamorphic record of the Stronie Formation, the Orlica-Śnieżnik Dome, SW Poland. *International Journal of Earth Sciences*, **98**, 1901-1923.

Jastrzębski, M., Żelaźniewicz, A., Nowak, I., Murtezi, M. & Larionov, A. N., 2010. Protolith age and provenance of metasedimentary rocks in Variscan allochthon units: U-Pb SHRIMP zircon data from the Orlica-Śnieżnik Dome, West Sudetes. *Geological Magazine*, **147**, 416-433.

Jeřábek, P., Faryad, W. S., Schulmann, K., Lexa, O. & Tajčmanová, L., 2008. Alpine burial and heterogeneous exhumation of Variscan crust in the West Carpathians: insight from thermodynamic and argon diffusion modelling. *Journal of the Geological Society*, **165**, 479-498.

Jolivet, L., Raimbourg, H., Labrousse, L., Avigad, D., Leroy, Y., Austrheim, H. & Andersen, T. B., 2005. Softening trigerred by eclogitization, the first step toward exhumation during continental subduction. *Earth and Planetary Science Letters*, **237**, 532-547.

Klápová, H., Konopásek, J. & Schulmann, K., 1998. Eclogites from the Czech part of the Erzgebirge: multi-stage metamorphic and structural evolution. *Journal of the Geological Society*, **155**, 567-583.

Klemd, R. & Bröcker, M., 1999. Fluid influence on mineral reactions in ultrahigh-pressure granulites: a case study in the Śnieżnik Mts. (West Sudetes, Poland). *Contributions to Mineralogy and Petrology*, **136**, 358-373.

Klemd, R., Bröcker, M. & Schramm, J., 1995. Characterization of amphibolite-facies fluids of Variscan eclogites from the Orlica-Śnieżnik Dome (Sudetes, SW Poland). *Chemical Geology*, **119**, 101-113.

Konopásek, J. & Schulmann, K., 2005. Contrasting Early Carboniferous field geotherms: evidence for accretion of a thickened orogenic root and subducted Saxothuringian crust (Central European Variscides). *Journal of the Geological Society*, **162**, 463-470.

Košuličová, M. & Štípská, P., 2007. Variations in the transient prograde geothermal gradient from chloritoid-staurolite equilibria: a case study from the Barrovian and Buchan-type domains in the Bohemian Massif. *Journal of Metamorphic Geology*, **25**, 19-35.

Koyi, H. A., Milnes, A. G., Schmeling, H., Talbot, C. J., Juhlin, C. & Zeyen, H., 1999. Numerical models of ductile rebound of crustal roots beneath mountain belts. *Geophysical Journal International*, **139**, 556-562.

Kröner, A., Jaeckel, P., Hegner, E. & Opletal, M., 2001. Single zircon ages and whole rock Nd isotopic systematics of early Palaeozoic granitoid gneisses from the Czech and Polish Sudetes (Jizerské hory, Krkonoše Mountains and Orlice-Sněžník Complex). *International Journal of Earth Sciences*, **90**, 304-324.

Kröner, A., Štípská, P., Schulmann, K. & Jaeckel, P., 2000. Chronological constraints on the pre-Variscan evolution of the northeastern margin of the Bohemian Massif, Czech Republic. In: *Orogenic processes; quantification and modelling in the Variscan Belt.* (eds Franke, W., Haak, V., Oncken, O. & Tanner, D.) *Geological Society of London Special Publications*, pp. 175-197, Geological Society of London. London, United Kingdom, 179, 175-197.

Kryza, R., Pin, C. & Vielzeuf, D., 1996. High-pressure granulites from the Sudetes (south-west Poland): evidence of crustal subduction and collisional thickening in the Variscan Belt. *Journal of Metamorphic Geology*, **14**, 531-546.

Lange, U., Bröcker, M., Armstrong, R., Trapp, E. & Mezger, K., 2005a. Sm-Nd and U-Pb dating of high-pressure granulites from the Zlote and Rychleby Mts (Bohemian Massif, Poland and Czech Republic). *Journal of Metamorphic Geology*, **23**, 133-145.

Lange, U., Bröcker, M., Armstrong, R., Żelaźniewicz, A., Trapp, E. & Mezger, K., 2005b. The orthogneisses of the Orlica-Śnieżnik complex (West Sudetes, Poland): geochemical characteristics, the importance of pre-Variscan migmatization and constraints on the cooling history. *Journal of the Geological Society*, **162**, 973-984.

Lange, U., Bröcker, M., Mezger, K. & Don, J., 2002. Geochemistry and Rb-Sr geochronology of a ductile shear zone in the Orlica-Śnieżnik dome (West Sudetes, Poland). *International Journal of Earth Sciences*, **91**, 1005-1016.

Lexa, O., Schulmann, K., Janoušek, V., Štípská, P., Guy, A. & Racek, M., 2011. Heat sources and trigger mechanisms of exhumation of HP granulites in Variscan orogenic root. *Journal of Metamorphic Geology*, **29**, 79–102.

Lexa, O., Štípská, P., Schulmann, K., Baratoux, L. & Kröner, A., 2005. Contrasting textural record of two distinct metamorphic events of similar P-T conditions and different durations. *Journal of Metamorphic Geology*, **23**, 649-666.

Mahar, E. M., Baker, J. M., Powell, R., Holland, T. J. B. & Howell, N., 1997. The effect of Mn on mineral stability in metapelites. *Journal of Metamorphic Geology*, **15**, 223-238.

Mazur, S., Aleksandrowski, P. & Szczepański, J., 2005. The presumed Teplá-Barrandian/Moldanubian terrane boundary in the Orlica Mountains (Sudetes, Bohemian Massif): structural and petrological characteristics. *Lithos*, **82**, 85-112.

Murtezi, M., 2006. The acid metavolcanic rocks of the Orlica-Śnieżnik Dome (Sudetes): Their origin and tectono-metamorphic evolution. *Geologia Sudetica*, **38**, 1-38.

Oliver, G. J. H., Corfu, F. & Krogh, T. E., 1993. U-Pb ages from SW Poland: evidence for a Caledonian suture zone between Baltica and Gondwana. *Journal of the Geological Society, London*, **150**, 355-369.

Parry, M., Štípská, P., Schulmann, K., Hrouda, F., Ježek, J. & Kröner, A., 1997. Tonalite sill emplacement at an oblique plate boundary: northeastern margin of the Bohemian Massif. *Tectonophysics*, **280**, 61-81.

Platt, J. P., 1987. The uplift of high-pressure low-temperature metamorphic rocks. *Philosophical Transactions of the Royal Society of London*, **A321**, 87-103.

Platt, J. P., 1993. Exhumation of high-pressure rocks; a review of concepts and processes. *Terra Nova*, **5**, 119-133.

Pouba, Z., Paděra, K. & Fiala, J., 1985. Omphacite granulite from the NE margin of the Bohemian Massif (Rychleby Mts). *Neues Jahrbuch für Mineralogie, Abhandlungen*, **151**, 29-52.

Powell, R., Holland, T. & Worley, B., 1998. Calculating phase diagrams involving solid solutions via non- linear equations, with examples using THERMOCALC. *Journal of Metamorphic Geology*, **16**, 577-588.

Racek, M., Štípská, P., Pitra, P., Schulmann, K. & Lexa, O., 2006. Metamorphic record of burial and exhumation of orogenic lower and middle crust: a new tectonothermal model for the Drosendorf window (Bohemian Massif, Austria). *Mineralogy and Petrology*, **86**, 221-251.

Ring, U., Brandon, M. T., Lister, G. S. & Willett, S. D., 1999. Exhumation processes: normal faulting, ductile flow and erosion. *Geological Society Special Publication*, **154**, 1-27.

Schmalholz, S. M., 2006. Scaled amplification equation: a key to the folding history of buckled viscous single-layers. *Tectonophysics*, **419**, 41-53.

Schneider, D. A., Zahniser, S. J., Glascock, J. M., Gordon, S. M. & Manecki, M., 2006. Thermochronology of the West Sudetes (Bohemian Massif): Rapid and repeated eduction in the Eastern Variscides, Poland and Czech Republic. *American Journal of Science*, **306**, 846-873.

Schulmann, K. & Gayer, R., 2000. A model for a continental accretionary wedge developed by oblique collision: the NE Bohemian Massif. *Journal of the Geological Society, London*, **157**, 401-416.

Schulmann, K., Konopásek, J., Janoušek, V., Lexa, O., Lardeaux, J. M., Edel, J. B., Štípská, P. & Ulrich, S., 2009. An Andean type Palaeozoic convergence in the Bohemian Massif. *Comptes Rendus Geoscience*, **341**, 266-286.

Schulmann, K., Lexa, O., Štípská, P., Racek, M., Tajčmanová, L., Konopásek, J., Edel, J. B., Peschler, A. & Lehmann, J., 2008. Vertical extrusion and horizontal channel flow of orogenic lower crust: key exhumation mechanisms in large hot orogens? *Journal of Metamorphic Geology*, **26**, 273–297.

Skjernaa, L., 1980. Rotation and deformation of randomly oriented planar and linear structures in progressive simple shear. *Journal of Structural Geology*, **2**, 101-109.

Skrzypek, E., Schulmann, K., Štípská, P., Chopin, F., Lehmann, J., Lexa, O. & Haloda, J., 2011a. Garnet porphyroblast growth in collisional orogens: insight from EBSD inclusion trails study and thermodynamic modelling. *Journal of Metamorphic Geology*, **in print**.

Skrzypek, E., Štípská, P., Schulmann, K., Lexa, O. & Lexová, M., 2011b. Prograde and retrograde metamorphic fabrics - a key for understanding burial and exhumation in orogens (Bohemian Massif). *Journal of Metamorphic Geology*, **in print**.

Smulikowski, K., 1967. Eclogites of the Śnieżnik Mts in the Sudetes. *Geologia Sudetica*, **3**, 157-174.

Steltenpohl, M. G., Cymerman, Z., Krogh, E. J. & Kunk, M. J., 1993. Exhumation of eclogitized continental basement during Variscan lithospheric delamination and gravitational collapse, Sudety Mountains, Poland. *Geology*, **21**, 1111-1114.

Štípská, P., Pitra, P. & Powell, R., 2006. Separate or shared metamorphic histories of eclogites and surrounding rocks? An example from the Bohemian Massif. *Journal of Metamorphic Geology*, **24**, 219-240.

Štípská, P., Schulmann, K. & Kröner, A., 2004. Vertical extrusion and middle crustal spreading of omphacite granulite: a model of syn-convergent exhumation (Bohemian Massif, Czech Republic). *Journal of Metamorphic Geology*, **22**, 179-198.

Štípská, P., Schulmann, K. & Powell, R., 2008. Contrasting metamorphic histories of lenses of high-pressure rocks and host migmatites with a flat orogenic fabric (Bohemian Massif, Czech Republic): a result of tectonic mixing within horizontal crustal flow? *Journal of Metamorphic Geology*, **26**, 623-646.

Štípská, P., Schulmann, K., Thompson, A. B., Ježek, J. & Kröner, A., 2001. Thermo-mechanical role of a Cambro-Ordovician paleorift during the Variscan collision: the NE margin of the Bohemian Massif. *Tectonophysics*, **332**, 239-253.

Turniak, K., Mazur, S. & Wysoczanski, R., 2000. SHRIMP zircon geochronology and geochemistry of the Orlica-Śnieżnik gneisses (Variscan belt of Central Europe) and their tectonic implications. *Geodinamica Acta*, **13**, 1-20.

White, R. W., Pomroy, N. E. & Powell, R., 2005. An in situ metatexite-diatexite transition in upper amphibolite facies rocks from Broken Hill, Australia. *Journal of Metamorphic Geology*, **23**, 579-602.

White, R. W., Powell, R. & Holland, T. J. B., 2007. Progress relating to calculation of partial melting equilibria for metapelites. *Journal of Metamorphic Geology*, **25**, 511-527.

White, R. W., Powell, R., Holland, T. J. B. & Worley, B. A., 2000. The effect of TiO_2 and Fe_2O_3 on metapelitic assemblages at greenschist and amphibolite facies conditions: mineral equilibria calculations in the system K_2O-FeO-MgO-Al_2O_3-SiO_2-H_2O-TiO_2-Fe_2O_3. *Journal of Metamorphic Geology*, **18**, 497-511.

Żelaźniewicz, A., Nowak, I., Larionov, A. & Presnyakov, S., 2006. Syntectonic Lower Ordovician migmatite and post-tectonic Upper Viséan syenite in the western limb of the Orlica-Śnieżnik Dome, West Sudetes: U-Pb SHRIMP data from zircons. *Geologia Sudetica*, **38**, 63-80.

25. **Štípská**, P., Schulmann, K. and Powell, R. (2008). Contrasting metamorphic histories of lenses of high-pressure rocks and host migmatites with a flat orogenic fabric (Bohemian Massif, Czech Republic): a result of tectonic mixing within horizontal crustal flow? *Journal of Metamorphic Geology*, **26,** 623–646. doi:10.1111/j.1525-1314.2008. 00781.x.

26. Hasalová, P., Janoušek, V., Schulmann, K., **Štípská**, P. & Erban, V. (2008a). From orthogneiss to migmatite: geochemical assessment of the melt infiltration model in the Gföhl Unit (Moldanubian Zone, Bohemian Massif). *Lithos*, **102**, 508–537. doi:10.1016 /j.lithos. 2007.07.021.

27. Hasalová, P., Schulmann, K., Lexa, O., **Štípská**, P., Hrouda, F., Ulrich, S., Haloda, J. & Týcová, P. (2008b). Origin of migmatites by deformation-enhanced melt infiltration of orthogneiss: a new model based on quantitative microstructural analysis. *Journal of Metamorphic Geology*, 26, 29-53. doi:10.1111/j.1525-1314.2007.00743.x.

28. Hasalová, P., **Štípská**, P., Powell, R., Schulmann, K., Janoušek, V. & Lexa, O. (2008c). Transforming mylonitic metagranite by open-system interactions during melt flow. *Journal of Metamorphic Geology*, 26, 55-80. doi:10.1111/j.1525-1314.2007.00744.x.

J. metamorphic Geol., 2008, **26,** 623–646 doi:10.1111/j.1525-1314.2008.00781.x

Contrasting metamorphic histories of lenses of high-pressure rocks and host migmatites with a flat orogenic fabric (Bohemian Massif, Czech Republic): a result of tectonic mixing within horizontal crustal flow?

P. ŠTÍPSKÁ,[1] K. SCHULMANN[1] AND R. POWELL[2]
[1]*Université Louis Pasteur, CGS/EOST, UMR CNRS 7517, 1 Rue Blessig, Strasbourg, France (stipska@gmail.com)*
[2]*School of Earth Sciences, University of Melbourne, Melbourne, Victoria 3010, Australia*

ABSTRACT Migmatites with sub-horizontal fabrics at the eastern margin of the Variscan orogenic root in the Bohemian Massif host lenses of eclogite, kyanite-K-feldspar granulite and marble within a matrix of migmatitic paragneiss and amphibolite. Petrological study and pseudosection modelling have been used to establish whether the whole area experienced terrane-wide exhumation of lower orogenic crust, or whether smaller portions of higher-pressure lower crust were combined with a lower-pressure matrix. Kyanite-K-feldspar granulite shows peak conditions of 16.5 kbar and 850 °C with no clear indications of prograde path, whereas in the eclogite the prograde path indicates burial from 10 kbar and 700 °C to a peak of 18 kbar and 800 °C. Two contrasting prograde paths are identified within the host migmatitic paragneiss. The first path is inferred from the presence of staurolite and kyanite inclusions in garnet that contains preserved prograde zoning that indicates burial with simultaneous heating to 11 kbar and 800 °C. The second path is inferred from garnet overgrowths of a flat foliation defined by sillimanite and biotite. Garnet growth in such an assemblage is possible only if the sample is heated at 7–8 kbar to around 700–840 °C. Decompression is associated with strong structural reworking in the flat fabric that involves growth of sillimanite in paragneiss and kyanite-K-feldspar granulite at 7–10 kbar and 750–850 °C. The contrasting prograde metamorphic histories indicate that kilometre-scale portions of high-pressure lower orogenic crust were exhumed to middle crustal levels, dismembered and mixed with a middle crustal migmatite matrix, with the simultaneous development of a flat foliation. The contrasting *P–T* paths with different pressure peaks show that tectonic models explaining high-pressure boudins in such a fabric cannot be the result of heterogeneous retrogression during ductile rebound of the whole orogenic root. The *P–T* paths are compatible with a model of heterogeneous vertical extrusion of lower crust into middle crust, followed by sub-horizontal flow.

Key words: Bohemian Massif; exhumation; high-pressure granulite; migmatite; *P–T* paths.

INTRODUCTION

The existence of regional-scale fabrics in orogens, where high-pressure lower-crustal boudins are embedded in an apparently lower-pressure effectively horizontal (flat) fabric provokes the question 'how was the lower crust exhumed?' A classical area in this regard is the Western Gneiss Region (WGR) in Norway, where eclogite boudins with a relict steep foliation are wrapped in flat amphibolite facies fabrics (e.g. Dewey *et al.*, 1993; Engvik & Andersen, 2000). In the WGR, Andersen *et al.* (1991), Dewey *et al.* (1993) and Engvik & Andersen (2000) suggested that eclogite facies orogenic crust with a steep fabric was heterogeneously reworked during terrane-wide exhumation of the deeply buried crustal material. Exhumation has been explained by isostatic rebound associated with an extensional mechanism because of convective removal of the tectospheric root (Andersen *et al.*, 1991; Dewey *et al.*, 1993; Johnston *et al.*, 2007) or by lateral variations in lithostatic pressure within the thickened continental crust (Koyi *et al.*, 1999; Milnes & Koyi, 2000).

Another area where amphibolite facies gneisses and migmatites with a flat fabric containing high-pressure boudins occur is in the Variscan orogen in Europe. In the Bohemian Massif, the widespread presence of subhorizontal fabrics is commonly explained by a continental underthrusting model. It assumes successive imbrication of underthrust lower plate followed by syn-convergent subhorizontal thrusting of lower crustal nappes over the middle crust, at distances of several hundred kilometres (Tollmann, 1982; Matte *et al.*, 1990; Matte, 1991; Finger & Steyer, 1995; Franke, 2000).

An alternative exhumation model has been proposed for the Variscan orogenic root in the Bohemian massif

stemming from an interpretation of the structural superposition of flat fabrics on steep foliations that are heterogeneously preserved along the eastern margin of the Bohemian Massif (Schulmann *et al.*, 2008). The model involves localized vertical extrusion of lower crust into middle crustal levels, where rocks from different depths are heterogeneously reworked within a flat fabric (Štípská *et al.*, 2004; Schulmann *et al.*, 2005; Racek *et al.*, 2006; Tajčmanová *et al.*, 2006). The development of the flat fabric along the eastern Variscan collisional front is attributed to the indentation of the Brunia continent to the east into the heterogeneous orogenic root. It is interpreted by Schulmann *et al.* (2008) to involve horizontal 'channel flow' of weak orogenic crust over the basement promontory (see also the models of Grujic *et al.*, 1996; Beaumont *et al.*, 2001; Jamieson *et al.*, 2002, 2007; Culshaw *et al.*, 2006). Once the lower crust material (e.g. high-pressure granulite and eclogite) is folded/extruded to mid-crustal levels, channel flow has the potential to tectonically mix the material with mid-crustal rocks, as well as account for the flat fabrics themselves.

Both the isostatic rebound and nappe stacking models (e.g. Matte, 1991; Dewey *et al.*, 1993) assume exhumation of the whole lower crust as a coherent high-pressure terrane affected by heterogeneous retrogression (for recent studies, see Engvik & Andersen, 2000; Ryan, 2001; Young *et al.*, 2007), whereas the vertical extrusion/subhorizontal flow model of Schulmann *et al.* (2008) or the 'heterogeneous' channel flow model of Beaumont *et al.* (2006) supposes that exhumation is heterogeneous and that rocks originally coming from different depths are mixed in a horizontally flowing matrix. Distinguishing between these amounts to establishing whether there is a concordance of *P–T* paths between the high-pressure boudins and surrounding matrix (see also Konopásek *et al.*, 2002; Štípská *et al.*, 2006). An area where this concordance may be tested occurs at the eastern margin of the Bohemian Massif, where eclogite and high-pressure granulite occur within a flat-fabric matrix dominated by paragneiss and amphibolite migmatite. As the high-pressure history of the eclogite boudins is well established (Štípská & Powell, 2005a), the focus in this paper will be on kyanite-K-feldspar granulite and especially on determination of prograde and peak conditions of the host matrix paragneiss via pseudosection modelling.

GEOLOGICAL SETTING

Field setting

The classical lithological division of the Variscan Moldanubian internal orogenic zone in the Bohemian Massif includes the Gföhl unit and Monotonous and Varied groups (e.g. Fuchs, 1986; Fig. 1). The Gföhl unit is characterized by high-grade rocks, recently interpreted as an orogenic lower crust (Schulmann *et al.*, 2005, 2008), and typically includes kyanite-K-feldspar granulite and Gföhl migmatite orthogneiss, hosting intermediate granulite and peridotite associated with eclogite (Carswell, 1991; Medaris *et al.*, 1995, 1998, 2005, 2006; O'Brien & Rötzler, 2003). The Monotonous group is composed of paragneisses with intercalated quartzite and amphibolite, whereas the Varied group paragneisses host marble and calcsilicate rocks in addition to amphibolite and quartzite intercalations. Generally, the Monotonous and Varied groups underwent upper amphibolite facies metamorphism and anatexis (Petrakakis, 1986, 1997; Schulmann *et al.*, 2008). In some places these groups contain eclogite boudins (Medaris *et al.*, 1995, 1998, 2005, 2006; O'Brien & Vrána, 1995; O'Brien, 1997).

This lithological and metamorphic subdivision can be only partly applied in the area studied, as shown in the east–west cross-section across the eastern margin of the Bohemian Massif (Fig. 2). In the west, migmatitic paragneisses of the Monotonous group typically contain numerous layers of quartzite and few amphibolite bodies. To the east, the migmatitic paragneisses contain numerous lenses of garnetiferous amphibolite, amphibolite associated with felsic fine-grained rocks (layered amphibolite) and abundant marble and calcsilicate. Such a lithological association is characteristic of the mid-crustal Varied group, but in places the marbles contain boudins of eclogite (quarry near Menhartice, Fig. 2). Around the town of Jemnice, the paragneisses include garnetiferous amphibolite, layered amphibolite, calcsilicate, eclogite (metre-scale boudins in the Police quarry and a several hundred metre body in the Jemnice town; Štípská & Powell, 2005a), and bodies of kyanite-K-feldspar granulite of up to several kilometres scale (Fig. 2). This assemblage has the lithological characteristics of the Gföhl lower crustal unit, as well as those of the mid-crustal Monotonous or Varied groups. To the east, a several hundred square kilometre-scale body of the Gföhl migmatite orthogneiss (Hasalová *et al.*, 2008a,b,c) with intercalated peridotites and serpentinites is surrounded by migmatitic paragneiss. Further to the east and structurally below, occurs an external orogenic zone represented by Brunia-derived crustal nappes with inverted Barrovian metamorphism (Štípská & Schulmann, 1995; Fritz *et al.*, 1996; Štípská *et al.*, 2000).

Structural evolution

The structural fabric of the westerly Monotonous group is marked by a steeply east-dipping foliation S1 that is folded by open to isoclinal recumbent folds with north–east-trending hinges and axial planes shallowly dipping to the east (Figs 2 & 3a). This folding commonly leads to the entire transposition of the early fabric into shallow east-dipping mylonitic and locally also migmatitic foliation S2 parallel to the axial planes of the recumbent folds. Both foliations are developed under amphibolite facies conditions.

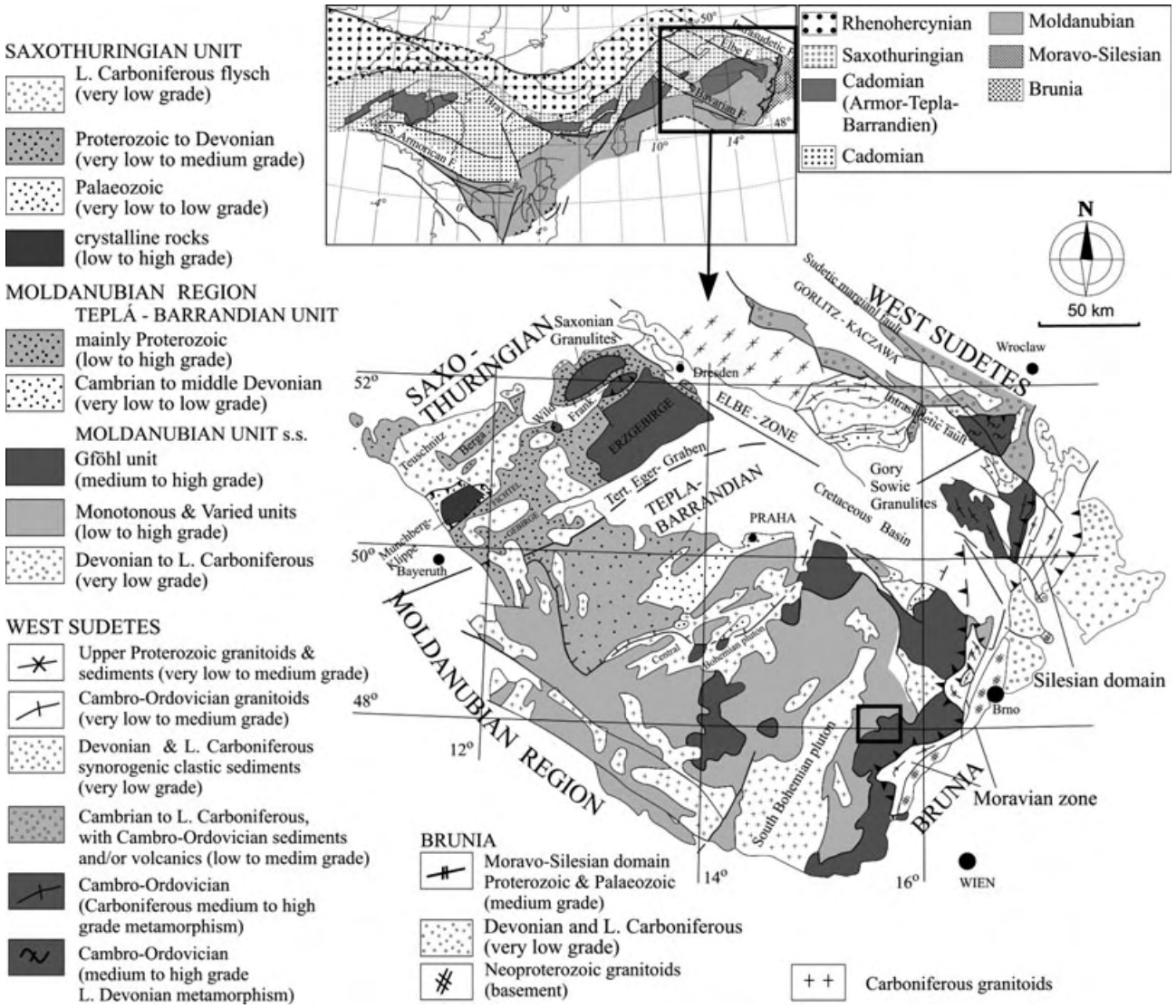

Fig. 1. Geological map of the Bohemian Massif with major units shown schematically (modified after Franke, 2000). Location of the study area (Fig. 2) is indicated. Upper left inset is position of study area in the framework of the European Variscides (modified after Edel *et al*., 2003).

The dominant structure further to the east, where the rocks cannot be clearly assigned to any of the classically distinguished units, is a generally flat-lying migmatitic foliation S2 that is either subhorizontal or shallowly dipping to the east or to the west (Figs 2 & 3b). This planar fabric is defined mostly by compositional layering, gneissosity, centimetre-scale coarse-grained leucosome bands in paragneiss and amphibolite, and by the oblate shape of eclogite boudins (Fig. 3b–f). In the felsic granulite and in the Gföhl orthogneiss, the flat foliation is also penetrative, defined by alternation of biotite-rich and biotite-poor layers and the orientation of biotite and recrystallized quartz and feldspar bands. Coarse-grained leucosomes are often developed in neck zones of intrafolial boudins in the amphibolite and paragneiss and in extensional gashes and shear bands affecting foliation of migmatites. A moderate north–south-trending subhorizontal mineral and stretching lineation L2 defined by sillimanite prisms and quartz rods is locally associated with asymmetrical boudinage and leucosome-filled shear bands that indicate predominantly top to the north-directed movement (Fig. 3e). The internal structure of eclogite is isotropic, not exhibiting the penetrative flat foliation that is characteristic of all other rock types (Fig. 3f). The flat foliation indicates a regime characterized by vertical shortening and a main NNE–SSW-stretching direction, with ductile flow in the presence of melt in a predominantly NNE direction (Schulmann *et al*., 1994).

Centimetre-scale isoclinal rootless folds that occur in layered amphibolite (Fig. 3d) may be interpreted as

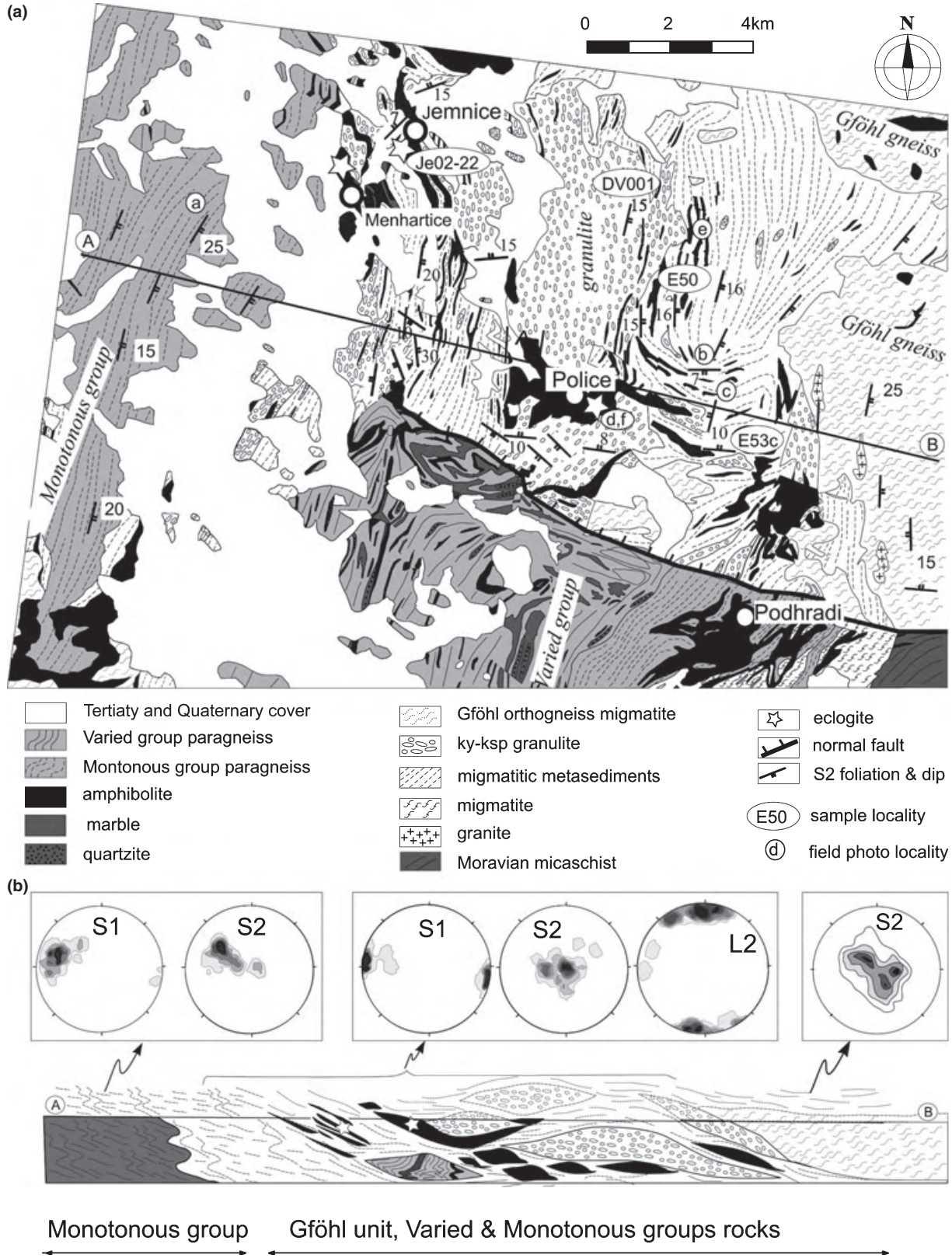

Fig. 2. (a) Simplified geological map of the area studied. Sample locations used for petrology, location of field photographs and the position of the structural profile are indicated. (b) Interpretative geological cross-section showing early steep fabric and style of superimposed subhorizontal deformation. Vertical axis not to scale.

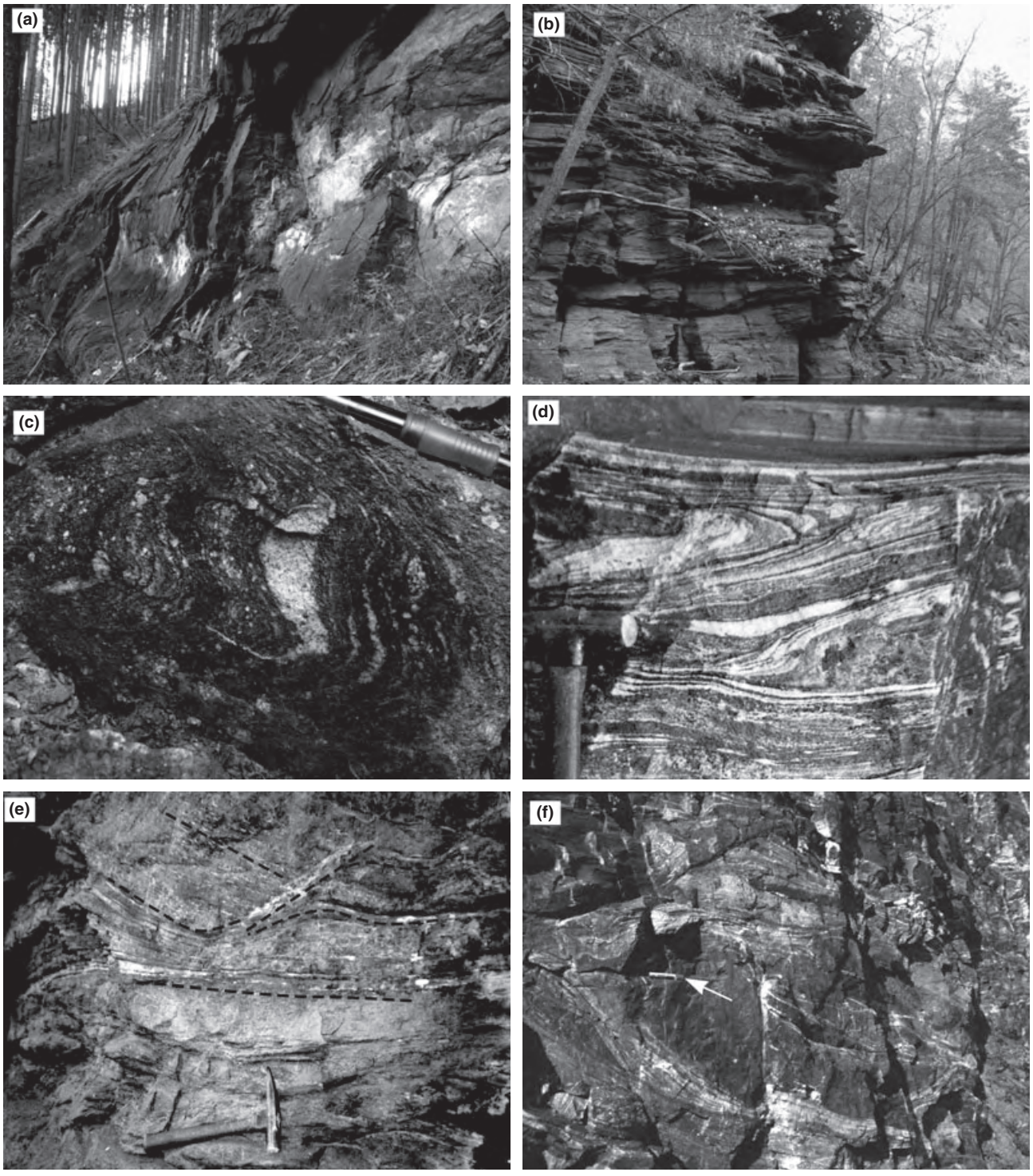

Fig. 3. Field photographs illustrating typical structural relationships (position indicated in Fig. 2). (a) Steep foliation folded by subhorizontal open folds in quartzite of the Monotonous group (Nové Hobzí). (b) Subhorizontal foliation in layered amphibolite and gneiss, typical for the areas west of the Monotonous group (Koberův mlýn). (c) Remnants of early steep foliation preserved within hinges of subhorizontal folds in a paragneiss (Peksův mlýn). (d) Isoclinal rootless folds within subhorizontal fabric of layered amphibolite (Police). (e) Shear bands filled with leucosome in migmatitic amphibolite indicate predominantly top to north movement (Tříletý mlýn). (f) Eclogite boudin wrapped in flat migmatitic fabric of layered amphibolite (the arrow shows a hammer, Police).

syn-schistosity folds developed during the formation of the flat foliation. However, an earlier steep north–south-trending migmatitic fabric refolded by centimetre- to metre-scale close to isoclinal folds with subhorizontal axial planes and north–south-trending subhorizontal hinges were identified in several outcrops (Fig. 3c). This disposition of steep fabric may indicate that the rootless folds are remnants of a regional-scale earlier steep foliation (Fig. 2b), a common feature in other areas along the eastern border of the Moldanubian domain (Štípská *et al.*, 2004; Schulmann *et al.*, 2005; Racek *et al.*, 2006; Tajčmanová *et al.*, 2006). However, in the area studied, the early steep fabric is commonly almost completely obliterated because of the NNE-directed ductile shearing (Schulmann *et al.*, 1994).

Geochronology at the eastern margin of the Bohemian Massif

Conventional multigrain zircon and U-Pb and Pb-Pb on single zircon methods in granulite yielded one group of ages between 400 and 370 Ma and a second group between 350 and 340 Ma (van Breemen *et al.*, 1982; Kröner *et al.*, 1988; Schulmann *et al.*, 2005). SHRIMP U-Pb zircon dating from granulite in Austria gave Ordovician *c.* 500 Ma cores, *c.* 345 Ma high-U inner rims and *c.* 335 Ma outer low-U rims (Friedl *et al.*, 2003). In addition, U-Pb multigrain dating of monazite from the Gföhl gneiss yielded 337 Ma (van Breemen *et al.*, 1982). The 500 Ma ages are interpreted as reflecting formation of the protolith, the 400–370 Ma ages as a result of Devonian back arc reworking (Finger & von Quadt, 1995; Schulmann *et al.*, 2005) or as the granulite protolith age (Wendt *et al.*, 1994; Janoušek *et al.*, 2006) and 350–340 Ma ages as the metamorphic peak (Friedl *et al.*, 2003; Schulmann *et al.*, 2005). The youngest ages around 335 Ma are considered as reflecting amphibolite facies retrogression. Cooling ages (Schulmann *et al.*, 2008) define an older group around 336 Ma from high closure temperature methods such as Sm-Nd whole-rock garnet (Brueckner *et al.*, 1991; Beard *et al.*, 1992; Medaris *et al.*, 1995, 1998, 2005, 2006) and $^{40}Ar/^{39}Ar$ in hornblende (Dallmeyer *et al.*, 1992), and a younger group between 331 and 325 Ma from low closure temperature methods such as $^{40}Ar/^{39}Ar$ in muscovite and biotite (Matte *et al.*, 1985; Dallmeyer *et al.*, 1992; Fritz *et al.*, 1996).

PETROGRAPHY

Analytical procedures and abbreviations

The minerals in the rocks were analysed using the Cameca SX100 at the Geological Institute of the Czech Academy of Sciences, in point-beam mode at 15 kV and 10 nA. Petrography is documented in Figs 4–6, representative mineral analyses are summarized in Tables 1–3 and garnet chemistry is shown in Fig. 7. The sign '= >' is used for indicating a trend in mineral composition or for zoning and the sign '–' for a range of mineral compositions. The mineral abbreviations used are listed in the footnote of Table 1.

Previous petrological studies

Štípská & Powell (2005a) studied eclogite boudins that occur within the flat fabric in Jemnice town (sample Je02-22 in Fig. 2). Garnet inclusions suggest that garnet grew in the presence of hornblende and plagioclase rather than zoisite, and garnet preserves prograde zoning. These features are compatible with isothermal burial at 730–750 °C up to about 17–18 kbar and indicate a steep geothermal gradient during prograde evolution. The plagioclase-hornblende coronas around garnet and symplectite of plagioclase and diopside with hornblende within the matrix indicate retrogression around 11 kbar within the hornblende stability field at a temperature of around 800 °C. Disappearance of garnet and its replacement by plagioclase and hornblende within the flat fabric in the marginal parts of the eclogite boudins are interpreted as resulting from further decompression.

Petrography of kyanite-K-feldspar granulite and migmatite paragneiss

As the *P–T* path of the eclogite is established (Štípská & Powell, 2005a), the focus is on the kyanite-K-feldspar granulite and particularly on the paragneiss matrix.

Kyanite-K-feldspar granulite

The kyanite-K-feldspar granulite is a foliated, fine-grained (0.1–0.2 mm) rock composed of plagioclase, K-feldspar, quartz, garnet, kyanite, sillimanite, biotite and rutile. The flat foliation (S2) is defined by recrystallized ribbons of quartz and feldspar, and planar orientation of kyanite, biotite and sillimanite and in some places by centimetre- to decimetre-scale alternation of biotite-rich and biotite-poor layers.

Sample DV001b is derived from a biotite-rich layer and is composed of bi-g-ky-sill-q-ru-pl-ksp and antiperthite. Garnet contains inclusions of quartz, plagioclase, antiperthite (0.5 mm), biotite and rutile (Fig. 4). Texturally, some garnet exhibit two stages of growth with a boundary marked by antiperthite, plagioclase and biotite (Fig. 4a–d). In Fig. 4b,c, antiperthite included in garnet has a K-feldspar lamellae-rich core with a plagioclase rim that contains a biotite inclusion. Plagioclase inclusions without K-feldspar exsolution lamellae are also included in garnet (Fig. 4b–d). Antiperthite also occurs as large relicts (Fig. 4e) within a finely recrystallized matrix of plagioclase, K-feldspar and quartz (0.1–0.2 mm). Oriented biotite, kyanite and sillimanite in the matrix, together with oriented

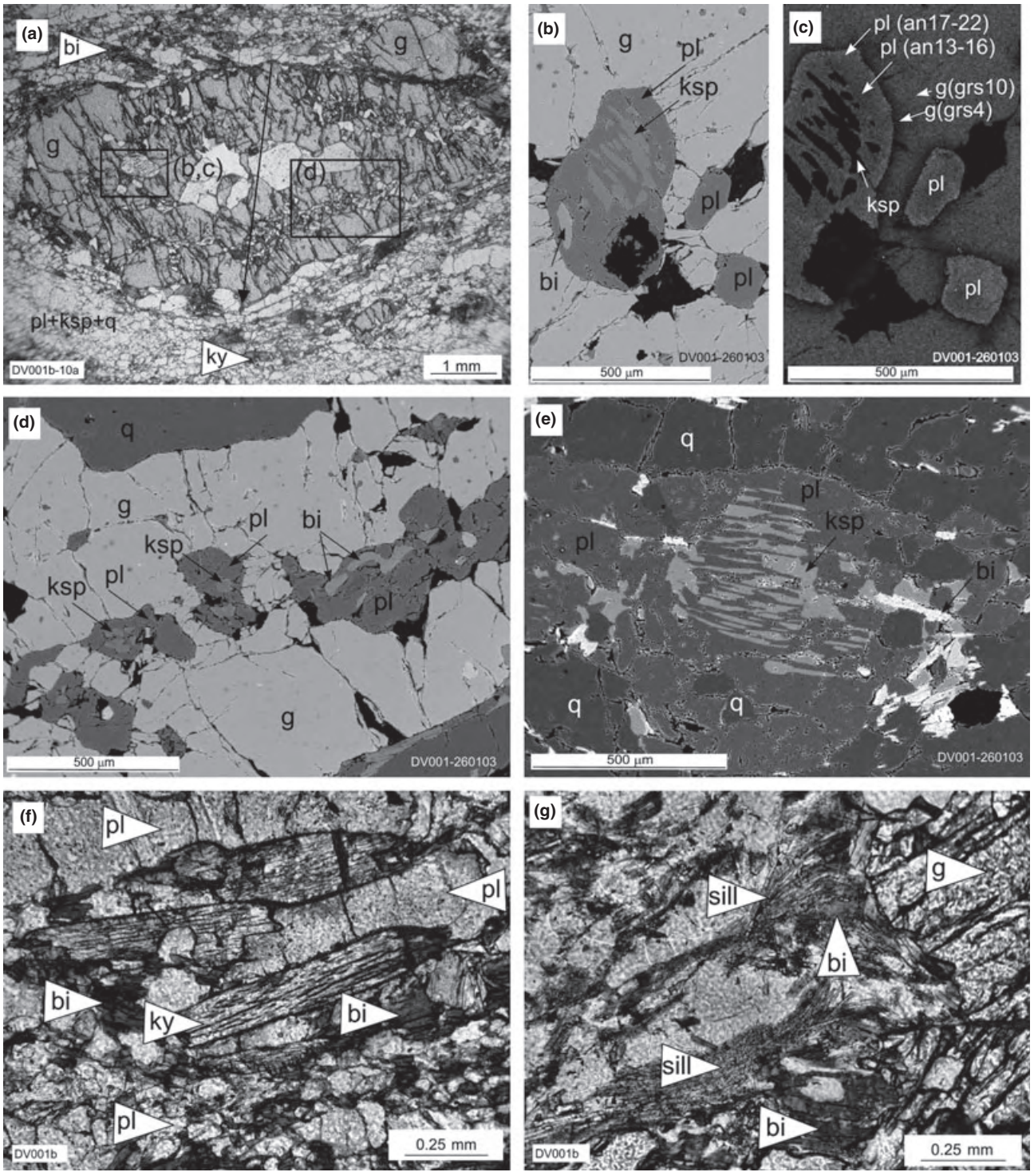

Fig. 4. Photomicrographs of kyanite-K-feldspar granulite (plane-polarized light and BSE). (a) Large texturally two-stage garnet in flat foliation. The arrow indicates profile in Fig. 7. (b & c) Detail of antiperthite, biotite and plagioclase included in garnet. (d) Detail of plagioclase, K-feldspar and biotite included at a boundary suggesting two stages of garnet growth. (e) Relic antiperthite within recrystallized matrix. (f) Kyanite in flat foliation with coronas of plagioclase separating it from the matrix. (g) Sillimanite-biotite intergrowth in S2 pressure shadows of garnet.

ribbons of recrystallized quartz, define the S2 foliation. However, kyanite is commonly isolated from the matrix by a plagioclase corona (Fig. 4f) (see also Tajčmanová *et al.*, 2007). Some biotite is also associated with sillimanite in S2 pressure shadows around garnet (Fig. 4g).

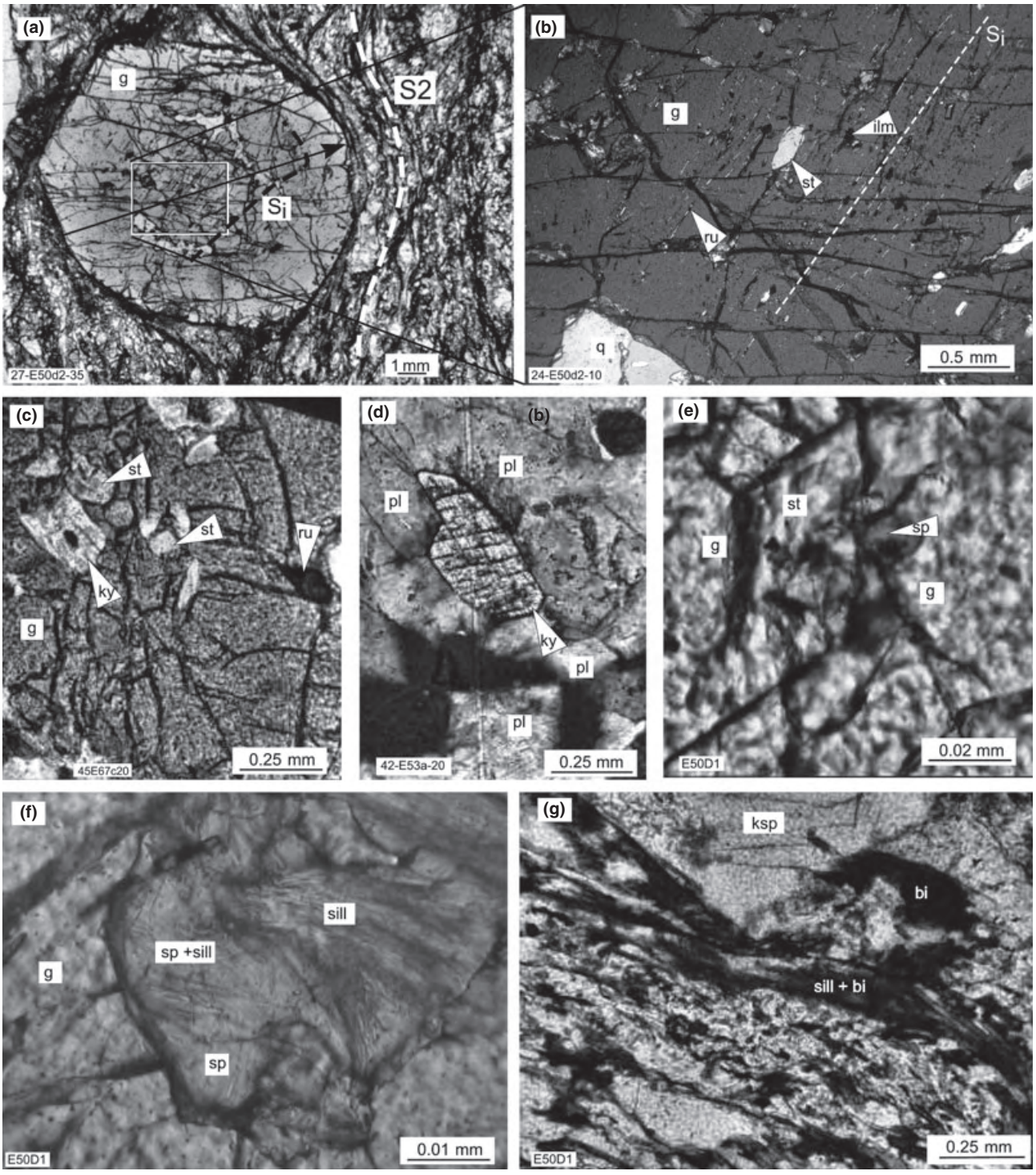

Fig. 5. Photomicrographs of kyanite and/or staurolite bearing paragneiss (plane-polarized light and BSE). (a) Large garnet in flat foliation. Direction of internal inclusion trails is underlined. The arrow indicates profile shown in Fig. 7. (b) Detail of oriented staurolite, ilmenite and rutile inclusions within garnet from (a). (c) Inclusions of kyanite, staurolite and rutile in garnet. (d) Kyanite separated by plagioclase corona from the matrix quartz and K-feldspar. (e) Spinel next to staurolite in garnet. (f) Spinel and sillimanite in garnet, interpreted as pseudomorphs after staurolite. (g) Sillimanite and biotite in matrix flat foliation.

In the two-stage garnet, the grossular profile is flat but decreases at garnet rims or at contact with plagioclase; X_{Fe} is also flat with a slight increase at the garnet rim ($alm_{0.51=>0.57}grs_{0.11=>0.03}py_{0.37–0.38}sps_{0.0–0.01}$; $X_{Fe} = 0.58 => 0.62$, Figs 4a & 7a). The anorthite content of plagioclase increases from core to rim,

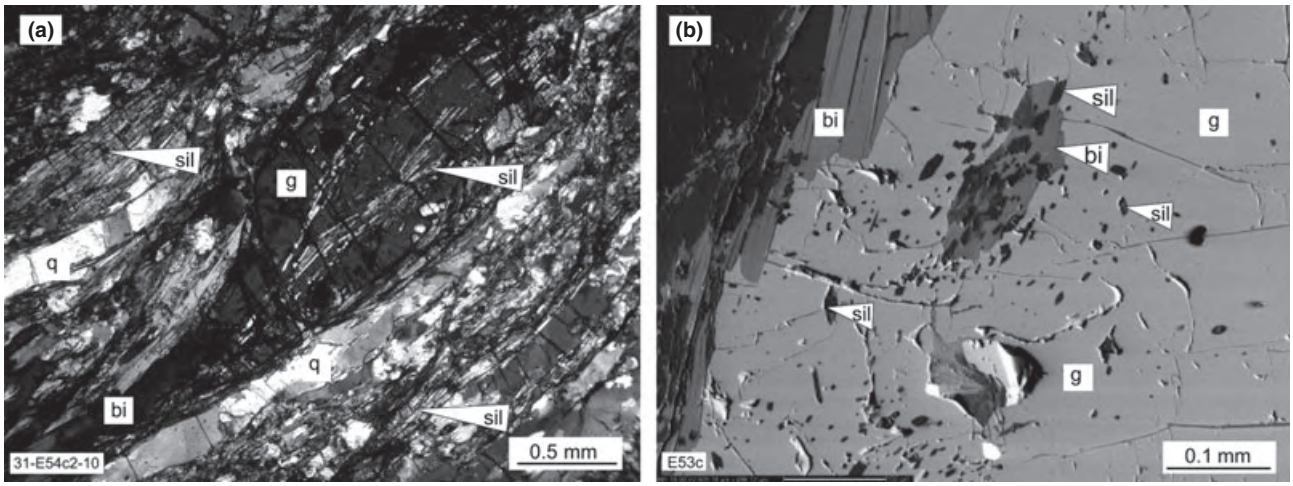

Fig. 6. Photomicrographs of paragneiss with texture of garnet including oriented sillimanite (plane polarized light and BSE). (a) Included sillimanite in garnet is oriented parallel to the external flat foliation. (b) Detail of sillimanite and biotite included at garnet rim.

Table 1. Representative mineral analyses: ky-ksp granulite DV001.

Mineral	g-core	g-rim	pl-mx-core	pl-mx-r	pl-cont-g	pl-exs	ksp-host	bi-in	bi-mx	bi-cont-g
Analysis	x1-1	x2-45	20	67	x6	x13	x14	x8	x23	x26
SiO_2	39.50	39.40	64.89	64.39	62.63	64.91	64.70	37.24	36.40	37.58
TiO_2	0.04	0.00	0.01	0.01	0.02	0.02	0.00	5.61	4.27	3.21
Al_2O_3	21.96	22.03	21.90	21.62	23.39	21.92	18.62	15.92	17.75	17.71
FeO	25.83	28.59	0.00	0.13	0.28	0.00	0.06	11.50	11.83	11.16
MnO	0.32	0.00	0.06	0.00	0.00	0.00	0.03	0.01	0.00	0.05
MgO	9.02	9.14	0.01	0.00	0.00	0.01	0.01	13.93	14.00	15.83
CaO	3.75	1.20	2.90	3.60	4.90	3.10	0.07	0.03	0.06	0.05
Na_2O	0.02	0.00	10.32	8.96	8.99	10.29	1.97	0.04	0.13	0.14
K_2O	0.01	0.00	0.22	0.84	0.57	0.20	14.44	10.01	9.88	9.70
Total	100.45	100.36	100.31	99.55	100.78	100.45	99.90	94.29	94.32	95.43
Oxygen	12	12	8	8	8	8	8	11	11	11
Si	3.02	3.02	2.84	2.87	2.75	2.84	2.97	2.87	2.79	2.80
Ti	0.00	0.00	0.00	0.00	0.00	0.00	0.00	0.33	0.25	0.18
Al	1.98	1.99	1.13	1.13	1.21	1.13	1.01	1.45	1.60	1.56
Fe^{3+}	0.00	0.00	0.00	0.00	0.01	0.00	0.00	0.00	0.00	0.00
Fe^{2+}	1.65	1.84	0.00	0.00	0.00	0.00	0.00	0.74	0.75	0.70
Mn	0.02	0.00	0.00	0.00	0.00	0.00	0.00	0.00	0.00	0.00
Mg	1.03	1.05	0.00	0.00	0.00	0.00	0.00	1.60	1.60	1.76
Ca	0.31	0.09	0.14	0.17	0.23	0.15	0.00	0.00	0.00	0.00
Na	0.00	0.00	0.88	0.77	0.77	0.87	0.18	0.00	0.02	0.02
K	0.00	0.00	0.01	0.05	0.03	0.01	0.84	0.99	0.97	0.92
cat	8.00	8.00	5.00	5.00	5.00	5.00	5.00	7.98	7.98	7.94
X_{Fe}	0.62	0.64						0.32	0.32	0.28
an/or/grs	grs = 0.10	grs = 0.03	an = 0.13	an = 0.17	an = 0.22	an = 0.14	or = 0.83			

in, inclusion in garnet; mx, matrix; exs, exsolutions in ternary feldspar; host, in ternary feldspar; cont-g, contact with garnet; mu, muscovite; q, quartz; chl, chlorite; g, garnet; st, staurolite; bi, biotite; ky, kyanite; sill, sillimanite; and, andalusite; cd, cordierite; pa, paragonite; ma, margarite, ep, epidote; pl, plagioclase; ksp, K-feldspar; liq, granitic liquid; o, omphacitic clinopyroxene; ilm, ilmenite; ru, rutile; sp, spinel; crn, corundum.
alm = Fe/(Ca + Fe + Mg + Mn), prp = Mg/(Ca + Fe + Mg + Mn), grs = Ca/(Ca + Fe + Mg + Mn), sps = Mn/(Ca + Fe + Mg + Mn), XFe = Fe/(Fe + Mg), an = Ca/(Ca + Na + K), ab = Na/(Ca + Na + K), or = K/(Ca + Na + K).
The isopleth notation used is: x(g, st) = Fe/(Fe + Mg) × 100, z(g) = Ca/(Ca + Fe + Mg) × 100, ca(pl) = Ca/(Ca + Na) × 100.

ranging from 0.13 to 0.16 in the matrix grains, and reaching 0.17–0.22 at direct contact with garnet. Relics of large matrix K-feldspar with perthitic exsolutions are more albitic ($or_{0.74–0.78}ab_{0.21–0.26}$) than recrystallized K-feldspar ($or_{0.90}ab_{0.10}$). In the antiperthite matrix grain (Fig. 4e), the average composition of the plagioclase host is $ab_{0.86}an_{0.13}or_{0.01}$ and the K-feldspar exsolution lamellae is $ab_{0.14}an_{0.00}or_{0.86}$. If the host and lamellae in the core are combined with the exsolution-free rim, giving pl = 78% and ksp = 22%, the reintegrated composition is $ab_{0.70}an_{0.10}or_{0.20}$. If only the host and lamellae in the core are combined (pl = 58% and ksp = 42%), the reintegrated composition is $ab_{0.55}an_{0.08}or_{0.37}$ (for details see also the discussion in Štípská &

Table 2. Representative mineral analyses: paragneiss E50d.

Mineral	g-core	g-rim	pl-mx	pl-mx	ksp-core	ksp-rim	bi-mx	st-in	sp-in
Analysis	x34-26	x34-53	65	14	3	7	26	3	41
SiO_2	37.54	37.79	66.36	62.47	65.62	67.83	35.30	25.89	0.02
TiO_2	0.03	0.02	0.00	0.00	0.00	0.00	3.52	1.04	0.02
Al_2O_3	21.09	21.06	20.88	23.02	18.66	20.07	17.66	54.34	58.24
FeO	31.12	32.29	0.00	0.00	0.02	0.00	20.35	12.44	27.41
MnO	3.22	1.51	0.00	0.00	0.01	0.00	0.06	0.20	0.19
MgO	2.33	4.94	0.00	0.00	0.00	0.00	9.78	2.13	4.68
CaO	5.08	2.23	2.33	4.92	0.21	0.61	0.00	0.00	0.02
Na_2O	0.00	0.01	10.36	8.76	4.22	10.42	0.14	0.00	Cr_2O_3 0.35
K_2O	0.00	0.00	0.14	0.29	10.80	1.12	9.64	0.00	ZnO 9.38
Total	100.41	99.85	100.07	99.46	99.54	100.05	96.45	96.04	100.31
Oxygen	12	12	8	8	8	8	11	24	6
Si	3.00	3.00	2.91	2.78	2.99	2.98	2.73	3.49	0.00
Ti	0.00	0.00	0.00	0.00	0.00	0.00	0.21	0.11	0.00
Al	1.99	1.97	1.08	1.21	1.00	1.04	1.61	8.63	1.94
Fe^{3+}	0.01	0.02	0.00	0.00	0.00	0.00	0.00	0.00	0.05
Fe^{2+}	2.07	2.12	0.00	0.00	0.00	0.00	1.32	1.40	0.60
Mn	0.22	0.10	0.00	0.00	0.00	0.00	0.00	0.02	0.00
Mg	0.28	0.59	0.00	0.00	0.00	0.00	1.13	0.43	0.20
Ca	0.44	0.19	0.11	0.24	0.01	0.03	0.00	0.00	0.00
Na	0.00	0.00	0.88	0.76	0.37	0.89	0.02	0.00 Cr	0.01
K	0.00	0.00	0.01	0.02	0.63	0.06	0.95	0.00 Zn	0.20
cat	8.00	8.00	5.00	5.00	5.00	5.00	7.97	14.08	3.00
X_{Fe}	0.88	0.78						0.77	0.75
an/or/grs	grs = 0.15	grs = 0.06	an = 0.11	an = 0.23	or = 0.62	or = 0.91			

in, inclusion in garnet; mx, matrix; cont-g, contact with garnet.

Table 3. Representative mineral analyses: paragneiss E53c.

Mineral	g-core	g-rim	pl		bi-mx
Analysis	42	62.00	22	ksp	16
SiO_2	37.82	37.77	62.552	65.214	35.571
TiO_2	0.12	0.00	0.000	0.000	4.959
Al_2O_3	21.17	21.05	23.402	18.839	18.046
FeO	32.13	33.30	0.000	0.000	19.336
MnO	1.00	1.60	0.000	0.000	0.000
MgO	5.77	4.26	0.000	0.000	8.613
CaO	2.05	1.95	5.075	0.000	0.000
Na_2O	0.00	0.00	8.787	2.550	0.330
K_2O	0.00	0.00	0.185	13.116	9.632
Total	100.05	99.93	100.00	99.72	96.49
Oxygen	12	12	8	8	11
Si	2.98	3.01	2.772	2.989	2.776
Ti	0.01	0.00	0.000	0.000	0.291
Al	1.97	1.98	1.222	1.018	1.660
Fe^{3+}	0.05	0.00	0.00	0.00	0.000
Fe^{2+}	2.07	2.22	0.000	0.000	1.262
Mn	0.07	0.11	0.000	0.000	0.000
Mg	0.68	0.51	0.000	0.000	1.002
Ca	0.17	0.17	0.241	0.000	0.000
Na	0.00	0.00	0.755	0.227	0.050
K	0.00	0.00	0.010	0.767	0.959
cat	8.00	8.00	5.00	5.00	8.00
X_{Fe}	0.75	0.81			0.560
an/or/grs	grs = 0.06	grs = 0.06	an = 0.24	or = 0.77	

in, inclusion in garnet; mx, matrix.

Powell, 2005b). These reintegrated compositions give, at 15 kbar, temperatures of 900 and 950 °C, respectively, using the Fuhrman & Lindsley (1988) calibration. The titanium content of biotite included in garnet is higher (X_{Fe} = 0.29–0.32 and Ti = 0.30–0.33 p.f.u.) than in the matrix biotite (X_{Fe} = 0.29–0.32 and Ti = 0.20–0.24 p.f.u.) or in biotite in direct contact with garnet (X_{Fe} = 0.29–0.32 and Ti = 0.18–0.19 p.f.u.).

Paragneisses

The paragneisses are opthalmitic with millimetre- to centimetre-scale quartzofeldspathic augen or centimetre-scale leucosome layers and lenses alternating with biotite-rich layers, defining the flat S2 foliation. Leucosomes are composed of quartz and up to 3 cm feldspar that shows locally reduced grain size (0.2–0.5 mm) interpreted to be due to recrystallization associated with the late stage of flat fabric development. The dominant assemblage in the paragneisses is bi-pl-ksp-q, commonly with prismatic and/or fibrolitic sillimanite and rare garnet (Fig. 5g). Kyanite relicts are rarely enclosed within matrix plagioclase or in garnet (Fig. 5c,d). Garnet also includes rare staurolite, sillimanite, and common quartz, plagioclase, rutile and ilmenite (Figs 5a–c & 6). Sillimanite and feldspar are rarely replaced by muscovite. Based on contrasting mineralogy and contrasting textural relationships that indicate different sequences of crystallization, two samples of paragneisses (E50 & E53) that contain garnet with inclusions were selected for a detailed study.

The sample E50 contains g-bi-sill-pl-ksp-q-ru-ilm-st-sp-crn. Garnet (up to 5 mm) includes staurolite, quartz, plagioclase, biotite, rutile and ilmenite (Fig. 5a,b). The core of the garnet has straight inclusion trails of tiny rutile and staurolite oriented perpendicular to the inclusion trails in the garnet rim and the external S2 foliation (Fig. 5a,b). These features are interpreted in terms of superposition of two nearly perpendicular foliations during garnet growth. Macroscopically, the latter (flat foliation) refolds the former (steep foliation). Garnet exhibits strong zoning

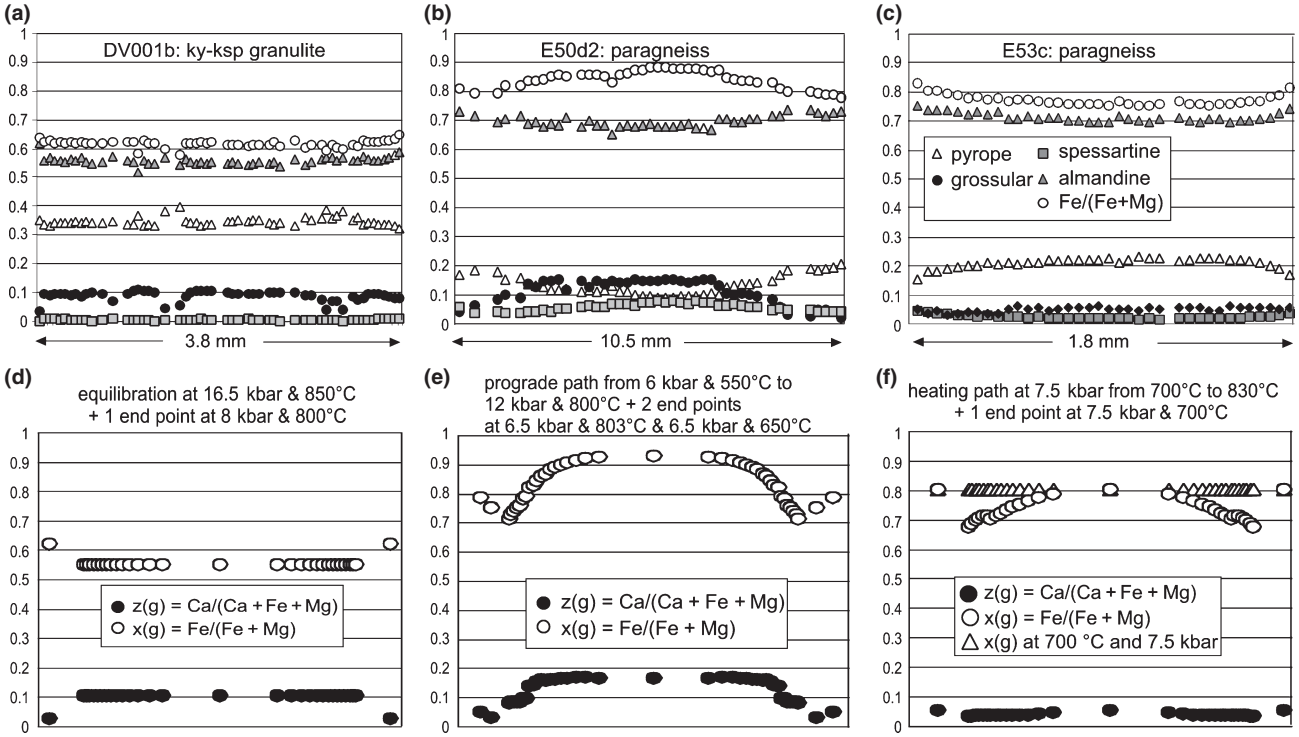

Fig. 7. Measured (a–c) and modelled (d–f) garnet profiles. See text for details.

characterized by increase in almandine and pyrope, and decrease in grossular, spessartine and X_{Fe} from core to rim ($alm_{0.65=>0.75}grs_{0.17=>0.03}$ $py_{0.10=>0.22}$ $sps_{0.10=>0.01}$; X_{Fe} = 0.90 = > 0.78; Figs 5a & 7b). The outermost rim shows an increase in spessartine and slight increase in X_{Fe} ($sps_{0.06}$; X_{Fe} = 0.82). Staurolite included in garnet has X_{Fe} = 0.75–0.80. Spinel with fibrolitic sillimanite and/or corundum occurs at some staurolite rims (Fig. 5e,f). The matrix foliation is defined by prismatic sillimanite that is commonly associated with red-brown biotite (X_{Fe} = 0.46–0.57; Ti = 0.18–0.23 p.f.u; Fig. 5g). Within the recrystallized felsic lenses, plagioclase (an = 0.22–0.27) occurs with up to 2 mm perthitic K-feldspar porphyroblasts (ab = 0.3). Matrix accessories are rare rutile and abundant ilmenite.

The sample E53c contains g-bi-sill-pl-ksp-q-ilm (Fig. 6). The foliation is defined by felsic layers formed by coarse-grained feldspar and quartz alternating with biotite-sillimanite-rich layers. Garnet includes oriented needles of prismatic sillimanite that continue to the external S2 foliation, the texture being interpreted as garnet overgrowing the biotite-sillimanite flat foliation (Fig. 6a). Garnet shows a relatively flat distribution of elements with slight increase in X_{Fe} from core to rim ($alm_{0.70=>0.74}$ $grs_{0.06=>0.03}py_{0.23=>0.15}sps_{0.02=>0.04}$; X_{Fe} = 0.76 = > 0.82; Fig. 7c). Biotite has X_{Fe} = 0.48–0.56 and Ti = 0.13–0.29 p.f.u, plagioclase contains 19–28% of anorthite and K-feldspar has 9–23% of albite.

PSEUDOSECTION MODELLING

Calculation methods

The pseudosections were calculated using THERMOCALC 3.25 (Powell *et al.*, 1998; 2007 version) and the DATASET 5.5 (Holland & Powell, 1998; November 2003 upgrade), in the system Na_2O-CaO-K_2O-FeO-MgO-Al_2O_3-SiO_2-H_2O-TiO_2-O (NCKFMASHTO) with the biotite and melt models from White *et al.* (2007), ilmenite and garnet from White *et al.* (2000), feldspar from Holland & Powell (2003), paragonite-muscovite from Coggon & Holland (2002) and other models from THERMOCALC documentation (Powell & Holland, 2004). The analysed rock compositions were used, with the amount of H_2O chosen after construction of *T–M*(H_2O) sections (not shown; see Hasalová *et al.*, 2008c for approach). Mineral composition and molar proportion isopleths (abbreviations listed in Table 1) were plotted for the phases of interest and especially in order to study garnet growth and its zoning along specified *P–T* trajectories.

Pseudosection for granulite sample DV001

The composition of the sample DV001, in wt%, is SiO_2 = 66.68, TiO_2 = 0.77, Al_2O_3 = 15.92, FeO_{tot} = 4.16, MnO = 0.04, MgO = 2.94, CaO = 1.43, Na_2O = 3.69, K_2O = 2.59, P_2O_5 = 0.18 (by standard wet chemical methods). This composition was modified

for modelling by adding 1 mol.% of kyanite to enable a small amount of aluminosilicate to be stable at the estimated peak metamorphic conditions (860°C and 14 kbar, see below) and on decompression, as it is observed in the thin section. H_2O = 1.65 mol.% in the rock composition allows the observed assemblage g-bi-sill-ru-pl-ksp-pl with garnet X_{Fe} = 0.60–0.62 to be stable on the pseudosection. Higher H_2O shifts the liquid-out line to lower temperature where x(g) is higher than that observed in the sample, and lower H_2O moves the liquid-out line to higher temperature where x(g) is lower than that observed (not shown).

The major features of the pseudosection involve melt being stable above 820 °C and the muscovite-out line located from 15 kbar at low temperature heading through 830 °C at 15 kbar to 950 °C at 25 kbar. Biotite is stable up to 21 kbar and 900 °C, omphacite is stable above 18 kbar, the plagioclase-out line is located above 19 kbar and the cordierite-out line is below 7 kbar.

The textural and compositional features of the sample DV001 suggest that kyanite and the second-stage, high-grossular garnet belong to the same assemblage. The antiperthite must have already been present in the rock when the second-stage garnet grew, and because biotite and plagioclase are also included, the second garnet growth occurred in the stability field of biotite and non-ternary feldspar. The antiperthite is therefore likely to be a relic that is not related to the peak pressure assemblage (see also Štípská & Powell, 2005b). The low grossular garnet rim, high anorthite plagioclase rim, and sillimanite plus biotite that formed at the expense of garnet, belong to a later assemblage related to the S2 foliation.

These features are compatible on the pseudosection with a decompression path that goes from the field g-bi-ky-liq-pl-ksp-q-ru to the g-bi-sill-liq-pl-ksp-q-ru field, followed or accompanied by cooling. Compositional isopleths z(g) = 10, x(g) = 58 and ca(pl) = 13 constrain the likely equilibration conditions of the early assemblage to 15–18 kbar and 840–870 °C (area A1 in Fig. 8) and the isopleths z(g) = 3, x(g) = 60–62 and ca(pl) = 17 indicate conditions of about 7–9 kbar and 800–840 °C for the second sillimanite-bearing assemblage associated with S2 (area A2 in Fig. 8). It grew at the expense of garnet (with X_{Fe} = 0.62) in S2 pressure shadows. In the pseudosection, it is compatible with equilibration on cooling to 840 °C in the presence of melt within the g-bi-sill-liq-pl-ksp-q-ru where garnet molar isopleths decrease and x(g) changes until x(g) = 60 (area A2 in Fig. 8). After the liq-out line is crossed, the garnet molar content remains constant, the spacing of x(g) isopleths is much larger, reaching x(g) = 62, the measured X_{Fe} value at the garnet rim.

A hypothetical garnet profile for diffusive equilibration at 16.5 kbar and 850 °C with rims that tend to be equilibrated towards compositions at 8 kbar and 800 °C is calculated from the pseudosection isopleths and shown in Fig. 7d. The trends and absolute values approximate the measured garnet profile (Fig. 7a), indicating that it is consistent with such a P–T path (path A, Fig. 8).

Pseudosections for paragneiss

The composition of the paragneiss sample E54c containing garnet-sillimanite-biotite-plagioclase-K-feldspar-quartz is used for modelling and discussion of observed petrographic features in both paragneiss samples studied (in wt%: SiO_2 = 61.50, TiO_2 = 1.18, Al_2O_3 = 18.30, FeO_{tot} = 8.90, MnO = 0.21, MgO = 2.69, CaO = 1.50, Na_2O = 2.01, K_2O = 2.07, P_2O_5 = 0.13; standard wet chemical methods). Because the rock composition does not come from the same sample as the thin sections described, the results should be taken only as a guide in determination of approximate P–T conditions, but should be able to allow discussion of the overall shape of the P–T paths. The reconstruction of a prograde path for paragneiss migmatites requires several steps. It involves the determination of H_2O in the final assemblage, consideration of open system behaviour with respect to melt, and modification of the whole-rock composition by adding (or subtracting) melt (White & Powell, 2002; White *et al.*, 2004). Tracking of the P–T path must therefore be undertaken backwards in time, from the matrix assemblage to the early prograde evolution. As the whole-rock composition is expected to change along the P–T path via loss of melt and/or H_2O, individual segments of the P–T path are modelled in pseudosections calculated for different whole-rock compositions. First, pseudosections are presented for the reconstruction of the P–T path for sample E50 (labelled as path B) and then the same pseudosections are used to discuss the evolution of sample E53c (labelled as path C).

Pseudosection for paragneiss with dry solidus: applied to sample E50

The first pseudosection is constructed for H_2O = 1.91 mol.% that allows stability of the observed assemblage g-bi-sill-ksp-pl-q-ilm at the solidus, with isopleths approximating the rim mineral compositions in sample E50 (Fig. 9). In a T–$M(H_2O)$ section (not shown), a larger H_2O amount causes K-feldspar not to be stable at subsolidus conditions, whereas a lower H_2O amount shifts the solidus to higher temperature and consequently the x(g) values at the solidus are too low compared with measured values. The major features of the pseudosection include a steep solidus at 770–810 °C, a steep biotite-out line at 800–840 °C, cordierite stability below 6.5 kbar for temperatures between 700 and 850 °C, stability of rutile above 6.5 kbar and stability of ilmenite below 8 kbar.

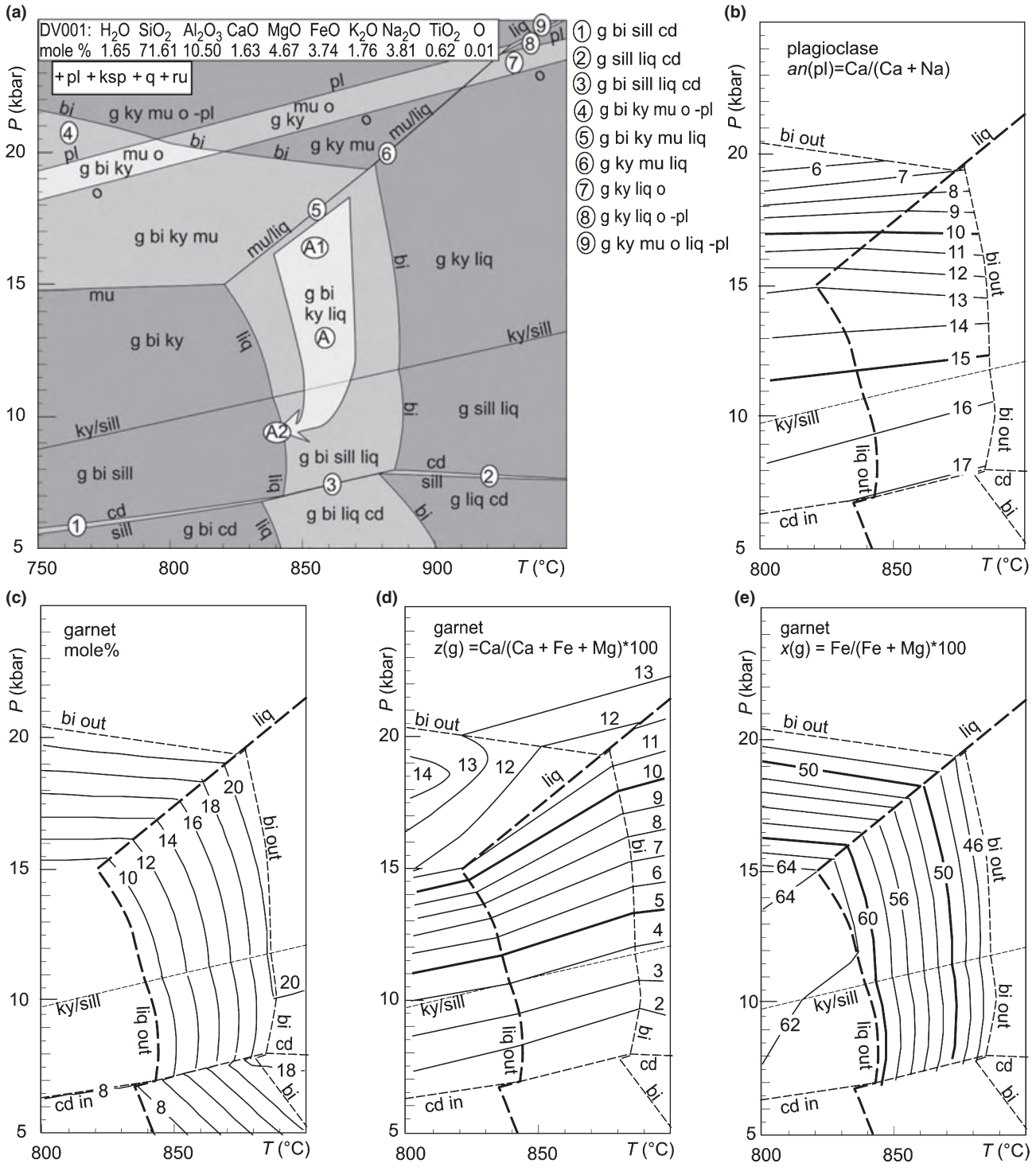

Fig. 8. Pseudosection calculated for the rock composition of the granulite sample DV001 (in moles adjusted to 100%). *P–T* path is derived by comparing the modelled assemblages and isopleths with assemblages, chemistry and zoning of minerals observed in the sample. See text for details. (b–e) Enlarged and simplified parts of the pseudosection with calculated isopleths of mineral composition and molar proportions.

The paragenetic relations in sample E50 involve oriented inclusions of staurolite, ilmenite and rutile in strongly zoned garnet. Staurolite inclusions in garnet are surrounded by hercynite and sillimanite and/or corundum, indicating their decomposition in an SiO_2-undersaturated environment within the garnet. The matrix comprises garnet, sillimanite, biotite, plagioclase, K-feldspar, ilmenite and quartz. The matrix

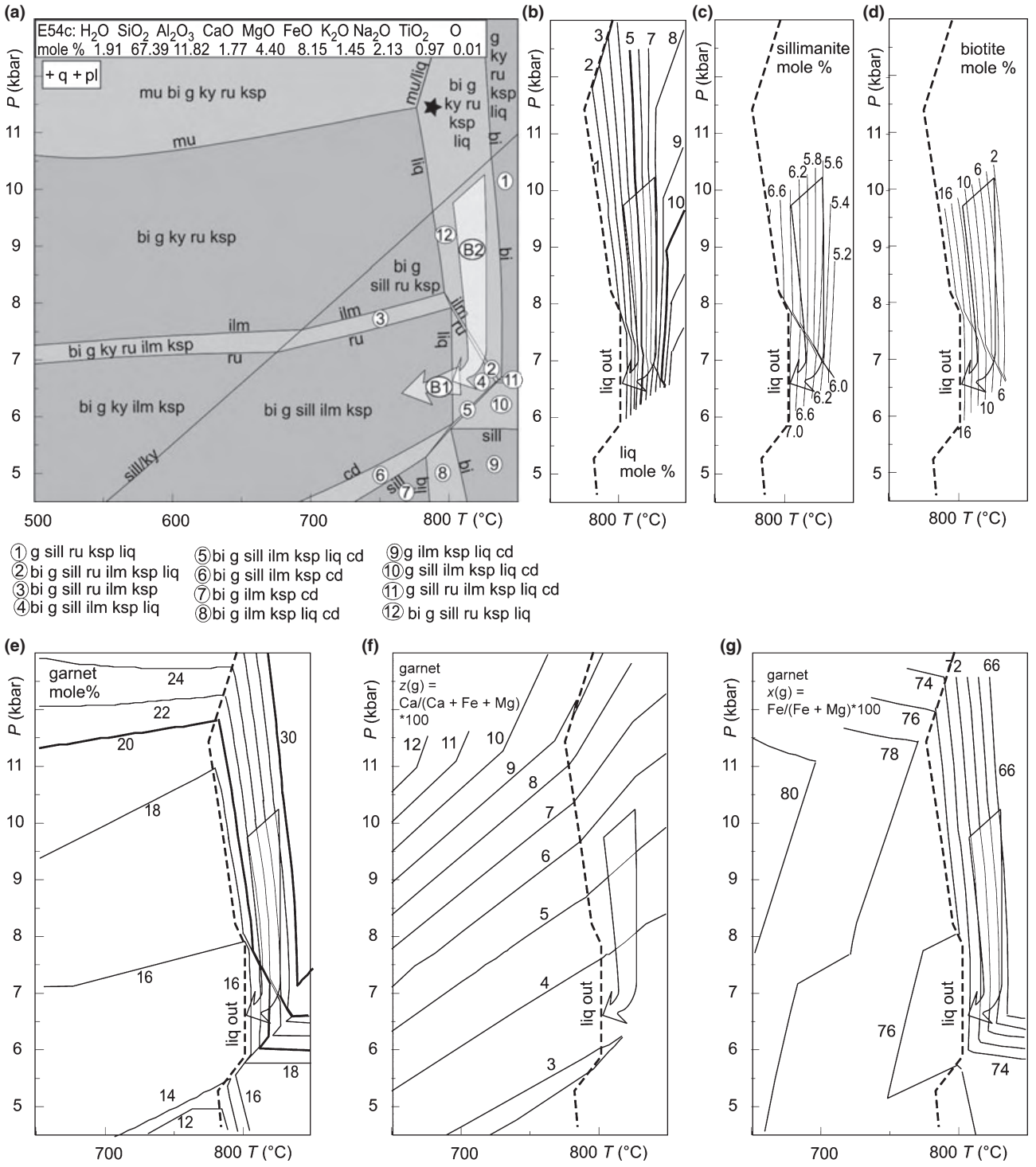

Fig. 9. Pseudosection calculated for the model rock composition of the paragneiss sample E54 (in moles adjusted to 100%). H_2O = 1.91 is set to explain the assemblages on retrogression. *P–T* path is derived by comparing the modelled assemblages and isopleths with assemblages, chemistry and zoning of minerals observed in the studied sample (E50d). Star indicates *P–T* conditions where melt is reintegrated. See text for details. (b–g) Enlarged and simplified parts of the pseudosection with calculated isopleths of mineral composition and molar proportions for the areas of interest.

assemblage is compatible with a cooling path in the bi-g-sill-ilm-ksp-pl-q field (Fig. 9), where the garnet rim composition (grs = 3–4%, X_{Fe} = 0.79–0.80) approximately matches the calculated isopleths. The occurrence of biotite and sillimanite in garnet pressure shadows is explained in the pseudosection by

decreasing the molar proportion of garnet (Fig. 9e) and increasing the proportion of biotite and sillimanite (Fig. 9c,d), with cooling in the bi-g-sill-ilm-ksp-pl-q-liq field until the liq-out line is reached (segment B1 of path B, Fig. 9). The absence of rutile within the matrix is explained by crossing the ilm-in and ru-out line as indicated by the arrow B2, suggesting decompression (Fig. 9). The earlier evolution cannot be explained in this pseudosection because staurolite-bearing assemblages are not stable on the diagram.

Pseudosection for paragneiss with H_2O-saturated solidus: applied to sample E50

The metasedimentary rocks are likely to have been H_2O-saturated during prograde metamorphism, until the H_2O-saturated solidus was reached. However, the pseudosection that reproduces the paragneiss matrix assemblage bi-g-sill-ilm-ksp-pl-q (Fig. 9) does not have a H_2O-saturated solidus. This is interpreted to be a consequence of melt (and thus H_2O) loss that occurred during metamorphism. In order to obtain a H_2O-saturated solidus on the diagram, the melt is reintegrated into the whole-rock composition from a point (indicated by a 'star' in Fig. 9) after muscovite-dehydration melting (for the procedure of melt reintegration, see White *et al.*, 2004). These are conditions where melt loss might be expected to occur in a rock because of the stepwise increase in modal % of melt because of destabilization of muscovite over a small interval of *P–T* conditions. However, the resulting melt composition is not very sensitive to the choice of *P–T* conditions for melt loss (see also White & Powell, 2002). The quantity of melt added into the rock composition controls the amount of H_2O added, and therefore also the position of the H_2O-saturation point on the solidus or the pressure at which the rock crossed the solidus. As this cannot be known exactly, the pressure has to be estimated.

The paragneiss E50 contains staurolite inclusions in garnet and other paragneisses of the same type have kyanite inclusions in garnet; therefore, a moderate-pressure and moderate-temperature prograde path is indicated. The probable pressure where the solidus was crossed is estimated to be around 10 kbar. For a path that crosses the H_2O-saturated solidus at around 10 kbar it is necessary to add approximately 7 mol.% of melt. A higher amount of melt added would cause the H_2O saturation point on the solidus to occur at progressively lower pressure and a lower amount of melt added would cause the saturation point to move up pressure. A diagram with a reintegrated whole-rock composition with 7 mol.% of melt added is presented in Fig. 10. Its major features include the absence of K-feldspar below 780 °C, and H_2O saturation between 620 °C and the H_2O-saturated solidus for a pressure interval of 4.5–10 kbar. Staurolite and kyanite stability extends to low temperature because of H_2O undersaturation at these conditions.

This pseudosection is used to discuss the part of the *P–T* path from the wet solidus until the point of melt loss (arrow B3 in Fig. 10). This part of the *P–T* path trends from the wet solidus at 10 kbar across the bi-mu-g-ky-ru-liq-pl-q field, then crosses the muscovite-out and K-feldspar-in lines and ends in the muscovite-absent bi-g-ky-ru-ksp-liq-pl-q field. Comparing the garnet chemistry (Fig. 7b) with the trend of compositional isopleths, it is probable that this sample experienced a *P–T* path through the kyanite stability field as indicated by the arrow on the pseudosection. The absence of kyanite in the thin section studied is explained by strong reworking of the matrix in the sillimanite stability field. However, kyanite is included in garnet and in matrix plagioclase in other samples of the same paragneiss type (Fig. 5c), indicating that in some paragneiss samples the assemblage corresponding to the field bi-g-ky-ru-ksp-liq-pl-q is developed. The absence of muscovite in the sample is explained by its decomposition during the formation of K-feldspar.

H_2O-saturated pseudosection for paragneiss: applied to sample E50

The early prograde path cannot be discussed using the diagram in Fig. 10, as only part of the subsolidus region is H_2O-saturated whereas the metasediments are thought to have been H_2O-saturated on the prograde path. Therefore, a pseudosection that is H_2O-saturated in the whole range of subsolidus conditions was calculated for the rock composition with reintegrated melt (Fig. 11). The major features with respect to the previous pseudosection involve limited staurolite stability between 550 and 680 °C and below 8.5 kbar, kyanite stability above 620 °C, a garnet-in line between 500 and 590 °C and the stability of chlorite and epidote at low temperature.

The paragenetic features of sample E50 that involve staurolite, ilmenite and rutile included in garnet are compared with a path on this pseudosection that crosses the garnet-, staurolite- and rutile-in lines sequentially, and ends in the mu-bi-g-ky-ru-q-pl-H_2O field (arrow B4 in Fig. 11). The molar proportion of garnet increases along this path, demonstrating that garnet in a rock following such a path can grow, and can include staurolite, ilmenite and rutile. Calculated garnet compositional isopleths also correlate with grossular and X_{Fe} trends in the measured garnet profile (Fig. 7b), and staurolite compositional isopleths correspond approximately to the observed values (X_{Fe} = 0.75–0.80).

Model of garnet zoning in sample E50

To test whether the garnet in sample E50 is consistent with growth zoning (Fig. 7b), a garnet zoning model is calculated from the series of pseudosections along the indicated *P–T* path B (segments B1–B3 in Figs 9–11).

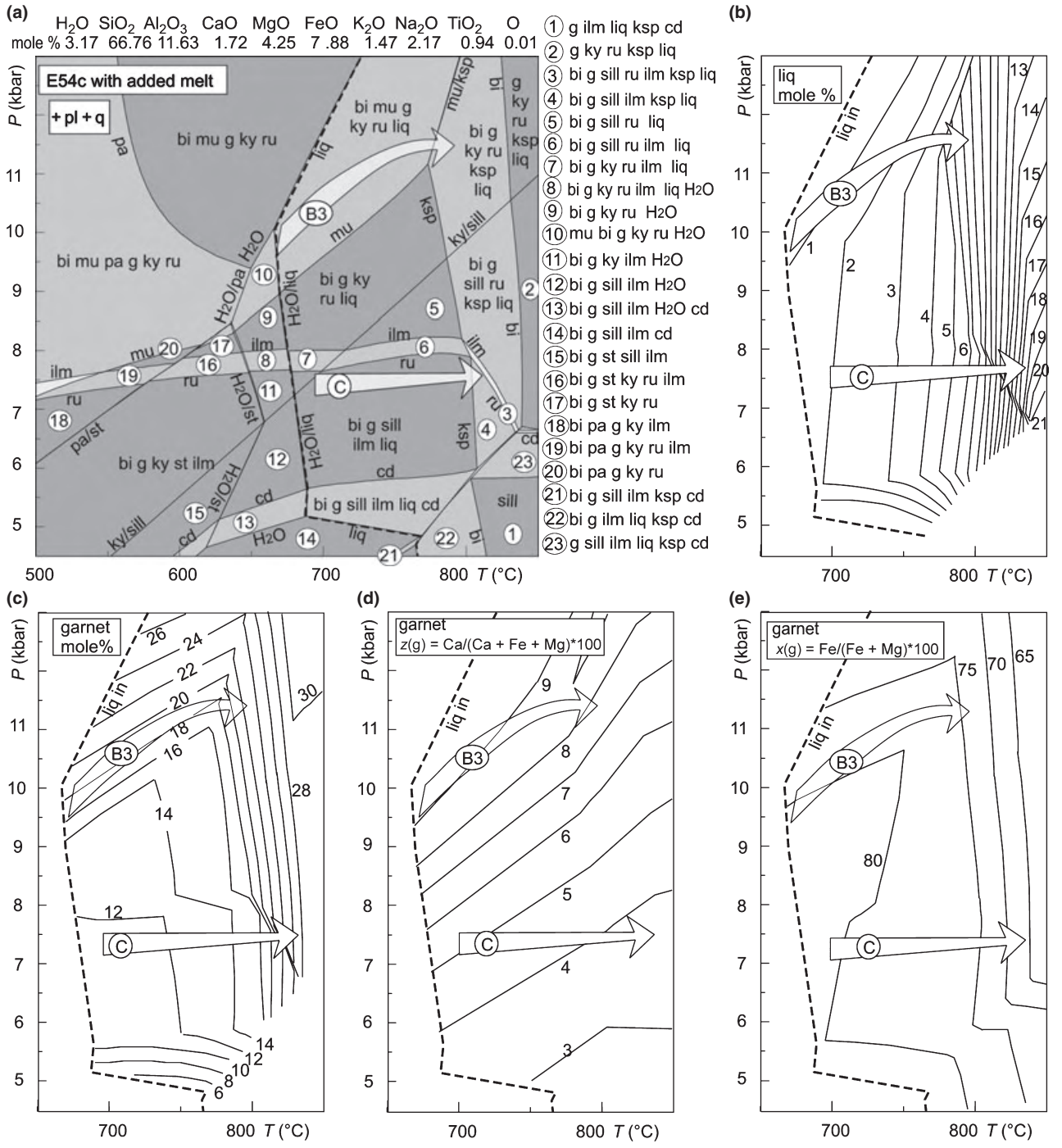

Fig. 10. Pseudosection calculated for the model rock composition of the paragneiss sample E54 with reintegrated melt (in moles adjusted to 100% after reintegration of melt). *P–T* path is derived by comparing the modelled assemblages and isopleths with assemblages, chemistry and zoning of minerals observed in the samples studied (E50d & E53c). See text for details. (b–e) Enlarged and simplified parts of the pseudosection with calculated isopleths of mineral composition and molar proportions.

With increasing pressure and temperature, garnet molar isopleths along path B increase from zero at the garnet-in line up to 22 mol.% at 12 kbar and 800 °C (Figs 9–11). The z(g) along this part of the path decreases from 0.18 to 0.08 and x(g) decreases from 0.93 to 0.70. Garnet molar proportion is calculated for points along the indicated path B at intervals of 1 mol.% increase. The effect of conversion of garnet proportion into radius (in arbitrary units, assuming radial symmetry) reproduces closely the garnet profile

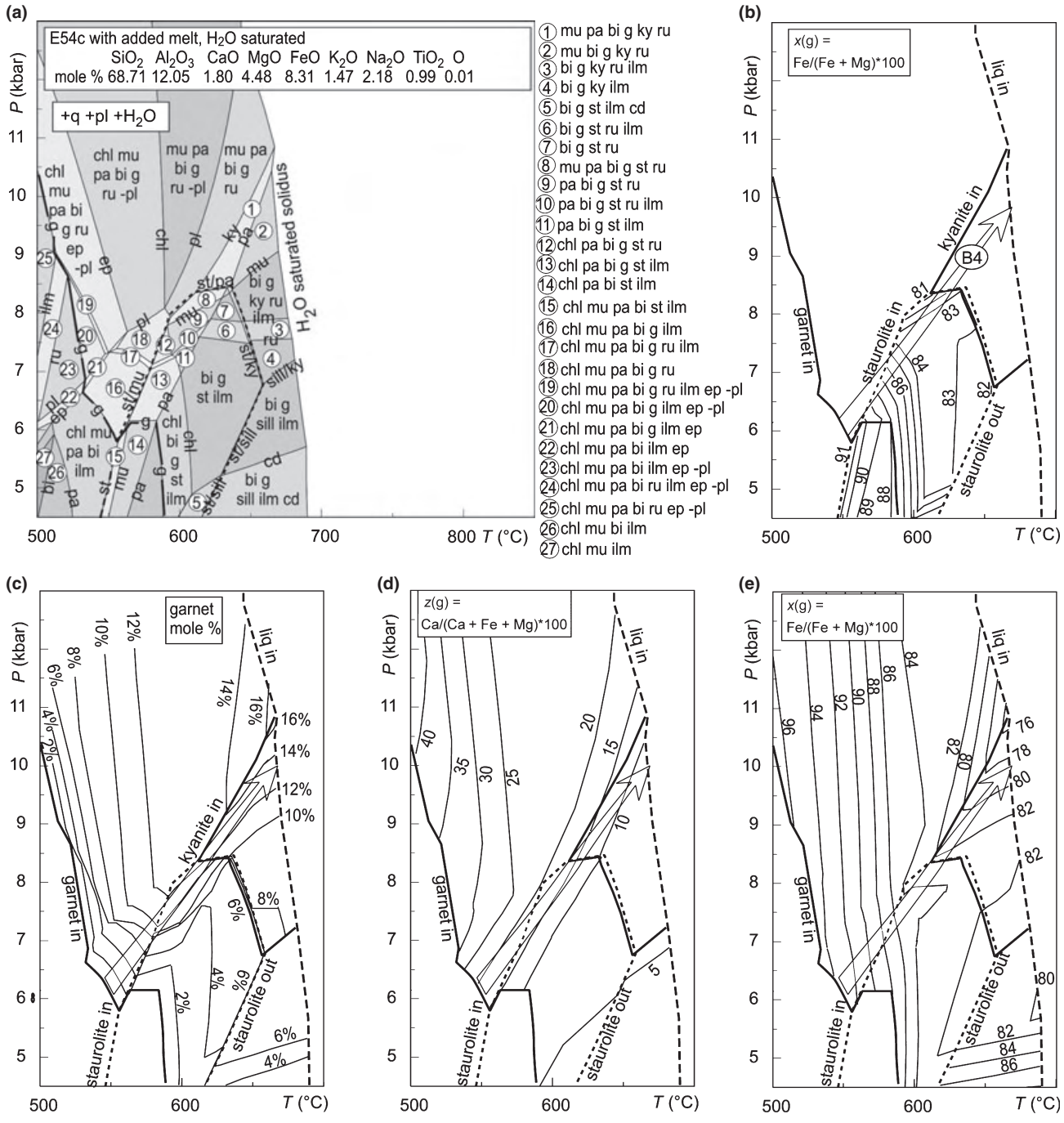

Fig. 11. Pseudosection calculated for the model rock composition of the paragneiss sample E54c with reintegrated melt and H_2O saturation below solidus (listed analysis is the same rock composition with reintegrated melt as used for Fig. 10, but presented on an anhydrous basis in moles adjusted to 100%). *P–T* paths are derived by comparing the modelled assemblages and isopleths with assemblages, chemistry and zoning of minerals observed in the sample studied (E50d). See text for details. (b–e) Enlarged and simplified parts of the pseudosection with calculated isopleths of mineral composition and molar proportions.

from the sample studied (Fig. 7e), so the zoning is interpreted as prograde growth zoning. Along the decompression part of the path (B2 in Fig. 9), garnet molar content remains approximately constant until cooling in the sillimanite stability field. There, garnet content decreases to 16 mol.% with $z(g) = 0.035$ and $x(g) = 0.77$ at the liquid-out line (B1 in Fig. 9). Further cooling to 6.5 kbar and 650 °C would cross the isopleths $z(g) = 0.05$ and $x(g) = 0.79$ (not indicated). These two compositions are plotted as the end-points in the theoretical garnet profile in Fig. 7e and are considered to approximate the composition

towards which garnet in a rock would tend to diffusionally equilibrate at these conditions. In the sample, in accordance with the prediction from the pseudosection, garnet is partially consumed and the low grossular garnet rims (grs = 2%) and relatively high X_{Fe} values = 0.80 are interpreted as diffusionally equilibrated at low pressure.

Pseudosection for paragneiss with H_2O-saturated solidus: applied to sample E53c

The paragneiss sample E53c shows simple mineralogy with bi-g-sill-ilm-pl-ksp-q, but with the remarkable textural feature that numerous sillimanite needles and biotite are included in garnet that are oriented parallel to the external matrix foliation (Fig. 6). This texture indicates garnet growth over the flat foliation fabric in which sillimanite and biotite were already stable.

This textural feature may be explained in the pseudosection for H_2O saturation at the solidus (Fig. 10). In the bi-g-sill-ilm-liq-pl-q field, the garnet molar isopleths are steep and increase only along paths that involve heating (e.g. along path C, Fig. 10). We therefore interpret the texture to be a result of heating in the sillimanite stability field around 7 kbar at the time when the sample had already developed the flat sill-bi-bearing foliation. The minimum temperature achieved needs to be around 800 °C where K-feldspar becomes stable. The preservation of the assemblage bi-g-sill-ilm-pl-ksp-q after cooling cannot be explained in this diagram, suggesting that melt loss must have occurred near the metamorphic peak in order to preserve K-feldspar on cooling (e.g. along path B1 in Fig. 9a).

Model of garnet zoning in sample E53c

The garnet in sample E53c is largely unzoned, with low grossular content (grs = 2–6%) and slightly increasing X_{Fe} from core to rim (Fig. 7c). A predicted garnet profile along path C (Fig. 10) is calculated at an interval of 1 mol.% increase and then converted to radius (in arbitrary units) (Fig. 7f). The resulting profile shows low and almost constant $z(g)$ = 0.03–0.05, whereas $x(g)$ decreases from 0.80 to 0.68 (open circles). One end-point shows the garnet composition at 7.5 kbar and 700 °C that would be the composition towards which the rims in a model system garnet would tend to equilibrate after cooling. The triangles show the $x(g)$ at 7.5 kbar and 700 °C that a garnet would have if it diffusionally equilibrated at these conditions. Comparison of the theoretical garnet profile with the measured garnet zoning favours the interpretation that the garnet in the rock results from the growth along a heating path with initially low grossular content, but its compositional X_{Fe} characteristic rather reflects modification by diffusion on cooling.

DISCUSSION AND CONCLUSIONS

P–T evolution

This metamorphic study and previous investigations have shown that the *P–T* paths for the eclogite (Štípská & Powell, 2005a), kyanite-K-feldspar granulite, and for the matrix of the paragneiss had different prograde histories and metamorphic peaks, indicating that these rocks came together at about 7–9 kbar (Figs 12 & 13c). From this depth, their exhumation would have been shared. The evidence for the *P–T* paths and their relation to the fabric development of the different rock types is now summarized and discussed.

Prograde paths, peak conditions and early retrogression are not shared

The eclogite boudins studied by Štípská & Powell (2005a) gave a prograde path based on garnet prograde zoning and the character of inclusions, peak conditions derived from garnet-omphacite thermometry and a decompression path within the hornblende stability field (Fig. 12a,e). The internal foliation within garnet is oriented at a high angle to the external foliation indicating that the prograde path is associated with a different fabric, most likely (from other evidence) with a steep orientation (Fig. 12a).

Opinions relating to the character of the protoliths and to the early and peak *P–T* conditions for the kyanite-K-feldspar granulite and associated rocks vary from crystallization of dry magma at high pressure, to ultrahigh-temperature/high-pressure metamorphism or even ultrahigh-pressure metamorphism (for recent discussion, see Štípská & Powell, 2005b; Racek *et al.*, 2008; O'Brien, 2008). In the kyanite-K-feldspar granulite sample, the earliest assemblage DV001b contained antiperthite included in garnet, as well as antiperthite relicts in the matrix. Reintegration of the feldspar composition gives a temperature of 900–950 °C, but the pressure at which it crystallized cannot be deduced because of a lack of clear textural relations with the rest of the mineral assemblage. The second-stage garnet that overgrew antiperthite also includes plagioclase and biotite (Fig. 12c), indicating that it has grown in the biotite and plagioclase stability field, at a lower temperature than crystallization of ternary feldspar (see also Štípská & Powell, 2005b). Flat garnet profiles (grs = 10–11%, X_{Fe} = 0.62) are interpreted as diffusionally equilibrated (Fig. 7a). In the pseudosection, corresponding isopleths cross in the field of g-ky-bi-liq-ru-pl-ksp-q at around 16.5 kbar and 850 °C that is compatible with the occurrence of relic kyanite in the matrix and the composition of matrix plagioclase cores (Fig. 12b). These conditions are considered to reflect the pressure peak. The assemblage g-bi-sill-ru-pl-ksp-q within the flat fabric, equilibrated with low grossular garnet rims (grs = 3%, X_{Fe} = 0.63), is

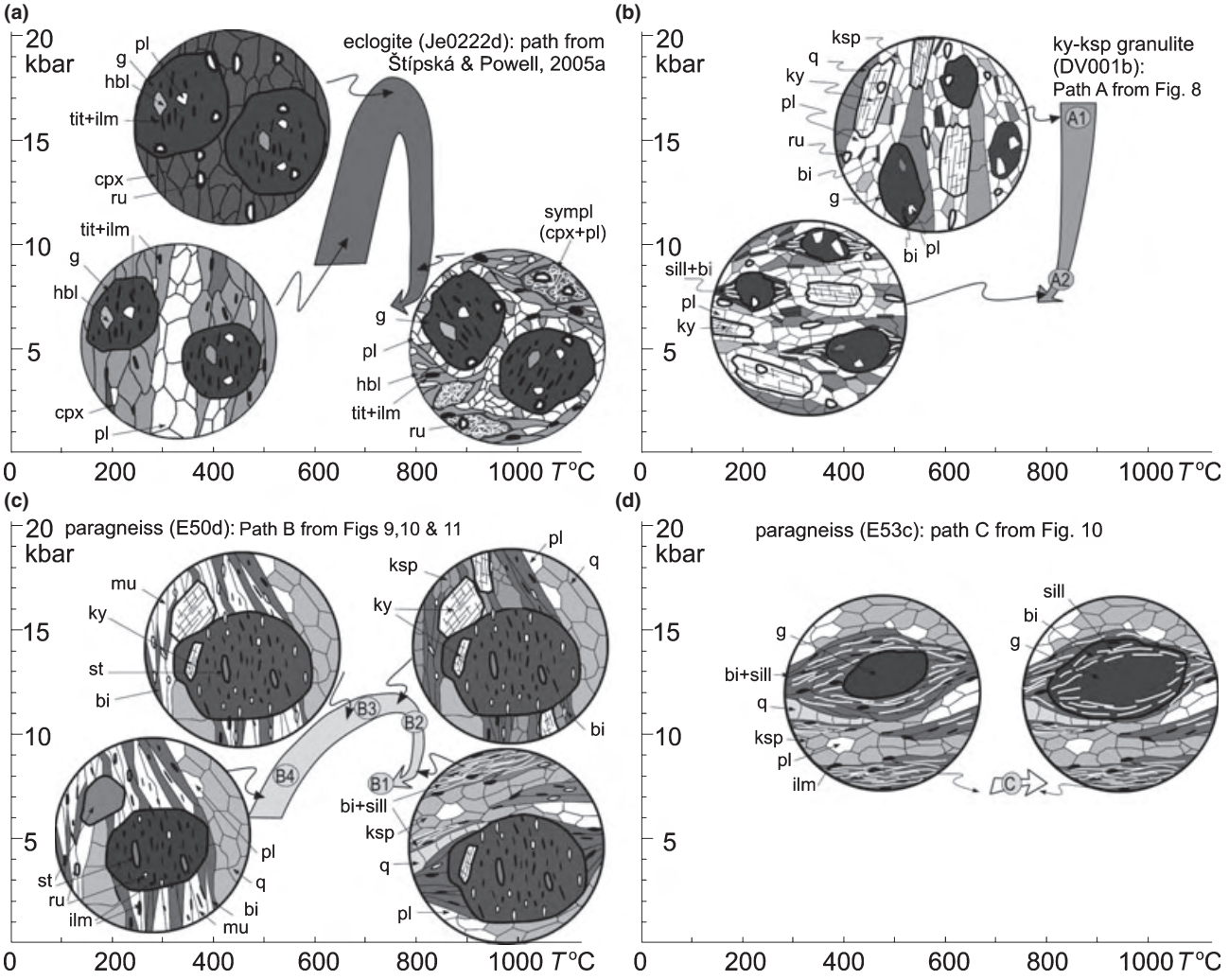

Fig. 12. (a–d) Sketches show petrological successions in individual samples and inferred *P–T* paths. The orientation of structures shows an attempt to interpret structural development of mineral assemblages before reworking by the flat foliation. For discussion see text.

compatible with conditions of about 800–850 °C and 8 kbar (Fig. 12b).

In the paragneiss sample E50 the inclusions of staurolite, ilmenite and rutile in garnet, together with garnet prograde zoning, allow a prograde *P–T* path to be inferred from 6 kbar and 550 °C to the pressure peak at around 11 kbar and 800 °C (Fig. 12c). The minimum peak temperature is well constrained via the muscovite dehydration melting equilibria with the formation of K-feldspar. Most probably, this occurred in the kyanite stability field, as kyanite (and staurolite) inclusions occur within garnet in other similar samples (Fig. 5c). However, within the sample studied the pressure peak is constrained only by a trend of garnet molar and compositional isopleths within the field of bi-g-ky-ru-ksp-liq-pl-q and its exact position is uncertain. Whether the sample continued burial until high pressure is impossible to resolve, but based on its moderate pressure, moderate temperature evolution marked by staurolite inclusions, the continuation of the path to high pressure is unlikely. The prograde path is connected with the development of the internal fabric within the garnet that is oriented at a high angle to the external foliation. It may indicate the existence of an earlier steep fabric developed during burial (Fig. 5a,b), but the general orientation of the foliation remains speculative in the absence of a macroscopically preserved steep foliation. The low-pressure reworking within the flat foliation is relatively well constrained by the presence of sillimanite, the absence of rutile, and garnet rim chemistry indicating *P–T* conditions around 7 kbar and 800 °C (Fig. 12c).

The paragneiss sample E53c contains a key texture involving numerous oriented sillimanite inclusions within garnet parallel to the external flat foliation, indicating garnet growth in the presence of sillimanite (Fig. 6). In the pseudosection, such a texture is explained by heating to about 800 °C at around

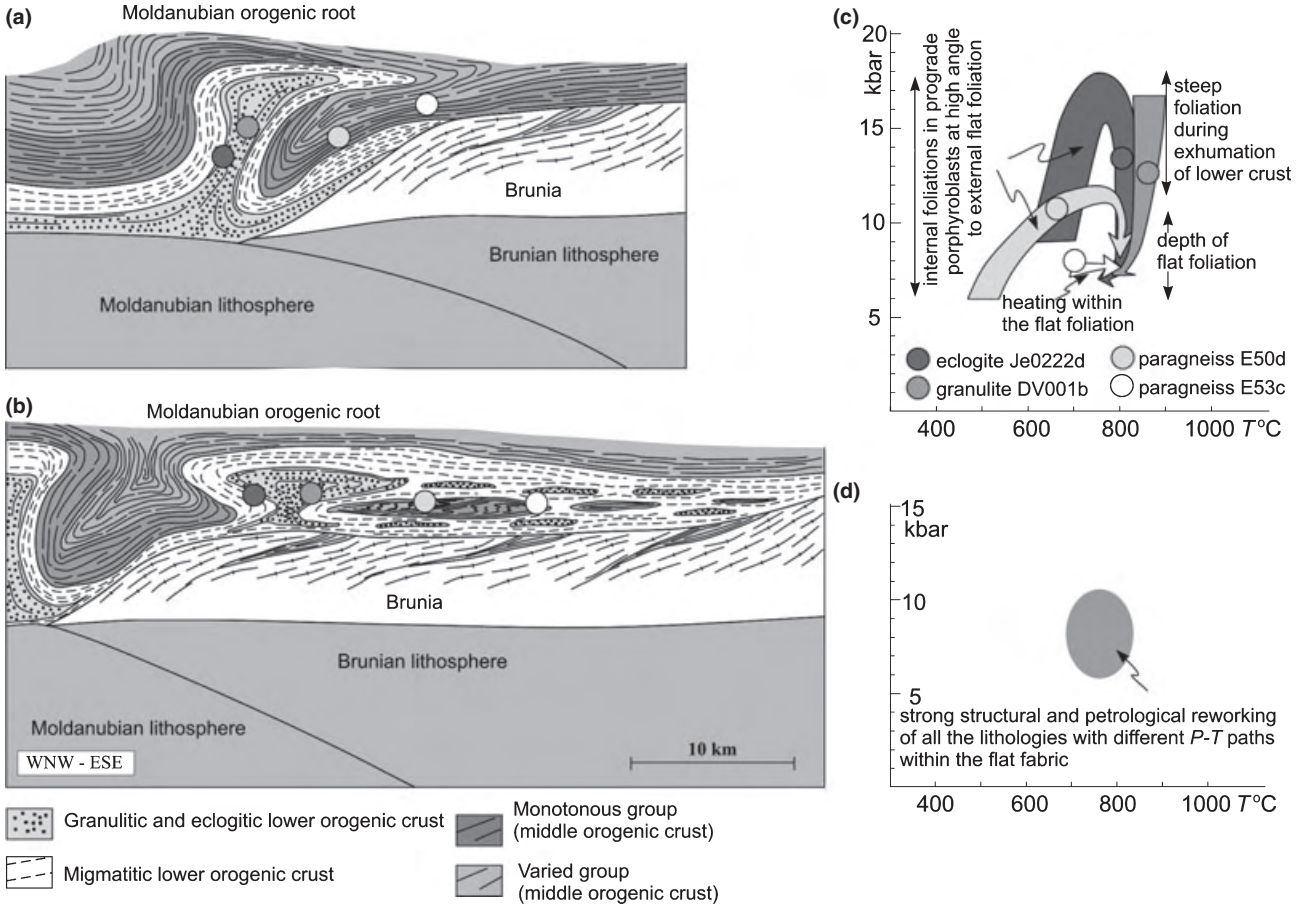

Fig. 13. Model of two-stage exhumation after Schulmann *et al.* (2008). Idealized position of the samples studied is indicated by circles. (a) Vertical displacements within the orogenic root cause exhumation of lower orogenic crust and burial of middle and upper orogenic crust. (b) Subhorizontal flow of the mixed lower and middle crustal portions over the Brunia basement. (c, d) Summary of *P–T* paths.

7 kbar, supported also by the garnet having a low grossular content (Fig. 12d).

Implications from the *P–T* paths

The *P–T* paths show that rocks with different prograde *P–T* histories and from different depths were exhumed and mixed within the flat fabric at mid-crustal conditions (Figs 12 & 13b,c). The prograde path of the eclogite indicates burial to the base of the lower orogenic crust corresponding to about 70 km, whereas the prograde path of the paragneiss (sample E50) shows burial to middle orogenic crust conditions, to 35–40 km. Both paths are likely to be connected with steep fabric development as indicated by the orientation of inclusion trails in prograde garnet and also by analogy with other regions where these relations have been studied (Romanová & Štípská, 2001; Štípská *et al.*, 2004; Racek *et al.*, 2006). However, in the absence of macroscopic preservation of the steep fabric in the area studied, its regional extent, or how much of the crust developed it, cannot be demonstrated.

Decompression of the eclogite and kyanite-K-feldspar granulite from their high-pressure peaks is essentially isothermal and it is joined by the *P–T* path of the paragneiss (E50) at 11 kbar. There is no structural record preserved for this decompression stage in any of the lithologies. However, in other areas studied, the early decompression path documented in granulite is connected with the steep fabric (Štípská *et al.*, 2004; Tajčmanová *et al.*, 2006). The almost constant temperature maintained by lower crustal rocks during exhumation to middle crustal levels indicates that hot lower crust was able to maintain its temperature over 8–10 kbar of vertical displacement. This will have been the result of interplay of several factors, but the most important one is likely to have been the relative rapidity of the decompression, as well as the volume of the decompressed material involved.

The first evidence for the development of the flat fabric comes from textures in the mineral assemblages developed during retrogression of the eclogite, at around 11 kbar (Štípská & Powell, 2005a). However it is not clear whether the first development of the flat fabric occurred at this pressure regionally. The

flat-fabric assemblages exemplified by the felsic granulite (DV001) and the paragneiss (E50) occur regionally in the area studied, with effective re-equilibration at 7–8 kbar. A high temperature of around 800 °C was maintained during this part of the exhumation path. The heating path that is recorded by the paragneiss sample E53c, in which the flat fabric was already developing, is interpreted to be the result of heating by juxtaposed lower crustal portions and middle crust with slightly lower temperature. The paths connected with the flat fabric show the convergence of temperatures towards 800 °C, including such heating paths. The pressure difference between the first vestiges of flat fabric development in the eclogite at around 11 kbar and re-equilibration of kyanite-K-feldspar granulite and paragneiss at 7–8 kbar shows that the flat fabric is associated with, and likely to be responsible for, a minimum of 10 km of vertical displacement of lower and middle orogenic crust and that this part of the exhumation occurred at about 800 °C (see also Hasalová *et al*., 2008c). This was then followed by cooling.

Implications for the exhumation model of the orogenic lower crust

The results presented here are inconsistent with a tectonic model in which one crustal level is exhumed from depth and no mixing of material with contrasting *P–T* histories is involved, as proposed for the WGR (Andersen *et al*., 1991; Dewey *et al*., 1993; Engvik & Andersen, 2000). The absence of crustal mixing in the WGR was confirmed by Engvik *et al*. (2000) who showed that the flat fabric originated at eclogite facies conditions and continued development heterogeneously while still flat during amphibolite facies reworking. The major result of their work and the subsequent studies of Young *et al*. (2007) and Johnston *et al*. (2007) is a model of exhumation of the eclogitic lower crust as a coherent crustal-scale body, consistent with earlier WGR models (e.g. Andersen *et al*., 1991; Dewey *et al*., 1993).

Even if the prograde part of the *P–T* paths of the eclogite and paragneiss samples of this study could be explained by different burial depth of the same continental crust, their recent close juxtaposition is difficult to reconcile using the WGR exhumation model or by the nappe stacking model suggested for the Variscan belt (e.g. Matte *et al*., 1990). The exhumation process needs to allow mixing of crustal portions coming from different depths. Such a model, based on superposition of two structural and metamorphic events that are observed in several profiles along the eastern margin of the Bohemian Massif, is that of Schulmann *et al*. (2008). Its two-stage scenario adopted for the area presented here is shown in Fig. 13. The interpretation also relies on previous work further north and south (Štípská *et al*., 2004; Racek *et al*., 2006; Tajčmanová *et al*., 2006), especially for the structures associated with the early exhumation stage that are not preserved in the area studied.

The first stage (Fig. 13a,c) is characterized by localized vertical extrusion of lower crust initiated by vertical crustal scale folding (Štípská *et al*., 2004) that leads to the development of the steep fabric. It develops also in the orogenic middle crust adjacent to where the high-pressure rocks are extruded. This mechanism juxtaposes lower crustal rocks at middle crustal levels with decompression *P–T* paths and rocks that just experienced burial and prograde *P–T* paths (Racek *et al*., 2006). The vertical material transfer occurred at about 340 Ma as indicated by zircon dating (e.g. Štípská *et al*., 2004; Schulmann *et al*., 2005).

The second exhumation stage, associated with the development of the subhorizontal fabric, appears to be related to the progressive indentation of the Brunia continent into weak and already vertically folded crust of the orogenic root (Fig. 13b,d). The root material above the indentor in which the flat fabric is developed corresponds to the area studied. It was heterogeneous as a consequence of the vertical folding, involving high-pressure granulite, eclogite, peridotite as well as mid-crustal gneiss, having a range of *P–T* histories (Fig. 13c). The rocks above the indentor predominantly record evidence for horizontal viscous flow at a depth corresponding to about 7 kbar (Fig. 13d) in the area studied. However, detailed study of migmatites close to the study area has shown that various migmatite types record exhumation in flat fabric rocks from 8 to 4 kbar (Hasalová *et al*., 2008c). The existence of the underthrust Brunia basement is documented by gravity surveying that places the subsurface margin of the Brunia promontory up to 100 km to the east from the present Moldanubian/Brunian surface boundary (Schulmann *et al*., 2008; Fig. 11). The Brunia continent itself is imbricated during the underthrusting, resulting in the formation of two large-scale crustal nappes with tectonically inverted Barrovian metamorphic zonation (Štípská & Schulmann, 1995; Štípská *et al*., 2000). Flat shearing in a deformed part of the Brunia basement and within the Moldanubian rocks above is oblique and NE-directed (Schulmann *et al*., 1994), and dated at 335 Ma using U-Pb SHRIMP on zircon (Friedl *et al*., 2003) and to 330–325 Ma using Ar^{40}/Ar^{39} method (Dallmeyer *et al*., 1992; Fritz *et al*., 1996).

Our two-stage exhumation model is similar in some aspects to the results of numerical modelling. Beaumont *et al*. (2006) proposed three major types of channel flow called 'homogeneous channel flow', 'heterogeneous channel flow' and the 'hot fold nappe', which differ in boundary conditions, heterogeneity of the crust and the possible presence of a strong lower crustal promontory. The exhumation process in the eastern Moldanubian domain can be related to both the 'hot fold nappe' and to the 'heterogeneous channel flow' models. The geometry and kinematics of the flat fabric is consistent with the development of a 'hot fold

nappe', with the arrival of a lower crustal promontory forcing weak crust to flow within large-scale gently inclined fold nappes over the basement (see also Jamieson *et al.*, 2007, and references therein, relating to the Grenville front). The mixing of rocks with contrasting *P–T* paths in a partially molten matrix is consistent with 'heterogeneous channel flow', involving, first, the deformation and exhumation of the orogenic lower crust to mid-crustal levels, then the development of subhorizontal channel flow acting on the heterogeneous crust created during first phase. Consequently, the heterogeneous channel flow may transport rocks with different *P–T* histories, including high-pressure granulites and eclogites.

ACKNOWLEDGEMENTS

Financial support of the French National Grant Agency (06-1148784 to K. Schulmann), of the Czech National Grant Agency (205/05/2187 to P. Štípská and L. Tajčmanová) and of the Charles University Grant Agency (149/2000/B-GEO/PrF to P. Štípská) is gratefully acknowledged. V. Böhmová from the Geological Institute of the Czech Academy of Sciences is thanked for operating the microprobe. RP acknowledges the support of ARC DP0451770. B. Jamieson, G. Clarke and G. Zhao are thanked for their detailed and constructive reviews, and M. Brown is thanked for his careful editorial work.

REFERENCES

Andersen, T. B., Jamtveit, B., Dewey, J. F. & Swensson, E., 1991. Subduction and eduction of continental crust: major mechanisms during continent-continent collision and orogenic extensional collapse, a model based on the south Norwegian Caledonides. *Terra Nova*, **3,** 303–310.

Beard, B. L., Medaris, L. G., Johnson, C. M., Brueckner, H. K. & Mísař, Z., 1992. Petrogenesis of Variscan high-temperature group A eclogites from the Moldanubian Zone of the Bohemian Massif, Czechoslovakia. *Contributions to Mineralogy and Petrology*, **111,** 468–483.

Beaumont, C., Jamieson, R. A., Nguyen, M. H. & Lee, B., 2001. Himalayan tectonics explained by extrusion of a low-viscosity crustal channel coupled to focused surface denudation. *Nature*, **414,** 738–742.

Beaumont, C., Nguyen, M. H., Jamieson, R. A. & Ellis, S., 2006. Crustal flow modes in large hot orogens. In: *Channel Flow, Ductile Extrusion and Exhumation in Continental Collision Zones, Special Publication 268* (eds Law, R. D., Searle, M. P. & Godin, L. *et al*), pp. 91–145. Geological Society, London.

van Breemen, O., Aftalion, M., Bowes, D. R. *et al.*, 1982. Geochronological studies of the Bohemian Massif, Czechoslovakia, and their significance in the evolution of Central Europe. *Transactions of the Royal Society of Edinburgh, Earth Sciences*, **73,** 89–108.

Brueckner, H. K., Medaris, L. G. & Bakun-Czubarow, N., 1991. Nd and Sr age and isotope patterns from Variscan eclogites of the eastern Bohemian Massif. *Neues Jahrbuch für Mineralogie, Abhandlungen*, **163,** 169–196.

Carswell, D. A., 1991. Variscan high P–T metamorphism and uplift history in the Moldanubian Zone of the Bohemian Massif in Lower Austria. *European Journal of Mineralogy*, **3,** 323–342.

Coggon, R. & Holland, T. J. B., 2002. Mixing properties of phengitic micas and revised garnet-phengite thermobarometers. *Journal of Metamorphic Geology*, **20,** 683–696.

Culshaw, N. G., Beaumont, C. & Jamieson, R. A., 2006. The orogenic superstructure-infrastructure concept: revisited, quantified, and revived. *Geology*, **34,** 733–736.

Dallmeyer, D., Neubauer, F. & Höck, V., 1992. $^{40}Ar/^{39}Ar$ mineral age controls on the chronology of late-Paleozoic tectonothermal activity in the southeastern Bohemian Massif, Austria (Moldanubian and Moravosilesian zone). *Tectonophysics*, **210,** 135–153.

Dewey, J. F., Ryan, P. D. & Andersen, T. B., 1993. Orogenic uplift and collapse, crustal thickness, fabrics and metamorphic phase changes; the role of eclogites. In: *Magmatic Processes and Plate Tectonics, Special Publications 79* (eds Prichard, H. M., Alabaster, T., Harris, N. B. W. & Neary, C. R.), pp. 325–343. Geological Society, London.

Edel, J. B., Schulmann, K. & Holub, F. V., 2003. Anticlockwise and clockwise rotations of the Eastern Variscides accommodated by dextral lithospheric wrenching: palaeomagnetic and structural evidence. *Journal of the Geological Society*, **160,** 209–218.

Engvik, A. K. & Andersen, T. B., 2000. Evolution of Caledonian deformation fabrics under eclogite and amphibolite facies at Vardalsneset, Western Gneiss Region, Norway. *Journal of Metamorphic Geology*, **18,** 241–257.

Engvik, A. K., Austrheim, H. & Andersen, T. B., 2000. Structural, mineralogical and petrophysical effects on deep crustal rocks of fluid-limited polymetamorphism, Western Gneiss Region, Norway. *Journal of the Geological Society*, **157,** 121–134.

Finger, F. & Steyer, H. P., 1995. A tectonic model for the eastern Variscides: indications from a chemical study of amphibolites in the south-eastern Bohemian Massif, Austria. *Geologica Carpathica*, **46,** 1–14.

Finger, F. & von Quadt, A., 1995. U/Pb ages from zircons from a plagiogranite-gneiss in the south-eastern Bohemian Massif, Austria – further evidence for an important early Paleozoic rifting episode in the eastern Variscides. *Schweizerische Mineralogische und Petrographische Mitteilungen*, **75,** 265–270.

Franke, W., 2000. The mid-European segment of the Variscides: tectonostratigraphic units, terrane boundaries and kinematic evolution. In: *Orogenic Processes: Quantification and Modelling in the Variscan Belt, Special Publication 179* (eds Franke, W., Haak, V., Oncken, O. & Tanner, D.), pp. 35–63. Geological Society, London.

Friedl, G., Cooke, R., Finger, F., McNaughton, N. J. & Fletcher, I., 2003. U-Pb shrimp dating and trace element investigations on multiple zircons from a South-Bohemian granulite. *Journal of the Czech Geological Society*, **48,** 51.

Fritz, H., Dallmeyer, R. D. & Neubauer, F., 1996. Thick-skinned *v.* thin-skinned thrusting: rheology controlled thrust propagation in the Variscan collisional belt (the Southeastern Bohemian Massif, Czech Republic – Austria). *Tectonics*, **15,** 1389–1413.

Fuchs, G., 1986. Zur Diskussion um den Deckenbau der Böhmischen Masse. *Jahrbuch der Geologischen Bundesanstalt*, **129,** 41–49.

Fuhrman, M. L. & Lindsley, D. H., 1988. Ternary-feldspar modeling and thermometry. *American Mineralogist*, **73,** 201–215.

Grujic, D., Casey, M., Davidson, C. *et al.*, 1996. Ductile extrusion of the Higher Himalayan Crystalline in Bhutan: evidence from quartz microfabrics. *Tectonophysics*, **260,** 21–43.

Hasalová, P., Janoušek, V., Schulmann, K., Štípská, P. & Erban, V., 2008a. From orthogneiss to migmatite: geochemical assessment of the melt infiltration model in the Gföhl Unit (Moldanubian Zone, Bohemian Massif). *Lithos*, doi:10.1016/j.lithos.2007.07.021.

Hasalová, P., Schulmann, K., Lexa, O. *et al.*, 2008b. Origin of migmatites by deformation-enhanced melt infiltration of

orthogneiss: a new model based on quantitative microstructural analysis. *Journal of Metamorphic Geology*, **26,** 29–53.
Hasalová, P., Štípská, P., Powell, R., Schulmann, K., Janoušek, V. & Lexa, O., 2008c. Transforming mylonitic metagranite by open-system interactions during melt flow. *Journal of Metamorphic Geology*, **26,** 55–80.
Holland, T. J. B. & Powell, R., 1998. An internally consistent thermodynamic data set for phases of petrological interest. *Journal of Metamorphic Geology*, **16,** 309–343.
Holland, T. & Powell, R., 2003. Activity-composition relations for phases in petrological calculations: an asymmetric multicomponent formulation. *Contributions to Mineralogy and Petrology*, **145,** 492–501.
Jamieson, R. A., Beaumont, C., Nguyen, M. H. & Lee, B., 2002. Interaction of metamorphism, deformation and exhumation in large convergent orogens. *Journal of Metamorphic Geology*, **20,** 9–24.
Jamieson, R. A., Beaumont, C., Nguyen, M. H. & Culshaw, N. G., 2007. Synconvergent ductile flow in variable-strength continental crust: numerical models with application to the western Grenville orogen. *Tectonics*, **26,** TC5005, doi: 10.1029/2006TC002036.
Janoušek, V., Gerdes, A., Vrána, S. *et al*., 2006. Low-pressure granulites of the Líšov Massif, Southern Bohemia: Visean metamorphism of Late Devonian plutonic arc rocks. *Journal of Petrology*, **47,** 705–744.
Johnston, S. M., Hacker, B. R. & Andersen, T. B., 2007. Exhuming Norwegian ultrahigh-pressure rocks: overprinting extensional structures and the role of the Nordfjord-Sogn Detachment zone. *Tectonics*, **26,** TC5001, doi: 10.1029/2005TC001933.
Konopásek, J., Schulmann, K. & Johan, V., 2002. Eclogite-facies metamorphism at the eastern margin of the Bohemian Massif – subduction prior to continental underthrusting? *European Journal of Mineralogy*, **14,** 701–713.
Koyi, H. A., Milnes, A. G., Schmeling, H., Talbot, C. J., Juhlin, C. & Zeyen, H., 1999. Numerical models of ductile rebound of crustal roots beneath mountain belts. *Geophysical Journal International*, **139,** 556–562.
Kröner, A., Wendt, I., Liew, T. C. *et al*., 1988. U-Pb zircon and Sm-Nd model ages of high grade Moldanubian metasediments, Bohemian Massif, Czechoslovakia. *Contributions to Mineralogy and Petrology*, **99,** 257–266.
Matte, P., 1991. Accretionary history and crustal evolution of the Variscan belt in Western Europe. *Tectonophysics*, **196,** 309–337.
Matte, P., Maluski, H. & Echtler, H., 1985. Cissaillements ductiles varisques vers l'Est – Sud-Est dans les nappes du Waldviertel (Sud-Est du Massif de Bohême, Autriche). Données microtectoniques et radiométriques 39Ar/40Ar. *Comptes rendus de l'Académie des Sciences Paris, série II*, **301,** 721–726.
Matte, P., Maluski, H., Rajlich, P. & Franke, W., 1990. Terrane boundaries in the Bohemian Massif: result of large-scale Variscan shearing. *Tectonophysics*, **177,** 151–170.
Medaris, L. G., Jelínek, E. & Mísař, Z., 1995. Czech eclogites: terrane settings and implications for Variscan tectonic evolution of the Bohemian Massif. *European Journal of Mineralogy*, **7,** 7–28.
Medaris, L. G., Fournelle, J. H., Ghent, E. D., Jelínek, E. & Mísař, Z., 1998. Prograde eclogite in the Gföhl Nappe, Czech Republic: new evidence on Variscan high-pressure metamorphism. *Journal of Metamorphic Geology*, **16,** 563–576.
Medaris, G., Wang, H., Jelínek, E., Mihaljevič, M. & Jakeš, P., 2005. Characteristics and origins of diverse Variscan peridotites in the Gföhl Nappe, Bohemian Massif, Czech Republic. *Lithos*, **82,** 1–23.
Medaris, L. G., Ghent, E. D., Wang, H. F., Fournelle, J. H. & Jelínek, E., 2006. The Spačice eclogite: constraints on the P–T-t history of the Gföhl granulite terrane, Moldanubian Zone, Bohemian Massif. *Mineralogy and Petrology*, **86,** 203–220.
Milnes, A. G. & Koyi, H. A., 2000. Ductile rebound of an orogenic root; case study and numerical model of gravity tectonics in the Western gneiss complex, Caledonides, southern Norway. *Terra Nova*, **12,** 1–7.
O'Brien, P. J., 1997. Garnet zoning and reaction textures in overprinted eclogites, Bohemian Massif, European Variscides: a record of their thermal history during exhumation. *Lithos*, **41,** 119–133.
O'Brien, P. J., 2008. Challenges in high-pressure granulite metamorphism in the era of pseudosections: reaction textures, compositional zoning and tectonic interpretation with examples from the Bohemian Massif. *Journal of Metamorphic Geology*, **26,** 235–251.
O'Brien, P. J. & Rötzler, J., 2003. High-pressure granulites: formation, recovery of peak conditions and implications for tectonics. *Journal of Metamorphic Geology*, **21,** 3–20.
O'Brien, P. J. & Vrána, S., 1995. Eclogites with a short-lived granulite facies overprint in the Moldanubian Zone, Czech Republic: petrology, geochemistry and diffusion modelling of garnet zoning. *Geologische Rundschau*, **84,** 473–488.
Petrakakis, K., 1986. Metamorphism of high-grade gneisses from the Moldanubian Zone, Austria, with particular reference to garnets. *Journal of Metamorphic Geology*, **4,** 323–344.
Petrakakis, K., 1997. Evolution of Moldanubian rocks in Austria: review and synthesis. *Journal of Metamorphic Geology*, **15,** 203–222.
Powell, R. & Holland, T., 2004. Course notes for "THERMOCALC Workshop 2004: Calculating Metamorphic Phase Equilibria" (ETH Zurich). CD ROM.
Powell, R., Holland, T. & Worley, B., 1998. Calculating phase diagrams involving solid solutions via non-linear equations, with examples using THERMOCALC. *Journal of Metamorphic Geology*, **16,** 577–588.
Racek, M., Štípská, P., Pitra, P., Schulmann, K. & Lexa, O., 2006. Metamorphic record of burial and exhumation of orogenic lower and middle crust: a new tectonothermal model for the Drosendorf window (Bohemian Massif, Austria). *Mineralogy and Petrology*, **86,** 221–251.
Racek, M., Štípská, P. & Powell, R., 2008. Garnet-clinopyroxene intermediate granulites in the St. Leonhard massif of the Bohemian Massif: ultrahigh-temperature metamorphism at high pressure or not? *Journal of Metamorphic Geology*, **26,** 253–271.
Romanová, M. & Štípská, P., 2001. Structural and metamorphic evolution of the Stronie formation near Javorník. *Mineralogical Society of Poland, Special Papers*, **19,** 147–149.
Ryan, P., 2001. The role of deep basement during continent-continent collision. In: *Continental Reactivation and Reworking, Special Publications 184* (eds Miller, J. A., Holdsworth, R. E., Buick, I. S. & Hand, M.), pp. 39–55. Geological Society, London.
Schulmann, K., Melka, R., Lobkowicz, M., Ledru, P., Lardeaux, J. M. & Autran, A., 1994. Contrasting styles of deformation during progressive nappe stacking at the southeastern margin of the Bohemian Massif (Thaya Dome). *Journal of Structural Geology*, **16,** 355–370.
Schulmann, K., Kröner, A., Hegner, E. *et al*., 2005. Chronological constraints on the pre-orogenic history, burial and exhumation of deep-seated rocks along the eastern margin of the Variscan orogen, Bohemian Massif, Czech Republic. *American Journal of Science*, **305,** 407–448.
Schulmann, K., Lexa, O., Štípská, P. *et al*., 2008. Vertical extrusion and horizontal channel flow of orogenic lower crust: key exhumation mechanisms in large hot orogens? *Journal of Metamorphic Geology*, **26,** 273–297.
Štípská, P. & Powell, R., 2005a. Constraining the P–T path of a MORB-type eclogite using pseudosections, garnet zoning and garnet-clinopyroxene thermometry: an example from the Bohemian Massif. *Journal of Metamorphic Geology*, **23,** 725–743.
Štípská, P. & Powell, R., 2005b. Does ternary feldspar constrain the metamorphic conditions of high-grade meta-igneous

rocks? Evidence from orthopyroxene granulites, Bohemian Massif *Journal of Metamorphic Geology*, **23,** 627–647.
Štípská, P. & Schulmann, K., 1995. Inverted metamorphic zonation in a basement-derived nappe sequence, eastern margin of the Bohemian Massif. *Geological Journal*, **30,** 385–413.
Štípská, P., Schulmann, K. & Höck, V., 2000. Complex metamorphic zonation of the Thaya dome: result of buckling and gravitational collapse of an imbricated nappe sequence. In: *Forced Folds and Fractures, Special Publications 169* (eds Cosgrowe, J. W. & Ameen, M. S.), pp. 197–211. Geological Society, London.
Štípská, P., Schulmann, K. & Kröner, A., 2004. Vertical extrusion and middle crustal spreading of omphacite granulite: a model of syn-convergent exhumation (Bohemian Massif, Czech Republic). *Journal of Metamorphic Geology*, **22,** 179–198.
Štípská, P., Pitra, P. & Powell, R., 2006. Separate or shared metamorphic histories of eclogites and surrounding rocks? An example from the Bohemian Massif *Journal of Metamorphic Geology*, **24,** 219–240.
Tajčmanová, L., Konopásek, J. & Schulmann, K., 2006. Thermal evolution of the orogenic lower crust during exhumation within a thickened Moldanubian root of the Variscan belt of Central Europe. *Journal of Metamorphic Geology*, **24,** 119–134.
Tajčmanová, L., Konopásek, J. & Connolly, J. A. D., 2007. Diffusion-controlled development of silica-undersaturated domains in felsic granulites of the Bohemian Massif (Variscan belt of Central Europe). *Contributions to Mineralogy and Petrology*, **153,** 237–250.
Tollmann, A., 1982. Großräumiger variszischer Deckenbau im Moldanubikum und neue Gedanken zum Variszikum Europas. *Geotektonische Forschungen*, **64,** 1–91.
Wendt, J. I., Kröner, A., Fiala, J. & Todt, W., 1994. U-Pb zircon and Sm-Nd dating of Moldanubian high-P/high-T granulites from south Bohemia, Czechoslovakia. *Journal of the Geological Society of London*, **151,** 83–90.
White, R. W. & Powell, R., 2002. Melt loss and the preservation of granulite facies mineral assemblages. *Journal of Metamorphic Geology*, **20,** 621–632.
White, R. W., Powell, R., Holland, T. J. B. & Worley, B. A., 2000. The effect of TiO_2 and Fe_2O_3 on metapelitic assemblages at greenschist and amphibolite facies conditions: mineral equilibria calculations in the system K_2O-FeO-MgO-Al_2O_3-SiO_2- H_2O-TiO_2-Fe_2O_3. *Journal of Metamorphic Geology*, **18,** 497–511.
White, R. W., Powell, R. & Halpin, J. A., 2004. Spatially-focused melt formation in aluminous metapelites from Broken Hill, Australia. *Journal of Metamorphic Geology*, **22,** 825–845.
White, R. W., Powell, R. & Holland, T. J. B., 2007. Progress relating to calculation of partial melting equilibria for metapelites. *Journal of Metamorphic Geology*, **25,** 511–527.
Young, D. J., Hacker, B. R., Andersen, T. B. & Corfu, F., 2007. Prograde amphibolite facies to ultrahigh-pressure transition along Nordfjord, western Norway: Implications for exhumation tectonics. *Tectonics*, **26,** TC1007. doi. 10.1029/2004TC001781.

Received 8 November 2007; revision accepted 10 March 2008.

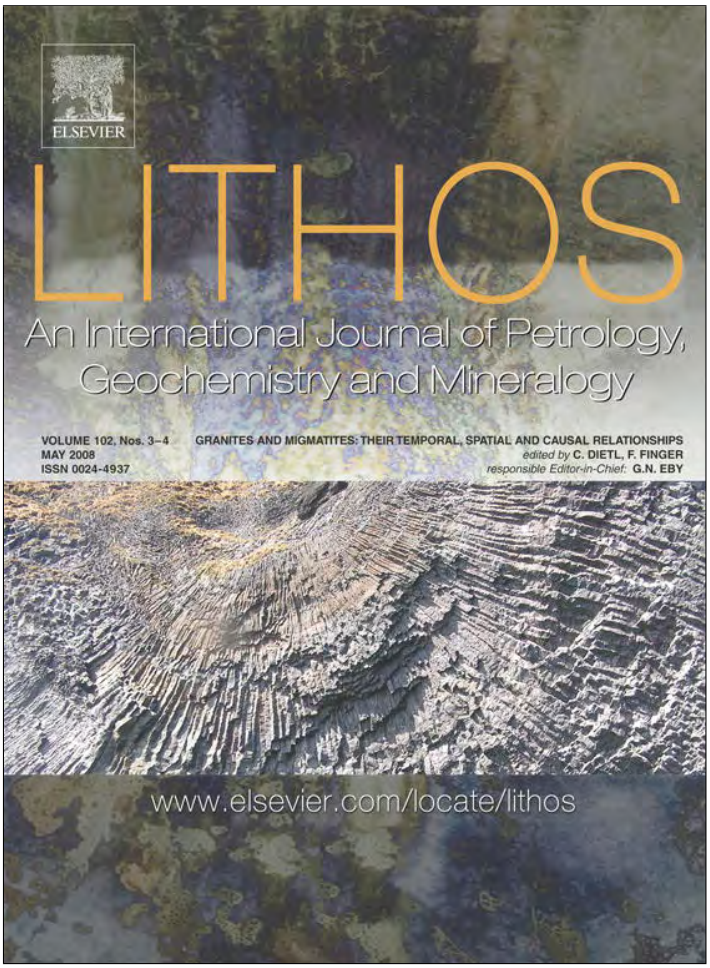

Available online at www.sciencedirect.com
ScienceDirect
Lithos 102 (2008) 508–537
LITHOS
www.elsevier.com/locate/lithos

From orthogneiss to migmatite: Geochemical assessment of the melt infiltration model in the Gföhl Unit (Moldanubian Zone, Bohemian Massif)

P. Hasalová [a,b,*], V. Janoušek [a,c], K. Schulmann [b], P. Štípská [b], V. Erban [c]

[a] *Institute of Petrology and Structural Geology, Charles University, Albertov 6, 128 43 Prague 2, Czech Republic*
[b] *Université Louis Pasteur, CGS/EOST, UMR 7517, 1 rue Blessig, Strasbourg 67084, France*
[c] *Czech Geological Survey, Klárov 3, 118 21 Prague 1, Czech Republic*

Received 9 September 2006; accepted 25 July 2007
Available online 27 August 2007

Abstract

The Gföhl Unit is the largest migmatite terrain of the Variscan orogenic root domain in Europe. Its genesis has been until now attributed to variable degrees of *in situ* partial melting. In the Rokytná Complex (Gföhl Unit, Czech Republic) there is a well-preserved sequence documenting the entire migmatitization process on both outcrop and regional scales. The sequence starts with (i) banded orthogneiss with distinctly separated monomineralic layers, continuing through (ii) migmatitic mylonitic gneiss, (iii) schlieren migmatite characterised by disappearance of monomineralic layering and finally to (iv) felsic nebulitic migmatite with no relics of the original banding.

While each type of migmatite shows a distinct whole-rock geochemical and Sr–Nd isotopic fingerprint, the whole sequence evolves along regular, more or less smooth trends for most of the elements. Possible mechanisms which could account for such a variation are that the individual migmatite types (i) are genetically unrelated, (ii) originated by equilibrium melting of a single protolith, (iii) formed by disequilibrium melting (with or without a small-scale melt movement) or (iv) were generated by melt infiltration from external source. The first scenario is not in agreement with the field observations and chemistry of the orthogneisses/migmatites. Neither of the remaining hypotheses can be ruled out convincingly solely on whole-rock geochemical grounds. However in light of previously obtained structural, petrologic and microstructural data, this sequence can be interpreted as a result of a process in which the banded orthogneiss was pervasively, along grain boundaries, penetrated by felsic melt derived from an external source.

In terms of this melt infiltration model the individual migmatites can be explained by different degrees of equilibration between the bulk rock and the passing melt. The melt infiltration can be modelled as an open-system process, characterised by changes of the total mass/volume and accompanied by gains/losses in many of the major- and trace elements. The modelling of the mass balance resulted in identification of a component added by a heterogeneous nucleation of feldspars, quartz and apatite from the passing melt. This is in line with the observed presence of new albitic plagioclase, K-feldspar and quartz coatings as well as resorption of relict feldspars. At the most advanced stages (schlieren and nebulitic migmatites) the whole-rock trace-element geochemical variations document an increasing role for fractional crystallization of the K-feldspar and minor plagioclase, with accessory amounts of monazite, zircon and apatite.

* Corresponding author. Université Louis Pasteur, CGS/EOST, UMR 7517, 1 rue Blessig, Strasbourg 67084, France.
E-mail address: hasalovap@seznam.cz (P. Hasalová).

0024-4937/$ - see front matter
doi:10.1016/j.lithos.2007.07.021

The penetrating melt was probably (leuco-) granitic, poor in mafic components, Rb rich, with low Sr, Ba, LREE, Zr, U and Th contents. It probably originated by partial melting of micaceous quartzo-feldspathic rocks.

If true and the studied migmatites indeed originated by a progressive melt infiltration into a single protolith resembling the banded orthogneiss, this until now underappreciated process would have profound implications regarding rheology and chemical development of anatectic regions in collisional orogens.

Keywords: Melt infiltration; Porous flow; Migmatites; Whole-rock geochemistry; Mass balance; Bohemian Massif (Gföhl Unit)

1. Introduction

The melt extraction from lower crustal rocks and its further transport to higher crustal levels are key issues of granite petrogenesis. Generally the melt fraction produced during anatexis is rather small; it is originally concentrated mainly at grain boundaries and along microfractures (Rushmer, 1995; Sawyer, 2000; Guernina and Sawyer, 2003). The mechanism of the melt segregation is still a controversial issue. It may be drained from the grain boundaries to melt-assisted sites, networks of leucosome-filled structures or dykes (see Lister and Kerr, 1991; Petford et al., 1994 for review) responsible for its further transport. The other, arguably more popular model involves pervasive flow through a porous space or fracture network (McKenzie, 1984; Wickham, 1987; Weinberg, 1999) and is strongly controlled by the permeability of the system.

Regardless of its exact mechanism, the segregation will be governed by the melt density and viscosity, which in turn reflect its composition, volatile contents and temperature (Brown et al., 1995; Petford et al., 2000). Important factor is also the thermal and mechanical state of the crust surrounding the melting zone (Weinberg and Searle, 1998). The efficiency of the melt extraction can be further boosted by active deformation in the source (McKenzie, 1984). At the grain-scale, the transport is controlled mainly by the melt geometry (wetting angle) (von Bargen and Waff, 1986) and its amount (Rushmer, 1995; Vigneresse et al., 1996). The grain-scale movement is possible as soon as the melt forms an interconnected network. Even when the wetting angle is low (von Bargen and Waff, 1986), an important prerequisite for the operation of pervasive porous flow is the lower solidus temperature of the country-rock compared to that of the penetrating melt.

The other passionately discussed problem is the further transport of the granitic melts. As an alternative to dyking (Petford et al., 1994, 2000), mesoscale pervasive magma migration, either channelized using the country-rock anisotropies (Collins and Sawyer, 1996; Weinberg and Searle, 1998; Brown and Solar, 1999; Vanderhaeghe, 1999; Weinberg, 1999; Leitch and Weinberg, 2002; Olsen et al., 2004), or penetrative through the whole-rock volume (Hasalová et al., in press-a) has been proposed for hot low-viscosity crustal rocks. For the latter model, the deformation is essential.

The whole-rock compositions of the migmatitic rocks, and the trace elements with radiogenic isotopes in particular, can be useful in constraining the nature of the source, residual mineralogy, as well as degree, mechanism and timescales of the crustal melting (see Whittington and Treloar, 2002 for review). For instance the water-saturated or dehydratation melting driven by decomposition of individual hydrous phases (muscovite, biotite or amphibole) will each leave its own geochemical imprint. Moreover, the chemistry of the melt will be substantially different depending on whether its bulk equilibrated with the restite (batch melting) or the extraction was in small increments with no mutual homogenization (fractional melting). Apart from these two models for the equilibrium melting, variable degrees of disequilibria seem commonplace. The disequilibrium melting takes over especially in collisional orogens, when the melt extraction was accelerated by deformation or the accessory phases were shielded by major phases in the source not participating in the melting reaction (e.g. Watt and Harley, 1993; Nabelek and Glascock, 1995; Bea, 1996; Harris and Ayres, 1998). Last but not least, the protolith is often not exposed, and thus its exact nature and composition are unknown.

The ideal elements for modelling of partial melting are those residing in the main rock-forming minerals. This is the case of LILE, whose main reservoirs are feldspars and micas (e.g. Harris and Inger, 1992). On the other hand, several trace elements are incompatible in the main rock-forming minerals but form essential structural components (ESC) in accessory phases (Hanson and Langmuir, 1978). The dissolution of such an accessory mineral at the contact with the melt will continue until either the appropriate saturation level is reached or the source is exhausted (Watson and Harrison, 1984). The saturation models are defined for the main accessories of interest in granitic magmas, zircon (Watson and Harrison, 1983), apatite

(Harrison and Watson, 1984) and monazite (Montel 1993). In reality, the dissolution of the accessory minerals is governed by a number of factors, including the temperature, melt composition, crystal size, the water activity in the magma, diffusivity, absolute solubility of the ESC coupled with the degree of the melt undersaturation and its distribution within the rock volume.

Taken together, balancing the element fluxes during partial melting is not an easy task, as the granitic melts can result from a complex interplay of a number of processes, operative on various scales (e.g. Barbey et al., 1996). For open systems, a promising approach are mass transfer calculations, which take into account the changes in the total mass or volume of the system concerned (Grant, 1986; Olsen and Grant, 1991).

The Gföhl Unit of the Moldanubian Zone, Czech Republic, offers an exceptional opportunity to study the origin of migmatitic rocks, because it is possible to observe the spatial and structural relationships between the migmatites with different proportion of melt directly in the field. This means that one is able, for rocks with the same orthogneiss protolith and increasing degrees of migmatization, to investigate gradual changes in modal proportions of the rock-forming minerals, their chemistry, microstructures and whole-rock geochemical signature.

The present contribution aims to describe the major- and trace-element as well as Sr–Nd isotopic whole-rock geochemical variation in the individual gneiss and migmatite types in this unit. This, together with information on field relations, petrography and textures is used to evaluate the possible genetic hypotheses. Using the mass transfer calculations and other arguments we test the feasibility of the possible genetic scenarios. Included among them is the newly defined melt infiltration model (Hasalová et al., in press-a,b), in whose terms the various types of the Gföhl gneisses and migmatites were interpreted by a process in which the banded orthogneiss was pervasively, along grain boundaries, penetrated by felsic melt derived from an external source. Such a melt infiltration model would have potentially large consequences for generation of granitic magmas and crustal rheology in collisional orogens.

2. Regional setting

The *Moldanubian Zone* represents the orogenic root domain of the Bohemian Massif, which developed during the Variscan collision in the Devonian to Carboniferous times (Fig. 1a) (Matte et al., 1990; Dallmeyer et al., 1995; Schulmann et al., 2005 and references therein). At its eastern extremity, the Moldanubian rocks were thrust over the Cadomian Brunia basement along a so-called Moldanubian Thrust. The associated deformation produced a crustal-scale shear zone in the basement (the Moravian Zone, MZ), which crops out as three NE–SW trending tectonic windows (Suess, 1912; Urban, 1992; Schulmann et al., 1994; Fritz et al., 1996) (Fig. 1b).

The Moldanubian Zone is a tectonic assemblage of medium- to high-grade metamorphic rocks, intruded by numerous large, mostly Carboniferous plutons (Finger et al., 1997). The Moldanubian sequence has been subdivided into mainly metasedimentary and gneissic middle crustal rocks of Proterozoic and Lower Palaeozoic protolith ages assigned to the Drosendorf Unit by some authors (e.g. Tollmann, 1982; Franke, 2000) and the structurally upper and higher grade Gföhl Unit (Fuchs and Matura, 1976; Petrakakis, 1997 and references therein). The middle crustal rock assemblage consists of the Monotonous Series (mainly migmatitic Grt–Bt–Sil paragneiss with minor orthogneiss and amphibolite) and the Varied Series (paragneiss with intercalations of amphibolite, calc-silicate gneiss, marble, quartzite and graphite schist).

The *Gföhl Unit* is dominated by high-grade felsic gneiss and migmatite and layered migmatitic amphibolites. It also includes a high-pressure felsic Grt–Ky–Kfs granulite, which encloses bodies of garnet and spinel peridotites, pyroxenites and eclogites (Carswell, 1991; O'Brien and Carswell, 1993; Medaris et al., 1995). The exhumation of high-grade rocks and their juxtaposition to the middle crust within the orogenic root has been recently attributed to vertical extrusion of orogenic lower crust followed by horizontal channelized spreading at middle crustal levels, associated with retrogression and widespread melting (Schulmann et al., 2005; Tajčmanová et al., 2006).

The Gföhl gneiss and migmatite vary from banded orthogneiss without signs of melting towards migmatite with isotropic (nebulitic) structure without traces of earlier fabrics. The protolith is considered to be granitic (Dudek et al., 1974; Matějovská, 1975). The U–Pb SHRIMP dating showed that the protolith was Early Palaeozoic (488 ± 6Ma: Friedl et al., 2004). The age of Variscan metamorphism of the Gföhl gneiss has been estimated at 341 ± 4 and 337 ± 3Ma (conventional U–Pb ages for zircon and monazite, respectively: van Breemen et al., 1982) in Moravia and at 340 ± 10Ma (SHRIMP ages of outer growth zones of zircons: Friedl et al., 1998) together with 339.9 ± 0.9Ma (U–Pb monazite: Friedl et al., 1994) in Austria.

The Gföhl gneisses and HP felsic granulites show in many places intimate mutual association (Dudek et al., 1974; O'Brien and Rötzler, 2003), which led some workers to propose that the gneisses may represent

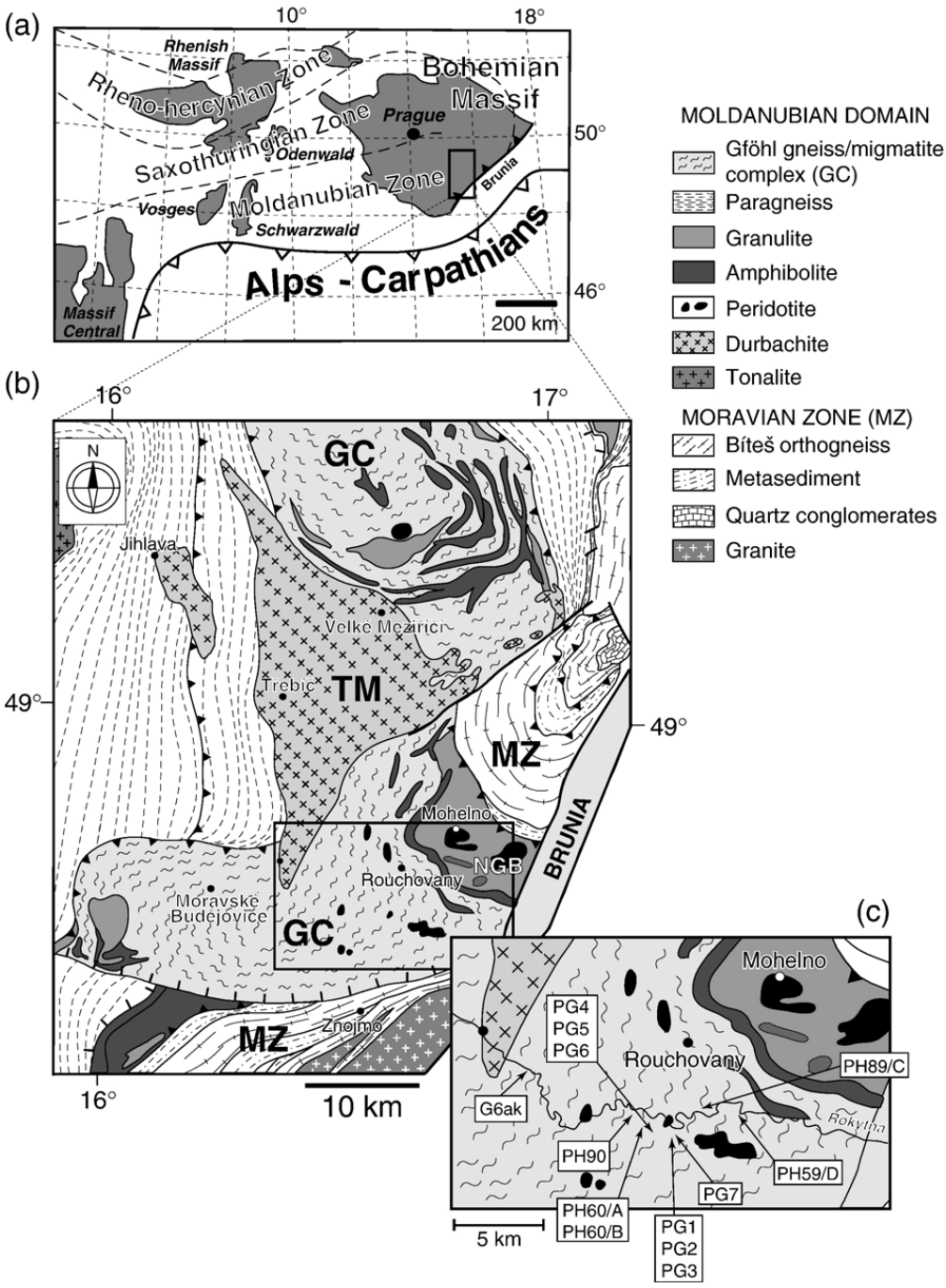

Fig. 1. (a) Location of the Gföhl Unit in the context of the Central European Variscides. (b) Geological map of the eastern part of the Bohemian Massif with location of the studied area (outlined). (c) Schematic map of the Rokytná Complex, showing the distribution of whole-rock samples collected in the course of this work.

retrogressed granulites (Cooke and O'Brien, 2001). The peak conditions in the granulite bodies, estimated by many workers at 1000°C and > 15kbar (see O'Brien, 2006 for review), have been recently constrained by others to *c.* 800–900°C and 18kbar (Medaris et al., 1998; Štípská and Powell, 2005; Tajčmanová et al., 2006). The peak pressure estimates have been interpreted as metamorphic conditions of the vertical extrusional fabric at *c*. 340Ma (Schulmann et al., 2005). The estimated pressure of re-equilibration associated with flat fabric that originated during the lateral spreading varies from 10kbar (Štípská et al., 2004), through 7kbar (Racek et al., 2006) to 4.0kbar (Tajčmanová et al., 2006), at temperatures between 700 and 800°C. In Austria the metamorphic conditions of the Gföhl gneiss and migmatite were estimated at 750°C

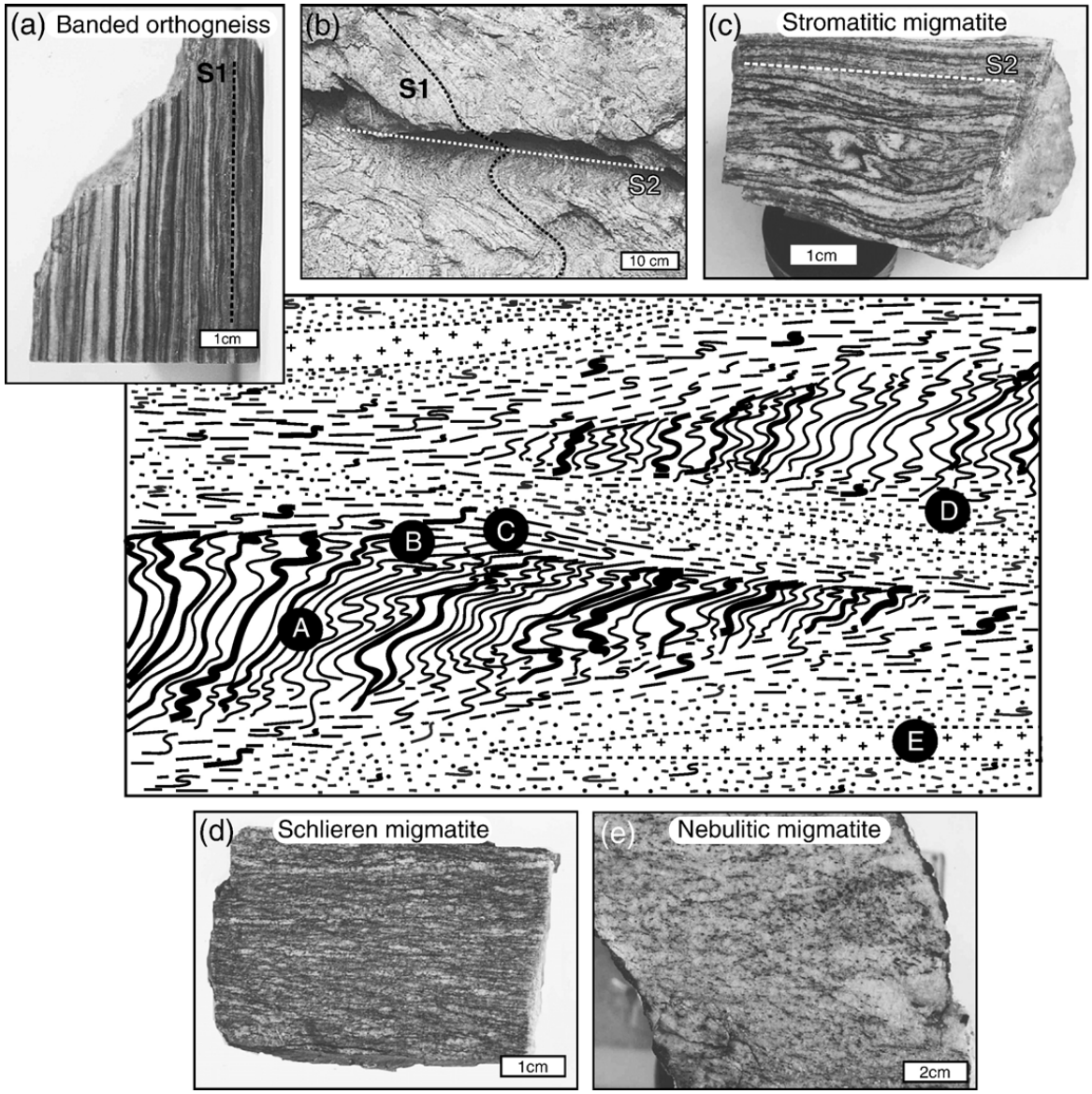

Fig. 2. Sketch showing the individual gneiss and migmatite types and their relationships within an outcrop (the width of the figure is 5m; modified after Hasalová et al., in press-a). Banded orthogneiss with distinct S_1 compositional layering (a) is folded and transposed (b) to the stromatitic migmatite (c) that passes gradually to the schlieren migmatite (d) and finally to the completely isotropic nebulitic migmatite with no relics of gneissosity (e). Shown are typical macrophotographs of each rock type.

and *c*. 7kbar (Petrakakis, 1986a,b), and nearly identical values were obtained by Owen and Dostal (1996) from western Moravia.

3. Field relations and migmatite occurrence

The studied area (Fig. 1b, c), the so-called *Rokytná Complex* (Svoboda et al., 1966), is situated at the eastern extremity of the Gföhl Unit close to its contact with the Moravian Zone. It is bound by the rocks of the Moravian Zone (MZ) in the East, by the Náměšť granulite body (NGB) in the North and by the Třebíč durbachite Massif (TM) in the West (Fig. 1b). The main rock types in the Rokytná Complex are high-grade orthogneisses and migmatites, enclosing minor bodies of amphibolites, granulites and paragneisses (Matějovská, 1975). The migmatites of the Rokytná Complex are texturally highly variable. In order to refer to individual rock types, the current paper employs migmatite terminology of Mehnert (1971), based on their macroscopic appearance.

Two major deformation events were recorded in this gneiss-migmatite complex (Urban, 1992; Schulmann et al., 1994; Hasalová et al., in press-a). The D_1 event most likely corresponded to early stages of lower crust exhumation, triggered by shortening of the thickened orogenic root (Schulmann et al., 2005). The D_2 shearing

has been attributed to horizontal spreading of lower crust at mid-crustal levels (e.g. Tajčmanová et al., 2006).

The deformation phase D_1 resulted in formation of steep, west dipping solid-state foliation S_1, represented by compositional layering in the *banded orthogneiss* (Fig. 2a). The D_2 deformation led to the development of a large crustal-scale shear zone and was associated with reworking and folding of S_1 compositional layering that is locally preserved in elongated relict domains (Fig. 2). These relict domains with gently folded S_1 fabric are surrounded by highly deformed zones with tightly folded S_1 fabric. Locally the S_1 fabric is completely transposed into the new S_2 foliation dipping gently to the SW. The resulting composite S_{1-2} fabric is characterized by banded structure with polymineralic K-feldspar- and plagioclase-rich domains resembling *stromatitic migmatite* (Fig. 2c). Detailed field study revealed that, with increasing degree of deformation, the stromatitic migmatite gradually passes into more isotropic *schlieren migmatite* (Fig. 2d) still containing rootless folds modifying the relics of the S_1 fabric. This rock type is alternating with irregular bodies or elongated lenses of felsic fine-grained *nebulitic migmatite* (Fig. 2e).

Such migmatite variations, which have originated through intense D_2 deformation superimposed on early steep anisotropy, can be identified both on the outcrop and the regional scales. In the studied area, stromatitic migmatites generally prevail over schlieren migmatites; the banded orthogneisses and nebulitic migmatites are subordinate. Macroscopically visible melt accumulations or granitic veins parallel to S_2 and tensional gashes perpendicular to S_2 are locally present.

3.1. Definition of individual rock types

Hasalová et al. (in press-a) showed the intimate relationship between different migmatite types suggesting that they all originated from the same protolith and that the banded orthogneiss and nebulitic migmatite can be considered as end-members of a continuous structural evolution.

All the studied samples contain stable mineral assemblage Pl + Kfs + Qtz + Bt ± Grt ± Sil; common accessory phases are apatite, monazite, zircon and xenotime. The modal proportion of feldspars remains in all rock types nearly the same, only the quartz shows a marked increase. On the other hand, the biotite and garnet contents decrease towards the nebulitic migmatite (Table 1).

The banded orthogneiss is characterized by monomineralic banding, defined by recrystallized K-feldspar, plagioclase aggregates and quartz bands, alternating with layers rich in biotite, garnet, sillimanite and apatite.

Table 1
Evolution of mineral chemistry and mineral proportions in the studied sequence

	Banded orthogneiss	Stromatitic migmatite	Schlieren migmatite	Nebulitic migmatite
X_{Fe} (Grt)	0.75–0.85	0.85–0.91	0.96–0.97	0.98–1.00
X_{Fe} (Bt)	0.43–0.50	0.55–0.59	0.76–0.79	0.91–0.93
An (Pl relict)	0.25–0.30	0.15–0.25	0.07–0.15	0.05–0.10
An (Pl new)	0.10–0.20	0.04–0.10	0.01–0.05	0.00–0.04
Or (Kfs)	0.80–0.95	0.80–0.95	0.80–0.95	0.80–0.95
Ti (Bt) (pfu)	0.20–0.30	0.20–0.25	0.18–0.20	0.02–0.05
Mineral proportions (wt.%)				
Kfs	19–34 (27)	28–31 (30)	28–31 (27)	29–34 (37)
Pl	26–32 (30)	28–35 (30)	24–29 (27)	21–28 (26)
Qtz	25–32 (28)	26–33 (31)	33–36 (35)	32–43 (37)
Bt	5–15 (10)	4–9 (7)	6–9 (7)	6–7 (6)
Grt	5–6 (5)	4–2 (2)	< 2	< 1
R^2	0.33–0.82	0.31–0.60	0.25–0.53	0.20–0.90

Grt garnet; *Bt* biotite; *Pl* plagioclase; *Kfs* K-feldspar; *Qtz* quartz; X_{Fe} = $Fe_t/(Fe_t+Mg)$; *An* anorthite = Ca / (Ca + Na + K); *Or* orthoclase = K / (Ca + Na + K). Mineral proportions were obtained by the constrained least-squares method (Albarède, 1995); shown are the ranges and (in brackets) average values; R^2 = goodness of fit (see text for details).

The stromatitic migmatite is marked by the onset of disintegration of the original monomineral banding and is composed of plagioclase and K-feldspar aggregates with subordinate quartz. These aggregates are rimmed by biotite locally overgrown by fibrolitic sillimanite.

The schlieren migmatite is made of K-feldspar–quartz-rich and plagioclase–quartz-rich aggregates. The original banding is distinguishable only from the modal content of the mineral phase dominant in these feldspar aggregates.

The nebulitic migmatite represents the most isotropic rock type, completely lacking relics of the original gneissosity. The migmatite occurs as irregular flat bodies or elongated lenses.

3.2. Mineral chemistry and microstructures

The banded orthogneiss always contains two chemically and microstructurally distinct *plagioclase* populations (Table 1 and Fig. 3a–d): (i) well-equilibrated grains with straight boundaries in plagioclase aggregates (An_{25-30}) and (ii) newly-grown plagioclase (An_{10-20}) forming interstitial grains or thin films coating the K-feldspar or plagioclase grains. In the stromatitic migmatite, the degree of albite coating increases and both the newly formed grains (An_{4-10}) and the relict grains (An_{15-25}) are more sodic (Table 1). In the schlieren migmatite large, corroded relict grains (An_{7-15}) are resorbed by new interstitial plagioclase (An_{1-5}) (Fig. 3c). This results, in the nebulitic migmatite, in

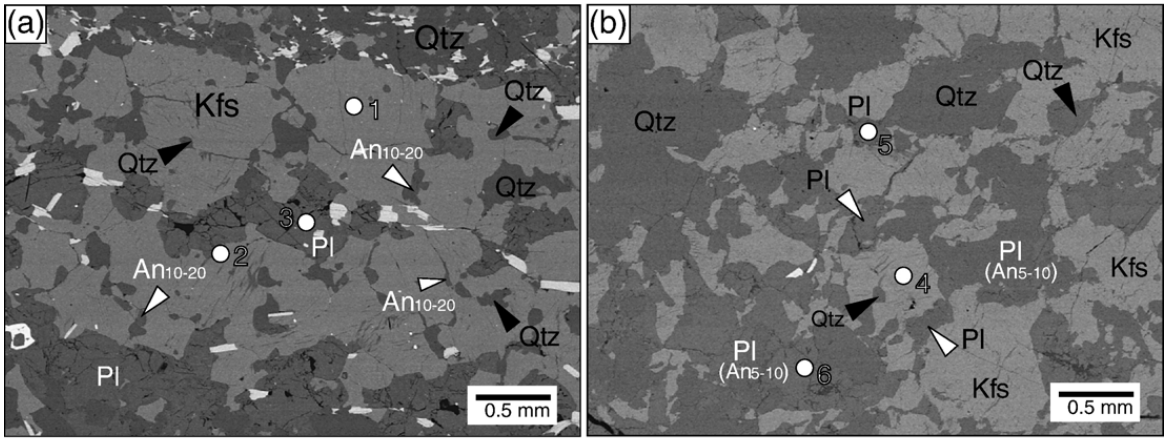

	Banded orthogneiss			Stromatitic migmatite			Schlieren migmatite			Nebulitic migmatite		
Mineral	Kfs	Pl	Pl	Kfs	Pl	Pl	Kfs	Pl	Pl	Kfs	Pl	Pl
Position	core	rim/films	core	core	rim/films	core	core	rim/films	core	core	rim/films	core
Wt. %	(1)	(2)	(3)				(7)	(8)	(9)	(4)	(5)	(6)
SiO_2	64.69	67.48	61.70	64.37	67.24	63.68	64.51	67.64	65.04	63.97	67.79	65.42
Al_2O_3	18.41	20.16	24.12	18.55	20.27	22.55	18.38	19.41	21.11	18.98	19.90	21.69
CaO	0.05	2.83	5.29	0.04	1.07	3.90	0.01	0.42	2.53	0.05	0.28	1.93
Na_2O	2.24	9.63	8.59	1.56	11.50	9.76	1.41	11.86	10.53	1.22	11.86	10.97
K_2O	13.96	0.12	0.43	15.04	0.10	0.23	15.18	0.10	0.15	15.65	0.02	0.18
BaO	0.39	0.00	0.00	0.13	0.00	0.00	0.08	0.00	0.00	0.00	0.00	0.00
Total	99.73	100.22	100.12	99.68	100.18	100.12	99.57	99.43	99.36	99.86	99.86	100.19

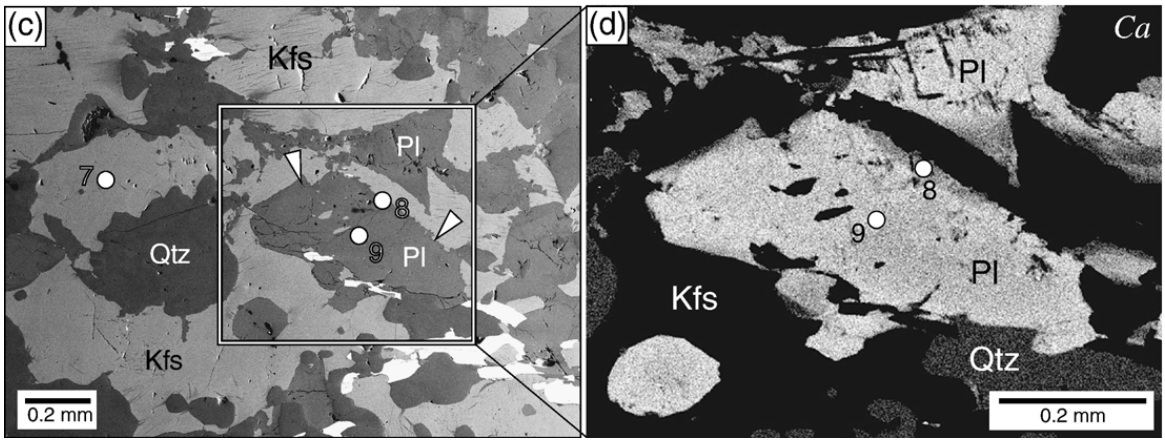

Fig. 3. Microscopic appearance and composition of feldspars in studied samples. (a–c) BSE images showing presence of melt and important changes in the feldspar textures within the studied sequence. (a) Typical microstructure of banded orthogneisses and stromatitic migmatites: recrystallized feldspar aggregate with numerous quartz (black arrows) and plagioclase (white arrows) interstitial grains/films tracing the K-feldspar boundaries (sample PH60/B). Relict plagioclase ($An_{24–30}$) is rimmed by more albitic plagioclase ($An_{10–20}$) and K-feldspar grains are traced by thin plagioclase ($An_{10–20}$) films (white arrows). This albitic plagioclase represents a component crystallized from the partial melt. (b) Typical appearance of schlieren and nebulitic migmatites featuring irregularly shaped feldspar and quartz grains. New interstitial plagioclase (white arrows), K-feldspar and quartz (black arrows) grains are tracing most of the feldspar boundaries. These newly crystallized feldspar and quartz resorb relict feldspar grains, causing their highly irregular shapes (sample PH59/C). (c) Detail of the irregular lobate K-feldspar grain completely embayed with newly crystallized quartz and plagioclase. Relict plagioclase grains are also surrounded by new albitic plagioclase (white arrows) (sample PH90). (d) Compositional map of the Ca distribution. It shows that a less sodic plagioclase is overgrown by albitic plagioclase crystallized from the melt (sample PH90). The feldspar compositions are summarized in the table. Note a continuous decrease in the Na_2O contents in each of the relict and newly crystallized plagioclases throughout the studied sequence.

complete overgrowths of small cuspate plagioclase ($An_{0–4}$) accompanied by K-feldspar and quartz on residual, strongly irregular plagioclase ($An_{5–10}$) grains. The newly-grown albitic plagioclase is, in agreement with Sawyer (1999, 2001) interpreted as having crystallized from the former melt.

Composition of *K-feldspar* is rather uniform (Table 1), however its microstructure evolves (Fig. 3). In the banded orthogneiss, recrystallized K-feldspar grains form almost monomineral bands (Fig. 3a). In the stromatitic migmatite, the K-feldspar bands start to be disintegrated with individual grains having slightly lobate boundaries traced by interstitial quartz and plagioclase. The schlieren migmatite shows K-feldspar relics that are highly irregular and surrounded by myrmekite and newly-grown interstitial quartz, plagioclase and K-feldspar (Fig. 3c). The degree of K-feldspar corrosion is highest in the nebulitic migmatite, where the residual grains are completely overgrown by cuspate plagioclase, accompanied by new K-feldspar and quartz (Fig. 3b).

Quartz occurs as recrystallized ribbons or interstitial grains and inclusions in the feldspar aggregates in the banded orthogneiss. Stromatitic, schlieren and nebulitic migmatite show gradual disappearance of the former quartz ribbons. Instead the quartz forms irregular polycrystalline aggregates with lobate grain boundaries or interstitial grains at feldspar boundaries, where it participates in resorption of the relict feldspar.

Biotite evolves texturally from elongated flakes in layers separating the feldspar-rich aggregates (banded orthogneiss) to grains dispersed in plagioclase-rich aggregates (stromatitic migmatite) or in the matrix composed of plagioclase, quartz and K-feldspar (schlieren and nebulitic migmatites). Cuspate biotite shapes, developed mostly in the nebulitic migmatite, were interpreted by Mehnert et al. (1973) and Büsch et al. (1974) as resulting from the reaction with the melt. The biotite chemistry evolves continuously, in the sequence from the banded orthogneiss to nebulitic migmatite, towards more Fe-rich and Ti-poor compositions (Table 1). Biotite is locally overgrown by fibrolitic *sillimanite*.

Garnet is unzoned almandine, with remarkable systematic increase in X_{Fe} from the banded orthogneiss to nebulitic migmatite (Table 1). Garnet in banded orthogneiss and stromatitic migmatite occurs as small idiomorphic grains along plagioclase and biotite layers. In schlieren and nebulitic migmatite, rare large atoll-shaped garnet appears in the matrix.

The most abundant among *accessory minerals* is apatite; characteristic but less common are monazite, zircon and xenotime. The Th content in monazite is continuously increasing towards the nebulitic migmatite, documenting an increasing brabantite substitution (Fig. 4 and Table 2). Monazite in the nebulitic migmatites is characterised by the highest contents of Th (up to 24wt.% ThO_2), with elevated U (< 4wt.% UO_2), Ca (up to 6wt.% CaO) and Y (< 2.2wt.% Y_2O_3).

Hasalová et al. (in press-a) assessed and quantified the microstructural changes from banded orthogneiss to nebulitic migmatite, finding out that the grain size of all felsic phases decreases continuously in the studied sequence. Resulting grain size distribution was interpreted to result from increasing nucleation rate and decreasing growth rate in the textural sequence. This is in accordance with the resorption of old/relict minerals and crystallization of new minerals from a melt along the feldspar boundaries. For further details on mineralogy and microstructures in the migmatite sequence the reader is referred to this publication.

4. Whole-rock geochemistry

4.1. Major elements

The studied samples are all broadly granitic in composition, as demonstrated for instance by the Q'-ANOR diagram of Streckeisen and Le Maître (1979) based on the CIPW normative mineralogy (Fig. 5). Whereas the banded orthogneisses and stromatitic migmatites correspond mostly to granite, schlieren migmatites straddle the boundary of the alkali feldspar granite domain occupied by the nebulitic migmatites.

Analogously, each of the groups shows a rather restricted range of major-element compositions. However there is a tendency for systematic changes in the whole migmatite sequence (Fig. 6 and Table 3). Thus the banded orthogneiss is are the least siliceous (SiO_2 = 68.09–72.93wt.%) and richest in most other

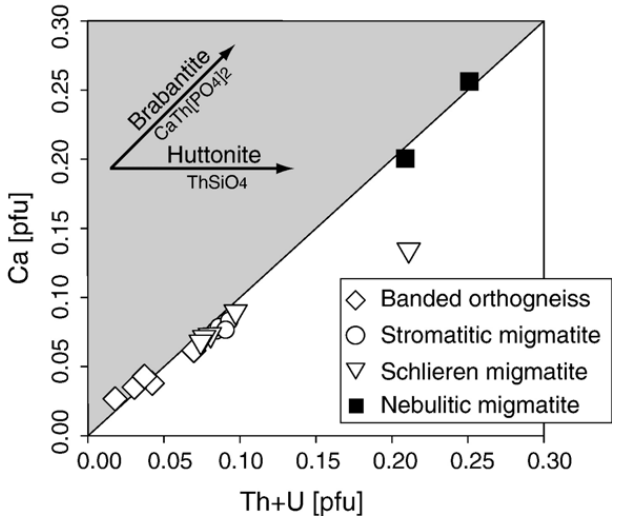

Fig. 4. Monazite compositions from the four studied rock types. Binary plot Th + U vs. Ca (pfu) demonstrates the importance of brabantite substitution, Ca (Th, U) REE_{-2} and only a minor role for the huttonite substitution, (Th, U) Si $REE_{-1}P_{-1}$.

Table 2
Representative microprobe analyses of monazite in individual rock types

Sample	Banded orthogneiss		Stromatitic migmatite		Schlieren migmatite		Nebulitic migmatite	
	PH60/B	PH60/B	PH14/N	PH14/N	PH63/C	PH63/C	PH59/D	PH59/D
Wt.%								
P_2O_5	29.97	30.40	28.87	29.24	29.83	30.18	29.62	28.86
SiO_2	0.31	0.14	0.55	0.52	0.54	0.49	0.77	0.91
ThO_2	4.04	2.59	8.53	8.85	10.08	8.53	22.01	24.10
U_2O_3	0.71	0.85	1.50	0.78	0.94	0.59	1.68	3.65
La_2O_3	13.42	13.04	10.87	11.24	10.01	10.39	8.00	6.82
Ce_2O_3	33.41	32.49	27.70	27.84	27.78	28.61	22.19	18.64
Pr_2O_3	3.08	3.00	2.51	2.80	2.90	2.65	2.16	1.68
Nd_2O_3	10.95	11.55	9.39	9.25	9.27	9.11	5.16	4.42
Sm_2O_3	1.16	1.45	1.24	1.38	1.31	1.57	1.03	0.42
Gd_2O_3	1.20	1.61	1.17	1.11	1.38	1.26	0.83	0.56
Y_2O_3	0.75	1.60	4.40	4.00	3.95	3.93	2.24	1.80
Al_2O_3	0.03	0.02	0.01	0.00	0.00	0.00	0.01	0.00
CaO	0.91	0.84	1.81	1.86	2.13	1.73	4.83	6.03
SrO	0.00	0.00	0.00	0.00	0.00	0.00	0.00	0.01
Total	99.91	99.57	98.54	98.88	100.11	99.02	100.52	97.90
P	1.002	0.992	0.969	0.974	0.982	0.978	0.971	0.969
Si	0.006	0.012	0.022	0.021	0.016	0.021	0.030	0.036
∑ (P→Si)	1.008	1.005	0.991	0.994	0.998	0.999	1.001	1.005
Th	0.023	0.036	0.077	0.079	0.072	0.089	0.194	0.218
U	0.008	0.006	0.014	0.007	0.005	0.008	0.015	0.033
La	0.187	0.194	0.159	0.163	0.161	0.143	0.114	0.100
Ce	0.463	0.478	0.402	0.401	0.427	0.394	0.315	0.271
Pr	0.043	0.044	0.036	0.040	0.037	0.041	0.030	0.024
Nd	0.161	0.153	0.133	0.130	0.129	0.128	0.071	0.063
Sm	0.019	0.016	0.017	0.019	0.017	0.017	0.014	0.006
Gd	0.021	0.016	0.015	0.015	0.017	0.018	0.011	0.007
Y	0.033	0.016	0.093	0.084	0.075	0.081	0.046	0.038
Al	0.001	0.001	0.001	0.000	0.000	0.000	0.000	0.000
Ca	0.035	0.038	0.077	0.079	0.070	0.088	0.200	0.256
Sr	0.000	0.000	0.000	0.000	0.000	0.000	0.000	0.000
∑ (Th→Sr)	0.993	0.997	1.023	1.016	1.009	1.008	1.011	1.016
Total	2.000	2.000	2.010	2.010	2.010	2.010	2.010	2.020
End-members								
Huttonite	0.56	1.23	2.15	2.03	1.58	2.06	2.93	3.57
Monazite	87.95	88.83	73.07	74.11	76.41	71.77	53.88	45.62
Xenotime	5.43	3.11	10.57	9.66	9.07	9.82	5.62	4.47
Brabantite	6.05	6.83	14.22	14.19	12.95	16.35	37.57	46.34

Huttonite = $ThSiO_4$; monazite = $(La–Sm)PO_4$; xenotime = $(Y, Gd–Lu)PO_4$; brabantite = $(Th, Ca, U, Pb)(PO_4)_2$.

oxides (TiO_2 = 0.29–0.56, Al_2O_3 = 11.50–15.40, FeOt = 1.98–3.39, MgO = 0.32–1.04, CaO = 0.95–1.66). Convex downward trends with an initial sharp decrease and an inflection point at SiO_2 *c.* 73–74 % are characteristic also of the mafic components TiO_2, FeOt, MgO and CaO. The compositional ranges observed in the most siliceous nebulitic migmatite are SiO_2 = 73.82–78.10, TiO_2 = 0.10–0.19, FeOt = 1.41–1.75, MgO = 0.15–0.30 and CaO = 0.95–1.66. On the other hand, the alkalis and P_2O_5 fail to define clear, non-scattered trends. All the studied samples are peraluminous; the values of the Shand's index A/CNK (molar Al_2O_3 / ($CaO + Na_2O + K_2O$), Table 3), decrease from 1.13–1.20 in the banded orthogneiss to 1.09–1.16 in the nebulitic migmatite.

4.2. Trace elements

4.2.1. Overall variation

While some of the trace elements show a more or less monotonous decrease with increasing silica (Ba, La, Eu and Zr) the trends for the others are more complicated (Fig. 7 and Table 4). The comparisons of trace-element concentrations between individual samples and their groups are facilitated by spider plots normalized to the

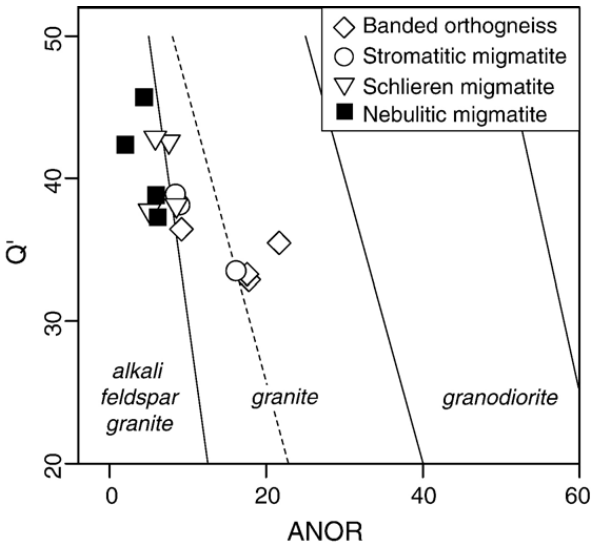

Fig. 5. Enlarged part of the Q'-ANOR classification for studied orthogneiss and migmatite samples (after Streckeisen and Le Maître, 1979; based on the CIPW norm). Banded orthogneiss and stromatitic migmatite correspond to granite. Schlieren migmatite straddles the boundary of the alkali feldspar granite domain, nebulitic migmatite falls purely into the alkali feldspar granite field.

average composition of the Earth's upper crust (Taylor and McLennan, 1985) (Fig. 8). The banded orthogneiss is characterised by having concentrations comparable with the upper crustal averages. Notable is only a slight (up to *c.* 2.5×) enrichment in the HREE, and remarkable troughs for Nb (0.3–0.5), Sr (0.18–0.42), Tb (0.40–0.54) and a less apparent one for Ti (0.48–0.93). The character of distribution patterns for other rock types is generally similar; however many of the trace elements show large variations and an overall tendency do decrease, especially in the more siliceous schlieren and nebulitic migmatites. The troughs for Sr, Tb and Ti progressively deepen. Later in the sequence conspicuous negative Ba, Th and, lesser, U, La, Ce, Nd, Sm, Zr and Hf anomalies also appear.

4.2.2. LILE

There is a marked Cs depletion in all samples from the Rokytná Complex. Without exception, the Rb/Cs ratios (Table 4) are significantly higher than in the average continental crust (Rb/Cs = 30; Taylor and McLennan, 1985 or 23; Wedepohl, 1995). The Rb/Cs ratios fall into a broad interval between 40 and 183, with the ratios increasing systematically in the sequence from the banded orthogneiss to nebulitic migmatite. On the other hand, the available analyses yield K/Rb ratios of 126–350 typical of ordinary crustal rocks (i.e. ranging between *c.* 120 and 500: Shaw, 1968; Rudnick et al., 1985) (Table 4). Therefore there is no evidence to support a notable Rb depletion.

4.2.3. REE

Like most major and other trace elements, the total REE contents also drop sharply in the sequence from banded orthogneiss to nebulitic migmatite, spanning a broad range (∑REE 36–220ppm, Table 4). At the same time the chondrite-normalized (Boynton, 1984) patterns (Fig. 9a–d) feature a strong progressive depletion in LREE and MREE; the HREE decrease is retarded. Thus a marked drop in La_N/Yb_N ratios (from 7.98 to 1.57; see also Fig. 9e) is accompanied with a rotation in the LREE segment (La_N/Sm_N 3.39 to 2.19; Fig. 9f). With rising degree of fractionation (expressed, for instance, by SiO_2 contents) there is an increase in the magnitude of the negative europium anomaly (Eu/Eu* dropping from 0.62 to 0.15). Banded orthogneiss, stromatitic and schlieren migmatites are fairly homogeneous in terms of their total REE contents and distributions. However, generally subparallel patterns for the samples of the nebulitic migmatite vary much in LREE and HREE contents, as they do in the magnitude of their negative Eu anomalies.

The REE patterns show a gradually developing M-type (or concave) lanthanide tetrad effect (Masuda et al., 1987). Its magnitude expressed as a parameter TE_{1-3} (Irber, 1999) ranges from negligible/none (banded orthogneiss, TE_{1-3} = 0.98–1.01, Table 4), through noticeable in stromatitic migmatite (1.02–1.04), schlieren migmatite (1.05–1.10) to pronounced in the nebulitic migmatite (1.04–1.17). In addition, the TE_{1-3} values correlate positively with some variables expressing fluid/melt or crystal/melt fractionation, such as Rb/Cs (Fig. 9g) and Eu/Eu* (Fig. 9h).

Most of the workers nowadays agree that the occurrence of M-type lanthanide tetrad effect is connected to fluorine-rich environments, being caused by melt/fluid (Irber, 1999; Monecke et al., 2002; Zhao et al., 2002) or melt/melt (Veksler et al., 2005) fractionation. However, the fluorine contents are constantly low (0.10–0.13) regardless of the migmatite type (Table 3) and thus this element does not seems to play a major role. In our case the reason for the formation of the tetrad effect remains enigmatic.

4.3. Zircon and monazite saturation temperatures

The calculated zircon saturation temperatures (Watson and Harrison, 1983; Hanchar and Watson, 2003) range from *c.* 830°C to 710°C (Table 3), and decrease monotonously in the structural sequence from banded orthogneiss to nebulitic migmatite (Fig. 10). The same trend is seen for the monazite saturation temperatures (Montel, 1993) spanning a comparable interval (*c.* 800°C to 680°C, Table 3).

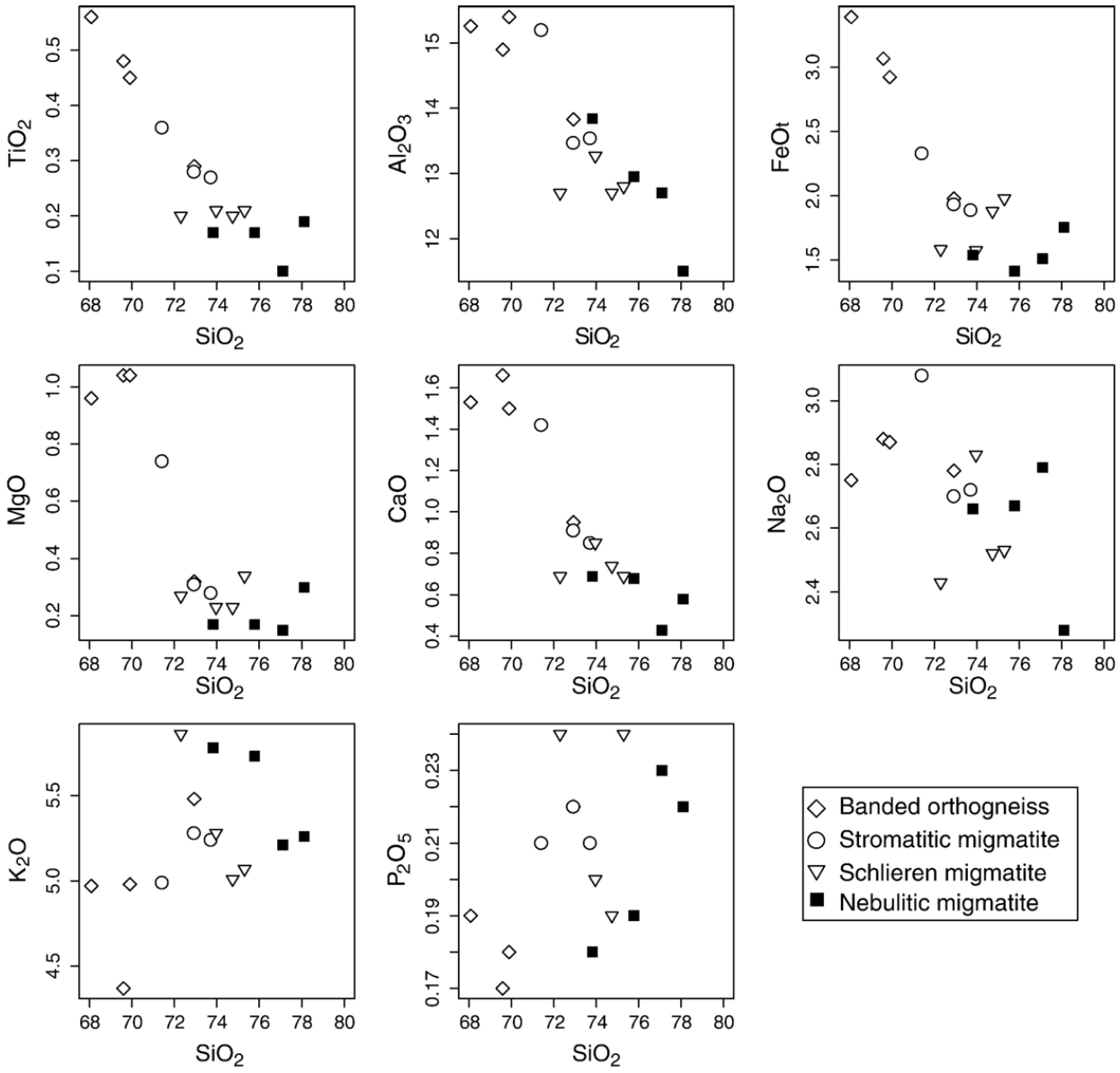

Fig. 6. Harker plots showing the major-element evolution from the banded orthogneiss to the nebulitic migmatite (wt.%). Note that some of the oxides show remarkable horizontal shifts at the end of the sequence, i.e. in the more siliceous schlieren and nebulitic migmatites. This is ascribed to an increasing role for the fractional crystallization. See text for explanation.

4.4. Radiogenic isotopes

Whole-rock Sr–Nd isotopic ratios for the four main varieties of the Rokytná gneisses and migmatites, age-corrected to 340Ma, are presented in the Table 5 and Fig. 11.

The two most basic banded orthogneisses (PG7 and PH60B) show an identical, most negative ε_{Nd}^{340} value of −6.7. The rest of the data set seems to contain Nd significantly more radiogenic (ε_{Nd}^{340} = − 5.6 to − 5.2). Altogether the data correspond to fairly uniform two-stage Nd depleted-mantle model ages (T_{Nd}^{DM} = 1.46–1.58Ga). There are, however, more pronounced differences in the Sr isotopic compositions (Fig. 11a). The Sr isotopic ratios correlate positively with silica spanning the broad range from 0.7153 for the most basic orthogneiss PG7 to 0.7332 and 0.7347 in the most siliceous nebulites PG1 and PG3 (Fig. 11b).

The Sr–Nd data for the Rokytná Complex resemble the previously published analyses from the Austrian outcrops of the Gföhl gneiss. Frank et al. (1990), as a part of their extensive study concerned with Rb–Sr whole-rock and thin slab dating, obtained a comparably broad range of Sr isotopic compositions ($^{87}Sr/^{86}Sr_{340}$ = 0.7192–0.7412).

Table 3
Major-element compositions (ICP-MS) and saturation temperature estimates for zircon (Zrn) and monazite (Mnz)

Sample	Banded orthogneiss				Stromatitic migmatite		
	G2A	PH60/B	PG5	PG7	PH60/A	PG4	PG6
Wt.%							
SiO_2	69.60	69.90	72.93	68.09	71.40	72.91	73.70
TiO_2	0.48	0.45	0.29	0.56	0.36	0.28	0.27
Al_2O_3	14.90	15.40	13.83	15.26	15.20	13.47	13.54
Fe_2O_3	3.41	3.25	2.20	3.77	2.59	2.15	2.10
MnO	0.04	0.04	0.03	0.05	0.03	0.03	0.03
MgO	1.04	1.04	0.32	0.96	0.74	0.31	0.28
CaO	1.66	1.50	0.95	1.53	1.42	0.91	0.85
Na_2O	2.88	2.87	2.78	2.75	3.08	2.70	2.72
K_2O	4.37	4.98	5.48	4.97	4.99	5.28	5.24
P_2O_5	0.17	0.18	0.22	0.19	0.21	0.22	0.21
F			0.11	0.08		0.10	0.10
Total	99.22	100.21	99.53	98.71	100.66	98.83	99.53
A/CNK	1.19	1.20	1.13	1.20	1.16	1.14	1.16
K_2O/Na_2O	1.5	1.7	2.0	1.8	1.6	2.0	1.9
CaO/Na_2O	0.6	0.5	0.3	0.6	0.5	0.3	0.3
Al_2O_3/TiO_2	31.2	34.3	48.4	27.1	41.9	48.7	51.0
FeOt[a] + MgO + TiO_2	4.6	4.4	2.6	4.9	3.4	2.5	2.4
(°C)							
Zrn saturation T	819	812	799	828	789	789	798
Mnz saturation T	801	797	796	836	785	794	796

Sample	Schlieren migmatite				Nebulitic migmatite			
	PH89/C	PH90	PG2	PH14/D	PH59/D	G6ak	PG1	PG3
Wt.%								
SiO_2	72.30	75.30	74.74	73.96	77.10	78.10	73.82	75.78
TiO_2	0.20	0.21	0.20	0.21	0.10	0.19	0.17	0.17
Al_2O_3	12.70	12.80	12.70	13.27	12.70	11.50	13.84	12.95
Fe_2O_3	1.76	2.20	2.09	1.75	1.68	1.95	1.71	1.57
MnO	0.03	0.03	0.03	0.02	0.03	0.03	0.03	0.02
MgO	0.27	0.34	0.23	0.23	0.15	0.30	0.17	0.17
CaO	0.69	0.69	0.74	0.85	0.43	0.58	0.69	0.68
Na_2O	2.43	2.53	2.52	2.83	2.79	2.28	2.66	2.67
K_2O	5.86	5.07	5.01	5.28	5.21	5.26	5.78	5.73
P_2O_5	0.24	0.24	0.19	0.20	0.23	0.22	0.18	0.19
F			0.13	0.10			0.12	0.11
Total	97.10	100.20	98.93	99.98	101.16	100.98	99.59	100.42
A/CNK	1.10	1.17	1.16	1.11	1.15	1.10	1.16	1.09
K_2O/Na_2O	2.4	2.0	2.0	1.9	1.9	2.3	2.2	2.1
CaO/Na_2O	0.3	0.3	0.3	0.3	0.2	0.3	0.3	0.3
Al_2O_3/TiO_2	62.3	61.8	62.1	63.7	130.9	60.2	80.1	77.4
FeOt[a] + MgO + TiO_2	2.1	2.5	2.3	2.0	1.8	2.2	1.9	1.8
(°C)								
Zrn saturation T	766	781	761	770	706	744	770	750
Mnz saturation T	743	747	782	761	679	708	780	766

[a]Total iron as FeO.

The only three Sr–Nd isotopic pairs for Gföhl gneisses were reported by Vellmer (1992): $^{87}Sr/^{86}Sr_{340}$ = 0.7237–0.7367 and ε_{Nd}^{340} = − 5.4 to − 6.7 (T_{Nd}^{DM} = 1.47–1.55 Ga).

The $^{87}Sr/^{86}Sr_{340}$–ε_{Nd}^{340} plot (Fig. 11a) shows clearly that the Sr–Nd isotopic compositions of the Rokytná gneisses fall within the compositional range of the typical Moldanubian granulites (Vellmer 1992; Valbracht et al., 1994; Becker et al., 1999; Janoušek et al., 2004). However they differ from the Czech Moldanubian metasediments (paragneisses and kinzigites;

Janoušek et al., 1995 and unpublished data), which have epsilon Nd values significantly lower than the gneisses described in the present work (Fig. 11a).

5. Discussion

Among the Gföhl gneisses and migmatites, several macroscopically distinct types can be distinguished. As shown by Hasalová et al. (in press-a), they apparently form a continuous structural sequence related to a disintegration of the parental orthogneiss. This distinctly banded rock is gradually transposed to stromatitic and schlieren migmatites. The migmatites are characterised by abundance of feldspar- and quartz-rich aggregates, presumably formed by fragmentation of the original banding. Eventually, the monomineralic layering vanishes and schlieren migmatite develops into isotropic nebulitic migmatite with no relics of gneissic morphology. At the first glance, this sequence resembles evolution of migmatite types described in classical works (e.g. Mehnert, 1971; Brown, 1973).

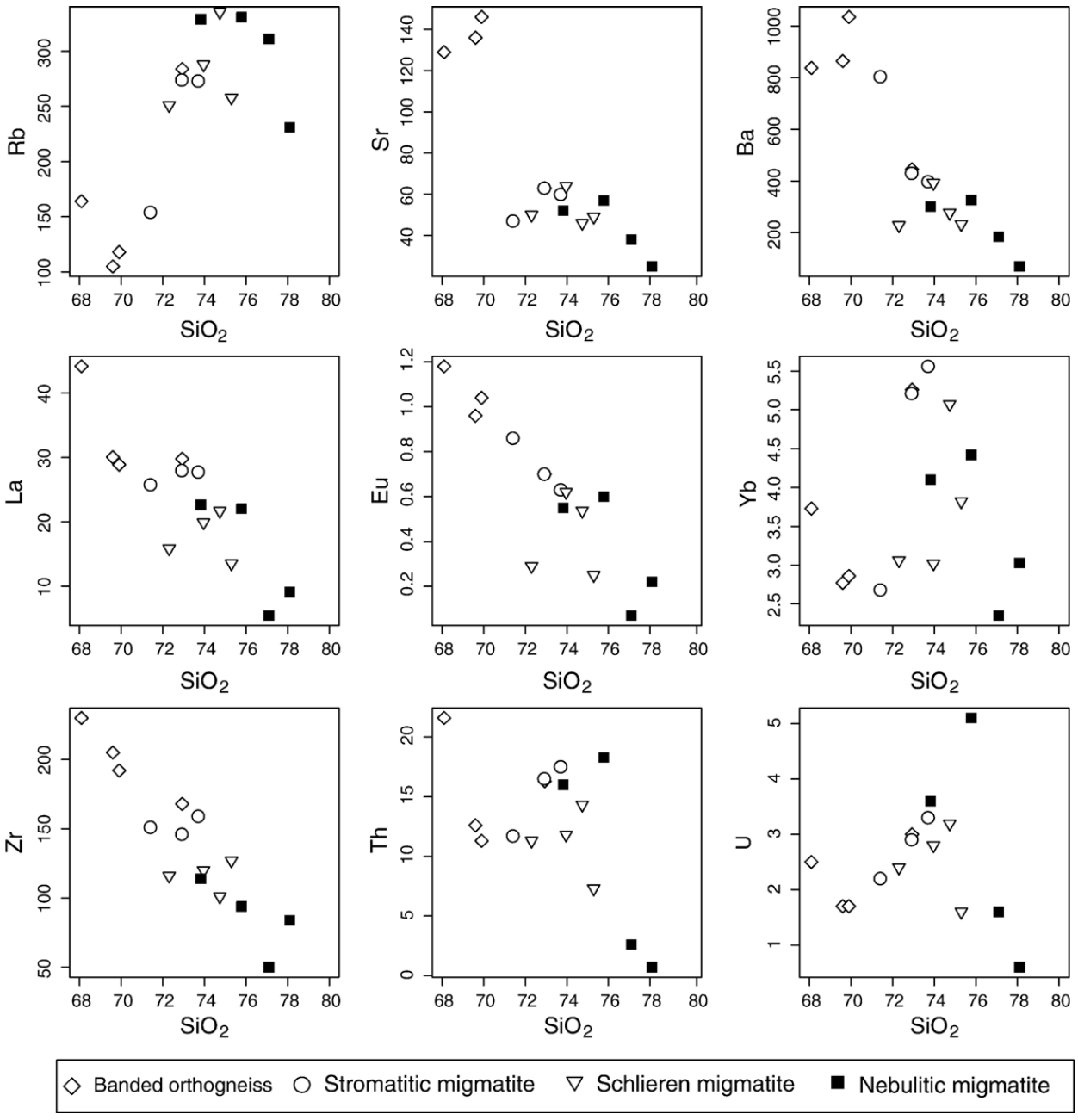

Fig. 7. Selected binary plots of SiO_2 vs. trace elements (typical LILE, REE and HFSE, in ppm). Some of the trace elements (Ba, La, Eu and Zr) show a more or less continuous decrease throughout the studied sequence, the trends for the others are more complicated.

Table 4
Trace-element compositions (ICP-MS)

Sample p.p.m.	Banded orthogneiss				Stromatitic migmatite			Schlieren migmatite				Nebulitic migmatite			
	G2A	PH60/B	PG5	PG7	PH60/A	PG4	PG6	PH89/C	PH90	PG2	PH14/D	PH59/D	G6ak	PG1	PG3
Rb	105	118	284	164	154	274	273	251	258	337	288	311	231	329	331
Sr	136	146	63	129	130	63	60	49	50	46	64	25	38	52	57
Ba	865	1035	445	838	226	430	397	232	228	276	392	69	184	301	326
Cs	2.4	2.4	5.5	4.1	3.0	5.6	5.7	3.4	2.4	5.8	5.0	1.7	1.6	6.3	6.0
Th	12.6	11.3	16.3	21.6	11.7	16.5	17.5	11.3	7.3	14.1	11.8	2.6	0.7	16.0	18.3
U	1.7	1.7	3.0	2.5	2.2	2.9	3.3	2.4	1.6	3.2	2.8	1.6	0.6	3.6	5.1
Pb	21	23	29	29	23	31	27	13	11	41	27	9	9	48	35
Cr	38	43	13	35	21	11	11	13	24	10	10	13	28	11	34
V	46	46	16	49	27	17	16	4	6	12	12	5	< 2[a]	10	9
K/Rb	345.5	350.3	160.2	251.6	269.0	160.0	159.3	193.8	163.1	123.4	152.2	139.1	189.0	145.8	143.7
Rb/Sr	0.8	0.8	4.5	1.3	1.2	4.4	4.5	5.1	5.2	7.3	4.5	12.5	6.1	6.3	5.8
Rb/Cs	43.4	48.7	51.2	40.0	50.7	49.3	48.2	74.9	106.4	57.7	57.7	182.0	144.4	52.6	54.9
Rb/Ba	0.1	0.1	0.6	0.2	0.7	0.6	0.7	1.1	1.1	1.2	0.7	4.5	1.3	1.1	1.0
Sc	8	8	4	9	3	4	4	3	4	3	3	4	4	3	3
Zn	68	61	21	45	53	22	17	39	54	20	14	65	35	14	446
Zr	205	192	168	230	172	146	159	127	116	101	120	84	50	114	94
Hf	4.0	4.2	5.7	6.8	3.6	5.0	5.5	3.2	2.8	3.8	3.8	1.7	2.0	4.2	3.9
Nb	8.1	7.7	10.6	12.3	7.2	9.6	10.0	9.9	8.1	8.6	8.0	6.8	5.5	7.5	8.5
Ta	1.9	2.0	0.8	1.0	2.5	0.7	0.8	3.7	3.1	0.6	0.7	3.0	2.0	0.6	0.8
La	30.0	28.9	29.8	44.1	25.8	28.0	27.7	15.9	13.6	21.6	19.9	5.5	9.1	22.7	22.1
Ce	60.4	57.1	61.8	88.7	51.8	58.2	57.5	34.9	30.3	45.4	41.3	12.5	20.2	46.6	45.4
Pr	7.0	6.7	7.2	10.5	6.1	6.9	6.8	4.1	3.6	5.5	4.8	1.5	2.5	5.5	5.3
Nd	25.8	24.7	26.9	39.4	22.3	25.7	24.8	14.4	12.8	19.9	17.6	4.8	9.0	19.8	18.7
Sm	5.7	5.4	6.2	8.2	5.0	6.0	5.9	3.7	3.4	5.2	4.3	1.5	2.6	4.8	4.6
Eu	0.96	1.04	0.70	1.18	0.86	0.70	0.63	0.29	0.25	0.53	0.62	0.07	0.22	0.55	0.60
Gd	5.1	4.8	5.9	7.4	4.4	5.5	5.4	3.6	3.3	4.9	4.1	1.4	2.6	4.5	4.5
Tb	0.92	0.88	1.12	1.19	0.84	1.11	1.09	0.80	0.79	1.08	0.89	0.37	0.64	0.90	0.95
Dy	5.5	5.7	8.3	8.1	5.3	8.3	8.1	5.6	5.8	8.4	6.7	2.9	4.8	6.9	7.5
Ho	1.25	1.29	1.90	1.71	1.18	1.91	1.86	1.27	1.35	2.0	1.47	0.64	1.12	1.53	1.78
Er	3.1	3.4	5.1	4.3	3.0	5.2	5.2	3.4	3.8	5.4	3.7	1.8	3.1	4.1	4.6
Tm	0.51	0.53	0.83	0.65	0.51	0.85	0.92	0.56	0.68	0.85	0.58	0.37	0.54	0.69	0.76
Yb	2.8	2.9	5.3	3.7	2.7	5.2	5.6	3.1	3.8	5.1	3.0	2.3	3.0	4.1	4.4
Lu	0.41	0.43	0.75	0.58	0.39	0.78	0.87	0.43	0.53	0.69	0.43	0.35	0.41	0.60	0.64
Y	41.0	42.0	44.1	42.3	46.0	43.7	43.9	45.0	42.0	44.4	37.3	38.0	23.0	35.6	39.1
Sum REE	149.6	143.7	161.8	219.8	130.1	154.2	152.4	91.9	83.9	126.6	109.5	35.9	59.8	123.2	121.9
La_N/Yb_N	7.31	6.81	3.82	7.98	6.49	3.62	3.36	3.50	2.39	2.85	4.44	1.57	2.02	3.73	3.36
La_N/Sm_N	3.29	3.36	3.04	3.39	3.24	2.94	2.95	2.73	2.50	2.62	2.89	2.35	2.19	2.95	2.99
Eu/Eu*	0.54	0.62	0.35	0.46	0.56	0.37	0.34	0.25	0.23	0.32	0.45	0.15	0.26	0.36	0.40
TE_{1-3}	1.00	1.00	1.01	0.98	1.02	1.03	1.04	1.09	1.10	1.05	1.06	1.17	1.10	1.04	1.04

[a]values given as < mean that the concentration is below the respective detection limit.

5.1. Genesis of the Gföhl migmatites

Partial melting of rocks with a broadly granitic composition is the generally accepted explanation for the petrogenesis of the Gföhl migmatites (Dudek et al., 1974; Matějovská, 1975). Even though such a conclusion is generally in line with the results presented in the current paper, the exact cause for the chemical variability observed in the Gföhl migmatites was never seriously discussed. The possible mechanisms involve: (i) tectonic or intrusive juxtaposition of genetically unrelated migmatites that have originated from distinct protoliths, (ii) equilibrium melting of a single metagranitic protolith, (iii) disequilibrium melting (with or without a small-scale melt movement) and (iv) infiltration of a melt derived from an external source into the parental orthogneiss. These hypotheses are evaluated below.

5.1.1. Distinct protoliths to each of the migmatite types

The first and arguably the most unrealistic is a model in which each of the migmatite types had its own, genetically unrelated protolith and their juxtaposition was purely accidental. This possibility can be first of all ruled out because of the observed gradual transposition of the S_1 banded gneisses into the S_2 stromatitic and schlieren migmatites (Hasalová et al., in press-a). These authors

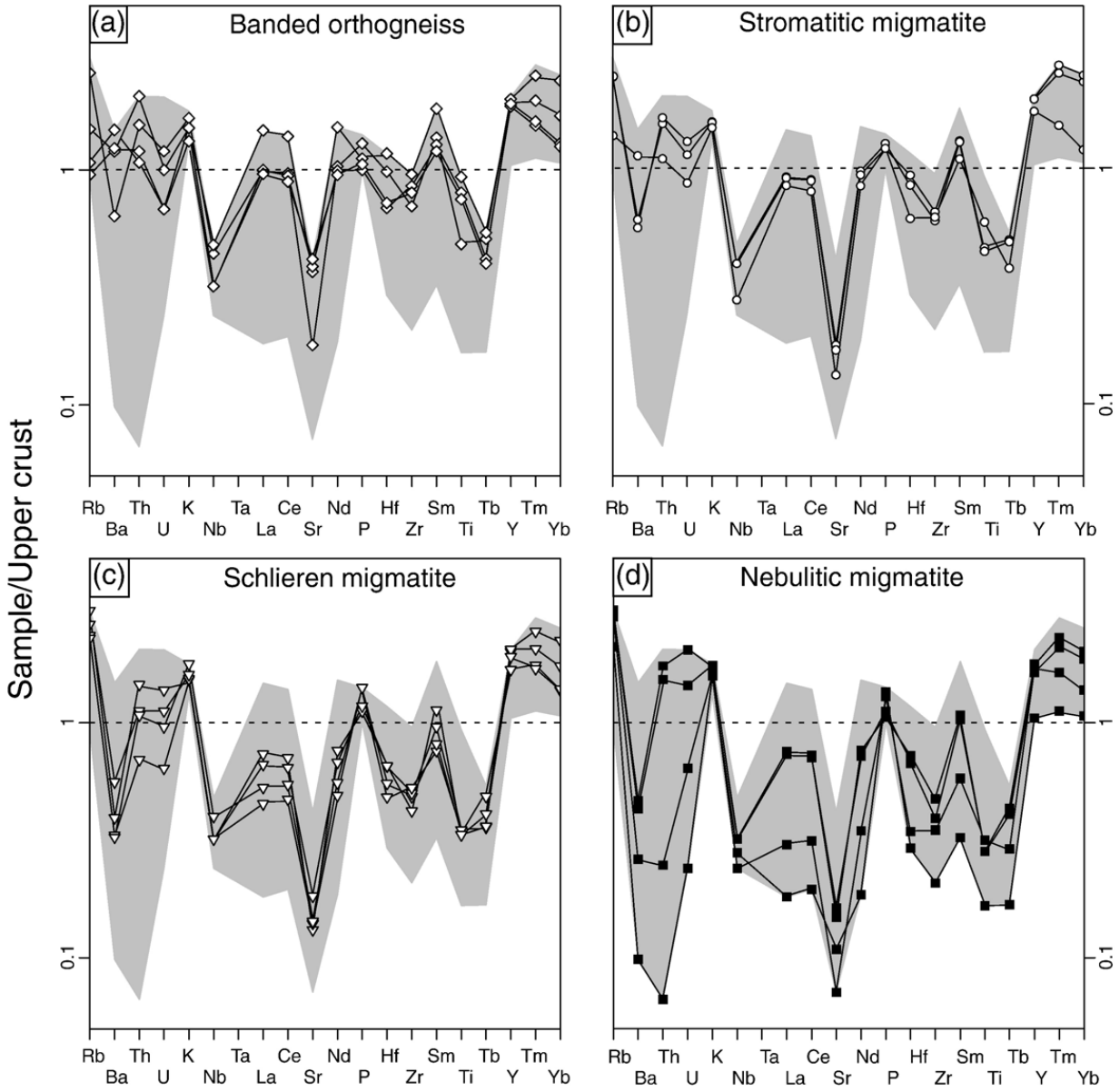

Fig. 8. Spider plots normalized to the composition of the average upper crust (Taylor and McLennan, 1985). The overall shape of the individual patterns for all rock types is similar. Broad ranges in compatible elements for the schlieren and nebulitic migmatites are interpreted as being due to the K-feldspar dominated fractional crystallization. Shaded field corresponds to the total variation in the whole dataset.

pointed out that the structural data are compatible with progressive deformation within a ductile shear zone resulting in generation of a continuous spectrum of variably deformed rock types ranging from pristine banded orthogneiss to the most affected schlieren migmatite. This interpretation is based on observed progressive folding of early steep orthogneiss fabric, in more advanced stages with development of isoclinal folds, leading eventually to complete fabric transposition and formation of schlieren migmatite. At the first glimpse, the elongated bodies of nebulitic migmatite can be viewed either as veins of isotropic granite penetrating parallel to the main S_2 mylonitic anisotropy (e.g. Brown and Solar, 1998) or as tectonically expelled granitic liquid injected into country rocks, which were hot thus preventing freezing (Weinberg and Searle, 1998). However, the nebulitic migmatite can be also regarded as the most extreme end-member of the structural sequence, i.e. completely disintegrated parental orthogneiss. This possibility is strongly supported by the microstructures, mineral chemistry (Table 1) and whole-rock geochemical parameters (Figs. 6–9) including the Sr–Nd isotopic compositions (Fig. 11 and Table 5) which change continuously from the banded orthogneiss to the nebulitic migmatite. Additionally, the overall resemblance in the trace-element distribution patterns and only gradual changes in the elemental concentrations

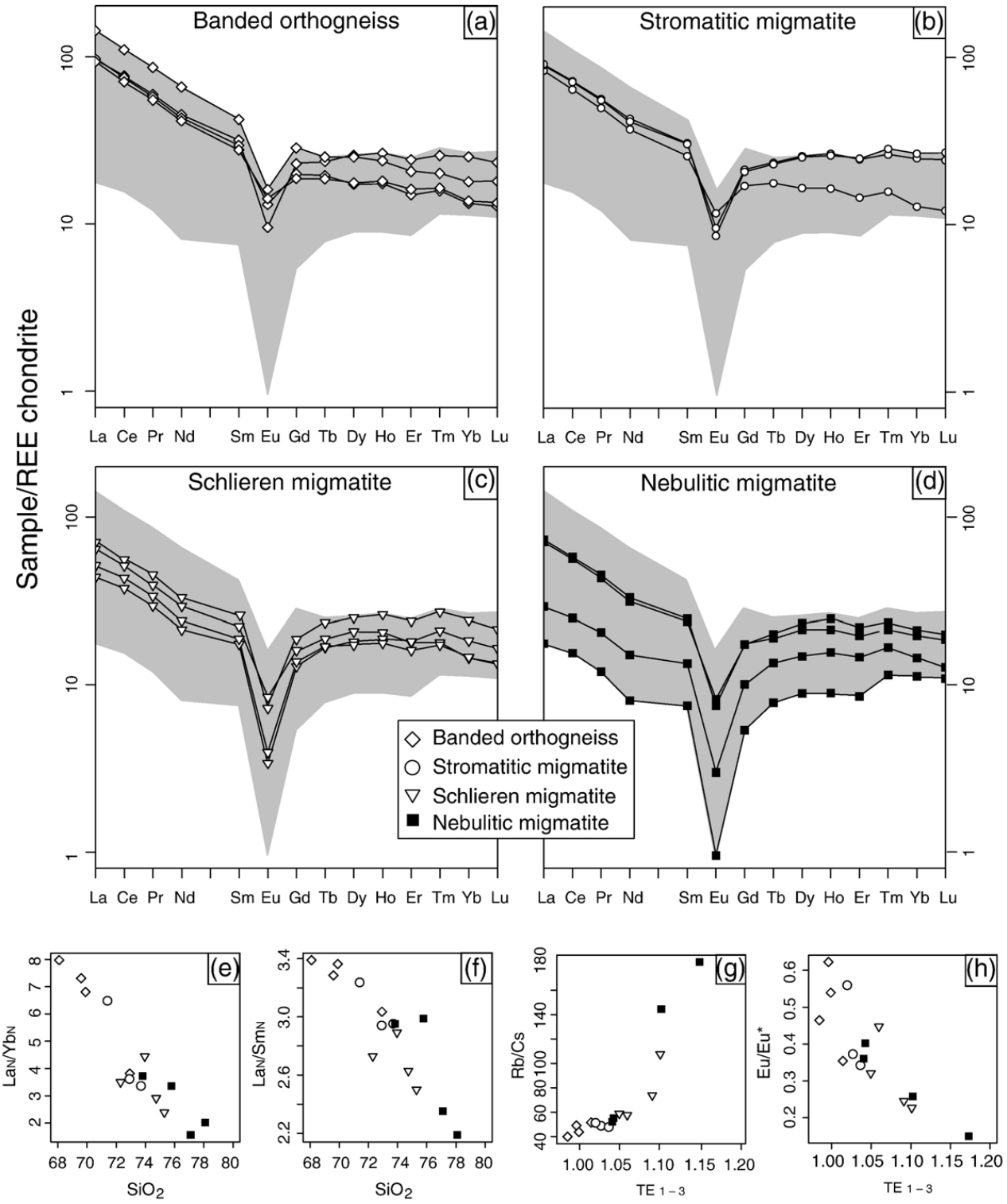

Fig. 9. (a–d) Chondrite-normalized (Boynton, 1984) REE patterns for the studied samples. The REE contents drop sharply in the sequence from banded orthogneisses to nebulitic migmatite, spanning a broad range. Magnitude of the negative Eu anomaly increases with degree of fractionation. Shaded field corresponds to the total variation in the whole dataset. (e–f) Binary plots of SiO_2 vs. La_N/Yb_N and La_N/Sm_N characterising the shape of the normalized REE patterns. (g–h) Binary plots exhibiting the magnitude of the tetrad effect (expressed as a parameter TE_{1-3}: Irber, 1999) vs. Rb/Cs and Eu/Eu*. The TE_{1-3} values correlate positively with Rb/Cs (g) and negatively with the Eu/Eu* (h) ratios.

(Figs. 8–9) together with the monotonously decreasing zircon/monazite saturation temperatures (Fig. 10) argue against significant differences in the protoliths. In other words, the available data for four studied orthogneiss and migmatite types suggest that they all have to have originated from the same protolith.

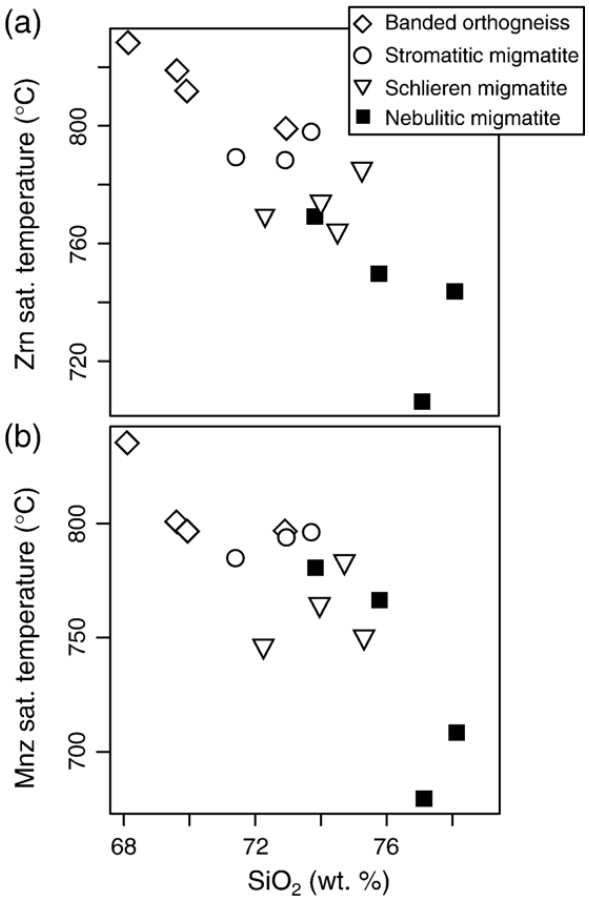

Fig. 10. Calculated saturation temperatures for (a) zircon (Watson and Harrison, 1983) and (b) monazite (Montel, 1993) plotted against SiO_2. The both sets of the saturation temperatures decrease continuously in the morphologic migmatite sequence.

5.1.2. Equilibrium melting

The equilibrium melting model rests upon an assumption that the anatexis was slow enough for the full equilibration between the solid residue and the *in situ* partial melt to be achieved. In the closed-system, equilibrium melting model, followed by homogenization of the individual melt batches, one would not expect any variations in their radiogenic isotope compositions (e.g. Briquet and Lancelot, 1979). However, the Sr–Nd isotope data in the Rokytná Complex display considerable variability and regular changes with independent geochemical parameters (see for instance the linear trend in the SiO_2–$^{87}Sr/^{86}Sr_i$ plot: Fig. 11b). This may reflect the source isotopic heterogeneity, perhaps due to *in situ* ^{87}Sr growth in the pre-Variscan protolith to the Gföhl gneisses (Frank et al., 1990). Such an isotopic heterogeneity is frequently observed on grain to meter scale in many high-grade metamorphic terrains and anatectic granites worldwide (e.g. Barbero et al., 1995).

Even though the variation in radiogenic isotope compositions does not preclude small-scale equilibria, the evolution of mineral compositions (Table 1) provides an independent argument disproving the equilibrium melting hypothesis. Assuming a closed-system, equilibrium melting along a prograde path, the X_{Fe} in garnet and biotite should decrease in accord with the decreasing modal proportion of garnet. In addition, the plagioclase should exhibit an increase in anorthite component with increasing degrees of melting. Such a compositional evolution was reported in a number of field and experimental studies (e.g. Vielzeuf and Holloway, 1988; Gardien et al., 1995; Dallain et al., 1999). However the compositional changes in the Rokytná Complex are just opposite, the X_{Fe} in garnet and biotite increase and the basicity of plagioclase drops (Table 1). This evolution is thus incompatible with a hypothesis invoking increasing degrees of melting in a closed-system.

Another possible argument is the strong textural and chemical disequilibrium between the rims and cores of the plagioclase crystals, demonstrating that it were apparently only their rims that have been in equilibrium with the melt (Fig. 3). However, because of the commonly slow diffusion of major and trace elements in the plagioclase (e.g. Blundy and Shimizu, 1991), this observation cannot exclude the *in situ* partial melting completely.

On this basis, the equilibrium melting hypothesis can be discounted as the main process responsible for the origin of the studied sequence, leaving the disequilibrium partial melting and open-system interactions as the only viable alternatives.

5.1.3. Disequilibrium melting

There is a growing evidence from experimental (e.g. Johannes 1980; Hammouda et al., 1996; Knesel and Davidson 1996, 2002) as well as from field observations and whole-rock geochemistry (e.g. Sawyer, 1991; Barbero et al., 1995; Bea, 1996; Harris and Ayres, 1998) indicating that the equilibrium between the melt and the solid residue does not have to be always attained in course of the crustal anatexis.

Firstly, the disequilibrium may occur when some accessory phases have remained armoured by main rock-forming minerals that have not participated in the melting reaction(s) (e.g. Watson and Harrison, 1984; Watt and Harley 1993; Nabelek and Glascock, 1995; Bea, 1996). However in the high-grade metamorphic rocks, the great majority of the accessory mineral grains is thought to be located at newly formed (or migrated) grain boundaries of the main rock-forming minerals and thus probably in contact with the partial melt (Watson et al., 1989). In lower-grade rocks, the accessories are mostly included in biotite and/or hornblende that in the course of the

Table 5
Sr–Nd isotopic data for gneisses/migmatites from the Rokytná Complex

Sample	Rock type	Rb (ppm)	Sr (ppm)	$^{87}Rb/^{86}Sr$	$^{87}Sr/^{86}Sr$ [a]	$(^{87}Sr/^{86}Sr)_i$ [b]
PG7	Banded orthogneiss	163.6	129.4	3.669	0.733034 (9)	0.715275
PH60/B	Banded orthogneiss	117.7	146.0	2.337	0.730249 (14)	0.718936
PG5	Banded orthogneiss	283.7	63.3	13.074	0.793691 (18)	0.730418
PG6	Stromatitic migmatite	273.2	60.3	13.215	0.795889 (19)	0.731933
PG2	Schlieren migmatite	337.4	46.3	21.329	0.829370 (18)	0.726143
PG1	Nebulitic migmatite	329.4	52.4	18.400	0.823759 (9)	0.734707
PG3	Nebulitic migmatite	331.0	57.4	16.873	0.814908 (14)	0.733248

Sample	Sm (ppm)	Nd (ppm)	$^{147}Sm/^{144}Nd$	$^{143}Nd/^{144}Nd$ [a]	$(^{143}Nd/^{144}Nd)_i$ [b]	ε^{i}_{Nd} [b]	T^{Nd}_{CHUR} (Ga)	T^{Nd}_{DM}(Ga) [c]
PG7	8.19	39.43	0.1255	0.512134 (8)	0.511855	−6.7	1.08	1.58
PG7 [d]	8.19	39.43	0.1255	0.512140 (8)	0.511861	−6.6	1.07	1.57
PH60/B	5.40	24.74	0.1318	0.512151 (9)	0.511858	−6.7	1.15	1.58
PG5	6.17	26.89	0.1387	0.512223 (9)	0.511914	−5.6	1.09	1.49
PG6	5.91	24.79	0.1441	0.512248 (7)	0.511927	−5.3	1.13	1.47
PG2	5.19	19.90	0.1573	0.512269 (6)	0.511919	−5.5	1.43	1.48
PG1	4.83	19.80	0.1473	0.512261 (9)	0.511933	−5.2	1.16	1.46
PG3	4.64	18.74	0.1498	0.512250 (9)	0.511916	−5.5	1.26	1.49

[a] values in parentheses are errors on the last decimal place (2SE).
[b] isotopic ratios with subscript "i" were all age-corrected to 340 Ma.
[c] two-stage Nd model ages calculated after Liew and Hofmann (1988).
[d] duplicated mesurement (including sample decomposition and column separation).

dehydratation melting would release them (Clemens, 2003).

The more common causes of disequilibrium are rapid melt production, extraction and segregation, not allowing enough time for the diffusional equilibration between the residual minerals and the melt. In normal granitic magmas derived by dehydratation crustal melting, the dissolution of zircon is assumed to be fast enough for the equilibrium to be attained (Harrison and Watson 1983; Watson 1996). However, achievement of equilibrium is less likely in the case of monazite and apatite, whose dissolution is controlled mainly by sluggish LREE and phosphorus diffusion (Harrison and Watson, 1984; Rapp and Watson, 1986). Swift extraction of low to moderate melt fractions can be promoted by a feedback mechanism between increasing melt production and deformation or shear-enhanced compaction, as was demonstrated for instance in the Himalayas (D'Lemos et al., 1992; Rutter and Neumann, 1995; Ayres et al., 1997). Muscovite dehydratation melting can as well cause high dilatation strain that may further boost melt segregation (Rushmer 1996, 2001).

Disequilibrium melting may have a profound influence on the radiogenic isotopic composition of granitic magmas. Their Sr isotopic signature is controlled mainly by the main rock-forming minerals in the source (principally the balance between feldspars with low Rb/Sr and micas with high Rb/Sr, and thus also high $^{87}Sr/^{86}Sr$ isotopic ratios). Consequently, the melts produced by disequilibrium dehydratation melting involving muscovite and/or biotite will tend to have a more radiogenic Sr than their source. On the other hand, the bulk of the Nd in the felsic magmas will be controlled mainly by monazite and apatite, and thus the Nd isotope ratios will be governed by dissolution kinetics of these minerals. As shown by modelling of Zeng et al. (2005), these two phases ought to show a contrasting behaviour. The apatite with high Sm/Nd ratio will develop, with time, a more radiogenic Nd. Thus the progressive dissolution of apatite will yield melts with Nd isotopic signature increasingly more radiogenic (higher epsilon Nd values) than the source. Monazite, which has relatively low Sm/Nd, will have an opposite effect.

Disequilibrium melting model can explain the observed variation in the $^{87}Sr/^{86}Sr_{340}$–ε^{340}_{Nd} as well as SiO_2–$^{87}Sr/^{86}Sr_{340}$ plots (Fig. 11a, b). The trends may theoretically argue for an increasing role of biotite dehydratation melting and apatite dissolution in the more siliceous samples. Two disequilibrium melting scenarios can be distinguished, one without, and one involving melt movement.

If there was *no melt movement*, the differences in the amount of melt should directly reflect the primary variations in the protolith fertility, starting from nearly zero in the most basic of the banded orthogneisses. This would imply that the more acid portions with presumably higher melt contents would correspond to more fertile protoliths. In the context of dehydratation melting

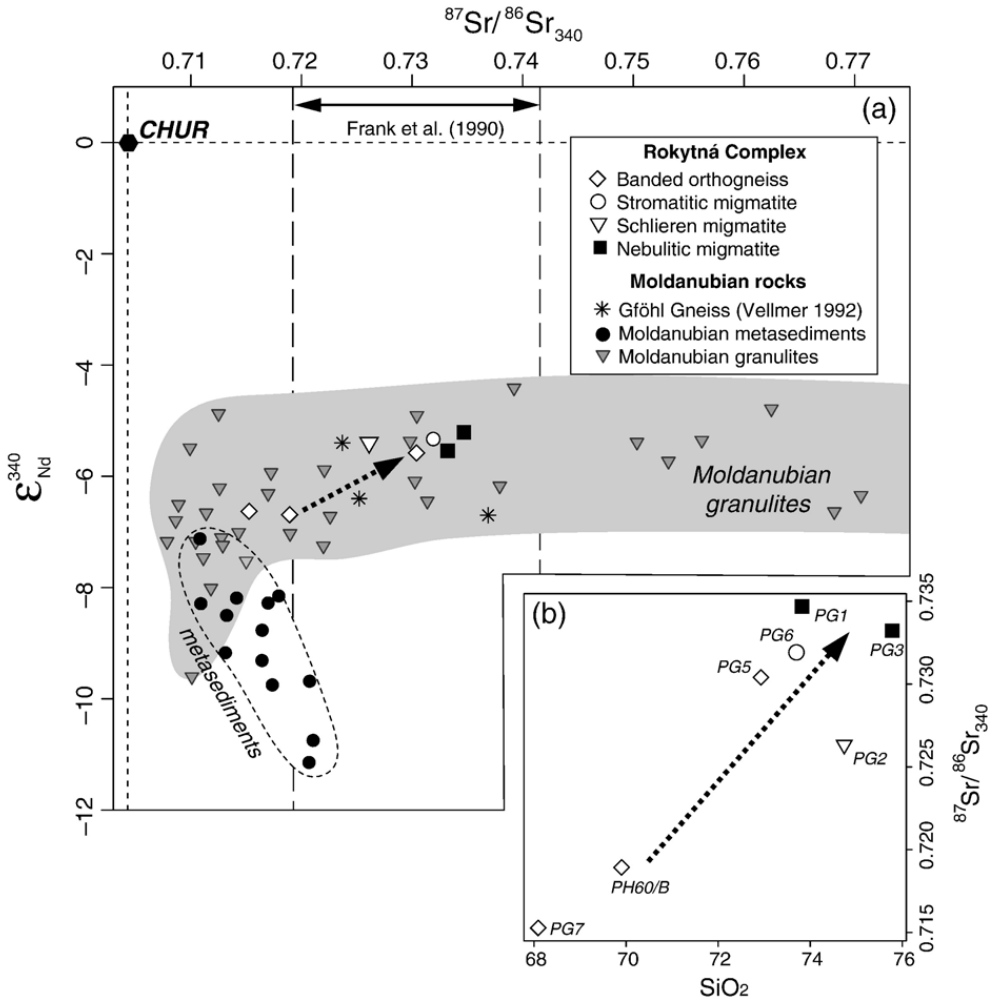

Fig. 11. Sr–Nd isotopic compositions of the Gföhl gneisses and migmatites. (a) $^{87}Sr/^{86}Sr_{340}$ vs. ε^{340}_{Nd} diagram. Selected rock types from the Moldanubian Zone of the Bohemian Massif are shown for comparison: metasediments (black circles) (Janoušek et al., 1995 and unpublished data), mostly felsic granulites (gray field) (Vellmer 1992; Valbracht et al., 1994; Becker et al., 1999; Janoušek et al., 2004) and Gföhl gneisses (black asterisks) (Vellmer 1992). The labelled range corresponds to the Sr isotopic analyses of the Gföhl gneisses from Frank et al. (1990). The samples from Rokytná Complex (this study) form a positive trend deep within the field of the Moldanubian granulites, far from the metasedimentary rocks. (b) Binary plot SiO_2 vs. $^{87}Sr/^{86}Sr_{340}$ for the analysed gneiss and migmatite samples shows a positive correlation. Dashed arrow denotes a tentative evolution of the individual rock types interpreted as being due to the melt infiltration into the banded gneiss (essentially a binary mixing). Closed-system fractional crystallization would result in horizontal shifts in this diagram.

model, they would have to contain more micas compared to their more basic (and more refractory) counterparts. This is unlikely in a co-genetic granitic suite of comparable silica range. More importantly, the obtained zircon and monazite saturation temperatures are mutually comparable and reasonably high for biotite dehydratation melting to be a feasible melting mechanism. This seems to indicate that there was enough time for equilibrium between the residual zircon/monazite and the liquid to be established.

The whole-rock geochemical data can also be used to prove or disprove whether the melts could have originated from protoliths resembling the banded orthogneiss. From the composition of the least siliceous nebulitic migmatite follows that the anatectic melt had to have been granitic, poor in most major- and minor-element oxides (TiO_2, MgO, CaO) albeit rather Fe- and K-rich (FeOt ~ 1.6%; K_2O/Na_2O = 1.9–2.3) (Table 3 and Fig. 6). As shown by Sylvester (1998), the CaO/Na_2O ratios in peraluminous magmas are controlled mostly by the plagioclase/clay ratio of the source. This enables the distinction between granites generated from plagioclase-poor (pelitic; low CaO/Na_2O) and plagioclase-rich (psammitic; high CaO/Na_2O) sources. The Rokytná migmatites are characterized by intermediate CaO/Na_2O (0.15–0.26) and high Al_2O_3/TiO_2 (61–127) ratios. The nebulitic migmatites are relatively rich in Rb (231–331ppm), as well as extremely poor in Ba (69–326ppm) and Sr (25–57ppm), translating to relatively high Rb/Sr (5.8–9.2) and Rb/Ba (1.0–3.4) ratios. This, together with the presence of marked negative Eu anomalies, are

compatible with generation via rather low-degree, dehydratation melting of muscovite–biotite-rich quartzo-feldspathic lithologies (Harris and Inger, 1992; Barbarin, 1996; Sylvester 1998 and references therein). Thus the chemistry of the nebulitic migmatite does not seem to match *in situ* melts of the rocks similar to the banded orthogneiss.

The more plausible is the possibility that the melt was *drained out on distances not exceeding the outcrop scale*. If the melt extraction was rapid, there would not be enough time for its full equilibration. Nowadays, the most accepted model for melt migration (low to moderate melt fraction) involves movement through the network of interconnected pores, driven by deformation. Ultimately the deformation results in pervasive melt migration utilizing the main rock anisotropies such as foliation planes, fold hinges and boudin necks as suggested by many field studies (e.g. Collins and Sawyer, 1996; Weinberg, 1999; Brown and Solar, 1999). Additionally, shear-enhanced compaction would drive melt into a network of melt-filled vein-like leucosomes. Porous flow through such a vein network would transfer the melt rapidly to the higher structural levels (Rutter and Neumann, 1995).

In this scenario, one would expect at least a rudimentary preservation of the melt flow network throughout the area affected. However no such structures have been observed in the field. Moreover, the distribution of migmatites in the studied region is not homogenous; there exist large regions that are formed by products of advanced migmatization (schlieren and nebulitic migmatites) that are however distributed rather randomly and definitely not structurally above the other two migmatite types as should be anticipated. On this basis, a small (outcrop) scale melt movement can be probably ruled out.

Additionally, we have calculated (using the whole-rock and mineral chemistries) the composition of a melt that would be in equilibrium with the stable mineral assemblage of the banded orthogneiss (Pl–Kfs–Qtz–Sil–Grt–Bt) at 6.5kbar and 740–760°C. The calculations were performed using THERMOCALC 3.25 (Powell et al., 1998) and the internally-consistent thermodynamic dataset 5.5 (Holland and Powell, 1998) in the $Na_2O–CaO–K_2O–FeO–MgO–Al_2O_3–SiO_2–H_2O$ (NCKFMASH) system. The obtained melt is granitic (SiO_2 = 68.3–69.3wt.%; alkali feldspar granite in CIPW-based Q'-ANOR plot of Streckeisen and Le Maître 1979), slightly peraluminous (A/CNK ~ 1.1), CaO poor (0.32–0.41%) and alkali rich ($K_2O + Na_2O$ = 8.8–8.9wt.%), with prevalence of potassium over sodium (K_2O/Na_2O ~ 1.35). Simple comparison with the composition of nebulitic migmatite reveals that the modelled melt has clearly too low SiO_2, CaO, MgO (0.07–0.09%), FeOt (0.27–0.33%), and exceedingly high alkalis (Na_2O = 3.7–3.8% and K_2O = 5.1%) (cf. Fig. 6). Even in this case, the nebulitic migmatite seem to be too different to represent rocks dominated by partial melts of the banded orthogneisses.

An alternative would be that the nebulitic migmatites represent diatexites that left behind some of their residue. In spite of its macroscopic appearance, the nebulitic migmatite probably never contained higher amounts of melt, regardless the fact that considerable melt volume had to have passed through the system to account for all the observed variations. Hasalová et al. (in press-a) presented the AMS (anisotropy of magnetic susceptibility) data on biotite that show strong degree of anisotropy of magnetic susceptibility even in the nebulitic migmatite. This is in contrast with AMS data from other migmatitic terrains (e.g. Ferré et al., 2004) and with results of numerical modelling (e.g. Blumenfeld and Bouchez, 1988) that both yielded significantly lower values of degree of magnetic anisotropy in diatexites. The high degree of AMS in the Rokytná Complex thus documents predominance of solid-state deformation with only minor contribution from melt. The system had to have been still matrix and not melt supported, precluding free rotation of biotite in viscously flowing melt.

5.1.4. Melt infiltration from an external source

By "melt infiltration" we mean a process, whereby melt derived from an external source passes pervasively, i.e. along grain boundaries, the whole rock volume. In this model, the textural and geochemical variations can be interpreted by different degrees of equilibration between the bulk rock and the passing melt. Melt infiltration is a well known process from studies concerned with metasomatism in the Earth's mantle and contact aureoles around igneous intrusions. In the mantle, melt infiltration, loosely termed reactive flow, corresponds to grain-scale porous flow along high porosity dissolution channels (e.g. McKenzie, 1989; Van der Wal and Bodinier, 1996; Kelemen et al., 1997; Reiners, 1998). The effects of reactive flow can be identified due to highly contrasting modal and chemical composition of the peridotite and the percolating basaltic melt (Godard et al., 1995). The large difference in viscosities between the melt and host rock is the reason why the porous flow in the mantle, albeit slow, does not require deformation to occur. Even though this mechanism has been invoked to explain the transport of basaltic magma in the mantle (Kelemen et al., 1997 and references therein), many workers still tend to prefer

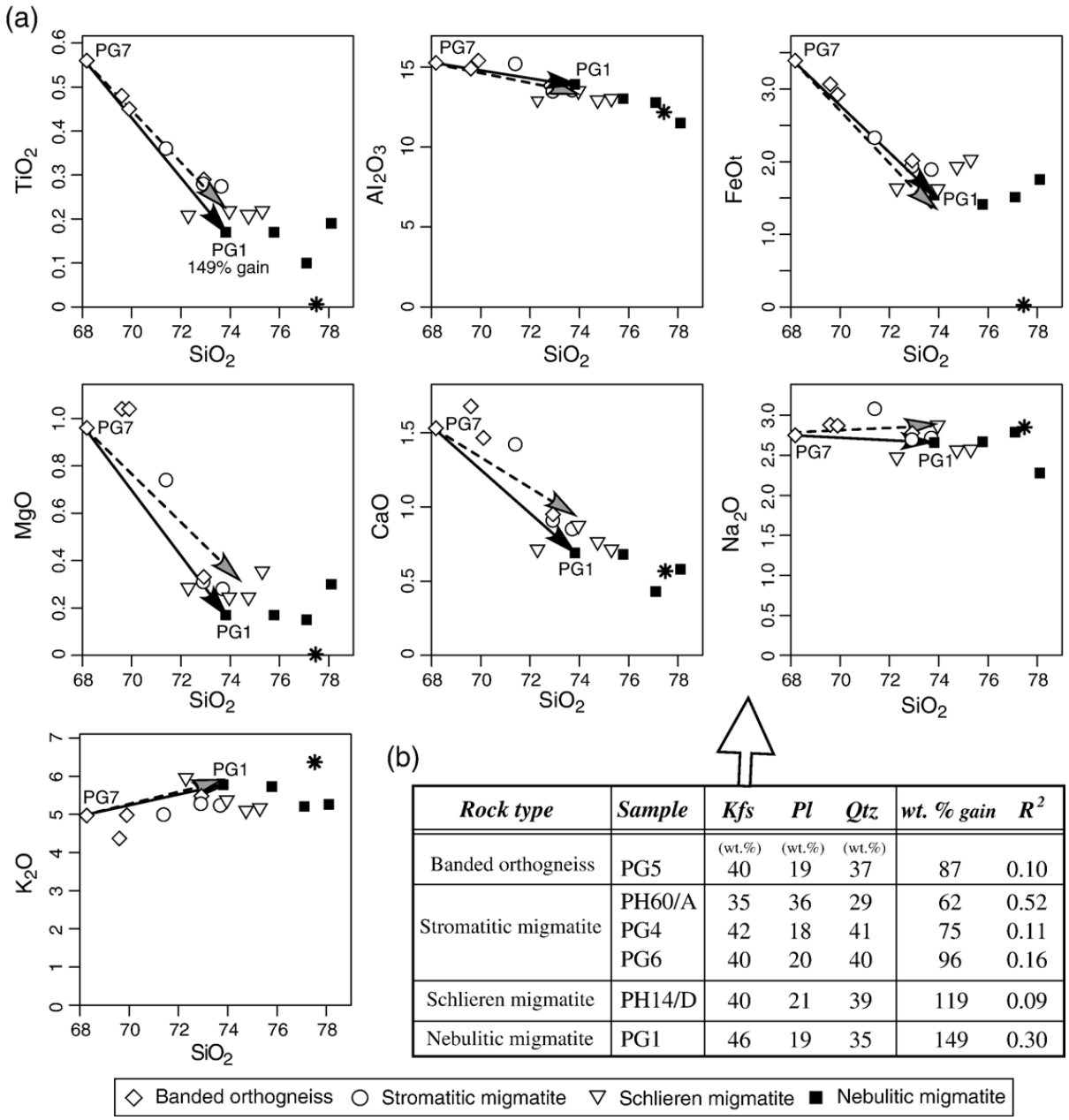

Rock type	Sample	Kfs (wt.%)	Pl (wt.%)	Qtz (wt.%)	wt. % gain	R^2
Banded orthogneiss	PG5	40	19	37	87	0.10
Stromatitic migmatite	PH60/A	35	36	29	62	0.52
	PG4	42	18	41	75	0.11
	PG6	40	20	40	96	0.16
Schlieren migmatite	PH14/D	40	21	39	119	0.09
Nebulitic migmatite	PG1	46	19	35	149	0.30

Fig. 12. (a) Modelling of chemical effects connected with the leucogranitic melt infiltration into the Rokytná Complex. As the melt passes through the system, K-feldspar, plagioclase and quartz crystallize/overgrow the corresponding phases in the matrix. The model treated various rock samples as mixtures of the banded orthogneiss and the crystallizing minerals from the melt. The compositions of the latter are listed in the table forming a part of the Fig. 3; as the starting material has been chosen the least evolved banded orthogneiss (PG7). Solid black arrows represent the tie line between the real compositions of the banded orthogneiss (PG7) and the nebulitic migmatite (PG1). The dashed arrows represent the outcome of the modelling. Note the good correspondence of the real and modelled trends. The stars portray the best-fit solution for the assemblage added. The results indicate that the whole compositional spectrum from the banded orthogneisses to the least siliceous nebulitic migmatites could have been produced by addition of up to *c.* 150wt.% of the both feldspars and quartz combined (if the original rock is taken as 100%, i.e. corresponding to a relative gain of 60%). (b) Summary of the modelling for various migmatite pairs. Presented are proportions of the minerals (Kfs, Pl, Qtz) added into the system, total percentages of these newly crystallized phases (protolith gneiss PG7 = 100%) and sum of squared residuals (R^2) indicating the goodness of the fit.

fracture-controlled melt flow (e.g. Spiegelman and Kenyon, 1992; Harte et al., 1993).

However, pervasive melt infiltration is even further from being generally accepted for melt transport mechanism in the crust. Melt percolation from/along grain boundaries has until now been reserved only for the scale of several centimetres (e.g. Sawyer, 2001) and it has been considered only rarely as a serious possibility for large-scale melt transport in the crust (Hasalová et al., in press-a,b).

The main problem consists in the fact that this process is considered too sluggish to be efficient. McKenzie (1984)

showed that the pervasive porous flow in crustal rocks would be possible only in a matrix which is able to compact, in other words they concluded that such a flow is essentially a deformation-driven process. This could have been the case in the Rokytná Complex, where a large, crustal-scale shear zone played an important role in its exhumation.

During the penetration by externally-derived melt, the rock complex would clearly display open-system behaviour, with components having been lost to, or introduced from, the passing melt of unknown volume. The whole-rock composition would then represent a net result of the changing system mass/volume, the contributions from newly precipitated minerals as well as the mass balance of geochemical species exchanged with the melt/fluid phase.

We have attempted to model the process as an addition of K-feldspar, plagioclase and quartz crystallized from the melt passing through the banded orthogneiss. The exact composition of the pristine orthogneiss is unknown; therefore we have opted for the presumably least influenced sample PG7. The mineral compositions employed were those of the newly formed rims overgrowing the relict mineral grains in the matrix (Fig. 3). A graphical representation of the modelling approach is shown in Fig. 12a. The whole compositional spectrum from the banded orthogneiss to the least siliceous nebulitic migmatite can be explained by a relative gain up to 60% of K-feldspar, plagioclase and quartz. The proportion of the three minerals changes from roughly balanced to a strong prevalence of K-feldspar (~ 40%) and quartz (~ 40%) over plagioclase (~ 20%).

Additionally, assessment of the mass balance in individual major- and trace elements during the orthogneiss transformation used the approach of Gresens (1967) in the form of isocon plots (Grant, 1986, 2005) (Fig. 13a). The results of individual isocon analyses were pulled together into binary plots of an immobile element vs. relative gains/losses (%) of individual elements (Fig. 13b). The most appropriate choice of immobile components seems to be high-field strength elements Zr, Hf, La, Sm, Nb and Th, as follows from examination of isocon plots as well as the ordered ratios of concentrations of individual elements in the 'altered' and 'original' rocks (Grant, 2005).

Slopes of the isocons fitted to these HFS elements are lower than unity in all cases, pointing to an increase in the overall mass of the system (an increase in volume if changes in density were negligible) (e.g. Fig. 13a). Many of the elements show coherent behaviour, with three groups emerging (Fig. 13b): (1) immobile elements that have been used in the construction of the isocons, oscillating around zero (e.g. Th, La, Sm and Nb), (2) hydrous fluid-mobile trace elements (LILE) showing extreme relative enrichments (Rb, Cs and U), and (3) significantly less affected major and minor elements Si, Al, K, Na and P. In accordance with the previous modelling (Fig. 12), the behaviour of the elements in the latter group (Si, Al, K, Na and P), can be interpreted as precipitation of new albitic plagioclase, K-feldspar, quartz and apatite. Variable but less pronounced depletion in Ca, Sr and Ba may point to instability and partial replacement of the original K-feldspar and more calcic plagioclase. This would explain the origin of the observed albitic plagioclase and K-feldspar overgrowths/films formed on older feldspars generation of the matrix (Fig. 3).

Taken together, both modelling approaches seem to support the model of melt infiltration, which is in accordance with the major- and trace-element variation and Sr–Nd isotopic data indicating open-system behaviour.

5.1.4.1. The possible role for fractional crystallization. While some major elements display consistent trends over the whole silica range, the others feature remarkable horizontal shifts at the end of the sequence, i.e. in the more siliceous schlieren and nebulitic migmatites (Fig. 6). In addition, the spider plots (Fig. 8) show large ranges for compatible elements in these two migmatite types, with the contents decreasing rapidly in the most silica-rich samples. This seems to indicate that there was an additional process involved.

Theoretically such a differentiation to more siliceous compositions could have been driven by the restite unmixing (Chappell et al., 1987; Barbero and Villaseca, 1992; Chappell, 1996; Williamson et al., 1997). However this does not agree with the observed limited variations in the ferromagnesian components, nearly constant A/CNK and sharp decrease in feldspar-compatible elements, such as Ba, Sr and Eu. Moreover this scenario would require separation of large volumes of refractory garnet-bearing residua, whose occurrence is unknown from the Gföhl Unit.

The major- and trace-element signatures of the most siliceous samples of the nebulitic migmatite are remarkably similar to felsic, strongly fractionated granites. The broad variation and progressive decrease in Ba, Sr, Eu, LREE, Th (Figs. 6 and 7) and, to some extent, Pb (not shown) seem to bear a testimony to fractional crystallization, a process very efficient in removing compatible elements from an evolving magma. This mechanism is expected to have operated already during the ascent and, more importantly, at the terminal stages of the melt infiltration process.

This hypothesis is corroborated for instance by the binary plot involving Sr and Ba (Fig. 14). The diagram

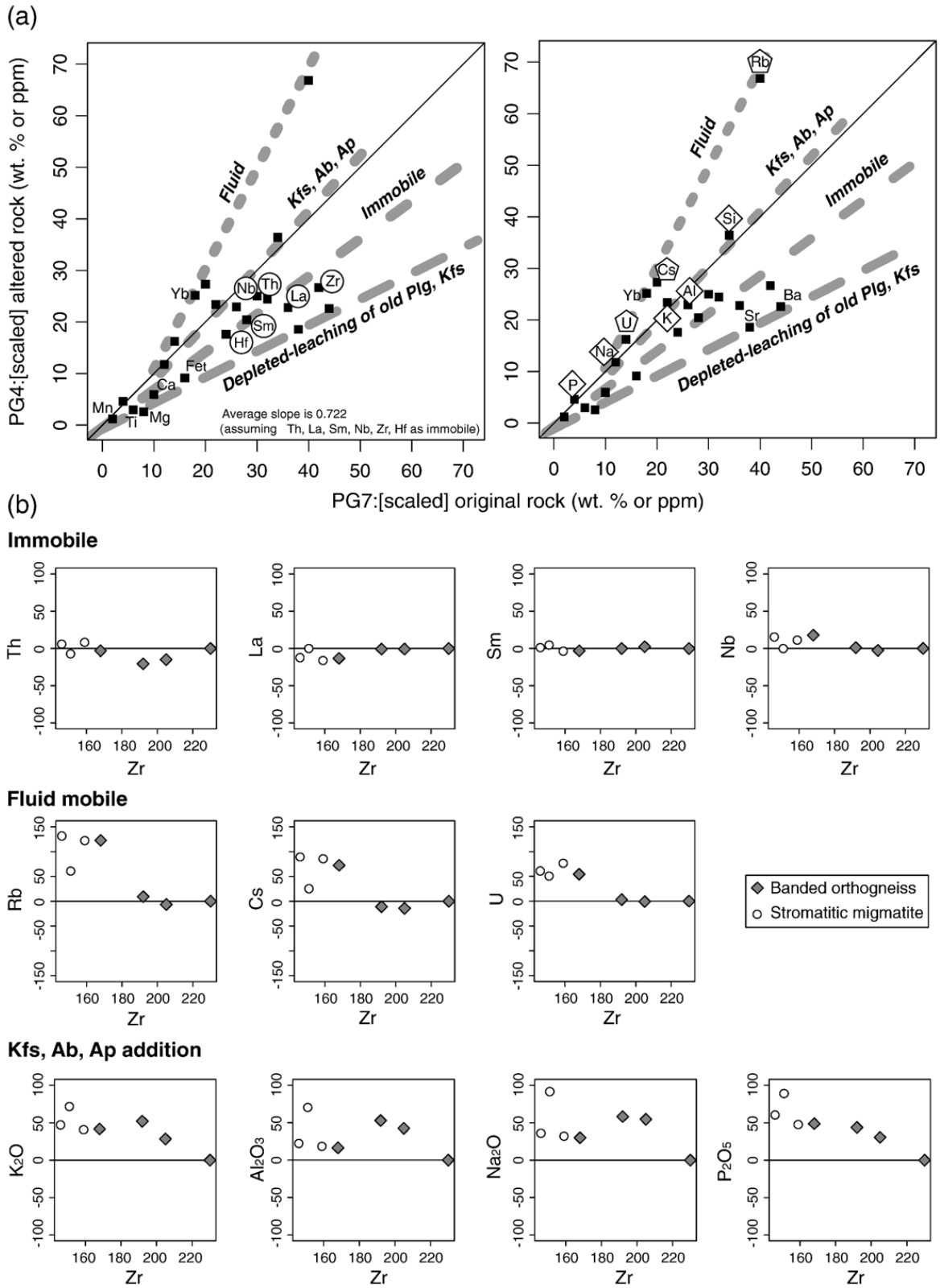

Fig. 13. Mass balance calculations of individual major- and trace elements (after Gresens, 1967) (a) Typical isocon plot (Grant, 1986; 2005) for transformation of banded orthogneiss (PG7) into schlieren migmatite (PG4). The slope of the isocon has been obtained taking the presumably immobile elements Zr, Hf, La, Sm, Nb and Th (circled) into consideration. The sample plot with highlighted elements that are interpreted as having been added to the system due to growth of new mineral phases (Pl, Kfs, Ap) and brought by hydrous fluid (Rb, Cs and U). (b) Plots of Zr vs. relative gains/losses (%: Grant, 2005) of individual elements. As a starting material was taken the least evolved orthogneiss (PG 7) with the highest Zr contents. This element has been chosen as it varies greatly, decreases monotonously (see also Fig. 7) and seems immobile in the course of the progressive breakdown of the orthogneiss matrix.

demonstrates that the entire compositional spectrum of the schlieren and nebulitic migmatites can be modelled by reasonable amounts of K-feldspar > albitic plagioclase and biotite fractionation.

In addition, some role for the accessory minerals is evident. The sharp decrease in LREE and Th with increasing silica (Figs. 7 and 8) points to monazite removal (Fig. 4), a phenomenon common in relatively LREE-poor granitic melts (Villaseca et al., 2003). Lastly, the drop in MREE can be accounted for by apatite fractionation.

5.1.4.2. P–T conditions of the orthogneiss-melt interaction. In order to understand better the mechanism of the migmatization, information on the *P–T* conditions is essential. Some constraints are provided by the saturation thermometry on accessory minerals. In slightly peraluminous, calcium-poor leucogranites the most important will be zircon (Watson and Harrison, 1983) and monazite (Montel, 1993).

Given that the amount of melt present in the banded orthogneiss was limited, the whole-rock geochemistry can be used as a proxy to assess the concentrations of

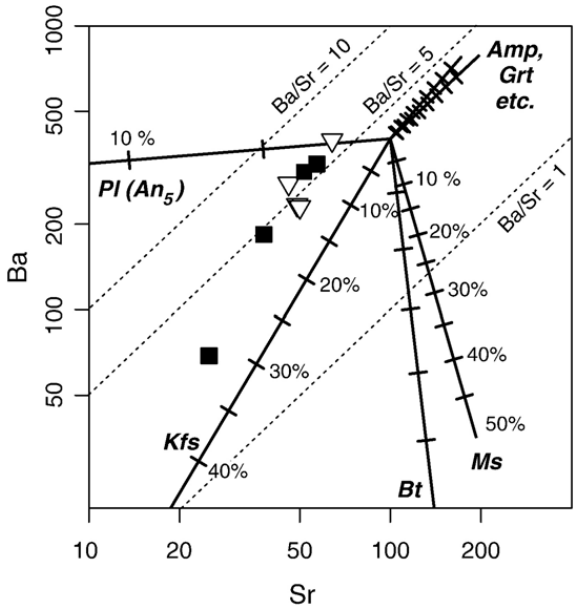

Fig. 14. Fractional crystallization modelling for schlieren and nebulitic migmatites. The results are plotted in Sr vs. Ba diagram (ppm). The diagram is in logarithmic coordinates in order to transform the exponential fractional crystallization trends into linear ones. Labelled vectors correspond to up to 50% fractional crystallization of the main rock-forming minerals. The starting point was chosen arbitrarily and the vectors can be shifted freely. Trace-element distribution coefficients are from Hanson (1978; Kfs, Amp, Rb in Pl), Icenhower and London (1995; Bt and Ms) and Blundy and Shimizu (1991; Sr in Pl, assuming 750°C, An_5). The whole compositional spectrum for the nebulitic migmatite can be reproduced by reasonable degree of fractionation of an assemblage dominated by K-feldspar, with minor plagioclase and biotite.

many elements in its Early Palaeozoic protolith. Even though inherited Precambrian components are by no means rare in the Gföhl gneiss zircons, at least in Austria (Friedl et al., 2004), their proportion by volume is small. Consequently, their influence on the Zr budget and thus the calculated Zr saturation temperatures should be negligible. Then the zircon (*c.* 815 ± 24°C, median ± 2σ) and monazite (*c.* 800 ± 38°C) saturation temperatures yield the upper constraints on the liquidus temperature of the magma parental to the granitic protolith (e.g. Hanchar and Watson, 2003; Miller et al., 2003; Janoušek, 2006). This agrees with the coincidence of the two independent saturation temperatures derived from both accessory minerals.

On the other hand, the nebulitic migmatite may provide information on the maximum liquidus temperature of the Variscan anatectic melt. The temperature is near 740°C, derived from zircon (747 ± 53°C) and monazite (740 ± 90°C). If the melt infiltration has indeed taken place, the apparent gradual decrease in zircon and monazite saturation temperatures in the whole-rock sequence (Fig. 10) may be an artefact, resulting from mixing of two dissimilar components.

The second approach, using the THERMOCALC calculations, was adopted by Hasalová et al. (in press-b). These authors calculated equilibration temperature of the banded orthogneiss, stromatitic, schlieren and nebulitic migmatites to be 790–850°C at 7.5kbar, 760–820°C at 6.5kbar, 715–770°C at 5.5kbar and 690–750°C at 4.5kbar, respectively. Moreover, the *P–T* calculations clearly show that the infiltrating melt equilibrated with the host rock on the retrograde branch of the *P–T* path.

5.2. Broader implications for the petrogenesis of felsic migmatites

Several authors have recently proposed a new mechanism for transport of felsic magma through hot, mid-crustal rocks, termed pervasive flow (Weinberg, 1999; Olsen et al., 2004). In this model, foliation-parallel veins/sheets of granitic composition invade hot country rocks, whose low-viscosity inhibits hydrofracturing and dyking (Weinberg and Searle, 1998). Additionally, their high temperature (higher than the solidus of the invading melt) enables the magma to migrate upwards without crystallizing. This process should result eventually in a formation of up to several km thick injection complexes, common in hot crustal terrains (Weinberg, 1999; Leitch and Weinberg, 2002). Hasalová et al. (in press-a) argued that the large-scale pervasive flow does not require formation of channelized pathways but can also occur penetratively, along grain boundaries. These authors

presented microstructural observations indicating that the porous flow commonly described in mantle rocks (McKenzie, 1984; Reiners, 1998) can in fact play a significant role in the crust as well.

The model of pervasive flow still contains several aspects that remain to be clarified. Firstly, its physical background is still poorly understood. So far there are only several theoretical papers (Leitch and Weinberg, 2002; Olsen et al., 2004), accompanied by works providing field and petrographic evidence from a handful of terrains worldwide (e.g. Collins and Sawyer, 1996; Weinberg and Searle, 1998; Vanderhaeghe, 1999).

A key problem is the expected involvement of small volumes of penetrating acid melt, which should theoretically have high viscosities. The process of reactive porous flow is very slow even for mantle-derived melts (tens to hundreds centimetres per year; McKenzie, 1984) and is likely to be even more so in the crust. This would make the system vulnerable to freezing, and subsequently render the long-distance melt percolation impossible.

These problems can be possibly less important for volatile-rich melts, as water, F and B dramatically decrease the viscosity of granitic melts (Dingwell et al., 1996; Giordano et al., 2004; Whittington et al., 2004). This was probably not the case in the Rokytná Complex, as the whole-rock fluorine contents are uniformly low (Table 1) and tourmaline, the main boron host, is absent. However, the pervasive melt migration, even at small volumes, can occur as soon as a sufficient porosity is created. This is associated with dilatation related either to cavitation process, known well from the material science (Čadek, 1988), in conjunction with melt underpressure or to grain-scale hydrofracturing related to melt overpressure and high differential stress (Závada et al., in press). The most straightforward scenario in our case seems that the pervasive porous flow was a deformation-driven process associated with diffusion creep deformation mechanism. It could have been connected to a crustal-scale shear zone, described in many previous works (e.g. Schulmann et al., 2005; Racek et al., 2006; Tajčmanová et al., 2006).

Generally speaking, we have not found in the course of the current research any arguments invalidating the melt infiltration model. In fact the whole-rock geochemistry may provide important constraints on the nature and source of the protolith, the penetrating melt and the overall mass balance. However, the crucial point that ought to be stressed here is that the whole-rock geochemical data by themselves, even though not contradicting the melt infiltration model, do not provide an unequivocal proof for its operation. They cannot rule out completely some common scenarios, such as disequilibrium melting with small-scale melt movement or *in situ* equilibrium melting, in which the individual small melt batches failed to homogenize with each other, still reflecting the geochemical/isotopic variation of their protolith. In order to disprove the other genetic possibilities microstructural, petrological and field data are essential. In this context the reader is referred to the complementary work providing the necessary additional information (Hasalová et al., in press-a-b).

6. Conclusions

Four types of gneisses and migmatites (banded orthogneiss, stromatitic, schlieren and nebulitic migmatites) were defined previously in the Rokytná Complex (Gföhl Unit, Bohemian Massif). While each of the types shows a distinct geochemical and Sr–Nd isotopic fingerprint, the whole sequence evolves along regular, more or less smooth trends for most of the elements. This evolution of the Rokytná Complex has been interpreted by (Hasalová et al., in press-a,b) as a result of *melt infiltration*. The melt infiltration has been defined as a process in which the banded orthogneiss was pervasively, along grain boundaries, penetrated by felsic melt derived from an external source. In this context the individual migmatite types can be explained by different degrees of equilibration between the bulk rock and the passing melt.

The current study is in agreement with this model, however the available whole-rock geochemical data alone are not unequivocal and need to be supported by field, microstructural and petrological observations. Nevertheless, the major- and trace-element as well as Sr–Nd isotopic compositions yield some important constraints concerning the nature of the protolith, the composition and possible source of the penetrating melt and the overall mass balance.

If true, the melt infiltration can be modelled as an open-system process, characterised by changes of the total mass/volume, accompanied by gains/losses in many of the major- and trace elements. The numerical modelling of the mass balance resulted in identification of a component added by a heterogeneous nucleation of feldspars, quartz and apatite from the passing melt. This is in accord with presence of new albitic plagioclase, K-feldspar and quartz coatings as well as resorption of relict feldspars. At the most advanced stages, the chemical variations in the schlieren and nebulitic migmatites require an increasing role for fractional crystallization of the K-feldspar and minor plagioclase, with accessory amounts of Th-rich monazite ± apatite.

In general, the melt infiltration model may potentially explain the origin of some of the felsic migmatites in other high-grade metamorphic terrains. If proven widespread, the process would have profound implications for

chemical development of large crustal segments overlaying anatectic regions and the melt transport therein. Melt infiltration would also strongly influence the rheology of large crustal domains, with potential consequences for deformation mechanism in collisional orogens. Clearly, much more work remains to be done before it could be truly established and well understood.

Acknowledgements

This work was financially supported by the Grant Agency of the Czech Academy of Sciences (Grant No. IAA311140), the Czech Grant Agency (No. 205/04/2065), the French National Agency (No. 06-1148784) and an internal CNRS funding (CGS/EOST). Stays of P. Hasalová at ULP Strasbourg were founded by the French Government Foundation (BGF). Our sincere thanks are due to R. Boutin, who has performed timely and precise ICP-MS analyses at ULP Strasbourg and to J. Míková with P. Denková from the Czech Geological Survey for the assistance in the isotopic laboratory. We gratefully acknowledge A. Langrová from the Institute of Geology at the Czech Academy of Sciences for operating the electron microprobe. Last but not least, the quality of this paper benefited from careful editorial handling by Carlo Dietl, as well as helpful reviews by Peter Nabelek and Malcolm Roberts.

Appendix 1. Analytical techniques

Four samples of each rock type were taken in order to document the compositional variation on both the outcrop as well as regional scale (Fig. 1c).

Minerals were analysed using the Cameca SX100 electron microprobe at the Czech Academy of Sciences in point beam mode at 15kV and 10nA. Representative analyses are summarized in the Table 2.

Following a lithium tetraborate fusion, major-element oxides and trace elements were determined by ICP MS VG PQ 2+ at the Centre de Géochimie de la Surface, Université Louis Pasteur, Strasbourg. The obtained results are listed in Tables 3 and 4. Fluorine was measured by an ion selective electrode in the laboratories of the Czech Geological Survey in Prague (Table 3). Data management, recalculation, plotting and statistical evaluation of the whole-rock geochemical data were facilitated using *GCDkit* (Janoušek et al., 2006).

For the isotopic study, samples were dissolved using a combined HF–HCl–HNO_3 attack. Strontium was isolated by exchange chromatography techniques on PP columns with Sr.spec Eichrom resin and bulk REE were isolated on PP columns filled with TRU.spec Eichrom resin (Pin et al., 1994). The Nd was further separated on PP columns with Ln.spec Eichrom resin (Pin and Zalduegui, 1997). Isotopic analyses were performed on Finnigan MAT 262 thermal ionization mass spectrometer in dynamic mode using a double Re filament assembly (CGS). The $^{143}Nd/^{144}Nd$ ratios were corrected for mass fractionation to $^{146}Nd/^{144}Nd = 0.7219$, $^{87}Sr/^{86}Sr$ ratios assuming $^{86}Sr/^{88}Sr = 0.1194$. External reproducibility is given by results of repeat analyses of the La Jolla ($^{143}Nd/^{144}Nd = 0.511852 \pm 14$ (2σ; $n = 23$)) and NBS 987 ($^{87}Sr/^{86}Sr = 0.710247 \pm 26$ (2σ; $n = 25$)) isotopic standards. The Rb, Sr, Sm and Nd concentrations were obtained by ICP-MS.

The decay constants applied to age-correct the isotopic ratios are from Steiger and Jäger (1977) (Sr) and Lugmair and Marti (1978) (Nd). The ε_{Nd}^{i} values and single-stage CHUR Nd model ages were obtained using Bulk Earth parameters of Jacobsen and Wasserburg (1980), the two-stage Depleted Mantle Nd model ages (T_{Nd}^{DM}) were calculated after Liew and Hofmann (1988). The Sr–Nd isotopic data for studied migmatites are listed in Table 5.

References

Albarède, F., 1995. Introduction to Geochemical Modeling. Cambridge University Press, Cambridge.

Ayres, M., Harris, N., Vance, D., 1997. Possible constraints on anatectic melt residence times from accessory mineral dissolution rates: an example from Himalayan leucogranites. Mineral. Mag. 61, 29–36.

Barbarin, B., 1996. Genesis of the two main types of peraluminous granitoids. Geology 24, 295–298.

Barbey, P., Brouand, M., Le Fort, P., Pecher, A., 1996. Granite–migmatite genetic link: the example of the Manaslu granite and Tibetan Slab migmatites in central Nepal. Lithos 38, 63–79.

Barbero, L., Villaseca, C., 1992. The Layos Granite, Hercynian Complex of Toledo (Spain): an example of parautochthonus restite-rich granite in a granulitic area. Trans. Roy. Soc. Edinb., Earth Sci. 83, 127–138.

Barbero, L., Villaseca, C., Rogers, G., Brown, P.E., 1995. Geochemical and isotopic disequilibrium in crustal melting: an insight from the anatectic granitoids from Toledo, Spain. J. Geophys. Res., 100, 15745–15765.

Bea, F., 1996. Controls on the trace element composition of crustal melts. Trans. Roy. Soc. Edinb., Earth Sci. 87, 33–41.

Becker, H., Wenzel, T., Volker, F., 1999. Geochemistry of glimmerite veins in peridotites from Lower Austria — implications for the origin of K-rich magmas in collision zones. J. Petrol. 40, 315–338.

Blumenfeld, P., Bouchez, J.-L., 1988. Shear criteria and migmatite deformed in the magmatic and solid states. J. Struct. Geol. 10, 361–372.

Blundy, J.D., Shimizu, N., 1991. Trace element evidence for plagioclase recycling in calc-alkaline magmas. Earth Planet. Sci. Lett. 102, 178–197.

Boynton, W.V., 1984. Cosmochemistry of the rare earth elements: meteorite studies. In: Henderson, P. (Ed.), Rare Earth Element Geochemistry. Elsevier, Amsterdam, pp. 63–114.

Briquet, L., Lancelot, J., 1979. Rb–Sr systematics and crustal contamination trends for calc-alkaline igneous rocks. Earth Planet. Sci. Lett. 43, 385–396.

Brown, M., 1973. The definition of metatexites, diatexites and migmatites. Proc. Geol. Assoc. 84, 371–382.

Brown, M., Solar, G.S., 1998. Granite ascent and emplacement during contractional deformation in convergent orogens. J. Struct. Geol. 20, 1365–1393.

Brown, M., Solar, G.S., 1999. The mechanism of ascent and emplacement of granite magma during transpression: a syntectonic granite paradigm. Tectonophysics 312, 1–33.

Brown, M., Averkin, Y.A., McLellan, E.L., Sawyer, E.W., 1995. Melt segregation in migmatites. J. Geophys. Res. 100, 15655–15679.

Büsch, W., Schneider, G., Mehnert, K.R., 1974. Initial melting at grain boundaries. Part II: melting in rocks of granodioritic, quartz dioritic and tonalitic composition. Neues Jahrb. Mineral., Monatsh. 8, 345–370.

Čadek, J., 1988. Creep in Metallic Materials. Elsevier, Amsterdam.

Carswell, D.A., 1991. Variscan high P–T metamorphism and uplift history in the Moldanubian Zone of the Bohemian Massif in Lower Austria. Eur. J. Mineral. 3, 323–342.

Chappell, B.W., 1996. Magma mixing and the production of compositional variation within granite suites: evidence from the granites of southeastern Australia. J. Petrol. 37, 449–470.

Chappell, B.W., White, A.J.R., Wyborn, D., 1987. The importance of residual source material (restite) in granite petrogenesis. J. Petrol. 28, 571–604.

Clemens, J.D., 2003. S-type granitic magmas — petrogenetic issues, models and evidence. Earth Sci. Rev. 61, 1–18.

Collins, W.J., Sawyer, E.W., 1996. Pervasive granitoid magma transfer through the lower-middle crust during non-coaxial compressional deformation. J. Metamorph. Geol. 14, 565–579.

Cooke, R.A., O'Brien, P.J., 2001. Resolving the relationship between high P–T rocks and gneisses in collisional terranes: an example from the Gföhl gneiss–granulite association in the Moldanubian Zone, Austria. Lithos 58, 33–54.

Dallain, C., Schulmann, K., Ledru, P., 1999. Textural evolution in the transition from subsolidus annealing to melting process, Velay Dome, French Massif Central. J. Metamorph. Geol. 17, 61–74.

D'Lemos, R.S., Brown, M., Strachan, R.A., 1992. Granite magma generation, ascent and emplacement within a transpressional orogen. J. Geol. Soc., London 149, 487–490.

Dallmeyer, R.D., Franke, W., Weber, K., 1995. Pre-Permian Geology of Central and Eastern Europe. Springer, Berlin.

Dingwell, D.B., Hess, K.U., Knoche, R., 1996. Granite and granitic pegmatite melts: volumes and viscosities. Trans. Roy. Soc. Edinb., Earth Sci. 87, 65–72.

Dudek, A., Matějovská, O., Suk, M., 1974. Gföhl orthogneiss in the Moldanubicum of Bohemia and Moravia. Krystalinikum 10, 67–78.

Ferré, E.C., Martín-Hernández, F., Teyssier, C., Jackson, M., 2004. Paramagnetic and ferromagnetic anisotropy of magnetic susceptibility in migmatites: measurements in high and low fields and kinematic implications. Geophys. J. Int. 157, 1119–1129.

Finger, F., Roberts, M.P., Haunschmid, B., Schermaier, A., Steyrer, H.P., 1997. Variscan granitoids of Central Europe: their typology, potential sources and tectonothermal relations. Mineral. Petrol. 61, 67–96.

Frank, W., Hammer, S., Popp, F., Scharbert, S., Thöni, M., 1990. Isotopengeologische Neuergebnisse zur Entwicklungsgeschichte der Böhmischen Masse. Österr. Beitr. Met. Geoph. 3, 185–228.

Franke, W., 2000. The mid-European segment of the Variscides: tectonostratigraphic units, terrane boundaries and plate tectonic evolution. In: Franke, W., Haak, V., Oncken, O., Tanner, D. (Eds.), Orogenic Processes: Quantification and Modelling in the Variscan Belt, vol. 179. Geological Society Special Publication, London, pp. 35–61.

Friedl, G., von Quadt, A., Finger, F., 1994. 340 Ma U/Pb-Monazitalter aus dem niederösterreichischen Moldanubikum und ihre geologische Bedeutung. Terra Nostra 94, 43–46.

Friedl, G., McNaughton, N.J., Fletcher, A., Finger, F., 1998. New SHRIMP-zircon ages for orthogneisses from the south-eastern part of the Bohemian Massif (Lower Austria). Acta Univ. Carol., Geol. 42, 251–252.

Friedl, G., Finger, F., Paquette, J.L., von Quadt, A., McNaughton, N.J., Fletcher, I.R., 2004. Pre-Variscan geological events in the Austrian part of the Bohemian Massif deduced from U/Pb zircon ages. Int. J. Earth Sci. (Geol. Rundsch.) 93, 802–823.

Fritz, H., Dallmeyer, R.D., Neubauer, F., 1996. Thick-skinned versus thin-skinned thrusting: rheology controlled thrust propagation in the Variscan collisional belt (the southeastern Bohemian Massif, Czech Republic-Austria). Tectonics 15, 1389–1413.

Fuchs, G., Matura, A., 1976. Zur Geologie des Kristallins der südlichen Böhmischen Masse. Jb. Geol. B.-A. 119, 1–43.

Gardien, V., Thompson, A.B., Grujic, D., Ulmer, P., 1995. Experimental melting of biotite + plagioclase + quartz + muscovite assemblage and implications for crustal melting. J. Geophys. Res. 100, 15581–15591.

Giordano, D., Romano, D.B., Dingwell, D.B., Poe, B., Behrens, H., 2004. The combined effects of water and fluorine on the viscosity of silicic magmas. Geochim. Cosmochim. Acta 68, 5159–5168.

Godard, M., Bodinier, J.-L., Vasseur, G., 1995. Effects of mineralogical reactions on trace element redistributions in mantle rocks during percolation processes: a chromatographic approach. Earth Planet. Sci. Lett. 133, 449–461.

Grant, J.A., 1986. The isocon diagram — a simple solution to Gresens' equation for metasomatic alteration. Econ. Geol. 81, 1976–1982.

Grant, J.A., 2005. Isocon analysis: a brief review of the method and applications. Phys. Chem. Earth, Parts A/B/C 30, 997–1004.

Gresens, R.L., 1967. Composition–volume relationships of metasomatism. Chem. Geol. 2, 47–55.

Guernina, S., Sawyer, E.W., 2003. Large-scale melt-depletion in granulite terranes: an example from the Archean Ashuanipi Subprovince of Quebec. J. Metamorph. Geol. 21, 181–201.

Hammouda, T., Pichavant, M., Chaussidon, M., 1996. Isotopic equilibration during partial melting: an experimental test of the behaviour of Sr. Earth Planet. Sci. Lett. 144, 109–121.

Hanchar, J.M., Watson, E.B., 2003. Zircon saturation thermometry. In: Hanchar, J.M., Hoskin, P.W.O. (Eds.), Zircon. Reviews in Mineralogy and Geochemistry, vol. 53. Mineralogical Society of America and Geochemical Society, Washington, pp. 89–112.

Hanson, G.N., 1978. The application of trace elements to the petrogenesis of igneous rocks of granitic composition. Earth Planet. Sci. Lett. 38, 26–43.

Hanson, G.N., Langmuir, C.H., 1978. Modelling of major elements in mantle-melt systems using trace element approaches. Geochim. Cosmochim. Acta 42, 725–741.

Harris, N., Ayres, M., 1998. The implications of Sr-isotope disequilibrium for rates of prograde metamorphism and melt extraction in anatectic terrains. In: Treloar, P., O'Brien, P.J. (Eds.), What Drives Metamorphism and Metamorphic Reactions?, vol. 138. Geological Society London, Special Publication, London, pp. 171–182.

Harris, N.B.W., Inger, S., 1992. Trace element modelling of pelite-derived granites. Contrib. Mineral. Petrol. 110, 46–56.

Harrison, T.M., Watson, E.B., 1983. Kinetics of zircon dissolution and zirconium diffusion in granitic melts of variable water content. Contrib. Mineral. Petrol. 84, 66–72.

Harrison, T.M., Watson, E.B., 1984. The behavior of apatite during crustal anatexis: equilibrium and kinetic considerations. Geochim. Cosmochim. Acta 48, 1467–1477.

Harte, B., Hunter, R.H., Kinny, P.D., 1993. Melting and melt movement in the Earth. Philos. Trans. R. Soc. Lond., A, 342, 1–21.

Hasalová, P., Schulmann, K., Lexa, O., Štípská, P., Hrouda, F., Ulrich, S., Haloda, J., Týcová, P., in press-a. Origin of migmatites by deformation enhanced melt infiltration of orthogneiss: a new model based on quantitative microstructural analysis. J. Metamorph. Geol.

Hasalová, P., Štípská, P., Powell, R., Schulmann, K., Janoušek, V., Lexa, O., in press-b. Transforming mylonitic metagranite by open-system interactions during melt flow. J. Metamorph. Geol.

Holland, T.J.B., Powell, R., 1998. An internally consistent thermodynamic data set for phases of petrological interest. J. Metamorph. Geol. 16, 309–343.

Icenhower, J., London, D., 1995. An experimental study of element partitioning among biotite, muscovite and coexisting peraluminous silicic melt at 200 MPa (H_2O). Am. Mineral. 80, 1229–1251.

Irber, W., 1999. The lanthanide tetrad effect and its correlation with K/Rb, Eu/Eu*, Sr/Eu, Y/Ho, and Zr/Hf of evolving peraluminous granite suites. Geochim. Cosmochim. Acta 63, 489–508.

Jacobsen, S.B., Wasserburg, G.J., 1980. Sm–Nd evolution of chondrites. Earth Planet. Sci. Lett. 50, 139–155.

Janoušek, V., 2006. Saturnin, R language script for application of accessory-mineral saturation models in igneous geochemistry. Geol. Carpath. 57, 131–142.

Janoušek, V., Rogers, G., Bowes, D.R., 1995. Sr–Nd isotopic constraints on the petrogenesis of the Central Bohemian Pluton, Czech Republic. Geol. Rundsch. 84, 520–534.

Janoušek, V., Finger, F., Roberts, M.P., Frýda, J., Pin, C., Dolejš, D., 2004. Deciphering petrogenesis of deeply buried granites: whole-rock geochemical constraints on the origin of largely undepleted felsic granulites from the Moldanubian Zone of the Bohemian Massif. Trans. Roy. Soc. Edinb., Earth Sci. 95, 141–159.

Janoušek, V., Farrow, C.M., Erban, V., 2006. Interpretation of whole-rock geochemical data in igneous geochemistry: introducing Geochemical Data Toolkit (GCDkit). J. Petrol. 47, 1255–1259.

Johannes, W., 1980. Metastable melting in the granite system Qz–Or–Ab–An–H_2O. Contrib. Miner. Petrol. 72, 73–80.

Kelemen, P.B., Hirth, G., Shimizu, N., Spiegelman, M., Dick, H.J.B., 1997. A review of melt migration processes in the adiabatically upwelling mantle beneath oceanic spreading ridges. Philos. Trans. R. Soc. Lond., A, 355, 283–318.

Knesel, K.M., Davidson, J.P., 1996. Isotopic disequilibrium during melting of granite and implications for crustal contamination of magmas. Geology 24, 243–246.

Knesel, K.M., Davidson, J.P., 2002. Insights into collisional magmatism from isotopic fingerprints of melting reactions. Science 296, 2206–2208.

Leitch, A.M., Weinberg, R.F., 2002. Modelling granite migration by mesoscale pervasive flow. Earth Planet. Sci. Lett. 200, 131–146.

Liew, T.C., Hofmann, A.W., 1988. Precambrian crustal components, plutonic associations, plate environment of the Hercynian Fold Belt of Central Europe: indications from a Nd and Sr isotopic study. Contrib. Mineral. Petrol. 98, 129–138.

Lister, J.R., Kerr, R.C., 1991. Fluid-mechanical models of crack propagation and their application to magma transport in dykes. J. Geophys. Res. 96, 10049–10077.

Lugmair, G.W., Marti, K., 1978. Lunar initial $^{143}Nd/^{144}Nd$: differential evolution line of the lunar crust and mantle. Earth Planet. Sci. Lett. 39, 349–357.

Masuda, A., Kawakami, O., Dohmoto, Y., Takenaka, T., 1987. Lanthanide tetrad effects in nature: two mutually opposite types, W and M. Geochem. J. 119–124.

Matějovská, O., 1975. The Moldanubian gneiss series of south-western Moravia and its relation to granulites. Věst. Ústř. Úst. Geol. 50, 345–351.

Matte, P., Maluski, H., Rajlich, P., Franke, W., 1990. Terrane boundaries in the Bohemian Massif: result of large-scale Variscan shearing. Tectonophysics 177, 151–170.

McKenzie, D., 1984. The generation and compaction of partially molten rock. J. Petrol. 25, 713–765.

McKenzie, D., 1989. Some remarks on the movement of small melt fractions in the mantle. Earth Planet. Sci. Lett. 95, 53–72.

Medaris Jr., L.G., Jelínek, E., Mísař, Z., 1995. Czech eclogites: terrane settings and implications for Variscan tectonic evolution of the Bohemian Massif. Eur. J. Mineral. 7, 7–28.

Medaris Jr., L.G., Fournelle, J.H., Ghent, E.D., Jelínek, E., Mísař, Z., 1998. Prograde eclogite in the Gföhl Nappe, Czech Republic: new evidence on Variscan high-pressure metamorphism. J. Metamorph. Geol. 16, 563–576.

Mehnert, K.R., 1971. Migmatites and the Origin of Granitic Rocks. Elsevier, Amsterdam.

Mehnert, K.R., Büsch, W., Schneider, G., 1973. Initial melting at grain boundary of quartz and feldspar in gneisses and granulites. Neues Jahrb. Mineral., Monatsh., 4, 165–183.

Miller, C.F., McDowell, S.M., Mapes, R.W., 2003. Hot and cold granites? Implications of zircon saturation temperatures and preservation of inheritance. Geology 31, 529–532.

Monecke, T., Kempe, U., Monecke, J., Sala, M., Wolf, D., 2002. Tetrad effect in rare earth element distribution patterns; a method of quantification with application to rock and mineral samples from granite-related rare metal deposits. Geochim. Cosmochim. Acta 66, 1185–1196.

Montel, J.M., 1993. A model for monazite/melt equilibrium and application to the generation of granitic magmas. Chem. Geol. 110, 127–146.

Nabelek, P.I., Glascock, M.D., 1995. REE-depleted leucogranites, Black Hills, South Dakota: a consequence of disequilibrium melting of monazite-bearing schists. J. Petrol. 36, 1055–1071.

O'Brien, P.J., 2006. Type-locality granulites: high-pressure rocks formed at eclogite-facies conditions. Mineral. Petrol. 86, 161–175.

O'Brien, P.J., Carswell, D.A., 1993. Tectonometamorphic evolution of the Bohemian Massif: evidence from high pressure metamorphic rocks. Geol. Rundsch. 82, 531–555.

O'Brien, P.J., Rötzler, J., 2003. High-pressure granulites: formation, recovery of peak conditions and implications for tectonics. J. Metamorph. Geol. 21, 3–20.

Olsen, S.N., Grant, J.A., 1991. Isocon analysis of migmatitization in the Front Range, Colorado, USA. J. Metamorph. Geol. 9, 151–164.

Olsen, S.N., Marsh, B.D., Baumgartner, L.P., 2004. Modelling mid-crustal migmatite terrains as feeder zones for granite plutons: the competing dynamics of melt transfer by bulk versus porous flow. Trans. Roy. Soc. Edinb., Earth Sci. 95, 49–58.

Owen, J.V., Dostal, J., 1996. Prograde metamorphism and decompression of the Gföhl gneiss, Czech Republic. Lithos 38, 259–270.

Petford, N., Lister, J.R., Kerr, R.C., 1994. The ascent of felsic magmas in dykes. Lithos 32, 161–168.

Petford, N., Cruden, A.R., McCaffrey, K.J.W., Vigneresse, J.-L., 2000. Granite formation, transport and emplacement in the Earth's crust. Nature 408, 669–673.

Petrakakis, K., 1986a. Gneisses from the Moldanubikum, Lower Austria, and the metamorphic evolution of the southern Bunte-Serie. Tschermaks Mineral. Petrogr. Mitt. 35, 243–259.

Petrakakis, K., 1986b. Metamorphism of high-grade gneisses from the Moldanubian Zone, Austria, with particular reference to the garnets. J. Metamorph. Geol. 4, 323–344.

Petrakakis, K., 1997. Evolution of Moldanubian rocks in Austria: review and synthesis. J. Metamorph. Geol. 15, 203–222.

Pin, C., Zalduegui, J.F.S., 1997. Sequential separation of light rare-earth elements, thorium and uranium by miniaturized extraction chromatography: application to isotopic analyses of silicate rocks. Anal. Chim. Acta 339, 79–89.

Pin, C., Briot, D., Bassin, C., Poitrasson, F., 1994. Concomitant separation of strontium and samarium-neodymium for isotopic analysis in silicate samples, based on specific extraction chromatography. Anal. Chim. Acta 298, 209–217.

Powell, R., Holland, T., Worley, B., 1998. Calculating phase diagrams involving solid solutions via non-linear equations, with examples using THERMOCALC. J. Metamorph. Geol. 16, 577–588.

Racek, M., Štípská, P., Pitra, P., Schulmann, K., Lexa, O., 2006. Metamorphic record of burial and exhumation of orogenic lower and middle crust: a new tectonothermal model for the Drosendorf window (Bohemian Massif, Austria). Mineral. Petrol. 86, 221–251.

Rapp, R.P., Watson, E.B., 1986. Monazite solubility and dissolution kinetics; implications for the thorium and light rare earth chemistry of felsic magmas. Contrib. Mineral. Petrol. 94, 304–316.

Reiners, P.W., 1998. Reactive melt transport in the mantle and geochemical signatures of mantle-derived magmas. J. Petrol. 39, 1039–1061.

Rudnick, R.L., McLennan, S.M., Taylor, S.R., 1985. Large ion lithophile elements in rocks from high-pressure granulite facies terrains. Geochim. Cosmochim. Acta 49, 1645–1655.

Rushmer, T., 1995. An experimental deformation study of partially molten amphibolite: application to low-melt fraction segregation. J. Geophys. Res. 100, 15681–15695.

Rushmer, T., 1996. Melt segregation in the lower crust: how have experiments helped us? Trans. Roy. Soc. Edinb. Earth Sci. 87, 73–83.

Rushmer, T., 2001. Volume change during partial melting reactions: implications for melt extraction, melt geochemistry and crustal rheology. Tectonophysics 342, 389–405.

Rutter, E.H., Neumann, D.H.K., 1995. Experimental deformation of partially molten Westerly Granite under fluid-absent conditions, with implications for the extraction of granitic magmas. J. Geophys. Res. 100, 15697–15715.

Sawyer, E.W., 1991. Disequilibrium melting and the rate of melt-residuum separation during migmatitization of mafic rocks from the Grenville Front, Quebec. J. Petrol. 32, 701–738.

Sawyer, E.W., 1999. Criteria for the recognition of partial melting. Phys. Chem. Earth (A) 24, 269–279.

Sawyer, E.W., 2000. Grain-scale and outcrop-scale distribution and movement of melt in a crystallising granite. Trans. Roy. Soc. Edinb. Earth Sci. 91, 73–85.

Sawyer, E.W., 2001. Melt segregation in the continental crust: distribution and movement of melt in anatectic rocks. J. Metamorph. Geol. 19, 291–309.

Schulmann, K., Melka, R., Lobkowicz, M.Z., Ledru, P., Lardeaux, J., Autran, A., 1994. Contrasting styles of deformation during progressive nappe stacking at the southeastern margin of the Bohemian Massif (Thaya Dome). J. Struct. Geol. 16, 355–370.

Schulmann, K., Kröner, A., Hegner, E., Wendt, I., Konopásek, J., Lexa, O., Štípská, P., 2005. Chronological constraints on the pre-orogenic history, burial and exhumation of deep-seated rocks along the eastern margin of the Variscan Orogen, Bohemian Massif, Czech Republic. Am. J. Sci. 305, 407–448.

Shaw, D.M., 1968. A review of K–Rb fractionation trends by covariance analysis. Geochim. Cosmochim. Acta 32, 573–601.

Spiegelman, M., Kenyon, P., 1992. The requirements for chemical disequilibrium during magma migration. Earth Planet. Sci. Lett. 109, 611–620.

Steiger, R.H., Jäger, E., 1977. Subcommission on Geochronology; convention on the use of decay constants in geo- and cosmochronology. Earth Planet. Sci. Lett. 36, 359–362.

Streckeisen, A., Le Maître, R.W., 1979. A chemical approximation to the modal QAPF classification of the igneous rocks. Neues Jahrb. Mineral., Abh. 136, 169–206.

Suess, F.E., 1912. Die moravische Fenster und ihre Beziehung zum Grundgebirge des Hohen Gesenkes. Denkschr. Österr. Akad. Wiss. Mat. Naturwiss. Kl. 88, 541–631.

Svoboda, J., et al., 1966. Regional Geology of Czechoslovakia. Part I The Bohemian Massif. Czech Geological Survey in the Publishing House of Czechoslovak Academy of Sciences, Prague.

Sylvester, P.J., 1998. Post-collisional strongly peraluminous granites. Lithos 45, 29–44.

Štípská, P., Powell, R., 2005. Does ternary feldspar constrain the metamorphic conditions of high-grade meta-igneous rocks? Evidence from orthopyroxene granulites, Bohemian Massif. J. Metamorph. Geol. 23, 627–647.

Štípská, P., Schulmann, K., Kröner, A., 2004. Vertical extrusion and middle crustal spreading of omphacite granulite: a model of syn-convergent exhumation (Bohemian Massif, Czech Republic). J. Metamorph. Geol. 22, 179–198.

Tajčmanová, L., Konopásek, J., Schulmann, K., 2006. Thermal evolution of the orogenic lower crust during exhumation within a thickened Moldanubian root of the Variscan belt of Central Europe. J. Metamorph. Geol. 24, 119–134.

Taylor, S.R., McLennan, S.M., 1985. The Continental Crust: Its Composition and Evolution. Blackwell, Oxford.

Tollmann, A., 1982. Größräumiger variszischer Deckenbau im Moldanubikum und neue Gedanken zum Variszikum Europas, 64. Geotektonische Forschungen, Stuttgart.

Urban, M., 1992. Kinematics of the Variscan thrusting in the Eastern Moldanubicum (Bohemian Massif, Czechoslovakia): evidence from the Náměšť granulite massif. Tectonophysics 201, 371–391.

Valbracht, P.J., Vrána, S., Beetsma, J.J., Fiala, J., Matějka, D., 1994. Sr and Nd isotopic determinations in three Moldanubian granulite massifs in southern Bohemia. J. Czech Geol. Soc. 39, 114.

van Breemen, O., Aftalion, M., Bowes, D.R., Dudek, A., Mísař, Z., Povondra, P., Vrána, S., 1982. Geochronological studies of the Bohemian Massif, Czechoslovakia, and their significance in the evolution of Central Europe. Trans. Roy. Soc. Edinb., Earth Sci. 73, 89–108.

Van der Wal, D., Bodinier, J.L., 1996. Origin of the recrystallisation front in the Ronda peridotite by km-scale pervasive porous melt flow. Contrib. Mineral. Petrol. 122, 387–405.

Vanderhaeghe, O., 1999. Pervasive melt migration from migmatites to leucogranite in the Shuswap metamorphic core complex, Canada: control of regional deformation. Tectonophysics 312, 35–55.

Veksler, I.V., Dorfman, A.M., Kamenetsky, M., Dulski, P., Dingwell, D.B., 2005. Partitioning of lanthanides and Y between immiscible silicate and fluoride melts, fluorite and cryolite and the origin of the lanthanide tetrad effect in igneous rocks. Geochim. Cosmochim. Acta 69, 2847–2860.

Vellmer, C., 1992. Stoffbestand und Petrogenese von Granuliten und granitischen Gesteinen der südlichen Böhmischen Masse in Niederösterreich. Unpublished PhD. thesis, Georg-August-Universität, Göttingen.

Vigneresse, J.-L., Barbey, P., Cuney, M., 1996. Rheological transitions during partial melting and crystallization with application to felsic magma segregation and transfer. J. Petrol. 37, 1579–1600.

Villaseca, C., Martin Romera, C., De la Rosa, J., Barbero, L., 2003. Residence and redistribution of REE, Y, Zr, Th and U during granulite-facies metamorphism: behaviour of accessory and major phases in peraluminous granulites of central Spain. Chem. Geol. 200, 293–323.

Vielzeuf, D., Holloway, J.R., 1988. Experimental determination of the fluid-absent melting relations in the pelitic system-consequences for crustal differentiation. Contrib. Mineral. Petrol. 98, 257–276.

von Bargen, N., Waff, H.S., 1986. Permeabilities, interfacial areas and curvatures of partially molten systems: results of numerical computations of equilibrium microstructures. J. Geophys. Res. 91, 9261–9276.

Watson, E.B., 1996. Dissolution, growth and survival of zircons during crustal fusion; kinetic principles, geological models and implications for isotopic inheritance. Trans. Roy. Soc. Edinb., Earth Sci. 87, 43–56.

Watson, E.B., Harrison, T.M., 1983. Zircon saturation revisited: temperature and composition effects in a variety of crustal magma types. Earth Planet. Sci. Lett. 64, 295–304.

Watson, E.B., Harrison, T.M., 1984. Accessory minerals and the geochemical evolution of crustal magmatic systems: a summary and prospectus of experimental approaches. Phys. Earth Planet. Inter. 35, 19–30.

Watson, E.B., Vicenzi, E.P., Rapp, R.P., 1989. Inclusion/host relations involving accessory minerals in high-grade metamorphic and anatectic rocks. Contrib. Mineral. Petrol. 101, 220–231.

Watt, G.R., Harley, S.L., 1993. Accessory phase controls on the geochemistry of crustal melts and restites produced during water-undersaturated partial melting. Contrib. Mineral. Petrol. 114, 550–566.

Wedepohl, K.H., 1995. The composition of the continental crust. Geochim. Cosmochim. Acta 59, 1217–1232.

Weinberg, R.F., 1999. Mesoscale pervasive felsic magma migration: alternatives to dyking. Lithos 46, 393–410.

Weinberg, R.F., Searle, M.P., 1998. The Pangong Injection Complex, Indian Karakoram: a case of pervasive granite flow through hot viscous crust. J. Geol. Soc. 155, 883–891.

Whittington, A.G., Treloar, P.J., 2002. Crustal anatexis and its relation to the exhumation of collisional orogenic belts, with particular reference to the Himalaya. Mineral. Mag. 66, 53–92.

Whittington, A., Richet, P., Behrens, H., Holtz, F., Scaillet, B., 2004. Experimental temperature-X(H_2O)-viscosity relationship for leucogranites and comparison with synthetic silicic liquids. Trans. Roy. Soc. Edinb., Earth Sci. 95, 59–71.

Wickham, S.M., 1987. The segregation and emplacement of granitic magmas. J. Geol. Soc. (London), 144, 281–297.

Williamson, B.J., Downes, H., Thirlwall, M.F., Beard, A., 1997. Geochemical constraints on restite composition and unmixing in the Velay anatectic granite, French Massif Central. Lithos 40, 295–319.

Závada, P., Schulmann, K., Konopásek, J., Ulrich, S., Lexa, O., in press. Extreme ductility of feldspar aggregates – melt enhanced grain boundary sliding (GBS) and creep failure: rheological implications for felsic lower crust. J. Geophys. Res.

Zhao, Z.H., Xiong, X.L., Hen, X.D., Wang, Y.X., Qiang, W., Bao, Z.W., Jahn, B., 2002. Controls on the REE tetrad effect in granites: Evidence from the Qianlishan and Baerzhe granites, China. Geochem. J. 36, 527–543.

Zeng, L., Asimow, P.D., Saleeby, J.B., 2005. Coupling of anatectic reactions and dissolution of accessory phases and the Sr and Nd isotope systematics of anatectic melts from a metasedimentary source. Geochim. Cosmochim. Acta 69, 3671–3682.

J. metamorphic Geol., 2008, **26,** 29–53 doi:10.1111/j.1525-1314.2007.00743.x

Origin of migmatites by deformation-enhanced melt infiltration of orthogneiss: a new model based on quantitative microstructural analysis

P. HASALOVÁ,[1,2] K. SCHULMANN,[1] O. LEXA,[1,2] P. ŠTÍPSKÁ,[1] F. HROUDA,[2,3] S. ULRICH,[2,4] J. HALODA[5] AND P. TÝCOVÁ[5]
[1]*Université Louis Pasteur, CGS/EOST, UMR 7517, 1 rue Blessig, Strasbourg 67084, France (hasalovap@seznam.cz)*
[2]*Institute of Petrology and Structural Geology, Charles University, Albertov 6, 12843 Prague, Czech Republic*
[3]*AGICO, Ječná 29a, 621 00 Brno, Czech Republic*
[4]*Institute of Geophysics, Czech Academy of Sciences, Boční II/1401, 14131 Praha 4, Czech Republic*
[5]*Czech Geological Survey, Klárov 3, 118 21 Prague 1, Czech Republic*

ABSTRACT A detailed field study reveals a gradual transition from high-grade solid-state banded orthogneiss via stromatic migmatite and schlieren migmatite to irregular, foliation-parallel bodies of nebulitic migmatite within the eastern part of the Gföhl Unit (Moldanubian domain, Bohemian Massif). The orthogneiss to nebulitic migmatite sequence is characterized by progressive destruction of well-equilibrated banded microstructure by crystallization of new interstitial phases (Kfs, Pl and Qtz) along feldspar boundaries and by resorption of relict feldspar and biotite. The grain size of all felsic phases decreases continuously, whereas the population density of new phases increases. The new phases preferentially nucleate along high-energy like–like boundaries causing the development of a regular distribution of individual phases. This evolutionary trend is accompanied by a decrease in grain shape preferred orientation of all felsic phases. To explain these data, a new petrogenetic model is proposed for the origin of felsic migmatites by melt infiltration from an external source into banded orthogneiss during deformation. In this model, infiltrating melt passes pervasively along grain boundaries through the whole-rock volume and changes completely its macro- and microscopic appearance. It is suggested that the individual migmatite types represent different degrees of equilibration between the host rock and migrating melt during exhumation. The melt topology mimicked by feldspar in banded orthogneiss forms elongate pockets oriented at a high angle to the compositional banding, indicating that the melt distribution was controlled by the deformation of the solid framework. The microstructure exhibits features compatible with a combination of dislocation creep and grain boundary sliding deformation mechanisms. The migmatite microstructures developed by granular flow accompanied by melt-enhanced diffusion and/or melt flow. However, an AMS study and quartz microfabrics suggest that the amount of melt present did not exceed a critical threshold during the deformation to allow free movements of grains.

Key words: crystal size distribution; melt infiltration; melt topology; migmatites; quantitative textural analysis.

INTRODUCTION

Movement of a large volume of granitic melt is an important factor in the compositional differentiation of the continental crust (Fyfe, 1973; Collins & Sawyer, 1996; Brown & Rushmer, 2006) and the presence of melt in rocks profoundly influences their rheology (Arzi, 1978). The migration of melt through the crust is controlled by melt buoyancy and pressure gradients resulting from the combination of gravity forces and deformation (Wickham, 1987; Sawyer, 1994). There are three major mechanisms controlling melt migration through the continental crust: (i) diapirism resulting in upward motion of low-density magma through higher density rocks (Chandrasekhar, 1961; Ramberg, 1981); (ii) dyking that describes melt migration by hydrofracturing of the host rock and transport of melt through narrow dykes (Lister & Kerr, 1991; Petford, 1995); (iii) and migration of a melt through a network of interconnected pores during deformation or compaction of solid matrix (McKenzie, 1984; Wickham, 1987).

Brown & Solar (1998a) and Weinberg & Searle (1998) proposed that during active deformation melt moves by pervasive flow and it is essentially pumped through the system parallel to the principal finite elongation in the form of foliation-parallel veins. Based on a number of field studies, pervasive melt migration at outcrop scale controlled by regional deformation has been suggested by various authors (Collins & Sawyer, 1996; Brown & Solar, 1998b; Vanderhaeghe, 1999; Marchildon & Brown, 2003).

These authors argued that magma intrudes pervasively, parallel to the main anisotropy represented by foliation planes (John & Stünitz, 1997), fold hinges and interboudin partitions (Brown, 1994; Brown *et al.*, 1995). It is also commonly observed that vein-like leucosomes are injected into extensional structures provided the magma pressure is high enough (Wickham, 1987; Lucas & St.Onge, 1995) or parallel to axial surfaces of folds (Vernon & Paterson, 2001).

Microscopic studies of natural rocks show orientations of former melt microstructures that are interpreted in terms of grain-scale channel networks (Sawyer, 2001). Melt migration pathways at the grain scale are commonly determined from distribution of melt films and pools (now glass) in experimentally prepared samples or by distribution of minerals supposed to preserve the original melt topology in natural rocks (Brown *et al.*, 1999; Rosenberg & Riller, 2000; Rosenberg, 2001). The melt topology in experiments is controlled mainly by differential stress, confining pressure and the amount of melt in the system (Rosenberg, 2001). At static conditions, the melt topology is characterized by equilibrium dihedral (wetting) angles at triple point junctions (Jurewicz & Watson, 1984; Laporte & Watson, 1995; Laporte *et al.*, 1997; Cmíral *et al.*, 1998; Walte *et al.*, 2003) and the mobility of the melt remains very low, even if the melt phase forms an interconnected network along triple-junction grain edges at dihedral angles lower than 60° (Laporte & Watson, 1995; Connolly *et al.*, 1997).

Experimental studies on rock analogues to investigate grain-scale melt flow under laboratory conditions show that during contemporaneous melting and deformation melt connection allows the nucleation of shear bands along which a melt is further segregated (Rosenberg & Handy, 2000, 2001; Barraud *et al.*, 2001). Rosenberg (2001) reviewed the experimental data and concluded that the melt migration and melt flow direction are controlled by incremental shortening and melt pressure gradients between source and areas of melt accumulation.

There have only been a few attempts to quantify melt distribution in rocks using methods of quantitative and computer aided microstructural analysis (Dallain *et al.*, 1999; Tanner, 1999; Marchildon & Brown, 2003). These studies commonly deal with grain contact frequency distributions, grain size evolution and orientation of former melt films (Dougan, 1983; McLellan, 1983; Rosenberg & Riller, 2000). However, modern quantitative microstructural analysis may provide further important information about: (i) reorganization of the rock structure associated with melt migration in terms of grain contact distributions (Lexa *et al.*, 2005); (ii) characterization of dynamic or static conditions of melt movement through rocks using analysis of grain boundaries and shape orientations (Rosenberg & Riller, 2000; Marchildon & Brown, 2002); and (iii) cooling or heating histories of rocks using crystal size distribution (CSD) theory (Higgins, 1998; Berger & Roselle, 2001).

In this work, a sequence of deformed felsic rocks is studied, ranging from high-grade banded orthogneiss to fine-grained isotropic migmatite both at macro- and microscale using structural, petrographic and quantitative microstructural analyses. It is shown that a sequence of banded orthogneiss, stromatic, schlieren and nebulitic migmatites results from progressive deformation in a crustal-scale shear zone in the presence of melt. The microstructural and fabric modifications connected with disintegration of parental banded orthogneiss and development of random mineral microstructure are quantified. The relationships of the individual rocks types and the possible origin of this sequence are discussed in terms of deformation and migmatization of different protoliths, melt infiltration from an external source or *in situ* melting of the same protolith during progressive deformation. It is argued that banded orthogneiss and nebulitic migmatites can be interpreted as end-members of a continuous sequence resulting from melt infiltration from an external source during deformation. Finally, the role of melt for activity of grain-scale deformation mechanisms and bulk rheological behaviour of crustal rocks during melt infiltration is discussed.

GEOLOGICAL SETTING

The Moldanubian zone represents the highest grade unit of the Bohemian Massif and is interpreted as an internal zone of the Variscan orogen developed during the Variscan convergence (Matte *et al.*, 1990). The Moldanubian zone is comprised essentially of high-grade gneisses and migmatites containing relicts of high-pressure felsic granulites, eclogites and peridotites that are intercalated with mid-crustal rocks (Fig. 1a). Schulmann *et al.* (2005) described the structural and metamorphic evolution of high-grade crustal rocks of the so-called Gföhl Unit and of the adjacent middle crustal units. For the mechanism of exhumation, they proposed a model of vertical extrusion of orogenic lower crust and its lateral spreading in mid-crustal levels due to an indentation of the easterly Brunia promontory. As a consequence of this process, the high-pressure rocks were thrust over adjacent middle crustal units in conjunction with retrogression of original mineral assemblages and partial melting of all the rock types (Štípská *et al.*, 2004).

Fig. 1. (a) Geological map of the eastern margin of the Bohemian Massif (modified after Schulmann *et al.*, 2005) with the location of the study area (black rectangle). The upper right inset shows the general location of the Bohemian Massif within the European Variscides. (b) Schematic block diagram displaying the main structural features in the study area (modified after Schulmann *et al.*, 2005). Dominant S_1 and S_2 fabrics with their orientations are shown. This block diagram is not vertically scaled.

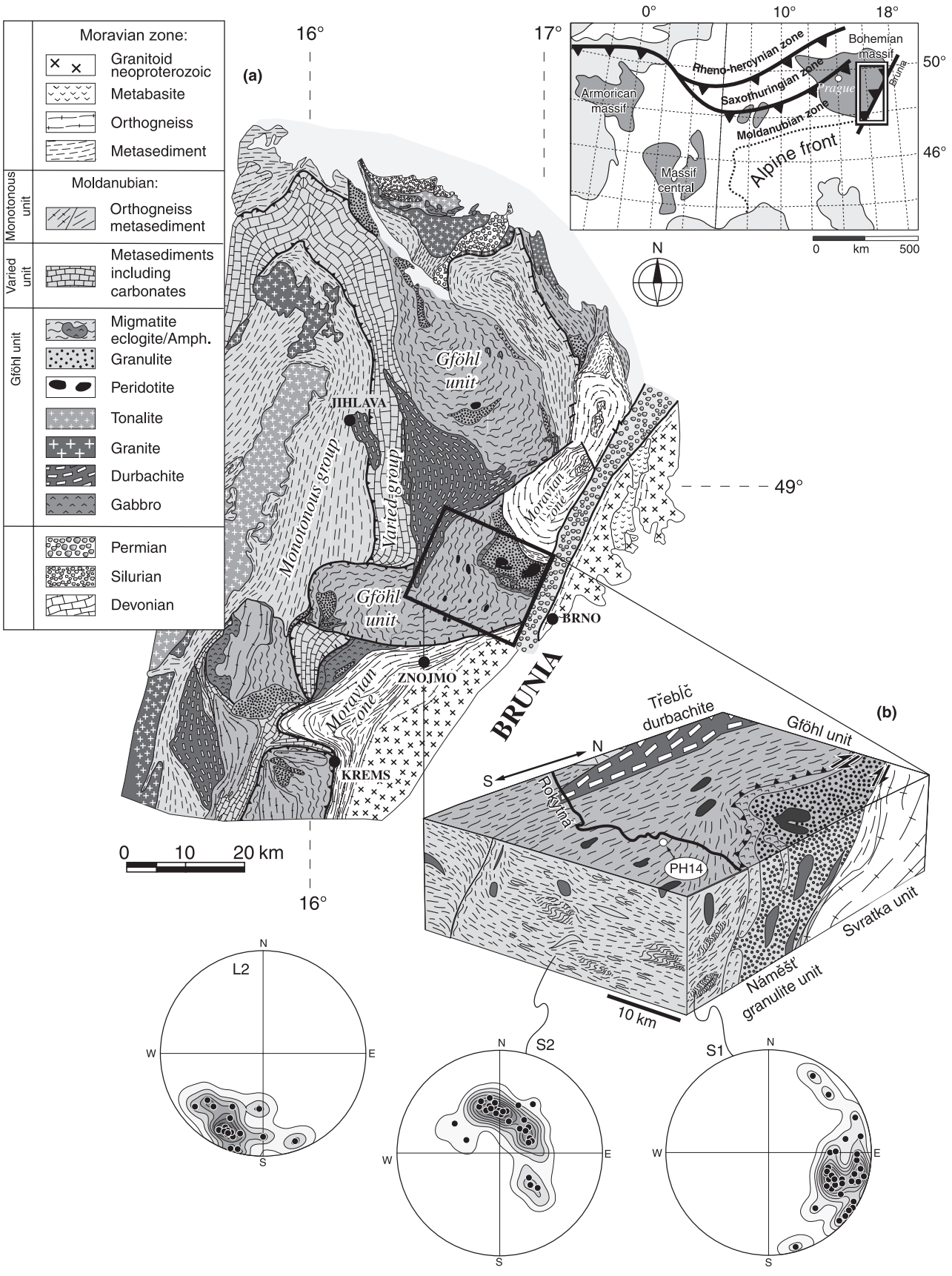

The onset of the exhumation process is dated by zircon U–Pb ages of *c.* 340 Ma on felsic granulites, migmatites and mantle-derived syn-tectonically emplaced plutons (van Breemen *et al.*, 1982; Kröner *et al.*, 1988; Holub *et al.*, 1997; Schulmann *et al.*, 2005). Tajčmanová *et al.* (2006) assigned metamorphic conditions of 840 °C at 18–19 kbar and 760–790 °C at 10–13 kbar to relict steep granulitic fabrics which originated by vertical extrusion of lower crust. These authors also estimated the conditions of re-equilibration of granulites associated with horizontal spreading stage to 720–770 °C and 4–4.5 kbar. High pressure rocks of the Gföhl Unit are accompanied by large bodies of biotite–sillimanite Gföhl orthogneiss spatially associated with K-feldspar–sillimanite paragneisses and leucocratic migmatites for which *P–T* conditions of 7–10 kbar and 750 °C were estimated by Racek *et al.* (2006).

The area of this study is located at the easternmost termination of the Gföhl Unit (Fig. 1a). The main rock type is represented by the Gföhl orthogneiss with protolith ages 488 ± 6 Ma (U–Pb SHRIMP: Friedl *et al.*, 2004) including small bodies of amphibolite, granulite, eclogite, ultrabasic rock and paragneiss. The Gföhl orthogneiss shows different stages of migmatization characterized by the assemblage of Kfs + Pl + Qtz + Bt ± Grt ± Sill. This migmatized orthogneiss complex is heterogeneously deformed by top to the NE shearing along a large-scale, gently dipping shear zone (Schulmann *et al.*, 1994). Consequently, the northern margin of this complex is thrust over a footwall comprised of the Náměšť granulite body and Neoproterozoic metagranites of the north-eastern continental margin (Urban, 1992).

STRUCTURAL EVOLUTION

Mesoscopic structures

Two major deformation events are recognized. The first event (D_1) is represented by a steep, west-dipping high-grade foliation S_1 (Fig. 1b). This fabric is preserved in banded orthogneisses (type I), as an alternation of recrystallized monomineralic K-feldspar, plagioclase and quartz layers, separated by bands of biotite ± sillimanite (Fig. 2a). Lineation L_1 is locally marked by alignment of biotite, sillimanite and by elongation of quartz and feldspar aggregates. This deformation is attributed to an early stage of exhumation of the lower crust along a vertical channel

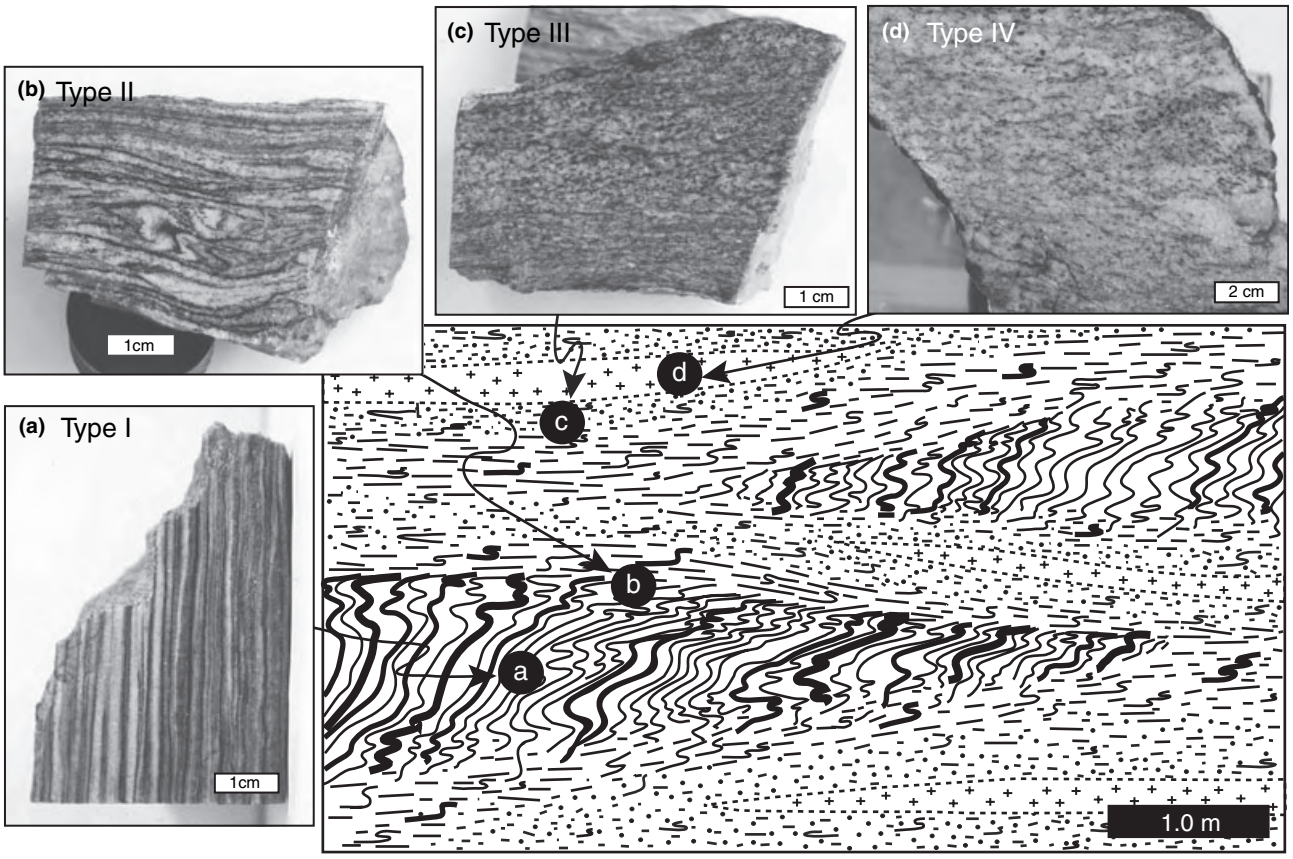

Fig. 2. Schematic representation of the rock relationships at an outcrop scale and photographs of the individual rock types. (a) Banded orthogneiss (type I); (b) stromatic migmatite (type II); (c) schlieren migmatite (type III); and (d) nebulitic migmatite (type IV). The position of this outcrop in the study area is shown in Fig. 1b.

during horizontal shortening of the thickened orogenic root (Schulmann *et al.*, 2005).

The second deformation (D_2) is associated with reworking and folding of the S_1 compositional layering in banded orthogneiss, so that S_1 is only preserved locally in elongate relict domains (Fig. 2a). The D_2 shearing is attributed to horizontal flow of hot lower crust in a zone up to 10 km wide at a mid-crustal level above the Brunia promontory over distances of several tens of kilometres (Schulmann *et al.*, 2005). Relic domains with gently folded S_1 fabric are surrounded by highly deformed zones with tightly folded S_1 fabric (Fig. 2). The composite S_{1-2} fabric is characterized by a banded structure with diffuse boundaries between polymineralic K-feldspar- and plagioclase-rich domains similar to a stromatic migmatite structure (type II) (Fig. 2b). Locally the S_1 fabric is completely transposed and a new S_2 foliation is dipping gently to the SW (Fig. 1b). A sub-horizontal, gently S–SW plunging L_2 lineation (Fig. 1b) is mostly defined by preferred orientation of sillimanite.

Detailed field observations reveal that with ongoing deformation the type II rock gradually pass into more isotropic rock (type III) composed of K-feldspar–quartz and plagioclase–quartz aggregates (Fig. 2c) and containing rootless folds of the deformed S_1 fabric. This rock type alternates with irregular bodies or elongate lenses of fine-grained isotropic felsic rock (type IV, Fig. 2d), which in this region traditionally has been described as a nebulitic migmatite (Matějovská, 1974). Such a structural sequence originated through intense D_2 deformation superimposed on an older steep anisotropy and was identified in outcrop scale along several sections. These observations are supported by the existence of macroscopically visible leucosomes or granitic veins that are also parallel to S_2 and form isolated elongate pockets and lock-up shear bands.

This area has been extensively studied by Matějovská (1974) and Dudek *et al.* (1974) who used the classical migmatite terminology of Mehnert (1971) for the above-described rock types. These authors identified type I rock as banded orthogneiss, rock type II as stromatic migmatite and rock type IV as nebulitic migmatite. Rock type III resembles the schlieren migmatite of Mehnert (1971). Because the Gföhl Unit is considered as one of the largest migmatitic terranes of the Variscan belt, the traditional migmatite terminology was adapted to these rocks.

MICROSTRUCTURAL OBSERVATIONS

The microstructural characteristics including grain size, grain shape and grain boundary geometry were studied in each of the four rock types and in K-feldspar- and plagioclase-rich domains. Thin sections were cut perpendicular to the foliation and parallel to L_2 lineation (XZ section). To discriminate K-feldspar from plagioclase, the thin sections were stained according to the method of Bailey & Stevens (1960).

Type I: banded orthogneiss

This rock type is a fine-grained orthogneiss with 0.25- to 2.0-mm-thick layers of recrystallized plagioclase (30 modal%), K-feldspar (40 modal%) and quartz (20 modal%), separated by discrete layers of biotite (10 modal%) commonly associated with minor sillimanite and garnet (Table 1, Fig. 3a).

K-feldspar forms completely recrystallized aggregates (0.2–0.8 mm grain size) with straight grain boundaries locally meeting in triple point junctions at 120° (Fig. 4a). Numerous rounded inclusions of quartz (0.05 mm) occur preferentially at triple points, along planar boundaries or in cores of feldspar (Fig. 4a). Plagioclase (An_{10-20}) is present in K-feldspar aggregates as small interstitial grains or forms thin films preferentially tracing those K-feldspar boundaries that are oriented at a high angle to the foliation (Fig. 5a). Rarely, tiny interstitial biotite is present in the K-feldspar-rich bands.

Plagioclase aggregates (0.2–0.5 mm) are composed of an equidimensional polygonal mosaic with straight boundaries, and minor interstitial quartz and biotite (Fig. 4b). The plagioclase grains show abundant twinning and form a foam-like texture with a perfect triple point network of grain boundaries. Plagioclase exhibits normal zoning with homogeneous oligoclase cores (An_{24-28}) and more sodic (An_{10-18}), clear, 2 to 10 μm-thick rims at boundaries with K-feldspar. Plagioclase grain size continuously decreases from the centre of an aggregate towards its borders. Quartz occurs as small (0.01–0.05 mm) rounded inclusions or interstitial grains, whereas K-feldspar exhibits characteristic cuspate shapes (Fig. 5b). Tiny biotite grains (0.1–0.5 mm in length; $X_{Fe} = 0.42–0.48$, Ti = 0.2–0.27 p.f.u.) commonly occur along the plagioclase boundaries that are sub-parallel to the foliation (Fig. 3a).

Quartz ribbons 0.3–1.0 mm wide are composed of elongate grains with straight grain boundaries perpendicular to the ribbon margin (Fig. 3a). Quartz–feldspar boundaries are gently curved, with cusps that point from feldspar to quartz. Biotite-rich layers commonly show decussate microstructure, which is a textural equivalent of the foam-like texture of the felsic minerals (Vernon, 1976). Contacts between biotite- and plagioclase-rich layers are marked by numerous (< 1 modal%) small idiomorphic garnets (0.05–0.10 mm in size; $X_{Fe} = 0.77–0.85$).

Type II: stromatic migmatite

This rock type is composed of plagioclase- and K-feldspar-rich aggregates with subordinate quartz and irregular quartz aggregates (Fig. 3b); modes are given in Table 1. These aggregates are rimmed by relicts of

Table 1. Representative data for the quantitative textural analysis.

		Banded orthogneiss		Stromatic migmatite		Schlieren migmatite		Nebulitic migmatite
		Kfs domain	P1 domain	Kfs domain	P1 domain	Kfs domain	P1 domain	
Grain size – Feret diameter (mm)								
Median	Kfs	0.430	0.121	0.345	0.065	0.172	0.138	0.137
	P1	0.134	0.224	0.086	0.225	0.094	0.119	0.110
	Qtz	0.079	0.076	0.071	0.079	0.070	0.076	0.074
Ql	Kfs	0.120	0.065	0.194	0.042	0.103	0.082	0.085
	P1	0.103	0.095	0.055	0.158	0.061	0.084	0.074
	Qtz	0.046	0.051	0.044	0.050	0.046	0.047	0.039
Q3	Kfs	0.630	0.170	0.556	0.101	0.263	0.211	0.237
	P1	0.257	0.373	0.161	0.350	0.172	0.164	0.160
	Qtz	0.105	0.114	0.119	0.127	0.105	0.121	0.127
Q3 – Q1	Kfs	0.510	0.105	0.362	0.059	0.161	0.129	0.152
	P1	0.154	0.278	0.107	0.192	0.111	0.080	0.086
	Qtz	0.059	0.063	0.075	0.077	0.060	0.074	0.089
Crystal size distribution (CSD)								
N0. (mm^{-4})	Kfs	0.0037	–	0.00487	–	0.053	–	0.2124
	P1	–	0.0303	–	0.0733	–	0.06812	0.1857
	Qtz	1.008	2.334	1.6448	3.73	2.093	0.6585	2.286
Gt	Kfs	0.347	–	0.286	–	0.148	–	0.1127
	P1	–	0.15731	–	0.1269	–	0.11	0.0689
	Qtz	0.0736	0.0569	0.0669	0.0547	0.0644	0.0813	0.0623
Shape preferred orientation (SPO)								
Eigenvalue ratio (Rg)	Kfs	1.48	1.42	1.42	1.32	1.21	1.13	1.15
	P1	1.17	1.42	1.1	1.23	1.21	1.14	1.13
	Qtz	1.25	1.47	1	1.24	1.1	1.33	1.32
Aspect ratio (median)	Kfs	1.66	1.69	1.6	1.5	1.59	1.6	1.55
	P1	1.51	1.6	1.59	1.44	1.65	1.5	1.61
	Qtz	1.5	1.5	1.46	1.5	1.5	1.5	1.49
	Bt	2.14	2.7	2	2.2	2.2	2.35	2.2
Grain boundary preferred orientation (GBPO)								
Eigenvalue ratio (Rb)	Kfs–Kfs	1.34	–	1.25	–	1.06	–	1.5
	Kfs–P1	1.15	1.18	1.09	1.13	1.14	1.13	1.12
	Kfs–Qtz	1.17	–	1.15	–	1.17	–	1.17
	P1–P1	–	1.18	–	1.15	–	1.15	1.36
Modal proportion (%)								
	Kfs	70–80	10	70–80	5	50	20–25	30
	P1	10	60	10	60	20	40	30
	Qtz	10–20	20	10–20	25	30	30	30
	Bt	< 1	< 10	< 1	~10	< 1	< 10	10
	Sill, Grt	0	< 1	0	< 1	0	< 1	< 2

biotite-rich layers commonly intergrown with fibrolitic sillimanite. The ill-defined and rather diffuse boundaries between individual aggregates are characteristic for this textural type (Fig. 3b).

K-feldspar-rich aggregates (0.2–0.8 mm grain size) include abundant small interstitial plagioclase (An_{17-20} in the core and An_{4-10} at the rim) and quartz. K-feldspar forms irregular grains with lobate boundaries. Most of the K-feldspar grain boundaries are decorated by thin interstitial plagioclase (An_{6-8}). Quartz is present as inclusions (0.01–0.06 mm) in K-feldspar or forms irregular grains (0.1–0.2 mm) along the K-feldspar boundaries. In plagioclase-rich aggregates (0.1–0.3 mm grain size, An_{17-20}), plagioclase grains have straight to lobate boundaries, whereas irregularly distributed interstitial quartz has irregular shapes. Similar to the type I orthogneiss, interstitial K-feldspar shows cuspate shapes.

Biotite (15 modal%; $X_{Fe} = 0.55–0.59$, Ti = 0.18–0.26 p.f.u) is variable in size and appears along plagioclase boundaries mostly parallel to the foliation (Fig. 3b). Small idiomorphic garnet (0.07–0.2 mm in size; $X_{Fe} = 0.84–0.91$) occurs in the plagioclase-rich aggregates and biotite-rich layers.

Type III: schlieren migmatite

This textural type does not show macroscopically visible feldspar-rich aggregates, but stained thin sections reveal the presence of plagioclase–quartz and K-feldspar–quartz-enriched domains (Fig. 3c); modes are given in Table 1. The foliation is marked by preferred orientation of biotite and sillimanite dispersed in the rock.

K-feldspar forms large irregularly shaped grains (0.1–0.3 mm in size) (Figs 3c & 4c) or small cuspate grains along plagioclase boundaries. The most characteristic feature is the presence of irregular embayments of quartz and plagioclase in the K-feldspar grains (Fig. 4d). Myrmekitic aggregates are commonly developed along the K-feldspar boundaries (Fig. 4c). Plagioclase occurs as large irregular twinned grains (An_{12-16} in the core, An_{2-4} at the rim) and as films (An_{1-4}) lining the K-feldspar boundaries (Fig. 5c). Entirely dispersed quartz forms large relict grains (0.7–1.0 mm) with undulatory extinction and highly lobate boundaries, abundant irregular interstitial grains lining the K-feldspar boundaries and rounded inclusions (0.02–0.05 mm) in K-feldspar and

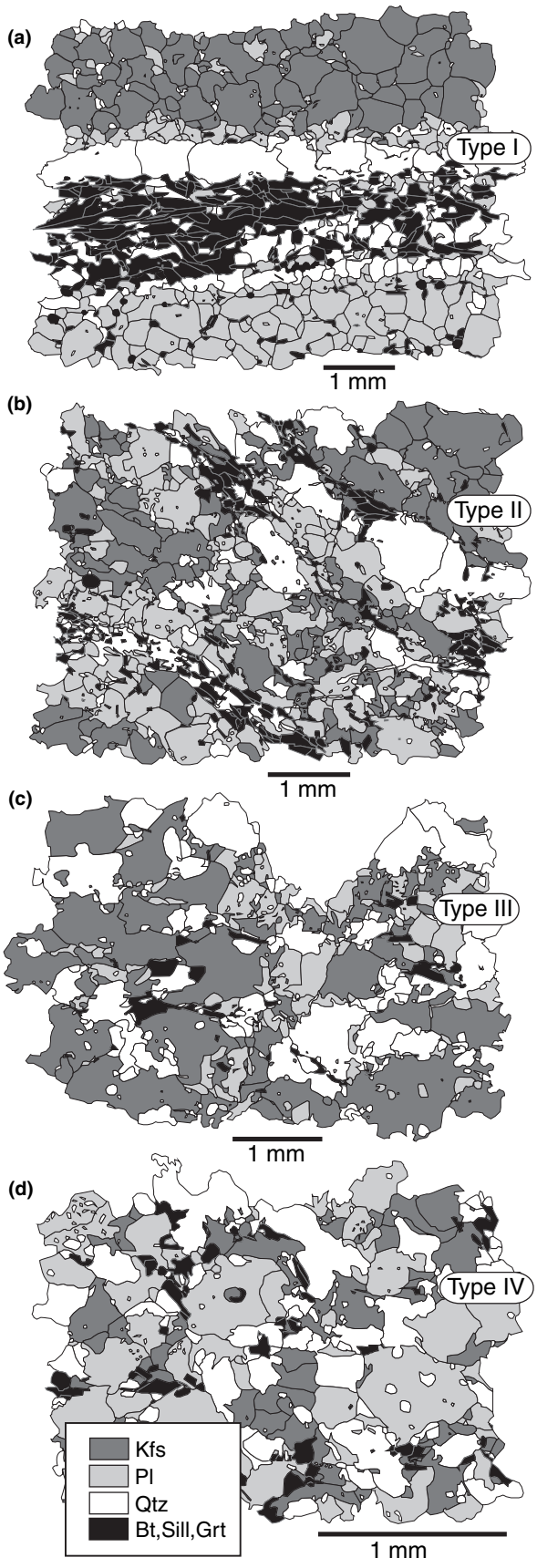

plagioclase (Fig. 4c). Biotite (10–15 modal%; X_{Fe} = 0.76–0.79, Ti = 0.18–0.19 p.f.u.) is homogeneously dispersed and is most prevalent in the plagioclase–quartz domains. Atoll-shaped garnet (0.05–0.25 mm in size; X_{Fe} = 0.96–0.97) appears inside the felsic aggregates, rather than along contacts with biotite.

Type IV: nebulitic migmatite

This type of rock is composed of almost equal amounts of plagioclase, K-feldspar and quartz, and contains minor biotite (X_{Fe} = 0.91–0.93, Ti = 0.01–0.04 p.f.u.), sillimanite and garnet (X_{Fe} = 0.98–1.00) (Fig. 3d), with a weakly developed preferred orientation of the biotite and sillimanite; modes are given in Table 1. K-feldspar (0.10–0.25 mm in size) occurs in the form of irregular grains embayed with quartz and plagioclase. Commonly, the intensity of quartz and plagioclase lobes correlates well with highly cuspate irregular forms of corroded relics of K-feldspar (Fig. 4e). Similarly, the relics of irregular plagioclase (0.05–0.15 mm in size; An_{6-10} in the core and An_{0-4} at the rim) show cuspate boundaries, but with curvature less pronounced than that of the corroded relics of K-feldspar grains. An important feature is the presence of new plagioclase (An_{0-1})–K-feldspar intergrowths embaying corroded relics of K-feldspar grains (Fig. 4f). Quartz (0.04–0.07 mm) with highly lobate boundaries is uniformly distributed in the rock. Biotite of low aspect ratio shows highly corroded cuspate forms filled with quartz, K-feldspar and plagioclase.

Summary of modal changes

Modal composition of the feldspar aggregates in the type II migmatite does not change significantly compared with the type I orthogneiss. However, the type III migmatite is characterized by an important increase in quartz content in feldspar domains (up to 30 modal%) associated with a slight increase in interstitial plagioclase in K-feldspar-rich domains and K-feldspar in plagioclase-rich domains. The proportions of the felsic minerals are equal in the type IV migmatite.

Fig. 3. Representative digitalized microstructures (XZ sections) for individual textural types (note differences in scales when making comparisons). (a) Banded orthogneiss (type I) with distinct monomineralic layers composed of a polygonal mosaic of well-equilibrated plagioclase, K-feldspar and quartz polycrystalline ribbons separated by discrete layers of biotite ± sillimanite ± garnet (sample PH60/B). (b) Stromatic migmatite (type II) composed of K-feldspar-rich, plagioclase-rich and quartz-rich aggregates separated by relicts of biotite ± sillimanite-rich layers (sample PH60/A). (c) Schlieren migmatite (type III) showing alternation of K-feldspar- and plagioclase-rich domains interpreted to correspond to an original spatial distribution (K-feldspar domain is shown, sample PH90). (d) Isotropic nebulitic migmatite without any gneissosity (type IV) composed of equal amounts of K-feldspar, plagioclase and quartz (sample PH59/D).

Evidence of melting

Sawyer (1999, 2001) summarized criteria for recognition of former melt at grain scale in metamorphic rocks. The three most important features are: (i) mineral pseudomorphs after thin melt films along crystal faces, a feature typically observed in melting experiments under dynamic conditions (Jin *et al.*, 1994); (ii) rounded and corroded reactant minerals embayed by surrounding mineral pseudomorphs after melt (Büsch

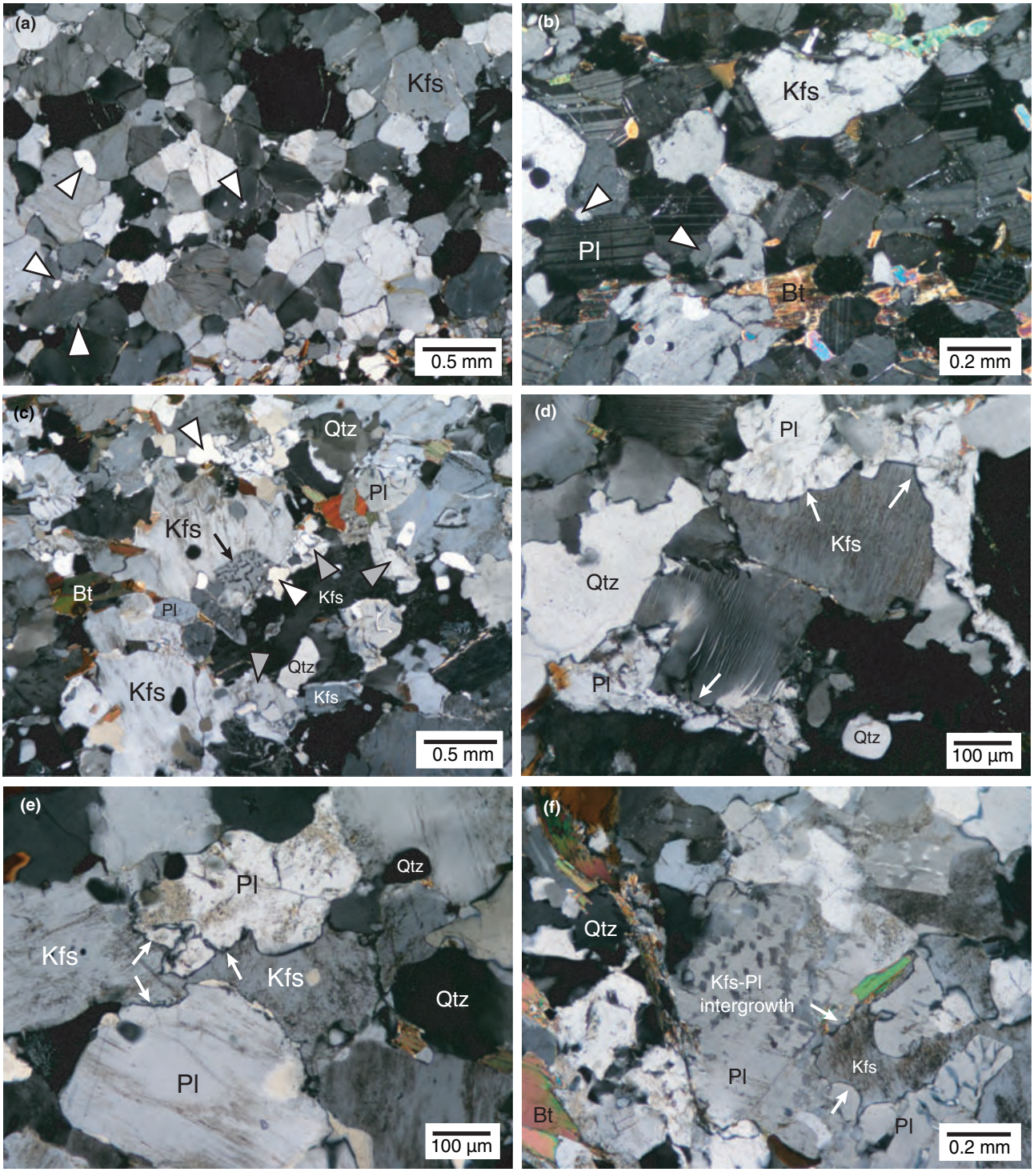

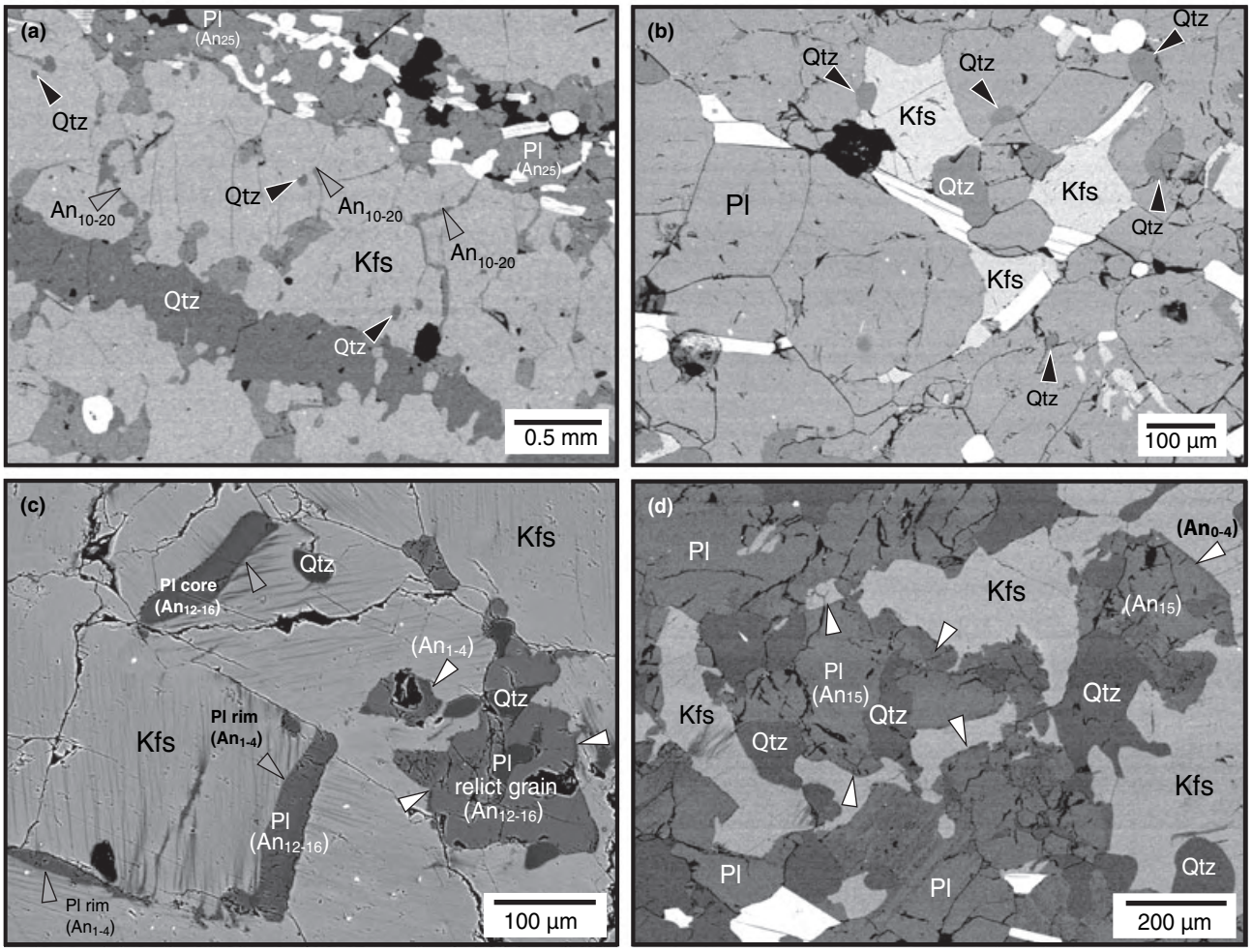

Fig. 5. SEM backscatter images showing the inferred former melt topology (note differences in scales when making comparisons). (a) Type I banded orthogneiss: interstitial plagioclase (An_{10-20}), representing the plagioclase component crystallized from the anatectic melt (grey arrow), tracing the K-feldspar boundaries sub-perpendicular to the foliation (sample PH60/B). Black arrows show small rounded quartz grains crystallized along feldspar boundaries. (b) Type I banded orthogneiss: inferred former melt pools with cuspate margins in a plagioclase band (sample PH60/B). The former melt has crystallized to K-feldspar (cuspate melt pools), plagioclase (growing on the old plagioclase grains) and quartz (forming small rounded grains along the feldspar boundaries (black arrow)). (c) Type III schlieren migmatite: more developed interstitial plagioclase (grey arrow) with normal zoning (core = An_{12-16}; rim = An_{1-4}) and distinct albite rims (An_{1-4}) on relict feldspar grains (white arrow) (sample PH90). The interstitial plagioclase is not in optical continuity with any residual plagioclase grains adjacent to it and does not show any preferred orientation, in contrast to plagioclase in types I and II. (d) Type III schlieren migmatite: new plagioclase inferred to have crystallized from melt (growing on an old plagioclase grain in the form of the discrete albite rims (white arrow)) and quartz grains that resorb relict K-feldspar grains (sample PH14/D).

Fig. 4. Photomicrographs showing characteristic textures of the rock sequence (note differences in scales when making comparisons). (a) Type I banded orthogneiss: recrystallized K-feldspar aggregate with straight grain boundaries and numerous smaller rounded quartz grains (white triangles) along the boundaries or in the cores of feldspar (sample PH60/B). (b) Type I banded orthogneiss: well-developed plagioclase polygonal foam-like texture with straight grain boundaries, interstitial quartz (white triangles) and biotite (sample PH60/B). (c) Type III schlieren migmatite: typical microstructure with irregularly shaped feldspar and quartz grains with highly lobate boundaries. Myrmekitic aggregates commonly develop along the K-feldspar boundaries (black arrow). New small interstitial plagioclase (grey triangles), K-feldspar and quartz (white triangles) grains trace almost all the relict feldspar boundaries. Interstitial quartz forms preferentially rounded shapes different from plagioclase which forms thin elongated grains/films coating K-feldspar boundaries (sample PH90). Such a microstructure is typical also for the type IV. (d) Type III schlieren migmatite: irregular cuspate K-feldspar grain embayed with newly crystallized quartz and plagioclase (sample PH90). (e) Type IV nebulitic migmatite: corroded relics of K-feldspar grains (sample PH59/D). (f) Type III nebulitic migmatite: plagioclase-K-feldspar intergrowths embaying relict K-feldspar grain (sample PH14/D). White arrows in (d), (e) and (f) point to irregular embayments of relict K-feldspar originated through resorption of old K-feldspar grains by newly crystallized material.

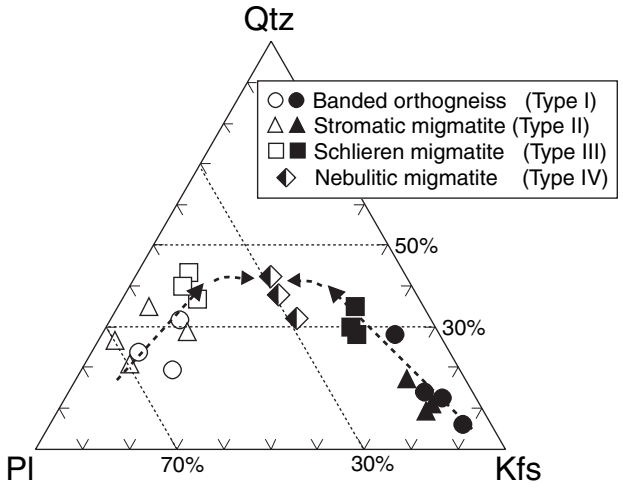

Fig. 6. Modal changes in both plagioclase (open symbols) and K-feldspar (closed symbols) aggregates in different rock types plotted in a quartz–plagioclase–K-feldspar triangle. Arrowed dashed lines indicate evolutionary trend from type I banded orthogneiss to type IV nebulitic migmatite.

et al., 1974); and (iii) cuspate and lobate areas inferred to represent pools of crystallized melt (Jurewicz & Watson, 1984).

The former presence of melt at grain scale was inferred from the following microstructures (Figs 4 & 5). (i) Plagioclase films between adjacent K-feldspar grains, inferred to represent a plagioclase component crystallized from melt (Fig. 5a, c). This plagioclase is characterized by more albitic composition and by different topology compared with original grains. (ii) Pl–Kfs–Kfs and Kfs–Kfs–Pl dihedral angles commonly lower than 30° (Fig. 5a, c), as observed in granitic melt crystallized under experimental conditions (e.g. Laporte *et al.*, 1997). (iii) Cuspate K-feldspar pools in plagioclase aggregates (Fig. 5b), inferred to represent a K-feldspar component crystallized from melt (Jurewicz & Watson, 1984; Sawyer, 1999, 2001). (iv) Normal zoning of plagioclase from An_{10-30} to An_{0-15} (Sawyer, 1998; Marchildon & Brown, 2001) lining K-feldspar boundaries (Fig. 5c, d). An important feature is the preferential orientation of plagioclase films coating K-feldspar boundaries in type I orthogneiss and type II migmatite sub-perpendicular to the foliation (Fig. 5a), in contrast to the types III and IV migmatites, where these films are wider and do not show any optically visible preferred orientation. Bulbous myrmekite (Fig. 4d) and new highly irregular lobate grains that overgrow partially resorbed corroded feldspar grains (e.g. Fig. 4c) are similar to microstructures described as typical of minerals reacting with melt (Mehnert *et al.*, 1973; Büsch *et al.*, 1974; McLellan, 1983).

QUANTITATIVE TEXTURAL ANALYSIS

The quantitative analysis of texture is based on statistical evaluation of grain size distributions (Kretz, 1966, 1994; Ashworth, 1976; Ashworth & McLellan, 1985; Cashman & Ferry, 1988; Cashman & Marsh, 1988; Higgins, 1998; Berger & Roselle, 2001), spatial distribution of minerals and GBPOs (Panozzo, 1983), and grain contact frequencies (Flinn, 1969; Kretz, 1969; McLellan, 1983; Kruse & Stünitz, 1999). In simple chemical systems, these textural parameters are more sensitive to changes of physical conditions than compositional characteristics. This is due to the high activation energies of chemical reactions needed to produce new crystal growth compared with the small amount of lattice strain energy and grain boundary energy required to drive recrystallization processes (Spry, 1969; Stünitz, 1998).

In this study, the textures of three samples were analysed from each rock type, and in each sample more than 1000 grains were evaluated in thin section. Due to significant textural variations, the individual K-feldspar-rich and plagioclase-rich domains were analysed separately. Maps of grains with full topology were manually traced into the ESRI ArcView Desktop GIS environment and grain boundaries were generated using the ArcView PolyLX extension (Lexa, 2003). The 'shapefiles' of individual digitalized thin sections are attached in Appendix S1 (*Supplementary material*). Analysis of grain size, CSD, grain shape preferred orientation (SPO), grain boundary preferred orientation (GBPO) and grain contact frequencies were obtained using the MATLAB™ PolyLX toolbox (Lexa, 2003; http://petrol.natur.cuni.cz/ ondro/). The grain sizes of the minerals were evaluated in terms of Feret diameter (diameter of a circle having the same area as the grain). Two methods were used to determine the grain SPO: (1) mean directions using circular statistics; and (2) eigenvalue analysis of Scheidegger's bulk orientation tensor calculated from individual long axes weighted by grain size (Lexa *et al.*, 2005), where degree of SPO is expressed as the eigenvalues ratio Rg. GBPO was assessed by similar techniques, but the bulk orientation tensor is formed from the decomposed grain boundaries between chosen phases (Lexa *et al.*, 2005) and the degree of GBPO is expressed as the eigenvalues ratio Rb. Grain contact frequency, used to examine statistical deviation from a random spatial distribution of contact relations between the individual minerals, was evaluated in a manner similar to the method of Kretz (1969, 1994), except that contact frequencies were obtained directly from grain map topologies instead of using line intercepts.

Results of the quantitative microstructural analyses show an evolutionary trend from the banded orthogneiss, through the migmatite types II and III to the nebulitic migmatite. Therefore, in the following sections the rock types are discussed as a sequence in which the type I orthogneiss and type IV nebulitic migmatite are considered to be end-members of a continuous microstructural evolution.

Grain size analysis

The CSD is an important tool to estimate residence time of magmas in magma chambers, cooling rates in rapidly quenched lavas, as well as to quantify textures related to phenocrysts accumulation and fractionation (Cashman & Marsh, 1988; Marsh, 1988; Higgins, 1998). In metamorphic petrology, CSD is used to obtain quantitative information concerning crystal nucleation and growth rates and nucleation density and/or annealing (Randolph & Larson, 1971; Cashman & Ferry, 1988; Carlson, 1989; Waters & Lovegrove, 2002). Hickey & Bell (1996) proposed that during dynamic recrystallization decreasing strain rate to temperature ratio ($\dot{e}/T$) leads to decrease in the ratio of nucleation and growth rate (N/G) and development of coarser grain size, whereas increasing $\dot{e}/T$ leads to increasing N/G and therefore to grain size decrease. This hypothesis is well documented in experimental studies with steel alloys (Sakai & Jonas, 1984) supported by Azpiroz & Fernández (2003) and Lexa *et al.* (2005) in naturally deformed rocks. These authors evaluate the role of recrystallization mechanisms on N/G ratio of the CSD. The CSD is commonly used in formerly partially molten rocks to evaluate combined process of resorption and grain size decrease in reacting phases in mesosome and nucleation and grain growth and coarsening of minerals crystallizing in leucosomes (Dougan, 1983; McLellan, 1983; Ashworth & McLellan, 1985; Dallain *et al.*, 1999). Because the processes controlling grain size distributions in the crystallization of partially molten rocks are complex and interpretations uncertain, CSD has only rarely been used to describe textural evolution of migmatites (Berger & Roselle, 2001). In this work, the CSD methods are used as a practical approach to parameterize grain size frequency histograms and visualize their trends in a simple manner.

Grain size statistics were evaluated for the four rock types for plagioclase, K-feldspar and quartz and the results are presented in the form of average grain size, expressed as a median value of the Feret diameter, and grain size range expressed as the difference between the third and first quartiles instead of standard deviation because of the log-normal distribution of measured data (Fig. 7a, Table 1). The results are also summarized as CSD curves (plot of logarithms of population density against crystal size) that were constructed using the method of Peterson (1996); values of the zero-size intercept (N_0 – population density interpreted as the ratio of nucleation rate to growth rate) and negative inverse of slope (Gt interpreted as a function of growth rate) of the linear parts of the CSD curves are plotted in Fig. 7b, c.

Both plagioclase and K-feldspar in the type I orthogneiss are characterized by log-normal grain size distribution exhibiting average grain size of ~0.2 and 0.2–0.5 mm respectively. Interstitial quartz yields significantly smaller average grain size of 0.05–0.1 mm in both domains. Quartz grains from polycrystalline ribbons were not evaluated statistically but their grain size of 0.5–2.0 mm was estimated using an optical microscope. The grain size of new interstitial plagioclase in the K-feldspar aggregates is close to 0.1 mm. The grain size distributions from type I orthogneiss to type II, type III and type IV migmatites are characterized by the following features. The average grain size of plagioclase and K-feldspar decreases compared with type I orthogneiss (Fig. 7a, Table 1). This is accompanied by a continuous decrease in grain size range for both feldspars. The interstitial quartz grain size remains fairly constant throughout all the stages of textural evolution, ranging between 0.05 and 0.1 mm, being larger in the K-feldspar than in the plagioclase domains (Fig. 7a). The grain size of minor plagioclase in the K-feldspar domains shows a bimodal distribution that is attributed to the presence of small newly nucleated grains (0.06–0.1 mm) and to larger plagioclase grains (0.2 mm) already present in the feldspar aggregates.

The CSD of plagioclase indicate continuous increase in N_0 (nucleation density) values coupled with a decrease in Gt (growth rate) values from type I orthogneiss towards type IV migmatite (Fig. 7b, Table 1). By contrast, K-feldspar shows a decrease in Gt values from type I orthogneiss to type III migmatite without significant increase in N_0 values, which remain very low. From type III to type IV migmatite a dramatic increase in N_0 values is observed for K-feldspar at almost constant Gt values (Fig. 7c). This evolution is clearly shown by steepening of the slopes of the CSD curves accompanied by increase in their upper intercept with the ordinate axis (insets in Fig. 7b, c).

Grain shapes and grain shape preferred orientation

Grain shape or grain aspect ratio together with grain SPO analyses provide important information about deformation during or after leucosome formation (Mehnert, 1971; McLellan, 1983) or about degree of inheritance of original anisotropy (Ashworth, 1979). Measurements of preferred orientations of inferred melt-filled grain boundaries in rocks give insights into processes of melt draining and melt transfer (Rosenberg & Handy, 2000, 2001; Sawyer, 2001).

Grain shape and SPO statistics were evaluated in all the textural types for plagioclase, K-feldspar, quartz and biotite. The results of SPO statistic are summarized in a boxplot-type diagram, where the axial ratios of the individual minerals are plotted against bulk SPO (Lexa *et al.*, 2005) for the corresponding minerals (Fig. 8).

Aspect ratios for both K-feldspar and plagioclase show small median values ranging from 1.5 to 1.7 throughout the whole microstructural sequence (Fig. 8, Table 1). Quartz exhibits slightly smaller and stable aspect ratio close to 1.5. An important feature is the continuous decrease in SPO of K-feldspar and

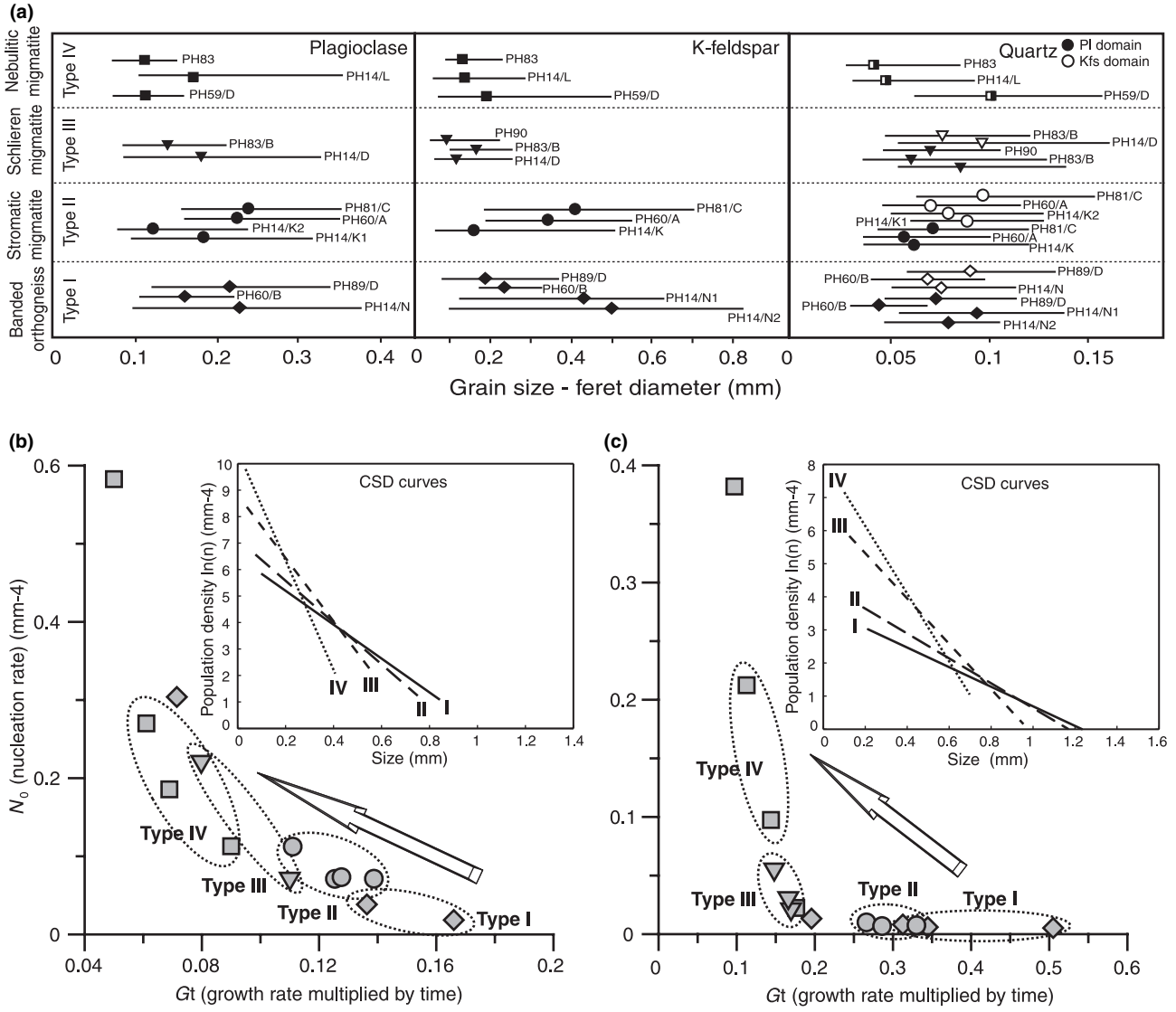

Fig. 7. Grain size statistics and CSD evolution for the rock sequence. (a) Calculated average grain size (median value of the Feret diameter) and range (difference of third and first quartiles) for plagioclase, K-feldspar and quartz. (b,c) Plots of crystal size distribution parameters N_0 (corresponding to the nucleation density per size per volume) and Gt (non-dimensional value dependent on the growth rate) with examples of linearized CSD curves (upper right insets) used for Gt and N_0 estimates. (b) Plagioclase, (c) K-feldspar. The CSD curves show single lines of four representative samples corresponding to the individual rock types.

plagioclase from type I orthogneiss to type IV nebulitic migmatite (Fig. 8, Table 1). Rose diagrams for the rock types I, II and III show that K-feldspar and plagioclase (Fig. 8b) have weakly inclined SPO with respect to the aggregate elongation direction at an angle of 15°–30°. Biotite shows a high aspect ratio for type I orthogneiss (Table 1) and strong SPO parallel with mesoscopic foliation for the types I, II and III migmatites. In the type IV migmatite, biotite aspect ratio and preferred orientation are lower and the latter parameter shows bimodal distribution with one maximum sub-parallel to the main foliation and a second one almost perpendicular to it. Interstitial K-feldspar, plagioclase and quartz exhibit always small aspect ratio and weakly developed SPO maxima at an angle of 40°–60° to the foliation for types I, II and III. The exception is type IV migmatite, where, in similar fashion to biotite, the interstitial plagioclase shows two maxima, one sub-parallel and one perpendicular to the foliation.

Grain contact frequency analysis and grain boundary preferred orientation

The grain contact frequency method (Kretz, 1969) allows an examination of the statistical deviation from the hypothesis of random distribution of phases in rocks. In random distribution, the number of

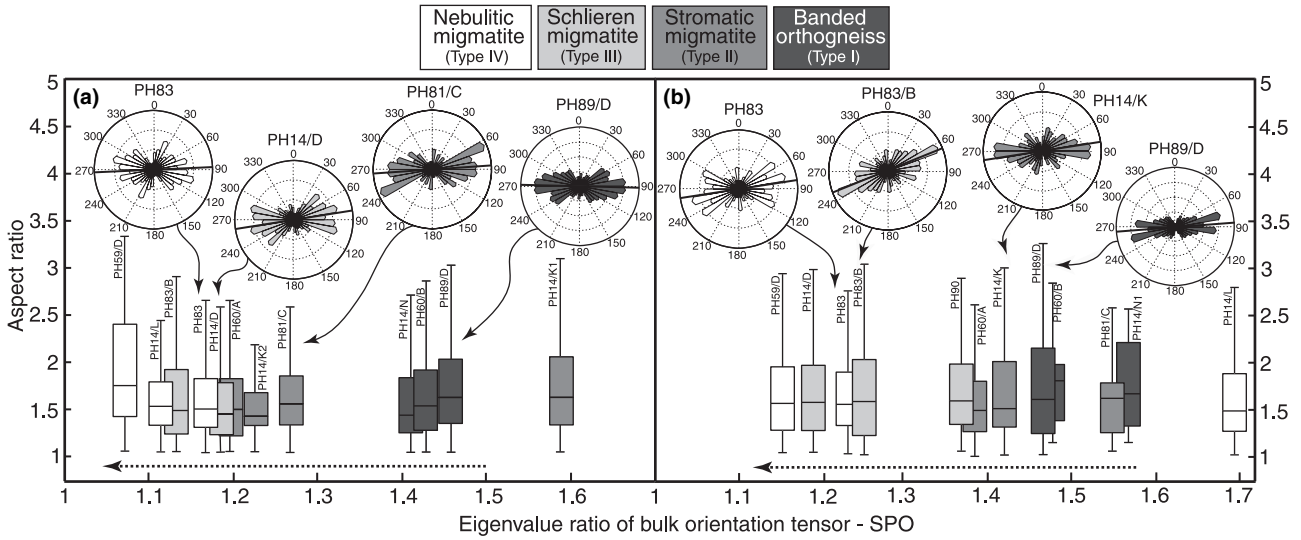

Fig. 8. Plot of grain shape preferred orientation (SPO) of K-feldspar (a) and plagioclase (b). The results are summarized in a box plot of aspect ratios (characterizing the shape of grains) *v*. eigenvalue ratios (showing the degree of preferred orientation). Individual boxes show median, and first and third quartiles of the aspect ratio. The whiskers represent a statistical estimate of the data range where outliers are not plotted. Representative rose diagrams for individual rock types show maxima orientation in respect to the aggregate elongation direction. The degree of shading corresponds to the individual rock types.

contacts of given phases depend only on the total number of grains of each phase present. There are two possible deviations from random distribution: (i) aggregate distribution, where grains of the same phase tend to occur in aggregates in which contacts between grains of the same phase (like–like contacts) predominate; and (ii) regular distribution, where the grains tend to occur in a regular (chessboard-like) pattern in which contacts between different phases (unlike contacts) are more common. McLellan (1983) reviewed processes responsible for different types of grain distributions. A random distribution should theoretically develop during rapid quenching of granitic melt, whereas regular distribution commonly is interpreted as resulting from extensive solid-state annealing under very high temperatures (Flinn, 1969; Vernon, 1976; McLellan, 1983; Lexa *et al*., 2005). These interpretations are based on the assumption of reducing surface energy (Seng, 1936; DeVore, 1959) by elimination of high-energy contacts (commonly non-coherent like–like contacts) either by reduction of grain boundary area or by nucleation and growth of new phases along such a boundary (Kim & Rohrer, 2004). In addition, Kruse & Stünitz (1999) and Baratoux *et al*. (2005) proposed that the regular distribution was induced by mechanical mixing and heterogeneous nucleation. According to Vernon (1976) and McLellan (1983), an aggregate distribution results from a solid-state differentiation associated mostly with dynamic recrystallization where development of monomineralic layers results from uneven efficiency of deformation mechanisms simultaneously operating in different phases (Jordan, 1988).

Grain contact frequency and the GBPO were evaluated for K-feldspar, plagioclase and quartz in all the textural types over the full digitized area of individual K-feldspar and plagioclase domains. The results are presented in Fig. 9, where the χ-value

$$\chi = \frac{\text{Observed} - \text{Expected}}{\sqrt{\text{Expected}}}$$

or deviation from the random distribution is plotted against the ratio of eigenvalues of the orientation tensor or the degree of GBPO (Lexa *et al*., 2005). Values of expected frequencies are estimated using Lafeber's method of testing for randomness (Lafeber, 1963; Kretz, 1969). This diagram offers a simple visual evaluation of the relationship between degree of deviation from expected random distribution of grain contacts and GBPOs of like–like and unlike boundaries.

The type I orthogneiss is characterized by a relatively small proportion of like–like K-feldspar and plagioclase contacts indicating a weak regular distribution (slightly negative χ-values for like–like and positive χ-values for unlike contacts; Fig. 9), despite a macroscopically banded texture in which a strong aggregate distribution should be observed. This feature is attributed to a great proportion of minor interstitial grains (Qtz, Bt, Kfs and Pl) lining the K-feldspar and the plagioclase boundaries. Additionally, the number of like–like K-feldspar and plagioclase contacts continuously decreases from type I orthogneiss to type IV migmatite, whereas the number of Pl–Kfs, Kfs–Qtz and Pl–Qtz unlike

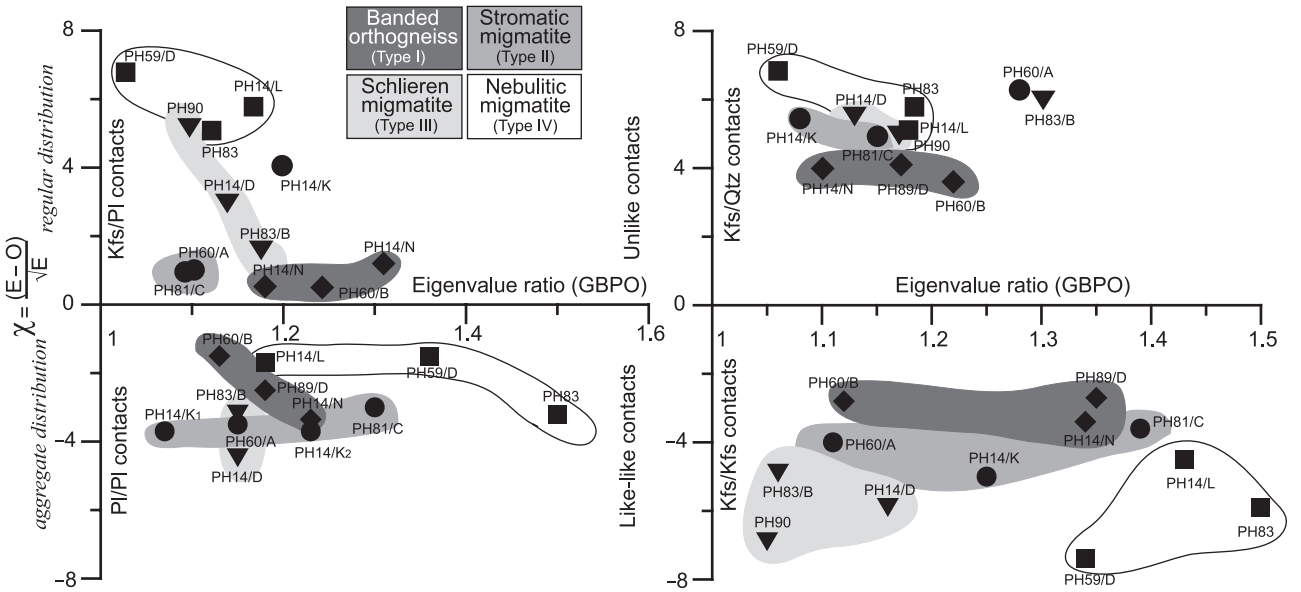

Fig. 9. Grain boundary statistics plotted as the deviation from a random spatial distribution (grain contact frequency) *v.* degree of grain boundary preferred orientation (GBPO). For details see text. The degree of shading corresponds to the individual rock types.

contact continuously increases (negative like–like χ-values and positive unlike χ-values) (Fig. 9). This is in a good accordance with the increasing amount of interstitial phases towards the type IV migmatite. Quartz exhibits the same strong regular distribution from the type I orthogneiss to the type IV migmatite in both feldspar domains.

In K-feldspar-rich aggregates, the degree of GBPO of the K-feldspar like–like boundaries slightly decreases from type I orthogneiss to type III migmatite, whereas type IV migmatite is characterized by an increase in the degree of K-feldspar like–like GBPO (Fig. 9, Table 1). The GBPO of plagioclase–plagioclase boundaries in the plagioclase-rich aggregates is similar to the evolution of K-feldspar like–like boundaries. The GBPO of the K-feldspar–quartz boundaries as well as those of K-feldspar–plagioclase boundaries are weak, and decrease throughout the textural evolution (Fig. 9, Table 1).

MINERAL FABRIC

In rocks deformed in the presence of melt, the textures of quartz and feldspar can be used to evaluate the deformation mechanisms of the solid fraction as well as the deformation of crystallizing intragranular melt (Závada *et al.*, 2007). The mineral fabrics of ferromagnesian phases can be indirectly assessed using anisotropy of magnetic susceptibility (AMS). The AMS method has been recently used to determine the degree of susceptibility, shape of the fabric ellipsoid and relative contribution of ferro- and para-magnetic minerals to the bulk fabric in migmatites (Ferré *et al.*, 2003, 2004).

Anisotropy of magnetic susceptibility

Types III and IV migmatites are macroscopically close to isotropic, so that the mineral alignment defined by the orientation of dispersed biotite is poorly defined (Fig. 2c, d). To better characterize the fabric, the AMS method was used to determine the internal fabric of these rocks. Oriented samples were collected using a portable drill at four sampling sites covering a section across the well-defined structural sequence. The AMS data were statistically evaluated using the Anisoft software package (Jelínek, 1978; Hrouda *et al.*, 1990). The low values of mean susceptibility ($< 250 \times 10^{-6}$ SI) indicate that biotite is the main carrier of the magnetic susceptibility (Ferré *et al.*, 2003). The AMS study reveals a homogeneous pattern of a south-dipping magnetic foliation (Fig. 10b) and SW sub-horizontally plunging magnetic lineation (Fig. 10b) that are consistent with the mesoscopic D_2 structural pattern.

According to the degree of AMS (expressed by parameter P′, Jelínek, 1981) and shape of the AMS ellipsoid (expressed by parameter T, Jelínek, 1981) the samples are divided in two groups (Fig. 10a). The banded orthogneiss and the type II migmatite exhibit a strong degree of magnetic anisotropy (P′ = 1.14–1.2) and planar shape of the ellipsoid of magnetic susceptibility ($T = 0.4$–1) (Fig. 10a). These values are typical for metamorphic rocks with well-developed compositional layering and biotite aligned in planar aggregates. Samples from types III and IV migmatites occur in a region of lower degree of anisotropy (P′ = 1.06–1.16) and correspond to a planar–linear fabric ($T = 0.1$–0.7) (Fig. 10a) marked by more intense magnetic lineation.

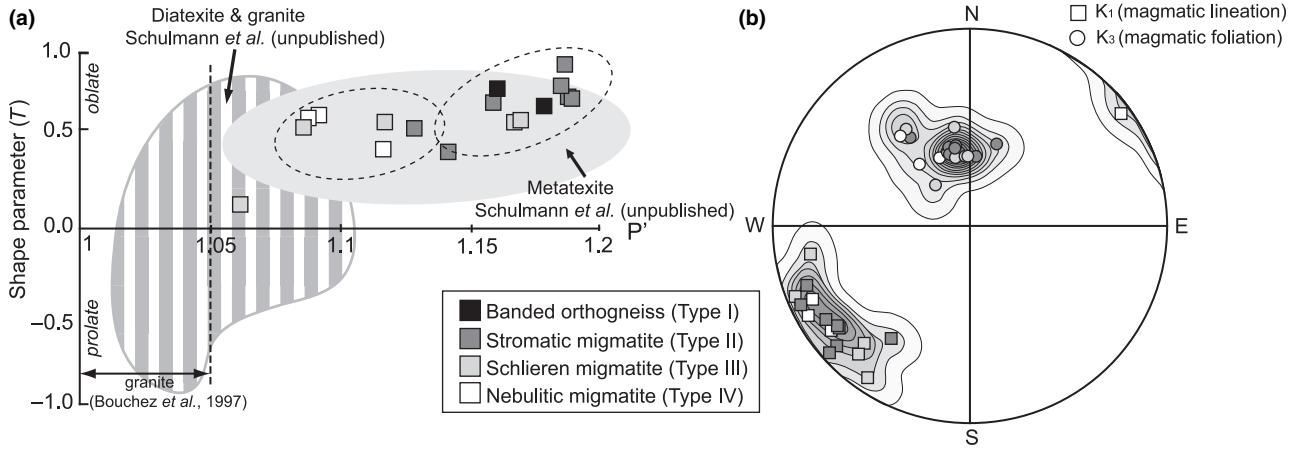

Fig. 10. Plots to show the anisotropy of magnetic susceptibility (AMS). (a) P'–T plot, where the P' parameter represents the degree of magnetic anisotropy and T is a shape parameter that describes the shape of the ellipsoid of magnetic susceptibility. T can take either positive values ($T > 0$), characteristic for a planar fabric, or negative values ($T < 0$), typical for a linear fabric. Dashed ellipses show two distinct datasets. For comparison, data obtained by Schulmann K., Edel J.-B., Hasalová P., Lexa O., Ježek J. & Cosgrove J. W. (unpublished data) and Bouchez (1997) are shown. (b) Magnetic foliation (circles), plotted as the minimal susceptibility direction (K_3), perpendicular to the magnetic foliation, and magnetic lineation (squares), plotted as the maximal susceptibility direction (K_1).

Lattice preferred orientation

To understand the deformation behaviour of individual phases, we measured and evaluated statistically the lattice preferred orientation (LPO) of aggregate grains (Pl, Kfs and Qtz) and grains apparently crystallized from melt (Pl, Kfs and Qtz) separately (Fig. 12g, h). The LPO of quartz, plagioclase and K-feldspar were measured on a scanning electron microscope Cam-Scan3200 in the Czech Geological Survey using the electron back-scattered diffraction technique (EBSD) and HKL technology (Adams *et al.*, 1993; Bascou *et al.*, 2001). Diffraction patterns were acquired at 20 kV of accelerating voltage, 5 nA of probe current and working distance of ~33 mm from the thin section prepared from the structural XZ plane. The procedure was carried out manually due to small differences in diffraction patterns. The chemistry and orientation of individual grains was controlled using a forescatter detector with combination of orientation and chemical contrast. Thus, each individual grain is represented by only one orientation measurement. The resulting pole figures are presented as lower hemisphere equal-area projections in which the trace of foliation is oriented along the equator and the stretching lineation is in the E–W direction.

Old quartz grains in ribbons of the type I orthogneiss show *c*-axes distributed in weak sub-maxima arranged along weakly developed small circles close to the S_1 foliation trace. The most intense sub-maxima are developed close to the lineation direction. This type of *c*-axis pattern may indicate preferential prism $\langle c \rangle$ slip-system activity and dominantly coaxial deformation. The *c*-axes of large quartz grains in types II, III and IV migmatites reveal strong maxima either parallel to the S_2 foliation pole or close to the centre of the diagram. These *c*-axis patterns indicate mainly activity of basal $\langle a \rangle$ or rhomb $\langle a + c \rangle$ slip-systems and less frequently prism $\langle a \rangle$ slip (Fig. 11a). Towards types III and IV migmatites, the LPO of the matrix quartz became less well developed, preserving activity of the same slip-systems as in the previous microstructural types (Fig. 11a). New quartz grains crystallized from melt in type I orthogneiss, and type II migmatite show very weak LPO and nearly random distribution of all quartz axes (Fig. 11b). Whereas old grains show progressive weakening of the LPO from type II to type IV migmatite, the new and randomly crystallized grains tends to develop weak crystal preferred orientation during the same microstructural evolution from type II to type IV migmatite (Fig. 11). It is difficult to distinguish old from new quartz grains in the type IV rock and therefore the LPO of quartz in this microstructure links LPO evolution between old and new grains in the final microstructural type.

K-feldspar and plagioclase commonly show weak LPO in all rock types regardless the origin of grains. K-feldspar shows crystallographic patterns which are compatible with dominant activity of the 1/2 [110](001) slip system (Willaime & Gandais, 1977; Willaime *et al.*, 1979) (Fig. 12a, c). Contribution of other slip systems as [100](010) (Fig. 12b) and [100](001) (Fig. 12d) has also been identified in both relict K-feldspar grains and in K-feldspar grains apparently crystallized from melt respectively.

Distribution of the main lattice directions of plagioclase revealed slip parallel either to $1/2[1\bar{1}0]$ on (001) and $(11\bar{1})$ planes (Fig. 12e) or to 1/2 [110] on (001) and $(1\bar{1}\bar{1})$ planes (Fig. 12f) for all types of rocks and both aggregate grains and plagioclase inferred to have crystallized from melt (Fig. 12g) (Olsen & Kohlstedt, 1984). The textures of plagioclase inferred to have

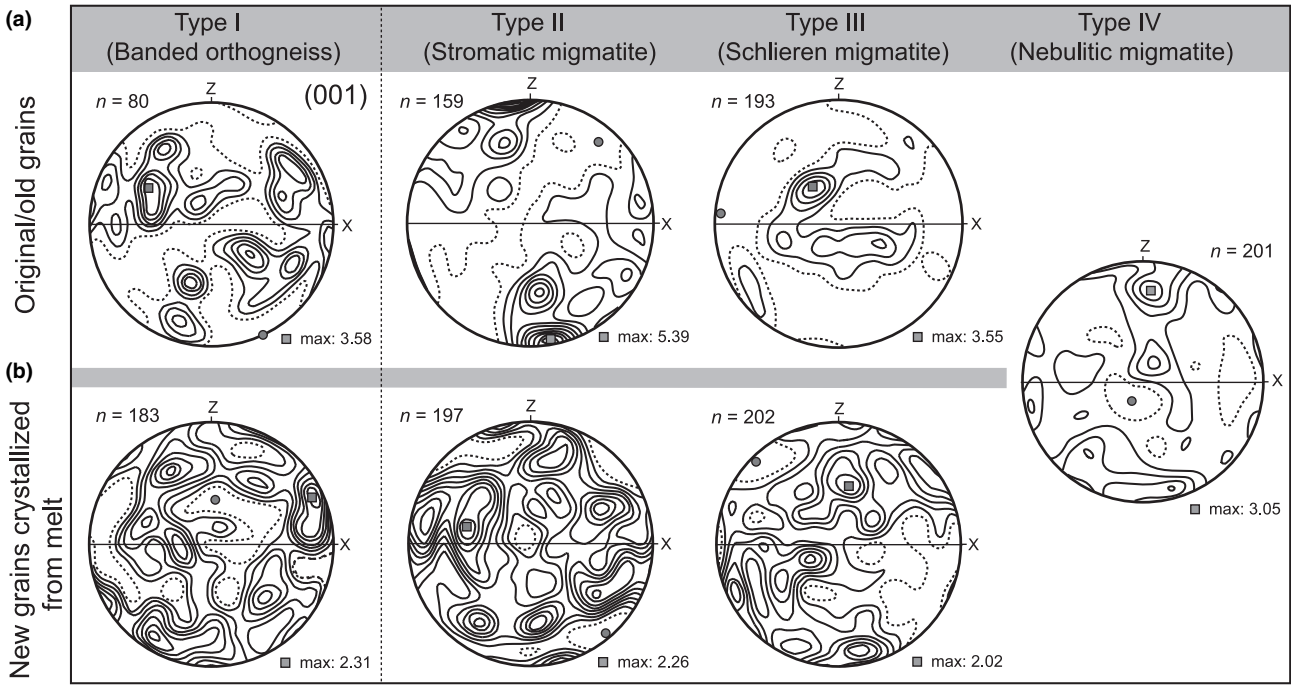

Fig. 11. Characteristic *c*-axes preferred orientations of (a) old/relict quartz grains and (b) new quartz grains crystallized from areas of inferred former melt for all rock types. The *c*-axis patterns of old/relict quartz grains in type I banded orthogneiss indicate prism ⟨*c*⟩ slip system activity whereas in type II, III and IV migmatites basal ⟨*a*⟩ or rhomb ⟨*a* + *c*⟩ slip systems are dominant with minor prism ⟨*a*⟩ slip. New quartz grains inferred to have crystallized from melt in type I banded orthogneiss to type IV nebulitic migmatite show very weak LPO and nearly isotropic distribution of all quartz axes. Equal area projections, lower hemisphere, contoured at interval of 0.5 times uniform distribution. Foliation is horizontal and lineation is in this plane in the E–W direction. *N* is the number of measured grains. Maximum densities are marked on the bottom right of each pole figure. The dashed line represents the lowest contour level and the grey circle corresponds to the minimum density value.

crystallized from melt are commonly weak with the exception of strong LPO of plagioclase in the type I orthogneiss (Fig. 12f). Such slip-systems are supposed to be secondary and active if grains are in unsuitable (hard) orientation to the dominant slip-system [100](010) (Kruse *et al.*, 2001).

DISCUSSION

This study presents a detailed microstructural and quantitative textural analysis of four types of migmatitic rocks identified in one of the largest (~5000 km^2) migmatitic complex of the eastern Variscan belt. The rock types are interpreted as representing a textural sequence from banded orthogneiss via stromatic and schlieren migmatites to nebulitic migmatite. The possible mechanisms that could account for the origin of this rock sequence involve: (i) genetically unrelated migmatites that have originated from distinct protoliths; (ii) variable degree of *in situ* partial melting of a single protolith or different protoliths; and (iii) melt infiltration from an external source through solid rock in which banded orthogneiss and nebulitic migmatite represent genetically linked end-members. These hypotheses are discussed further below.

Spatial relationships of individual migmatite types within the shear zone

The structural sequence described in this work indicates an intimate relationship between types I to III migmatites and nebulitic type IV migmatite sheets that can be interpreted in terms of a shear zone, which was exploited by rising magma (Brown *et al.*, 1995; Collins & Sawyer, 1996; Brown & Solar, 1998b). We have shown that the D_2 flat fabrics that cross-cut the steep foliation S_1 developed at high-temperature solid-state conditions (Fig. 1). Tajčmanová *et al.* (2006) and Racek *et al.* (2006) described a similar sequence of superposed fabrics in lower crustal rocks several tens of kilometres to the north and south of the studied area respectively. These authors proposed that the flat D_2 deformation fabrics originated due to thrusting of orogenic lower crust over middle crustal units along a large-scale retrograde shear zone. In agreement with these authors, we suggest that the D_2 fabrics developed in a thrust related crustal-scale shear zone reported already by Urban (1992), Schulmann *et al.* (1994) and redefined later by Schulmann *et al.* (2005). The main difference between other regions is in the degree of D_2 reworking, which is so high in the studied area that

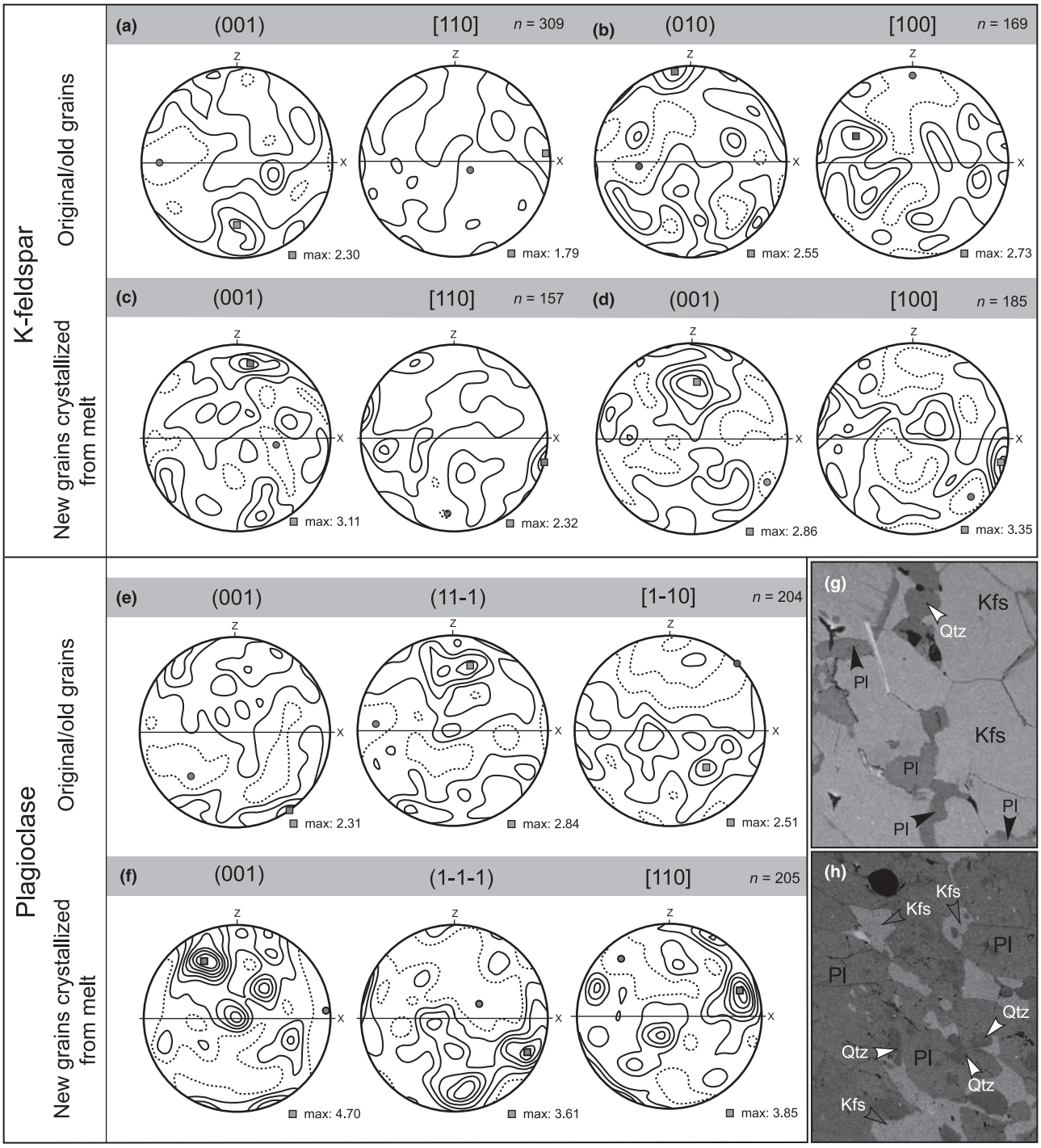

Fig. 12. Characteristic LPO patterns of K-feldspar (a–d) and plagioclase (e,f). Both feldspars commonly show weak LPO in all rock types regardless of the origin of the grains. An exception is the strong LPO of new plagioclase grains in the type I banded orthogneiss (f). K-feldspar usually shows activity of 1/2[110](001) (a,c; type I), but also of [100](010) (b; type IV) and [100](001) (d; type IV) slip systems. Plagioclase reveals activity of secondary slip systems such as 1/2[1$\bar{1}$0] on (001) and (11$\bar{1}$) or 1/2 [1$\bar{1}$0] on (001) and (111) (e,f; type I). Equal area projections, lower hemisphere, contoured at intervals of 0.5 times uniform distribution. Foliation is horizontal and lineation is in this plane in the E–W direction. *N* is the number of measured grains. Maximum densities are marked on the bottom right of each pole figure. The dashed line represents the lowest contour level and the grey circle corresponds to the minimum density value. (f,g) BSE images depicting the microstructural appearance of examples of the measured phases (sample PH60/B). Original plagioclase (g) and K-feldspar (h) aggregates with newly crystallized quartz (white arrow), plagioclase (black arrows) and K-feldspar (grey arrows) are shown.

steep D_1 fabrics are preserved only as rare relics shown in Fig. 2.

Our structural observations are compatible with progressive transposition within the ductile shear zone ranging from type I banded orthogneiss to highly reworked type III schlieren migmatite. This interpretation is based on progressive folding of early steep orthogneiss fabric, development of isoclinal folds and complete fabric transposition and development of type III migmatite in a ductile shear zone (Fig. 2; Turner & Weiss, 1963). In such a context, the elongated bodies of type IV nebulitic migmatite can be seen as veins of isotropic granite penetrating parallel to the main S_2 mylonitic anisotropy (e.g. Cosgrove, 1997; Brown & Solar, 1998a). Alternatively, the type IV nebulitic migmatites could be interpreted in terms of injected melt into hot country rocks (called also magma wedging, Weinberg & Searle, 1998) preventing magma freezing during D_2 shearing. Finally, the nebulitic migmatite can be also regarded as the most extreme end-member of the structural sequence, i.e. completely disintegrated parental orthogneiss.

In summary, the type I orthogneiss to type III migmatite show intimate spatial relationships suggesting that they have originated from the same protolith and that they are genetically linked. However, the macroscopic observations alone cannot distinguish the origin of type IV migmatite and further arguments are required.

Microstructural and petrological arguments for melt–rock interaction during exhumation

We suggest, in agreement with Sawyer (1999, 2001), that the position and topology of new plagioclase, quartz and K-feldspar grains in type I orthogneiss and type II migmatite may be interpreted in terms of melt products crystallized along boundaries of the feldspar in individual aggregates (Fig. 5a–c). The main difference between type I orthogneiss and type II migmatite is a more albitic composition of plagioclase and a greater modal content of new phases in the latter. Types III and IV migmatites show development of highly corroded shapes of K-feldspar, plagioclase and biotite (Fig. 4c–f). This indicates that all rock types exhibit features compatible with the presence of melt and its interaction with the solid rock. Additionally, the degree of melt–rock interaction is inferred to increase from type I orthogneiss towards type IV nebulitic migmatite (Fig. 4).

The structural sequence exhibits a distinct trend in modal composition of originally monomineralic layers that are progressively converted into polymineralic aggregates of granitic composition (Fig. 6). The compositional paths show evolutionary trends from type I orthogneiss to type III migmatite, interpreted as being associated with crystallization of melt, culminating in the type IV migmatite, which has equal amounts of plagioclase, K-feldspar and quartz (Fig. 6).

Plagioclase shows systematic decrease in anorthite content for both original plagioclase grains (An_{30} to An_{25}), their rims and inter-granular aggregates (An_{20} to An_{10}) towards type IV nebulitic migmatite. Both garnet and biotite exhibit systematically increasing X_{Fe} towards type IV migmatite (from 0.7 to 1.00 and from 0.4 to 0.9 respectively) coupled with decrease in Ti content in biotite (from 0.2 to 0.04 p.f.u.). The mineral compositional data suggest systematic equilibration of garnet, biotite and plagioclase compositions in the stability field of sillimanite with decreasing temperature. The full petrological data and P–T estimates for melt–rock interaction are presented in a companion paper (Hasalová *et al.*, 2008a). Here, we quote the P–T estimates based on thermodynamic modelling using THERMOCALC (Powell *et al.*, 1998) to point out the decrease in temperature from 790 to 850 °C at 7.5 kbar for type I orthogneiss to 690–770 °C at 4.5 kbar for type IV nebulitic migmatite.

Taken together, the microstructural and petrological data show paradoxically an increasing degree of apparent melt–rock interaction coupled with decreasing equilibration temperature with textural evolution from type I to type IV rock type. The microstructural and modal composition data do not exclude either partial melting or infiltration of melt from an external source. However, the systematic modification of chemical composition of minerals across the migmatite sequence is in contradiction with the model of *in situ* partial melting. Namely, as suggested by many field and experimental studies, the composition of plagioclase would be shifted towards more anorthitic contents and the X_{Fe} of garnet and biotite would decrease during partial melting process (Le Breton & Thompson, 1988; Vielzeuf & Holloway, 1988; Gardien *et al.*, 1995; Greenfield *et al.*, 1998; Dallain *et al.*, 1999).

Interpretation of quantitative microstructural data

Microstructural studies of partially molten rock have revealed systematic changes in grain size, grain SPO and spatial distribution of individual phases during increasing degree of partial melting (e.g. Vernon, 1976; McLellan, 1983; Dallain *et al.*, 1999). Here these trends are compared with our quantitative microstructural data, and the alternative origins that may result in the observed microstructural sequence are discussed.

Interpretation of crystal size distributions

The most significant result of this study is the systematic decrease in average grain size (Fig. 7a) and systematic increase in a population density (nucleation rate) associated with possible decrease in growth rate for all feldspar from type I orthogneiss to type IV migmatite (Fig. 7b, c).

Results from migmatitic terranes show that the CSD associated with partial melting is characterized by

production of coarse-grained felsic mineral aggregates resulting from increase in temperature (e.g. Dougan, 1983; McLellan, 1983). This process is commonly followed by textural coarsening (Ashworth & McLellan, 1985; Dallain *et al*., 1999; Berger & Roselle, 2001) explained by two competing approaches: the Lifshitz–Slyozov–Wagner (LSW) model (Lifshitz & Slyozov, 1961), and the communicating neighbour theory (CN of DeHoff, 1991). Higgins (1998) showed that textural coarsening results in progressive decrease in N_0 value and decrease in the slope of the CSD curve; he interpreted this trend as a result of rapid undercooling during solidification of magma followed by reduced undercooling, suppression of nucleation and textural coarsening. However, our textural sequence exhibits the opposite trend in evolution of CSD curves, which is interpreted as indicating that *in situ* partial melting and textural coarsening are not responsible for the origin of observed CSDs.

The observed CSD trend may be explained by one of three different mechanisms: (1) solid-state deformation under decreasing temperature and or increasing strain rate (Hickey & Bell, 1996; Azpiroz & Fernández, 2003; Lexa *et al*., 2005); (2) a different degree of reaction overstepping (Waters & Lovegrove, 2002; Moazzen & Modjarrad, 2005); and (3) a different degree of undercooling (Marsh, 1988).

The grain size for dynamically recrystallized grains in a power-law creep regime is a function of differential stress (Twiss, 1977). Such grains are characterized by strong shape and LPO and commonly solid-state differentiation (Baratoux *et al*., 2005; Lexa *et al*., 2005). However, this microstructural study does not reveal any features in quartz, plagioclase and K-feldspar of rock types II, III and IV which may indicate a dynamic recrystallization processes operating under decreasing temperature. Differences in the degree of reaction overstepping have been documented in contact aureoles, but may be rejected in this case due to the regional nature of the metamorphism. However, the role of different degrees of undercooling relating to an overall decrease in equilibration temperature cannot be excluded.

Our data indicate that the sequence of rock types reflects the progressive resorption of residual grains and crystallization of new grains from melt in intergranular spaces. Moreover, the trend of CSD curves suggest a progressive increase in nucleation rate and decrease in growth rate from type I orthogneiss to type IV nebulitic migmatite. This trend could be explained by an increase in undercooling consistent with the decreasing equilibration temperature we report.

The CSD trend is compatible with crystallization of melt in a progressively exhuming and rapidly cooling system. This is in accordance with exceptionally high cooling rates up to several hundred degrees celsius per million years estimated for nearby granulites by Tajčmanová *et al*. (2006).

Interpretation of spatial distributions of phases

The quantitative analysis of spatial distributions of individual phases shows that the intensification of regular distribution (increasing amount of unlike contacts; Fig. 9) correlates with an increasing degree of host rock–melt equilibration. The process of melt crystallization leads to new mineral growth on the surfaces of residual grains. This is responsible for the increase in unlike grain boundaries, which commonly retain melt–solid geometries. Our case study shows that the development of a regular distribution of felsic phases is not related to solid-state annealing, as supposed by some authors (Flinn, 1969; McLellan, 1983; Lexa *et al*., 2005), but to the process of crystallization of melt, consistent with precipitation of the minor phase on triple points in granular polygonal aggregates to achieve lower total interfacial energy (Spry, 1969; Vernon, 1974). This process was documented by Dallain *et al*. (1999), who showed that the predominance of unlike contacts in polycrystalline aggregates originated through wetting of grain boundaries by fluids or melt, and subsequent precipitation of other phases on like–like contacts. However, we cannot exclude the possibility that a regular distribution reported from granulites and high-grade gneisses (Flinn, 1969; Kretz, 1994) results from solid-state annealing of rocks where melt crystallized. Therefore, the regular distribution developed during melt crystallization may be inherited and perhaps further accentuated during later thermal and textural re-equilibration.

Origin of microstructural and compositional trends

The sequence from type I orthogneiss to type IV migmatite exhibit continuous trends in all quantitative parameters (Table 1). The grain size decreases (Fig. 7a) and there is a progressive development of a regular distribution of all felsic phases (Fig. 9), which is linked with mineral compositional trends indicating temperature decrease. These clear evolutionary trends are incompatible with a process of partial melting of different protoliths. Partial melting of the same protolith may develop continuous trends, but these should show increase in grain size of individual felsic phases (Dallain *et al*., 1999) and different mineral compositional evolution (e.g. Gardien *et al*., 1995; Greenfield *et al*., 1998). Additionally, we show that the degree of regular distribution for K-feldspar- and plagioclase-dominated aggregates evolves in the same manner throughout the microstructural sequence (Fig. 9). However, Dallain *et al*. (1999) reported significantly more advanced regular distribution of plagioclase-compared with K-feldspar-rich aggregates in the microstructural sequence originated by partial melting. These authors proposed that this microstructural contrast originated due to melting process preferentially operating in mica–plagioclase rich aggregates, whereas the K-feldspar-rich aggregates were more

refractory. In the present case, Hasalová *et al.* (2008b) report continuous trends in whole-rock geochemistry and mineral compositions for the sequence of rock types, but different Nd isotopic composition for the type I orthogneiss compared with the rest of the sequence, which precludes of *in situ* anatexis in a closed system.

Melt infiltration model

The discrepancies between the evolutionary trends we report and generally accepted trends for anatectic terranes require an appropriate explanation that is consistent with the structural, quantitative microstructural and mineral compositional data. As a possible explanation, we introduce the concept of *melt infiltration* from an external source, where melt passes pervasively along grain boundaries through the whole-rock volume and changes macroscopic (Fig. 2) and microscopic (Fig. 3) appearance of the rock. This process is characterized by resorption of old phases, nucleation of new phases along high-energy like–like grain boundaries and modification of mineral and whole-rock compositions. These gradual changes are accompanied by grain size reduction (Fig. 7) and progressive disintegration of former aggregate (layered) distribution of original phases (Fig. 9). We suggest that the individual migmatite types represent different degrees of equilibration between the host rock and migrating melt. It should be emphasized, that all these processes occur along a retrograde path during exhumation of the Gföhl Unit. We are aware that a decrease in P–T conditions during melt infiltration is a fundamental and limiting factor for the model proposed.

The amount of melt and its connectivity are critical parameters controlling melt mobility and the rheological behaviour of melt-present rocks. To constrain these parameters both AMS and EBSD were used. Using AMS, it is possible to distinguish between solid-state dominated deformation mechanisms in the melanosome and free rigid body particle rotation in the leucosome (e.g. Ferré *et al.*, 2003). On the other hand, using the EBSD technique enables us to distinguish deformation mechanisms in the solid framework and to constrain the mechanical role of melt during the deformation.

AMS fabric origin: solid framework or melt controlled deformation

The AMS study shows that the magnetic anisotropy is dominated by biotite. The oblate shape of magnetic ellipsoid and high degree of anisotropy of type I orthogneiss and type II migmatite (Fig. 10a) are consistent with strong preferred orientation of biotite and the fact that biotite has a intrinsically oblate shape of the single-grain magnetic ellipsoid (Zapletal, 1990; Martín-Hernandéz & Hirth, 2003). The type III and IV migmatites reveal partly resorbed biotite flakes uniformly dispersed in the rock marked by slightly weaker degree of magnetic anisotropy and less oblate fabric ellipsoid compared with types I and II migmatite (Fig. 10a). This contrasts with common granites and diatexites from other migmatitic terranes which show significantly lower values of degree of anisotropy and highly variable shapes of AMS ellipsoids (Fig. 10a; Bouchez, 1997; Ferré *et al.*, 2003).

Numerous natural studies supported by numerical modelling indicate that the magnetic susceptibility in viscously flowing magmas is characterized by a very low degree of anisotropy, pulsatory fabrics and dominantly a plane strain AMS ellipsoid shape (Blumenfeld & Bouchez, 1988; Hrouda *et al.*, 1994; Arbaret *et al.*, 2000). A comparison of the AMS fabrics with those of diatexites and results of numerical models indicate that the intensity of the AMS fabric of types III and IV migmatites does not originated from freely rotated biotite in viscously flowing melt. On the contrary, we argue that the AMS fabric in all types of migmatites resembles fabrics usually acquired through solid-state deformation of a load-bearing framework, similar to melanosomes in migmatites (Ferré *et al.*, 2003). To understand the mechanisms responsible for development of such fabrics the grain-scale deformation mechanisms and melt behaviour in individual rock types is discussed.

Deformation mechanisms

Experimental studies of low melt fraction rocks deformed under high differential stress show that matrix minerals deform by grain boundary migration accommodated dislocation creep (Dell' Angelo *et al.*, 1987; Walte *et al.*, 2005). Strong shape and GBPO of feldspar (Figs 8 & 9) as well as LPO of residual quartz grains (Fig. 11a) in the type I orthogneiss may be interpreted in terms of plastic deformation consistent with a dislocation creep deformation mechanism (Rosenberg & Berger, 2001). However, the weak LPO of residual grains of both feldspars (Fig. 12a, e) in the type I orthogneiss suggests a contribution of grain boundary sliding during the development of the microstructure. In other words, the type I microstructure corresponds to a transient microstructure in terms of decreasing activity of dislocation creep and enhancement of diffusion controlled processes.

Decrease in SPO and GBPO and constantly weak LPO in feldspar of type II migmatite (Figs 8 & 9) may be interpreted as a result of melt-enhanced diffusion creep (Garlick & Gromet, 2004). However, the large quartz grains reveal intense activity of basal $\langle a \rangle$ slip suggesting important plastic yielding of this mineral (Fig. 11a). Elongate pockets inferred to represent former melt oriented at a high angle to the stretching lineation in the type I orthogneiss (Fig. 5a) and type II migmatite indicate that the melt distribution was controlled by the deformation. This is supported by the

strong LPO of interstitial plagioclase (Fig. 12f). Rosenberg & Riller (2000) reported that pockets within quartz aggregates inferred to have been former melt are oriented at high angle to the foliation plane, possibly close to σ_1. Melt distribution in our samples is similar to their results and also to experiments at high differential stresses (Dell' Angelo & Tullis, 1988) and high confining pressures. In these experiments, melt accumulated in pockets along faces of the grains subparallel to the main compressional stress direction σ_1 (Dell' Angelo & Tullis, 1988; Daines & Kohlstedt, 1997). Such a melt topology is also termed 'dynamic wetting' (Jin *et al*., 1994).

In types III and IV migmatites both residual and new grains of K-feldspar and plagioclase exhibit low SPO, GBPO and LPO (Figs 8, 9 & 12), indicating absence of dislocation creep, in contrast to quartz, which exhibits relatively strong crystallographic preferred orientation (Fig. 11a). The topology of former melt is poorly constrained in both types III and IV migmatite but, the SPO of the minor phases interpreted to have crystallized from melt shows a bimodal distribution sub-perpendicular and sub-parallel to the S_2 foliation. These observations are neither compatible with high differential stress nor low differential stress experiments, in which the melt occurs primarily in triple point junctions without any SPO (Dell' Angelo *et al*., 1987; Gleason *et al*., 1999). However, in some natural samples, former melt pockets are preferentially located along grain boundaries parallel to the foliation (John & Stünitz, 1997; Sawyer, 1999; Rosenberg & Berger, 2001), indicating that the orientation of melt pocket in nature is not always in agreement with experimental studies (Rosenberg, 2001). In this study, the melt pocket orientation sub-parallel to the foliation may indicate low differential stress and high fluid/melt pressure as suggested by Cosgrove (1997).

We conclude that during evolution from type I banded orthogneiss to type IV nebulitic migmatite melt wetted a majority of grain contacts. The AMS study and quartz microfabrics in types II to IV migmatites suggest that the melt fraction did not exceed the critical amount to allow free relative movement of grains without interference, i.e. the melt fraction is below the critical threshold (e.g. RCMP of Arzi, 1978; RPT of Vigneresse *et al*., 1996). Rosenberg & Handy (2005) argued that melt fractions of only $\phi = 0.07$ (melt connectivity threshold, MCT) will enable the formation of interconnected networks of melt under dynamic conditions which will lead to a substantial strength drop. These authors suggested that weakening at the MCT probably involves localized, inter- and intragranular microcracking, as well as limited rigid body rotation of grains, without an important contribution of dislocation creep and diffusion processes at grain boundaries. However, we do not observe any strain localization associated with brittle failure and therefore it is suggested that the deformation has to be accommodated by mechanisms operating homogeneously across significant rocks volumes. Material science experiments (Mabuchi *et al*., 1997) show that weakening due to melt-enhanced grain boundary sliding at low melt fraction is an efficient mechanism allowing homogeneous deformation. We suggest that deformation of both feldspars and quartz in the type II to type IV migmatites occurred by melt-enhanced grain boundary sliding with a contribution to the overall deformation by dislocation creep. These characteristics are compatible with granular flow as described by Paterson (2001) accompanied by melt-enhanced diffusion and/or direct melt flow.

CONCLUSIONS

Based on a detail field and microstructural study, we distinguish four types of gneiss/migmatite in the Gföhl gneiss complex: (i) banded orthogneiss (type I), with distinct layers of recrystallized plagioclase, K-feldspar and quartz separated by layers of biotite; (ii) stromatic migmatite (type II), composed of plagioclase and K-feldspar aggregates with subordinate quartz and irregular quartz aggregates – the boundaries between individual aggregates are ill defined and rather diffuse; (iii) schlieren migmatite (type III), which consists of plagioclase–quartz- and K-feldspar–quartz-enriched domains with a foliation marked only by preferred orientation of biotite and sillimanite dispersed in the rock; and, (iv) nebulitic migmatite (type IV), with no relicts of gneissosity. It is demonstrated that this is a continuous sequence developed by melt-present deformation, in which the type I banded orthogneisses and type IV nebulitic migmatites are end-members.

The progressive disintegration of the banded microstructure and the development of nebulitic migmatite is characterized by several systematic textural changes. The grain size of all felsic phases continuously decrease whereas the population density of precipitated phases increases. The new phases preferentially nucleate along high-energy like–like boundaries, causing the development of a regular distribution of individual phases. Simultaneously, the modal proportions of felsic phases evolve towards a 'granite minimum' composition. Further, this evolutionary trend is accompanied by a decrease in grain SPO of all felsic phases. To explain these textural and compositional changes we introduce a model of melt infiltration from an external source in which melt is argued to pass pervasively along grain boundaries through the whole-rock volume. It is suggested that the individual migmatite types represent different degrees of equilibration between the host rock and migrating melt during the retrograde metamorphic evolution.

The inferred melt topology in type I orthogneiss exhibits elongated pockets of melt oriented at a high angle to the compositional banding, indicating that the melt distribution was controlled by deformation the solid framework. Here, the microstructure exhibits features compatible with a combination of dislocation

creep and grain boundary sliding deformation mechanisms. The types II–IV microstructures developed by granular flow accompanied by melt-enhanced diffusion and/or melt flow. However, the amount of melt present never exceeded a critical threshold during the deformation to allow free rotation of biotite grains.

The model of melt infiltration based on structural and microstructural observation is supported by thermodynamic (Hasalová *et al*., 2008a) and geochemical modelling (Hasalová *et al*., 2008b). Although our data seem to be consistent with such a model, there are still a number of issues to be resolved (e.g. time-scale of the process, the character of the melt and the grain-scale deformation mechanisms enabling pervasive flow of viscous melt). Nevertheless, our model has profound consequences for the petrogenesis of migmatites, the rheology of anatectic regions during syn-orogenic exhumation and melt transport in the crust.

ACKNOWLEDGEMENTS

This work was financially supported by the Grant Agency of the Czech Academy of Science (Grants No. IAA311140 and No. 205/04/2065) by an internal CNRS funding (CGS/EOST) and by the French National Agency (No. 06-1148784). Visits by P. Hasalová to ULP Strasbourg were funded by the French Government Foundation (BGF). We gratefully acknowledge A. Langrová from the Institute of Geology at the Czech Academy of Sciences for operating the microprobe. We also thank the reviewers C. Rosenberg, R. Weinberg and H. Stünitz for their constructive comments and suggestions for improving this paper, and the Journal editor M. Brown for his careful handling of the manuscript. R. Powell and M. Brown are thanked for helpful discussions.

REFERENCES

Adams, B. L., Wright, S. I. & Kunze, K., 1993. Orientation imaging: the emergence of a new microscopy. *Metallurgical Transactions A*, **24,** 819–831.

Arbaret, L., Fernandez, A., Ježek, J., Ildefonse, B., Launeau, P. & Diot, H., 2000. Analogue and numerical modeling of shape fabrics: application to strain and flow determination in magma. *Transactions of the Royal Society of Edinburgh: Earth Sciences*, **90,** 97–109.

Arzi, A. A., 1978. Critical phenomena in the rheology of partially melted rocks. *Tectonophysics*, **44,** 173–184.

Ashworth, J. R., 1976. Petrogenesis of migmatites in the Huntly-Portsoy area, north-east Scotland. *Mineralogical Magazine*, **40,** 661–682.

Ashworth, J. R., 1979. Comparative petrography of deformed and undeformed migmatites from the Grampian Highlands of Scotland. *Geological Magazine*, **116,** 445–456.

Ashworth, J. R. & McLellan, E. L., 1985. Textures. In: *Migmatites* (ed. Ashworth, J.R.), pp. 180–204, Blackie, Glasgow.

Azpiroz, M. D. & Fernández, C., 2003. Characterization of tectono-metamorphic events using crystal size distribution (CSD) diagrams. A case study from the Acebuches metabasites (SW Spain). *Journal of Structural Geology*, **25,** 935–947.

Bailey, E. H. & Stevens, R. H., 1960. Selecting straining of K-feldspar and plagioclase on rock lobes and thin sections. *American Mineralogist*, **45,** 1020–1025.

Baratoux, L., Schulmann, K., Ulrich, S. & Lexa, O., 2005. Contrasting microstructures and deformation mechanisms in metagabbro mylonites contemporaneously deformed under different temperatures (c. 650 °C and c. 750 °C). In: *Deformation Mechanisms, Rheology and Tectonics: From Minerals to Lithosphere*. (eds Gapais, D., Brun, J.P. & Cobbold, P.R.), *Geological Society Special Publications*, pp. 97–125, Geological Society of London, London, UK.

Barraud, J., Gardien, V., Allemand, P. & Grandjean, P., 2001. Analogue modelling of melt segregation and migration during deformation. *Physics and Chemistry of the Earth (A)*, **26,** 317–323.

Bascou, J., Barruol, G., Vauchez, A., Mainprice, D. & Egydio-Silva, M., 2001. EBSD-measured lattice-preferred orientations and seismic properties of eclogites. *Tectonophysics*, **342,** 61–80.

Berger, A. & Roselle, G., 2001. Crystallization processes in migmatites. *American Mineralogist*, **86,** 215–224.

Blumenfeld, P. & Bouchez, J.-L., 1988. Shear criteria and migmatite deformed in the magmatic and solid states. *Journal of Structural Geology*, **10,** 361–372.

Bouchez, J.-L., 1997. Granite is never isotropic: an introduction to AMS studies of granitic rocks. In: *Granite: From Segregation of Melt to Emplacement Fabrics* (eds Bouchez, J.-L., Hutton, D.H.W. & Stephens, W.E.), pp. 95–112. Kluwer, Dortrecht.

van Breemen, O., Aftalion, M., Bowes, D. R. *et al*., 1982. Geochronological studies of the Bohemian Massif, Czechoslovakia, and their significance in the evolution of Central Europe. *Transactions of the Royal Society of Edinburgh, Earth Sciences*, **73,** 89–108.

Brown, M., 1994. The generation, segregation, ascent and emplacement of granite magma: the migmatite-to-crustally-derived granite connection in thickened orogens. *Earth-Science Reviews*, **36,** 83–130.

Brown, M. & Rushmer, T., 2006. *Evolution and Differentiation of the Continental Crust*. Cambridge University Press, Cambridge, 553 pp.

Brown, M. & Solar, G. S., 1998a. Granite ascent and emplacement during contractional deformation in convergent orogens. *Journal of Structural Geology*, **20,** 1365–1393.

Brown, M. & Solar, G. S., 1998b. Shear zone systems and melts: feedback relations and self-organization in orogenic belts. *Journal of Structural Geology*, **20,** 211–227.

Brown, M., Averkin, Y., McLellan, E. L. & Sawyer, E. W., 1995. Melt segregation in migmatites. *Journal of Geophysical Research*, **100,** 15655–15679.

Brown, M. A., Brown, M., Carlson, W. D. & Denison, C., 1999. Topology of syntectonic melt-flow networks in the deep crust: inferences from three-dimensional images of leucosome geometry in migmatites. *American Mineralogist*, **84,** 1793–1818.

Büsch, W., Schneider, G. & Mehnert, K. R., 1974. Initial melting at grain boundaries. Part II. Melting in rocks of granodioritic, quartz dioritic and tonalitic composition. *Neues Jahrbuch Für Mineralogie Monatshefte*, **8,** 345–370.

Carlson, W. D., 1989. The significance of intergranular diffusion to the mechanism and kinetics of porphyroblast crystallization. *Contributions to Mineralogy and Petrology*, **103,** 1–24.

Cashman, K. V. & Ferry, J. M., 1988. Crystal size distribution (CSD) in rocks and the kinetics and dynamics of crystallization. 3. Metamorphic crystallization. *Contributions to Mineralogy and Petrology*, **99,** 401–415.

Cashman, K. V. & Marsh, B. D., 1988. Crystal size distribution (CSD) in rocks and the kinetics and dynamics of crystallization. 2. Makaopulu lava lake. *Contributions to Mineralogy and Petrology*, **99,** 292–305.

Chandrasekhar, S., 1961. *Hydrodynamic and Hydromagnetic Stability*. Oxford University Press, London.

Cmíral, M., Fitz Gerald, J. D., Faul, U. H. & Green, D. H., 1998. A close look at dihedral angles and melt geometry in olivine-basalt aggregates: a TEM study. *Contributions to Mineralogy and Petrology*, **130,** 336–345.

Collins, W. J. & Sawyer, E. W., 1996. Pervasive granitoid magma transfer through the lower-middle crust during non-coaxial compressional deformation. *Journal of Metamorphic Geology*, **14,** 565–579.

Connolly, J. A. D., Holness, M. B., Rubie, D. C. & Rushmer, T., 1997. Reaction-induced microcracking: an experimental investigation of a mechanism for enhancing anatectic melts extraction. *Geology*, **25,** 591–594.

Cosgrove, J. W., 1997. The influence of mechanical anisotropy on the behaviour of the lower crust. *Tectonophysics*, **280,** 1–14.

Daines, M. J. & Kohlstedt, D. L., 1997. Influence of deformation on melt topology in peridotites. *Journal of Geophysical Research*, **102,** 10257–10271.

Dallain, C., Schulmann, K. & Ledru, P., 1999. Textural evolution in the transition from subsolidus annealing to melting process, Velay Dome, French Massif Central. *Journal of Metamorphic Geology*, **17,** 61–74.

DeHoff, R. T., 1991. A geometrically general theory of diffusion controlled coarsening. *Acta Metallica and Materialia*, **39,** 2349–2360.

Dell' Angelo, L. N. & Tullis, J., 1988. Experimental deformation of partially melted granitic aggregates. *Journal of Metamorphic Geology*, **6,** 495–515.

Dell' Angelo, L. N., Tullis, J. & Yund, R. A., 1987. Transition from dislocation creep to melt-enhanced diffusion creep in fine-grained granitic aggregates. *Tectonophysics*, **139,** 325–332.

DeVore, G. W., 1959. Role of minimum interfacial free energy in determining the macroscopic features of minerals assemblages. *Journal of Geology*, **67,** 211–227.

Dougan, T. W., 1983. Textural relations in melanosomes of selected specimens of migmatitic pelitic schists: implications for leucosome-generating process. *Contributions to Mineralogy and Petrology*, **83,** 82–98.

Dudek, A., Matějovská, O. & Suk, M., 1974. Gföhl orthogneiss in the Moldanubicum of Bohemia and Moravia. *Krystalinikum*, **10,** 67–78.

Ferré, E. C., Teyssier, C., Jackson, M., Thill, J. W. & Rainey, E. S. G., 2003. Magnetic susceptibility anisotropy: a new petrofabric tool in migmatites. *Journal of Geophysical Research*, **108,** B2, doi: 10.1029/2002JB001790

Ferré, E. C., Martín-Hernández, F., Teyssier, C. & Jackson, M., 2004. Paramagnetic and ferromagnetic anisotropy of magnetic susceptibility in migmatites: measurements in high and low fields and kinematic implications. *Geophysical Journal International*, **157,** 1119–1129.

Flinn, D., 1969. Grain contacts in crystalline rocks. *Lithos*, **2,** 361–370.

Friedl, G., Finger, F., Paquette, J., Quadt, A., McNaughton, N. & Fletcher, I., 2004. Pre-Variscan geological events in the Austrian part of the Bohemian Massif deduced from U–Pb zircon ages. *International Journal of Earth Sciences*, **93,** 802–823.

Fyfe, W. S., 1973. The granulite facies, partial melting and the Archaean crust. *Royal Society of London Philosophical Transactions, Series, A*, **273,** 457–461.

Gardien, V., Thompson, A. B., Grujic, D. & Ulmer, P., 1995. Experimental melting of biotite + plagioclase + quartz + muscovite assemblage and implications for crustal melting. *Journal of Geophysical Research*, **100,** 15581–15591.

Garlick, S. R. & Gromet, L. P., 2004. Diffusion creep and partial melting in high temperature mylonitic gneisses, Hope Valley shear zone, New England Appalachians, USA. *Journal of Metamorphic Geology*, **22,** 45–62.

Gleason, G. C., Bruce, V. & Green, H. W., 1999. Experimental investigation of melt topology in partially molten quartzo-feldspathic aggregates under hydrostatic and non-hydrostatic stress. *Journal of Metamorphic Geology*, **17,** 705–722.

Greenfield, J. E., Clarke, G. L. & White, R. W., 1998. A sequence of partial melting reactions at Mt. Stafford, central Australia. *Journal of Metamorphic Geology*, **16,** 363–378.

Hasalová, P., Štípská, P., Powell, R., Schulmann, K., Janoušek, V. & Lexa, O., 2008a. Transforming mylonitic metagranite by open-system interactions during melt flow. *Journal of Metamorphic Geology*, doi: 10.1111/j.1525-1314.2007.00744.x

Hasalová, P., Janoušek, V., Schulmann, K., Štípská, P. & Erban, V., 2008b. From orthogneiss to migmatite: geochemical assessment of the melt infiltration model in the Gföhl Unit (Moldanubian Zone, Bohemian Massif). *Lithos*, doi: 10.1016/j.lithos.2007.07.021

Hickey, K. A. & Bell, T. H., 1996. Syn-deformational grain growth: matrix coarsening during foliation development and regional metamorphism rather than by static annealing. *European Journal of Mineralogy*, **8,** 1351–1373.

Higgins, M. D., 1998. Origin of anorthosite by textural coarsening: quantitative measurements of a natural sequence of textural development. *Journal of Petrology*, **39,** 1307–1323.

Holub, F. V., Cocherie, A. & Rossi, P., 1997. Radiometric dating of granitic rocks from the Central Bohemian Plutonic Complex (Czech Republic): constraints on the chronology of thermal and tectonic events along the Moldanubian–Barrandian boundary. *Earth and Planetary Sciences*, **325,** 19–26.

Hrouda, F., Jelínek, V. & Hrušková, L., 1990. A package of programs for statistical evaluation of magnetic anisotropy data using IBM-PC computers. *EOS, Transactions, American Geophysical Union*, **71,** 1289.

Hrouda, F., Melka, R. & Schulmann, K., 1994. Periodical changes in fabric intensity during simple shear deformation and its implications for magnetic susceptibility anisotropy of sedimentary and volcanic rocks. *Acta Universitatis Carolinae Geologica*, **38,** 37–56.

Jelínek, V., 1978. Statistical processing of anisotropy of magnetic susceptibility measured on groups of specimens. *Studia Geophysica et Geodaetica*, **22,** 50–62.

Jelínek, V., 1981. Characterization of magnetic fabric of rocks. *Tectonophysics*, **79,** 63–67.

Jin, Z., Green, H. W. & Zhou, Y., 1994. Melt topology in partially molten mantle peridotite during ductile deformation. *Nature*, **372,** 164–167.

John, B. E. & Stünitz, H., 1997. Evidence for magmatic fracturing and small-scale melt segregation during pluton emplacement. In: *Processes of Melt Segregation* (eds Bouchez, J.-L. & Clemens, J.), pp. 55–74, Kluwer Press, Amsterdam.

Jordan, P., 1988. The rheology of polymineralic rocks: an approach. *Geologische Rundschau*, **77,** 285–294.

Jurewicz, S. R. & Watson, E. B., 1984. Distribution of partial melt in a felsic system – the importance of surface energy. *Contributions to Mineralogy and Petrology*, **85,** 25–29.

Kim, C.-S. & Rohrer, G. S., 2004. Geometric and crystallographic characterization of WC surfaces and grain boundaries in WC–Co composites. *Interface Science*, **12,** 19–27.

Kretz, R., 1966. Grain-size distribution for certain metamorphic minerals in relation to nucleation and growth. *Journal of Geology*, **74,** 147–173.

Kretz, R., 1969. On the spatial distribution of crystals in rocks. *Lithos*, **2,** 39–66.

Kretz, R., 1994. *Metamorphic Crystallization*. Wiley, New York.

Kröner, A., Wendt, I., Liew, T. C. *et al*., 1988. U–Pb zircon and Sm–Nd model ages of high grade Moldanubian metasediments, Bohemian Massif, Czechoslovakia. *Contributions to Mineralogy and Petrology*, **99,** 257–266.

Kruse, R. & Stünitz, H., 1999. Deformation mechanisms and phase distribution in mafic high-temperature mylonites from the Jotun Nappe, southern Norway. *Tectonophysics*, **303,** 223–249.

Kruse, R., Stünitz, H. & Kunze, A., 2001. Dynamic recrystallization processes in plagioclase porphyroclasts. *Journal of Structural Geology*, **24,** 587–589.

Lafeber, D., 1963. On the spatial distribution of fabric elements in rock and soil fabric. *Proceedings of the 4th Australia-New Zealand Conference on Soil Mechanics and Foundation Engineering*, University of Adelaide, Adelaide, **11,** 185–199.

Laporte, D. & Watson, E. B., 1995. Experimental and theoretical constraints on melt distribution in crustal sources: the effect of crystalline anisotropy on melt interconnectivity. *Chemical Geology*, **124,** 161–184.

Laporte, D., Rapaille, C. & Provost, A., 1997. Wetting angle, equilibrium melt geometry, and the permeability threshold of partially molten crustal protoliths. In: *Granite: From Segregation of Melt to Emplacement Fabrics* (eds Bouchez, J.L., Hutton, D.H.W. & Stephens, W.E.), pp. 31–54. Kluwer, Dordrecht.

Le Breton, N. & Thompson, A. B., 1988. Fluid-absent (dehydration) melting of biotite in metapelites in the early stages of crustal anatexis. *Contributions to Mineralogy and Petrology*, **99,** 226–237.

Lexa, O., 2003. *Numerical approaches in structural and microstructural analyses*, Unpublished PhD Thesis. Charles University, Prague.

Lexa, O., Štípská, P., Schulmann, K., Baratoux, L. & Kröner, A., 2005. Contrasting textural record of two distinct metamorphic events of similar P–T conditions and different durations. *Journal of Metamorphic Geology*, **23,** 649–666.

Lifshitz, I. M. & Slyozov, V. V., 1961. The kinetics of precipitation from supersaturated solid solutions. *Journal of Physics and Chemistry of Solids*, **19,** 35–50.

Lister, J. R. & Kerr, R. C., 1991. Fluid-mechanical models of crack propagation and their application to magma-transport in dykes. *Journal of Geophysical Research*, **96,** 10049–10077.

Lucas, S. B. & St.Onge, M. R., 1995. Syn-tectonic magmatism and the development of compositional layering, Ungava Orogen (northern Quebec, Canada). *Journal of Structural Geology*, **17,** 475–491.

Mabuchi, M., Jeong, H. G., Hiraga, K. & Higashi, K., 1997. Partial melting at interfaces and grain boundaries for high-strain-rate superplastic materials. *Interface Science*, **4,** 357–368.

Marchildon, N. & Brown, M., 2001. Melt Segregation in late syn-tectonic anatectic migmatites: an example from the Onawa Contact Aureole, Maine, USA. *Physics and Chemistry of the Earth*, **26,** 225–229.

Marchildon, N. & Brown, M., 2002. Grain-scale melt distribution in two contact aureole rocks: implications for controls on melt localization and deformation. *Journal of Metamorphic Geology*, **20,** 381–396.

Marchildon, N. & Brown, M., 2003. Spatial distribution of melt-bearing structures in anatectic rocks from Southern Brittany, France: implications for melt transfer at grain-to orogen-scale. *Tectonophysics*, **364,** 215–235.

Marsh, B. D., 1988. Crystal size distribution (CSD) in rocks and the kinetics and dynamics of crystallization; 1, Theory. *Contributions to Mineralogy and Petrology*, **99,** 277–291.

Martín-Hernandéz, F. & Hirth, A. M., 2003. Paramagnetic anisotropy of magnetic susceptibility in biotite, muscovite and chlorite single crystals. *Tectonophysics*, **367,** 13–28.

Matějovská, O., 1974. *Petrographic Characteristic of Gneiss Series between Mohelno and Bitov, SW Moravia*. MS Geofond, Prague (in Czech).

Matte, P., Maluski, H., Rajlich, P. & Franke, W., 1990. Terrane boundaries in the Bohemian Massif: Result of large-scale Variscan shearing. *Tectonophysics*, **177,** 151–170.

McKenzie, D., 1984. The generation and compaction of partially molten rock. *Journal of Petrology*, **25,** 713–765.

McLellan, E. L., 1983. Contrasting textures in metamorphic and anatectic migmatites – an example from the Scottish Caledonides. *Journal of Metamorphic Geology*, **1,** 241–262.

Mehnert, K. R., 1971. *Migmatites and the Origin of Granitic Rocks*. Elsevier, Amsterdam.

Mehnert, K. R., Büsch, W. & Schneider, G., 1973. Initial melting at grain boundary of quartz and feldspar in gneisses and granulites. *Neues Jahrbuch Für Mineralogie Monatshefte*, **4,** 165–183.

Moazzen, M. & Modjarrad, M., 2005. Contact metamorphism and crystal size distribution studies in the Shivar aureole, NW Iran. *Geological Journal*, **40,** 499–517.

Olsen, T. S. & Kohlstedt, D. L., 1984. Analysis of dislocations in some naturally deformed plagioclase feldspars. *Physics of The Earth and Planetary Interiors*, **11,** 153–160.

Panozzo, R., 1983. The two-dimensional analysis of shape fabric using projections of lines in a plane. *Tectonophysics*, **95,** 279–295.

Paterson, M. S., 2001. A granular flow theory for the deformation of partially molten rock. *Tectonophysics*, **335,** 51–61.

Peterson, T. D., 1996. A refined technique for measuring crystal size distributions in thin section. *Contributions to Mineralogy and Petrology*, **124,** 395–405.

Petford, N., 1995. Segregation of tonalitic–trondhjemitic melts in the continental crust: the mantle connection. *Journal of Geophysical Research*, **100,** 15735–15743.

Powell, R., Holland, T. & Worley, B., 1998. Calculating phase diagrams involving solid solutions via non-linear equations, with examples using THERMOCALC. *Journal of Metamorphic Geology*, **16,** 577–588.

Racek, M., Štípská, P., Pitra, P., Schulmann, K. & Lexa, O., 2006. Metamorphic record of burial and exhumation of orogenic lower and middle crust: a new tectonothermal model for the Drosendorf window (Bohemian Massif, Austria). *Mineralogy and Petrology*, **86,** 221–251.

Ramberg, H., 1981. *Gravity, Deformation and the Earth's Crust in Theory, Experiments and Geological Applications*. Academic Press, London.

Randolph, A. D. & Larson, M. A., 1971. *Theory of Particle Processes*. Academic Press, New York.

Rosenberg, C., 2001. Deformation of partially molten granite: a review and comparison of experimental and natural case studies. *International Journal of Earth Sciences*, **90,** 60–76.

Rosenberg, C. & Berger, A., 2001. Syntectonic melt pathways in granitic gneisses, and melt-induced transitions in deformation mechanisms. *Physics and Chemistry of the Earth (A)*, **26,** 287–293.

Rosenberg, C. L. & Handy, M. R., 2000. Syntectonic melt pathways during simple shearing of a partially molten rock analogue (norcamphor-benzamide). *Journal of Geophysical Research*, **105,** 3135–3149.

Rosenberg, C. & Handy, M. R., 2001. Mechanisms and orientation of melt segregation paths during pure shearing of a partially molten rock analogue (norcamphor-benzamide). *Journal of Structural Geology*, **23,** 1917–1932.

Rosenberg, C. L. & Riller, U., 2000. Partial-melt topology in statically and dynamically recrystallized granite. *Geology*, **28,** 7–10.

Rosenberg, C. L. & Handy, M. R., 2005. Experimental deformation of partially melted granite revisited: implications for the continental crust. *Journal of Metamorphic Geology*, **23,** 19–28.

Sakai, T. & Jonas, J. J., 1984. Dynamic recrystallization: mechanical and microstructural consideration. *Acta Metallurgica*, **32,** 198–209.

Sawyer, E. W., 1994. Melt segregation in the continental crust. *Geology*, **22,** 1019–1022.

Sawyer, E. W., 1998. Formation and evolution of granite magmas during crustal reworking: the significance of diatexites. *Journal of Petrology*, **39,** 1147–1167.

Sawyer, E. W., 1999. Criteria for the recognition of partial melting. *Physics and Chemistry of the Earth*, **24,** 269–279.

Sawyer, E. W., 2001. Melt segregation in the continental crust: distribution and movement of melt in anatectic rocks. *Journal of Metamorphic Geology*, **19,** 291–309.

Schulmann, K., Melka, R., Lobkowicz, M., Ledru, P., Lardeaux, J. M. & Autran, A., 1994. Contrasting styles of deformation during progressive nappe stacking at the south-

eastern margin of the Bohemian Massif (Thaya Dome). *Journal of Structural Geology*, **16,** 355–370.
Schulmann, K., Kröner, A., Hegner, E. *et al.*, 2005. Chronological constraints on the pre-orogenic history, burial and exhumation of deep-seated rocks along the eastern margin of the Variscan orogen, Bohemian Massif, Czech Republic. *American Journal of Science*, **305,** 407–448.
Seng, H., 1936. Die Migmatitfrage und der Mechanismus parakristalliner Prägung. *Geologische Rundschau*, **27,** 471–492.
Spry, A. H., 1969. *Metamorphic Textures*. Pergamon Press, Oxford.
Štípská, P., Schulmann, K. & Kröner, A., 2004. Vertical extrusion and middle crustal spreading of omphacite granulite: a model of syn-convergent exhumation (Bohemian Massif, Czech Republic). *Journal of Metamorphic Geology*, **22,** 179–198.
Stünitz, H., 1998. Syndeformational recrystallization – dynamic or compositionally induced? *Contributions to Mineralogy and Petrology*, **131,** 219–236.
Tajčmanová, L., Konopásek, J. & Schulmann, K., 2006. Thermal evolution of the orogenic lower crust during exhumation within a thickened Moldanubian root of the Variscan belt of Central Europe. *Journal of Metamorphic Geology*, **24,** 119–134.
Tanner, D. C., 1999. The scale-invariant nature of migmatite from the Oberpfalz, NE Bavaria and its significance for melt transport. *Tectonophysics*, **302,** 297–305.
Turner, F. J. & Weiss, L., 1963. *Structural Analysis of Metamorphic Tectonites*. McGraw Hill, New York.
Twiss, R. J., 1977. Theory and applicability of a recrystallized grain size paleopiezometer. *Pure and Applied Geophysics*, **115,** 227–244.
Urban, M., 1992. Kinematics of the Variscan thrusting in the Eastern Moldanubicum (Bohemian Massif, Czechoslovakia): evidence from the Náměšť granulite massif. *Tectonophysics*, **201,** 371–391.
Vanderhaeghe, O., 1999. Pervasive melt migration from migmatites to leucogranite in the Shuswap metamorphic core complex, Canada: control of regional deformation. *Tectonophysics*, **312,** 35–55.
Vernon, R. H., 1974. Controls of mylonitic compositional layering during non-cataclastic ductile deformation. *Geological Magazine*, **111,** 121–123.
Vernon, R. H., 1976. *Metamorphic Processes: Reactions and Microstructure Development*. Wiley, New York.
Vernon, R. H. & Paterson, S. R., 2001. Axial-surface leucosomes in anatectic migmatites. *Tectonophysics*, **335,** 183–192.
Vielzeuf, D. & Holloway, J. R., 1988. Experimental determination of the fluid-absent melting relations in the pelitic system-consequences for crustal differentiation. *Contributions to Mineralogy and Petrology*, **98,** 257–276.
Vigneresse, J.-L., Barbey, P. & Cuney, M., 1996. Rheological transitions during partial melting and crystallization with application to felsic magma segregation and transfer. *Journal of Petrology*, **37,** 1579–1600.
Walte, N. P., Bons, P. D., Passchier, C. W. & Koehn, D., 2003. Disequilibrium melt distribution during static recrystallization. *Geology*, **31,** 1009–1012.
Walte, N. P., Bons, P. D. & Passchier, C. W., 2005. Deformation of melt-bearing systems – insight from *in situ* grain-scale analogue experiments. *Journal of Structural Geology*, **27,** 1666–1679.
Waters, D. J. & Lovegrove, D. P., 2002. Assessing the extent of disequilibrium and overstepping of prograde metamorphic reactions in metapelites from the Bushveld aureole. *Journal of Metamorphic Geology*, **20,** 135–149.
Weinberg, R. F. & Searle, M. P., 1998. The Pangong Injection Complex, Indian Karakoram: a case of pervasive granite flow through hot viscous crust. *Journal of Geological Society*, **155,** 883–891.
Wickham, S. M., 1987. The segregation and emplacement of granitic magmas. *Journal of the Geological Society of London*, **144,** 281–297.
Willaime, C. & Gandais, M., 1977. Electron microscope study of plastic defects in experimentally deformed alkali feldspars. *Bulletin de la Societe Francaise de Mineralogie et de Cristallographie*, **100,** 263–271.
Willaime, C., Christie, J. M. & Kovacs, M.-P., 1979. Experimental deformation of K-feldspar single crystals. *Bulletin de Mineralogie*, **102,** 168–177.
Zapletal, K., 1990. Low-field susceptibility anisotropy of some biotite crystals. *Physics of the Earth and Planetary Interiors*, **63,** 85–97.
Závada, P., Schulmann, K., Konopásek, J., Ulrich, S. & Lexa, O., 2007. Extreme ductility of feldspar aggregates – melt enhanced grain boundary sliding (GBS) and creep failure: rheological implications for felsic lower crust. *Journal of Geophysical Research*, doi: 10.1029/2006JB004820.2007

Received 14 February 2006; revision accepted 25 September 2007.

SUPPLEMENTARY MATERIAL

The following material is available online at http://www.blackwell-synergy.com:

Appendix S1 Digitalized thin sections (separated plagioclase and K-feldspar domains) that have been used for the quantitative analyses.

J. metamorphic Geol., 2008, **26,** 55–80 doi:10.1111/j.1525-1314.2007.00744.x

Transforming mylonitic metagranite by open-system interactions during melt flow

P. HASALOVÁ,[1,2] P. ŠTÍPSKÁ,[2] R. POWELL,[3] K. SCHULMANN,[2] V. JANOUŠEK[1,4] AND O. LEXA[1,2]
[1]*Institute of Petrology and Structural Geology, Charles University, Albertov 6, 128 43, Prague 2, Czech Republic (hasalovap@seznam.cz)*
[2]*Université Louis Pasteur, CGS/EOST, UMR 7517, 1 Rue Blessig, Strasbourg, France*
[3]*School Earth Sciences, University of Melbourne, Melbourne, Vic. 3010, Australia*
[4]*Czech Geological Survey, Klárov 3, 118 21, Prague 1, Czech Republic*

ABSTRACT Gneisses and migmatites of the Gföhl unit (Moldanubian Zone, Bohemian Massif) range from banded mylonitic orthogneiss with recrystallized monomineralic bands, through stromatic (metatexite) and schlieren (inhomogeneous diatexite) migmatite, to isotropic nebulite (homogeneous diatexite). This sequence was classically attributed to increasing degree of anatexis. Under the microscope, the evolution is characterized by progressive destruction of the monomineralic banding that characterizes the original mylonitic orthogneiss. Throughout, the mineral assemblage is biotite–K-feldspar–plagioclase–quartz ± garnet ± sillimanite, but the mineral compositions exhibit systematic changes with progressive disintegration of the layering. From banded orthogneiss to nebulite, the garnet composition changes systematically, $Alm_{75 \rightarrow 94}Prp_{17 \rightarrow 0.8}Grs_{2.5 \rightarrow 1.2}Sps_{2 \rightarrow 11}$ and $X_{Fe} = 0.45 \rightarrow 0.99$ and for biotite, $X_{Fe} = 0.80 \rightarrow 1$. This is consistent with a decrease in equilibration temperature and pressure of 790 °C and 8.5–6 kbar, to 690 °C and 5–4 kbar respectively. There is also a systematic change of whole-rock composition, marked by an increase in SiO_2 (71 → 77 wt%) and X_{Fe} (0.62 → 0.85) and by a decrease in Al_2O_3 (16 → 13 wt%) and CaO (1.50 → 0.43 wt%). Assuming that the rocks started with the same composition, these systematic changes indicate open-system behaviour. The predicted consequences of various open-system processes are assessed using thermodynamic modelling. The observed variations are interpreted as being a consequence of melt flow through, and interaction with the rocks, and, to change the rock composition sufficiently, a large volume of melt must have been involved.

Key words: diatexite; infiltration migmatite; melt transport; metasomatism by melt; metatexite; thermodynamic modelling.

INTRODUCTION

In the most frequently used descriptive classification scheme, migmatites form a continuum from stromatite to nebulite (e.g. Mehnert, 1971), or from metatexite to diatexite if interpretation of origin is taken into account (e.g. Brown, 1973). Stromatite and metatexite exhibit migmatitic banding that was produced by metamorphic differentiation, mainly associated with partial melting, while nebulite and diatexite do not show continuous migmatitic banding. The textural transition from stromatite to nebulite is commonly interpreted as being the result of increasing degree of partial melting, whereby the solid matrix loses its cohesion and becomes melt supported. When such a process is demonstrated or when such an interpretation is accepted, the textural varieties are referred to as metatexite and diatexite respectively (Sawyer, 1998; Milord *et al.*, 2001). Estimated melt contents in diatexites deduced from field studies vary between 20 and 40 mol.% (e.g. Sawyer, 1998; Milord *et al.*, 2001; White *et al.*, 2003), which is consistent with the experimentally determined 'solid to liquid' transition (Arzi, 1978; Wickham, 1987; Vigneresse *et al.*, 1996). In felsic rocks, such an amount of melt may only be attained at upper amphibolite facies conditions if melt or H_2O are introduced, or if the temperature reached granulite facies conditions (e.g. White *et al.*, 2005 and references therein). However, it has been shown that the destruction of pre-migmatite or migmatite banding may also occur at lower melt fractions (McLellan, 1983; Sawyer, 1994, 1996; Dallain *et al.*, 1999). These authors suggest that solid state annealing in conjunction with incipient anatexis can result in apparent 'granite-like' texture. Hence, apparently, several distinct processes may lead to the formation of nebulites and not all nebulites may be interpreted as diatexites.

When melt is present in a rock, the melt can move, and therefore such metamorphism may be a closed or an open-system process. In a generally accepted scheme, called here the *melt loss* model, the melt is thought to form or collect for example around

porphyroblasts, parallel to the foliation or in dilatant structures. With increasing melt production, a meso-scale interconnected network develops, capable of allowing the draining of melt (Marchildon & Brown, 2003). Given the commonly observed lack of re-hydration reactions on cooling (Powell & Downes, 1990; Brown, 2001; White & Powell, 2002), most migmatites have lost melt and such systems are considered as open with respect to melt loss.

The second open-system model considers *melt redistribution* involving the existence of rock volumes from which melt is lost and volumes into which melt is introduced (Marchildon & Brown, 2001; Milord *et al.*, 2001). The third open-system model may be called *transformation by melt* and relates to melt movement through rocks that causes chemical changes of the protolith (e.g. Mehnert, 1971, p. 285). This model was largely abandoned several decades ago for crustal rocks, although such a mechanism has been invoked in recent studies concerned with metasomatic processes in the mantle, being referred to as reactive porous melt flow (e.g. Nielson & Wilshire, 1993; Van der Wal & Bodinier, 1996; Kelemen *et al.*, 1997; Reiners, 1998).

The first model is the most generally accepted one, and arises from studies that have been carried out almost exclusively on metasedimentary rocks (Barbey *et al.*, 1996; Fitzsimons, 1996; Greenfield *et al.*, 1996, 1998; Milord *et al.*, 2001; Milord & Sawyer, 2003). However, granitic orthogneiss is another abundant crustal lithology capable of producing granitic melt, but with some exceptions (e.g. Sawyer & Barnes, 1988; Hand & Dirks, 1992; Sawyer, 1998; Dallain *et al.*, 1999), they have not been the focus of studies of anatexis and melt transport. Processes that operate at sub-solidus conditions on a prograde path in orthogneiss are dominated by textural modifications, involving various recrystallization mechanisms, rather than changes that affect the stable mineral assemblage. Recrystallization leads to the formation of augen and ribbons of recrystallized aggregates of plagioclase, K-feldspar, quartz and mica, and may result in monomineralic bands (Gapais, 1989; Schulmann *et al.*, 1996; Závada *et al.*, 2007). In studying the melting process, the lack of prograde changes in stable mineral assemblages in a granitic orthogneiss may be taken as an advantage because, in most cases, they begin to melt with mineralogy identical to their protolith, similar from one granitic orthogneiss to another, e.g. with quartz–plagioclase–K-feldspar ± biotite ± muscovite. The rock structure, commonly characterized by monomineralic recrystallized bands and augen of felsic minerals, starts to disintegrate progressively in the presence of melt (Dallain *et al.*, 1999). Such disintegration of K-feldspar, plagioclase and quartz bands cannot be studied in metasediments where such monomineralic banding of felsic minerals does not occur. It may also be expected that a deformed granitic orthogneiss starts to melt with whole-rock chemistry more or less unchanged from that of the protolith granite. Therefore, geochemical and mineralogical changes may be interpreted as resulting mainly from the melting process.

Textural variations between banded mylonite orthogneiss, stromatic and nebulitic migmatites are observed within the Gföhl orthogneiss complex in the Bohemian Massif, and have been considered as reflecting increasing degree of anatexis (Dudek *et al.*, 1974; Matějovská, 1974). However, Hasalová *et al.* (2008a) studied the Gföhl gneiss using microstructural analysis and interpreted the variations as originating from a single protolith by progressive disintegration of banded mylonite orthogneiss by interaction with infiltrating melt. In this model, melt passes through and interacts with a rock volume and changes its macroscopic and microscopic appearance. Consequently, the individual migmatite types represent different degrees of interaction with melt. Hasalová *et al.* (2008b) studied whole-rock major-element, trace-element and Sr–Nd isotopic data and concluded that the systematic variations reflect open-system behaviour during transformation from banded orthogneiss into nebulitic migmatite. However these approaches could not, for example, determine *P–T* conditions of equilibration and could not quantify the volume of melt involved.

In the first part of the current paper, the variations in mineral chemistry of the four rock types are used to determine the *P–T* conditions of equilibration of the Gföhl migmatites, based on mineral equilibria modelling. These *P–T* conditions are interpreted as reflecting an exhumation path along which equilibration of orthogneiss occurred while melt was still present, the equilibration becoming progressively localized between rock volumes that became melt-absent with decreasing temperature. In the second part, forward modelling is used to discuss possible open-system processes that may have operated in the rocks to assess the conclusion of Hasalová *et al.* (2008a) that melt infiltration must be the main process involved in the rock transformations. The mineral equilibria and rock chemistry consequences of melt infiltration are then considered in detail.

GEOLOGICAL SETTING AND PREVIOUS STUDIES

The area studied is situated at the eastern extremity of the Gföhl Unit (Moldanubian Zone, Bohemian Massif), one of the largest Variscan migmatite terranes in Europe (Fig. 1). This terrane is formed mainly of high-grade felsic gneisses and migmatites (the so-called Gföhl gneiss) showing a range of varieties from banded orthogneiss without macroscopic signs of melting through to isotropic nebulitic migmatite. The gneisses and migmatites include large bodies of high-pressure felsic granulite, eclogite and peridotite (for review, see Schulmann *et al.*, 2005; Fig. 1).

The structural succession in the area studied ~10 km north of Znojmo (Fig. 1) is defined by vertical S_1 structures that are locally preserved in low strain

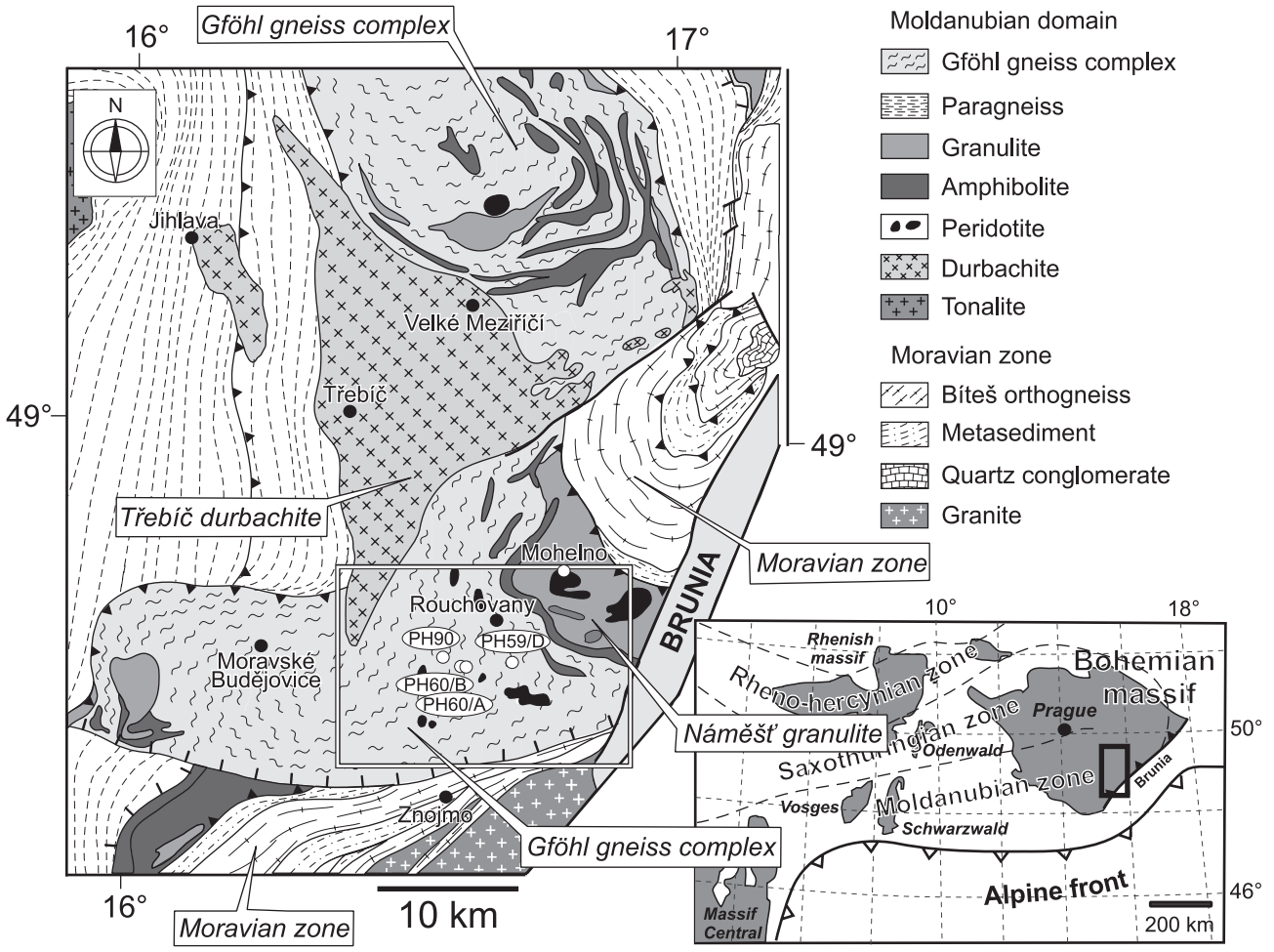

Fig. 1. Geological map of the eastern part of the Bohemian Massif (the area studied is outlined). Location of four characteristic samples used in this study is shown. The lower right inset displays the general location of the Bohemian Massif within the European Variscides.

domains of a flat S_2 foliation (Fig. 2) that is connected with the development of a large crustal-scale shear zone (Urban, 1992; Hasalová *et al*., 2008a). The transition from the S_1 to the S_2 fabric is marked by centimetre- to metre-scale open-to-isoclinal folds with NE–SW oriented axes and sub-horizontal axial planes. This structural evolution has been explained in terms of vertical extrusion of orogenic lower crust and its lateral spreading at mid-crustal levels (Štípská *et al*., 2004; Schulmann *et al*., 2005; Franěk *et al*., 2006; Racek *et al*., 2006). This exhumation was accompanied by a profound textural modification of rocks that is the focus of the present study. The conditions of retrogression in the proximity of the area studied were determined to be 770–720 °C and 4.5–4 kbar for the HP granulites (Tajčmanová *et al*., 2006). The metamorphism is dated at *c*. 340–323 Ma (van Breemen *et al*., 1982).

Hasalová *et al*. (2008a) established a continuous structural succession for the Gföhl orthogneiss (Fig. 2), in four 30-km-long NW–SE profiles across the Gföhl orthogneiss complex. The rocks in the succession have been classified in terms of the descriptive scheme of Mehnert (1971), as used by Matějovská (1974) in this area, as follows: banded orthogneiss (type I), stromatic migmatite (type II), schlieren migmatite (type III) and nebulitic migmatite (type IV).

The migmatite variations are identified both on outcrop and regional scales. The banded orthogneiss (type I) is relatively rare, the size of individual occurrences ranging from centimetre- to outcrop-scale relicts commonly surrounded by an anastomosing network of type II migmatites. The types II and III migmatites are the most common, having diffuse and gradational contacts between them. The nebulitic migmatite (type IV) is rare, forming irregular or elongated bodies, several centimetres to several metres across, with relatively sharp boundaries towards type III migmatite that surrounds them (Fig. 2).

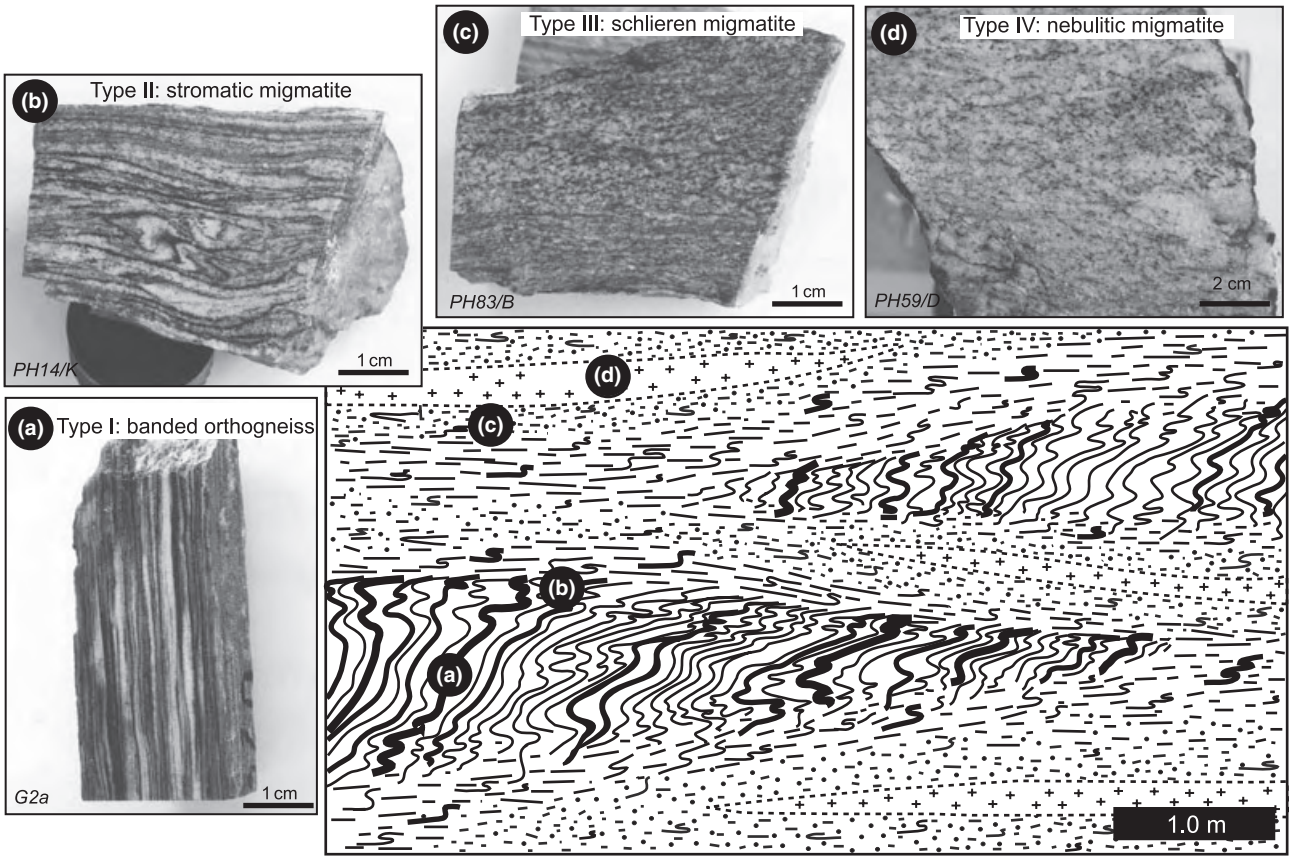

Fig. 2. Individual gneiss and migmatite types, and a sketch of the outcrop relationships (modified after Hasalová *et al.*, 2008a). (a) Banded orthogneiss with S_1 monomineralic layering, (b) stromatic migmatite in folded and transposed S_1 foliation by S_2 fabric, (c) schlieren migmatite surrounds stromatic migmatite in S_2 foliation, (d) macroscopically isotropic nebulitic migmatite forms elongated lenses that are inferred to be interconnected in the S_2 foliation.

The banded orthogneiss (type I) (Fig. 2a), characterized by the presence of monomineralic layers of plagioclase, K-feldspar, quartz and biotite, is folded and reworked by the D_2 deformation. This S_1 compositional banding is locally preserved in elongated relict domains (Fig. 2) that are surrounded by a tightly folded S_1 fabric. The S_1 fabric is commonly transposed into the new S_2 foliation and the resulting fabric is characterized by banded structure with polymineralic K-feldspar- and plagioclase-rich domains resembling stromatic migmatite (type II, Fig. 2b). The stromatic migmatite gradually passes into more isotropic rock resembling schlieren migmatite (type III, Fig. 2c) that still contains rootless folds modifying the relicts of the S_1 fabric. This rock type alternates with irregular bodies or elongated lenses of felsic nebulitic migmatite (type IV, Fig. 2d). The field observations suggest that the type I banded orthogneiss is progressively transformed into types II and III migmatites. Whether type IV is transformed from type III cannot be assessed from field observations, because of the lack of S_1 structures in type IV and the relatively sharp boundaries between type III and type IV.

PETROLOGY, MINERAL AND WHOLE-ROCK CHEMISTRY

Analytical procedures and abbreviations

Minerals were analysed using the scanning electron microscope CamScan S4 with attached Link ISIS 300 EDX microanalytical system at Charles University in Prague, Czech Republic, in point beam mode at 20 kV and 10 nA, and using the Cameca SX100 at the Geological Institute of the Czech Academy of Sciences in point beam mode at 15 kV and 10 nA. Representative mineral analyses are summarized in Tables 1–4. Whole-rock major-element analyses (Table 5) were carried out on the ICP-MS at the University Louis Pasteur in Strasbourg. The mineral abbreviations used are mu = muscovite, qtz = quartz, g = garnet, bi = biotite, ky = kyanite, sill = sillimanite, and = andalusite, pl = plagioclase, cd = cordierite, liq = liquid; ilm = ilmenite; ru = rutile; Alm = Fe/(Ca + Fe + Mg + Mn), Prp = Mg/(Ca + Fe + Mg + Mn), Grs = Ca/(Ca + Fe + Mg + Mn), Sps = Mn/(Ca + Fe + Mg + Mn), X_{Fe} = Fe/(Fe + Mg), An = Ca/(Ca + Na + K),

Table 1. Representative analyses of garnet and biotite.

	Banded orthogneiss (type I)		Stromatic migmatite (type II)		Schlieren migmatite (type III)		Nebulitic migmatite (type IV)	
Sample	G2A		PH60/A		PH90	G3c	PH59/D	
Mineral	g	bi	g	bi	g	bi	g	bi
wt% oxide								
SiO_2	37.75	35.98	36.92	36.14	36.03	35.00	36.68	36.18
TiO_2	0.00	3.85	0.00	3.96	0.00	2.99	0.00	0.17
Al_2O_3	21.50	17.97	21.20	18.66	20.43	19.52	21.15	22.38
FeO	34.57	17.78	35.77	19.96	36.88	24.49	40.14	27.14
MnO	1.13	0.00	2.64	0.00	4.97	0.00	1.89	0.00
MgO	4.26	11.03	2.63	8.01	0.67	4.20	0.41	1.34
CaO	1.12	0.00	0.72	0.12	0.58	0.24	0.41	0.00
Na_2O	0.00	0.00	0.00	0.00	0.04	0.00	0.00	0.00
K_2O	0.00	9.66	0.00	9.31	0.02	9.75	0.00	9.39
Total	100.33	96.28	99.88	96.17	99.62	96.18	100.68	96.61
Cations/charges	8/24	8/24	8/24	8/24	8/24	8/24	8/24	8/24
Si	3.00	2.78	2.99	2.84	2.98	2.81	3.00	2.91
Ti	0.00	0.22	0.00	0.23	0.00	0.18	0.00	0.01
Al	2.02	1.63	2.02	1.73	1.99	1.85	2.04	2.12
Fe^{3+}	0.00	0.00	0.00	0.00	0.07	0.00	0.00	0.00
Fe^{2+}	2.30	1.15	2.42	1.31	2.48	1.64	2.75	1.83
Mn	0.08	0.00	0.18	0.00	0.35	0.00	0.13	0.00
Mg	0.51	1.27	0.32	0.94	0.08	0.50	0.05	0.16
Ca	0.10	0.00	0.06	0.01	0.05	0.02	0.04	0.00
Na	0.00	0.00	0.00	0.00	0.01	0.00	0.00	0.00
K	0.00	0.95	0.00	0.93	0.00	1.00	0.00	0.96
Total	8.00	8.00	8.00	8.00	8.00	8.00	8.00	8.00
X_{Fe}	0.82	0.47	0.88	0.58	0.97	0.77	0.98	0.92
Alm	0.77		0.81		0.84		0.93	
Prp	0.17		0.11		0.03		0.02	
Grs	0.03		0.02		0.02		0.01	
Sps	0.03		0.06		0.11		0.04	

X_{Fe} = Fe/(Fe + Mg); Alm = Fe/(Fe + Mg + Ca + Mn); Prp = Mg/(Fe + Mg + Ca + Mn); Grs = Ca/Fe + Mg + Ca + Mn); Sps = Mn/(Fe + Mg + Ca + Mn).

Ab = Na/(Ca + Na + K), Or = K/(Ca + Na + K). The isopleths notations used are x(g) =Fe/(Fe + Mg), z(g) = Ca/(Ca + Fe + Mg + Mn), m(g) = Mn/(Ca + Fe + Mg + Mn), x(bi) = Fe/(Fe + Mg), ca(pl) = Ca/(Ca + Na).

Microstructures and mineralogy

The mineral assemblage in all rock types is biotite, K-feldspar, plagioclase and quartz; all the migmatite types commonly also contain garnet and sillimanite. Kyanite was not found in thin section, but was identified rarely in mineral concentrates. Apatite, monazite, zircon, xenotime, ilmenite and rutile are present as accessory phases.

Microstructure of felsic phases

The most obvious difference in microstructures between the individual migmatite types involves the different distribution of K-feldspar, plagioclase and quartz that ranges from monomineralic recrystallized bands to an isotropic distribution, and also involves a different amount and distribution of interstitial felsic phases.

The banded orthogneiss (type I) shows alternation of monomineralic bands of recrystallized K-feldspar, quartz and plagioclase separated by discrete bands rich in biotite, garnet and sillimanite (Figs 2a & 3a). Some feldspar boundaries in K-feldspar and plagioclase bands are coated by small interstitial plagioclase, quartz and K-feldspar grains (arrows in Figs 3a,b & 4a). The stromatic migmatite (type II) is composed of plagioclase-rich, K-feldspar-rich and quartz-rich aggregates (Fig. 3c). The limits between individual aggregates are ill defined and commonly traced only by biotite–sillimanite-rich layers. The interstitial quartz and feldspar grains coat the majority of feldspar boundaries (arrows in Fig. 3c,d). In the schlieren migmatite (type III), plagioclase–quartz-rich and K-feldspar–quartz-rich domains are present (Fig. 3e). Most of the large feldspar grains show cuspate boundaries that are completely coated by interstitial feldspar and quartz (arrows in Fig. 3f). The type IV (nebulitic migmatite) is isotropic, without banding, resembling the characteristic texture of diatexites (Figs 2d & 3g). The microstructure of this migmatite shows cuspate shapes of large feldspar and quartz grains and high proportion of interstitial grains along feldspar boundaries (Fig. 3g,h).

According to Sawyer (1999, 2001), interstitial grains as observed in the migmatites are interpreted as having crystallized from a granitic melt, and the cuspate shapes of feldspar as a result of its dissolution in the presence of melt. The progressively higher proportion of interstitial grains and more cuspate form of feldspar towards the types III and IV migmatites is interpreted according to Mehnert (1971) and Sawyer (1999) to result from an increasing degree of melt-rock interaction involving dissolution and precipitation. The microstructural evolution of the type I orthogneiss to type IV migmatites are interpreted as resulting from the progressive disintegration of monomineralic banding of a single mylonitic orthogneiss in the presence of melt.

Microstructural position of biotite, garnet and sillimanite

Whereas biotite is found in all thin sections, garnet and sillimanite are present in most of them. These minerals display different textural appearance and position in four rock types. In type I orthogneiss and type II migmatite, small idiomorphic garnet is typically arranged into aggregates or appears as individual grains that are commonly associated with biotite and sillimanite along or within the plagioclase bands (Fig. 4b, c). In types III and IV migmatites the garnet is atoll shaped and randomly distributed in the matrix; garnet also tends to be bigger and the proportion lower than in types I and II (Fig. 4d). Biotite defines the foliation in all the migmatite types. In rock types I and II biotite appears as large elongated flakes in layers separating felsic bands (Figs 2a & 4c) and in types III and IV migmatites it is dissipated in the matrix, commonly exhibiting highly corroded shapes (Fig. 4e). Sillimanite is in all the migmatite types associated with biotite, and also defines the foliation

Table 2. Representative analyses of plagioclase.

	Banded orthogneiss (type I)						Stromatic migmatite (type II)					
Sample	PH60/B		PH60/B		PH60/B		PH14/K	PH60/A	PH60/A		PH14/K	PH60/A
Position	pl core		pl rim		pl film		pl core		pl rim		pl film	
Wt% oxide												
SiO_2	61.70	61.24	66.12	66.49	67.48	66.39	63.41	66.94	63.21	64.65	64.57	67.24
Al_2O_3	24.12	24.18	20.99	20.81	20.16	21.20	22.54	20.58	23.81	22.78	22.61	20.27
CaO	5.29	5.88	3.05	1.88	2.83	3.25	3.94	0.80	3.72	2.55	2.78	1.07
Na_20	8.59	8.65	9.81	10.79	9.63	9.46	9.63	10.93	9.00	9.42	10.03	11.50
K_2O	0.43	0.17	0.10	0.17	0.12	0.08	0.19	0.14	0.51	0.83	0.17	0.10
Total	100.12	100.11	100.07	100.14	100.22	100.37	99.75	99.48	100.25	100.23	100.16	100.18
Cations/charges	5/16	5/16	5/16	5/16	5/16	5/16	5/16	5/16	5/16	5/16	5/16	5/16
Si	2.73	2.71	2.91	2.91	2.98	2.93	2.80	2.95	2.79	2.85	2.84	2.93
Al	1.26	1.26	1.09	1.07	1.05	1.10	1.17	1.07	1.24	1.18	1.17	1.04
Ca	0.25	0.28	0.14	0.09	0.13	0.15	0.19	0.04	0.18	0.12	0.13	0.05
Na	0.74	0.74	0.84	0.92	0.83	0.81	0.83	0.93	0.77	0.80	0.85	0.97
K	0.02	0.01	0.01	0.01	0.01	0.00	0.01	0.01	0.03	0.05	0.01	0.01
Total	5.00	5.00	5.00	5.00	5.00	5.00	5.00	5.00	5.00	5.00	5.00	5.00
End-members												
Ab	0.73	0.72	0.85	0.90	0.85	0.84	0.81	0.95	0.79	0.83	0.86	0.95
An	0.25	0.27	0.15	0.09	0.14	0.16	0.18	0.04	0.18	0.12	0.13	0.05
Or	0.02	0.01	0.01	0.01	0.01	0.00	0.01	0.01	0.03	0.05	0.01	0.01

	Schlieren migmatite (type III)						Nebulitic migmatite (type IV)					
Sample	PH90		PH90		PH90		PH59/D		PH59/D		PH59/D	
Position	pl core		pl rim		pl film		pl core		pl rim		pl film	
wt% oxide												
SiO_2	65.04	64.89	68.19	67.64	67.73	67.98	65.97	65.57	67.79	66.70	67.39	67.50
Al_2O_3	21.11	21.62	19.51	19.41	19.65	19.51	21.51	21.59	19.90	22.39	20.28	20.25
CaO	2.53	2.86	0.29	0.42	0.67	0.35	2.07	1.70	0.28	0.00	0.20	0.35
Na_2O	10.53	10.23	11.87	11.86	11.73	11.73	10.46	11.03	11.86	10.81	11.76	11.89
K_2O	0.15	0.20	0.15	0.10	0.09	0.17	0.14	0.30	0.02	0.22	0.11	0.05
Total	99.36	99.80	100.01	99.43	99.87	99.74	100.15	100.19	99.86	100.12	99.75	100.03
Cations/charges	5/16	5/16	5/16	5/16	5/16	5/16	5/16	5/16	5/16	5/16	5/16	5/16
Si	2.87	2.87	2.97	2.96	2.96	2.97	2.89	2.86	2.96	2.92	2.94	2.94
Al	1.10	1.10	1.00	1.00	1.01	1.01	1.11	1.11	1.02	1.15	1.04	1.04
Ca	0.12	0.11	0.01	0.02	0.03	0.02	0.10	0.08	0.01	0.00	0.01	0.02
Na	0.90	0.89	1.00	1.01	0.99	0.99	0.89	0.93	1.00	0.92	1.00	1.00
K	0.01	0.02	0.01	0.01	0.01	0.01	0.01	0.02	0.00	0.01	0.01	0.00
Total	5.00	5.00	5.00	5.00	5.00	5.00	5.00	5.00	5.00	5.00	5.00	5.00
End-members												
Ab	0.88	0.87	0.98	0.98	0.96	0.97	0.89	0.91	0.99	0.99	0.98	0.98
An	0.12	0.11	0.01	0.02	0.03	0.02	0.10	0.08	0.01	0.00	0.01	0.02
Or	0.01	0.02	0.01	0.01	0.00	0.01	0.01	0.02	0.00	0.01	0.01	0.00

An = Ca/(Ca + Na + K); Ab = Na/(Ca + Na + K); Or = K/(Ca + Na + K).

(Fig. 4c), although in types III and IV migmatites it also may occur in aggregates and nodules that are up to 5 cm in size (Fig. 4f).

Mineral chemistry

Garnet

Garnet in all rock types is rich in almandine with minor pyrope, spessartine and grossular and does not exhibit compositional zoning. In type I orthogneiss it has the lowest X_{Fe} of rock types ($Alm_{73–81}Prp_{15–21}$ $Sps_{2–3}Grs_{2–3.5}$, $X_{Fe} = 0.77–0.85$; Figs 5 & 6a). Garnet in type II migmatite has higher almandine and spessartine and lower pyrope contents ($Alm_{78–84}$ $Prp_{8–15}$ $Sps_{4–7}Grs_{2–2.5}$, $X_{Fe} = 0.84–0.91$). In types III and IV migmatites the garnet composition is $Alm_{84–86}Prp_{2–3}$ $Sps_{9–13}Grs_{1.7–2}$, $X_{Fe} = 0.96–0.97$ and $Alm_{91–94}Prp_{0–2}$ $Sps_{4–15}Grs_{1.2–2}$, $X_{Fe} = 0.99–1.0$. Consequently, garnet displays systematic changes that involve progressive increase in almandine (73 → 91 mol.%) and spessartine (2 → 13 mol.%), and increase in X_{Fe} (0.77 → 1.0 mol.%) that are accompanied by a decrease in pyrope (15 → 0 mol.%) and grossular (3.5 → 1.2 mol.%) (Figs 5 & 6a, Tables 1 & 4).

Biotite

Within each type, biotite does not display significant chemical variation. In the type I orthogneiss biotite has $X_{Fe} = 0.45$, Ti = 0.18–0.27 p.f.u. and $Al^{VI} = 0.36–0.80$ p.f.u. Towards type IV migmatite X_{Fe} and Al^{VI} exhibit systematically higher values ($X_{Fe} = 0.57$, $Al^{VI} = 0.44–0.53$ p.f.u. in type II; $X_{Fe} = 0.78$, $Al^{VI} = 0.60–0.76$ p.f.u. in type III and $X_{Fe} = 0.92$, $Al^{VI} = 0.85–1.05$ p.f.u. in type IV), while the amount of Ti

Table 3. Representative analyses of K-feldspar.

	Banded orthogneiss (type I)		Stromatic migmatite (type II)		Schlieren migmatite (type III)		Nebulitic migmatite (type IV)	
Sample	PH60/B	PH60/B	PH14/K	PH14/K	PH90	PH90	PH59/C	PH59/C
wt% oxide								
SiO_2	64.69	64.36	64.37	64.50	64.51	64.89	63.97	64.19
Al_2O_3	18.41	18.26	18.55	18.70	18.38	18.38	18.98	18.79
FeO	0.00	0.00	0.10	0.09	0.10	0.09	0.00	0.00
CaO	0.05	0.06	0.04	0.05	0.01	0.05	0.05	0.01
Na_20	2.24	1.35	1.56	2.15	1.41	1.55	1.22	1.41
K_20	13.96	15.37	15.04	14.16	15.18	15.11	15.65	15.22
BaO	0.39	0.40	0.13	0.10	0.08	0.07	0.00	0.02
Total	99.73	99.79	99.78	99.74	99.67	100.15	99.86	99.62
Cations/charges	5/16	5/16	5/16	5/16	5/16	5/16	5/16	5/16
Si	2.97	2.97	2.97	2.96	2.98	2.98	2.94	2.96
Al	0.99	1.00	1.01	1.01	1.00	0.99	1.03	1.02
Ca	0.00	0.00	0.00	0.00	0.00	0.00	0.00	0.00
Na	0.12	0.20	0.14	0.19	0.13	0.14	0.11	0.13
K	0.90	0.82	0.88	0.83	0.89	0.88	0.92	0.89
Ba	0.01	0.01	0.00	0.00	0.00	0.00	0.00	0.00
Total	5.00	5.00	5.00	5.00	5.00	5.00	5.00	5.00
End-members								
Ab	0.12	0.19	0.14	0.19	0.12	0.13	0.10	0.12
An	0.00	0.00	0.00	0.00	0.00	0.00	0.00	0.00
Or	0.88	0.80	0.86	0.81	0.88	0.86	0.89	0.88

An = Ca/(Ca + Na + K); Ab = Na/(Ca + Na + K); Or = K/(Ca + Na + K).

Table 4. Summary of important changes in mineral chemistry throughout the studied sequence.

	Banded orthogneiss (type I)	Stromatic migmatite (type II)	Schlieren migmatite (type III)	Nebulitic migmatite (type IV)
Garnet				
X_{Fe}	0.77–0.85 (0.81)	0.84–0.91 (0.87)	0.96–0.97 (0.97)	0.98–1.00 (0.99)
Alm	0.73–0.81 (0.77)	0.78–0.84 (0.81)	0.84–0.86 (0.85)	0.91–0.94 (0.93)
Prp	0.15–0.21 (0.18)	0.08–0.15 (0.12)	0.02–0.03 (0.03)	0.00–0.02 (0.01)
Sps	0.02–0.03 (0.02)	0.04–0.07 (0.05)	0.09–0.13 (0.11)	0.04–0.07 (0.05)
Grs	0.02–0.03 (0.02)	0.02–0.03 (0.02)	0.01–0.02 (0.02)	0.01–0.02 (0.02)
Biotite				
X_{Fe}	0.42–0.48 (0.45)	0.55–0.59 (0.57)	0.77–0.79 (0.78)	0.91–0.94 (0.92)
Ti (p.f.u.)	0.18–0.27 (0.22)	0.20–0.28 (0.23)	0.16–0.20 (0.19)	0.01–0.04 (0.02)
Al^{IV} (p.f.u.)	1.06–1.33 (1.25)	1.18–1.30 (1.23)	1.18–1.20 (1.20)	1.08–1.16 (1.10)
Al^{VI} (p.f.u.)	0.36–0.80 (0.42)	0.44–0.53 (0.50)	0.60–0.76 (0.68)	0.85–1.05 (1.00)
Plagioclase				
An (pl core)	0.19–0.28 (0.25)	0.11–0.26 (0.19)	0.11–0.17 (0.14)	0.05–0.10 (0.08)
An (pl rim)	0.05–0.22 (0.14)	0.01–0.18 (0.06)	0.00–0.13 (0.05)	0.00–0.10 (0.03)
K-feldspar				
Ba (p.f.u.)	0.06–0.20 (0.13)	0.02–0.08 (0.04)	0.00–0.05 (0.02)	0.00–0.02 (0.00)
Or	0.79–0.90 (0.85)	0.81–0.94 (0.88)	0.79–0.93 (0.88)	0.86–0.95 (0.89)

X_{Fe} = Fe/(Fe + Mg); An = Ca/(Ca + Na + K); Or = K/(Ca + Na + K). Shown are the ranges and average values (in brackets).

decreases (Ti = 0.20–0.28 p.f.u. in type II; Ti = 0.16–0.20 p.f.u. in type III; Ti = 0.01–0.04 p.f.u. in type IV) (Fig. 6b, Tables 1 & 4).

K-feldspar

K-feldspar composition does not vary significantly, except for barium and higher albite contents in cores of large highly cuspate K-feldspar grains that commonly show preferentially oriented exsolved albite. In both the K-feldspar and plagioclase aggregates the composition is $Or_{79-95}Ab_{5-8}An_{0-1}$ (Tables 3 & 4). Barium shows progressively lower contents from type I orthogneiss to type IV migmatite (Ba = 0.06–0.20 p.f.u. for type I; 0.02–0.08 for type II: 0.00–0.05 for type III and 0.00–0.02 for type IV).

Plagioclase

Plagioclase composition within each of the individual rock types varies according to the microstructural position (Fig. 7 & Table 2), with less sodic plagioclase (An_{15-30}) forming the matrix and small interstitial grains or films and rims of larger grains being more albitic (An_{0-15}). Interstitial grains or thin films trace K-feldspar boundaries in the K-feldspar aggregates, whereas albitic rims occur on more calcic plagioclase grains in plagioclase aggregates (Fig. 7).

The most anorthite-rich plagioclase occurs in the plagioclase domains in the type I orthogneiss. It exhibits homogeneous oligoclase cores (An_{19-28}) and more sodic (An_{5-22}), clear 2- to 10-μm-thick rims at the boundaries with K-feldspar (Fig. 7). Simultaneously with progressively thicker albite rims on plagioclase grains from type I orthogneiss to type IV migmatite, both the plagioclase grains and their rims become more sodic (the variation in compositions from core to rim is: type II – $An_{11-26} \rightarrow An_{1-18}$; type III – $An_{11-17} \rightarrow An_{0-13}$; type IV – $An_{5-10} \rightarrow An_{0-5}$) (Tables 2 & 4). The orthoclase component of plagioclase remains nearly constant at 1–2 mol.% (Table 2).

Small interstitial plagioclase grains and films in the K-feldspar aggregates (Figs 3a & 7) are generally more sodic than the grains in the plagioclase aggregates. The anorthite content of this interstitial plagioclase decreases in a fashion similar to the trend in the plagioclase aggregates, but with lower anorthite contents (type I – $An_{12-17}Ab_{75-91}Or_{0-1}$; type II – $An_{4-8}Ab_{91-95}Or_{0-1}$; type III – $An_{2-5}Ab_{95-99}Or_{0-1}$; type IV – $An_{0-3}Ab_{98-100}Or_{0-1}$) (Fig. 7).

Whole-rock chemistry

Representative whole-rock chemical analyses are given for the four rock types in Table 5. The whole suite is slightly peraluminous (A/CNK = 1.1–1.2) and broadly granitic in composition (SiO_2 = 68–78 wt%). There is a tendency to smooth, systematic changes in many geochemical parameters from type I orthogneiss to type IV migmatite. After an initial dramatic drop (from type I to type III), the concentrations of most of the major-element oxides (Al_2O_3, TiO_2, FeO_t, MgO and CaO) level off at SiO_2 of 73–74 wt% and do not change significantly thereafter (type IV migmatite). Alkalis (Na_2O and K_2O) and P_2O_5 are rather scattered or show a feeble tendency to increase from the type I orthogneiss to the type IV migmatite. The X_{Fe} increases towards the nebulitic migmatite (Table 5). Additional detailed information on the whole-rock geochemistry is given in Hasalová *et al.* (2008b).

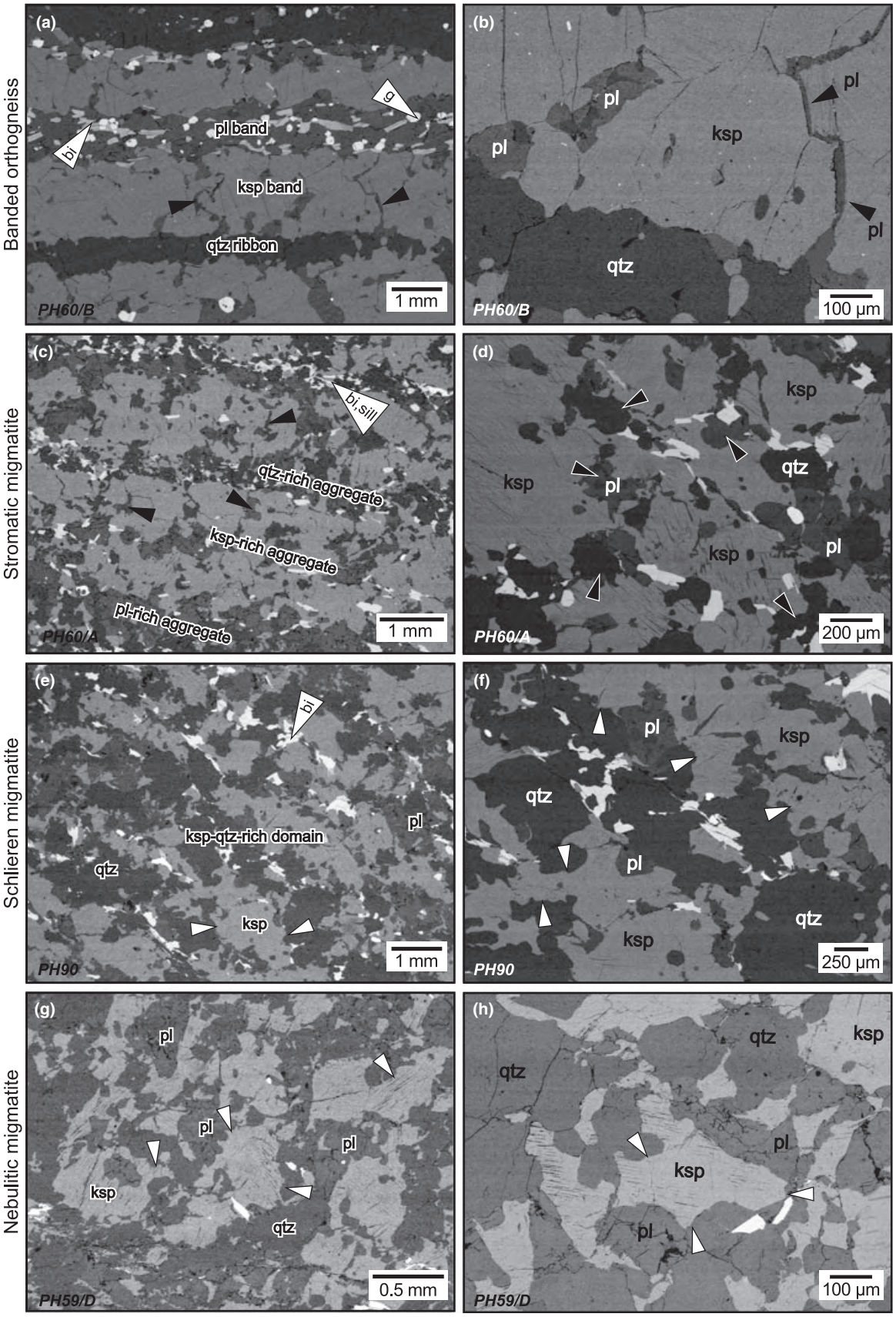

The whole-rock compositions and mineral chemistries are related for higher variance mineral assemblages, whereas the mineral compositions reflect *P–T* conditions in lower variance mineral assemblages. The rock and mineral compositions are plotted in the Al_2O_3–FeO–MgO compositional diagram where tie triangles of sillimanite–biotite–garnet plot at progressively higher X_{Fe} values from type I orthogneiss to type IV migmatite, corresponding to the rock compositional changes (Fig. 8). However, the assemblage garnet–sillimanite–biotite–K-feldspar–quartz–plagioclase–ilmenite–rutile–melt is trivariant in the NCKFMASHTO system and quadrivariant in the more complete MnNCKFMASHTO system. Therefore, the observed changes in X_{Fe} of the minerals in the four rock types are most likely to reflect also changes in *P–T* conditions (as established in the pseudosection modelling below).

The progressive shift of rock compositions to higher X_{Fe} values could be explained by originally different protoliths. However, as progressive evolution from type I orthogneiss to type IV migmatite is suggested in the field, the rocks are considered to have originally the same protolith and variations of the whole-rock chemistry are ascribed to open-system processes during metamorphism.

PSEUDOSECTION MODELLING

The aim of this section was to assess the ability of various closed- and open-system processes to account for the observed mineral and whole-rock chemistry variations and to estimate the amount of melt involved and/or produced. To achieve this, the *P–T* conditions of equilibration for each migmatite type are estimated. Then the likely rock composition and mineral assemblage of the granite protolith is estimated to allow the forward modelling of the processes.

Calculation methods

The calculations were performed using THERMOCALC 3.25 (Powell *et al.*, 1998, 2005 upgrade) and the internally consistent thermodynamic data set 5.5 (Holland & Powell, 1998; November 2003 upgrade). The pseudosections for the four rock types were calculated in the system MnO–Na_2O–CaO–K_2O–FeO–MgO–Al_2O_3–SiO_2–H_2O–TiO_2–O (MnNCKFMASHTO). The rock compositions were used with the molar amounts of these oxides normalized to 100% (Table 5). The amount of H_2O to include in the rock compositions was chosen after construction of *T–M*(H_2O) sections, to explain the observed mineral assemblage and chemistry of the minerals.

In the absence of activity–composition models for all minerals in the MnNCKFMASHTO system, for some minerals a choice had to be made between activity–composition models that involve Mn and models that involve Fe^{3+} and Ti. Garnet stability at low temperatures depends largely on Mn; therefore, the Mn-bearing activity–composition model (THERMOCALC documentation, Powell & Holland, 2004) was preferred to the Fe^{3+}-bearing model (White *et al.*, 2007) as the solubility of Fe^{3+} in garnet is small. A consequence of garnet being the only Mn-bearing mineral is that it is stable in the whole range of modelled *P–T* conditions, but this is likely to be realistic in the range of *P–T* conditions of interest. For biotite, the activity–composition model that includes Ti–Fe^{3+} substitution (White *et al.*, 2007) was chosen for calculations rather than a Mn-bearing activity–composition model, as Mn incorporation in biotite is minor but Ti and Fe^{3+} influence considerably the stability of biotite. The activity–composition relationship for ilmenite is from White *et al.* (2000), for melt is from White *et al.* (2007), for the feldspar is from Holland & Powell (2003) and for paragonite–muscovite is from Coggon & Holland (2002).

Modelling of the likely protolith composition and modelling of closed-system melting was also performed in the MnNCKFMASHTO system. Modelling of the open-system processes involving melt loss, melt gain and simulation of the equilibration of the rock with infiltrating melt was performed in the NCKFMASH system, because the available activity–composition model for melt does not include Ti, Fe^{3+} and Mn. The activity–composition relationships used are as follows: for melt, from White *et al.* (2007); for feldspar, from Holland & Powell (2003); for paragonite–muscovite, from Coggon & Holland (2002); and, for other NCKFMASH phases, from White *et al.* (2001).

P–T conditions of last equilibration

In determining the conditions of last equilibration, it is assumed that the assemblage tends to continuously equilibrate until it becomes fluid or melt absent (Guiraud *et al.*, 2001; Powell *et al.*, 2005; Štípská & Powell, 2005). For migmatites, this is likely to correspond to the *P–T* conditions on the retrograde path where the rock becomes melt poor, or possibly when it crosses the solidus. As the position of the solidus in a *P–T*

Fig. 3. Textural features of the types I–IV (SEM backscatter images). (a,b) Type I: alternation of monomineralic bands of recrystallized K-feldspar, quartz and plagioclase separated by discrete bands rich in biotite, garnet and sillimanite. Some K-feldspar grains are traced by interstitial plagioclase and quartz (black arrows). (c,d) Type II: plagioclase-rich, K-feldspar-rich and quartz-rich aggregates. Interstitial feldspar and quartz coat most of the feldspar boundaries (black arrows). (e,f) Type III: alternation of plagioclase–K-feldspar-rich and K-feldspar–quartz-rich domains. Large irregular K-feldspar grains with highly lobate boundaries (white arrows) are embayed in plagioclase, K-feldspar and quartz. (g,h) Type IV: isotropic structure with large feldspar with highly lobate shapes (white arrows), note the different scale.

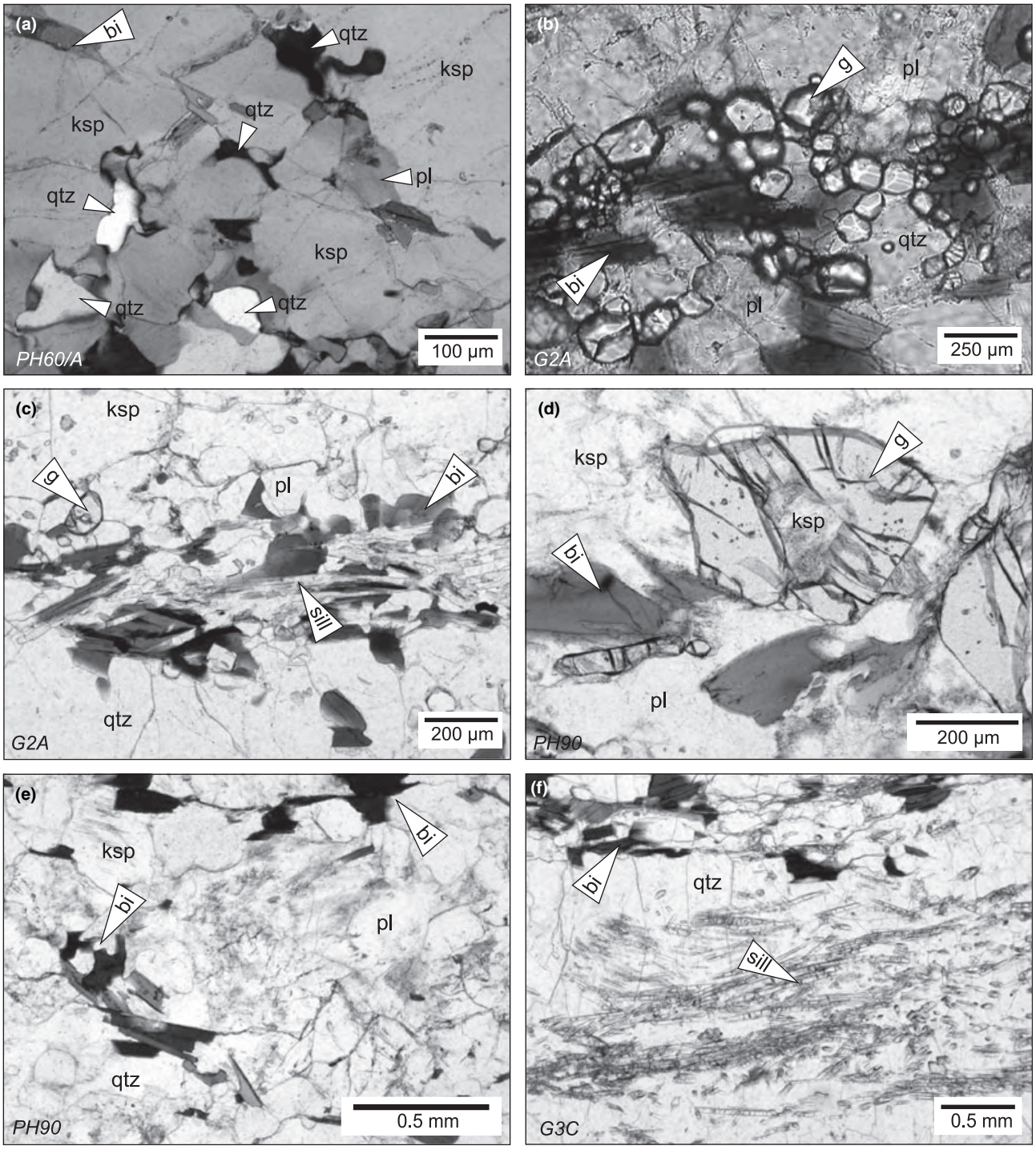

Fig. 4. Photomicrographs showing typical textures and mineral assemblages. (a) K-feldspar with highly cuspate interstitial plagioclase and quartz (example from type II). (b) Small idiomorphic garnet associated with biotite along the boundary of plagioclase band (in types I & II). (c) Biotite is locally associated with fibrolitic sillimanite (type I). (d) Large atoll-shaped garnet with biotite in felsic matrix (in types III & IV). (e) K-feldspar–quartz-rich domain with random distribution of biotite. Biotite preferred orientation emphasizes the foliation (type III). (f) Large sillimanite nodules parallel to the foliation (in types III and IV).

pseudosection depends largely on the amount of H_2O present in the rock, the amount of H_2O that should be used in the calculation of a P–T pseudosection must be evaluated using a T–$M(H_2O)$ pseudosection.

The T–$M(H_2O)$ calculations are shown only for the type I orthogneiss (Fig. 9). The observed assemblage is g–sill–bi–pl–ksp–qtz–ru–ilm, with garnet $X_{Fe} = 0.70$–0.84, biotite $X_{Fe} = 0.42$–0.58 and spessartine in garnet

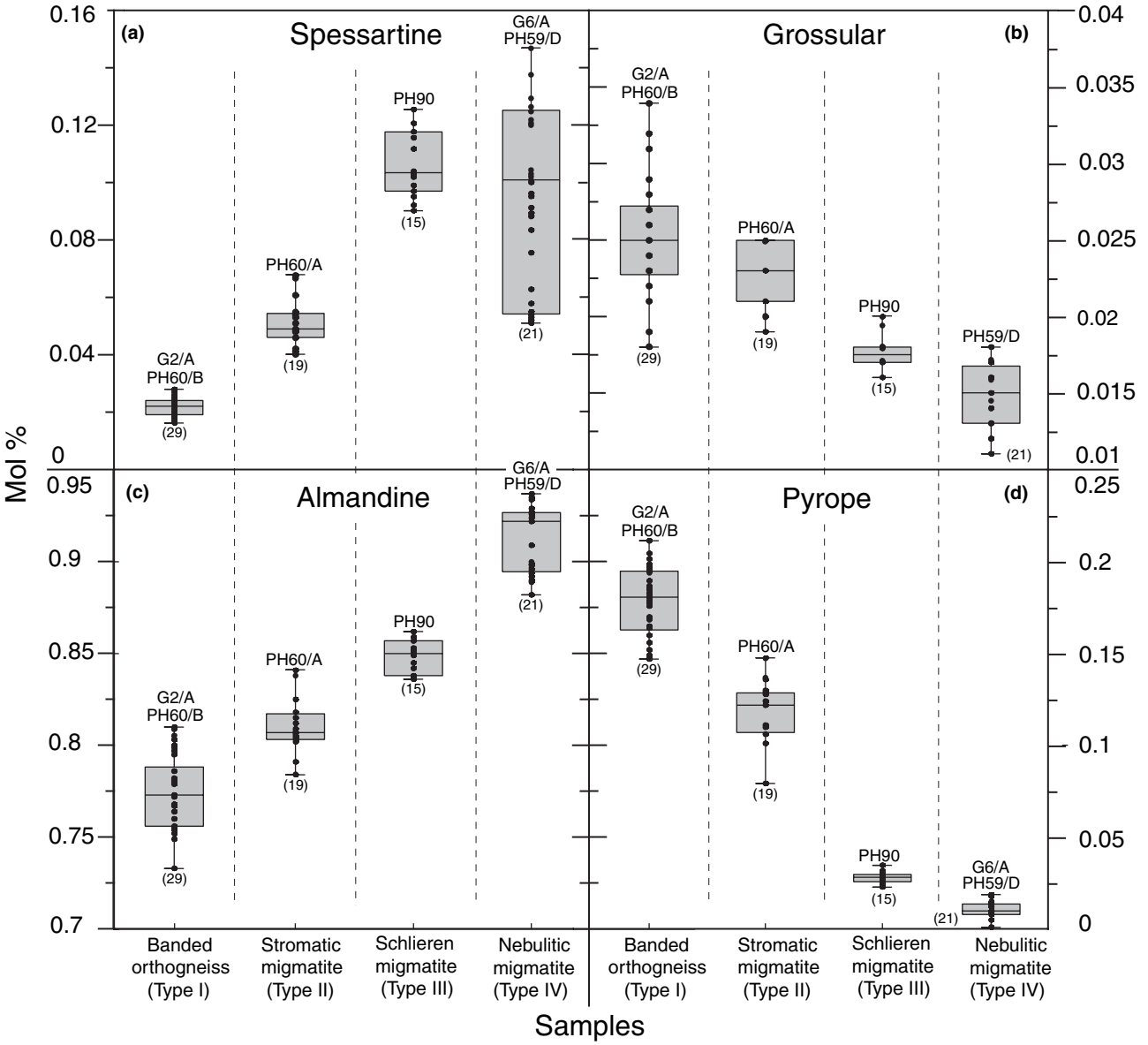

Fig. 5. Garnet composition trends of (a) spessartine, (b) grossular, (c) almandine, (d) pyrope. The data are summarized in box-plots of individual component content (mol.%) *v.* rock type. Individual boxes show median and first and third quartile of the component content. The whiskers represent a statistical estimate of the data range, where outliers are not plotted. The number of analyses is marked.

of 1–4 mol.%; therefore, a section at 7 kbar in the stability field of sillimanite was chosen for modelling.

The major features of the diagram involve the assemblage g–sill–bi–liq–pl–ksp–qtz–ru–ilm at high temperatures and high $M(H_2O)$, the liquid-out line that appears at low $M(H_2O)$ at high temperature and the muscovite-in line at ~715 °C for $M(H_2O)$ higher than ~1.54 mol.%. From the point of view of a cooling path for a hypothetical rock at high $M(H_2O)$ (arrow A, Fig. 9), there is a molar increase in biotite coupled with molar decrease in garnet, muscovite becomes stable just before sillimanite-out is crossed at 715 °C. Such a rock would have a preserved assemblage of g–bi–liq–mu–pl–ksp–qtz–ru. This does not correspond to the observed mineral assemblage. For a rock at intermediate $M(H_2O)$ (black arrow B, Fig. 9), the molar proportions of garnet and melt decrease in favour of biotite until the liquid-out line is reached and muscovite appears. Such a rock would have a preserved assemblage g–sill–bi–mu–pl–ksp–qtz–ru–ilm (along the grey arrow B, Fig. 9) that, again, does not correspond to the observed assemblage.

For a rock at low $M(H_2O)$ (black arrow C, Fig. 9), the molar proportions of garnet and melt decrease in

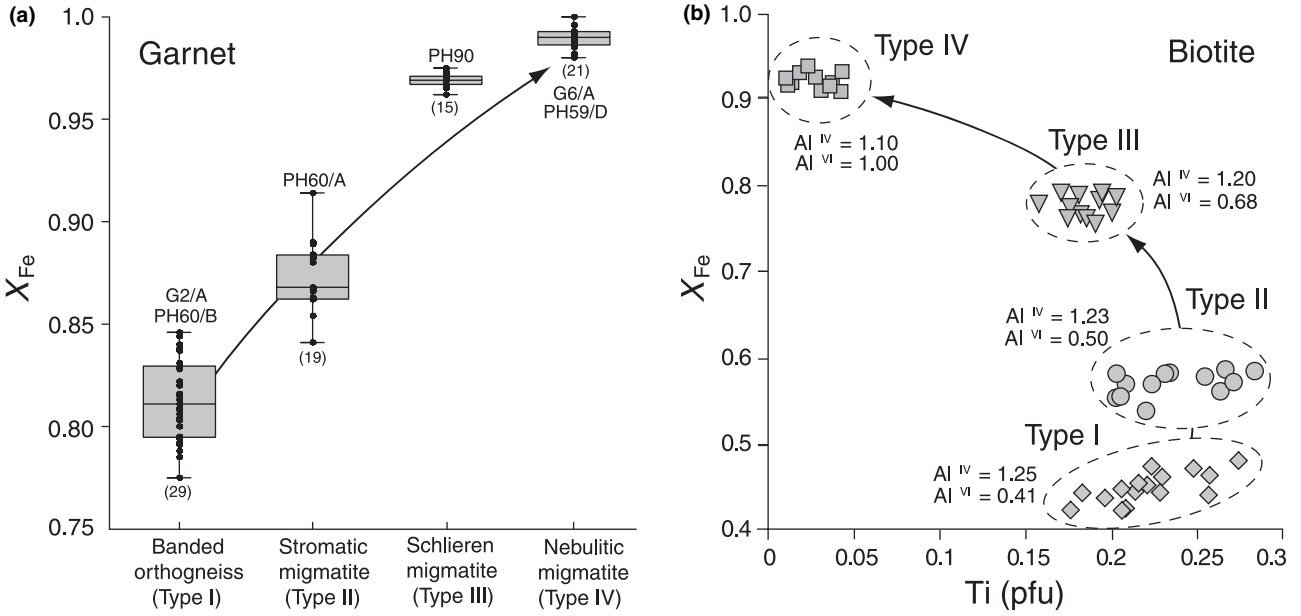

Fig. 6. (a) Garnet X_{Fe} plotted in a form of box-plot diagram (X_{Fe} *v.* rock type). For details see caption of Fig. 4. (b) Compositional changes of biotite.

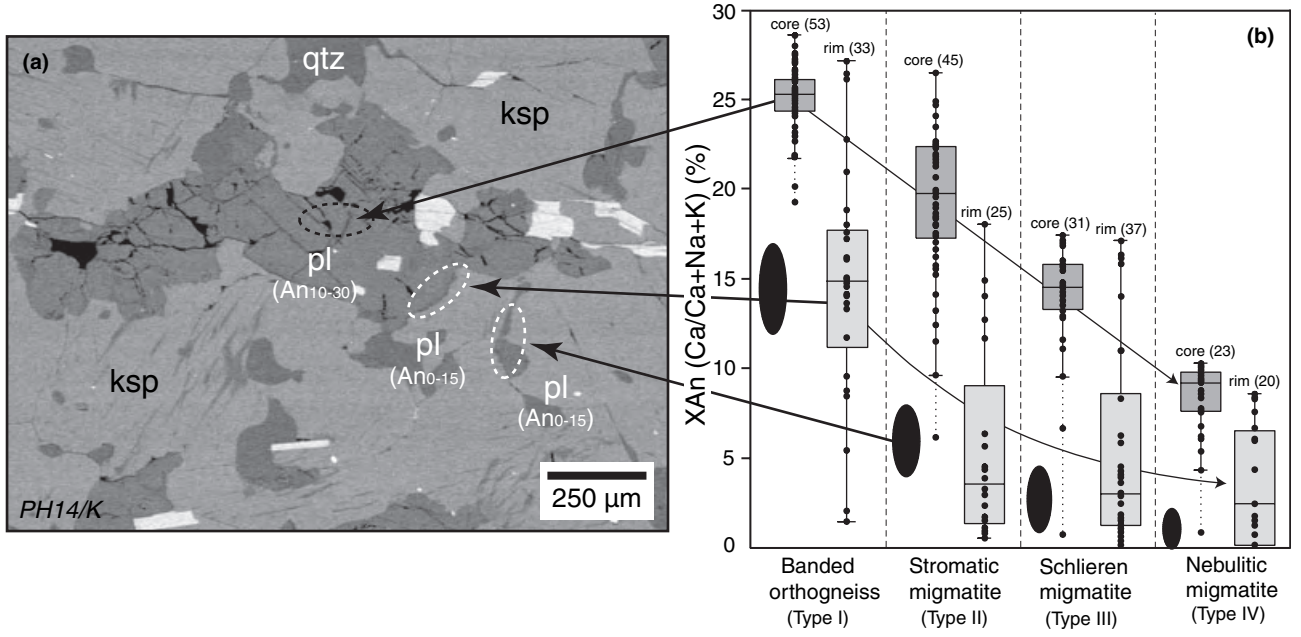

Fig. 7. Plagioclase composition with respect to its microstructural position. (a) SEM backscatter image shows typical microstructural varieties of plagioclase (example from type II migmatite). Large plagioclase from plagioclase aggregates (black dashed circle), interstitial plagioclase tracing the K-feldspar boundaries or rims of large plagioclase (white dashed circles). (b) Composition of texturally different plagioclase. In each rock type cores are more anorthite-rich than adherent rims and interstitial plagioclase (shown as black ellipses). From type I to IV, each plagioclase microstructural type displays enrichment in sodium. The compositional data are summarized in box-plots of anorthite content (mol.%) *v.* rock type (for detail see caption of Fig. 4, the outliers are plotted), with number of analyses in brackets.

favour of biotite, associated with important changes in x(g), m(g) and x(bi), until the liquid-out line is reached. Here the mineral assemblage g–sill–bi–pl–ksp–qtz–ru–ilm is likely to be the preserved one, and this does correspond to the mineral assemblage observed in the rocks. The calculated mineral compositions are x(g) =

Table 5. Whole-rock compositions.

	Whole-rock compositions (ICP-MS)				Whole-rock compositions from modelling		
Rock type	Banded orthogneiss (type I)	Stromatic migmatite (type II)	Schlieren migmatite (type III)	Nebulitic migmatite (type IV)	Reconstructed mu–bi granite	Melt loss composition after 11 mol.% of melt loss in a closed system (820 °C/9 kbar)	Melt loss compositions after 40 mol.% of melt loss in H_2O saturated system (800 °C/9 kbar)
Sample	PH60/B	PH 60/A	PH89/C	PH59/D			
wt%							
SiO_2	69.90	71.40	72.30	77.10	69.57	69.21	67.62
TiO_2	0.45	0.36	0.20	0.10	0.46	0.51	0.71
Al_2O_3	15.40	15.20	12.70	12.70	16.02	16.06	16.26
$Fe_2O_3^a$	3.25	2.59	1.76	1.68	2.91	3.13	4.14
MnO	0.04	0.03	0.03	0.03	0.07	0.07	0.10
MgO	1.04	0.74	0.27	0.15	0.98	1.06	1.43
CaO	1.50	1.42	0.69	0.43	1.74	1.84	2.23
Na_2O	2.87	3.08	2.43	2.79	2.90	2.81	2.50
K_2O	4.98	4.99	5.86	5.21	5.35	5.31	4.99
P_2O_5	0.18	0.21	0.24	0.23	–	–	–
Total	99.61	100.02	96.48	100.42	100.00	100.00	99.99
A/CNK	1.20	1.17	1.10	1.15	1.17	1.17	1.20
X_{Fe}	0.61	0.64	0.77	0.85	0.63	0.62	0.62

[a]Total iron as Fe_2O_3.

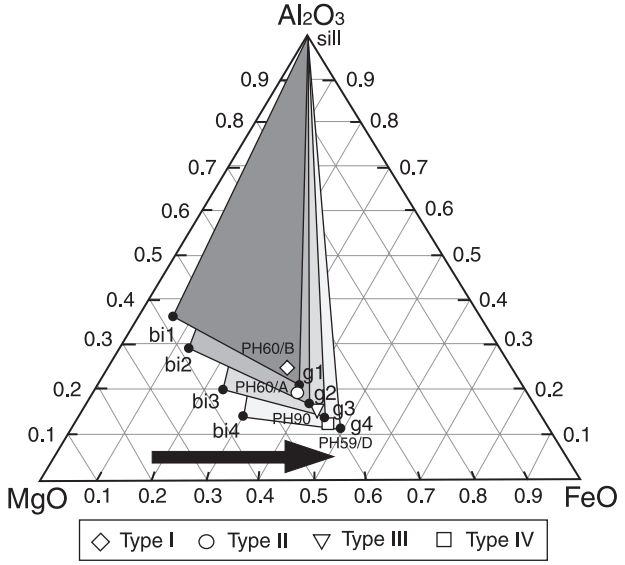

Fig. 8. Al_2O_3–FeO–MgO compositional diagram. Type I orthogneiss to type IV migmatite mineral compositions (black symbols, mol.%) and whole-rock analyses (opens symbols, mol.%) plot at progressively higher X_{Fe} values.

0.77, x(bi) = 0.5 and m(g) = 0.03 (compare type I, X_{Fe} of the garnet = 0.77–0.85, X_{Fe} of the biotite = 0.45 and Sps in garnet of 2–3 mol.%). For arrow C, $M(H_2O)$ = 0.88, and therefore this amount of $M(H_2O)$ is used for the construction of a P–T pseudosection for type I orthogneiss. In this way, the amount of H_2O necessary to preserve the assemblage and mineral chemistry was determined for construction of pseudosections for the whole-rock chemistry of types II, III and IV migmatites.

The major features and topology of H_2O-undersaturated pseudosections for types I–IV (Figs 10 & 11) are similar, but with the exact position of fields and curves varying in P–T space dependent on the X_{Fe} of the rock and on $M(H_2O)$. They show a steeply inclined solidus at progressively lower temperature. The muscovite-in line is temperature sensitive and steep at suprasolidus conditions and pressure sensitive at subsolidus conditions. Cordierite-bearing assemblages are restricted to the low pressure part of the pseudosections and the biotite upper temperature limit decreases from 850 °C for type I orthogneiss to 780 °C for type IV migmatite.

The transition from g–sill–bi–liq–pl–ksp–qtz–ru–ilm into g–sill–bi–pl–ksp–qtz–ru–ilm at the solidus occurs on pseudosections on cooling at progressively lower temperature between 800 and 790, 770–750, 720–710 and 690–680 °C for type I orthogneiss to type IV migmatite. Conditions of this transition are also limited by the muscovite-in line from the high-pressure side and by the cordierite-in line from the low-pressure side. These correspond to 9–5.3, 8.6–4.8, 6.6–4 and 5.2–4 kbar, and can be considered to be pressure windows through which mineral assemblage preservation is likely to have occurred, indicated by grey arrows.

The P–T conditions of equilibration can be further refined by comparing the observed chemistry of garnet, and biotite and garnet modal proportions, with chemical variables and molar proportions calculated in pseudosections (Figs 10 & 11). From the point of view of decreasing P–T conditions, in the field of g–sill–bi–liq–pl–ksp–qtz–ru–ilm the molar proportions of garnet and melt decrease in favour of biotite and the molar proportion of garnet is progressively lower at the liquid-out line for the types I–IV. This is in accordance with the observed decrease in modal proportion of garnet from the type I orthogneiss to the type IV migmatite. In the diagrams, during the continuous reaction involving g–sill–bi–liq–pl–ksp–qtz–ru–ilm, the x(g) and x(bi) increase until the solidus is

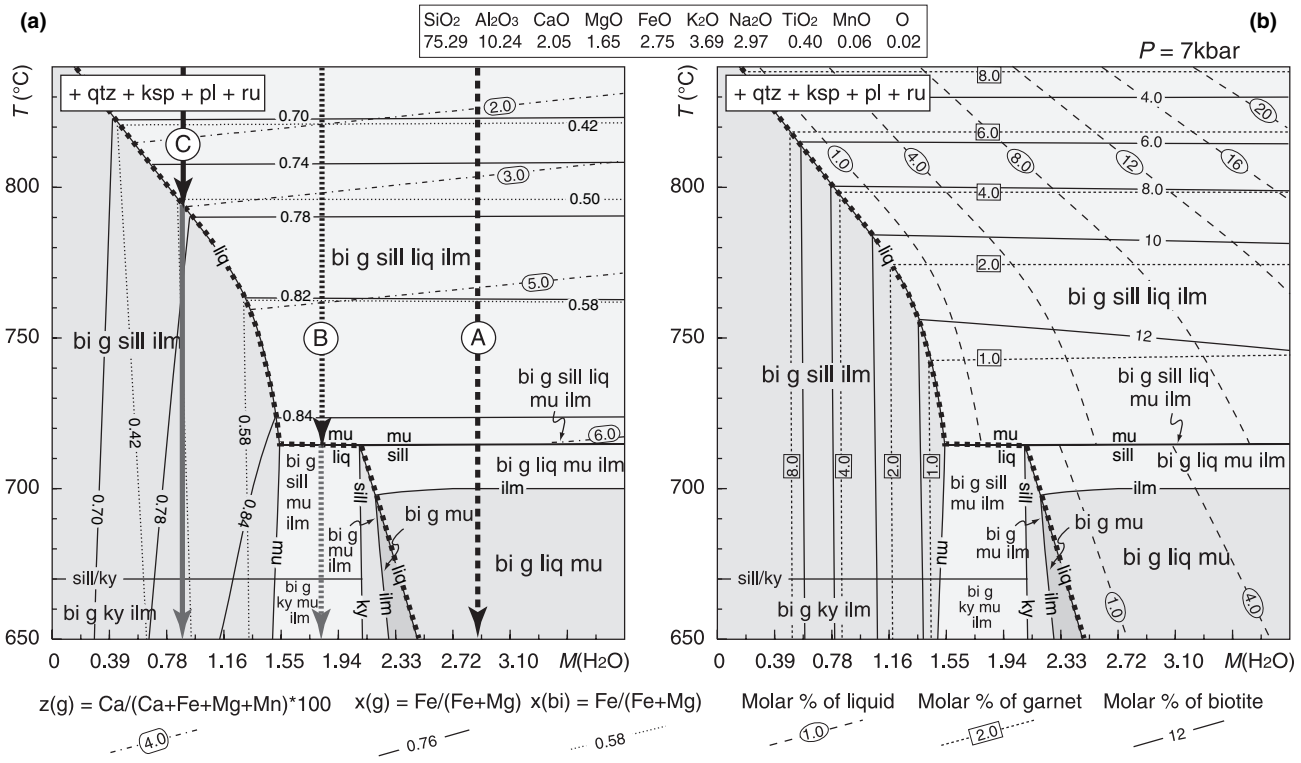

Fig. 9. *T*–*M*(H_2O) pseudosection for type I orthogneiss at 7 kbar contoured for (a) *x*(g), *z*(g), *x*(bi) and (b) molar proportions of liquid, garnet and biotite. Three cooling paths at different proportions of H_2O are discussed in the text.

crossed (Figs 10 & 11), where the continuous reaction is stopped as biotite loses its source of H_2O. On further cooling, the only reaction that operates is exchange of Fe–Mg between garnet and biotite.

Regarding the spacing of *x*(g) and *x*(bi) isopleths in the g–sill–bi–pl–ksp–qtz–ru–ilm and g–sill–bi–liq–pl–ksp–qtz–ru–ilm fields, the Fe–Mg exchange is much less efficient in changing garnet and biotite chemistry than is the continuous reaction in the presence of melt. Therefore, the observed decrease in X_{Fe} of garnet and biotite in types I–IV is attributed to the decreasing temperature of last melt crystallization. The isopleths of *z*(g) are pressure sensitive and decrease in the field of g–sill–bi–liq–pl–ksp–qtz–ru–ilm from 6.5 to 3 kbar with decreasing pressure. Therefore, the decreasing grossular content in garnet from the type I orthogneiss to the type IV migmatite is interpreted as reflecting the decreasing pressure of last melt crystallization in the rocks (Fig. 10 & Table 4).

Based on the pseudosection modelling, the mineral assemblage and mineral chemistry of type I orthogneiss to type IV migmatite is interpreted as recording the last re-equilibration in the presence of melt that occurred along an exhumation path. The equilibration *P*–*T* conditions in the pseudosections for types I, II, III and IV are therefore inferred to be 790 °C and 9–5 kbar, 760 °C and 8.5–4.5 kbar, 710 °C and 6.5–4 kbar and 690 °C and 5–3 kbar respectively. Because the calculations were performed in the relatively complete MnNCKFMASHTO system, these *P*–*T* conditions are likely to be realistic.

P–T path before the last equilibration

Because it is likely that open-system processes have operated during metamorphism, the bulk-rock composition of each rock type is not likely to correspond to an original protolith composition. For this reason, the *P*–*T* evolution before the last equilibration cannot be evaluated from pseudosections calculated for observed bulk-rock compositions. The general *P*–*T* evolution may be constrained, however, because the presence of kyanite in mineral concentrates suggests that the *P*–*T* evolution was likely to have involved decompression from the kyanite stability field.

FORWARD MODELLING OF OPEN-SYSTEM PROCESSES

Prior to considering melt infiltration, the melt amount that it might be possible to produce by various processes is modelled to assess whether the change from banded, metatexite-like structure, into isotropic, diatexite-like structure may be caused by loss of coherence due to high melt production in the rocks themselves. The amount of melt is modelled for: (1) temperature increase for an appropriate protolith composition (closed-system model); and (2) H_2O

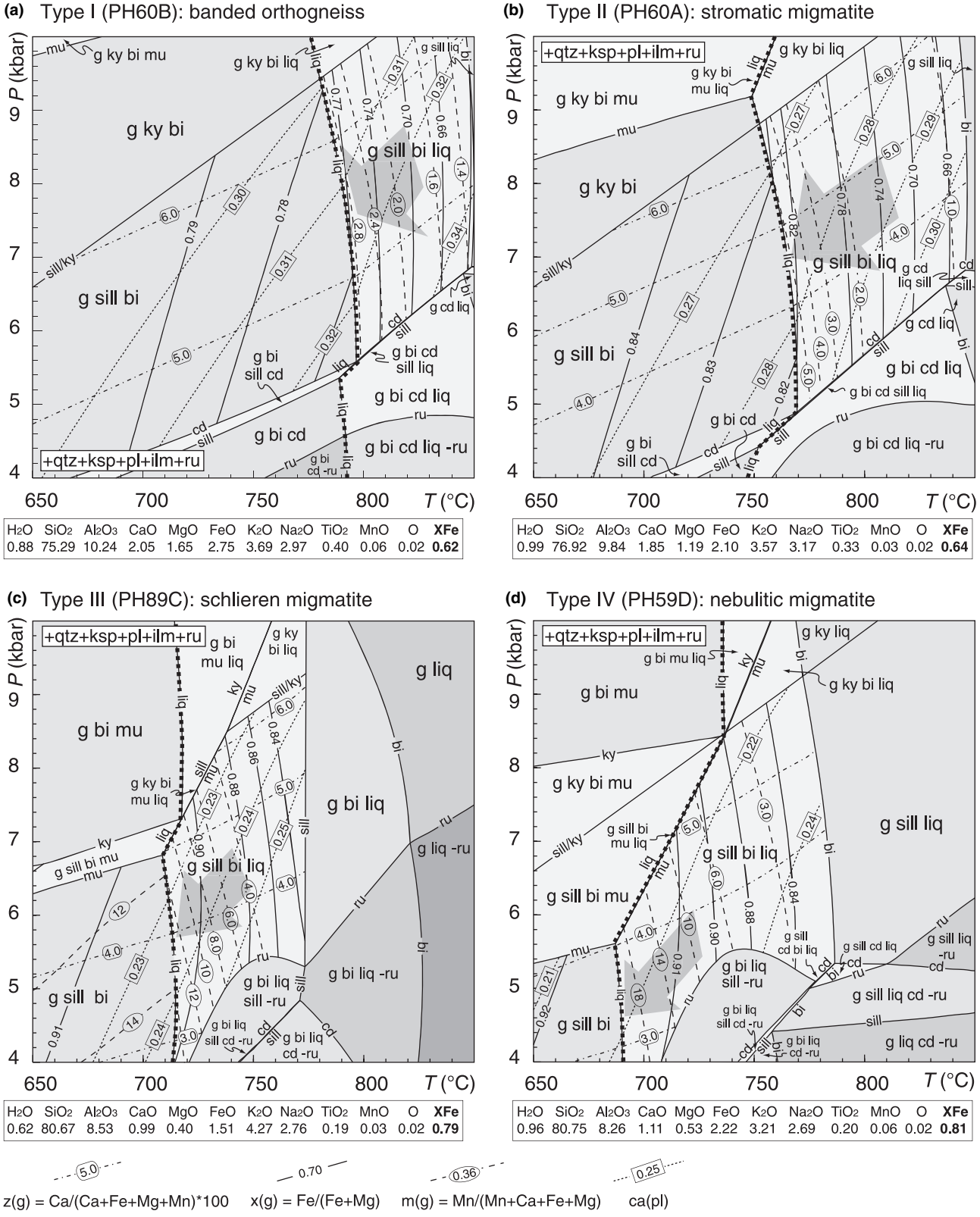

Fig. 10. H_2O-undersaturated MnNCKFMASHTO *P–T* pseudosections for the rock compositions of (a) banded orthogneiss (type I), (b) stromatic migmatite (type II), (c) schlieren migmatite (type III) and (d) nebulitic migmatite (type IV). For the H_2O content used, see text. Solidus is underlined by a dashed line and isopleths of *x*(g), *z*(g), *m*(g) and *ca*(pl) are shown.

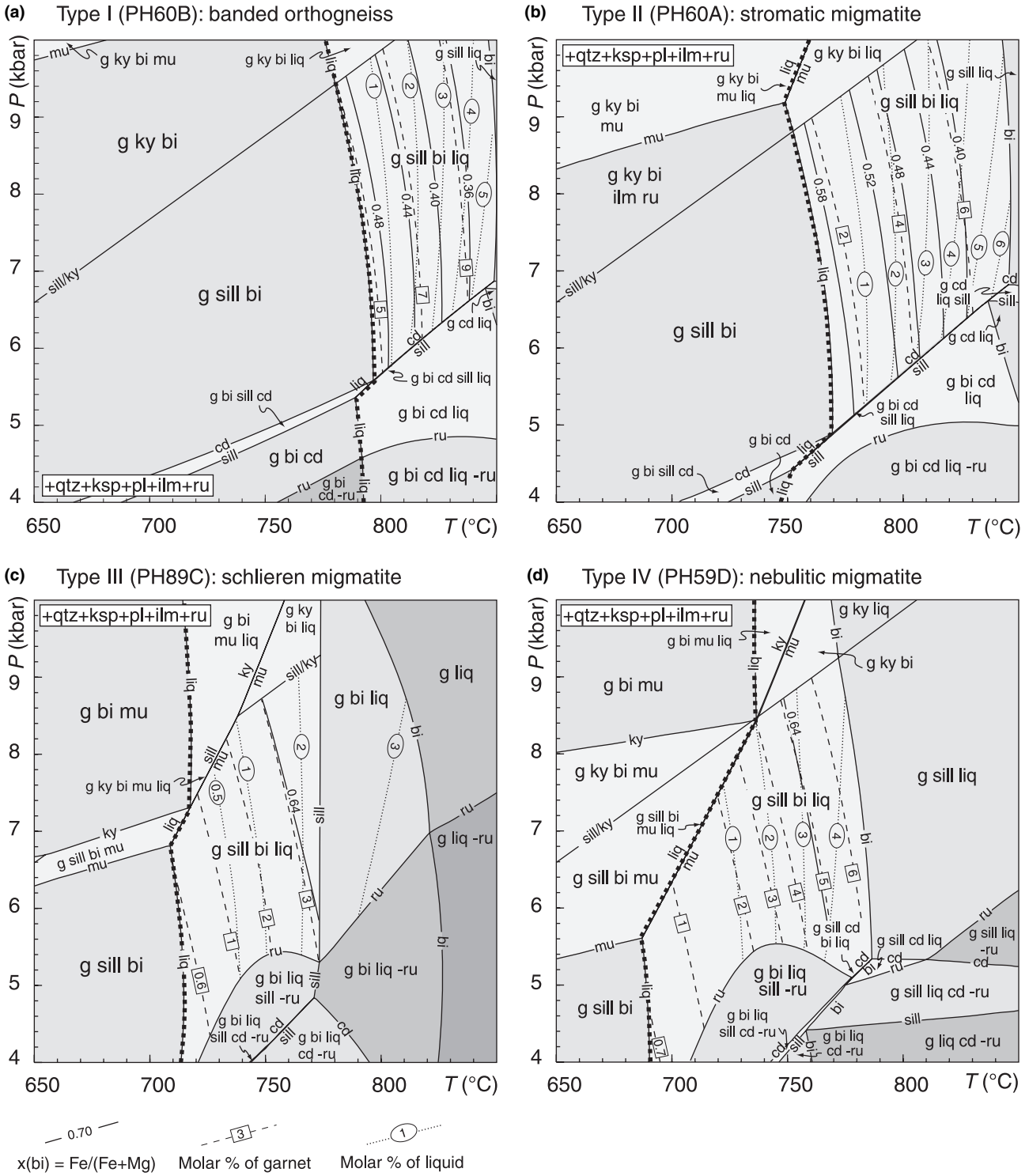

Fig. 11. *P–T* pseudosections of types I–IV (same as in Fig. 10) contoured for x(bi) and for molar proportions of liquid and garnet.

introduction (fluid infiltration model). Also examined are processes that may alter the rock composition, including melt loss and its influence on the resulting whole-rock composition. Reaction sequences, and the evolution of mineral proportions and mineral compositions of the assemblages are discussed for the various cases in the context of the observed trends in types I–IV. Before these calculations can be undertaken the

protolith is reconstructed using the composition of type I orthogneiss, the least modified rock composition available.

Reconstruction of the protolith

The likely protolith is reconstructed to estimate the maximum amount of melt that such protolith would produce along a prograde path (can a diatexite be formed?) and to examine compositional trends of phases with increasing degree of melting (do they correspond to observed compositional trends?). The least modified rock is type I banded orthogneiss that contains sillimanite and kyanite. However, it is likely that the original granitic protolith before metamorphism and mylonitization did not involve aluminosilicate, but that aluminosilicate was a product of muscovite-breakdown melting along the prograde path. To preserve the aluminosilicate from reaction at the solidus during the retrograde path, some melt must have been lost (Brown, 2002; White & Powell, 2002), and such melt loss is likely to occur after muscovite dehydration melting (White & Powell, 2002). The chemistry of the melt to be introduced is taken from a point located on a prograde path after muscovite-breakdown melting in the g–ky–bi–liq–pl–ksp–qtz–ru–ilm field and conditions of 11.5 kbar and 790 °C were chosen, but the results are insensitive to this P–T choice. It is necessary to add 7 mol.% of melt to obtain a kyanite-absent assemblage on the prograde path prior to muscovite breakdown. An upper limit of melt addition, only slightly larger than 7 mol.%, results in H_2O saturation at the solidus. The pseudosection for the composition of the type I rock with 7 mol.% of reintegrated melt is presented in Fig. 12a, b.

Melting of the protolith in a closed system and with melt loss

The pseudosection in Fig. 12a is used to estimate the maximum amount of melt that a biotite–muscovite protolith with the starting assemblage g–bi–mu–pl–ksp–qtz–ru–ilm would produce along a prograde path to discuss whether the degree of closed-system melting is sufficient to form a diatexite. This pseudosection is also used for examination of compositional trends of phases with increasing degree of melting and on the retrograde path (Fig. 12b), and to infer the whole-rock compositional trends caused by melt loss.

The major prediction from the pseudosection from the point of view of a simple prograde heating path (Fig. 12a, path A) are the appearance of first liquid at 650 °C, disappearance of muscovite associated with the appearance of kyanite at 745 °C (Fig. 12a, b) and the kyanite/sillimanite transformation at 755 °C. A similar evolution occurs along path B, involving an increase in P and T followed by decompression, with kyanite formed on the prograde path, then being transformed into sillimanite on decompression (Fig. 12a, b).

The melt amount is controlled by the P–T path and the H_2O content in the mica. The amount of melt produced before muscovite dehydration melting is ~2 mol.% and then the amount of melt increases over a small interval by 3 mol.%, when muscovite-breakdown melting connected with the appearance of kyanite occurs at 740–750 °C. The dehydration of biotite continues up to 850 °C and the total amount of melt reaches 12–15 mol.% by the point at which all the biotite is consumed. The amount of melt does not increase significantly on decompression, so the degree of melting is controlled only by heating on the prograde path. The mineral chemistry changes involve increasing anorthite content of plagioclase, decreasing X_{Fe} of garnet and biotite (Fig. 12a, b) and decreasing grossular content in garnet (Fig. 12b). In addition to the increasing amount of melt, the phase changes involve disappearance of muscovite, appearance of kyanite and sillimanite, increasing molar content of garnet and decreasing molar content of biotite. On a retrograde path garnet and sillimanite are consumed by continuous reactions producing biotite and muscovite respectively. When the hypothetical rock becomes melt absent the stable assemblage is g–bi–mu–pl–ksp–qtz–ru–ilm.

These predictions are now discussed in terms of evolutionary trends observed in the migmatites. If the protolith was biotite–muscovite granite that was by deformation and metamorphism converted into a bi–mu orthogneiss, then the first melt has been produced at 650 °C and the fertility of the rock was controlled by dehydration melting of biotite and muscovite. The amount of melt produced at peak (800–850 °C) may have reached up to 12–15 mol.%. If the protolith was a bi–ky(sill) orthogneiss, then the maximum melt production in the biotite stability field would have been only 5 mol.% (Fig. 11a). Thus, the amount of melt in both cases is not likely to be sufficient to produce a melt-supported structure required for diatexite formation, but may be sufficient to allow melt-assisted granular flow (at ~7 vol%: Rosenberg & Handy, 2005).

Additionally, modal, and especially the compositional evolution of minerals (e.g. X_{Fe} of garnet and biotite and anorthite content in plagioclase) from type I orthogneiss to type IV nebulite do not fit the evolution on the prograde path in the pseudosection (Table 4). To preserve the observed assemblage g–sill–bi–pl–ksp–qtz–ru–ilm, some melt must have been lost before retrogression. The melt loss alters the rock composition, but the whole-rock composition after melt loss (calculated at 820 °C and 9 kbar, point 2 in Fig. 12a, b) shows $X_{Fe} = 0.62$, $SiO_2 = 69.21$, $Al_2O_3 = 16.06$, $CaO = 1.74$ and $Na_2O = 2.90$, which are changes that are opposite to the trend observed from type I orthogneiss to type IV migmatite ($X_{Fe} = 0.62 \rightarrow 0.85$, $SiO_2 = 69.90 \rightarrow 77.10$, $Al_2O_3 = 15.40 \rightarrow 12.70$, $CaO = 1.50 \rightarrow 0.43$) (Table 5). Therefore, the whole-rock compositional changes from type I

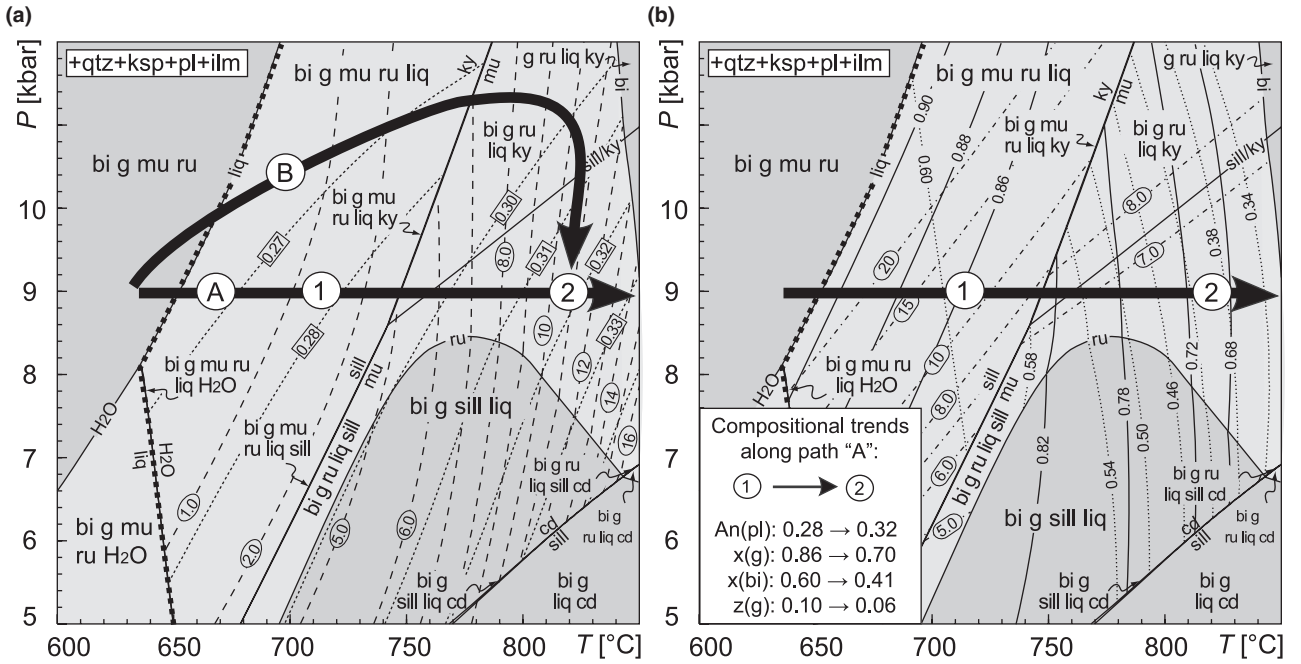

H_2O	SiO_2	Al_2O_3	CaO	MgO	FeO	K_2O	Na_2O	TiO_2	MnO	O
2.58	74.17	10.06	1.96	1.55	2.59	3.64	3.00	0.37	0.06	0.02

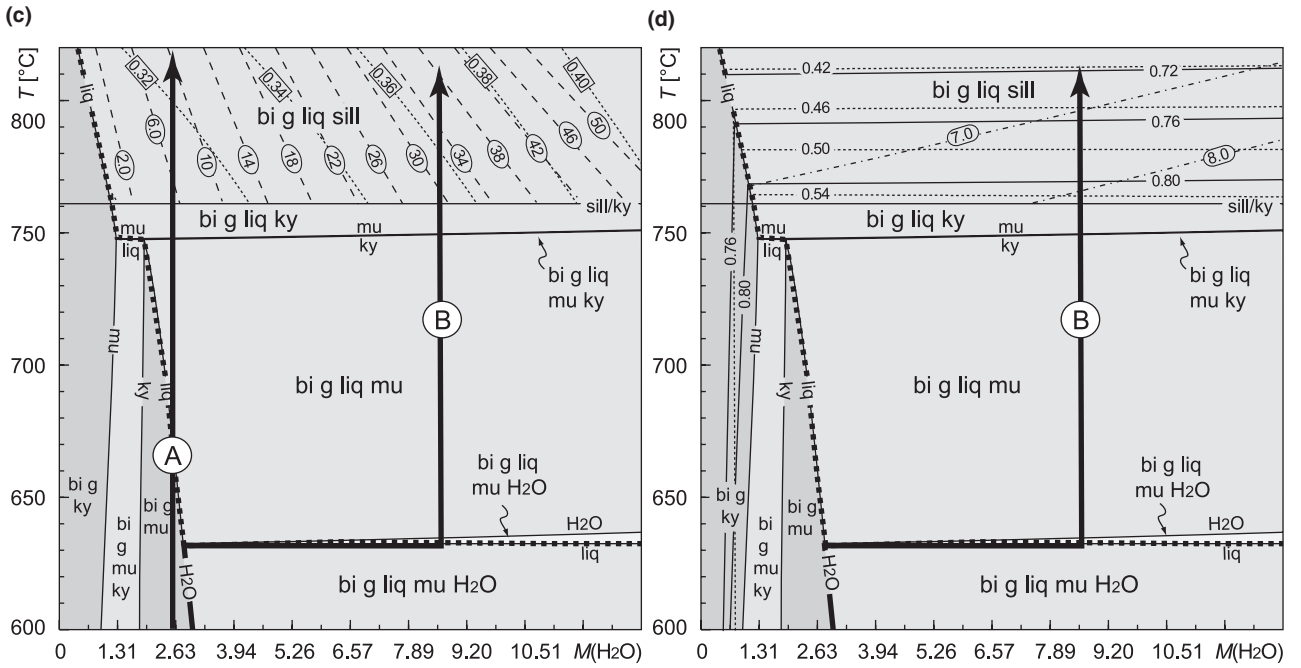

SiO_2	Al_2O_3	CaO	MgO	FeO	K_2O	Na_2O	TiO_2	MnO	O
75.30	10.24	2.05	1.65	2.75	3.69	2.97	0.40	0.06	0.02

z(g) = Ca/(Ca+Fe+Mg+Mn)*100 x(g) = Fe/(Fe+Mg) x(bi) = Fe/(Fe+Mg) molar % of liquid ca(pl)

orthogneiss to type IV migmatite cannot be explained by melt loss in a closed-system melting model.

H_2O infiltration model

The amount of melt necessary to form a diatexite may be obtained if H_2O is introduced from an external source, for example from associated dehydrating metasediments at near-solidus conditions (White *et al.*, 2005). Therefore, we assess the possibility that the type I orthogneiss to type IV migmatite evolution can result from the addition of external H_2O using a T–$M(H_2O)$ pseudosection. For the path A in Fig. 12c the melting of a mu–bi-bearing protolith is controlled only by mica-breakdown melting, and the path corresponds to path A in the P–T pseudosection in Fig. 12a. To the right side may be shown paths with additional H_2O. For example in path B, a bi–mu-bearing protolith is dehydrating until the H_2O saturated solidus is reached at 630 °C and at these conditions additional H_2O is introduced (Fig. 12c, d). The melt production is then controlled by the P–T path and the amount of H_2O introduced, and for path B it may reach 38 mol.% of melt at 810 °C (Fig. 12c). The augmented degree of melting due to the addition of H_2O along the prograde path has little influence on the molar content of garnet and biotite, although both become more magnesian (see horizontal x(g) and x(bi) isopleths in Fig. 12d), but influences more significantly the composition of plagioclase and the grossular content in garnet, plotted as ca(pl) and z(g) isopleths (Fig. 12c, d). If the high amount of melt produced along path B is accompanied by subsequent melt loss, the whole-rock composition is altered and for melt loss at 800 °C shows $X_{Fe} = 0.62$, $SiO_2 = 67.62$, $Al_2O_3 = 16.26$, $CaO = 2.23$ and $Na_2O = 2.50$ (Table 5).

The transformation of type I mylonitic orthogneiss into type IV nebulitic migmatite might be explained by increased degree of melting due to H_2O influx. However, the decrease in anorthite content of plagioclase and the increasing X_{Fe} of biotite and garnet would remain unexplained. Also the model, even if it is accompanied by melt loss (into $X_{Fe} = 0.62$, $SiO_2 = 67.62$, $Al_2O_3 = 16.26$, $CaO = 2.23$; Table 5) cannot account for the observed whole-rock trends (see Table 5).

Melt infiltration model

A model in which melt moves through and equilibrates with a rock is assessed, to evaluate the change of rock composition that such a continuing equilibration with infiltrating melt produces. The infiltrating melt may have been lost from similar protoliths at any point on the P–T path, moving up through the rock pile, or it can be of foreign derivation, for example from granulitic migmatites outside the Gföhl orthogneiss migmatite body. This melt then equilibrates with the rock and leaves it with slightly different composition, the rock also changing composition. Additionally, the infiltration may occur during exhumation, corresponding to the implied decreasing equilibration P–T conditions from type I orthogneiss to type IV migmatite, and therefore the equilibration of the melt with the rock may also be complicated by decompression and cooling. As the processes involved may be complex, the modelling is undertaken for simplified situations. It will be assumed that the rock had time to equilibrate during the melt infiltration.

Estimation of melt composition

The modelling is performed in the NCKFMASH subsystem as noted above. For this, the P–T conditions used for calculations are displaced to slightly lower temperature to be approximately equivalent to the calculations in MnNCKFMASHTO (740 °C at 7–5 kbar, 720 °C at 6.5–5 kbar, 690 °C at 5–4 kbar and 670–660 °C at 5–3 kbar for types I, II, III and IV, respectively, using Fig. 13).

There is no direct evidence for the composition of the melt present during metamorphism, apart from the mineral compositions preserved in the rocks. Assuming that the infiltrating melt tends to be in equilibrium with the minerals (at least with their rim compositions) and that this equilibrium evolves as temperature decreases, the composition of the percolating melt can be estimated from the preserved assemblages and their mineral chemistry.

From the phase rule it follows that a melt composition that is in equilibrium with garnet–sillimanite–biotite–plagioclase–K-feldspar–quartz in the NCKFMASH system can be calculated if three variables are fixed. In the following calculations pressure, temperature and anorthite content of plagioclase are fixed (Table 6). For example, the melt composition that is in equilibrium with 15 mol.% anorthite content in plagioclase at 6.5 kbar and 740 °C in a rock with the assemblage garnet–sillimanite–biotite–liquid–plagioclase–K-feldspar–quartz is $H_2O = 23.02$, $SiO_2 = 62.74$, $Al_2O_3 = 7.32$, $CaO = 0.21$, $MgO = 0.10$, $FeO = 0.24$, $K_2O = 2.71$, $Na_2O = 3.66$ (in mol.%),

Fig. 12. Reconstruction of the granite protolith and forward modelling of closed-system melting and H_2O infiltration. Pseudosections calculated for the bi–mu granite, reconstructed by adding 7 mol.% of melt into the rock composition of the type I. (a,b) P–T pseudosections contoured for x(g), z(g), x(bi), ca(pl) and mol.% of liquid. Closed-system model is discussed for two prograde paths A and B. Inset shows calculated mineral compositions along path A. Rock composition after melt loss at 820 °C and 9 kbar is shown in Table 5. (c,d) T–$M(H_2O)$ pseudosection. Path A illustrates closed-system melting of bi–mu granite and path B H_2O infiltration at the solidus. Melt proportion and mineralogical changes are discussed in the text, the rock composition after melt loss at 800 °C is listed in Table 5.

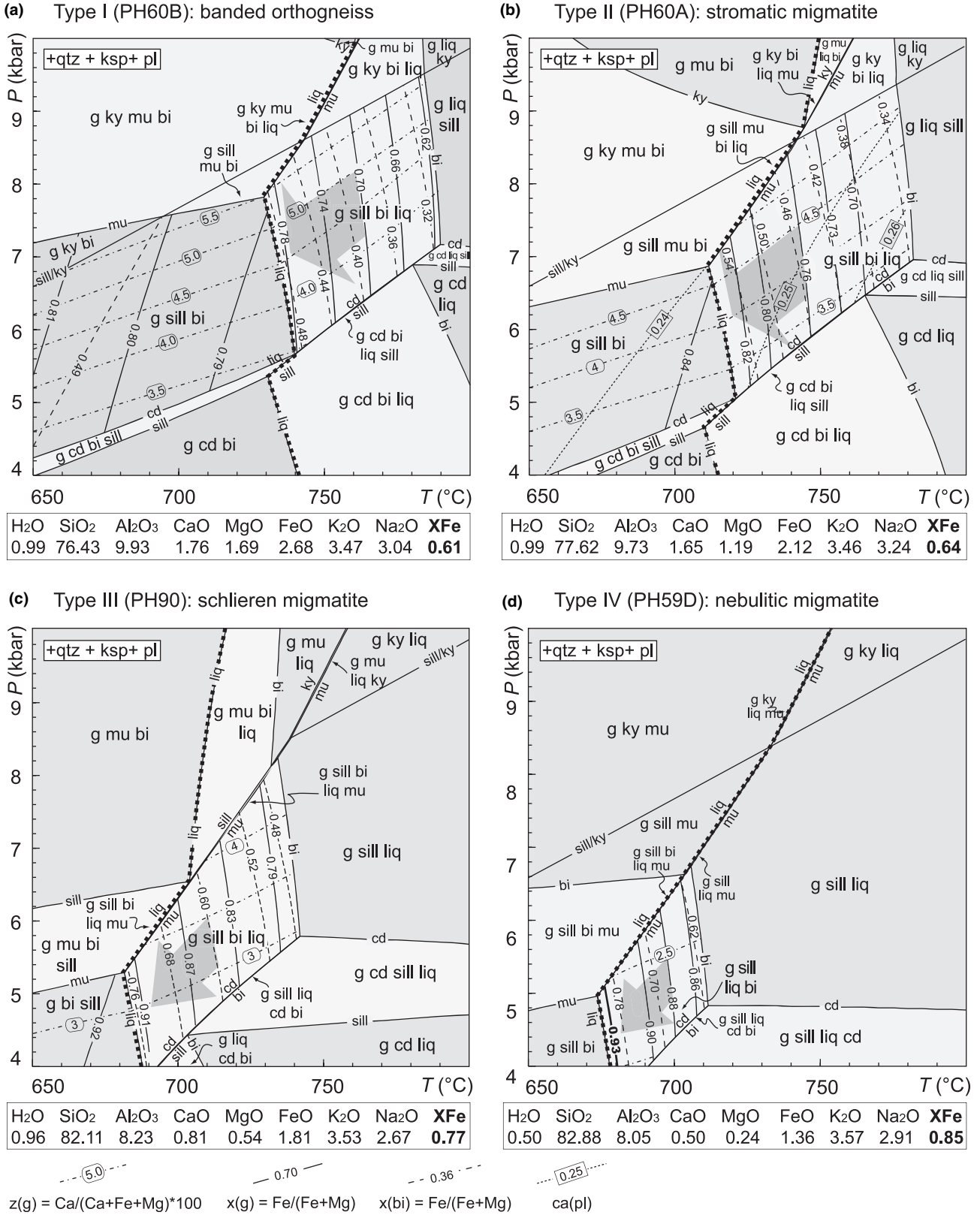

H_2O	SiO_2	Al_2O_3	CaO	MgO	FeO	K_2O	Na_2O	**XFe**
0.99	76.43	9.93	1.76	1.69	2.68	3.47	3.04	**0.61**

H_2O	SiO_2	Al_2O_3	CaO	MgO	FeO	K_2O	Na_2O	**XFe**
0.99	77.62	9.73	1.65	1.19	2.12	3.46	3.24	**0.64**

H_2O	SiO_2	Al_2O_3	CaO	MgO	FeO	K_2O	Na_2O	**XFe**
0.96	82.11	8.23	0.81	0.54	1.81	3.53	2.67	**0.77**

H_2O	SiO_2	Al_2O_3	CaO	MgO	FeO	K_2O	Na_2O	**XFe**
0.50	82.88	8.05	0.50	0.24	1.36	3.57	2.91	**0.85**

Fig. 13. H_2O-undersaturated NCKFMASH *P–T* pseudosections for the whole-rock composition of (a) type I, (b) type II, (c) type III and (d) type IV, contoured for *x*(g), *z*(g), *x*(bi), and *ca*(pl). Solidus is shown as a dashed line.

Table 6. Melt compositions.

	T (°C)	P (kbar)	An(pl)	H_2O	SiO_2	Al_2O_3	CaO	MgO	FeO	K_2O	Na_2O	x(g)	z(g)	x(bi)
Melt I	740	6.50	0.15 (mol.%)	23.02	62.74	7.32	0.21	0.10	0.24	2.71	3.66	0.77	0.03	0.47
(PH60/B)			(wt%)	7.61	69.22	13.71	0.22	0.07	0.32	4.69	4.17			
Melt II	720	5.50	0.07 (mol.%)	22.76	63.17	7.26	0.09	0.09	0.28	2.57	3.78	0.82	0.02	0.55
(PH60/A)			(wt%)	7.52	69.63	13.58	0.09	0.07	0.37	4.44	4.30			
Melt III	690	4.50	0.04 (mol.%)	23.27	63.21	6.97	0.09	0.05	0.23	2.51	3.68	0.90	0.01	0.72
(PH90)			(wt%)	7.74	70.12	13.13	0.09	0.04	0.31	4.37	4.21			
Melt IV	660	3.50	0.02 (mol.%)	23.64	63.49	6.72	0.02	0.01	0.16	2.46	3.50	0.98	0.01	0.94
(PH59/D)			(wt%)	7.90	70.81	12.72	0.02	0.01	0.21	4.30	4.03			

which is taken to approximate the melt composition in equilibrium with the rim compositions of the minerals in the type I orthogneiss (Table 6). In the same way melt compositions were calculated for decreasing P–T conditions at 5.5 kbar and 720 °C and 4.5 kbar and 690 °C and 3.5 kbar and 660 °C, in equilibrium with $X_{An} = 0.07$, 0.04 and 0.02, that are taken to approximate the melt compositions in equilibrium with rim compositions of the phases in type II, III and IV migmatites respectively (Table 6). The choice of fixed variables was assessed by comparing the calculated garnet and biotite compositions with observed values in the rocks.

Equilibration with infiltrating melt

Modelling the equilibration of host rock with infiltrating melt is presented for a model situation in which the rock is kept at fixed P–T conditions (6.5 kbar, 740 °C) and equilibrates with infiltrating melt of fixed composition (melt II, III or IV in Table 6) (Fig. 14a). The starting composition is that of the type I orthogneiss (sample PH60/B) in which the mineral assemblage is g–sill–bi–liq–pl–ksp–qtz. Melt infiltration is simulated in cycles, each consisting of addition of 10 mol.% of melt, equilibration and melt loss, as schematically presented in the T–X section (Fig. 14b), where X links the rock to the melt composition. Following equilibration of infiltrating melt with the host minerals, a new rock composition named $solids_{(1)}$ is calculated for the modified mineral compositions. The equilibrated melt leaves the rock to be replaced with 10 mol.% of new melt of the same composition as the first infiltrating batch. Following equilibration of $solids_{(1)}$ and melt, a new rock composition is calculated named $solids_{(2)}$, and so on. These 'metasomatic' runs are repeated and the changes of major oxides in the evolving rock composition for infiltration by melt composition III are reported in Fig. 14c–f. The procedure was also undertaken for melt of compositions II and IV, shown in the insets in Fig. 14c–f.

The rock composition that equilibrates with melts II, III and IV shows similar trends of increasing SiO_2, decreasing CaO and Al_2O_3, constant Na_2O and decreasing K_2O, irrespective of the melt composition used (Fig. 14). The X_{Fe} ratio increases only slightly (0.60–0.67, not shown). To change the whole-rock composition as indicated by the arrows in Fig. 14 by melts II, III and IV it was necessary to produce 60, 60 and 40 runs respectively. Similar trends were obtained for simulations where the rock changes P–T conditions and equilibrates with melt of fixed composition, and where the rock changes P–T conditions and equilibrates with melt that changes composition (from melt II, to melt III to melt IV, not shown).

The trends obtained for the major oxides SiO_2, CaO, Al_2O_3 and, to a lesser extent, Na_2O are very similar to the trends in types I–IV (large arrow in Fig. 14 c–f), with best fits for equilibration with melts III and IV. In the model, the rock composition may change significantly by equilibration with infiltrating melt and that this process may explain major chemical trends in types I–IV. However, with the calculated melt compositions the trends of the types I–IV in K_2O and X_{Fe} are not well reproduced. The most likely explanation for this is that the melt compositions used do not correspond to the melt infiltrating, the necessary approximation having been made that they correspond to the melt already in equilibrium with the rocks (see above). The trends may indicate that the melts infiltrating the rocks have a somewhat different K/(Na + K) than those used in the modelling. Given the low FeO and MgO contents in haplogranitic melts (White *et al.*, 2001, 2007), modification of X_{Fe} is inevitably limited. Arbitrarily increasing these contents does allow the observed trends to be reproduced.

Melt redistribution

In the melt redistribution model (Marchildon & Brown, 2001; Milord *et al.*, 2001), the resulting composition of the rock should lie between the protolith and melt composition. The whole-rock compositions of types I–IV do not lie exactly on the line between type I and calculated melt compositions (stars in Fig. 14c–f) but follow similar trends. An important consequence of interpreting the observed trends as a result of melt redistribution is that the types II to IV migmatites gained a significant and progressively increasing proportion of melt. The melt loss from type I orthogneiss or from a theoretical mu–bi granite protolith (calculated to be a maximum of 15 mol.% of melt for a closed system, Fig. 12a) is clearly not enough to change significantly the chemistry of types II

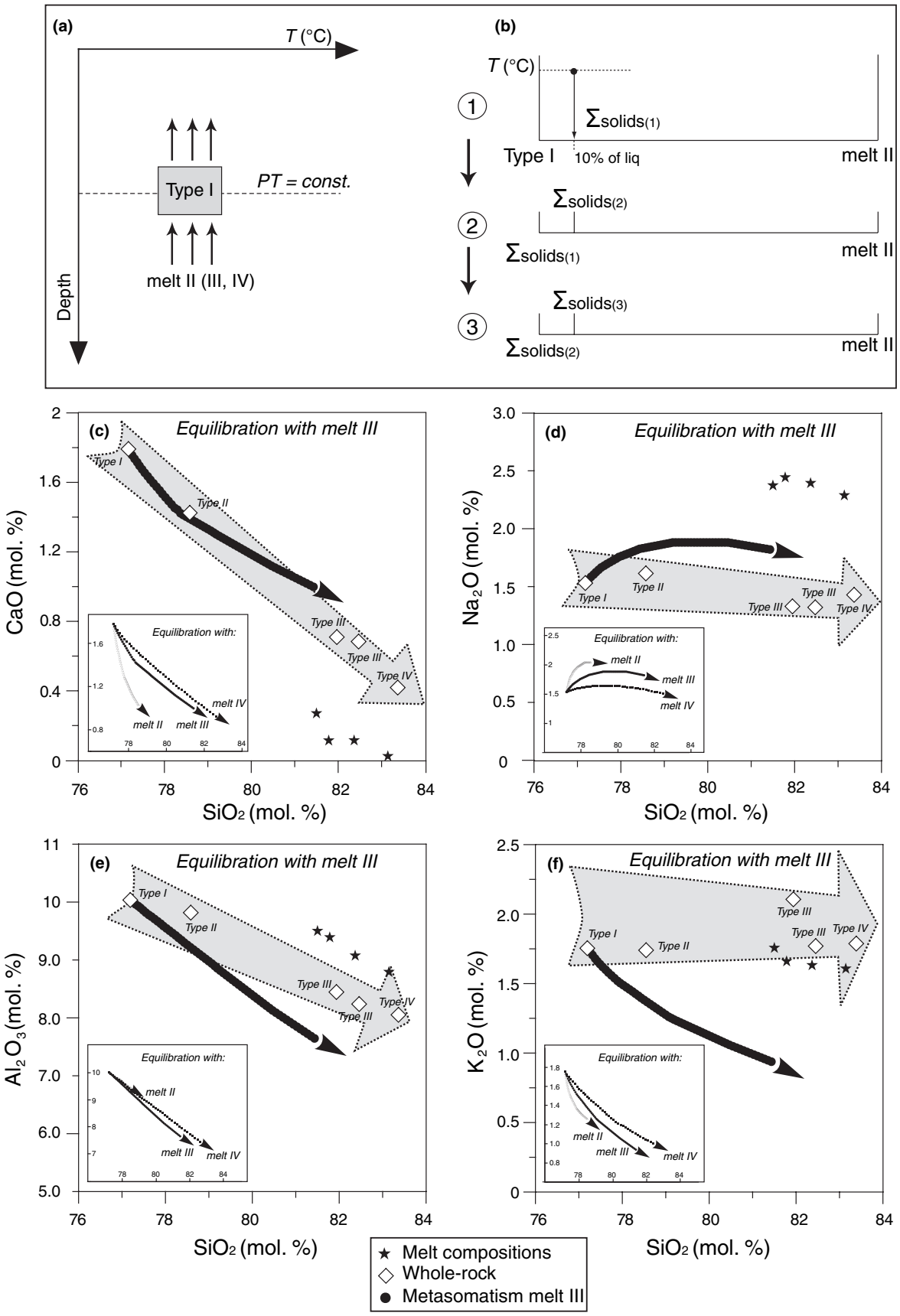

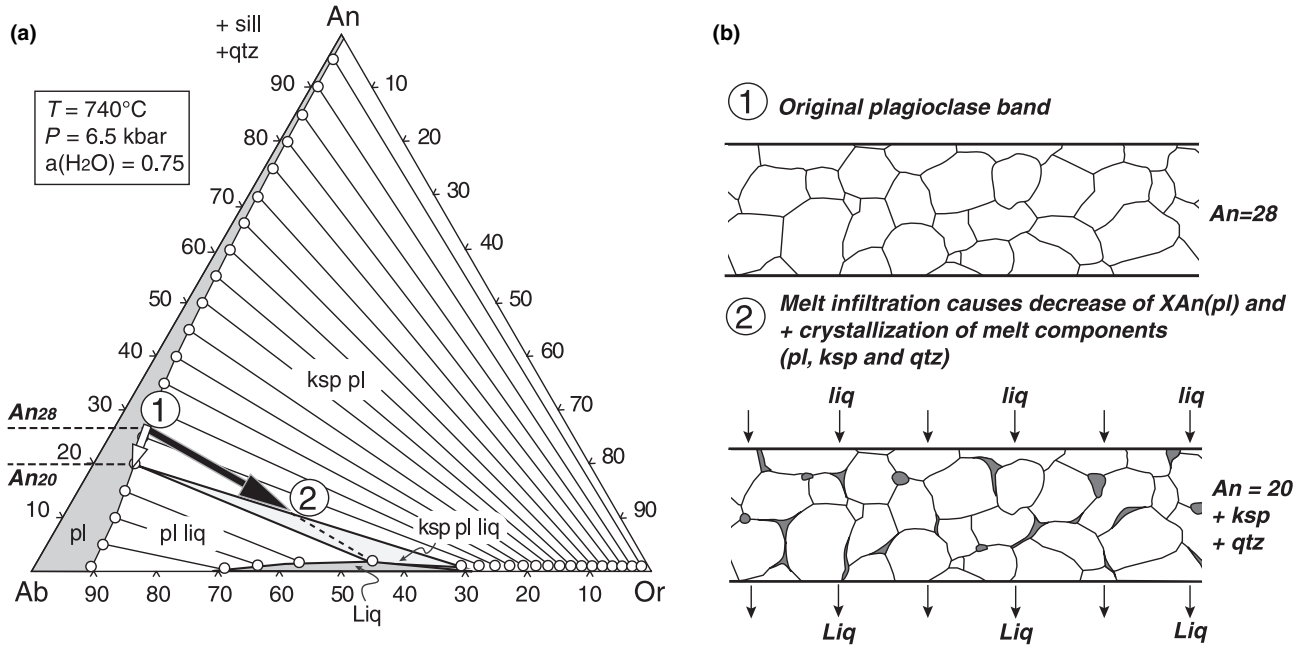

Fig. 15. (a) Ab–An–Or compatibility diagram calculated for 740 °C, 6.5 kbar and $a(H_2O) = 0.75$. For details see text. (b) Schematic sketch illustrating the disintegration of monomineralic banding.

to IV migmatites. However, some contribution of melt gain on the rock chemistry changes cannot be excluded, but it is likely to be of minor importance.

Destruction of monomineralic banding

An aspect of the evolution of the rocks, as seen progressively in type I orthogneiss to type III migmatite, is the destruction of the monomineralic banding. Accepting that infiltrating melt is largely responsible for the evolution from type I to type IV, the response of the original monomineralic layers to melt infiltration is investigated. In this, the original monomineralic layers of recrystallized plagioclase and K-feldspar are considered as equilibration volumes. In a reduced NCKASH system, the assemblage liquid–plagioclase–K-feldspar–quartz–sillimanite is divariant if $a(H_2O)$ is fixed. An albite–anorthite–K-feldspar compatibility diagram can then be calculated for any point in P–T space if sillimanite and quartz are in excess (Fig. 15). A diagram is calculated for 740 °C and 6.5 kbar with $a(H_2O) = 0.75$, chosen such that the plagioclase in equilibrium with K-feldspar and the infiltrating melt is An_{20}. This divariant assemblage liq–ksp–pl appears as a tie triangle involving K-feldspar with Ab_{29}. The tie lines in the trivariant fields of pl–ksp and pl–liq join the coexisting compositions, on the left side a quadrivariant field of plagioclase is located and at the bottom a quadrivariant field of liquid. The composition of the plagioclase layer which has higher anorthite content than this occurs outside the divariant assemblage liq–pl–ksp. A plagioclase layer infiltrated by melt is therefore drawn towards the liquid composition along the black arrow. As there exists a miscibility gap in feldspar, the vector is decomposed, and plagioclase composition is drawn to anorthite 20 mol.% (white arrow), at the same time K-feldspar crystallizes in the layer. In such a way the composition of the original plagioclase layer (Fig. 15, circle 1) is shifted into the pl–ksp trivariant field. Equilibration with melt pulls the composition to the pl–ksp tie line forming one edge of the liq–pl–ksp divariant (Fig. 15, circle 2). A similar process occurs in the K-feldspar layer (not shown in Fig. 15).

CONCLUSIONS

In the Gföhl gneiss, eastern Bohemian Massif, a sequence of felsic orthogneiss migmatites shows macroscopic features typical of evolution from metatexites to diatexites. They are divided into four stages that involve a progressive evolution of a banded mylonitic orthogneiss (type I) through stromatite migmatite (type II) and schlieren migmatite (type III)

Fig. 14. Model of the melt infiltration. (a) Sketch of the rock at fixed P–T conditions equilibrating with infiltrating melt; (b) modelling steps of rock equilibration with melt in the T–X section. For explanation see text. (c–f) Major oxides changes in the infiltration model compared with type I to IV rock composition (white diamonds) and calculated melt compositions (black stars, compositions from Table 6). The lower left insets show compositional variations for infiltration by melt composition II, III and IV. For details see text.

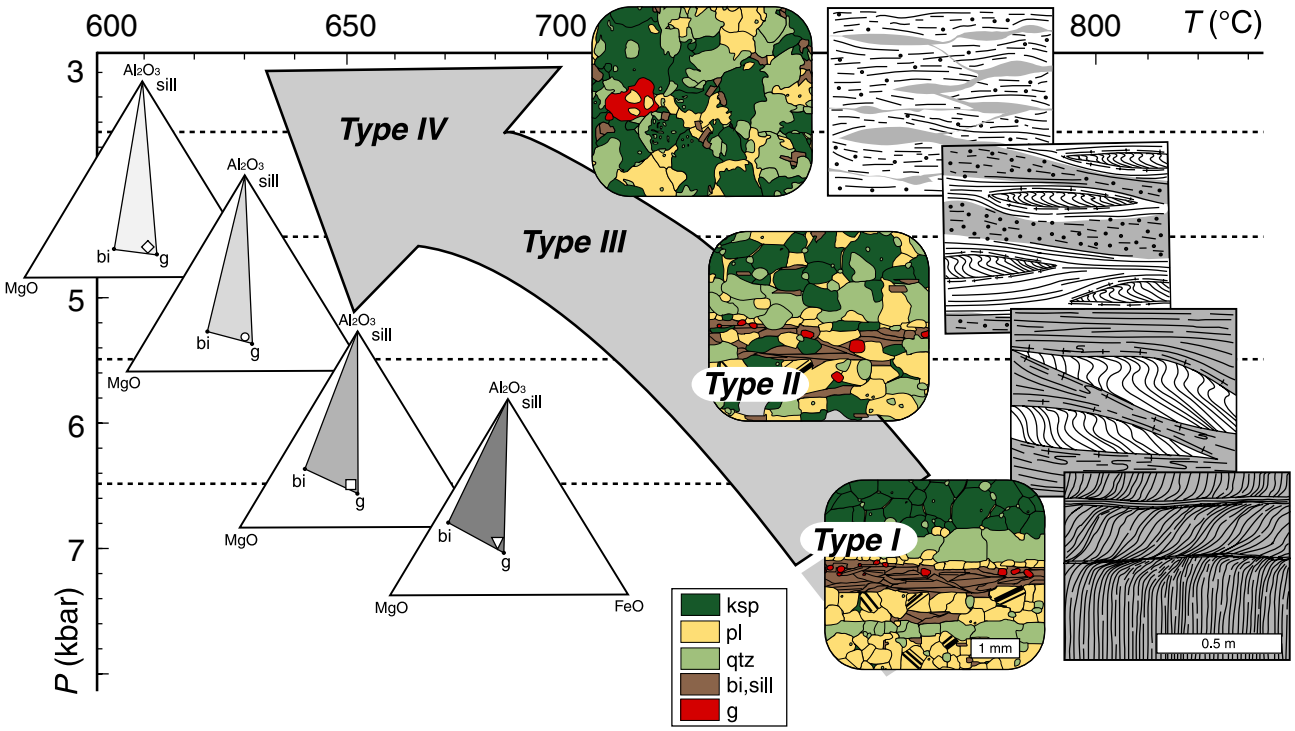

Fig. 16. Exhumation *P–T* path deduced from four migmatite types in the Gföhl orthogneiss complex. Shown are mineral and rock chemistry changes, microstructures of banding disintegration and a schematic model of melt distribution (shaded areas) within the complex during exhumation.

into nebulitic migmatite (type IV). The transformation of the rocks occurred during superposition of a flat D_2 deformation on a steep S_1 foliation, and microscopically it is characterized by progressive destruction of monomineralic banding and its replacement by a random microstructure typical of diatexites (Hasalová *et al.*, 2008a).

The rocks contain the assemblage g–sill–bi–liq–pl–ksp–qtz–ru–ilm. The mineral composition trends of banded orthogneiss changing into nebulitic migmatite involve mainly increase in X_{Fe} of garnet and biotite, and decrease in grossular content in garnet. These variations reflect decreasing temperature and pressure conditions of equilibration in the presence of melt, according to pseudosection modelling in MnNCKFMASHTO system (Figs 10 & 11).

The major-element whole-rock compositional changes involve mainly an increase in SiO_2 and X_{Fe} and a decrease in CaO and Al_2O_3 (Table 5). These appear to be inconsistent with closed-system melting or by an H_2O-infiltration model accompanied by melt loss. However, they are largely compatible with rock equilibration with an infiltrating melt. The open-system simulation was undertaken at essentially constant volume. Otherwise, the rock composition changes requiring infiltration by a large quantity of melt would result in an unacceptable increase in rock volume, although a small (< 10 mol.%) final accumulation of melt in type IV nebulitic migmatite is implied by the microstructural results of Hasalová *et al.* (2008a).

The textural and whole-rock chemical changes from banded orthogneiss to nebulitic migmatite are attributed to an increasing volume of melt that infiltrated through and interacted with the parental banded orthogneiss. The *P–T* path suggests that the melt infiltration proceeded at progressively lower *P–T* conditions for types I–IV (Fig. 16), which implies that melt flow changed from pervasive to channelized during exhumation (Fig. 16) corresponding to the observed relationships between the four rock types in the field (Fig. 2).

ACKNOWLEDGEMENTS

This work was financially supported by the Grant Agency of the Czech Academy of Science (No. IAA311140), the Czech National Grant Agency (No. 205/05/2187) and the French National Agency (No. 06-1148784 to K. Schulmann). Visits by P. Hasalová to ULP Strasbourg were funded by the French Government Foundation (BGF). A. Langrová from the Geological Institute of the Czech Academy of Sciences and J. Haloda from the Czech Geological Survey are thanked for operating the microprobe. RP acknowledges the support of ARC DP0451770. R. White is thanked for suggestions concerning how to model the

melt infiltration. We also thank R. White, R. Weinberg and P. Barbey for their constructive reviews and the journal editor M. Brown for all his editorial work on the manuscript.

REFERENCES

Arzi, A. A., 1978. Critical phenomena in the rheology of partially melted rocks. *Tectonophysics*, **44,** 173–184.

Barbey, P., Brouand, M., Le Fort, P. & Pêcher, A., 1996. Granite-migmatite genetic link: the example of the Manaslu granite and Tibetan Slab migmatites in central Nepal. *Lithos*, **38,** 63–79.

van Breemen, O., Aftalion, M., Bowes, D. R. *et al*., 1982. Geochronological studies of the Bohemian Massif, Czechoslovakia, and their significance in the evolution of Central Europe. *Transactions of the Royal Society of Edinburgh: Earth Sciences*, **73,** 89–108.

Brown, M., 1973. The definition of metatexites, diatexites and migmatite. *Proceedings of the Geologist's Association*, **84,** 371–382.

Brown, M., 2001. Crustal melting and granite magmatism: key issues. *Physics and Chemistry of the Earth*, **26,** 201–212.

Brown, M., 2002. Retrograde processes in migmatites and granulites revised. *Journal of Metamorphic Geology*, **20,** 25–40.

Coggon, R. & Holland, T., 2002. Mixing properties of phengitic micas and revised garnet–phengite thermobarometers. *Journal of Metamorphic Geology*, **20,** 683–696.

Dallain, C., Schulmann, K. & Ledru, P., 1999. Textural evolution in the transition from subsolidus annealing to melting process, Velay Dome, French Massif Central. *Journal of Metamorphic Geology*, **17,** 61–74.

Dudek, A., Matějovská, O. & Suk, M., 1974. Gföhl orthogneiss in the Moldanubicum of Bohemia and Moravia. *Krystalinikum*, **10,** 67–78.

Fitzsimons, I. C. W., 1996. Metapelitic migmatites from Brattstrand Bluffs, East Antarctica – metamorphism, melting and exhumation of the mid crust. *Journal of Petrology*, **37,** 395–414.

Franěk, J., Schulmann, K. & Lexa, O., 2006. Kinematic and rheological model of exhumation of high pressure granulites in the Variscan orogenic root: example of the Blanský les granulite, Bohemian Massif, Czech Republic. *Mineralogy and Petrology*, **86,** 253–276.

Gapais, D., 1989. Shear structures within deformed granites; mechanical and thermal indicators. *Geology*, **17,** 1144–1147.

Greenfield, J. E., Clarke, G. L., Bland, M. & Clark, D. J., 1996. In-situ migmatite and hybrid diatexite at Mt Stafford, central Australia. *Journal of Metamorphic Geology*, **14,** 413–426.

Greenfield, J. E., Clarke, G. L. & White, R. W., 1998. A sequence of partial melting reactions at Mt. Stafford, central Australia. *Journal of Metamorphic Geology*, **16,** 363–378.

Guiraud, M., Powell, R. & Rebay, G., 2001. H_2O in metamorphism and unexpected behaviour in the preservation of metamorphic mineral assemblages. *Journal of Metamorphic Geology*, **19,** 445–454.

Hand, M. & Dirks, P. H. G. M., 1992. The influence of deformation on the formation of axial-planar leucosomes and the segregation of small melt bodies within the migmatitic Napperby Gneiss, central Australia. *Journal of Structural Geology*, **14,** 591–604.

Hasalová, P., Schulmann, K., Lexa, O. *et al*., 2008a. Origin of migmatites by deformation enhanced melt infiltration of orthogneiss: a new model based on quantitative microstructural analysis. *Journal of Metamorphic Geology*, doi: 10.1111/j.1525-1314.2007.00743.x.

Hasalová, P., Janoušek, V., Schulmann, K., Štípská, P. & Erban, V., 2008b. From orthogneiss to migmatite: geochemical assessment of the melt infiltration model in the Gföhl Unit (Moldanubian Zone, Bohemian Massif). *Lithos*, doi: 10.1016/j.lithos.2007.07.021.

Holland, T. J. B. & Powell, R., 1998. An internally consistent thermodynamic dataset for phases of petrological interest. *Journal of Metamorphic Geology*, **16,** 309–343.

Holland, T. & Powell, R., 2003. Activity–composition relations for phases in petrological calculations: an asymmetric multicomponent formulation. *Contributions to Mineralogy and Petrology*, **145,** 492–501.

Kelemen, P. B., Hirth, G., Shimizu, N., Spiegelman, M. & Dick, H. J. B., 1997. A review of melt migration processes in the adiabatically upwelling mantle beneath oceanic spreading ridges. *Philosophical Transactions of the Royal Society of London Series A: mathematical physical and engineering sciences* , **355,** 283–318.

Marchildon, N. & Brown, M., 2001. Melt segregation in late syntectonic anatectic migmatites: an example from the Onawa contact aureole, Maine, USA. *Physics and Chemistry of the Earth*, **26,** 225–229.

Marchildon, N. & Brown, M., 2003. Spatial distribution of melt-bearing structures in anatectic rocks from Southern Brittany, France: implications for melt transfer at grain- to orogen-scale. *Tectonophysics*, **364,** 215–235.

Matějovská, O., 1974. *Petrographic Characteristic of Gneiss Series between Mohelno and Bítov, SW Moravia*. MS Geofond, Prague (in Czech).

McLellan, E. L., 1983. Contrasting textures in metamorphic and anatectic migmatites – an example from the Scottish Caledonides. *Journal of Metamorphic Geology*, **1,** 241–262.

Mehnert, K. R., 1971. *Migmatites and the Origin of Granitic Rocks*. Elsevier, Amsterdam.

Milord, I. & Sawyer, E. W., 2003. Schlieren formation in diatexite migmatite: examples from the St Malo migmatite terrane, France. *Journal of Metamorphic Geology*, **21,** 347–362.

Milord, I., Sawyer, E. W. & Brown, M., 2001. Formation of diatexite migmatite and granite magma during anatexis of semi-pelitic metasedimentary rocks: an example from St. Malo, France. *Journal of Petrology*, **42,** 487–505.

Nielson, J. E. & Wilshire, H. G., 1993. Magma transport and metasomatism in the mantle: a critical review of current geochemical models. *American Mineralogist*, **78,** 1117–1134.

Powell, R. & Downes, J., 1990. Garnet porphyroblast-bearing leucosomes in metapelites: mechanisms, phase diagrams, and an example from Broken Hill, Australia. In: *High Temperature Metamorphism and Crustal Anatexis* (eds Ashworth, J.R. & Brown, M.), pp. 105–123. Unwin Hyman, London, UK.

Powell, R. & Holland, T., 2004. *Course Notes for 'THERMOCALC Workshop 2004: Calculating Metamorphic Phase Equilibria' (ETH Zurich)*. (CD-ROM).

Powell, R., Holland, T. & Worley, B., 1998. Calculating phase diagrams involving solid solutions via non-linear equations, with examples using THERMOCALC. *Journal of Metamorphic Geology*, **16,** 577–588.

Powell, R., Guiraud, M. & White, R. W., 2005. Truth and beauty in metamorphic phase equilibria: conjugate variables and phase diagrams. *Canadien Mineralogist*, **43,** 21–33.

Racek, M., Štípská, P., Pitra, P., Schulmann, K. & Lexa, O., 2006. Metamorphic record of burial and exhumation of orogenic lower and middle crust: a new tectonothermal model for the Drosendorf window (Bohemian Massif, Austria). *Mineralogy and Petrology*, **86,** 221–251.

Reiners, P. W., 1998. Reactive melt transport in the mantle and geochemical signatures of mantle-derived magmas. *Journal of Petrology*, **39,** 1039–1061.

Rosenberg, C. L. & Handy, M. R., 2005. Experimental deformation of partially melted granite revisited: implications for the continental crust. *Journal of Metamorphic Geology*, **23,** 19–28.

Sawyer, E. W., 1994. Melt segregation in the continental crust. *Geology*, **22,** 1019–1022.

Sawyer, E. W., 1996. Melt segregation and magma flow in migmatites: implications for the generation of granite magmas.

Transactions for the Royal Society of Edinburgh: Earth Sciences, **87,** 85–94.

Sawyer, E. W., 1998. Formation and evolution of granite magmas during crustal reworking: the significance of diatexites. *Journal of Petrology*, **39,** 1147–1167.

Sawyer, E. W., 1999. Criteria for the recognition of partial melting. *Physics and Chemistry of the Earth*, **24,** 269–279.

Sawyer, E. W., 2001. Melt segregation in the continental crust: distribution and movement of melt in anatectic rocks. *Journal of Metamorphic Geology*, **19,** 291–309.

Sawyer, E. W. & Barnes, S.-J. 1988. Temporal and compositional differences between subsolidus and anatectic migmatite leucosomes from the Quetico metasedimentary belt, Canada. *Journal of Metamorphic Geology*, **6,** 437–450.

Schulmann, K., Mlčoch, B. & Melka, R., 1996. High-temperature microstructures and rheology of deformed granite, Erzgebirge, Bohemian Massif. *Journal of Structural Geology*, **18,** 719–733.

Schulmann, K., Kröner, A., Hegner, E. *et al*., 2005. Chronological constraints on the pre-orogenic history, burial and exhumation of deep-seated rocks along the eastern margin of the Variscan orogen, Bohemian Massif, Czech Republic. *American Journal of Science*, **305,** 407–448.

Štípská, P. & Powell, R., 2005. Does ternary feldspar constrain the metamorphic conditions of high-grade meta-igneous rocks? Evidence from orthopyroxene granulites, Bohemian Massif. *Journal of Metamorphic Geology*, **23,** 627–647.

Štípská, P., Schulmann, K. & Kröner, A., 2004. Vertical extrusion and middle crustal spreading of omphacite granulite: a model of syn-convergent exhumation (Bohemian Massif, Czech Republic). *Journal of Metamorphic Geology*, **22,** 179–198.

Tajčmanová, L., Konopásek, J. & Schulmann, K., 2006. Thermal evolution of the orogenic lower crust during exhumation within a thickened Moldanubian root of the Variscan belt of Central Europe. *Journal of Metamorphic Geology*, **24,** 119–134.

Urban, M., 1992. Kinematics of the Variscan thrusting in the Eastern Moldanubicum (Bohemian Massif, Czechoslovakia): evidence from the Náměšť granulite massif. *Tectonophysics*, **201,** 371–391.

Van der Wal, D. & Bodinier, J.-L., 1996. Origin of the recrystallization front in the Ronda peridotite by km-scale pervasive porous melt flow. *Contributions to Mineralogy and Petrology*, **122,** 387–405.

Vigneresse, J.-L., Barbey, P. & Cuney, M., 1996. Rheological transitions during partial melting and crystallization with application to felsic magma segregation and transfer. *Journal of Petrology*, **37,** 1579–1600.

White, R. W. & Powell, R., 2002. Melt loss and the preservation of granulite facies mineral assemblages. *Journal of Metamorphic Geology*, **20,** 621–632.

White, R. W., Powell, R., Holland, T. J. B. & Worley, B. A., 2000. The effect of TiO_2 and Fe_2O_3 on metapelitic assemblages at greenschist and amphibolite facies conditions: mineral equilibria calculations in the system K_2O–FeO–MgO–Al_2O_3–SiO_2–H_2O–TiO_2–Fe_2O_3. *Journal of Metamorphic Geology*, **18,** 497–511.

White, R. W., Powell, R. & Holland, T. J. B., 2001. Calculation of partial melting equilibria in the system Na_2O–CaO–K_2O–FeO–MgO–Al_2O_3–SiO_2–H_2O (NCKFMASH). *Journal of Metamorphic Geology*, **19,** 139–153.

White, R. W., Powell, R. & Clarke, G. L., 2003. Prograde metamorphic assemblage evolution during partial melting of metasedimentary rocks at low pressures: migmatites from Mt Stafford, Central Australia. *Journal of Petrology*, **44,** 1937–1960.

White, R. W., Pomroy, N.E. & Powell, R., 2005. An in situ metatexite–diatexite transition in upper amphibolite facies rocks from Broken Hill, Australia. *Journal of Metamorphic Geology*, **23,** 579–602.

White, R. W., Powell, R. & Holland, T.J.B., 2007. Progress relating to calculation of partial melting equilibria for metapelites. *Journal of Metamorphic Geology*, **25,** 511–527.

Wickham, S. M., 1987. Crustal anatexis and granite petrogenesis during low-pressure regional metamorphism: the Trois Seigneurs Massif, Pyrenees, France. *Journal of Petrology*, **28,** 127–169.

Závada, P., Schulmann, K., Konopásek, J., Ulrich, S. & Lexa, O., 2007. Extreme ductility of feldspar aggregates – melt enhanced grain boundary sliding (GBS) and creep failure: rheological implications for felsic lower crust. *Journal of Geophysical Research*, doi: 10.1029/2006JB004820.2007.

Received 13 December 2006; revision accepted 25 September 2007.